Vol. 79, No. 2 / 2026

e: ISSN 2068 – 2239
p: ISSN 2068 – 4215

INMATEH –

AGRICULTURAL ENGINEERING

MAY - AUGUST

No liability is assumed by the editorial staff for the content of scientific papers and opinions published in this volume. They represent the author's point of view

Managing Editorial Board - INMA Bucharest

Editor in Chief

Lucian-Ionel CIOCA, Professor, PhD.Eng., "Lucian Blaga" University of Sibiu

Executive Editor

Lucreţia POPA
PhD.Eng, SR I

Assistant Editor

Nicolae-Valentin VLADUŢ
PhD.Eng, SR I

Mihai-Gabriel MATACHE
PhD.Eng, SR I

Logistic support, database

Virgil MURARU
PhD.Eng, SR I

Official translator

RADU Daniela-Cristina, English

Editorial Board

- *QUENDLER Elisabeth – Austria, Vienna, Univ. of Natural Resources & Applied Life Sciences;*
- *Ir. HUYGHEBAERT Bruno – Belgia, Walloon Agricultural Research Center CRA-W;*
- *Van IMPE F.M. Jan – Belgia, KU Leuven University*
- *FABBRO Dal Inacio Maria - Brazil, Campinas State University;*
- *ATANASOV Atanas – Bulgaria, "Angel Kanchev" University of Rousse*
- *MOLINOS-SENANTE María – Chile, Pontificia Universidad Católica - Vicedecana, Escuela de Ingeniería UC*
- *BILANDZIJA Nikola – Croatia, Zagreb University, Faculty of Agriculture;*
- *KOSUTIC Silvio – Croatia, Zagreb University, Faculty of Agriculture;*
- *KOVACEV Igor - Croatia, Zagreb University, Faculty of Agriculture;*
- *GONZÁLEZ Omar – Republic of Cuba, Central University "Marta Abreu" de las Villas;*
- *KATHIJOTES Nicholas – Cyprus, University of Nicosia;*
- *HERAK David - Czech Republic, Czech University of Agriculture Prague;*
- *BORCHARD Nils – Finland, Natural Resources Institute Finland (Luke);*
- *SAUER Johannes – Germany, Technical University Munich;*
- *FENYVESI László – Hungary, Hungarian Institute of Agricultural Engineering Godolo;*
- *PEEYUSH Soni - India, Indian Institute of Technology, Kharagpur;*
- *MOHAMMADREZA Alizadeh – Iran, Department of Agricultural Engineering, Rice Research Institute of Iran (RRII);*
- *De WRACHIEN Daniele - Italy, State University of Milan;*
- *BIOCCA Marcello - Italy, Agricultural Research Council, Agricultural Engineering Research Unit;*
- *COLANTONI Andrea – Italy, University Viterbo;*
- *SARAUSSKIS Egidijus – Lithuania, Vytautas Magnus University, Faculty of Agricultural Engineering;*
- *KRIAUCIUNIENE Zita - Lithuania, Vytautas Magnus University;*
- *DUKE Mike – New Zealand, University of Waikato, Faculty of Science and Engineering;*
- *EWEMOJE Temitayo Abayomy – Nigeria, University of Ibadan, Faculty of Technology, Department of Agricultural and Environmental Engineering;*
- *SKIERUCHA Wojciech – Poland, Institute of Agro-physics Polish Academy of Sciences, Lublin;*
- *EKIELSKI Adam - Poland, Warsaw University of Life Sciences;*
- *KOT Sebastian - Poland, Czestochowa University of Technology*
- *SAVIN Lazar– Serbia, University of Novi Sad, Faculty of Agriculture, Department of Agricultural Engineering;*
- *SIMIKIC Mirko– Serbia, University of Novi Sad, Faculty of Agriculture, Department of Agricultural Engineering;*
- *MARTINOV Milan - Serbia, Faculty of Agriculture, Department of Agricultural Engineering,*
- *TURAN Jan – Slovakia, Technical University Kosice, Dept Elect & Multimedia Commun, Kosice;*
- *MADYIRA M. Daniel - South Africa, University of Johannesburg, Mechanical Engineering Science Department*
- *COZ FERNANDEZ Alberto – Spain, University of Cantabria, School of Nautical Studies, Department of Chemistry and Process & Resource Engineering;*
- *ERTEKIN Can - Turkey, Akdeniz University Antalia;*
- *KABAŞ Önder –Turkey, Antalia, Agricultural Scientific Research Institute of Batı Akdeniz;*
- *SELVİ Kemal Çağatay - Turkey, Samsun, University of Ondokuz Mayıs, Faculty of Agriculture, Department of Machines for Agriculture;*
- *ÖTLEŞ Semih - Turkey, Ege University, Engineering Faculty, Food Engineering Department;*
- *MARUSCHAK Pavlo - Ukraine, Ternopil Ivan Pul'uj National Technical University, Department of Technical Mechanics and Agricultural Engineering;*
- *BULGAKOV Volodymyr – Ukraine, National University of Life and Environmental Sciences of Ukraine;*
- *PARASCHIV Gigel - Romania, Politehnica University of Bucharest;*
- *VOICU Gheorghe - Romania, Politehnica University of Bucharest;*
- *BIRIŞ Sorin - Romania, Politehnica University of Bucharest;*
- *MAICAN Edmond - Romania, Politehnica University of Bucharest;*
- *FILIP Nicolae - Romania, Technical University Cluj Napoca;*
- *COZAR Onuc-Romania, „Babes-Bolyai" University of Cluj-Napoca Romania, Faculty of Physics;*
- *VLASE Sorin - Romania, "Transilvania" University of Braşov;*
- *ŢENU Ioan - Romania, USAMV Iaşi;*
- *HERIŞANU Nicolae - Romania, Politehnica University of Timisoara;*
- *MARSAVINA Liviu - Romania, Politehnica University of Timisoara*
- *MARINCA Vasile - Romania, Politehnica University of Timisoara*
- *GERGEN Iosif - Romania, USAMVB Timişoara;*
- *BORDEAN Despina-Maria - Romania, USAMVB Timişoara;*
- *BUNGESCU Sorin - Romania, USAMVB Timişoara;*
- *RODINA Steliana – Romania, ICEADR, Bucharest;*
- *VOICEA Iulian - Romania, INMA Bucharest;*
- *DEAK Gyorgy - Romania, INCDPM Bucharest;;*
- *BELC Nastasia - Romania, IBA Bucharest;*
- *BUŢU Alina - Romania, INCDSB Bucharest;*
- *PAUN Mihaela - Romania, INCDSB, Bucharest*

INMATEH - Agricultural Engineering **journal is indexed in the next international databases:**
ELSEVIER /SciVerse SCOPUS, CLARIVATE - WEB of SCIENCE- Emerging Sources Citation Index (ESCI), ULRICHS Web: Global Serials Directory, CABI, SCIPIO, Index COPERNICUS International, EBSCO Publishing, Elektronische Zeitschriftenbibliothek

INMATEH - Agricultural Engineering
vol. 79, no.2 / 2026
e-ISSN: 2068–2239; p: ISSN: 2068–4215

https://inmateh.eu/ *E-mail: inmatehjournal@gmail.com*

Edited by: INMA Bucharest
Copyright: INMA Bucharest / Romania
National Institute for Research-Development of Machines and Installations
Designed for Agriculture and Food Industry - INMA Bucharest
6, Ion Ionescu de la Brad Bvd., sector 1, Bucharest, ROMANIA

	CONTENT Vol.79	Pag.
1.	**DESIGN AND SIMULATION OF A COMBINED SEED AGITATION PLATE FOR AN AIR-SUCTION PRECISION SEED METERING DEVICE WITH MULTIPLE-SEED-PER-HILL BASED ON DEM / *基于离散元的一穴多粒气吸式精密排种器组合型搅种盘设计与仿真*** **Zhiwei WANG[1)], Deyi ZHANG[1)], Sugirbay ADILET[2)], Naishuo WEI[1)], Yanwu JIANG[1)], Jianguo ZHOU[1)], Jun CHEN[1*)]** [1)] College of Mechanical and Electronic Engineering, Northwest A&F University, Yangling, Shaanxi, China; [2)] Research School of Veterinary Medicine and Agriculture, Shakarim University, Semey, Kazakhstan	**15**
2.	**SIMULATION AND OPTIMIZATION OF THE SEED METERING PLATE FOR AN AIR-SUCTION PRECISION SEED METERING DEVICE WITH MULTIPLE-SEED-PER-HILL BASED ON CFD / *基于CFD的一穴多粒气吸式精密排种器排种盘仿真与优化*** **Zhiwei WANG[1)], Yanwu JIANG[1)], Deyi ZHANG[1)], Sugirbay ADILET[2)], Naishuo WEI[1)], Jianguo ZHOU[1)], Jun CHEN[1*)]** [1)] College of Mechanical and Electronic Engineering, Northwest A&F University, Yangling, Shaanxi, China [2)] Research School of Veterinary Medicine and Agriculture, Shakarim University, Semey, Kazakhstan	**28**
3.	**DESIGN AND OPTIMIZATION OF A HUMAN–MACHINE COLLABORATIVE VIBRATION HARVESTING SYSTEM FOR LYCIUM BARBARUM L. / *枸杞人机协同振动采收系统设计与优化*** **Yahao GE[1)], Zeyu WANG[1)], Min WANG [1)], Yifan ZHANG [1)], Jun CHEN[1*)], Ming ZHANG [2)]** [1)] College of Mechanical and Electronic Engineering, Northwest A&F University, Yangling, Shaanxi, China [2)] Ningxia Zhengqi Hong Lycium barbarum L. Industrial Development Co., Ltd， Guyuan, China	**40**
4.	**STUDY ON NON-PARAMETRIC EXTRAPOLATION METHOD OF TRACTOR PTO LOAD BASED ON DBSCAN / *基于DBSCAN对拖拉机PTO的载荷非参数外推方法研究*** **Yin TANG, Shuaijie MA, Fuxi SHI*** College of Mechanical and Electronic Engineering, Northwest A&F University, Yangling /China	**51**
5.	**GRIPPING FORCE ESTIMATION FOR AN ROV ROBOTIC ARM IN INTENSIVE AQUACULTURE *ESTIMAREA FORȚEI DE PRINDERE PENTRU UN BRAȚ ROBOTIC ROV ÎN ACVACULTURĂ INTENSIVĂ*** **Dan CUJBESCU[1)], Iulian VOICEA[*1)], Cătălin PERSU[1)], Iuliana GĂGEANU[1)], Carmen Bălțatu[1)], Viorel FĂTU[2)], Vlad ARSENOAIA[3)]** [1)] National Institute of Research – Development for Machines and Installations Designed to Agriculture and Food Industry, Romania; [2)] Research Development Institute for Plant Protection (ICDPP); [3)] Faculty of Agriculture, Ion Ionescu de la Brad University of Agricultural Sciences and Veterinary Medicine, Iasi / Romania	**61**
6.	**DESIGN AND EXPERIMENTAL RESEARCH OF SELF-PROPELLED TOBACCO STEM HARVESTER / *自走式烟杆收获机设计与试验研究*** **Liquan YANG[1,2)], Guangyu YIN[1,2)], Rui FENG[1)], Junya HUANG[1)], Xiaodong LIU[1)], Jianbo WANG[1)], Dongwei YAN[1)], Qingqing L、[1, *)], Guangxi LI[1, *)]** [1)] Henan Province Engineering Research Centre of Ultrasonic Technology Application, [2)] Pingdingshan University, Pingdingshan, Henan, China; [2)] Pingdingshan Company, Henan Tobacco Company, Pingdingshan, Henan, China	**70**
7.	**DESIGN AND EXPERIMENTAL STUDY OF A RESIDUAL FILM BALING DEVICE / *残膜打包装置的设计与试验研究*** **Guan WANG[1)], Haolin WANG[2)], Zhihong TIAN[1)], Qi Wang[1)], Dong JI[1)], Fengbo LIU[1)*]** [1)] Liaoning Agricultural Vocational and Technical College, 76 Yucai Road, Yingkou, China; [2)] Design Department of Liaoning liaotuo Dayi Agricultural Machinery Co., Ltd, Fushun, China	**83**
8.	**APP-ENABLED WIRELESS LOOP RESISTANCE TESTING FOR EFFICIENT EVALUATION OF AGRICULTURAL POWER SYSTEM EQUIPMENT / *基于APP的无线回路电阻测试实现农业电力系统设备的高效评估*** **Yue YAO, Yanquan HOU*, Wei LI, Juntao ZHAO, Chen HUANG, Cen LI** State Grid Heilongjiang Electric Power Co., Ltd. Qitaihe Power Supply Company / P.R.China	**93**
9.	**DESIGN AND EXPERIMENT OF IWOA-OPTIMIZED FUZZY PID VARIABLE FERTILIZATION CONTROL SYSTEM FOR RICE BASED ON N-P-K HYBRID PRESCRIPTION GRAPH / *基于 N-P-K 融合处方图的 IWOA 优化模糊 PID 水稻变量施肥控制系统设计与试验*** **Kun ZHANG[1)], Lin WAN[*1,2)], Gang CHE[1,2)], Chun-sheng WU[3)], Xi-lu LI[*3)]** [1)] College of Engineering, Heilongjiang Bayi Agricultural University, Daqing, China [2)] Key Laboratory of Intelligent Agricultural Machinery Equipment in Heilongjiang Province, Daqing, China; [3)] Heilongjiang Province Agricultural Machinery Science Research Institute - Jiamusi Branch, Jiamusi China	**104**
10.	**THE BEHAVIOR OF VEGETABLE SEED PICK-UP USING A VACUUM SEED-METERING UNIT (VSMU) / *سلوك التقاط بذور الخضروات باستخدام وحدة تلقيم البذور بالشفط*** **Mohamed ABO-HABAGA[1)], Zakaria ISMAIL[1)], Mohamed SHALABY[1)], Mahmoud OKASHA[*2,3)]** [1)]Agricultural Engineering Department, Faculty of Agriculture, Mansoura University / Egypt [2)]Agricultural Engineering Research Institute (AEnRI), Agricultural Research Center (ARC), Giza / Egypt [3)]Department of Agricultural, Food, Environmental and Animal Sciences (DI4A), University of Udine, Udine / Italy	**115**

11.	**APPLICATION OF LLM + ZERO-SHOT LARGE MODELS FOR FRUIT OBJECT DETECTION /** *应用LLM + Zero-Shot大模型实现水果目标检测* **Yingdong QIN [1,2,3,*], Haoyu SONG [1,2,3], Jingyi LI [4], Keyao WEN [1]** [1] College of Artificial Intelligence and Low-Altitude Technology, South China Agricultural University, Guangzhou, China; [2] National Center for International Collaboration Research on Precision Agricultural Aviation Pesticides Spraying Technology (NPAAC), South China Agricultural University, Guangzhou, China; [3] Center for International Cooperation and Disciplinary Innovation of Precision Agricultural Aviation Applied Technology ('111 Center'), South China Agricultural University, Guangzhou, China; [4] School of Statistics and Data Science, Guangdong University of Finance & Economics, Guangzhou, China	**125**
12.	**A LIGHTWEIGHT TEA BUD DETECTION METHOD FOR ONLINE GRADING OF FRESH TEA LEAVES BASED ON IMPROVED YOLOV11N /** *一种基于改进YOLOv11n的面向茶鲜叶在线分级的轻量化茶芽检测方法* **Wenguang ZHENG *), Xinyong SHI, Rongyang WANG** School of Mechanical Engineering & Automation, University of Science and Technology Liaoning, Anshan, China School of Intelligent Manufacturing and Elevator Mechanics, Huzhou Vocational and Technical College, Huzhou, China	**134**
13.	**PRECISION INTEGRATED DECISION-MAKING AND CONTROL SYSTEM FOR WATER AND FERTILIZER MANAGEMENT IN ORCHARDS BASED ON THE INTERNET OF THINGS AND CLOUD PLATFORM /** *基于物联网与云平台的果园水肥一体化精准决策控制系统设计* **Kang NIU*, Hongze GUO, Weipeng ZHANG, Bo ZHAO, Guopeng ZHANG, Liming ZHOU** State Key Laboratory of Agricultural Equipment Technology, Chinese Academy of Agricultural Mechanization Sciences Group Co., Ltd., Beijing, China	**149**
14.	**THERMAL ENVIRONMENT IMPROVEMENT AND PARAMETER OPTIMIZATION OF WET CURTAIN FAN VENTILATION IN A GREENHOUSE: A CFD STUDY WITH EXPERIMENTAL VALIDATION /** *温室湿帘风机通风热环境改善与参数优化：CFD研究与实验验证* **Huanran SUN[1, 2], Binguang JIA[*3], Ziye SONG[4]** [1]Shandong Huayu University of Technology, Dezhou, China; [2]Shandong Engineering Research Center of Low-Carbon Energy Internet of Things Technology, Dezhou, China; [3]Department of Mechanical and Electrical Engineering, Jinan Engineering Polytechnic, Jinan, China; [4]Civil and Transportation Engineering College, Weifang University, Weifang, China	**163**
15.	**A REVIEW ON THE DEVELOPMENT STATUS AND TRENDS OF KEY TECHNOLOGIES FOR HYBRID TRACTORS /** *混合动力拖拉机关键技术发展现状及趋势综述* **Zhaoyue LIU[1], Jikang XU※[1], Xiaodong LV[1], Jinliang LI[2]** [1] Qingdao Agricultural University/ China; [2] Lingong Agricultural Equipment Co., Ltd. / China	**175**
16.	**EXPERIMENTAL STUDY AND ANALYSIS ON MECHANICAL PROPERTIES OF CASSAVA ROOTS AT HARVESTING STAGE /** *收获期木薯块根力学特性试验研究与分析* **Guanghao XU[1], Wenwen LI[1,3], Jiannong SONG[2], Binfeng SUN[1], Zhongsheng CAO[1], Junbao HUANG[1], Xinyi PENG[1], Yanda LI[1*]** [1] Institute of Agricultural Engineering, Jiangxi Academy of Agricultural Sciences, Nanchang / China; [2] College of Engineering, China Agricultural University, Beijing / China [3] College of Engineering, Jiangxi Agricultural University, Nanchang / China	**204**
17.	**RESEARCH AND ANALYSIS ON THE OPERATING PERFORMANCE OF RIDGE ROLLERS UNDER DIFFERENT OPERATING MODES /** *起垄机不同作业模式下作业性能研究与分析* **Xin ZHANG[1], Yucheng LIANG[1*], Lu GAN[1], Yanliang ZHANG[1], Yiwen YUAN[2]** [1] Heilongjiang Academy of Agricultural Machinery Engineering Sciences, Harbin, China [2] College of Mechanical and Electrical Engineering, Heilongjiang University, Harbin, China	**216**
18.	**REAL-TIME AND PRECISE DETECTION OF FIELD SOYBEAN RUST AND BACTERIAL SPOT BASED ON IMPROVED YOLOV11N /** *基于改进 YOLOv11n 的田间大豆豆锈病与细菌性斑点病实时精准检测* **Tianhao WU, Yongcai MA*, Hanyang WANG** College of Engineering, Heilongjiang Bayi Agricultural University, Daqing / China	**229**
19.	**DESIGN AND IMPLEMENTATION OF A VISUAL MONITORING SYSTEM FOR PADDY FLOW INSTABILITY IN INTELLIGENT HUSKERS /** *面向智能砻谷机的稻谷料流失稳视觉监测系统设计与实现* **Min CHENG[*1], Shihao ZHOU[1], Yong PAN[2], Xingchuang WANG[1]** [1] School of Mechanical and Electrical Engineering, Henan University of Technology, Zhengzhou / China; [2] School of Intelligent Engineering, Henan Mechanical and Electrical Vocational College, Zhengzhou / China	**239**

20.	**LENGTH OF CLOSED FISHTAIL-SHAPED TURNS AND HEADLAND WIDTH WHEN PLOUGHING WITH A REVERSIBLE PLOUGH IN AN IRREGULARLY SHAPED FIELD / *ДЪЛЖИНА НА ЗАТВОРЕНИ ГЪБОВИДНИ ЗАВОИ И ШИРОЧИНА НА ИВИЦАТА ЗА ЗАВИВАНЕ ПРИ ОРАН С ОБРЪЩАТЕЛЕН ПЛУГ В ПОЛЕ С НЕПРАВИЛНА ФОРМА*** **Krasimir TRENDAFILOV** Trakia University – Stara Zagora, Faculty of Technics and Technologies – Yambol, Department of Mechanical Engineering/ Bulgaria	**249**
21.	**ENAS-BASED YOLOv8 IMPROVEMENT WITH JOINT STRUCTURE AND LOSS SEARCH FOR CORN SEEDLING AND WEED DETECTION /** ***基于ENAS的YOLOv8改进方法：结合结构与损失函数搜索实现玉米幼苗与杂草检测*** **Junnan HU [1)], Hanyang WANG *[11)], Yongcai MA [1)], Dan LIU [2)]** [1)] College of Engineering, Heilongjiang Bayi Agricultural University, Daqing, Heilongjiang/ China [2)] College of Civil Engineering and Water Conservancy, Heilongjiang Bayi Agricultural University, Daqing, Heilongjiang / China	**259**
22.	**RESEARCH ON MULTI-OBJECT TRACKING OF PIGS BASED ON IMPROVED BYTE TRACK / *基于改进ByteTrack的多目标生猪跟踪研究*** **Jinhang MU[1,2)] , Yiran LIU[1)] , Lingqing FENG*[,1)]** [1)] College of Information Science and Engineering, Shanxi Agricultural University, Taigu, China [2)] School of Computer Science and Technology, North University of China, Taiyuan, China	**269**
23.	**EXPERIMENTAL INVESTIGATION OF A MACHINE FOR LOCAL STRIP APPLICATION (MLSA) OF SAPROPEL-BASED ORGANIC FERTILIZER MIXTURES / *ЕКСПЕРИМЕНТАЛЬНІ ДОСЛІДЖЕННЯ МАШИНИ ДЛЯ ЛОКАЛЬНОГО СМУГОВОГО ВНЕСЕННЯ (МЛСВ) ОРГАНІЧНИХ ДОБРИВ НА ОСНОВІ САПРОПЕЛЮ*** **Igor TSIZ, Volodymyr DIDUKH, Serhiy KHOMYCH, Victor TARASYUK, Roman KHLOPETSKYI** Lutsk National Technical University / Ukraine	**278**
24.	**STUDY ON THE EFFECTS OF MOISTURE CONTENT ON THE COMPRESSIVE MECHANICAL PROPERTIES OF SWEET POTATO ROOTS / *含水率对甘薯块根压缩力学特性的影响研究*** **Shuai GAO, Yuecheng WU, Kaiyan XIN, Ping ZHAO[*)]** College of Engineering, Shenyang Agricultural University, Shenyang, Liaoning, China	**288**
25.	**FROM HARVEST TO PACKAGE: AN AUTONOMOUS ROBOT FOR INTEGRATED TOMATO PICKING AND BAGGING / *用于番茄一体化采摘与包装的自主机器人*** **Yanhua YING, Dongya LI *, Jiahui HU, Yujie ZHOU, Yubo LI** College of Engineering, Applied Technology College of Soochow University, Suzhou, China	**299**
26.	**STRUCTURAL DESIGN AND VISION-BASED TARGET DETECTION AND LOCALIZATION OF A DESERT SHRUB STUBBLE-CUTTING MACHINE / *沙生灌木平茬机的结构设计与基于视觉的目标检测与定位*** **Weiqi WU[1)], Haitang CEN*[1)], Wang GUO[2)], Wei ZHANG[1)]** [1)] School of Mechanical Engineering, Inner Mongolia University of Technology, Hohhot / China; [2)] Inner Mongolia Academy of Science and Technology, Hohhot / China	**311**
27.	**SMOOTH-PLANNER: A ROBUST GRADIENT-BASED LOCAL TRAJECTORY PLANNING METHOD FOR NON-HOLONOMIC ORCHARD ROBOTS/** ***SMOOTH-PLANNER：一种面向非完整约束果园机器人基于梯度的鲁棒局部轨迹规划方法*** **Fanjun MENG, Fa SUN, Mengmeng NI, Zhisheng ZHAO, Lili YI*** School of Agricultural Engineering and Food Science, Shandong University of Technology, Zibo / China	**323**
28.	**RECENT ADVANCES SURVEY IN COMPUTER VISION AND ARTIFICIAL INTELLIGENCE FOR FRUIT DETECTION / *TINJAUAN KEMAJUAN TERKINI TEKNOLOGI PENGLIHATAN KOMPUTER DAN KECERDASAN BUATAN DALAM PENGESANAN BUAH*** **Qi LIU[1)], Puteri Suhaiza binti SULAIMAN[1*)], Mas Rina binti MUSTAFFA[1)], Zainal bin Abdul KAHAR[1)], Lian BAI[2)], Huicai XU[1)]** [1)] Faculty of Computer Science and Information Technology, Universiti Putra Malaysia, Serdang, Selangor, Malaysia [2)] College of Software, Shanxi Agricultural University, Taigu, Shanxi, China	**332**
29.	**DESIGN AND PERFORMANCE TESTING OF AN AUTOMATIC ORIENTATION AND CONVEYING DEVICE FOR POSTHARVEST CABBAGE TRIMMING BASED ON A CONICAL TREAD / *基于圆锥踏面的采后甘蓝自动定向输送装置设计及试验*** **Gongpei CUI [1)], Yu ZHANG [1)], Huanhuan CHEN [1)], Yongjie CUI [2,3,4)], Jing ZHANG [1)], Dongdong LI [1)], He LI [1)], Wanzhang WANG [*1)]** [1)] College of Mechanical and Electronic Engineering, Henan Agricultural University, Zhengzhou, China; [2)] College of Mechanical and Electronic Engineering, Northwest A&F University, Yangling, China; [3)] Key Laboratory of Agricultural Internet of Things, Ministry of Agriculture and Rural Affairs, Yangling, China; [4)] Shaanxi Key Laboratory of Agricultural Information Perception and Intelligent Service, Yangling, China	**351**

30.	**KINEMATIC ANALYSIS AND OPTIMAL DESIGN OF THE SEPARATION CONVEYOR DEVICE FOR *PANAX NOTOGINSENG* COMBINE HARVESTER** **Ibrahim Issa Mohamed ISSA[1,3*)], Zhaoguo ZHANG[1,2,3*)], Faan WANG[2,3)], Altyeb Ali Abaker OMER[4)], Wael EL-KOLALY[5)]** [1)] Faculty of Mechanical and Electrical Engineering, Kunming University of Science and Technology, Kunming, China; [2)] Faculty of Modern Agricultural Engineering, Kunming University of Science and Technology, Kunming, China; [3)] Research Center on Mechanization Engineering of Chinese Medicinal Materials in Yunnan Universities, Kunming, China; [4)] School of Tea and Coffee, Puer University, Puer, China; [5)] Agricultural Engineering Research Institute (AEnRI), Agricultural Research Center (ARC), Ministry of Agriculture, 256 Dokki, Giza, Egypt	**365**
31.	**DESIGN AND EXPERIMENT OF A SPOON-CLAMP TYPE GARLIC SEED METERING DEVICE / *勺夹式大蒜排种器设计与试验*** **Xinyan ZHANG, Lin LUO, Dongming ZHANG, Shu-juan YI *)** College of Engineering, Heilongjiang Bayi Agricultural University, Daqing / P. R. China	**387**
32.	**MECHANIZED DETASSELING TECHNOLOGY FOR CORN SEED PRODUCTION: GLOBAL PROGRESS, KEY CHALLENGES, AND OPTIMIZATION STRATEGIES / *制种玉米机械化去雄技术：全球进展、核心挑战与优化策略*** **Yang LI [1,2)], Yiteng LEI [*1)], Luochuan XU[1)], Wei DONG [1)]** [1)] College of Electronic Engineering, Yili Normal University, Yining, China; [2)] Key Laboratory of Micro Nano Electric Sensing Technology and Bionic Instruments, Yili Normal University, Yining, China.	**404**
33.	**DEVELOPMENT AND PERFORMANCE EVALUATION OF A ROTARY POWER WEEDER FOR PADDY CULTIVATION / रोटरी पावर वीडर का विकास एवं धान की खेती में मूल्यांकन** **Subhash CHANDRA, Sanjay KUMAR, Sanjay Kumar PATEL, Adityanshu TRIPATHI, Shreesh Sanjay AMIN, Priyanshu KUMAR*** Department of Farm machinery and Power Engineering, College of Agricultural Engineering and Technology, Dr. Rajendra Prasad Central Agricultural University, Pusa (Samastipur)-848125, Bihar, India	**421**
34.	**EXPERIMENTAL STUDY ON THRESHING POWER CONSUMPTION OF AN AXIAL-FLOW THRESHING DEVICE WITH ADJUSTABLE THRESHING INTENSITY / *脱粒力度可调式轴流脱粒装置脱粒功耗试验研究*** **Yuejiang TENG[1,2)], Chengqian JIN[*3)], Fuxiang XIE[1,2)], Jian SONG[1,2)]** [1)] School of Machinery and Power Engineering, Weifang University, Weifang / China; [2)] Shandong Key Laboratory of Intelligent Manufacturing Technology for Advanced Power Equipment, Weifang/China; [3)] Nanjing Institute of Agricultural Mechanization, Ministry of Agriculture and Rural Affairs, Nanjing / China	**432**
35.	**DESIGN AND EXPERIMENT OF AUTOMATIC STRIP-ZONING PESTICIDE APPLICATION CONTROL SYSTEM FOR SOYBEAN-MAIZE STRIP INTERCROPPING BASED ON MACHINE VISION / *基于机器视觉的大豆玉米带状复合种植自动分带施药控制系统设计与试验*** **Gongpei CUI, Huanhuan CHEN, Yu ZHANG, Zishang YANG, Lele WANG, He LI *)** College of Mechanical and Electrical Engineering, Henan Agricultural University, Zhengzhou, Henan, China	**444**
36.	**OPTIMISATION AND EXPERIMENTAL RESEARCH OF FURROWING TOOL BASED ON EDEM/ *基于EDEM的开沟刀具优化与试验研究*** **Jian YAN[1)], Jing MI[2*)], Fei XIA[3)], Guangwen YANG[2)], Chenjun HU[2)], Bin YANG[2)], Yan ZHOU[2)], Bo ZHANG[4)], Po NIU[5*)]** [1)] Chongqing Three Gorges Vocational College, School of Automotive Engineering, People's Republic of China; [2)]Yibin Academy of Agricultural Sciences, People's Republic of China; [3)]Chongqing Kaizhou District Agriculture Service Centre, Chongqing, People's Republic of China; [4)]Chongqing Wanzhou District Agricultural Technology and Machinery Promotion Centre, People's Republic of China; [5)]College of Mechanical Engineering, Chongqing Three Gorges University, People's Republic of China	**461**
37.	**PARAMETER CALIBRATION OF THE BONDING MODEL FOR ASTRAGALUS ROOT BASED ON DISCRETE ELEMENTS / *基于离散元的黄芪根BONDING模型参数标定*** **Jun YOU, Xin DU *), Qi-xin SUN, Shu-fa CHEN, Jing-yi MAO** Jiangsu Ocean University, Lianyungang / China	**472**
38.	**DETECTION OF COMBINE-HARVESTER FEED QUANTITY BASED ON MULTI-SOURCE INFORMATION FUSION / *基于多信息融合的联合收割机喂入量检测方法研究*** **Jizhong WANG[1)*], Wei DONG[1)], Yong WU[2)], Yangchun LIU[3)], Hongze GUO[3)]** [1)] Weifang University, Weifang, China [2)] Shandong Maritime Vocational College. Weifang, China [3)] State Key Laboratory of Agricultural Equipment Technology, China Academy of Agricultural Mechanization Science Group Co., Ltd. Beijing, China	**484**

39.	**YOLO11-RCSP: CHERRY TOMATO FLOWER POLLINATION STATUS RECOGNITION BASED ON MULTI-SCALE FEATURE FUSION /** *YOLO11-RCSP：融合多尺度特征的圣女果花授粉状态识别* **Jianhua CUI, XinYU LI, FuZhun LI, XiaoYing ZHANG** College of Software, Shanxi Agricultural University, Taigu, Shanxi / China	**497**
40.	**RESEARCH ON GRAPE DISEASE DETECTION METHOD BASED ON PWE-YOLO /** *基于PWE-YOLO的葡萄病害检测方法* **Haoyue LIU [1], Benzhi YANG [1], Mingyang Gao [1], Dong WANG [1], Yuepeng SONG[1,2,*], Longlong REN[1,2,*]** [1] Shandong Agricultural University, College of Mechanical and Electrical Engineering/ China; [2] Shandong Provincial Engineering Laboratory of Agricultural Equipment Intelligence/ China	**501**
41.	**DESIGN AND EXPERIMENTAL STUDY OF A SELF-PROPELLED ELECTRIC TRACKED CHASSIS FOR *PANAX NOTOGINSENG* TRANSPLANTER IN HILLY AND MOUNTAINOUS REGIONS /** *丘陵山区自走式三七移栽机电动履带底盘设计与试验研究* **Wei SU[1], Congcong LIAO[1], Qingxu YU*[2], Yi ZENG[1], Qinghui LAI[1], Cantong SU[1]** [1]University of Science and Technology Kunming, Kunming, China; [2]Nanjing Institute of Agricultural Mechanization, Ministry of Agriculture and Rural Affairs, Nanjing, China	**514**
42.	**IMPROVED DBO ALGORITHM FOR FIXED-WING UAV MOUNTAIN CROP IRRIGATION PATH PLANNING /** *改进的DBO算法用于固定翼无人机山地作物灌溉路径规划* **Shengfu WU[1], Peng ZHOU[1,2*], Jin LUO[1], Linjia CHUAN[1], Jing LIU[1], Fugui ZHANG[1,2*]** [1] School of Mechanical Engineering, Guizhou University, Guiyang, Guizhou/ China [2] Guizhou Provincial Key Laboratory of Mountainous Intelligent Agricultural Machinery, Guiyang, Guizhou/ China	**534**
43.	**HOW CAN SMARTPHONE DEVICES BE INTEGRATED WITH SPECTRAL SIGNATURES TO DETECT MATAG HYBRID? /** ***BAGAIMANAKAH PERANTI TELEFON PINTAR DAPAT DIINTEGRASIKAN DENGAN TANDA TANGAN SPEKTRAL UNTUK MENGESAN HIBRID MATAG?*** **Nur Adibah MOHIDEM[1], Nik Norasma CHE'YA[2,3,4*], Mohammadmehdi SABERIOON[5], Mohamad Syukri TAN SHILAN[6], Nur Annisa MAT NORDIN[2]** [1]Public Health Unit, Department of Primary Health Care, Faculty of Medicine and Health Sciences, University Sains Islam Malaysia, Bandar Baru Nilai, Nilai, Negeri Sembilan, Malaysia. [2]Department of Agriculture Technology, Faculty of Agriculture, University Putra Malaysia, Serdang, Selangor, Malaysia. [3]Institute of Plantation Studies, University Putra Malaysia, Serdang, Selangor, Malaysia. [4]Centre for Advanced Lightning, Power and Energy Research (ALPER), Univ.Putra Malaysia, Serdang, Selangor, Malaysia. [5]German Research Centre for Geosciences (GFZ), Telegrafenberg, Potsdam, Germany. [6]Crop Industry Development Division, Department of Agriculture Malaysia, Pusat Pertanian Lekir, Perak, Malaysia.	**552**
44.	**DEEP LEARNING-BASED TARGET RECOGNITION AND LOCALIZATION IN CITRUS PICKING ROBOT /** *基于深度学习的柑橘采摘机器人目标识别与定位方法研究* **Yu YANG*[1], Linhui WANG[1], Shuwei DENG[1], Zhengqi ZHOU[1], Zhizhuang LIU[1]** [1] Hunan University of Science and Engineering, Yongzhou, Hunan, China	**575**
45.	**A COUPLED CFD–DEM NUMERICAL STUDY OF THE AERODYNAMIC SORTING OF *ZANTHOXYLUM BUNGEANUM* SHELLS AND SEED-BEARING PARTICLES /** *基于CFD-DEM耦合的红花椒果壳与带籽椒粒气动分选数值模拟研究* **Ruiqiang XU [1], Zhongbin LIU *[1], Hongwei XIAO [2], Chunglim LAW [3], Fengkui XIONG *[1, 2]** [1] College of Mechanical Engineering, Sichuan University of Science and Engineering, Yibin, Sichuan, P.R.China; [2] College of Engineering, China Agricultural University, Beijing, P. R. China; [3] Taylor's University, Subang Jaya, Malaysia	**584**
46.	**DESIGN AND EXPERIMENT OF AN INTEGRATED AUTOMATIC TRANSPLANTING SYSTEM WITH A FLEXIBLE END-EFFECTOR FOR PLUG SEEDLINGS /** *基于柔性末端执行器的钵苗全自动移栽系统的设计与试验* **Chao HE [1,2], Tian JIAO [1], Tie YE [1], Mingyuan WEI [3], Wanrui SONG *[4]** [1] School of Intelligent Manufacturing and Electrical Engineering, Nanyang Normal University / China; [2] Collaborative Innovation Center of Intelligent Explosion-proof Equipment, Henan Province / China; [3] College of Engineering, China Agricultural University / China [4] Nanyang Vocational College of Agriculture, Nanyang / China	**594**
47.	**CITRUS FLOWER, FRUIT, AND SHOOT RECOGNITION BASED ON IMPROVED YOLOv10 /** *基于改进YOLOv10的柑橘花果梢识别* **Wenfeng GUO*[1], ZhiFang BI[1], Linjuan WANG[1], Qinqin WU[2], Han WANG[3]** [1] Department of Basic Science, Shanxi Agricultural University, Taigu, Shanxi / China; [2] School of Mega Data, Jiangxi Institute of Fashion Technology, Nanchang, Jiangxi / China; [3] College of Information Science and Engineering, Shanxi Agricultural University, Taigu, Shanxi / China	**606**

48.	**DESIGN AND PERFORMANCE EVALUATION OF A TOBACCO-CLIP LOADING AND UNLOADING DEVICE FOR BULK-CURING BARNS /** ***密集烤房烟夹装卸装置设计及性能试验*** **Qingqing LÜ[1)], Yunlan MAO[1)], Ruixue LIU[1)], Kun ZHAO[1)], Xiaodong LIU[1)], Guangxi LI[1)], Liquan YANG[1,2*)], Guangyu YIN[2*)]** [1)] Henan Province Engineering Research Centre of Ultrasonic Technology Application, Pingdingshan University, Pingdingshan, China; [2)] Pingdingshan Company, Henan Tobacco Company, Pingdingshan, China	**617**
49.	**MECHANISM AND EFFICACY EVALUATION OF ATMOSPHERIC PRESSURE DBD PLASMA TREATMENT FOR FORAGE GRASS SEEDS /** ***面向牧草种子应用的常压DBD等离子体种子处理机制与效能评估*** **Jun-hui XI[1)], Xiao-juan ZHAO[2)], Xiang-yang WU[3)], Zhen-hua WANG[3)], Jia-jia SU[2)], Yun-ting HUI*[1,2)], Yan-ying GUO[1)], Yang-yang LIAO[3)], De-cheng WANG*[1)]** [1)] College of Engineering, China Agricultural University, Beijing / China; [2)] Hohhot Branch of Chinese Academy of Agricultural Mechanization Sciences Co., Ltd., Hohhot/ China; [3)] Chinese Academy of Agricultural Mechanization Sciences Group Co., Ltd., Beijing / China	**632**
50.	**OPTIMIZATION OF FUZZY PID CONTROL USING AN IMPROVED SPARROW SEARCH ALGORITHM FOR SOYBEAN FOLIAR FERTILIZER SPRAYING /** ***基于改进麻雀搜索算法的大豆叶面肥喷施模糊PID控制优化研究*** **Yue CHEN[1)], Hailiang GONG[1)], Weidong ZHUANG*[1)]** College of Engineering, Heilongjiang Bayi Agricultural University, Daqing, Heilongjiang, China	**644**
51.	**COMPARATIVE ASSESSMENT OF RANDOM FOREST, XGBOOST AND MLP MODELS FOR PREDICTIVE GREENHOUSE CONTROL USING WIRELESS SENSOR NETWORK DATA /** ***EVALUAREA COMPARATIVĂ A MODELELOR RANDOM FOREST, XGBOOST ŞI MLP PENTRU CONTROLUL PREDICTIV AL UNEI SERE, FOLOSIND DATE DINTR-O REȚEA DE SENZORI WIRELESS*** **Mihai Gabriel MATACHE[1)], Carmen BĂLȚATU*[1)], Dragoș SĂCĂLEANU[2)], Adrian IOSIF[2)], Tudor Adrian ENE[3)], Cristina Mihaela DOBRE[4)]** [1)] INMA Bucharest/ Romania; [2)] National University for Science and Technology POLITEHNICA Bucharest, Romania; [3)] ICDP Brașov; [4)] Beia Consult International SRL	**657**
52.	**AN EFFICIENT RICE PEST DETECTION METHOD BASED ON YOLOV11N /** ***基于 YOLOv11n 的高效水稻害虫检测方法*** **Xiaoke WANG, Zhichao ZHAO, Qiuyang HU, Jiyu LAI, Tiefeng WU*** School of Information and Control Engineering, Qingdao University of Technology, Qingdao / China	**671**
53.	**DESIGN AND EXPERIMENT OF A SMALL SELF-PROPELLED LIQUID-FERTILIZER INJECTOR /** ***小型自走式液肥注射机设计与试验*** **Ting GUO[1)], Xi XIAO[1)], Ming LIU[2)], Chengsong LI[2)], Linji LI[1)], Lin ZHU[1)], Wanneng LI*[2)]** [1)] Hunan Provincial Tobacco Company, Chenzhou City Company, Hunan / China [2)] College of Engineering and Technology, Southwest University, Chongqing / China	**683**
54.	**PERFORMANCE ANALYSIS AND TESTING OF A CONICAL DEFLECTOR-TYPE SEED-METERING DEVICE UNDER VIBRATION /** ***振动工况下锥面导流式排种器性能分析与试验*** **Jianxin DONG[1)], Hui QU*[1)], Wenxue DONG**[1)], Shilin ZHANG[2)], Xiaojun GAO[3)], Zuoli FU[4)], Lei WANG[5)]** [1)] College of Mechanical and Electrical Engineering, Inner Mongolia Agricultural University, Huhhot, China; [2)] Mechanical and Electrical Engineering College, Gansu Agricultural University, Lanzhou, China; [3)] College of Engineering, Nanjing Agricultural University, Nanjing, China; [4)] College of Mechanical and Electronic Engineering, Northwest A&F University, Yangling, China; [5)] National Technology Innovation Center for Prataculture, Huhhot, China	**697**
55.	**SOIL–AIR THERMAL ENVIRONMENT IN CHINESE SOLAR GREENHOUSES WITH EARTHEN WALLS /** ***中国土墙日光温室土壤-空气热环境研究*** **Kaixiao CHENG[2)], Hong YANG[1*)], Weiwei CHENG[1)]** [1)] Shanxi Agricultural University, College of Urban and Rural Construction, Taigu / China [2)] Shanxi Agricultural University, College of Agricultural Engineering, Taigu / China	**707**
56.	**ARTIFICIAL INTELLIGENCE–BASED ANALYSIS OF SUSTAINABLE AGRICULTURE DISCOURSE /** ***SÜRDÜRÜLEBILIR TARIM SÖYLEMLERININ YAPAY ZEKA TABANLI ANALIZI*** **Mehmet KAYAKUŞ[1)], Onder KABAS [2*)], Valentin VLADUT [3*)], Aylin KABAS [4)]** [1)] Department of Biomedical Engineering, Faculty of Engineering, Akdeniz University, Antalya, Türkiye; [2)] Department of Machine, Technical Science Vocational School, Akdeniz University, Antalya, Türkiye; [3)] National Institute of Research—Development for Machines and Installations Designed for Agriculture and Food Industry—INMA Bucharest, Bucharest, Romania [4)] Department of Organic Farming, Manavgat Vocational School, Akdeniz University, Antalya, Türkiye	**716**

57.	**PATH PLANNING FOR AGRICULTURAL PICKING MANIPULATORS USING A GRID-NUMBER-GUIDED IMPROVED RRT ALGORITHM /** *基于栅格编号引导的改进RRT算法的农业采摘机械臂路径规划* **Wei ZHAO[*1)], Yang PAN[1)], Bangbo LIU[1)], Xi XU[1)], Tianle SHI[1)], Weijian SU[1)], Xiaobiao SHANG[1)], Hao PENG[1)], Hongfu ZHANG[*1)]** College of Mechanical and Electrical Engineering, Yunnan Agricultural University, Kunming，Yunnan / China	732
58.	**RESEARCH PROGRESS ON MECHANICAL-TYPE AND PNEUMATIC-TYPE PRECISION SEED METERING DEVICES: A REVIEW /** *机械式与气力式精量排种器研究进展综述* **Wenting JIN [1,2)], Jinhui ZHAO [1)], Jie WANG [1)], Yunfei LV [*1)], Wenpeng LI [1)]** [1)] Hebei Petroleum University of Technology, Chengde / P.R. China; [2)] State Key Laboratory of Agricultural Equipment Technology, Beijing / P.R. China	747
59.	**DESIGN AND EXPERIMENTAL STUDY OF FURROW OPENER FOR SELF-PROPELLED CODONOPSIS PILOSULA TRANSPLANTER BASED ON DISCRETE ELEMENT METHOD /** *基于离散元的自走式党参移栽机开沟器设计与试验研究* **Qingxu YU [1,2,3)], Ying LANG[1)], Yan GONG[1)] *, Xiao ZHANG[1)], Jianling HU[1)], Dehuan ZHOU[1)],** [1)] Nanjing Institute of agricultural mechanization, Ministry of agriculture and rural areas, Nanjing, China; [2)] Key Laboratory of Modern Agricultural Equipment, Ministry of Agriculture and Rural Affairs, Nanjing, China; [3)] Institute of Western Agriculture, Chinese Academy of Agricultural Science, Changji, China	763
60.	**DESIGN AND INSERTION PERFORMANCE OPTIMISATION OF A COMPOSITE INSERTION PIN FOR A CORN STALK SAND BARRIER LAYING DEVICE /** *玉米秸秆沙障铺设装置复合插针设计及插入性能优化* **Qidong SUN, Weiqiang ZHENG*), Liping ZHANG, Bolin LI, Zhiqiang FENG, Senyu NIU, Chengqian XIE** College of Mechanical Engineering, Xinjiang University, Urumqi 830046 / China	778
61.	**DESIGN AND EXPERIMENTAL EVALUATION OF A DIRECT-INJECTION WINGED SHOVEL FOR A DEEP STRAW INCORPORATION MACHINE /** *秸秆深埋还田机直注翼铲设计与试验评价* **Sicheng YANG[1)], Lihua WEI*[1)], Fanbowen MENG[1)], Deshuai LI[1)], Jiantian LI[2)], Zhengqing WANG[1)], Ruili WANG*[1)]** [1)]College of Engineering, Shenyang Agricultural University, Shenyang / China; [2)]Fengcheng Caohe Machinery Manufacturing Co., Ltd., Dandong / China	792
62.	**PARAMETER CALIBRATION OF THE DISCRETE ELEMENT MODEL FOR THE AGRICULTURAL MACHINERY-LATERITIC SOIL-PANAX NOTOGINSENG INTERACTION DURING THE TRANSPLANTING PROCESS /** *三七移栽过程机具-红土-三七交互离散元模型参数标定* **Wei SU[1)], Yi ZENG [1)], Qingxu YU*[2)], Congcong LIAO[1)], Qinghui LAI[1)], Cantong SU[1)]** [1)]University of Science and Technology Kunming, Kunming, China; [2)]Nanjing Institute of Agricultural Mechanization, Ministry of Agriculture and Rural Affairs, Nanjing, China	805
63.	**BODY CONDITION SCORING METHOD FOR JERSEY CATTLE BASED ON ME-POINTNEXT /** *基于ME-PointNeXt的娟姗奶牛体况评分方法* **Yu Zhenwei[1,2)], Shi Xiaolong[1)], Li Baotong[1)], CI-REN Duoji[3)], Zhang Ji[1)], Tian Fuyang[*1,2)]** [1)] College of Mechanical and Electronic Engineering, Shandong Agricultural University, Tai'an / China; [2)] Shandong Engineering Research Centre of Agricultural Equipment Intelligentization, Tai'an / China; [3)] Tibet Nianxiongziji Animal Husbandry Co., Ltd., Rikaze/China	818
64.	**DESIGN AND EXPERIMENTAL EVALUATION OF A CELL-WHEEL SEED-METERING DEVICE FOR RAPESEED BLANKET SEEDLING PRODUCTION /** *窝眼轮式油菜毯状苗育苗排种器的设计与试验* **Yaodong WU[1)], Jing LUO[2)], Qing TANG[1,2)], Jixuan WANG[2)], Qun LI[1)], Meng BAI[2)] , Jinhui CHEN[2)], Tong WU[1)]** [1)] Jiangsu Yunma Agricultural Machinery Manufacturing Co., Ltd., Yancheng, China [2)]Nanjing Institute of Agricultural Mechanization, Ministry of Agriculture and Rural Affairs, Nanjing, China	830
65.	**INTELLIGENT ANIMAL FEEDING SYSTEM BASED ON MULTISOURCE INFORMATION ACQUISITION /** *基于多源信息采集的动物智能饲喂系统* **Linwei LI[1,7)], Jie BAI[2)], Xinyu ZHAO[1)], Guanzhen LI[3)], Yuanrong TIAN[4)], Peng CHENG[5)], Dongyao LIU[6)], Zhenyu LIU [8,9)], Senhao YANG[1)], Tao ZHAO[2)], Xiaoping JI[*4)]** [1)] College of Information Science and Engineering, Shanxi Agricultural University, Taigu 030801, Shanxi/China; [2)] Department of Big Data and Intelligent Engineering, Shanxi Institute of Technology, Yangquan, Shanxi/China;[3)] College of Computer Science and Software Engineering, Hohai University, Nanjing, Jiangsu/China; [4)] Faculty of Software Technologies, Shanxi Agricultural University, Taigu, Shanxi/China; [5)] Combat Support Academy, Rocket Force University of Engineering, Xi'an, Shanxi/China; [6)] Department of Mechanical Engineering, Shanxi Institute of Technology, Yangquan, Shanxi/China; [7)] Key Laboratory of Equipment and Informatization in Environment Controlled Agriculture, Ministry of Agriculture and Rural Affairs, Hangzhou, Zhejiang/China; [8)] Dryland Farm Machinery Key Technology and Equipment Key Laboratory of Shanxi Province, Taigu, Shanxi/China; [9)] College of Agricultural Engineering, Shanxi Agricultural University, Taigu, Shanxi/China	846

66.	**RESEARCH PROGRESS AND DEVELOPMENT TRENDS OF KEY TECHNOLOGIES FOR ELECTRIC TRACTORS / *纯电动拖拉机关键技术研究进展与发展趋势*** **Xiaodong LV[1)], Zhaoyue LIU[1)], Jikang XU[*1)]** [1)] Qingdao Agricultural University, Qingdao / China	**861**
67.	**A REVIEW ON RESEARCH OF MECHANIZED RESIDUAL FILM RECOVERY TECHNOLOGIES AND EQUIPMENT / *机械化残膜回收技术与装备研究综述*** **Hongjian ZHANG*[1)], Junyi LU[1)], Yufeng LI[1)], Linlong JING[1)], Shuo KANG[1)], Jinxing WANG[1)]** [1)]School of Mechanical and Electronic Engineering, Shandong Agricultural University, Shandong/China	**877**
68.	**YOUNG APPLE FRUIT DETECTION METHOD FOR ENTIRE DWARF AND DENSELY PLANTED APPLE TREES BASED ON CHUNKING STRATEGY / *基于分块策略的矮砧密植苹果整株果树幼果识别方法研究*** **Yu YANG[1)], Xingchen QIAO[1)], Huijun ZHAO[2)], Yicheng YANG[1)], Zhaohui ZHENG[3)], Gang ZHANG[4)], Xiaole WANG[1)], Zhenchao WU*[1)]** [1)]School of Engineering, Anhui Agricultural University, Hefei, Anhui, China; [2)] Himile Industrial Park, Economic Development Zone, Weifang, Shandong, China [3)] College of Mechanical and Electrical Engineering, Shihezi University, Shihezi, China [4)] School of Intelligent Manufacturing, Anhui Science and Technology University, Chuzhou, China	**895**
69.	**EXPERIMENTAL EVALUATION OF BUCKWHEAT DEHULLING USING A NOVEL DEHULLING DEVICE WITH A ROTATING DRUM AND A SHAPE-ADAPTIVE PRESSURE DECK / *Эргэх хүрд ба сагаг будааны хэлбэрт тохируулсан шинэ хийцийн шахах дектэй хальслах төхөөрөмжөөр сагаг будааг хальсалсан туршилтын үр дүн*** **Amartuvshin OIDOV [1)]; Baatarkhuu DORJSUREN[1*)] ; Dovchinvanchig MAASHAA[2*)]** [1)] School of Engineering and Technology, Mongolian University of Life Sciences, Ulaanbaatar, Mongolia [2)] School of Applied Sciences, Mongolian University of Life Sciences, Ulaanbaatar, Mongolia	**910**
70.	**TRAJECTORY TRACKING APPROACH FOR ORCHARD INSPECTION VEHICLE BASED ON IMM-EKF AND IMPROVED STANLEY CONTROLLER / *基于IMM-E F与改进STANLEY的果园巡检车轨迹跟踪方法*** **Junling HU [1)], Xiaofan LIU [2)], Meixia JIA [1,*)]** [1)] Chongqing Jianzhu College, School of Intelligent Manufacturing, Chongqing, China [2)] Communication University of China, School of Economics and Management, Beijing, China	**920**
71.	**BGE-YOLOV11: A LIGHTWEIGHT MODEL FOR DETECTING MAIN STEM NODES IN SOYBEAN *基于大豆主茎节点检测的BGE-YOLOv11轻量化模型研究*** **Hao BI, Xiuying Xu[1*)], Yiting LIU, Yanxu JIAO, Lingfeng ZHU** College of Engineering, Heilongjiang Bayi Agricultural University, Daqing / China	**932**
72.	**DISCRETE ELEMENT MODELING AND PARAMETER CALIBRATION OF THE WHEAT ROOT–SOIL COMPOSITE / *小麦根土复合体离散元模型建立与标定试验*** **Chengcheng GUO[1)], Zhiping YANG*[2)], Junchang ZHANG[2)], Huiyan YIN[1)], Cui LI[1)]** [1)]College of Agricultural Machinery and Automotive Engineering, Gansu Polytechnic College of Animal Husbandry & Engineering, Wuwei / China; [2)]College of Mechanical and Electronic Engineering, Northwest A&F University, Yangling / China	**943**
73.	**STUDY OF THE MOTION STABILITY AND OPERATIONAL SMOOTHNESS OF AN AGRICULTURAL ROBOTIC PLATFORM / *ԳՅՈՒՂԱՏՆՏԵՍԱԿԱՆ ՆՇԱՆԱԿՈՒԹՅԱՆ ՌՈԲՈՏ-ՀԱՐԹԱԿԻ ՇԱՐԺՄԱՆ ԿԱՅՈՒՆՈՒԹՅԱՆ ԵՎ ԸՆԹԱՑՔԻ ՍԱՀՈՒՆՈՒԹՅԱՆ ՈՒՍՈՒՄՆԱՍԻՐՈՒԹՅՈՒՆ*** **Arshaluys TARVERDYAN[1)], Aghavard KHACHATRYAN[2)], Artur ALTUNYAN[1*)], Sergey PAPYAN[1)], Albert GRIGORYAN[1)]** [1)]Scientific Research Institute for Agricultural Mechanization and Automation, Armenian National Agrarian University, Yerevan, Armenia; [2)]Chair of Higher Mathematics and Physics, Armenian National Agrarian University, Yerevan, Armenia	**954**
74.	**SIMULATION ANALYSIS AND PARAMETER OPTIMIZATION OF A TWIN-ROLL SOIL-CRUSHING DEVICE FOR A POTATO HARVESTER *优化*** **Yangbiao HUANG[1)], Song CHEN[1)], Zihao OU[1)], Qingmiao XIANG[1)], Bei WU*[1,2)], Bang JI[1,2)], Zhichao FANG[1,2)], Fangping XIE[1,2]** [1)] Hunan Agricultural University, College of Mechanical and Electrical Engineering, Changsha / China; [2)] Hunan Key Laboratory of Intelligent Agricultural Machinery and Equipment, Changsha / China	**970**
75.	**ARTIFICIAL NEURAL NETWORK FOR OPTIMIZING THE CONVECTIVE DRYING PROCESS OF PEAR SLICES / *REŢEA NEURALĂ ARTIFICIALĂ PENTRU OPTIMIZAREA PROCESUL DE USCARE CONVECTIVĂ A FELIILOR DE PERE*** **Alexandru-Polifron CHIRIȚĂ[*1)], Vitali VIȘANU[2)], Radu RĂDOI[1)], Victor POPESCU[2)], Gabriela MATACHE[1)], Mihai BALAN[2)], Gheorghe ȘOVĂIALĂ[1)], Mihail MELENCIUC[2)]** [1)] National Institute of Research & Development for Optoelectronics / INOE 2000, Subsidiary Hydraulics and Pneumatics Research Institute / IHP / Romania. [2)] Technical University of Moldova, Department of Mechanical Engineering / Republic of Moldova	**980**

76.	**NUMERICAL SIMULATION STUDY ON FALLING-FILM EVAPORATION OF MOLASSES ETHANOL WASTEWATER / *甘蔗糖蜜酒精废水降膜蒸发的数值模拟研究*** **Liang WANG[1,3], Mingzhe HU[2], Xiaole WANG[2]** [1]College of Energy and Architectural Engineering, Shandong Huayu University of Technology, Dezhou, China; [2]School of Thermal Engineering, Shandong Jianzhu University, Jinan, Shandong, China; [3]Shandong Engineering Research Center of Low-Carbon Energy Internet of Things Technology, Dezhou, China	**989**
77.	**LIGHTWEIGHT DETECTION OF EGG SURFACE DEFECTS UNDER CONVEYOR-BELT CONDITIONS USING YOLOv11N-DAL / *传送带条件下基于 YOLOv11n-DAL 的鸡蛋外观缺陷轻量化检测*** **Xianyong MENG[1,2], Haoran GUO[1,2], Jun YAN[1,2], Qimiao WANG[1,2,*], Qinyou SUN[1,2,*]** [1] School of Information Science and Engineering, Shandong Agricultural University, Taian, China; [2] Key Laboratory of Huanghuaihai Smart Agricultural Technology, Ministry of Agriculture and Rural Affairs, Taian, China	**999**
78.	**DESIGN AND TESTING OF AN AUTOMATIC SEEDLING-LOADING SYSTEM FOR A HIGH-SPEED RIDE-ON RICE TRANSPLANTER / *高速乘坐式插秧机自动装秧系统设计与试验*** **Fengpeng NING, Jinping CAI, Yihan ZHOU, Qilong ZHANG, Xianhao DUAN, Zhaopeng LIU, Muhua LIU, Xiongfei CHEN, Peng XU *** Jiangxi Provincial Key Laboratory of Modern Agricultural Equipment. College of Engineering Jiangxi Agricultural University, Nanchang, China	**1011**
79.	**STUDY ON ORTHOGONAL STRAIN CHARACTERISTICS OF BRASSICA NAPUS STEMS DURING TENSILE PROCESS BASED ON DIGITAL IMAGE CORRELATION / *基于DIC的油菜茎秆拉伸过程正交应变特性试验研究*** **Guangchao ZHAN[1], Yi YANG[1], Guodang LIAN*[2], Peng ZHANG[1], Wangyuan ZONG[3]** [1]School of Electromechanical and Intelligent Manufacturing, Huanggang Normal University, Huanggang, Hubei, China; [2] School of Mechanical and Electrical Engineering, Lanzhou University of Technology, Lanzhou, Gansu; China; [3]College of Engineering, Huazhong Agricultural University, Wuhan, Hubei, China	**1026**
80.	**SUSTAINABLE CONTROL OF *BOTRYTIS CINEREA* IN VITICULTURE USING BIOACTIVE PLANT EXTRACTS OBTAINED BY HYBRID ULTRASOUND-PERCOLATION TECHNOLOGY / *CONTROLUL SUSTENABIL AL FUNGULUI BOTRYTIS CINEREA ÎN VITICULTURĂ UTILIZÂND EXTRACTE BIOACTIVE DIN PLANTE OBȚINUTE PRIN TEHNOLOGIA HIBRIDĂ ULTRASUNETE-PERCOLARE*** **Ana-Maria TĂBĂRAȘU[1], Florin NENCIU*[1], Cristina FĂTU[2], Lorena-Diana POPA *[3], Nicolae-Valentin VLĂDUȚ[1], Iuliana GĂGEANU[1], Teofil-Alin ONCESCU[1], Diana COCÂRȚĂ[4], Dragoș-Nicolae ANGHELACHE[1], Andra-Maria LĂCUREANU[4], Iulian VOICEA[1], Elena-Valeria VLĂDUȚ[4],** [1]INMA Bucharest / Romania; [2] Research Development Institute for Plant Protection / Romania; [3] Agricultural Research and Development Station Secuieni / Romania; [4] National University of Science and Technology POLITEHNICA Bucharest / Romania	**1036**
81.	**STUDY ON KEY PARAMETERS AND FERTILIZATION PERFORMANCE OF A FLUTED-WHEEL FERTILIZER METERING DEVICE BASED ON EDEM / *基于EDEM的外槽轮式排肥器关键参数和施肥性能研究*** **Chang WAN[1,2,3], Jiajun ZHANG[1], Zhihui QI[1], Zilun ZHOU[1], Yu WANG[1], Qingqing FAN[4], Ling ZHOU*[1,2,3]** [1] College of Mechanical and Electrical Engineering, Tarim University, Alar, Xinjiang / China [2] Key Laboratory of Modern Agricultural Engineering of Xinjiang Uygur Autonomous Region, Alar, Xinjiang / China [3] Xinjiang Production and Construction Corps (XPCC) Key Laboratory of Utilization and Equipment of Special Agricultural and Forestry Products in Southern Xinjiang, Alar, Xinjiang / China [4] Alar Runong Modern Agricultural Technology Co., Ltd., Alar, Xinjiang / China	**1049**
82.	**OPERATIONAL RELIABILITY OF UAV-BASED WASTE SITE DETECTION FOR ENVIRONMENTAL MONITORING / *FIABILITATEA OPERAȚIONALĂ A IDENTIFICĂRII ZONELOR CU DEȘEURI UTILIZÂND UAV-URI ÎN MONITORIZAREA MEDIULUI*** **Adrian IOSIF [1], Edmond MAICAN[1], Sorin-Ștefan BIRIȘ[1], Gabriel-Alexandru CONSTANTIN[1], Mihai-Gabriel MATACHE[2]** [1]Department of Biotechnical Systems, Faculty of Biotechnical Systems Engineering, National University of Science and Technology Politehnica Bucharest, Romania [2]INMA Bucharest / Romania	**1070**
83.	**PERFORMANCE EVALUATION OF MOBILE AND STATIONARY FISH SMOKING TECHNOLOGIES / *የተንቀሳቃሽ እና የቋሚ የዓሣ ማጨሻ ቴክኖሎጂዎች የአፈጻጸም ግምገማ*** **Amanuel ERCHAFO*} Maney AYALEW** Ethiopian Institute of Agricultural Research, Melkassa Agricultural Research Centre, Department of Agricultural Engineering, P.O. Box 436, Adama, Ethiopia	**1085**

84.	**MULTIBODY DYNAMICS SIMULATION AND TESTING OF A SMALL ELECTRONICALLY CONTROLLED TRACKED CHASSIS FOR HILLY AND MOUNTAINOUS TERRAIN / *丘陵山地小型履带式电控底盘多体动力学仿真与试验*** **Xiaolian LÜ[1)], Jiankang HUANG[1)], Ruijuan SU[1)], Yang ZHANG[2)], Xiaorong LÜ*[2)]** [1)] College of Mechanical & Electrical Engineering, Chuzhou University, Chuzhou, China; [2)] College of Machinery & Electronics, Sichuan Agricultural University, Yaan, China	**1102**
85.	**AUTOMATIC RADICLE LENGTH ESTIMATION OF GERMINATED CUCUMBER SEEDS BASED ON GERMHRNET / *基于GermHRNet的发芽黄瓜种子胚根长度自动估测方法*** **Rui ZHAO[1)], Heng ZHAO[1)], Feng ZHANG[1)], Wenjie LI[2)], Bei WANG[2)], Qi WANG[4)], Yiting SU[1)], Qiulan WU[*1)], Bo ZHOU[*2,3)],** [1)]College of Information Science and Engineering, Shandong Agricultural University, Tai'an/China [2)]College of Life Sciences, Shandong Agricultural University, Tai'an/China [3)]Eukaryotic Biotechnology (Shandong) Co., Ltd., Tai'an/China [4)]Yoheng Biotechnology (Ningbo) Co., Ltd., Ningbo/China	**1114**
86.	**DESIGN AND EXPERIMENTAL STUDY OF AN INCLINED SPOON-DISC MAIZE SEED-METERING DEVICE / *倾斜勺盘式玉米排种器的设计与试验研究*** **Ziyu WANG[1)], Xingkang LIU[1)], Wentao LI[2)], Hongchao WANG*[2)], Junlei LIU[2)], Qinglong TANG[2)], Jiakai XU[2)], Xinying DONG[1)]** [1)] College of Information and Electrical Engineering, Heilongjiang Bayi Agricultural University, Daqing, China [2)] College of Engineering, Heilongjiang Bayi Agricultural University, Daqing, China	**1129**
87.	**CONSTRUCTION AND PARAMETER CALIBRATION OF A DISCRETE ELEMENT MODEL FOR SEED GINGER IN SOWING OPERATIONS / *播种期生姜离散元模型构建与参数标定*** **Jinbiao ZHANG[1)], Jin CHENG*[1)], Lin LIU[1)], Jialin HOU[1)], Rui HOU[2)], Qiwei ZHAO[3)], Yuhua LI[1)]** [1)] Shandong Agricultural University, Tai'an / China; [2)] Beijing University of Posts and Telecommunications, Beijing / China [3)] Dezhou Chunming Agricultural Machinery Company Limited, Dezhou / China	**1143**
88.	**AUTONOMOUS NAVIGATION FOR ORCHARD INTER-TREE WEEDING ROBOTS BASED ON AN IMPROVED A*-DWA FUSION ALGORITHM / *基于改进A*-DWA融合算法的果园株间除草机器人自主导航研究*** **Yan XU, Qing YUAN, Dazhong WANG, Yinan LIU, Xiangchen MENG, Xiang YUE** College of Engineering, Shenyang Agricultural University, Shenyang, China	**1155**
89.	**DETERMINATION OF PHYSICAL PROPERTIES AND CALIBRATION OF DISCRETE ELEMENT SIMULATION PARAMETERS FOR YIMENG MOUNTAIN JUJUBES / *沂蒙山红枣颗粒物性参数测定与离散元仿真参数标定*** **Fandi ZENG[1)], Hao ZHANG[2)], Yinzeng LIU[1)], Xiaofei CHENG[1)], Yuzhen DONG[1)], Zhihuan ZHAO[*1)], Haocheng LIU[1)]** [1)]Shandong Agriculture and Engineering University, College of Mechanical and Electronic Engineering, Jinan, China; [2)] Shandong Agriculture and Engineering University, College of Food Science and Engineering, Jinan, China	**1169**
90.	**WIND-BLOWN SAND EROSION OF A POLYCARBONATE LAMP COVER FOR AGRICULTURAL MACHINERY AT DIFFERENT WIND SPEEDS AND YAW ANGLES / *不同风速与偏航角下农用机械聚碳酸酯灯罩的风沙冲蚀特性*** **Sheng JIANG[1)], Afang JIN*[1)], Mengyao XU[1)]** [1)] College of Mechanical Engineering, Xinjiang University, Urumqi / China	**1179**
91.	**LIQUID SLOSHING SUPPRESSION EFFECT OF DOUBLE-LAYER ELASTICALLY CONSTRAINED FLOATING PLATE USED FOR PLANT PROTECTION UAVS / *双层弹性约束浮板液体晃动抑制实验研究*** **Jizhou ZHENG[1),2)], Chengbin ZHANG[3)], Yixuan SUN[1)], Lin ZHU[1)], Yan ZHANG*[4)5)]** [1)] College of Mechanical and Electronic Engineering, Shandong Agricultural University, Taian, China [2)] Shandong Key Laboratory of Intelligent Production Technology and Equipment for Facility Horticulture, Taian, China [3)] Shandong Taikai Power Electronic CO. LTD, Taian, China [4)] College of Information Science and Engineering, Shandong Agricultural University, Taian, China [5)] Smart Agriculture Technology Laboratory of the Ministry of Agriculture and Rural Affairs, Taian, China	**1191**
92.	**FAILURE MECHANISMS IN REPAIRABLE AGRICULTURAL TRACTORS ACROSS ENGINE OPERATING-HOUR CLASSES/*MECHANIZMY POWSTAWANIA USZKODZEŃ W CIĄGNIKACH ROLNICZYCH W ZALEŻNOŚCI OD CZASU PRACY SILNIKA*** **Karol DURCZAK[*1)]; Tomasz ŻELAZIŃSKI[2)]; Adam EKIELSKI[2)]** [1)] Department of Biosystems Engineering, Faculty of Environmental and Mechanical Engineering, Poznan University of Life Sciences, Poznań / Poland; [2)] Department of Production Engineering, Faculty of Production Engineering, University of Life Sciences in Warsaw, Warsaw / Poland	**1201**

93.	**COMPUTER VISION-BASED CORN STALK IMAGE RECOGNITION RESEARCH /** ***基于计算机视觉的玉米秆图像识别研究*** **Wenlong LI[1)], Ning DAI[*1),2)], Qiuyan LIANG[*1)], Liuxuan MA[1)], Lianyang WANG[1)]** [1)] School of Mechanical Engineering, Jiamusi University, Jiamusi, Heilongjiang; [2)] The First Affiliated Hospital of Jiamusi University, Jiamusi, Heilongjiang	**1211**
94.	**A REVIEW OF INTELLIGENT TOBACCO TRANSPLANTERS: KEY TECHNOLOGIES AND DEVELOPMENT TRENDS /** ***烟草智能化移栽机械关键技术演进与发展趋势综述*** **Lichang CHEN[1)], Guangliang LI[1)], Wuli DUAN[2*)], Xiaolei SONG[1)], Ran RAN[2)], Jianmin XU[3)], Wutai DONG[1)]** [1)] College of Mechanical and Electrical Engineering, Yunnan Agricultural University, Kunming, Yunnan / China [2)] Baoshan Branch of Yunnan Provincial Tobacco Company, Baoshan, Yunnan / China [3)] Yunnan Agricultural Machinery Research Institute Co., Ltd., Kunming, Yunnan / China	**1222**
95.	**CONTRIBUTIONS TO THE INVESTIGATION OF THE MECHANICAL BEHAVIOUR OF ROSE HIP SEEDS UNDER COMPRESSION AND CREEP TESTS: EXPLORATORY UNSUPERVISED CLASSIFICATION OF COMPRESSION RESPONSES /** ***CONTRIBUȚII LA CERCETAREA COMPORTAMENTULUI MECANIC AL SEMINȚELOR DE MĂCEȘE PRIN TESTE DE COMPRESIUNE ȘI FLUAJ: CLASIFICAREA EXPLORATORIE PRIN TEHNICI DE ÎNVĂȚARE AUTOMATĂ NESUPRAVEGHEATĂ A RĂSPUNSURILOR LA COMPRESIUNE*** **George IPATE*[1)], Iuliana GĂGEANU*[2)], Alina Corina DUMITRAŞCU[3)]** [1)]National University of Science and Technology Politehnica Bucharest / Romania; [2)] National Institute of Agricultural Machinery, Bucharest, Romania [3)] "Gheorghe Asachi" Technical University, Iasi, Romania	**1244**
96.	**TOBACCO COATED SEED RECOGNITION AND CLASSIFICATION METHOD BASED ON IMPROVED YOLOv10N /** ***基于改进YOLOv10n的烟草包衣种子识别分类方法*** **Limin XIE[1,2)], Xinghong ZOU[2,3)], Bing FANG[1,2)], Changling YIN[4)], Zhihui LIN[4)], Zhansheng JIANG[4*)]** [1)] College of Mechanical and Electrical Engineering, Fujian Agriculture and Forestry University, Fuzhou, China [2)] Fujian Key Laboratory of Agricultural Information Sensing Technology, Fuzhou, China [3)] College of Computer and Information Sciences, Fujian Agriculture and Forestry University, Fuzhou, China) [4)] Fujian Tobacco Company Sanming Company	**1256**
97.	**COMPARATIVE EVALUATION OF AEROPONIC, HYDROPONIC AND CONVENTIONAL SYSTEMS FOR POTATO MINITUBER PRODUCTION /** ***EVALUAREA COMPARATIVĂ A SISTEMELOR AEROPONICE, HIDROPONICE ȘI CONVENȚIONALE UTILIZATE PENTRU PRODUCEREA MINITUBERCULILOR DE CARTOF*** **Andreea TICAN*, Carmen CHELMEA, Mihaela CIOLOCA, Monica POPA** National Institute of Research and Development for Potato and Sugar Beet Brașov, Romania	**1267**
98.	**A STUDY OF THE QUALITY OF CARROT ROOT CLEANING WITH A SPIRAL CLEANER: SOIL SEPARATION AND MECHANICAL DAMAGE /** ***ДОСЛІДЖЕННЯ ЯКОСТІ ОЧИЩЕННЯ КОРЕНЕПЛОДІВ МОРКВИ СПІРАЛЬНИМ ОЧИСНИКОМ: ВІДОКРЕМЛЕННЯ ҐРУНТУ ТА МЕХАНІЧНІ ПОШКОДЖЕННЯ*** **Volodymyr BULGAKOV[1)], Oleksandr MATSUIEV[2,*)], Lucretia POPA[3)], J¸ ri OLT[4)]** [1)] National University of Life and Environmental Sciences of Ukraine, Kyiv, Ukraine [2)] Institute of Mechanics and Automation of Agroindustrial Production of the National Academy of Agrarian Sciences of Ukraine, Hlevakha, Ukraine [3)] Research Institute for Agriculture Economy and Rural Development – ICEADR Bucharest, Romania [4)] Estonian University of Life Sciences, Institute of Forestry and Engineering, Chair of Biosystems Engineering, Tartu, Estonia	**1278**
99.	**DESIGN AND EXPERIMENTAL STUDY OF A SOIL PICKUP AND SEPARATION DEVICE FOR AN AUTOMATIC FLOWER TRANSPLANTER /** ***花卉自动移栽机取分土装置设计与试验研究*** **Xiang ZOU[1)], Lihua WEI*[1,2)], Denghui ZHAO[1)], Jian KANG[1)], Xiaohu BAI[1,2)] and Subo TIAN*[1,2)]** [1)]College of Engineering, Shenyang Agricultural University, Shenyang/ China; [2)]Key Laboratory of Agricultural Equipment for Horticultural Crops, Ministry of Agriculture and Rural Affairs, Shenyang / China	**1287**
100.	**KINEMATICS OF A ROTARY TILLER EQUIPPED WITH A TURNING MECHANISM FOR TREE-TRUNK BYPASS /** **ՇՐՋԱԴԱՐՁԱՅԻՆ ՄԵԽԱՆԻԶՄՈՎ ՀՈՂԱՄՇԱԿ ՖՐԵԶԻ ԿԻՆԵՄԱՏԻԿԱՆ ԾԱՌԱԲՆԵՐԻ ՇՐՋԱՆՑՄԱՆ ԺԱՄԱՆԱԿ** **Albert GRIGORYAN, Artur ALTUNYAN*), Seryozha PAPYAN, Arman SIMONYAN, Aram MAZMANYAN, Arshaluys TARVERDYAN** Scientific Research Institute for Agricultural Mechanization and Automation, Armenian National Agrarian University, Yerevan, Armenia	**1298**

101.	**OPTIMAL DESIGN AND SIMULATION-BASED VALIDATION OF A TOBACCO PLANTER BASED ON MULTIPLE BIRD-BEAK CHARACTERISTIC CURVES /** ***基于多鸟喙特征曲线的烟草栽植器优化设计与仿真验证*** **Sheng DING[1)], Ao SHAN[2)], Chencan XIAO [3)], Qing JIANG[1,2,*)]** [1)] School of Mechanical and Vehicle Engineering, Anhui Agricultural University, Hefei / China; [2)] Anhui Provincial Engineering Research Center of Intelligent Agricultural Machinery, Hefei / China	**1310**
102.	**DUST GENERATION MECHANISMS AND EFFECTS OF OPERATING PARAMETERS IN A FLAIL-TYPE STRAW PICKUP HEADER USING DEM AND CFD /** ***基于DEM与CFD的锤爪式秸秆捡拾割台扬尘机理与作业参数影响*** **Jinghao FAN[1,2)], Haiqing TIAN*[1,2)], Chunxiang ZHUO[1,2)], Kai ZHAO[1,2)], Qiang YUE[1,2)], Ruiyi XU[1,2)]** [1)] College of Mechanical and Electrical Engineering, Inner Mongolia Agricultural University, Hohhot, China. [2)] Inner Mongolia Engineering Research Centre of Intelligent Equipment for the Entire Process of Forage and Feed Production, Hohhot, China.	**1326**
103.	**DESIGN AND TESTING OF A COMPOSITE POTATO PICKUP DEVICE BASED ON EDEM /** ***基于EDEM的复合式马铃薯捡拾装置设计与试验*** **Zheng MA[1,2)], Jianjiao HUANG[1,2)], Shuai WANG[1,2,*)], Yaoming LI[1,2)], Zhiqiang SONG[1,2)]** [1)] School of Agricultural Engineering, Jiangsu University, Zhenjiang, Jiangsu, China; [2)] Key Laboratory for Theory and Technology of Intelligent Agricultural Machinery and Equipment, Jiangsu University, Zhenjiang, Jiangsu, China	**1340**
104.	**BASELINE CHARACTERISATION AND MULTI-YEAR ELEMENTAL MONITORING OF BIOMASS CROPS ON POST-MINING LAND IN PETRILA, ROMANIA/** ***CARACTERIZAREA INIȚIALĂ ȘI MONITORIZAREA MULTIANUALĂ A COMPOZIȚIEI ELEMENTARE A CULTURILOR DE BIOMASĂ PE TEREN POST-MINIER DIN PETRILA, ROMÂNIA*** **Emilia-Cornelia DUNCA[1)], Sorin Mihai RADU[1)], Mădălina-Flavia IONIȚĂ[1)], Sabin Ioan IRIMIE[1)], Daniela-Ionela CIOLEA[1)], Cristian Marian SORICĂ[2*)]** [1)] Universitatea din Petroșani, 20 Universității Street, Petroșani, Romania; [2)] INMA Bucharest, 6 Ion Ionescu de la Brad Blvd., Bucharest, Romania	**1352**
105.	**INTEGRATION OF SMART TRAPS AND WEATHER SENSORS INTO A DIGITAL PRECISION AGRICULTURE SYSTEM //** ***INTEGRAREA CAPCANELOR INTELIGENTE ȘI A SENZORILOR METEO ÎNTR-UN SISTEM DIGITAL PENTRU AGRICULTURA DE PRECIZIE*** **Cătălin PERSU[1)], Dan CUJBESCU[1)], Florin-Cristian MARIN[2)], Alin ONCESCU[1)], Iuliana GĂGEANU[1)], Robert CRISTEA[1)], Alexandru IONESCU[1)], Carmen BĂLȚATU[1)], Ana-Maria TĂBĂRAȘU[1)]** [1)] National Institute of Research – Development for Machines and Installations Designed to Agriculture and Food Industry, Romania [2)] Research Institute for Fruit Growing Pitesti-Maracineni, 117450 Maracineni, Arges, Romania	**1363**
106.	**RESEARCH ON THE INFLUENCE OF TEMPORARY GRASSLAND ROTATION ON ARABLE CROPS SUITABLE FOR THE FAGARAS COUNTRY /** ***CERCETĂRI PRIVIND INFLUENȚA ROTAȚIEI PAJIȘTILOR TEMPORARE ASUPRA CULTURILOR ARABILE PRETABILE PENTRU ȚARA FĂGĂRAȘULUI*** **Tudor Adrian ENE *[1)], Vasile MOCANU [1)]** [1)] Research-Development Institute for Grassland Brașov / Romania;	**1373**
107.	**ENERGY AND EXERGY ANALYSES OF TWO-TEMPERATURE-LEVEL VAPOR COMPRESSION REFRIGERATION SYSTEMS FOR APPLICATIONS IN THE FOOD INDUSTRY /** ***ANALIZA ENERGETICĂ ȘI EXERGETICĂ A SISTEMELOR FRIGORIFICE CU COMPRIMARE MECANICĂ DE VAPORI CU DOUĂ NIVELURI DE TEMPERATURĂ DESTINATE APLICAȚIILOR DIN INDUSTRIA ALIMENTARĂ*** **Daniel DIMA [1)], George Daniel GHIȚĂ *[1)], Mihai Florin BIZDADEA *[1)], Horațiu POP [1)], Valentin APOSTOL [1)], Valentin CIOBANU [1)], Cristian Marian SORICĂ [2*)]** [1)] National University of Science and Technology POLITEHNICA Bucharest / Romania; [2)] National Institute of Research – Development for Machines and Installations Designed to Agriculture and Food Industry - INMA Bucharest, Romania	**1383**
108.	**SORGHUM GRAIN CLASSIFICATION AND DETECTION USING YOLOv8 WITH DECOUPLED FULLY CONNECTED ATTENTION MECHANISM AND MULTI-SCALE FEATURE FUSION /** ***融合解耦全连接注意力机制与多尺度特征融合的 YOLOv8 高粱籽粒分类检测方法*** **Yinzeng LIU[1)], Chengpeng CUI[1,2)], Kaixing ZHANG[3)], Lu LIU [4)], Fandi ZENG[1)], Mingming LIU[1)], Hongwei DIAO[1)], Tiexin WANG[2)], Zhihuan ZHAO[*1)]** [1)] Mechanical and Electronic Engineering College, Shandong Agriculture and Engineering University, Jinan / China; [2)] Shandong Unia Agricultural Machinery Co., Ltd, Dezhou / China; [3)] College of Mechanical and Electrical Engineering, Shandong Agricultural University, Tai'an / China; [4)] Production Unit Directly-Affiliated to Xinjiang Production and Construction Corps / China	**1395**

109.	**SA-YOLO FOR MAIZE SEEDLING ROW SEGMENTATION: TOWARD RELIABLE NAVIGATION LINE EXTRACTION IN AGRICULTURAL FIELDS / *基于改进YOLOv12n-seg网络的苗期玉米作物行识别方法*** **Delin SHANG[1,2)], Yu YANG[3)], Xingchen QIAO[3)], Zhiwei HU[3)], Changchun FAN[3)], Yuanwei JIANG[3)], Ziyang QIN[3)], Kuanyan ZHANG[3)], Xiaole WANG[3)], Tie ZHANG*[1,2)], Zhenchao WU*[3)], Gang ZHANG*[4)]** [1)] State Key Laboratory of Agricultural Equipment Technology, Beijing, China; [2)] Chinese Academy of Agricultural Mechanization Sciences Group Co., Ltd., Beijing, China; [3)] School of Engineering, Anhui Agricultural University, Anhui 230036, Hefei, China; [4)] School of Intelligent Manufacturing, Anhui Science and Technology University, Chuzhou, China	**1410**
110.	**PERFORMANCE EVALUATION OF A SURFACE-MOUNTED THERMOELECTRIC GENERATOR, DESIGNED FOR RECOVERING RESIDUAL HEAT / *EVALUAREA PERFORMANȚEI UNUI GENERATOR TERMOELECTRIC MONTAT PE SUPRAFAȚĂ, PROIECTAT PENTRU RECUPERAREA CĂLDURII REZIDUALE*** **Alexandru IONESCU[1)], Florin NENCIU[1)], Mihai MATACHE[1)], Costin MIRCEA[1)], Nicolae-Valentin VLĂDUȚ[1)], Cătălin PERSU[1)], Laurențiu VLĂDUȚOIU[1)], Nicoleta VANGHELE[1)*], Robert BLEJAN[2)]** [1)] National Institute of Research – Development for Machines and Installations Designed to Agriculture and Food Industry - INMA Bucharest / Romania; [2)] National Institute of Research & Development for Optoelectronics / INOE 2000, Subsidiary Hydraulics and Pneumatics Research Institute / IHP / Romania	**1430**
111.	**DESIGN AND TESTING OF AN AIR SUCTION ORCHARD FRUIT-BAG COLLECTION MACHINE / *气吸式果园套袋纸回收机设计与试验*** **Caiqi HU[1,2)], Junbo WANG[1,2)], Fengjie TENG[1,2)], Rendong SUI*[1,2)]** [1)] College of Mechanical and Electrical Engineering, Qingdao Agricultural University, Shandong / China; [2)] Shandong Provincial Key Laboratory of Smart Agricultural Equipment for Protected Horticulture / China	**1444**
112.	**DESIGN AND TESTING OF A PRESS-GROOVE UNIFORM SEEDING MACHINE FOR WHEAT IN HIGH-MOISTURE RICE-STUBBLE FIELDS/*高湿地稻茬麦压沟定深匀播机设计与试验*** **Zhang XIAO[1)], Tong JIAN[2)], Chen WEI*[1)], Zhaxi LUOBU*[2)], Wu JINJI[1)], Zhu JIPING[1)], Ding YAN[1)], Ma LINGJUAN[3)]** [1)] Nanjing Institute of Agricultural Mechanization, Ministry of Agriculture and Rural Affairs, Nanjing / China; [2)] Tibet Academy of Agricultural and Animal Husbandry Sciences, Lhasa / China; [3)] Agricultural Mechanization General Station of the Ministry of Agriculture and Rural Affairs	**1457**

DESIGN AND SIMULATION OF A COMBINED SEED AGITATION PLATE FOR AN AIR-SUCTION PRECISION SEED METERING DEVICE WITH MULTIPLE-SEED-PER-HILL BASED ON DEM

/

基于离散元的一穴多粒气吸式精密排种器组合型搅种盘设计与仿真

Zhiwei WANG[1)], Deyi ZHANG[1)], Sugirbay ADILET[2)], Naishuo WEI[1)], Yanwu JIANG[1)], Jianguo ZHOU[1)], Jun CHEN[1*)]

[1)] College of Mechanical and Electronic Engineering, Northwest A&F University, Yangling, Shaanxi, 712100, China

[2)] Research School of Veterinary Medicine and Agriculture, Shakarim University, Semey 071400, Kazakhstan

Corresponding author: Jun Chen. E-mail address: chenjun_jdxy@nwsuaf.edu.cn

DOI: https://doi.org/10.35633/inmateh-79-01

Keywords: *Small-seeded crops, Seed filling, Particle mobility, Multi-sphere modelling, Response surface methodology (RSM), Bench validation*

ABSTRACT

To improve the seed-filling performance of pneumatic precision seed metering devices for small-seeded crops, a U-shaped seed agitation plate and a combined-type agitation plate were developed. The agitation performance of cylindrical, U-shaped, and combined-type agitation plates was evaluated using the average and maximum velocities of the seed population as quantitative indicators. A three-factor, three-level simulation experiment based on the Discrete Element Method (DEM) was conducted, with agitation plate type, rotational speed, and knob height as the main factors. The optimal parameter combinations were determined as follows: for millet, a combined-type agitation plate with a rotational speed of 24.85 r/min and a knob height of 8.36 mm; for broomcorn millet, 24.17 r/min and 7.96 mm; and for rapeseed, 22.93 r/min and 8.57 mm. Bench experiments were carried out to validate the optimized combined-type agitation plate. The seed-filling rates reached 99.3%, 100%, and 99.7% for millet, broomcorn millet, and rapeseed, respectively. The results indicate that the combined-type agitation plate significantly improves seed mobility and filling performance, providing an effective solution for precision seeding of small-seeded crops.

摘要

针对小籽粒气吸式排种器搅种效果不佳而使得排种盘充种效果差的问题，本研究设计了一种 U 型搅种钮和组合型搅种钮。为了对比和验证圆柱型、U 型、组合型三种搅种盘的搅种质量，以种群在搅种过程中的平均速度和最大速度为评价指标，选取搅种盘类型、搅种盘转速、搅种钮高度为试验因素利用 EDEM 离散元仿真软件对其进行了三因素三水平正交仿真试验，得到了谷子最佳参数组合为组合型搅种盘、作业速度 24.85r/min、搅种钮高度 8.36 mm，糜子最佳参数组合为组合型搅种盘、作业速度 24.17 r/min、搅种钮高度 7.96mm，油菜籽最佳参数组合为组合型搅种盘、作业速度 22.93 r/min、搅种钮高度 8.57 mm。通过台架试验对谷子，糜子，油菜籽种群搅种钮高度分别为 8.4 mm、8.0 mm、8.6 mm 时在最低工作速度 10r/min 时的搅种效果进行验证，组合型搅种盘对应三类种子的充种率分别为 99.3%、100%和 99.7%，优于圆柱形和 U 型搅种盘。试验证明组合型搅种盘具有良好的搅种效果，能够满足小籽粒种子的搅种需求。

INTRODUCTION

Millet, broomcorn millet, and rapeseed are important grain and economic crops in Northwest China. Due to the region's arid climate, limited precipitation, and relatively low temperatures, plastic film mulching is widely adopted in crop production *(Bai et al., 2025)*. In addition, because of the low emergence rate of small-seeded crops, hill-drop sowing with multiple seeds per hole is commonly used *(Tan et al., 2025)*.

To improve the seeding quality and efficiency of small seeds, pneumatic precision seed metering devices capable of multi-grain seeding per hole have been increasingly developed *(Gaikwad et al., 2008; Zhang et al., 2015; Rezaei et al., 2019; Yu et al., 2024)*. However, the small size, low mass, and impurity content of these seeds often result in poor flowability within the seed chamber. This leads to insufficient seed filling or seed leakage at the suction holes of the metering plate, thereby reducing seeding stability. To address this issue, seed agitation devices are introduced to enhance seed flowability and improve seed-filling performance. During operation, agitation knobs interact with seeds through contact, extrusion, and collision, promoting particle mobility within the seed chamber *(Yazgi et al., 2007; Onal et al., 2012; Ibrahim et al., 2018; Wang et al., 2023; Li et al., 2025; Li et al., 2026)*.

Previous studies have proposed various methods to improve seed flowability and filling performance. For example, *Shi et al. (2020)* designed a pneumatic combined-hole precision seed metering device with an integrated agitation mechanism, which enhanced seed filling through shaped holes and guided airflow. *Cong et al. (2014)* developed a dual-purpose pneumatic seed metering device with embedded guiding strips to improve seed distribution. *Ren et al. (2024)* improved seed flowability by arranging curved grooves and shaped holes in a staggered configuration. *Lei et al. (2016)* proposed a cylindrical double-helix agitation device to enhance wheat seed mobility, while *Wang et al. (2019)* designed a wedge-shaped agitation structure to improve seeding accuracy in rice seeders. *Li et al. (2019)* and *Li et al. (2024)* further optimized agitation structures to improve seed filling and reduce seed damage under high-speed conditions. International studies have likewise shown that the operating parameters and auxiliary filling structures of pneumatic seed metering devices strongly affect metering performance and crop adaptability *(Singh et al., 2005; Karayel et al., 2022)*, and a recent review further highlighted the growing importance of coupled numerical and experimental approaches in the development of pneumatic seed-metering devices *(Bustos-Gaytán et al., 2025)*.

Although these studies have demonstrated the importance of agitation devices in improving seed flowability and filling performance, most designs focus on specific crops or operating conditions. Systematic research on universal agitation devices suitable for multiple small-seeded crops remains limited. The novelty of this paper lies in the design of a combined-type agitation plate, the DEM-based mechanistic comparison of three knob configurations, and the parameter optimization of a single structure applicable to three representative small-seeded crops.

Preliminary experiments in this study revealed that, for millet, broomcorn millet, and rapeseed, insufficient agitation leads to seed leakage and blockage of suction holes by impurities. Therefore, a U-shaped and a combined-type seed agitation plate were designed to improve seed flowability and stability. Based on DEM simulations using EDEM, the key factors affecting agitation performance were analyzed. A three-factor, three-level experimental design was then conducted to determine the optimal parameter combination of the agitation plate. The results provide a theoretical and technical basis for the design of universal pneumatic precision seed metering systems for small-seeded crops.

MATERIAL AND METHODS

Design and working principle of the seed agitation plate

As shown in Fig. 1, three agitation-knob configurations were designed for the seed agitation plate: cylindrical, U-shaped, and combined types (a combination of cylindrical and U-shaped structures). The agitation plate was designed to be positioned close to the circumferential region of the suction holes on the seed metering plate, while avoiding interference with the seed-cleaning mechanism. In addition, the height of the agitation knobs was optimized to ensure effective seed disturbance without interfering with surrounding components such as the seed chamber housing.

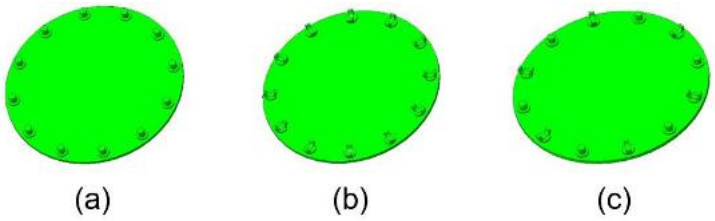


Fig. 1 - Agitation-knob configurations of the seed agitation plate

(a) Cylindrical type; (b) U-shaped type; (c) Combined type

As shown in Fig. 2, the geometric parameters of the seed agitation plate and agitation knobs are illustrated. To ensure effective interaction between the agitation knobs and the seed population, while maintaining sufficient clearance for the seed-cleaning mechanism, the diameter of the agitation plate (D) and the spacing between symmetrically arranged knobs (d_1) were designed according to the dimensions of the seed metering plate. Simulation-based pre-experiments demonstrated that many factors have negligible effects on the seed-agitating performance. Therefore, considering the matching compatibility with the seed metering plate, the parameters were set as follows: D = 160 mm, d_1 = 140 mm, h_{12} = 2 mm, k_{12} = 10 mm, k_{21} = 3 mm, and d_2 = 10 mm.

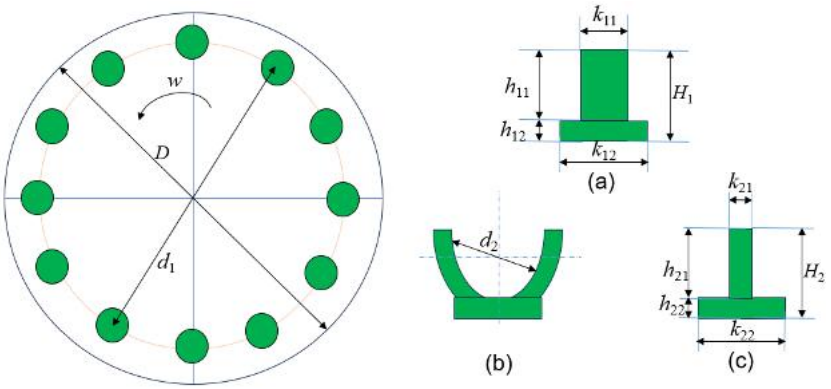


Fig. 2 - Geometric configuration of the seed agitation

(a) Front view of cylindrical type; (b) Front view of U-shaped type; (c) Front view of combined type

A pedestal structure was first introduced on the metering plate, on which the cylindrical and U-shaped agitation knobs were mounted. The number and arrangement of the knobs were determined based on uniform circumferential distribution and sufficient interaction coverage with the seed population. In this study, twelve agitation knobs were evenly distributed along the circumference of the agitation plate.

Considering key factors such as knob geometry, rotational speed of the metering plate, and knob height, the agitation performance was further analyzed using DEM simulations.

DEM-based simulation and analysis of the seed agitation process

Seed particle modeling

Statistical analysis indicated low variability among the effective seed samples. Therefore, one representative seed from each type (millet, broomcorn millet, and rapeseed) was selected for three-dimensional (3D) reconstruction.

Each selected seed was scanned using a portable 3D scanner (EinScan, accuracy ≤ 0.02 mm, Shenzhen Xinlin 3D Co., Ltd., China) to obtain its geometric morphology. The scanned data were processed in VxElements software, including calibration, alignment, mesh generation, and surface reconstruction. The resulting 3D models were exported in STL format.

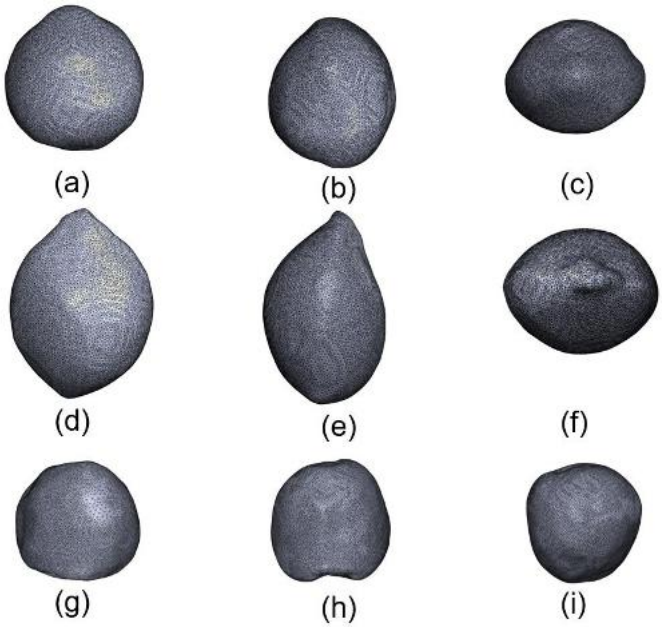


Fig. 3 - 3D reconstructed models of seeds

(a–c) Millet; (d–f) Broomcorn millet; (g–i) Rapeseed

The STL models were subsequently imported into SolidWorks 2021 for visualization, and the corresponding views of the three seed types are shown in Fig. 3.

For DEM simulation in EDEM, the Hertz–Mindlin (no-slip) contact model was used in this simulation, the seed particles were constructed using a multi-sphere approximation method based on the scanned 3D geometries. The millet, broomcorn millet, and rapeseed models were composed of six, eight, and seven spheres, respectively, to balance computational efficiency and shape accuracy.

Because the effective seed samples exhibited relatively small dimensional variation, one representative seed from each crop was used to establish the multi-sphere model. This strategy is suitable for comparative analysis of knob configuration and operating parameters, but it cannot fully represent seed-size dispersion, broken seeds, or impurity particles in real seed lots. Therefore, the present DEM model should be regarded as a simplified but representative model, and its engineering validity was further checked through bench experiments.

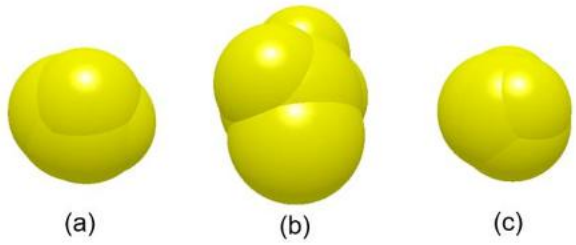


Fig. 4 - Multi-sphere particle models used in EDEM

(a) Millet; (b) Broomcorn millet; (c) Rapeseed

The material and contact parameters used in the simulation were defined based on experimental measurements and literature values *(Yazgi et al., 2007; Onal et al., 2012; Ibrahim et al., 2018; Cui et al., 2025; He et al., 2025; Wang et al., 2025; Zhang et al., 2025)*, as summarized in Table 1.

Table 1

The mechanics parameters of different parts

Item	Value （millet, broomcorn millet, and rapeseed）
Poisson's ratio of seeds	0.27/0.33/0.29
Shear modulus of seeds [Pa]	（1.4/2.6/0.53）×10^8
Seed density [kg/m³]	1015.6/907.7/1132.5
Coefficient of restitution (seed–metering plate)	0.37/0.35/0.41
Dynamic friction coefficient (seed–metering plate)	0.015/0.019/0.017
Static friction coefficient (seed–metering plate)	0.481/0.317/0.387
Coefficient of restitution (seed–agitation knob)	0.35/0.30/0.33
Dynamic friction coefficient (seed–agitation knob)	0.009/0.006/0.011
Static friction coefficient (seed–agitation knob)	0.406/0.331/0.371
Coefficient of restitution (seed–seed)	0.23/0.21/0.27
Dynamic friction coefficient (seed–seed)	0.022/0.015/0.019
Static friction coefficient (seed–seed)	0.46/0.38/0.41
Coefficient of restitution (seed–housing)	0.37/0.33/0.45
Dynamic friction coefficient (seed–housing)	0.021/0.013/0.019
Static friction coefficient (seed–housing)	0.577/0.467/0.517

Construction of DEM model and simulation setup

The three-dimensional model of the seed metering device was developed in SolidWorks 2021, exported in STL format, and imported into EDEM for simulation. The material properties and contact parameters were assigned according to the values listed in Table 1.

A particle generation region was defined at the seed inlet to simulate seed feeding. The particle generation rate of 10,000 particles/s and the total particle number of 40,000 were determined through preliminary simulation trials to ensure rapid chamber filling, continuous particle coverage in the working region around the agitation plate, and stable response values without excessive computational cost. The initial falling velocity of 2 m/s was assigned to allow the particles generated at the inlet to enter the seed chamber smoothly and to avoid artificial accumulation near the particle factory.

Particle generation lasted for 4 s to complete chamber filling, followed by a settling period of approximately 2 s. When the particle velocity decreased below 0.01 m/s, the seed bed was considered to reach a quasi-static state, after which the rotational simulation was initiated.

The metering plate and agitation plate were then assigned rotational motion. Taking a rotational speed of 20 r/min as an example, the angular velocity was set to 120°/s, with rotation about the central axis of the metering plate. The simulation time step was set to 20% of the Rayleigh time step, and the total simulation time was 3 s so that a sufficiently long stable agitation interval could be captured for statistical analysis.

Post-processing and evaluation indices

In the EDEM post-processing module, the velocity distribution of seed particles was visualized using a color scale, where red indicates high velocity and blue indicates low velocity (Fig. 5). The velocity field reflects the agitation intensity induced by the agitation plate.

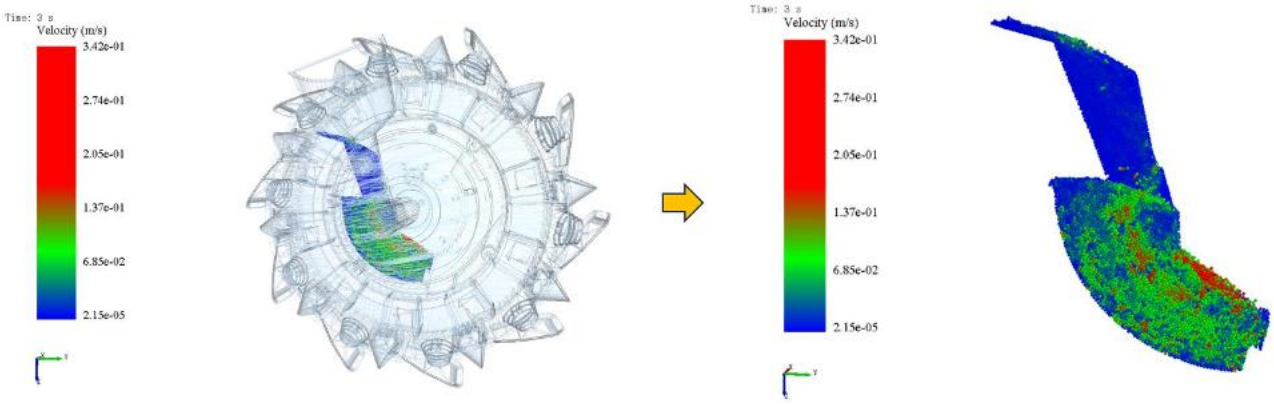


Fig. 5 - Velocity distribution of seed particles during agitation

To quantitatively evaluate the agitation performance, the average velocity and maximum velocity of the seed population were selected as the primary DEM indicators. These two indices reflect the overall particle mobility and the local disturbance intensity in the filling zone, respectively, and are therefore closely related to the seed replenishment capacity near the suction-hole circumferential region. In addition, the seed-filling rate obtained from the bench test was used as an engineering validation index. Because the present DEM model was simplified to facilitate comparative structural optimization, contact frequency and spatial uniformity of particles were not extracted in this study and are discussed as limitations.

Preliminary simulation results

As shown in Fig. 6, the temporal variations of average and maximum velocities for different agitation plate configurations are presented. During the initial stage (0–0.3 s), the velocity curves fluctuate due to startup effects. After 0.3 s, the system reaches a relatively stable state. Therefore, the interval of 0.3–3.0 s was selected for statistical analysis.

Under a rotational speed of 20 r/min and an agitation knob height of 8.0 mm, the average velocities of the seed population for the cylindrical, U-shaped, and combined-type agitation plates were 0.0148 m/s, 0.0153 m/s, and 0.0167 m/s, respectively. The corresponding maximum velocities were 0.3593 m/s, 0.3641 m/s, and 0.4086 m/s.

These results indicate that the geometry and configuration of agitation knobs significantly influence seed agitation performance. The combined-type agitation plate exhibited superior performance compared with the other configurations. Therefore, further analysis considering additional factors is necessary.

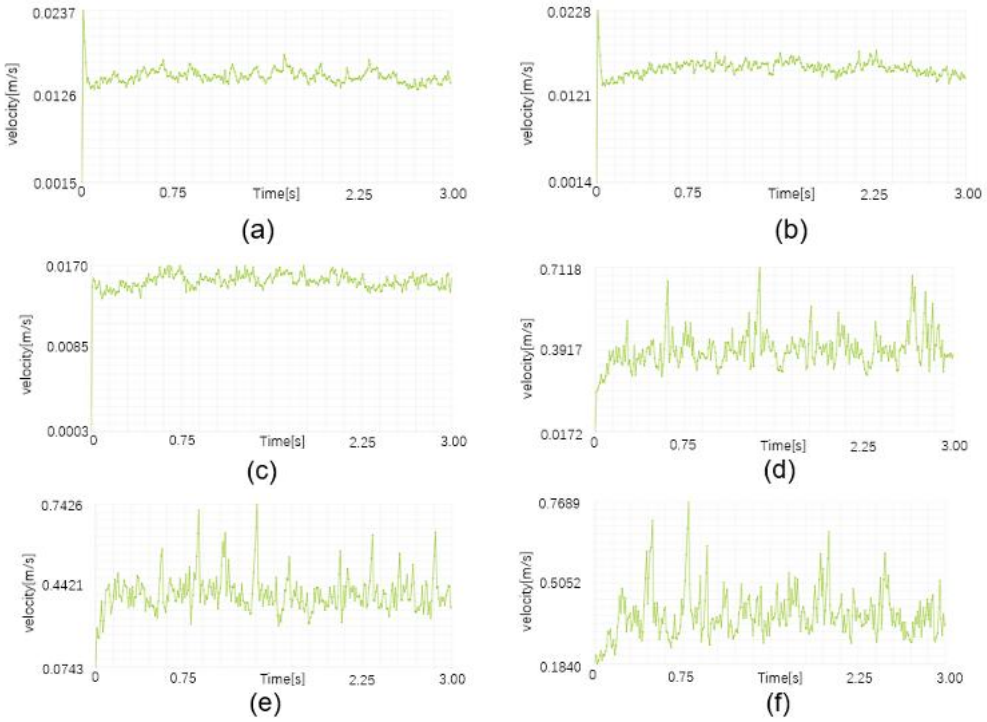


Fig. 6 - Time-dependent velocity curves of seed particles

(a–c) Average velocity each for millet, broomcorn millet, rapeseed;
(d–f) Maximum velocity each for millet, broomcorn millet, rapeseed

Response surface design

Based on the simulation results and preliminary analysis, the agitation knob type, rotational speed of the agitation plate, and agitation knob height were identified as the primary factors influencing seed agitation performance.

Three types of agitation knobs—cylindrical, U-shaped, and combined—were selected as factor X_1. According to the typical operating speed range of seed metering devices (2.0–5.0 km/h), the corresponding rotational speed of the metering plate ranges from 10 to 27 r/min. Therefore, three representative levels (15, 20, and 25 r/min) were selected for factor X_2. Considering the structural constraints and clearance between the agitation knobs and adjacent components (e.g., seed chamber housing and seed-cleaning mechanism), the feasible range of knob height was determined to be 0–15 mm. Accordingly, three levels (6.0, 8.0, and 10.0 mm) were selected for factor X_3 *(Han et al., 2018; Liu et al., 2022; Gao et al., 2023; Ding et al., 2024)*.

A three-factor, three-level response surface design generated in Design-Expert 8.0.6 was adopted, resulting in 17 simulation runs with five center-point replications. Quadratic regression models were then established for the two response variables, and the coded levels of the factors are listed in Table 2.

Table 2

Factor levels used in the experimental design

Code	Agitation knob type (X_1)	Rotational speed (X_2) [r/min]	Agitation knob height (X_3) [mm]
-1	A: Cylindrical	15	6.0
0	B: U-shaped	20	8.0
1	C: Combined	25	10.0

Bench validation of seed-filling performance

Because low rotational speed provides the weakest particle disturbance and therefore the most stringent condition for maintaining seed filling, bench experiments were conducted at the minimum operating condition of the seed metering device (10 r/min, corresponding to a forward speed of 2.0 km/h). Validation under this condition was used to verify whether the optimized structure could still ensure adequate seed replenishment under the least favorable agitation state. The agitation knob height was set according to the optimized simulation results.

However, the present validation was limited to low-speed bench conditions, and further experiments over the full operating-speed range are still required.

The experiments were carried out using a JPS-12 seed metering performance test bench (Heilongjiang Provincial Agricultural Machinery Research Institute, China). The system mainly consists of a seedbed belt, a metering device mounting frame, a hydraulic system, and a high-speed imaging system. The bench has a total length of 9.5 m, a belt width of 0.7 m, and an adjustable forward speed range of 1.5–12.0 km/h. The high-speed camera was operated at 300 frames per second (fps), and the recorded images were processed using i-SPEED Control Software.

Due to the difficulty in directly quantifying seed agitation through visual observation, the seed-filling rate was selected as the engineering validation index of agitation performance. Improved agitation enhances seed mobility in the filling zone, weakens local seed crowding, and reduces the probability of insufficient filling at the suction holes.

For each seed type (millet, broomcorn millet, and rapeseed), corresponding to three different types of seed agitating plates (cylindrical, U-shaped, and combined), 300 consecutive seeding events were recorded for each treatment. The filling and missing conditions of seeds in each hill were captured through a transparent seed chamber using both a high-speed camera and a mobile camera. The average seed-filling rate was calculated based on the recorded data.

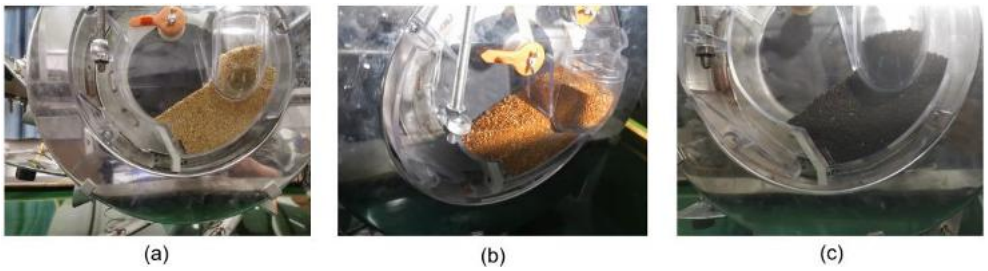


Fig. 7 - Bench validation of seed-filling performance

(a) Millet; (b) Broomcorn millet; (c) Rapeseed

RESULTS AND DISCUSSION

Results and analysis of the experimental design

A three-factor, three-level response surface experiment was conducted using Design-Expert software, resulting in 17 simulation runs. The average velocity (Y_1) and maximum velocity (Y_2) of the seed population were selected as response variables to evaluate agitation performance. The experimental design and corresponding results are summarized in Table 3.

Table 3

Experiment scheme and results

No.	X_1	X_2	X_3	Y_1 [m/s]	Y_2 [m/s]
1	-1	-1	0	0.0152	0.3593
2	1	-1	0	0.0153	0.3651
3	-1	1	0	0.0158	0.3742
4	1	1	0	0.0166	0.4029
5	-1	0	-1	0.0150	0.3621
6	1	0	-1	0.0154	0.3642
7	-1	0	1	0.0152	0.3733
8	1	0	1	0.0161	0.3821
9	0	-1	-1	0.0148	0.3599
10	0	1	-1	0.0153	0.3707
11	0	-1	1	0.0155	0.3642
12	0	1	1	0.0166	0.3964
13	0	0	0	0.0159	0.3848

No.	X_1	X_2	X_3	Y_1 [m/s]	Y_2 [m/s]
14	0	0	0	0.0157	0.3774
15	0	0	0	0.0160	0.3753
16	0	0	0	0.0163	0.3842
17	0	0	0	0.0163	0.3898

Regression modeling and ANOVA

The experimental results were analyzed to obtain polynomial regression equations, in which the average population velocity and the maximum population velocity were taken as the response variables, and the coded values of the factors were used as independent variables, as follows:

$$Y_1 = 0.016 + 0.000275X_1 + 0.0004375X_2 + 0.0003625X_3 + 0.000175X_1X_2 + 0.000125X_1X_3 + 0.00015X_2X_3 - 0.00022X_1^2 - 0.000095X_2^2 - 0.000395X_3^2 \quad (1)$$

$$Y_2 = 0.38 + 0.005675X_1 + 0.012X_2 + 0.007388X_3 + 0.005725X_1X_2 + 0.001675X_1X_3 + 0.00535X_2X_3 - 0.00465X_1^2 - 0.002275X_2^2 - 0.007225X_3^2 \quad (2)$$

Quadratic regression models were developed for both response variables (Y_1 and Y_2) based on the coded factors. Analysis of variance (ANOVA) results (Tables 4 and 5) indicate that both models are statistically significant ($p < 0.05$), with no significant lack-of-fit ($p > 0.05$), confirming the adequacy of the regression models.

Table 4

ANOVA of the seed population average speed Y_1

Sources	Sum of squares	Degree of freedom	Mean square	*F*	*p*
Model	4.43×10^{-6}	9	4.93×10^{-7}	7.59	0.0070
X_1	6.05×10^{-7}	1	6.05×10^{-7}	9.32	0.0185
X_2	1.53×10^{-6}	1	1.53×10^{-6}	23.58	0.0018
X_3	1.05×10^{-6}	1	1.05×10^{-6}	16.19	0.0050
X_1X_2	1.2325×10^{-7}	1	1.2325×10^{-7}	1.8867	0.2119
X_1X_3	6.2516×10^{-8}	1	6.2516×10^{-8}	0.9626	0.3592
X_2X_3	9.2145×10^{-8}	1	9.2145×10^{-8}	1.3861	0.2775
X_1^2	2.0403×10^{-7}	1	2.0403×10^{-7}	3.1387	0.1198
X_2^2	3.8624×10^{-8}	1	3.8624×10^{-8}	0.5853	0.4693
X_3^2	6.5746×10^{-7}	1	6.5746×10^{-7}	10.1180	0.0155
Lack of fit	1.83×10^{-7}	3	6.08×10^{-8}	0.89	0.5171
Pure error	2.72×10^{-7}	4	6.81×10^{-8}		
Total	4.89×10^{-6}	16			

Table 5

ANOVA of the seed population maximum speed Y_2

Sources	Sum of squares	Degree of freedom	Mean square	*F*	*p*
Model	2.46×10^{-3}	9	2.73×10^{-4}	8.67	0.0047
X_1	2.58×10^{-4}	1	2.58×10^{-4}	8.18	0.0244
X_2	1.15×10^{-3}	1	1.15×10^{-3}	36.33	0.0005
X_3	4.37×10^{-4}	1	4.37×10^{-4}	13.85	0.0074
X_1X_2	1.3112×10^{-4}	1	1.3112×10^{-4}	4.1601	0.0808
X_1X_3	1.1277×10^{-5}	1	1.1277×10^{-5}	0.3561	0.5695
X_2X_3	1.1403×10^{-4}	1	1.1403×10^{-4}	3.6330	0.0983
X_1^2	9.1227×10^{-5}	1	9.1227×10^{-5}	2.8889	0.1330

Sources	Sum of squares	Degree of freedom	Mean square	*F*	*p*
X_2^2	2.1873×10^{-5}	1	2.1873×10^{-5}	0.6915	0.4331
X_3^2	2.2746×10^{-4}	1	2.2746×10^{-4}	6.9743	0.0334
Lack of fit	8.15×10^{-5}	3	2.72×10^{-5}	0.78	0.5632
Pure error	1.39×10^{-4}	4	3.48×10^{-5}		
Total	2.68×10^{-3}	16			

For both response variables, the main factors X_1 (agitation knob type), X_2 (rotational speed), and X_3 (knob height) significantly affected the results ($p < 0.05$), while interaction terms were generally insignificant. The quadratic term X_3^2 also showed a significant effect, indicating a nonlinear relationship between knob height and agitation performance.

Effect of factors on average velocity (Y_1)

The response surfaces for the average velocity are shown in Fig. 8. Among the three factors, rotational speed (X_2) exhibited the most significant influence, followed by knob height (X_3), while knob type (X_1) had a relatively smaller effect.

As the knob configuration changed from cylindrical to U-shaped and then to the combined type, the average velocity of the seed population increased. The cylindrical part mainly breaks the compact seed layer and promotes upward and radial displacement, whereas the U-shaped part provides a temporary guiding and holding space for particles. Their combination extends the particle-structure interaction path, increases the disturbance depth, and reduces the low-mobility region near the chamber wall, thereby improving continuous seed replenishment around the suction-hole zone.

With increasing rotational speed, the average velocity increased monotonically because more kinetic energy was transferred from the rotating structure to the seed population per unit time. In contrast, knob height exhibited a quadratic effect. When the height was too small, the disturbance depth was insufficient and only the superficial seed layer was mobilized. When the height became excessive, particles were overly squeezed toward the chamber wall, leading to local congestion and a reduction in overall particle circulation.

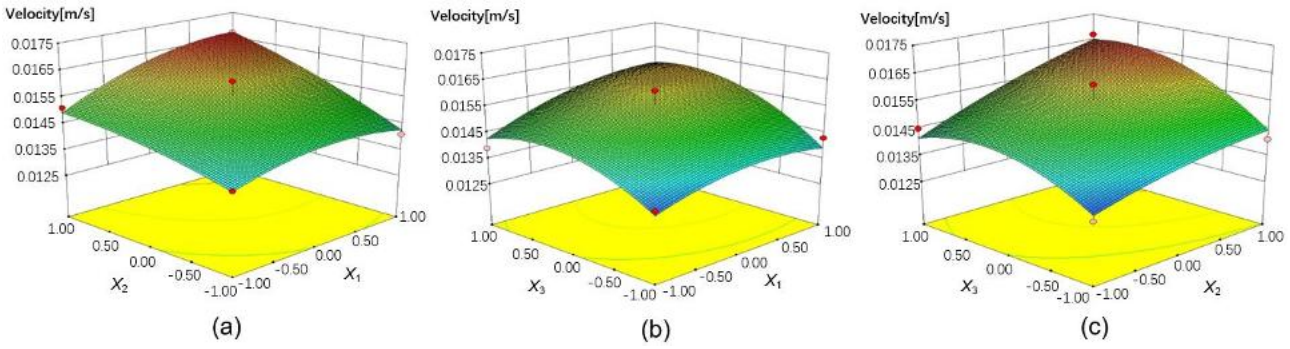


Fig. 8 - Response surfaces to influences of different factors on the seed population average speed

(a) X_1 and X_2; (b) X_1 and X_3; (c) X_2 and X_3

Effect of factors on maximum velocity (Y_2)

The response surfaces for maximum velocity are presented in Fig. 9. Similar trends were observed for Y_2 as for Y_1. Rotational speed remained the most influential factor, followed by knob height, while knob type had the least effect. Compared with the average velocity, the maximum velocity responds more sensitively to local strong interactions between the knob and nearby particles.

Increasing rotational speed significantly enhanced the maximum velocity of seed particles because the instantaneous particle-structure interaction became stronger. The influence of knob height also exhibited a nonlinear effect. An excessively large knob height reduced the free-movement space of particles and converted part of the agitation effect into compressive crowding rather than effective acceleration.

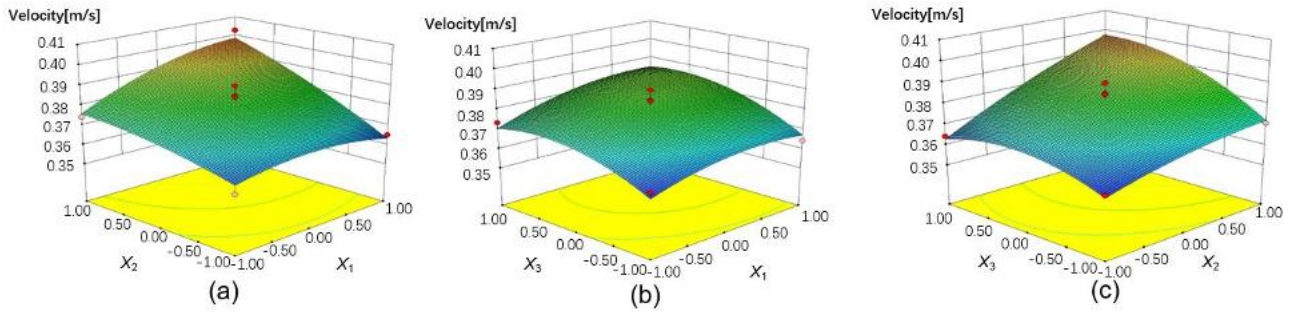


Fig. 9 - Response surfaces to influences of different factors on the seed population maximum speed
(a) X_1 and X_2; (b) X_1 and X_3; (c) X_2 and X_3

The consistent trends observed for both response variables confirm the reliability of the simulation results. From an engineering perspective, the superior performance of the combined-type agitation plate indicates that a moderate increase in particle mobility is beneficial to low-speed seed filling. Because the agitation mechanism is mounted on the existing rotating plate and operates within a relatively low speed range, its additional energy demand is expected to be limited. Moreover, the disturbance mode is dominated by pushing and rolling rather than high-energy impact, so obvious seed damage is not expected. However, direct seed-damage and germination tests were not conducted in this study, and these aspects should be included in future work. The proposed structure can also be extended to other small-seeded crops by re-matching the knob height, chamber clearance, and rotational speed according to seed size and flowability.

Optimization of parameters

Based on the regression models, the optimal parameter combinations were obtained for each seed type. For millet, the optimal configuration was a combined-type agitation plate with a rotational speed of 24.85 r/min and a knob height of 8.36 mm. For broomcorn millet, the optimal parameters were 24.17 r/min and 7.96 mm, while for rapeseed, the optimal values were 22.93 r/min and 8.57 mm.

The results indicate that the combined-type agitation plate consistently provides superior agitation performance across all seed types.

The simulation results demonstrate that agitation performance improves with increasing rotational speed. However, to ensure practical applicability, the optimized design must also perform effectively under low-speed conditions. Therefore, validation experiments were conducted at the minimum operating speed (10 r/min) using the optimized knob heights for each seed type. This choice represents the most unfavorable agitation condition for the device; nevertheless, the present experimental verification is still limited to low-speed bench conditions, and future studies should extend the validation to the full operating-speed range and integrated field conditions.

Bench test validation results

As shown in Fig. 10, the seed-filling performance of the seed holes on the seed plate after the agitation process is presented.

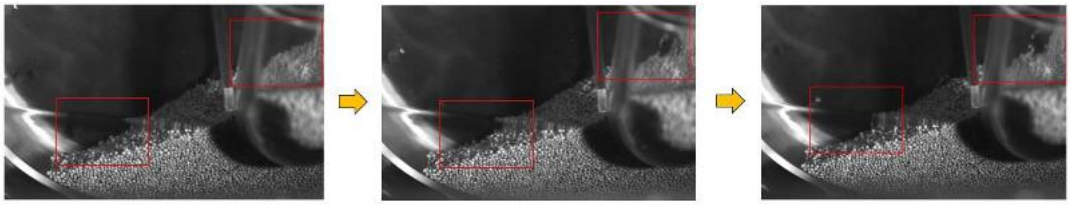


Fig. 10 - Variation of the millet population under the action of the combined agitation plate

The filling condition was analyzed and statistically evaluated on a hole-by-hole basis using recordings from a high-speed camera and a mobile phone. Under the conditions where multiple-seed adsorption was neglected and the seed-cleaning device was not activated, the results indicate that at an operating speed of 10 r/min, for the combined agitation plate, the seed-filling rates of millet, broomcorn millet, and rapeseed were 99.3%, 100%, and 99.7%, respectively; for the cylindrical seed agitation plate, the corresponding seed-filling rates were 94.3%, 97.0%, and 96.3%, respectively; and for the U-shaped seed agitation plate, the corresponding values were 97.3%, 98.7%, and 98.0%, respectively. These results demonstrate that the combined seed agitation plate exhibits superior agitation performance compared with the other two types, thereby satisfying the design requirements of the seed agitation mechanism of the seed metering device.

CONCLUSIONS

This study developed U-shaped and combined-type agitation plates to improve the agitation performance of pneumatic seed metering devices for small-seeded crops. Based on DEM simulations and bench validation experiments, the following conclusions were obtained.

(1) The agitation performance of cylindrical, U-shaped, and combined-type configurations was systematically evaluated using the average and maximum velocities of seed particles as response variables. The combined-type agitation plate exhibited superior performance compared with the other two configurations.

(2) A three-factor, three-level experimental design was conducted to analyze the effects of agitation plate type, rotational speed, and knob height. The optimal parameter combinations were identified as follows: for millet, 24.85 r/min and 8.36 mm; for broomcorn millet, 24.17 r/min and 7.96 mm; and for rapeseed, 22.93 r/min and 8.57 mm, all with the combined-type agitation plate.

(3) Bench validation experiments confirmed that, under the minimum operating speed of 10 r/min, the optimized agitation configurations achieved high seed-filling rates of 99.3%, 100%, and 99.7% for millet, broomcorn millet, and rapeseed, respectively. These results demonstrate that the proposed agitation plate effectively enhances seed-filling performance and meets the operational requirements of precision seeding under the least favorable agitation condition.

The proposed design provides a practical structural option for improving the low-speed filling stability of pneumatic precision seed metering devices for millet, broomcorn millet, and rapeseed. Future studies should incorporate seed-size distributions and impurity particles into the DEM model and carry out seed-damage, germination, full-speed bench, and integrated field validations.

ACKNOWLEDGEMENT

This study was supported by the National Natural Science Foundation of China (32272001), the Shaanxi Key Research and Development Project (2023-ZDLNY-62), and the Shaanxi Key Research and Development Project (grant number 2022NY-205).

REFERENCES

[1] Bai S., Yuan Y., Niu K., Zhou L., Zhao B., & Yu Y. (2025). Design and test of operation quality monitoring system for cotton precision film-laying hole seeder (棉花精量铺膜穴播机作业质量监测系统设计与试验). *Transactions of the Chinese Society for Agricultural Machinery*, 56(5), 49-58. https://doi.org/10.6041/j.issn.1000-1298.2025.05.005

[2] Bustos-Gaytán A., Saldaña-Robles N., Joya-Cárdenas D.R., Gutiérrez-Vaca C., Alfaro-Ayala J.A., Barco-Burgos J., & Saldaña-Robles A. (2025). Advancements in pneumatic seed-metering devices: A review of numerical and experimental approaches. *Results in Engineering*, 26, 105626. https://doi.org/10.1016/j.rineng.2025.105626

[3] Cong J., Liao Q., Cao X., Liao Y., Yu J., & Wang L. (2014). Seed filling performance of dual-purpose seed plate in metering device for both rapeseed & wheat seed (油菜小麦兼用排种盘的排种器充种性能). *Transactions of the Chinese Society of Agricultural Engineering*, 30(8), 30-39. https://doi.org/10.3969/j.issn.1002-6819.2014.08.004

[4] Cui Y., Ye S., Feng S., & Zheng D. (2025). Calibration of discrete element simulation parameters for buckwheat seeds. *INMATEH Agricultural Engineering*, 75(1), 110-120. https://doi.org/10.35633/inmateh-75-09

[5] Ding L., Yuan Y., Dou Y., Li C., He Z., Guo G., Zhang Y., Chen B., & Li H. (2024). Design and experiment of air-suction maize seed-metering device with auxiliary guide. *Agriculture*, 14(2), 169. https://doi.org/10.3390/agriculture14020169

[6] Gaikwad B.B., & Sirohi N.P.S. (2008). Design of a low-cost pneumatic seeder for nursery plug trays. Biosystems Engineering, 99(3), 322-329. https://doi.org/10.1016/j.biosystemseng.2007.10.017

[7] Gao X., Xie G., Li J., Shi G., Lai Q., & Huang Y. (2023). Design and validation of a centrifugal variable-diameter pneumatic high-speed precision seed-metering device for maize. *Biosystems Engineering*, 227, 161-181. https://doi.org/10.1016/j.biosystemseng.2023.02.004

[8] Han D., Zhang D., Jing H., Yang L., Cui T., Ding Y., Wang Z., Wang Y., & Zhang T. (2018). DEM-CFD coupling simulation and optimization of an inside-filling air-blowing maize precision see

d-metering device. *Computers and Electronics in Agriculture*, 150, 426-438. https://doi.org/10.1016/j.compag.2018.05.006

[9] He Y., Ji X., Dun G., Liu X., Mu A., & Ma, C. (2025). Discrete element simulation calibration of contact parameters for millet seeds. *INMATEH Agricultural Engineering*, 76(2), 686-696. https://doi.org/10.35633/inmateh-76-58

[10] Ibrahim, E. J., Liao, Q., Wang, L., Liao, Y., & Yao, L. (2018). Design and experiment of multi-row pneumatic precision metering device for rapeseed. *International Journal of Agricultural and Biological Engineering*, 11(5), 116-123. https://doi.org/10.25165/j.ijabe.20181105.3544

[11] Karayel D., Barut Z.B., & Özmerzi A. (2022). Estimation of optimum vacuum pressure of air-suction seed-metering device of precision seeders using artificial neural network models. *Agronomy*, 12(7), 1600. https://doi.org/10.3390/agronomy12071600

[12] Lei X., Liao Y., Li Z., Zhang W., Li S., & Liao Q. (2016). Design of seed churning device in air-assisted centralized metering device for rapeseed and wheat and experiment on seed filling performance (油菜小麦兼用气送式集排器搅种装置设计及充种性能试验). *Transactions of the Chinese Society of Agricultural Engineering*, 32(18), 26-34. https://doi.org/10.11975/j.issn.1002-6819.2016.18.004

[13] Li H., Yang Li, Zhang D., Cui T., He X., & Li Z. (2026). Seed motion and force characteristics in pneumatic seed delivery device based on CFD-DEM coupling (基于 CFD-DEM 耦合的气力式导种装置中种子运动与受力研究). *Transactions of the Chinese Society for Agricultural Machinery*, 57(6), 104-118. https://doi.org/10.6041/j.issn.1000-1298.2026.06.010

[14] Li X., Liao Q., Du W., Wang X., Liao Y., & Yuan J. (2024). Damage patterns and germination experiments of rice seeds using high-speed air-assisted centralized seed metering device (高速气送集排器水稻种子损伤规律及发芽试验). *Transactions of the Chinese Society of Agricultural Engineering*, 40(21), 46-55. https://doi.org/10.11975/j.issn.1002-6819.202406072

[15] Li Z., An S., Yang Li, Zhang D., He X., & Cui T. (2025). Analysis and structural optimization of filling and releasing mechanism for pneumatic high-speed precision maize seed-metering device. *Transactions of the CSAM*, 56(9), 62-72，128. https://doi.org/10.6041/j.issn.1000-1298.2025.09.005

[16] Li Z., Yang W., Zhang T., Wang W., Zhang S., & Chen L. (2019). Design and suction performance test of sucking-seed plate combined with groove-tooth structure on high speed precision metering device of rapeseed (油菜高速精量排种器槽齿组合式吸种盘设计与吸附性能试验). *Transactions of the Chinese Society of Agricultural Engineering*, 35(1), 12-22. https://doi.org/10.11975/j.issn.1002-6819.2019.01.002

[17] Liu R., Liu Z., Zhao J., Lu Q., Liu L., & Li Y. (2022). Optimization and experiment of a disturbance-assisted seed filling high-speed vacuum seed-metering device based on DEM-CFD. *Agriculture*, 12(9), 1304. https://doi.org/10.3390/agriculture12091304

[18] Onal, I., Degirmencioglu, A., & Yazgi, A. (2012). An evaluation of seed spacing accuracy of a vacuum type precision metering unit based on theoretical considerations and experiments. *Turkish Journal of Agriculture and Forestry*, 36(2): 133-144. https://doi.org/10.3906/tar-1010-1316.

[19] Ren D., Liu Tao, Xia S., Chen Y., Wang W., & Li Z. (2024). Design and seed filling performance test of cavity plate combination hole type seeding plate for corn and soybean (玉米大豆兼用腔盘组合孔式排种盘设计与充种性能试验). *Transactions of the Chinese Society for Agricultural Machinery*, 55(2), 73-89. https://doi.org/10.6041/j.issn.1000-1298.2024.02.007

[20] Rezaei Asl A., Roudbari M., & Esmailzadeh E. (2019). Fabrication and evaluation of vacuumed metering drum performance for row planting of soybean with grease belt. *Agricultural Engineering International: CIGR Journal*, 21(4), 96-106.

[21] Shi S., Liu H., Wei G., Zhou J., Jian S., & Zhang R. (2020). Optimization and experiment of pneumatic seed metering device with guided assistant filling based on EDEM-CFD (基于 DEM-CFD 的驱导辅助充种气吸式排种器优化与试验). *Transactions of the Chinese Society for Agricultural Machinery*, 51(5), 54-66. https://doi.org/10.6041/j.issn.1000-1298.2020.05.006

[22] Singh R.C., Singh G., & Saraswat D.C. (2005). Optimisation of design and operational parameters of a pneumatic seed metering device for planting cottonseeds. *Biosystems Engineering*, 92 (4), 429-438. https://doi.org/10.1016/j.biosystemseng.2005.07.002

[23] Tan Y., Zhang Y., Jin Y., Liao Q., Li W., & Liao Y. (2025). Design and experiment of pneumatic-assisted seed collector for rapeseed and wheat. *Transactions of the CSAM*, 56(9), 105-116，187. https://doi.org/10.6041/j.issn.1000-1298.2025.09.009

[24] Wang B., Wang Z., Luo X., Zhang M., Fang L., Liu S., & Xu P. (2019). Design and experiment of wedge churning device for pneumatic cylinder-type seed metering device for hybrid rice (杂交稻气力滚筒集排式排种器楔形搅种装置设计与试验). *Transactions of the Chinese Society of Agricultural Engineering*, 35(23), 1-8. https://doi.org/10.11975/j.issn.1002-6819.2019.23.001

[25] Wang J., Sun W., Simionescu P. A., & Ju Y. (2023). Optimization of the fluted force-feed seeder meter with the helical roller using the discrete element method and response surface analysis. *Agriculture*, 13(7), 1400. https://doi.org/10.3390/agriculture13071400

[26] Wang Z., Hou Z., Bao L., Liu Y., Li B., & Guo F. (2025). Construction of ellipsoidal particle discrete element model and calibration of simulation parameters. *INMATEH - Agricultural Engineering*. 77(3), https://doi.org/10.35633/inmateh-77-108

[27] Yazgi, A., & Degirmencioglu, A. (2007). Optimisation of the seed spacing uniformity performance of a vacuum-type precision seeder using response surface methodology. *Biosystems Engineering*, 97(3): 347-356. https://doi.org/10.1016/j.biosystemseng.2007.03.013.

[28] Yu D., Peng F., Zeng Z., Zhang M., Yang W., Zang Y., He J., Huang Y., Wu Y., Zhong W., Guo Z., Liu J., Li G., Qin X., & Wang Z. (2024). Vibrational dynamics of rice precision hole seeders and their impact on seed dispensation efficacy. *Agriculture*, 14(2), 324. https://doi.org/10.3390/agriculture14020324

[29] Zhang D., Huang Z., Chen Y., Yi S., & Li Y. (2025). Discrete element method based modeling and parameter calibration for millet threshing mixture. *Transactions of the CSAM*, 56(12), 354-365. https://doi.org/10.6041/j.issn.1000-1298.2025.12.032

[30] Zhang G., Zang Y., Luo X., Wang Z., Zhang Q., & Zhang S. (2015). Design and indoor simulated experiment of pneumatic rice seed metering device. *International Journal of Agricultural and Biological Engineering*, 8(4), 10–18. https://doi.org/10.3965/j.ijabe.20150804.162645

SIMULATION AND OPTIMIZATION OF THE SEED METERING PLATE FOR AN AIR-SUCTION PRECISION SEED METERING DEVICE WITH MULTIPLE-SEED-PER-HILL BASED ON CFD

/

基于 CFD 的一穴多粒气吸式精密排种器排种盘仿真与优化

Zhiwei WANG[1)], Yanwu JIANG[1)], Deyi ZHANG[1)], Sugirbay ADILET[2)], Naishuo WEI[1)], Jianguo ZHOU[1)], Jun CHEN[1*)]

[1)] College of Mechanical and Electronic Engineering, Northwest A&F University, Yangling, Shaanxi, 712100, China

[2)] Research School of Veterinary Medicine and Agriculture, Shakarim University, Semey 071400, Kazakhstan

** Corresponding author: Jun Chen. E-mail address: chenjun_jdxy@nwsuaf.edu.cn*

DOI: https://doi.org/10.35633/inmateh-79-02

Keywords: *Small-seed crops, Pneumatic adsorption, Hill-drop sowing, Suction-hole pressure, Airflow-field mapping, Parameter optimization*

ABSTRACT

To enhance the seeding accuracy of multi-seed-per-hole operations for small-seed crops, a combined experimental-CFD optimization method for an air-suction seed metering plate was developed. Single-factor tests established that the suitable suction-hole diameter was 0.4-0.6 times the equivalent seed diameter, and threshold-based negative-pressure tests were used to define the acceptable suction-hole negative-pressure range for millet, broomcorn millet, and rapeseed. CFD pressure-tracing analysis was then performed to quantify the mapping between suction-hole pressure and air-chamber inlet negative pressure. On this basis, a three-factor, three-level optimization test was conducted using inlet negative pressure, suction-hole diameter, and suction-hole thickness as variables, with the qualification rate of suction-hole pressure as the response. The optimized parameter combinations were 2.51 kPa, 0.88 mm, and 0.31 mm for millet; 2.97 kPa, 1.12 mm, and 0.35 mm for broomcorn millet; and 2.35 kPa, 0.93 mm, and 0.32 mm for rapeseed. Bench validation showed seed-filling rates of 93%, 97%, and 96%, respectively. The results demonstrate that the proposed method can effectively reduce empirical trial workload and provide a practical basis for the design of pneumatic precision seed metering plates for small-seed crops.

摘要

为提高小籽粒作物一穴多粒作业的播种精度，本文提出了一种针对气吸式排种盘的 CFD 仿真试验联合优化方法。通过单因素试验确定，适宜的吸孔直径应为种子当量直径的 0.4～0.6 倍；同时，基于基准压力试验界定了谷子、糜子和油菜籽适宜的吸孔负压范围。随后，采用 CFD 压力追踪分析方法，定量建立了吸孔负压与气室入口负压之间的映射关系。在此基础上，以入口负压、吸孔直径和吸孔厚度为试验因素，以吸孔负压合格率为响应指标，开展了三因素三水平优化试验。优化结果表明：谷子的最优参数组合为 2.51 kPa、0.88 mm 和 0.31 mm；糜子的最优参数组合为 2.97 kPa、1.12 mm 和 0.35 mm；油菜籽的最优参数组合为 2.35 kPa、0.93 mm 和 0.32 mm。台架验证结果显示，三者的充种率分别达到 93%、97%和 96%。结果表明，所提出的方法能够有效减少经验试验工作量，并可为小籽粒作物气力式精密排种盘的设计提供实用依据。

INTRODUCTION

Millet, broomcorn millet, and rapeseed are important economic crops in Northwest China, where sowing practices include manual broadcasting, drill sowing, and hill-drop sowing, while the level of mechanization in some mountainous and hilly areas remains relatively low *(Cong et al., 2014; Gao et al., 2022; Cao et al., 2026)*. The regional climate is characterized by low temperature, aridity, and limited precipitation, which are unfavorable for seed germination and early growth. Consequently, plastic-film mulching and multi-seed-per-hole sowing are commonly adopted to improve seedling establishment. Under these agronomic conditions, single-seed precision sowing is generally unsuitable for small-seed crops.

Precision sowing technology can significantly improve sowing quality by placing a controlled number of seeds at specified row spacing, plant spacing, and sowing depth, while simultaneously completing operations such as fertilization, soil compaction, and mulching *(Gao et al., 2026; Wei et al., 2026)*. The seed metering device is the core component of precision sowing systems and can be broadly classified into mechanical and pneumatic types *(Gaikwad and Sirohi, 2008; Karayel et al., 2022; Bustos-Gaytán et al., 2025)*.

Among them, pneumatic seed metering devices are widely used because of their strong adaptability to seed-size variation, low mechanical damage, and suitability for relatively high-speed operation *(Wang et al., 2017; Li et al., 2023; Yang et al., 2026)*.

Previous studies have shown that vacuum pressure, hole geometry, plate speed, and seed delivery conditions jointly determine the performance of precision seeders *(Ibrahim et al., 2018; Rezaei Asl et al., 2019)*. *Karayel et al. (2004)* mathematically analyzed the vacuum-pressure requirement of a precision seeder, *Yazgi and Degirmencioglu (2007)* optimized seed-spacing uniformity through response surface methodology, *Panning et al. (2000)* evaluated laboratory and field methods for planter spacing assessment, and *Onal et al. (2012)* examined the theoretical and experimental accuracy of a vacuum-type precision metering unit. In China, related studies have further improved seed filling by using dual-chamber structures, grooved-tooth disturbance, wedge-shaped agitation, and protrusion-assisted seed plates *(Ding et al., 2018; Li et al., 2019; Wang et al., 2019; Xing et al., 2020)*. However, most available studies focus on single-seed precision sowing or general spacing performance, whereas the coupled pressure-matching problem of small seeds under multi-seed-per-hole conditions remains insufficiently clarified.

Accordingly, the novelty of this study lies in three aspects: (1) an engineering matching rule between seed size and suction-hole diameter was established for small-seed multi-seed-per-hole sowing; (2) the mapping between suction-hole pressure and air-chamber inlet pressure was quantified through CFD-assisted pressure tracing; and (3) the coupled effects of inlet negative pressure, suction-hole diameter, and suction-hole thickness were optimized and validated experimentally for three representative small-seed crops. These results provide a more directly applicable design route for pneumatic seed metering plates than empirical parameter selection alone.

MATERIAL AND METHODS

Selection of suction hole diameter range

The geometry of suction holes, including shape, diameter, and thickness, plays a critical role in the performance of seed metering plates *(Dun et al., 2019; Gao et al., 2022; Ren et al., 2024)*. Considering the seed cleaning and unloading mechanisms employed in this study, concave–convex hole structures were excluded due to their incompatibility with the operational requirements.

To determine the appropriate suction hole diameter range, three types of seeds—millet, broomcorn millet, and rapeseed—were matched with a series of hole diameters ranging from 0.3 mm to 2.0 mm at intervals of 0.1 mm. The holes were fabricated using laser cutting on a steel plate with a thickness of 0.5 mm.

To ensure stable seed adsorption and transport while avoiding excessive cleaning and seed damage during release, a geometric matching method was adopted. Seeds were placed on suction holes of varying diameters, and the interaction between seed geometry and hole size was evaluated. The criterion for suitable matching was defined as the condition at which the seed just began to enter the suction hole without falling through.

Based on repeated observations and statistical screening, the relationship between suction-hole diameter and equivalent seed diameter was expressed as:

$$d_k = (0.4-0.6)\ d_z \quad (1)$$

where: d_k – the diameter of the seed metering plate suction hole, mm; d_z - the equivalent diameter of small-seed crops, mm.

Table 1

Range of suction hole diameters for different seed types

Item	Millet	Broomcorn millet	Rapeseed
Equivalent diameter [mm]	1.5717	2.5290	2.1331
Suction hole diameter [mm]	0.629-0.943	1.012-1.517	0.853-1.280
Median suction hole diameter [mm]	0.786	1.265	1.067

This empirical relationship is consistent with the geometric compatibility requirements between seed size and suction hole diameter, ensuring stable adsorption without multiple seed pickup. Accordingly, the suitable ranges of suction hole diameters for each seed type were determined, as summarized in Table 1. It can be observed that the suction hole diameter increases proportionally with seed size, which is consistent with the relationship d_k = (0.4–0.6)d_z.

Selection of negative pressure range

The negative pressure at the suction hole is a key parameter governing seed adsorption, transport, and release in pneumatic seed metering devices *(Hu et al., 2025; Shi et al., 2025)*. An appropriate negative pressure range should ensure stable seed pickup, prevent excessive seed removal during cleaning, and allow reliable seed release.

To determine the feasible range of suction hole negative pressure, a threshold-based experimental method was employed. Two types of brushes were used to simulate external disturbances during the seed cleaning process: a soft nylon brush (bristle diameter 0.09 mm) and a stiff bristle brush (diameter 0.20 mm). The lower limit of negative pressure was defined as the minimum pressure at which the seed remained attached to the suction hole when lightly contacted by the soft brush. The upper limit was defined as the pressure at which the seed was just removed when subjected to the stiff brush. Each measurement was repeated 20 times, and the average values were used to reduce experimental uncertainty. The difference between these two thresholds was taken as the effective negative pressure range for seed adsorption. This range ensures sufficient holding force during seed transport while avoiding excessive adhesion that may hinder seed release.

The experimental setup is shown in Fig. 1 and mainly consisted of a fixed frame, a PVC suction tube with a diameter of 6 mm, a vacuum pump (OL 750 AD, rated suction capacity 125 L/min), a pressure-regulating device (IRV 20-C06, adjustment range -0.5 to -100.0 kPa), and the corresponding power supplies. During the experiment, the suction tube was sealed to the back side of a single suction hole to eliminate air leakage, and the negative pressure was increased stepwise by 0.1 kPa from an initial value of -0.1 kPa until the defined threshold conditions were reached.

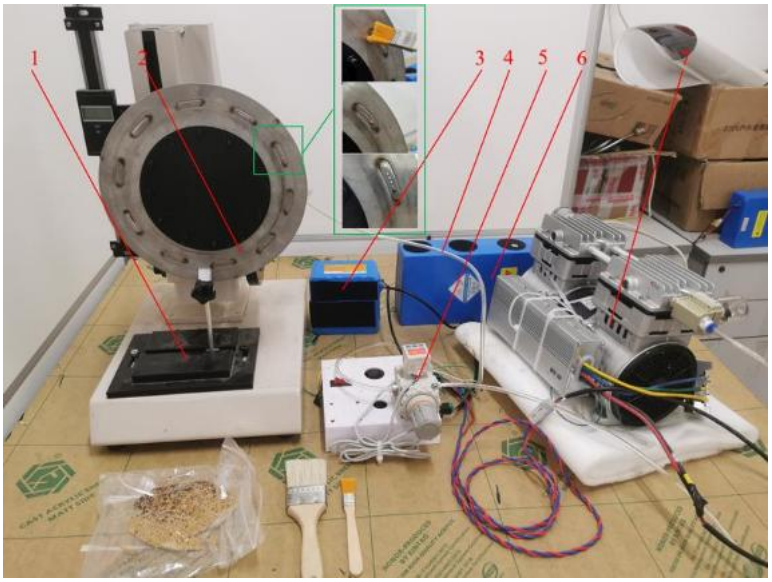


Fig. 1 - Experimental setup for the single-factor test of the seed metering plate

1. seed plate support frame; 2. seed metering plate; 3. 24V power supply for the pressure regulator; 4. suction tube; 5. pressure regulating device; 6. 36V power supply for the vacuum pump; 7. vacuum pump

As shown in Table 2, the effective negative-pressure ranges for millet, broomcorn millet, and rapeseed were 0.77-2.67 kPa, 0.97-3.25 kPa, and 0.92-2.81 kPa, respectively. Although only 0.22, 0.31, and 0.27 kPa were sufficient for the initial adsorption of the three seeds at the median suction-hole diameters, these values were below the engineering working range defined by the brushing-threshold criterion and therefore were not used for subsequent optimization.

Table 2

Range of suction hole negative pressure for different seed types

Item	Millet	Broomcorn millet	Rapeseed
Median suction hole diameter [mm]	0.8	1.2	1.0
Suction hole negative pressure range [kPa]	0.77-2.67	0.97-3.25	0.92-2.81
Median suction hole negative pressure [kPa]	1.72	2.11	1.87

Potential sources of experimental variation in the negative-pressure tests included seed-size dispersion after grading, manual differences during brush contact, the 0.1 kPa pressure-setting resolution, and local sealing variability between the suction tube and the plate. These effects were reduced by seed grading, repeated measurements, and the use of averaged values in all subsequent analyses. The obtained pressure ranges therefore provide a practical basis for balancing seed retention and release during pneumatic metering.

Simulation-based determination of air chamber suction inlet pressure range

To establish the relationship between the air-chamber inlet negative pressure and the suction-hole pressure of the seed metering plate, CFD simulations were conducted on the airflow field within the chamber.

As shown in Fig. 2, a three-dimensional model of the air chamber was developed in SolidWorks and imported into ANSYS Fluent for numerical simulation. Considering the circumferential symmetry of the chamber around the central axis of the suction inlet, a symmetric cross-sectional model was used to reduce computational cost while retaining the dominant pressure-transfer characteristics relevant to the present study *(Zhang et al., 2022; Zhao et al., 2023; Zhong et al., 2024)*.

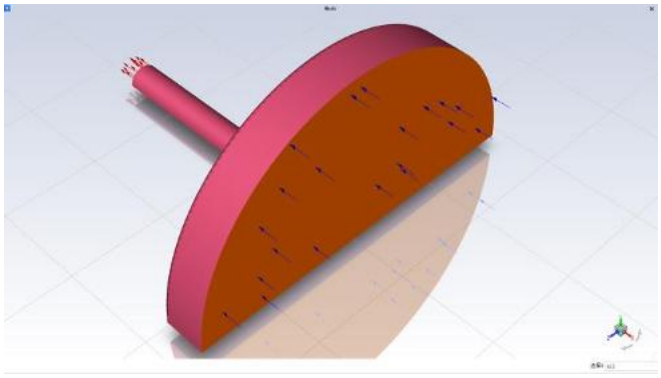


Fig. 2 - 3D model of air chamber flow field

As shown in Fig. 3, a two-dimensional symmetric cross-sectional model extracted from the 3D geometry was used for the CFD calculations. To improve the accuracy of pressure extraction, the cross-sectional model shown in Fig. 3(b) was discretized using a hexagonal-dominant cell, with local refinement applied in the suction inlet passage and suction-hole region, where the pressure gradient changed markedly. The global mesh size was approximately 0.20 mm, while the local mesh size in the refined region was reduced to 0.05 mm. Three mesh schemes were tested for mesh-independence analysis, containing approximately 28,436, 46,912, and 71,385 cells, respectively. The average pressure at three monitoring points near the suction-hole outlet was used as the mesh-independence criterion. When the number of cells increased from 46,912 to 71,385, the relative deviation of the monitored pressure was only 0.84%, indicating that further mesh refinement had a negligible effect on the simulation results. Therefore, considering both computational cost and numerical accuracy, the mesh with 46,912 cells was adopted for the subsequent simulations.

Millet was selected as the representative case for the pressure-tracing analysis. The suction inlet diameter was 30 mm, the suction-hole diameter was 0.8 mm, and the hole thickness was 0.5 mm. Three monitoring points were arranged near the suction-hole outlet, three monitoring points were arranged symmetrically near the suction-hole outlet, and their average pressure was used as the evaluation index. The inlet negative pressure was increased stepwise by 0.1 kPa.

In the simulations, air was treated as an incompressible fluid under steady turbulent flow conditions. Because the airflow inside the chamber was mainly characterized by internal negative-pressure flow, and the objective of this study was to determine the pressure-transfer relationship between the chamber inlet and the suction hole rather than to capture transient vortex evolution, the standard k–ε turbulence model was selected. Compared with more complex turbulence models, the standard k–ε model provides better numerical robustness and computational efficiency for steady engineering flows, and it has been widely used in airflow simulations of pneumatic seed-metering devices to achieve stable predictions of chamber pressure fields. The ambient conditions were set at 25 °C and 101 kPa *(Yu et al., 2014; Zhang et al., 2022; Tang et al., 2023; Wang et al., 2023; Zhong et al., 2024)*.

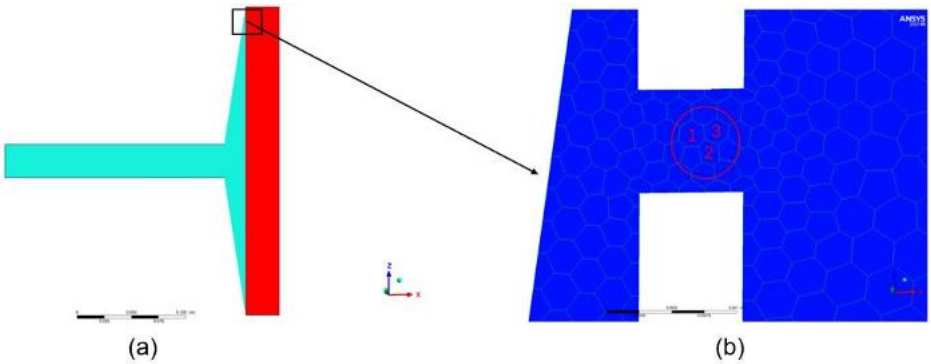
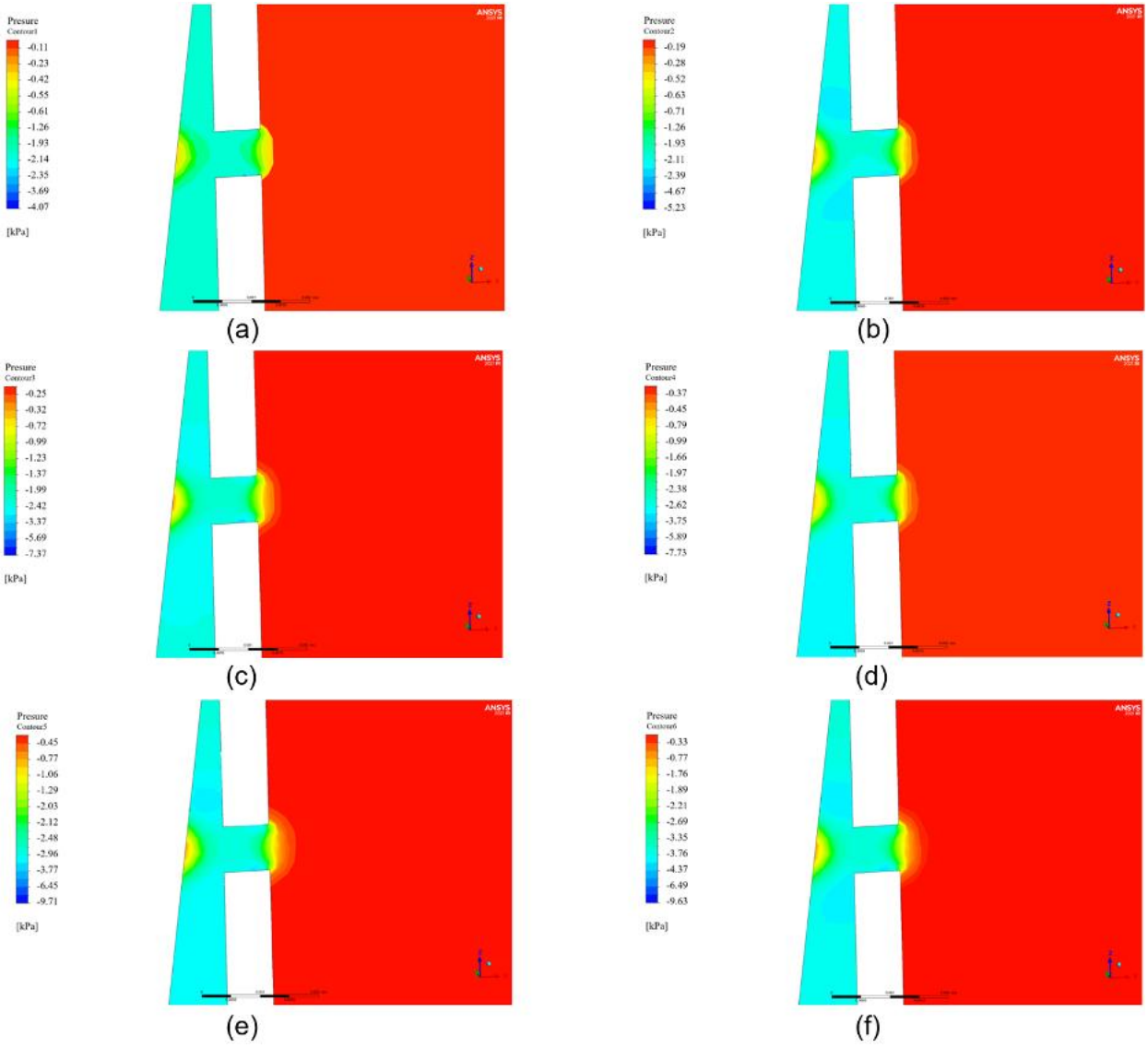


Fig. 3 - Computational domain and mesh of the airflow field

(a) Geometry of the air chamber; (b) Mesh of the cross-sectional plane.

Pressure–velocity coupling was handled using the SIMPLE algorithm, and second-order discretization schemes were applied to the pressure and momentum equations. The solution was considered converged when the residuals of the continuity and momentum equations were reduced below 1×10^{-5}, and the monitored suction-hole pressure remained stable with no further noticeable variation.

Eight representative inlet-pressure conditions, namely 1.9, 2.1, 2.4, 2.7, 3.1, 3.5, 3.9, and 4.1 kPa, were extracted from the stepwise simulation process. The corresponding suction-hole pressures were 0.62, 0.74, 1.24, 1.67, 2.06, 2.25, 2.61, and 2.73 kPa, respectively.



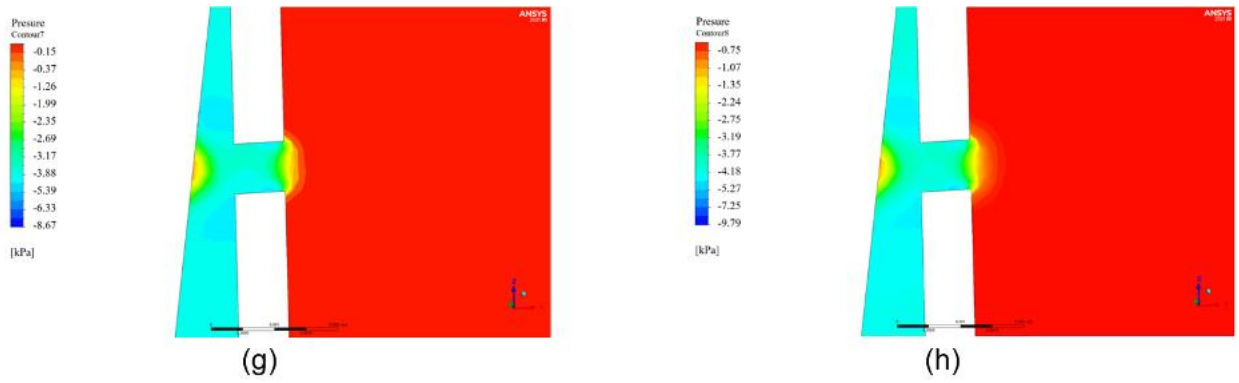


Fig. 4 - Pressure contours at suction holes under different air chamber inlet pressures

(a) 1.9 kPa; (b) 2.1 kPa; (c) 2.4 kPa; (d) 2.7 kPa; (e) 3.1 kPa; (f) 3.5 kPa; (g) 3.9 kPa; (h) 4.1 kPa

As shown in Fig. 4, the pressure contours at the suction hole changed regularly with increasing inlet negative pressure. When the chamber inlet pressure was lower than about 2.1 kPa, the suction-hole pressure was below the experimentally acceptable lower limit for millet. When the chamber inlet pressure exceeded about 3.9-4.1 kPa, the suction-hole pressure approached or exceeded the upper limit of the qualified range, indicating a risk of over-adsorption. Therefore, the corresponding inlet pressure range for millet was determined to be 2.11-3.95 kPa, which matches the experimentally defined suction-hole pressure range of 0.77-2.67 kPa.

Using the same tracing method, the inlet pressure ranges for broomcorn millet and rapeseed were obtained as 2.37-4.22 kPa and 2.23-4.16 kPa, respectively. These results establish a quantitative mapping between chamber inlet pressure and suction-hole pressure, thereby providing a direct basis for subsequent optimization of the seed metering plate.

Table 3

Relationship between air chamber inlet pressure and suction hole pressure

Item	Millet	Broomcorn millet	Rapeseed
Median suction hole diameter [mm]	0.8	1.2	1.0
Suction hole negative pressure range [kPa]	0.77-2.67	0.97-3.25	0.92-2.81
Air chamber suction inlet negative pressure range [kPa]	2.11-3.95	2.37-4.22	2.23-4.16

Experimental design for seed metering plate optimization

To determine the appropriate combination of suction hole diameter, suction hole thickness, and air chamber inlet negative pressure for different seed types, the factor ranges were defined based on the preliminary single-factor experiments and CFD simulation results. Using millet as an example, the selected ranges were 2.0–4.0 kPa for inlet negative pressure, 0.6–1.0 mm for suction hole diameter, and 0.3–0.7 mm for suction hole thickness.

A three-factor, three-level Box–Behnken response-surface design was employed, and the coded factor levels are listed in Table 4. The experimental design matrix and corresponding results are presented in Table 5. The design with 17 runs was employed, including five center-point replicates to estimate pure error. For each parameter combination, pressure values were extracted at 100 suction-hole positions along the metering plate, and the percentage of qualified pressure values was calculated as the response.

Table 4

Factor levels used in the experimental design

Code	Inlet negative pressure (X_1) [kPa]	Suction hole diameter (X_2) [mm]	Suction hole thickness (X_3) [mm]
-1	2	0.6	0.3
0	3	0.8	0.5
1	4	1.0	0.7

The qualification rate of suction-hole pressure was selected as the response variable. For millet, the acceptable suction-hole pressure range was defined as 0.8-2.7 kPa. Analysis of variance and response-surface optimization were performed in Design-Expert 8.0.6. In the statistical interpretation, the main sources of experimental error considered were seed-size variability after grading, pressure-setting resolution, and repeated positioning differences during testing.

Table 5

Experimental design matrix and results

No.	X_1	X_2	X_3	Y_1 [%]
1	-1	-1	0	74
2	1	-1	0	92
3	-1	1	0	70
4	1	1	0	76
5	-1	0	-1	81
6	1	0	-1	93
7	-1	0	1	72
8	1	0	1	80
9	0	-1	-1	93
10	0	1	-1	82
11	0	-1	1	88
12	0	1	1	78
13	0	0	0	97
14	0	0	0	94
15	0	0	0	89
16	0	0	0	90
17	0	0	0	95

RESULTS AND DISCUSSION

Regression modeling and analysis of variance

Based on the experimental results, a quadratic regression model was established using Design-Expert 8.0.6, with the pressure qualification rate at the suction hole (Y_1) as the response variable and the coded factors (X_1, X_2, X_3) as independent variables:

$$Y_1 = 93 + 5.5X_1 - 5.12X_2 - 3.88X_3 - 3X_1X_2 - X_1X_3 + 0.25X_2X_3 - 9.38X_1^2 - 5.63X_2^2 - 2.12X_3^2 \quad (2)$$

Analysis of variance (ANOVA) was performed to evaluate the significance of the regression model, as summarized in Table 6. The results indicate that the model is statistically significant ($p < 0.05$), while the lack-of-fit term is not significant ($p > 0.05$), confirming that the model adequately describes the experimental data.

Table 6

Analysis of variance (ANOVA) for the regression model

Sources	Sum of squares	Degree of freedom	Mean square	*F*	*p*
Model	1177.69	9	130.85	13.23	0.0013
X_1	242.00	1	242.00	24.46	0.0017
X_2	210.13	1	210.13	21.24	0.0025
X_3	120.13	1	120.13	12.14	0.0102
X_1X_2	36.0000	1	36.0000	3.6390	0.0981
X_1X_3	4.0000	1	4.0000	0.4043	0.5451

Sources	Sum of squares	Degree of freedom	Mean square	*F*	*p*
X_2X_3	0.2500	1	0.2500	0.0253	0.8782
X_1^2	370.0658	1	370.0658	37.4074	0.0005
X_2^2	133.2237	1	133.2237	13.4667	0.0080
X_3^2	19.0132	1	19.0132	1.9219	0.2082
Lack of fit	23.25	3	7.75	0.67	0.6116
Pure error	46	4	11.50		
Total	1246.94	16			

Among the factors, X_1 (inlet negative pressure), X_2 (suction hole diameter), X_3 (suction hole thickness), as well as the quadratic terms X_1^2 and X_2^2, show significant effects on the response ($p < 0.05$). In contrast, the interaction terms are not significant, indicating weak coupling effects among the factors.

Effect of factors and response surface analysis

The effects of the factors on the pressure qualification rate are illustrated in Fig. 5. Among the three variables, inlet negative pressure exerted the strongest influence on the response, followed by suction-hole diameter, whereas suction-hole thickness showed a smaller but still significant main effect. The curved surface in Fig. 5(a) indicates that the qualified rate can be maximized only within a moderate pressure-diameter window; excessively low inlet pressure leads to insufficient suction-hole pressure, whereas excessive inlet pressure increases the risk of over-adsorption.

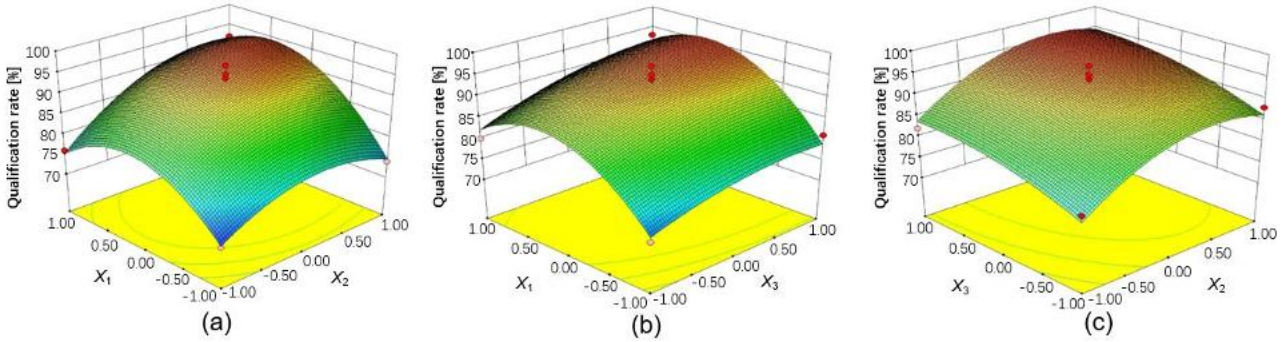


Fig. 5 - Response surfaces to influences of different factors on qualified rate of pressure at the suction hole

(a) X_1 and X_2; (b) X_1 and X_3; (c) X_2 and X_3

As shown in Fig. 5, the qualified rate first increased and then decreased with increasing inlet negative pressure. This trend reflects the transition from insufficient adsorption to an over-strong pressure field. A similar non-monotonic pattern was observed for suction-hole diameter: when the hole was too small, pressure transfer was insufficient, whereas an excessively large hole caused the local pressure to move outside the qualified range. By contrast, increasing suction-hole thickness tended to reduce the qualified rate because the longer flow passage increased local pressure loss and weakened effective pressure transmission near the hole exit.

Parameter optimization and engineering interpretation

Based on the regression model, the optimal parameter combination for millet was an inlet negative pressure of 2.51 kPa, a suction-hole diameter of 0.88 mm, and a suction-hole thickness of 0.31 mm.

Separate Box–Behnken designs were conducted for the three seed types, and only the millet design matrix is shown here as a representative example due to space limitations; the optimized results for the other two seed types are summarized in Table 7. Using the same methodology, the optimal combinations for broomcorn millet and rapeseed were determined to be 2.97 kPa, 1.12 mm, and 0.35 mm, and 2.35 kPa, 0.93 mm, and 0.32 mm, respectively.

The results further confirm that the empirical relationship between seed size and suction-hole diameter, namely that the hole diameter should be approximately 0.4-0.6 times the equivalent seed diameter, is applicable to the present metering system.

Table 7

Optimal parameter combinations for different seed types

Seed type	Inlet negative pressure [kPa]	Suction hole diameter [mm]	Suction hole thickness [mm]
Millet	2.51	0.88	0.31
Broomcorn millet	2.97	1.12	0.35
Rapeseed	2.35	0.93	0.32

Test bench validation experiment

To verify the rationality of the optimized parameter combinations and reduce the influence of random experimental error, a validation bench was established, as shown in Fig. 6. The test bench mainly consisted of a negative-pressure fan, the seed metering device, a high-speed camera, a seed bed belt, and an oil pump. The validation was carried out without seed-cleaning operations so that the filling performance of the seed metering plate itself could be evaluated independently.

According to the optimal simulation results, the parameter combination for millet was a negative pressure of 2.5 kPa, a suction hole diameter of 0.9 mm, and a suction hole thickness of 0.3 mm; for broomcorn millet, the optimal parameters were 3.0 kPa, 1.1 mm, and 0.4 mm, respectively; and for rapeseed, they were 2.4 kPa, 0.9 mm, and 0.3 mm, respectively.

Under the optimized parameter combinations, 100-hole validation tests were conducted for millet, broomcorn millet, and rapeseed. The seed-filling rates reached 93.0 ± 1.4%, 97.0 ± 0.9%, and 96.0 ± 1.1%, respectively. These results indicate that the CFD-based pressure tracing and response-surface optimization provided parameter combinations sufficiently close to the experimental optimum, and therefore can be used as an efficient preselection method for subsequent metering-plate design.

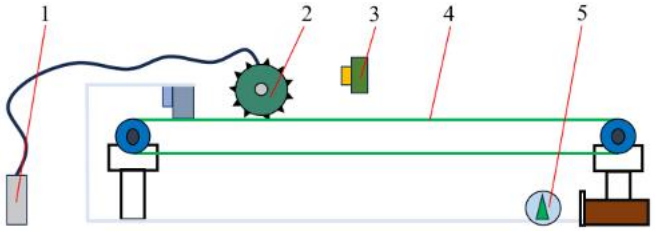


Fig. 6 - Schematic diagram of the seed metering performance test bench

1. negative pressure fan; 2. seed metering device; 3. high-speed camera; 4. seed bed belt; 5. oil pump

CONCLUSIONS

This study systematically investigated the key parameters affecting the performance of a pneumatic seed metering plate for small-seed crops through a combination of experiments, CFD simulation, and optimization analysis. The main conclusions are as follows:

(1) Single-factor tests established the engineering matching relationship between suction-hole diameter and seed size for the present metering system, namely that the suitable suction-hole diameter was 0.4-0.6 times the equivalent seed diameter.

(2) Brushing-threshold experiments and the dedicated adsorption test platform determined the acceptable suction-hole negative-pressure ranges for millet, broomcorn millet, and rapeseed as 0.77-2.67 kPa, 0.97-3.25 kPa, and 0.92-2.81 kPa, respectively.

(3) CFD pressure-tracing analysis clarified the mapping between suction-hole pressure and chamber inlet negative pressure, thereby converting the experimentally defined adsorption range into a directly usable chamber-pressure range for design and adjustment.

(4) Response-surface optimization identified the optimal parameter combinations for the three seed types, and bench validation produced seed-filling rates of 93%, 97%, and 96%, confirming the reliability of the optimized results.

From an engineering perspective, the proposed workflow can be used to narrow the parameter-search space of pneumatic seed metering plates for small-seed crops and reduce repeated physical trials. However, the CFD model was based on a steady and symmetric airflow field and did not explicitly account for transient leakage, plate rotation, or gas-solid coupling with moving seeds. These factors should be incorporated in future transient CFD-DEM studies to further improve predictive accuracy.

ACKNOWLEDGEMENT

This study was supported by the National Natural Science Foundation of China (32272001), the Shaanxi Key Research and Development Project (2023-ZDLNY-62), and the Shaanxi Key Research and Development Project (grant number 2022NY-205).

REFERENCES

[1] Bustos-Gaytán A., Saldaña-Robles N., Joya-Cárdenas D.R., Gutiérrez-Vaca C., Alfaro-Ayala J.A., Barco-Burgos J., & Saldaña-Robles A. (2025). Advancements in pneumatic seed-metering devices: A review of numerical and experimental approaches. *Results in Engineering*, 26, 105626. https://doi.org/10.1016/j.rineng.2025.105626

[2] Cao Z., Yi S., Wang S., Chen T., & Li Y. (2026). Detection method of hole formation in foxtail millet based on K-value (基于 K 值法的谷子穴播成穴性检测方法). *Transactions of the Chinese Society for Agricultural Machinery*, 57(6), 119-128. https://doi.org/10.6041/j.issn.1000-1298.2026.06.011

[3] Cong J., Liao Q., Cao X., Liao Y., Yu J., & Wang L. (2014). Seed filling performance of dual-purpose seed plate in metering device for both rapeseed & wheat seed (油菜小麦兼用排种盘的排种器充种性能). *Transactions of the Chinese Society of Agricultural Engineering*, 30(8), 30-39. https://doi.org/10.3969/j.issn.1002-6819.2014.08.004

[4] Ding L., Yang L., Liu S., Yan B., He X., & Zhang D. (2018). Design of air suction high speed precision maize seed metering device with assistant seed filling plate (辅助充种种盘玉米气吸式高速精量排种器设计). *Transactions of the Chinese Society of Agricultural Engineering*, 34(22), 1-11. https://doi.org/10.11975/j.issn.1002-6819.2018.22.001

[5] Dun G., Yu C., Yang Y., Ye J., Du J., & Zhang J. (2019). Parameter simulation optimization and experiment of seed plate type hole for soybean breeding (大豆育种排种盘型孔参数仿真优化与试验). *Transactions of the Chinese Society of Agricultural Engineering*, 35(19), 62-73. https://doi.org/10.11975/j.issn.1002-6819.2019.19.008

[6] Gaikwad B.B., & Sirohi N.P.S. (2008). Design of a low-cost pneumatic seeder for nursery plug trays. Biosystems Engineering, 99(3), 322-329. https://doi.org/10.1016/j.biosystemseng.2007.10.017

[7] Gao L., Shi B., Liao Q., Zhang B., Zheng J., & Liao Y. (2022). Seeding performance of conical-hole seeding plate of the positive and negative pressure combination precision seed metering device for rapeseed (正负气压组合油菜精量排种器锥孔盘排种性能). *Transactions of the Chinese Society of Agricultural Engineering*, 38(6), 22-33. https://doi.org/10.11975/j.issn.1002-6819.2022.06.003

[8] Gao X., Zhao P., Li J., Xu Y., Huang Y., & Wang L. (2022). Design and experiment of quantitative seed feeding wheel of air-assisted high-speed precision seed metering device. *Agriculture*, 12(11), 1951. https://doi.org/10.3390/agriculture12111951

[9] Hu M., Zhang J., Chen Y., Xu C., & Li, B. (2025). Parameter optimization and experiment of an inside-filling pneumatic high-speed precision seed-metering device for cotton. *INMATEH Agricultural Engineering*, 76(2), 1334-1351. https://doi.org/10.35633/inmateh-76-111

[10] Ibrahim E.J., Liao Q., Wang L., Liao Y., & Yao L. (2018). Design and experiment of multi-row pneumatic precision metering device for rapeseed. *International Journal of Agricultural and Biological Engineering*, 11(5), 116-123. https://doi.org/10.25165/j.ijabe.20181105.3544

[11] Karayel D., Barut Z.B., & Ozmerzi A. (2004). Mathematical modelling of vacuum pressure on a precision seeder. *Biosystems Engineering*, 87(4), 437-444. https://doi.org/10.1016/j.biosystemseng.2004.01.011

[12] Karayel D., Barut Z.B., & Özmerzi A. (2022). Estimation of optimum vacuum pressure of air-suction seed-metering device of precision seeders using artificial neural network models. *Agronomy*, 12(7), 1600. https://doi.org/10.3390/agronomy12071600

[13] Li X., Liao Q., Wang L., Li M., & Du W. (2023). Design and experiments of the type-hole wheel with high-speed air-assisted centralized metering device for rice, wheat and rapeseed (稻麦油兼用高速气送式集排器型孔轮设计与试验). *Transactions of the Chinese Society of Agricultural Engineering*, 39(14), 35-48. https://doi.org/10.11975/j.issn.1002-6819.202303044

[14] Li Z., Yang W., Zhang T., Wang W., Zhang S., & Chen Li. (2019). Design and suction performance test of sucking-seed plate combined with groove-tooth structure on high speed precision metering device of rapeseed (油菜高速精量排种器槽齿组合式排种盘设计与吸附性能试验). *Transactions of the Chinese Society of Agricultural Engineering*, 35(1), 12-22. https://doi.org/10.11975/j.issn.1002-6819.2019.01.002

[15] Liao Y., Wang L., & Liao Q. (2017). Design and test of an inside-filling pneumatic precision centralized seed-metering device for rapeseed. *International Journal of Agricultural and Biological Engineering*, 10(2), 56–62, https://doi.org/10.3965/j.ijabe.20171002.2061

[16] Liu D., Ma J., Qiao X., Xin P., Zhang X., Wang J., & Zheng D. (2023). The design of and experiments with a double-row seed-metering device for buckwheat breeding in an experimental area. *Agronomy*, 13(12), 2857. https://doi.org/10.3390/agronomy13122857

[17] Onal I., Degirmencioglu A., & Yazgi A. (2012). An evaluation of seed spacing accuracy of a vacuum type precision metering unit based on theoretical considerations and experiments. *Turkish Journal of Agriculture and Forestry*, 36(2), 133-144. https://doi.org/10.3906/tar-1010-1316

[18] Panning J.W., Kocher M.F., Smith J.A., & Kachman S.D. (2000). Laboratory and field testing of seed spacing uniformity for sugarbeet planters. *Applied Engineering in Agriculture*, 16(1), 7-13. https://doi.org/10.13031/2013.4985

[19] Ren D., Liu Tao, Xia S., Chen Y., Wang W., & Li Z. (2024). Design and seed filling performance test of cavity plate combination hole type seeding plate for corn and soybean (玉米大豆兼用腔盘组合孔式排种盘设计与充种性能试验). *Transactions of the Chinese Society for Agricultural Machinery*, 55(2), 73-89. https://doi.org/10.6041/j.issn.1000-1298.2024.02.007

[20] Rezaei Asl A., Roudbari M., & Esmailzadeh E. (2019). Fabrication and evaluation of vacuumed metering drum performance for row planting of soybean with grease belt. *Agricultural Engineering International: CIGR Journal*, 21(4), 96-106.

[21] Shi Y., Zhang X., Yan J., Ma X., Li H., & Han C. (2025). Calibration and optimization of discrete element parameters for tiger nuts. *INMATEH Agricultural Engineering*, 76(2), 978-993. https://doi.org/10.35633/inmateh-76-84

[22] Singh R.C., Singh G., & Saraswat D.C. (2005). Optimisation of design and operational parameters of a pneumatic seed metering device for planting cottonseeds. *Biosystems Engineering*, 92(4), 429-438. https://doi.org/10.1016/j.biosystemseng.2005.07.002

[23] Tang H., Xu F., Xu C., Zhao J., & Wang Y. (2023). The influence of a seed drop tube of the inside-filling air-blowing precision seed-metering device on seeding quality. *Computers and Electronics in Agriculture*, 204, 107555. https://doi.org/10.1016/j.compag.2022.107555

[24] Wang B., Liao Q., Wang L., Shu C., Cao M., & Du W. (2023). Design and test of air-assisted seed-guiding device of precision hill-seeding centralized seed-metering device for sesame. *Agriculture*, 13(2), 393. https://doi.org/10.3390/agriculture13020393

[25] Wang B., Wang Z., Luo X., Zhang M., Fang L., Liu S., & Xu P. (2019). Design and experiment of wedge churning device for pneumatic cylinder-type seed metering device for hybrid rice (杂交稻气力滚筒集排式排种器楔形搅种装置设计与试验). *Transactions of the Chinese Society of Agricultural Engineering*, 35(23), 1-8. https://doi.org/10.11975/j.issn.1002-6819.2019.23.001

[26] Wang F., Lv B., Wang H., & Zhao M. (2017). Structural design and test of seed-suction hole of air-sucking seed-metering device for millet (气吸式谷子排种装置吸种孔的结构设计与试验). *Transactions of the Chinese Society of Agricultural Engineering*, 33(8), 30-36. https://doi.org/10.11975/j.issn.1002-6819.2017.08.004

[27] Wei S., Ding Y., Dong W., Liao Q., Wang S., Nong F., & Huang Q. (2026). Design and experiment of precision pneumatic seed metering device with adjustable seeds per hole for cotton (穴粒数可调气吸式棉花精量排种器设计与试验). *Transactions of the Chinese Society for Agricultural Machinery*, 57(2), 32-45. https://doi.org/10.6041/j.issn.1000-1298.2026.02.004

[28] Xing H., Zhang G., Han Y., Gao Y., & Zha X. (2020). Development and experiment of double cavity pneumatic rice precision direct seeder (双腔气力式水稻精量水田直播机设计与试验). *Transactions of the Chinese Society of Agricultural Engineering*, 36(24), 29-37. https://doi.org/10.11975/j.issn.1002-6819.2020.24.004

[29] Yang R., He Y., Chen D., Chen L., Li G., & Zha X. (2026). Design and experiment of air-suction double disc combined maize plot seed meter (气吸双盘组合式玉米小区排种器设计与试验). *Transactions of the Chinese Society for Agricultural Machinery*, 57(6), 67-77. https://doi.org/10.6041/j.issn.1000-1298.2026.06.007

[30] Yazgi A., & Degirmencioglu A. (2007). Optimisation of the seed spacing uniformity performance of a vacuum-type precision seeder using response surface methodology. *Biosystems Engineering*, 97(3), 347-356. https://doi.org/10.1016/j.biosystemseng.2007.03.013

[31] Yu J., Liao Y., Cong J., Yang S., & Liao Q. (2014). Simulation analysis and match experiment on negative and positive pressures of pneumatic precision metering device for rapeseed. *International Journal of Agricultural and Biological Engineering*, 7(3), 1-12. https://doi.org/10.3965/j.ijabe.20140703.001

[32] Zhang X., Wen Z., Wang Q., Li H., Zhang Z., & Liu J. (2022). Research on characteristics of airway pressure loss in seeding-wheel-type pneumatic seeder. *Agriculture*, 12(12), 2021. https://doi.org/10.3390/agriculture12122021

[33] Zhao X., Zhang T., Liu F., Li N., & Li J. (2023). Sunflower seed suction stability regulation and seeding performance experiments. *Agronomy*, 13(1), 54. https://doi.org/10.3390/agronomy13010054

[34] Zhong W., Zhao X., Liu F., Bai H., Dong W., Hu H., & Kong X. (2024). Design and experiment of precision seed metering device for flow adsorption of quinoa seeds. *Agriculture*, 14(3), 434. https://doi.org/10.3390/agriculture14030434

DESIGN AND OPTIMIZATION OF A HUMAN–MACHINE COLLABORATIVE VIBRATION HARVESTING SYSTEM FOR *LYCIUM BARBARUM L.*

/

枸杞人机协同振动采收系统设计与优化

Yahao GE[1)], Zeyu WANG[1)], Min WANG [1)], Yifan ZHANG [1)], Jun CHEN[1*)], Ming ZHANG [2)]
[1)] College of Mechanical and Electronic Engineering, Northwest A&F University, Yangling, Shaanxi, 712100, China
[2)] Ningxia Zhengqi Hong Lycium barbarum L. Industrial Development Co., Ltd， Guyuan 756000, China
DOI: https://doi.org/10.35633/inmateh-79-03

Keywords: *Lycium barbarum L., Human–Machine Collaboration, Vibration Harvesting, Selective t Harvesting, Performance Optimization*

ABSTRACT

To address the challenges of labor-intensive and inefficient manual harvesting of Lycium barbarum L. grown on a double-layer trellis, this study proposes a human–robot collaborative system. The system consists of a hand-held high-frequency rocker-oscillator harvester and an electric receiving cart. Mechanical property measurements of fruits and branches revealed detachment forces of 1.2 to 1.8 N for mature fruits and 2.5 to 3.0 N for immature fruits, with an average bending elastic modulus of 548.9 MPa for fruit-bearing branches, providing a basis for selective harvesting. A Box–Behnken design was employed to optimize vibration frequency, harvesting duration, and inter-rod spacing, and response surface analysis identified the optimal parameters as 18 Hz, 4.5 s, and 26 mm. Next, a central composite design optimized the receiving cloth tilt angle and radius to maximize collection efficiency, defined as the ratio of fruits collected by the cart to the total number of detached fruits. Field validation demonstrated a mature fruit harvesting rate of 96.2%, a mis-harvesting rate of 4.3%, a damage rate of 3.7%, and a collection efficiency of 96.1%, with relative errors below 0.5% compared to model predictions. These results confirm the system's effectiveness and provide technical support for standardized, low-damage mechanized fruit harvesting of Lycium barbarum L..

摘要

为解决双层篱架栽培枸杞人工采摘劳动强度大、效率低下的问题，本研究提出了一种人机协作采摘系统。该系统由手持高频摇摆振动采摘机与电动接果车组成。对果实及枝条力学特性的测定结果显示，成熟果实的脱离力为 1.2 至 1.8 N，未成熟果实为 2.5 至 3.0 N，果枝的平均弯曲弹性模量为 548.9 Mpa，为实现选择性采摘提供了理论依据。研究采用 Box–Behnken 试验设计对振动频率、采摘时长及振动杆间距进行了优化，并通过响应面分析确定最佳参数为振动频率 18 Hz、采摘时长 4.5 s 以及振动杆间距 26 mm。随后，利用中心复合试验设计对接果布的倾角与半径进行了优化，以最大化接果效率，接果效率定义为接果车收集到的果实数量占脱落果实总量的比例。田间验证结果显示，成熟果实采摘率达到 96.2%，误采率为 4.3%，损伤率为 3.7%，接果效率为 96.1%，各项指标实测值与模型预测值的相对误差均低于 0.5%。上述结果表明该系统具有高效、低损伤的应用潜力，为双层篱架栽培枸杞的标准化机械化果实采摘提供了技术支撑。

INTRODUCTION

The transition toward mechanization and intelligent technologies is of great significance for improving the production efficiency of *Lycium barbarum* L. *(Torregrosa et al., 2014)*. Owing to its indeterminate inflorescences and continuous multi-cropping fruiting, harvesting operations are frequent and labor-intensive *(Chen et al., 2025)*. At present, high-cost and low-efficiency manual harvesting remains predominant, constituting a major bottleneck for high-quality development of the industry. Therefore, the development of efficient and low-damage mechanized harvesting equipment is imperative.

Vibrational harvesting is the principal method for mechanized harvesting of *L. barbarum*, with notable progress in both hardware and operational strategies. The impact of shaker design, shaking position, and duration on fruit detachment efficiency has been experimentally tested in stone fruits such as apricots *(Erdogan et al., 2003)*. Canopy shaker systems for late-season oranges have also been studied to evaluate the effect of vibration parameters on fruit motion and detachment *(Castro-García et al., 2018)*, and the application of arrayed excitation units further enhances operational efficiency *(Mei et al., 2024)*.

Additionally, a variable-pitch combing brush device has been developed to achieve effective fruit detachment with reduced damage *(Zhang et al., 2018)*. Modifications to excitation methods can effectively increase harvesting efficiency *(Chen et al., 2025)*, while batch-specific parameter optimization improves overall yield *(Liu et al., 2025)*. Simulation and field trials have validated optimal parameter combinations *(Wang et al., 2025; Wang et al., 2026)*, and studies on energy transmission have revealed optimal excitation positions and resonance frequency for vibrational harvesting of *L. barbarum (Deng et al., 2025; Su et al., 2025; Zhao et al., 2021)*.

However, existing studies have mainly focused on fruit detachment, with limited attention to the receiving system. Portable harvesters typically rely on manually spread collection mats, resulting in high labor demands and significant fruit loss. Research on blueberries has shown that soft receiving surfaces can effectively reduce impact damage *(Yu et al., 2014)*, and rigid–flexible coupled collision models further optimize harvesting parameters *(Takeda et al., 2017; Wang et al., 2022)*. Additionally, proper selection of excitation frequency can improve picking rate *(Yu et al., 2024)*. Recent studies on mechanical harvesting systems in olives provide insights for power requirements and trunk shaker optimization *(Ghonimy et al., 2023)*, and analysis of coffee fruit-peduncle systems reveals vibration transmissibility and energy transfer for efficient harvesting *(Villibor et al., 2023)*. Studies on other small berry crops indicate that integrating harvesting and receiving functions can enhance efficiency and minimize fruit damage; multiple excitations improve fruit detachment, whereas mechanical analysis and transport optimization further reduce damage *(Sim et al., 2024; Komarnicki, 2025; Lyu et al., 2024)*. Nevertheless, systematic integration studies for *L. barbarum* remain lacking.

To address this gap, the present study proposes a human–machine collaborative harvesting approach with a portable vibrational harvester and an electric receiving cart. By integrating agronomic measurement, mechanical analysis, simulation, and field trials, key operational parameters are optimized to improve efficiency and reduce fruit damage, providing systematic support for mechanized harvesting of *L. barbarum*.

MATERIALS AND METHODS

Agronomic Parameter Measurement

Key agronomic parameters of goji berries, including plant height, row spacing, layer height, and layer width, were measured and are summarized in Table 1. These data serve as a reference for the design of subsequent harvesting equipment.

Table 1

Agronomic Parameters of Standard Double-Layer Trellis Cultivation

Agronomic Parameter	Description	Mean ± SD
Plant height (m)	Height from ground to the top of the plant	1.71 ± 0.12
Plant spacing (m)	Distance between centers of adjacent plants in a row	1.32 ± 0.10
Layer 1 height (m)	Height of first fruit-bearing branch layer from ground	0.73 ± 0.06
Layer 2 height (m)	Height of second fruit-bearing layer from ground	1.51 ± 0.30
Layer 1 width (m)	Horizontal width of the first layer fruit crown	1.27 ± 0.16
Layer 2 width (m)	Horizontal width of the second layer fruit crown	1.15 ± 0.23
Row spacing (m)	Distance between centers of adjacent rows	3.19 ± 0.35

The field study was conducted on goji plants cultivated by Ningxia Zhengqi Hong Industrial Development Co., Ltd. in Guyuan City, Ningxia, China. A standard double-layer trellis system was employed, with branches pruned to droop naturally, thereby minimizing inter-branch entanglement and facilitating mechanized harvesting (Fig. 1). The overall cultivation environment is depicted in Fig. 2.



Fig. 1 - Single Goji Plant Model

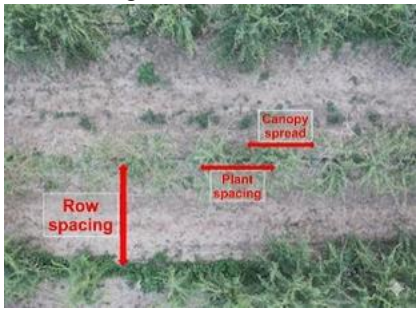


Fig. 2 - Cultivation Environment

Fruit Detachment Mechanical Parameters

The mechanical properties of goji berries at different physiological stages are crucial for designing vibration-based harvesting devices. Structural and compositional changes during maturation influence how easily the fruit detaches. The relationship between detachment force and moisture content is therefore critical for developing effective harvesting strategies.

To measure detachment force, a tensile load was applied along the peduncle at a constant speed, and the peak force at fracture was recorded. Mature fruits with 85–90% moisture content show peduncle shear forces of 1.2–1.8 N, whereas immature green fruits, despite sometimes exceeding 90% moisture, have more lignified peduncles and require higher detachment forces of 2.5–3.0 N.

As shown in Fig. 3, detachment force is negatively correlated with moisture content across all maturity stages. When moisture rises from 75% to 90%, mature fruits' detachment force decreases by ~30% to 1.2–1.8 N, while immature fruits decrease by only ~15%, remaining 2.5–3.0 N. This difference underlies the harvest-ripe, leave-unripe strategy, essential for selective mechanical harvesting and preventing damage to developing fruits.

Based on this relationship, vibration parameters can be adjusted in real time. For mature fruits with moisture above 85%, 15–20 Hz efficiently detaches them without stressing branches. Green fruits below 80% moisture require higher energy, naturally remaining attached under tuned excitation. These findings provide a theoretical basis for precise vibration control and intelligent, adaptive harvesting systems.

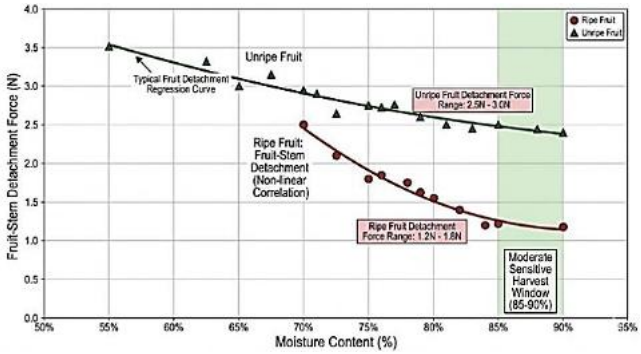


Fig. 3 - Hematic Illustration of the Relationship Between *Lycium barbarum L.* Detachment Force and Moisture Content

Analysis of Vibration Mechanisms

During operation of the portable goji harvester, the excitation rod induces forced vibrations in the "fruit–peduncle–branch" system. Statistical analysis identified three detachment modes: tensile break, fling-off, and impact detachment, with tensile break being predominant. The sequential stages of this process are illustrated in Fig. 4.

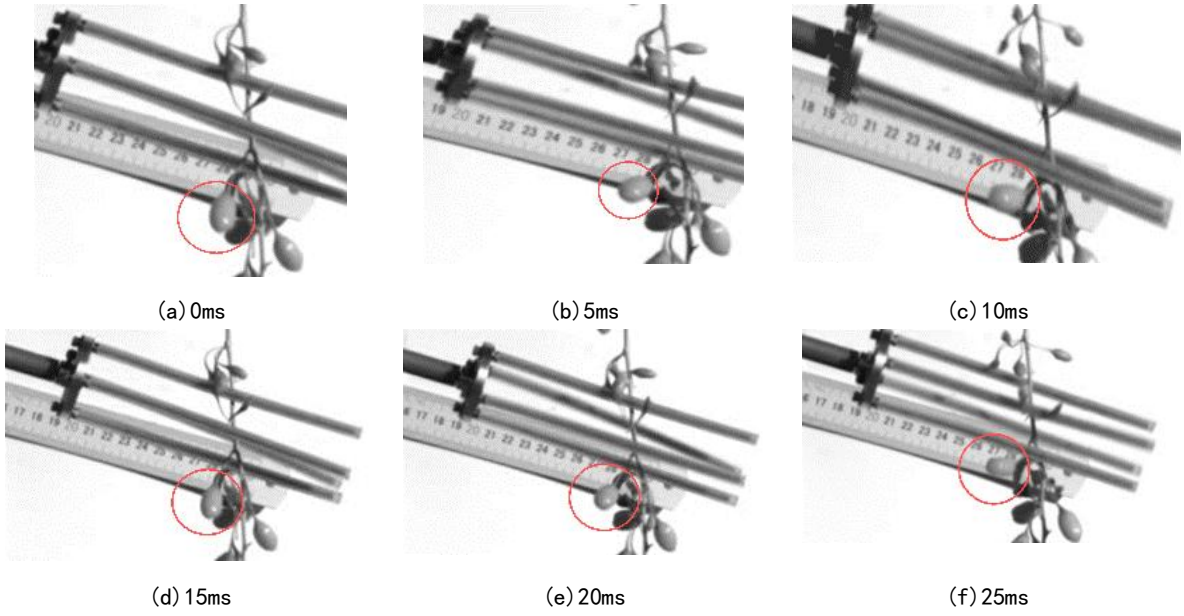


Fig. 4 - Sequence Diagram of Fruit Detachment During Vibration Harvesting

In the tensile break mode, vibration-induced tension in the peduncle generates a velocity difference between the branch and the fruit, while branch acceleration produces an inertial force exceeding the fruit–peduncle adhesion, causing detachment. As shown in Fig. 4a–f, the process follows six stages: (a) initial excitation and peduncle tensioning; (b) inertial sliding of the fruit after branch acceleration; (c) reverse branch motion and impact interaction; (d) secondary sliding after collision; (e) repeated peduncle tensioning during cyclic vibration; and (f) final fruit detachment. This sequence reveals that mature fruit removal is primarily driven by the accumulation of vibration-induced inertial force exceeding fruit–peduncle adhesion, which is essential for understanding the mechanism of selective harvesting. Notably, the repeated tensioning during cyclic vibration progressively weakens the peduncle connection, making final detachment more efficient.

A staged dynamic analysis of this vibration-induced detachment is summarized in Fig. 5, which illustrates the key mechanical interactions involved. During vibration harvesting, the fruit-bearing branch is regarded as an excitation carrier, and the fruit–peduncle system is simplified as a forced vibration system. The inertial force generated by vibration can be expressed as:

$$F_i = ma = m\omega^2 r \tag{1}$$

where F_i is the inertial force acting on the fruit (N), m is the fruit mass (kg), a is the vibration acceleration $(m \bullet s^{-2})$, ω is the angular velocity of vibration $(rad \bullet s^{-1})$, and r is the equivalent vibration radius (m).

Considering the combined effects of inertial force and gravity, the resultant tensile force acting along the fruit–peduncle connection can be described as:

$$F = \sqrt{(I\sin\theta + m\omega^2 r)^2 + (I\cos\theta - G)^2} \tag{2}$$

where F is the resultant tensile force acting on the fruit–peduncle connection (N), G is the fruit gravity (N), and θ is the angle between the peduncle and the vibration direction $(°)$. Fruit detachment occurs when $F > F_d$, where F_d is the measured fruit detachment force (N). Therefore, under appropriate vibration conditions, mature fruits with lower detachment force can be detached preferentially, while immature fruits with higher detachment force remain attached, thereby providing a clear mechanical basis for selective vibration harvesting. This principle ensures that only ripe fruits are removed during operation, leaving unripe fruits to continue maturing for subsequent harvests.

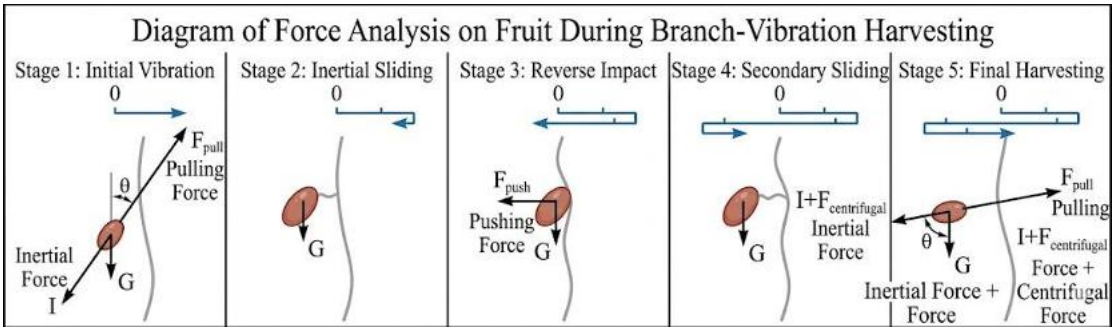


Fig. 5 - Schematic Diagram of the Dynamic Analysis of Fruit Detachment During Vibration Harvesting

During harvesting, the excitation rod applies direct vibration to fruit-bearing branches, inducing forced vibrations in the "fruit–peduncle–branch" system. Detachment forces differ among tissues: mature fruits require the least force, followed by flowers, while immature fruits and leaves require higher forces, with some overlap.

Vibration-based harvesting relies on inertial forces, and controlling vibration intensity is critical. By adjusting acceleration appropriately, mature fruits can be detached selectively while minimizing unintended detachment of other tissues. Calculated detachment accelerations rank in the order: mature fruits, immature fruits, leaves, and flowers, with minimal overlap, supporting effective selective harvesting.

Harvesting System Platform

A coordinated system was developed for mechanized Lycium barbarum L. harvesting, comprising a portable hand-held harvester and an electric fruit-collecting cart. During operation, the harvester is guided by an operator to detach fruits using the excitation rod, while the cart positions a receiving cloth beneath the branches to collect the detached fruits. The platform is mounted on a mobile chassis, manually navigated along orchard rows, with a fixed frame supporting all components.

Design of the Harvesting Device

The portable harvester improves *Lycium barbarum L.* harvesting efficiency and reduces labor through mechanized vibration. Its rocker-oscillator mechanism ensures smooth, continuous oscillation, and the harvesting head is adjustable. The oscillating rod length can be varied to control vibration amplitude and angle, enabling precise excitation at the fruit–peduncle junction (Fig. 6). Goji berries of different maturity often coexist on the same branch, requiring selective harvesting. During operation, the excitation rod acts on fruit-bearing branches, transmitting high-frequency torsional torque. Mature fruits detach when inertial force exceeds peduncle adhesion, while immature fruits remain attached, achieving selective harvesting of ripe fruits (Fig. 7).

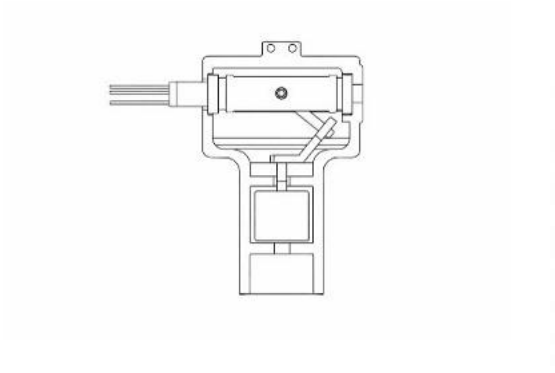


Fig. 6 - Schematic Diagram of the Hand-Held Harvesting Device Structure

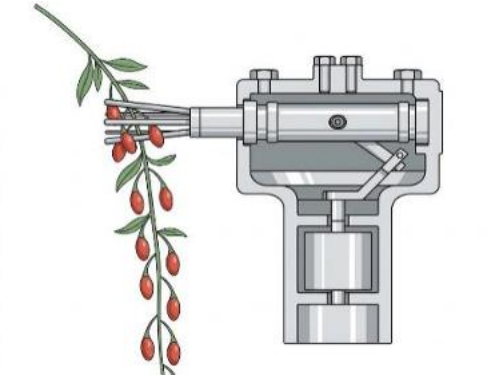


Fig. 7 - Operation Diagram of the Portable Harvesting Device

Design of the Receiving Device

A coordinated system combines a hand-held harvester with an electric collection cart. The operator vibrates fruit-bearing branches while the cart deploys a cloth to collect detached fruits, improving efficiency and reducing labor. The cart chassis fits the standardized double-layer trellis, with row spacing 3.19 m, canopy width 1.27 m, and inter-row corridor 1.92 m. Its width is 0.6 m, height 0.4 m, and length 1.6 m, allowing side-by-side operation and clearance under lower branches (first-layer branches average 0.73 m, lower traction line 0.61 m). The design lowers the center of gravity to enhance stability while accommodating 1.32 m plant spacing.

Based on its chassis dimensions, the receiving cart's structure and workflow were designed to reduce fruit loss and labor intensity. The operator guides the cart along orchard rows using a push handle, while an electric-driven, manually assisted mechanism deploys flexible side cloths to form a semi-enclosed collection surface. The low-center-of-gravity chassis with wide wheel track ensures stability, and the worm-gear motor maintains position under impact. The canopy, tilted 20° downward with a cushioning layer, absorbs shocks and directs detached fruits into the storage basket. Fruits are collected as branches are vibrated by the hand-held harvester, and the canopy is retracted after harvesting (Fig. 9).

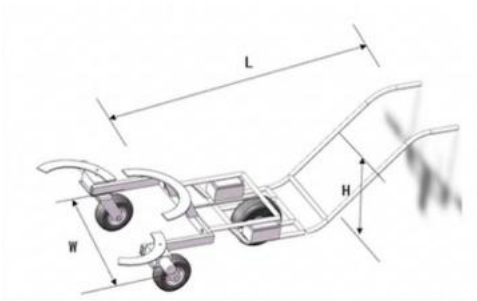


Fig. 8 - Three-Dimensional Structural Model of the Receiving Cart Chassis



Fig. 9 - Field Operation Diagram of the Receiving Cart

RESULTS

Experimental Design

To investigate the effects of vibration frequency X_1, harvesting duration X_2, and inter-rod spacing X_3 on harvesting performance, a Box–Behnken design was employed. The factor coding is summarized in Table 2.

Table 2

Factor Coding for the Portable Harvesting Device

Code	Vibration frequency X1 (Hz)	Harvesting duration X2 (s)	Inter-rod spacing X3 (mm)
1	20	5	40
0	15	3	30
-1	10	1	20

The mature fruit harvesting rate Y_1, mis-harvesting rate of immature fruits Y_2, and damage rate of mature fruits Y_3 were calculated as follows:

$$Y_1 = \frac{N_{hm}}{N_{hm} + N_{rm}} \times 100\% \quad (3)$$

$$Y_2 = \frac{N_{hi}}{N_{hi} + N_{ri}} \times 100\% \quad (4)$$

$$Y_3 = \frac{N_{dm}}{N_{hm}} \times 100\% \quad (5)$$

where N_{hm} is the number of harvested mature fruits, N_{rm} is the number of residual mature fruits, N_{hi} is the number of harvested immature fruits, N_{ri} is the number of residual immature fruits, and N_{dm} is the number of damaged mature fruits.

During each trial, the receiving device was carefully positioned precisely beneath the canopy, and the collection surface was fully deployed to ensure complete coverage of the target area and to maximize fruit capture efficiency (Fig. 10). The collection surface consists of a fixed central cloth and two motor-driven lateral arms that together envelop the trunk, forming a fully enclosed annular collection area around the base of the plant, effectively capturing all detached fruits and preventing losses. The harvester then applied controlled high-frequency excitation to fruit-bearing branches via the vibrating rods (Fig. 11), with vibration carefully tuned to avoid excessive stress. Detached fruits fell directly onto the tilted collection surface, rolled smoothly downward along the 20° slope, and gradually accumulated into the storage basket located at the lowest point. This carefully designed gravity-driven flow completely eliminates the need for manual fruit collection, minimizes handling, and effectively reduces impact damage by controlling both the distance and speed at which fruits fall before contacting the soft, cushioned collection surface.



Fig. 10 - Field Positioning of the Receiving Device



Fig. 11 - Vibration Harvesting Operation

Data Analysis

Using vibration frequency X_1, harvesting duration X_2, and inter-rod spacing X_3 as independent variables, and the harvesting rate of mature fruits Y_1, mis-harvesting rate of immature fruits Y_2, and damage rate of mature fruits Y_3 as dependent variables, trials were conducted sequentially for each treatment combination. The data are summarized in Table 3.

Table 3

Statistical Data of *Lycium barbarum L.* Vibration Harvesting Experiments

Index	X1	X2	X3	Y1/%	Y2/%	Y3/%
1	-1	-1	0	73.62	1.85	8.97
2	1	-1	0	69.34	5.2	6.5
3	-1	1	0	85.97	3.31	3.99
4	1	1	0	99.74	6.13	3.07
5	-1	0	-1	71.55	0.83	9.91
6	1	0	-1	90.16	1.77	6.6
7	-1	0	1	87.2	6.12	4.87
8	1	0	1	98.4	10.87	1.89
9	0	-1	-1	69.01	0.73	11.38
10	0	1	-1	85.88	2.6	7.12
11	0	-1	1	85.47	4.2	4.78
12	0	1	1	94.88	10.07	3.48
13	0	0	0	87.96	3.3	2.68
14	0	0	0	85.2	5.85	3.84
15	0	0	0	94.6	2.26	4.08
16	0	0	0	94.55	4.72	1.2
17	0	0	0	93.6	4.8	4.28

The experimental data were fitted using a second-order polynomial regression model, expressed as:

$$Y = \beta_0 + \sum \beta_i X_i + \sum \beta_{ii} X_i^2 + \sum \beta_{ij} X_i X_j \quad (6)$$

Where Y represents the response variable, β_0 is the intercept coefficient, β_i, β_{ii} and β_{ij} are the linear, quadratic, and interaction coefficients, respectively, and X_i and X_j are the coded independent variables.

Based on the definitions of Y_1, Y_2 and Y_3 (Eq.3 – Eq.5), a second-order polynomial regression was applied to obtain models for each evaluation indicator, as given in Eq. 7 – Eq. 9:

$$Y_1 = 91.18 + 4.91X_1 + 8.63X_2 + 6.17X_3 - 6.02X_2^2 \quad (7)$$

$$Y_2 = 4.19 + 1.48X_1 + 1.27X_2 + 3.17X_3 \quad (8)$$

$$Y_3 = 3.22 - 1.21X_1 - 1.75X_2 - 2.50X_3 + 1.64X_2^2 + 1.83X_3^2 \quad (9)$$

Analysis of variance (ANOVA) showed that the regression model for the harvesting rate of mature fruits Y_1 was significant $(P = 0.0095)$, with a non-significant lack-of-fit $(P = 0.3376)$ and $R^2 = 0.8980$. The model for the mis-harvesting rate of immature fruits Y_2 was highly significant $(P = 0.0083)$, with a non-significant lack-of-fit $(P = 0.5318)$ and $R^2 = 0.9020$. The model for the damage rate of mature fruits Y_3 was also highly significant $(P = 0.0025)$, with a non-significant lack-of-fit $(P = 0.7476)$ and $R^2 = 0.9321$. All three models showed good fit and high predictive reliability.

Parameter Optimization

The response surface analysis is shown in Fig. 12. Figs. 12(a–c) show the effects of harvesting duration, vibration frequency, and inter-rod spacing on the mature fruit harvest rate. Both duration and frequency initially increase the harvest rate, but saturation occurs beyond a certain threshold, indicating that most easily detached fruits have already been removed. Inter-rod spacing further improves overall harvest efficiency by reducing excitation blind zones, enhancing detachment from inner branches, and ensuring more uniform fruit removal across the canopy.

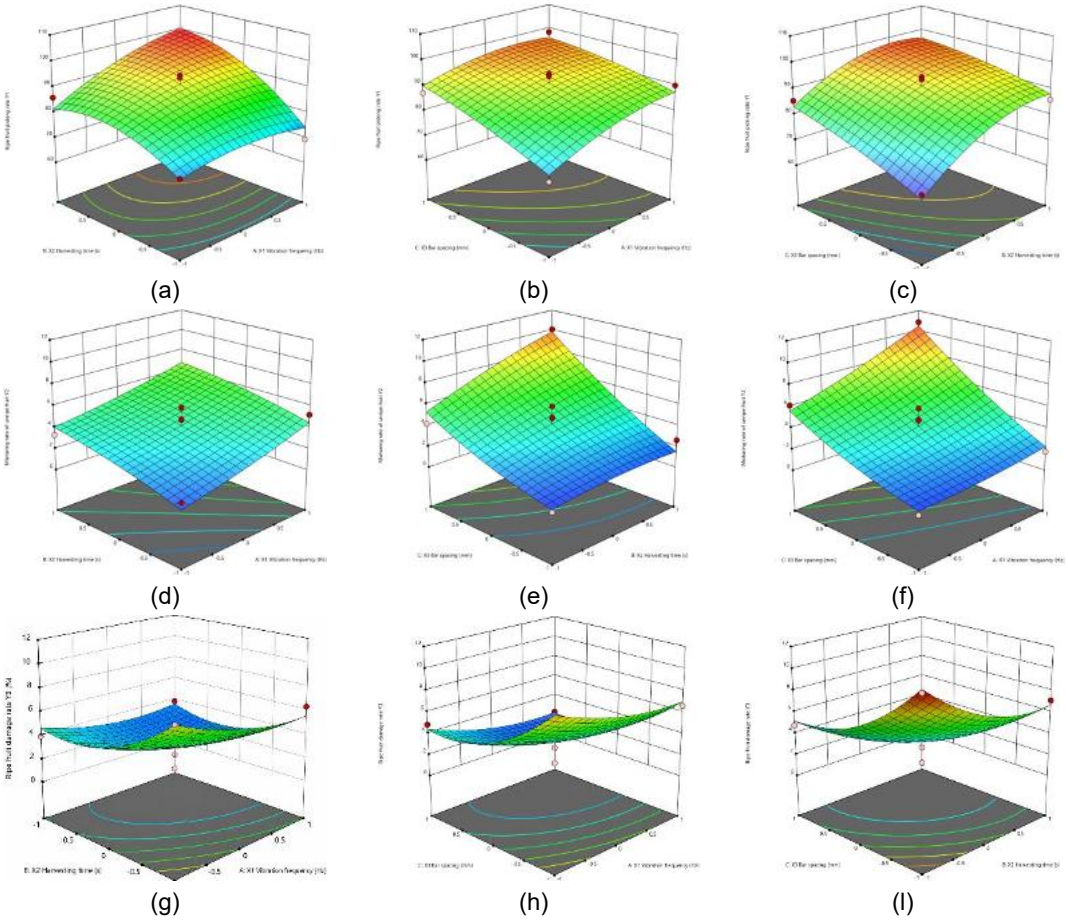


Fig. 12 - Response Surface Analysis

Figs 12(d–f) show the effects on mis-harvesting of immature fruits. Inter-rod spacing has the strongest influence, as wider spacing allows deeper penetration into the canopy, increasing unintended detachment. Vibration frequency and harvesting duration also contribute, with high-frequency, long-duration excitation potentially inducing peduncle fatigue.

Figs 12(g–i) illustrate effects on mature fruit damage, which exhibits a U-shaped trend. Narrow spacing leads to surface bruising, moderate spacing minimizes damage, and excessive spacing or duration causes secondary collisions, increasing peel rupture.

Multi-objective optimization identified the optimal combination as 18 Hz vibration frequency, 4.5 s harvesting duration, and 26 mm inter-rod spacing, predicting 96.47% harvest, 4.18% mis-harvesting, and 3.59% damage, balancing efficiency and fruit quality.

Based on the harvesting parameter optimization, the performance of the receiving device was further optimized. A central composite design (CCD) was used, with the receiving cloth tilt angle (20–40°) and radius (70–100 cm) as independent variables. The factor coding is summarized in Table 4.

Table 4

Factor Coding for the Lycium barbarum L. Receiving Device

Index	Tilt Angle of Receiving Cloth A_1 (°)	Radius of Receiving Cloth A_2 (cm)
1	40	100
0	30	85
-1	20	70

The collection efficiency of the receiving device Y_4 was used as the evaluation indicator, as expressed in Eq.10:

$$\eta = \frac{m_1}{m_2} \times 100\% \tag{10}$$

where m_1 is the number of fruits collected by the receiving device, and m_2 is the total number of detached fruits. Upon completion of the trials, the results are summarized in Table 5.

Table 5

Statistical Data of Lycium barbarum L. Receiving Experiments

Index	Tilt Angle of Receiving Cloth A1 (°)	Radius of Receiving Cloth A2 (cm)	Collection Efficiency B (%)
1	20	70	88.4
2	40	70	88.9
3	20	100	67.1
4	40	100	67.6
5	20	85	85.7
6	40	85	86.2
7	30	70	95.5
8	30	100	74.5
9	30	85	92.8
10	30	85	93.1
11	30	85	92.6
12	30	85	93.2
13	30	85	92.9

A second-order polynomial regression was applied to the experimental data to obtain the regression model for the collection efficiency of the receiving device Y4, as expressed in Eq.11:

$$\eta = 92.92 + 0.25A_1 - 10.60A_2 - 6.98A_1^2 - 7.93A_2^2 \tag{11}$$

The regression model was highly significant $(P < 0.0001)$ with a coefficient of determination $R^2 = 0.9998$, indicating an excellent fit. Response surface analysis showed that collection efficiency increased and then decreased with both tilt angle and cloth radius, revealing a single optimum within the experimental range. Optimization to maximize collection efficiency yielded a tilt angle of 29.72° and a cloth radius of 76.83 cm, corresponding to a predicted efficiency of 96.33%. For practical control, these parameters were rounded to 30° and 77 cm.

Validation experiments under these conditions produced a harvesting rate of mature fruits of 96.2%, a mis-harvesting rate of 4.3%, a damage rate of 3.7%, and a collection efficiency of 96.1%. The relative errors compared to model predictions (96.47%, 4.18%, 3.59%, and 96.33%, respectively) were all below 0.5%, confirming the reliability of the optimization and the accuracy of the model.

CONCLUSIONS

This study developed a human–machine collaborative harvesting system for double-layer trellis-cultivated goji berries, integrating a hand-held high-frequency rocker-oscillator harvester and an electric receiving cart. Mature fruits had detachment forces of 1.2–1.8 N and immature fruits 2.5–3.0 N, with the average bending elastic modulus of fruit-bearing branches being 548.9 MPa, providing a basis for selective harvesting and simulation. The harvester, equipped with a flexible silicone-coated comb head and Hall-effect speed monitoring, delivered precise excitation at 15–20 Hz. The receiving cart, with a 1.6 × 0.6 × 0.4 m chassis and side-mounted cantilever canopy, formed a ring-shaped collection area of 50–180 cm diameter with a 20° downward tilt. Response surface optimization identified operational parameters of 18 Hz vibration frequency, 4.5 s harvesting duration, 26 mm inter-rod spacing, 30° cloth tilt, and 77 cm radius. Field validation achieved a mature fruit harvesting rate of 96.2%, mis-harvesting rate of 4.3%, damage rate of 3.7%, and collection efficiency of 96.1%, with relative errors below 0.5%, demonstrating the platform's effectiveness for high-efficiency, low-damage harvesting.

ACKNOWLEDGEMENT

This study was supported by the Key R&D and Transformation Program of Qinghai Province (Project No.: 2024-NK-141S-1), titled "Research on Key Technologies for Mechanized Harvesting of Goji Berries and Their Integrated Application."

REFERENCES

[1] Castro-Garcia, S., Sola-Guirado, R., Gil-Ribes, J. (2018). Vibration analysis of the fruit detachment process in late-season 'Valencia' orange with canopy shaker technology. *Biosystems Engineering*, 170, 130-137. DOI: https://doi.org/10.1016/j.biosystemseng.2018.04.007

[2] Chen Q., Wei N., Fan Y., Wang Z., Zhou J., Gao Z., Chen Y., Chen J., (2025). Fruit-flower-leaf dynamic response of *Lycium barbarum* L. for vibration harvesting. *Smart Agricultural Technology*, 10, 100722. DOI: https://doi.org/10.1016/j.atech.2024.100722

[3] Chen Q., Zhang S., Wei N., Fan Y., Zhang W., Wang Z., Chen J., Chen Y., (2025). Simulation and Experimental Study of Goji Berry Vibration Harvesting under Different Excitation Modes (不同激振方式下枸杞振动采摘仿真与试验). *Transactions of the Chinese Society of Agricultural Engineering*, vol.41 no.03, 32-42. DOI: http://doi.org/10.11975/j.issn.1002-6819.202408110

[4] Deng B., Wang X., Wang K., Song H., Gao S., Tu Y., Zhang X., (2025). Analysis of energy transfer characteristics in multi-level branches of *Lycium barbarum* L. under vibration excitation. *Computers and Electronics in Agriculture*, 239, 110992. DOI: http://doi.org/10.1016/j.compag.2025.110992

[5] Erdoğan, D., Güner, M., Dursun, E., Gezer, İ. (2003). Mechanical harvesting of apricots. *Biosystems Engineering*, 85(1), 19-28. DOI: http://dx.doi:10.1016/S1537-5110(03)00024-2

[6] Ghonimy, M., Ibrahim, M., Helmy, H., Alzoheiry, A. (2024). Power requirements for olive mechanical harvesting using trunk shaker. *Scientific Reports*, 14(1), 25585. DOI: https://doi.org/10.1038/s41598-024-77571-8

[7] Komarnicki, P., Cieniawska, B. (2025). The Effect of Foliar Calcium Spraying on Changes in the Mechanical Properties of Blueberry (*Vaccinium corymbosum* L.). *Agriculture*, 15(4), 438. DOI: https://doi.org/10.3390/agriculture15040438

[8] Liu Y., Liu J., Zhao J., Wang F., Zhang H., Su, X., Sun Y., Liu J., Zhao, D. (2025). Effects of Different Excitation Parameters on Mechanized Harvesting Performance and Postharvest Quality of First-Crop Organic Goji Berries in Saline–Alkali Land. *Agriculture*, 15(13), 1377. DOI: https://doi.org/10.3390/agriculture15131377

[9] Lyu X., Wang H., Xu G., Chu C. (2024). Research on fruit picking test of blueberry harvesting machinery under transmission clearance. *Heliyon*, 10(15). DOI: https://doi.org/10.2139/ssrn.4620409

[10] Mei S., Wang J., Song Z., Tang D., Shen C., (2024). Mechanism and experimental study on the fruit detachment of Chinese wolfberry through reciprocating vibration. *International Journal of Agricultural and Biological Engineering*, 17(2), 47-58. DOI: https://doi.org/10.25165/j.ijabe.20241702.8482

[11] Sim A., Pearse J., McGuinness B., Williams H., Duke M. (2024). Evaluation of a low-cost selective shaking device and soft surface catchment for fresh market blueberry harvesting. In *2024 IEEE 20th International Conference on Automation Science and Engineering (CASE)* (pp. 2813-2818). IEEE. DOI: https://doi.org/10.1109/case59546.2024.10711523

[12] Su X., Liu Y., Liu J., Zhao D., (2025). Analysis and Experiment on the Vibration Response of Fruit-Bearing Goji Branches (枸杞挂果枝条振动响应分析与试验). *Scientia Silvae Sinicae*, vol.61 no.08, 25-31. DOI: https://doi.org/10.11707/j.1001−7488.LYKX20240470

[13] Takeda F., Yang W., Li C., Freivalds A., Sung K., Xu R., Hu B., Williamson J., Sargent S., (2017). Applying New Technologies to Transform Blueberry Harvesting. *Agronomy*, 7(2), 33. DOI: https://doi.org/10.3390/agronomy7020033

[14] Torregrosa, A., Albert, F., Aleixos, N., Ortiz, C., Blasco, J. (2014). Analysis of the detachment of citrus fruits by vibration using artificial vision. *Biosystems Engineering*, 119, 1-12. DOI: http://dx.doi.org/10.1016/j.biosystemseng.2013.12.010

[15] Villibor, G., Santos, F., Queiroz, D., Khoury, J., Pinto, F. (2023). Vibration Transmissibility of the Coffee Fruit-Peduncle System: a Forced Vibration Study of High Frequency Aiming Mechanical Harvesting. *Engenharia Agrícola*, 43(1), e20220201. DOI: http://dx.doi.org/10.1590/1809-4430-Eng.Agric.v43n1e20210201/2023

[16] Wang H., Chu C., Li Y., Liu G., (2025). Coupled Rigid-Flexible Simulation Analysis and Experimental Study of a Portable Blueberry Harvester (便携式蓝莓采摘机刚柔耦合仿真分析与试验). *Scientia Silvae Sinicae*, vol.61 no.10, 175-189. DOI: http://doi.org/10.11707/j.1001−7488.LYKX20240478

[17] Wang H., Huang X., Song J., Zhao J., Zhao L., Na R., Zhao X., Yan W., (2026). Design and Testing of Key Components for a Blueberry Harvester Based on the Multi-Excitation Vibration Picking Principle (基于多激励振动采摘原理的蓝莓采收机关键部件设计与试验). *Transactions of the Chinese Society for Agricultural Machinery*, 57(02), 58-69+275. DOI: http://doi.org/10.6041/j.issn.1000-1298.2026.02.006

[18] Wang H., Lv X., Xiao F., Sun L. (2022). Analysis and testing of rigid–flexible coupling collision harvesting processes in blueberry plants. *Agriculture*, 12(11), 1900. DOI: https://doi.org/10.3390/agriculture12111900

[19] Yu P., Li C., Takeda F., Krewer G., Rains G., Hamrita T. (2014). Measurement of mechanical impacts created by rotary, slapper, and sway blueberry mechanical harvesters. *Computers and Electronics in Agriculture*, 101, 84-92. DOI: http://doi.org/10.1016/j.compag.2013.12.001

[20] Yu Z., Wu J., Jiang F., Xing H., Yan L., Yang J. (2024). Kinematic Analysis of the Vibration Harvesting Process of *Lycium barbarum* L. Fruit. *Agriculture*, 14(10), 1715. DOI: https://doi.org/10.3390/agriculture14101715

[21] Zhang W., Li Z., Tan Y., Li W., (2018). Optimized Design and Experimentation of a Variable-Pitch Comb-Brush Type Goji Berry Harvesting Device (变间距梳刷式枸杞采收装置优化设计与试验). *Transactions of the Chinese Society for Agricultural Machinery*, 49(08), 83-90. DOI: https://doi.org/10.6041/j.issn.1000-1298.2018.08.010

[22] Zhao, J., Tsuchikawa, S., Ma, T., Hu, G., Chen, Y., Wang, Z., Chen Q., Gao Z., Chen, J. (2021). Modal analysis and experiment of a *Lycium barbarum* L. Shrub for efficient vibration harvesting of fruit. *Agriculture*, 11(6), 519. DOI: https://doi.org/10.3390/agriculture11060519

STUDY ON NON-PARAMETRIC EXTRAPOLATION METHOD OF TRACTOR PTO LOAD BASED ON DBSCAN

/

基于 DBSCAN 对拖拉机 PTO 的载荷非参数外推方法研究

Yin TANG[1)], Shuaijie MA[1)], Fuxi SHI[1*)], Huipeng QIU[2)], Xiao ZHANG[2)], Jianmin GAO[2)]

[1)] College of Mechanical and Electronic Engineering, Northwest A&F University, Yangling 712100 / China

[2)] Automotive Transmission Engineering Research Institute, FAST Auto Drive Group Co., Ltd, Xi'an 710119 / China

Tel: +8613541853577; E-mail: 1135209658@qq.com

DOI: https://doi.org/10.35633/inmateh-79-04

Keywords: *Tractor, Load spectrum, Non-parametric extrapolation, DBSCAN clustering, Kernel density estimation*

ABSTRACT

The power take-off (PTO) shaft of a tractor is subjected to complex and variable random loads during field operations, and the accuracy of the resulting load spectrum directly affects the reliability of fatigue life prediction. To address the limitations of traditional parametric extrapolation methods, particularly their inadequate fitting performance, a non-parametric extrapolation method based on DBSCAN clustering is proposed. Field test validation demonstrates that the proposed method effectively captures the multi-modal distribution characteristics of the load. The extrapolated results show good agreement with the measured data in terms of cycle count distribution and pseudo-damage indicators. Compared with the fixed-bandwidth method, the proposed approach increases the coefficient of determination by 3.401% and reduces the mean squared error (MSE) by 39.154%, while yielding pseudo-damage values closer to 1. These findings provide a novel technical approach for the construction of load spectra under complex operating conditions of agricultural machinery.

摘要

拖拉机动力输出轴在田间作业过程中承受复杂多变的随机载荷，其载荷谱编制的准确性直接影响疲劳寿命预测的可信度。针对传统参数化外推方法难以精确拟合的问题，提出一种基于 DBSCAN 聚类的非参数外推方法。田间实测数据验证表明，该方法能有效刻画载荷的多模态分布特征，外推结果在循环计数分布与伪损伤等指标上与实测数据具有良好的一致性。结果表明本文提出的方法决定系数相比于固定带宽提高了 3.401%，均方误差降低了 39.154%，伪损伤值更接近 1。研究结果为农业装备复杂工况下载荷谱编制提供了新的技术途径。

INTRODUCTION

In the development of modern agriculture, tractors are widely used and play a crucial role in agricultural mechanization and efficiency improvement *(Yu et al., 2023; Yang et al., 2018)*. The tractor power take-off (PTO) shaft is an important component of the tractor transmission system and a key part affecting the durability and reliability of the entire tractor. The tractor load spectrum can reflect the load history experienced by the whole tractor or its key components, serving as the foundation for tractor fatigue analysis and reliability assessment *(Liu et al., 2011)*. Load extrapolation is a critical step in load spectrum compilation, and its effectiveness directly affects the accuracy of the compiled load spectrum. Therefore, researching load extrapolation methods suitable for the tractor PTO shaft is of great significance for improving the credibility of tractor durability and reliability tests, as well as enhancing the operational performance of the tractor *(Wang et al., 2022)*.

In recent years, the combination of clustering algorithms and kernel density estimation has provided new ideas for load extrapolation (*Chen et al., 2017*). Kernel density estimation is a statistical method that directly infers the population probability density surface based on the sample data itself without any prior theoretical distribution assumptions. Research has shown that grouping load data using the Density-Based Spatial Clustering of Applications with Noise (DBSCAN) algorithm allows for the calculation of optimal bandwidths for different clusters of data, thereby effectively addressing the limitations of a global fixed-bandwidth. The DBSCAN algorithm can identify clusters of arbitrary shapes and automatically exclude noise points, which aligns naturally with the multi-operating condition and multi-modal distribution characteristics commonly found in load data *(He et al., 2018; Wang et al., 2016)*.

Based on the above analysis, this paper proposes a non-parametric extrapolation method for tractor PTO loads based on DBSCAN clustering *(Li et al., 2025)*. First, the PTO torque time history under typical operating conditions is collected through field tests. Second, the rain-flow counting method is used to extract the mean and amplitude of load cycles, and the DBSCAN algorithm is applied to perform cluster analysis on the mean-amplitude data. The rain-flow counting method is a counting method for calculating the amplitude and mean of load cycles, which conforms to the inherent characteristics of fatigue loads and is widely used in the statistical analysis of load time history. Then, based on the clustering results, bandwidth-optimized kernel density estimation is performed for the data of each cluster to establish a load probability distribution model. Finally, extrapolation is carried out through Monte Carlo simulation to obtain a PTO load spectrum covering the full life cycle. The research results can provide more accurate load input for tractor PTO fatigue strength design and bench durability tests, while also offering a methodological reference for load spectrum compilation under complex operating conditions in the field of agricultural equipment.

MATERIALS AND METHODS

Testing System Setup

The tractor wireless torque measurement system is mainly composed of a torque sensor, a data acquisition module, a wireless transmission module, and host computer software. The wireless torque sensor, model TQ201, primarily consists of a strain measurement circuit, a data processing unit, a wireless communication unit, and a power supply unit. The strain gauges and the sensor are fixed on the output shaft, forming the basic sensor. When the output shaft rotates, the resistance of the strain bridge changes, causing the voltage at the measurement terminal to change. The voltage signal is transmitted to the data processing unit, where it passes through the node's built-in high-precision resistive bridge circuit and amplification conditioning circuit. Subsequently, the signal is transmitted to the wireless receiving module via the wireless communication unit. Throughout the entire process, the power supply unit provides power to all components.

A schematic diagram of the ultimately constructed wireless torque testing system is shown in Figure 1 below.



Fig. 1 – Schematic diagram of wireless torque testing system

Field Test Load Collection

From May 20 to 25, 2025, a field test of tractor power take-off (PTO) shaft torque was conducted in the suburbs of Yangling District, Xianyang City, Shaanxi Province. The test prototype was a YCX504D tractor, and the operating condition was rotary tillage using a 1GQN-180Z rotary tiller. Based on the tractor wireless torque testing system, the PTO shaft torque load is displayed and recorded in real time.

Load Signal Preprocessing

During the real-vehicle testing of tractor PTO torque, the original load signal is often contaminated with singular points that do not represent true loads due to the harsh field environment, electrical system interference, and occasional instability of the sensor. These abnormal data can severely distort the statistical characteristics of the load distribution, thereby affecting the accuracy of fatigue damage calculations. Therefore, this study adopts a strategy combining the amplitude threshold method and the gradient threshold method to eliminate and smooth the original load signal.

The amplitude threshold method is primarily used to identify and eliminate outliers that significantly exceed the extreme values of the physical system or violate statistical laws. For load signals with stationary or pseudo-stationary random characteristics, such as tractor PTO torque, this study employs the classic criterion as the basis for determination.

$$\mu = \frac{1}{N}\sum_{i=1}^{N} x_i \quad (1)$$

$$\sigma = \sqrt{\frac{1}{N-1}\sum_{i=1}^{N}(x_i - \mu)^2} \quad (2)$$

According to statistical principles, if the data obey or approximately obey a normal distribution, the probability of abnormal points is extremely small. The discrimination criterion of the amplitude threshold method is as follows.

$$|x_i - \mu| > K\sigma \quad (3)$$

Among them, x_i is the load amplitude at the sampling point, μ is the mean of the load signal sequence, σ is the standard deviation of the load signal sequence, and K is the threshold coefficient, typically taken as 3.

When the signal point satisfies the above condition, it is determined as a gross error. To maintain the continuity of the time series, the point is usually not directly removed; instead, it is replaced by linear interpolation using adjacent valid data points, i.e.

$$x_i^* = \frac{x_{i-1}+x_{i+1}}{2} \quad (4)$$

Although the amplitude threshold method can effectively eliminate global extreme outliers, it cannot identify local abrupt signals where the amplitude does not exceed the limit but unreasonable mutations occur between adjacent sampling points. When a tractor encounters gravel or experiences sudden implement jamming, certain impacts may occur; however, limited by the inertia of the mechanical system, the instantaneous rate of change of the load has a physical upper bound. Therefore, the gradient threshold method is introduced to eliminate high-frequency abnormal sudden-change signals.

The gradient threshold method determines anomalies by calculating the difference between two adjacent sampling points (i.e., the local gradient) and comparing it with a set critical threshold. Its discrimination criterion can be expressed as:

$$|\Delta x_i| = |x_i - x_{i-1}| > \varepsilon \quad (5)$$

To avoid misidentifying actual transient impact loads as outliers, it is usually necessary to perform bidirectional gradient verification in conjunction with adjacent points. That is, a data point is determined as an outlier only when the gradients between it and both the previous and subsequent points are greater than the set threshold and are in opposite directions.

The improved discrimination criterion is as follows:

$$\begin{gathered} |x_i - x_{i-1}| > \varepsilon \\ |x_i - x_{i+1}| > \varepsilon \\ (x_i - x_{i-1})(x_i - x_{i+1}) > 0 \end{gathered} \quad (6)$$

In the formula, x_i is the current load signal point to be detected; x_{i-1} is the previous valid load signal point; x_{i+1} is the next load signal point; and ε is the gradient threshold. This threshold is typically determined based on the physical characteristics (maximum stiffness and response frequency) of the tractor's power transmission system or suspension system.

When a data point is identified as a gradient anomaly, polynomial interpolation is similarly employed for smoothing correction to restore the true physical profile of the signal, ensuring the accuracy of cycle amplitude extraction during subsequent rain-flow counting.

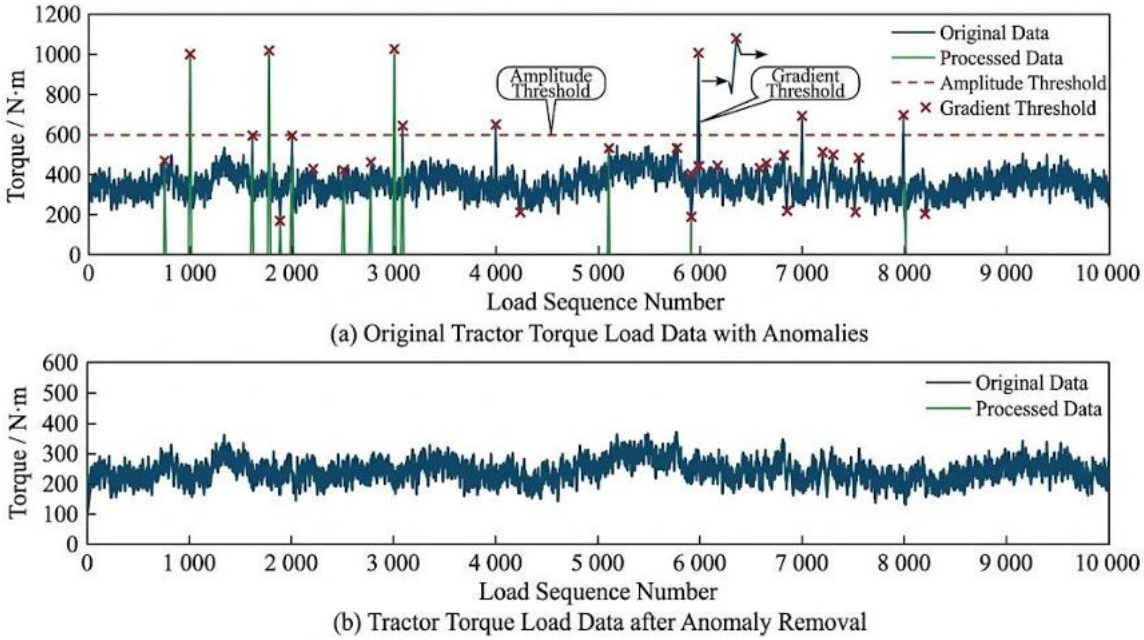


Fig. 2 – Comparison chart for removing singular points

After removing singular points from the load signal, the signal often still contains random high-frequency interference caused by tractor engine vibration, high-frequency excitation from the transmission system, and the inherent thermal noise of the sensor. To ensure that the subsequent rain-flow counting method can accurately extract the true load amplitudes that affect fatigue life, further smoothing and noise reduction of the signal are required.

For load spectrum compilation, traditional moving average filtering tends to flatten the peaks and valleys of the signal, thereby underestimating the true fatigue damage. Therefore, this paper adopts the S-G polynomial smoothing filter method for signal noise reduction. The core advantage of the S-G filter lies in its ability to filter out high-frequency noise while preserving the local extreme characteristics and waveform width of the original load signal to the greatest extent.

The S-G filter is essentially a sliding window filtering method based on local polynomial least squares fitting. Let the width of the smoothing sliding window be 2m+1; the set of data points within the window is denoted as $\{(ti,xi)|i=-m, \ldots, 0, \ldots, m\}$, where the center point corresponds to i=0. Within each sliding window, a k-order polynomial is used to fit the data points in the window.

The fitting polynomial can be expressed as:

$$p(j) = \sum_{r=0}^{k} a_r \, j^r \tag{7}$$

In order to solve for the coefficients of the polynomial, the principle of the least squares method is applied to minimize the sum of squared residuals between the fitted values and the actual observed values within the window.

$$E = \sum_{j=-m}^{m} \left(\sum_{r=0}^{k} a_r \, j^r - x_{i+j} \right)^2 \tag{8}$$

In order to minimize the error function, the partial derivatives with respect to each coefficient are taken and set to zero, allowing the coefficient matrix to be solved. In practical applications, through complex matrix operations and derivations, the smoothed fitting value at the center point is actually equivalent to the linearly weighted combination of the data points within the window. Therefore, the final smoothed output of the S-G filter can be expressed in the form of a convolution sum.

$$x_i^* = \sum_{j=-m}^{m} C_j \, x_{i+j} \tag{9}$$

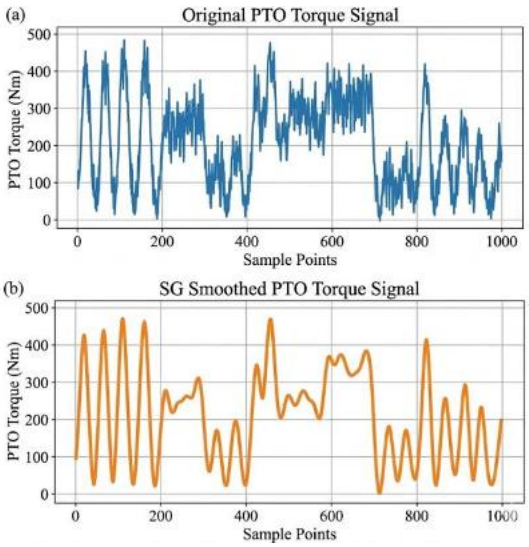


Fig. 3 – Comparison chart before and after noise reduction treatment

RESULTS

Load Counting Statistical Processing

After preprocessing, the data can be further screened and streamlined to improve analysis efficiency. The rain-flow counting method is a widely used statistical counting technique for measured load time histories, which extracts information on the amplitude and mean of load cycles, aligning with the inherent characteristics of fatigue loads. For the preprocessed load signal, the four-point rain-flow counting method is employed to perform statistical counting processing on the measured load, resulting in a mean-amplitude matrix of load cycles.

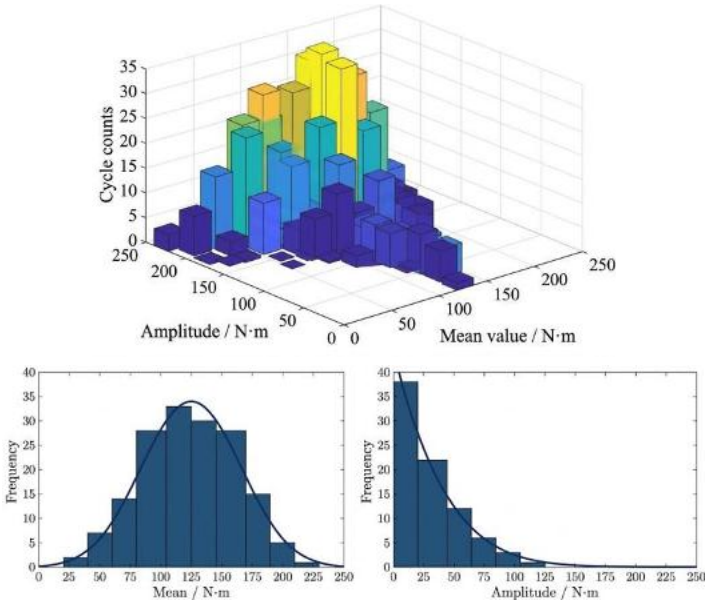


Fig. 4 – Schematic diagram of rainflow matrix

Kernel Density Extrapolation Based on DBSCAN Clustering

After completing the preprocessing of the tractor PTO load signal, the rain-flow counting method is used to extract load cycles from the torque time history, transforming the random load into a series of complete mean-amplitude cycles to form a sample set.

$$X = \{(m_i, a_i) \mid i = 1,2, \ldots, N\} \quad (10)$$

Among them, m_i is the mean value of the cycle, and a_i is the amplitude. This two-dimensional feature space serves as the foundation for subsequent clustering and probabilistic modeling. Due to the complex operating conditions of tractors, PTO loads often exhibit multi-modal distribution characteristics. Therefore, the DBSCAN density clustering algorithm is introduced to partition the sample set. DBSCAN identifies clusters of arbitrary shapes based on density reach-ability and automatically eliminates noise points.

The ε of a sample point x_i is defined as:

$$N_\varepsilon(x_i) = \{x_j \in X \mid d(x_i, x_j) \leq \varepsilon\} \quad (11)$$

The Euclidean distance is usually used as the distance metric d(·). If the number of sample points within the neighborhood satisfies

$$|N_\varepsilon(x_i)| \geq MinPts \quad (12)$$

Then x_i is a core point. Clusters are continuously expanded through direct density-reachability and density-reachability relationships, ultimately partitioning the samples into K clusters C_1, C_2, …, C_K and several noise points. The selection of the parameters ε and $MinPts$ is crucial: the k-distance graph method is used to determine ε (taking k=$MinPts$), that is, the distance from each sample to its nearest neighbor is calculated and sorted in descending order, and the distance corresponding to the inflection point of the curve is taken as ε; $MinPts$ is empirically tuned between 4 and 10. The clustering algorithm is shown in the figure.

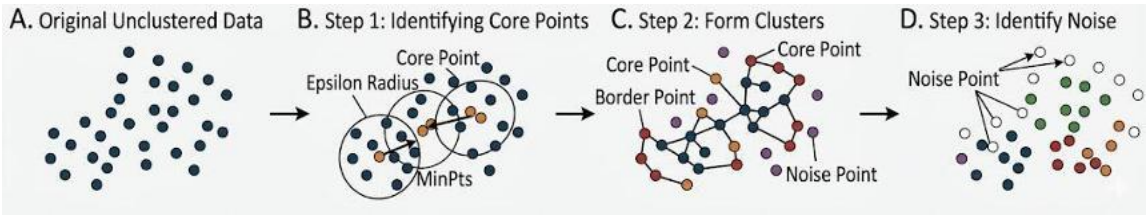


Fig. 5 – DBSCAN algorithm schematic diagram

After clustering is completed, a two-dimensional probability density function is established for each cluster C_j (with sample sizen_j), and kernel density estimation is used to describe its distribution. For the cluster, the probability density estimate is given by:

$$\hat{f}_j(m, a) = \frac{1}{n_j}\sum_{i=1}^{n_j} K_{H_j}(m - m_{ji}, a - a_{ji}) \quad (13)$$

where $K_{H_j}(\cdot)$ is the two-dimensional Gaussian kernel function.

$$K_{H_j}(u) = \frac{1}{2\pi|H_j|^{1/2}} exp\left(-\frac{1}{2}u^T H_j^{-1} u\right) \quad (14)$$

H_j is the bandwidth matrix. The selection of bandwidth directly affects the estimation accuracy, and the traditional global fixed-bandwidth struggles to accommodate the differences in data distribution across clusters. Therefore, the optimal bandwidth is calculated separately based on the characteristics of each cluster. The Rule-of-Thumb method is used to determine the bandwidth matrix. For two-dimensional data, n rule can be adopted:

$$.H_j = n_j^{-1/6}\hat{\Sigma}_j^{1/2} \quad (15)$$

where $\hat{\Sigma}_j$ is the sample covariance matrix of the cluster, estimated by the following formula:

$$\hat{\Sigma}_j = \frac{1}{n_j - 1}\sum_{i=1}^{n_j}\begin{bmatrix} (m_{ji} - \bar{m}_j)^2 & (m_{ji} - \bar{m}_j)(a_{ji} - \bar{a}_j) \\ (m_{ji} - \bar{m}_j)(a_{ji} - \bar{a}_j) & (a_{ji} - \bar{a}_j)^2 \end{bmatrix} \quad (16)$$

In the formula, $\bar{m}_j$ and $\bar{a}_j$ are the sample means of the mean and amplitude for that cluster, respectively. This adaptive bandwidth method preserves details in data-dense regions while providing smooth estimation in sparse regions, thereby improving the goodness of fit. After obtaining the probability density functions for each cluster, Monte Carlo simulation is used for load extrapolation. First, the sampling weights for each cluster are calculated:

$$w_j = \frac{n_j}{\sum_{j=1}^{K} n_j} \quad (17)$$

Noise points are not involved in modeling. The extrapolation factor is determined based on the operating time T_0 corresponding to the measured data and the design life T_{target}:

$$\lambda = \frac{T_{target}}{T_0} \quad (18)$$

The total number of extrapolated cycles is approximately:

$$N_{target} = \lambda N \quad (19)$$

The sampling process is as follows: a cluster is randomly selected according to the weight w_jj, and then a sample point is drawn from the kernel density mixture distribution of that cluster.

Specifically, a sample (m_{ji},a_{ji}) within the cluster is first randomly selected as the kernel center, and then a new sample $(m_{\text{new}i},a_{\text{new}i})$ is drawn from a two-dimensional Gaussian distribution with the center as the mean and a covariance matrix of H_{j2}. This process is repeated until N_{target} samples are obtained. To ensure the physical rationality of the extrapolated loads, boundary constraints are applied to the sampling results. Samples that exceed the boundaries are discarded and resampled. Finally, the extrapolated load cycle set is obtained:

$$X_{ext} = \{(m_k, a_k) \mid k = 1,2, \ldots, N_{target}\} \quad (20)$$

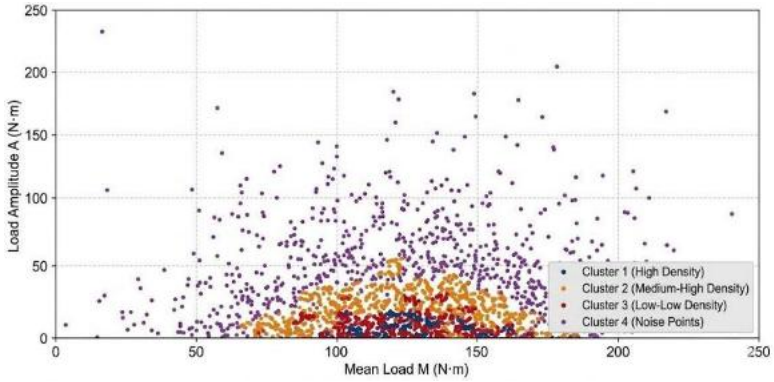


Fig. 6 – DBSCAN clustering effect diagram

Figure 6 shows the identification of load distribution based on DBSCAN clustering. Combined with adaptive bandwidth kernel density estimation and Monte Carlo sampling, it enables high-precision non-parametric extrapolation of complex tractor PTO loads.

Extrapolated Load Verification

To verify the effectiveness and accuracy of the proposed method, a comparison is made with the traditional load extrapolation based on fixed-bandwidth kernel density estimation. The evaluation is conducted in terms of two aspects, namely goodness of fit and pseudo-damage.

The fixed-bandwidth method and the DBSCAN clustering method proposed in this paper were both used to extrapolate to five times the original load. The coefficient of determination and mean square error were introduced as two parameters to compare the extrapolation effects, and the results are shown in Table1. The results indicate that, compared with the fixed-bandwidth method, the coefficient of determination of the proposed method increased by 3.401%, while the mean square error decreased by 39.154%. It can be concluded that the clustering-based load extrapolation with clustered data significantly improves the extrapolation performance, verifying the feasibility and effectiveness of the proposed method.

Table 1

Comparison of Extrapolation Effects

Extrapolation model	Coefficient of determination	Mean square error
Fixed-bandwidth	0.941	8.745
DBSCAN clustering	0.973	5.321

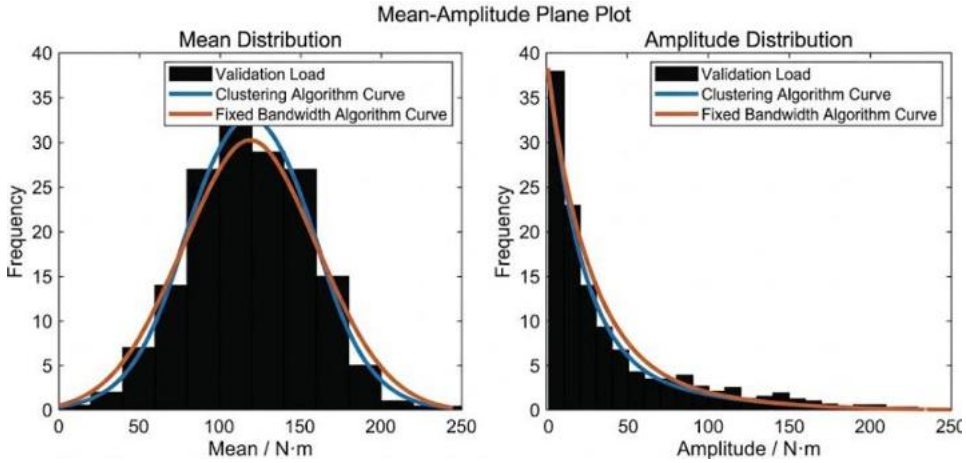


Fig. 7 – Mean amplitude probability fitting curve

To verify the accuracy of the extrapolated load spectrum generated by the DBSCAN based non-parametric estimation method, this paper introduces the pseudo-damage theory for equivalence testing. Pseudo-damage is an engineering indicator used to evaluate the severity of a load spectrum from the perspective of fatigue damage, comprehensively reflecting the influence of load amplitude distribution and cycle count on the fatigue life of components. The calculation of pseudo-damage is based on Miner's linear cumulative damage criterion and the S-N curve.

$$D_p = \sum_{i=1}^{k} n_i S_{ai}^m \quad (21)$$

In the formula, D_p represents the total pseudo-damage of the load spectrum; k is the total number of load levels after rain flow counting and two-dimensional grid division of the load spectrum; S_{ai}^m is the torque amplitude of the load level; $n_i$is the cycle count corresponding to the load level; and m is taken as 6.

The pseudo-damage ratio R_d is defined as the ratio of the pseudo-damage of the extrapolated load spectrum to the pseudo-damage of the proportionally scaled original load spectrum.

$$R_d = \frac{D_{p,ext}}{D_{p,ori} \times E_f} \quad (22)$$

In the formula, R_d is the pseudo-damage ratio, $D_{p,ext}$ is the pseudo-damage value of the full-life load spectrum generated by two-dimensional non-parametric extrapolation, $D_{p,ori}$ is the pseudo-damage value of the original measured load, and E_f is the extrapolation factor.

Table 2

Pseudo-damage ratio at different multiples

Different multiples	Fixed-bandwidth	The proposed method
10	1.098	1.032
20	1.112	1.038
30	1.103	1.041
40	1.113	1.043
50	1.121	1.045

Based on the comparison data of pseudo-damage ratios under different extrapolation factors, the adaptive bandwidth method based on DBSCAN clustering proposed in this paper demonstrates significantly superior performance compared to the traditional fixed-bandwidth method at all extrapolation factors. The pseudo-damage ratio of the fixed-bandwidth method fluctuates between 1.098 and 1.121, showing a clear upward trend as the extrapolation factor increases. In contrast, the pseudo-damage ratio of the proposed method remains stable between 1.032 and 1.045, not only closer to the ideal value of 1, but also exhibiting an increase of only 1.260% as the extrapolation factor rises, demonstrating excellent accuracy retention and factor insensitivity.

From a quantitative perspective, the method proposed in this paper reduces the deviation of the pseudo-damage ratio by an average of approximately 6.512% compared to the fixed-bandwidth method. The fundamental reason for this difference lies in the fact that the fixed-bandwidth kernel density estimation adopts a globally uniform smoothing parameter, which makes it difficult to simultaneously achieve fitting accuracy in both dense and sparse regions when dealing with the multi-modal distribution characteristics of tractor PTO loads, leading to distortion of the distribution tail features that is amplified with increasing extrapolation factors. In contrast, the DBSCAN clustering method effectively identifies natural clusters corresponding to different operating conditions through density-based clustering, and computes adaptive bandwidths based on the sample covariance of each cluster, thereby more accurately preserving the original load distribution morphology and fatigue damage characteristics.

The results indicate that the proposed method can more accurately replicate the fatigue damage potential of loads under different extrapolation requirements, exhibiting higher accuracy and robustness, and is suitable for load spectrum compilation throughout the full life cycle of tractor PTO.

ACKNOWLEDGMENTS

This study was funded by the key project "Collection and Compilation of High Power Tractor Operating Load Spectrum"(number: HTSP-20251217004) of Shaanxi FAST Auto Drive Group Co., Ltd.

CONCLUSIONS

（1）The clustering effectiveness of the DBSCAN algorithm is highly dependent on the selection of the neighborhood radius ε and the minimum number of samples MinPts. The current approach based on the k-distance graph combined with empirical tuning has a certain degree of subjectivity.

Future research can explore automatic parameter optimization methods based on clustering validity indices or introduce adaptive DBSCAN variants to achieve full adaptability in the clustering process, further enhancing the robustness and generality of the method. In non-parametric rain-flow extrapolation based on kernel density estimation, the kernel bandwidth is the most critical factor affecting the extrapolation performance. More accurate and effective selection algorithms can be introduced for the choice of kernel bandwidth.

（2）This study only considered the load characteristics in the two dimensions of mean and amplitude, whereas actual fatigue damage is also influenced by factors such as load sequence and frequency components. Subsequent research could attempt to incorporate additional features such as load duration and rise/fall rates into the analysis dimension to construct a higher-dimensional probability model. At the same time, methods for reconstructing time series with realistic temporal characteristics from extrapolated cycle distributions can be explored to meet the requirements of bench tests that demand full time-domain signals.

（3）The method proposed in this paper was validated based on PTO load data from a specific tractor model. Future work should extend the validation to load data from more tractor models and a wider range of operation types (such as plowing, rotary tillage, transportation, etc.) to verify the scalability of the method. More importantly, indoor bench durability tests using the extrapolated load spectrum should be conducted. By comparing the actual fatigue life of components with the life predicted by the extrapolated spectrum, a quantitative evaluation system for method accuracy can be established, providing a more solid foundation for engineering applications.

REFERENCES

[1] Anonymous (2018). Developing an accelerated flight load spectrum based on the n(z)-N curves of a fleet. *Journal of Technology & Science*, pp. 986, United States.

[2] Bučar, T., Nagode, M., Fajdiga, M. (2003). Reliability approximation using finite Weibull mixture distributions. *Reliability Engineering and System Safety*, Vol. 84, pp. 241-251, Netherlands.

[3] Chen, C., Yang, Z., He, J., (2017). Load spectrum generation of machining center based on rainflow counting method. *Journal of Vibroengineering*, Vol. 19, pp. 5767-5779, Lithuania.

[4] Chen, D., Xiang, C., Chen, X. (2002). Load spectrum establishment for power train parts of military vehicle. *Journal of Mechanical Strength*, Vol. (02), pp. 310-314, China.

[5] He, J., Wang, S., Li, G., (2018). Compilation of NC lathe dynamic cutting force spectrum based on two-dimensional mixture models. *The International Journal of Advanced Manufacturing Technology*, Vol. 98, pp. 251-262, United Kingdom.

[6] Jin, X., Zhang, S. (2019). Nonparametric fitting extrapolation based on measured load of high-speed axle. *Journal of Beijing Jiaotong University*, Vol. 43, pp. 97-103+130, China.

[7] Liu, Y., Zhang, X., Wang, Z., (2011). Comparison of load spectrum extrapolation methods. *Modern Manufacturing Engineering*, Vol. (11), pp. 8-11, China.

[8] Liu, Y., Chang, L., Sun, L. (2012). Research on load spectrum compilation method for wheel loader driveline. *China Mechanical Engineering*, Vol. 23, pp. 1412-1416, China.

[9] Li, Y., Zhao, P., Gu, Z., Cheng, L., Li, S. (2025). Transformer-Based Load Spectrum Compilation for Rolling Bearings. *Journal of Engineering*, Vol. 2025, pp. 5876690-5876690, United Kingdom.

[10] Li, S., Zhai, Y., Wang, X., (2021). Load extrapolation method for tractor drive shaft based on kernel density estimation. *Journal of China Agricultural University*, Vol. 26, pp. 175-184, China.

[11] Li, Y. (2016). Research on nonparametric extrapolation method in load spectrum compilation of wheel loader [D]. Jilin University, China.

[12] Liu, H., Zhang, W., Xu, Y., (2017). Load spectrum compilation of tracked vehicle drive shaft based on kernel density estimation. *Acta Armamentarii*, Vol. 38, pp. 1830-1838, China.

[13] Nagode, M., Klemenc, J., Fajdiga, M. (2001). Parametric modelling and scatter prediction of rainflow matrices. *International Journal of Fatigue*, Vol. 23, pp. 525-532, Netherlands.

[14] Tian, W., Song, X., Wan, Y. (2019). Overview of common load spectrum extrapolation algorithms. *Southern Agricultural Machinery*, Vol. 50, pp. 103+108, China.

[15] Wang, L., Zong, J., Wang, Y., (2022). Compilation of Tractor Three-Point Hitch Traction Load Spectrum and Bench Test Based on Optimal Distribution Fitting. *Transactions of the Chinese Society of Agricultural Engineering*, Vol. 38, pp. 41-49, China.
[16] Wang, J., Chen, X., (2016). A Review of the Extrapolation Method in Load Spectrum Compiling. *Journal of Mechanical Engineering*, Vol. 62, pp. 60-75, China.
[17] Wang, J., Zhang, X., Liu, C., (2017). Determination of the Threshold for Extreme Load Extrapolation Based on Multi-Criteria Decision-Making Technology. *Strojniški vestnik - Journal of Mechanical Engineering*, Vol. 63, pp. 201-211, Slovenia.
[18] Wang, J., Zhang, Z., Luo, L., (2021). SwinGD: A robust grape bunch detection model based on Swin transformer in complex vineyard environments. *Horticulturae*, Vol. 7, pp. 492, Switzerland.
[19] Yang, Z., Song, Z., Luo, Z., (2022). Time domain extrapolation method for key component loads of tractor based on EMD-POT model. *Journal of Mechanical Engineering*, Vol. 58, pp. 252-262, China.
[20] Yu, L., An, Y., He, J., (2023). Research progress and development trend of load spectrum extrapolation technology for electromechanical equipment. *Journal of Jilin University (Engineering and Technology Edition)*, Vol. 53, pp. 941-953, China.
[21] Zhang, T., Wu, F., Wang, M., (2023). Grape-bunch identification and picking point location on occluded fruit axes based on YOLOv5-GAP. *Horticulturae*, Vol. 9, pp. 498, Switzerland.

GRIPPING FORCE ESTIMATION FOR AN ROV ROBOTIC ARM IN INTENSIVE AQUACULTURE
/
ESTIMAREA FORȚEI DE PRINDERE PENTRU UN BRAȚ ROBOTIC ROV ÎN ACVACULTURĂ INTENSIVĂ

Dan CUJBESCU[1)], Iulian VOICEA[*1)], Cătălin PERSU[1)], Iuliana GĂGEANU[1)], Carmen Bălțatu[1)], Viorel FĂTU[2)], Vlad ARSENOAIA[3)]

[1)] National Institute of Research – Development for Machines and Installations Designed to Agriculture and Food Industry, Romania

[2)] Research Development Institute for Plant Protection (ICDPP)

[3)] Faculty of Agriculture, Ion Ionescu de la Brad University of Agricultural Sciences and Veterinary Medicine, 700490 Iasi / Romania

Tel: 0752161780; E-mail: voicea_iulian@yahoo.com

DOI: https://doi.org/10.35633/inmateh-79-05

Keywords: *Remotely Operated Vehicle, ROV manipulator, gripping force estimation, underwater robotics, force reconstruction, aquaculture systems, robotic manipulation*

ABSTRACT

This paper presents a theoretical framework for estimating the gripping force of a three-degree-of-freedom robotic arm mounted on a remotely operated underwater vehicle, intended for sampling operations in intensive aquaculture systems. Using the static relationship based on the Jacobian transpose, the proposed method reconstructs the force and moment vectors acting at the end-effector from the estimated joint torques. The gripping force is determined by projecting the Cartesian force onto the normal directions of a two-finger gripper. Transmission efficiency and joint friction are incorporated into the model through the definition of an effective torque. The influence of hydrodynamic forces is treated as an external disturbance during quasi-static manipulation. The internal consistency of the model is evaluated through a numerical validation based on representative design parameters for compact underwater manipulators. The analysis indicates that a gripping force of approximately 150–200 N satisfies the friction-based stability condition for typical sampling loads of approximately 100 N. Furthermore, the resulting joint torques remain within the realistic operating limits of actuators commonly used in ROV-mounted manipulators. The findings confirm the dimensional consistency and physical plausibility of the proposed estimation framework, which may be applied to assisted underwater force estimation in aquaculture applications.

REZUMAT

Lucrarea dezvoltă un cadru teoretic pentru estimarea forței de prindere a unui braț robotic cu trei grade de libertate montat pe un vehicul subacvatic acționat de la distanță, care va fi utilizat în operațiunile de eșantionare într-un sistem intensiv de acvacultură. Folosind relația statică bazată pe transpunerea iacobiană, metoda reconstruiește vectorul forțelor și vectorul momentelor care apar la efectorul final de la cuplurile estimate în articulații. Forța de prindere este determinată prin proiectarea unei forțe carteziene pe direcțiile normale ale unui dispozitiv de prindere cu două degete. Eficiența transmisiei și frecarea articulară sunt încorporate în model printr-un cuplu efectiv. Efectul forțelor hidrodinamice este tratat ca forțe perturbatoare în timpul manipulării cvasi-statice. Consistența internă a modelului este evaluată prin intermediul unei validări numerice bazate pe parametri de proiectare reprezentativi pentru manipulatoare subacvatice compacte. Conform analizei, o forță de prindere de aproximativ 150–200 N îndeplinește condiția de stabilitate bazată pe frecare pentru sarcini tipice de eșantionare de aproximativ 100 N. Cuplurile articulare rezultate se încadrează în limitele realiste ale actuatoarelor utilizate în mod obișnuit în manipulatoarele montate pe ROV. Rezultatele analizei numerice confirmă coeziunea dimensională și plauzibilitatea fizică a cadrului de estimare sugerat, care poate fi utilizat în determinarea forței de manipulare subacvatică asistată în acvacultură.

INTRODUCTION

Recent developments in precision aquaculture have created a growing need to identify reliable solutions for underwater inspection and intervention, driven by the rapid expansion of intensive aquaculture (*Akram et al., 2022; Akram et al., 2025*).

Recent experimental studies have demonstrated the increasing use of remotely operated underwater vehicles for the inspection and monitoring of aquaculture nets, since these systems can operate efficiently in confined underwater environments and can integrate vision and control systems suitable for fish farm monitoring (*Cai et al., 2025*). In addition, the continuous evolution of autonomous and semi-autonomous strategies for the inspection of large fish cages has been observed. This trend has encouraged the integration of robust robotic manipulators on underwater platforms. The practical deployment of underwater robotic arms confirms the usefulness of these systems for maintenance, inspection, and intervention operations (*Vasileiou et al., 2025*).

For performing sampling operations, a robotic arm mounted on an ROV must be able to generate sufficient gripping force to prevent the manipulated object from slipping and, at the same time, limit contact loads to avoid damage to fragile or deformable samples. In current practice, direct force measurement at the end effector is frequently influenced by various factors such as operating costs, sealing requirements, space available for sensor integration, as well as long-term operational reliability. Thus, especially when the manipulation is performed slowly and the process is dominated by contact mechanics rather than fast dynamic effects, force estimation based on actuator signals and mathematical model relationships becomes a practical solution (*Bicchi, 1995; Yoshikawa, 1985*). The feasibility of coordinated vehicle–manipulator operation in complex environments has been validated through multibody models and control architectures in realistic underwater scenarios (*Di Vito et al., 2021*). Motion planning and coordinated control strategies have been proposed and implemented to deal with inertial effects and coupling between vehicle and manipulator (*Han et al., 2020*). Also, experiments have been performed to increase the robustness of the system to external disturbances through hybrid controllers and methods based on disturbance observers (*Li et al., 2019*). Studies on unmanned systems for aquaculture monitoring emphasized the growing integration of underwater robotic platforms, sensor technologies, and intelligent monitoring approaches for improving operational efficiency and environmental supervision in fish farming systems (*Ganie et al., 2025; Ubina and Cheng, 2022*). Recent experiments highlight adaptive approaches and model-free methods for interacting with unknown environments, highlighting the importance of robust force and motion control in underwater manipulation (*Yang et al., 2024*).

Since the robot must simultaneously manage model uncertainties, hydrodynamic perturbations, and contacts with deformable elements, its control plays a critical role in its underwater manipulation. Experimental research has been conducted to address this challenge, which has developed complex interaction control schemes for underwater vehicle–manipulator systems that ensure stable behavior during contact operations (*Heshmati-Alamdari et al., 2018*). Recent data-driven control studies for autonomous underwater vehicles have also demonstrated the potential of robust Koopman operator-based approaches for improving system stability and dynamic response under uncertain underwater operating conditions (*Liu et al., 2026; Rahmani and Redkar, 2024*). Studies have also been conducted that highlight the rapid development of underwater robots and the essential technologies required for their operational control, including dynamic modeling, sensor systems, and environmental interaction strategies, which have highlighted that interaction forces are essential for achieving safe and efficient underwater operations (*Sun et al., 2024*).

Classical robot modeling provides the mathematical foundation for relating joint variables to forces acting on the end effector, with standard kinematic and static relationships using the Jacobian matrix to transform joint torques into Cartesian vectors of forces and moments, which allows for force estimation when joint torques can be directly measured or inferred from motor currents (*Craig, 2005; Siciliano et al., 2009*). Experimental research has shown that underwater vehicle–manipulator systems introduce additional effects that influence the balance between torques and forces, including buoyancy, hydrodynamic drag, added mass, and coupling between vehicle motion and manipulator action (*Antonelli, 2014; Fossen, 2011*). Studies dedicated to underwater manipulators also show that real underwater systems are limited by joint friction, structural compliance, and sensor constraints, factors that directly affect interaction control and force reconstruction (*Sivčev et al., 2018*). Experiments on force and interaction control methods for underwater vehicle–manipulator systems have also been carried out, highlighting the need for high robustness against model uncertainties and deformable contacts, important aspects for gripping and sampling operations in aquaculture applications (*Heshmati-Alamdari et al., 2018*).

The novelty of this work consists in the development of an integrated theoretical framework that combines actuator signal interpretation, Jacobian-based static force reconstruction, transmission loss compensation, and gripper contact modeling for gripping force estimation in ROV-mounted underwater

manipulators dedicated to aquaculture sampling operations. The proposed approach provides a physically consistent and modular methodology suitable for underwater environments where direct force sensing is difficult due to sealing, space, and reliability constraints.

MATERIALS AND METHODS

1. System Overview and Assumptions

In order to carry out the experimental research, a system was analyzed that includes: a remotely operated underwater vehicle (ROV that ensures positioning and coarse movements) equipped with a serial robotic manipulator and a parallel gripper with two fingers, intended for sampling operations in intensive aquaculture environments that performs fine positioning and gripping operations. The present paper focuses on the manipulator-gripper subsystem and treats the vehicle as a rigid base, whose movement is slow in relation to the handling load, and for the theoretical development the following hypotheses are adopted:

1. The handling load is quasi-static, and inertial effects are negligible in relation to the contact forces.
2. The gripper applies symmetric normal forces on the object.
3. The torques in the joints can be estimated based on the actuator signals.
4. Hydrodynamic effects are treated as external perturbations and are not included in the main static model.
5. The manipulated object is rigid or weakly deformable, and the contact occurs at well-defined points.

These assumptions are consistent with standard approaches used in robotic manipulation and in the analysis of underwater vehicle–manipulator systems (*Craig, 2005; Siciliano et al., 2009; Antonelli, 2014*).

2. Kinematic Model of the Manipulator

The manipulator is modeled as a serial kinematic chain with n revolute or prismatic joints. The joint coordinate vector is defined as:

$$q = [q_1, q_2, \dots, q_n]^T \tag{1}$$

where:

q – the joint coordinate vector of the manipulator, [rad] or [m];

$q_1, q_2, \dots q_n$– the individual joint coordinates, and each term represents either a rotation angle for a revolute joint [rad] or a linear displacement for a prismatic joint, [m];

n – the total number of degrees of freedom of the manipulator, equal to the number of independently actuated joints, [-];

$[\,]^T$ – the transpose operator, which indicates that q is written as a column vector of size n x 1.

The kinematic structure of the ROV-mounted manipulator is illustrated in Fig. 1. The scheme defines the joint coordinates q_1, q_2, q_3, the end-effector frame, and the wrench F applied at the gripper, together with the joint torques τ_1, τ_2, τ_3. This representation provides the geometric basis for the derivation of the Jacobian matrix and for the static force mapping used.

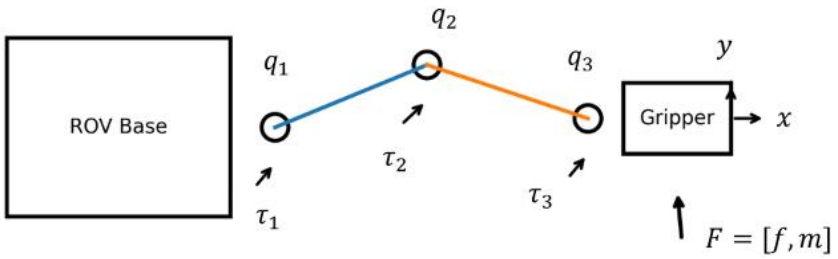


Fig. 1 – Kinematic scheme of the ROV-mounted manipulator and definition of joint variables and end-effector wrench

The pose of the end-effector is described by the vector:

$$x = [p^T, \varphi^T]^T \tag{2}$$

where:

p– the position, [m];

φ– the orientation, [rad].

The forward kinematics is expressed as:

$$x = f(q) \tag{3}$$

The differential kinematics is obtained by differentiation with respect to time:

$$\dot{x} = J(q)\dot{q} \tag{4}$$

where:

$J(q)$ – the manipulator Jacobian matrix.

The Jacobian relates joint velocities to end-effector linear and angular velocities and is computed using standard methods based on the chosen kinematic representation (*Craig, 2005; Siciliano et al., 2009*).

3. Static Force Relationship

Under quasi-static conditions, the relationship between joint torques τ and the wrench applied at the end-effector F is given by the principle of virtual work:

$$\tau = J^T(q)F \tag{5}$$

Here, F is defined as:

$$F = [f^T,\ m^T]^T \tag{6}$$

where:

f– force vector [N],

m – moment vector at the end-effector [N·m].

If the Jacobian transpose is full rank, or if a suitable pseudoinverse is used, the end-effector wrench can be estimated as:

$$F = (J^T(q))^{\dagger}\tau \tag{7}$$

where:

† represents the Moore–Penrose pseudoinverse operator.

From a dimensional point of view, the proposed formulation is coherent, with the electric current being expressed in amperes, the joint torques expressed in newton-meters, and the Cartesian forces expressed in newtons, and the Jacobian matrix and its transpose provide a physically meaningful correspondence between the joint space and the Cartesian space. This dimensional consistency allowed the estimated grip force to be directly correlated with the grip stability conditions, determined by friction and external loads. This relationship forms the basis for force estimation based on information on joint torques, a standard approach used in force control and interaction modeling in robotics (*Siciliano et al., 2009*).

4. Joint Torque Estimation from Actuator Signals

For electrically actuated joints, the motor torque τ_m is proportional to the motor current I

$$\tau_m = k_t I \tag{8}$$

where:

τ_m– the torque generated by the electric motor at its shaft, [N·m];

k_t– motor torque constant. It expresses the proportionality between the motor current and the produced torque, [N·m/A];

I– motor current supplied to the actuator, [A].

The joint torque τ is obtained by considering the transmission ratio r and the mechanical efficiency η:

$$\tau = \eta r \tau_m \tag{9}$$

where:

τ– the torque available at the robot joint after the transmission, [N·m];

η– mechanical efficiency of the transmission, it accounts for losses due to friction and other dissipative effects, [-];

r– transmission ratio (gear ratio), it relates the motor shaft torque to the joint torque, [-].

This relation shows how the motor torque is transformed into joint torque through the transmission mechanism, taking into account the gear ratio and the mechanical losses (*Craig, 2005; Siciliano et al., 2009*).

Friction and other parasitic effects can be represented by an additional torque term τ_f, leading to:

$$\tau_{eff} = \tau - \tau_f \tag{10}$$

where:

τ_{eff}– the torque actually available for producing motion or for balancing external forces at the joint, after subtracting losses, [N·m];

τ_f– the torque loss due to joint friction, seals, and other dissipative effects in the transmission, [N·m].

In this theoretical framework, τ_f is treated as an uncertainty term or as a parameter that can be compensated using standard friction models.

5. Gripper Contact Model and Gripping Force Definition

The gripper is modeled as a two-finger parallel mechanism applying normal forces F_n on opposite sides of the object. The total gripping force F_g is defined as:

$$F_g = 2F_n \tag{11}$$

where:

F_g– total gripping force applied by the gripper on the object, [N];

F_n– normal contact force applied by one gripper finger on the object surface, it is the force perpendicular to the contact surface at one finger, [N].

For static equilibrium, the gripping force must be sufficient to resist the external load W acting on the object. Assuming Coulomb friction with coefficient μ, the no-slip condition can be written as:

$$F_n \geq \frac{W}{2\mu} \tag{12}$$

where:

W– external load acting on the object (in practice, it represents the effective weight of the object, corrected by buoyancy in underwater conditions), [N];

μ– coefficient of friction between the gripper finger and the object surface, [-].

This relation is derived from basic grasp mechanics and is widely used for preliminary grasp force estimation (*Cutkosky, 1989; Salisbury and Mason, 1985*). In underwater conditions, the effective load W is corrected by buoyancy, but the same equilibrium principle applies (*Fossen, 2011*).

6. Extraction of Gripping Force from End-Effector Wrench

The estimated end-effector force vector $f$contains the interaction forces between the gripper and the object. The gripping force is obtained by projecting this force onto the normal directions of the gripper fingers. Let n_1 and n_2 be the unit normal vectors at the two contact points. The normal contact forces are:

$$F_{n1} = fn_1, \quad F_{n2} = fn_2 \tag{13}$$

where:

f– the resultant interaction force between the gripper and the object, expressed in Cartesian coordinates (the end-effector force vector acting at the gripper), [N].

Under symmetric grasp conditions:

$$F_{n1} \approx F_{n2} \approx F_n \tag{14}$$

and the gripping force is estimated as:

$$F_g = F_{n1} + F_{n2} \tag{15}$$

This procedure links the joint-level measurements to a physically meaningful gripping force value at the gripper-object interface.

7. Treatment of Underwater Effects

Hydrodynamic forces such as drag and added mass introduce additional torques at the joints and additional forces at the end-effector. For slow manipulation tasks, these effects are assumed to be small compared to contact forces and are treated as disturbances, following common practice in underwater manipulation modeling (*Antonelli, 2014; Fossen, 2011*).

The estimated force can therefore be expressed as:

$$F_{est} = F_{contact} + F_{dist} \tag{16}$$

where:

F_{est}– the force vector obtained from the model-based estimation process, which includes both the contact interaction force and additional disturbance effects, [N];

$F_{contact}$– the actual contact interaction force at the gripper–object interface, [N];

F_{dist}– disturbance force vector (it groups the contributions of unmodeled or parasitic effects, such as hydrodynamic drag, added mass effects, structural compliance, and measurement noise), [N].

This relation states that the force obtained from estimation is the sum of the actual contact force and additional disturbance-related force components.

RESULTS

This section presents the theoretical and numerical validation of the proposed gripping force estimation framework for a three-degree-of-freedom (3-DoF) serial manipulator mounted on an ROV, as illustrated in Fig. 1. The analysis focuses on the internal consistency of the mathematical formulation and on verifying whether the predicted force and torque levels are realistic for underwater sampling operations performed with compact robotic manipulators.

1. Logical workflow of the force estimation method

The estimation procedure follows the sequence illustrated in Fig. 2.

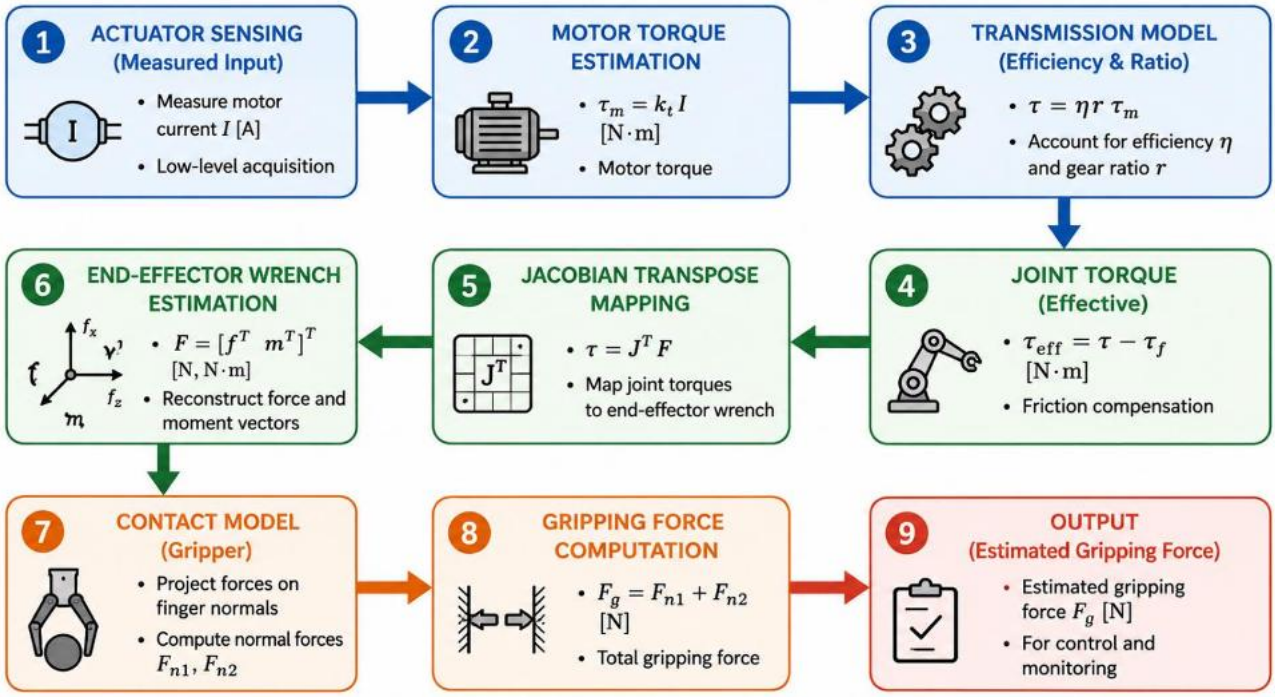


Fig. 2 – Logical block diagram for gripping force estimation

The process begins with actuator measurements, where the electric motor current is used to estimate motor torque. The transmission model converts the motor torque into joint torque, while mechanical losses are accounted for through an effective torque term.

2. Validation of gripping force requirements

To evaluate the physical plausibility of the model, representative design values typical for compact underwater manipulators were considered. Parallel grippers used for sampling tasks usually provide a nominal clamping capability in the range of 150–200 N. A representative external load associated with pulling or detaching a biological sample from a structure was assumed as:

$$W = 100 \text{ N} \tag{17}$$

From equations (12), (14), (15):

$$F_g \geq \frac{W}{\mu} \tag{18}$$

The minimum gripping force becomes:

$$F_{g,min} = \frac{100}{\mu} \tag{19}$$

The required gripping force therefore depends directly on the contact friction conditions:

- For $\mu = 0.5$

$$F_{g,min} = 200 \text{ N} \tag{20}$$

which corresponds to the upper bound of the considered gripper capability.

- For $\mu = 0.6$

$$F_{g,min} \approx 167 \text{ N} \tag{21}$$

which lies within the nominal operating range of compact parallel grippers.

- For a mid-range gripping force of approximately $F_{min} = 147$ N, the friction coefficient required to prevent slip becomes:

$$\mu_{min} = \frac{W}{F_g} = \frac{100}{147} \approx 0.68 \tag{22}$$

This result shows that grasp stability strongly depends on the contact interface. High-friction pads or textured surfaces significantly improve the safety margin of the grasp.

3. Joint torque validation for a 3-DoF manipulator

To validate the model, the external force was propagated through the kinematic chain of a 3-DoF planar manipulator corresponding to the structure shown in Fig. 1. The relationship between the Cartesian force and the joint torques is given by Eq. (5).

For a planar 3R manipulator, the end-effector position can be written as:

$$x = l_1 \cos q_1 + l_2 \cos(q_1 + q_2) + l_3 \cos(q_1 + q_2 + q_3) \tag{23}$$

$$y = l_1 \sin q_1 + l_2 \sin(q_1 + q_2) + l_3 \sin(q_1 + q_2 + q_3) \tag{24}$$

Hence, the Jacobian matrix associated with the planar force components is:

$$J(q) = \begin{bmatrix} -l_1 \sin q_1 - l_2 \sin(q_1 + q_2) - l_3 \sin(q_1 + q_2 + q_3) & -l_2 \sin(q_1 + q_2) - l_3 \sin(q_1 + q_2 + q_3) & -l_3 \sin(q_1 + q_2 + q_3) \\ l_1 \cos q_1 + l_2 \cos(q_1 + q_2) + l_3 \cos(q_1 + q_2 + q_3) & l_2 \cos(q_1 + q_2) + l_3 \cos(q_1 + q_2 + q_3) & l_3 \cos(q_1 + q_2 + q_3) \end{bmatrix} \tag{25}$$

For the considered case, the external force is purely vertical,

$$f = [0, -100]^T \quad \text{N} \tag{26}$$

Therefore:

$$\tau = J^T(q) f \tag{27}$$

reduces to: $\tau_i = J_{y,i} F_y$ (28)

where $J_{y,i}$ represents the element on row y, column i of the Jacobian matrix. Using l_1 = 0.20 m, l_2 = 0.18 m, l_3 = 0.156 m and $q_1 = 30°$, $q_2 = -45°$, $q_3 = 20°$, the following values are obtained:

$$J_{y,1} = 0.5025 \text{ m}; \; J_{y,2} = 0.3293 \text{ m}; \; J_{y,3} = 0.1554 \text{ m} \tag{29}$$

which yield the following joint torques

$$\tau_1 = -50.25 \text{ N} \cdot \text{m}; \; \tau_2 = -32.93 \text{ N} \cdot \text{m}; \; \tau_3 = -15.54 \text{ N} \cdot \text{m} \tag{30}$$

It is observed that the obtained torque values decrease from the base joint to the distal joint, which is consistent with the mechanical advantage of the serial manipulator. It is also found that the first joint supports the cumulative moment generated by all downstream segments, while the distal joint is mainly influenced by the local lever arm of the end effector, this evolution confirming the physical plausibility of the static relationship based on Jacobian used in the proposed model.

The value obtained for the third joint is practically identical to the direct moment balance around the wrist:

$$M = W \cdot l = 100 \cdot 0.156 = 15.6 \text{ N} \cdot \text{m} \tag{31}$$

This correspondence indicates that the Jacobian transpose mapping correctly captures the relationship between the external force applied at the gripper and the torques generated in the manipulator joints for the configuration illustrated in Fig. 1.

4. Interpretation of the validation results

The estimated gripping force lies inside the typical capability band of small parallel grippers, while the corresponding joint torques remain compatible with actuator sizes commonly employed in ROV-mounted robotic arms. In particular, the torque levels derived from the Jacobian-based mapping are consistent with those obtained from a direct mechanical moment balance, reinforcing the physical credibility of the model. The method can serve as a practical tool for monitoring and regulating gripping forces during underwater manipulation tasks, especially in situations where integrating dedicated force sensors at the end-effector is impractical due to sealing constraints, limited space, or cost considerations.

CONCLUSIONS

The paper presented a theoretical framework for estimating the gripping force of an ROV-mounted robotic arm intended for sampling operations in intensive aquaculture systems. The proposed approach combines actuator signal interpretation, transmission modeling, Jacobian-based force reconstruction, and gripper contact analysis to estimate the interaction force at the gripper-object interface.

The numerical validation demonstrated that the estimated gripping forces and joint torques remain within realistic operating ranges for compact underwater manipulators. The obtained torque distribution was consistent with the mechanical behavior of serial robotic structures, confirming the physical plausibility of the proposed model.

The modular structure of the method allows independent improvement of actuator, friction, hydrodynamic, and contact models, making the framework suitable for future extensions and experimental implementation in underwater manipulation applications.

Future research will focus on experimental validation under real operating conditions and on the integration of dynamic and hydrodynamic effects into the estimation process.

ACKNOWLEDGEMENT

This research was supported by the Romanian Ministry of Research Innovation and Digitalization, through the project “Underwater Intelligent System (Robot) for the Protection of Life, Health and Growth Environment” – PN 23 04 01 03 – Ctr. 9N/01.01.2023 and by the Ministry of Agriculture and Rural Development – Romania - MADR through the Sectoral Project ADER 25.2.2 “Vertical Aquaponic Farm Adapted To Current Climate Changes”, Ctr. 18.07.2023.

REFERENCES

[1] Akram, W., Casavola, A., Kapetanović, N., Mišković, N.A., 2022. A visual servoing scheme for autonomous aquaculture net pens inspection using ROV. *Sensors*, 22(9), 3525. https://doi.org/10.3390/s22093525

[2] Akram, W., Din, M.U., Heshmat, M., Casavola, A., Seneviratne, L., Hussain, I., 2025. Active vision-based real-time aquaculture net pens inspection using ROV. *Scientific Reports*, 15, 32690. https://doi.org/10.1038/s41598-025-21083-6

[3] Antonelli, G., 2014. *Underwater Robots. Motion and Force Control of Vehicle-Manipulator Systems*. Springer, London. https://doi.org/10.1007/978-3-319-02877-4
[4] Bicchi, A., 1995. On the closure properties of robotic grasping. *The International Journal of Robotics Research*, 14(4), pp. 319–334. https://doi.org/10.1177/027836499501400402
[5] Cai, K., Li, C., Sun, Q., Liu, Y., Ye, H., Xu, Y., 2025. Autonomous inspection strategies and simulation for large aquaculture net cages based on deep visual perception. *Journal of Marine Science and Engineering*, 13(9), 1736. https://doi.org/10.3390/jmse13091736
[6] Craig, J.J., 2005. *Introduction to Robotics: Mechanics and Control*. 3rd ed., Pearson Prentice Hall, Upper Saddle River, NJ.
[7] Cutkosky, M.R., 1989. On grasp choice, grasp models, and the design of hands for manufacturing tasks. *IEEE Transactions on Robotics and Automation*, 5(3), pp. 269–279. https://doi.org/10.1109/70.34763
[8] Di Vito, D., De Palma, D., Simetti, E., Indiveri, G., Antonelli, G., 2021. Experimental validation of the modeling and control of a multibody underwater vehicle manipulator system for sea mining exploration. *Journal of Field Robotics*, 38, pp. 171–191. https://doi.org/10.1002/rob.21982
[9] Fossen, T.I., 2011. *Handbook of Marine Craft Hydrodynamics and Motion Control*. Wiley, Chichester. https://doi.org/10.1002/9781119994138
[10] Ganie, P.A., Khatei, A., Posti, R., Bhat, F.A., Dar, S.A., Yaseen, T., Rather, M.A., 2025. Unmanned aerial vehicles in fisheries and aquaculture: a comprehensive overview. *Environmental Monitoring and Assessment, 197*, 503. https://doi.org/10.1007/s10661-025-13920-y
[11] Han, H., Wei, Y., Ye, X., Liu, W., 2020. Motion planning and coordinated control of underwater vehicle-manipulator systems with inertial delay control and fuzzy compensator. *Applied Sciences*, 10(11), 3944. https://doi.org/10.3390/app10113944
[12] Heshmati-Alamdari, S., Bechlioulis, C.P., Karras, G.C., Nikou, A., Dimarogonas, D.V., Kyriakopoulos, K.J., 2018. A robust interaction control approach for underwater vehicle manipulator systems. *Annual Reviews in Control*, 46, pp. 315–325. https://doi.org/10.1016/j.arcontrol.2018.10.003
[13] Li, J., Huang, H., Wan, L., Zhou, Z., Xu, Y., 2019. Hybrid strategy-based coordinate controller for an underwater vehicle manipulator system using nonlinear disturbance observer. *Robotica*, 37(10), pp. 1710–1731. https://doi.org/10.1017/S0263574719000213
[14] Liu, Y., Cheng, T., Zheng, H., Wang, C., Dai, Y., Zhang, S., Fan, W., Wu, Z., Fang, H. 2026. Preliminary Exploration of an Informatized Management Model for Deep-Sea Aquaculture: From Land-Based Farming to Offshore Marine Ranches. *Fishes, 11*(3), 134. https://doi.org/10.3390/fishes11030134
[15] Rahmani, M., Redkar, S. 2024. Enhanced Koopman operator-based robust data-driven control for 3 degree of freedom autonomous underwater vehicles: *A novel approach. Ocean Engineering, 307*, 118227. https://doi.org/10.1016/j.oceaneng.2024.118227
[16] Salisbury, J.K., Mason, M.T., 1985. *Robot Hands and the Mechanics of Manipulation*. MIT Press, Cambridge, MA.
[17] Siciliano, B., Sciavicco, L., Villani, L., Oriolo, G., 2009. *Robotics: Modelling, Planning and Control*. Springer, London. https://doi.org/10.1007/978-1-84628-642-1
[18] Sun, L., Wang, Y., Hui, X., Ma, X., Bai, X., Tan, M., 2024. Underwater robots and key technologies for operation control. *Cyborg and Bionic Systems*, 5, 0089. https://doi.org/10.34133/cbsystems.0089
[19] Ubina, N. A., Cheng, S.-C., 2022. A Review of Unmanned System Technologies with Its Application to Aquaculture Farm Monitoring and Management. *Drones*, *6*(1), 12. https://doi.org/10.3390/drones6010012
[20] Vasileiou, M., Vlontzos, G., 2025. A hybrid remotely operated underwater vehicle for maintenance operations in aquaculture: practical insights from Greek fish farms. *Computers and Electronics in Agriculture*, 233, 110045. https://doi.org/10.1016/j.compag.2025.110045
[21] Yang, X., Chen, C., Yan, J., Hua, C., Guan, X., 2024. Model-free control of underwater vehicle-manipulator system interacting with unknown environments. *Ocean Engineering*, 298, 116924. https://doi.org/10.1016/j.oceaneng.2024.116924
[22] Yoshikawa, T., 1985. Manipulability of robotic mechanisms. *The International Journal of Robotics Research*, 4(2), pp. 3–9. https://doi.org/10.1177/027836498500400201

DESIGN AND EXPERIMENTAL RESEARCH OF SELF-PROPELLED TOBACCO STEM HARVESTER

/

自走式烟杆收获机设计与试验研究

Liquan YANG[1,2)], Guangyu YIN[1,2)], Rui FENG[1)], Junya HUANG[1)], Xiaodong LIU[1)], Jianbo WANG[1)], Dongwei YAN[1)], Qingqing L[1, *)], Guangxi LI[1, *)]

[1)] Henan Province Engineering Research Centre of Ultrasonic Technology Application, Pingdingshan University, Pingdingshan, Henan 467000, China

[2)] Pingdingshan Company, Henan Tobacco Company, Pingdingshan, Henan 467000, China

** Corresponding author: Qingqing Lü, Guangxi LI*

Tel: +8618339975718; E-mail: 2696@pdsu.edu.cn, 2677@pdsu.edu.cn

DOI: https://doi.org/10.35633/inmateh-79-06

Keywords: *Self-Propelled, Tobacco Stem Harvester, SolidWorks, ANSYS Simulation, Field Experiment*

ABSTRACT

To promote the mechanization of the tobacco industry, a self-propelled tobacco stem harvester was designed in this study. To improve harvesting efficiency under varying terrain and planting conditions, the machine integrates key functional components, including a chain-clamp conveyor and a loosening shovel with optimized structural parameters. The performance of these core components was analysed using 3D modelling and finite element simulations conducted in ANSYS. Field experiment optimization indicated that the optimal operating parameters were a clamping chain speed of 0.7 m/s, a forward travel speed of 0.4 m/s, and a clamping chain gap of 12 mm. Experimental results showed that the harvester achieved a leakage rate of 3% and a breakage rate of 7%. Overall, the machine demonstrated reliable performance and satisfied practical operational requirements. This study provides an effective technical solution for the mechanization of tobacco stem harvesting, contributing to reduced production costs and the advancement of agricultural modernization.

摘要

为推进烟草产业机械化发展，解决烟杆后处理机械化清理的难题，设计了一种自走式烟杆收获机，针对不同地形及种植条件，旨在提升烟杆收获效率。采用 SolidWorks 三维建模、Ansys 有限元仿真和 Adams 运动分析软件，设计并优化了松土铲、链夹式夹持输送链、粉碎刀辊等核心零部件。为验证烟杆收获机的作业性能，以烟杆漏拔率和拔断率为试验目标，设计了单因素试验和正交试验进行了田间测试，综合分析结果表明夹持链运动速度 0.7m/s、机器前进速度 0.4 m/s、夹持链间隙 12 mm 时综合作业效果最佳，收获漏拔率 3%、拔断率 7%，烟杆粉碎后颗粒长度主要集中在 40-50mm，作业性能优良，满足使用需求。本研究为烟杆收获机械化提供了可行的技术方案，对降低生产成本、促进农业现代化具有重要意义。

INTRODUCTION

Tobacco is one of the world's most important cash crops *(Zeng et al., 2024; Mo, 2023; Wu, 2007)*, particularly in Asia, Africa, and South America, where many countries' economies rely heavily on the tobacco industry *(Zhang, 2016)*. As the world's largest producer and consumer of tobacco, China plays a significant role in generating farmers' income and local economic development through tobacco cultivation. Tobacco stems and roots are the residues left after tobacco leaf harvesting *(Yang et al., 2015)*. Due to their high lignin and cellulose content, they provide an ideal overwintering site for harmful microorganisms, such as bacteria and viruses, serving as hosts for various pathogens *(Li et al., 1999)*. They cannot be used as fertilizers for on-site application *(Zhang, 2007)*; therefore, they must be promptly removed from tobacco fields. Tobacco roots are large in volume and tightly bound to the rhizosphere soil, making them difficult to remove completely *(Li et al.,2010)*. After tobacco leaf harvesting each year, many tobacco stems and roots are discarded in fields, ditches, or riverbanks, forming agricultural waste that pollutes the soil and severely impacts the development and growth of the next crop season *(Zhang, 2007; Li, 2009; Reynaldo et al., 2000; Jin et al.,1999)*. Manual collection of tobacco stems and roots faces issues such as high labour intensity and low collection efficiency. Existing tobacco stem removal machinery primarily uses counter-rotating blades to remove stems and roots, which can cause root system fractures and severe residue problems. Therefore, an efficient tobacco field root removal mechanism is urgently required to address these issues *(Tu, 2006)*.

Some developed countries, such as the United States, France, and Japan, have been at the forefront of research into tobacco stem cleaning machinery, with advanced technology and rapid development *(Guo et al., 2023)*. These machines are characterized by multi-functionality, high power, and high levels of integration. However, their large size and working width render them unsuitable for the small-scale cultivation practices of Chinese tobacco farmers. Domestic machinery in China is mostly single-function, primarily designed for stem removal, with few machines capable of integrating functions such as stem removal, transportation, crushing, and collection.

Therefore, this study designed a self-propelled tobacco stem harvester capable of simultaneously completing tobacco stem pulling, root removal, transportation, and crushing operations, effectively addressing the issues of single functionality and low mechanization levels in existing tobacco stem cleaning equipment. Kinematic and dynamic analyses, finite element simulations, and field trials were conducted on the mechanism.

MATERIALS AND METHODS

1. Overall structural design of the self-propelled tobacco stem harvester

The self-propelled tobacco stem harvester completes the tasks of deep loosening of tobacco roots, pulling up tobacco stems, conveying, crushing, and collecting in a single operation. The main transmission system of the machine primarily uses a chain drive and gear meshing transmission. Power is provided by two 74-horsepower engines, one for machine movement and the other for the pulling stem operation. Based on the overall structural and functional requirements, the lifting arm assembly was designed at a 45° angle to the horizontal ground, with the initial clamping position set at 60° to enhance contact between the tobacco stems and conveyor chain and reduce the risk of missed lifting. Twelve bearing mounting sleeves were symmetrical welded to the outer side of the conveyor chain, providing stable pulling power through the gear transmission system. The integrated soil-loosening blade structure at the front significantly reduced the pulling force required to lift the tobacco stems. Additionally, the inner side of the clamping chain is equipped with a spring-loaded clamping mechanism that dynamically adjusts the gap between the two chains through elastic deformation, ensuring reliable clamping of the tobacco stems during lifting and effectively preventing slippage. The overall structural design is illustrated in Fig. 1.

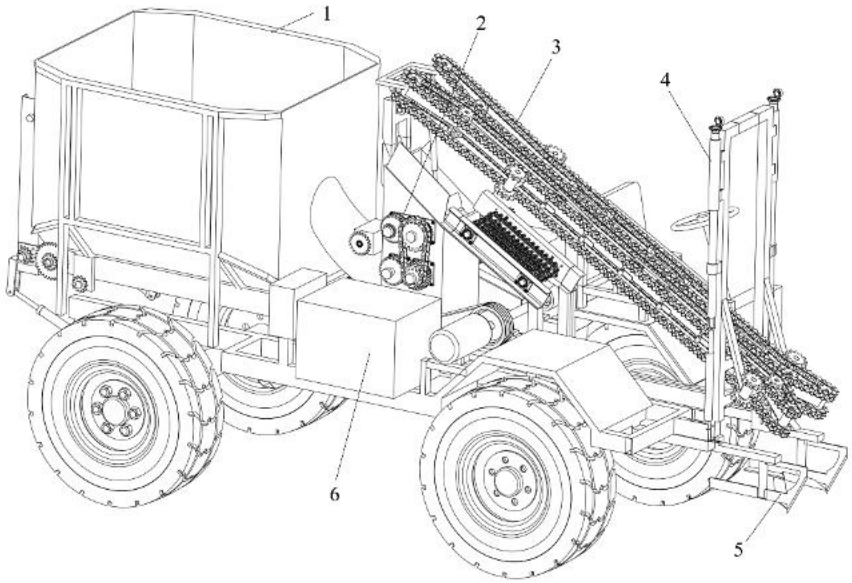


Fig. 1 – Structural diagram of a self-propelled tobacco pole harvester

1. Material-receiving hopper 2. Crusher 3. Clamping chain 4. Lifting hydraulic cylinder 5. Soil loosening blade 6. Engine

1.1. Overall design of clamping conveyor chain

The clamping stem mechanism *(Gao et al., 2025)* rotates counterclockwise under the drive of the drive wheel, conveying the clamped tobacco stems to the crusher for crushing them. Although the clamping-type conveying method uses elastic components to secure tobacco stems, they may slip or shift during conveying, leading to blockages. Considering that tobacco stems ultimately need to be shredded and returned to the field, there is no need to maintain their original shape. After a comprehensive comparison and analysis, this study selected a chain-clamping stem device as the core conveying structure to ensure the stability of tobacco stem conveyance and operational continuity.

To ensure that the clamping chain maintains a stable clamping force and efficient transmission performance during tobacco stem conveying, an internal tensioning wheel staggered layout design was adopted, with external tensioning wheels installed to effectively avoid clamping force reduction and derailment risks caused by chain elongation. By welding U-shaped brackets to the top of both side supports, the structural integrity was enhanced to prevent component separation. To address the complex terrain of tobacco fields, bearings were installed in the bearing brackets, and a hydraulic cylinder was integrated at the front end of the clamping mechanism. These two components work in tandem to achieve dynamic height adjustment of the lifting stem assembly, thereby enhancing the environmental adaptability of the equipment. The power transmission mechanism is as follows: the universal joint driveshaft transmits power to the drive sprocket, driving the driven sprocket to rotate in the counterclockwise direction. After the tobacco stems are loosened by the soil loosening blade, they are fed into the clamping and pulling stem device inlet, immediately clamped by the clamping chain, and pulled out of the soil. Under the coordinated action of the tensioning wheels, the tobacco stems were smoothly conveyed to the shredding device inlet, as shown in Fig. 2.

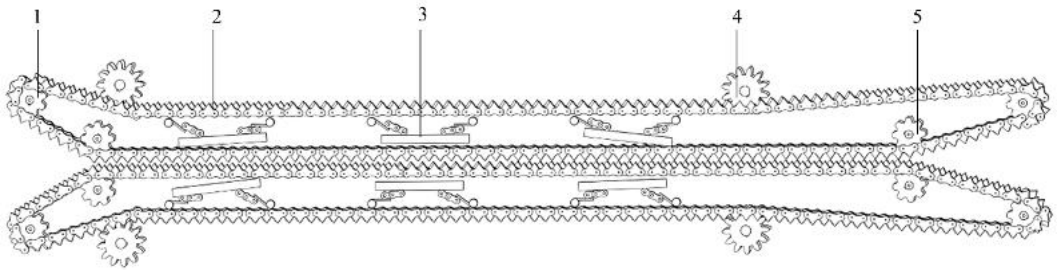


Fig. 2 – Clamping chain structure

1. Drive sprocket 2. Clamping chain 3. Clamping plate 4. External tension sprocket 5. Gap adjusting sprocket

1.2. Loosening Shovel Design

Loosening shovels can be classified into chisel-, arrow-, and wing-shaped shovels *(Fan, 2022)*, duck-foot shovels, vibrating loosening shovels, and combination shovels. Based on the soil type of the tobacco field, a combination shovel type was selected to adapt to different working environments. According to the research findings in *Yu et al., (2007), and Tong et al., (2005)*, the operational resistance of a soil loosening shovel is primarily influenced by factors such as shovel type, operational speed, operational depth, and angle of penetration. Because the shovel structure and operational speed were already finalized in this study, the research focus was on determining the operational depth and angle of penetration parameters of the soil loosening shovel.

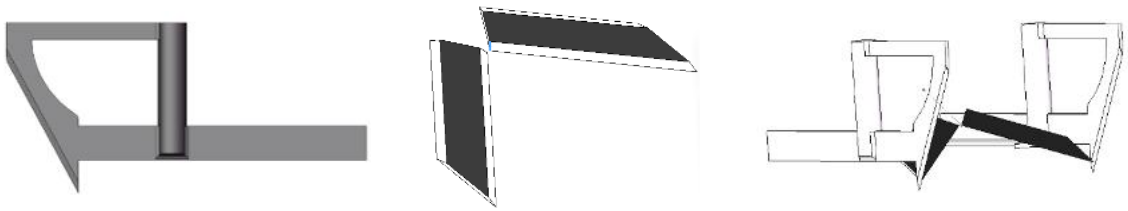
(1) Working depth

The appropriate selection of working depth is crucial for reducing working resistance, protecting the soil structure, and ensuring operational effectiveness. Excessively deep working depths increase the working resistance, leading to higher energy consumption, component wear, and damage to the soil's original aggregate structure. Conversely, excessively shallow depths do not meet the operational requirements for effectively loosening tobacco stems. According to relevant research *(Guo, 2023),* when the working depth is between 200 and 300 mm, effective loosening can be ensured while balancing energy consumption and soil protection. After careful consideration, this study selected 250 mm as the working depth of the loosening blade to achieve a balanced optimization of the working performance and energy consumption.

(2) Angle of Entry

The size of the angle of entry directly affects the ease of entry of the loosening blade *(Zhang 2014)*. An excessively small angle makes penetration difficult and reduces work efficiency, whereas an excessively large angle increases resistance and accelerates tool wear. According to the literature *(Wang et al., 2007)*, the optimal penetration angle is 60°–70°; therefore, 60° was selected.

After determining the parameters, the tillage blade was modelled, as shown in Fig. 3.



(a) Shovel frame (b) Shovel blade (c) Assembly

Fig. 3 – General assembly drawing of ripper shovel

1.3. Analysis of the dimensions of the crushing roller

The tobacco stem *(Chen et al., 2025)* was crushed using a multi-roller crusher *(Jiang et al., 2019)*, and the model and spatial arrangement of the roller are shown in Fig. 4.



(a) Knife roller model (b) Four knife roller arrangement configurations

Fig. 4 – Knife roller model and its arrangement

According to *Yang et al., (2024)*, the cutting speed of tobacco stems is generally between 16 and 30 m/s. The diameter of the cutting roller was 240 mm, and the minimum cutting speed of the cutting roller was:

$$n_{\min} = \frac{30v}{\pi R} = \frac{30 \times 14}{\pi \times 0.24} = 557 \text{ r} \cdot \text{min}^{-1} \quad (1)$$

where: $n_{\min}$ is the minimum cutting speed of the cutting roller, r·min^{-1}; v is minimum linear velocity, m·s^{-1}.

Maximum cutting speed:

$$n_{\max} = \frac{30v}{\pi R} = \frac{30 \times 30}{\pi \times 0.24} = 1193.7 \text{ r} \cdot \text{min}^{-1} \quad (2)$$

where: $n_{\max}$ is the maximum cutting speed of the cutting roller, r·min^{-1}; v is maximum linear velocity, m·s^{-1}.

The rotational speed of the cutting roller was selected as 800 r·min^{-1}.

According to the Agricultural Machinery Design Manual *(Wang et al., 2007)*, the relationship is expressed as follows:

$$H = d + \frac{rv_m}{v_d} \quad (3)$$

where: H is the distance between the knife holder and the centre of the spindle, mm; d is the diameter of the tobacco stem, mm; r is the rotation radius of the cutting roller blade, mm; v_m is the conveying speed of the conveyor chain, m·s^{-1}; v_d is the linear speed of the cutting roller blade, m·s^{-1}.

1.4. Design of the Transmission System for the Tobacco Stem Harvester

The self-propelled tobacco stem harvester's transmission system uses a combination of chain and belt drives. The output shaft of the main motor transmits power to the transfer case, which is then distributed by gear z1 to the symmetrically arranged bevel gears z2 and z3 on both sides. The bevel gears drive the clamping chains at equal speeds in opposite directions, thereby providing the required power for tobacco stem clamping. Auxiliary motor 2 transmits power via a belt drive to gear z8, which subsequently drives z10, z11, and z12. These four gears operate in coordination to realize the synchronous counter-rotation of the four cutting rollers, as shown in Fig. 5.

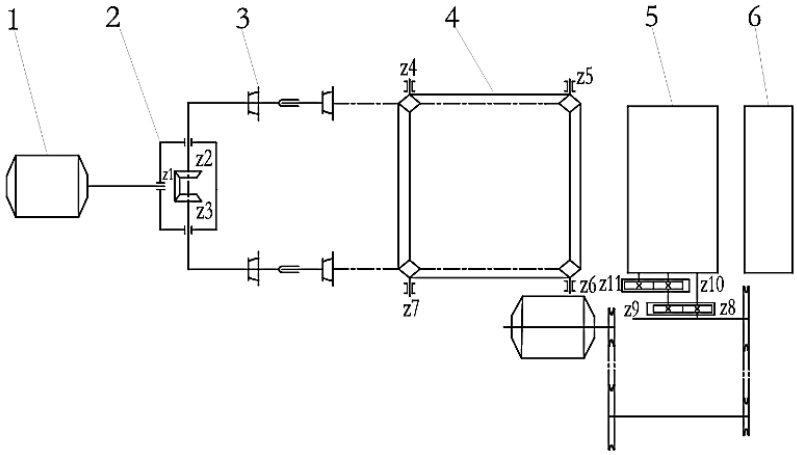


Fig. 5 – Transmission system of the tobacco harvester

1. Motor 2. Transfer case 3. Universal drive shaft 4. Clamping chain 5. Crushing device 6. Collection bin

1.5. Design of the Hydraulic System for the Tobacco Stem Harvester

To enable the tobacco stem harvester to adapt to varying field terrain conditions, two hydraulic cylinders were installed on both sides of the clamping chain. When operating on elevated terrain, the clamping chain can be raised, whereas on lower terrain it can be lowered accordingly, ensuring efficient and accurate tobacco stem harvesting. The hydraulic system mainly consists of a hydraulic pump, a relief valve, a three-position four-way directional control valve, and a check valve, as shown in Fig. 6.

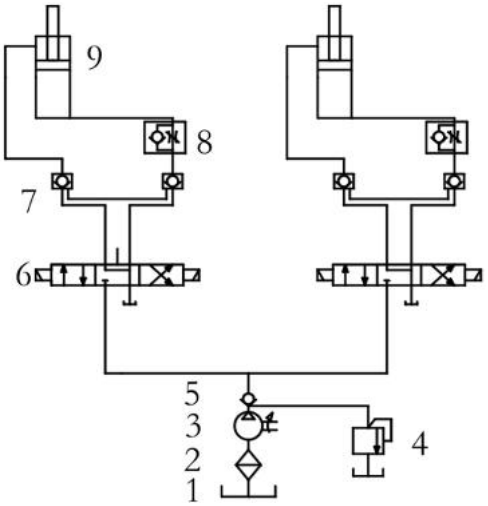


Fig. 6 – Hydraulic system of tobacco stem harvester

1. Oil tank; 2. Filter; 3. Hydraulic pump; 4. Relief valve; 5. Check valve; 6. Three-position, four-way directional control valve; 7. Pilot-operated check valve; 8. Throttle check valve; 9. Hydraulic cylinder

Hydraulic pump *3* serves as the power source of the system, supplying pressurized hydraulic oil and constituting the core of the hydraulic system. Hydraulic cylinder *9* acts as the actuator, converting hydraulic energy into mechanical energy to drive the movement of the working components. Relief valve *4*, check valve *5*, control check valve *7*, throttle check valve *8*, and the three-position four-way directional control valve *6* function as control and regulating components, governing the pressure, flow rate, and flow direction of the hydraulic oil. Oil tank 1 and filter *2* are auxiliary components that ensure reliable and stable system operation. During operation, hydraulic oil stored in oil tank *1* is filtered by filter *2* and then drawn in and pressurized by hydraulic pump *3*. The pressurized oil passes through check valve *5*, which prevents reverse flow, and enters the directional control valve *6*. By switching positions, the directional control valve controls the flow direction of the hydraulic oil. When the valve is set to the corresponding working position, the pressurized oil flows through its internal passages, passes through control check valve *7*, and enters either the rodless chamber or the rod chamber of hydraulic cylinder *9*. The piston extends when oil enters the rodless chamber and retracts when oil enters the rod chamber. The throttle check valve *8* regulates the flow rate of the hydraulic oil entering and leaving the hydraulic cylinder, thereby controlling the piston movement speed. Relief valve *4* limits the system pressure; when the pressure exceeds the preset value, the valve opens to return oil to the tank, ensuring system safety.

2. Stress Analysis and Motion Simulation of Key Components

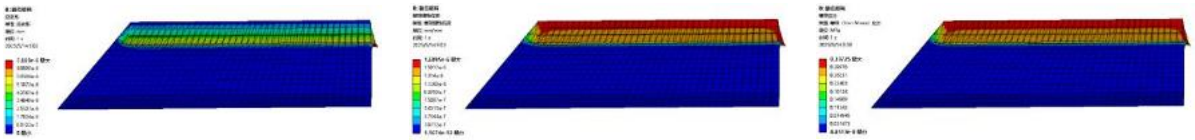
2.1. Force analysis of deep loosening plough

An Ansys finite element simulation was used to determine the material properties and mesh division for the loosening plough model, and a constraint force of 500 N was applied. The equivalent stress and total deformation cloud diagrams are shown in Fig. 7 and 8, respectively.



(a) Total deformation (b) Equivalent elastic strain (c) Equivalent stress

Fig. 7 – Stress contour diagram of ripper shovel 1



(a) Total deformation (b) Equivalent elastic strain (c) Equivalent stress

Fig. 8 – Stress contour diagram of soil loosening shovel 2

The maximum stress on the soil loosening blade frame during operation was 39.91 MPa, primarily concentrated in the middle and lower sections of the blade edge. This value is significantly below the allowable stress of the material, ensuring structural safety and reliability. Under the influence of operational bending moments, the maximum deformation of the soil loosening blade was 0.13322 mm, which is an imperceptible micro-deformation not visible to the naked eye and does not affect harvesting operations, indicating that the soil loosening blade design meets the requirements. The maximum stress on the soil loosening blade was 0.33725 MPa, and the maximum deformation was 7.661×10^{-6} mm. The maximum stress on the soil loosening blade was far below the material yield strength of 250 MPa, and the deformation was small. Therefore, the design is safe, reliable, and meets operational requirements.

2.2. Simulation of the clamping and pulling stem mechanism

2.2.1. Modelling of the clamping process

The tobacco stem is the main test object, and its parameters significantly affect the final test results. Through research on the physical characteristics of the tobacco stem, it was determined that the length, diameter, and mass of the tobacco stem were approximately 1200 mm, 25 mm, and 695 g, respectively.

The volume of the tobacco stem can be obtained from Equation (4)

$$V=\pi r^2 h=\frac{\pi D^2 h}{4}=\frac{3.14\times25^2\times1200}{4}=588.75\ \text{cm}^3 \tag{4}$$

where: V is the volume of the tobacco stem, cm³; D is tobacco diameter, cm; h is tobacco length, mm.

Using the density formula $\rho = m/v$, the density of the tobacco stem was approximately 1.18 g/cm³. According to *Wang et al., (2007)*, the elastic modulus of the tobacco stem is 1147 MPa, and the Poisson's ratio is 0.33.

During the clamping and pulling processes, owing to the complexity of the simulation process, most components did not significantly affect the simulation results. Therefore, simplifying the model not only provides a more intuitive representation of the motion process but also significantly reduces simulation complexity.

In SolidWorks, components such as the frame, clamping chain, and bearings were simplified, parameters were set, and the model was saved in the '*.xt' file format before being imported into Adams for simulation analysis. The simplified model is illustrated in Fig. 9.

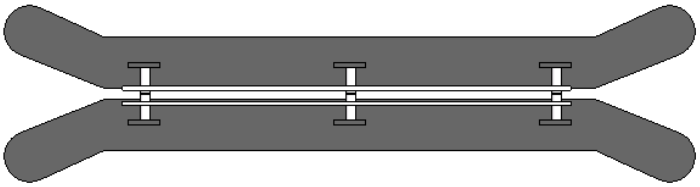


Fig. 9 – Simplified model of the clamping mechanism

The clamping device operates through the coordinated action of various mechanisms, and simulating its motion requires constraints between the mechanisms. Specifically, the operational state of the mechanisms is equivalent to the linear motion of the model, the spring tension state when the tobacco holder is clamped is equivalent to the linear motion of the stopper plate, and the tobacco holder clamping process is equivalent to the linear motion of the tobacco holder. When the tobacco stem is clamped, it comes into contact with the clamping link, thereby generating a contact force. According to reference *(Pu, 2005),* the contact force between the tobacco stem and clamping link is continuous. In the Adams software, the formula for calculating the contact stiffness coefficient K of the object contact system is shown in Equation (5).

$$K=\sqrt{\frac{16RE^2}{9}}=\frac{4}{3}E\sqrt{R} \tag{5}$$

where: R is the contact radius，mm; E is the moment of inertia, MPa.

$$\frac{1}{R}=\frac{1}{R_1}+\frac{1}{R_2} \tag{6}$$

where: R_1 and R_2 represent the contact radius of the object during the contact process. If the contact surface is flat, the contact radius becomes infinite.

$$\frac{1}{E}=\frac{(1-\mu_1^{\ 2})}{E_1}+\frac{(1-\mu_2^{\ 2})}{E_2} \tag{7}$$

where: E_1 and E_2 are the Young's moduli between the two contacting objects，MPa, and μ_1 and μ_2 are the Poisson's ratios between the two contacting objects.

During the simulation process, the material selected for the clamping chain was 45 steel, with a Young's modulus of 2.09 × 10⁵ MPa and Poisson's ratio of 0.269. The Young's modulus of the tobacco stem was 1147 MPa, and the Poisson's ratio was 0.33. The simulated motion of the tobacco stem in Adams is the contact between the tobacco stem and guard plate, which can be regarded as the contact between a cylindrical surface and plane. Based on the modelling of the tobacco stem, the contact radius of the tobacco stem was set to 12.5 mm. Substituting the data into Equations (8) and (9) yields:

$$\frac{1}{R}=\frac{1}{12.5}+\frac{1}{\infty} \tag{8}$$

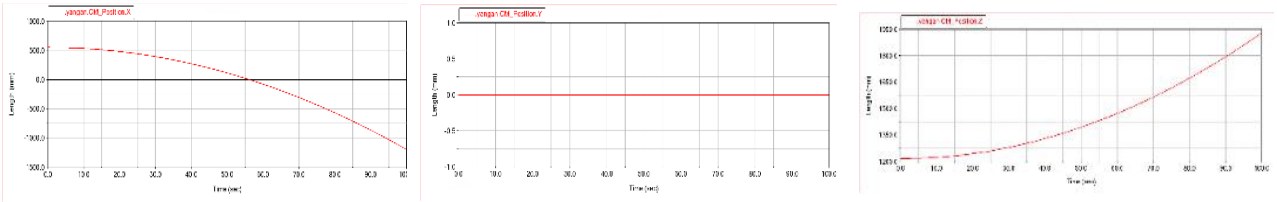
$$\frac{1}{E}=\frac{(1-0.3^2)}{2.05\times10^5}+\frac{(1-0.33^2)}{1147} \tag{9}$$

Substituting the data into Equation (2) yields the contact stiffness coefficient K:

$$K=\frac{4}{3}E\sqrt{R}=\frac{4}{3}\times1279.9\times\sqrt{12.5}=6033.6 \tag{10}$$

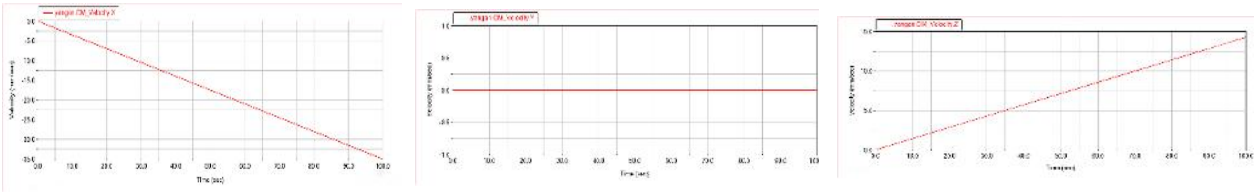
2.2.2. Simulation analysis of the clamping process motion

The simulation analysis of the clamping process motion mainly analyses the displacement, velocity, and acceleration of the tobacco stem as it moves from the lower to the upper end of the clamping chain. The simulation results obtained using Adams software are shown in Figs. 10–12.



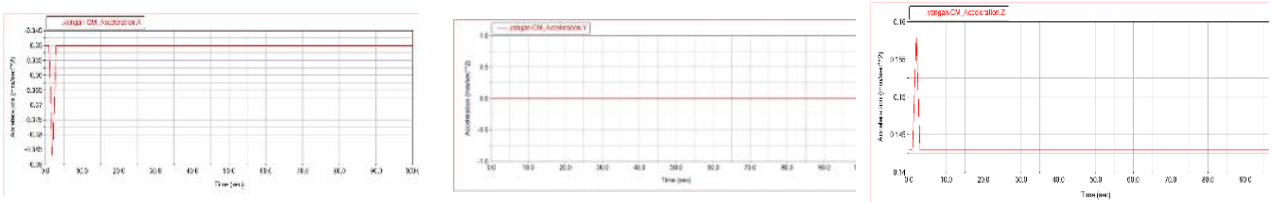
(a) Displacement in the X direction (b) Displacement in the Y direction (c) Displacement in the Z direction

Fig. 10 – Displacement curve of the tobacco holder clamping point



(a) Displacement in the X direction (b) Displacement in the Y direction (c) Displacement in the Z direction

Fig. 11 – Speed curve of the tobacco holder clamping point



(a) Displacement in the X direction (b) Displacement in the Y direction (c) Displacement in the Z direction

Fig. 12 – Acceleration curve of the tobacco holder clamping point

By analysing the displacement curve shown in Fig. 10, it can be seen that tobacco stem 1 exhibits a negative displacement trend along the X-axis, as the displacement direction is opposite to the positive direction of the coordinate axis, effectively increasing the displacement magnitude; the displacement along the Y-axis remains constant, while the displacement along the Z-axis continues to increase. This result directly reflects the actual operating conditions of the tobacco stem moving backward along the longitudinal (Z-axis) direction under the influence of the conveyor chain after being clamped and pulled out, which is consistent with the theoretical expectations.

Fig. 11 shows that the velocity of the tobacco stem along the X and Z axes increased in opposite directions in a synchronized manner, whereas the velocity along the Y axis remained zero throughout, further validating the directional conveying characteristics of the tobacco stem within a two-dimensional plane.

Fig. 12 indicates that the acceleration along the Y-axis is zero, whereas the acceleration along the X- and Z-axes remains relatively stable during motion, although significant fluctuations occur between 0 and 5 s. The analysis indicates that this fluctuation is caused by an instantaneous change in acceleration due to inertial forces when the smoke stem is lifted. As the smoke stem entered the stable conveying phase, the acceleration gradually returned to a steady state.

Based on the analysis results of the displacement, velocity, and acceleration, the clamping and lifting stem mechanism operated smoothly, and its dynamic performance met the design specifications.

3. Field Trial of Tobacco Stem Harvester

The trial site was selected in the tobacco fields of the Yilong Machinery Factory in Henan Province, using tobacco stems from the current season. The tobacco stems used in the trial were those remaining after tobacco leaf harvesting, with an average height of approximately 1200 mm, an average diameter of 30.6 mm, and plant spacing of 60 mm. The tobacco field ridges were 50 cm wide, 30 cm high, and spaced 80 cm apart from each other. The trial site had no recent rainfall, with clear weather and moderate soil moisture content, which made it suitable for the trial operations.

Typically, mechanical operations require that the rate of harvest omission and the rate of tobacco stem breaking (the roots are not pulled out, but the stems are broken) should both be below 10%. The formulas for calculating the rate of harvest omission (Y_1) and the rate of stem breaking (Y_2) are as follows:

Stem removal performance indicators

$$\text{Harvest omission rate: } Y_1=W_1/W \tag{11}$$

$$\text{Stem breaking rate: } Y_2=W_2/W \tag{12}$$

where: Y_1 represents the rate of tobacco harvest omission, Y_2 represents the rate of tobacco stem breaking, W_1 represents the number of tobacco harvest omissions, W_2 represents the number of broken tobacco stems, and W represents the total number of tobacco stems tested.

The primary operational parameters affecting the tobacco harvest omission and stem breaking rates were the clamping chain transmission speed, harvester forward speed, and clamping chain clearance. These parameters were tested to determine their influence on the tobacco harvest omission and stem breaking rates. The field trial process is illustrated in Fig. 13.



(a) Test process (b) Condition of tobacco fields after testing

Fig. 13 – Field experiments

3.1. Single-factor field test

3.1.1. Effect of clamping chain transmission speed on tobacco harvest omission rate and stem breaking rate

The forward speed of the tobacco-stem harvester can be adjusted using a transmission gearbox. The transmission speed of the dual-row clamping chain was controlled by the drive system, whereas the clamping chain gap was finely adjusted using nuts on the compression springs. In the first field trial, the forward speed of the harvester was set to 0.6 m/s, and the clamping gap was set to 9 mm. Five gradient clamping chain transmission speeds of 0.6, 0.8, 1.2, 1.5, and 1.8 m/s were selected for testing. During the trial, 100 tobacco stems were pulled for each parameter set. The results of the field trials are shown in Fig. 14.

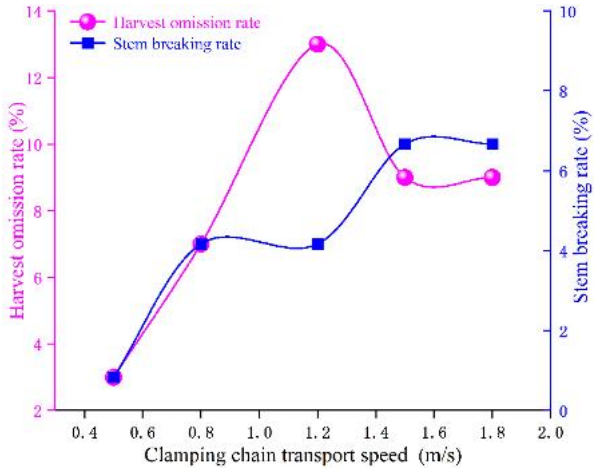


Fig. 14 – The harvest omission rate and stem breaking rate of tobacco stems under different speeds of clamping chain

Fig. 14 shows that when the conveying speed of the clamping chain is within the range of 0.6–1.2 m/s, the leakage rate increases linearly with the speed. However, when the speed increased to 1.2–1.5 m/s, the harvest omission rate decreased slightly and stabilized at 1.5 m/s. The stem breaking rate continued to increase with increasing conveying speed, reaching a peak near 1.5 m/s before stabilizing. Considering the dual optimization requirements of the harvest omission and stem breaking rates, the overall performance of tobacco stem removal was optimal when the conveying speed of the clamping chain was controlled between 0.6 and 0.8 m/s.

3.1.2. Effect of harvester forward speed on tobacco harvest omission rate and stem breaking rate

The conveying speed of the clamping chain was set to 0.7 m/s, and the forward speeds of the tobacco stem harvester were set to 0.4, 0.5, 0.6, and 0.7 m/s, respectively, while maintaining a constant chain gap of 9 mm. A total of 100 tobacco stems were pulled, and the harvest omission and stem breaking rates were recorded. The test results are presented in Fig. 15.

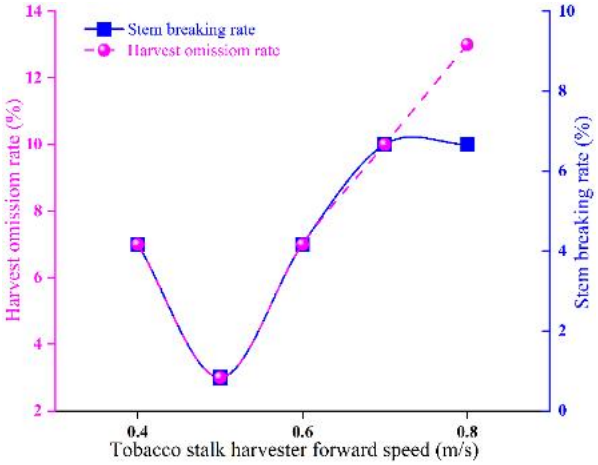


Fig. 15 –The harvest omission rate and stem breaking rate of tobacco stems under different harvester forward speeds

According to the experimental data in Fig. 15, when the forward speed of the tobacco stem harvester was within the range of 0.4–0.5 m/s, the harvest omission rate decreased as the speed decreased.

However, within the range of 0.5–0.7 m/s, the stem breaking rate increased with speed, reaching a peak at 0.7 m/s and then stabilizing. Combining the harvest omission rate and stem breaking rate change curve, within the 0.4–0.5 m/s speed range, the stem breaking rate decreased as speed increased, and within the 0.4–0.6 m/s range, the stem breaking rate showed an upward trend. Through a comprehensive dual-indicator optimization analysis of the harvest omission and stem breaking rates, when the forward speed of the tobacco stem harvester was controlled between 0.4 and 0.6 m/s, the overall operational performance of the equipment reached its optimal level. This parameter effectively reduces the risk of harvest omission and stem breakage while ensuring operational efficiency of the harvester.

3.1.3. Effect of clamping chain spacing on tobacco harvest omission rate and stem breaking rate

The clamping chain conveying speed was set to 0.7 m/s, and the tobacco stem harvester forward speed was set to 0.5 m/s. Clamping chain gaps of 7, 9, 12, 15, and 18 mm were selected. Under these conditions, 100 tobacco stems were pulled, and the harvest omission and stem breaking rates were recorded. The test results are presented in Fig. 16.

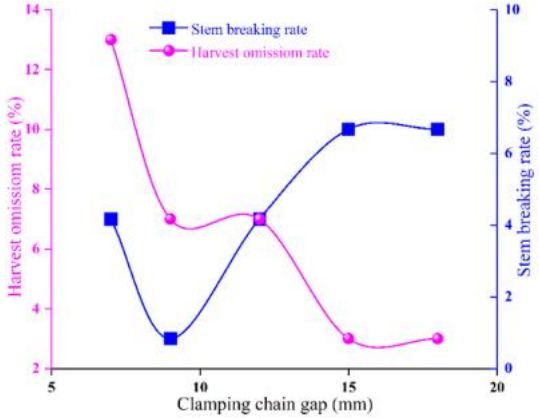


Fig. 16 – The harvest omission rate and stem breaking rate of tobacco stems under different clamping chain gaps

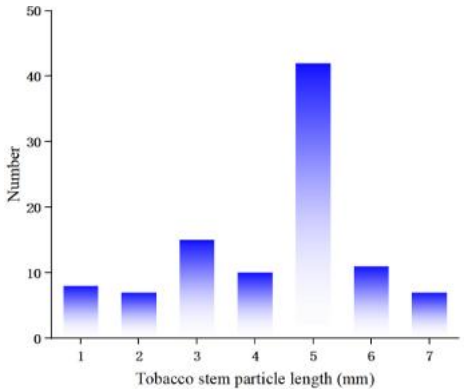
As shown in Fig. 16, when the clamping chain gap was between 7 and 9 mm, the harvest omission rate decreased as the clamping chain gap increased. When the clamping chain gap was between 9 and 15 mm, the harvest omission rate increased as the clamping chain gap increased, reaching a maximum at 15 mm and then stabilizing. The stem-breaking rate decreased as the clamping chain gap increased. Therefore, the optimal clamping chain gap for the removal efficiency was 9–15 mm.

3.1.4. Analysis of Tobacco Stem Crushing Performance

The primary factors affecting tobacco stem crushing efficiency are the conveyor chain transmission speed and the cutting roller rotational speed *(Guo et al., 2023)*. The conveyor chain speed was set to 0.7 m/s, and the cutting roller rotational speed was set to 800 r·min^{-1}. For each test, a random sample of 100 crushed tobacco stems was selected for length measurement. The experiment was repeated three times, and the average value of the three measurements was calculated. The experimental test setup is shown in Fig. 17(a).



(a) Automatic unloading process of crushed tobacco stems



(b) Statistical distribution of tobacco stem crushing effectiveness

Fig. 17 – Tobacco stem crushing effectiveness

As shown in Fig. 17(b), the number of crushed tobacco stem particles was primarily concentrated in the 40–50 mm range, followed by the 20–40 mm and 50–70 mm ranges. No particles larger than 70 mm were observed, which generally aligns with a normal distribution. The crushing results met the design expectations.

3.2. Multi-factor orthogonal experiment

3.2.1. Experimental design

To analyse the interactive effects between the clamping chain speed, harvester forward speed, and clamping chain gap, a multi-factor orthogonal experimental design was developed based on single-factor experiments. The clamping chain transport speed was set to 0.6, 0.7, and 0.8 m/s, the forward speed of the tobacco stem harvester was set to 0.4, 0.5, and 0.6 m/s, and the clamping chain gap was set to 9, 12, and 15 mm. An $L_9(3^3)$ orthogonal array was employed, consisting of nine experimental runs, with the experimental scheme presented in Table 1.

Table 1

Table of orthogonal test protocols

Number	Forward speed (m/s)	Clamping chain transport speed (m/s)	Clamping chain gap (mm)
1	0.4	0.6	9
2	0.4	0.7	12
3	0.4	0.8	15
4	0.5	0.6	12
5	0.5	0.7	15
6	0.5	0.8	9
7	0.6	0.6	15
8	0.6	0.7	9
9	0.6	0.8	12

3.2.2. Test Results and Analysis

In each test group, 100 tobacco stems were pulled out, and the number of stems that were not pulled out and the number of broken stems were counted. The harvest omission and stem-breaking rates for each group were calculated, and the test results are presented in Table 2.

Table 2

Orthogonal test results

No.	Forward Speed (m/s)	Clamping Chain Transport Speed (m/s)	Clamping Chain Gap (mm)	Harvest Omission Rate (%)	Stem Breaking Rate (%)
1	0.4	0.6	9	6	10
2	0.4	0.7	12	4	2
3	0.4	0.8	15	12	2
4	0.5	0.6	12	8	6
5	0.5	0.7	15	14	2
6	0.5	0.8	9	10	16
7	0.6	0.6	15	12	4
8	0.6	0.7	9	8	18
9	0.6	0.8	12	10	6

Although orthogonal experiments can determine the optimal combination of working parameters for equipment field operations, it is difficult to intuitively quantify the extent to which travel speed, clamping chain speed, and clamp gap affect the harvest omission and stem breakage rates. Therefore, to accurately identify the significant differences between each factor and their impact on operational performance, it is necessary to further use the range analysis method to conduct an in-depth analysis of the experimental data. The results of the range analysis for the rate of harvest omission and stem breaking are shown in Tables 3 and Table 4.

Table 3

Range analysis of the harvest omission rate

Value	Forward Speed (m/s)	Clamping Chain Speed (m/s)	Clamping Chain Gap (mm)
K1	7.333	8.667	8.000
K2	10.667	8.667	7.333
K2	10.000	0.667	12.667.
Extreme Difference	3.334	2.000	5.334

Table 4

Range analysis of the stem breaking rate

Value	Forward speed (m/s)	Clamping chain speed (m/s)	Clamping chain gap (mm)
K1	4.667	6.667	14.667
K2	8.000	7.333	4.667
K2	9.333	8.000	2.667
Extreme difference	4.666	1.333	12.000

Different factors, levels, and response indicators yield varying effects, and a larger range value indicates a greater influence of a factor on the experimental results. As shown in Table 3, the order of influence of the factors on the harvest omission rate was clamping chain gap > forward speed > clamping chain speed. Similarly, as shown in Table 4, the order of influence of the factors on the stem breakage rate was clamping chain gap > forward speed > clamping chain speed.

Based on the analysis of the above experimental results, when the forward speed is 0.4 m/s, the clamping chain speed is 0.7 m/s, and the clamping chain gap is 12 mm, the comprehensive operational performance of the tobacco stem harvester is optimal.

4. CONCLUSIONS

This study focuses on the design and experimental research of a self-propelled tobacco stem harvester. The main design parameters of the self-propelled tobacco stem harvester were established through field testing of tobacco stems and soil physical properties, combined with literature analysis to determine key component parameters, and validated through simulation and field trials. The main conclusions are as follows.

(1) A chain-clamp-holding and transport device was designed, which integrated a spring-loaded clamping mechanism and hydraulic adjustment system to achieve a dynamic adaptive adjustment of the clamping gap. This effectively addresses issues such as slippage and missed extraction during tobacco stem transportation, significantly enhancing the harvesting reliability.

(2) Based on the Ansys static simulation analysis, the maximum stress of the soil loosening blade structure under operational conditions was 22.35 MPa, and the maximum deformation was 0.0125 mm, both of which were below the material's allowable strain value, thus verifying the structural strength and stability. Based on Adams' dynamic simulation results, the entire machine operated smoothly and met the design performance requirements.

(3) Through field single-factor experiments, the optimal parameter ranges were determined as follows: clamping chain transmission speed of 0.6–0.8 m/s, clamping gap of 9–15 mm, and harvester forward speed of 0.4–0.6 m/s. Further optimization through multi-factor orthogonal experiments yielded the optimal parameter combination: forward speed of 0.4 m/s, clamping chain transport speed of 0.7 m/s, and clamping chain gap of 12 mm. Crushing performance tests showed that the particle size of crushed tobacco stems was primarily distributed between 40 and 50 mm, with a size distribution conforming to a normal distribution pattern, achieving the design-expected crushing effect.

ACKNOWLEDGEMENT

This research was funded by the Key R&D and Promotion Special Tackling Key Problems in Science and Technology in Henan Province, China (grant no. 242102111173, 242102111172); Henan Province Tobacco Company Pingdingshan Company Science and Technology Project (PYKJ202204); Key Research Fund of Pingdingshan University (grant no. 2023-JYZD01).

REFERENCES

[1] Chen, T., Yi, S.J., Wang, S., Sun, W.S. (2025). Working Mechanism Analysis and Experimental Study of Grass Crusher. *INMATEH-Agricultural Engineering*, 75, 334-345. doi: https://doi.org/10.35633/inmateh-75-28.

[2] Fan, W. (2022). *Design and research on key components of Small Self-walking White Radish Harvester*, Guizhou University. doi: 10.27047/d.cnki.ggudu.2022.001679.

[3] Gao, S.B., Yuan Y.W., Niu, K., Zhao B., Zhou, L.M., Lv, C.X., Bai, S.H., Zhang, S.Y., An, R. (2025). Design And Experiment of Clamping and Conveying Device for Tracked Self-Propelled Chinese Cabbage Harvester. *INMATEH - Agricultural Engineering*, 1, 376-389. doi: https://doi.org/10.35633/inmateh-75-32.

[4] Guo, T.S., Zhang, Q., Wang, X., Yang, B.K., Yin, Z.C., Liu, H.X., Li, X., Ye, W.R., Cao, X.C., Luo, K.P., Shi, L. (2023). Current Situation and Development Suggestions of Tobacco Stalk Cleaning Machinery in China. *South Agricultural Machinery*, 12, 19-37+27. doi: 10.3969/j.issn.1672-3872.2023.12.005.

[5] Guo, T.S. (2023). Design and research on key components of tobacco straw cleaning machinery in field. *Yunnan Agricultural University*. doi: 10.27458/d.cnki.gynyu.2023.000636.

[6] Jin, B.H., Cha, Z.G., Chen, L., Jin, W.B. (1999). Study on the Extraction of Pectin from Tobacco. *Anhui Chemical Industry*, 3, 7-9.

[7] Jiang, Y.J., Liao, Y.T., Liao, Q.X. (2019). Design and Experiment on Cylinder-type Chopping Device of Harvester for Fodder Rapeseed in Winter and Spring. *Transactions of the Chinese Society for Agricultural Machinery*, 2, 102-111. doi: 10. 6041/j. issn. 1000-1298. 2019. 02. 011

[8] Li, X.W., Li, G.P. (1999). New Approaches to Industrial Utilization of Tobacco Stems. *China Dairy*, 4, 30-31.

[9] Li, J., Li, J.C., Wu, X.H., Zi, W.H., Yang, Y.F., Liu, Y.S. (2010). Progress in Research on Comprehensive Utilization of Tobacco Waste. *Yunnan Chemical Technology*, 2, 44-49. doi: 10.3969/j.issn.1004-275X.2010.02.010.

[10] Li, Y. (2009). Influence of Tobacco Plant Residues on the Occurrence of Diseases and Pests and Their Removal Measures. *XianDai NongYe KeJi*, 23, 182. doi: 10.3969/j.issn.1007-5739.2009.23.126.

[11] Mo, Z.J. (2023). *Study on the Formation Mechanism of Nicotine Transport Heterosis in Tobacco Hybrids*. Guizhou University. doi: 10.27047/d.cnki.ggudu.2023.000040.

[12] Pu, M.H. (2005). *The Virtual Design and Simulation for Small-Scale Type* [MA thesis]. Guangxi University.

[13] Reynaldo C.C., Shirley C.A., Julie L.L. (2000). Study on the Manufacture of Fiberboard from Tobacco Stalks. *Tobacco Science & Technology*, 7, 32-34. doi: 10.3969/j.issn.1002-0861.2000.07.015.

[14] Tu, J.H. (2006). *Study on Preparation and Characterization of Tobacco-stem-based Lignoceramics*. Kunming University of Science and Technology.

[15] Tong J, Moayad Z B. (2005). Effects of rake angle of chisel plough on soil cutting factors and power requirements: A computer simulation. *Soil & Tillage Research*, 1, 55-64.

[16] Wu, Z.L. (2007). *Purification and Some Properties of Sucrase from Tobacco (Nicotiana Tabacum L) Leaves*. Southwest University. doi: 10.7666/d.y1074057.

[17] Wang, W.J., Hu, Z. (2007). Agricultural Machinery Designing Handbook. *Beijing: Agricultural Science and Technology Press*.

[18] Yang, B., Sun, S.L., Li, J.Z., Zhang, W.J., Xun, Z.F. (2015). Design and Experiment for Stem Pulling and Stump Cutting Device of Tobacco Stem Pulling Machine. *Journal of Hunan Agricultural University (Natural Sciences)*, 4 446-449. doi: 10.13331/j.cnki.jhau.2015.04.021.

[19] Yu, Y.C., Liu, W.Y., Zhao, Y.F., Sun, J.Q. (2007). Force Mathematical Model and Examination Analysis of the Column Subsoiler. *Transactions of the Chinese Society of Agricultural Engineering*, 6, 109-113. doi: 10.3321/j.issn:1002-6819.2007.06.021.

[20] Yang, T.Y., Zhang, D.F., Shu, C.S., Yu, C.J., Cao, Y. (2024). Vibration Characteristics and Dynamic Analysis of Knife Roll of Tobacco Stalk Pulling and Crushing Machine. *Journal of Chinese Agricultural Mechanization*, 12, 9-14+29. doi: 10.13733/j.jcam.issn.2095-5553.2024.12.002.

[21] Zeng, J.J., Li, J.Z., He, W., Duan, M.Z., Peng, Z.G., Zhou, D.F. (2024). Analysis of the Current Status of Tobacco Fertilisation Machinery Research and Recommendations for Development. *Agriculture & Technology*, 6, 9-11, doi: 10.19754/j.nyyjs.20240330003.

[22] Zhang, J.F. (2016). An Analysis of the Impact of the Tobacco Industry on Local Economies Under Government Regulation. *China Market Marketing*, 50, 68+70. doi: 10.13939/j.cnki.zgsc.2016.50.068.

[23] Zhang, L.P. (2007). *Study on the Preparation of Tobacco-stem-based Activated Carbon and Its Adsorption Treatment of Heavy Metal-containing Wastewater* [PhD dissertation]. Kunming University of Science and Technology.

[24] Zhang, L. (2014). *Design of Chain-type Plastic Film Collector for Potato* [MA thesis]. Shandong Agricultural University.

DESIGN AND EXPERIMENTAL STUDY OF A RESIDUAL FILM BALING DEVICE
/
残膜打包装置的设计与试验研究

Guan WANG[1)], Haolin WANG[2)], Zhihong TIAN[1)], Qi Wang[1)], Dong JI[1)], Fengbo LIU[1)*]
[1)] Liaoning Agricultural Vocational and Technical College, 76 Yucai Road, Yingkou 115009, China;
[2)] Design Department of Liaoning liaotuo Dayi Agricultural Machinery Co., Ltd, Fushun, 113000, China;
Tel: 18341895506; E-mail: j18341895506@126.com
Corresponding author: Fengbo LIU
DOI: https://doi.org/10.35633/inmateh-79-07

Keywords: *residual film baling device; discrete element method (DEM); Rocky DEM; parameter optimization; response surface methodology (RSM).*

ABSTRACT
To address the problems of low bale-forming rate and loose compaction during the mechanized recovery of residual plastic film in farmland, a three-stage residual film baling device was developed. Based on the discrete element method (DEM), a flexible thin-shell model of the residual film was established, and dynamic simulation and parameter optimization of the baling process were carried out using Rocky DEM software. Combined with single-factor experiments and response surface methodology, the effects of baling chamber inclination angle, belt type, belt linear speed, and upper belt inclination angle on bale integrity and compaction were analyzed. The results showed that the bale-forming rate of the three-stage device reached 99.13%, and the bale density reached 83.75 kg/m³ under the optimal conditions: baling chamber inclination angle of 30°, upper belt inclination angle of 30°, belt linear speed of 2.3 m/s, and the use of a rough-surface belt. Field validation tests showed that the average density of the residual film bales was 91.4 kg/m³, with a prediction error of only 2.23 kg/m³ compared with the simulation results. The device operated stably and reliably. This study presents a high-efficiency residual film baling device with improved bale-forming rate and compaction performance through structural optimization and parameter tuning, providing technical support for efficient recovery and pollution control of residual plastic film in farmland.

摘要
针对机械化农田残膜回收过程中出现的袋装率低和薄膜包装松散的问题，本研究开发了一种三阶段残膜包装装置。基于离散元方法，建立了残膜的柔性薄壳模型，并使用 rockydem 完成了残膜包装过程的动态模拟和参数优化。结合单因素实验和响应面分析，探讨了包装腔角度、包装带类型、线速度和上带安装角度对包装完整性和紧凑性的影响规律。结果表明，三阶段装置的包装率达到了 99.13%，薄膜密度为 83.75 千克/立方米，当包装腔方位角为 30°、上带安装倾斜度为 30°、线速度为 2.3 米/秒且使用粗糙带时。现场验证显示，残膜袋的平均密度为 91.4 千克/立方米，与模拟预测的误差仅为 2.23 千克/立方米。该装置的运行稳定可靠。在本研究中，通过结构创新和参数优化，开发出了一种高回收率且结构紧凑的残膜包装装置，为农田残膜的高效回收和污染控制提供了技术支持。

INTRODUCTION
The extensive use of plastic films in agriculture has significantly enhanced crop productivity and efficiency in modern farming residual film. However, the improper disposal of agricultural plastic waste, particularly plastic films used for mulching, poses substantial environmental threats, contributing to soil pollution and microplastic contamination in agroecosystems (*Li et al., 2021; Zhang et al., 2020*). As the agricultural sector strives for sustainability, the development of effective residual film recovery technologies has become paramount (*Wang et al., 2021; Liu et al 2019*).

Recent advancements in machine design and technology have led to the emergence of residual film recovery machines, which facilitate the collection, recycling, and reprocessing of used plastic films (*Chen et al., 2020; Torres et al., 2022*). These machines not only streamline the waste recovery process but also significantly reduce labor costs and enhance recovery efficiency, thereby promoting sustainable agricultural practices (*Xu et al., 2023; Gao et al., 2022*).

Studies have demonstrated that implementing residual film recovery systems can result in considerable economic benefits for farmers (*Smith et al., 2019; Kim et al., 2021*). For instance, the recovery of used films allows for the recycling of valuable polymers back into the production cycle, reducing raw material dependency and lowering overall production costs (*Mao et al., 2022; Huang et al., 2020*). Moreover, these technologies contribute to closing the loop in agricultural plastics management, aligning with circular economy principles (*Anderson et al., 2021; Roberts et al., 2022*).

Despite significant strides in technology, challenges remain in achieving widespread adoption of residual film recovery machines (*Yuan et al., 2023; Deng et al., 2022*). Factors such as initial costs, maintenance, and the need for farmer education on proper usage significantly influence their implementation (*Liu et al., 2022; Choi et al., 2021*).

In conclusion, residual film recovery machines play a crucial role in mitigating the environmental impact of plastic films used in agriculture. Ongoing research and development efforts should focus on overcoming existing barriers, optimizing machine efficiency, and enhancing the circular economy in agriculture to ensure sustainable development. During the compression stage of the belt-type baling device, the residual film is still prone to probabilistic scattering and the movement trajectory is difficult to control, which is not conducive to the formation of high-density and stable formed residual film bales. Therefore, based on an in-depth analysis of the forming mechanism of the residual film in the baling chamber, structural constraints and parameter optimization are used to suppress the scattering and winding behaviors and improve the forming quality of the residual film package (*Xie et al., 2020; Tan et al., 2022*).

To address key problems such as the low bale-forming rate and loose baling during the mechanized recovery of residual plastic film in farmland, a three-stage belt-type residual film baling device was developed based on DEM and flexible thin-shell modeling technology *(Potyondy et al., 2004; Roessler et al., 2018)*. By establishing a dynamic model of residual film behavior in the baling chamber and performing three-dimensional simulations and parameter optimization using Rocky DEM software, the effects of key factors—including the inclination angle of the baling chamber, the type and linear speed of the baling belt, and the installation angle of the upper baling belt—on the integrity and compaction density of the residual film bales were systematically analyzed. The performance of the optimized parameter combination was further verified through field experiments.

MATERIALS AND METHODS

Overall structure and working principle

The residual film baling device mainly consists of a lower baling belt, a rear baling belt, and two side plates. Compared with conventional steel-roller-type baling systems, the belt-type baling structure reduces the overall machine weight and prevents film leakage between the rollers. Driven by the rear belt, the residual film rotates within the baling chamber and is gradually compacted to form a residual film bale. The overall structure of the device is shown in Fig. 1.

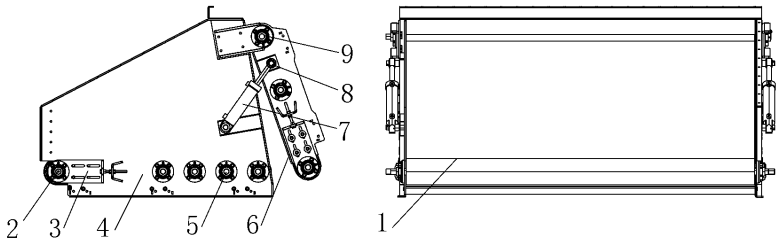


Fig. 1 - Basic structure of the residual film baling device

1. Discharge belt; 2. Lower belt drive roller; 3. Tension adjustment mechanism; 4. Side plates; 5. Support roller; 6. Rear baling belt; 7 Hydraulic cylinder; 8. Rear belt drive roller 9. Drive roller.

The lower baling belt is tensioned over the drive roller by means of a tension adjustment mechanism. The drive roller is fixed to the two side plates by bolted connections. For unloading, the rear baling mechanism can be lifted by a hydraulic cylinder to form a discharge channel. During operation, the lower belt captures the residual film discharged from the upstream collection device and conveys it toward the rear baling belt. After contacting the lower belt, the residual film is lifted and then falls back onto the accumulated film layer, forming an initial core through a winding process. As material continues to be supplied, the core grows progressively into a compact residual film bale. The formed bale is finally discharged from the rear of the device under the combined action of gravity and belt motion.

Baling Mechanism Design

The baling mechanism mainly consists of a lower baling mechanism and a rear baling mechanism. The lower baling mechanism includes a lower baling belt, a front drive roller, a rear drive roller, and support rollers. The rear baling mechanism consists of a rear baling belt, an upper drive roller, a lower drive roller, and support rollers. The two baling mechanisms are arranged symmetrically in a V-shaped configuration. Based on theoretical analysis and considering potential interference with the residual film recovery machine, the optimal angle between the two mechanisms was determined to be 70°.

The V-shaped space forms the baling chamber of the device, in which the residual plastic film is effectively compressed to form a residual film bale. To facilitate field operation and transportation, and to ensure that the bales can be discharged in a single operation, positioning blocks are installed on both sides of the belts to prevent lateral deviation caused by uneven tension during the baling process.

Due to the complex spatial structure of the baling chamber and the difficulty of precise analytical calculation, an estimation method based on the bale diameter is proposed to determine the appropriate size of the baling chamber. The calculation method is given as follows:

$$m = \rho \frac{\pi d^2}{4} l > \lambda LWX \quad (1)$$

In the formula, m represents the mass of a single residual film bale (kilograms), ρ is the density of the bale at discharge (kg/m^3), d is the diameter of the bale (m), l is the length of the bale (m), L is the maximum length of the field working row (m), W is the working width of the front-end residual film recovery machine (m), X is the mass of residual film per unit area (kg/m^2) and λ is the impurity coefficient of the bale.

The derivation of Equation (1) is based on the mass-volume equivalence principle. The mass of a single residual film bale (m) can be expressed as the product of the bale volume (V) and the mixture density (ρ) at the moment of discharge. Assuming that the bale is approximately cylindrical, with diameter (d) and length (l), its volume can be expressed as: $V = \frac{\pi d^2}{4} l$. Meanwhile, the total mass of residual film collected during a single operation can be expressed as the product of the working width (W), operation row length (L), residual film mass per unit area (X), and impurity coefficient (λ). By equating the two expressions and solving for (d) Equation (1) can be obtained.

To determine the impurity content of residual film per unit area in the experimental field, the following method was adopted. Random sampling was conducted in the test field, and five operation rows were selected. For each row, a standard sampling area of 8 m × 2.1 m was defined. The sampling process is illustrated in Fig. 2.

After the residual film within the sampling area was collected into the collection box using the residual film recovery machine, the data were analyzed. The corresponding measurement results are presented in Table 1.



Fig. 2 - Sampling and measurement of residual film during mechanical recovery

(1) Experimental field *(2) Residual film collection by the machine*

Table 1

Residual film mass in the experimental field

No.	Residual film mass / g	Residual film mass per unit area / kg/m ²
1	180.63	11.15×10-3
2	178.55	11.02×10-3
3	181.32	11.19×10-3
4	177.48	10.95×10-3
5	181.29	11.19×10-3
Average value	**179.85**	**11.10×10-3**

According to Table 1, the residual film mass per unit area (*X*) was taken as 9.46×10-3kg/m². Considering that the working width (*W*) of the residual film recovery machine is 2.1 m, the operating width of the proposed device was designed to match that of the 11CM-2100 residual film recovery machine; therefore, *W* was set to 2.1 m. The maximum measured operation row length (*L*) in the test field was 1000 m. The density of the residual film bale (ρ) was taken as 122.7 kg/m³ based on test results obtained from a roll-type residual film baling machine.

Eight groups of samples were randomly collected from the residual film mixture recovered by the machine. The analysis showed that the average volume ratio of residual film to impurities was 2.18:1.

Considering regional and crop-dependent variations in impurity content, and to ensure a sufficient design margin, the impurity coefficient (λ) was finally set to 2. Substituting these values into Equation (1) yields a minimum bale diameter of $d \geq 0.45\text{m}$. Taking into account the structural dimensions of the 11CM-2100 residual film recovery machine and avoiding interference with the baling device, a diameter of $d = 0.5\text{m}$ was selected as the design parameter. According to Equation (1), the corresponding bale mass (*m*) was calculated to be 57.33 kg. The designed residual film baling system is suitable for both manual handling and mechanized operation and meets ergonomic requirements.

Discrete element modelling of residual film

The residual film was modeled in Rocky DEM using the “flexible membrane” contact model, which allows for large deformation and bending behavior. Each film element was represented by a triangular mesh with assigned elastic properties: Young’s modulus of 0.2 GPa, Poisson’s ratio of 0.4, and a thickness of 0.05 mm. The contact interaction between film elements and the baling belts was defined using a linear spring-dashpot model, with a coefficient of restitution of 0.45, a static friction coefficient of 0.6, and a rolling friction coefficient of 0.15. These parameters were calibrated by comparing the simulated film stacking behavior with results from physical drop tests. The calibration process involved adjusting the friction coefficients until the simulated angle of repose matched the experimentally measured value of 38° for field-collected residual film samples. The simulation time step was set to 20% of the Rayleigh time step, and the total simulation time corresponded to 15 s of real operating conditions.

Establishment of the three-stage baling device model

During the simulation, observation of the dynamic behavior of the residual film revealed a stochastic scattering phenomenon, as shown in Fig. 3.

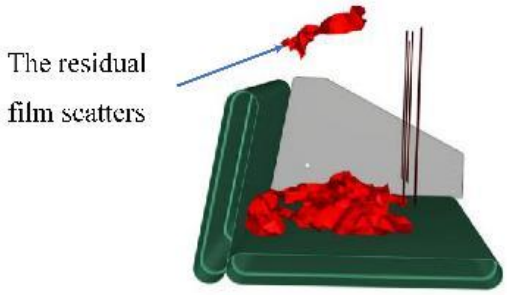


Fig. 3 - Residual film scattering phenomenon

When the residual film comes into contact with the rear baling belt, its relatively rough surface produces a hooking effect, leading to a sudden increase in frictional resistance. As a result, the residual film tends to scatter along the direction of belt motion. In actual operation, scattered film is prone to entanglement with transmission components or accumulation in structural gaps, which reduces operational efficiency and may cause blockage or mechanical failure. To address this issue, a third (upper) baling belt was introduced above the original lower and rear belts, forming a three-stage constraint system. This configuration significantly improves control over the motion trajectory of the residual film and effectively suppresses scattering

The upper belt serves two main functions. First, it intercepts residual film that deviates from the intended trajectory and redirects its motion through frictional interaction. Second, during bale formation, it works in coordination with the lower and rear belts to apply multi-directional compressive forces, resulting in improved compaction uniformity, higher bale density, and enhanced forming stability. The optimized three-stage structure is shown in Fig. 4.

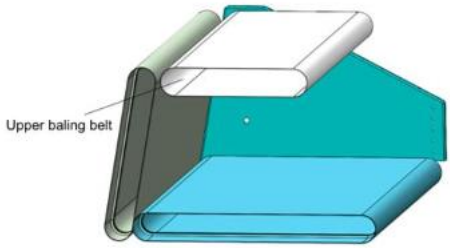


Fig. 4 - Three-stage residual film baling device

To investigate the influence of installation parameters on the baling performance, the installation inclination angle of the baling belt, the inclination angle of the baling chamber, and the belt linear speed were selected as experimental factors. The bale-forming rate and bale density were used as evaluation indicators, and single-factor experiments were conducted on the three-stage baling device.

The effect of the installation inclination angle on the device performance is shown in Fig. 5.

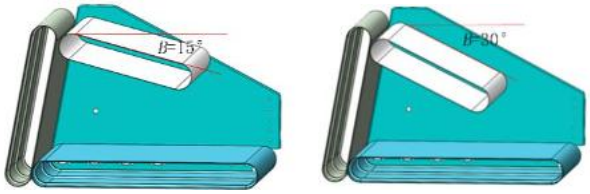


Fig. 5 - Installation inclination angle of the upper baling belt

The baling belt was selected as a rough-surface belt. The inclination angle of the baling chamber was set to 0°, the belt linear speed was fixed at 1.5 m/s, and the installation inclination angle of the upper belt was varied at 0°, 5°, 10°, 15°, 20°, 25°, and 30°. Each experiment was repeated five times, and the average values were used for analysis. The results are presented in Fig. 6.

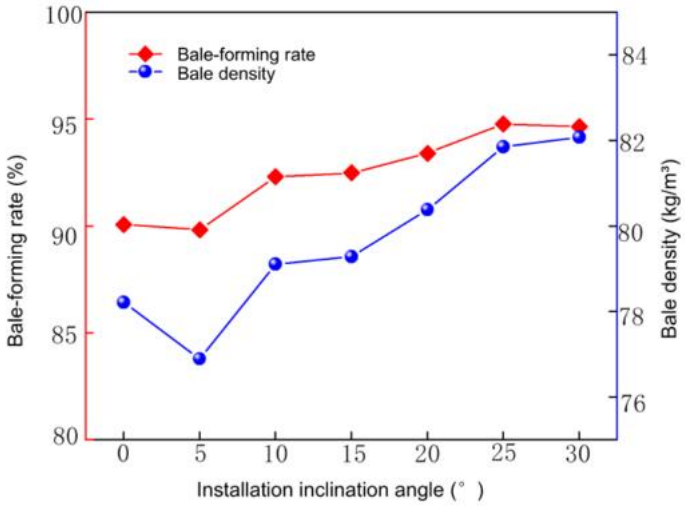


Fig. 6 - Effect of installation inclination angle on baling performance

It can be seen from Fig. 6 that the installation inclination angle of the upper baling belt has a significant influence on the forming quality of the residual film bales. As the inclination angle increases, both the bale-forming rate and bale density show an increasing trend, reaching optimal values at 30°. This behavior can be attributed to the fact that a larger inclination angle enhances the wrapping and normal constraint effects of the belt on the residual film. As a result, scattering during the compaction process is effectively suppressed, and the motion trajectory of the film becomes more stable, leading to improved bale formation and higher density.

A single-factor experiment was further conducted to investigate the effect of belt linear speed on the performance of the three-stage baling device. The installation inclination angle was fixed at 30°, and the inclination angle of the baling chamber was set to 0°. The belt linear speed was varied at 0.5 m/s, 1.0 m/s, 1.5 m/s, 2.0 m/s, and 2.5 m/s. Each experiment was repeated five times, and the average values were used for analysis. The results are shown in Fig. 7.

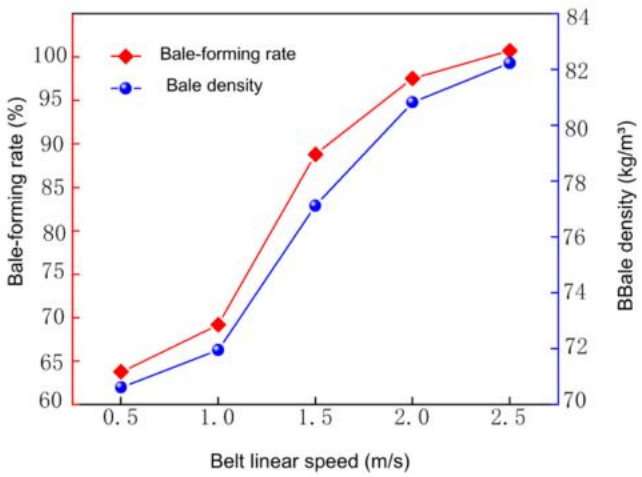


Fig. 7 - Effect of belt linear speed on baling performance

As shown in Fig. 7, compared with the conventional two-stage structure, the three-stage device exhibits clear advantages in terms of bale-forming rate and bale density. As the belt linear speed increases, both indicators show a continuous upward trend, reaching optimal values at 2.5 m/s. This behavior can be explained by the enhanced compaction effect provided by the third-stage belt. When the volume of the residual film bale reaches a certain level, the upper belt applies additional compressive force. By increasing the normal pressure and contact area, the overall frictional interaction and constraint on the residual film are significantly enhanced, resulting in improved bale integrity and higher density.

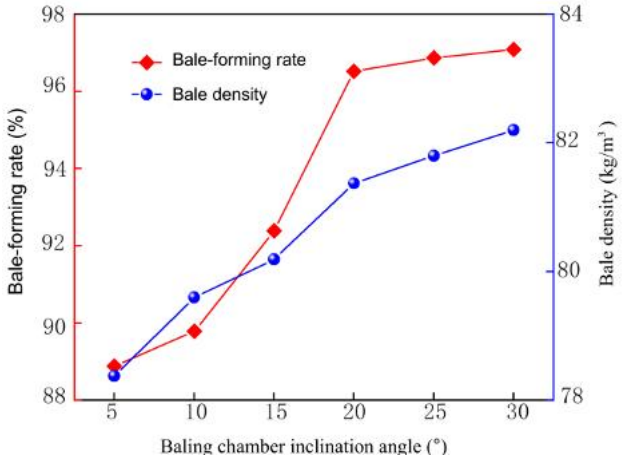


Fig. 8 - Effect of baling chamber inclination angle on baling performance

A single-factor experiment was conducted to investigate the effect of the baling chamber inclination angle on the performance of the three-stage baling device. The installation inclination angle of the upper belt was fixed at 30°, and the belt linear speed was set to 1.5 m/s. The results are presented in Fig. 8. As the baling chamber inclination angle increases, both the bale-forming rate and bale density exhibit an increasing trend. This is because a larger inclination angle enhances the spatial constraint during the compaction process. In combination with the three-stage belt system, a multi-directional constraint is formed, which effectively controls the motion trajectory of the residual film, improves material aggregation, enhances compaction, and reduces scattering.

RESULTS

Simulation performance test of three-stage baling device

To investigate the performance variation of the three-stage residual film baling device under multi-factor conditions, and to identify the key variables affecting bale density and bale-forming rate, an orthogonal experimental design was adopted to determine the optimal operating parameter combination. The belt linear speed, the installation inclination angle of the upper belt, and the inclination angle of the baling chamber were selected as experimental factors. The corresponding factor levels are presented in Table 2.

Table 2

Factor levels of the three-stage baling device

Level	Baling chamber inclination angle A/°	Upper belt inclination angle B/°	Belt linear speed C/m·s^{-1}
-1	20	20	2.1
0	25	25	2.3
1	30	30	2.5

Analysis of experimental data

A simulation experiment was designed using the Box–Behnken method. A total of 17 experimental runs were conducted, including five replications at the center point. The experiments were designed to investigate the interaction effects between the bale-forming rate, bale density, and three key factors.

Regression model for bale-forming rate

Analysis of variance (ANOVA) and significance tests of the regression coefficients were performed for the regression model of the residual film bale-forming rate (Y_1). The regression equation for Y_1 is given as follows:

$$\hat{Y}_1 = 97.38 + 0.635A + 0.8345B + 0.6162C + 0.0075AB - 0.1042AC + 0.11BC + 0.3117A^2 - 0.1008B^2 - 1.52C^2 \quad (2)$$

Taking the bale-forming rate as the response variable, the regression model established for the baling chamber inclination angle (A), the upper belt inclination angle (B), and the belt linear speed (C) was found to be highly significant (F = 402.8). The linear terms (A, B, C), interaction terms (AC, BC), and quadratic terms (A^2, B^2, C^2) were all statistically significant. The lack-of-fit term was not significant (F = 2.0, p = 0.2565), indicating good model adequacy. The coefficient of determination was R^2 = 0.9981, with an adjusted R^2 of 0.9956 and a predicted R^2 of 0.9803, demonstrating excellent model fit and strong predictive capability.

Based on response surface methodology (RSM), the experimental data were analyzed to investigate the interaction effects between the bale-forming rate and its key influencing factors, as shown in Fig. 9.

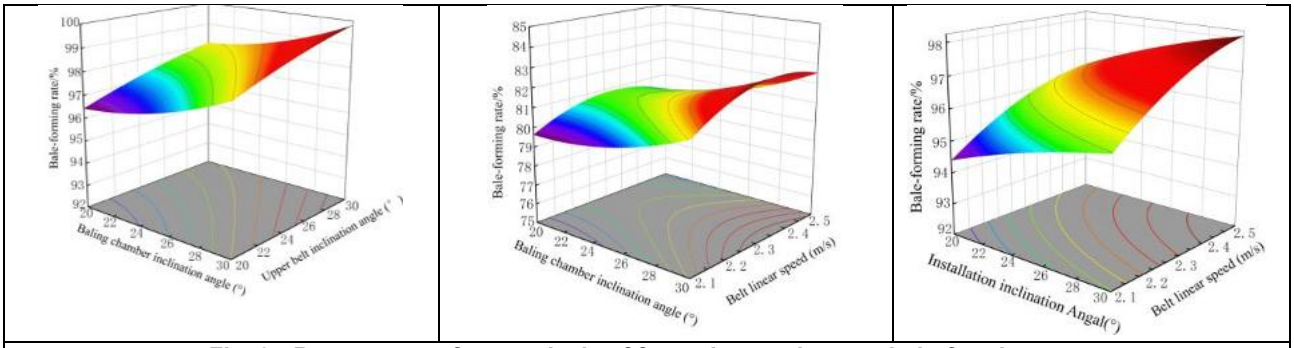


Fig. 9 - Response surface analysis of factor interactions on bale-forming rate

(a) Interaction between baling chamber inclination angle and upper belt inclination angle

(b) Interaction between baling chamber inclination angle and belt linear speed

(c) Interaction between upper belt inclination angle and belt linear speed

Figure 9(a) shows that the bale-forming rate increases with the increase in the upper belt inclination angle, and its influence is more significant than that of the baling chamber inclination angle. This trend can be explained by the change in force components acting on the residual film. As the inclination angle increases, the normal force component exerted by the upper belt becomes more effective in constraining the film, while the tangential (conveying) component also increases, improving both compaction and motion control. Consequently, the probability of film scattering is reduced.

Figure 9(b) indicates that, under the interaction between belt linear speed and baling chamber inclination angle, the bale-forming rate initially increases and then decreases with increasing belt speed, reaching a peak value (approximately 81.5%) at around 2.3 m/s. The influence of belt linear speed is more pronounced than that of the baling chamber inclination angle.

Figure 9(c) shows that the response surface for the interaction between belt linear speed and upper belt inclination angle is convex, indicating the presence of an optimal parameter region. The effect of the upper belt inclination angle on the bale-forming rate is more significant than that of belt linear speed.

The variation in bale density follows a similar trend. The maximum density is also achieved at approximately 2.3 m/s, as optimal compaction requires both sufficient compressive force and adequate residence time for interlayer bonding of the residual film. At excessively high belt speeds, the residence time in the compression zone is reduced, limiting effective compaction.

According to the response surface analysis, the order of influence of each factor on the bale-forming rate is: upper belt inclination angle > baling chamber inclination angle > belt linear speed

Regression model for bale density

The regression model for residual film bale density (Y_2) was analyzed using ANOVA and significance tests of the regression coefficients. The regression equation for Y_2 is given as follows:

$$\hat{Y}_2 = 81.35 + 1.03A + 1.21B + 0.4217C - 0.0075AB - 0.055AC + 0.11BC + 0.5051A^2 - 0.3983B^2 - 0.9424C^2 \quad (3)$$

The developed regression model for bale density was found to be highly significant (F = 875.1). The linear terms (A, B, C), interaction terms (AC, BC), and quadratic terms (A^2, B^2, C^2) were all statistically significant. The lack-of-fit term was not significant (F = 4.73, p = 0.0838), indicating good model adequacy. The coefficient of determination was R^2 = 0.9988, with an adjusted R^2 of 0.9973 and a predicted R^2 of 0.9849, demonstrating excellent agreement between the model and experimental data, as well as strong predictive capability.

Based on response surface methodology, the interaction effects of each factor on bale density were analyzed, and the corresponding response surface plots are shown in Fig. 10.

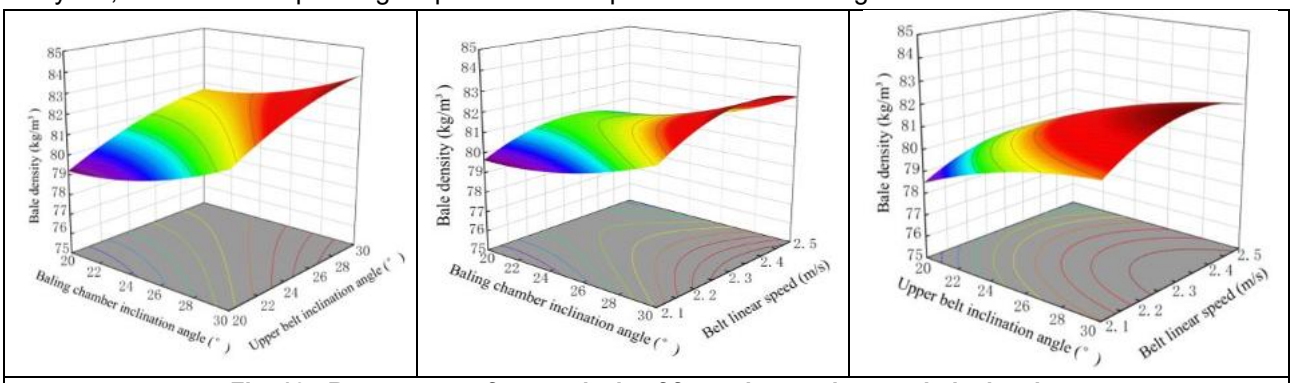


Fig. 10 - Response surface analysis of factor interactions on bale density

(a) Interaction between baling chamber inclination angle and upper belt inclination angle	*(b) Interaction between baling chamber inclination angle and belt linear speed*	*(c) Interaction between upper belt inclination angle and belt linear speed*

Figure 10(a) shows that bale density increases with increasing upper belt inclination angle, and its influence is more significant than that of the baling chamber inclination angle. Figure 10(b) indicates that, under the interaction between belt linear speed and baling chamber inclination angle, bale density initially increases and then decreases with increasing belt speed, reaching a peak value of approximately 81.2 kg/m³ at around 2.3 m/s. The interaction between these two factors is significant. Figure 10(c) shows that, under the interaction between belt linear speed and upper belt inclination angle, the influence of the upper belt inclination angle on bale density is more pronounced than that of belt linear speed.

To determine the optimal operating parameters, the regression models were optimized using Design-Expert software. The constraints were set as follows: baling chamber inclination angle of 25°–30°, upper belt inclination angle of 20°–30°, and belt linear speed of 2.1–2.5 m/s. The optimization results indicate that the maximum bale density (83.75 kg/m³) is achieved at a baling chamber inclination angle of 29.92°, an upper belt inclination angle of 29.64°, and a belt linear speed of 2.3 m/s. Meanwhile, the maximum bale-forming rate (99.13%) is obtained at a baling chamber inclination angle of 29.96°, an upper belt inclination angle of 30.11°, and a belt linear speed of 2.33 m/s.

Considering manufacturing feasibility and operational convenience, the final selected parameter combination was a baling chamber inclination angle of 30°, an upper belt inclination angle of 30°, and a belt linear speed of 2.3 m/s.

Performance tests of the residual film baling device were then conducted. Based on the average of 10 trials, the results (Table 6) show that the measured bale density was 91.4 kg/m³, and the bale-forming rate reached 100%. The experimental results are in good agreement with the simulation predictions, demonstrating the feasibility and accuracy of the proposed simulation model. The operational performance of the machine is shown in Fig. 11.



Fig. 11 - Experimental setup for performance testing of the residual film baling device

Table 3

Experimental results of bale density and bale-forming rate

Test Number	**1**	**2**	**3**	**4**	**5**
bale-forming rate Y_1**/(%)**	91.3	92.5	90.8	89.4	93.7
Test Number	6	7	8	9	10
bale-forming rate Y_1**/(%)**	88.5	91.1	90.2	93.8	92.7
Average value	91.4				
Test Number	1	2	3	4	5
bale density Y_2**(kg·m^{-3})**	100	100	100	100	100
Test Number	6	7	8	9	10
bale density Y_2**%(kg·m^{-3})**	100	100	100	100	100
Average value	100				

CONCLUSIONS

(1) The proposed three-stage baling structure significantly improved baling performance. By introducing an upper baling belt to the conventional two-stage configuration, a three-dimensional constraint system was formed. This effectively suppressed residual film scattering and enhanced bale compactness. Both the bale-forming rate and bale density were significantly improved compared with the traditional two-stage structure.

(2) The optimal combination of operating parameters was determined using response surface methodology. For the three-stage baling device, the optimal conditions were a baling chamber inclination angle of 30°, an upper belt inclination angle of 30°, a belt linear speed of 2.3 m/s, and the use of a rough-surface belt. Under these conditions, the maximum bale-forming rate reached 99.13%, and the bale density reached 83.75 kg/m³, indicating optimal operational performance.

(3) Field tests verified the reliability of the simulation results and the practicality of the device. Under the optimized parameters, the measured average bale density was 91.4 kg/m³. The experimental results were in good agreement with the simulation predictions, demonstrating the high predictive accuracy of the developed model. The device operated stably and reliably, meeting the requirements for residual film recovery in farmland conditions.

(4) This study provides a feasible technical solution for efficient residual film recovery and pollution control. Through structural innovation and systematic parameter optimization, the device achieved high bale-forming rates and high-density compaction. This contributes to improved recovery efficiency and reduced post-processing costs, with positive implications for mitigating residual film pollution in agricultural fields.

Although the DEM model captures the main flexible behavior of residual film, it simplifies the material as a homogeneous elastic shell and does not account for tear propagation or variable impurity adhesion. The model parameters were calibrated under dry, low-impurity conditions; their applicability to wet or high-impurity environments requires further validation. In addition, the scalability of the optimal parameters to different crop types (e.g., maize vs. cotton) and field conditions has not been systematically investigated. The long-term durability of the three-stage belt system (e.g., belt wear and tension stability) will be evaluated in future multi-season field trials.

ACKNOWLEDGEMENT

Fund Project: Key Research Project of Basic Scientific Research of Liaoning Provincial Department of Education in 2022, Project Number (LJKZZ20220158)

Project of Liaoning Vocational College of Agriculture: Design of Farmland Film Recovery Device (LnzkA202405).

REFERENCES

[1] Anderson, G., Smith, L., Roberts, K. (2021). Plastic waste management in agriculture: Policy implications. *Environmental Policy and Governance*, 31(2):101-109.

[2] Chen, L., Wang, F., Xu, P. (2020). Efficiency of agricultural film recovery machines. *Applied Engineering in Agriculture*, 36(5):745-751.

[3] Choi, J., Park, S., Lee, H. (2021). Engagement strategies for effective film recovery implementation. *Sustainable Development*, 29(6):660-670.

[4] Deng, Y., Liu, J., He, W. (2022). Assessing farmer attitudes towards plastic film recovery. *Agricultural Systems*, 197:103-110.

[5] Gao, J., Liu, Y., Zhao, X. (2022). Enhancing recovery efficiency in agricultural practices. *Bioresource Technology Reports*, 10:123-132.

[6] Huang, X., Zhang, D., Wei, J. (2020). Circular economy in agriculture: A review of plastic recovery systems. *Sustainable Production and Consumption*, 24:33-42.

[7] Kim, S., Lee, D., Park, J. (2021). Recycling potential of agricultural films: Challenges and opportunities. *Waste Management*, 120:54-62.

[8] Li, J., Zhang, H., Wang, L. (2021). Environmental impacts of agricultural plastic waste. *Waste Management*, 119:35-45.

[9] Liu, H., Zhang, H. (2019). Assessment of agricultural plastic waste management. *Resources, Conservation and Recycling*, 148:55-62.

[10] Liu, L., Zhang, D., Qiu, F. (2022). The importance of education in plastic waste management. *International Journal of Agricultural Sustainability*, 20(3):227-237.

[11] Mao, Q., Liu, T., Chen, Y. (2022). The role of plastic recovery in sustainable agriculture. *Journal of Environmental Management*, 303:113-120.

[12] Potyondy, D.O., Cundall, P.A. (2004). A bonded-particle model for rock. International Journal of Rock Mechanics and Mining Sciences, 41(8):1329-1364.

[13] Roberts, K., Brown, S., Wang, T. (2022). The circular economy in agricultural management. *Journal of Sustainable Agriculture*, 35(4):789-800.

[14] Roessler, T., Katterfeld, A. (2018). DEM parameter calibration of cohesive bulk materials using a simple angle of repose test. Particulate Science and Technology, 36(8):982-992.

[15] Smith, R., Brown, A., Taylor, M. (2019). Economic impacts of film recycling on farmers. *Agricultural Economics*, 50(1):110-120.

[16] Tan, C., Gao, H., Wu, F. (2022). Future directions in agricultural film recovery research. *Journal of Cleaner Production*, 350:131-145.

[17] Torres, A., Kim, S., Garcia, R. (2022). Cost-benefit analysis of film recovery systems. *Journal of Cleaner Production*, 345:131-140.

[18] Wang, T., Liu, P., Sun, Z. (2021). Innovations in plastic film recovery technologies. *Journal of Agricultural Engineering*, 8(3):123-133.

[19] Xie, F., Liu, Z., Cheng, B. (2020). Sustainable technologies for agricultural waste management. *Journal of Environmental Science and Health*, 55(12):1450-1460.

[20] Xu, P., Zhang, J., Li, Q. (2023). Labor savings through automated film recovery techniques. *Frontiers in Sustainable Food Systems*, 7:220-230.

[21] Yuan, T., Zhang, L., Chen, H. (2023). Overcoming barriers to film recovery technology adoption. *Renewable Agriculture and Food Systems*, 38(1):56-68. Zhang, Y., Chen, L., Li, C. (2020). Microplastic pollution in agricultural soils: A review. *Agronomy for Sustainable Development*, 40(2):15.

APP-ENABLED WIRELESS LOOP RESISTANCE TESTING FOR EFFICIENT EVALUATION OF AGRICULTURAL POWER SYSTEM EQUIPMENT

/

基于 APP 的无线回路电阻测试实现农业电力系统设备的高效评估

Yue YAO, Yanquan HOU*, Wei LI, Juntao ZHAO, Chen HUANG, Cen LI
State Grid Heilongjiang Electric Power Co., Ltd. Qitaihe Power Supply Company / P.R.China
Tel: +8613398601690; E-mail: 965660634@qq.com
Corresponding author: Yanquan Hou
DOI: https://doi.org/10.35633/inmateh-79-08

Keywords: *High-Voltage Switchgear; Loop Resistance Test; Abnormal Contact Resistance; Contact Wear; Agricultural power distribution network*

ABSTRACT

Agricultural power networks accelerate contact wear and reduce the accuracy of conventional loop resistance testing. This study presents an APP-based wireless three-phase synchronous measurement system integrating UC3854-driven multi-stage power factor correction (0–100 A, 82–83.17% efficiency, PF 0.99) and a supercapacitor pulse module (16 V trigger, 230 V charge). The system achieves 0.01 μΩ resolution and >10,000 MΩ insulation resistance. Field validation on 110 kV GIS reduced wiring and testing times by 67% (≤1% deviation), while 500 kV GIL measurements improved efficiency by 80%. The platform enables high-current stability, strong interference immunity, and digitalized operation.

摘要

农业配电网运行于潮湿、多尘、腐蚀性环境，加速接触磨损并降低传统回路电阻测试仪的精度。本研究开发了一种基于 APP 的无线三相同步回路电阻测试系统，采用基于 UC3854 的多级功率因数校正架构（0–100 A 恒流输出，效率 82–83.17%，功率因数 0.99）和超级电容脉冲放电模块（16 V 触发，230 V 充电）。系统实现 0.01 μΩ 测量分辨率和>10,000 MΩ 绝缘电阻，优于商用回路电阻测试仪典型的 0.1 μΩ 分辨率。现场测试表明：110 kV GIS 设备接线时间由 30 min 缩短至 10 min，测量时间由 3 min 缩短至 1 min（效率提升 67%，偏差 ≤1%）；500 kV GIL 区段（1.2 km）将传统五段测试整合为单次连续测量（效率提升 80%）。该系统为高电流稳定输出、强抗干扰、快速接线和数字化管理的农业配电网提供了高效可靠的测试解决方案。

INTRODUCTION

The rural power distribution network is a critical infrastructure in modern agriculture, supporting not only livestock production, irrigation systems, and primary processing, but also the integration of distributed energy and agricultural IoT. Consequently, the reliability of high-voltage switchgear—responsible for circuit control and protection—has become a key determinant of grid security (*Li, 2022*). Compared with urban systems, rural equipment is more exposed to humidity, dust, corrosive gases, and temperature fluctuations, which accelerate contact degradation and increase the risk of abnormal loop resistance, potentially leading to overheating, protection failure, and system outages (*Li et al, 2022*). Loop resistance measurement is widely used to evaluate the operational condition of GIS and GIL switchgear. According to standards such as GB 50150 and DL/T 596, resistance values should not exceed 120% of factory references, and significant phase deviations indicate potential faults. However, conventional testers face substantial limitations in rural applications. Fixed-spacing clamps often fail to meet GB/T 3048.4–2007 requirements, especially for large or irregular conductors, resulting in poor measurement reliability (*Ma et al., 2022; Deng, 2021*). Temperature variations introduce resistance drift and reduce testing efficiency due to thermal stabilization requirements *(Zhang et al., 2021*). In addition, strong electromagnetic interference in substations distorts measurement signals (*Fang, 2020; Fang, 2020b*), while traditional instruments lack real-time data transmission capabilities, hindering digital management (*Wu & Zhang, 2020*). Condition-based maintenance (CBM) has been extensively studied worldwide.

Early work by EPRI in the 1970s introduced reliability-centered maintenance concepts (*Yuan et al., 2020*), followed by developments in Japan and Europe emphasizing online monitoring and integrated diagnostic systems (*Wang et al., 2018; Ban et al., 2018*). In contrast, existing loop resistance testing technologies in China still rely on single-phase sequential measurement and wired control, limiting efficiency and data reliability (*Xiao et al., 2014*).

To address these challenges, this study develops a three-phase synchronous loop resistance testing system tailored for rural environments. The system integrates wireless APP-based control, a high power-factor constant-current source, supercapacitor-assisted pulse discharge, enhanced electromagnetic compatibility design, and optimized Bluetooth communication. It enables rapid deployment, high-precision measurement, and automated data management, thereby facilitating the transition toward condition-based and digitalized operation of agricultural power distribution systems.

MATERIALS AND METHODS

System Architecture of the Tester

Within this system, the overall topology presents a hierarchical structure composed sequentially of the front-end power equipment, sensor unit, data acquisition and processing module, signal-processing chain, and fault-diagnosis module. During operation, the power equipment generates current, voltage, and loop-impedance states that are first captured in real time by high-sensitivity sensors. After entering the data acquisition unit, the sensing signals are quantized and preprocessed according to the required sampling accuracy and bandwidth, followed by preliminary data structuring and anomaly elimination performed by an embedded processor. The signal-processing module applies filtering, denoising, feature decomposition, and parameter modeling to the acquired signals, enabling the dynamic characteristics and state parameters of the electrical circuit to be presented with an enhanced signal-to-noise ratio. The fault-diagnosis module identifies abnormal conditions—such as loop-resistance deviation, contact erosion, and poor contact—based on the extracted key features, and transmits the diagnostic results to the App interface via a wireless communication link, allowing maintenance personnel to monitor equipment health in real time and perform remote control and decision support.

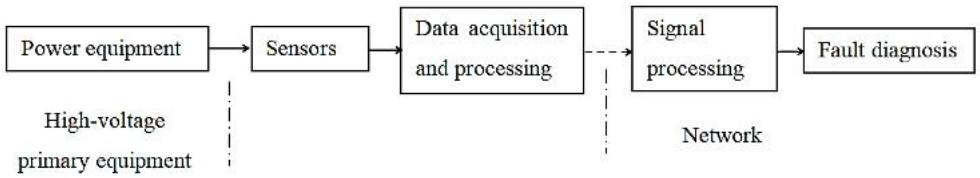


Fig. 1 – Topology of an App-Wireless-Controlled Loop-Resistance Tester for Switchgear

To eliminate the influence of temperature on the measurement results, an automatic temperature-compensation technique is employed. The ambient temperature is continuously monitored using a DHT11 temperature–humidity sensor, and the measured resistance is corrected to its equivalent value at the standard reference temperature of 20°C using the resistance–temperature conversion formula $R_t=R_o(1+\alpha t)$ (*Lai et al., 2019*). In this equation, R_o denotes the standard resistance at 20℃, R_t is the measured resistance under the current ambient temperature, and α represents the temperature coefficient of the conductor material. This correction ensures the comparability of measurement data across different environments and seasons. The main controller adopts the STM32F103C8T6, a 32-bit microcontroller operating at a clock frequency of 72 MHz, integrating a 12-bit ADC, DMA controller, and multiple communication interfaces. These features meet the requirements of three-phase data acquisition and Bluetooth communication, while its low-power operation mode supports long-duration field testing (*Chen et al., 2016*). The design schematic is shown in Figure 2.

Interference suppression is achieved through power-supply filtering, Bluetooth AFH frequency hopping, and electromagnetic-compatibility design. For GIS/GIL applications, a dedicated wireless auxiliary short-circuiting module is integrated, enabling long-distance testing within 3 km via LoRa communication. After the system is powered on, the main program performs initialization, defining system variables and assigning initial values, configuring the I/O modules, and setting parameters for the display, serial ports, and other functional modules. Once initialization is completed, the program enters a keypad-scanning routine (i.e., scanning touch-keys on the display) and responds to user operations.

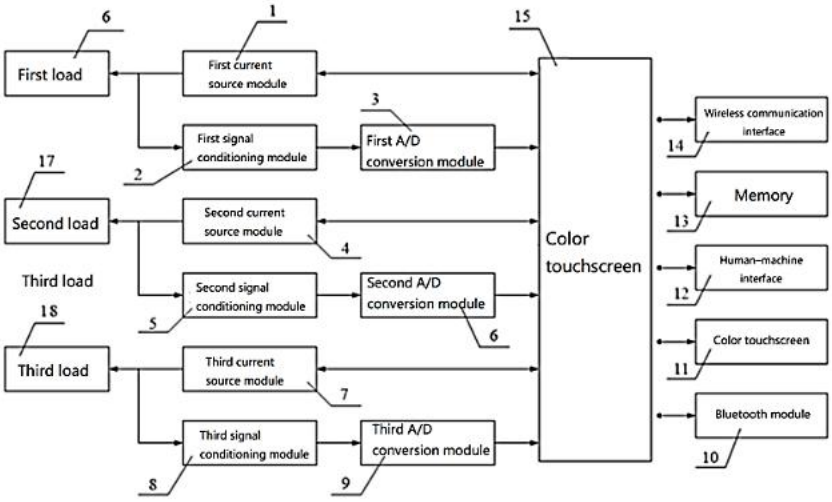


Fig. 2 – The structural schematic diagram of the tester

The GC7135B A/D converter synchronously samples three-phase current, voltage, and temperature; the STM32 computes resistance, resistivity, and temperature-corrected values transmitted to a mobile APP. The APP supports Bluetooth pairing, time sync, parameter configuration, command execution, real-time data reception, validity assessment (inter-phase deviation ≤5% as qualified), WORD report generation, and PMS interface reservation. To counter 2.4-GHz ISM band EMI (*Kusuma Neerugatti & Pakala, 2025*), a hierarchical anti-interference architecture integrates FEC, ARQ, AFH, and packet-length adaptation (*Golaghazadeh et al., 2022; Labiod et al., 2014*). Bluetooth uses 1/3-rate repetition and 2/3-rate shortened Hamming coding; ARQ with CRC enables fast retransmission via ACK/NACK (Type-I Hybrid ARQ). AFH dynamically excludes interfered channels, while variable packet lengths mitigate high-interference transmission risks. A two-tier validation framework (laboratory and field) evaluates functionality, stability, communication reliability, and applicability. Laboratory tests assess Bluetooth communication, data-display sync, constant-current output (0–100 A), measurement range/resolution, HMI, insulation, and EMC using standard resistors, calibrators, and EMI injection. Field tests on 110-kV GIS and 500-kV GIL systems (*Chen et al., 2025*) verify three-phase synchronous measurement, long-distance wireless triggering, and integrated operation; the 1.2 km GIL test validates coordinated main/remote module operation under practical grid conditions.

Development and Testing of the High-Power-Factor Power Supply

The design of the current source employs the UC3854 as the core controller to realize active power-factor correction. Based on the preset current value, the controller automatically adjusts the PWM duty ratio and regulates the switching frequency of the MOSFETs, ensuring that the output current remains stable at the specified level.



Fig. 3 – Photograph of the power supply unit

This study employs a multi-stage AC/DC/AC/DC topology with active power correction and PWM modulation for a high-power, high-power-factor intelligent DC supply (Figure 4). Module (1): rectification; (2): BOOST step-up; (3): half-bridge conversion; (4): high-frequency transformer; (5): secondary rectification; (6): temperature sensor; (7): protection unit; (8): PWM modulator; (9): UC3854-based PFC controller; (10): control interface.

Working process: Mains AC is rectified by (1) to DC bus voltage, then conditioned via the PFC loop (2, 9) to improve power factor. PWM modulator (8) drives half-bridge converter (3) to invert DC to high-frequency AC; transformer (4) provides isolation and step-down; module (5) rectifies and filters to final DC output. Temperature sensor (6) monitors power semiconductors, feeding protection unit (7) to adjust PWM (8) or activate cooling. Control interface (10) manages current setting and display. UC3854-based PFC (9) regulates BOOST input current in-phase with voltage, pushing power factor >0.95; PFC auto-activates under heavy load and disables under light load. PWM modulator (8) serves as the core control unit, adjusting duty cycle and switching frequency per preset current from (10) to stabilize output. The multi-stage structure delivers 100 A at 10 V, exceeding 500 A at 5 V.

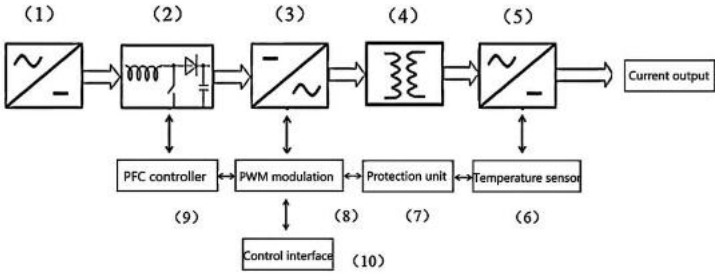


Fig. 4 – Block diagram of the current source principle

In this design, the UC3854 integrated circuit, produced by Texas Instruments for active power factor correction (APFC), is adopted. By incorporating input-voltage feed-forward technology together with the internal multiplier and divider, the loop gain of the control circuitry becomes independent of input-voltage fluctuations. This enables stable operation across the full input-voltage range while ensuring excellent dynamic response and load-regulation performance. The application schematic of the UC3854 is shown in Figure 5.

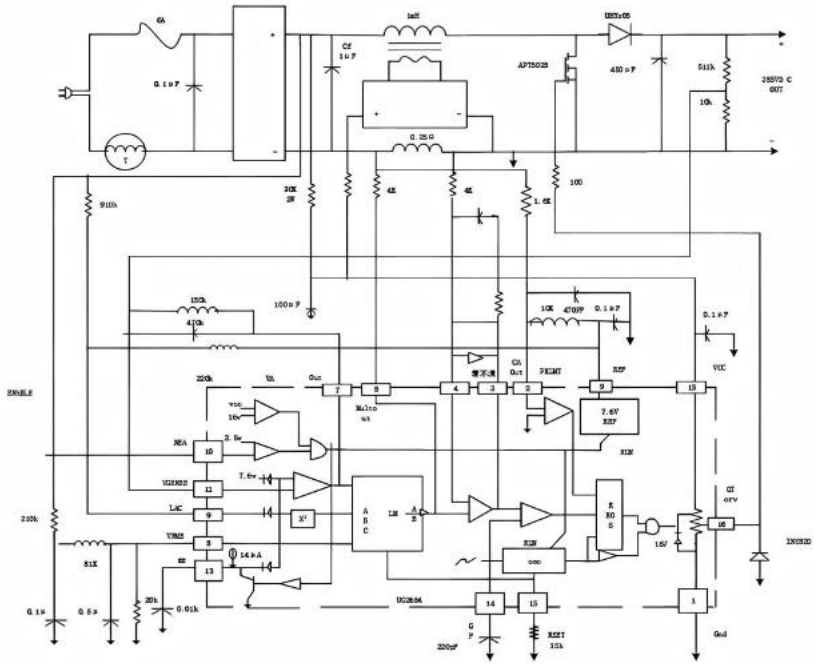


Fig. 5 – Schematic diagram of the UC3854 application circuit

Although the AC/DC and DC/AC stages provide sufficient power, the output voltage remains excessive and current capacity inadequate. A step-down transformer with rectification is therefore introduced to obtain a stable high-current DC output (*Yuan et al., 2020*). Performance evaluation focuses on efficiency, harmonics, waveform quality, thermal behavior, and electromagnetic compatibility under controlled conditions (20 ± 5 ℃, 30%–70% RH). The input is connected to a calibrated power analyzer, and the output to a programmable electronic load. Efficiency is measured from 10% to 100% load with 60 s stabilization per point. Harmonic spectra and total harmonic distortion (THD) are measured under full-load conditions, while waveform distortion, ripple characteristics, and dynamic response are evaluated using high-bandwidth oscilloscopic measurements.

Thermal performance is assessed 60 min full-load operation using thermocouples or infrared imaging to determine steady-state distribution. Electromagnetic compatibility is verified through EFT, surge, and ESD tests applied to power and signal ports, with continuous monitoring of system stability. This framework enables systematic validation of key metrics and supports subsequent system optimization.

Design of the Test Power Supply Based on Supercapacitors

Supercapacitors provide rapid charge–discharge, high power density, long cycle life (>500,000), and wide-temperature operation (−40 to 70 °C). Compared with batteries and electrolytic capacitors, they offer 30–40× higher capacitance at equal volume, faster charging (~95% within 10 s), lower ESR, and significantly enhanced instantaneous power capability. These properties enable high-current pulse generation for loop-resistance measurement. Peak current and duration depend on initial voltage U, capacitance C, inductance L, and resistance R. Large parasitic inductance induces voltage spikes, mitigated by series inductance (validated by simulation). Peak current scales with voltage, exceeding kA levels above 16 V (~2200 A at 32 V), while higher voltage or capacitance extends pulse duration. The discharge path is modeled as a series RLC circuit. Based on the zero-input response of a second-order system, pulse current generation is realized. The 220 V AC input is isolated and half-wave rectified. A microcontroller controls relay-based charging and SCR-based discharging, with a diode preventing reverse current. Charging and discharging are coordinated via optocoupler-driven switching. Experimental validation employs C=1500μF, L=15mH, shunt 100 A/45 mV, and R=0.5Ω, confirming feasibility of the proposed design.

Research on Anti-Strong-Electric-Field and Anti-Strong-Magnetic-Field Interference Techniques

Testing equipment relies on microelectronic components (ICs, digital circuits) for control, signal transmission, measurement, monitoring, and diagnostics, making it highly sensitive to transient disturbances and substation electromagnetic environments. EMC tests are essential to ensure sufficient immunity and reliable operation of intelligent high-voltage devices (*Zhang et al., 2021*). Laboratory analysis of electromagnetic environments guides controlled EMC testing to guarantee field reliability under complex scenarios. This study incorporates strong electric and magnetic field interference considerations into enclosure, high-current power source, functional/signal/communication port designs for robust field usability. For the high-current power source, differential-mode (L1) and common-mode (L3, C2, C3) filters mitigate interference from switching operations, pump start/stop transients, and transformer excitation in agricultural grids. X-class capacitor C1 (phase-neutral) provides high-frequency discharge during voltage spikes to suppress differential-mode noise coupling. Common-mode choke L3 with symmetrically arranged Y-class capacitors C2 and C3 attenuates common-mode interference from lightning, capacitor switching, and long-line transients. The combined filters ensure stable input under weak grids, long transmission lines, and strong interference, providing clean front-end power for subsequent rectification and constant-current output.

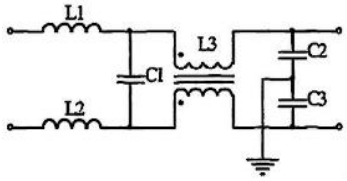


Fig. 6 – Input-End Filter Circuit of the Power Supply

An active PFC circuit at the front-end rectification stage synchronizes input current with grid voltage, maintaining near-sinusoidal waveforms to suppress harmonic injection and high-frequency distortion—critical in rural/agricultural grids where complex loads, voltage fluctuations, and high line impedance cause low-order harmonics, current distortion, sampling noise, ADC instability, and control-loop oscillations. The PFC stage stabilizes energy input, reduces conducted interference, and prevents high-frequency noise from propagating into the filter network and constant-current module. RC snubber networks across MOSFETs and IGBTs attenuate high dv/dt transients and voltage spikes, mitigating reverse voltage ringing and parasitic oscillations in inductive agricultural grid environments. This reduces radiated and conducted EMI while protecting sensors, amplifiers, and microcontrollers. A hybrid single-point and low-impedance grounding strategy minimizes grounding inductance/impedance, rapidly diverting high-frequency currents during transients to limit internal noise propagation. Critical components (drivers, communication modules, ADC units) are protected via localized shielding combined with low-impedance grounding, ensuring interference currents discharge preferentially through the shielding structure—enhancing system robustness against electromagnetic disturbances in harsh agricultural conditions.

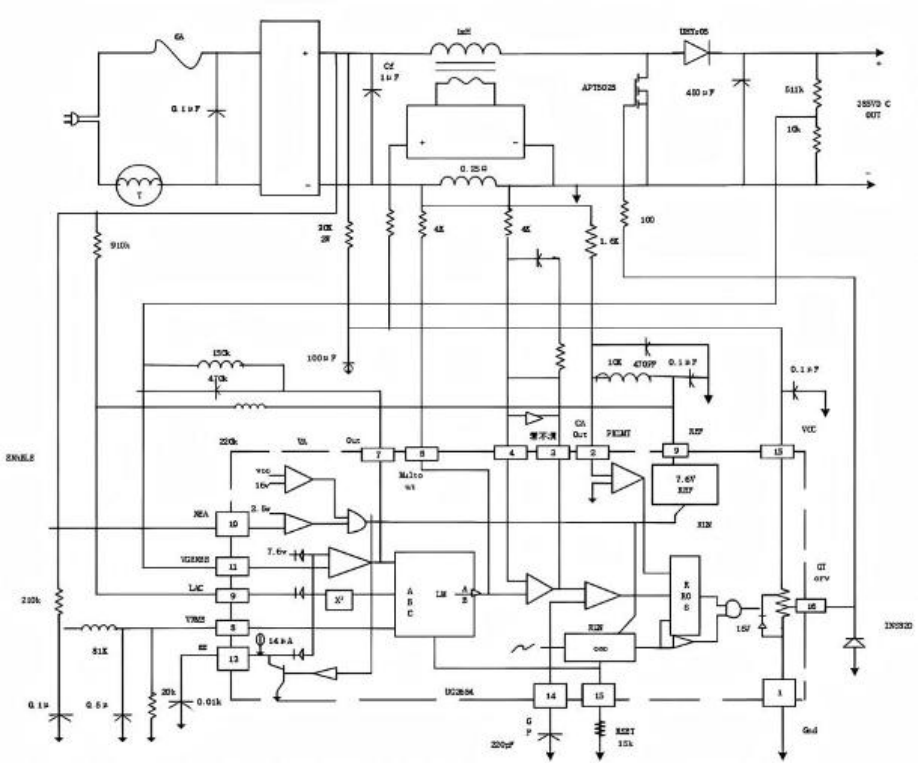


Fig. 7 – Schematic diagram of the UC3854 application circuit

Following the initial design, the AC/DC–DC/AC stages provide sufficient power but yield excessively high voltage and insufficient current capacity. To meet system requirements, a step-down transformer combined with rectification is introduced to generate a stable high-current DC output. Performance evaluation of the high-power-factor supply targets five key metrics: efficiency, harmonic characteristics, waveform quality, thermal behavior, and electromagnetic compatibility, all conducted under controlled conditions (20 ± 5 ℃, 30%–70% RH) using calibrated instrumentation. Efficiency is assessed across 10%–100% load with 60 s steady-state measurements to derive efficiency curves, while harmonic performance is evaluated at full load to obtain spectral distribution and total harmonic distortion. Waveform characteristics are captured via high-bandwidth oscilloscopic sampling to analyze distortion, ripple, and dynamic response. Thermal performance is determined through a 60 min full-load test, with temperature evolution monitored at critical components to establish steady-state distribution. Electromagnetic compatibility is verified by applying EFT, surge, and ESD disturbances to power, enclosure, and signal ports, while continuously tracking system stability and measurement integrity. This unified framework ensures systematic validation of electrical, thermal, and anti-interference performance, providing a robust basis for subsequent optimization and system integration.

RESULTS

Performance Testing of the High Power Factor Power Supply

To satisfy on-site testing requirements in rural grids, the high power factor DC supply was experimentally validated across 10%–100% load conditions. The efficiency curve demonstrates that, despite minor fluctuations at low load due to unstable grid quality, efficiency stabilizes beyond 40% load and exceeds 82% at full load, with a peak of 83.17%. This ensures stable current delivery under intermittent agricultural loads and enhances the consistency of loop resistance measurements. Harmonic analysis under full-load conditions shows low total harmonic distortion with a dominant fundamental component, confirming that the PFC design effectively suppresses harmonic amplification in weak rural distribution networks, thereby preventing measurement instability caused by harmonic interference. Thermal testing indicates that after 60 min full-load operation, key components stabilize at 113 °C (transformer) and 117–118 °C (rectifier), remaining within safe limits under a 23°C ambient environment and demonstrating suitability for prolonged field operation. Electromagnetic compatibility results further reveal that, under EFT, ESD, and RF disturbances typical of rural grids, the system maintains stable output without data interruption or fluctuation. Overall, the proposed power module exhibits high efficiency, thermal reliability, and strong anti-interference capability, providing a robust energy foundation for three-phase high-current loop resistance testing.

Table 1

Values under different load conditions

	Efficiency test value 220 Vac -50 Hz	Target efficiency value	Conclusion
Efficiency at 20% load	93.20%	>82%	Through
Efficiency at 50% load	94.30%	>85%	
Efficiency at 100% load	92.80%	>82%	
Power factor at 100% load	0.991	>0.9	

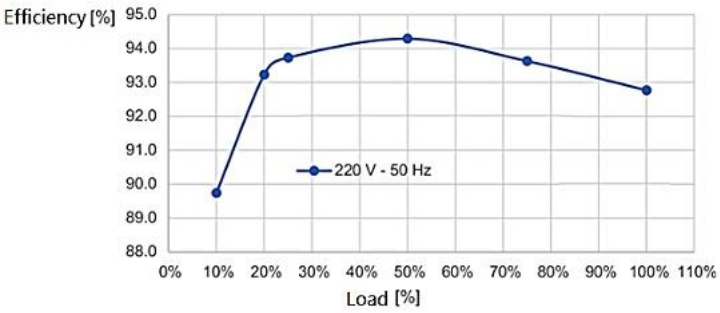


Fig. 8 – Efficiency curve under different load conditions

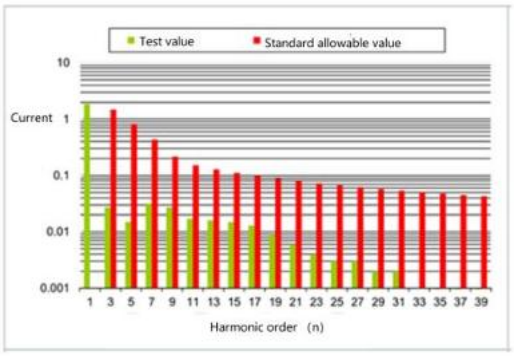


Fig. 9 – Harmonics under full-load conditions

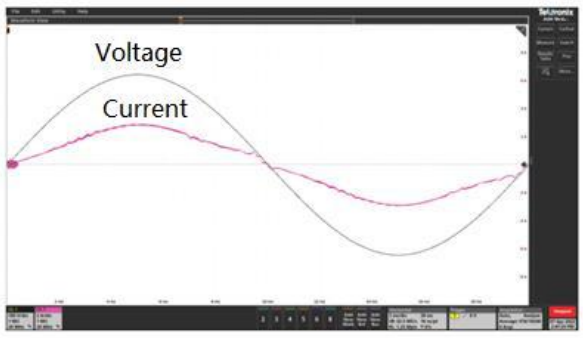


Fig. 10 – Voltage and current waveforms

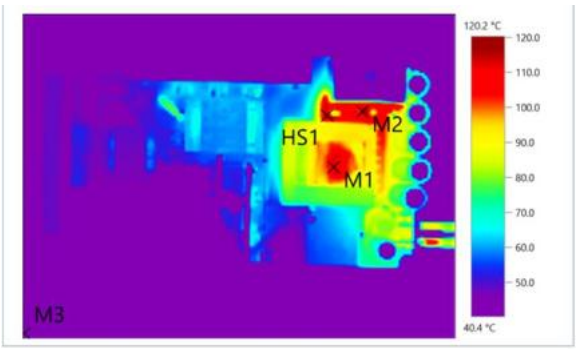


Fig. 11 – Temperature measurements

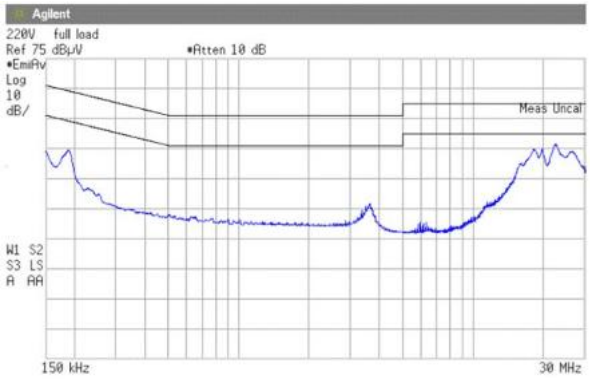


Fig. 12 – Electromagnetic compatibility (EMC) testing under full-load conditions

Supercapacitor Performance Testing

Figure 13 presents the supercapacitor discharge waveform at (U=16\text{ V}), where the current rapidly reaches its peak with a smooth rising edge and no observable spike interference, confirming that the current-limiting inductor and conduction control effectively suppress inductive transient distortion typical of rural grids. When the capacitor bank is charged to 230 V, the output current stabilizes at 100 A and remains steady throughout discharge without collapse induced by line inductance, contact instability, or humidity variations, demonstrating its capability to provide a reliable pulse source for high-impedance test circuits.

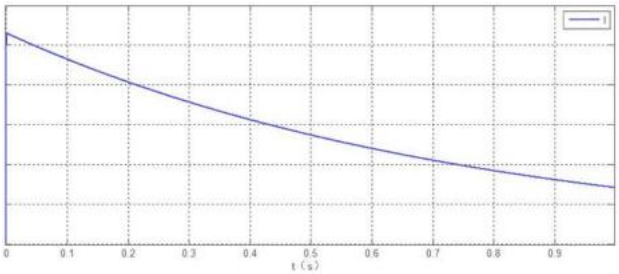


Fig. 13 – Discharge Current Waveform of the Supercapacitor at a Charging Voltage of U = 16

Figure 14 further exhibits an underdamped RLC response with low oscillation amplitude and smooth decay, indicating proper impedance matching. Compared with conventional capacitor discharge, which often produces voltage spikes and abrupt current transitions under humid and variable-temperature conditions, the proposed design suppresses initial peaks via series inductance, ensuring stable loop current and preventing false triggering of protection mechanisms. These results collectively confirm that the supercapacitor-based power supply offers high stability, reliability, and environmental adaptability, making it well-suited for deployment in rural distributed power testing scenarios.

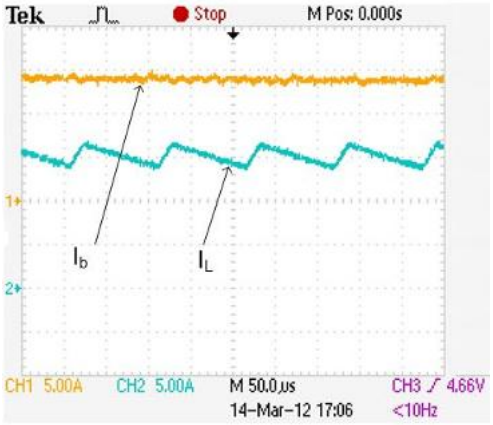


Fig. 14 – Discharge Current Waveform of the RLC Circuit

Performance Testing of the Tester

Comprehensive performance evaluation, conducted in accordance with technical specifications, confirms that the system fulfills all critical functional and operational requirements. Stable Bluetooth communication and WORD-format report export compatible with PMS platforms are achieved. The system provides real-time display of resistance, voltage, current, resistivity, and temperature-corrected values with design-level precision. The DC constant current source operates within 0–100 A, ensuring smooth regulation without overshoot. Measurement range covers 0–19,999 μΩ with 0.01 μΩ resolution, meeting micro-ohm accuracy demands. The human–machine interface integrates a 7-inch 800×480 touchscreen and high-speed thermal printing for rapid reporting. Insulation resistance exceeds 10,000 MΩ, far above the ≥0.5 MΩ requirement. Under full-load conditions (100 A), stable multi-module operation is maintained, with power conversion efficiency ≥82% and power factor up to 0.99 (GB/T14549-93 compliant). Electromagnetic compatibility testing further verifies that all ports satisfy immunity requirements, with no functional degradation or data distortion observed.

Table 2

Test Report Indicators

Testing Item	Technical Requirement	Test Result
Bluetooth Functionality	Must be able to upload data, export data documents, control data acquisition, and generate documents; meet PMS system requirements for document format and data.	Successfully uploads data, exports documents, allows control and generation of documents, meeting PMS system format and data requirements.
Data Display	Must display resistance, voltage, current, resistivity, and resistance values at standard temperature.	Successfully displays resistance, voltage, current, resistivity, and resistance values at standard temperature.

Testing Item	Technical Requirement	Test Result
DC Constant Current Source	Must output 0–100 A test current, with built-in stepwise current increase function.	Outputs 0–100 A test current with stable stepwise increase.
Measurement Range & Resolution	Range: 0–19,999 μΩ; Resolution: 0.01 μΩ	Range: 0–19,999 μΩ; Resolution: 0.01 μΩ
Human–Machine Interface	Equipped with 800×480 HD color 7-inch touchscreen for user interaction.	Equipped with 800×480 HD color 7-inch touchscreen, fully operational.
Insulation Performance	Insulation resistance between instrument casing or panel and ground must be ≥0.5 MΩ.	Measured >10,000 MΩ, far exceeding requirement.

Field tests were conducted on 110 kV GIS equipment at a 220 kV substation in Liaoning Province. The results demonstrate the following advantages of the proposed method:

Connection Efficiency: Simultaneous three-phase connection reduced the setup time from 30 min, required for conventional sequential single-phase connection, to 10 min, representing a 67% improvement.

Testing Duration: Simultaneous three-phase testing completed the full testing procedure within 1 min, compared with 3 min for conventional sequential testing, resulting in a further 67% reduction in testing time.

Data Reliability: The measured phase resistances were 35.95 μΩ (phase A), 36.04 μΩ (phase B), and 35.61 μΩ (phase C). The inter-phase deviation was less than 1%, satisfying the qualification criteria, while the deviation from laboratory-calibrated reference values remained within 0.5%, demonstrating higher accuracy than conventional testing instruments.

For 500 kV GIL testing over a distance of 1.2 km, a wireless auxiliary short-circuit device was coordinated with the main testing unit. Conventional segmented measurement, requiring five segments and approximately 5 min of total testing time, was replaced by single-connection testing completed within 1 min, corresponding to an 80% improvement in testing efficiency. The measured loop resistance was 72.5 μΩ, with a deviation of less than 1% compared with the conventional measurement result of 73.1 μΩ, thereby verifying the accuracy of long-distance testing.



Fig. 15 – Field measurement image of the loop resistance tester

CONCLUSIONS

This study develops a high-power constant-current source based on an AC/DC/AC/DC multi-stage architecture integrated with a UC3854 PFC circuit, achieving a power factor of 0.99 and efficiency above 82% under full load, while maintaining stable output in rural grid conditions characterized by voltage fluctuation and harmonic disturbance. Coupled with an RLC-optimized supercapacitor pulse module, the system delivers smooth, controllable high-current waveforms, ensuring stable excitation even in high-impedance and high-inductance loops, thereby overcoming current collapse issues and improving measurement repeatability. To ensure operational reliability, a comprehensive electromagnetic compatibility framework is established, incorporating differential/common-mode filtering, PFC shaping, RC snubber circuits, single-point grounding, and shielding structures. Experimental validation confirms stable performance in communication, data acquisition, and micro-ohm-level measurement without data drift under EFT, ESD, and RF interference, demonstrating strong anti-interference capability. Field applications further verify system effectiveness.

In 110 kV GIS testing, connection and measurement times are reduced by 67%, while in 500 kV GIL systems, integrated wireless testing improves efficiency by 80%. Across all scenarios, phase deviation remains below 1% and measurement error within 0.5%, confirming high consistency and reliability. Overall, the proposed APP-based wireless three-phase synchronous loop resistance testing system integrates high-efficiency power supply, supercapacitor pulse discharge, and robust EMC design to achieve accurate, efficient, and reliable testing in rural power grids, providing a practical solution for condition monitoring and digitalized operation of agricultural distribution systems.

ACKNOWLEDGEMENT

This work is supported by the Science and Technology Project of State Grid Heilongjiang Electric Power Co., Ltd (The Research and Application Circuit Resistance Testing Method of Switch Equipment Based on wireless synchronization)(522424250002).

REFERENCES

[1] Ban, L., Zheng, B., Zhou, P., Han, B., Xiang, Z., Sun, G., Wang, X., Wang, D., Liu, B., Teng, W., & Liu, Y. (2018). Research and engineering application of phase selection closing technology for UHV AC transformers. *Power System Technology*, 42(04), 1226–1233.

[2] Chen, J., Dong, J., & Zhao, Y. (2016). Analysis of GIS equipment conductive loop resistance testing. *Yunnan Electric Power Technology*, (S2).

[3] Chen, Y., Yan, J., Wang, Y., Wu, Y., & Liu, Z. (2025). A novel localization method for partial discharge in GIS based on electromagnetic time reversal technique. *Measurement*, 253(B), 117599. https://doi.org/10.1016/j.measurement.2025.117599

[4] Deng, M. (2021). Efficiency improvement of fixed switchgear loop resistance testing. *Journal of Chongqing College of Electric Power*, 26(06), 1–3.

[5] Fang, C. (2020). Discussion and innovation of loop resistance measurement methods. *Power Equipment Management*, (06), 181–182.

[6] Fang, H. (2020). Discussion and innovation of loop resistance testing methods. *China Electric Power Enterprise Management*, (21), 94.

[7] Gao, F. (2003). *Intelligent testing of switch loop resistance* (Master's thesis). Dalian University of Technology.

[8] Golaghazadeh, F., Coulombe, S., & Robert, J.-M. (2022). Residual packet loss rate analysis of 2-D parity forward error correction. *Signal Processing: Image Communication*, 102, 116597. https://doi.org/10.1016/j.image.2021.116597

[9] Labiod, H., Zeadally, S., & Tebchrany, E. (2014). Performance analysis of a cross-layered incremental redundancy hybrid automatic repeat request (CL IR-HARQ) mechanism. *Ad Hoc Networks*, 23, 109–120. https://doi.org/10.1016/j.adhoc.2014.06.006

[10] Lai, J., Peng, H., Jiang, Y., Hu, J., Huang, S., & Wang, W. (2019). Research on rapid GIS conductive loop resistance measurement without disassembling grounding lines. *Electric Measurement & Instrumentation*, (15), 1–6.

[11] Li, J.; Wu, X.; Chow, S.K.W.; Zhuang, Q.; Habert, G. (2023). Thermal Comfort Comparison and Cause Analysis of Low-Temperature High-Humidity Indoor Environments of Rural Houses in Gansu Province, China. *Sustainability*, 15, 16428. https://doi.org/10.3390/su152316428

[12] Li, L. (2022). Study on the measurement of conductive loop resistance of 500 kV GIS circuit breakers. *Hydropower and Pumped Storage*, 8(01), 90–93.

[13] Ma, Y., Li, X., Zhou, X., Liu, W., Ai, S., & He, N. (2022). Research on transformer excitation inrush current suppression based on high-voltage vacuum rapid circuit breakers. *High Voltage Apparatus*, 58(10), 136–142.

[14] Neerugatti, K., & Pakala, V. (2025). Design of 2.54 GHz active inductor-based LC-voltage controlled oscillator for Bluetooth/WLAN applications. *Integration*, 105, 102487. https://doi.org/10.1016/j.vlsi.2025.102487

[15] Wang, W., Wang, X., & Tang, H. (2018). Field test method of high-voltage circuit breaker loop resistance. *Electrical Technology and Economy*, (06), 27–29.

[16] Wu, H., Jiao, C., Cui, X., Liu, X., & Ji, J. (2017). Transient electromagnetic disturbance induced on the ports of intelligent component of electronic instrument transformer due to switching operations in 500 kV GIS substations. *IEEE Access*, 5, 5104–5112.

[17] Wu, Y., Yan, W., Chen, H., Zhang, W., & Ma, H. (2022). Research on interferences of VFTO to irregular distributions of secondary side cables. *IEEE Transactions on Power Delivery*. https://doi.org/10.1109/TPWRD.2022.3197318

[18] Wu, Z., & Zhang, C. (2020). Research and design of a novel loop resistance tester. *Electronic Testing*, (09), 108–109+111.

[19] Xiao, J., Wang, Y., Lü, J., & Han, W. (2014). Research on a novel circuit breaker loop resistance testing system. *Electric Measurement & Instrumentation*, 51(05), 67–72.

[20] Yuan, C., Wei, D., & Liu, K. (2020). Research on a novel circuit breaker loop resistance tester. *China New Technology & New Products*, (01), 24–26.

[21] Zhang, J., Zhen, C., Lü, B., Wei, C., Niu, L., & Ji, K. (2021). Verification method of circuit breaker breaking capacity based on final current half-wave energy. *Electrical Appliances and Energy Efficiency Management Technology*, (07), 56–60.

DESIGN AND EXPERIMENT OF IWOA-OPTIMIZED FUZZY PID VARIABLE FERTILIZATION CONTROL SYSTEM FOR RICE BASED ON N-P-K HYBRID PRESCRIPTION GRAPH

/

基于 N-P-K 融合处方图的 IWOA 优化模糊 PID 水稻变量施肥控制系统设计与试验

Kun ZHANG[1)], Lin WAN[*1,2)], Gang CHE[1,2)], Chun-sheng WU[*3)], Xi-lu LI[3)]

[1)] College of Engineering, Heilongjiang Bayi Agricultural University, Daqing 163319, China

[2)] Key Laboratory of Intelligent Agricultural Machinery Equipment in Heilongjiang Province, Daqing 163319, China

[3)] Heilongjiang Province Agricultural Machinery Science Research Institute - Jiamusi Branch, Jiamusi 154004, China

Tel:+86-459-13555523188; E-mail: 381995603@qq.com

Corresponding author: Lin Wan

Tel:+86-459-18546403666; E-mail: wcs70@163.com

Corresponding author: Chun-sheng Wu

DOI: https://doi.org/10.35633/inmateh-79-09

Keywords: *Rice, variable fertilization, three-dimensional prescription map, whale optimization algorithm, fuzzy PID control*

ABSTRACT

Traditional uniform fertilization in rice paddy fields is associated with low fertilizer-use efficiency and severe agricultural non-point source pollution. Existing variable-rate fertilization equipment commonly presents limitations such as reliance on single-source prescription information and insufficient control precision. To address these issues, this study uses an impeller-type fertilizer applicator as the working platform and, considering the characteristics of cold-region rice cultivation in Heilongjiang Province, constructs an integrated ternary nitrogen-phosphorus-potassium fertilization prescription map. A mapping model between fertilizer application rate and motor speed is established, and a fuzzy PID controller optimized using an improved whale optimization algorithm (IWOA) is designed. Fertilizer-discharge calibration tests and field trials were conducted. The results showed that the coefficient of determination (R^2) between fertilizer discharge rate and motor speed reached 0.9912. The IWOA-fuzzy PID algorithm achieved a step-response overshoot of only 3.3% and a settling time of 1.55 s, while the relative error of field fertilization was controlled within ±5%.

摘要

水稻格田传统均匀施肥模式存在肥料利用率低、农业面源污染突出等问题，现有变量施肥装备普遍存在处方信息单一和控制精度不足等缺陷。针对上述问题，本文以叶轮式施肥装置为作业载体，结合黑龙江寒地水稻种植特点，构建氮磷钾三元融合施肥处方图。建立施肥量 - 电机转速映射模型，设计基于改进鲸鱼算法（IWOA）优化的模糊 PID 控制器。开展排肥标定试验，以及田间试验。试验结果表明：排肥量与电机转速拟合决定系数 R^2=0.9912，IWOA - 模糊 PID 算法阶跃响应超调量仅 3.3%，调节时间 1.55 s，田间施肥相对误差控制在 ±5% 以内。

INTRODUCTION

The area of rice cultivation in our country is vast, and it is a pillar industry for ensuring national food security. The traditional fertilization model has led to increasingly prominent issues of resource waste and ecological problems (*Wang et al., 2024; Ren et al., 2023*). In the scenario of large-scale production of rice fields, the extensive and uniform fertilization method causes a decline in fertilizer utilization rate and an increase in agricultural non-point source pollution (*Li et al., 2022; Liu et al., 2012*). With the rapid iteration of smart agriculture and precise agricultural machinery technology, variable fertilization control in rice fields has become the mainstream direction of industry development. However, during the implementation of this technology, there are always two major challenges: the complex operation environment of paddy fields and the limited computing power of edge terminals of agricultural machinery (*Hu et al., 2023; Hu et al., 2021*).

The rice field operation environment is complex and variable, and the movement of machinery is prone to skidding and jolting. Coupled with the continuous fluctuations in field humidity and soil moisture content, it not only changes the load state of the impeller fertilizer distribution mechanism but also causes problems such as fertilizer deliquescence, caking, and blockage (*Wang et al., 2024; Ding et al., 2025*).

Various interference factors in the field can mask the operation characteristics of the fertilization mechanism, making it difficult for traditional fertilization control methods to accurately identify changes in working conditions and dynamically match the fertilizer demand in the field. This is also an important cause for the current low control accuracy of variable fertilization equipment (*Bai et al., 2022; Wang et al., 2023*).

At present, variable fertilization for rice is mainly divided into two technical routes: real-time sensing and prescription map. Both schemes have their own advantages and inherent defects (*Wang et al., 2024*). Real-time sensing fertilization relies on dynamic collection of nutrient data by field sensors, with fast decision response speed, but the sensors are prone to interference from paddy mud water and dust, resulting in poor long-term operational stability and high equipment modification costs (*Li et al., 2024*). Prescription map fertilization relies on the pre-mapped nutrient layers in the field for operations, with clear decision logic and lower hardware costs, and is also the mainstream choice in domestic rice-growing areas. However, the existing prescription maps are mostly single nutrient layers and cannot meet the agronomic requirements for coordinated fertilization of nitrogen, phosphorus, and potassium (*Ding et al., 2025; Qin et al., 2025*).

In recent years, domestic and foreign research institutions and agricultural machinery enterprises have conducted a large number of research projects on variable fertilization equipment for rice, prescription map technology, and intelligent control algorithms. The team from Huazhong Agricultural University in China developed an electrically driven side-drip fertilization device for rice, optimizing the synchronization of fertilization points (*Li et al., 2024*). Northeast Agricultural University based on Kriging interpolation method constructed a fertilization prescription map for rice, combined with neural network to optimize control parameters. Xi'an University of Science and Technology used Kalman filtering to optimize sensor data, reducing fertilization control error to 2.7% (*Li et al., 2024*). Guizhou University based on the GIS platform built a fertilization decision system to achieve spatial analysis of field nutrients (*Mou et al., 2017*). Foreign enterprises such as John Deere, Kubota, and Igus have launched complete sets of intelligent fertilization agricultural machinery, relying on high-precision positioning technology to achieve dynamic variable operations (*Abdalla & Nafchi, 2024*); several domestic agricultural technology enterprises have also introduced mass-produced variable fertilization equipment, achieving certain fertilizer-saving effects in large-field operations (*Wang et al., 2004; Chen Li et al., 2008*). These studies have advanced variable fertilization technology from different dimensions such as equipment structure, data processing, and algorithm optimization, providing a solid theoretical and practical foundation for subsequent research.

PID and fuzzy PID algorithms are the most widely used mainstream technologies in the field of agricultural mechanical control (*Wang et al., 2023*). The traditional PID algorithm has a simple structure and is easy to implement in engineering, but its parameters are fixed and have poor control effect when facing nonlinear loads of the impeller fertilizer distribution mechanism and system time delays (*Chen et al., 2008*); the basic fuzzy PID can achieve online self-adaptive adjustment of parameters, but the fuzzy rules and initial parameters are mostly set based on manual experience, which is prone to fall into local optimal solutions and easily causes excessive overshoot and lag in dynamic working conditions such as sudden changes in vehicle speed and load disturbances (*Qin et al., 2025; Bai et al., 2022*). The limitations of existing algorithms further restrict the operational accuracy and working condition adaptability of variable fertilization equipment.

MATERIALS AND METHODS

Fertilizer application device structure and working principle

The wheeled fertilizer distributor uses the separated blades of the impeller to form independent fertilizer chambers for fertilizer filling and discharge. Since the fertilizer is not forcibly squeezed during operation, problems such as particle breakage, deliquescence, adhesion, and blockage in compound fertilizers can be effectively avoided. At the same time, the continuous and smooth fertilizer-discharge process during impeller rotation ensures a good linear relationship between discharge amount and impeller speed, thereby meeting the dynamic regulation requirements of prescription-chart-based variable-rate fertilization.

The device adopts a centrifugal fertilizer application device, which consists of a fertilizer box, a centrifugal fertilizer discharger, a fertilizer discharging motor, a fan, etc. The discharge port at the bottom of the fertilizer box is connected to the fertilizer inlet of the discharger. After receiving the control instructions, the motor drives the centrifugal fertilizer wheel to rotate. Under the influence of gravity, the fertilizer particles fall into the Venturi tube. The stable air pressure output by the air system transports the fertilizer along the fertilizer guiding pipe outward. At the same time, under the action of the high-speed airflow, the fertilizer enters the mud ditch to complete the variable fertilizer application for rice.

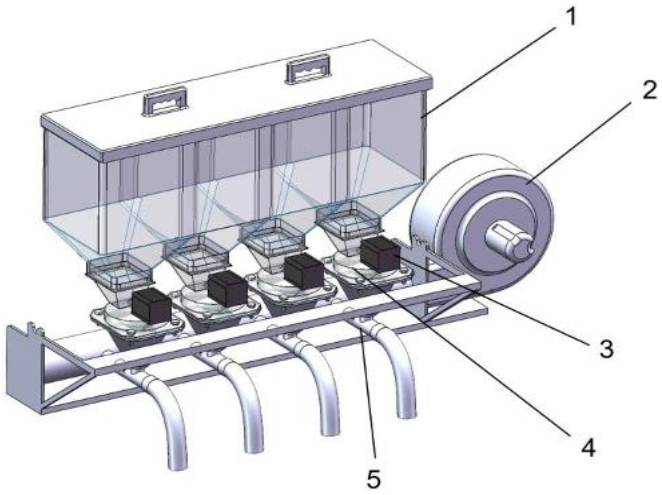


Fig. 1 - Fertilizer apparatus

1. Manure box; 2. Fan; 3.57-step motor; 4. Impeller type manure discharger; 5. Venturi tube

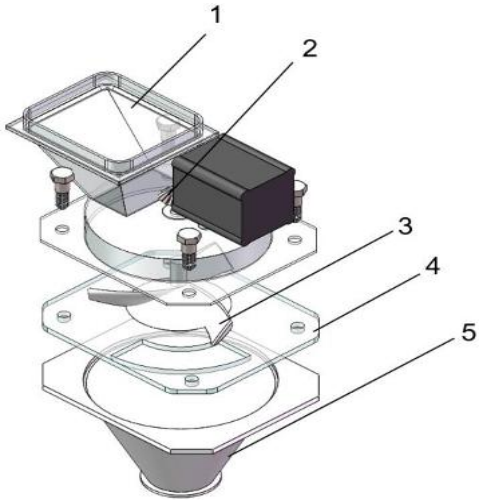


Fig. 2 - Impeller fertilizer distributor

1. Upper housing; 2. Transmission gear; 3. Impeller blade; 4. Baffle; 5. Lower housing

Overall structure and working principle of the fertilization system

A closed-loop control architecture of upper-level computer decision-making and lower-level machine execution is adopted. During the operation process, the upper-level computer matches the pre-established grid prescription map with the real-time obtained GNSS-RTK positioning information, completes spatial grid addressing based on the current position, and further calculates the target fertilization amount corresponding to the current operation position. The lower-level machine uses the ESP32 controller as the control unit. After receiving the fertilization instructions issued by the upper-level computer, it combines the real-time operation vehicle speed and converts the target fertilization amount into the theoretical rotational speed command for the fertilizer distribution motor. The lower-level machine introduces a fuzzy PID control strategy optimized based on the improved whale optimization algorithm (IWOA) to adjust the rotational speed of the fertilizer distribution motor in real time, and outputs pulse signals to drive the TB6600 stepper motor driver, thereby controlling the 57 stepper motors to complete the fertilizer distribution operation. At the same time, a Hall sensor is installed at the fertilizer distribution shaft end to collect the actual rotational speed of the motor in real time, and the feedback signal is transmitted back to the microcontroller, together with the control instructions, to form the bottom-level rotational speed closed-loop.

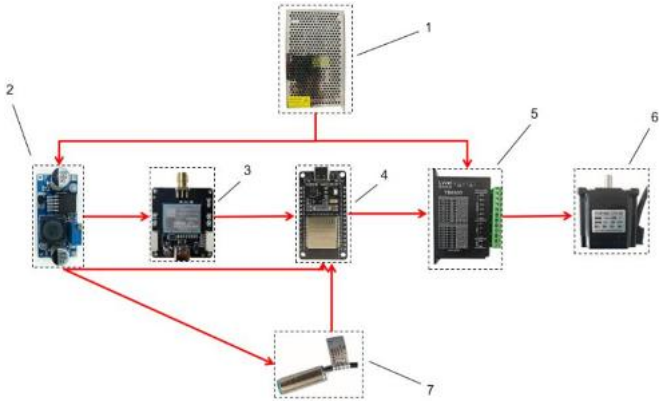


Fig. 3 - Control system hardware architecture diagram

1. 24V power supply; 2. Blood pressure reduction module; 3.RTK positioning module; 4. ESP32 microcontroller; 5. TB6600 Motor Driver; 6.57-step motor; 7. Hall sensor

CONSTRUCTION OF INTEGRATED FERTILIZATION PRESCRIPTION MAP

Nutrient spatial interpolation and rasterization

Converting the scattered and point-like vector data in the database into continuous planar control maps that the system can read is the key step in establishing the prescription map. In the ArcGIS software, rasterization processing is carried out using the ordinary Kriging spatial interpolation algorithm. Ordinary Kriging is an unbiased optimal linear estimation method and its mathematical model is shown in Eq. (1):

$$\hat{Z}(x_0)=\sum_{i=1}^{n}\lambda_i Z(x_i) \quad (1)$$

where:

$\hat{Z}(x_0)$ is the estimated nutrient value at the grid point x_0 that needs to be predicted, $Z(x_i)$ is the is the measured value at the known sampling point x_i, n is the number of adjacent measured points involved in the interpolation, λ_i is the weight coefficient of the i-th measured point for the predicted point.

The determination of the weight coefficient λ_i relies on the fitting of the semi-variance function, which is used to measure the spatial autocorrelation degree of soil nutrients in a certain direction and distance. The formula is expressed as follows:

$$\gamma(h)=\frac{1}{2N(h)}\sum_{i=1}^{N(h)}[Z(x_i)-Z(x_i+h)]^2 \quad (2)$$

where:

$\gamma(h)$ is the half-mutation value for a step size of h, $N(h)$ is the number of sample point pairs with a spatial distance of h.

The conventional interpolation results in a continuous gradient surface, while the actual fertilization operation is carried out based on discrete units and requires a rasterization reconstruction. Considering the 2.1-meter working width of the transplanting machine used in the experiment, the nearest neighbor method is selected for spatial resampling. The pixel scale of the prescription map is divided into 2.1m × 2.1m squares, and from a logical perspective, the geographic information is mapped into a two-dimensional control array that the microcontroller can directly read.

Calculation of target fertilizer application rate

Based on the actual operation requirements of the fertilizer application machine, practical modifications were made to the classic model. The modified model uses the absolute nutrient gap as the base, removes the low utilization compensation term that is prone to causing data fluctuations, and adds the base application ratio coefficient R.

For any grid i within the operation area, the formula for calculating the target amount of compound fertilizer to be applied based on the single-nutrient balance is as shown in Eqs. (3), (4), and (5):

$$W_{Ni}=\frac{Y\times(U_N/100)-C_{Ni}\times K_s\times E_{sN}}{F_N}\times R_N \quad (3)$$

$$W_{Fi}=\frac{Y\times(U_P/100)-C_{Pi}\times K_s\times E_{sP}}{F_P}\times R_P \quad (4)$$

$$W_{Ki}=\frac{Y\times(U_K/100)-C_{Ki}\times K_s\times E_{sK}}{F_K}\times R_K \quad (5)$$

where:

W_{Ni},W_{Fi},W_{Ki} is the theoretical amount of compound fertilizer base fertilizer calculated based on the individual requirements of nitrogen, phosphorus and potassium at grid point i for the target yield of the experimental field rice, (kg/hm^2); Y is the target yield of the rice in the experimental field, (kg/hm^2); UN, UP, UK is the amount of pure nutrients required for each 100 kilograms of rice to be formed, (kg); C_{Ni},C_{Pi},C_{Ki} is the background contents of available nitrogen, available phosphorus and available potassium obtained through kriging interpolation at grid point i, (mg/kg); K_s is the conversion constant for converting soil nutrient measurement values to the actual total nutrient content of the topsoil per hectare; E_{sN},E_{sP},E_{sK} is the seasonal utilization rate of the soil's own nutrients; F_N,F_P,F_K is the mass fraction of the corresponding effective components in the compound fertilizer; R_N,R_P,R_K is the proportion coefficients for the application of base fertilizers with different nutrient compositions.

The sampling depth for the experiment was set at the standard plough layer, which is 20 cm deep. Considering that the average bulk density of the soil in this area is approximately 1.15 g/cm^3, the total weight of the plough layer soil is approximately 2.3 × 10^6 kg. Therefore, when the soil nutrient concentration is 1 mg/kg, its equivalent absolute nutrient quantity per hectare is 2.3 kg, so the constant K_s is set as 2.3.

The selected fertilizer is a controlled-release compound fertilizer. The specific N-P205-K2O ratio is 21-15-16. By dividing the formula denominator by this mass fraction, the actual nutrient requirements can be converted into the total weight of the compound fertilizer. This fertilizer contains more than 8% controlled-release fertilizer, which can effectively delay the release of nitrogen.

Table 1

Target fertilization amount calculation parameters table

Symbol	Numerical value	Units
Y	9500	kg/hm²
U_N	2.1	kg
U_P	1.1	kg
U_K	2.5	kg
F_N	0.21	%
F_P	0.15	%
F_K	0.16	%
E_{sN}	0.35	%
E_{sP}	0.4	%
E_{sK}	0.5	%
R_N	0.75	%
R_P	0.45	%
R_K	0.35	%
K_s	2.3	%

Generation of diversified and integrated prescription diagrams

The fusion weight ratio of N, P, and K was set as 0.6 : 0.3 : 0.1. On the ArcGIS software platform, the weighted overlay operation of three independent raster maps was carried out using the map algebra module. The mathematical fusion model is expressed as Eq. (6):

$$W_f(i,j)=\omega_N \cdot W_N(i,j)+\omega_P \cdot W_P(i,j)+\omega_K \cdot W_K(i,j) \quad (6)$$

where: $W_f(i,j)$ is the Integrated coordinates; Y is the target yield of the rice in the experimental field,(kg/hm²); (i,j) is the final target amount of fertilizer application at the plot level; ω_N, ω_P, ω_K are the decision weights for nitrogen, phosphorus, and potassium; W_N, W_P, W_K calculated theoretical target quantity of the single-factor compound fertilizer.

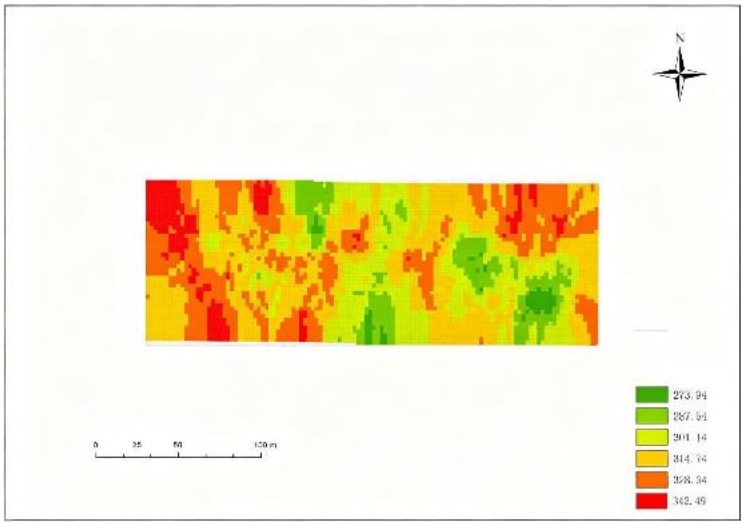


Fig. 4 - Variable fertilization integration prescription chart

IWOA - FUZZY PID ALGORITHM DESIGN

Design of fuzzy PID controller

Proportional-Integral-Derivative, abbreviated as PID, is the most widely used and mature classic algorithm in mechanical and electrical control engineering. It achieves precise regulation of the controlled object by linearly combining the error signal. The expression of PID control in continuous time is as follows:

$$u(t)=K_p\left[e(t)+\frac{1}{T_i}\int_0^t e(\tau)d\tau+T_d\frac{de(t)}{dt}\right] \quad (7)$$

where:

$u(t)$ is the controller output; $E(t)$ is the system error; Kp is the final target amount of fertilizer application at the plot level; T_i *is the integral time constant, (s);* T_d is the differentiating time constant, (s); $e(t)$ is the speed error.

If the traditional position-based PID algorithm is used directly, the program must continuously accumulate all historical rotational speed errors throughout the entire operation cycle. This not only excessively consumes the limited memory resources of the microcontroller, but the more fatal risk lies in the fact that when field operations cross the prescription map grid and the target fertilization amount instructions undergo a step-like sudden change, the accumulated massive errors will instantly trigger the integral saturation effect. Therefore, the bottom-level fertilizer application control selects the incremental digital PID control algorithm. Instead of directly outputting the absolute value of the control quantity, it outputs the incremental $\Delta u(k)$ of the control variable frequency pulse frequency. The core difference equation derivation formula is:

$$\Delta u(k)=u(k)-u(k-1) \quad (8)$$

Discretizing Eq. (7) yields the underlying running formula for the incremental PID on the microcontroller:

$$\Delta u(k)=K_p[e(k)-e(k-1)]+K_i e(k)+K_d[e(k)-2e(k-1)+e(k-2)] \quad (9)$$

where:

$K_i = K_p\frac{T}{T_i}$ is the discrete integral coefficients, $K_d=K_p\frac{T_d}{T}$ is the discrete differential coefficient.

The above incremental PID algorithm has solved the engineering implementation problems of the underlying control. However, the fixed PID parameters are difficult to adapt to complex working conditions such as load fluctuations and sudden changes in target fertilization amounts during field operations, and may lead to large control overshoot and lag in response. Therefore, this paper introduces the fuzzy control algorithm to perform online dynamic tuning of the three parameters of the PID controller. The equation is as follows:

$$\begin{cases} K_p(k)=K_{p0}+E_p\cdot\Delta K_p(k) \\ K_i(k)=K_{i0}+E_i\cdot\Delta K_i(k) \\ K_d(k)=K_{d0}+E_d\cdot\Delta K_d(k) \end{cases} \quad (10)$$

The fuzzy basic domains of the input variables e, ec and the output variables ΔK_p, ΔK_i, ΔK_d are uniformly set to the range [-3, 3]. The fuzzy domain is divided into 7 fuzzy linguistic levels, which are defined as: NB (very large negative), NM (moderately negative), NS (small negative), ZO (zero), PS (small positive), PM (moderately positive), and PB (very large positive).

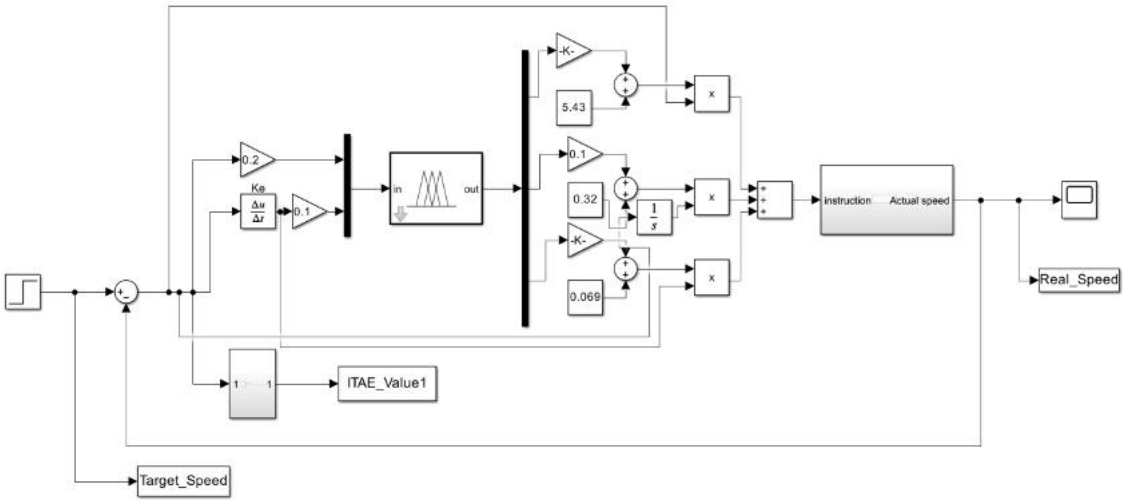


Fig. 5 - Architecture diagram of the fuzzy PID control system

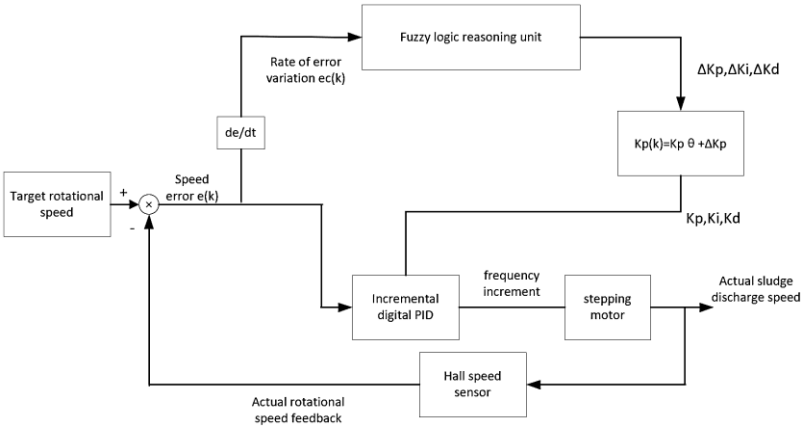


Fig. 6 - Fuzzy PID simulation model

Improvement of population initialization with tent mapping introduction

The standard WOA uses pseudo-random numbers to generate the initial population, which may cause individuals to cluster within the optimization space, thereby reducing the search efficiency of the algorithm in the early stage. The Tent mapping has a strict uniform probability density distribution and pure chaotic characteristics within the [0,1] interval. Its mathematical expression is:

$$z_{i+1} = z_i/\alpha, \quad 0 \le z_i < \alpha \tag{11}$$

$$z_{i+1}(1 - z_i)/(1 - \alpha), \quad \alpha \le z_i \le 1 \tag{12}$$

The value of α is set to the typical value of 0.499. A chaotic sequence is generated using the Tent mapping, and then it is transformed into the initial positions of the fuzzy PID parameters through the inverse mapping. This enables the initial population of pilot whales to evenly cover the entire parameter domain, thereby improving the global optimization starting point of the algorithm from the very beginning.

Nonlinear convergence factor strategy based on cosine function

The linearly decreasing approach results in less global exploration time in the initial stage of the algorithm, and too rapid attenuation in the local development stage later on, which makes it easy to miss the optimal solution. The actual parameter optimization process is a highly complex nonlinear dynamic process. Therefore, this paper proposes a nonlinear convergence factor update strategy based on the cosine function, and the mathematical model is modified as:

$$a = 2 \cdot \cos\left(\frac{\pi}{2} \cdot \frac{t}{T_{max}}\right) \tag{13}$$

The improved α value maintains a relatively slow decay rate in the early stage of iteration, providing the population with more ample time for global and extensive search, thus avoiding premature convergence of the algorithm. In the later stage of iteration, as the slope of the cosine function increases, the α value rapidly decays to 0, prompting the algorithm to converge quickly to the high-precision local extremum point.

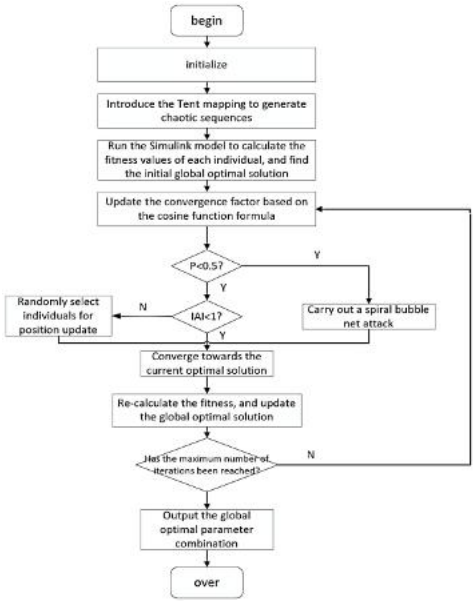


Fig. 7 - Fuzzy PID simulation model

Algorithm simulation analysis

A simulation model was built on the MATLAB/Simulink platform, and step response simulations were conducted for the traditional PID, basic fuzzy PID, and IWOA-fuzzy PID. The optimal physical operating range of the system is 10 to 60 r/min. Therefore, in this section, the target rotational speed command of the system is set to the median value within this range, which is 30 r/min.

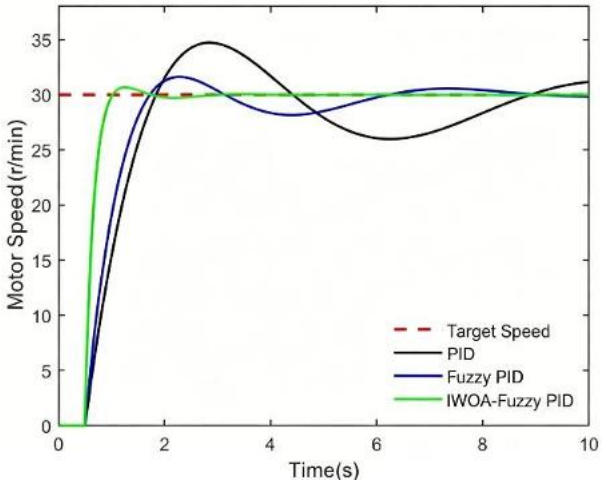


Fig. 8 - Fuzzy PID simulation model

Table 2

Comparison of step response performance indicators

Control algorithm	Rise time [s]	Overshoot [%]	Accommodation time[s]
PID	2.45	16.7	8.8
Fuzzy PID	1.68	6.7	6.02
IWOA - Fuzzy PID	0.92	3.3	1.55

In the PID algorithm, the initial parameters are K_p = 1.23, K_i = 0.84, and K_d = 0.05. Due to the presence of a 0.485-second pure lag in the motor speed response, the relatively large integral coefficient accumulated a huge error energy within the starting dead zone, resulting in a severe integral saturation phenomenon. The weak differential damping was unable to effectively restrain it, directly causing the response curve to soar to around 35 r/min, with a severe overshoot and long-term oscillation. In the fuzzy PID algorithm, the system introduced error and error rate change K_e = 0.2 and Kec = 0.1, and the three compensation quantities ΔK_p, ΔK_i, and ΔK_d were 0.57, 0.1, and 0.05 respectively. Due to the limitation of manual experience setting, the system could not fully exert its potential. Eventually, after 50 generations of deep evolution using the IWOA algorithm, the system successfully escaped from the local optimal trap and locked onto the global optimal parameters K_p = 5.43, K_i = 0.32, and K_d = 0.069. After generating only 1.8% overshoot and a brief real mechanical micro-vibration, it quickly stabilized and precisely matched the target rotational speed command of 30 r/min.

Calibration test of the relationship between fertilizer discharge amount and rotational speed

In this experiment, the calibration speed range of the fertilizer discharge shaft was set at 10 to 60 r/min, and the step size of the test speed was set at 10 r/min. All these were strictly repeated for 6 independent sampling measurements. When calculating the data later, the average values of each group were extracted as the actual fertilizer discharge amount at that speed.

Table 3

Test data on fertilizer discharge amount at different rotational speeds

Rotate speed [r/min]	Measure-ment 1 [g]	Measure-ment 2 [g]	Measure-ment3 [g]	Measure-ment 4 [g]	Measure-ment 5 [g]	Measure-Ment 6 [g]	Average fertilizer application rate [g/min]
10	1121.2	1135.4	1128.5	1119.8	1138.1	1129.2	1128.7
20	2650.3	2681.2	2658.5	2675.9	2645.1	2679.6	2665.1
30	3405.6	3448.2	3415.9	3438.1	3395.4	3454	3426.2
40	4610.2	4655.8	4625.5	4648.1	4602.4	4667.4	4634.9
50	5145.2	5205.6	5168.4	5192.1	5130.5	5219	5176.8
60	6250.5	6345.2	6280.4	6325.8	6240.1	6338.8	6296.8

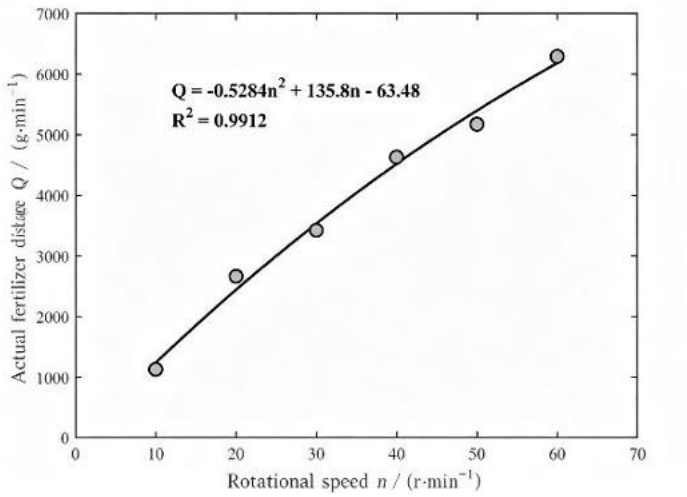


Fig. 9 - Speed and fertilizer discharge rate calibration curve

The coefficient of determination R^2 of the fitted equation is 0.9912. In the system's global closed-loop, this equation is used to convert the fertilizer application rate specified by the prescription map into a dynamic rotational speed executable by the hardware. After the controller obtains the local target displacement Q issued by the prescription chart, it needs to perform real-time reverse optimization calculation to convert it into the target rotational speed n_t of the stepper motor. The underlying control relationship is expressed as Eq. (14):

$$n_t = \frac{-135.8 + \sqrt{135.8^2 - 4 \times (-0.5284) \times (-63.48 - Q)}}{2 \times (-0.5284)} \tag{14}$$

Field trial

The experiment adopted the IWOA-fuzzy PID algorithm as the core driving strategy. The experiment was conducted at the Erliuhe Farm. The experimental equipment was a Jinjiang riding-type rice transplanting machine with a working width of 2.1 meters and equipped with a fan-type fertilizer distributor.

The test equipment includes an ESP32 microcontroller, a GNSS-RTK positioning receiver, a TB6600 stepper motor driver, a 24V power supply, a high-precision electronic balance, and a measuring tape.

The actual fertilizer discharge amount was measured using the box difference weighing method. Before starting the experiment, an adequate initial fertilizer mass W_1 was placed in the fertilizer box and weighed. After the transplanting machine completed the experiment, the remaining fertilizer mass W_2 in the box was weighed again. By calculating the difference between the two measurements ($\Delta W = W1 - W2$), the actual fertilizer discharge amount was obtained. The initial fertilizer mass in the box was 15 kg.



Fig. 10 - Field trial

The travel speed of the transplanting machine was fixed at 1 m/s. Six paths corresponding to different prescription grades were planned in the field, with each path having a length of 20 m. A fertilizer collection bag was attached to the fertilizer discharge outlet, and the fertilizer discharge system was started at the beginning of each path. The motor pulse signal was stopped at the end of the 20 m path. The remaining fertilizer mass in the fertilizer box was then weighed using an electronic balance. The actual fertilizer application rate was calculated using Eq. (15), and the relative error δ was calculated using Eq. (16):

$$M_a = \frac{10000 \times m_a}{L \times W} \quad (15)$$

$$\delta = \frac{M_a - M_t}{M_t} \times 100\% \quad (16)$$

where:

M_a is the actual fertilizer application rate per unit area, (kg/hm^2); m_a is the total mass of discharged fertilizer, (kg); L is the working length, (m); W is the working width, (m); δ is the fertilizer application error; M_t is the target fertilizer application rate, (kg/hm^2).

RESULTS

The fertilizer mass measured for each prescription level was substituted into the formula for calculation, and the results of the constant-rate fertilizer application test are shown in Table 4.

Table 4

The results of the fertilizer application test

Prescription chart level	Target fertilizer application rate [kg/hm^2]	Total discharged fertilizer mass [ma/kg]	Actual fertilizer application rate [kg/hm^2]	Relative error [%]
1	273.94	1.167	277.86	1.43
2	287.54	1.176	280	-2.62
3	301.14	1.317	313.57	4.13
4	314.74	1.31	311.9	-0.9
5	328.34	1.409	335.48	2.17
6	342.49	1.384	329.52	-3.79

CONCLUSIONS

This study addressed the key challenges of fertilization operations in cold-region paddy fields and developed an intelligent variable-rate fertilization system driven by integrated prescription maps. Based on measured field soil data, the study completed the integration and rasterization of multiple nutrient prescriptions for nitrogen, phosphorus, and potassium, thereby solving the problem that traditional single-nutrient prescriptions cannot meet the coordinated fertilizer-supply requirements of rice cultivation. Based on the impeller-type fertilizer discharge device, a mechanism analysis was conducted, and a correlation model between fertilizer application rate and motor speed was established. In addition, a spatiotemporal delay compensation strategy was introduced to effectively correct fertilizer placement deviations caused by machine travel and fertilizer transport. The improved whale optimization algorithm was used to optimize the parameters of the fuzzy PID controller, significantly enhancing the dynamic control capability of the system. The test results showed a strong linear correlation between fertilizer application rate and motor speed, with a coefficient of determination of 0.9912. The optimized control algorithm achieved a step-response overshoot of 3.3% and a settling time of only 1.55 s, while the fertilizer application errors under different field operating conditions were controlled within ±5%, meeting the field agronomic requirements of rice cultivation.

ACKNOWLEDGEMENT

This research is funded by the following projects: the Jiansanjiang Rice Industry Research Institute Project（JCY202403）; the Special Project for Central Government to Guide Local Science and Technology Development（ZY20B05）.

REFERENCES

[1] Chen, L.P., Huang, W.Q., Meng, Z.J. (2008). Design of variable fertilization controller based on CAN bus (基于 CAN 总线的变量施肥控制器设计) [J]. *Journal of agricultural machinery science*, (08):101-104+185.

[2] Dong, S., Shu, X. D., Chung, G.B. (2020). Improved whale optimization algorithm based on the tent chaotic mapping and nonlinear convergence factor[J]. *Journal of physics: conference series*,1682(1):012055.
[3] Dou, H., Hu, L. (2026). Precision variable-rate fertilizer application method based on real-time field soil electrical conductivity sensing [J]. *Computers and Electronics in Agriculture*, 241111267-111267.
[4] Kun, H., Lian, Z., Ping, L. (2023). Side-Deep fertilization stabilizes double-cropping rice yield, increases N and P utilization, and reduces N and P losses [J]. *Land*, 12(3):724-724.
[5] Li, T., Li, J. (2024). Fuzzy PID control based on genetic algorithm optimization inverted pendulum system [J]. *Journal of Physics: Conference Series*, 2816(1):012001-012001.
[6] Li, Y. (2025). Research on variable sowing and fertilization control system - based on financial accounting precision (变量播种施肥控制系统的研究——基于财务会计精细化) [J]. *Agricultural mechanization research*, 46(02):216-220.
[7] Li, Z.P., Liang, C.Y., Li, P. (2022). *Research status and prospects of precision fertilization technology (*精准施肥技术研究现状和展望*)* [J]. *Tropical agricultural engineering*, 46(03):47-50.
[8] Liu, Y.C. (2012). *Research on key technologies for variable-fertilizer application and precision farming equipment* (变量配肥施肥精准作业装备关键技术研究) [D]. Chinese academy of agricultural mechanization sciences.
[9] Luo, L., Zhang, F.G., Li, Y.T. (2018). Research on variable fertilization control system without GPS positioning (基于无 GPS 定位的变量施肥控制系统的研究) [J]. *Agricultural mechanization research*, 40(01):96-100.
[10] Ma, X., Zhao, X., Liu, S.S. (2023). Design and experiment of variable fertilizer application device for solid particles fertilizer in high-speed rice transplanter (水稻高速插秧机固体颗粒肥料变量施肥装置设计与试验) [J]. *Journal of agricultural machinery science*, 54(09):99-110
[11] Mou, G.T., Feng, Y.J., Li, J. (2017). *Research on recommended fertilizer amount for rice in mountain villages based on GIS (*基于 GIS 的山地村域水稻推荐施肥量研究*)* [J]. *Chinese rice*, 23(04):119-122.
[12] Qi, W.Z., Wang, J.X., Liu, S.X. (2019). Design and experiment of the variable fertilizer application system for rice and wheat machines (稻麦变量施肥机控制系统设计与试验) [J]. *Agricultural mechanization research*, 41(08):72-79.
[13] Xu, Y., Jin, Y., Sun, Z. (2025). PSO-Based System Identification and Fuzzy-PID Control for EC Real-Time Regulation in Fertilizer Mixing System[J]. *Agronomy*, 15(5):1259-1259.
[14] Wang, B.W. (2024). *Design and experimental research of impeller-type sub-surface fertilization device for rice (叶轮式水稻侧深施肥装置设计与试验研究)* [D]. Heilongjiang Bayi Agricultural University.
[15] Wang, J.F., Lv, Z.Y., Zhao, M.Y. (2024). Design and experiment of a variable fertilizer application system for rice based on prescription maps (基于处方图的水稻侧深变量施肥控制系统设计与试验) [J]. *Journal of agricultural machinery science*, 55(09):151-162.
[16] Wang, N., Zhuang, W.D. (2024). Research status and development suggestions of variable fertilization technology (变量施肥技术的研究现状与发展建议) [J]. *Modernized agriculture*, 03:77-79.
[17] Wang, Z.Y., Wang, L. (2025). Multi-strategy improved whale optimization algorithm and its applications(多策略改进的鲸鱼优化算法及其应用) [J]. Journal of Harbin Engineering university, 46(05):997-1004.
[18] Zhou, C., Liu, K., Yao L.L. (2025). Research status and prospects of key technologies for prescription-type variable fertilization (处方图变量施肥关键技术研究现状与展望) [J]. *Chinese journal of agricultural machinery chemistry*, 46(08):238-245.

THE BEHAVIOR OF VEGETABLE SEED PICK-UP USING A VACUUM SEEDMETERING UNIT (VSMU)

/

سلوك التقاط بذور الخضروات باستخدام وحدة تلقيم البذور بالشفط

Mohamed ABO-HABAGA[1)], Zakaria ISMAIL[1)], Mohamed SHALABY[1)], Mahmoud OKASHA[*2,3)]

[1)]Agricultural Engineering Department, Faculty of Agriculture, Mansoura University/ Egypt

[2)]Agricultural Engineering Research Institute (AEnRI), Agricultural Research Center (ARC), Giza 12611/ Egypt

[3)]Department of Agricultural, Food, Environmental and Animal Sciences (DI4A), University of Udine, 33100 Udine/ Italy

Tel: +20-1003133841; E-mail: mahmoudokasha1988@yahoo.com & mahmoud.okasha@uniud.it

Corresponding author: Mahmoud Okasha

DOI: https://doi.org/10.35633/inmateh-79-10

Keywords: *Automatic seeding; Precision seeding; Vacuum pressure; Vegetable seeds*

ABSTRACT

This study aimed to evaluate the performance of a vacuum seed-metering unit (VSMU) developed for sowing vegetable seeds in trays under different vacuum pressures. Laboratory experiments were conducted using three seed types with markedly different physical and geometric properties: pepper, Armenian cucumber, and okra. Metering performance was evaluated in terms of the accuracy, miss, and multiple indices. The results showed that seed physical and geometric properties affected the optimal vacuum pressure, which was 1.52, 7.5, and 8.5 kPa for pepper, Armenian cucumber, and okra seeds, respectively. The corresponding accuracy indices were 93.54%, 91.25%, and 96.04%. Seeds with a relatively large mass, such as okra seeds, or low sphericity, such as Armenian cucumber seeds, required higher vacuum pressures than the flat, approximately circular pepper seeds. The developed VSMU therefore demonstrated its ability to handle seeds with diverse physical and geometric characteristics and achieve accurate seed metering.

الملخص

تهدف هذه الدراسة إلى تقييم وحدة شفط البذور المُصمَّمة لزراعة بذور الخضراوات بدقةٍ عالية، عند مستويات مختلفة من ضغط الشفط. تم إجراء التجارب المعملية على ثلاثة أصناف من البذور المختلفة في الخصائص الفيزيائية والهندسية: بذور الفلفل، القثاء الأرمني والبامية. تم تقييم الأداء باستخدام مؤشر جودة البذر، ومؤشر الفقد، ومؤشر المتعدد. وأظهرت النتائج أن الخصائص الفيزيائية للبذور تُؤثِّر بدرجة كبيرة على قيم ضغط الشفط المثلى، والتي بلغت 1.52، و7.5، و8.5 كيلو باسكال لبذور الفلفل، والقثاء الأرمني، والبامية على التوالي. وبلغت نسبة دقة البذر 93.54% و91.25% و96.04% على التوالي. تؤكد هذه النتائج أن البذور ذات الكتلة الكبيرة، كالبامية، أو ذات الكروية القليلة، كالقثاء الأرمني، تحتاج إلى ضغوط شفط أعلى مما تحتاجه بذور الفلفل الدائرية المُسطَّحة. وهكذا أظهرت وحدة الشفط المُطوَّرة القدرةَ على التعامل بدقة مع أشكال البذور المختلفة، وتطوير تقنيات الزراعة الدقيقة لمحاصيل الخضروات المتعددة.

INTRODUCTION

The Egyptian agricultural sector requires numerous physically demanding tasks and a large workforce. However, the sector faces several challenges: a shortage of skilled labor, high wages, and a lack of interest among young people in pursuing agricultural careers (*Abo-Habaga et al., 2024 a, b*). Meanwhile, vegetables are the most economical source of vitamins and minerals vital for a healthy lifestyle and are widely recognized as a fundamental element of food and nutrition security. To maintain an adequate supply of vegetables, further investment in agricultural output, post-harvest management, food safety, and market accessibility is necessary (*Zamuco et al., 2023*). Many agricultural operations, including sowing, transplanting, harvesting, and packaging, still require considerable manual labor. It leads to higher overall production costs (*Arteaga et al., 2020*). Sowing is the first critical operation in commercial vegetable seedling production. Depositing a single seed in each cell of a plug tray is essential because multiple seeds per cell result in excess seedlings, whereas missed seeds leave empty cells. These faults increase the labor required to add or remove seedlings later in the production process. Therefore, precision single-seed sowing is important for high-quality, efficient seedling production (*Xia et al., 2021*). Nevertheless, the overall mechanization level for vegetables is currently approximately 20%, much lower than that for food crops. Given the growing scale of vegetable cultivation, adopting mechanization for seeding is essential (*Li et al., 2025*). Sowing seeds is a crucial step after soil preparation. Among the many cultivation methods, tray planting is one of the most important, efficient, and reliable. This ensures increased productivity, uniform growth and seedling quality, and independent development of each seedling (*Lin and Lee, 2023*).

[1] *Mohamed Abo-habaga, Associate Professor; Zakaria Ismail, Professor; Mohamed Shalaby, M.Sc. Student; Mahmoud Okasha, Researcher*

However, manual sowing in trays is inaccurate and time-consuming, especially with small seeds, as one worker can sow 100 trays in 8 hours, producing approximately 9800 seedlings (*Gaikwad and Sirohi 2008*). It limits production accuracy and capacity due to fatigue and human error. Thus, solutions are moving towards the use of machinery for sowing, which can be complex at times due to variations in seed physical and geometrical properties (*Arteaga et al., 2020*). Tray planting systems require continuous preparation and filling of the soil before sowing. The seed placement process is crucial, as it directly affects the accuracy of placing seeds at the appropriate depth and location (*López et al., 2018*). Numerous machines and technologies were designed and developed for sowing, including mechanical and electrical components and intelligent robots, to improve plant production. Among these, pneumatic seeders have proven to be the most effective, enhancing plant uniformity and offering several other advantages (*Liu et al., 2024*; *Pradhan et al., 2024*). Several studies on vacuum seed meters emphasize the impact of the physical dimensions of the seed pick-up mechanism, including negative pressure, forward speed, and various operational variables, on measurement performance (*Liu et al., 2021*). *Karayel et al. (2004)* reported optimal suction levels for several vegetable seeds and emphasized the high accuracy of air suction in precision agriculture. Other research has discussed the mechanics of seed suction as a combination of differential pressure and pressure-gradient forces (*Shi et al., 2020*; *Li et al., 2021*). *Gaikwad and Sirohi (2008)* developed an inexpensive machine that pneumatically sows trays and found that suction pressure is the primary determinant of sowing accuracy, followed by nozzle diameter. Results under ideal seeding conditions were over 90% for both pepper and tomato seeds.

Similarly, *Li et al*. (2025) developed a precision seeding machine with a vacuum cylinder for irregularly shaped vegetable seeds. They applied computational fluid dynamics (CFD) modeling to study airflow distribution and the relationships among suction pressure, vibration frequency, and key seeding indices. *Ding et al*. (2024) developed a seed-planting machine for seedling trays and noted that seeds with different morphological characteristics require specific planting criteria. Failure to dynamically consider these criteria results in reduced accuracy and increased planting errors.

Zamuco et al. (2023) reported that the accuracy of their planting machine for seedling trays was significantly affected by pressure and seed surface area, with both factors strongly influencing machine performance. The vacuum seed-metering unit (VSMU) uses vacuum as its primary operating mechanism to achieve single, stable seed separation. Suction level is the primary operational factor affecting the efficiency of the capture and individualization process. The main purpose of this study is to evaluate the behavior of vegetable seed pick-up with various physical and geometric properties (pepper, Armenian cucumber, and okra) using a vacuum seed-metering unit (VSMU).

MATERIALS AND METHODS

The VSMU system (Fig. 1) was developed, and the research work was carried out at the AGRI-TRONICS laboratory, Department of Agricultural Engineering, Faculty of Agriculture, Mansoura University, Mansoura, Egypt, during the period January-May 2026.

The VSMU system

VSMU was developed for precision seed sowing, using a pneumatic mechanism that changes vacuum pressure based on seed physical and geometric parameters. The unit is composed of two basic components: the suction unit and the electrical control unit. The combination enabled precision single-seed pick-up with minimal seed misses and enhanced sowing accuracy across a range of seed types.

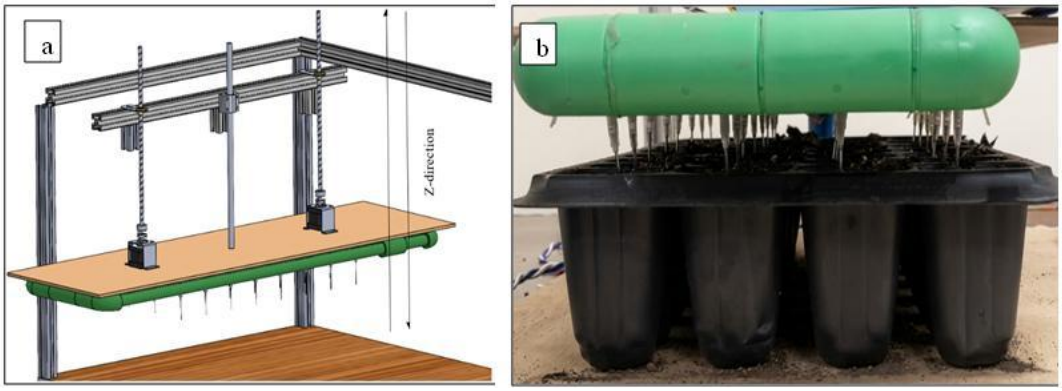


Fig. 1 – The VSMU system: (a) 3D design showing the direction of the z-axis, (b) photo of the VSMU during seed placement into the tray

Suction unit:

The suction unit picks up the seeds using needles with suction nozzles, driven by a suction motor connected to a flexible hose and PPR plastic pipes. The nozzle's picking surface was made flat by smoothing the needle's pointed nose to avoid seed damage, and its length was kept at 30 mm to facilitate picking seeds even as the seed level in the seed box declined (Fig. 2).

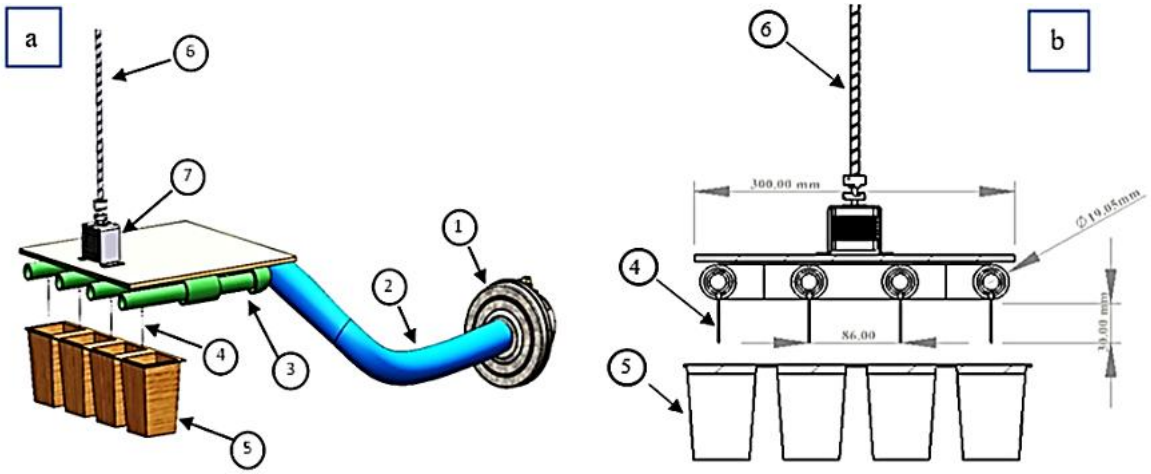


Fig. 2 – VSMU (a) Conceptual drawing and (b) Line diagram (Dim. in mm)

1 – Suction motor; 2 – Flexible vacuum hose; 3 – PPR plastic pipes; 4 – Nozzles; 5 – Seeds box; 6 – Lead Screw; 7 – Stepper motor

Seed box

A wooden seed box was designed measuring 550 × 270 mm with a depth of 30 mm, featuring cells with inward-inclined hive walls to centralize the seeds, thereby enhancing seed extraction during the unit's continuous operation.

Suction pipes and manifold

The VSMU's airflow system was designed using PPR plastic pipes of two different diameters. A 1-inch pipe was connected directly to the flexible hose supplying the suction motor, while 3/4-inch parallel pipes—matched to the cell arrangement in the tray—distributed airflow to the suction needles mounted on them.

Suction motor

A 2200 W suction motor, functioning at 220 V and 50 Hz, was incorporated to generate the pneumatic suction necessary for seed collection. This assembly facilitates the secure attachment of seeds from the seed box and prevents them from being ejected from the nozzle until they reach the tray.

Vacuum intensity adjustment mechanism

Servo motor

The SG90 servo motor served as a precise actuator, connecting the digital control system to the analogue AC dimmer. The servo was mechanically connected to the AC dimmer mechanism to adjust its displacement, enabling indirect control of suction strength via the user interface. It converted PWM control signals into accurate rotational velocities, enabling modulation of the suction operation level. The SG90 functions within a voltage range of 4.8 to 6.0 V. It provides a stall torque of 1.8 kg·cm (0.176 N·m) at 4.8 V and 2.0 to 2.2 kg·cm (0.196 to 0.215 N·m) at 6.0 V. It is compatible with PWM signals and possesses a rotational range of 0° to 180°. The no-load speed is approximately 0.12 seconds per 60 degrees.

AC dimmer

The SCR Voltage Regulator Module is a 2200 W, 220 VAC-type SCR control device for the smooth, continuous control of the effective voltage to the suction motor. It allows for accurate speed control of the suction motor to match the suction it produces. The SCR VC module phase angle controls AC for the SCR. Using phase-control technology, the SCR operates at an angle that reduces the effective load voltage relative to the RMS load voltage. The module simultaneously controls the motor's effective speed and the output voltage to the load, with no discrete switching. The module requires a 220VAC power source. It has a maximum capacity of 2200 Watts, making it suitable for controlling many high-wattage AC load motors, including Universal and AC motor types. The SCR VC module can be used as a VR for motor speed control and, in some applications, as a standard PID-compatible power modulation module. The SCR module's output voltage is modulated to provide adjustable suction, depending on system requirements, allowing precise control of suction pressure in the VSMU system to accommodate differences in seed properties. Based on initial experiments conducted on the studied seeds, the appropriate suction levels for sowing ranged from 1 to 9 kPa.

Operational pressures were measured at the flexible hose interface near the vacuum source using a calibrated pressure gauge. To guarantee experimental consistency and pressure stability, measurements were verified and stabilized before each trial run.

Seed release mechanism

After picking the seeds, the suction unit moves to the tray where the seeds will be placed, down into the soil. The needles penetrate the soil to a depth predetermined by the user, depending on the type of seed. When the specified depth is reached. Experimentally, the dimmer automatically pauses the suction motor for 10 seconds to ensure that the negative pressure is fully discharged, leaving the seeds for the needle nozzle. The suction unit then moves, leaving the seeds inside the soil.

Electrical and control components:

Arduino Mega

The Arduino Mega 2560 served as the principal microcontroller for system control and the integration of all electronic components. The system analyzed input signals from the user interface and sensors to produce control outputs that operated the servo motor and managed the AC voltage controller. It is predicated on the ATmega2560 microcontroller. It possesses a clock speed of 16 MHz. It functions at 5 volts. The device features 54 digital input/output pins, 15 of which support PWM output, 16 analogue input pins, and several serial communication interfaces, including 4 UARTs, facilitating simultaneous connections to multiple devices. The system comprises 256 KB of flash memory (8 KB allocated to the bootloader), 8 KB of SRAM, and 4 KB of EEPROM. The Mega 2560 was deemed suitable for overseeing the multi-component control architecture of the developed system owing to its superior I/O capacity and greater memory than smaller Arduino boards.

RAMPS 1.6 expansion control board

The RAMPS 1.6 extension control board was used to interface with and coordinate the system's motion-control components. It is based on a multi-axis control architecture using an Arduino-compatible shield. It supports up to 5 stepper motor drivers and modular connectors for end stops, heaters, and sensors and is normally run at 12–24 V DC. It has MOSFET power outputs for controlled loads and a heatsink assembly for optimized thermal dissipation at high current.

User interface – UI

The LCD2004 module was used as a human-machine interface (HMI) to monitor the system and select parameters. It consists of a 20 × 4-character LCD, an integrated rotary encoder, and an SD card interface. It runs on 5V direct current and communicates with the main controller over a standard parallel or I2C link. With this setup, the embedded firmware is in charge and can autonomously tune the system.

Power supply

A regulated 12 V DC switching-mode power supply (SMPS) powered the control and actuation subsystems. The SMPS accepts a wide input voltage range of 100-240 VAC, provides a stable 12 V DC output, and has a maximum current rating of 15 A, for a total rated output power of 180 W. The SMPS has built-in protections against overload, overvoltage, short circuits, and other hazards, helping extend its lifespan and ensuring normal operation with a wide variety of loads.

Stepper motor

The NEMA 17 stepper motor provides accurate positional control of the mechanical actuation components. The NEMA 17 stepper motor is a bipolar hybrid model with a standard step angle of 1.8° (200 steps per revolution). The electrical specification of the NEMA 17 stepper motor is a phase current rating of 1.2 to 2.0 A and a holding torque rating of 30-70 N·cm. The NEMA 17 stepper motor can be interfaced with drivers that use either pulse-width modulation (PWM) or step/direction control signals to provide accurate open-loop positioning. The general geometric specifications of the NEMA 17 stepper motor include a standard 42 × 42 mm frame size with a variety of different shaft combinations.

Stepper motor driver module

The DRV8825 driver was used to control the stepper motor, leveraging its high precision microstepping capabilities. In addition, the module provides a motor supply voltage range of 8.2 to 45 V and a maximum of 2.2 A per phase with sufficient thermal management. It supports microstepping resolutions up to 1/32 step, driven by STEP and DIR logic signals. Moreover, the driver includes built-in protection circuitry, including overcurrent, thermal shutdown, and under-voltage lockout (UVLO).

Studied factors

The developed VSMU was evaluated under various working conditions. The key elements assessed were seed morphology and vacuum intensity, as these factors directly affect seed pick-up efficiency and deposition accuracy.

1. Morphology: Three types of seeds were chosen to determine the performance of the metering unit for a variety of seed sizes, shapes, surface textures, and masses (Table 1): pepper *(Capsicum annuum L.)*, Armenian cucumber *(Cucumis melo var. flexuosus)*, and okra *(Abelmoschus esculentus L.)* seeds. For each type, length (L), width (W), and thickness (T) were measured on 30 seeds using a digital caliper (accuracy 0.01 mm), and thousand-seed mass (M) was determined with a digital balance. Sphericity (φ) and aspect ratio (R_a) were determined by Eqs. (1) and (2), according to *Mohsenin (1970).*

$$\phi = \frac{(L \times W \times T)^{1/3}}{L} \times 100 \quad (1)$$

$$R_a = \frac{W}{L} \times 100 \quad (2)$$

Table 1

The physical and geometrical properties of the studied seeds

Seed type	Parameter	L (mm)	W (mm)	T (mm)	φ (%)	Ra (%)	M (g/1000 seeds)
Pepper	Mean	3.71	3.87	0.89	62.96	104.31	3.5
	±SD	0.50	0.19	0.16			
	CV (%)	13.47	4.91	17.98			
Armenian cucumber	Mean	5.21	2.22	1.59	50.61	42.61	30.2
	±SD	0.60	0.22	0.49			
	CV (%)	11.52	9.91	30.82			
Okra	Mean	4.71	4.02	3.59	86.64	85.35	81.4
	±SD	0.30	0.24	0.36			
	CV (%)	6.37	5.97	10.02			

The data in Table 1 demonstrate significant differences in physical attributes among the three seed varieties evaluated. Okra seeds exhibited the largest dimensions (L = 4.71, W = 4.02, T = 3.59 mm), highest φ (86.64%) and R_a (85.35%), and greatest thousand-seed mass (81.4 g), suggesting a compact, near-spherical form. On the other hand, the Armenian cucumber seeds exhibited the largest elongation, the lowest φ (50.61%) and *Ra* (42.61%), and an intermediate thousand-seed mass of 30.2 g. The pepper seeds had a considerably low T of 0.89 mm, which resulted in a flat morphology, a moderate φ of 62.96%, and the smallest thousand-seed mass of 3.5 g. Such diversity in seed geometry and mass among the three varieties is likely to result in different pick-up reactions at varying suction pressures.

2. Vacuum pressure levels: The stability of pick-up and reliability of singulation were examined across different suction levels. The control system regulated the vacuum motor speed to generate the required pneumatic pressure, and the suction strength was electronically controlled. The experiment was performed at pressure levels ranging from 1 to 9 kPa.

Operation of the suction unit

Each seed type and suction pressure level had 15 trial replications for that specific combination. In each replication, 32 tray cells/nozzles were tested; therefore, the total sample size was 480 cells per treatment. The suction pressure was adjusted to the target value before each trial, allowed to stabilize, and verified with the vacuum gauge before beginning the seed pick-up cycle. After the user determines the required suction power variables, the suction unit moves to the seed box. The servo motor then automatically adjusts the dimmer to the specified suction level. At that time, the seeds are drawn toward the needle nozzle by the suction. Then the suction unit moves to the tray to be planted, and the seeds are placed inside the soil. The servo moves to close the suction motor for 10 seconds as a rest time to ensure all seeds fall and remain in the soil. Then, the suction unit returns to its position to start a new circuit, and the process repeats until the user-specified number of circuits is completed. The workflow procedure is shown in Fig. 3.

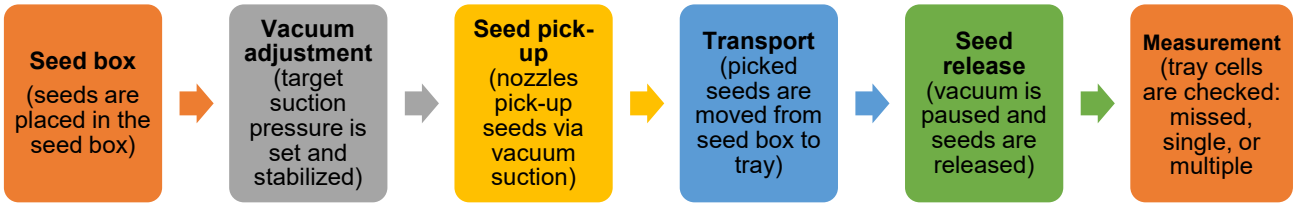


Fig. 3 – Workflow procedure of VSMU

Measurements

The total miss index (I_m), total multiple index (I_d), and accuracy percentage (S) were calculated according to Eqs. (3-5), respectively, according to *Kachman and Smith* (1995) and *Ismail et al. (2023).*

$$I_m = \frac{N_m}{N_t} \times 100 \quad (3)$$

$$I_d = \frac{N_d}{N_t} \times 100 \quad (4)$$

$$S = \frac{N_{success}}{N_t} \times 100 \quad (5)$$

where: S is the accuracy percentage, [%]; N_m is the number of cells that were "lost", and no seeds were sown; N_d is the number of cells in which "two seeds" (Doubles) descended; N_t is the total number of cells; $N_{success}$ is the number of successful cells.

Instruments:

1) A digital caliper was used to measure the seeds' dimensions. The digital caliper has a measurement range of 0 to 150 mm with an accuracy of 0.01 mm.
2) A digital balance was used to measure the mass of the seeds. It has a maximum capacity of 200 g with an accuracy of 0.001 g.
3) The vacuum pressure inside the system was measured by a vacuum gauge. The device's measuring range is -1 to 0 bar (0 to -30 inHg), and its accuracy class is 1.6 (±1.6% full scale).

RESULTS AND DISCUSSION

The VSMU system was evaluated using three parameters: the accuracy percentage index (S), the missing index (I_m), and the multiple index (I_d). In experimental trials, for each seed type, the S of vacuum seed placement was determined at different theoretical suction levels using these indicators. I_m shows a seed not captured due to insufficient suction pressure. I_d occurs when more than one seed is picked up at once, which can be caused by excessive vacuum pressure or by seeds clumping together around the nozzle. The accuracy index was calculated as the ratio of successful single-seed pickup events to the total number of pickup attempts, with both missed and multiple-seed pickups classified as unsuccessful events. Tests were conducted to determine the effects of different vacuum pressures on seed-pickup performance and singulation efficiency.

The experimental results were used to determine the optimal suction level for each seed type, defined as the level at which the accuracy percentage was maximized and the missing- and multiple-seed indices were minimized. For each seed type, 15 replications were conducted at each suction pressure level. The tested pressure levels ranged from 1 to 9 kPa (Figs. 4-7).

1. Pepper

Increasing the vacuum pressure from 1 to 9 kPa, the total miss index (I_m) changed slightly from 3% to 2%; the total multiple index (I_d) rose from 4% to 21%, while the accuracy percentage (S) decreased from 93% to 77%. As vacuum pressure increased, metering accuracy declined, mainly because (I_d) increased rather than (I_m) decreased (Fig. 4).

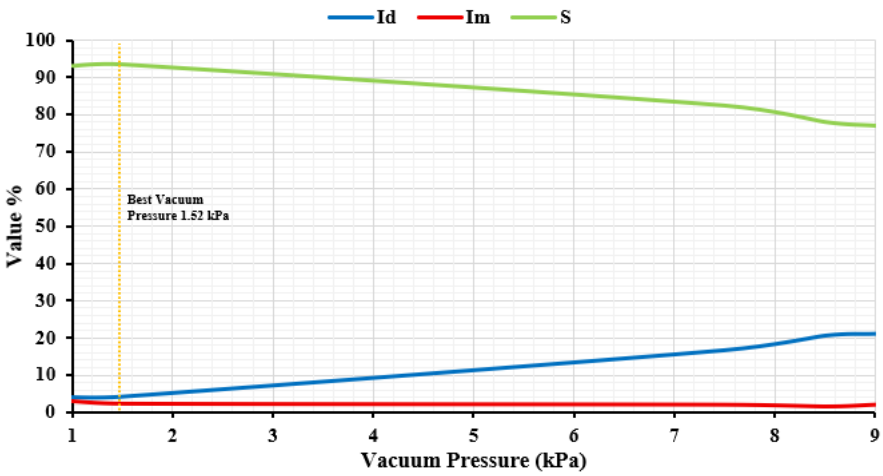


Fig. 4 – Effect of suction pressure on I_d, I_m, and S for pepper seeds

2. Armenian cucumber

Increasing vacuum pressure from 1 to 9 kPa, the total miss (I_m) index decreased from 14% to 2.3%; the total multiple index rose from 2% to 10.2%; and then the accuracy percentage (S) continued to rise from 84% to 91.25% at 7.5 kPa -Best Vacuum Pressure- and then decreased again to 87.5% at 9 kPa. As vacuum pressure increased, the reduction in the total miss index (I_m) was the dominant effect at lower pressures, while the rise in the total multiple index (I_d) became more pronounced at higher pressures (Fig. 5).

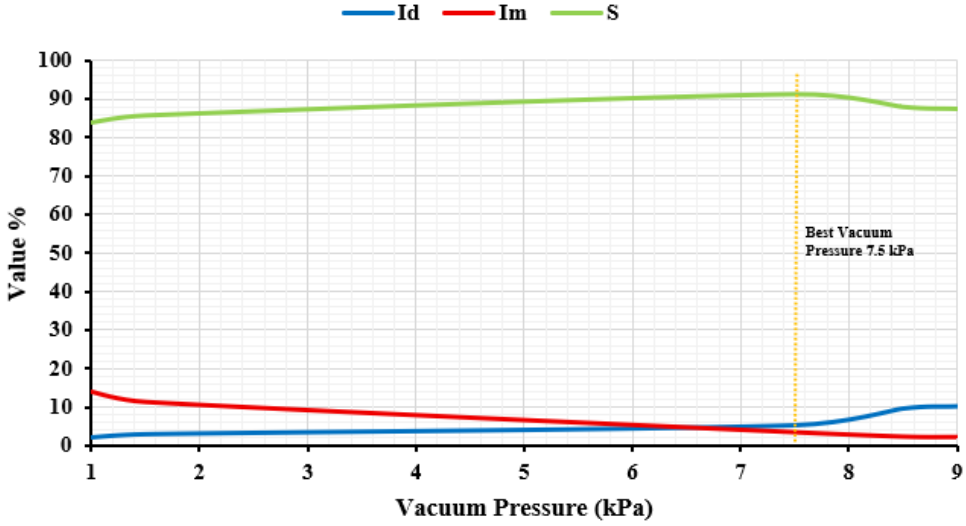


Fig. 5 – Effect of suction pressure on I_m, I_d, and S for Armenian cucumber seeds

3. Okra

Increasing vacuum pressure from 1 to 9 kPa, the total miss index (I_m) decreased from 15% to 2.4%; the total multiple index (I_d) rose from 0.1% to 2% and then the accuracy percentage (S) continued to rise from 84.9% to 96.04% at 8.5 kPa -Best Vacuum Pressure- and then decreased again to 95.6% at 9 kPa. As vacuum pressure increased, the reduction in the total miss index (I_m) was the dominant effect at lower pressures. In comparison, the rise in the total multiple index (I_d) became more pronounced at higher pressures (Fig. 6).

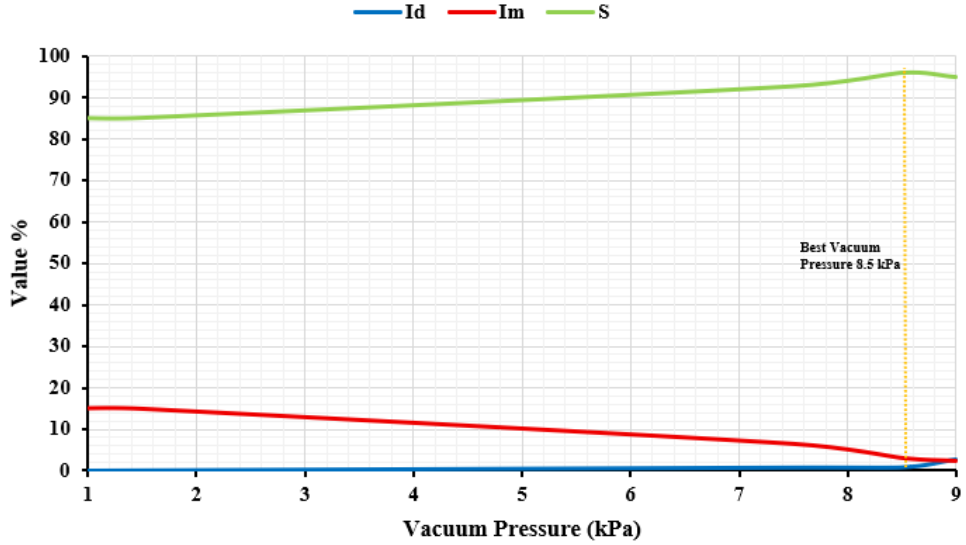


Fig. 6 – Effect of suction pressure on I_m, I_d, and S for *okra* seeds

Comparative seed singulation performance across crop types

The VSMU accuracy percentage varied across seed types at their respective optimum suction settings. For each crop, the best operating condition was selected based on the maximum accuracy percentage index (S) and minimum missing (I_m) and double (I_d) indices. The best suction pressures were 1.52, 7.5, and 8.5 kPa for pepper, Armenian cucumber, and okra seeds. Values of missing and multiple-seeds are expressed as mean ± standard deviation based on 15 replications. At the optimum suction pressures, pepper seeds at 1.52 kPa recorded 1.20 ± 1.01 missing events and 2.07 ± 1.22 multiple-seed events.

Armenian cucumber seeds at 7.5 kPa recorded 1.27 ± 0.70 missing events and 3.27 ± 1.03 multiple-seed events. Meanwhile, okra seeds at 8.5 kPa recorded 1.00 ± 0.65 missing events and 0.27 ± 0.46 multiple-seed events. These results indicate that the selected suction pressure for each seed type yielded stable seed pick-up performance, with acceptable variation across replications. The values obtained for *S*, I_m, and I_d for pepper seeds under these conditions were 93.54%, 2.29%, and 4.16%, respectively. Armenian cucumber seeds were recorded at 91.25%, 3.54%, and 5.2%, respectively. Okra seeds performed best overall with an *S* value of 96.04% and I_m and I_d values of 3.12% and 0.83%, respectively. The variation in singulation performance was attributed to differences in seed size, shape, and surface contact characteristics under pneumatic suction conditions.

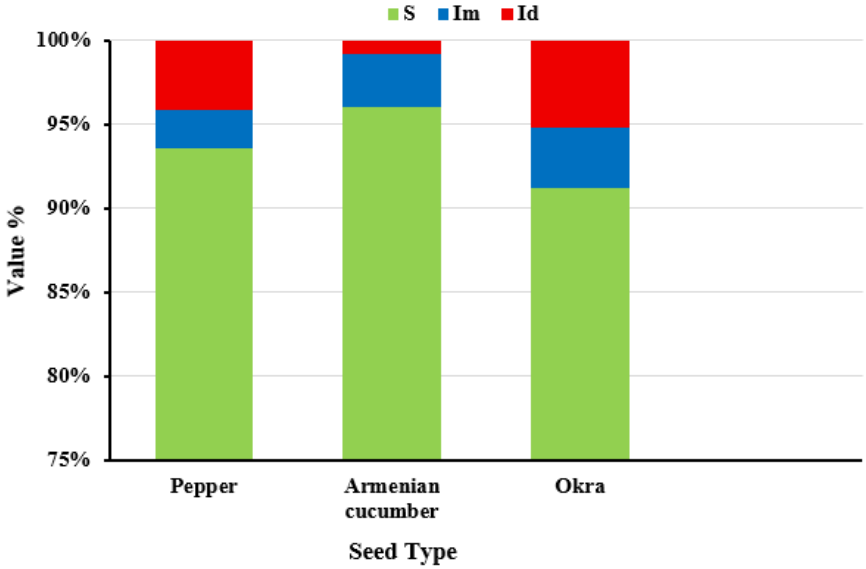


Fig. 7 – Seed singulation performance

Pepper seeds have a lower optimum vacuum pressure primarily because of their low seed weight and flat shape. This setup provides enough suction force to lift the pepper seeds at very low vacuum pressures. In contrast, the low sphericity and length of Armenian cucumber seeds would inhibit stable contact with the nozzle, thereby requiring higher vacuum levels to pick up the seeds reliably. Okra seeds, while highly spherical, have the highest seed weight and thus require more suction force to maintain stable attachment during transport than either of the other two seed types. Thus, the optimum vacuum pressure depends on the interaction between the seed's physical characteristics and the nozzle design, rather than on the seed's size alone. The results are in agreement with those of *Karayel et al.* (2022), determined in laboratory experiments conducted under controlled conditions, that the optimum vacuum pressure of the air-suction seed-metering device changed depending on the seed type and was 3.0 kPa for soybean, 4.0 kPa for maize, 2.5 kPa for melon and watermelon, 2.0 kPa for sugar beet, and 1.5 kPa for onion seeds. In the present investigation, a similar trend was observed, with pepper seeds requiring the lowest optimum vacuum pressure (1.52 kPa). This value closely matches that of onion seeds, due to their similar small seed size and reduced mass. In contrast, cucumber and okra seeds required much greater vacuum pressures, 7.5 kPa and 8.5 kPa, respectively. This trend is reconcilable with the higher vacuum pressure level observed for larger seeds such as melon, watermelon, soybean, and maize. This shows that the different morpho-physical properties of the seeds also determine the optimal vacuum pressure, with seed size and weight being the most significant factors. VSMU's success in providing accurate, repeatable seed singulation across all seed types confirmed prior theories that vacuum pressure depends on both seed type and the system employed. The findings that are used to assign optimum vacuum pressures (1.52 kPa for pepper, 7.5 kPa for Armenian cucumber and 8.5 kPa for okra) are consistent with previous research of pneumatic seeding systems in which small seeds typically require less suction (1.5-4.0 kPa) in controlled lab conditions (*Karayel et al., 2004*; *Karayel et al., 2022*). The findings are also similar to those for other small vegetable seeds, such as onion and sugar beet. The interaction between the physical properties of the seeds and the operational characteristics of the VSMU led to higher vacuum requirements for okra and Armenian cucumbers due to their irregular shapes and low sphericity. Because of these properties, the effective contact area between the seed and the suction area of the orifices is reduced; therefore, pick-up stability is reduced, which increases the amount of vacuum necessary to achieve proper seed singulation.

Higher suction demand during steady-state operation can result from operating modes and measured conditions that differ from those in the laboratory. Seed metering studies using vacuum systems have established that both seed characteristics and operational conditions can affect vacuum requirements, and that many observed deviations from ideal values can be attributed to seed–orifice interactions rather than to defects in the vacuum system (*Karayel et al., 2004; Jabir and Alfadil, 2022*). Therefore, it can be concluded that the optimal vacuum pressure arises from the interaction between the seed and the system, rather than being determined solely by the seed's characteristics.

CONCLUSIONS

The VSMU provided highly repeatable seed pick-up performance at a range of vacuum pressures and seed physical characteristics. Seed capture performance was influenced by vacuum pressure, as indicated by the single-seed pick-up accuracy percentage (S), miss index (I_m), and multiple index (I_d). The test results indicated that the vacuum pressure providing the best performance depends upon the seed characteristics, including seed shape/size, mass, and surface. The vacuum pressure at which the best pick-up performance for pepper seeds occurred was 1.52 kPa, corresponding to a single-seed pick-up (S) of 93.54%, a miss index of 2.29%, and a multiple index of 4.16%. The pick-up pressure for okra seed pick-up performance was 8.5 kPa, resulting in a single-seed pick-up accuracy percentage (S) of 96.04%, a miss index of 3.12%, and a multiple index of 0.83%. The pick-up performance for Armenian cucumber seeds was 7.5 kPa, yielding a single-seed pick-up accuracy percentage (S) of 91.25%, a miss index (I_m) of 3.54%, and a multiple index (I_d) of 5.20%. Overall, optimizing vacuum pressure improved single-seed capture efficiency and reduced missed and multiple-seed pick-ups, thereby minimizing erroneous seed placement by the vacuum pick-up system. Thus, the VSMU can be regarded as an efficient and versatile mechanism for precision sowing applications of seeds with different physical properties. Nevertheless, this study was conducted under controlled laboratory conditions and was limited to only three types of vegetable seeds. Future work should include other seed types and nozzles with different geometries, be tested across a wider range of operating conditions, and include nursery-scale validation.

REFERENCES

[1] Abo-Habaga, M.M., Ismail, Z.E., Moustafa, N.E., & Okasha, M.H. (2024a). Development of an automated Cartesian arm for planting seeds in pots. *Journal of Soil Sciences and Agricultural Engineering*, *15*(7), 217–224. https://doi.org/10.21608/jssae.2024.305809.1238

[2] Abo-Habaga, M., Ismail, Z., Moustafa, N., & Okasha, M. (2024b). Developing an automatic precision seeding unit (APSU) for pot seed planting. *INMATEH - Agricultural Engineering*, *74*(3), 260–272. https://doi.org/10.35633/inmateh-74-22

[3] Arteaga, O., Amores, K., Terán, H., Cangui, R.S., Ramírez, A., Hurtado, S., Inlago, D., & Chuquimarca, B. R. (2020). Automation of a seed on tray seeder machine. IOP Conference Series: Materials Science and Engineering, 872, 012003. https://doi.org/10.1088/1757-899X/872/1/012003

[4] Ding, X., Hao, W., Liu, K., Wang, B., He, Z., Li, W., & Yang, Q. (2024). Development of a universal plug tray seeder for small seeds based on electrostatic adsorption. *Computers and Electronics in Agriculture*, *227*, 109651. https://doi.org/10.1016/j.compag.2024.109651

[5] Gaikwad, B.B., & Sirohi, N.P.S. (2008). Design of a low-cost pneumatic seeder for nursery plug trays. *Biosystems Engineering*, *99*(3), 322–329. https://doi.org/10.1016/j.biosystemseng.2007.10.017

[6] Ismail, Z.E., Khdar, Kh.A.A., & Shawky, M.S. (2023). Connection of the Radish Seed's Physical Characteristics with the Bottom Holes Design of the Seeder Device. *Journal of Soil Sciences and Agricultural Engineering, Mansoura University*, *14*(7), 203–207. https://doi.org/10.21608/jssae.2023.216279.1166

[7] Jabir, E., & Alfadilb, A.D. (2022). An evaluation of a vacuum distribution device for seed pick-up regularity of a multiple-rows pneumatic plate. *International Research Journal of Multidisciplinary Technovation*, *4*(6), 14–25. https://doi.org/10.54392/irjmt2262

[8] Kachman, S.D., & Smith, J.A. (1995). Alternative measures of accuracy in plant spacing for planters using single seed metering. *Transactions of the ASAE*, *38*(2), 379–387. https://doi.org/10.13031/2013.27843

[9] Karayel, D., Barut, Z.B. & Özmerzi, A. (2004). Mathematical Modelling of Vacuum Pressure on a Precision Seeder. *Biosystems Engineering*, *87*(4), 437–444. https://doi.org/10.1016/j.biosystemseng.2004.01.011

[10] Karayel, D., Güngör, O., & Šarauskis, E. (2022). Estimation of Optimum Vacuum Pressure of Air-Suction Seed-Metering Device of Precision Seeders Using Artificial Neural Network Models. *Agronomy*, *12*(7), 1600. https://doi.org/10.3390/agronomy12071600

[11] Li, J.H., Lai, Q.H., Zhang, H., Zhang, Z.G., Zhao, J.W., & Wang, T.T. (2021). Suction force on high-sphericity seeds in an air-suction seed-metering device. *Biosystems Engineering*, *211*, 125–140. https://doi.org/10.1016/j.biosystemseng.2021.08.031

[12] Li, Y., Liu, Y., Ning, Y., Wu, H. & Zhao, Y. (2025). Design and experiment of air-suction drum-type seedling seeder for irregular-shaped vegetable seeds. *Scientific Reports*, *15*(1), 4694. https://doi.org/10.1038/s41598-024-83635-6

[13] Lin, H.-T., & Lee, Y.-H. (2023). Implementing a Precision Pneumatic Plug Tray Seeder with High Seeding Rates for Brassicaceae Seeds via Real-Time Trajectory Tracking Control. *Actuators*, *12*(9), 340. https://doi.org/10.3390/act12090340

[14] Liu, W., Xu, M. & Jiang, H. (2024). Design, integration, and experiment of transplanting robot for early plug tray seedling in a plant factory. *AgriEngineering*, *6*(1), 678–697. https://doi.org/10.3390/agriengineering6010040

[15] Liu, Z.Q., Zhang, M., Han, J., Zhuang, Y.J., Lan, Y.B. & Chen, Y.L. (2021). Effect of seed filling and releasing angles on the performance of compound vacuum seed metering device. *INMATEH - Agricultural Engineering*, *65*(3), 153–162. https://doi.org/10.35633/inmateh-65-16

[16] López, R. M. D. A., Paz, I.T., & Gutierrez, H.A. (2018). Modelación y simulación de sistema dosificador de semillas para sembradora automática de charolas de germinación. [Master's thesis, CIATEQ]. Repositorio CIATEQ. https://ciateq.repositorioinstitucional.mx/jspui/handle/1020/278

[17] Mohsenin, N.N. (1970). *Physical properties of plant and animal materials: Structure*. Gordon and Breach.

[18] Pradhan, N.C., Naik, M.A., Chowdhury, M., Kushwah, A., Asha, K.R., Dhar, T., & Satpute, A.N. (2024). Robotic seeding or sowing system in smart agriculture. In Artificial Intelligence and Smart Agriculture: Technology and Applications (pp. 495-520). Singapore: Springer Nature Singapore. https://doi.org/10.1007/978-981-97-0341-8_23

[19] Shi, S., Liu, H., Wei, G.J., Zhou, J.L., Jian, S.C., & Zhang, R.F. (2020). Optimization and experiment of pneumatic seed metering device with guided assistant filling based on EDEM-CFD. *Transactions of the Chinese Society for Agricultural Machinery, 51*(5), 54–66. https://doi.org/10.6041/j.issn.1000-1298.2020.05.006

[20] Xia, H., Zhen, W., Liu, Y., & Zhao, K. (2021). Optoelectronic measurement system for a pneumatic roller-type seeder used to sow vegetable plug-trays. *Measurement*, *170*, 108741. https://doi.org/10.1016/j.measurement.2020.108741

[21] Zamuco, C.T., Amongo, R.M.C., Suministrado, D.C., & Peralta, E.K. (2023, September). Development of an automated precision planter for solanaceous vegetable seeds. In IOP Conference Series: Earth and Environmental Science (Vol. 1241, No. 1, p. 012063). IOP Publishing. https://doi.org/10.1088/1755-1315/1241/1/012063

APPLICATION OF LLM + ZERO-SHOT LARGE MODELS FOR FRUIT OBJECT DETECTION
/
应用 LLM + Zero-Shot 大模型实现水果目标检测

Yingdong QIN [1,2,3,*], Haoyu SONG [1,2,3], Jingyi LI [4], Keyao WEN [1]

[1] College of Artificial Intelligence and Low-Altitude Technology, South China Agricultural University, Guangzhou 510642, China;
[2] National Center for International Collaboration Research on Precision Agricultural Aviation Pesticides Spraying Technology (NPAAC), South China Agricultural University, Guangzhou 510642, China;
[3] Center for International Cooperation and Disciplinary Innovation of Precision Agricultural Aviation Applied Technology ('111 Center'), South China Agricultural University, Guangzhou 510642, China;
[4] School of Statistics and Data Science, Guangdong University of Finance & Economics, Guangzhou 510220, China.
*Correspondent author: Qin Yingdong, E-mail: qinyingd@foxmail.com, ORCID: 0009-0008-3403-0554
DOI: https://doi.org/10.35633/inmateh-79-11

Keywords: Fruit Recognition, LLM, Vision Transformer, Zero-Shot, Smart Agriculture

ABSTRACT

Efficient and flexible agricultural image annotation is crucial for intelligent crop monitoring in smart agriculture, yet conventional detection models are limited by fixed class labels and require extensive manual annotations. This study presents a zero-shot annotation framework that integrates OWLv2, Google's second-generation open-vocabulary vision model, with large language models (e.g., GPT-3.5, DeepSeek V1) to enable multilingual, natural language-driven fruit recognition in smart agriculture. A user-friendly interface was developed to support individual or batch image annotation with adjustable sensitivity to meet diverse field requirements. Experimental evaluations demonstrated the framework's strong generalizability and semantic understanding capabilities, allowing recognition of unseen fruit categories and attributes such as ripeness or color. The system significantly reduces annotation time and labor costs, while enhancing accessibility through natural language interaction. To ensure a robust evaluation of generalizability, a cross-domain protocol was employed using a novel dataset from 2025. Results showed that OWLv2 achieved an F1-score of 0.80 and an mAP of 0.8301, significantly outperforming the pre-trained YOLO11 (F1: 0.74, mAP: 0.60) in zero-shot scenarios. OWLv2 exhibited superior flexibility and required no task-specific dataset retraining, although its computational demands remain higher than lightweight models like YOLO11. Notably, while the LLM (DeepSeek) introduced a total one-time API latency of 598.3 ms (called only once for processing multiple images). the actual core computational latency of OWLv2 was only 257.7 ms per image. Despite a total processing time of 891.9 ms (including visualization output), the framework demonstrates superior recall (0.9080) and semantic flexibility without retraining. These results verify the enormous application potential of OWLv2 and similar zero-shot models in agriculture, providing scalable solutions for automated annotation, real-time monitoring, and large-scale data collection.

摘要

在智慧农业领域，传统农业领域图像目标检测模型受限于固定的类别标签，并依赖大量人工标注。本研究提出了一种可以语言交互的零样本（zero-shot）标注框架，将 Google 第二代开放词汇视觉模型 OWLv2 与大语言模型（GPT-3.5、DeepSeek V1）相结合，以实现面向智慧农业的多语言、自然语言驱动的果实识别。为此，我们开发了一个交互界面，支持单张或批量图像标注，并可根据实际田间需求调节检测灵敏度。实验评估结果表明，该框架具备优异的泛化能力与语义理解能力，能够识别未曾在训练集中出现的果品类别及其属性（如成熟度、颜色等）。基于 2025 年果园数据集的跨域评估表明，OWLv2 的 F1 分数（0.80）与 mAP（0.8301）显著优于零样本场景下的预训练 YOLO11（F1: 0.74, mAP: 0.60）。相较于传统模型，OWLv2 展现出更强的灵活性，且无需针对特定任务重新训练数据集；时延分析显示，LLM（DeepSeek）仅引入 598.3 ms 的单次调用延迟（多张图只调一次），OWLv2 的核心计算耗时仅为 257.7 ms/幅。尽管包含图像输出的总处理时间为 891.9 ms，但该框架在无需重训的情况下展现了极高的召回率（0.9080）与语义灵活性。上述结果验证了 OWLv2 及同类零样本模型在农业领域具有为自动化标注、实时监测及大规模数据采的巨大潜力。

INTRODUCTION

In recent years, the emergence of transformer-based architectures has significantly advanced the field of computer vision, with growing implications in agricultural automation and precision farming. One notable breakthrough was Google's Vision Transformer (ViT), which introduced the concept of dividing images into fixed-size patches (e.g., 16×16) and treating them as sequential data, similar to words in natural language processing (*Dosovitskiy et al., 2020*). This approach enabled visual models to benefit from the scalability and learning efficiency of transformer networks, paving the way for a wide range of vision tasks with reduced reliance on task-specific architectures.

Following ViT, transformer-based vision models have evolved rapidly. Notably, OpenAI's CLIP model (*Radford et al., 2021*) demonstrated that joint vision-language pretraining on web-scale data can result in powerful zero-shot capabilities. Similarly, research from institutions such as Google and NVIDIA (*Xu J. et al., 2023*) has explored large-scale multimodal models for open-vocabulary learning, where systems are trained not on fixed class labels but on flexible language prompts. These developments are highly relevant to agriculture, where the diversity of crops, growing conditions, and field scenarios presents a challenge to traditional classification-based systems.

To address the need for more adaptable models, Google introduced the Open-Vocabulary Learner (OWL) framework. The first generation, OWL-ViT (*Minderer et al., 2022*), combined ViT backbones with vision-language pretraining in the style of CLIP, enabling zero-shot object detection based on textual input. However, it still relied heavily on annotated data for downstream adaptation. In response, OWLv2 was released in 2023 (*Minderer et al., 2023*), introducing a self-labelling mechanism called OWL-self. This technique allows the model to automatically generate pseudo-annotations via bounding box proposals, which are then refined through loss computation and further model updates. The concept aligns with the iterative self-supervision loop proposed by Meta AI in its Segment Anything (SA) model (*Kirillov et al., 2023*), which reduces dependence on manual labels by enabling scalable training on unlabeled image datasets.

Compared to chemical methods for fruit detection, image-based methods are more intuitive (*Qin et al., 2023*). *Wei et al. (2023)* verified that imaging techniques enhance the accuracy of conventional sensing methods for food detection. In smart agriculture, open-vocabulary models excel in dynamic environments like orchards or greenhouses, enabling tasks such as fruit recognition, disease monitoring, and crop growth assessment (*Espinoza et al., 2023; Mimma et al., 2022; Zhang et al., 2025*). *Li et al. (2025)* developed an improved YOLOv8n model for strawberry detection, which achieved high precision and lightweight deployment but still relied on labeled fruit datasets and fixed class definitions. *Tang et al. (2025)* proposed an enhanced YOLOv11n model for kiwifruit flower detection under occlusion, demonstrating strong performance in complex orchard environments but requiring task-specific training data. Their work underscores the value of open-vocabulary zero-shot models that support flexible, unannotated fruit and flower recognition. *Tan et al. (2021)* early explored the zero-shot paradigm but were hindered by limited datasets, methods, and computational resources, resulting in unsatisfactory performance.

In this study, the application of OWLv2 to agricultural image segmentation is investigated, with particular emphasis on fruit recognition and annotation under diverse field conditions. OWLv2 was locally deployed using Google's open-source implementation and integrated with the ChatGPT 3.5 API to enhance natural language interaction capabilities. Systems incorporating large language models (LLMs), such as ChatGPT, generally exhibit improved usability and broader user acceptance in practical applications (*Qing et al., 2023*). The proposed system enables users to submit free-form agricultural queries, ranging from crop names to complex descriptions such as "ripe citrus under leaves", and generates corresponding segmentation masks in a zero-shot manner. In addition, a user-friendly interface with configurable parameters was developed to support both single-image and batch annotation workflows.

MATERIALS AND METHODS

Experimental Environment and Hardware

The proposed framework was implemented using Python 3.7 on an Ubuntu 22.04 LTS workstation. To ensure reproducibility, all visual inference tasks were executed on a consistent hardware setup: an Intel Core i7-10700K CPU, 32 GB of DDR4 RAM, and an NVIDIA GeForce RTX 3060 GPU with 12GB of VRAM. The OWLv2 model (google/owlv2-base-patch16) was deployed via the Hugging Face Transformers library.

Logic Architecture and Feature Matching Mechanism

This section describes the deployment of OWLv2 in combination with GPT-3.5 or DeepSeek V1 for open-vocabulary fruit image annotation in an agricultural context. The method involves four key stages: (1) environment setup and model loading, (2) query preprocessing via GPT-3.5 or DeepSeek V1, (3) image inference and prediction using OWLv2, and (4) postprocessing and visualization. The technical schematic of the developed zero-shot annotation framework with language interaction capability is shown in **Fig. 1**.

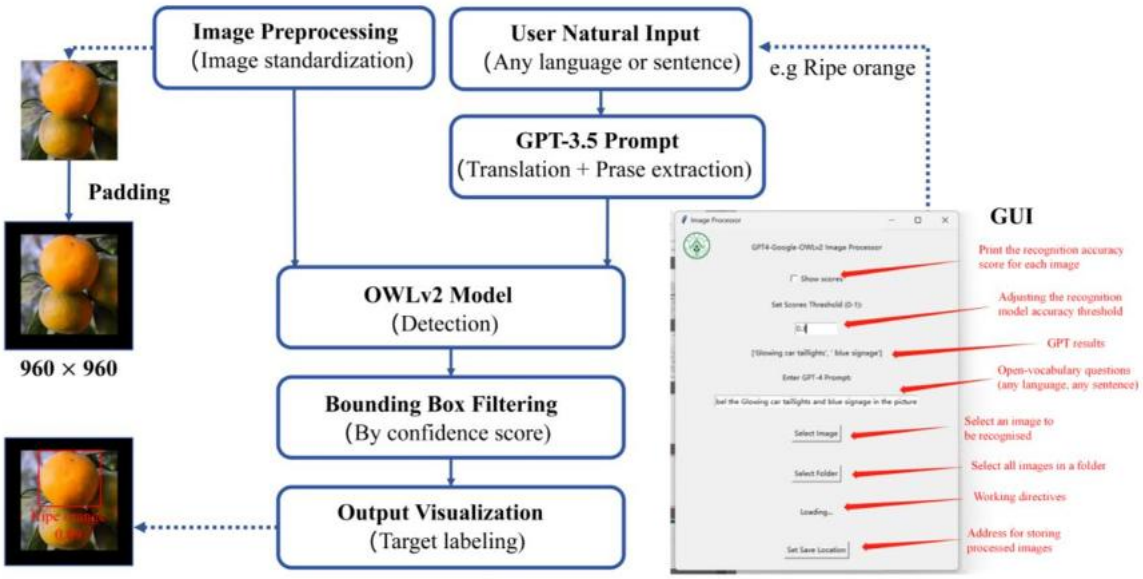


Fig. 1 - Zero-Shot Models for Fruit Object Detection Steps

Since it is based on Transformer architecture, the library is housed in the public repository NielsRogge/Transformers-Tutorials on GitHub*, where the OWLv2 model can be located. Additionally, the SAM model is available for those interested, despite its distinct functionality, exhibiting similar characteristics during application. First and foremost, the installation of the library is crucial.

Subsequently, the workflow involves loading the OWLv2 model, processor, and input image. After completing these steps, a query vocabulary must be defined for object retrieval. In the original OWLv2 framework, queries are required to be provided as comma-separated vocabulary terms in string format, which limits usability and flexibility. To improve user interaction, the proposed system directly integrates the outputs of ChatGPT 3.5 or DeepSeek V1 through a predefined system prompt. First, the user input is translated into English and converted into concise noun phrases representing the target objects. Several examples are included in the prompt design to facilitate few-shot learning by the large language model (LLM). During inference, the user input is first processed by ChatGPT or DeepSeek, and the generated output is subsequently used as the query input for OWLv2. This strategy enables the system to accept arbitrary sentence structures and multilingual inputs while maintaining compatibility with the OWLv2 query format. To ensure deterministic keyword extraction, the LLM API temperature was fixed at 0.0, and the prompt design followed a strict JSON-like few-shot template, as illustrated in **Tab. 1**.

The core of the zero-shot detection lies in the similarity matching between image tokens and text queries. To eliminate mathematical redundancy, the similarity score $S_{i,j}$ is calculated as the normalized dot product (cosine similarity) between the visual and textual embeddings:

$$S_{i,j} = \frac{f_{image}(x_i) \cdot f_{text}(q_j)}{\|f_{image}(x_i)\| \|f_{text}(q_j)\|} \quad (1)$$

where: x_i denotes the i-th visual token, q_j is the j-th text query embedding, f_{image} and f_{text} represent the respective encoders. This score determines the confidence level for each bounding box proposal.

Subsequent steps involve the local deployment of OWLv2, including image standardization through padding to achieve a fixed shape and size (torch size of 960 x 960). After the forward pass, the model's output is obtained. Finally, coordinate annotation and visualization are carried out based on the model's output, accompanied by the labeling of their similarities for later adjustments to the model's sensitivity.

*: NielsRogge/Transformers-Tutorials: https://github.com/NielsRogge/Transformers-Tutorials

Table 1

System prompt used for keyword extraction

Prompt
You are a keyword extraction machine. Your main responsibility is to extract key target words and determine the action objects of the questioner. For instance, when statements like 'I want to find an apple', 'Search for bananas', or 'Where is the watermelon' are given, the targets for the questioner are the apple, bananas, and watermelon, respectively. Only output the object, including object phrases. If there are multiple objects, separate them with commas. If the input is in another language, it is considered to be English. Use English output only. Cannot output the word 'picture'. Regardless of the syntax used by the questioner, your answer can only be an object (a noun or noun phrase with modifying qualifiers, if there are no modifiers only nouns are output). Preferably output modified nouns, e.g., 'girl in a skirt' instead of 'skirt' and 'girl'

Evaluation Protocol and Metrics

To rigorously validate the system's performance beyond a simple demonstration, a cross-domain evaluation protocol was established.

Baseline Model Dataset (YOLO11): To provide a robust benchmark, the YOLO11 model (Released in late 2024) was pre-trained on a specific agricultural dataset consisting of 1,217 RGB images of oranges (1,017 for training and 200 for validation). These images were captured between 2024 and 2025 across various locations in Guangdong, China, covering diverse environmental challenges such as standard lighting, minor occlusions, and fruit clustering.

Test Dataset Definition: A test set of 50 high-resolution images was independently collected in 2025 at a citrus orchard in Sihui, Guangdong. These images include complex variables such as heavy occlusion, variable lighting (noon vs. evening), and fruit clustering.

Quantitative Metrics: The detection performance is quantified using standard computer vision metrics:

1. Precision and Recall: To evaluate accuracy and coverage.
2. F1-Score: The harmonic mean of precision and recall.
3. mAP (mean Average Precision): Calculated at an IoU (Intersection over Union) threshold of 0.5.
4. Inference Latency: Measured in milliseconds (ms) to assess real-time potential.

Ground Truth: Manual annotation was performed by two researchers using the LabelImg tool to provide the benchmark for Comparison with the OWLv2 outputs.

RESULTS

Q&A-annotation Tool

A graphical user interface (GUI) for annotation was developed using Tkinter, a lightweight Python library. The tool supports common image formats, including *.jpg* and *.png*, and allows users to process either individual images or image folders in batch mode. User input is provided through a simple text input box, while the corresponding output information is displayed directly within the interface, as shown in **Fig. 1**. The main functional parameters of the tool are summarized in **Tab. 2**.

Table 2

Q&A-Semantic Annotation Tool Parameters

Performance indicators	parameter
Single Operation Time	1~2 s
Batch Operation Time (30 sheets)	~25 s per sheet
Startup Time	~20 s
Supported File Formats	.jpg, .png, etc.
Interaction Languages	English, Chinese, French, German, Spanish, etc.
Semantic Conversion Tools	ChatGPT, DeepSeek
LLM API Latency	~1 s

The batch processing capability of our program is demonstrated in **Fig. 2**. This function enables rapid and efficient annotation of large image datasets with high accuracy, significantly reducing the time and labor costs associated with manual labeling.

As noted in Google's documentation, such automated annotation avoids errors caused by fatigue during repetitive labeling tasks. The source code of the program is publicly available in the supplementary materials.

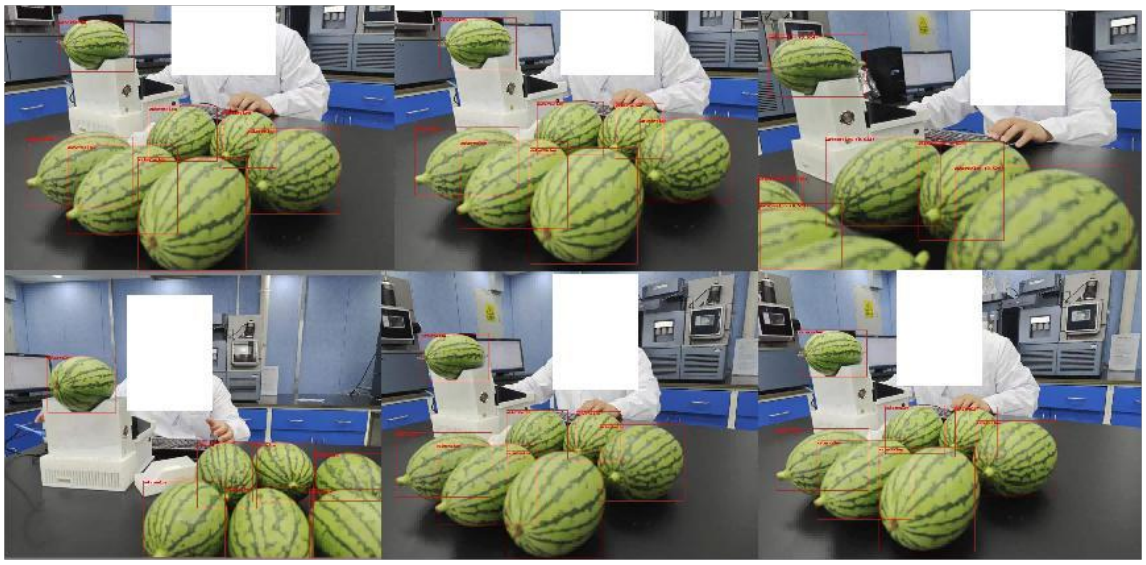


Fig. 2 - Batch Labeling of Watermelon Targets

Understanding of Word Semantics and Generalizability

Compared to traditional object detection models, OWLv2 demonstrates the ability to interpret semantic descriptors, enabling it to analyze attributes such as fruit ripeness without additional fine-tuning. As shown in **Fig. 3**, the model correctly inferred the "ripe" status of Shatangju mandarins produced in Sihui, Guangdong, China. In **Fig. 3b**, the AI-generated maturity scores are visually presented and align closely with human perception, although some misclassifications remain. These can be filtered out using thresholding strategies as demonstrated in **Fig. 3c**.

It is hypothesized that such human-like image-semantic understanding arises from the model's interpretation of not only color features (e.g., the word "yellow" used as a prompt did not strictly correspond to the model's assigned maturity scores) but also more comprehensive features such as orange, red, or green hues, as well as texture information, as indicated in the model's official documentation. Moreover, the proposed open-ended, natural language querying approach facilitates voice-based usage by farmers and enhances accessibility for farmers speaking different languages worldwide. Apart from maturity assessment, citrus images also hold significant potential for semantic applications in pest and disease monitoring (*Zongyin et al., 2025*).

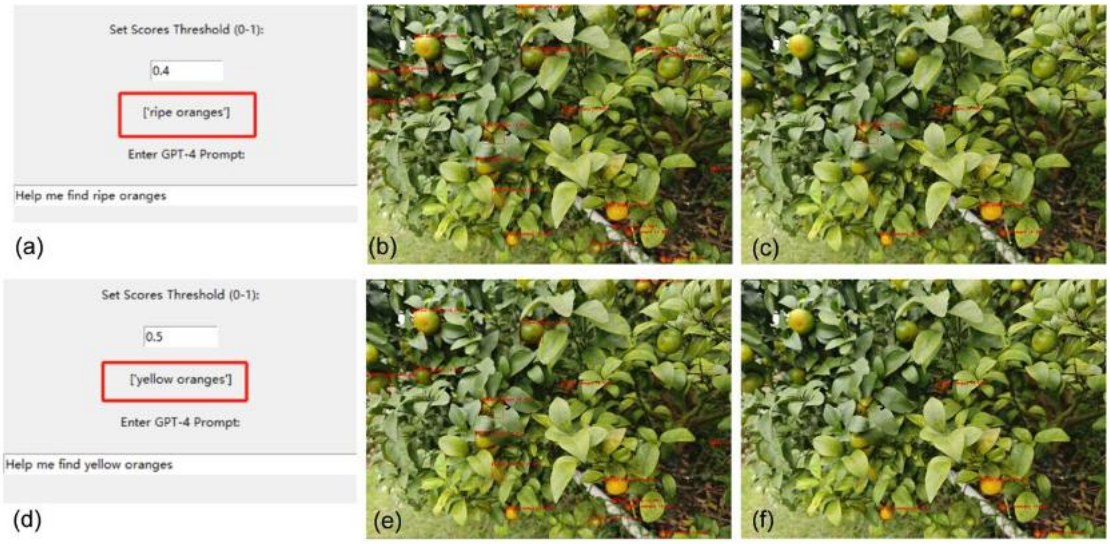


Fig. 3 - Semantic understanding ability.

(a) Questioning and extracting vocabulary (the meaning of ripe fruit); (b) The threshold score is 0.25; (c) The threshold score is 0.4; (d) Questioning and extracting vocabulary (the meaning of fruit color); (e) The threshold score is 0.35; (f) The threshold score is 0.5.

Differences from other model applications

Fig. 4 compares OWLv2 with two widely used publicly available models on Hugging Face, using both network resource images and our own dataset. Targets with a screening score greater than 0.5 were marked for evaluation. OWLv2 was more aggressive in detecting oranges and identified a greater number of fruits overall, though it also produced some misclassifications. It is important to note that these comparison models are not zero-shot models; they require training with annotated datasets. Despite this, OWLv2, trained on a billion-level text-image dataset with strong computational support, demonstrated comparable or even superior performance in certain tasks. While general-purpose models remain effective for simple detection tasks, integrating OWLv2 with APIs such as GPT or DeepSeek further lowers the barrier to its practical application.

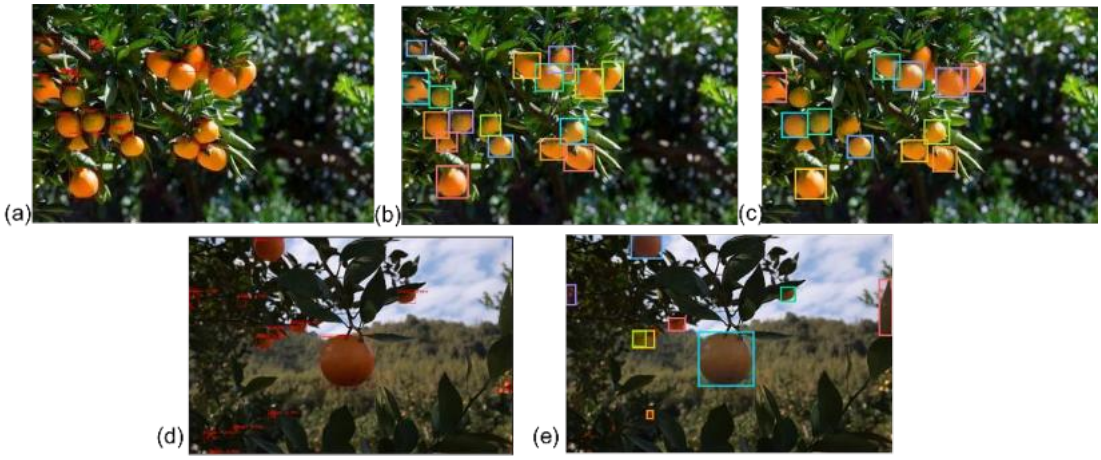


Fig. 4 - Comparison of annotation capabilities across models

(a) Google/owlv2 (network diagram); (b) Facebook/detr-resnet-50 (network diagram); (c) Hustvl/yolos-tiny (network diagram); (d) Google/owlv2 (real-world image); (e) Facebook/detr-resnet-50 (real-world image).

Comparative Evaluation of Zero-shot Foundation Model and YOLO11 for Cross-Domain Object Detection

To benchmark local deployment, zero-shot OWLv2 was compared with a pre-trained YOLO11 model. To prioritize generalization, a cross-domain evaluation was conducted using a novel, independent dataset. This protocol ensures a fair comparison by testing YOLO11 on unseen, heterogeneous data rather than its original training distribution, matching the zero-shot conditions of OWLv2. On its internal validation set, the pre-trained YOLO11 achieved a Precision of 0.9250, a Recall of 0.8333, an F1-score of 0.88, and an mAP of 0.9199. For the comparative test, 50 representative images were selected as the common test set for both the zero-shot OWLv2 and the pre-trained YOLO11 models.

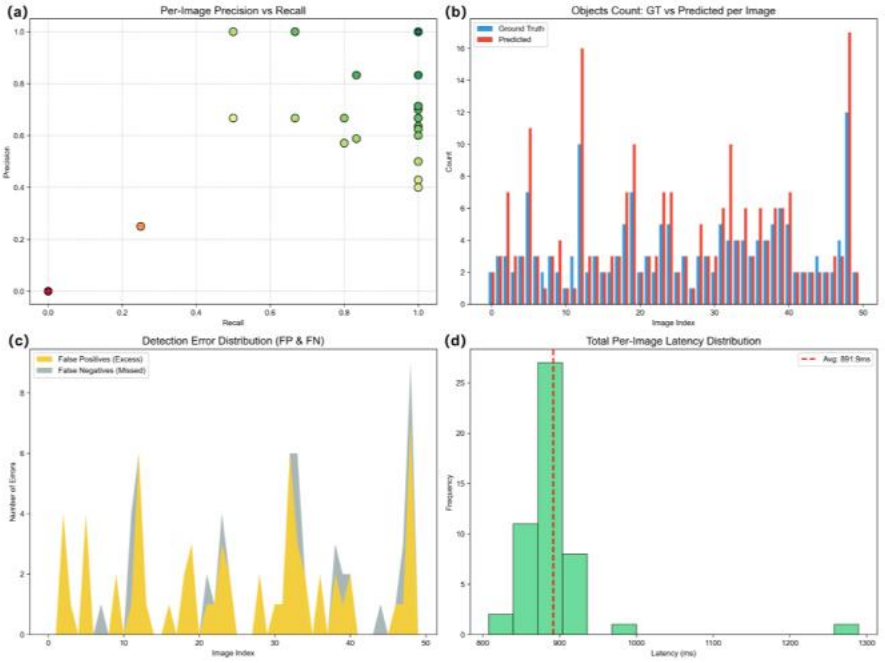


Fig. 5 - Comprehensive performance evaluation of the zero-shot OWLv2 model

(a) PR scatter plot showing per-image precision and recall distribution; (b) Object count consistency between GT and predicted labels; (c) Error distribution identifying fluctuations in FP and FN; (d) Latency distribution with a mean processing time of 891.9 ms.

Table 3

Performance comparison between zero-shot OWLv2 and YOLO11 on the orange dataset

Method	TP	FP	FN	Precision	Recall	F1-Score	mIoU	mAP	Avg. Computation Latency (ms)
OWLv2	158	63	16	0.7149	0.908	0.8000	0.8482	0.8301	257.7
YOLO11	120	27	54	0.8163	0.6897	0.7477	0.8438	0.6055	116.2

The performance of OWLv2 is evaluated from four dimensions **(Fig. 5)**. As illustrated in the Per-Image Precision vs. Recall plot, a significant majority of the data points are clustered in the high-recall and high-precision region (upper right), demonstrating the model's robustness. The Objects Count comparison reveals a high degree of consistency between the Ground Truth (GT) and predicted labels across varying object densities. Regarding error analysis, the Detection Error Distribution suggests that False Positives (FP) constitute the primary source of error compared to False Negatives (FN), indicating a slight tendency towards over-detection in cluttered environments. Furthermore, the Latency Distribution analysis confirms the model's computational efficiency; the total per-image latency follows a near-normal distribution with an average of 891.9 ms. In fact, this is because the program additionally outputs annotated images, while the actual computation latency is only 257.7 ms (**Tab. 3**) and Average DeepSeek latency (Run once before the computational procedure) is only 598.3 ms.

Although the original YOLO validation set achieved a Precision of 0.9250 and an F1-score of 0.88, validation performance typically exceeds that of the test set. Upon switching to the specific test dataset, YOLO11 yielded a Precision of 0.8163 and an F1-score of 0.74, which are considered reasonable within this context. However, owing to a more aggressive detection strategy, OWLv2 significantly outperformed YOLO in terms of Recall (0.9080 vs. 0.6897) while maintaining a respectable Precision of 0.7149. Consequently, OWLv2 achieved a superior F1-score of 0.80. While both models exhibited comparable Mean Intersection over Union (mIoU) values (0.8482 and 0.8438, respectively), OWLv2 demonstrated superior robustness with a substantially higher mAP (0.8301 vs. 0.6055), making it more suitable for detection tasks in complex environments.

Error Analysis of Zero-Shot Foundation Model Annotation via Local Deployment

A comparative review of the OWLv2 outputs against the manually annotated dataset reveals that human annotators often overlook small or partially concealed targets due to visual fatigue or resolution constraints. Consequently, traditional supervised training sets may not fully encompass all ground-truth oranges present in a scene. The zero-shot foundation model consistently identifies minute targets that are only discernible upon magnification, highlighting its significant utility for pre-annotation workflows. This suggests a paradigm shift where foundation models perform automated labeling, leaving humans to act solely as verifiers to mitigate the experiential errors commonly introduced during manual dataset construction.

Detailed manual verification of the detection errors indicates that false positives are primarily driven by extreme texture variations resulting from lighting and shadow fluctuations. Specifically, overexposure (pure white) and deep shadows (black) can lead the model to fragment a single fruit into 2 or 3 separate detections (e.g., as shown on the **Fig. 6** left, where one orange is misidentified as two).



Fig. 6 - Comparison of Zero-Shot OWLv2 and Manual Annotation

(a) Annotations generated by the foundation model under zero-shot conditions;
(b) Standard manual annotations derived from the laboratory's existing dataset.

Discussion

The performance of the zero-shot model demonstrates a "detect-at-all-costs" strategy, prioritizing comprehensive recall over strict precision. This "detect-all" capability is effective not only for close-range operations but also for long-distance path planning by identifying distant fruits in advance. *Jin (2020)* applied visual servo control to agricultural picking robots, emphasizing accurate target positioning as critical for automated harvesting but limited by conventional image detection pipelines. In practice, orange localization was also achieved to assist grasping using traditional object recognition schemes in the previous work, but the factor that most significantly affected operational efficiency was unrelated to fruit coordinate positioning *(Lan et al., 2026).* In this study, switching the detection framework from YOLO11 to OWLv2 only increased the average inference time by approximately 140 ms.

Beyond validating its basic feasibility, the primary advantage of such foundation models lies in their rich semantic information. For instance, the model can theoretically analyze crop growth stages based on prompts like "ripe oranges". However, since the foundation model is pre-encapsulated, the exact semantic threshold for concepts like "maturity" remains a "black box" during API calls. Because both semantic prompts and image features are likely abstracted into high-dimensional vectors, the internal understanding of these concepts can only be calibrated through iterative adjustments of the confidence scores.

In this study, the integration of the Segment Anything Model (SAM) was investigated, as illustrated in **Fig. 7**. SAM offers general image segmentation based on object boundaries, complementing OWLv2's semantic recognition. While SAM does not always outperform OWLv2, their combination could enable instance detection and area measurement for applications such as yield estimation and disease monitoring. Future versions like SAM2 may also support video stream segmentation for real-time use in agricultural machinery or UAVs.

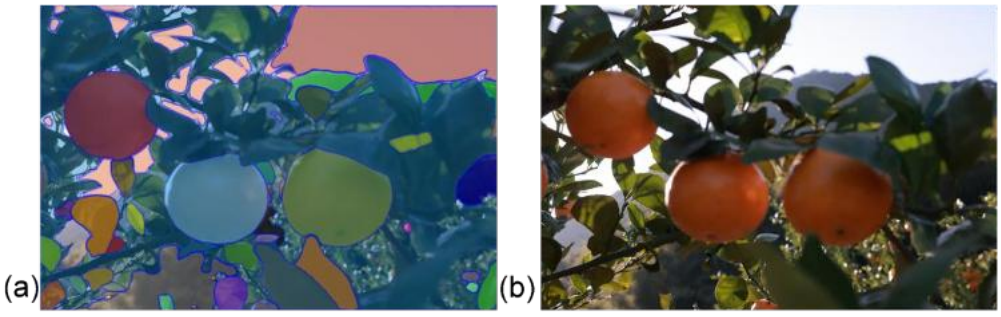


Fig. 7 - Using the SAM model to segment oranges
(a) segmentation image; (b) visible light image.

Moreover, OWLv2 shows certain advantages over models like YOLO, as it requires no annotated datasets or retraining to recognize new classes or descriptive attributes. This makes it suitable for backend decision-making, semantic analysis, and rapid dataset annotation. Its ability to interpret terms like "ripe" or color variations via natural language is valuable in diverse crop scenarios. However, for real-time orchard operations requiring high-speed and lightweight models, YOLO remains more appropriate due to its faster inference and computational efficiency.

CONCLUSIONS

This work presented a zero-shot fruit recognition and annotation tool by integrating OWLv2 with GPT or DeepSeek to support multilingual, natural language queries. The system showed strong generalizability and semantic understanding, allowing recognition of unseen fruit categories and descriptive attributes without retraining. Its ability to interpret complex human language inputs makes it practical for deployment in diverse agricultural environments. Cross-domain experimental results verified that the framework possesses superior generalization capabilities compared to traditional supervised models like YOLO11 when encountering unseen environments. Future work will focus on integrating segmentation models and optimizing inference speed to meet the real-time requirements of smart agriculture.

ACKNOWLEDGEMENT

This study was funded by The Special Fund for Science and Technology Innovation Strategy of Guangdong province (the "Climbing Plan"), [pdjh2025bc042], the University Students' Innovation and Entrepreneurship Training Program [S202510564054S], the "111 Center" [D18019].

DATA AVAILABILITY

Code and data are available upon request from the corresponding author.

DECLARATIONS OF INTEREST

The authors declare no competing financial interest.

REFERENCES

[1] Dosovitskiy, A., Beyer, L., Kolesnikov, A., Weissenborn, D., Zhai, X., Unterthiner, T., ... & Houlsby, N. (2020). An image is worth 16x16 words: Transformers for image recognition at scale. *arXiv preprint arXiv:2010*.11929.

[2] Espinoza, S., Aguilera, C., Rojas, L., & Campos, P. G. (2023). Analysis of fruit images with deep learning: a systematic literature review and future directions. *IEEE Access*, 12, 3837-3859.

[3] Jin, Y. (2020). Recognition technology of agricultural picking robot based on image detection technology. *INMATEH-Agricultural Engineering*, 62(3).191-200.

[4] Kirillov, A., Mintun, E., Ravi, N., Mao, H., Rolland, C., Gustafson, L., ... & Girshick, R. (2023). Segment anything. *arXiv preprint arXiv:2304*.02643.

[5] Lan, Y. B., Bian, Z. H., Qin, Y. D., et al. (2026). Current status and future prospects of agricultural drones in multi-scenario application in China. *Transactions of the Chinese Society of Agricultural Engineering (Transactions of the CSAE)*, x(x), 611-627. doi: 10.11975/j.issn.1002-6819.202510102.

[6] Lan, Y., Song, H., Wang, Y., Liu, X., Li, X., & Li, Y. (2026). Collision-free grasp path planning for citrus-picking manipulator based on ALH-SAC algorithm. Nongye Jixie Xuebao / *Transactions of the Chinese Society of Agricultural Machinery*, 57(5), 82–94.

[7] LI, Z., LI, S., LAN, W., LI, S., CHEN, Y., & LV, P. (2025). Strawberry Fruit Detection Method Based on Improved YOLOv8n. *INMATEH-Agricultural Engineering*, 76(2).697-710.

[8] Minderer, M., Gritsenko, A., & Houlsby, N. (2023). Scaling Open-Vocabulary Object Detection. *arXiv preprint arXiv:2306*.09683.

[9] Mimma, N. E. A., Ahmed, S., Rahman, T., & Khan, R. (2022). Fruits classification and detection application using deep learning. *Scientific Programming*, 2022(1), 4194874.

[10] Minderer, M., Gritsenko, A., Stone, A., Neumann, M., Weissenborn, D., Dosovitskiy, A., ... & Shen, Z. Simple open-vocabulary object detection with vision transformers. *arXiv (2022). arXiv preprint arXiv:2205*.06230.

[11] Qin Y, Jia W. Real-time monitoring system for rabbit house environment based on NB-IoT network. *Smart Agric*. (2023) 5:155–65. doi: 10.12133/j. smartag.SA202211008.

[12] Qin, Y., Jia, W., Sun, X., & Lv, H. (2023). Development of electronic nose for detection of micro-mechanical damages in strawberries. *Frontiers in Nutrition*, 10, 1222988.

[13] Qing, J., Deng, X., Lan, Y., & Li, Z. (2023). GPT-aided diagnosis on agricultural image based on a new light YOLOPC. *Computers and electronics in agriculture*, 213, 108168.

[14] Radford, A., Kim, J. W., Hallacy, C., Ramesh, A., Goh, G., Agarwal, S., ... & Sutskever, I. (2021, July). Learning transferable visual models from natural language supervision. In *International conference on machine learning*. pp. 8748-8763. PMLR.

[15] Tang, Y., Sun, J., Zhang, Y., Wang, C., Zhang, Z., & Shi, F. (2025). Kiwifruit Flower Detection Using an Optimized YOLOv11n Architecture. *INMATEH-Agricultural Engineering*, 77(3). 44-53.

[16] Tan, C., Xu, X., & Shen, F. (2021). A survey of zero-shot detection: Methods and applications. *Cognitive Robotics*, 1, 159–167.

[17] Wei, X., Wang, B., Cao, X., Zhou, H., Wu, Z., & Wang, Z. L. (2023). Dual-sensory fusion self-powered triboelectric taste-sensing system towards effective and low-cost liquid identification. *Nature Food*, 4(8), 721-732.

[18] Xu, J., Liu, S., Vahdat, A., Byeon, W., Wang, X., & De Mello, S. (2023). Open-vocabulary panoptic segmentation with text-to-image diffusion models. In *Proceedings of the IEEE/CVF Conference on Computer Vision and Pattern Recognition*. pp. 2955-2966.

[19] Zhang, Y., Shao, Y., Tang, C., Liu, Z., Li, Z., Zhai, R., ... & Song, P. (2025). E-CLIP: An Enhanced CLIP-Based Visual Language Model for Fruit Detection and Recognition. *Agriculture*, 15(11), 1173.

[20] Zongyin, C., Cui, L., Yan, X., Han, Y., Yang, W., Yilong, Z., ... & Yubin, L. (2025). Field Evaluation of Different Unmanned Aerial Spraying Systems Applied to Control Panonychus citri in Mountainous Citrus Orchards. *Agriculture*, 15(12), 1283.

A LIGHTWEIGHT TEA BUD DETECTION METHOD FOR ONLINE GRADING OF FRESH TEA LEAVES BASED ON IMPROVED YOLOV11N

/

一种基于改进 YOLOv11n 的面向茶鲜叶在线分级的轻量化茶芽检测方法

Wenguang ZHENG *), Xinyong SHI, Rongyang WANG
School of Mechanical Engineering & Automation, University of Science and Technology Liaoning, Anshan 114000, China
School of Intelligent Manufacturing and Elevator Mechanics, Huzhou Vocational and Technical College, Huzhou 313000, China
Tel: +8618641268671; E-mail: zhengwg@ustl.edu.cn
Corresponding author: Wenguang Zheng
DOI: https://doi.org/10.35633/inmateh-79-12

Keywords: *object detection, fresh tea leaves, YOLOv11, lightweight model*

ABSTRACT

To address the limitations of computational resources and the stringent real-time stability requirements in post-harvest online grading of fresh tea leaves, this study proposes a lightweight object detection method oriented toward efficient deployment. The YOLOv11n network was selected as the baseline model. A StarNet backbone was introduced to enhance nonlinear inter-channel interactions while reducing the complexity of feature extraction. In addition, a DySample dynamic upsampling module was employed to predict content-adaptive sampling locations, thereby improving multi-scale feature reconstruction under lightweight constraints. Furthermore, a wavelet-based pooling structure was designed to perform structure-aware frequency-domain decomposition, preserving critical edge and texture information while reducing redundant computation. The Inner-MPDIoU loss function was also adopted to calculate overlap consistency within a compact core region, thereby improving bounding-box localization stability for fine-grained structures. Based on these integrated improvements, the lightweight YOLOv11-SDWI detection model was developed. Experimental results demonstrated that the proposed model achieved an accuracy of 89.5%, with only 4.9 GFLOPs and 1.89 M parameters. To further verify its engineering applicability, the algorithm was encapsulated into a complete visual software system specifically designed for fresh tea leaf sorting. The developed system provides a functional interface for real-time detection, effectively bridging theoretical algorithm design and practical agricultural applications, and establishing a solid software foundation for future deployment on physical sorting equipment.

摘要

为了解决采后鲜茶在线分级中计算资源有限以及对高实时稳定性的严格要求，本文研究了一种面向高效部署的轻量化目标检测方法。以 YOLOv11n 网络为基线模型。引入 StarNet 主干网络以增强非线性通道间交互并降低特征提取复杂度。采用 DySample 动态上采样模块来预测内容自适应的采样位置，从而在轻量化约束下改善多尺度特征重建。进一步设计了基于小波的池化结构来执行结构感知的频域分解，在保留关键边缘和纹理信息的同时减少冗余计算。此外采用 Inner MPDIoU 损失在紧凑的核心区域上计算重叠一致性，增强了细粒度结构的边界框定位稳定性。基于这些系统性改进，构建了 YOLOv11 SDWI 轻量化检测模型。实验结果表明，所提模型实现了 89.5%的精度，同时仅需 4.9 G 浮点运算数和 1.89 M 参数量。为了验证其工程应用潜力，该算法被封装成专为鲜茶分拣量身定制的完整视觉软件系统。这种系统级实现为实时检测提供了功能性界面，成功弥合了理论算法设计与实际农业应用之间的差距，并为未来在物理分拣设备上的部署奠定了坚实的软件基础。

INTRODUCTION

Tea grading has become a crucial process in modern tea production, as stable and efficient quality classification directly affects product value, consumer acceptance, and processing efficiency.

In practical production, fresh tea leaves are typically graded according to external characteristics such as bud–leaf morphology, tenderness, integrity, and size. Common grading categories include single bud, one bud with one leaf, one bud with two leaves, and broken leaves. Early studies on tea quality analysis and classification mainly relied on traditional image processing and machine learning methods.

Wenguang Zheng, Assoc. Prof. Ph.D. Eng; Xinyong Shi, M.S. Stud. Eng.; Rongyang Wang, Prof. Ph.D. Eng.

For example, multispectral features were extracted using wavelet transforms, and Chinese famous tea classification was achieved via a multi-class least square support vector machine *(Li X. et al., 2011)*. Hyperspectral imaging was employed to model and quantitatively characterize the evolution of color and category during the tea drying process *(Xie C. et al., 2014)*. In addition, tea image classification was achieved based on handcrafted texture features, such as local binary patterns *(Tang Z. et al., 2015)*. These methods typically depend on manually designed features combined with shallow classifiers, and can achieve reasonable performance under controlled experimental conditions. However, due to the lack of end-to-end learning capability, their generalization ability is limited, making it difficult to meet the comprehensive requirements for robustness, accuracy, and scalability in practical applications.

With the rapid development of computer vision and deep learning technologies, convolutional neural network (CNN)–based object detection methods have demonstrated significant advantages in target recognition and localization under complex backgrounds by automatically learning hierarchical feature representations from large-scale data. The Faster R-CNN framework was applied to tea bud recognition and detection, demonstrating significant effectiveness in handling complex poses, occlusions, and background interference *(Xu G. et al., 2020; Zhu H. et al., 2022)*. In addition, a variety of deep learning paradigms have been explored for tea-related visual perception tasks. These include discriminative pyramid networks for semantic segmentation *(Hu G. et al., 2021)*, Mask R-CNN for joint detection and picking-point localization *(Wang T. et al., 2023)*, SSD-based feature fusion models for enhanced bud detection *(Chen B., Yan J., 2021)*, and Transformer-based frameworks such as RT-DETR-Tea to strengthen global feature modeling and multi-scale semantic fusion in complex environments *(Chen Y. et al., 2024)*. These studies indicate that, compared with traditional approaches, deep learning–based object detection algorithms achieve higher detection accuracy and better efficiency in complex environments.

The YOLO family of models represents a typical class of single-stage object detection methods. Through continuous optimization of network architectures and feature fusion strategies, these models have achieved a favorable balance between detection accuracy and computational efficiency and have gradually been introduced into complex agricultural vision scenarios. In tea bud detection research, existing studies have mainly focused on suppressing background interference and modelling scale variation. A two-level fusion framework, combining YOLOv3-based detection with DenseNet201-based classification, was constructed to improve the recognition accuracy of tea bud targets *(Xu W. et al., 2022)*. In addition, a refined TBC-YOLOv7 algorithm was developed by integrating Transformer modules, a bidirectional feature pyramid, and coordinate attention mechanisms, while employing the SIOU loss function to accelerate convergence and enhance detection accuracy *(Wang S. et al., 2023)*. Regarding the YOLOv8 framework, various optimization strategies have been explored. For instance, an occlusion-aware dual-attention mechanism was introduced to enhance model robustness under complex backgrounds and partial occlusions for tea pest and disease detection *(Wu Y. et al., 2025)*. Furthermore, YOLOv8-based models have been improved through attention mechanisms, multi-scale feature fusion, enhanced convolutional structures, Transformer modeling, and regression loss optimization, effectively increasing tea leaf detection and grading accuracy under leaf stacking conditions in complex environments *(Tang X. et al., 2025; Xia Y. et al., 2024; Zhao X. et al., 2024)*. In summary, existing studies indicate that YOLO-series models are capable of effectively handling target scale variation and complex background interference while maintaining real-time performance, thereby providing a solid technical foundation for the development of online tea leaf detection and grading systems.

Although the YOLO family has demonstrated strong performance in real-time object detection, there remains considerable room for optimization in specific application scenarios. In recent years, lightweight optimization of YOLO-based models has become an active research topic, with improvements explored in backbone design, feature fusion, sampling strategies, and training objectives. For instance, the YOLO-PEFL model was developed by replacing the YOLOv4 backbone with ShuffleNetV2 and adjusting anchor sizes, reducing model size by approximately 80% while maintaining 96.71% accuracy for efficient pear flower detection *(Wang C. et al., 2022)*. Similarly, the PAG-YOLO architecture was introduced, incorporating spatial and channel attention mechanisms with a specialized loss function to improve small-ship detection accuracy with negligible computational overhead *(Hu J. et al., 2021)*. To further reduce complexity, the GhostNet-YOLOv5 framework was proposed by integrating a GhostNet backbone, achieving 76.31% accuracy with only 5.94 million parameters and a 10 MB weight size *(Cao M. et al., 2022)*. Another approach involved adopting ShuffleNetV2 as the YOLOv5 backbone combined with channel pruning in the neck and detection head, compressing the model to 27% of its original size *(Zhang S. et al., 2023)*.

Additionally, a lightweight tea bud detection model was constructed by introducing GhostConv, bottleneck attention modules, and weighted feature fusion into YOLOv5, which increased mAP by 9.66% while significantly reducing FLOPs and parameters *(Gui Z. et al., 2023)*. Recent studies have also focused on optimizing bounding box regression loss functions to enhance training stability and performance under constrained model capacities.

However, existing studies have mainly focused on object detection during tea garden picking or in complex natural scenes, while relatively less attention has been paid to post-harvest grading, which is a critical stage in the processing pipeline. Therefore, this paper focuses on the research scenario of post-harvest fresh tea leaf grading equipment. Under this operating condition, fresh tea leaves, after mechanical pre-screening, are fed into intelligent sorting equipment, within which multi-stage single-row conveying devices are used to orderly transport and spread the tea leaves, so that they present a low-occlusion and relatively regular arrangement during the visual detection stage. Therefore, under this application background, how to construct a lightweight detection model that balances computational efficiency, detection accuracy, and engineering deplorability remains an urgent problem to be solved. Based on this, this paper proposes an improved lightweight object detection framework, YOLOv11-SDWI. The proposed method performs coordinated optimization from both the network architecture and training strategy levels, enhancing feature representation capability and regression stability while maintaining a compact model structure. At the same time, a fresh tea leaf dataset oriented toward post-harvest online grading scenarios is constructed to provide data support for subsequent model training and evaluation. Experimental results show that the proposed method can maintain competitive detection performance while significantly reducing computational complexity and parameter scale, verifying its engineering application potential in practical tea sorting systems.

MATERIALS AND METHODS

YOLOv11 network improvements

The YOLO family has continuously evolved in the field of object detection, becoming a representative technical framework with significant influence and broad practical adoption *(Ge Z. et al., 2021; Redmon J., Farhadi A., 2017)*. Multi-scale feature representation and extraction capabilities have been further enhanced in YOLOv11 through improved backbone and neck architectures, as well as the introduction of modules such as C3K2, SPPF, and C2PSA, demonstrating superior performance for small-object detection in complex scenes *(Khanam R., Hussain M., 2024)*. Given that tea buds are small targets and traditional methods often suffer from insufficient accuracy or excessive computational overhead, YOLOv11n was selected as the baseline model for further design and optimization in this study.

To address the real-time requirements and computational constraints in fresh tea leaf sorting, this study develops the YOLOv11-SDWI model based on the YOLOv11n baseline. This architecture integrates the StarNet backbone, the DySample dynamic upsampling module, the Wavelet Pooling downsampling module, and the Inner-MPDIoU bounding box regression loss function. The structural details of the proposed YOLOv11-SDWI network are illustrated in Figure 1.

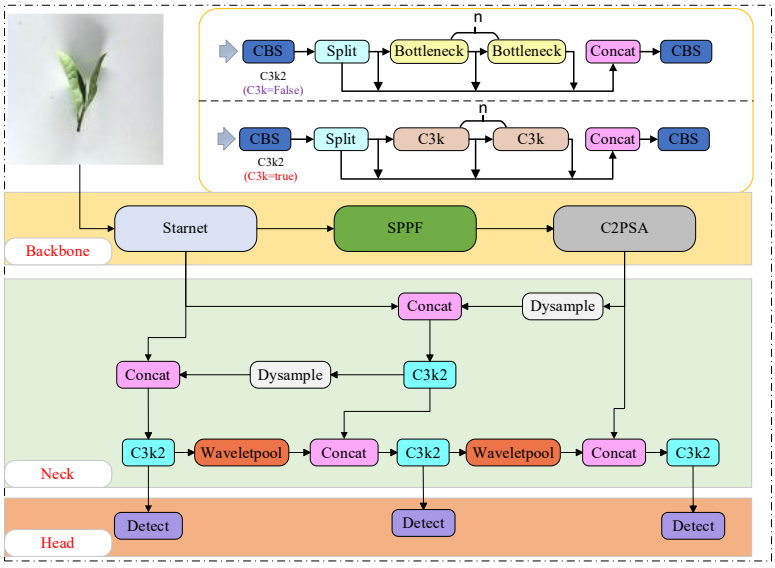


Fig. 1 - Architecture of the proposed YOLOv11-SDWI lightweight fresh tea leaf detection network

Lightweight Backbone Optimization Using StarNet

In post-harvest fresh tea leaf online grading scenarios, detection models are typically deployed on edge devices, where computational and storage resources are limited and long-term stable real-time operation is required. Therefore, the backbone network must maintain sufficient feature representation capability under low computational cost and a small parameter budget. Traditional convolutional backbones usually enhance representation by increasing network depth or channel width, which significantly increases computational and storage overhead, while channel interactions are mainly modelled through linear aggregation, limiting their ability to capture complex feature combinations. To address these issues, this study introduces StarNet into the YOLOv11n backbone *(Ma X. et al., 2024)***Error! Reference source not found.**, leveraging star-shaped operations to enhance nonlinear inter-channel interactions. This design improves the effective feature output per unit of computation while preserving a compact architecture, thereby enabling a more efficient lightweight feature extraction backbone.

As illustrated in Fig. 2, StarNet adopts a stage-wise hierarchical architecture. After the initial convolutional stem, feature maps are progressively processed by multiple stages (Stage1–Stage4). Each stage consists of a down-sampling convolution followed by several stacked StarBlocks, enabling multi-scale semantic feature extraction with gradually increasing receptive fields. StarBlock is the fundamental building unit of StarNet, and its internal data flow is explicitly shown in the figure. Given an input feature with channel dimension d, the feature is first processed by a depth wise convolution (DW-Conv) to extract spatial information with low computational overhead. The resulting feature is then fed into two parallel fully connected (FC) branches that expand the channel dimension to 4d.One branch is activated by ReLU6, and the outputs of the two branches are fused through an element-wise multiplication operation. This operation introduces nonlinear inter-channel interactions without explicitly increasing the output channel dimension. The fused feature is subsequently projected back to dimension d through an FC layer and further refined by a DW-Conv. A residual connection is finally applied to combine the block input and output, ensuring stable feature propagation across stacked StarBlocks.

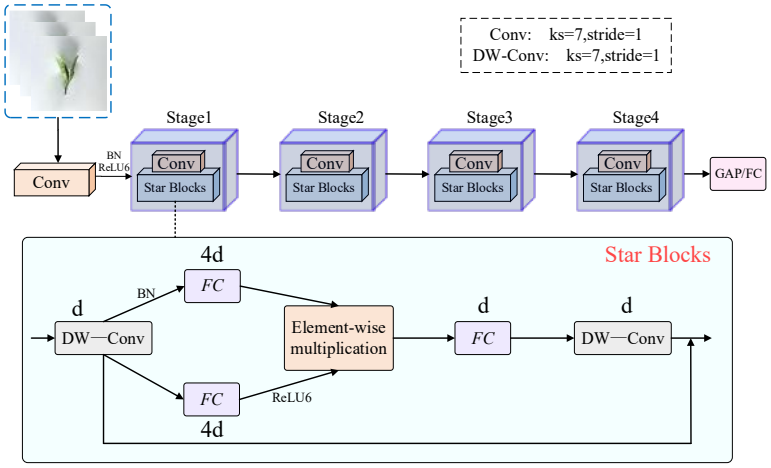


Fig. 2 - Schematic diagram of the StarNet backbone architecture

By stacking multiple StarBlocks within each stage, StarNet progressively enhances feature representation from low-level details to high-level semantics while maintaining a compact structure. When integrated into the YOLOv11 backbone, the input tea leaf image is sequentially processed by the stem convolution, StarNet backbone stages, and the subsequent neck for multi-scale feature fusion. This design provides compact yet discriminative feature representations for the detection head, which is particularly beneficial for lightweight deployment under resource-constrained edge environments.

DySample Upsampling Module

During multi-scale feature fusion, the upsampling module directly determines the spatial reconstruction quality of high-level semantic features. Conventional nearest-neighbor or bilinear interpolation relies on fixed sampling over regular grids that is independent of feature content; while computationally efficient, such methods often fail to accurately recover spatial structures near object boundaries, fine-grained textures, or regions with significant structural variation. To address this limitation, this paper introduces the DySample *(Liu W. et al., 2023)* upsampling module into the Neck of YOLOv11.

By predicting content-adaptive sampling locations, DySample enables learnable feature reconstruction, thereby enhancing the representation capability of multi-scale feature fusion under lightweight constraints.

As illustrated in Fig. 3, the overall workflow of DySample consists of two components: sampling coordinate construction and feature resampling. Given an input feature map $X \in \mathrm{R}^{C \times H \times W}$, the module first predicts a set of two-dimensional offset information through a lightweight linear mapping, and constructs a high-resolution sampling coordinate set S based on a regular initial grid. Subsequently, differentiable bilinear resampling is performed on the input feature X according to S, generating an output feature X' whose spatial resolution is increased to $sH \times sW$. Since the resampling process is differentiable with respect to the sampling coordinates, the prediction of sampling locations can be jointly optimized with the detection objectives during training, thereby enabling end-to-end adaptive upsampling.

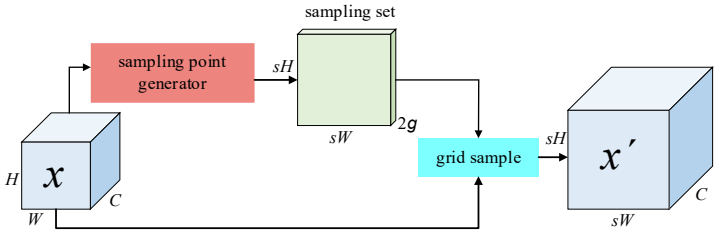


Fig. 3 - Overall workflow of the DySample upsampling module

During the construction of sampling coordinates, DySample achieves a balance between representation capability and computational complexity by adopting a grouped sampling + scope control strategy. As shown in the upper part of Fig. 4, under the static scope control mode, the module predicts an offset map O in the low-resolution feature domain via a linear mapping and applies a fixed scaling factor to constrain its magnitude, so that the initial sampling points are distributed around a regular grid. The offsets are then mapped to the high-resolution sampling grid through a spatial–channel rearrangement operation and added to the regular initial grid to obtain the final sampling coordinate set S. By constraining the maximum displacement of sampling points with a fixed scope, this strategy ensures structural stability of the sampling pattern while avoiding severe resampling instability caused by excessive offsets, making it suitable for regions with relatively smooth structural variations.

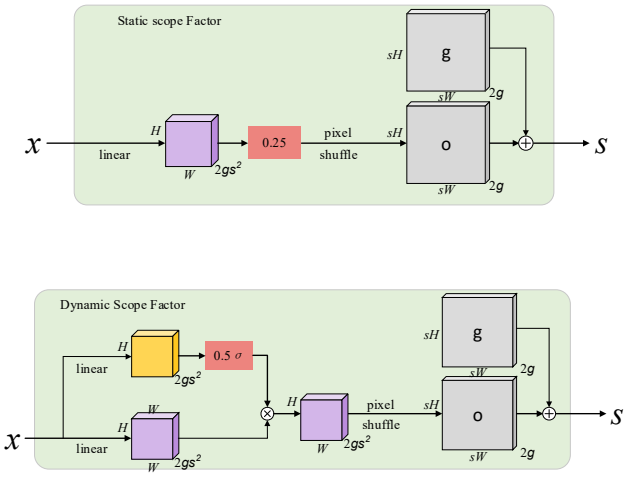


Fig. 4 - Static and dynamic scope control mechanisms in DySample

As illustrated in the lower part of Fig. 4, under the dynamic scope control mode, DySample further introduces an input-adaptive scale modulation factor on top of offset prediction. This factor is jointly applied with the predicted offsets to dynamically adjust the sampling displacement magnitude at each spatial location. Specifically, in flat regions or structurally simple areas, the displacement magnitude is automatically suppressed, causing sampling positions to remain close to the regular grid; in contrast, in edge regions or areas with significant structural variations, the displacement magnitude is adaptively amplified, thereby enhancing the sensitivity of sampling locations to spatial structure changes. Through this mechanism, DySample enables region-aware adaptive sampling without introducing a significant increase in computational cost, effectively accommodating spatial heterogeneity across different regions of the feature map.

As shown in Fig. 5, DySample provides the LP (Low-resolution to Pixel Shuffle) and PL (Pixel Shuffle to Low-resolution) offset prediction schemes. The LP structure predicts offsets directly in the low-resolution feature domain and maps them to the high-resolution sampling grid via spatial-channel rearrangement. The PL structure projects features into the high-resolution domain first to predict offsets, which are then reshaped to match the sampling coordinates. Both structures ultimately generate a sampling coordinate set *S* for the subsequent differentiable resampling process.

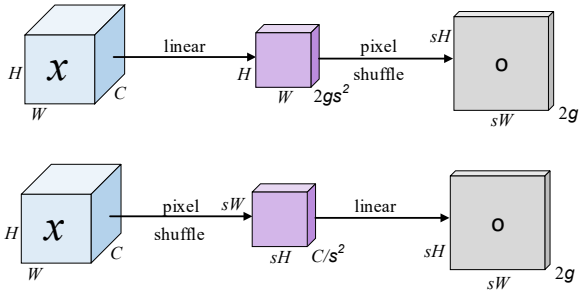


Fig. 5 - Offset prediction structures of DySample: LP and PL schemes

In summary, DySample reformulates the traditional rule-based upsampling process into a learning framework that integrates regular priors with content-adaptive offsets, enabling the upsampling module to actively adapt to object structures and scale variations during end-to-end training. In this work, simply replacing the original fixed-interpolation upsampling module in the YOLOv11 neck with DySample can significantly improve feature reconstruction quality with almost no increase in computational complexity.

Structure-Aware Downsampling Method Based on Wavelet Transform

In convolutional neural networks, downsampling operations are commonly employed to enlarge the receptive field and reduce feature resolution. However, traditional downsampling methods based on strided convolution or pooling essentially perform direct spatial subsampling, which easily introduces aliasing effects during resolution reduction and leads to irreversible loss of high-frequency structural information such as edges and textures. For post-harvest fresh tea leaf grading tasks, bud contours, leaf-edge morphology, and local structural variations constitute critical discriminative cues; degradation of such structural information at the downsampling stage can directly impair subsequent feature fusion and detection accuracy. To address this issue, this study introduces the WaveletPool downsampling module *(Williams T., Li R., 2018)*, which replaces conventional spatial downsampling with a structure-aware frequency-domain decomposition mechanism.

As shown in Fig. 6, WaveletPool applies a two-dimensional Discrete Wavelet Transform (DWT) to the input feature map. Given an input feature map *X*, WaveletPool does not perform spatial downsampling directly; instead, it first applies fixed wavelet filtering operations independently to each channel. Specifically, the module employs four fixed two-dimensional Haar wavelet kernels to convolve the input features in parallel, thereby decomposing the original feature representation into four sub-band components with clear physical interpretations: LL, LH, HL, and HH. Among them, LL represents the low-frequency approximation component, which mainly preserves global structure and contour information, while LH, HL, and HH correspond to high-frequency detail components in different directions, characterizing edges, textures, and local structural variations, respectively.

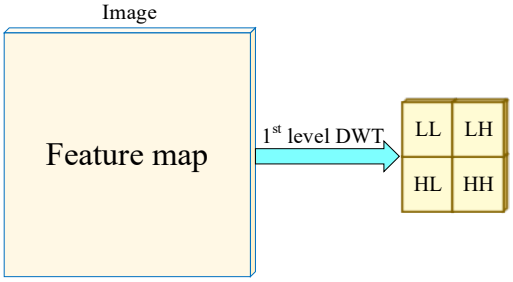


Fig. 6 - Schematic diagram of WaveletPool-based feature downsampling

This frequency-domain reorganization ensures structural integrity across scales. By preserving essential discriminative cues, WaveletPool facilitates precise feature reconstruction and target localization, effectively mitigating the information loss common in conventional lightweight designs.

Bounding Box Regression Constraint Based on Internal Region Consistency

In the post-harvest fresh tea leaf detection task, bud–leaf targets are often slender, small in scale, and subject to pronounced boundary variations. When bounding box regression is optimized solely by global overlap, it may suffer from boundary deviations that are difficult to further converge once the predicted and ground-truth boxes enter a high-overlap regime. To address this issue, this work introduces an Inner-IoU *(Wang D. et al., 2025)* based regression strategy: it computes overlap consistency on a more compact core region defined inside both boxes, and incorporates key geometric position offset constraints to strengthen the joint alignment of the target body and boundary structure under a lightweight setting.

As illustrated in Fig. 7, let the spatial resolution of the input feature map be $h \times w$. The predicted bounding box width and height in the feature space are denoted as w_{pred} and h_{pred}, respectively, while the corresponding ground-truth width and height are denoted as w_{gt} and h_{gt}. The top-left and bottom-right coordinates of the predicted bounding box are (x_1^{pred}, y_1^{pred}) and (x_2^{pred}, y_2^{pred}), respectively, and the corresponding ground-truth coordinates are (x_1^{gt}, y_1^{gt}) and (x_2^{gt}, y_2^{gt}).

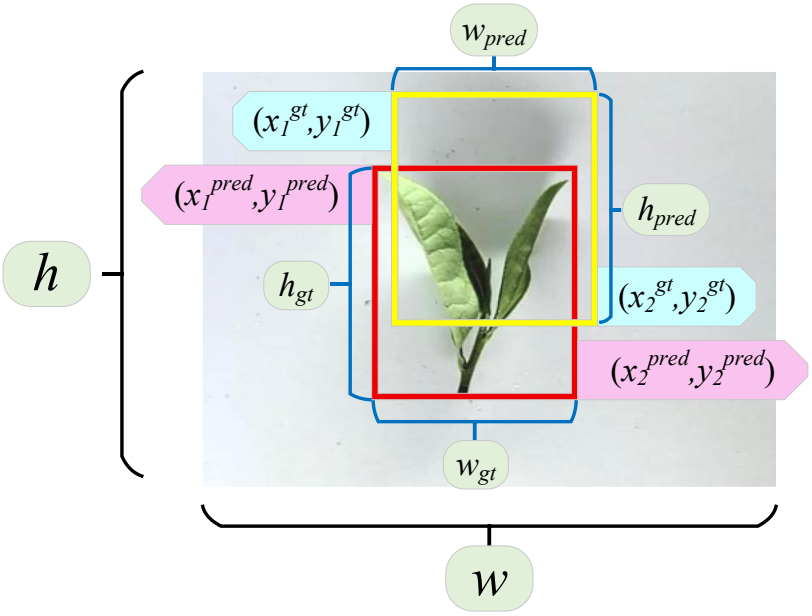


Fig. 7 - Illustration of Bounding Box Regression under Inner-IoU Constraint

At the level of region constraint, the regression supervision is not directly imposed on the complete predicted box and ground-truth box. Instead, a more compact core region is constructed inside both boxes, focusing exclusively on the effective area covered by the target body. This internal region is spatially constrained jointly by the predicted box and the ground-truth box, such that the overlap computation is concentrated on the target itself. As a result, interference from background regions and boundary redundancy is effectively reduced during the regression process. Under scenarios where the target size is small or the two boxes already exhibit a high degree of overlap, this constraint strategy can still maintain stable optimization signals, thereby improving the continuity and convergence of the regression process.

At the level of geometric position constraint, explicit modelling of the positional offsets between the predicted box and the ground-truth box is further introduced. As illustrated in Fig. 7, the spatial discrepancies at both the top-left and bottom-right corners of the predicted and ground-truth boxes are jointly incorporated into the regression constraint, enabling coordinated correction of boundary geometry across position, width, and height dimensions. To prevent imbalance in optimization strength across targets of different scales during regression, these positional offsets are normalized using the minimum enclosing region jointly formed by the two boxes. This normalization ensures that targets of varying sizes are subject to a consistent geometric constraint scale during training.

Through the combined effect of internal region consistency constraints and key positional distance awareness, the regression process no longer focuses solely on whether the predicted box covers the target, but further strengthens fine-grained alignment in terms of boundary geometry and spatial structure. Without introducing additional inference overhead, this strategy effectively improves the localization accuracy and stability of detection boxes in scenarios involving fine-grained structural details.

Intelligent Sorting Software System Design

To apply the proposed YOLOv11 SDWI model to actual fresh tea leaf sorting scenarios, a visual software system is designed in this study. The complete operational workflow of the software system is illustrated in Figure 8.

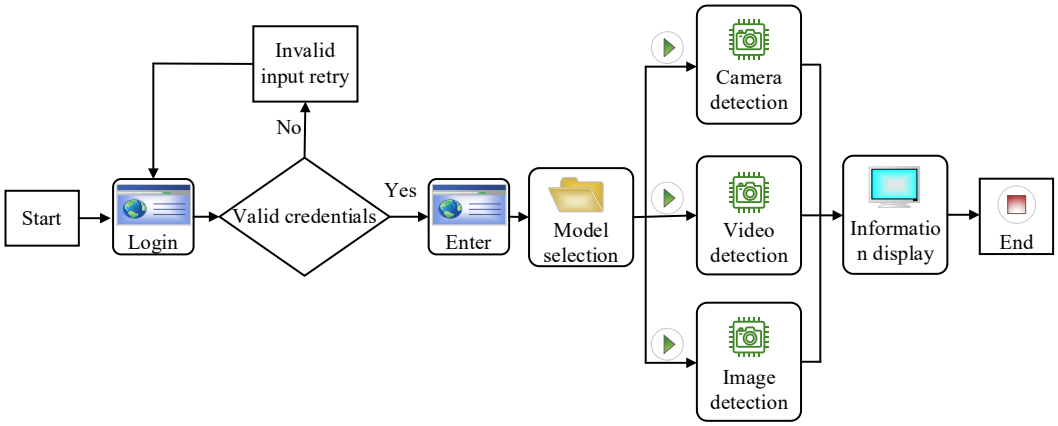


Fig. 8 - Operational workflow of the visual software system for fresh tea leaf sorting

The process begins with a user authentication stage where users input their account and password to log in. If the credentials are incorrect, the system prompts an error and requires re login. Upon successful authentication, the user enters the main interface and proceeds to the model selection module. Here the core inference engine loads the trained lightweight model weights. To accommodate diverse practical needs, the system offers 3 distinct detection modes including camera detection, video detection, and image detection. Once a specific mode is selected and visual data is input, the backend immediately executes feature extraction and bounding box regression. The system then continuously outputs target categories and confidence scores and bounding box coordinates to the front end information display module before ending the process. This logic ensures a seamless transition from data input to result visualization. The initial login interface of the developed intelligent system is presented in Figure 9, demonstrating a user friendly design tailored for practical agricultural applications.

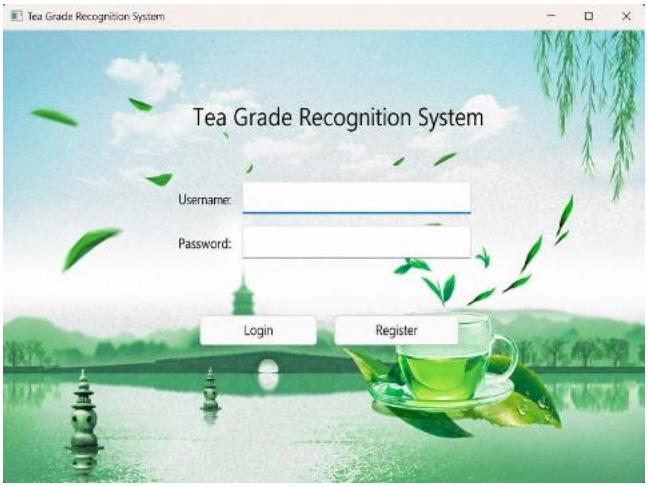


Fig. 9 - Initial graphical user interface of the developed intelligent sorting software

Image Acquisition and Dataset Construction

This study constructs an image dataset of post-screened fresh tea leaves for tea grade recognition and online grading. To address the stacking and occlusion that can occur during conveyance in intelligent sorting equipment and consequently degrade visual recognition, the multi-stage single-file conveying unit of the sorting system is used to spread and separate the leaves, so that they present a low-occlusion and relatively orderly arrangement on the conveyor belt, enabling the acquisition of image samples with clearer contours and texture details. Images are captured frame by frame using a Canon 6D II camera at a fixed viewpoint, covering diverse poses, scales, and local detail variations of fresh tea leaves during conveyance to enhance data diversity and representativeness.

During dataset construction, the raw images are first screened and organized, and samples with obvious blur, abnormal exposure, missing targets, or severe occlusion are removed. Ultimately, 1,563 valid images of fresh tea leaves of different grades are obtained to build the grading dataset. To ensure objective and reproducible training and evaluation, all images are randomly split into training, validation, and test sets at a ratio of 7:2:1.

Data Screening and Image Annotation

In this study, the collected fresh tea leaf images were manually annotated using the bounding-box labelling tool Labellmg to obtain object category labels and spatial localization information. According to the main picking morphology, fresh tea leaves were divided into four classes: one bud and one leaf, one bud and two leaves, one bud and three leaves, and one bud with multiple leaves, encoded as 0, 1, 2, and 3, respectively. To ensure a comprehensive dataset representation, a total of 8,267 instances were annotated across 1,563 images. According to the picking morphology, the instances were categorized into four classes: one bud with one leaf (1,923 instances), one bud with two leaves (2,196 instances), one bud with three leaves (1,747 instances), and one bud with multiple leaves (2,401 instances). The class definitions and index mapping are listed in Table 1.

Table 1

Categories of fresh tea leaves and corresponding codes

Category	Code
One bud with one leaf	0
One bud with two leaves	1
One bud with three leaves	2
One bud with multiple leaves	3

After annotation, labels were saved as XML files in the PASCAL VOC format. Each bounding box corresponds to a target instance, and a single image may contain multiple instances; the number of boxes varies with the number of fresh tea leaf targets in the image. Representative appearances and poses of the four classes are shown in Figure 10.

To support subsequent YOLO-based training and inference, a Python script was further used to convert the annotations from the VOC format to the YOLO format. After conversion, each image is associated with a TXT label file, where each target is represented as n, x, y, w, h. Here, n denotes the class index, x and y are the normalized horizontal and vertical coordinates of the bounding-box center, and w and h are the normalized width and height of the bounding box. To enhance the generalization ability of the model, data augmentation is applied to the training set during training to increase sample diversity.



Fig. 10 - Examples of fresh tea leaf samples from different grade categories

RESULTS

Experimental Environment and Training Strategy

The experimental platform in this study is based on the Ubuntu 20.04 operating system with Python 3.8. The deep learning framework used is PyTorch 1.10.0, with CUDA 11.3 configured to enable GPU-accelerated computation. In terms of hardware, the platform is equipped with a single NVIDIA GeForce RTX 3090 GPU with 24 GB of memory, an AMD EPYC 7642 48-Core Processor (20 vCPU), and 90 GB of system memory.

To ensure a rigorous and fair comparison, all models evaluated in this study, including the proposed YOLOv11-SDWI and various baseline architectures, were trained from scratch for 300 epochs without utilizing any pre-trained weights. Furthermore, a uniform input resolution was maintained across all experiments, and the standard data augmentation strategies provided by YOLOv11 were adopted. No individual hyperparameter tuning was performed for any specific model, as all hyperparameters were kept strictly consistent with the default configurations of the baseline YOLOv11 model.

Evaluation Metrics

This study evaluates model performance from two aspects: detection accuracy and computational efficiency. Commonly used metrics in object detection are adopted, including *Precision (P), Recall (R), and Mean Average Precision (mAP)*, as well as indicators reflecting model complexity and inference cost, such as the number of parameters (Params), floating-point operations (FLOPs), real-time inference speed measured in Frames Per Second (FPS), and model weight file size. These metrics are used to comprehensively and quantitatively assess the performance of the proposed improved model, and their definitions and meanings are described as follows.

$$P = \frac{TP}{TP + FP} \tag{1}$$

$$R = \frac{TP}{TP + FN} \tag{2}$$

$$AP = \int_0^1 (P \times R) dx \tag{3}$$

$$mAP = \frac{1}{N} \sum_{i=1}^{N} AP(i) \tag{4}$$

In the above definitions:

True Positives (TP) denote the number of actual positive samples that are correctly predicted as positive, that is, the number of targets correctly detected by the model;

False Negatives (FN) denote the number of actual positive samples that are incorrectly predicted as negative, that is, the number of targets missed by the model;

False Positives (FP) denote the number of actual negative samples that are incorrectly predicted as positive, that is, the number of background regions mistakenly detected as targets.

Ablation Experiments

To verify the effectiveness of the proposed lightweight improvement strategies, YOLOv11 is adopted as the baseline model, and multiple modifications are introduced from both network architecture and training strategy perspectives. Ablation experiments are conducted to analyze the impact of different module combinations on model performance. At the network architecture level, improvements are applied to the backbone network, feature fusion process, and downsampling strategy; at the training strategy level, the bounding box regression loss function is optimized. For clarity in ablation analysis, the symbols a, b, c, and d are used to denote the four modules StarNet, DySample, Wavelet Pooling, and Inner-MPDIoU, respectively, with their corresponding relationships listed in Table 2.

Table 2

Module Notation Used in Ablation Experiments

Module	StarNet	DySample	Wavelet Pooling	Inner-MPDIoU
Symbol	a	b	c	d

The ablation results are shown in Table 3. Introducing StarNet (a) effectively reduces the model parameters from 2.58 M to 1.95 M and the FLOPs from 6.3 G to 5.2 G, while improving the detection accuracy to 87.9%, demonstrating efficient model compression with stable performance. Further incorporating DySample (a+b) or Wavelet Pooling (a+c) leads to additional accuracy gains and reduced computational cost, indicating that these lightweight modules contribute positively when combined with an optimized backbone. When StarNet, DySample, and Wavelet Pooling are jointly integrated (a+b+c), the FLOPs and parameter count are reduced to 4.9 G and 1.89 M, corresponding to reductions of 22.2% and 26.7% compared with the baseline,

while achieving an accuracy of 89.1%. By further introducing Inner-MPDIoU to form the complete YOLOv11-SDWI model, the detection accuracy is increased to 89.5% without additional computational overhead, demonstrating effective synergy among the proposed components.

Table 3

Results of network ablation experiments

Model	Mean Average Precision mAP@0.5(%)	Floating Point Operations (FLOPs)/G	Number of Parameters (Params)(×10⁶)
YOLOv11	87.0	6.3	2.58
YOLOv11-SDWI	89.5	4.9	1.89
YOLOv11+a	87.9	5.2	1.95
YOLOv11+a+b	88.5	5.0	1.94
YOLOv11+a+c	88.1	5.2	2.11
YOLOv11+a+d	88.5	5.0	1.94
YOLOv11+b+c	88.7	6.3	2.53
YOLOv11+a+b+c	89.1	4.9	1.89

Backbone Network Comparison

To verify the applicability and advantages of the selected backbone network in lightweight object detection tasks, comparative experiments were conducted on several mainstream lightweight backbones under the same detection framework and unified training strategy. The compared backbones include StarNet, EfficientViT, FasterNet, MobileNetV4, and UniRepLKNet. The performance of different backbone networks was comprehensively evaluated from three aspects: detection accuracy, floating-point operations (FLOPs), and parameter scale. The corresponding results are presented in Table 4. Among these metrics, detection accuracy is measured using the mean average precision at an IoU threshold of 0.5.

Table 4

Performance Comparison of Different Lightweight Backbone Networks

Module	Mean Average Precision mAP@0.5(%)	Floating Point Operations (FLOPs)/G	Number of Parameters (Params)(×10⁶)
Starnet	87.9	5.2	1.95
efficientViT	87.3	7.9	3.73
Fasternet	86.8	9.2	3.90
Mobilenetv4	85.7	21.0	5.43
unireplknet	86.4	14.1	5.80

As shown in Table 4, StarNet achieves a mean average precision of 87.9% at an IoU threshold of 0.5, which is comparable to EfficientViT (87.3%) and higher than FasterNet, UniRepLKNet, and MobileNetv4. Despite similar detection accuracy, StarNet exhibits significantly lower computational complexity, requiring only 5.2G FLOPs, which is markedly less than EfficientViT (7.9G), FasterNet (9.2G), UniRepLKNet (14.1G), and MobileNetv4 (21.0G). In addition, StarNet contains only 1.95M parameters, approximately half of those in EfficientViT and FasterNet, and substantially fewer than UniRepLKNet and MobileNetv4.

Overall, these results indicate that while some backbone networks achieve competitive accuracy, they do so at the cost of increased computation or model size. In contrast, StarNet provides a more favorable balance between detection performance and efficiency, making it better suited for real-time, resource-constrained tea leaf sorting applications. Accordingly, StarNet is selected as the backbone network of the proposed lightweight detection framework.

Comparative Experiments with Different Detection Models

To comprehensively evaluate the potential and efficiency of the proposed YOLOv11-SDWI model for intelligent post-harvest tea leaf sorting, an extensive comparative analysis is conducted against a diverse range of mainstream object detection baselines. These baselines encompass classic two-stage detectors, conventional single-stage architectures, and multiple representative iterations within the YOLO series, thereby ensuring a thorough evaluation across different network paradigms. To guarantee fairness, all models are trained and validated on the identical dataset using strictly unified evaluation protocols. The assessment

focuses on the critical trade-off between detection accuracy and computational complexity, which is a key consideration for agricultural equipment with limited computing resources: the mean Average Precision at an IoU threshold of 0.5 (mAP@0.5) is utilized to quantify detection precision, while the parameter scale (Params) and floating-point operations (FLOPs) are simultaneously reported to gauge the lightweight characteristics and theoretical deployment feasibility. The detailed quantitative results are summarized in Table 5.

Table 5

Comparative evaluation of mainstream object detection models.

Model	Mean Average Precision mAP@0.5(%)	Floating Point Operations (FLOPs)/G	Precision *P*	Recall *R*	Number of Parameters (Params)(×10⁶)	MB
YOLOv5	83.5	4.1	77.4	78.3	1.76	77.3
YOLOv7-tiny	86.3	13.0	81.9	85.4	6.01	44.6
YOLOv8n	86.3	8.1	82.2	80.4	3.06	39.5
YOLOv9t	86.9	11.0	80.8	79.3	2.66	90.5
YOLOv10n	85.6	8.2	78.4	78.8	2.67	71.2
YOLOv11n	87.0	6.3	82.1	81.2	2.58	23.8
YOLOv12n	84.9	6.5	76.9	77.4	2.50	25.2
YOLOv13n	83.1	5.9	76.6	75.8	2.64	16.4
Fast RCNN	87.7	370.3	81.3	80.9	13.7	241.5
SSD	84.3	62.7	80.2	80.7	26.4	76.4
RTDETR	78.5	100.6	73.8	72.6	28.4	113.6
Ours	89.5	4.9	85.4	84.9	1.89	19.3

Based on the detailed data in Table 5, the proposed YOLOv11-SDWI model significantly outperforms mainstream detection networks across multiple core performance indicators. Compared to the baseline YOLOv11n model, our network not only reduces the parameter count from 2.58M to 1.89M but also increases the mean average precision from 87.0% to 89.5%, achieving a dual optimization of performance and computational complexity. This leading position remains robust during horizontal comparisons with other lightweight versions. For instance, YOLOv12n has a computational overhead of 6.5G floating point operations with a precision of only 84.9%, meaning our model delivers a detection capability 4.6% higher while maintaining a lower computational cost. Similarly, YOLOv13n exhibits a higher computational cost of 5.9G but only achieves a mean average precision of 83.1%. When compared with heavy two stage networks like Fast RCNN, the latter reaches an accuracy of 87.7% but imposes a computational burden over 75 times that of our model, making it entirely unsuitable for real-time processing in hardware restricted environments. On the other end of the spectrum, YOLOv5 possesses a slightly smaller calculation volume leading by 0.8G, yet its detection precision is 6.0% lower than our model. This substantial precision gap renders it inadequate for fresh tea processing tasks that demand high sorting quality.

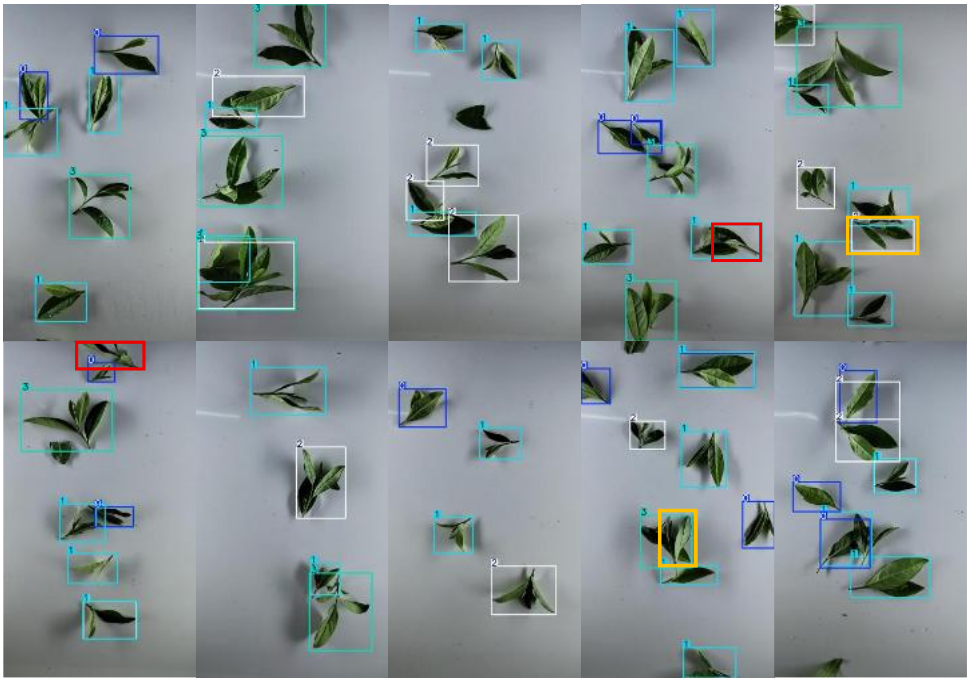
Synthesizing the experimental results above, the YOLOv11-SDWI model discovers an ideal balance between detection accuracy and lightweight design. It provides a high mean average precision of 89.5% and a precision rate of 85.4% using a minimal storage space of 19.3 MB. The data fully validate that the model effectively eliminates redundant computations and strengthens the recognition ability for tiny tea bud targets without sacrificing feature representation. This architecture combining high efficiency and accuracy demonstrates strong competitiveness in the specific agricultural application of intelligent fresh tea sorting. It offers solid technical support for portable agricultural equipment with limited computing resources, presenting significant theoretical value and practical deployment potential.

Model Visualization Analysis

Beyond computational efficiency, the proposed YOLOv11-SDWI demonstrates enhanced localization stability in complex backgrounds. Figure 11 presents a comparative visualization of 10 randomly selected representative test samples. Quantitative observation of these specific images reveals that the baseline model produced 4 false negatives (missed detections) and 3 false positives (misclassifying background leaves as buds). Following the structural optimizations, YOLOv11-SDWI successfully reduced the false negatives to 2 and the false positives to 2. This targeted reduction in visual detection errors confirms that the lightweight modifications effectively preserve critical structural features, minimizing both target omission under occlusion and background interference in practical grading scenarios.



YOLOv11 Detection Results



YOLOv11-SDWI Detection Results

False Negative False Positive

Fig. 11 - Comparison of actual detection effect before and after model improvement

Intelligent Sorting System Visualization and Functional Testing

Based on the preliminary software architecture design, this study successfully developed the fresh tea grade recognition system. The actual operational interface is illustrated in Figure 12. After importing the test image or video stream, the built in lightweight core inference engine executes target feature extraction and classification localization. The right information statistics panel is designed to monitor operational metrics including processing time and target count. This functional layout ensures that operators can intuitively observe the working status of the detection algorithm.



Fig. 12 - Main detection interface of the fresh tea grade recognition system

In the central main display area, the system precisely marks the spatial position of each tea bud through visualized colored bounding boxes and overlays the corresponding confidence scores above the targets. The detection results and location information data table at the bottom synchronously records the specific attributes of all tracked targets including categories and precise bounding box coordinate ranges. These structured coordinate and category output data are formatted to be directly transmittable as control commands to downstream mechanical sorting execution mechanisms in future applications. The overall software implementation proves that the lightweight model constructed in this study can be effectively packaged into an independent application with comprehensive visualization features. This development provides a necessary and reliable software foundation for the future physical integration of post-harvest fresh tea online grading equipment.

CONCLUSIONS

This paper proposes a lightweight object detection framework YOLOv11 SDWI for post-harvest fresh tea leaf online grading. By systematically optimizing the network architecture and training strategy of the baseline YOLOv11n model the proposed method achieves a comprehensive enhancement in both detection accuracy and computational efficiency. Experimental results demonstrate that the YOLOv11 SDWI model outperforms the baseline model across all accuracy metrics. The mean average precision increases from 87.0 % to 89.5 %. The precision rises from 82.1 % to 85.4 %. The recall also improves from 81.2 % to 84.9 %. Simultaneously the proposed model significantly reduces computational costs. The floating point operations are decreased from 6.3 G to 4.9 G. The parameter count is reduced from 2.58 M to 1.89 M. The model weight size is compressed from 23.8 MB to 19.3 MB. This proves that the improved model successfully strikes an optimal balance between high performance and lightweight design.

Overall, the proposed method exhibits strong potential for practical deployment in post-harvest tea sorting systems. Building upon the visual software system developed in this study future work will focus on expanding the dataset to include multiple tea varieties and further improving detection accuracy. Most importantly the plan is to integrate the proposed software architecture with mechanical sorting hardware to conduct real world physical deployment and joint debugging on actual production lines ultimately achieving the complete engineering application of the intelligent tea grading equipment.

ACKNOWLEDGEMENT

This work was supported by the Fundamental Research Funds for the Liaoning Universities LJ242410146044 and the Huzhou Public Welfare Application Research Project 2024GZ226.

REFERENCES

[1] Cao, M., Fu, J., Zhu, J., Cai, C., (2022). Lightweight tea bud recognition network integrating GhostNet and YOLOv5. *Mathematical Biosciences and Engineering*, Vol. 19, pp. 12897-12914, USA.

[2] Chen, B., Yan, J., Wang, K., (2021). Fresh Tea Sprouts Detection via Image Enhancement and Fusion SSD. *Journal of Control Science and Engineering*, Vol. 2021, pp. 6614672, United Kingdom.

[3] Chen, Y., Guo, Y., Li, J., Zhou, B., Chen, J., Zhang, M., Cui, Y., Tang, J., (2024). RT-DETR-Tea: A Multi-Species Tea Bud Detection Model for Unstructured Environments. *Agriculture*, Vol.14, pp.2256, Switzerland.

[4] Ge, Z., Liu, S., Wang, F., Li, Z., Sun, J., (2021). YOLOX: Exceeding YOLO series in 2021. *arXiv preprint*, arXiv:2107.08430, USA.
[5] Gui, Z., Chen, X., Wang, Y., Zhang, H., (2023). A lightweight tea bud detection model based on Yolov5. *Computers & Electronics in Agriculture*, Vol. 205, pp. 107636, Netherlands.
[6] Hu, G., Li, S., Wan, M., et al., (2021). Semantic segmentation of tea geometrid in natural scene images using discriminative pyramid network. *Applied Soft Computing*, Vol. 113, pp. 107984, Netherlands.
[7] Hu, J., Zhi, Y., Chen, M., Liu, P., (2021). PAG-YOLO: A Portable Attention-Guided YOLO Network for Small Ship Detection. *Remote Sensing*, Vol. 13, pp. 3059, Switzerland.
[8] Khanam, R., Hussain, M., (2024). YOLOv11: An overview of the key architectural enhancements. *Computer Vision and Pattern Recognition*, Vol. 10, pp. 17725, USA.
[9] Li, X., Nie, P., Qiu, Z., He, Y., (2011). Using wavelet transform and multi-class least square support vector machine in multi-spectral imaging classification of Chinese famous tea. *Expert Systems with Applications*, Vol. 38, pp. 11149-11159, United Kingdom.
[10] Liu, W., Lu, H., Fu, H., Cao, Z., (2023). Learning to Upsample by Learning to Sample. *2023 IEEE/CVF International Conference on Computer Vision (ICCV)*, pp. 5027-5037, Paris/France.
[11] Ma, X., Dai, X., Bai, Y., Wang, Z., (2024). Rewrite the Stars. *2024 IEEE/CVF Conference on Computer Vision and Pattern Recognition (CVPR)*, pp. 1213-1224, Seattle/USA.
[12] Redmon, J., Farhadi, A., (2017). YOLO9000: Better, Faster, Stronger. *2017 IEEE Conference on Computer Vision and Pattern Recognition (CVPR)*, pp. 7263-7271, Piscataway/USA.
[13] Tang, X., Tang, L., Li, J., Guo, X., (2025). Enhancing multilevel tea leaf recognition based on improved YOLOv8n. *Frontiers in Plant Science*, Vol. 16, pp. 1540670, Switzerland.
[14] Tang, Z., Su, Y., Er, M., Qi, F., Zhang, L., Zhou, J., (2015). A local binary pattern based texture descriptors for classification of tea leaves. *Neurocomputing*, Vol. 168, pp. 1011-1023, Netherlands.
[15] Wang, C., Wang, Y., Liu, S., He, P., Zhang, Z., Zhou, Y., (2022). Study on Pear Flowers Detection Performance of YOLO-PEFL Model Trained With Synthetic Target Images. *Frontiers in Plant Science*, Vol. 13, pp. 911473, Switzerland.
[16] Wang, D., Lv, H., Zhu, X., Zheng, Y., (2025). Detection and identification of fish skin lesions in the underwater environment based on improved YOLOv8 model for aquaculture. *Aquaculture*, Vol. 608, pp. 742722, Netherlands.
[17] Wang, S., Wu, D., Zheng, X., (2023). TBC-YOLOv7: a refined YOLOv7-based algorithm for tea bud grading detection. *Frontiers in Plant Science*, Vol. 14, pp. 1223410, Switzerland.
[18] Wang, T., Zhang, K., Zhang, W., Liu, H., (2023). Tea picking point detection and location based on Mask-RCNN. *Information Processing in Agriculture*, Vol. 10, pp. 267-275, Netherlands.
[19] Williams, T., Li, R., (2018). Wavelet Pooling for Convolutional Neural Networks. *Proceedings of the International Conference on Learning Representations (ICLR)*, Vancouver/Canada.
[20] Wu, Y., Wan, S., Wu, L., Zhao, Y., (2025). DAONet-YOLOv8: An occlusion-aware dual-attention network for tea leaf pest and disease detection. *arXiv preprint*, arXiv:2511.23222, USA.
[21] Xia, Y., Zhang, L., Wang, Q., Li, H., (2024). Recognition Model for Tea Grading and Counting Based on the Improved YOLOv8n. *Agronomy*, Vol. 14, pp. 1251, Switzerland.
[22] Xie, C., Li, X., Shao, Y., He, Y., (2014). Color Measurement of Tea Leaves at Different Drying Periods Using Hyperspectral Imaging Technique. *PLoS ONE*, Vol. 9, pp. e113422, USA.
[23] Xu, G., Zhang, X., et al., (2020). Recognition approaches of tea bud image based on faster R-CNN depth network (基于 Faster R-CNN 深度网络的茶芽图像识别方法). *Journal of Optoelectronics Laser*, Vol. 31, pp. 1131-1139, Tianjin/China.
[24] Xu, W., Zhao, X., Liu, P., Chen, S., (2022). Detection and classification of tea buds based on deep learning. *Computers & Electronics in Agriculture*, Vol. 192, pp. 106547, Netherlands.
[25] Zhang, S., Chen, H., Wu, J., Yang, L., (2023). Edge device detection of tea leaves with one bud and two leaves based on ShuffleNetv2-YOLOv5-Lite-E. *Agronomy*, Vol. 13, pp. 577, Switzerland.
[26] Zhao, X., Wang, F., Li, C., Sun, Y., (2024). A quality grade classification method for fresh tea leaves based on an improved YOLOv8x-SPPCSPC-CBAM model. *Scientific Reports*, Vol. 14, pp. 4166, United Kingdom.
[27] Zhu, H., Li, X., et al., (2022). Tea Bud Detection Based on Faster R-CNN Network (基于 Faster R-CNN 网络的茶芽检测). *Transactions of the Chinese Society for Agricultural Machinery*, Vol. 53, pp. 217-224, Beijing/China.

PRECISION INTEGRATED DECISION-MAKING AND CONTROL SYSTEM FOR WATER AND FERTILIZER MANAGEMENT IN ORCHARDS BASED ON THE INTERNET OF THINGS AND CLOUD PLATFORM

/

基于物联网与云平台的果园水肥一体化精准决策控制系统设计

Kang NIU*, Hongze GUO, Weipeng ZHANG, Bo ZHAO, Guopeng ZHANG, Liming ZHOU
State Key Laboratory of Agricultural Equipment Technology, Chinese Academy of Agricultural Mechanization Sciences Group Co., Ltd., Beijing 100083, China
Tel: +86-18600808820; E-mail: niukag@163.com
Correspondent author: Kang NIU
DOI: https://doi.org/10.35633/inmateh-79-13

Keywords: *IoT, water and fertilizer integration, intelligent control decision-making, orchard, cloud platform*

ABSTRACT

Addressing the issues of severe resource wastage, low automation levels, and insufficient control precision in traditional orchard water and fertiliser management, this paper proposes a multi-dimensional, collaborative integrated water and fertiliser management system for orchards. This system combines IoT sensing technology, wireless communication technology, cloud platform computing, and intelligent control algorithms. Through a layered architecture design, this system innovatively enhances the perception layer, transmission layer, data layer, and application layer. It integrates diverse communication protocols such as ZigBee, LoRa and NB-IoT, combines sensors for irrigation, fertilisation, and other aspects, and merges intelligent algorithms including PID closed-loop control and fuzzy neural networks. This enables precise water-fertiliser ratio formulation, remote real-time monitoring, and adaptive regulation. Field validation at a demonstration orchard in Guangdong demonstrated water savings of 30%–65%, fertiliser reductions of 40%–50%, and crop yield increases of 20%–135%. Research findings indicate that the deep integration of IoT and cloud platforms significantly enhances water and fertiliser utilisation efficiency in orchards while reducing labour costs. This provides technical support for standardised orchard cultivation, aligning with the demands for precision and intelligent development in modern agriculture.

摘要

针对传统果园水肥管理中资源浪费严重、自动化程度低、管控精度不足等问题，结合物联网感知技术、无线通信技术、云平台计算与智能控制算法，提出一套多维度协同的果园水肥一体化管控体系。该体系通过分层架构设计，分别对感知层、传输层、数据层与应用层进行了改良创新，整合 ZigBee、LoRa 等多元通信协议，集成灌溉，施肥等多方面传感器，融合 PID 闭环控制、模糊神经网络等智能算法，实现水肥精准配比、远程实时监控与自适应调控。通过广东示范果园田间验证，系统可节水 30%~65%、节肥 40%~50%，作物增产 20%~135%，研究结果表明，物联网与云平台的深度融合可显著提升果园水肥利用效率、降低人工成本，为果园标准化栽培提供技术支撑，符合现代农业精细化、智能化发展需求。

INTRODUCTION

China ranks as the world's foremost fruit producer, with orchard cultivation spanning 19.33 million hectares and total fruit output exceeding 261 million tonnes *(Lu et al., 2022).* However, traditional orchard water and fertiliser management predominantly relies on flood irrigation, furrow irrigation combined with manual fertiliser application *(Singh et al., 2025; Kun et al., 2021; Yang et al., 2025),* presenting three significant challenges. Firstly, resource utilisation efficiency is low, with an irrigation water use coefficient of merely 0.536 and chemical fertiliser utilisation rates below 40%, significantly trailing developed nations' standards *(Zhang et al., 2025)*. Secondly, labour intensity is high, as manual irrigation and fertilisation in large-scale orchards are time-consuming and labour-intensive, exacerbated by an ageing workforce and labour shortages *(Lin et al., 2020; Zheng et al., 2024; Zhao et al, 2025; Ji et al, 2023; Liu et al, 2025).* Thirdly, there are pronounced ecological risks, with excessive water and fertiliser leading to environmental issues such as soil acidification, salinisation, nitrate leaching, and groundwater contamination *(Jian et al, 2021; Li et al, 2024; Song et al, 2025)*.

As agricultural supply-side reforms advance, the "one control, two reductions" strategy has become a core objective for green agricultural development, rendering traditional water and fertiliser management models inadequate for meeting the demands of high-quality industrial development *(Zhu et al, 2023; Tran et al, 2023)*.

As a core precision agriculture technology, water-fertiliser integration delivers water and nutrients directly to root zones in precise, crop-specific ratios. This significantly enhances water and fertiliser utilisation rates, reduces environmental pollution, and improves crop yield and quality *(Fu et al., 2021; Wongchai et al., 2022; Adamo et al., 2025)*.

Overseas adoption of water-fertiliser integration commenced earlier, with Israel, the United States, and the Netherlands achieving large-scale implementation. Over 90% of Israeli agricultural production employs integrated water-fertiliser management (*Meng et al., 2022*); 33% of American fruit tree cultivation utilises this technology, forming a variable fertilisation system based on GPS navigation and prescription maps; while the Netherlands has achieved synergistic optimisation of water-fertiliser coupling and environmental control in protected orchards *(Nie et al., 2023; An et al., 2022; Sun et al., 2025)*. These systems exhibit high water and fertiliser utilisation rates, significantly reducing labour intensity for farmers. However, their limitations—including weak system integration, single-dimensional control, limited communication range, and lack of cloud-based coordination—make direct application to China's diverse topographical orchards challenging *(Sheng et al., 2023)*.

The emergence of IoT and cloud platform technologies offers novel solutions to these challenges *(Xu et al., 2025)*. Through multi-sensor collaborative sensing, wireless data transmission, and cloud-based data analysis, remote, automated, and precision water and fertiliser management becomes feasible. Moreover, cloud platforms enable unified multi-region control, substantially enhancing large-scale management efficiency *(Xing et al., 2024)*.

This study aims to construct an integrated IoT-cloud platform system for water-fertiliser management tailored to complex orchard environments. It addresses challenges including multi-parameter precision sensing with stable long-distance transmission, intelligent decision-making and adaptive regulation of water-fertiliser ratios, and cloud-based collaborative control with multi-terminal user-friendly operation. Adaptable to diverse orchard scenarios—mountainous, protected, and large-scale contiguous plots—this system provides a comprehensive technical solution for intelligent water-fertiliser management, holding significant potential for widespread application. The proposed orchard water-fertiliser integration control system design integrates IoT and cloud platform technologies, achieving precision, remote operation, and automation in water-fertiliser management. Research findings indicate that this system significantly enhances water-fertiliser utilisation efficiency, reduces labour costs, increases crop yield and quality, and is adaptable to diverse complex orchard environments. It holds considerable significance for advancing the intelligent and green development of modern agriculture.

MATERIALS AND METHODS

Precision decision control system

System design proposal

Design of a precision decision control system for water and fertiliser application in field crops this system employs a dual-layer architecture comprising a local head-end control system and a remote intelligent cloud platform. The head-end control system serves as the central hub managing multiple devices, undertaking tasks including water extraction, filtration, fertiliser injection, water distribution, and associated controls. It enables real-time control and operational status monitoring of critical components such as water sources, pumps, filters, motors, and electrical control cabinets. It continuously monitors and alerts on critical metrics such as outlet pressure and flow rate of the main pipeline network, filter differential pressure, and three-phase electrical parameters of pump motors. This ensures equipment safety by protecting pumps, motors, filters, and pipelines during system malfunctions.

Addressing the varying water and fertiliser requirements of different fruit tree varieties and growth stages throughout their lifecycle, the orchard water and fertiliser precision control system employs a closed-loop control method combining servo drive with state feedback. It receives prescription data issued by the remote cloud platform in real time, parses it, and transmits valve start/stop control signals to the valve control system. By executing actions such as valve opening, closing, or partial opening, it achieves automated management for the precise application of water, fertiliser, and pesticides. The variable irrigation and fertilisation ratio decision model, constructed based on knowledge engineering theory, is embedded within the integrated water

and fertiliser system to achieve intelligent dynamic adjustment of water and fertiliser ratios. The system dynamically adjusts pump group operation based on real-time orchard conditions, comprehensively optimising field moisture ratios and enhancing water resource utilisation efficiency through refined management. Closed-loop control automatically activates solenoid valve operation triggered by prescription decisions from the cloud platform, establishing a precision decision-making framework based on prescription map data and real-time field parameters. This ensures irrigation operations automatically cease at the time points specified in the prescription map.

Primary controller

As the control core of the entire water-fertiliser integration system, the head controller possesses bidirectional data interaction and control capabilities. Downstream, it connects wirelessly via IoT to various monitoring nodes including valve controllers, pump station controllers, and data loggers. Through these nodes, it collects data such as pipeline valve status, pipe pressure, and pump operating parameters. Based on this collected data, it executes control commands including solenoid valve opening/closing, pump start/stop, and variable frequency regulation to achieve precise application of water, fertiliser, and pesticides. Upstream, it communicates with the cloud platform for data storage, processing, and remote intelligent control.

The head unit serves as the operational vehicle for the water-fertiliser integration system. It comprises core components including an irrigation tank, chemical application tank, fertiliser tank, pipeline booster pump, filter, integrated water-fertiliser tank assembly, automatic water-fertiliser application controller, differential pressure butterfly valve, solenoid valves, and flow meters. Its fundamental structure is illustrated in Figure 1.

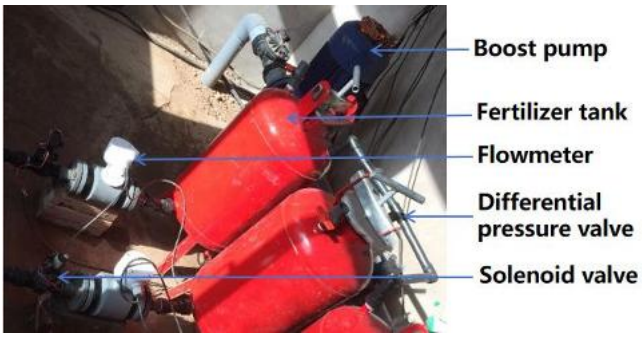


Fig. 1 - Primary equipment configuration plan

The primary controller also incorporates intelligent gateway functionality, establishing communication links between the control system and remote cloud servers via its RTU communication module. This facilitates bidirectional data exchange and control command transmission between the control system and precision management platform, ensuring effective remote command execution and real-time field data uploads. It employs IoT communication protocols such as ZigBee, LoRa, or custom 433 MHz for field monitoring nodes, delivering stable IoT connectivity. Whether utilising broadcast or polling communication mechanisms, it ensures uninterrupted communication links and reliable data transmission. Through each monitoring node, it manages the entire process of sensor data collection, transmission, storage, local display, and cloud uploading for parameters including pressure, flow rate, valve status, and pump operation.

The master controller visually presents the communication status of IoT nodes within the control system, core operational parameters, and the working status of actuators such as valves and pump stations through diverse formats including data lists, trend curves, and graphical representations. This provides maintenance personnel with a clear, comprehensive overview of system operations. It features automatic control parameter configuration, enabling manual/automatic mode switching based on preset requirements to flexibly adapt to varying management scenarios. Users may remotely access the precision crop management platform via smartphones, computers, or other smart terminals to operate various control systems.

On-site controller

The on-site controller serves as an IoT node within the control system. It comprises a power management module, IoT communication module, sensor data acquisition module, relay output module, node enclosure, solar panel array, storage battery, and high-gain communication antenna, and is mounted on field node poles.

The controller's input interface employs an RS-485 serial port for connecting various sensors to gather field data. Its output interface utilises relay outputs capable of driving actuators such as solenoid valves and pump station motors, with a pulse voltage of ±12 V when interfacing with solenoid valves.

On-site controllers perform dual functions of data acquisition and control signal output. Depending on monitored objects and control tasks, they are categorised as integrated monitoring controllers, valve controllers, pump station controllers, and various signal acquisition units. When integrated with corresponding control objects, on-site controllers form intelligent terminal devices such as wireless smart electrically controlled valves, wireless smart pump controllers, wireless smart soil moisture monitors, wireless pipeline pressure measurement and control units, and wireless flow monitors.

Variable rate fertiliser application system

Overall technical approach

The variable fertiliser application control system, serving as the core execution module for precision water-fertiliser integration control, comprises five functional units: the host computer control system, microcontroller system, fertiliser hopper detection module, discharge port fertiliser weighing module, and fertiliser discharge motor control module, as illustrated in Figure 2. Its core operational mechanism functions as follows: the microcontroller, serving as the heart of the micro-control system, simultaneously acquires two critical signals—fertiliser weight within the hopper and discharge chute—via an AD acquisition card. This data is then transmitted to the host computer through an RS-232 serial communication link. The host computer integrates the preset prescription chart information with the two feedback signals. Through algorithmic analysis, it derives precise fertiliser blending ratios and application rate parameters. Control commands are then issued to the microcontroller system, which executes the instructions. This system implements coordinated position and speed control of the fertiliser discharge chute motor. By adjusting the chute wheel speed, variable regulation of the fertiliser blending and application process is ultimately achieved.

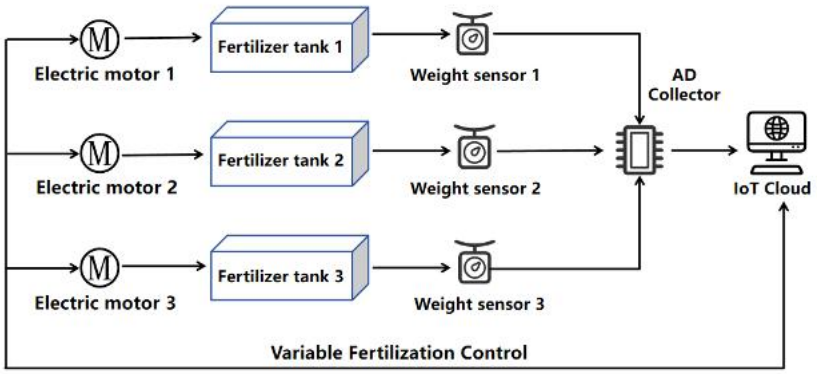


Fig. 2 - Schematic diagram of variable-rate fertiliser application control system

Specific functions of each unit

(1) Host computer control system: Real-time acquisition of fertiliser weight variations within the hopper and feedback signals from the discharge chute via RS-232 serial communication. Integrates prescription maps to precisely match target area fertiliser requirements and blending ratios, generating tailored control commands transmitted to the microcontroller system. This enables coordinated decision-making for variable-rate fertiliser blending and application.

(2) Microcontroller system: Undertakes dual core functions. Firstly, it acquires and pre-processes weight signals from both the hopper and discharge chute, transmitting these via RS-232 serial bus to the host computer. Secondly, based on prescription parameters and vehicle speed signals received from the host, it employs servo control technology to regulate variable fertiliser application throughout the mixing and dispensing process.

(3) Fertiliser hopper detection module: Utilises pressure sensors for real-time monitoring of hopper contents. The process involves: changes in hopper weight causing fluctuations in sensor output signals; the microcontroller system acquiring these voltage variations via an AD acquisition card; signal conditioning followed by transmission to the host computer via RS-232 interface; the host computer calibrating and converting the voltage signals to derive real-time hopper weight changes, representing actual fertiliser application monitoring data.

(4) Discharge outlet fertiliser weighing module: Employing a suspended pressure sensor to perform real-time verification of fertiliser application rates at the discharge outlet. The specific process is as follows: Fertiliser falling from the hopper into the discharge outlet hopper triggers signal changes in the suspended pressure sensor. The microcontroller system acquires this voltage signal via an AD acquisition card and transmits it to the host computer. The host computer processes the data, converting it into the actual weight value of fertiliser at the discharge outlet, thereby forming a closed-loop feedback verification of the fertiliser application rate.

Irrigation control system design

Facility composition

The orchard intelligent irrigation system, serving as a crucial operational component of the precision decision-making control system for water and fertiliser application, comprises core hardware including remote pressure transmitters, remote electromagnetic flow meters, intelligent irrigation controllers, pulse solenoid valves, intelligent irrigation gateways, and a cloud-based decision platform.

The remote pressure gauge collects pipeline pressure signals from the irrigation system, transmitting them via 5G communication to the cloud decision platform. Based on pipeline pressure conditions, the platform assesses system functionality, identifies faults such as leaks, and feeds this information back to the decision control platform. Alarm devices then alert farmers to faults, ensuring timely maintenance. Remote electromagnetic flow meters capture dynamic flow data from orchard irrigation pipelines, transmitting this via 5G to the cloud platform. The platform analyses instantaneous flow rates to assess pipeline operational status and detect leaks, while accumulating flow statistics to quantify water consumption per irrigation cycle across zones. This provides data-driven support for scientific decision-making within the orchard irrigation system.

The cloud decision platform serves as the central brain of the orchard's intelligent drip irrigation system. It collects and stores parameter information transmitted by field irrigation controllers, processes this data to generate precise control commands, and supports the expansion of orchard zone controller units according to user requirements. Concurrently, the cloud decision platform provides 24/7 real-time monitoring, parameter querying, data storage, and analytical capabilities. Its web interface displays orchard, pipeline, and environmental parameters, enabling users to remotely regulate zone solenoid valves via control buttons. All historical parameter data is archived in the server database for user retrieval and download, providing traceability support for irrigation system maintenance and optimisation. Furthermore, the system continuously monitors pump parameters including power consumption, flow rate, and pressure, enabling remote metering control and management of water usage. Through intelligent control technology, pump operation can be regulated to achieve precise flow regulation, thereby conserving water resources.

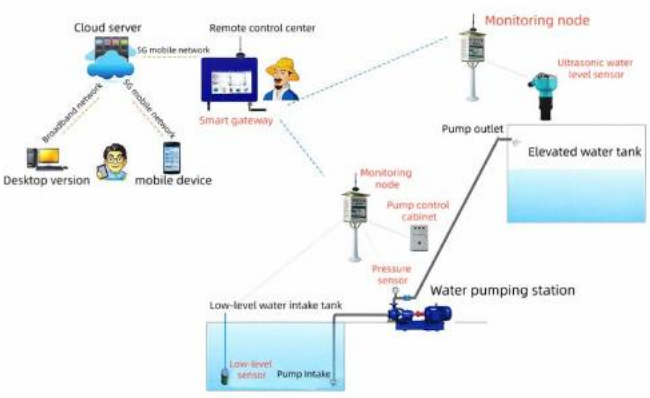


Fig. 3 - Pump station control for irrigation systems

First wireless gateway

The primary wireless gateway serves as the core communication convergence node for the system, primarily facilitating data aggregation and remote transmission for intelligent devices such as pump controllers, wireless valve controllers, and wireless water level sensors, as illustrated in Figure 4. This gateway accesses the internet via GPRS/CDMA/5G mobile communication technology (utilising an IoT SIM card), establishing a direct data exchange link with the cloud-based irrigation management platform. Field intelligent nodes—including pump controllers, valve controllers, soil moisture sensors, and pressure sensors—support two communication access modes: firstly, integrating gateway communication functionality to connect directly with the cloud platform; secondly, forming internal node networking via IoT wireless protocols such as LoRa, with

aggregated data subsequently transmitted to the cloud platform via the master gateway. Furthermore, the master gateway may be integrated with the head controller to form an intelligent head controller with gateway functionality. This enables remote real-time monitoring and control of the precision application system for water, fertiliser and pesticides in the field, while reducing system operation and communication costs. The wireless head gateway offers precise, efficient, secure and stable long-range information transmission, alongside advantages of operational simplicity and high signal recognition rates, ensuring the reliability of the system's communication links.

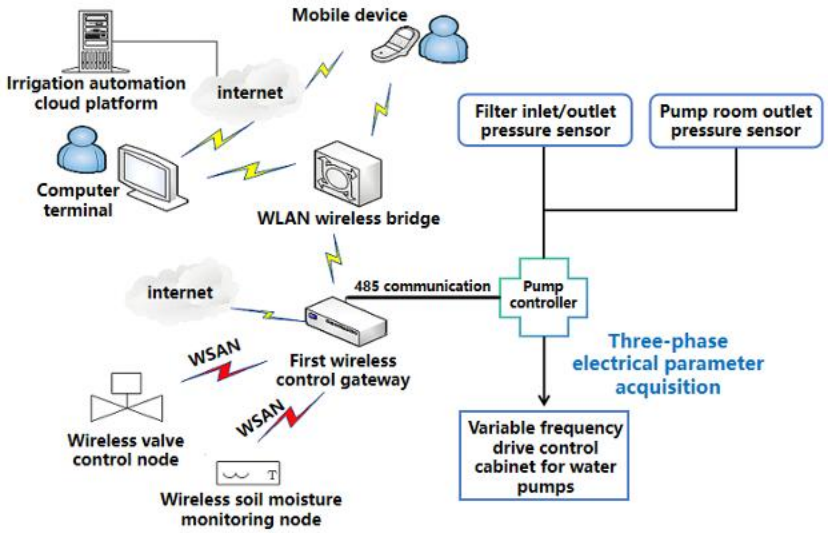


Fig. 4 - First control system architecture diagram

Automated monitoring management

Based on the aforementioned communication architecture, the system enables remote centralised management of pump stations alongside granular monitoring of irrigation water usage and energy efficiency. Total irrigation water consumption is controlled through real-time monitoring and statistical analysis, implementing an authorised water withdrawal control mechanism to provide technical support for managing irrigation water volume within prescribed limits. Real-time energy efficiency monitoring automatically collects electrical parameters such as pump station voltage, current, and power consumption. Combined with operational data including pressure, flow rate, and filter operational status, this enables multi-dimensional statistical analysis. It accurately assesses the rationality of field irrigation patterns, providing foundational data support for optimising water resource allocation and power dispatch.

Users can access comprehensive remote monitoring of pump station operations via cloud-based servers, overcoming spatial (any internet-covered area), temporal (all-hour), and device (compatible with PCs, mobiles, tablets, and other terminals) constraints. Specific monitoring functions include: real-time monitoring of outlet pressure and flow rate, monitoring of variable frequency drive cabinet operational status, and dynamic monitoring of well water levels. The system also features low water level alarms for wells, enabling timely alerts for abnormal water levels to ensure pump station operational safety and continuity of irrigation operations.

Multi-protocol converged communications technology

Internet of Things information transmission

By leveraging a multi-protocol converged communication scheme, perception data collected from the orchard environment is transmitted to the cloud platform with high throughput via 5G cellular networks, where an adaptive protocol selection mechanism is implemented based on the topographical complexity of the orchard: specifically, ZigBee technology is deployed in flat orchard scenarios, which delivers a transmission range of 50-300 m with ultra-low power consumption characteristics and thus is suitable for large-scale sensor node deployment in low-relief terrain, whereas LoRa technology is adopted for mountainous orchard environments featuring complex terrain and long communication distances, enabling an extended communication range of up to 8 km with robust anti-interference capability to mitigate signal attenuation caused by obstacles such as fruit tree canopies and undulating terrain, and the specific configuration and selection criteria of wireless communication modules are elaborated in Table 1.

Table 1

Communication module selection guide

Communication protocol	Core parameters	Suitable scenarios	Model selection
ZigBee	Transmission distance: 50–300 m; Operating current ≤30 mA; Frequency band: 2.4 GHz	Facility orchard/greenhouse	When node spacing is small (< 100 m) and the number of nodes is large (≥50)
LoRa	Transmission distance: 1–8 km; Operating current ≤100mA; Frequency bands: 433/868/915MHz	Mountain orchards/sloping land	Transmission distance > 500 m, complex terrain with numerous obstructions
NB-IoT	Transmission distance: 1–10 km; Operating current ≤20mA; Carriers: China Mobile/China Unicom/China Telecom	Wide-area dispersed orchards (multi-parcel, cross-regional)	When there is no self-built gateway and nodes are dispersed (across townships)

Remote communication mechanism

The remote decision-making control system necessitates the establishment of an effective and reliable remote wireless transmission network. The GSM network's short message service data transmission method has inherent limitations: it suffers from poor real-time performance, is prone to peak congestion during holidays, imposes byte-count restrictions on communication traffic, and carries high tariff costs, rendering it ill-suited for large-volume data transmission requirements. By contrast, GPRS offers distinct advantages: higher data transmission reliability and throughput rates, built upon the Internet Protocol to enable global internet access, permanent connectivity, and pay-as-you-go pricing. This platform utilises the GPRS network as its transmission medium, specifically employing the Transmission Control Protocol within the IP suite for remote data transfer.

The data communication service programme employs multithreading technology to achieve real-time monitoring, reception, and processing of requests sent by the remote data transmission module. This service continuously monitors a predefined port. Upon detecting a request signal from the remote data transmission module, it creates a dedicated thread to process the request. The thread first parses the function code within the request packet, directing it to the appropriate processing workflow based on the function code's specificity. Subsequently, the workflow parses the request data according to predefined communication protocol specifications and completes data persistence by writing it to the database. The communication interaction flow and data transmission link between the server and client are illustrated in Figure 5.

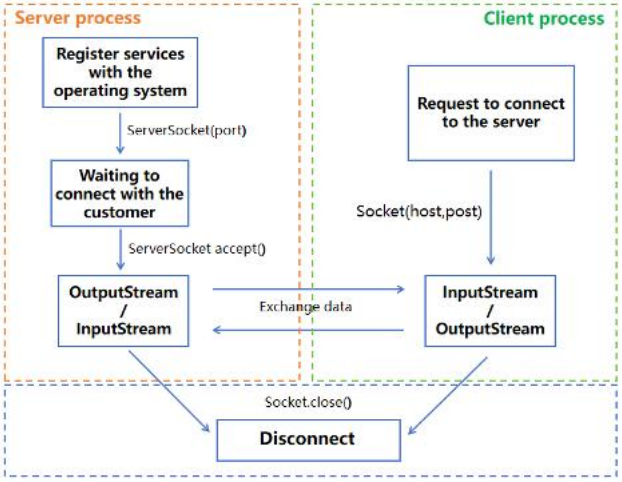


Fig. 5 - Server-client communication process

Cloud platform collaborative control technology

Core architecture of the cloud platform

The cloud platform is built upon the Spring 3.0 MVC framework, employing a MySQL+Redis database architecture to deliver data storage, intelligent decision-making, and remote management capabilities. It provides multi-dimensional analytical reports covering water and fertiliser utilisation efficiency, crop growth trends, and cost-benefit assessments, generating regional water and fertiliser management plans. This enables unified oversight across multiple orchards, with support for data export and visualisation.

Parameters and selection

When selecting hardware for cloud platforms, compatibility should be prioritised to ensure protocol alignment across all component layers. Consideration must also be given to the protection of outdoor components and their environmental adaptability to temperature variations. Wide-temperature models should be selected for cold regions, while anti-condensation models are required for high-humidity areas. Finally, cost and provisions for future scalability must be factored in. Specific selection parameters are detailed in Table 2.

Table 2

Selection criteria for modules of the cloud platform

Core parameters	Technical specifications	Suitable scenarios	Model selection
Data storage	Real-time data storage: ≥100,000 entries; Historical data storage: ≥1 billion entries; Storage type: Relational	Large-scale orchards (≥5 sites)	For long-term data analysis, select "Cloud Server + Local Backup"; For small orchards, consider "Lightweight Cloud" (low cost).
Concurrent access	Supported concurrent users: ≥100; Device connections: ≥1000; Response time: ≤2 seconds	Multi-team collaboration (e.g. growers + technicians)	Cooperatives / Enterprise users should select the “High Concurrency' model”; Individual orchards may opt for the “Basic Edition”.
Security level	Permission Management: Data Encryption for Transmission and Storage; Automatic Backup Frequency: daily	Sensitive data (such as output/cost)	Cross-regional management supports multi-tenant independent administration.
Functional module	Core functions: data monitoring, remote control, alarm management, etc; Extended functions: water-fertiliser models, yield forecasting, energy consumption analysis, etc.	High demand for intelligent solutions	For orchards requiring only basic management controls, the Standard Edition without extended features is available.

Software and system interface design

Control and execution system software

The system software comprises two components: the host computer control software and the microcontroller execution software. The host computer control software reads weight data from the microcontroller and, in conjunction with pre-stored fertiliser application rates for specific plot locations and implement points, calculates the servo motor's rotational speed. It then transmits commands to the microcontroller. Figure 6 illustrates the operational interface of the host computer control software.

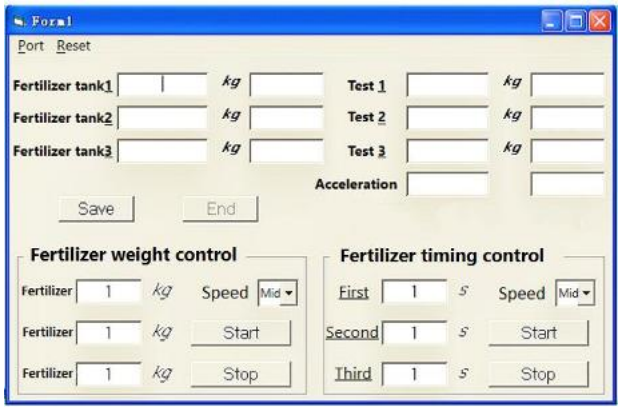


Fig. 6 - Host computer control software operating interface

The specific operational procedure is as follows: click the Port button to access the serial port parameter configuration interface, which includes settings for port number, baud rate, parity bit, data bits, and stop bits. Clicking Reset will clear the fertiliser hopper weight data. Upon system power-up, the host computer software displays real-time weighing values for all three fertiliser hoppers and flow measurements for all three feeders.

Within the fertiliser control panel, pre-set fertiliser quantities for each hopper may be manually input according to operational requirements, or automatically retrieved from the prescription chart by the software. Fertiliser application rate dynamically adjusts in direct correlation with the implement's forward speed: increased forward speed synchronously accelerates fertiliser application, while reduced forward speed correspondingly decelerates it. After completing the above parameter presets, click the "Start" button to initiate fertilisation operations. Data from detection results is saved by clicking the "Save" button. If data saving is unnecessary, clicking the "Cancel" button will prompt a warning dialogue box alerting to the risk of unsaved data. Table 3 summarises the control equipment selection.

Table 3

Control equipment selection table

Controller type	Core technical parameters	Suitable scenarios	Model selection
Edge controller	Interfaces: ≥8 channels; Protection rating: IP65; Power supply: DC 24V	Large-scale orchards (≥10 hectares)	Requirement for basic functionality to be maintained when offline
Local PLC controller	Interfaces: ≥4 channels; Protection rating: IP30; Power supply: AC 220V	Small to medium-sized orchards (≤5 hectares)	When on-site operational requirements are numerous
Industrial touchscreen	Screen size: 7–10 inches; Communication: RS485 / Ethernet; Protection rating: IP65	Local operational requirements (e.g., campus control room)	Supports one-touch start/stop quick operation
Mobile terminal (app)	Functionality: Remote control, data viewing, alert notifications; Communication: 4G/5G/Wi-Fi; Response time: ≤3 seconds	Remote inspection / Multi-orchard management	Multi-site manager selection

The core software module of the microcontroller comprises AD data acquisition and pulse signal output. Upon system power-up or AD7706 reset, the initialisation configuration of the microcontroller's SPI interface is completed first. Data exchange between the microcontroller and AD7706 employs a bidirectional synchronous serial communication method. The AD7706's DIN pin receives control commands issued by the microcontroller, while the converted digital signal is returned to the microcontroller via the DOUT pin. The DRDY register is set to low to receive information from the microcontroller, with the communication frequency set to 2 Mbps. The AD7706 is configured with an update frequency of 50 Hz, yielding a -3 dB cutoff frequency of 13.1 Hz and a gain amplification factor of 1. The microcontroller can output pulses of varying frequencies by configuring the registers of its PWM module. The detailed execution flow of the microcontroller software is illustrated in Figure 7.

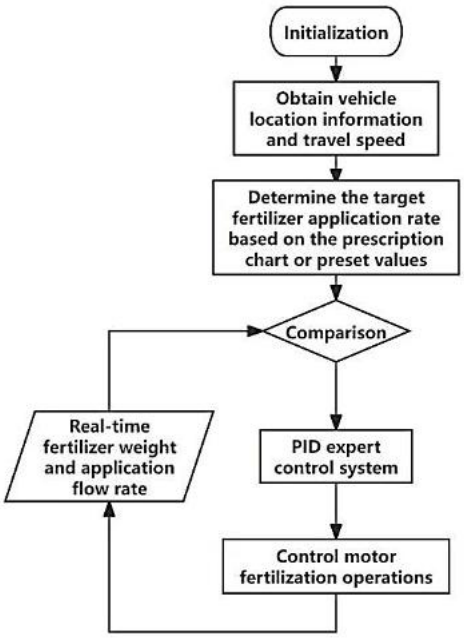


Fig. 7 - Software flowchart

Web application development

The application platform is built upon the Spring MVC framework, with its technical architecture illustrated in Figure 8.

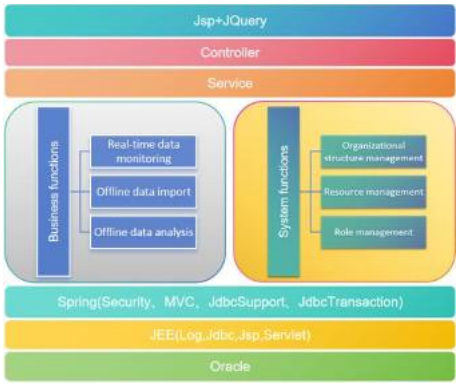


Fig. 8 - Application platform technical architecture

The system employs a Browser/Server architecture for web application development, deployed on cloud server nodes. It supports dual-platform access via mini-programs and mobile applications (Apps), utilising responsive design for multi-device compatibility. The human-machine interface adheres to ergonomic design standards, ensuring excellent usability. Users may monitor core hydrological parameters—including irrigation pressure and flow rates across demonstration zone sub-sections—alongside valve operational statuses in real-time via web browsers or mobile terminals at any location. Concurrently, remote irrigation and fertilisation control commands may be issued to implement time-segmented, zone-specific, and scheduled precision application of water, fertilisers, and pesticides. Historical monitoring data and operational logs can be queried, enabling data-driven analysis for optimising crop irrigation and fertilisation parameters. This design achieves full-process visualised control over irrigation and fertilisation operations, providing data-driven technical support for precision agricultural management decisions. Figure 9 illustrates the zone control interface and display screens for spray flow rates and pipeline pressure within the remote intelligent monitoring system application.

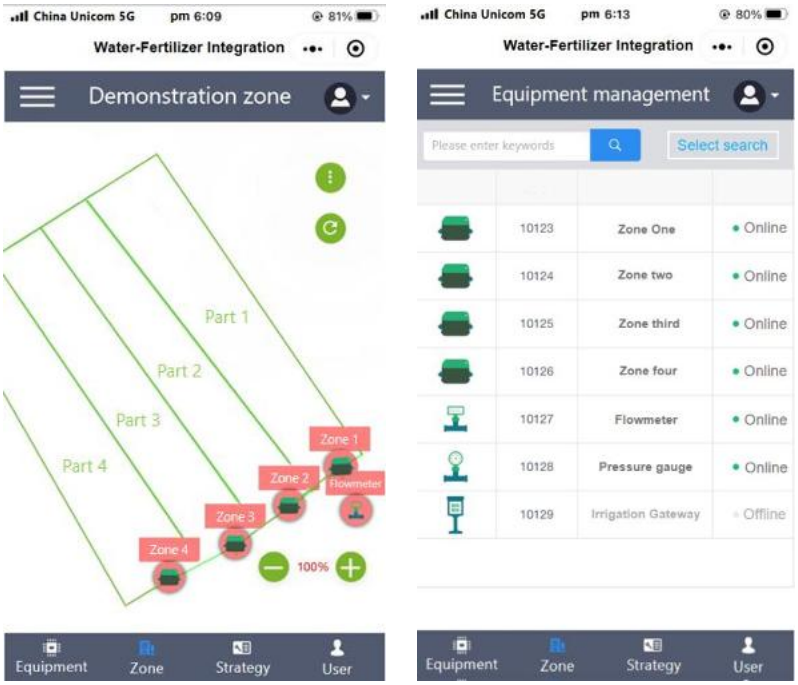


Fig. 9 - Remote intelligent monitoring system App interface

Database selection analysis

As the core repository for system information storage, databases underpin the entire process of data operations including insertion, deletion, modification, and retrieval. Their performance directly determines the overall operational efficiency of the system. Therefore, selecting a suitable database tailored to specific system requirements is crucial for reducing response latency and enhancing overall system performance.

Different database types possess distinct technical characteristics and applicable scenarios, necessitating targeted selection based on the specific application requirements of the monitoring system, as illustrated in Table 4. From the perspective of current market applications, relational databases have long held a dominant position. This category organises data using a two-dimensional tabular structure, achieving efficient CRUD operations through standardised data models and mature algorithmic mechanisms.

Table 4

Database selection comparison

Name	Type	Core features	Applicable scenarios
Oracle Database	Relational	Comprehensive data management capabilities, robust transaction processing power, and a rich product ecosystem	Large-scale enterprise applications
MySQL	Relational	Open-source and free of charge, with outstanding performance, compact size, and cross-platform compatibility	Website development for small and medium-sized enterprises, lightweight applications
SQL Server	Relational	SQL-based, easy to operate, user-friendly management interface, low operational costs	Development of various web projects
NoSQL	Non-relational	Supports dynamic mode, capable of storing semi-structured data, predominantly key-value storage.	High-concurrency, massive-scale data storage scenarios

Taking into account the operational requirements and technical compatibility of this monitoring system, the final configuration has been determined as follows: MySQL 1.8 will be employed to store harvester operational data, whilst Redis will be utilised as a caching database for frequently accessed data. This approach ensures an optimal balance between storage performance and operational demands.

RESULTS

The field trial scene at the citrus orchard demonstration base in Huizhou, Guangdong Province is depicted in Figure 10. Key indicators including citrus fruit growth status and yield were recorded both before and after implementing this water-fertiliser integrated control system. The relevant statistical results are presented in Table 6.

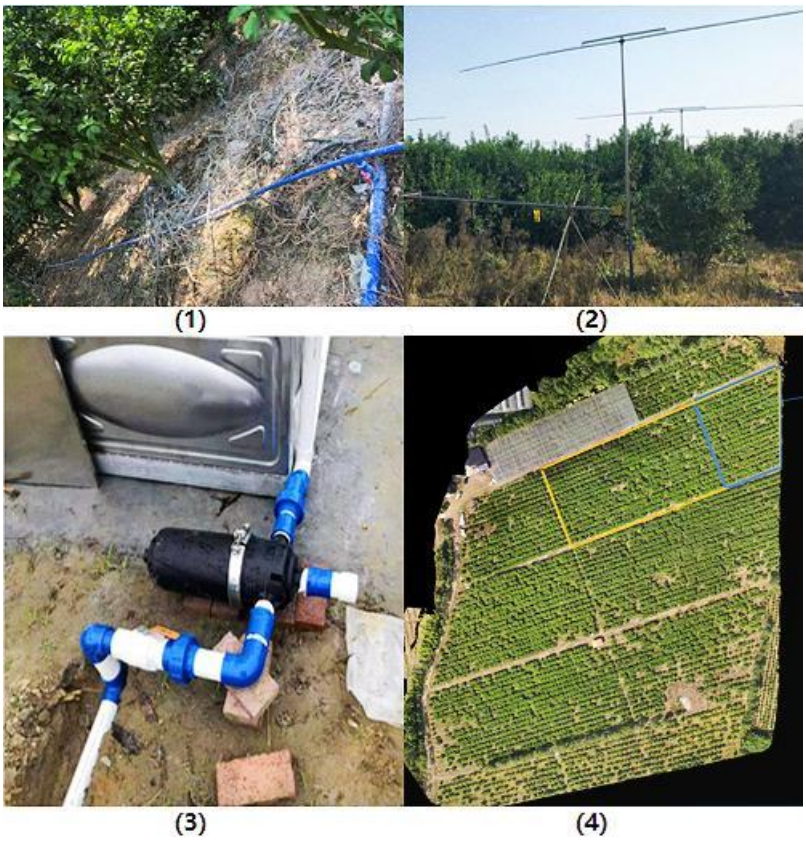


Fig. 9 - Field trial scenario

(1) Drip irrigation pipeline; (2) Dribble board; (3) Fertiliser pipeline; (4) Citrus orchard plot

Table 6

Comparison of citrus growth and yield indicators

Indicator	Experimental group	Control group	Increase rate
Number of fruits per individual tree	445	334	33.2%
Single fruit weight	0.23 kg	0.16 kg	43.8%
High-quality fruit yield	89.1%	70.0%	19.1%
Total output	3180 kg/hm²	2050 kg/hm²	55.1%

The field trial established a precision management system utilising IoT and cloud platforms as the experimental group, with a conventional manual management area serving as the control group. The trial period spanned one year, monitoring indicators including: water and fertiliser use efficiency, crop growth metrics, and system operational stability.

Experimental results demonstrated superior crop growth metrics in the experimental group compared to the control group, indicating that this orchard's integrated water and fertiliser control system effectively enhances fruit quality and yields.

CONCLUSIONS

(1) The system employs irrigation-fertilisation coupling technology, enabling full-growth-cycle requirement design tailored to crop needs. Water and nutrients are delivered directly to crops in precise quantities, at scheduled times, and in proportioned ratios. Statistical analysis and evaluation have been conducted on the selection of all necessary hardware and software components for this process.

(2) The precision control decision system remotely regulates the timing and volume of water and fertiliser application based on crop growth monitoring and detailed prescription information from decision models. It automatically activates and deactivates solenoid valves for unattended operation. Alternatively, by configuring application modes on the controller, the system dynamically applies water, fertiliser, and pesticides according to input instructions.

(3) The precision water and fertiliser decision-making employs the following management methods: operational condition monitoring, closed-loop control, zone management, time-division multiplexing, and platform-based decision-making. This study incorporates a tailored system interface design and optimises the communication network and cloud platform architecture, enabling real-time display of field water and fertiliser status on the remote monitoring interface. Future applications may incorporate multi-source sensor fusion technology combined with machine vision for crop growth monitoring, establishing specialised water and fertiliser models for multiple crops. This would extend applicability to field crops and protected horticulture. Continuous refinement of intelligent algorithms, alongside integration of big data analytics and machine learning, could enable predictive regulation of water and fertiliser requirements, further enhancing the system's adaptability and control precision.

ACKNOWLEDGEMENT

This research was supported by National Key Research and Development Program Project (Grant No. 2023YFD2001103).

REFERENCES

[1] Adamo, T., Caivano, D., Colizzi, L., Dimauro, G., & Guerriero, E. (2025). Optimization of irrigation and fertigation in smart agriculture: An IoT-based micro-services framework. *Smart Agricultural Technology*, Vol. 11, 100885, Italy. DOI: https://doi.org/10.1016/j.atech.2025.100885

[2] An, S., Wang, X., Xue, B., Yin, Y., Wang, H., Rao, C., & Guo, H. (2022). Research and Development of Intelligent Water and Fertilizer Integrated Machine Control System Based on Cloud Platform (基于云平台的智能水肥一体机控制系统研发). *Agricultural Engineering*, Vol. 12, pp. 29-34, China. DOI: https://doi.org/10.19998/j.cnki.2095-1795.2022.07.006

[3] Fu, C., Ma, X., & Zhang, L. (2021). Fuzzy-PID strategy based on PSO optimization for pH control in water and fertilizer integration. *IEEE Access*, Vol. 10, pp. 4471-4482, United States. DOI: https://doi.org/10.1109/ACCESS.2021.3138910

[4] Jian, L., Li, B., Chen, J., & Han, L. (2021). Design of Monitoring System for Electric Vehicle Charging Facilities Based on Cloud Platform. *Journal of Physics: Conference Series*, Vol. 1873, 012016, United Kingdom. DOI: https://doi.org/10.1088/1742-6596/1873/1/012016

[5] Ji, Z., Hui, L., Sun, D., Cui, Y., Zhang, F., Zhao, W., Xu, B., & Zhou, M. (2023). Water and Fertilizer Integration System Based on Internet of Things (基于物联网的水肥一体化系统). *Agricultural Engineering*, Vol. 13, pp. 68-75, China. DOI: https://doi.org/10.19998/j.cnki.2095-1795.2023.11.012

[6] Kun, T., Sanmin, S., Liangzong, D., & Shaoliang, Z. (2021). Design of an intelligent irrigation system for a jujube orchard based on IoT (基于物联网的枣园智能灌溉系统设计). *INMATEH-Agricultural Engineering*, Vol. 63, No. 1, Romania. DOI: https://doi.org/10.35633/inmateh-63-19

[7] Li, R., Bai, J., Li, D., Ren, X., He, D., Du, R., Feng, Z., & Zhang, Z. (2024). Water and fertilizer decision model for synergistic optimization of yield, quality and efficiency of cherry tomato based on combination evaluation. *Computers and Electronics in Agriculture*, Vol. 224, 109224, Netherlands. DOI: https://doi.org/10.1016/j.compag.2024.109224

[8] Lin, N., Wang, X., Zhang, Y., Hu, X., & Ruan, J. (2020). Fertigation management for sustainable precision agriculture based on Internet of Things. *Journal of Cleaner Production*, Vol. 277, 124119, United Kingdom. DOI: https://doi.org/10.1016/j.jclepro.2020.124119

[9] Liu, X., Zhao, Z., & Rezaeipanah, A. (2025). Intelligent and automatic irrigation system based on internet of things using fuzzy control technology. *Scientific Reports*, Vol. 15, 14577, United Kingdom. DOI: https://doi.org/10.1038/s41598-025-98137-2

[10] Lu, Y., Liu, M., Li, C., Liu, X., Cao, C., Li, X., & Kan, Z. (2022). Precision fertilization and irrigation: Progress and applications. *AgriEngineering*, Vol. 4, pp. 626-655, Switzerland. DOI: https://doi.org/10.3390/agriengineering4030041

[11] Meng, Z., Zhang, L., Wang, H., Ma, X., Li, H., & Zhu, F. (2022). Research and design of precision fertilizer application control system based on PSO-BP-PID algorithm. *Agriculture*, Vol. 12, 1395, China. DOI: https://doi.org/10.3390/agriculture12091395

[12] Nie, X., Huang, Z., Huang, D., & Zhang, H. (2023). Design of Water and Fertilizer Integration System Based on Internet of Things (基于物联网的水肥一体化系统设计). *Agricultural Engineering*, Vol. 13, pp. 43-49, China. DOI: https://doi.org/10.19998/j.cnki.2095-1795.2023.03.008

[13] Sheng, Q., Li, X., Han, Y., Li H., & Zhang, M. (2023). Design of Crop Irrigation Decision-Making System Based on ZigBee Technology (基于 ZigBee 技术的作物灌溉决策系统设计). *International Journal of Robotics and Automation Technology*, Vol. 10, pp. 96-109, China. DOI: https://doi.org/10.31875/2409-9694.2023.10.09

[14] Singh, A. K., Khatoon, S., Chaturvedi, D. K., Choudhury, U., Yadav, A. K., & Sharma, G. (2025). A comprehensive review of recent advances in intelligent controller development for smart irrigation systems. *Discover Computing*, Vol. 28, pp. 1-25, India. DOI: https://doi.org/10.1007/s10791-025-09762-4

[15] Song, Y., Xu, J., Zhang, S., Xing, J., Wang, X., Wang, L., Hu, C., & Li, W. (2025). Regulation of photosynthetic performance and dry matter accumulation through water and fertilizer management to enhance yield of tomato cultivated in yellow sand substrate. *Agricultural Water Management*, Vol. 319, 109795, Netherlands. DOI: https://doi.org/10.1016/j.agwat.2025.109795

[16] Sun, X., Tian, G., Guo, C., Yan, Z., & Zhen, Y. (2025). The application status and development prospects of water and fertilizer integration technology in modern agriculture. *Advances in Resources Research*, Vol. 5, pp. 1004-1024, China. DOI: https://doi.org/10.50908/arr.5.2_1004

[17] Tran, D. T., Le, H. S., & Huh, J. H. (2023). Building an automatic irrigation fertilization system for smart farm in greenhouse. *IEEE Transactions on Consumer Electronics*, Vol. 70, pp. 4685-4698, South Korea. DOI: https://doi.org/100410.1109/TCE.2023.3304554

[18] Wongchai, A., Shukla, S. K., Ahmed, M. A., Sakthi, U., & Jagdish, M. (2022). Artificial intelligence-enabled soft sensor and internet of things for sustainable agriculture using ensemble deep learning architecture. *Computers and Electrical Engineering*, Vol. 102, 108128, United Kingdom. DOI: https://doi.org/10.1016/j.compeleceng.2022.108128

[19] Xing, Y., & Wang, X. (2024). Precise application of water and fertilizer to crops: challenges and opportunities. *Frontiers in Plant Science*, Vol. 15, 1444560, Switzerland. DOI: https://doi.org/10.3389/fpls.2024.1444560

[20] Xu, Y., Zhang, Z., Li, M., Xia, S., Liu, W., Xu, X., & Li, Q. (2025). Cross-scale synergistic optimization for irrigation allocation and fertilizer management under uncertainty. *Agricultural Water Management*, Vol. 317, 109672, Netherlands. DOI: https://doi.org/10.1016/j.agwat.2025.109672

[21] Yang, J., Li, X., Zheng, Q., & Liu, L. (2025). Particle Swarm Optimization-Enhanced Fuzzy Control for Electrical Conductivity Regulation in Integrated Water–Fertilizer Irrigation Systems. *Automation*, Vol. 6, 76, Switzerland. DOI: https://doi.org/10.3390/automation6040076

[22] Zhang, W., Tong, J., Zhang, F., Zhang, W., Zhang, J., Zhang, J., Sun, H., Northwood, D. O., Waters, K. E., & Ma, H. (2025). Integrated irrigation of water and fertilizer with superior self-correcting fuzzy PID control system. *Plos one*, Vol. 20, e0324448, United States. DOI: https://doi.org/10.1371/journal.pone.0324448

[23] Zhao, Q., Feng, J., Guo, S., Yang, S., Jing, R., Zhang, X., Zhou, X., & Li, D. (2025). Water-fertilizer regulation improves yield, quality, and water-fertilizer use efficiency of greenhouse lettuce by altering the bacterial community in nutrient solutions. *Journal of Agriculture and Food Research*, Vol. 21, 101976, United States. DOI: https://doi.org/10.1016/j.jafr.2025.101976

[24] Zheng, Y., Jiang, Z., Kozlov, O. V., & Kondratenko, Y. P. (2024). Fuzzy automatic control of the irrigation process for the IoT-based smart farming systems. *Journal of Ambient Intelligence and Smart Environments*, Vol. 16, pp. 337-363, Belgium. DOI: https://doi.org/10.3233/AIS-23040

[25] Zhu, F., Zhang, L., Hu, X., Zhao, J., Meng, Z., & Zheng, Y. (2023). Research and design of hybrid optimized backpropagation (BP) neural network PID algorithm for integrated water and fertilizer precision fertilization control system for field crops. *Agronomy*, Vol. 13, 1423, China. DOI: https://doi.org/10.3390/agronomy13051423

THERMAL ENVIRONMENT IMPROVEMENT AND PARAMETER OPTIMIZATION OF WET CURTAIN FAN VENTILATION IN A GREENHOUSE: A CFD STUDY WITH EXPERIMENTAL VALIDATION

/

温室湿帘风机通风热环境改善与参数优化：CFD 研究与实验验证

Huanran SUN[1, 2)], Binguang JIA[*3)], Ziye SONG[4)]

[1)]Shandong Huayu University of Technology, Dezhou, 253023, China;
[2)]Shandong Engineering Research Center of Low-Carbon Energy Internet of Things Technology, Dezhou, 253023, China;
[3)]Department of Mechanical and Electrical Engineering, Jinan Engineering Polytechnic, Jinan, 250200 China;
[4)]Civil and Transportation Engineering College, Weifang University, Weifang 261000, China.
Tel:13688624631; E-mail: jiabinguang78@163.com
DOI: https://doi.org/10.35633/inmateh-79-14

Keywords: *Greenhouse, Wet curtain, Temperature, Velocity*

ABSTRACT

Effective cooling is crucial for maintaining suitable thermal environments in greenhouses during hot summers. This study developed a coupled numerical model to investigate the cooling performance of a wet curtain system in a multi-span plastic greenhouse in Weifang, China. Relative deviations were less than 5.88% for wet curtain outlet temperature and below 7% for average greenhouse temperature. Results indicated that the wet curtain reduced the average greenhouse temperature by 2.33 ~ 4.20 ℃, with the maximum reduction of 4.20 ℃ occurring at 12:00. The cooling capacity increased with rising solar radiation in the morning and then diminished in the afternoon. The cooled air entered as a floor-level jet, accumulated near the crop zone, and subsequently rose due to buoyancy, forming two large recirculation vortices that enhanced vertical mixing and improved temperature uniformity. Consequently, the average indoor air velocity increased by 8.38% ~ 22.40% compared to ventilation without the wet curtain. Parametric analysis revealed that the average greenhouse temperature decreased nonlinearly with increasing inlet velocity, and the marginal cooling benefit dropped significantly when the inlet velocity exceeded 0.75 m/s. An optimal inlet velocity range of 0.75 ~ 1.0 m/s is recommended. The model accurately captured the thermal performance and airflow patterns of the greenhouse with wet curtain cooling.

摘要

在炎热的夏季，有效的降温对维持温室适宜的热环境至关重要。本研究建立了一个耦合数值模型，用于研究山东潍坊一座连栋塑料温室中湿帘系统的降温性能。湿帘出口温度的相对偏差小于 5.88%，温室平均温度的相对偏差小于 7%。结果表明，湿帘使温室平均温度降低了 2.33 ~ 4.20 ℃，其中 12:00 时降幅最大，达 4.20 ℃。上午降温能力随太阳辐射增强而提高，午后则逐渐减弱。冷却后的空气以贴地射流形式进入温室，在作物区附近积聚，随后因浮力作用上升，形成两个大型回流涡，增强了垂直混合，改善了温度均匀性。因此，与无湿帘的通风相比，室内平均风速提高了 8.38% ~ 22.40%。参数分析显示，温室平均温度随入口风速的增加呈非线性下降，当入口风速超过 0.75 m/s 时，边际降温效益显著降低。推荐的最佳入口风速范围为 0.75 ~ 1.0 m/s。该模型准确捕捉了湿帘降温温室的热工性能和气流流型。

INTRODUCTION

With the global population projected to reach 8.5 billion by 2030 (*Abedrabboh et al., 2024*), the demand for food is explosive growth, with an estimated increase of 50% (*Bergman et al., 2011*), thereby placing greater pressure on water resources and arable land. Consequently, enhancing food yield has become a critical issue in addressing food security.

Greenhouse is a facility that utilize solar energy to enable off-season crop cultivation (*Dietz et al., 2011*). Greenhouses transmit shortwave solar radiation while blocking longwave radiative loss, thus maintaining a favorable thermal environment for off-season cultivation (*Zhang et al., 2025*).

Huanran Sun, M.S. Eng.; Binguang Jia, Prof. Ph.D.; Ziye Song, Prof. Ph.D.

Compared with open-field cultivation, the greenhouse contributes to a notable increase in overall crop yield, as greenhouse can monitor and regulate growing conditions (*Garcia et al., 2026*). At the same land area, tomato production in greenhouse can achieve yields approximately 15 times higher than those obtained in open-field systems (*Abedrabboh et al., 2024*). Furthermore, off-season crop marketing can significantly elevate market prices, which contributes to enhance the economic profitability of agricultural production (*Lei et al., 2023*). Although greenhouses can maintain suitable internal conditions for the growth for horticultural products in winter, the greenhouse effect intensifies internal temperatures during summer, leading to increased pest and disease incidence and, in severe cases, dehydration and crop mortality (*Rahman et al., 2021*). Therefore, effectively providing an optimal growing environment under high-temperature summer conditions has become a prominent research focus in the horticulture (*Krishna et al., 2024*).

Based on cooling strategies, summer greenhouse cooling can be categorized into passive and active approaches (*Zhang et al., 2022*). Passive cooling relies on natural ventilation driven by indoor–outdoor temperature gradients. Although optimizing vent configurations can improve airflow and temperature distribution (*Park et al., 2022*). Some researchers (*Moreno-Teruel et al., 2022*) noted that the increase in the greenhouse width could enhance crop radiation interception and elevate internal CO_2 concentrations for the passive cooling strategy. The greenhouse designed by Yang et al. demonstrated superior performance over front roof and side vent configurations under both sunny and overcast conditions, resulting in improved crop growing environments and a 7.9% increase in tomato yield (*Yang and Liu, 2024*). Despite extensive research on passive cooling techniques, the limited temperature gradient between the interior and exterior renders passive cooling insufficient to ensure adequate crop growth conditions during summer.

Active cooling techniques employ fans to forcibly introduce outdoor air or cold air generated by mechanical cooling systems into the greenhouse (*Peng et al., 2023*). Depending on the cold source, active cooling can be divided into artificial cooling and natural cooling. Compared with natural ventilation, forced ventilation can provide the required airflow rates in summer but may still induce spatial temperature heterogeneity (*Jerszurki et al., 2021*; *Yoon et al., 2024*).

When the environment temperature was greater than the suitable temperature for crop growth in summer, wet curtain systems, which relied on the core mechanism of evaporative cooling, could produce air cooler than ambient conditions, emerging as a critical solution for summer greenhouse cooling (*Shen et al., 2026*). As wet curtain achieved temperature reductions of 5 to 15 °C while consuming only one-quarter to one-third of the energy required by conventional air conditioning, wet curtain greenhouse cooling systems have attracted considerable research interest (*Chen et al., 2023*).

However, a critical shortcoming persists in most CFD studies on wet curtain greenhouses. To simplify computation, the cooling effect of the wet curtain is typically predefined as a fixed temperature drop or a fixed cooling efficiency based on empirical correlations. Although this empirical boundary treatment is computationally efficient, it neglects the dynamic interactions among the incoming air velocity, the heat and mass transfer within the water film, and the fluctuating outdoor climatic conditions (solar radiation and air humidity). Consequently, such simplifications cannot capture the transient response of the cooling system, and under highly variable solar radiation loads, they may cause significant deviations in the predicted spatial distributions of airflow and temperature. This study proposes a mechanistic-coupling modeling approach. Unlike conventional empirical methods, the heat and mass transfer equations of the wet curtain are embedded into the greenhouse mathematical model via user-defined functions (UDFs). This integration enables the inlet boundary conditions at the wet curtain to dynamically respond to real-time outdoor environmental parameters, rather than being prescribed in advance.

MATERIALS AND METHODS

Description of experimental greenhouse

The experimental facility employed in this study was a large-scale multi-span plastic greenhouse in Weifang City, China (118°32′E, 36°41′N). As illustrated in **Fig. 1**, the greenhouse were 36 m in length, 16 m in width and 4.5 m in height. Along the longitudinal direction, the structure was divided into four identical modules, each with a length of 9 m. Each module was equipped with an air inlet and an outlet, both measuring 4 m in width and 1.5 m in height. A wet curtain pad matching the inlet dimensions was installed at the air intake, with a fan positioned downstream of the pad. The roof adopted an arched configuration, reaching a maximum height of 4.5 m, while the surrounding sidewalls, which connect to the arched roof, have a height of 3 m.

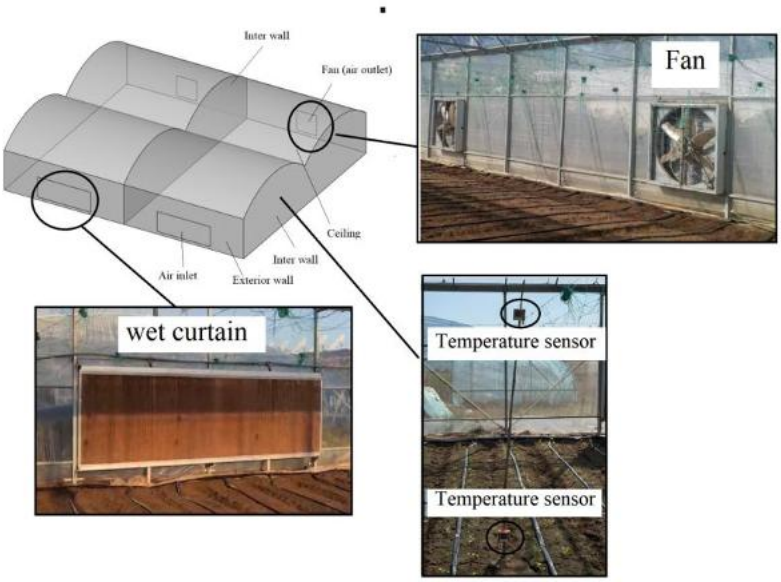


Fig. 1 - Experimental greenhouse structure and location of observation points

Cooling experiments were conducted on September 17, 2025, between 8:00 and 17:00. This date was deliberately chosen to avoid interfering with the ongoing crop production cycle, as the greenhouse is a commercial cultivation facility. Measurements were therefore scheduled during a non-planting window while the house was empty, and the day itself was a typical clear, hot day representative of the late-summer climatic conditions requiring cooling. The ambient temperature ranged from 18.8 ℃ to 28.2 ℃, and the relative humidity varied between 39.4% and 58.8%. The wet curtain pad was supplied with recirculating water maintained at a controlled temperature of 18–20 ℃. The water flow rate was set according to the pad manufacturer's specification to ensure complete wetting of the pad surface, approximately 30 L·min-¹. The evaporative cooling efficiency of the pad under these operating conditions is approximately 80%. A total of 10 temperature monitoring points were arranged inside the greenhouse, distributed between the upper and lower regions to capture vertical temperature variations. Temperature measurements were performed using Testo 174H data loggers (operating range: -20 ~ 70 ℃; accuracy: ±0.5 ℃). Solar radiation, which was mounted above the west side of the greenhouse roof, was recorded using a TBQ-2 pyranometer (measurement range: 0 ~ 2000 W/m; accuracy: 5 %; sensitivity: 8.963 μV·W/m²; spectral range: 0.3 ~ 3.0 μm). Ambient wind speed was monitored using a YGC-FS anemometer (measurement range: 0 ~ 45 m/s; resolution: 0.1 m/s; accuracy: ± (0.3 + 0.03 V) m/s) positioned on the western side of the greenhouse.

Physical model and mesh generation

The physical model of the greenhouse was established and meshed by Gambit software. As illustrated in **Fig. 2**, the experimental greenhouse could be divided into several geometrically identical modules; therefore, to reduce computational expense, only one module was selected for physical modeling. After the model construction, mesh generation was performed. The mesh configuration of the greenhouse was depicted in **Fig. 2**. Mesh quality assessment revealed a maximum skewness of 0.82, with 93.8% of grid elements exhibiting a skewness below 0.6, indicating satisfactory mesh quality suitable for subsequent simulations.

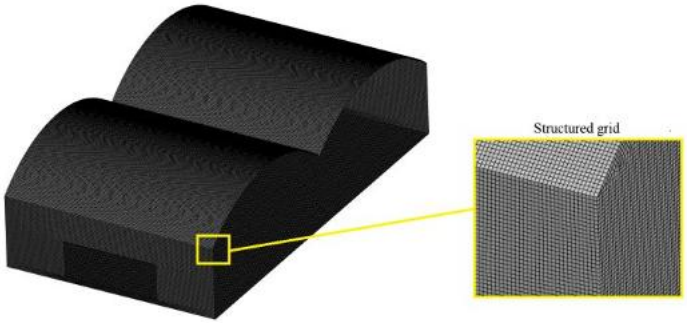


Fig. 2 – Grid generated in greenhouse computational domain

To achieve a balance between computational speed and accuracy, a grid independence test was performed using seven systematically refined meshes under conditions without wet curtain ventilation. The resulting average temperatures were plotted in **Fig. 3**. As the mesh was refined, the predicted average temperature decreased monotonically and the variation became negligible beyond 3.49 × 10⁶ elements. To quantitatively assess the discretization error, the Grid Convergence Index (GCI) was calculated. GCI for the fine-grid solution was determined to be 1.36%, confirming that the discretization uncertainty is sufficiently small. Consequently, the mesh with 3.49 × 10⁶ elements was selected as an appropriate compromise between accuracy and computational cost.

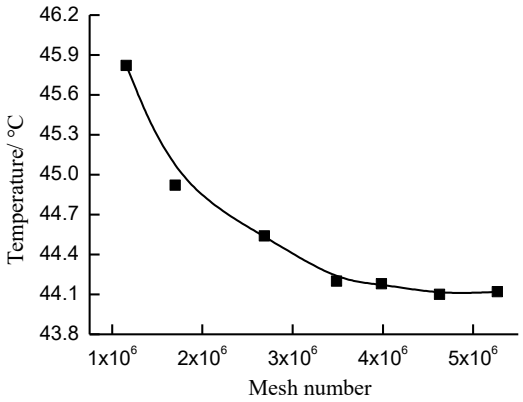


Fig. 3 - Average temperature with respect to mesh number

Governing equations

Computational fluid dynamics simulation techniques could discretize the system of partial differential equations governing fluid flow in both space and time, and obtain physical quantities (e.g., velocity, pressure, temperature) at discrete points through iterative solution of the resulting algebraic equations. This approach provided a convenient and effective means for parametric investigations of greenhouse cooling using wet curtain systems.

Prior to conducting the numerical simulations, the following assumptions were adopted (*Jiao et al., 2024*):

(1) The effects of crop respiration and transpiration on the temperature and velocity distributions of air inside the greenhouse are neglected;

(2) The Boussinesq approximation is employed to account for the influence of buoyancy forces on airflow;

(3) Infiltration of cold air into the greenhouse is disregarded.

(4) There are no crops being cultivated in the greenhouse.

The continuity, momentum, and energy equations for the air region within the greenhouse are expressed as follows (*Fu et al., 2023*):

$$\frac{\partial \rho}{\partial t} + \nabla\left(\rho \vec{v}\right) = 0 \tag{1}$$

$$\frac{\partial}{\partial t}\left(\rho \vec{v}\right) + \nabla\left(\rho \vec{v}\vec{v}\right) = -\nabla P + \nabla \cdot \left(\bar{\bar{\tau}}\right) + \rho \vec{g} \tag{2}$$

$$\frac{\partial}{\partial t}\left(\rho E\right) + \nabla \cdot \left(\vec{v}\left(\rho E + P\right)\right) = \nabla \cdot \left(k_{eff}\nabla T - \sum_j h_j \vec{J}_j + \left(\bar{\bar{\tau}}_{eff} \cdot \vec{v}\right)\right) \tag{3}$$

where: ρ was the air density (kg/m³); t was time (s); v was velocity vector (m/s); P was the pressure (Pa); τ was the stress tensor (Pa); g was the gravitational acceleration vector (m/s²); E was the total energy per unit mass (J/kg); k_{eff} was the effective thermal conductivity (W/(m·K)); T was Temperature (K); h_j was the enthalpy of species (J/kg); J_j was diffusion flux of species (kg/(m²·s)); τ_{eff} was the effective stress tensor (Pa).

Given that the airflow in a greenhouse typically exhibits complex turbulent characteristics, specifically manifested as high-strain-rate flow formed when cold air jets impinge on the ground, and large-scale recirculation vortices driven by buoyancy after heating (*Allali et al. 2024*). To more accurately predict the velocity and temperature distributions inside the greenhouse, this study adopts the RNG *k-ε* turbulence model

based on renormalization group theory. Compared with the standard k-ε model, the RNG *k-ε* model introduces an additional source term into the ε equation and modifies the calculation formula for turbulent viscosity, thereby enabling more effective handling of high strain rates, streamline curvature, and the nonlinear effects of buoyancy on the turbulent structure (*Chen, 2015*). This model has been widely applied in CFD simulations of greenhouse environments and similar building ventilation, and can reasonably resolve the temperature stratification and vortex structures of interest in this study.

$$\frac{\partial(\rho k)}{\partial t}+\frac{\partial(\rho k u_i)}{\partial x_i}=\frac{\partial}{\partial x_j}\left[\alpha_k \mu_{eff}\frac{\partial k}{\partial x_j}\right]+G_k+\rho\varepsilon \tag{4}$$

$$\frac{\partial(\rho \varepsilon)}{\partial t}+\frac{\partial(\rho \varepsilon u_i)}{\partial x_i}=\frac{\partial}{\partial x_j}\left[\alpha_\varepsilon \mu_{eff}\frac{\partial \varepsilon}{\partial x_j}\right]+\frac{C_{1\varepsilon}^{*}}{k}G_k-C_{2\varepsilon}\frac{\beta\varepsilon^2}{k} \tag{5}$$

where: G_k was the generation term of turbulent kinetic energy; k caused by the average velocity gradient; $C_{1\varepsilon}$ and $C_{2\varepsilon}$ were empirical constants; $C_{1\varepsilon}$=1.42, $C_{2\varepsilon}$ = 1.68.

The discrete ordinates (DO) radiation model implemented in the CFD framework enables the incorporation of solar radiation as a function of longitude and latitude. The DO radiation model was selected for calculating solar radiation, with the relevant governing equations provided below (*Jiao et al., 2024*).

$$\nabla\left(I_\lambda\left(\vec{r},\vec{s}\right)\vec{s}\right)+\left(\alpha_\lambda+\sigma_s\right)I_\lambda\left(\vec{r},\vec{s}\right)=\alpha_\lambda n^2\frac{\sigma T^4}{\pi}+\frac{\sigma_s}{4\pi}\int_0^{4\pi}I_\lambda\left(\vec{r},\vec{s}\right)\Phi\left(\vec{s}\cdot\vec{s}'\right)d\Omega' \tag{6}$$

The physical properties employed in the governing equations are summarized in Table 1.

Where: $\vec{r}$ was the position vector; $\vec{s}$ was the direction vector, *a* was the absorption coefficient, n was the refractive index, σs was the scattering coefficient, σ was the Stefan-Boltzmann constant (5.672×10^{-8} W·m^{-2}·K^{-4}); *I* was the radiation intensity (W·m^{-2}), Φ was the phase function, Ω' was the solid angle.

The physical properties employed in the governing equations are summarized in Table 1 (*He et al., 2018*).

Table 1

Physical property parameters in mathematical model

Name	Density/ Kg/m^3	Specific heat capacity/ J/(kg·K)	Thermal conductivity/ W/(m·K)	Absorptivity	Transmittance	Viscosity/ Pa·s	Coefficient of thermal expansion/ 1/K
Air	0.91	1006.4	0.0242	0	1	1.79×10^{-5}	3.34×10^{-3}
Soil	1300	800	1.3	0.4	0	-	-
Polycarbonate	920	2300	0.4	0.3	0.7	-	-

Boundary conditions

Near-wall regions were treated using the standard wall function approach. The roof, sidewalls, and ground surface of the greenhouse were all configured as wall boundary conditions. For these boundaries, the free-stream temperature was set to the ambient temperature, and the convective heat transfer coefficient was assigned a value of 15 W/ (m²·K). At the greenhouse inlet, fans were installed to force outdoor air through the wet curtain, where it was cooled before being delivered into the greenhouse interior. A velocity inlet boundary condition was prescribed at the inlet. The corresponding inlet velocities were set as 0.25 ~ 1.50 m/s. The temperature variation of the incoming air was determined by solving the heat and mass transfer processes within the wet curtain. The outlet air temperature was calculated using the following expression (*Jiang et al., 2021*):

$$T_{wc,out}=T_{wb,in}+\left[\frac{T_{w,in}+T_{wc,out}}{2}+\left(T_e-T_{wb,in}\right)e^{-NTU}\right] \tag{7}$$

where: $T_{wc,out}$ was the air temperature at the outlet of the wet curtain, ℃; $T_{wb,in}$ was the temperature of the water in the wet curtain, ℃; T_e was the environment temperature, ℃; *NTU* was the number of heat transfer units.

The number of heat transfer units (NTU) was defined as (*Bergman et al., 2011*):

$$NTU=\frac{A_{total}}{\dot{m}_a C_{p,eff}}\frac{k_{da}}{I}\left[0.1\left(\frac{I}{b}\right)^{0.12}\left(\frac{u_a I}{\nu_a}\right)^{0.8}Pr^{0.33}\right] \tag{8}$$

where: I was the specific surface area of the wet curtain, m^2/m^3; b was the thickness of the wet curtain, m; u_a was the velocity at which air passes through the wet curtain, m/s; Pr was Prandtl number; v_{da} was the kinematic viscosity of air, m^2/s.

The parameters employed in the mathematical model and boundary conditions were summarized in Table 2.

Table 2

Parameters of boundary conditions

Time	Environment temperature/℃	External radiation temperature/℃	Solar radiation/ W/m^2
8:00:00	27.00	13.83	522.90
9:00:00	29.00	16.70	569.41
10:00:00	31.00	19.58	595.24
11:00:00	32.50	21.75	609.10
12:00:00	33.50	23.20	614.64
13:00:00	34.00	23.92	613.14
14:00:00	34.50	24.65	604.26
15:00:00	34.00	23.92	585.85
16:00:00	33.00	22.48	552.59
17:00:00	31.50	20.31	491.56

RESULTS AND DISCUSSION

Validation

The experimental data (*Al-Ismaili, 2009*) were employed to validate the wet curtain model. The results in **Fig. 4** indicated that the relative deviation of the temperature values model ranged from 3.96% to 5.88%. In summary, the proposed mathematical model could effectively predict the heat transfer performance wet curtain in greenhouse.

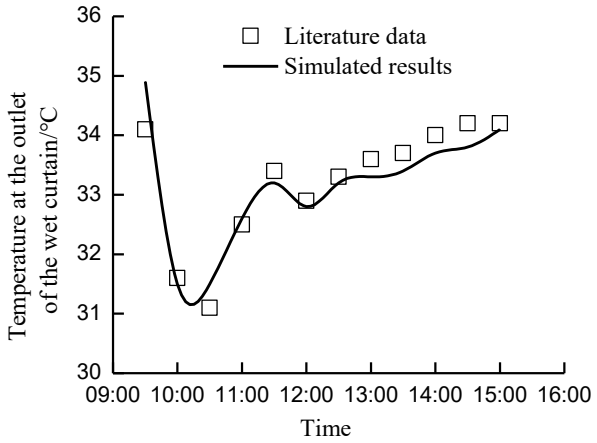


Fig. 4 - Comparison of the predicted and the measured temperature at the outlet of the wet curtain

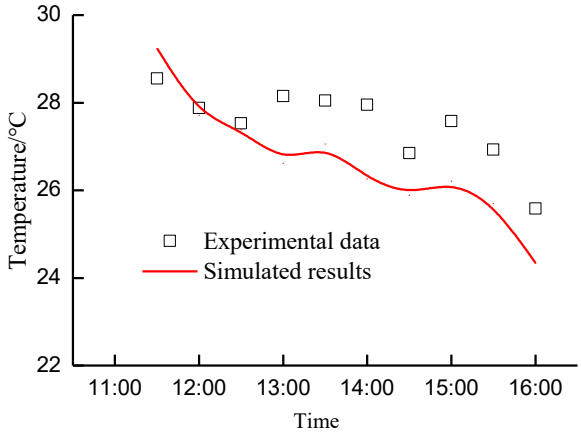


Fig. 5 - The average temperature of the greenhouse

To further substantiate the accuracy of the developed mathematical model, a comparison was conducted between the experimentally measured and numerically simulated average temperatures in the greenhouse. As illustrated in **Fig. 5**, the experimentally obtained average greenhouse temperatures were in strong agreement with the predicted results, exhibiting a relative deviation of less than 7%. The relative deviation between the experimental and simulated results might be attributed to the fact that the numerical simulation employed hourly average values of ambient temperature and solar radiation, whereas during the experimental process, these parameters exhibited fluctuations within the given hour. Based on the analyses presented in **Fig. 4** and **Fig. 5**, it could be concluded that the established mathematical model not only accurately predicted the operational performance of the wet curtain but also effectively characterized the temperature distribution within the greenhouse.

Comparison between greenhouse and wet curtain

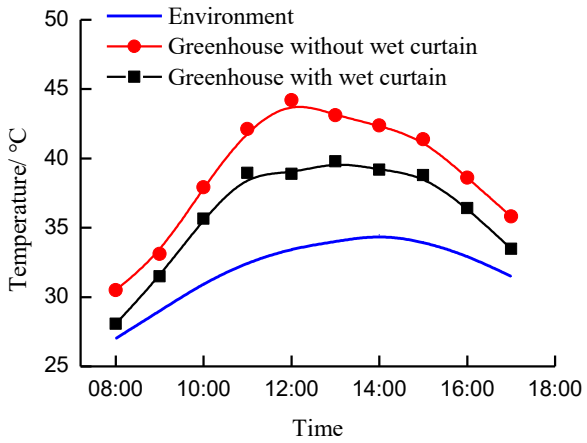


Fig. 6 - Averages temperature in greenhouse with and without wet curtain

Fig. 6 illustrated the average temperature in greenhouse with and without wet curtain on a typical day. Starting from 8:00, the initial temperatures were recorded at 30.49 °C (without wet curtain) and 28.07 °C (with wet curtain); then, given the rising ambient temperature and solar radiation, the indoor temperature progressively increased, peaking between 12:00 and 13:00 at 44.20 °C (without wet curtain) and 39.79 °C (with wet curtain); finally, temperatures gradually declining as solar radiation intensity diminished. A comparative analysis of the cooling effect of the wet curtain revealed that, during the period from 8:00 to 17:00, the wet curtain effectively reduced the ambient temperature within the greenhouse, with its cooling efficacy initially increasing and then decreasing throughout the day. At 8:00, wet curtain achieved an additional temperature reduction of 2.42 ℃ in the average greenhouse temperature, whereas at 12:00, the reduction attributable to the wet curtain reached 4.20 ℃. Subsequently, as solar radiation increased, the cooling effect of the wet curtain gradually weakened, diminishing to 2.33 °C by 17:00. The cooling capacity of the wet curtain was directly governed by its evaporation efficiency. From 8:00 to 12:00, as solar radiation intensified, the temperature difference between the outdoor air and the water in the wet curtain progressively increased, promoting the water evaporation and enhancing the actual cooling capacity of the wet curtain. After 12:00, the decrease in the solar radiation and air temperature, and the increase in the relative humidity resulted in the fact that the differences in both water vapor partial pressure and temperature between the air and the wet curtain water diminished, ultimately leading to a gradual attenuation of the cooling performance of the wet curtain.

Fig. 7 presented the temperature distribution within the greenhouse at 12:00.

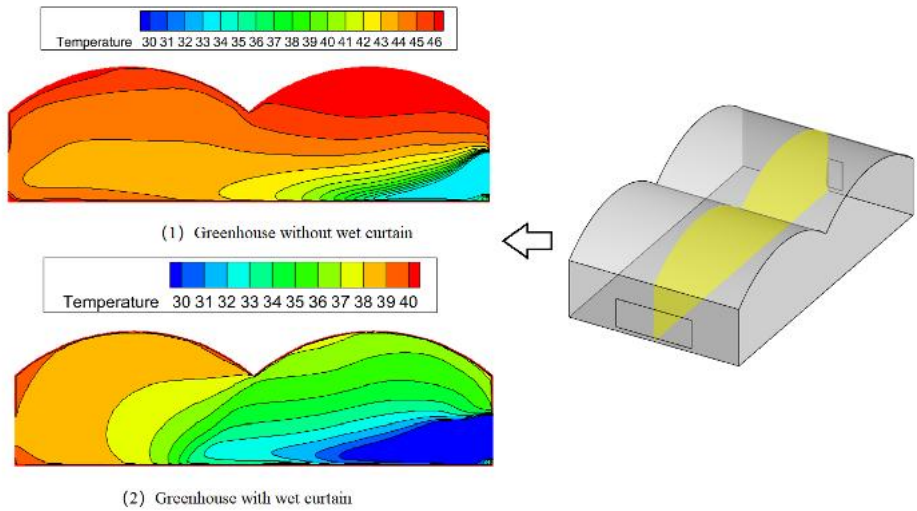


Fig. 7 - Temperature distributions in greenhouse

As illustrated in **Fig. 7**, two distinct temperature gradients appeared in the greenhouse, oriented horizontally and vertically. Owing to the transparent covering material, a substantial portion of solar radiation penetrated the greenhouse, resulting in indoor temperatures considerably higher than ambient levels.

The incoming air, either ambient or pre-cooled by the wet curtain, mixed with the warmer indoor air, thereby reducing the greenhouse temperature. The gradual intermingling of warm and cool air generated a temperature gradient along the direction of airflow. The vertical temperature gradient was influenced by two primary factors. First, because the air inlet was located at the lower portion of the greenhouse, the relatively cool air tended to accumulate near the floor under gravitational forces. Second, the polycarbonate material at the greenhouse ceiling directly absorbed a portion of the solar radiation, raising its own temperature and consequently creating a high-temperature zone near the roof.

A comparison between **Fig. 7** (1) and (2) revealed that the implementation of wet curtain substantially lowered the temperature in the crop-growing zone near the greenhouse floor. This phenomenon could be attributed to two key factors: (1) As outdoor air flowed through the wet curtain, the evaporation of water could absorb heat from the air, reducing the inlet air temperature below ambient levels. As a result, the air entering the greenhouse possessed an enhanced capacity to extract heat from the interior. (2) As depicted in **Fig. 7** (2), the cool air generated by the wet curtain gradually warmed upon entering the greenhouse. The heated air, driven by buoyancy forces, induced the natural convection beneath the greenhouse arch, as illustrated in **Fig. 9**. Such natural convection accelerates the mixing between the lower and upper regions of the greenhouse, thereby improving the uniformity of the indoor temperature distribution.

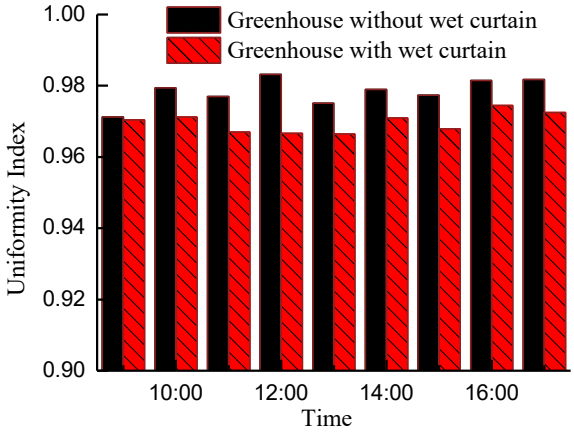


Fig. 8 - Uniformity Index of temperature with times

To better quantify the temperature distribution inside the greenhouse, **Fig. 8** presented the variation of the Uniformity Index of temperature over time.

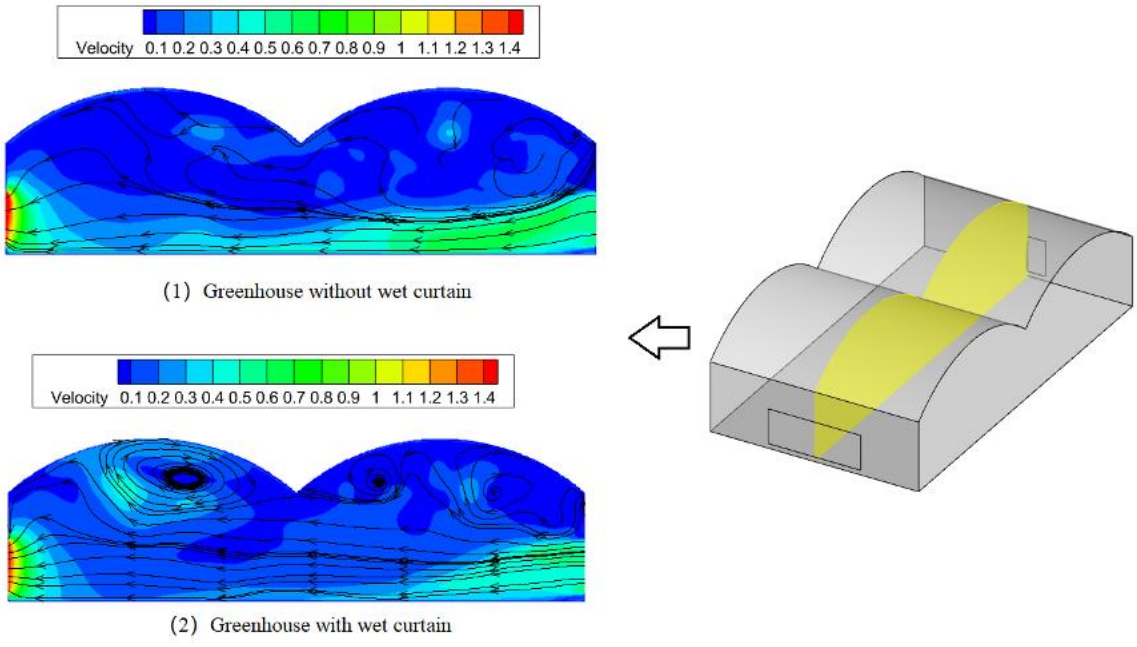


Fig. 9 - Velocity distributions in greenhouse

It could be seen from **Fig. 8**, the uniformity index under both conditions remained above 0.96 between 9:00 and 17:00, with relatively small overall fluctuations. It should be noted, however, that the uniformity index in the greenhouse without a wet curtain was slightly higher than that in the greenhouse with a wet curtain at most time points. Combined with the preceding analysis of temperature gradients, this can be explained by the fact that after the wet curtain system introduces cool air into the greenhouse, a distinct cold–hot interface forms in the horizontal airflow direction, causing a slight statistical decline in the uniformity index that measures the overall spatial distribution. Nevertheless, it is precisely this pronounced horizontal temperature difference that acts as the key driving force for the natural convection described earlier. As pointed out in the text, the cool air gradually warms after entering the greenhouse and rises under buoyancy, effectively accelerating the mixing between the cooler lower zone and the warmer upper zone of the greenhouse.

It could be found from **Fig. 9** (1) and (2) that, introducing wet curtain in greenhouse, the low-temperature air cooled by the wet curtain entered through the air inlet at a relatively high velocity, forming a stable cold air jet. This jet advanced along the ground while tending to accumulate near the greenhouse floor due to its lower temperature and higher density. As the flow developed, the cold air mixed with the warm air within the greenhouse, resulting in the decrease in its density. Under the effect of buoyancy, the warmed air gradually raised, eventually forming an updraft near the greenhouse arch. After reaching the top of the greenhouse, the ascending airflow was redirected by the enclosure. Part of the airflow moved forward and the others reversed, thereby generating two relatively regular large-scale recirculating vortices across the greenhouse cross-section. In contrast, if the greenhouse did not introduce wet curtain, the air inlet temperature was equal to the ambient temperature, resulting in a negligible density difference and weak buoyancy effects. The airflow advanced primarily in the horizontal direction, failing to establish effective vertical stratification or uplift.

Fig. 10 illustrated the temporal variation of the average air velocity in the two greenhouses. It could be seen from Fig. 10 that from 8:00 to 12:00, the average air velocity gradually increased with times, and reached maximum values of 0.16 m/s (without wet curtain) and 0.18 m/s (with wet curtain) at 12:00, respectively. After 12:00, the average air velocity decreased. During the 8:00 ~ 12:00 period, the intensifying solar radiation raised the temperature in the greenhouse, thereby increasing the vertical temperature gradient within the greenhouse and promoting fluid mixing.

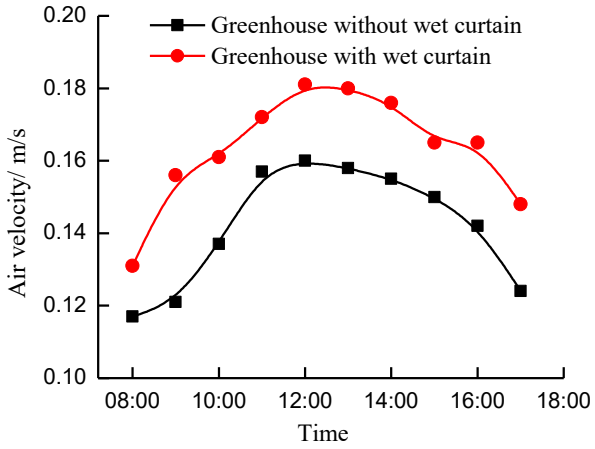


Fig. 10 - Average velocity with times

As also shown in **Fig. 10**, the implementation of pad ventilation enhances indoor air velocity, achieving an increase ranging from 8.38% to 22.40% during the 8:00 ~ 17:00 period.

The effect of the inlet velocity

Fig. 11 illustrated the average temperature in greenhouse for different inlet air velocity at 12:00. As depicted in **Fig. 11**, an increase in inlet velocity led to a gradual decline in the average greenhouse temperature, albeit with a decreasing rate of reduction. When the inlet velocity increased from 0.25 m/s to 0.5 m/s, the average greenhouse temperature decreased from 41.44 ℃ to 37.88 ℃, representing a cooling

rate of 8.59%. In contrast, when the inlet velocity rose from 1.25 m/s to 1.5 m/s, the temperature reduction rate was merely 0.64%.

At low inlet velocities, the residence time of air within the wet curtain was relatively prolonged, allowing sufficient heat and moisture exchange between the air and the water in the wet curtain, thereby enabling substantial cooling. Consequently, an increase in inlet velocity effectively augmented the influx of cooled air into the greenhouse, significantly reducing the average indoor temperature.

However, as the inlet velocity continued to increase, the residence time shortened, and the heat and mass transfer between the water film and the airstream became incomplete, resulting in a diminished decline in outlet air temperature. Moreover, high inlet velocities enhanced the inertial dominance of the cold jet, causing the low-temperature air to traverse the crop zone rapidly without adequate mixing with the warm air in the greenhouse before advancing toward the outlet, thereby compromising the effectiveness of heat exchange. Hence, the reduction in average greenhouse temperature exhibited a nonlinear pattern. A comprehensive analysis of the average greenhouse temperature trends presented in **Fig. 11** indicated that once the inlet velocity exceeded 0.75 m/s, the temperature decline slowed markedly, and the marginal cooling benefit diminished. Accordingly, this study identified an inlet velocity range of 0.75 ~ 1.0 m/s as optimal for pad operation.

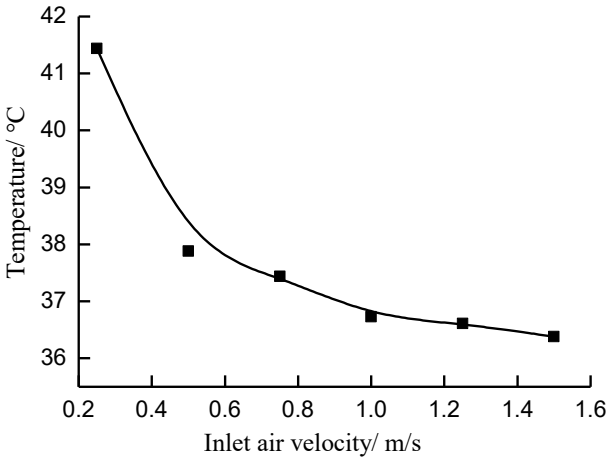


Fig. 11 - Average temperature in greenhouse for different inlet air velocity

CONCLUSIONS

A coupled numerical model of the wet curtain and greenhouse was developed and validated to investigate the mechanisms governing the influence of the wet curtain cooling system on the greenhouse thermal environment in summer. The main conclusions were as follows:

(1) The established mathematical model could accurately describe its cooling processes. The air cold by wet curtain implemented as a boundary condition for greenhouse simulations, the relative deviation between the simulated and measured average greenhouse temperatures was less than 7%, indicating that the established model effectively predicted the thermal performance of the greenhouse with wet curtain.

(2) The cooling performance of the wet curtain pronounced diurnal variation. During the period from 8:00 to 12:00, the temperature difference between the outdoor air and the water in wet curtain increased with intensifying solar radiation, enhancing the driving force for water evaporation and progressively improving cooling efficacy. After 12:00, as solar radiation weakened, the cooling capacity gradually declined. Over a typical day, the pad reduces the average greenhouse temperature by 2.33 ℃ to 4.20 ℃, with the maximum cooling effect occurring at 12:00.

(3) The cold air produced wet curtain could modify the airflow pattern within the greenhouse. Low-temperature air entered through the lower inlet as a jet, accumulated near the crop zone under gravitational forces, and subsequently rose upon heating due to buoyancy, forming two large-scale recirculating vortices across the greenhouse cross-section. This configuration effectively promoted mixing between the upper and lower air layers, resulting in a more uniform temperature distribution. Compared with forced ventilation without pad operation, the pad increased the average air velocity within the greenhouse by 8.38% to 22.40%.

(4) Parametric analysis of inlet velocity revealed that the average greenhouse temperature decreases nonlinearly with increasing inlet velocity, with the rate of reduction gradually slowing. Once the inlet velocity

exceeded 0.75 m/s, the marginal cooling benefit declined significantly. An inlet velocity in the range of 0.75 ~ 1.0 m/s was recommended.

ACKNOWLEDGMENTS

This work was supported by Doctoral Fund of Dezhou University (NO. 4022504135).

REFERENCES

[1] Abedrabboh, O., Koç, M., & Biçer, Y. (2024). Comparative thermoeconomic assessment of renewable-driven hybrid-cooled sustainable greenhouses for subtropical regions. *Energy Conversion and Management*, Vol. 300, pp.117990, Qatar.

[2] Al-Ismaili, A. M. (2009). Modeling of a humidification-dehumidification greenhouse in Oman [Doctoral dissertation, Cranfield University], United Kingdom.

[3] Allali, F. E., Fatnassi, H., Demrati, H., Molina Aiz, F. D., Gourdo, L., Errami, Y., Wifaya, A., & Aharoune, A. (2024). CFD-based optimization of Direct evaporative cooling systems for Canarian greenhouses in Semi-Arid regions. Energy & Buildings, Vol. 323(2024), pp. 114767, Morocco.

[4] Bergman, T. L., Lavine, A. S., Incropera, F. P., & DeWitt, D. P. (2011). *Introduction to heat transfer*. John Wiley & Sons, United States.

[5] Chen, L., Xu, L., & Wei, R. (2023). Energy-saving control algorithm of Venlo greenhouse skylight and wet curtain fan based on reinforcement learning with soft action mask. *Agriculture*, 13(1), 141, Shanghai, China.

[6] Chen J.R., (2015). Study of Indoor Environment Dynamic Simulation of Layer-House Based on the Model of Caged Pens of Porous Media, Master dissertation (基于笼养鸡只多孔介质模型的蛋鸡舍内环境动态模拟研究), Hebei University of Technology, China.

[7] Dietz, K. J., Zörb, C., & Geilfus, C. M. (2021). Drought and crop yield. *Plant Biology*, Vol. 23(6), pp. 881-893, Germany.

[8] Fu, Q., Li, X., Zhang, G., & Li, X. (2023). A temperature and vent opening couple model in solar greenhouses for vegetable cultivation based on dynamic solar heat load using computational fluid dynamics simulations. *Journal of Food Process Engineering*, Vol. 46(2), pp. e14240, Beijing/China.

[9] Garcia, G., Treccarichi, S., Ciccarello, L., Al Achkar, N., Arena, D., Soler, S., Prohens, J., & Branca, F. (2026). Agronomic performance of tomato rootstocks under Mediterranean greenhouse organic farming. *Agronomy*, Vol.16(5), pp. 515, Italy.

[10] He, X., Wang, J., Guo, S., Zhang, J., Wei, B., Sun, J., & Shu, S. (2018). Ventilation optimization of solar greenhouse with removable back walls based on CFD. *Computers and Electronics in Agriculture*, Vol. 149, pp. 16-25, Nanjing/China.

[11] Jerszurki, D., Saadon, T., Zhen, J., Agam, N., Tas, E., Rachmilevitch, S., & Lazarovitch, N. (2021). Vertical microclimate heterogeneity and dew formation in semi-closed and naturally ventilated tomato greenhouses. *Scientia Horticulturae*, Vol. 288, pp. 110271, Israel.

[12] Jiang, R., Li, Q., & Guo, F. (2023). Influence of outdoor environmental parameters on brackish water desalination system in greenhouse (室外环境参数对温室苦咸水淡化系统的影响). *Gas & Heat*, Vol. 43(5), pp. 28-34, Jinan/China.

[13] Jiao, N., Zhu, D., Jing, Y., Liu, M., & Liu, C. (2024). Research on determination method of greenhouse wet pad-fan operating parameters based on numerical simulation (基于数值模拟的温室湿帘—风机运行参数确定方法研究). *Journal of Chinese Agricultural Mechanization*, Vol. 45(5), pp. 79-84, Yangling, Shaanxi/China. DOI: 10.13733/j.jcam.issn.2095-5553.2024.05.012

[14] Krishna, H., Hebbar, S., Kumar, P., Sharma, S., Kumar, R., Tiwari, S., Maurya, S., Srivastava, K., Pal, G., Bahadur, A., & Behera, T. K. (2024). Navigating challenges and prospects in off-season vegetable production. *Vegetable Science*, 51, pp. 97-105 India.

[15] Lei, W., Lu, H., Qi, X., et al. (2023). Field measurement of environmental parameters in solar greenhouses and analysis of the application of passive ventilation. *Solar Energy*, Vol. 263, pp. 111851, Shandong/ China.

[16] Moreno-Teruel, M. Á., Molina-Aiz, F. D., López-Martínez, A., Marín-Membrive, P., Peña-Fernández, A., & Valera-Martínez, D.L. (2022). The influence of different cooling systems on the microclimate, photosynthetic activity and yield of a tomato crops (*Lycopersicum esculentum Mill*.) in Mediterranean greenhouses. *Agronomy*, Vol. 12(2), pp. 524, Spain.

[17] Park, S. J., Lee, I. B., Lee, S. Y., Kim, J. G., Choi, Y. B., Decano-Valentin, C., Cho, J. H., Jeong, H. H., & Yeo, U. H. (2022). Numerical analysis of ventilation efficiency of a Korean Venlo-type greenhouse with continuous roof vents. *Agriculture,* Vol.12(9), pp. 1349, Korea.

[18] Peng, Y., Ma, X., Wang, Y., Li, M., Gao, F., Zhou, K., & Aemixay, V. (2023). Energy performance assessment of photovoltaic greenhouses in summer based on coupled optical-electrical-thermal models and plant growth requirements. *Energy Conversion and Management,* Vol. 287, pp. 117086, Kunming, China.

[19] Rahman, M. S., Manjira, S., Majumder, M. K., & Rahman, S. (2021). Socio-economic determinants of off-season summer tomato cultivation. *International Journal of Vegetable Science*, Vol. 27(3), pp. 252-259, Bangladesh.

[20] Shen, L., Xue, K., Xiao, B., & Chen, Y. (2026). Simulation of Heat Flow Field in Venlo Greenhouse in South China and Optimization of Its Cooling and Dehumidification System. *Processes*, 14(9), 1331, Guangzhou, China.

[21] Yang, Y., & Liu, Y. (2024). The impact of different natural ventilation methods on the performance of desert solar greenhouses (不同自然通风方式对沙漠日光温室性能的影响). *Agriculture and Technology*, Vol. 44(10), pp. 18-23, Tarim/China. DOI: 10.19754/j.nyyjs.20240530005

[22] Yoon, J., Song, H., & Jang, E. S. (2024). Computational fluid dynamics analysis of ventilation characteristics with various design parameters in single-span greenhouses. *Energy Sources, Part A: Recovery, Utilization, and Environmental Effects*, Vol. 46(1), pp. 11938-11951, Korea.

[23] Zhang, J., Zhao, S., Dai, A., et al. (2022). Greenhouse natural ventilation models: How do we develop with Chinese greenhouses? *Agronomy*, Vol.12(9), pp. 1995, Beijing/China.

[24] Zhang, J., Zhao, S., Dai, A., Wang, P., Liu, Z., Liang, B., & Ding, T. (2025). Microclimate prediction of solar greenhouse with pad-fan cooling systems using a machine and deep learning approach. *Agriculture*, Vol.15(20), pp. 2107, Dalian/China.

[25] Zhang, Y., Sun, W., Jin, L., Yang, H., Wang, J., & Shu, S. (2025). Computational Fluid Dynamics-Based Simulation of Ventilation in a Zigzag Plastic Greenhouse. *Horticulturae*,11(2), 175, Nanjing, China

A REVIEW ON THE DEVELOPMENT STATUS AND TRENDS OF KEY TECHNOLOGIES FOR HYBRID TRACTORS

/

混合动力拖拉机关键技术发展现状及趋势综述

Zhaoyue LIU[1)], Jikang XU[*1)], Xiaodong LV[1)], Jinliang LI[2)]

[1)] Qingdao Agricultural University/ China;

[2)] Lingong Agricultural Equipment Co., Ltd. / China

Corresponding author: Jikang Xu; E-mail: xujikang@qau.edu.cn

DOI: https://doi.org/10.35633/inmateh-79-15

Keywords: *Power Topological Structure; Energy Management Strategy; Energy Source Configuration; Technical Bottlenecks; Research Prospects*

ABSTRACT

Driven by global agricultural mechanization and green low-carbon transformation, hybrid tractors have become a key focus in agricultural machinery competition due to fuel economy and operational adaptability. Using literature review and comparative analysis, this paper summarizes global and domestic technological development and characteristics of typical models. It analyzes three core power topological structures, compares energy configurations and management strategies, clarifies applicable scenarios and pros and cons of different routes, and points out bottlenecks in power coupling, energy storage and control, as well as industrial dilemmas like high costs and poor supporting facilities.

摘要

在全球农业机械化与绿色低碳转型的双重驱动下，混合动力拖拉机凭借其燃油经济性与作业适应性优势，成为全球农机技术竞争的焦点。为厘清混合动力拖拉机关键技术的发展现状与现存问题，为该领域技术的进一步优化和规模化推广提供参考，本文采用文献梳理与对比分析的方法，系统归纳了该领域国内外技术发展格局与代表机型技术特征，深入剖析了三类核心动力拓扑结构的工作原理与性能差异，对比了不同能量源配置方案、能量管理策略的应用效果与验证方法。研究明确了各类技术路线的适用场景与优劣势，指出了当前该领域在动力耦合、储能系统、控制策略方面的研发瓶颈，以及成本、配套设施等产业化应用难题。

INTRODUCTION

Currently, global agriculture is transforming toward industrial model upgrading and sustainable development, and the problems of high emissions and high energy consumption commonly existing in traditional agricultural machinery have become increasingly prominent. As the core power equipment in agricultural production, the energy consumption control and emission management of tractors have become critical to industrial development. Pure electric tractors are limited by shortcomings such as insufficient horsepower, short endurance and operating time, and poor environmental adaptability, and it will take time to overcome these problems. Against this background, hybrid tractors, which integrate traditional fuel power and electric power and realize collaborative energy distribution through a power coupling system, have become a key transitional technology. With remarkable effects on energy conservation and emission reduction as well as great potential for improving operational efficiency, they also represent an important direction for the iterative upgrading of agricultural machinery and equipment. Policies from various countries have gradually increased support. China's 14th Five-Year Plan clearly includes high-end intelligent and new energy agricultural machinery in key supported areas, creating a favorable environment for the technical research and development and industrialization of hybrid tractors (*Yin et al., 2025*).

At present, the technology of hybrid tractors has formed a diversified pattern with three mainstream technical routes, namely series hybrid, parallel hybrid and series-parallel hybrid, developing in parallel. Meanwhile, energy management strategies have gradually evolved from rule-based control to optimization algorithms and intelligent strategies, which has become a current research hotspot. Nevertheless, this field still faces core controversial issues and technical bottlenecks as follows: the low collaborative efficiency of the power coupling system restricts the performance improvement of the whole machine.

The excessively high cost of power batteries leads to the high price of the complete machine, affecting its market promotion; energy management strategies are highly complex and difficult to adapt to diverse operating scenarios, and their stability and reliability need to be further enhanced. These problems jointly hinder the industrialization process of hybrid tractors, and further exploration in technological breakthroughs and path optimization is required to realize their large-scale application (*Li, 2026*). Current reviews of hybrid tractors only discuss individual technologies (topology or energy management) without systematic comparisons across the full technical chain: topology, coupling, components, strategies and configurations. Most reviews focus on regional research rather than establishing a global framework covering European, North American and Asian technical routes, and seldom summarize core debates and industrial limitations from practical engineering cases.

This paper reviews global advances in hybrid tractor technologies, compares three typical topologies and various energy management schemes, identifies industrialization barriers and technical disputes, and predicts future trends to offer systematic support for further research and engineering implementation.

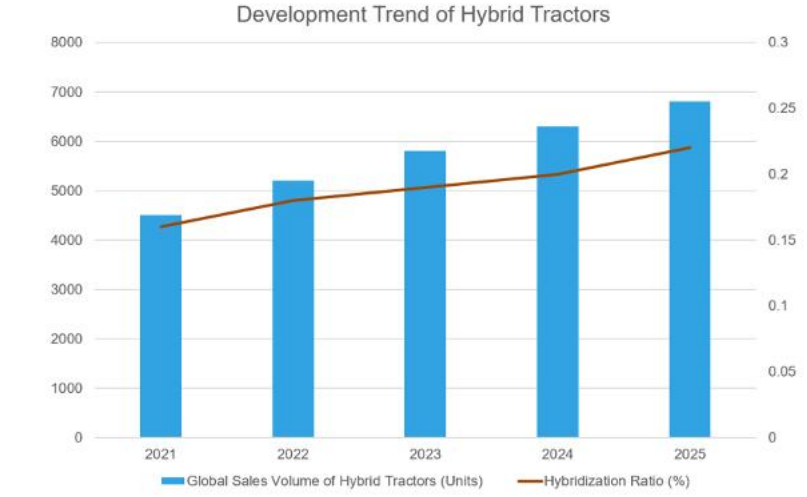
The objective of this review is to systematically analyze the technical routes, key bottlenecks, and development trends of hybrid tractors, aiming to provide a reference for their performance optimization and industrial promotion.

Development Background and Driving Forces

Agricultural machinery, as an important part of non-road mobile machinery, has attracted increasing attention concerning its emission problems. Traditional agricultural tractors are usually equipped with oversized diesel engines and emit large quantities of pollutants and carbon dioxide during field operation. Studies have shown that agricultural machinery and equipment are among the major contributors to emissions in the agricultural sector. This situation runs counter to the trend of global sustainable development, prompting various countries to pursue more environmentally friendly power solutions for agricultural applications **Error! Reference source not found.**.

Policy-driven support serves as a critical impetus for the development of hybrid tractors. The key special project on Key Technologies for Factory Agriculture and Intelligent Agricultural Machinery Equipment implemented under China's 14th Five-Year Plan has accelerated the research, development and industrial application of high-end intelligent agricultural power equipment. The Agricultural Mechanization Station of the Ministry of Agriculture and Rural Affairs has provided clear directional guidance for the industry by organizing technical seminars on the test and appraisal of power machinery, focusing on technological innovation and test certification of new energy agricultural machinery and equipment. The field trials and verification of new energy and high-end intelligent tractors carried out in Tacheng, Xinjiang in 2025 systematically assessed key indicators including product reliability and operating efficiency, providing an important basis for technological optimization and industrialization of such equipment **Error! Reference source not found.**.

Market demand is also a key factor in the development of hybrid tractors. With the increase in the number of large-scale farms, the demand for hybrid tractors—agricultural machinery featuring high efficiency and low operating costs—is growing steadily, as shown in Figure 1 and Figure 2.



Data sources: Market reports on hybrid tractors from 2021 to 2025 by authoritative institutions such as Global Info Research, Market Research Future, and QYResearch, compiled through cross-validation.

Fig. 1 - Development Trends of Hybrid Tractors

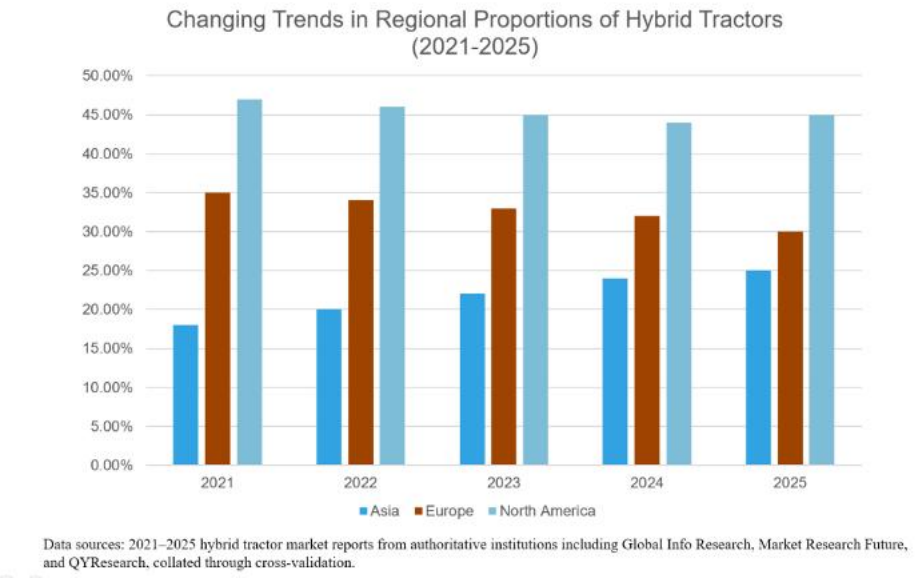


Fig. 2 - Trend of Regional Proportion Change of Hybrid Tractors

Taking the world's largest hybrid wheeled tractor launched by Zoomlion as an example, it is specially designed for high-intensity and high-efficiency operations in ultra-large-scale farms. It can achieve a continuous operating area of 7,200 mu within 12 hours, with a 15% improvement in operating efficiency and a 10% reduction in fuel consumption. Such remarkable performance advantages endow it with strong competitiveness in the international market. This high-quality agricultural machinery equipped with cutting-edge technology can effectively solve the pain points of modern agriculture (*Han, 2023*).

Development History

Since the 19th century, the development of hybrid tractors has gradually realized the leap from conceptual prototype to commercial explosion, as shown in Table 1. From the hybrid system combining steam and internal combustion engines, to the research and development of modern hybrid technologies, and then to the formation of a multi-architecture product matrix, it indicates that hybrid power technology has become increasingly mature (*Niu, 2025; Wen et al., 2025*).

Table 1

The Development History of Hybrid Tractors

Stage	Time Range	Core Progress	Representative Events
Technical Embryonic Stage	1970s–1999	Integration of steam and internal combustion engines, accumulation of hydraulic transmission technology.	1970s: US initiated research on hybrid power for construction and agricultural machinery; 1997: John Deere launched the world's first hybrid tractor prototype.
Exploration Stage	2000-2016	European and American enterprises launched research and development of modern hybrid power technology.	India's ITL launched commercial prototypes.
Independent Innovation Stage	2017-2024	Domestic enterprises broke through core technologies and broke the foreign monopoly.	Yuchai IE-POWER powertrain was implemented; LiuGong 350 hp-class hybrid models were mass-produced.
Commercial Explosion Stage	From 2025	Formation of a multi-architecture product matrix and implementation of policy subsidies.	Zoomlion series-parallel hybrid models were mass-produced; special subsidies were implemented in Jiangsu and other regions.

Stage Achievements

A number of iconic prototype models have emerged in the field of hybrid tractors at present, with major breakthroughs achieved in core performance. A collaborative development pattern of multiple configurations has been formed, and a complete industrial ecosystem centered on "configuration innovation — control optimization — independent component development — standard support" has been gradually built, driving the industry to achieve leapfrog development.

Hybrid configurations have become the mainstream direction for heavy-duty hybrid tractor models. The hydraulic-electric hybrid configuration based on HMCVT (Hydromechanical Continuously Variable Transmission) enables efficient power transmission. HMCVT transmits power in parallel through dual flows, namely the hydraulic branch and the mechanical branch, and its overall efficiency depends on the synergistic cooperation between the two branches. The hydraulic branch, i.e., the pump-motor system, features relatively low efficiency (generally 60% to 80%), while the mechanical branch boasts high efficiency (up to over 95%). The overall transmission efficiency of the system is improved by optimizing the power split ratio between the two branches *(Wang, 2018; Xu et al., 2012*).

Currently, a virtuous cycle has taken shape among policy subsidies, technological R&D, production and manufacturing, and market application, laying a solid foundation for the sustainable development of the hybrid tractor industry. It has driven the sector to achieve leapfrog development, gradually shifting from "foreign technological monopoly" to "domestic independent innovation" and from "single-point demonstration application" to "full scenario coverage".

Research Progress Abroad

Research progress on hybrid tractors varies in different regions abroad, with characteristic technical routes formed in accordance with local farming scenarios, accompanied by high technical maturity and industrialization levels.

North America focuses on high-horsepower models, with power-split hybrid technology as the core, featuring mature commercialization and comprehensive experimental data, which are suitable for large-scale farming. As shown in Figure 3(a), studies on the American John Deere 8R 410 Hybrid series-parallel power-split tractor demonstrate that control strategies such as MPC are adopted to improve energy efficiency. The Case NH Puma Hybrid series has a rated power of 250 kW and a comprehensive fuel-saving rate of 24%, and has been put into large-scale batch production (*Zhou et al., 2024; Wang et al., 2025*).

In Europe, plug-in hybrid technology serves as the core, with emphasis on multi-energy coupling to adapt to diverse low-carbon operating scenarios. As shown in Figure 3(b), the Italian Antonio Carraro SRX Hybrid, a parallel-torque-coupled hybrid tractor, integrates a 55 kW Stage 5 internal combustion engine and a 20 kW electric motor. It supports multiple operating modes including pure electric, hybrid, energy recovery, and power assist, and features a compact articulated narrow body for flexible orchard operations. It combines the advantages of fuel saving and low emissions, and is also integrated with an Industry 4.0 intelligent control system to achieve high efficiency, environmental protection, and operational stability. In 2019, Germany's Fendt launched the X concept series, a series hybrid tractor without energy storage devices, as illustrated in Figure 3(c). Figure 3(d) presents the series-parallel hybrid topology adopted by Austria's STEYR, with a peak power of 250 kW. This model achieves a maximum gradeability of 35° and a fuel saving rate of 25% in tests conducted in the Alpine region. Relevant studies also indicate that control strategies such as MPC are employed (*Wang, 2024; Varlese et al., 2025*).

Relying on their technological advantages in small and medium-horsepower models, Japan and South Korea focus on research and development in this field, promoting the integration of electrification and intelligence to adapt to small-scale and refined farming operations. Some scholars have carried out relevant experimental verifications, laying a foundation for industrialization (*Xu, 2021*).

Research Progress in China

In recent years, the hybrid tractor industry in China has developed rapidly. A number of leading enterprises, including China YTO Group Corporation, Yuchai Group and Zoomlion Heavy Industry, have launched a variety of innovative products suitable for different scenarios, achieving breakthroughs in high-horsepower models, small and medium-sized facility horticulture models and other fields. For example, more than 20 types of power equipment were displayed at the on-site demonstration of high-end intelligent agricultural power equipment held in Yangling, Shaanxi Province in 2025, highlighting the progress of China in this field.

As a leading enterprise in China's agricultural machinery industry, China YTO Group launched the Dongfanghong HB 2204 series hybrid tractor in 2022, which is equipped with a 161.7 kW China IV diesel engine and an Electric Continuously Variable Transmission (E-CVT) system, with a localization rate of over 85%. Field tests conducted in the corn planting area of Zhoukou, Henan Province show that this model has a plowing fuel consumption of 15.2 L/h, which is 23% lower than that of traditional tractors, an operating efficiency of 6.5 hectares per hour, and a brake energy recovery efficiency of 18% (Anon., 2023). Yuchai Group boasts mature powertrain technology. As shown in Figure 3(e), the IE-POWER series hybrid powertrain released in 2021 consists of an engine, a generator, a drive motor and an electric-shift gearbox, suitable for tractors with 200–260 horsepower. Applications in the sugarcane planting areas of Guangxi show that this powertrain reduces the comprehensive fuel consumption of tractors by 10%-30%, and decreases the failure rate by 5%-30% compared with traditional transmission systems (*Anonymous, 2022*).



(a) John Deere 8R 410 Hybrid (USA) (Series-Parallel Power-Split Type, 2024)



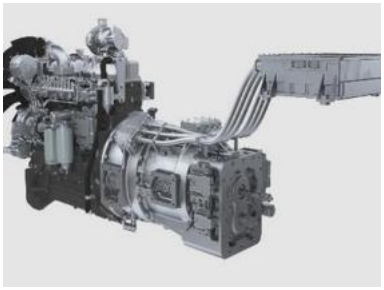
(b) Antonio Carraro SRX Hybrid (Italy) (Parallel-Torque Coupling Type, 2018)



(c) Germany Fendt X concept series (Series Type without Energy Storage Device, 2019)



(d) STEYR Hybrid CVT Tractor (Asymmetric Power Distribution + Intelligent Coupling Control, 2023)



(e) IE-POWER Hybrid Powertrain (Centralized Electric Drive Continuously Variable Power System, 2021)



(f) "Honghu" T300 High-Power Hybrid Tractor (400 HP New Energy Intelligent Agricultural Machinery, 2022)



(g) Guangxi Liugong LT3504-CE Tractor (Conventional Series Type, 2023)



(h) SDLG T3204-7E Tractor (Series-Parallel Power-Split Type, 2024)



(i) ZOOMLION Hybrid Wheeled Tractor (Series-Parallel Hybrid Configuration, 2025)

Fig. 3 - Typical hybrid electric tractor products worldwide

SDLG Agricultural Machinery adopts the power-split technical route. Studies have shown that power-split technology transmits power through the parallel combination of hydraulic and mechanical systems, which can significantly improve transmission efficiency. Especially under medium and low-speed working conditions such as plowing, the hydraulic power split ratio can be lower than 20%, with a high proportion of mechanical transmission, and the efficiency is close to that of pure mechanical transmission (*Li et al., 2026*). In vegetable greenhouse operations in Shouguang, Shandong Province, this model features a turning radius of only 1.8 m, a gradeability of 25°, reduces comprehensive fuel consumption by 28% compared with conventional models, and is equipped with an electric output function to adapt to various agricultural implements. Zoomlion focuses on small and medium-sized hybrid tractors.

The CA504ET distributed drive model launched in 2023 has a power of 74.6 kW, adopts wheel motor differential steering with a turning radius of less than 1.5 m, and supports 1-hour fast charging. In tea planting operations in the hilly areas of Hunan Province, this model achieves a pure electric driving range of 80 km and a comprehensive energy-saving rate of 22%, making it the first facility horticulture hybrid tractor practically promoted in China (*Zhang et al., 2003*).

In addition, as shown in Figure 3(f), the 300-horsepower "Honghu" T300 pure electric intelligent tractor launched by the Chinese Academy of Sciences in 2022 is customized for black soil farmland. It adopts a pure electric drive configuration without internal combustion engine and hybrid energy storage system, achieving high efficiency and stability in power output. This design optimizes energy utilization through the hybrid power system and significantly improves continuous operation capacity, with a single operation duration of up to 10 hours and an operation efficiency of 12 hectares per hour, representing an efficiency improvement of approximately 30% compared with traditional models. This indicates that China has joined the ranks of international advanced levels in the field of high-power pure electric intelligent tractors (*Ren et al., 2022*).

Notably, although some domestic models have achieved a high localization rate, China still has weak independent research and development capabilities for high-end core components, whose performance indicators lag behind international advanced levels, leading to high import dependence. This has become the primary bottleneck restricting the development of the industry. The constraints are mainly concentrated in core modules of high-end Electric Continuously Variable Transmission (E-CVT), high-performance motor controllers, special sensors and other fields (*Mocera, 2020*). Compared with the independently developed CVT gearboxes of international brands with a transmission efficiency of over 95%, domestically produced E-CVT gearboxes in China still have gaps in transmission efficiency, load-bearing capacity and service life. Problems such as wear and shift shock are more likely to occur under long-term high-load operation. For high-horsepower models, the permanent magnet synchronous motors independently developed in China are inferior to international counterparts in terms of power density and heat dissipation performance. In addition, the insufficient precision manufacturing level of core components and the poor quality stability of basic parts such as high-end bearings and seals also contribute to the performance gaps (*Wu, 2019; Huang et al., 2025*).

On the other hand, compared with the intelligent optimization algorithms widely adopted internationally, such as Model Predictive Control (MPC) and Equivalent Consumption Minimization Strategy (ECMS), most enterprises in China still apply simple logic threshold control strategies, which can only realize basic power mode switching and fail to optimize energy flow distribution in real time according to load fluctuations and varying operating scenarios in field farming (*Qiu, 2026*). For example, although the Zoomlion CA504ET model has achieved breakthroughs in pure electric range and comprehensive energy-saving rate during tea planting operations in the hilly areas of Hunan Province, the energy switching response lags under sudden load changes, resulting in partial energy waste.

Horizontal Comparison of Technical Routes for Hybrid Tractors Worldwide

As shown in Table 2, the differences in the technological development of hybrid tractors worldwide are not prominent, and several key distinctions mainly originate from variations in technological accumulation, industrial foundations, and market demands. Foreign manufacturers focus on the optimization of power-split series-parallel hybrid technology, which is adaptable to multiple horsepower ranges and operating scenarios with mature industrialization. Series, parallel, and series-parallel configurations each have their own emphases and are suitable for regional application scenarios, among which the series-parallel configuration acts as the core technology with extensive coverage of application scenarios.

The domestic technical route emphasizes practicality and presents a diversified development trend. Series and extended-range configurations represent the mainstream, parallel configurations have achieved gradual breakthroughs, and series-parallel configurations remain in the research and development (R&D) and pilot stage. Series configurations are widely applied, parallel configurations are dedicated to refined agricultural operations, and the core technologies of series-parallel configurations rely on imports, failing to realize large-scale industrialization.

In terms of energy sources, foreign countries feature a diversified pattern, with lithium-ion batteries as the primary energy source and composite energy storage as the auxiliary; new energy sources such as hydrogen fuel have already been industrialized. In China, lithium-ion batteries are the absolute mainstream, composite energy storage is in pilot application, and hydrogen fuel is still in the R&D and demonstration stage (*Hu et al., 2025*).

In terms of intelligence, foreign countries have formed a complete intelligent operation system. Combined with technologies such as intelligent algorithms and autonomous navigation, adaptive operating conditions and full life cycle management have been realized. In contrast, China is still in the basic stage, with core focus on navigation and simple operating condition switching, poor system coordination, and lack of full life cycle management functions.

At the supply chain level, foreign countries have an extremely high localization rate of core components and a complete supply chain. In China, the localization of medium and low-end components is mature, while high-end components rely on imports, resulting in polarized cost control. Overall, foreign countries focus on high-end and diversified intelligence, while China emphasizes practicality and economy. With technological breakthroughs and the improvement of the industrial chain in the future, the gap is gradually narrowing (*Yu, 2022*).

Table 2

Horizontal Comparison of Technical Routes for Hybrid Tractors Worldwide

Comparison Dimension	Foreign Status	Domestic Status	Core Differences
Topology Configuration	Dominated by series-parallel (power-split) configuration;	Dominated by series/extended-range configuration; series-parallel configuration is in pilot stage	Foreign countries focus on high-end development; China focuses on practicality
Energy Source	Mature industrialization application of Lithium-ion battery + hybrid energy storage + hydrogen fuel	Lithium-ion battery as the main energy source, hybrid energy storage in pilot application; hydrogen fuel in R&D stage	Diversified energy sources abroad; single energy type in China
Intelligence Level	MPC/ECMS algorithms + autonomous navigation + remote diagnosis	Basic navigation + logic threshold control	Mature system collaboration abroad; domestic intelligence at basic stage
Localization Rate of Core Components	Localization rate of core components ≥ 95%	Independent production for medium and low-end components; 15%–30% of high-end components imported	Complete supply chain abroad; domestic high-end components rely on imports

Multi-Energy Coupling Mechanism

The multi-energy coupling mechanism serves as the foundation of a hybrid power system. Its core function is to coordinate, superpose, or distribute the power from different sources such as the engine and drive motor. Through three core coupling modes, it adapts to the varying load demands of tractors in different operations, ensuring smooth and efficient power output while maximizing energy utilization. The three coupling modes have clear divisions of labor and different applicable scenarios. There is no absolute superiority or inferiority among them, as all are designed to balance the overall power performance and energy efficiency of the tractor.

Power coupling is the most commonly used coupling mode. Its core logic is to superpose or distribute the output power of the engine and the drive motor, and dynamically allocate the power proportion of the two power sources according to the operating load, so as to avoid overload or inefficient operation of a single power source. The core equation is as follows:

$$P_{total} = P_{engine} \pm P_{motor} \text{ or } \tau_{output} = \tau_1 + \tau_2 \quad (1)$$

where: P_{total} is the total output power of the hybrid power system [kW];P_{engine} is the output power of the internal combustion engine [kW]; P_{motor} is the output power of the drive motor [kW]; τ_{output} is the total output torque of the hybrid power system [N·m]; τ_1 is the output torque of the internal combustion engine [N·m]; τ_2 is the output torque of the drive motor [N·m].

Its working process does not require strict synchronization of the rotational speed and torque of the power sources; power coordination is only realized through the coupling device, making it suitable for scenarios with large load fluctuations (*Wang et al., 2026*).

Speed coupling mechanisms typically employ planetary gears, differentials, or dedicated transmission devices to synthesize the speeds of the engine and motor in a fixed ratio, enabling continuously variable transmission or power splitting. In a study by Zuo Tiantian et al., Lagrange equations and dynamic models were established to analyze the differential transmission characteristics of the power coupling device for hybrid

tractors, verifying the effectiveness of speed coupling mechanisms in coordinating the speeds of different power sources (*Zuo et al., 2013*). Deng Xiaoting (*Deng, 2012; Deng et al., 2026*) and his colleagues designed a test bench for parallel hybrid electric tractors. Torque and speed sensors were used to monitor the speed difference between the engine and the motor in real time, and the coupling device was adopted to realize dynamic matching, which significantly improved the transmission efficiency.

Torque coupling directly superimposes the output torque of the engine and the drive motor and transmits it to the drive wheels through a coupling device. Its core advantage is fast dynamic response, making it suitable for scenarios requiring instant high torque such as slope climbing and heavy-load starting (*Wang et al., 2026*). Its working principle is that the torques of the two power sources are directly superimposed through gear meshing, clutches and other structures, without complicated speed coordination, enabling rapid output of high torque and improving the overall power performance. Torque coupling technology resolves the contradiction between instantaneous high-torque demand and system energy efficiency through efficient coordination of multiple power sources. Future research can further explore the dynamic response optimization of electromagnetic couplers, torque distribution strategies for hybrid energy systems, and thermal management schemes for high-power-density motors (*Dong, 2026*).

Power Mode Switching Logic

Power mode switching logic serves as the control center of a hybrid power system. Its core function is to automatically or manually switch among the four primary power modes based on real-time parameters such as tractor operating conditions, load magnitude, and energy storage status, so as to realize “on-demand energy supply” and maximize energy-saving effects and operational efficiency. The switching process is smooth without power interruption, adapting to the complex operating environment in farmland. Currently, the four core power modes are: pure electric drive mode; hybrid drive mode; regenerative braking mode; and idle stop mode. The specific trigger conditions and operating states are shown in Figure 4.

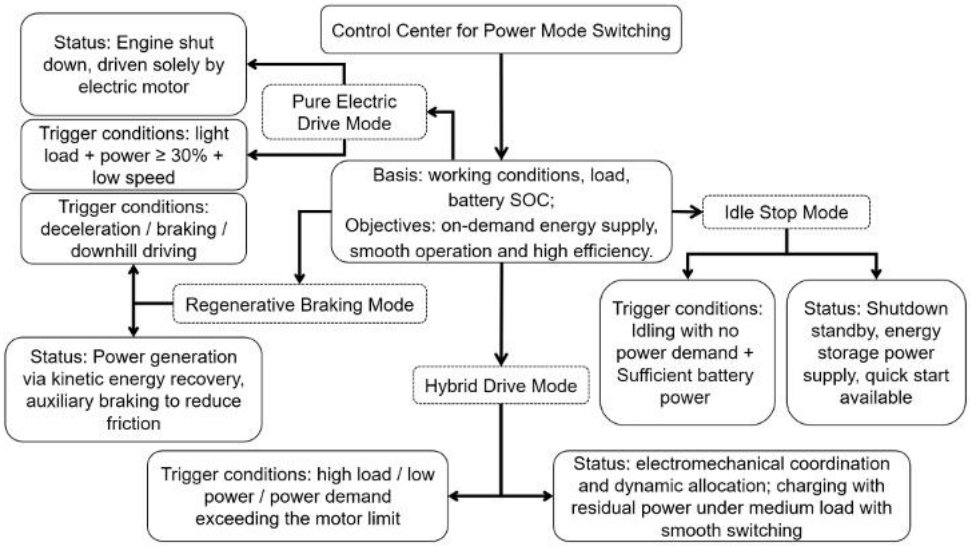


Fig. 4 - Block Diagram of Power Mode Switching Conditions and Operating States

Dynamic Regulation Principle of Energy Flow

The dynamic regulation principle of energy flow is the core of energy saving in hybrid power systems. It focuses on establishing a closed-loop mechanism of "energy recovery–storage–reuse". Through an intelligent control system, it monitors the generation, consumption and storage status of energy in real time, recovers and stores otherwise wasted energy, and redistributes it according to operational requirements, thus maximizing energy utilization efficiency.

Energy recovery marks the starting point of the closed-loop mechanism. Its core is to capture redundant energy generated during tractor operation and convert it into storable and utilizable electric energy, which mainly includes two types of recovery scenarios. The first is braking energy recovery, corresponding to the regenerative braking mode mentioned earlier. When the tractor decelerates, brakes or travels downhill, the motor operates in reverse, converting the kinetic energy of the whole machine into electric energy. The energy flow path is: Kinetic energy → Motor (generator mode) → Electric energy → Energy storage device. This is the primary scenario for energy recovery (*Wang et al., 2023*). The second is excess engine power recovery.

When the tractor operates under medium load, the engine maintains a high-efficiency speed range, and the part of output power exceeding the operational demand drives the generator to produce electricity, recovering the excess power and avoiding energy waste.

Energy storage acts as the core hub of the closed-loop mechanism. Its key lies in classified storage via different energy storage devices according to energy characteristics, balancing the requirements of "short-term rapid storage" and "long-term stable power supply". The mainstream storage scheme adopts a hybrid energy storage system of "hydraulic accumulator + power battery", and some high-end models are equipped with supercapacitors. Among them, hydraulic accumulators focus on short-term rapid energy storage and release, mainly storing the instantaneous large amount of energy generated during braking with fast response speed, which can quickly provide auxiliary power for high-load operations (*Wang et al., 2026*). Power batteries focus on long-term stable storage, storing electric energy recovered from excess engine power and braking, ensuring power supply for pure electric drive mode and auxiliary equipment. Supercapacitors are used for supplementary storage to improve the response speed of energy recovery and release, adapting to scenarios with frequent load fluctuations (*Ren et al., 2018*).

Energy reuse is the final stage of the closed-loop mechanism. Its core lies in rationally distributing the stored electric energy to various power components through an intelligent energy regulation system according to the real-time operational demands of the tractor, thereby achieving efficient energy utilization. It specifically includes three application scenarios:

First, driving energy supply. The stored electric energy is converted into power via the drive motor to assist the engine or independently provide power for the tractor's travel and operation, adapting to pure electric drive and hybrid drive modes.

Second, auxiliary energy supply. It supplies power to auxiliary components such as the whole-machine control system, hydraulic system, and navigation equipment, reducing energy loss caused by the engine driving the generator for power supply.

Third, emergency energy supply. When the engine malfunctions or the energy storage device has sufficient power, the pure electric drive mode can be used to complete emergency operations or field transfer, avoiding delays to the work progress (*Li et al., 2024*).

In summary, the core operating logic of a hybrid power system is as follows: it achieves power coordination through the multi-energy coupling mechanism, adapts to different operating scenarios relying on flexible power mode switching logic, and maximizes energy utilization efficiency via the closed-loop energy regulation of "recovery-storage-reuse". This ultimately fulfills the dual goals of energy conservation, consumption reduction and power performance enhancement, meeting the diverse and complex field operation demands of hybrid tractors.

Typical Structures and Extensions

The series hybrid topology, also known as the electrically coupled hybrid system, is characterized as shown in Figure 5.

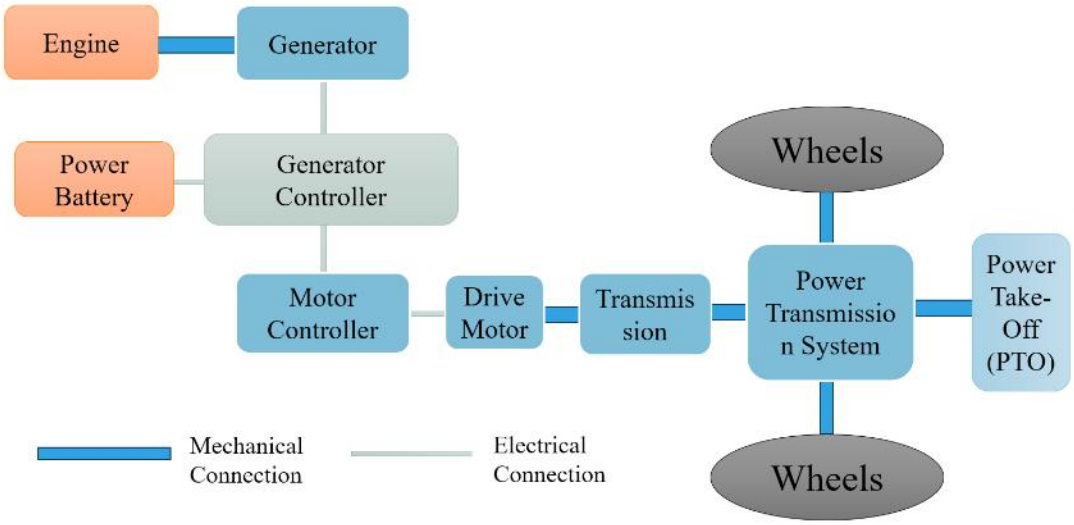


Fig. 5 - Topology Diagram of Series Hybrid Tractor Power System

There is no mechanical connection between the engine and the drive wheels; the engine directly drives the generator to produce electricity, and the electric energy is converted into mechanical energy by the motor to drive the wheels. The advantage of this structure is that the engine can always operate in its high-efficiency range regardless of actual driving conditions, thus significantly improving fuel economy. Another merit of the series configuration is the simplified transmission system. However, since energy undergoes two conversions (mechanical energy → electric energy → mechanical energy), efficiency losses may occur under certain operating conditions. Therefore, this structure is particularly suitable for working scenarios with large load fluctuations and frequent start-stop operations (*Wen et al., 2025; Luo, 2025; Lu et al., 2017*).

The parallel hybrid topology is characterized by the fact that both the engine and the motor can directly drive the wheels, with a mechanical coupling relationship between them. This structure offers the advantage of a more direct energy transfer path, avoiding losses caused by multiple conversions, resulting in higher energy efficiency especially under high-speed and steady working conditions. Parallel hybrid tractors show significant potential in energy optimal control (*Wang et al., 2020*).

Figure 6 shows a torque-coupled parallel hybrid configuration. Mechanical power from the diesel engine and power from the electric motor supplied by the power battery are combined via a torque coupler, then transmitted to the rear wheels through the transmission and final drive. Meanwhile, the transmission is also connected to the PTO, enabling independent output of working power to realize coordinated power supply for both driving and field operations.

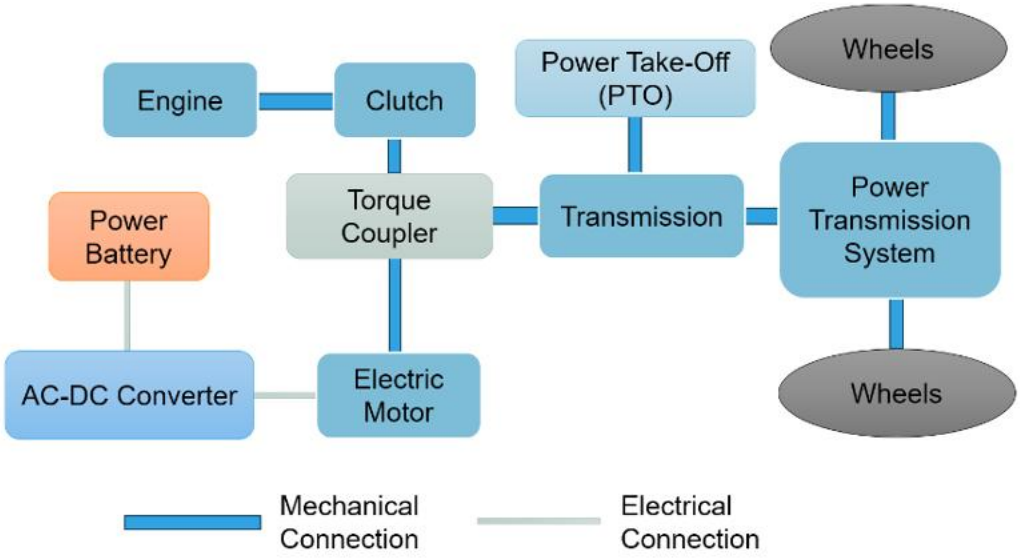


Fig. 6 - Schematic Diagram of Torque-Coupling Parallel Hybrid Powertrain Configuration

Figure 8 shows the power-split series-parallel hybrid topology, which combines the characteristics of series and parallel configurations. It can not only decouple the engine from the drive wheels, but also retain a direct mechanical drive path, enabling more flexible energy flow. This structure typically realizes power splitting via a planetary gear mechanism or complex transmission device, yet also introduces challenges of structural complexity and higher cost. Among series-parallel layouts, the planetary gear-based electric continuously variable transmission (ECVT) has become a research focus due to its multi-node and multi-power-source arrangement. ECVT often adopts a dual or triple planetary row configuration, and realizes multiple operating modes through the combination of actuators such as clutches and brakes.

For instance, in Tan Mengqi's research on the energy management strategy of a dual planetary row hybrid system, the dual planetary row hybrid powertrain was systematically designed using the equivalent tree graph method. Its tree graph representation is shown in Figure 7(a).

The configuration mainly consists of an engine (E), two motors (MG1, MG2), two planetary gear sets (S1, C1, R1) and (S2, C2, R2), two brakes (B1, B2), and three clutches (CL1, CL2, CL3), with its structural diagram shown in Figure 7(b) (*Tan, 2025*).

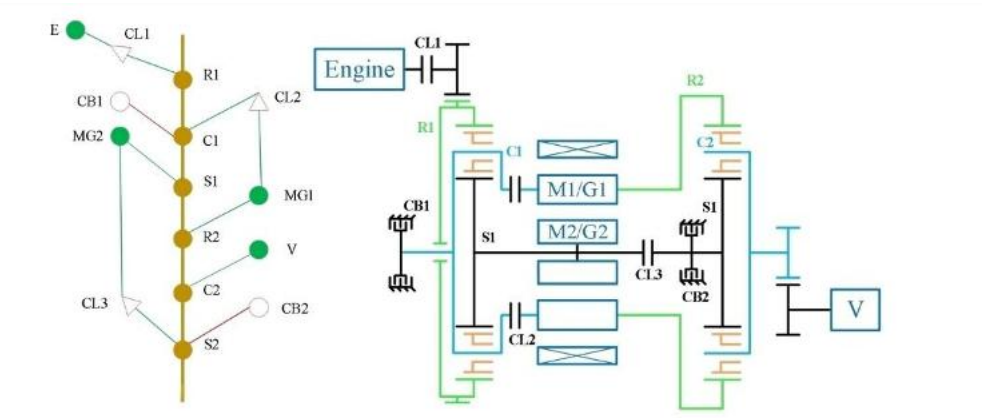


Fig. 7 - Schematic of Dual Planetary Gear Hybrid Powertrain (*Tan, 2025*)

The advantage of the series-parallel hybrid structure lies in its ability to intelligently select the optimal operating mode according to different working conditions. Under low-speed and heavy-load conditions, the system can adopt series mode to ensure the engine operates in its high-efficiency range. Under high-speed and steady working conditions, it can switch to parallel mode or direct mechanical drive mode to reduce the number of energy conversions. Under heavy-load conditions such as rapid acceleration or climbing, the engine and motor can output power simultaneously to provide maximum driving capability *(Yan, 2023)*.

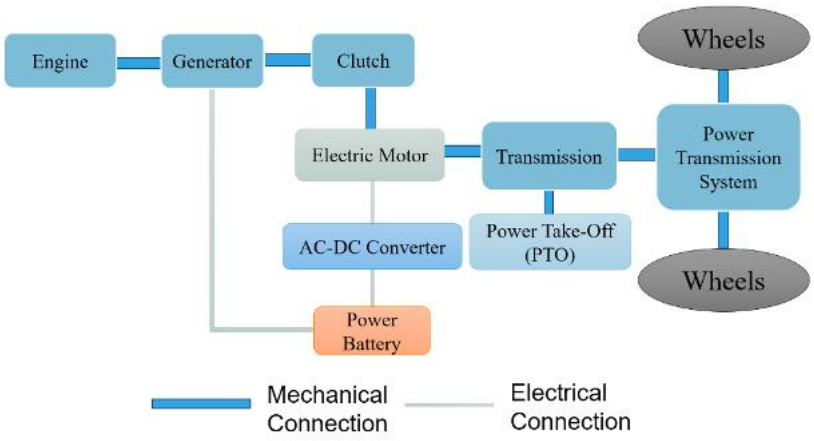


Fig. 8 - Series-Parallel Hybrid Drive Schematic

Extended topologies are optimized and extended hybrid forms based on series, parallel and series-parallel basic configurations, combined with the requirements of operating scenarios and energy-saving goals. They mainly fall into two categories: range-extended hybrid and plug-in hybrid. Both adopt the principle of "electric drive as the main, fuel as the auxiliary", but differ significantly in power transmission, energy replenishment methods and scenario adaptability. They are the mainstream extended directions for the industrial promotion of current hybrid tractors, suitable for farming conditions and infrastructure levels in different regions (*Zhao et al., 2018*).

The configuration innovation and technological extension of hybrid tractors mainly center on three core objectives, namely energy conservation and efficiency enhancement, scenario adaptability, and cost optimization. On the basis of basic topologies and extended topologies, and in combination with emerging energy storage technologies, intelligent technologies and actual field operation demands, the diversified upgrading of power configurations and cross-border extension of core technologies are realized. Meanwhile, such innovation and extension make up for the inherent shortcomings of conventional configurations, promoting the development of hybrid power systems toward high-end, diversified and adaptive trends while balancing technological advancement and engineering feasibility. Furthermore, technological extension should cover the independent localization of core components. Domestic enterprises have gradually broken through the technical bottlenecks of key components such as high-end CVT gearboxes and high-performance motor controllers, promoted the collaborative matching between core components and hybrid power configurations, and continuously reduced the dependence on imported key parts.

Performance Comparison

Based on relevant domestic and international research data, field test results of benchmark models and simulation analysis conclusions, three typical hybrid power topologies, namely the power-split type, series type and series-parallel type, present significant differences in four core dimensions: power performance, fuel economy, emission characteristics, and reliability and maintainability, making them adaptable to different operating scenarios and application demands. The performance differences, main advantages and disadvantages of the three topologies are shown in Table 3 and Table 4. In terms of comprehensive performance comparison, different hybrid power technical routes show distinct characteristics. For fuel economy, the power-split topology achieves the optimal performance, with a fuel consumption rate as low as 10.8 L/h during tillage operations and an energy-saving rate of 32%; the series topology has prominent advantages in low-speed operations, with a fuel consumption rate of 15.2 L/h during seeding operations and an energy-saving rate of 23%; the series-parallel topology features excellent multi-condition adaptability, with a comprehensive energy-saving rate of up to 28%. In terms of power performance, the series-parallel topology holds remarkable advantages: the maximum gradeability of series-parallel models can reach 35°, and the power response time is only 0.2 s, making it particularly suitable for complex hilly terrains; the power-split topology ranks second, with a power split efficiency exceeding 90% in some models and a 15% improvement in acceleration performance; while the power output of the series topology is 10% to 15% lower than that of the series-parallel topology under high-load operations. In terms of cost and reliability, the assembly price of the series topology is about 30% lower than that of the series-parallel topology, and the failure rate is reduced by 40%; the power-split topology has a 20% lower maintenance cost than the series-parallel topology due to its moderate structural complexity; the series-parallel topology has a relatively high control system failure rate owing to multi-mode switching requirements, and the failure probability of the coupling device reaches 8% after 1000 hours of continuous operation (*Tong, 2025; Liu et al., 2018; Liu et al., 2025*). Hybrid tractor schemes rely on industry, supply chains and markets instead of mere performance. Series topology suits domestic mass production for low R&D costs. Power-split series-parallel types excel in Western high-power tractors. For hilly and greenhouse farms, simple series/parallel structures are more cost-effective.

Table 3

Comparison of Performance Indicators for Different Hybrid Powertrain Configurations

Performance Indicators	Series Type	Power-Split Type	Series-Parallel Type
Fuel consumption rate (L/h, plowing condition)	15.2~18.0	10.5~12.8	12.0~14.5
Energy-saving rate (compared with conventional models)	20%~30%	25%~35%	22%~32%
Power response time (s)	0.2~0.4	0.1~0.2	0.15~0.3
Maximum gradeability (°)	25~30	30~35	32~38
Structural complexity	Low	Medium	High
Manufacturing cost (relative value)	1.0	1.3~1.5	1.4~1.6
Battery capacity requirement (kWh)	20~40	15~25	25~50
Applicable operating conditions	Long-term operation at low speeds	Continuous operation at medium and high speeds	Operation under complex working conditions

Data source: Original Strength Document "What Are the Respective Characteristics of Series and Parallel Hybrid Electric Vehicles?"

Table 4

Comparison of Characteristics for Hybrid Tractors with Different Powertrain Configurations

Drive Configu-ration	Sub - Configu-ration	Core Characteristics	Key Advantages	Main Disadvantages
Series Type	Range-extended type / General type	Load decoupling; range-extended type is dominated by pure electric drive, while the general type mainly relies on the engine-generator set.	Continuously variable transmission; simplified transmission system.	High energy conversion loss; relatively large system weight.
Parallel Type	Torque / speed / traction coupling type	Torque/speed/traction coupling; adaptable to time-varying loads and complex terrains.	Efficient engine operation; satisfactory load response; simplified transmission system.	Dependence on large-capacity batteries; high control complexity; high development cost.

Drive Configu-ration	Sub - Configu-ration	Core Characteristics	Key Advantages	Main Disadvantages
Series-Parallel Type	Series-parallel type / Power-split type	A power generation system is added on the basis of the coupling system, supporting the switching of multiple driving modes.	Multi-mode drive; maximized energy efficiency.	Complex power system; high development cost; difficult control.

Analysis of Key Component Technologies

The performance, reliability and domestic localization level of hybrid tractors mainly depend on the technical maturity of four key components: power source, energy storage system, power coupling device and electronic control system. Combined with the current industry technology status, authoritative test data and domestic localization progress, this paper systematically analyzes the detailed technical points of each component, identifies the technical bottlenecks and development directions, and explains the root causes of the performance differences among the three topologies mentioned above.

The power source is the core driving unit of hybrid tractors, which is divided into two major categories: diesel engines and new energy motors. The cooperative operation of the two determines the power output and energy-saving effect of the topology, and its technical level directly affects the operation adaptability of tractors. At present, mainstream hybrid tractors are equipped with China IV emission diesel engines, and some high-end models have been upgraded to China V emission standards. The core of the upgrade focuses on three goals: reducing emissions, improving efficiency, and adapting to hybrid collaboration. Currently, domestic diesel engines for agricultural machinery have achieved domestic localization of China IV emission technologies, but some core aftertreatment components for China V emission standards still rely on imports (*Liu, 2023*).

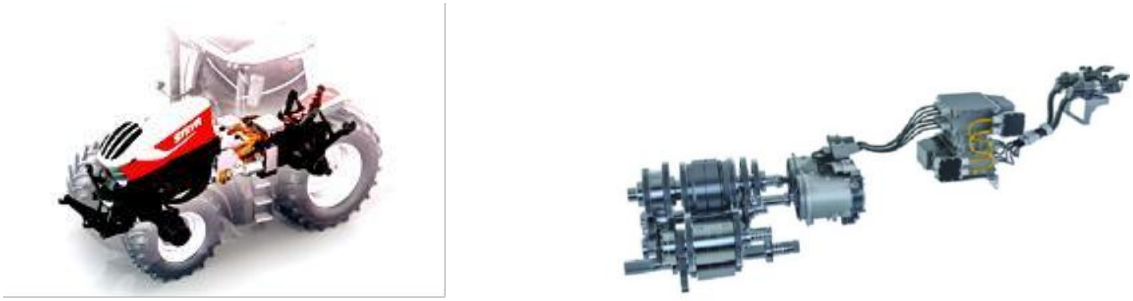
New energy motors constitute the core of the electric drive for hybrid tractors. The performance differences among the three mainstream motor types determine their adaptability to different topological structures and operating scenarios, as detailed below.

(1) Permanent magnet synchronous motors feature high power density, high operating efficiency, excellent speed regulation performance, and stable low-speed torque output. They are suitable for the high-frequency mode switching requirements of series-parallel and power-split topologies, and can accurately match the load fluctuations in complex hilly terrains, making them the mainstream choice for high-end hybrid tractors at present. Their shortcomings lie in the relatively high cost and the tendency of permanent magnets to demagnetize under high temperature and vibration. Additional protective structures are required when adapting to the high-dust and high-temperature field operating environment of tractors, resulting in slightly higher maintenance costs (*Lu, 2023; Zhu, 2025; Zhao et al., 2021*).

(2) Asynchronous motors feature a simple structure, high reliability, and moderate cost, with outstanding high-temperature resistance and anti-vibration performance. They are suitable for the “engine generation + motor drive” mode of series topology and can meet the continuous power output demand of long-term low-speed operation. Their shortcomings include low power density, poor low-speed efficiency, and relatively slow dynamic response, making them unsuitable for series-parallel topologies with high-frequency load fluctuations and rapid mode switching (*Gui, 2026*).

(3) Switched reluctance motors have relatively high power density, robust structure, low cost, and large starting torque, making them suitable for high-load operating scenarios. Furthermore, they have no risk of permanent magnet demagnetization and feature low maintenance costs. However, their shortcomings include complex control logic, significant noise and vibration during operation, and poor low-speed running smoothness. At present, they are mainly applied in low-end series hybrid tractors for light and medium-load operations, and have not been widely used in high-end models (*Li, 2026*).

In conventional tractors, continuously variable transmission (CVT) refers to a technology that realizes uninterrupted speed regulation of the whole machine by continuously adjusting the transmission ratio between the input and output shafts of the transmission system without changing the engine speed. In the field of hybrid tractors, this technology has been further extended to the smooth and continuous control of the whole machine’s operating speed. The current mainstream technical routes include the centralized electric-drive CVT system shown in Figure 3(c), the distributed electric-drive CVT system shown in Figure 9, and the electromechanical coupling CVT system. Their technical characteristics and typical products are presented in (*Wen et al., 2025*).



(a) *STEYR Konzept Continuously Variable Transmission Power System (Wheel-Hub Electric Drive)*

(b) *John Deere eAutoPower Continuously Variable Transmission System (Electromechanical Coupling Type)*

Fig. 9 - Main Technical Characteristics and Typical Products of CVT Power System and Engine

The energy storage system serves as the core carrier for energy recovery and power compensation of hybrid tractors. It is responsible for storing energy generated by the engine and recovered via braking, and supplementing energy to the drive system under high-load conditions. Its performance directly affects the energy-saving rate and power response speed of the topology, and is mainly divided into three categories: power batteries, supercapacitors, and fuel cells.

Power battery technology functions to store surplus engine energy and braking recovery energy, providing high-energy-density supplementary energy support for electric motors. Most hybrid tractors adopt lithium-ion batteries, which feature high energy density but relatively low power density. In the single-motor drive hybrid system proposed by Wang Zhiguo et al., efficient collaboration between the internal combustion engine and the electric motor was achieved through optimized control strategies, raising the charge-discharge efficiency of power batteries to over 90%. However, the core problems of power battery technology lie in low-temperature performance attenuation and limited cycle life *(Scolaro et al., 2021, Troncon et al., 2019)*.

Supercapacitor technology is designed to compensate for the low power density of batteries and quickly respond to instantaneous load demands (e.g., tractor startup or climbing). It has a power density of 5–10 kW/kg and a charge-discharge efficiency exceeding 95%, making it suitable for frequent start-stop operating conditions. Yue Dongpeng et al. pointed out that supercapacitors in hybrid systems can realize short-term energy buffering, reduce peak current pressure on batteries, and extend their service life (*Sunil et al., 2026*). Their limitation is low energy density, requiring combined use with batteries (*Wang et al., 2026; Wang, 2015*).

Fuel cell technology, as an auxiliary power source, provides continuous electric energy output through hydrogen energy conversion, but has not yet been promoted or piloted.

The power coupling device is the core of power distribution for hybrid tractors, responsible for coupling and splitting the power of diesel engines and new energy motors to realize the switching of different power modes. Its technical bottlenecks and domestic localization progress directly restrict the performance and cost control of hybrid topologies, and are mainly divided into three categories: clutches, planetary gear sets, and electronic control couplers.

The electronic control system is responsible for the overall coordinated control of the power source, energy storage system, and power coupling device. It mainly consists of an Engine Control Unit (ECU), Vehicle Control Unit (VCU), and Battery Management System (BMS). The coordinated control capability, as well as the technical level of chips and algorithms, directly determines the performance and reliability of the hybrid topology.

For the coordinated control architecture of ECU/VCU/BMS, the three units form a "hierarchical control and collaborative linkage" architecture, which is the core of power mode switching and optimal energy distribution for hybrid tractors. As the main control unit, the VCU receives real-time data from the ECU, BMS, and field operation sensors, formulates optimal control strategies according to operating conditions, sends control commands for engine speed and fuel injection volume to the ECU, charge-discharge control commands to the BMS, and power distribution and mode switching commands to the power coupling device (*Sunil et al., 2026*) ; the ECU executes VCU commands, optimizes the engine operating state to ensure the engine maintains a high-efficiency speed range, and feeds back real-time engine operating data; the BMS monitors the real-time status of power batteries and supercapacitors, controls charge-discharge speed and current to prevent overcharging and over-discharging, extends the service life of energy storage components, and feeds back the energy status of the energy storage system.

At present, the coordinated control architecture of domestic hybrid tractors has achieved initial maturity and can meet basic power distribution and mode switching requirements. However, high-end models lack sufficient coordinated control accuracy and slow response speed, and the data interaction efficiency of the three units still needs to be optimized. Chips and algorithms are the core of the electronic control system and also the main technical bottleneck of domestic hybrid tractors (*Zhang, 2024; Cheng et al., 2026*).

In terms of chips, high-computing-power Microcontroller Unit (MCU) chips and power chips required for high-end ECU/VCU/BMS mainly rely on imports. Although domestic chip enterprises have launched mid-end chips, their computing power, high-temperature resistance, and vibration resistance are insufficient to meet the high-frequency control demands of high-end hybrid tractors, and they also suffer from poor stability and high failure rates. Domestic substitution of chips is currently the core development direction (*Zhang, 2024; Jing et al., 2020*).

In terms of algorithms, the core challenge lies in adaptive control algorithms for operating conditions. The field operating conditions of tractors are complex, and traditional logic threshold control algorithms can no longer meet precise control demands. Intelligent algorithms such as Model Predictive Control (MPC) and reinforcement learning are required to realize condition-adaptive power distribution and mode switching. At present, domestic enterprises are still in the research and development and testing stage of intelligent algorithms. The adaptability and stability of the algorithms are insufficient to accurately match complex field conditions, and the compatibility between algorithms, topologies, and key components is poor, resulting in the failure to fully exert the performance of some high-end hybrid tractors *(Xie et al., 2018*).

In summary, the technical maturity and domestic localization level of the four key components directly determine the performance, cost, and reliability of hybrid tractors. At present, domestic hybrid tractors have realized the localization of mid-to-low-end components, and core shortcomings are concentrated in high-end motors, electronic control chips, high-end electronic control couplers, hydrogen fuel cells and other fields. In the future, it is necessary to carry out industry-university-research collaborative research to break through core technical bottlenecks, promote the domestic substitution of key components, and optimize the collaborative compatibility of each component to support the high-quality development of the hybrid tractor industry (*Chen, 2024*).

Energy Source Configuration and Matching Strategy

The core of energy source configuration for hybrid tractors lies in the type selection and parameter matching of diesel engines and energy storage devices. Its primary objective is to adapt to complex field operating conditions and achieve a balance between dynamic performance, energy-saving efficiency and service life. Combined with industrial research and practical applications of tractor models, three mainstream technical routes have been formed at present. The following section systematically analyzes the configuration by focusing on three core aspects: the comparison between single and composite energy source configurations, parameter matching methods, and case studies of 300-horsepower-class models, in conjunction with the technical characteristics of energy storage systems *(Paciolla et al., 2024, Sayed et al., 2024)*.

Comparative Study on Single Energy Source and Composite Energy Source Configurations

The energy source configuration of hybrid tractors can be divided into two categories: the engine plus single energy storage device configuration and the hybrid energy storage configuration. Based on different theoretical foundations, they show significant differences in performance, applicable scenarios and cost control (*Zhu et al., 2025*).

The single energy source configuration, centered on "matching a single energy storage device with the engine", features a simple structure and low development difficulty, making it the mainstream basic configuration for current hybrid tractors. Most engines adopt China IV/Euro V emission diesel engines, and lithium iron phosphate batteries are preferred as power batteries, which adapt to the high-temperature and vibratory field operating environment of agricultural machinery. With a thermal runaway temperature ≥ 600 ℃, their safety performance is superior to that of ternary lithium batteries, and the battery capacity is matched to 15–50 kWh according to the horsepower class (*Liu et al., 2025*). The IE-POWER electric continuously variable transmission powertrain released by Yuchai Group adopts a series hybrid architecture, which collaborates a single energy storage device (battery) with the engine, achieving a 10%–30% improvement in operating efficiency and a 10%–30% increase in fuel saving rate (*Huang, 2021*). This configuration simplifies the transmission system layout and reduces development complexity, and is especially suitable for 200–260 HP

heavy-duty tractors (*Wang, 2024*). Its core advantages include simple structure and moderate cost, adapting to light and medium-load long-term operation scenarios. The main limitation is that battery life is significantly affected by the agricultural machinery operating environment; continuous high temperature and high-frequency vibration in the field accelerate battery degradation, resulting in a short actual service life. In addition, the peak power output is limited, making it difficult to adapt to high-load scenarios such as deep tillage and heavy-load transfer.

The composite energy source configuration is an optimized upgrade based on the single configuration, with the core logic of "integrating the high energy density of power batteries and the high power density of supercapacitors". Its theoretical foundation is "energy-power dual complementarity": power batteries undertake continuous energy supply, while supercapacitors provide instantaneous power compensation and rapid energy recovery. The two cooperate to match the engine power output and achieve optimal comprehensive performance *(Song et al., 2019*). Its core advantage is balanced comprehensive performance, which not only solves the problems of insufficient peak power and short service life of the single battery configuration, but also makes up for the shortcomings of low energy density of single supercapacitors and inability to operate in pure electric mode for a long time (*Liu et al., 2019*). The main limitation is the complex structure and high cost. A special energy cooperative control strategy needs to be designed, and the parameter matching of multiple energy storage devices is difficult. The manufacturing cost is 30%–40% higher than that of the single battery configuration. At present, it is mainly used in high-end high-horsepower hybrid tractors to adapt to complex operating conditions (*Li et al., 2026, Mocera, 2021*).

In summary, the single energy source configuration focuses on "low cost and adaptation to basic working conditions", with the core advantages of simple structure and convenient maintenance, but limited comprehensive performance. The composite energy source configuration focuses on "high performance and adaptation to complex working conditions", with the core advantages of balanced power and energy saving as well as longer component service life, but suffers from high cost and complex control. The choice between the two mainly depends on the operating scenarios, horsepower requirements and cost budget. The single energy source configuration is preferred for small and medium-horsepower tractors in basic operations, while the composite energy source configuration is prioritized for high-horsepower tractors in complex working conditions.

Energy Source Parameter Matching Method

The core of energy source parameter matching lies in optimizing the parameter combination of engine power and energy storage devices (capacity and power) according to the operating condition requirements of the typical operating cycles of hybrid tractors, so as to achieve the optimization objectives of "meeting power demand, minimizing energy consumption and maximizing service life". Its core process is "operating condition modeling - target setting - parameter optimization - verification and iteration" *(Mocera et al., 2022, Pascuzzi et al., 2024, Paciolla et al., 2024)*.

Operating condition modeling is the foundation of parameter matching, which focuses on quantifying key parameters such as load characteristics, speed variations and braking frequency of the typical operating cycles of hybrid tractors through field tests and simulation analysis, and constructing an operating condition model that conforms to actual operations. At present, the mainstream modeling method in the industry is "field tests + MATLAB/Simulink simulation". Firstly, real-time data including load power, travel speed, braking time and slope variations of tractors under typical operating conditions such as plowing, rotary tillage, sowing, transfer and braking are collected by sensors, and the proportion of different operating conditions is determined based on accumulated field operation data of more than 1000 hours. Subsequently, based on the collected data, an operating condition load spectrum model is constructed to clarify the basic power demand of the engine, as well as the peak power and energy storage requirements of the energy storage device, and a power demand time series $P_{req}(t)$ is established. Key parameters include average power P_{avg}, peak power P_{max}, load factor $\eta_L = \frac{P_{avg}}{P_{max}}$, and cycle period T, which provide data support for parameter matching. During the modeling process, the particularities of agricultural machinery operations—such as large fluctuations in field loads and complex operating environments—must be emphatically considered. Therefore, environmental impact factors should be integrated into the model to avoid the disconnection between theoretical modeling and practical applications. For example, battery capacity degradation must be considered in high-temperature environments, and power redundancy should be reserved under vibratory conditions to ensure the rationality

of parameter matching. Parameter matching optimization takes "maximum energy-saving rate, satisfactory power performance, longest service life, and minimum cost" as the multi-objective optimization objective. Combined with the operating data, intelligent optimization algorithms are adopted to collaboratively optimize the engine power and parameters of the energy storage device. The details are as follows:

A multi-objective optimization framework is constructed, and the objective function is established as follows:

$$\min\left\{w_1\frac{f_1}{f_{1,ref}}+w_2\frac{f_2}{f_{2,ref}}+w_3\frac{f_3}{f_{3,ref}}\right\} \quad (2)$$

where:

f_1 is the energy consumption [kwh/m]; f_2 is the battery degradation rate [%/1000 h]; f_3 is the proportion of time with insufficient power [%]; $f_{i,ref}$ are the respective reference benchmark values of the three indicators; division is performed to normalize indicators with different dimensions and magnitudes for summation. w_i is the weight coefficient, which needs to be determined using the Analytic Hierarchy Process.

Constraint conditions are set as follows:

Power constraint:

$$P_{eng}+P_{bat}\geq P_{req}(t)+\Delta P_{margin} \quad (3)$$

where:

P_{eng} is the engine output power [W], P_{bat} is the battery output/input power [W]; P_{req} is the vehicle total required power at time t (varies in real time with driving conditions) [W], ΔP_{margin} is the reserved power margin [W].

SOC boundary:

$$SOC_{min}\leq SOC(t)\leq SOC_{max} \quad (4)$$

where:

SOC is the State of Charge [%].

Engine operating range:

$$\omega_{eng}\in[\omega_{idle},\omega_{rated}] \quad (5)$$

where:

ω_{eng} is the engine rotational speed [r/min]; ω_{idle} is the minimum idle rotational speed [r/min]; ω_{rated} is the rated maximum operating rotational speed [r/min].

In terms of optimization algorithm applications, the industry currently mainly adopts intelligent optimization algorithms such as genetic algorithm and particle swarm optimization. Combined with Simulink simulation models, multi-objective optimization is performed on the parameters of engines and energy storage devices, and parameter combinations are iteratively optimized to finally determine the optimal matching scheme (*Liu et al., 2017; Li et al., 2025; Zhang et al., 2025*).

In summary, the core of energy source configuration for hybrid tractors lies in "operating condition adaptation, parameter optimization, and type matching". The single energy source configuration is suitable for basic operations and cost control, while the composite energy source configuration adapts to complex working conditions and improves comprehensive performance. The parameter matching method based on operating condition modeling and intelligent optimization algorithms can achieve the optimal balance of energy source configuration. Case studies of 300-horsepower-class models show that the hybrid energy storage configuration represents the development trend of high-end models, but the bottlenecks of cost and control complexity need to be broken through. Meanwhile, the technical characteristics of the energy storage system directly affect the selection and performance of energy source configuration. In the future, it is necessary to further optimize the performance of energy storage devices, promote the collaborative upgrading of energy source configuration with topological structures and electronic control systems, and support the high-end development of the hybrid tractor industry.

Research Progress of Typical Energy Management Strategies

For hybrid electric vehicles, there are generally two or more power sources. Therefore, it is necessary to design reasonable energy management strategies according to the power demand under different road conditions and rationally distribute the output power of each power source to achieve the optimal control objectives. At present, domestic and foreign research on energy management strategies for hybrid power systems mainly focuses on the fields of automobiles and buses. Existing multi-energy energy management strategies can be mainly divided into three categories (*Gao, 2024*), as shown in Figure 10.

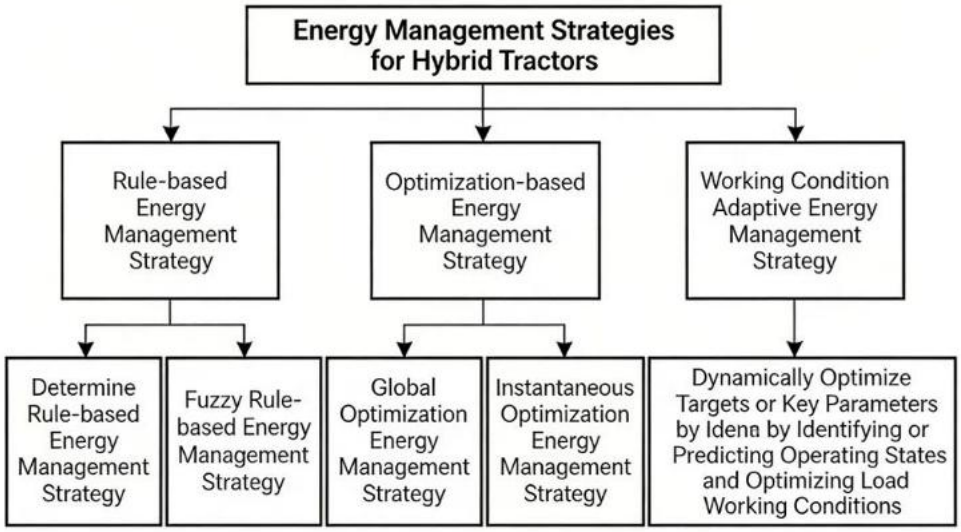


Fig. 10 - Classification of EMS for Hybrid Tractors

Rule-based energy management strategies can be divided into deterministic rule-based strategies and fuzzy rule-based strategies. Deterministic rule-based strategies predefine control rules based on engineering experience or expert knowledge to realize power distribution among multiple power sources. They are simple, practical and highly implementable, with representative ones including state machine strategy, power-following control rules and thermostat control rules. Unlike the simple switching thresholds of deterministic rule-based strategies, fuzzy rule-based strategies are a nonlinear control technology formed by combining fuzzy mathematics and mathematical logic. They can predict future driving states through fuzzy logic inference based on known driving states, exhibiting strong robustness (*Yao et al., 2023;*).

Ding Axin et al. (*2021*) used dynamic programming energy management strategy to obtain the optimal energy distribution results for a fuel cell/battery hybrid power system, and on this basis, designed an improved state machine energy management strategy. Simulation results showed that the strategy can realize real-time control and effectively reduce the system hydrogen consumption.

Chen X.R. et al. (2022) proposed an external energy efficiency maximization strategy based on power decoupling for the fuel cell + battery architecture, and compared it with traditional control strategies. The results showed that the proposed strategy can meet the power demand of ships under typical working conditions, effectively reduce hydrogen fuel consumption, improve battery utilization, and enable efficient operation of the entire system.

Fei Peng et al. (2017) further proposed a processing compensation strategy based on fuzzy logic hysteresis state machine and differential power strategy, which improved the dynamic coordination efficiency of the hybrid system and increased fuel efficiency by 7%.

Optimization-based management strategies achieve optimal system control under preset constraints, and can be mainly divided into global optimization control and instantaneous optimization control. The former takes a given driving cycle as the premise and conducts global search optimization analysis combined with modern optimization algorithms and control theory, mainly including dynamic programming control, stochastic dynamic programming, etc. The latter takes a certain working condition and driving state as the optimization interval, establishes an objective function to minimize fuel consumption in this interval, and optimizes the system energy distribution in real time online. Compared with the former, it can realize real-time dynamic optimization, mainly including Pontryagin's Minimum Principle, Equivalent Consumption Minimization Strategy, etc. (*Wang et al., 2022*).

Dima Fares et al. (2015) proposed an offline optimization algorithm based on weighted improved dynamic programming, combined with online optimization using a PID controller. The results showed that the algorithm converges faster than the ordinary dynamic programming algorithm and achieves higher fuel economy compared with rule-based algorithms. *Peng et al. (2021)* proposed an offline optimal energy management strategy combining Pontryagin's Minimum Principle and dynamic programming, and introduced a damping coefficient into the cost function, which effectively reduced the dynamic fluctuation of fuel cell output power. The feasibility of the strategy was verified through experiments.

Ding Chenguang et al. (2026) innovatively proposed an energy management strategy based on frequency division decoupling. The strategy aims to design a low-pass filtering algorithm, enabling the fuel cell to provide the main power output and low-frequency fluctuating power, while the lithium battery recovers braking energy and provides high-frequency fluctuating power. The effectiveness of the strategy was verified under Chinese urban bus driving cycles and actual bus operating conditions. In addition, with the rapid development of the automotive manufacturing industry, some control strategies based on intelligent algorithms have been applied to the energy management of hybrid power systems, typically including machine learning, artificial neural networks and model predictive control. Such strategies are relatively complex and difficult to implement, but are of far-reaching significance for in-depth research and innovation in the automotive field. *Chen Zeyu et al.* (*2022*) proposed an energy management strategy based on deep reinforcement learning, which determines the optimal variable power through the deep deterministic policy gradient algorithm. The effectiveness of the strategy was verified by real-vehicle tests and comparison with the particle swarm optimization strategy (*Kebriaei et al., 2015*).

Huang Zhenzhen et al. (*2021*) designed an online multi-objective energy management strategy for fuel cell vehicles based on BP neural network. The strategy trained simulation datasets obtained based on Pontryagin's Minimum Principle to establish neural network sub-models, and combined the obtained sub-models into a multi-neural network model. Finally, the feasibility of the strategy was verified through online software simulation and hardware-in-the-loop simulation tests respectively.

Li X. et al. (2019) proposed an energy management strategy based on explicit model predictive control, formulated the optimal control problem as a multi-parameter quadratic programming optimization problem, and realized real-time control by solving the multi-parameter quadratic programming problem offline, which effectively improved fuel economy and reduced online computation time.

Gao Zhi et al. (2024) conducted research on the energy management strategy of a fuel cell tractor hybrid power system. Taking a hydrogen fuel cell hybrid tractor as the research object, they determined the fuel cell/lithium battery/supercapacitor three-power-source topology, completed component selection and matching, and built a simulation model. The EEMS strategy was designed and compared with SMC and ECMS. Hardware-in-the-loop test verification showed that EEMS can ensure stable system operation, significantly reduce hydrogen consumption, and alleviate power impact on the fuel cell.

Through the analysis of existing literature, it can be found that although rule-based energy management strategies are simple, effective and easy to implement, they rely on given expert experience or rules, are difficult to adapt to real-time dynamic working conditions, and cannot guarantee optimal control of the hybrid system. Although optimization-based control strategies have outstanding theoretical performance, can maximize the optimization of hybrid systems and improve system performance and fuel economy, they have high requirements for hardware and control accuracy, and require long computation time, resulting in high production costs and difficulty in practical application. Some literatures also fail to consider field interference factors, leading to limitations in test results. Future development directions need to expand multi-field working conditions, optimize the real-time performance of EEMS to promote engineering application, improve system reliability with intelligent algorithms, and perfect the test system to adapt to actual field scenarios. Hybrid tractor energy management strategies mostly adopt road vehicle frameworks, poorly adapting to violent, irregular field operation loads. Dynamic programming is hard to engineer; MPC faces high hardware cost barriers; widely used rule-based strategies have limited energy-saving potential. Balancing accuracy, cost and adaptability is the core challenge (*Brudeli G et al.,2026*).

Research Review on Strategy Optimization Directions

The core of the energy management strategy for hybrid tractors is to dynamically allocate the power output of the engine and motor, and maintain the stability of the battery State of Charge (SOC) to achieve optimal fuel economy (*Wang et al., 2015*).

Strategies that allocate power based on preset logical rules mainly include the thermostat strategy and the power-following strategy. Among them, the thermostat strategy sets an SOC threshold range of 30%-70%: the engine starts to generate electricity when the SOC is below the threshold, and the system switches to pure electric drive when the SOC exceeds the threshold. The power-following strategy dynamically adjusts the engine output according to the real-time power demand of the tractor, enabling the engine to match real-time load fluctuations (*Dobretsov et al., 2024*).

Optimization strategies with minimum fuel consumption as the objective function optimize power distribution through algorithms, including dynamic programming (which solves the optimal solution based on global operating condition information and serves as an offline optimization benchmark), model predictive control (which realizes real-time control relying on receding horizon optimization), and nonlinear programming genetic algorithm (which optimizes key parameters via genetic algorithm to improve control accuracy) (*Wang et al., 2015*).

Intelligent algorithm strategies integrating machine learning, reinforcement learning and other technologies include fuzzy PID control, which combines fuzzy logic and PID algorithm to optimize the response characteristics of the power generation system, and deep reinforcement learning, which learns the optimal strategy through the interaction between agents and the operating environment to adapt to complex and variable field working conditions.

The selection of technical routes for hybrid tractors is restricted by three core factors: operating scenarios, power level and cost budget.

(1) Operating scenarios: Large-area plain field operations are suitable for series configuration and engine-battery energy source layout and rule-based strategy, highlighting the advantages of endurance and cost control; complex hilly field operations are suitable for series-parallel configuration and engine-battery-supercapacitor energy source layout and model predictive control strategy, emphasizing dynamic performance and environmental adaptability; facility horticulture operations are suitable for power-split configuration and engine-supercapacitor energy source layout and fuzzy PID strategy, focusing on operational flexibility and low noise.

(2) Power level: Small-horsepower tractors with a power rating lower than 50kW mainly adopt series configuration and engine-battery energy source layout; high-horsepower tractors with a power rating higher than 150kW tend to use series-parallel configuration and engine-battery-supercapacitor energy source layout.

(3) Cost budget: Economical users such as individual farmers choose series configuration and engine-battery energy source layout and rule-based strategy, with the complete machine price 10%~15% higher than that of conventional tractors; large-scale farms prefer series-parallel configuration and engine-battery-supercapacitor energy source layout and optimization-based strategy. Although the initial investment is 30%~40% higher, the annual operating cost is reduced by 24%~30%, with an investment payback period of about 3~4 years (*Zhou, 2026*).

Review on Verification Methods of Energy Management Strategies

Verification of energy management strategies for hybrid tractors is the key to their transformation from theoretical models to engineering applications. Combined with the characteristics of field operating conditions, there are four core verification methods:

(1) As a low-cost and efficient preliminary method, simulation verification builds powertrain system and strategy models relying on platforms such as MATLAB/Simulink, and completes preliminary iterations combined with field operating condition load spectra. It has the advantages of low cost, short cycle and the ability to simulate extreme working conditions, but is limited by dependence on model accuracy and detachment from the actual environment, which is suitable for the initial stage of strategy research and development (*Wang et al., 2021*);

(2) As a bridge between simulation and real-vehicle tests, bench test verification simulates field operating conditions in a controllable environment through powertrain system or complete vehicle benches to realize semi-physical verification. It features accurate data and high safety, but is difficult to simulate the complex interaction among soil, farm implements and tractors, which is suitable for the strategy optimization stage (*Li et al., 2026*);

(3) Field real-vehicle test verification is the final standard for engineering implementation, which verifie s the adaptability, reliability and economy of strategies in real field scenarios. It has high result credibility, but is restricted by long cycle, high cost and great interference from natural factors, which is suitable for the strat egy application stage (*Wu et al., 2014*);

(4) As a high-end intelligent development trend, Hardware-in-the-loop (HIL) test verification integrates virtual models and physical hardware with strong real-time performance, making it suitable for the verification of intelligent strategies. However, it has high equipment cost and technical threshold, which is applicable to t he research and development of high-end intelligent strategies (*Qiao et al., 2022*).

In practical applications, a full-process integrated system of "simulation verification→HIL test verification→bench test verification→field real-vehicle test verification" is generally adopted. In the future, it will develop towards the standardization of operating condition load spectra, the integration of digital twin and HIL, and the improvement of multi-objective verification systems.

Technical R&D Bottlenecks

In terms of power coupling and transmission efficiency, the series configuration suffers from large energy conversion losses, and the conversion efficiency of the "engine-generator-motor" chain needs to be improved; its energy consumption under high-speed operating conditions is higher than that of the series-parallel configuration. The power-split configuration has high requirements for the machining accuracy of planetary gear mechanisms, and the gear meshing efficiency of domestic enterprises is 5%~8% lower than the international advanced level. The mode switching shock problem of the series-parallel configuration has not been completely solved, and the switching shock of some models reaches 0.3g, which affects operation comfort and component service life.

In terms of energy storage system performance, batteries account for 20%~30% of the complete machine cost, and the service life of batteries in agricultural machinery operating environments is only 1/2~2/3 of that in electric vehicles. Supercapacitors have low energy density and must be matched with large-capacity batteries to meet long-time operation requirements, which increases system complexity and cost. The energy distribution strategy of hybrid energy storage systems is not yet mature, and the cooperative control accuracy between batteries and supercapacitors needs to be enhanced.

In terms of control strategies, optimization-based and intelligent algorithm strategies rely on accurate operating condition prediction models. However, agricultural operating conditions are greatly affected by soil, climate and crops with strong uncertainty, leading to reduced control accuracy. The weight distribution of multi-objective optimization strategies lacks a unified standard and requires recalibration in different operating scenarios, increasing R&D difficulty. The synergy between the control system and the operation system is insufficient, failing to achieve integrated power-operation optimization. The above shortcomings in technical R&D have led to divergences in the technical route selection of hybrid tractors.

Research Focuses and Controversies

Research and development of hybrid tractor technologies center on three core links: power coupling, energy storage system, and control strategy. Clear research focuses have been formed for key technological breakthroughs, while significant academic and industrial controversies exist due to differences in technical route selection and performance priority setting. Such controversies mainly involve three aspects: research focuses and divergences of power coupling and transmission efficiency, energy storage system performance, and control strategy.

The research focus of power coupling and transmission efficiency lies in breaking through the performance shortcomings of three topological structures:

- Firstly, optimizing the energy conversion loss of the series topology, reducing the multi-stage conversion loss of the "engine-generator-motor" chain by improving the matching parameters of generators and motors and enhancing the energy distribution accuracy of the electronic control system;
- Secondly, upgrading the processing technology of core components for the power-split topology, conquering the high-precision processing technology of planetary gear mechanisms, and narrowing the meshing efficiency gap with the international advanced level;
- Thirdly, suppressing the mode switching shock of the series-parallel topology, developing adaptive buffer control algorithms to reduce the impact load in the process of multi-mode switching. The divergences are reflected in the priority of technical routes. Some studies argue that priority should be given to the low-cost optimization of the series topology to meet the demand for large-scale promotion; other studies advocate tackling the mode switching technology of the series-parallel topology to seize the high-end market with its comprehensive performance advantages. The two sides hold different views on the route selection between "cost priority" and "performance priority".

In terms of research focuses and divergences of energy storage system performance, they mainly focus on three core issues:

- Firstly, cost control and service life extension of power batteries, improving battery reliability in agricultural machinery operating environments by developing special battery PACK technologies with vibration resistance and high temperature resistance, and exploring battery recycling and echelon utilization paths to reduce costs;
- Secondly, optimizing the collaborative mechanism of hybrid energy storage composed of supercapacitors and batteries, breaking through the precise control technology of energy distribution strategies, and balancing the advantages of high power density of supercapacitors and high energy density of batteries.

Thirdly, simplifying the structure of the hybrid energy storage system, reducing system complexity and complete machine layout difficulty through integrated design.

The divergences mainly concentrate on the selection of energy storage technical routes. For the research focuses and divergences of control strategies, they mainly focus on the precision and integration of strategies:

- Firstly, constructing a high-precision prediction model suitable for agricultural operating conditions, integrating multi-source data such as soil, climate and crops to improve the adaptability of intelligent algorithms to complex operating conditions;
- Secondly, establishing a dynamic weight adjustment mechanism for multi-objective optimization strategies to achieve balanced optimization of fuel economy, power performance and component service life;
- Thirdly, promoting the collaborative integration of control system and operation system, developing an integrated algorithm of "power control-farm implement control-navigation control" to realize optimal energy distribution in the whole operation process.

The divergences are mainly reflected in the technical implementation path, with differences in the route selection between "adaptive algorithm optimization" and "systematic standardized research and development".

Industrialization Application Bottlenecks

Hybrid tractors face multiple challenges in popularization and application, especially in terms of cost and cost performance. Their selling price is 30%~60% higher than that of traditional tractor models. For instance, the Dongfanghong HB2204 is 250,000 yuan more expensive than traditional models with the same horsepower, and the price of imported hybrid tractors is even higher. Although their operating cost can be reduced by 24%~30%, the investment payback period is relatively long. In terms of infrastructure and after-sales service, there are also prominent problems including a rural charging pile coverage rate of less than 5%, which restricts the application of pure electric mode, as well as a high technical threshold and high cost for hybrid system maintenance.

Core Technology Development Trends

(1) Develop integrated power coupling devices to reduce structural complexity and improve transmission efficiency; explore novel transmission technologies such as electromagnetic coupling transmission and the integration of Hydro-mechanical Continuously Variable Transmission (HMCVT) with electric drive, breaking through the limitations of traditional mechanical transmission. For high-horsepower models, focus on the optimization of series-parallel topology, and develop lightweight and highly reliable multi-mode coupling devices to reduce manufacturing costs by 15~20%.

(2) Develop special high-power-density batteries for agricultural machinery, such as solid-state batteries, to extend endurance and reduce costs; optimize hybrid energy storage systems and dynamically adjust the energy distribution ratio between batteries and supercapacitors based on operating conditions; develop battery thermal management and vibration protection technologies to extend battery life to 5–6 years, close to the level of electric vehicle batteries.

(3) Integrate multi-source sensor technology to construct adaptive operating condition prediction models and improve the real-time performance and accuracy of optimization strategies; develop intelligent algorithms combining deep learning and reinforcement learning to realize self-learning and self-optimization of control strategies, adapting to complex and variable agricultural operating environments; develop an integrated "power-operation" control platform to collaboratively optimize energy management with implement control and path planning, improving overall operating efficiency.

Innovation of Research Methods and Verification Systems

(1) Reduce costs through large-scale production to approach the level of traditional high-end tractor models; adopt modular design to realize the standardization and generalization of powertrain, energy storage system and control system, so as to lower research and development and manufacturing costs.

(2) Build an "agricultural machinery cooperatives and charging piles" model, and deploy fast charging piles in major agricultural production areas to solve the charging difficulty; establish a professional after-sales service network, carry out technical training for maintenance personnel to shorten the fault maintenance cycle; build a remote diagnosis and operation and maintenance platform, and realize predictive maintenance via big data analysis to reduce the failure rate.

(3) Improve the technical standard system, and formulate national standards for hybrid tractors covering energy saving rate test methods, safety requirements and electromagnetic compatibility; strengthen policy support, increase the proportion of purchase subsidies, set up special research and development funds, and encourage collaborative innovation between enterprises and universities; promote the "combination of lease and purchase" and "trade-in for new" models to reduce users' initial investment proportion and accelerate the popularization and application.

CONCLUSIONS

(1) Hybrid tractors have become the core development direction under the background of global agricultural mechanization and green low-carbon transformation, forming a diversified technological pattern and industrialization promotion trend. Driven by policy support, market demand and technological innovation, this field has achieved leapfrog development from conceptual prototype to commercial explosion, and distinctive technical routes adapted to local farming scenarios have been formed both domestically and internationally. Foreign countries are represented by high-horsepower power-split hybrid tractors in North America, plug-in multi-energy coupling hybrid tractors in Europe, and small and medium-horsepower refined hybrid tractors in Japan and South Korea, with high industrialization maturity and complete core technology and supply chain systems. China has made remarkable breakthroughs in the period of independent innovation, with leading enterprises such as YTO Group Corporation, Yuchai Group and Zoomlion emerging, forming a gradient product layout covering 200~320 horsepower heavy-duty models and light and small facility agricultural models. Core indicators such as fuel saving rate and operation efficiency have reached the international advanced level. For example, the plowing fuel consumption of Dongfanghong HB2204 is 23% lower than that of traditional models with the same horsepower, and the operation efficiency of the "Honghu" T300 developed by the Chinese Academy of Sciences is increased by 30%. However, the whole industry is still in the transition stage from "domestic independent substitution" to "high-end breakthrough".

(2) The topological structure and technical level of key components determine the upper limit of the complete machine performance, and different technical routes present distinct differentiated adaptation characteristics. The three core topological structures of series, parallel and series-parallel have their own advantages and disadvantages. The series structure has become the mainstream choice for light and medium load and long-time operation scenarios due to its simple structure and moderate cost, but its energy conversion loss and energy consumption under high-speed working conditions are relatively high. The power-split structure, with a plowing fuel consumption rate of 10.5~12.8L/h and a fuel saving rate of 25%~35%, is the technical route with optimal fuel economy, suitable for medium and high-speed continuous operation. The series-parallel structure realizes adaptive operation under complex working conditions through multi-mode switching, with a maximum climbing gradient of 32~38° and a power response time of only 0.15~0.3s, making it suitable for complex terrains such as hills and mountains, but it has the shortcomings of complex structure and high manufacturing cost. In terms of key components, China has achieved domestic production of National Stage IV diesel engines and medium and low-end power batteries, but core components such as high-end E-CVT gearboxes, high-performance permanent magnet synchronous motors and high-computing power electronic control chips still rely on imports. There is a 5~8% gap in transmission efficiency, power density and other indicators compared with the international advanced level, and the lack of precision manufacturing and collaborative adaptation capabilities of core components has become the primary technical bottleneck restricting the improvement of complete machine performance.

(3) The optimization of energy management strategies and energy source configuration is the core to improve system energy efficiency, and currently faces dual challenges of working condition adaptability and real-time performance. Two routes have been formed for energy source configuration: single energy storage and hybrid energy storage. The single energy storage configuration, centered on lithium iron phosphate

batteries, is suitable for small and medium-horsepower basic operations with significant cost advantages. The hybrid energy storage configuration integrates the "energy-power dual complementarity" advantages of power batteries and supercapacitors, becoming the first choice for 300-horsepower high-end models, but its control complexity and manufacturing cost are 30~40% higher than those of the single configuration. Energy management strategies have evolved from traditional rule-based strategies to optimization algorithms and intelligent algorithms. However, most domestic enterprises still rely on logic threshold control, which is difficult to adapt to field load fluctuations and scenario changes. Although intelligent algorithms such as MPC and ECMS, which are mainstream applications abroad, can maximize energy efficiency, they have high requirements for hardware computing power and the accuracy of working condition prediction models, making large-scale engineering application difficult. In terms of verification system, the full-process integrated verification of "simulation-bench-field-hardware-in-the-loop" has become a trend, but problems such as insufficient standardization of working condition load spectra and shallow application of digital twin technology lead to deviations between strategy verification and actual operation scenarios.

(4) Multiple bottlenecks still exist in technological research and development and industrialization promotion, and core controversies focus on the priority of technical routes and performance balance. At the technological R&D level, three prominent problems are insufficient power coupling efficiency (energy conversion loss of series structure and mode switching shock of series-parallel structure up to 0.3g), limited performance of energy storage system (batteries account for 20~30% of the complete machine cost, and the service life is only 1/2~2/3 of that of electric vehicle batteries), and poor coordination of control strategies (lack of integrated "power-operation" optimization). Academic and industrial controversies are reflected in the choice between "cost priority" and "performance priority" routes, the adaptation of energy storage technical routes, and the trade-off between algorithm optimization and system standardization. At the industrialization level, the selling price of complete machines is 30~60% higher than that of traditional models, with a long investment payback period; the coverage rate of rural charging piles is less than 5%, restricting the application of pure electric mode; the high technical threshold for hybrid system maintenance and imperfect after-sales service network jointly restrict large-scale promotion.

(5) Future development needs to focus on core technological breakthroughs, improvement of industrialization ecology and innovation of policy mechanisms to promote the transformation of hybrid tractors towards high-end, intelligent and low-cost development. At the technical level, focus should be placed on developing integrated power coupling devices, special high-power-density solid-state batteries for agricultural machinery, thermal management and vibration protection technologies to extend battery life to 5~6 years; integrate multi-source sensors and deep learning algorithms to build a working condition adaptive prediction model, and develop an integrated "power-operation-navigation" control platform. At the industrialization level, realize the standardization and generalization of core components through modular design, and reduce manufacturing costs through large-scale production; build an infrastructure network of "agricultural machinery cooperatives and charging piles" and establish a professional after-sales service and remote diagnosis system; improve technical standards such as energy saving rate testing and safety requirements, increase support for purchase subsidies and special R&D funds, and promote the "combination of lease and purchase" and "trade-in for new" models to reduce users' initial investment. With the breakthrough of core technical bottlenecks and the maturity of the industrial ecology, hybrid tractors will gradually transform from "transitional technology" to "mainstream equipment", providing core power support for the sustainable development of global agriculture.

ACKNOWLEDGEMENT

This research was supported by the Key Research and Development Program of Shandong Province under (Grant Nos. 2024TSGC0754 and 2022CXGC020702). The authors sincerely acknowledge the financial support provided by these programs.

REFERENCES

[1] Anonymous. (2022). Yuchai Powertrain Helps Tractors Realize Stepless Speed Change (玉柴动力总成助力拖拉机实现无级变速). *Agricultural Machinery*, (7), 31.

[2] Anonymous. (2023). Dongfanghong HB2204 Hybrid Tractor: Electronically Controlled Intelligent Control and Manipulation, 0–40 km/h Stepless Speed Driving! (东方红 HB2204 混合动力拖拉机：电控智能化控制操纵). *Hebei Agricultural Machinery*, (17), 3.

[3] Brudeli, G., de Souza Rebouças, G.F., Vestgaard, B., Fagerås, H. (2026). Innovating Hybrid Power. In: Heintzel, A. (eds) Internationaler Motorenkongress 2025. Int.Engine.Congr. 2025 2025. *Proceedings. Springer Vieweg*, Wiesbaden. https://doi.org/10.1007/978-3-658-49720-0_2

[4] Chen W. (2024). Research on Intelligent Development of New Energy Vehicle Energy Control (新能源汽车能源控制智能化发展研究). *Auto Weekly*, (3), 64-66.

[5] Chen X. R. (2022). Research on Energy Management Strategy of Fuel Cell-Battery Hybrid Power Ship. *In Proceedings of SPIE*, 12164, 121640W.

[6] Chen Z. Y., Fang Z. Y., Yang R. X., et al. (2022). Energy Management Strategy for Hybrid Electric Vehicle Based on Deep Reinforcement Learning (基于深度强化学习的混合动力汽车能量管理策略). *Transactions of China Electrotechnical Society*, 37 (23), 6157-6168.

[7] Cheng F., & Hao Y. G. (2026). *A Fuel Cell Energy Management System for Hydrogen Energy Vehicle (一种氢能汽车的燃料电池能量管理系统).* Patent No. CN201910830891.

[8] Cui M., & Zhu L. H. (2025). Accelerating the Maturation and Application of Advanced Technology Agricultural Machinery Equipment (加快推进先进技术农机装备熟化应用). *Agricultural Machinery Quality and Supervision*, (5), 5.

[9] Deng X. T. (2012). *Research on Dynamic Characteristics of Hybrid Tractor (混合动力拖拉机动力特性的研究)*. Nanjing Agricultural University, Nanjing, China.

[10] Deng X. T., Lei Y., & Lu Z. X. (2026). *A Test Bench for Series Hybrid Tractor (一种串联式混合动力拖拉机试验台)*. Patent No. CN201711263692.9.

[11] Dima S., Fares R., Riad K., et al. (2015). Dynamic Programming Technique for Optimizing Fuel Cell Hybrid Vehicles. *Int. J. Hydrogen Energy*, 40 (34), 11234-11245.

[12] Ding A. X., Zhang C. Y., & Shen Y. (2021). Research on Improved State Machine Energy Management Strategy for Fuel Cell Vehicle (燃料电池汽车改进型状态机能量管理策略研究). *Machinery Manufacturing & Automation*, (6), 1-5.

[13] Ding C. G. (2026). *Research on Energy Management Strategy of Hydrogen Fuel Cell Hybrid System (氢燃料电池混合动力系统能量管理策略研究)*. University of Electronic Science and Technology of China, Chengdu, China.

[14] Dobretsov, R.Y., Tcheremisin, K.V., Voinash, S.A. et al. Control of Power Distribution in the Transmission of an Integral Tractor. *Russ. Engin. Res*. 44, 1257–1262 (2024). https://doi.org/10.3103/S1068798X24702204

[15] Dong H. (2026). *Research on Structural Scheme and Energy Control of Parallel Hydraulic Hybrid Vehicle (并联式液压混合动力车辆结构方案与能量控制研究).* Jilin University, Changchun, China.

[16] Fei P., Peng Y. Z., Yuan Z., et al. (2017). Development of Master-Slave Energy Management Strategy Based on Fuzzy Logic Hysteresis State Machine and Differential Power Processing Compensation for a PEMFC-LIB-SC Hybrid Tramway. *Applied Energy*, 202, 362-375.

[17] Gao Z. (2024). *Research on Energy Management Strategy of Fuel Cell Tractor Hybrid System (燃料电池拖拉机混合动力系统能量管理策略研究).* Henan University of Science and Technology, Luoyang, China.

[18] Gui C. D. (2026). *Design of Permanent Magnet Synchronous Motor Driver for Vehicle Engine Cooling System (车载发动机冷却系统永磁同步电机驱动器设计).* University of South China, Hengyang, China.

[19] Han H. B. (2023). Zoomlion's Intelligent Agricultural Machinery Matrix Shines at International Agricultural Machinery Exhibition (中联重科智能农机矩阵点亮国际农机展). *Agricultural Machinery Market*, (11), 35.

[20] Hu B., Yue Y., Tan S. L., et al. (2025). Research on Hierarchical Energy Management Strategy for Fuel Cell Hybrid Electric Vehicle Considering Speed Planning (考虑速度规划的燃料电池混合动力汽车分层能量管理策略研究). *Journal of Chongqing University of Technology (Natural Science)*, 39 (6), 1-12.

[21] Huang L. L. (2021). Yuchai Releases Two Powertrains: New Energy and CVT (玉柴发布新能源和 CVT 两款动力总成). *Agricultural Machinery Quality and Supervision*, (11), 44.

[22] Huang L. P., Hou L. C., & Zhang M. (2025). Research on Electromagnetic Characteristics of Permanent Magnet Synchronous Direct Drive Drum Based on Maxwell Simulation Analysis (基于 Maxwell 仿真分析的永磁同步直驱滚筒电磁特性研究). *Mechanical Engineering and Technology*, 14 (6), 592-601.

[23] Huang Z. Z. (2021). *Research on Online Multi-Objective Energy Management Strategy for Fuel Cell Vehicle Based on BP Neural Network (基于 BP 神经网络的燃料电池汽车在线多目标能量管理策略研究)*. Chongqing University, Chongqing, China.

[24] Jing J., Liu Y., & Huang W. (2020). Research on Voltage Control of P2.5 Hybrid System. In *Proceedings of the Conference*.

[25] Kebriaei M., Niasar A. H., & Asaei B. (2015). Hybrid electric vehicles: an overview. In 2015 *International Conference on Connected Vehicles and Expo (ICCVE)*. *IEEE*, Shenzhen, China, pp. 299-305. https://doi.org/10.1109/ICCVE.2015.84

[26] Lang Z. Z., Li J. Z., Li L. C., et al. (2026). Current Situation and Control Requirements of Noise and Emission of Agricultural Machinery in China (中国农业机械噪声、排放现状及控制要求). *Tractor, Agricultural Transporter, Agricultural Engine Industry Background Information* (Seventh Volume).

[27] Li H., Ying X. E., Li C., et al. (2026). *Engine Bench Test Device for Electric Air Compressor of Agricultural Machinery (农业机械电动空气压缩机的发动机台架试验装置).* Patent No. CN202222306784.3.

[28] Li J. (2026). *Performance Analysis and Optimal Design Method of Switched Reluctance Motor (开关磁阻电机的性能分析及其优化设计方法研究).* Hebei University of Technology, Tianjin, China.

[29] Li J. F., Zhang X. M., Song Z. H., et al. (2025). Design and Verification of Power System for Distributed Hybrid Tractor Based on TRIZ Theory (基于 TRIZ 理论的分布式混合动力拖拉机动力系统设计与验证). *Journal of Jilin University (Engineering and Technology Edition)*, (1), 1-10.

[30] Li L. Q., Ran G. W., Gao Z. Y., et al. (2024). Adaptive Energy Management and Capacity Configuration of Composite Power Supply System for Pure Electric Tractor (纯电动拖拉机复合供电系统自适应能量管理与容量配置). *Transactions of the Chinese Society of Agricultural Engineering*, 40 (23), 38-46.

[31] Li M. B. (2026). *Research on System Structure and Control Strategy of Hybrid Electric Vehicle (混合动力电动汽车系统结构及控制策略研究).* Shandong Agricultural University, Tai'an, China.

[32] Li W., Li S., Du C., & Yan F. (2026). Cross-type transfer of fuel cell hybrid vehicles energy management strategies based on deep reinforcement learning. *Energy Conversion and Management*, 356, 121371. https://doi.org/10.1016/j.enconman.2026.121371

[33] Li X., Han L., Liu H., et al. (2019). Real-Time Optimal Energy Management Strategy for a Dual-Mode Power-Split Hybrid Electric Vehicle Based on an Explicit Model Predictive Control Algorithm. *Energy*, 172, 1161-1178.

[34] Liu C., & Huang Y. C. (2025). Hierarchical Energy Management Method for Durability Optimization of Fuel Cell Hybrid System Based on Finite State Machine Architecture (基于有限状态机架构的燃料电池混合动力系统耐久性优化分层能量管理方法). *Railway Locomotive & Car*, 45 (3), 73-80.

[35] Liu C., Chen Y., & Zhao L. (2019). Research on Energy Management Strategy of HEV Hybrid Power Supply Based on Stream Mining (基于流挖掘 HEV 复合电源能量管理策略研究). *Chinese Journal of Power Sources*, 43 (7), 1123-1126.

[36] Liu M. N., Zhou Z. L., Xu L. Y., et al. (2017). Optimal Design of Tractor Transport Unit Based on Multi-Performance Objectives (基于多性能目标的拖拉机运输机组优化设计). *Transactions of the Chinese Society of Agricultural Engineering*, 33 (8), 56-63.

[37] Liu Q. (2023). Looking at the Best-Selling Agricultural Machinery Products in the National IV Era (且看国四时代的畅销农机产品). *Agricultural Machinery Quality and Supervision*, (2), 46-47.

[38] Liu X. Y., Du P. H., Li Y., et al. (2025). Simulation Research on Thermal Runaway Mechanism of Lithium Iron Phosphate Battery Based on Temperature Rise Rate (基于温升速率的磷酸铁锂电池热失控机理仿真研究). *Southern Agricultural Machinery*, (Suppl.1), 1-6.

[39] Liu Y. N., Deng X. T., Zhang W. H., et al. (2018). Research on Design Theory and Method of Drive System for Series Hybrid Tractor (串联式混合动力拖拉机驱动系统设计理论和方法研究). *Agricultural Equipment & Vehicle Engineering*, 56 (2), 49-54.

[40] Lu Z. H. (2023). Design of Hybrid Electric Drive Stepless Speed Powertrain for Heavy Tractor (重型拖拉机混动电驱无级变速动力总成设计). *Modern Manufacturing Technology & Equipment*, 59 (7), 51-53.

[41] Lu Z. X., Hou X. F., & Deng X. T. (2017). Design, Matching and Traction Test of Drive System for Series Hybrid Tractor (串联式混合动力拖拉机驱动系统设计匹配与牵引试验). *Journal of Nanjing Agricultural University*, 40 (5), 912-920.

[42] Luo G. J. (2025). *Research on Energy Management Strategy of Series Diesel-Electric Hybrid Tractor (串联式柴电混合动力拖拉机的能量管理策略研究).* Nanjing Agricultural University, Nanjing, China.

[43] Mocera F. (2021). A Model-Based Design Approach for a Parallel Hybrid Electric Tractor Energy Management Strategy Using Hardware in the Loop Technique. *Vehicles*, 3(1), 1-19. https://doi.org/10.3390/vehicles3010001

[44] Mocera F., & Somà A. (2020). Analysis of a Parallel Hybrid Electric Tractor for Agricultural Applications. *Energies*, 13(12), 3055. https://doi.org/10.3390/en13123055

[45] Mocera F., Martini V., & Somà A. (2022). Comparative Analysis of Hybrid Electric Architectures for Specialized Agricultural Tractors. *Energies*, 15(5), 1944. https://doi.org/10.3390/en15051944

[46] Niu B. G. (2025). Hybrid Tractor Technology Is Becoming Mature and Ushering in Market Dawn (混动拖拉机技术日渐成熟，正迎来市场曙光). *Agricultural Machinery*, (7), 43-45.

[47] Pascuzzi S., Łyp-Wrońska K., Gdowska K., & Paciolla F. (2024). Sustainability Evaluation of Hybrid Agriculture-Tractor Powertrains. *Sustainability*, 16 (3), 1184. https://doi.org/10.3390/su16031184

[48] Paciolla, F., Patimisco, P., Farella, A., Quartarella, T., Pascuzzi, S. (2024). Performance Evaluation of Hybrid-Electric Architectures for Agricultural Tractors. In: Lorencowicz, E., Huyghebaert, B., Uziak, J. (eds) Farm Machinery and Processes Management in Sustainable Agriculture. FMPMSA 2024. Lecture Notes in Civil Engineering, vol 609. *Springer*, Cham. https://doi.org/10.1007/978-3-031-70955-5_38

[49] Peng H., Chen Z., Li J., et al. (2021). Offline Optimal Energy Management Strategies Considering High Dynamics in Batteries and Constraints on Fuel Cell System Power Rate: From Analytical Derivation to Validation on Test Bench. *Applied Energy*, 282, 116170.

[50] Qiao B. Z., & Liu Y. B. (2022). Research on FADEC Reliability Test HIL Simulation Automation Technology (FADEC 可靠性试验 HIL 仿真自动化技术研究). *Measurement & Control Technology*, 41 (10), 94-98.

[51] Qiu D. Y. (2026). Research on Energy Management of Hybrid Electric Vehicle Based on Driving Condition Identification and Prediction (基于行驶工况识别与预测的混合动力汽车能量管理研究). Hefei University of Technology, Hefei, China.

[52] Ren H., & Zeng Y. (2022). Chinese Academy of Sciences Releases Phased Achievements of the "Black Soil Granary" Science and Technology Campaign (中国科学院发布“黑土粮仓”科技会战阶段性成果). *Bulletin of the Chinese Academy of Sciences*, 37 (10), F0003.

[53] Ren L., Zhang H. J., Jin B. Q., Gao Y., & Song C. F. (2018). Study on Charging and Discharging Characteristics of Supercapacitors in Braking Energy Recovery System (制动能量回收系统中超级电容充放电特性研究). *Electrical Measurement & Instrumentation*, 55 (24), 35-39.

[54] Sayed, H.A.A., Abdelhamid, M.A., Abdelkader, T.K. et al. Machine learning and analytic hierarchy process integration for selecting a sustainable tractor. *Sci Rep* 14, 26735 (2024). https://doi.org/10.1038/s41598-024-78023-z

[55] Scolaro E, Alberti L, Barater D. Electric Drives for Hybrid Electric Agricultural Tractors. In: 2021 IEEE Workshop on Electrical Machines Design, Control and Diagnosis (WEMDCD). *IEEE*; 2021. p 331–336. https://doi.org/10.1109/wemdcd51469.2021.9425671.

[56] Sunil K., Mari D., Natarajan S., et al. (2026). Thermal Management Control Strategy for Primary & Secondary Drive Cooling Hybrid Electric Tractor. *SAE Int. J. Altern. Powertrains.*

[57] Tan M. Q. (2025). *Research on Energy Management Strategy of Dual Planetary Gear Hybrid System (双行星排式混合动力系统能量管理策略研究)*. Chongqing Jiaotong University, Chongqing, China.

[58] Tong Y. K. (2025). *Research on Optimal Matching of Power System for Hybrid Tractor (混合动力拖拉机动力系统优化匹配研究).* Henan University of Science and Technology, Luoyang, China.

[59] Troncon D, Alberti L, Mattetti M. A (2019). Feasibility Study for Agriculture Tractors Electrification: Duty Cycles Simulation and Consumption Comparison. In: *2019 IEEE Transportation Electrification Conference and Expo (ITEC). IEEE*; p.1–6. https://doi.org/10.1109/itec.2019.8790502.

[60] Varlese C., Konrad J., Volf T., et al. (2025). Predictive Power Demand for Energy Management of Hybrid Electric Tractors. *Smart Agricultural Technology*, 11, 100628.

[61] Wang B. (2015). *Research and Development of Test Bench for Series Hybrid Tractor (串联式混合动力拖拉机试验台的研究与开发).* Nanjing Agricultural University, Nanjing, China.

[62] Wang C. G., & Li H. (2020). Research on Energy Management Control Strategy of Parallel Hybrid Tractor (并联式混合动力拖拉机能量管理控制策略探究). *Journal of Kaifeng University*, 34 (1), 91-96.

[63] Wang K. Y., & Feng B. Q. (2021). Modeling and Simulation of Hybrid Electric Vehicle Power System Based on MATLAB/Simulink (基于 Matlab/Simulink 的混合动力汽车动力系统建模与仿真). *Equipment Repair Technology*, (5), 50-57.

[64] Wang R. C., Shao K., Ye Q., et al. (2026). *A Hydraulic Recovery and Comprehensive Utilization System of Automobile Wheel Inertia Energy and Its Control Method (一种汽车车轮惯性能量的液压式回收和综合利用系统及其控制方法)*. Patent No. CN201610183233.9.

[65] Wang S., Wu X., Zhao X., et al. (2025). An Integrated Control Strategy for Reducing Equivalent Fuel Consumption and Improving Traction Efficiency of a Distributed Hybrid Electric Tractor Considering Farmland Terrain Adaptability. *Energy*, 334, 127440.

[66] Wang T. (2024). Research on the Energy Management Strategy of a Hybrid Tractor OS-ECVT Based on a Dynamic Programming Algorithm. *Agriculture*, 14 (10), 1678.

[67] Wang T. (2024). Research on the Energy Management Strategy of a Hybrid Tractor OS-ECVT Based on a Dynamic Programming Algorithm. *Agriculture*, 14.

[68] Wang T. X. (2023). Research on Energy Management Strategy of Fuel Cell Hybrid Vehicle (燃料电池混动汽车能量管理策略研究). *Henan Science and Technology*, 42 (10), 26-29.

[69] Wang W. D., Xiang C. L., Han L. J., et al. (2026). Analysis of Dual-Mode Power-Split Hybrid System and Research on Energy Management Strategy (双模式功率分流混合动力系统分析与能量管理策略研究). In *Proceedings of the 32nd Chinese Control Conference*.

[70] Wang Y., & Sun Z. (2015). Dynamic Analysis and Multivariable Transient Control of the Power-Split Hybrid Powertrain. *IEEE/ASME Transactions on Mechatronics*, 20 (6), 3085-3097.

[71] Wang Z. F., Luo W., Xu S., et al. (2022). Review on Energy Management Strategy of Fuel Cell Vehicle (燃料电池汽车能量管理策略综述). *Battery Bimonthly*, (3), 312-316.

[72] Wang Z. G., Yan W., Zhou Z. H., et al. (2026). *A Control Device for Power Optimization System of Single-Motor Drive Hybrid Tractor (一种单电机驱动混合动力拖拉机动力优化系统控制装置).* Patent No. CN202323357927.4.

[73] Wen C. K., Zhao Z. H., Xie B., et al. (2025). Review on Key Technologies of Hybrid Tractors (混合动力拖拉机关键技术研究综述). *Transactions of the Chinese Society for Agricultural Machinery*, 56 (12), 1-23.

[74] Wu X. (2019). *Research on High-Efficiency and Wide-Range Control of Vehicle-Mounted Permanent Magnet Synchronous Motor (车用永磁同步电机高效与宽域控制研究).* China University of Mining and Technology, Xuzhou, China.

[75] Xie H.H., & Sun Y.T. (2018). Discussion on BMS/VCU Production Process (浅谈 BMS/VCU 生产工艺流程). *Auto Time*, (3), 8-9.

[76] Xu R.Z.M. (2021). Dynamic Obstacle Detection Based on Panoramic Vision in the Moving State of Agricultural Machineries. *Comput. Electron. Agric.*, 184, 106080.

[77] Yan Y.X. (2023). *Research on Control Strategy of Power System of Hybrid Tractor (混合动力拖拉机动力系统控制策略研究).* Henan University of Science and Technology, Luoyang, China.

[78] Yao Y.Q., & Zhou Y.Y. (2023). Overview of Energy Management Strategy for Hybrid Electric Vehicle Based on Rule Strategy (基于规则策略的混合动力汽车能量管理策略概述). *Auto Time*, (5), 10-12.

[79] Yin B.F. (2025). Research on Rule-Based Energy Management Strategy for Series Hybrid Tractor (基于规则的串联式混合动力拖拉机能量管理策略研究). *Agricultural Machinery Quality and Supervision*, (6), 10-12.

[80] Yu Z.G. (2022). New Energy Development and Modern Technology Application Trend of Tractors (拖拉机的新能源化发展及其现代化技术应用趋势). *Agricultural Machinery Using & Maintenance*, (7), 32-34.

[81] Zhang K., Wang L., Deng X.T., et al. (2025). Improved Method and Verification of ECVT Energy Management Strategy for Hybrid Tractor Based on Pontryagin's Minimum Principle (基于庞特里亚金极小值原理的混合动力拖拉机 ECVT 能量管理策略改进方法与验证). *Transactions of the Chinese Society for Agricultural Machinery*, (9), 1-12.

[82] Zhang M.Z., Zhou Z.L., Xu L. Y., et al. (2003). Design of Multi-Stage Hydro-Mechanical Continuously Variable Transmission for Agricultural Tractor (农业拖拉机用多段液压机械无级变速器设计). *Transactions of the Chinese Society of Agricultural Engineering*, 19 (6), 126-130.

[83] Zhang S.H. (2024). Research on Optimization of Overcharge/Overdischarge Protection of Low-Temperature Battery Based on a Hybrid Vehicle (基于某混动车型的低温电池过充 / 过放保护优化研究). *Auto Electric Appliances*, (3), 12-14.

[84] Zhao J.H., Xu L. Y., Liu E.Z., et al. (2018). Design of Drive System for Extended-Range Electric Tractor (增程式电动拖拉机驱动系统设计). *Journal of Agricultural Mechanization Research*, 40 (11), 246-250.

[85] Zhao X.C., Zhou Z.G., Zhang J., et al. (2021). Torque Coordination Control of Engine Starting During Driving of Dual-Motor PHEV Based on Dynamic Programming (基于动态规划的双电机 PHEV 行进间启动发动机转矩协调控制). *Tractor & Farm Transporter*, 48 (5), 53-60.

[86] Zhou R., Wang L., & Deng X. (2024). Research on Energy Distribution Strategy of Tandem Hybrid Tractor Based on the Pontryagin Minimum Principle. *Agriculture*, 14 (3), 412.

[87] Zhou R.D. (2026). *Research on Energy Distribution Strategy of Series Hybrid Tractor Under Different Working Conditions (不同工况下串联式混合动力拖拉机能量分配策略研究).* Nanjing Agricultural University, Nanjing, China.

[88] Zhu L.H. (2025). Yuchai Hybrid" Accelerates the Transformation of Tractor Industry (玉柴混动" 加速拖拉机产业变革). *Agricultural Machinery Quality and Supervision*, (11), 40-41.

[89] Zhu M.J., Zhao J.H., Wu X.H., et al. (2025). Energy Management Strategy of Distributed Hybrid Tractor Based on Clustering Optimization Equivalent Factor (基于聚类优化等效因子的分布式混动拖拉机能量管理策略). *Transactions of the Chinese Society of Agricultural Engineering*, 42 (Suppl.), 460-468.

[90] Zuo T.T., Zhu S.H., & Deng X.T. (2013). Research on Dynamic Characteristics of Power Coupling Device of Hybrid Tractor (混合动力拖拉机动力耦合装置动力学特性研究). *Tractor & Farm Transporter*, (4), 12-15.

EXPERIMENTAL STUDY AND ANALYSIS ON MECHANICAL PROPERTIES OF CASSAVA ROOTS AT HARVESTING STAGE

/

收获期木薯块根力学特性试验研究与分析

Guanghao XU[1)], Wenwen LI[1,3)], Jiannong SONG[2)], Binfeng SUN[1)], Zhongsheng CAO[1)], Junbao HUANG[1)], Xinyi PENG[1)], Yanda LI[1*)]

[1)] Institute of Agricultural Engineering, Jiangxi Academy of Agricultural Sciences, Nanchang 330200 / China;
[2)] College of Engineering, China Agricultural University, Beijing 100083 / China
[3)] College of Engineering, Jiangxi Agricultural University, Nanchang; 330045 / China
* Corresponding author: Yanda LI
Tel: +86-15870656983; E-mail: liyanda2008@126.com
DOI: https://doi.org/10.35633/inmateh-79-16

Keywords: *harvesting stage, cassava roots, mechanical properties, mechanical damage, experimental study*

ABSTRACT

During mechanized harvesting operations, including excavation, root–soil separation, collection, and transportation, cassava roots are susceptible to multiple mechanical loads such as shear, compression, and impact, which easily induce mechanical damage and seriously deteriorate the processing quality and storage performance of cassava roots. To reveal the mechanical variation characteristics and damage thresholds of cassava roots under primary mechanical damage modes during harvesting and transportation, this study took harvest-stage cassava roots as the research object and conducted systematic mechanical property tests. Three typical mechanical tests, including compression, shear, and bending tests, were performed to explore the mechanical response rules of cassava roots under typical loads, obtain key mechanical parameters and damage thresholds, and clarify the failure characteristics and mechanical mechanisms under different loading modes. The research results clarify the internal relationship between mechanical properties and mechanical damage of cassava roots at the harvesting stage. This study provides reliable basic data and theoretical support for the parameter optimization of key working components, operational parameter matching of specialized cassava harvesters, and the optimal selection of tool edge angles for cassava slicing machinery, and possesses practical engineering significance for reducing mechanical harvesting damage and improving the post-harvest commodity rate and processing performance of cassava roots.

摘要

木薯块根在机械化收获的挖掘、薯土分离、收集及转运作业中，易受到剪切、挤压、撞击等多种机械载荷作用而产生损伤，严重影响块根加工品质与存储期。为揭示收获与运输过程中木薯块根主要机械损伤形式下的受力变化特性及阈值，本研究以收获期木薯块根为研究对象，系统开展了力学特性试验研究。通过开展压缩、剪切、弯曲三项力学性能试验，测定收获期木薯块根在典型载荷作用下的力学响应规律，获取其关键力学参数与损伤阈值，明确不同受力形式下的破坏特征与力学机制。研究结果阐明了收获期木薯块根的力学特性与机械损伤的内在关联，为专用木薯收获机关键工作部件参数优化、作业参数匹配以及木薯切片机械刀具刃角的合理选取提供可靠的基础数据与理论支撑。在降低木薯机械化收获损伤、提升产后商品率与加工性能方面具有重要的应用价值。

INTRODUCTION

Cassava, a species of the genus Manihot in the *Euphorbiaceae* family, is ranked among the world's three major tuber crops together with potato and sweet potato *(FAO., 2001)*. Having a cultivation history of more than 200 years in China, cassava is mainly grown in tropical and subtropical provinces including Guangxi, Guangdong, Hainan, Yunnan, Fujian, Hunan and Jiangxi *(Fu et al., 2018; Li et al., 2024; Xu et al., 2025)*. Notably, Guangxi Zhuang Autonomous Region accounts for over 60% of China's total cassava planting area and fresh tuber yield *(Feng et al., 2022)*.

Guanghao Xu, Assistant Researcher Ph.D. Eng.; Wenwen Li, M.S. Eng. Stud.; Jiannong Song, Prof. Ph.D. Eng.; Binfeng Sun, Associate Researcher Ph.D.; Zhongsheng Cao, Associate Researcher Ph.D.; Junbao Huang, Assistant Researcher Ph.D.; Xinyi Peng, Assistant Researcher M.S. Eng.; Yanda Li, Senior Researcher Ph.D.

Restricted by the limited area of tropical and subtropical zones in China, as well as the high labor intensity and low mechanization level of cassava cultivation, domestic cassava output has long failed to meet the demand of national industrial production *(Liang et al., 2016; Li et al., 2025)*.

According to the latest statistics released by the Food and Agriculture Organization of the United Nations (FAO), China's cassava planting area reached approximately 3.42×10^5 hectares and the fresh tuber yield was about 7.92×10^6 tons in 2024 *(FAO., 2026)*. Since 2009, China's imports of dried cassava chips have consistently made up more than 80% of the global trade volume of this product *(Tan et al., 2018; FAO., 2026)*.

During mechanized harvesting, cassava roots sustain various types of mechanical damage in the processes of digging, root-soil separation, collection and transportation *(Yang et al., 2026)*. Common damage forms include shearing by the cutting edge of digging blades, compression from digging and separating components, and impact between roots or between roots and container walls during collection and conveying. Such mechanical damage severely impairs the subsequent processing quality and thus reduces the commercial value of cassava roots *(Li et al., 2023; Dankwa et al., 2025; Sreekumar et al., 2026)*.

After harvesting, cassava roots are first sliced, followed by natural or mechanical drying to reduce the moisture content of slices for the production of dried cassava chips *(Simo-Tagne et al., 2021; Gao et al., 2022; Krishnakumar et al., 2022)*. Therefore, investigating the mechanical properties of fresh cassava roots at the harvesting stage is of great significance for the structural design, parameter optimization and operational parameter selection of cassava harvesters and dedicated cassava slicers. To date, numerous experimental studies have been conducted worldwide on the mechanical properties of common crop materials, mainly focusing on crop rhizomes, fruits, stems and leaves *(Fan et al., 2022; Hostetler et al., 2022; Jin et al., 2024; Zhang et al., 2025)*.

Yang Wang et al. prepared cylindrical and polyhedral specimens from cassava roots and measured their tensile, compressive and shear strengths as well as elastic modulus via physical tests *(Yang et al., 2011)*.

Yan Mei et al. adopted cuboid specimens of cassava roots to investigate their compressive and shear mechanical characteristics *(Yan et al., 2013; Yan et al., 2013)*. Nevertheless, these studies only tested partial tissues of cassava roots rather than the whole root. Cassava roots at the harvesting stage have a complex structure, with distinct mechanical performances among the outer cortex, inner cortex, parenchyma and pith. Mechanical parameters obtained from partial tissues fail to reflect the actual mechanical properties of intact cassava roots.

In this study, intact fresh cassava roots at the harvesting stage were selected as test materials. Combined with the main damage characteristics during harvesting and the subsequent slicing process, physical experiments were carried out to investigate the effects of major test factors on the compressive, shear and bending mechanical properties of cassava roots. Based on the analysis of experimental results, the variation laws of mechanical properties affected by each factor were summarized. The findings can provide fundamental data and theoretical support for the structural design of key components and the selection of operational parameters of low-damage and high-efficiency cassava harvesters and slicers.

MATERIALS AND METHODS

Compression mechanical property test

Preparation of compression specimens

The test materials were collected from the full mechanization demonstration base for cassava and pineapple production at the Agricultural Machinery Research Institute, Chinese Academy of Tropical Agricultural Sciences, Zhanjiang City, Guangdong Province.

The cassava variety used was *Nanzhi 199*. Intact cassava roots with uniform shape, free from diseases, pests and mechanical damage were selected and cleaned to remove surface soil for standby.

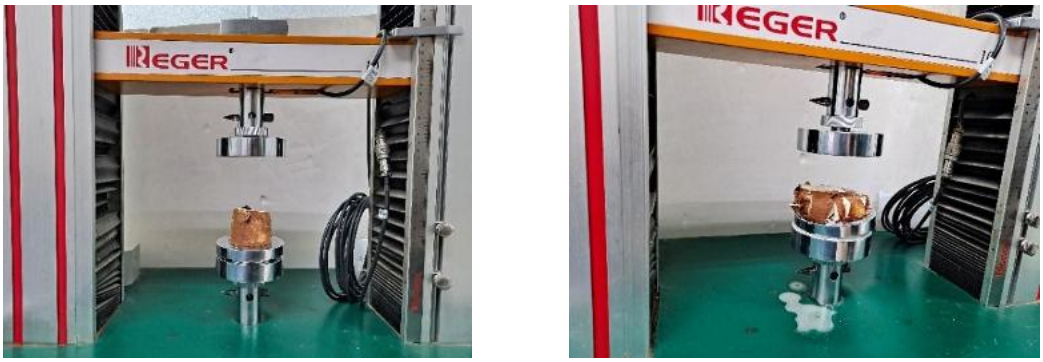
Shear specimens with a length of 50 mm were prepared from the head, middle and tail parts of the cassava roots, and the average diameter at the middle of each specimen was recorded. Both cut ends of the finished specimens were immediately sealed with paraffin to mitigate test errors caused by water loss.



Fig. 1 - Compressive specimens

Test apparatus

The testing device adopted was the RGM-4005 microcomputer-controlled fully digital electronic universal material testing machine manufactured by Reger Instruments. This equipment is mainly used to determine the mechanical properties and related physical parameters of various materials under tension, compression, bending and shear conditions. Equipped with different fixtures, it can also perform tests such as tearing, peeling and puncture. A disc-type compression fixture was used in this experiment. The structural appearance and technical parameters of the testing machine are presented below. Other auxiliary tools included a vernier caliper, paraffin, utility knife and steel ruler.



a. Universal material testing machine **b. Post-compression state of samples**

Fig. 2 - Reer RGM-4005 electronic universal testing machine

Table 1

Nameplate parameters of electronic universal testing machine

Item	Parameter value
Tester model	RGM-4005
Maximum load capacity	5 kN
Test speed range	0.001–500 mm/min
Relative error of test force	Within ±1% of indicated value
Relative error of speed	Within ±1% of indicated value
Relative error of displacement	Within ±1% of indicated value
Tensile test stroke	800 mm
Effective test width	400 mm
Motor power	0.4 kW
Overall dimension of main machine	975 × 460 × 2170 mm
Weight of main machine	Approx. 200 kg

Experimental design and methods

Cassava roots are generally quasi-cylindrical, conical, or spindle-shaped, and their compressive mechanical properties differ among the head, middle, and tail regions *(Yang et al., 2011)*. Based on the structural characteristics of cassava roots and previous literature *(Yang et al., 2022; Dai et al., 2026)*, three experimental factors were selected for this study, namely loading direction, loading speed, and root position. The experimental factors and corresponding levels are listed in Table 2.

Table 2

Factors and levels for compression test

Level	Loading direction (A)	Loading speed (B) / (mm/min)	Root position (C)
1	Axial	50	Head
2	Major radial	100	Middle
3	Minor radial	150	Tail

According to the selected experimental factors and levels, an $L_9(3^4)$ orthogonal array was adopted for the compression mechanical property test of cassava tuberous roots. A total of 9 groups of tests were conducted in each run, and all tests were repeated once, resulting in 18 test groups in total. The compression fixture was correctly mounted on the electronic universal testing machine. A cassava tuberous root sample was placed at the center of the lower platen of the compression fixture, and the upper platen was adjusted until its bottom surface just contacted the sample. After setting the operating parameters of the testing machine, the test was initiated by clicking the "Run" button. The compressive load increased gradually. When the compression deformation reached the maximum value, the cassava tuberous root fractured, accompanied by a sharp drop in load reading, and the test was terminated. All experimental data were automatically recorded by the computer.

The compressive stress calculation formula for cassava roots is expressed as:

$$\sigma_y = \frac{F_y}{A} \quad (1)$$

In equation:

σ_y- Maximum compressive stress of specimen, [MPa];

F_y- Maximum compressive load in compression test, [N];

A - Cross-sectional area of specimen, [mm^2].

The calculation formula for the cross-sectional area under axial compression is expressed as:

$$A_y = \pi \left(\frac{D_b + D_s}{4}\right)^2 \quad (2)$$

In equation:

A_y- Axial cross-sectional area of specimen, [mm^2];

D_b- Maximum outer diameter at the middle of specimen, [mm];

D_s- Minimum outer diameter at the middle of specimen, [mm].

The calculation formula for cross-sectional area under radial compression is expressed as:

$$A_{y1} = 50 D_b \quad (3)$$

$$A_{y2} = 50 D_s \quad (4)$$

In equation:

A_{y1}- Cross-sectional area of specimen at major diameter, [mm^2];

A_{y2}- Cross-sectional area of specimen at minor diameter, [mm^2].

Shear mechanical property test

Preparation of shear specimens

Test materials were sourced from the same batch used in the compressive mechanical property test. Specimens with a length of 50 mm were prepared from the head, middle and tail portions of cassava roots, and the average diameter at the middle position of each specimen was recorded. After preparation, the cut ends of specimens were immediately sealed with paraffin to minimize experimental errors induced by moisture loss.

Test apparatus

A computer-controlled fully digital universal material testing machine (Model RGM-4005, Reger Instrument, Shenzhen, China) was adopted for the test. A self-designed shear fixture dedicated to cassava roots was equipped in this experiment. The fixture consists of two components: a blade clamping seat and a specimen supporting base, wherein the supporting base enables adjustment of the angle between the blade and the axial line of cassava root specimens. Additional experimental accessories include shear blades, vernier calipers, paraffin, utility knives and steel rulers. The operation mode of shear test and fixture structure are shown in figure 3.

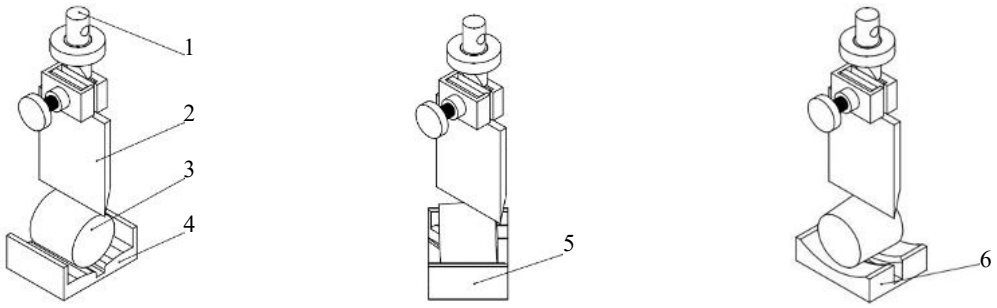


Fig. 3 - Shear mode and fixture

1. Blade clamping seat; 2. Shear blade; 3. Shear specimen; 4. Axial shear supporting base; 5. Lateral 45° shear supporting base; 6. Radial shear supporting base

Experimental design and methods

Based on previous studies on shear mechanical properties of rhizome crops and the actual slicing operation of cassava roots *(Yan et al., 2013; Chen et al., 2024)*, four experimental factors including shear angle (D), blade cutting edge angle (E), root position (F) and loading speed (G) were selected to investigate the shear mechanical characteristics of cassava roots. The shear angle is defined as the included angle between the cutting edge of the blade and the central axis of specimens, with three levels of 0°, 45° and 90°. A single-edge cutter was adopted in this test, and the blade cutting edge angles were set as 15°, 30° and 45°. Three root positions (head, middle and tail of cassava roots) were chosen, and loading speeds were designed at 50 mm/min, 100 mm/min and 150 mm/min. The experimental factors and corresponding levels are listed in Table 3.

Table 3

Factors and levels for shear test

Level	Shear angle (D)	Blade cutting edge angle (E)	Root position (F)	Loading speed (G) / (mm/min)
1	0°	15°	Head	50
2	45°	30°	Middle	100
3	90°	45°	Tail	150

According to the selected experimental factors and levels, an orthogonal array test $L_9(3^4)$ was adopted for the shear mechanical property test of cassava roots. Nine groups of tests were conducted per trial, and each test was replicated once, resulting in a total of 18 experimental groups. A tension-compression load cell was mounted on the sensor holder of the universal material testing machine. Subsequently, the blade fixture and specimen supporting base of the self-made cassava root shear fixture were connected to the upper and lower fixture joints of the testing machine, respectively, to complete the assembly of the load cell, fixture and testing equipment. The shear specimen was placed on the specimen supporting base. The moving crosshead of the universal testing machine was adjusted to make the cutting edge tangent to the outer cylindrical surface of the specimen. The specimen base of the fixture was further adjusted to set a specified included angle between the central axis of cassava root and the blade cutting edge. After parameter configuration on the testing machine, the test was initiated by clicking the “Run” button and terminated once the specimen was completely cut off by the blade. All test data were automatically recorded by the supporting software of the universal material testing system.

The shear stress calculation formula of cassava roots is expressed as:

$$\sigma_j = \frac{F_j}{A_j} \tag{5}$$

where:

σ_j- Maximum shear stress of specimen, [MPa];

F_j- Maximum shear load during shear test, [N];

A_j- Shear cross-sectional area of specimen, [mm^2].

The calculation formula for cross-sectional area under axial shear is given as:

$$A_j = 50D_j \tag{6}$$

where:

D_j- Average outer diameter of specimen, [mm].

The calculation formula for cross-sectional area under both axial 45° and 90° shear is defined as:

$$A_j = {\pi\left(\frac{D_j}{2}\right)^2}\Big/{\sin\alpha} \quad (7)$$

where: α- Included angle between blade cutting edge and specimen central axis, [rad].

Bending mechanical property test

Preparation of bending specimens

Test materials were consistent with those used for the compression mechanical property test. Referring to relevant literatures *(Yan et al., 2013; Chen et al., 2024)*, ten bending specimens with a length of 200 mm were prepared. In the preparation process, the head and tail of cassava roots were cut off and only the middle nearly cylindrical part was reserved. The outer diameters at the front, middle and rear positions of each specimen were measured and recorded by a vernier caliper, and the average value was regarded as the specimen diameter. After specimen fabrication, both end cross-sections were sealed with paraffin wax, and the bending test was conducted immediately.

Test apparatus

A computer-controlled fully digital universal material testing machine (Model RGM-4005, Reger Instrument, Shenzhen, China) was adopted for the test. The fixture consisted of the original indenter matched with the tester and self-fabricated lower supports, as shown in Figure 4. Other experimental tools included a vernier caliper, paraffin wax, utility knife and steel ruler.

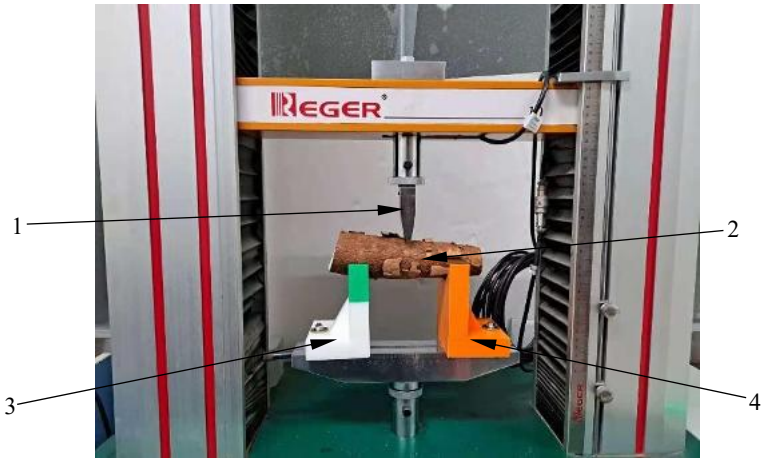


Fig. 4 - Bending test of cassava roots

1. Upper indenter; 2. Compression specimen; 3. Left lower support; 4. Right lower support

Experimental design and methods

The three-point bending method was adopted for the bending mechanical property test. The span of the three-point bending fixture on the universal testing machine was adjusted to 100 mm, with the midpoint of the span set as the indentation position of the upper indenter. The prepared cassava root specimen was placed on the supports, and the test was performed at a loading speed of 2 mm/min until complete fracture of the specimen. The double-layer peel of cassava root is approximately 2 mm thick and tightly bonded to the flesh; thus, cassava roots are simplified as cylindrical materials. Based on the load data recorded by the testing machine, the flexural modulus of elasticity and flexural strength of cassava roots can be calculated.

The bending moment equation for three-point bending test of cylindrical specimens is given as *(Liu., 2004)*:

$$M_w = \frac{F_w L}{4} \quad (8)$$

In equation:

M_w- Bending moment of specimen, [N·mm];

F_w - Maximum bending load of specimen, [N];

L - Bending span of specimen, [mm].

The moment of inertia and flexural section modulus of cylindrical specimens are expressed as *(Liu., 2004)*:

$$I_w = \frac{\pi d_w^4}{64} \quad (9)$$

$$W_w = \frac{\pi d_w^3}{4} \quad (10)$$

where:

I_w- Moment of inertia of specimen, [mm^4];

d_w- Diameter of specimen, [mm];

W_w- Flexural section modulus of specimen, [mm^3].

The calculation formula for flexural elastic modulus of the specimen is as follows:

$$E_w = \frac{F_w L^3}{48 y_w I_w} \quad (11)$$

where:

E_w- Flexural elastic modulus of specimen, [MPa];

y_w- Bending deflection of specimen, [mm].

The calculation formula for flexural strength of the specimen is as follows *(Liu., 2004)*:

$$\sigma_w = \frac{M_w}{W_w} \quad (12)$$

where: σ_w- Flexural strength of specimen, [MPa].

RESULTS AND ANALYSIS

Compression mechanical property test results and analysis

Test results

Loading direction, loading speed and root position were selected as influencing factors for compression tests of cassava roots at harvest stage, while compressive stress and compression deformation were taken as evaluation indices. After data calculation and screening, the measured values of compressive stress and compression deformation are listed in Table 4.

Table 4

Compression test results of harvest-stage cassava roots

Test No.	Level combination	Compressive stress (MPa)		Compression deformation (mm)	
		I	II	I	II
1	$A_1B_1C_1$	1.12	1.00	15.94	12.42
2	$A_1B_2C_2$	1.09	1.73	15.05	15.18
3	$A_1B_3C_3$	1.28	1.56	14.38	13.98
4	$A_2B_1C_2$	0.32	0.30	8.29	7.66
5	$A_2B_2C_3$	0.45	0.56	5.79	11.85
6	$A_2B_3C_1$	0.40	0.21	7.29	9.49
7	$A_3B_1C_3$	0.70	0.34	15.84	8.99
8	$A_3B_2C_1$	0.40	0.35	10.25	6.66
9	$A_3B_3C_2$	0.26	0.38	10.69	7.99

Results analysis

ANOVA of compression test data for cassava roots was conducted with SPSS, and the results are shown in Tables 5 and 6.

Table 5

ANOVA of compressive stress results

Source	Type III Sum of Squares	df	Mean Square	f	Sig.
Corrected Model	1.831[a]	8	0.229	7.953	0.003
Intercept	5.422	1	5.422	188.38	<0.001
Loading direction (A)	1.427	2	0.713	24.79	<0.001
Loading speed (B)	0.251	2	0.126	4.38	0.047
Root position (C)	0.153	2	0.077	2.67	0.122
Error	0.259	9	0.029	—	—
Total	7.512	18	—	—	—
Corrected Total	2.090	17	—	—	—

Note: R^2 = 0.876 (Adjusted R^2 = 0.765)

Table 6

ANOVA for compression deformation results

Source	Type III Sum of Squares	df	Mean Square	f	Sig.
Corrected Model	168.720[a]	8	21.090	3.757	0.032
Intercept	2215.920	1	2215.920	394.70	<0.001
Loading direction (A)	135.611	2	67.806	12.07	0.003
Loading speed (B)	21.352	2	10.676	1.900	0.202
Root position (C)	11.757	2	5.879	1.046	0.389
Error	50.530	9	5.614	—	—
Total	2435.170	18	—	—	—
Corrected Total	219.250	17	—	—	—

Note: R^2 = 0.770 (Adjusted R^2 = 0.565)

Loading direction (A) exerted an extremely significant effect on both compressive stress and compression deformation of cassava roots (P < 0.001 and P = 0.003, respectively). Loading speed (B) significantly affected compressive stress (P = 0.047) but showed insignificant influence on compression deformation (P > 0.05), while root position (C) had no significant impact on the two indicators (P > 0.05). The factor influence order was loading direction > loading speed > root position, and the determination coefficients indicated satisfactory fitting of the two ANOVA models.

As shown in the experimental data in Table 4, the average axial compressive stress is 3.45 times and 3.24 times the average compressive stress under large radial and small radial compression, respectively. The compressive stress varies from 0.21 MPa to 1.73 MPa with an overall average of 0.69 MPa. Loading direction exerts the most significant influence on the compressive stress of cassava roots, and the axial compressive strength is higher than the radial compressive strength.

Shear mechanical property test results and analysis

Test results

The load-displacement curves automatically recorded by the software of an electronic universal testing machine during shear tests on harvest-stage cassava roots were processed to obtain the maximum shear force of each sample. Combined with the premeasured root diameter of each replicate group, the maximum shear stress was calculated in accordance with the specified data processing method, and the calculated results are listed in Table 7.

Table 7

Shear test results of harvest-stage cassava roots

Test No.	Level combination	Maximum shear stress (kPa)	
		Ⅰ	Ⅱ
1	$D_1E_1F_1G_1$	37.99	87.86
2	$D_1E_2F_2G_2$	68.78	95.13
3	$D_1E_3F_3G_3$	100.50	97.25
4	$D_2E_1F_2G_3$	99.98	59.24
5	$D_2E_2F_3G_1$	86.48	64.15
6	$D_2E_3F_1G_2$	154.22	128.93
7	$D_3E_1F_3G_2$	77.90	67.75
8	$D_3E_2F_1G_3$	71.07	90.48
9	$D_3E_3F_2G_1$	112.28	78.96

Results analysis

ANOVA of shear test data for cassava roots was conducted with SPSS, and the results are shown in Tables 8.

Table 8

ANOVA for maximum shear stress results

Source	Type III Sum of Squares	df	Mean Square	f	Sig.
Corrected Model	8449.965[a]	8	1056.246	2.508	0.096
Intercept	7919.111	1	7919.111	18.806	0.002

Source	Type III Sum of Squares	df	Mean Square	f	Sig.
Shear angle (D)	1121.622	2	560.811	1.332	0.311
Blade cutting edge angle (E)	5487.648	2	2743.824	6.516	0.018
Root position (F)	523.623	2	261.812	0.622	0.559
Loading speed (G)	1317.072	2	658.536	1.564	0.261
Error	3789.928	9	421.103	—	—
Total	150744.510	18	—	—	—
Corrected Total	12239.893	17	—	—	—

Note: R^2 = 0.690 (Adjusted R^2 = 0.415)

ANOVA results indicated that blade cutting edge angle (E) exerted a significant effect on the maximum shear stress of cassava roots (P < 0.05), which was the dominant factor governing the shear mechanical properties of cassava roots. Shear angle (D), root position (F) and loading speed (G) had no statistically significant influence on maximum shear stress (P > 0.05). The priority of factor influence followed the order: blade cutting edge angle (E) > loading speed (G) > shear angle (D) > root position (F). The determination coefficient R^2 = 0.690 and adjusted R^2 = 0.415 indicated that the regression model had acceptable fitting performance for experimental analysis.

Cassava roots consist of epidermis, endodermis and flesh, with respective mass proportions of 1.0% – 2.0%, 10.0% – 14.0% and 80.0% – 90.0%, showing relatively uniform internal composition. At the initial cutting stage, shear load increases nearly linearly with rising displacement, and the load-displacement curve approximates a straight line. After the shear load reaches its peak value, further increase of cutting displacement leads to two distinct load-falling patterns: sharp cliff-type drop and fluctuating stepwise decline. The difference originates from specimen dimension, loading speed and blade cutting edge angle. Larger outer diameter, loading speed or blade cutting edge angle causes wedge-induced fracture inside cassava roots during cutting, resulting in abrupt cliff-like load reduction; in contrast, wedge-induced fracture disappears when any of the three parameters is set at a low level. According to shear test data, the maximum shear stress of harvest-stage cassava roots ranges from 37.99 kPa to 154.22 kPa with an average value of 87.72 kPa. ANOVA confirms that blade cutting edge angle imposes a statistically significant effect on the shear strength of cassava roots.

Bending mechanical property test results and analysis

Test results

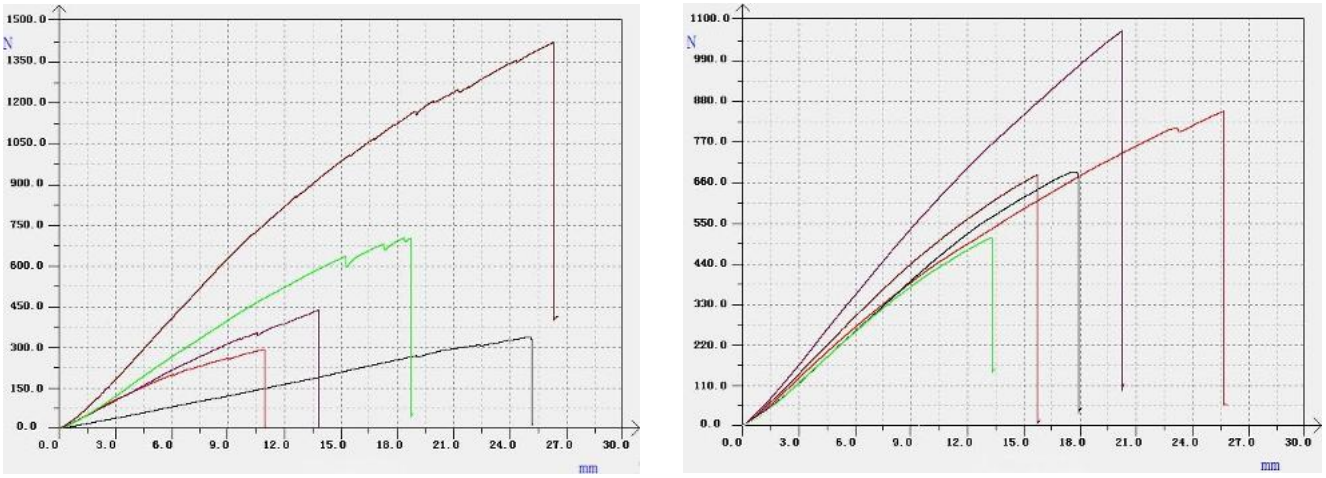
In the bending test of harvest-stage cassava roots, the maximum bending load F_w and bending deflection y_w for each specimen were obtained from load–displacement curves automatically recorded by the electronic universal testing machine. The bending elastic modulus E_w and flexural strength σ_w were calculated according to Eqs. (8) – (12), and the results are summarized in Table 9.

Table 9

Bending test results of harvest-stage cassava roots

Test No.	Specimen diameter d_w (mm)	Bending deflection y_w (mm)	Maximum bending load F_w (N)	Bending elastic modulus E_w (MPa)	Flexural strength σ_w (MPa)
1	37.33	9.40	227.04	5.28	1.11
2	39.35	10.95	290.92	4.70	1.22
3	43.30	25.03	336.58	1.62	1.06
4	46.07	13.81	436.13	2.98	1.14
5	52.99	18.38	700.71	2.05	1.20
6	53.59	17.74	686.50	1.99	1.14
7	54.78	15.73	678.38	2.03	1.05
8	55.70	25.70	850.04	1.46	1.25
9	61.66	20.24	1065.83	1.55	1.16
10	61.78	26.34	1416.46	1.57	1.53

Figure 5 shows the load-displacement curves obtained from three-point bending tests of harvest-stage cassava root specimens.



a. Test 1 b. Test 2

Fig. 5 - Bending load–deformation curves

Results analysis

As listed in Table 9, the maximum bending load of cassava roots specimens increases gradually with rising specimen diameter. Quadratic regression fitting was conducted between measured maximum bending load and specimen diameter, and the fitted equation is expressed as $F_w = 1.56d_w^2 - 112.3d_w + 2311$ with a determination coefficient R^2 = 0.9429, revealing that the ultimate bearing bending load has a positive quadratic correlation with root diameter. The bending elastic modulus generally declines as specimen diameter increases, while bending strength fluctuates slightly within the range of 1.05 - 1.53 MPa with an average value of 1.19 MPa. Owing to the high moisture content inside cassava roots, a great deal of sap exudes from loading and supporting positions during bending test, which imposes a certain influence on the measured bending strength. As illustrated in Figure 5, the whole bending process of harvest-stage cassava roots can be divided into two stages: quasi-elastic deformation stage and brittle fracture stage. At the initial loading phase, bending deformation is approximately proportional to the applied load. Once the load reaches the critical yield point, the specimens rupture instantly without apparent plastic deformation accompanied by crisp cracking sound, meanwhile the bending load drops sharply in cliff-type form, which demonstrates obvious brittle fracture property of cassava roots.

CONCLUSIONS

In this study, mechanical tests including compression, shear and bending were carried out on intact cassava roots at the harvesting stage. Based on systematic experimental analysis, the main research conclusions are summarized as follows:

(1) The compression test results show that the loading direction has a significant influence on the compressive stress of cassava roots, while the loading speed and root position have no significant effect. All three experimental factors (loading direction, loading speed and root position) exhibit insignificant effects on the compressive deformation of cassava roots. The compressive stress of harvest-stage cassava roots ranges from 0.21 MPa to 1.73 MPa, with an average value of 0.69 MPa, and the axial compressive strength is generally higher than the radial compressive strength.

(2) The shear test results indicate that the influencing order of each factor on the maximum shear stress of cassava roots is blade cutting edge angle (E) > loading speed (G) > shear angle (D) > root position (F). Only the blade cutting edge angle presents a significant effect on the shear mechanical properties, while the other factors have no significant influence. The shear stress of harvest-stage cassava roots varies from 37.99 kPa to 154.22 kPa, with an average value of 87.72 kPa.

(3) The bending test results demonstrate that the bending elastic modulus decreases gradually with the increase of cassava root diameter, while the bending strength fluctuates slightly in the range of 1.05–1.53 MPa, with an average of 1.19 MPa. Quadratic regression fitting was conducted between the maximum bending load and root diameter, and the coefficient of determination (R^2) reaches 94.29%, which indicates high fitting accuracy and verifies the reliability of the test data and the applicability of the regression model.

(4) By comparing the average failure stress obtained from compression, shear and bending tests, the damage priority of cassava roots under mechanical load is determined as shear damage, compressive damage and bending damage. This study systematically clarifies the basic mechanical response rules and mechanical damage characteristics of harvest-stage cassava roots. The research results can provide reliable theoretical support and basic test data for the structural parameter optimization of key components of dedicated cassava harvesters, the matching of field operation parameters, and the optimal selection of tool edge angles for cassava slicing machinery.

ACKNOWLEDGEMENT

This work was supported by Jiangxi Provincial Natural Science Foundation (No. 20232BAB215029) and Jiangxi Province Agricultural Machinery Equipment R&D, Manufacturing, Promotion, and Application Integrated Pilot Project (No. YCTY202405).

REFERENCES

[1] Chen, L., Li, K., Mou, X., Liu, Z., Jiang, H., Mabrouk, M., Pan, J., & Atwa, E. M. (2024). Evaluating the impact of moisture content and loading orientation on the geometrical characteristics and mechanical behavior of cassava tubers. *Agronomy*, 14(10), 2254. https://doi.org/10.3390/agronomy14102254

[2] Dai, M., Sun, Y., Miao, H., Zhang, S., & Su, W. (2026). Study on the biomechanical properties of stalks of different ginger varieties. *INMATEH - Agricultural Engineering*, 78(1), 387-396. https://doi.org/10.35633/inmateh-78-31

[3] Dankwa, K.O., Gimode, W., & Olasanmi, B. (2025). A review of global cassava (Manihot esculenta Crantz) production trends, post-harvest physiological deterioration (PPD) challenge, and control strategies. *Discover Food*, 5, 307. https://doi.org/10.1007/s44187-025-00629-7

[4] Fan, J., Li, Y., Wang, B., Gu, F., Wu, F., Yang, H., Yu, Z., & Hu, Z. (2022). An experimental study of axial Poisson's ratio and axial young's modulus determination of potato stems using image processing. *Agriculture*, 12(7), 1026. https://doi.org/10.3390/agriculture12071026

[5] Feng, S., Fu, D., Han, X., & Wang, X. (2022). Impacts of the extension of cassava soil conservation and efficient technology on the reduction of chemical fertilizer input in China. *Sustainability*, 14(22), 15052. https://doi.org/10.3390/su142215052

[6] Food and Agriculture Organization of the United Nations. (2001). *Impact of cassava production on the environment*. https://www.fao.org/4/y2413e/y2413e07.htm

[7] Food and Agriculture Organization of the United Nations. (2026). *FAOSTAT database: Production – Crops and livestock products [Dataset]*. https://www.fao.org/faostat/en/#data/QCL

[8] Fu, H., Qu, Y., & Pan, Y. (2018). Efficiency of cassava production in China: empirical analysis of field surveys from six provinces. *Applied Sciences*, 8(8), 1356. https://doi.org/10.3390/app8081356

[9] Gao, Y., Yang, X., Chu, L., Zhang, Y., & Li, Q. (2022). Experimental investigation and thin-layer modelling of cassava slice drying. *Journal of Thermal Analysis and Calorimetry*, 147(2), 1379-1387. https://doi.org/10.1007/s10973-020-10401-x

[10] Hostetler, A.N., Erndwein, L., Ganji, E., Reneau, J.W., Killian, M.L., & Sparks, E.E. (2022) Maize brace root mechanics vary by whorl, genotype and reproductive stage. *Annals of Botany*, 129, 657–667. https://doi.org/10.1093/aob/mcac029

[11] Jin, Y., Song, Z., Zhang, R., & Zhang, J. (2024). Experiment and analysis of physical, mechanical, and viscoelastic properties of the roots and stalks of green leafy vegetables. *PLOS One*, 19(7), e0305572. https://doi.org/10.1371/journal.pone.0305572

[12] Krishnakumar, T., Sajev, M.S., Pradeepika, C., Namrata, A.G., Sanket, J.M., Jeevarathinam, G., & Muthusamy, V. (2022). Physical and mechanical properties of cassava (Manihot esculenta Crantz) cultivars: Implications for the design of mechanical peeling machines. *Journal of Food Process Engineering*, 45(6), e13923. https://doi.org/10.1111/jfpe.13923

[13] Li, G., Zhou, S., Deng, G., Zheng, S., He, F., Cui, Z., Dai, Y., Li, L., Yan, B., Qin, S., Wang, X., Chen, P., & Liu, Z. (2024). Research progress on mechanization technology and equipment for cassava field production. *Agriculture*, 14(11), 1926. https://doi.org/10.3390/agriculture14111926

[14] Li, J., Liu, Y., Tan, Y., & Yang, L. (2025). Global cassava germplasm resources: industrial and technological development. *Food and Energy Security*, 14(5), 70131. https://doi.org/10.1002/fes3.70131

[15] Li, R., Yuan, S., Zhou, Y., Wang, S., Zhou, Q., Ding, Z., Wang, Y., Yao, Y., Liu, J., & Guo, J. (2023). Comparative transcriptome profiling of cassava tuberous roots in response to postharvest physiological deterioration. *International Journal of Molecular Sciences*, 24(1), 246. https://doi.org/10.3390/ijms24010246

[16] Liang, H., Wei, Y., Song, E., & Huang, J. (2016). Enlightenment of world cassava production to China (世界木薯生产对中国的启示). *Chinese Agricultural Science Bulletin*, 32(9), 94-99. https://doi.org/10.11924/j.issn.1000-6850.casb15090068

[17] Liu, H. (2004). Mechanics of Materials I 4th edition (材料力学I, 第四版). *Higher Education Press*, Beijing, China.

[18] Simo-Tagne, M., Tagne Tagne, A., Ndukwu, M. C., Bennamoun, L., Obounou Akong, M. B., El Marouani, M., & Rogaume, Y. (2021). Numerical study of the drying of cassava roots chips using an indirect solar dryer in natural convection. *AgriEngineering*, 3(1), 138-157. https://doi.org/10.3390/agriengineering3010009

[19] Sreekumar, J., Asok, K., & Chandra, C.V. (2026). Computer vision-based classification of post-harvest physiological deterioration in cassava (Manihot esculenta Crantz) roots using deep learning models. *Journal of Stored Products Research*, 118, 103097. https://doi.org/10.1016/j.jspr.2026.103097

[20] Tan, Y., Li, C., & Zeng, H. (2018). Analysis on the development of cassava production and trade in China (中国木薯生产和贸易发展分析). *World Agriculture*, 2018(10), 163-168. https://doi.org/10.13856/j.cn11-1097/s.2018.10.024

[21] Xu, G., Song, J., Cao, Z., Sun, B., Huang, J., Peng, X., Li, W., & Li, Y. (2025). Kinematic characteristics analysis and test of double-row vibrating cassava harvester. *INMATEH - Agricultural Engineering*, 77(3), 904-917. https://doi.org/10.35633/inmateh-77-74

[22] Yan, M., Wang, T., Li, M., & Li Y. (2013). Experimental study on compressive mechanical properties of cassava roots (木薯块根压缩力学特性试验研究). *Food & Machinery*, 29(3), 194-196.

[23] Yan, M., Wang, T., Li, M., & Li Y. (2013). Study on the mechanical properties of cassava root cutting (木薯块根切割力学特性研究). *Food & Machinery*, 29(4), 88-91.

[24] Yang, H., Wang, B., Gu, F., Wu, F., Zhang, Y., & Hu, Z. (2022). Determination of some physical and mechanical properties of onion. *INMATEH - Agricultural Engineering*, 68(3), 324-332. https://doi.org/10.35633/inmateh-68-32

[25] Yang, W., Yang, J., Zheng, X., Wang, Q., Jia, F., & Zhao, J. (2011). Experiment on mechanical properties of cassava (木薯力学特性测试). *Transactions of the Chinese Society of Agricultural Engineering*, 27(S2), 50-54.

[26] Yang, W., Xi, J., Li, X., Zheng, X., & Lu, Z. (2026). Numerical simulation of the eccentric cassava tuber harvest lifting[J]. *Biosystems Engineering*, 265,104437. https://doi.org/10.1016/j.biosystemseng.2026.104437

[27] Zhang, Z., Bao, G., Yuan, Y., Lv, Z., Chen, X., Chen, X., & Yang, W. (2025) Mechanical properties of radish petioles and calibration of cohesion parameters in discrete element models. *Frontiers in Plant Science*, 16,1634962. https://doi.org/10.3389/fpls.2025.1634962

RESEARCH AND ANALYSIS ON THE OPERATING PERFORMANCE OF RIDGE ROLLERS UNDER DIFFERENT OPERATING MODES
/
起垄机不同作业模式下作业性能研究与分析

Xin ZHANG[1)], Yucheng LIANG[1*)], Lu GAN[1)], Yanliang ZHANG[1)], Yiwen YUAN[2)]
[1)] Heilongjiang Academy of Agricultural Machinery Engineering Sciences, Harbin 150081, China
[2)] College of Mechanical and Electrical Engineering, Heilongjiang University, Harbin, 150080, China
Tel: +86-18249059533; E-mail: xinzhang135689@163.com
DOI: https://doi.org/10.35633/inmateh-79-17

Keywords: *ridge roller, operating mode, resistance, ridge formation, experiment*

ABSTRACT
To explore the operational performance of a ridge roller under two different working modes, namely, linear arrangement (LA) and interleaved arrangement (IA) of adjacent ridging shovels, firstly, theoretical analysis was conducted to conclude that the operational resistance of IA is greater than that of LA. Secondly, a discrete element simulation method was employed to establish a discrete element simulation model. The extracted data verified the conclusions of the theoretical analysis. Qualitative analysis was conducted based on the formed ridge profile, indicating that LA has a better ridge forming effect than IA. Finally, field experiments were conducted, with the operating speed of the ridge roller (1.5 km/h, 3 km/h, 4.5 km/h) and different installation distances between adjacent ridging shovels (0, 240 mm, 480 mm) as experimental factors. The average operational resistance, the distance between adjacent ridge tops, and the height difference at the bottom of the ridge furrow were used as indicators for a full-factor experiment. It was concluded that under the same conditions, LA has the best ridge forming effect but requires the greatest resistance, while IA can effectively reduce resistance but has a poorer ridge forming effect. This study provides a theoretical basis and guidance for tillage and soil preparation operations.

摘要
为探究起垄机两种不同作业模式，即相邻起垄铲直线排布（LA）和交错排布（IA）下的作业性能，首先通过理论分析得出 IA 的作业阻力大于 LA；其次采用离散元仿真模拟方法，建立离散元仿真模型，通过提取数据验证了理论分析的结论，并通过形成的垄体断面轮廓进行定性分析，得出 LA 的垄体成型效果优于 IA；最后通过田间试验，以起垄机作业速度（1.5 km/h、3 km/h、4.5 km/h）和相邻起垄铲不同前后安装距离（0、240 mm、480 mm）为试验因素，以平均作业阻力和相邻垄体垄顶距离和垄沟最底端高度差为指标进行全因素试验，得出其他条件相同情况下，LA 的垄体成型效果最好，但是所需阻力最大，IA 阻力能有效降低但是垄体成型效果较差。本研究可为耕整地作业过程提供一定的理论依据和指导作用。

INTRODUCTION

The Northeast region is China's foremost grain production base, predominantly utilizing the ridge tillage method. This approach facilitates increasing soil temperature, enhancing water infiltration, and creating an optimal environment for crop root growth *(Zhao et al., 2025; Zhang et al., 2022; Yuan et al., 2019).* Therefore, rotary tillage and ridging operations are crucial components of agricultural mechanized production *(Shen et al., 2020; Guan et al., 2021).*

A large amount of research has been conducted both domestically and internationally on the issues of operational resistance and ridge formation effectiveness during rotary tillage and ridging operations. Scholars from the Nanjing Research Institute of Agricultural Mechanization under the Ministry of Agriculture have designed a sweet potato double-row ridging machine. The plow body primarily serves the function of furrowing, with a large amount of backfill soil *(Wang et al., 2025).* Researchers from Hunan Agricultural University have designed a plow-rotating combined rapeseed ditching and ridging machine. Compared to traditional ridging machines, it significantly improves soil fallback and achieves better ridging results (*Bao et al., 2017*). Some foreign researchers have also conducted comparisons on the ditching performance and fuel consumption of different ditching implements (*Kumar Sahu et al., 2018*).

Researchers from Henan Agricultural University optimized key components of the tobacco ridger and conducted experiments, resulting in reduced operational resistance and better consistency in ridge formation *(Song et al., 2024; Chen et al., 2022).* Scientific researchers and others have developed hillside land-leveling machines, but their functions are relatively limited, and the ridging effect is poor *(Zheng et al., 2021).*

Overall, current research on the operational resistance and ridge formation effectiveness of ridging machines primarily revolves around optimizing key components, with almost no theoretical research conducted on the most basic operational modes. Therefore, this paper focuses on two different operational modes of ridging machines, LA and IA, to study the factors affecting the operational resistance and ridge formation of ridging machines, aiming to provide theoretical support for rotary tillage and ridging operations.

MATERIALS AND METHODS

Ridge tiller operating mode

The ridger operates in two modes during its working process, and the top views of these two modes are illustrated in Fig. 1. The first mode involves the ridging shovels being aligned in a straight line. This ridging method ensures high uniformity and consistency in the ridges. However, on deeply plowed or rototilled soil, where there are numerous stems and stubble, and if the soil viscosity is high, the operational resistance increases, potentially leading to blockages and affecting the working efficiency, as depicted in Fig. 1(a). To address the blockage issue and reduce operational resistance, the second mode was developed, where adjacent ridging shovels are arranged in a staggered manner, maintaining a certain installation distance in the forward direction. This mode significantly reduces the likelihood of blockages, but it suffers from poor consistency in the shape of the ridges, as shown in Fig. 1(b).



(a) Linear arrangement (LA) *(b) Interleaved arrangement (IA)*

Fig. 1 – Two ridge-forming modes

1. ridge shovel; 2. soil

Regardless of which operation mode the ridger adopts, the operation process will encounter significant resistance, requiring a power machine to provide substantial energy. To understand the force conditions on the ridging shovel under the two operation modes, a force analysis was conducted on one side plate of a single ridging shovel.

Force analysis of LA

When the ridging shovel is arranged in a straight line, the squeezing action between the inner plates of two adjacent ridging shovels will push the soil from a width of a_1 to a ridge width of b_1, thereby directly forming a ridge. At this time, the two side plates that help form the ridge platform are subjected to the force of the soil. In this operation mode, both sides of the ridge are squeezed by the side plates, and the soil can only move in a limited space, being completely constrained. In soil mechanics, this situation is referred to as the presence of infinite soil complete constraint on both sides of the ridge, assuming that the soil has a low moisture content or is dry and loose soil. A force analysis is conducted on any mass point O with a depth of h embedded in the soil on the side plate as it moves forward at a constant speed, as shown in Fig. 2.

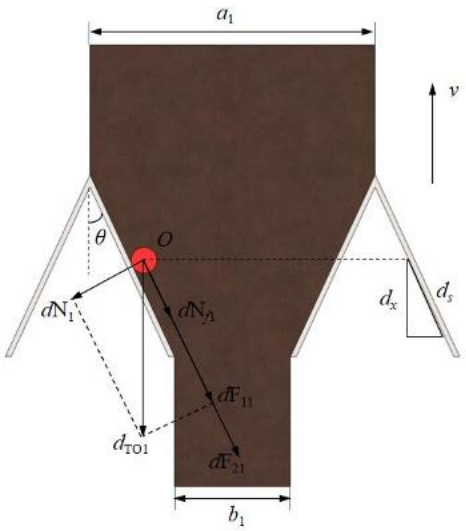


Fig. 2 – Force analysis of LA

In the figure, v represents the advancing direction of the ridging shovel, θ denotes the half-apex angle of the ridging shovel, dx signifies the displacement of particle O along the advancing direction, and ds indicates the displacement of particle O along the side plate. Calculations are performed based on Rankine's theory and assuming uniform normal pressure distribution on the side plate *(Waldron L.J., 1977*; *Waldron L.J. et al., 1981).*

$$\begin{cases} dA = hds \\ ds = \dfrac{dx}{\cos\theta} \\ dN_1 = pdA \\ dN_{f1} = \mu dN_1 \\ dF_{11} = \dfrac{dN_1}{\tan\theta} \\ dF_{21} = dN_{f1} + dF_{11} \\ p_1 = \xi\left(K_p\gamma h + 2c\sqrt{K_p}\right) \\ K_p = \dfrac{1+\sin\phi}{1-\sin\phi} \\ \xi = 1+\left(K_p - 1\right)\dfrac{\tan\theta}{\tan\phi} \end{cases} \quad (1)$$

where:

dA—when the displacement in the forward direction is x, the area swept by the side plate in a small unit, m^2;

dN_1—normal pressure acting on a micro-unit area, N;

p_1—normal pressure per unit area, N;

dN_{f1}—friction force, N;

μ—coefficient of friction;

d_{F11}—the component of the total resistance of soil to the side plate in the direction of the side plate, N ;

d_{F21}—total resistance in the direction of the side plate, N;

K_p—soil resistance coefficient under the condition of complete constraint on both sides of the side plate;

γ—soil bulk density;

β—the angle between the soil failure surface and the horizontal plane, （°）;

Φ—Soil internal friction angle, (°) ;

c—Soil cohesion, typically ranging from 5 to 100 kPa for cohesive soil;

ξ—For the three-dimensional shape factor, when there is complete constraint from infinite soil on both sides of the ridge, based on Coulomb's passive earth pressure theory, this parameter needs to be introduced for three-dimensional correction.

By processing Eq. (1), the total drag force of the micro-unit in the direction of the side plate is obtained:

$$dF_{21}=\left[1+\left(\frac{1+\sin\phi}{1-\sin\phi}-1\right)\frac{\tan\theta}{\tan\phi}\right]\left[\frac{1+\sin\phi}{1-\sin\phi}\gamma h^2+2hc\sqrt{\frac{1+\sin\phi}{1-\sin\phi}}\right]\left(\mu\frac{dx}{\cos\theta}+\frac{dx}{\sin\theta}\right) \quad (2)$$

Force analysis of IA

When the ridging shovels are arranged in a staggered manner, during operation, the two adjacent ridging shovels at the front will first extrude soil from a width of a_2 to a ridge width of b_2, forming a large ridge. Subsequently, the middle ridging shovel located behind them will divide the ridge width b_2 into two ridges with a width of c_2. Unlike the analysis in the previous section, when two ridges with a width of c_2 are formed, there are no other ridging shovels on either side of the rear ridging shovel to press against its side plates. The two sides of the formed ridge are in free constraints, which is referred to as the absence of infinite soil body complete constraints on both sides of the ridge. A force analysis is conducted on any mass point O with a depth of h into the soil on the side plate, as shown in Fig. 3.

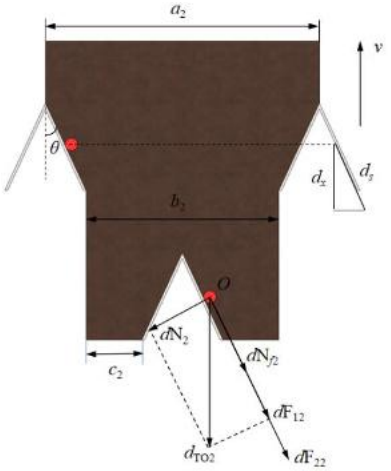


Fig. 3 – Force analysis of IA

Similar to the analysis in the previous section, there are:

$$\begin{cases} dA=hds \\ ds=\dfrac{dx}{\cos\theta} \\ dN_2=pdA \\ dN_{f2}=\mu dN_2 \\ dF_{12}=\dfrac{dN_2}{\tan\theta} \\ dF_{22}=dN_{f2}+dF_{12} \\ p=K_f\gamma h \\ K_f=\dfrac{\tan\beta+\cot(\beta+\theta)}{\tan\beta+\cot(\beta+\theta+\delta)}\dfrac{\sin\beta}{\sin\theta}\cos(\beta+\theta+\delta) \end{cases} \quad (3)$$

where: dN_2—normal pressure acting on a micro-unit area, N;

P_1—normal pressure per unit area, N;

dN_{f2}—friction force, N;

d_{F12}—the component of the total resistance of soil to the side plate in the direction of the side plate, N;

d_{F22}—total resistance in the direction of the side plate, N;

K_f—Soil resistance coefficient under free constraints on both sides of the side plate;

δ—The friction angle between the side plate and the soil, (°).

By processing Eq. (2), the total drag force of the micro-unit in the direction of the side plate is obtained:

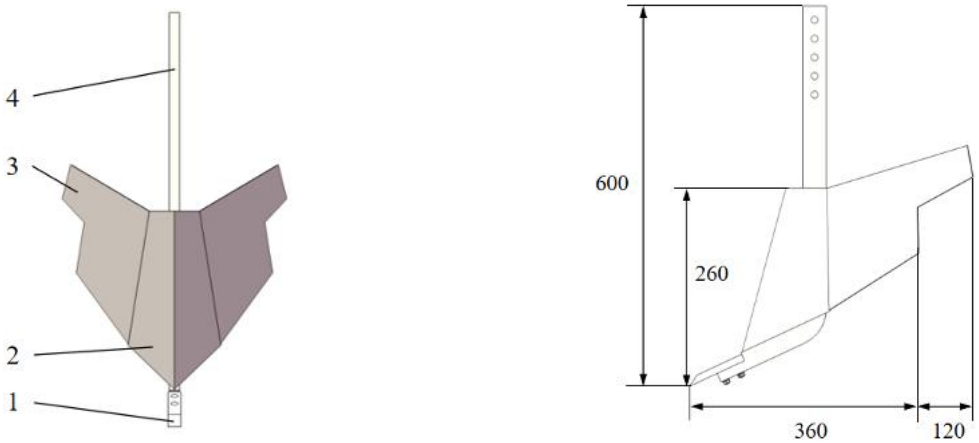
$$dF_{22} = \frac{\tan\beta + \cot(\beta+\theta)}{\tan\beta + \cot(\beta+\theta+\delta)} \frac{\sin\beta}{\sin\theta} \cos(\beta+\theta+\delta)\gamma h^2 \left(\mu \frac{dx}{\cos\theta} + \frac{dx}{\sin\theta} \right) \quad (4)$$

Based on the above analysis, it can be concluded that when the ridger operates in two different modes, the force conditions on the ridging shovel are completely different. When the friction force on the side plate of the ridging shovel is large, the corresponding power consumption of the entire machine is also high, and the wear on the side plate is also faster. Therefore, in order to reduce fuel consumption and extend the service life of the side plate of the ridging shovel, discrete element simulation analysis is conducted on the ridging shovel under the two operating modes, with the aim of qualitatively analyzing the force conditions on the ridging shovel and the consistency of the ridges in the two operating modes.

Ridge roller model establishment

The agricultural practice for corn cultivation in Northeast China primarily involves standard ridges with a ridge spacing of 650 mm. Therefore, the ridge spacing of the ridge roller model used in the simulation is set to 650 mm. To more clearly observe the simulated resistance of the two ridge-forming operation modes, the number of ridges is appropriately increased. Taking the example of forming four ridges with five ridge shovels, the simulation is conducted.

As the core component of the ridger, the ridging shovel bears almost all the operational resistance of the entire machine. Due to variations in ridging agronomic requirements across different regions, and considering only the differences in operational resistance of the ridging shovel under different arrangement modes and the consistency of ridge formation in this paper, the model is simplified. The digging shovel tip adopts a chisel-type tip and is installed at the bottom of the shovel handle using countersunk square root bolts. The soil divider plate is mounted on the lifting plate through a hinged shaft and can rotate at the hinged shaft to adjust the opening and closing angle. The three-dimensional diagram and key dimensions of the ridging shovel are shown in Fig. 4.

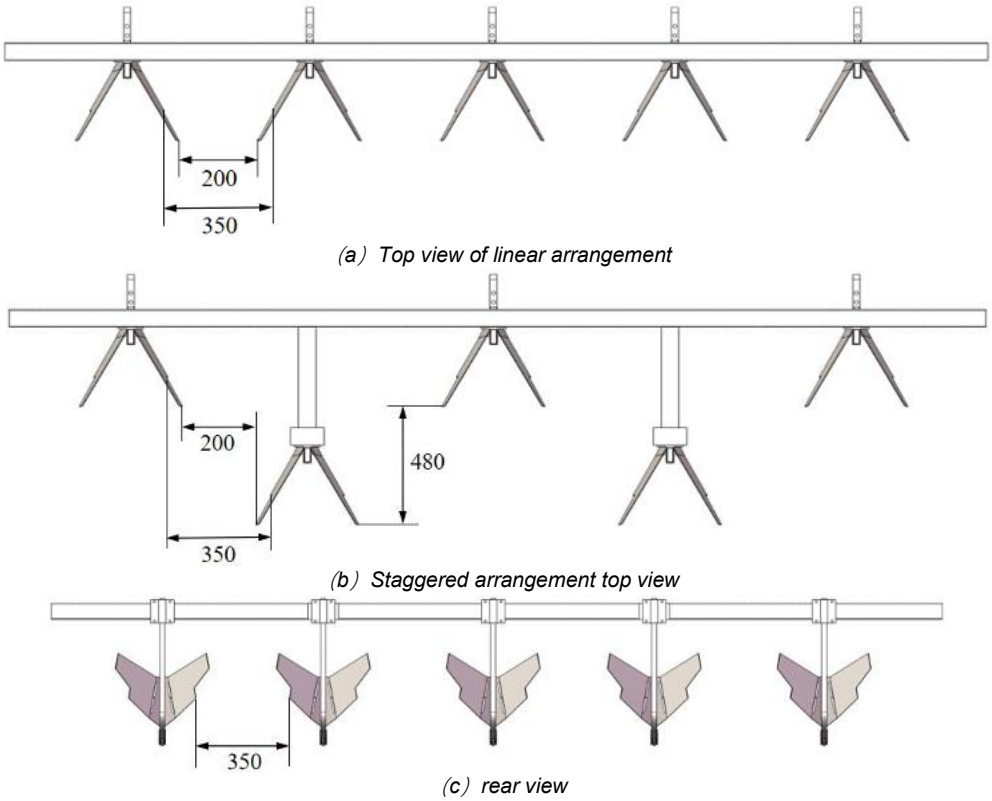


(a) Front view of ridging shovel
1.blade tip; 2.lifting board; 3.partition board; 4.shovel handle

(b) Side view of ridging shovel

Fig. 4 – Structural diagram of ridging shovel

During the simulation, based on agronomic requirements, the ridge top width is set at 250 mm. Using the 3D software SolidWorks 2020 (Dassault systems France, originally developed in USA), a model of the ridger is created according to the ridge forming conditions. The 3D models and key operational parameters of the ridger for two ridging modes are shown in Fig. 5. Since the ridge platform is formed by the contour created after the ridging process and subsequent compaction by the compaction wheel, this simulation analysis does not consider the factor of the compaction wheel. Therefore, the design specifies a distance of 200 mm between the ends of two adjacent soil divider plates (which is less than the top width of the ridge platform, which is 250 mm), a distance of 350 mm between the bottom ends of two soil divider plates, and a distance of 480 mm between the front and rear of two adjacent ridging shovels in the staggered arrangement mode.



(a) Top view of linear arrangement

(b) Staggered arrangement top view

(c) rear view

Fig. 5 – Ridge roller operating mode

Establishment of discrete element simulation model

This study takes black soil in Northeast China as the research object. Based on the physical characteristics of Northeast black soil, a soil model is established using the discrete element software EDEM 2018 (USA). The simulation parameters are shown in Table 1 *(Zhao et al., 2021; Zeng et al., 2020; Ucgul M. et al., 2015; Zhang et al., 2023; Kojo A.et al., 2021; Hadi Z. et al., 2022)*.

Table 1

Parameters of Soil Model

Parameters	Values
Poisson's ratio	0.41
Shear modulus / MPa	1.24
Density / (kg·m^{-3})	2150
Coefficient of restitution between soil particles	0.6
Static friction coefficient between soil particles	0.3
Rolling friction coefficient between soil particles	0.2
Normal contact bonding stiffness between soil particles / (N·m^{-3})	3.4×10^{8}
Shear contact bonding stiffness between soil particles / (N·m^{-3})	1.5×10^{8}
Critical normal stress / Pa	2×10^{5}
Critical shear stress / Pa	6.8×10^{4}
Bond radius / mm	5.5

Assuming that the field has undergone rotary tillage before ridging, resulting in fine and uniform soil, the external dimensions of the soil bin are determined based on the overall dimensions of the ridger, the ridging depth, the ridge-platform dimensions, and the ability of the ridger to form a distinct ridge in the simulation. Accordingly, the external dimensions of the soil bin are set to 3500 mm × 1500 mm × 300 mm (length × width × height). Due to the large volume of this soil bin, to shorten simulation time, the soil particle radius is set to 5 mm, and the soil particle generation type is selected with no limit on quantity, with a generation rate of 50,000 particles per second, and particle positions are randomly generated. The particles generated by the particle factory fill the soil bin under gravity. To make the bonding force between soil particles more consistent with field conditions, the soil bin is settled after being filled, and then continues to be filled until it is completely filled.

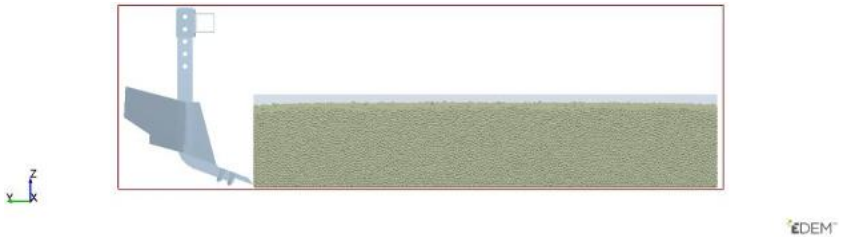
Save the overall model of the ridger in .stp format and import it into the EDEM soil bin model. The material is selected as 65 Mn, the depth of the ridging plate into the soil is 190 mm, and the forward speed is set to 3 km/h *(Liao et al., 2022)*. The simulation parameters of the ridger are shown in Table 2 *(Wang, 2019)*.

Table 2

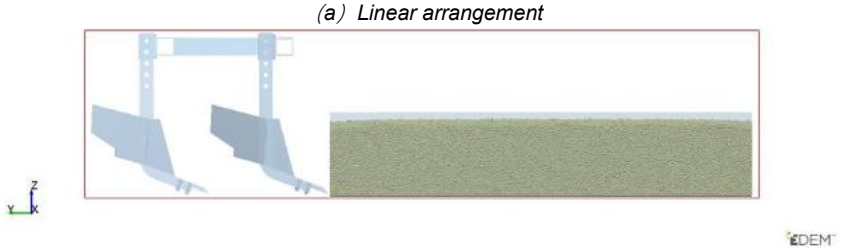
Parameters of soil model

Parameters	Values
Poisson's ratio	0.3
Shear modulus / MPa	7.9×10^4
Density / (kg·m^{-3})	7865
Coefficient of restitution between the subsoiler and soil	0.6
Static friction coefficient between the subsoiler and soil	0.6
Rolling friction coefficient between the subsoiler and soil	0.05

The overall model under the two operating modes is shown in Fig. 6.



(a) Linear arrangement



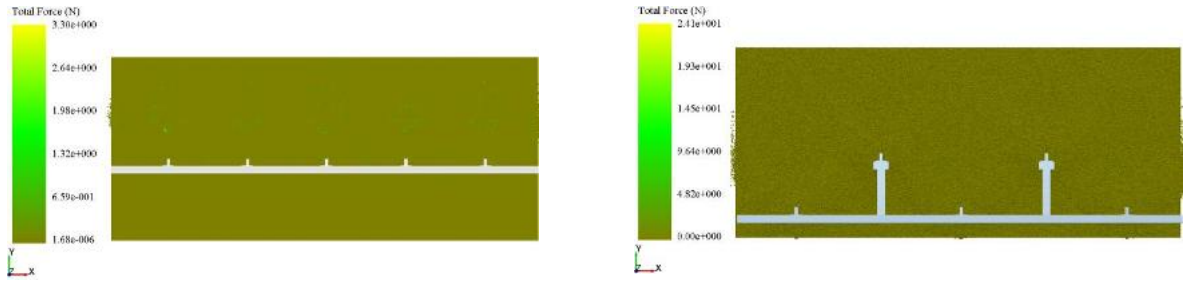
(b) Interleaved arrangement

Fig. 6 – Overall Model Construction

RESULTS

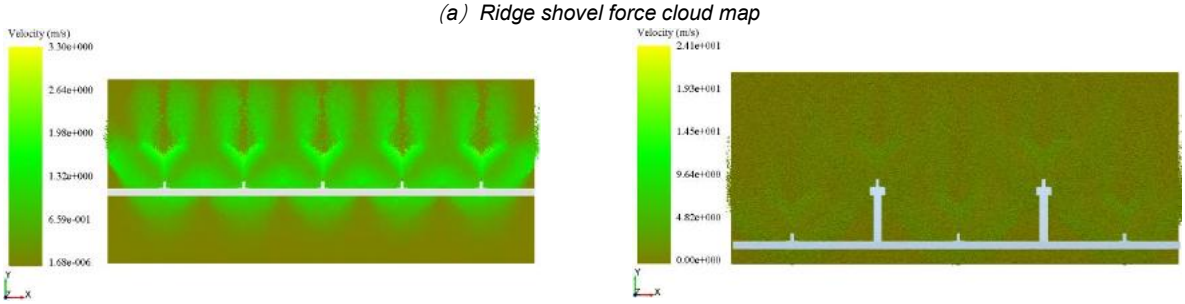
Simulation result of force analysis

The force and soil-velocity nephograms of the ridging shovel under the two operating modes of the ridger at the same time point are shown in Fig. 7.



LA *IA*

(a) Ridge shovel force cloud map



LA *IA*

(b) Soil velocity nephogram

Fig. 7 – Cloud Map Display

By extracting the force data at multiple identical time points after the ridging shovel is fully buried in soil under the two modes, and plotting the curves by Excel 2020, the results are shown in Fig. 8.

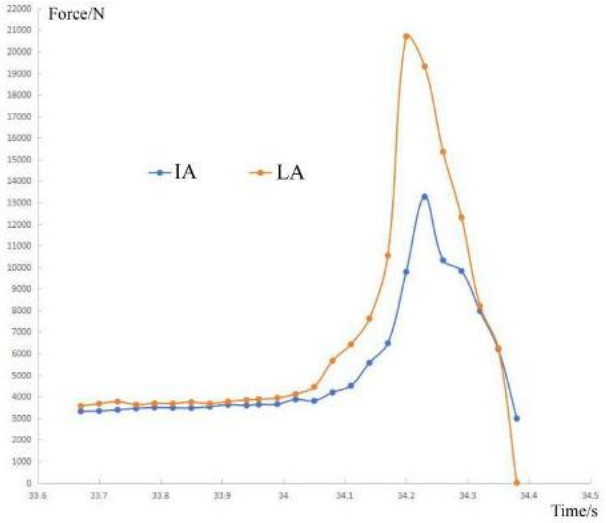


Fig. 8 – Force Line Graph of Ridging Shovel

Based on the analysis of the force cloud diagram and force polygonal line diagram of the ridging shovel, it can be concluded that the force exerted on the straight-line arrangement is greater than that on the staggered arrangement. According to the analysis of the soil particle velocity cloud diagram, the disturbance to soil particles caused by the straight-line arrangement is more pronounced than that caused by the staggered arrangement. This indicates that the closer the distance between two adjacent soil boards, the more pronounced the squeezing effect on soil particles during operation, and the greater the frictional force exerted on the adjacent soil boards. Consequently, the straight-line arrangement results in greater operational resistance and soil particle disturbance compared to the staggered arrangement.

Simulation result of ridge formation analysis

After the simulation of the ridging shovel is completed and the state of the soil particles in the soil bin has stabilized, cross-sections are taken at the same position on the ridge. The screenshots of the cross-sections under the two operating states are shown in Fig. 9.



（a）LA （b）IA

Fig. 9 – Cross-sectional View of the Ridge

Through observation and comparison, it can be seen that the shape of ridges formed by the straight arrangement is more consistent, with the depth of furrows being basically uniform. The bottom ends of the furrows are generally on the same straight line, and the distances l_1 and l_2 between the ridges of two adjacent ridges are basically consistent, as shown in Fig. 9(a). However, in the staggered arrangement, after the two ridging shovels located at the rear operate, the separated soil will move to both sides, causing soil to slide off the side of the ridge that is farther from the soil divider plate. This results in a height difference h_1 at the bottom end of the furrow, leading to poor consistency in the ridges, making the depth of the ridge platforms and furrows inconsistent, and there is a certain gap in the distance between the ridges of two adjacent ridges, with l_3 being slightly smaller than l_4, as shown in Fig. 9(b).

Based on the above analysis, it is preliminarily concluded that the linear arrangement mode results in greater resistance for the ridging machine but produces ridges with better consistency, while the staggered arrangement mode results in less resistance for the ridging machine but produces ridges with poorer consistency.

Field performance test

In the previous force analysis, it was conducted from a microscopic perspective, assuming low soil moisture content or dry soil, aiming to theoretically analyze the different forces exerted on the ridging shovel under two operating modes. According to relevant literature, the forward speed during operation also affects the force exerted on the ridging machine *(Tong et al., 2013; Jia et al., 2018).*

To explore the impact of different operating modes of the ridger on anti-blocking effect and ridge formation effect during actual operation, this chapter conducts a full-factor experiment based on the same structural parameters of the ridging shovel, using forward speed and the installation distance between adjacent ridging shovels as experimental factors, and taking operating resistance, the distance between the ridges of two adjacent ridges, and the height difference at the bottom of the furrow as indicators *(Wu, 2021).*

Test conditions and preparation

The field experiment was conducted at the experimental base of the Heilongjiang Academy of Agricultural Mechanization Engineering and Science in May 2025. The average stubble height of corn stalks was 103 mm, with soil hardnesses of 487 kPa (100 mm) and 1235 kPa (200 mm). The average soil moisture content was 16.2%, and the average root stubble moisture content was 38.6%. The experiment utilized a 1GZL-2 rotary tillage and ridging machine, which features rotary tilling at the front, three ridging shovels attached at the back, and an intermediate ridging shovel with an extension rod that allows for adjustment of the distance between adjacent shovels. This machine can form two ridges in a single operation. A photo of the rotary tillage and ridging machine is shown in Fig. 10.



Fig. 10 – Picture of rotary tillage and ridging machine

The equipment required for the experiment includes a Lovol 604 tractor (Shan dong, China), a GPS-10A multi-function testing device (Huade Soil Instrument Manufacturing Co., Ltd., Nanjing, China) for motor vehicles, a level ruler (Ningbo Deli Tools Co., Ltd., Zhejaing, China), a tape measure (Ningbo Deli Tools Co., Ltd., Zhejaing, China), a soil hardness meter (Huade Soil Instrument Manufacturing Co., Ltd., Nanjing, China), and a cutting ring assembly (Huade Soil Instrument Manufacturing Co., Ltd., Nanjing, China). The testing system is shown in Fig. 11.



Fig. 11 – Field experiment

The forward speeds were selected as 1.5 km/h, 3 km/h, and 4.5 km/h. As shown in Fig. 5(b), considering the front-to-rear dimension of the ridging shovel is 480 mm, the installation distances were chosen as 0, 240 mm, and 480 mm. To ensure a noticeable difference in resistance during each test, the forward distance for each test was set at 110 m, which includes a 10 m buffer zone and a 100 m effective working length. Each test was repeated three times. During the test, the forward speed was controlled by the tractor's electronic throttle, and the installation distance of the ridging shovel was adjusted by changing extension rods of different lengths. The coding of experimental factors is shown in Table 3.

Table 3

Experimental Factors and Levels

Level	Factors	
	Forward speed (km/h)	Front-to-rear installation distance (mm)
1	1.5	0
2	3	240
3	4.5	480

The operational resistance is represented by the average resistance within an effective operational length of 100 meters. The data acquisition method for the distance between the top of adjacent ridges and the height difference at the bottom of the furrow is as follows: within the experimental group corresponding to the effective operational length of 100 meters, three sets of data are randomly collected every 10 meters for recording.

The average operational resistance results are presented in Table 4.

Table 4

Analysis of Average Operational Resistance

Forward speed / (km·h^{-1})	Operating resistance of adjacent ridging shovels under different installation distances / N		
	0	240	480
1.5	1542	1346	1295
	1608	1377	1230
	1588	1285	1192
3	1830	1602	1452
	1857	1588	1389
	1760	1590	1490
4.5	1944	1750	1633
	2013	1681	1584
	2036	1684	1592

Analysis of the results in Table 4 reveals that when the forward speed remains constant, the operating resistance gradually decreases as the installation distance between adjacent ridging shovels increases. This trend aligns with the results of the theoretical analysis mentioned earlier, and the operating resistance is at its maximum when the installation distance between adjacent ridging shovels is zero. When the installation distance between adjacent ridging shovels remains constant, the operating resistance gradually increases as the forward speed increases.

The distance between the ridges of adjacent furrows is shown in Table 5.

Table 5

Distance Between the Tops of Adjacent Ridges

Forward speed / (km·h^{-1})	Distance between the ridges of adjacent furrows under different installation distances of adjacent ridge shovels / mm		
	0	240	480
1.5	203	205	206
	202	205	203
	203	204	206
3	202	208	209
	202	205	209
	201	207	208
4.5	203	213	215
	201	210	214
	203	211	217

Based on the analysis of the results in Table 5, it can be seen that when the forward speed remains constant, the distance between the ridges of adjacent furrows increases with the increase in the installation distance between adjacent furrowing shovels. When the installation distance between adjacent furrowing shovels is 0, the distance between the ridges of adjacent furrows is almost unaffected by speed. As the installation distance between adjacent furrowing shovels increases, the distance between the ridges of adjacent furrows is more significantly affected by speed, and the increase is more pronounced.

The height difference at the lowest end of adjacent ridges and furrows is presented in Table 6.

Table 6

Height difference at the lowest end of adjacent ridges and furrows

Forward speed / (km·h^{-1})	The height difference at the bottom of adjacent ridges and furrows under different installation distances between adjacent ridge shovels / mm		
	0	240	480
1.5	3	8	9
	2	8	8
	3	6	8
3	2	10	15
	1	11	18
	2	13	14
4.5	4	17	30
	3	20	41
	1	23	36

Based on the analysis of the results in Table 6, it can be seen that when the forward speed is constant, the height difference at the bottom of adjacent ridges and furrows increases with the increase of the installation distance between adjacent ridging shovels. When the installation distance between adjacent ridging shovels is 0, the height difference at the bottom of adjacent ridges and furrows is almost unaffected by speed. As the installation distance between adjacent ridging shovels increases, the height difference at the bottom of adjacent ridges and furrows is more significantly affected by speed, and the increase is more pronounced.

In all experimental groups, no blockage occurred, and it did not reach the level that required stopping the machine for cleaning. However, as the installation distance between adjacent ridging shovels increased, the accumulation of soil, straw, and stubble at the ridging shovel during operation was significantly alleviated.

CONCLUSIONS

(1) This article conducts a force analysis of the ridging shovel under two operating modes of the ridging machine (i.e., whether there is a front-to-back installation distance between two adjacent ridging shovels). Through theoretical analysis, it is concluded that the operating mode where the front-to-back installation distance between two adjacent ridging shovels is 0 results in a greater force on the ridging machine than the other mode.

(2) Using the discrete element simulation method, a discrete element model of the tiller-soil system was established. Under the condition of consistent other parameters, discrete element simulation tests were conducted for two operating modes with installation distances of 0 and 400 mm between adjacent tilling blades. This not only verified the previous conclusion, but also observed through the simulated ridges that the consistency of the ridges was also affected.

(3) A full-factorial field experiment was conducted, considering the forward speed of the ridger (1.5 km/h, 3 km/h, 4.5 km/h) and the installation distance between adjacent ridging shovels (0, 240 mm, 480 mm) as experimental factors. The experiment evaluated the ridger force, the distance between the ridges, and the height difference at the bottom of adjacent ridges as indicators. The results indicated that when the installation distance between adjacent ridging shovels was 0, the operational resistance was the highest, but the ridge formation effect was the best. As the forward speed and the installation distance between adjacent ridging shovels increased, the ridge formation effect gradually deteriorated. No blockage occurred during the experiment, but there was accumulation of soil, stems, and stubble at the ridging shovel, which could be effectively alleviated by increasing the installation distance between adjacent ridging shovels.

ACKNOWLEDGEMENT

This study was Supported by the Project of Laboratory of Advanced Agricultural Sciences, Heilongjiang Province (ZY04JD05-013); Heilongjiang province key research and development plan project (2024ZXDXB35) funding.

REFERENCES

[1] Bao, P., Wu, M., Guan, C., Luo, H., He, Y., Xiang, W., (2017). Design of plow-rotary style ditching and ridging device for rapeseed seeding (犁旋组合式油菜播种开沟起垄装置设计). *Transactions of the CSAE*, Vol. 33(20), pp. 23-31. China.

[2] Chen, X. (2022). *Design and Test of Successive Compaction Device of Tobacco Ridging, Fertilization and Compaction Machine (烟草起垄施肥机逐级压实装置设计与试验).* Zhengzhou: Henan Agricultural University. China.

[3] Guan, C., Cui, Z., Gao, Q., Wang, S., Chen, Y., Yang, Y., (2021). Design of biaxial rotary tillage soil test bench and layered tillage test (双轴旋耕碎土试验台设计与分层耕作试验). *Transactions of the CSAE*, Vol. 37(10), pp. 28-37. China.

[4] Hadi, A., Seyed, H., Mojtaba, N., (2022). Weed seed burial as affected by mouldboard design parameters, ploughing depth and speed: DEM simulations and experimental validation. *Biosystems Engineering*, Vol.216, pp.79-92. Iran.

[5] Jia H., Wang, W., Wang, W., Zheng, J., Wang, Q., Zhang, J., (2018). Application of anti-adhesion structure based on earthworm motion characteristics. *Soil & Tillage Research*, Vol.178, pp.159-166. China.

[6] Waldron L J., Dakessian S., (1981). Soil reinforcement by roots: calculation of increased soil shear strength from root properties. *Soil Science*, Vol.132(6), pp. 427-35. America.

[7] Kumar Sahu S., Tiwari K.B., Shrivastava P., (2018). Optimization of the kinematic parameter and fuel consumption for the side-shift offset rotavator using L and J-shape soil cutting blades. *International Journal of Current Microbiology and Applied Sciences,* Vol.7(8), pp. 1970-1982. India.

[8] Kojo, A., James, B., Diogenes, L., Antille, D., Mustafa, U., Troy, A., (2021). Analysis of effect of bent leg opener geometry on performance in cohesive soil using the discrete element method. *Biosystems Engineering*, Vol.209, pp.106-124. Ghana.

[9] Liao, Q., Du, W., Zhang, Q., Lin, J., Chen, Z., Zhang, J., (2022). Design and Experiment of Cigar Tobacco Adjustable Seed-plot Ridging and Film Spreading Machine (雪茄烟叶可调式苗床起垄铺膜机设计与试验). *Transactions of the Chinese society for agricultural machinery*, Vol.01, pp.1-13. China.

[10] Shen, H., Wang, B., Hu, L., Wang, G., Ji, L., Shen, G., Wu, T., (2020). Design of potato connecting and conveying mechanism for 4UZL-1 type sweet potato combine harvester device (4UZL-1 型甘薯联合收获机薯块交接输送机构设计). *Transactions of the CSAE*, Vol. 36(17), pp. 9-17. China.

[11] Song, Q. (2024). Design and Experiment of Compaction Device for Single-row Ridging Fertilizer Machine (单行起垄施肥作业机镇压装置设计与试验). Zhengzhou: Henan Agricultural University. China.

[12] Tong, J., Zhang, Q., Chen, D., Chang, Y., Wang, H., (2013). Effects of Bionic Geometric Structure Press Rollers on Reducing Rolling Resistance and Adhesion against Soil. *Applied Mechanics and Materials*, Vol.461, pp.63-72. China.

[13] Ucgul M., Fielke J M., Saunders C. (2015). Three dimensional discrete element modeling DEM of tillage accounting for soil cohesion and adhesion. *Biosystems Engineering*, Vol.129, pp. 298-306. Australia.

[14] Waldron L J. (1977). The Shear Resistance of Root-Permeated Homogeneous and Stratified Soil. *Soil Science Society of America Journal,* Vol. 41(5), pp. 843-9. America.

[15] Wang, B., Hu, L., Wang, S., Wang, B., Yu, Z., Wang, G., (2018). Design and Experiment of Sweet Potato Transplanting Operation Machine with Rotary Tillage, Ridging and Covering Film Functions (甘薯双垄旋耕起垄覆膜机的设计及试验研究). *Journal of China Agricultural University*, Vol. 23(7), pp. 116-125. China.

[16] Wang, J. (2019). *Design and Experiment of Subsoiler-stubble Chopper Device in No-tillage (免耕条件下破茬深松装置设计与 试验).* Harbin: Northeast Agricultural University. China.

[17] Wu, Y. (2021). *Design and experiment of an integrated machine for tobacco ridging, fertilizing and shaping (烟草起垄施肥整形一体机的设计与试验).* Zhengzhou: Henan Agricultural University. China.

[18] Yuan, T. (2019). *Experimental Study on Water-saving Effect of Summer Maize Under Ridge Tillage and Furrow Irrigation with Straw Mulching (秸秆覆盖条件下垄作沟灌夏玉米节水效应试验研究).* Zhengzhou: North China University of Water Resources and Electric Power. China.

[19] Zeng, Z., Ma, X., Chen, Y., Qi, L., (2020). Modelling residue incorporation of selected chisel ploughing tools using the discrete element method (DEM). *Soil and Tillage Research*, Vol.197, pp. 104505. China.

[20] Zhang, G., Yang, Y., Liu, Y., Wang, Z., (2022). Advances and Prospects of Soil Erosion Research in the Black Soil Region of Northeast China (东北黑土区土壤侵蚀研究进展与展望). *Journal of Soil and Water Conservation*, Vol. 36(02), pp. 1-12. China.

[21] Zhang, S., Zhao, H., Wang, X., Dong, J., Zhao, P., Yang, F., Chen, X., Liu, F., Huang, Y., (2023). Discrete element modeling and shear properties of the maize stubble-soil complex. *Computers and Electronics in Agriculture*, Vol.204:104579, China.

[22] Zhao, S., Liu, H., Yang, C., Yang, L., Gao, L., Yang, Y., (2021). Design and Discrete Element Simulation of Interactive Layered Subsoiler with Maize Straw Returned to Filed (玉米秸秆还田交互式分层深松铲设计与离散元仿真). *Transactions of the Chinese society for agricultural machinery*, Vol.52(3), pp.75-87. China.

[23] Zhao, S., Zhao, G., Leng， M., Liu, Z., Jiang, C., Yuan, Y., Yang, Y., (2025). Design and Testing of Serrated Stubble-breaking Blade with Interaction type with Subsoiler (与深松铲互作锯齿式灭茬刀设计与试验). *Transactions of the Chinese society for agricultural machinery*, Vol.56(04), pp.151-162. China.

[24] Zheng, Z., Fu, Z., Wang, C., (2021). Design and experimental research on soil covering device with linkage and differential adjustment of potato planter. *Agriculture,* Vol. 11, pp. 665. China.

REAL-TIME AND PRECISE DETECTION OF FIELD SOYBEAN RUST AND BACTERIAL SPOT BASED ON IMPROVED YOLOV11N

/

基于改进 YOLOv11n 的田间大豆豆锈病与细菌性斑点病实时精准检测

Tianhao WU, Yongcai MA*, Hanyang WANG
College of Engineering, Heilongjiang Bayi Agricultural University, Daqing 163319/China
Tel: +86-18745952020; E-mail: myc1631@163.com
Corresponding author: Yongcai MA
DOI: https://doi.org/10.35633/inmateh-79-18

Keywords: *Soybean Disease Detection, YOLOv11, Lightweight Model, Real-time Detection*

ABSTRACT

To overcome YOLOv11's limitations in complex field environments, this paper proposed SDD-YOLOv11n, a lightweight real-time detector for soybean diseases. The model reconstructed the backbone using GhostConv to minimize redundancy and integrates a C3k2_Star module to enhance small lesion detection against background noise. Additionally, a Detect Efficient (DE) head further compressed the architecture. Experimental results verified the model's efficiency, achieving a parameter count of 1.88 M and a weight size of 3.9 MB—reductions of 27.3% and 25% compared to YOLOv11n, respectively. Furthermore, the model maintained high detection performance with a Mean Average Precision (mAP50) of 75.6% and an F1-score of 69.3%, demonstrating its effectiveness in balancing architectural efficiency and accuracy in complex field environments.

摘要

针对 YOLOv11 在复杂田间环境下存在的局限性，本文提出了一种轻量化的大豆病害实时检测模型——SDD-YOLOv11n。该模型利用 GhostConv 重构主干网络以最大限度地降低特征冗余，并引入 C3k2_Star 模块，旨在抑制背景噪声干扰的同时增强对微小病斑的检测能力。此外，设计了 Detect Efficient (DE) 检测头以进一步压缩模型架构。试验结果验证了该模型的高效性，其参数量仅为 1.88 M，权重文件大小为 3.9 MB，较 YOLOv11n 分别降低了 27.3%和 25%。同时，该模型在 mAP50 和 F1-Score 上分别达到了 75.6%和 69.3%，证明了其在检测精度和架构效率之间的良好平衡，能够有效应对复杂田间环境下的检测任务。

INTRODUCTION

As a vital oil and protein source, soybean production in China is integral to the national economy. However, prevalent diseases like soybean rust and bacterial spot can cause yield losses of 10%–80% or even total failure (*Liu et al., 2014*). Since traditional manual identification is inefficient and subjective, developing rapid, accurate detection technologies is essential for precision agriculture and food security (*Xiao et al., 2024*).

In recent years, to address issues regarding the accuracy and efficiency of crop disease identification, numerous scholars have focused on improving deep learning algorithms (*Xu et al., 2025*). *Zhu* proposed the CBF-YOLO algorithm, incorporating CSE-ELAN, Bi-PAN, and FFE modules, to detect common soybean pests in complex environments, significantly enhancing the model's detection capabilities (*Zhu et al., 2024*). *Korade* utilized YOLO for leaf extraction and applied various deep learning models to predict disease status. Their findings indicated that ResNet-50 was superior in capturing images from farms for soybean condition prediction, achieving the highest accuracy across all metrics; furthermore, they generated a confusion matrix to evaluate classification accuracy, verifying the model's robustness *(Korade et al., 2025)*. Using the public RiceDisease dataset, *Gan* proposed the G-YOLO model to improve rice leaf disease detection. By combining a lightweight efficient detection head with a multi-scale pyramid pooling layer, the model increased detection speed while maintaining considerable accuracy, making it highly suitable for deployment on resource-constrained edge devices (*Gan et al., 2025*). Similarly, to facilitate edge deployment for peanut disease identification, Sun developed YOLO-PLNet, a lightweight real-time detector specifically optimized for resource-constrained hardware *(Sun et al., 2025*).

To improve localization capabilities for tiny lesion features on cucumbers, Liu proposed the DCNSE-YOLOv7 algorithm, which introduced deformable convolutions and the SENet attention mechanism to strengthen effective target extraction, employed the K-means++ algorithm for anchor box reclustering, and replaced the loss function with Focal-EIOU (Liu *et al., 2023*). To enhance the identification accuracy of ginger leaf pests and diseases in natural environments, *Lan* introduced the GhostNet network and CA attention mechanism to propose Ginger-YOLOv5s, an improved model based on YOLOv5s that met real-time detection requirements while reducing missed and false detections (*Lan et al.,2024*). *Yang* proposed a lightweight tomato leaf pest and disease model based on YOLOv8n (*Yang et al., 2025*).

By reconstructing the original C2f with the StarBlock module and introducing the MLCA attention mechanism to reduce features along the channel dimension, further lightweighting of the original model was achieved. However, despite these advancements, existing studies generally encounter difficulties in balancing detection efficiency with accuracy. Common issues include excessive model parameters, high memory footprint, and a lack of universality in experimental data.

In summary, although deep learning is widely applied in agriculture, existing high-performance models (e.g., ResNet-50, Faster R-CNN) possess large parameter counts, making them difficult to deploy on agricultural drones and edge devices with limited computing power. While attempts have been made to lightweight the YOLO series, there remains a critical deficiency in maintaining a balance between extreme lightweighting (<4 MB) and performance preservation. Furthermore, optimizations targeting the YOLOv11 architecture for this context are currently insufficient. Consequently, this paper proposes SDD-YOLOv11n. By introducing GhostConv to reconstruct the backbone, integrating the C3k2_Star module, and designing a Detect Efficient (DE) head, this study aims to resolve the aforementioned challenges.

MATERIALS AND METHODS

IMAGE ACQUISITION AND DATASET CONSTRUCTION

The soybean disease dataset utilized in this study was collected at Jianshan Farm in Nenjiang, Heihe City, Heilongjiang Province. The dataset comprises three categories of leaf conditions: Healthy, Bean Rust, and Angular Leaf Spot (as shown in Fig. 1). To enhance image diversity and improve the algorithm's generalization capability, original images were acquired using a Redmi K60 smartphone under varying lighting conditions, weather scenarios, and growth backgrounds. Subsequently, the captured images underwent a manual screening process to select high-quality samples. All selected images were standardized to JPEG format, resulting in a total of 6,523 images.

To ensure the diversity of training samples and mitigate model overfitting, data augmentation techniques were applied to the existing dataset. Common augmentation methods employed include rotation, cropping, brightness adjustment, translation, background masking, and Gaussian noise injection. Specifically, noise injection was utilized to simulate environmental uncertainties encountered in real-world scenarios, thereby enhancing the model's robustness and generalization in complex field conditions (*Sulaiman et al., 2022*). Following data augmentation, the expanded dataset was manually annotated using LabelImg. The class labels were defined as "Healthy," "Bean_Rust," and "Angular_Leaf_spot." Finally, the dataset was randomly partitioned into training, validation, and test sets in a ratio of 8:1:1.

Despite the application of various data augmentation techniques to simulate complex field environments, the current dataset presents certain limitations. The images were exclusively acquired from a single geographic location (Jianshan Farm) using a specific capture device (Redmi K60), and encompass only three primary leaf conditions (Healthy, Bean Rust, and Angular Leaf Spot). Consequently, this restricted range of geographic, climatic, and disease category variations may inherently constrain the model's generalization capability when deployed across more diverse real-world agricultural scenarios. Acknowledging this, future data collection efforts will prioritize expanding the dataset across varied regions, diverse lighting scenarios, and encompassing a broader spectrum of soybean diseases to further enhance model robustness.

As a significant evolution in the series, YOLOv11 integrates novel feature extraction modules to maintain high speed and accuracy (*Khanam et al.,2024*). Its backbone, optimized from YOLOv9's GELAN architecture, features the C3k2 module. Compared to the C2f module in YOLOv8, C3k2 offers superior feature extraction with reduced parameter count and complexity, facilitating deployment across diverse environments (*Wu et al., 2025*). Among the five variants, this study selects YOLOv11n as the baseline. Its minimal computational footprint makes it particularly suitable for resource-constrained agricultural IoT devices (*Wang et al., 2025*).



a. Healthy b. Bean_Rust c. Angular_Leaf_spot

Fig. 1 - H (healthy) vs D (diseased) leaves of soybean

To further optimize the trade-off between detection accuracy and efficiency in YOLOv11n, this study proposes three structural enhancements. First, GhostConv substitutes standard convolutions to minimize computational redundancy and parameter volume. Second, a novel C3k2_Star module is introduced to refine the original C3k2 structure, offering a lighter and more flexible solution for resource-constrained field environments. Finally, a Detect Efficient (DE) head is implemented to replace the standard detection head, significantly reducing computational load while maintaining detection performance. The architecture of the improved SDD-YOLOv11n is illustrated in Figure 2.

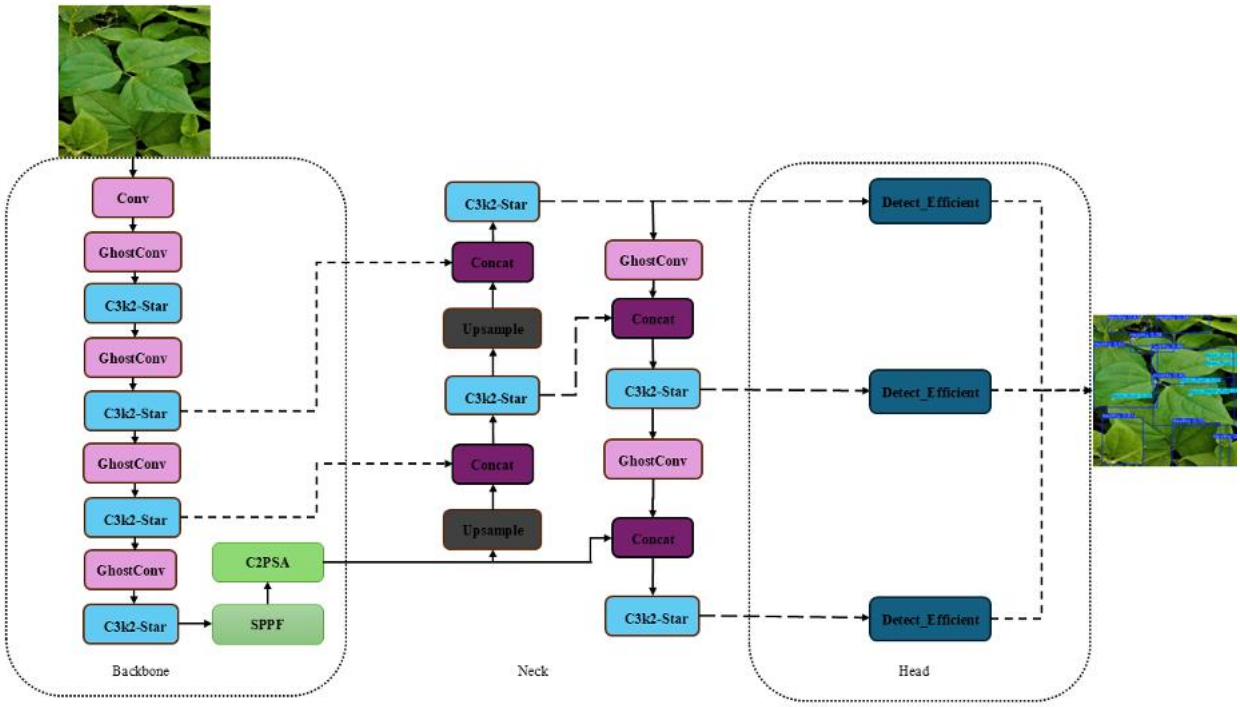


Fig. 2 - The architecture of the SDD-YOLOv11n network

Ghostconv Module

To accommodate resource-constrained edge devices in field applications, the substantial computational overhead caused by redundant feature maps in YOLOv11's standard convolutions presents a challenge (*Han et al., 2020*). Consequently, this study integrates the GhostNet architecture into YOLOv11n by substituting standard convolutions (excluding the initial layer) with GhostConv modules. By leveraging "cheap linear operations" to generate feature maps, this approach significantly compresses parameter volume while preserving critical spatial information. GhostConv achieves efficient feature learning by decoupling primary feature extraction from "ghost" feature generation.

The specific process is as follows:

1) Primary Feature Generation:

A small subset of convolution kernels is selected to extract core primary features. Assuming the input feature map is $X \in \mathbb{R}^{H\times W\times C}$, the number of primary feature channels is m (where $m \ll N$), and the number of

convolution kernels is m, the calculation for the primary feature map $Y^{'}$ is defined as shown in Equation (1):

$$Y^{'} = X * f^{'} \quad (1)$$

where $f^{'}$ represents the primary convolution kernels, and the computational cost is approximately $\frac{1}{s}$ of that of standard convolution.

2) Ghost Feature Generation:

For each primary feature, $s-1$ ghost features are generated via cost-effective linear operations, where s represents the generation ratio controlling the total number of features $N = m \times s$. Letting the i-th primary feature be $y_i^{'}$, its corresponding ghost feature generator is $\Phi_{i,j}$. The calculation for the ghost features is defined as shown in Equation (2):

$$y_{i,j} = \Phi_{i,j}(y_i^{'}),\ \forall i = 1,\ldots,m,\ \ j = 1,\ldots,s-1 \quad (2)$$

Upon completion of these two steps, the primary features and ghost features are concatenated to obtain the final output feature map Y.

In contrast to the full-channel operations in YOLOv11, GhostConv executes standard convolution on a subset of channels and generates the remainder via linear transformations. This mechanism significantly reduces computational complexity and parameter volume while preserving robust feature expression, thereby achieving model lightweighting without compromising detection accuracy.

C3k2_star Module

Derived from the Cross Stage Partial (CSP) architecture, the C3k2 module optimizes gradient flow and reduces redundancy through feature partitioning and fusion. However, to address the strict computational constraints of field environments, further lightweight optimization is required. Consequently, this study introduces the C3k2_Star module to replace the standard C3k2 in both the backbone and neck networks, thereby enhancing deployment efficiency.

The core of the C3k2_Star module lies in the stacking of n Star_Block instances. Derived from StarNet (*Ma et al., 2024*), the Star_Block employs element-wise multiplication for feature modulation. Inputs are processed via two parallel branches to generate a gating signal and a feature stream, respectively, which are then fused through element-wise multiplication to enhance feature representation (*Li et al., 2020)*.

Letting the input feature be X, this core interaction process is defined by Equation (3):

$$Y = (W_1 X) * f(W_2 X) \quad (3)$$

Where W_1 and W_2 represent the weight matrices of the two branches, respectively; f denotes the non-linear activation function; and $*$ represents element-wise multiplication. The structure of the StarBlock module is illustrated in Figure 3.

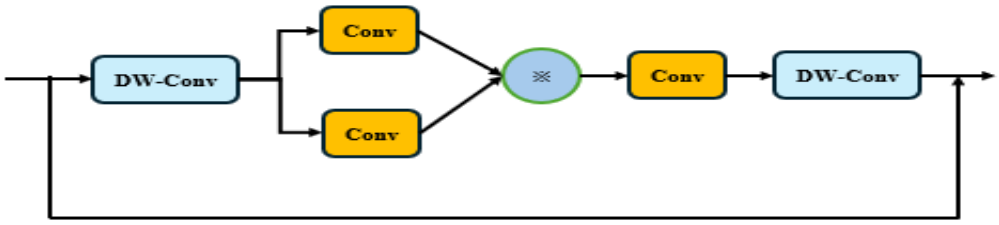


Fig. 3 - Structure of the StarBlock Module

Through element-wise multiplication, the module achieves dynamic channel re-weighting, effectively isolating minute disease symptoms from complex backgrounds by suppressing noise and amplifying relevant features. This "Star operation" significantly enhances representational capability via high-dimensional mapping Figure 3: Structure of the StarBlock Module maintaining a low parameter count, avoiding the substantial computational overhead associated with global attention mechanisms.

The final output undergoes a linear mapping to restore the channel dimensions, incorporating a residual connection as defined in Equation (4):

$$Y_{out} = W_3(Y_{star}) + X \quad (4)$$

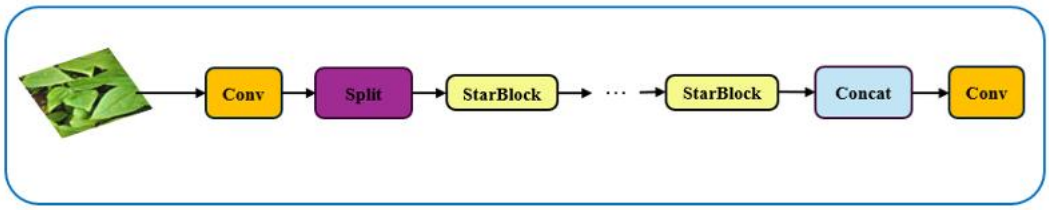


Fig. 4 - Structure of the C3k2_Star Module

Where W_3 represents the output projection matrix, and the addition operation denotes the residual connection. The structure of the C3k2_Star module is illustrated in Figure 4.

Detect_Efficient Module

To address parameter redundancy in YOLOv11n's decoupled head and enhance inference efficiency, this study introduces the DE module. While retaining Distribution Focal Loss (DFL) and Anchor-free strategies to ensure localization precision and multi-scale adaptability, the design implements lightweight optimizations to mitigate the high computational overhead associated with standard dense convolutional layers. The core principle of DFL is defined in Equation (5):

$$\hat{y} = \sum_{i=0}^{n} P\,(y_i) y_i \tag{5}$$

Where $\hat{y}$ represents the predicted bounding box coordinate, and $P(y_i)$ denotes the predicted probability density function. During the discretization process, the continuous regression range is discretized into the interval $[y_0, y_n]$, where $\sum P\,(y_i) = 1$.

To mitigate the high computational cost of dense convolutions, the DE module substitutes standard layers with stacked 3×3 Grouped Convolutions at the input of each branch. This design significantly lowers parameter count and complexity via independent channel processing, achieving an optimal speed-accuracy trade-off suitable for agricultural deployment.

RESULTS

Training Environment and Experimental Setup

Experiments were conducted on a Linux platform featuring an NVIDIA RTX 4090D (24GB) GPU and an 18-core 2.6GHz CPU, utilizing PyTorch 2.2.0 (CUDA 12.1). Training employed the SGD optimizer (momentum=0.937, initial $lr = 0.01$) with an input resolution of 640×640, a batch size of 64, and a duration of 300 epochs. Performance was evaluated via Precision(P), Recall(R), mAP, Parameters, GFLOPs, FPS, and Model Size(M-S).

Model Performance Evaluation

Upon evaluation on the test set, the computational complexity and inference efficiency of the optimized SDD-YOLOv11n model are presented in Table 1.

Table 1

The computational complexity and inference efficiency of the optimized SDD-YOLOv11n

GFLOPs	Parameters	FPS（Inference）	FPS(Comprehensive)	M-S/MB
4.4	1877017	503.59	285.05	3.9

Experimental results demonstrate that SDD-YOLOv11n exhibits significant lightweight efficiency, characterized by 1.88 M parameters, 4.4 GFLOPs, and a 3.9 MB file size, rendering it ideal for edge deployment. Furthermore, the model achieves exceptional speed—503.59 FPS for pure inference and 285.05 FPS for comprehensive processing—fully satisfying the stringent real-time requirements of agricultural disease detection.

The quantitative evaluation results for the SDD-YOLOv11n model are detailed in Table 2.

Table 2

Quantitative Evaluation Results of the SDD-YOLOv11n Model

P / %	R / %	F1-Score / %	mAP50 / %	mAP50-95 /%
68.9	70.3	69.3	75.6	54.2

Results indicate that the model demonstrates robustness with an mAP of 75.6% and a high-threshold mAP of 54.2%. Furthermore, an overall F1-score of 69.3% signifies a well-balanced trade-off between precision and recall.

Ablation Studies of Proposed Improvements

To validate the efficacy of the proposed improvements, a comprehensive ablation study was conducted on the YOLOv11n baseline. By incrementally integrating GhostConv, C3k2_Star, and the DE Head, the specific quantitative results are presented in Table 3.

Table 3

Ablation experiment

Model	Parameters	GFOLPs	M-S/MB	FPS	P%	R/%	mAP50)/%
Base	2582737	6.3	5.2	290.56	68.9	72.0	76.9
Base+a	2257041	5.5	4.6	298.38	69.3	69.9	76.3
Base+b	2472393	6.4	5.1	267.92	69.7	71.1	76.4
Base+c	2313041	5.1	4.7	290.47	68.9	71.5	76.9
Base+a+b	2146713	5.6	4.5	302.05	70.1	69.6	76.1
Base+a+b+c	1877017	4.4	3.9	285.05	68.9	70.3	75.6

Note: "Base" refers to the YOLOv11n model; "a", "b", and "c" denote the GhostConv module, the C3k2_Star module, and the DE module, respectively.

Combining all three modules yielded the best performance, validating the effectiveness of each component and their synergy.

Comparative Analysis of Different Detection Models

To benchmark SDD-YOLOv11n, quantitative comparisons were conducted against mainstream detectors—including Faster R-CNN(F-R) (*Ren et al., 2016*), SSD (*Liu et al., 2024*), and recent YOLO iterations (*Tian et al., 2025, Lei et al., 2025*)—under identical experimental conditions. Performance was evaluated via mAP, Parameters, GFLOPs, FPS, Recall, and Memory Size, with specific results detailed in Table 4.

Table 4

Contrast test

Model	Parameters	GFOLPs	M-S/MB	FPS	P/%	R/%	mAP50)/%
YOLOv11n	2582737	6.3	5.2	290.56	68.9	72.0	76.9
YOLOv12n	2508929	5.8	5.2	266.42	70.2	70.3	76.7
YOLOv13n	2448480	6.1	5.2	250.64	70.1	69.6	76.1
SSD	24103280	30.5	12.5	55.20	61.5	64.0	68.5
F-R	41350110	180.2	25.4	18.50	71.0	68.5	74.5
Ours	1877017	4.4	3.9	285.05	68.9	70.3	75.6

Comparative analysis reveals that while Faster R-CNN achieved the highest Precision (71%), its extensive computational overhead (41.3 M parameters, 18.5 FPS) and SSD's sub-optimal performance limit their practical utility. This aligns with the findings of *Korade*, whose international study demonstrated that while heavy architectures like ResNet-50 can achieve superior accuracy in soybean disease prediction, they often pose significant challenges for real-time farm deployment due to their complexity. In contrast, SDD-YOLOv11n surpasses these traditional models in comprehensive efficiency, demonstrating superior feature fusion in complex farmland environments. Against state-of-the-art YOLO variants (v12n, v13n), the proposed model reduces parameters and GFLOPs by approximately 25% while enhancing inference speed by 18–34 FPS. Achieving this lightweight design with negligible accuracy loss, SDD-YOLOv11n strikes a critical balance for energy-constrained drone applications.

Ultimately, SDD-YOLOv11n addresses the hardware constraints of smart agriculture. With only 1.87 M parameters (approx. 1/22 of Faster R-CNN) and the lowest computational load (4.4 GFLOPs), its minimal memory footprint (3.9 MB) facilitates cost-effective deployment on embedded systems like Raspberry Pi and Jetson Nano. The model's exceptional inference speed (285.05 FPS) not only extends operational endurance but also reserves ample computational margin for real-time decision-making systems.

Visualization of Detection Results

In this section, the detection results obtained from the trained YOLOv11n, YOLOv12n, YOLOv13n, and SDD-YOLOv11n models are visualized. The resulting comparison is illustrated in Figure 5, where bounding boxes are color-coded as follows: dark blue denotes “Healthy” leaves, sky blue indicates “Bean Rust,” and white represents “Angular Leaf Spot.”

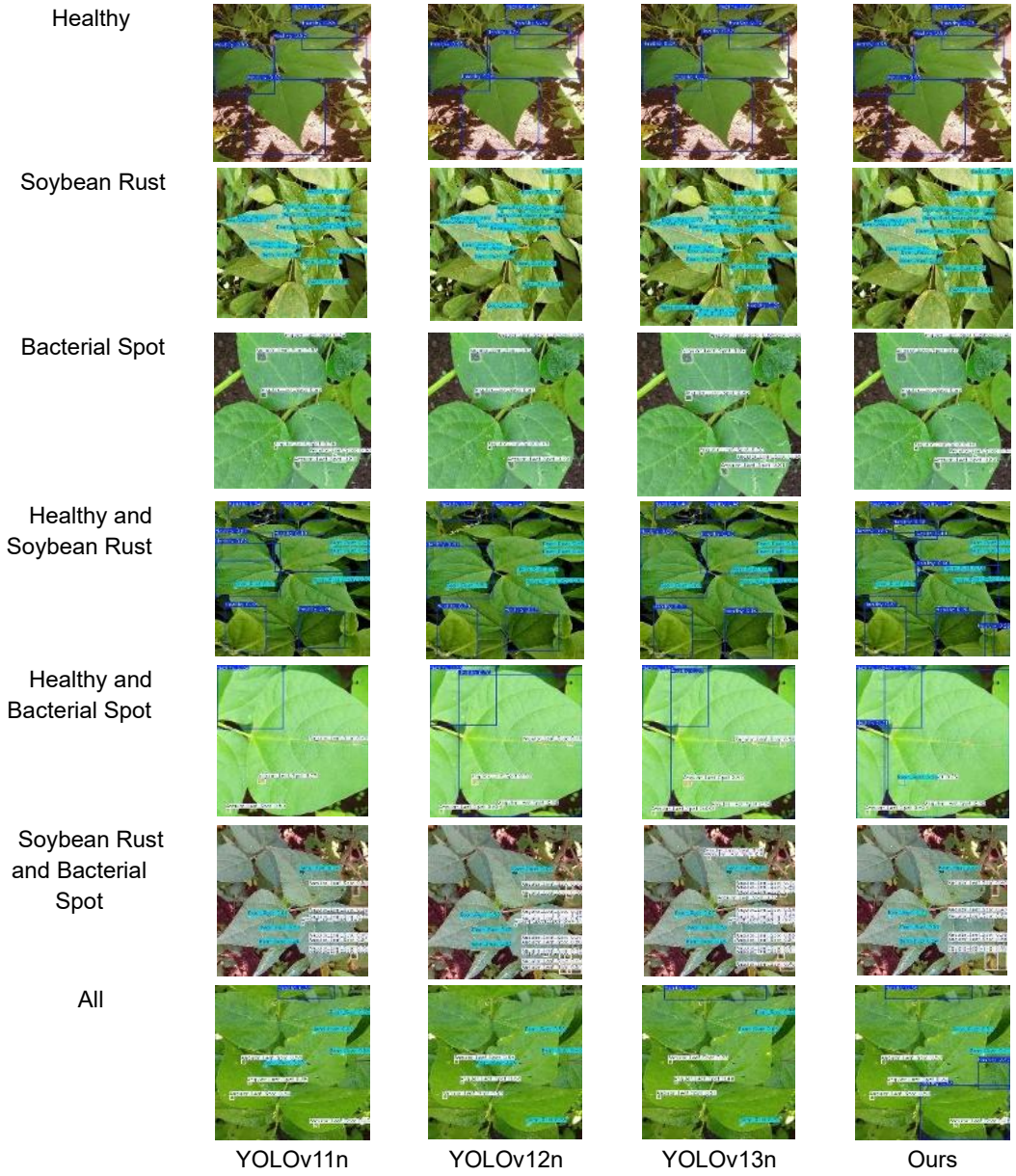


Fig. 5 – Visual Comparison of Detection Results Across Different Models

As illustrated, SDD-YOLOv11n achieves detection accuracy comparable to state-of-the-art benchmarks (YOLOv11n, v12n, v13n). Notably, it demonstrates superior robustness in classifying “bean rust,” avoiding the misclassifications observed in YOLOv12n and v13n. The results confirm the model’s efficacy in distinguishing between healthy, rust-infected, and angular leaf spot samples. Furthermore, by maintaining high detection speeds with minimal resource consumption, SDD-YOLOv11n is highly conducive to real-time deployment on edge devices.

Error Analysis and Robustness Evaluation

Figure 6 illustrates the confusion matrix of SDD-YOLOv11n on the test set, demonstrating exceptional classification consistency within complex field environments. Specifically, the “Healthy” category achieves near-perfect recognition. Misclassifications between the visually similar “Bean Rust” and “Angular Leaf Spot” (104 and 187 instances, respectively) are negligible relative to their vast true positive baselines. This confirms the robust discriminative feature extraction capability of the proposed GhostConv backbone and C3k2_Star module.



Fig. 6 – Confusion matrix of the SDD-YOLOv11n model on the test set

However, the matrix's background row and column reveal the primary error source: false negatives and false positives induced by background interference, with "Angular Leaf Spot" exhibiting a notably higher missed detection rate. To further interpret these error mechanisms and validate the model's decision-making process, Grad-CAM visualizations (Fig. 7) were evaluated on representative scenarios. This interpretability approach follows the recent advancements by Alhammad, who utilized deep learning combined with explainable AI (XAI) to ensure the transparency and reliability of disease classification in plant pathology *(Alhammad et al., 2025)*. As shown in Fig. 7(a), the model demonstrates exceptional feature focusing capabilities; even under severe leaf overlapping, the high-response regions (dark red) precisely localize on minute, early-stage bean rust lesions, visually confirming the efficacy of the proposed modules. Conversely, Fig. 7(b) and 7(c) expose the model's limitations under severe background noise. Fig. 7(b) illustrates a typical missed detection where a diseased leaf is ignored because the model's attention is erroneously drawn to surrounding weeds, resulting in a low feature response (cold tones) on the actual lesion. Furthermore, Fig. 7(c) presents a false-positive case where a non-target weed is misclassified as a "Healthy" leaf. Crucially, this uncovers an attention defocusing mechanism: the high-response areas are severely scattered across the background soil. This hallucination-like misclassification indicates that homologous green backgrounds and extreme lighting remain the main bottlenecks for the lightweight model's spatial attention allocation. Future work will integrate multi-scale feature fusion strategies to enlarge the global receptive field and optimize detection performance in such challenging scenarios.



(a) Accurate feature focusing on early-stage bean rust

(b) A false-negative case caused by severe background distraction

(c) A false-positive case showing attention defocus caused by complex background noise

Fig. 7 - Grad-CAM visualizations of representative detection results

CONCLUSIONS

To address the requirements for field-based soybean disease detection, this study successfully constructed a high-quality soybean disease image dataset. Based on this dataset and the YOLOv11n architecture, an efficient detection model for soybean rust and bacterial spot—SDD-YOLOv11n—was designed and implemented. The proposed model significantly reduces parameter count, GFLOPs, and model size while maintaining commendable accuracy, thereby providing a theoretical foundation for subsequent applications in actual field environments. The specific conclusions are as follows:

1. Structural Improvements: This study introduced structural optimizations to the YOLOv11n baseline. Specifically, standard convolutional layers were replaced with Ghost modules from the GhostNet architecture. Furthermore, the C3k2_Star module, inspired by StarNet principles, was proposed to supersede the original C3k2 module. Finally, a highly efficient detection head, Detect_Efficient, was developed. Experimental results indicate that, at the cost of a marginal decrease of approximately 1% in Mean Average Precision (mAP), the model achieved reductions of roughly 27.3% in parameter count, 30.1% in floating-point operations, and 25% in model size, while simultaneously increasing the frame rate by 5.5 FPS. This demonstrates a substantial reduction in computational demand while maintaining robust accuracy, thereby satisfying the conditions required for practical detection.
2. Comparative Advantage: Compared to current mainstream detection models, SDD-YOLOv11n exhibits significant advantages in terms of lightweight characteristics. While ensuring high accuracy, the model volume is merely 3.9 MB, and the floating-point operations are limited to 4.4 GFLOPs. In conclusion, SDD-YOLOv11n demonstrates superior performance regarding parameter count, model size, and computational complexity.

Although the SDD-YOLOv11n model proposed in this study achieved promising detection results on the self-constructed soybean leaf disease dataset, there remains room for improvement. Limitations exist regarding the diversity of disease types and the environmental complexity within the dataset due to the challenging nature of data acquisition. Future research will focus on expanding the scale and diversity of the data. Additionally, model compression techniques such as pruning and knowledge distillation will be applied to further lightweight the model, thereby continuing to reduce computational resource consumption and hardware dependency. Future work will also prioritize deployment experiments on edge devices to evaluate the model's real-time performance and stability in actual field environments.

ACKNOWLEDGEMENT

This study was funded by the Key Research and development Plan of Heilongjiang Province(2024ZXDXB45), (LJGXCG2022-107).

REFERENCES

[1] Sarah M. Alhammad, Doaa Sami Khafaga, Walaa M. El hady, Farid M. Samy & Khalid M. Hosny. (2025). Deep learning and explainable AI for classification of potato leaf diseases. *Frontiers in Artificial Intelligence,* Vol. 7, pp. 1449329-1449329, Riyadh/Saudi Arabia

[2] Gan B., Pu G., Xing W. (2025). Enhanced YOLOv8 with SDD weight and efficient detection head for detecting rice leaf diseases. *Scientific Reports*, Vol. 15, pp. 22179, London/UK.

[3] Han K., Wang Y., Tian Q. (2020). GhostNet: More features from cheap operations. *Conference on Computer Vision and Pattern Recognition*, pp. 1577-1586, Seattle/USA.

[4] Khanam R., Hussain M. (2024). YOLOv11: An overview of the key architectural enhancements. *arXiv preprint* arXiv:2410.17725, Ithaca/USA.

[5] Korade N.B., Salunke M.B., Bhosle A. (2025). Proactive Soybean Disease Detection through YOLO Leaf Extraction and ResNet-50 Classification to Reduce Crop Loss and Boost Productivity. *International Journal of Engineering Trends and Technology*, Vol. 73, pp. 133, Maharashtra/India.

[6] Lan Y., Sun B., Zhang L. (2024). Identification of ginger leaf diseases and pests in natural scenes based on improved YOLOv5s (基于改进 YOLOv5s 的自然场景下生姜叶片病虫害识别). *Transactions of the Chinese Society of Agricultural Engineering*, Vol. 40, pp. 210-216, Beijing/China.

[7] Lei M., Li S., Wu Y. (2025). YOLOv13: Real-Time Object Detection with Hypergraph-Enhanced Adaptive Visual Perception. *arXiv preprint* arXiv:2506.17733, Ithaca/USA.

[8] Li X., Wang W., Wu L. (2020). Generalized focal loss: Learning qualified and distributed bounding boxes for dense object detection. *Advances in Neural Information Processing Systems*, Vol. 33, pp. 21002-21012, Vancouver/Canada.

[9] Liu M., Liepold C., Swaminathan S. (2014). Progress in research on Asian soybean rust (亚洲大豆锈病研究进展). *Chinese Journal of Oil Crop Sciences*, Vol. 36, pp. 676-684, Wuhan/China.

[10] Liu S., Hu B., Zhao C. (2023). Detection and identification of cucumber leaf diseases and insect pests based on improved YOLOv7 (基于改进 YOLOv7 的黄瓜叶片病虫害检测与识别). *Transactions of the Chinese Society of Agricultural Engineering*, Vol. 39, pp. 163-171, Beijing/China.

[11] Liu W., Anguelov D., Erhan D. (2016). SSD: Single shot multibox detector. *European Conference on Computer Vision*, pp. 21-37, Cham/Switzerland.

[12] Ma X., Dai X., Bai Y. (2024). Rewrite the stars. *Proceedings of the IEEE/CVF Conference on Computer Vision and Pattern Recognition*, pp. 5694-5703, Seattle/USA.

[13] Ren S., He K., Girshick R. (2016). Faster R-CNN: Towards real-time object detection with region proposal networks. *IEEE Transactions on Pattern Analysis and Machine Intelligence*, Vol. 39, pp. 1137-1149, New York/USA.

[14] Sulaiman, N., Che'Ya, N. N., Mohd Roslim, M. H., Juraimi, A. S., Mohd Noor, N., & Fazlil Ilahi, W. F. (2022). The application of hyperspectral remote sensing imagery (HRSI) for weed detection analysis in rice fields: A review. *Applied Sciences*, Vol. 12(5), pp. 2570-2570, Serdang/Malaysia

[15] Sun, J., Feng, Z., Han, J., Xu, F., Zhang, H., & Guo, Y. (2025). YOLO-PLNet: a lightweight real-time detection model for peanut leaf diseases based on edge deployment. *Frontiers in Plant Science*, Vol. 16, pp. 1707501, Zhengzhou/China

[16] Tian Y., Ye Q., Doermann D. (2025). YOLOv12: Attention-centric real-time object detectors. *arXiv preprint* arXiv:2502.12524, Ithaca/USA.

[17] Wang J., Li S., Wang C. (2025). Lightweight tomato pest detection model based on improved YOLOv8n (基于改进 YOLOv8n 的轻量级番茄虫害检测模型). *Transactions of the Chinese Society of Agricultural Engineering*, Vol. 41, pp. 185-195, Beijing/China.

[18] Wu S., Mao Y., Hu H. (2025). Grape fruit and leaf disease detection method based on improved YOLO11n (基于改进 YOLO11n 的葡萄果叶病害检测方法). *Transactions of the Chinese Society of Agricultural Engineering*, Vol. 41, pp. 140-147, Beijing/China.

[19] Xiao C. (2024). Symptom identification and prevention methods of several common soybean diseases (大豆几种常见病害的症状识别及防治方法). *Modernizing Agriculture*, pp. 15-17, Heilongjiang/China.

[20] Xu Y., Wu Q., Zhang B. (2025). Application progress of lightweight deep learning network in crop object detection (轻量级深度学习网络在农作物目标检测的应用进展). *Journal of Chinese Agricultural Mechanization*, Vol. 46, pp. 261-270, Nanjing/China.

[21] Yang S., Zhang P., Wang L. (2025). Lightweight tomato leaf disease and pest identification method integrating improved YOLOv8n and channel pruning (集成改进 YOLOv8n 与通道剪枝的轻量化番茄叶片病虫害识别方法). *Transactions of the Chinese Society of Agricultural Engineering*, Vol. 41, pp. 206-214, Beijing/China.

[22] Zhu Linqi, Li Xiaoming, Sun Hongmin & Han Yingpeng. (2024). Research on CBF-YOLO detection model for common soybean pests in complex environment. *Computers and Electronics in Agriculture,* Vol. 216*,* pp. 108515, Harbin/China.

DESIGN AND IMPLEMENTATION OF A VISUAL MONITORING SYSTEM FOR PADDY FLOW INSTABILITY IN INTELLIGENT HUSKERS

/

面向智能砻谷机的稻谷料流失稳视觉监测系统设计与实现

Min CHENG [*1], Shihao ZHOU[1], Yong PAN[2], Xingchuang WANG[1]

[1] School of Mechanical and Electrical Engineering, Henan University of Technology, Zhengzhou / China;

[2] School of Intelligent Engineering, Henan Mechanical and Electrical Vocational College, Zhengzhou / China

Corresponding author: Min Cheng, Tel: +86-18623710936; E-mail: chengminhappy2006@163.com,

DOI: https://doi.org/10.35633/inmateh-79-19

Keywords: *Rubber roll husker; Paddy flow; Machine Vision; Real-time monitoring*

ABSTRACT

To achieve precise prevention and control of rubber roll wear in huskers, this study established a complete experimental platform integrating mechanical transmission, feeding control, and visual acquisition units, and subsequently developed a real-time monitoring system for paddy flow instability based on machine vision. An image acquisition system composed of a CMOS camera and a customized light source was built to construct a dedicated dataset for paddy flow states. Based on the lightweight YOLOv8n detection model, Python programming was adopted in the PyCharm environment with the Ultralytics library integrated, realizing real-time recognition and quantitative analysis of paddy flow states. The results demonstrated that the system realized a real-time detection efficiency of 14 FPS on a local workstation, and the YOLOv8n model achieved a recognition accuracy of 90.8% in terms of mean Average Precision at IoU threshold 0.5 (mAP@0.5) for sparse and overlapping grain states. The system could effectively capture key abnormal states, including inclined paddy grains entering the rolling zone, sparse paddy flow lasting more than 5 seconds, and overlapping paddy flow density exceeding 10 grains/cm². This study transformed the mechanical characteristics of paddy flow instability into pixel-level quantitative indicators and established an integrated visual monitoring paradigm of "perception-analysis-decision", providing effective technical support for the intelligent management and control of huskers.

摘要

为实现砻谷机胶辊磨损的精准防控，本研究搭建了集成机械传动、喂料控制与视觉采集单元的完整实验平台，开发了基于机器视觉的稻谷料流失稳实时监测系统。采用 CMOS 相机与定制光源构建图像采集系统，构建稻谷料流状态专用数据集；基于 YOLOv8n 轻量化检测模型，在 PyCharm 环境中采用 Python 编程集成 ultralytics 库，实现料流状态的实时识别与量化解析。结果表明，该系统在本地工作站可实现 14FPS 的实时检测效率，YOLOv8n 模型对颗粒稀疏与堆叠状态的识别精度（交并比 0.5 阈值下的平均精度均值，mAP@0.5）达到 90.8%，可有效捕捉稻谷颗粒入轧倾斜、料流稀疏持续时间大于 5 秒、料流堆叠密度超过 10 粒/cm²等关键异常状态。本研究将料流失稳的力学特征转化为像素级量化指标，构建"感知-解析-决策"一体化视觉监测范式，为砻谷机智能管控提供了有效的技术支撑。

INTRODUCTION

During the operation of a rubber roll husker, the uniform wear condition of rubber rolls is crucial for maintaining a stable hulling process (*Prabhakaran et al., 2017*). Studies indicate that the dynamic imbalance in paddy flow distribution is the fundamental cause of uneven rubber roll wear (*Yehia & Katab, 2018*). However, constrained by the complex environment of the rolling zone, existing industrial sensors struggle to accurately monitor dynamic paddy flow conditions. To address this, there is an urgent need to develop a machine vision-based monitoring system. By enabling online recognition and analysis of the paddy flow before it enters the rolling zone, the system can accurately capture unstable flow patterns and provide real-time data support for subsequent control. The technology enables the prevention of rubber roll wear from the source and offers a new paradigm for the intelligent upgrading of grain processing equipment.

Early monitoring technologies primarily focused on mechanical parameters. For instance, Zhancheng Grain Machinery Factory in Zhejiang developed a real-time roll pressure monitoring system that uses sensors to provide immediate feedback on pressure data, offering visual guidance for manual operation (*Xiang and Ruan, 2009; Zhou et al., 2025*).

Wang et al. (2013) introduced a PLC control system into the rubber roll husker, integrating functions such as equipment start-stop, flow regulation, and fault alarm, thereby preliminarily achieving automated management of the hulling process. *Wang (2016)* designed a real-time monitoring system that breaks through single-dimensional limitations by simultaneously collecting parameters such as rubber roll speed, roll pressure, and flow rate, enabling intelligent management of operational parameters. Furthermore, uneven feeding during rubber roll husker operation leads to uneven wear of the rubber rolls, which can cause vibration and noise. *Wu et al. (2024)* conducted real-time detection and identification of abnormal wear conditions on the rubber rollers of a husker based on point cloud data, effectively addressing the challenge of accurately monitoring the wear state of rubber rollers. *Zhu (1979)* pointed out that rubber roll eccentricity is caused by vibration during the hulling process. To address this issue, *Liu (2020)* applied a multi-link vibration isolation concept within the rolls and designed an impact isolator, which mitigated shock vibration transmission and acoustic radiation in the rubber roll husker. Future studies should further investigate the influence of uneven rubber roll wear on rotor dynamic characteristics to mitigate vibration and noise.

In the field of material flow monitoring, although existing bulk material monitoring technologies are quite diverse, specialized research on paddy flow remains scarce. Current achievements mainly focus on belt conveyor scenarios in industries such as coal, while the physical and chemical characteristics of paddy differ significantly from other materials, imposing higher requirements on monitoring technology. For material flow monitoring on belt conveyors, *Wen et al. (2023),* integrated line laser and binocular vision techniques to detect coal flow on the conveyor belt, and achieved high-precision volumetric flow calculation through host computer processing. The method exhibits limited adaptability to complex conditions in paddy flow, such as overlapping and inclination. *Xu et al. (2022)* integrated RFID technology with point cloud data processing methods to achieve real-time measurement of the mass flow rate of bulk materials on a conveyor belt, obtaining high-precision results on fine sand materials, which can provide a reference for similar applications in paddy flow monitoring. *Yan et al. (2023)* employed a dual-array capacitive sensor combined with the BP-Adaboost algorithm to realize multi-parameter measurement of gas–solid two-phase flow, effectively improving the identification capability for complex flow conditions such as sparse or stacked particles. *Zhu et al. (2024)* evaluated the measurement performance of an array capacitive sensor for particle concentration in gas–solid two-phase flow through a CFD-DEM coupling method, thereby laying a theoretical foundation for precise monitoring of particle flow. However, this method requires adaptive optimization for the specific characteristics of paddy flow to enhance the accuracy and stability of the monitoring system.

Current paddy flow monitoring faces three challenges: the difficulty in balancing accuracy with adaptability, the insufficient reliability of low-cost sensors, and the disconnection between monitoring and control processes. Therefore, this paper proposes an integrated visual monitoring paradigm of "perception-analysis-decision". By converting the mechanical characteristics of paddy flow instability into pixel-level quantitative indicators, it establishes a closed-loop feedback channel for the full-cycle intelligent management of rubber rolls.

MATERIALS AND METHODS

The feeding device and the visual acquisition unit form the hardware core of the system, working in coordination with the host computer to establish a comprehensive paddy flow status monitoring framework.

Mechanical system structure and functional implementation

The structure and control performance of the feeding device directly determine the data reliability of the monitoring system. This apparatus adopts a combined long and short chute board structure and employs modular design to achieve precise simulation and regulation of paddy flow conditions. As shown in Fig. 1(a), the device consists of a hopper, feeding roller, electric motor, long and short chute boards, chute adjustment mechanism, and support frame.

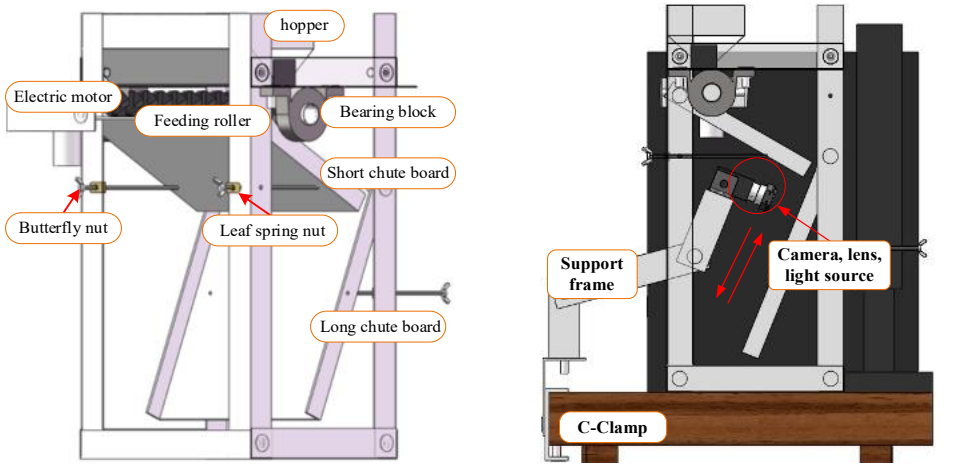
The electric motor drives the feeding roller at a constant speed, ensuring continuous and stable material conveyance. The long and short chute boards facilitate uniform material distribution and guided flow through their uniquely designed inclination angles. The integrated Q312B leaf spring nut and butterfly bolt assembly enables stepless adjustment of the chute inclination, thereby allowing precise control over paddy flow velocity and density distribution. The support frame employs a rigid connection design to effectively suppress mechanical vibration interference with the paddy flow state. Through coordinated mechatronic control, the entire setup provides stable and reliable experimental conditions for the visual monitoring system.

Software architecture and data processing flow

The vision acquisition system establishes a comprehensive technical framework for paddy flow monitoring through the integration of hardware and software algorithms. As shown in Fig. 1(b), the vision acquisition unit adopts a modular design incorporating a Hikvision MV-CU013-A0UC CMOS industrial camera, MVL-HF0628M-6MPE 6mm fixed-focus lens, and ring LED light source (*Yu, 2024*).

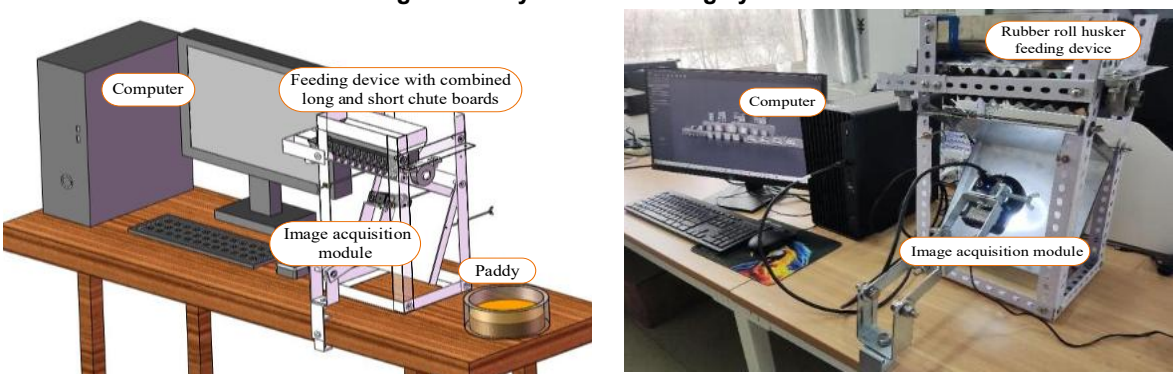
The system utilizes a C-mount interface and USB 3.0 protocol to establish a high-speed data transmission channel. The camera ensures complete capture of dynamic paddy flow characteristics through its high-frame-rate acquisition capability. The lens maintains geometric imaging accuracy with a low distortion rate of -0.103%. The ring light source effectively suppresses localized shadows and enhances grain texture features through multi-angle uniform illumination. Under the centralized management of MVS V4.4.0 professional software, the unit achieves unified control of parameters including acquisition frequency, resolution, and image format. All hardware components operate in coordination with the computer-based main control system through standard communication protocols, collectively forming a stable and reliable visual perception foundation. Feeding device with combined long and short chute boards (*Zhang et al., 2024*).

The system software employs a multi-threaded architecture developed in a Python-OpenCV environment, implementing three core functional modules. The image acquisition module captures 640×640 resolution video streams at 168 FPS through the VideoCapture interface, performing color space conversion and image preprocessing. The model inference module utilizes the Ultralytics library to load an optimized YOLOv8 model, executing object detection with preset confidence and IoU thresholds to output particle localization and classification data. The visualization module integrates functions for rendering detection bounding boxes, annotating categories, and counting particles, supporting real-time display and result storage. Each module exchanges data through asynchronous message queues, working in conjunction with MVS professional software to manage device control and parameter configuration, thereby establishing a complete "acquisition-analysis-display" processing pipeline. By integrating the computer, image acquisition module, and feeding device, an efficient and stable image acquisition platform was established. The structural model diagram of this platform is shown in Fig. 2, providing a foundation for subsequent object detection and analysis.



(a) Schematic diagram of feeding device (b) Diagram of camera mount position adjustment

Fig. 1 - Paddy flow monitoring system



(a) Design diagram of the visual monitoring platform (b) Physical photograph of the visual monitoring platform

Fig. 2 - 3D structural design and physical experimental platform for the flow monitoring system

Paddy flow dataset construction

YOLOv8 is an object detection algorithm based on convolutional neural networks. Building upon the YOLO series, it enhances detection performance by incorporating novel features and architectural improvements (*Ma et al., 2024; Paul et al., 2024; Tian., 2024*). The algorithm requires a large volume of image data with corresponding annotations as training samples. Through learning from these samples, it extracts features such as shape and color of paddy, thereby establishing a mapping relationship between input images and target detection results. To accurately identify paddy flow conditions, this study constructed a dedicated image dataset *(Ma et al., 2024)*. The dataset comprises a total of 530 images, including 220 static scenes and 310 dynamic scenes, divided into training and validation sets in an 8:2 ratio. Due to limitations in dataset size and annotation cost, only a training set and a validation set have been currently divided, with no separate test set established. Model performance evaluation is primarily conducted based on the validation set, while the model's generalization capability is further verified through dynamic real-time monitoring experiments. Future work will expand the dataset and introduce an independent test set to refine the evaluation framework. Using the LabelImg tool, manual annotations were performed in YOLO format, generating label files containing target bounding box coordinates and category labels. During annotation, sparse and overlapping paddy flow conditions were labeled as Sparse Grains (SG) and Pile-up Scenes (PS) tags respectively (*Song, 2025*). As shown in Fig. 3, for sparsely distributed grains, each grain was individually annotated with SG tags; for overlapping regions, whether single-layer or multi-layer distribution, they were uniformly labeled as PS tags to ensure the model can effectively learn morphological features of grains under different density conditions.

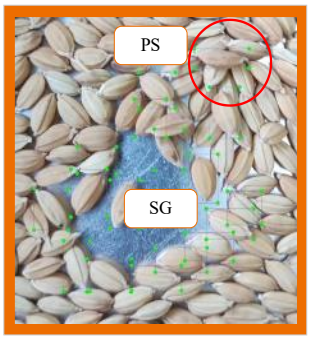


Fig. 3 - Labeling of paddy condition data

Model training via comparative experiments

During the model training phase, the YOLOv8 training parameters were configured within the PyCharm development environment. The yolov8n.pt, yolov8s.pt, and yolov8m.pt pre-trained models were selected for a comparative experiment to evaluate their performance on the paddy flow dataset. For data configuration, the dataset path was explicitly specified via a configuration file, with "SG" and "PS" defined as the two target categories. In the hyperparameter settings, the number of training epochs was set to 100, the batch size was set to 4, the initial learning rate (lr0) was 0.01, and the final learning rate (lrf) was 0.01, using a cosine annealing scheduling strategy. All models were trained under identical experimental settings to ensure comparability of the results (*Ma, 2021*). The complete algorithm workflow is shown in Fig. 4.

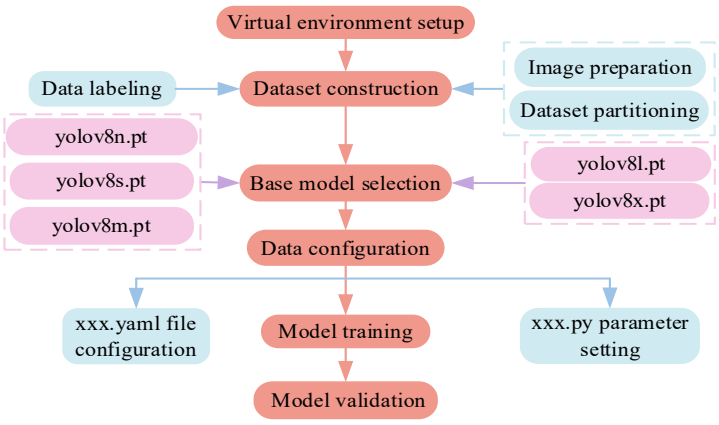


Fig. 4 - YOLOv8 application flowchart

RESULTS

Comprehensive model performance evaluation

Based on the YOLOv8 architecture, a comparative experiment was conducted using three model specifications named yolov8n.pt, yolov8s.pt and yolov8m.pt on a self-built paddy flow dataset. Through comprehensive evaluation using metrics including mAP@0.5, FPS and model size, the most suitable model architecture for dynamic monitoring scenarios was successfully identified (*Ma et al., 2025*).

Table 1

Performance metrics of different model specifications on the paddy flow dataset

Method	mAP0.5(%)	mAP0.5:0.95(%)	Frame Rate (FPS)	Model Size(MB)
YOLOv8n	90.8	73.1	14	6.3
YOLOv8s	89.5	74.2	9	22.5
YOLOv8m	92.4	77.2	3	52

Experimental results demonstrate notable performance disparities among the YOLOv8 series models in paddy flow detection tasks. As shown in Table 1, the nano model YOLOv8n achieves the optimal balance between accuracy and speed, attaining 90.8% mAP@0.5 with a compact model size of 6.3MB and an inference speed of 14 FPS. This demonstrates its strong capability in identifying sparse paddy flow conditions, making it suitable for deployment in computationally constrained small-scale rubber roll huskers. However, its mAP@0.5:0.95 of 73.1% falls below that of the medium model, indicating insufficient precision in target localization at lower IoU thresholds. The small model YOLOv8s shows suboptimal performance in both detection accuracy (89.5%) and processing speed (9 FPS), primarily attributable to increased network depth causing loss of shallow features. In contrast, YOLOv8m demonstrates comprehensive leadership in detection accuracy, achieving 92.4% mAP@0.5 and 77.2% mAP@0.5:0.95. Its deep feature pyramid effectively integrates multi-scale information, successfully addressing occlusion problems caused by paddy flow accumulation. Nevertheless, its practical application remains constrained by an inference speed of 3 FPS and a substantial model size of 52MB. Additionally, setting the training batch size to 4 may theoretically have a slight impact on model generalization performance. As shown in Table 1, all three models completed effective training in the paddy flow detection task, yielding stable and reliable detection results. The core focus of this study is to verify the monitoring feasibility of lightweight models, and the negative impact of this parameter setting on the final detection performance is within an acceptable range.

Table 2

Comparative analysis of performance metrics for different model variants on the paddy flow dataset

Parameter	YOLOv8n	YOLOv8s	YOLOv8m
Detection accuracy	Strong in sparse scenes Weak in overlapping scenes	Lowest overall performance	Optimal for all scenarios
Inference speed	14 FPS (Excellent real-time performance)	9 FPS (Suboptimal efficiency)	3 FPS (Severe delay)
Hardware compatibility	Embedded device friendly	Cost-ineffective	Requires GPU server support
Data dependency	Sensitive to low-resolution input	Sensitive to feature distribution	Requires high-quality training data

As shown in Table 2, comparative analysis of performance metrics from different model specifications on the paddy flow dataset demonstrates that although YOLOv8m achieves optimal detection accuracy, the final selection was determined to be YOLOv8n as the core model for paddy flow monitoring, considering the system's stringent requirements for real-time performance and embedded deployment. This model achieves the best balance between accuracy and speed, with its compact 6.3MB size and 14 FPS inference speed better aligning with practical engineering applications, thereby establishing a reliable technical foundation for real-time monitoring of paddy flow states in rubber roll huskers.

Evaluation of model prediction results

During the training of the YOLOv8 model, the convergence curve serves as a critical indicator for evaluating training effectiveness.

As shown in Fig. 5(a), the YOLOv8n model demonstrates favorable convergence characteristics on the paddy flow dataset. The bounding box regression loss decreases from 1.2 to 0.6, while the classification loss on the validation set exceeds that of the training set by 0.1, suggesting mild overfitting. Fluctuations in the object confidence loss within the validation set indicate that the model's adaptability to complex scenarios requires further improvement. Performance metrics reveal a precision of 0.8 and a recall of 0.75, with mAP50 reaching 0.82.

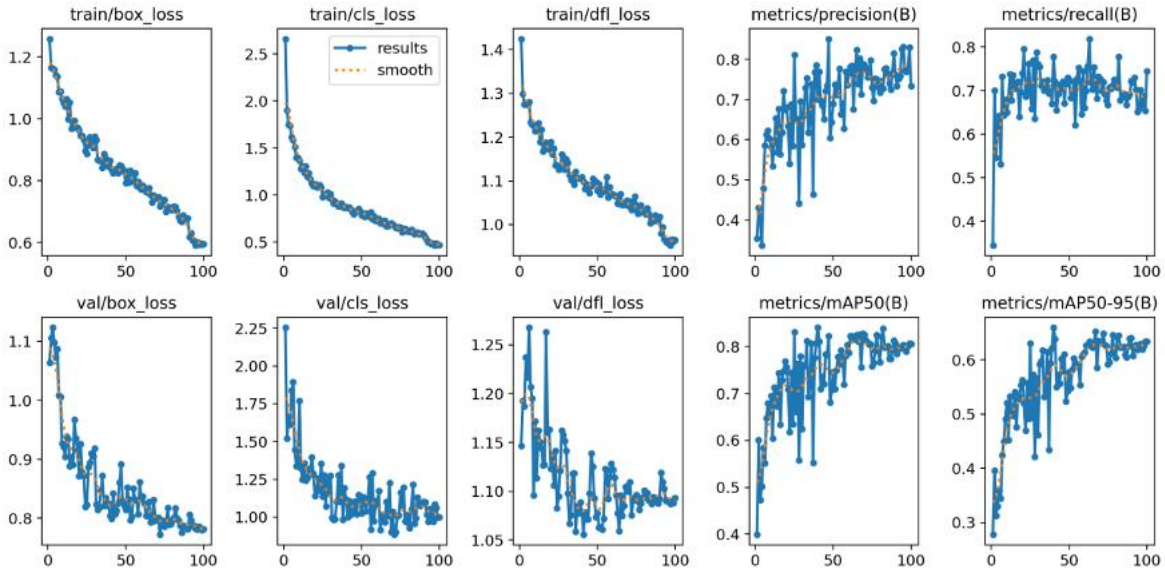
However, mAP50-95 plateaus at 0.68, indicating a performance bottleneck in detection under high IoU thresholds. After 50 training epochs, the model stabilizes, with the performance gap between the training and validation sets controlled within 5%, demonstrating robust generalization capability.

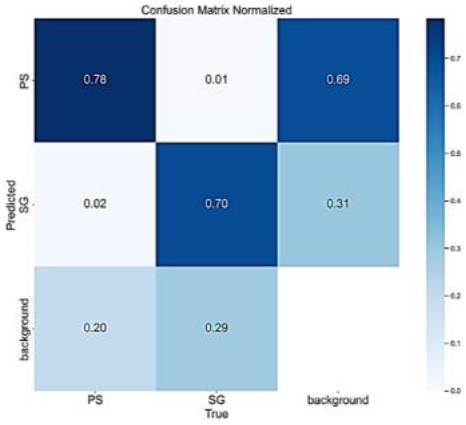
Analysis of convergence curves for YOLOv8s and YOLOv8m on the paddy flow dataset reveals distinct training patterns. YOLOv8s shows a decrease in bounding box loss from 1.2 to 0.6, with the validation set converging at 0.8, demonstrating progressive improvement in localization capability. However, the model displays noticeable overfitting as evidenced by a validation classification loss of 1.0 significantly exceeding the training loss of 0.5. Additionally, fluctuations in objectness loss reaching 1.2 on the validation set indicate limited generalization capability. The performance metrics show precision and recall values of 0.8 and 0.7, respectively, on the validation set, with mAP50 reaching 0.8, while mAP50–95 plateaus at 0.6 and shows slower growth.

Similarly, YOLOv8m exhibits a decline in bounding box regression loss from 1.2 to 0.6 in training and 0.8 in validation, confirming continuous localization improvement. Nevertheless, the model demonstrates pronounced overfitting with a validation classification loss of 1.0 compared to the training loss of 0.5. Objectness loss fluctuations up to 1.2 in validation further reveal inadequate generalization capacity. Performance metrics indicate validation precision of 0.8, recall of 0.7, and mAP50 of 0.8, while mAP50-95 stabilizes at 0.6 with decelerated growth. Both architectures consequently face limitations in high-threshold detection performance despite their steady progress in localization accuracy.

Convergence curve analysis reveals that YOLOv8s exhibits elevated validation loss with overfitting tendencies, while YOLOv8m demonstrates rapid initial convergence but subsequent instability. In contrast, YOLOv8n delivers optimal performance on the paddy flow dataset, characterized by synchronized and stable decline in both training and validation losses, demonstrating superior generalization capability that best aligns with the requirements of this monitoring task.

Classification accuracy is regarded as a vital metric for evaluating the classification capability of YOLOv8 models. When a model maintains high accuracy on both training and validation sets, it indicates effective fitting while possessing strong generalization capability. As shown in Fig. 5(b), the confusion matrix analysis of YOLOv8n demonstrates 78% recognition accuracy for overlapping paddy flow and 70% accuracy for sparse paddy flow, with cross-misclassification rates between both categories remaining below 3%. However, the background misclassification rates reach 20% for overlapping flow and 29% for sparse paddy flow, indicating the current model's capability to distinguish complex backgrounds requires further enhancement.





(a) Convergence curve of Yolov8n on the paddy flow dataset (b) Confusion matrix of YOLOv8n

Fig. 5 - Training dynamics and classification performance of YOLOv8n

Confusion matrix analysis of YOLOv8s indicates 65% recognition accuracy for overlapping paddy flow and 68% for sparse conditions, with a cross-misclassification rate of merely 2% between these two categories. However, the background misclassification rates reach critically high levels of 34% and 32% respectively, suggesting inadequate learning of background features and heightened susceptibility to interference from target characteristics. For YOLOv8m, the recognition accuracy for SG reaches 86%, while its predictive accuracy for PS remains notably low at 55%, demonstrating strong SG identification capability but significant errors in PS detection. The absence of cross-misclassification between categories confirms high accuracy in single-target recognition. Additionally, PS and SG instances are misclassified as background at substantial rates of 45% and 14% respectively, indicating prevalent background misclassification issues.

Classification accuracy analysis demonstrates that YOLOv8n achieves optimal overall performance in paddy flow detection, with recognition accuracies of 78% for overlapping paddy flow and 70% for sparse paddy flow, while maintaining cross-misclassification rates below 3% between categories. Despite background misclassification rates ranging from 20% to 29%, it still exhibits superior performance compared to other models. Both YOLOv8m and YOLOv8s exhibit specific limitations, either in particular scenario recognition capabilities or overall performance deficiency, accompanied by notably high background misclassification rates. Comprehensive evaluation confirms YOLOv8n as the preferred solution for achieving simultaneous accurate identification of both sparse and overlapping states in paddy flow.

Validation of the paddy flow monitoring system

To verify the practical performance of the material flow monitoring system, this study conducted system validation based on a dynamic material flow simulation platform in a local workstation environment equipped with a 12th-generation Intel Core i7 processor, 32 GB of RAM, and no GPU acceleration. A graded quantitative characterization system was proposed to systematically describe sparse and overlapping unstable states of paddy flow by defining grain density levels within a unit area. For sparse paddy flow conditions, three severity levels were established based on grain count per unit area: mild (10~20 grains), moderate (25~40 grains), and severe (45~60 grains). For overlapping paddy flow conditions, both single-layer and multi-layer structures were uniformly annotated as overlapping regions using the same grain quantity classification criteria. The system implements dynamic visualization of detection results through Python programming, enabling real-time display of distributed sparse and overlapping paddy flow regions at different severity levels.

The system achieves deep integration with the CMOS camera SDK through Python-OpenCV. Within the PyCharm development environment, it utilizes the Ultralytics library to load the trained YOLOv8n model weights and employs a multi-threaded architecture for synchronous processing of image acquisition and model inference tasks. For the dynamic and non-stationary monitoring scenario of paddy flow, the system must achieve real-time image sensing, instant processing, and fast inference. It should synchronously perform acquisition, detection, and recognition during transient changes in the flow state, ensuring high synchronization between the output results and the actual flow state, thereby meeting the timeliness and real-time decision-making requirements of online dynamic material flow monitoring (*He et al., 2025*). The system achieves real-time monitoring of dynamic paddy flow parameters via an asynchronous message queue mechanism, stably outputting key state information such as sparse and overlapping grain distributions. The real-time monitoring performance is illustrated in Fig. 6.

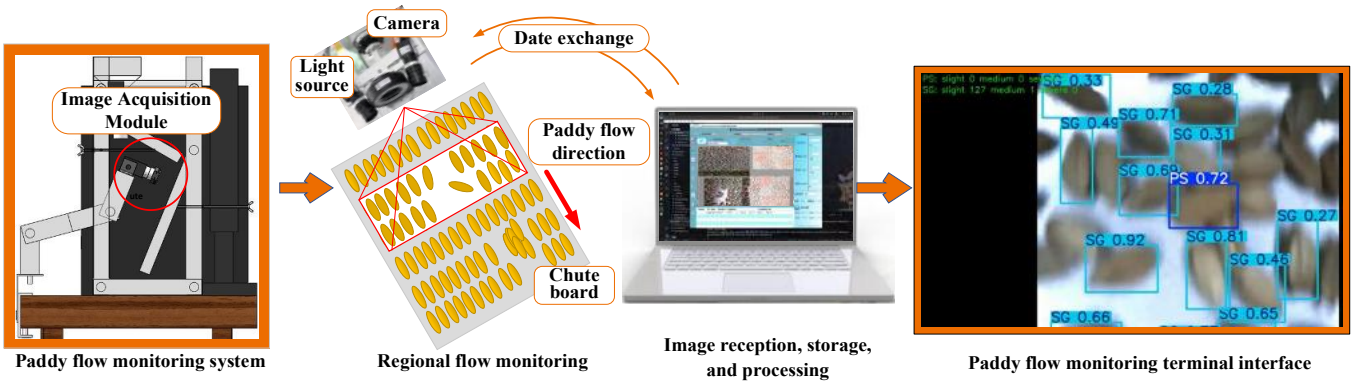


Fig. 6 - Real-time monitoring of sparse and overlapping paddy flow

Validation results demonstrate that the system maintains a stable frame rate of 14 FPS when processing 640×640 resolution video streams, meeting the real-time monitoring requirements. *Chen et al. (2020)* developed a real-time vision-based detection system for dynamic grain flow monitoring in rice combine harvesters and showed that a frame rate of 10~20 FPS is sufficient to capture transient changes in agricultural material flow and fulfill the engineering requirements for online detection. The comprehensive recognition accuracy for sparse and overlapping paddy flow states reaches 89.7%, enabling synchronous output of critical information including sparse and overlapping paddy flow conditions. The asynchronous message queue mechanism ensures stable data exchange, with memory usage remaining stable at approximately 1.8 GB during testing. The system demonstrates excellent engineering applicability and robustness, providing effective technical support for intelligent control of rubber roll huskers.

CONCLUSIONS

Addressing the issue of uneven wear in rubber roll huskers caused by unstable paddy flow, this paper systematically investigates machine vision-based monitoring methods for paddy flow conditions.

By constructing a dedicated image dataset, developing an optimized lightweight detection model, and integrating hardware-software systems, the feasibility and effectiveness of this technical approach in engineering applications have been verified.

The main conclusions are as follows:

(1) A comprehensive technical solution for paddy flow status monitoring has been proposed. This solution systematically establishes a technical framework encompassing image acquisition platform construction, multi-scenario data collection, specialized dataset development, and monitoring system integration, providing a reusable methodological foundation for dynamic paddy flow monitoring.

(2) Comparative experiments based on the YOLOv8 architecture demonstrate that the YOLOv8n nano model achieves the best balance between accuracy and speed. Although its mAP@0.5 of 90.8% is lower than that of YOLOv8m, its inference speed and model size are superior to the latter, while maintaining a real-time processing speed of 14 FPS, thereby fully meeting the real-time requirements of the husker operation scenario.

(3) The real-time paddy flow monitoring system exhibits significant engineering application value. Through coordinated hardware-software design, the system accurately identifies unstable paddy flow conditions including sparse and overlapping states in dynamic paddy flow, providing effective technical support for wear control in rubber roll huskers.

This research validates the application potential of machine vision technology based on lightweight deep learning models in agricultural mechanization. The proposed monitoring solution not only offers a novel approach for quality control in rice processing but also serves as a technical reference for real-time monitoring of other agricultural materials. Future research may further explore the model's adaptability under more complex working conditions and its integration with data from other sensors.

ACKNOWLEDGEMENT

The authors acknowledge the financial support from Science and Technology Research Project of Henan (No.262102111069), the Joint Fund of Henan Provincial Science and Technology Research and Development Plan (No.232103810087), the R&D Special Fund Subsidy Research Project of Zhengzhou (No. 22ZZRDZX14).

REFERENCES

[1] Chen J., Lian Y., Zou R., Zhang S., Ning X., Han M. (2020). Real-time grain breakage sensing for rice combine harvesters using machine vision technology. *International journal of agricultural and biological engineering*, vol. 13, no. 3, pp. 194-199. DOI: https://doi.org/10.25165/j.ijabe.20201303.5478

[2] He X., Liu Z., Hu S., Liu C., Zhou D. (2025). Real-time safety assessment techniques of dynamic systems (动态系统的实时安全性评估技术). *Acta Automatica Sinica*, vol. 51, no. 2, pp. 249-270. DOI: https://doi.org/10.16383/j.aas.c240096

[3] Liu P. (2020). *Research on impact vibration isolation technology in rubber roll husking process (胶辊式砻谷的冲击振动隔离技术研究)*, MSc dissertation, Xihua University. DOI: https://doi.org/10.27411/d.cnki.gscgc.2020.000028

[4] Ma B., Hua Z., Wen Y., Deng H., Zhao Y., Pu L., Song H. (2024). Using an improved lightweight YOLOv8 model for real-time detection of multi-stage apple fruit in complex orchard environments. *Artificial Intelligence in Agriculture*, vol. 11, pp. 70-82. DOI: https://doi.org/10.1016/j.aiia.2024.02.001

[5] Ma F., Li S., Li J., Li Y., Duan L., Li L., Tan J., Wang Y. (2025). Millet ear detection method in UAV images based on improved YOLOx. *INMATEH-Agricultural Engineering*, vol. 75, no.1, pp.680-690. DOI: https://doi.org/10.35633/inmateh-75-59

[6] Ma N., Li Z., Kong Q. (2024). Wheat grains automatic counting based on lightweight YOLOv8. *INMATEH-Agricultural Engineering*, vol. 73, no.2, pp.592-602. DOI: https://doi.org/10.35633/inmateh-73-50

[7] Ma S. (2021). *Research and implementation of belt material flow detection algorithm based on machine vision (基于机器视觉的皮带料流检测算法研究与实现)*, MSc dissertation, Yanshan University. DOI: https://doi.org/10.27440/d.cnki.gysdu.2021.001282

[8] Paul A., Machavaram R., Kumar D., Nagar H. (2024). Smart solutions for capsicum Harvesting: Unleashing the power of YOLO for Detection, Segmentation, growth stage Classification, Counting, and real-time mobile identification. *Computers and Electronics in Agriculture*, vol. 219, pp. 108832. DOI: https://doi.org/10.1016/j.compag.2024.108832

[9] Prabhakaran P., Ranganathan R., Muthu Kumar V., Rajasekar R., Devakumar L., Pal S. (2017). Review on parameters influencing the rice breakage and rubber roll wear in sheller. *Archives of metallurgy and materials*, vol. 62, no. 3, pp. 1875-1880. DOI: https://doi.org/10.1515/amm-2017-0284

[10] Song J., Wu Z. (2025). Research on traffic sign detection based on YOLOv8n (基于 YOLOv8n 的交通标志检测研究). *Internet of Things Technologies*, vol. 15, no. 4, pp. 21-24+28. DOI: https://doi.org/10.16667/j.issn.2095-1302.2025.04.005

[11] Tian Y., Qin S., Yan Y., Wang J., Jiang F. (2024). Blueberry maturity detection in complex field environments based on improved YOLOv8 (基于改进 YOLOv8 的田间复杂环境下蓝莓成熟度检测). *Transactions of the Chinese Society of Agricultural Engineering*, vol. 40, no. 16, pp. 153-162. DOI: https://doi.org/10.11975/j.issn.1002-6819.202312044

[12] Wang H. (2016). *Design and research of automatic adjustment system for rubber roll husker (胶辊砻谷机自动调节系统的设计与研究)*, MSc dissertation, Shanxi Agricultural University.

[13] Wang Y., Liu Y. (2013). Application of PLC automatic control technology in rice milling production lines (自动控制技术 PLC 在碾米生产线中的应用). *Heilongjiang Grain*, no. 5, pp. 55-56. DOI: https://doi.org/10.3969/j.issn.1671-6019.2013.05.025

[14] Wen L., Liang B., Zhang L., Hao B., Yang Z. (2023). Research on coal volume detection and energy-saving optimization intelligent control method of belt conveyor based on laser and binocular visual fusion. *IEEE Access*, vol. 12, pp. 75238-75248. DOI: https://doi.org/10.1109/ACCESS.2023.3261335

[15] Wu Z., Jin T., Liu X., Zhang Z., Zhao B., Zhang Y., He X. (2024). Research on the Wear State Detection and Identification Method of Huller Rollers Based on Point Cloud Data. *Coatings*, vol. 14, no. 9, pp. 1209. DOI: https://doi.org/10.3390/coatings14091209

[16] Xiang G., Ruan J. (2009). Current status and development overview of rubber roll huskers in domestic and international markets (国内外胶辊砻谷机现状及发展概述). *Grain Processing*, vol. 34, no. 5, pp. 60-65. DOI: https://doi.org/10.3969/j.issn.1007-6395.2009.05.019

[17] Xu S., Cheng G., Cui Z., Jin Z., Gu W. (2022). Measuring bulk material flow—Incorporating RFID and point cloud data processing. *Measurement*, vol. 200, pp. 111598. DOI: https://doi.org/10.1016/j.measurement.2022.111598

[18] Yan W., Yang D., Zhang Y., Li B. (2023). Twin-array capacitance sensor for multi-parameter measurement of gas-solid particle flow based on BP-Adaboost. *Flow Measurement and Instrumentation*, vol. 94, pp. 102445. DOI: https://doi.org/10.1016/j.flowmeasinst.2023.102445

[19] Yehia M.E., Katab A.R. (2018). Effect of hulling machines on hulling characteristics and quality of rice grains. *Misr Journal of Agricultural Engineering*, vol. 35, no. 1, pp. 259-274. DOI: https://doi.org/10.21608/mjae.2018.96055

[20] Yu Z. (2024). *Research and application of industrial image anomaly detection model based on deep learning (基于深度学习的工业图像异常检测模型研究与应用)*, MSc dissertation, Xi'an University of Architecture and Technology. DOI: https://doi.org/10.27393/d.cnki.gxazu.2024.001092

[21] Zhang H., Qi S., Yang R., Pan Z., Guo X., Wang W., Liu S., Liu Z., Mu J., Geng B. (2024). Design and experimentation of a potato planter missed and repeated planting detection system based on yolov7-tiny model. *INMATEH--Agricultural Engineering*, vol. 72, pp. 106-116. DOI: https://doi.org/10.35633/inmateh-72-10

[22] Zhou S., Cheng M., Xu X., Cao X. (2025). Research status and advances in perception monitoring and quality control technology for intelligent rubber roll huskers (智能胶辊砻谷机感知监测与品质调控技术研究现状及进展). Food & Machinery, vol. 41, no. 05, pp. 241-248. DOI: https://doi.org/10.13652/j.spjx.1003.5788.2024.80979

[23] Zhu Z. (1979). Preliminary study on severe rubber roll eccentricity and intense machine vibration in cantilever counterweighted rubber roll huskers (关于悬臂式重铊紧辊胶辊砻谷机的胶辊严重失圆及机体强烈振动问题的初步探讨). *Grain Industry*, no. 4, pp. 25-37.

[24] Zhu Z., Wang Y., Wang D., Yang G., Xie Z. (2024). Evaluation of array capacitive sensor for local concentration measurement of gas–solid particles flow by coupled fields based on CFD-DEM. *Measurement*, vol. 229, pp. 114457. DOI: https://doi.org/10.1016/j.measurement.2024.114457

LENGTH OF CLOSED FISHTAIL-SHAPED TURNS AND HEADLAND WIDTH WHEN PLOUGHING WITH A REVERSIBLE PLOUGH IN AN IRREGULARLY SHAPED FIELD / *ДЪЛЖИНА НА ЗАТВОРЕНИ ГЪБОВИДНИ ЗАВОИ И ШИРОЧИНА НА ИВИЦАТА ЗА ЗАВИВАНЕ ПРИ ОРАН С ОБРЪЩАТЕЛЕН ПЛУГ В ПОЛЕ С НЕПРАВИЛНА ФОРМА*

Krasimir TRENDAFILOV
Trakia University – Stara Zagora, Faculty of Technics and Technologies – Yambol, Department of Mechanical Engineering/ Bulgaria
Tel: +359 887 708 603; E-mail krasimir.trendafilov@trakia-uni.bg
DOI: https://doi.org/10.35633/inmateh-79-20

Keywords: *headland, closed fishtail turn, turning, headland width, length of turn*

ABSTRACT
The efficiency of agricultural operations depends on the length of non-working passes in the headlands. Therefore, the aim is to minimize both turn length and headland width. Various methods are used to construct turn trajectories, allowing them to be compared under specific conditions and enabling the most efficient movement pattern to be selected. This article examines closed fishtail-shaped turns composed of arcs with a given radius and straight-line segments. Analytical relationships were derived to determine the headland width and the length of closed fishtail-shaped turns for different travel directions of a machine-tractor unit equipped with a mounted reversible plough in an irregularly shaped field. It was found that, at a positive angle between the travel direction of the unit and the field boundary, movement of the unit across the field from right to left results in shorter closed fishtail-shaped turns and requires a narrower headland than movement from left to right.

РЕЗЮМЕ
Ефективността на извършване на земеделските операции зависи от дължината на неработните ходове в ивиците за завиване. Стремежът е дължината на завоите и широчината на ивицата за завиване да бъдат минимални. За построяване на траекторията на завоите се използват различни методи, които позволяват те да бъдат сравнявани при определени условия и да бъде избиран най-ефективният начин на движение. В настоящата статия са разгледани затворени гъбовидни завои изградени от дъги с определен радиус и прави линии. Изведени са аналитични зависимости за определяне на широчината на ивицата за завиване и дължината на гъбовидни затворени завои при различни направления на движение на машинно-тракторен агрегат с навесен обръщателен плуг в поле с неправилна форма. Установено е, че при положителен ъгъл между посоката на движение на агрегата и границата на полето и движение на агрегата по полето отдясно наляво гъбовидните затворени завои са с по-малка дължина и изискват по-тясна ивица за завиване в сравнение с движението отляво надясно.

INTRODUCTION

To increase the efficiency of the movement of autonomous machine-tractor units in the field, it is necessary to determine the most suitable trajectories of movement not only inside the field, but also in the headlands. If when moving in the field, efficiency is determined mainly by the direction and sequence of work movements, then when moving in the headlands, a choice must be made between different types of turns. The goal is to reduce the time for making turns, their length and the headland width. This, in turn, will lead to an increase in the productivity of the units and a decrease in soil compaction in the headlands. Ward et al. divided the headland into three zones – transition area, turning area and area located near to the field edge. The authors found that yields in these zones were lower than yields in the field. The main characteristic of the turning area was traffic, and this zone consistently reported worse yields than those in the field area. The outer zone also yielded significantly less, indicating that there were factors other than traffic that had an impact (*Ward et al., 2020*).

To select the most effective way of turning, the authors compare different types of turns, using the following approaches to build the turns:

1. The turns consist of primitives – straight lines and arcs with a certain radius. This allows the turns to be compared without considering factors such as driving speed and wheel turning speed.

Jeon et al. consider a stretched turn and a closed fishtail turn, which are created from arcs with the minimum turning radius of the tractor and straight lines. When performing a closed fishtail turn, the shape of the turn does not change depending on the angle between the direction of the working move and the field boundary, which leads to an additional path when entering or leaving the headland, depending on this angle (*Jeon et al., 2021*). In another study, the turns were built in the same way and again the shape of the turns was not adjusted to the angle between the working move and the field boundary. This results in a larger headland width *(Wang et al., 2025*). The authors point out that the length of the non-working move decreases by 18%, which is due to the different way of moving in the field.

Han et al. conducted a simulation study of three types of turns in the headland. In the proposed algorithm, the turns are built from curves with a certain turning radius of the tractor and straight sections. The highest field efficiency is achieved when performing a fishtail turn (X-shaped) due to the shorter path in the headland, which leads to less total field processing time. The authors recommend this turn for fields with a larger width, while for small widths (30 m) the efficiency is higher when performing a stretched turn (C-shaped) (*Han et al., 2019*).

An algorithm for performing a closed fishtail turn with an arcuate reverse is presented in (*Wang and Noguchi, 2018*). Unlike other algorithms, the turning radii in the two directions are different. The authors indicate that compared to a fishtail turn with a straight reverse movement, their proposed movement algorithm provides a smaller lateral deviation (3.9 cm), and the time and trajectory of the turn are reduced by 17% and 21%, respectively. The headland width is also smaller.

Chen et al. derived relationships for the turn length and turning time in the headland for four types of turns, but the type of turn depends on the angle between the travel direction and the field boundary, as well as on the direction in which the turn is performed. According to the authors, the largest reduction in turn length, the turning time and the headland width is achieved for the semicircular turn to the left (*Chen et al., 2023*).

2. The turns are made up of straight lines, arcs with a certain radius and connecting curves with a variable radius

When the turns are made up of arcs with a minimum radius and straight lines, it is necessary for the unit to stop or the turning of the wheels to be done very quickly, which leads to a large jerk of the machine. Therefore, Boryga proposes to use trigonometric transition curves to perform turns in the headland. They have a gradually changing curvature, which provides a smooth transition between the segments of the trajectory. This reduces sudden changes in direction and improves the dynamics of movement (*Boryga et al., 2025*).

Sabelhaus et al. analysed three forward turns in which clothoids were used to connect straight-line segments and circular arcs *(Sabelhaus et al., 2015)*. A clothoid has a curvature that varies progressively up to the reciprocal of the minimum turning radius, thereby providing a smooth transition between the other elements of the trajectory. Sabelhaus et al. also examined seven different headland turns constructed using clothoids. The authors indicated that the headland width is smallest in the fishtail turn, and the turn length and the time of its execution depend on the distance between the working moves. At a short distance of 3 m, the fishtail turn has the shortest turn length and the shortest driving time. While at 10 m the values of these indicators are lower in the Ω-turn (*Sabelhaus et al., 2013*).

Koc presents an analytical approach to modeling the curvature of the connecting curve using differential equations. The method can be applied to identify various types of transition curves. The author gives examples of solving the problem involving linear change of curvature and the curvature in polynomial and trigonometric form (*Koc, 2014*).

3. Turns involve curves with variable radius and follow a guiding curve that usually copies the field boundary

An algorithm is used to determine the field boundary based on images, then a reference line for turning is generated at a certain distance from the field boundary, and the turning trajectory is designed based on Bezier curves. The authors found that when turning at a lower speed, there is less lateral deviation and better trajectory tracking effect, but the turning time is longer (*Gao et al., 2023*).

Another study presented a field boundary detection algorithm based on DeepLabv3+, which also uses Bezier curves to calculate the turning trajectory. It was found that the robot can successfully perform a turn with a maximum deviation of 0.09 m, demonstrating precise navigation control in complex agricultural environments (*Wu et al., 2025*).

A similar algorithm is described in the patent (*Kakkar et al., 2021*). The turn is made along a guide line, which has the shape of the field boundary. A different turn trajectory can be selected, which can be displayed on the screen. The algorithm can select a trajectory according to various optimization criteria - road length, fuel economy, etc.

4. The turns are composed of two symmetrical curves described by polynomials

Boryga et al. propose an algorithm for planning a trajectory in which the movement proceeds along two transitional curves, constituting the so-called transition bi-curve. The authors consider turns of 90, 180, 270 and 360 degrees. According to them, the trajectories, the curvature of which is described by a polynomial of the third degree are the most favourable. They are characterized by the smallest absolute values of maximal acceleration and jerk and to lack jerk discontinuity (*Boryga, et al., 2020*).

Since the low efficiency of turning (turn length, time for its execution, headland width) is caused by the large turning radius of the tractor, a headland turning system has been created, including a steering auxiliary wheel in front of the tractor. This provides a large turning angle of ± 180º. This way of turning reduces the time for turning by about 50%, the turn length by about 80%, and the headland width by an average of about 50% for different types of turns (*Yang et al., 2022*). Such a turning system is more effective for units with a small and medium working width - up to 9 – 11 m (*Trendafilov and Delchev, 2018*). Systems with a fifth wheel on the tractor have not yet gained popularity.

The steering system built into the tractor can be supplemented with control of the breaking force of the wheels when turning. This will result in a reduction in the turning radius by about 15% to 35% compared to a manually operated vehicle without breaking (*Bharadwa, et al., 2021*).

Fishtail turns usually have the smallest length and width of headland. Therefore, they are preferred when making turns by implements with mounted machines. The aim of this study is to determine the headland width and the length of fishtail closed turns performed by a reversible plough in different directions of movement in an irregularly shaped field.

MATERIALS AND METHODS

Previous publications examined the movement of trailed and semi-mounted reversible ploughs in the headlands of an irregularly shaped field (*Trendafilov, 2010; Trendafilov, 2017*). In these cases, the turns were performed in forward motion. Trendafilov derived relationships for determining the turn length and headland width when performing open fishtail-shaped turns with reverse movement *(Trendafilov, 2025)*. The same methodology is used in the present article and is described again for the reader's convenience.

Fig. 1 shows a diagram of the machine-tractor unit. Its designations are:

- α is the angle between the direction of movement of the unit and the headland. It varies between 0º and 90º. It is assumed that the angle is positive when it is on the right side of the unit when moving towards the headland (Fig. 1a), and negative – on the left side of the unit (Fig. 1b);
- B – the working width of the unit;
- l_a– the kinematic length of the unit;
- l_n – the distance from the center of the unit (the middle of the rear axle of the tractor) to the top of the share of the first plough body;
- g – the distance from the axis of symmetry of the tractor to the top of the share of the last plough body;
- y – the distance from the tractor's axis of symmetry to the end of the share of the first plough body (or to the inner edge of the wheel of the tractor, which moves in the furrow left during the previous working stroke);
- R – the turning radius of the unit;
- M – the distance between the outer edges of the rear wheels of the tractor;
- H – the longitudinal base (distance between the front and rear axles) of the tractor;
- E – the headland width.

A closed fishtail turn is considered with two directions of movement of the machine-tractor unit in the field – from left to right and from right to left. The turn is made up of three circular segments with a radius equal to the minimum turning radius of the unit. The turn length in the headland includes the length of the circular segments and the length of the rectilinear path travelled by the unit until reaching the inner border of the headland. The headland width is determined by summing straight segments, the length of which can be determined from the parameters of the unit. The headland width and the turn length are determined for an interval of change of angle α from 10º to 90º, since below 10º a headland is not needed.

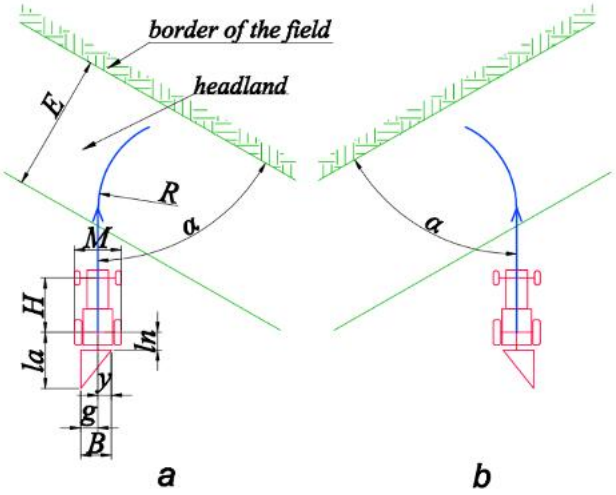


Fig.1 - Scheme of the machine-tractor unit and angle between its direction of movement and the field boundary (*Trendafilov, 2025*)

a – positive angle; b – negative angle

Only the case in which angle α is positive is considered, since a symmetric image is obtained at a negative angle. As indicated by *Trendafilov (2010)*, the relationships are the same, but their positions are interchanged. Thus, the relationships for movement across the field from left to right at a positive angle apply to movement across the field from right to left at a negative angle, while the relationships for movement from right to left at a positive angle α apply to movement from left to right at a negative angle.

Using the obtained relationships, the headland width and turn length were determined for a ploughing unit with the following parameters: $H = 2\ m$; $M = 1.8\ m$; $R = 3.2\ m$; $B = 1.2\ m$; $l_a = 2\ m$; $l_n = 0.6\ m$; $y = 0.5\ m$; $g = 0.7\ m$. The results are presented graphically and analysed.

RESULTS

Closed fishtail turn - movement from left to right

As shown in Fig. 2a, the turn is composed of three circular arcs, whose central angles satisfy the following relationship:

$$\beta_1 + \beta_2 + \beta_3 = 180° \quad (1)$$

Hence, the turn length is obtained as:

$$l_T = \pi R \quad (2)$$

The width of headland E can be determined by summing the segments of known length:

$$x = l_a.\sin\alpha + (R - g)\cos\alpha - R\cos(\alpha + \beta_1) \quad (3)$$

$$y = H.\sin(\alpha + \beta_1) \quad (4)$$

$$z = -0.5M.\cos(\alpha + \beta_1) \quad (5)$$

Therefore, the headland width is obtained as:

$$E = x + y + z = l_a \sin\alpha + (R - g)\cos\alpha + H.\sin(\alpha + \beta_1) - (R + 0{,}5M)\cos(\alpha + \beta_1) \quad (6)$$

Angle β_1 is determined from triangles O_1CO_2 and O_2DO_3. The following equations are used:

$$2R\cos\beta_1 + 2R\cos\beta_3 = 2R - B \quad (7)$$

$$2R\sin\beta_1 + l_a + l_n = 2R\sin\beta_3 \quad (8)$$

Thus angle β_1 is obtained as:

$$\beta_1 = \cos^{-1}\left[\frac{2R-B}{4R\cos\left[\tan^{-1}\left(\frac{l_a+l_n}{2R-B}\right)\right]}\right] - \tan^{-1}\left(\frac{l_a+l_n}{2R-B}\right) \quad (9)$$

When angle α decreases without changing angles β, the headland is bounded by the front left wheel of the tractor, which reaches the field boundary, and by the rear plough body. At a certain value of the angle α, the headland is additionally bounded, besides the last plough body, by the rear right wheel of the tractor at the end of its reverse movement (Fig. 2b). This condition is necessary to prevent the tractor from entering the already worked part of the field. In this case, the segments used to determine the headland width have the following lengths: y – determined using Eq. (4); z – determined using Eq. (5); and

$$e = (R + 0{,}5M)\cos(\beta_3 - \alpha) \tag{10}$$

$$d = R\cos(\alpha + \beta_1) \tag{11}$$

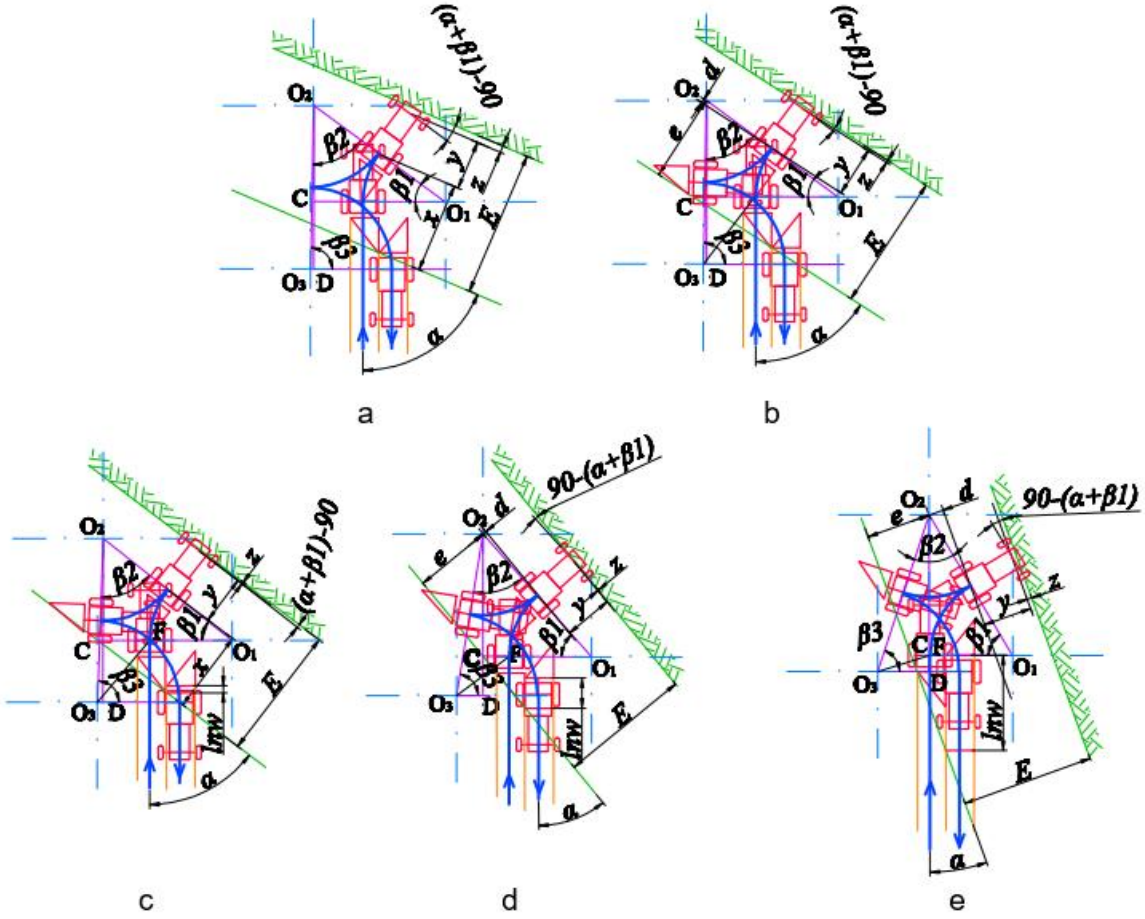


Fig. 2 - Scheme of a closed fishtail turn when moving from left to right

The headland width is given by:

$$E = e - d + y + z = (R - 0{,}5M)\cos(\alpha + \beta_1) + H.\sin(\alpha + \beta_1) + (R + 0{,}5M)\cos(\beta_3 - \alpha) \tag{12}$$

From Eqs. (7) and (8), angle β_3 is determined as follows:

$$\beta_3 = \tan^{-1}\left(\frac{l_a + l_n}{2R - B}\right) + \cos^{-1}\left[\frac{2R - B}{4R\cos\left[\tan^{-1}\left(\frac{l_a + l_n}{2R - B}\right)\right]}\right] \tag{13}$$

After equating Eqs. (6) and (12), the value of angle α at which the transition between the two equations occurs is determined as follows:

$$\alpha = \tan^{-1}\left[\frac{(R+0{,}5M)\cos\beta_3 - (R-g) + 2R\cos\beta_1}{l_a + 2R\sin\beta_1 - (R+0{,}5M)\sin\beta_3}\right] \tag{14}$$

Both front wheels of the tractor reach the end of the field simultaneously when:

$$\alpha + \beta_1 = 90 \tag{15}$$

For values of angle α lower than:

$$\alpha = \tan^{-1}\left(\frac{l_a + l_n}{R - B}\right) \tag{16}$$

the values of angles β change. The boundary of the headland passes through the last plough body and the rear right wheel of the tractor (Fig. 2c).

After completing the turn, the tractor must perform a straight-line non-working pass of length l_{nw} until the front plough body reaches the headland boundary. The headland width is determined using Eq. (12). The straight-line non-working pass is given by:

$$l_{nw} = l_a + l_n - (R - B)\tan\alpha \quad (17)$$

The turn length is given by:

$$l_T = \pi R + l_{nw} = \pi R + l_a + l_n - (R - B)\tan\alpha \quad (18)$$

The values of angles β are determined from triangles O_1CO_2 and O_2DO_3 using Eq. (7) and the following equation:

$$2R\sin\beta_1 + (R - B)\tan\alpha = 2R\sin\beta_3 \quad (19)$$

In this expression, angle α is used for simplification, since angle DO_3F is approximately equal to α. Thus, the angles β are obtained as follows:

$$\beta_1 = \cos^{-1}\left[\frac{2R-B}{4R\cos\left[\tan^{-1}\left(\frac{(R-B)\tan\alpha}{2R-B}\right)\right]}\right] - \tan^{-1}\left(\frac{(R-B)\tan\alpha}{2R-B}\right) \quad (20)$$

$$\beta_3 = \tan^{-1}\left(\frac{(R-B)\tan\alpha}{2R-B}\right) + \cos^{-1}\left[\frac{2R-B}{4R\cos\left[\tan^{-1}\left(\frac{(R-B)\tan\alpha}{2R-B}\right)\right]}\right] \quad (21)$$

When angle α decreases and reaches the value

$$\alpha = \tan^{-1}\left(\frac{B}{l_a - l_n}\right) \quad (22)$$

the headland boundary becomes parallel to the beam carrying the plough bodies (Fig. 2d). At a smaller angle, the headland boundary is no longer determined by the last plough body, but by the first plough body when the unit enters the headland and by the rear right wheel of the tractor (Fig. 2e). The front right wheel of the tractor reaches the field boundary. The lengths of the segments used to determine the headland width are as follows: e, determined using Eq. (10); d, determined using Eq. (11); y, determined using Eq. (4); and

$$z = 0{,}5M.\cos(\alpha + \beta_1) \quad (23)$$

For the headland width, the following expression is obtained:

$$E = e + d + y + z = (R + 0{,}5M)\cos(\alpha + \beta_1) + H.\sin(\alpha + \beta_1) + (R + 0{,}5M)\cos(\beta_3 - \alpha) \quad (24)$$

By equating Eqs. (12) and (24), it can be seen that they are equal when condition (15) is satisfied. This corresponds to the transition between the variants shown in Fig. 2c and Fig. 2e.

The length of the straight-line non-working pass in the headland after the turn increases as angle α decreases. It is determined as follows:

$$l_{nw} = \frac{B}{\tan\alpha} + l_n - (R - B)\tan\alpha \quad (25)$$

The turn length is:

$$l_T = \pi R + l_{nw} = \pi R + \frac{B}{\tan\alpha} + l_n - (R - B)\tan\alpha \quad (26)$$

By equating Eqs. (18) and (26), the angle at which the turn lengths for the two variants are equal is obtained:

$$\alpha = \tan^{-1}\left(\frac{B}{l_a}\right) \quad (27)$$

Closed fishtail turns - movement from right to left

At a large angle α, the front right wheel of the tractor reaches the field boundary (Fig. 3 a). During reverse movement, the tractor does not reach the field boundary. The turn length is also determined using Eqs. (1) and (2). The lengths of the segments used to determine the headland width are as follows:

$$x = l_a\sin\alpha + (g - R)\cos\alpha + R\cos(\alpha - \beta_1) \quad (28)$$

$$y = H.\sin(\alpha - \beta_1) \quad (29)$$

$$z = 0{,}5M.\cos(\alpha - \beta_1) \quad (30)$$

The headland width is:

$$E = x + y + z = l_a\sin\alpha + (g - R)\cos\alpha + H\sin(\alpha - \beta_1) + (R + 0{,}5M)\cos(\alpha - \beta_1) \quad (31)$$

Angles β_1 and β_3 are determined using equations (9) and (13) respectively. When angle α decreases and reaches a certain value, the rear wheels of the tractor also reach the field boundary during reverse movement (Fig. 3 b). The figure shows the limiting case in which the front and rear wheels of the tractor reach the field boundary. In this case, the headland width can be determined using Eq. (31) or by using the following segments:

$$m = -(R + 0{,}5M)\cos(\alpha + \beta_3) \quad (32)$$

$$n = (R - y)\cos\alpha \quad (33)$$

$$q = l_n \sin\alpha \tag{34}$$

$$E = m + n - q = -(R + 0{,}5M)\cos(\alpha + \beta_3) + (R - y)\cos\alpha - l_n \sin\alpha \tag{35}$$

After equating Eqs. (31) and (35), angle α is obtained as follows:

$$\alpha = \tan^{-1}\left[\frac{H\sin\beta_1 - (R+0{,}5M)(\cos\beta_3 + \cos\beta_1) - (B-2R)}{H\cos\beta_1 + (R+0{,}5M)(\sin\beta_1 - \sin\beta_3) + l_a + l_n}\right] \tag{36}$$

At smaller values of angle α the headland width is determined using Eq. (35). At the angle α determined using Eq. (22), the line of all plough bodies becomes parallel to the headland boundary.

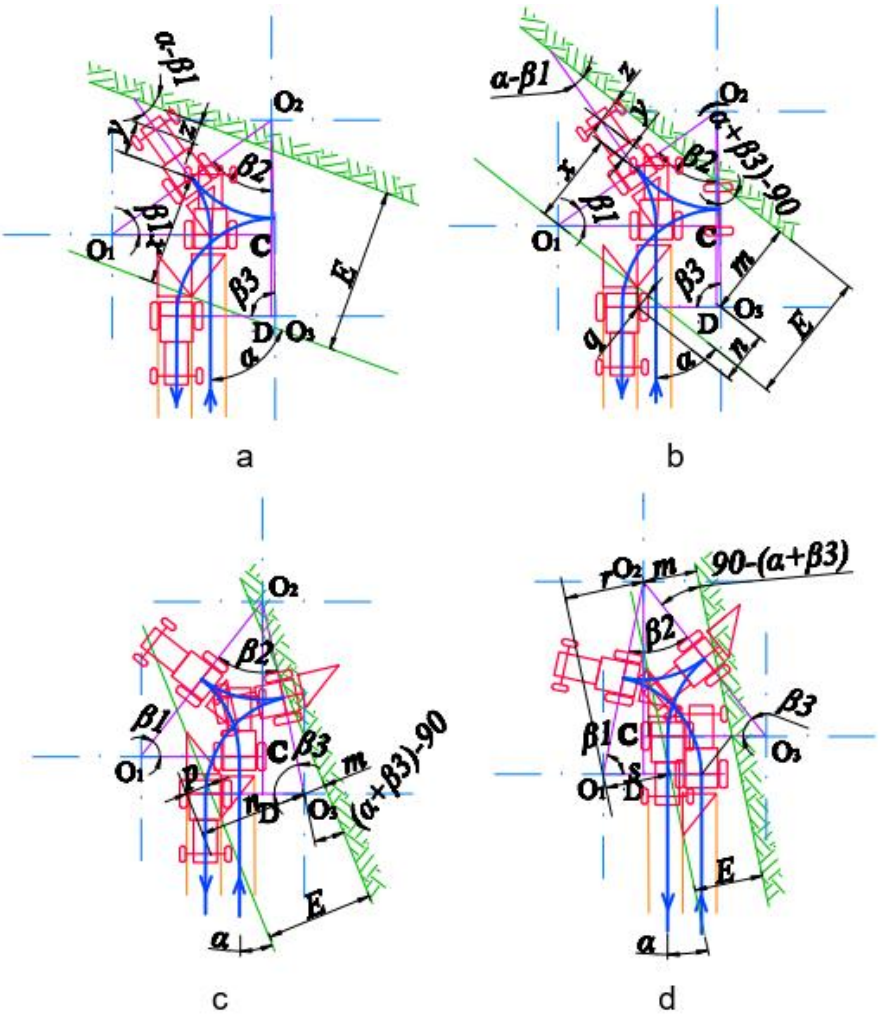


Fig. 3 - Scheme of a closed fishtail turn when moving from right to left

For values of angle α smaller than that determined by Eq. (22), the headland boundary is determined by the last plough body when the unit enters and leaves the headland (Fig. 3c). It can be seen that the front left wheel of the tractor enters the field; however, this is permissible because this part of the field has not yet been processed.

The relationships used to determine the headland width are as follows: (m), determined using Eq. (32), and:

$$p = l_a \sin\alpha \tag{37}$$

$$n = (R + g)\cos\alpha \tag{38}$$

$$E = m + n - p = -(R + 0{,}5M)\cos(\alpha + \beta_3) + (R + g)\cos\alpha - l_a \sin\alpha \tag{39}$$

Angles β vary depending on angle α and are determined using Eq. (7) and the following equation:

$$2R\sin\beta_3 - 2R\sin\beta_1 = 2l_a - \frac{B}{\tan\alpha} \tag{40}$$

The equations for determining angles β are as follows:

$$\beta_1 = \cos^{-1}\left[\frac{2R-B}{4R\cos\left[\tan^{-1}\left(\frac{2l_a-\frac{B}{\tan\alpha}}{2R-B}\right)\right]}\right] - \tan^{-1}\left(\frac{2l_a-\frac{B}{\tan\alpha}}{2R-B}\right) \quad (41)$$

$$\beta_3 = \tan^{-1}\left(\frac{2l_a-\frac{B}{\tan\alpha}}{2R-B}\right) + \cos^{-1}\left[\frac{2R-B}{4R\cos\left[\tan^{-1}\left(\frac{2l_a-\frac{B}{\tan\alpha}}{2R-B}\right)\right]}\right] \quad (42)$$

The rear axle of the tractor becomes parallel to the field boundary when:

$$\alpha + \beta_3 = 90 \quad (43)$$

As angle α decreases further, the rear right wheel reaches the field boundary (Fig. 3 d). In this case, the following relationships are used to determine the headland width:

$$m = (R + 0{,}5M)\cos(\alpha + \beta_3) \quad (44)$$

$$r = 2R\cos(\beta_1 - \alpha) \quad (45)$$

$$s = (R - g)\cos\alpha - l_a\sin\alpha \quad (46)$$

$$E = m + r - s = (R + 0{,}5M)\cos(\alpha + \beta_3) + 2R\cos(\beta_1 - \alpha) - (R - g)\cos\alpha + l_a\sin\alpha \quad (47)$$

The variants shown in Fig. 3c and Fig. 3d are equivalent at the angle:

$$\alpha = \tan^{-1}\left(\frac{(R+0{,}5M)\cos\beta_3 + R\cos\beta_1 - R}{(R+0{,}5M)\sin\beta_3 - R\sin\beta_1 - l_a}\right) \quad (48)$$

At an angle α smaller than that determined by

$$\alpha = \tan^{-1}\left(\frac{B}{2l_a}\right) \quad (49)$$

angles β are determined using Eq. (7) and the following equation:

$$2R\sin\beta_1 - 2R\sin\beta_3 = \frac{B}{\tan\alpha} - 2l_a \quad (50)$$

Their values are obtained as follows:

$$\beta_1 = \tan^{-1}\left(\frac{\frac{B}{\tan\alpha}-2l_a}{2R-B}\right) + \cos^{-1}\left[\frac{2R-B}{4R\cos\left[\tan^{-1}\left(\frac{\frac{B}{\tan\alpha}-2l_a}{2R-B}\right)\right]}\right] \quad (51)$$

$$\beta_3 = \cos^{-1}\left[\frac{2R-B}{4R\cos\left[\tan^{-1}\left(\frac{\frac{B}{\tan\alpha}-2l_a}{2R-B}\right)\right]}\right] - \tan^{-1}\left(\frac{\frac{B}{\tan\alpha}-2l_a}{2R-B}\right) \quad (52)$$

Fig. 4 shows the variation in headland width depending on the angle between the direction of the working pass and the field boundary for a specific machine-tractor unit. It can be seen that when the turn is performed from right to left, a narrower headland is required. Its width decreases as angle α decreases. When the unit moves across the field from left to right, the headland width changes only slightly and remains constant at angles below 50°.

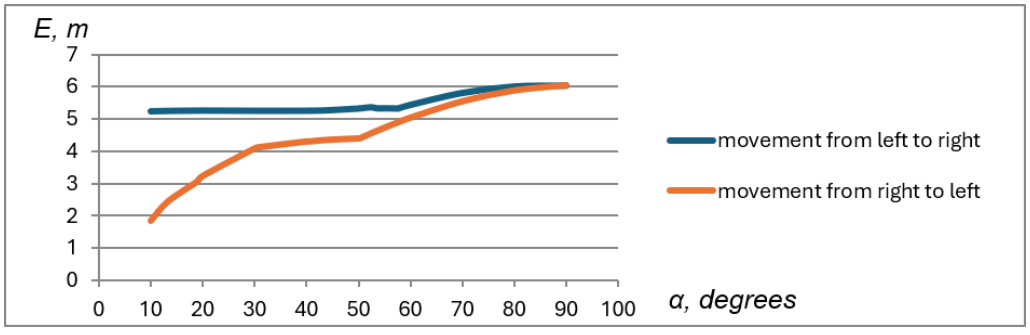


Fig. 4 - Headland width when making fishtail closed turns in different directions of movement depending on the angle α

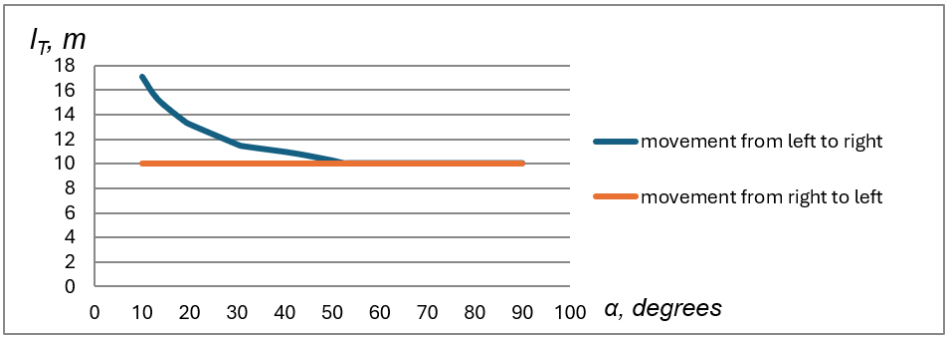


Fig. 5 - Turn length in the headland when performing fishtail closed turns in different directions of movement depending on the angle α

Fig. 5 shows the turn length for different travel directions. The turn length remains constant when the unit moves from right to left, whereas it increases significantly at smaller values of angle α when the unit moves from left to right. This is due to the presence of an additional straight-line path in the headland under this movement mode, which occurs at small values of angle α.

CONCLUSIONS

Analytical relationships were derived for determining the headland width and the length of closed fishtail-shaped turns during the movement of a machine-tractor unit equipped with a mounted reversible plough in an irregularly shaped field. It was established that, at a positive angle between the travel direction of the unit and the field boundary, movement of the unit across the field from right to left results in shorter closed fishtail-shaped turns and requires a narrower headland compared with movement from left to right. Future research should include a comparative analysis of open and closed fishtail-shaped turns in terms of turn length and headland width, and should provide relevant practical recommendations.

REFERENCES

[1] Bharadwa A., Jayachander S., Subramani M., Kishore A., Gunnam J., & Shahi K. (2021). *A headland turning system for an agricultural machine*. International Publication Number WO 2021/005406 A1, International Application No.PCT/IB2019/056951, World Intellectual Property Organization, Publication Date 14 January 2021

[2] Boryga M., Kołodziej P., Gołacki K. (2020). Application of Polynomial Transition Curves for Trajectory Planning on the Headlands, *Agriculture*, 10, 144; doi:10.3390/agriculture10050144

[3] Boryga M., Kołodziej P., & Gołacki K. (2025). Modification of Typical Headland Manoeuvres Using Transition Curves. *Appl. Sci*., 15, 8817, https://doi.org/10.3390/app15168817

[4] Chen T., Xu L., Ahn H. S., Lu E., Liu Y., & Xu R. (2023). Evaluation of headland turning types of adjacent parallel paths for combine harvesters. *Biosystems engineering*, 233, 93–113. https://doi.org/10.1016/j.biosystemseng.2023.07.009

[5] Gao G., Guo H., Zhang J., Zhang Z., Wu T., Lu H., Qiu Z., Chen H., & Lingxuan Z. (2023). An efficient headland-turning navigation system for a safflower picking robot. *Journal of Agricultural Engineering*, volume LIV:1539

[6] Han X., Kim H.J., Jeon C.W. *et al.* (2019). Simulation Study to Develop Implement Control and Headland Turning Algorithms for Autonomous Tillage Operations. *J. Biosyst. Eng.* 44, 245–257. https://doi.org/10.1007/s42853-019-00035-9

[7] Jeon C.W., Kim H.J., Yun C., Han X., & Kim J. H. (2021). Design and validation testing of a complete paddy field-coverage path planner for a fully autonomous tillage tractor. *Biosystems engineering*, 208, 79-97

[8] Kakkar S., Santamaria J. C., Creaby J., & Sights B. (2021). *Headland - following turns*. Pub. No.: US 2021/0339768 A1, Patent Application Publication, United States, Pub. Date: Nov. 4 , 2021

[9] Koc W. (2014). Analytical Method of Modelling the Geometric System of Communication Route. *Mathematical Problems in Engineering*, 2014, 1-13, http://dx.doi.org/10.1155/2014/679817

[10] Sabelhaus D., Lammers P. S., Meyer zu Helligen L. P., & Röben F. (2015). Path planning of headland turn manoeuvres. *Landtechnik* 70(4), 123–131, DOI:10.15150/lt.2015.2666

[11] Sabelhaus D., Röben F., Meyer zu Helligen L. P., & Lammers P. S. (2013). Using continuous-curvature paths to generate feasible headland turn manoeuvres, *Biosystems engineering*, 116, 399 – 409, http://dx.doi.org/10.1016/j.biosystemseng.2013.08.012

[12] Trendafilov K. (2010). Theoretical determination of the width of strip for turning when ploughing with trailed and semi-mounted reversible ploughs in a field with irregular shape. *Agricultural Science and Technology*, 2(4), 2010, 218-220.

[13] Trendafilov K. (2017). Analysis of non-working moves performed by semi-mounted reversible plough in a headland. *Applied Researches in Technics, Technologies and Education*, 5(2), 2017, 79-84, doi: 10.15547/artte.2017.02.001

[14] Trendafilov K. (2025). Length of Open Fishtail Turns and Width of the Headland When Plowing with a Mounted Reversible Plow in an Irregularly Shaped Field. *Applied Researches in Technics, Technologies and Education*, 13(2),.88-97, doi: 10.15547/artte.2025.02.004

[15] Trendafilov K., & Delchev N. (2018). Headland turns using the tractor's "fifth wheel" steering device instead of front steering wheels. *Bulgarian Journal of Agricultural Science*, 24(6), 1137–1147

[16] Wang H, & Noguchi N. (2018). Adaptive turning control for an agricultural robot tractor. *Int J Agric & Biol Eng*, 2018, 11(6), 113–119.

[17] Wang N., Jin Z., Wang T., Xiao J., Zhang Z., Wang H., & Zhang M., Li H. (2025). Hybrid path planning methods for complete coverage in harvesting operation scenarios. *Computers and Electronics in Agriculture,* 231, 109946, https://doi.org/10.1016/j.compag.2025.109946

[18] Ward M., Forristal P.D., McDonnell K. (2020). Impact of field headlands on wheat and barley performance in a cool Atlantic climate as assessed in 40 Irish tillage fields. *Irish Journal of Agricultural and Food Research,* 59, 85-97, doi:10.15212/ijafr-2020-0113

[19] Wu T., Guo H., Zhou W., Gao G., Wang X., & Yang C. (2025). Navigation path extraction for farmland headlands via red-green-blue and depth multimodal fusion based on an improved DeepLabv3+ model. *Engineering Applications of Artificial Intelligence*, 151, 110681. https://doi.org/10.1016/j.engappai.2025.110681

[20] Yang Y., Zhang G., Chen Z., Wen X., Cheng S., Ma Q., Qi J., Zhou Y., & Chen L. (2022). An independent steering driving system to realize headland turning of unmanned tractors. *Computers and Electronics in Agriculture,* 201, 107278, https://doi.org/10.1016/j.compag.2022.107278

ENAS-BASED YOLOv8 IMPROVEMENT WITH JOINT STRUCTURE AND LOSS SEARCH FOR CORN SEEDLING AND WEED DETECTION

/

基于 ENAS 的 YOLOv8 改进方法：结合结构与损失函数搜索实现玉米幼苗与杂草检测

Junnan HU [1], Hanyang WANG *[1], Yongcai MA [1], Dan LIU [2]

[1] College of Engineering, Heilongjiang Bayi Agricultural University, Daqing, Heilongjiang/ China

[2] College of Civil Engineering and Water Conservancy, Heilongjiang Bayi Agricultural University, Daqing, Heilongjiang/ China

Tel: +8613005357555; E-mail: michaelyang198217@163.com

Corresponding author: Wang Hanyang

DOI: https://doi.org/10.35633/inmateh-79-21

Keywords: *Corn seedling-weed detection; Efficient neural architecture search; YOLOv8; Edge deployment; Virtual spraying signal; Precision weeding*

ABSTRACT

Corn seedling and weed detection during the 2–5-leaf stage is essential for precision weeding, but similar morphology, field background interference, and the accuracy-efficiency trade-off limit the practical use of lightweight detectors. To address these problems, this study proposes Corn-Weed-ENAS, an improved YOLOv8-based detection model with joint structure and loss-function search. A differentiated ENAS search space was constructed for the backbone, neck, detection head, and loss function to automatically identify a compact architecture suitable for corn seedling-weed detection. A field image dataset of 2–5-leaf corn seedlings and weeds were collected in Heilongjiang Province, and comparative and ablation experiments were conducted against mainstream detectors. The proposed model achieved 97.3% mAP@0.5 with 2.5M parameters and 6.7 GFLOPs, showing a favorable balance between detection accuracy and lightweight deployment. To further verify its agricultural engineering applicability, an indoor simulated operation test was conducted on a Jetson Orin Nano Super platform using 20 pots of corn seedlings and weeds and a moving test vehicle at 1.2 m/s. In the virtual spraying signal verification, YOLOv8n produced five missed detections and one false detection, whereas Corn-Weed-ENAS produced three missed detections and no false detection. These results indicate that Corn-Weed-ENAS can provide more reliable weed localization and virtual trigger outputs for selective spraying decision support.

摘要

玉米 2~5 叶期苗草识别是精准除草的重要基础，但玉米幼苗与杂草形态相近、田间背景干扰复杂，且轻量化检测模型常存在精度与效率难以兼顾的问题。针对上述问题，本文提出一种结合结构搜索与损失函数搜索的 YOLOv8 改进模型 Corn-Weed-ENAS。该方法面向骨干网络、颈部网络、检测头和损失函数构建差异化 ENAS 搜索空间，自动获得适用于玉米苗草检测任务的紧凑型网络结构。本文采集黑龙江省 2~5 叶期玉米幼苗与杂草图像数据集，并与主流目标检测模型开展对比和消融试验。结果表明，所提出模型在 2.5M 参数量和 6.7 GFLOPs 条件下取得 97.3% mAP@0.5，实现了检测精度与轻量化部署之间的较好平衡。为进一步验证其农业工程应用适应性，本文基于 Jetson Orin Nano Super 平台开展了室内模拟作业试验，采用 20 盆玉米苗与杂草盆栽以及 1.2 m/s 移动试验车进行虚拟喷药信号验证。结果显示，YOLOv8n 出现 5 次漏检和 1 次误检，而 Corn-Weed-ENAS 仅出现 3 次漏检且无误检。结果说明，Corn-Weed-ENAS 能够为选择性喷药决策支持提供更可靠的杂草定位与虚拟触发输出。

INTRODUCTION

Weeds compete with crops for water, nutrients, and sunlight, suppressing crop growth and reducing yield and quality (*Hamuda et al., 2016; Islam et al., 2021*). Effective weed control during critical growth stages is thus essential for agricultural productivity (*Knezevic and Datta, 2015; Ramesh et al., 2021*). Current weed management relies on manual, mechanical, biological, and chemical methods (*Bajwa et al., 2015; Christensen et al., 2009; Wang et al., 2013*), with chemical control dominating globally due to its efficiency (*Harker and O'Donovan, 2013; Wei et al., 2010*). The 2–5-leaf stage is a critical weeding window for corn, where seedlings and weeds exhibit minimal morphological differences.

While targeted herbicide application can reduce weed damage, mechanical weeding is inefficient and labor-intensive, and chemical weeding causes pesticide waste and soil pollution, conflicting with green agriculture principles. Developing precise seedling-weed detection algorithms therefore holds significant academic and practical value for modernizing corn production and advancing sustainable agriculture (*Zhang, 2021*).

Driven by the growth of smart agriculture, machine vision and deep learning have become mainstream for agricultural target detection. The YOLO series of single-stage detectors is widely adopted for its balanced speed and accuracy (*Miao et al., 2025; Tang et al., 2025*). Among these, YOLOv8, with superior feature extraction, inference efficiency, and edge-deployment suitability, has been applied to corn seedling and weed detection (*Chu et al., 2025; Wang et al., 2026*). However, standard YOLOv8 faces notable limitations in real agricultural scenarios, including lighting variations, soil interference, seedling-weed occlusion, and morphological similarity at the 2–5-leaf stage. Existing studies have improved accuracy and lightweighting via complex dataset collection and module optimization, laying a foundation for seedling-stage weed detection (*Liu et al., 2022; Wang et al., 2026; Zhao et al., 2026*).

Recent studies have explored deep-learning-based crop and weed detection under natural field conditions. For example, MSRCR-YOLOv4-tiny was used to improve field corn weed detection under complex illumination, while improved YOLO-based models have been developed for corn-field weed detection and target spraying system design. These studies demonstrate the feasibility of lightweight object detection for agricultural weed control. However, most existing methods mainly focus on image-level detection accuracy and module-level network improvement. The connection between detection outputs and agricultural machinery decision signals, such as weed target-point localization and selective spraying triggering, is still insufficiently discussed.

Most current improvements rely on manually adding attention mechanisms and optimizing feature fusion modules, which depend heavily on researcher experience and consume substantial computational resources and time (*Ghosh et al., 2025; Jin et al., 2023; Yang et al., 2021*). Neural Architecture Search (NAS) addresses the limitations of manual network design; in particular, Efficient Neural Architecture Search (ENAS) drastically reduces search time and cost via parameter sharing, enabling automatic discovery of task-specific lightweight, high-performance networks, and has been widely used in computer vision (*Pham et al., 2018*). Currently, ENAS applications in object detection are limited to single-module local optimization, with scarce research in agriculture.

To meet the precision weed control needs of intelligent agricultural machinery, this study constructs a seedling-weed dataset for realistic corn seedling scenarios, focusing on 2–5-leaf corn and common weeds. A full-module ENAS-based joint optimization strategy is implemented for the YOLOv8 network, including fine-grained search of the backbone, neck, detection head, and loss function. Compared with manual module design, the proposed search strategy aims to obtain a compact architecture with better task adaptability. In addition to offline comparative and ablation experiments, this study further conducts an indoor simulated deployment experiment on a Jetson Orin Nano Super platform. The detection outputs are converted into weed center points and software-level virtual spraying trigger signals, thereby evaluating the potential of the proposed model as a perception and decision-support module for selective spraying or intelligent weeding equipment.

MATERIALS AND METHODS

Data collection

Data for this study were collected in Longfeng Town, Longfeng District, Daqing City, Heilongjiang Province. The corn varieties planted were Xianyu 696 and Xianyu 335. The collection environment and growth conditions are shown in Fig 1. The corn was planted in single rows on ridges, with a row spacing of 65 cm. Sampling took place from May to June 2025, when the corn was in the 2–5-leaf stage. Images were captured using a D435i stereo depth camera positioned 40-70 cm above the ground, with the camera's downward angle set between 60°and 90°. The dataset includes various lighting conditions (sunny, cloudy, overcast, etc., as well as early morning, morning, noon, afternoon, evening), different weed growth stages and species (such as Chenopodium, Apium, and Kochia), as well as varying levels of occlusion and weed density to ensure the dataset's generalizability. The dataset exhibits sufficient diversity, aiming to ensure its robustness in real-world application scenarios (*Le et al., 2021; Yang et al. 2025*).

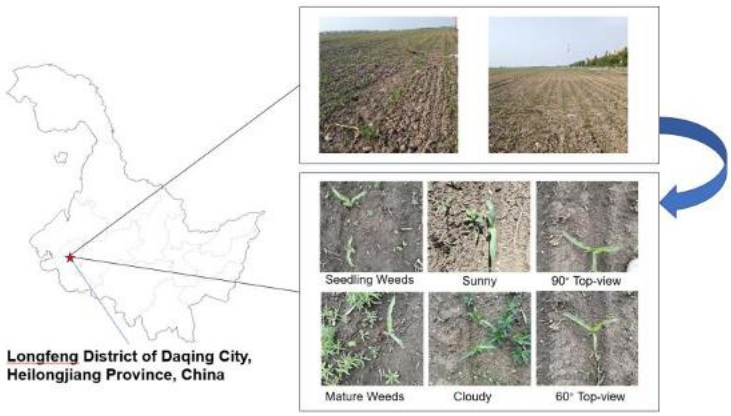


Fig. 1 - Data collection environment and dataset details

The data was manually screened to remove low-quality images with exposure issues (overexposure or underexposure) or blurriness, resulting in a total of 4,000 images, all saved in JPG format. During the preprocessing stage, a differentiated preprocessing strategy was employed to enhance the model's robustness in complex real-world scenarios. Specifically, while ensuring that the main content of the images remains recognizable, some images with slight blurring and uneven lighting were selectively retained with the aim of enabling the model to learn to perform recognition under suboptimal conditions. At the same time, all images were cropped to a uniform size to establish a standard input format. To further enhance the model's generalization ability and stability, this study implemented systematic data augmentation techniques to expand the training dataset by simulating a wider range of imaging variations. During the data augmentation phase, to enhance the model's robustness and generalization capabilities for corn seedling-weed detection recognition in complex field environments, a comprehensive augmentation strategy that included rotation, resizing, noise addition, and brightness adjustment was employed. The images were then annotated using the LabelImg tool and classified into two categories: corn and weeds. The dataset was randomly divided into training, validation, and test sets in an 8:1:1 ratio, ensuring that each set contained images from different environments (*Li et al., 2023*).

Development of the ENAS framework

This study builds upon the ENAS framework proposed by Pham et al. in 2018, retaining its core modules—the controller, hypernetwork, and reward signal—to construct a fine-grained search space covering all components of YOLOv8. An optimized ENAS network is proposed to achieve end-to-end automatic optimization of YOLOv8. Unlike traditional methods, this study focuses on the four key components of YOLOv8—the Backbone, Neck, Head, and loss function—to design differentiated, fine-grained search spaces and strategies that balance detection accuracy with model lightweighting, thereby improving search efficiency and convergence stability. The search process is as follows: the controller makes decisions regarding the architecture, the sub-architectures evaluate composite metrics on the hypernetwork validation set, and the controller updates the reinforcement learning policy based on these results, guiding the search toward a lightweight, high-performance solution. This framework integrates both global and local features required for identifying corn seedlings and weeds during the 2–5-leaf stage, striking a balance between accuracy and efficiency. The optimized, lightweight architecture selected is used for real-time, high-precision detection of corn seedlings and weeds in the field, achieving a Pareto optimal balance of accuracy, size, and speed.

Corn-Weed-ENAS searchable object detection model architecture

This study proposes the Corn-Weed-ENAS searchable object detection model, which centers on a weight-sharing supernetwork that integrates the ENASChoice module. It natively supports end-to-end architecture search and is tailored to meet the deployment requirements of agricultural embedded scenarios. The hypernetwork is designed according to the principle of layer-by-layer reconfigurability, which enables the construction of a fine-grained search space covering the entire network pipeline, including the core network components and supervisory signals. The search space consists of two main levels. First, fine-grained end-to-end search is performed across the Backbone, Neck, and Head. The backbone, neck, and detection head layers are encapsulated in ENASChoice modules, each integrating more than ten types of operation primitives, including standard convolutions, ghost convolutions, depthwise separable convolutions, attention mechanisms, and lightweight modules.

During the search process, the controller selects the optimal operation for each ENASChoice module, enabling end-to-end customization of the microarchitecture, from backbone feature extraction and multi-scale feature fusion to detection output. Second, flexible loss-function configuration is introduced. By incorporating multiple loss functions into the search space, the proposed method enables the joint optimization of the network architecture and the supervisory signal.

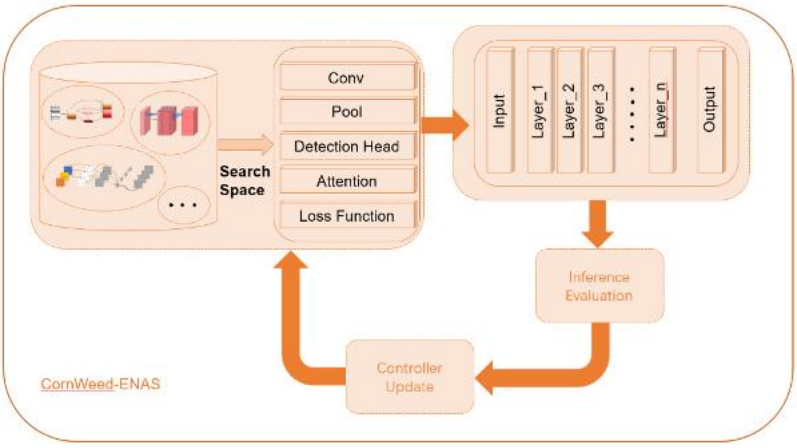


Fig. 2 – Corn-weed-ENAS Workflow

Cooperative optimization algorithms and architecture mapping mechanisms

Most traditional NAS algorithms are limited to optimizing the backbone network. To address this inherent limitation, this study proposes an improved Corn-Weed-ENAS co-optimization algorithm. Within the weight-sharing framework, the algorithm simultaneously performs joint optimization of architectural parameters and network weights, fully expanding the search space to encompass all critical dimensions that determine the model's final performance, covering the four core modules: Backbone, Neck, Head, and loss function. Throughout the architecture exploration process, the controller can dynamically balance multiple sets of interdependent key metrics. These metrics include model accuracy, computational complexity, and on-device inference speed. The ultimate goal of an algorithm is not the extreme optimization of a single metric. Its goal is to collaboratively identify the globally optimal architecture across multiple metrics, thereby achieving a paradigm shift from local component optimization to global system-level coordination. To achieve an efficient mapping from architectural decisions to an executable network topology, this study introduces a layer-by-layer mapping mechanism. The controller outputs a discrete selection index for each searchable unit. Using a prebuilt lookup dictionary, the system precisely maps indices to predefined operation keys or module instances, establishing a direct and stable link between high-level architectural decisions and low-level network implementation. Once the search is complete, the system instantiates a deterministic subnetwork from the hypernetwork based on the optimal selection sequence sampled by the controller. The subnet retains only the selected operations and modules. It also fully inherits the pre-trained weights from the hypernetwork, ultimately enabling a seamless transition from architecture search to a deployable model.

Automatic search algorithms and implementation

In the Corn-Weed-ENAS framework proposed in this study, the hyperparameters of the controller design and search process are set as follows. Architectural decisions are made using independent classification controllers, with each ENASChoice module and configurable component corresponding to a separate classification distribution. The maximum number of search rounds is set to 300. In each round, the controller samples a complete architectural configuration, corresponding to a specific subnet instance within the predefined full-stack search space. The key hyperparameters for policy-gradient updating include a baseline decay rate of 0.9 and an entropy regularization coefficient of 0.01.

After initializing the controller and the weight-sharing hypernetwork, the search iteration process is started. In each iteration, the current controller policy is evaluated as follows. First, the controller samples an architectural configuration, which is represented as a sequence of choice indices. Then, using a predefined lookup dictionary, this index sequence is mapped to specific operations and modules. Next, the selected subnet is activated in the hypernetwork, and 10% of the full dataset is selected for training to enable efficient subnet evaluation.

Finally, a reward value is calculated using a multi-objective function that balances detection accuracy and inference efficiency, thereby guiding the direction of the architecture search. The reward function is defined as follows:

$$R = R_{gating} + R_{main} + R_{bonus\_all} + R_{bonus\_pareto} \quad (1)$$

wherein: R_{gating} is the gating penalty:

$$R_{gating} = -base_{penalty} - \alpha \times \max(0, map_{[0.5]min} - map_{[0.5]}) - \beta \times \max(0, map_{[0.5-0.95]min} - map_{[0.5-0.95]}) \quad (2)$$

where $base_{penalty} = 2.0, \alpha = 50.0, \beta = 30.0, map_{[0.5]min}$ and $map_{[0.5-0.95]min}$ are the minimum acceptable $map_{[0.5]}$ and $map_{[0.5-0.95]}$ values;

$R_{main} = \sum w_i \times gain_i + \sum w_j + save_j$, where $gain_i$ denotes the relative improvement of metrics (precision, recall, $map_{[0.5]}$, $map_{[0.5-0.95]}$) over the baseline (normalized via tanh function with $s_{metric} = 0.01$, and $save_j$ denotes the relative reduction of resources (parameters, FLOPs, weight size) compared to the baseline (normalized via tanh function with $s_{cost=0.05}$.

R_{bonus_all} is the "all-improve" bonus: a fixed value if the architecture outperforms the baseline in all metrics and underperforms in all resource indicators (zero if identical to the baseline);

R_{bonus_pareto} is the Pareto front bonus: scaled by the number of dominated architectures when the candidate is added to the Pareto front (Pareto tolerance tol= $1e-12$).

After receiving the reward, the algorithm executes the policy update step. The advantage function is computed as Advantage = Reward - Baseline, where Baseline refers to the exponential moving average of historical rewards. The controller's loss function is defined as follows:

$$L_{controller} = -log\pi_\theta(a) \cdot A - \lambda H(\pi_\theta) \quad (3)$$

Specifically, $\pi_\theta(a)$ denotes the joint probability that the IndependentCategoricalController samples the architectural configuration a under the current policy θ (product of independent categorical distribution probabilities for each configurable component). The negative logarithm of this probability, $-log\pi_\theta(a)$, corresponds to '-log_prob' in the code and serves as the core component of policy gradient computation. A denotes the advantage function, computed as $A = R - B$; here, R is the multi-objective reward calculated via Formula (1), and B is the global exponential moving average baseline (independent of search state). This advantage value quantifies the relative quality of the current architectural configuration against the average performance. $H(\pi_\theta)$ represents the average entropy of the controller's categorical distributions (across all configurable components), weighted by the coefficient λ to encourage architectural exploration.

The aforementioned iterative process proceeds cyclically until any of the following termination conditions is satisfied: (1) The preset maximum number of epochs is reached; (2) Algorithm performance converges, i.e., the improvement in the best fitness reward obtained over N consecutive generations falls below a preset threshold ε. Upon termination of the search, the architectural decision individual with the highest historical fitness is selected as the optimal solution. Subsequently, the system instantiates the corresponding operations and modules via the two-stage mapping process based on this optimal decision, directly extracts the corresponding weights from the pre-trained supernetwork, and assembles them into the final deployable lightweight detection model, thus completing the entire workflow from automated architecture search to efficient model derivation.

Edge deployment and indoor simulated virtual spraying signal verification

To further evaluate the practical applicability of the proposed Corn-Weed-ENAS model in agricultural machinery scenarios, an indoor simulated operation experiment was conducted using a Jetson Orin Nano Super development board. The development board was equipped with 8 GB memory and a 1024-core NVIDIA Ampere architecture GPU. A driver-free USB camera with a resolution of 0.3 megapixels was used as the image acquisition device. During the experiment, the camera center was installed 60 cm above the ground, and the optical axis of the camera was set at a downward angle of 60° relative to the horizontal plane. This configuration was used to simulate the visual perception condition of a small selective spraying or intelligent weeding platform.

Twenty pots of potted plants were arranged to construct the indoor simulated operation scene. Each pot contained 1–5 corn seedlings and weeds, forming different crop-weed distributions and partial occlusion conditions. During the experiment, the test vehicle moved along the horizontal line of the potted plants at a speed of 1.2 m/s.

The trained YOLOv8n and Corn-Weed-ENAS models were deployed on the Jetson Orin Nano Super platform for real-time detection. For each detected weed target, the center point of the bounding box was calculated and regarded as the potential spraying target point. A virtual spraying trigger signal was generated when the detected weed target satisfied the predefined trigger condition. Since no actual herbicide spraying device was connected in this experiment, the generated signal was used as a software-level virtual spraying signal to evaluate whether the model could provide usable perception outputs for subsequent selective spraying control.

This verification focused on the transformation from visual detection results to application-oriented decision signals. Missed detection was recorded when a weed target requiring a trigger signal was not detected by the model. False detection was recorded when a non-weed object or background region was incorrectly detected as a weed target and could lead to an unnecessary virtual spraying signal. The number of missed detections and false detections was compared between YOLOv8n and Corn-Weed-ENAS to evaluate the reliability of the proposed model in the simulated selective spraying scenario.

RESULTS

Evaluation metrics and parameter settings

To comprehensively and objectively evaluate the detection accuracy and target-recognition robustness of the detection models identified by the Corn-Weed-ENAS framework for corn seedling and weed detection, as well as their engineering deployment efficiency and lightweight characteristics when adapted to agricultural edge devices, this study combines conventional accuracy metrics from object detection with engineering-oriented deployment metrics to construct a multidimensional evaluation framework. The names, physical meanings, and descriptions of each evaluation metric are presented in Table 1. All subsequent calculations of these metrics follow the standard conventions used in the field of object detection.

Table 1

Evaluation metrics

Index	Description
IoU=0.5	The ratio of the intersection to the union between the model-predicted bounding box and the actual bounding box
AP	Average Accuracy at Different Recall Rates
mAP@0.5	Mean Average Precision for corn seedling and weed detection at an IOU threshold of 0.5
F1 score	Harmonic Mean of Precision and Recall
FPS	Number of images the model can process per second
Precision（P）	The ratio of accurately detected corn seedlings and weeds in the image to the total number of detected corn seedlings and weeds
Recall(R)	The proportion of correctly identified corn seedlings and weeds in the image relative to the total number of corn seedlings and weeds in the dataset
Weights	Weight Size(MB)
Parameters	Number of parameters in a model(M)

Among these, IoU, AP, mAP@0.5, precision, recall and F1 score are accuracy metrics for quantifying the target localization and classification performance of corn seedling and weed detection models; FPS, model weight and parameter count are deployment metrics to evaluate inference speed and compactness, meeting the demands of agricultural edge computing applications. All tests were conducted on a Windows 11 system with an Intel Core i7-13700KF CPU and NVIDIA GeForce RTX 4070 Ti Super GPU, with PyCharm as the IDE and the core software stack: Python 3.10.19, PyTorch 2.7.1 and CUDA 12.6. For fair and comparable experimental results across all models, a unified set of hyperparameters was adopted: 640×640 input resolution, stochastic gradient descent (SGD) as the optimization algorithm, and 300 training epochs.

Comparative study

Comparison models are categorized into three types covering object detectors of different generations and architectural paradigms: (1) YOLO baseline models (YOLOv5s, YOLOv7-tiny, and YOLOv8n, the search benchmark in this study); (2) the latest lightweight YOLO models (YOLOv11n, YOLOv12) representing state-of-the-art advances in lightweight visual recognition; (3) the classic two-stage detector Faster R-CNN, selected as the accuracy-oriented baseline. Detailed comparison results are presented in Fig. 3.

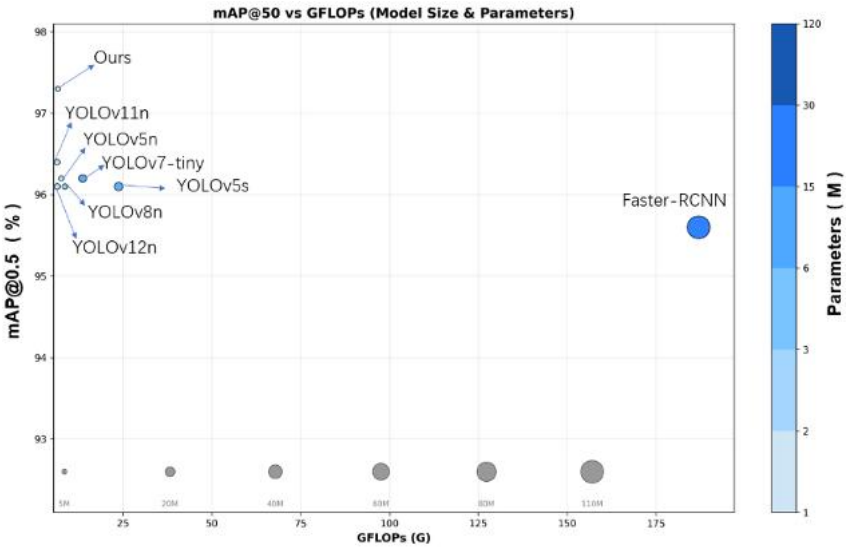


Fig. 3 - Performance Comparison of Different Object Detectors on a Dataset of Corn Seedlings and Weeds

Table2

Other indicators not included in Fig 2

Indicator	YOLOv5s	YOLOv5n	YOLOv7	YOLOv8n	YOLOV11n	YOLOV12n	Faster-RCNN	Ours
P	93.9	93.6	93.7	92.7	93.6	93.6	77.9	94.6
R	92.1	93.0	93.3	93.2	92.6	93.2	96.1	96
FPS	66	204	119	180	241	240	8	234

The results show that the model identified by the Corn-Weed-ENAS framework achieved a 97.3% accuracy rate (mAP@0.5), with precision, recall, and F1 scores all outperforming the comparison algorithms, demonstrating the highest recognition accuracy. At the same time, with 5.2 million model weights, 2.5 million parameters, and only 6.7 billion FLOPs, it achieves improved performance while remaining lightweight.

Results of edge deployment and virtual spraying signal verification

The indoor simulated deployment experiment showed that both YOLOv8n and Corn-Weed-ENAS could be deployed on the Jetson Orin Nano Super platform and could output weed detection results and virtual spraying trigger signals under the moving operation condition. The test was conducted using 20 pots of potted corn seedlings and weeds. The camera was mounted 60 cm above the ground with a 60° downward viewing angle, and the test vehicle moved along the potted plants at a speed of 1.2 m/s.

Under the same deployment platform, camera configuration, operation speed, and virtual trigger strategy, YOLOv8n produced five missed detections and one false detection, whereas Corn-Weed-ENAS produced three missed detections and no false detection. Compared with YOLOv8n, Corn-Weed-ENAS reduced the number of missed detections by 40.0% and reduced the number of false detections from one to zero. This result indicates that the proposed Corn-Weed-ENAS model had more stable weed localization performance and lower risk of unnecessary virtual spraying signals in the simulated operation scenario.

Although this experiment did not involve actual herbicide spraying, it provided a software-level verification of the transformation from detection results to spraying decision signals. The results demonstrate that Corn-Weed-ENAS can not only achieve high detection accuracy in offline image evaluation, but also generate target-point outputs and virtual trigger signals on an edge device. Therefore, the proposed model has potential as a perception and decision-support module for selective spraying or intelligent weeding equipment.

Table3

Edge deployment and virtual spraying signal verification results under the indoor simulated operation scenario

Model	Platform	Test scene	Missed detections	False detections	Relative change
YOLOv8n	Jetson Orin Nano Super	Indoor potted-plant simulated operation	5	1	Baseline

Model	Platform	Test scene	Missed detections	False detections	Relative change
Corn-Weed-ENAS	Jetson Orin Nano Super	Indoor potted-plant simulated operation	3	0	Missed detections reduced by 40.0%; false detections reduced to 0



Fig. 4 - Indoor simulated operation platform for edge deployment and virtual spraying signal verification.
(a) Overall indoor experimental platform with the test vehicle, deployment terminal, and potted samples;
(b) Jetson Orin Nano Super development board used for model deployment and real-time inference;
(c) Camera view of potted corn seedlings and weeds during vehicle movement.

Ablation experiment

To validate the effectiveness of each structural module in the model and demonstrate the performance advantages of the Corn-Weed-ENAS model proposed in this paper, this section presents a systematic set of ablation experiments. The experiment uses the YOLOv8n model as the baseline and systematically decomposes it into four core search modules: the backbone network, the neck structure, the detection heads, and the loss function. It compares the detection accuracy and computational cost of the model under different combinations of these modules. Additionally, the experiment compares the final optimized model with the baseline model and the step-by-step search models to comprehensively evaluate the effectiveness of the model optimization. The evaluation metrics used in this experiment are the same as those in the comparative experiments. The experimental results are shown in Table 4.

Table 4

Results of the ablation experiment

Model configuration	mAP@0.5 (%)	Precision (%)	Recall (%)	Weights (M)	Parameters (M)	FLOPs (G)
YOLOv8n (Baseline)	96.1	92.7	93.2	6.3	3.0	8.1
Only Backbone	96.7	93.7	93.4	5.8	2.9	7.6
Previous + Neck	96.8	94.4	94.0	5.4	2.7	7.1
Previous + Detection Head	97.1	94.9	94.4	5.2	2.5	6.7
Corn-Weed-ENAS	97.3	95.1	94.6	5.2	2.5	6.7

Ablation experiments show that each module has a significant impact on model performance: Experiments show that the selection of the backbone, neck, head, and loss function all have a significant impact on model performance. The model offers notable advantages in terms of compactness, with 5.2 million weights, 2.5 million parameters, and 6.7 billion FLOPs. Its mAP@0.5 reached 97.3%, with the best performance across all accuracy metrics. It effectively addresses the challenge of balancing accuracy with lightweight design, outperforms both the baseline model and stepwise improvement models in overall performance, and offers significant practical value.

CONCLUSIONS

Comparative and ablation experiments validated the effectiveness of the proposed Corn-Weed-ENAS model for corn seedling and weed detection. Compared with mainstream detectors including YOLO series models and Faster R-CNN, Corn-Weed-ENAS achieved 97.3% mAP@0.5 with 2.5M parameters and 6.7 GFLOPs, showing a favorable balance between detection accuracy, compactness, and deployment efficiency.

The ablation results further confirmed that the searched backbone, neck, detection head, and loss-function configuration jointly contributed to the final model performance.

To strengthen the agricultural engineering application of the study, an indoor simulated deployment experiment was conducted on a Jetson Orin Nano Super platform. Under a simulated moving operation condition with 20 pots of corn seedlings and weeds, YOLOv8n produced five missed detections and one false detection, whereas Corn-Weed-ENAS produced three missed detections and no false detection. The proposed model reduced missed detections by 40.0% and eliminated false detections compared with YOLOv8n. These results indicate that Corn-Weed-ENAS can provide more reliable weed localization and virtual spraying trigger outputs on an edge device.

Overall, Corn-Weed-ENAS can serve as a lightweight perception and decision-support module for selective spraying or intelligent weeding equipment. However, the deployment experiment in this study was a software-level virtual signal verification under an indoor simulated potted-plant scenario, and actual herbicide spraying and field weeding performance were not evaluated. Future work will connect the model with physical spraying or mechanical weeding actuators and conduct field-level operational tests to further verify its engineering applicability.

ACKNOWLEDGEMENT

This study was financially supported by Accurate monitoring of soil crop information acquisition and real-time precision application technology and equipment research and development of medicine and fertilizer (No.: 2024ZXDXB45) Key Research and development Plan of Heilongjiang Province and Heilongjiangb Bayi Agricultural University Support Program from Daqing City, Grant No.ZRCPY202121.

REFERENCES

[1] Bajwa, A. A., Mahajan, G., Chauhan, B. S. (2015). Nonconventional Weed Management Strategies for Modern Agriculture. *Weed Science*, Vol. 63(4), pp. 723-747, United States.

[2] Christensen, S., Søgaard, H. T., Kudsk, P., Nørremark, M., Lund, I., Nadimi, E. S., Jørgensen, R. (2009). Site-specific Weed Control Technologies. *Weed Research*, Vol. 49, pp. 233-241, United Kingdom.

[3] Chu, Y., Wei, Y. L., Liang, H. J., et al. (2025). Lightweight YOLOv8 Weed Detection Algorithm. *Journal of North China University (Natural Science Edition)*, Vol. 46, No. 4, pp. 489-498, Hebei/China.

[4] Ghosh, D., Ghosh, S., Jana, N. D., Biswas, S., Mallipeddi, R. (2025). Designing optimal Vision Transformer architecture using differential evolution for tomato leaf disease classification. *Computers and Electronics in Agriculture*, Vol. 238, pp. 110824, Netherlands.

[5] Hamuda, E., Glavin, M., Jones, E. (2016). A Survey of Image Processing Techniques for Plant Extraction and Segmentation in the Field. *Computers and Electronics in Agriculture*, Vol. 125, pp. 184-199, Netherlands.

[6] Harker, K. N., O'Donovan, J. T. (2013). Recent Weed Control, Weed Management, and Integrated Weed Management. *Weed Technology*, Vol. 27(1), pp. 1-11, United States.

[7] Islam, N., Rashid, M. M., Wibowo, S., Xu, C.-Y., Morshed, A., Wasimi, S. A., Moore, S., & Rahman, S. M. (2021). Early Weed Detection Using Image Processing and Machine Learning Techniques in an Australian Chilli Farm. *Agriculture*, Vol. 11(5), pp. 387, Netherlands.

[8] Jin, X., Xiong, J. H., Rao, Y., Zhang, T., Ba, W. J., Gu, S. F., Zhang, X. D., Lu, J. (2023). TranNas-NirCR: A method for improving the diagnosis of asymptomatic wheat scab with transfer learning and neural architecture search. *Computers and Electronics in Agriculture*, Vol. 213, pp. 108271, Netherlands.

[9] Knezevic, S. Z., Datta, A. (2015). The Critical Period for Weed Control: Revisiting Data Analysis. *Weed Science*, Vol. 63(SP1), pp. 188-202, United States.

[10] Le, V. N. T., Truong, G., & Alameh, K. (2021). Detecting Weeds from Crops Under Complex Field Environments Based on Faster RCNN. In: *IEEE 8th International Conference on Communications and Electronics (ICCE)*, pp. 350-355, Vietnam.

[11] Li, H. S., Shi, L., Fang, S., et al. (2023). Real-time Detection of Apple Leaf Diseases in Natural Scenes Based on YOLOv5. *Agriculture*, Vol. 13, No. 4, pp. 878, Switzerland.

[12] Liu, M. C., Gao, T. T., Ma, Z. X., et al. (2022). Field Weed Detection Model for Maize Based on MSRCR-YOLOv4-tiny. *Transactions of the Chinese Society for Agricultural Machinery*, Vol. 53, No. 2, pp. 246-255+335, Beijing/China.

[13] Miao, X., Wu, X., & Zhang, X. (2025). Lightweight corn leaf disease detection model based on YOLOV8N-LSCSBD. *INMATEH Agricultural Engineering*, Vol. 77, pp.373-382. DOI: https://doi.org/10.35633/inmateh-77-30. Romania.

[14] Pham, H., Guan, M. Y., Zoph, B., Le, Q. V., Dean, J. (2018). Efficient neural architecture search via parameter sharing. In: *Proceedings of the 35th International Conference on Machine Learning (ICML),* Vol. 80, Stockholm, Sweden.

[15] Ramesh, K., Kumar, S. V., Upadhyay, P. K., Chauhan, B. S. (2021). Revisiting the Concept of the Critical Period of Weed Control. *The Journal of Agricultural Science*, Vol. 159(9-10), pp. 636-642, United Kingdom.

[16] Tang, Y., Sun, J., Zhang, Y., Wang, C., Zhang, Z., & Shi, F. (2025). Kiwifruit flower detection using an optimized YOLOv11n architecture. *INMATEH Agricultural Engineering*, Vol. 77, No. 3, pp. 44-53, Romania.

[17] Wang, H. Z., Liu, H. T., Li, X. L., et al. (2025). Lightweight Lawn Heterogeneous Weed Detection Algorithm Based on Improved YOLOv8n. *Transactions of the CSAE*, Vol. 41, No. 10, pp. 157-165, Beijing/China.

[18] Wang, N., Shang, Z., Chen, K., et al. (2026). Weed Detection Method in Corn Field Based on Improved YOLOv5s. *Journal of China Agricultural University*, Vol. 31, No. 2, pp. 192-204, Beijing/China.

[19] Wang, P., Tang, Y., Luo, F., Wang, L., Li, C., Niu, Q., Li, H. (2022). Weed25: A Deep Learning Dataset for Weed Identification. *Frontiers in Plant Science*, Vol. 13, Switzerland.

[20] Wei, D., Chen, L., Ma, Z., Wang, G., & Zhang, R. (2010). Review of Non-chemical Weed Management for Green Agriculture. *International Journal of Agricultural and Biological Engineering*, Vol. 3(4), pp. 52-60, Beijing/China.

[21] Yang, X. J., Guo, M., Lyu, Q. S., Ma, M. (2021). Detection and classification of damaged wheat kernels based on progressive neural architecture search. *Biosystems Engineering*, Vol. 208, pp. 176-185, Netherlands.

[22] Yang, Z. J., Zhang, J. H., Liu, J. Q., et al. (2025). Lightweight Detection and Segmentation Method of Red Soil Aggregate Cracks Based on YOLOv8n-seg. *Transactions of the CSAE*, Vol. (Online), pp. 1-10, [2025-12-09], Beijing/China.

[23] Zhang, J. Y. (2021*). Design and Experiment of Intelligent Mechanical Weeding Device for Ridge Corn*. Harbin: Northeast Agricultural University, Heilongjiang/China.

[24] Zhao, J. G., An, M. L., Zhao, X. G., et al. (2026). Weed Detection Method and Target Spraying System Design of Corn Based on WEED-YOLOv10. *Transactions of the CSAE*, Vol. (Online), pp. 1-10, [2026-01-25], Beijing/China.

RESEARCH ON MULTI-OBJECT TRACKING OF PIGS BASED ON IMPROVED BYTE TRACK

基于改进 ByteTrack 的多目标生猪跟踪研究

Jinhang MU[1,2)] , Yiran LIU[1)] , Lingqing FENG*,[1)]

[1)] College of Information Science and Engineering, Shanxi Agricultural University, Taigu, 030801, China
[2)] School of Computer Science and Technology, North University of China, Taiyuan, 030051, China
** Corresponding author: Lingqing Feng*
Tel: +86-13834837537; E-mail: fenglq@sxau.edu.cn
DOI: https://doi.org/10.35633/inmateh-79-22

Keywords: *live pigs; multi-object tracking; trajectory smoothing; smart farming; improved ByteTrack*

ABSTRACT

As the pig farming industry evolves towards intelligence and large-scale operations, multi-object tracking technology plays a pivotal role in enhancing farming efficiency and optimizing health management. Addressing the issues of trajectory interruption and jitter caused by frequent occlusion of targets, significant scale variations, rapid motion, and sudden turns in large-scale breeding scenarios, an improved ByteTrack method is presented. This method employs YOLOv8 as the detector and enhanced the ByteTrack framework. By incorporating an Exponential Moving Average (EMA) trajectory smoothing module, it optimizes the trajectory jitter issues encountered by traditional Kalman filtering in fast-moving or sudden turning scenarios, resulting in smoother and more continuous tracking trajectories. Experimental results on a real-world livestock farm video dataset demonstrate that the proposed method achieves improvements across several key evaluation metrics. Specifically, the Multi-Object Tracking Accuracy (MOTA) increased by 1.61%, Identification F1 Score (IDF1) improved by 2.55%, and the Recall rose by 9.68%. The results demonstrate that the proposed method can effectively track pigs in complex farming environments with frequent occlusions, large scale variations, and abrupt motion, providing reliable underlying data support for downstream applications, such as abnormal behavior identification and automated physical activity statistics in intelligent pig farming systems.

摘要

随着养猪业向智能化与规模化发展，多目标跟踪技术对提升养殖效率与优化健康管理具有关键作用。针对规模化养殖场景中目标频繁遮挡、尺度变化显著、快速运动及突然转向导致的轨迹中断与抖动问题，本文提出一种基于改进 ByteTrack 算法的生猪多目标追踪方法，旨在应对规模化养殖场景中目标频繁遮挡、尺度变化显著及轨迹中断等挑战，以提升养殖智能化管理效率。该方法以 YOLOv8 作为目标检测器，并在 ByteTrack 多目标追踪框架基础上，引入指数移动平均（EMA）轨迹平滑模块，有效缓解了传统卡尔曼滤波在目标快速运动或突然转向时出现的轨迹抖动问题，从而获得更为平滑、连续的追踪轨迹。在实际养殖场视频数据集上的实验结果表明，本方法在多项关键评价指标上均有显著提升，其中多目标跟踪准确率（MOTA）提升 1.61%，身份一致性（IDF1）提升 2.55%，召回率提升 9.68%。该方法能够有效应对复杂场景下的目标追踪任务，通过缓解遮挡与尺度变化对追踪精度的影响，能够为后续生猪异常行为识别、运动量自动化统计等实际生产应用提供稳定的底层数据支撑。

INTRODUCTION

The pig farming industry occupies a crucial position in the agricultural economic system, and its development directly affects the stability of meat supply in the market as well as farmers income. With the increasing scale and intensification of pig farming, high labor costs, difficulties in disease prevention, and environmental pollution have become bottlenecks for healthy pig farming (*Reza et al., 2025*). In this context, smart farming has become an important development trend in the pig farming industry (*Trabachini et al., 2025*). Monitoring the health status of pigs is a key aspect of pig production and an important step in achieving intelligent monitoring.

Traditional group pig monitoring mainly relies on manual inspection, which is inefficient, labor-intensive, and unable to provide continuous monitoring. Although sensor-based methods can achieve effective monitoring, they require expensive equipment and may cause stress responses in pigs. In contrast, vision-based multi-object tracking enables continuous and non-contact monitoring by providing identity and location information for each pig, thereby supporting timely abnormal behavior detection and disease prevention.

Monitoring the health status of pigs is a critical component of pig production and a key step in achieving intelligent farming (*Devi et al., 2024*). Traditional manual inspection methods are inefficient, costly, and cannot provide continuous monitoring. Sensor-based approaches are expensive and may induce stress in pigs, negatively impacting their health (*Pandey et al., 2021*). Utilizing multi-object tracking technology, farm staff can monitor pigs' locations, movements, and behavior patterns continuously and without contact, enabling timely detection of diseases, stress, and other abnormalities, and allowing for prompt intervention, thereby effectively preventing disease spread (*Jaoukaew et al., 2024*).

In recent years, methods for multi-object tracking of pigs have shifted from approaches based on handcrafted features to those based on deep learning. Deep learning-based multi-object tracking methods for pigs can be broadly categorized into key-point recognition-based methods, image segmentation-based methods, and object detection-based methods (*Lu et al., 2024*). Key-point recognition methods track targets by detecting their key skeletal points (such as the snout, base of the tail, and four hooves in pigs) (*Psota et al., 2020*). These methods can estimate target poses or behaviors during tracking but rely heavily on key-point visibility, making them unsuitable for densely populated or highly obstructed environments (*Yin et al., 2025*). Methods based on image segmentation precisely extract the target from the background through pixel-level segmentation and then track the mask (*Compte et al., 2025*). However, pixel-level processing is very computationally intensive (*Liang et al., 2025*). The object detection-based approach is currently the mainstream method. It first obtains the bounding boxes of objects through a detector and then matches these boxes between frames to acquire object identities and trajectories (*Li et al., 2025*).

To address challenges in pig farming scenarios, including frequent occlusions, large target scale variations, and abrupt target motion, this paper proposes an improved ByteTrack-based multi-pig tracking framework for achieving more stable and continuous trajectory association in complex breeding environments. The main contributions of this paper are as follows:

(1) YOLOv8 is adopted as the object detector to improve bounding box regression accuracy and enhance detection robustness under complex backgrounds, scale variations, and mutual occlusions;

(2) An Exponential Moving Average (EMA)-based trajectory smoothing module is introduced to improve the ByteTrack framework. By computing a weighted average of historical trajectory positions, this module compensates for the limitations of Kalman filtering during abrupt changes in the target motion state, thereby significantly reducing tracking-box jitter and ensuring the continuity of target trajectories. This makes it particularly suitable for practical applications in complex dynamic scenarios.

(3) A real-world multi-pig tracking dataset covering multiple scenes and camera viewpoints is constructed, and extensive experiments are conducted to validate the effectiveness of the proposed method.

MATERIALS AND METHODS

Dataset construction

In order to ensure the diversity of data scenarios, videos were collected from different farms, with some videos coming from a farm in Taiyuan, Shanxi (Pig Farm 1), some from a farm in Yuncheng, Shanxi (Pig Farm 2), and some from publicly available online datasets. Figure 1 shows samples from the dataset.

As shown in Figure 1, (a) and (c) are taken from an oblique angle, capturing a more comprehensive view of the pigs' bodies, with the main challenge being mutual occlusion. The individuals in (c) have a very high similarity, making identity recognition difficult. (b) is taken from a side view, which is severely obstructed by the pen bars and is also more prone to mutual occlusion. (d) is taken from a top-down view, which reduces occlusion but limits the coverage area and the information that can be collected about the pigs.

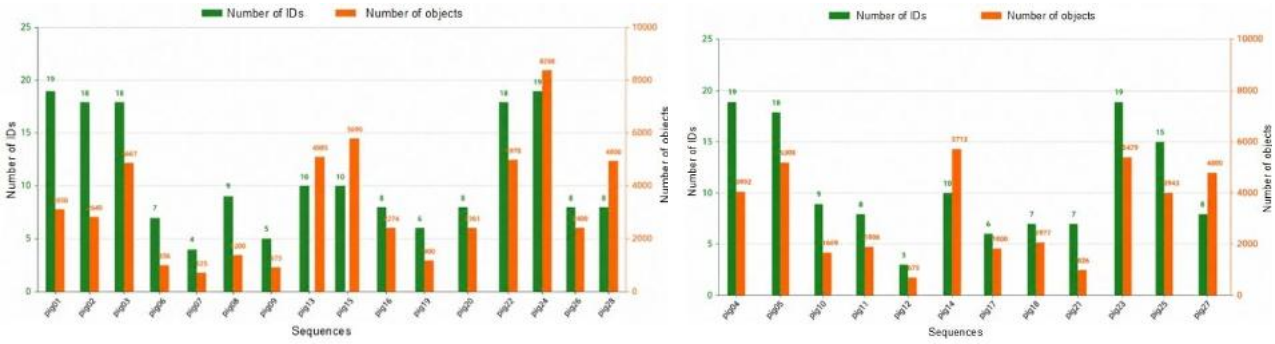
In order to train a multi-object tracking model for pigs, long videos were divided into clips ranging from 150 to 600 frames, and the collected videos were annotated in the MOT format. A total of 28 videos were annotated, with 16 used as the training set, containing 4,980 frames, and 12 used as the test set, containing 4,050 frames. The detailed information of the videos is shown in Figure 2. The entire dataset includes a total of 9,030 frames, 304 IDs, and 88,067 annotated objects.



(a) Oblique top view (b) Side view

(c) Oblique top view (d) Side view

Fig. 1 - Samples in the dataset



(a) Training set (b) Test set

Fig. 2 – Dataset description

Overall architecture

Many online tracking methods rely on Kalman filtering for trajectory prediction (*Stanojevic et al., 2024*). Although Kalman filtering can predict the positions of targets, its predictions are susceptible to noise, resulting in unsmooth trajectories. This is manifested as jumps or jitters in the tracking boxes, which in turn affect the stability of tracking. The workflow of the improved ByteTrack method is shown in Figure 3.

In pig farming scenarios, the movement trajectories of pigs are usually irregular, often accompanied by rapid movements, sudden turns, or body tremors. Based on this, this study introduces the Exponential Moving Average (EMA) algorithm (*Haynes et al., 2012*), which smooths prediction results by performing a weighted average on historical trajectory positions. Unlike Kalman filtering, which assumes relatively smooth linear motion, EMA smoothing is more tolerant to abrupt short-term motion fluctuations commonly observed in pig movement behaviors. This characteristic makes EMA particularly suitable for livestock tracking scenarios with frequent irregular motion patterns.

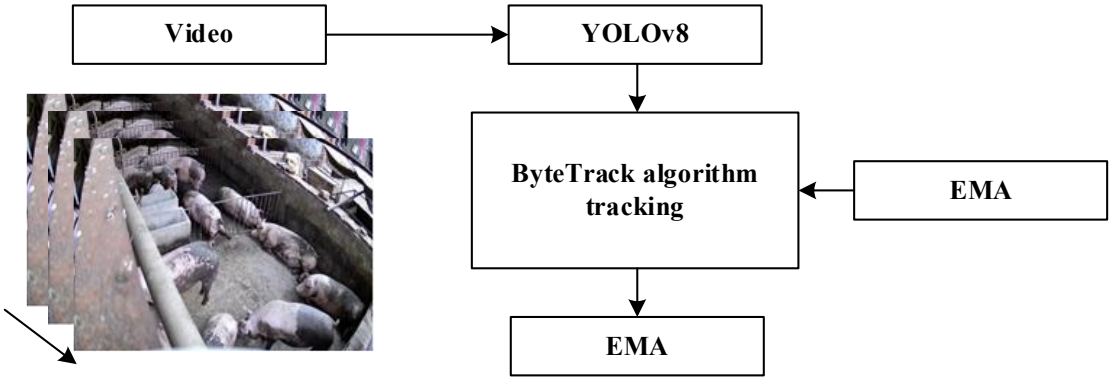


Fig. 3 - Overall architecture of the improved ByteTrack multi-object tracking method

Furthermore, the performance of ByteTrack strongly depends on the stability of object detections, since its association process relies on confidence scores and IoU similarity across consecutive frames. In pig farming scenarios, frequent occlusions, abrupt motion, and similar appearances often lead to unstable detections when conventional detectors are used.

To address these challenges, YOLOv8 is adopted for its stronger feature extraction and localization capability, especially for small-scale and partially occluded targets. Meanwhile, the EMA-based trajectory smoothing module further reduces trajectory jitter caused by sudden motion and detector noise.

ByteTrack Tracking Method

ByteTrack is a lightweight and efficient multi-object tracking algorithm that does not require the integration of a Re-ID module or depend on additional training processes (*Zhang et al., 2022*). When an object undergoes significant occlusion, the confidence of the detection boxes generated by the detection algorithm typically decreases. The most notable improvement of this system is the reasonable reuse of low-confidence detection boxes, which effectively suppresses object loss in occlusion scenarios.

The tracking process of the ByteTrack is shown in Figure 4.

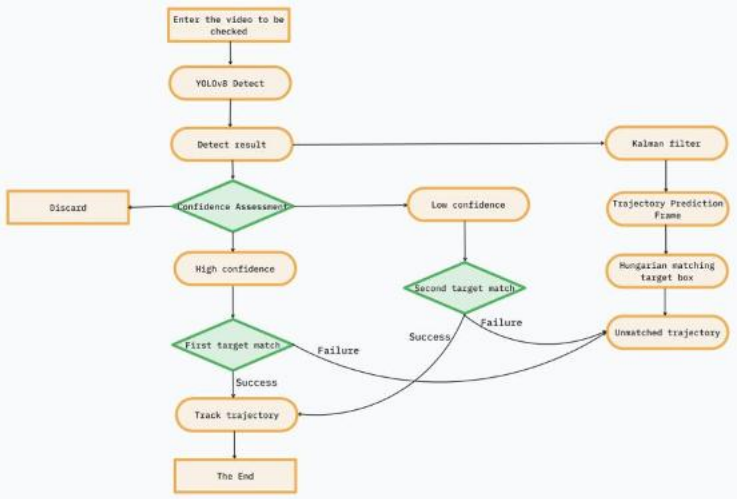


Fig. 4 – Flowchart of ByteTrack

Specifically, the system first divides the detection boxes based on a confidence threshold. In the initial matching stage, the trajectory boxes predicted by the Kalman filter are associated with high-confidence detection boxes through the IoU matrix and the Hungarian algorithm; subsequently, the remaining unmatched trajectories are matched with low-confidence detection boxes in a secondary matching stage. Ultimately, only unmatched detection boxes are discarded, while successfully matched targets are used to update trajectories or initialize new trajectories.

YOLOv8 Detection Method

YOLOv8 is a mature detector widely used in multiple real-world scenarios. These successful applications fully validate YOLOv8's strong adaptability and high performance in various contexts, providing a reliable technical foundation for the pig detection tasks in this study (*Sohan et al., 2024*). The network architecture of YOLOv8 is shown in Figure 5.

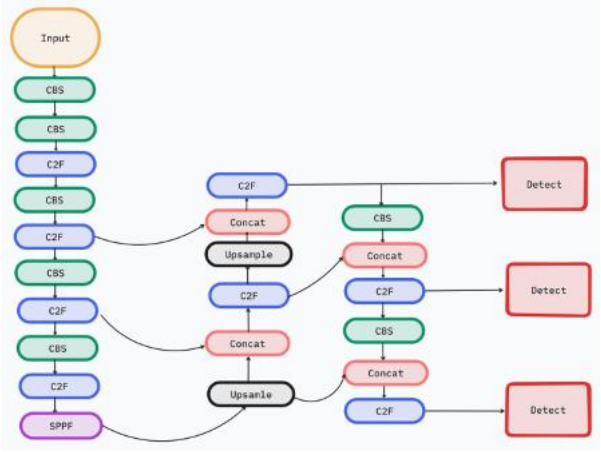


Fig. 5 - YOLOv8 network structure diagram

In Figure 5, the overall architecture of the YOLOv8 model mainly consists of four parts: Input, Backbone, Neck, and Head.

The Input end is responsible for performing data augmentation on the input images to improve the model's generalization ability. The Backbone is used to extract multi-level features from the images and mainly consists of modules such as CBS (*Conv BN SiLU*), C2f (lightweight residual module), and SPPF (spatial pyramid pooling). Through multiple downsampling and feature refinement steps, the Backbone gradually compresses the feature map size while enhancing semantic information.

The Neck section is designed to integrate feature information at different scales to enhance detection performance. This section draws on the design concepts of FPN and PANet, effectively combining shallow and deep features, significantly improving the detection of small targets.

The Head outputs multi-scale feature maps and generates feature maps of three different sizes. Each scale network outputs the target's bounding box, confidence score, and class label.

Evaluation Method

The model evaluation metrics include: $MOTA$, $IDF1$, IDP, MT, ML, IDS, FP(False Positives), FN(False Negatives), precision, and recall (*Dendorfer et al., 2020*).

MOTA is as shown in formula (1):

$$MOTA = 1 - \frac{\sum_t (FN_t + FP_t + IDSW_t)}{\sum_t GT_t} \quad (1)$$

It measures the overall accuracy of the entire tracking system, taking into account missed detections, false positives, and ID switches. IDS is the number of times a target's identity changes. GT is the total number of targets in the ground truth. FP is the false detected targets, and FN is the missed detections.

$IDF1$ is as shown in formula (2):

$$IDF1 = \frac{2 \times IDTP}{2 \times IDTP + IDFP + IDFN} \quad (2)$$

$IDF1$ is the harmonic mean of ID Precision and $ID\ Recall$, used to measure the consistency of identity preservation. $IDTP$ is the correctly predicted identities, $IDFP$ is the incorrectly assigned identities, and $IDFN$ is the missed identities that should have been detected.

The precision and recall is calculated as formula (3) and (4):

$$Precision = \frac{TP}{TP + FP} \quad (3)$$

$$Recall = \frac{TP}{TP + FN} \quad (4)$$

FN (False Negatives) refers to missed detections, meaning that the target in the ground truth was not detected. TP (True Positive) means the model successfully detected a target that actually exists.

RESULTS AND DISCUSSION

Experimental Setup

This experiment was conducted on a hardware platform equipped with an Intel® Core™ i5-11260H processor, 15.7GB of memory, and an NVIDIA GeForce RTX 3050 GPU, with Windows 11 as the operating system. The algorithm was implemented based on Python 3.10 and the PyTorch 2.6.0 framework, and accelerated using CUDA 11.8. The detection model is based on the YOLO architecture and was trained using YOLOv8s, with the training process consisting of 50 epochs.

During the model training phase, the batch size was set to 16, the initial learning rate was set to 0.001, and the weight decay coefficient was 0.0005. The loss function weight allocation was as follows: BoxLoss was 0.05, the classification loss weight was 0.3, and DflLoss was 1.5. To further improve the model's accuracy and recall, the experiment introduced a data augmentation strategy.

Model Training Results

As shown in Figure 6, the trends of key metrics during the model training process are displayed. After training converges, the model's accuracy remains above 0.95, and the recall stays above 0.87.

For each video sequence, the frame rate is maintained at 10 FPS, and the total inference time is approximately 5 minutes.

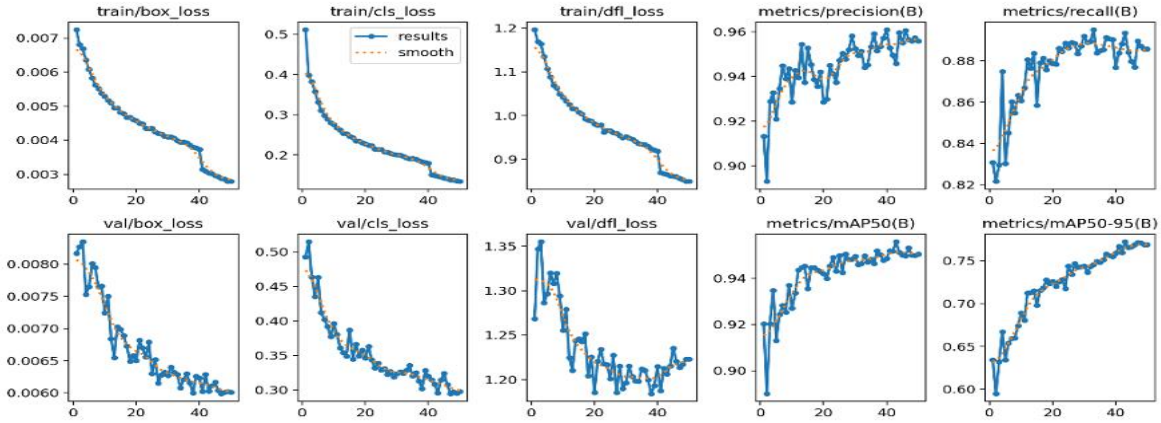


Fig. 6 - Training Results of YOLOv8 Model

Muti-Target Tracking Results Of Live Pigs

The results of multi-pig tracking using the improved ByteTrack algorithm are shown in Table 1.

The improved ByteTrack algorithm performs well in the task of tracking pigs. Although the MOTA metric is relatively low in some specific scenarios (pig12), overall, this improvement is significantly effective.

Table 1

Experimental Results of Multi-object Tracking of Pigs

Video	MOTA	IDF1	IDP	IDR	FP	FN	IDS	precision	recall
pig04	92.84%	92.95%	92.79%	93.11%	145	131	10	96.38%	96.72%
pig05	94.10%	89.66%	89.07%	90.26%	187	116	10	96.52%	97.81%
pig10	72.98%	78.29%	76.50%	80.17%	259	179	13	85.19%	89.28%
pig11	81.34%	67.20%	69.49%	65.06%	104	219	14	93.85%	87.87%
pig12	30.81%	83.52%	72.17%	99.11%	357	105	5	61.49%	84.44%
pig14	84.09%	71.41%	67.63%	75.63%	781	105	23	87.78%	98.16%
pig17	81.00%	91.32%	84.50%	99.33%	328	12	2	84.50%	99.33%
pig18	83.21%	92.05%	91.25%	92.87%	182	147	3	90.95%	92.56%
pig21	79.66%	87.05%	84.34%	89.95%	111	56	1	87.40%	93.22%
pig23	93.63%	83.75%	83.07%	84.45%	210	119	20	96.23%	97.83%
pig25	86.63%	89.52%	84.93%	94.62%	482	32	13	89.03%	99.19%
pig27	99.08%	99.83%	100.00%	99.67%	14	30	0	99.71%	99.38%

Ablation Experiment Results

To evaluate the impact of the improved module on the tracking system, an ablation experiment was conducted on the video pairs in the test set, and the results are shown in Table 2.

Table 2

Ablation Experiment Results

Ablation module	Evaluation metrics								
EMA	MOTA	IDF1	IDP	IDR	IDS	FP	FN	precision	recall
×	80.00%	83.00%	87.79%	79.21%	79	1225	4857	94.58%	84.97%
√	81.61%	85.55%	82.98%	88.69%	114	3160	1251	89.09%	94.65%

Figure 7 shows a comparison of the effects before and after adding the EMA module. (a) and (b) are consecutive video frames without using the EMA module, while (c) and (d) show the results of processing the same two video frames after adding the EMA module. As shown in Figure 6, by introducing the EMA trajectory smoothing algorithm, the consistency between the size of the tracking box and the actual size of the pig's body has been significantly improved.

Comparative Experiment

To verify the effectiveness of the improved ByteTrack algorithm, the experiment compared it with two multi-object tracking algorithms, OCSORT and DeepSORT (*Wojke et al., 2017; Cao et al., 2023*). All three algorithms follow the Tracking-by-Detection paradigm, which first uses an object detector to obtain targets in each frame and then matches the detected boxes with existing trajectories through an association strategy. To ensure a fair comparison, all three used YOLOv8s as the base detection model and conducted multi-object tracking tests on the same video sequences. Table 4 shows the results of the comparative experiment.



(a) Frame 1 without EMA module added (b) Frame 2 without EMA module added (c) Add EMA module frame 1 (d) Add EMA module to frame 2

Fig. 7 - Comparison of effects with or without the EMA module

Table 3

Comparison of Experimental Results

Algorithm Name	Evaluation metrics								
	MOTA	IDF1	IDP	IDR	IDS	FP	FN	precision	recall
DeepSORT	81.10%	85.55%	82..98%	88.69%	114	263	104	89.09%	94.65%
OCSORT	84.10%	85.52%	89.25%	81.89%	149	374	3651	96.90%	87.59%
Improved ByteTrack	81.61%	85.55%	82.98%	88.69%	114	3160	1251	89.09%	94.65%

As shown in Table 3, among the three trackers, DeepSORT performed the worst overall. This is because in complex scenarios, DeepSORT is prone to higher ID switches and missed detections. OC-SORT has relatively high multi-object tracking accuracy, but it also has a high false detection rate, indicating that it often loses track, resulting in poor trajectory continuity. In contrast, the improved ByteTrack algorithm performs well overall, although its accuracy and stability are slightly inferior to OC-SORT. It can be seen that the improved ByteTrack achieves the best overall performance.

Practical Application Discussion

The data from Pig Farm 1 were collected in Taiyuan, Shanxi Province, from April 19 to April 30, 2019. The pigsty consisted of 10 pens (6 m × 5 m × 1.2 m), each housing 5–6 sows. A Hikvision DS-2CD3T86FWDV2-I3S high-definition network camera was installed on the side wall and ceiling (approximately 2 m height) of each pen for video collection.

Multi-object tracking technology enables continuous and non-contact monitoring of pigs by providing stable identity and trajectory information for each individual. Based on this advantage, the proposed improved ByteTrack method can continuously analyze pig movement trajectories and behavioral patterns, offering reliable data support for abnormal behavior detection, activity analysis, and livestock health management. In practical deployment, the system requires only standard HD cameras and GPU-based edge computing devices. By integrating YOLOv8 with the ByteTrack+EMA framework, the system enables real-time pig tracking and trajectory smoothing while remaining compatible with existing farm management systems.

CONCLUSIONS

This study focuses on the challenges in multi-object tracking of pigs, such as variable target scales, mutual occlusion, and complex scenes, and proposes a pig multi-object tracking method based on an improved ByteTrack. By introducing the EMA trajectory smoothing algorithm, the method performs weighted averaging of the targets' historical position information, effectively suppressing the jitter of detection boxes.

Experimental results show that the proposed improved method achieves significant performance gains in real-world applications. Compared with the baseline model ByteTrack, MOTA increased by 1.61%, IDF1 increased by 2.55%, Recall improved by 9.68%, and the FN was greatly reduced. The results indicate that the improved ByteTrack performs stably in complex scenarios with high pig density, frequent occlusions, and highly similar appearances, demonstrating strong practical application potential.

ACKNOWLEDGEMENT

This research was financed by the Basic Research Program of Shanxi Province, China (No.202303021222058).

REFERENCES

[1] Cao J., Pang J., Weng X., Khirodkar R., Kitani K., (2023). Observation-centric sort: Rethinking sort for robust multi-object tracking. *Proceedings of the IEEE/CVF Conference on Computer Vision and Pattern Recognition*, pp. 9686-9696, IEEE, Vancouver / Canada. DOI: https://doi.org/10.1109/CVPR52729.2023.00934.

[2] Compte A., Yan Y., Cortés X., Escalera S., Jacques-Junior J.C., (2025). Housed pig identification and tracking for precision livestock farming. *Expert Systems with Applications*, Vol.293, p.128466, Elsevier, Oxford/UK. DOI: https://doi.org/10.1016/j.eswa.2025.128466.

[3] Dendorfer P., Rezatofighi H., Milan A., Shi J., Cremers D., Reid I., Leal-Taixé L., (2020). MOT20: A benchmark for multi object tracking in crowded scenes. *arXiv preprint arXiv:2003.09003*. DOI: https://doi.org/10.48550/arXiv.2003.09003.

[4] Devi S.J., Doley J., Bharati J., Mohan N.H., Gupta V.K., (2024). Analysis of pig posture detection in group-housed pigs using deep learning-based mask scoring instance segmentation. *Animal Science Journal*, Vol.95, no.1, p.e13975, Wiley, Hoboken/USA. DOI: https://doi.org/10.1111/asj.13975.

[5] Haynes D., Corns S., Venayagamoorthy G.K., (2012). An exponential moving average algorithm. *Proceedings of the 2012 IEEE Congress on Evolutionary Computation (CEC)*, pp.1-8, IEEE, Brisbane/Australia. DOI: https://doi.org/10.1109/CEC.2012.6252962.

[6] Jaoukaew A., Suwansantisuk W., Kumhom P., (2024). Robust individual pig tracking. *International Journal of Electrical and Computer Engineering*, Vol.14, no.1, pp.279-293, IAES, Yogyakarta/Indonesia. DOI: https://doi.org/10.11591/ijece.v14i1.

[7] Li W., Yuan H., Zhu X., Yang X., (2025). EOD-EMDA: A method for automatically identifying and tracking individual pigs in herds. *Smart Agricultural Technology*, Vol.12, p.101259, Elsevier, Amsterdam/Netherlands. DOI: https://doi.org/10.1016/j.atech.2025.101259.

[8] Liang Z., Xu A., Ye J., Zhou S., Weng X., Bao S., (2024). An automatic movement monitoring method for group-housed pigs. *Animals*, Vol.14, no.20, p.2985, MDPI, Basel/Switzerland. DOI: https://doi.org/10.3390/ani14202985.

[9] Lu J., Chen Z., Li X., Fu Y., Xiong X., Liu X., Wang H., (2024). ORP-Byte: A multi-object tracking method of pigs that combines Oriented RepPoints and improved Byte. *Computers and Electronics in Agriculture*, Vol. 219, p. 108782, Elsevier, Amsterdam / Netherlands. DOI: https://doi.org/10.1016/j.compag.2024.108782.

[10] Pandey S., Kalwa U., Kong T., Guo B., Gauger P.C., Peters D.J., Yoon K.J., (2021). Behavioral monitoring tool for pig farmers: Ear tag sensors, machine intelligence, and technology adoption roadmap. *Animals*, Vol.11, no.9, p.2665, MDPI, Basel / Switzerland. DOI: https://doi.org/10.3390/ani11092665.

[11] Psota E.T., Schmidt T., Mote B., Pérez L.C., (2020). Long-term tracking of group-housed livestock using keypoint detection and MAP estimation for individual animal identification. *Sensors*, Vol.20, no.13, p.3670, MDPI, Basel/Switzerland. DOI: https://doi.org/10.3390/s20133670.

[12] Reza M.N., Kabir M.S., Haque M.A., Jin H., Kyoung H., Choi Y.K., Chung S.O., (2025). Instance segmentation and automated pig posture recognition for smart health management. *Journal of Animal Science and Technology*, Vol.67, no.3, p.677, Korean Society of Animal Sciences and Technology, Seoul/Korea. DOI: https://doi.org/10.5187/jast.2024.e112.

[13] Sohan M., Sai Ram T., Rami Reddy C.V., (2024). A review on YOLOv8 and its advancements. *Proceedings of the International Conference on Data Intelligence and Cognitive Informatics (ICDICI)*, pp.529-545, Springer, Singapore. DOI: https://doi.org/10.1007/978-981-99-7962-2_39.

[14] Stanojevic V.D., Todorovic B.T., (2024). BoostTrack: Boosting the similarity measure and detection confidence for improved multiple object tracking. *Machine Vision and Applications*, Vol.35, no.3, p.53, Springer, Berlin/Germany. DOI: https://doi.org/10.1007/s00138-024-01531-5.

[15] Trabachini A., Moreira M.D.R., Harada …D.S., Amorim M.D.N., Silva-Miranda K.O.D., (2025). Precision livestock farming applied to swine farms—A systematic literature review. *Animals*, Vol.15, no.14, p.2138, MDPI, Basel/Switzerland. DOI: https://doi.org/10.3390/ani15142138.

[16] Wojke N., Bewley A., Paulus D., (2017). Simple online and realtime tracking with a deep association metric. *Proceedings of the 2017 IEEE International Conference on Image Processing (ICIP)*, pp.3645-3649, IEEE, Beijing/China. DOI: https://doi.org/10.1109/ICIP.2017.8296962.

[17] Yin Z., Wang Z., Ye J., Zhou S., Xu A., (2025). GCNTrack: A pig-tracking method based on skeleton feature similarity. *Animals*, Vol.15, no.7, p.1040, MDPI, Basel/Switzerland. DOI: https://doi.org/10.3390/ani15071040.

[18] Zhang Y., Sun P., Jiang Y., Yu D., Weng F., Yuan Z., Wang X., (2022). ByteTrack: Multi-object tracking by associating every detection box. *Proceedings of the European Conference on Computer Vision (ECCV)*, pp.1-21, Springer, Cham/Switzerland. DOI: https://doi.org/10.1007/978-3-031-20047-2_1.

EXPERIMENTAL INVESTIGATION OF A MACHINE FOR LOCAL STRIP APPLICATION (MLSA) OF SAPROPEL-BASED ORGANIC FERTILIZER MIXTURES

/

ЕКСПЕРИМЕНТАЛЬНІ ДОСЛІДЖЕННЯ МАШИНИ ДЛЯ ЛОКАЛЬНОГО СМУГОВОГО ВНЕСЕННЯ (МЛСВ) ОРГАНІЧНИХ ДОБРИВ НА ОСНОВІ САПРОПЕЛЮ

Igor TSIZ, Volodymyr DIDUKH, Serhiy KHOMYCH, Victor TARASYUK, Roman KHLOPETSKYI
Lutsk National Technical University / Ukraine
Tel: +38 050 147 28 44; E-mail: igor-71@ukr.net
DOI: https://doi.org/10.35633/inmateh-79-23

Keywords: *sapropel, organic fertilizer mixture, local strip application, applicator machine, torque, mass flow rate*

ABSTRACT

An alternative approach to the utilization of lake sapropel is its mixing with available organic sorbents, such as chopped cereal straw. The application of such mixtures in strips into the soil ensures the formation of a moisture-holding nutrient layer during crop cultivation. To form these strips, an experimental prototype of a single-row machine was developed. Under laboratory conditions, the torque M required to drive the machine and the mixture mass flow rate Q were investigated. The variable parameters included the rotational speed of the metering beater shaft n, the blade inclination angle ξ, the width of the hopper outlet opening a, and the opening position of the metering beater housing gate Δ. To obtain mathematical models of the machine drive torque $M(a,\Delta,\xi,n)$ and the mixture mass flow rate $Q(a,\Delta,\xi,n)$ in the form of regression equations, a statistical design of experiments method for a four-factor experiment based on the Box–Behnken design was applied. Analysis of the obtained regression equations showed that, in order to reduce the energy consumption of the machine drive, it is advisable to maintain the beater rotational speed within the range of $n = 550$–600 rpm, the blade inclination angle at $\zeta = 45 - 50^0$, and the maximum opening of the metering beater housing gate $\Delta = 0.06$ m. A nomogram was developed for regulating the mixture feeding rate of the machine by changing the width of the hopper gate opening a. It was also established that, at the maximum mass flow rate of $Q = 3.5$ kg/s, the torque required for the machine drive M ranged from 6.9 to 7.2 N·m.

РЕЗЮМЕ

Альтернативним способом використання озерного сапропелю є його змішування із доступними органічними сорбентами, наприклад, січкою соломи злакових культур. Внесення таких сумішей смугами у ґрунт забезпечує формування вологоутримуючого поживного шару під час вирощування сільськогосподарських культур. Для формування таких смуг розроблено експериментальний зразок однорядної машини. В умовах лабораторії досліджували крутний момент M, необхідний на привід машини та продуктивність подачі суміші Q. Змінними параметрами були частота обертання вала дозуючого бітера n, кут нахилу лопаті ξ, ширина вихідного отвору бункера a машини та положення заслінки дозуючого бітера Δ. Для отримання математичних моделей крутного моменту приводу машини $M(a,\Delta,\xi,n)$ та продуктивності подачі суміші $Q(a,\Delta,\xi,n)$ у вигляді рівняння регресії було використано математичний метод планування для чотирифакторного експерименту, який базувався на плані Бокса-Бенкіна. Аналізуючи отримані рівняння регресії встановили, що для зменшення енергетичних затрат на привід машини доцільно забезпечувати частоту обертання бітера у межах $n = 550$-600 об/хв., кут нахилу лопаті - $\zeta = 45 - 50^0$ та максимальну величину відкривання заслінки корпусу дозуючого бітера $\Delta = 0.06$ м. Отримано номограму для регулювання продуктивності подачі суміші машиною шляхом зміни ширини відкривання заслінки бункера a. Також встановлено, що під час досягнення максимальної продуктивності у $Q = 3.5$ кг/с значення крутного момент на привід машини M знаходиться у межах 6.9 до 7.2 Н·м.

INTRODUCTION

A distinctive feature of lake sapropels is their complex influence on all factors determining soil fertility. In particular, numerous studies have reported a positive effect of sapropel and sapropel-based fertilizers on the soil water–air regime and thermal conditions. When sapropel is applied to the soil, an increase in total and capillary water capacity, water-holding capacity, and moisture content of the upper soil horizon is observed (*Baksiene et al., 2015; Edesi et al., 2020; Shevchuk, 1996; Skrylnyk et al., 2021*). It has also been established that the extent of improvement in the water–physical properties of soil depends both on the application rate of sapropel fertilizers and on their quality, particularly their chemical and mechanical composition.

At the same time, the commonly known methods of using sapropel as a fertilizer involve its dewatering from the natural moisture content of deposits, typically ranging from 92–98%, down to approximately 60% *(Booth et al., 2007; Bulgakov et al., 2017; Zarina et al., 2023*). Dewatering sapropel to such a moisture level is associated with significant energy consumption and financial costs, which in turn increases the cost of fertilizers produced on its basis.

It is also well known that achieving high yields of agricultural crops is largely constrained by climate change in general and, in particular, by the catastrophic depletion of soil moisture reserves. Recent studies (*Didukh et al., 2024*) have demonstrated the possibility of forming a nutrient, moisture-holding layer from sapropel and sapropel-based mixtures capable of accumulating water and, when necessary, releasing it to the surrounding soil layers and plants.

Climate change, the energy crisis, and ongoing soil degradation processes are forcing farmers to move away from conventional farming systems and to adopt energy- and resource-saving technologies, such as Mini-till, No-till, Strip-till, and Verti-till (*Jaskulska et al., 2020; Kargwal et al., 2022; Kosolap and Krotinov, 2011*). Among these systems, Strip-till technology has become increasingly widespread. This approach replaces traditional row cultivation with strip cultivation, typically characterized by inter-row spacings ranging from 30 to 75 cm.

These trends create favorable conditions for the local application of fertilizers based on sapropel of natural moisture content for crops grown using wide-row planting systems. This solution is particularly relevant for soils with a light mechanical composition that are located in close proximity to sapropel deposits. Such fertilizers may consist of sapropel mixtures with readily available organic sorbents, for example, chopped cereal straw (*Didukh et al., 2024*).

Existing designs and studies of equipment for the local strip application of organic fertilizers in orchards and for row crops (*Glancey and Adams, 1996; LaguÎ et al., 2006; Popa et al., 2025; manufacturer data: Renmark*) are generally based on conventional manure spreaders additionally equipped with transverse belt or screw conveyors, or with horizontal spreading discs. These machines enable the placement of organic fertilizer strips on the soil surface near tree trunks, berry bushes, vineyards, or within the inter-rows of row crops. For the local strip application of liquid organic fertilizers into the soil, tank units equipped with cultivators have been developed. Such systems perform soil tillage according to the Strip-till concept and typically form from 4 to 12 fertilizer strips, with inter-row spacings varying from 45 to 75 cm *(manufacturer data: Vogelsang*). For the subsurface strip application of solid organic fertilizers, machines employing flexible screw-type distribution devices have also been developed and tested (*Landry et al., 2011*). However, the aforementioned machines are not suitable for the application of sapropel-based mixtures or for the formation of a moisture-holding nutrient layer due to specific design features that prevent their working elements from handling materials with increased stickiness and viscosity. Taking into account the advantages and limitations of the existing machine designs, a modernized organic fertilizer spreader was developed to enable the formation of subsurface strips of high-moisture solid organic fertilizers for the cultivation of wide-row crops (*Didukh et al., 2024*).

The primary quality parameter of machines designed for uniform surface application of organic fertilizers is the uniformity of distribution. Consequently, numerous experimental and theoretical studies have been devoted to determining the influence of spreading unit parameters on the uniformity of fertilizer distribution over the field surface (*Duhovnik et al., 2004; Cârdei et al., 2019; Ştefan (Popa) et al., 2015; Stefan et al., 2021*).

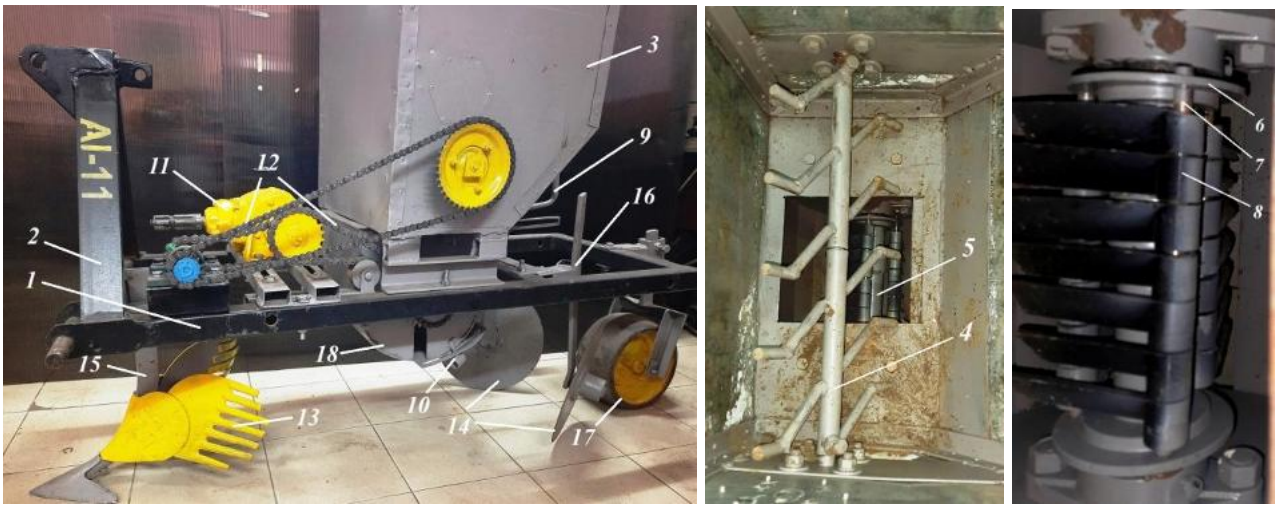
Well-known theoretical and experimental studies of organic fertilizer application machines have also focused on evaluating the influence of hopper geometry and conveying system parameters on machine energy consumption and on the characteristics of the outgoing fertilizer flow (*Landry et al., 2005; Ştefan et al., 2017*).

For machines performing strip application of organic fertilizers, experimental investigations have established specific energy consumption values and deviations in application rates for individual strips (*LaguÎ et al., 2006; Landry et al., 2011*). In recent years, there has also been a widespread implementation of advanced computer-aided design and simulation tools for the development and modeling of organic fertilizer spreaders and their working elements (*Sengottaian et al., 2019; Stefan et al., 2025*).

The aim of this study is to investigate the influence of the main design and technological parameters of the working elements of a modernized organic fertilizer spreader (*Didukh et al., 2024*) on the drive torque and the mixture mass flow rate of the machine.

MATERIALS AND METHODS

To investigate the developed design of the modernized organic fertilizer spreader (*Didukh et al., 2024*), an experimental prototype of a single-row machine for the local strip application (MLSA) of sapropel-based mixtures was manufactured (Fig. 1a). The machine is based on a frame *1*, on which the hitch mechanism *2* and the fertilizer hopper *3* are mounted. An agitator *4* is installed inside the hopper (Fig. 1b), while a metering beater *5* is located beneath the hopper within its own housing. The metering beater 5 (Fig. 1c) consists of a central shaft fitted with two flanges *6*, each carrying three shafts *7*. Blades 8 are pivotally mounted on the shafts *7*. Regulation of the fertilizer flow supplied from the hopper *3* to the metering beater *5* is performed using a gate *9*, whereas the overall fertilizer application rate is controlled by a gate *10* of the metering beater housing *18*.



a b c

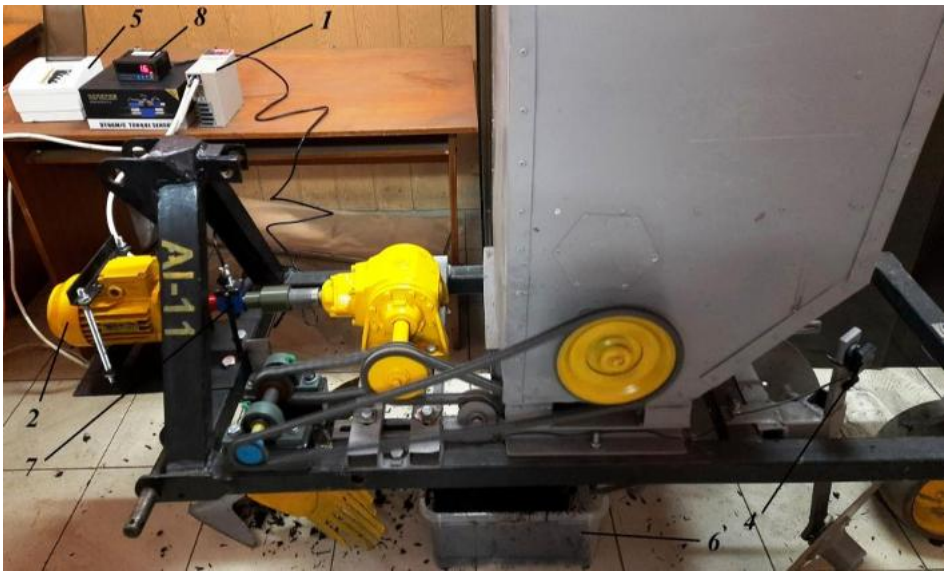
Fig. 1 - Experimental prototype of the MLSA machine for sapropel and sapropel-based mixtures
***(a)** general view; **(b)** internal part of the hopper; **(c)** metering beater*

To form the furrow, the machine is equipped with a furrow opener *13*, while furrow covering is performed by disc closers *14*. The furrow depth and the ridge height formed during furrow covering are adjusted by the mechanisms controlling the working depth of the opener *15* and the position of the disc closers *16*, respectively. To ensure a horizontal operating position of the machine, a support wheel *17* is provided, which simultaneously performs the function of soil compaction above the applied fertilizers.

Based on theoretical analysis and literature sources (*Didukh et al., 2024; LaguÎ et al., 2006*), it was established that the drive torque and the mixture mass flow rate are significantly influenced by the following design and technological parameters: the rotational speed of the metering beater shaft, the angle between the working surface of the blade and the axis of rotation of the metering beater (hereinafter referred to as the blade inclination angle), the width of the machine hopper outlet opening (determined by the position of the hopper gate), and the opening angle of the metering beater housing gate (determined by the position of the metering beater gate).

To investigate the influence of these factors on the torque required to drive the machine M and on the mixture mass flow rate Q, laboratory tests were conducted. For this purpose, the experimental machine prototype was additionally equipped with an asynchronous motor *2*, an electronic rotational speed controller *1*, and a torque sensor *7* with a monitoring unit *8* (Fig. 2). To obtain mathematical models describing the

variation of the machine drive torque M and the mixture mass flow rate Q in the form of regression equations, a design of experiments approach for a four-factor experiment based on a second-order, symmetric, non-composite Box–Behnken design, originally proposed by *Box and Behnken, (1960)*, was applied. The factors investigated in the experiment are presented in Table 1. The ranges of variation in the rotational speed of the metering beater shaft and the blade inclination angle were selected based on the results reported by *Didukh et al., (2024)*.



a)



b)



c)

Fig. 2 - MLSA machine equipment used for laboratory investigations of sapropel and sapropel-based mixtures:
(a) general view; (b) installation of the Hall-effect sensor; (c) rotational speed monitor.

Table 1

Investigated factors and their variation ranges

Variation level	Factors			
	Width of the hopper outlet opening, *a*	**Opening of the metering beater housing gate, *Δ* (m)**	**Blade inclination angle, *ζ***	**Rotational speed of the metering beater shaft, *n***
	[m]	**[m]**	**[deg.]**	**[rpm]**
	x_1	x_2	x_3	x_4
Upper (+1)	0.14	0.08	50	850
Central (0)	0.10	0.06	45	700
Lower (-1)	0.06	0.04	40	550

The investigated factors were fixed at the specified levels as follows. To vary the rotational speed of the metering beater shaft n, a frequency inverter Veichi AC01-T3-1R5G-B (1) was used to control the rotational speed of the asynchronous drive motor (2) (Fig. 2).

The achieved rotational speed of the metering beater shaft was monitored using a Hall-effect sensor (3) and recorded based on the readings of the monitor (4). To vary the blade inclination angle ζ, three sets of blades were manufactured from PLA plastic using 3D printing, with each set consisting of 21 blades (Fig. 3) and corresponding to the angle values listed in Table 1. The suitability of using plastic for blade manufacturing was substantiated in *Tsiz et al., (2026)*. The blade length from the mounting axis was 100 mm, while the width and thickness of the working part were 30 mm and 5 mm, respectively.



a) b)

Fig. 3 – Photograph of the blade manufacturing process with an inclination angle of $\zeta = 45^0$ by 3D printing (a) and the manufactured blades with inclination angles of $\zeta = 40^0$ and $\zeta = 50^0$ (b).

The experiments were carried out using a mixture consisting of 87% sapropel with a moisture content of $W = 92.2$ %, and 11% chopped winter wheat straw with a moisture content of $W = 13.6$ % and a cutting length of 5–20 mm. The moisture content of the mixture was $W = 81.7$ %. The stickiness characteristics of this and other sapropel-based mixtures are presented in *Tsiz et al., (2026).*

After setting the factor values specified by the experimental design in the form of parameters of the experimental setup, the hopper was filled with the above-described mixture, and the power supply of the frequency inverter Veichi AC01-T3-1R5G-B (1) was switched on using the control panel (5). Subsequently, the electric current frequency corresponding to the rotational speed of the beater shaft required by the experimental plan was set on the inverter display, and the power supply of the electric motor (2) was switched on. During the experiment, the mixture delivered by the metering beater was collected in a container (6) (Fig. 2). Each experimental run involved operating the machine for 20 s, after which the drive was switched off. During the experiment, between the 15th and 20th second of machine operation, the torque value measured by the sensor (7) was recorded based on the readings of the monitor (8).

The mixture mass flow rate of the machine, expressed in kg/s, was determined by dividing the mass of the mixture collected in the container (6) (Fig. 2) during one experimental run by the duration of the experiment (20 s). All experiments aimed at determining the drive torque and the mixture mass flow rate at the factor levels specified by the experimental design were performed in three replicates.

RESULTS

To process the experimental data obtained for the drive torque and the mixture mass flow rate, the methodology described in *Box and Behnken, (1960)* and *Tsiz and Homich, (2013)* for a four-factor experimental design was applied. The calculations were performed using Mathcad software. The reproducibility of the experiment was confirmed using Cochran's test. For the drive torque, the calculated value of the Cochran criterion satisfied the condition $G^{calc} = 0.110 < G^{tab}(0.05;27;2) = 0.318$ and for the mixture mass flow rate of the machine, the corresponding condition – $G^{calc} = 0.213 < G^{tab}(0.05;27;2) = 0.318$ was also fulfilled. The maximum standard deviation of the experimental torque values was $S = 0.49$ N·m, whereas the corresponding value for the mixture mass flow rate was $S = 0.22$ kg/s.

The significance of the regression coefficients was evaluated using confidence intervals determined according to Student's *t*-test. The tabulated value of this criterion at a 5% significance level and with the corresponding number of degrees of freedom of the reproducibility variance $f_1 = 2$ was $t = 4.3$.

After excluding the terms with statistically insignificant coefficients, the regression equations took the following form:

– for the drive torque

$$y_1 = 4.7 + 1.467 \cdot x_1 - 0.233 \cdot x_2 - 0.133 \cdot x_3 + 1.017 \cdot x_4 + \\ +0.275 \cdot x_1 \cdot x_4 + 0.188 \cdot x_1^2 - 0.388 \cdot x_2^2 + 0.187 \cdot x_4^2 \quad (1)$$

– for the mixture mass flow rate

$$y_2 = 1.29 + 1.007 \cdot x_1 + 0.101 \cdot x_2 + 0.455 \cdot x_4 + 0.156 \cdot x_1 \cdot x_4 + 0.436 \cdot x_1^2 + 0.262 \cdot x_4^2 \quad (2)$$

where: x_1, x_2, x_3, x_4 - are the coded values corresponding to the following factors: the width of the hopper outlet opening a, the opening of the metering beater housing gate Δ, e blade inclination angle ζ, and the rotational speed of the metering beater shaft n, respectively.

The adequacy of the regression equations was verified using Fisher's test. The calculated value of this criterion for the drive torque, with the variance of inadequacy $S_{n.}^2 = 0.00502$ and the variance of experimental reproducibility $S_y^2 = 0.01$ was $F^{calc} = 5.02$. The tabulated value of Fisher's criterion at the adopted 5% significance level was:

$$F^{tab}(0.05; f_2; f_1) = 19.43 \quad (3)$$

where: $f_2 = 18$ - is the number of degrees of freedom of the inadequacy variance;

$f_1 = 2$ - is the number of degrees of freedom of the experimental reproducibility variance.

Since

$$F^{calc.} = 5.02 < F^{tab}(0.05; f_2; f_1) = 19.43 \quad (4)$$

the hypothesis of adequacy of the regression equation, for which the response function is the drive torque required for machine operation, is confirmed.

The calculated value of Fisher's criterion for the mixture mass flow rate, with the inadequacy variance $S_{n.}^2 = 0.011$ and the experimental reproducibility variance $S_y^2 = 3.612 \times 10^{-3}$ was equal to $F^{calc} = 3.011$. The tabulated value of Fisher's criterion at the adopted 5% significance level was:

$$F^{tab}(0.05; f_2; f_1) = 19.44 \quad (5)$$

where: $f_2 = 20$ - is the number of degrees of freedom of the inadequacy variance;

$f_1 = 2$ - is the number of degrees of freedom of the experimental reproducibility variance.

Since

$$F^{calc.} = 3.011 < F^{tab}(0.05; f_2; f_1) = 19.44 \quad (6)$$

the hypothesis of adequacy of the regression equation, for which the response function is the mixture mass flow rate, is confirmed.

After converting the factors to their natural values, the regression equations (7) for the drive torque and (8) for the mixture mass flow rate of the machine were obtained. The reported precision of the regression coefficients was required to ensure the adequacy of the developed regression equations. Based on equation (7), response surfaces were constructed (Fig. 3a–c), whereas two-dimensional cross-sections of the response surface were generated based on equation (8) (Fig. 3d).

$$M = 3.14627778 - 18.90833333 \cdot a + 104.75 \cdot \Delta - 0.0266 \cdot \xi - 0.00943889 \cdot n + \\ +0.04583333 \cdot a \cdot n + 117.5 \cdot a^2 - 970.0 \cdot \Delta^2 + 8.31 \cdot 10^{-6} \cdot n^2; \quad (7)$$

$$Q = 6.59694444 - 47.525 \cdot a + 5.05 \cdot \Delta + 0.01586889 \cdot n + \\ +0.026 \cdot a \cdot n + 272.5 \cdot a^2 + 1.164 \cdot 10^{-5} \cdot n^2, \quad (8)$$

where: M - the drive torque required for machine operation [N·m];

Q - the mixture mass flow rate of the machine [kg/s].

The analysis of the regression equation for the drive torque required for machine operation (1) and the corresponding response surfaces (Fig. 4a–c) indicates a significant influence of all the investigated factors on this parameter. An increase in the drive torque is caused by an increase in the hopper outlet width a and the rotational speed of the metering beater shaft n. For factor a, this effect is associated with an increase in the mass of the mixture supplied by the metering beater per unit time, whereas for factor n, it is explained by the increased aerodynamic resistance acting on the rotating rotor blades.

In turn, an increase in the blade inclination angle ζ leads to a reduction in the projected area of the blade surface onto the plane perpendicular to the direction of rotation, which results in a decrease in aerodynamic resistance. The reduction in the drive torque with increasing opening of the metering beater housing gate Δ is evidently caused by a decrease in resistance during the discharge of the mixture from the rotor blades through the outlet opening of the housing.

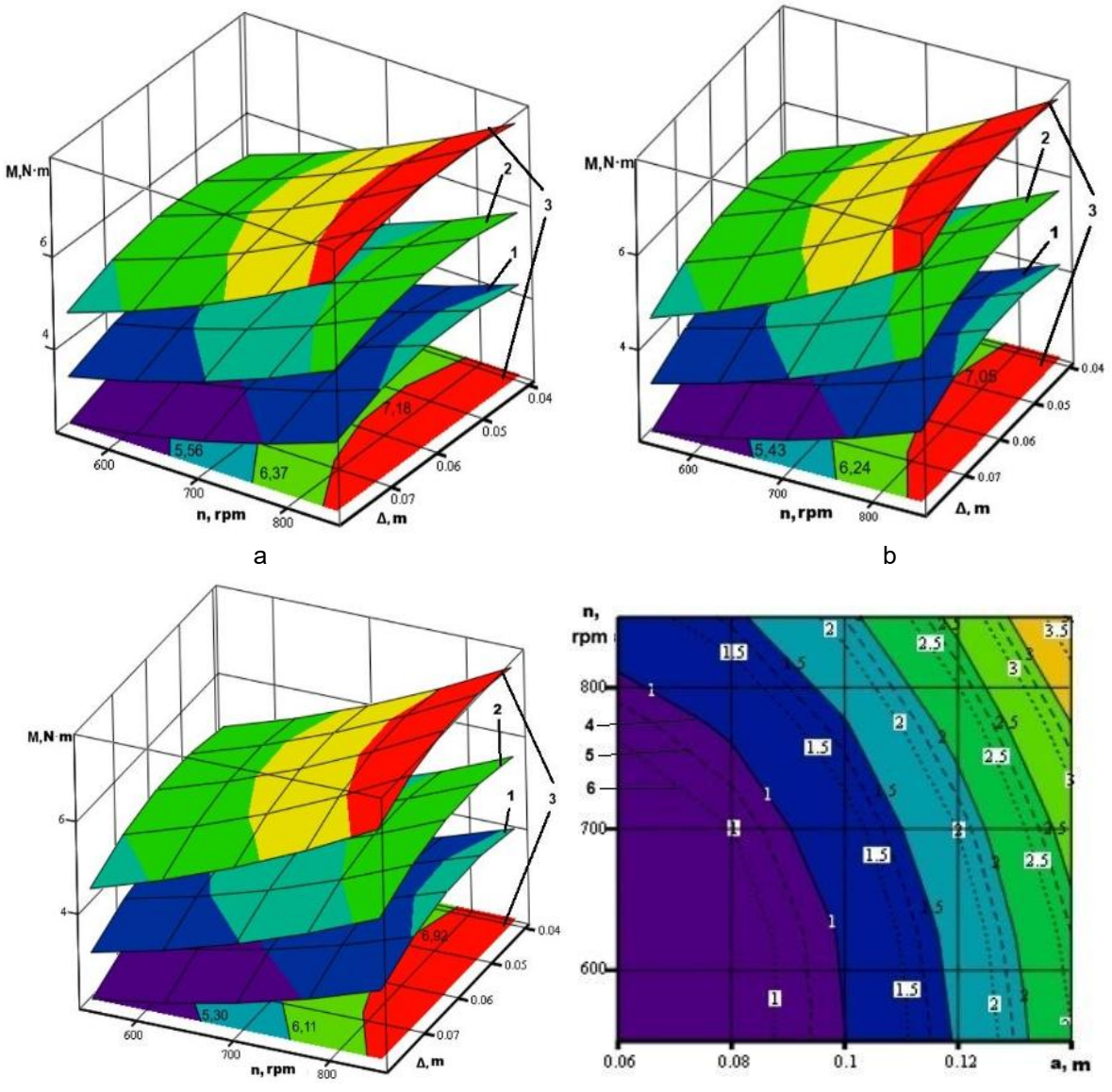


Fig 4 – Response surfaces constructed using equation (7) (a–c) and contour plots generated based on equation (8) (d).

a - $\zeta = 40^0$; b - $\zeta = 45^0$, c - $\zeta = 50^0$; 1 - $a = 0.06$ m; 2 - $a = 0.10$ m; 3 - $a = 0.14$ m; 4 - $\Delta = 0.04$ m; 5 - $\Delta = 0.06$ m; 6 - $\Delta = 0.08$ m

At the same time, the analysis of Equation (2) and the corresponding plots (Fig. 4d) indicates that the blade inclination angle ζ has no significant effect on the mixture mass flow rate. An increase in the mixture mass flow rate is observed with increasing rotor rotational speed n and hopper outlet width a.

Based on a comparison of the plots for the drive torque M (Fig 4, a-c) and the mixture mass flow rate Q (Fig 4, d) it was established that an increase in productivity Q is accompanied by an increase in the drive torque required for machine operation M. In order to achieve the maximum productivity $Q = 3.5$ kg/s the maximum drive torque values M in the range of 6.9–7.2 N·m are required.

Visual observations of the MLSA operation demonstrated stable performance without adhesion of the moist mixture to the working surfaces of the beater blades over the entire investigated range of factor variation (Table 1).

Therefore, in order to reduce energy consumption for machine operation, it is advisable to maintain the beater rotational speed within the range of $n = 550–600$ rpm, a blade inclination angle of $\zeta = 45 – 50^0$, and the maximum opening of the metering beater housing gate $\Delta = 0.06$ m.

Under these conditions, the required fertilizer application rate should be adjusted by selecting the hopper outlet width a using the plot shown in Fig. 4d as a regulating nomogram.

To compare the experimentally obtained values of drive torque M and productivity Q with the results obtained in studies of similar machines mentioned above, it is necessary to test the MLSA under field conditions. Laboratory investigations confirmed the operability of the developed design and the correctness of the adopted design solutions, which ensure self-cleaning of the blades when working with mixtures of increased stickiness.

A further development of the conducted research is the design of a multi-row machine capable of forming strips of a moisture-holding nutrient fertilizer layer during the cultivation of crops with different inter-row spacings. The design of such a machine can be developed by modernizing existing organic fertilizer spreaders using the proposals described in *Didukh et al., (2024)*.

CONCLUSIONS

Based on previous studies and existing designs of machines for organic fertilizer application, an experimental prototype of a single-row MLSA was developed. Equipping the MLSA with an electric drive, a frequency controller, and a torque sensor enabled experimental investigations of its operation under laboratory conditions.

The conducted MLSA studies, using a mathematical design of experiments approach, made it possible to obtain regression-based mathematical models describing the dependence of the drive torque $M(a,\Delta,\xi,n)$ and the mixture mass flow rate $Q(a,\Delta,n)$ on the investigated factors.

It was established that achieving the maximum productivity $Q = 3.5$ kg/s requires the maximum drive torque M values in the range from 6.9 to 7.2 N·m. In order to reduce energy consumption during machine operation, it is advisable to maintain the beater rotational speed within the range of $n = 550$-600 rpm, the blade inclination angle $\zeta = 45 – 50^0$ and the maximum opening of the metering beater housing gate $\Delta = 0.06$ m. Under these operating conditions, the required fertilizer application rate should be set by selecting the hopper outlet width a, using the plot shown in Fig. 4d as a regulating nomogram.

Future research will focus on field testing of the MLSA and on the development of a multi-row machine capable of forming strips of a moisture-retaining nutrient fertilizer layer for crops grown with different row spacings.

REFERENCES

[1] Baksiene E., Asakaviciute R., Romanovskaja D., Tripolskaja L., Razukas A., (2015). The influence of lake sediments on sandy loam soil properties and crop yield, *Romanian agricultural research*, No. 32., ISSN 1222-4227, pp. 183-190.

[2] Booth C.A., Baksiene E., Fullen M.A., Ciunys A., (2007). Long-term agrochemical dynamics: engineering, application and challenges of calcareous sapropel as a soil fertilizer. *International Journal of Ecodynamics*, 2(2), pp. 108–116. https://doi.org/10.2495/ECO-V2-N2-108-116

[3] Box G.E.P., Behnken D.W., (1960) Some new three level designs for the study of quantitative variables. *Technometrics,* Vol.2, No. 4. pp. 425-475.

[4] Bulgakov V.P., Konishchuk V.V., Lozovitska O. V., Cherednyk Yu. S., (2017). Analysis of the properties of sapropel when used on degraded soils of western Polissya (Аналіз властивостей сапропелю при використанні на деградованих грунтах західного Полісся), *Scientific Journal ´ScienceRise»* №1/1(30), pp. 27-31. https://doi.org/10.15587/2313-8416.2017.90394

[5] Cârdei P., Stefan V., Popa L., Ciupercă R., (2019). Statistical models for the working process carried out by the organic fertilizer spreading machine. *INMATEH Agricultural Engineering,* Vol. 58 (2), pp. 121-128. https://doi.org/10.35633/INMATEH-58-13

[6] Didukh V., Tsiz I., Satsiuk V., Khlopetscyi R., (2024). Research in processes and machines for local strip application of moisture-holding organic fertilizers. *Proceedings of 23rd International Scientific Conference "Engineering for Rural Development".* Jelgava, 22.-25.05.2024. pp. 212-219. https://doi.org/10.22616/ERDev.2024.23.TF044

[7] Duhovnik J., Benedičič J., Bernik R., (2004). Analysis and design parameters for inclined rotors used for manure dispersal on broadcast spreaders for solid manure. *Transactions of the ASAE*, Vol. 47 (5), pp. 1389−1404. https://doi.org/10.13031/2013.17604

[8] Edesi L., Kangor T., Loide V., Vettik R., Tamm I., Kennedy H.J., Haljak M., Tamm U., Vosa T., Tamm K., Talve T., Karron E., (2020). Effects of lake sediment on soil chemical composition, dehydrogenase activity and grain yield and quality in organic oats and spring barley succession. *Agronomy Research*. 18(3), pp. 2022-2032. https://doi.org/10.15159/AR.20.197

[9] Glancey J. L., Adams R. K., (1996). Applicator for sidedressing row crops with solid wastes. Transactions of the ASAE. Vol. 39(3), pp. 829-835. https://doi.org/10.13031/2013.27567

[10] Jaskulska I., Romaneckas K., Jaskulski D., Gałęzewski L., Breza-Boruta B., Dębska B., Lemanowicz J., (2020). Soil properties after eight years of the use of strip-till one-pass technology. *Agronomy*, 10(10). pp. 1-16. https://doi.org/10.3390/AGRONOMY10101596

[11] Kargwal R., Yadvika, Kumar A., Garg M., Chanakaewsomboon I., (2022). A review on global energy use patterns in major crop production systems. *Environmental Science:* Adv. 1., pp. 662-679. https://doi.org/10.1039/d2va00126h

[12] Kosolap M.P., Krotinov O.P. (2011) *Farming system No-till (Система землеробства No-till)*. Kyiv, Logos.

[13] Laguë C., Agnew J., Landry H., Roberge M., Iskra C., (2006). Development of a precision applicator for solid and semi-solid manure. *Applied Engineering in Agriculture,* Vol. 22 (3), pp. 345-350. https://doi.org/10.13031/2013.20451

[14] Landry H., King T., Schoenau J.J., Laguë C., Agnew J.M., (2011). Development and evaluation of subsurface application technology for solid organic fertilizers. *Applied Engineering in Agriculture,* Vol. 27 (4), pp. 533-549. https://doi.org/10.13031/2013.38200

[15] Landry H., Piron E., Agnew J.M., Laguë C., Roberge M., (2005). Performances of conveying systems for manure spreaders and effects of hopper geometry on output flow. *Applied Engineering in Agriculture*, Vol. 21(2), pp. 159−166. https://doi.org/10.13031/2013.18147

[16] Popa L., Zaica A., Ştefan V., (2025). Technology and technical equipment for organic fertilization in orchards, *Fruit Growing Research*, Vol. XLI, pp. 169-177. https://doi.org/10.33045/fgr.v41.2025.18

[17] Sengottaian K., Mohanrajhu N., Palani S., Jayabalan C., (2019). Design of manure spreader machine for agricultural farm field. *International Journal of Innovative Technology and Exploring Engineering,* Vol. 9 (1), pp. 4280-4284. https://doi.org/10.35940/ijitee.A4877.119119

[18] Shevchuk M.Yo., (1996). *Sapropel of Ukraine: reserves, quality and perspectives of use (Сапропелі України: запаси, якість та перспективи використання)*. Lutsk, Nadstyr'ya.

[19] Skrylnyk I., Hetmanenko V., Xiao Y., Kutova A., Artemieva K., Zheng Y., Shi R., (2021). Sorption ability of soil improvers based on sapropel and biochar to mineral fertilizer nutrients. *Earth and Environmental Science* 792(1):012006. https://doi.org/10.1088/1755-1315/792/1/012006

[20] Ştefan (Popa) V., Ciupercă R., Popa L., Nedelcu A., Lazăr G., Petcu A.S., Zaica A., (2015). The influence of physical characteristics of solid organic fertilizers on quality of land spreading. *INMATEH Agricultural Engineering,* Vol. 46 (2), pp. 77-84.

[21] Ştefan V., David L., Popa L., Zaica A., (2017). Use of theoretical mathematical relations for calculating the application and mass flow rate of a rear delivery vertical-axis manure spreader. *Proceedings of* 16th International Scientific Conference *´Engineering for Rural Development»,* Jelgava, 24.-26.05.2017, pp. 1284-1291. https://doi.org/10.22616/ERDev2017.16.N279

[22] Stefan V., Popa L., Harabagiu A., Ciupercă R., Zaica A., Vișan A. (2025). Optimization of organic fertilizer distribution using EDEM simulation analysis. *INMATEH Agricultural Engineering*, pp.1217-1230. https://doi.org/10.35633/inmateh-76-102

[23] Stefan V., Zaica A., Iosif A., (2021). Research on the uniformity degree of solid organic fertilizers distribution. *INMATEH Agricultural Engineering,* Vol. 65 (3) *pp.* 495-504. https://doi.org/10.35633/inmateh-65-51

[24] Tsiz I., Homich S., (2013), Experimental research of working process of pneumatic intake device for sapropel extraction, *INMATEH, Agricultural Engineering,* Vol. 40, No. 2., pp. 67-72.

[25] Tsiz I., Khomych S., Tsyz T., Holii V., (2026). Study of tangential stickiness force of mixtures based on organic sapropel. Proceedings of 25nd International Scientific Conference “Engineering for Rural Development”. Jelgava, 27.-29.05.2026. pp. 127-132. https://doi.org/10.22616/ERDev.2026.25.TF024

[26] Zarina L., Cerina S., Proskina L., (2023). Effect of sapropel fertilizer on the quality of the yield of some field crops. *Agronomy Research* 21(3), pp.1328–1337. https://doi.org/10.15159/ar.23.045
[27] https://www.renmark.it/vendita-spandiletame-jolly-spazi-stretti-distribuzione-a-ventolino/
[28] https://www.vogelsang.info/en/products/liquid-manure-spreading-technology/soil-cultivation-systems/xtill

STUDY ON THE EFFECTS OF MOISTURE CONTENT ON THE COMPRESSIVE MECHANICAL PROPERTIES OF SWEET POTATO ROOTS
/
含水率对甘薯块根压缩力学特性的影响研究

Shuai GAO, Yuecheng WU, Kaiyan XIN, Ping ZHAO*)
College of Engineering, Shenyang Agricultural University, Shenyang, LIAONING, 110161, China
Tel: +86 13591675814; E-mail addresses: zhaopingxdg@syau.edu.cn
Corresponding author: Ping Zhao
DOI: https://doi.org/10.35633/inmateh-79-24

Keywords: *Sweet potato, Compressive mechanical properties, Moisture content, Elastic modulus, Maximum rupture force.*

ABSTRACT
To investigate the effects of moisture content on the compressive mechanical properties of sweet potato roots, this study used three sweet potato varieties (Zishu, Hongyao, and Xiguahong) cultivated in the Tianjin region as experimental materials. Experiments were conducted between October 8, 2025, and January 8, 2026, in a laboratory environment maintained at 20°C ± 2°C and 50% ± 5% relative humidity. The test employed a moisture content measurement method based on storage duration, measuring moisture content every 10 days. Simultaneously, compressive mechanical property tests were performed using an INSTRON 3344 series universal material testing machine under conditions of a 10 mm/min loading speed and a maximum pressure of 1500 N. The maximum rupture force, maximum deformation, and elastic modulus of sweet potatoes at different moisture contents were determined. Data analysis was conducted using Design-Expert 13 software. The results indicated that the variation patterns of moisture content were similar across the different sweet potato varieties. The moisture content decreased rapidly during the initial storage period, showed a brief increase in the middle stage, and then continued to decline at a slower rate in the later stage. Moisture content significantly affected the compressive mechanical properties of sweet potatoes. As the moisture content decreased, the elastic modulus and maximum rupture force increased, while the maximum deformation decreased.

摘 要
为探究水分含量对甘薯块根压缩力学特性的影响，本研究以天津地区种植的紫薯、红瑶、西瓜红三个甘薯品种为试验材料，于 2025 年 10 月 8 日至 2026 年 1 月 8 日，在温度保持为 20℃±2℃、相对湿度保持为 50%±5%的实验室环境中开展试验。本试验采用基于贮藏时长的水分含量测定方法，每 10 天测定一次甘薯水分含量；同时使用英斯特朗 3344 系列万能材料试验机，在加载速率 10 毫米 / 分钟、最大压力 1500 牛的试验条件下开展压缩力学特性测试，测定不同水分含量下甘薯的最大断裂力、最大变形量及弹性模量，并采用 Design-Expert 13 软件对试验数据进行分析。试验结果表明，不同甘薯品种的水分含量变化规律具有一致性：贮藏初期水分含量快速下降，贮藏中期出现短暂上升，贮藏后期则以较慢速率持续降低。水分含量对甘薯的压缩力学特性存在显著影响，随着水分含量的降低，甘薯的弹性模量和最大断裂力呈上升趋势，而最大变形量呈下降趋势。

INTRODUCTION

Sweet potato is an important food crop, rich in nutrients such as protein, carotenoids, flavonoids, anthocyanins, various vitamins, and minerals (*Alam M.K., 2020; Khatun T., 2025*). The physical and mechanical property parameters of sweet potato roots serve as crucial theoretical basis for the design of related machinery and are essential parameters for establishing models when studying the interaction mechanisms between sweet potatoes, soil, and machinery using numerical simulation methods (*Zhao Ping, 2024*). Furthermore, the compressive characteristics of sweet potatoes are also a theoretical guide for designing machinery used in storage, transportation, and processing. Since moisture content significantly influences compressive mechanical properties, studying the compressive mechanical properties of sweet potatoes at different moisture levels is of great importance. Additionally, the deep processing methods for sweet potatoes are closely related to their moisture content.

Different moisture levels determine the most suitable processing techniques; for instance, slicing, juicing, and mashing are more appropriate at high moisture content, while baking, frying, and grinding into flour are better suited for lower moisture content. Therefore, investigating the variation pattern of sweet potato moisture content during storage is particularly important, providing references for selecting preservation methods, processing techniques, and optimal timing.

Currently, researchers domestically and internationally have conducted studies on the relationship between the compressive mechanical properties of root and tuber crops and moisture content. Foreign scholar studied the relationship between the mechanical properties and moisture content of cassava roots, measuring the mechanical response of cassava roots under compression and other loads at different moisture contents and analyzing the effect of moisture content on mechanical indicators such as hardness and elastic modulus (*Bo M.W. et al, 2016*). *Agboola et al, (2024*), experimentally studied the mechanical properties of sugarcane stalks, analyzing compressive strength, Young's modulus, and other mechanical performance indicators based on compression tests conducted at different growth stages and among different varieties. *Bulan R et al, (2020),* investigated the relationship between moisture content and mechanical properties of arecanut fruits by measuring various engineering properties of fresh arecanut fruits at three different moisture levels. Their findings revealed that a reduction in moisture content led to increases in most dimensional, frictional and compressive indicators, while sphericity, thousand-fruit mass and bulk density decreased. *Teshome A et al, (2025),* measured grain size, thousand-kernel weight, bulk density, angle of repose, friction coefficient and other indicators under multiple moisture contents and conducted statistical analyses. The results demonstrated that rising moisture content enlarged grain dimensions, thousand-kernel weight, angle of repose and friction coefficient yet lowered bulk density, with significant disparities in grain properties across treatments, indicating that differentiated seeding equipment should be matched for wheat varieties with varying cultivars and moisture contents. Domestic researcher conducted tests on the mechanical physical characteristics of sweet potato tubers at harvest, demonstrating that sweet potato tubers can be considered isotropic materials (*Shen Haiyang, 2020*). An overview of these studies reveals that relatively little attention has been paid to the patterns of moisture content variation and its specific effects on compressive mechanical properties. *Zhang Lingzhi et al, (2025)*, explored the variation laws of moisture content in various plant organs, grain starch content, and membrane puncture properties at different grain positions during ripening. They verified that the grain dehydration rate had an extremely significant positive correlation with the moisture contents of stalks and cobs. When the grain moisture content fell below 25%, the yield load and elastic modulus at the side and top positions of grains in the desiccant treatment group were superior to those in the natural dehydration group. *Cui Qingliang et al, (2022),* measured the tensile, bending, shear and dynamic cutting mechanical properties of buckwheat stalks, analyzed the influences of moisture content, stalk height above ground and cutting parameters. The results revealed that buckwheat stalks with higher moisture content exhibited greater tensile and cutting-related indicators yet weaker bending performance; the overall mechanical strength of stalks declined with the increase of height above ground. Cutting speed and blade bevel angle had significant effects on cutting stress and cutting energy consumption, and the optimal ranges of cutting parameters were put forward.

However, reviewing literature on crops similar to sweet potatoes, conducted block experiments on cassava stems and determined stem mechanical parameters, finding that the moisture content at different growth locations significantly affected the maximum compression load, indicating a significant influence of moisture content on compressive mechanical properties (*Wang Wei, 2017*). *Wang Juxia, (2024*), through completely randomized compression mechanical property tests on mung bean seeds, found that under the same loading speed, seed moisture content significantly affected the yield load and apparent elastic modulus of the seeds. Based on the above analysis, this paper aims to study the effect of moisture content on the compressive mechanical properties of sweet potato roots.

MATERIALS AND METHODS

Test Materials

This experiment was conducted in a sweet potato test field established through cooperation between Shenyang Agricultural University and Yuelong Town, Tianjin. Three cultivated sweet potato varieties, namely Zishu, Hongyao, and Xiguahong, were used as experimental materials. Manual harvesting took place on October 8, 2024 (*Liao J., 2025*).

Thirty tubers of each variety were selected based on uniform size, absence of damage, pests, and diseases, ensuring consistent maturity. After harvest, The length, width, and thickness of the fresh sweet potatoes for each variety were measured using a vernier caliper, and tubers of similar size and shape were selected, labeled, and stored, as shown in Figure 1. All test sweet potatoes were stored in the Agricultural Product Processing and Storage Laboratory of Shenyang Agricultural University from October 8, 2025, to January 8, 2026, totaling 3 months.



Fig. 1 - Sweet potato samples used for the experiment

Test Equipment and Instruments

The test equipment included a 101-type electric drum drying oven (Tianjin Tonglixinda Instrument Factory), an INSTRON 3344 series universal material testing machine (INSTRON, USA), an electronic balance (precision 0.01 g), a vernier caliper (measurement range 0-300 mm, accuracy 0.02 mm), plastic bags, and labels. The universal testing machine was used to test the compressive mechanical properties of sweet potatoes at different moisture contents. It can display compression load, displacement, speed, and test curves in real-time. The electronic balance and the 101 electric drum drying oven were used to determine the moisture content of the sweet potatoes. The vernier caliper was used to measure the diameter and thickness of the sweet potato samples.



Fig. 2 - Universal material physical testing machine



Fig. 3 - Electric drum drying oven

Experimental Procedure

Detailed elaboration of the adopted test method and its advantages over conventional laboratory testing methods

The integrated storage-stage moisture monitoring combined with uniaxial compression test adopted in this work is a customized composite testing scheme for fresh tuber crops. Conventional single standard laboratory analysis methods are divided into two independent tests: one-time destructive drying for moisture measurement and separated compression tests on randomly sampled tuber blocks, which have two obvious defects: first, the moisture sample and mechanical sample are taken from different sweet potato individuals, leading to inconsistent actual moisture levels between mechanical test specimens and measured moisture data; second, traditional instant dehydration treatment will destroy the original internal tissue structure of fresh sweet potatoes and cannot reflect the natural tissue state of tubers during actual storage.

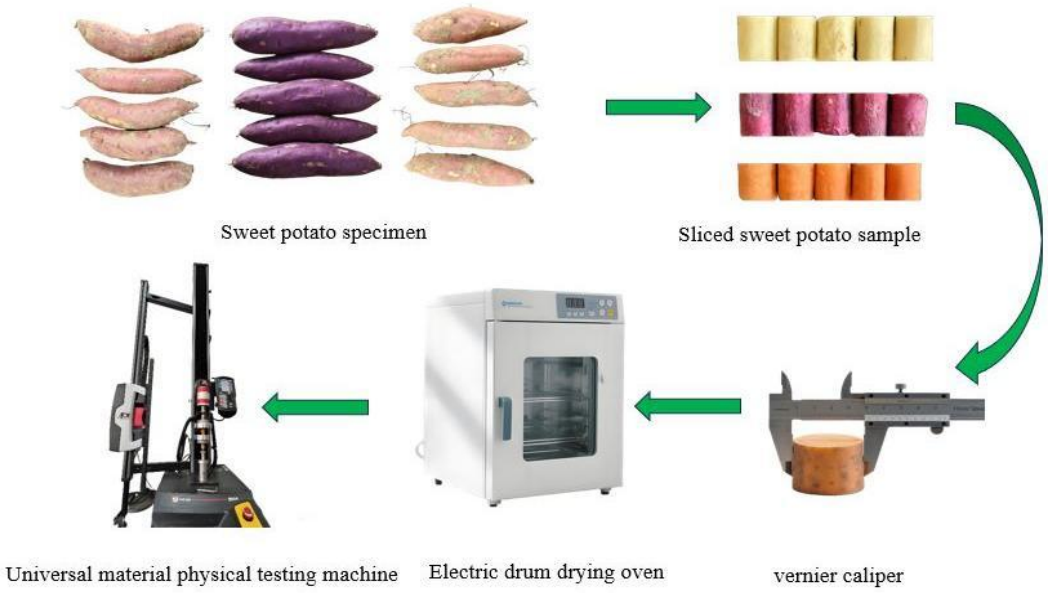


Fig. 4 - Test Procedure

The present testing method synchronously completes moisture tracking and compression measurement on the same batch of sweet potato tubers under natural storage environment, without artificial forced dehydration before mechanical testing. Cylindrical samples are cut from the same intact tuber for moisture detection and compression loading respectively, which ensures the complete consistency of tissue state and moisture background of test specimens. Besides, continuous 90-day periodic sampling avoids the error caused by discrete single-point sampling in short-term static tests. Compared with vacuum drying independent mechanical test and rapid oven drying mechanical test, this method can truly restore the natural water migration and tissue hardening law of sweet potato during postharvest storage, and the data correlation between moisture and mechanical indicators is higher, which is more suitable for exploring the continuous variation law of mechanical properties of fresh root crops with moisture content.

Sample repetition setting for guaranteeing test accuracy

Sweet potatoes were cut into cylindrical pieces approximately 15 mm thick using a sampling tool. The slices were made flat, avoiding cracks or unevenness, as shown in Figure 4. The universal testing machine was turned on and preheated for 10-15 minutes to ensure instrument stability. Test machine parameters were set: loading speed at 10 mm/min, maximum pressure set to 1500 N based on expected compression degree. The cut sweet potato sample was placed on the compression platform of the testing machine, ensuring it was centered, as shown in Figure 5. The testing machine was started, applying pressure to the sample at the set loading speed, and the deformation under different pressures was recorded. The deformation of the sample was observed, and any anomalies were recorded. Changes in the moisture content of sweet potatoes during storage are affected by temperature and humidity (*Guo Lianghu, 2020*). Therefore, environmental temperature and humidity were kept stable to avoid affecting the experimental results. Experiments were conducted in a laboratory environment maintained at 20°C ± 2°C and 50% ± 5% relative humidity. For each sweet potato variety under every single storage time/moisture level, 5 parallel tuber individuals were selected, and 3 cylindrical specimens were cut from each tuber for repeated compression tests; a total of 15 replicate compression samples were measured per treatment group. Meanwhile, 5 parallel thin slice samples were prepared for moisture content measurement at each test node. Multi-layer repetition design (individual tuber repetition + specimen repetition) can eliminate random errors caused by individual differences of sweet potato tubers, cutting thickness deviation and instrument micro-fluctuation, effectively improving the stability and reproducibility of test data.

The above steps were repeated for multiple sweet potato samples to ensure the repeatability and accuracy of the results. Based on the recorded pressure and deformation data, the elastic modulus of the sweet potato samples was calculated. The elastic modulus is an indicator reflecting the material's ability to resist deformation (*Long Che, 2024*).



Fig. 5 - Sweet potato samples placed on the testing machine platform

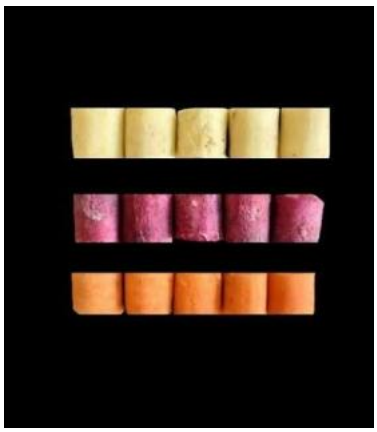


Fig. 6 - Cylindrical samples of sliced sweet potatoes

Test Design and Methods

To study the effect of moisture content on the compressive mechanical properties of sweet potatoes, this test adopted a moisture content testing method based on storage time. After harvest, the first moisture content determination and compression mechanical test were conducted; the second test was performed after 10 days; the third after 20 days; the fourth after 30 days; the fifth after 40 days; continuing this pattern, moisture content was tested every 10 days, resulting in 10 measurements over a total of 90 days. Through these tests, the variation patterns of moisture content with storage time for the three sweet potato varieties were obtained.

There are many methods for measuring moisture content; currently, internationally common methods include vacuum drying and convection oven drying (*Ge Naijun, 2025; Chen Siyu, 2025*). Based on available laboratory conditions and referencing GB/T 12078-2008, the convection oven drying method and mass weighing method were used to determine the moisture content of sweet potatoes. First, 10 samples were prepared for each sweet potato variety, cut into thin slices of similar thickness, and numbered separately. The weight of the samples was measured and the initial weight recorded. They were evenly placed on trays and in a convection oven at 100°C, dried for 0, 1, 2, 3, and 4 hours respectively. During the drying process, at specified times, samples of the three varieties were taken out, weighed, and the data recorded. If the weight no longer changed, it signified the end of drying; samples not meeting the specified drying standard were returned to the convection oven for continued drying.

$$x = \frac{m_1 + m_2}{m_1} \quad (1)$$

where: x is the moisture content of the crop, m_1 is the mass of the sample in grams, m_2 is the mass of the sample dried to constant weight in grams.

The procedure for testing the compressive properties of sweet potatoes was as follows: the loading speed was fixed at 10 mm/min, and the loading direction was vertical (*Ruan B., 2024*). Samples from the three sweet potato varieties were compressed at their natural moisture content levels after different storage periods to obtain the maximum rupture force, maximum deformation, and elastic modulus. The influence of moisture content on compressive mechanical properties was then studied through static load mechanical performance analysis. For each of the three sweet potato varieties tested, five replicate tests were conducted at the same moisture content level. For each of the three sweet potato varieties tested, five independent intact tubers were selected at the same moisture content level, and three cylindrical test pieces were cut from each tuber for compression test, forming 15 repeated test replicates for one treatment to reduce random test error. Data were statistically analyzed, and the mean and variance were calculated. During the test, a rigid plate was used as the loading device (*Barnett M.R., 2004*). The test sweet potato sample was placed in the center of the platen, and the upper platen was adjusted so that it did not contact the sweet potato. Entering the test program control interface, the control parameters were selected in the method settings, including a loading rate of 10 mm/min, an upper load limit of 1500 N, an upper displacement limit of 25 mm, an upper load drop percentage of 20%, and an upper load drop value of 10 N. In the test interface, the steps were followed by clicking load zero, reset extensometer, start, and finish sequentially. To reduce test error, each test was repeated five times under the same conditions, and the average value was taken finally.

This paper selected sweet potato moisture content as the experimental factor. The maximum rupture force at sample fracture, maximum deformation, and elastic modulus were used as test indicators. A three-factor, three-level experimental design was implemented, and response surface analysis was conducted to explore the interaction between these three factors and their effect on moisture content. The factor levels are shown in Table 1:

Table 1

Factor level table

Factor	level		
	-1	0	1
A（N）	300	390	480
B（mm）	5	7.5	10
C（MPa）	3	4.5	6

Note: A denotes maximum breaking force, B denotes maximum deformation, and C denotes elastic modulus.

To explore the interactive effects of the three factors on moisture content, simulation analyses were performed for each model sequentially. The data obtained from the simulation process were integrated, and the monitoring results are shown in Table 2.

Table 2

Orthogonal experimental design of moisture content

Test Number	A Maximum breaking force / N	B Maximum deformation / mm	C Modulus of elasticity / MPa	Y_1- Moisture content （%）
1	390	5	3	71.5
2	390	10	6	72.5
3	390	7.5	4.5	75.3
4	390	10	3	74.2
5	390	5	6	74.1
6	480	7.5	3	73.3
7	390	7.5	4.5	75.0
8	300	5	4.5	72.1
9	480	7.5	6	74.3
10	480	10	4.5	74.1
11	390	7.5	4.5	75.3
12	390	7.5	4.5	75.1
13	300	7.5	6	73.1
14	300	10	4.5	73.8
15	300	7.5	3	73.2
16	480	5	4.5	74.0
17	390	7.5	4.5	75.2

Based on Design-Expert 13 software, data were analyzed to perform significance tests and analysis of variance (ANOVA) for the mean Y_1 moisture content regression equation.

RESULTS AND DISCUSSION

Variation Pattern of Moisture Content in Different Varieties

The moisture content measurement results for the three varieties from 0 to 3 months after harvest were collected and analyzed, as shown in Figure 6. It can be observed that the moisture content of the three sweet potato varieties at harvest reached 74%-76%, but as storage time increased, the moisture content showed a decreasing trend: during the first 0-30 days of storage, the moisture content decreased rapidly; around 45 days, the decreasing trend slowed down further, reaching about 72%-74%. At 60 days of storage, the Zishu variety had the lowest moisture content and tended to stabilize. Starting from day 50, the moisture content of the Hongyao, Xiguahong, and Zishu varieties also slightly increased. Taking Xiguahong as an example, the moisture content of freshly harvested tubers initially reached 74.8%; after 20 days, it decreased to 74.3%, a drop of about 0.5%. The moisture content on day 90 was 72.7%, and the data stabilized. For different sweet potato varieties, their moisture content also differed. Overall, despite the different varieties, the variation pattern of moisture content in sweet potato tubers was similar. In the initial storage period, the moisture content decreased relatively quickly.

This is because physiological activities within the sweet potato continue after harvest, and respiration consumes a certain amount of water. The moisture content showed a brief increasing trend in the middle stage, possibly due to high humidity in the storage environment and poor ventilation, causing the sweet potato surface to absorb moisture from the air, leading to an increase in its moisture content. Microbial metabolic activities can also produce water, causing local increases in moisture content. However, this increase is temporary. As storage time increases, the moisture content of sweet potatoes continues to decrease, but the rate of decrease gradually slows down. Considering that sweet potatoes contain starch, sugars, and other carbohydrates besides water, it is certain that the tubers are not fully mature immediately after harvest, the skin is still tender, the cork layer has not formed, the water content is high, and they are prone to peeling. At this stage, sweet potatoes have sufficient moisture and a relatively soft texture, making them suitable for direct processing into mashed or pulped sweet potato for fillings in pastries. They can also be used to make sweet potato beverages or processed into ready-to-eat products such as steamed or roasted fresh sweet potato products.

Through compression mechanical tests, the compressive mechanical properties of different sweet potato varieties at various moisture contents were obtained (Table 3).

Table 3

The values of compressive mechanical properties under different moisture contents

Variety	Moisture content /%	Maximum breaking force / N	Maximum deformation / mm	Modulus of elasticity / MPa
Xiguahong	74.8	302.45	6.10	4.85
	74.3	389.54	9.45	4.11
	73.8	460.75	7.35	5.70
	73.3	487.68	10.45	5.33
	73.1	517.68	7.40	5.25
	72.8	562.25	17.50	3.92
	72.9	540.59	8.30	5.81
	73.0	506.61	13.05	3.26
	72.8	480.55	7.25	5.01
	72.7	473.50	8.52	4.71
Hongyao	75.3	299.85	6.32	4.19
	74.6	370.57	5.90	5.04
	74.0	424.75	10.21	4.15
	73.5	484.65	8.25	4.82
	73.4	494.35	7.45	5.68
	73.5	477.28	8.85	5.08
	73.7	457.92	6.54	5.42
	73.6	436.05	7.25	4.35
	73.5	427.52	8.65	4.11
	73.5	415.28	8.14	4.48
Zishu	74.3	344.69	4.85	5.44
	73.8	408.45	7.65	4.71
	73.4	464.15	6.35	6.22
	73.1	514.74	8.71	5.32
	72.9	542.72	6.45	7.04
	73.1	560.31	5.32	7.87
	73.2	542.56	5.21	7.18
	73.1	521.15	6.23	7.89
	73.0	506.45	7.15	6.38
	73.0	495.51	6.45	6.11

The rupture force of sweet potato primarily refers to the maximum value of the external load sustained by the sweet potato at the point of rupture. From Table 3, it can be seen that as the moisture content decreases, the compressive load that the sweet potato can withstand increases. The moisture content of all varieties was above 70% at the initial harvest stage. During the first 20 days of natural storage, the moisture content decreased rapidly. For example, for Hongyao, the maximum rupture force increased from 299.85 N to 370.57 N. Then, after about 50 days of storage, the change in maximum rupture force tended to stabilize. With further increase in storage time, around 90 days, when the moisture content was lower, the rupture force showed a subsequent decrease in some cases.

The elastic modulus of sweet potato is a measure of its resistance to deformation. A larger elastic modulus indicates that a greater external load pressure is required to cause elastic deformation. From the experimental data in Table 3, it can be observed that the modulus for the three varieties increased as the moisture content decreased. However, after 50 days, the trend of change in the elastic modulus was similar for the three varieties, with Zishu having the highest elastic modulus, followed by Xiguahong, and Hongyao having the smallest. A higher elastic modulus value indicates better firmness of the tuber. Analysis suggests that after the moisture content decreases, the elastic viscosity of the sweet potato decreases, and the density increases. The sweet potato becomes closer to a rigid body, is less prone to deformation under pressure, and possesses a certain load-bearing capacity.

The compressive deformation of sweet potato refers to its deformation under external compressive load, specifically the maximum displacement at the fracture point. From the experimental data in Table 3, it can be seen that as the moisture content decreases, the deformation tends to decrease, and the trend of change is consistent across different varieties. For example, for the Hongyao variety, the change in sweet potato deformation with moisture content is shown in Figure 7 (Note: Referenced but not provided in original text).

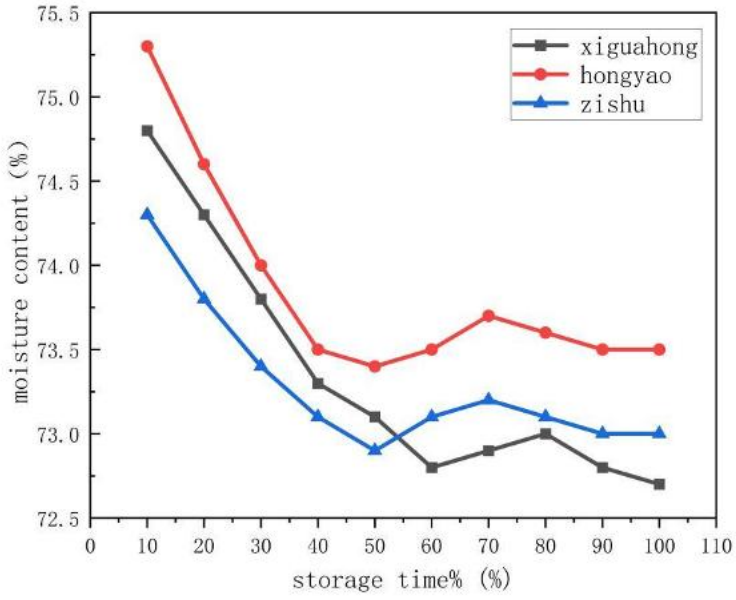


Fig. 7 - The variation law of moisture content of sweet potatoes with storage time

When the moisture content decreased from 75.3% to 73.5%, the deformation showed a decreasing trend, but overall, the decrease was relatively slow. After 50 days of storage, when the moisture content dropped to around 73.4%, the change in deformation was small. Other varieties exhibited their own characteristics, but the overall trend was consistent. As storage time increases and moisture content gradually decreases, the internal tissue of the sweet potato becomes more compact. Additionally, increased maturity and hardness enhance its ability to resist external loads, resulting in reduced deformation. At this stage, the moisture content is moderate, and the texture has a certain toughness, making it suitable for producing sweet potato dried strips by natural air-drying or oven-drying to remove some moisture while retaining flavor. They can also be processed into sweet potato flour through dehydration and grinding, which can be used for thickening or making pastries.

Based on Design-Expert 13 software, the significance of the regression equation and the analysis of variance for the mean Y_1 moisture content are shown in Table 4. Due to space limitations, this paper only presents the analysis for one sweet potato variety, Hongyao.

Table 4

Significance and analysis of variance of mean regression equation

Source	Sum of Squared Deviations	degree of freedom	Mean Square	F-value	p-value	Significance
Model	20.83	9	2.31	70.28	＜0.0001	**
A	1.53	1	1.53	46.50	0.0002	**
B	1.05	1	1.05	31.92	0.0008	**
C	0.41	1	0.40	12.30	0.009	**
AB	0.64	1	0.64	19.44	0.003	**
AC	0.30	1	0.30	9.19	0.019	*
BC	4.62	1	4.62	140.386	＜0.0001	**
A2	1.72	1	1.72	52.37	0.0002	**
B2	4.55	1	4.55	138.30	＜0.0001	**
C2	4.77	1	4.78	145.03	＜0.0001	**
residual	0.2305	7	0.03			
Missing item	0.1625	3	0.05	3.186	0.146	ns
Pure error	0.0680	4	0.02			
total	21.05	16				

Note: P < 0.01 indicates highly significant results, denoted by **; P < 0.05 indicates significant results, denoted by *; P > 0.05 indicates non-significant results, denoted by ns.

According to the table data, the significance test result for the model (p-value less than 0.0001) indicates that the model is statistically highly significant. Simultaneously, the p-value for the lack of fit is 0.146, indicating that the lack of fit is not significant. The fit statistic $R_1^2 = 0.9891$, indicating a high degree of fit for the regression model. The regression equation for moisture content is given by Equation 2:

$$Y_1=75.18+0.4375^*A+0.3625^*B+0.225^*C-0.4^*AB+0.275^*\mathrm{AC}-1.07^*\mathrm{BC}-0.64^*\mathrm{A}^2-1.04^*\mathrm{B}^2-1.06^*\mathrm{C}^2 \quad (2)$$

where: Y_1: Moisture content of crop. A: Maximum rupture force. B: Maximum deformation. C: Elastic modulus. AB, AC, BC: Interaction terms of two factors. A^2, B^2, C^2: Quadratic terms of each single factor.

The response surfaces showing the interactive effects of the three factors on Y_1 moisture content are shown in Figure 8:

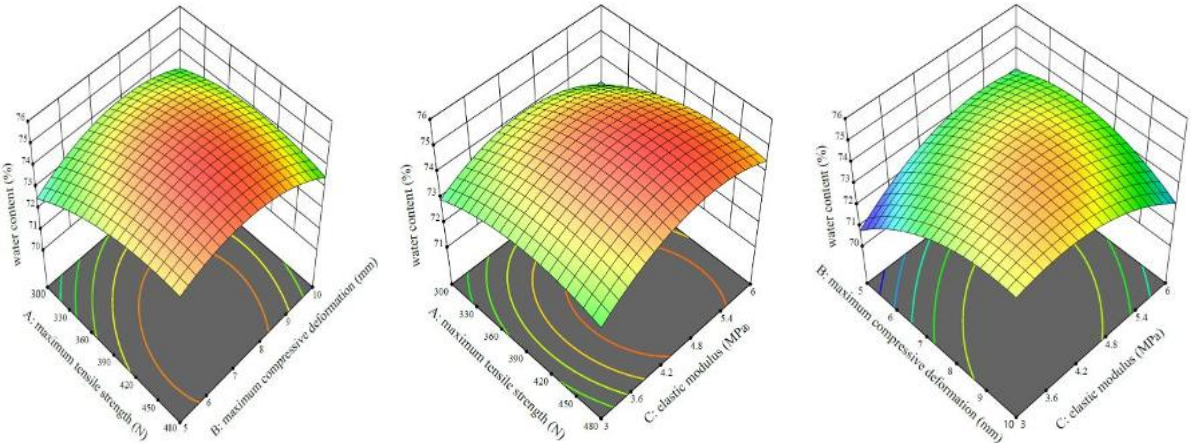
(a) Response surface of maximum rupture force (A) and maximum deformation (B) on sweet potato moisture content;

(b) Response surface of maximum rupture force (A) and elastic modulus (C) on sweet potato moisture content;

(c) Response surface of maximum deformation (B) and elastic modulus (C) on sweet potato moisture content.

Fig. 8 - Three-dimensional response surface plots showing the interactive effects between every two mechanical indicators (maximum rupture force, maximum deformation, elastic modulus) on the moisture content of Hongyao sweet potato tubers. Each subfigure corresponds to the coupling effect of two independent mechanical factors on the moisture content response value, while the third factor is fixed at the zero central level (A =390 N, B =7.5 mm, C =4.5 MPa). The vertical axis of each 3D surface represents the predicted moisture content; the two horizontal axes represent the two selected mechanical indicators respectively. The gradient change of surface height intuitively reflects the changing trend of moisture content under different factor combinations. The curved shape of the response surface demonstrates that there exists obvious nonlinear interaction between every pair of mechanical indicators, consistent with the significance results of AB, AC and BC interaction terms in ANOVA table. The surface shows an overall rising trend first and then falling, which is caused by the negative quadratic terms of A, B and C in the regression equation. The BC coupling surface has the steepest curvature, indicating that the interaction between maximum deformation and

elastic modulus exerts the most prominent influence on sweet potato moisture content, which matches the extremely significant p-value of BC item ($p<0.0001$) in the analysis of variance.



（a） A and B （b） A and C （c） B and C

Fig. 8 - Response surfaces of test factors to the effects of soil disturbance

CONCLUSIONS

Through moisture content tests and mechanical property tests on different sweet potato varieties from the Tianjin region, this study investigated the effect of moisture content on the mechanical properties of sweet potato roots and their variation patterns. The influence of moisture content on the maximum rupture force, maximum deformation, and elastic modulus for three sweet potato varieties was analyzed. The main conclusions are as follows:

The moisture content of three sweet potato varieties was studied over 3 months post-harvest. The variation pattern of moisture content was similar across different sweet potato varieties. During the initial storage period, the moisture content decreased rapidly, showed a brief increase in the middle stage, and continued to decrease in the later period.

Moisture content had a highly significant effect on the mechanical properties of sweet potatoes, including the maximum rupture force, maximum deformation, and elastic modulus. The elastic modulus and maximum rupture force increased with decreasing moisture content, while the maximum deformation decreased with decreasing moisture content.

In the early storage period, when sweet potatoes have high moisture content, they are suitable for direct processing into mash or pulp for use as fillings in pastries. They can also be used to make sweet potato beverages or processed into ready-to-eat products like steamed or roasted fresh sweet potatoes. In the later storage period, when the moisture content is moderate and the texture has a certain toughness, they are suitable for making sweet potato dried strips by natural air-drying or oven-drying to remove partial moisture while retaining flavor. They can also be processed into sweet potato flour through dehydration and grinding, which can be used for thickening or making pastries.

ACKNOWLEDGEMENT

Basic Scientific Research Program of the Department Education of Liaoning Province of China, Grant/Award Number: LJKMZ20220999.

REFERENCES

[1] Alam, M. K., Sams, S., Rana, Z. H., Akhtaruzzaman, M., & Islam, S. N. (2020). Minerals, vitamin C, and effect of thermal processing on carotenoids composition in nine varieties orange-fleshed sweet potato (Ipomoea batatas L.). *Journal of Food Composition and Analysis*, 92, 103582. https://doi.org/10.1016/j.jfca.2020.103582

[2] Barnett, M. R., Keshavarz, Z., Beer, A. G., & Atwell, D. (2004). Influence of grain size on the compressive deformation of wrought Mg–3Al–1Zn. *Acta materialia*, 52(17), 5093-5103. https://doi.org/10.1016/j.actamat.2004.07.015

[3] Bo, M. W., Choa, V., Chu, J., Arulrajah, A., & Horpibulsuk, S. (2016). Laboratory investigation on the compressibility of Singapore marine clays. *Marine Georesources & Geotechnology*, 35(6), 847–856. https://doi.org/10.1080/1064119X.2016.1256922

[4] Bulan R., Devianti D., Ayu E. S., Sitorus A. (2020), Effects of Moisture Content on Some Engineering Properties of Arecanut (Areca Catechu L.) Fruit Which Are Relevant to the Design of Processing Equipment, *INMATEH Agricultural Engineering*, Technologies and technical equipment for agriculture and food industry, Volume 60 / No.1, pp.61-70; https://doi.org/10.35633/inmateh-60-07

[5] Che, L., Pan, L. & Gu, X. (2024) Experimental study on dynamic elastic modulus loss of concrete broken by high voltage pulse discharge based on orthogonal design. *Sci Rep* 14, 21299. https://doi.org/10.1038/s41598-024-71905-2

[6] Chen, S. Y., Song, W. X., Liu, C. S., Yu, T., Qiao, R., & Wu, W. F. (2025). Analysis of influencing factors and heat transfer process simulation of corn hot air drying. *Journal of Agricultural Mechanization Research*, 47(7), 279–284. https://doi.org/10.13427/j.issn.1003-188X.2025.07.042

[7] Cui Q L, Wang C, Li H B, Zhang Z Y, Zhang Y Q. (2022). Test and analysis of mechanical properties of buckwheat stem during harvest [J]. *INMATEH Agricultural Engineering*, 68(3): 275-282. https://doi.org/10.35633/inmateh-68-27

[8] Ge, N. J. (2025). Research and application of vacuum drying technology in processing production lines. *Neijiang Science and Technology*, 46(3), 14-15+154.

[9] Guo, L. H., Wang, Z., Li, N., Lu, L. H., Gao, W., Guo, Y. X., & Wu, Z. X. (2020). Effects of temperature and humidity on storage quality of purple sweet potato. *Journal of Agricultural Science and Technology*, 22(2), 107-114. https://doi.org/10.13304/j.nykjdb.2019.0145

[10] Khatun, T., & Asaduzzaman, Md. (2025). Effect of sweet potato flash powder on the proximate, functional, and bioactive properties of fortified confectionery products. *Food and Humanity*, 5, 100771. https://doi.org/10.1016/j.foohum.2025.100771

[11] Liao, J., Chen, Z., Lu, H., & Huang, L. (2025). Effects of specimen dimensions on the compressive mechanical properties of mongolian scots pine: Experimental investigation and quantitative analysis. *Structures*, 80, 109786. https://doi.org/10.1016/j.istruc.2025.109786

[12] Ma, X., Li, H., Ge, Y., Li, S., Zhao, Y., & Yu, S. (2020). Experimental study on mechanical properties of tomato potted seedling stems. *Journal of Agricultural Mechanization Research*, 42(8), 161–167. https://doi.org/10.13427/j.cnki.njyi.2020.08.030

[13] Pan, L.Y. (2025). Hongyao sweet potato industrial cluster in Ninghe District YueLong Town makes small sweet potatoes a "trendy product". Qiuxian, (04), 12-13.

[14] Ruan, B., Li, J., Gan, Y., & Huang, J. (2024). Mesoscopic simulation of the mechanical behaviour of foam concrete subjected to large compressive deformation. *Construction and Building Materials*, 418, 135367. https://doi.org/10.1016/j.conbuildmat.2024.135367

[15] Shen, H., Ji, L., Hu, L., Wang, B., Wang, G., & Bao, G. (2020). Study on mechanical-physical property parameters of sweet potato tubers at harvest stage. *Journal of Chinese Agricultural Mechanization*, 41(12), 55–61. https://doi.org/10.13733/j.jcam.issn.2095-5553.2020.12.011

[16] Teshome A., Olaniyan A. M., Fanta A., Alemayehu H., Abebe M., Alemu D., Mohammed M., Aseffa T. (2025). Effect of moisture content on some physical and mechanical properties of wheat (Triticum Aestivum L.) Seeds, *INMATEH Agricultural Engineering*, Vol. 76, No.2, pp. 272-281. https://doi.org/10.35633/inmateh-76-24

[17] Wang, J. X., Yin, Y., & Zhang, Y. Q. (2024). Effects of grain moisture content and loading speed on compression characteristics of mung bean grains. *Journal of Agricultural Engineering*, 14(11), 100-106. https://doi.org/10.19998/j.cnki.2095-1795.202411315

[18] Wang, W., Li, C. B., Liao, Y. L., & Wang, J. L. (2017). Experiment and research on mechanical properties of cassava stems. *Journal of Chinese Agricultural Mechanization*, 38(5), 6-11. https://doi.org/10.13733/j.jcam.issn.2095-5553.2017.05.002

[19] Zhang L., Zhong M., LU W., Xie F., Wu Y., Ji B. (2025), Effects of moisture, starch, and microstructure on the mechanical Properties of Maize Kernels During Mechanical Harvest After Physiological Maturity, *INMATEH Agricultural Engineering*, Volume 77 / No. 3, pp. 227-237, https://doi.org/10.35633/inmateh-77-18

[20] Zhao, P., Zhang, H., Li, B., Xu, Q., & Tang, X. (2024). Experimental study on physical and mechanical properties of sweet potato roots. *Journal of Shenyang Agricultural University*, 55(5), 545–551. https://doi.org/10.3969/j.issn.1000-1700.2024.05.001

FROM HARVEST TO PACKAGE: AN AUTONOMOUS ROBOT FOR INTEGRATED TOMATO PICKING AND BAGGING
/
用于番茄一体化采摘与包装的自主机器人

Yanhua YING, Dongya LI *, Jiahui HU, Yujie ZHOU, Yubo LI [1]
College of Engineering, Applied Technology College of Soochow University, Suzhou 215000, China
**Corresponding author: Dongya Li, Email: lidongya@suda.edu.cn*
DOI: https://doi.org/10.35633/inmateh-79-25

Keywords: *Tomato picking robot; Heat-sealing automatic bagging machine; Bagging function; Picking actuator; Robot vision recognition*

ABSTRACT
In addressing the high labor costs and low operational efficiency of greenhouse tomato harvesting and separate packaging workflows, this study develops an integrated tomato harvesting robotic system embedded with RGB-D machine vision, 5-degree-of-freedom manipulator and vertical heat-sealing net bag packaging mechanism. The YOLOv8s lightweight detection model trained on self-built multi-light greenhouse tomato dataset (1260 annotated images covering unobstructed, semi-occluded and heavily occluded fruits) is adopted to identify ripe tomatoes with a recognition accuracy of 95.2%, and ImageJ software is introduced to conduct secondary maturity screening via RGB chromatographic analysis. A global path planning combined with TEB local trajectory optimization realizes autonomous obstacle avoidance navigation of the wheeled mobile platform, while RRT-Connect bidirectional random tree algorithm is applied for obstacle-free grasping trajectory planning inside dense tomato canopies. A total of 120 valid cyclic tests are carried out in simulated greenhouse environment to verify the full-chain automation including fruit detection, in-situ picking and instant bagging. Experimental results show that the average single-fruit processing cycle is 12.1 s, with a picking success rate of 90.8% and bagging success rate of 98.3%. Compared with skilled manual picking and packaging, the overall working efficiency is improved by approximately 30%. This system firstly realizes continuous integrated harvesting and commercial packaging operation for greenhouse tomatoes, providing a feasible technical solution for full-process intelligent protected agriculture.*

摘要
针对温室番茄采摘、包装分离作业带来的高人力成本与低效问题，本文研发一套集成 RGB-D 机器视觉、五自由度机械臂与立式热封网袋包装机构的一体化番茄采收机器人。系统采用 YOLOv8s 轻量化检测模型，基于自建多光照温室番茄数据集（1260 张标注图像，覆盖无遮挡、半遮挡、重度遮挡样本）实现成熟番茄识别，识别精度 95.2%；配套 ImageJ 软件通过 RGB 色谱分析完成果实成熟度二次校验。采用 A 全局路径规划结合 TEB 局部轨迹优化实现轮式移动底盘自主避障导航，RRT-Connect 双向随机树算法完成密植冠层内无碰撞抓取轨迹规划。在模拟温室环境完成 120 组完整循环试验，验证识别、就地采摘、即时套袋全流程自动化。试验结果表明，机器人单果平均处理周期 12.1 秒，采摘成功率 90.8%，套袋成功率 98.3%；相较熟练人工采摘包装综合效率提升约 30%。本系统首次实现温室番茄采收与商品化包装连续一体化作业，为设施农业全程智能化提供可行技术方案。*

INTRODUCTION
Facility agriculture, through controlled-environment production, is crucial for ensuring stable and efficient food supply. As a primary protected-field crop, tomatoes face significant harvesting challenges: concentrated fruit ripening leads to a surge in labor demand, resulting in tight operation cycles, high-intensity work, and rising costs. The aging workforce and global labor shortage trends further exacerbate this issue, making large-scale manual harvesting increasingly economically unsustainable. Consequently, developing autonomous harvesting robot systems has become an imperative for agricultural sustainability.

[1] *Yanhua Ying, Undergraduate student; Dongya Li, Professor; Jiahui Hu, Undergraduate student; Yyjie Zhou, Undergraduate student; Yubo Li, Undergraduate student.*

To this end, extensive research has been conducted in the field of agricultural harvesting robots. International projects, such as the EU's CROPS *(Goulart, 2023)* have developed modular multi-crop operation platforms integrating perception and manipulation. Research on crops like cucumbers and grapes has also advanced solutions combining machine vision, flexible end effectors, and motion planning. While these systems have made significant strides in fruit recognition and separation, their functionality largely remains confined to the "identify-harvest" stage. Harvested fruits typically require separate manual processes for sorting and packaging, adding handling steps and increasing damage risks, thereby hindering the realization of continuous automation from plant to packaged product. Particularly, the technology for immediate online automated commercial packaging (such as protective netting bags) post-harvest remains a critical bottleneck for achieving end-to-end automation *(Marin et al., 2025).*

To advance full automation of the "harvesting-packaging" process for greenhouse tomatoes, this study designed and validated a multi-sensor fusion robotic system. This system integrates a highly compact mechanical platform (incorporating an end-effector, vertical heat-sealing bagging mechanism, and buffer collection bin) with collaborative intelligent algorithms (YOLO-based visual detection, A*/TEB and RRT-Connect/visual servo hierarchical planning, and behavior tree scheduling). It combines ripe fruit identification, precise picking, on-site bagging, and collection into a single continuous operational cycle. Simulated greenhouse experiments demonstrated a 90.8% picking success rate, 98.3% bagging success rate, and an average processing cycle of approximately 12 seconds per fruit. Overall efficiency significantly surpassed manual labor, providing a highly efficient and feasible solution for automated greenhouse tomato production *(Liu et al., 2025)*.

Matache et al. (2026) developed an AI greenhouse tomato harvesting robot that only supports fruit picking without on-site packaging, requiring repeated manual fruit transfer and causing peel damage, which fails to realize end-to-end production. Current tomato harvesting robots have three core research gaps:

Most platforms lack integrated heat-sealing bagging actuators, separating harvesting and packaging procedures. Visual systems rarely combine YOLO detection with image-based maturity grading, and few reports fully disclose YOLO version, dataset and occlusion detection performance;

No unified collaborative scheduling system exists for mobile chassis, manipulator and bagging module.

To address the above bottlenecks, this study proposes a multi-sensor fusion robot integrated with 5-axis manipulator and vertical bagging mechanism. YOLOv8s combined with ImageJ chromatographic analysis realizes precise fruit screening, while A*/TEB navigation and RRT-Connect arm planning support lossless canopy picking. The system achieves continuous identification-picking-bagging-collection operation to fill the gap of integrated post-harvest packaging.

MATERIALS AND METHODS

OVERALL DESIGN AND INTEGRATION OF THE HARVESTING ROBOT SYSTEM

System Architecture and Workflow

To achieve full automation of tomato picking, bagging, and collection, this system employs a layered, collaborative hardware-software architecture Fig. 1 *(Adochiei et al., 2025)*, thereby enabling a closed-loop operational workflow Fig. 2.

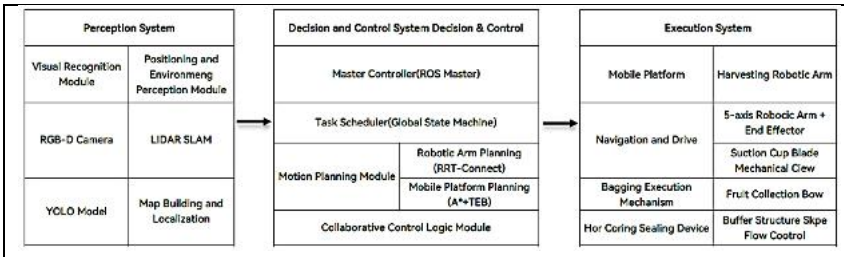


Fig. 1 - Overall System Architecture

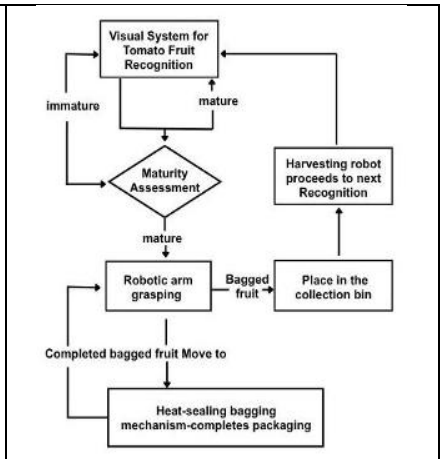


Fig. 2 - Workflow

Key Technical Parameters of the Harvesting Robot

Key design parameters are shown in Table 1.

Table 1

Summary of Key Performance Indicators for Tomato Harvesting Robots

Parameter	Technical Index
Overall Dimensions	Length 1200 mm × Width 880 mm × Height 960 mm
Whole Machine Weight	6 kg
Maximum Working Radius (Range)	2–5 m
Battery Endurance Time	2-5 h
Harvest Success Rate	85%-93 %
Bagging success rate	88%-95 %
Ripe Tomato Recognition Accuracy	95.2 %
Single Fruit Processing Cycle	10-15 s
Hourly Processing Capacity	249-400 fruits/h

In mechanical and structural design, overall dimensions must strictly comply with relevant specification constraints *(He et al., 2025)*. Concurrently, the vision system must operate stably under complex lighting conditions and identify partially obscured or overlapping fruits, achieving millimeter-level positioning accuracy to ensure precise grasping *(Wang & Liu, 2025)*.

DESIGN AND IMPLEMENTATION OF ROBOTIC MECHANICAL SYSTEMS

1. Overview of mobile platforms

A front-wheel-drive wheeled chassis with long wheelbase is adopted to enhance driving stability. The picking manipulator, heat-sealing bagging unit and fruit bin are arranged sequentially along the travel direction to match the picking-bagging-collection workflow *(Luo et al., 2017).*

After grasping, the fruit is transferred to the bagging mechanism and slides down a 20° inclined chute into the rear buffer bin. This integrated layout shortens fruit conveying paths and forms the mechanical foundation for continuous automatic operation (Fig. 3).

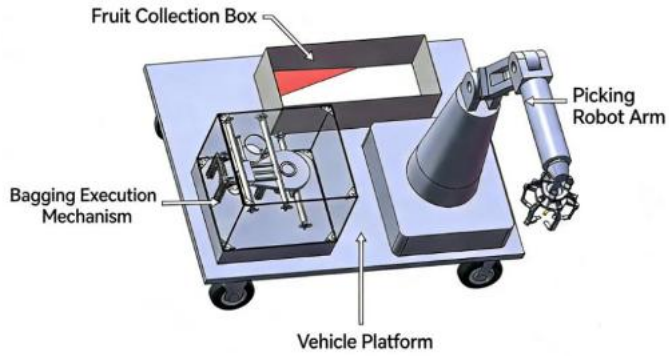


Fig. 3 - Mobile Platform

2. Design of harvesting robotic arm and end-effector

A 5-axis manipulator is equipped with 360° rotating base and wrist joints, plus a 270° elbow joint. The gripper integrates flexible protective sleeves, retractable vacuum cups and cable-driven cutting blades *(Bu et al., 2025)*. Three parallel cylinders' control gripper opening and closing for 50-100 mm diameter tomatoes. Vacuum assistance realizes gentle fruit transfer before bagging (Figs. 4-6).

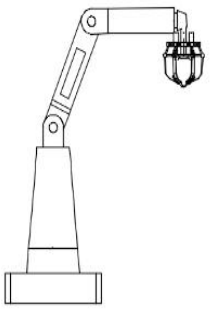


Fig. 4 - Manipulator



Fig. 5 - Gripper



Fig. 6 - Gripper Finger

3. Bagging actuator design

A vertical hot-cut net bagging device is proposed to replace inefficient manual packaging. Its three core modules work sequentially: net bag feeding, conical expansion, and thermal sealing & cutting.

Dual friction rollers deliver mesh bags; the tapered guide expands bag openings to fit variable fruit sizes. A cam-driven hot blade completes simultaneous cutting and sealing, with adjustable speed and temperature controlled by PLC (Figs. 7-8).

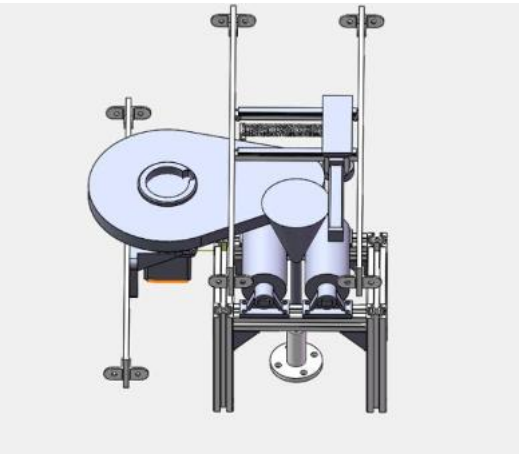


Fig. 7 - Structural Diagram of the Bagging Mechanism

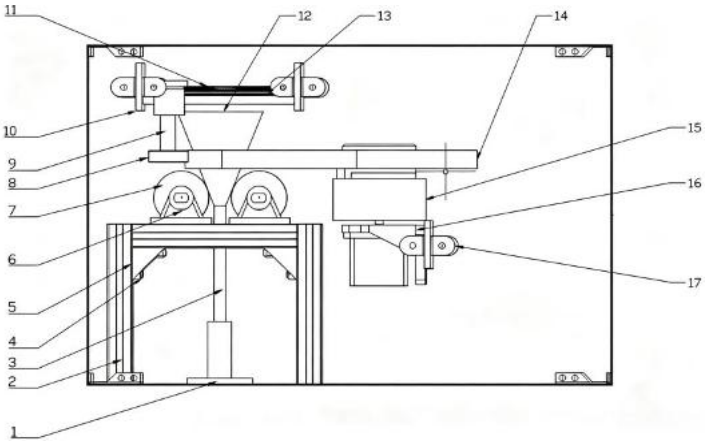


Fig. 8 - Schematic of the Bagging Mechanism

1-External Threaded Flange; 2-Support Profile; 3-Support Steel Pipe; 4-Nuts and Bolts; 5-Angle Bracket; 6-Support Frame; 7-Dual Active Friction Wheel Mechanism; 8-Rollers; 9-Connectors; 10-Support Plate; 11-Tension spring; 12-Guide cone; 13-Linear slide rail; 14-Cam mechanism; 15-Coupling; 16-Drive motor; 17-Triangular iron

4. Fruit collection bin design

The storage bin is fitted with foam anti-collision cushions and a 20°- 30° slope connecting the bagging device. Adjustable flexible partitions separate fruits by size to reduce extrusion damage while maintaining storage density (Fig. 9).

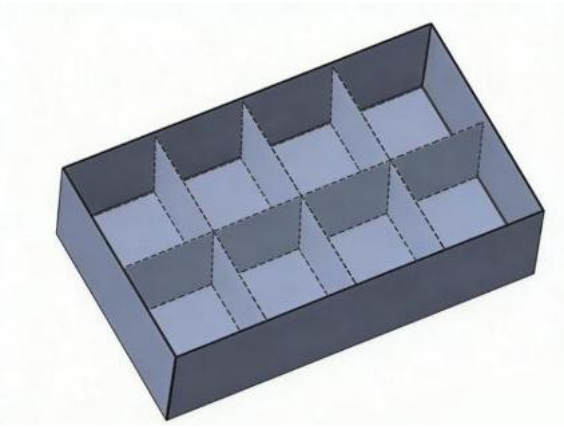


Fig. 9 - Fruit Collection Bin

MACHINE VISION-BASED TOMATO IDENTIFICATION AND HARVESTING LOCALISATION

1. Visual system hardware configuration

As shown in Fig. 10, the visual system hardware primarily consists of an industrial control computer, power supply, depth camera, robotic arm with its controller, and an electric gripper. The system employs an MK-GEB013GC-M1 camera paired with an MK-FC23M35F28-10M-A lens to capture tomato fruit images *(Yuan et al., 2023)*, meeting requirements for color recognition and spatial perception. The Model K280L Industrial Control Computer runs the visual recognition model, performs deep learning inference, controls the electric gripper, and communicates with the robotic arm controller. The robotic arm control system employs a dedicated controller equipped with a teach pendant, enabling automatic planning of the shortest motion path based on the target coordinates of the end-effector.

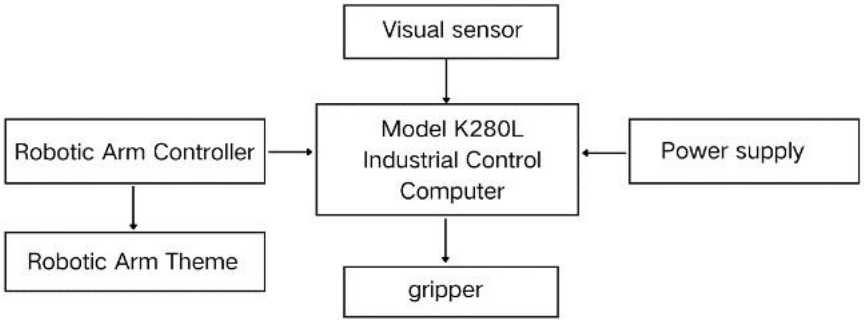


Fig. 10 - Block Diagram of the Vision System

2. Tomato recognition and localization algorithm

First, calibrate the robot to establish three Cartesian coordinate systems: the flange coordinate system, the gripper coordinate system, and the camera coordinate system *(El-sheikha et al., 2024).* As this robot employs an 'eye-on-hand' mounting configuration, measurements reveal the X, Y, and Z deviation values between the camera coordinate system origin and the gripper coordinate system origin: X=20, Y=0, Z=30 (mm).

The coordinate transformation relationship between a point P in space within the flange coordinate system and the gripper coordinate system is as follows:

If a point P in space is represented as P_b in the flange coordinate system and P_g in the gripper coordinate system, then:

$$P_b = {}^{b}R_g P_g + {}^{b}t_g \quad (1)$$

$${}^{b}R_g = R_z R_y R_x \quad (2)$$

represents the rotation matrix, and ${}^{b}t_g$ denotes the translation vector calculated from the X, Y, Z offsets. When expressed in homogeneous coordinates, the transformation matrix takes the form:

$$\begin{bmatrix} X_b \\ Y_b \\ Z_b \\ 1 \end{bmatrix} = \begin{bmatrix} {}^{b}R_g & {}^{b}t_g \\ O^T & 1 \end{bmatrix} \begin{bmatrix} X_g \\ Y_g \\ Z_g \\ 1 \end{bmatrix} = {}^{b}T_g \begin{bmatrix} X_g \\ Y_g \\ Z_g \\ 1 \end{bmatrix} \quad (3)$$

Here, ${}^{b}T_g$ represents a 4×4 homogeneous transformation matrix. After image acquisition, the computer performs feature extraction (including edge detection and corner operations), classifying features into three categories: fruit stalks, leaves, and fruits. Subsequently, path planning is conducted using the RRT algorithm to navigate around stem and leaf obstacles during harvesting *(Meng et al., 2025).*

3. Determining fruit maturity and harvest readiness

Tomatoes with diameters of 30-50 mm were selected, and fruit size was determined from the images captured by the camera. As illustrated in Fig. 11, ImageJ software was used to extract the RGB intensity values of the tomato fruit images. These values were then compared with reference color characteristics to evaluate fruit ripeness, as shown in Fig. 12 *(Sep˙ lveda et al., 2020).*



Fig. 11 - Representative image of a tomato fruit

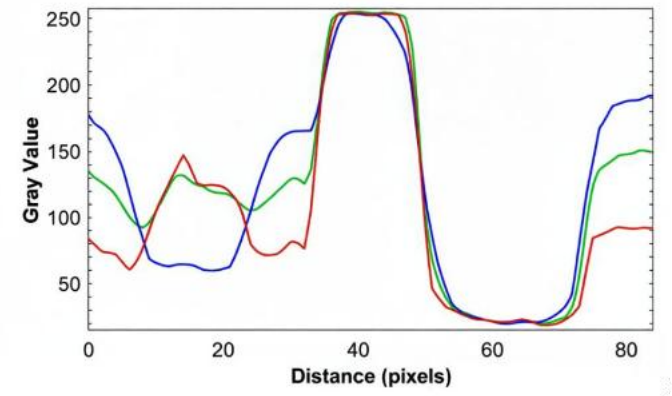


Fig. 12 - Chromatographic Range

YOLO VISUAL DETECTION MODEL AND TRAINING DATASET

This work adopts lightweight YOLOv8s for tomato recognition, leveraging C2f multi-scale backbone and decoupled detection heads to enhance detection of occluded fruits and reduce ripeness misclassification.

1. Self-Built Tomato Dataset

RGB-D images were captured under morning weak light, midday strong light and evening diffuse light, totaling 1260 samples categorized by occlusion: 520 unobstructed, 460 semi-occluded (10%-50% leaf coverage), 280 heavily occluded (>50% leaf coverage). Four labels (ripe_tomato, unripe_tomato, leaf, branch) were annotated via LabelImg. The dataset was split 7:2:1 for training, validation and testing, with random cropping, brightness jitter, flip and blur augmentation applied during training.

2. Model Training Parameters and Evaluation Metrics

Training ran on Model K280L PC with RTX 3060 GPU; BatchSize=16, initial lr=0.001, cosine annealing decay, total 150 epochs. Loss combines CIoU and cross-entropy. Evaluation metrics include mAP@0.5, Precision, Recall and single-frame inference latency, analyzed in Results.

3. Data Flow Between YOLO and ImageJ Software

The ROS vision node feeds frames into YOLOv8s to extract bounding boxes of ripe tomatoes;

Target regions are auto-cropped and batch-exported for ImageJ analysis.

ImageJ extracts RGB gray curves to match standard ripeness thresholds.

Only qualified fruit coordinates are transmitted to the manipulator planning module; underripe targets are discarded.

This two-stage screening reduces mis-harvest caused by contour-only YOLO judgment.

ROBOT MOTION PLANNING AND COLLABORATIVE CONTROL

Mobile Platform Path Planning

Equation (4) is the heuristic cost function of A* algorithm, used to search the shortest collision-free global path in greenhouse crop rows.

The A* algorithm employs a heuristic function *(Shao, 2025)*:

$$f(n) = g(n) + h(n) \tag{4}$$

to guide the search, ensuring the shortest path while enhancing efficiency.

The TEB (Timed Elastic Band) algorithm models the robot's future trajectory as a timestamped sequence of poses:

$$B = \{Q_i\}_{i=0}^{n},\ Q_i = [x_i, y_i, \theta_i, \Delta t_i]^T \tag{5}$$

and achieves smooth, safe local motion by minimizing the total cost function:

$$F(B) = \sum_k \omega k \cdot f_k(B) \tag{6}$$

to achieve smooth and safe local motion *(Li, 2025)*.

Equations (5) and (6) model robot pose sequence and overall trajectory cost, realizing real-time local obstacle avoidance based on LiDAR point cloud data.

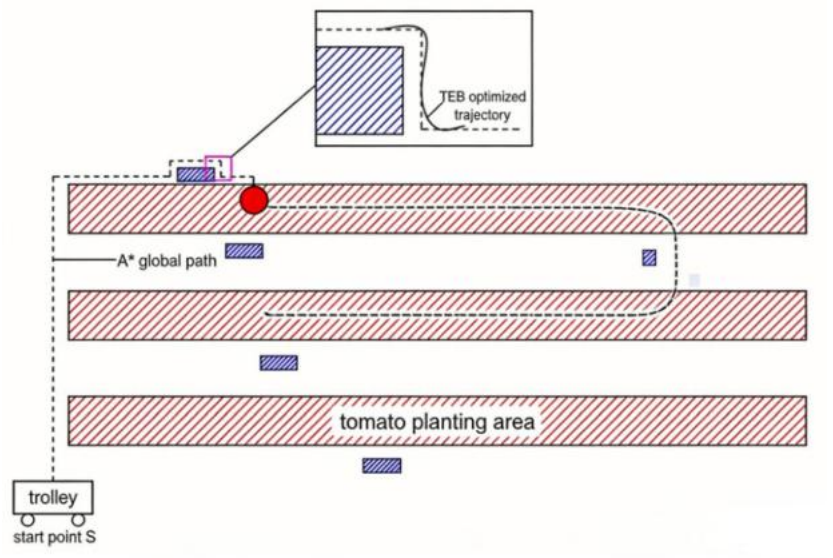


Fig. 13 - Tomato Planting Area and Mobile Platform Path

The system adopts a two-layer planning architecture of “global guidance—local optimization”. The flowchart of the A* algorithm Fig. 14 and the complete operational flowchart of A* working in tandem with TEB are shown in Fig. 15. *(Ji et al., 2023).*

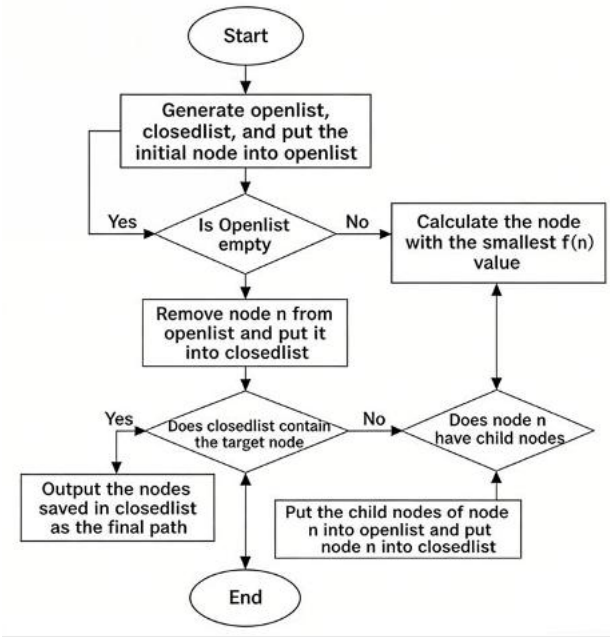


Fig. 14 - A* Algorithm Flowchart

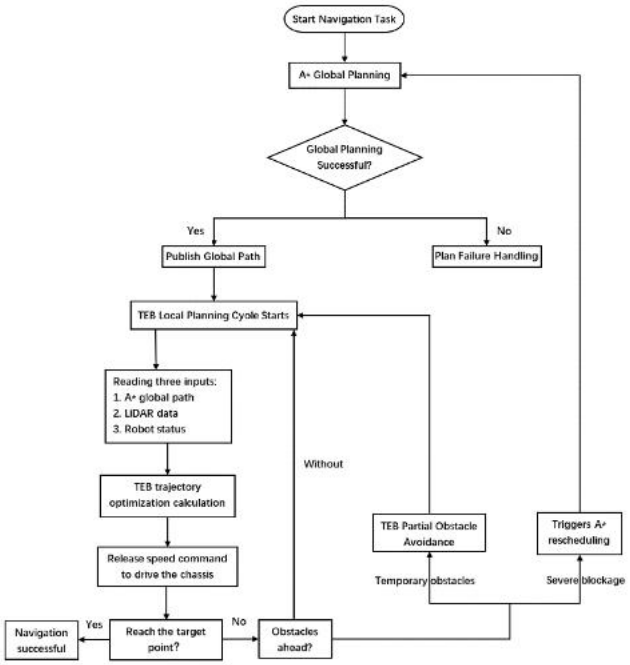


Fig. 15 - Collaborative Workflow Diagram

Robotic Arm Picking Motion Path Planning

The picking robotic arm must operate within dense, unstructured canopy structures, presenting challenges of high-dimensional configuration space search and dynamic obstacle avoidance *(Yuan & Shen, 2017)*. To address this, the system employs a comprehensive strategy combining ‘Global Sampling Planning (RRT-Connect) *(Yu et al., 2017)* + Local Visual Servoing Fine-Tuning + Semantic Layered Obstacle Avoidance’.

Global Path Planning: Employing the RRT-Connect bidirectional random tree algorithm, random trees are simultaneously grown from the start point q_{start} and the goal point q_{goal}. Through random sampling, node expansion, and collision detection, it rapidly searches for feasible paths in high-dimensional spaces with probabilistic completeness.

The node-expansion rule is defined as follows:

$$q_{new} = q_{near} + \varepsilon \cdot \frac{q_{rand} - q_{near}}{\|q_{rand} - q_{near}\|} \quad (7)$$

Equation (7) defines the node-expansion rule used in the bidirectional RRT-Connect algorithm, enabling rapid collision-free path planning within a dense tomato canopy.

Semantics-Based Hierarchical Obstacle Avoidance Strategy: See Table 2 below for details:

Table 2

Parameter Table for Stratified Obstacle Avoidance Strategy

Grade	Obstacle type	Safe distance	Constraint nature		Handling principles
Level 1	Such as greenhouse skeleton, support columns, etc.	70 mm	Hard constraint		Touching is strictly prohibited, and intrusion is regarded as a collision
Level 2	Tomato branches, leaves, vines	1 mm	Soft constraints (continuous costs)		Allow slight contact to guide the detour with a continuous penalty function
Level 3	Other fruits to be protected	3 mm	Strong repulsion constraint		Active protection gives a very high cost of repulsion to avoid collisions

System Collaborative Control and Communication Framework

To ensure the coordinated and orderly operation of the mobile platform, robotic arm, and bagging device, the system manages the temporal dependencies, spatial conflicts, and exception-handling requirements associated with the different tasks, as illustrated in Fig. 16.

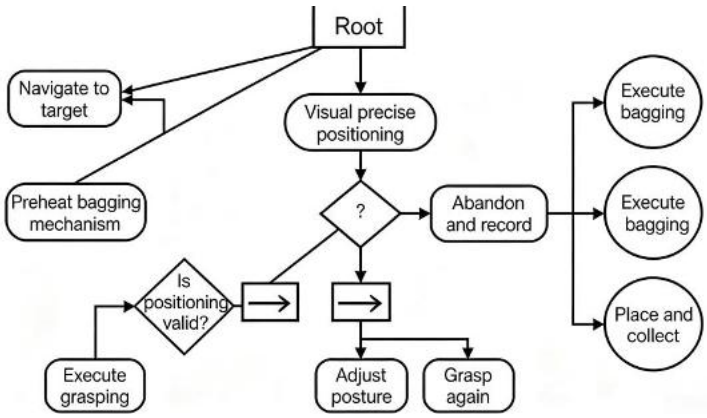


Fig. 16 - Multi-Task Coordinated Control System

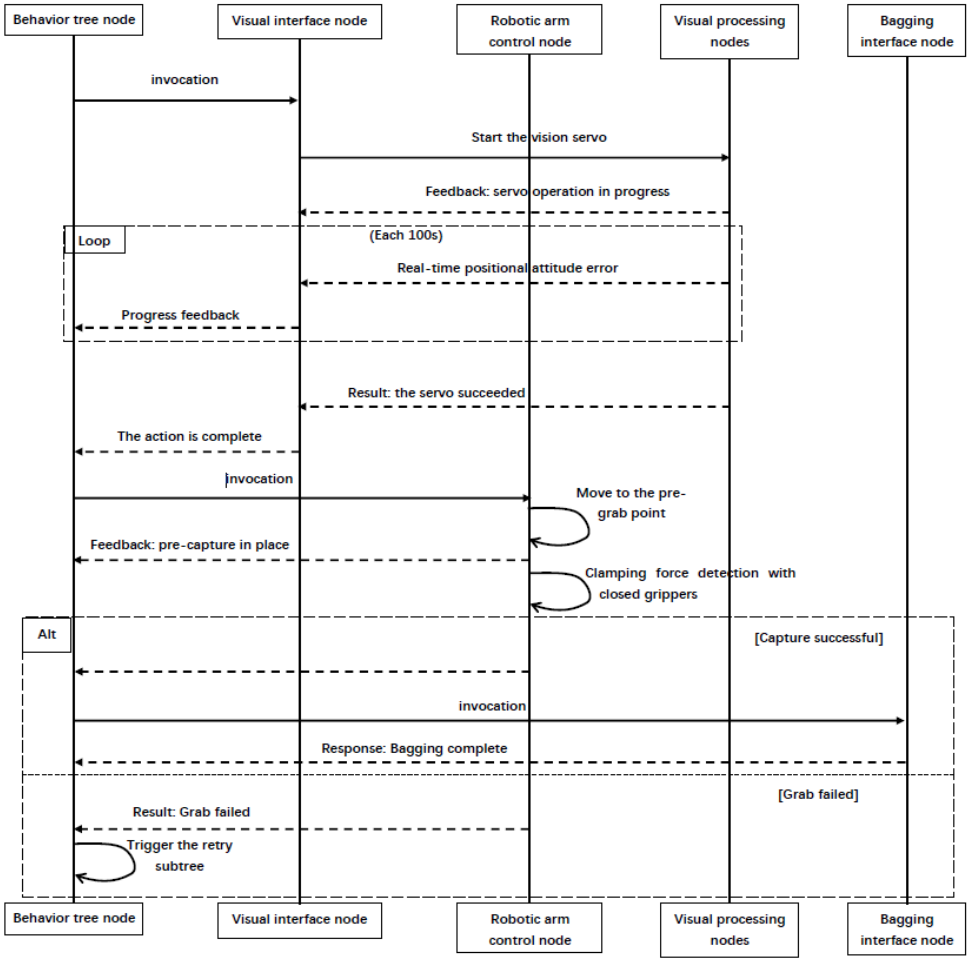


Fig. 17 - Internal Execution Logic and Multi-System Coordination Mechanism

To clearly illustrate the internal execution logic of critical action nodes within the behavior tree and the multi-system coordination mechanism, the 'Execute Harvesting Action' node serves as an example. Internally, it invokes sub-services such as visual servo, grasping, and bagging to achieve a seamless sequence from visual fine positioning to fruit grasping and bagging. Fig. 17 details this node's execution flow and the invocation relationships between its modules.

The system employs a ROS-based modular communication network, where functional nodes exchange data and execute tasks via Topics, Services, and Actions. A TF tree manages coordinate transformations, enabling real-time coordination and synchronization among the mobile platform, robotic arm, and packaging device under behavior tree scheduling.

RESULTS

System Integration and Experimental Analysis

Quantitative Performance Analysis of YOLOv8s Visual Detection Model

Detection performance under three occlusion grades is tested on the test set, as listed in Table 3.

Table 3

YOLOv8s detection performance under different fruit occlusion conditions

Occlusion Level	mAP@0.5	Precision /%	Recall /%	Single-frame Inference Time /ms
Unobstructed ripe tomato	98.6	97.3	96.8	28.6
Semi-occluded ripe tomato	94.1	94.5	93.2	29.1
Heavily occluded ripe tomato	87.3	88.1	86.5	30.2

The mAP declines with increased leaf coverage but still meets picking requirements. Combined with ImageJ secondary screening, the overall maturity discrimination accuracy reaches 93.5%. The average 29 ms inference time ensures real-time grasping response on the K280L industrial computer.

Navigation Experiment of Mobile Platform Based on A and TEB Algorithm*

A* global + TEB local dual planning is verified in simulated greenhouse ridges with static and dynamic obstacles, 20 repeated trials for each group. Comparative results are shown in Table 4.

Table 4

Comparative navigation results of A* single planning and A*+TEB dual planning

Evaluation Index	A* + TEB Dual Planning	Single A* Global Planning	Performance Improvement Rate
Global path length of standard ridge / m	18.62	18.62	-
Average single navigation time / s	22.4	28.7	22.0%
Maximum lateral deviation during obstacle avoidance / mm	36.2	94.7	-
Total collision times within 20 groups of tests	0	12	-
Average terminal positioning error / mm	±8.3	±15.6	46.8%

TEB optimizes local trajectories based on LiDAR data, eliminating collision risks and improving docking precision for manipulator picking.

Classification Statistical Test of Independent Net Bagging Operation

The robot completes single-fruit independent heat-sealed packaging. Special bagging tests are carried out for tomatoes with diameters ranging from 50 mm to 100 mm. 120 valid experimental samples are grouped by fruit size to count bagging success rate and fault distribution, as shown in Table 5.

Table 5

Bagging performance statistics of tomatoes with different diameters

Tomato Diameter Range / mm	Number of Test Samples	Successful Bagging Cases	Bagging Success Rate / %	Main Fault Types
50–70 (small fruit)	42	41	97.6	Slight net bag offset (1 case)
70–85 (medium fruit)	50	49	98.0	Thermal sealing adhesion (1 case)
85–100 (large fruit)	28	27	96.4	Fruit jamming on guide cone (1 case)
Total Summary	120	118	98.3	Total faults: 2 cases

Overall bagging reliability meets commercial standards; large-fruit jamming can be mitigated by optimizing the conical guide stroke in future work.

Efficiency Quantitative Comparison Between Robotic System and Manual Operation

120 continuous robotic cycles yield an average single-fruit runtime of 12.1 ± 1.5 s. Three skilled workers achieved 17.3 ± 2.8 s per fruit under identical operations.

Hourly throughput: Robot ≈ 298 fruits/h; Manual ≈ 208 fruits/h, corresponding to ~30% efficiency improvement, consistent with Abstract claims.

Manual efficiency drops 23% after 4 h due to fatigue, while the robot maintains stable output without labor attenuation and extra transfer steps.

Experiments and Results

To validate system performance, testing was conducted in a simulated greenhouse environment. The experiment utilized tomato plants at varying stages of maturity, requiring the system to perform continuous integrated operations on ripe fruit *(Wu and Miao, 2025).* Through over 120 effective cycles, the system's performance metrics were evaluated and compared with manual operations, with results shown in Table 6.

Table 6

System Key Performance Indicator Test Results

Experimental Parameters	Experimental Parameters Average Value/Success Rate	Note
Total number of experiments (fruit)	120 times	Includes tests under different lighting conditions (morning/afternoon)
Average total time required per fruit	12.1 ± 1.5 s	The entire process time from identification to completion of bagged recycling
Accuracy rate for identifying ripe fruit	95.2%	The proportion of mature fruit correctly identified as “ready for harvest”
Comprehensive Accuracy Rate for Maturity Assessment	93.5%	Overall classification accuracy for green-ripe, color-changing, and fully ripe fruit stages
Harvest Success Rate	90.8%	The percentage of fruit stems successfully gripped and severed without causing damage to the fruit
Accuracy of Harvest Location Positioning	96.7%	Precision of the robotic arm's end effector reaching the predetermined fruit stalk cutting point
Bagging success rate	98.3%	Percentage of successful bagging operations
Average time required for manual operations (for comparison)	17.3 ± 2.8 seconds per fruit	The average time required for skilled workers to complete picking and bagging

Table 6 summarizes all key comprehensive indicators of the integrated robot prototype under simulated greenhouse tests.

System Comparison Analysis and Summary of Advantages

To objectively evaluate the comprehensive performance and innovative value of this design, this section compares it with three representative studies from recent years: a greenhouse tomato harvesting robot focused on sequence optimization *(Li, 2024)*, a strawberry harvesting robot investigating dual-arm coordination *(Liu et al., 2026),* and the latest row-planted strawberry harvesting robot designed for narrow ridge-edge environments *(Wang et al., 2025)*. Key systematic comparisons are presented in the table below.

Table 7

Systematic Comparative Analysis Chart

Comparison Dimensions	This Design: Tomato Harvesting Robot	Greenhouse Tomato Harvesting Robot	Dual-Arm Strawberry Picking Robot	Row-planted strawberry picking robot
Perception System Solution	Multi-source Fusion Perception: Integration of RGB-D cameras (target recognition/localization) and LiDAR (SLAM navigation).	Visual Perception: Utilizes an enhanced Ghost-CAE YOLOv5 model with a depth camera (D435).	Visual and 3D Reconstruction: Employs YOLOv8-segment for instance segmentation, combined with COLMAP for scene modeling.	Visual and End-Point Sensing: YOLOv5-based picking point localization combined with end-point fiber optic sensors for trigger detection.
Planning and Control Strategy	Hierarchical Collaborative Planning: A* (global path planning), TEB (local obstacle avoidance), RRT-Connect (robot arm path planning) integrated with vision servo closed-loop control.	Harvest Sequence Optimization: We propose the “K-G method,” which integrates K-means clustering with a Gaussian kernel function to optimize sequences.	Dual-Arm Task Planning: Proposes a coordinated algorithm integrating genetic and cheetah optimization (GCO), with path planning employing RRT*.	Task Decision Model: Priority-Based Harvesting Strategy Based on Fruit Spatial Relationships; Four-Degree-of-Freedom “PRPR” Configuration Manipulator.
Key Performance Indicators	Recognition success rate: 95.2%; Picking success rate: 90.8%; Bagging success rate: 98.3%; Single fruit full cycle: ~12.1 s.	mAP Recognition Rate: 95.12%; Picking Success Rate: 95.56%; Average Picking Cycle: ~6.7 s per fruit.	(Algorithm Performance) Reduces total job time by up to 34.5% and reduces dual-arm idle time by 81.9%.	Single-arm picking cycle: 5.0 s; Average dual-arm cycle: 4.57 s; Damage-free picking success rate: 59.56%.

Mechanical and Actuator Systems	Dedicated bagging mechanism (integrated heat sealing), flexible cushioning collection bin, vacuum-assisted end-effector for transfer.	Universal Six-Axis Robotic Arm (AUBO-i5) with Adaptive Flexible Four-Finger Gripper.	A composite end effector integrating active obstacle clearance (low-voltage blower) with passive obstacle avoidance (soft gripper).	Non-destructive mechanical gripper employing a spatial cam and spring steel plate for rapid gripping and shearing.
System Autonomy and Collaboration	Based on ROS and behavior trees, achieve adaptive coordination and task scheduling among the mobile platform, robotic arm, and bagging unit.	Achieved a closed-loop autonomous picking system for a single arm, without involving complex multi-motor unit coordination.	Establish a “dual cargo bay-dual workstation” model to optimize temporal and spatial conflicts between dual arms within overlapping work zones.	Features a distributed four-wheel independent drive/steering chassis with multiple steering modes to accommodate narrow aisle navigation.

CONCLUSIONS

This study designs and validates a fully integrated tomato harvest-and-packaging robot. The 12.1 s single-fruit cycle delivers ~30% higher efficiency than manual labor, with 95.2% fruit recognition, 90.8% picking and 98.3% bagging success rates.

The system’s performance relies on four coordinated technologies: YOLOv8s+ImageJ dual ripeness detection, A*/TEB inter-row navigation, RRT-Connect canopy obstacle avoidance and behavior tree multi-unit scheduling.

Different from single-function harvesting robots, the built-in vertical heat-sealing bagger realizes on-site commercial packaging to reduce fruit damage. This prototype provides a complete hardware and algorithm reference for full-process intelligent greenhouse agriculture.

ACKNOWLEDGEMENT

Fund support: The Innovation and Entrepreneurship Training Program for College Students in Jiangsu Province(S202513984014)

REFERENCES

1. Adochiei, IR., Argatu, F.C., Enache, BA., Banica, C.K., Grigorescu, S.D., Adochiei, FC. (2025). Modular Mobile Robotic Platform for Smart City and Indoor Service Applications. In: Sontea, V., Tiginyanu, I., Railean, S. (eds) *7th International Conference on Nanotechnologies and Biomedical Engineering. ICNBME 2025. IFMBE Proceedings, Vol. 135*, 624-634. Springer, Cham. https://doi.org/10.1007/978-3-032-06497-4_61
2. Bu, L., Sugirbay, A., & Li, T. (2025). Optimal combination of picking motions for robotic apple harvesting based on experimental and simulation analysis. *Tehnicki Vjesnik, Vol. 32*(5), 1607-1613. https://doi.org/10.17559/tv-20240701001813
3. El-sheikha, A. M., Darwesh, M. R., Hegazy, R., Okasha, M., Mohamed, N. H. (2024). Study the thermal performance of drying tomatoes process using a solar energy system. *INMATEH agricultural engineering, Vol. 73*, 13-29. https://doi.org/10.35633/inmateh-73-01.
4. Goulart, N. D. S. R. (2023). Efficiency evaluation of an automated mango harvesting unit. Rockhampton: *Central Queensland University.* https://doi.org/10.25946/26156437
5. He, L.L., Gu, Y., Xia, M., Li, R., Zhang, Q., Fu, L.S. (2025). Research progress of the kiwifruit operation robots and prospects for fully intelligent production (猕猴桃作业机器人研究进展及全程智能化生产展望). *Transactions of the Chinese Society of Agricultural Engineering*, *Vol. 41*, 1-14. DOI: 10.11975/j.issn.1002-6819.2025.17.001 *(in Chinese)*
6. Ji, J., Zhao, J.-S., Misyurin, S. Y., & Martins, D. (2023). Precision-driven multi-target path planning and fine position error estimation on a dual-movement-mode mobile robot using a three-parameter error model. *Sensors*, *Vol.* 23(1), 517. https://doi.org/10.3390/s23010517
7. Li, Y. J. (2024). Research on the Method of Operation Path Planning for Tomato Picking Robot Based on Reinforcement Learning (基于强化学习的番茄采摘机器人操作路径规划方法研究). *Hunan Agricultural University*, 2024. DOI: 10.27136/d.cnki.ghunu.2024.000057 *(in Chinese)*
8. Li, Z. M. (2025). Research on Path Planning and Path Tracking Control Technology of Picking Robot Mobile Platform (采摘机器人移动平台路径规划与路径跟踪控制研究). *Yanshan University*, 2025. DOI: 10.27440/d.cnki.gysdu.2024.001391. *(in Chinese)*

9. Liu, X., Song, Z., Tan, Y., Yang, S., & Ma, Y. (2026). Conflict avoidance task planning strategy for dual-arm cooperative strawberry harvesting robots. *Computers and Electronics in Agriculture, Vol. 241*. DOI: 10.1016/J.COMPAG.2025.111067
10. Liu, X.G., Ma, B. J., Wang, C.C., Zhang, J., Zhang, H. M., Wei, D. (2025). Research status and development trend of autonomous mobile robots in orchard (果园自主移动机器人研究现状及发展趋势). *Journal of Chinese Agricultural Mechanization, Vol. 46*, pp.120-127. DOI: 10.13733/j.jcam.issn.2095-5553.2025.06.018. *(in Chinese)*
11. Luo, L. F., Zou, X. J., Cheng, T. C., Yang, Z. S., Zhang, C., Mo, Y. D. (2017). Design of virtual test system based on hardware-in-loop for picking robot vision localization and behavior control (采摘机器人视觉定位及行为控制的硬件在环虚拟试验系统设计). *Transactions of the Chinese Society of Agricultural Engineering, Vol. 33*, pp. 39-46. DOI: 10.11975/j.issn.1002-6819.2017.04.006. *(in Chinese)*
12. Marin, F. B., Matache, M. G., Marin, M., Gurau, G., Cristea, R., Tanase, A. (2025). Computer vision-based grasp detection for a metamaterial soft gripper in robotic vegetables harvesting. *INMATEH Agricultural Engineering, Vol. 77*(3), 872-881, https://doi.org/10.35633/inmateh-77-71
13. Matache, M.G., Marin, F.B., Persu, C.I., Cristea, R.D., Nenciu, F., Atanasov, A.Z. (2026). Autonomous Tomato Harvesting System Integrating AI-Controlled Robotics in Greenhouses. *Agriculture, Vol.* 16, 847. https://doi.org/10.3390/agriculture16080847
14. Meng, T., Zhou, R., & Ren, Z. (2025). Implementation of a visual positioning and robotic arm grasping algorithm for handling robots. *In Proceedings of 2025 2nd International Conference on Industrial Automation and Robotics, Vol. 2025*, 68-77. https://doi.org/10.1145/3778886.3778897
15. Sepúlveda, D., Fernández, R., Navas, E., Armada, M., & González-de-Santos, P. (2020). Robotic aubergine harvesting using dual-arm manipulation. *IEEE Access, Vol.* 8, 121889-121904. doi: 10.1109/ACCESS.2020.3006919
16. Shao, Y.X. (2025). Research on optimal obstacle avoidance motion planning technology of oyster mushroom picking robot (平菇采摘机器人避障最优运动规划技术研究). *Central South University*, 2025. DOI: 10.27661/d.cnki.gzhnu.2024.003174. *(in Chinese)*
17. Wang, G., Liu, J. (2025). Structural design of an eggplant harvesting robot based on SolidWorks (基于SolidWorks 的茄子采摘机器人结构设计). *Hebei Agricultural Machinery*, *Vol.* 2025, 4-6. DOI: 10.15989/j.cnki.hbnjzzs.2025.16.011. *(in Chinese)*
18. Wang, K., Yang, S., Liu, X., Song, J., Li, Y., & Xie, F. (2025). Research on target recognition, localization, and picking sequence planning for tomato-picking robots in greenhouse environments. *Smart Agricultural Technology, Vol. 12*,101628. DOI: 10.1016/J.ATECH.2025.101628
19. Wen, B.-J., & Liu, T.-W. (2023). Automatic assembly with dual robotic arms based on mutual visual tracking and positioning. *Science Progress, Vol. 106*(2), 1-24. https://doi.org/10.1177/00368504231172667
20. Wu, J., Miao, R. (2025). Strawberry identification and key points detection for picking based on improved yolov8-pose at red ripe stage (基于改进 YOLOV8-POSE 的红熟期草莓识别与采摘关键点检测). *INMATEH Agricultural Engineering, Vol. 76*, 89-99. https://doi.org/10.35633/inmateh-76-08
21. Yu, X.Y., Zhan, Y.A., Hong X.J.F., Ou, L.L. (2017). Parameter identification of a 6-degree-of-freedom robotic arm kinematic model using particle swarm optimisation (基于粒子群算法的 6 自由度机械臂动力学模型参数辨识). *High Technology Communications, Vol. 27*, 625-632. DOI: 10.3772/j.issn.1002-0470.2017.07.006 *(in Chinese)*
22. Yuan, T., Zheng, X.J., Fu, J., Rong, J.C., Zhang, Z.Q., Yang, Y., Zhang, J.X., Li, W. (2023). Small watermelon harvesting robot and harvesting method based on greenhouse three-dimensional cultivation model: China (基于温室立体栽培模式下小型西瓜采摘机器人及采摘方法), CN116965236A[P]. 2023-04-28. *(in Chinese)*
23. Yuan, Z., Shen Y. G. (2017). Research on trajectory optimization of self-seeking path and obstacle avoidance for fruit-picking robot based on heuristic intelligent algorithm (水果采摘机器人自主寻径避障轨迹优化研究—基于启发式智能算法). *Agricultural Mechanisation Research*, *Vol. 39*. DOI: 10.13427/j.cnki.njyi.2017.07.042 *(in Chinese)*

STRUCTURAL DESIGN AND VISION-BASED TARGET DETECTION AND LOCALIZATION OF A DESERT SHRUB STUBBLE-CUTTING MACHINE
/
沙生灌木平茬机的结构设计与基于视觉的目标检测与定位

Weiqi WU[1)], Haitang CEN*[1)], Wang GUO[2)], Wei ZHANG[1)]
[1)] School of Mechanical Engineering, Inner Mongolia University of Technology, Hohhot, 010000 / China;
[2)] Inner Mongolia Academy of Science and Technology, Hohhot, 010000 / China
Tel: +86-13514712360; E-mail: 1054949591@qq.com
DOI: https://doi.org/10.35633/inmateh-79-26

Keywords: *desert shrubs, machine vision, structural design, stubble cutting machine*

ABSTRACT
Current research on shrub stubble cutting machines primarily focuses on mechanical structure design and operational performance, whereas shrub localization and cutting status still rely on manual judgment. To address this issue, an intelligent desert shrub stubble cutting machine integrating structural design with vision-assisted operation was developed. The overall structure and key component parameters were determined through theoretical analysis, and the disc cutting process was validated via Workbench simulation. The YOLOv5s model incorporating a Focal-CIoU loss function was adopted to enhance shrub detection under complex background conditions. Image processing and binocular vision were employed to obtain the three-dimensional coordinates of shrub roots. Experimental results demonstrate that the cutting device meets the operational requirements; the improved model achieves an accuracy of 91.9%, a recall of 96.5%, and a mAP of 98.3%; and the maximum relative errors for root depth and height measurements are 3.19% and 6.51%, respectively, satisfying the detection and localization requirements for shrub stubble cutting.

摘要
当前灌木平茬机的研究主要集中于机械结构设计与作业性能，而灌木定位和切割状态仍依赖人工判断。针对该问题，本文研制了一种将结构设计与视觉辅助作业相结合的智能荒漠灌木割茬机。通过理论分析确定了整机结构和关键部件参数，并利用Workbench仿真验证了圆盘切割过程。采用引入Focal-CIoU损失函数的YOLOv5s模型，以增强复杂背景条件下的灌木检测能力。利用图像处理和双目视觉获取了灌木根部的三维坐标。实验结果表明：切割装置满足作业要求；改进模型的准确率达到91.9%，召回率为96.5%，mAP为98.3%；根部深度和高度测量的最大相对误差分别为3.19%和6.51%，满足灌木平茬检测与定位要求。

INTRODUCTION
Land desertification represents a major obstacle to ecological restoration and sustainable development. As of 2024, desertified land in China accounts for approximately 26.8% of the country's total terrestrial area. Xerophytic shrubs, such as *Salix psammophila* and *Haloxylon ammodendron*, are widely used for windbreak and sand fixation as well as ecological restoration due to their pronounced drought tolerance and significant sand-binding capacity (*Gao S. et al., 2022*). These shrubs exhibit a growth characteristic known as "rejuvenation after pruning": prolonged absence of pruning leads to gradual branch senescence and even whole-plant mortality, which may in turn induce secondary desertification (*Pei et al., 2019*). Therefore, regular pruning is an essential measure to maintain the long-term vitality of these shrubs. At present, pruning of xerophytic shrubs in China relies predominantly on manual labor and semi-automatic backpack pruning machines, which suffer from low operational efficiency and high labor intensity. Moreover, prolonged use is associated with occupational health risks, including vibration-induced disorders and noise-induced hearing loss (*Tian, 2013*).

Existing research on pruning machines has primarily focused on mechanical structures and operational parameters. *Ma et al., (2015),* developed a tracked, self-propelled shrub pruning machine that improved adaptability to sandy terrain through a floating cutting mechanism. *Wang et al., (2025),* designed a hydraulic scissor-type Caragana pruning machine and reduced both branch breakage rate and cutting power consumption via parameter optimization. Although these studies have enhanced the operational performance of the equipment, the pruning process remains largely manual, with limited perception of shrub distribution and ground surface variations.

Regarding intelligent pruning operations, *Ren (2021)* integrated machine vision into Caragana pruning tasks, enabling the identification of root collar positions and supporting adaptive adjustment of the cutting platform height. However, this work focused on visual recognition in isolation and lacked full integration with the machine's structural design and practical operational workflows. In agricultural machinery research, machine vision has been successfully applied to identification and localization tasks in field operations—for example, *Fan et al., (2025),* achieved cotton row detection for spraying robots in cotton fields. Nevertheless, these studies targeted regularly spaced row crops, whose spatial distribution differs markedly from the sparse, irregular, and clustered arrangement of desert shrubs, rendering the direct transfer of such methods impractical for shrub pruning applications.

To address the aforementioned challenges, this paper proposes the design of an intelligent pruning machine for xerophytic shrubs. The machine is built upon a tracked mobile platform and integrates cutting and baling functions. It incorporates a visual recognition system based on an improved YOLOv5s model, synergistically combining image processing with binocular stereo vision measurement. Simulation analyses and prototype experiments were conducted to validate the machine's capabilities in accurate shrub identification, three-dimensional localization, and adaptive cutting. The findings provide a technical reference for the development of intelligent pruning equipment for xerophytic shrubs.

MATERIALS AND METHODS

Machine structure design

The intelligent shrub-topping machine developed in this study consists of a cutting unit, a baling unit, a binocular stereo camera, a tracked locomotion system, a conveying mechanism, a header lifting mechanism, a motor, and a battery. The overall configuration and key design parameters are illustrated in Fig. 1 and listed in Table 1, respectively (*Zhang B. et al., 2022; Georges R. et al., 2014*).

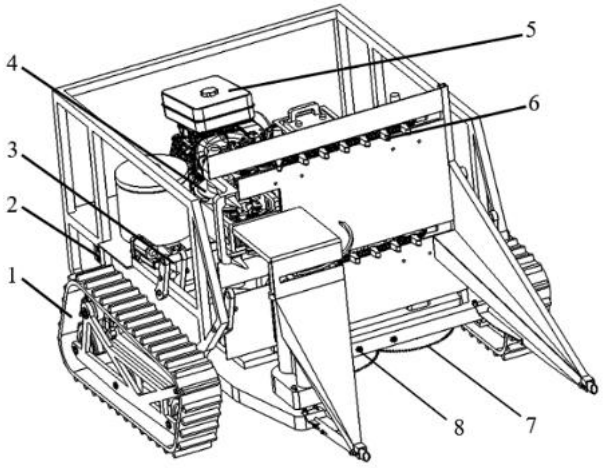


Fig. 1 - Overall structure of the shrub stubble cutting machine

1 – Traveling mechanism; 2 – Traveling drive assembly; 3 – Header lifting device; 4 – Baling device; 5 – Powertrain; 6 – Conveying device; 7 – Cutting device; 8 – Binocular camera sensor

Table 1

Technical parameters of the shrub trimmer for sandy land

Parameter	Value
Overall machine weight (kg)	<500
Overall dimensions (length × width × height) (mm)	1450×1342×1000
Diameter of coppiced shrubs (mm)	0~20
Working width (mm)	700
Pruning height (mm)	10-100
Power of a single travelling motor (kW)	2

Operating principles

During operation, the rubber-tracked chassis propels the machine toward the target shrub stand. The cutting platform height is adjusted to a preset cutting position via an electric linear actuator (*Johnson P.C. et al., 2012*), after which the cutting motor is activated.

As the machine advances, the V-shaped guide plate mounted at the front end aligns and directs the shrubs, facilitating smooth entry into the cutting zone and enabling precise severance. The cut shrubs are continuously conveyed into the baling unit by a conveyor chain and progressively compacted under the compressive force exerted by the baling tines. Once the diameter of the shrub bundle within the baling unit reaches a preset threshold, the baling clutch engages automatically; the rope feed needle then delivers twine to the knotting mechanism to complete the binding process. Subsequently, the bound shrub bundle is ejected laterally from the machine. The clutch then disengages, and the baling unit ceases operation, thereby completing one full pruning cycle.

Main structure design of the cutting device

The cutting unit is one of the most critical components of the brush cutter designed for xerophytic shrubs. In this study, a disc-type cutting unit is adopted, as illustrated in Fig. 2. The cutting platform is connected to the frame via a four-bar linkage and secured with bolts. Power from the cutting motor is transmitted to the main shaft, and the ground clearance of the cutting unit is regulated by the extension and retraction of electric linear actuators mounted on both sides of the frame.

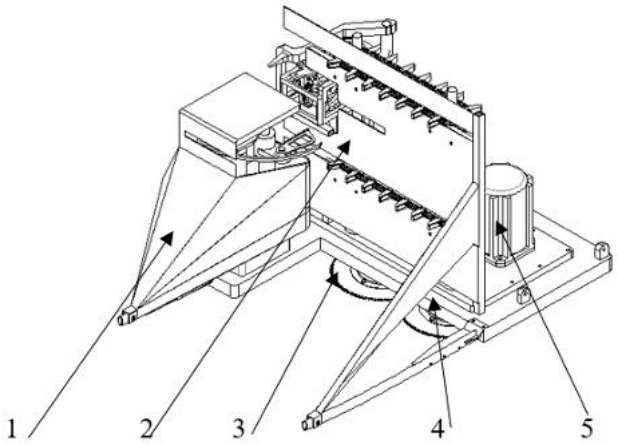


Fig. 2 - Schematic diagram of the cutting unit

1 – Branch gathering frame; 2 – Cutting baffle; 3 – Cutting component; 4 – Bottom plate drive; 5 – Cutting motor

Design and calculations of the cutting unit

1) Transmission system design

The transmission system of the cutting unit consists of gears, sprockets, and transmission shafts. Power from the motor is transmitted to cutting spindles I and II via gear trains. Spindle I additionally transmits power to the conveying unit and the baling unit to facilitate transport and compaction of the severed shrubs. The corresponding schematic diagram is presented in Fig. 3. At the lower end of the extended shaft of spindle I, the cutter head is attached, while the upper end is coupled to the gearbox via a keyway, enabling power transmission to the conveying unit.

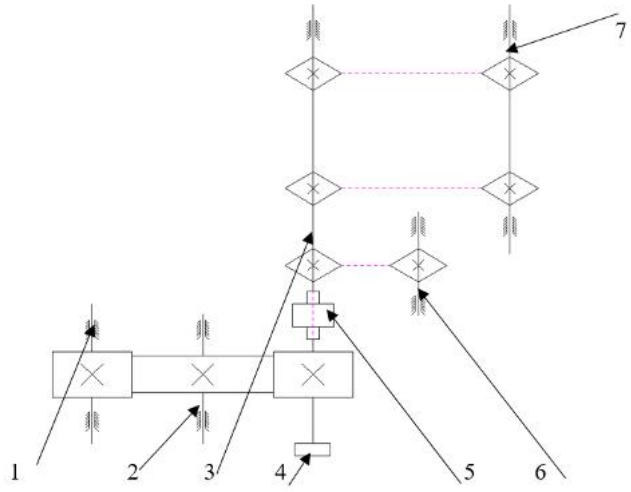


Fig. 3 - Schematic diagram of the transmission system

1 – Power input shaft; 2 – Intermediate shaft; 3 – Drive shaft of transmission chain; 4 – Cutting component; 5 – Planetary reducer; 6 – Power input shaft of baling mechanism; 7 – Transmission shaft of transmission chain

2) Circular saw blade selection

The principal parameters of the saw blade include the outer diameter D, thickness S, number of teeth T, rake angle γ_1, and clearance angle α_1. Based on the diameter of the shrub roots and in accordance with circular saw blade standards, the blade diameter is selected as D = 350 mm. The thickness of the blade is determined by Equation (1):

$$S = \eta_1 K \sqrt{D} \tag{1}$$

where:

η_1 is the safety factor, taken as 1.68; K is the thickness safety coefficient, taken as 0.075. After calculation, the thickness S of the circular saw blade is determined to be 2.3 mm. The number of teeth T is 100, the rake angle γ_1 is 20°, and the clearance angle α_1 is 15°.

3) Calculation of cutting power

The total power P_Z consumed during shrub cutting consists of the no-load rotational power P_K of the saw blade and the cutting power P_L. The corresponding formulas for calculating these three power components are given in Equations (2) - (4):

$$P_k = \frac{mv_c^2 + J\omega^2}{2} \tag{2}$$

$$P_L = \frac{v_f Al}{102} \tag{3}$$

$$P_Z = P_K + P_L \tag{4}$$

where:

m is the mass of the circular saw blade, 1.625 kg; v_c is the peripheral speed of the saw blade, 26 m/s; J is the moment of inertia of the saw blade, 0.49 kg·m^2; ω is the angular speed of the saw blade, rad/s; v_f is the feed velocity of the brush cutter, 0.5 m/s; A is the cutting width, m; l is the specific cutting energy required for shrubs, 490 J/m^2. Finally, P_K is 0.82 kW, P_L is 0.84 kW, and P_Z is 1.66 kW.

Main structure and working principle of the baling unit

This study adopts a side-baling configuration. The baling unit consists of a knotter, a power input chain, the knotter main shaft, a rope feed rocker, a rope feed rocker transmission shaft, and a stem compression rod. The power input shaft of the baling unit is connected to the conveyor chain main shaft via a chain drive. When the clutch lever is actuated—i.e., depressed and rotated by a specified angle—the power input shaft engages with the knotter main shaft, thereby initiating knotter operation. The rope feed rocker main shaft and the knotter main shaft are interconnected by a chain drive. The transmission chain is housed within the baseplate, and the chain type selected is the C08A roller chain. A schematic diagram of the baling unit is presented in Fig. 4.

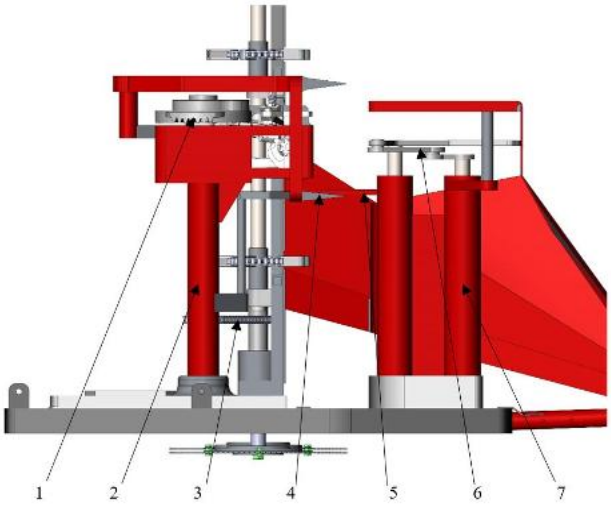


Fig. 4 - Structure of the baling mechanism

1 – Knotting device; 2 – Drive shaft sleeve I; 3 – Power input chain; 4 – Clutch control lever; 5 – Stem-pressing rod; 6 – Rope-feeding rocker; 7 – Drive shaft sleeve II

Design of the main components of the baling unit

1) Design of the knotter structure

The knotter consists of a conical gear disc, a rope-clamping device, and knotting pliers, as illustrated in Fig. 5. The phase difference between the inner and outer teeth of the conical gear disc is 58°, which governs the timing coordination between the rope-clamping device and the knotting pliers. The phase difference between the outer teeth and the cam's far stop point is 111°, which controls the timing coordination between the knotting pliers and the rope-cutting knife.

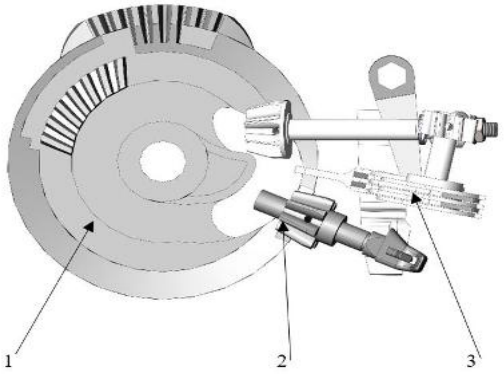


Fig. 5 - Structure of the knotting mechanism

1 – Conical-toothed disc; 2 – Looping pliers; 3 – Rope clamp

2) Design of the rope-feeding rocker

The rope feed rocker, as the most critical auxiliary component of the baling unit, is designed to deliver rope accurately and rapidly to the knotter, thereby facilitating the baling operation. To minimize the time required for rope feeding and baling, a crank-rocker mechanism is adopted in the design of the rope feed rocker. A simplified motion analysis diagram is presented in Fig. 6 (*Mutlu H., 2021*). Based on this diagram, the motion parameters of the rocker can be determined. Through empirical design, the rotation radius of the driving crank l_1 is set to 63 mm. Using the crank-rocker mechanism calculation formulas, the lengths of the remaining three links—l_2, l_3, and l_4—are determined as 124 mm, 124 mm, and 134 mm, respectively.

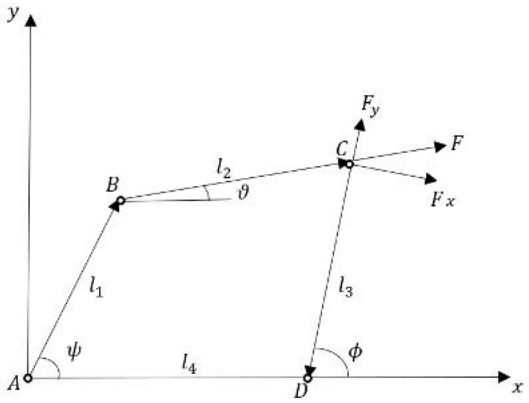


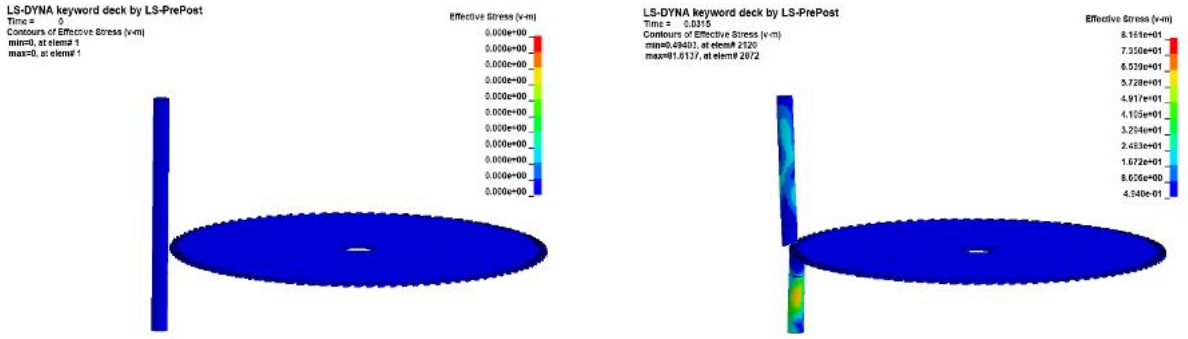
Fig. 6 - Force diagram of the crank-rocker mechanism

Simulation analysis on the stubble-cutting process of the cutting device

To ensure the accuracy of the simulation results while maintaining computational efficiency, the following simplifications were applied to the circular-disc cutting model: (1)The cross-section of the desert shrub was approximated as a circular profile; (2) The taper variation along the shrub stem was neglected, and the stem was modelled as a cylinder of uniform cross-sectional area; (3)The upper and lower clamping plates, transmission system, and bolts of the circular saw blade were omitted, and the bolt mounting holes were removed (*Wu G., Zhang D.D., 2022*).

Based on the aforementioned simplifications, the model was developed using SolidWorks. The saw blade was modelled with a diameter of 350 mm, a rake angle γ_1 = 20°, the clearance angle α_1 = 15°, and a tooth count T=100. As the primary target of cutting in this study was shrubs with a stem height of 0–20 mm, the shrub was simplified as a cylinder of 20 mm diameter and 200 mm height, with the cutting height set to 70 mm.

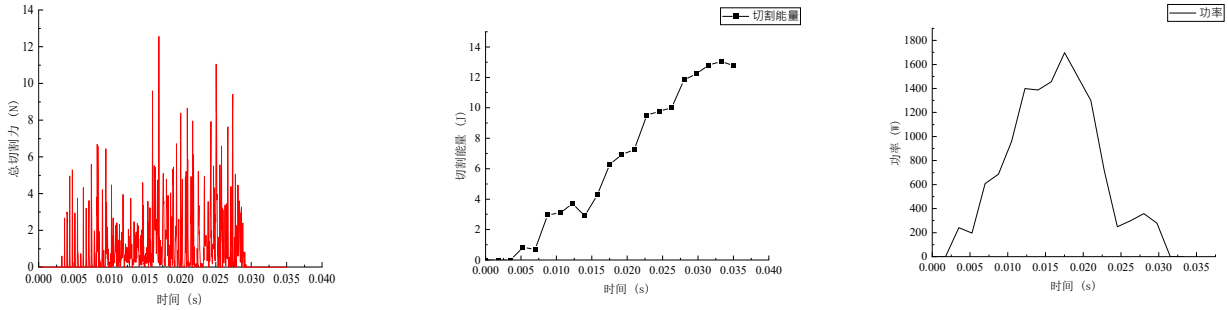
In Workbench, the material of the circular saw blade was defined as 65Mn steel, with a density of 7.85×10³ kg/m³, a Poisson's ratio of 0.3, and an elastic modulus of 210 GPa. Desert shrub stems are characterized as nonlinear, non-homogeneous, and anisotropic elastic materials (*Gangwar T., Schillinger D., 2019*). To reduce model complexity while satisfying the analysis requirements, the stem was simplified as an isotropic linear-elastic material. The corresponding material parameters were assigned from the Workbench material library as follows: density of 480 kg/m³, Poisson's ratio of 0.33, and elastic modulus of 5034 MPa. The stress distribution cloud diagram obtained from the simulation is presented in Fig. 7.



a. Initial moment of the simulation b. Moment of shrub cutting

Fig. 7 - Stress variation during the four stages of the simulated sawing process

The curves of total cutting force, required energy, and cutting power of the circular saw blade over time during shrub cutting are presented in Fig. 8. As shown in Fig. 8a, the maximum total cutting force acting on the shrub stem reaches 13 N at a simulation time of 0.175 s. From Fig. 8b, it can be observed that cutting initiates at 0.026 s; the shrub stem bends under load and accumulates strain energy. At 0.03 s, the stem releases all the stored energy due to elastic deformation. The maximum energy required for cutting the shrub is 13 J. As illustrated in Fig. 8c, the maximum power required for cutting is 1670 W, which is consistent with the power consumption obtained from the theoretical calculation presented earlier. These simulation results indicate that the cut-ting device designed in this study meets the operational requirements for shrub cutting.



a. Total cutting force b. Cutting energy c. Cutting power

Fig. 8 - Curve of energy change during shrub cutting

Model training and evaluation of the visual recognition algorithm

Following the structural design of the pruning machine and the simulation analysis of the cutting components, this study investigates an image recognition algorithm for shrub detection during pruning operations. Model training and testing were conducted in a Windows 11 environment using a 12th Gen Intel(R) Core(TM) i5-12490F processor, an NVIDIA GeForce RTX 3060 Ti graphics card, 16 GB of RAM, and Python version 3.10.

In this experiment, 50 images were collected through online image retrieval and manual capture. The dataset was then augmented using techniques including horizontal flipping, brightness adjustment, rotation, scaling, cropping, high-frequency noise addition, Gaussian blurring, and histogram equalization. The final augmented shrub image dataset comprised 1,000 images and was randomly partitioned into training, validation, and test sets in an 8:1:1 ratio, corresponding to 80% for training, 10% for validation, and 10% for testing. During model training, the batch size was set to 8, the initial learning rate to 0.01, the weight decay coefficient to 0.0005, the momentum factor to 0.937, and the total number of epochs to 150.

Focal-CIoU-based improved loss function

In the original YOLOv5s network architecture, Complete Intersection over Union (CIoU) is employed as the bounding box regression loss function. CIoU quantifies the degree of matching between predicted and ground-truth bounding boxes by jointly considering the intersection over union (IoU), the Euclidean distance between their center points, and the consistency of their aspect ratios (*Li T. et al., 2023*). The corresponding formulas are given in Equations (5) - (7):

$$L_{CIoU} = 1 - \mathrm{IoU} + \frac{\rho^2\left(b, b^{gt}\right)}{c^2} + \alpha v = 1 - \frac{\left|B \cap B^{gt}\right|}{\left|B \cup B^{gt}\right|} + + \frac{\rho^2\left(b, b_{gt}\right)}{c^2} + \alpha v \quad (5)$$

$$v = \frac{4}{\pi}(\arctan\frac{w}{h} - \arctan\frac{w}{h}) \quad (6)$$

$$\alpha = \frac{v}{(1 - \mathrm{IoU}) + v} \quad (7)$$

where:

IoU is the intersection over union between the predicted box and the ground-truth box; B and B^{gt} are the predicted box and the ground-truth box, respectively; b and b^{gt} are the centers of B and B^{gt}, respectively; ρ^2 is the squared Euclidean distance between the two centers; c is the diagonal length of the smallest enclosing rectangle covering both boxes; α is the control parameter for the convergence speed of the loss; v is the measure of the aspect ratio difference.

In practical shrub detection, the sparse distribution of shrubs in desert environments results in some collected images where the shrubs occupy a significantly smaller proportion of the image area compared to the desert background. This imbalance hinders the model's ability to effectively learn discriminative shrub features, thereby reducing detection accuracy. To address this issue, this study adopts the computational principle of Focal Loss and integrates it with CIoU to formulate the Focal-CIoU loss function (*Peng H. et al., 2023*), as presented in Equation (8):

$$L_{Focal-CIoU} = IoU^{\gamma} L_{CIoU} \quad (8)$$

where:

γ represents the degree of outlier suppression.

By introducing the IoU modulation term, Focal-CIoU reduces the influence of samples with high IoU values in the loss computation, enabling the model to focus more on shrub targets with large localization errors during training—thereby improving localization accuracy and detection performance in complex backgrounds.

Experimental results and analysis of the visual recognition algorithm

To evaluate the shrub detection performance of the improved YOLOv5s network, comparative experiments were conducted using YOLOv5s, YOLOv7-Tiny, YOLOv8s, as well as the lightweight backbones MobileNetV3 and ShuffleNetV2 integrated into the YOLOv5 framework. All models were trained under identical conditions using the same dataset. The experimental results are presented in Table 2.

Table 2

Comparison of detection performance across different models

Models	Precision [%]	Recall [%]	mAP@0.5 [%]	Params [M]	FLOPs [G]
YOLOv5s	91.1	94.3	97.7	7.01	15.8
YOLOv7-Tiny	91.4	91.2	96.4	6.14	13.6
YOLOv8s	91.8	92.4	96.8	11.12	28.4
MobileNetV3	73.8	85.3	85.4	2.39	3.5
ShuffleNetV2	75.2	77.0	82.3	1.8	2.8
This paper	91.9	96.5	98.3	7.01	15.8

As shown in Table 2, YOLOv8s achieves the highest accuracy among all models evaluated; however, it also has the largest number of parameters and the highest computational cost, making it the most complex model.

Although MobileNetV3 and ShuffleNetV2 have fewer parameters and lower computational costs, their accuracy is insufficient to ensure reliable detection performance. The improved model achieves higher accuracy and recall than all other detection models in the experiment. Compared with YOLOv5, YOLOv7‑Tiny, and YOLOv8s, the improved model increases accuracy by 0.8, 0.5, and 0.1 percentage points, respectively, and recall by 2.2, 5.3, and 4.1 percentage points, respectively. Therefore, the proposed network model not only achieves higher accuracy and recall but also has fewer parameters and lower computational cost, making it more suitable for deployment on brush cutters for shrub detection.

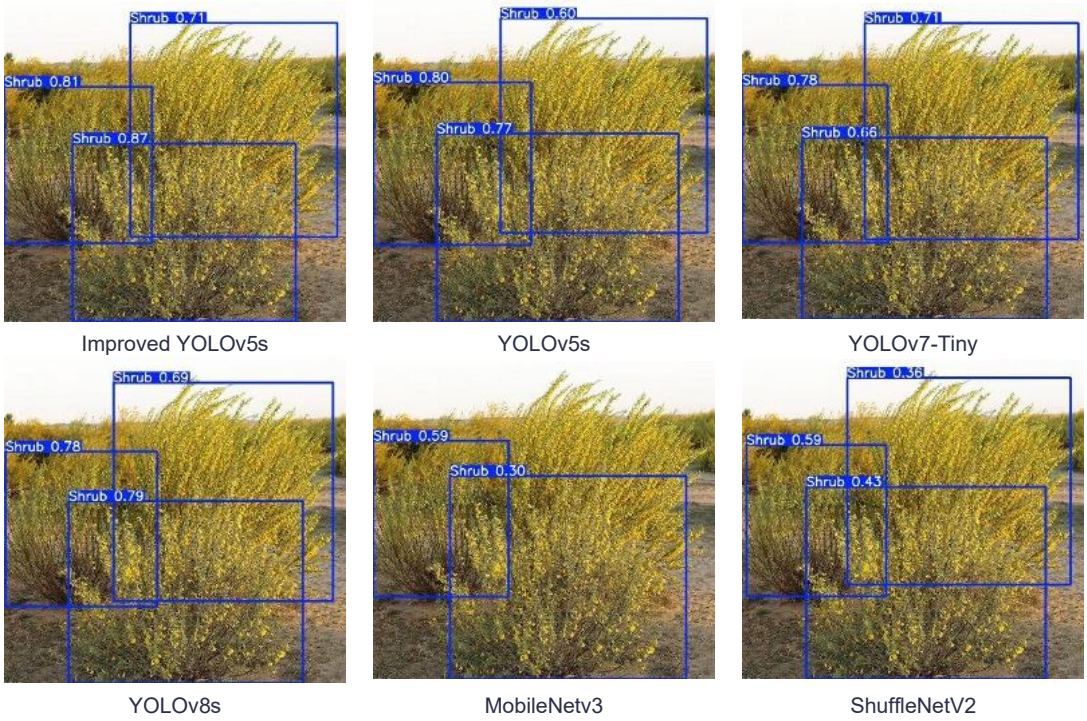


Fig. 9 - Shrub detection results across different network models

Figure 9 presents the shrub detection results of the six models. With the exception of ShuffleNetV2, which missed one shrub, all other models correctly detected three shrubs. Among them, the detection confidence of MobileNetV3 was significantly lower than that of the remaining four models, indicating weaker detection performance. Compared with the other network models, the improved YOLOv5s model achieves more accurate shrub localization and higher confidence scores, demonstrating superior detection performance.

Image processing-based shrub root detection and 3D measurement method

The shrub root image processing algorithm employs digital image processing techniques to isolate shrub root branches from complex backgrounds. To remove irrelevant information, the acquired image undergoes a series of preprocessing steps. First, the image is converted to grayscale using the maximum intensity method (*Chun P.J. et al., 2021*) to enhance the contrast between roots and background. Second, median filtering is applied for noise suppression (*Cao et al., 2024*). Third, Otsu's thresholding method (*Hu J. et al., 2024*) is used for segmentation, followed by intensity inversion to highlight root contours. Finally, a morphological closing operation (consisting of erosion followed by dilation) with a 10×10 structuring element (*Zhou R.G. et al., 2015*) is performed to suppress shadows and residual leaf fragments. The largest connected foreground region is then selected, and its contour is outlined in green to complete shrub root segmentation. The complete processing pipeline is illustrated in Fig. 10.



a. Original shrub image

b. Grayscale conversion using maximum intensity projection

c. Median-filtered image



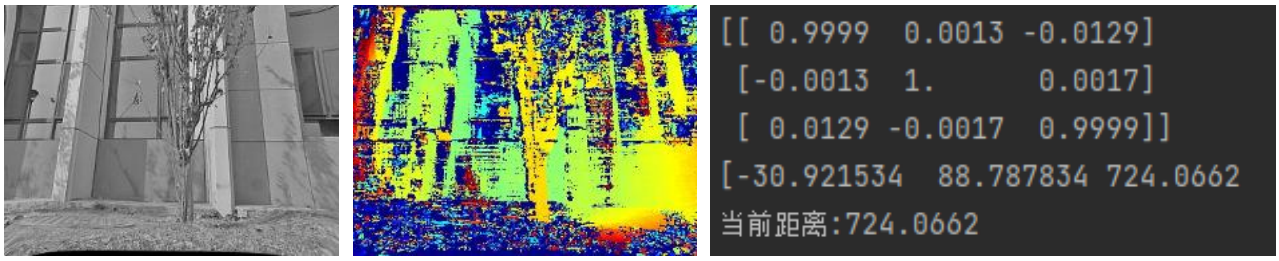
d. Otsu-thresholded binary image e. Morphologically closed image f. Root segmentation result

Fig. 10 - Image processing process of shrub roots

Experimental validation of shrub root localization accuracy

Using the parallax between the left and right cameras of the binocular stereo system and applying the principle of similar triangles, the distance from each three-dimensional scene point to the camera is computed (*Ren Z. et al., 2022; Hu W. et al., 2021; Zhai G. et al., 2020*). Camera calibration is then performed to estimate the intrinsic and extrinsic camera parameters and to correct lens distortion (*Wang Q. et al., 2022*). Finally, the Semi-Global Block Matching (SGBM) algorithm is employed for stereo correspondence, yielding the depth maps shown in Figs. 11a and 11b (*Almatrouk B. et al., 2024*).

The three-dimensional coordinate visualization of the shrub in the image is presented in Fig. 11c, where the y-axis represents the vertical height of the shrub relative to the camera plane, and the z-axis represents the depth (i.e., the distance along the optical axis) from the camera.



a. Grayscale shrub image b. Shrub depth map c. Coordinate Output Diagram

Fig. 11 - Grayscale and depth images of shrubs in the test scene

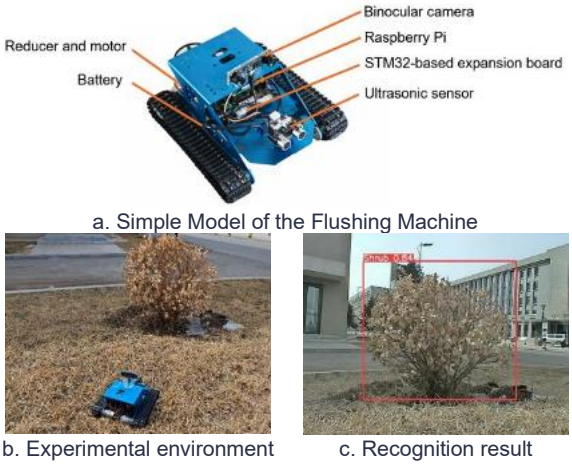
RESULTS

Construction and experimental validation of a simplified shrub stubble-cutting prototype

The simplified prototype of the pruning machine developed in this study is shown in Fig. 12a. Its main components include a gear reducer and a DC motor, a Raspberry Pi microcontroller unit, an STM32-based expansion board, a binocular stereo camera, an ultrasonic distance sensor, and a power supply unit.

Shrub detection experiment

In this experiment, an area with shrub vegetation on a university campus was selected as the test site, and the pruning machine prototype was deployed at the location shown in Fig. 12b. The prototype is equipped with YOLOv5s for real-time object detection, enabling the acquisition of image and spatial coordinate information. The shrub recognition results are presented in Fig. 12c, which demonstrates that the prototype achieves robust shrub detection performance.



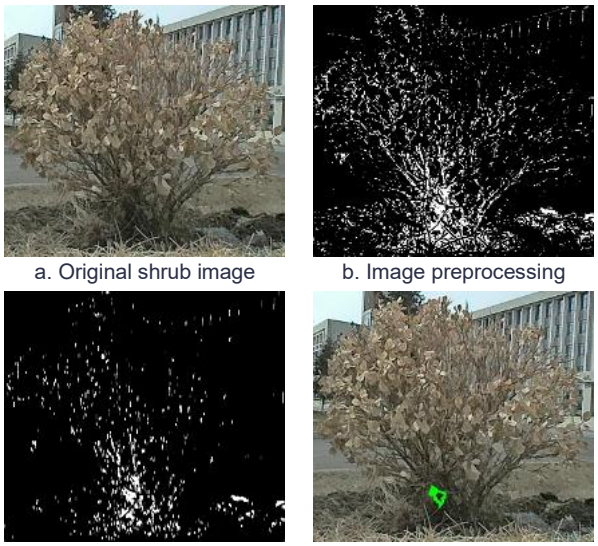
a. Simple Model of the Flushing Machine

b. Experimental environment c. Recognition result

Fig. 12 - Shrub identification experiment

Image processing-based shrub root detection experiment

To verify the effectiveness of the image processing algorithm, further processing was performed on the image containing the shrub with the largest bounding box area, thereby providing data support for shrub pruning. The shrub root detection results are presented in Fig. 13. As shown in the resulting images, the image preprocessing and morphological operations are effective, and the detection outcomes are accurate.



a. Original shrub image b. Image preprocessing

c. Morphological operations d. Detection results

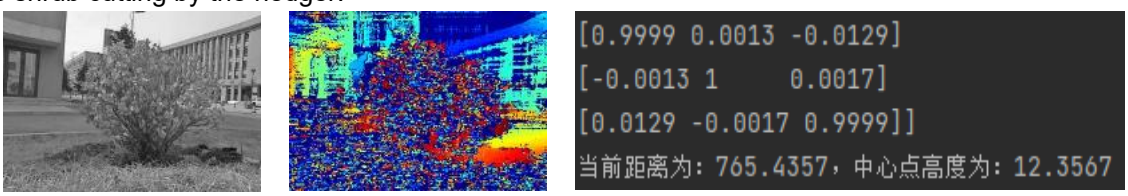
Fig. 13 - Results of the shrub root detection experiment

Experimental validation of shrub root localization accuracy

To verify the effectiveness of the proposed shrub root detection algorithm, images were captured using a binocular camera, and feature points were matched via the Semi-Global Block Matching (SGBM) algorithm. A depth map was then reconstructed based on binocular stereo vision principles. The experimental results are presented in Figs. 14a and 14b.

The depth image and the shrub root identification image were overlaid to integrate the root detection results into the shrub's depth map and to output the coordinates of the center point. The measured shrub root height and depth are shown in Fig. 14c, where the center point height corresponds to the vertical coordinate of the center of the shrub root bounding box relative to the camera plane. The relative errors in this trial were 2.51% for depth measurement and 5.59% for height measurement.

To evaluate the reliability of the algorithm for shrub depth and height estimation, 12 independent trials were conducted following the same procedure. The three-dimensional coordinates of each detected root center were extracted and compared against ground-truth distance and height measurements. The detailed results are listed in Table 3. The experimental results indicate that the maximum relative errors in depth and height estimation are 3.19% and 6.51%, respectively—both within the tooling alignment tolerance required for precise shrub cutting by the hedger.



a. Grayscale shrub image b. Shrub depth map c. Three-dimensional shrub root coordinate visualization

Fig. 14 - Experimental results of shrub depth map drawing

CONCLUSIONS

Based on the operational requirements for pruning sand-dwelling shrubs, this study completed the overall structural design of the pruning machine and the selection of key component parameters. A simulation analysis of the circular-saw cutting process was also performed. The results demonstrate that the power demand during cutting is consistent with theoretical calculations, and that the designed cutting device meets both the power requirements and the operational specifications for shrub pruning.

This study introduced the Focal‑CIoU loss function into the YOLOv5s model and developed a shrub target detection model specifically tailored for desert environments with sparse backgrounds. The improved model achieves an accuracy of 91.9%, a recall of 96.5%, and an mAP@0.5 of 98.3%. While significantly enhancing detection performance, the model maintains a low parameter count, which is sufficient to meet the real‑time detection requirements of the shrub pruning machine.

Based on image processing and binocular stereo vision, this study achieved shrub root region segmentation and three-dimensional coordinate estimation. Experimental results demonstrate that under complex background conditions, the proposed shrub root detection method robustly extracts root contours. The maximum relative errors for depth and height measurements are 3.19% and 6.51%, respectively—both within the positioning accuracy tolerance required for shrub pruning operations.

ACKNOWLEDGEMENT

This work was supported by the Major Science and Technology Project of Inner Mongolia Autonomous Region (2020ZD0002).

REFERENCES

[1] Almatrouk B., Meng H., & Swash M.R. (2024). Holoscopic elemental-image-based disparity estimation using multi-scale, multi-window semi-global block matching, *Applied Sciences*, vol.14, no.8, Article 3335, London/United Kingdom. https://doi.org/10.3390/app14083335

[2] Cao N., & Liu Y. (2024). High-noise grayscale image denoising using an improved median filter for the adaptive selection of a threshold, *Applied Sciences*, vol.14, no.2, Article 635, Zhengzhou/China. https://doi.org/10.3390/app14020635

[3] Chun P., Izumi S., & Yamane T. (2021). Automatic detection method of cracks from concrete surface imagery using two-step light gradient boosting machine, *Computer-Aided Civil and Infrastructure Engineering*, vol.36, no.1, pp.61-72, Tokyo/Japan. https://doi.org/10.1111/mice.12564

[4] Fan X.P., Xu Y., & Zhou J.P. (2025). Visual navigation method and field experiment of a cotton field spraying robot (棉田施药机器人视觉导航方法与田间试验), *Transactions of the Chinese Society of Agricultural Engineering*, vol.41, no.6, pp.52-61, Beijing/China. https://doi.org/10.11975/j.issn.1002-6819.202408183

[5] Gangwar T., & Schillinger D. (2019). Microimaging-informed continuum micromechanics accurately predicts macroscopic stiffness and strength properties of hierarchical plant culm materials, *Mechanics of Materials*, vol.130, pp.39-57, Twin Cities/USA. https://doi.org/10.1016/j.mechmat.2019.01.009

[6] Gao S., Wu J., Ma L., Gong X., & Zhang Q. (2023). Introduction to sand-restoration technology and model in China, *Sustainability*, vol.15, no.1, Article 98, Hohhot/China. https://doi.org/10.3390/su15010098

[7] Georges R., Auchet S., & Méausoone P.J. (2014). A dynamic measurement of a disc chipper cutting forces, *Biomass and Bioenergy*, vol.64, pp.269-275, Reggio Calabria/Italy. https://doi.org/10.1016/j.biombioe.2014.02.033

[8] Hu J., Wang H., Zhou Y., Yang S., Lv H., & Yang L. (2024). Research on internal quality testing method of dry longan based on terahertz imaging detection technology, *Journal of Food Measurement and Characterization*, vol.18, no.7, pp.5507-5522, Nanchang/China. https://doi.org/10.1007/s11694-024-02583-x

[9] Hu W., Wang W., Ai C., Wang J., Wang W., Meng X., Liu H., Tao H., & Qiu S. (2021). Machine vision-based surface crack analysis for transportation infrastructure, Automation in Construction, vol.132, Article 103973, Changsha/China. https://doi.org/10.1016/j.autcon.2021.103973

[10] Johnson P.C., Clementson C.L., Mathanker S.K., Grift T.E., & Hansen A.C. (2012). Cutting energy characteristics of *Miscanthus* × *giganteus* stems with varying oblique angle and cutting speed, *Biosystems Engineering*, vol.112, no.1, pp.42-48, Urbana IL/USA. https://doi.org/10.1016/j.biosystemseng.2012.02.003

[11] Li T., Ren L., Hu B., Wang S., Zhao M., Zhang Y., & Yang M. (2023). Grading detection of tomato hole-pan seedlings using improved YOLOv5s and transfer learning (改进 YOLOv5s 和迁移学习对番茄穴盘苗的分级检测), *Transactions of the Chinese Society of Agricultural Engineering*, vol.39, no.23, pp.174-184, Xinjiang/China. https://doi.org/10.11975/j.issn.1002-6819.202308078

[12] Ma A.J., Chen Z.J., Yu G.S., Yuan X.Y., & Du K. (2015). Development and application of a crawler self-propelled stubble cutter for desert shrub forest (履带自行式沙地灌木林平茬机的研制及应用), *Scientia Silvae Sinicae*, vol.51, no.7, pp.99-106, Beijing/China. https://doi.org/10.11707/j.1001-7488.20150711

[13] Mutlu H. (2021). Design of the crank-rocker mechanism for various design cases based on the closed-form solution, *Sādhanā*, vol.46, Article 4, Mersin/Turkey. https://doi.org/10.1007/s12046-020-01529-5

[14] Pei Z.Y., Duan G.D., Hao S.R., Qiao J.W., & Qin W. (2019). Optimization of stumping method based on wind control benefit for *Salix psammophila* shrub in Mu Us sandy land (基于防风效益的毛乌素沙地沙柳灌丛平茬方法优选), *Transactions of the Chinese Society of Agricultural Engineering*, vol.35, no.4, pp.153-161, Hohhot/China. https://doi.org/10.11975/j.issn.1002-6819.2019.04.019

[15] Peng H., Liang M., Yuan C., & Ma Y. (2024). EDF-YOLOv5: An improved algorithm for power transmission line defect detection based on YOLOv5, *Electronics*, vol.13, no.1, Article 148, Zhengzhou/China. https://doi.org/10.3390/electronics13010148

[16] Ren K. (2021). *Machine vision technology for Caragana stubble cutting machine (柠条平茬机的机器视觉技术研究)*, MSc thesis, Harbin Engineering University, Harbin/China.

[17] Ren Z., Fang F., Yan N., & Wu Y. (2022). State of the art in defect detection based on machine vision, *International Journal of Precision Engineering and Manufacturing-Green Technology*, vol.9, no.2, pp.661-691, Tianjin/China. https://doi.org/10.1007/s40684-021-00343-6

[18] Tian Z.Q. (2013). Development status and trend of Caragana shrub harvester (柠条收割机发展现状及趋势), *Agricultural Engineering*, no.4, pp.9-11, Jinzhong/China.

[19] Wang Q., Yan C., Tan R., Feng Y., Sun Y., & Liu Y. (2022). 3D-CALI: Automatic calibration for camera and LiDAR using 3D checkerboard, *Measurement*, vol.203, Article 111971, Nanjing/China. https://doi.org/10.1016/j.measurement.2022.111971

[20] Wang Y., Zhang J., Gao Y., Qu A., Wen X., & Hou Y. (2025). Design and test of the hydraulic shear-type *Caragana korshinskii* Kom. coppicing machine (液压剪式柠条平茬机的设计与试验), *Transactions of the Chinese Society of Agricultural Engineering*, vol.41, no.14, pp.71-81, Yinchuan/China. https://doi.org/10.11975/j.issn.1002-6819.202412022

[21] Wu G., & Zhang D.D. (2022). Thermal-mechanical coupling analysis of disc brake based on ANSYS Workbench (基于 ANSYS Workbench 的盘式制动器热机耦合分析), *Lubrication Engineering*, vol.47, no.10, pp.126-133, Yichang/China. https://doi.org/10.3969/j.issn.0254-0150.2022.10.018

[22] Zhai G., Zhang W., Hu W., & Ji Z. (2020). Coal mine rescue robots based on binocular vision: A review of the state of the art, *IEEE Access*, vol.8, pp.130561-130575, Beijing/China. https://doi.org/10.1109/ACCESS.2020.3009387

[23] Zhang B., Liu Y., Zhang H., Shen C., & Fu W. (2022). Design and evaluation of a shaping and pruning machine for dwarf and densely planted jujube trees, *Applied Sciences*, vol.12, no.5, Article 2699, Haikou/China. https://doi.org/10.3390/app12052699

[24] Zhou R.G., Chang Z.B., Fan P., Li W., & Huan T.T. (2015). Quantum image morphology processing based on quantum set operation, *International Journal of Theoretical Physics*, vol.54, no.6, pp.1974-1986, Nanchang/China. https://doi.org/10.1007/s10773-014-2402-4

SMOOTH-PLANNER: A ROBUST GRADIENT-BASED LOCAL TRAJECTORY PLANNING METHOD FOR NON-HOLONOMIC ORCHARD ROBOTS
/
SMOOTH-PLANNER:一种面向非完整约束果园机器人基于梯度的鲁棒局部轨迹规划方法

Fanjun MENG, Fa SUN, Mengmeng NI, Zhisheng ZHAO, Lili YI*
School of Agricultural Engineering and Food Science, Shandong University of Technology, Zibo / China
Tel: +86 18553308656; E-mail: yili0001@sdut.edu.cn
DOI: https://doi.org/10.35633/inmateh-79-27

Keywords: *Obstacle avoidance, trajectory optimization, B-spline, non-holonomic constraints*

ABSTRACT
This study proposes Smooth-Planner, a robust gradient-based local trajectory planning method for non-holonomic orchard robots operating in narrow row environments. The method employs a B-spline–based optimization framework that explicitly considers kinematic feasibility and collision avoidance without relying on dense global maps. Field experiments conducted in a standardized orchard demonstrate stable and repeatable performance, with lateral deviations effectively constrained and a minimum safety clearance of 0.90 m consistently maintained from crop rows. The results validate the practical safety and reliability of the proposed approach for autonomous agricultural operations.

摘要
本文提出了一种面向果园非完整约束移动机器人的稳健局部轨迹规划方法——Smooth-Planner。该方法基于 B 样条轨迹表示与梯度优化框架，在不依赖高精度全局地图的条件下，显式约束运动学可行性与避障安全性。标准化果园实地试验结果表明，该方法运行稳定、重复性良好，横向偏差得到有效控制，并始终保持不小于 0.90 m 的作物行安全间距。实验结果验证了该方法在自主农业作业中的安全性与实用性。

INTRODUCTION
With the rapid development of smart agriculture and digital orchard management, ground-based inspection robots are increasingly employed for tasks such as tree growth monitoring, precision spraying, and environmental data collection *(Dou et al., 2024; Hua et al., 2025)*. Unlike structured roads or open outdoor environments, orchard scenarios exhibit distinct spatial and perceptual characteristics, such as GNSS-denied canopy areas, narrow inter-row passages, and irregular branch protrusions *(Bayar et al., 2016)*. These features pose significant challenges to reliable autonomous navigation. Specifically, the complexity of the unstructured environment demands that the robot possesses high autonomy and strict safety awareness.

Local path planning is the core enabling technology for ensuring the safe and stable operation of these robots *(Cai et al., 2007)*. During routine inspection, robots must navigate continuously within confined corridors while coping with dynamic uncertainties, such as wind-blown branches and seasonal canopy variations. Crucially, the stability of local planning directly impacts operational efficiency and system safety. Frequent oscillations or abrupt stops caused by poor planning not only reduce task efficiency but also increase energy consumption and mechanical wear on the chassis *(Hu et al., 2015; Bai et al., 2019)*. Therefore, developing a local planner that satisfies requirements for real-time performance, robustness, and trajectory feasibility is of paramount importance.

A variety of local planning approaches have been applied in agricultural robotics. Classical sampling-based or search-based methods, such as the Dynamic Window Approach (DWA) *(Guo et al., 2024; Wang et al., 2024)* and Timed Elastic Band (TEB) *(Zai et al., 2023; Zheng et al., 2023)*, rely heavily on grid-based cost maps. In orchard environments characterized by sparse and noisy point clouds, maintaining a high-resolution grid map is computationally expensive, and discretization errors often lead to trajectory jitters or overly conservative behaviors *(Xie et al., 2018)*. More recently, gradient-based trajectory optimization methods *(Zhou et al., 2021)* have demonstrated superior smoothness and computational efficiency. However, most existing gradient-based planners are originally designed for holonomic aerial vehicles (UAVs). They often neglect the non-holonomic kinematic constraints of ground robots. Directly applying these methods to orchard robots typically results in infeasible trajectories that the vehicle hardware cannot execute, leading to tracking errors or collisions.

To address these challenges, this paper proposes a robust local trajectory planning method tailored for differential-drive orchard inspection robots, referred to as Smooth-Planner. The proposed approach adopts a gradient-based continuous trajectory optimization framework. Unlike traditional methods that depend on constructing explicit Euclidean Signed Distance Fields (ESDF) *(Han et al., 2019)* or grid maps *(Li et al., 2014)*, Smooth-Planner directly optimizes local trajectories by jointly considering smoothness, collision avoidance, and motion feasibility. By embedding geometry-aware obstacle avoidance constraints and non-holonomic motion limits into a continuously differentiable optimization formulation, the method generates high-quality executable trajectories even with incomplete perception.

The main contributions of this work are summarized as follows: (1) A map-free local trajectory optimization framework is established to handle the challenges of narrow orchard corridors and sparse perception, significantly reducing the dependency on high-precision environmental mapping. (2) A novel formulation of continuous collision and kinematic penalties is introduced, which strictly enforces non-holonomic constraints to ensure the generated trajectories are dynamically feasible for tracked ground robots. (3) Extensive field experiments in real orchard scenarios validate that the proposed method achieves high stability and maintains sufficient safety margins, proving its practical value for autonomous orchard inspection.

MATERIALS AND METHODS

System overview and problem formulation

The experimental platform used in this study is an electrically driven tracked robot designed for autonomous orchard inspection (Fig.1). To accurately account for collision risks in narrow inter-row environments, the robot geometry is abstracted as a bounding box with length L and width W. The perception system consists of an Ouster 3D LiDAR for local environment perception and a GNSS-RTK module for global pose estimation, while all planning algorithms are executed on an onboard NVIDIA AGX Orin computing platform. Under nominal operating conditions, the robot demonstrates high-precision trajectory tracking and reliable localization. This consistent baseline ensures that the deviations observed during obstacle avoidance are solely attributable to the proposed planning strategy rather than sensing noise or control instability.

Considering the differential steering mechanism, the robot is subject to non-holonomic kinematic *(Zhang et al., 2025)* constraints that prohibit instantaneous lateral motion. Under these constraints, the local trajectory planning problem is formulated as finding an optimal trajectory Φ within a receding horizon that minimizes a compound cost function J, while satisfying collision avoidance and kinematic feasibility requirements. Detailed formulations of the cost function and constraints are presented in the following sections.

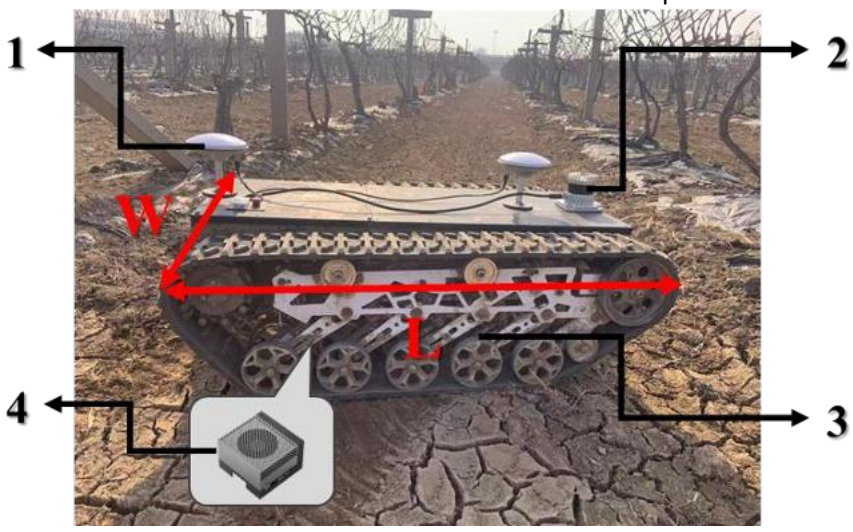


Fig. 1 -Tracked mobile platform for orchard robots

1. GNSS-RTK; 2. 3D LiDAR; 3. Crawler-Type Mobile Chassis; 4. Jetson AGX Orin.

Trajectory representation and motion modeling

To ensure smooth motion on uneven orchard terrain, the local trajectory is parameterized using a uniform B-spline curve *(Sun et al., 2024)*. The trajectory is uniquely defined by a set of control points $Q_i = \{Q_1, Q_2, \ldots, Q_{Nc}\}$, the spline degree P_b, and a uniform knot interval Δt, which enables direct adjustment of the trajectory during optimization.

Fig. 2 demonstrates the key geometric characteristics leveraged in this study **(1) Local Support**, which ensures that each trajectory segment is determined by only P_b+1 neighboring control points, allowing optimization constraints to be decoupled locally; **(2) Convex Hull**, implying that the continuous curve lies within the polygon formed by its control points, which simplifies collision checking; and **(3) Derivative Consistency**, allowing velocity and acceleration to be expressed as linear combinations of control points, enabling kinematic constraints to be enforced directly without explicit integration.

At low speed (< 1 m/s), lateral slip is neglected and the robot is modeled using a kinematic non-holonomic approximation *(Mínguez et al., 2002)*. Under this assumption, discrete velocity and acceleration associated with adjacent control points are approximated using finite differences with a constant time interval Δt as follows:

$$V_i = \frac{Q_{i+1}-Q_i}{\Delta t},\ A_i = \frac{V_{i+1}-V_i}{\Delta t} \tag{1}$$

where:

V_i and A_i denote the discrete velocity and acceleration, respectively; Q_i denotes the $i\text{-}th$ control point of the B-spline trajectory; Δt is the uniform time interval between adjacent control points.

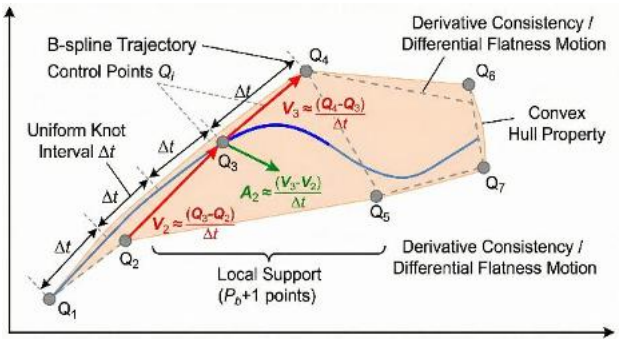


Fig. 2 - Illustration of B-spline trajectory properties

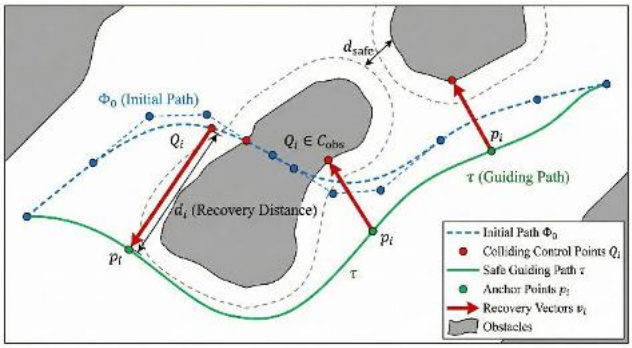


Fig. 3 --Front-end Logic - Optional

Collision-free Initial Trajectory Generator

To incorporate environmental awareness into the local planner, a collision-free initial trajectory generator is adopted as the front-end of the proposed method. Fig. 3 Schematic of the collision-free initial trajectory generation. The navigation layer initially outputs a globally smooth B-spline path Φ_0 that satisfies boundary constraints. When a colliding segment is detected, A^* search *(Hart et al., 1968)* is employed to generate a collision-free guiding path τ based on the topological structure of the environment. Unlike methods that rely on unstable gradients from irregular obstacle surfaces, τ serves as a safe topological attractor to guide the trajectory generation.

To precisely quantify collision risks, a safety threshold d_{safe} is first defined based on the robot's circumscribed radius *(Howell et al., 2022)*:

$$d_{safe} = \sqrt{\left(\frac{L}{2}\right)^2 + \left(\frac{W}{2}\right)^2} + \delta \tag{2}$$

where δ is a safety buffer.

For each control point Q_i, its distance to the nearest obstacle $d_{obs}(Q_i)$ is queried from the local obstacle cloud. Control points satisfying $d_{obs}(Q_i)<d_{safe}$ are identified as colliding points and grouped into a collision set C_{obs}.

For every colliding index i in C_{obs}, a unique anchor point p_i is assigned on the guiding path τ. Based on this correspondence, a collision recovery distance d_i and a recovery gradient vector $\boldsymbol{v_i}$ are defined as follows:

$$d_i = \|Q_i - p_i\| \tag{3}$$

$$\boldsymbol{v_i} = p_i - Q_i \tag{4}$$

where:

d_i denotes the Euclidean distance measuring the deviation of the colliding point from the safe path; $\boldsymbol{v_i}$ represents the gradient direction vector that pulls the control point Q_i back towards the safe anchor p_i.

Through this procedure, the feasible geometric references (p_i) and the associated recovery metrics (d_i, $\boldsymbol{v_i}$) are successfully generated, providing the essential collision-free initialization terms required for the subsequent gradient-based trajectory optimization.

Cost Function Formulation

To generate safe and executable trajectories, the local planning problem is formulated as a weighted multi-objective optimization (Fig. 4). The total cost function J is defined as:

$$\min_{Q} J = \lambda_s J_s + \lambda_c J_c + \lambda_k J_k \tag{5}$$

where:

J_s, J_c, and J_k represent smoothness, collision, and kinematic feasibility penalties, respectively. The coefficients λ_s, λ_c and λ_k are weighting factors that balance the trade-off between trajectory quality, safety, and feasibility.

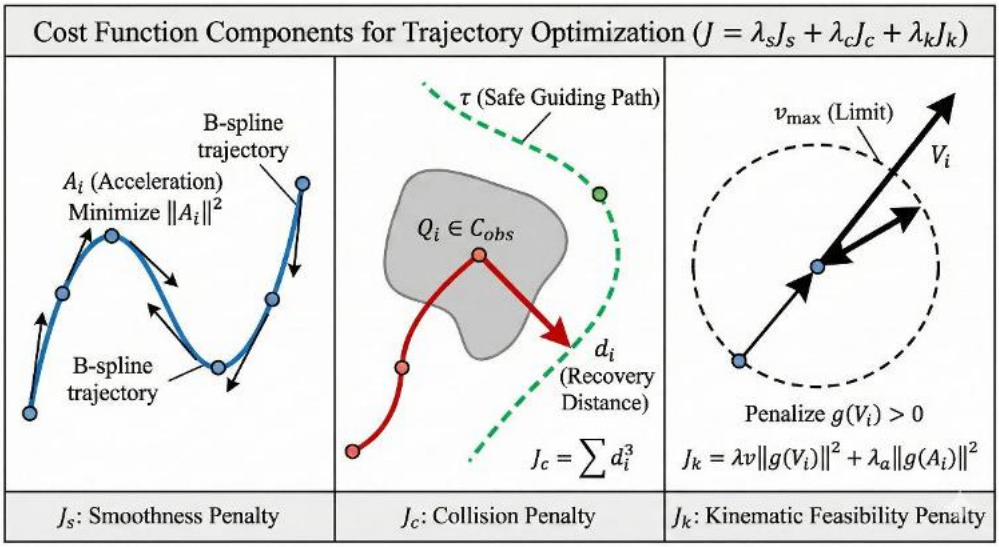


Fig. 4 - Cost function components

- Smoothness Penalty

Orchard environments are characterized by uneven terrain and varying soil conditions. Excessive acceleration can lead to chassis vibration, track slippage, or damage to onboard inspection sensors. To ensure trajectory smoothness and minimize control effort, a penalty on the control point acceleration is applied:

$$J_s = \sum_{i=1}^{N_c-2} \| A_i \|^2 \tag{6}$$

where:

N_c is the total number of control points in the B-spline trajectory, and A_i is the discrete acceleration vector derived in Equation (1).

The use of the squared L_2 norm serves two critical purposes. Mathematically, it provides a convex and continuously differentiable cost landscape, which facilitates rapid convergence for gradient-based optimization. Physically, the quadratic form heavily penalizes abrupt acceleration spikes, ensuring that the generated motion is gentle enough to prevent track slippage on soft orchard ground.

- Collision Penalty

The collision penalty strictly enforces the safety constraints. Unlike traditional methods that rely on computing gradients from irregular obstacle surfaces, this study leverages the recovery distance d_i derived from the safe guiding path. The penalty term J_c is formulated as:

$$J_c = \sum_{i \in C_{obs}} (d_i)^3 \tag{7}$$

This cubic formulation is applied exclusively to the set of colliding control points C_{obs} identified by the front-end. It ensures a continuous gradient that grows steeply as the control point deviates further from the safe anchor p_i, generating a strong restoring force that effectively pulls the trajectory back into the collision-free corridor defined by the guiding path.

- Kinematic Feasibility Penalty

To guarantee that the planned trajectory is executable by the hardware, dynamical limits are imposed as soft constraints. Velocities and accelerations exceeding the system limits (v_{max}, a_{max}) are penalized to ensure the generated commands remain within the robot's physical capabilities. The kinematic feasibility penalty J_k is formulated as:

$$J_{kinematic} = \sum_{i=1}^{N_c-1} \lambda_v \cdot g(V_i, v_{max}) + \sum_{i=1}^{N_c-2} \lambda_a \cdot g(A_i, a_{max}) \quad (8)$$

where:

$g(\cdot)$ is a squared penalty function activated only when constraints are violated:

$$g(x, x_{lim}) = \begin{cases} (\|x\|^2 - x_{lim}^2)^2 & \|x\| > x_{lim} \\ 0 & \|x\| \leq x_{lim} \end{cases} \quad (9)$$

where:

V_i and A_i are the discrete velocity and acceleration vectors, v_{max} and a_{max} denote the maximum linear velocity and acceleration allowed by the chassis, and λ_v and λ_a are the weighting coefficients.

This formulation provides a continuously differentiable gradient that grows quadratically with the violation magnitude, effectively pulling the trajectory back into the feasible state space without introducing unnecessary computational complexity.

Gradient-based Trajectory Optimization

Given the composite cost function J, the trajectory generation is resolved by finding the optimal control points Q_i that minimize this cost. To ensure rapid convergence and avoid infeasible local minima, the optimization is initialized using the collision-free geometric reference. This initialization strategy provides a high-quality initial guess that naturally lies within the safe topological corridor, allowing the gradient-based solver to focus on local smoothing and refinement rather than global search.

Let x denote the decision variable vector formed by flattening the control points Q_i. The optimization is solved using an iterative gradient update rule:

$$x_{k+1} = x_k - \alpha_k \mathrm{H}_k^{-1} \nabla \mathrm{J}(x_k) \quad (10)$$

where:

$\nabla J(x_k)$ is the gradient of the cost function, α_k is the step size determined by line search, and H_k^{-1} represents the inverse Hessian matrix. To solve this efficiently within the limited computing budget, the L-BFGS (Limited-memory Broyden–Fletcher–Goldfarb–Shanno) *(Liu et al., 1989)* algorithm is adopted. Unlike standard Newton methods, L-BFGS approximates H_k^{-1} using a limited history of past updates, significantly reducing memory consumption and computational complexity for the high-dimensional B-spline problem.

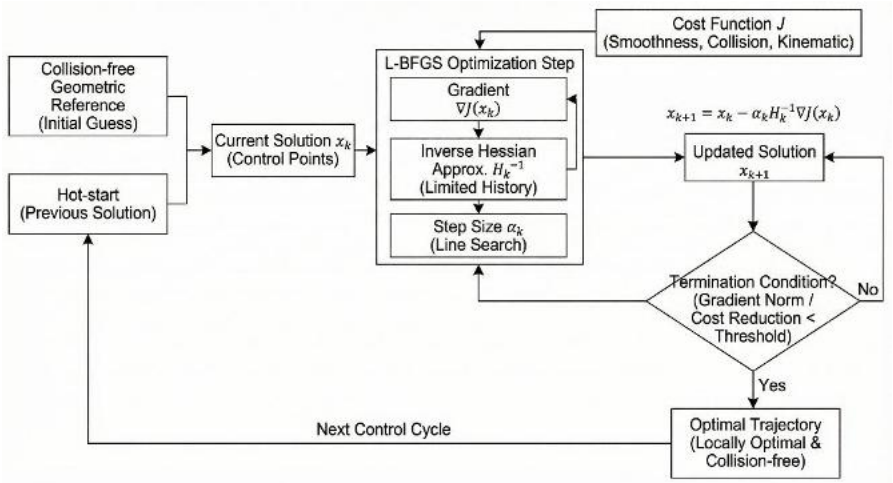


Fig. 5 - Flowchart of numerical optimization algorithm

In the dynamic context of orchard inspection, the optimizer employs a hot-start strategy, utilizing the solution from the previous control cycle as the initial guess for the current frame. The iteration terminates when either the gradient norm or the relative cost reduction falls below a predefined threshold, ensuring that a stable, locally optimal, and collision-free trajectory is regenerated in real-time.

RESULTS

Experimental Setup and Baseline Validation

Field experiments were conducted in a standard orchard environment in Shandong Province, China. The test site featured typical inter-row characteristics with an average row spacing of 4.5 m and a plant spacing of 1.5 m. The robot was tasked to follow predefined global paths, with all sensor data and trajectory logs recorded at 0.2 s intervals. throughout the trials, a constant forward speed of 0.6 m/s was maintained to ensure consistent motion dynamics.

Prior to the obstacle avoidance tests, the baseline path tracking accuracy was verified. The results showed that the robot maintained a lateral tracking error of less than 3.0 cm on straight paths. This high-precision baseline ensures that the significant deviations observed in subsequent experiments were solely driven by the active obstacle avoidance algorithm rather than control instability.

Local Obstacle Avoidance Performance

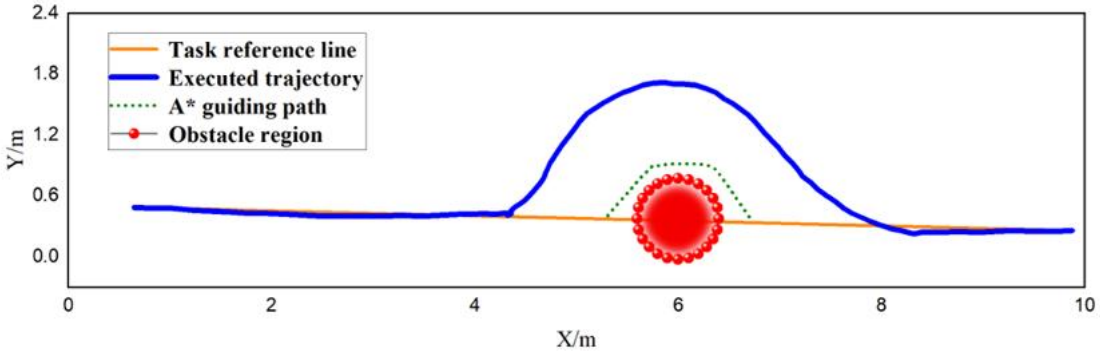


Fig. 6 -Obstacle avoidance trajectory

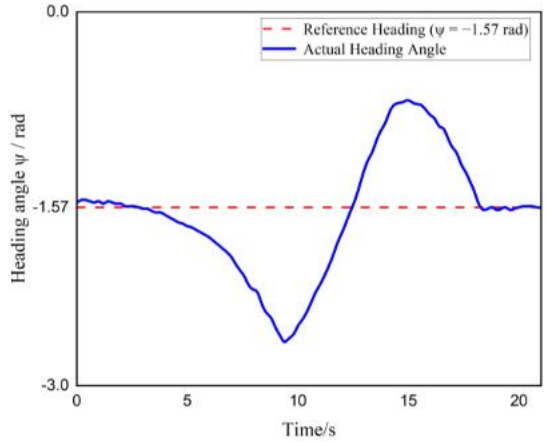


Fig. 7 - The curve of the heading angle over time

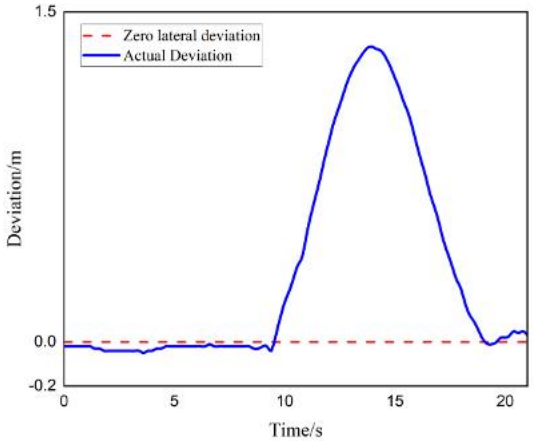


Fig. 8 - The curve of lateral deviation over time

Fig. 6 illustrates the spatial trajectory of the robot during a representative avoidance maneuver. The local avoidance process is initiated at approximately x = 4.35 m, where the robot smoothly deviates from the task path guided by the optimized B-spline trajectory. The maneuver is completed at around x = 8.32 m. Although a slight overshoot occurs immediately after obstacle clearance, it is rapidly attenuated by the feedback controller, allowing the trajectory to converge asymptotically back to the global reference path without persistent oscillations. The corresponding heading angle response is presented in Fig. 7. It is noteworthy that while the reference heading remains constant, the actual heading exhibits an anticipatory deviation as the robot perceives the obstacle, reaching a maximum difference of approximately 1.07 rad at t = 9.4 s. This heading-first response precedes significant lateral displacement, demonstrating the kinematic feasibility of the smooth transition into the avoidance maneuver. Fig. 8 quantifies the lateral deviation relative to the global path. The deviation profile exhibits a single-peak structure with a maximum amplitude of 1.34 m. Given the orchard row spacing of 4.5 m, the operational boundary lies at 2.25 m from the path centerline. Consequently, the maximum deviation of 1.34 m preserves a substantial safety margin of approximately 0.9 m from the vine rows. This result confirms that the proposed Smooth-Planner effectively utilizes the available free space to bypass obstacles while strictly adhering to the agronomic safety constraints of the orchard environment.

Stability and Robustness Validation

To further evaluate the practical applicability of the proposed method under realistic field conditions, additional experiments were conducted. Fig. 9 visualizes the onboard local point cloud perception during the obstacle avoidance maneuver, alongside corresponding real-world snapshots. As observed, despite the unstructured environmental noise typical of orchards, the obstacle geometry is distinctly captured by the LiDAR. The robot successfully executes a smooth bypass within the 4.5 m inter-row space. The strong consistency between the point cloud data and the physical environment confirms the reliability of the perception-planning pipeline.

To quantitatively assess the repeatability and stability of the system, the obstacle avoidance experiment was replicated in ten independent trials under identical conditions. Key performance indicators were extracted from each trial, and the statistical results are summarized in Table 1.

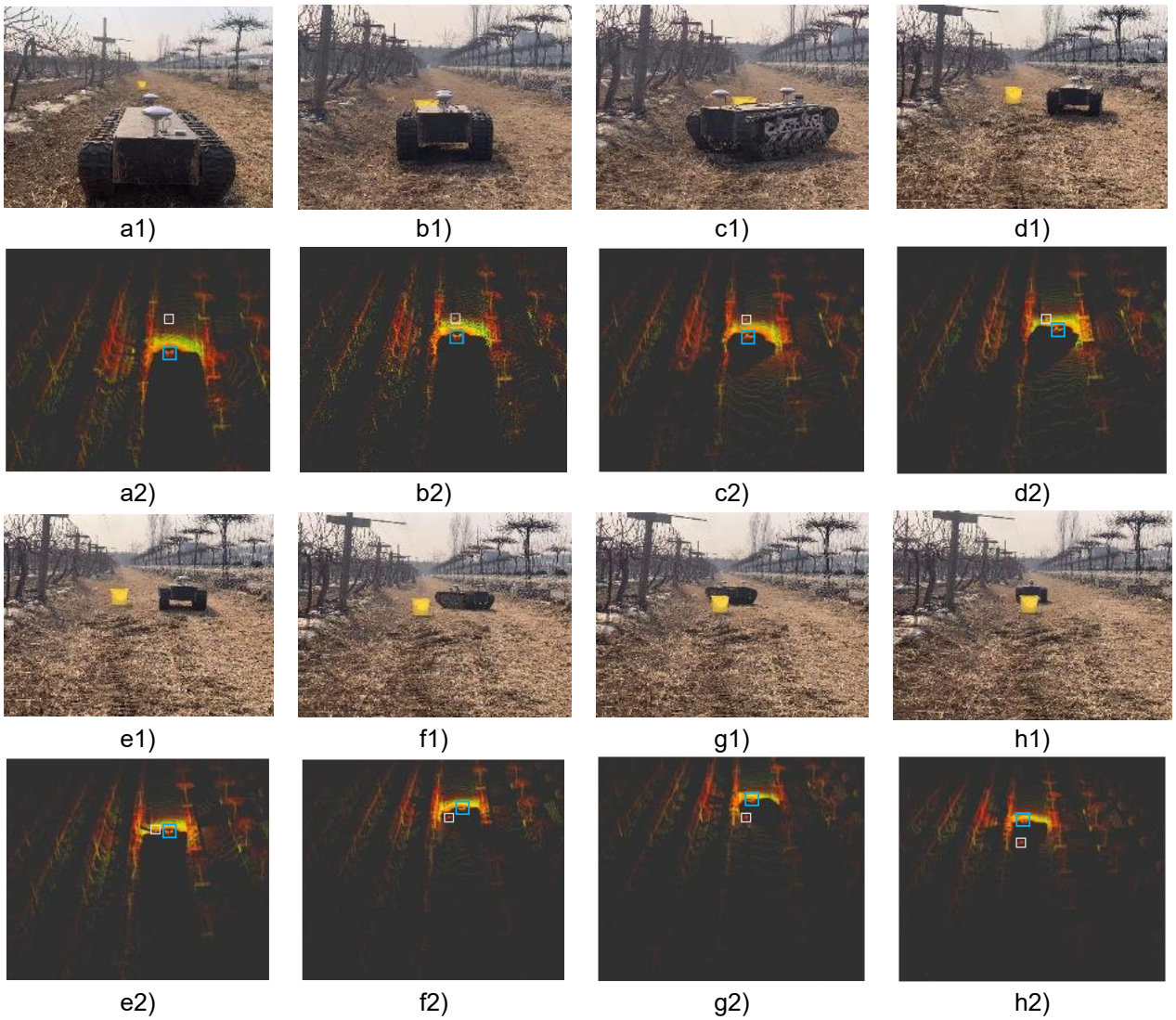


Fig. 9 – Real-world images and point cloud diagrams of obstacle avoidance operation

a1)–h1) – real-world images; a2)–h2) – LiDAR point cloud

Table 1

Statistical Metrics of Obstacle Avoidance Performance (N=10)

Performance Metric	Mean	Std. Dev.	Description
Max. Lateral Deviation(m)	1.32	0.08	Peak deviation from the global path
Min. Safety Margin(m)	0.9	0.07	Distance to the crop row boundary
Avoidance Duration(s)	9.65	0.15	Time elapsed during the maneuver
Total Path Length(m)	4.12	0.05	Length of the executed trajectory

As indicated in Table 1, the system demonstrates high repeatability. The Max. Lateral Deviation averaged 1.32 m with a standard deviation of only 0.08 m. This minimal variance is critical for agricultural automation, as it indicates that the robot's trajectory is highly predictable and robust against sensor noise across different runs.

Furthermore, by correlating these statistics with the 4.5 m row spacing, the Minimum Safety Margin is calculated to be approximately 0.9 m. Even accounting for the variance, the robot consistently maintains a sufficient buffer from the vine rows, thereby effectively mitigating collision risks with the crop canopy. The consistent values for Lateral Deviation RMSE and Avoidance Duration further validate that the proposed Smooth-Planner generates stable, feasible, and robust trajectories suitable for continuous orchard inspection tasks.

CONCLUSIONS

In this study, a robust local trajectory planning method, Smooth-Planner, was developed to address the challenges of autonomous navigation in narrow and unstructured orchard environments. By integrating a collision-free topological guiding path with a gradient-based continuous optimization framework, the proposed method generates smooth trajectories that strictly satisfy the non-holonomic kinematic constraints of differential-drive robots.

Field experiments conducted in a standardized orchard validated the effectiveness of the system. The results demonstrated that the robot could stably bypass obstacles with highly repeatable behavior, exhibiting an average maximum lateral deviation of 1.32 m with a minimal standard deviation of 0.08 m. Crucially, quantitative analysis confirmed that even during avoidance maneuvers, a minimum safety margin of approximately 0.93 m was maintained from the crop rows, ensuring agronomic safety. Overall, this work provides a reliable, map-free, and practical solution for the deployment of inspection robots in complex agricultural scenarios.

ACKNOWLEDGEMENT

The project supported by the R&D of low-speed unmanned autonomous navigation controller Project under Grant (No.2022TSGC1175).

REFERENCES

[1] Bai, G., Liu, L., Meng, Y., Luo, W., Gu, Q., & Liang, C. (2019). Study of obstacle avoidance controller of agricultural tractor-trailers based on predictive control of nonlinear model (基于非线性模型预测控制的农用拖挂车避障控制器研究). *Transactions of the Chinese Society for Agricultural Machinery*, 50(4), 356–362. https://doi.org/10.6041/j.issn.1000-1298.2019.04.041

[2] Bayar, G., Bergerman, M., Konukseven, E. I., & Koku, A. B. (2016). Improving the trajectory tracking performance of autonomous orchard vehicles using wheel slip compensation. *Biosystems Engineering*, 146, 149–164. https://doi.org/10.1016/j.biosystemseng.2015.12.019

[3] Cai, J., Zhao, J., Rath, T., & Kawollek, M. (2007). Path planning for obstacle avoidance of fruit harvesting robot (水果收获机器人避障路径规划). *Transactions of the Chinese Society for Agricultural Machinery*, 38(3), 102–105. https://doi.org/10.3969/j.issn.1000-1298.2007.3.070325

[4] Dou, H., Chen, Z., Zhai, C., Zhang, B., Ding, X., & Wang, X. (2024). Research progress on autonomous navigation technology for orchard intelligent operation equipment (果园智能化作业装备自主导航技术研究进展). *Transactions of the Chinese Society for Agricultural Machinery*, 55(4), 1–22. https://doi.org/10.6041/j.issn.1000-1298.2024.04.001

[5] Guo, H., Li, Y., Wang, H., Wang, C., Zhang, J., Wang, T., Rong, L., Wang, H., Wang, Z., Huo, Y., Guo, S., & Yang, F. (2024). Path planning of greenhouse electric crawler tractor based on the improved A* and DWA algorithms. *Computers and Electronics in Agriculture*, 227, 109596. https://doi.org/10.1016/j.compag.2024.109596

[6] Han, L., Gao, F., Zhou, B., & Shen, S. (2019). FIESTA: Fast incremental Euclidean distance fields for online motion planning of aerial robots. *2019 IEEE/RSJ International Conference on Intelligent Robots and Systems (IROS)*, 4423–4430. https://doi.org/10.1109/IROS40897.2019.8968199

[7] Hart, P. E., Nilsson, N. J., & Raphael, B. (1968). A formal basis for the heuristic determination of minimum cost paths. *IEEE Transactions on Systems Science and Cybernetics*, 4(2), 100–107. https://doi.org/10.1109/TSSC.1968.300136

[8] Howell, T. A., Le Cleac'h, S., Singh, S., Florence, P., Manchester, Z., & Sindhwani, V. (2022). Trajectory optimization with optimization-based dynamics. *IEEE Robotics and Automation Letters*, 7(3), 6750–6757. https://doi.org/10.1109/LRA.2022.3152696

[9] Hu, J., Gao, L., Bai, X., Li, T., & Liu, X. (2015). Review of research on automatic guidance of agricultural vehicles (农业机械自动导航技术研究进展). *Transactions of the Chinese Society of Agricultural Engineering*, 31(10), 1–10. https://doi.org/10.11975/j.issn.1002-6819.2015.10.001

[10] Hua, W., Zhang, Z., Zhang, W., Liu, X., Hu, C., He, Y., Mhamed, M., Li, X., Dong, H., Saha, C. K., Khan, W. U., Abid, F., & Abdelhamid, M. A. (2025). Key technologies in apple harvesting robot for standardized orchards: A comprehensive review of innovations, challenges, and future directions. *Computers and Electronics in Agriculture*, 235, 110343. https://doi.org/10.1016/j.compag.2025.110343

[11] Li, H., Tsukada, M., Nashashibi, F., & Parent, M. (2014). Multivehicle cooperative local mapping: A methodology based on occupancy grid map merging. *IEEE Transactions on Intelligent Transportation Systems*, 15(5), 2089–2100. https://doi.org/10.1109/TITS.2014.2309639

[12] Liu, D. C., & Nocedal, J. (1989). On the limited memory BFGS method for large scale optimization. *Mathematical Programming*, 45(1–3), 503–528. https://doi.org/10.1007/BF01589116

[13] Mínguez J., Montano L., & Santos-Victor J. (2002). Reactive navigation for non-holonomic robots using the ego-kinematic space. *Proceedings of the 2002 IEEE International Conference on Robotics and Automation*, 3, 3074–3080. https://doi.org/10.1109/ROBOT.2002.1013699

[14] Sun, Y., & Wang, H. (2024). Research on B-spline curve trajectory planning method considering curvature. *8th International Conference on Robotics, Control and Automation (ICRCA),* 211–216. https://doi.org/10.1109/ICRCA60878.2024.10649358

[15] Wang, Y., Fu, C., Huang, R., Tong, K., He, Y., & Xu, L. (2024). Path planning for mobile robots in greenhouse orchards based on improved A* and fuzzy DWA algorithms. *Computers and Electronics in Agriculture*, 227, 109598. https://doi.org/10.1016/j.compag.2024.109598

[16] Xie, Y., Yin, J., Yu, C., He, K., Hu, X., & Li, R. (2018). Obstacle avoidance navigation algorithm and analog experiment for wheeled AGV running along vineyard ridge road (轮式 AGV 沿葡萄园垄道行驶避障导航算法与模拟试验). *Transactions of the Chinese Society for Agricultural Machinery*, 49(7), 13–22.

[17] Zai, W., Lin, Q., Wang, S., & Lin, X. (2023). Path planning for wheeled robots based on the fusion of improved A* and TEB algorithms. *2023 China Automation Congress (CAC)*, 3257–3261. https://doi.org/10.1109/CAC59555.2023.10451976

[18] Zhang, W., Sun, T., Li, Y., He, C., Xiu, X., & Miao, Z. (2025). Optimal motion planning and navigation for nonholonomic agricultural robots in multi-constraint and multi-task environments. *Computers and Electronics in Agriculture*, 238, 110822. https://doi.org/10.1016/j.compag.2025.110822

[19] Zheng, H., Dai, M., Zhang, Z., Xia, Z., Zhang, G., & Jia, F. (2023). The navigation based on hybrid A star and TEB algorithm implemented in obstacles avoidance. *29th International Conference on Mechatronics and Machine Vision in Practice (M2VIP),* 1–6. https://doi.org/10.1109/M2VIP58386.2023.10413435

[20] Zhou, X., Wang, Z., Ye, H., Xu, C., & Gao, F. (2021). EGO-planner: An ESDF-free gradient-based local planner for quadrotors. *IEEE Robotics and Automation Letters*, 6(2), 478–485. https://doi.org/10.1109/LRA.2020.3047728

RECENT ADVANCES SURVEY IN COMPUTER VISION AND ARTIFICIAL INTELLIGENCE FOR FRUIT DETECTION
/
TINJAUAN KEMAJUAN TERKINI TEKNOLOGI PENGLIHATAN KOMPUTER DAN KECERDASAN BUATAN DALAM PENGESANAN BUAH

Qi LIU[1)], Puteri Suhaiza binti SULAIMAN[1*)], Mas Rina binti MUSTAFFA[1)], Zainal bin Abdul KAHAR[1)], Lian BAI[2)] and Huicai XU[1)]

[1)] Faculty of Computer Science and Information Technology, Universiti Putra Malaysia, Serdang, Selangor, Malaysia
[2)] College of Software, Shanxi Agricultural University, Taigu, Shanxi, China
**Corresponding author: +60 39769 1717; psuhaiza@upm.edu.my*

DOI: https://doi.org/10.35633/inmateh-79-28

Keywords: *Fruit Detection, CV, AI, DL, ML*

ABSTRACT

With the development of society and the advancement of science and technology, the object detection technology driven by Artificial Intelligence is also constantly innovating. As an important task in the field of agricultural Computer Vision, fruit detection in real environments faces many challenges. This paper reviews and analyzes the latest breakthroughs and representative studies in this field. Based on the existing research, the existing fruit detection algorithms are roughly divided into 5 categories: (1) the traditional fruit detection algorithm based on manual features; (2) the fruit detection algorithm based on two stages; (3) the fruit detection algorithm based on one stage; (4) the fruit detection algorithm based on anchor-free frame, and (5) the fruit detection algorithm based on transfer learning. This paper also discusses various application scenarios, such as multi-object detection, complex backgrounds, and edge computing. It also summarizes the classic and cutting-edge technical methods at the current time point, providing valuable insights for fruit detection in agricultural production.

ABSTRAK

Dengan perkembangan masyarakat dan kemajuan sains dan teknologi, teknologi pengesanan objek yang dipacu oleh kecerdasan buatan juga sentiasa berinovasi. Sebagai tugas penting dalam bidang penglihatan komputer pertanian, pengesanan buah-buahan dalam persekitaran sebenar menghadapi banyak cabaran. Kertas kerja ini mengulas dan menganalisis penemuan terkini dan kajian-kajian yang mewakili bidang ini. Berdasarkan kajian, algoritma pengesanan buah-buahan sedia ada secara kasarnya dibahagikan kepada lima kategori, iaitu: (1) algoritma pengesanan buah-buahan tradisional berdasarkan ciri manual; (2) algoritma pengesanan buah-buahan berdasarkan dua peringkat; (3) algoritma pengesanan buah-buahan berdasarkan satu peringkat; (4) algoritma pengesanan buah-buahan berdasarkan tanpa sauh; dan (5) algoritma pengesanan buah-buahan berdasarkan pembelajaran pemindahan. Kertas kerja ini juga membincangkan pelbagai senario aplikasi seperti pengesanan berbilang objek, latar belakang kompleks dan pengkomputeran tepi. Ia juga meringkaskan kaedah teknikal klasik dan canggih pada masa kini, memberikan pandangan berharga untuk pengesanan buah-buahan dalam pengeluaran pertanian.

INTRODUCTION

Agriculture is one of the most important sectors and plays a vital role in ensuring global food security, rural development, and economic growth. As agricultural technology advances and modernizes, several challenges need to be addressed, such as climate change, pests and diseases, labor shortages, and the need for sustainable resource management (*Devlet A., 2021*). The fusion of artificial intelligence (AI) and computer vision (CV) can alleviate these challenges and open up new opportunities to improve the efficiency, accuracy, and yield of agricultural processes. Object detection has become a key technology that helps to autonomously identify, locate, and classify objects such as leaves, fruits, pests, and diseases from images or video frames (*Gupta, S., &Tripathi, A.K., 2024*). There are a variety of technologies used for object detection in agriculture, including IoT sensors with cameras that can monitor leaves, fruits, vegetables, and crops in real time. Other technologies include drones and satellites for capturing large-scale crop images for analysis and pest detection, and robotic harvesters for automated sowing and harvesting of fruits and vegetables.

In addition, due to the advancement of deep learning (DL), object detection methods have shifted from feature-based models to data-driven methods, such as convolutional neural networks (CNNs) (*O'shea K. & Nash R., 2015*), YOLO (You Only Look Once) (*Redmon J. et al., 2016*), and region-based CNN (R-CNN) *(Girshick R. et al., 2015*), which are used to detect pests and diseases and growth stages. In addition, the recent developments of Vision Transformers (ViT) (*Dosovitskiy A. et al., 2020*), EfficientDet (*Tan M. et al., 2020*), and hybrid CNN-Transformer architectures have significantly improved the detection performance in harsh field environments.

In recent years, with the development of DL technology, the progress of AI has brought great development prospects to object detection. This paper sorts out the mainstream methods and their evolution in the current object detection field, summarizes their core features and application effects, reveals key influencing factors, and evaluates scalability and deployment feasibility, aiming to provide a reference for academia and engineering and help the digital upgrade of the industry.

Fruit Detection

As a core technology of CV, object detection aims to achieve dual perception of object location and classification in images. In the agricultural field, the goal of object detection is to use images or videos to identify and locate certain objects, such as fruits, leaves, vegetables, and pests on crops. This article focuses on the application of fruit-related aspects in agricultural planting and production. In the fruit detection scenario, its core task is to extract the feature representation of the object from complex farmland images, and then realize applications such as automatic picking, yield assessment, and quality grading. Figure 1 shows the evolution of the main technical methods for object detection.

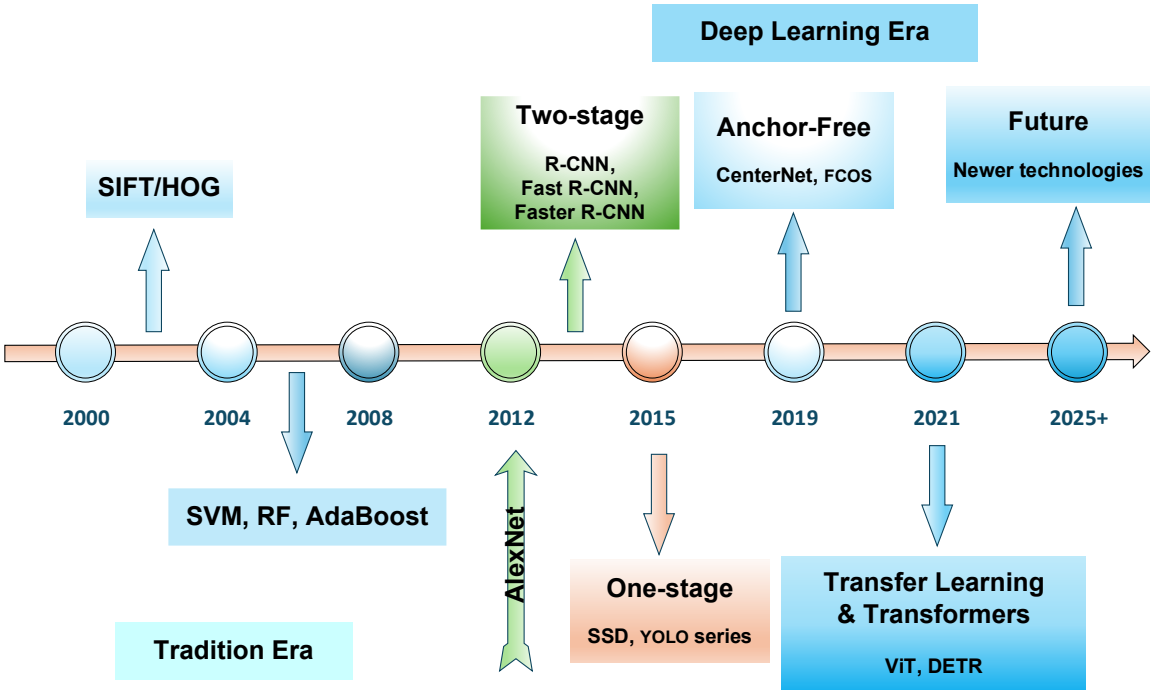


Fig. 1 - The evolution of the main technical methods for object detection

Traditional Methods

Traditional methods have been widely used in tasks such as fruit detection, counting, and grading. The core relies on the feature engineering technology route, and detection is mainly achieved through manual feature extraction and rule definition, such as color, shape, and texture. Its process usually includes four stages: image preprocessing, feature extraction, threshold setting, and classification rules. In image preprocessing, Gaussian or median filtering methods are often used for denoising, and color space conversion is used to enhance fruit features. Subsequently, the tomato area is extracted from the complex background through color segmentation (such as fixed threshold, Otsu method), and morphological operations (erosion, expansion, opening operations, and closing operations) are used to optimize the segmentation results. For the candidate area, edge detection and Hough transform are combined to fit the contour, and the real fruit is screened out using geometric features. At the same time, some fine-grained recognition tasks introduce texture analysis to improve accuracy.

The traditional algorithm is based on the image recognition model, and its detection process always consists of two parts. First, the image is feature extracted based on methods such as scale-invariant feature transform (SIFT) (*Lowe D.G., 2004*) and histogram of oriented gradient (HOG) (*Dalal N., &Triggs B., 2005*), and then the object in the image is classified using methods such as support vector machine (SVM) *(Burges C.J., 1998*) and adaptive boosting (Adaboost) *(Freund Y., & Schapire R.E., 1995*). *Ji et al. (2012)* proposed an apple recognition algorithm based on an SVM by extracting the color and shape features of the fruit in the image, and got good results on apple picking robots. However, the strategies for handling situations involving leaf shading and densely overlapping fruits are still not perfect and fall short compared to extreme conditions in real orchards. *Si et al. (2015)* proposed a fruit recognition algorithm based on color difference and its ratio, which determines the fruit by calculating the color difference and its ratio of pixels. It effectively eliminates the influence of shadows and soil in the natural environment, and achieves a recognition rate of 85%. However, the experiment used a small data scale, a single experimental scenario, and lacked systematic verification under complex conditions. *Mehra et al. (2016)* transformed images from RGB to Lab* color space, clustered pixels using k-means clustering, and then determined maturity based on color characteristics of these clusters. By integrating tomato maturity assessment with disease detection within a single CV framework, they demonstrated the practical value of multi-task recognition while validating the feasibility of image features for fruit quality monitoring and health evaluation. This approach exhibits significant systemic innovation and application significance. However, the feature extraction and classification methods employed exhibit insufficient robustness to lighting variations, fruit occlusion, and scenarios involving multiple concurrent diseases. Furthermore, the limited dataset size and diversity weaken the model's generalization capability, making it difficult to detect automated in real environments. *Al-Mashhadani et al. (2020)* used OpenCV combined with the HSV color space to estimate tomato ripeness and perform counting. They determined the colors of ripe and nearly ripe fruits through thresholding in the HSV color space. While this technique could identify fruits that were ripe and about to change color when grouped, it could not distinguish differences between them.

Traditional algorithms always rely on manually designed feature extraction methods, which are prone to false positives and false negatives when faced with complex scenarios such as changes in light, occlusion, and overlap. They also suffer from high computational complexity, low robustness, and poor adaptability. Although traditional image processing methods based on manual design have the advantages of simple implementation, low computational cost, and low hardware requirements, and have played an important role in early research, their limitations, such as slow processing speed and high computational complexity, have become increasingly apparent (*Bello R.-W. et al., 2025*).

Compared with traditional recognition methods, DL-based methods are self-learning directly from the image's own features and expression relationships. They have a strong ability to express fruit features, high generalization, and high accuracy, solving the problem that traditional methods cannot meet the real-time requirements. At the same time, with the improvement of computer computing power, more researchers have turned their attention to DL. *Girshick et al. (2014)* proposed the R-CNN algorithm, and the use of CNNs greatly improved the speed of object detection. AlexNet *(Krizhevsky A. et al., 2017*) defeated traditional object detection algorithms in the ImageNet Large-Scale Visual Recognition Challenge, and its speed and accuracy are far superior to traditional detection algorithms. So far, DL methods have begun to be widely used in various object detection and recognition algorithms. So, there are several main categories of commonly used methods for detecting fruits on plants based on DL. First is the Two-Stage-Based Algorithm, second is the One-Stage-Based Algorithm, third is the Anchor-Free-Based Algorithm, and the last is the Transformer-Based Algorithm.

Two-Stage-Based Detection Algorithm

The two-stage object detection algorithm is a classic paradigm for object detection in CV. Its core logic is to split the detection task into two stages: "candidate region generation" and "region fine detection" to achieve high-precision object positioning and classification. With their powerful feature learning and expression capabilities, CNNs have gradually replaced traditional image processing methods and become one of the mainstream technologies for detection. As an important representative of the two-stage detection framework, the R-CNN series algorithms have promoted the advancement of object detection technology.

Girshick et al. (2014) proposed the original R-CNN framework, which used a CNN to extract high-level features of candidate regions for the first time, significantly improving detection accuracy. The original R-CNN uses selective search to generate candidate regions, extracts features one by one through CNN, and combines SVM classification and bounding box regression to optimize the detection effect.

Although it improves accuracy, it still has a high computational cost and slow speed, making it difficult to meet real-time requirements. For this, Fast R-CNN (*Girshick R., 2015*) and Faster R-CNN (*Ren S. et al., 2015*) have been introduced. Fast R-CNN reduces redundant calculations and improves detection speed by sharing feature maps and ROIPooling. Faster R-CNN is later than Fast R-CNN. It introduces the region proposal network (RPN) to achieve end-to-end training of candidate region generation and detection, further improving efficiency and accuracy, realizing the integration of detection processes, and laying the foundation for a two-stage detection framework. Mask R-CNN (*He K. et al., 2017*) introduced an instance segmentation function based on Faster R-CNN, adds a mask branch, replaces ROIPooling with ROIAlign to eliminate quantization error, and realizes end-to-end training of object detection, classification, and instance segmentation. It has high accuracy and is extended to tasks such as panoramic segmentation, becoming the basic framework for multimodal vision tasks. It is particularly suitable for scenes with densely clustered fruits, and can effectively distinguish overlapping fruits and improve detection results. Figure 2 shows the basic principle of the two-stage-based detection algorithm.

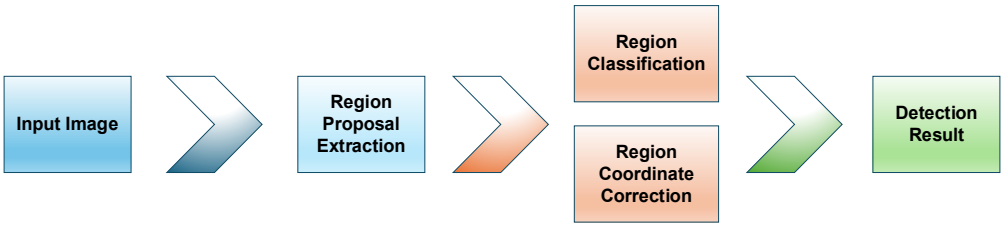


Fig. 2 - The basic principle of the two-stage-based detection algorithm

Ganesh et al. (2019) implement orange detection and instance segmentation based on Mask R-CNN. Its advantage lies in the use of a powerful two-stage segmentation framework, which enables the model to maintain high segmentation accuracy under complex backgrounds. However, Mask R-CNN itself has a large structure and slow inference speed, which makes it difficult to meet the application requirements of real-time picking or drone inspection. Furthermore, it doesn't conduct in-depth discussions on the model's cross-scene generalization, robustness, and data diversity. *Afonso et al. (2020)* proposed a tomato detection algorithm based on the Mask R-CNN approach. This algorithm detects objects and their corresponding pixels, utilizing RealSense cameras to capture tomato images from greenhouses for identifying four distinct stages of tomato ripeness. Results demonstrate the model's excellent performance in detecting and classifying tomatoes within the challenging greenhouse environment, indicating that Mask R-CNN can implicitly learn object depth—a critical factor for background elimination. However, the model exhibits strong dependence on the dataset and lacks validation for generalization. *Wang et al. (2021)* integrated an attention mechanism into the Faster R-CNN model to address the challenge of detecting young tomato against near-color backgrounds. Results show this method achieves a mAP of 98.46% with an average detection time of just 0.084 seconds per image. It enables real-time, accurate, and efficient detection of young tomato fruits, providing a robust solution for fruit detection under near-color backgrounds. But the more complex model structure increases hardware costs and deployment complexity. *Zu et al. (2021)* built a model using Mask R-CNN with a ResNet50-FPN backbone to detect and segment green tomatoes in greenhouses. The model uses ROIAlign bilinear interpolation to compute object regions generated from training feature maps. It achieves detection and segmentation of ripe green tomatoes through parallel operations of ROI object classification, bounding box regression, and mask generation. At an IOU threshold of 0.5, the model achieves an F1 score of 92.0%. And the model remains limited as experiments were conducted solely on green tomatoes, and performance degrades when fruits overlap. *Xu et al. (2022)* used a bimodal feature map and a balanced multi-task loss model, which improved stem segmentation accuracy during cherry tomato harvesting. Nevertheless, challenges persist regarding color and shape similarity, loss of stem features, and category differences. *Yan et al. (2024)* built a comprehensive recognition framework based on an improved Faster R-CNN, integrating apple detection, quantity statistics, localization, and quality estimation. Its advantage lies in unifying multiple tasks into a single model. Through feature pyramid optimization and region proposal modules, it improves detection accuracy and stability in complex orchard environments, effectively addressing real-world challenges such as occlusion and varying lighting conditions. However, while multi-task coupling enhances functionality, it also increases training complexity. Furthermore, the mechanisms of interaction between tasks have not been systematically analyzed, and the limited dataset size means that the demonstration of generalization ability remains insufficient.

Cong et al. (2025) proposed the TQVG Model based on Mask R-CNN for tomato quality grading. Results demonstrate that the model achieves higher mAP and faster inference speeds with fewer parameters. The model exhibits high dependence on training data, sensitivity to annotation quality, and lacks performance validation for real-time and mobile deployment. Furthermore, optimization is still needed in terms of inference efficiency.

While the R-CNN series offer high detection accuracy, they still have some significant limitations for widespread application in fruit detection. Their reliance on a two-stage process of "candidate region generation + classification and regression" results in high overall computational cost, slow inference speed, large file size, and cumbersome workflow, making edge deployment difficult and hindering real-time detection. Although improvements over the original R-CNN, independent steps such as candidate region generation still exist, leading to complex structures, high training costs, high computational resource requirements, and difficulties in end-to-end optimization. They also tend to miss information about dense, small objects, making them less effective against both small and dense objects.

Therefore, although they have significantly advanced object detection technology by optimizing feature extraction and candidate region generation, and perform well in high-accuracy detection and robustness against complex backgrounds, real-time deployment on mobile terminals and edge devices remains challenging due to limitations in detection speed and model size. So, it is necessary to combine lightweight design with efficient feature extraction strategies to further improve their practicality and versatility. Figure 3 shows the mAP values of some Two-stage detectors on the COCO dataset.

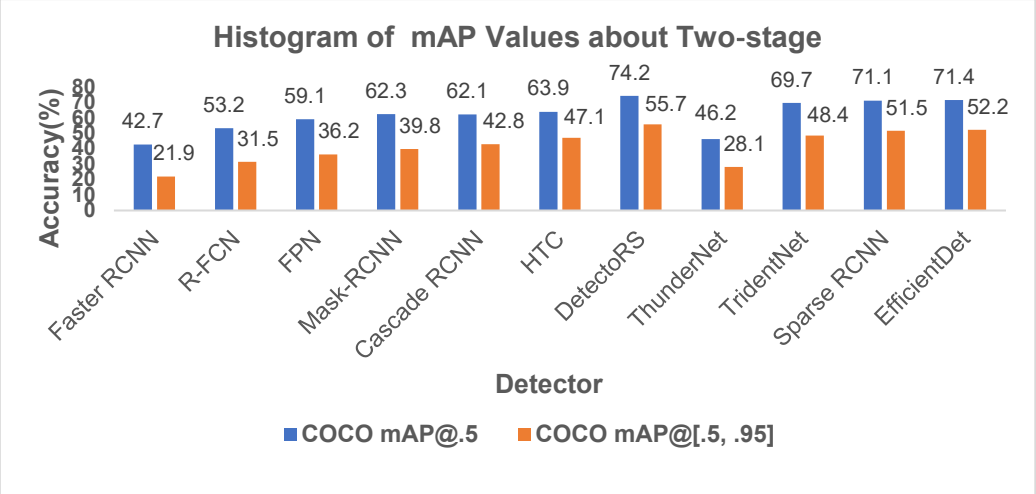


Fig. 3 - The mAP values of some Two-stage detectors on COCO dataset. There're Faster-RCNN *(Ren S. et al., 2015)*, R-FCN (*Dai J. et al., 2016*), FPN (*Lin T.-Y. et al., 2017*), Mask-RCNN (*He K. et al., 2017*), Cascade RCNN *(Cai Z., Vasconcelos, N., 2018*), HTC (*Chen K. et al., 2019*), DetectoRS (*Qiao S. et al., 2021*), ThunderNet *(Qin Z. et al., 2019*), TridentNet (*Li Y. et al., 2019*), Sparse RCNN (*Sun P. et al., 2021*), EfficientDet (*Tan M. et al., 2020*).

One-Stage-Based Detection Algorithm

The regression-based one-stage fruit detection and recognition method does not need to generate candidate regions, but directly obtains the category probability and position of the object, making its network structure simpler and sacrificing some accuracy, but the detection and recognition speed of the algorithm is improved.

YOLO *(Redmon, J. et al., 2016)* series are a typical representative of one-stage detection. With its end-to-end structure, fast speed, and high accuracy, it has become the mainstream technical route for fruit detection. Since YOLO was proposed, it has been iterated on many versions and widely used in agricultural visual inspection, especially in real-time and deployment flexibility scenarios. With the iteration, the YOLO series continues to optimize detection accuracy, efficiency, and generalization ability. YOLO9000 *(Redmon J., & Farhadi A., 2017*) adopted Darknet-19, anchor box and multi-scale training to improve the performance of small object detection; YOLOv3 *(Redmon J. & Farhadi A., 2018*) adopted a deeper Darknet-53 to enhance feature expression; YOLOv4 (*Bochkovskiy A. et al., 2020*) and YOLOv5 integrated CSPNet, Mish activation function, and Mosaic data enhancement, significantly improving speed and accuracy, and are widely used; YOLOv7 (*Wang C.-Y. et al., 2023*) proposed the ELAN (Efficient Layer Aggregation Network) architecture, which improves feature utilization through grouped convolution and residual connection, and performs expansion and compound scaling, supplemented by dynamic label allocation optimization, with strong robustness, and can adapt to complex lighting and occlusion scenes.

YOLOv8 adopts a unified framework for all tasks, enhanced features, and improved loss functions, and introduces adaptive strategies to achieve real-time deployment optimization. And YOLOX (*Ge Z. et al., 2021*) in the YOLO series is also a model based on an anchor-free architecture. YOLOX divides the input image into multiple smaller grids, so that predictions can be made quickly and grid by grid. YOLOX-PAI (*Wu Z. et al., 2022*) is an improved version of YOLOX. Its core part uses an adaptive spatial feature fusion strategy for feature enhancement and an attention mechanism to organize tasks. Figure 4 shows the basic principle of the one-stage-based detection algorithm.

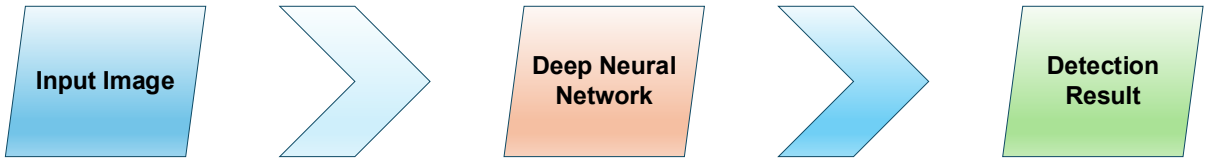


Fig. 4 - The basic principle of the one-stage-based detection algorithm

Mirhaji et al. (2021) utilize various YOLO models to detect and estimate fruit load in citrus orchards, and systematically evaluate the impact of different imaging methods and lighting conditions on detection performance. The results show that the model's precision, recall, F1 score, and mAP are 91.23%, 92.8%, 92%, and 90.8%, respectively, and the overall performance difference between nighttime and daytime imaging is not significant. But the model lacks specific optimization for orchard shading, dense fruit distribution, or strong light interference, and its robustness requires further verification.

Hernández et al. (2023) proposed a tomato ripeness detection model based on YOLOV3-tiny, achieving an F1 score of 90%. Although YOLOv3-tiny is sufficiently lightweight to significantly boost inference speed while maintaining detection accuracy, its overly simplified architecture limits feature extraction capabilities. This results in insufficient recognition accuracy under complex lighting, occlusion, and color transition conditions, necessitating further improvements in model robustness.

Zhang et al. (2023) employed YOLOv4-Tiny + FENB to detect tomatoes under occluded backgrounds during both daytime and nighttime. The nighttime mAP value reached 94.72%, with test results consistently outperforming both YOLOv4 and YOLOv4-Tiny, demonstrating the model's robust performance under nighttime and occluded conditions. However, the authors provided limited validation of the model's robustness and adaptability in complex backgrounds.

Li et al. (2023) proposed the YOLOv5s-Tomato model to identify four distinct tomato maturity stages. They enhanced small object detection performance using techniques like Mosaic data augmentation, the Focus module, and the CSPNet network architecture, while employing EIoU as the loss function. This approach yielded significant improvements in model size and detection speed. Results demonstrate that the model effectively meets greenhouse detection requirements while improving recognition accuracy for occluded and small tomatoes. Since all training images originated from a single greenhouse, further research is needed to evaluate its generalization in complex environments.

Zhang et al. (2024) proposed a cascaded DL network based on YOLOv5 for tomato detection and classification, achieving 82.4% accuracy and 90.9% recall in detecting unobstructed tomatoes. Additionally, the network achieved an average accuracy of 96.9% for tomato ripeness classification and a detection speed of 20 FPS. The validation dataset primarily relied on a single greenhouse scenario, leaving its generalization capability in complex backgrounds insufficiently validated. Furthermore, the analysis of trade-offs between accuracy, stability, and real-time performance for pose classification was inadequate.

Wang et al. (2024b) proposed the NVW-YOLOv8s model for real-time detection and segmentation of tomatoes at three distinct ripeness stages. This model addresses challenges such as sample imbalance, small object detection, and occlusion by introducing a foreground-foreground category balancing method and the C2f-N module, significantly enhancing detection and segmentation performance. The results show that both the mAP@0.5 and F1-Score outperform the baseline model YOLOv8s. However, this study lacks validation of the model's generalization ability across different geographical regions, growth conditions, or tomato varieties.

Wu et al. (2024) proposed a tomato ripeness recognition and stem detection model to address occlusion and overlap issues. The model incorporates CBAM attention and EfficientVMamba modules to enhance feature extraction from tomatoes at different maturity stages and improve small object detection. Experimental results demonstrate that the model achieves higher mAP, precision, recall, and F1 scores than the original YOLOv8n model when identifying tomatoes of varying ripeness in complex environments.

However, due to the limited diversity of scenarios, further validation of robustness and generalization capabilities is lacking.

Zhao et al. (2025) proposed a more lightweight and efficient ripeness detection algorithm, YOLO-DGS, to achieve precise detection of tomato fruit ripeness in natural environments. Experimental results demonstrate that the improved model achieves notable enhancements in inference speed, parameter count, F1 score, recall, and mAP. The study does not explore the lightweight nature or its application on edge devices.

Teng et al. (2025) propose a lightweight improved YOLOv8 model, DS-YOLO, for efficient strawberry fruit detection. By introducing depthwise separable convolutions and a lightweight feature fusion module, the model significantly reduces the number of parameters and computational cost, while maintaining or slightly improving detection accuracy and achieving higher real-time performance.

Experimental results show improvements in mAP@0.5, recall, and precision, while reducing the number of parameters and computational cost. Limited by the relatively small experimental dataset and limited scenarios, the model's generalization ability was not adequately validated. Furthermore, the model's robustness improvement was also limited for small strawberries, dense fruit clusters, and extreme lighting conditions.

The YOLO series are driving the development of detection technology towards real-time, lightweight, and industrial applications thanks to its excellent balance between speed and accuracy, flexible architecture, and complete ecosystem. However, due to its high downsampling and low feature map resolution, the YOLO series algorithms are prone to overlooking small objects or inaccurately locating them. Detection quality tends to degrade when objects are densely packed, overlapping, or when there is strong background interference. Since it relies primarily on manual resolution of class imbalances, its generalization ability is limited, and lightening the model significantly reduces its performance, making it difficult to achieve both accuracy and speed. In the future, it is hoped that solutions or approaches such as integrating Transformers, NAS optimization, and integrated detection-segmentation-tracking functions can further improve the performance of intelligent fruit detection models. Figure 5 shows the mAP of One-stage detectors on COCO dataset.

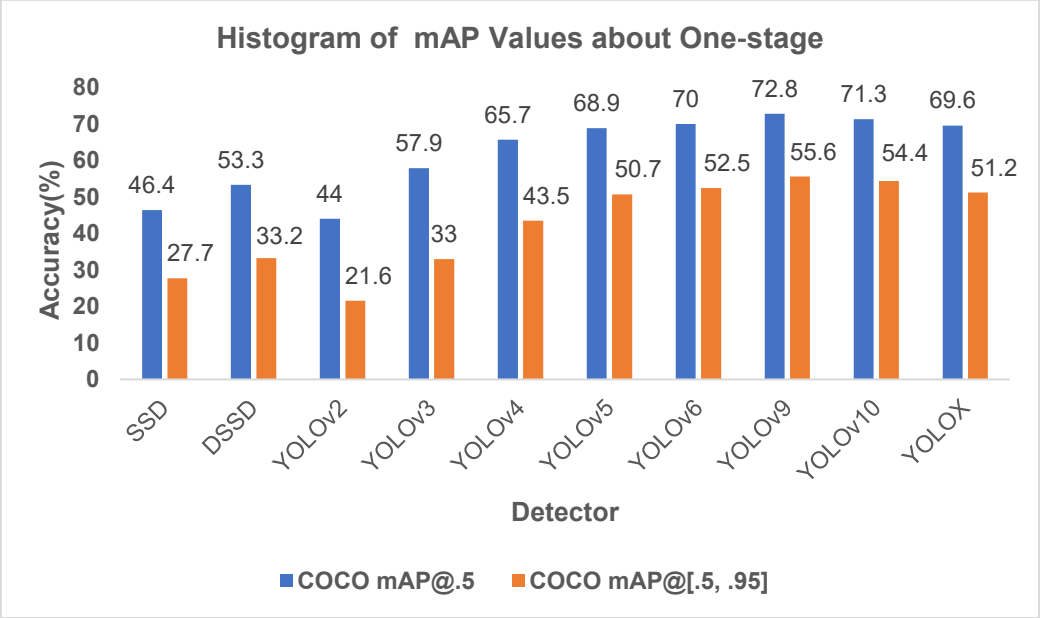


Fig. 5 - The *mAP* of One-stage detectors on *COCO* dataset.

There're SSD (*Liu W. et al., 2016*), DSSD *(Fu C.-Y. et al., 2017*), YOLOv2 (*Redmon J. & Farhadi, A., 2017*), YOLOv3 (*Redmon J. & Farhadi, A., 2018*), YOLOv4 (*Bochkovskiy A. et al., 2020*), YOLOv5 (*Jocher G. et al., 2022*), YOLOv6 (*Li C. et al., 2022*), YOLOv9 *(Wang C.-Y. et al., 2024*), YOLOv10 (*Wang A. et al., 2024a*), YOLOX (*Ge Z. et al., 2021*).

Anchor-Free-Based Detection Algorithm

Although the anchor-free-based algorithm can select positive samples for box regression, it relies on pre-defined boxes and brings some obvious limitations. When too many negative samples are generated, there will be class imbalance; the anchor box of the object class also has the problem of object positioning; the hyperparameters introduced by the anchor box can only be adjusted based on experience, which may be a huge challenge when the workload is large. Based on the idea of eliminating the pre-defined anchor box, the anchor-free-based algorithm is proposed to solve these potential problems. The algorithms can be divided into key-point-based methods and anchor-point-based (also called center-point-based) methods.

Key-point-based detection algorithms use multiple preset keypoints to detect objects and make bounding box predictions based on grouping these keypoints. The first algorithm is CornerNet *(Law H., Deng, J., 2018*), which uses keypoint pairs at the top left and bottom right corners of the bounding box to detect objects and introduces a pooling layer to better locate the bounding box corners. And the CornerNet-Lite *(Law H. et al., 2019*) improves efficiency by introducing an attention mechanism to reduce the number of pixels processed. Then, Matrix networks (xNets) (*Rashwan A. et al., 2019*) provide a lightweight architecture based on scale and aspect ratio, making detection faster. Besides, CenterNet (*Duan K. et al., 2019*) addresses the limitations of CornerNet by adding a third keypoint in the bounding box.

Zhao & Yan (2021) selected the CenterNet framework as the model for solving the problem of fruit detection in digital images. It achieves end-to-end prediction in a single-stage detection process, omitting the candidate box generation step of the traditional two-step method and improving detection speed.

Experiments demonstrate that the model can maintain high detection accuracy even in complex backgrounds, reflecting the potential of CenterNet for small and dense objects. The experiments lack comparisons with more advanced or lightweight models, making it difficult to evaluate their practical advantages in current fruit detection research. Furthermore, the detection capability for multiple categories or fruits of different ripeness levels is not verified to validate the model's generalization ability, and its robustness in occluded, low-light, or multi-view scenarios is not validated. *Wang et al. (2024)* proposed a novel model called CenterNet-LW-SE based on CenterNet. Experimental results show that the model outperforms the original CenterNet in precision, recall, model size, and detection speed, achieving a 2.1% performance improvement while reducing model size by 16.69% and shortening average detection time by 30.40%. It enhances feature representation capabilities to address the challenges of small objects, strong camouflage, and complex backgrounds of camellia fruit in natural environments, particularly excelling in fine-grained feature enhancement. However, the overall model architecture still relies on CenterNet, and it lacks sufficient comparison with more advanced lightweight models (such as YOLOv8n, RT-DETR, and MobileOne), making it difficult to demonstrate its competitive advantage among current lightweight detection frameworks. Generalization validation is insufficient, lacking cross-regional, cross-seasonal, and cross-device dataset testing; model stability requires further verification. Although it claims to be lightweight, it does not provide a complete evaluation of inference time and hardware deployment, lacking edge performance metrics to support its deployment value. *Fan et al (2024)* employed the CenterNet neural network as the detection framework, which improved keypoint prediction accuracy while maintaining low computational cost and achieving a lightweight design. They also implemented structural reinforcement and feature enhancement for complex orchard environments, significantly improving the model's robustness in unstructured environments. Experimental results show that the model achieves an AP of 96.80% on the test set, with 18.91 FPS, a size of only 17.56 MB, and a RMSE of 4.405 mm for localization accuracy. Due to its relatively limited testing scenarios, its generalization and robustness under complex occlusion conditions are an important challenge.

Anchor-point-based detection algorithms use preset anchors and perform detection pixel by pixel. DenseBox (*Huang L. et al., 2015*) is an excellent anchor-point-based detection algorithm. And some years later, the fully convolutional single-stage (FCOS) (*Tian Z. et al., 2019*) model was proposed as a representative model, which uses FPN for multi-level prediction and forces classification of positive and negative anchors, and adds a prediction branch to the classification branch to eliminate the interference of anchors. The FCOS model is not only fast in calculation speed, but also can be customized to meet more requirements.

Liu et al. (2022) propose an accurate detection and segmentation method based on the FCOS object detection model for detecting and segmenting occluded green fruits. Results show that on the apple dataset, the detection and segmentation accuracies for green fruits reach 81.2% and 85.3%, respectively. On the Apple-ape dataset, the detection accuracy and segmentation accuracy reach 77.2% and 79.7%, respectively. The model has 39.7 M parameters and 169.8 G floating-point operations. The model addresses the problem of green fruits easily blending with the background leaves in natural scenes, resulting in weak contrast. An improved model is proposed to significantly enhance the distinguishability of fruits under the "occlusion + same-color background" condition. Combined with enhanced feature extraction and segmentation mechanisms (such as attention modules or multi-scale fusion), it effectively and robustly improves the segmentation boundary quality for fruits with weak texture and partial occlusion. But the model structure is relatively complex and computationally intensive, and the dataset coverage is still limited, so the bottlenecks in lightweight design and adaptability may still exist.

Zhao et al. (2023) propose a novel fruit detection model called FCOS-LSC based on FCOS to better address the challenge of identifying green fruits. This model can directly predict the object's center point and size, avoiding the complexity and parameter tuning issues of traditional anchor-box methods. It effectively enhances the ability to identify low-contrast fruits in complex backgrounds and efficiently identifies and locates green fruit images affected by overlapping occlusion, lighting conditions, and shooting angles. Experiments are insufficient to verify the model's generalization ability under different lighting conditions, different varieties, or multiple fruit categories, indicating room for improvement in robustness. Specific analysis of deployment efficiency, model parameter count, and computational cost is lacking, limiting its guidance for practical mobile or edge applications. Figure 6 shows the mAP of Anchor-free detectors on the COCO dataset.

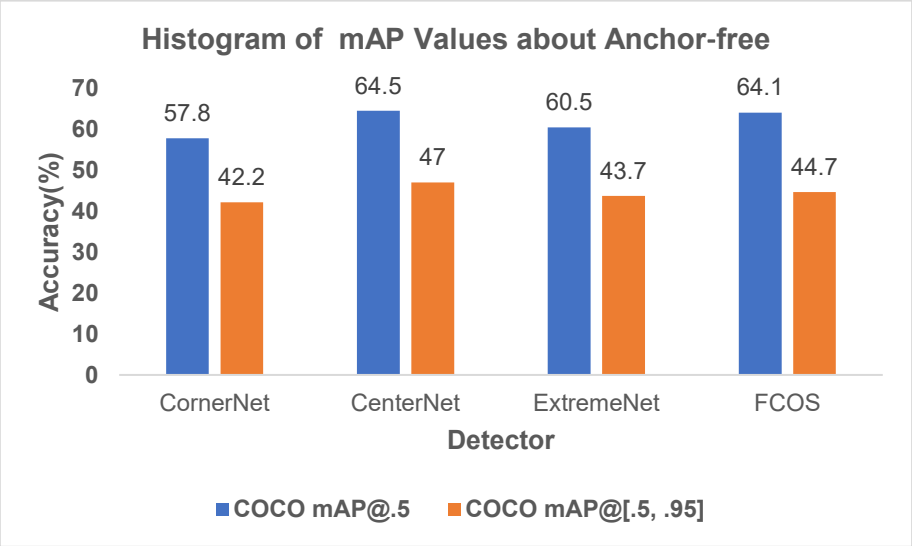


Figure 6. The mAP of Anchor-free detectors on the COCO dataset. There're CornerNet (*Law H., &Deng J., 2018*), CenterNet (*Zhou X. et al., 2019a*), ExtremeNet (*Zhou X. et al., 2019b*), FCOS (*Tian Z. et al., 2019*).

Transformer-Based Detection Algorithm

With the widespread application of the Transformer architecture in the field of CV, object detection technology has achieved a breakthrough. In 2020, the Facebook AI Research team proposed DETR (DEtection TRansformer) (*Carion N. et al., 2020*), which for the first time used a full Transformer structure to achieve end-to-end detection, eliminating traditional modules such as anchors and NMS. DETR has opened up a new path for object detection, especially in complex backgrounds and overlapping occlusions, showing good robustness and high accuracy, and has attracted attention in the field of intelligent agricultural monitoring.

DETR is the first end-to-end framework that introduces the Transformer into object detection. It eliminates NMS and anchor boxes through binary matching, directly outputs detection results, and simplifies the process. The first generation of DETR has high accuracy but slow training and limited small object detection capabilities, which affects the promotion of agricultural applications; the subsequent Deformable DETR *(Zhu X. et al., 2020*) proposed a deformable attention mechanism, introduced deformable convolution to strengthen local feature learning, and only focused on key sampling points, greatly improving small object detection performance and training efficiency; Conditional DETR *(Meng D. et al., 2021*) accelerated training convergence through the conditional cross-attention mechanism, which is faster than DETR; DN-DETR *(Li F. et al., 2022*) proposed a denoising training strategy, accelerated convergence by adding noise queries and reconstructing labels, and enhanced cross-scenario generalization capabilities through dynamic training strategies; DINO (*Zhang H. et al., 2022*) integrated DN-DETR's denoising training and conditional attention to achieve SOTA performance and support few-sample detection; RT-DETR (*Zhao Y. et al., 2024*) was improved based on DINO to achieve real-time end-to-end detection, balance accuracy and speed, and improve model performance; ViDT++ (*Song H. et al., 2021b*) combines visual Transformer and DETR to propose a sparse attention mechanism to achieve efficient detection on high-resolution images (*Zhu X. et al., 2020*). The DETR series is easy to integrate with multi-task learning, supports fruit detection, maturity grading, and size estimation, promotes the integrated development of intelligent monitoring, and is evolving towards lightweight and edge device adaptation, with good industrial application prospects. The Figure 11 shows the architecture of RT-DETR, and Figure 12 shows the mAP values of some classic transfer learning-based object detection models on the coco dataset.

Huang et al. (2024) designed a lightweight Transformer architecture-based pear detection model for natural environments, using the RT-DETR model. The improved model achieves accuracy, recall, and mean accuracy of 93.7%, 91.9%, and 98%, respectively. Compared with the original model, the number of parameters, computational cost, and weight memory are reduced by 48.47%, 56.2%, and 48.31%, respectively. This successfully combines the strong feature modeling capabilities of the Transformer with real-time requirements, alleviating the problems of large parameter count and high computational consumption in traditional ViT models. This research does not fully address the issue of insufficient training data, which may affect the model's generalization ability, and its adaptability to scenarios with extreme lighting changes and dense fruit occlusion is insufficient, requiring further strengthening of robustness. The model complexity is still higher than most lightweight CNNs, limiting its feasibility for deployment on low-power MCUs or edge devices with extremely low computing power. *Zhang (2025)* proposed PG-DETR based on DETR for detecting small, occluded early-stage pomegranate fruits in complex orchard environments. Experimental results show that PG-DETR requires only 6.7 million parameters and has a computational cost of 12.4 GFLOPs/s, achieving a mAP50 of 93.37%. Compared to the RT-DETR-R18 baseline model, our model reduces parameters by 66.2%, GFLOPs by 78.2%, and inference speed by 3.2 times, reaching 173.58 FPS. Despite its "lightweight" design, the DETR framework still incurs some computational overhead compared to YOLO-like frameworks, and its deployment advantage on truly low-power devices is not significant. Furthermore, the model's training is highly dependent on factors such as convergence speed and data size requirements, and its generalization ability may still be limited in small-sample agricultural scenarios. *Tang et al. (2025)* proposed a novel multi-scale lightweight DETR (ML-DETR) for the identification of ripe cherry tomatoes. The ML-DETR model achieves an accuracy of 91.36%, an mAP50 of 0.8875, a floating-point computation of 13.9 GFLOPs, and a frame rate of 81.2 FPS, outperforming the original RT-DETR model. This research primarily focuses on ripe fruit detection, with insufficient validation of its generalization ability to immature, occluded, and densely packed fruits, and incomplete coverage of real-world application scenarios. Furthermore, deployment experiments on real-world edge hardware are lacking, and the value of its lightweight design has not been fully validated in terms of actual device power consumption or real-time performance. *Liu et al. (2024)* proposed a green apple detection model based on an optimized deformable DETR. Experimental results show that the improved detection model significantly improves accuracy, with an overall AP of 54.1, an AP50 of 80.4, an AP75 of 58.0, an AP of 35.4 for small objects, an mAP of 60.2 for medium objects, and an AP of 85.0 for large objects. The model, based on a deformable DETR structure optimization, effectively enhances the detection capability for low-contrast, camouflaged objects like green apples, especially performing well in natural environments with leaf shading and complex lighting conditions. However, the experimental comparison range is relatively narrow, mainly focusing on green apples; cross-crop generalization ability was not tested, and scalability and universality are insufficient. Furthermore, the model's actual deployment performance is lacking, and the real-time harvesting or monitoring needs in agricultural scenarios have not been fully validated. Figure 7 shows the mAP values of some classic transfer learning-based object detection models on the coco dataset.

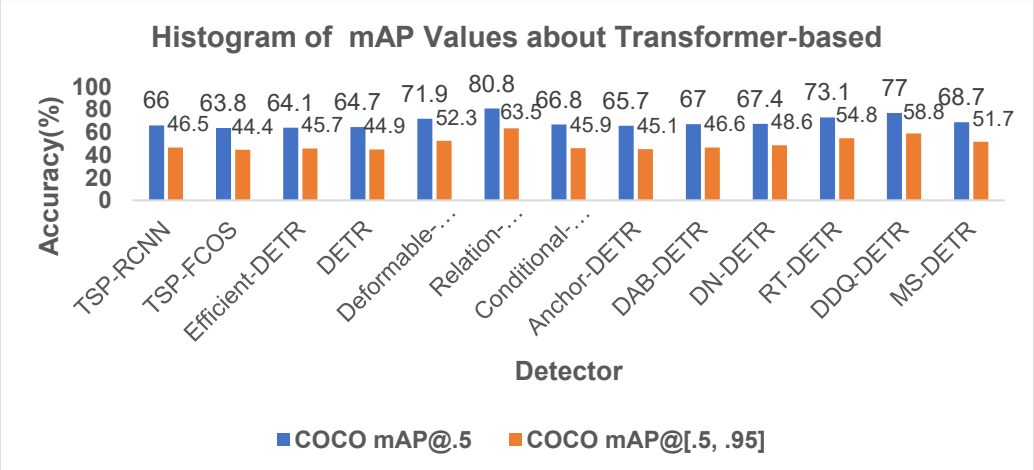


Fig. 7 - The mAP values of some classic Transformer-based detectors on the COCO dataset

They're TSP-RCNN (*Sun Z. et al., 2021*), TSP-FCOS (*Sun Z. et al., 2021*), Efficient-DETR *(Yao Z. et al., 2021*), DETR *(Carion N. et al., 2020*), Deformable-DETR (*Zhu X. et al., 2020*), Relation-DETR (*Hou X. et al., 2024*), Conditional-DETR *(Meng D. et al., 2021*), Anchor-DETR (*Wang Y. et al., 2022*), DAB-DETR (*Liu S. et al., 2022*), DN-DETR *(Li F. et al., 2022*), RT-DETR (*Zhao Y. et al., 2024*), DDQ-DETR (*Zhang S. et al., 2023*), MS-DETR (*Zhao C. et al., 2024*).

Key Challenges

Fruit detection technology can realize automatic fruit recognition, counting, and status analysis through DL algorithms, and is widely used in fields such as yield estimation, intelligent picking, and quality grading. Algorithms such as YOLOv8 and Faster R-CNN achieve a balance between detection accuracy and speed through multi-scale feature fusion and attention mechanism optimization. The Anchor-Free architecture is more adaptable to irregular fruits, and the introduction of the Transformer architecture improves the segmentation of overlapping and occluded objects. Current technology faces challenges such as missed detection of small objects, complex background interference, and insufficient real-time performance. Table 1 shows the main characteristics, advantages, and disadvantages of the backbone networks of some typical object detection models.

Table 1

The main characteristics, advantages, and disadvantages of the backbone networks of some typical object detection models.

Author	Net	Innovations	Advantages	Disadvantages
(Krizhevsky, A. et al., 2012)	AlexNet	The first employed a deep CNN, used sequential convolutional layers, and used a wide sensory field.	First pioneering DL for visual tasks; overall ease of understanding and implementation of the model; significant results for small datasets.	Although a deep network is used, the network has only 8 layers with limited depth; the computational cost of the model is high.
(Simonyan, K., & Zisserman, A., 2014)	VGGNets	Modeled with small convolutional filters (3×3); built a depth architecture; innovative use of miniature convolutional filters.	Strong model performance; performs well across datasets; good at capturing spatial hierarchies.	The model requires high computational power; the number of parameters in the model is large; the model is memory-intensive.
(He, K. et al., 2016)	ResNets	Innovative use of residual connectivity; first use of ultra-deep networks; enables batch normalization of applications.	Effectively mitigates the gradient vanishing problem; the model is highly scalable; it is faster and smaller compared to VGG.	The model requires more computational power; the model is too parameterized; the model is complex to train.
(Szegedy, C. et al., 2017)	Inception-ResNet	Used the Inception module with residual concatenation; established a multi-scale feature extraction mechanism; applied the residual Inception module	The model has more accuracy; the model is very efficient in extracting features; it effectively combines the advantages of Inception and ResNet.	Higher complexity of model architecture; high model requirements on computational resources; smaller range of applications
(Huang, G. et al., 2017)	DenseNets	The model has a compact architecture, and the input of the next layer comes from the output of the previous layer.	The model achieves efficient reuse of features, etc.; the model effectively mitigates the gradient vanishing problem.	Models are memory-intensive; internal connections are complex; memory consumption is high.
(Hu, J. et al., 2018)	SENet	Enables channel-level feature recalibration and lightweight modules	Improved channel interdependency and accuracy while enabling efficient integration with other architectures	Increases computational overhead and thus training time; slower than ResNets
(Tan, M., &Le, Q., 2019)	EfficientNets	A composite scaling method is used; depth separation of the convolution is achieved; and it is lightweight and efficient.	Higher precision and better efficiency with fewer parameters.	Requires tuning of scaling parameters; costly for computation and data movement; one-dimensional scaling only

Author	Net	Innovations	Advantages	Disadvantages
(Wang, C.-Y. et al., 2020)	CSPResNeXt	Implementing partial connectivity across stages, aggregating residual transforms; class does EfficientNet-like scaling	Reduced memory costs while not only maintaining accuracy but also obtaining better inference rates	Increased complexity, long training time, edges, and poor generalization
(Wang, C.-Y. et al., 2021)	CSPDarkNet	Partial connectivity enhancement across phases; available for YOLOv4; efficient feature extraction	Effectively balances speed and accuracy; reduces memory costs; can be used for real-time inspection programs.	Increased design complexity of the architecture leads to reduced ease of use and increased training time.
(Liu, Z. et al., 2022)	ConvNeXt	Simpler architecture with fewer activation and normalization layers	High performance; simple design; good generalization across different datasets	Requires more validation, high computational effort, and high computational power requirements
(Oquab, M. et al., 2023)	DINOv2	A self-supervised vision converter is employed to enable more efficient feature extraction.	Strong generalization ability and self-supervised learning without labeled data	It is data and computation-intensive, with high equipment requirements, while being less effective for small data sets.
(Matszangosz, K.K., &Wendt, M., 2024)	SAM	It's a base model created by the Facebook team that can be used in a wide range of applications.	Highly adaptable and can be used without adjustment or with fine-tuning	Extremely demanding on computing and storage resources, and real-time detection is not currently possible

Difficulty in Dense Detection of Small Objects

In the fruit detection task, “small object dense detection” is a key challenge, where the fruit size is often less than 2%-5% of the image resolution, and in the processing is easy to lose the features, resulting in a decline in the detection accuracy or even failure to detect the object. At the same time, the dense cluster distribution of fruits, accompanied by mutual overlap and branch and leaf occlusion, makes it difficult for the detection network to distinguish between neighboring small objects, and easy to miss detection and false detection. Researchers use multi-scale feature fusion, high-resolution input, attention mechanism, Deformable Convolution, and Transformer feature enhancement to improve the detection of dense small objects *(Bai Y. et al., 2024; Luo Q. et al., 2024; Song H. et al., 2021a*). However, the detection of dense small objects in complex environments is still a bottleneck (*Gong X., &Wu Q.*).

The Effects of Occlusion and Overlap

Fruits grow in the plant, are mostly obscured by leaves, or often grow in clusters and densely, which brings about seriousness between pairs of branches and leaves and fruits, resulting in blurred fruit outlines and making it difficult to distinguish the boundaries, which becomes a key challenge affecting the detection accuracy. Traditional detection methods and early CNN models are difficult to effectively deal with occluded or overlapping objects due to the limited local feature expression capability, and are prone to miss detection and false detection, while networks such as YOLO series and Faster R-CNN can hardly accurately distinguish overlapping objects (*Dalal M., Mittal P., 2025*).

To improve the detection performance, the researchers introduced the attention mechanism to enhance the attention of occlusion area, deformable convolution to improve the ability of local complex morphology perception, combined with instance segmentation to achieve pixel-level differentiation, and utilized the Transformer architecture to enhance the model's understanding of the complex spatial relationship between branches, leaves, and fruits (*Lin Y. et al., 2024; Singh P., Krishnamurthi R., 2024*). Despite these advancements, occlusion and object overlap remain significant challenges affecting detection robustness. Future work should focus on optimizing model architectures and data augmentation strategies to improve detection performance in complex environments.

The Impact of Light Variations

Light variations (e.g., sunlight intensity, shadows, high light reflections, backlighting, and low light) are the key challenges affecting the stability and generalization ability of the detection model, especially more

prominently in the open-air planting and greenhouse transparent coverage models, where the relationship between light and shadow is complex. Under strong sunlight, high light on the fruit surface leads to color distortion; low light or a cloudy environment reduces image contrast and blurs the boundary; under partial shade, the fruit is easily overwhelmed by shadows, which seriously affects the detection accuracy *(Jiang C. et al., 2022*). At the same time, the change of sunlight angle makes the fruit morphology and shadows constantly changing, which puts forward higher requirements on model robustness.

Although the mainstream algorithms have a certain degree of light invariance, there are still performance fluctuations under extreme environments. The researcher has enhanced the light change data, introduced light enhancement broadening, adaptive exposure compensation, attention mechanism, and global modeling ability of the Transformer to alleviate the light and shadow interference *(Dritsas E., 2025*). However, there is still room for improvement in detection performance under strong dynamic lighting scenarios.

The Interference of Complex Background

Different planting environments pose great challenges to the generalization ability and robustness of detection algorithms (*Dickinson S., 2009*). The greenhouse environment can be controlled, with stable light, clean background, the algorithm is easy to achieve high accuracy; while the open-air environment has a complex background, changing light, messy plant branches and leaves, and large differences in fruit morphology, which often leads to the same model in the two scenarios, resulting in performance fluctuations. In addition, the color and maturity of fruits in the open-air environment are greatly affected by natural factors, and the differences between different batches and plots are significant, which can easily lead to misdetection and omission; different planting management methods also increase the difficulty of the model in adapting to changes in spatial layout.

The generalization of the model can be improved to a certain extent through large-scale multi-scene datasets, cross-domain migration learning, style migration, scene adaptive mechanism, and fusion Transformer architecture. However, highly robust detection across scenes, regions, and species is still a challenge that needs to be broken (*Edozie E. et al., 2025*).

DISCUSSION

The Bright Future of Lightweight Networks

In the field of fruit object detection, lightweight networks are becoming an important direction to promote the scale application of smart agriculture. The demand for automated devices (e.g., drones, mobile robots, etc.) in agricultural production has increased, and there is an urgent need for “high-performance + low-computing power demand” detection models (*Zhang P. et al., 2022*). Although traditional high-precision networks have high accuracy, the models are large and energy-consuming, which are not suitable for low-power devices. Lightweight network design is accelerating, striving to balance detection accuracy and operational efficiency. MobileNet, ShuffleNet, SqueezeNet, and other CNN lightweight backbone networks significantly reduce model complexity by means of deep separable convolution, channel rearrangement, etc. MobileNetV3, combined with the optimized design of NAS, has been widely used in tomato detection and grading (*Tan Y. et al., 2025*).

The lightweight versions of the YOLO series (e.g., YOLOv4-Tiny, YOLOv5-Nano, YOLOv7-Tiny, etc.) can be efficiently deployed through pruning optimization and sparse training, with detection speeds up to 30-60 FPS, and are suitable for both embedded and mobile applications (*Li Z. et al., 2024*). Lightweight Transformer architectures (MobileViT) are gradually applied to crop detection, combining global modeling capability and high efficiency, showing good prospects.

The Potential of Transformer Architecture

As a breakthrough DL architecture, Transformer has been extended from NLP to CV by virtue of its powerful global feature modeling capability through the self-attention mechanism, and has been widely used in object detection, yield estimation, and ripening grading, etc. Compared with CNNs, Transformers can effectively capture long-range dependencies in images and improve the robustness and accuracy of detection and grading under complex backgrounds, dense fruit distribution, occlusion, and multi-scale changes. Compared with CNNs, Transformers can effectively capture long-range dependencies in images and improve the robustness and accuracy of detection and grading in complex backgrounds, dense fruit distribution, occlusion, and multi-scale change scenes *(Jackulin C., Murugavalli S., 2022; Zhao Z. et al., 2023*).

The DETR series simplifies the detection process and enhances the detection of small and occluded objects through the query matching mechanism without an anchor, and has already outperformed the traditional YOLO architecture in dense detection scenes.

The Importance of Dataset Construction

In the application of fruit detection, the construction of high-quality datasets is the core foundation to promote technological progress and industrialized applications. Despite the rapid development of DL and Transformer architecture, the lack of standardized data still restricts algorithm performance and generalization ability. Currently, tomato datasets are generally characterized by fragmented data, non-standardized annotations, and a lack of multimodal and multitasking data (*Chen L. et al., 2020*), leading the algorithms into the strange circle of "good results in the laboratory, but difficult to promote in the field".

The variable environment of agricultural scenarios and cultivation management measures leads to high costs and difficulty in data collection and labeling. Data enhancement and simulation data technology are becoming an important means to break through the data bottleneck and improve model robustness. Datasets with high-quality and uniform standards are an important factor in enhancing the generalization ability of models across cultivars and environments (*Akbar J.U.M. et al., 2024*).

The Prospects of Edge Computing

Edge computing has become an important trend as the demand for real-time, portability, and low cost in smart agriculture increases (*Dhiman P. et al., 2023*). Compared with traditional cloud computing, edge computing processes data directly on local devices such as cell phones, drones, and robots, reducing transmission latency, enhancing system real-time and stability, and adapting to complex and changing agricultural environments (*Sathyadhas G.N. et al., 2025*).

Smartphones have become mainstream edge computing terminals due to their powerful computing power (GPU/ NPU), convenience, and low cost. With lightweight models (e.g., MobileNet, YOLOv5-Nano, MobileViT) and AI frameworks (TF Lite, N-CNN), cell phone apps can realize real-time fruit detection and grading, and support intelligent management in the field (*Zheng H. et al., 2025*). With the help of high-performance edge equipment, lightweight Transformer, and NAS-optimized network, object detection technology will be available to everyone and everywhere, promoting smart agriculture to a new stage of universality and efficiency (*Liu H.I. et al., 2024*).

CONLCUSIONS

This paper systematically reviews the applications and significant advancements of CV and DL in fruit detection. Fruit detection technology has rapidly evolved from traditional algorithms to advanced architectures such as CNNs, YOLO, and DETR. However, this analysis shows that these technologies all face specific trade-offs in practical applications. While traditional CNNs provide reliable feature extraction benchmarks, their computational redundancy often fails to meet the real-time requirements of mobile devices. Single-stage detectors like YOLO, by sacrificing some fine-grained accuracy, greatly improve inference speed, making them the preferred choice for edge computing; however, their performance tends to bottleneck when dealing with densely clustered or severely occluded small target fruits. Conversely, Transformer-based models (such as DETR), with their global attention mechanism, have demonstrated breakthrough accuracy in solving complex occlusion problems, but their large number of parameters and high computational cost remain the biggest obstacles to their widespread deployment on low-power agricultural devices. Therefore, at this juncture, finding the optimal balance between computational efficiency and the ability to understand complex scenarios is the core challenge currently facing practical applications. To overcome the limitations of the aforementioned single model, experts and scholars are exploring and attempting to integrate lightweight architecture with the Transformer mechanism to reshape the research paradigm in this field. This hybrid network design not only addresses the low-cost requirement for easy deployment at the edge but also ensures high detection accuracy in complex environments, making it an inevitable trend for the true implementation of smart agriculture.

REFERENCES

[1] Afonso, M., Fonteijn, H., Fiorentin, F.S., Lensink, D., Mooij, M., Faber, N., Polder, G., & Wehrens, R. (2020). Tomato fruit detection and counting in greenhouses using deep learning. *Frontiers in plant science*, *11*, 571299.

[2] Akbar, J.U.M., Kamarulzaman, S.F., Muzahid, A.J.M., Rahman, M.A., & Uddin, M. (2024). A comprehensive review on deep learning assisted computer vision techniques for smart greenhouse agriculture. *IEEE Access*, *12*, 4485-4522.

[3] Al-Mashhadani, Z., & Chandrasekaran, B. (2020). Autonomous ripeness detection using image processing for an agricultural robotic system. 2020 11th IEEE Annual Ubiquitous Computing, Electronics & Mobile Communication Conference (UEMCON),

[4] Bai, Y., Yu, J., Yang, S., & Ning, J. (2024). An improved YOLO algorithm for detecting flowers and fruits on strawberry seedlings. *Biosystems engineering*, 237.
[5] Bello, R.-W., Owolawi, P.A., van Wyk, E.A., & Tu, C. (2025). Object Detection Algorithms for Digital Imaging Applications: A Review. *Available at SSRN 5236924*.
[6] Bochkovskiy, A., Wang, C.-Y., & Liao, H.-Y.M. (2020). Yolov4: Optimal speed and accuracy of object detection. *arXiv preprint arXiv:2004.10934*.
[7] Burges, C.J. (1998). A tutorial on support vector machines for pattern recognition. *Data mining and knowledge discovery*, *2*(2), 121-167.
[8] Cai, Z., & Vasconcelos, N. (2018). Cascade r-cnn: Delving into high quality object detection. Proceedings of the IEEE conference on computer vision and pattern recognition,
[9] Carion, N., Massa, F., Synnaeve, G., Usunier, N., Kirillov, A., & Zagoruyko, S. (2020). End-to-end object detection with transformers. European conference on computer vision,
[10] Chen, K., Pang, J., Wang, J., Xiong, Y., Li, X., Sun, S., Feng, W., Liu, Z., Shi, J., & Ouyang, W. (2019). Hybrid task cascade for instance segmentation. Proceedings of the IEEE/CVF conference on computer vision and pattern recognition,
[11] Chen, L., Penney, D., & Jiménez, D. (2020). AI for Computer Architecture: Principles, Practice, and Prospects. *Synthesis Lectures on Computer Architecture*, *15*(5), 1-142.
[12] Cong, P., Wang, K., Liang, J., Xu, Y., Li, T., & Xue, B. (2025). TQVGModel: Tomato Quality Visual Grading and Instance Segmentation Deep Learning Model for Complex Scenarios. *Agronomy*, *15*(6), 1273.
[13] Dai, J., Li, Y., He, K., & Sun, J. (2016). R-fcn: Object detection via region-based fully convolutional networks. *Advances in neural information processing systems*, *29*.
[14] Dalal, M., & Mittal, P. (2025). A Systematic Review of Deep Learning-Based Object Detection in Agriculture: Methods, Challenges, and Future Directions. *Computers, Materials & Continua*, *84*(1), 57-91. https://doi.org/10.32604/cmc.2025.066056
[15] Dalal, N., & Triggs, B. (2005). Histograms of oriented gradients for human detection. 2005 IEEE computer society conference on computer vision and pattern recognition (CVPR'05),
[16] Devlet, A. (2021). Modern agriculture and challenges. *Frontiers in Life Sciences and Related Technologies*, *2*(1), 21-29.
[17] Dhiman, P., Kaur, A., Hamid, Y., Alabdulkreem, E., Elmannai, H., & Ababneh, N. (2023). Smart Disease Detection System for Citrus Fruits Using Deep Learning with Edge Computing. *Sustainability*, *15*(5), 4576. https://doi.org/10.3390/su15054576
[18] Dickinson, S. (2009). The Evolution of Object Categorization and the Challenge of Image Abstraction. *Object Categorization: Computer and Human Vision Perspectives*. https://doi.org/10.1017/CBO9780511635465.002
[19] Dosovitskiy, A., Beyer, L., Kolesnikov, A., Weissenborn, D., Zhai, X., Unterthiner, T., Dehghani, M., Minderer, M., Heigold, G., & Gelly, S. (2020). An image is worth 16x16 words: Transformers for image recognition at scale. *arXiv preprint arXiv:2010.11929*.
[20] Dritsas, E. (2025). A Comprehensive Survey of Machine Learning Techniques and Models for Object Detection. *Sensors*, *25*.
[21] Duan, K., Bai, S., Xie, L., Qi, H., Huang, Q., & Tian, Q. (2019). Centernet: Keypoint triplets for object detection. Proceedings of the IEEE/CVF international conference on computer vision,
[22] Edozie, E., Shuaibu, A.N., John, U.K., & Sadiq, B.O. (2025). Comprehensive review of recent developments in visual object detection based on deep learning. *Artificial Intelligence Review*, *58*(9).
[23] Fan, P., Zheng, C., Sun, J., Chen, D., Lang, G., & Li, Y. (2024). Enhanced real-time target detection for picking robots using lightweight centernet in complex orchard environments. *Agriculture*, *14*(7), 1059.
[24] Freund, Y., & Schapire, R.E. (1995). A desicion-theoretic generalization of on-line learning and an application to boosting. European conference on computational learning theory,
[25] Fu, C.-Y., Liu, W., Ranga, A., Tyagi, A., & Berg, A.C. (2017). Dssd: Deconvolutional single shot detector. *arXiv preprint arXiv:1701.06659*.
[26] Ganesh, P., Volle, K., Burks, T., & Mehta, S. (2019). Deep orange: Mask R-CNN based orange detection and segmentation. *IFAC-PapersOnLine*, *52*(30), 70-75.
[27] Ge, Z., Liu, S., Wang, F., Li, Z., & Sun, J. (2021). Yolox: Exceeding yolo series in 2021. *arXiv preprint arXiv:2107.08430*.
[28] Girshick, R. (2015). Fast r-cnn. Proceedings of the IEEE international conference on computer vision,
[29] Girshick, R., Donahue, J., Darrell, T., & Malik, J. (2014). Rich feature hierarchies for accurate object

detection and semantic segmentation. Proceedings of the IEEE conference on computer vision and pattern recognition,
[30] Girshick, R., Donahue, J., Darrell, T., & Malik, J. (2015). Region-based convolutional networks for accurate object detection and segmentation. *IEEE transactions on pattern analysis and machine intelligence*, *38*(1), 142-158.
[31] Gong, X., & Wu, Q. Fruit Detection Methods Based on Deep Learning in Agricultural Planting: A Systematic Literature Review. *IEEE Access*, *13*.
[32] Gupta, S., & Tripathi, A.K. (2024). Fruit and vegetable disease detection and classification: Recent trends, challenges, and future opportunities. *Engineering Applications of Artificial Intelligence*, *133*, 108260.
[33] He, K., Gkioxari, G., Dollár, P., & Girshick, R. (2017). Mask r-cnn. Proceedings of the IEEE international conference on computer vision,
[34] He, K., Zhang, X., Ren, S., & Sun, J. (2016). Deep residual learning for image recognition. Proceedings of the IEEE conference on computer vision and pattern recognition,
[35] Hernández, G.A.A., Olguin, J.C., Vasquez, J.I., Uriarte, A.V., & Torres, M.C.V. (2023). Detection of tomato ripening stages using yolov3-tiny. *arXiv preprint arXiv:2302.00164*.
[36] Hou, X., Liu, M., Zhang, S., Wei, P., Chen, B., & Lan, X. (2024). Relation detr: Exploring explicit position relation prior for object detection. European Conference on Computer Vision,
[37] Hu, J., Shen, L., & Sun, G. (2018). Squeeze-and-excitation networks. Proceedings of the IEEE conference on computer vision and pattern recognition,
[38] Huang, G., Liu, Z., Van Der Maaten, L., & Weinberger, K.Q. (2017). Densely connected convolutional networks. Proceedings of the IEEE conference on computer vision and pattern recognition,
[39] Huang, L., Yang, Y., Deng, Y., & Yu, Y. (2015). Densebox: Unifying landmark localization with end to end object detection. *arXiv preprint arXiv:1509.04874*.
[40] Huang, Z., Zhang, X., Wang, H., Wei, H., Zhang, Y., & Zhou, G. (2024). Pear fruit detection model in natural environment based on lightweight transformer architecture. *Agriculture*, *15*(1), 24.
[41] Jackulin, C., & Murugavalli, S. (2022). A comprehensive review on detection of plant disease using machine learning and deep learning approaches. *Measurement: Sensors*, *24*, 100441. https://doi.org/10.1016/j.measen.2022.100441
[42] Ji, W., Zhao, D., Cheng, F., Xu, B., Zhang, Y., & Wang, J. (2012). Automatic recognition vision system guided for apple harvesting robot. *Computers & Electrical Engineering*, *38*(5), 1186-1195.
[43] Jiang, C., Ren, H., Ye, X., Zhu, J., Zeng, H., Nan, Y., Sun, M., Ren, X., & Huo, H. (2022). Object detection from UAV thermal infrared images and videos using YOLO models. *International Journal of Applied Earth Observation and Geoinformation*, *112*, 102912. https://doi.org/10.1016/j.jag.2022.102912
[44] Jocher, G., Chaurasia, A., Stoken, A., Borovec, J., Kwon, Y., Michael, K., Fang, J., Wong, C., Yifu, Z., & Montes, D. (2022). ultralytics/yolov5: v6. 2-yolov5 classification models, apple m1, reproducibility, clearml and deci. ai integrations. *Zenodo*.
[45] Krizhevsky, A., Sutskever, I., & Hinton, G.E. (2012). Imagenet classification with deep convolutional neural networks. *Advances in neural information processing systems*, *25*.
[46] Krizhevsky, A., Sutskever, I., & Hinton, G.E. (2017). ImageNet classification with deep convolutional neural networks. *Communications of the ACM*, *60*(6), 84-90.
[47] Law, H., & Deng, J. (2018). Cornernet: Detecting objects as paired keypoints. Proceedings of the European conference on computer vision (ECCV),
[48] Law, H., Teng, Y., Russakovsky, O., & Deng, J. (2019). Cornernet-lite: Efficient keypoint based object detection. *arXiv preprint arXiv:1904.08900*.
[49] Li, C., Li, L., Jiang, H., Weng, K., Geng, Y., Li, L., Ke, Z., Li, Q., Cheng, M., & Nie, W. (2022). YOLOv6: A single-stage object detection framework for industrial applications. *arXiv preprint arXiv:2209.02976*.
[50] Li, F., Zhang, H., Liu, S., Guo, J., Ni, L.M., & Zhang, L. (2022). Dn-detr: Accelerate detr training by introducing query denoising. Proceedings of the IEEE/CVF conference on computer vision and pattern recognition
[51] Li, R., Ji, Z., Hu, S., Huang, X., Yang, J., & Li, W. (2023). Tomato maturity recognition model based on improved YOLOv5 in greenhouse. *Agronomy*, *13*(2), 603.
[52] Li, Y., Chen, Y., Wang, N., & Zhang, Z. (2019). Scale-aware trident networks for object detection. Proceedings of the IEEE/CVF international conference on computer vision,
[53] Li, Z., Wang, J., Gao, G., Lei, Y., Zhao, C., Wang, Y., Bai, H., Liu, Y., Guo, X., & Li, Q. (2024). SGSNet: a lightweight deep learning model for strawberry growth stage detection. *Front Plant Sci*, *15*, 1491706.

https://doi.org/10.3389/fpls.2024.1491706
[54] Lin, T.-Y., Dollár, P., Girshick, R., He, K., Hariharan, B., & Belongie, S. (2017). Feature pyramid networks for object detection. Proceedings of the IEEE conference on computer vision and pattern recognition,
[55] Lin, Y., Huang, Z., Liang, Y., Liu, Y., & Jiang, W. (2024). AG-YOLO: A Rapid Citrus Fruit Detection Algorithm with Global Context Fusion. *Agriculture*, *14*(1), 114. https://doi.org/10.3390/agriculture14010114
[56] Liu, H.I., Galindo, M., Xie, H., Wong, L.K., Shuai, H.H., Li, Y.H., & Cheng, W.H. (2024). Lightweight Deep Learning for Resource-Constrained Environments: A Survey. *ACM Computing Surveys*, *56*(10).
[57] Liu, M., Jia, W., Wang, Z., Niu, Y., Yang, X., & Ruan, C. (2022). An accurate detection and segmentation model of obscured green fruits. *Computers and Electronics in Agriculture*, *197*, 106984.
[58] Liu, Q., Meng, H., Zhao, R., Ma, X., Zhang, T., & Jia, W. (2024). Green apple detector based on optimized deformable detection transformer. *Agriculture*, *15*(1), 75.
[59] Liu, S., Li, F., Zhang, H., Yang, X., Qi, X., Su, H., Zhu, J., & Zhang, L. (2022). Dab-detr: Dynamic anchor boxes are better queries for detr. *arXiv preprint arXiv:2201.12329*.
[60] Liu, W., Anguelov, D., Erhan, D., Szegedy, C., Reed, S., Fu, C.-Y., & Berg, A.C. (2016). Ssd: Single shot multibox detector. Computer Vision–ECCV 2016: 14th European Conference, Amsterdam, The Netherlands, October 11–14, 2016, Proceedings, Part I 14,
[61] Liu, Z., Mao, H., Wu, C.-Y., Feichtenhofer, C., Darrell, T., & Xie, S. (2022). A convnet for the 2020s. Proceedings of the IEEE/CVF conference on computer vision and pattern recognition,
[62] Lowe, D.G. (2004). Distinctive image features from scale-invariant keypoints. *International journal of computer vision*, *60*, 91-110.
[63] Luo, Q., Wu, C., Wu, G., & Li, W. (2024). A Small Target Strawberry Recognition Method Based on Improved YOLOv8n Model. *IEEE Access*, 12.
[64] Matszangosz, K.K., & Wendt, M. (2024). 4-torsion classes in the integral cohomology of oriented Grassmannians.
[65] Mehra, T., Kumar, V., & Gupta, P. (2016). Maturity and disease detection in tomato using computer vision. 2016 Fourth international conference on parallel, distributed and grid computing (PDGC),
[66] Meng, D., Chen, X., Fan, Z., Zeng, G., Li, H., Yuan, Y., Sun, L., & Wang, J. (2021). Conditional detr for fast training convergence. Proceedings of the IEEE/CVF international conference on computer vision,
[67] Mirhaji, H., Soleymani, M., Asakereh, A., & Mehdizadeh, S.A. (2021). Fruit detection and load estimation of an orange orchard using the YOLO models through simple approaches in different imaging and illumination conditions. *Computers and Electronics in Agriculture*, *191*, 106533.
[68] O'shea, K., & Nash, R. (2015). An introduction to convolutional neural networks. *arXiv preprint arXiv:1511.08458*.
[69] Oquab, M., Darcet, T., Moutakanni, T., Vo, H., Szafraniec, M., Khalidov, V., Fernandez, P., Haziza, D., Massa, F., & El-Nouby, A. (2023). Dinov2: Learning robust visual features without supervision. *arXiv preprint arXiv:2304.07193*.
[70] Qiao, S., Chen, L.-C., & Yuille, A. (2021). Detectors: Detecting objects with recursive feature pyramid and switchable atrous convolution. Proceedings of the IEEE/CVF conference on computer vision and pattern recognition,
[71] Qin, Z., Li, Z., Zhang, Z., Bao, Y., Yu, G., Peng, Y., & Sun, J. (2019). ThunderNet: Towards real-time generic object detection on mobile devices. Proceedings of the IEEE/CVF international conference on computer vision,
[72] Rashwan, A., Kalra, A., & Poupart, P. (2019). Matrix Nets: A new deep architecture for object detection. Proceedings of the IEEE/CVF international conference on computer vision workshops,
[73] Redmon, J., Divvala, S., Girshick, R., & Farhadi, A. (2016). You only look once: Unified, real-time object detection. Proceedings of the IEEE conference on computer vision and pattern recognition,
[74] Redmon, J., & Farhadi, A. (2017). YOLO9000: better, faster, stronger. Proceedings of the IEEE conference on computer vision and pattern recognition,
[75] Redmon, J., & Farhadi, A. (2018). Yolov3: An incremental improvement. *arXiv preprint arXiv:1804.02767*.
[76] Ren, S., He, K., Girshick, R., & Sun, J. (2015). Faster r-cnn: Towards real-time object detection with region proposal networks. *Advances in neural information processing systems*, *28*.
[77] Sathyadhas, G.N., Gladston, A., & Nehemiah, K.H. (2025). LwSANet: Light Weight Self-Attention Network Model to Recognize Fruits from Images. *Traitement du Signal*, *42*(1).
[78] Si, Y., Liu, G., & Feng, J. (2015). Location of apples in trees using stereoscopic vision. *Computers and*

Electronics in Agriculture, *112*, 68-74.
[79] Simonyan, K., & Zisserman, A. (2014). Very deep convolutional networks for large-scale image recognition. *arXiv preprint arXiv:1409.1556*.
[80] Singh, P., & Krishnamurthi, R. (2024). IoT-based real-time object detection system for crop protection and agriculture field security. *Journal of Real-Time Image Processing*, *21*(4), 1-19.
[81] Song, H., Jiang, M., Wang, Y., & Song, L. (2021a). Efficient detection method for young apples based on the fusion of convolutional neural network and visual attention mechanism. *Nongye Gongcheng Xuebao/Transactions of the Chinese Society of Agricultural Engineering*, *37*, 297-303. https://doi.org/10.11975/j.issn.1002-6819.2021.09.034
[82] Song, H., Sun, D., Chun, S., Jampani, V., Han, D., Heo, B., Kim, W., & Yang, M.-H. (2021b). Vidt: An efficient and effective fully transformer-based object detector. *arXiv preprint arXiv:2110.03921*.
[83] Sun, P., Zhang, R., Jiang, Y., Kong, T., Xu, C., Zhan, W., Tomizuka, M., Li, L., Yuan, Z., & Wang, C. (2021). Sparse r-cnn: End-to-end object detection with learnable proposals. Proceedings of the IEEE/CVF conference on computer vision and pattern recognition,
[84] Sun, Z., Cao, S., Yang, Y., & Kitani, K.M. (2021). Rethinking transformer-based set prediction for object detection. Proceedings of the IEEE/CVF international conference on computer vision,
[85] Szegedy, C., Ioffe, S., Vanhoucke, V., & Alemi, A. (2017). Inception-v4, inception-resnet and the impact of residual connections on learning. Proceedings of the AAAI conference on artificial intelligence,
[86] Tan, M., & Le, Q. (2019). Efficientnet: Rethinking model scaling for convolutional neural networks. International conference on machine learning,
[87] Tan, M., Pang, R., & Le, Q.V. (2020). Efficientdet: Scalable and efficient object detection. Proceedings of the IEEE/CVF conference on computer vision and pattern recognition,
[88] Tan, Y., Liu, X., Zhang, J., Wang, Y., & Hu, Y. (2025). A Review of Research on Fruit and Vegetable Picking Robots Based on Deep Learning. *Sensors (Basel)*, *25*(12), 3677. https://doi.org/10.3390/s25123677
[89] Tang, Z., Fang, L., Sun, S., Gong, Y., & Li, Q. (2025). ML-DETR: Multiscale-Lite Detection Transformer for identification of mature cherry tomatoes. *IEEE Transactions on Instrumentation and Measurement*.
[90] Teng, H., Sun, F., Wu, H., Lv, D., Lv, Q., Feng, F., Yang, S., & Li, X. (2025). DS-YOLO: A Lightweight Strawberry Fruit Detection Algorithm. *Agronomy*, *15*(9), 2226.
[91] Tian, Z., Shen, C., Chen, H., & He, T. (2019). Fcos: Fully convolutional one-stage object detection. Proceedings of the IEEE/CVF international conference on computer vision,
[92] Wang, A., Chen, H., Liu, L., Chen, K., Lin, Z., & Han, J. (2024a). Yolov10: Real-time end-to-end object detection. *Advances in neural information processing systems*, *37*, 107984-108011.
[93] Wang, A., Qian, W., Li, A., Xu, Y., Hu, J., Xie, Y., & Zhang, L. (2024b). NVW-YOLOv8s: An improved YOLOv8s network for real-time detection and segmentation of tomato fruits at different ripeness stages. *Computers and Electronics in Agriculture*, *219*, 108833.
[94] Wang, C.-Y., Bochkovskiy, A., & Liao, H.-Y.M. (2021). Scaled-yolov4: Scaling cross stage partial network. Proceedings of the IEEE/cvf conference on computer vision and pattern recognition,
[95] Wang, C.-Y., Bochkovskiy, A., & Liao, H.-Y.M. (2023). YOLOv7: Trainable bag-of-freebies sets new state-of-the-art for real-time object detectors. Proceedings of the IEEE/CVF conference on computer vision and pattern recognition,
[96] Wang, C.-Y., Liao, H.-Y.M., Wu, Y.-H., Chen, P.-Y., Hsieh, J.-W., & Yeh, I.-H. (2020). CSPNet: A new backbone that can enhance learning capability of CNN. Proceedings of the IEEE/CVF conference on computer vision and pattern recognition workshops,
[97] Wang, C.-Y., Yeh, I.-H., & Mark Liao, H.-Y. (2024). Yolov9: Learning what you want to learn using programmable gradient information. European conference on computer vision,
[98] Wang, P., Niu, T., & He, D. (2021). Tomato young fruits detection method under near color background based on improved faster R-CNN with attention mechanism. *Agriculture*, *11*(11), 1059.
[99] Wang, Y., Deng, H., Wang, Y., Song, L., Ma, B., & Song, H. (2024). CenterNet-LW-SE net: integrating lightweight CenterNet and channel attention mechanism for the detection of Camellia oleifera fruits. *Multimedia Tools and Applications*, *83*(26), 68585-68603.
[100] Wang, Y., Zhang, X., Yang, T., & Sun, J. (2022). Anchor detr: Query design for transformer-based detector. Proceedings of the AAAI conference on artificial intelligence,
[101] Wu, Z., An, R., Zhou, L., & Che, X. (2024). Recognition of Tomato Fruit Maturity and Fruit Stems Based on Improved YOLOv8. Proceedings of the International Conference on Image Processing, Machine

Learning and Pattern Recognition,
[102] Wu, Z., Zou, X., Zhou, W., & Huang, J. (2022). YOLOX-PAI: an improved YOLOX, stronger and faster than YOLOv6. *arXiv preprint arXiv:2208.13040*.
[103] Xu, P., Fang, N., Liu, N., Lin, F., Yang, S., & Ning, J. (2022). Visual recognition of cherry tomatoes in plant factory based on improved deep instance segmentation. *Computers and Electronics in Agriculture*, *197*, 106991.
[104] Yan, Z., Zhang, H., & Li, L. (2024). An Integrated Target Recognition Method Based on Improved Faster-RCNN for Apple Detection, Counting, Localization, and Quality Estimation. 2024 IEEE 4th International Conference on Power, Electronics and Computer Applications (ICPECA),
[105] Yao, Z., Ai, J., Li, B., & Zhang, C. (2021). Efficient detr: improving end-to-end object detector with dense prior. *arXiv preprint arXiv:2104.01318*.
[106] Zhang, F., Chen, Z., Ali, S., Yang, N., Fu, S., & Zhang, Y. (2023). Multi-class detection of cherry tomatoes using improved Yolov4-tiny model. *International Journal of Agricultural and Biological Engineering*, *16*(2), 225-231.
[107] Zhang, H., Li, F., Liu, S., Zhang, L., Su, H., Zhu, J., Ni, L.M., & Shum, H.-Y. (2022). Dino: Detr with improved denoising anchor boxes for end-to-end object detection. *arXiv preprint arXiv:2203.03605*.
[108] Zhang, J., Xie, J., Zhang, F., Gao, J., Yang, C., Song, C., Rao, W., & Zhang, Y. (2024). Greenhouse tomato detection and pose classification algorithm based on improved YOLOv5. *Computers and Electronics in Agriculture*, *216*, 108519.
[109] Zhang, P., Liu, X., Yuan, J., & Liu, C. (2022). YOLO5-spear: A robust and real-time spear tips locator by improving image augmentation and lightweight network for selective harvesting robot of white asparagus. *Biosystems engineering*(218-), 218.
[110] Zhang, S., Wang, X., Wang, J., Pang, J., Lyu, C., Zhang, W., Luo, P., & Chen, K. (2023). Dense distinct query for end-to-end object detection. Proceedings of the IEEE/CVF conference on computer vision and pattern recognition,
[111] Zhang, X. (2025). PG-DETR: A Lightweight and Efficient Detection Transformer for Early Stage Pomegranate Fruit Detection. *IEEE Access*.
[112] Zhao, C., Sun, Y., Wang, W., Chen, Q., Ding, E., Yang, Y., & Wang, J. (2024). Ms-detr: Efficient detr training with mixed supervision. Proceedings of the IEEE/CVF conference on computer vision and pattern recognition,
[113] Zhao, K., & Yan, W.Q. (2021). Fruit detection from digital images using CenterNet. International symposium on geometry and vision,
[114] Zhao, M., Cui, B., Yu, Y., Zhang, X., Xu, J., Shi, F., & Zhao, L. (2025). Intelligent Detection of Tomato Ripening in Natural Environments Using YOLO-DGS. *Sensors*, *25*(9), 2664.
[115] Zhao, R., Guan, Y., Lu, Y., Ji, Z., Yin, X., & Jia, W. (2023). FCOS-LSC: A novel model for green fruit detection in a complex orchard environment. *Plant Phenomics*, *5*, 0069.
[116] Zhao, Y., Lv, W., Xu, S., Wei, J., Wang, G., Dang, Q., Liu, Y., & Chen, J. (2024). Detrs beat yolos on real-time object detection. Proceedings of the IEEE/CVF conference on computer vision and pattern recognition,
[117] Zhao, Z., Hao, K., & Liu, K, Zheng, T, Xu, J, Cui, S, He, C, Zhou, J, Zhao, G. (2023). MCANet: Hierarchical cross-fusion lightweight transformer based on multi-ConvHead attention for object detection. *Image and vision computing*, *136*(Aug.), 104715.104711-104715.104714.
[118] Zheng, H., Liu, C., Zhong, L., Wang, J., Huang, J., Lin, F., Ma, X., & Tan, S. (2025). An android-smartphone application for rice panicle detection and rice growth stage recognition using a lightweight YOLO network. *Front Plant Sci*, *16*, 1561632. https://doi.org/10.3389/fpls.2025.1561632
[119] Zhou, X., Wang, D., & Krähenbühl, P. (2019a). Objects as points. *arXiv preprint arXiv:1904.07850*.
[120] Zhou, X., Zhuo, J., & Krahenbuhl, P. (2019b). Bottom-up object detection by grouping extreme and center points. Proceedings of the IEEE/CVF conference on computer vision and pattern recognition,
[121] Zhu, X., Su, W., Lu, L., Li, B., Wang, X., & Dai, J. (2020). Deformable detr: Deformable transformers for end-to-end object detection. *arXiv preprint arXiv:2010.04159*.
[122] Zu, L., Zhao, Y., Liu, J., Su, F., Zhang, Y., & Liu, P. (2021). Detection and segmentation of mature green tomatoes based on mask R-CNN with automatic image acquisition approach. *Sensors*, *21*(23), 7842.

DESIGN AND PERFORMANCE TESTING OF AN AUTOMATIC ORIENTATION AND CONVEYING DEVICE FOR POSTHARVEST CABBAGE TRIMMING BASED ON A CONICAL TREAD

/

基于圆锥踏面的采后甘蓝自动定向输送装置设计及试验

Gongpei CUI [1], Yu ZHANG [1], Huanhuan CHEN [1], Yongjie CUI [2,3,4], Jing ZHANG [1], Dongdong LI [1], He LI [1], Wanzhang WANG [*1]

[1] College of Mechanical and Electronic Engineering, Henan Agricultural University, Zhengzhou 450002, China;
[2] College of Mechanical and Electronic Engineering, Northwest A&F University, Yangling 712100, China;
[3] Key Laboratory of Agricultural Internet of Things, Ministry of Agriculture and Rural Affairs, Yangling 712100, China;
[4] Shaanxi Key Laboratory of Agricultural Information Perception and Intelligent Service, Yangling 712100, China
Tel: +86 13513711991; E-mail: wangwz@henau.edu.cn
Corresponding author: Wanzhang WANG
DOI: https://doi.org/10.35633/inmateh-79-29

Keywords: *postharvest cabbage, automatic orientation, conical tread, kinematic analysis, parameter optimization*

ABSTRACT

Automatic orientation and conveying are critical to enhancing the operational efficiency of postharvest cabbage commercial processing (e.g., trimming), reducing labor input costs, and boosting commodity added value. To address this demand, this study presents the optimal design of an automatic orientation and conveying device for postharvest cabbages based on conical treads, leveraging the moment of inertia principle. Through dynamic modeling and analysis, the key structural parameters governing orientation performance and their feasible ranges were quantified. Furthermore, the orientation reliability of the proposed structure was validated via ADAMS-based motion simulation. A prototype of the postharvest cabbage orientation and conveying device was fabricated, and parameter optimization experiments were conducted to determine the optimal operating conditions. The results indicate that the device achieves superior operational performance when the orientation roller angle is set to 20°, the axial clearance is 60 mm, and the conveying chain linear speed is 300 mm/s. Under these optimal parameters, the orientation success rate of postharvest cabbages reaches 98.67 ± 1.05%, with an orientation angle deviation of 5.18 ± 0.39°. This design remarkably improves the orientation and conveying precision of postharvest cabbages, laying a solid theoretical foundation and providing technical support for subsequent commercial processing operations such as root cutting.

摘 要

自动定向输送可有效提升采后甘蓝整修等商品化处理的作业效率，减少人工成本，提升其商品附加值。本文根据转动惯量原理优化设计了一种基于圆锥踏面的采后甘蓝自动定向输送装置，通过动力学分析确定了影响定向效果的关键结构参数及范围，并基于 ADAMS 运动仿真分析进一步验证了该结构的定向可行性。搭建采后甘蓝定向输送装置样机并进行参数优化试验，结果表明：定向辊锥度角度为 20°，轴向间隙为 60 mm，输送链条线速度为 300 mm/s 时作业效果最佳，采后甘蓝定向成功率为 98.67±1.05%，其夹角为 5.18±0.39°，进一步提升了采后甘蓝的定向输送性能，为后续根茎整修等商品化处理提供理论依据和技术支撑。

INTRODUCTION

Cabbage is one of the most widely cultivated and consumed vegetables in China. In 2024, its cultivation area amounted to 1.03×10^6 hectares with a total yield of 3.68×10^7 tons (*FAO, 2026*). Commercial processing represents an effective means to elevate the commodity added value of postharvest cabbage, and automatic orientation and conveying constitutes a pivotal procedural step in this workflow (*Du et al., 2019; Xiong et al., 2025*). Specifically, this process entails adjusting randomly arranged cabbages into a standardized posture via external force intervention, thereby facilitating subsequent postharvest operations including trimming, grading, packaging and storage (*Cui et al., 2023*).

Currently, scholars at home and abroad have conducted extensive relevant research in the field of automatic orientation and conveying for postharvest fruit and vegetable processing. Nevertheless, the majority of these studies focused on small and medium-sized spherical fruits and vegetables.

Bennedsen et al., (2005), developed an apple orientation and rotation device based on the differences in physical characteristics between apple stalks and calyxes. On this basis, *Li et al., (2009)*, added freely rotatable positioning wheels to adapt to apples of different diameters. Moreover, *Lefcourt et al., (2008, 2009)*, proposed an automatic apple orientation method based on two parallel tracks, which relies on the rotational inertia effect.

Mizushima and Lu., (2013), found that the orientation of apples could also be achieved using a double-cone roller structure. *Li et al., (2014)*, utilized the offset center-of-gravity position of lychees and the structural characteristics of curved rollers to realize automatic posture adjustment and single-row oriented conveying of lychees through counter-rotating rollers.

Kang et al., (2017, 2018), employed the rolling friction effect to keep jujubes in a stable state with minimum momentum during rotation, thereby gradually achieving sequential oriented arrangement of individual jujubes.

Zheng et al., (2015), adopted a pair of rollers with different diameters and a certain inclination angle to realize the oriented conveying of peppers. Considering the significant differences in the three-axis dimensions of fresh apricots and their symmetry along the suture plane, *Liu et al., (2012, 2016)*, proposed a differential belt-type dynamic orientation and conveying method based on the minimum action principle of space geometry.

Lin et al., (2017), optimized the design of a strawberry guiding roller with an hourglass-like geometric structure; strawberries completed the orientation process at the depressions between two adjacent rollers.

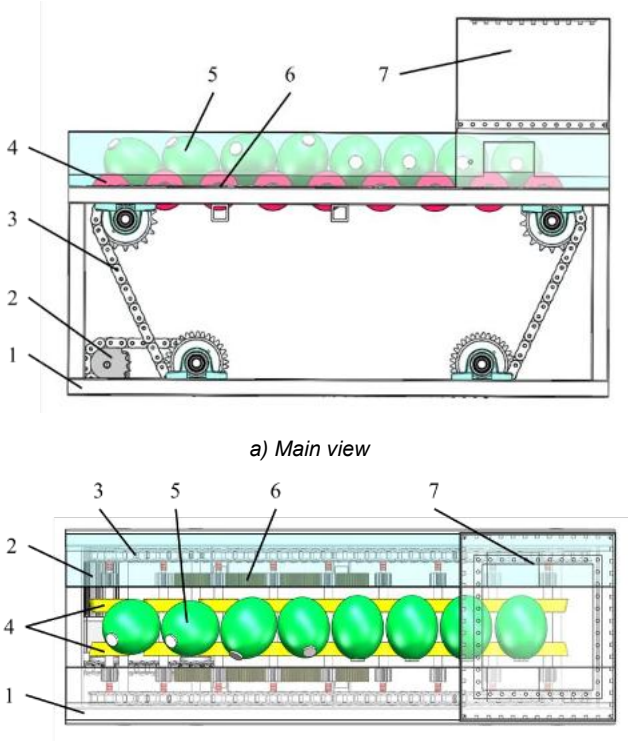
Wang et al., (2020), designed an oriented arrangement vertical and horizontal cutting machine suitable for large-scale processing of potato seed tubers, whose orientation arrangement device can effectively adjust the position and posture of seed tubers. However, unlike the aforementioned small and medium-sized quasi-spherical fruits and vegetables, cabbage presents structural characteristics of non-homogeneous mass distribution and axial offset of the mass center (*Cui et al., 2020*). Conventional cylindrical rollers fail to satisfy the automatic orientation requirements of cabbage. Hence, a novel orientation device is proposed, which can counteract the eccentric effect of cabbage's mass center through lateral friction torque.

To further enhance the orientation and conveying performance of postharvest cabbage, this study proposed an automatic orientation and conveying method for postharvest cabbage based on conical treads, building on previous research findings (*Cui et al., 2020; Zheng et al., 2021; Wang et al., 2021*). Conical rollers feature tapered surfaces with variable diameters. The constraint space formed by such rollers generates lateral friction torque on cabbages to counteract the influence induced by the axial offset of cabbage's mass center. Under the combined effect of the moment of inertia and the principle of minimum action, cabbages are guided to rotate stably around their minimum inertia axis, delivering superior automatic orientation performance. Through dynamic analysis, the key structural parameters and their feasible ranges affecting the orientation effect were determined, followed by the implementation of ADAMS motion simulation. Subsequently, a prototype of the postharvest cabbage orientation and conveying device was fabricated, and parameter optimization experiments were conducted to obtain the optimal combination of operating parameters. This research provides a solid theoretical basis and technical support for subsequent commercial processing operations of postharvest cabbage, such as root cutting.

MATERIALS AND METHODS

Automatic orientation and conveying device for postharvest cabbage based on conical treads

Automatic orientation and conveying device for postharvest cabbage based on conical treads was simplified as illustrated in Figure 1. It is composed of a frame, a drive motor, a chain transmission mechanism, a conical tread orientation roller group, a rack-and-pinion pair, an image detection mechanism, and other auxiliary components. Among these components, the conical tread orientation roller group comprises orientation rollers symmetrically fixed on the roller shaft. Gears engaged with the rack for transmission are symmetrically installed on the outer side of the roller shaft. Both ends of the roller shaft are connected to the chain transmission mechanism through couplings. Both the rack and the chain transmission mechanism are fixedly mounted on the frame.



a) Main view

b) Top view

Fig.1 - Schematic diagram of the structure of an automatic orientation conveying device for postharvest cabbage based on conical treads

1 – Rack; 2 – Drive motor; 3 – Chain transmission mechanism; 4 – Conical tread orientation roller group; 5 –Postharvest cabbage; 6 – Rack and pinion pair; 7 – Image detection mechanism.

Specifically, the drive motor drives the chain transmission mechanism to operate backward at a constant speed. Through the couplings, the conical tread orientation roller group is also driven to move backward at a constant speed. Meanwhile, under the drive of the rack-and-pinion pair, the conical tread orientation roller groups rotate passively, and adjacent conical tread orientation roller groups form a stable orientation space. According to the kinematic transmission relationship, a conversion relationship exists between the linear velocity of the conveying chain and the angular velocity of the rollers, as expressed in Eq. (1).

$$v = \omega r \tag{1}$$

where v is the linear velocity of the conveying chain, [m/s]; ω is the angular velocity of the rollers, [rad/s]; r is the pitch radius of the pinion in the rack-and-pinion pair, [m].

When postharvest cabbages fall into this orientation space, the conical tread orientation rollers exert forces on them, enabling the cabbages to achieve automatic orientation under the combined action of rotational inertia and the principle of minimum action, and then be conveyed backward under the drive of the chain transmission mechanism. When the gears leave the action area of the rack, no external force acts on the conical tread orientation rollers. Under the action of gravity and friction, the conical tread orientation rollers form a stable state with the oriented cabbages and continue to be conveyed backward. Finally, the cabbages reach the area of the image detection mechanism, where pose images are collected to evaluate the orientation effect, providing data support for subsequent commercial processing such as trimming.

Kinematics analysis of postharvest cabbage orientation

The conical tread possesses excellent self-centering and curve-guiding capabilities (*Zhong et al., 2016; Ren et al., 2010*). Furthermore, the orientation movement of postharvest cabbage on this structure conforms to the principles of moment of inertia and least action. Therefore, the orientation kinematics of postharvest cabbage was analyzed, as illustrated in Figure 2, and the structure was optimized to enhance the orientation and conveying performance of postharvest cabbage. At this point, the postharvest cabbage on the conical tread orientation roller group is subjected to the combined action of its own gravity, as well as the supporting force and frictional force from each conical tread orientation roller rotating in the same direction at the same speed. As a result, it gradually achieves stable rotational motion around its central axis, and the circumferences of the trajectories of the two contact points formed between the cabbage and the conical tread orientation rollers are equal.

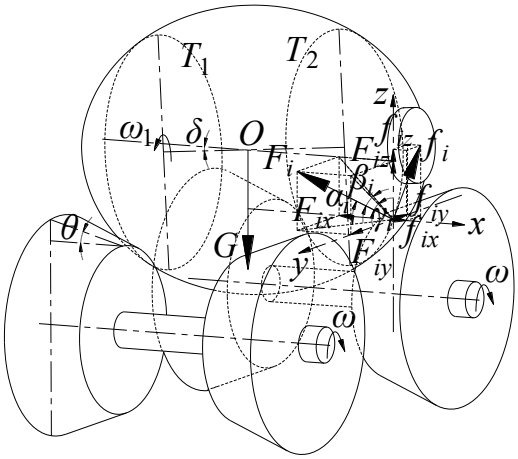


Fig. 2- Force analysis of postharvest cabbage movement on the conical tread orientation roller groups

Note: F_i denotes the support force exerted by the conical tread-oriented roller on postharvest cabbage, while f_i represents the frictional force exerted by the roller wheel on postharvest cabbage. F_{ix}, F_{iy}, and F_{iz} denote the component forces of the support force along the x, y, and z axes respectively, whereas f_{ix}, f_{iy}, and f_{iz} denote the component forces of the frictional force along the x, y, and z axes respectively. G denotes the gravitational force of the postharvest cabbage itself, ω represents the rotational angular velocity of the roller, ω_1 denotes the rotational angular velocity of the postharvest cabbage, α_i, β_i, γ_i denote the angles between the support force and the planes of the three coordinate axes respectively, θ denotes the taper angle of the roller, δ denotes the angle between the central axis of the postharvest cabbage and the roller axis, T_1 and T_2 denote the motion trajectories of contact points between the postharvest cabbage and the conical tread-oriented roller, and O represents the center of mass of the postharvest cabbage.

In this state, the postharvest cabbage moves dynamically and stably on the conical tread orientation rollers; that is, the force system within its rigid-body inertial force system reaches equilibrium. Therefore, it can be concluded that:

$$\sum M_x = \sum M_e + \sum M_{Ix} = 0 \tag{2}$$

where: M_x is the torque generated by postharvest cabbage rotating about the x-axis at angular velocity ω_x, [N·m]; M_e is the torque produced by external forces when postharvest cabbage rotates about its central axis, [N·m]; M_{Ix} is the principal moment of inertia of postharvest cabbage in the inertial coordinate system, [N·m].

As shown in Figure 2, the instantaneous forces acting on the postharvest cabbage in all directions have reached equilibrium. Furthermore, the angle between the support force exerted by the conical tread orientation roller on the postharvest cabbage and the component force at its point of contact is equal to the taper angle of the conical tread orientation roller. Therefore, when the postharvest cabbage rotates about its central axis, the torque generated by the external force is:

$$M_e = \sum \left| \vec{f}_{iy} + \vec{f}_{iz} \right| L_i = \mu_0 \sum F_i \cos\gamma_i L_i = \mu_0 \sum F_i \cos\theta L_i \tag{3}$$

where: f_{iy} and f_{iz} are the components of the friction force exerted by the conical tread-oriented roller on the postharvest cabbage along the y and z axes respectively, [N]; L_i is the perpendicular distance from the contact point between the postharvest cabbage and the roller to the rotational axis, [m]; μ_0 is the coefficient of friction between the roller and the postharvest cabbage; F_i is the support force exerted by the roller on the postharvest cabbage, [N]; γ_i is the angle between the support force and the component force at the contact point's cross-section, [°]; θ is the taper angle of the roller, [°].

Meanwhile, based on the theorem of motion of the center of mass and D'Alembert's principle in the center-of-mass frame, the rigid-body inertial force system of postharvest cabbage is simplified. The calculation methods for the principal vector of the inertial forces of the particle system and the principal moment of the inertial forces about the central axis are given in Eq. (4).

$$\begin{cases} \vec{F}_{IO} = \sum \vec{F}_{Ii} = -m\vec{a}_O \\ M_{Ix} = \sum M_x(F_{Ii}^{\mathrm{n}}) + \sum M_x(F_{Ii}^{\mathrm{t}}) \end{cases} \tag{4}$$

where: F_{I0} is the principal vector of the inertial force of the particle system, [N]; F_{Ii} is the inertial force of the center of mass of the postharvest cabbage, [N]; m is the mass of the postharvest cabbage, [kg]; a_O is the acceleration of the center of mass, [m/s]; F_{Ii}^{n} is the normal component of the inertial force of the center of mass

of the postharvest cabbage, [N]; F_{Ii}^{t} is the tangential component of the inertial force of the center of mass of the postharvest cabbage, [N].

Among these, the magnitudes of the various components of the inertial forces acting on the postharvest cabbage pith are as follows

$$\begin{cases} F_{Ii}^{\mathrm{t}} = m_i a_i^{\mathrm{t}} = m_i r_i \alpha \\ F_{Ii}^{\mathrm{n}} = m_i a_i^{\mathrm{n}} = m_i r_i \omega_1^2 \end{cases} \tag{5}$$

where: m_i is mass of any particle in the postharvest cabbage, [kg]; a_i^t is tangential component of acceleration for that particle, [m/s]; r_i is perpendicular distance from a given particle in the postharvest cabbage to the rotational axis, [m]; α is angular acceleration of the postharvest cabbage rotating about its central axis, [rad/s²]; a_i^n is normal acceleration component of the particle, [m/s]; ω_1 is angular velocity of the postharvest cabbage around the x-axis under slight disturbance, [rad/s].

As previously established, postharvest cabbage undergoes stable rotational motion about its central axis on the conical tread orientation roller group assembly, with its center of gravity positioned along the central axis. Therefore, it follows that:

$$\begin{cases} F_{IO} = 0 \\ \sum M_x(F_{Ii}^{\mathrm{n}}) = 0 \end{cases} \tag{6}$$

According to the simplified mathematical model of postharvest cabbage, the moments of inertia in the three directions of the x, y, and z axes can be calculated, and it can be obtained that:

$$\begin{cases} I_x = \dfrac{1}{5}\rho_2 V\left(b^2+c^2\right) + \dfrac{1}{2}V_1\left(\rho_1-\rho_2\right)r^2 \\ I_y = \dfrac{1}{5}\rho_2 V\left(a^2+c^2\right) + \dfrac{1}{2}V_1\left(\rho_1-\rho_2\right)\left(\dfrac{1}{6}\left(3r^2+h^2\right)+2\left(a-\dfrac{h}{2}\right)^2\right) \\ I_z = \dfrac{1}{5}\rho_2 V\left(a^2+b^2\right) + \dfrac{1}{2}V_1\left(\rho_1-\rho_2\right)\left(\dfrac{1}{6}\left(3r^2+h^2\right)+2\left(a-\dfrac{h}{2}\right)^2\right) \end{cases} \tag{7}$$

where: *Ix, Iy, and Iz* are moments of inertia of postharvest cabbage along the x, y, and z axes respectively, [kg·m²]; V is volume of postharvest cabbage, [m³]; V_1 is volume of the central column, [m³]; ρ_1 is density of the central column, [kg/m³]; ρ_2 is density of the head, [kg/m³]. The density of the above two tissue structures was calculated following the method proposed by *Zheng et al., 2021*, and their volumes were measured via the water displacement method; r is radius of the central column, [m]; h is length of the central column, [m]*; a, b* and c are radii of the postharvest cabbage along the x, y, and z axes, respectively, [m].

By combining Eqs. (4) to (7), the following expression is obtained:

$$M_{Ix} = \sum M_x(F_{Ii}^{\mathrm{t}}) = -\sum F_{Ii}^{\mathrm{t}} \cdot r_i = -\sum (m_i r_i^2)\alpha = -I_x\alpha = -\left[\frac{1}{5}\rho_2 V\left(b^2+c^2\right) + \frac{1}{2}V_1\left(\rho_1-\rho_2\right)r^2\right]\alpha \tag{8}$$

By combining Eqs. (2) to (8), the following expression is obtained:

$$\alpha = \frac{10\mu_0 \sum F_i \cos\theta L_i}{2\rho_2 V\left(b^2+c^2\right) + 5V_1\left(\rho_1-\rho_2\right)r^2} \tag{9}$$

In addition, for the conical tread orientation roller set to achieve orientation operation, it should meet the basic geometric position relationship and have no assembly interference. That is, postharvest cabbage in random orientations should not fall off during transport. Meanwhile, to ensure smooth execution of subsequent rhizome cutting, the rhizomes of postharvest cabbage must be positioned outside the conical tread orientation roller group. Therefore, the structural design and spatial arrangement of the conical tread orientation roller must meet these functional requirements:

$$\begin{cases} \min(D_x, D_y) > D_{\min} > D_A - D_R \\ \min(H) > C_A + 2T_R > \min(D_x, D_y) > C_A \\ D_A > D_R + 2T_R \tan\theta \end{cases} \tag{10}$$

where: D_x is the postharvest cabbage transverse diameter, [mm]; D_y is the postharvest cabbage longitudinal diameter, [mm]; D_{min} is the minimum diameter of the contact point trajectory between postharvest cabbage and roller, [mm]; D_A is center distance between axes of conical tread-oriented rollers, [mm]; D_R is Inner diameter of roller, [mm]; H is plant height of postharvest cabbage, [mm]; C_A is axial clearance of roller, [mm]; T_R is thickness of roller, [mm].

Calculated from Eq. (10):

$$\begin{cases} \theta < \arctan\left[\dfrac{\min(D_x, D_y)}{2T_R}\right] \\ \min(D_x, D_y) - 2T_R < C_A < \min(H) - 2T_R \end{cases} \tag{11}$$

Eqs. (9) and (11) demonstrate that during postharvest cabbage orientation on the conical tread orientation roller assembly, its motion state is influenced not only by the physical parameters of the cabbage itself but also by structural parameters such as the taper angle of the conical tread orientation roller and its positional relationship. This provides a theoretical basis for selecting factors in subsequent experiments aimed at optimizing the automatic orientation parameters for postharvest cabbage.

Simulation and Analysis of Orientation Movement of Postharvest Cabbage Based on ADAMS

Firstly, SolidWorks software was employed to establish a three-dimensional simulation model for the orientation motion of postharvest cabbage. By integrating the physical parameters of postharvest cabbage with the results of orientation kinematic analysis, the inner diameter of the conical tread orientation roller was determined to be 70 mm, with a taper angle of 20° and a thickness of 30 mm. The structural parameters of the roller were derived from the optimal parameter combinations reported in previous studies (*Cui et al., 2020; 2021*), with the radial and axial clearances set at 50 mm and 60 mm, respectively. Furthermore, postharvest cabbage was modeled as an isotropic elastic body (*Duet et al., 2019*) and simplified into two components: a central stem solid and a head solid. Both the physical parameters and material properties were kept consistent with the settings in *Cui et al., (2020),* to better verify the orientation performance of the conical tread orientation roller assembly. Subsequently, this three-dimensional model was converted into the universal IGS format and imported into ADAMS software. The simulation model for the orientation movement of postharvest cabbage is shown in Figure 3.

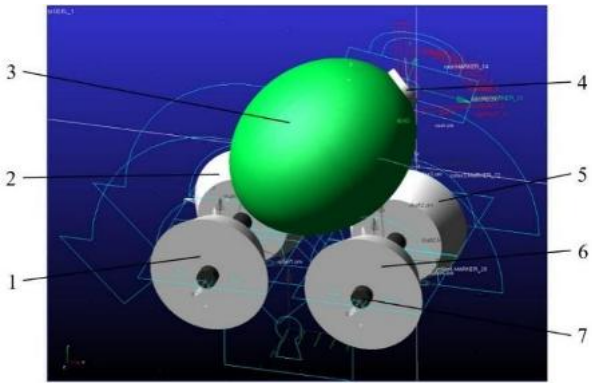


Fig. 3 - Postharvest cabbage automatic orientation simulation model

1 – Conical tread orientation roller 1; 2 – Conical tread orientation roller 2; 3 – Blade ball; 4 – Central column; 5 – Conical tread orientation roller 3; 6 – Conical tread orientation roller 4; 7 – Support shaft.

The simulation analysis workflow for postharvest cabbage orientation essentially followed that of *Cui et al.*, *2020*, with the specific steps outlined below:

(1) Material definition. The material properties of key components, including the orientation roller, leaf head, central stem, and support shaft, were set.

(2) Motion constraint conditions. Constraints were added to the conical tread orientation roller model, including fixed pairs, rotating pairs, drive mechanisms, and contact forces. The impact function method was adopted to define the contact forces between the central stem and head of postharvest cabbage and the roller.

The stiffness coefficient, collision index, maximum damping coefficient, static friction coefficient, and dynamic friction coefficient were set to 278 N/mm, 1.5, 0.3 N·s/mm, 0.5, and 0.48, respectively (*Zheng et al., 2021*).

(3) Marker point addition. One marker point was selected at the center of the base of the central stem and another at the center of the head, designated as point A (x_1, y_1, z_1) and point B (x_2, y_2, z_2), respectively. Both marker points are located along the central axis of postharvest cabbage.

(4) Motion parameter configuration. The initial pose of postharvest cabbage was divided into 26 distinct configurations (*Cui et al., 2020*) for simulation testing. The drive parameters were set to 12.00 rad/s, 15.00 rad/s, and 18.00 rad/s, respectively. The simulation duration was uniformly set to 10.0 seconds, with 500 simulation steps for each configuration.

(5) Orientation metric calculation method. In this study, orientation was analyzed solely based on the angle between the central axis of postharvest cabbage and the axis of the conical orientation roller, which was calculated according to Eq. (12).

$$\begin{cases} \delta = \arccos\left|\dfrac{l_{AB}^2 + l_{AC}^2 - l_{BC}^2}{2 l_{AC} l_{AB}}\right| \\ l_{BC} = \sqrt{(x_1 - x_2)^2 + (y_1 - y_2)^2 + (z_1 + k - z_2)^2} \\ l_{AC} = \sqrt{(x_1 - x_2)^2 + (y_1 - y_2)^2 + (z_1 + k - z_1)^2} = k \\ l_{AB} = \sqrt{(x_1 - x_2)^2 + (y_1 - y_2)^2 + (z_1 - z_2)^2} \end{cases} \quad (12)$$

where: δ is angle between the central axis of the postharvest cabbage and the roller axis, [°]; l_{BC}, l_{AC} *and* l_{AB} are lengths of line segments BC, AC, and AB respectively, [mm]; wherein the parameter *k* of the marked point *C* (x_1, y_1, $z_1 + k$) is a constant value set at 150 (*Cui et al., 2020).*

Automatic orientation performance optimization test based on conical treads

Based on the aforementioned kinematic and simulation analyses of the automatic orientation of postharvest cabbage using conical treads, a conical tread orientation conveying device for postharvest cabbage was designed and trial-manufactured, as illustrated in Figure 4. A total of 120 postharvest cabbages of the "Zhonggan 15" variety were selected as test samples. Their transverse diameters ranged from 114 to 128 mm, longitudinal diameters from 108 to 124 mm, plant heights from 132 to 155 mm, masses from 527 to 795 g, and sphericities from 87% to 94%.

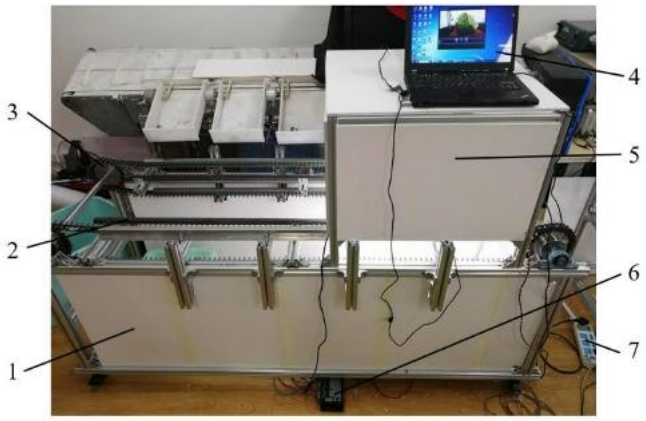


Fig. 4 - Prototype of a Postharvest Cabbage Cone-Tread Oriented Conveying Device

1 – Frame; 2 – Rack and pinion assembly; 3 – Chain drive mechanism; 4 – Laptop computer; 5 – Image acquisition system; 6 – Motor control system; 7 – Power supply.

In addition, the test equipment included a digital vernier caliper (accuracy: 0.01 mm, measuring range: 0–300 mm, manufactured by AIRAJ, Germany) and an AR926 laser tachometer (accuracy: ±0.05%, measuring range: 2.5–99999 r/min, manufactured by Dongguan Wanchuang Electronic Products Co., Ltd., China).

In this experiment, an orthogonal test was carried out with the taper angle of the conical tread orientation roller, the axial clearance, and the linear velocity of the conveyor chain as experimental factors, and the orientation angle of postharvest cabbage and the orientation success rate as experimental indicators, with details shown in Table 1.

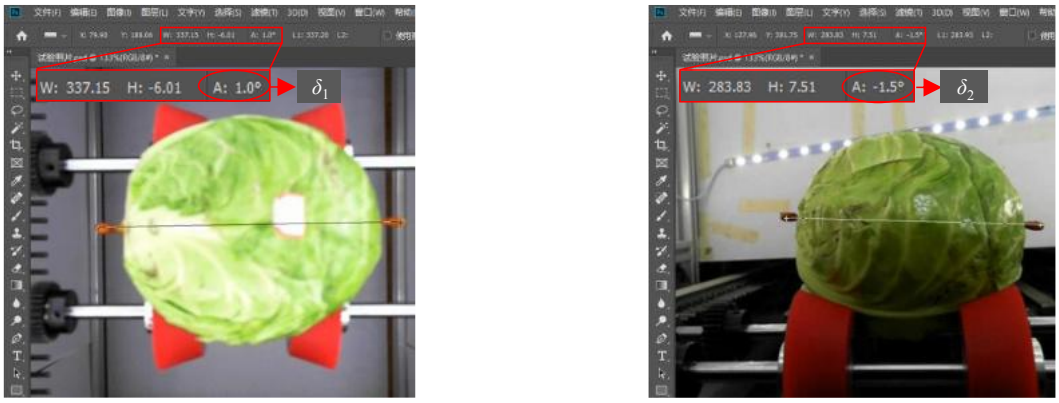
The taper angle of the conical tread orientation roller was adjusted by replacing custom-made rollers with different taper angles, where the inner diameter and thickness of the rollers were fixed at 70 mm and 30 mm, respectively. The axial clearance was measured and adjusted using a digital vernier caliper, while the linear velocity of the conveyor chain was regulated by measuring the angular velocity of the sprocket with a laser tachometer. Each experimental group consisted of 30 cabbages, and each group was repeated three times; the average value was taken as the final experimental result.

Table 1

Orthogonal Test Factors and Levels for Conical Tread Orientation

Levels	Factors		
	Taper angle (°)	Axial clearance (mm)	Linear velocity of chain (mm/s)
1	10	40	225
2	20	50	300
3	30	60	375

The experimental indicators, including the orientation angle and orientation success rate of postharvest cabbage, were calculated based on the calibration results of the angle between the central axis of postharvest cabbage and the axis of the rollers, which were obtained from the top-view and side-view images using Photoshop software. This measurement method was consistent with that reported by *Cui et al., (2020)*, as illustrated in Figure 5.



(a) Included angle from top-view δ_1 (b) Included angle from side-view δ_2

Fig. 5 - Method for determining the orientation angle of postharvest cabbage on a conical tread orientation roller

The calculation methods for the cabbage angle and orientation success rate are shown in Eqs. (13) and (14).

$$\delta = \arcsin\sqrt{\frac{\tan^2\delta_1 + \tan^2\delta_2}{1+\tan^2\delta_1 + \tan^2\delta_2}} \tag{13}$$

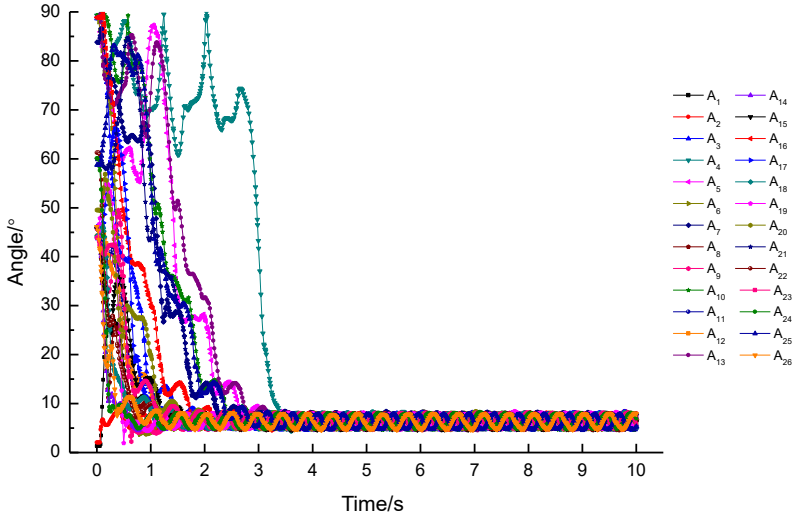
$$\eta_o = \frac{n_o}{N}\times 100\% \tag{14}$$

where: η_o is postharvest cabbage orientation success rate, [%]; n_o is number of postharvest cabbage achieving successful orientation (rotating around their central axis at a relatively small and stable angle), [heads]; N is total number of postharvest cabbage, [heads].

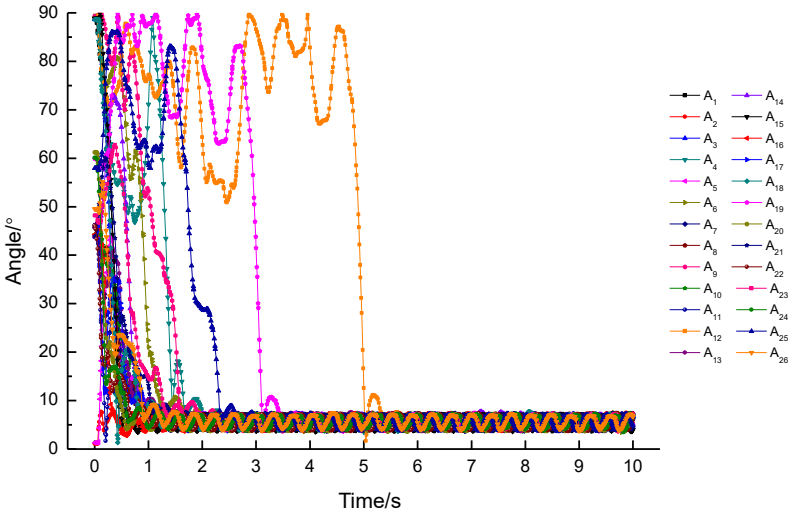
RESULTS

Analysis of the Simulation Results on the Orientation Movement of Postharvest Cabbage on Conical Tread Surfaces

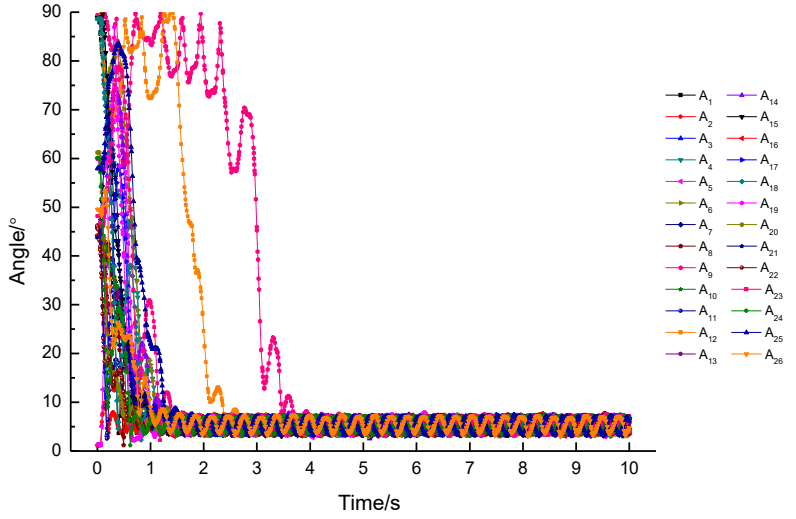
The pattern of angular variation during the automatic orientation of postharvest cabbage on the conical tread orientation roller group is illustrated in Figure 6.



(a) Roller angular velocity: 12.00 rad/s.



(b) Roller angular velocity: 15.00 rad/s.



(c) Roller angular velocity: 18.00 rad/s

Fig. 6 - Pattern of Angular Movement Between the Central Axis of Postharvest Cabbage and the Axis of the Conical Orientation Roller

Specifically, as shown in Figure 6(a), the angle stabilizes at 6.62 ± 0.12° when the roller's angular velocity is 12.00 rad/s. The longest time required for angular stabilization is 3.52 seconds (for initial pose A_4). For initial poses A_{13} and A_5, the time required for angular stabilization decreases gradually, while the remaining postharvest cabbage poses take no more than 2.50 seconds to achieve angular stabilization.

Similarly, as shown in Fig. 6(b), the orientation angle of postharvest cabbages stabilized at 5.90 ± 0.07° when the angular velocity reached 15.00 rad/s. The maximum stabilization time was 5.42 s, which was observed for the initial pose A_{12}. For the initial poses A_{19} and A_3, the stabilization time decreased in turn, whereas the orientation angles for all other initial poses stabilized within 2.08 s. As depicted in Fig. 6(c), at an angular velocity of 18.00 rad/s for the conical tread orientation roller group, the orientation angle of postharvest cabbages stabilized at 5.74 ± 0.13°. The maximum stabilization time was 3.76 s for the initial pose A_9; the stabilization time for A_{12} was relatively shorter, and that for all other initial poses did not exceed 1.44 s.

It is worth noting that in the above cases, the initial poses of postharvest cabbages (A4, A12 and A9) that required the longest angular motion stabilization time all corresponded to rotational motion about a principal axis of inertia other than the central axis. Nevertheless, no orientation failure was observed, and all initial poses were successfully oriented. In comparison with the orientation accuracy of cylindrical orientation rollers (6.72 ± 1.23°; *Cui et al., 2020*), the conical tread-based automatic orientation and conveying structure for postharvest cabbages thus exhibits superior orientation performance and efficiency.

Analysis of the experimental results on the performance optimization of automatic orientation based on conical treads

As shown in Table 2, range analysis indicated that the experimental factors affecting the orientation angle of postharvest cabbages were ranked by significance as follows: axial clearance > taper angle > linear velocity of the conveyor chain. The optimal parameter combination for achieving the target orientation angle was determined as $A_2B_3C_3$. Similarly, for the orientation success rate, the factors were ranked by significance in the order of taper angle > axial clearance > linear velocity of the conveyor chain, with the optimal parameter combination identified as $A_2B_3C_2$.

Table 2

Results of Postharvest Cabbage Cone Tread Orientation Orthogonal Experiment

Test number	*A*	*B*	*C*	Orientation angle (°)	Orientation success rate (%)
1	1	1	1	8.39	80.00
2	1	2	2	7.54	81.11
3	1	3	3	5.51	87.78
4	2	1	2	6.63	94.44
5	2	2	3	6.78	90.00
6	2	3	1	6.17	96.67
7	3	1	3	7.72	82.22
8	3	2	1	7.07	90.00
9	3	3	2	5.88	92.22
$k_{\delta 1}$	7.15	7.58	7.21		
$k_{\delta 2}$	6.53	7.13	6.68		
$k_{\delta 3}$	6.89	5.85	6.67		
R_{δ}	0.62	1.72	0.54		
$k_{\eta 1}$	82.96	85.56	88.89		
$k_{\eta 2}$	93.70	87.04	89.26		
$k_{\eta 3}$	88.15	92.22	86.67		
R_{η}	10.74	6.67	2.59		

Note: A is the taper angle of conical roller, B is the axial clearance, C is the linear velocity of the chain.

A comparison of the optimal parameter combinations for the orientation angle and orientation success rate of postharvest cabbages shows consistency in the operational parameters for the taper angle and axial clearance of the conical orientation rollers: specifically, the taper angle at A_2 and axial clearance at B_3. In contrast, a variation was observed in the linear velocity of the conveyor chain.

Notably, the orientation success rate was relatively high at conveyor chain linear velocity C_2, and the orientation angle achieved at this velocity was essentially identical to that obtained at C_3. For this reason, conveyor chain linear velocity C_2 was selected, yielding the overall optimal parameter combination of $A_2B_3C_2$ for the conical orientation of postharvest cabbages.

Meanwhile, analysis of variance (ANOVA) was performed on the test results to judge whether the effect of each factor possessed statistical significance. Specifically, the ANOVA results for orientation deflection angle are listed in Table 3. The F-values of the three factors followed the order axial clearance > taper angle > linear velocity of the conveyor chain, which was entirely consistent with the factor sequence obtained from range analysis. Nevertheless, all F-values were far lower than the critical value at the significance level of 0.05. This indicated that within the parameter range selected for the test, none of the three factors induced statistically significant differences in the orientation angle. This phenomenon could be attributed to the compensation effect among different factor levels a smaller axial clearance can make up for the insufficient lateral friction torque for automatic orientation generated by rollers with a small taper angle, which restrains drastic fluctuations of cabbage orientation deflection angle as a whole and ultimately weakens the statistical discrimination ability of a single factor.

Table 3

ANOVA Results of Orientation Angle

Factors	Sum of squares	Freedom	*F* value
A	0.582	2	0.293
B	4.814	2	2.421
C	0.569	2	0.286
Error	5.965	6	

The ANOVA results for orientation success rate are presented in Table 4. The sequence of F-values follows taper angle > axial clearance > linear velocity of the conveyor chain, consistent with the ranking derived from range analysis. The surface structure of conical rollers directly determines the lateral friction torque for automatic orientation that corrects the posture of cabbages, so the roller taper angle always acts as the dominant control variable to achieve stable orientation. However, the F-values of all factors remain below the critical value corresponding to the significance level of 0.05. This implies that within the parameter range set in this study, none of the factors exhibited a significant regulatory effect. Subsequent research can appropriately expand the value interval of factor levels and add more gradient levels to further explore their underlying influence rules.

Table 4

ANOVA Results of Orientation Success Rate

Factors	Sum of squares	Freedom	F value
A	173.091	2	2.009
B	73.591	2	0.854
C	11.786	2	0.137
Error	258.468	6	

Optimal parameter combination trial validation

Sixty randomly selected Zhonggan 15 cabbages were used as experimental samples to verify the postharvest orientation performance of the conical tread orientation and conveying device for postharvest cabbages, which was operated at a taper angle of 20°, an axial clearance of 60 mm, and a linear velocity of 300 mm/s for the conveyor chain. The experimental results are summarized in Table 5.

Table 5

Postharvest Cabbage Cone Tread Orientation Validation Test Results

Test number	Number of cabbage successfully orientated (piece)	Orientation success rate (%)	Orientation angle (°)
1	59	98.33	5.37
2	59	98.33	5.14

Test number	Number of cabbage successfully orientated (piece)	Orientation success rate (%)	Orientation angle (°)
3	60	100	4.53
4	59	98.33	5.39
5	59	98.33	5.92
6	60	100	4.81
7	60	100	5.47
8	59	98.33	5.04
9	58	96.67	5.2
10	59	98.33	4.89
Standard	59.20	98.67	5.18
Deviation	0.63	1.05	0.39

The results demonstrate that under this optimal parameter combination, the orientation success rate of postharvest cabbages reaches 98.67±1.05%, with the orientation angle at 5.18±0.39°. Further analysis on the processing capacity of the prototype indicates that the rack length of the rack-and-pinion pair is 1 m, namely the actual effective length of the orientation section is 1 m. At the optimal chain linear velocity of 300 mm/s, the corresponding cabbage residence time for orientation section is approximately 3.33 s, which provides sufficient duration to complete automatic orientation. For individual cabbages with occasional orientation failure, they can be identified, rejected and circulated back into the orientation mechanism for secondary posture adjustment. Meanwhile, the uniform feeding spacing between adjacent cabbages is set to 150 mm, and the calculated theoretical hourly throughput reaches 7200 cabbages per hour, which satisfies the demand for large-scale commercial processing of cabbages. There exists a trade-off between orientation performance and processing capacity. If higher production efficiency is required in practical application, the conveying speed can be moderately increased at the cost of reduced orientation accuracy. For precision rhizome cutting scenarios with extremely strict requirements on trimming quality, the chain conveying speed can be reduced to extend the residence time for orientation, sacrificing partial throughput to acquire more stable orientation performance. These findings further enhance the orientation performance of postharvest cabbages and provide more favorable technical conditions for subsequent commercial processing operations, such as root and stem trimming.

CONCLUSIONS

(1) Based on the moment of inertia and the principle of minimum action, this study develops an automatic conveying and orientation device for postharvest cabbages equipped with conical tread rollers. The axially variable-diameter tread surfaces of conical rollers generate lateral friction torque acting on cabbages, counteracting orientation deviation caused by non-homogeneous mass distribution and axial offset of the mass center, and guiding cabbages to rotate steadily around their minimum inertia axis to achieve automatic orientation. Meanwhile, ADAMS dynamic simulation results reveal that cabbages with 26 types of initial poses can all complete automatic orientation on this device, with the maximum posture stabilization convergence time reaching 5.42 s, which further verifies the superiority and feasibility of the conical tread orientation mechanism.

(2) Range analysis and analysis of variance (ANOVA) of orthogonal tests indicate that the significance order of experimental factors affecting the orientation deflection angle of postharvest cabbages is axial clearance > taper angle > linear velocity of the conveying chain. The significance order of factors influencing orientation success rate is taper angle > axial clearance > linear velocity of the conveying chain. Within the parameter range set in this study, none of the experimental factors exerted a statistically significant regulatory effect on the orientation deflection angle or orientation success rate of postharvest cabbages. Future research can appropriately expand the value range of factor levels and add more gradient levels to further explore their underlying influence rules.

(3) The optimal combination of operating parameters was determined as follows: taper angle of 20°, axial clearance of 60 mm, and conveying chain linear velocity of 300 mm/s. Under this working condition, the orientation success rate reaches 98.67±1.05%, the average orientation deflection angle is 5.18±0.39°, and the theoretical processing throughput is 7200 cabbages per hour, which can basically meet the requirements of postharvest commercial treatment of cabbages. Nevertheless, all performance tests in this paper were only

carried out with the cabbage cultivar "Zhonggan No.15" as the research object, which brings certain limitations to this study. Follow-up research will investigate the automatic orientation adaptability of flatter, elongated and highly asymmetrical cabbage cultivars.

(4) Test results of the prototype performance reveal that occasional orientation failures are inevitable during long-term continuous orientation operation. Excluding failures caused by cabbage jamming due to oversized dimensions or cabbage slipping through roller gaps, all remaining failures stem from insufficient residence time for orientation. Cabbages rotating around non-central principal axes with large moments of inertia cannot complete automatic orientation within the limited available duration. To address the above problems, our research team plans to conduct follow-up studies on cabbage size grading and orientation posture recognition based on machine vision. Specifically, cabbages will be classified by size grading prior to orientation and delivered to dedicated orientation production lines matching their respective dimensions, so as to eliminate orientation failures induced by mismatches between cabbage size and structural parameters of the orientation device. After orientation, machine vision posture recognition will judge the orientation quality. Cabbages identified as orientation failures will be separated and recirculated into the orientation mechanism for secondary adjustment, thereby improving the orientation success rate for cabbages of various sizes.

ACKNOWLEDGEMENT

This work was supported by the China Postdoctoral Science Foundation (307923), the Henan Agricultural University High-Level Talent Special Support Fund (30501381), the Henan Provincial Science and Technology Special Envoys Program (30804295), and the Henan Provincial Key Scientific and Technological Research Program (242102111175).

REFERENCES

[1] Bennedsen BS. , Peterson DL., Tabb A. 2005. Identifying defects in images of rotating apples. *Computers and Electronics in Agriculture*, 48(2): 92-102 Kearneysville/West Virginia,DOI:10.1016/j.compag.2005.01.003

[2] Cui G P., Wang Z J., Wen S T., Wei Y Z., Cui Y J., Niu Z J. 2021. Design and Experiment of Post-Harvest Cabbage Individual Sorting and Orientation Conveying Device (采后甘蓝单体排序定向输送装置设计与试验). *Transactions of the Chinese Society for Agricultural Machinery,* 52 (6): 351-360 Yangling/Shaanxi, China. DOI: https://doi.org/10.6041/j.issn.1000-1298.2021.06.037

[3] Cui G P., Zheng X M., Cui Y J., Wang Z J., Shi Y G., Fu L S. 2020. Research on Automatic Orientation Method of Postharvest Cabbage Based on Moment of Inertia (基于转动惯量的采后甘蓝自动定向方法研究). *Transactions of the Chinese Society for Agricultural Machinery*, 51 (11): 183-195 Yangling/Shaanxi, China. DOI: https://doi.org/10.6041/j.issn.1000-1298.2020.11.020

[4] Cui Y J., Wang M H. (2023). Analysis of Research Progress in Automatic Orientation Technology in the Agricultural Field (农业领域自动定向技术研究进展分析). *Transactions of the Chinese Society for Agricultural Machinery*, 54 (04): 1-20 Yangling/Shaanxi, China. DOI: https://doi.org/10.6041/j.issn.1000-1298.2023.04.001

[5] Du D., Wang J., Xie L., Deng F. 2019. Design and field test of a new compact self-propelled cabbage harvester. *Transactions of the ASABE*, 62(5): 1243-1250 Hangzhou/Zhejiang, China. DOI: https://doi.org/10.13031/trans.13327

[6] FAOSTAT. 2026. Production of cabbages and other brassicas in 2024 [DB/OL]. Retrieved from http://www.fao.org/faostat/en/#data, 2026-1-11

[7] Kang N B., Qiang F., Wu L G., Wang S G., He J G. 2017. Design and Experiment of Fresh Jujube Grading Machine Based on Electromagnetic Synchronous Actuator (基于电磁式同步执行机构的鲜枣分级机设计与试验). *Transactions of the Chinese Society of Agricultural Engineering*, 33 (7): 254-260 Yinchuan/Ningxia, China. DOI: https://doi.org/10.11975/j.issn.1002-6819.2017.07.033

[8] Kang N B., Shang M Y., He J G., Liu G S., Wang S L., Wu L G. 2017. Design of a Chain Pneumatic Punching Automatic Seed-removing Machine for Dried Red Dates (链式气动冲切自动化干红枣去核机设计). *Transactions of the Chinese Society of Agricultural Engineering*, 34 (22): 19-26 Yinchuan/Ningxia, China. DOI: https://doi.org/10.11975/j.issn.1002-6819.2018.22.003

[9] Lefcourt AM., Narayanan P., Tasch U., Kim MS., Reese D., Rostamian R., Lo YM. 2009. Orienting apples for imaging using their inertial properties and random apple loading. *Biosystems Engineering*, 104(1): 64-71 Baltimore/Maryland, USA. DOI: https://doi.org/10.1016/j.biosystemseng.2009.06.002

[10] Lefcourt AM., Narayanan P., Tasch U., Rostamian R., Kim MS., Chen YR. 2008. Algorithms for parameterization of dynamics of inertia-based apple orientation. *Applied Engineering in Agriculture*, 24(1): 123-129 Beltsville/Maryland, USA. DOI：10.13031/2013.24152

[11] Li C Y., Ma X Z., Cheng H S., Chen Z. 2014. Design and Testing of a Lychee-Specific Pitting and Shelling Machine (荔枝定向去核剥壳机设计与试验). *Transactions of the Chinese Society for Agricultural Machinery*, 45 (8): 93-100 Guangzhou/Guangdong, China. DOI: https://doi.org/10.6041/j.issn.1000-1298.2014.08.015

[12] Li J., Zhang D X., Liu B. 2009. Design of Conveying and Tilting Mechanism for Apple Grading Machine (苹果分级机输送与翻转机构设计). *Transactions of the Chinese Society for Agricultural Machinery*, 40 (5): 158-161+157 Beijing, China.

[13] Lin J., Holmes M., Vinson R., Ge CR., Pogoda FC., Mahon L., Gentry R., Seibel GE., Chen X., Tao Y. 2017. Design and testing of an automated high-throughput computer vision guided waterjet knife strawberry calyx removal machine. *Journal of Food Engineering*, 211: 30-38 College Park/Maryland, USA. DOI: https://doi.org/10.1016/j.jfoodeng.2017.05.002

[14] Liu X D., Liang Q A., Li S., Liu X L., Zhang J. 2012. Design and Experiment of Single-channel Apricot Cutting and Pitting Machine (单通道杏切分去核机的设计与试验). *Xinjiang Agricultural Mechanization*, (6): 5-7 Urumqi/Xinjiang, China. DOI:10.13620/j.cnki.issn1007-7782.2012.06.013

[15] Liu X D., Wang X N., Wang C Y., Liu X L., Yang H M., Gan L X. 2016. Design and Experiment of a Differential Three-Channel Dynamic Orientation Conveying Device for Fresh Apricots (差速式三通道鲜杏动态定向输送装置设计与试验). *Transactions of the Chinese Society for Agricultural Machinery*, 47 (10): 35-43 Shenyang/Liaoning, China. DOI: https://doi.org/10.6041/j.issn.1000-1298.2016.10.005

[16] Mizushima A, Lu R. 2013. A low-cost color vision system for automatic estimation of apple fruit orientation and maximum equatorial diameter. Transactions of the ASABE, 56(3): 813-827 East Lansing/Michigan, USA. DOI:https://doi.org/10.13031/trans.56.9343

[17] Ren ZS., Sun SG., Xie G. 2010. A method to determine the two-point contact zone and transfer of wheel–rail forces in a turnout. *Vehicle System Dynamics,* 48(10): 1115-1133 Beijing, China. DOI: https://doi.org/10.1080/00423110903337281

[18] Wang X Y., Zhu S., Li X Q., Li T X., Wang L L., Hu Z X. 2020. Design and Experiment of a Potato Seed Tuber Cutter with Oriented Arrangement and Vertical-Horizontal Cutting (定向排列纵横切分马铃薯种薯切块机设计与试验). *Transactions of the Chinese Society for Agricultural Machinery*, 51 (6): 334-345 Zibo/Shandong, China. DOI: https://doi.org/10.6041/j.issn.1000-1298.2020.06.036

[19] Wang Z J., Cui G P., Zheng X M. 2021. Analysis of Motion and Damage in the Cabbage Flipping and Unloading Process Based on EDEM (基于 EDEM 的甘蓝翻转卸料过程运动与损伤分析). [J] *Journal of Agricultural Mechanization Research*, 43 (02): 16-22+77 Yangling/Shaanxi, China. DOI: https://doi.org/10.13427/j.cnki.njyi.2021.02.003

[20] Xiong W., Zhou L C., Yu H. 2025. Research Progress and Prospect of Sorting Technology and Equipment for Thin-Skinned Fruits and Vegetables (薄皮果蔬分选技术与设备研究进展与展望). [J] *Transactions of the Chinese Society for Agricultural Machinery*, 56 (08): 665-683

[21] Zheng X M., Cui G P., Wang Z J. 2021. Design and Experiment of Automatic Orientation Adjustment Device for Postharvest Trimming System of Cabbage (甘蓝采后整修系统自动调向装置设计与试验). *Journal of Agricultural Mechanization Research*, 43 (02): 64-70 Yangling/Shaanxi, China. DOI: https://doi.org/10.13427/j.cnki.njyi.2021.02.011

[22] Zheng X S., Wang C Y., Tang W B., Guo Y P., Lu F. 2015. Design of Orientation Conveying Mechanism for Chili Seed Removing Machine (辣椒去核机定向输送机构的设计). *Journal of Agricultural Mechanization Research*, 37 (10): 112-115 Urumqi/Xinjiang, China. DOI: https://doi.org/10.13427/j.cnki.njyi.2015.10.024

[23] Zhong X B., Tao G A., Luo Y Y., Yi X L. 2016. Optimisation Method for the Tread Profile of Independently Rotating Wheels (独立旋转车轮踏面外形优化设计方法). *Journal of Sichuan University of Science & Engineering (Natural Science Edition)*, 29 (3): 33-38 Zhuzhou/Hunan, China. DOI: https://doi.org/10.11863/j.suse.2016.03.08

KINEMATIC ANALYSIS AND OPTIMAL DESIGN OF THE SEPARATION CONVEYOR DEVICE FOR *PANAX NOTOGINSENG* COMBINE HARVESTER

Ibrahim Issa Mohamed ISSA[1,3*)], Zhaoguo ZHANG[1,2,3*)], Wael EL-KOLALY[4)], Altyeb Ali Abaker OMER[5)], Faan WANG[2,3)], Jie SONG[2,3)]

[1)] Faculty of Mechanical and Electrical Engineering, Kunming University of Science and Technology, Kunming 650500, China;
[2)] Faculty of Modern Agricultural Engineering, Kunming University of Science and Technology, Kunming 650500, China;
[3)] Research Center on Mechanization Engineering of Chinese Medicinal Materials in Yunnan Universities, Kunming 650500, China;
[4)] Agricultural Engineering Research Institute (AEnRI), Agricultural Research Center (ARC), Ministry of Agriculture, 256 Dokki, Giza, Egypt;
[5)] School of Tea and Coffee, Puer University, Puer, China

Corresponding authors: Ibrahim Issa Mohamed Issa, E-mail: ibrahimeisa14@gmail.com, Zhang Zhaoguo, E-mail: zzg@kust.edu.cn
DOI: https://doi.org/10.35633/inmateh-79-30

Keywords: *Panax notoginseng; Hilly and Mountainous Areas; Separation Conveyor; EDEM Simulation; SolidWorks*

ABSTRACT

Panax notoginseng is a high-value medicinal rhizome crop widely cultivated in the hilly and mountainous regions of southwest China, where traditional manual harvesting remains labor-intensive and inefficient. To address these challenges, this study focuses on the design, kinematic analysis, optimization, and validation of a separation conveyor device for a self-propelled Panax notoginseng combine harvester. The separation conveyor was developed based on the agronomic characteristics of Panax notoginseng and the mechanical requirements of soil-rhizome separation. A comprehensive methodology integrating theoretical modeling, kinematic and mechanical analysis, coupled discrete element-multibody dynamics (DEM-MBD) simulations using EDEM and RecurDyn, and laboratory experiments was employed. Key operational parameters, including conveyor speed, vibration frequency, and lifting angle, were systematically evaluated through quadratic regression and orthogonal experimental design. Simulation results indicated that effective soil separation could be achieved within 2.25 s, with fine soil particles separating earlier than larger aggregates. Laboratory tests identified optimal parameters of 0.8 m·s⁻¹ conveyor speed, 1.5 Hz vibration frequency, and a 20° lifting angle. Field validation experiments confirmed the reliability of the optimized design, achieving average separation and conveying rates of 96.87% and 96.42%, respectively, with a low rhizome damage rate of 1.88%. The results demonstrate that the proposed separation conveyor provides an effective solution for mechanized harvesting of Panax notoginseng and offers valuable reference for similar rhizome crop harvesters.

INTRODUCTION

Panax notoginseng is unique to southwest China, a well-known rhizome-based traditional Chinese medicine with excellent medicinal and economic value, which removes blood stasis and prevents cardiovascular and cerebrovascular diseases (*Issa et al., 2025c; Jiang et al., 2022; Lin et al., 2022*). Flowers, leaves, stems, and rhizomes can all be used as medicine. Modern medical research has found that *Panax Notoginseng* is rich in saponins, flavonoids, and various amino acids (*Zhou et al., 2010*). It is mainly cultivated in hilly and mountainous areas (*Zhang et al., 2016; Zhaoguo et al., 2023*). *Panax notoginseng* is mainly produced in mountainous and hilly areas such as Yunnan, Guangxi, and Sichuan *(Guiyun and Ying, 2012; Guo Jingjing et al., 2014*). Yunnan Province is located in the southwest of China and has mountainous plateau terrain. 87.21% of Yunnan Province's land area is located in the 1000~3000m medium altitude area. Mountains, hills, plains, and terraces account for 88.64%, 4.96%, 4.85% and 1.55% of Yunnan Province's area, respectively. Most of them are hilly and mountainous (*Thomas, 1992*). In recent years, the *Panax notoginseng* industry has entered a stage of large-scale, base-based, and standardized development *(Lihong et al., 2017*). However, *Panax notoginseng* is mainly harvested by traditional manual harvesting, which has low harvesting efficiency, high labor intensity, and is time-consuming and labor-intensive *(Zhenmeng et al., 2018*). Mechanized harvesting of *Panax notoginseng* can reduce farmers' work intensity and improve work efficiency *(Faan et al., 2024*).

Guo Siwei and others designed and developed a self-propelled *Panax notoginseng* combine harvester. The machine consists of an excavator, a primary conveying and separation device, a secondary conveying and separation device, a lifting device, a collection device, a hydraulic transmission system, a control system, and a crawler system. It integrates excavation, separation, conveying, and collection, achieving mechanized harvesting of *Panax notoginseng* and effectively reducing labor intensity (*Siwei, 2024*).

There is limited research on separation conveyor devices for rhizome crop harvesters from research institutes, while most research comes from agricultural machinery manufacturers (*Issa et al., 2025b*). For example, Johnson et al. applied the separation conveyor device to the technology of separation and loading conveyance using a hydraulic system to achieve highly controllable separation and conveying. The American Lockwood company developed a potato harvester that uses two-stage separation and conveying technology to load the harvester into the collection box, thereby improving separation and conveying efficiency *(Yitao et al., 2020*). The Japanese Matsuyama GSA600 harvester uses a rubber conveyor belt to improve durability without damaging rhizome and tuber tissue. The vibration device uses a three-speed adjustable setting to deliver different vibration frequencies for various crops and soil conditions (*Cheng et al., 2023*).

Recent research on conveying and separation devices for rhizome crop harvesters in China has primarily used DEM-MBD coupling simulations to design separation and conveying devices, study the movement of rhizomes and soil during the separation process, and assess the crushing effect *(Chen et al., 2024; Issa et al., 2025a; Wang et al., 2023b; Wang et al., 2023c*). For example, Wei Zhongcai from Shandong University of Science and Technology designed a wave-shaped conveyor suitable for potatoes *(Zhongcai et al., 2020*). To address the issue of high potato damage and skin breakage rates, he analyzed the key factors and structural parameters of the potato-soil separation process, utilizing a dual separation method that combines vibration and wave techniques to reduce these rates; additionally, Wang Feng from Gansu Agricultural University designed a double-layer separation conveyor for Pinellia Ternata, which employed a method of first conveying and then separating, while configuring the separation operation separately to enhance the rhizome-soil separation effect (*Feng, 2022*).

In summary, most rhizome and tuber harvesters in China, especially those for Chinese medicinal materials, have simple structures, small operating widths, and are mostly specialized harvesters for single medicinal materials. The conveying and separation components mainly include bar-type lifting chains, connecting-rod vibrating conveyors, roller conveyor chains, and cylindrical screens. In combination with previous research, the heavy soil in the *Panax notoginseng* planting area makes rhizome and soil separation more difficult, and the *Panax notoginseng* rhizome is rigid. It is challenging to break parameters during the conveying and separation process. Therefore, to ensure the separation of the rhizome and soil.

This study focused on the development and optimization of a separation conveyor for a self-propelled *Panax notoginseng* harvester to improve soil–rhizome separation efficiency. The separation conveyor was designed using computer-aided design tools and analyzed through coupled discrete element and multibody dynamics simulations. EDEM and RecurDyn software were used to simulate the conveying and separation processes and investigate the interactions among soil particles, rhizomes, and conveyor components. Key operating factors, including conveyor speed, vibration frequency, and lifting angle, were systematically evaluated using quadratic regression analysis to identify optimal parameter combinations. Field experiments were conducted to verify the simulation model and assess separation performance under practical operating conditions. The combined simulation and experimental approach provided a scientific basis for optimizing the structure and operating parameters of the separation conveyor system.

MATERIALS AND METHODS

Self-propelled combine harvester structure and working principle

Based on the agronomic conditions for *Panax notoginseng* cultivation in Yunnan and the basic physical parameters of *Panax notoginseng* and the soil, a self-propelled *Panax notoginseng* combine harvester was designed. *Panax notoginseng* is mainly planted in hilly and mountainous areas. Considering the influence of slopes, the entire machine should be smaller to meet the working requirements and deliver excellent performance. At the same time, it should meet the design requirements of relevant national and local standards. The strong adaptability and possibility of the crawler chassis, which can turn around at the end of fields, and adapt to different working conditions. Therefore, this study aims to design key components of a crawler self-propelled *Panax notoginseng* combined harvester to enable joint operations for *Panax notoginseng* excavation, separation, transportation, lifting, collection, and unloading, thereby adapting to small-plot operations in hilly and mountainous areas.

The *Panax notoginseng* combine harvester designed in this research comprises an excavation device, a separation conveyor device, a lifting device, a collection device, an engine, a hydraulic caterpillar chassis, and a wheelhouse, as shown in Figure 1. The entire vehicle utilizes hydraulic control. The engine drives the hydraulic pump, supplying power to the combine harvester. The hydraulic valve group then distributes this power to each system, moving the hydraulic motor and hydraulic cylinder to enable walking and harvesting operations.

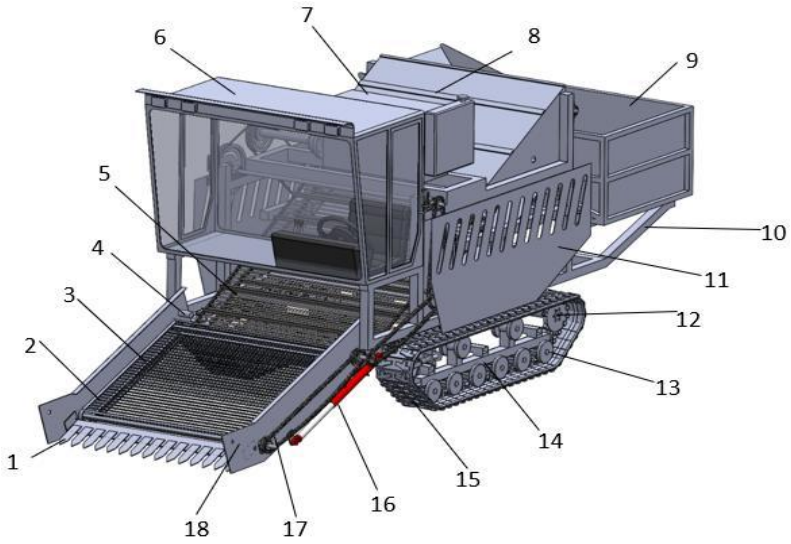


Fig. 1 - Self-propelled *Panax Notoginseng* Combine Harvester

1. Excavation shovel; 2. Separation conveyor; 3. Vibration device; 4. Pillar; 5. Lifting device 6. Wheelhouse; 7. Engine; 8. Lifting device cover 9. Collecting box; 10. Chassis; 11. Frame; 12. Drive wheel; 13. Support wheels; 14. Crawler chassis walking frame; 15. V Rubber tracks; 16. Hydraulic cylinder for collecting box; 17. Transmission chain18. Separation conveyor device frame.

When the *Panax notoginseng* combine harvester is operating, the excavation shovel is aligned with the *Panax notoginseng* ridge and the corresponding height is adjusted to meet the depth and angle of *Panax notoginseng* harvesting; the speed of the separation conveyor and the vibrating wheel are adjusted so that the excavated *Panax notoginseng* rhizome-soil complex can achieve a relatively ideal separation effect during the soil separating operation; the excavation shovel digs and crushes the *Panax notoginseng* rhizome-soil complex to facilitate the subsequent conveying and soil removal process; the separation conveyor is transported backward, and the *Panax notoginseng* rhizome-soil complex is shaken by the vibrating wheel to achieve soil removal; the *Panax notoginseng* after soil removal is thrown from the separation conveyor to the lifting device, and transported upward under the drive of the chain; after reaching the top, it is thrown into the aggregate box to complete the entire harvesting operation; after the collection is completed, the hydraulic cylinder flips it over to complete the unloading operation.

Design and analysis of the separation conveyor device

The separation conveyor is designed to separate soil from rhizomes and transport them. In contrast, the lifting device's primary role is transportation. During operation, the excavation device gathers the rhizome-soil mixture and delivers it to the separation conveyor. Here, soil is removed, and the *Panax notoginseng* rhizomes are conveyed onward. Finally, the cleaned rhizomes, along with any residual soil, are transferred to the lifting device for further transport.

Commonly used conveying devices can be divided into belt conveyor, roller push-type, chain-type lifting, bucket elevator, and throwing wheel type, according to structural form. Among them, the bar-type structure is more suitable for harvesting *Panax notoginseng* rhizome. It is simple to operate and has strong separation performance. It can ensure good conveying capacity at a large lifting angle (*Issa et al., 2020; Xiaohong, 2023*). It mainly includes guide wheels, plum blossom-shaped drive wheels, lifting chains, vibration wheels, driven wheels, and supporting wheels. After *Panax notoginseng* is excavated, it enters the separation conveyor device. During transport, fine impurities are directly deposited on the ridge through the bars. Part or all of the rhizome-soil complex, and large soil blocks, are further separated from the vibration wheel by vibration and then transported to the lifting device of the working components. The three-dimensional model of the separation conveyor components is shown in Figure 2. The primary power source is hydraulic transmission.

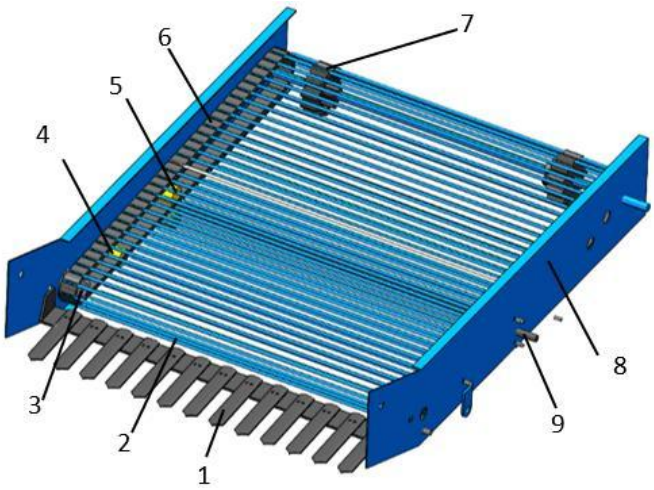


Fig. 2 - Structural diagram of the separation conveyor device

1. Excavation shovel; 2. Rod; 3. Driven wheel; 4. Supporting wheel 5. Vibration device; 6. Separation conveyor belt; 7. Drive wheels; 8. Separation conveyor frame; 9. Vibration device pillar

The working principle is that the excavation device removes the *Panax notoginseng* rhizome-soil complex, and the complex is transported to the separation conveyor device by friction and inertia. The soil is then broken, separated, and dropped by the vibration wheel. Finally, the *Panax notoginseng* is thrown to the lifting device at the rear end of the lifting chain. The main technical parameters are shown in Table 1.

Table 1

Main technical parameters of the separation conveyor device

Parameter	Numerical value
Device diameters (length × wide × Height)	1988×1540×1080 mm
Device weight	410 kg
Number of harvested ridges	1
Working width	1500 mm
Operating speed	≥0.4 m/s
Conveying speed	0.4 ~ 1.0 m/s

According to the previous planting site survey, the working width was determined to be 1500 mm. According to the design requirements of the bar elevator in the Agricultural Machinery Design Manual (*Hongwei, 2024*). The conveyor belt length should be 1200~1500 mm, and the selected length is 1400 mm. The bar gap was determined based on the minimum triaxial dimensions of the *Panax notoginseng* rhizome-soil complex. According to the previous research, the bar diameter was selected as 12 mm, the bar gap was 38 mm, and the bar center distance was 50 mm, as shown in Figure 3.

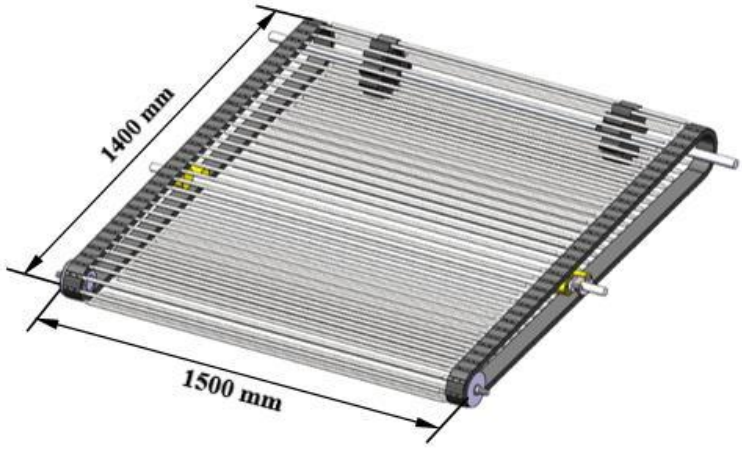


Fig. 3 - Separation conveyor size

On rhizome harvesters in many countries around the world, the distance between the harvester bars on the vibrating screen is 25~28 mm, 40~48 mm in the United States, and 30~40 mm in Japan and South Korea (*Wang et al., 2025; Zhaoguo et al., 2021*). The two-dimensional design scheme of the bar is shown in Fig. 4.

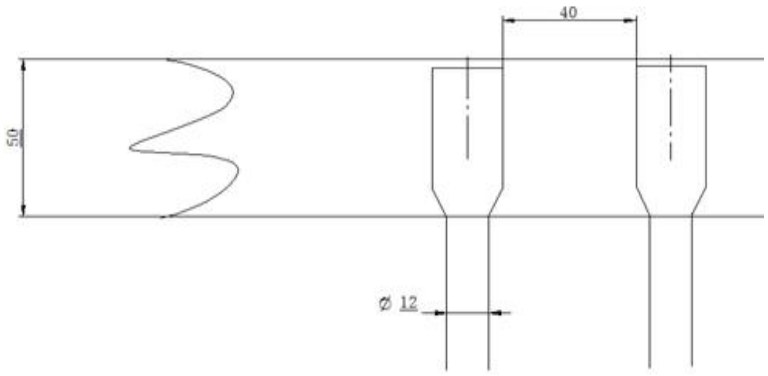


Fig. 4 - Design scheme of the bar

Determination of the drive wheel

The driving wheel is the main working part of the *Panax notoginseng* combined harvester movement transmission. It is also the main power-consumption component, driving the rotation of the entire conveyor belt and the movement of the vibration wheel, driven wheel, and supporting wheel. The actual production of the drive wheel is also complicated. The wheel hub is made of metal material and covered with plum blossom rubber. It is fixed on the drive shaft with a flange. The rotary shaft is first processed during manufacturing. Then the caster is matched with the conveyor belt to ensure the thick elastic rubber on the surface of the rotary shaft is matched. Through the driving wheel and the conveyor belt, the line contacts the flexible curved surface during movement, reducing rigid contact between the harvester parts and increasing overall harvester reliability. Due to the large span of the conveyor belt, four drive wheels are arranged symmetrically in pairs. The drive wheel is shown in Figure 5.

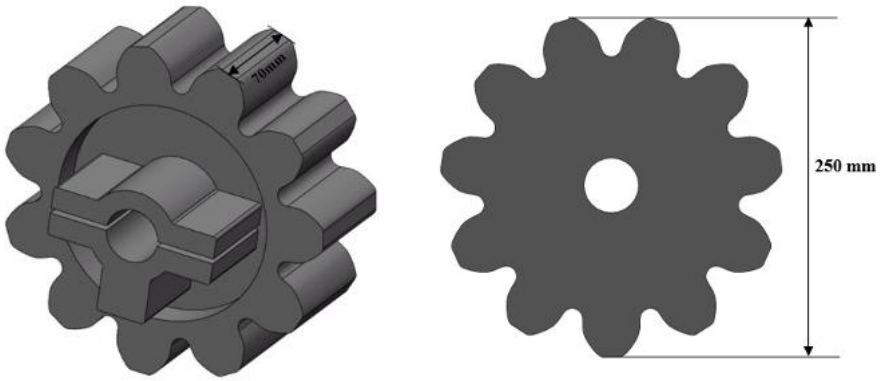


Fig. 5 - Drive wheel diagram

The separation conveyor speed is a key parameter of the separation conveyor device and is mainly controlled by the drive wheel. If the speed is too high, the vibration time of *Panax notoginseng* on the separation conveyor will be reduced, the rhizome-soil separation effect will be poor, the soil and impurities will not fall easily, and the excessive speed will also cause the tooth jump phenomenon; if the speed is too low, the soil will be piled up at the connection position between the excavation device and the separation conveyor device, reducing the harvesting efficiency. According to the supporting project's requirements, production efficiency should be ≥ 3 mu per hour. Combined with the operating width of the whole machine, it can be seen that the operating speed of the entire machine should be ≥ 0.38 $m \cdot s^{-1}$, so the speed of the separation conveyor should be greater than 0.38 $m \cdot s^{-1}$.

The drive wheel can be simplified as a polygonal rotating mechanism that drives the separation conveyor. By substituting the speed, number of teeth, and pitch into Eq. (1), the rotational speed *n* of the drive wheel can be obtained.

$$V_s = \frac{zpn}{60\times 1000} \quad (1)$$

where:

V_s is the separation conveyor speed [m·s^{-1}]; p is the pitch of the drive wheel [mm]; n is the drive wheel speed [r·min^{-1}]; z is the number of teeth of the drive wheel.

As shown in Figure 6, the velocity analysis of the separation conveyor indicates that the bar velocity can be decomposed into horizontal and vertical components.

$$\begin{cases} V_x = R\omega_1 cos\varphi' \\ V_y = R\omega_1 sin\varphi' \end{cases} \quad (2)$$

where:

R is the pitch radius of the drive wheel [mm]; ω_1 is the angular velocity of the drive wheel [rad·s^{-1}]; φ' is the phase angle [°], i.e. the angle between the line connecting the center of the bar with the center of the drive wheel and the vertical center line.

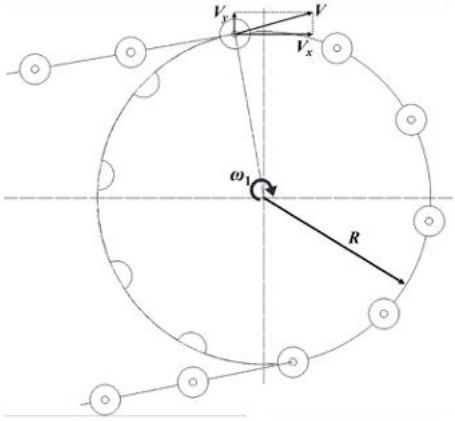


Fig. 6- Velocity analysis of the separation conveyor device

Based on the velocity analysis, the horizontal velocity component of the bar is responsible for conveying the material and therefore represents the conveying speed. Since the phase angle range is $-\frac{\pi}{2} \leq \varphi \leq \frac{\pi}{2}$, the following conclusions can be drawn.

$$\begin{cases} V_{\min} = R\omega_1 cos\frac{\pi}{2} = 0 \\ \varphi' = \pm\frac{\pi}{2} \end{cases} \quad (3)$$

When the phase angle is 90°, the separation conveyor bar and the drive wheel just come into contact and mesh, and the minimum lifting velocity is 0.

When the lifting velocity reaches its maximum value:

$$\begin{cases} V_{\max} = R\omega_1 \\ \varphi' = 0 \end{cases} \quad (4)$$

When the phase angle is 0, the bar coincides with the vertical centerline, and the velocity of the separation conveyor reaches its maximum value. At the next moment, the *Panax notoginseng* roots are thrown toward the lifting device. Therefore, to ensure smooth connection with the lifting-chain device, the radius and angular velocity of the drive wheel should be increased as much as possible. Accordingly, a drive wheel with 13 teeth, a diameter of 250 mm, and a width of 70 mm is selected and fixed to the drive shaft by means of a flange.

Determination of the vibration wheel

The vibration wheel is the main component of the separation conveyor device and the most critical component. The system realizes the rotation of the vibration wheel driven by the conveyor belt; the vibration wheel is an active double-roller vibration wheel (as shown in Figure 7). According to the overall configuration of the separation conveyor device and the transmission design requirements, the vibration wheel is installed between the front-driven wheel and the drive wheel. The upper part contacts the tight side of the conveyor belt. The single roller can rotate around its own fixed axis. The size is 70 mm in diameter and 75 mm in width. It is fixedly connected to the vibration shaft by a vibration wheel fixing plate.

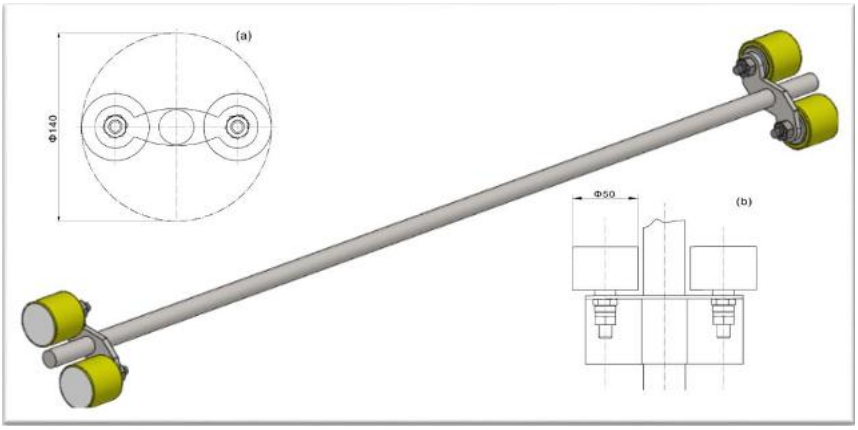


Fig. 7 - Structure diagram of the active vibration device

The active vibration device uses a hydraulic motor and is adjustable in speed. The vibration wheel shakes the separation conveyor twice for each rotation of the vibrating shaft. The vibration frequency is calculated as follows:

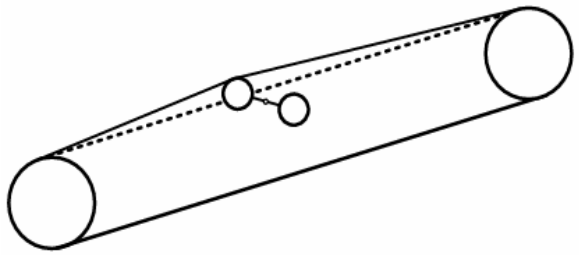


Fig. 8 - Vibration wheel working process diagram

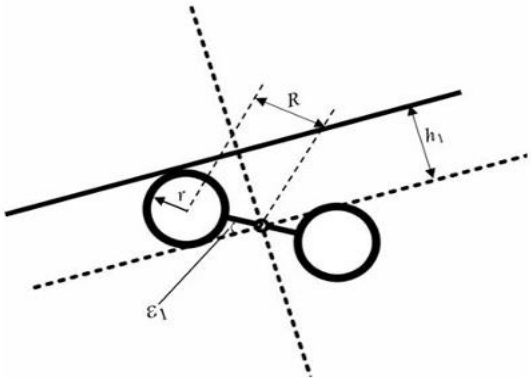


Fig. 9 - The vibration wheel lifts the separation conveyor

The calculation equation for the rotation angle of the vibration wheel is:

$$\varepsilon = \pm \arcsin\left(\frac{h_1 - r}{R}\right) + k\pi \quad (6)$$

where:

ε is the rotation angle of the vibration wheel [°]; h_1 is the distance between the vibration axis and the conveyor belt [mm]; r is the radius of the vibration wheel roller, [mm]; R is the distance from the origin to the center of the roller [mm]; k: natural number, k=0,1,2, …

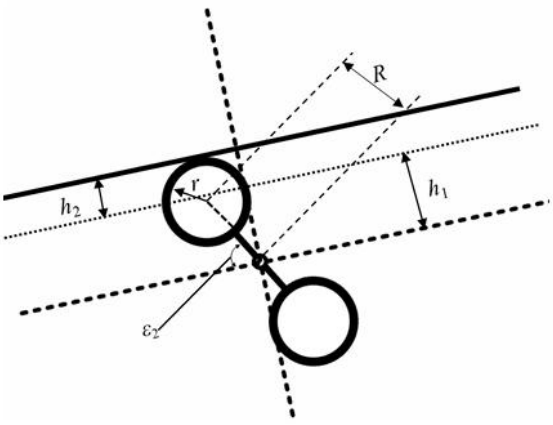


Fig. 10 - Schematic diagram of the conveyor belt lifted by the vibration wheel

As shown in Figure 10, when the vibration wheel lifts the conveyor belt, the contact point between the roller and the screen surface is displaced. The displacement can be divided into D_1 in the direction perpendicular to the conveyor belt and D_2 parallel to the conveyor belt. The displacement components are calculated using Eq. 7.

$$\begin{cases} D_1 = R|sin\varepsilon_2| + r - h_1 \\ D_2 = R|cos\varepsilon_1| - R|cos\varepsilon_1| \\ k\pi + \varepsilon_1 \geq \varepsilon_2 \geq (k+1)\pi - \varepsilon_1 \end{cases} \quad (7)$$

where:

ε_1 is the rotation angle before the vibration wheel lifts the screen surface [°]; ε_2 is the rotation angle after the vibration wheel lifts the screen surface [°].

The calculation equation for the rotation angle ε_2 after the vibration wheel lifts the screen surface is shown in equation 8.

$$\varepsilon_2 = \omega_2 t \quad (8)$$

where:

t is the rotation time of the vibration wheel (s).

Combining Eqs (7) and (8), the following equation can be obtained:

$$\begin{cases} D_1 = R|sin\omega_2 t| + r - h_1 \\ D_2 = R|cos\omega_2 t| - R|cos\varepsilon_1| \\ k\pi + \varepsilon_1 \geq \omega_2 t \geq (k+1)\pi - \varepsilon_1 \end{cases} \quad (9)$$

Taking the derivative of the above equation, the velocity of the screen contact point under the action of the vibration wheel can be obtained as follows:

$$\begin{cases} V_1 = \frac{Dd_1}{dt} = \omega_2 R\cos\omega_2 t \\ V_2 = \frac{Dd_2}{dt} = \omega_2 R sin\omega_2 t \end{cases} \quad (10)$$

The acceleration of the screen contact point under the action of the vibration wheel can then be obtained as follows:

$$\begin{cases} a_1 = \frac{dV_1}{dt} = {\omega_2}^2 R\sin\omega_2 t \\ a_2 = \frac{dV_2}{dt} = {\omega_2}^2 R\cos\omega_2 t \end{cases} \quad (11)$$

Mechanical analysis of the separation conveyor device

The movement of the *Panax notoginseng* rhizome on the separation conveyor device can be roughly divided into four stages (*Wang et al., 2023a*): from the front guide wheel to the front end of the vibration wheel, the vibration wheel action stage, from the rear end of the vibration wheel to the end of the drive wheel, and from the end of the drive wheel to the lifting chain device. Since the movement of the *Panax notoginseng* rhizome from the front guide wheel to the end of the drive wheel is similar, only the two movement conditions on the separation conveyor device, and when thrown out from the end of the drive wheel are discussed and analyzed.

The *Panax notoginseng* rhizome is transported along the inclined surface on the separation conveyor device. When the screen surface is approximated as a straight line, and the air resistance is not considered, the force analysis of the *Panax notoginseng* rhizome is performed, as shown in Figure 11. To ensure the smooth transportation of the *Panax notoginseng* rhizome and the separation of the rhizome and soil, the following conditions should be met:

$$\begin{cases} f_s - \mathrm{mgsin}\alpha_\mathrm{s} \geq \mathrm{ma_x} \\ F_\mathrm{N} - \mathrm{mgcos}\alpha_\mathrm{s} \geq \mathrm{ma_y} \end{cases} \quad (12)$$

where:

f_s is the friction between *Panax notoginseng* rhizome and screen surface, [N]; m is the mass of Panax notoginseng rhizome, [kg]; F_N is the support force of screen surface on *Panax notoginseng* rhizome, [N]; α_s is the angle between screen surface and horizontal plane, [N]; $\mathrm{a_x}$: tangential acceleration of *Panax notoginseng* rhizome along screen surface, m·s^{-2}; $\mathrm{a_y}$ is the normal acceleration of *Panax notoginseng* rhizome along screen surface, m·s^{-2}.

To ensure that the rhizome of *Panax notoginseng* is hit by the vibration wheel and thrown up, the following conditions should be met:

$$\begin{cases} \frac{mg}{z}\omega_2{}^2(R+r)cos\alpha_s > mg \\ \omega_2 = \frac{nb}{30} \end{cases} \quad (13)$$

where:

n is the vibration wheel speed, [r·min^{-1}]; b is constant, [b=π^2].

Simplifying equation (13), the vibration wheel speed should satisfy:

$$n > 30\sqrt{\frac{1}{(R+r)cos\alpha_s}} \quad (14)$$

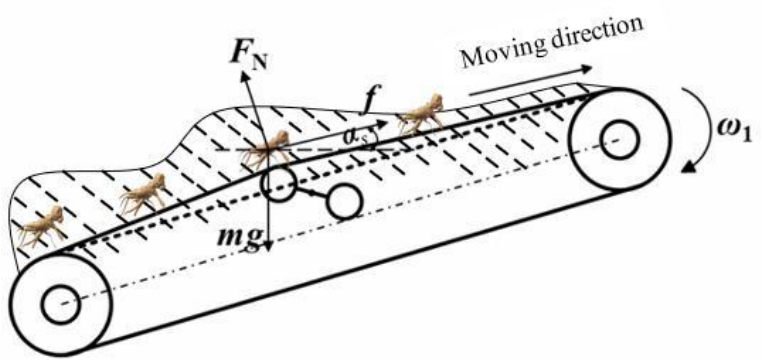


Fig. 11 - Mechanical analysis of the separation conveyor device

Analysis of the throwing motion at the end of the conveyor belt

After the rhizome of *Panax notoginseng* passes through the front end of the conveyor belt and the vibration wheel, it reaches the end and first does an oblique throwing motion, then a horizontal throwing motion, and finally goes to the lifting device. During the analysis, the screen surface is regarded as a plane, with the center of mass of the rhizome of *Panax notoginseng* as the origin, the horizontal right is the positive direction of the X-axis, and the vertical upward is the positive direction of the Y-axis. Without considering the air resistance, the displacement and velocity of the rhizome of *Panax notoginseng* are analyzed, as shown in Figure 12. Assume that the initial velocity of the rhizome of *Panax notoginseng* is v_a, which can be decomposed into the velocity vax in the X-axis direction and the velocity v_{ay} in the Y-axis direction, and satisfies the following relationship:

$$\begin{cases} v_{ax} = v_a cos\theta_s \\ v_{ay} = v_a sin\theta_s \end{cases} \quad (15)$$

where: θ_s: screen surface inclination [°]; v_{ax}: X-axis speed [m·s^{-1}]; v_{ay}: Y-axis speed [m·s^{-1}].

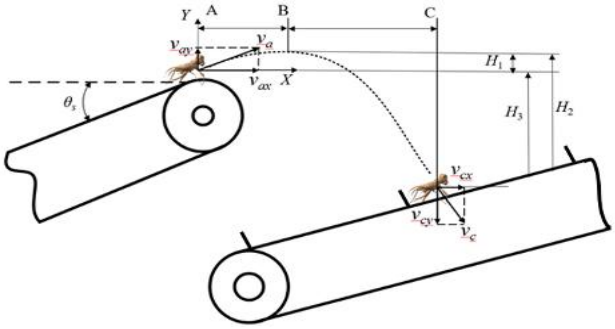


Fig. 12 - Throwing-motion analysis of *Panax notoginseng* rhizomes

The rhizome of *Panax notoginseng* performs oblique projectile motion in the AB section and horizontal projectile motion in the BC section. The displacement and velocity analyses of the two sections have been performed. The displacement analysis of the oblique projectile motion in the AB section is shown in equations (16), (17), and (18) since point B is the end point of the oblique projectile motion of the rhizome of *Panax notoginseng*, the vertical velocity v_{by} = 0 and the horizontal velocity v_{bx} = cosθ of the rhizome of *Panax notoginseng* at point B.

$$H_1 = \frac{v_{ay}{}^2}{2g} \quad (16)$$

$$X_1 = v_{\mathrm{ax}} t_1 \tag{17}$$

$$t_1 = \frac{v_{\mathrm{ay}}}{\mathrm{g}} \tag{18}$$

where:

H_1 is the vertical displacement of segment AB, [m]; X_1 is the horizontal displacement of segment AB, [m]; t_1 is the time taken for segment AB, [s]; g is the gravitational acceleration, [m·s^{-2}], g=9.8 m·s^{-2}.

The displacement analysis of the BC segment horizontal projection motion is shown in equations (19), (20), and (21):

$$H_2 = H_1 + H_3 \tag{19}$$

$$X_2 = v_{\mathrm{ax}} t_2 \tag{20}$$

$$t_2 = \sqrt{\frac{2H_2}{\mathrm{g}}} \tag{21}$$

where:

H_2 is the vertical displacement of BC segment, [m]; H_3 is the drop height of *Panax notoginseng* rhizome from the end of the separation conveyor to the lifting chain device, [m]; t_2 is the time taken for BC process, [s]. By combining and simplifying Eqs. (16)–(21), the displacement and time required for the *Panax notoginseng* rhizomes to be thrown from the end of the separation conveyor to the lifting-chain device can be obtained, as shown in the following equations:

$$H_2 = \frac{{v_{ay}}^2}{2\mathrm{g}} + H_3 \tag{22}$$

$$t = \frac{v_{\mathrm{ay}}}{\mathrm{g}} + \sqrt{\frac{2\left(\frac{{v_{ay}}^2}{2\mathrm{g}} + H_3\right)}{\mathrm{g}}} \tag{23}$$

$$t = v_{\mathrm{ax}}\left(\frac{v_{\mathrm{ay}}}{\mathrm{g}} + \sqrt{\frac{2\left(\frac{{v_{ay}}^2}{2\mathrm{g}} + H_3\right)}{\mathrm{g}}}\right) \tag{24}$$

Since point C is the end point of the horizontal motion, the horizontal velocity of point C $v_{\mathrm{cx}} = v_{\mathrm{a}}\cos\theta$, and the vertical velocity and the resultant velocity are shown in the following equation.

$$v_{\mathrm{cy}} = \mathrm{g}t_2 = \sqrt{{v_{ay}}^2 + 2gH_3} \tag{25}$$

$$v_{\mathrm{c}} = \sqrt{{v_{cx}}^2 + {v_{cy}}^2} = \sqrt{(v_a cos\theta)^2 + {v_{ay}}^2 + 2\mathrm{g}H_3} \tag{26}$$

In summary, the speed and displacement of *Panax notoginseng* rhizome from the end of the separation conveyor to the lifting device are primarily determined by the initial speed, screen surface inclination, and drop height. To ensure that the *Panax notoginseng* rhizomes can fall smoothly from the separation conveyor to the lifting device, the initial speed and drop height should be increased as much as possible, and the screen surface angle should be reduced. The conveying speed is taken as 0.6~1.4 m·s^{-1}, and the inclination angle is 15~35°.

Simulation analysis and test of the separation conveyor device

Establishing the separation conveyor simulation environment

Soil particle size and distribution data were measured, and the soil discrete element particle model was divided into three categories. The default spherical particles in EDEM were used. The soil particle shape, size, and proportions are shown in Table 2 and were added as the second category of bulk particles.

In RecurDyn, create a Wall file from the completed multibody dynamics model. Enable the RecurDyn-EDEM coupling interface and import the metal model's Wall file into EDEM's Geometry window, as shown in Figure 13. Create a solid thin plate at the bottom and end of the lifting chain to simulate the soil drop and the transition between the *Panax notoginseng* rhizome-soil complex and the next-level working component. Set the physical properties of the *Panax notoginseng* rhizome, soil particles, and metal model, enter the contact parameters, select the JKR contact model, and set the surface energy parameters for the contact.

Table 2

Soil discrete element particle model

Name	Model	Diameter / mm	Scale / %
Single spherical particles		1.6	33.9
Double-spherical particles		3.6	25.2
Triple-spherical particles		5.2	41.3

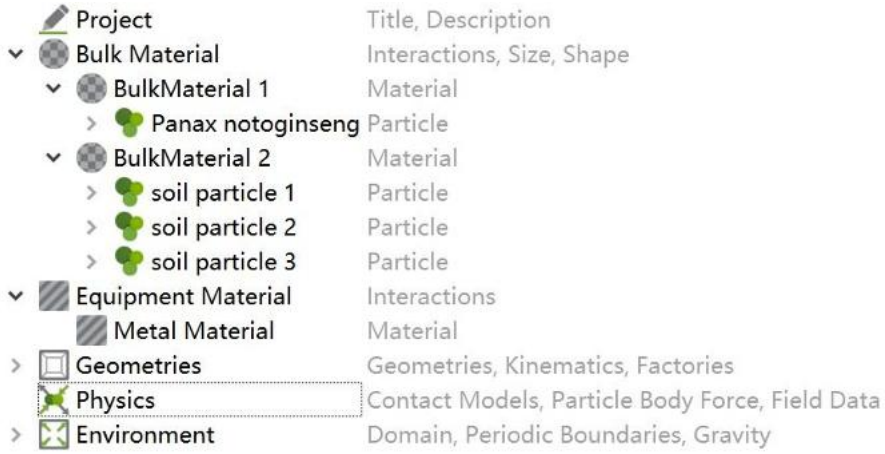


Fig. 13 - Establishment of granular and metallic materials

A virtual cube with an edge length of 0.2 m is generated at the front of the elevator chain. The Y-direction is defined as the gravity direction, and the acceleration is 0.98 m·s^{-2}, as shown in Figure 14.

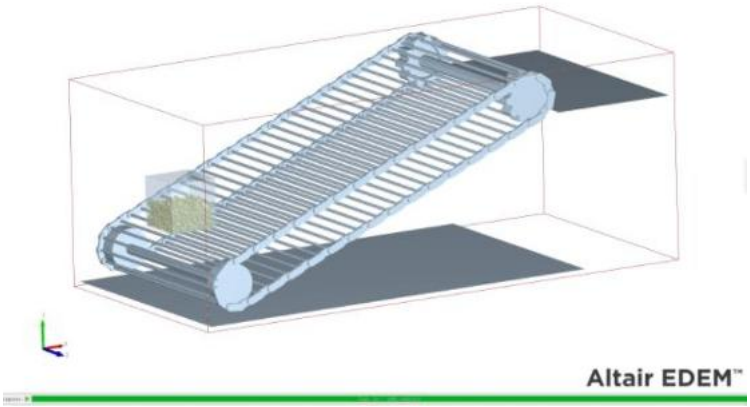


Fig. 14 - Establishment of coupled simulation environment

A discrete element model of the *Panax notoginseng* rhizome stem is generated within the box, enclosing a predetermined proportion of soil particles. This simulates the actual production process of the *Panax notoginseng* rhizome-soil complex as it is transported and separated by the elevator chain. At this point, the simulation environment is set up, and the coupled simulation can begin. Set the simulation time to 4 s and the step size to 0.01 s.

Simulation test results of the separation conveyor device

Overall movement of the *Panax notoginseng* rhizome-soil complex

The simulation results show that the rhizome-soil separation of the *Panax notoginseng* rhizome-soil complex was essentially complete within 2.25 seconds of simulation. Therefore, the main focus was on observing the conveying and separation movement characteristics of the *Panax Notoginseng* rhizome-soil complex during the period 0 to 2.2 seconds. The lifting velocity was 0.8 m·s^{-1} and the lifting angle was 25°, as shown in Figure 15.

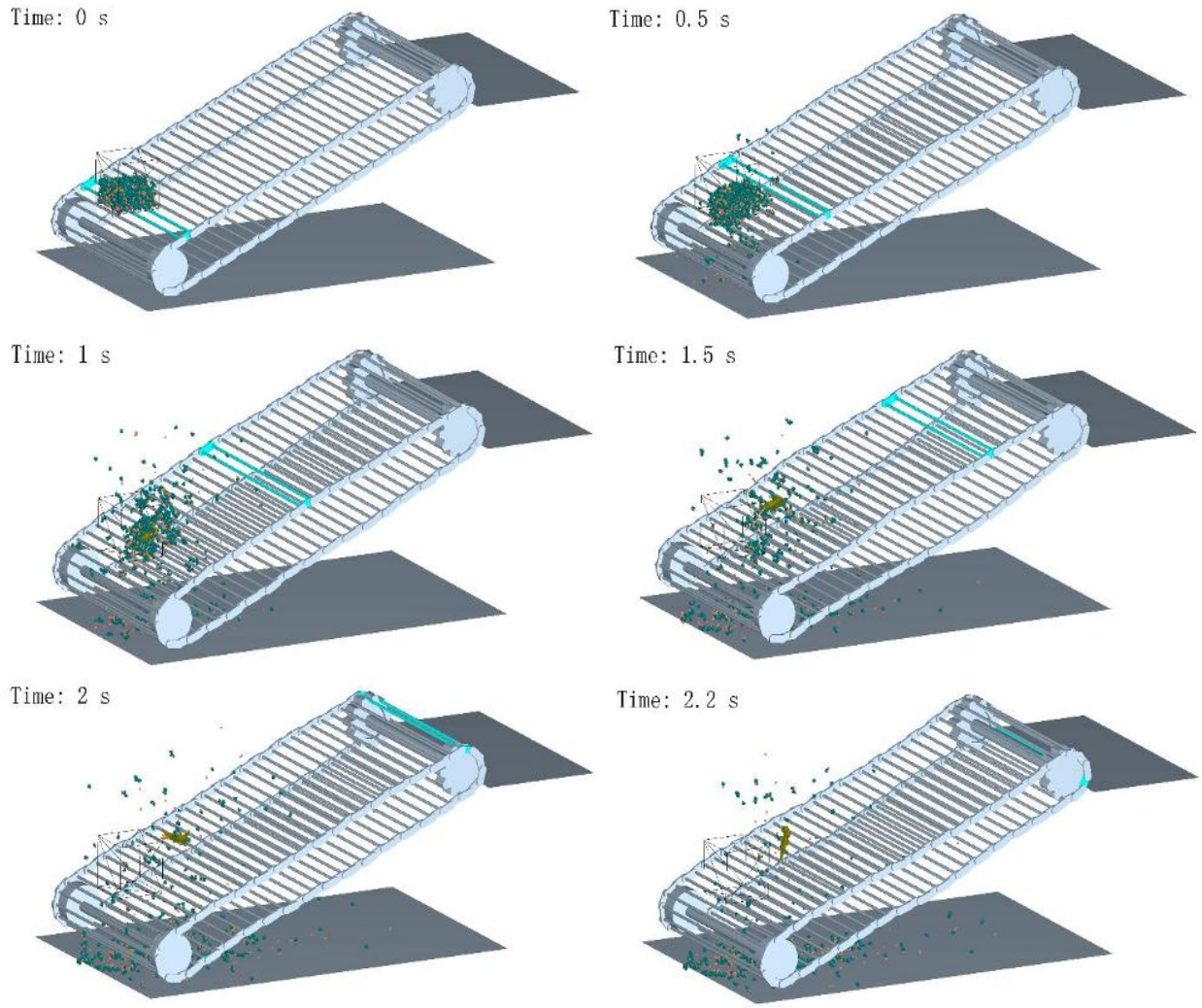


Fig. 15 - Movement trajectory of the *Panax notoginseng* rhizome-soil composite

To observe the relative motion of the *Panax notoginseng* rhizome soil complex and the lifting chain, use the blue bar below the virtual box as the observation point. The *Panax notoginseng* rhizome-soil complex freely falls onto the screen surface. Some loose, fine soil particles escape directly through the gaps between the bars, while the majority of the soil adheres to the surface of the *Panax notoginseng*. The relative friction between the *Panax notoginseng* rhizome-soil complex and the screen surface tends to transport the material diagonally upward. The vibration of the elevator chain gradually separates the *Panax notoginseng* roots from the soil particles, and the separation efficiency gradually increases as the amount of soil in the *Panax notoginseng* rhizome-soil complex decreases. Due to the low gravity, the soil particles are struck by the bars and scattered, resulting in significant variations in their velocities. However, the velocity of the *Panax notoginseng* rhizome on the screen surface does not change significantly, and the conveying speed is lower than the lifting speed. In EDEM post-processing, the *Panax notoginseng* particles were set to Steam mode. The *Panax notoginseng* rhizome exhibits "bouncing" and "backflowing" on the elevator chain. The degree of "bouncing" and "backflowing" becomes more pronounced as the number of soil particles attached to the rhizome decreases.

Rhizome-soil separation of Panax notoginseng rhizome-soil complex

To observe the effect of rhizome-soil separation in the coupled simulation of the *Panax notoginseng* rhizome-soil complex, the 3D Viewer-Setup Selections-Grid Bin Group function in the EDEM post-processing module was used to partition the particle computational domain. Three soil particle groups were selected for computational particle grouping. The dimensions and position of the Gind Bin Group were set, along with the number of bins. The computational domain was rotated along the Z-axis to an angle parallel to the elevator chain screen surface. Using a 0.4s time frame as an example, the soil particle computational domain partitioning is shown in Figure 16.

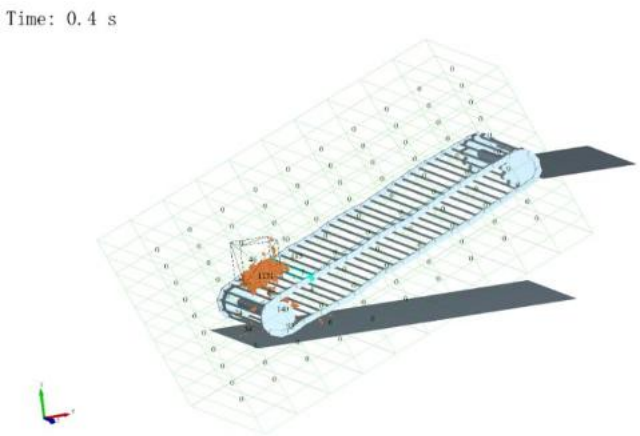


Fig. 16 - Gind Bin Group setting

The separation of the rhizome and soil in the *Panax notoginseng* rhizome-soil complex is expressed as the sieving rate. There are 1,800 soil particles of varying sizes and shapes. By counting the number of particles attached to the *Panax notoginseng* at each step, the sieving rate of the *Panax notoginseng* rhizome-soil complex can be calculated. The calculation equation is as follows:

$$Z_s = \frac{n_s}{N_s} \times 100\% \quad (27)$$

where: Z_s is the Simulated sieving efficiency of the *Panax notoginseng* root-soil complex, [%]; n_s is the Number of soil particles attached to the *Panax notoginseng*; T_s is the Total number of soil particles.

The sieving rate of the *Panax notoginseng* rhizome-soil composite was calculated for each step length, ranging from 0 to 2.20 seconds. The trajectory of soil particle motion is plotted in Figure 17. The sieving rate curve is plotted in Figure 18. Single spherical particles are purple, double spherical particles are orange, and triple spherical particles are green. The sieve clearance rate of the *Panax notoginseng* rhizome-soil complex increased rapidly within 0.25 s, then slowly increased until it approached 100%. This is because finely divided single-spherical particles separated preferentially; double-spherical particles separated in the middle section; and triple-spherical particles had strong adhesion to the *Panax notoginseng* rhizome, bouncing on the sieve surface with the *Panax notoginseng* and gradually separating.

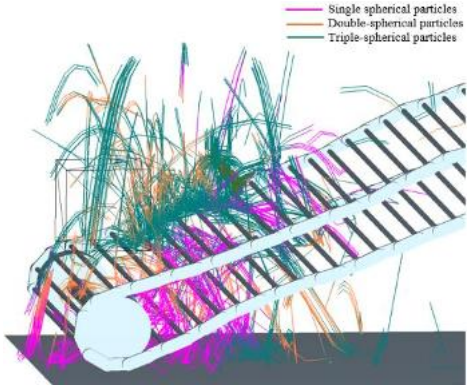


Fig. 17 - Soil particle motion trajectory

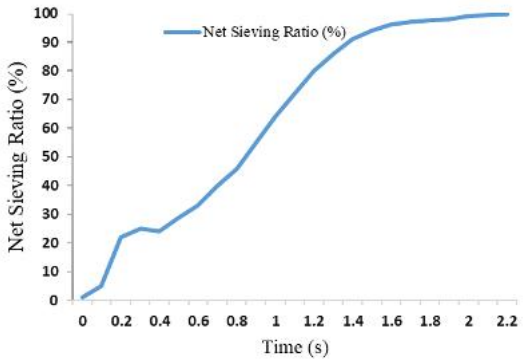


Fig. 18 - Sieve clearance rate curve

Dynamic analysis of Panax notoginseng rhizome

To investigate the motion and forces acting on *Panax notoginseng* rhizome on the separation conveyor, a triaxial force curve for *Panax Notoginseng* particles was plotted, as shown in Figure 19. At the front end of the separation conveyor, the *Panax Notoginseng* rhizome-soil complex exhibits high soil adhesion and is relatively heavy, making it difficult to lift. Therefore, from 0 to 0.75 s, the forces acting on the *Panax Notoginseng* rhizome are uneven and exhibit irregular variations. After 0.75 s, the forces acting on the *Panax Notoginseng* rhizome fluctuate dramatically at regular intervals, primarily due to the vibration of the separation conveyor. The moment the rod strikes the rhizome, the forces acting on the rhizome vary significantly. The *Panax notoginseng* rhizome is mainly subjected to the force in the X-axis and Y-axis directions on the inclined plane of the separation conveyor.

The friction between the *Panax notoginseng* rhizome-soil composite and the separation conveyor mainly provides the force on the X-axis. At the moment when the rod hits the *Panax notoginseng* rhizome, the *Panax notoginseng* rhizome is mainly subjected to the force in the normal direction of the separation conveyor, which is manifested as the force in the positive direction of the Y-axis and the force in the negative direction of the X-axis. After being thrown up, the force received by the *Panax notoginseng* is the gravity in the negative direction of the Y-axis, and the forces on the X-axis and Z-axis are close to zero.

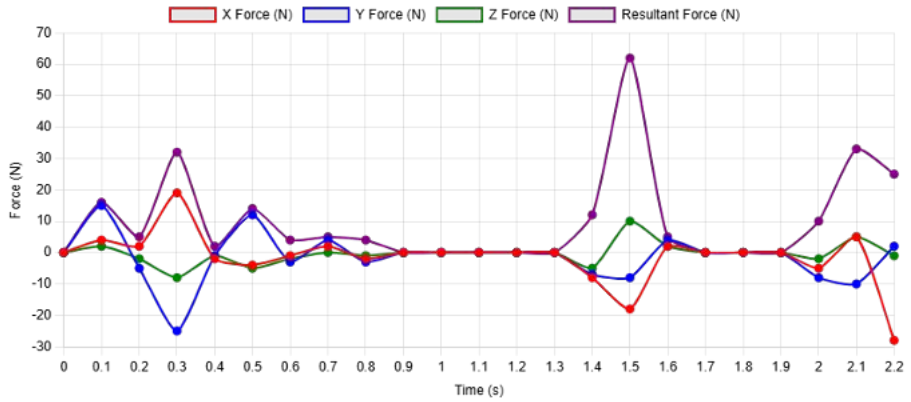


Fig. 19 - Force variation curve of Panax notoginseng rhizome

The forces acting on the three axes of the *Panax notoginseng* rhizome drive the changes in its velocity along these three axes, as shown in Figure 20. The velocity on the Z axis changes slightly, at around 0 $m \cdot s^{-1}$, indicating that the movement of the *Panax notoginseng* rhizome in the axial direction of the rod is not apparent; the velocity on the X axis is positive within 0-1.7 s, indicating that the *Panax notoginseng* lifting effect is significant; the velocity on the X axis is negative within 1.7-2.2 s, indicating that the movement direction of the *Panax notoginseng* rhizome is rolling downward along the separation conveyor, with "backflow" occurring; the velocity on the Y axis fluctuates regularly in the positive and negative directions, indicating that the *Panax notoginseng* rhizome vibrates significantly on the separation conveyor, and the greater the fluctuation amplitude, the greater the height to which the Panax notoginseng is thrown.

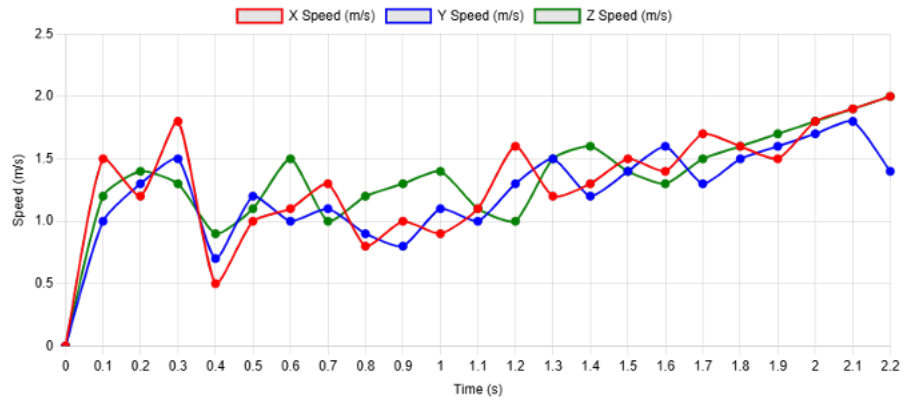


Fig. 20 - Speed variation curve of *Panax notoginseng* rhizome

Lab Test of the separation conveyor

To assess the performance of the separation conveyor device in the *Panax notoginseng* harvester, a bench test was conducted at the Research Center on Mechanization Engineering of Chinese Medicinal Materials in Yunnan. The lab test utilized a separation conveyor device capable of adjusting multiple operational parameters. The drive shaft's height, which influences the lifting angle, is adjustable via a two-link worm-gear lift, while vibration amplitude is controlled by varying the distance between the vibration shaft and the working surface. An inverter controls the conveyor's speed and vibration frequency by driving two three-phase asynchronous motors. The frame comprises a 6 mm-thick Q235 steel plate and a galvanized square tube, with adjustment mechanisms for inclination angle and vibration amplitude, facilitated by a drive shaft and laser-cut sliding grooves. Asynchronous motors power two turbine screw lifters synchronously to maintain the setup's stability. The primary *Panax notoginseng* harvester separation conveyor device is shown in Figure 21.

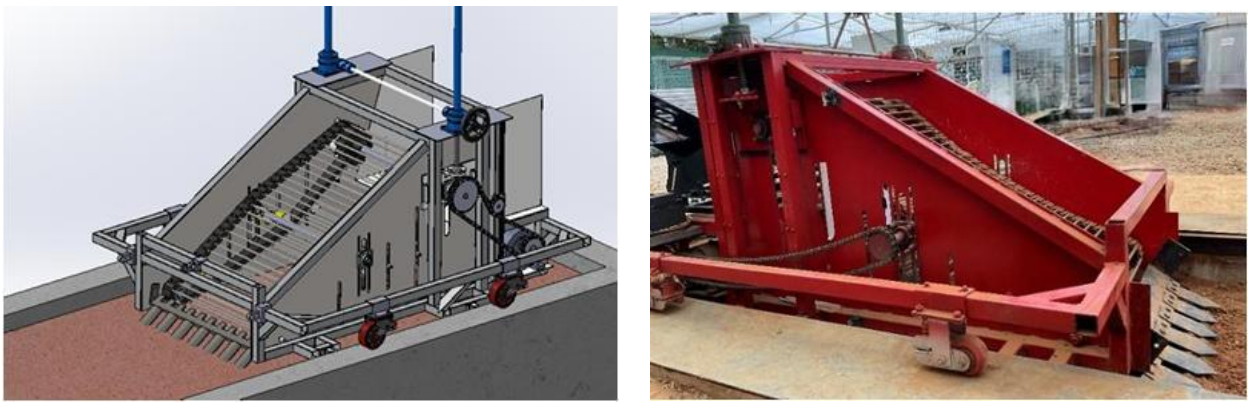


Fig. 21 - The separation conveyor device lab test prototype

Test plan and evaluation indicators

According to theoretical calculations and operational requirements, the main factors affecting the performance of the separation conveyor device are conveyor speed, conveyor inclination angle, and vibration frequency. Referring to the design and analysis of key component parameters, it is known that the conveyor inclination is changed by adjusting the platform separation conveyor device, and the preset range is 15°~35°; the YVR-1 digital tachometer of Yatai Optoelectronics is used to measure the conveying shaft speed of the two three-phase asynchronous motors under no-load conditions (Figure 22). The conveyor drive wheel ratio converts the drive wheel and vibration wheel speeds, and then the conveyor speed and vibration frequency are calculated. The preset conveyor speed is 0.6~1.4 m·s^{-1}, and the preset vibration frequency is 1~3 Hz.



Fig. 22 - Rotational speed measurement

Experiments were conducted to determine the optimal operating parameters of the separation conveyor device, using the separation and conveying rates as evaluation criteria. The conveying rate Y_1 refers to the ratio of the number of *Panax notoginseng* transported by the separation conveyor to the next stage of working components within a specific period to the number of *Panax notoginseng* entering the separation conveyor, and the calculation equation is:

$$Y_1 = \frac{N}{M} \times 100\% \tag{28}$$

where: Y_1 is the conveying rate, [%]; N is the number of particles passing through the separation conveyor; M is the number of particles entering the separation conveyor.

The separation rate Y_2 is the percentage of the actual mass of the separated material to the mass of the material that should be separated. The mass of soil and other impurities separated by the separation conveyor device per unit time, and the mass of impurities attached to the rhizome of *Panax notoginseng* after separation, are measured to facilitate detection of the separation process. The separating rate calculation equation is:

$$Y_2 = \frac{m_1}{m_1+m_2-m_3} \times 100\% \tag{29}$$

where: Y_2 is the separation rate, [%]; m_1 is the mass of impurities separated after separating, [g]; m_2 is the mass of *Panax notoginseng* rhizome and soil after separating, [g]; m_3 is the mass of *Panax notoginseng* rhizome, [g].

Orthogonal test design

To explore the influence of each experimental factor and its interaction on the quality of conveying and separation operation, the lifting speed X_1 is 0.6, 0.8, and 1.0 m·s^{-1}, the vibration frequency X_2 is 1 Hz, 1.5 Hz, and 2 Hz, and the lifting angle X_3 is selected as 15°, 20°, and 25°. The conveying and separating rates are used as experimental indicators in the orthogonal rotation combination test for quadratic regression (Figure 23). The level coding of the experimental factors is shown in Table 3.



Fig. 23 - Separation conveyor device lab test

Table 3

Experimental factors and codes

Code	Experimental factor		
	Lifting speed X_1/m·s^{-1}	Vibration frequency X_2/Hz	Lifting angle X_3 /°
1.682	1.14	2.34	28.40
1	1.0	2.0	25
0	8.0	1.5	20
-1	0.6	1.0	15
-1.682	0.46	0.66	11.60

Orthogonal Experimental results

The Experimental plan and results are shown in Table 4. A total of 23 test groups were conducted, and the test was repeated 3 times at each combination level. The arithmetic mean was taken as the test value of the conveying and separating rates.

Table 4

Experimental plan and results

Serial Number	Factor			Conveying rate	Separation rate
	X_1	X_2	X_3	Y_1/%	Y_2/%
1	-1	-1	-1	92.45	90.78
2	1	-1	-1	91.63	92.02
3	-1	1	-1	82.96	92.47
4	1	1	-1	88.69	91.21
5	-1	-1	1	92.47	90.18
6	1	-1	1	94.33	91.62
7	-1	1	1	87.58	93.07
8	1	1	1	96.85	93.31
9	-1.682	0	0	82.36	90.29
10	1.682	0	0	90.72	93.00
11	0	-1.682	0	94.74	90.89
12	0	1.682	0	90.14	93.94
13	0	0	-1.682	92.15	92.57
14	0	0	1.682	92.84	94.11
15	0	0	0	95.63	93.92
16	0	0	0	95.74	94.44

Serial Number	Factor			Conveying rate	Separation rate
	X_1	X_2	X_3	Y_1/%	Y_2/%
17	0	0	0	94.97	94.36
18	0	0	0	96.04	93.98
19	0	0	0	95.47	94.25
20	0	0	0	96.16	94.23
21	0	0	0	94.89	94.08
22	0	0	0	95.72	94.35
23	0	0	0	95.36	94.00

$$Y_1 = 95.53866 + 2.20391X_1 - 1.65008X_2 + 1.21982X_3 + 1.74500X_1X_2 + 0.777500X_1X_3 + 1.25750X_2X_3 - 3.04412{X_1}^2 - 0.958665{X_2}^2 - 0.939224{X_3}^2 \quad (30)$$

$$Y_2 = 94.19028 + 0.455272X_1 + 0.775363X_2 - 0.314116X_3 - 0.462500X_1X_2 + 0.212500X_1X_3 + 0.462500X_2X_3 - 1.00566{X_1}^2 - 0.733492{X_2}^2 - 0.406535{X_3}^2 \quad (31)$$

Design-Expert 13 software was used to analyze the conveying and separation rates test results using variance ANOVA. The significance test results are shown in Table 5. The results in the table show that the experimental model is highly statistically significant ($p < 0.0001$), indicating that the designed test is reasonable and practical. The determination coefficient R^2 for Y_1 and Y_2 are 0.9589 and 0.9360, respectively, implying that the regression equation has a high degree of fitting; in summary, the models can be used for analysis and optimization. The experimental factors lifting speed X_1, vibration frequency X_2, and lifting angle X_3 all significantly affect the conveying rate Y_1 and the separation rate Y_2 ($p < 0.05$). The interaction term between lifting speed and vibration frequency ($X_1 X_2$), as well as the vibration frequency and lifting angle ($X_2 X_3$), has a significant influence on the conveying Y_1 and separation Y_2 rates ($p < 0.05$), the interaction term between lifting speed and lifting angle ($X_1 X_3$) had a non-significant effect on the conveying Y_1 and separation Y_2 rates ($P>0.05$). The squared terms X_1^2, X_2^2, and X_3^2 significantly affected the Y_1 and Y_2 ($p < 0.01$).

Table 5

Variance analysis

Source of variation	Conveying rate					Separation rate				
	Sum of squares	Freedom	Mean square	*F*	*P*	Sum of squares	Freedom	Mean square	*F*	*P*
Model	340.17	9	37.80	33.73	< 0.0001***	43.11	9	4.79	21.11	< 0.0001***
X_1	66.34	1	66.34	59.20	< 0.0001***	2.83	1	2.83	12.48	0.0037***
X_2	37.19	1	37.19	33.18	< 0.0001***	8.21	1	8.21	36.19	< 0.0001***
X_3	20.32	1	20.32	18.13	0.0009***	1.35	1	1.35	5.94	0.0299**
X_1X_2	24.36	1	24.36	21.74	0.0004***	1.71	1	1.71	7.54	0.0167**
X_1X_3	4.84	1	4.84	4.32	0.0582*	0.3613	1	0.3613	1.59	0.2292
X_2X_3	12.65	1	12.65	11.29	0.0051***	1.71	1	1.71	7.54	0.0167**
X_1^2	147.30	1	147.30	131.44	< 0.0001***	16.08	1	16.08	70.86	< 0.0001***
X_2^2	14.61	1	14.61	13.04	0.0032***	8.55	1	8.55	37.69	< 0.0001***
X_3^2	14.02	1	14.02	12.51	0.0036***	2.63	1	2.63	11.58	0.0047***
Residual	14.57	13	1.12			2.95	13	0.2269		
Lack of fit	13.07	5	2.61	13.96	0.0009***	2.66	5	0.5326	14.88	0.0007***
Error	1.50	8	0.1872			0.2863	8	0.0358		
Sum	354.73	22				46.06	22			

Note: * indicates significant impact (0.05<P<0.1), * * indicates significant impact (0.01<P<0.05), and * * * indicates extremely significant impact (P<0.01).

The *Panax Notoginseng* rhizome conveying rate constantly changes during operation, and the average value during the period of constant speed stability is the *Panax notoginseng* rhizome conveying rate. The changes in the conveying rate obtained are shown in Figure 24. Response surface plots were generated using Design-Expert 13 to visualize the effects of the factors above on the conveying rate. Figure 24a shows that the *Panax notoginseng* rhizome conveying rate Y_1 decreases slightly with increased vibration frequency X_2. With the increase in lifting speed X_1, the conveying rate Y_1 first increases and then decreases. Figure 24b shows that the conveying rate Y_1 increases with the lifting angle X_3, first and then decreases, as the ratio of lifting speed X_1 to lifting angle X_3 increases. Figure 24c shows that the conveying rate Y_1 decreases significantly with the increase in vibration frequency X_2, and the conveying rate Y_1 is not considerably affected by the lifting angle X_3 ratio to vibration frequency X_2.

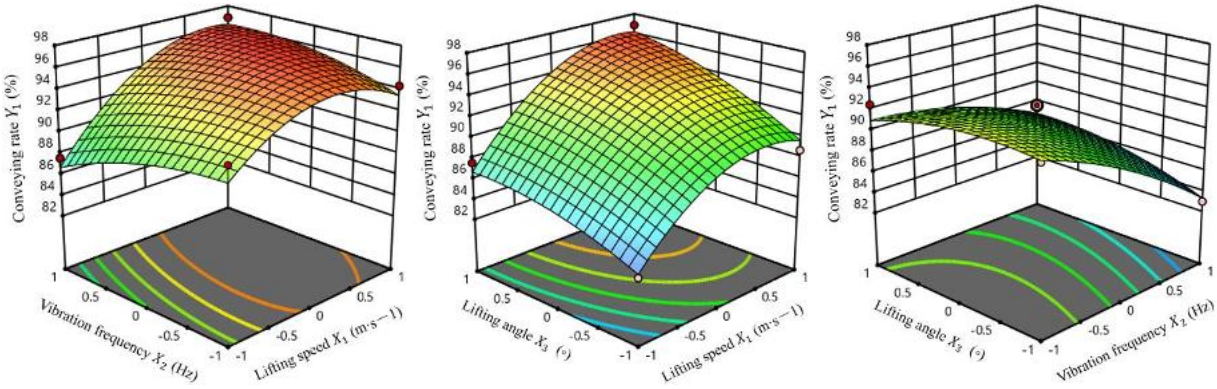


Fig. 24 - Response surface of interaction factors to the *Panax Notoginseng* rhizome conveying rate Y_1
(a) response surface under factors X_1 and X_2; (b) response surface under factors X_1 and X_3; and (c) response surface under factors X_2 and X_3

Figure 25 indicates the *Panax notoginseng* rhizome separation rate Y_2. Figure 25d shows that the separation rate Y_2 increases with an increasing lifting speed X_1 and vibration frequency X_2 from -1 to 1. Figure 25e shows that the conveying rate Y_2 increases slightly with increasing lifting speed X_1 and lifting angle X_3, and first increases and then decreases as X_1 increases from 0 to 1. The rhizome separation rate Y_2 gradually increases as the vibration frequency X_2 from -1 to 1 increases, and the separation rate Y_2 is not considerably affected by the lifting angle X_3 ratio to vibration frequency X_2, as shown in Figure 25f.

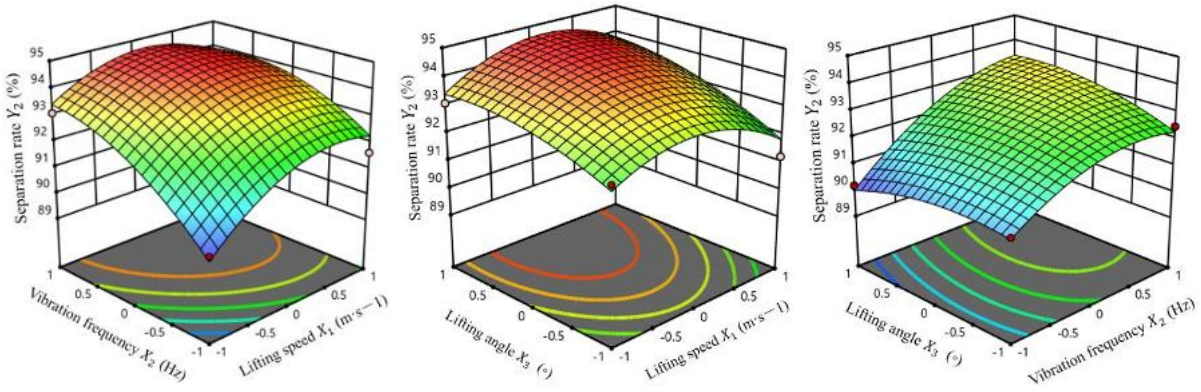


Fig. 25 - Response surface of interaction factors to the *Panax Notoginseng* rhizome separation rate Y_2
(d) response surface under factors X_1 and X_2; (e) response surface under factors X_1 and X_3; and (f) response surface under factors X_2 and X_3

Field validation experiment

Experimental design

The machining and assembly of the whole machine were completed based on the structural parameters of the separation conveyor device. Field validation tests were conducted in November 2025 at the *Panax notoginseng* farm in Shilin County, Kunming City, Yunnan Province, to evaluate the practical applicability and reliability of the device under real-world agricultural conditions. The operation parameters of the separation conveyor device during the field harvesting experiment are shown in Table 6.

Figure 26 depicts the scenario for field harvesting operations. Test tools include a steel tape measure, an electronic stopwatch, an electronic balance, a temperature and humidity meter, a soil moisture tester, and a digital display soil hardness meter. The experiment design of the field during the harvest period of *Panax Notoginseng* is as follows: the average ridge width of *Panax Notoginseng* is 1400 mm, the average ridge height is 200 mm, the average thickness of the mixture of *Panax Notoginseng* and soil is 100-150 mm, and the average diameter of rhizome is 26.3 mm, soil moisture content 13.2%, the soil is soft and sticky, with moderate cohesion. The weather is sunny, and the average temperature at harvest is 24°, with a relative humidity of 71%.

Table 6

Operation parameters of the separation conveyor device

Parameter	Numerical value
Working inclination angle of separation conveyor (◦)	20
Working speed of separation conveyor (m·s^{-1})	0.8
Vibration frequency (Hz)	1.5



Fig. 26 - Field harvesting experiment

Test measurements

(1) *Panax Notoginseng* conveying rate:

The *Panax Notoginseng* conveying rate (T) was calculated to determine how the mass of the *Panax Notoginseng* remained unconveyed. It was defined as follows:

$$T = \frac{W_1}{W_1+W_2} \times 100\% \quad (32)$$

where W_1 is the total mass of harvested Panax Notoginseng (kg), and W_2 is the total mass of unharvested *Panax Notoginseng* (kg).

(2) *Panax Notoginseng* damage rate:

After *Panax Notoginseng* was harvested by machine, the harvested rhizomes were categorized into two groups: reasonable and damaged. The weight of each rhizome group was measured individually. The total damage rate (D) of the *Panax notoginseng* can be gained from the following equation:

$$D = \frac{W_4}{W_3+W_4} \times 100\% \quad (33)$$

where W_3 is the total mass of good *Panax Notoginseng* (kg); W_4 is the mass of damaged *Panax Notoginseng* by the harvester machine (kg).

(3) Separation rate:

$$S = \frac{m_1}{m_1+m_2-m_3} \times 100\% \quad (34)$$

where S is the separation rate, %; m_1 is the mass of impurities separated after separating, (kg); m_2 is mass of *Panax notoginseng* rhizome and soil after separating, (kg); m_3 is the mass of *Panax notoginseng* rhizome, (kg).

Field experiment results

The treatments were randomly distributed in the main subplot and sub-subplot; the sub-subplot area was 52.5 m² (35×1.5 m), with 1.5 m between sub-subplots and 10 m at the end of each sub-subplot. After each subplot of experiments is completed, the data collection is carried out within half an hour to ensure consistent rhizome moisture evaporation. The average value is then calculated using the test data from the sub-subplots. The average value of all measured data is used as the final evaluation indicator. The results of the field test are listed in Table 7.

Table 7

Experimental results

Serial Number	Separation rate/%	Conveying rate/%	Damage rate/%
1	96.45	95.25	2.07
2	97.16	95.44	1.86
3	96.38	96.85	2.18
4	96.67	97.13	1.55
5	97.11	96.71	1.93
6	95.92	96.83	1.28
7	97.23	97.14	2.05
8	98.06	95.94	2.13
Average	96.87	96.42	1.88

DISCUSSION

The average values for the efficiency of *Panax notoginseng*-soil separation, the conveying rate of *Panax notoginseng*, and the rhizome damage rate for the separation conveyor device are 96.87%, 96.42%, and 1.88%, respectively. The relative errors between the laboratory and field test results for the efficiency of *Panax notoginseng*-soil separation and the rhizome conveying rate are 0.97% and 1%, respectively. These values are consistent with the optimized parameters and meet the agronomic requirements for *Panax notoginseng* harvesting. The separation rate of *Panax notoginseng* increased by 0.10%, and the damage rate decreased by 0.99% compared to the reference (*Zhenmeng et al., 2018*). The results indicate that the separation conveyor device yields a higher harvest of *Panax notoginseng* in hilly areas.

CONCLUSIONS

(1) This study systematically investigated the design, analysis, and optimization of a separation conveyor device for a self-propelled *Panax notoginseng* combine harvester, addressing the challenges of harvesting in hilly and mountainous regions of southwest China. By integrating agronomic characteristics of *Panax notoginseng* with mechanical design principles, a crawler-type harvester capable of excavation, separation, conveying, lifting, and collection was successfully developed to improve harvesting efficiency and reduce labor intensity.

(2) Through detailed kinematic and mechanical analyses, the separation conveyor structure and key components such as the drive wheel, vibration wheel, and bar-type conveyor were theoretically modeled and optimized. Coupled DEM–MBD simulations using EDEM and RecurDyn provided insights into soil–rhizome interaction, particle separation behavior, and dynamic forces acting on *Panax notoginseng* rhizomes. Simulation results demonstrated that effective soil separation could be achieved within approximately 2.25 s, with finer soil particles separating earlier than larger aggregates.

(3) Laboratory experiments and quadratic regression orthogonal tests further validated the simulation outcomes. Conveyor speed, vibration frequency, and lifting angle were identified as significant factors influencing conveying and separation performance. Optimal parameters were determined as a conveyor speed of 0.8 $m \cdot s^{-1}$, vibration frequency of 1.5 Hz, and lifting angle of 20°, achieving separation and conveying rates exceeding 95% under laboratory conditions.

(4) Field validation experiments confirmed the reliability and applicability of the optimized design. The separation conveyor achieved an average separation rate of 96.87%, conveying rate of 96.42%, and a low rhizome damage rate of 1.88%, meeting agronomic and mechanization requirements. Overall, this research provides a solid theoretical and experimental foundation for advancing mechanized harvesting of *Panax notoginseng* and similar rhizome crops.

ACKNOWLEDGEMENT

We would like to express our sincere appreciation to all those who supported and contributed to this research. Special thanks to the Research Center on Mechanization Engineering of Chinese Medicinal Materials in Yunnan Universities for providing invaluable resources and support throughout this study, under project number 2022YFD2002004. We also extend our gratitude to the Faculty of Mechanical and Electrical Engineering and Faculty of Modern Agricultural Engineering, Kunming University of Science and Technology, Kunming, China, for their collaboration and valuable contributions, Additionally, we acknowledge the School of Tea and Coffee, Puer University, Puer, China. and the Agricultural Engineering Research Institute (AEnRI), Agricultural Research Center (ARC), 256 Dokki, Giza, Egypt.

REFERENCES

[1] Chen, M., Liu, X., Hu, P., Zhai, X., Han, Z., Shi, Y., Zhu, W., Wang, D., He, X., Shang, S., (2024), Study on rotor vibration potato-soil separation device for potato harvester using DEM-MBD coupling simulation, *Computers and Electronics in Agriculture* Vol. 218, https://doi.org/10.1016/j.compag.2024.108638.

[2] Cheng, Z., Yang, D., Wang, X., Liu, M., Li, Y., Chen, X., (2023), Development Status and Prospect of Potato Mechanized Harvest in Hilly and Mountainous Areas, *AGRICULTURAL ENGINEERING* Vol. 13, no.11, pp. 5-12, DOI：10.19998/j.cnki.2095-1795.2023.11.001.

[3] Faan, W., Chang, N., Zhaoguo, Z., Hongwei, X., Kaiting, X., Boyang, W., (2024), Analysis and experiment on drag reduction characteristics of digging shovel of *Panax notoginseng* harvester, *Nongye Jixie Xuebao/Transactions of the Chinese Society of Agricultural Machinery* Vol. 55, no.7.

[4] Feng, W., (2022). *Design and experiment of double-layer flat screen tuber harvester for Pinellia ternata*. Master's Thesis, Gansu Agricultural University, Gansu/China.

[5] Guiyun, S., and Ying, L., (2012), Processing, Production and Identification of Orally Taken *Panax notoginseng* Powder, *Capital Medicine (Chuan Tong Zhong Yi Yao)*, no.9, pp. 45－45,

[6] Guo Jingjing, Lailai, L., Huichao, Z., Yang, X., (2014), Research Progress on the Main Components of *Panax notoginseng* and Their Immunomodulatory Effects, *Journal of Tianjin University of Traditional Chinese Medicine* Vol. 33, no.2, pp. 119－124, 0.11656/j.issn.1673-9043.2014.02.17.

[7] Hongwei, X., (2024). *Research on Digging and Conveying Separation Device for Self-propelled Panax Notoginseng Combine Harvester*. Master's Thesis, Kunming University of Science and Technology, Kunming/China.

[8] Issa, I. I. M., Zhang, Z., El-Kolally, W., Wang, F.A., Wang, Y., (2025a), Innovated design, simulation and evaluation of potato harvester excavation and separation conveyors, *International Journal of Agricultural and Biological Engineering* Vol. 18, no.2, pp. 132-145, DOI: 10.25165/j.ijabe.20251802.9164.

[9] Issa, I. I. M., Zhang, Z., El-Kolaly, W., Yang, X., Wang, H., (2020), Design, ansys analysis and performance evaluation of potato digger harvester, *International Agricultural Engineering Journal* Vol. 29, no.1, pp. 60-73,

[10] Issa, I. I. M., Zhang, Z., Omer, A. A. A., Kaiting, X., Zhuma, G., (2025b), A Comprehensive Review of Harvesting Equipment for Rhizome and Tuber Crops: A Bibliometric and Thematic Analysis of Trends, Influences, Intellectual Structures, and Future Directions, *Revista De La Facultad De Ciencias Agrarias* Vol. 57, no.1, pp. 93-121,

[11] Issa, I. I. M., Zhaoguo, Z., El-Kolaly, W., Faan, W., (2025c), Design, Simulation Analysis, and Experiment on Excavation Device of Self-Propelled Panax Noto-ginseng Combine Harvester, *AMA, Agricultural Mechanization in Asia, Africa and Latin America* Vol. 56, no.9, pp. 384-407, DOI: 09.13658/Ama.28.09.2025.01

[12] Jiang, D., Liu, Y., Lin, Z., Wang, W., (2022), Effects of combined infrared and hot-air drying on ginsenosides and drying characteristics of *Panax notoginseng* (Araliaceae) roots, *International Journal of Agricultural and Biological Engineering* Vol.15, no.1, pp. 267-276, DOI: 10.25165/j.ijabe.20221501.6210

[13] Lihong, L., Ying, L., Fen, W., Shilei, L., Huize, H., Wensheng, Z., Wenfeng, X., (2017), The Current Development Situation and Suggestion of Panar notoginseng in Yunnan Pronince, *Modern Chinese Medicine* Vol. 19, no.9, pp. 1331-1335,

[14] Lin, Y., Zhang, F., Li, L. X., Shi, L., Zhu, Y., Wang, J., (2022), Identification of *Panax notoginseng* powder in different parts based on the electronic nose and time-domain feature extraction, *Journal of the Electrochemical Society* Vol. 169, no.4, pp. 047510, DOI: 10.1149/1945-7111/ac62bf.

[15] Siwei, G., (2024). *Research on The Whole Machine Monitoring and Control System of Self-propelled Panax notoginseng Combine Harvester*. Master's Thesis, Kunming University of Science and Technology, Kunming/China.

[16] Thomas, A., (1992), Agricultural water balance of Yunnan Province, PR China: agroclimatic zoning with a Geographical Information System, *Agricultural water management* Vol. 21, no.4, pp. 249-263,

[17] Wang, F., Wen, B., Xie, X., Xie, K., Guo, S., Zhang, Z., (2023a), Operation mechanism analysis and parameter optimization of conveying and separating device of *Panax notoginseng* harvester, *Trans. Chin. Soc. Agric. Mach* Vol. 54, pp. 201-211,

[18] Wang, L., Sun, W., Zhang, L., Zhao, M., and Simionescu, P. A., (2025), Design and Testing of a Self-Propelled Fork-Tooth Harvester for Medicinal Plant Rhizomes, *Agriculture* Vol. 15, no.7, pp. 694,

[19] Wang, L. H., Liu, F., Wang, Q., Zhou, J. Q., Fan, X. Y., Li, J. R., Zhao, X., Xie, S. S., (2023b), Design of a spring-finger potato picker and an experimental study of its picking performance, *Agriculture* Vol. 13, no.5, pp. 945, https://doi.org/10.3390/agriculture13050945.

[20] Wang, W., Yang, R., Pan, Z., Qing, Y., Zhang, J., Chen, D., Guo, X., Lyu, S., (2023c), Design and experimental study of single plant harvester for potato breeding experiments, *Agriculture* Vol. 14, no.1, pp. 71,

[21] Xiaohong, X., (2023). *Experimental Study on Transportation and Separation of Panax Notoginseng Soil Complex*, Kunming University of Science and Technology.

[22] Yitao, L., Chengliang, L., Qingxi, L., Lei, W., (2020), Research progress of seed guiding technology and device of planter, *Nongye Jixie Xuebao/Transactions of the Chinese Society of Agricultural Machinery* Vol. 51, no.12, pp. 1-14,

[23] Zhang, Z., Wang, F., Zhang, Y., Zhang, D., Tian, R., (2016), Design and Experiment of Self-propelled *Panax notoginseng* Harvester, *Journal of Agricultural Machinery* Vol.47, no.1, pp. 234-240, 10．6041/j issn．1000-1298．2016．S0．036.

[24] Zhaoguo, Z., Haiyi, W., Yanbin, L., Xi, Y., Issa, I., Zhendong, Z., (2021), Design and experiment of multi-stage separation buffer potato harvester, *Nongye Jixie Xuebao/Transactions of the Chinese Society of Agricultural Machinery* Vol. 52, no.2, pp. 96-106,

[25] Zhaoguo, Z., Hongwei, X., Haotian, X., Chang, N., Chao, W., (2023), Calibration and experiment of discrete element parameters of *Panax notoginseng* stem, *Transactions of the Chinese Society for Agricultural Machinery* Vol. 54, no.11, pp. 61-70, 91,

[26] Zhenmeng, C., Zhaoguo, Z., Faan, W., Dan, Z., Haihui, Y., (2018), Kinematic analysis and optimal design of vibration-type device for *Panax notoginseng* root-soil separation, *Journal of Northwest A&F University (Natural Science Edition)* Vol. 46, no.11, pp. 146-154,

[27] Zhongcai, W., Guoliang, S., Xueqiang, L., Faming, W., Chuanzhu, S., Pengxiang, M., (2020), Parameter optimization and test of potato harvester wavy sieve based on EDEM, *Nongye Jixie Xuebao/Transactions of the Chinese Society of Agricultural Machinery* Vol. 51, no.10, pp. 109-122,

[28] Zhou, J., Ye, Z., Cui, X., Zeng, J., Zhao, A., Zhu, L., (2010), Study on the pharmacodynamics of notoginsenosides R1, R2 and ginsenoside R b1 *Chinese Patent Medicine* Vol. 32, no.09, pp. 1494-1497.

DESIGN AND EXPERIMENT OF A SPOON-CLAMP TYPE GARLIC SEED METERING DEVICE

/

勺夹式大蒜排种器设计与试验

Xinyan ZHANG, Lin LUO, Dongming ZHANG, Shu-juan YI *)
College of Engineering, Heilongjiang Bayi Agricultural University, Daqing/P. R. China
Tel: +86–13836961877; E-mail: yishujuan_2005@126.com;
Corresponding author: Shu-juan Yi
DOI: https://doi.org/10.35633/inmateh-79-31

Keywords: *precision seeding, single-clove metering, discrete element method, bench test, garlic mechanization*

ABSTRACT

To reduce miss-seeding and improve the stability of single-clove pickup in garlic seed metering devices, a spoon-clamp type garlic seed metering device was designed. The proposed mechanism combined spoon-type seed pickup with spring-assisted clamping, so garlic cloves with irregular surfaces could be picked up, carried, cleaned, and discharged more stably. Based on the geometric characteristics of three garlic varieties, the key parameters of the seed plate, seed pickup spoon, and opening-closing mechanism were determined by theoretical analysis. A three-dimensional model of the seed metering device and garlic-clove models were established using the discrete element method. Single-factor simulations were then performed to analyze the effects of seed plate speed and seed pickup spoon diameter on the qualified seeding index, reseeding index, and miss-seeding index. The suitable simulated operating range was 1–7 r/min for seed plate speed and 25–35 mm for seed pickup spoon diameter. Bench tests showed that the suitable parameter combination for "Acheng Purple Garlic" and "Nong'an Purple Garlic" was a seed plate speed of 4 r/min and a seed pickup spoon diameter of 32 mm. For "Zhaozhou White Garlic", the suitable combination was 5.5 r/min and 28 mm. These results showed that the spoon-clamp mechanism was feasible for improving single-clove garlic metering stability under controlled bench-test conditions.

摘要

针对大蒜蒜瓣形状不规则导致排种器漏播率高、单粒取种稳定性不足等问题，本文设计了一种勺夹式大蒜排种器。该装置将取种勺取种与弹簧辅助夹持相结合，使蒜瓣在取种、携种、清种和投种过程中保持较稳定的约束状态。基于三种大蒜蒜瓣的几何特性，通过理论分析确定排种盘、取种勺及开合机构等关键参数。采用离散元法建立排种器三维模型和蒜瓣颗粒模型，并通过单因素仿真分析排种盘转速和取种勺直径对合格指数、重播指数和漏播指数的影响。仿真结果表明，排种盘转速为 1–7 r/min、取种勺直径为 25–35 mm 时排种性能较优。台架试验结果表明，"阿城紫皮蒜"和"农安紫皮蒜"的适宜参数组合为排种盘转速 4 r/min、取种勺直径 32 mm；"肇州白皮蒜"的适宜参数组合为排种盘转速 5.5 r/min、取种勺直径 28 mm。研究结果说明，勺夹式取种机构在受控台架条件下具有提高大蒜单粒取种稳定性的可行性。

INTRODUCTION

Garlic is one of the main specialty cash crops in China. Precision garlic seeding technology is important for improving the quality and efficiency of mechanized garlic sowing *(Wei et al., 2022; Xie et al., 2015)*. Garlic cloves have irregular curved surfaces and differ greatly in variety, shape, and size. These characteristics can easily cause miss-seeding, reseeding, and unstable seed carrying during mechanical sowing. Improving the stability of single-clove pickup and transport is therefore an important issue in the development of garlic seed metering devices. Existing garlic seeding devices mainly include spoon-chain, spoon-belt, cell-type, and pneumatic seed metering devices *(Liu et al., 2019; Zhang et al., 2014)*. Reviews and recent studies have also emphasized the need for improved single-clove pickup, directional control, and adaptability *(Cui et al., 2018; Fang et al., 2024; Jiang, 2018; Shao et al., 2025)*. These devices can meet some agronomic requirements, but their performance is still limited by seed leakage, unstable single-clove pickup, high structural complexity, or poor adaptability to different garlic varieties.

Previous studies have improved garlic seed metering performance through different technical routes. *Li et al. (2020)* designed a wheel-spoon type single-clove seed picking device, but different spoon structures were needed for different garlic grades. *Li et al. (2017)* and *Geng et al. (2016)* designed seed-box delivery mechanisms, but manual replanting was still required when serious miss-seeding occurred. Other mechanical garlic planting devices were reported by *Choi et al. (2003)*, *Dong et al. (2015)*, *Han (2011)*, and *Kang (2000)*. *Bakhtiari et al. (2009)* developed a precision garlic seeder with good performance, although the sensors and control system increased the manufacturing cost. *Xie et al. (2022)* proposed a tooth-assisted pneumatic garlic seed metering device, and *Hou et al. (2024)* designed a multi-disturbance seed-cleaning device. These studies indicate that seed pickup stability, miss-seeding control, and structural adaptability remain important problems. Most spoon-type mechanisms mainly depend on passive seed filling or spoon carrying, and the clove is not actively constrained during transport. A clove may slip, fall, or be picked up together with other cloves under shape variation and collision disturbance. A metering mechanism that combines spoon pickup with controlled clamping is therefore needed to improve carrying stability while reducing seed damage.

Accordingly, this study aimed to: (1) design a spoon-clamp type garlic seed metering device that combines spoon pickup with spring-assisted clamping; (2) determine the key structural parameters of the seed plate, seed pickup spoon, and opening-closing mechanism based on garlic-clove dimensions and theoretical analysis; (3) analyze the effects of seed plate speed and seed pickup spoon diameter using DEM simulation; and (4) verify the suitable parameter combinations through bench tests with three garlic varieties. This study provides a basis for further optimization and field validation of garlic precision seeding devices.

MATERIALS AND METHODS

Dimensional Measurement

The geometric characteristics of garlic cloves are the basis for designing the key components and selecting the control parameters of the seed metering device. The axial dimension method is commonly used to measure seed materials *(Liu et al., 2018)*. In this study, clove morphology was described by length L, width W, thickness H, and tail length T. As shown in Fig. 1, a three-axis spatial coordinate system XYZ was established with the centroid of the garlic clove as the origin O. The length, width, and thickness directions were defined as the X-, Y-, and Z-axes, respectively. To keep the design parameters consistent, garlic cloves with similar moisture content and intact appearance were selected. Each dimension was measured using a Vernier caliper with an accuracy of 0.01 mm.

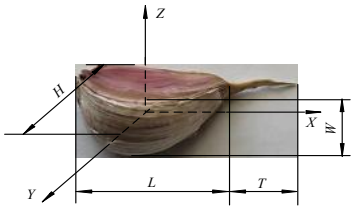


Fig. 1 – Determination of the geometric dimensions of garlic cloves

A total of 300 cloves were randomly selected from each variety, including “Acheng Purple Garlic”, “Zhaozhou White Garlic”, and “Nong’an Purple Garlic”. Each dimension was measured three times with equal precision. The probability density distribution of garlic dimensions was analyzed using Excel *(Tang, 2018)*, and the mean and standard deviation were calculated, as shown in Table 1.

Table 1

Geometrical dimensions of three garlic varieties

Tested varieties	Length [mm]		Width [mm]		Thickness [mm]		Tail Length [mm]	
	Mean	Standard Deviation	Mean	Standard Deviation	Mean	Standard Deviation	Mean	Standard Deviation
Acheng Purple Garlic	28.43	0.93	16.95	0.82	17.05	0.97	10.71	1.02
Zhaozhou White Garlic	32.80	2.94	14.34	1.31	10.13	0.70	12.04	0.99
Nong’an Purple Garlic	25.37	1.61	16.26	0.79	15.93	0.78	12.40	0.82

Table 1 shows clear differences in the geometric dimensions of the three garlic varieties. The average length, width, thickness, and tail length of “Acheng Purple Garlic” were 28.43, 16.95, 17.05, and 10.71 mm, respectively. The corresponding values for “Zhaozhou White Garlic” were 32.80, 14.34, 10.13, and 12.04 mm. For “Nong’an Purple Garlic”, the values were 25.37, 16.26, 15.93, and 12.40 mm. These data provide a basis for designing the seed pickup spoon parameters.

Overall Structure and Working Principle of the Seed Metering Device

The spoon-clamp garlic seed metering device mainly consists of seed pickup spoons, torsion springs, a seed plate, limit rods, and other components, as shown in Fig. 2. The working process of the device includes four zones: seed pickup, seed clamping, seed cleaning, and seed discharge.

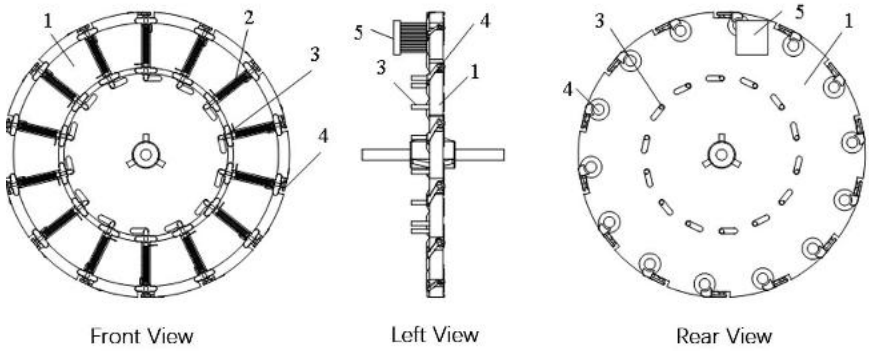


Fig. 2 – Overall structure of spoon-clamp garlic seed metering device

1 – Seed Plate; 2 – Torsion Spring; 3 – Limit Rod; 4 – Seed Pickup Spoon; 5 – Seed Cleaning Brush

During operation, the seed plate rotates around the main shaft and drives the seed pickup spoons, torsion springs, and clamping components. When a seed pickup spoon reaches the seed pickup zone, the limit rod opens the spoon through the torsion spring shaft. After the spoon passes the limit block, the elastic force of the torsion spring closes the spoon and clamps a garlic clove. The clamped clove then moves with the seed plate. When the spoon passes through the seed cleaning brush, excessive or unstable cloves are removed. At the seed discharge position, the second limit rod opens the spoon and releases the clove. This process integrates seed pickup, clamping, cleaning, and discharge. It is also the main structural difference between the proposed mechanism and ordinary spoon-type carrying devices.

Design of Key Components

Design of Seed Plate

The seed plate of the precision garlic seed metering device adopts a disc structure. Its main parameters include seed plate diameter, rotational speed, and the number of seed pickup spoons. A relationship among seed plate diameter, rotational speed, forward speed, and the number of seed pickup spoons was therefore established.

A larger seed plate diameter and more seed pickup spoons can reduce angular velocity and increase the curvature radius at the seed drop point, which helps stabilize seed pickup. Increasing the seed plate diameter can also increase spring deformation and improve control of the squeezing force during seed carrying. However, an excessive diameter increases the size, weight, and power consumption of the metering mechanism. Considering the relationship among seed plate radius, rotational speed, and forward speed, the seed plate diameter was set to 400 mm in the prototype design.

The linear speed of the seed plate refers to the linear speed at the seed pickup spoon. As the rotational speed increases, the time for the seed pickup spoon to pass through the seed area decreases. This may increase miss-seeding and cause picked cloves to fall under collision disturbance. Therefore, the linear speed of the seed pickup spoon should generally not exceed 0.35 m/s.

The maximum linear speed was set to 0.35 m/s, and the maximum rotational speed of the seed plate was calculated according to Equation (1).

$$\frac{d_p n_p \pi}{60} = 0.35 m/s \quad (1)$$

where d_p is the seed plate diameter, [m]; and n_p is the seed plate rotational speed, [r/min].

During operation, the garlic seeder mainly relies on ground-wheel transmission. According to the coordination between seed metering and forward movement, the time required for a garlic clove to rotate through the arc distance between adjacent seed pickup spoons should be equal to the time required for the seeder to move forward by one hill spacing. The relationship between seed pickup spoon spacing and garlic plant spacing is expressed as follows:

$$S_p = r\theta = \frac{n_p d_p \pi t}{60} \tag{2}$$

$$(1+\delta)\ \upsilon_c t = S_c \tag{3}$$

where S_p is the arc distance between adjacent seed pickup spoons on the seed plate, [m]; r is the seed plate radius, [m]; θ is the angular displacement, [rad]; n_p is the seed plate rotational speed, [r/min]; d_p is the seed plate diameter, [m]; t is the travel time, [s]; δ is the ground-wheel slip rate; υ_c is the forward speed of the machine, [m/s]; and S_c is the garlic plant spacing, [m].

By combining the above two formulas, the expression for the seed pickup spoon spacing can be obtained as follows:

$$S_p = \frac{S_c n_p d_p \pi}{(1+\delta)60\upsilon_c} \tag{4}$$

According to the agronomic requirements for garlic planting, the plant spacing S_c is 80–120 mm, the forward speed of the seeder υ_c is 0.2–0.4 km/h, and the ground-wheel slip rate δ is 0.05–0.12. When δ = 0.08, the calculated arc distance S_p between adjacent seed pickup spoons on the seed plate is 58–116 mm.

$$n_s = \frac{\pi d_p}{S_p} \tag{5}$$

where n_s is the number of seed pickup spoons, [pcs]; d_p is the seed plate diameter, [m]; and S_p is the arc distance between adjacent seed pickup spoons, [m].

The calculation showed that the arc distance between adjacent seed pickup spoons on the seed plate was 116 mm, and the number of seed pickup spoons was 14.

Design of Seed Pickup Spoon

A spoon-clamp seed pickup structure was proposed because garlic cloves differ greatly in three-dimensional morphology and have uneven curved surfaces. The seed pickup spoon is used for seed pickup and carrying. During seed plate rotation, the spoon should carry the garlic clove to the discharge position without damage or falling. A larger spoon can reduce miss-seeding, but an excessively large spoon may increase reseeding. The spoon size was therefore determined according to the external dimensions of the garlic cloves. The three-dimensional shape of garlic cloves was approximately regarded as an ellipsoid. The spoon opening was initially designed as a circular opening similar to a small hemisphere. To reduce miss-seeding and reseeding, the diameter of the spoon opening should be greater than the average clove width and smaller than the average clove length. The initial diameter was set to 30 mm. The minimum and maximum diameters were 16 mm and 36 mm, respectively, and the spoon depth was about 4 mm, which was about two-thirds of the maximum clove thickness. The structure of the seed pickup spoon is shown in Fig. 3.

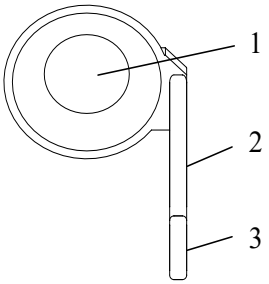


Fig. 3 – Structure diagram of seed pickup spoon
1 – Spoon Body; 2 – Spoon Handle; 3 – Fixing Hole

Design of Opening and Closing Mechanism

The seed pickup process of the precision garlic seed metering device mainly depends on the opening and closing mechanism. The fixed end contacts the limit rod and continuously opens the seed pickup spoon. As the seed plate rotates, the elastic potential energy of the torsion spring increases. When the fixed end is separated from the limit rod, the stored elastic potential energy is released, and the seed pickup spoon closes rapidly under the action of the torsion spring. The operating performance of this mechanism directly affects seed clamping, transport, and discharge. It is therefore an important component for precision seed pickup in garlic planting. The opening and closing mechanism are shown in Fig. 4.

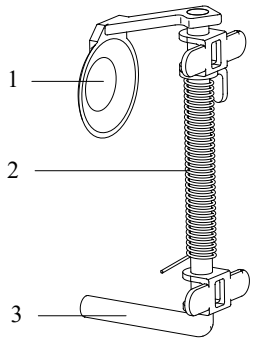


Fig. 4 – Opening and closing mechanism of the garlic seed metering device
1 – Seed Pickup Spoon; 2 – Torsion Spring; 3 – Limit Rod

The opening-closing mechanism realizes the opening and closing movement of the seed pickup spoon through the combined action of the torsion spring and limit rod. During opening, elastic potential energy is stored in the torsion spring and then released to generate the clamping force of the seed pickup spoon. The clamping force affects both seed pickup stability and clove damage. Because the clamping force is difficult to adjust directly during operation, different spring wire diameters were used as equivalent clamping force levels in the experiment. The relationship between spring wire diameter and clamping force is expressed by Eq. (6).

$$\begin{cases} P = k\Delta s \\ k = \dfrac{1000 d_w}{\left(\dfrac{d}{d_w}\right)^3} \end{cases} \quad (6)$$

where P is the clamping force of the seed pickup spoon, [N]; k is the spring stiffness coefficient, [N/mm]; Δs is the spring deformation, [mm]; d_w is the spring wire diameter, [mm]; and d is the mean spring diameter, [mm].

"Acheng Purple Garlic" was selected for the single-factor test on clamping force to clarify its effect on seed damage rate. The spring wire diameters were set to 0.5, 0.6, 0.7, 0.8, 0.9, and 1.0 mm. For each spring wire diameter, 300 garlic cloves were selected and evenly divided into three groups for repeated seed pickup tests. The seed damage rate was determined according to visible damage to the garlic body after the skin was peeled off. Considering the practical requirements of agricultural production and the adjustable range of the mechanism, the spring wire diameter was set within 0.5–1.0 mm. The number of damaged cloves among the effectively clamped cloves was counted, and the seed damage rate was used as the evaluation indicator. The test plan and results are shown in Table 2.

Table 2
Single-factor test scheme and results for spring wire diameter

Spring Wire Diameter [mm]	0.5	0.6	0.7	0.8	0.9	1.0
Seed Damage Rate [%]	0	0	0	5.33	6.66	8.00

The single-factor results showed that the seed damage rate was 0% when the spring wire diameter was 0.5–0.7 mm. Visible damage began to appear when the spring wire diameter exceeded 0.7 mm. The spring wire diameter was therefore set to 0.7 mm, corresponding to a clamping force of approximately 2.401 N. This value was selected to maintain clamping stability while reducing garlic-clove damage.

Determination of Seed Discharge Port Position

The position of the seed discharge port directly affects the falling height and initial state of the garlic clove, and is therefore an important parameter for device coordination.

Fig. 5 shows the seed pickup process and the falling process from the discharge port.

To determine the discharge port position, the seed pickup process was assumed to be uniform. The horizontal and vertical coordinates of the garlic clove during movement with the seed plate are denoted as x and y. When the garlic clove falls from the discharge port, its initial horizontal and vertical velocities are denoted as v_x and v_y. The horizontal and vertical displacements after falling are denoted as X and Y. The expressions for these variables are given in Equation (7).

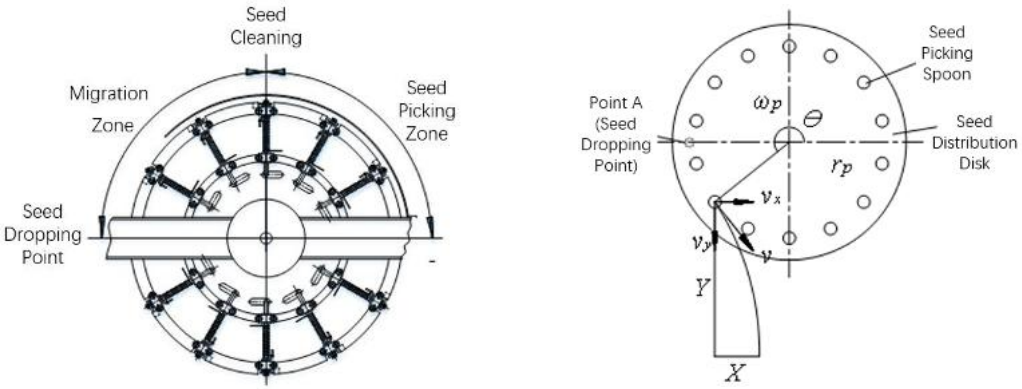


Fig. 5 – Motion analysis of seeding process

$$\begin{cases} x = r_p \cos\theta \\ y = r_p \sin\theta \\ \dot{x} = -r_p \sin\theta \\ \dot{y} = r_p \cos\theta \\ X = r_p \omega_p t \cos\theta \\ Y = r_p \omega_p t \sin\theta + \dfrac{gt^2}{2} \end{cases} \quad (7)$$

where x and y are the horizontal and vertical coordinates of the garlic clove, [m]; $\dot{x}$ and $\dot{y}$ are the corresponding velocity components, [m/s]; X and Y are the horizontal and vertical falling displacements, [m]; r_p is the seed plate radius, [m]; θ is the garlic-clove discharge angle, [rad]; ω_p is the angular velocity of the seed plate, [rad/s]; t is the falling time, [s]; and g is the gravitational acceleration, [m/s²].

To reduce the horizontal velocity during discharge and obtain zero horizontal displacement after the garlic clove falls from the discharge port, the discharge position was determined according to the motion relationship in Equation (7). Among the solutions, −90° corresponds to the initial seed pickup position. Therefore, point A in Fig. 5 was selected as the seed discharge port position.

Discrete Element Simulation

A model of the precision garlic seed metering device and garlic-clove models were constructed using the discrete element method (DEM), and simulation experiments were then conducted *(Hu, 2010)*. The control-variable single-factor method was used to clarify the independent effects of seed plate speed and seed pickup spoon diameter at the prototype design stage. The qualified seeding index, reseeding index, and miss-seeding index were selected as evaluation indicators. EDEM software was used for the virtual simulation tests, which provided data support for structural improvement and operational parameter selection of the precision garlic seed metering device.

Establishment of Seed Metering Device Geometric Model

The geometric model of the seed metering device is an important factor affecting the accuracy of seed pickup simulation. The precision garlic seed metering device was modeled using NX/UG 3D software *(Bertrand et al., 2005; Cundall and Strack, 1979; Hou et al., 2019; Li et al., 2003; Qian, 2008; Sakaguchi et al., 2001; Sharma et al., 2011; Yang and Hsiau, 2000; Yu et al., 2005)*, as shown in Fig. 6. To improve calculation efficiency while preserving the main contact boundaries, small fillets, threaded holes, and other non-critical details were simplified before importing the model into EDEM.

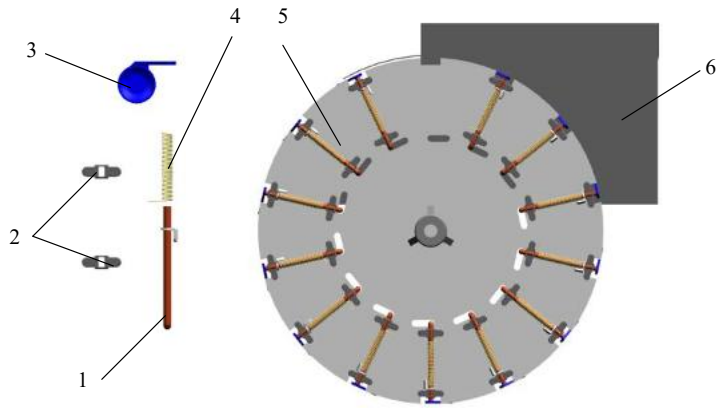
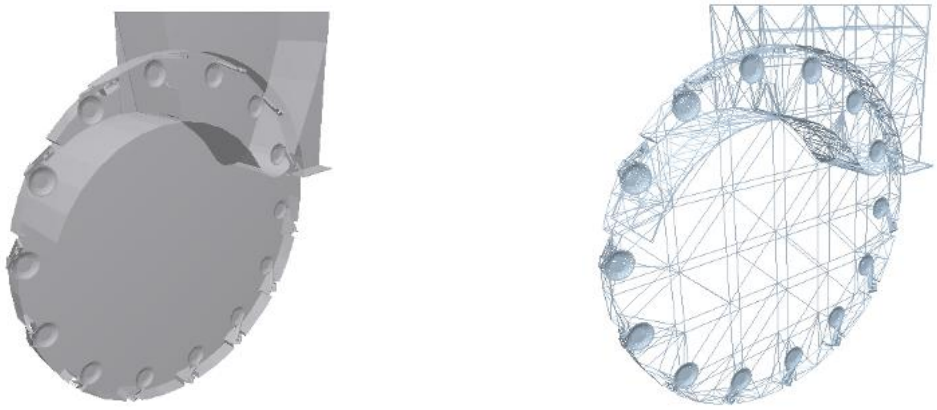


Fig. 6 – Three-dimensional model of garlic seed metering device
1 – Opening and Closing Limit Rod; 2 – Fixing Washer; 3 – Seed Pickup Spoon; 4 – Spring; 5 – Seed Plate; 6 – Seed Box

According to the requirements of prototype development and preliminary material property measurements, the seed pickup spoon was set as 65 Mn steel, with a Poisson's ratio of 0.40, a shear modulus of 7.85×10^9 Pa, and a density of 7800 kg/m^3. The seed plate and seed box were set as aluminum alloy, with a Poisson's ratio of 0.42, a shear modulus of 1.7×10^{10} Pa, and a density of 2700 kg/m^3.



a) Garlic seed metering device in filled format *b) Garlic seed metering device in mesh format*

Fig. 7 – Virtual simulation model of spoon-clamp garlic precision seed metering device

Establishment of Discrete Element Model for Garlic Cloves

The shape and size of garlic cloves are important factors affecting the seeding performance of the seed metering device. In this study, the seeding performance of three garlic varieties was analyzed. According to the morphological and dimensional characteristics of the three varieties, the clove shapes were divided into two categories. "Acheng Purple Garlic" and "Nong'an Purple Garlic" were classified as drum-shaped, while "Zhaozhou White Garlic" was classified as slender. Based on the parameters measured in previous material property studies, multi-sphere filling was carried out for the two clove shapes. The filled garlic-clove particles are shown in Fig. 8.

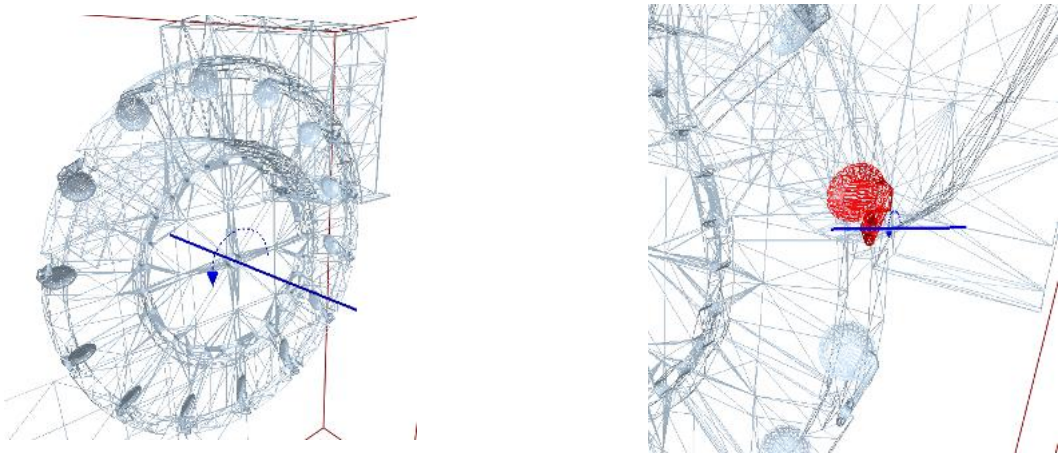


a) Drum-shaped *b) Slender*

Fig. 8 – Filling condition of two kinds of garlic cloves

Numerical Simulation Test of Seed Metering Device Performance

The seeding performance of the garlic seed metering device is affected by garlic variety and size, seed plate speed, and seed pickup spoon diameter. In this study, seed plate speed and seed pickup spoon diameter were selected as the main design variables. The qualified seeding index, reseeding index, and miss-seeding index were used as evaluation indicators. A single-factor control-variable simulation was adopted to determine the suitable parameter range before bench-test validation. The possible interaction between factors was not the focus of this prototype-stage study and should be further analyzed in later optimization work.



a) Rotation direction of the seed plate and seed pickup spoon *b) Self-rotation direction of the seed pickup spoon*

Fig. 9 – Simulation of component motion settings

Factors and Evaluation Indicators for Virtual Simulation Experiments

The rotational speed of the seed plate was matched with the revolution speed of the seed pickup spoons. A rotating model was used to set the rotational speed of the seed plate and each seed pickup spoon, and the self-rotation motion of the seed pickup spoons was also added. A factory model was used to establish a virtual particle factory above the seed box for dynamic particle generation. The operating parameters of the spring were set through the Application Programming Interface, as shown in Fig. 9.

Virtual simulation experiments were conducted using the same structural parameters of the spoon-clamp precision garlic seed metering device. The effects of seed plate speed and seed pickup spoon diameter on seeding performance and the suitable parameter range were analyzed for drum-shaped and slender garlic cloves. Based on theoretical analysis, preliminary tests, agronomic requirements, and actual operating conditions, the seed plate speed was set to 1–13 r/min, and the seed pickup spoon diameter was set to 15–45 mm. Single-factor virtual simulation experiments were conducted separately for the two garlic-clove types.

Referring to the national standards GB/T 6973–2005 “Test Methods for Single Seed (Precision) Planters” and NY/T 503–2015 “Quality of Single Seed (Precision) Planter Operations,” the qualified seeding index, reseeding index and miss-seeding index were selected to evaluate the operational performance, suitable parameter range and stability of the precision garlic seed metering device. Considering the differences between simulation and bench tests and the operability of the virtual statistics, the calculation formulas for each simulation indicator were defined as follows:

$$S_f = \frac{n_{0f}}{N_f} \times 100\% \tag{8}$$

$$D_f = \frac{n_{1f}}{N_f} \times 100\% \tag{9}$$

$$M_f = \frac{n_{2f}}{N_f} \times 100\% \tag{10}$$

where S_f is the simulation qualified seeding index, [%]; D_f is the simulation reseeding index, [%]; M_f is the simulation miss-seeding index, [%]; n_{0f} is the single-seed pickup count, [pcs]; n_{1f} is the count of two or more seeds picked up, [pcs]; n_{2f} is the no-seed pickup count, [pcs]; and N_f is the theoretical seed pickup count, [pcs].

Bench-Test Materials and Equipment

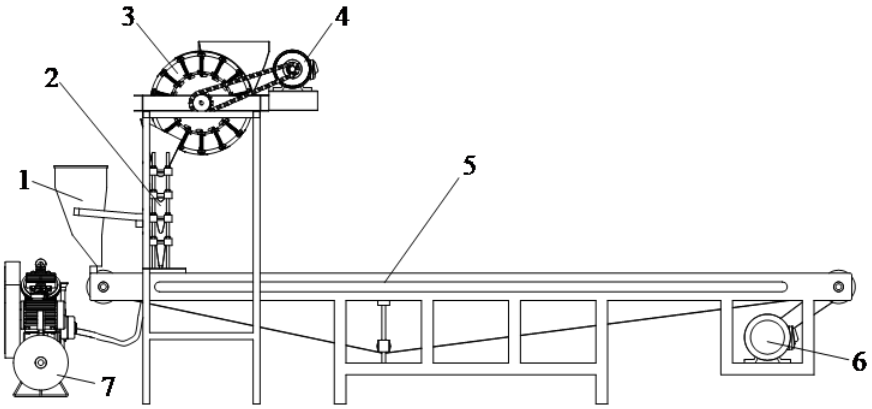


Fig. 10 – Test-bed of spoon-clamp garlic precision seeding device

1 – Soil Spreading Device; 2 – Three-stage Alignment Mechanism; 3 – Spoon-clamp Precision Garlic Seed Plate; 4 – Speed-regulating Motor for Seed Metering Device; 5 – Conveyor Belt; 6 – Speed-regulating Motor for Conveyor Belt; 7 – Air Pump

The test materials were three garlic varieties widely planted in the Heilongjiang region: “Acheng Purple Garlic”, “Zhaozhou White Garlic”, and “Nong’an Purple Garlic”. The cloves were manually graded and screened to ensure a moisture content of 55%–65%, plump and symmetrical shapes, and no scars, rot, or pest damage. Garlic cloves with similar specifications were selected for single-factor performance testing and validation of the seeding device.

A self-made spoon-clamp precision garlic seeding test bench was used, and its overall structure is shown in Fig. 10. The bench mainly consisted of a spoon-clamp precision garlic seed metering device, a seed alignment mechanism, a soil spreading device, a conveyor belt, and a speed-regulating motor. The seed metering device and alignment mechanism completed seed pickup and alignment. The positioning bowl in the alignment mechanism was opened and closed by an air pump. The soil spreading device mainly consisted of a soil box and adjustable baffles. It spread soil evenly on the conveyor belt, allowing the garlic cloves to fall into the soil on the conveyor belt after alignment.

The motors of the seed metering device and conveyor belt were controlled by frequency converters, which adjusted the working speeds and improved the operability of the test bench. The JPS-12 frequency converter was selected to ensure precise motor speed adjustment and stable bench operation. According to the agronomic requirements for garlic seeding spacing, a conversion relationship between the working speed of the seed metering device and the forward speed of the machine was needed. During the experiment, the forward speed of the machine was represented by the forward speed of the conveyor belt. The conversion relationship is expressed as follows:

$$N_P = \frac{60V_D}{S_Q N_Q} \cdot 1000 \tag{11}$$

where N_P is the rotational speed of the seed plate, [r/min]; V_D is the conveyor-belt speed, [m/s]; S_Q is the theoretical plant spacing, [mm]; and N_Q is the number of seed pickup spoons, [pcs].

Based on the mechanism analysis, DEM simulation, and production requirements, the main factors affecting the operational quality and suitable seeding range of the spoon-clamp precision garlic seeding device are seed plate speed and seed pickup spoon diameter. Bench tests were conducted to verify the effects of these two structural and operational parameters and to determine suitable parameter combinations for the tested garlic varieties.

Division of Sections and Variable Calculation

The measured spacing between adjacent garlic cloves was recorded as x_i, and the reference (theoretical) plant spacing was recorded as X_{ref}. The samples were divided into intervals with a step of $0.1X_{ref}$. The dimensionless spacing ratio for each observation was calculated using Equation (12).

$$X_i = \frac{x_i}{X_{ref}} \tag{12}$$

where X_i is the dimensionless spacing ratio; x_i is the measured spacing between adjacent garlic cloves, [mm]; and X_{ref} is the reference (theoretical) plant spacing, [mm].

The spacing of the tested garlic seed samples was divided into qualified intervals, reseeding intervals, and miss-seeding intervals. The division methods for each interval are as follows:

$$\begin{cases} \boldsymbol{n}_1' = \sum \boldsymbol{n}_i (\boldsymbol{X}_i \in \{0.0-0.5\}) \Rightarrow Reseeing\ Interval \\ \boldsymbol{n}_2' = \sum \boldsymbol{n}_i (\boldsymbol{X}_i \in \{0.5-1.5\}) \Rightarrow Qualified\ Interval \\ \boldsymbol{n}_3' = \sum \boldsymbol{n}_i (\boldsymbol{X}_i \in \{1.5-2.5\}) \Rightarrow Miss-Seeding\ Interval \\ \boldsymbol{n}_4' = \sum \boldsymbol{n}_i (\boldsymbol{X}_i \in \{2.5-3.5\}) \\ \boldsymbol{n}_5' = \sum \boldsymbol{n}_i (\boldsymbol{X}_i \in \{3.5-+\infty\}) \\ \boldsymbol{N} = \boldsymbol{n}_1' + \boldsymbol{n}_2' + \boldsymbol{n}_3' + \boldsymbol{n}_4' + \boldsymbol{n}_5' \quad \Rightarrow Number\ of\ Interval \end{cases} \tag{13}$$

The qualified count, reseeding count, and miss-seeding count of the measured garlic seed hill spacing can be expressed by Equation (14) as follows:

$$\begin{cases} \text{Qualified Count:}\ \ n_1 = N - 2n_2 \\ \text{Reseeding Count:}\ \ n_2 = n_1' \\ \text{Miss-seeding Count:}\ \ n_0 = n_3' + 2n_4' + 3n_5' \\ \text{Number of Intervals:}\ \ N' = n_2' + 2n_3' + 3n_4' + 4n_5' \\ \text{Average Qualified Spacing:}\ \ \bar{X} = \dfrac{\sum n_i X_i}{n_2} \qquad Xi \in \{> 0.5 \sim \leq 1.5\} \end{cases} \tag{14}$$

where n'_j (j = 1,…,5) is the number of observations in the *j-th* spacing interval; n_i is the frequency in interval i; X_i is the dimensionless spacing ratio; N is the total number of observations; n_1, n_2, and n_0 are the qualified, reseeding, and miss-seeding counts, respectively; N' is the equivalent total interval count; and $\bar{X}$ is the mean qualified spacing ratio.

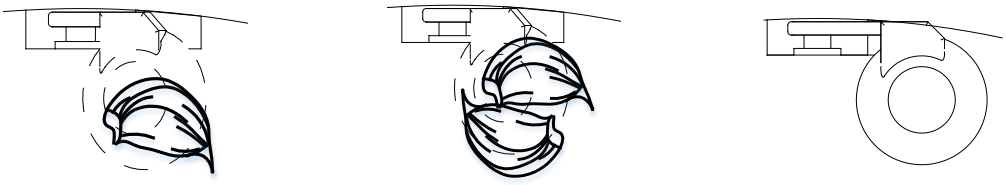
Calculation Methods for Seeding Performance Evaluation Indicators

Qualified Seeding Index, Miss-seeding Index, Reseeding Index, and Qualified Plant Spacing Index. The calculation methods for each performance indicator of the garlic seeding device in this study are shown in Equation (15) as follows:

$$\begin{cases} Qualified\ Seeding\ Index:\ \ \boldsymbol{S}_0 = \dfrac{\boldsymbol{n}_n}{\boldsymbol{N}'} \times 100\% \\ Qualified\ Plant\ Spacing\ Index:\ \ \boldsymbol{S} = \dfrac{\boldsymbol{n}_1}{\boldsymbol{N}'} \times 100\% \\ Reseeding\ Index:\ \ \boldsymbol{D} = \dfrac{\boldsymbol{n}_2}{\boldsymbol{N}'} \times 100\% \\ Miss-seeding\ Index:\ \ \boldsymbol{M} = \dfrac{\boldsymbol{n}_0}{\boldsymbol{N}'} \times 100\% \end{cases} \tag{15}$$

where S_0 is the qualified seeding index, [%]; S is the qualified plant spacing index, [%]; D is the reseeding index, [%]; M is the miss-seeding index, [%]; n_n is the single-seed pickup count, [pcs]; n_1 is the qualified single-seed discharge count, [pcs]; n_2 is the count of two or more seeds discharged, [pcs]; n_0 is the miss-seeding count, [pcs]; and N' is the total number of hill-spacing intervals in the sample, [pcs].

The evaluation criteria were as follows. In the single-factor tests of seed plate speed and seed pickup spoon diameter, the seed pickup spoon was judged as qualified if it held only one garlic clove after passing through the seed box, as shown in Fig. 11(a). If it held two or more garlic cloves, it was judged as reseeding, as shown in Fig. 11(b). If it did not hold any garlic clove, it was judged as miss-seeding, as shown in Fig. 11(c).



a) Qualified *b) Reseeding* *c) Miss-seeding*

Fig. 11 – Seed collection judgment: qualified, reseeding, and miss-seeding

RESULTS

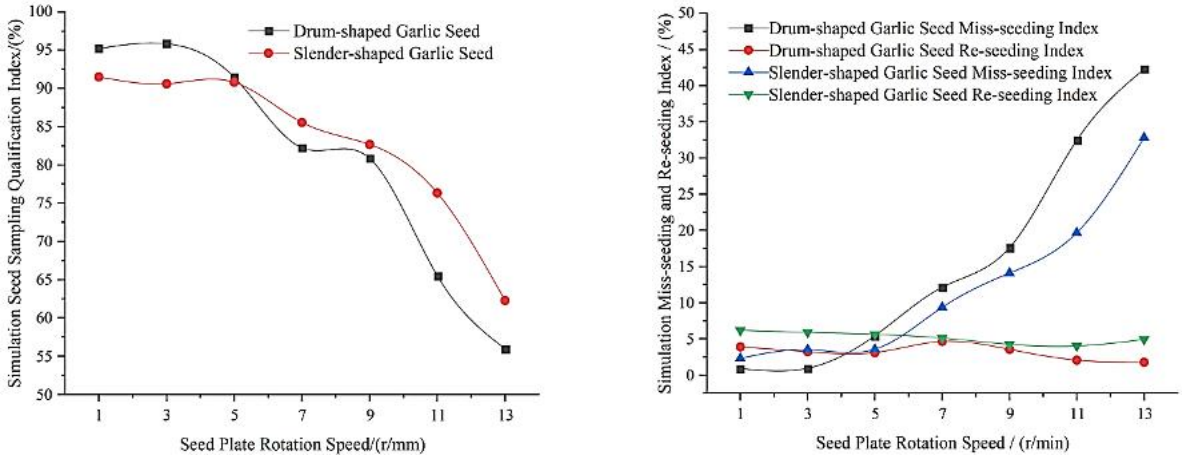
Simulation Results and Analysis

Seed plate speed and seed pickup spoon diameter were used as experimental factors, while qualified seeding index, reseeding index, and miss-seeding index were used as evaluation indicators. Single-factor DEM simulations were conducted for drum-shaped garlic cloves, represented by “Acheng Purple Garlic” and “Nong’an Purple Garlic”, and slender garlic cloves, represented by “Zhaozhou White Garlic”. These simulations were used to analyze the effect of each factor on seeding performance. Based on the structural dimensions of the seed metering device and the agronomic requirements for garlic seeding, the seed plate speeds were set to 1, 3, 5, 7, 9, 11, and 13 r/min. The seed pickup spoon diameter was fixed at 30 mm for the single-factor simulation on seed plate speed. The simulation results are shown in Table 3.

Table 3

Virtual simulation scheme and results for seed plate speed

Test Number	Operating Speed [r/min]	Drum-shaped			Slender		
		Qualified Index [%]	Reseeding Index [%]	Miss-seeding Index [%]	Qualified Index [%]	Reseeding Index [%]	Miss-seeding Index [%]
1	1	95.21	3.89	0.90	91.51	6.17	2.32
2	3	95.84	3.22	0.94	90.60	5.89	3.51
3	5	91.46	3.10	5.44	90.81	5.63	3.56
4	7	82.23	4.64	13.13	85.55	5.10	9.35
5	9	80.85	3.55	15.60	81.67	4.24	14.09
6	11	65.50	2.06	32.44	76.33	4.00	19.67
7	13	55.96	1.77	42.27	62.27	4.93	32.80



a) Simulation of qualified index *b) Simulation of reseeding and miss-seeding indices*

Fig. 12 – Single-factor simulation test of the rotation speed of seed metering plate

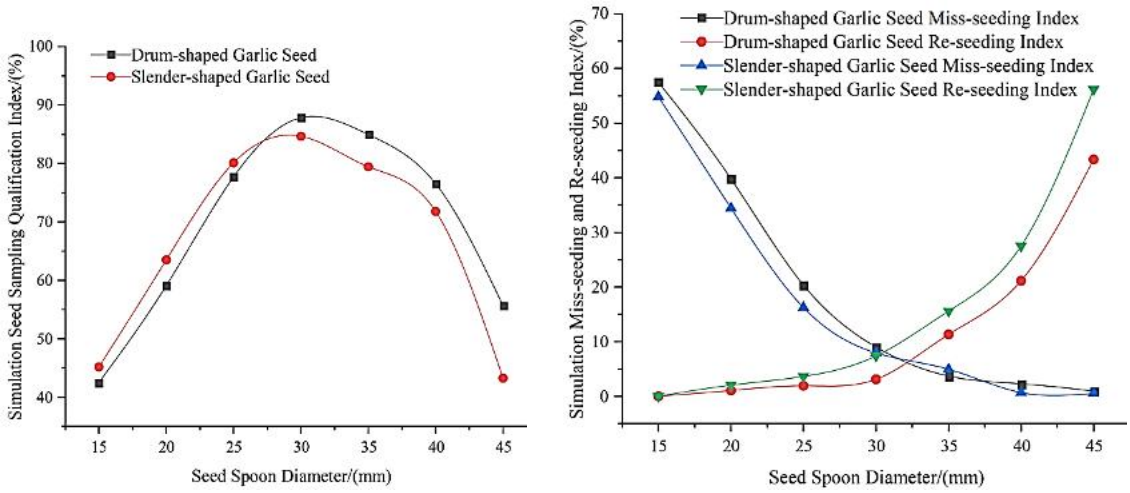
As shown in Fig. 12, the virtual simulation results showed that the qualified seeding index of both garlic-clove types first remained relatively stable and then decreased as seed plate speed increased. At low to medium speeds, the seed pickup spoon had sufficient contact time with the seed population, and the clamping mechanism could complete stable pickup and carrying. When the speed exceeded the suitable range, the contact time between the spoon and garlic cloves decreased. Collision disturbance also increased, which led to unstable pickup and higher miss-seeding. Under simulation conditions, the qualified seeding index was relatively high within 1–7 r/min, while the miss-seeding index increased continuously at higher speeds. The reseeding index was less affected by seed plate speed.

The seed pickup spoon diameters were set to 15, 20, 25, 30, 35, 40, and 45 mm. Other experimental conditions were fixed at a seed plate speed of 5 r/min for the single-factor simulation on seed pickup spoon diameter. The simulation results are shown in Table 4.

Table 4

Virtual simulation scheme and results for seed pickup spoon diameter

Test Number	Seed pickup spoon diameter [mm]	Qualified Index [%]	Drum-shaped Reseeding Index [%]	Miss-seeding Index [%]	Qualified Index [%]	Slender Reseeding Index [%]	Miss-seeding Index [%]
1	15	42.52	0	57.48	45.18	0	54.82
2	20	59.1	1.08	39.82	63.5	2.05	34.45
3	25	77.7	1.94	20.36	80.12	3.63	16.25
4	30	87.85	3.12	9.03	84.66	7.39	7.95
5	35	84.96	11.34	3.7	79.44	15.6	4.96
6	40	76.55	21.14	2.31	71.8	27.52	0.68
7	45	55.68	43.36	0.96	43.25	56.18	0.57



a) Simulation of qualified index *b) Simulation of reseeding and miss-seeding indices*

Fig. 13 – Single-factor simulation test of seed pickup spoon diameter

As shown in Fig.13, the qualified seeding index first increased and then decreased as seed pickup spoon diameter increased. A smaller spoon diameter reduced the effective contact area between the spoon and garlic clove, which resulted in a higher miss-seeding index. As the spoon diameter increased, the clove was more easily captured and carried. However, an excessively large spoon increased the probability of holding two or more cloves, and the reseeding index increased. The seed pickup spoon diameter should therefore match the size distribution of each garlic variety. Based on the single-factor simulation results, the suitable parameter range under DEM conditions was 1–7 r/min for seed plate speed and 25–35 mm for seed pickup spoon diameter.

Experimental Results and Analysis

"Acheng Purple Garlic", "Zhaozhou White Garlic", and "Nong'an Purple Garlic" were used as test materials to verify the influence of the selected factors on metering performance. Seed plate speed and seed pickup spoon diameter were taken as experimental factors. The qualified seeding index, miss-seeding index, reseeding index, and qualified plant spacing index were used as test indicators *(Xing et al., 2015)*. The seed plate speed ranged from 1 r/min to 10 r/min, and the seed pickup spoon diameter ranged from 20 mm to 44 mm.

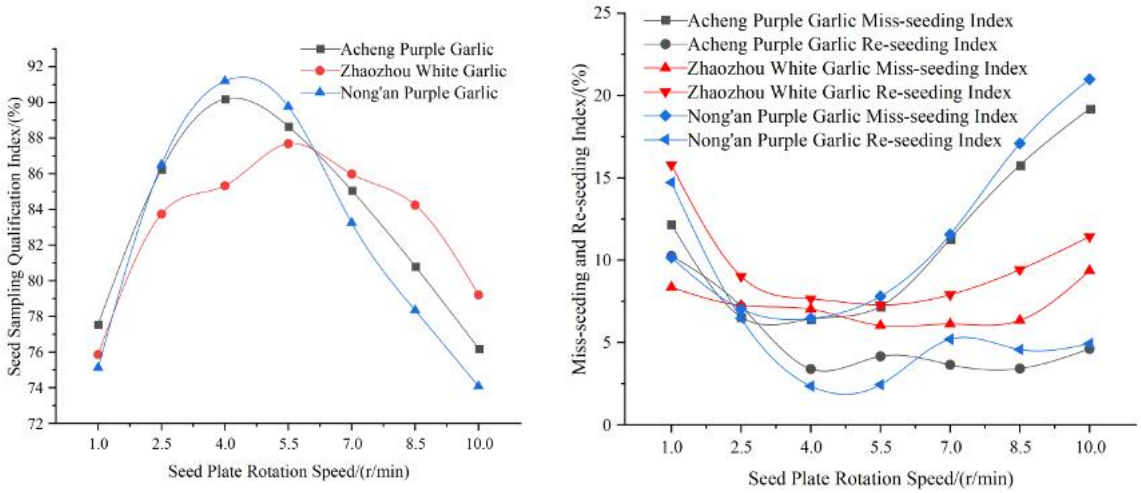
Influence of Seed Plate Working Speed on Seeding Performance

With the seed pickup spoon diameter fixed at 32 mm, the seed plate speed was set to seven levels: 1, 2.5, 4, 5.5, 7, 8.5, and 10 r/min. Each level was tested three times. The average values of the qualified seeding index, miss-seeding index, and reseeding index were used for analysis. The single-factor bench-test plan and results for seed plate speed with the three garlic varieties are shown in Table 5.

Table 5

Single-factor test scheme and results for seed plate speed

Garlic Variety	Test Number	Seed Plate Rotation Speed [r/min]	Test Indicators [%]		
			Qualified seeding Index	Miss-seeding Index	Reseeding Index
Acheng Purple Garlic	1	1	77.56	12.18	10.26
	2	2.5	86.26	6.55	7.19
	3	4	90.19	6.42	3.39
	4	5.5	88.65	7.19	4.16
	5	7	85.06	11.3	3.64
	6	8.5	80.81	15.77	3.42
	7	10	76.21	19.19	4.61
Zhaozhou White Garlic	8	1	75.86	8.35	15.79
	9	2.5	83.74	7.25	9.01
	10	4	85.33	7.02	7.65
	11	5.5	87.69	6.03	7.28
	12	7	85.98	6.12	7.9
	13	8.5	84.24	6.34	9.42
	14	10	79.21	9.36	11.43
Nong'an Purple Garlic	15	1	75.12	10.16	14.72
	16	2.5	86.51	7.03	6.46
	17	4	91.20	6.45	2.35
	18	5.5	89.77	7.80	2.43
	19	7	83.25	11.56	5.19
	20	8.5	78.34	17.09	4.57
	21	10	74.08	20.99	4.93



a) Influence of seed plate rotation speed on qualified seeding index

b) Influence of seed plate rotation speed on miss-seeding and reseeding indices

Fig. 14 – Single-factor test result curve of the rotation speed of the seed metering plate

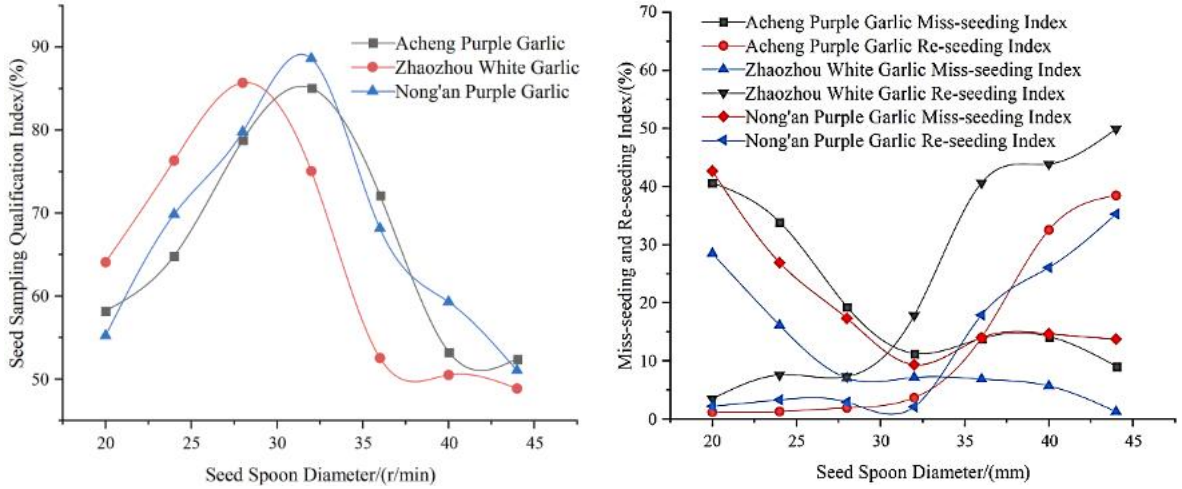
As shown in Fig. 14, the qualified seeding index of all three garlic varieties first increased and then decreased as seed plate speed increased. For "Acheng Purple Garlic" and "Nong'an Purple Garlic", the qualified index reached its maximum at 4 r/min. For "Zhaozhou White Garlic", the maximum value was obtained at 5.5 r/min. At a very low speed, the disturbance to the seed population was insufficient, which reduced the probability of stable single-clove pickup. At an excessively high speed, the spoon passed through the seed zone too quickly, and the cloves were more easily affected by collision and vibration. As a result, the miss-seeding index increased. The difference among varieties was mainly related to clove shape. The slender "Zhaozhou White Garlic" required a slightly higher speed to improve pickup probability, while the two drum-shaped varieties reached their suitable speed at 4 r/min.

Influence of Seed Pickup Spoon Diameter on Seeding Performance

Table 6

Single-factor test scheme and results for seed pickup spoon diameter

Garlic Variety	Test Number	Seed pickup spoon diameter [mm]	Test Indicators [%] Qualified seeding Index	Miss-seeding Index	Reseeding Index
Acheng Purple Garlic	1	20	58.21	40.64	1.15
	2	24	64.84	33.89	1.27
	3	28	78.78	19.32	1.9
	4	32	85.06	11.3	3.64
	5	36	72.15	13.84	14.01
	6	40	53.29	14.19	32.52
	7	44	52.46	9.1	38.44
Zhaozhou White Garlic	8	20	64.07	28.47	3.46
	9	24	76.32	16.12	7.56
	10	28	85.69	7.03	7.28
	11	32	75.05	7.14	17.81
	12	36	52.52	6.86	40.62
	13	40	50.49	5.66	43.85
	14	44	48.85	1.25	49.9
Nong'an Purple Garlic	15	20	55.21	42.64	2.15
	16	24	69.84	26.89	3.27
	17	28	79.78	17.32	2.9
	18	32	88.62	9.3	2.08
	19	36	68.15	13.99	17.86
	20	40	59.29	14.66	26.05
	21	44	51.02	13.72	35.26



a) Influence of seed pickup spoon diameter on qualified seeding index

b) Influence of seed pickup spoon diameter on miss-seeding and reseeding indices

Fig. 15 – Single-factor test result curve of seed pickup spoon diameter

As shown in Fig.15, the qualified seeding index of all three garlic varieties first increased and then decreased as seed pickup spoon diameter increased. The miss-seeding index decreased with increasing spoon diameter because the effective clamping and carrying area became larger. However, the reseeding index increased when the spoon diameter was too large, because two or more cloves could be picked up at the same time. The qualified seeding index reached its maximum at a spoon diameter of 32 mm for "Acheng Purple Garlic" and "Nong'an Purple Garlic", and at 28 mm for "Zhaozhou White Garlic". These results were consistent with the garlic-clove size differences measured in Table 1. Compared with the simulation results, the bench-test qualified indexes were lower because the real cloves had irregular surfaces, skin deformation, and non-uniform contact states. Therefore, the DEM simulation was used to determine the suitable parameter range, while the final parameter combination was verified by bench tests. Because the validation was conducted on a laboratory bench, field conditions such as vibration, soil resistance, ground-wheel slip, and non-uniform seed supply may affect the actual sowing performance. Further field validation and multi-factor optimization are needed in future work.

CONCLUSIONS

A spoon-clamp type garlic seed metering device was designed to improve the stability of single-clove pickup and carrying. The device integrates spoon pickup, spring-assisted clamping, seed cleaning, and controlled discharge. This structure is suitable for garlic cloves with irregular shapes and size variation.

DEM simulations were conducted to analyze the effects of seed plate speed and seed pickup spoon diameter. The qualified seeding index decreased at excessive seed plate speeds because seed pickup time was reduced and collision disturbance increased. Under simulation conditions, the suitable parameter range was 1–7 r/min for seed plate speed and 25–35 mm for seed pickup spoon diameter.

Bench tests verified the feasibility of the proposed mechanism under controlled test conditions. The suitable parameter combination was 4 r/min and 32 mm for “Acheng Purple Garlic” and “Nong’an Purple Garlic”, and 5.5 r/min and 28 mm for “Zhaozhou White Garlic”. Future work should focus on field validation, vibration adaptability, and multi-factor optimization of the garlic seed metering device.

ACKNOWLEDGEMENT

This study was funded by the Experimental Study on the Mechanism and Parameter Optimization of High-efficiency and Low-loss Screening of Trommel Screen of Flat Fritillary Harvester (XDB202401), and by the Heilongjiang Province “Double First-Class” Discipline Collaborative Innovation Achievement Projects of the Education Department of Heilongjiang Province (Grant Nos. LJGXCG2023–050 and LJGXCG2022–112).

REFERENCES

[1] Bakhtiari M.R., Loghavi M., (2009). Development and evaluation of an innovative garlic clove precision planter. *Journal of Agricultural Science and Technology*, Vol. 11, no. 2, pp. 125–136, Tehran/Iran.

[2] Bertrand F., Leclaire L.-A., Levecque G., (2005). DEM-based models for the mixing of granular materials. *Chemical Engineering Science*, Vol. 60, no. 8–9, pp. 2517–2531, Amsterdam/Netherlands. DOI: https://doi.org/10.1016/j.ces.2004.11.048

[3] Choi D.K., Park W.K., Kang T.G., Park S.H., Kim H.J., Kwak T.Y., Kim Y.K., (2003). *Garlic upright-positioning and planting device*. Patent, No. US6619219B2, USA.

[4] Cui R., Huang J., Zhang Z., Wang X., Jian S., (2018). Research status of garlic mechanized sowing technology (大蒜机械化播种技术研究现状). *Agricultural Equipment & Vehicle Engineering*, Vol. 56, no. 6, pp. 54–56, China.

[5] Cundall P.A., Strack O.D.L., (1979). A discrete numerical model for granular assemblies. *Géotechnique*, Vol. 29, no. 1, pp. 47–65, London/United Kingdom. DOI: https://doi.org/10.1680/geot.1979.29.1.47

[6] Dong X., Lu J., Wu Y., Sha Y., (2015). Research and development on automatic garlic planting machine. *Proceedings of the International Conference on Logistics, Engineering, Management and Computer Science*, Advances in Intelligent Systems Research, Atlantis Press, pp. 1531–1535, Paris/France, ISBN: 978-94-6252-102-5, ISSN: 1951-6851. DOI: https://doi.org/10.2991/lemcs-15.2015.305

[7] Fang F.H., Song J.L., Wang Z., Li K.Q., Zhang Y.Z., Zhou L., Li C., (2024). Design and experiment of air-suction precision seed-metering device for garlic (大蒜气吸式精量排种器的设计与试验). *INMATEH Agricultural Engineering*, Vol. 74, no. 3, pp. 721–731, Bucharest / Romania. DOI: https://doi.org/10.35633/inmateh-74-64

[8] GB/T 6973-2005, (2005). *Test methods for single-seed (precision) planters (单粒（精密）播种机试验方法)*. Standard, China.

[9] Geng A.J., Zhang Z.L., Song Z.H., Yang J.N., Li R.X., Hou J.L., Liu S.Q., (2016). Kinematic analysis and parameter optimized experiment of garlic box putting process (蒜种盒机械投放过程运动学分析与参数优化试验). *Transactions of the Chinese Society of Agricultural Engineering*, Vol. 32, no. 5, pp. 29–35, Beijing/China. DOI: https://doi.org/10.11975/j.issn.1002-6819.2016.05.004

[10] Han X., (2011). *Cone-plate type seed metering garlic dibbling machine (锥盘式排种器大蒜点播机)*. Patent, No. CN201911025U, China.

[11] Hou J.L., Fang L.Z., Zhang H.K., Zhou K., Li T.H., Li Y.H., (2024). Design and experiment of multi-disturbance cleaning and single-seed sowing device for garlic (多重扰动清种式大蒜单粒取种排种器设计与试验). *Nongye Jixie Xuebao / Transactions of the Chinese Society for Agricultural Machinery*, Vol. 55, no. 1, pp. 65–75, Beijing/China. DOI: https://doi.org/10.6041/j.issn.1000-1298.2024.01.006

[12] Hou J.L., Wang H.X., Niu Z.R., Xi R., Li T.H., (2019). Discrete element simulation and experiment of picking and clearing performance of garlic seed-picking device (大蒜取种装置取种清种性能离散元模拟与试验). *Transactions of the Chinese Society of Agricultural Engineering*, Vol. 35, no. 24, pp. 48–57, Beijing/China. DOI: https://doi.org/10.11975/j.issn.1002-6819.2019.24.006

[13] Hu G., (2010). *Discrete element method analysis and simulation of particulate systems: Industrial applications of DEM and introduction to EDEM software (颗粒系统的离散元素法分析仿真：离散元素法的工业应用与 EDEM 软件简介)*, Wuhan University of Technology Press, Wuhan/China, ISBN: 978-7-5629-3169-0.

[14] Jiang H., (2018). Research status and development trend analysis of garlic planters (大蒜播种机研究现状及发展趋势分析). *Southern Agricultural Machinery*, Vol. 49, no. 17, p. 58, China.

[15] Kang B.J., (2000). *Garlic sowing machine*. Patent, No. KR1020000056342, Korea.

[16] Li J., Webb C., Pandiella S.S., Campbell G.M., (2003). Discrete particle motion on sieves—a numerical study using DEM simulation. *Powder Technology*, Vol. 133, no. 1–3, pp. 190–202, Amsterdam/Netherlands. DOI: https://doi.org/10.1016/S0032-5910(03)00092-5

[17] Li X.Y., Geng A.J., Hou J.L., Zhang J., Zhang Z.L., (2017). Design and experiment of full-automatic lifting and releasing device of garlic seed box (全自动蒜种盒提取投放装置设计与试验). *Transactions of the Chinese Society of Agricultural Engineering*, Vol. 33, no. 23, pp. 29–35, Beijing/China. DOI: https://doi.org/10.11975/j.issn.1002-6819.2017.23.005

[18] Li Y.H., Zhang Z.L., Li T.H., Wu Y.Q., Niu Z.R., Hou J.L., (2020). Design and experiment of wheel-spoon type garlic precision seed-picking device (轮勺式大蒜单粒取种装置设计与试验). *Nongye Jixie Xuebao / Transactions of the Chinese Society for Agricultural Machinery*, Vol. 51, no. 3, pp. 61–68, Beijing/China.

[19] Liu J., Geng A., Li X., Hou J., Han X., (2019). Research status of single-seed picking and reseeding technology for garlic planters (大蒜播种机单粒取种及补种技术研究现状). *Journal of Agricultural Mechanization Research*, Vol. 41, no. 2, pp. 262–268, China.

[20] Liu W., He J., Li H., Li X., Zheng K., Wei Z., (2018). Calibration of simulation parameters for potato minituber based on EDEM (基于离散元的微型马铃薯仿真参数标定). *Nongye Jixie Xuebao / Transactions of the Chinese Society for Agricultural Machinery*, Vol. 49, no. 5, pp. 125–135, Beijing/China. DOI: https://doi.org/10.6041/j.issn.1000-1298.2018.05.014

[21] NY/T 503-2015, (2015). *Operational quality of single-seed (precision) planters (单粒（精密）播种机作业质量)*. Standard, China.

[22] Qian L.B., (2008). *Digital design methodology of openers based on the discrete element method (基于离散元法的开沟器数字化设计方法研究)*, PhD dissertation, Jilin University, Changchun/China.

[23] Sakaguchi E., Suzuki M., Favier J.F., Kawakami S., (2001). PH—postharvest technology: Numerical simulation of the shaking separation of paddy and brown rice using the discrete element method. *Journal of Agricultural Engineering Research*, Vol. 79, no. 3, pp. 307–315, London/United Kingdom. DOI: https://doi.org/10.1006/jaer.2001.0706

[24] Shao M.X., Zhang X.M., Fang L.Z., Ma G.C., Tian J., Fu S.H., (2025). Research progress on mechanized garlic seeding technology in China. *International Journal of Agricultural and Biological Engineering*, Vol. 18, no. 2, pp. 9–20, Beijing/China. DOI: https://doi.org/10.25165/j.ijabe.20251802.9035

[25] Sharma V., Das L., Pradhan R.C., Naik S.N., Bhatnagar N., Kureel R.S., (2011). Physical properties of tung seed: An industrial oil-yielding crop. *Industrial Crops and Products*, Vol. 33, no. 2, pp. 440–444, Amsterdam/Netherlands. DOI: https://doi.org/10.1016/j.indcrop.2010.10.031

[26] Tang H., (2018). *Design and mechanism study of a corrugated-surface finger-clamping precision maize seed metering device (波纹曲面指夹式玉米精量排种器设计及其机理研究)*, PhD dissertation, Northeast Agricultural University, Harbin/China.

[27] Wei H., Wang X., Chen J., Cui R., (2022). Discussion on the present situation and development of mechanized garlic production in China (中国大蒜机械化生产现状与发展思路探讨). *Journal of Chinese Agricultural Mechanization*, Vol. 43, no. 4, pp. 175–182, China. DOI: https://doi.org/10.13733/j.jcam.issn.2095-5553.2022.04.025

[28] Xie D.B., Zhang C.L., Wu X.Q., Wang W.W., Liu L.C., Chen L.Q., (2022). Design and test of garlic seed placer with seed-disturbing-tooth-assisted air suction (扰种齿辅助气吸式大蒜排种器设计与试验). *Nongye Jixie Xuebao / Transactions of the Chinese Society for Agricultural Machinery*, Vol. 53, no. 2, pp. 47–57, Beijing/China. DOI: https://doi.org/10.6041/j.issn.1000-1298.2022.02.005

[29] Xie X., Zhang Y., Liu Z., Cheng Y., Liu C., Bi L., (2015). Design of planting mechanism for garlic planter (大蒜播种机种植机构的设计). *Transactions of the Chinese Society of Agricultural Engineering*, Vol. 31, no. 1, pp. 34–39, Beijing/China. DOI: https://doi.org/10.3969/j.issn.1002-6819.2015.01.005

[30] Xing H., Zang Y., Wang Z., Luo X., Zhang G., Cao X., Gu X., (2015). Design and experiment of stratified seed-filling room on rice pneumatic metering device (水稻气力式排种器分层充种室设计与试验). *Transactions of the Chinese Society of Agricultural Engineering*, Vol. 31, no. 4, pp. 42–48, Beijing/China. DOI: https://doi.org/10.3969/j.issn.1002-6819.2015.04.006

[31] Yang S.C., Hsiau S.S., (2000). Simulation study of the convection cells in a vibrated granular bed. *Chemical Engineering Science*, Vol. 55, no. 18, pp. 3627–3637, Amsterdam/Netherlands. DOI: https://doi.org/10.1016/S0009-2509(00)00040-3

[32] Yu J.Q., Fu H., Li H., Shen Y.F., (2005). Discrete element method and its application in the research and design of agricultural machinery working components (离散元法及其在农业机械工作部件研究与设计中的应用). *Transactions of the Chinese Society of Agricultural Engineering*, Vol. 21, no. 5, pp. 1–6, Beijing/China.

[33] Zhang D.Q., Wu Y.J., Zhang C.K., (2014). Vertical planting structure design for planter. *Applied Mechanics and Materials*, Vol. 654, pp. 87–90, Switzerland. DOI: https://doi.org/10.4028/www.scientific.net/AMM.654.87

MECHANIZED DETASSELING TECHNOLOGY FOR CORN SEED PRODUCTION: GLOBAL PROGRESS, KEY CHALLENGES, AND OPTIMIZATION STRATEGIES

/

制种玉米机械化去雄技术：全球进展、核心挑战与优化策略

Yang LI [1,2], Yiteng LEI [*1], Luochuan XU[1], Wei DONG [1]

[1] College of Electronic Engineering, Yili Normal University, Yining, 835000, China;

[2] Key Laboratory of Micro Nano Electric Sensing Technology and Bionic Instruments, Yili Normal University, Yining, 835000, China.

Tel: +8615699398577; E-mail: younger1425580067@163.com

DOI: https://doi.org/10.35633/inmateh-79-32

Keywords: *Seed production of corn, Mechanized elimination of male dominance, Intelligent recognition, Integration of agricultural machinery and agronomy, constraints.*

ABSTRACT

Detasseling the female parent plants is a critical operation in hybrid corn seed production. This article systematically reviews global developments in mechanized detasseling technology for corn seed production. First, it provides an in-depth analysis of two key technologies supporting mechanized detasseling: the biomechanical characteristics of corn tassels and intelligent tassel-detection technologies based on machine vision and photoelectric sensing. Second, the current development of mechanized detasseling equipment is reviewed, and the technical parameters and field performance of representative domestic and international machines are compared in detail. The comparison identifies four major constraints limiting the wider adoption of this technology in China: an insufficient single-pass detasseling rate, poor coordination between machinery and agronomic practices, a high crop-damage rate, and low acceptance among farmers. Finally, three targeted optimization strategies are proposed: developing intelligent and precision detasseling equipment, promoting closer integration of agricultural machinery and agronomy, and strengthening field demonstration and extension activities. This review aims to provide a theoretical basis and practical reference for improving mechanized detasseling processes and supporting the development of more effective detasseling equipment.

摘要

母本去雄是制种玉米的核心生产环节。本文系统综述了全球制种玉米机械化去雄技术的发展动态。首先，深入分析了支撑机械化去雄的两大关键技术：雄穗生物力学特性研究与基于机器视觉、光电传感的智能识别技术。其次，梳理了机械化去雄装备的发展现状，详细对比了国内外主流机型的技术参数与作业性能。通过国内外发展现状比较，明确指出当前制约我国技术推广的四大瓶颈：一次性去净率不足、农机农艺不匹配、作业损伤率高以及农户接受度低。最后，针对性地提出三大优化策略：研发智能精细化装备、促进农机农艺深度融合、加强示范推广。本文旨在为优化机械去雄工艺与装备研发提供理论依据和参考。

INTRODUCTION

Corn can not only be used as a food crop, but also widely applied in various fields such as feed, food processing, medical and health care, light industry, chemical industry, and bioenergy *(Liu et al., 2024; Jahangirlou et al., 2023; Chukwutem et al., 2023)*. According to statistics from the Food and Agriculture Organization of the United Nations (FAO), corn has always been the second largest crop in terms of global cultivation area, second only to wheat. Its total yield and yield per unit area are higher than other major grains such as wheat and rice *(Rosegrant et al., 2009)*. High quality corn seeds are the foundation for ensuring high and stable yield of corn *(Singh et al., 2025)*. China's corn varieties are mainly hybrid varieties, and their hybrid advantage is mainly reflected in the first generation. From the second generation onwards, the advantage gradually decreases, so annual seed production is needed to maintain their potential for increased yield *(Wang et al., 2013; Su et al., 2003)*.

Seed production of corn refers to the process of selecting, breeding, producing, and processing high-quality seeds from superior species of corn through multiple techniques, such as selection, breeding, production, and processing, to be suitable for replanting, expansion, or sowing *(Wych et al., 1988; Liu et al., 2024)*. Compared to regular corn, seed corn has better economic benefits and the planting area has been increasing year by year in recent years *(Shahrokhi et al., 2024; Si et al., 2026)*.

Yang LI, lecturer; Yiteng LEI, Associate Professor; Luochuan XU, lecturer;Wei DONG, lecturer.

In China, the planting area of seed corn accounts for about 98% of the total planting area of corn *(Shi et al., 2014)*. Therefore, the sustained high yield and high quality of seed corn are of great significance for food security and economic stability *(Huang et al., 2024)*.

The removal of male parents is the core production process of seed corn. Timely and complete tassel removal effectively prevents self-pollination in seed-production fields, thereby ensuring the genetic purity and quality of the hybrid seed. It may also help reduce the risk of certain field diseases and pests *(Felkl et al., 1988; Darrah et al., 2019)*. Seed purity is a key indicator for evaluating the quality of corn hybrids *(Liu et al., 2024)*, and male removal is the most difficult and difficult key step to accurately control in the hybrid seed production process *(Liu et al., 2014; Tian et al., 2014)*. This article systematically analyzes the current development status of male elimination technology and equipment, identifies the main problems in male elimination operations, and proposes targeted improvement suggestions, in order to provide theoretical basis and reference for optimizing mechanical male elimination processes and equipment research and development.

AGRONOMY OF MALE REMOVAL IN CORN SEED PRODUCTION

To ensure the production of high-quality hybrid seed that meets purity standards, all tassels on the female parent plants must be removed before pollen shedding and preferably before full tassel emergence. The operation should follow the principles of timeliness, completeness, and thoroughness *(Tian et al., 2014; Moreira et al., 2010)*. According to the national standard *(GB/T 17315-2011)*, when the cumulative loose powder plant rate exceeds 1% during the entire male removal process, the seed field is scrapped. At present, there are two main methods for male removal in seed production of corn: manual male removal and mechanical male removal.

Manual detasseling commonly follows the principle of removing the tassels before they fully emerge from the leaf whorl. This operation may involve manually opening or removing the leaves enclosing the tassel, or removing one or two upper leaves before tassel emergence. Care must be taken to ensure that no tassel branches remain and that the plants are not broken or otherwise damaged during the operation *(Han et al., 2011; Czepak et al., 2019)*. Detasseling is preferably carried out in the morning and should be avoided on rainy days. It must be completed before the tassels fully emerge and begin shedding pollen *(Bai et al., 2022)*. The main advantage of manual detasseling is that it can reduce damage to the leaves and plants while allowing the operation to be performed at the most appropriate stage according to the growth condition of each plant *(Lu et al., 2010)*. However, it also has several evident disadvantages, including low working efficiency, high labour intensity, high production costs, unfavorable working conditions, and strong dependence on weather conditions *(Asefa et al., 2026; Han et al., 2011; Cui et al., 2010)*. In addition, manual detasseling generally requires five to seven repeated passes to meet pollination-control requirements. The first three or four passes mainly involve tassel removal, whereas the subsequent passes focus on identifying and removing missed or late-emerging tassels *(Tang et al., 2017; Fan et al., 2021)*.

Mechanical detasseling involves using a dedicated detasseling machine to remove tassels from the female parent plants. This method is particularly suitable for varieties with a relatively high number of upper leaves and a low ear position. The operation is generally initiated when approximately one-third of the tassel has emerged above the uppermost leaf.

During tassel removal, no more than two leaves should preferably be removed, with three leaves regarded as the maximum acceptable number *(Ghețe et al., 2020; Nicoletti et al., 2023)*. After mechanical detasseling, a timely manual follow-up inspection is required to remove missed tassels and any residual tassel branches *(Liu et al., 2010; Wu et al., 2013)*.

However, mechanical detasseling may cause substantial damage to the plants and consequently reduce yield. In addition, detasseling performance remains relatively unstable, with reported removal rates generally ranging from 80% to 90% *(Wilhelm et al., 1995; Wang et al., 2024; Prodanović et al., 2022)*.

Compared with manual detasseling, this method offers several important advantages, including high operational efficiency, less dependence on environmental and human factors, good maneuverability, suitability for large-scale field deployment, and improved working conditions for operators *(Sabljak et al., 2019)*. Therefore, the development and wider adoption of mechanical detasseling remain essential for promoting efficient and large-scale corn seed production *(Zhang et al., 2024; Ghimire et al., 2025)*.

RESEARCH STATUS OF DETASSELING TECHNIQUES FOR SEED PRODUCTION CORN

Mechanical Properties of Tassels

The mechanical properties of corn tassels in seed-production fields are key physical parameters for the design and optimization of detasseling equipment *(Jia et al., 1990)*, and have been studied for many years.

In 1990, American researchers *Jia et al.* pioneered the measurement of the manual pulling force required to remove tassels from different varieties of seed corn. They also analyzed the effects of gripping position, field location, and operating time on the pulling force. The results indicated that the average and maximum manual pulling forces for tassel removal were 58.3 N and 92.5 N, respectively. It was found that the corn variety, gripping position, and field location had a significant impact on the pulling force, whereas the time of day during which the operation was performed showed no significant effect *(Jia et al., 1990)*.

Subsequently, *Zhang et al.* conducted correlation and path analysis on nine stalk traits and the unit volume stalk rupture resistance (UVSRP) using a set of diallel cross combinations. The study found that the length of the tassel main axis showed a highly significant positive correlation with UVSRP, whereas the fresh weight of biomass below the ear, the length of the stalk below the ear, the fresh weight of the stalk, ear height, and the stalk length-to-thickness ratio exhibited highly significant negative correlations with UVSRP. Therefore, an appropriate tassel main axis length can serve as an important reference trait for breeding corn varieties with enhanced stalk lodging resistance *(Zhang et al., 2006)*. Wang conducted experimental and theoretical analyses on the tassel pulling force characteristics, plant elastic modulus, and spatial distribution traits of seed corn plants during the detasseling period. The study obtained the range of pulling forces for two inbred lines, Zheng 58 and PH6WC, at different growth stages, and determined their elastic modulus during detasseling as well as the natural spatial distribution patterns of the plants *(Wang et al., 2016)*. Jin further investigated the pulling force characteristics of tassels during the detasseling period, using Xianyu 335, a corn variety widely cultivated in Northeast China, as the research subject. The results showed that during the stage when the tassel had grown 5-10 cm and before pollen shedding, the maximum pulling force was 56.5 N, and the maximum cross-sectional area was 31.2 mm², with the pulling force being proportional to the cross-sectional area *(Jin et al., 2019)*.

Recently, *Ou et al.* systematically calibrated the physical property parameters of tassels in seed corn. Through mechanical tests, the bending modulus and shear strength were determined to be 46.41 MPa and 0.76 MPa, respectively. Furthermore, simulation tests involving rotary cutting components for tassel removal revealed that vertical feed cutting had the least impact on tassel bending deformation *(Ou et al., 2024)*.

Tassel recognition technology

With the advancement of agricultural modernization and intelligentization, the deep integration of computer technology into agricultural machinery and equipment has become a significant development trend *(Kasal et al., 2025; Rodene et al., 2024)*. Currently, achieving automatic recognition of corn tassels using advanced sensing technologies is a key link in enhancing the precision and intelligence of detasseling operations. Researchers both domestically and internationally have actively explored this direction, primarily focusing on two technical pathways: machine vision recognition and photoelectric sensing *(Shepard et al., 2024; Cao et al., 2025)*.

Machine vision recognition technology

Machine vision technology offers several advantages, including nondestructive operation, high accuracy and efficiency, substantial information-processing capacity, strong real-time performance, and flexibility. It has therefore received considerable attention and has been widely applied in precision *agriculture (Gong et al., 2007)*.

The earliest application of this technology to corn tassel recognition research in China was conducted by Tang Wenbing from China Agricultural University. Tang et al. designed and constructed a corn tassel recognition system based on binocular stereo vision, as shown in Figure 1. The hardware of the system primarily consisted of two CMOS color cameras of the same model, a pan-tilt, lenses, a conversion box, and a laptop computer. The workflow was as follows: first, preprocessing the captured images, using color features as the main basis for tassel extraction; then, obtaining the effective tassel regions through image segmentation techniques, and performing image matching based on the segmentation results using binocular stereo vision technology; finally, calculating depth information to determine the specific three-dimensional spatial position of the tassels *(Tang et al., 2011)*.



a) b)

Fig. 1 - Recognition Effect Diagram (Tang et al., 2011)

a) Original image; b) Segmented image

Kumar et al. proposed a novel method for corn ear detection based on k-means clustering and adaptive threshold segmentation. The study, focusing on the task of corn panicle detection in UAV images, developed a semi-automatic image annotation method to facilitate the rapid construction of labeled datasets for corn crops. A tool developed based on this method can be integrated with machine learning models to provide initial annotation results for given images and supports interactive user modification and refinement *(Kumar et al., 2021).*

Wang et al. compared three object detection models-Faster R-CNN, SSD, and YOLO_X-using UAV imagery and a transfer learning approach. The results showed that transfer learning significantly improved model performance, with YOLO_X performing the best, achieving a recognition precision of 97.16% and a mean average precision (mAP) of 93.60%. The study also found significant differences in detection adaptability across varieties, with Zhengdan 958 showing the best detection results. Moreover, as planting density increased, the mean absolute error of detection rose from 0.19 to 0.75. This research provides a reliable method for high-throughput detection of corn tassels in the field *(Wang et al., 2022)*.

Kurtulmuş et al. developed a corn tassel detection algorithm suitable for outdoor field environments. The algorithm utilizes color information and a Support Vector Machine (SVM) classifier for image binarization based on standard RGB images. It achieves tassel cutting position detection while effectively controlling the false positive rate. On the test set, the correct detection rate of this method reached 81.6% *(Kurtulmuş et al., 2014).*

National standards and seed purchasers impose stringent requirements on the tassel removal rate in seed corn production. Consequently, the identification of missed tassels has become a research hotspot *(Falahat et al., 2023; Ding et al., 2026). Li et al.* proposed a lightweight tassel detection model named MLCE-RTMDet. Based on the RTMDet-tiny architecture, this model employs MobileNetV3 as the backbone feature extraction network to reduce computational load and incorporates the CBAM attention mechanism to enhance multi-scale feature extraction capability for tassels, thereby mitigating the potential performance degradation associated with lightweight networks. Furthermore, the model utilizes EIOU Loss instead of GIOU Loss, further improving the accuracy of tassel detection. This research can provide effective technical support for detecting missed tassels after manual detasseling in corn seed production fields *(Li et al., 2024).*

Yang et al. integrated machine vision and UAV remote sensing technologies to collect visible-light images of corn during the tasseling stage. To construct a dataset and enhance model robustness, they employed the Segment Anything Model (SAM) for semi-automatic annotation and applied image augmentation techniques to simulate environmental variations. The study improved the YOLOv5 framework by introducing the lightweight MobileNetV3 network to reduce parameters and optimizing the network architecture for accurate detection of missed tassels. Experiments demonstrated that this method can automatically identify missed female tassels in the field, effectively evaluate detasseling performance, and provide precise location guidance for follow-up removal operations *(Yang et al., 2026)*.

Computer vision technology plays a central role in image recognition, and deep learning-based object detection algorithms (such as Faster R-CNN, SSD, and the YOLO series) have been widely applied to corn tassel recognition *(Duangpapeng et al., 2018; Alzadjali et al., 2021; Niu et al., 2024)*. Researchers train models using large, annotated datasets of tassel images, enabling the models to learn key information about tassel appearance, color distribution, and texture features. The trained models can then accurately identify tassels in new images captured by UAVs, providing reliable, high-throughput information on tasseling status for breeders *(Qi et al., 2025)*. However, the recognition accuracy of such models for small-target tassels remains insufficient, and their algorithmic performance requires further optimization.

Optoelectronic sensing recognition technology

Gu et al. designed an infrared detection-based corn detasseling machine, as shown in Figure 2. The machine mainly consists of a frame, a lifting device, a detasseling device, and an infrared detection unit. Its core innovation lies in the integration of an infrared detection unit in front of the detasseling unit, which contains multiple sets of infrared sensor pairs for precisely locating the height of the tassels. During field operation, when the top of the corn plant interrupts the optical path of the infrared sensor pairs, the control mechanism adjusts the working height of the hydraulic detasseling device in real time based on multiple height signals, thereby achieving precise alignment and adaptive control of the detasseling position *(Gu et al., 2013)*.

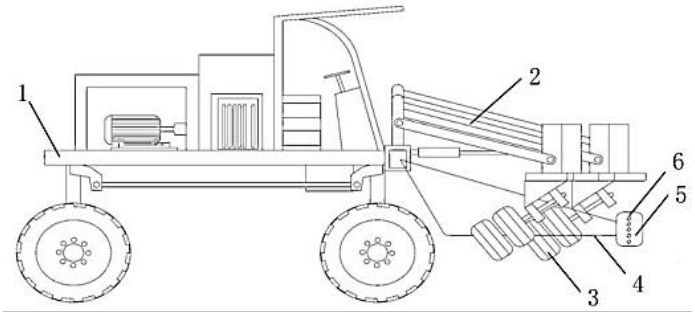


Fig. 2 - Infrared-guided corn detasseling machine *(Gu et al., 2013)*

1. Frame; 2. Lifting mechanism; 3. Profiling mechanism; 4. Connecting rod; 5. Infrared detection unit; 6. Infrared sensor

Liu et al. developed a height-adaptive corn detasseling device, as shown in Fig.3. The device primarily consists of a detasseling bracket and a control module. Two detasseling discs are mounted on the bracket, which is also equipped with a bracket hydraulic cylinder and a hydraulic cylinder for the sensor support rod. A reflector mechanism and a photoelectric sensor mechanism are installed at the front end of the bracket. During operation, the photoelectric sensor continuously detects tassel height and transmits the signal to the control module. The control module then actuates the bracket hydraulic cylinder to extend or retract, thereby adjusting the working height of the detasseling discs and profiling rollers. This enables the device to adapt to variations in corn tassel height during detasseling *(Liu et al., 2025)*.

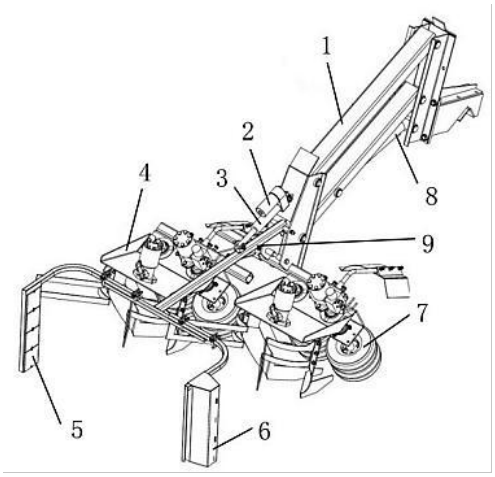


Fig. 3 - Height-adaptive corn detasseling header *(Liu et al., 2025)*

1. Frame; 2. Control module; 3. Hydraulic cylinder for the photoelectric-sensor support rod; 4. Profiling disc; 5. Reflector mechanism; 6. Photoelectric sensor mechanism; 7. Profiling roller; 8. Bracket hydraulic cylinder; 9. Profiling bracket

Wang et al. designed a single-row profiling and lifting mechanism for corn detasseling, as shown in Fig.4. The device mainly consists of a hydraulic lifting cylinder, a parallel four-bar linkage, a hydraulic motor, and photoelectric sensors. The photoelectric sensors are installed at the front of the frame on both sides of the sensor mounting bracket. The detasseling wheels are mounted behind the sensors and connected to an electric push rod. The entire detasseling assembly is connected to the parallel four-bar linkage, whose vertical movement is controlled by the hydraulic cylinder. A displacement sensor is mounted on the hydraulic cylinder and connected to the piston rod to monitor changes in piston displacement and convert them into pulse signals. Based on the signals received from the photoelectric sensors and the displacement sensor, the controller regulates the extension and retraction of the hydraulic cylinder and electric push rod. This enables the detasseling unit to follow variations in tassel height and perform adaptive detasseling *(Wang et al., 2015)*.

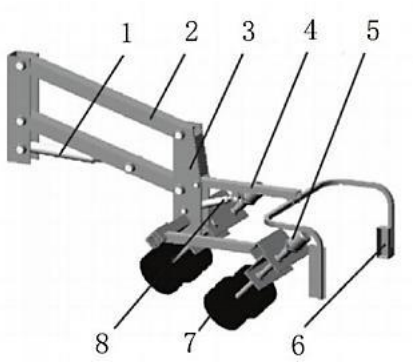


Fig. 4 - Single-row profiling and lifting mechanism for corn detasseling *(Wang et al., 2015)*

1. Hydraulic cylinder; 2. Parallel four-bar linkage; 3. Detasseling-wheel mounting bracket; 4. Sensor mounting bracket; 5. Hydraulic motor; 6. Photoelectric sensor; 7. Detasseling wheel; 8. Electric push rod

KEY TECHNOLOGIES FOR MECHANIZED DETASSELING

Existing mechanized detasseling technologies can be classified into two categories according to the removal method: extraction-type and cutting-type systems. Extraction-type detasseling commonly uses rotating wheels, belts, or rollers to grip and pull the tassel, together with a portion of the upper stem and leaves, from the corn plant through a clamping and pulling action *(Costa et al., 2019)*. Cutting-type detasseling primarily uses reciprocating or rotating blades to remove the tassel and portions of the attached upper stem and leaves through a shearing action *(Zou et al., 2020)*.

Cutting-Type Detasseling Technology

Research on cutting-type corn detasseling technology began in developed countries as early as the 1970s. Gildersleeve et al. designed a clamping-and-cutting detasseling device, as shown in Fig.5. The device mainly consisted of a frame, hydraulic motor, flexible drive shaft, drive chain, fixed blade, clamping wheels, and related components. During operation, the hydraulic motor transmitted power through the flexible drive shaft and drive chain to a pair of clamping wheels, causing them to rotate in the same direction. Under the force of a tension spring, the left clamping wheel was pressed against the lower portion of the right clamping wheel, thereby creating frictional contact between them. As the machine advanced, corn plants were guided toward the center by a crop divider and entered the contact region between the clamping wheels. The tassels were then cut by the combined action of the clamping wheels and the fixed blade *(Gildersleeve et al., 1973)*.

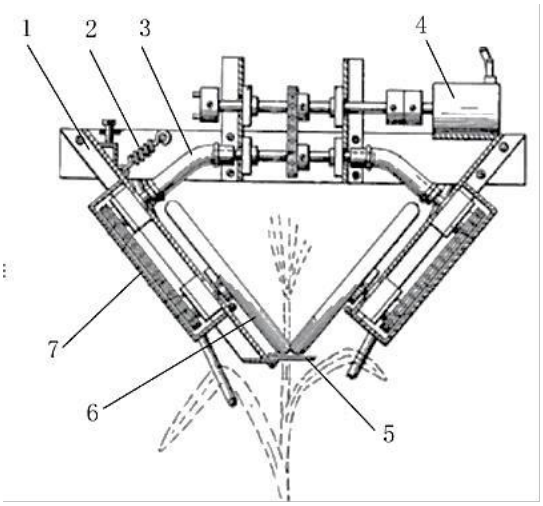


Fig. 5 - Clamping-and-cutting detasseling device *(Gildersleeve et al., 1973)*

1. Frame; 2. Tension spring; 3. Flexible drive shaft; 4. Hydraulic motor; 5. Fixed blade; 6. Clamping wheel; 7. Drive chain

Meiners et al. developed a horizontal cutting-type detasseling device, as shown in Fig.6. The device mainly consists of a drive belt, blades, guide rods, a crop divider, guide plates, and related components. During operation, corn plants are gathered toward the center by the crop divider and guided into the space formed between adjacent guide rods or between a guide rod and the protective shield. The tassels are then cut by blades arranged in a linear configuration. A notable feature of this device is that the multiple guide rods not only guide the plants but also help prevent leaves from entering the blade cutting zone, thereby reducing leaf damage and loss *(Meiners et al., 1973)*.

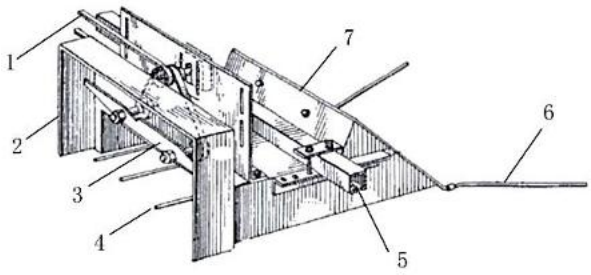


Fig. 6 - Horizontal cutting-type detasseling device (Meiners et al., 1973)

1. Drive belt; 2. Protective shield; 3. Blade; 4. Guide rod; 5. Frame; 6. Crop divider; 7. Guide plate

Grandinetti et al. designed an airflow-assisted corn detasseling device, as shown in Fig.7. The device mainly consists of a paddle wheel, a crop divider, air ducts and nozzles, an arcuate backing plate, and related components. During operation, the drive shaft rotates the paddle wheel to generate airflow, which is directed through the ducts and nozzles to separate the upper leaves. After the plants leave the airflow zone, the vertical plates maintain the leaves in the separated position. The tassel then enters the space between the two vertical plates and is snapped or cut off through the combined action of the paddle wheel, its blades, and the arcuate backing plate. The airflow system and vertical plates effectively separate the tassel from the upper leaves and prevent leaf rebound, thereby reducing damage to the upper leaves of the corn plants *(Meiners et al., 1990)*.

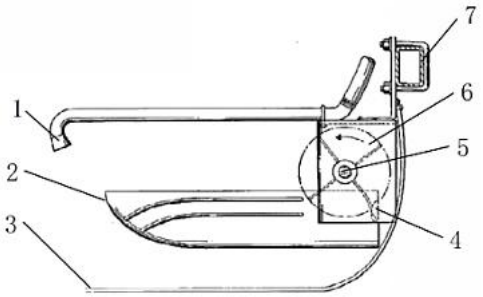


Fig. 7 - Airflow-assisted cutting-type detasseling device *(Meiners et al., 1990)*

1. Air duct and nozzle 2. Vertical plate 3. Crop divider 4. Arcuate backing plate 5. Drive shaft 6. Paddle wheel 7. Frame

Based on the phenotypic characteristics of corn plants and the principles of manual detasseling, Song et al. proposed a downward cutting-and-rotating detasseling method designed to reduce damage to the leaves surrounding the tassel. To implement this method, they developed a compact corn detasseling device comprising an RGB camera, left and right gripping mechanisms (Claw-L and Claw-R), a sliding mechanism, and a rotating mechanism. The complete operating sequence of the device is illustrated in Fig.8. Field experiments showed that the device achieved a tassel-removal success rate of 88.33% *(Song et al., 2024)*.

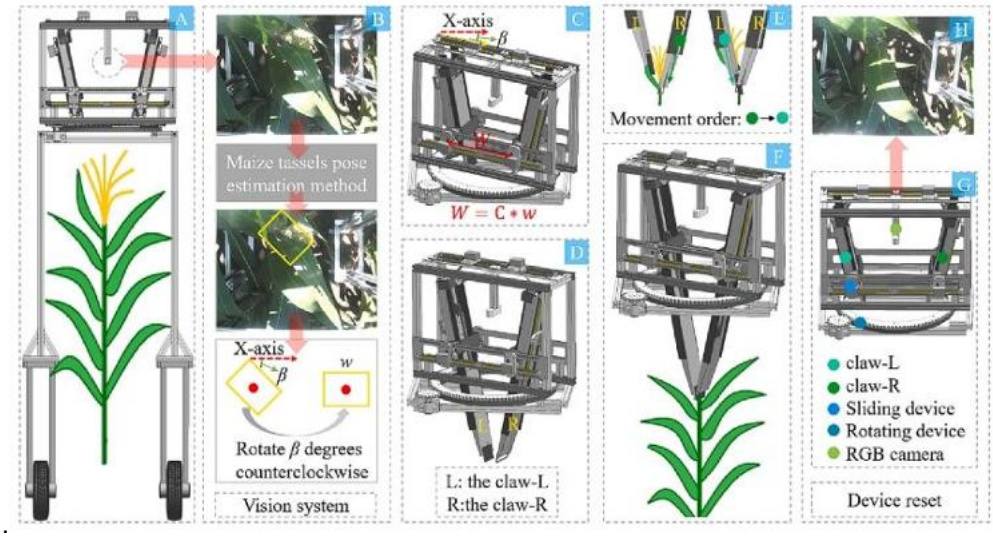


Fig. 8 - Operating sequence of the corn detasseling device *(Song et al., 2024)*

A. Schematic of the device during operation; B. Vision system; C. Movement of the device to the specified angle and position; D. Movement of Claw-L and Claw-R to the specified positions; E. Movement sequence of the two claws during detasseling; F. Device configuration upon completion of detasseling; G. Return of the device to its initial position; H. Removed corn tassel

Extraction-Type Detasseling Technology

In 1970, *Spry et al.* developed a belt-type extraction detasseling device, as shown in Fig.9. The device mainly consisted of a pressure wheel, a hydraulic motor, a leaf-pressing roller, and related components. During operation, as the implement advanced, corn plants were guided toward the center by a crop divider. Under the continuous action of the leaf-pressing roller, the tassel was separated from the surrounding leaves and then entered the gripping zone formed by two elastic belts. The tassel was gradually pulled from the plant and either discharged onto the ground or collected. A helical metal strip was mounted on the surface of the leaf-pressing roller to improve its gripping and downward-pressing performance *(Spry et al., 1970)*.

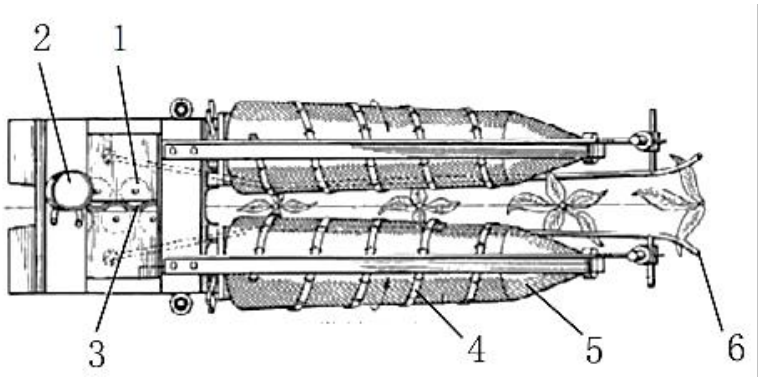


Fig. 9 - Belt-type extraction detasseling device *(Spry et al., 1970)*

1. Compression wheel; 2. Hydraulic motor; 3. Elastic belt; 4. Helical metal strip; 5. Leaf-pressing roller; 6. Crop divider

Kenneth et al. designed a pneumatic-wheel extraction detasseling device, as shown in Fig.10. The device primarily consists of a main frame, a support frame, a hydraulic motor, a drive shaft, a driven shaft, pneumatic rubber wheels, and related components. During operation, the drive wheel and driven wheel rotate in opposite directions, gripping and pulling the corn tassel together with a portion of the attached upper stem and leaves. The removed material is then discharged into the interrow space. The pneumatic rubber wheels provide flexible gripping, thereby improving the adaptability of the detasseling mechanism to variations in tassel size and position. In addition, the tread pattern on the wheel surfaces enhances gripping performance *(Kenneth et al., 1970)*.

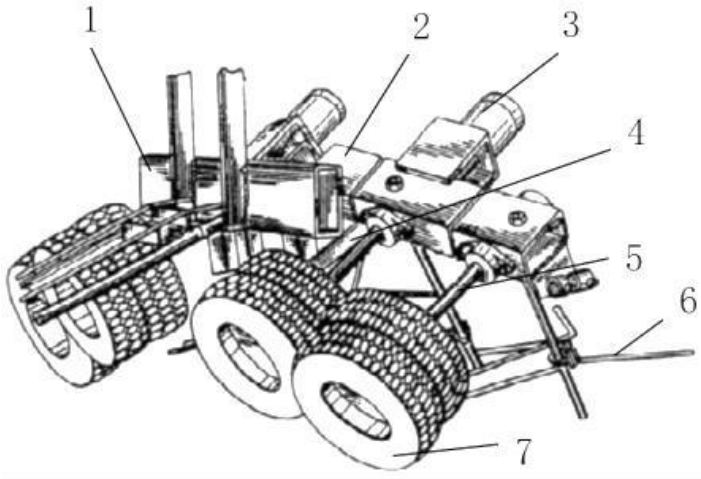


Fig. 10 - Pneumatic-wheel extraction detasseling device *(Kenneth et al., 1970)*

1. Frame; 2. Fixed frame; 3. Hydraulic motor; 4. Drive shaft; 5. Driven shaft; 6. Crop divider; 7. Pneumatic rubber wheel

Bourgoin developed a flexible-disk extraction detasseling unit, as shown in Fig.11. The unit mainly consists of a crop divider, two flexible disks, an opening roller, a pressure roller, and related components. During operation, as the detasseling unit advances, corn plants are guided toward the center by the crop divider and enter the V-shaped space formed by the two flexible disks. Under the combined effects of disk rotation and forward travel, the plants move progressively into the contact zone, where the gap between the disks gradually narrows until the disks come into full contact. The tassel is then firmly gripped by the flexible disks under the action of the pressure roller, pulled from the plant, and discharged forward. A limitation of this design is that the removed tassels may become entangled with or remain caught on the corn plants.

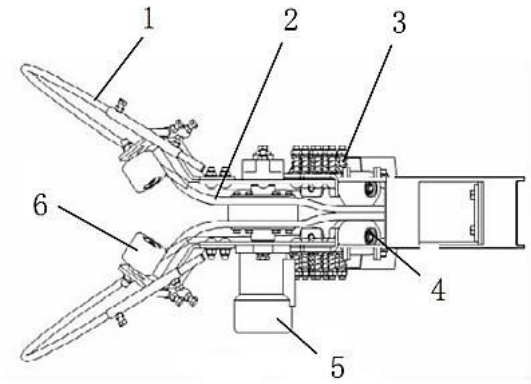


Fig. 11 - Flexible-disk extraction detasseling unit

1. Crop divider; 2. Flexible disc; 3. Compression spring; 4. Opening roller; 5. Hydraulic motor; 6. Pressing roller

DEVELOPMENT STATUS OF MECHANIZED DETASSELING EQUIPMENT FOR CORN SEED PRODUCTION

Mechanized Detasseling Equipment Developed Outside China

Research on mechanized detasseling equipment for corn seed production began relatively early in other countries. In 1937, the first mechanized corn detasseling machine was developed in the United States. As shown in Fig.12, the machine featured a high-clearance chassis equipped with six operator platforms and supported by three ground wheels, allowing it to travel slowly between corn rows. However, tassel removal was still performed manually by workers standing on the platforms. Therefore, the machine essentially provided mechanized transport and elevation for manual detasseling rather than fully mechanized tassel removal *(Seeber et al., 1937)*. By 1950, a second-generation detasseling machine had been developed, as shown in Fig. 13 *(Hagle et al., 1950)*. Compared with the earlier model, it provided improved travel stability, operator safety, and field efficiency. Nevertheless, because the detasseling operation still depended heavily on manual labor and the level of automation remained limited, the machine was not widely adopted.



Fig. 12 - Early mechanically assisted corn detasseling machine *(Seeber et al., 1937)*



Fig. 13 - Second-generation mechanically assisted corn detasseling machine *(Hagle et al., 1950)*

In recent years, various corn detasseling machines have been widely adopted in Europe, the United States, and other regions as alternatives to manual labor. These machines are technologically mature, highly efficient, and adaptable to different field conditions. Representative models include the 204SP and DTB series manufactured by Hagie in the United States; the TS4, 5175, and 5180 manufactured by Oxbo in the United States; the PDF752D manufactured by Big John in the United States; the BD864 manufactured by Bourgoin in France; the FALCON 140 manufactured by Frema in France; and the S series manufactured by Castrix in Italy. The Hagie 204SP is one of the earliest commercially available self-propelled corn detasseling machines, as shown in Fig.14. It uses a four-wheel hydrostatic drive system and has a chassis ground clearance of 193 cm. Its track width can be adjusted from 214.6 to 304.8 cm, allowing operation at common corn row spacings of 51–76 cm. Depending on operational requirements, the front of the machine can be equipped with either extraction-type or cutting-type detasseling units. The operating height of these units can be adjusted over a range of 0–167.6 cm, and the machine can be configured to operate on 4 to 18 rows, in even-numbered configurations *(Ma et al., 2012)*.



Fig. 14 - Hagie 204SP self-propelled corn detasseling machine
(Ma et al., 2012)



Fig. 15 - Hagie DTB-series corn detasseling machine

In addition, the Hagie DTB-series corn detasseling machines have been well received because of their operational versatility. Machines in this series can also be readily converted for use as self-propelled sprayers, as shown in Fig. 15. Several other representative corn detasseling machines are presented in Fig.16, and their principal performance parameters are summarized in Table 1.



a)



b)



c)



d)



e)



f)

Fig. 16 - Representative corn detasseling machines
a) Oxbo TS4; b) Oxbo 5175; c) Big John PDF752D; d) Bourgion BD864; e) Frema FALCON140; f) Castrix S4C

Table 1

Key specifications of representative corn detasseling machines developed outside China

Model	Rated power	Row spacing	Track width	Ground clearance	Number of rows	Turning radius	Field capacity	Detasseling rate
	[kW]	[cm]	[cm]	[mm]	-	[m]	[ha/h]	[%]
Oxbo TS4	95.61	60 ~ 80	6000 ~ 8000	1900	12/16	-	5.8 ~ 7.7	≈95
Oxbo 5175	127	60 ~ 76	2290 ~ 3000	1830	12	4.8 ~ 8.7	-	≈95
PDF752D	92	40 ~ 90	2000 ~ 2600	1850	8	4.3 ~ 5.6	2 ~ 2.5	≥92
BD864	82	-	2000 ~ 3000	2100	4/6/8/9	-	-	≥90
FALCON140	103	-	2000 ~ 2600	2000	6/8/9/12	5.5 ~ 7.0	3.5 ~ 5.6	≥90
S4C	55.4/57.6	60	1600 ~ 2200	1600	4/6	3.4 ~ 4.8	1.8 ~ 2.3	≈95

Corn detasseling machines developed outside China are generally technologically mature. Their typical configurations include a self-propelled power unit, hydraulically driven working components, and cutting-type or pneumatic-wheel extraction-type detasseling mechanisms. These machines also commonly incorporate intelligent technologies, such as optical sensing for tassel detection and automatic height adjustment, to improve operating precision. However, this high level of technological integration also leads to substantial equipment costs, which typically exceed RMB 1 million per unit *(Liu et al., 2025)*. Such high prices significantly limit their adoption by farms in China, which generally operate on a smaller scale.

Mechanized Detasseling Equipment Developed in China

Research on corn detasseling machines in China began relatively late. During the early stages, development efforts focused primarily on importing and adapting foreign designs. One representative achievement was the 3QXZ-6 corn detasseler, developed by the Chinese Academy of Agricultural Mechanization Sciences in 2016. However, because of limitations in technological maturity and market adaptability at that time, the machine was not produced on a large scale *(Wang et al., 2016)*. At present, the corn detasseling machines that have entered mass production and practical use in China are mainly manufactured by Jiuquan Ouke Seed Machinery Co., Ltd. Representative models include the OK104-3CX and 3CX-6A corn detasseling machines, shown in Figs. 17 and 18, respectively. Together with the 3QXZ-6, these machines use both cutting-type and pneumatic-wheel extraction-type detasseling mechanisms. Their principal performance parameters are summarized in Table 2 *(Xu et al., 2015; Zhu et al., 2015; Feng et al., 2024)*.



Fig. 17 - OK104-3CX



Fig.18 - 3CX-6A

Table 2

Key specifications of three corn detasseling machines developed in China

Model	Rated power	Row spacing	Drive configuration	Track width	Ground clearance	Number of rows	Turning radius	Field capacity	Detasseling rate
	[KW]	[cm]	-	[cm]	[mm]	-	[m]	[ha/h]	[%]
3QXZ-6	88.2	60	self-propelled	2000～2600	1800	4/6	-	-	≈87.7
OK104-3CX	160	-	self-propelled	1900～2300	1900～1960	8/12	6.6	1～2.3	≥85
3CX-6A	120	-	self-propelled	1900～2300	1900	4/6	3.2～4	0.8～1.5	≥85

In July 2024, a fully electric corn detasseling robot independently developed by Xinjiang Jiuyu Technology Co., Ltd. was introduced and deployed for field operations in Guangming Village, Ergong Town, Changji City, as shown in Fig. 19. The robot integrates the BeiDou Navigation Satellite System with LiDAR point-cloud data and AI-based image-recognition algorithms to generate precise operating paths in real time. During operation, it detects the positions of the leaves and tassels and autonomously determines the required lowering distance of the detasseling actuators. The robot can accommodate corn plants ranging from 1.5 to 2.3 m in height, provides millimeter-level positioning accuracy, and achieves a tassel-removal rate of 90%. It can detassel four rows in a single pass, with a field capacity of 0.47–0.74 ha/h and an energy consumption of approximately 6 kWh/ha. Compared with conventional methods, the robot can reduce labor costs by more than RMB 40 per *mu* and substantially shorten the detasseling period. The deployment of this machine represents an important step toward the intelligent automation of detasseling operations in China's corn seed-production industry.



Fig. 19 - Fully electric corn detasseling robot

Corn detasseling equipment developed in Europe and the United States has established a relatively mature technological system characterized by high-powered self-propelled chassis, hydraulically driven cutting- or extraction-type working units, and basic optical height-profiling systems. Although this system provides high field efficiency, it is also associated with high equipment costs and limited adaptability to diverse agronomic practices. By contrast, although technological development in China began later, substantial progress has been made in lightweight machinery for small- and medium-sized fields and in intelligent recognition technologies based on machine vision and photoelectric sensing. Notable advances have also been achieved in fully electric drive systems and intelligent detasseling robots integrating the BeiDou Navigation Satellite System with AI-based technologies.

FACTORS LIMITING THE MECHANIZATION OF CORN DETASSELING

(1) Corn detasseling machinery continues to face important technical limitations. Although mainstream machines developed in China and other countries generally achieve satisfactory detasseling performance, they often fail to meet seed-purity requirements in a single pass. As a result, growers must rely on manual follow-up removal or repeated machine passes to eliminate missed tassels. The effective detasseling window is only 7–10 days. Manual inspection and removal are labor-intensive and inefficient and may not consistently ensure the required quality. Repeated passes by ground-based machinery, however, substantially increase operating costs and may cause soil compaction and crop damage. Therefore, the efficient and accurate detection and removal of missed tassels remains a central challenge in improving the quality and efficiency of detasseling operations.

(2) The requirements of agricultural machinery and agronomic practices remain insufficiently coordinated. The absence of unified standards for planting parameters, including row spacing and female-to-male row configuration, increases the difficulty of mechanized detasseling in corn seed production. China's principal corn seed-production areas are concentrated in regions such as Gansu and Xinjiang. In Gansu, however, fields are relatively fragmented, and plots larger than 30 *mu* account for less than 5% of the total cultivated area. This limits the ability of large detasseling machines to fully realize their field-efficiency advantages. In addition, the large number of corn varieties used for seed production results in substantial differences in tassel height and attachment strength. Even within the same field, individual plants may vary in height and morphology because of differences in seed vigor, water and nutrient availability, and localized soil conditions. These factors place greater demands on the adaptability and control accuracy of detasseling machinery.

(3) Mechanical damage caused by detasseling operations remains a significant problem. Manual detasseling can generally remove tassels from female parent plants with minimal damage to other plant tissues. In contrast, mechanical detasseling relies primarily on cutting or roller-clamping extraction mechanisms, which may tear or crush the leaves surrounding the tassel. This problem is particularly serious in varieties with relatively few leaves above the ear, because damage to these leaves can directly reduce photosynthetic capacity and impair assimilate transport, ultimately decreasing seed yield. Reported data indicate that mechanical detasseling may reduce the yield of such sensitive varieties by approximately 15%.

(4) Growers' acceptance of detasseling machinery remains relatively low. On the one hand, imported machines involve high purchase and maintenance costs, whereas the operating window for corn detasseling is short. Consequently, annual machine utilization is low and the investment payback period is long. On the other hand, although labor costs continue to rise, reaching approximately RMB 300 per worker per day, the advantages of existing machinery in terms of field efficiency and cost-effectiveness are not yet sufficiently pronounced. This is particularly true under complex agronomic conditions, where machine performance may remain unstable. In addition, traditional production practices continue to influence decision-making in some rural areas. Growers may therefore be cautious about adopting new technologies and may prefer to rely on experienced workers for detasseling operations.

OPTIMIZATION STRATEGIES FOR MECHANIZED CORN DETASSELING

(1) Promote the development of intelligent and precision detasseling equipment

Future research and development should focus on improving the overall performance of detasseling equipment. The primary objective should be to balance a high tassel-removal rate with a low plant-damage rate by minimizing mechanical damage to the leaves while maintaining effective detasseling performance. Efforts should also focus on improving equipment adaptability. Dedicated machine series and modular configurations should be developed for different production systems, including large-scale operations on expansive fields and fragmented production on small plots. The long-term goal is to develop a new generation of intelligent, precision detasseling equipment. Achieving this goal will require breakthroughs in key technologies, including intelligent tassel-recognition algorithms, high-precision height-profiling actuators, and adaptive control systems for complex field terrain. These developments are expected to address persistent limitations such as high plant-damage rates and large turning radii.

(2) Promote closer integration of agricultural machinery and agronomic practices

Efficient and stable mechanized detasseling requires coordinated optimization of agronomic standards and variety development. First, standardized planting protocols should be established and promoted to unify key agronomic parameters, including row spacing and female-to-male row ratios, thereby creating favorable conditions for mechanized operations. Second, breeding programs should target varieties with uniform plant height and ear position, together with tassel characteristics suitable for mechanical removal. Such varieties would provide stronger biological and agronomic support for mechanized detasseling. Finally, collaboration between agricultural machinery engineers and agronomists should be strengthened. A permanent, integrated mechanism for research, development, field validation, and extension should be established so that agronomic requirements guide machine design and machinery performance supports agronomic objectives. This coordinated approach will promote the systematic advancement and sustainable development of full-process mechanization in corn seed production.

(3) Strengthen demonstration, extension, and service support

First, the systematic development of high-standard farmland should be promoted. Land consolidation, field leveling, supporting farm roads, and improved field-layout planning can create more favorable operating conditions for mechanized detasseling and, ultimately, full-process mechanization. Second, an effective demonstration and extension system should be established. Large-scale growers, specialized cooperatives, and other qualified organizations should be selected and supported in establishing demonstration bases. Field comparison trials can then be used to clearly demonstrate the efficiency and economic benefits of mechanized detasseling, thereby increasing growers' awareness of and willingness to adopt the technology. Finally, new models of agricultural service provision should be actively explored. Cooperatives, agricultural enterprises, and other service providers should be encouraged to offer specialized contract detasseling services. Large-scale service operations can improve machinery utilization, spread investment and operating risks across multiple users, and support the development of a sustainable mechanism for technology adoption and expansion.

CONCLUSIONS

This paper systematically reviews and compares the historical development, current technological status, and equipment characteristics of mechanized detasseling for corn seed production worldwide. At present, the wider adoption of mechanized detasseling remains constrained by several factors, including insufficient single-pass tassel-removal rates, poor coordination between agricultural machinery and agronomic practices, high plant-damage rates, and limited economic viability. However, with continued advances in artificial intelligence, robotics, and precision agriculture, detasseling technology is expected to become increasingly intelligent, precise, and integrated. These developments may substantially reduce reliance on manual labor and create the conditions for mechanized detasseling to replace most, or potentially all, manual operations in corn seed production.

ACKNOWLEDGEMENT

This work is supported by the Yili Prefecture Science and Technology Plan Project (YZ2022Y011).

REFERENCES

[1] Alzadjali, A., Alali, M. H., Veeranampalayam Sivakumar, A. N., Deogun, J. S., Scott, S., Schnable, J. C., Shi, Y. (2021). Maize tassel detection from UAV imagery using deep learning. *Frontiers in Robotics and AI,* 8, 600410. https://doi.org/10.3389/frobt.2021.600410

[2] Asefa, G., Bedane Gudeta, B. T., Azemach, G., Abakemal, D., Kaske, K., Abebe, B., ... & Tujuba, C. (2026). Review of Maize Seed Research in Ethiopia (2012-2021). *VOLUME II*.

[3] Bai, Y. (2022). Technical measures of corn field scientific management. *Modern Agriculture Research,* 28(1), 100-102. https://doi.org/10.19704/j.cnki.xdnyyj.2022.01.033

[4] Cao, Y., Liu, Y., Gao, X., Jia, Y., & Dong, S. (2025). LightTassel-YOLO: A Real-Time Detection Method for Maize Tassels Based on UAV Remote Sensing. *Smart Agriculture,* 7(6), 96-110. https://doi.org/10.12133/j.smartag.SA202505021

[5] Costa, L., Carvalho, I., Ferreira, L., Szareski, V., Pimentel, J., Troyjack, C., & Aumonde, T. Z. (2019). The effects of different mechanical detasseling methods on hybrid maize seed production. *Genet Mol Res,* 18(4), 10-4238. https://doi.org/10.4238/gmr18207

[6] Czepak, M. P., Kliemann, M., Schmildt, O., Araujo, R. N., de Sousa Oliveira, V., Junior, L. M. B., ... & Schmildt, E. R. (2019). Effect of artificial detasseling and defoliation on maize seed production. *Int. J. Plant Soil Sci,* 28(4), 1-9.

[7] Chukwutem, I. B. (2023). Design and construction of corn thresher machine using locally sourced materials. *BW Academic Journal,* 10.

[8] Darrah, L. L., McMullen, M. D., Zuber, M. S. (2019). Breeding, genetics and seed corn production Corn. *Chemistry and Technology,* 19-41. https://doi.org/10.1016/B978-0-12-811971-6.00002-4

[9] Ding, C., Zhang, R., Qi, J., Xie, Y., Yi, T., Li, L., Bao, Z. (2026). Precision detection and geolocation of missed pre-tassels in hybrid maize seed production using UAV-based deep learning. *European Journal of Agronomy*, *173*, 127923. https://doi.org/10.1016/j.eja.2025.127923

[10] Duangpapeng, P., Ketthaisong, D., Lomthaisong, K., Lertrat, K., Scott, M. P., Suriharn, B. (2018). Corn tassel: A new source of phytochemicals and antioxidant potential for value-added product development in the agro-industry. *Agronomy,* 8(11), 242.

[11] Fan, Y. Z., Zhao, G. M., Hou, X. M. (2021). Production technology of maize hybrid in Tacheng area of Xinjiang. *Heilongjiang Agricultural Sciences,* (5),135-140.

[12] Falahat, S., & Karami, A. (2023). Maize tassel detection and counting using a YOLOv5-based model. *Multimedia Tools and Applications*, *82*(13), 19521-19538. https://doi.org/10.1007/s11042-022-14309-6

[13] Felkl, G. (1988). Economic aspects of detasseling corn plants and insecticide use to control Asian corn borer, Ostrinia furnacalis Guenée (Lep., Pyralidae), in the Philippines. *Journal of Applied Entomology,* 105(1-5), 379-386. https://doi.org/10.1111/j.1439-0418.1988.tb00200.x

[14] Feng, Z. R., Zhao, L., Li, Y. W., Fu, Q. F. (2024). Development and Experimental Verification of 3CX-6A Small and Lightweight Seed Production Corn Male Removal Machine. *Agriculture Machinery Technology Extension,* (01), 45-47.

[15] GB/T 17315-2011. *Operational Procedures for Hybrid Maize Seed Production Technology*, State Administration for Market Regulation, China.

[16] Ghețe, A. B., Haș, V., Vidican, R., Copândean, A., Ranta, O., Moldovan, C. M., Duda, M. M. (2020). Influence of detasseling methods on seed yield of some parent inbred lines of Turda maize hybrids. *Agronomy,* 10(5), 729. https://doi.org/10.3390/agronomy10050729
[17] Gildersleeve, B. T. (1973). *Machine for detasseling corn.* Patent, No.3712035, United States.
[18] Gong, R. H., Qi, L. J., Fu, Z. T. (2007). Advance in Precision Agriculture Based on the Machine Vision Technology (机器视觉技术在精细农业中的研究进展). *Journal of Agricultural Mechanization Research,* https://doi.org/10.13427/j.cnki.njyi.2007.11.026
[19] Grandinetti, D. L. (1990). C*orn Detasseling Machine,* Patent, No.4890447, United States.
[20] Ghimire, B., Shrestha, S., Kandel, B. P., Bhandari, A., & Rijal, M. (2025). Effects of Detasseling Timing and Intensity on Yield and TSS of Sweet Corn. *Agronomy Journal of Nepal,* 9, 189-194. https://doi.org/10.3126/ajn.v9i1.91457
[21] Gu, J. C., Yang, J. H., Tan, C. P. (2013). *Sensitivity corn male removal machine,* Patent, No.CN202819217U, China.
[22] Hagle, R. W., Clarion., Collins, E. V., Iowa, A. (1950). *Corn Detasseling Machine*, Patent, No.2508605A, United States.
[23] Han, F. T. (2011). Corn seed production technology (玉米制种技术). *Modern Agricultural Science and Technology*, (23), 123.
[24] HAGIE. (2024). *Cutting type detasseling device of 204SP detasseling machine.* Available: https://www.hagie.com/equipment/204sp/
[25] Huang, G. J. (2025). Exploration of Strategies for Improving Hybrid Seed Production and Breeding Technology of Corn. *Seed Science & Technology,* 43(19), 104-106+118. https://doi.org/10.19904/j.cnki.cn14-1160/s.2025.19.033
[26] Jahangirlou, M. R., Morel, J., Akbari, G. A., Alahdadi, I., Soufizadeh, S., Parsons, D. (2023). Combined use of APSIM and logistic regression models to predict the quality characteristics of maize grain. *European Journal of Agronomy,* 142, 126629. https://doi.org/10.1016/j.eja.2022.126629
[27] Jia, J., Gibson, H. G., Krutz, G. W. (1990). Forces Required to Remove Tassels from Dent Seed Corn. *Applied Engineering in Agriculture,* 6(5), 553-556. https://doi.org/10.13031/2013.26427
[28] Jin, S. (2019). *Design and Experimental Study on Key Components of Corn Detasseling Machine.* [Master's degree thesis, Jilin Agricultural University]. https://doi.org/10.27163/d.cnki.gjlnu.2019.000099
[29] Jiu Quan Ok Seed Machinery CO., LTD. (2024). *OK104-3CX detasseling machine.* Available: http://www.woksm.com/productinfo/1156378.html.
[30] Kasal, Y. G., Singh, S., & Khan, S. (2025). Emerging trends in agricultural robotics: Integration of artificial intelligence, machine vision, and IoT in farm machinery. *Int J Agric Nutr,* 7(10), 70-74. https://doi.org/10.33545/26646064.2025.v7.i10b.303
[31] Kenneth, P. C. (1991). *Corn detasseling head, Patent,* No.4989399. United States.
[32] Kumar, A., Desai, S. V., Balasubramanian, V. N. (2021). Efficient Maize Tassel-Detection Method using UAV based remote sensing. *Remote Sensing Applications: Society and Environment, 23, 100549*. https://doi.org/10.1016/j.rsase.2021.100549
[33] Kurtulmuş, F., Kavdir, I. (2014). Detecting corn tassels using computer vision and support vector machines. *Expert Systems with Applications*, 41(16), 7390-7397. https://doi.org/10.1016/j.eswa.2014.06.013
[34] Li, J. R. (2024). *Research on Tassel Detection Method of Seed Maize Based on Deep Learnin.* [Doctoral dissertation, Northwest A&F University]. https://doi.org/10.27409/d.cnki.gxbnu.2024.002358
[35] Li, J. R., Du, J. J., Zhang, H. M., Guo, X. Y., Zhao, C. J. (2024). Maize Tassel Detection Algorithm after Artificial Emasculation Based on Lightweight MLCE-RTMDet (基于轻量化 MLCE-RTMDet 的人工去雄后玉米雄穗检测算法). *Transactions of the Chinese Society for Agricultural Machinery,* 55(11), 184-192+503.
[36] Liu, C. (2025). *Design and Experimental Study of Extraction Type Maize Seed Production Machine*. [Master's thesis, Northeast Forestry University]. https://doi.org/10.27009/d.cnki.gdblu.2025.000834
[37] Liu, P., Liu, D. M. (2024). Discussion on high-yield and high-efficiency cultivation mode of corn planting(玉米种植高产高效栽培模式探讨). *Seed Science & Technology,* 42(04), 56-58.
[38] Liu, L., Li, F. H. (2010). Maize hybrid seed production technology in Jiuquan region. *Modern rural technology,* (15), 11-12.
[39] Liu, Y. G., Shi, Q., Gao, Q. (2014). Measures to improve the quality of male removal of maize maternal parent in seed production (提高制种玉米母本去雄质量的措施). *Seed Science & Technology,* 32(09), 47-48.

[40] Liu, D. X., Zheng, Y. X., Yu, H. T. (2025). *Highly adaptive corn male removal head unit*, Patent. No.CN120092700A. China.
[41] Liu, L., Meng, L., Li, F. H., Hu, S. R. (2024). Mechanization technology for seed corn production in Xinjiang: Detasseling. *Xinjiang Agricultural Mechanization,* (03), 5-7+34. https://doi.org/10.13620/j.cnki.issn1007-7782.2024.03.001
[42] Lu, Y. T., Li, Y. X., Li, B. (2010). Comparative analysis of characteristics between manual and mechanical emasculation in hybrid maize seed production (制种玉米人工去雄与机械去雄特点对比分析). *Xinjiang Agricultural Mechanization*, (01), 25-26. https://doi.org/110.13620/j.cnki.issn1007-7782.2010.01.025
[43] Ma, J. F. (2012). Application of Haiji 204 Seed Production Corn Male Removal Machine in Changji City. *Xinjiang Agricultural Mechanization,* (06), 36-37.
[44] Meiners, E. R. (1973). *Corn detasseler head.* Patent, No.3717982, United States.
[45] Moreira, J. N., Silva, P. S. L., Silva, K. M., Dombroski, J. L., & Castro, R. S. (2010). Effect of detasseling on baby corn, green ear and grain yield of two maize hybrids. *Horticultura Brasileira,* 28(4), 406-411. https://doi.org/10.1590/S0102-05362010000400005
[46] Nicoletti, M. A., Ortiz, T. A., Takahashi, L. S. A. (2023). Yield and physiological quality of corn seeds after application of detasseling techniques in two cropping seasons. *Australian Journal of Crop Science,* 17(1), 69-73.
[47] Nithinkumar, K., Singh, S.P., Prakash, V., Saikia, N. (2024). Nitrogen and detasseling influences growth, yield and economics of male sterile baby corn (Zea mays). *Indian Journal of Agronomy,* 69(2), 211-215. https://doi.org/10.59797/ija.v69i2.5510
[48] Niu, S., Nie, Z., Li, G., & Zhu, W. (2024). Multi-altitude corn tassel detection and counting based on UAV RGB imagery and deep learning. *Drones,* 8(5), 198. https://doi.org/10.3390/drones8050198
[49] Ou, H. (2024). *Design and Development of Rotary-cutting Device for Corn Seed production Detasseling UAV*. [Master's degree thesis, Guangxi University].
[50] Prodanović, R., Subić, J., Sabljak, V. (2022). Grain Yield Seed Hybrids Maize per Different Way of Detasseling. *Rom Biotechnol Lett,* 27(4), 3617-3622. https://doi.org/10.25083/rbl/27.4/3617.3622
[51] Qi, J., Ding, C., Zhang, R., Xie, Y., Li, L., Zhang, W., Chen, L. (2025). UAS-based MT-YOLO model for detecting missed tassels in hybrid maize detasseling. *Plant Methods*, *21*(1), 21.
[52] Rodene, E., Fernando, G.D., Piyush, V., Ge, Y., Schnable, J. C., Ghosh, S., & Yang, J. (2024). Image filtering to improve maize tassel detection accuracy using machine learning algorithms. *Sensors,* 24(7), 2172. https://doi.org/10.3390/s24072172
[53] Rosegrant, M. R., Ringler, C., Sulser, T. B., Ewing, M., Palazzo, A., Zhu, T., ... & Batka, M. (2009). Agriculture and food security under global change: Prospects for 2025/2050. *International Food Policy Research Institute*, Washington, DC, 254.
[54] Seeber, P. (1937). C*orn Detasseling Machine,* Patent, No.2081681, United States.
[55] Shahrokhi, M., Khorasani, K. S., Ortez O. (2024). Grain yield and its contributing traits in promising sweetcorn hybrids. *Agrosystems, Geosciences & Environment,* 7(1), e20477. https://doi.org/10.1002/agg2.20477
[56] Shepard, N. R., DeSalvio, A. J., Arik, M., Adak, A., Murray, S. C., Varela, J. I., & de Leon, N. (2024). Deep learning-based high-throughput phenotyping of maize (Zea mays L.) tasseling from UAS imagery across environments. *bioRxiv,* 600506. https://doi.org/10.1101/2024.06.24.600506
[57] Shi, J. D., Lu, J. L., Qian, X. F., Lu, Y. M. (2014). Mechanized seed production technology of hybrid maize using combined parents. *China Seed Ind,* 233(8), 89-90.
[58] Si, X. Y., Liu, Y., Hou, Q. X. (2026). Research status and development prospects of emasculation machine for seed maize. *Journal of Chinese Agricultural Mechanization,* 47(01), 312-317. https://doi.org/10.13733/j.jcam.issn.2095-5553.2026.01.042
[59] Spry, R. H. (1970). *Detasseler apparatus, Patent,* No.3524308. United States.
[60] Su, Q. Y. (2003). Reasons and improvement measures affecting the purity of maize hybrid seed production. *Journal of Maize Sciences,* (s1), 70-71. https://doi.org/10.13597/j.cnki.maize.science.2003.s1.031
[61] Song, C., Zhang, F., Xie, J., Yang, C., Li, J., Zhang, J. (2024). Development and evaluation of a novel maize detasseling device. *Computers and Electronics in Agriculture,* 221, 108944. https://doi.org/10.1016/j.compag.2024.108944
[62] Sabljak, V., Prodanović, R., Ožegović, L., Đurićb, K., & Ivanišević́a, D. (2019). Effectiveness in the production of seed maize per different way of detasseling. *Annals of Agronomy,* 43(2).101-108.

[63] Singh, T. N., Saharia, D. D., Devi, E. L., Biswas, D., Chongtham, S. K., Bhupenchandra, I., ... & Kumar, B. (2025). Seed Production Techniques in Maize: Principles and Practices. In Hybrid Seed Production for Boosting Crop Yields: Applications, Challenges and Opportunities. *Singapore: Springer Nature Singapor*e, 127-152.

[64] Tang, W. (2017). Key Technical Points and Management Measures for Hybrid Maize Seed Production and Emasculation in Yili Region (伊犁地区杂交玉米制种去雄技术要点及管理措施). *Seed World,* (07), 43-44.

[65] Tang, W. B., Zhang, Y., Zhang, D. X., Yang, W., Li, M. Z. (2011). Corn tassel detection based on image processing. *International Workshop on Image Processing and Optical Engineering*, 8335, 123-129. https://doi.org/10.1117/12.917672

[66] Tian, F. D., Gao, L. H., Xiong, J. L. (2014). Overview of Maize Seed Production Technology (玉米制种技术综述). *Modern Agricultural Science and Technology,* (18), 43-44+51.

[67] Wang, B. B., Yang, G. J., Yang, H. (2022). UAV images for detecting maize tassel based on YOLO_X and transfer learning. *Transactions of the Chinese Society of Agricultural Engineering,* 38(15), 53-62.

[68] Wang, J. J. (2016). *Research on mechanized extraction technology and device for male tassel of hybrid maize.* [Doctoral Dissertation, Chinese Academy of Agricultural Mechanization Sciences].

[69] Wang, J. J., Chen, Z., Yang, X. J., Wang, J. (2016). Design and Experiment of 3QXZ-6 Seed Corn Detasseling Machine. *Transactions of the Chinese Society for Agricultural Machinery,* 47(07), 112-118.

[70] Wang, L., Kong, D. S., Wang, L. M. (2024). Agronomic factors affecting the mechanized emasculation of maize seed production. *Journal of Chinese Agricultural Mechanization,* 45(09), 15-20. https://doi.org/10.13733/j.jcam.issn.2095-5553.2024.09.003

[71] Wang, T. (2015). *Design of corn tassel single profile automatic lifting system.* Master's thesis from Shihezi University.

[72] Wang, X. R. (2013). Brief Discussion on the Key Points of Mechanized Technology in the Whole Process of Corn Seed Production. *Xinjiang Agricultural Mechanization,* (02), 24-25. https://doi.org/10.13620/j.cnki.issn1007-7782.2013.02.022

[73] Wilhelm, W. W., Johnson, B. E., Schepers, J. S. (1995). Yield, Quality, and Nitrogen Use of Inbred Corn with Varying Numbers of Leaves during Detasseling. *Seed Physiology, Production & Technology,* 35(1), 209-212. https://doi.org/10.2135/cropsci1995.0011183X003500010039x

[74] Wu, J., He, X. L., Wei, L. P. (2013). Requirements and application effects of mechanical tasseling technology for corn. *Xinjiang Farm Research of Science and Technology, 3*6(08), 28.

[75] Wych, R. D. (1988). Production of hybrid seed corn. *Corn and corn improvement,* 18, 565-607. https://doi.org/10.2134/agronmonogr18.3ed.c9

[76] Xu, T., Xie, B., Mao, E. R., Du, Y. F. (2015). Design and Experiment of the Control System for the Male Removal Operation of Corn Male Removal Machine. *Transactions of the Chinese Society of Agricultural Engineering*, 31(04), 49-54.

[77] Yang, J. X., Chen, L. P., Zhang, R. R. (2026). Identification and Detection of Omitted Tassels in Maize for Seed Based on Machine Vision (基于机器视觉的制种玉米遗漏雄穗识别检测). *Journal of Agricultural Mechanization Research,* 48(01),182-189+198. https://doi.org/10.13427/j.issn.1003-188X.2026.01.024

[78] Yu, X., Ying, D. M., Nie, C. W. (2023). Dynamic monitoring of corn tassel area based on U-Net. Proceedings of the 20th Annual Academic Conference of the Chinese Society of Crop Sciences. Changsha, Hunan. https://doi.org/10.26914/c.cnkihy.2023.082716

[79] Zhang, F. K., Huo, S. P., Zhang, J. (2006). Correlation and path analysis between maize stalk traits and breaking resistance (玉米茎秆性状与抗折断力的相关和通径分析). *Journal of Maize Sciences,* (06), 46-49.

[80] Zou, Z. R., Wang, J. J., Zhao, Q. N. (2020). Research Status of Seed Corn Emasculation Technology and Equipment. *Agricultural Engineering,* 10(07), 19-23.

[81] Zhang, R. R, Yang, J. X., Chen, L. P., Chen, C. D., Li, L. L, Zhang, L. H. (2024). Review of the detasseling techniques for maize (Zea mays L.) hybrid seed production. *International Journal of Agricultural and Biological Engineering,* 17(3), 1-11.

DEVELOPMENT AND PERFORMANCE EVALUATION OF A ROTARY POWER WEEDER FOR PADDY CULTIVATION
/
रोटरी पावर वीडर का विकास एवं धान की खेती में मूल्यांकन

Subhash CHANDRA, Sanjay KUMAR, Sanjay Kumar PATEL, Adityanshu TRIPATHI, Shreesh Sanjay AMIN, Priyanshu KUMAR*
Department of Farm machinery and Power Engineering, College of Agricultural Engineering and Technology, Dr. Rajendra Prasad Central Agricultural University, Pusa (Samastipur)-848125, Bihar, India
Corresponding Author: Priyanshu Kumar, Email: pkfmpe@gmail.com, Tel: 9113443855
DOI: https://doi.org/10.35633/inmateh-79-33

Keywords: *Benefit–Cost Ratio, Direct-Seeded Paddy, Economic Performance, Weeding Efficiency, Forward Speed, Mechanized Weeding*

ABSTRACT
Manual weeders reduce labour requirements compared with hand weeding but remain time-consuming and physically demanding in paddy cultivation. A rotary power weeder powered by a 4.5 hp single-cylinder, air-cooled engine and equipped with three rotary units was developed for direct-seeded paddy and evaluated under field conditions. The machine was tested at three forward speeds and compared with manual weeding using a khurpi. Weeding efficiency decreased with increasing forward speed, whereas plant damage and power requirement increased. The highest grain yield and benefit–cost ratio were obtained at 1.27 km h^{-1}, which was identified as the optimum operating speed. Field evaluation demonstrated that the developed machine reduced labour requirements, provided effective weed control, and improved the operational efficiency of mechanical weed management in direct-seeded paddy cultivation.

सारांश
मैनुअल वीडर हाथ से निराई की तुलना में श्रम की आवश्यकता को कम करते हैं, किंतु धान की खेती में ये अभी भी समय-साध्य एवं श्रमसाध्य बने रहते हैं। डायरेक्ट सीडेड धान के लिए 4.5 हार्सपावर एकल-सिलेंडर वायु-शीतित इंजन तथा तीन रोटरी इकाइयों से युक्त एक रोटरी पावर वीडर का विकास कर क्षेत्रीय परिस्थितियों में मूल्यांकन किया गया। मशीन का परीक्षण तीन अग्र गतियों पर किया गया तथा इसकी तुलना खुरपी द्वारा मैनुअल निराई से की गई। अग्र गति बढ़ने पर निराई दक्षता में कमी, जबकि पौधा क्षति एवं शक्ति आवश्यकता में वृद्धि पाई गई। सर्वाधिक उपज एवं लाभ–लागत अनुपात 1.27 किमी प्रति घंटा की गति पर प्राप्त हुआ, जिसे सर्वोत्तम कार्य गति पाया गया। क्षेत्रीय मूल्यांकन से श्रम आवश्यकता में कमी, प्रभावी खरपतवार नियंत्रण एवं धान की खेती में यांत्रिक निराई द्वारा बेहतर परिचालन दक्षता सिद्ध हुई।

INTRODUCTION
Paddy is the main crop of the Asia and the world with share 60% and 25% of its global production, respectively (*Timmer, 2010*). Paddy is cultivated in 43.86 million hectares in India with 104.80 million tonne production and 2.39 tonne/ha productivity (*Ministry of Agriculture & Farmers Welfare, 2022*). Bihar is progressing fast in paddy production with present productivity level 4.02 tonne/ha (Finance Department, 2023).

Intensive need of resources in traditional method of paddy cultivation has forced the scientists and policy makers for advocacy of direct seeded paddy cultivation. Paddy production by direct seeding method is adversely affected by the heavy infestation of weed resulting into reduction in grain yield 40-65% (*Farooq et. al., 2011b; Kumar et. al., 2016, Roy et. al., 2011*). Weeds reduce the yield between 40-65%. Weed eradication or its effect control is the critical challenge for the paddy growing farmers (*Sharma et. al., 1977*). Weeding alone contributes to one-third of the total cost of cultivation as the loss in total estimated cost of production of paddy (*Rangasamy et. al., 1993*). The loss of yield due to weed in direct seeding method may be up to 70-80% (*Singh et. al., 2007; Hussain et. al., 2008; Mahajan et. al., 2009*). Cultivation of direct seeded rice may give 27-30% more yield than the transplanted rice under effective weed management practices (*Mishra et. al., 2012*). Use of traditional tools and equipment for mechanical weeding increases the cost of operation besides enhanced drudgery, wastage of inputs as well as damage to the produce (*Shrivastava, 2000*).

Chemical weeding method is highly adopted practice by the farmers in paddy cultivation, where yield is reduced significantly in comparison to mechanical weeding method. Mechanical weeding method retards the growth rate of the weed without adversely affecting the growth of the plants (*Kwangwaropas, 1999*). However, hand held mechanical weeders or tools require lot of time, energy and labour (*Patel et. al., 2018*). Development of effective power weeder may reduce the time of weeding and associated drudgery to the operators in weeding operation. Power weeding in maize requires approximately 10 labour-hours per hectare, compared with 167 labour-hours per hectare for manual weeding using traditional tools (*Dixit and Syed, 2008*). Undoubtedly, power weeder is advantageous for the farmers on account of enhanced field capacity in comparison to all types of manually and animal driven weeders (*More et. al., 2020*).

Agricultural mechanization is essential for improving labour productivity and operational timeliness, particularly in weed management, which remains one of the most labour-intensive field operations (*Hunt, 2001*). In small and medium landholdings, tractor-mounted implements are often unsuitable due to economic and field constraints; consequently, self-propelled and engine-operated rotary power weeders have emerged as effective intermediate mechanization options (*FAO, 2011*). These machines perform shallow soil working and weed uprooting using rotary tools, offering higher field capacity, reduced drudgery and improved weeding efficiency compared with manual methods (*Manuwa, 2009; Tewari et al., 2014;Kumar et al., 2023*). Several studies have reported labour savings exceeding 60% and significant improvements in operational efficiency in row crops and horticultural systems (*Singh and Singh, 2012; Kumar, et al., 2026*). However, the performance of rotary power weeders is strongly influenced by design parameters, soil conditions and crop geometry, underscoring the need for systematic design and field-level performance evaluation (*Kepner et al., 2018*).

Manual weeding remains the most widely adopted method of weed control in India; however, it is highly labour-intensive, time-consuming, and significantly increases the cost of cultivation. Weeding requires approximately 900–1200 labour-hours per hectare, accounting for nearly 25% of the total labour requirement in crop production (*Nag and Dutta, 1979*). Delayed or inadequate weeding can reduce crop yield by 30–60% (*Singh, 1988*), while yield losses due to weeds alone have been reported to range from 16–42%, depending on crop and location, contributing nearly one-third of the cultivation cost (*Rangasamy et al., 1993*). In India, approximately ₹4.2 billion is spent annually on weed control, and nearly 40 million tonnes of major food grains are lost each year due to weed infestation (*Singh and Sahay, 2001*). Yield losses of 5–60% have been reported under different weed intensities and management conditions and may reach 80% when weeds are not controlled during the critical stage of crop growth (*Dutta, 1981; Goel et al., 2008; Paraforos, et al., 2018*).

Several mechanical weeders, including manual, push–pull, bullock-drawn, and self-propelled rotary weeders, have been developed to reduce labour dependency. However, their adoption remains limited due to labour scarcity, increasing wage rates, low field efficiency, dependence on optimum soil moisture, and inconsistent weed control performance. In particular, most commercially available self-propelled rotary weeders require multiple passes for inter-row weeding in wide-row crops, resulting in lower effective field capacity, increased fuel consumption, higher operational cost, and reduced overall productivity.

Despite these developments, limited research has focused on designing and evaluating a high-capacity rotary power weeder capable of simultaneously improving field capacity, field efficiency, weeding efficiency, and operational economy under wide-row crop conditions. Furthermore, comprehensive field performance evaluation considering operational parameters such as forward speed, field efficiency, fuel consumption, power requirement, and weeding effectiveness is scarce. This knowledge gap limits the optimization and wider adoption of rotary power weeders in Indian farming systems.

Therefore, the present study was undertaken to develop and evaluate an improved rotary power weeder with enhanced operational performance under field conditions. The study aims to optimize key operational parameters to improve weeding efficiency, reduce labour requirement and operating cost, minimize operator drudgery, and enhance crop productivity.

MATERIALS AND METHODS

The power weeder was developed in the Department of Farm Machinery and Power Engineering, College of Agricultural Engineering and Technology (CAET), Pusa. The design procedure is described below.

Drive Wheel

The design of the power weeder wheel is critical for ensuring effective traction, stability and soil engagement during operation. The wheel has a diameter of 44.80 cm and a hub bore diameter of 2.50 cm, providing sufficient clearance for mounting on the drive shaft while maintaining structural integrity.

The overall width of the wheel is 9.00 cm, with the spiked tread extending 7.00 cm, allowing adequate soil contact for propulsion and minimal slippage on soft or wet soils. The depth and geometry of the spikes, measured at 4.92 cm in height with a radial spacing of 6.45 cm, are designed to penetrate the soil effectively, loosening the top layer without causing excessive compaction. Triangular cut-outs on the wheel body reduce weight without compromising strength, while the rounded edges with radii R1.25 cm and R2.50 cm provide wear resistance and facilitate smooth rotation. The lateral thickness of the tines, ranging from 3.67 cm to 4.66 cm, ensures durability under repetitive loading and abrasive soil conditions as shown in fig. 1. Overall, the wheel design balances traction, mechanical strength and soil interaction to optimize the performance of the power weeder in various field conditions.

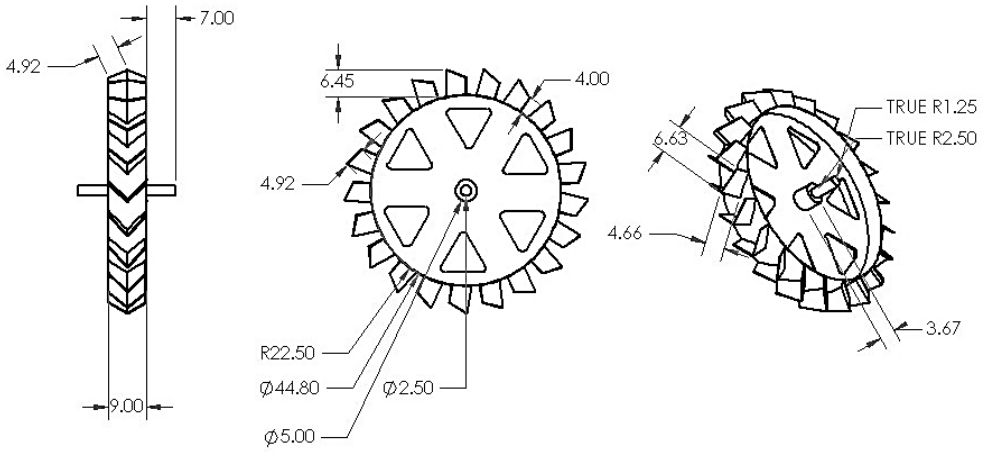


Fig. 1 - Different views of drive wheel

Vertical Rotary Blade

The power weeder blade design incorporates three rotary blades mounted on a 92.0 cm wide chain-driven assembly, with individual blade offset of 12.0 cm, ensuring balanced soil penetration and weed uprooting across varied field conditions. Key structural parameters include a 20.0 cm vertical height for the assembly, 9.50 cm and 4.0 cm horizontal spans for mounting stability, blade thickness of 0.5 cm, hub dimensions of 1.0 cm width by 12.0 cm length and a 12.0 cm base separation, which collectively optimize cutting width, torsional strength and minimal soil compaction during operation as shown in fig. 2. These dimensions support highly efficient weeding efficiency in multi-crop applications while maintaining operational safety and durability.

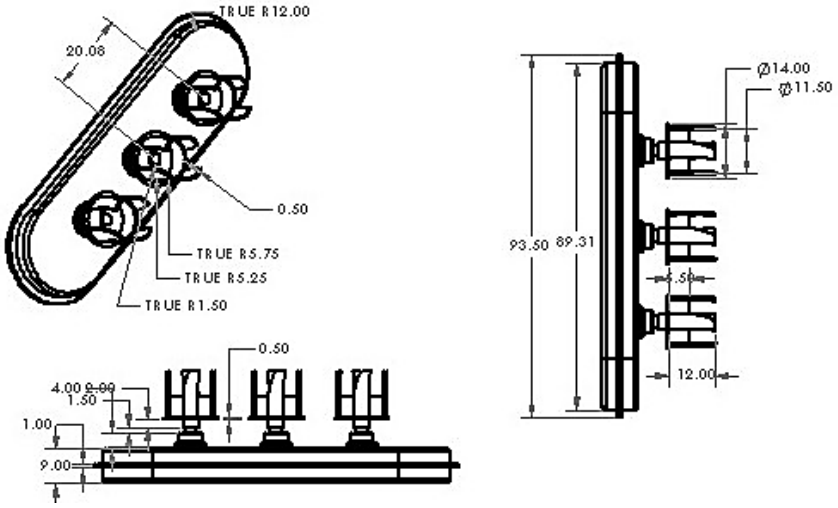
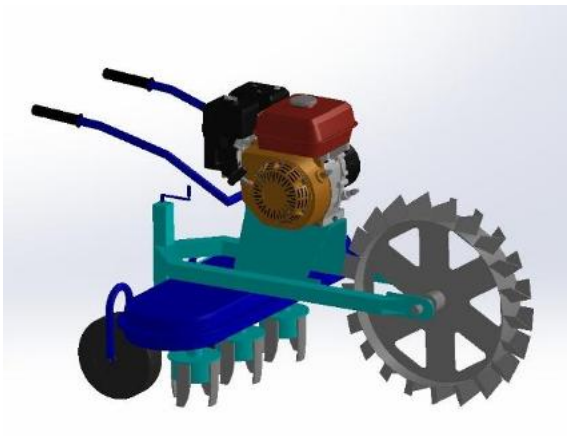
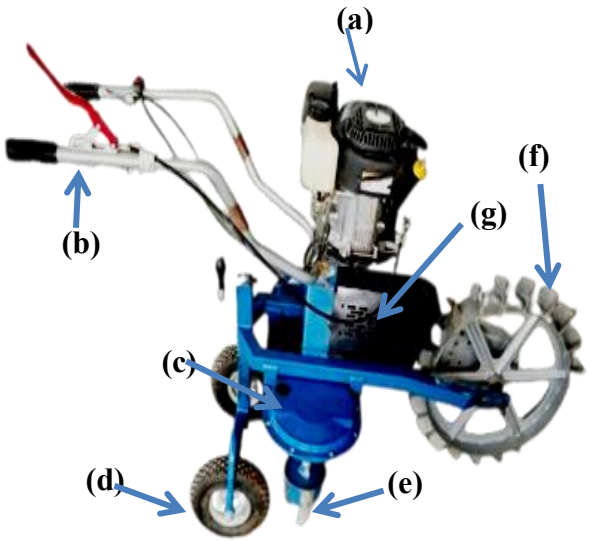


Fig. 2 - Different views of vertical rotary blade

Isometric view of the developed power weeder modeled in Solid Edge, illustrating the overall machine layout and spatial arrangement of major functional components and schematic diagram as shown in fig. 3. The view highlights the integration of the power unit, transmission system, rotary weeding mechanism and operator controls for design visualization and analysis.



(i)



(ii)

Fig. 3 - (i) 3-D model and (ii) a view of Schematic diagram of rotary power weeder showing major functional components;
(a) Engine; (b) Handle; (c) Gear box; (d) Depth control wheel; (e) Vertical rotor blade; (f) Drive wheel; (g) Gear Box

Component of Power Paddy Weeder

The drive wheel generates power for the forward movement of the machine. The vertical rotor wheel has a conical-shaped blade that cuts the soil as it rotates and helps the machine achieve the desired working depth. The Gear Box-I multiplies the engine speed (rpm) and transmits it to the rotor shaft, while Gear Box-II reduces the engine speed and delivers a lower rpm (about 10) to the drive wheel. The depth control wheel maintains a uniform cutting depth across the field.

The engine supplies power to operate all the other components of the machine. The specifications of the developed power weeder are given in Table 1. The cost of the machine was considered as ₹90,000.00 per unit for the purpose of cost calculation.

Table 1

Specification of developed power paddy weeder

Sl. No.	Machine components		Specification
1.	**Overall dimensions, mm (L×W×H)**	:	1600×740×1050
2.	**Type**	:	Self-propelled 3 row, walk behind type vertical axis rotary weeder,
3.	**Engine**		
	Type	:	4.5 hp, single cylinder, 4 stroke, 175 cc, air cooled, petrol engine
	Engine speed (recommended)		
	High idle speed, rpm	:	3600±100
	Lower idle speed, rpm	:	1900±100
	Rated speed, rpm	:	3600
	Speed at maximum torque, rpm	:	2500±100
4.	**Machine weight, kg**	:	85
5.	**Ground clearance, mm**	:	60
6.	**Rotor speed, rpm**	:	545
7.	**Fuel tank**		
	Material	:	Plastic
	Capacity, l	:	1.2
8.	**Drive wheel**		
	Material	:	G.I.
	Method of drive	:	Through chain & sprocket
	No. of sprocket teeth		
	Drive	:	18
	Driven	:	27
	No. of sprocket	:	02

Sl. No.	Machine components		Specification
9.	**Transmission ratio**		
	Primary reduction		
	Type	:	Crown and pinion
	No. of teeth on pinion	:	9
	No. of teeth on crown	:	29
	Ratio	:	3.2:1
	Secondary reduction		
	Type	:	Crown and pinion
	No. of teeth on pinion	:	16
	No. of teeth on crown	:	40
	Ratio	:	2.5:1
10.	**Rotor**		
	Rotor shaft		
	Type	:	Round
	Material	:	Medium carbon steel (EN9)
	Type of disc and number	:	Round and 3
	Rotor blades		
	Type	:	'J' shape
	Material	:	High carbon steel (EN42J)
	Number	:	12
	Cutting angle	:	45°
	Hardness(HRC)		
	At the cutting edge	:	42.67 (Average)
	At the shank	:	40.67 (Average)

Experimental Field

The evaluation of developed paddy power weeder was carried out in the research farm of Dr. Rajendra Prasad Central Agricultural University in Kharif 2023. The experimental plot was located at Latitude 25°98' N, Longitude 85°67' E and altitude 53.0 meter above the mean sea level. The soil of the plot was calcareous sandy loam with pH 8.5, composed with 90.3% sand, 9.7% silt and clay, 10-12% $CaCO_3$, 0.06% organic matter. The bulk density of the experimental plot was 1.43g/cm^3. The Rajendra Bhagwati paddy variety was grown by direct seeding method in a plot having area 1200 m^{2}and size 40×30m (Table 2) under dry condition.

Table 2

Crop and field parameters

Crop parameters		
Variety	**:**	Rajendra Bhagwati
Method of planting	**:**	Direct seeding
Field parameter and performance		
Plot size	**:**	40m x 30m
Soil type	**:**	Sandy loam
Soil P_H	**:**	8.1
Average soil moisture, %	**:**	10.80 to 12.40
Average bulk density, g/cc	**:**	1.84 to 1.90
Average depth of cut, mm	**:**	23.3 to 27.7
Average width of cut, mm	**:**	6 to 6.1
Average fuel consumption, l/h	**:**	0.88 to 1.20
Weed parameters		
Type of weed	**:**	Seasonal (Motha, *Cyperus rotundus*) (Sama or Sanwa, *Echinochloa colona*)
Height of weed, mm	**:**	80 to 120 (At the time of weeding)

Experimental Procedure

The experiment was conducted under the Randomized Block Design by operating the power weeder at three variable speeds i.e. 1.10 km/h, 1.27 km/h and 1.45 km/h. Weeding by hand tool *Khurpi* was taken as check treatment in the present experiment. Data were recorded in five replications of each treatment. Machine, crop, and economic parameters were evaluated to assess the performance of the developed machine and its effects on paddy yield and production economics. The results were compared with the farmers' commonly adopted practice of manual weeding using a khurpi or trowel.

The average working depth was 27.7 mm, with an engine speed of 3600 rpm and a rotor speed of 545 rpm. During the field evaluation, operator feedback regarding ease of operation and machine vibration was recorded qualitatively at the end of each experimental run. The standard formulae adopted for calculating the performance parameters of the developed power weeder are presented in Table 3.

Table 3

Standard formulae used for evaluating the performance of a power weeder

No.	Parameter	Formula [Units]	Citation
1.	Theoretical field capacity (TFC)	$\text{TFC} = \frac{S \times W}{10}$ [ha h^{-1}]	*Kepner et al., 2018; Ragesh et al., 2018*
2.	Effective field capacity (EFC)	$EFC = \frac{Effective\ coverage\ area\ by\ the\ machine\ (m^2)}{Total\ time\ taken\ in\ in\ hour\ (t) \times 1000}$ [ha h^{-1}]	*Kepner et al., 2018; Ragesh et al., 2018*
3.	Field efficiency (FE)	$FE = \frac{Effective\ field\ capacity\ (ha/h)}{Theoretical\ field\ capacity\ (ha/h)} \times 100$ [%]	*Islam et al. 2017; Ragesh et al., 2018*
4.	Weeding efficiency (WE)	$WE = \frac{w_1 - w_2}{w_1} \times 100$ [%]	*Thorat et al. 2014; Ragesh et al., 2018*
5.	Performance index (PI)	$PI = \frac{Effective\ field\ capacity \times (100 - Damage\ factor) \times Weeding\ index}{Input\ power}$ [ha hp^{-1}h^{-1}]	*Thorat et al. 2014; Ragesh et al., 2018*

Assessment of Grain and Straw Yield

The grain yield was recorded by using a wire square of 1m^2 by throwing it randomly in each treatment. In each treatment grain yield was recorded at five different locations, treated as replications. The straw yield was worked out by considering the grain straw ratio 1:1.15 for Rajendra Bhagwati paddy variety. The evaluation of machine parameters, including theoretical and effective field capacities, field and weeding efficiencies, fuel consumption and power consumption, was carried out as per the methodology outlined by *Sanjay (2024)*. Whereas, the performance index of weeder was determined by method described by *Rangasamy et al. (1993.)*

Cost Economics of Paddy and Straw

It was taken as per local market rate available in Samastipur town of Bihar. The paddy and straw cost were Rs 19.00/kg and 1.50 Rs/ kg, respectively. The cost of machine was carried out as per the methodology mentioned by *Sanjay (2024).*

RESULTS AND DISCUSSIONS

The average data of the replications with regards to the field capacity and field efficiency of the machine in all the treatments is presented in Table 4 and at the end of the operation, the operator reported that the machine was easy to operate and produced minimal vibration.

Table 4

Determination of Field Capacity & Field Efficiency of the machine in different treatments

Treatments	TFC (ha/h)	Theoretical Time (h/ha)	No. of Turns	Turning time/ turn (s)	Turning time (h/ha)	Actual Time (h/ha)	AFC (ha/h)	Field Efficiency (%)
T_1	0.0825	12.12	39	16	1.44	13.56	0.074	89.69
T_2	0.0953	10.49	39	16	1.44	11.93	0.084	85.45
T_3	0.1087	9.20	39	19	1.72	10.92	0.092	84.63

From the data recorded in Table 3 above, it was observed that the highest field capacity was recorded in treatment T_3 (0.092 ha/h) followed by treatment T_2 (0.084 ha/h) & treatment T_1 (0.074 ha/h). The field efficiency of machine was found having antagonistic relationship with the field capacity. The field efficiency of machine was maximum 89.69% in treatment T_1 followed by treatment T_2 (85.45%) and the minimum in treatment T_3 (84.63%).

Since the actual field capacity (AFC) is not dependent on the theoretical field capacity, which in turn is influenced by the forward speed of the machine, the AFC was observed to increase with the increase in forward speed from treatment T1 (1.10 km/h) to treatment T3 (1.45 km/h) *(Kumar et al., 2018; Verma et al., 2020)*. When the machine speed was increased, operational control at the terminal points and near the headland required more time, resulting in higher turning time (*Bhoi & Dash, 2021*). Consequently, this adversely affected the overall field efficiency of the machine, which was found minimum (84.63%) in treatment T3 (*Ghosh et al., 2022; Yadav & Patel, 2023*). Field efficiency decreased with increasing forward speed because the actual field capacity did not increase proportionally with the theoretical field capacity. At higher operating speeds, turning losses at headlands, implement overlap, missed areas requiring correction, and time required for machine adjustments increased. In addition, higher speeds reduced the operator's ability to maintain precise machine guidance, resulting in greater operational inefficiencies. Consequently, the ratio of actual field capacity to theoretical field capacity declined, leading to a reduction in field efficiency.

The weeding efficiency of the machine as well as *khurpi* as control treatment was determined at 25 and 45 days after seeding (Table 5). There was a similar trend in variation of weeding efficiency of the machine both at 25 and 45 days after seeding (DAS).

Table 5

Determination of weeding efficiency (%) of machine in different treatments

Treatment	Forward speed of the machine (km/h)	Weeding at 25 DAS			Weeding at 45 DAS		
		Weed count/m² area before weeding	Weed count/m² area after weeding	Weeding efficiency (%)	Weed count/m² area before weeding	Weed count/m² area after weeding	Weeding efficiency (%)
T_1	1.10	134	18	86.57	63	7	88.89
T_2	1.27	169	23	86.39	63	8	87.30
T_3	1.45	161	27	83.23	60	10	83.33
T_4	-	152	7	95.39	66	3	95.45

At 25 days after seeding, the weeding efficiency in treatment T_1 and T_2 were 86.57% and 86.39%, respectively. In treatment T_3, the machine had exhibited lower weeding efficiency i.e. 83.23%. At 45 days after seeding, the weeding efficiency in treatment T_1 and T_2 were 88.89% and 87.30% respectively. However, the same was 83.33% in treatment T_3 at 45 days after seeding.

The manual weeding by *khurpi* in control treatment had registered highest weeding efficiency among all the treatments with values 95.39% and 95.45% at 25 and 45 days after seeding respectively.

The weeding efficiency of the machine at 45 DAS was found to be slightly higher, possibly due to the vigorous growth of paddy plants, which restricted the survival of weeds around the root zone (*Devi et al., 2021; Mehta et al., 2020*).

However, when the forward speed of the machine exceeded 1.27 km/h, there was a significant decline in the weeding efficiency of the vertical rotary weeder. This reduction occurred due to the smaller overlapping portion of the tilth soil during each blade rotation, which caused incomplete uprooting and allowed some weeds to survive within the tilled zone (*Rajendran & Manian, 2019; Dash et al., 2021; Singh et al., 2023*).

The plant damage reported in percentage (%) was increasing with increase in forward speed of the machine (Table 6). The trend in variation of plant damage by the machine recorded in different treatments had the antagonistic relationship with the performance index (Table 6).

The plant damage at 25 DAS was ranging between 2.63% to 2.98% in treatments from T_1 to T_3. However, at 45 DAS the same was minimum (5.34%) in treatment T_1, followed by treatment T_2 (5.81%) and treatment T_3 (6.78%) respectively. The power requirement of the machine for weeding was minimum 3.2 hp in treatment T_1 and maximum 4.1 hp in treatment T_3 followed by 3.8 hp in treatment T_2. However, the weeding efficiency of machine was increasing marginally in all the treatments at 45 DAS in comparison to weeding efficiency reported at 25 DAS. The performance index of the machine was maximum in treatment T_1, both at 25 DAS (190.19%) and 45 DAS (189.85%). The minimum performance index 181.98% was recorded at 25 DAS in treatment T_3 followed by 175.06% at 45 DAS.

Table 6

Determination of performance index of the machine

Treatments	AFC (ha/h)	Power (hp)	Weeding efficiency (%)		Plant damage (%)		Performance Index	
			At 25 DAS	At 45 DAS	At 25 DAS	At 45 DAS	At 25 DAS	At 45 DAS
T_1	0.0722	3.2	86.57	88.89	2.63	5.34	190.19	189.85
T_2	0.0825	3.8	86.39	87.30	2.46	5.81	182.94	178.52
T_3	0.0924	4.1	83.23	83.33	2.98	6.78	181.98	175.06

There was more plant damage in all the treatments at 45 DAS, probably due to the higher tillering per hill in the paddy crop, where plants often came in contact with the rotating blades, causing mortality during the forward movement of the machine (*Patel et al., 2020; Reddy et al., 2020*). The trend of increased plant damage percentage and decreased weeding efficiency with an increase in the forward speed of the machine resulted in the highest performance index in treatment T1 and the lowest in treatment T3 (*Kumar & Singh, 2022*).

The power requirement of the machine from treatment T1 to T3 was found to be in increasing order, primarily due to the higher operational speed during the weeding process (*Sharma et al., 2021*). Therefore, the observed increase in both plant damage percentage and power requirement for weeding from treatment T1 to T3 was responsible for the decreasing trend of the performance index of the machine across treatments (*Deshmukh & Tiwari, 2019*). Power requirement increased with increasing forward speed because the rotary blades engaged a larger volume of soil and weed biomass per unit time. This increased the soil-cutting force, draft resistance, and torque required to rotate the blades. Consequently, the engine was required to deliver higher power to overcome the increased operational load while maintaining the desired rotor speed. Additionally, the higher rate of soil fragmentation and biomass cutting at elevated forward speeds contributed to greater energy demand, resulting in an increase in power consumption.

The data of plant height recorded from 30 days after seeding in different treatments at successive interval of 15 days clearly indicates that the plant growth in all the treatments were symmetric and presented in Table 7. The plant height recorded at 45 days after seeding shown maximum growth of the crop (48.48 cm) in treatment T_1 and minimum (44.42 cm) in treatment T_4 (Control Treatment). However, after 60 days of seeding the plant height in treatment T_1, T_3 and T_4 were at par. In treatment T_1, there was maximum plant growth with crop height 780.8 mm.

Table 7

Measurement of plant height at different stages during crop growth

Treatments	Average of plant height after 30 days, mm	Average of plant height after 45 days, mm	Average of plant height after 60 days, mm
T_1	258.4	484.8	780.8
T_2	254.2	464.0	776.9
T_3	243.6	478.8	765.0
T_4	254.6	444.2	762.5

The weeding in paddy crop by machine had a positive effect on plant growth due to inter-row soil pulverization, which enhanced soil aeration and nutrient availability for the plants (*Deshmukh & Tiwari, 2019; Patel et al., 2020*). The change in machine speed had no significant impact on the extent of soil pulverization and therefore, only marginal variation was observed in plant height at 45 and 60 days after seeding across all treatments (*Kumar & Singh, 2022*).

The weeding by *khurpi* was also found to be equally effective because of its high weeding efficiency, coupled with improved soil aeration near the root zone of the plants (*Sharma et al., 2021*). The plant height in the control treatment at 45 and 60 DAS was statistically at par with the plant height in treatment T3, where the machine operated at a higher forward speed (1.45 km/h), indicating that increased speed did not significantly affect crop growth (*Reddy et al., 2020*).

The cost of cultivation of paddy crop by using power weeder and khurpi for weeding operation were worked out to determine the Benefit-cost ratio in all the treatments. The data with regards to B-C ratio in different treatments of machine operation and weeding by khurpi as control treatment is presented in Table 8.

Table 8

Economic assessment of Power Weeder vis-à-vis manual weeding in paddy crop

Treatments	Cost of common operation (Land preparation, Sowing, Irrigation & Harvesting and Threshing (Rs/ha)	Cost of weeding (Rs/ha)	Total Cost of cultivation (Rs/ha)	Cost of Produce (Rs/ha)			Benefit in cultivation in comparison to the traditional method (Rs/ha)	B-C ratio
	(1)	(2)	(3)=(1+2)	Grain (4)	Straw (5)	Total 6=(4+5)	(7)	(8)=(7/3)
T_1	16800	2974.57	19774.57	82608.2	7499.95	90108.15	70333.58	**3.56**
T_2	16800	2604.73	19404.73	83448.0	7576.20	91024.20	71619.47	**3.69**
T_3	16800	2326.30	19126.30	82239.6	7466.49	89706.09	70579.79	**3.69**
T_4	16800	9000.00	25800.00	81795.0	7426.12	89221.12	63421.12	**2.46**

From perusal of the data presented in the Table 7, it is evident that the benefit-cost ratio was in higher range (3.56 to 3.69) in weeding by machine from treatment T_1 to T_3, as compared to the manual weeding, by *Khurpi* (2.46). The B-C ratio was maximum in treatment T_2 and T_3 (3.69) and minimum (3.56) in treatment T_1, when the weeding was done by the use of power weeder. The weeding by *Khurpi* was found least economical on account of lowest B-C ratio among all the treatments.

The highest grain and straw yield were recorded in the paddy crop when weeding was done using a power weeder. This was probably due to the fact that the rotating blades pulverized the soil, leading to better aeration in the root zone and improved nutrient availability for plant growth and development (*Deshmukh & Tiwari, 2019; Singh et al., 2021*). In weeding by *Khurpi*, although the weeding efficiency was higher, the lower yield of the crop in comparison to machine weeding (treatments T_2 and T1) may be attributed to less soil pulverization, resulting in restricted aeration near the root zone of the plants (*Patel et al., 2020*). The highest B–C ratio in treatment T2, over treatments T1 and T3, was due to the higher yield of grain and straw in T1 compared to other machine operations. The lowest B–C ratio in the control treatment (T4) was mainly due to the reduced grain and straw yield and the higher cost of cultivation associated with *Khurpi* weeding, which required a large amount of manual labour for operation (*Kumar & Singh, 2022*).

CONCLUSIONS

The study evaluated the effect of forward speed of a rotary power weeder on field performance, crop yield and economic efficiency in paddy cultivation. Results revealed that an increase in forward speed enhanced the actual field capacity but led to higher plant damage, power requirement and a decline in field efficiency. The treatment operated at a moderate speed of 1.27 km h^{-1} (T_2) exhibited the most desirable combination of performance indicators, with superior weeding efficiency, lower crop damage and a balance between time efficiency and operational cost. Consequently, T_2 also recorded the highest grain and straw yields, resulting in the maximum benefit–cost ratio among all treatments. The findings suggest that maintaining an optimum forward speed of approximately 1.27 km h^{-1} ensures effective weed control, improved soil conditions and enhanced profitability in paddy cultivation. Adoption of rotary power weeders at this operational speed can significantly reduce labour dependency and promote sustainable mechanization in wetland paddy farming.

REFERENCES

[1] Dash S.K., Pradhan P.L., Swain S., (2021), Effect of machine parameters on the performance of rotary weeders in paddy fields, *Agricultural Mechanization in Asia, Africa and Latin America*, Vol. 52, No. 4, pp. 65–72.

[2] Deshmukh S.P., Tiwari G.S., (2019), Comparative evaluation of commercial vegetable transplanters for small-scale farming, *Journal of Agricultural Engineering*, Vol. 56, No. 4, pp. 22–28.

[3] Devi, K. S., Neeraja, T., Prasuna, V. (2021). Performance Evaluation of Manually Operated Weeders Developed in ANGRAU. *Int. J. Curr. Microbiol. App. Sci*, 10(08), 636-652. https://doi.org/10.20546/ijcmas.2021.1008.074

[4] Dixit J., Syed I., (2008), Field evaluation of power weeder for rain-fed crops in Kashmir Valley, *Agricultural Mechanization in Asia, Africa and Latin America*, Vol. 39, No. 1, pp. 53–56.

https://www.researchgate.net/publication/268502977_Field_Evaluation_of_Power_Weeder_for_Rain-fed_Crops_in_Kashmir_Valley

[5] Dutta S.K., (1981), *Principles and Practices of Rice Production*, John Wiley and Sons, New Jersey, USA. http://books.irri.org/0471097608_content.pdf

[6] FAO, (2011), *Agricultural Mechanization in Asia, Africa and Latin America*, Food and Agriculture Organization of the United Nations, Rome, Italy.

[7] Farooq M., Siddique K.H.M., Rehman H., Aziz T., Lee D.J., Wahid A., (2011), Rice direct seeding: Experiences, challenges and opportunities, *Soil and Tillage Research*, Vol. 111, No. 2, pp. 87–98. https://doi.org/10.1016/j.still.2010.10.008

[8] Finance Department, (2023), *Economic Survey of Bihar – 2023*, Government of Bihar. https://instituteofpublicservices.com/2024/02/16/bihar-economic-survey-2023-24/

[9] Ghosh M., Pradhan P., Nayak R., (2022), Effect of operational parameters on field efficiency and performance of power weeders in paddy fields, *Journal of Agricultural Engineering*, Vol. 59, No. 1, pp. 15–22.

[10] Goel A.K., Behera D., Behera B.K., Mohanty S.K., Nanda S.K., (2008), Development and ergonomic evaluation of manually operated weeder for dry land crops, *Agricultural Engineering International: The CIGR E-Journal*, Vol. 10, Manuscript PM 08 009, pp. 1–11. https://api.semanticscholar.org/CorpusID:55558971

[11] Hunt D., (2001), *Farm Power and Machinery Management*, 10th ed., Iowa State University Press, Ames, Iowa, USA. https://www.scribd.com/document/413228196/Farm-Power-and-Machinery-Management

[12] Hussain S., Ramzan M., Akhter M., Aslam M., (2008), Weed management in direct seeded rice, *Journal of Animal and Plant Sciences*, Vol. 18, No. 2–3, pp. 86–89. https://thejaps.org.pk/docs/18_2-3_2008/08-838.pdf

[13] Kepner R.A., Bainer R., Barger E.L., (2018), *Principles of Farm Machinery*, 4th ed., AVI Publishing. https://doi.org/10.1097/00010694-195602000-00021

[14] Kumar, P., Meena, S. S., Shekhawat, R. S., Agarwal, N. K., & Khidiya, M. S. (2023). Pruning and plucking equipment in horticulture: a review. https://doi.org10.15740/HAS/IJAS/19.2/724-729

[15] Kumar, P., Khatri, S., Maurya, M., Tripathi, A., Kumar, N., (2026) Transforming Indian agriculture: Role and benefits of farm mechanization using modern machinery. International Journal Advanced Biochemistry Research;10(1S):485-490. https://doi.org10.33545/26174693.2026.v10.i1Sf.7026

[16] Kumar A., Singh B., (2022), Economic analysis of mechanical and manual weeding operations in rice cultivation, *Journal of Farm Machinery and Power Engineering*, Vol. 14, No. 1, pp. 12–18.

[17] Kumar R., Singh A., Mehta C.R., (2018), Influence of forward speed and operational width on field capacity and efficiency of self-propelled paddy weeders, *International Journal of Agricultural Engineering*, Vol. 11, No. 2, pp. 89–95. https://doi.org/10.12944/CARJ.6.3.24

[18] Kumar S., (2024), *A Numerical Approach in Agricultural Engineering with Objective*, 4th ed., Kalyani Publishers.

[19] Kwangwaropas M., (1999), Study and research of the equipment used for weeding under mango tree, *Proceedings of the 4th National Plant Protection Conference*, Chonburi, Thailand, pp. 256–263.

[20] Mahajan G., Chauhan B., Johnson D., (2009), Weed management in aerobic rice in Northwestern Indo-Gangetic Plains, *Journal of Crop Improvement*, Vol. 23, No. 4, pp. 366–382. https://doi.org/10.1080/15427520902970458

[21] Manuwa S.I., (2009), Performance evaluation of a rotary weeder in vegetable production, *Soil and Tillage Research*, Vol. 103, No. 1, pp. 78–82.

[22] Mehta C.R., Singh K., Verma R., (2020), Evaluation of self-propelled paddy weeder for energy efficiency and crop performance, *Journal of Agricultural Engineering*, Vol. 57, No. 3, pp. 23–30.

[23] Ministry of Agriculture & Farmers Welfare, (2022), *Agricultural Statistics at a Glance 2022*, Government of India. https://agriwelfare.gov.in/Documents/CWWGDATA/Agricultural_Statistics_at_a_Glance_2022_0.pdf

[24] Mishra J., Singh V., (2012), Tillage and weed control effects on productivity of a dry seeded rice–wheat system on a Vertisol in Central India, *Soil and Tillage Research*, Vol. 123, pp. 11–20. https://doi.org/10.1016/j.still.2012.02.003

[25] Mor, A., Bansal, N.K., Parveen, Karwasra, N., & Kumar, S. (2020). Performance evaluation of different weeders in cotton. International Journal of Agricultural Engineering, 13(2), 227–236. https://doi.org10.15740/HAS/IJAE/13.2/227-236

[26] Nag P.K., Dutta P., (1979), Effectiveness of some simple agricultural weeders with reference to physiological responses, *Journal of Human Ergonomics*, Vol. 8, pp. 11–21. https://doi.org/10.11183/jhe1972.8.13

[27] Paraforos, D. S., Hübner, R., Griepentrog, H. W. (2018). Automatic determination of headland turning from auto-steering position data for minimising the infield non-working time. *Computers and electronics in agriculture*, 152, 393-400. https://doi.org/10.1016/j.compag.2018.07.035

[28] Patel S.P., Guru P.K., Borkar N.T., Debnath M., Lal B., Gautam P., Kumar A., Bhaduri D., Shahid M., Tripathi R., Nayak A.K., Pathak H., (2018), *Energy Footprints of Rice Production* (NRRI Research Bulletin No. 14), ICAR–National Rice Research Institute, Cuttack, India. https://icar-crri.in/wp-content/uploads/2019/07/6.-Energy-Footprints-of-Rice-Production_14.pdf

[29] Patel S., Verma R.K., Yadav M., (2020), Performance of different weeding methods on soil properties and crop productivity in rice, *Agricultural Mechanization in Asia, Africa and Latin America*, Vol. 51, No. 2, pp. 45–50.

[30] Rajendran P., Manian R., (2019), Optimization of operational parameters of rotary weeders for wetland paddy cultivation, *Journal of Agricultural Science and Technology*, Vol. 21, No. 6, pp. 1543–1552.

[31] Ragesh, K. T., Jogdand, S. V., & Victor, D. V. (2018). Field performance evaluation of power weeder for paddy crop. Current Agriculture Research Journal, 6(3), 441-448. http://dx.doi.org/10.12944/CARJ.6.3.24

[32] Rangasamy K., Balasubramanium M., Swaminathan K.R., (1993), Evaluation of power weeder performance, *Agricultural Mechanization in Asia, Africa and Latin America*, Vol. 24, No. 4, pp. 16–18. https://www.shin-norin.co.jp/english/pdf/VOL_24_NO4_AUTUMN_1993.pdf

[33] Reddy G.P., Naik R.K., Kumar D., (2020), Influence of forward speed of power weeder on soil pulverization and crop growth in paddy, *International Journal of Agricultural Sciences*, Vol. 12, No. 6, pp. 87–92.

[34] Sharma H.C., Singh H.B., Fireson G.H., (1977), Competition from weeds and their control in direct seeded rice, *Weed Research*, Vol. 17, No. 2, pp. 103–108. https://doi.org/10.1111/j.1365-3180.1977.tb00452.x

[35] Sharma R., Jat M.L., Singh S., (2021), Effect of mechanical weeders on weed control efficiency and yield attributes of rice crop, *Indian Journal of Weed Science*, Vol. 53, No. 2, pp. 105–110.

[36] Shrivastava N.S.L., (2000), Role of mechanisation of horticultural crops with emphasis on automation, *Agricultural Engineering Today*, Vol. 24, No. 1–2, pp. 13–28.

[37] Singh G., Singh S., (2012), Performance evaluation of engine-operated weeder in different crops, *Journal of Agricultural Engineering*, Vol. 49, No. 3, pp. 11–17.

[38] Singh G., Sahay K.M., (2001), *Research Development and Technology Dissemination: A Silver Jubilee Publication*, Central Institute of Agricultural Engineering (CIAE), Bhopal, India.

[39] Singh R., Sharma V., Kumar N., (2021), Effect of mechanical and manual weeding on yield and economics of paddy crop, *Indian Journal of Agronomy*, Vol. 66, No. 3, pp. 341–346.

[40] Singh R.P., Patel N.K., Yadav V.S., (2023), Impact of forward speed on soil pulverization and weed control efficiency in vertical rotary weeders, *Current Agriculture Research Journal*, Vol. 11, No. 2, pp. 198–206.

[41] Singh S., Ladha J.K., Gupta R.K., Bhushan L., Rao A.N., Sivaprasad A., Singh P., (2007), Evaluation of mulching, intercropping with *Sesbania* and herbicide use for weed management in dry-seeded rice (*Oryza sativa* L.), *Crop Protection*, Vol. 26, No. 4, pp. 518–524. https://doi.org/10.1016/j.cropro.2006.04.024

[42] Tewari V.K., Kumar A., Kumar S., (2014), Development and performance evaluation of a power weeder for row crops, *Biosystems Engineering*, Vol. 118, pp. 55–64.

[43] Timmer C.P., (2010), *The Changing Role of Rice in Asia's Food Security* (ADB Sustainable Development Working Paper Series No. 15), Asian Development Bank, Metro Manila, Philippines. http://adb.org/sites/default/files/publication/28552/adb-wp15-rice-food-security.pdf

[44] Verma R.K., Sinha N., Tiwari S., (2020), Evaluation of field performance of walk-behind rotary weeders in wetland rice, *Agricultural Science Digest*, Vol. 40, No. 4, pp. 298–304.

EXPERIMENTAL STUDY ON THRESHING POWER CONSUMPTION OF AN AXIAL-FLOW THRESHING DEVICE WITH ADJUSTABLE THRESHING INTENSITY

/

脱粒力度可调式轴流脱粒装置脱粒功耗试验研究

Yuejiang TENG[1,2], Chengqian JIN[*3], Fuxiang XIE[1,2], Jian SONG[1,2]

[1)] School of Machinery and Power Engineering, Weifang University, Weifang / China;

[2)] Shandong Key Laboratory of Intelligent Manufacturing Technology for Advanced Power Equipment, Weifang / China;

[3)] Nanjing Institute of Agricultural Mechanization, Ministry of Agriculture and Rural Affairs, Nanjing / China

Tel: +86-19525369138; E-mail: tyj2021to2026@163.com

Correspondent author: Chengqian JIN

DOI: https://doi.org/10.35633/inmateh-79-34

Keywords: *axial-flow threshing device, adjustable threshing intensity, threshing power consumption, mechanical efficiency, parameter optimization*

ABSTRACT

To address the high power consumption, limited load adaptability, and inadequate parameter matching of conventional axial-flow threshing devices, power-consumption tests were conducted on an axial-flow threshing device with adjustable threshing intensity using rice as the test material. The tests examined different threshing-intensity modes, separating-screen types, and operating parameters. The effects of these factors on no-load power consumption, effective power consumption, total power consumption, and mechanical efficiency were analyzed. The results showed that total power consumption was minimized when the threshing-intensity adjustment plates were fully open and the rectangular-hole separating screen was used. Total power consumption increased with increasing drum speed, deflector angle, and feed rate, but decreased with increasing concave clearance. Mechanical efficiency initially remained stable and then decreased as drum speed increased, whereas it increased with increasing deflector angle and feed rate. The specific threshing power consumption, expressed per unit feed rate, ranged from 4.4 to 5.2 kW/(kg/s). It increased with increasing drum speed, deflector angle, and feed rate, and decreased with increasing concave clearance. This study provides a reference for reducing power consumption and optimizing parameter matching in axial-flow threshing devices with adjustable threshing intensity.

摘要

针对传统轴流脱粒装置功耗偏高、负荷适应性差、参数匹配粗放等问题，以水稻为试验材料，在一种脱粒力度可调式轴流脱粒装置上，开展不同脱粒力度模式、分离筛板类型及不同工作参数条件下的脱粒功耗试验，分析各试验因素对空载功耗、有效功耗、总功耗及机械效率的影响规律。结果表明：脱粒力度调节板全部打开、采用长方形筛孔式分离筛板时总功耗最低；总功耗随滚筒转速、导流板角度、喂入量的增大而上升，随凹板筛间隙的增大而下降；机械效率随转速的升高先稳后降，随导流板角度及喂入量的增大而提高。装置单位喂入量脱粒功耗为 4.4～5.2 kW/(kg/s)，随滚筒转速、导流板角度、喂入速率的增加而升高，随凹板筛间隙的增大而降低。该研究可为脱粒力度可调式轴流脱粒装置低功耗优化与参数匹配提供参考。

INTRODUCTION

As the core working component of a grain combine harvester, the threshing device accounts for the highest proportion of the total power consumption of the whole machine. The characteristics of threshing power consumption directly affect the power matching, operating efficiency and performance, as well as fuel economy of the combine harvester *(Song et al., 2022; Li et al., 2011; Mousaviraad et al., 2020)*. In practical harvesting operations, operating parameters such as drum speed, concave clearance and feed rate jointly determine the threshing power consumption and the mechanical efficiency of the device *(Kiniulis et al. 2017; Qin et al., 2025; Yu et al., 2025)*. At present, harvesting equipment generally suffers from problems such as extensive parameter matching, high operating power consumption, large fluctuations in mechanical efficiency and poor load adaptability *(Lu et al., 2012; Chen et al., 2025; Vlăduț et al., 2022)*.

Yuejiang Teng, Lecturer, Ph.D.; Chengqian Jin, Prof., Ph.D.; Fuxiang Xie, Prof., Ph.D.; Jian Song, Prof., Ph.D.

Especially under complex field conditions with uneven feeding and drastic changes in crop moisture content, problems such as blockage, sharp increase in energy consumption, incomplete threshing or excessive grain damage frequently occur, which seriously restrict the upgrading and development of combine harvesters toward high efficiency, low consumption, intelligence and lightweight *(Jin et al., 2015; Ren et al., 2013; Steponavičius et al. 2023; Vlăduţ et al., 2023; Zhang et al., 2026)*.

In recent years, scholars worldwide have conducted extensive research on the structural optimization, parameter matching, and power consumption characteristics of axial-flow threshing devices. *Waree et al. (2016)* investigated the effects of structural parameters on the power consumption of an axial-flow corn threshing device using the response surface methodology. The results indicated that increasing the tine clearance, concave grate clearance, and concave clearance could significantly reduce threshing power consumption. Meanwhile, a power consumption prediction model with high fitting accuracy was established, which provided a theoretical basis for the low-energy structural parameter optimization of threshing devices. *Fan et al. (2022)* developed an adaptive feed-rate threshing clearance control system to address the excessive power consumption caused by non-adjustable threshing clearance under varying feed rates. Tests showed that the system could match the optimal threshing clearance, with the average power consumption increased by only 3.45%. The system significantly improved operating performance while maintaining basically stable energy consumption, providing a feasible approach for the energy-saving control of threshing devices. *Ali et al. (2024)* optimized the rotor structure of sunflower threshers to conduct experiments for energy consumption reduction. Their test results verified that rotor rotary speed and concave clearance exert remarkable impacts on the specific energy consumption during threshing operations. When adopting the tine-bar rotor under the working condition of 300 r/min rotor speed and 10 mm concave clearance, the specific energy consumption was reduced from 9.65 kWh/ton to 5.09 kWh/ton. This finding demonstrated that structural improvement of threshing rotors was an effective method to reduce the power consumption of threshing operations. *Xing et al. (2024)* designed a longitudinal-axial flow threshing device with a measurement and control system to tackle the high energy consumption and poor parameter matching of corn ear threshing under high moisture content. Parameter optimization tests were carried out with drum speed, concave clearance, and deflector angle as variables. A regression model of unit energy consumption was established and the optimal parameters were obtained. Results showed that the unit energy consumption was reduced by 14.74% after optimization with high model accuracy, offering a reference for the low-power consumption optimization of threshing devices.

Most existing studies focused on threshing devices with fixed structures and single adjustment mode, and there is a lack of research on the power consumption characteristics of novel axial-flow threshing devices with adjustable threshing intensity, multi-mode switching and multi-parameter collaborative regulation *(Wang et al., 2025; Xie et al., 2021)*. In particular, studies on the variation laws of power consumption and mechanical efficiency under the coupling effects of different threshing intensity modes, separating screen types, concave clearance, deflector angle and other parameters are insufficient.

Therefore, this study took an axial-flow threshing device with adjustable threshing intensity as the research object. The device integrated an adjustable-intensity threshing concave, a 360° separation device, a concave clearance adjustment mechanism, and a deflector angle adjustment mechanism, which could realize the switching of four threshing intensity modes and multi-parameter collaborative regulation. Threshing power consumption tests were carried out under different threshing intensity modes, separating screen types, drum speeds, deflector angles, concave clearances and feed rates. The variation laws of no-load power consumption, effective threshing power consumption, total threshing power consumption and mechanical efficiency were systematically analyzed, and the influence mechanism of each parameter on threshing power consumption was revealed. This study could provide experimental evidence and theoretical support for the low-energy optimization and parameter matching of adjustable axial-flow threshing devices

MATERIALS AND METHODS

Structure of the longitudinal-axial flow threshing device with adjustable threshing intensity

The threshing intensity required during harvesting varies considerably among crop varieties, moisture contents, and feed-rate conditions. The complexity of practical threshing conditions therefore imposes greater requirements on the adaptability of the threshing device. To address these requirements, a longitudinal axial-flow threshing device with adjustable threshing intensity was designed, as shown in Fig. 1. The device mainly consists of a screw feeder, a trapezoidal threshing drum, an adjustable-intensity threshing concave, a 360° separation device, concave-clearance adjustment mechanisms, deflectors, and a deflector-angle adjustment mechanism.

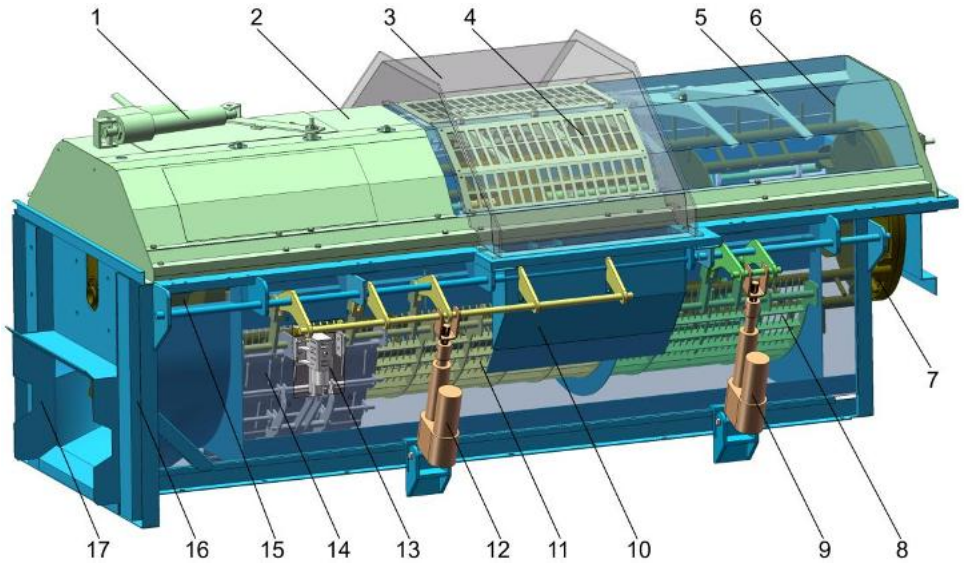
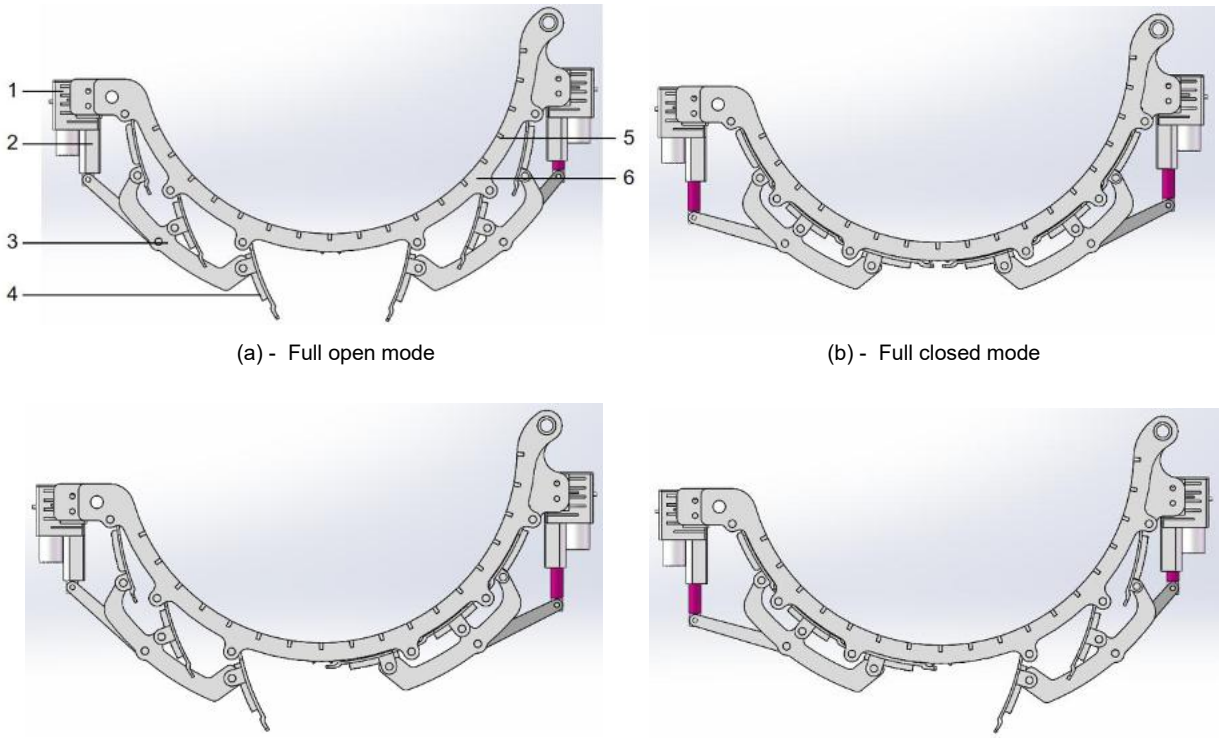


Fig. 1 - Structure of the longitudinal-axial flow threshing device with adjustable threshing intensity

1 – deflector angle adjustment mechanism; 2 – top cover; 3 – 360° separation device; 4 – upper sieve plate of 360° separation device; 5 – deflector; 6 – threshing element; 7 – trapezoidal threshing drum; 8 – separating concave; 9 – separating concave clearance adjustment mechanism; 10 – return plate of 360° separation device; 11 – threshing concave; 12 – threshing concave clearance adjustment mechanism; 13 – adjustable-intensity threshing concave; 14 – threshing-intensity adjustment plate; 15 – screw feeder;16 – frame; 17 – feed inlet

The structure of the adjustable-intensity threshing concave is shown in Fig. 2. It mainly consists of threshing intensity adjustment plates, transverse grids, concave bars, side arc plates, electric actuator mounts, electric actuators and transmission rods.



(a) - Full open mode

(b) - Full closed mode

(c) - Left open and right closed mode

(d) - Left closed and right open mode

Fig. 2 - Structure and operating modes of the adjustable-intensity threshing concave

1 – electric actuator mount; 2 – electric actuator; 3 – transmission rod; 4 – threshing-intensity adjustment plate; 5 – transverse partition plate; 6 – Side arc plate

The threshing-intensity adjustment plates were divided into left and right parts. Each part contained 9 adjustment plates arranged in 3 rows and 3 columns.

Each adjustment plate was hinged on one side to the concave frame, and the other side was uniformly controlled by an electric actuator through a transmission mechanism to switch between open and closed states. The left and right electric actuators were both fixed on the concave frame. According to the required threshing intensity during operation, the threshing-intensity adjustment plates could be adjusted to four modes: fully open, fully closed, left open and right closed (viewed from the rear of the threshing device), and left closed and right open (viewed from the rear of the threshing device), as shown in Fig. 2.

Test materials

Compared with other grains, rice grains and stems have higher moisture content, resulting in relatively high power consumption during threshing. Therefore, rice was selected as the test material in this study to investigate threshing power consumption. The relevant material properties of rice are listed in Table 1.

Table 1

Relevant material characteristic parameters of the test crop

Test crop	Plant height [mm]	Straw-to-grain ratio	Grain moisture content [%]	Stem moisture content [%]	Thousand-grain weight [g]	Yield per unit area [kg·hm^{-2}]
Rice	865	1:1.1	23.2	58.6	27.5	8960

Test Method

The power consumption of the threshing device measured in the experiment included no-load power consumption, effective threshing power consumption, and total threshing power consumption. No-load power consumption referred to the power required to maintain the rotation of the threshing drum. Effective threshing power consumption was the power consumed for crop threshing. Total threshing power consumption, which is the sum of no-load power consumption and effective threshing power consumption, represented the total power required for the threshing operation of the device. The power consumption of the threshing device *(Wan et al., 2005; Zhang et al., 2010)* was calculated using Equation (1).

$$P=\frac{Mn}{9550} \tag{1}$$

where: P is power consumption of the threshing device, kW; M is torque acting on the threshing drum during operation, N·m; n is rotational speed of the threshing drum, r/min.

The experimental measurement equipment included a wireless torque measuring device, a data receiving device, a drum rotational speed measuring device, etc., as shown in Fig. 3. Before the experiment, the strain gauges of the torque acquisition device were adhered to the ground surface of the main shaft of the threshing drum with glue and fixed with adhesive tape. The wireless torque node and battery were also fixed on the main shaft of the threshing drum with adhesive tape. During the test, the torque data acting on the drum was transmitted to a computer through a wireless gateway. An encoder was installed at the rear of the threshing drum and connected to the main shaft of the drum via a coupling. The real-time rotational speed of the threshing drum could be measured by the encoder when the threshing device was in operation. The threshing power consumption could be obtained by substituting the torque and rotational speed parameters into Equation (1).



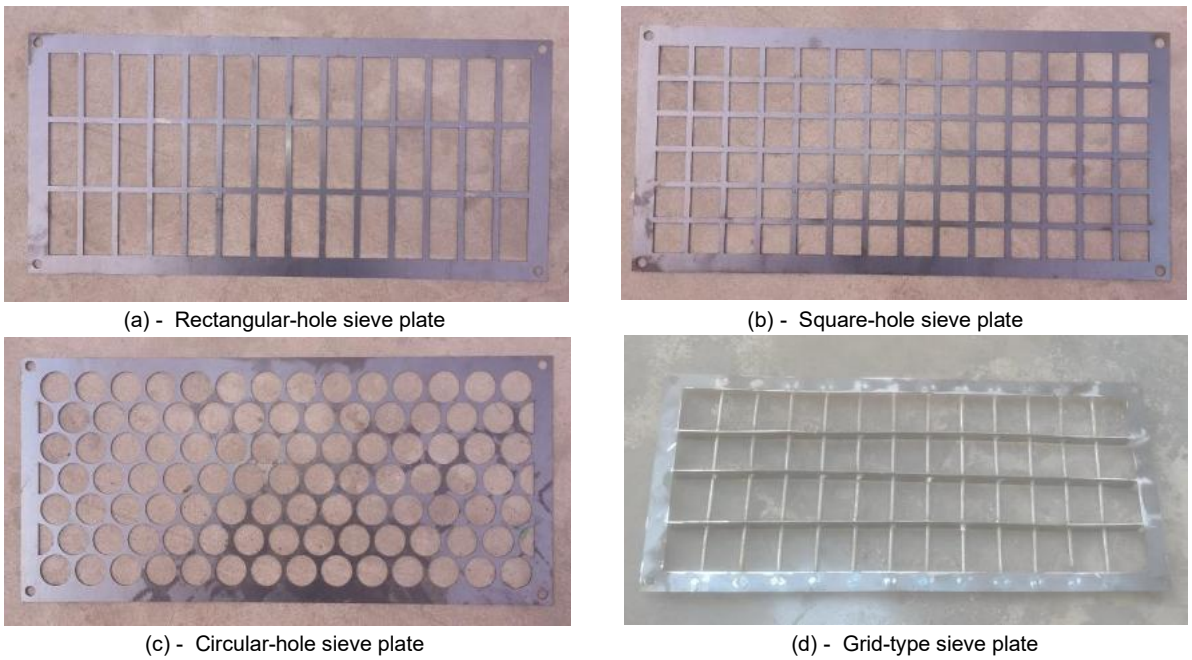
(a) - Data receiving and processing device

(b) - Drum torque acquisition device

(c) - Drum rotational speed measurement device

Fig. 3 - Equipment used to measure threshing power consumption

To investigate the influence laws of different structural parameters of the threshing device on its power consumption, comparative experiments were carried out on the threshing power consumption under different switching modes of the adjustable threshing force concave sieve (as shown in Fig. 2) and different types of separation sieve plates at the upper part of the 360°separation device (as shown in Fig. 4), respectively.



(a) - Rectangular-hole sieve plate (b) - Square-hole sieve plate

(c) - Circular-hole sieve plate (d) - Grid-type sieve plate

Fig. 4 - Different types of sieve plates used in the upper separation device

The basic operating parameters of the threshing device were set as follows *(Jiang et al., 2025; Zhou et al., 2022; Liu et al., 2025)*: drum rotational speed of 900 r/min, deflector angle of 60°, concave sieve clearance of 20 mm, and Feed rate of 4 kg/s. In the comparative experiment of threshing power consumption under different switching modes of the adjustable threshing force concave sieve, the upper part of the 360° separation device was equipped with a rectangular-hole separation sieve plate. In the comparative experiment of threshing power consumption with different types of separation sieve plates for the 360° separation device, the threshing force adjustment plates were fully opened.

To investigate the influence law of operating parameters on the threshing power consumption of the threshing device, single-factor tests were conducted by selecting rotational speed of the threshing drum, deflector angle, concave sieve clearance and feed rate as influencing factors. During the experiments, the threshing force adjustment plates were fully opened, and the upper part of the 360° separation device was equipped with a rectangular-hole separation sieve plate. The adjustment method of the operating parameters is shown in Fig. 5. The level coding design of the experimental influencing factors is presented in Table 2.



(a) -Drum rotational speed adjustment device (b) - Deflector angle adjustment device (c) Concave sieve clearance adjustment device

Fig. 5 - Operating parameters adjustment devices

Table 2

Experimental factors coding

Coded Value	Drum rotational speed [r·min^{-1}]	Deflector angle [°]	Concave clearance [mm]	Feed rate [kg·s^{-1}]
-1	800	50	10	3
-0.5	850	55	15	3.5
0	900	60	20	4
0.5	950	65	25	4.5
1	1000	70	30	5

RESULTS AND DISCUSSION

The results of the comparative tests on threshing power consumption under the different operating modes of the adjustable-intensity threshing concave are shown in Fig. 6. Among the four modes, total threshing power consumption was lowest, at 27.14 kW, when the threshing-intensity adjustment plates were fully open, and highest, at 27.67 kW, when they were fully closed. When the adjustment plates were fully open, the effective separation area of the concave was larger, which reduced the amount of crop material retained in the threshing chamber and decreased threshing resistance. Consequently, total threshing power consumption was minimized. When viewed from the rear of the device toward the front, the threshing drum rotated counterclockwise. Under this direction of rotation, threshing resistance was lower in the left-open/right-closed mode than in the left-closed/right-open mode. Accordingly, the total threshing power consumption was lower in the left-open/right-closed mode.

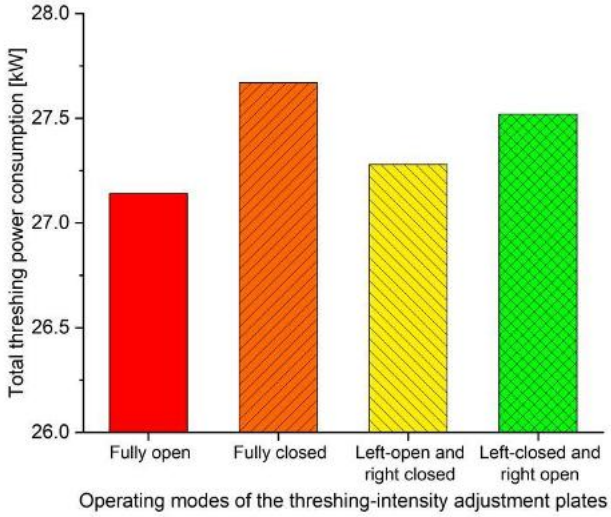


Fig. 6 - Comparison of total threshing power consumption among the operating modes of the threshing-intensity adjustment plates

The results of the comparative tests on threshing power consumption using different separation sieve plates in the 360° separation device are shown in Fig. 7.

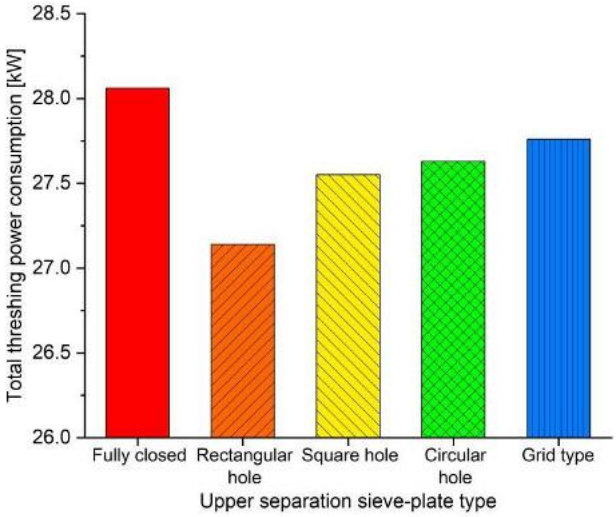


Fig. 7 - Comparison of total threshing power consumption among different upper separation sieve-plate types

As shown in Fig. 7, when the upper concave sieve of the 360° separation device was fully closed, the threshing power consumption was 28.06 kW, which was significantly higher than that under the open condition.

This phenomenon could be attributed to the reduced separation area of the concave sieve in the fully closed state, which prolonged the threshing and separation duration of crops in the threshing chamber and thus increases the threshing power consumption of the drum. The order of threshing power consumption for different types of separation sieve plates from low to high was as follows: rectangular-hole sieve plate, square-hole sieve plate, circular-hole sieve plate, and grid-type sieve plate. The underlying reason for this result was that, for separation sieve plates of the same overall size, the separation area of the rectangular-hole sieve plate was larger than that of the other types. Although the grid-type sieve plate also exhibited a large separation area in the front view, a considerable amount of threshed material exits the threshing chamber at a certain angle relative to the sieve plate during separation, and the protruding structure of the grid-type sieve plate impeded the separation process. Therefore, among the different types of separation sieve plates, the rectangular-hole sieve plate achieved the lowest total threshing power consumption of 27.14 kW.

The effects of drum rotational speed on the threshing power consumption and mechanical efficiency of the threshing device are depicted in Fig. 8. The no-load power consumption of the threshing device exhibited a gradual upward trend with increasing drum rotational speed, rising from approximately 7.32 kW at 800 r/min to about 9.21 kW at 1000 r/min. This phenomenon was attributed to the increased mechanical losses, such as bearing friction and air resistance, at higher drum speeds, which elevated the basic energy consumption required to maintain the idling of the drum. The effective threshing power consumption of the device increased continuously with the rise in drum rotational speed, from approximately 17.76 kW at 800 r/min to around 20.68 kW at 1000 r/min. The increased rotational speed intensified the impact and kneading actions of the threshing components on the crop materials, thereby raising the effective energy consumption for threshing, with a growth rate slightly higher than that of the no-load power consumption. As the sum of the no-load power consumption and the effective threshing power consumption, the total threshing power consumption also presented a linear increasing trend with the elevation of drum speed, increasing from about 25.08 kW at 800 r/min to roughly 29.89 kW at 1000 r/min. The overall variation trend was steady without drastic fluctuations, demonstrating the stable operation of the device within the tested rotational speed range.

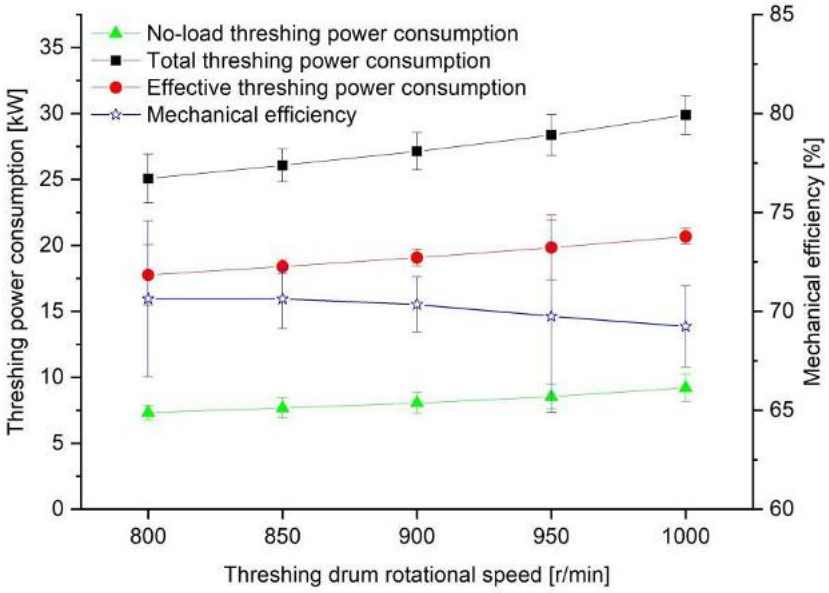


Fig. 8 - Effects of threshing-drum rotational speed on threshing power consumption and mechanical efficiency

As shown in Fig. 8, the mechanical efficiency of the threshing device remained relatively constant initially and then decreased as the drum rotational speed increased. Within the range of 800 ~ 900 r/min, the mechanical efficiency was stabilized at approximately 70.50%, indicating a high and stable energy utilization efficiency of the device in this speed interval. When the rotational speed exceeded 900 r/min, the mechanical efficiency began to decrease noticeably, dropping to about 69.76% at 950 r/min and further to 69.24% at 1000 r/min. The primary reason for the decline in mechanical efficiency was that the growth rate of no-load power consumption surpasses that of effective threshing power consumption at high speeds, with more energy dissipated in mechanical losses rather than being directly utilized for threshing operations, thus reducing the energy utilization efficiency.

The effects of deflector angle on the threshing power consumption and mechanical efficiency of the threshing device are illustrated in Fig. 9. The no-load power consumption remained basically stable at approximately 8.06 kW as the deflector angle increased from 50° to 70°.

This indicated that the variation in deflector angle exerted a negligible influence on mechanical losses during drum idling (such as bearing friction and air resistance), and the no-load power consumption was only determined by the inherent structure and operating state of the device. With the increase of the deflector angle, the effective threshing power consumption of the device exhibited a steady upward trend, rising gradually from approximately 18.68 kW at 50° to 19.60 kW at 70°. A larger deflector angle prolonged the residence time of crops in the threshing drum, promoted more uniform material distribution, and enhanced the interaction between threshing components and crops, thereby leading to a slight increase in effective threshing energy consumption. As the sum of no-load power consumption and effective threshing power consumption, the total threshing power consumption also increased slowly with the rise in deflector angle, from 26.74 kW at 50° to approximately 27.66 kW at 70°. The overall variation was gentle without obvious abrupt changes, demonstrating the stable operation of the device within the tested angle range.

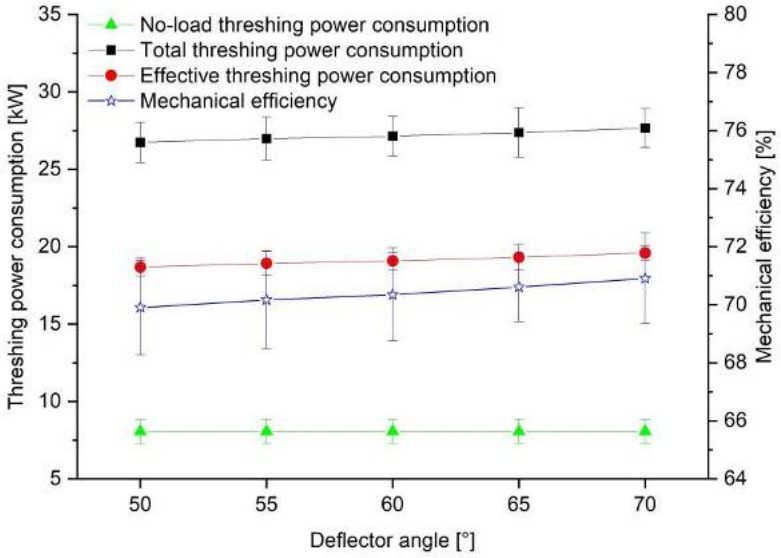


Fig. 9 - Effects of deflector angle on threshing power consumption and mechanical efficiency

As shown in Fig. 9, the mechanical efficiency of the threshing device displayed a continuous and steady upward trend with the increase in deflector angle, rising gradually from approximately 69.90% at 50° to about 70.91% at 70°. Although the increase amplitude was small, the trend was stable. The primary reason for the improved efficiency was that the growth rate of effective threshing power consumption was slightly higher than that of total power consumption, with more energy being efficiently utilized for threshing operations rather than mechanical losses, thus resulting in a slight optimization of energy utilization efficiency as the deflector angle increased.

The effects of concave sieve clearance on the threshing power consumption and mechanical efficiency of the threshing device are presented in Fig. 10. The no-load power consumption remained essentially constant at approximately 8.06 kW as the concave sieve clearance increased from 10 mm to 30 mm. This indicated that the adjustment of concave sieve clearance exerted no significant influence on the mechanical losses during drum idling, and the no-load power consumption was solely determined by the operating state of the device itself. The effective threshing power consumption of the device exhibited a gradual downward trend with the increase in concave sieve clearance, decreasing from 20.48 kW at 10 mm to 18.28 kW at 30 mm. A larger clearance weakened the squeezing and kneading interaction between the threshing components and the crop materials, and reduced the resistance of materials passing through the threshing zone, thereby lowering the effective energy consumption directly used for threshing operations. As the sum of the no-load power consumption and the effective power consumption, the total threshing power consumption also decreased steadily with the increase in clearance, from 28.54 kW at 10 mm to 26.34 kW at 30 mm. The overall variation was gentle without drastic fluctuations, indicating the stable operation of the device within the tested clearance range.

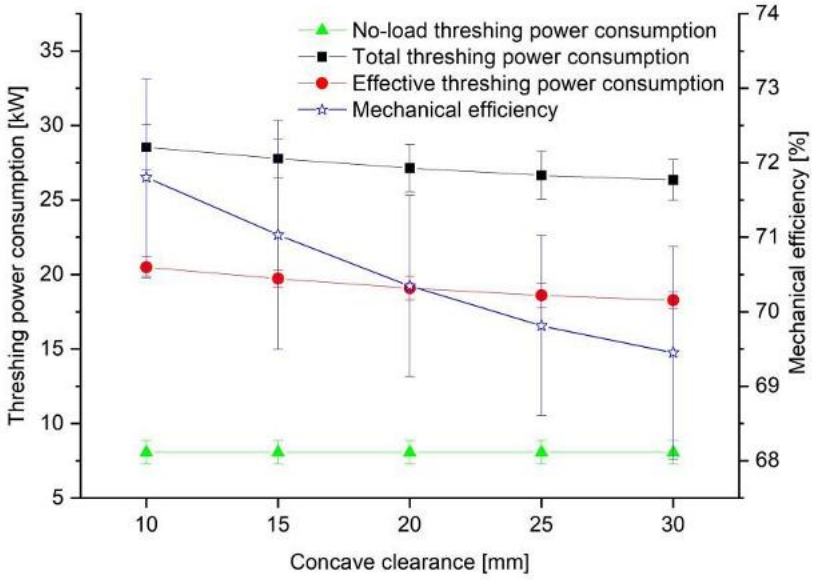


Fig. 10 - Effects of concave clearance on threshing power consumption and mechanical efficiency

As shown in Fig. 10, the mechanical efficiency of the threshing device decreased continuously as the concave clearance increased, declining from approximately 71.80% at 10 mm to 69.45% at 30 mm, a reduction of about 2.35 percentage points. This decrease occurred because effective threshing power consumption declined more rapidly than total power consumption. Consequently, a greater proportion of the total input power was associated with mechanical losses, such as those required to maintain drum rotation, rather than being used directly for threshing. Therefore, energy-use efficiency gradually decreased with increasing concave clearance.

The effects of feed rate on the threshing power consumption and mechanical efficiency of the device are illustrated in Fig. 11. Within the experimental range where the feed rate increased from 3.0 kg/s to 5.0 kg/s, the no-load power consumption remained stable at 8.06 kW without noticeable fluctuations. This indicated that the variation in feed rate exerted no significant influence on mechanical losses during drum idling. The no-load power consumption was determined only by the inherent structure and operating state of the device, independent of the working load, which conformed to the basic characteristics of the no-load power consumption of threshing devices. The effective threshing power consumption presented an approximately linear upward trend with the increase in feed rate, rising from about 13.98 kW at 3.0 kg/s to approximately 25.2 kW at 5.0 kg/s. The underlying reason was that a higher feed rate corresponded to a greater amount of crop material entering the threshing chamber per unit time, which synchronously enhanced the frequency and intensity of impact and kneading actions exerted by threshing components on the crop.

Consequently, the effective energy consumption directly employed for threshing operations increased substantially, with a stable growth rate and no obvious inflection point as the feed rate rose. As the sum of the no-load power consumption and the effective threshing power consumption, the total threshing power consumption exhibited a variation trend highly consistent with that of the effective threshing power consumption, increasing rapidly and approximately linearly from 22.04 kW at 3.0 kg/s to 33.26 kW at 5.0 kg/s. The continuous growth of total power consumption demonstrated that feed rate was a core sensitive factor affecting the overall energy consumption of the threshing device. The greater the operation load, the higher the energy consumption of the whole machine.

The mechanical efficiency of the threshing device increased continuously and rapidly with the rise in feed rate, from approximately 63.49% at 3.0 kg/s to 75.81% at 5.0 kg/s, with an increase of 12.32 percentage points, and the rising rate accelerated slightly with a higher feed rate. The essential reason was that the no-load power consumption remained constant. Meanwhile, the effective threshing power consumption increased linearly with feed rate. This led to a continuous rise in the proportion of effective threshing power consumption in total power consumption and a continuous decline in the proportion of mechanical losses. Therefore, energy utilization efficiency was significantly optimized. This regularity indicated that a proper increase in feed rate could considerably improve the energy utilization efficiency of threshing operations and reduce the energy consumption per unit grain mass. The premise was that the structural strength and threshing quality of the device were satisfied.

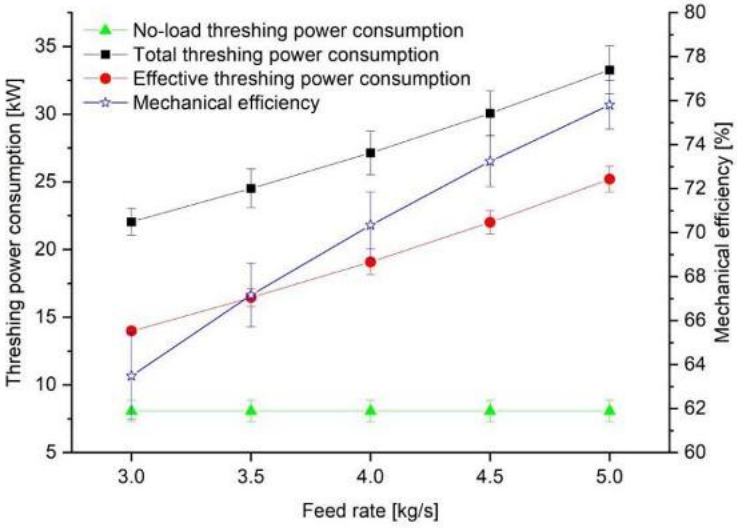


Fig. 11 - Effects of feed rate on threshing power consumption and mechanical efficiency

To further investigate the effects of operating parameters on the threshing power consumption of the device, the variation laws of these parameters on the threshing power consumption per unit feed rate of the threshing device were obtained, as shown in Fig. 12. The threshing power consumption per unit feed rate generally ranged from 4.4 kW/(kg/s) to 5.2 kW/(kg/s). It increased with the rise of drum rotational speed, deflector angle and feed rate, while decreasing with the increase of concave sieve clearance.

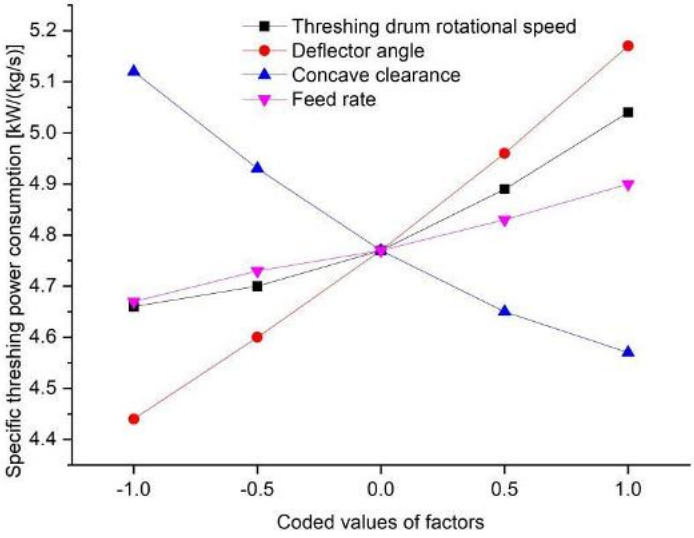


Fig. 12 - Effects of operating parameters on specific threshing power consumption

CONCLUSIONS

1) The effects of device structural parameters on the total threshing power consumption were clarified. Among the four modes of the threshing force adjustable concave sieve, the total threshing power consumption reached the minimum value of 27.14 kW when the threshing force adjustment plates were fully open, whereas the maximum value of 27.67 kW was obtained when the plates were fully closed. For different types of separation sieve plates on the upper part of the 360° separation device, the rectangular-hole sieve plate achieved the lowest total threshing power consumption of 27.14 kW.

2) Within the experimental range of drum rotational speed from 800 to 1000 r/min, with the increase of rotational speed, the no-load power consumption rose from 7.32 kW to 9.21 kW, the effective threshing power consumption increased from 17.76 kW to 20.68 kW, and the mechanical efficiency decreased from 70.63% to 69.24%. Within the deflector angle range of 50° to 70°, the no-load power consumption remained stable at 8.06 kW, the effective threshing power consumption increased from 18.68 kW to 19.60 kW, and the mechanical efficiency rose from 69.90% to 70.91%. Within the concave sieve clearance range of 10 to 30 mm, the no-load

power consumption was constant at 8.06 kW. The effective threshing power consumption decreased from 20.48 kW to 18.28 kW, and the mechanical efficiency dropped from 71.80% to 69.45%.

3) Within the feed rate range of 3.0 to 5.0 kg/s, with the increase of feed rate, the no-load power consumption remained stable at 8.06 kW, the effective threshing power consumption rose from 13.98 kW to 25.20 kW, and the mechanical efficiency increased from 63.49% to 75.81%. The threshing power consumption per unit feed rate of the device ranged from 4.4 kW/(kg/s) to 5.2 kW/(kg/s). It increased with the rise of drum rotational speed, deflector angle and feed rate, while decreasing with the increase of concave sieve clearance.

ACKNOWLEDGEMENT

This work was supported by Weifang City Science and Technology Development Plan Project (grant numbers 2025GX010) and the doctoral research start-up fee (grant numbers 44122025).

REFERENCES

[1] Ali K.A.M., Li C., Wang H., Mousa, A.M., Mohamed M.A.-E., (2024). Enhancing the performance of sunflower threshing machine through innovative enhancements, *Agriculture,* 14(2), 312, DOI: https://doi.org/10.3390/agriculture14020312

[2] Chen, L., Zhu, J., Liu, C., Zhang, C., Zhang, H., & Cai, Z., (2025). Optimal design and test of wheat plot breeding threshing device (小麦小区育种脱粒装置优化设计与试验), *Transactions of the Chinese Society for Agricultural Machinery*, 56(7), 72-81.

[3] Fan, C., Zhang, D., Li Y., Cui, T., He, X., Dong, J., & Zhao, H., (2022). Power consumption and performance of a maize thresher with automatic gap control based on feed rate monitoring, *Biosystems Engineering*, 216, 147-164.

[4] Jin, X., Zhu, X., Jin, C., & Cao, G., (2015). Research on the power consumption model of g rain threshing cylinder (谷物脱粒滚筒的功耗模型研究), *Journal of Chinese Agricultural Mechanization*, 36(3), 30-33+38.

[5] Jiang, T., Li, H., Huang, M., Zhang, M., Jin, M., & Guan, Z., (2025). Design and experiment of spiral Interlaced threshing cylinder for combine harvester (联合收获机螺旋交错排布式脱粒滚筒设计与试验), *Transactions of the Chinese Society for Agricultural Machinery*, 56(2), 314-324.

[6] Kiniulis V., Steponavičius D., Andriušis A., Kemzūraitė A., Jovarauskas D., (2017). Comparing performance of filler-plate-covered threshing cylinders. *Mechanics*, 23(5), 714-722.

[7] Li, Y., Tang, Z., Xu, L., Zhao, Z., & Li, H., (2011). Power analysis and experiment on longitudinal axial-threshing unit test- bed (纵轴流脱粒分离装置功耗分析与试验), *Transactions of the Chinese Society for Agricultural Machinery*, 42(6), 93-97.

[8] Liu, A., Xie, F., Zhu, L., Wang, X., Ji, B., & Kang, J., (2025). Design and experiment of adaptive threshing gap device for soybean combine harvester (大豆联合收获机脱粒间隙自适应装置设计与试验), *Journal of Chinese Agricultural Mechanization*, 56(12), 322-330+342.

[9] Lu, W., Zhang, D., (2012). Research on the power consumption model of threshing cylinder (谷物联合收获机脱粒滚筒功耗模型研究), *Journal of Agricultural Mechanization Research*, 34(12), 44-47.

[10] Mousaviraad M., Tekeste M.Z., (2020). Effect of grain moisture content on physical, mechanical, and bulk dynamic behaviour of maize. *Biosystems Engineering*, 195, pp. 186-197. DOI: https://doi.org/10.1016/j.biosystemseng.2020.04.012

[11] Qin, Y., Chen, M., Yang, T., Zhang, G., Jin, C., & Mo, G., (2025). Wheat harvesting quality online detection system and experimental verification, *INMATEH - Agricultural Engineering*, 76(2), 945-953.

[12] Ren, S., Xie, F., Luo, X., & Sun, S., (2013). Analysis and test of power consumption in paddy threshing using flexible and rigid teeth (柔性齿与刚性齿脱粒水稻功耗比较分析与试验), *Transactions of the Chinese Society of Agricultural Engineering*, 29(5), 12-18.

[13] Song, Z., Diao, P., Cui, P., Wei, M., Miao, H., & Yao, W., (2022). Design and experimental study of flexible threshing device for Longitudinal axial flow corn, *INMATEH - Agricultural Engineering*, 67(2), 155-165.

[14] Steponavičius D., Kemzūraitė A., Pužauskas E., Domeika R., Grigas A., Karalius D., (2023). Shape optimization of concave crossbars to increase threshing performance of moist corn ears. *Agriculture*, 13, pp. 983-1003. DOI: https://doi.org/10.3390/agriculture13050983

[15] Vlăduț N.-V., Biriș S.-Ș., Cârdei P., Găgeanu I., Cujbescu D., Ungureanu N., Popa L.-D., Perişoară L., Matei G., & Teliban G.-C., (2022). Contributions to the mathematical modeling of the threshing and

separation process in an axial flow combine, *Agriculture,* 12(10), 1520, DOI: https://doi.org/10.3390/agriculture12101520

[16] Vlăduț N.-V., Ungureanu N., Biriș S.-S., Voicea I., Nenciu F., Găgeanu I., Cujbescu D., Popa L.-D., Boruz S., Matei G., Ekielski A., Teliban G.-C., (2023). Research on the identification of some optimal threshing and separation regimes in the axial flow apparatus, *Agriculture*, 13(4): 838, DOI: https://doi.org/10.3390/agriculture13040838

[17] Wan, L., Yi, S., & Ma, Y., (2005). Study on power consumption of single axial flow threshing and separating unit of paddy (纵置单轴流滚筒脱粒与分离装置功耗性能试验研究), *J.of Heilongjiang August First Land Reclamation University*, 17(2), 56-58.

[18] Wang, W., Li, C., Chen, X., Liu, F., Wu, S., Qiao, X., Zhang, J., & Wang, B., (2025). Design and experiment of a threshing and separation system for a comb-type wheat plot harvester based on CFD-DEM, *INMATEH - Agricultural Engineering*, 77(3), 773-782.

[19] Waree, S., Somchai, C., & Khwantri, S., (2016). Design factors affecting losses and power consumption of an axial flow corn shelling unit, *Songklanakarin Journal of Science and Technology*, 38(5), 591-598.

[20] Xie, G., Zhang, G., Fu, J., Zhou, Y., Wang, Y., Gao, Y., Wang, W., & Mohamed, A., (2021). Comparing power consumption of drum and cylindrical rod-tooth longitudinal axial flow threshing roller (鼓形与圆柱形杆齿式纵轴流脱粒滚筒功耗对比试验), *Journal of Huazhong Agricultural University*. 40(1), 202-209.

[21] Xing, S., Cui, T., Zhang, D., Yang, L., He, X., Li, C., Dong, J., Jiang, Y., Wu, W., Zhang, C., & Du, Z., (2024). Design and optimization for a longitudinal-flow corn ear threshing device of low loss and low energy consumption, *Computers and Electronics in Agriculture*, 226, 1-16.

[22] Yu, Q., Yin, J., Cui, Y., Zha, Z., Guan, P., Wang, Y., Wang, X., & Geng, D., (2025). Study and experiment on a corn flexible threshing technology with single-point hinged structure based on DEM-MBD coupling, *INMATEH - Agricultural Engineering*, 76(2), 1190-1202.

[23] Zhang, J., Hu, J., Zhou, Z., Li, S., Liu, X., He, X., & Zhang, H., (2026). Design and experimental study of the rigid-flexible coupled structure for longitudinal axial-flow threshing device in high-moisture corn (高含水率玉米纵轴流脱粒装置刚柔耦合结构设计与试验), *Transactions of the Chinese Society of Agricultural Engineering*, 42(1), 58-70.

[24] Zhang, M., Wu, C., Lu, Y., Yu, S., & Yu, X., (2010). Experimental study of power consumption on threshing and separating of canola indirect harvest (油菜分段收获脱粒分离功率消耗试验研究), *Journal of China Agricultural University*, 15(4), 120-123.

[25] Zhou, X., Wang, Z., Tian, L., Su, Z., & Ding, Z., (2022). Innovative design and performance test of threshing-separating device for horizontal axial-flow combine harvester, *INMATEH - Agricultural Engineering*, 67(2), 497-508.

DESIGN AND EXPERIMENT OF AUTOMATIC STRIP-ZONING PESTICIDE APPLICATION CONTROL SYSTEM FOR SOYBEAN-MAIZE STRIP INTERCROPPING BASED ON MACHINE VISION

/

基于机器视觉的大豆玉米带状复合种植自动分带施药控制系统设计与试验

Gongpei CUI, Huanhuan CHEN, Yu ZHANG, Zishang YANG, Lele WANG, He LI *)
College of Mechanical and Electrical Engineering, Henan Agricultural University, Zhengzhou, Henan, China
Tel: +86 15515549801; E-mail: lihenjx@henau.edu.cn
Corresponding author: He Li
DOI: https://doi.org/10.35633/inmateh-79-35

Keywords: *soybean-maize strip intercropping; machine vision; peak method; ROI; precision zoning; least squares method*

ABSTRACT

The soybean-maize strip intercropping mode has been widely popularized, yet existing plant protection machinery fails to dynamically adjust pesticide application according to crop zones, suffers from poor pesticide application accuracy, and is prone to causing crop damage. Aiming at the above problems, this study proposed a precise strip-zoning pesticide application method for soybean and maize and established an automatic strip-zoning pesticide application control system based on machine vision. Perspective transformation was adopted to correct image viewing angles; after subsequent processing via excess green binarization and opening-closing operations, a dynamic ROI (Region of Interest) positioning and recognition algorithm for crop rows based on the peak value method was applied. The least square method was used to extract crop row lines, the offset was calculated according to the geometric relationship of the centerlines of soybean and maize zones, and an automatic strip-zoning offset compensation model was constructed to achieve precise strip-zoning. Field experiment results show that: under conditions with little shadow and stable light, the recognition algorithm achieved the optimal performance with an accuracy of up to 92%. At operating speeds of 2–5 km/h, the automatic strip-zoning pesticide application control system had a mean strip-zoning deviation of ≤3.16 cm, with the proportion of deviations within 5 cm reaching 84% (up to 94%). Under wind speeds of 1.4–2.9 m/s, the maximum droplet drift deposition amount of the closed anti-drift device was 9.41 droplets per cm², delivering favorable strip-zoning pesticide application performance, which provides data support and a reference for field precision plant protection operations under the strip intercropping mode.

摘 要

大豆玉米带状复合种植模式广泛推广，但现有植保机械无法随作物带进行动态调整施药，且施药精度差，易造成伤害。针对上述问题，本文基于机器视觉，提出一种大豆玉米精准分带施药方法并搭建自动分带施药控制系统。采用透视变换校正图像视角，再经超绿二值化与开闭运算处理后，基于峰值法的作物行动态 ROI（Region of interesting）定位识别算法，采用最小二乘法提取作物行线，依据大豆玉米带中心线的几何关系计算偏移量并构建自动分带偏移补偿模型以实现精准分带。田间试验结果表明：在阴影少、光照稳定条件下，识别算法效果最佳，准确率可达 92%。自动分带施药控制系统在 2-5km/h 的速度下分带偏差均值≤3.16cm，5cm 内偏差占比达 84%（最高 94%）。1.4m/s~2.9m/s 风速条件下，封闭式防飘移装置的雾滴飘移沉积量最高为 9.41 个/cm2，具有较好的分带效果，为复合种植模式下的田间精准植保作业提供数据支撑与参考。

INTRODUCTION

Soybean and maize are important food crops, and efficient and precise plant protection operations constitute a key measure to improve their yield *(Cui et al., 2023; Zhang et al., 2025)*. At present, the mainstream pesticide application equipment for the soybean-maize strip intercropping mode is the traditional fixed zoned boom sprayer *(Khan et al., 2024; Zhang et al., 2024)*. Although it can realize zoned pesticide application to a certain extent, it is unable to perceive the dynamic information of field crop zones and achieve precise pesticide application when confronted with problems such as inconsistent inter-zone spacing and irregular sowing rows in the sowing process. Therefore, there is an urgent need to develop a technical scheme for field precision plant protection adapted to this cropping mode.

At present, scholars at home and abroad have carried out extensive research in the field of precision control such as crop row line extraction. *Zhao et al., (2016),* proposed an operation line extraction method suitable for wheat harvesting, which adopted the cross-correlation function method to detect the boundary points between the harvested area and the to-be-harvested area, and fitted the target line via the Hough transform. *Chen et al., (2019)* mapped the fitting straight lines obtained from different accumulation thresholds of the Hough transform to the parameter space, clustered the parameter space data by K-means clustering, and regarded the cluster centroids in the parameter space under the optimal accumulation threshold as the identified actual crop rows. *Chen et al., (2020)* adopted a median point Hough transform based on an optical system for navigation line fitting, which was 24 ms faster than the traditional Hough transform. In addition, *Yang et al., (2020),* used the least square method to obtain navigation lines in the dynamic ROI area on the basis of static ROI, with a recognition accuracy of 96%. *Liao. et al., (2019),* counted the pixel points of crop rows by sub-region and took them as candidate feature points, retained valid feature points based on the distance threshold, and performed straight line fitting on the feature points using the least square method, with an extraction accuracy of 95.6%. *Hossein et al., (2014),* extracted crop row center lines using the Hough transform and centroid image processing algorithm respectively, with the average time consumption of the two algorithms being 0.7 s and 0.4 s. *Montalvo et al., (2012),* proposed a crop row detection method based on the moving window method for maize fields with high weed density, which was superior to the traditional Hough transform in processing efficiency. However, the above methods are restricted by factors such as application scenarios and algorithm time consumption, and their robustness and accuracy need to be further improved. Meanwhile, all these studies are conducted for homogeneous crops, leading to poor applicability.

Aiming at the above problems, this study established an automatic strip-zoning pesticide application control system and proposed a dynamic ROI positioning and recognition algorithm for crop rows based on the peak value method, which fused perspective transformation, vertical projection, strip segmentation and the least square method for crop row fitting. Meanwhile, the offset was calculated according to the geometric relationship of the centerlines of soybean and maize zones, and an offset compensation model was constructed. The traditional PID control algorithm was introduced to enhance the regulation capability of the actuation output of the automatic strip-zoning pesticide application control system, thereby enabling rapid response and correction of deviations caused by changes in the field environment. Finally, the system was deployed on a strip-type boom sprayer to conduct field performance experiments. The results show that the recognition algorithm has a certain robustness under different light conditions. At different operating speeds, the system can effectively perform strip-zoning pesticide application and reduce crop phytotoxicity, which holds certain practical significance for strip-zoning pesticide application under the strip intercropping mode.

MATERIALS AND METHODS

1. Automatic Strip-zoning Pesticide Application Control System for Soybean-maize Intercropping Based on Machine Vision

1.1 Structural Composition of the Automatic Strip-zoning Pesticide Application Control System

The overall structure of the automatic strip-zoning boom sprayer for pesticide application based on machine vision is shown in Fig. 1, which is mainly composed of a power system, travel assembly, image acquisition and processing module, strip-zoning control module, and soybean-maize pesticide application module. The sprayer has a wheel base of 1.8 m and is powered by a single-cylinder diesel engine with a rated power of 14.7 kW, which can meet the requirements of normal field operations for the automatic strip-zoning pesticide application control system.



Fig. 1 - Structural Schematic Diagram of Automatic Strip-zoning Boom Sprayer

1 - Lateral adjustment spray boom mechanism; 2 - Soybean-maize pesticide application module; 3 - Travel assembly; 4 - Power system; 5 - Image acquisition and processing module

The structure of the automatic strip-zoning pesticide application control system is mainly composed of a lateral adjustment spray boom mechanism, a control unit and an image acquisition and processing module. Among them, the lateral adjustment spray boom mechanism consists of a middle spray boom frame, side spray boom frames and a lifting mechanism. One end of the central electric push rod is fixed to the lifting bracket, and the other end is connected to the middle spray boom frame. The sliders are arranged between the slide rails and the middle spray boom frame, and the two side spray boom frames are in sliding contact with the middle spray boom frame respectively, with a maximum operating width of 4.2 m. The control unit is mainly composed of a Delta PLC (Programmable Logic Controller), a Leadshine driver and a stepping push rod motor; the stepping push rod motor has a maximum stroke of 0.5 m and a maximum telescopic speed of 0.2 m/s. For the image acquisition and processing module, the acquisition device is an LT-USB 1080P depth camera (Lantian Technology Co., Ltd.), with a frame rate of 30 frames per second and a maximum video image resolution of 1920×1080. It is equipped with a 2.8–16 mm zoom lens and installed at a height of 1200 mm, which can effectively cover the target crop area. The built-in computer is configured with an Intel Core i5 processor, 16 GB of ROM, 512 GB of storage and 8 GB of RAM, which can basically meet the field operation requirements.

1.2 Working Principle of the Automatic Strip-zoning Pesticide Application Control System

As shown in Fig. 2, during field operation, the field crop row information (RGB images) collected by the LT-USB 1080P depth camera is transmitted to the upper computer via USB. The upper computer software calculates the lateral offset of the boom in real time and transmits it to the lower computer controller (PLC) through the RS485 serial port. The lower computer controller controls the left and right movement of the push rod motor via the Leadshine driver, and the Oedila rope displacement sensor feeds back the telescopic length of the push rod motor to the lower computer controller in real time, thereby achieving precise control of the boom's movement position. A speed sensor (E6B2-CWZ6C1000P incremental encoder, Omron Corporation) collects the operating speed of the sprayer in real time.

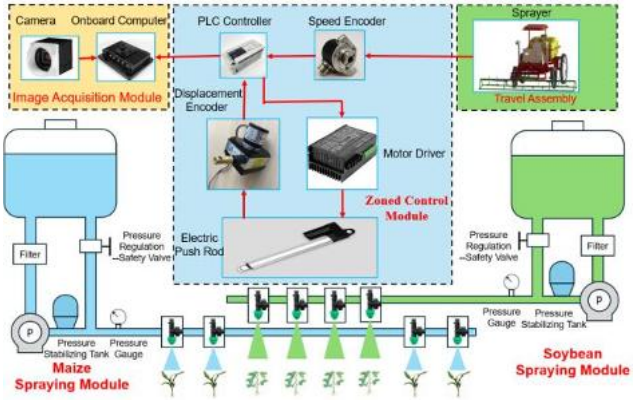


Fig. 2 - Flow Chart of Working Principle of Automatic Strip-Zoning Pesticide Application Control System

2. Recognition Method of Crop Zone Row Line Based on Machine Vision

Recognition of crop zone row lines is a prerequisite for achieving precision strip-zoning pesticide application. This paper adopts the peak value method for the fitting of soybean and maize crop zone row lines, and the specific process is illustrated in Fig. 3.

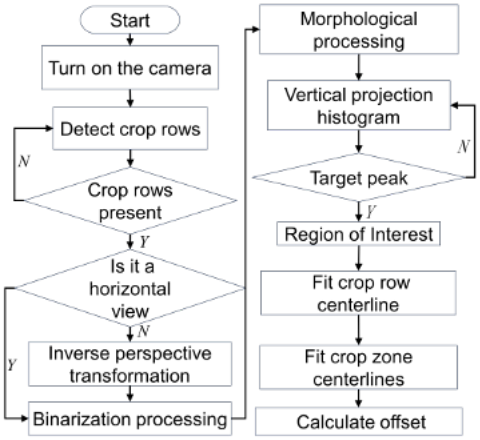


Fig. 3 - Flow Chart of Crop Zone Centerline Fitting

2.1 Image Acquisition and Preprocessing

2.1.1 Image Acquisition

Images were captured in a soybean-maize strip intercropping test field in Xinzheng City, Henan Province, with the shooting conducted from May to June 2025. The camera was mounted at a height of 1200 mm with an inclination angle of 30°. For subsequent research and analysis, soybean-maize videos with a resolution of 1280×720 pixels under different light conditions were selected, as shown in Fig. 4(a).

2.1.2 Image Preprocessing

2.1.2.1 Inverse Perspective Transformation

To maintain clear, parallel and equally wide boundaries of soybean and maize rows, effectively segment different crop zones, and avoid zonal segmentation errors caused by the convergence and overlap of distant crop zones in crop images, inverse perspective transformation was performed on the collected images *(Li et al., 2024; Tang et al., 2018; Zhao et al., 2019; Zhang et al., 2023)*.

As shown in Fig. 4, during plant protection operations, on the premise that the machine operates at a constant speed in a straight line while the camera angle and image size remain unchanged, four sets of valid pixel coordinates were selected from the image containing the target crop rows to form the boundary for inverse perspective transformation, and the target region was extracted accordingly. The inverse perspective transformation from Fig. 4(b) to Fig. 4(d) can be realized by means of the homography matrix (H matrix). From the transformation results, the crop rows are arranged in parallel without converging to infinity. This method can effectively reduce the computational complexity of the subsequent algorithm and facilitate the follow-up crop row line fitting *(Khan et al., 2024)*.

$$x' = H.x \tag{1}$$

where: H is the 3×3 homography matrix; x' is the corresponding plane coordinates in the transformed image, [Pixel]; x is the corresponding plane coordinates in the original image, [Pixel].

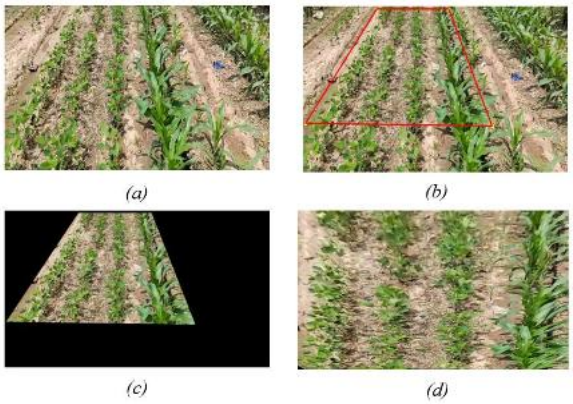


Fig. 4 - Inverse Perspective Transformation

(a) Original image; (b) Region division; (c) Region of Interest; (d) Perspective transformation

2.1.2.2 Image Segmentation

Segmenting crop regions from complex backgrounds such as soil and weeds is crucial for improving algorithm efficiency and achieving precision strip-zoning. Currently, image segmentation algorithms are mainly categorized into three types: color index-based segmentation, threshold-based segmentation, and deep learning-based segmentation *(Guerrero et al., 2013; Sun et al., 2022; Pérez-Ruíz et al., 2014; Jiang et al., 2014)*.

On this basis, this paper selected three typical segmentation algorithms, and ultimately determined the one with the optimal performance by comparing the time consumption and segmentation effectiveness of single-channel grayscale images under different climatic conditions.

(1) The VARI (Vegetation Index)-based image segmentation algorithm is mainly used to identify green vegetation regions from RGB images. Its core lies in utilizing the characteristic that the green component (*G*) is significantly higher than the red component (*R*), and reducing the impact of illumination intensity variations through normalization processing. The algorithm is presented as follows.

$$\begin{cases} VARI = (G - R) / D & (-1,1) \\ D = G + R - B & D \neq 0 \end{cases} \tag{2}$$

Based on this algorithm, green feature extraction was performed on the images, and the binarized images were further optimized via morphological operations, as shown in Fig. 5(b).

(2) An image preprocessing method based on the HSV color space. By adjusting the threshold ranges of hue, saturation and value, i.e., setting the values of the H, S and V channels within the green threshold range, the pixel values of green crops are enhanced while the non-green background is suppressed. To achieve effective segmentation of crop plants from the background, this paper combines the H and S channels: the green regions are filtered out by adjusting the threshold of the H channel, the S channel of the green regions is retained, and grayscale conversion is performed subsequently. The processing results are shown in Fig. 5(c).

(3) $2G\text{-}R\text{-}B$ based on the Excess Green Index is a green feature enhancement algorithm rooted in the RGB color space. It strengthens the weight of the green component and suppresses the red and blue components simultaneously, which makes the green regions more prominent after processing and facilitates subsequent segmentation and feature extraction. Its grayscale image is shown in Fig. 5(d).

$$ExG = 2G - R - B \tag{3}$$

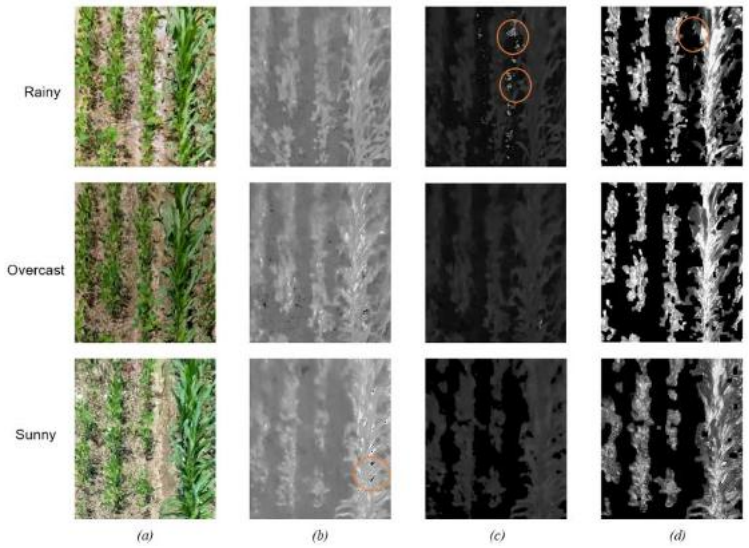


Fig. 5 - Grayscale Image Effect Comparison

(a) Original image; (b) VARI grayscale image; (c) HSV grayscale image; (d) 2G-R-B grayscale image

As shown in Fig. 5, a comparative analysis of the segmentation performance of the three different algorithms revealed that VARI could completely segment crops from the background under all three weather conditions, yet the resulting images were blurry with a time consumption of 201 ms. In comparison with the Excess Green algorithm, HSV leads to target loss and was prone to noise in rainy weather, which interfered with subsequent binarization processing. By contrast, the Excess Green-based segmentation algorithm could well preserve green crops; the time consumption of the Excess Green algorithm was 109 ms and that of the HSV algorithm is 98 ms. Considering the segmentation performance, time consumption and post-processing requirements comprehensively, the Excess Green algorithm was adopted as the preprocessing segmentation algorithm in this study. In view of the enhanced processing of green features by the Excess Green algorithm, to better constrain the range of green regions, this paper adopted the HSV threshold method in color space binarization for binarization processing, and the corresponding binary mask was generated by setting the threshold ranges of each HSV channel.

The expression is presented as follows.

$$\begin{cases} hsv\text{-}low = (H_{min},\ S_{min},\ V_{min}) \\ hsv\text{-}high = (H_{max},\ S_{max},\ V_{max}) \end{cases} \tag{4}$$

After completing the segmentation of the image foreground and background, there still exist noise and holes caused by interfering factors such as dew and shadows. These defects impair the image segmentation performance and hinder the subsequent detection of crop rows. In this study, morphological processing involving a closing operation followed by an opening operation was applied to the images, which can effectively fill gaps, eliminate noise, reduce interference from irrelevant detailed information, and enhance the algorithm's adaptability to complex environments.

Fig. 6 illustrates the corresponding processes of grayscale conversion, binarization and morphological processing.

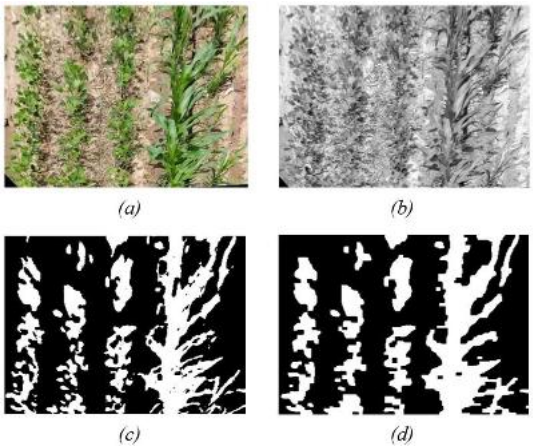


Fig. 6 - Binarization Processing Effect

(a) Original; (b) Grayscale; (c) Binarized; (d) Morphologically processed

2.2. Extraction of the Crop Zone Centerline

After acquiring the crop canopy characteristics, further post-processing is required for the preprocessed images to fit the geometric centerlines of the crop row canopy, laying a solid foundation for the extraction of the crop zone centerline.

2.2.1. Adaptive ROI Acquisition

The research object of this study is the test field under the soybean-maize strip intercropping mode. To achieve precision strip-zoning pesticide application, the recognition targets should be focused on the inter-zone areas between soybean zones and maize zones. In view of the complex field environment under the intercropping mode, which is likely to impair the algorithm recognition accuracy, this study adopts the peak value method to demarcate the ROI for the purpose of reducing interference from non-recognition areas *(Ota et al., 2022; Ramesh et al., 2016; Zhang et al., 2023)*. Given the known width (Width) and height (Height) of the preprocessed images, the expression for vertical projection is as follows:

$$S(j) = \sum_{i=1}^{H} P(i,j) \tag{5}$$

where: (i,j) is the pixel coordinates of the vertical projection, [Pixel]; $P(i,j)$ is the target pixel coordinates, [Pixel]; $S(j)$ is the cumulative value of target pixels in the j-th column, [Pixel].

Images are susceptible to noise caused by factors such as illumination and soil. To prevent minor wave crests from interfering with the subsequent identification of peak points, this study adopted mean filtering to perform denoising processing on the images.

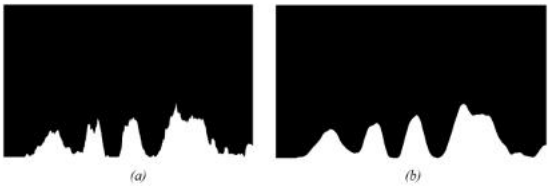


Fig. 7 - Vertical Projection Filtering Effect

(a) Before filtering; (b) After filtering

As shown in Fig. 7, four white vertical projections correspond to the position information of the four crop rows. Statistics of the cumulative pixel values and inspection of each contour are carried out on the vertical projection histogram. A height threshold T_k is set, which can filter out minor noise peaks. In this study, the height threshold is determined based on the mean value plus the standard deviation of the projection data.

Let the mean value be denoted as μ and the standard deviation as σ. The mean value represents the average value of each pixel array in the vertical projection, and the standard deviation characterizes the degree of dispersion of the array. In the vertical projection, the total pixel value of the "Target Peaks" (the columns corresponding to crop rows) is inevitably higher than the background mean value, while "noise" refers to random values that fluctuate slightly around the mean value. To obtain an optimal height threshold, 1σ and 2σ are selected to achieve a balance between the risk of peak missing and anti-noise capability. The expression is given as follows.

$$\mu + 1\sigma \le T_k \le \mu + 2\sigma \tag{6}$$

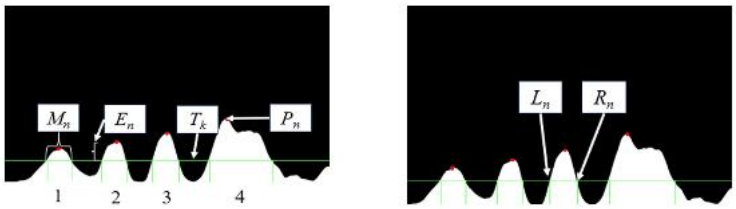


Fig. 8 - Algorithm Processing Effect

The research object of this study is limited to the adjacent vertical projection contours of soybean and maize, and valid contours are filtered out based on the global peak difference and peak width difference, for which the following expression is derived:

$$P_n = S(j)_{max} \tag{7}$$

where: $S(j)_{max}$ is the maximum cumulative value of target pixels, [Pixel].

Compare the M_n values of each contour from 1 to 4 and select the maximum value, then calculate the peak difference with its adjacent contour. The contour with the largest difference is retained to obtain the target contour, which narrows the ROI. To acquire complete crop rows, the peak values of the two contours are taken as reference points, with one target width ($\bar{M}$) expanded to the left and right respectively. The expression is as follows:

$$\bar{M} = \frac{1}{k}\sum_{i=1}^{n} M_i \tag{8}$$

where: k is the coefficient (related to crop growth conditions); n is the number of contours, which is known to be 2.

Analysis of program operation reveals that the value range of k is [2, 5]. The k value was screened using 200 images: different k coefficients were adopted with an increase step of 1, and the crop row retention effect was observed, from which it was concluded that k=3 meets the requirements. The positioning effect of the first ROI is shown in Fig. 9(a).

To extract the crop zone centerline and reduce the computational load of the recognition algorithm, a second ROI demarcation is performed for the soybean and maize row regions. On the basis of the first ROI, the rising edge boundaries and falling edge boundaries of the vertical projection contours of the soybean seedling rows and maize seedling rows were searched for and recorded. The ROI region was identified by acquiring the known height threshold T_k and boundary positioning points, as shown in Fig. 9(b).



Fig. 9 - ROI Localization Effect

(a) First ROI; (b) Second ROI

2.2.2. Crop Zone Centerline Fitting

As the core reference benchmark for an agricultural machinery vision plant protection system to complete offset detection and compensation, the crop zone centerline can clearly distinguish the spatial boundaries and central positions of soybean zones and maize zones, provide accurate displacement control commands for the automatic strip-zoning pesticide application control system, and ensure that operating components such as the spray boom and nozzles are accurately aligned with the crop zones. Its fitting process is illustrated in the figure below:

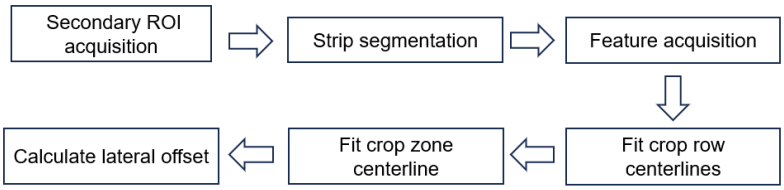


Fig. 10 - Flow Chart of The Crop zone Centerline Extraction

Strip segmentation was carried out on the basis of the second ROI. To reduce the computational load, the number of strips is set to N, and N is taken as 10 in this study. Vertical projection processing is performed on the pixels within each strip. Given the width W and height H of the ROI, the height of each strip is denoted by the mathematical expression ΔH. The mathematical expressions for the strips are given as follows.

$$S(j) = \sum_{i=1}^{\Delta H} P(i, j) \tag{9}$$

In the preprocessed images, the higher the leaf area ratio in the column direction, the larger the value of $S(j)$. The algorithm traverses $S(j)$ of each strip from left to right, excludes the values lower than the threshold, identifies the first and last qualified columns, and takes their average value to obtain the feature point ($\Delta H/2$, j). Subsequently, it traverses downward with a step size of ΔH within the ROI, collecting the feature points until all horizontal strips are completely traversed. The performance of the algorithm is shown in Fig. 11.

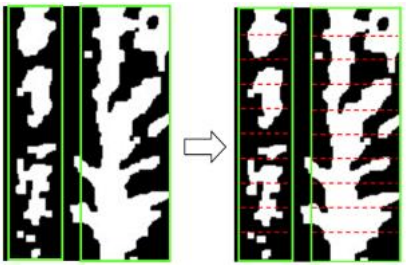


Fig. 11 - Strip Segmentation Effect

The crop row feature points obtained from each of the aforementioned strips are stored in a point set, and the fitting of the centerlines of soybean rows and maize rows is achieved based on the Least Squares Method *(Liao et al., 2019; McInnes et al., 2017; Ota et al., 2022; Vidovic et al., 2016; Yang et al., 2022)*. Ultimately, the crop zone centerline is derived by virtue of *the Parallel Centerline Principle*, with the results shown in Fig. 12.



Fig. 12 - Extraction Results of the Crop Zone Centerline

3. Realization of Offset Compensation Model and Strip-Zoning Control

3.1. Offset Calculation

3.1.1. Coordinate System Transformation

Coordinate System Transformation is a prerequisite for calculating the actual offset information of crop rows. To convert the identified row position information in the image into the actual displacement data in the world coordinate system, it is necessary to perform camera calibration and eliminate the errors caused by camera distortion.

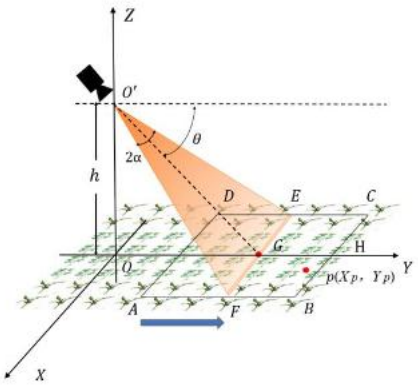


Fig. 13 - Geometric Relationship of the Camera Field of View in the World Coordinate System

As shown in Fig. 13, $ABCD$ in the figure represents the field of view (FOV) of the camera on the ground, point O' denotes the camera optical center, and point O is the projection coordinate of the camera on the ground, which also serves as the origin of the world coordinate system. Point P is the actual ground coordinate point corresponding to a pixel point p on the image, with the coordinate of (X_p,Y_p). G is the intersection point of the optical axis and the ground. The resolution of the industrial camera is $m \times n$, 2β is the vertical field of view angle ($\angle HO'O$), and 2α is the horizontal field of view angle ($\angle EO'F$). The calculation formulas are as follows:

$$\beta = arctan(\frac{Vc}{2f}) \tag{10}$$

$$\alpha = arctan(\frac{Vc'}{2f}) \tag{11}$$

where: β represents the half the vertical field of view angle, [°]; α represents the half the horizontal field of view angle, [°]; V_c is the sensor height, [mm]; V_c' is the sensor width, [mm].

From the camera sensor parameters, V_c is 2.92 mm, V_c' is 5.18 mm and f is 3.6 mm, from which β is calculated as 22.07 ° and α as 35.75 °.

Given a camera installation angle of 30°, the depression angle θ of the camera can be calculated as follows:

$$\theta = 30^\circ + \beta \tag{12}$$

θ is calculated as 52.07 °.

From the deduction based on the inverse perspective mapping formula, the corresponding coordinates of pixel point p in the world coordinate system can be obtained. Its expression is given as follows:

$$u = \frac{mY_p - htan\theta}{2Y_p tan\theta tan\alpha + 2htan\alpha} \tag{13}$$

$$v = \frac{nX_p}{2tan\alpha\sqrt{h^2 + Y_p^2}}\sqrt{1+\left(\frac{2utan\beta}{m}\right)^2} \tag{14}$$

where: u is the x-coordinate of point p on the image plane, [Pixel]; v is the y-coordinate of point p on the image plane, [Pixel].

Four coordinate systems are involved in the image processing process, namely the image coordinate system UO_0V, the image physical coordinate system XOY, the camera coordinate system $X_cO_cY_c$, and the world coordinate system $X_wO_wY_w$, as shown in Fig.15. The transformation relationship between the coordinates of any point in the image coordinate system and its corresponding coordinates in the world coordinate system is as follows:

$$Z_c\begin{bmatrix} u \\ v \\ 1 \end{bmatrix} = \begin{bmatrix} \frac{f}{dx} & 0 & 0 & 0 \\ 0 & \frac{f}{dy} & 0 & 0 \\ 0 & 0 & 1 & 0 \end{bmatrix}\begin{bmatrix} R & T \\ 0 & 1 \end{bmatrix}\begin{bmatrix} X_w \\ Y_w \\ Z_w \\ 1 \end{bmatrix} = M_1 M_2 \begin{bmatrix} X_w \\ Y_w \\ Z_w \\ 1 \end{bmatrix} \tag{15}$$

where: O_w-$X_wY_wZ_w$ is the world coordinate system, used to describe the camera position, [m]; O_c-$X_cY_cZ_c$ is the camera coordinate system, with the optical center as the origin, [m]; o-xy is the image coordinate system, with the midpoint of the imaging plane as the origin, [mm]; p is the point in the world coordinate system, i.e., a real physical point in the actual scene, [mm]; (u,v) are the coordinates of point p in the pixel coordinate system, [Pixel]; (x,y) are the coordinates of point p in the image coordinate system, [Pixel]; M_1 is the intrinsic parameter matrix ; M_2 is the extrinsic parameter matrix, which contains the rotation matrix R and the translation matrix T ; f is the camera focal length, i.e., [mm]. the distance between o and Oc, as shown in Fig. 14.

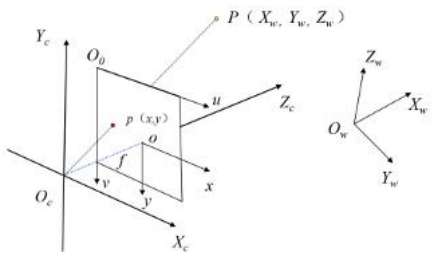


Fig. 14 - Schematic Diagram of Coordinate System Transformation

Two camera calibration methods based on OpenCV and MATLAB are currently available: the former is susceptible to image quality with relatively large calibration errors, while the latter requires manual extraction of corner points and features high accuracy with low calibration error. This study adopted the MATLAB-based calibration method: the calibration toolbox was invoked via the calib_gui command to import 20 calibration images, the checkerboard used had a square side length of 20 mm, and the results of corner point extraction are shown in Fig. 15.

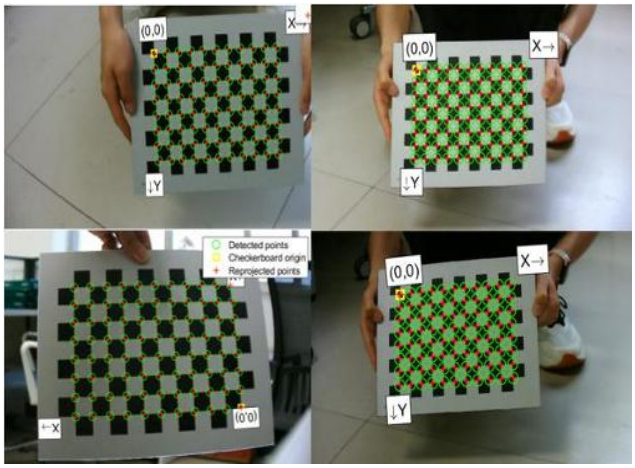


Fig. 15 - Corner Point Extraction Effect of the Calibration Board

As shown in Table 1 are the intrinsic and extrinsic parameter matrices of the target camera obtained via the MATLAB calibration toolbox.

Table 1

Camera Calibration Results

Property	Parameter
K	[763.1029,0,0;0,762.2424,0;629.5229,345.8421,1]
Radial Distortion	[0.130846983244061, -0.150301138293976]
Tangential Distortion	[0,0]

3.1.2. Lateral Offset Compensation Control Variable

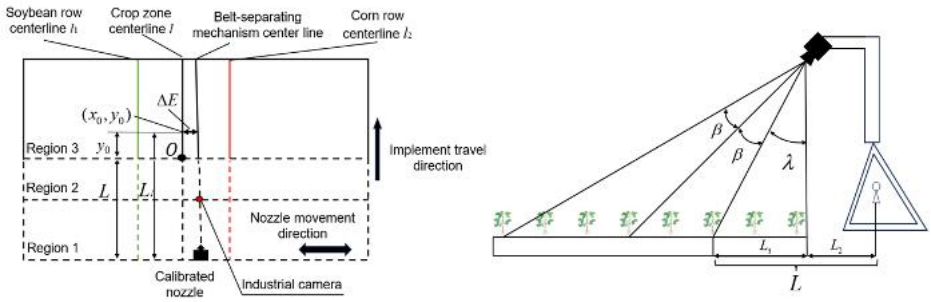
To achieve precise strip-zoning spraying, it is necessary to calculate the offset information of the crop zone centerline. The linear distance in the horizontal direction from the calibrated nozzle fixed on the anti-drift baffle to the crop zone centerline is defined as the offset. In the offset compensation model shown in Fig. 16(a), Zones 1 and 2 are the blind areas of the camera's field of view, among which Zone 1 refers to the area corresponding to the distance from the nozzle to the camera, and Zone 3 is the camera's field of view area. The crop zone centerline l: $Ax+By+C=0$ is derived from the soybean row centerline l_1: $Ax+By+C_1=0$ and the maize row centerline l_2: $Ax+By+C_2=0$ in accordance with the Parallel Centerline Principle. The point (x_0, y_0) represents the relative coordinate of a point on the crop zone centerline within Zone 3 with respect to the absolute coordinate system O, and ΔE denotes the actual lateral distance from this point to the nozzle, as given by the following formula:

$$\Delta E = \frac{\left|Ax_0 + By_0 + C\right|}{\sqrt{A^2 + B^2}} \tag{16}$$

The installation position coordinates and mounting angle of the industrial camera are shown in Fig. 16. The nozzle is fixed on the spray boom frame, and the actual distance L_1 from point (x_0, y_0) to the nozzle is jointly composed of y_0, L_2 and L_3, which can be expressed as:

$$\begin{cases} L_1 = y_0 + L \\ L = L_3 + L_2 \\ L_3 = h\tan\lambda \end{cases} \tag{17}$$

where: λ is the included angle between the lower boundary plane of the camera's field of view and the vertical direction, [°]; L_2 is the straight-line distance between the nozzle and the camera, [m]; L_3 is the straight-line distance between the camera and the field of view boundary, [m].



(a) *(b)*

Fig. 16 - Schematic Diagram of the Offset Compensation Model

(a) Top View; (b) Side View

When the automatic strip-zoning pesticide application control mechanism receives the execution signal, it cannot act immediately, and speed regulation control is thus required. The speed sensor mounted on the wheels captures the operating speed v_1, from which the safety boundary of the delayed execution time for the strip-zoning control system, t_1, is derived.

$$t_1 \leq \frac{L_1}{v_1} \tag{18}$$

Only when the time taken for the sprayer to operate a distance L satisfies the safety boundary condition can the row alignment mechanism complete the compensation for the offset ΔE. On this basis, an offset compensation model is established, yielding the response speed of the strip-zoning control mechanism as follows:

$$v_2 = \frac{\Delta E}{t_1} \tag{19}$$

To optimize the dynamic response characteristics of the offset compensation system, a position closed-loop control scheme based on a PD trajectory tracking strategy with PID control is designed in accordance with the established kinematic model of the row alignment mechanism (Fig. 16). This scheme is intended to significantly improve the response speed and accuracy of the system during target trajectory tracking by optimizing the controller design *(Ding et al., 2019; Han et al., 2022; Zheng et al., 2023)*. The expression is given as follows:

$$O_{pd} = K_p r + K_d \Delta r_0 + K_i \sum_{n=0}^{k} \Delta r_n \tag{20}$$

where: O_{pd} is the pulse output frequency, [Hz]; K_p is the proportional coefficient; K_d is the differential coefficient; K_i is the integral coefficient; Δr is the offset error, [mm]; Δr_0 is the offset error at the previous moment, [mm]; $\sum_{n=0}^{k} \Delta r_n$ is the cumulative offset error, [mm].

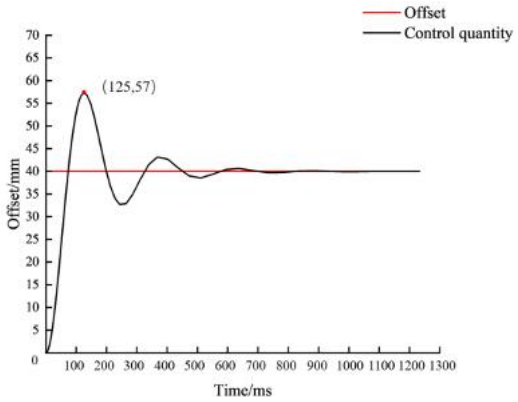


Fig. 17 - PD Control Curve

The results are shown in Fig. 17. When the target value was set to 40 mm, the maximum deviation of PD control reached 57 mm with a response time of 125 ms. To reduce the oscillation and instability phenomena occurring during the error adjustment process and enable the response speed of the actuator to be rapidly improved in a short time, the proportional coefficient K_p was determined as 2 and the differential coefficient K_d as 15 through manual tuning.

4 Experiment metrics and Determination Methods

4.1 Experiment metrics

This study selected the following core indicators to evaluate the system performance: mean recognition deviation and recognition accuracy reflect the recognition precision of the algorithm; mean deviation and the proportion of deviations within 50 mm reflect the strip-zoning accuracy of the system; droplet deposition density verifies the effect of strip-zoning pesticide application. The expressions are as follows:

$$\mu = \frac{1}{N}\sum_{i=1}^{N} x_i \tag{21}$$

$$P = \frac{N_{correct}}{N_{total}} \times 100\% \tag{22}$$

$$D = \frac{N_C}{S_T} \tag{23}$$

where: μ is the mean value of recognition deviation; $N_{correct}$ is the Number of correctly identified samples; N_{total} is the Total number of identified samples; D is the droplet deposition density, [droplet/cm²]; N_C is the number of droplets collected by the water-sensitive paper, [droplet]; S_T is the area of the water-sensitive test paper, [cm²].

4.2 Determination Methods

To verify the various performance metrics of the automatic strip-zoning pesticide application control system, the experiment was conducted in a soybean-maize strip intercropping test field in Xinzheng City, Henan Province (*34.3791°N, 113.6489°E*).

For the performance measurement of the recognition algorithm, light detection software was used to acquire field light intensity information at different time periods throughout the day, and videos of crop rows were collected and subjected to frame segmentation. The algorithm recognition system was applied to measure recognition deviations, with deviations exceeding 5 cm defined as recognition errors (*Wang, Q. et al., 2021; García et al., 2017*).

In the experiments for the system and droplet anti-drift performance, as is shown in Fig. 18, a strip intercropping plant protection sprayer was adopted, and the automatic strip-zoning pesticide application control system was mounted on the boom sprayer. A speed sensor was installed inside the sprayer's wheels, and a rope displacement sensor was fitted on the spray boom to measure the offset of the actuator. An industrial camera was installed at the front of the sprayer and positioned at the mid-stroke of the electric push rod. A calibrated nozzle was fixed inside the anti-drift device directly below the industrial camera to record the trajectory of the droplet strip. A rectangular area with a length of 20 m and a width equal to the inter-zone spacing was demarcated in the crop zone area; within this area, a piece of water-sensitive paper and a warning line of the same length as the area were laid every 40 cm as reference benchmarks. Meanwhile, water-sensitive test paper was laid on the canopies of soybean and maize plants (Fig. 22). During the experiment, the operating speed of the plant protection sprayer was controlled at 2 km/h, 3 km/h, 4 km/h and 5 km/h. After the system received control commands, the nozzles sprayed uniformly, and the droplet positions were visualized by utilizing the characteristic of water-sensitive paper turning red upon contact with water. The experiment wind speed was measured at 1.4–2.9 m/s. Upon completion of the experiment, the coordinate positions of droplet centers on the water-sensitive paper were manually recorded, and the number of blue spots on the surface of the water-sensitive test paper was counted to verify the overall performance of the automatic strip-zoning pesticide application control system.



Fig. 18 - Field Experiment

RESULTS

5. Field Experiment and Analysis

5.1. Performance Experiment of the Recognition Algorithm

To verify the robustness of the algorithm's recognition performance, this study conducted performance tests under different light intensities, with the mean recognition deviation and recognition accuracy adopted for evaluation.

The experimental results are shown in Table 2. The algorithm's recognition performance is dependent on light intensity: during the period of 14:30–16:30, the light was uniform and stable without direct strong light or shadow occlusion, and the crop row recognition accuracy reached the peak of the entire experiment period under both forward and backlighting conditions. The distinct crop-background feature boundaries facilitated target segmentation and contour extraction; during 9:30–14:30, the light intensity rose to the maximum, and local overexposure of images led to the loss of texture features in crop canopies and a decrease in the contrast between targets and the background, resulting in an increase in the mean recognition deviation and a subsequent decline in accuracy; during 16:30–18:30, the light intensity diminished, the area of shadows from crop canopies and the machine expanded with a complex distribution, and blurred pixel features caused a reduction in positioning accuracy, with the mean recognition deviation reaching 3.53 cm, which was significantly higher than that in the previous two periods. Overall, the recognition accuracy of the algorithm remained above 84% throughout the entire experiment period, indicating a certain level of its adaptability to the field environment.

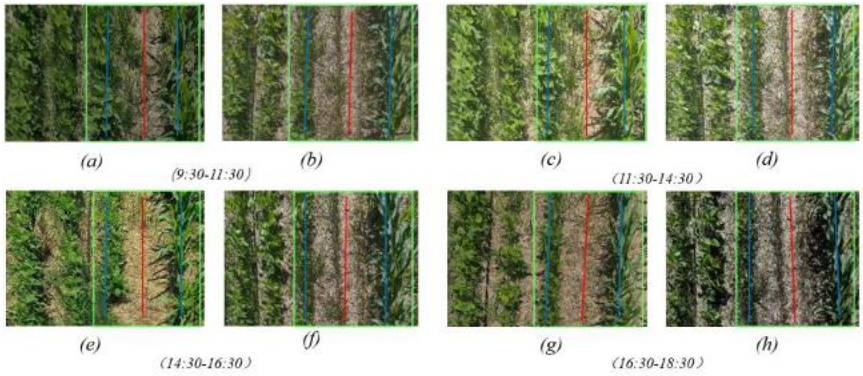


Fig. 19 - Light intensity experiment results

(a), (c), (e), (g)-- Frontlight; (b), (d), (f), (h)-- Backlight

Table 2

Light intensity experiment results

Time Interval	Light Intensity / Lux	Light Direction	Mean Recognition Deviation / cm	Recognition Accuracy / %
9:30-11:30	**1.66×10^4**	Frontlight	3.34	88
		Backlight	3.37	90
11:30-14:30	**1.79×10^4**	Frontlight	3.44	88
		Backlight	3.36	91
14:30-16:30	**1.39×10^4**	Frontlight	3.00	90
		Backlight	3.32	92
16:30-18:30	**1.15×10^4**	Frontlight	3.53	86
		Backlight	3.46	84

5.2. System Performance Experiment

To quantitatively analyze the real-time response characteristics of the visual recognition module and the automatic strip-zoning actuation mechanism, 20 groups of continuous and typically representative sample data were selected in this study while the sprayer was operating at an operating speed of 2 km/h, and the Trend Chart of Vision-Actuation Offset Variation (Fig. 20) was plotted accordingly.

As can be seen from Fig. 20, the strip-zoning actuation offset generally exhibits the characteristic of converging toward the visual recognition detection results. When the sprayer operated to Zone I, the crops grew uniformly with a reasonable planting density, and the crop row contours were clear and highly continuous. The automatic strip-zoning actuation mechanism featured a small displacement adjustment range and a rapid response, which reduced the offset to the minimum value of 0.3 cm throughout the entire operation process.

In contrast, when the sprayer operated to Zone II, the offset exhibited significant abnormal fluctuations, with the maximum offset reaching 4.9 cm, which was significantly higher than that in other operating areas.

This was due to the crop seedling absence in this zone, which led to the weakening of crop row contour features and the breakage of their continuity. This prevented the system's visual recognition module from accurately capturing the complete position of the crop zone centerline, which in turn caused a lag in the displacement adjustment of the automatic strip-zoning actuation mechanism and ultimately resulted in an increase in the offset.

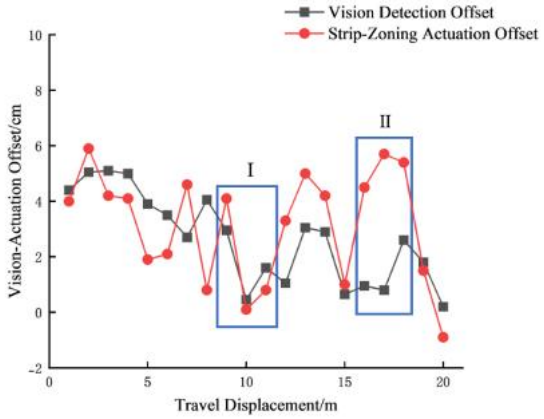


Fig. 20 - Trend Chart of Vision-Actuation Offset Variation

Meanwhile, the experiment set different operated speed gradients, and 50 groups of valid samples were selected for each gradient to plot the dynamic trend chart of the offset between the droplet zone center and the crop zone centerline (Fig. 21).

It can be seen from the trend characteristics in Fig. 21 that the offset exhibited a significant positive correlation with the increase in operating speed. The statistical characteristics of the crop zone trajectory offset under different speed gradients are shown in Table 3. Under the four operating speeds, the mean maximum deviation of the trajectory offset was all controlled within 50 mm. Among them, the mean offset fluctuated sharply at speeds of 2–4 km/h, with a maximum difference of 0.98 cm between adjacent speeds.

The main reasons are as follows: First, the nozzle and the boom frame are connected via a hinged joint. During the operating of the sprayer, the nozzle is prone to irregular lateral oscillation due to the unevenness of the field road surface and the inertial effect of the machine, which causes the droplet spray landing points to deviate from the preset area. Second, with the increase in the sprayer's operating speed, the video images collected by the system's visual recognition module suffer from insufficient resolution, which results in blurred boundary features between crop zones and a significant decline in contour recognizability. This makes it impossible to accurately extract the spatial position information of the inter-zone centerline, and thus the strip-zoning control actuation mechanism lacks a reliable visual perception basis for generating accurate offset compensation commands. This ultimately leads to continuous error accumulation, resulting in an obvious increasing trend of the mean offset with the rise in operating speed.

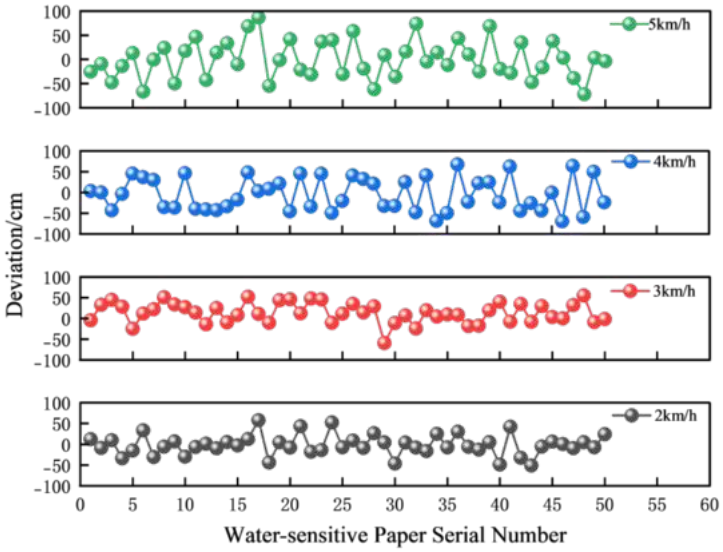


Fig. 21 - Deviation at Different Speeds

Table 3

Crop Strip Trajectory Deviation Statistics

Speed / km·h⁻¹	Mean Deviation / cm	Proportion of Deviations Within 50 mm / %
2	1.83	94.00
3	2.81	92.00
4	3.55	88.00
5	3.56	84.00

5.3 Drift Prevention Performance Experiment of Droplets

To further evaluate the strip-zoning effect of the automatic strip-zoning pesticide application control system, droplet cross-zone drift prevention performance experiment were conducted.

By calculating the droplet deposition density (Eq. 23), the deposition status of droplets per unit crop area can be determined *(Ma et al., 2023; Ni et al., 2020; Zhou et al., 2021)*. The results are shown in Tables 4 and 5.



Fig. 22 - Water-Sensitive Test Paper

Table 4

Maize Liquid Droplet Drift Deposition

Speed / km/h	Droplet Deposition Amount / (droplet /cm²)			Mean Droplet Deposition Amount / (droplet /cm²)
	1	2	3	
2	0.20	0.24	0.11	0.18
3	0.44	0.66	1.19	0.76
4	1.69	1.61	1.71	1.67
5	6.38	4.81	6.65	5.94

Table 5

Soybean Liquid Droplet Drift Deposition

Speed / km/h	Droplet Deposition Amount / (droplet /cm²)			Mean Droplet Deposition Amount / (droplet /cm²)
	1	2	3	
2	0.55	0.41	0.76	0.57
3	1.65	1.27	1.67	1.53
4	1.92	1.83	2.78	2.18
5	8.78	10.29	9.17	9.41

From the experimental results, the amount of droplet cross-zone drift is positively proportional to the operating speed, and the drift deposition amount of droplets is no more than 9.41 cm², which indicates that the system can effectively reduce droplet cross-zone drift.

CONCLUSIONS

(1) Taking soybean and maize under the strip intercropping mode as the research object, a crop row recognition algorithm and a strip-zoning spray control system were designed, and a vision-based strip-zoning pesticide application control system was established.

(2) Research is conducted on the crop row recognition method based on machine vision. A dynamic ROI positioning and crop row line extraction algorithm for soybean and maize crop rows based on the peak value method was proposed, and a strip-zoning offset compensation model was constructed accordingly.

(3) Field experiment results show that the light intensity at different times of the day causes slight fluctuations in the algorithm's recognition accuracy, while the recognition accuracy remains no less than 87% consistently. At operating speeds of 2 to 5 km/h, the mean strip-zoning deviation of the automatic strip-zoning pesticide application control system can be controlled within 3.61 cm, and the proportion of strip-zoning deviations within 5 cm reaches 84%, with a maximum of 94%. Under wind speeds of 1.4 to 2.9 m/s, the droplet drift deposition amount of the closed anti-drift device is directly proportional to the operating speed, with a maximum of 9.41 number/cm², which meets the plant protection operation standards for the soybean-maize strip intercropping mode. This study provides a practical technical reference for the development of precise plant protection operations under the soybean-maize intercropping mode.

ACKNOWLEDGEMENT

This work was supported by the Special Support Fund for High-level Talents of Henan Agricultural University (30501381), the Henan Provincial Science and Technology Commissioner Project (30804295), and the Henan Provincial Science and Technology Research and Development Program (242102111175).

REFERENCES

[1] Chen Z. W., Li W., Zhang W. Q., Li Y. W., Li M. S., Li H., (2019). Research on vegetable crop row extraction method based on automatic Hough transform accumulation threshold (基于自动 Hough 变换累加阈值的蔬菜作物行提取方法研究), *Transactions of the Chinese Society of Agricultural Engineering*, vol.35, no.22, pp.314-322, Chongqing/China. DOI: 10.11975/j.issn.1002-6819.2019.22.037

[2] Cui G. P., Sun X. J., Liu J. W., Shi Y. H., Li J. Y., Li Y. Q., Yu C. C., Cheng S. S., Li H., (2023). Design and test of strip-divided boom sprayer for soybean and corn strip compound planting (大豆玉米带状复合种植分带式喷杆喷雾机设计与试验), *Journal of Henan Agricultural University*, vol.57, no.5, pp.752-763, Zhengzhou/China. DOI:10.16445/j. cnki.1000-2340.20230828.001

[3] Ding Y. C., He Z. B., Xia Z. Z., Peng J. Y., Wu T. H., (2019). Design of immune PID controller for navigation of small crawler rapeseed seeder (小型履带式油菜播种机导航免疫 PID 控制器设计), *Transactions of the Chinese Society of Agricultural Engineering*, vol.35, no.7, pp.12-20, Wuhan/China. DOI: 10.11975/j.issn.1002-6819.2019.07.002

[4] García-Santillán I., Guerrero J., Montalvo M., Pajares G., (2017). Curved and straight crop row detection by accumulation of green pixels from images in maize fields, *Precision Agriculture*, vol.19, pp.18–41, Spain. DOI:10.1007/s11119-016-9494-1

[5] Jiang G. Q., Wang Z. H., Liu H. M., (2014). Automatic detection of crop rows based on multi-ROIs, *Computers and Electronics in Agriculture*, vol.42, no.5, pp.2429–2441, Jiaozuo/China. DOI: 10.1016/j.compag.2014.10.033

[6] Khan M. N., Rahi A., Rajendran V. P., Al Hasan M., Anwar S., (2024). Real-time crop row detection using computer vision-application in agricultural robots, *Frontiers in Artificial Intelligence*, vol.7, Article ID 1435686, IN/USA. DOI:10.3389/frai.2024.1435686

[7] Liao J., Wang Y., Yin J. N., Zhang S., Liu L., Zhu D. Q., (2019). Seedling row center line extraction based on sub-regional feature point clustering (基于分区域特征点聚类的秧苗行中心线提取), *Transactions of the Chinese Society for Agricultural Machinery*, vol.50, no.11, pp.34-41, Hefei/China. DOI: 10.6041/j.issn.1000-1298.2019.11.004

[8] Li Y. F., Wright B., Ha M. R. Z., (2024). Deep learning-based perspective distortion correction for outdoor photovoltaic module images, *Solar Energy Materials and Solar Cells*, vol.277, Article ID 113107, Sydney/Australia. DOI: 10.1016/j.solmat.2024.113107

[9] Ma K., Zhang Z. Y., Dong X. Y., Qiu B. J., (2023). Design and test of portable droplet deposition detection system (便携式雾滴沉积检测系统的设计与试验), *Journal of Agricultural Mechanization Research*, vol.45, no.5, pp.49-54, Zhenjiang/China. DOI: 10.13427/j.cnki.njyi.2023.05.045

[10] McInnes L., Healy J., Astels S., (2017). Hdbscan: hierarchical density based clustering, *Journal of Open Source Software*, vol.2, Article ID 205, Canada. DOI:10.21105/joss.00205.

[11] Montalvo M., Pajares G., Guerrero J. M., et al., (2012). Automatic detection of crop rows in maize fields with high weeds pressure, *Expert Systems with Applications*, vol.39, no.15, pp.11889–11897, Madrid/Spain. DOI:10.1016/j.eswa.2012.05.065

[12] Ni J. S., Ru Y., Wang S. J., Sun X. X., (2020). Experimental research on droplet drift prediction (雾滴飘移预测试验研究), *Journal of Agricultural Mechanization Research*, vol.42, no.10, pp.152-157, Nanjing/China. DOI: 10.13427/j.cnki.njyi.2020.10.026

[13] Ota K., Kasahara J. Y. L., Yamashita A., Asama H., (2022). Weed and crop detection by combining crop row detection and k-means clustering in weed infested agricultural fields, in 2022 *IEEE/SICE International Symposium on System Integration (SII)*, pp.985–990, Narvik/Norway. DOI:10.1109/SII52469.2022.9708815.

[14] Pérez-Ruíz M., Slaughter D. C., Fathallah F. A., Gliever C. J., Miller B. J., (2014). Co-robotic intra-row weed control system, *Biosystems Engineering*, vol.126, pp.45–55, Davis, CA/USA. DOI: 10.1016/j.biosystemseng.2014.07.009

[15] Ramesh K. N., Chandrika N., Omkar S. N., Meenavathi M. B., Rekha V., (2016). Detection of Rows in Agricultural Crop Images Acquired by Remote Sensing from a UAV, I.J. Image, *Graphics and Signal Processing*, vol.8, no.11, pp.25-31, Bangalore/India. DOI:10.5815/ijigsp.2016.11.04

[16] Sun B. F., Ye C., Li Y. D., Shu S. F., Cao Z. S., Wu L. F., Zhu Y., He Y., (2022). Paddy field image segmentation based on color index and threshold method (基于颜色指数与阈值法的稻田图像分割), *Journal of China Agricultural University*, vol.27, no.5, pp.86-95, Nanchang/China. DOI: 10.11841/j.issn.1007-4333.2022.05.08

[17] Tang J. L., Huang H. N., Shi L. C., Chen Z. B., Lu Y. Y., Chen H. C., (2018). An Improved Perspective Transform for Image Distortion Correction, *2018 IEEE International Conference on Consumer Electronics-Taiwan (ICCE-TW)*, pp.1-2, Taiwan/China. DOI:10.1109/ICCE-China.2018.8448538

[18] Vidovic I., Cupec R., Hocenski Z., (2016). Crop row detection by global energy minimization, *Pattern Recognition*, vol.55, pp.68–86, Croatia. DOI: http://dx.doi.org/10.1016/j.patcog.2016.01.013

[19] Wang Q., Meng Z. J., Fu W. Q., Liu H., Zhang Z. G., (2021). Multi-row crop line detection algorithm for maize seedling stage based on machine vision (基于机器视觉的玉米苗期多条作物行线检测算法), *Transactions of the Chinese Society for Agricultural Machinery,* vol.52, no.4, pp.208-213, Beijing/China. DOI: 10.6041/j.issn.1000-1298.2021.04.022

[20] Yang Z. L., Yang Y., Li C. R., Zhou Y., Zhang X. S., Yu Y., Liu D., (2022). Tasseled Crop Rows Detection Based on Micro-Region of Interest and Logarithmic Transformation, *Frontiers in Plant Science*, vol.13, Article ID 916474, Hefei/China. DOI:10.3389/fpls.2022.916474

[21] Zhai Z. Q., Zhu Z. X., Du Y. F., Song Z. H., Mao E. R., (2016). Multi-crop-row detection algorithm based on binocular vision, *Biosystems Engineering*, vol.150, pp.89-103, Beijing/China. DOI: 10.1016/j.biosystemseng.2016.08.004

[22] Zhang J. F., Wei Y. Q., Ye X. H., Liu Z. X., Qi Y. C., Maimaiti Y. S., (2025). Research Progress of Strip Compound Planting Technology of Maize and Soybean (玉米大豆带状复合种植技术研究进展), *Modern Agricultural Science and Technology*, no.11, pp.33-37, Aksu/China. DOI: 10.3969/j.issn.1007-5739.2025.11.009

[23] Zhang S., Liu Y., Xiong K., Tian Y. H., Du Y. F., Zhu Z. X., Du M. W., Zhai Z. Q., (2024). A review of vision-based crop row detection method: Focusing on field ground autonomous navigation operations, *Computers and Electronics in Agriculture*, vol.217, Article ID 109086, Beijing/China. DOI: 10.1016/j.compag.2024.109086

[24] Zhang X. Y., Wang Q. J., Wang X. H., Li H. W., He J., Lu C. Y., Yang Y., Jiang S., (2023). Automated detection of Crop-Row lines and measurement of maize width for boom spraying, *Computers and Electronics in Agriculture*, vol.211, Article ID 108406, Beijing/China. DOI: 10.1016/j.compag.2023.108406

[25] Zhao T., Noguchi S., Yang L. L., Ishii I., Chen J., (2016). Fast Edge Detection Method for Wheat Field Based on Visual Recognition (基于视觉识别的小麦收获作业线快速获取方法), *Transactions of the Chinese Society for Agricultural Machinery*, vol.47, no.11, pp.32-37, Yangling/China. DOI: 10.6041/j.issn.1000-1298.2016.11.005

[26] Zhao X. G., Ma W., Gao Y. Y., Zang Y. F., He Y. C., Wang X., (2019). Identification of early crop row for drill crops based on reverse perspective transformation (基于逆透视变换的条播作物早期作物行识别), *Journal of Jiangsu University (Natural Science Edition)*, vol.40, no.6, pp.668-675, Beijing/China. DOI: 10.3969/j.issn.1671-7775.2019.06.008

[27] Zheng K., Zhao X. G., Han C. J., He Y. K., Zhai C. Y., Zhao C. J., (2023). Design and Experiment of an Automatic Row-Oriented Spraying System Based on Machine Vision for Early-Stage Maize Corps, *Agriculture*, vol.13, Article ID 691, Beijing/China. DOI:10.3390/agriculture13060691

[28] Zhou M. C., Jiang H. Y., Bing Z. S., Su H., Knoll A., (2021). Design and evaluation of the target spray platform, *International Journal of Advanced Robotic Systems*, vol.18, pp.1-17, China. DOI:10.1177/1729881421996146

OPTIMISATION AND EXPERIMENTAL RESEARCH OF FURROWING TOOL BASED ON EDEM
/
基于 EDEM 的开沟刀具优化与试验研究

Jian YAN[1)], Jing MI[2*)], Fei XIA[3)], Guangwen YANG[2)], Chenjun HU[2)], Bin YANG[2)], Yan ZHOU[2)], Bo ZHANG[4)], Po NIU[5*)]

[1)] Chongqing Three Gorges Vocational College, School of Automotive Engineering, People's Republic of China;
[2)]Yibin Academy of Agricultural Sciences, People's Republic of China;
[3)]Chongqing Kaizhou District Agriculture Service Centre, Chongqing, People's Republic of China;
[4)]Chongqing Wanzhou District Agricultural Technology and Machinery Promotion Centre, People's Republic of China;
[5)]College of Mechanical Engineering, Chongqing Three Gorges University, People's Republic of China
Tel: +86 17726251480; E-mail: 1478807149@qq.com; niupo205@163.com
Corresponding author: Jing Mi, Po Niu
DOI: https://doi.org/10.35633/inmateh-79-36

Keywords: *furrowing tool; EDEM; response surface analysis; parameter optimisation.*

ABSTRACT
Mechanised furrowing and fertiliser application is an effective engineering solution for improving operational efficiency and reducing labour intensity in hilly and mountainous orchards. In this study, a systematic optimisation methodology for a disc-type furrowing tool is proposed by integrating discrete element method (DEM) simulations using EDEM with quadratic orthogonal regression experiments and response surface analysis. Key structural parameters, including bending radius, bending angle, and alpha angle, were selected as design variables, and their individual and interactive effects on furrowing power consumption were investigated. The results of the response surface analysis indicate that appropriate structural optimisation can significantly reduce trenching power consumption. The optimal structural parameters were determined as follows: bending radius of 36.79 mm, bending angle of 126.94°, and alpha angle of 43.65°. Under these conditions, the predicted power consumption was 0.85 kW, representing a reduction of 8.88% compared with the original tool design. Soil bin experiments were conducted to validate the DEM simulation results, and the experimental trends showed good agreement with the simulation predictions, demonstrating the reliability of the proposed optimisation approach. This study provides a practical reference for the engineering design and performance improvement of soil-engaging tools.

摘要
果园机械化开沟施肥技术是提高丘陵山区果园作业效率、降低劳动强度的关键手段之一。本文基于EDEM仿真技术，结合二次正交回归试验与响应曲面分析，优化了圆盘式开沟刀具的结构参数。研究重点分析了弯折半径、弯折角度和阿尔法角等关键参数，并通过响应曲面分析揭示了这些参数之间对开沟功耗的交互影响。优化结果表明，合理调整刀具结构能够显著降低开沟功耗，优化后的刀具参数为：弯折半径 X_1 = 36.79 mm、弯折角度 X_2 = 126.94°、阿尔法角 X_3 = 43.65°，优化后的功耗为 0.85 kW，相较未优化刀具，功耗降低了约 8.88%。土槽实验验证了仿真结果的准确性，为进一步优化开沟刀具提供了理论依据。

INTRODUCTION
Fertilisation is a fundamental management practice in orchard production because it directly influences tree growth, fruit yield, and fruit quality. In modern orchard management, strip fertilisation along the tree drip line is widely adopted to improve nutrient availability and root uptake. This practice requires efficient furrowing and subsequent backfilling to ensure uniform fertiliser placement and favourable soil conditions for root development *(Chen M. et al., 2024; Chen P. et al., 2024)*. However, conventional furrowing methods generally exhibit high energy consumption and low operational efficiency, particularly when traditional soil-engaging tools are employed. These limitations become more pronounced in hilly and mountainous orchards, where steep terrain, irregular planting layouts, and limited accessibility restrict the use of conventional agricultural machinery *(Fang et al., 2024; Jian et al., 2024)*. Consequently, fertilisation in these regions still relies heavily on manual labour, resulting in low productivity and high labour intensity. With the continuing shortage of agricultural labour, the development of efficient and energy-saving furrowing equipment has become an important prerequisite for improving the mechanisation of orchard fertilisation in hilly and mountainous areas.

As the key soil-engaging component of a furrowing machine, the structural design of the furrowing tool directly determines soil cutting performance, soil disturbance characteristics, and power consumption during operation *(Aikins et al., 2019; Madhusudan et al., 2024).* An appropriately designed tool not only improves trenching efficiency but also reduces energy consumption and enhances fertiliser placement quality, thereby improving both the economic and environmental sustainability of orchard production *(Wang et al., 2015; Yi et al., 2024).* These studies indicate that optimising the structural parameters of furrowing tools is an effective engineering approach for reducing power consumption and improving operational performance.

As a core component, tool structure significantly affects efficiency and energy demand. Extensive research has been conducted in this field. For instance, *Kang et al., (2016),* reduced power consumption by optimizing blade geometry, while *Yang et al., (2018)* developed a cut-and-throw furrowing tool tailored for tea plantations, thereby improving soil displacement performance. *Kim et al., (2021)* employed discrete element method simulations to optimise soil–tool interaction, achieving considerable reductions in power consumption and offering valuable guidance for tool design. Despite these advances, traditional furrowing tools still suffer from low efficiency and excessive power consumption when used in orchards located in hilly and mountainous regions—where high soil viscosity and sloughing are prevalent—indicating a clear need for further optimisation. Improving tool configuration is essential to enhance efficiency, reduce power consumption, and improve adaptability to diverse soils and fertilisation needs.

In this study, DEM simulations (EDEM) and soil trench tests were conducted to investigate the effects of bending radius, bending angle, and alpha angle on power consumption. A quadratic orthogonal regression model was established to optimise tool parameters.

MATERIALS AND METHODS

MAIN STRUCTURE AND PARAMETERS OF FURROWING TOOL

In this study, a disc-type furrowing cutter was adopted as the research object, and its structural design was developed based on the working principles of a wetland furrowing curved cutter, as illustrated in Figure 1. The tool mainly consists of a lateral cutting edge, a frontal cutting edge, a central shaft, and mounting apertures. The lateral cutting edge is formed along an Archimedean helix to facilitate soil cutting and conveyance, while the frontal cutting edge is designed with a circular arc profile to enhance soil penetration and stabilise the furrowing process *(Aikins et al., 2020; Amantayev et al., 2018; Barr et al., 2020; Mi et al., 2025).*

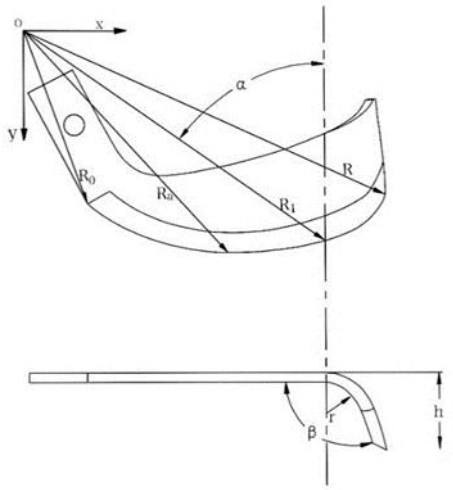


Fig. 1 - Tool structure diagram. O-centre of rotation

O-centre of rotation, R-radius of rotation, R_0-radius of the starting point of the side cutting edge, R_1-radius of the end point of the side cutting edge, R_α-radius of any point on the side cutting edge, α-angle between the end point of the side cutting edge and the bending line, r-bending radius, β-bending angle, h-working width.

The key structural parameters of the furrowing tool are listed in Table 1. These geometric parameters were obtained by measuring the manufactured prototype and were used to establish the three-dimensional model for DEM simulation.

Table 1

Main structural parameters of furrowing tool.

Parameter	Value
Radius of rotation [R]	245 mm
Bending radius [r]	45 mm
Bending angle [β]	145°
Alpha angle [α]	40°
Working width [h]	35 mm
Blade edge thickness	1.5 mm
Blade back thickness	5 mm
Working depth [H]	20 mm

Tool-soil coupling model based on EDEM

To ensure accuracy and reliability, a representative orchard soil from a hilly region was selected as the simulation medium. Measured soil properties were combined with literature values to define DEM input parameters *(Fang et al., 2016; HAO et al., 2023; Li et al., 2018; Liu et al., 2024; Liu et al., 2019; Zhu et al., 2020).* The soil is shaly and clayey, composed of fine particles that are difficult to measure directly at the particle scale. Thus, assumptions were made to balance computational efficiency and realistic soil behaviour. The Hertz–Mindlin with JKR model was used to simulate soil–soil and soil–tool interactions, with particle diameter set to 5 mm. Simulation parameters for the soil and tool are listed in Table 2.

Table 2

Tool-soil coupling model parameters

Parameter	Value	Parameter	Value
Machine forward speed [m/s]	0.3	Soil-soil recovery factor	0.28
Tool speed [rpm]	300	Soil- steel recovery factor	0.6
Soil density [kg/m³]	2500	Soil-soil static factor	0.5
Poisson's ratio for soil	0.32	Soil-steel static factor	0.5
Soil shear modulus [Pa]	1×10^{6}	Soil-soil rolling factor	0.37
Steel density [kg/m³]	7850	Soil-steel rolling factor	0.05
Shear modulus of steel [Pa]	7.962×10^{10}	Steel Poisson's ratio	0.3

Test equipment

The experimental system consisted of soil bin testing and processing equipment. The soil bin system included a P71 magnetic tachometer for speed measurement, an APN1211E-U power tester, a TAILI three-phase AC motor, and a TAILI S18 frequency converter. Processing equipment included a CNC machining centre (Huazhong CNC Co., Ltd.) for tool fabrication.

EDEM simulation test

A three-dimensional furrowing tool model was built in UG NX12 using the geometry and soil parameters from the previous section. The model was exported in STL format and imported into EDEM for simulation. The tool–soil coupling model was established by assigning material and contact properties to the tool and soil particles. Figure 2 shows the model generated using these methods and parameters.

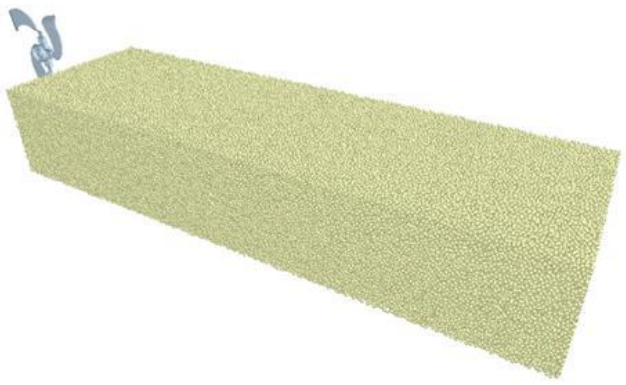


Fig. 1 - Tool-soil simulation model diagram

As EDEM does not directly provide tool power consumption as an output, the torque acting on the furrowing tool was first obtained from the simulation results and then converted into power consumption using the following Eq. 1:

$$P = \frac{T \cdot n}{9549} \quad (1)$$

where:

P-power consumption, [kW];

T-torque, [Nm];

n-tool speed, [rpm].

Soil bin experiment

To validate the EDEM simulation, a soil bin test bench was constructed. The soil bin measured 2500 × 600 × 500 mm, and the same disc-type tool as in the simulations was used. During testing, the tool was driven by an electric motor, and power consumption was recorded in real time. Each condition was repeated three times, and no-load power was subtracted to obtain net cutting power. Motor speed was controlled by a variable-frequency drive, while forward speed was manually adjusted. To reduce uncertainty, data were collected in the central region of the soil bin. Figure 3 shows the setup.

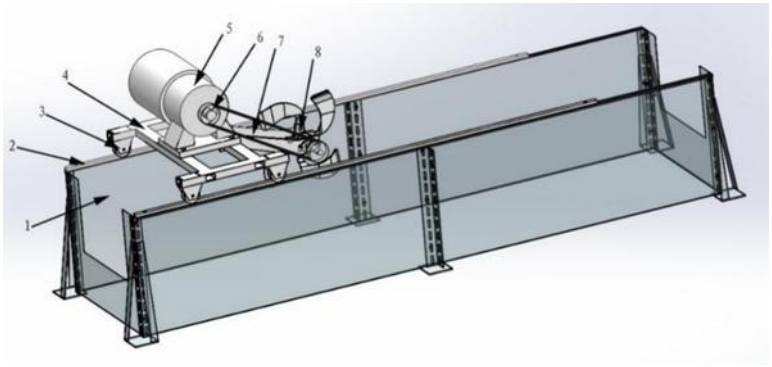


Fig. 2 - The schematic diagram of soil trough experimental scheme

1. soil tank; 2. guide rail; 3. pulley; 4. motor mounting; 5. motor; 6. chain drive; 7. tool arm; 8. cutter plate.

The constructed soil-tank experimental stand is illustrated inFig. **3** 3.



Fig. 3 - Soil trough test bench

Optimisation of furrowing tool parameters

This section optimises the parameters of the disc-type furrowing tool. Based on DEM simulations and soil bin tests, three parameters—bending radius (X_1), bending angle (X_2), and alpha angle (X_3)—were selected. The objective was to reduce power consumption and improve efficiency, thereby enhancing tool performance under typical orchard conditions.

Quadratic regression orthogonal experimental design

The orthogonal combination design includes a two-level test m_c, an asterisk test $2m_\gamma$ and zero-level experiment m_0. The total number of tests, n is calculated using the following Eq.(1):

$$n = m_c + 2m_\gamma + m_0 \quad (1)$$

In accordance with the orthogonality requirement, the arm length parameter, denoted as γ, must satisfy the following Eq. (2):

$$\gamma = \sqrt{\frac{\sqrt{(m_c + 2m_\gamma + m_0)m_c} - m_c}{2}} \quad (2)$$

The present experiment was a three-factor, two-level full-scale trial, which resulted in $\gamma = 1.353$.

In the context of the given factors, the arithmetic mean is defined as the zero level of factor x_j, denoted x_{j0}, where x_{j2} and x_{j1} represent the upper and lower levels of factor x_j, respectively. Let $x_{j\gamma}$ and $x_{-j\gamma}$ denote the upper and lower asterisk arm levels of factor x_j, respectively. These values correspond to the upper and lower levels of factor x_j(3).

$$x_{j0} = \frac{x_{j1} + x_{j2}}{2} = \frac{x_{j\gamma} + x_{-j\gamma}}{2} \quad (3)$$

Therefore, the variation in this factor is as Eq. (4):

$$\Delta_j = \frac{x_{j\gamma} - x_{j0}}{\gamma} \quad (4)$$

The factor levels and their corresponding coding results for this trial are shown in Table 3.

Table 3

Test factors and levels

coding	X_1 (bend radius)	X_2 (bending angle)	X_3 (Alpha angle)
γ (1.353)	58.53	145.15	46.77
1	55.00	142.50	45.00
0	45	135	40
-1	35.00	127.50	35.00
$-\gamma$ (-1.353)	31.47	124.85	33.23
Δ_j	3.6954	11.0864	3.6954

The quadratic regression orthogonal test design and the corresponding operating power consumption of the furrowing tool are presented in Table 4.

Table 4

Experimental arrangement and results

	X_1(Bending radius)	X_2(bending angle)	X_3(Alpha Angle)	Y（kW）
1	-1.000	-1.000	-1.000	0.901936
2	1.000	-1.000	-1.000	0.887035
3	-1.000	1.000	-1.000	0.943716
4	1.000	1.000	-1.000	0.954311
5	-1.000	-1.000	1.000	0.856537
6	1.000	-1.000	1.000	0.908795
7	-1.000	1.000	1.000	0.909632
8	1.000	1.000	1.000	0.987465
9	-1.353	0.000	0.000	0.882938
10	1.353	0.000	0.000	0.905925
11	0.000	-1.353	0.000	0.855001
12	0.000	1.353	0.000	0.93794
13	0.000	0.000	-1.353	0.920778
14	0.000	0.000	1.353	0.884145
15	0.000	0.000	0.000	0.879881
16	0.000	0.000	0.000	0.879881
17	0.000	0.000	0.000	0.879881

The objective was to minimize power consumption by optimising the structural parameters of the disc-type furrowing tool. A quadratic regression model was established to quantify the relationship between structural parameters and power consumption. The optimal parameters were obtained by solving the objective function in MATLAB.

RESULTS AND DISCUSSION

EDEM simulation results analysis

The torque acting on the disc-type furrowing tool during the furrowing process was obtained using the EDEM post-processing module, as shown inFig. 4. The mean torque was determined to be 29.79 Nm, and the corresponding furrowing power consumption was calculated to be 0.94 kW.

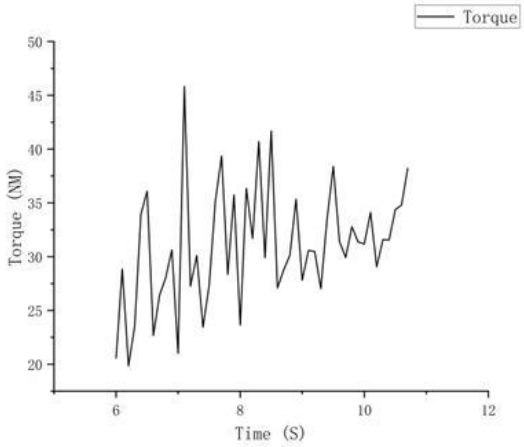


Fig. 4 - Tool furrowing torque diagram

The operation of the disc-type furrowing tool in the soil trench demonstrated its effectiveness in soil cutting and trench formation. During the furrowing process, the soil was lifted and displaced, with the majority returning to the trench, while a small portion of soil was ejected outside the simulation domain. This behaviour confirms the appropriateness of the tool's selected structural parameters for efficient trenching. The furrowing process is illustrated inFig. 5.

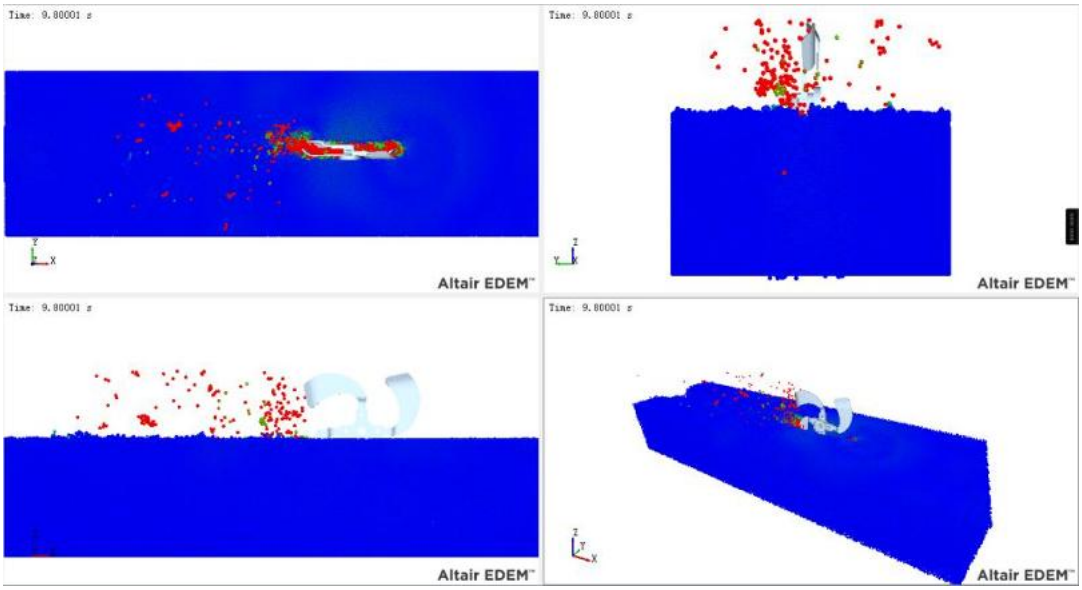


Fig. 5 - Schematic diagram of tool furrowing process

Comparative analysis of simulation test and soil tank test results

This section presents a comparative analysis of the simulation results and soil bin test data. Analysis of the soil bin experiments indicates that, during the furrowing process, the tool's lateral cutting edge initially engages and cuts the soil, followed by plastic deformation of the soil. As the disc-type furrowing tool rotates, the operating depth gradually increases, and the main cutting edge comes into contact with the soil, enlarging the contact area. This interaction results in shearing and extrusion of the soil, culminating in soil fragmentation, overturning, and partial ejection, thereby completing the furrowing and backfilling operations (Fig. **6**).



Fig. 6 - Effect diagram after furrowing

A detailed analysis of the soil bin test data indicated that the average power consumption of the disc-type furrowing tool was 1.07 kW. In comparison, the EDEM simulation predicted a furrowing power of 0.94 kW, yielding a relative error of 13.83%. The discrepancy can be attributed to fluctuations in the tool's forward speed, machining and assembly tolerances, and variations in soil properties. Nevertheless, this relative error is within an acceptable range for agricultural machinery, particularly for furrowing and tillage implements. These results demonstrate that the EDEM simulation can accurately predict the power consumption of the furrowing tool and can be effectively used to guide its structural optimisation.

Analysis of optimisation results of furrowing tool parameters

Quadratic regression orthogonal test results analysis

The results of the quadratic orthogonal regression experiments were imported into the statistical analysis software Design-Expert 13 for further evaluation. The outcomes of the analysis are summarised in Table **5**.

Table 5

Variance analysis

Source	Sum of Squares	df	Mean Square	F-value	p-value	VIF
Model	0.0196	9	0.0022	28.52	0.0001	1
A	0.0021	1	0.0021	27.70	0.0012	1
B	0.0107	1	0.0107	140.26	< 0.0001	1
C	0.0005	1	0.0005	6.19	0.0418	1
AB	0.0003	1	0.0003	4.28	0.0774	1
AC	0.0023	1	0.0023	29.63	0.0010	1
BC	0.0001	1	0.0001	0.8459	0.3883	1
A^2	0.0009	1	0.0009	11.62	0.0113	1
B^2	0.0011	1	0.0011	13.98	0.0073	1
C^2	0.0017	1	0.0017	22.18	0.0022	1

Note: $p \leq 0.01$ (highly significant), $p \leq 0.05$ (significant).

As shown in Table 5, the model has an F-value of 28.52, indicating statistical significance. The P-value indicates significance, with values < 0.05 denoting significant effects. Factors A, B, C, AC, and A^2, B^2, C^2 significantly affect power consumption. SS, DF, MS, and VIF denote sum of squares, degrees of freedom, mean square, and variance inflation factor, respectively; VIF = 1 indicates factor orthogonality.

ANOVA confirms that the model is statistically significant. Factor B (X_2) has the greatest effect, followed by C (X_3) and A (X_1). The interaction A × C also significantly affects power consumption. The analysis also yielded regression coefficients and model fit metrics.

The regression model is:

$$Y = +0.8770 + 0.0135 * X_1 + 0.0303 * X_2 - 0.0064 * X_3 + 0.0064 * X_1X_2 + 0.0168 * X_1X_3 + 0.0028 * X_2X_3 + 0.0115 * X_1^2 + 0.0126 * X_2^2 + 0.0159 * X_3^2 \quad (5)$$

Table 6

Fit degree analysis results

Std. Dev.	0.0087	R^2	0.9735
Mean	0.9045	Adjusted R^2	0.9393
C.V. %	0.9651	Predicted R^2	0.8023
		Adeq Precision	18.9286

The regression model exhibited an R^2 of 0.9735, an adjusted R^2 of 0.9393, and a P-value of 0.0001, indicating that the model fits the experimental data well, is highly reliable, and statistically significant. The predicted R^2 of 0.8023 is reasonably close to the adjusted R^2, with a difference of less than 0.2, further confirming the stability and predictive capability of the model.

Model adequacy was also evaluated using the Adeq Precision, which should ideally exceed 4. In this study, the Adeq Precision was 18.929, demonstrating that the model has sufficient signal strength and applicability. Additionally, the normality of the standardized residuals was assessed, showing that they approximately follow a normal distribution and converge along a standard normal probability plot, as illustrated in Fig. 7.

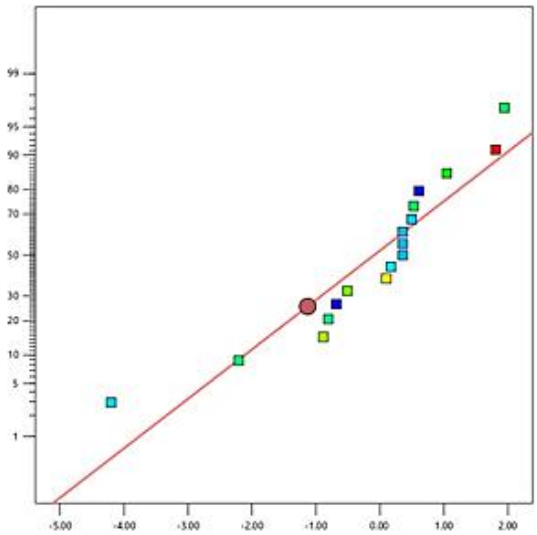


Fig. 7 - The distribution map of residual research

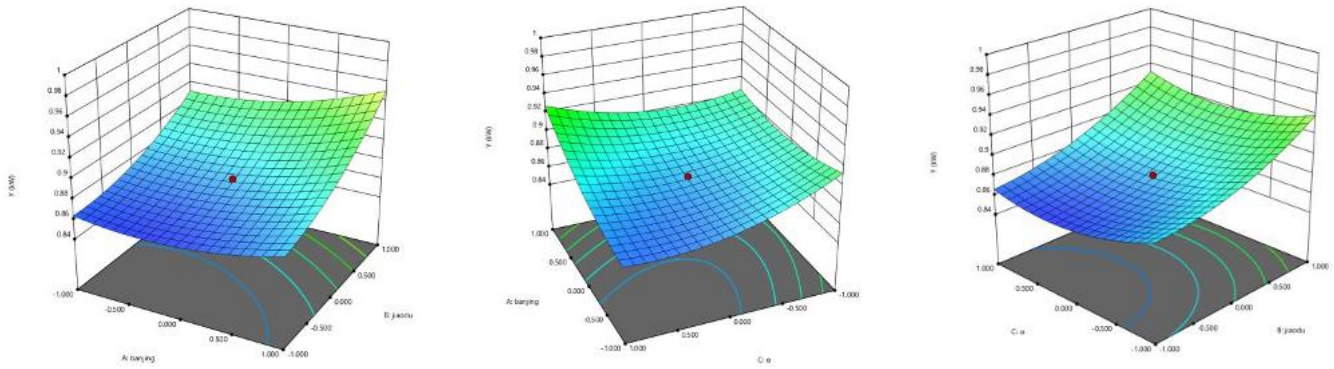
As shown in Fig. 7, the data points exhibit a linear trend and closely follow a normal distribution. This indicates a high degree of confidence in the predictive regression model and demonstrates strong agreement with the assumptions underlying the analysis of variance (ANOVA).

Optimisation analysis of tool structure parameters

The effect of tool structural parameters on furrowing power consumption.

Fig**. 8** illustrates the interaction effects of the disc-type furrowing tool's structural parameters on power consumption, as generated using Design-Expert 13. The figure indicates that an increase in the bending radius (X_1, factor A) leads to a gradual increase in furrowing power consumption, while an increase in the bending angle (X_2, factor B) also results in higher power consumption. In contrast, increasing the alpha angle (X_3, factor C) reduces furrowing power consumption.

Simulation analysis further revealed the underlying mechanisms of these effects. The bending radius strongly affects the tool–soil contact area and cutting characteristics. A smaller bending radius concentrates the cutting force and reduces the thickness of the soil layer being removed, but may increase soil reaction forces. Conversely, a larger bending radius allows deeper soil penetration but results in higher power consumption. The bending angle primarily influences the direction and efficiency of the shear force: smaller angles are more suitable for shallow cutting but may cause soil accumulation, whereas larger angles facilitate deeper cutting and improve the fragmentation of compacted soil layers. The alpha angle affects both the cutting depth and soil dispersion direction, with smaller angles promoting deeper penetration but increasing power requirements.



(a) (b) (c)

Fig. 8 - The interaction effect of tool structure parameters on power consumption

(a) The interaction between A (X1) and B (X2) on power consumption. (b) The interaction between C (X3) and B (X2) on power consumption. (c) The interaction between C (X3) and A (X1) on power consumption.

Optimisation of tool structure parameters

The objective of the optimisation was to minimise the furrowing power consumption by appropriately selecting the structural parameters of the disc-type furrowing tool. To achieve this, a regression model was established to quantify the relationship between the tool's structural parameters and power consumption, providing a quantitative foundation for optimisation.

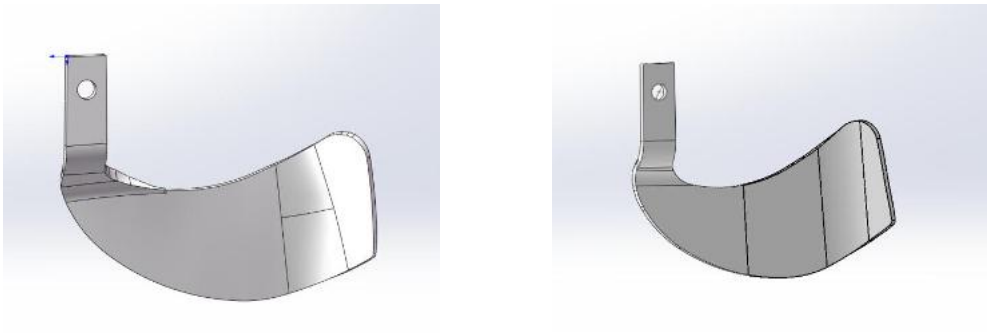
The following constraints were applied during the optimisation process:

$$\begin{cases} X_1 = [-1.353, 1.353] \\ X_2 = [-1.353, 1.353] \\ X_3 = [-1.353, 1.353] \end{cases} \quad (6)$$

The objective function was solved using MATLAB, yielding the optimal solution as follows:

$$\begin{cases} X_1 = 36.7939 \\ X_2 = 126.938 \\ X_3 = 43.6471 \end{cases} \quad (7)$$

The optimised parameters were applied to the regression equation, resulting in a furrowing power of 0.853 kW.



(a) (b)

Fig. 10 - Comparison of cutting tools before and after optimisation.

(a) Optimizing the front tool. (b) Optimised tool.

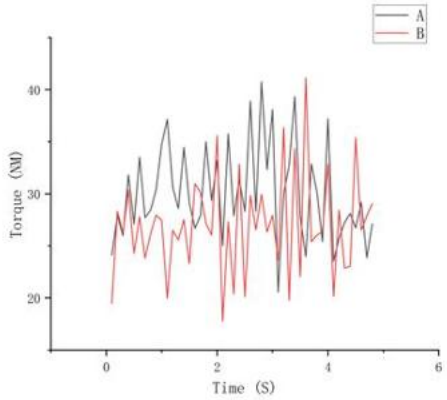


Fig. 11 - Comparison of furrowing torque before and after optimisation.

A Pre-optimisation torque. B Optimised furrowing torque

Simulation verification was performed to evaluate the furrowing power, which was determined to be 0.85 kW under the optimised tool parameters. The regression model predicted a furrowing power with a relative error of 0.6% compared to the simulation results. When compared with the pre-optimisation power of 0.94 kW, the optimised tool exhibited an 8.88% reduction in furrowing power consumption.

CONCLUSIONS

This study systematically optimised a disc-type furrowing tool using EDEM simulations combined with quadratic orthogonal regression. Results show that bending radius, bending angle, and alpha angle are key factors influencing furrowing power consumption. Response surface analysis revealed interactions: increasing bending radius or angle raises power, while increasing alpha angle reduces it. Tool optimisation reduced furrowing power by 8.88%.

Soil bin tests verified the simulation, showing a 13.8% relative error between experimental and simulated power. Discrepancies arose from soil property variations and experimental uncertainties. The error is acceptable for agricultural machinery, confirming the reliability of the EDEM simulation and structural optimisation approach.

Overall, this study offers a practical approach to improve open-furrow fertilisation in hilly orchards and a foundation for tool design and optimisation. Future work could refine soil parameters, improve model accuracy, and explore better tool configurations for more energy-efficient furrowing.

ACKNOWLEDGEMENT

This research was supported by the Yibin Science and Technology Program (No. 2025NY001), the Scientific and Technological Research Program of the Chongqing Municipal Education Commission (No. KJQN202503522), the Key Scientific and Technological Project of the Chongqing Municipal Education Commission (No. KJZD-K202201201), the Chongqing Natural Science Foundation (No. CSTB2025NSCQ-WZQLHJJMSX0017), and the Project of the Sichuan Innovation Team of the National Modern Agricultural Industry Technology System (No. Sccxtd-2026-20).

REFERENCES

[1] Aikins, K. A., Antille, D. L., Jensen, T. A., & Blackwell, J. (2019). Performance comparison of residue management units of no-tillage sowing systems. *Engineering in Agriculture, Environment and Food*, 12(2), 181-190. http://doi.org/10.1016/j.eaef.2018.12.006

[2] Aikins, K. A., Barr, J. B., Ucgul, M., Jensen, T. A., Antille, D. L., & Desbiolles, J. M. A. (2020). No-tillage furrow opener performance: a review of tool geometry, settings and interactions with soil and crop residue. *Soil Researchsoil Research*, 58(7), 603-621. http://doi.org/10.1071/SR19153

[3] Amantayev, M., Gaifullin, G., Kravchenko, R., Kushnir, V., & Nurushev, S. (2018). Investigation of the furrow formation by the disc tillage tools. *Bulgarian Journal of Agricultural Science*, 24(4)

[4] Barr, J., Desbiolles, J., Ucgul, M., & Fielke, J. M. (2020). Bentleg furrow opener performance analysis using the discrete element method. *Biosystems Engineering*, 189, 99-115.

[5] Chen, M., Guangfei, X., Yuanzhen, W., Yinping, Z., Peisong, D., & Huanxiao, P. (2024). Design and experiment analysis of the small maize harvester with attitude adjustment in the hilly and mountainous areas of China. *International Journal of Agricultural and Biological Engineering*, 17(1), 118-127.

[6] Chen, P., Jianghong, S., Jing, X., & Muhua, L. (2024). Design and Experiment of Hilly Orchard Vertical Spiral Ditching-fertilizing Machine. (丘陵果园立式螺旋开沟施肥机设计与试验) *Transactions of the Chinese Society for Agricultural Machinery*, 55(10), 223-233.

[7] Fang, H., Changying, J., Qingyi, Z., & Jun, G. (2016). Transactions of the Chinese Society of Agricultural Engineering [Force analysis of rotary blade based on distinct element method]. *Transactions of the Chinese Society of Agricultural Engineering*, 32(21), 54-59. http://doi.org/10.11975/j.issn.1002-6819.2016.21.007

[8] Fang, L., Xiaojun, G., Xian, J., Yuxiang, H., & Chongqin, Z. (2024). Design and Experiment of Archimedean Spiral-type Arc Double-toothed Disc Soil-covering Device for High-speed Precision Planter. (高速精量播种机阿基米德螺线型弧面双齿盘覆土装置设计与试验). *Transactions of the Chinese Society for Agricultural Machinery*, 6(2024,55), 91-100, 120. https://DOI.10.6041/j.issn.1000-1298.2024.06.009

[9] Hao, Z., Enlai, Z., Xun, L. I., Haoping, Y., Xiaochan, W., Shengyue, Q., Weixun, L. I., & Min, Z. (2023). Performance analysis of the soil-contacting parts for no-tillage planters and optimization of blade structure. *Transactions of the Chinese Society of Agricultural Engineering*, 39(2), 1-13. http://doi.org/10.11975/j.issn.1002-6819.202209196

[10] Jian, F., Jianxi, Z., & Aiping, Y. (2024). The current situation and trend of mechanized ditching and fertilization in hilly and mountainous orchards in China. *Agricultural Equipment & Vehicle Engineering*, 62(10), 30-35.

[11] Kang JianMing, K. J., Li ShuJun, L. S., Yang XueJun, Y. X., Liu LiJing, L. L., & Zhu RongGuang, Z. R. (2016). Virtual simulation and power test of rotary ditcher based on multi-body dynamics. Vol. 25 (4)

[12] Kim, Y. S., Siddique, M. A. A., Kim, W. S., Kim, Y. J., & Lim, R. G. (2021). DEM simulation for draft force prediction of moldboard plow according to the tillage depth in cohesive soil. *Computers and Electronics in Agriculture*, 189, 106368. https://DIO.10.1016/j.compag2021.106368

[13] Li, S., Xiaobing, C., Wei, C., Shiping, Z., Yunwu, L., Ling, Y., Shouyong, X., & Mingjin, Y. (2018). Soil-cutting simulation and parameter optimization of handheld tiller's rotary blade by Smoothed Particle Hydrodynamics modelling and Taguchi method. *Journal of Cleaner Production*, 179, 55-62. https://doi.org/10.1016/j.jclepro.2017.12.228

[14] Liu, M., Fangping, X., Dawei, L., & Xiushan, W. (2024). Analysis and experiment of the power of blade roller in reverse-rotary ditching machine based on the granular scale effect [Analysis and experiment of the power of blade roller in reverse-rotary ditching machine based on the granular scale effect]. *Transactions of the Chinese Society of Agricultural Engineering*, 40(7), 83-92. http://doi.org/10.11975/j.issn.1002-6819.202309134

[15] Liu, M., Yadong, L., Haofeng, K., Long, C., Jun, W., & Bailin, X. (2019). Research on the Cutting Performance of Ridger Based on Discrete Element Method. *Journal of Agricultural Mechanization Research*, 41(10), 129-134. http://doi.org/10.13427/j.cnki.njyi.2019.10.024

[16] Madhusudan, B. S., Kushwaha, H. L., Kumar, A., Parray, R. A., Swain, S. S., Chowdhury, M., Nag, R. H., Asha, K. R., Rathod, S. K., Kumar, P., Anand, R., Al-Ansari, N., Dewidar, A. Z., & Mattar, M. A. (2024). Critical assessment of furrow openers and operational parameters for optimum performance under conservation tillage. *Scientific Reports*, 14(1), 20928. http://doi.org/10.1038/s41598-024-70569-2

[17] Mi, J., Xie, H., & Niu, P. (2025). Design and optimisation of rotary tiller blade for orchards in hilly mountainous areas based on the discrete element method. *INMATEH - Agricultural Engineering*, 76(2) http://doi.org/https://doi.org/10.35633/inmateh-76-16

[18] Wang, P., Guo, L., Xianbing, W., Zhonghua, C., & Jian, C. (2015). The Research Situation and Development Ideas of Orchard Ditcher in China. *Agricultural Equipment & Vehicle Engineering*, 53(7), 30-33. http://doi.org/10.3969/j.issn.1673-3142.2015.07.007

[19] Yang, Y., Fielke, J., Ding, Q., & He, R. (2018). Field experimental study on optimal design of the rotary strip-till tools applied in rice-wheat rotation cropping system. (基于DEM-MBD的油茶林分层切抛式开沟刀组研制) *International Journal of Agricultural and Biological Engineering*, 11(2), 88-94. https://DIO.10.25165/j.ijabe.20181102.3347

[20] Yi, Z., Xiaohu, J., Mingliang, W., Zhihao, Z., Lewei, T., & Pengcheng, L. (2024). Development of the layered cut and throw ditching blade groups for oil tea forest based on DEM-MBD. *Transactions of the Chinese Society of Agricultural Engineering*, 40(08), 30-42. https://DOI.10.11975/j.issn.1002-6819.202311152

[21] Zhu, L., Sun, Y., Wang, H., Leng, Z., Yang, L., & Yang, M. (2020). Simulation of cutting soil of the mini-tiller rotary blade roller based on Finite Element Method. *J. Agric. Mech. Res*, 42, 39-43.

PARAMETER CALIBRATION OF THE BONDING MODEL FOR ASTRAGALUS ROOT BASED ON DISCRETE ELEMENTS

/

基于离散元的黄芪根 BONDING 模型参数标定

Jun YOU, Xin DU *), Qi-xin SUN, Shu-fa CHEN, Jing-yi MAO [1]
Jiangsu Ocean University, Lianyungang 222005/China
Tel: 0086-0518-85895322; E-mail: xindu @jou.edu.cn
Corresponding author: Xin Du
DOI: https://doi.org/10.35633/inmateh-79-37

Keywords: *Astragalus Membranaceus Root; Bonding Model; Placket-Burman; Steepest ascent; Box-Behnken; Discrete Element Method*

ABSTRACT

To address the issue of uneven fracture during the processing of Astragalus slices, this study first establishes a discrete element Bonding model for Astragalus roots, filling the gap in the calibration of its bonding parameters. Through uniaxial compression tests and multiple optimization experiments, the optimal parameters were determined, with simulation errors below 1.6% and validation errors for the fracture rate ≤ 12.7%, providing theoretical support for the development of processing equipment for Astragalus slices.

摘要

针对黄芪饮片加工断裂不均问题，本研究首次建立黄芪根离散元 Bonding 模型，填补其黏结参数标定空白。经单轴压缩试验与多组优化试验确定最优参数，仿真误差低于 1.6%，破碎率验证误差≤12.7%，可为黄芪饮片加工设备研发提供理论支撑。

INTRODUCTION

Astragalus membranaceus is a valuable traditional Chinese medicinal herb that functions in invigorating qi and enhancing body immunity. Its dried root has a long medicinal history and was incorporated into the medicine-food homologous catalogue in 2023, reflecting its significant medicinal value and industrial prospects (*Xi et al., 2023; Ji et al., 1998*). With the development of the modern Astragalus industry, promoting the mechanization and precision of processing operations such as root slicing and crushing has become essential. However, owing to the complex internal fibrous structure and unique mechanical properties of Astragalus root, uneven fractures and excessive powder production often occur during processing, which severely reduce the quality of prepared slices and production efficiency (*Duan, 2005*). The Discrete Element Method (DEM) coupled with the Bonding Model provides an effective means to simulate the bonding and fracture behaviors of granular materials and accurately reflect their mechanical responses, which has been widely applied in agricultural engineering (*Zhao et al., 2021; Zeng et al., 2021*). Nevertheless, existing DEM studies on Astragalus root lack accurate calibration of key Bonding Model parameters, including cohesion and elastic modulus, which limits the simulation accuracy of mechanical property evolution and fracture behaviors during processing. Therefore, calibrating these bonding parameters and establishing a high-precision DEM model is of great theoretical and practical importance for revealing tool-material interaction mechanisms, optimizing equipment design, and improving slice quality and active ingredient retention. Since DEM was proposed for soil mechanics by *Cundall et al.* (*1979*), it has been widely used in granular material operations such as mixing, conveying, filling and crushing (*Lu et al., 2015; Shen et al., 2016*). The Bonded Particle Model proposed by *Potyondy et al.* (*2004*) realizes fracture simulation via inter-particle bonding and has been widely adopted in agricultural research. Previous studies have completed bonding parameter calibration for various agricultural materials (e.g., coated fertilizer, garlic cloves, crop stems, corn ears) via mechanical tests such as uniaxial compression (*Du et al., 2022; Li et al., 2025; Xu et al., 2024; Gao et al., 2024; Xie et al., 2023; Li et al., 2025*). Relevant calibrations have also been conducted for banana stalks, walnuts and cotton seeds (*Zhang et al., 2023; Zhou et al., 2023; Hu et al., 2022*), and the model has been applied to analyze fracture mechanisms in Cyperus esculentus harvesting (*Zhu et al., 2022*).

[1] *Jun You, MA. Eng Stud.; Xin Du*, Lecturer Ph.D. Eng; Qixin Sun, Prof. Ph.D. Eng; Shufa Chen, Prof. Ph.D. Eng; Jingyi Mao, B.S Stud.*

These studies have promoted the application of the Bonding Model and parameter calibration in agricultural material processing. Building on existing research (*Du et al., 2022; Li et al., 2023; Xu et al., 2024; Gao et al., 2024; Xie et al., 2023; Li et al., 2025*), this study focuses on Astragalus root. Using the ultimate crushing load and displacement obtained from uniaxial compression tests, the Bonding Model parameters are optimized by combining the Plackett-Burman test, the Steepest Ascent test and the Box-Behnken test. The reliability of the calibrated parameters is verified through comparative tests between physical experiments and simulations.

This study aims to provide accurate basic parameters for DEM simulation of Astragalus processing equipment and support the intelligent development of related machinery. It fills the gap in DEM parameter calibration for Astragalus root and provides a new reference for mechanical simulation of granular traditional Chinese medicinal materials.

MATERIALS AND METHODS

Bonding Model

In discrete element numerical simulations, the bond-based contact model, designed by *Potyondy et al.* (*2004*), is a core method for studying material fracture. This model abstracts the interaction between particles as virtual connecting bonds, constructing a mechanical transmission network to simulate the fracture process. Although differing in theory and scale from the finite element method, it complements FEM in multi-physics field coupling. Bond elements possess multi-dimensional mechanical responses, undergoing tension, compression, torsion, and other deformations under load, following Hooke's law. The force-deformation relationship can be quantified using elastic moduli. When stress or torque exceeds a critical threshold, the bond breaks, simulating material crack propagation. The bonding contact model assumes that the bond between two particles is a virtual flat plate or cylinder, as illustrated in Figure 1.

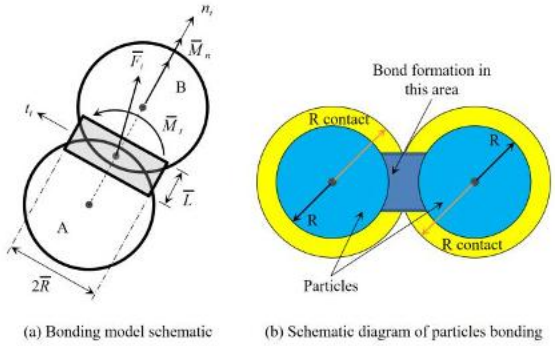


Fig. 1 - Schematic diagram of Bonding Model principle and particle bonding

During relative displacement between two particles, the plate or cylindrical structure is subjected to mechanical actions such as tension, bending, and shear. The force and moment increments on the bond are calculated as follows:

$$\begin{cases} \delta F_n = -v_n S_n A \delta t \\ \delta F_t = -v_t S_t A \delta t \\ \delta M_n = -\omega_n S_t J \delta t \\ \delta M_t = -\omega_t S_n \dfrac{J}{2} \delta t \end{cases} \quad (1)$$

$$\begin{cases} A = \pi R_B^2 \\ J = \dfrac{1}{2} \pi R_B^4 \end{cases} \quad (2)$$

where:

δF_n is the normal force, N; δF_t is the tangential force, N; v_n is the normal velocity, m/s; v_t is the tangential velocity, m/s; S_n is the normal stiffness, N/m; S_t is the tangential stiffness, N/m; δ_t is the simulation time step, s; A is the contact area between particles, m²; δM_n is the normal moment increment, N·m; δM_t is the tangential moment increment, N·m; ω_n is the normal angular velocity, rad/s; ω_t is the tangential angular velocity, rad/s; J is the particle moment of inertia, mm⁴; R_B is the bonded disk radius, mm.

Discrete Element Modeling of Astragalus Root Segment Particles

Astragalus roots from Dingxi, Gansu (density 0.912g/cm³) were cut into 37.5 mm-long uniform segments for geometric modeling. The Bonded Particle Method (BPM) (*Su et al., 2021*) was adopted to establish the discrete element model (DEM) for Astragalus root fracture analysis, where equal-diameter spherical particles are bonded to represent the root structure. A cylindrical bonding model was constructed, and 0.5 mm-radius spherical particles were finally selected for parameter calibration after comprehensive comparison of different particle sizes.

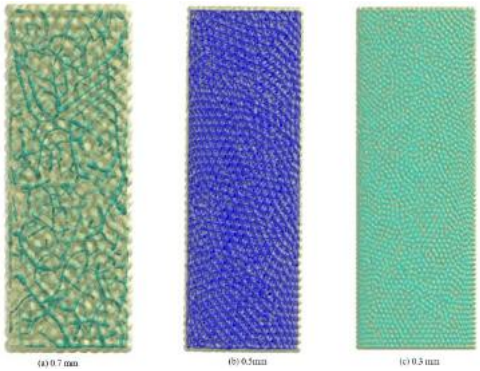


Fig. 2 - Filling diagrams using spherical particles of different diameters

Uniaxial Compression Test

Physical Experiment

Astragalus root segments with a diameter of 14 mm and length of 37.5 mm were selected. Uniaxial compression tests were performed on the segments using a universal testing machine. Loading was applied at a constant speed of 0.1 mm/s until specimen failure occurred. The loading process of a specimen during the uniaxial compression test is shown in Figure 3. The test was repeated 8 times, and the average displacement-load curve for the Astragalus segments is presented in Figure 4.

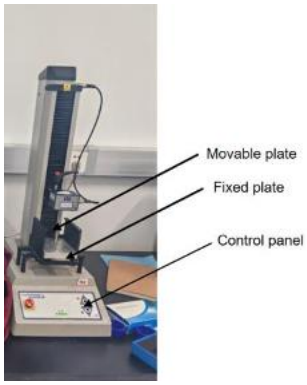


Fig. 3 - Universal testing machine

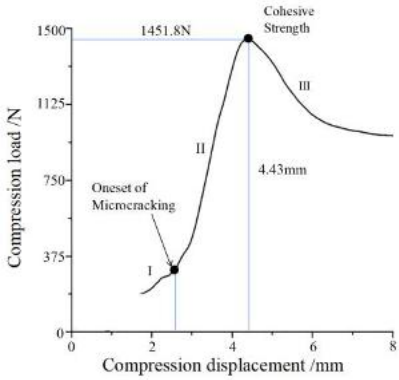


Fig. 4 - Displacement-load curve

Simulation Experiment

A uniaxial compression simulation model consistent with physical tests was established in EDEM 2022 (Figure 5). Material parameters are listed in Table 1. Simulation settings: total time 4 s, time step 8.5×10^{-6} s, data interval 0.01 s, grid size 3 times the radius of the smallest spherical particle.

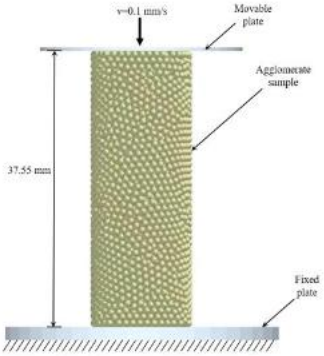


Fig. 5 - Uniaxial compression experiment simulation setup

Table 1

Physical property parameters of materials

Item	Parameter	Value
Astragalus	Poisson's Ratio	0.25
	Density (kg/m³)	912
	Shear Modulus (Pa)	2.17×10^{6}
Steel	Poisson's Ratio	0.3
	Density (kg/m³)	7850
	Shear Modulus (Pa)	8×10^{9}
Astragalus-Steel	Coefficient of Restitution	0.45
	Static Friction Coefficient	0.22
	Rolling Friction Coefficient	0.10
Astragalus-Astragalus	Coefficient of Restitution	0.51
	Static Friction Coefficient	0.43
	Rolling Friction Coefficient	0.15

Plackett-Burman Experimental Design

The Plackett-Burman design assesses factor significance by comparing two-level responses for each factor, taking ultimate crushing load (F_R) and displacement (L) as optimization objectives. Five factors (normal stiffness A, tangential stiffness B, critical normal stress C, critical tangential stress D, bonding radius E) were set at two levels. An 11-run design with 6 dummy terms for error analysis was used, and detailed factor levels are given in Table 2.

Table 2

Plackett-Burman experimental factor levels

No.	A	B	C	D	E
1	1.0×10^{7}	8.0×10^{6}	6.1×10^{6}	4.7×10^{6}	0.55
2	1.1×10^{7}	9.0×10^{6}	7.3×10^{6}	5.8×10^{6}	0.60

The simulation experimental design results are shown in Table 3.

Table 3

Plackett-Burman experimental design

No.	A	B	C	D	E	F_R/(N)	L/(mm)
1	1.1×10^{7}	9.0×10^{6}	6.1×10^{6}	5.8×10^{6}	0.60	1511	4.85
2	1.0×10^{7}	9.0×10^{6}	7.3×10^{6}	4.7×10^{6}	0.60	1484	5.05
3	1.1×10^{7}	8.0×10^{6}	7.3×10^{6}	5.8×10^{6}	0.55	1252	4.41
4	1.0×10^{7}	9.0×10^{6}	6.1×10^{6}	5.8×10^{6}	0.60	1480	5.15
5	1.0×10^{7}	8.0×10^{6}	7.3×10^{6}	4.7×10^{6}	0.60	1398	4.65
6	1.0×10^{7}	8.0×10^{6}	6.1×10^{6}	5.8×10^{6}	0.55	1207	4.49
7	1.1×10^{7}	8.0×10^{6}	6.1×10^{6}	4.7×10^{6}	0.60	1421	4.15
8	1.1×10^{7}	9.0×10^{6}	6.1×10^{6}	4.7×10^{6}	0.55	1315	3.95
9	1.1×10^{7}	9.0×10^{6}	7.3×10^{6}	4.7×10^{6}	0.55	1311	4.25
10	1.0×10^{7}	9.0×10^{6}	7.3×10^{6}	5.8×10^{6}	0.55	1278	4.72
11	1.1×10^{7}	8.0×10^{6}	7.3×10^{6}	5.8×10^{6}	0.60	1419	4.39
12	1.0×10^{7}	8.0×10^{6}	6.1×10^{6}	4.7×10^{6}	0.55	1207	4.45

Steepest Ascent Experimental Design

The Plackett-Burman results indicated that factor C had no significant effect on the experimental outcomes; therefore, C was fixed at 6.7×10^{6} Pa. A steepest ascent experiment was conducted to identify parameter combinations closer to the true values, with the experimental plan and results shown in Table 4.

Table 4

Steepest ascent experimental design

No.	A	B	D	E	F_R/(N)	L/(mm)
1	1.05×10^{7}	8.50×10^{6}	5.25×10^{6}	0.575	1357.9	4.20
2	9.65×10^{6}	8.63×10^{6}	5.80×10^{6}	0.585	1372.2	4.23
3	8.80×10^{6}	8.76×10^{6}	6.35×10^{6}	0.595	1401.1	4.28
4	7.95×10^{6}	8.89×10^{6}	6.90×10^{6}	0.605	1409.5	4.31
5	7.10×10^{6}	9.02×10^{6}	7.45×10^{6}	0.615	1430.9	4.35

No.	A	B	D	E	F_R/(N)	L/(mm)
6	6.25×10^6	9.15×10^6	8.00×10^6	0.625	1437.3	4.39
7	5.40×10^6	9.28×10^6	8.55×10^6	0.635	1458.1	4.41
8	4.55×10^6	9.41×10^6	9.10×10^6	0.645	1470.2	4.50

Box-Behnken Experimental Design

Design-Expert software was utilized to construct a Box-Behnken simulation experimental system for the significant contact parameters. The 7th level from the steepest ascent test was set as the central reference point (coded value 0). The 6th and 8th levels were defined as the low level (coded value -1) and high level (coded value +1), respectively, as shown in Table 5.

Table 5

Coding table for significant factor levels

Level	A	B	D	E
-1	6.25×10^6	9.15×10^6	8.00×10^6	0.625
0	5.40×10^6	9.28×10^6	8.55×10^6	0.635
+1	4.55×10^6	9.41×10^6	9.10×10^6	0.645

The experimental plan and results are shown in Table 6.

Table 6

Box-Behnken experimental design

No.	A	B	D	E	F_R/(N)	L/(mm)
1	4.55×10^6	9.15×10^6	8.55×10^6	0.635	1398.4	3.90
2	6.25×10^6	9.15×10^6	8.55×10^6	0.635	1449.7	4.34
3	4.55×10^6	9.41×10^6	8.55×10^6	0.635	1439.3	3.51
4	6.25×10^6	9.41×10^6	8.55×10^6	0.635	1501.0	5.25
5	5.40×10^6	9.28×10^6	8.00×10^6	0.625	1416.0	3.85
6	5.40×10^6	9.28×10^6	9.10×10^6	0.625	1415.6	4.05
7	5.40×10^6	9.28×10^6	8.00×10^6	0.645	1484.4	4.68
8	5.40×10^6	9.28×10^6	9.10×10^6	0.645	1485.0	4.78
9	4.55×10^6	9.28×10^6	8.55×10^6	0.625	1351.9	3.21
10	6.25×10^6	9.28×10^6	8.55×10^6	0.625	1453.3	4.35
11	4.55×10^6	9.28×10^6	8.55×10^6	0.645	1459.2	4.44
12	6.25×10^6	9.28×10^6	8.55×10^6	0.645	1522.7	5.08
13	5.40×10^6	9.15×10^6	8.00×10^6	0.635	1444.6	4.24
14	5.40×10^6	9.41×10^6	8.00×10^6	0.635	1475.0	4.36
15	5.40×10^6	9.15×10^6	9.10×10^6	0.635	1455.0	4.37
16	5.40×10^6	9.41×10^6	9.10×10^6	0.635	1474.9	4.35
17	4.55×10^6	9.28×10^6	8.00×10^6	0.635	1420.0	3.54
18	6.25×10^6	9.28×10^6	8.00×10^6	0.635	1501.7	4.57
19	4.55×10^6	9.28×10^6	9.10×10^6	0.635	1418.4	3.51
20	6.25×10^6	9.28×10^6	9.10×10^6	0.635	1502.0	4.56
21	5.40×10^6	9.15×10^6	8.55×10^6	0.625	1414.4	3.65
22	5.40×10^6	9.41×10^6	8.55×10^6	0.625	1430.3	3.95
23	5.40×10^6	9.15×10^6	8.55×10^6	0.645	1492.9	4.45
24	5.40×10^6	9.41×10^6	8.55×10^6	0.645	1510.6	5.40
25	5.40×10^6	9.28×10^6	8.55×10^6	0.635	1462.0	4.25
26	5.40×10^6	9.28×10^6	8.55×10^6	0.635	1452.0	4.45
27	5.40×10^6	9.28×10^6	8.55×10^6	0.635	1471.0	4.37
28	5.40×10^6	9.28×10^6	8.55×10^6	0.635	1447.0	4.51
29	5.40×10^6	9.28×10^6	8.55×10^6	0.635	1458.0	4.65

RESULTS AND ANALYSIS

Uniaxial Compression Test Results

As shown in Figure 4, the force-displacement curve of Astragalus root segments consists of three stages. Stage I involves local damage with rapid initial force growth followed by a slow increase, while the main body remains intact. Stage II is the main failure process: the load exceeds the bearing capacity, force peaks at the failure point. Stage III shows force decreasing with displacement, presenting oblique shear fracture.

The average ultimate crushing load of eight segments (14 mm diameter, 37.5 mm length) is 1451.8 N, with a corresponding ultimate displacement of 4.43 mm.

Plackett-Burman Test Significance Analysis

Design-Expert software was used to conduct ANOVA and t-tests (Table 7, Figure 6). For ultimate crushing load F_R, the influencing order was E > B > A > D > C; E, B and A posed significant effects (P<0.05) with all positive effect values, as confirmed by the Pareto chart. For ultimate crushing displacement L, the order was A > E > D > B > C; A, E and D showed significant effects (P<0.05), with positive effects for E, D, B, C and negative effect for A, as confirmed by the Pareto chart.

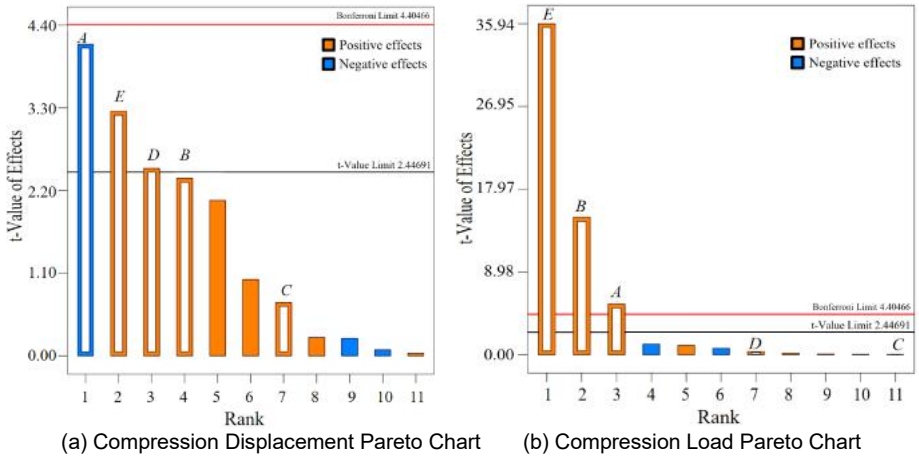
Table 7

Plackett-Burman test significance analysis

F_R					
Source of Variation	Sum of Squares	df	Mean Square	F-value	P-value
Model	1.302×10^5	5	26047.02	308.69	< 0.0001**
A	2552.08	1	2552.08	30.27	0.0015**
B	18802.08	1	18802.08	223.02	< 0.0001**
C	0.0833	1	0.0833	0.0010	0.9759
D	10.08	1	10.08	0.1196	0.7413
E	1.089×10^5	1	1.089×10^5	1291.38	< 0.0001**
Residual	505.83	6	84.31		
Total	1.307×10^5	11			

L					
Source of Variation	Sum of Squares	df	Mean Square	F-value	P-value
Model	1.22	5	0.2448	8.04	0.0123*
A	0.5250	1	0.5250	17.23	0.0060**
B	0.1704	1	0.1704	5.59	0.0559
C	0.0154	1	0.0154	0.5058	0.5037
D	0.1900	1	0.1900	6.24	0.0467*
E	0.3234	1	0.3234	10.62	0.0173*
Residual	0.1828	6	0.0305		
Total	1.41	11			

Note: * indicates significant difference (P<0.05), ** indicates highly significant difference (P<0.01). The same applies below.



(a) Compression Displacement Pareto Chart (b) Compression Load Pareto Chart

Fig. 6 - Pareto charts

Steepest Ascent Test Analysis

Combining the data in Table 4, it can be observed that the error between the simulated ultimate crushing load/displacement and the real values first decreased and then increased during the steepest ascent experiment. The 7th test group exhibited the highest agreement between the simulated F_R and L values and the real values.

Box-Behnken Test Significance Analysis and Parameter Optimization

Design-Expert 13 software was used to analyze the experimental data in Table 6. The ANOVA results are presented in Table 8. From Table 8, it can be seen that the quadratic regression models for both F_R and L were highly significant (P < 0.0001), and the lack-of-fit terms were not significant (P > 0.05), indicating high model accuracy. Factors A, B, and E were significant for both responses. For F_R, the order of influence was E > A > B. For L, the order of influence was also E > A > B.

The regression equations relating the factors to the ultimate crushing load F_R and ultimate crushing displacement L are:

$$\begin{cases} F_R = 1458 + 36.93A + 14.67B + 0.7667D + 39.44E + 2.6AB + 0.475AD - 9.47AE \\ \quad -2.63BD + 0.45BE + 0.25DE - 6.65A^2 + 1.92B^2 + 2.73D^2 - 4.31E^2 \\ L = 4.45 + 0.5033A + 0.1558B + 0.0317D + 0.4808E + 0.325AB + 0.005AD - 0.125AE \\ \quad -0.035BD + 0.1625BE - 0.025DE - 0.2067A^2 - 0.018B^2 - 0.1318D^2 - 0.003E^2 \end{cases} \quad (3)$$

Table 8

Box-Behnken test significance analysis

F_R					
Source of Variation	Sum of Squares	df	Mean Square	F-value	P-value
Model	38595.97	14	2756.85	18.41	< 0.0001**
A-A	16368.85	1	16368.85	109.29	< 0.0001**
B-B	2584.27	1	2584.27	17.26	0.0010*
D-D	7.05	1	7.05	0.0471	0.8313
E-E	18667.74	1	18667.74	124.64	< 0.0001**
AB	27.04	1	27.04	0.1805	0.6774
AD	0.9025	1	0.9025	0.0060	0.9392
AE	359.10	1	359.10	2.40	0.1438
BD	27.56	1	27.56	0.1840	0.6745
BE	0.8100	1	0.8100	0.0054	0.9424
DE	0.2500	1	0.2500	0.0017	0.9680
A²	286.49	1	286.49	1.91	0.1883
B²	23.83	1	23.83	0.1591	0.6960
D²	48.31	1	48.31	0.3226	0.5791
E²	120.40	1	120.40	0.8039	0.3851
Residual	2096.76	14	149.77		
Lack of Fit	1754.76	10	175.48	2.05	0.2547
Total	40692.73	28			

L					
Source of Variation	Sum of Squares	df	Mean Square	F-value	P-value
Model	7.07	14	0.5053	17.58	< 0.0001**
A-A	3.04	1	3.04	105.78	< 0.0001**
B-B	0.2914	1	0.2914	10.14	0.0066*
D-D	0.0120	1	0.0120	0.4187	0.5281
E-E	2.77	1	2.77	96.53	< 0.0001**
AB	0.4225	1	0.4225	14.70	0.0018*
AD	0.0001	1	0.0001	0.0035	0.9538
AE	0.0625	1	0.0625	2.17	0.1624
BD	0.0049	1	0.0049	0.1705	0.6859
BE	0.1056	1	0.1056	3.68	0.0759
DE	0.0025	1	0.0025	0.0870	0.7724
A²	0.2773	1	0.2773	9.65	0.0077*
B²	0.0021	1	0.0021	0.0731	0.7908
D²	0.1126	1	0.1126	3.92	0.0678
E²	0.0001	1	0.0001	0.0020	0.9647
Residual	0.4024	14	0.0287		
Lack of Fit	0.3124	10	0.0312	1.39	0.4022
Total	7.48	28			

To precisely determine the optimal parameter combination for each factor, the constraint range needed to be further narrowed. The target values for F_R and L were known to be 1451.8 N and 4.43 mm, respectively. Combining the data from Table 6, experimental runs 2, 11, 26, and 28 exhibited F_R and L values closest to the actual values. Based on the ANOVA results, since factor D had the lowest influence on both F_R and L, it was fixed at its central level (8.55×10^{6}Pa). The constraint ranges were set as follows:

$$\begin{cases} F = 1451.8\text{N} \\ L = 4.43\text{mm} \\ 4.55\times10^6\,\text{N/m}^3 \le A \le 6.25\times10^6\,\text{N/m}^3 \\ 9.15\times10^6\,\text{N/m}^3 \le B \le 9.41\times10^6\,\text{N/m}^3 \\ D = 8.55\times10^6\,Pa \\ 0.635 \le E \le 0.645 \end{cases} \quad (4)$$

Optimization solving was performed using Design-Expert 13. The optimal solution yielded values of A=5.3603×10^6 N/m³, B=9.23842×10^6 N/m³, D=8.55×10^6 Pa, E=0.635 mm. At this point, the predicted values for F_R and L were 1451.8 N and 4.38 mm, respectively. A simulation verification run using this parameter combination resulted in simulated F_R and L values of 1451.2 N and 4.31 mm, respectively. The relative errors compared to the real values were 0.04% and 1.6%, respectively.

As shown in Figure 7, the simulation results for load and displacement are generally consistent with the experimental data. The relative errors of the simulated values compared to the actual measurements are 0.04% and 1.6%, respectively. These findings suggest that the aforementioned parameters exhibit a high degree of reliability, thereby validating the applicability of the discrete element method for simulating the mechanical behavior of Astragalus roots.

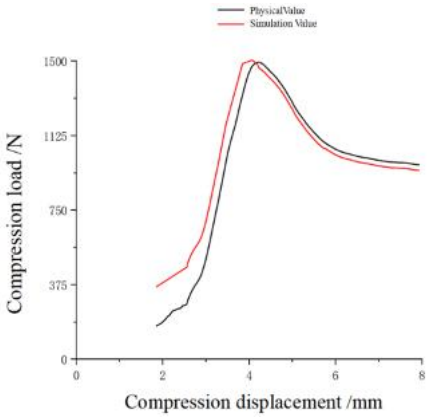


Fig. 7 - Deviation diagram of simulation value and test value

Verification test of the Bonding model breakage of Astragalus Root Granules

Experimental purpose

To verify the reliability of the parameter combination for the Astragalus root granule bonding model, this study simulated its actual crushing process in a hammer mill (including hammer impact, cavity wall extrusion and toothed ring shearing). The bond state and velocity distribution data were obtained to validate the model's characterization ability for Astragalus root crushing mechanics. The results provide theoretical support for the rotational speed optimization and structural improvement of traditional Chinese medicine hammer mills.

Test Equipment and Model Construction

Test equipment and materials

A small hammer-type pulverizer for Chinese medicinal materials (Figure 8) was used in the experiment. Its core parameters include a crushing chamber inner diameter of 165 mm and a screen mesh diameter of 0.5 mm. During operation, the high-speed rotating hammers impact and shear the material with toothed rings, and the screen controls the particle size. The experimental material was Astragalus roots from Dingxi, Gansu, cut into standard segments of 37.5 mm in length and 14 mm in diameter. Five intact and uniform segments were selected for the test.

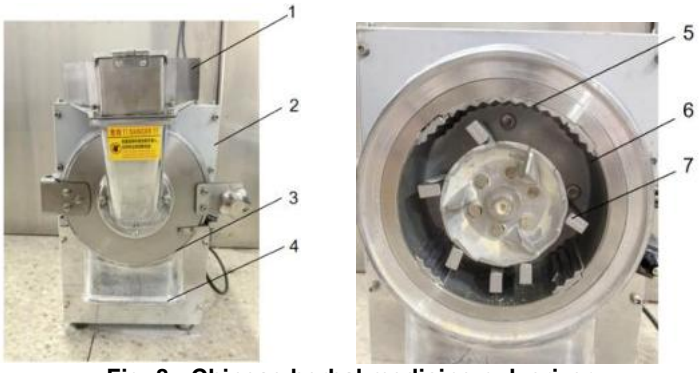


Fig. 8 - Chinese herbal medicine pulverizer

1. feed inlet; 2. electrical control box; 3. crushing chamber; 4. Discharge outlet; 5. toothed ring; 6. screen; 7. hammers

3D model and simulation Settings

The three-dimensional model of the inner wall of the crusher was constructed using SolidWorks 2024 (as shown in Figure 9a), including the crushing chamber, hammer pieces, toothed ring and other structures. The model was exported in .STL format and then imported into the Discrete element software EDEM 2022.

The virtual simulation test was conducted at the same rotor speed as the real test. The calculation formula for the particle breakage rate η of Astragalus root under each condition is:

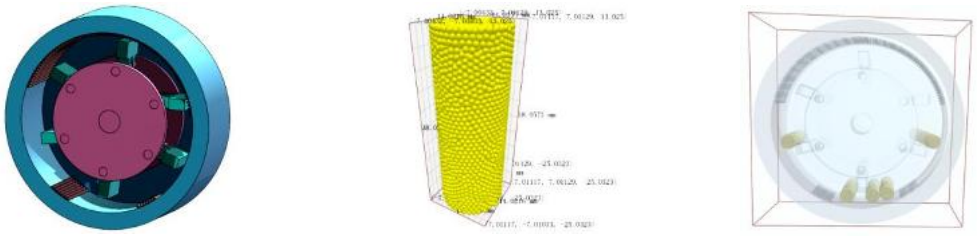
$$\eta = \frac{m_1}{m_0} \times 100\% \tag{5}$$

In the formula:

m_1 represents the mass of the powder, (g)'

m_0-total mass of Astragalus membranaceus roots in the test, 20.5 g

A total of 7,200 1 mm-diameter Astragalus granules were bonded to construct the Astragalus root granule model using the bonding model (Figure 9b). According to the material parameters in Table 1, the Poisson's ratio, density and shear modulus of Astragalus granules and steel crushing components were defined, and the collision recovery coefficient, static and rolling friction coefficients between Astragalus and steel, as well as those between Astragalus granules were set. The crusher geometry and Astragalus root granule model were imported into the discrete element software (Figure 9c). The simulation was run for 30 s with a time step of 7.0×10^{-6} s and data saved every 0.01 s to reproduce the actual crushing process of Astragalus root.



(a) Three-dimensional model of the inner wall; (b) Astragalus Root Granules Bonding model; (c) Simulation diagram

Fig. 9 - Schematic diagram of simulation modeling for crushing Astragalus root

Test method

Real crushing experiment

A real crushing test of Astragalus roots was conducted using the traditional Chinese medicine hammer crusher shown in Figure 10. Before the test, the equipment was pre-started, and Astragalus roots were fed slowly after the rotor speed stabilized. In the crushing chamber, roots were crushed by hammer impact, chamber wall compression and inter-particle collision, with crushed products discharged from the lower outlet. During the test, samples from the outlet and chamber inner wall were collected every 5 seconds. Morphology photos were taken at 5, 10, 15, 20, 25 and 30 seconds (right side of Figure 10), and the test was terminated at 30 seconds.

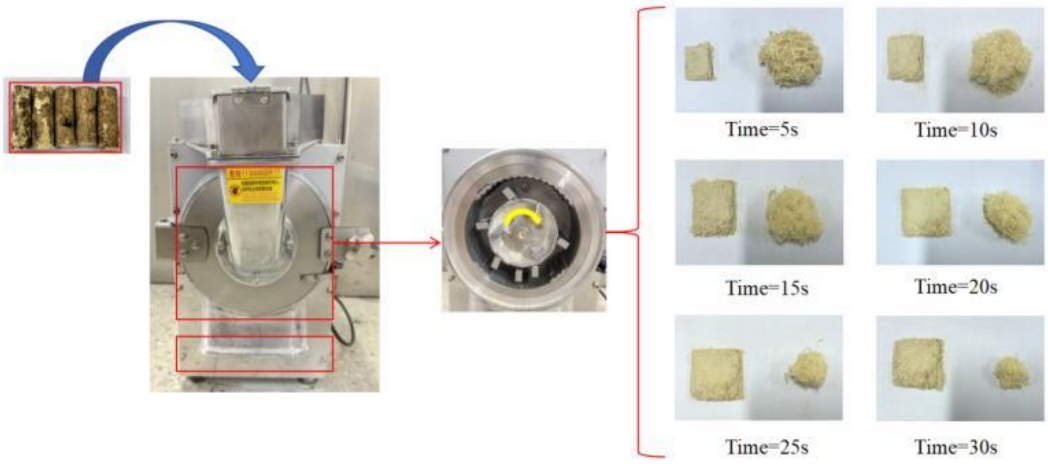


Fig. 10 - Bench test

Simulation crushing test

In EDEM 2022, rotor speed was set to 2840 r/min to match physical conditions. The discrete element model of Astragalus root particles, constructed based on the Bonding model, was imported to simulate the crushing process. Velocity field, vector distribution, and bond status evolution were recorded at 0, 5, 10, 15, 20, 25, and 30 s, with results shown in Figure 11.

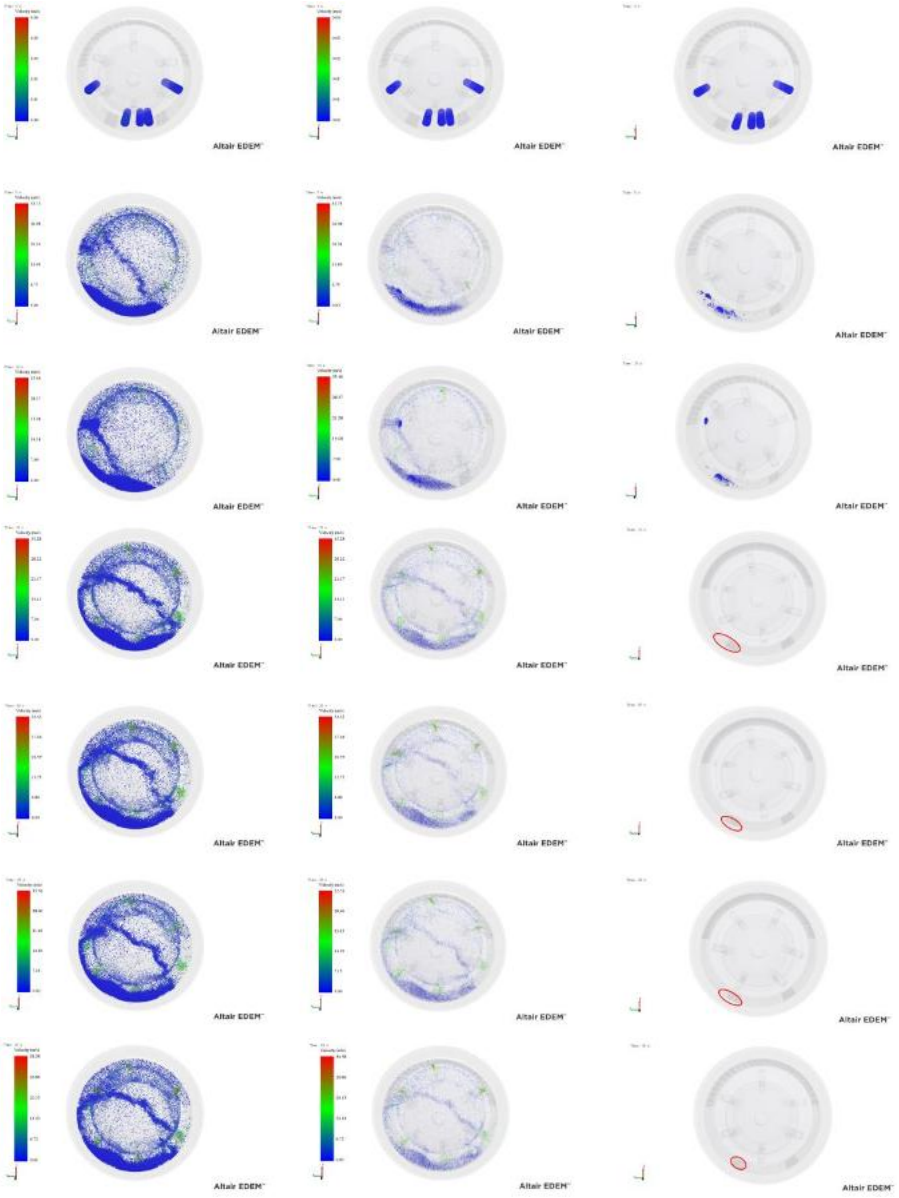


Fig. 11 - Simulation process of crushing Astragalus Root Granules

Test results

At a crusher speed of 2840 r/min, the error between the simulated and actual crushing rates of Astragalus root granules is 6.3%–12.7% as shown in Figure 12, which verifies the high accuracy of the calibrated bonding model parameters.

The crushing simulation presents three successive stages: initially, particles are agglomerated and static with complete bonds; subsequently, particles disperse and refine with increased velocity differences and large-scale bond breakage; finally, particles become fine and uniform, accompanied by a stable velocity field and nearly full bond dissociation.

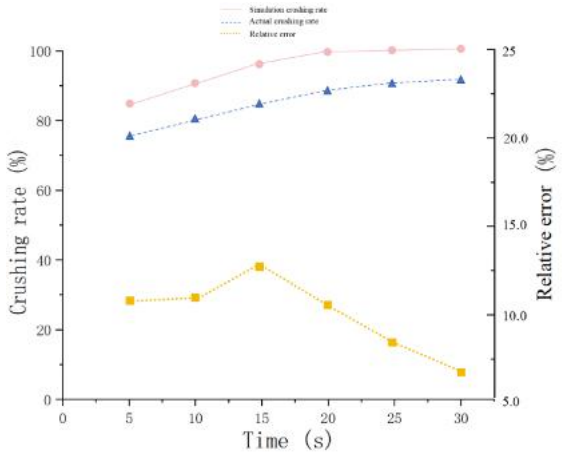


Fig. 12 - The breakage rate at different times

CONCLUSIONS

Uniaxial compression tests of Astragalus root segments were carried out to obtain its mechanical properties, with an ultimate crushing load of 1451.8 N and an ultimate crushing displacement of 4.43 mm. Significant factors were screened via the Plackett-Burman design, the parameter range was narrowed by the steepest ascent test, and the optimal Bonding Model parameters were determined by Box-Behnken optimization: normal stiffness per unit area 5.3603×10^{6} N/m³, shear stiffness per unit area 9.23842×10^{6} N/m³, critical shear stress 8.55×10^{6}Pa, bonded disk radius 0.635 mm. Uniaxial compression simulation verification shows that the relative errors of ultimate crushing load and displacement are only 0.04% and 1.6%, respectively. The parameters were applied to Astragalus root crushing simulation, accurately characterizing the evolution of velocity field, vector distribution and bond state, with a crushing rate error of 6.3%–12.7%, verifying their reliability. This study provides accurate parameter support for DEM simulation and intelligent design of Astragalus processing equipment, and offers a new reference for mechanical simulation of granular Chinese medicinal materials.

ACKNOWLEDGEMENT

This study was supported by Natural Science Foundation of Jiangsu Province, China (BK20241058).

REFERENCES

[1] Cundall, P.A., Strack, O.D.L. (1979). A Discrete Numerical Model for Granular Assemblies. *Géotechnique*, 29(1), 47–65. https://doi.org/10.1680/geot.1979.29.1.47.

[2] Duan, Q.M. (2005). *Study on Biological Characteristics of Astragalus membranaceus*. [Master's Thesis], Northwest A&F University, Yangling, China.

[3] Du, X., Liu, C.L., Jiang, M., Yuan, H., Dai, L., Li, F.L. (2022). Calibration of Bonding Model Parameters for Coated Fertilizers Based on Discrete Element Method. *Transactions of the Chinese Society for Agricultural Machinery*, 53, 141-149. http://doi.org/10.6041/j.issn.1000-1298.2022.07.014.

[4] Gao, Q., Cheng, L., Wang, R., Chen, M., Zhao, W., Fu, J., Wang, Z. (2024). Discrete Element Model Building and Optimization of Tomato Stalks at Harvest. *Agriculture*, 14, 531. http://doi.org/10.3390/agriculture14040531.

[5] Hu, M., Xia, J., Zhou, Y., Luo, C., Zhou, M., Liu, Z. (2022). Measurement and Calibration of the Discrete Element Parameters of Coated Delinted Cotton Seeds. *Agriculture*, 12, 286. http://doi.org/10.3390/agriculture12020286.

[6] Ji, X.M., Wang, W.Q., Liu, L. (1998). Brief Summary on Efficacy Research of Astragalus membranaceus. *Journal of Shandong University of Traditional Chinese Medicine*, 22(3), 65-67. https://doi.org/10.16294/j.cnki.1007-659x.1998.03.030.

[7] Li, C., Liu, Z., Geng, L., Xu, T., Feng, W., Liu, M., Qiao, D., Wang, Y., Wang, J. (2025). The Establishment of a High-Moisture Corn Ear Model Based on the Discrete Element Method and the Calibration of Bonding Parameters. *Agriculture*, 15, 752. http://doi.org/10.3390/agriculture15070752.

[8] Li, H., Meng, Y.B., Qi, X.D, Wang, Y.J., Li, Y.Q., Li, M.Y. (2025). Discrete Element Modeling Method and Parameter Calibration for Garlic Cloves Based on Bonding V2 Model. *Transactions of the Chinese Society for Agricultural Machinery*, 54, 1-11. http://doi.org/10.6041/j.issn.1000-1298.2025.07.013.

[9] Lu, G., Third, J.R., Müller, C.R. (2015). Discrete Element Models for Non-Spherical Particle Systems: From Theoretical Developments to Applications. *Chemical Engineering Science*, 127, 425-465. http://dx.doi.org/10.1016/j.ces.2014.11.050.

[10] Mu, X., Li, H., Wang, Z., Wang, Q., Geng, D., Zhu, J. (2023). Comparison of Crushing Effect of Differently Shaped Crushing Rollers on Whole-Plant Silage Maize. *Agriculture*, 13, 1276. http://doi.org/10.3390/agriculture13071276.

[11] Potyondy, D.O., Cundall, P.A. (2004). A Bonded-Particle Model for Rock. *International Journal of Rock Mechanics and Mining Sciences*, 41, 1329-1364. http://doi.org/10.1016/j.ijrmms.2004.09.011.

[12] Shen, Z., Jiang, M., Thornton, C. (2016). DEM Simulation of Bonded Granular Material. Part I: Contact Model and Application to Cemented Sand. *Computers and Geotechnics*, 75, 192-209. http://dx.doi.org/10.1016/j.compgeo.2016.02.007.

[13] Su, Y., Xu, Y., Cui, T., Gao, X., Xia, G., Li, Y., Qiao, M. (2021). Determination and Interpretation of Bonded-Particle Model Parameters for Simulation of Maize Kernels. *Biosystems Engineering*, 210, 193-205. http://doi.org/10.1016/j.biosystemseng.2021.08.022.

[14] Xi, J.Y., Su, Y.J., Zhao, K.P., Feng, J.L., Yang, F.D. (2023). Research Progress on the Dual-Use of Astragalus as Medicine and Food. *West China Journal of Pharmaceutical Sciences*, 38, 718-724. http://doi.org/10.13375/j.cnki.wcjps.2023.06.023.

[15] Xie, W., Peng, L., Jiang, P., Meng, D., Wang, X. (2023). Establishment and Optimization of Dual-Layer Bonding Discrete Element Model for Oilseed Rape Stem at Harvest. *Transactions of the Chinese Society for Agricultural Machinery*, 54, 112-120. http://doi.org/10.6041/j.issn.1000-1298.2023.05.011.

[16] Xu, J., Sun, S., Li, X., Zeng, Z., Han, C., Tang, T., Wu, W. (2024). Research on the Population Flow and Mixing Characteristics of Pelleted Vegetable Seeds Based on the Bonded-Particle Model. *Agriculture*, 14, 752. http://doi.org/10.3390/agriculture14050752.

[17] Zeng, Z.W., Ma, X., Cao, X.L., Li, Z.H., Wang, X.C. (2021). Critical Review of Applications of Discrete Element Method in Agricultural Engineering. *Transactions of the Chinese Society for Agricultural Machinery*, 52, 1-20. http://doi.org/10.6041/j.issn.1000-1298.2021.04.001.

[18] Zhang, H., Wen, Z., Chen, Y., Liu, J., Liu, H., Zhang, Z., Zhang, X. (2023). Research on Cutting Angle Design Optimization of Rubber Cutter Based on Discrete Element Method. *Agriculture*, 13, 1894. http://doi.org/10.3390/agriculture13101894.

[19] Zhang, X., Hu, X., Liu, J., Yang, Y., Li, Y. (2023). Discrete Element Simulation Bonding Model Parameter Calibration and Testing of Banana Stems. *Transactions of the Chinese Society for Agricultural Machinery*, 54, 121-130. http://doi.org/10.6041/j.issn.1000-1298.2023.05.012.

[20] Zhao, H., Huang, Y., Liu, Z., Liu, W., Zheng, Z. (2021). Applications of Discrete Element Method in the Research of Agricultural Machinery: A Review. *Agriculture,* 11, 425. http://doi.org/10.3390/agriculture11050425.

[21] Zhong, G., Li, H., He, J., Wang, Q., Lu, C., Wang, C., Tong, Z., Cui, D., He, D. (2023). Design and Test of Single-Disc Opener for No-Till Planter Based on Support Cutting. *Agriculture*, 13, 1635. http://doi.org/10.3390/agriculture13081635.

[22] Zhou, B., Zuo, Y., Hou, L. (2023). Parameter Calibration of Xinjiang Paperbark Walnut Kernels by Discrete Element Simulation. *Agriculture*, 13, 353. http://doi.org/10.3390/agriculture13020353.

[23] Zhu, H., He, X., Shang, S., Zhao, Z., Wang, H., Tan, Y., Li, C., Wang, D. (2022). Evaluation of Soil-Cutting and Plant-Crushing Performance of Rotary Blades with Double-Eccentric Circular-Edge Curve for Harvesting Cyperus esculentus. *Agriculture*, 12, 862. http://doi.org/10.3390/agriculture12060862.

DETECTION OF COMBINE-HARVESTER FEED QUANTITY BASED ON MULTI-SOURCE INFORMATION FUSION

/

基于多信息融合的联合收割机喂入量检测方法研究

Jizhong WANG[1)*], Wei DONG[1)], Yong WU[2)], Yangchun LIU[3)], Hongze GUO[3)]

[1)] Weifang University, Weifang, 261061, China

[2)] Shandong Maritime Vocational College. Weifang, 261061, China

[3)] State Key Laboratory of Agricultural Equipment Technology,

China Academy of Agricultural Mechanization Science Group Co., Ltd. Beijing 100083, China

Tel: +86-13651380575; E-mail: 780227311@qq.com-

DOI: https://doi.org/10.35633/inmateh-79-38

Keywords: *combine harvester; information fusion; feed quantity; harvest loss; grey relational analysis*

ABSTRACT

This study proposes a real-time method for detecting combine-harvester feed quantity based on multi-source information fusion and error correction, with the aim of addressing control delays caused by information lag. Field tests were conducted to obtain key parameters, including feeding-auger torque and threshing-drum torque, determine their relational weights, and establish a prediction model. The model achieved a maximum relative error of 9.64% and a mean relative error of 4.55%, meeting the requirements of practical field operation.

摘要

本研究旨在提出一种基于多信息融合与误差修正的联合收割机喂入量实时检测方法，以解决信息滞后导致的控制延迟问题。通过田间试验获取喂入搅龙转矩和脱粒滚筒转矩等关键参数，确定其关联权重，并建立预测模型。模型检测最大相对误差 9.64%，平均相对误差 4.55%，可满足实际作业需求。

INTRODUCTION

Combine harvesters possess the capability to carry out integrated multi-harvesting operations that encompass the direct harvesting of grain from the field. To maximize operational efficiency, parameters such as the feed quantity of the harvester and the width of the header have been progressively increasing in recent years (*Mathanker et al., 2015; Jiang et al., 2025; Chen et al., 2019*). Nevertheless, achieving an effective match between the separation, cleaning capabilities, and feed quantity of the harvester remains a pressing concern in practical operations. This is due to the challenges posed by excessive grain loss and high impurity content during the operational process. Consequently, it holds great significance to investigate a precise and efficient method for predicting the feed quantity of harvesters (*Li et al., 2024; Sun et al., 2022; Zhang et al., 2025*), which would facilitate comprehensive performance control and harvest loss reduction (*Wang et al., 2026*). The feed quantity of the harvester is defined as the total mass of harvested crops that are conveyed to the harvester feeding auger per unit time. The feed quantity is a crucial performance parameter of harvesters during harvesting operations, as it reflects the overall performance of the operation (*Li et al., 2026; Liang et al., 2024; Zhang et al., 2024*). The performance of the harvester can be affected by an excessive or insufficient feed quantity (*Saeys et al., 2009; Zhang et al., 2022*). A larger feed quantity, for instance, may cause the harvester to become overloaded, thus diminishing the overall performance of the operation, while increasing the rate of grain loss and damage. Conversely, a smaller feed quantity can lead to a significant decrease in operational efficiency and an increase in entrainment loss during operation, resulting in a reduced overall performance of the harvester. Consequently, accurate detection of the feed quantity of the harvester is highly significant and merits attention (*Wang et al., 2023; Abdeen et al., 2022; Chen et al., 2025; Yang et al., 2025*).

Four main approaches are currently used to detect or estimate combine-harvester feed quantity. The first estimates feed quantity by directly measuring the grain flow rate within the harvester *(Liu et al., 2018; Sangeetha et al., 2024)*. The second predicts feed quantity from the power consumption of the threshing mechanism. The third combines real-time grain-flow measurements with threshing-drum power consumption to improve feed-quantity estimation. The fourth predicts feed quantity by monitoring the torque and compressive force of key harvester components during operation *(Fricke et al., 2011; Ebrahimi et al., 2009; Wang et al., 2026)*.

Firstly, the correlation weight is employed to scrutinize and define the correlation extent of every influential factor towards the forecasting of feed quantity. Subsequently, by scrutinizing the feed quantity time lag of the data samples procured from sensors that exert a significant impact on the indicators, a multi-information integration-based error correction technique is proposed to rectify the model. Finally, a field validation experiment is formulated and executed to authenticate the efficiency of the formulated feeding prediction model.

First, grey relational analysis was used to determine the relative influence of each factor on feed-quantity prediction. Next, the time delays in the sensor data associated with the parameters having the greatest influence on feed quantity were analyzed, and an error-correction method based on multi-source information fusion was developed to improve the prediction model. Finally, field-validation experiments were designed and conducted to evaluate the effectiveness of the proposed feed-quantity prediction model.

MATERIALS AND METHODS

Sample data acquisition test design

The field experiment was conducted at the wheat plantation base of Qingdao Jimo Shengfa Cooperative, using the GM series wheat combine harvesters of Lovol Geso as the experimental prototype. The experimental procedures were carried out in strict accordance with the national standard GB/T8097-2008 Equipment for Harvesting — Combine Harvesters — Test Procedure. According to this standard, the test plot was selected with a length of no less than 30 m and a width sufficient to accommodate the full working width of the header, ensuring stable and representative operating conditions. For each test run, the combine harvester was operated at a constant preset speed over a total distance of 30 m in a straight line. The first 10 m served as the preliminary acceleration and stabilization phase, during which no data were recorded. Once the harvester reached the steady operating state, data were collected over the remaining 20 m sampling distance. Each test condition was repeated three times, and the mean values of each parameter were used for subsequent analysis to minimize random experimental errors, as illustrated in Fig. 1.

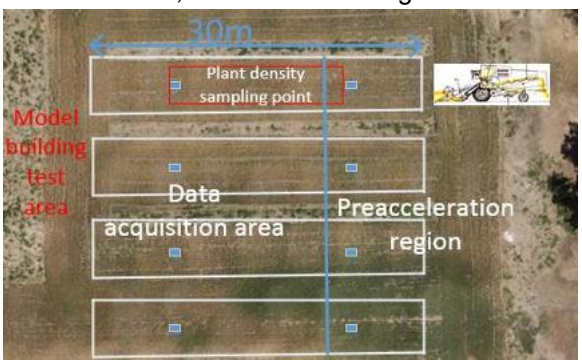
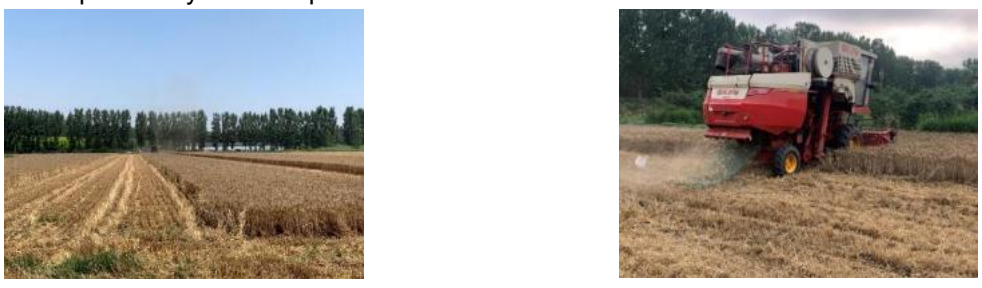


Fig. 1 - Schematic diagram of combine harvester field test scheme

Prior to the formal tests, a preliminary sampling survey of wheat crop properties was conducted within the test plot. Five representative 1 m × 1 m sampling areas were randomly selected to determine crop density, with the above-ground biomass harvested, oven-dried to constant weight at 105 °C, and weighed using an electronic balance (accuracy ±0.01 kg). The results indicated that the wheat had fully ripened, with a grain moisture content of 14.2% ± 0.5%, as measured by a grain moisture meter (PM-8188, Kett Electric Laboratory, Japan), which satisfied the harvesting standards specified in GB/T8097-2008. The test terrain was flat and the wheat growth was uniform with minimal weed presence, as illustrated in Fig. 2. These site conditions ensured the reliability and repeatability of the experimental data.



a) ***b)***

Fig. 2 - Wheat growth and field test

a) Field harvesting operation scene; b) Field harvesting operation scene

In the sampling area, a mesh collection bag was securely attached to the rear of the harvester to collect all impurities and threshed straw discharged during operation. After the harvester completed a 20 m test run, the contents of the bag were removed, sorted, and weighed, and a portion was retained as samples for subsequent tests. Ten tests were conducted following this procedure. For each test, the mean value of each performance index was used as the dataset for the corresponding group, as shown in Table 1.

Table 1

Field test data of operation parameters of key components of combine harvester

No.	Average feeding Quantity (kg/s)	Harvest speed (m/s)	Feeding auger torque(Nm)	Feeding auger rotation speed (r/min)	Threshing drum torque (Nm)	Threshing drum rotation speed (r/min)	Fan speed (r/min)
1	0.98	0.48	4.35	140.56	22.53	671.09	890.21
2	2.29	0.79	13.64	180.98	48.97	930.87	902.37
3	2.61	1.06	15.21	204.73	45.38	972.01	1005.70
4	3.56	1.41	24.98	192.31	74.89	990.58	990.38
5	4.04	1.37	45.47	118.93	85.31	598.49	1156.10
6	5.21	1.84	38.96	150.96	140.92	776.87	1056.26
7	5.70	1.91	58.69	155.89	128.69	909.31	998.39
8	6.13	2.11	49.24	200.14	149.25	1021.34	1156.19
9	6.52	2.84	54.68	188.20	145.39	1100.52	1200.47
10	7.69	3.31	62.38	220.56	162.11	1245.36	1099.68

Analysis of the feed-quantity prediction model

Analysis of the relative influence of different factors

Feed quantity is affected by multiple operating parameters, and analyzing it on the basis of a single variable may introduce considerable uncertainty. Therefore, the grey relational weighting method was used to evaluate the relative influence of each factor on feed quantity and to clarify the effects of the different operating parameters. The procedure for determining the relational weights included establishing the reference sequence, normalizing the comparison sequences, calculating the relational coefficients between the reference and comparison sequences, and determining the grey relational grades. Feed quantity was selected as the reference sequence, while operating speed, feed-auger torque and rotational speed, and threshing-drum torque and rotational speed were used as the comparison sequences. The grey relational weighting method was then applied to determine the relative contribution of each factor to feed quantity, as shown in Fig. 3. The factors were ranked according to their relational weights as follows: harvester operating speed, 0.89; feeding auger torque, 0.84; and threshing drum torque, 0.72.

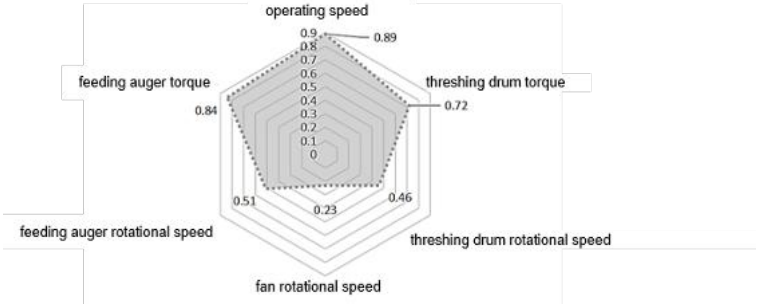


Fig. 3 - Influence weight of various factors on feed quantity

Analysis of the feed-quantity prediction model

Feed quantity is influenced not only by the operating parameters of the combine harvester but also by field crop characteristics, among which crop density is a key factor. To simplify the analysis and incorporate the measured crop-density data, crop density was divided into three categories: low, medium, and high. The corresponding ranges were 0.7~1.0kg/m^2, 1.0~1.3 kg/m^2, and 1.3~1.8 kg/m^2, respectively. By analyzing the relationship between the different crop-density ranges and feed quantity, a more accurate feed-quantity prediction model can be established.

Relationship between operating speed and feed quantity

Figure 4 presents the curve-fitting results based on the experimental data and shows the relationship between operating speed and feed quantity under low-, medium-, and high-crop-density conditions.

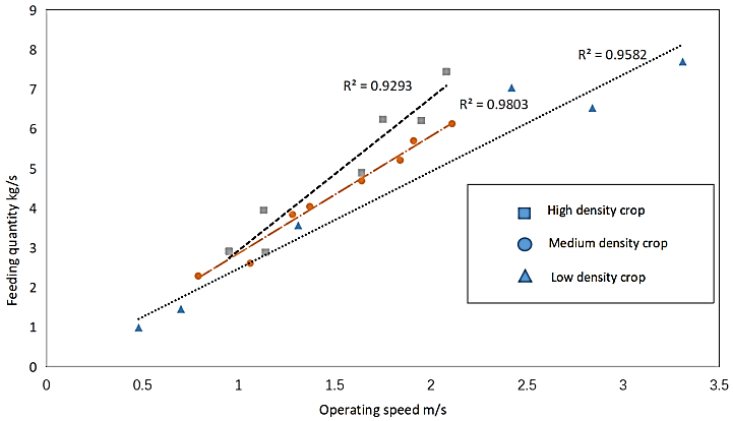


Fig. 4 - Regression curve between operating speed and feed quantity

The results shown in Fig. 4 indicate that, at the same operating speed, harvester feed quantity generally increased with crop density under low- and medium-speed conditions. However, under high-speed conditions, feed quantity was lower in the medium- and high-density crop regions than in the low-density crop region. To account for the combined effects of crop density and operating speed, their product was used as a composite influencing factor. A scatter plot describing the relationship between this factor and feed quantity is presented in Fig. 5.

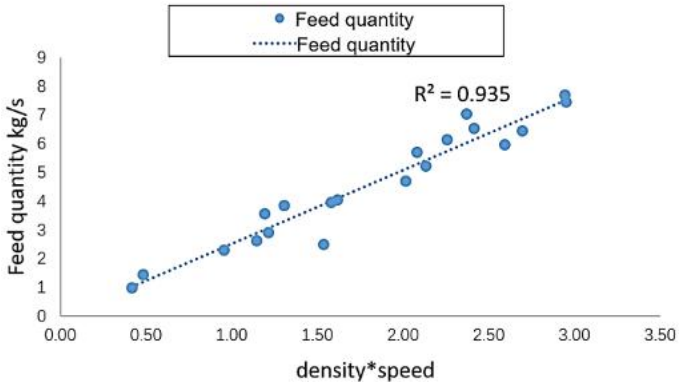


Fig. 5 - Regression relationship between the product of operating speed and wheat crop density and feed quantity

Table 2 presents the least-squares linear regression model for feed quantity, obtained by regressing harvester feed quantity against the product of operating speed and crop density.

Table 2

Regression relationship between the product of operating speed and wheat density and feed quantity

Model form	Regression equation	Coefficient of determination
y=a x+b	y=2.5668x+0.0632	0.935

Relationship between threshing-drum torque and feed quantity

Fig. 6 presents the curve-fitting results obtained from the experimental data and shows the relationship between threshing-drum torque and feed quantity under different crop-density conditions.

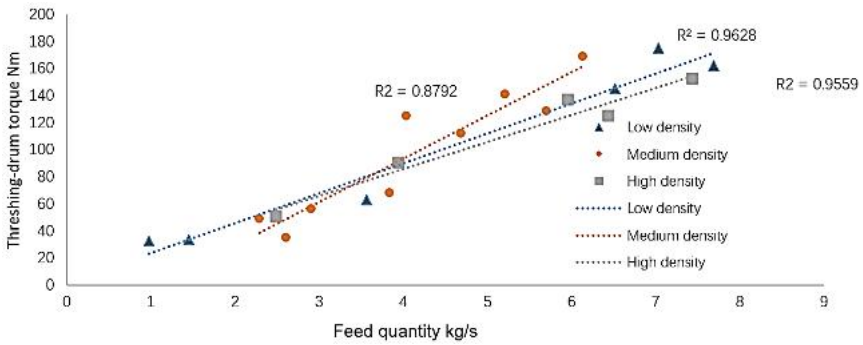


Fig. 6 - Relationship between threshing-drum torque and feed quantity under different crop-density conditions

As shown in Fig. 6, threshing-drum torque exhibited a strong linear relationship with feed quantity under low- and high-crop-density conditions. Under medium-crop-density conditions, the coefficient of determination was lower than those obtained for the other two density levels, although the linear relationship remained relatively strong. The corresponding regression models are presented in Table 3. These results indicate that a piecewise feed-quantity prediction model based on crop-density level is appropriate.

Table 3

Regression models relating feed quantity to threshing-drum torque under different crop-density conditions

Crop-density level	Model form	Regression equation	Coefficient of determination
Low density	y=a x+b	y=22.102x+34.83	0.9628
Medium density	y=a x+b	y=32.039x-34.837	0.8792
High density	y=a x+b	y=19.911x+34.83	0.9559

A multi-model regression analysis was conducted for the medium-crop-density condition to identify the most appropriate relationship between feed quantity and threshing-drum torque. The fitted models and their corresponding parameters are presented in Table 4, while the regression curves for the different model forms are shown in Fig. 7.

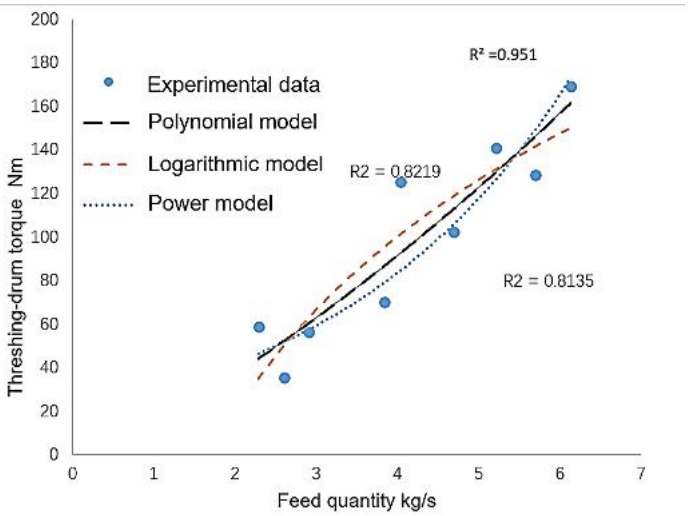


Fig. 7 - Regression curves relating feed quantity to threshing-drum torque using different model forms

As shown in Fig. 7, the quadratic model provided the best fit, with a higher coefficient of determination than the logarithmic and power models. Therefore, the quadratic model was selected to predict feed quantity under medium-crop-density conditions. The parameters and coefficients of determination of the fitted models are presented in Table 4.

Table 4

Comparison of regression models relating feed quantity to threshing-drum torque under medium-crop-density conditions

Crop-density level	Model form	Regression equation	Coefficient of determination
Low density	y=a x+b	y=22.102x+34.83	0.9628
Medium density	y=a x+b	y=32.039x-34.837	0.8792
High density	y=a x+b	y=19.911x+34.83	0.9559

In conclusion, linear regression models were suitable for describing the relationship between feed quantity and threshing-drum torque under low- and high-crop-density conditions, whereas a quadratic regression model was more appropriate under medium-crop-density conditions. The final piecewise prediction models are summarized in Table 5.

Table 5

Piecewise regression models relating feed quantity to threshing-drum torque

Crop-density level	Model form	Regression equation	Coefficient of determination
Low density	y=a x+b	y=22.102x+34.83	0.9628
Medium density	y=ax2+bx+c	y=1.3429x2+19.212x -6.7705	0.951
High density	y=a x+b	y=19.911x+34.83	0.9559

Analysis of the relationship between feeding-auger torque and feed quantity

Based on the experimental data, scatter plots were generated to illustrate the relationship between feeding-auger torque and feed quantity under different crop-density conditions. Regression analysis was then performed, and the fitted curves are presented in Fig. 8.

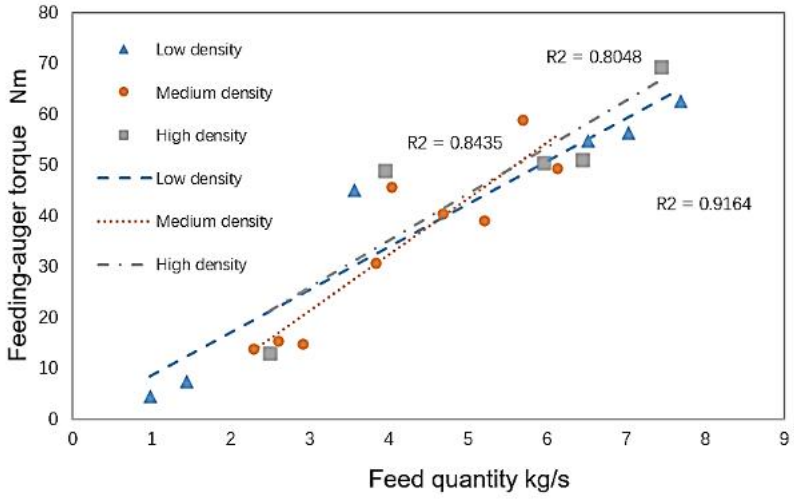


Fig. 8 - Regression curves relating feeding-auger torque to feed quantity under low-, medium-, and high-crop-density conditions

As shown in Fig. 8, feeding-auger torque exhibited a clear linear relationship with feed quantity under all three crop-density conditions. The strength of the relationship was highest under high-crop-density conditions, followed by medium- and low-crop-density conditions. The corresponding linear regression models are presented in Table 6.

Table 6

Linear regression models relating feeding-auger torque to feed quantity under different crop-density conditions

Crop-density level	Model form	Regression equation	Coefficient of determination
Low density	y=a x+b	y=22.102x+34.83	0.9628
Medium density	y=ax2+bx+c	y=1.3429x2+19.212x -6.7705	0.951
High density	y=a x+b	y=19.911x+34.83	0.9559

The analysis results indicated the presence of anomalous data points in the medium-crop-density dataset, which were attributed to irregular sensor measurements. After these anomalous points were removed, the remaining data exhibited a pronounced linear relationship between feeding-auger torque and feed quantity. Therefore, the valid samples obtained under medium-crop-density conditions were combined with those obtained under low-crop-density conditions for linear regression analysis. On this basis, the regression relationship for the medium-crop-density dataset was reconstructed, and the resulting fitted curve is presented in Fig. 9.

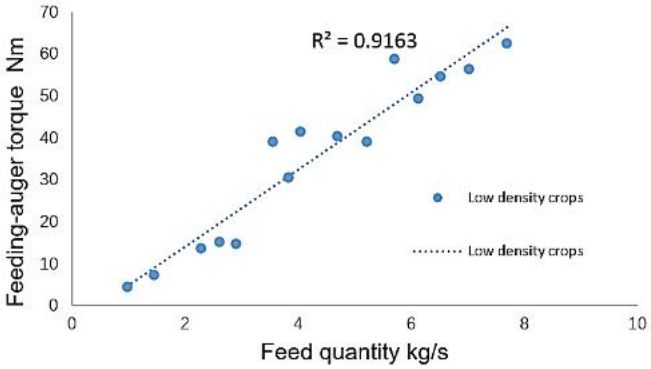


Fig. 9 - Regression relationship between feeding-auger torque and feed quantity under low-crop-density conditions

The data distribution for the high-crop-density condition was plotted, and regression analysis was performed. The resulting fitted curve is presented in Fig. 10.

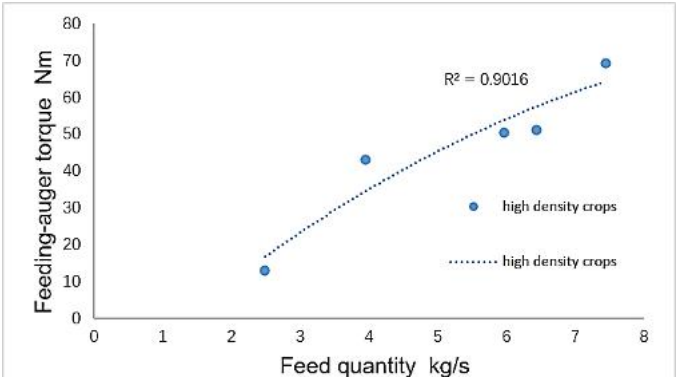


Fig. 10 - Regression relationship between feeding-auger torque and feed quantity under high-crop-density conditions

By comparing Figs. 9 and 10, it can be seen that different regression models were used to describe the relationship between feeding-auger torque and feed quantity under different crop-density conditions. A linear model was used for the combined low- and medium-crop-density data, whereas a quadratic model was used for the high-crop-density data. Both models exhibited relatively high coefficients of determination, indicating good fitting performance. In conclusion, the regression models describing the relationship between feed quantity and feeding-auger torque are presented in Table 7.

Table 7

Regression models relating feeding-auger torque to feed quantity under different crop-density conditions

Crop-density level	Model form	Regression equation	Coefficient of determination
Low and Medium density	y=a x+b	y = 9.1987x - 4.5299	0.9163
High density	y=ax2+bx+c	y=-0.7333x2+16.88x-20.796	0.9016

Analysis of the feed-quantity prediction model

During harvester operation, crop material passes through a series of conveying and processing stages. The wheat plants are first cut at the header and then enter the feeding auger, where they undergo initial compression before being transferred to the conveyor. The crop material is subsequently conveyed through the feeder house to the threshing drum, where threshing takes place. The straw is then separated and discharged, while the grain and impurities pass through the cleaning sieves. Finally, the cleaning system removes the remaining impurities and produces clean grain. Analysis of this material-flow process reveals a spatiotemporal delay between the feeding auger and the threshing drum during crop feeding. Consequently, the data collected from the different harvester components do not correspond to the same crop-material segment at the same instant and therefore cannot directly provide accurate real-time feedback on feed quantity for automatic harvester control.

To achieve spatiotemporal alignment between feed-quantity detection and the signals obtained from the feeding auger and threshing drum, and to reduce prediction delays caused by differences in material transport time, a model describing the crop-material conveying time through the harvester was established. The material-flow process is illustrated in Fig. 11.

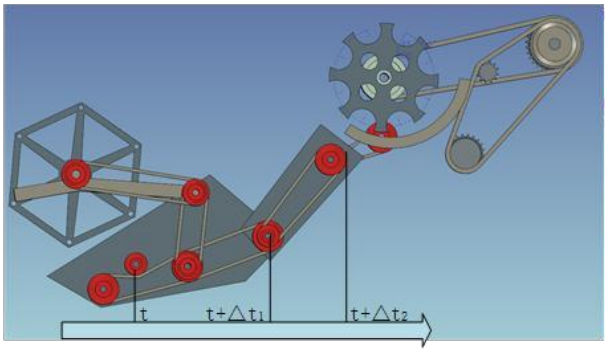


Fig. 11 - Crop-material conveying path through the combine harvester

As shown in Fig. 11, the crop-material conveying process begins when the crop enters the header and is subsequently transported from the feeding auger to the feeder house and then to the threshing drum. The transport time required for these two successive stages produces a delay in the crop-material flow. Neglecting frictional effects between the crop material and the conveying components, the time delay associated with crop transport from the feeding auger to the front end of the feeder house can be expressed by Eq. (1):

$$\Delta t_1 = \frac{L_1}{\omega_1 R_1} \tag{1}$$

where, L_1 is the effective conveying distance from the feeding auger to the front end of the feeder house, m; ω_1 is the rotational speed of the feeding auger, r/min; R_1 is the radius of the feeding-auger drive shaft, m.

The time delay associated with crop transport from the feeder house to the threshing drum was then analyzed and can be expressed by Eq. (2).

$$\Delta t_2 = \frac{L_2}{\omega_2 R_2} \tag{2}$$

where, L_2 is the effective conveying distance from the front end of the feeder house to the threshing drum, m; ω_2 is the rotational speed of the feeder-house conveyor drive shaft, r/min; R_2 is the radius of the feeder-house conveyor drive shaft, m.

Therefore, the total time delay required for the crop material to travel from the feeding auger to the threshing drum can be expressed by Eq. (3):

$$\Delta t = \Delta t_1 + \Delta t_2 = \frac{L_1}{\omega_1 R_1} + \frac{L_2}{\omega_2 R_2} = \frac{L_1 \omega_2 R_2 + L_2 \omega_1 R_1}{\omega_1 \omega_2 R_1 R_2} \tag{3}$$

Analysis of the crop-material transport delay from the header to the threshing drum indicates that, for a feed quantity $Q(t)$ entering the feeding system at time t, the corresponding operating parameters are the feeding-auger torque $T_1(t)$ and the threshing-drum torque $T_2(t + \Delta t_1 + \Delta t_2)$. The time shift in the threshing-drum torque signal results from the crop-material transport delays between the feeding auger, feeder house, and threshing drum.

By analyzing the relationships among key operating parameters, including feed quantity, operating speed, feeding-auger torque, and threshing-drum torque, this study determines the relative influence of each parameter and evaluates the time delay associated with the threshing-drum torque signal. On this basis, a multi-source information-fusion error-correction model based on relational weights is proposed for feed-quantity prediction. First, the pre-measured crop-density value is entered into the model. The real-time operating speed, feeding-auger torque, and threshing-drum torque are then integrated to obtain a preliminary estimate of feed quantity. Subsequently, the regression model relating threshing-drum torque to feed quantity is used to correct the error caused by the transport delay. The corrected value is then used as feedback to

refine the preliminary prediction. After the correction is completed, the model proceeds to the next feed-quantity prediction cycle.

First, the initial feed-quantity prediction model is formulated as:

$$Q(t) = \varphi_1 Q_1(T_1(t)) + \varphi_2 Q_v(v(t), \rho) + \Delta E(t) \tag{4}$$

where, φ_1 and φ_2 are the weighting coefficients of the prediction model, $Q(T_1)$ is the functional relationship between feed quantity and feeding-auger torque, $Q_v(v, \rho)$ is the functional relationship between feed quantity, operating speed, and crop density, $\Delta E(t)$ is the time-delay error-correction term.

The time-series error obtained from the current prediction cycle is used to correct the subsequent prediction, and the resulting correction term is denoted by $\Delta E(t)$.

First, the initial error sequence is defined as:

$$\Delta E^{(0)}(t) = \{e^{(0)}(t-nT), e^{(0)}(t-(n-1)T), e^{(0)}(t-(n-2)T), \cdots, e^{(0)}(t-(n-m)T), \cdots, e^{(0)}(t)\}$$

$$\begin{cases} n = 1, 2, 3, \ldots \\ m = 1, 2, 3, \ldots, n \end{cases} \tag{5}$$

where, T is the sampling interval of the threshing-drum torque signal. The sampling interval must be shorter than both transport-delay components, such that $T \leq \triangle t_1$ and $T \leq \triangle t_2$.

The elements of the initial error sequence are then expressed as:

$$\begin{aligned} e^{(0)}(t-(n-m)T) = \varphi_3 (Q_2(T_2(t-(n-m)T)) - Q(t-(n-m)\Delta t_1 T)) \\ - Q(t-(n-m)(\Delta t_1 + \Delta t_2)T)) \end{aligned} \tag{6}$$

where, $Q_2(T_2)$ is the functional relationship between threshing-drum torque and feed quantity, and φ_1, φ_2 and φ_3 are the relational weighting coefficients corresponding to operating speed, feeding-auger torque, and threshing-drum torque, respectively.

By applying the accumulated generating operation to △E(0)(t), the following accumulated sequence is obtained:

$$\begin{aligned} \Delta E^{(1)}(t) &= \left\{e^{(1)}(t-nT), e^{(1)}(t-(n-1)T), e^{(1)}(t-(n-2)T), \ldots, e^{(1)}(t-(n-m)T), \ldots, e^{(1)}(t)\right\} \\ e^{(1)}(t-(n-m)T) &= \sum_{i=1}^{m} e^{(0)}(t-(n-i)T) \end{aligned} \tag{7}$$

A first-order whitening differential equation is then established for the elements of the accumulated error sequence, as expressed in Eq. (8):

$$\frac{de^{(1)}}{dt} + ae^{(1)} = w \tag{8}$$

By discretizing Eq. 8, Eq. (9) is obtained:

$$\Delta^{(1)}(e^{(1)}(m+1)) + az^{(1)}(e(m+1)) = w \tag{9}$$

where, a and w are parameters to be determined.

The restored value of the sequence at time $m+1$ is then obtained by applying the inverse accumulated generating operation, as expressed in Eq. (10):

$$\begin{aligned} \Delta^{(1)}(e^{(1)}(m+1)) &= \Delta^{(0)}[e^{(1)}(m+1)] - \Delta^{(0)}[e^{(1)}(m)] = e^{(1)}(m+1) - e^{(1)}(m) = u^{(0)}(m+1) \\ z^{(1)}(e(m+1)) &= \frac{1}{2}(e^{(1)}(m+1) + e^{(1)}(m)) \end{aligned} \tag{10}$$

Substituting Eq. (10) into Eq. (9) yields Eq. (11):

$$e^{(0)}(m+1) = a[-\frac{1}{2}(e^{(1)}(m) + e^{(1)}(m+1))] + w \tag{11}$$

By expanding Eq. (11) in series form, Eq. (12) is obtained:

$$\begin{bmatrix} e^{(0)}(2) \\ e^{(0)}(3) \\ \cdot \\ \cdot \\ \cdot \\ e^{(0)}(m) \end{bmatrix} = \begin{bmatrix} -\frac{1}{2}(e^{(1)}(1)+e^{(1)}(2)) & 1 \\ -\frac{1}{2}(e^{(1)}(2)+e^{(1)}(3)) & 1 \\ \cdot & \cdot \\ \cdot & \cdot \\ \cdot & \cdot \\ -\frac{1}{2}(e^{(1)}(m-1)+e^{(1)}(m)) & 1 \end{bmatrix} \begin{bmatrix} a \\ w \end{bmatrix} \tag{12}$$

The auxiliary expressions are defined as follows:

$$Y = \begin{bmatrix} e^{(0)}(2) \\ e^{(0)}(3) \\ \cdot \\ \cdot \\ \cdot \\ e^{(0)}(m) \end{bmatrix} \tag{13}$$

$$B = \begin{bmatrix} -\frac{1}{2}(e^{(1)}(1)+e^{(1)}(2)) & 1 \\ -\frac{1}{2}(e^{(1)}(2)+e^{(1)}(3)) & 1 \\ \cdot & \cdot \\ \cdot & \cdot \\ \cdot & \cdot \\ -\frac{1}{2}(e^{(1)}(m-1)+e^{(1)}(m)) & 1 \end{bmatrix} \tag{14}$$

$$\Phi = [a \quad w]^T \tag{15}$$

Substituting Eqs. (13)–(15) into Eq. (12) yields the corresponding sequence:

$$Y = B\Phi \tag{16}$$

The parameter vector Φ can then be estimated using the least-squares method, as expressed in Eq. (17):

$$\Phi = [a, w]^T = (B^T B)^{-1} B^T Y \tag{17}$$

Accordingly, the time-response sequence can be derived as:

$$\hat{e}^{(1)}(m+1) = [e^{(1)}(1) - \frac{w}{a}]e^{-am} + \frac{w}{a} \tag{18}$$

By substituting Eq. (11), the restored original sequence is obtained as follows:

$$\hat{e}^{(0)}(m+1) = \hat{e}^{(1)}(m+1) - \hat{e}^{(1)}(m) = (1-e^{a})[e^{(1)}(1) - \frac{w}{a}]e^{-am} \tag{19}$$

For the known weighting-coefficient vector ϕ=[$\phi 1, \phi 2, \phi 3, \phi 4$], the grey relational grade vector is defined as shown in Eq. (20):

$$\hat{e}^{(0)}(m+1) = \hat{e}^{(1)}(m+1) - \hat{e}^{(1)}(m) = (1-e^{a})[e^{(1)}(1) - \frac{w}{a}]e^{-am} \tag{20}$$

The weighting coefficients corresponding to operating speed, feeding-auger torque, threshing-drum torque, and the fourth model parameter can then be determined as follows:

$$\varphi_k = \frac{\gamma_i}{\sum_{k=1}^{k=i} \gamma_k} \tag{21}$$

Experimental validation of the feed-quantity prediction model

The experiment was conducted at the wheat-growing base of Shengfa Cooperative in Jimo District, Qingdao. A modified GM-series combine harvester manufactured by Lovol was used, and the tested wheat cultivar was Jinan No. 17. Before the field tests, samples were collected from the experimental plot to determine key crop characteristics, including crop density and grain moisture content.

During each test, the harvester operated at a constant forward speed, while the crop material was fed manually to determine the actual feed quantity for the corresponding test plot. A total of 12 tests were conducted, and the validation results are presented in Table 8.

Table 8

Validation results for the feed-quantity prediction model

No.	Predicted feed quantity (kg/s)	Measured feed quantity (kg/s)	Absolute error	Relative error (%)
1	0.91	0.83	0.08	9.64
2	3.88	3.75	0.13	3.47
3	4.09	4.28	-0.19	4.44
4	1.5	1.65	-0.15	9.09
5	5.01	4.89	0.12	2.45
6	5.18	5.26	-0.08	1.52
7	3.38	3.16	0.22	6.96
8	5.72	5.9	-0.18	3.05
9	6.44	6.33	0.11	1.74
10	5.29	5.34	-0.05	0.94

After excluding the data from Tests 11 and 12, the maximum absolute error among the remaining samples was 0.22 kg/s, the maximum relative error was 9.64%, and the mean relative error was 4.33%. All relative errors were below 10%, indicating that the prediction model satisfied the specified measurement-error requirements.

In conclusion, the accuracy of detection and errors of the prediction model differ based on various feeding conditions. To analyze the variances in the feed quantity prediction models at different stages, the test data samples are divided into regions of low feed quantity, medium feed quantity, and high feed quantity. A comparative column chart is depicted in Fig. 12 to illustrate the differences.

Overall, the prediction accuracy and error varied under different feeding conditions. To evaluate the performance of the feed-quantity prediction model across different operating ranges, the validation samples were divided into low-, medium-, and high-feed-quantity groups. A comparative bar chart illustrating the prediction results and errors for these three groups is presented in Fig. 12.

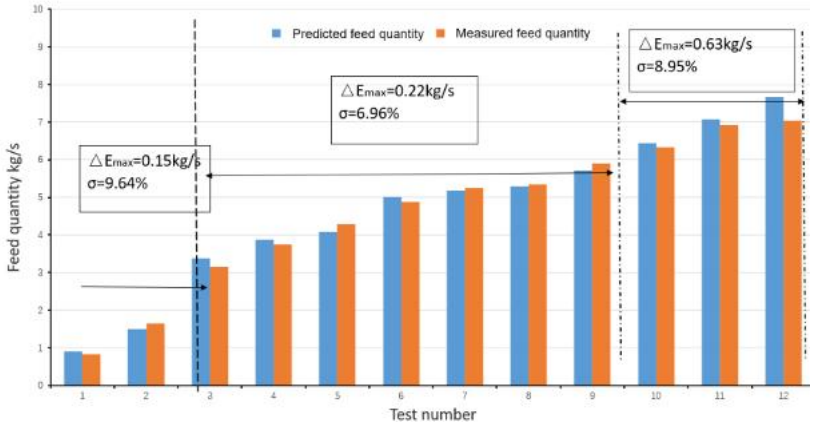


Fig. 12 - Comparison of measured and predicted feed quantities across different feed-quantity ranges

As shown in Fig. 12, the feed-quantity range was divided into three intervals: 0-3 kg/s, 3-6 kg/s, and 6-8 kg/s. The maximum relative errors in these intervals were 9.64%, 6.96%, and 8.95%, respectively. Comparison of the prediction results indicates that the model produced larger errors at low and high feed quantities, whereas its prediction performance was more accurate within the medium feed-quantity range.

CONCLUSIONS

(1) Grey relational weight analysis was used to determine the relative influence of the main operating parameters on feed quantity. Harvester operating speed had the highest relational weight (0.89), followed by feeding-auger torque (0.84) and threshing-drum torque (0.72). These results indicate that variations in feed quantity are primarily governed by changes in operating speed, whereas variations in feeding-auger and threshing-drum torque reflect the dynamic relationship between crop intake, material conveying, and threshing load.

(2) A piecewise modelling approach was adopted for different crop-density conditions. Under low- and high-crop-density conditions, feed quantity exhibited a strong linear relationship with threshing-drum torque, with coefficients of determination of R^2 = 0.9628 and 0.9559, respectively. Under medium-crop-density conditions, a quadratic model provided a better fit, with R^2 = 0.951. This result suggests that crop-flow and separation processes within the threshing system become more complex under medium-crop-density conditions and cannot be adequately described using a simple linear relationship.

(3) To compensate for the time delay in the signals collected from different harvester components, an error-corrected feed-quantity prediction model was developed. Field-validation results showed that, across the 12 test groups, the maximum absolute error was 0.63 kg/s, the maximum relative error was 9.64%, and the mean relative error was 4.55%. Further analysis by feed-quantity range showed that the maximum relative errors for the low (0–3 kg/s), medium (3–6 kg/s), and high (6–8 kg/s) ranges were 9.64%, 6.96%, and 8.95%, respectively. The model achieved the highest prediction accuracy within the medium feed-quantity range, whereas larger errors occurred at low and high feed quantities. These differences may be attributed to weaker sensor signals and a lower signal-to-noise ratio under low-feed conditions, as well as increased crop accumulation and greater torque fluctuations under high-feed conditions.

ACKNOWLEDGEMENT

This work was supported by the Opening Fund of State Key Laboratory of Agricultural Equipment Technology (SKL2025006); Doctoral Research Startup Fund Project of Weifang University(2024BS38)

REFERENCES

[1] Abdeen, M. A. M., Xie, G., Salem, A. E., Fu, J., & Zhang, G. (2022). Longitudinal axial flow rice thresher feeding rate monitoring based on force sensing resistors. *Scientific Reports*, Vol. 12, 1369, United Kingdom.

[2] Chen, D., & Wang, S. M. (2019). Design and Test of Feed Rate Monitoring System for Combine Harvester (联合收割机喂入量监测系统设计与试验). *Transactions of the Chinese Society for Agricultural Machinery*, Vol. 50, No. 6, pp. 85-92, China.

[3] Chen, X., Wu, S., Li, C., Liu, F., Yuan, L., & Wang, W. (2025). Design and experiment of feed rate monitoring system based on the action force of grain combine harvester reel. *Computers and Electronics in Agriculture*, Vol. 228, 109837, Netherlands.

[4] Ebrahimi-Nik, M., Khademolhosseini, N., Abbaspour-Fard, M. H., Mahdinia, A., & Alami-Saied, K. (2009). Optimum utilisation of low-capacity combine harvesters in high-yielding wheat farms using multi-criteria decision making. *Biosystems Engineering*, Vol. 103, No. 3, pp. 382-388, United Kingdom.

[5] Fricke, T., Richter, F., & Wachendorf, M. (2011). Assessment of forage mass from grassland swards by height measurement using an ultrasonic sensor. *Computers and Electronics in Agriculture*, Vol. 79, No. 2, pp. 142-152, Netherlands.

[6] Jiang, L., Wang, G., Xu, B., Husnain, N., & Wang, Q. (2025). Intelligent Systems for Combine Harvesters: A Comprehensive Review of Technologies and Trends. *IEEE Transactions on Industrial Informatics*, Vol.21, No. 12, pp. 1-15, United States.

[7] Li, Q., Yu, Y., Guo, G., Hu, J., Liu, P., Chai, X., Wang, Y., & Xu, L. (2024). Design and experiment of array-based fingerplate differential flow sensor for rice grain monitoring. *INMATEH - Agricultural Engineering*, Vol. 74, No. 3, pp. 358-369, Romania.

[8] Li, X. H., Qiu, Z. P., Jiang, J. C., Zhang, Y., Xing, C. X., & Wu, X. (2026). Magnetoelastomer-based grain flow sensor for combine harvesters. *Computers and Electronics in Agriculture*, Vol. 244, 111447, Netherlands.

[9] Liang, Z., Qin, Y., & Su, Z. (2024). Establishment of a Feeding Rate Prediction Model for Combine Harvesters. Agriculture, Vol. 14, No. 4, 589, Switzerland.

[10] Liu, A., Li, P., Xie, F., Zeng, L., & Ji, B. (2026). A feed rate monitoring system based on light loss in the conveyor trough of soybean combine harvester. *Computers and Electronics in Agriculture*, Vol. 238, 111005, Netherlands.
[11] Mathanker, S. K., Buss, J. C., Gan, H., Larsen, J. F., & Hansen, A. C. (2015). Stem bending force and hydraulic system pressure sensing for predicting napiergrass yield during harvesting. *Computers and Electronics in Agriculture*, Vol. 111, pp. 174-180, Netherlands.
[12] Saeys, W., Lenaerts, B., Craessaerts, G., & De Baerdemaeker, J. (2009). Estimation of the crop density of small grains using LIDAR sensors. *Biosystems Engineering*, Vol. 102, No. 1, pp. 22-30, United Kingdom.
[13] Sangeetha, C., Moond, V., Rajesh G. M., Damor, J. S., Pandey, S. K., Kumar, P., & Singh, B. (2024). Remote Sensing and Geographic Information Systems for Precision Agriculture: A Review. *International Journal of Environment and Climate Change*, Vol. 14, No. 2, pp. 287-309, India.
[14] Sun, Y., Liu, R., Zhang, M., Li, M., Zhang, Z., & Li, H. (2022). Design of feed rate monitoring system and estimation method for yield distribution information on combine harvester. *Computers and Electronics in Agriculture*, Vol. 201, 107322, Netherlands.
[15] Wang, F., Chen, L. P., Wang, Q., Qin, W. C., & Meng, Z. J. (2026). Design and experimental validation of a flow-guided weighing-based grain mass flow sensor for wheat combine harvester. *Computers and Electronics in Agriculture*, Vol. 240, 111224, Netherlands.
[16] Wang, J., Fang, X., Wang, F., Liu, Y., & Zhao, B. (2023). Study on the loss control system of wheat combine harvester. *INMATEH - Agricultural Engineering*, Vol. 69, No. 1, pp. 471-480, Romania.
[17] Wang, Q., Yin, Y., Meng, Z., Qin, W., & Geng, D. (2026). Research on Feeding Rate Measurement Method for Combine Harvester Based on Multimodal Information Fusion. *IEEE Journal of Selected Topics in Signal Processing*, Vol. 20, No. 2, pp. 115-128, United States.
[18] Yang, X., Li, P., Zhao, Z., Lei, C., & Jin, C. (2025). A review of the feed rate detection and stability control methods in combine harvesters. *INMATEH - Agricultural Engineering*, Vol. 75, No. 1, pp. 143-157, Romania.
[19] Zhang, C., Li, Q., Ye, S., & Zheng, D. (2025). Design and test of a wireless monitoring system for feed rate in combine harvester based on bottom plate pressure of chain-rake conveyor. *INMATEH - Agricultural Engineering*, Vol. 77, No. 3, pp. 894-903, Romania.
[20] Zhang, Y., Yin, Y., Meng, Z., Chen, D., Qin, W., Wang, Q., & Dai, D. (2022). Development and testing of a grain combine harvester throughput monitoring system. *Computers and Electronics in Agriculture*, Vol. 200, 107253, Netherlands.
[21] Zhang, Y., Zhang, B., Shen, C., Liu, H., Huang, J., Tian, K., & Tang, Z. (2024). Review of the field environmental sensing methods based on multi-sensor information fusion technology. International *Journal of Agricultural and Biological Engineering*, Vol. 17, No. 2, pp. 1-13, United States.

YOLO11-RCSP: CHERRY TOMATO FLOWER POLLINATION STATUS RECOGNITION BASED ON MULTI-SCALE FEATURE FUSION

/

YOLO11-RCSP：融合多尺度特征的圣女果花授粉状态识别

Jianhua CUI, XinYU LI, FuZhong LI, Xiaoying ZHANG

Faculty of Software Technologies, Shanxi Agricultural University, Taigu, Shanxi / China
Corresponding authors: FuZhong Li; Tel: +86-13734008985; E-mail: lifuzhong@sxau.edu.cn
Corresponding authors: Xiaoying Zhang; Tel: +86-15803449361; E-mail: xiaoyingzhang@sxau.edu.cn

DOI: https://doi.org/10.35633/inmateh-79-39

Keywords: *Deep learning, Object detection, YOLO11, Pollination status recognition, Cherry tomato*

ABSTRACT

In greenhouse cultivation of cherry tomatoes, the accurate identification of pollination status is a key prerequisite for achieving automated robotic pollination. As the site of direct interaction during pollination, changes in the colour and morphology of the stigma most accurately indicate whether pollination has been successful. However, due to the minuscule size of the stigma and the extremely subtle visual differences among the three states—unpollinated, pollinated, and fruiting—combined with interference from fluctuating lighting conditions and complex backgrounds in greenhouse environments, traditional methods struggle to provide high-precision visual perception data for pollination robots. To address this issue, this paper proposes an improved model, YOLO11-RCSP, which focuses on the stigma as the core recognition object to achieve automatic classification of the three pollination states: introducing a novel attention mechanism, RFA (Receptive Field Attention), adding an enhancement module (CPA-Enhancer) to the original model, and incorporating SAConv switchable dilated convolutions. In addition, the loss function is improved using the Powerful-IoU method (adaptive penalty factor and gradient adjustment function based on anchor box quality). The precision rate of the improved model reached 88.40%, the recall rate reached 84.60%, and the average precision was 90.80% when the IoU was 0.50. The average precision ranged from 0.50 to 0.95, reaching 63.20%. These metrics represent improvements of 5.20%, 3.30%, 4.40%, and 5.30%, respectively, compared to the original YOLO11 network model, demonstrating stronger feature extraction capabilities and robustness. Ablation experiments further confirm that the attention mechanism and multi-scale optimization have a synergistic effect on enhancing the performance of stigma pollination status recognition. This research will be applied to pistil-level pollination status recognition tasks, helping to advance the development and application of pollination robots, and providing critical technical support for the development of automated pollination equipment in protected agriculture.

摘要

在圣女果温室栽培中，授粉状态的精准识别是实现机器人自动化授粉作业的核心前提。柱头作为授粉过程的直接作用部位，其颜色、形态变化能够最准确地反映授粉是否成功。然而柱头目标尺度微小，未授粉、授粉和结果三类状态的视觉差异极为细微，而且受温室环境中光照变化与复杂背景的干扰，传统方法难以为授粉机器人提供高精度的视觉感知决策依据。针对该问题，本文提出一个改进模型 YOLO11-RCSP，以柱头为核心识别对象，实现三类授粉状态的自动分类：引入一种新型的注意力机制 RFA（感受野注意力）；在原有模型中添加一种增强模块（CPA-Enhancer）；添加 SAConv 可切换空洞卷积；改进损失函数采用 Powerful-IoU(自适应惩罚因子和基于锚框质量的梯度调节函数) 的方法。改进后模型的准确率达到 88.40%，召回率达到 84.60%，平均精度在 IoU=0.50 时为 90.80%，在 0.50 至 0.95 的 IoU 平均精度达到 63.20%，各项指标相较于原 YOLO11 网络模型分别提高了5.20%，3.30%，4.40%，5.30%，拥有更强的特征提取能力和鲁棒性。消融实验进一步证实注意力机制与多尺度优化对提升柱头授粉状态识别性能具有协同效应。本研究将应用于柱头级别的授粉状态识别任务，有助于推动授粉机器人的研发与应用，为设施农业自动化授粉装备的研发提供关键技术支撑。

INTRODUCTION

Cherry tomatoes are an important fruit and vegetable crop widely cultivated in China's protected agriculture, known for their extensive planting area and significant economic benefits. According to statistics, the area under protected tomato cultivation in China has exceeded 1 million hectares, with cherry tomatoes being particularly favoured by the market due to their excellent taste and rich nutritional content. Cherry tomatoes are monoecious plants with unisexual flowers. In natural environments, pollination can be achieved through natural wind or insect vectors; however, in enclosed environments such as greenhouses, the absence of natural wind and insect activity leads to poor pollination, which can result in flower and fruit drop, as well as deformed fruit, severely affecting the yield and quality of cherry tomatoes *(Wang et al., 2016)*. Currently, greenhouse cherry tomato production primarily relies on manual pollination, bumblebee pollination or hormone-dipped flowers. Manual pollination is inefficient, labour-intensive and difficult to control for uniformity; bumblebee pollination is affected by environmental factors such as temperature and humidity within the greenhouse and is relatively costly *(Wang et al., 2013)*; hormone dipping, meanwhile, tends to increase the incidence of deformed fruit, severely affecting the economic efficiency of cherry tomato production. Consequently, pollination robots have emerged as a solution. Pollination robots can significantly reduce labour costs, accelerate pollination speed and improve cherry tomato pollination efficiency. However, the complex growing environment of greenhouse cherry tomatoes—characterised by small, numerous and overlapping flowers—complicates their identification and detection. This represents both a key challenge and a focal point in pollination robot research *(Hou et al., 2024)*.

In recent years, object detection methods based on deep learning have been widely used in crop detection, providing technical support for the precise localization and recognition of crops *(Kang et al., 2023; Hu et al., 2023; Jia et al., 2024)*. In the field of agricultural robot vision, most existing studies focus on fruit picking or flower localization, while studies related to pollination mostly take the whole flower as the recognition unit. To meet the demand for pollination detection of kiwifruit flowers, Pan et al. proposed a lightweight model KIWI-YOLO, which enhances the model's perception of flower contour details through a frequency-domain feature fusion module, and effectively recognized four states including bud, female flower, male flower, and successful pollination on a self-built kiwifruit flower dataset, with mAP@50 reaching 91.6% *(Pan et al., 2024)*. To solve the detection difficulty caused by the dense distribution of kiwifruit flowers in complex orchard environments, Tang et al. proposed an improved model YOLOv11-TYW based on the YOLOv11n architecture, which verified the applicability of the YOLOv11 architecture in orchard flower object detection tasks and provided a technical reference for flower recognition in subsequent pollination robots *(Tang et al., 2025)*.

Isabel Pinheiro et al. adopted deep learning methods to detect kiwifruit flowers and determine their gender to address the problems that kiwifruit is a dioecious plant with no nectar to attract pollinators and existing technologies lack gender-based flower detection methods; four pre-trained models including YOLOv5, YOLOv8, RT-DETR, and DETR were evaluated, K-fold cross-validation was used to test model performance, and a manually annotated kiwifruit flower gender classification dataset was constructed, among which the YOLOv5s model performed best with a detection accuracy of 97%, providing technical support for the precise operation of automated kiwifruit pollination robots *(Pinheiro et al., 2024)*. Manzoor et al. proposed an improved model based on YOLOv5s; by replacing the backbone network with MobileNetV3 and introducing Ghost convolutions from GhostNet, the model achieved a lightweight effect in apple blossom detection with about 85% reduction in model size and about 89% reduction in GFLOPs, while maintaining an accuracy of 90.6% and mAP@50 of 91.2%, verifying the applicability and lightweight potential of the YOLO series in flower detection for pollination scenarios *(Manzoor et al., 2024)*. Touko Mbouembe et al. proposed an improved YOLOv5s model, which significantly enhanced feature representation ability and detection robustness for occluded objects by integrating the SE attention mechanism, BiFPN multi-scale feature fusion network, CARAFE upsampling operator, and Soft-NMS algorithm *(Touko Mbouembe et al., 2024)*. However, using the whole flower as the recognition target has shortcomings: although the overall size of the flower is large, its morphological characteristics are affected by petal opening angles, variety differences, and environmental factors; the key changes determining successful pollination actually occur at the stigma level, such as stigma colour, surface gloss, and ovary expansion, and these subtle changes are often blocked by petals or disturbed by background in whole-flower images, making them difficult for models to capture accurately. Therefore, methods using the whole flower as the recognition object have obvious deficiencies in the accuracy and interpretability of pollination status recognition.

As the direct site of pollination, the stigma's colour and morphological changes most sensitively reflect whether pollination has been successful. Lorberboym et al. employed a YOLOv8 segmentation model to perform instance segmentation of cannabis stigmas, assessing flower maturity through the proportion of stigma colour, further demonstrating the potential of stigma visual analysis in automated agriculture *(Lorberboym et al., 2026)*.

The Swin Transformer proposed by *Gao et al.* utilises a hierarchical self-attention mechanism to construct robust multi-scale feature representations, offering a new approach to small-object detection in complex visual tasks *(Gao et al., 2024)*. Addressing the issues of low efficiency and high costs associated with manual saffron stigma harvesting, *Priyadharshini et al.* proposed a saffron harvesting system based on an autonomous mobile robot. This system utilises a CNN module to identify mature flowers and the position of their stigmas, and integrates a 6-degree-of-freedom robotic arm onto a mobile platform to achieve precise grasping and separation of the stigmas via vision-guided servo control *(Priyadharshini et al., 2023)*.

Yang et al. addressed the challenges of detecting the minute scale and difficult-to-identify rotational orientation of forsythia pistils by proposing the PSTL-Orient method to detect the area and orientation of rotating pistils. By combining servo technology with flower detection, they achieved precise autonomous pollen delivery to the pistils by a robot *(Yang et al., 2023)*.

However, the identification of stigmas presents multiple technical challenges: due to the minute scale of the stigma target, which occupies very few pixels in an image, traditional object detection methods struggle to effectively extract subtle features; the visual differences between the three states—unpollinated, pollinated and fruiting—are extremely subtle, manifesting only as gradual changes in stigma colour, glossiness and the morphology of the surrounding ovary; these differences require the model to possess a high level of discriminatory ability; lighting conditions in greenhouse environments are complex, with changes in the angle of light in the morning and evening, and fluctuations in brightness caused by shade net coverage, whilst the varied background further increases the difficulty of recognition.

Based on the above analysis, this paper proposes the YOLO11-RCSP method for identifying the pollination status of cherry tomato stigmas, based on an improved YOLO11. This is achieved by introducing a novel attention mechanism, RFA (Receptive Field Attention), adding an enhancement module (CPA-Enhancer) to the original model, adding SAConv switchable dilated convolutions, and improving the loss function by adopting Powerful-IoU (adaptive penalty factors and gradient adjustment functions based on anchor box quality). These four improvement strategies enable the model to adaptively cope with changes in greenhouse lighting and occlusion, whilst also allowing the receptive field to be adjusted according to stigma scale, balancing small-target details with large-scale context to enhance recognition accuracy and robustness. Validation results show that the model achieves a precision of 88.40% and a recall of 84.60%. The average precision at IoU=0.50 is 90.80%, and the average precision across the IoU range of 0.50 to 0.95 is 63.20%. Compared to the original YOLO11 network model, these metrics have improved by 5.20%,3.30%, 4.40% and 5.30% respectively compared to the original YOLO11 network model.

MATERIALS AND METHODS

MATERIALS

DATA AND ACQUISITION

The cherry tomato flower dataset used in this study was captured in an earthen-walled greenhouse at the Innovation and Entrepreneurship Practice Base of the School of Software Engineering, Shanxi Agricultural University, Shanxi Province, China, as shown in Figure 1.

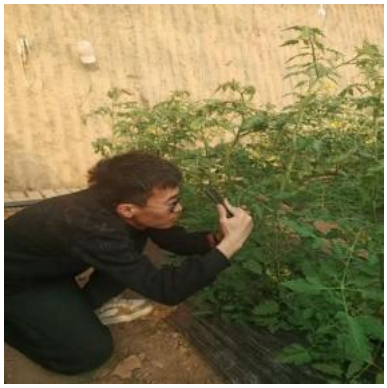


Fig. 1 - Scene of data capture

To enable the model to adapt to changes in stigma scale at different distances, three shooting distances were adopted: close-up (approximately 10–20 cm), medium (approximately 30–40 cm) and far (approximately 50–60 cm). The shooting angles included front, side and upward views to cover the various orientations a pollination robot might encounter during operation. Furthermore, to account for variations in greenhouse lighting conditions, data was collected during three time slots: 8:00–9:30 am, 12:00–1:30 pm and 3:30–5:00 pm. A total of 2,044 images of cherry tomato flowers were captured.

Photographs taken at the three different distances are shown in Figure 2:



Close-up *Medium range* *Long distance*

Fig. 2 - Images captured at different shooting distances

CONSTRUCTION OF THE DATASET

The 2,044 photographs collected were divided into training, validation and test sets in a ratio of 8:1:1, comprising 1,636 images in the training set, 204 in the validation set and 204 in the test set. Adhering to the principle of avoiding duplication and omissions, the LabelImg annotation tool was used to label the stigma of each image, categorising them into three states: unpollinated, pollinated and fruiting *(Li et al., 2024; Song et al., 2024; Sun et al., 2024)*. The specific data labels are shown in Figure 3.

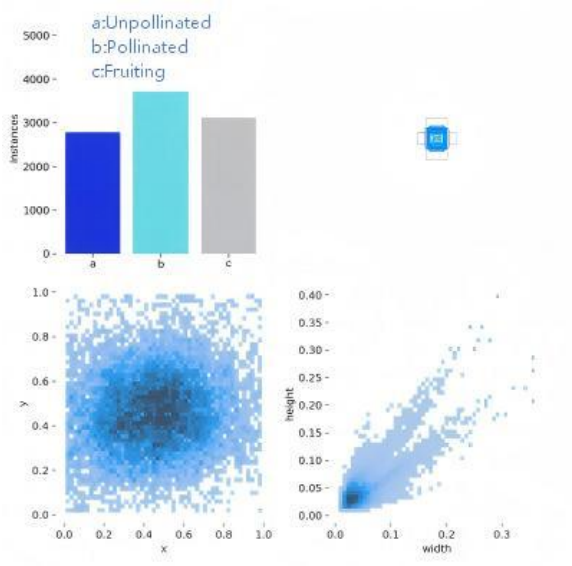


Fig. 3 - Data Labelling

IMPROVED METHOD

To address multiple technical challenges, including the minute scale of the stigma target, subtle visual differences between the three states, and complex lighting conditions in greenhouse environments, this paper proposes YOLO11-RCSP, a stigma pollination status recognition method based on an improved YOLO11. (1) Introducing RFAConv receptive field attention, which resolves the issue of parameter sharing by dynamically adjusting convolution kernel parameters, thereby enhancing the model's ability to perceive both local details and spatial context of the stigma; (2) Adding a CPA-Enhancer adaptive enhancement module to the original model, utilising thought chain prompts to encode degraded information, enabling the model to adaptively cope with changes in greenhouse lighting and occlusion; (3) Replacing the original C3k2 module with the

C3k2_SAConv module, which deeply integrates switchable dilated convolutions with C3k2, enabling the model to adaptively adjust the receptive field according to the scale of the stigma, balancing small-object details with large-scale context; (4) Modifying the loss function to Powerful-IoU, introducing an adaptive penalty factor and a gradient adjustment mechanism based on anchor box quality to improve small-object localisation accuracy and training stability. The diagram of the improved framework is shown in Figure 4.

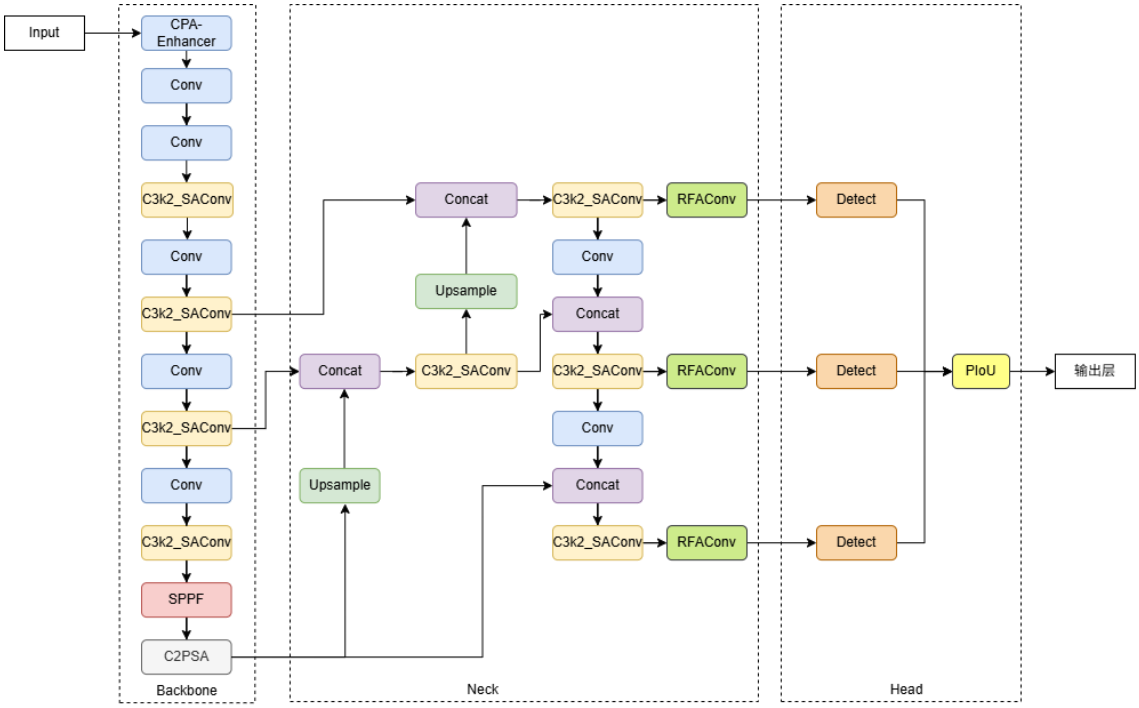


Fig. 4 - Diagram of the improved framework

RFACONV RECEPTIVE FIELD ATTENTION

The core idea of RFAConv is to introduce receptive field attention, allowing convolution kernel parameters to be dynamically adjusted based on the position and contextual information of the receptive field region, thereby addressing the issue of shared convolution kernel parameters *(Zhang et al., 2023)*. Unlike traditional spatial attention mechanisms, RFA not only focuses on spatial features within the image but also places greater emphasis on the spatial feature distribution within each receptive field. By dynamically weighting the importance of various features within the receptive field, it achieves the effect of 'different convolutional kernel parameters for different regions', as illustrated in Figure 5.

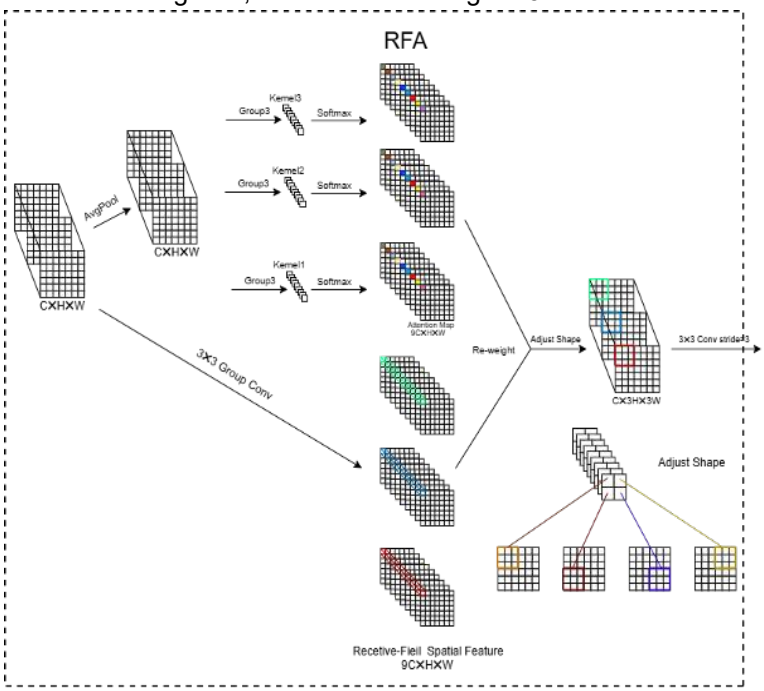


Fig. 5 - RFAConv architecture diagram

This study integrates the RFAConv module into the multi-scale feature fusion stage of YOLO11's neck network. This not only further enhances feature discrimination capabilities and strengthens the model's multi-scale perception but also controls computational overhead whilst improving performance. This design enables the model to dynamically adjust the size of the receptive field based on the scale characteristics of the stigmas in the input image. For smaller, unpollinated stigmas, the model assigns higher weights to branches with smaller receptive fields to preserve fine-scale details; for pollinated stigmas, it assigns higher weights to branches with medium and large receptive fields to capture broader spatial context.

CPA-ENHANCER MODULE

The CPA-Enhancer is specifically designed to enhance object detection performance under unknown degradation conditions. Its core innovation lies in utilising Chain of Thought (CoT) prompts to encode degradation-related information and gradually adjust the enhancement strategy under the step-by-step guidance of the CoT prompts, enabling the model to adaptively address unknown degradation types without prior knowledge of the degradation type *(Zhang et al., 2024)*.This is the first work to apply CoT prompts to object detection tasks; its modular design allows it to be seamlessly integrated into any general-purpose detector, achieving significant performance gains under various unknown degradation conditions. Its structure is shown in Figure 6.

The characteristics of the CPA-Enhancer module are well-suited to the requirements of this study. The identification of pollination status in tomato stigmas faces various complex factors, such as changes in greenhouse lighting and leaf occlusion, which traditional enhancement methods struggle to comprehensively address. Upon adding the CPA-Enhancer to the YOLO11 backbone network, the model can adaptively adjust its enhancement strategy based on the degraded features of the input image, thereby improving the robustness of detection for the small stigmas. Furthermore, as this module has a small number of parameters and low computational overhead, it effectively enhances the accuracy of pollination status recognition whilst maintaining YOLO11's real-time inference capability, providing a more reliable visual perception module for pollination robots.

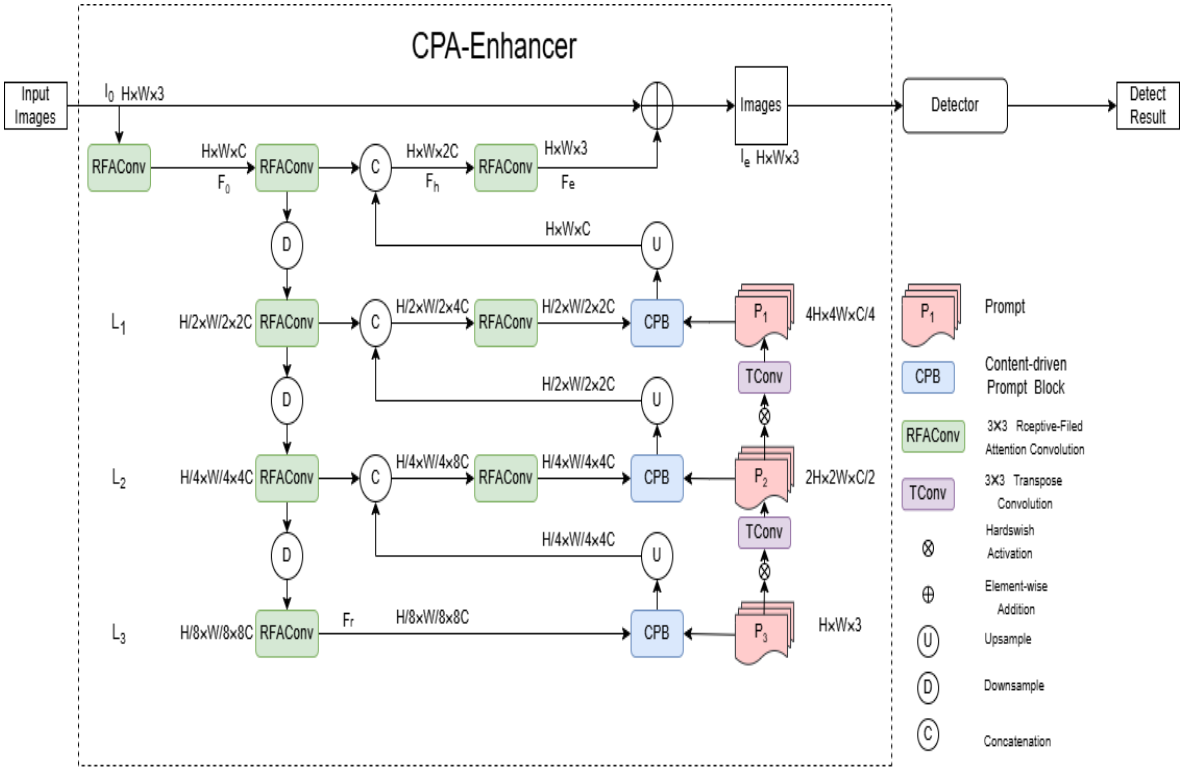


Fig. 6 - CPA-Enhancer architecture diagram

SACONV MODULE

SAConv is a convolutional operation capable of dynamically switching the stranding rate. Its core concept involves introducing a learnable routing mechanism that allows the convolutional kernel to select from or weight-blend multiple stranding rates *(Qiao et al., 2020)*.

This routing module first performs global average pooling on the input features, compressing them into a feature vector, then generates weight coefficients for each branch via two fully connected layers, and finally performs a weighted summation of the outputs from each branch. The expression is given by Eq. (1):

$$F_{out}=\sum_{i=1}^{3} \mathrm{comv}_{d_i}(F_{in}) \quad (1)$$

where '3' denotes the number of parallel dilated convolution branches configured in the SAConv module, i.e. three dilated convolution branches with different dilation rates; d_i is the dilation rate of the i-th branch; w_i is the weight coefficient generated by the dynamic routing module, satisfying Eq. (2):

$$\sum w_i=1 \quad (2)$$

This improvement enables the model to dynamically adjust the void ratio based on input features, allowing it to flexibly capture multi-scale context whilst preserving fine-grained details; its structure is shown in Figure 7.

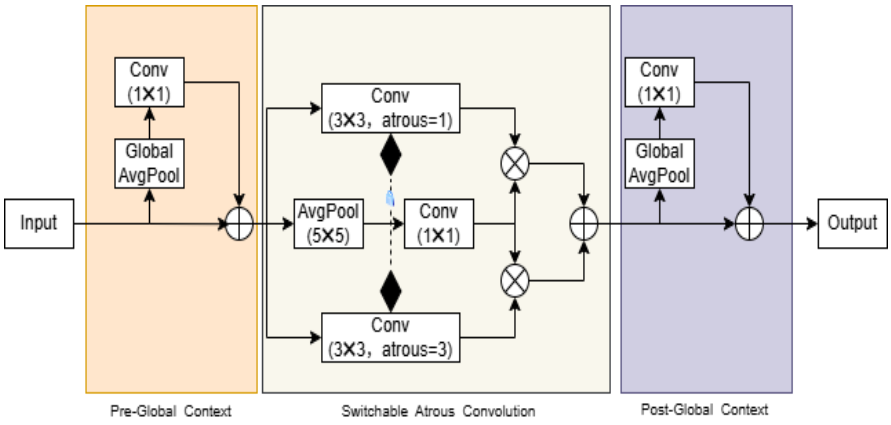


Fig. 7 - SAConv architecture diagram

Wang et al. integrated SAConv into YOLOv8n to construct the LSD-YOLO model, which was applied to the detection of surface diseases on lemons, thereby validating the effectiveness of this module in agricultural small-object detection tasks *(Wang et al., 2024)*. In this study, we propose the C3k2_SAConv module by deeply integrating the SAConv module with the C3k2 module. This enables the C3k2_SAConv module to retain the original lightweight advantages of C3k2 whilst enhancing the model's dynamic perception of features at different scales through the introduction of the SAConv module. It is particularly suitable for fine-grained recognition tasks, such as stigma detection, where scale varies significantly and the requirements for receptive fields change dynamically.

POWERFUL-IOU LOSS FUNCTION

Existing IoU-based loss functions first increase the size of the anchor boxes during regression to achieve overlap with the target box. Even when the area of the anchor box is already larger than that of the target box, this regression method is complex and slow, requiring more iterations to converge. Furthermore, their penalty terms contain unreasonable components that fail to accurately reflect the differences between the anchor and target boxes, and they do not fully account for the target size, which may lead to degradation in certain cases. To address issues such as anchor box enlargement, this paper proposes a size-adaptive penalty term that guides the anchor boxes to regress directly and efficiently. This paper combines this penalty term with a function that adjusts the gradient based on anchor box quality, resulting in a new IoU-based loss term called the Powerful-IoU (PIoU) loss.

PIoU is an improved bounding box regression loss function proposed by Liu et al., which has achieved superior performance compared to traditional loss functions such as CIoU and GIoU on mainstream detectors including YOLOv8 and DINO *(Liu et al., 2023)*. Its core innovation lies in the introduction of an adaptive penalty factor and a gradient adjustment mechanism based on anchor quality, enabling the model to dynamically adjust the loss contribution according to anchor quality, thereby enhancing its adaptability to small objects and high-precision localisation tasks. Its expression is given by Eq. (3):

$$L_{PIoU}=\gamma(1-IoU)^2 \quad (3)$$

Here, '$(1\text{-IOU})^2$' serves as the base loss term, assigning a higher loss weight to samples with low IoU; ` $\gamma$ ` acts as a gradient adjustment factor, dynamically adjusting the gradient contribution based on the quality of the anchor boxes.

This design enables PIoU to combine the dual advantages of rapid convergence and stable refinement, making it particularly suitable for the high-precision localisation requirements of small targets such as the stigma.

Evaluation Metrics

For object detection models, this paper primarily employs precision (P), recall (R), average precision (mAP@50), and mean average precision (mAP@50–95) as the main metrics for evaluating model performance. P represents the proportion of all targets correctly identified by the algorithm's bounding boxes, reflecting the model's accuracy; R represents the proportion of correctly identified samples out of the total number of samples; mAP@50 is a key metric reflecting the comprehensive performance of the detection model; mAP@50-95 denotes the average of the mean average precision across different IoU thresholds. The calculations for precision, recall, average precision and mean average precision are shown in Eqs. (4) to (7):

$$\mathrm{P}=\frac{TP}{TP+FP} \tag{4}$$

$$\mathrm{R}=\frac{TP}{TP+FN} \tag{5}$$

$$\mathrm{AP}=\int_0^1 P(r)dr \tag{6}$$

$$mAP=\frac{1}{C}\sum_{i=1}^{c} AP_i \tag{7}$$

TP denotes the number of correctly detected positive samples; FP denotes the number of incorrectly detected negative samples; FN denotes the number of missed positive samples; C represents the number of classes; AP_i represents the average precision of the i-th class.

EXPERIMENTAL ENVIRONMENT

For detailed experimental configuration parameters, see Table 1.

Table 1

Experimental Environment Configuration

Configuration Name	Version and Model
GPU Model and Quantity	NVIDIA GeForce RTX 4080
CPU Model	13th Gen Intel® Core™ i7-13700K
System Memory	32.0GB
Operating System	Windows 11 Home Chinese Edition (22H2 build)
Deep learning framework	Torch 2.2.0 + cu118
CUDA and cuDNN versions	CUDA 11.8 + cuDNN 8.9.7
Programming Languages and Dependencies	timm == 0.9.12, mmcv-full == 2.2.0, numpy=1.26.3

The training parameters are summarized in Table 2.

Table 2

Training Parameter Configuration

Parameter Name	Parameter Value
epoch	200
batch	8
workers	4
optimizer	SGD
size	640
patience	30
amp	False
iou	0.7
lr0	0.01
lrf	0.01

RESULTS AND DISCUSSION

To ensure the validity and reliability of both ablation and comparative experiments, this study strictly controlled extraneous variables by employing identical training configurations for all participating models, and fixed random seeds across all runs to eliminate stochastic fluctuations, thus ensuring that any observed performance variations arise exclusively from network architectural improvements.

ABLATION STUDIES

In the ablation experiments, individual modules (A, B, C, D) were incorporated into the base model to assess their impact on performance. A denotes the RFAConv module; B denotes the CPA-Enhancer module; C denotes the C3k2_SAConv module; D denotes the PIoU loss function. The results are shown in Table 2.

Table 2

Results of the ablation experiments

Model	Module				P	R	mAP@50	mAP@50–95	GFLOPs	FPS
	A	B	C	D						
1					0.832	0.813	0.864	0.579	6.3	210.1
2	√				0.826	0.817	0.87	0.574	14.8	37.7
3		√			0.83	0.819	0.867	0.6	9.6	10.3
4	√	√			0.843	0.829	0.882	0.614	13.87	8.4
5			√		0.84	0.833	0.881	0.568	5.9	93.6
6				√	0.832	0.813	0.865	0.581	6.3	207.1
7			√	√	0.867	0.807	0.878	0.569	5.9	97.6
8	√		√		0.855	0.821	0.868	0.576	14.6	33.8
9	√		√	√	0.838	0.827	0.878	0.584	14.6	33.9
10	√	√	√	√	0.884	0.846	0.908	0.632	13.75	36.3

Based on the results of the comprehensive ablation experiments, the final improved scheme is Model 10: A+B+C+D. It achieved the best performance across core accuracy metrics such as precision, recall and mAP, significantly outperforming the baseline model and other module combinations, thereby fully validating the effectiveness of the multi-module joint optimisation strategy. However, compared to the baseline model, the computational cost of this scheme increased from 6.3 to 13.75, whilst inference speed decreased from 210.1 to 36.3. This change is primarily attributable to the inherent complexity of the introduced modules: RFAConv and C3k2_SAConv enhance feature representation capabilities but increase computational overhead; the serial processing mechanism of the CPA-Enhancer reduces real-time frame rates; and the PIoU loss function introduces additional floating-point operations. Nevertheless, these trade-offs do not detract from the value of the findings of this study. This study prioritises the improvement of detection accuracy; exchanging controllable computational redundancy for a 4.4% improvement in mAP@50 and a 5.3% improvement in mAP@50-95 represents a typical reasonable trade-off between accuracy and efficiency. Furthermore, compared to other high-accuracy combinations, such as Model 4, which achieves only 8.4 FPS, this approach maintains 36.3 FPS whilst achieving the highest accuracy, demonstrating a superior overall balance. Finally, the baseline model itself is designed to be extremely lightweight, with its 210 FPS far exceeding practical application requirements, whilst the computational load of this approach remains within an efficient and acceptable range, providing a clear direction for subsequent engineering optimisation. Therefore, variations in computational load and speed do not diminish the innovative contribution of this study at the algorithmic level; rather, they further highlight the significant advantages in terms of accuracy improvement.

MULTI-MODEL COMPARISON

To validate the superiority of YOLO11 in detecting the pollination status of cherry tomatoes, this paper trained seven models for detecting the pollination status of cherry tomato flowers using the same cherry tomato dataset under identical conditions. Precision (P), Recall (R), Average Precision (mAP@50) and Mean Average Precision (mAP@50-95) were adopted as the primary metrics for evaluating model performance. The comparison results are shown in Table 3.

Table 3

Comparison of model performance

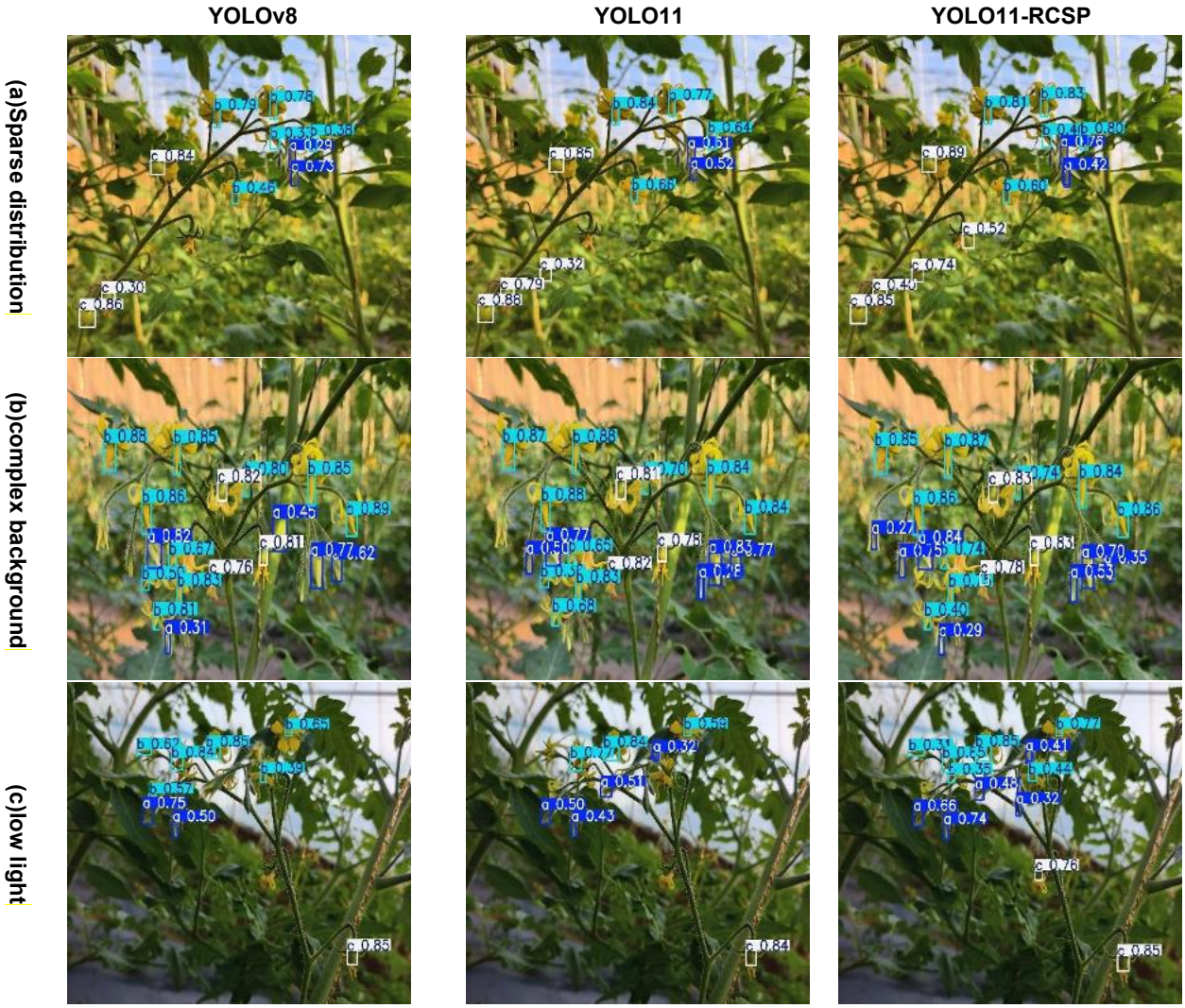
Model	Precision (P)	Recall (R)	mAP@50	mAP@50–95	GFLOPs	FPS
YOLOv5	0.827	0.798	0.865	0.552	5.8	260.1
YOLOv6	0.834	0.796	0.855	0.533	11.5	242.8
YOLOv8	0.829	0.788	0.858	0.547	6.8	256.6
YOLOv9t	0.837	0.815	0.873	0.549	6.4	103.6
YOLOv10n	0.835	0.79	0.858	0.545	8.2	184.1
YOLO11	0.832	0.813	0.864	0.579	6.3	210.1
YOLO11-RCSP	0.884	0.846	0.908	0.632	13.75	36.3

As summarised in Table 3, which compares the results of several mainstream models on the same cherry blossom pollination dataset, the YOLO11-RCSP model proposed in this paper leads comprehensively across core accuracy metrics, achieving a precision of 88.4% and a recall of 84.6%, with mAP@50 and mAP@50-95 reaching as high as 90.8% and 63.2%, respectively, significantly outperforming six comparison models ranging from YOLOv5 to YOLO11. For example, compared to the original YOLO11, mAP@50 is improved by 4.4%, and mAP@50-95 by 5.3%; compared to the similarly performing YOLOv9t, mAP@50 is improved by 3.5%, fully demonstrating the significant advantage of this improved approach in detection accuracy. In terms of computational efficiency, YOLO11-RCSP achieves 13.75 GFLOPs and 36.3 FPS. Although this exceeds some lightweight models, the improvement in accuracy far outweighs the computational cost when compared to YOLOv6 and YOLOv10n. However, whilst YOLOv9t maintains 103.6 FPS, its mAP@50 and mAP@50-95 are both significantly lower than those of our model. The 36.3 FPS fully meets the real-time requirements of agricultural detection scenarios, whilst the 210.1 FPS of the baseline YOLO11 is over-engineered. Therefore, trading a moderate loss in efficiency for a significant gain in accuracy aligns with the core requirements for detection accuracy in practical applications, fully validating the superiority of YOLO11-RCSP in the comprehensive trade-off between accuracy and efficiency.

VISUALISATION

VISUAL ANALYSIS OF DETECTION RESULTS

In this experiment, the performance of the YOLO11-RCSP model and other models in the object detection task was evaluated using six sets of cherry tomato images with distinct characteristics, as shown in Figure 8.



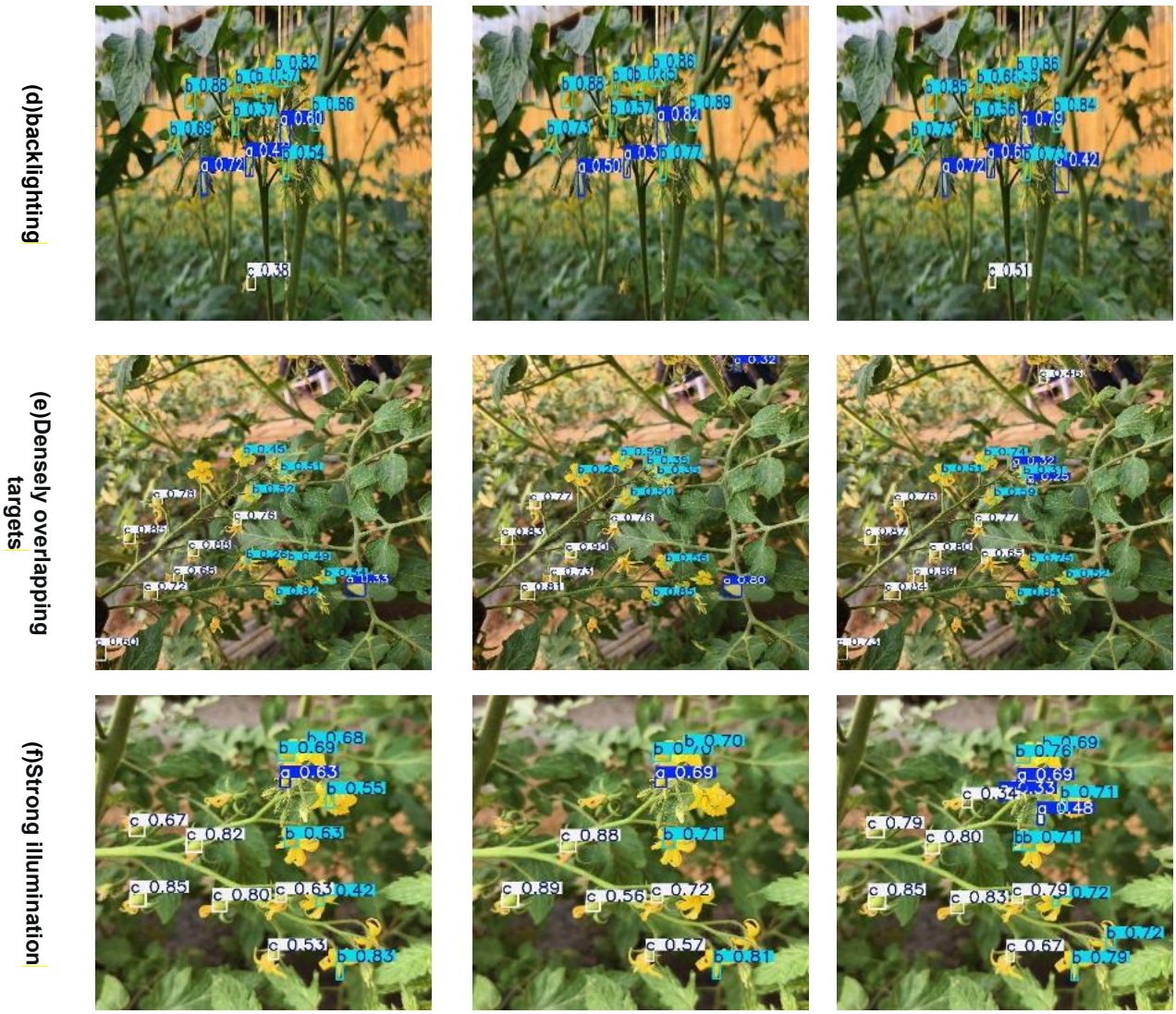


Fig. 8 - Detection comparison among different models and the improved model under various cherry tomato scenarios

The blue, green, and white bounding boxes indicate detected unpollinated styles, detected pollinated styles, and detected cherry tomato fruits, respectively.

In sparsely distributed and complex background scenarios, other models generally suffer from missed detections or misaligned bounding boxes. For example, YOLOv5 and YOLOv8 exhibit a weak response to unpollinated stigmas obscured by leaves, or fail to detect them entirely, whereas YOLO11-RCSP can accurately localise the stigma region, with bounding boxes closely matching the actual targets and a significantly higher accuracy rate than other models.

In scenes with dense targets, such as Column e, YOLOv6 and YOLOv9t exhibited overlapping detection boxes and false positives between multiple targets, misidentifying adjacent petals or ovaries as stigmas; whilst YOLOv10n and the original YOLOv11 detected most stigmas, their localisation accuracy was insufficient, and the detection boxes failed to tightly enclose the stigmas. In contrast, YOLO11-RCSP not only correctly detected all stigmas but also produced compact detection boxes with high accuracy.

In low-light images, the accuracy of other models generally declined, with some models even failing to detect stigmas, whilst YOLO11-RCSP maintained a high detection rate and localisation accuracy.

Visual Analysis of Heatmaps

In this experiment, to intuitively evaluate the areas of focus of different models regarding the pollination status of cherry tomato pistils, this study utilised the GradCAM method to generate heatmaps for each model and conducted a comparative analysis, as shown in Figure 9.

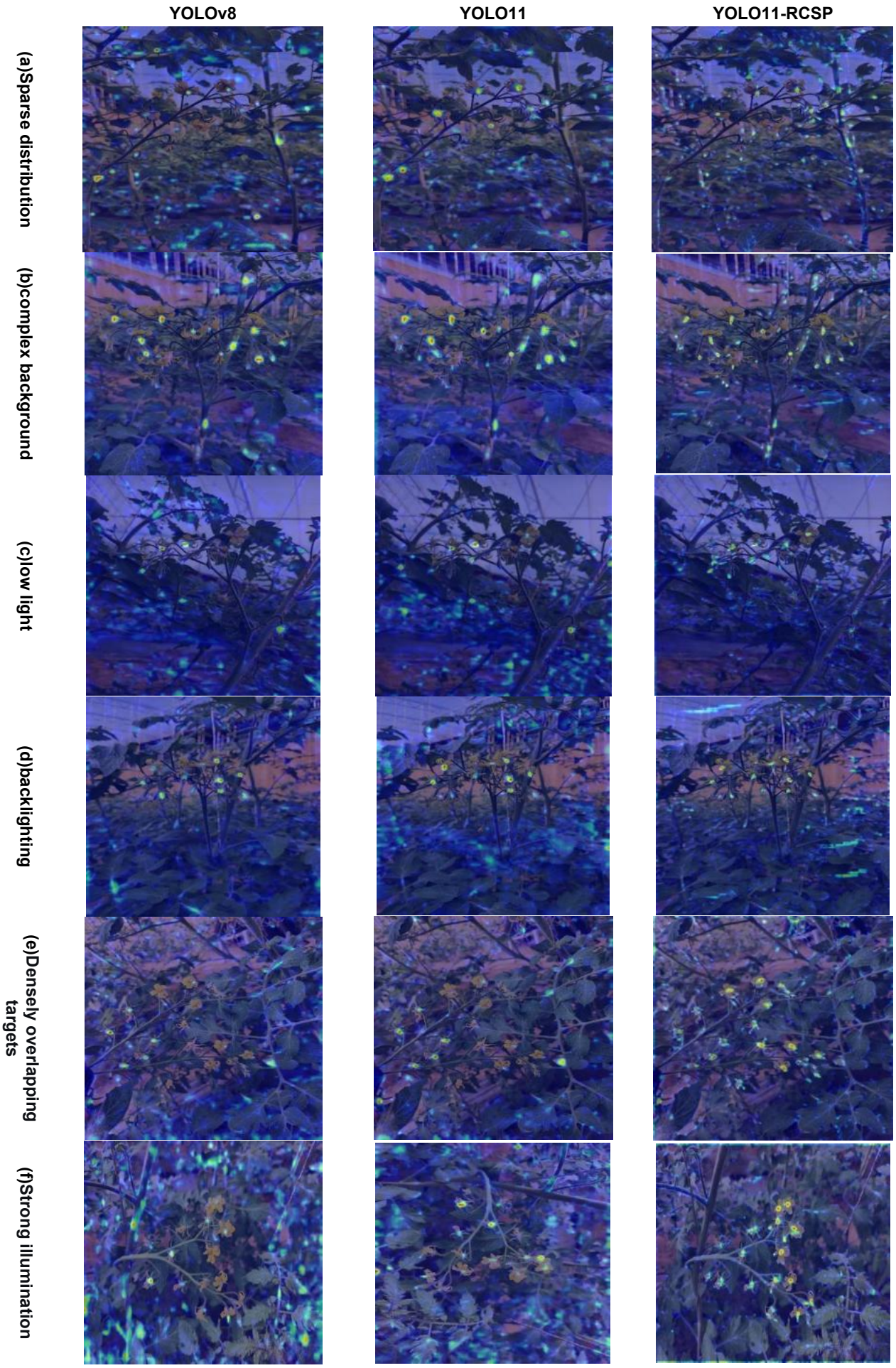


Fig. 9 - Comparison of heatmaps generated by different models and the improved model on various cherry tomato scenes

In scenarios featuring sparse cherry tomato distributions and complex backgrounds, the heatmaps demonstrate that the YOLO11-RCSP model focuses more accurately on the target regions compared to other models, effectively reducing unnecessary background activations. This indicates that the improved model can more effectively extract and focus on key features when handling complex backgrounds or sparse target distributions, exhibiting stronger robustness against interference.

For dense cherry tomato distributions, the YOLO11-RCSP model maintains high recognition accuracy even when targets are densely packed, accurately distinguishing individual targets and reducing false activations or missed detections. In contrast, other models are more susceptible to interference between targets in such scenarios, leading to a decline in detection performance.

Scene Application

Real-scene image collection was carried out in a ridge-planted facility tomato greenhouse using a DJI mobile phone gimbal combined with a smartphone, to verify the actual deployment effect of the model. During collection, the camera advanced uniformly along the planting ridges with wide-angle framing to include multiple tomato flowers in a single frame. By traversing each ridge, moving evenly and slightly adjusting the gimbal angle, repeated frames and overlapping regions were avoided, and the flowering and fruiting areas of the whole greenhouse were fully covered. A total of 218 field test images were obtained.

Inference deployment and acceleration of the optimal weight model best.pt were implemented based on PyTorch. A tomato flower detection system was constructed using Python and OpenCV, which enabled automatic image inference and detection. Unpollinated flowers, pollinated flowers and developed fruits were marked with bounding boxes of different colours, and quantity statistics and visual output were completed.

A field comparison test was conducted with reference to manually annotated ground truth. A total of 1530 valid targets were detected, including 445 unpollinated flowers, 820 pollinated flowers and 265 developed fruits, corresponding to the ground truth values of 454, 811 and 271 respectively. The results show that the model can accurately identify tomato organs at different developmental stages in the field environment with low quantity statistics error, and can provide intelligent support for flowering management, pollination effect evaluation and yield prediction of facility tomatoes.

CONCLUSIONS

To address the core requirement for the accurate recognition of stigma pollination status in cherry blossom pollination robots, along with technical challenges including the tiny size of stigma targets, subtle visual differences among three states, and complex lighting conditions in greenhouse environments, this paper proposes a YOLO11-RCSP model based on the improved YOLO11. The model incorporates four key enhancements: introducing RFAConv receptive field attention convolution to solve parameter sharing issues; adding a CPA-Enhancer adaptive enhancement module to improve adaptability to greenhouse lighting variations and occlusions; replacing the original C3k2 module with the C3k2_SAConv module to dynamically adjust the receptive field; and adopting the Powerful-IoU loss function to optimize small-object localization accuracy. On the self-built cherry tomato pistil dataset, the model achieves 88.40% precision, 84.60% recall, 90.80% mAP@50, and 63.20% mAP@50–95, representing improvements of 5.20%, 3.30%, 4.40%, and 5.30% respectively over the baseline YOLO11, and significantly outperforms mainstream detectors such as YOLOv5, YOLOv6, YOLOv8, YOLOv9t, and YOLOv10n, thereby validating the effectiveness and superiority of the proposed method.

Although the YOLO11-RCSP model has achieved significant improvements in detection accuracy, computational complexity has increased and inference speed has decreased following the model enhancements; whilst it meets real-time requirements, there is still room for optimisation. Future work will focus on model lightweighting and adaptive methods for cross-scenario data augmentation to further enhance the model's deployment efficiency and generalisation robustness.

This research is expected to be deployed in the visual perception module of a tomato pollination robot, enabling precise determination of pollination status and providing a basis for decision-making in automated pollination operations.

ACKNOWLEDGEMENT

This study received support from two projects: the Science and Technology Innovation Enhancement Project under the Scientific Research Initiatives of Shanxi Agricultural University (No. CXGC2025057), the Smart Agricultural Machinery and Rural Governance Project funded by the Shanxi Provincial Key Research and Development Project (No. 202202140601021). The authors express sincere gratitude for the financial and institutional support provided by these initiatives.

REFERENCES

[1] Gao, P., Zhang, X.-Y., Yang, X.-L., et al. (2024). Robust Visual Tracking Using Hierarchical Vision Transformer with Shifted Windows Multi-Head Self-Attention: Regular Section. *IEICE Transactions on Information and Systems*, E107.D(1), 161--164.

[2] Hou, B. F., Li, X. M., Mou, X. W., et al. (2024). Design and experiment of cherry tomato greenhouse inspection robot system. *Chinese Journal of Agricultural Mechanization*, *45*(1), 285--294. https://doi.org/10.13733/j.jcam.issn.2095-5553.2024.01.039

[3] Hu, Y. F., Zhao, X. L., Li, P. J., et al. (2023). Tomato fruit detection in natural environment based on improved YOLOv5. *Chinese Journal of Agricultural Mechanization*, *44*(10), 231--237. https://doi.org/10.13733/j.jcam.issn.2095-5553.2023.10.032

[4] Jia, G. G., Wang, B., & Zhao, Y. (2024). Simulation of apple picking machinery based on visual recognition. *Journal of Agricultural Mechanization Research*, *46*(12), 22--27+112. https://doi.org/10.13427/j.cnki.njyi.2024.12.004

[5] Kang, Y., Li, J. Y., Qiu, J. K., et al. (2023). Soybean seedling identification from ultra-low altitude UAV based on EfficientDet network. *Journal of Agricultural Mechanization Research*, *45*(9), 7--13. https://doi.org/10.13427/j.cnki.njyi.2023.09.013

[6] Li, Z. C., Luo, W. P., Ling, X. J., et al. (2024). Detection method of chestnut burr in natural environment based on improved YOLOv8. *Chinese Journal of Agricultural Mechanization*, *45*(12), 251--258. https://doi.org/10.13733/j.jcam.issn.2095-5553.2024.12.037

[7] Liu, C., Wang, K., Li, Q., et al. (2023). Powerful-IoU: More straightforward and faster bounding box regression loss with a nonmonotonic focusing mechanism. *Neural Networks*, *170*, 276--284.

[8] Lorberboym, E., Lazare, S., Golshmid, P., & Shani, G. (2026). Estimating Cannabis Flower Maturity in Greenhouse Conditions Using Computer Vision. *Agriculture*, *16*, 460. https://doi.org/10.3390/agriculture16040460

[9] Manzoor, S. H., Zhang, Z., Li, X., et al. (2024). Lightweight and Robust YOLOv5s with MobileNetV3 and GhostNet for Precision Apple Flower Detection for Pollination Drones. In Y. Liu, L. Yang, Y. Shi, et al. (Eds.), New Technologies Applied in Apple Production: Sensing and Autonomous Systems (pp. 81--108). *Singapore: Springer Nature Singapore*.

[10] Pan, F., Hu, M., Duan, X., Zhang, B., Xiang, P., Jia, L., Zhao, X., & He, D. (2024). Enhancing kiwifruit flower pollination detection through frequency domain feature fusion: a novel approach to agricultural monitoring. *Frontiers in Plant Science*, *15*, 1415884. https://doi.org/10.3389/fpls.2024.1415884

[11] Pinheiro, I., Moreira, G., Magalhães, S., et al. (2024). Deep learning based approach for actinidia flower detection and gender assessment. *Scientific Reports*, *14*(1), 24452. https://doi.org/10.1038/s41598-024-75432-0

[12] Priyadharshini, J., Arunn, T., Rithick Roshan, B., et al. (2023). Saffron Harvesting using Robotic Arm Embedded on a Rover. *In 2023 2nd International Conference on Automation, Computing and Renewable Systems (ICACRS) (pp. 1745--1750)*. Pudukkottai: IEEE.

[13] Qiao, S., Chen, L.-C., & Yuille, A. (2020). DetectoRS: Detecting Objects with Recursive Feature Pyramid and Switchable Atrous Convolution. *CoRR*, *abs/2006.02334*.

[14] Song, Y. L., Wang, C., Li, D. Y., et al. (2024). UAV small target detection algorithm based on improved YOLOv5s. *Journal of Zhejiang University (Engineering Edition),* *58*(12), 2417--2426.

[15] Sun, J. F., Wang, L., & Wang, J. P. (2024). Research on fruit freshness detection algorithm based on improved YOLOv5s. *Modern Electronic Technology*, *47*(22), 37--43. https://doi.org/10.16652/j.issn.1004-373x.2024.22.007

[16] Tang, Y., Sun, J. Y., Zhang, Y. F., et al. (2025). Kiwifruit flower detection using an optimized YOLOv11n architecture. *INMATEH Agricultural Engineering*, *77*(3), 44--53.

[17] Touko Mbouembe, P. L., Liu, G., Park, S., & Kim, J. H. (2024). Accurate and fast detection of tomatoes based on improved YOLOv5s in natural environments. *Frontiers in Plant Science*, *14*, 1292766. https://doi.org/10.3389/fpls.2023.1292766

[18] Wang, J. S., Liu, Q. Y., & Zhao, P. S. (2016). Study on effect of vibrator pollination on tomato in winter-spring greenhouse. *Vegetables*, (4), 21--23.

[19] Wang, S., Li, Q., Yang, T., et al. (2024). LSD-YOLO: Enhanced YOLOv8n Algorithm for Efficient Detection of Lemon Surface Diseases. *Plants*, *13*(15), 2069. https://doi.org/10.3390/plants13152069

[20] Wang, X. F., Zhang, Q., & Su, A. H. (2013). Application effect of bumblebee pollination technology on greenhouse cherry tomato. *Northern Horticulture*, (11), 45--47.

[21] Yang, M., Lyu, H., Zhao, Y., et al. (2023). Delivery of pollen to forsythia flower pistils autonomously and precisely using a robot arm. *Computers and Electronics in Agriculture*, *214*.

[22] Zhang, X., Liu, C., Yang, D., Song, T., Ye, Y., Li, K., & Song, Y. (2023). RFAConv: Innovating Spatial Attention and Standard Convolutional Operation. *CoRR*, *abs/2304.03198*.

[23] Zhang, Y., Wu, Y., Liu, Y., & Peng, X. (2024). CPA-Enhancer: Chain-of-Thought Prompted Adaptive Enhancer for Object Detection under Unknown Degradations. *arXiv preprint arXiv*:2403.11220.

RESEARCH ON GRAPE DISEASE DETECTION METHOD BASED ON PWE-YOLO
/
基于 PWE-YOLO 的葡萄病害检测方法

Haoyue LIU [1)], Benzhi YANG [1)], Mingyang Gao [1)], Dong WANG [1)], Yuepeng SONG[1,2,*)] Longlong REN[1,2,*)]
[1)] Shandong Agricultural University, College of Mechanical and Electrical Engineering/ China;
[2)] Shandong Provincial Engineering Laboratory of Agricultural Equipment Intelligence/ China
E-mail: uptonsong@sdau.edu.cn
DOI: https://doi.org/10.35633/inmateh-79-40

Keywords: *Grape diseases; Deep learning; Object detection; Lightweight model; YOLO v11*

ABSTRACT

Accurate detection of grape diseases in controlled facility environments is of significant importance. In this study, a novel detection model, PWE-YOLO, is proposed based on YOLO v11. In this model, the C3k2 modules in the Neck network are replaced with C3k2-PConv modules, which maintain high-precision feature extraction while reducing model parameters and memory consumption. Furthermore, a WaveletPool module is introduced to replace all Conv modules in the model, except for the 0th and 1st layers, enhancing feature representation and detection accuracy for grape diseases while further reducing model parameters and floating-point operations. EMA attention modules are incorporated at the 17th and 24th layers to improve small-object detection capabilities, thereby increasing overall detection precision. Experimental results demonstrate that PWE-YOLO achieves a precision of 85.0%, recall of 83.6%, and mAP of 86.9%, with 1.96 × 10^6 parameters and 5.1 × 10^9 floating-point operations. Compared with the original YOLO v11 model, precision, recall, and mAP increase by 4.5, 1.4, and 1.9 percentage points, respectively, while parameters and floating-point operations decrease by 24.03% and 10.05%. Relative to YOLO v8, v9, v10, v12, and v13, precision improves by 2.2%, 5.3%, 3.3%, 2.2%, and 2.5%, recall by 6.0%, 2.8%, 5.2%, 8.8% and 3.8%, and mAP by 1.9%, 1.8%, 2.8%, 5.0%, and 2.3%, respectively, with corresponding reductions in model parameters and floating-point operations. These results indicate that PWE-YOLO not only provides high-accuracy detection for grape diseases but also reduces computational complexity, achieving a lightweight architecture and faster detection speed, making it suitable for deployment in resource-constrained target detection scenarios.

摘要

为实现设施环境中葡萄病害目标的准确检测，本文在 YOLO v11 的基础上，提出一种适用于设施环境葡萄病害目标检测模型 PWE-YOLO。将颈部网络中的 C3 2 模块替换为 C3 2-PConv 模块，在保持高精度特征提取能力的基础上，降低模型参数量和内存占用量；同时在模型中引入 WaveletPool 模块，替换模型中除第 0 层、第 1 层外的所有 Conv 模块，提高葡萄病害的特征表达能力与检测精度，进一步降低模型参数量和浮点运算量；且在模型的第 1 层和第 24 层中添加 EMA 注意力机制模块，增强模型对小目标的检测能力，提升模型的检测精度。结果显示，PWE-YOLO 模型的精确率为 85.0%、召回率为 83.6%、mAP 为 86.9%、参数量为 1.96×10^6、浮点运算量为 5.1×10^9。与原始 YOLO v11 模型相比，该模型的精确率、召回率和 mAP 分别提高 4.5、1.4、1.9 个百分点，参数量和浮点运算量分别降低 24.03%、10.05%。与 YOLO v8、YOLO v9、YOLO v10、YOLO v12、和 YOLO v13 模型相比，其精确率分别提高 2.2、5.3、3.3、2.2、和 2.5 个百分点，召回率分别提高 6.0、2.8、5.2、8.8、和 3.8 个百分点，mAP 分别提高 1.9、1.8、2.8、5.0、和 2.3 个百分比，参数量分别减少 34.88%、25.19%、2 .40%、21.91%和 20.00%，浮点运算量分别减少 3 .03%、52.34%、3 .80%、12.0 %和 1 . 4%。结果表明，本文提出的 PWE-YOLO 模型在葡萄病害检测任务中不仅能够提供高准确性的检测性能，同时也有效降低了计算复杂度，具有较轻的模型结构和较快的检测速度，适合应用于对计算资源要求较高的目标检测任务中。

INTRODUCTION

Grapes, as one of the most important economic crops worldwide, are known to be highly susceptible to fungal diseases, including downy mildew, powdery mildew, and gray mold, during their growth period. Premature leaf senescence and fruit rot are caused by these diseases, which severely affect yield and quality *(Rahman et al, 2024)*.

Haoyue Liu, M.Sc. Stud. Eng.; Benzhi Yang, M.Sc. Stud. Eng.; Mingyang Gao, M.Sc. Stud. Eng.; Dong Wang, M.Sc. Stud. Eng.; Longlong Ren Lecturer Ph.D. Eng; Yuepeng Song, Prof. Ph.D. Eng.

Therefore, early detection and effective control of these diseases are considered crucial for ensuring the sustainable development of the grape industry. However, in the early stages of infection, disease symptoms are often subtle and typically manifest as small spots or slight discoloration on leaves, which can be easily mistaken for leaf changes induced by environmental stress. Traditional manual identification methods are largely dependent on expert judgment, resulting in relatively low accuracy and making comprehensive monitoring in large-scale vineyards difficult to achieve *(Poblete-Echeverría et al, 2025)*.

In recent years, with the rapid advancement of computer vision and deep learning technologies, image recognition methods based on convolutional neural networks (CNNs) have made remarkable progress in crop disease detection *(Zhang et al, 2022)*. Among these methods, the YOLO series of algorithms has been extensively applied in agricultural settings, particularly for the identification and detection of grape diseases, due to its end-to-end architecture and high real-time performance. For example, Liu et al. proposed an improved CNN-based detection framework for multiple grape leaf diseases, in which preprocessing and data augmentation techniques were applied to simulate real-world environments, enhancing the model's robustness and generalization ability, and achieving a precision of 97.22% on the test set *(Liu et al, 2020)*. Zhen Yuanyuan et al. introduced the CBAM attention mechanism on top of the YOLOv8 model to enhance the feature representation of key disease spots on grape leaves, while the ShuffleNet V2 module was incorporated for network lightweight modification, which improved both detection accuracy and speed, achieving a mAP of 94.6% and an inference speed of 52.06 FPS *(Yang et al, 2024)*. Zhang et al. proposed the DLVTNet model, combining generative data augmentation with a lightweight Transformer, and achieved a precision of 98.48% on the grape leaf disease dataset *(Zhen et al, 2025)*. Fu et al. combined YOLO and Transformer concepts to develop the MHDI-DETR model, balancing computational efficiency and detection accuracy, and achieving a mAP of 92.6% in detecting grape leaf diseases such as black rot and black spot *(Fu et al, 2024)*. Zhang Lin et al. proposed a detection method combining StyleGAN2-ADA augmentation with an improved YOLOv7 model to enhance localization of small early-stage disease spots, and by utilizing attention mechanisms and feature fusion, the model was able to detect small targets effectively, achieving a mAP of 95.4%, a precision of 94.1%, and an inference speed of 77.12 FPS *(Zhang et al, 2025)*.

Nevertheless, existing studies remain limited, as deep network models typically involve large numbers of parameters and high computational complexity, which hinder efficient deployment on resource-constrained agricultural edge devices. To address these challenges, an early detection method for grape diseases based on PWE-YOLO is proposed in this study. The proposed model enhances detection accuracy for grape diseases, reduces model parameters and memory consumption, and improves detection speed. Notably, in resource-limited environments, the model demonstrates superior real-time detection and on-site deployment capabilities, thereby exhibiting increased practicality and robustness.

MATERIALS AND METHODS

Data Collection and Preprocessing

Image data were collected at the Yantai Academy of Agricultural Sciences, Fushan District, Yantai City (37.5076°N, 121.255°E), from September 2024 to August 2025. The images were captured under natural lighting conditions using an iPhone 15 Pro smartphone, which took multi-angle shots of grape leaves. A total of approximately 3,000 images were collected, covering both healthy leaves and five major disease types: downy mildew, powdery mildew, gray mold, canker, and Grapevine Leafroll-associated Virus (GLRaV) disease. To ensure sample diversity, the images were captured under varying lighting intensities, humidity levels, and leaf age stages. The collected images were manually screened to remove blurred and occluded samples, after which they were resized to 600×400 pixels and normalized to ensure consistency in input for model training. After screening, a final dataset consisting of 1,785 high-quality images was created. Table 1 presents the number of images for each disease category in the dataset.

Table 1

Number of images in grape disease dataset

Type	downy mildew	powdery mildew	gray mold	canker	GLRaV
Primitive	456	359	321	369	280

Disease annotation was performed using the LabelImg tool, with the annotation categories including five types: downy mildew, powdery mildew, gray mold, canker, and GLRaV; the annotation results are shown in Figure 1.

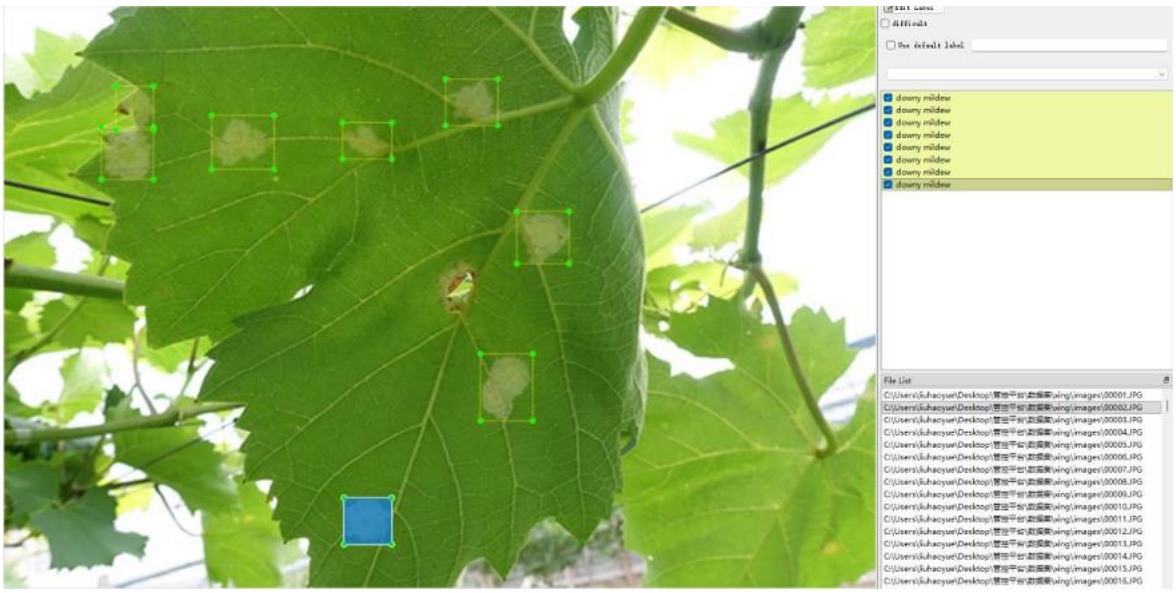


Fig. 1 - Annotation of the Grape Disease Dataset

The dataset was divided into training, validation, and test sets with a ratio of 70%, 20%, and 10%, respectively. To improve the model's robustness and generalization ability, data augmentation was applied to the images in the dataset. Specifically, six augmentation techniques were used: adding Gaussian noise, random rotation, random cropping, horizontal flipping, brightness adjustment, and Gaussian blur. For each original image, three techniques were randomly selected) from the six listed and applied in combination, repeated three times. This process produced three augmented samples per original image, effectively enlarging the dataset and improving the model's adaptability to complex imaging conditions. The dataset was ultimately expanded to 7,140 images, with 4,998 images in the training set, 1,428 in the validation set, and 714 in the test set. Representative examples of the augmented dataset images are shown in Figure 2.

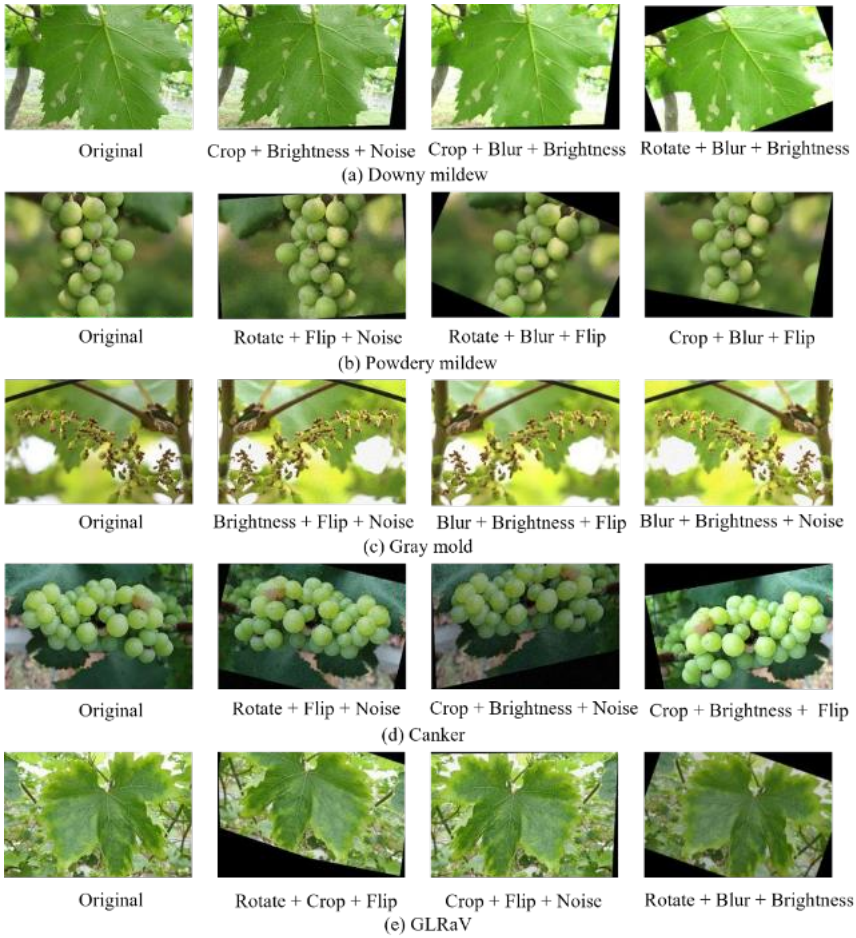


Fig. 2 - Image Examples of the Grape Disease Dataset

Construction of the PWE-YOLO-Based Grape Disease Detection Model

In agricultural object detection tasks, YOLO v11 adopts an efficient single-stage architecture and demonstrates strong small-object feature representation capabilities, enabling high-precision real-time detection of targets such as pests and diseases in complex scenarios, while maintaining a lightweight design and ease of deployment *(Badgujar et al, 2024)*. To enhance the detection performance of grape diseases in controlled environments, the YOLO v11 model was improved in this study.

First, the C3k2-PConv module was introduced to replace the C3k2 module in the Neck network. This modification reduces the model's parameter count and memory usage while preserving high-precision feature extraction capabilities. Consequently, real-time detection performance is improved, and model robustness and detection accuracy are simultaneously enhanced.

Second, the WaveletPool module was introduced to replace all Conv modules in the model, except for the 0th and 1st layers. This modification reduces the model's parameter count and floating-point operations, maintaining a lightweight architecture while effectively suppressing downsampling aliasing. Moreover, it enhances the retention of high-frequency features in disease regions, such as edges, patterns, and color variations, thereby improving feature representation and detection accuracy for early-stage grape diseases.

Finally, the EMA attention mechanism module was added to the 17th and 24th layers to mitigate background interference, enhance the model's robustness in complex environments, and improve precision and mAP values. The architecture of the proposed PWE-YOLO model is illustrated in Figure 3.

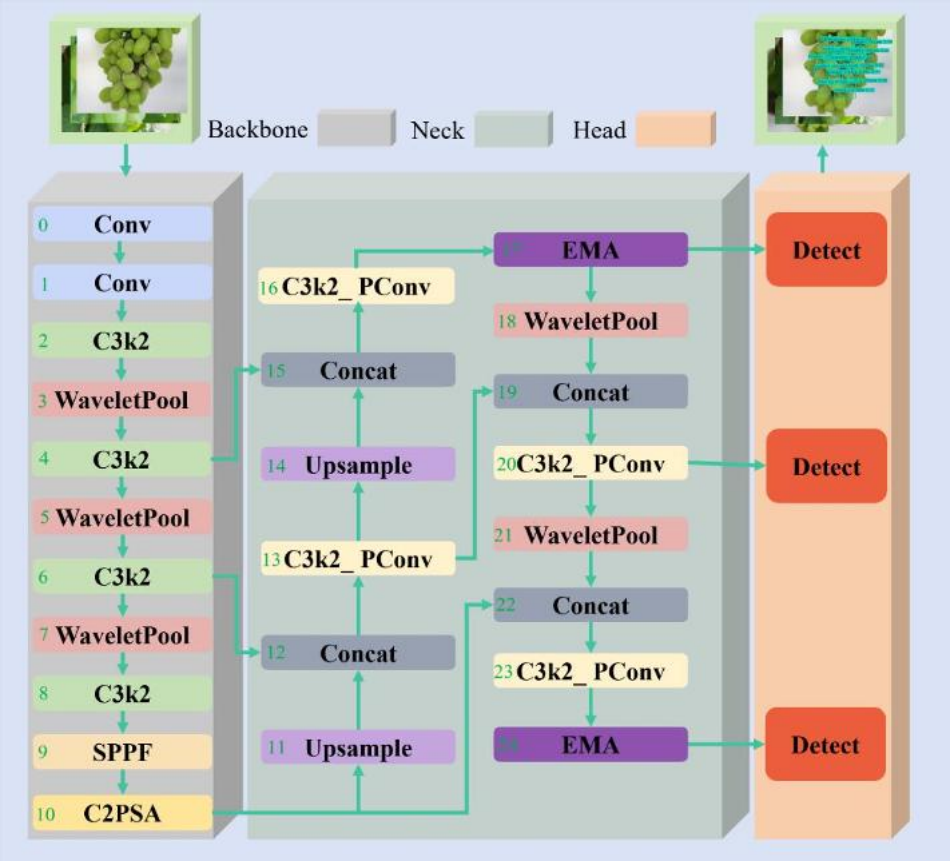


Fig. 3 - Architecture of the PWE-YOLO Model

C3k2-PConv Module

Partial Convolution (PConv) *(Chen et al, 2023)* performs convolution operations on the valid regions of the input feature map, reducing redundant computations and memory accesses, thereby improving the efficiency of spatial feature extraction *(Jiang et al, 2025)*. Unlike traditional convolution and depth/group convolutions, PConv applies the convolution kernel only to valid channels, leaving other channels unchanged. This approach reduces the number of floating-point operations, maintains high detection accuracy, reduces the model's parameter count, and increases computational speed *(Zhang and Zeng, 2024)*, The structure of PConv is illustrated in Figure 4. The C3k2 module extracts multidimensional features from the input image by combining convolutions at different levels. The C3 layer is generally used to capture feature information at multiple scales more effectively, thereby enhancing the model's ability to perceive complex image content *(Jin et al, 2025; Zhang et al, 2026)*.

The C3k2-PConv module combines the deep feature extraction capability of Convolutional Neural Networks (CNN) with the selective convolution ability of partial convolutions. Through flexible convolution kernel combinations and localized convolution operations, it enhances the processing of complex image content while effectively addressing the impact of missing or invalid data. The structure of the C3k2-PConv module is shown in Figure 5.

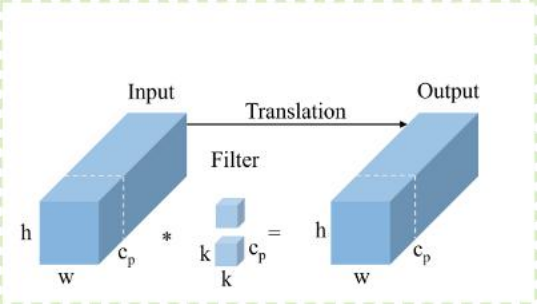


Fig. 4 - Architecture of the PConv Module

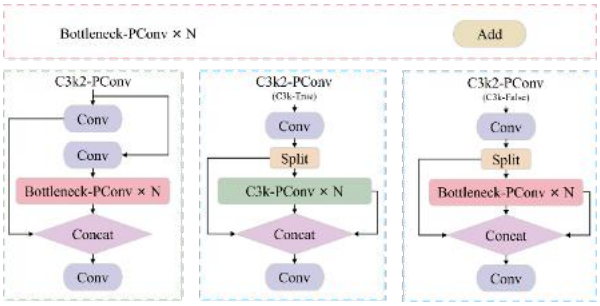


Fig. 5 - Architecture of the C3k2-PConv Module

For the early detection of grape diseases, the C3k2-PConv module substantially reduces the model's parameter count and memory usage while maintaining high-precision feature extraction capabilities, thereby enhancing real-time detection speed. Particularly in cases of feature loss or damaged regions caused by insufficient lighting or suboptimal shooting angles, C3k2-PConv performs convolution operations exclusively on valid regions, avoiding interference from missing or corrupted areas in the final detection results. Consequently, the module improves the model's robustness and detection accuracy under challenging imaging conditions.

WaveletPool Module

The WaveletPool module is an efficient downsampling method based on discrete wavelet transform *(Sun et al, 2022)*. By performing two-dimensional wavelet decomposition on the input feature map, the module extracts a low-frequency structural subband (LL) and three types of high-frequency detail subbands (LH, HL, HH), using the LL subband as the downsampling output. This approach reduces feature dimensionality while retaining key information such as edges and textures of the target *(Qu and Zhang, 2025; Xu and Wang, 2023)*. Compared with traditional max pooling or average pooling, WaveletPool module effectively suppresses aliasing in the downsampling process in the transform domain, preventing small target features from being overly smoothed or lost in deep networks. It is particularly suitable for small object recognition and detection tasks in agricultural scenarios characterized by significant scale variations and complex backgrounds *(Raj et al, 2025)*. Furthermore, WaveletPool features low computational cost and a lightweight structure, making it appropriate for deployment on mobile devices or in real-time detection systems. Its advantages in enhancing accuracy and feature stability have been validated in several lightweight detection networks. The structure of the WaveletPool module is shown in Figure 6.

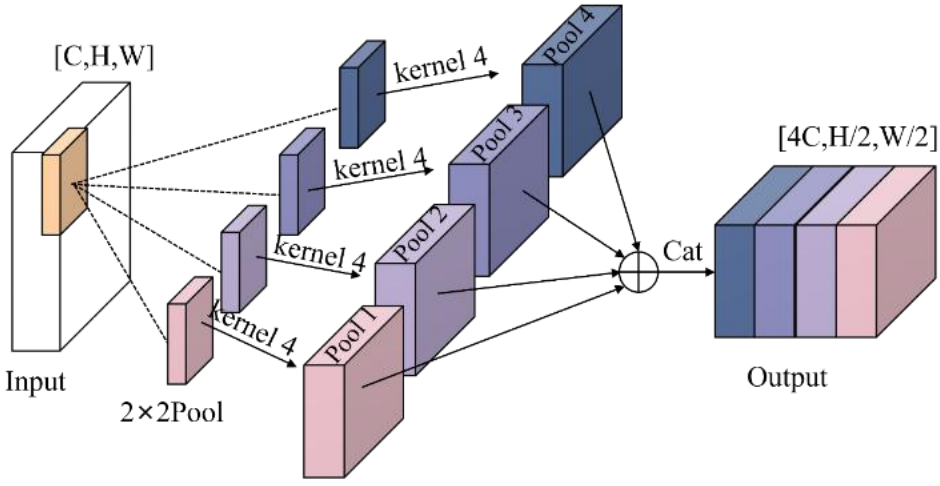


Fig. 6 - Architecture of the WaveletPool module

For grape disease detection tasks, the WaveletPool module, based on discrete wavelet transform, effectively suppresses aliasing during downsampling while maintaining the network's lightweight design, enhancing the retention of high-frequency features such as edges, patterns, and color variations in disease regions. This module stabilizes the model under conditions of low texture contrast, complex background lighting, and micro-scale variations in early-stage disease spots, thereby improving feature representation and detection accuracy for early-stage grape diseases.

EMA Attention Module

The EMA (Efficient Multi-scale Attention) *(Ouyang et al, 2023)* mechanism is an efficient feature extraction module designed to enhance the fusion of multi-scale features. Integrating the EMA attention mechanism into the YOLO model can improve the detection accuracy of agricultural targets, including crop diseases and small objects such as buds. The EMA module divides the input feature map into multiple sub-feature groups and utilizes parallel 1×1 and 3×3 convolution paths to extract fine-grained and large-scale features, respectively. The 1×1 path employs global average pooling and convolution operations to encode channel information, enhancing inter-channel interaction, while the 3×3 path captures broader spatial features, expanding the receptive field for feature extraction *(Li et al, 2025)*. This design allows the EMA attention mechanism to focus on target regions without compromising computational efficiency, improving robustness to small targets and complex backgrounds *(Williams et al, 2018)*. Following its integration, the YOLO model demonstrates enhanced capability in detecting small targets and handling complex backgrounds, thereby improving its suitability for agricultural application, effectively improving the detection of small objects such as buds and early-stage disease spots. The structure of the EMA attention mechanism is shown in Figure 7.

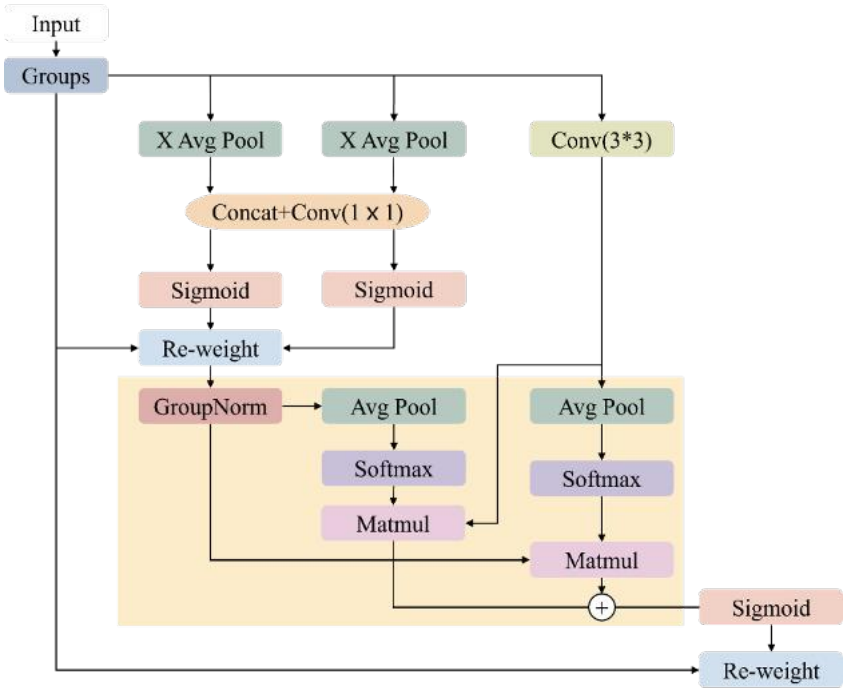


Fig. 7 - Architecture of the EMA module

In grape disease detection tasks, the EMA attention mechanism enhances the model's sensitivity to early-stage grape diseases, such as small lesions, through multi-scale feature extraction and information fusion. It effectively captures features at different scales via parallel 1×1 and 3×3 convolution paths, while reinforcing attention to small targets, thereby improving detection accuracy for small lesions. Additionally, EMA reduces background interference, enhancing model robustness in complex environments and enabling more accurate and stable early detection of grape diseases.

Model Deployment Methodology

The operating system used is Linux Ubuntu 22.04, with an Intel(R) Xeon(R) Platinum 8474C CPU model, an NVIDIA GeForce RTX 4090 GPU with 24GB of video memory. The programming language is Python 3.10, the deep learning framework is PyTorch 2.1.0, and the GPU acceleration library is CUDA 12.1.

RESULTS

Experimental Setup and Evaluation Metrics

To evaluate the performance of the network model in object detection tasks, Precision, Recall, mean Average Precision (mAP), the number of parameters, and the number of floating-point operations are used as the primary evaluation metrics *(Xie et al, 2025)*. During training, the input image size was set to 400 × 600 pixels, the number of epochs was set to 100, and the batch size was set to 64. The SGD optimizer was used for model optimization. The cache mechanism was enabled, the number of data loading workers was set to 8, and automatic mixed precision training was adopted.

Comparison Experiment of C3k2-PConv Module

To evaluate the performance of the C3k2-PConv module proposed in this study, alternative modules—C3k2-WTConv, C3k2-FasterBlock, and C3k2-RepVGG—were used to replace the corresponding module at the same position in the model, and comparison experiments were conducted. The results are summarized in Table 2.

Table 2

Effects of different C3k2 modules on detection performance

Model	P/%	R/%	mAP/%	Parameters	FLOPs
YOLO v11	80.5	82.2	85.0	2.58×10^6	6.3×10^9
YOLO v11-C3k2-PConv	81.5	82.7	85.7	2.37×10^6	5.9×10^9
YOLO v11-C3k2-WTConv	80.5	81.8	85.5	2.53×10^6	6.3×10^9
YOLO v11- C3k2-FasterBlock	82.0	82.5	85.1	2.54×10^6	6.2×10^9
YOLO v11-C3k2-RepVGG	80.9	82.5	85.2	2.60×10^6	6.4×10^9

As shown in the table, the YOLO v11-C3k2-PConv model achieves improvements of 1.0, 0.5, and 0.7 percentage points in Precision, Recall, and mAP, respectively, compared with the baseline YOLO v11 model, while reducing the number of parameters and floating-point operations by 8.1% and 6.3%, respectively. Compared with the other alternative modules, the YOLO v11-C3k2-PConv model exhibits slightly lower Precision than the YOLO v11-C3k2-FasterBlock model, but outperforms the remaining models across all other evaluation metrics. In particular, its Recall, mAP, number of parameters, and floating-point operations are superior to those of the alternative models, demonstrating a lower computational cost. These results suggest that the YOLO v11-C3k2-PConv model is well adapted to object detection tasks under constrained computational resources and demonstrates superior performance in the grape disease detection task evaluated in this study.

Comparison Experiment of WaveletPool Module

The performance of the WaveletPool module proposed in this study was evaluated by replacing it with alternative modules—SAConv, ContextGuided, and ADown—at the same position in the model, and comparison experiments were conducted. The results are summarized in Table 3.

Table 3

Comparison of detection results for different modules

Model	P/%	R/%	mAP/%	Parameters	FLOPs
YOLO v11	80.5	82.2	85.0	2.58×10^6	6.3×10^9
YOLO v11-WaveletPool	83.2	80.0	85.5	2.17×10^6	5.4×10^9
YOLO v11-SAConv	83.2	79.9	84.3	3.42×10^6	4.7×10^9
YOLO v11-ContextGuided	81.2	78.8	86.0	2.83×10^6	6.8×10^9
YOLO v11-ADown	83.0	80.0	83.7	2.11×10^6	5.3×10^9

As shown in the table, compared with the original YOLO v11 model, the YOLO v11-WaveletPool model exhibits a slight decrease in Recall, while Precision and mAP increase by 2.7 and 0.5 percentage points, respectively. Additionally, the number of parameters and floating-point operations decrease by 15.89% and 14.29%, respectively. Compared with the alternative modules, YOLO v11-WaveletPool demonstrates higher Precision and Recall. Although its mAP is slightly lower than that of the YOLO v11-ContextGuided model, it outperforms the other models in overall detection performance. In comparison with the YOLO v11-ADown model, the YOLO v11-WaveletPool model has slightly higher numbers of parameters and floating-point operations, but its Precision, Recall, and mAP remain superior. Moreover, the total number of parameters and floating-point operations in the YOLO v11-WaveletPool model is substantially lower than in the remaining models, contributing to better overall efficiency and detection performance.

Comparison Experiment of EMA Attention Module

The performance of the EMA attention mechanism proposed in this study was evaluated by integrating alternative attention mechanisms—including SCSA, MSDA, LSKA, iRMB, CGA, and SEAM—at the corresponding positions in the model. Performance comparisons were then conducted, and the results are presented in Figure 8.

As shown in Figure 8, compared with the baseline YOLO v11 model, the YOLO v11-EMA model achieves increases of 1.7, 0.4, and 0.7 percentage points in Precision, Recall, and mAP, respectively. Relative to the YOLO v11-MSDA model, the YOLO v11-EMA model exhibits a slightly lower Recall, while its Precision and mAP are improved by 0.4 and 1.2 percentage points, respectively. For the YOLO v11-iRMB model, although its mAP is comparable to that of the YOLO v11-EMA model, its Precision and Recall remain lower. Furthermore, compared with the YOLO v11-SCSA, YOLO v11-LSKA, YOLO v11-CGA, and YOLO v11-SEAM models, the YOLO v11-EMA model demonstrates superior performance in all three metrics. Collectively, these results indicate that the YOLO v11-EMA model exhibits the best overall performance in grape disease detection tasks.

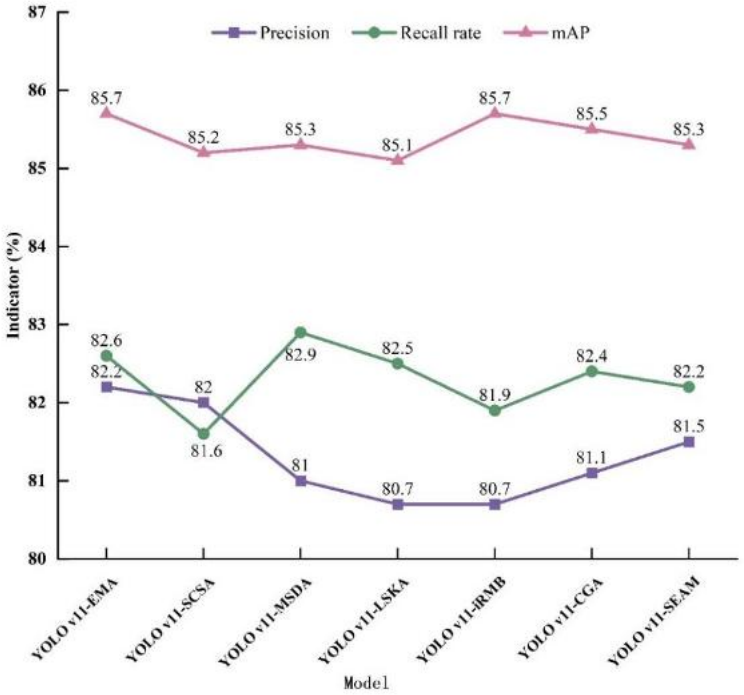


Fig. 8 - Comparative results of different attention modules

Ablation Experiment

The effectiveness of the improved PWE-YOLO model was evaluated through ablation experiments conducted on the custom-built grape disease dataset, with YOLO v11 serving as the baseline model. These experiments were designed to assess the impact of each individual module on overall model performance. The results of the ablation study are presented in Table 4, where "√" indicates the inclusion of a module and "×" indicates its exclusion. Here, P represents the C3k2-PConv module, W corresponds to the WaveletPool module, and E denotes the EMA attention mechanism.

Table 4

Results of ablation experiment

Model	WaveletPool	EMA	C3k2-PConv	P/%	R/%	mAP/%
YOLO v11	×	×	×	80.5	82.2	85.0
YOLO v11-P	×	×	√	81.5	82.7	85.7
YOLO v11-W	√	×	×	83.2	80.0	85.5
YOLO v11-E	×	√	×	82.2	82.6	85.7
YOLO v11-PW	√	×	√	83.9	83.2	85.8
YOLO v11-PE	×	√	√	84.5	83.4	86.6
YOLO v11-WE	√	√	×	83.3	83.1	86.4
PWE-YOLO	√	√	√	85.0	83.6	86.9

As presented in Table 4, the introduction of the C3k2-PConv module into the YOLO v11 model results in the YOLO v11-P model. Compared with the baseline YOLO v11 model, YOLO v11-P achieves improvements of 1.0, 0.5, and 0.7 percentage points in Precision, Recall, and mAP, respectively, while its number of parameters and floating-point operations are reduced by 8.13% and 6.35%, respectively. The integration of the WaveletPool module into YOLO v11 produces the YOLO v11-W model. Compared with YOLO v11, YOLO v11-W improves Precision and mAP by 2.7 and 0.5 percentage points, respectively, while its number of parameters and floating-point operations are reduced by 15.89% and 14.29%, respectively. Similarly, the addition of the EMA attention mechanism results in the YOLO v11-E model. Compared with the baseline model, YOLO v11-E achieves improvements of 1.7, 0.4, and 0.7 percentage points in Precision, Recall, and mAP, respectively, while its number of parameters and floating-point operations slightly increase. These results indicate that the individual incorporation of the C3k2-PConv, WaveletPool, and EMA modules can effectively enhance the detection performance of the model.

The simultaneous integration of the C3k2-PConv and WaveletPool modules into the YOLO v11 model produces the YOLO v11-PW model. Compared with the YOLO v11-P and YOLO v11-W models, YOLO v11-PW achieves improvements in Precision, Recall, and mAP, while its number of parameters and floating-point operations is significantly reduced relative to YOLO v11, YOLO v11-P, and YOLO v11-W. The combination of the C3k2-PConv module and the EMA attention mechanism results in the YOLO v11-PE model. YOLO v11-PE demonstrates enhanced Precision, Recall, and mAP compared with YOLO v11-P and YOLO v11-E, while its number of parameters and floating-point operations are reduced compared with YOLO v11 and YOLO v11-E, with a slight increase in floating-point operations relative to YOLO v11-P. Similarly, the integration of the WaveletPool module and the EMA attention mechanism yields the YOLO v11-WE model. Compared with YOLO v11-W and YOLO v11-E, YOLO v11-WE achieves improvements in Precision, Recall, and mAP, while its number of parameters and floating-point operations is significantly lower than in YOLO v11 and YOLO v11-E, with a slight increase in floating-point operations relative to YOLO v11-W.

The simultaneous integration of the C3k2-PConv module, the WaveletPool module, and the EMA attention mechanism into the YOLO v11 model produces the PWE-YOLO model. Compared with the baseline YOLO v11 model, PWE-YOLO achieves improvements of 4.5, 1.4, and 1.9 percentage points in Precision, Recall, and mAP, respectively, while reducing the number of parameters and floating-point operations by 24.03% and 10.05%, respectively. PWE-YOLO outperforms all other improved models across the evaluated metrics, demonstrating superior detection performance. The results of the ablation experiments confirm the effectiveness and rationality of the proposed design. By integrating the C3k2-PConv, WaveletPool, and EMA modules, the model's detection accuracy is effectively enhanced, while the computational cost is substantially reduced. These improvements make the proposed method particularly suitable for target detection tasks under constrained computational resources, highlighting its clear advantage for grape disease detection in controlled environments.

Comparative Experiment of Different Models

To further validate the advancement of the PWE-YOLO model proposed in this paper, a comparative experiment was conducted between the PWE-YOLO model and the YOLO v8 *(Ren et al, 2024)*, YOLO v9 *(Kalezhi and Shumba, 2025)*, YOLO v10 *(Zheng et al, 2025)*, YOLO v11, YOLO v12 *(Zhao et al, 2025)*, and YOLO v13 models. In the experimental design, all models were trained and tested under the same hardware and software environment to eliminate the influence of external environmental factors on the experimental results. The grape disease dataset constructed in this study was used, and reasonable hyperparameters were set to ensure the reliability and accuracy of the experimental results. The results are summarized in Table 5.

Table 5

Performance comparison of different models

Model	P/%	R/%	mAP/%	Parameters	FLOPs
YOLO v8	82.8	77.6	85.0	3.01×10^6	8.1×10^9
YOLO v9	79.7	80.8	85.1	2.62×10^6	10.7×10^9
YOLO v10	81.7	78.4	84.1	2.70×10^6	8.2×10^9
YOLO v11	80.5	82.2	85.0	2.58×10^6	6.3×10^9
YOLO v12	83.8	74.8	81.9	2.51×10^6	5.8×10^9
YOLO v13	83.5	79.8	84.6	2.45×10^6	6.2×10^9
PWE-YOLO	85.0	83.6	86.9	1.96×10^6	5.1×10^9

As shown in Table 5, the PWE-YOLO model achieves a Precision of 85.0%, Recall of 83.6%, and mAP of 86.9%, with a parameter count of 1.96×10^6 and floating-point operations of 5.1×10^9. Compared with YOLO v8, YOLO v9, YOLO v10, YOLO v11, YOLO v12, and YOLO v13, the Precision of PWE-YOLO increases by 2.2, 5.3, 3.3, 4.5, 2.2, and 2.5 percentage points, respectively; Recall increases by 6.0, 2.8, 5.2, 1.4, 8.8, and 3.8 percentage points, respectively; and mAP improves by 1.9, 1.8, 2.8, 1.9, 5.0, and 2.3 percentage points, respectively. In terms of computational complexity, PWE-YOLO demonstrates significant advantages over the compared models. The number of parameters is reduced by 34.88%, 25.19%, 27.40%, 24.03%, 21.91%, and 20.00%, respectively, while floating-point operations are decreased by 37.03%, 52.34%, 37.80%, 19.05%, 12.07%, and 17.74%, respectively. These results indicate that PWE-YOLO not only achieves higher accuracy in grape disease detection but also reduces computational complexity, featuring a lightweight architecture and faster inference speed. Overall, the proposed model demonstrates superior performance across Precision, Recall, and mAP, underscoring its effectiveness and suitability for real-time target detection in resource-constrained agricultural environments.

Analysis of Detection Results for Different Diseases

This study focuses on the recognition of multiple grape diseases, including downy mildew, powdery mildew, gray mold, canker, and Grapevine Leafroll-associated Virus (GLRaV) disease. Given the distinct manifestations of these diseases, the performance of the proposed PWE-YOLO model was evaluated separately for each disease type. To verify the recognition accuracy, comparative analyses were conducted between the original model and the improved PWE-YOLO model for all five disease categories.

Table 6

Comparison of model recognition accuracy for five diseases before and after improvement

Model	mAP (%)	Precision				
		downy mildew (%)	powdery mildew (%)	gray mold (%)	canker (%)	GLRaV (%)
YOLO v11	85.0	79.6	81.1	77.9	83.9	80.0
PWE-YOLO	86.9	84.8	85.5	82.2	87.0	85.5

Table 6 presents the recognition results for five grape diseases obtained using both the baseline YOLO v11 model and the improved PWE-YOLO model. The introduction of the C3k2-PConv module allows the model to perform convolution operations exclusively on valid regions during disease detection, effectively mitigating the impact of feature loss or damaged areas caused by insufficient lighting or unfavorable shooting angles. This approach prevents interference from missing regions in the final detection outcomes. The incorporation of the WaveletPool module enables effective suppression of downsampling aliasing while maintaining a lightweight network structure, significantly improving the retention of high-frequency features such as edges, patterns, and color variations in disease regions. Furthermore, the addition of the EMA attention mechanism enhances the model's focus on small targets, thereby increasing the detection accuracy of small lesions. As shown in Table 6, the integration of these three improvements leads to increases of 5.2, 4.4, 4.3, 3.1, and 5.5 percentage points in detection accuracy for the five grape diseases, respectively, compared with the baseline YOLO v11 model.

As shown in Table 6, through the three proposed improvements, the detection accuracy of the five grape diseases in the PWE-YOLO model increased by 5.2, 4.4, 4.3, 3.1, and 5.5 percentage points, respectively, compared with the original YOLO v11 model. These results indicate that the proposed PWE-YOLO model demonstrates superior performance across all disease types.

Analysis of Detection Results for Different Diseases

To comprehensively evaluate the detection performance of the proposed PWE-YOLO model, both PWE-YOLO and the baseline YOLO v11 models were applied to images from the test set. The visual detection results produced by the two models were compared, as illustrated in Figure 9.

The detection results are presented in Figure 9. For grape disease images with few targets, such as gray mold and Grapevine Leafroll-associated Virus (GLRaV) disease, the PWE-YOLO model accurately detects the disease regions, whereas the YOLO v11 model, although capable of detecting both diseases, exhibits slightly lower accuracy. For images containing multiple disease targets, such as downy mildew, powdery mildew, and canker, detection is challenged by overlapping symptoms and subtle disease manifestations, resulting in higher rates of missed and false detections.

Nevertheless, the PWE-YOLO model successfully detects a larger number of disease instances while maintaining lower rates of missed and false detections, whereas the YOLO v11 model exhibits missed detections for downy mildew and canker, and false detections for powdery mildew. These visualization results further validate the superiority and practical applicability of the PWE-YOLO model in grape disease detection tasks.

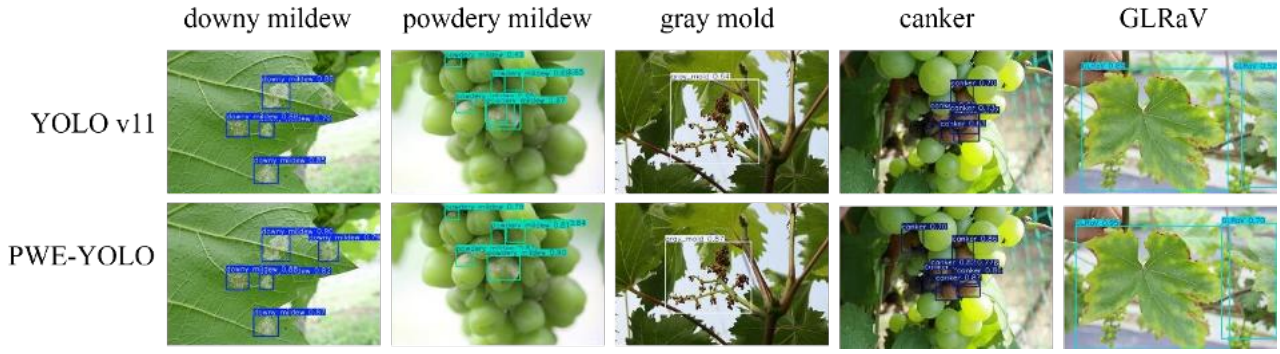


Fig. 9 - Detection results of different models

Practical Application in Vineyard Disease Inspection

To further demonstrate the practical applicability of the proposed method, a vineyard inspection robot platform was employed for field image acquisition. The platform consists of a mobile inspection robot, a robotic arm, and a depth camera mounted at the end of the robotic arm. During field operation, the robot moves along the vineyard rows, while the robotic arm adjusts the position and viewing angle of the camera to capture grape leaf images under natural environmental conditions. The acquired images are then input into the improved PWE-YOLO model for disease detection. The model outputs the disease category, confidence score, and location of the diseased region. Therefore, the integration of the inspection robot platform and the proposed detection model provides a feasible technical solution for intelligent grape disease monitoring, early warning, and precision vineyard management.

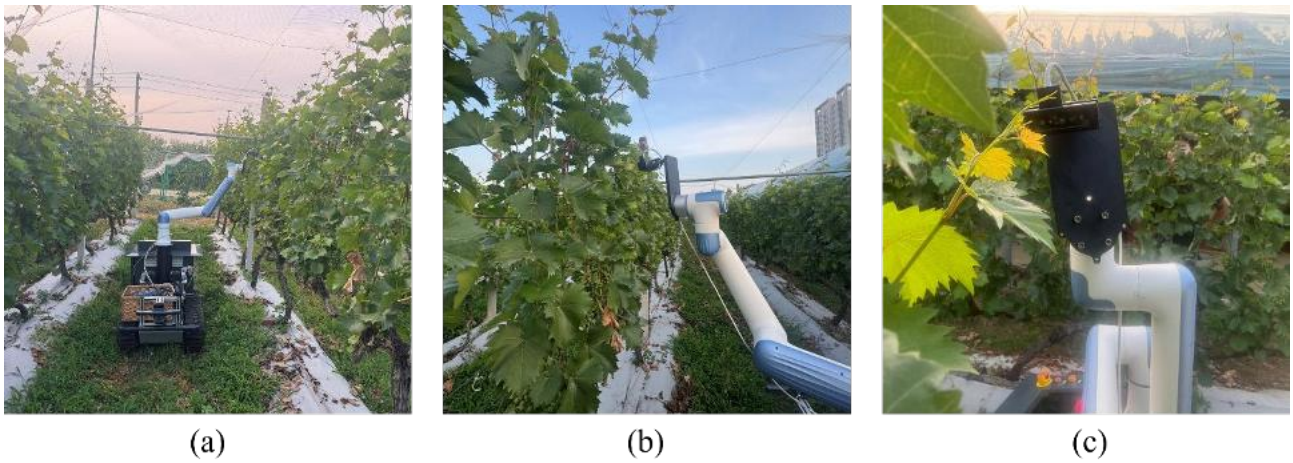


Fig. 10 - Field application of the vineyard inspection robot for grape disease detection

(a) Overall view of the mobile inspection robot in vineyard rows;
(b) image acquisition using the robotic arm and depth camera;
(c) close-up view of the depth camera mounted at the end of the robotic arm.

CONCLUSIONS

To achieve accurate detection of grape diseases in controlled environments, a PWE-YOLO model was proposed based on YOLO v11. By integrating the C3k2-PConv module, WaveletPool module, and EMA attention mechanism, the PWE-YOLO model improves detection accuracy, reduces floating-point operations and parameter count, and enhances inference speed.

The PWE-YOLO model achieves a Precision of 85.0%, Recall of 83.6%, and mAP of 86.9%, with a parameter count of 1.96×10^6 and floating-point operations of 5.1×10^9. Compared with the original YOLO v11 model, Precision, Recall, and mAP are improved by 4.5, 1.4, and 1.9 percentage points, respectively,

while the number of parameters and floating-point operations are reduced by 24.03% and 10.05%, respectively. Furthermore, when compared with YOLO v8, YOLO v9, YOLO v10, YOLO v11, YOLO v12, and YOLO v13, PWE-YOLO demonstrates clear advantages across multiple key metrics, including Precision, Recall, and mAP. In practical detection scenarios, PWE-YOLO effectively reduces missed detections, demonstrating its potential for real-time, accurate, and efficient grape disease monitoring in facility environments.

ACKNOWLEDGEMENT

We would like to acknowledge the financial support from Innovation Team Fund for Fruit Industry of Modern Agricultural Technology System in Shandong Province (SDAIT-06-12), the Key R&D Program of Shandong Province, China (2024TZXD038,2024TZXD045), and Yantai Major Scientific and Technological Innovation Project (2024ZDCX025).

REFERENCES

[1] Badgujar, C. M., Poulose, A., & Gan, H. (2024). Agricultural object detection with You Only Look Once (YOLO) Algorithm: A bibliometric and systematic literature review. *Computers and Electronics in Agriculture*, 223, 109090.

[2] Chen, J., Kao, S. H., He, H., Zhuo, W., Wen, S., Lee, C. H., & Chan, S. H. G. (2023). Run, don't walk: chasing higher FLOPS for faster neural networks. In *Proceedings of the IEEE/CVF conference on computer vision and pattern recognition* (pp. 12021-12031).

[3] Fu, Z., Yin, L., Cui, C., & Wang, Y. (2024). A lightweight MHDI-DETR model for detecting grape leaf diseases. *Frontiers in plant science, 15*, 1499911.

[4] Jiang, Y., Fang, Y., & Deng, L. (2025). PDCNet: A lightweight and efficient robotic grasp detection framework via Partial Convolution and knowledge distillation. *Computer Vision and Image Understanding, 259*, 104441.

[5] Jin, T., Shen, Z., & Geng, H. (2025). Optimized YOLOv11m for real-time high-speed railway catenary defect detection. *Scientific Reports*.

[6] Kalezhi, J., & Shumba, L. (2025). Cassava crop disease prediction and localization using object detection. *Crop Protection, 187,* 107001.

[7] Liu, B., Ding, Z., Tian, L., He, D., Li, S., & Wang, H. (2020). Grape leaf disease identification using improved deep convolutional neural networks. *Frontiers in plant science, 11,* 1082.

[8] Li, X., Hou, H., Yu, Y., Fan, Z., & Zhao, X. (2025). YOLO-LitePV: a lightweight detection algorithm for photovoltaic panel defects. *Nondestructive Testing and Evaluation*, 1-28.

[9] Ouyang, D., He, S., Zhang, G., Luo, M., Guo, H., Zhan, J., & Huang, Z. (2023, June). Efficient multi-scale attention module with cross-spatial learning. In *ICASSP 2023-2023 IEEE international conference on acoustics, speech and signal processing (ICASSP)* (pp. 1-5). IEEE.

[10] Poblete-Echeverría, C., Hernández, I., Iñiguez, R., Gutiérrez, S., Barrio, I., & Tardáguila, J. (2025). Using Artificial intelligence for automatic and fast detection of downy mildew symptoms in grapevine canopies. *European Journal of Agronomy, 170,* 127755.

[11] Qu, Y., & Zhang, F. (2025). FWL-YOLO: a lightweight model for barcode detection and recognition in express delivery waybills. *Signal, Image and Video Processing, 19*(3), 261.

[12] Ren, J., Zhang, H., Wang, G., Dai, C., Teng, F., & Li, M. (2024). Real-time grape disease detection model based on improved YOLOv8s. *INMATEH-Agricultural Engineering, 72*(1).

[13] Rahman, M. U., Liu, X., Wang, X., & Fan, B. (2024). Grapevine gray mold disease: Infection, defense and management. *Horticulture Research, 11*(9), uhae182.

[14] Raj, A., Dawale, M., Wayal, S., Khandagale, K., Bhangare, I., Banerjee, S., ... & Gawande, S. (2025). YOLO-ODD: an improved YOLOv8s model for onion foliar disease detection. *Frontiers in Plant Science, 16*, 1551794.

[15] Sun, J., Li, Y., Zhao, Q., Guo, Z., Li, N., Hai, T., ... & Chen, D. (2022). Cascade wavelet transform based convolutional neural networks with application to image classification. *Neurocomputing, 514*, 285-295.

[16] Williams, T., & Li, R. (2018, February). Wavelet pooling for convolutional neural networks. In *International conference on learning representations*.

[17] Xie, Y., Du, D., & Liu, Y. (2025). RE-YOLO: Vehicle Detector Based on Knowledge Distillation YOLOv8 for Autonomous Driving Scenarios. *Journal of Computing in Civil Engineering, 39*(6), 04025084.

[18] Xu, W., & Wang, R. (2023). ALAD-YOLO: An lightweight and accurate detector for apple leaf diseases. *Frontiers in plant science, 14*, 1204569.

[19] Yang, Y., Jiao, L., Liu, X., Li, L., Liu, F., Yang, S., & Zhang, X. (2024). Efficient LWPooling: Rethinking the wavelet pooling for scene parsing. *IEEE Transactions on Circuits and Systems for Video Technology, 34*(9), 8481-8493.

[20] Zhen, Y., Liu, P., Jin, Y., & Yang, G. (2025). Grape leaf disease detection and identification based on improved YOLOv8. *Transactions of the Chinese Society of Agricultural Engineering, 41*(14), 148-154.

[21] Zhang, N., Zhang, E., Qi, G., Li, F., & Lv, C. (2025). Lightweight grape leaf disease recognition method based on transformer framework. *Scientific Reports, 15*(1), 28974.

[22] Zhang, L., & Zeng, Q. (2024). Grape disease detection method based on styleGAN2-ADA and improved YOLOv7. *Trans. Chin. Soc Agric. Machinery., 55*, 241-252.

[23] Zhang, Z., Feng, B., & Liu, H. (2026). TS-YOLO: a small traffic sign detection algorithm for various harsh driving conditions in bad weather. *Scientific Reports*.

[24] Zheng, B., Angkawisittpan, N., Huang, L., & Sonasang, S. (2025). RSP-YOLOv11n multi-module optimized algorithm for insulator defect detection in UAV images. *Scientific Reports, 15*(1), 35426(13)

[25] Zhao, M., Cui, B., Yu, Y., Zhang, X., Xu, J., Shi, F., & Zhao, L. (2025). Intelligent Detection of Tomato Ripening in Natural Environments Using YOLO-DGS. *Sensors, 25*(9), 2664.

[26] Zhang, X., Zhanfeng, H. O. U., & Chuanzhong, X. (2022). Design and experiment of recognition system for coated red clover seeds based on machine vision. *INMATEH-Agricultural Engineering, 66*(1), pp.62-72. DOI: https://doi.org/10.35633/inmateh-66-06

DESIGN AND EXPERIMENTAL STUDY OF A SELF-PROPELLED ELECTRIC TRACKED CHASSIS FOR *PANAX NOTOGINSENG* TRANSPLANTER IN HILLY AND MOUNTAINOUS REGIONS

/

丘陵山区自走式三七移栽机电动履带底盘设计与试验研究

Wei SU[1)], Congcong LIAO[1)], Qingxu YU*[2)], Yi ZENG[1)], Qinghui LAI[1)], Cantong SU[1)]

[1)]University of Science and Technology Kunming, Kunming 650093, China;

[2)]Nanjing Institute of Agricultural Mechanization, Ministry of Agriculture and Rural Affairs, Nanjing 210014, China;

***** *Correspondent authors: Qingxu YU; E-mail: yqx5205@163.com*

DOI: https://doi.org/10.35633/inmateh-79-41

Keywords: *Panax notoginseng transplanter; fully electric intelligent tracked chassis; speed-measuring encoder; speed-synchronized cooperative transplanting control; hilly and mountainous regions; straight-line deviation correction control*

ABSTRACT

To address the challenges of low transplanting efficiency, poor planting accuracy, and high labor intensity associated with manual Panax notoginseng transplanting in the hilly and mountainous regions of Yunnan, as well as the limited adaptability of existing transplanting equipment to narrow ridged fields and steep, complex terrain, this study developed a self-propelled, fully electric tracked chassis tailored to the agronomic requirements of Panax notoginseng transplanting. The study included the overall structural design, selection and matching of the power battery and drive transmission system, and development of a dimensionless ratio-coefficient control model relating planting spacing to travel and transplanting speeds under the constraint of the manual seedling-feeding speed. An integrated electronic control system was developed to provide remote-controlled travel, speed-synchronized transplanting control, and straight-line deviation correction. The stability and dynamic performance of the chassis were analyzed theoretically and subsequently validated through field tests under multiple operating conditions. Theoretical results showed that the chassis had a maximum lateral roll angle of 39.19°, a maximum traction force of 7,524 N, and sufficient power reserve for operation on slopes of up to 25°. Field tests demonstrated that, after correction using the speed-adjustment coefficient, the straight-line deviation over a travel distance of 30 m was limited to within 1.1%, exceeding the requirements of the relevant national standard. The measured pivot-turning offset was approximately 191 mm, in close agreement with the theoretical value. Key performance indicators, including slope-climbing stability, ridge-travel stability, and motor thermal stability, all met the applicable national standards. The developed chassis effectively improves the adaptability of transplanting equipment for Panax notoginseng production in hilly and mountainous regions and significantly enhances the automation level and planting accuracy of transplanting operations. This study provides theoretical and technical support for the intelligent development of transplanting equipment for rhizomatous medicinal plants.

摘要

针对云南丘陵山区三七人工移栽效率低、栽植精度差、劳动强度大，且现有移栽装备难以适配垄上窄幅作业与陡坡复杂地形的产业痛点，本文设计一款适配三七移栽农艺需求的丘陵山区自走式纯电动履带底盘。完成整机结构方案设计、动力电池与驱动传动系统的选型匹配，基于人工投苗速度极限建立株距与行走-移苗速度的无量纲配比系数调控模型，开发集遥控行走控制、随速协同移栽控制、直线度纠偏控制于一体的电控系统，并开展整机稳定性与动力性能的理论计算，以及多工况田间性能验证试验。理论计算结果表明：该底盘横向极限倾翻角达 39.19°，最大牵引力 524 N，动力储备满足 25° 陡坡作业；田间试验结果显示：经速度修正系数纠偏后，整机 30 m 行程直线度误差可控制小于 1.1%，优于国家标准限值；原地转向中心偏移量实测约 191 mm，符合理论计算值；爬坡稳定性、垄上行驶稳定性及电机热稳定性等核心性能指标均满足相关国标要求。该底盘有效解决丘陵山区三七移栽的装备适配难题，显著提升移栽作业的自动化水平与栽植精度，可为根茎类中药材移栽装备的智能化升级提供理论与技术支撑。

---

[1] *Wei SU, Ph. D. Professor; Qingxu YU, Ph. D. Assistant Researcher; Qinghui LAI, Ph. D. Professor; Congcong LIAO, Master Candidate; Yizeng ZENG, Master Candidate; Cantong SU, Master Candidate.*

INTRODUCTION

To address the practical challenges associated with manual transplanting of *Panax notoginseng* in the hilly and mountainous regions of Yunnan—including low efficiency, poor planting accuracy, and high labor intensity—as well as the limited adaptability of existing transplanting equipment to narrow ridges and steep, complex terrain *(Liu et al., 2025; Zhang, 2025; Zhu, 2025)*, an electric direct-drive, remote-controlled chassis is needed. The chassis should provide rapid dynamic response, stable operation *(Xu et al., 2023)*, and reliable remote-control capability, enabling it to operate effectively under narrow-width field conditions. By coordinating travel speed with the seedling-transplanting speed, the system can maintain accurate planting spacing and meet the operational requirements of ridged *Panax notoginseng* transplanting.

In the field of tracked chassis research, scholars worldwide have conducted extensive investigations, providing a solid theoretical and technical foundation for performance optimization. International studies have primarily focused on three directions: stability control, motion resistance analysis, and design evaluation versatility. *Rocha et al., (2023),* proposed an attitude controller integrating dual quaternions with the differential kinematics of a Stewart platform, enabling active track flap adjustments for terrain adaptation on rough ground. *Shafaei* & *Mousazadeh, (2023),* investigated the resistance characteristics of rubber track landing gears for autonomous towed robots, clarifying the effects of speed and load on resistance and suggesting optimization directions. *Dobretsov et al., (2021),* introduced a deterministic calculation method based on the Bernstein–Letoshnev relationship to effectively assess chassis–soil mechanical parameters. Validation using an eight-ton chassis demonstrated that this method outperforms stochastic approaches.

Chinese researchers have proposed various optimization strategies to address common challenges in the autonomous navigation and motion control of tracked chassis *(Liu et al., 2025; Zhao et al., 2024)*. *Qi et al., 2024,* developed a three-tangent path planning algorithm to mitigate the control deficiencies of single-side braking steering in tracked chassis, significantly improving path tracking stability and reducing steering control frequency. In response to the operational demands of complex environments such as hilly and mountainous regions and orchards, Chinese researchers have conducted targeted design and development efforts focusing on critical performance indicators, including trafficability and stability *(Chen et al., 2025; Zhang et al., 2025; Li et al., 2025; Wang et al., 2025)*. *Nie Jianjun et al., (2025),* designed an arch-shaped agricultural robot chassis with an adjustable posture tailored for hilly terrains, verifying its superior terrain adaptability and travel performance.

Addressing specific planting patterns and operational requirements, domestic researchers have also developed specialized chassis and their control systems *(Hao et al., 2024; Zhu et al., 2023)*. *Yu et al., (2025)*, tackling the challenges in rhizome transplanting of medicinal materials, designed an electronic control system for transplanters based on STM32 and fuzzy PID, validating its superior performance over traditional PID schemes, thereby providing theoretical and technical support for the mechanization of medicinal material transplanting. Additionally, some scholars have conducted foundational research on chassis performance prediction and validation, offering critical support for design optimization *(Liu et al., 2025)*. *Zhang et al., 2023*, addressing the performance deficiencies of a *Panax notoginseng* combined harvester chassis, investigated chassis trafficability under heavy clay soil conditions, providing theoretical references for the design of rhizomatous crop harvester chassis in hilly and mountainous regions.

In summary, the application of fully electric tracked chassis in the transplanting of rhizomatous medicinal materials remains underexplored. To address this gap, this study proposes a fully electric tracked chassis specifically designed for *Panax notoginseng* transplanting, integrating the characteristics of ridged planting and the steep terrain typical of hilly and mountainous regions. The chassis is tailored to the operational requirements of *Panax notoginseng* transplanting, with a core focus on the demanding conditions of low-speed, high-load operation. This capability to accommodate low travel speeds under substantial load during transplanting constitutes a key advantage distinguishing it from general-purpose chassis. To validate its performance under such conditions, a series of tests were conducted, including speed measurement, straight-line deviation correction, and pivot turning offset evaluation. Furthermore, a speed-synchronized control system was developed to precisely measure the travel speed of the transplanter. Using this measured speed as the target, a PID control algorithm was employed to regulate the seedling conveying belt motor, enabling coordinated control between the seedling conveying belt and travel motors, ultimately achieving precise transplanting.

MATERIALS AND METHODS

Test materials

The design, fabrication, and assembly of the chassis system and core working components of the *Panax notoginseng* transplanter developed in this study were completed by Sanniu Agricultural Machinery Manufacturing Co., Ltd. in Dingxi City, Gansu Province. After preliminary debugging and performance baseline tests of the prototype were conducted at the company's experimental field, comprehensive performance validation tests were carried out on January 19, 2026, at the Engineering Training Center of Kunming University of Science and Technology to fully verify the operational stability of the whole machine and optimize key working parameters.

Test equipment

All measuring instruments used in these tests were calibrated, with accuracy meeting the relevant requirements of the test specifications. Environmental parameter collection and measurement were strictly conducted in accordance with GB/T 5262—2008, "General Rules for Measuring Methods of Agricultural Machinery Test Conditions" *(General Administration of Quality Supervision, Inspection and Quarantine of P.R.China & Standardization Administration of P.R.China, 2008)*. The data obtained provide a reliable foundation for subsequent analysis of operational performance and optimization of key parameters.

Machine structure and working principle

Given the complex terrain of Yunnan's hilly and mountainous regions and the specific transplanting mode under *Panax notoginseng* shade shelters, the structural parameters of the tracked self-propelled transplanter chassis significantly affect critical performance metrics such as passability on sloping terrain *(Han et al., 2022)*. Through specialized chassis design, this study achieves a marked improvement in the trafficability of irregular pathways between planting ridges.

Table 1

Design Parameters of the Tracked Chassis

Parameters	Value	Parameters	Value
Overall length/mm	1400	Effective drive-wheel diameter/mm	150
Overall width/mm	1360	Total mass/kg	780
Overall height/mm	1050	Minimum ground clearance/mm	350
Track width/mm	230	Inner distance between tracks/mm	900
Idler wheel diameter/mm	150	Ground contact length/mm	850
Guide wheel diameter/mm	200	Maximum climbing angle/(°)	≥25

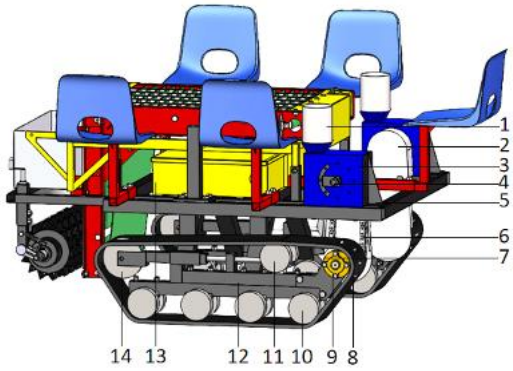


Fig. 1 - Schematic of the tracked chassis of the *Panax notoginseng* transplanter

1. Motor; 2. Chain guard; 3. NMRV110 gearbox; 4. Encoder; 5. Gearbox mounting plate; 6. Drive chain; 7. Track drive sprocket; 8. Track 9. FC207 bearing housing; 10. Idler wheel; 11. Drive wheel; 12. Chassis; 13. Battery box; 14. Guide wheel

The structure of the tracked chassis for the *Panax notoginseng* transplanter is illustrated in Figure 1. The machine employs a brushless DC motor coupled with an NMRV110 reducer, driving the tracked traveling mechanism via chain transmission. The power transmission path follows the sequence: motor, reducer, output shaft, sprocket and chain, drive wheel, and tracks, with assistance from supporting rollers and guide wheels to enable movement.

Given the operational demands of steep slopes in hilly regions, the electric chassis is required to achieve a climbing capability of no less than 25° and must not tip over when traversing laterally on slopes. The frame adopts a 1360 mm wide-base design with a low-center-of-gravity layout. Combined with the independent support on both sides of the tracks and the large ground contact area, this configuration significantly enhances anti-overturning capability and operational stability on complex slopes *(Mo, 2025; Mu et al., 2024; Quan & Ma, 2010)*.

Design and Selection of Key Chassis Components

To address the power requirements, agronomic compatibility, and intelligent control objectives for *Panax notoginseng* transplanting operations in the hilly and mountainous regions of Yunnan, this chapter focuses on the core working systems of the chassis. It presents the specialized design, parameter selection, and performance matching of the power battery system, drive motor system, and control system. These efforts ensure stable power output, precise coordination between travel and seedling transplanting operations, and flexible and reliable field maneuverability, thereby fully meeting the demands of narrow ridged field operations and steep, complex terrains.

Design and Selection of the Power Battery System

To meet the continuous operation and operational stability requirements of the traveling, transplanting, and electronic control systems of the *Panax notoginseng* transplanter, a dual-power supply architecture is adopted. The traveling power circuit is powered by a high-capacity battery pack consisting of sixteen 12 V/65 Ah lead-acid batteries configured in series-parallel to provide 48 V/260 Ah. The seedling transplanting power circuit is powered by a dedicated battery pack composed of two 12 V/20 Ah lead-acid batteries connected in series to supply 24 V/20 Ah, providing exclusive power to the seedling transplanting actuator. The control circuit employs an independent lithium battery module to deliver a stable 5 V power supply to controllers, sensors, and other components, achieving isolation between high-voltage and low-voltage electrical systems, thereby ensuring control accuracy and signal transmission stability. Under a rated operating voltage of 48 V supplied by the 260 Ah battery pack, the chassis operates in the field at full power of 4.4 kW. The endurance time of the traveling system is calculated using the following formula:

$$T = \frac{CkU}{P} \tag{1}$$

where: C — capacity of lead-acid battery pack (260 Ah)

U — rated voltage of travel motor (48 V)

P — actual power of travel motor (4400 W)

k — actual usable capacity factor of lead-acid batteries (0.8)

According to calculation, the full-power field operation duration of the chassis is approximately 2.3 hours.

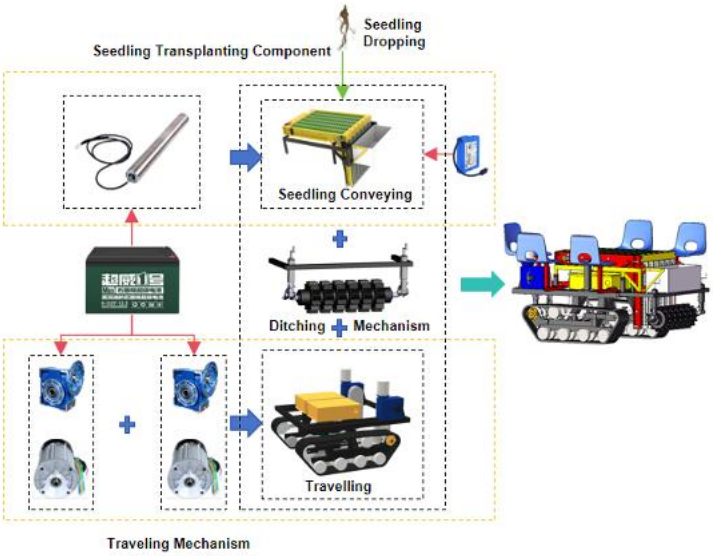


Fig. 2 - Schematic diagram of the power supply system for a transplanter

Design of the Drive Motor and Transmission System

The drive motor system serves as the power core for the chassis traveling and transplanting operations. Its parameter selection, transmission system matching, and coordinated design of operating speed directly determine the traction performance, climbing capability, and transplanting spacing accuracy of the whole machine.

Based on the agronomic requirements of *Panax notoginseng* transplanting and the limits of manual seedling feeding speed, this study completes the selection and design of the drive motor and transmission components, establishes a coordinated matching model for traveling and seedling transplanting speeds, thereby ensuring both dynamic performance and operational precision.

Coordinated Matching Model of Traveling and Seedling Transplanting Speeds under Manual Feeding Constraint

The transplanting operation of *Panax notoginseng* adopts a manual seedling feeding method, where the feeding rate serves as a critical constraint affecting the overall operating speed, seedling conveyor belt speed, and planting spacing. Experimental results indicate that the upper limit of manual feeding rate per person is 0.5 plants/s, with the machine employing four operators working simultaneously. Based on this constraint, a dimensionless ratio coefficient regulation model correlating planting spacing with traveling and seedling transplanting speeds was established, as illustrated in Figure 3.

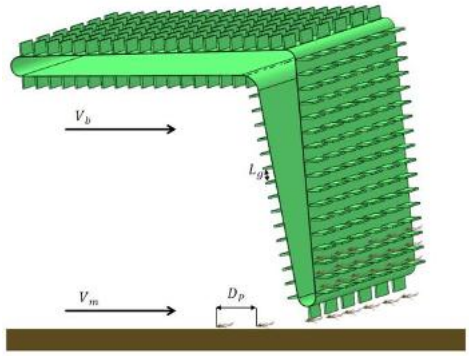


Fig. 3 - Schematic of seedling transplanting

The transplanting spacing is defined as the linear distance traveled by the transplanter along its direction of travel during the interval between the moment a preceding seedling drops into the planting soil and the moment the next seedling reaches the exit of the seedling conveyor belt. The underlying principle is illustrated in Figure 3.

The time interval for the subsequent seedling to reach the exit of the seedling conveyor belt can be expressed as $t=L_g/V_b$. Based on the physical definition of planting spacing D_p, the calculation formula for planting spacing can be derived as follows:

$$D_p=V_m t=V_m \frac{L_g}{V_b} \tag{2}$$

Introducing the dimensionless ratio coefficient $K=V_m/V_b$, which relates the traveling speed of the transplanter to the seedling conveyor belt speed, and substituting it into the above formula, the theoretical relationship between planting spacing and the ratio coefficient can be simplified as follows:

$$D_p=KL_g \tag{3}$$

where:

D_p— planting spacing (mm)

t — time interval for the next seedling to reach the outlet (min)

V_m — travel speed of transplanter (m/min)

V_b — conveying speed of seedling belt (m/min)

L_g — spacing between partition baffles on seedling conveyor belt (40 mm)

K — dimensionless matching coefficient between transplanter travel speed and seedling belt conveying speed (dimensionless)

To achieve convenient and precise regulation of *Panax notoginseng* transplanting spacing, the dimensionless ratio coefficient K is adopted as the core control parameter, addressing the limitations of traditional dual-speed synchronization methods. Based on the agronomic spacing requirement of Dp=80～200 mm for *Panax notoginseng* and the partition plate spacing Lg=40 mm on the seedling conveyor belt, the reasonable range of $K$is derived as 2～5, enabling precise matching of the corresponding planting spacing requirements.

In the control system, the operator only needs to set the target Kvalue, and the system automatically matches V_m and V_b to achieve single-parameter online regulation of planting spacing.

This approach simplifies operation, ensures regulation accuracy, and enhances equipment adaptability while precisely aligning with the limits of manual seedling feeding, thereby establishing an accurate correlation between operating speed and planting spacing.

Based on the limit of manual seedling feeding speed, the maximum allowable speed of the seedling conveyor belt is derived. Let the operation time be t, then the displacement of the seedling conveyor belt during time t is given by:

$$S_b = V_b t \tag{4}$$

Combined with the planting spacing D_p, the total number of seedlings planted within time t can be calculated as:

$$N = 6 \times \frac{S_b}{D_p} \tag{5}$$

Given that the maximum manual seedling feeding rate per person is 0.5 plants/s, equivalent to 30 plants/min, the number of seedlings fed per person within t minutes is less than $30t$, i.e., $N_S < 4 \times 30t$. Substituting $S_b = V_b t$ into the inequality and simplifying yields:

$$V_b < \frac{30 \times 4D_p}{6} = 20D_p \tag{6}$$

where:

N_s — total maximum fry output of four seedling distributors within a fixed time period (plant)

S_b — moving distance of seedling conveyor belt within a fixed time period (m)

t — operation assignment time (min)

6 — coefficient for simultaneous six-row transplanting (dimensionless)

4 — coefficient corresponding to four seedling planting units (dimensionless)

Based on the *Panax notoginseng* transplanting spacing control range of D_p=0.08～0.2 m, the constraint conditions for the seedling conveyor belt speed are derived as follows: when D_p=0.08 m, Vb<1.6 m/min; when D_p=0.2 m, V_b<4 m/min. These constraints ensure that the seedling conveyor belt speed matches the maximum manual seedling feeding rate, preventing missed placements or misalignment caused by excessive belt speed.

Combined with the previously derived formula for planting spacing $D_p = V_m L_g / V_b$, the calculation formula for the transplanter traveling speed can be rearranged to obtain:

$$V_m = \frac{D_p V_b}{L_g} \tag{7}$$

Under the constraint of the maximum manual seedling feeding rate, combined with the limit values of the seedling conveyor belt speed and the planting spacing range, the maximum traveling speed of the transplanter can be calculated as follows: when the planting spacing D_p=0.08 m, the maximum traveling speed is 3.2 m/min; when D_p=0.2 m, the maximum traveling speed is 20 m/min. The traveling speed of the transplanter must match the manual seedling feeding limit. In practical operation, a speed range of 3.2 m/min to 20m/min is recommended to accommodate the planting spacing requirement of 80 mm to 200 mm, ensuring coordinated matching among traveling speed, seedling feeding, and seedling conveying speed.

Matching Calculation of the Transmission Ratio for the Traveling System

Based on the design requirement of adopting the recommended speed range of 3.2~20 m/min in actual operation, and considering factors such as ground slip during tracked field operation and elastic slip in the chain transmission, sufficient margin is reserved for the theoretical traveling speed. Consequently, 22 m/min is ultimately determined as the theoretical maximum reference speed for the matching calculation of the sprocket-chain transmission ratio. The calculation formula for the straight-line traveling speed of the whole machine is:

$$V_m = \frac{\pi n_0 D(1-\delta)}{i_1 i_2} \tag{8}$$

where: V_m — theoretical maximum reference speed (22 m/min)

n_0 — rated speed of brushless DC motor (3000 r/min)

D — effective diameter of track driving wheel (0.15 m)

i_1 — reduction gear ratio (60)

i_2 — gear-chain transmission ratio (dimensionless)

δ— total slip coefficient of transmission system, including chain elastic slip and track-ground slip (0.26)

The calculated transmission ratio i_2≈0.79. Accordingly, the number of teeth on the driving sprocket of the reducer output shaft was selected as 15, and the number of teeth on the driven sprocket of the track drive wheel was selected as 19. This parameter matching scheme enables precise adaptation between the machine's traveling speed, the rated motor speed, and each stage of the transmission system, thereby effectively ensuring traveling stability and synchronization with seedling transplanting during field operations.

Control System Design

To ensure operational flexibility, accurate straight-line travel, and coordinated travel–transplanting performance during field operation of the *Panax notoginseng* transplanter, an electronic control system was developed that integrates remote travel control, speed-synchronized transplanting control, and straight-line deviation correction. The system enables remote control of chassis travel, steering, and emergency stopping, as well as real-time closed-loop coordination between seedling-conveying speed and travel speed. These functions improve the level of operational intelligence and enhance transplanting-spacing accuracy.

The control logic of the remote-control system for the tracked chassis is illustrated in Figure 4. Upon power-up, the system first initializes, followed by communication link verification of the wireless remote-control module, with the verification result indicated via an indicator light: if the module is not successfully connected, the light remains constantly on without flashing; if the connection is normal, the light flashes continuously, and the system enters the command-ready state. The remote controller issues three types of commands: travel commands control the chassis forward/backward movement, steering, and emergency stop; mode switching commands enable switching of operation modes such as cruise control; and motor correction coefficient commands adjust the track motor deviation correction parameters. After executing a command, the system verifies the completion status in real time; if incomplete, the command continues to execute, and upon completion, the control process terminates.

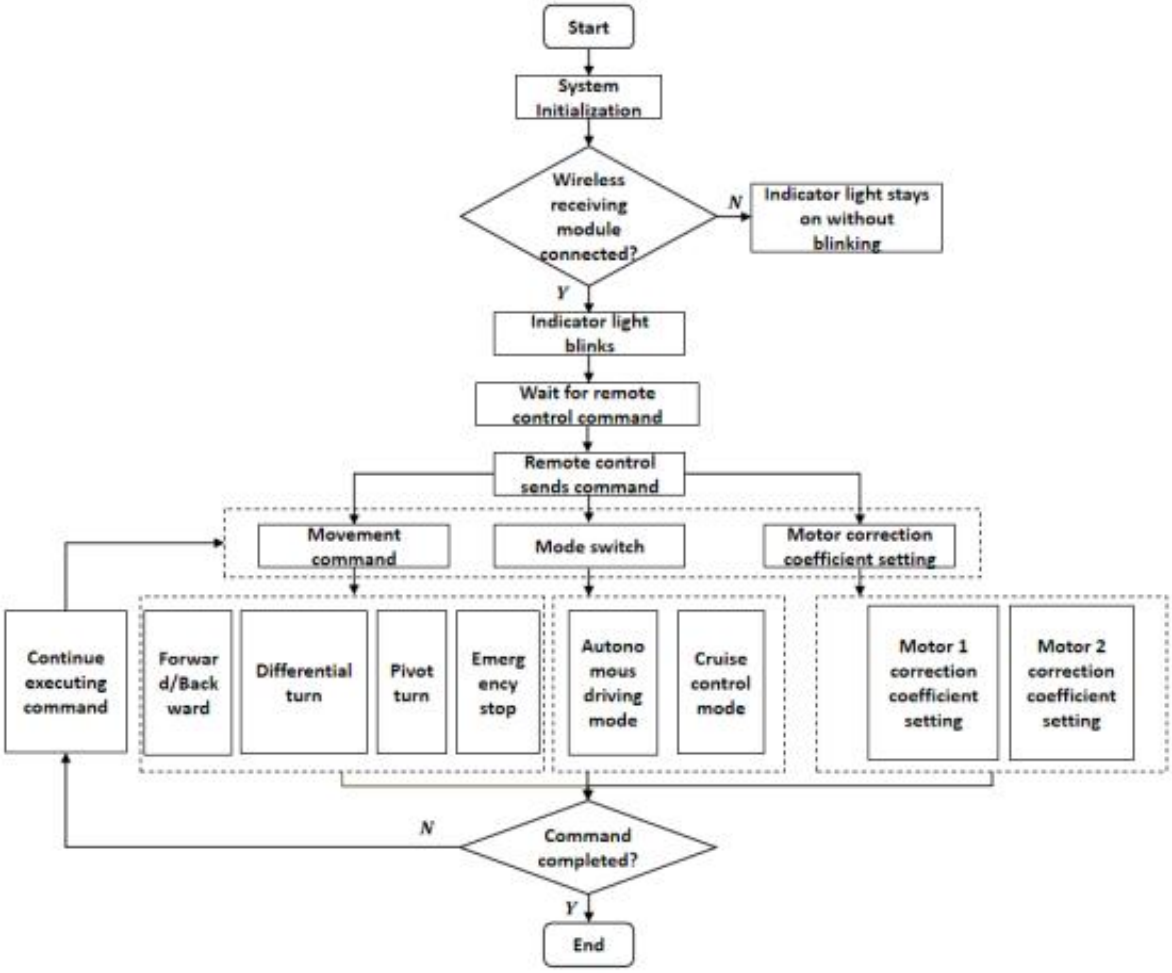


Fig. 4 - Control logic diagram of the remote control system

The speed-synchronized control system designed in this paper operates according to a three-stage architecture of "signal acquisition – main control processing-execution drive," with the core function of achieving real-time coordinated control between the seedling conveyor belt speed and the chassis traveling speed, thereby ensuring the stability and consistency of transplanting spacing. The schematic diagram of the control system is shown in Figure 5.

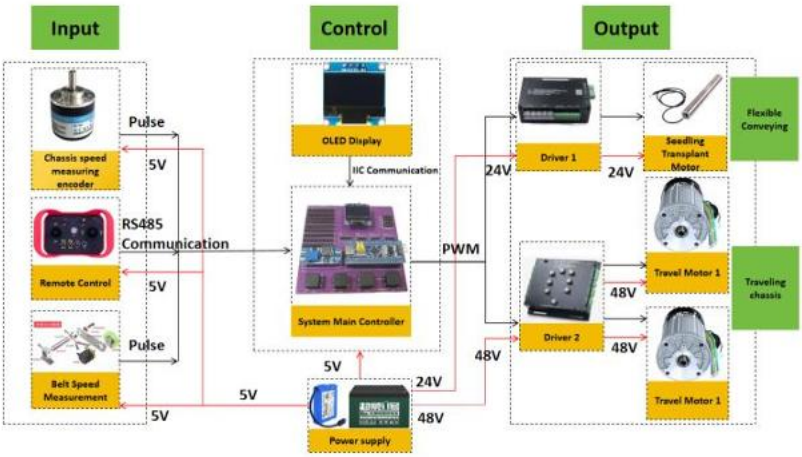


Fig. 5 - Schematic of the control system

During the signal acquisition stage, the chassis speed-measuring encoder and belt speed-measuring encoder at the input end collect pulse signals from one side of the traveling motor and seedling transplanting motor in real time with a sampling period of 100 ms. The remote controller synchronously transmits operation commands, such as travel control and transplanting operations, via the RS485 communication protocol. The aforementioned multi-source signals and commands are transmitted in real time to the system's main controller, providing the data foundation for subsequent coordinated computation.

During the main control processing and status display stage, the system's main controller, after receiving and parsing the multi-source signals, performs coordinated computation of the machine's operational logic and timing scheduling. The real-time speed feedback value of the traveling motor is multiplied by the preset dimensionless ratio coefficient K to serve as the target value for the PID control of the seedling transplanting motor speed, completing the core computation of speed-synchronized control. Simultaneously, operational status data—including real-time motor speeds, operation progress, and set planting spacing values—are transmitted to the OLED display via the IIC communication protocol, enabling real-time visualization of the machine's operating status.

Execution drive stage: The system's main controller outputs PWM speed regulation signals to the corresponding motor drivers, driving each actuator to complete the preset actions. The 24 V seedling transplanting motor driver controls the operation of the seedling transplanting motor, enabling gentle conveying of seedlings. The two 48 V traveling motor drivers independently control the two traveling motors, achieving traveling drive and differential steering control of the tracked chassis. Through closed-loop regulation using the speed-synchronized PID control algorithm, the real-time speed of the seedling transplanting motor continuously approaches the target speed, ultimately realizing precise matching between the chassis traveling speed and the seedling transplanting speed. This fundamentally ensures high consistency between the actual transplanting spacing and the preset value.

Straight-line deviation control is a key technical requirement in chassis design because it directly affects transplanting-row accuracy and helps prevent the machine from damaging the ridges or departing from the intended transplanting path. This study proposes a manual deviation-correction method based on a speed-correction coefficient. Straight-line travel is corrected by adjusting the rotational speeds of the left and right track motors.

The speed of a single track under the correction coefficient is calculated as follows:

$$\begin{cases} V_l = \dfrac{k_l n_1 \pi D(1-\delta)}{i_1 i_2} \\ V_r = \dfrac{k_r n_2 \pi D(1-\delta)}{i_1 i_2} \end{cases} \quad (9)$$

where:

V_l — corrected travel speed of the left track (m/min)

k_l — speed correction factor for left track motor (initial value = 1; manually adjustable via remote control) (dimensionless)

n_1 — rotational speed of left brushless DC motor before correction factor compensation (r/min)

D — effective diameter of track driving wheel (0.15 m)

δ — total slip coefficient of transmission system, including chain elastic slip and track-ground slip (0.26)

i_1 — reduction gear ratio (60)

i_2 — sprocket-chain transmission ratio (0.79)

V_r — corrected travel speed of the right track (m/min)

k_r — speed correction factor for right track motor (default value = 1; manually adjustable via remote control) (dimensionless)

n_2 — rotational speed of right brushless DC motor before correction factor compensation (r/min)

The specific deviation correction control logic is as follows: the motor speed is determined by the duty cycle of the PWM signal output by the main controller, with the duty cycle being positively correlated with the motor speed. By multiplying the correction coefficient by the current duty cycle, precise adjustment of the motor speed is achieved, thereby altering the traveling speed of the single-side track. When the transplanter deviates to the right, the correction coefficients are adjusted to increase the speed of the right traveling motor and decrease the speed of the left traveling motor （k_r>1, k_l<1）, generating a leftward corrective torque that returns the machine to the preset straight trajectory. Conversely, the reverse adjustment strategy is applied for trajectory correction. This approach ultimately ensures the straight-line traveling accuracy of the whole machine, meeting the field operation requirements for *Panax notoginseng* seedling transplanting.

Test method

The overall stability of the *Panax notoginseng* transplanter is not only crucial for the safety of the remote operator and seedling feeders but also plays a key role in improving transplanting quality. In this study, the maximum roll angle is adopted to evaluate the stability of the whole machine on ridges and under longitudinal operating conditions *(Jiang et al., 2023)*.

Lateral Stability Analysis

Under no-load condition, the force diagram of the *Panax notoginseng* transplanter when stationary or moving straight at a uniform speed on a transverse slope is illustrated in Figure 6.

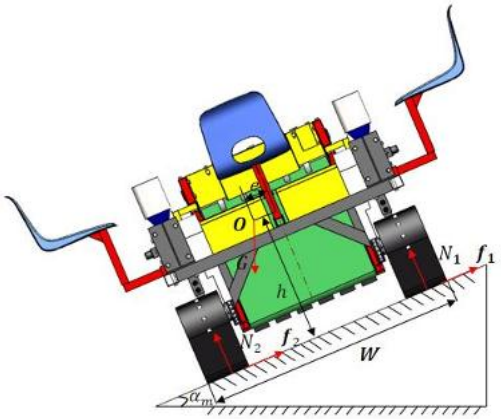


Fig. 6 - Schematic of lateral force analysis of crawler chassis for *Panax notoginseng* transplanter

The maximum roll angle α_m refers to the maximum slope angle at which the machine does not overturn when positioned on a transverse slope. According to the moment balance principle, when the machine is about to overturn about the edge of one track, the supporting force on that side becomes zero, and the moment of gravity about the pivot point is also zero.

Let the outer distance between the two tracks be W, the height of the center of mass be h, and the horizontal offset of the center of mass be e (positive to the left). The distances from the center of mass to the edges of the left and right tracks are then expressed as shown in Equation (10).

$$\begin{cases} L_L = \dfrac{W}{2} - e \\ L_R = \dfrac{W}{2} + e \end{cases} \tag{10}$$

where:

L_L — distance from mass center to the edge of left track (m)

L_R — distance from mass center to the edge of right track (m)

W — distance between outer edges of two tracks (m)

e — horizontal offset of mass center (m)

As shown in the figure, when the slope is inclined downward to the left, the critical condition for overturning about the left edge is as follows:

$$GL_L \cos \alpha_m = Gh \sin \alpha_m \tag{11}$$

The maximum roll angle formula can be derived as follows:

$$\alpha_m = \tan^{-1} \frac{\frac{W}{2} - e}{h} \tag{12}$$

If $W/2$-e≤0, the *Panax notoginseng* transplanter is already prone to overturning on level ground, and thus $\alpha_m=0$.

Based on theoretical calculations of relevant parameters for the *Panax notoginseng* transplanter and subsequent analysis using Equation (11), it can be determined that increasing the outer distance between the two tracks and lowering the height of the center of mass effectively enhances the lateral stability of the chassis. A larger maximum lateral roll angle α_m indicates superior lateral stability of the whole machine. Using the actual structural dimensions of the *Panax notoginseng* transplanter, the position of the center of mass was measured with SolidWorks software. The vertical distance from the center of mass to the ground was determined to be h=650 mm, the outer distance between the two tracks W=1360 mm, and the lateral offset of the center of mass relative to the longitudinal central plane e=150 mm. Substituting these parameters into the model yields a maximum lateral roll angle α_m=39.19° for the whole machine.

Ridging Stability Analysis

Deviation of the transplanter chassis or unevenness of the ridge may cause the tracks to ride onto the ridge slope, resulting in tilting of the transplanter and thereby increasing the risk of overturning. During *Panax notoginseng* transplanting operations, the ridge bottom width W_b is 850 mm, the ridge top width W_t is 720 mm, and the ridge height h ranges from 250 to 300 mm. The ridging state of the *Panax notoginseng* transplanter is illustrated in Figure 7.



(a)Normal Ridge Alignment (b)Abnormal Ridge-Straddling State

Fig. 7 - Schematic of ridge-riding state of *Panax notoginseng* transplanter

$$\alpha = \tan^{-1} \frac{2h}{W_b - W_t} \tag{13}$$

$$\alpha_t = \tan^{-1} \frac{2hh_0}{2hW_b - h_0(W_b - W_t)} \tag{14}$$

where:

α — slope angle of ridge side (\(^\circ\))

h — ridge height (mm)

W_b — base width of ridge (mm)

W_t — top width of ridge (mm)

h_0 — vertical distance between the bottom of side track and ridge bottom under tilting state of transplanter (mm)

α_t — tipping angle (°)

Under the limit state where h=h_0, the inclination angle of the transplanter reaches its maximum operational value. Substituting h=h_0=300 mm, W_b=850 mm, and W_t=720 mm into the calculation yields α=77.8° and α_t=20.9°. This critical roll angle is smaller than the previously calculated maximum lateral roll angle α_m=39.19◦. Therefore, even if the transplanter unexpectedly rides onto the ridge surface, there is no risk of overturning.

Theoretical Calculation of Dynamic Performance

When operating in hilly and mountainous regions, the chassis must not only meet the requirements for lateral and ridge stability but also possess sufficient power reserve to handle extreme steep slope conditions reaching up to 25° or more in certain areas of Yunnan Province (*Guo et al., 2025*). Based on the parameters of the drive motor and transmission system outlined in Section 2.2, a theoretical verification of the maximum traction force and climbing capability of the chassis is conducted, providing performance expectations for subsequent field climbing tests.

The whole machine adopts a dual-motor synchronous drive configuration. After two stages of transmission, the maximum traction force of the chassis can be calculated using the following formula:

$$\begin{cases} T_0 = \dfrac{9550 P_0}{n_0} \\ F_{max} = \dfrac{2 T_0 i_1 i_2 \eta}{r} \end{cases} \tag{15}$$

where: T_0 — rated torque of motor (N·m)

P_0 — rated power of motor (2.2 kW)

n_0 — rated rotational speed of motor (3000 r/min)

F_{max} — maximum traction force (N)

i_1 — transmission ratio of worm gear reducer (60)

i_2 — sprocket-chain transmission ratio (0.79)

η — total mechanical efficiency (0.85)

r — radius of driving wheel (0.075 m)

After calculation, the maximum traction force of the chassis is 7524 N, which meets the operational requirements of low-speed, high-load conditions.

Using the total resistance formula for slope traveling, the climbing capability under extreme operating conditions is verified for a design slope angle of 25°:

$$F_f = fG\cos\alpha + G\sin\alpha \tag{16}$$

where: F_f — maximum resistance force (N)

f — rolling resistance coefficient (0.15, dimensionless)

G — total gravity load (N)

α — slope inclination angle (25°)

The formula for the traction force reserve coefficient is given in Equation (17).

$$S = \frac{F_{max}}{F_f} \tag{17}$$

where: S — traction reserve coefficient (dimensionless)

F_{max} — maximum traction force of chassis (N)

F_f — maximum total running resistance on slope (N)

The total no-load mass of the whole machine is 780 kg, and the full-load mass is 1080 kg (including five operators). Calculations indicate that under full-load conditions, the maximum total resistance is approximately 5912 N, with a traction force reserve coefficient of about 1.27; under no-load conditions, the maximum total resistance is approximately 4270 N, with a traction force reserve coefficient of about 1.76. The traction force reserve is sufficient under all operating conditions, enabling stable adaptation to the steep slope requirements of ≥25° in the mountainous regions of Yunnan.

Steering Performance

Steering performance is a core indicator for the adaptability of the *Panax notoginseng* transplanter to narrow-row operations in mountainous areas, directly determining the machine's compatibility with complex terrain and its operational efficiency. This model adopts a pivot turning design, which fundamentally avoids issues such as damaging ridges or seedlings during turning. Therefore, the offset distance of the pivot turning center is selected as the key evaluation indicator for steering performance. During pivot turning of tracked vehicles in the field, longitudinal slip and lateral skid occur between the tracks and the ground due to soil characteristics, leading to deviations in the actual rotation center. Consequently, the calculation of the actual pivot turning center offset requires the introduction of correction terms for slip and skid. Based on the steering dynamics of tracked vehicles, the calculation formula (18) incorporating the effects of slip and skid is established.

$$R_{0,\delta}=\frac{Bk}{2(1-k)} \tag{18}$$

where: $R_{0,\delta}$ — actual offset of turning center under slipping turning condition (m)

B — track gauge of chassis (distance between centerlines of two tracks) (1.13 m)

k — steering slip coefficient (0.25, dimensionless)

Therefore, the theoretical offset distance of the pivot turning center during field operation is calculated to be 188 mm.

RESULTS AND ANALYSIS

Straight-line Traveling Speed Test

To verify the speed control accuracy of the traveling system and the reliability of the encoder speed measurement, and to provide data support for the coordinated matching between traveling speed and the seedling planting mechanism, a straight-line traveling speed test of the tracked chassis was conducted in accordance with GB/T 5668—2017, "Rotary Tillers"*(General Administration of Quality Supervision, Inspection and Quarantine of P.R.China & Standardization Administration of P.R.China, 2017)* .

The encoder is installed at the output shaft end of the traveling reducer, with a speed sampling period set to 100 ms. The output shaft speed is calculated by collecting the number of pulses per unit time, and the chassis traveling speed is estimated by combining transmission parameters, driving wheel dimensions, and slip rate correction. The speed measurement model is expressed as shown in Equation (19):

$$V_e=\frac{CN_0\pi D(1-\delta)}{Ni_2} \tag{19}$$

where: V_e — chassis travel speed calculated by encoder (m/min)

N_0 — encoder pulse count collected within 100 ms sampling period (1)

D — effective diameter of track driving wheel (0.15 m)

δ — total slip coefficient of transmission and travel system, including chain elastic slip and track-ground slip (0.26)

N — encoder resolution (10000 pulses per revolution)

i_2 — transmission ratio of sprocket-chain mechanism between reducer output shaft and driving wheel (0.79)

C — time conversion factor converting 100 ms sampling interval to minutes (600, dimensionless)

The test site was selected on a level and compacted field road surface within the Engineering Training Center of Kunming University of Science and Technology, with a road length of ≥30 m and longitudinal and transverse slopes of ≤1%, meeting the specifications for traveling performance testing of agricultural machinery.

During the test, the duty cycle of the PWM speed regulation signal for the traveling motor was set to 20%, 40%, 60%, 80%, and 100% via the remote controller, respectively, to control the whole machine to travel straight for 30 m at the corresponding set speeds. An electronic stopwatch was used to record the travel time for each pass. The test was repeated three times for each duty cycle parameter, and the arithmetic mean of the three measurements was taken to calculate the actual average traveling speed, which was then compared and analyzed with the speed synchronously measured by the encoder.

Table 2

Driving speed test results

Duty Cycle /%	Test No.	Time /s	Average Time /s	Actual Travel Speed (m/min)	Encoder-measured Travel Speed (m/min)
20	1	367.38	360.92	4.99	4.40
	2	357.36			
	3	358.02			
40	1	187.44	191.12	9.42	9.13
	2	197.22			
	3	188.7			
60	1	125.88	127.76	14.09	13.9
	2	127.50			
	3	129.90			

Duty Cycle /%	Test No.	Time /s	Average Time /s	Actual Travel Speed (m/min)	Encoder-measured Travel Speed (m/min)
80	1	97.38	96.06	18.74	17.85
	2	98.04			
	3	92.76			
100	1	83.92	83.47	21.56	21.32
	2	81.24			
	3	85.26			

The test results are presented in Table 2. The deviation between the encoder-measured speed and the actual average speed gradually decreases as the duty cycle increases. Under low-speed operating conditions, the deviation mainly arises from real-time fluctuations in track ground slip, elastic deformation of the transmission system, and differences in sampling scales between the long-stroke average speed and the short-period instantaneous speed. By calibrating and correcting the comprehensive slip rate coefficient, the encoder speed measurement can accurately approximate the actual traveling speed of the transplanter, thereby providing reliable data support for the coordinated speed control between traveling and seedling transplanting.

Straight-line deviation Test and Correction for the Transplanter During Traveling

The straight-line deviation test was conducted in accordance with the technical requirements and relevant test specifications for deviation under Clause 3.3.9 of the national standard GB/T 15370.4—2012, "Agricultural Tracked Tractors—Part 4: Technical Specifications for Belt Drive Tracked Tractors." The standard specifies that on a dry, hard, and level road surface with longitudinal and transverse slopes not exceeding 1%, the deviation of an agricultural tracked tractor over 100 m shall not exceed 6 m, which serves as the acceptance criterion for straight-line deviation *(General Administration of Quality Supervision, Inspection and Quarantine of P.R.China & Standardization Administration of P.R.China, 2012)*.

The straight-line deviation test of the transplanter was conducted by laying out a 30 m reference line in the test field, with marking points set every 5 m along the line. The initial position of the transplanter was aligned with the reference line, and the machine was driven at a uniform speed along the line. According to the aforementioned standard, the deviation over a 30 m travel distance shall not exceed 1.8 m, corresponding to a straight-line deviation of no more than 6%. The lateral deviation of the transplanter's traveling trajectory was measured using a tape measure. The field test setup for evaluating the straight-line deviation of the transplanter is shown in Figure 8.

Straight-line deviation is a core indicator for evaluating the degree of deviation, and its calculation expression is given as:

$$\gamma = \frac{max|y(x)-y_0(x)|}{L} \times 100\% \quad (20)$$

where: γ — straight-line deviation rate (%)

$y(x)$ — lateral coordinate of the actual travel path of the transplanter (dimensionless)

$y_0(x)$ — lateral coordinate of the ideal straight path, generally set to 0

L — straight-line test distance (30 m)



Fig. 8 - Straight-line travel deviation test of the transplanter

The straight-line traveling performance of the transplanter chassis directly determines the quality of ridged transplanting operations and the uniformity of plant distribution for *Panax notoginseng*. In this test, the straight-line deviation of the transplanter was measured under PWM duty cycles of 20%, 40%, 60%, 80%, and 100%, respectively. Through parameter calibration, the straight-line deviation was minimized as much as possible to enhance the precision and effectiveness of *Panax notoginseng* transplanting operations. The test results of the straight-line deviation before correction are shown in Table 3.

Table 3

Straight-line travel deviation of the transplanter before correction

Duty Cycle /%	Field Offset (Before Correction) /m			Mean straight-line deviation rate (Before Correction) /%
	Test 1	Test 2	Test 3	
20	1.63	1.67	1.72	5.58
40	2.23	1.92	2.13	6.98
60	2.16	2.09	2.2	7.17
80	2.06	2.45	2.36	7.63
100	2.48	2.39	2.56	8.26

As shown in the data in the table, the straight-line deviation of the transplanter gradually increases with the duty cycle, with most deviation values under each duty cycle exceeding the 6% limit specified in the national standard. If operated directly under such conditions, the transplanter would exhibit significant deviation during travel, leading to a high risk of the chassis riding onto the ridge. To avoid this problem, the remote operator would need to frequently apply minor steering corrections to maintain a stable travel path during operation. Therefore, this study introduces a straight-line deviation correction coefficient to address the issue of path deviation during transplanting operations. The straight-line deviation of the transplanter after correction is shown in Table 4, with the minimum value from three replicates used to determine the optimal correction coefficient.

Table 4

Straight-line travel deviation of the transplanter after correction

Duty Cycle /%	Lateral deviation after correction /m			Deviation rate corresponding to the minimum value /%
	Test 1	Test 2	Test 3	
20	0.32	0.26	0.29	0.87
40	0.34	0.24	0.28	0.8
60	0.45	0.38	0.25	0.83
80	0.78	0.43	0.32	1.07
100	0.32	0.47	0.36	1.07

Table 5

Correction coefficients of left and right motors under different duty cycles

Duty Cycle /%	Correction Parameters					
	Test 1		Test 2		Test 3	
	Right Motor	Left Motor	Right Motor	Left Motor	Right Motor	Left Motor
20	1	1.033	1	1.017	1	1.023
40	1	1.057	1	1.039	1	1.046
60	1	1.091	1	1.086	1	1.077
80	1	1.1	0.979	1.1	0.965	1.1
100	0.867	1.1	0.901	1.1	0.889	1.1

The correction coefficients for the left and right motors under different duty cycles are shown in Table 5. The test results indicate that the transplanter exhibits an overall leftward deviation when traveling on flat surfaces, which is attributed to the lower traveling speed of the left track compared to the right track. As the control duty cycle increases, the straight-line deviation of the whole machine tends to increase. To compensate for the speed difference between the two tracks and improve straight-line traveling accuracy, the correction coefficient for the left motor should be set greater than 1, while the correction coefficient for the right motor is either maintained at 1 or adjusted to less than 1.

The recommended correction coefficients for the left and right motors under different duty cycles are as follows: at 20% duty cycle, right motor 1, left motor 1.017; at 40% duty cycle, right motor 1, left motor 1.039; at 60% duty cycle, right motor 1, left motor 1.077; at 80% duty cycle, right motor 0.965, left motor 1.1; at 100% duty cycle, right motor 0.867, left motor 1.1.

Pivot Turning Center Offset Measurement

Steering performance is a core indicator of the field adaptability of tracked transplanters, directly determining the flexibility of inter-ridge turning and headland turning, as well as operational safety. This test was conducted in accordance with the steering performance test specifications for tracked tractors specified in GB/T 19040—2016, "Agricultural Tractors—Requirements for Steering" *(General Administration of Quality Supervision, Inspection and Quarantine of P.R.China & Standardization Administration of P.R.China, 2016)*. The pivot turning performance test of the transplanter was carried out on a typical soft field surface used for *Panax notoginseng* cultivation, where the track steering trajectory was measured and the turning center offset was determined.



(a) On-site turning test (b)Actual steering trajectory measurements

Fig. 9 - In-situ turning test of the transplanter

The test results indicate that the transplanter achieves stable pivot turning, with a measured turning center offset of approximately 191 mm, which is in close agreement with the previously calculated theoretical value. The turning accuracy and stability meet the operational requirements for *Panax notoginseng* transplanting in the field. The pivot turning test site and trajectory measurement results are shown in Figure 9.

Climbing Stability Test

In accordance with GB/T 3871.21—2015, "Agricultural Tractors—Test Procedures—Part 21: Stability" *(General Administration of Quality Supervision, Inspection and Quarantine of P.R.China & Standardization Administration of P.R.China, 2015)*, the climbing stability test of the *Panax notoginseng* transplanter was conducted. The test was performed on a slope with an inclination of 27°, and the machine was driven longitudinally and transversely on the slope at a travel speed of 10 m/min. The results showed that the transplanter successfully climbed the 27° slope during longitudinal travel and exhibited no instability or rollover during transverse travel on the 27° slope. The overall stability of the machine is excellent, meeting the operational requirements for ridged *Panax notoginseng* transplanting in the hilly and mountainous regions of Yunnan.



Fig.10 - Site of the vertical climb test



Fig.11 - Site of the lateral slope stability test

Ridged Traveling Stability Test

To verify the traveling stability of the transplanter under ridged slope conditions, a single-side ridge-crossing tilt travel test was conducted. One side of the transplanter's tracks was positioned to ride onto the ridge slope, and the machine was driven straight for 10 m along the ridge length at a uniform speed under different duty cycles. The traveling status of the whole machine was recorded, and no instability or overturning was observed throughout the process.



Fig.12 - On-ridge stability test

To verify the traveling stability of the transplanter under ridged slope conditions, a single-side ridge-crossing tilt travel test was conducted. The ridge parameters were fixed (ridge bottom width 850 mm, ridge top width 720 mm), and only the ridge height was varied to adjust the roll angle of the machine under different operating conditions. Three typical ridge heights for *Panax notoginseng* cultivation—200 mm, 250 mm, and 300 mm—were selected, corresponding to roll angles of 14.3°, 17.7°, and 20.9°, respectively, thereby establishing varying tilt operating conditions.

Table 6

Ridge-riding stability test results

Duty Cycle (%)	Working Condition Lateral Tilt Angle (°)		
	14.3	**17.7**	**20.9**
20	Pass	Pass	Pass
40	Pass	Pass	Pass
60	Pass	Pass	Pass
80	Pass	Pass	Pass
100	Pass	Pass	Pass

For each roll angle under different operating conditions, the transplanter was operated at five PWM speed regulation duty cycles of 20%, 40%, 60%, 80%, and 100%. The test was repeated three times for each condition, and the machine status was recorded. The test results are shown in Table 6. Under all combined conditions, the transplanter passed stably without overturning, verifying its traveling stability within this tilt range and across different operating parameters.

Motor Thermal Stability Test

Motor thermal stability is a core indicator determining the reliability of continuous field operation and the insulation service life of the transplanter's motors. In accordance with the mandatory requirements of Chapters 15 and 20 of GB/T 14711—2025, "General Requirements for Safety of Small and Medium-Sized Rotating Electrical Machines," concerning thermal testing and insulation structures, a thermal stability test was conducted on the variable-frequency speed-regulated brushless DC traveling motor with Class F insulation *(State Administration for Market Regulation & Standardization Administration of P.R.China, 2025)*. The test simulated load conditions of the transplanter under different operating speeds. The motor was operated continuously for 190 minutes under gradient PWM speed regulation duty cycles ranging from 20% to 90%, and the winding temperature was monitored in real time using a calibrated digital thermometer. Based on the heat resistance requirements for Class F insulation and accounting for a 20–30°C temperature margin between the motor housing and the winding, the evaluation criteria were established as follows: a safe operating range of 70°C to 90°C, and a forced shutdown protection threshold of 125°C to prevent insulation thermal aging.

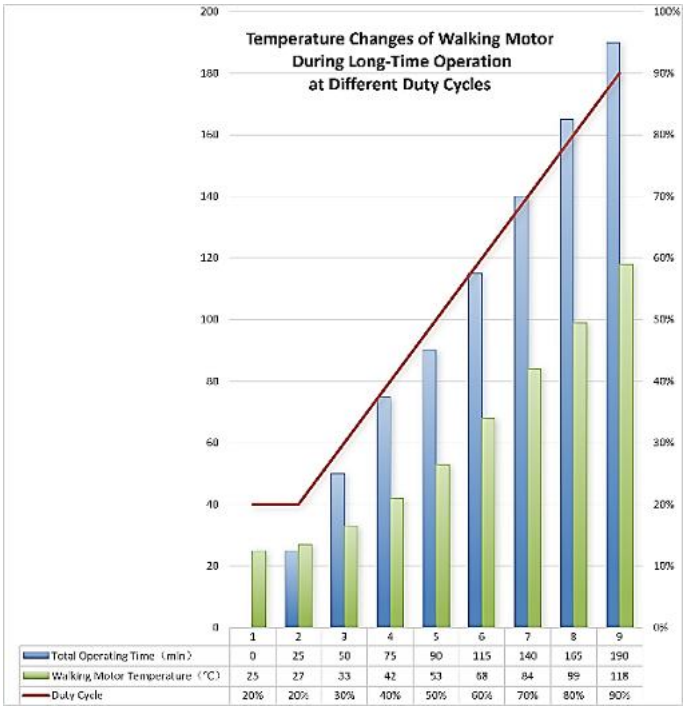


Fig.13 - Temperature change of driving motors under different duty cycle

The test results are shown in Figure 13: the motor temperature rise rate shows a clear positive correlation with the PWM duty cycle, consistent with the typical heating characteristics of small and medium-sized rotating electrical machines.

After 190 minutes of continuous operation, the final motor temperature reached 118°C, which did not reach the 125°C shutdown threshold, and remained within the safe operating range of 70°C to 90°C for most of the operation period. The test results meet the thermal safety requirements for continuous motor operation specified in GB/T 14711—2025, verifying that the traveling motor and transmission system possess good thermal stability and are capable of meeting the demands of prolonged continuous field operation for *Panax notoginseng* transplanting.

CONCLUSION AND DISCUSSION

An innovative design and theoretical modeling of a specialized tracked chassis for hilly and mountainous regions were completed. Addressing the complex agronomic requirements of ridged *Panax notoginseng* transplanting in Yunnan, the overall structure of a fully electric intelligent tracked chassis was designed. Based on the manual seedling feeding speed limit, a dimensionless ratio coefficient regulation model correlating

planting spacing with traveling and seedling transplanting speeds was innovatively established. This enabled precise matching of the transmission ratio and theoretical calculation of the overall machine stability, laying the theoretical foundation for subsequent control system development.

A coordinated control system for traveling and seedling transplanting, along with a straight-line deviation correction scheme, was developed. A speed-synchronized PID control system based on speed-measuring encoders was designed to achieve real-time coordinated control between seedling conveying speed and chassis traveling speed. A manual deviation correction method utilizing a speed correction coefficient was proposed, effectively addressing the issue of traveling deviation in tracked chassis. Field tests demonstrated that, after correction, the straight-line deviation of the whole machine over a 30 m travel distance was controlled to within 1.1%, which is superior to the national standard limit.

The key performance indicators of the whole machine were verified to meet the operational requirements of hilly and mountainous regions. The chassis achieved a maximum traction force of 7524 N, a maximum climbing angle of ≥25°, and a maximum lateral roll angle of 39.19°, with the pivot turning center offset closely matching the theoretical value. Performance indicators including slope climbing stability, ridged traveling stability, and motor thermal stability all satisfied the requirements of relevant national standards. This chassis effectively enhances the automation level and operational accuracy of *Panax notoginseng* transplanting in hilly and mountainous regions, providing technical support for the intelligent upgrade of transplanting equipment for rhizomatous medicinal herbs.

ACKNOWLEDGEMENT

We would like to thank all colleagues for their advice and support throughout the research process.

REFERENCES

[1] Chen W.H., Li K.Z., Yang Y.F., Yang L., & Wang F. (2025). Design and experiment of a gantry-type electric crawler work vehicle (龙门式电动履带作业车设计与试验). *Forestry Machinery & Woodworking Equipment*, 53(12), 36-40. https://doi.org/10.13279/j.cnki.fmwe.2025.0154

[2] Dobretsov, R. Y., Sokolova, V. A., Teterina, I. A., et al. (2021). Interaction feature of caterpillar tracks with soil under significant axial displacements of pressure center. *IOP Conference Series: Earth and Environmental Science*, 839, 052023. https://doi.org/10.1088/1755-1315/839/5/052023

[3] General Administration of Quality Supervision, Inspection and Quarantine of P.R.China, & Standardization Administration of P.R.China. (2012). *General technical conditions for agricultural tractors Part 4: tracked tractors (GB/T 15370.4-2012)* (GB/T 15370.4-2012 农业拖拉机通用技术条件第 4 部分：履带拖拉机). China Standards Press, Beijing.

[4] General Administration of Quality Supervision, Inspection and Quarantine of P.R.China, & Standardization Administration of P.R.China. (2016). *Steering requirements for agricultural tractors (GB/T19040-2016)*(GB/T19040-2016 农业拖拉机转向要求). China Standards Press, Beijing.

[5] General Administration of Quality Supervision, Inspection and Quarantine of P.R.China, & Standardization Administration of P.R.China. (2015). *Agricultural tractor test code Part 21: stability (GB/T3871.21-2015)*(GB/T3871.21-2015 农业拖拉机试验规程第 21 部分：稳定性). China Standards Press, Beijing.

[6] General Administration of Quality Supervision, Inspection and Quarantine of P.R.China, & Standardization Administration of P.R.China. (2008). *General rules for determination of agricultural machinery test conditions (GB/T5262-2008)* (农业机械试验条件测定方法的一般规定:GB/T5262-2008). China Standards Press, Beijing.

[7] General Administration of Quality Supervision, Inspection and Quarantine of P.R.China, & Standardization Administration of P.R.China. (2017). *Rotary tiller (GB/T5668-2017)* (GB/T5668-2017 旋耕机). China Standards Press, Beijing.

[8] Guo G.Z., Jin G.Y., Luo Y.N., Luo H.T., Xie F.H., & He J.Y. (2025). Effects of slope on the service life of agricultural monorail surface (坡度对农用单轨轨面运行寿命的影响). *Transactions of the Chinese Society of Agricultural Engineering*, 41(15), 40–47. https://doi.org/10.11975/j.issn.1002-6819.202502045

[9] Han Z H, Zhu L C, Yuan Y W, et al. (2022). Passability analysis and optimal design of tracked chassis for mountain orchards on slope（山地果园履带底盘坡地通过性能分析与优化设计）. *Transactions of the*

Chinese Society for Agricultural Machinery, 53, 413–421, 448. https://doi.org/10.6041/j.issn.1000-1298.2022.05.045

[10] Hao J.J., Ai Q.H., Yuan D.C., Li Z.W., Yang S.H., & Zhao J.G. (2024). Design and experiment of electric self-propelled maize-peanut strip compound planting pesticide applicator (电动自走式玉米-花生带状复合种植模式施药机设计与试验). *Transactions of the Chinese Society for Agricultural Machinery*, 55(9), 216–225. https://doi.org/10.6041/j.issn.1000-1298.2024.09.018

[11] Jiang Y., Sun Z.Y., Wang R.C., Xia C.G., Ye Q., & Guo Y.F. (2023). Design and performance test of omnidirectional leveling system for crawler work machine in hilly areas（丘陵山区履带式作业机全向调平系统设计与性能试验）. *Transactions of the Chinese Society of Agricultural Engineering*, 39(18), 64-73. https://doi.org/10.11975/j.issn.1002-6819.202304190

[12] Li S.J., Peng J.B., Niu C.Q., Gao X.D., Qian Z.Y., Li M.Z., (2025), Design and Test of Articulated Steering Profiling Extended Range Wheeled Power Chassis for Hilly Orchards (丘陵果园铰接转向仿形增程轮式动力底盘设计与试验). *Transactions of the Chinese Society for Agricultural Machinery*, Vol.56, No.9, Wuhan/China, ISSN 1000-1298, pp.363-376, https://doi:10.6041/j.issn.1000-1298.2025.09.028

[13] Liu, C. K., Wang, L., & Meng, J. J. (2025). Theoretical analysis and empirical test of the impact of agricultural mechanization on agricultural ecological efficiency（农业机械化影响农业生态效率的理论分析及实证检验） *Chinese Journal of Eco-Agriculture*, 33, 1219–1234. https://doi.org/10.12357/cjea.20240202

[14] Liu H.Y., Zou S., Tang J.C., et al. (2025). Path tracking algorithm of tracked agricultural chassis based on parameter pre-adjusted super-twisting sliding mode control（基于参数预调型超螺旋滑模控制的履带农用底盘路径跟踪算法研究）. *Transactions of the Chinese Society for Agricultural Machinery*, 56, 136-144.https://doi.org/10.6041/j.issn.1000-1298.2025.02.013

[15] Liu Q., Ji Y.X., Yang F.Z., Zhang L.H., Du Z.X., Liu Z.J., & Zhu X.Y. (2025). Development and validation of traction performance prediction model for mountain tracked chassis on slopes (山地履带式底盘坡地牵引性能预测模型构建与试验). *Transactions of the Chinese Society for Agricultural Machinery*, 56(5), 597–607. https://doi.org/10.6041/j.issn.1000-1298.2025.05.058

[16] Mo F.Y. (2025). Design and optimization of chassis structure for tractors adapted to hilly and mountainous areas (丘陵山地适应性拖拉机底盘结构设计与优化). *Farm Machinery Using & Maintenance*, (11), 20-23.

[17] Mu X.D., Yang F.Z., Duan L.J., et al. (2024). Research status and development trend of key technologies of leveling and anti-overturn for hilly mountain tractors（丘陵山地拖拉机调平与防翻关键技术研究现状与发展趋势）. *Smart Agriculture*, 6, 1-16.

[18] Nie J.J., Xia K.T., Xie X.L., Lü Y.L., & Li C.M. (2025). Mobile chassis design and passability of arched waist agricultural robot（拱腰式农业机器人移动底盘设计与通过性研究）. *Transactions of the Chinese Society for Agricultural Machinery*, 56(10), 736-745. https://doi.org/10.6041/j.issn.1000-1298.2025.10.067

[19] Qi Z.Z., Zhou J., Ye Z.W., Zhou X.J., & Yang H.Y. (2024). Local path planning method in automatic walking of single-side brake steering track chassis（单侧制动式转向履带底盘自主行走局部路径规划方法）. *Transactions of the Chinese Society for Agricultural Machinery*, 55(6), 52-59. https://doi.org/10.6041/j.issn.1000-1298.2024.06.005

[20] Quan Q. & Ma S. (2010). Controllable postures of a dual-crawler-driven robot. *Mechatronics*, 20, 281-292. https://doi.org/10.1016/j.mechatronics.2010.01.001

[21] Rocha, F., Cid, A., Delunardo, M., et al. (2023). Body posture controller for actively articulated tracked vehicles moving over rough and unknown terrains. In 2023 *IEEE/RSJ International Conference on Intelligent Robots and Systems (IROS),* pp. 2330-2337. https://doi.org/10.1109/IROS55552.2023.10341528

[22] Shafae S.M., & Mousazadeh H. (2023). An operational scrutinization of autonomous tractor-trailer robot considering motion resistance force of rubber tracked undercarriage. *Cognitive Robotics*, 3, 173-184. https://doi.org/10.1016/j.cogr.2023.06.002

[23] State Administration for Market Regulation, & Standardization Administration of P.R. China. (2025). General safety requirements for small and medium rotating electrical machines (GB/T14711-2025) (中小型旋转电机通用安全要求：B/T14 11-2025) China Standards Press, Beijing.

[24] Wang P F, Yi J A, Zhu J X. (2025). Design and test of hydraulic system of power chassis for hilly and mountainous orchards (丘陵山地果园动力底盘液压系统设计与试验). *Transactions of the Chinese Society for Agricultural Machinery*, 56, 702–711, 722. https://doi.org/10.6041/j.issn.1000-1298.2025.06.066

[25] Xu L Y, Zhang J J, Yan X H. (2023). Review on electrification technology of agricultural equipment (农业装备电动化技术研究综述). *Transactions of the Chinese Society for Agricultural Machinery*, 54, 1–12. https://doi.org/10.6041/j.issn.1000-1298.2023.09.001

[26] Yu Q., Zhang X., Cao G., et al. (2025). Design and experiment of electric control system for self-propelled Chinese herbal materials transplanter. *Agriculture*, 15, 621. https://doi.org/10.3390/agriculture15060621

[27] Zhang X. (2025). *Design and test of precise transplanting control system for Panax notoginseng* (三七精准移栽控制系统设计与试验)[Master's thesis]. Kunming University of Science and Technology.

[28] Zhang X., Wang B.B., & Li M.T. (2025). Design and experiment of a multifunctional remote-controlled electric tracked chassis for hilly orchards in southern China (南方丘陵果园多功能遥控电动履带底盘设计与试验). *Modern Agricultural Equipment*, 46(6), 77-83. https://doi.org/10.3969/j.issn.1673-2154.2025.06.011

[29] Zhang Z.G., Deng Y.X., Wang F.A., Cao Q.Z., & Xie K.T. (2023). Trafficability analysis and scaling model experiment of self-propelled Panax notoginseng combine harvester chassis (自走式三七联合收获机底盘通过性能分析与模型试验). *Transactions of the Chinese Society for Agricultural Machinery*, 54(9), 164–177. https://doi.org/10.6041/j.issn.1000-1298.2023.09.016

[30] Zhao Z.Z., Zhang G.Z., Luo C.M., Liu W.R., Tang N.R., Kang Q.X., & Wang W.K. (2024). Path tracking algorithm of the dual motor tracked chassis considering skid and slip (考虑滑移滑转的双电机履带底盘路径跟踪算法). *Transactions of the Chinese Society of Agricultural Engineering*, 40(12), 46-54. https://doi.org/10.11975/j.issn.1002-6819.202401021

[31] Zhu L.C., Zhao Z.Y., Han Z.H., Wang R.X., Zhou L.M., & Zhao B. (2023). Design and experiment of dual-steering motion control system based on active disturbance rejection control (基于自抗扰控制的双重转向运动控制系统设计与试验). *Transactions of the Chinese Society for Agricultural Machinery*, 54(S1), 391–401. https://doi.org/10.6041/j.issn.1000-1298.2023.S1.042

[32] Zhu L.H. (2025). "Yuchai hybrid" accelerates the industrial reform of tractors (玉柴混动"加速拖拉机产业变革). *Agricultural Machinery Quality and Supervision*, (11), 40-41.

IMPROVED DBO ALGORITHM FOR FIXED-WING UAV MOUNTAIN CROP IRRIGATION PATH PLANNING
/
改进的 DBO 算法用于固定翼无人机山地作物灌溉路径规划

Shengfu WU[1)], Peng ZHOU[1,2*)], Jin LUO[1)], Linjia CHUAN[1)], Jing LIU[1)], Fugui ZHANG[1,2*)]
[1)] School of Mechanical Engineering, Guizhou University, Guiyang, Guizhou / China
[2)] Guizhou Provincial Key Laboratory of Mountainous Intelligent Agricultural Machinery, Guiyang, Guizhou / China
Tel: 15286617318; E-mail: w15286617318@163.com
Corresponding author: Peng Zhou
Email address: pzhou@gzu.edu.cn, Guiyang, China
DOI: https://doi.org/10.35633/inmateh-79-42

Keywords: *Fixed-wing UAV; Path planning; Improved DBO algorithm; Safe turning radius; Pitch angle; Overlap ratio; Coverage uniformity*

ABSTRACT
To address the contradiction between obstacle avoidance safety and irrigation operation quality in 3D path planning of fixed-wing UAVs for mountainous agricultural crop irrigation, this paper proposes a multi-strategy improved dung beetle optimization (MDBO) algorithm. First, safe turning radius and pitch angle constraints are embedded into the optimization objective to restrict flight attitude, ensure flight stability under complex mountain terrain, reduce collision risk, and maintain consistent spray deposition. Second, four improvement strategies, including Bernoulli chaotic mapping initialization, golden sine position update mechanism, dynamic adaptive weight, and adaptive Gaussian-Cauchy hybrid mutation perturbation, are integrated into the basic DBO algorithm to enhance global search capability, local exploitation accuracy and convergence performance. Comparative tests on 9 benchmark functions show that MDBO outperforms the basic DBO in convergence speed and solution stability. Furthermore, three irrigation performance indicators (coverage rate, overlap ratio and coverage uniformity) are constructed for posterior evaluation of spray distribution quality. Simulation experiments under three mountainous terrain scenarios verify that MDBO achieves better path accuracy, convergence performance and irrigation effect than traditional algorithms, and can meet the efficient irrigation path requirements of mountainous agricultural crops.

摘要
为解决固定翼无人机在山区农业作物灌溉三维路径规划中避障安全性与灌溉作业质量之间的矛盾，本文提出一种多策略改进的蜣螂优化（MDBO）算法。首先，将安全转弯半径和俯仰角约束嵌入优化目标函数中，以限制飞行姿态，确保复杂山地地形下的飞行稳定性，降低碰撞风险，并保持喷洒沉积的一致性。其次，将伯努利混沌映射初始化、黄金正弦位置更新机制、动态自适应权重以及自适应高斯-柯西混合变异扰动等四种改进策略融入基本 DBO 算法，以提升全局搜索能力、局部开发精度和收敛性能。在 9 个基准函数上的对比实验表明，MDBO 在收敛速度和解的稳定性方面优于基本 DBO 算法。此外，构建了三个灌溉性能指标（覆盖率、重叠率和覆盖均匀性），用于对喷洒分布质量进行后评估。在三种山地地形场景下的仿真实验验证了 MDBO 算法在路径精度、收敛性能和灌溉效果方面优于传统算法，能够满足山地农作物高效灌溉路径的需求。

INTRODUCTION
In agricultural and forestry mountainous planting scenarios, irrigation is a key link in ensuring crop yield *(Ma, 2025)*. However, mountainous crop areas are restricted by objective conditions such as complex terrain (with interlaced slopes and gullies) *(Hu, 2023)* and uneven crop distribution (fruit tree clusters, terraced crops). Traditional ground irrigation equipment struggles to access these areas, and manual irrigation faces the dilemma of low efficiency and high cost.

Against this background, fixed-wing UAVs, with the advantages of long endurance and wide coverage, have become an ideal carrier for irrigation in agricultural and forestry mountainous areas—by carrying spray or drip irrigation components, they can achieve large-area and efficient irrigation operations.

As one of the core issues in fixed-wing UAV irrigation operations, the quality of irrigation path planning *(Giagkiozis et al., 2015)* directly determines the irrigation effect: it is necessary to ensure that the path fully covers all areas to be irrigated, while avoiding obstacles such as fruit tree canopies and slope shoulders, and to maintain a stable flight process to prevent uneven irrigation caused by severe attitude changes. In agricultural aviation, flight stability and path smoothness are critical not only for geometry but also for spray deposition uniformity, droplet drift mitigation, and operational continuity. Studies on UAV-based spraying have shown that flight parameters such as altitude, velocity, and operational stability significantly influence droplet coverage, deposit consistency, and drift risk *(Wang et al., 2017; Wang et al., 2017; Pan et al., 2016)*. Furthermore, the spray distribution from a UAV is inherently non-uniform, and the coverage uniformity is critically affected by flight speed and pass width *(Nanavati et al., 2023)*. Therefore, optimizing path planning for irrigation requires not only obstacle avoidance and path length minimization but also consideration of spray coverage uniformity and overlap control.

In terms of flight parameter constraints *(Deng et al., 2022)*, in traditional path planning, UAVs are often simplified as point masses. However, fixed-wing UAVs have a large volume and may collide with obstacles during flight; moreover, they require long takeoff and landing distances. In addition, UAVs need to frequently adjust their flight trajectories between crops and slopes in agricultural and forestry mountainous areas. If parameter constraints are not fully considered in traditional planning, a series of problems are likely to occur: if the turning radius is too small, UAVs are prone to colliding with fruit trees or slope ridges; if the pitch angle fluctuates too much, it will lead to unstable flight altitude (excessively high altitude causes uneven diffusion of irrigation liquid/droplets, while excessively low altitude may scratch crops). Therefore, it is crucial to introduce constraints on the two flight parameters of safe turning radius and pitch angle in irrigation path planning for agricultural and forestry mountainous areas—which is also the key that distinguishes this scenario from ordinary mountain path planning, as the irrigation scenario has more prominent requirements for "path coverage integrity" and "flight attitude stability."

In terms of path planning algorithms, traditional path planning algorithms such as Dijkstra's algorithm *(Fadzli et al., 2015)*, artificial potential field (APF) method *(Zhou et al., 2015)*, and simulated annealing (SA) algorithm *(Zhu et al., 2006)* have the problem of slow convergence, making it difficult to adapt to the dynamically changing needs of crop distribution in agricultural and forestry mountainous areas. Although existing intelligent optimization algorithms such as the A* algorithm *(Wang et al., 2023)*, genetic algorithm (GA) *(Zhao et al., 2023)*, ant colony optimization (ACO) algorithm *(Wen et al., 2023)*, and particle swarm optimization (PSO) algorithm *(Chen et al., 2023)* have been applied in related fields, they still have the defect of being prone to falling into local optimality (e.g., only avoiding local fruit tree clusters while ignoring marginal irrigation areas). *Zhu et al., 2006,* proposed a path planning method for plant protection UAVs based on the genetic algorithm: by converting intra-regional operation paths and inter-regional scheduling paths into virtual nodes or arcs to construct a super network, it verified the feasibility of this method in the multi-plot path planning problem of UAV pesticide spraying. *Wang et al., (2023),* improved the ant colony algorithm by introducing a height factor, making the ant colony search more directional. *Zhao et al., (2023),* proposed an improved particle swarm UAV trajectory planning algorithm: by combining the "stepwise" adjustment strategy of inertia weight and the strategy of jumping out of local optimal solutions, it improved the optimality and real-time performance of the planning algorithm.

In the context of agricultural spraying operations, coverage path planning has been extensively studied. *Vazquez-Carmona et al., (2022),* proposed a CPP method for spraying drones that models the sprinkler footprint as a paraboloid and restricts flight within the region of interest to avoid collisions. *Plessen, (2025),* combined the traveling salesman problem with area coverage path planning for spot spraying, demonstrating that the inclusion of headland paths significantly reduces coverage gaps. *Meron et al., (2025),* employed high-resolution thermal and visible light imagery to quantify irrigation uniformity across surface, linear move, and solid-set irrigation systems, using the Crop Water Stress Index and Christiansen Uniformity Coefficient as evaluation metrics. *Cui et al., (2025),* utilized UAV multispectral imagery to estimate soil salinity under sunflower cover, demonstrating the feasibility of UAV-based monitoring for precision irrigation management.

Although the above algorithms can improve path planning performance to some extent, their application to mountainous crop irrigation remains limited when coverage continuity and terrain-adaptive flight stability must be considered simultaneously. For irrigation or spraying UAVs, trajectory optimization is not only a geometric problem; it also affects the continuity of the effective spray swath, local overlap/gap formation, and the stability of relative altitude above the crop canopy.

Existing studies on spraying path planning have shown that coverage-gap avoidance and area-coverage organization are essential for practical aerial application, rather than only minimizing route length. In addition, studies on UAV aerial spraying have reported that flight parameters such as height, velocity, and operational stability directly influence droplet coverage, deposit consistency, and drift risk.

Therefore, in the irrigation of mountain crops, a feasible approach should simultaneously meet the requirements of obstacle avoidance, fixed-wing kinematic constraints, and flight stability for irrigation. To address these challenges, the basic DBO framework was retained and enhanced by Bernoulli chaotic initialization, a golden sine strategy, dynamic adaptive weights, and an adaptive Gaussian-Cauchy mixed perturbation strategy, thereby proposing a multi-strategy DBO (MDBO). The optimization objective of this algorithm is to search for the shortest feasible path that satisfies the flight constraints such as smooth turning, stable pitch, and terrain adaptability, while ensuring the safety constraints. On this basis, this study introduces three irrigation performance indicators - coverage, repetition, and coverage uniformity - after the path planning is completed for posterior evaluation of the spray distribution quality of the optimized path. This design effectively overcomes the problems of local optimization and poor stability of fixed-wing unmanned aircraft in path planning in this scenario, and provides a quantitative evaluation basis for the applicability of the planned path for irrigation.

MATERIALS AND METHODS

Fixed-Wing UAV Path Planning Modelling

Mountain Modelling

To simulate the real mountainous irrigation environment, a 3D terrain model is constructed by superposition of multiple Gaussian hills, which can accurately reflect the elevation fluctuation characteristics of mountainous areas, as shown in Fig. 1.

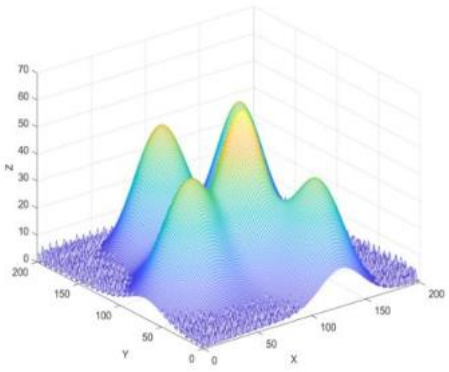


Fig. 1 - Mountain model

The mathematical expression is:

$$Z(x,y)=\sum_{i=1}^{N} h_i \exp[\left(\frac{x-x_{ic}}{x_{ir}}\right)^2-\left(\frac{y-y_{ic}}{y_{ir}}\right)^2 \tag{1}$$

where: N is the number of hills; h_i is the height; (x_{ic}, y_{ic}) is the center coordinate; x_{ir} is the gradient along the x-axis; and y_{ir} is the gradient along the y-axis.

Objective Function

Suppose that a fixed-wing UAV passes through N nodes during operation, with coordinate (x_1, y_1, z_1), (x_2, y_2, z_2), …, (x_N, y_N, z_N). The objective function consists of four core terms:

(1) The total length of the fixed-wing UAV path:

$$F_1=\sum_{i=1}^{N-1}\sqrt{dx_i^2+dy_i^2+dz_i^2} \tag{2}$$

where: F_1 represents the total length of the entire path, dx_i is the distance between two path nodes in the X-axis direction, dy_i is the distance between two path nodes in the Y-axis direction, dz_i is the distance between two path nodes in the Z-axis direction, and N represents the total number of path nodes.

(2) Path altitude of fixed-wing UAV:

$$F_2 = \sum_{i=1}^{N} \left| Z_i - \bar{Z} \right| \tag{3}$$

where: F_2 represents the path height, Z_i represents the z-coordinate of the i-th path point, $\bar{Z}$ represents the mean of all z-coordinates, and N represents the total number of path nodes.

(3) Safe turning radius for fixed-wing UAV:

$$F_3 = \sum_{i=1}^{N-2} \left(\cos\frac{\pi}{2} - \frac{dx_i \cdot dx_{i+1} + dy_i \cdot dy_{i+1} + dz_i \cdot dz_{i+1}}{\sqrt{dx_i^2 + dy_i^2 + dz_i^2} \cdot \sqrt{dx_{i+1}^2 + dy_{i+1}^2 + dz_{i+1}^2}} \right) \tag{4}$$

where: F_3 represents the safe turning radius, dx_i represents the variation of the i-th path segment on the x-coordinate, dy_i represents the variation of the i-th path segment on the y-coordinate, dz_i represents the variation of the i-th path segment on the z-coordinate, and dx_{i+1} represents the variation of the i+1st path segment on the x-coordinate, dy_{i+1} represents the variation of the i+1st path segment on the Y-coordinate, dz_{i+1} represents the variation of the i+1st path segment on the Z-coordinate, and N_2 represents the total number of path nodes.

(4) Pitch Angle of fixed-wing UAV flight:

$$F_4 = \tan^{-1}\left(\frac{dz}{\sqrt{dx^2 + dy^2}} \right) \tag{5}$$

where: F_4 represents the pitch Angle.

(5) Overall objective function expression:

$$F = \sum_{i=1}^{4} w_i \times F_i \tag{6}$$

where: $w_1 \sim w_4$ are weight coefficients, balancing path efficiency, flight safety and irrigation performance. The optimal weight combination is determined by ablation experiments.

Irrigation Performance Indicators

Different from ordinary path planning, irrigation path planning needs to evaluate the actual operation effect. Three quantitative indicators are proposed for posterior evaluation of spray distribution quality, which are not involved in the optimization process.

(1) Coverage rate: The proportion of grids sprayed at least once in the target area, reflecting the integrity of irrigation coverage.

$$CR = \frac{|\{(i,j) \mid c_{i,j} \geq 1\}|}{N_x \times N_y} \tag{7}$$

where: $c_{i,j}$ represents the coverage times of the grid (i,j), N_x and N_y represent the total number of grids in each dimension.

(2) Overlap ratio: The proportion of grids with spray times exceeding the ideal threshold, reflecting the degree of resource waste caused by repeated spraying.

$$OR = \frac{|\{(i,j) \mid c_{i,j} > c_{\text{ideal}}\}|}{N_x \times N_y} \tag{8}$$

where: c_{ideal} represents the ideal coverage threshold.

(3) Coverage uniformity: Quantifying the uniformity of spray distribution in the covered area. The closer the value is to 1, the more uniform the spray distribution.

$$U = 1 - \frac{\sigma(c_{\text{covered}})}{\mu(c_{\text{covered}})} \tag{9}$$

where: μ and σ represent the mean and standard deviation of the total number of times all covered grids have been covered, respectively.

Dung Beetle Optimization Algorithm

Dung Beetle Optimization Algorithm (DBO) is a novel population-based intelligence optimization algorithm inspired by social behaviors of dung beetles during the acquisition and handling of dung balls *(Xue et al., 2023)*.

As an innovative algorithm, dung beetles search rolling burying and guarding dung balls to implement the meta-heuristic as a means of dealing with complex optimization problems. More specifically, the DBO simulates 5 main behaviors of dung beetles — rolling of the ball, dance, mating, foraging and pill stealing *(Jin et al., 2023)*.

Rolling beetles move forward along a straight trajectory with the aid of light sources; dancing behavior adjusts moving direction when encountering obstacles; breeding beetles update positions within local optimal areas for oviposition; foraging beetles search for food near the global optimum with normal distribution perturbation; thief beetles compete for dung balls near the optimal food source to increase population diversity.

The basic DBO algorithm has fast initial convergence, but it still has limitations in solving complex 3D path planning problems: random initialization leads to insufficient population diversity, and population aggregation in the late iteration stage easily causes premature convergence and falls into local optimum. To address these defects, this paper improves the algorithm from four aspects to enhance its adaptability to mountainous irrigation path planning scenarios.

An Advanced Multiple Strategies Dung Beetle Optimization Algorithm

Aiming at the defects of basic DBO algorithm, four improvement strategies are integrated to construct a multi-strategy improved dung beetle optimization (MDBO) algorithm, so as to balance global exploration and local exploitation capability and avoid premature convergence.

Bernoulli Chaotic Mapping Strategy

Random initialization easily leads to uneven population distribution and insufficient diversity, limiting the early global search range. Chaotic mapping features ergodicity, randomness and regularity, which can generate initial populations with wider distribution and better diversity. In this paper, Bernoulli chaotic mapping is used to generate initial population positions *(Saito et al., 2016)*. The mapping expression is:

$$z_{n+1} = \begin{cases} \dfrac{z_n}{1-\beta}, & 0 \le z_n \le 1-\beta \\ \dfrac{z_n - (1-\beta)}{\beta}, & 1-\beta \le z_n \le 1 \end{cases} \tag{10}$$

where: $\beta \in (0,1)$.

Golden Sine Strategy

In the basic DBO algorithm, the position update of rolling beetles lacks sufficient information interaction with the optimal individual, which is easy to cause premature convergence. The golden sine algorithm combines the golden section ratio with the sine position update mechanism, which can effectively balance global exploration and local exploitation.

This paper introduces the golden sine strategy to optimize the position update of rolling beetles. The update formula is:

$$X_i^{t+1} = X_i^t \times |\sin(R_1)| + R_2 \times \sin(R_1) \times |x_1 \times P_i^t - x_2 \times X_i^t| \tag{11}$$

where: $R_1 \in (0, 2\pi)$, $R_2 \in (0, 2\pi)$, $x_1 = -\pi + (1-\tau) * 2\pi$, $x_2 = -\pi + (1-\tau) * 2\pi$, $\tau(\tau = (\sqrt{5}-1)/2)$.

In the second part of the position update expression, if $R_2 < ST$, the dung beetle gradually reduces its angle; otherwise $R_2 \geqslant ST$, the dung beetle has a random walk in normal distribution in the same region. While this design allows the algorithm to converge to the global best solution at the start of the fitness iteration, it also increases the potential to converge too quickly and get stuck at local optima. In order to remedy this defect, the present work proposed the golden sine, to optimize the DBO algorithm partition update mechanism. Below is the updated version of position update Equation:

$$X_{i,j}^{t+1} = \begin{cases} X_{ij}^t \times |sin(R_1)| + R_2 \times sin(R_1) \times |x_1 \times X_{best}^t - x_2 \times X_{ij}^t|, R_2 < ST \\ X_{i,j}^t + Q \cdot L, \qquad R_2 \ge ST \end{cases} \tag{12}$$

The improved position update scheme enhances algorithm performance in two aspects. First, all individuals interact with the current optimal individual per iteration to fully exploit optimal information, which

remedies the deficiency of inter-individual information exchange in the original DBO. Second, the golden sine strategy broadens the search range to avoid local optima, and the golden section coefficient fine-tunes the search distance and direction of dung beetles, thus achieving a balanced trade-off between global exploration and local exploitation.

Strategy For Dynamic Adaptability Weight

While, given many early iterations of the DBO algorithm, the algorithm may over-focus onto local areas, causing local convergence. To overcome this drawback, in this paper, the position update formula is changed by adding between its own position the global optimal solution from last generation, which means during the current position update, the position will be affected not only by itself but its optimal solution in the previous generation. Moreover, dynamic weight coefficient is proposed to improve global search ability in the early stage, whilst increasing local search and convergence processes in the latter stages by reducing adaptation. The new coefficient *w* and the new position update equations are as follows:

$$w = \frac{e^{2(1-t/iter_{max})} - e^{-2(1-t/iter_{max})}}{e^{2(1-t/iter_{max})} + e^{-2(1-t/iter_{max})}} \tag{13}$$

$$X_{i,j}^{t+1} = \begin{cases} (X_{i,j}^{t} + w(f_{j,g}^{t} - X_{i,j}^{t})) \cdot rand, R_2 < ST \\ \\ X_{i,j}^{t} + Q, \qquad\qquad R_2 \geq ST \end{cases} \tag{14}$$

where: $f_{j,g}^{t}$ is the j-th dimensional global optimal solution of the previous generation; Q is the stochastic number; $R_2 \in (0,1)$; and $ST \in (0.5,1)$.

Adaptive Gauss-Cauchy Mixed-Variance Perturbation Strategy

In later iterations, the basic DBO suffers from severe population aggregation around local optima. While accelerating convergence, this phenomenon sharply reduces population diversity, trapping the algorithm in local minima and even causing search stagnation. Mutation perturbation is a widely adopted technique to restore population diversity and assist the algorithm in escaping local optima *(Du et al., 2024)*.

Among common mutation operators, Gaussian mutation achieves fine local exploitation with small step sizes, whereas Cauchy mutation performs broader global exploration with larger step sizes but may generate lower-quality offspring. To fully leverage the strengths of both, this paper proposes an adaptive Gaussian-Cauchy hybrid mutation perturbation strategy. It only applies perturbation to the current best individual, and retains the mutated position only when its fitness is improved, thus effectively expanding population diversity while guaranteeing solution quality. The specific expression is given as follows:

$$H^b(t) = X^b(t) * (1 + \mu_1 * Gauss(\sigma) + \mu_2 * cauchy(\sigma)) \tag{15}$$

where: $\mu_1 = t / T_{max}$, $\mu_2 = 1 - t / T_{max}$, $X^b(t)$ indicates the individual's optimal position at the t-th iteration, $H^b(t)$ represents the position of the optimal position post a mixed Gauss-Cauchy perturbation, $Gauss(\sigma)$ is the Gaussian variational operator, and $cauchy(\sigma)$ is the Cauchy variational operator.

The strategy applies adaptive perturbation throughout iterations, with mutation modes dynamically tuned to the population distribution state. In early iterations, Cauchy distribution with large-amplitude perturbations is adopted for the widely dispersed population, which enhances population diversity, boosts global search capability, and prevents premature trapping in local optima. As iterations proceed and the population gradually converges, Gaussian distribution with small-amplitude perturbations dominates to perform precise local exploitation, accelerating convergence while maintaining algorithmic robustness in complex high-dimensional spaces. This adaptive switching mechanism effectively achieves a balanced trade-off between global exploration and local exploitation.

The mechanics and flow of this approach are encapsulated in the pseudo-code for the MDBO algorithm, which is detailed in Table 1 below.

Table 1

Pseudo-code for the MDBO algorithm

Pseudo-code for the MDBO algorithm
Inputs: maximum number of iterations T_{max} , population size N .
Output: optimal position X^b and its fitness value f_b .
1 Randomly initialize the dung beetle population, defining the relevant parameters
2 Initialization of population positions using Bernoulli's chaotic mapping
3 **while** $(t \le T_{max})$ **do**
4 **for** $i \leftarrow 1$ *to* N **do**
5 **if** $i ==$ Dung Beetle Roller **then**
5 $\delta = \text{rand}(1)$
6 **if** $\delta < 0.9$ **then**
7 Use the golden sine strategy to update the position of the rolling dung beetle;
8 **else**
9 Update the position of the rolling dung beetle;
10 **end if**
11 **end if**
12 **if** i ==Breeding Dung Beetles **then**
13 Update the location of breeding dung beetles;
14 **end if**
15 **if** i ==Foraging Dung Beetle **then**
16 The location of the foraging dung beetle was updated;
17 **end if**
18 **if** i ==Stealing Dung Beetles **then**
19 Updating the location of the stealing dung beetle using a equation that incorporates dynamic weighting factors;
20 **end if**
21 **end for**
22 **If** the newly generated position is better than before
23 Update Location;
24 **end if**
25 Applying an adaptive Gauss-Cauchy mixed-variance perturbation strategy to the current optimal solution
26 **if** the position is better after perturbation
27 Accept new position;
28 **end if**
29 $t = t + 1$
30 **end while**
31 **Return the** fitness value

Application of the MDBO Algorithm to Fixed-Wing UAV Path Planning

The procedure for applying the MDBO algorithm to fixed-wing UAV path planning is as follows:

Step1: Define start and end points, and construct a detailed map of complex mountain terrain;

Step2: Enter the objective function and associated parameters to guide the search;

Step3: Position the dung beetles using Bernoulli's chaotic mapping to ensure diverse starting points;

Step4: Calculate the fitness of each individual based on the objective function within the designated fitness landscape;

Step5: Apply the golden sine algorithm to adjust the positions of all dung beetles towards optimal paths;

Step6: Verify that no dung beetle exceeds the predefined map boundaries;

Step7: Modify current positions by integrating influences from both the previous positions and the current best solution using a dynamic adaptive weighting strategy;

Step8: Refresh the best-known solution and its corresponding fitness score;

Step9: Employ an adaptive Gauss-Cauchy mixed-variance perturbation strategy to further refine the current best solution, creating potential new optimal paths;

Step10: Determine if the end condition is met; if not, loop back to Step 4; if yes, proceed to the final step;

Step11: Deliver the optimal path solution with its fitness value and conclude the algorithm.

Refer to the flowchart depicted in Fig. 2 for a graphical representation of the MDBO algorithm steps.

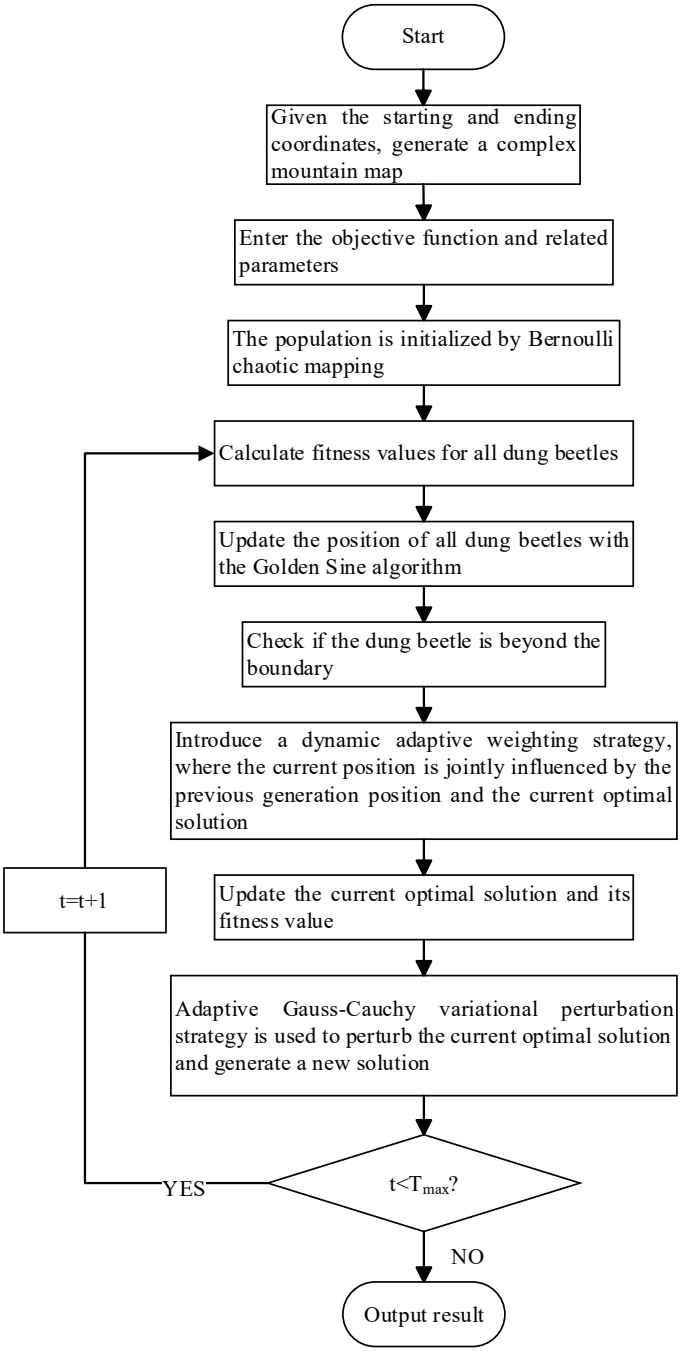


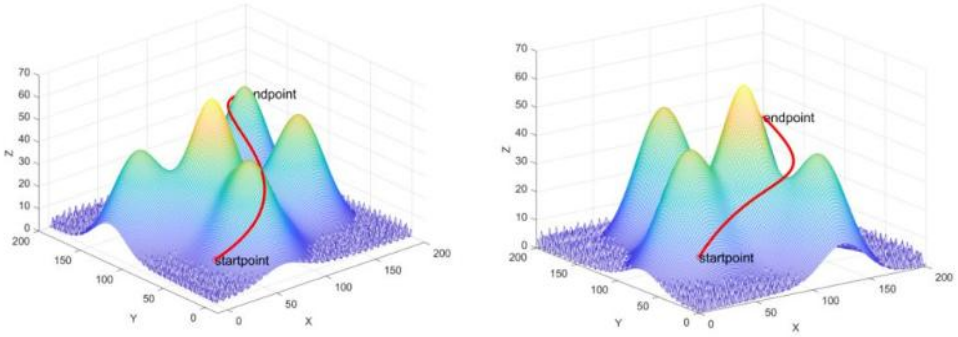
Fig. 2 - The flowchart of the MDBO algorithm

RESULTS

The experiments were conducted on a computer equipped with an Intel® Core™ i5-8250U processor operating at 1.60–1.80 GHz and 16 GB of RAM. The system ran the 64-bit version of Windows 11, and MATLAB R2022b was used for all simulations.

Security Constraints Impact Analysis

Safe turning radius and pitch angle are critical constraints for fixed-wing UAV path planning. Neglecting these constraints will induce excessively sharp turns and abrupt pitch maneuvers, which degrade flight efficiency, elevate collision risks and reduce spray uniformity in complex terrain. Comparative experiments with and without the above constraints are carried out, with results shown in Fig. 3. It is verified that introducing the constraints yields a smoother flight path with gentler turning and climbing maneuvers, thus effectively improving flight safety and operational reliability.



a) b)

Fig. 3 - Comparison of experiments with and without constraints

(a) No safe turning radius and pitch angle constraints; (b) Add safe turning radius and pitch angle constraints

Performance Analysis of the Algorithm Using Benchmark Test Functions

To gauge the effectiveness of the modified MDBO algorithm, this research utilized nine benchmark test functions outlined in Table 2. These functions were used to test and compare the MDBO algorithm against the original DBO algorithm. The chosen benchmarks encompass single-peak, multi-peak, and fixed-dimension functions, providing a comprehensive evaluation across various optimization scenarios. For each algorithm, the testing conditions were standardized with a population size of 30 and a limit of 500 iterations.

Each algorithm was independently run 30 times on the nine benchmark test functions, and the optimal value, mean, and standard deviation of the function values were recorded. The computational results are displayed in Table 3. As shown in Table 3, the results of the comprehensive experiments across the nine test functions indicate that the MDBO algorithm achieves optimal values comparable to the DBO algorithm on the 7th and 8th functions. Additionally, for the 9th function, both algorithms yield identical results. For the remaining six functions, the MDBO algorithm demonstrates superior optimization accuracy compared to the DBO algorithm. Furthermore, in terms of computational stability, the MDBO algorithm exhibits a lower standard deviation over 30 runs, indicating higher consistency and enhanced search capability compared to the DBO algorithm.

Table 2

Benchmark test function

Benchmark test function	Dimension	Definition	f_{min}
$F_1(x)=\sum_{i=1}^{n}x_i^2$	30	[-100,100]	0
$F_2(x)=\sum_{i=1}^{n}\lvert x_i\rvert+\prod_{i=1}^{n}\lvert x_i\rvert$	30	[-10,10]	0
$F_3(x)=\sum_{i=1}^{n}\left(\sum_{j-1}^{i}x_i\right)^2$	30	[-100,100]	0
$F_4(x)=\sum_{i=1}^{n}ix_i^4+random[0,1)$	30	[-128,128]	0
$F_5(x)=\sum_{i=1}^{n}\left[x_i^2-10\cos(2\pi x_i)+10\right]$	30	[-5.12,5.12]	0
$F_6(x)=-20\exp\left(-0.2\sqrt{\frac{1}{n}\sum_{i=1}^{n}x_i^2}\right)-exp\left(\frac{1}{n}\sum_{i=1}^{n}\cos(2\pi x_i)\right)+20+e$	30	[-32,32]	0
$F_7(x)=\frac{1}{4000}\sum_{i=1}^{n}x_i^2-\prod_{i=1}^{n}cos\left(\frac{x_i}{\sqrt{i}}\right)+1$	30	[-600,600]	0
$F_8(x)=\sum_{i=1}^{11}\left[a_i-\frac{x_1\left(b_i^2+b_ix_2\right)}{b_i^2+b_ix_3+x_4}\right]^2$	4	[-5,5]	0.0003075
$F_9(x)=\left(x_2-\frac{5.1}{4\pi^2}x_1^2+\frac{5}{\pi}x_1-6\right)^2+10\left(1-\frac{1}{8\pi}\right)cosx_1+10$	2	[-5,5]	0.398

Table 3

Benchmark test function experimental results

Function	Evaluation indicators	DBO	MDBO
F1	optimal value	4.7424E-158	0.00E+00
	mean	2.5287E-114	0.00E+00
	standard deviation	1.3785E-113	0.00E+00
F2	optimal value	1.2751E-167	0.00E+00
	mean	3.737E-109	0.00E+00
	standard deviation	2.0468E-108	0.00E+00
F3	optimal value	1.3035E-79	0.00E+00
	mean	4.0589E-59	3.4453E-293
	standard deviation	1.9479E-58	0.00E+00
F4	optimal value	8.6575E-4	24572E-4
	mean	0.5819	0.0328
	standard deviation	0.3549	0.0549
F5	optimal value	2.3283E-4	1.7876E-06
	mean	1.4341E-3	1.2686E-4
	standard deviation	9.4036E-4	1.2383E-4
F6	optimal value	2.7046E-188	0.00E+00
	mean	3.5662E-115	0.00E+00
	standard deviation	1.8311E-114	0.00E+00
F7	optimal value	0.00E+00	0.00E+00
	mean	0.1005	0.00E+00
	standard deviation	0.5503	0.00E+00
F8	optimal value	3.0749E-4	3.0749E-4
	mean	6.4466E-4	3.1581E-4
	standard deviation	3.5861E-4	2.6591E-05
F9	optimal value	0.3979	0.3979
	mean	0.3979	0.3979
	standard deviation	0.00E+00	0.00E+00

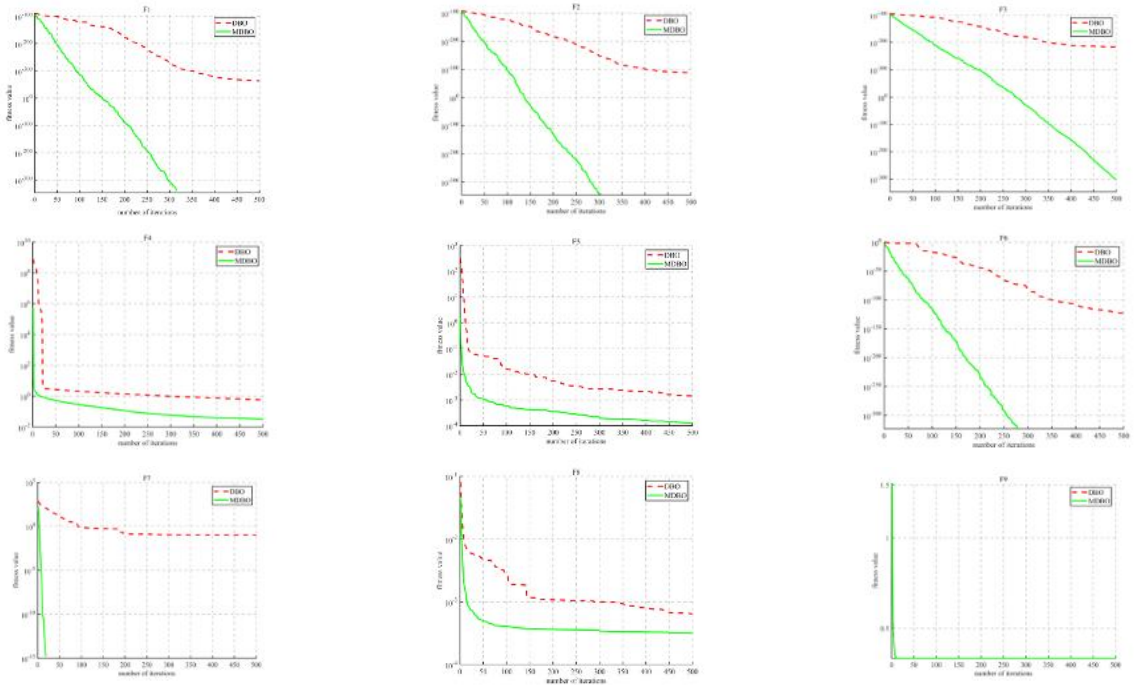


Fig. 4 - Convergence curves for each algorithm

Performance Analysis of the Algorithm Using Benchmark Test Functions

As the weight parameters of the multi-objective function directly determine path planning performance, this section adopts the single-factor control variable method in ablation experiments to analyze the influence law of each weight on fixed-wing UAV mountain irrigation path planning, and determines the optimal weight combination applicable to mountain agricultural irrigation scenarios.

The objective function consists of four core terms: path length, altitude fluctuation, turning radius constraint and pitch angle constraint, corresponding to weights w_1, w_2, w_3 and w_4 respectively. During the experiment, three weights are fixed at the final determined values, and only the target weight is adjusted within the range of [0, 1] with a step size of 0.1. Each parameter set undergoes 30 independent repeated experiments, and the error bars in the figures represent the standard deviation of results to quantify the operational stability of the algorithm.

Figs. 5–8 present the influence of each weight coefficient on path planning performance obtained via single-factor ablation experiments.

For the path length weight w_1 (Fig. 5): increasing w_1 within 0–0.3 significantly reduces altitude fluctuation, turning cost and pitch angle cost without notable path length degradation. At w_1 = 0.3, altitude fluctuation and pitch angle cost reach the global minimum, and turning cost stays within the optimal range. Values above 0.3 cause sharp deterioration of attitude-related indicators despite marginal reduction in path length, so w_1 = 0.3 is selected.

For the altitude fluctuation weight w_2 (Fig. 6): as w_2 rises from 0 to 0.3, altitude fluctuation drops sharply from 1200 m to 220 m, accompanied by optimized turning and pitch angle costs. When w_2 exceeds 0.3, altitude fluctuation oscillates without further improvement, while path length and attitude-related costs all deteriorate. Thus w_2 = 0.3 is adopted.

For the turning radius weight w_3 (Fig. 7): as a hard safety constraint for fixed-wing UAVs, insufficient turning radius directly leads to aerodynamic stall and crash. Increasing w_3 below 0.65 gradually optimizes turning cost without obvious degradation of other indicators, while values above 0.65 cause significant deterioration of path length, altitude fluctuation and pitch angle cost. Prioritizing flight safety, w_3 = 0.65 is determined.

For the pitch angle weight w_4 (Fig. 8): pitch angle cost keeps optimizing with the growth of w_4. Within the range of w_4 in [0.3, 1], pitch angle cost stabilizes in the optimal interval of 0.09–0.11, and no significant degradation occurs in path length, altitude fluctuation or turning cost. Given that pitch angle constraint directly determines operational feasibility, w_4 = 1.0 is chosen.

Based on the above experimental results, the final multi-objective weight combination applicable to mountain agricultural irrigation scenarios is determined as w_1 = 0.3, w_2 = 0.3, w_3 = 0.65, w_4 = 1.0.

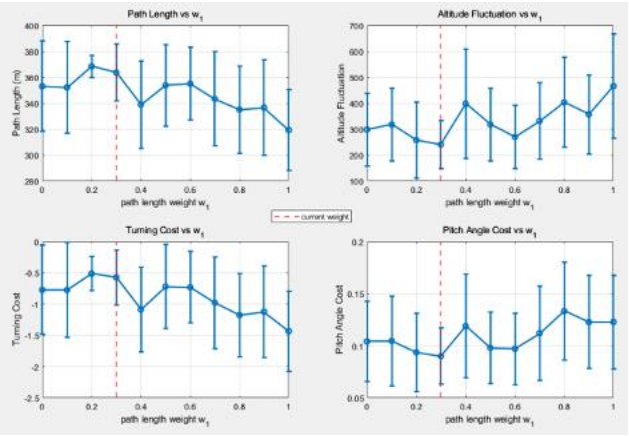


Fig. 5 - The influence of path length weight w_1 on the performance of path planning

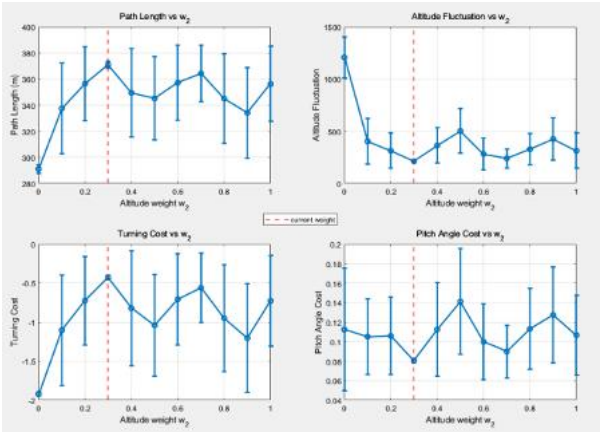


Fig. 6 - The influence of the highly fluctuating weight w_2 on the performance of path planning

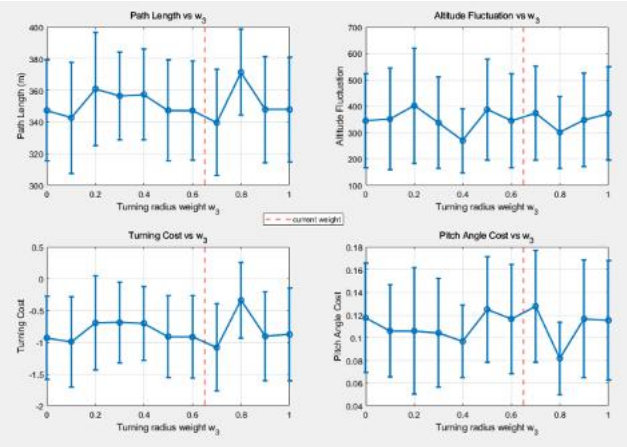


Fig. 7 - The influence of the turning radius weight w_3 on the performance of path planning

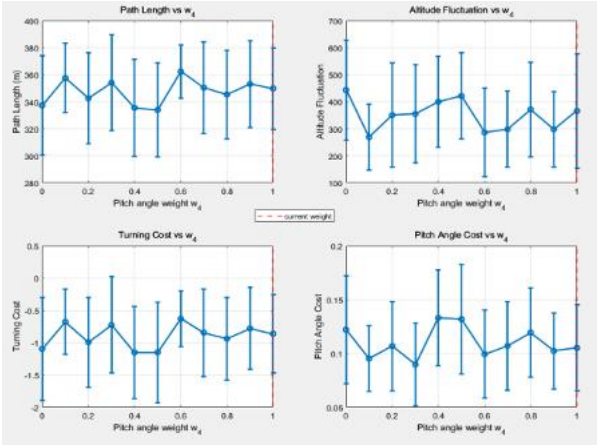


Fig. 8 - The influence of the pitch angle weight w_4 on the performance of path planning

Analysis Of Path Planning Simulation Results

To verify the robustness and effectiveness of the improved algorithms, this study conducted comparative experiments between the MDBO algorithm and several others, including PSO, COA, NGO, WOA, SSA, and DBO, in three mountainous environments with varying levels of complexity using MATLAB. The specific parameter settings for each algorithm are presented in Table 4.

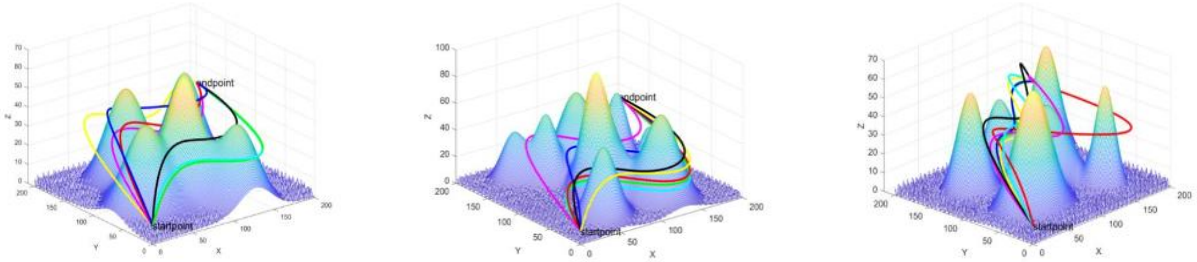
Table 4

Parameter variable settings

Arithmetic	Algorithmic parameter	Numerical value
PSO	w	1
	c_1	1.5
	c_2	2.0
COA	w	Reduction from 1 to 0.1
	SF	1.5
NGO	w	Reduced linearly from 1 to 0.1
WOA	a	Decrease from 2 to 0
SSA	w	Reduced linearly from 1 to 0.1
	R	0.2
DBO	a	-1 or 1
	R	1(decreases linearly during iterations)
MDBO	R_1	$(0, 2\pi)$
	R_2	$(0, \pi)$
	τ	$(\sqrt{5}-1)/2$
	a	-1 or 1
	R	1(decreases linearly during iterations)

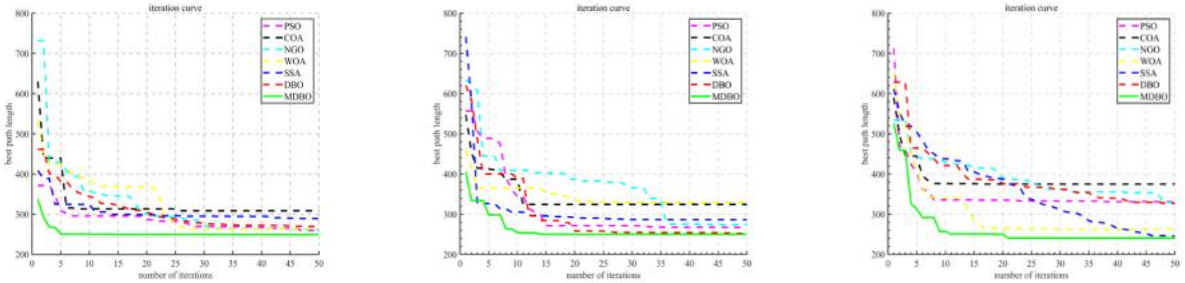
To ensure the neutrality of the experimental outcomes, the parameters for all tested algorithms were uniformly configured. The starting point was set at coordinates (0, 0, 10), while the endpoint was at (200, 200, 30). The experiments maintained a population size of 50 and were capped at a maximum of 50 iterations.

The evaluation of path optimization performance across three different mountainous terrains of increasing complexity is depicted in Figures 9 and 10. Figure 9 provides a visual comparison of the pathfinding results of each algorithm, and Figure 10 explores the correlation between the number of iterations and the achievement of optimal values.



(a) Map 1 (b) Map 2 (c) Map 3

Fig. 9 - Comparison of air path planning effects



(a) Map 1 (b) Map 2 (c) Map 3

Fig. 10 - The iterations vs optimal value curve

The iteration curves of three maps are shown in Fig. 10. The improved MDBO achieves faster convergence and stronger early exploration capability than the basic DBO. All algorithms tend to converge before the 8th iteration, while MDBO consistently yields the best convergence value at each iteration, with both higher convergence speed and solution accuracy than other comparison algorithms. The golden sine strategy accelerates convergence, the dynamic adaptive weight prevents premature local trapping, and the adaptive Gaussian-Cauchy hybrid mutation further helps the algorithm escape from local optima. The phenomenon that the basic DBO is easily trapped in local optima during iteration also verifies the effectiveness of the above improvements.

To eliminate the influence of randomness, 30 independent runs are conducted for each map. As shown in Table 5, the proposed MDBO outperforms all other algorithms in terms of maximum, minimum and average path length. More importantly, MDBO achieves the minimum standard deviation, indicating higher stability and consistency in path planning performance.

Table 5

Individual evaluation indicators in different maps

Map	Algorithm	Longest path	Shortest path	Mean	Standard deviation
Map 1	PSO	340.42	272.02	299.21	19.08
	COA	366.97	263.53	298.23	30.52
	NGO	335.07	260.22	275.48	20.05
	WOA	364.10	251.00	301.20	34.24
	SSA	341.80	252.86	279.61	27.18
	DBO	326.14	246.52	267.60	21.02
	MDBO	**311.33**	**234.52**	**253.24**	**14.06**
Map 2	PSO	336.36	245.26	280.85	21.26
	COA	359.23	252.24	288.22	30.23
	NGO	319.55	247.83	275.73	20.52
	WOA	361.83	255.13	302.19	30.53
	SSA	324.33	243.64	265.02	20.10
	DBO	339.86	235.58	261.63	21.56
	MDBO	**301.84**	**220.90**	**245.17**	**16.98**
Map 3	PSO	339.05	255.56	292.94	18.39

Map	Algorithm	Longest path	Shortest path	Mean	Standard deviation
	COA	368.35	242.49	295.18	31.45
	NGO	326.61	238.14	279.57	23.70
	WOA	344.89	254.13	297.90	27.58
	SSA	333.16	238.35	269.99	29.11
	DBO	328.05	232.38	254.62	20.58
	MDBO	**296.99**	**226.94**	**239.47**	**14.26**

Ablation Experiment

The modified versions of the DBO algorithm are denoted in Table 6: DBO123 indicates the DBO algorithm equipped with the Bernoulli's chaotic mapping strategy, golden sine strategy and dynamic adaptive weighting strategy; DBO124 represents the DBO algorithm with the Bernoulli's chaotic mapping strategy, golden sine strategy and adaptive Gauss-Cauchy mixed-variance perturbation strategy; DBO234 means that the DBO algorithm uses golden sine strategy, dynamic adaptive weighting strategy and adaptive Gauss-Cauchy mixed-variance perturbation strategy.

Table 6

MDBO algorithm and its variants

Algorithm	Bernoulli's chaotic mapping	Golden sine	Dynamic adaptive weighting	Gauss-Cauchy mixed-variance perturbation
DBO123	√	√	√	
DBO124	√	√		√
DBO134	√		√	√
DBO234		√	√	√
MDBO	√	√	√	√

To confirm that simultaneously introducing the four strategies can improve the performance of the MDBO algorithm, a series of ablation experiments were designed. In three mountainous environments with different level of complexity, comparative experiments between MDBO with its variants DBO123, DBO124 and DBO234 were implemented using MATLAB. The parameter settings for all the experiments were the same, that is, the starting coordinate is (0,0,10), end coordinate is (200,200,30), population size 50 and maximum 50 iterations.

The path finding optimization of each algorithm across three mountain maps with varying levels of complexity is illustrated in Fig. 11 and Fig. 12. Fig. 11 presents a comparison of the path planning effectiveness, while Fig. 12 depicts the relationship between the number of iterations and the optimal values. A total of 30 experiments were conducted on each of the three maps, and the longest path, shortest path, average value, and standard deviation of the fixed-wing UAV in these experiments were statistically analyzed, as shown in Table 7.

Experimental results demonstrate that the complete MDBO algorithm outperforms all variant algorithms across all evaluation metrics, including maximum, minimum and mean path length, as well as standard deviation. Iteration curves further confirm that MDBO converges significantly faster on all test maps, and the synergy among multiple strategies substantially enhances its path planning capability in complex mountainous terrain.

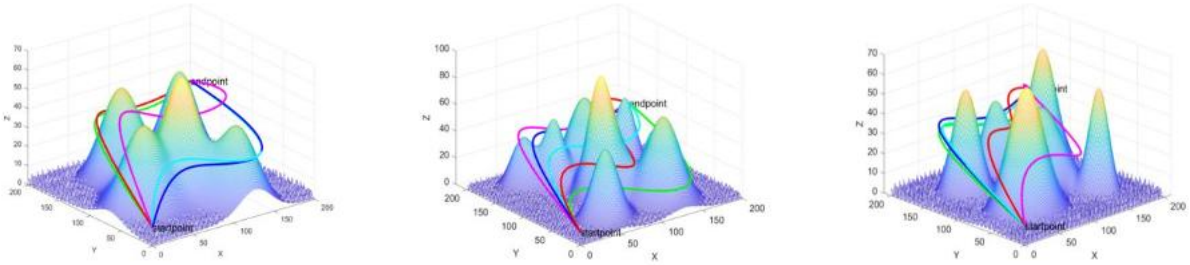
These four complementary strategies empower MDBO to achieve superior 3D path planning for fixed-wing UAVs. Bernoulli mapping diversifies initial solutions, and the golden sine strategy accelerates convergence. Dynamic adaptive weights balance exploration and exploitation, while Gaussian-Cauchy hybrid mutation introduces stochastic perturbations to effectively escape local optima.

Table 7

Individual evaluation indicators in different maps

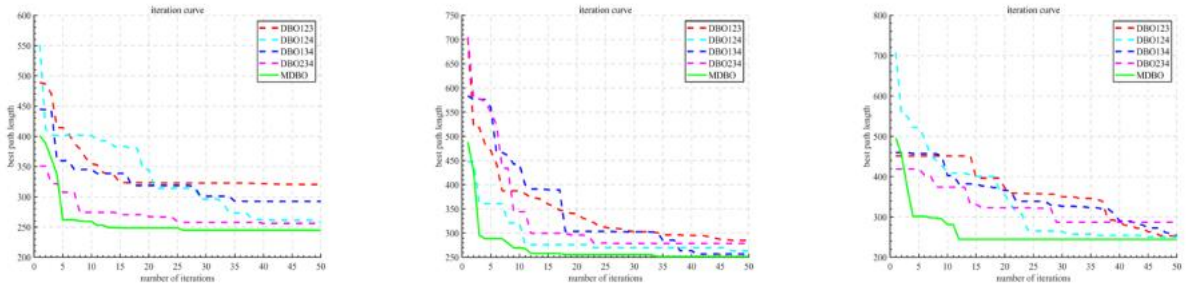
Map	Algorithm	Longest path	Shortest path	Mean	Standard deviation
Map 1	DBO123	323.27	240.17	259.09	23.60
	DBO124	322.76	243.04	260.92	19.78
	DBO134	314.13	243.16	259.15	18.86
	DBO234	322.06	243.14	257.30	17.64

Map	Algorithm	Longest path	Shortest path	Mean	Standard deviation
Map 2	**MDBO**	**298.55**	**230.32**	**250.38**	**12.77**
	DBO123	318.19	236.69	252.32	20.91
	DBO124	326.34	238.33	252.83	20.45
	DBO134	319.58	240.09	254.04	20.72
	DBO234	310.48	230.42	250.48	20.84
Map 3	**MDBO**	**295.11**	**220.50**	**246.09**	**16.32**
	DBO123	328.51	231.40	245.64	22.63
	DBO124	314.55	233.62	246.45	24.74
	DBO134	318.25	234.09	246.17	21.34
	DBO234	314.45	234.05	244.89	23.07
	MDBO	**296.71**	**220.89**	**238.68**	**16.26**



(a)Map 1 (b)Map 2 (c)Map 3

Fig. 11 - Comparison of air path planning effects



(a)Map 1 (b)Map 2 (c)Map 3

Fig. 12 - The iterations vs optimal value curve

Evaluation of Irrigation Effectiveness

Spray distribution quality of five algorithms (DBO123, DBO124, DBO134, DBO234 and MDBO) is evaluated on Map 1, with 30 independent runs conducted for each algorithm. Table 8 presents the statistical results of three irrigation indicators — coverage rate, overlap ratio and coverage uniformity, including the maximum, minimum, mean and standard deviation across all runs.

As shown in Table 8, MDBO achieves the highest coverage rate with the smallest standard deviation, indicating both optimal coverage performance and operational stability. The overall coverage rate of all algorithms is relatively low, mainly because fixed start and end points restrict path freedom, making a single flight unable to cover the entire map area; the safe turning radius and pitch angle constraints further narrow the feasible path space. Even under these limitations, MDBO still realizes relatively optimal coverage performance.

In addition, MDBO obtains the lowest overlap ratio, verifying its superior ability to avoid excessive spraying and minimize resource waste while maintaining adequate coverage. It also delivers the highest coverage uniformity, demonstrating its advantage in achieving balanced spray distribution. Comprehensive analysis confirms that the proposed MDBO algorithm achieves excellent overall irrigation performance.

Table 8

The irrigation index results of each algorithm in Map 1

Map	Performance indicators	Algorithm	Max	Min	Mean	Standard deviation
Map 1	Coverage rate	DBO123	0.1547	0.1121	0.1312	0.0089
		DBO124	0.1604	0.1158	0.1365	0.0100
		DBO134	0.1648	0.1294	0.1399	0.0114
		DBO234	0.1587	0.1163	0.1346	0.0099
		MDBO	**0.1734**	**0.1313**	**0.1449**	**0.0088**
	Overlap ratio	DBO123	0.1711	0.1087	0.1331	0.0133
		DBO124	0.1593	0.1258	0.1328	**0.0081**
		DBO134	0.1579	0.1262	0.1377	0.0117
		DBO234	0.1515	0.1203	0.1340	0.0083
		MDBO	**0.1474**	**0.1102**	**0.1267**	0.0091
	Uniformity	DBO123	0.6528	0.6054	0.6208	0.0139
		DBO124	0.6534	0.6046	0.6178	0.0151
		DBO134	0.6545	0.6057	0.6229	0.0175
		DBO234	0.6500	0.6058	0.6216	**0.0133**
		MDBO	**0.6617**	**0.6060**	**0.6362**	0.0167

CONCLUSIONS

This study addresses the core challenge of balancing obstacle avoidance safety and irrigation effectiveness in 3D path planning of fixed-wing UAVs for mountainous agricultural irrigation, and proposes a multi-strategy improved DBO (MDBO) algorithm with embedded flight kinematic constraints. Safe turning radius and pitch angle constraints are introduced to stabilize flight attitude and maintain irrigation consistency. Four improvement strategies (Bernoulli chaotic mapping, golden sine mechanism, dynamic adaptive weight, adaptive Gaussian-Cauchy hybrid mutation) are integrated to balance global exploration and local exploitation capability. Benchmark function tests and scenario simulation experiments verify the effectiveness of the proposed method.

Three irrigation performance indicators are established for posterior evaluation of spray distribution quality. Simulation results demonstrate that MDBO achieves superior performance in both path length optimization and irrigation effect, which fully meets the efficient irrigation path demands of mountainous crops.

This study is limited to simulation environment without considering practical factors such as wind disturbance, sensor noise and environmental variability, and irrigation indicators are applied for post-evaluation rather than being incorporated into the optimization objective. Future research will embed irrigation indicators into the objective function to balance path efficiency and irrigation quality, and further validate the algorithm via hardware-in-the-loop simulation and field tests.

ACKNOWLEDGEMENT

The authors were funded for this project by the Guizhou University Project (Guida Renjihezi (2023)52), (Guida Jichu [2023] 20), the Science and Technology Support Project of Guizhou Province, China (Qiankehe Support [2024] General 098), and the National Natural Science Foundation of China (Grant No.52465058), and the Guizhou Provincial Key Laboratory of Mountainous Intelligent Agricultural Machinery (Qiankehe Platform ZSYS[2025]013).

REFERENCES

[1] Chourasia S K, Vishwakarma S K, Pandey A. (2026). Can Micro-Irrigation in Canal Command Areas Increase Water Use Efficiency? A Feasibility Study for Sustainable Water Resources. *Water Conservation Science and Engineering*, Vol. 11, pp. 73, Roorkee/India.

[2] Hu R. P. (2023). Effectiveness of agricultural planting technology and agricultural mechanized production (农业种植技术与农业机械化生产的有效性). *Hebei Agricultural Machinery*, pp. 25-27, Hebei/China.

[3] Giagkiozis I, Purshouse R C, Fleming P J. (2015). An overview of population-based algorithms for multi-objective optimisation. *International Journal of Systems Science*, Vol. 46, pp. 1572-1599, Sheffield/United Kingdom.
[4] Wang S L, Song J L, He X K, et al. (2017). Performances evaluation of four typical unmanned aerial vehicles used for pesticide application in China. *Int J Agric & Biol Eng*, Vol. 10, pp. 22-31, Beijing/China.
[5] Wang C, Song J, He X, et al. (2017). Effect of flight parameters on distribution characteristics of pesticide spraying droplets deposition of plant-protection unmanned aerial vehicle (植保无人机飞行参数对施药雾滴沉积分布特性的影响). *Transactions of the Chinese Society of Agricultural Engineering*, Vol. 33, pp. 109-116, Beijing/China.
[6] Pan Z, Lie D, Qiang L, et al. (2016). Effects of citrus tree-shape and spraying height of small unmanned aerial vehicle on droplet distribution. *International Journal of Agricultural and Biological Engineering*, Vol. 9, pp. 45-52, Chongqing/China.
[7] Nanavati R V, Meng Y, Coombes M, et al. (2023). Generalized data-driven optimal path planning framework for uniform coverage missions using crop spraying UAVs. *Precision Agriculture*, Vol. 24, pp. 1497-1525, Loughborough/United Kingdom.
[8] Deng B C, Xu R, Huang C Y et al. (2022). Three-dimensional trajectory planning for unmanned aerial vehicles based on Kersey's variational sparrow search algorithm (基于柯西变异麻雀搜索算法的无人机三维航迹规划). *Mechanical Design and Research*, Vol. 38, pp. 62-66, Guangdong/China.
[9] Fadzli S A, Abdulkadir S I, Makhtar M, et al. (2015). Robotic indoor path planning using Dijkstra's algorithm with multi-layer dictionaries. *2015 2nd International Conference on Information Science and Security (ICISS)*, *IEEE*, pp. 1-4, Seoul/Korea.
[10] Zhou L, Li W. (2014). Adaptive artificial potential field approach for obstacle avoidance path planning. *2014 Seventh International Symposium on Computational Intelligence and Design*, *IEEE*, Vol. 2, pp. 429-432, Hangzhou/China.
[11] Zhu Q D, Yan Y J, Xing Z Y. (2006). Robot Path Planning Based on Artificial Potential Field Approach with Simulated Annealing. *Sixth international conference on intelligent systems design and applications*, Vol. 2, pp. 622-627, Jinan/China.
[12] Wang X, Liu Z, Liu J. (2023). Mobile robot path planning based on an improved A* algorithm. *International conference on computer graphics, artificial intelligence, and data processing (ICCAID 2022)*, Vol. 12604, pp. 1093, Guangzhou/China.
[13] Zhao Y, Li Y F. (2023). UAV pesticide spraying trajectory planning based on genetic algorithm (基于遗传算法的无人机农药喷洒航迹规划). *Intelligent Computer and Application*, Vol. 13, pp. 88-93+99, Shanghai/China.
[14] Wen J L, Liang F, Xu W. (2023). Research on three-dimensional path planning of unmanned aerial vehicle based on improved ant colony algorithm (基于改进蚁群算法的无人机三维路径规划研究). *Modern Information Technology*, Vol. 7, pp. 84-87+91, Zhejiang/China.
[15] Huang C. (2021). A Novel Three-Dimensional Path Planning Method for Fixed-Wing UAV Using Improved Particle Swarm Optimization Algorithm. *International Journal of Aerospace Engineering*, Vol. 1, pp. 7667173, Shenyang/China.
[16] Vazquez-Carmona E V, Vasquez-Gomez J I, Herrera-Lozada J C, et al. (2022). Coverage path planning for spraying drones. *Computers & Industrial Engineering*, Vol. 168, pp. 108125, Ciudad de México/México.
[17] Plessen M. (2025). Path planning for spot spraying with UAVs combining TSP and area coverages. *Smart Agricultural Technology*, Vol. 11, pp. 100965, Zug/Switzerland.
[18] Meron M, Peres M, Levin-Orlov V, et al. (2025). Irrigation uniformity assessment with high-resolution aerial sensors. *International Journal of Applied Earth Observation and Geoinformation*, Vol. 137, pp. 104446, Kiryat Shmona/Israel.
[19] Cui X, Han W, Zhang H, et al. (2023). Estimating soil salinity under sunflower cover in the Hetao Irrigation District based on unmanned aerial vehicle remote sensing. *Land Degradation & Development*, Vol. 34, pp. 84-97, Yangling/China.
[20] Xue J, Shen B. (2023). Dung beetle optimizer: a new meta-heuristic algorithm for global optimization: J. Xue, B. Shen. *The journal of Supercomputing*, Vol. 79, pp. 7305-7336, Shanghai/China.

[21] Jin H, Ji H, Yan F. (2023). An effective obstacle avoidance and motion planning design for underwater telescopic arm robots based on a tent chaotic dung beetle algorithm. *Electronics*, Vol. 12, pp. 4128, Huainan/China.
[22] Saito A, Yamaguchi A. (2016). Pseudorandom number generation using chaotic true orbits of the Bernoulli map. *Chaos: An Interdisciplinary Journal of Nonlinear Science*, Vol. 26, Hakodate/Japan.
[23] Du Y, Tian X Q, et al. (2024). Software defect detection method based on improved whale algorithm optimized SVM (基于改进鲸鱼算法优化 SVM 的软件缺陷检测方法). *Information Network Security*, Vol. 24, pp. 1152-1162, Beijing/China.

HOW CAN SMARTPHONE DEVICES BE INTEGRATED WITH SPECTRAL SIGNATURES TO DETECT MATAG HYBRID?
/
BAGAIMANAKAH PERANTI TELEFON PINTAR DAPAT DIINTEGRASIKAN DENGAN TANDA TANGAN SPEKTRAL UNTUK MENGESAN HIBRID MATAG?

Nur Adibah MOHIDEM[1)], Nik Norasma CHE'YA[2,3,4*)], Mohammadmehdi SABERIOON[5)], Mohamad Syukri TAN SHILAN[6)], Nur Annisa MAT NORDIN[2)]

[1)]Public Health Unit, Department of Primary Health Care, Faculty of Medicine and Health Sciences, University Sains Islam Malaysia, Bandar Baru Nilai, 71800 Nilai, Negeri Sembilan, Malaysia.
[2)]Department of Agriculture Technology, Faculty of Agriculture, University Putra Malaysia, 43400 Serdang, Selangor, Malaysia.
[3)]Institute of Plantation Studies, University Putra Malaysia, 43400 Serdang, Selangor, Malaysia.
[4)]Centre for Advanced Lightning, Power and Energy Research (ALPER), University Putra Malaysia, Serdang 43400, Selangor, Malaysia.
[5)]German Research Centre for Geosciences (GFZ), Telegrafenberg, 14473 Potsdam, Germany.
[6)]Crop Industry Development Division, Department of Agriculture Malaysia, Pusat Pertanian Lekir, 32600, Perak, Malaysia.
Tel: +603-97694892; E-mail: niknorasma@upm.edu.my
DOI: https://doi.org/10.35633/inmateh-79-43

Keywords: *MATAG; smartphone; spectral signature; species detection*

ABSTRACT

Smartphones have become a convenient tool in agriculture due to their mobility, affordability, and capacity to enhance more efficient crop monitoring, including MATAG variety identification. Detecting MATAG hybrid varieties remains challenging because their morphological traits are difficult to differentiate macroscopically, but reflectance values can be generated using a spectral signature graph. This review aims to explore the development of an intelligent identification system for the MATAG variety based on spectral signature analysis using a smartphone device. It discusses characterisation of MATAG hybrids, spectral signature differences between each coconut species, the development of spectral signature libraries, and the potential of smartphone-spectral signature-based applications compared with manual inspection and laboratory analysis. It also highlights the mechanisms of MATAG variety detection based on spectral signature analysis using a smartphone and practical considerations for farmers. Case studies and testimonials from farmers on how smartphone devices have revolutionised crop monitoring practices were also discussed, together with the potential benefits of using this technology for the agricultural industry. It also elaborates on the opportunities and challenges of detecting MATAG variety using smartphone-spectral approaches, which will be a useful resource for app developers to solve the problems in the field. Overall, this review provides a comprehensive overview of smartphone-spectral signature integration for MATAG detection that eventually helps farmers in the plantation.

ABSTRAK

Telefon pintar telah menjadi alat yang mudah digunakan dalam pertanian kerana mobiliti, kemampuan dan keupayaannya untuk meningkatkan pemantauan tanaman yang lebih cekap, termasuk pengenalan kepelbagaian MATAG. Mengesan kepelbagaian hibrid MATAG kekal mencabar kerana ciri-ciri morfologinya sukar dibezakan melalui mikroskop, tetapi nilai pantulan dapat dijana menggunakan graf tanda tangan spektral. Ulasan artikel ini bertujuan untuk meneroka pembangunan sistem pengenalan pintar untuk kepelbagaian MATAG berdasarkan analisis tanda tangan spektral menggunakan peranti telefon pintar. Ia membincangkan ciri-ciri hibrid MATAG, perbezaan tanda tangan spektral antara setiap spesies kelapa, pembangunan perpustakaan tanda tangan spektral, dan potensi aplikasi berasaskan tanda tangan spektral telefon pintar berbanding dengan pemeriksaan manual dan analisis makmal. Ia juga menyoroti mekanisme pengesan kepelbagaian MATAG berdasarkan analisis tanda tangan spektral menggunakan telefon pintar dan pertimbangan praktikal bagi petani. Kajian kes dan testimoni daripada petani tentang bagaimana peranti telefon pintar telah merevolusi amalan pemantauan tanaman juga dibincangkan, bersama dengan faedah berpotensi menggunakan teknologi ini untuk industri pertanian. Ia juga membincangkan peluang dan cabaran mengesan kepelbagaian MATAG menggunakan pendekatan spektral telefon pintar, yang akan menjadi sumber berguna bagi pembangun aplikasi untuk menyelesaikan masalah di lapangan. Secara keseluruhan, artikel ini memberikan gambaran menyeluruh tentang integrasi tanda tangan spektral telefon pintar untuk mengesan MATAG yang akhirnya membantu petani di ladang.

1. INTRODUCTION

Coconut (*Cocos nucifera L.*) is one of the most important plantations, particularly in tropical countries. Indonesia, the Philippines, and India are the world's biggest coconut producers, accounting for up to 75% of global production (*Halim et al., 2018*). Almost every part of the coconut tree can be consumed for human benefit. There are three types of coconut trees: tall, dwarf, and hybrid. Hybrids have earlier flowering, higher fruit yield, higher copra production, and higher copra and oil quality than the parent. The most popular hybrid is the 'MATAG' cultivar. The 'MATAG' results from intervarietal crosses between 'Malayan Yellow Dwarf' or 'Malayan Red Dwarf' with 'Tagnanan Tall'. The MATAG could generate drinking fruit juice, whereas the husk fibres are denser and more suitable for coir production.

MATAG is also widely used in the industry of processing products. Therefore, the agro-based ministry of the respective countries is always trying to increase the amount of MATAG trees planted (*Halim et al., 2018*). Thus, seedling producers attempt to keep up with the high demand. However, MATAG plantations need help in producing uniform and high-quality seedlings, resulting in a shortage of plantations for farmers (*Hassan et al., 2021*). The reasons for this issue are a less true-to-type MATAG variety identification and poor seedling quality caused by non-systematic and imprecise nursery management, which enhances the inefficient distribution of water and nutrients to seedlings (*Yusof et al., 2017*).

The standard MATAG variety detection technique in coconut nurseries is expert visual assessment based on the parent's colour. This approach is time-consuming and prone to human error (*Bisi et al., 2020*). Therefore, the seedlings will be culled based on the assessor's visual ability and experience. MATAG variety detection could be improved using computer vision techniques, including machine learning and support vector machines (*Che'Ya et al., 2022*). The efficiency for plant species identification using machine learning could reach up to 99.8% (*Borraz-Martínez et al., 2022*). As a result, the cost of production can be reduced, and the nursery's output of high-quality MATAG seedlings could be increased.

Nevertheless, the differences between MATAG varieties are hard to distinguish by visual comparison due to their similar shapes and colours. Because different substances have specific spectral signatures and reflectance, remote sensing techniques can be used with high altitude imaging sensors to obtain spectral information of the Earth's surface, including MATAG varieties. Therefore, spectral signatures can identify each MATAG according to its unique value and characteristics, which are displayed through the spectral signature graph (*Ahansal et al., 2022*).

Some farmers cannot identify MATAG variety and their characteristics in the field because they need up-to-date data related to MATAG, including leaves information for sensor imagery such as its width, length, area, perimeter, area of white space, area of the bounding box, area of hull, the perimeter of the hull, colour, texture, morphology, and structure, as well as seedling information for spectral signature analysis such as only germinated, normal seedlings, and seedling age (*Zaki et al., 2023*). As an alternative, a spectral library can be developed to compare the reflectance of the MATAG variety and include other applications such as image processing, estimating the infestation percentage, identifying the trees' location, and providing information on managing crops from planting to harvesting (*Rosle et al., 2019*). The spectral signature graph can be stored in the library using an online database and a mobile app to avoid losing data and allow researchers to access it worldwide easily (*Roslin et al., 2021*). The apps could help the farmers to process the image on the sensor via smartphone and visualise the MATAG variety mapping in the nurseries.

Some digital databases of the spectral library for crop variety identification, including the Johns Hopkins Spectral Library, United States Geological Survey (USGS) Spectral Library, ASTER Spectral Library, MedSpec, Jet Propulsion Laboratory Spectral Library, and LILIAN, were inaccessible to the public (*Kokaly et al., 2017; Adam, 2012*). While general crop monitoring apps exist, none specifically address MATAG variety detection through spectral signatures. Developing a spectral library for the MATAG variety is a proactive starting point for storing spectral signatures for future usage. Therefore, this review aims to discuss and elaborate on developing an intelligent identification system for the Matag variety based on spectral signature analysis using a smartphone device. Rather than being separate approaches, smartphones, UAVs, and sensors form a complementary ecosystem. Data collected across different spatial and temporal scales are integrated, analysed, and communicated back to the farmer via the smartphone platform, creating a seamless workflow for precision MATAG detection and farm management.

2. CHARACTERISATION MATAG HYBRID

MATAG is currently the most commercialised coconut variety planted in Malaysia, followed by Aromatic Dwarf, known as PANDAN and other dwarf varieties. The name “MATAG” refers to a new hybrid coconut, based on the original coconut from Malaysia, which is Malayan Yellow Dwarf (MYD) or Malayan Red Dwarf (MRD), a female parent crossing with Tagnanan Tall coconut (from the Philippines) as a male parent. MATAG produces large, rounded fruits that mature rapidly and provide high yields. Due to the increasing demand for raw materials in cooking and virgin coconut oil, MATAG has been identified as a suitable source for commercial cultivation in several states in Malaysia (*Raj et al., 2024*). The main producing states are Johor, Perak, Selangor, and Kelantan, where the favourable climatic conditions are well suited to coconut cultivation (*Man and Shah et al., 2020*).

MATAG can reach a height of 15 m, has orange or green leaves, and may initiate to bloom mostly in the third year of cultivation. The MATAG is a new variety of coconut that can produce more coconuts annually than other hybrid or normal coconut trees, up to 40,000 coconuts per hectare. MATAG begins bearing fruit in the third year after planting and can be harvested at approximately 48 months *(DOA, 2016)*. Compared with other hybrid cultivars, MATAG produces a higher number of coconuts, typically about 10–22 fruits per bunch. MATAG has a high nut production rate, yielding approximately 25,000-30,000 nuts per hectare yearly, which is more than the other hybrid types (*PRESSREADER, 2016*). Its average output yield during the first six years of harvest is 18,467, compared to 5,050 nuts for Malayan Tall.

The benefits of MATAG coconuts include their ability to produce higher copra per yield, i.e., 53.9%, because they have thicker plump fruit than other hybrids such as Aromatic Green Dwarf (AGD), CAMMA, and normal coconuts (*Kingimi et al., 2023*). When compared to a normal coconut, the size of the coconut is also larger, which makes the copra thicker and, thus, increases the production of grated coconut and coconut milk (Fig. 1). The MATAG hybrid is more flexible in terms of suitability for both tender and dry nuts due to its ease of dehusking for dry nut purposes, larger nut size that results in a higher amount of water, and reduced husk thickness. In addition, the MATAG coconut’s flavour is tastier because the coconut water is sweeter than regular or other hybrid coconuts, making it more pleasant to drink.



Fig. 1 - Nursery centre for the MATAG variety at DoA, Jorak (Johor)

3. OVERVIEW OF MATAG VARIETY DETECTION BASED ON SPECTRAL SIGNATURE LIBRARIES

Plant pigments absorb light primarily within the photosynthetically active radiation range of 400–700 nm. For example, chlorophyll strongly absorbs blue-violet and red light while reflecting green light, which gives leaves their characteristic green appearance *(Virtanen et al., 2020)*. Carotenoids, in contrast, reflect light in the yellow, orange, and red regions of the spectrum while absorbing mainly blue-green and violet light *(Liu and Van Iersel, 2021)*. Different coconut cultivars often have similar shapes and colours, making visual

discrimination difficult. However, they can be differentiated and identified based on their distinctive spectral signatures. Each plant pigment exhibits a characteristic spectral response defined by its reflectance across different spectral bands. Plant spectral signatures generally show low reflectance in the visible region of the electromagnetic spectrum because photosynthetic pigments strongly absorb visible light *(Kutser et al., 2020)*.

Coconut tree fronds with varying degrees of Coconut Scale Insect (CSI) infestation are healthy (young), slightly healthy, moderately healthy, and severely infected. Therefore, the identification of CSI in spectral signatures, even at low level, can evaluate the efficacy of control measures (biological and chemical) (*Franco et al., 2018*). Furthermore, a previous study (*Noor Azmi et al., 2020*) found that various degrees of disease infestation on coconut can be differentiated based on spectral signature using 8-band Worldview-2 satellite imagery, with the NIR-1 and NIR-2 bands, followed by the Red Edge band.

Reflectance generally decreases across the measured wavelength range as leaf health declines from healthy to infected. However, the spectral curves may show substantial variability because infection affects only part of the leaf area, often up to 50%, and measurements may randomly include both infected and healthy tissue within the sensor's field of view *(Rodríguez Machado et al., 2020)*. These differences can be visualized using reflectance-wavelength curves. Reflectance is measured at discrete intervals over a specified wavelength range. The width of these intervals represents the spectral resolution of the sensor, while the reflectance recorded within each interval corresponds to an individual spectral band. A spectral signature is characteristic of a material because its reflectance and emittance properties vary with its physical condition and surrounding environment *(Meerdink et al., 2019)*.

The real-time monitoring of spectral signatures has been improved by using field-based devices. The portable spectrometer is a device that can measure the spectral signature of plants, in which the signature can be used to recognise the plant species. Accordingly, because reflectance readings rely on incident sunlight, the device can only capture valid spectral signatures throughout the day under a clear skyline view with no significant cloud cover or precipitation (*Musiol-ková et al., 2021*). This aspect is why comparing the spectral signature graph of the same plant species between earlier studies is challenging and depends on the sampling environment during the measurement, such as humidity, cloud cover, type temperature, wind speed and direction, and aerosols (*Torresani et al., 2024*) The other reasons are viewing geometry (fore optic degree and field of view or FOV and instantaneous-field-of-view or IFOV, fore optic height above terrain, and ground), and illumination geometry, such as date, azimuth and orientation, position and sun altitude, time, and smoke and haze (*Jafarbiglu and Pourreza, 2023*). Hence, different conditions that influence the spectra of vegetation are shown in Fig. 2.

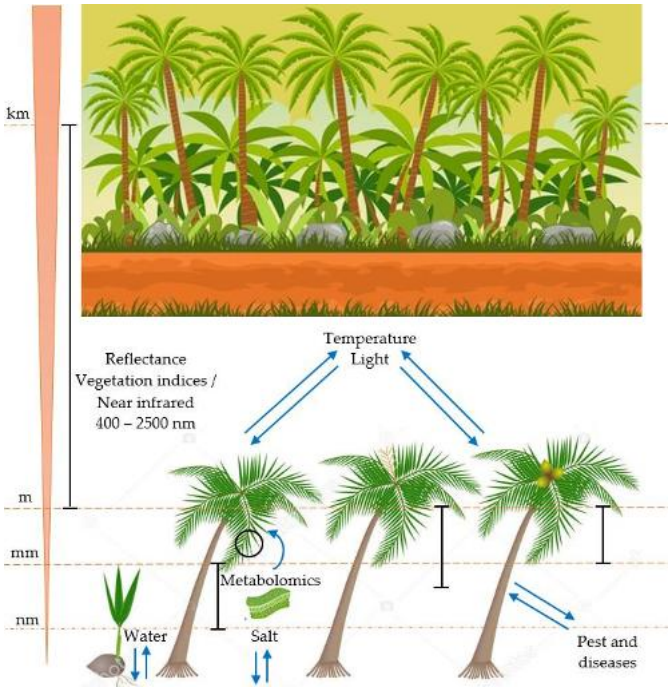


Fig. 2 - Different conditions which influence the spectra of vegetation

Plant reflectance can be measured using a handheld device, such as a spectroradiometer, to measure canopy spectral reflectance. These devices have developed into a helpful alternative for identifying or differentiating objects pertaining to spectral information using conventional methods, such as texture analysis and colour segmentation (*Soca-Muñoz et al., 2020*). Regarding vegetation, they can be used in the field to measure the spectral signatures of the visible light spectrum of various plant species, including different coconut species, i.e., MATAG. The spectral signature of the crop is attributed to low reflectance values in the visible zone of the electromagnetic spectrum due to significant light absorption by photosynthetic pigments (*Kutser et al., 2020*). The absorption maxima for chlorophyll a and b are in the blue (400 nm to 500 nm) and red (around 670 nm) zones, respectively, whereby carotenoids (i.e., xanthophylls and carotenes combined) absorb in the blue range as well (*Agostini et al., 2024*). Any disease that causes pigment degradation, chlorosis, or tissue necrosis may result in visible reflectance changes. Near-infrared (near-IR) reflectance values are high between 700 nm and 1000 nm. Hence, there is a need to develop a database to store spectral signature data. However, the database adopted from other studies requires an evaluation of dataset applicability for the specific task, such as detecting MATAG variety (*Imanian et al., 2021*). Furthermore, creating a large database of crop spectral signatures is difficult because it requires continuous monitoring of crops from seeding to harvesting.

For example, spectral signature libraries for agricultural research are accessible, such as the SPECCHIO Spectral online database held by the University of Zurich's Remote Sensing Laboratories in the Department of Geography (*SPECCHIO, 2022*). The library can display the spectral signature of significant crops such as wheat and potatoes. The database includes biophysical parameters of yields and soil characteristics. The library has been tested, but several things could be improved, including the lack of a multi-criteria query. A lengthy list containing hundreds of records is visualised for each search. Instead, it should be more systematic to include the crop's plantation date and location. Other agriculture libraries and databases are being developed. However, some are no longer available, such as the Vegetation Spectral Library, created with National Science Foundation funding by the Systems Ecology Laboratory at the University of Texas in El Paso (*Systems Ecology Laboratory, 2017*). Based on the published literature, no suitable library exists to be used for detecting MATAG. Hence, future studies are proposed to fill this limitation by developing a library specifically used to identify MATAG.

MATAG detection necessitates images during different growth stages, making fieldwork problematic in terms of labour and costly when using conventional visual assessment techniques based on the human eye (*Chu et al., 2025*). Conventional crop mapping is time-consuming and needs ongoing field research to validate and classify the images from RGB, multispectral, and hyperspectral sensors (*Zhang et al., 2025*). These problems can be solved by collecting spectral signatures for MATAG at various growth stages and mapping the reflectance of MATAG in the spectral signature library using sensors such as RGB and hyperspectral. Therefore, detecting MATAG using spectral signatures is highly desirable. The spectral signature can precisely map the MATAG variety as a spectral signature graph. Coconut species have specific spectral signatures with unique graph curves based on their characteristics. Then, a spectral library can compare the reflectance of MATAG in a field, estimating the infestation proportion (*Yang and Kong, 2017*). Moreover, it can identify plant locations through mapping coconut varieties. The spectral signature graph is stored in a digital database to prevent loss and provide easy access to researchers worldwide (*Rossel et al., 2016*). To the best of our knowledge, no study used spectral signatures to detect MATAG variety in any growing stages, starting from seeding, sprouting, growing, reaching maturity, and blooming. Only a few studies use the spectral signature analysis for coconut monitoring, and not specific for the detection of different coconut species (Table 1). Therefore, this approach could contribute to new knowledge and guide researchers to apply MATAG in the future.

Table 1

Examples of previous studies related to applying a spectral signature to coconut variety detection

Research focus	Findings	Reference
Select new antagonistic Trichoderma strains capable of protecting wild rocket and baby lettuce from harmful soil-borne pathogens.	Significant changes in the spectral signatures of healthy, infected, and bio-protected plants. OSAVI, SAVI, TSAVI, and TVI were strongly correlated with DSI.	*Manganiello et al. (2021)*
Use a portable spectrometer device for acquiring spectral signatures of various plant classifications.	Scanned spectral signatures of avocado, banana, cacao, coconut, mango, sugar cane, and cotton fruit/santol crops recognised by Mapua-Phil-Lidar-2 crops classification.	*Lazaro et al. (2019)*
Create a mechanism for identifying the spectral signature of tropical plants that	The FFT-processed reflectance demonstrates how the spectral signatures of each plant per location differ from	*Ballado et al. (2017)*

Research focus	Findings	Reference
grow in arid, wet, and near-sea environments.	one another. The peak value of Reflectance – FFT results for coconut is 1.1278 @194Hz (Arid Land).	
Collect field spectral signatures of CSI-affected coconut plants at various stages of infestation.	The spectral signatures of coconuts with varying degrees of infestation are different in the 8-band Worldview-2 satellite imagery, primarily in the NIR-1 and NIR-2 bands, followed by the Red Edge band.	*Parangit et al. (2014)*
Investigate the potential use of high-resolution data for horticultural crop type classification and delineation using a semi-automatic classification method versus traditional visual interpretation techniques.	Plantations that were older and more mature were classified more accurately, whereas young and recently planted plantations (3 years or less) had poor classification accuracy due to a mixed spectral signature, wider spacing, and poor plantation stands.	*Hebbar et al. (2014)*

4. COMPARISON BETWEEN TRADITIONAL METHODS AND SMARTPHONE-SPECTRAL SIGNATURE-BASED APPROACHES FOR DETECTING MATAG HYBRID

Traditional methods of MATAG variety cultivation include visual inspection and laboratory analysis. These methods have both advantages and disadvantages. The collected data are manually recorded in notebooks or logbooks, making them simple to adopt and applicable to different age groups of farmers because they require no digital infrastructure. It uses basic tools such as measuring tapes, poles, and even binoculars to identify the characteristics of crop species. The farmers will also physically evaluate the seedling colour and seedling age using morphological observation, thus allowing for direct assessment and decision-making. Although it is inexpensive, monitoring is subjective and inconsistent. Only surface-level problems can be observed, resulting in a lack of precision and depth (*Mahant and Pal, 2025*). It is also time-consuming and labour-intensive to accurately identify different Matag variety species, as limited to the farmer's knowledge and experience (*Arumugam and Hatta, 2022*). It is unsuitable for large-scale operations due to the need for extensive skills by qualified experts, with significant resources. Data retrieval and aggregation are inefficient, with limited data integration possibilities. Manual data collection and interpretation using items such as magnifying glasses, soil kits, and moisture meters can be prone to errors (*Mihrete and Mihretu, 2025*). Furthermore, laboratory analysis is suitable for less common MATAG samples, is costly, takes a longer time to produce the results, and is not suitable for large-scale MATAG monitoring due to the requirement for laboratory facilities and qualified personnel.

The monitoring of MATAG has improved substantially as technology has become more sophisticated. Farmers can use smartphone devices as an interface to capture the high-resolution images and spectral data of MATAG seedlings collected from unmanned aerial vehicles (UAVs) equipped with cameras and sensors. Images of the trees are then analysed using artificial intelligence and machine learning algorithms by a mobile application (*Singh et al., 2021*). When reflectance data are collected using external devices such as a UAV, the processed reflectance data can be uploaded to a cloud database or server. These processed spectral datasets are then retrieved by the apps and displayed in a user-friendly interface for farmers (*Heim et al., 2024*). In this context, the smartphone serves mostly as the end-user platform, while external devices provide additional spectral information. This approach allows for the early identification of problems in the field, frequently before obvious signs occur. It also provides detailed aerial views, allowing for early detection of pest infestations, disease outbreaks, and nutrient deficits on the trees. Farmers can take a picture of an infected tree and send it to the mobile application, which can figure it out within minutes. It has user-friendly interfaces that include GPS mapping, automated alerts, data analytics, and cloud storage. It offers instructional tools and advice on best practices in the plantation. It can be used to detect diseases in real-time across large areas. It is portable since farmers may receive information directly (*Ibrahim et al., 2025*). However, the accuracy may vary based on the quality of the provided smartphone camera and sensors, as well as the specificity of the algorithms. The initial setup cost is high, and technical skills through training are required to configure, operate, and interpret the data efficiently. It also requires consistent internet connectivity (*Liu et al., 2023*).

MATAG variety identification can be monitored using spectral signature libraries, which analyse the specific wavelengths of light reflected by various plant tissues. These libraries store data on the spectral signatures of healthy and unhealthy coconut leaves, which can be utilised for determining disease transmission across large areas (*Roslin et al., 2021*). Mobile applications can be created to display the spectral signature of MATAG leaves through smartphones while also providing farmers with control measures of the disease. Smartphones can detect plant species using processed images from RGB, multispectral, or hyperspectral sensors, as well as an algorithm (*Che'Ya et al., 2022*). By connecting mobile devices with UAVs, images of

coconut tree crowns can be captured, and it is used to estimate total leaf area, number of bunches and fruits, and other phenotypic traits (*Arumugam and Md Hatta, 2022*). Such a connection can help to minimise data collection time and costs while also improving phenotyping data accuracy. Most smartphones are equipped only with RGB cameras. Hence, spectral signature analysis on smartphones is either limited to RGB-based indices or supported by add-on accessories (i.e., clip-on portable spectrometers) that increase the spectral range (*Schlemitz and Mezhuyev, 2024*). As an alternative, smartphones can be connected to external databases of pre-collected spectral libraries, which enables the phone to be utilised as the interface for spectral data visualisation and decision support.

While traditional methods for recognising MATAG diseases remain acceptable, smartphones with built-in cameras or that connect to external spectral sensors to evaluate the light reflected from coconut trees provide a more efficient, accurate, and cost-effective alternative. Smartphones can give precise data, detecting diseases that are invisible to the naked eye in real-time. Furthermore, smartphones are highly scalable, making them appropriate for large-scale plantations. Traditional approaches, on the other hand, have limited scalability due to labour constraints. Smartphones allow for seamless data integration, analysis, and storage, usually set up with cloud-based systems, whereas traditional methods rely on manual records that are difficult to analyse and prone to loss or damage. Traditional methods are less expensive initially. Despite the higher initial costs of smartphones, they provide better long-term cost reductions and benefits through optimised resource usage and increased yields, making them a good investment. Smartphones are designed to be user-friendly, but they need a certain amount of digital literacy, whereas traditional methods do not require technological proficiency but can be time-consuming and inconsistent (*Padhiary et al., 2025*). The combination of traditional and modern approaches might leverage the strengths of each to provide an efficient system for MATAG variety identification and farm management. The comparison between the advantages and disadvantages of traditional methods with smartphone-spectral signature-based approaches is presented in Fig. 3.

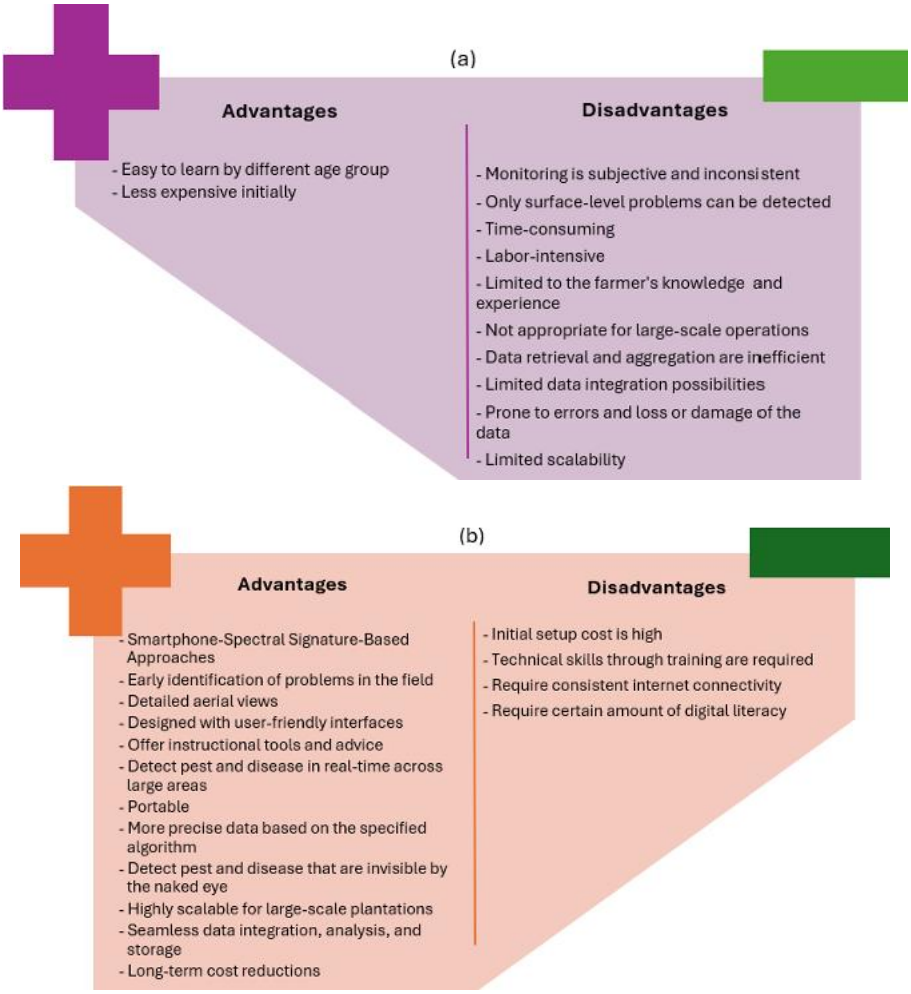


Fig. 3 - Advantages and Disadvantages between Traditional Methods (a) and Smartphone-Spectral Signature-Based Approaches (b) for Detecting MATAG Hybrid

5. MECHANISM OF MATAG VARIETY DETECTION BASED ON SPECTRAL SIGNATURE ANALYSIS USING A SMARTPHONE

5.1. Collection of Reflectance Data and Spectral Signatures

At first, the farmers need to ensure that the GPS in the smartphone is turned on to tag the location of the MATAG trees. After collecting the on-leaf surface of the seedlings, the reflectance of the spectral data is collected using a Handheld Spectroradiometer, under clear sky field conditions. It has a highly sensitive detector array with a low stray light grating, a built-in shutter, DriftLock dark current compensation, and second-order filtering, which produces a high signal-to-noise spectrum with second. Spectral data collection involves two primary steps, which include spectral sampling (Fig. 4) and spectral library compilation. During calibration, the white panel diffuses around 99% of incident light across its spectral range. Specifically, the reflectance value of the white reference panel is almost one for each wavelength (*Buddenbaum et al., 2019*). The MATAG trees should be chosen at random for 10 samples, with a spacing of 5 cm between the optical sensor and the sample. Accordingly, this method works to record data without inaccuracy or noise (*Che'Ya, 2016*). Reflectance data and spectral signature images for identifying MATAG species should be captured through RGB or hyperspectral sensors (*Strauss et al., 2021*).

The images are then divided into digital segments, and objects within the images are analysed using computer vision techniques such as machine learning and support vector machines. Hence, the spectral signature of a crop cannot be accurately assessed by parametric approaches such as regression or functional statistics. Non-parametric methods for hyperspectral spectroscopy include PCA, Fuzzy logic, SVM, CA, PLS, and NNs. Fisher's Linear Discriminant Analysis (LDA) classifies imaging and non-imaging hyperspectral data into two or more classes (*Golhani et al., 2018*). The generated images are examined for spectral signature differences among several MATAG types.

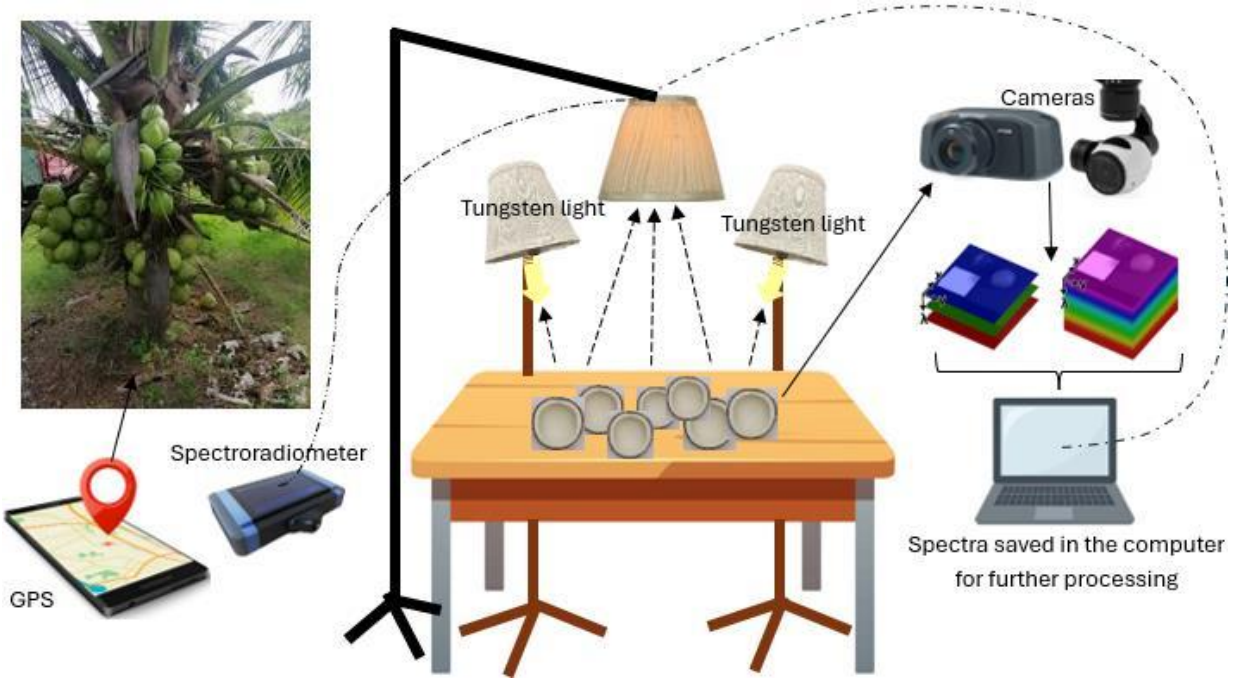


Fig. 4 - Configuration of spectral sampling in MATAG variety detection

5.2. Image Processing for Pest and Disease Monitoring Using the Mobile Application

Image preparation uses an algorithm incorporated into the system (*Miao et al., 2018*). The preprocessing phase ensures that the image collects only the analyses of hybrid components and excludes the other coconut species, also known as the separation technique. The colour of the images will be restored using colour constancy and uniformity (*Mendes et al., 2020*). The plant's various characteristics will next be retrieved and compared to the MATAG hybrid model to verify their uniqueness. The user receives findings that include the type of MATAG, the causing agent, a technique to control the infection, and prevention guidelines for overcoming the infection (*Ouhami et al., 2021*).

MATAG variety detection could be accomplished by capturing images of crops with seedlings using a camera. Under certain conditions, the camera may capture the image and detect the status of the plant

harbouring the different MATAG species based on light reflectance (*Areni, 2020*). Implementing hyperspectral sensors in smartphone devices is one way to improve the limits. A hyperspectral sensor can measure hundreds of electromagnetic spectrum bands within its range. The hyperspectral sensor's spectral bands monitor only a few nanometres of the electromagnetic spectrum, generating a wavelength with great spectral resolution (*Ko, 2019*). As a result, each pixel in a hyperspectral image acquires a specific set of data about the reflectance (or transmittance) of each spectral band (*Che'Ya, 2013*).

The total amount of these data is known as a spectral signature (or spectral profile), and it is captured by a non-imaging hyperspectral sensor (i.e., point spectroscopy) without the need for additional spatial information (*Park et al., 2020*). Hyperspectral sensors detect the spectral bands of each pixel in an image and merge the spectrum and spatial resolutions. As a result, each pixel in the image has a unique spectral signature, which comprises reflectance values for all spectrum bands detected by the hyperspectral sensor (*Hassanzadeh, 2020*). From another perspective, the final image is a hyperspectral data cube with two dimensions of spatial information and a single size for spectral information. In general, hyperspectral sensors can measure the NIR (700-1000 nm) and SWIR (1000-2500 nm) wavelengths of the electromagnetic spectrum (400-700 nm) (*Contreras, 2020*).

The interaction between spectral signature information and ground data demonstrated that the rate of MATAG variety detection in the crop may be predicted. Spectral reflectance can reveal species variances at specific wavelengths. *Roslin et al. (2021)* discovered that in the visible spectrum (450 nm to 700 nm), numerous weed spectral signatures were quite comparable, and several overlapped. Undoubtedly, not all MATAG have the same spectral signature on the coconut species, hence calibration and validation are still needed to identify MATAG. At the same time, in the infrared region (700 nm to 990 nm), different species' spectra are recognised by their wavelengths. Because each coconut has its own unique features, the significant bands for each species can be discovered in a specific region (710 nm to 750 nm), including MATAG. The damaged area could serve as an indicator for identifying MATAG species using spectral signatures. As a result, information on the spectral signature of the MATAG, as well as other sorts of pests and diseases, must be stored in a user-friendly manner.

The image data can be collected in red, green, and blue (RGB), and the MATAG will be identified based on its shape and colour using image processing. Thus, utilising a smartphone, the user can identify MATAG using apps connected to a cloud-based data processing machine. The spectroradiometer will capture spectral signatures (hyperspectral data) that can be used to classify MATAG. Thus, RGB, spectral, and hyperspectral information can be utilised to identify and refer to hyperspectral data. Certain smartphones only record RGB images. They can, however, process the RGB information and generate the results using artificial intelligence (AI) on the cloud server. The spectral signature of plants is already stored in the spectral library, which may be accessed if the user has a hyperspectral sensor and compares it to the spectral library in smartphone devices.

5.3. Generation of Spectral Signature Graph

The following subsection illustrates how spectral reflectance profiles can be analysed for MATAG and related coconut varieties. Applications for MATAG variety detection should rely on the ability to obtain a spectral signature that is related to tree features and plant health. Hence, a spectral signature graph could be associated with a variety of tree features, including age category, varietal difference, density, and shade composition (*Che'Ya et al., 2022a*). Other factors include healthy and unhealthy trees, with spectral signature values varying according to the types of MATAG hybrid. For data analysis, all raw data were sent to a computer. The data was saved in a Microsoft Excel file. In addition, the data should be arranged into 10 nm spectral bands, rather than its original 1 nm value (Fig. 5). The spectral signature may be seen in the spectral reflectance graph for each MATAG species. To further analyse subtle differences among coconut varieties, the first derivative of spectral reflectance is often used, as reported in a previous study (*Che'Ya et al., 2022c*). The general formula for calculating the first derivative between two adjacent reflectance values is given in Equation 1:

i. Visualising Spectral Reflectance. Construct a graphic illustration that shows spectral reflectance for MATAG.
ii. First Derivative Analysis. Use Equation (1) to calculate the first derivatives and then generate the spectral signature and first derivative graphs.

(1)

$$FD = \frac{R}{R} = \frac{Ry_2 - Ry_1}{\lambda x_2 - \lambda x_1}$$

where:

FD = First Derivative.

Ry_1, Ry_2= Reflectance of the first and second reflectance pairs n1 and n2.

λx_1, λx_2= Wavelength of first and second reflectance pairs n1 and n2.

n = Position of reflectance.

Fig. 5 presents an example of spectral reflectance profiles for MATAG seedlings. These curves can be further analysed using the derivative approach shown in Equation 1, which enhances the detection of small variations between overlapping spectra. The spectral reflectance profile of the three different coconut seedlings shows a similar trend. According to the graph, the spectral reflectance showed a low reflectance in the visible region with a small peak in the green region, and an increase begins at 680 nm. However, it is observed that numerous noises are clearer at certain points in the near-infrared region. The spectral data of the three coconut seedlings were similar in the visible region, and many overlapped each other. In the near-infrared region, the spectra of different seedlings also showed quite similar patterns, but they can be observed between 733 nm and 1000 nm. The reflectance of MRD coconut seedlings showed the highest NIR reflectance, and the lowest belongs to the reflectance of MATAG coconut seedlings. However, this study only detects and classifies MATAG coconut seedlings based on spectral data using a machine learning algorithm, without any integration with the mobile application. Future studies are needed to develop an intelligent identification system for the MATAG variety based on spectral signature analysis using a smartphone device.

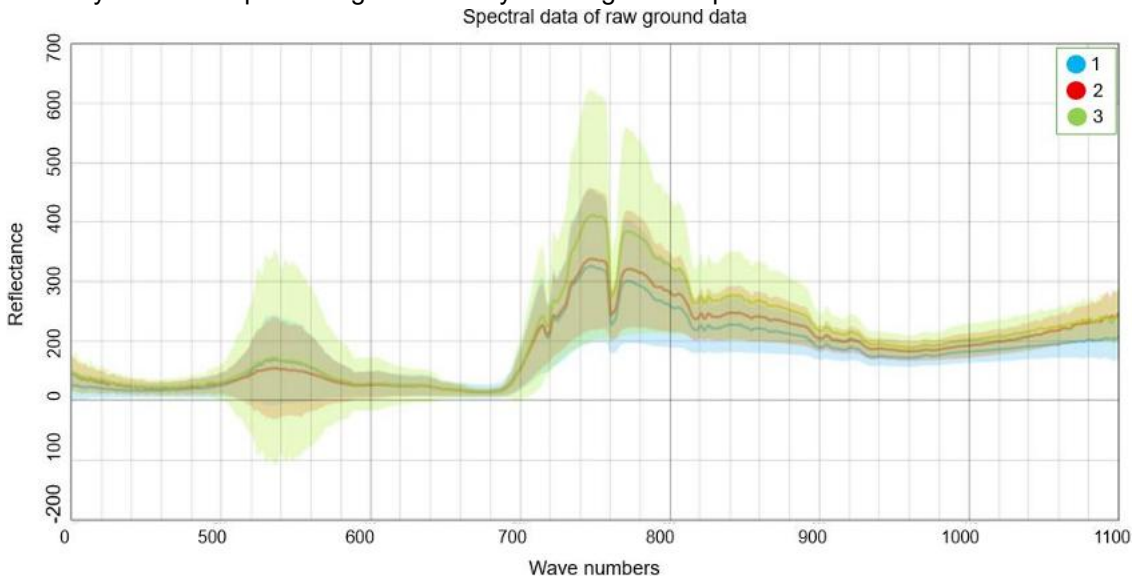


Fig. 5 - Spectral data of coconut seedlings of MATAG, MYD and MRD

5.4. Proposed Framework for Incorporating Spectral Libraries into Mobile Application

While no mobile applications currently exist for MATAG variety detection using spectral signatures, this section presents a conceptual application framework for how such applications could be developed and implemented. Farmers should choose a smartphone with a high-resolution camera capable of taking good pictures. Some smartphones have multi-spectral sensors, but basic smartphones can also be used using apps developed for MATAG variety identification and spectral analysis. The apps use algorithms to evaluate spectral data and associate it with several MATAG species. Plantix and Cropio are two applications for crop monitoring that can be connected with MATAG variety detection. To ensure accurate spectral analysis, images must be captured under consistent lighting conditions. The smartphone will improve the image quality by adjusting brightness, contrast, and reducing noise. It will also extract spectral information from the images, then transmit the results to a server for further assessment. This outcome includes examining the light reflected by the MATAG trees in various electromagnetic spectrum wavelengths, including red, green, blue, and near-infrared. The server detects the unique MATAG variety via spectral signature analysis. The selected variety is then reported back to the farmer via mobile apps, giving them correct information about the trees.

Creating an online database via smartphone from the processed images of spectral signatures for MATAG requires continuous monitoring of the plantation. The database should have a list of MATAG varieties

that can be used to identify specific characteristics as either the true-to-type or off-type seedlings, on an image. Therefore, MATAG classification demands images from various seedling ages to harvesting stages, as well as dates that coincide with crop growth stages. Aerial images should adjust the spectral resolution to fit the spectral signatures in the database. Other metadata, such as instrument characteristics, date of acquisition, vegetation biophysical parameters, soil characteristics, and other significant data, can also be displayed in this database.

The camera attached to a smartphone can be used to obtain imagery data for MATAG trees collected on the ground and varying levels of canopy decline, and stored in the database. With that, developers have created a smartphone attachment and application for simple spectroscopy. It uses a camera and a small spectrometer to collect the spectral data in MATAG trees. Farmers can identify with the MATAG variety using all the processing links to the server, including image preprocessing, transformation, and clustering (*Nesarajan et al., 2020*). The additional information includes the specific date and time, percentage of cloud cover, temperature, humidity, species homogeneity, the health of MATAG, size of the surveyed area, illumination and viewing setting, device calibration, and instrument settings that can be inserted into the smartphone.

Therefore, a spectrum library must be created to store MATAG variety data, identify different disease severity levels across a large area, and provide users with an action plan for crop management. The spectral library also contains normatively measured and processed background situation parameters for the specified MATAG species. The five components of the spectral library system include a knowledge database, a measured spectral library, an auxiliary library, spectral analysis, and an end-user application demonstration. Certain information, i.e., background knowledge on pest and disease species, could be identified in a knowledge database. Then, all of the calculated spectra of different species could be saved in the measured spectral library, and the auxiliary library can store several of the ancillary data of the species measured. The spectra gathered in the spectral analysis could be pre-analysed to verify the accuracy of the library before end-users use it in practical tasks. Fig. 6 presents an example of the data model of the spectral library system of MATAG.

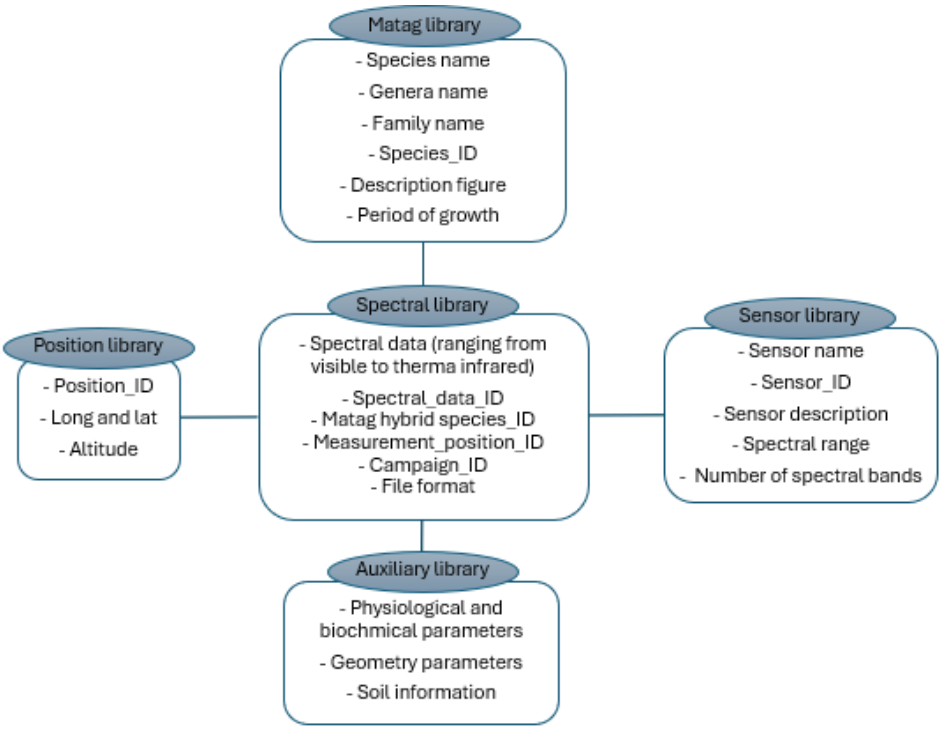


Fig. 6 - The data model of the Spectral Library System of MATAG variety detection

The spectral signature graph can be stored in a multifunctional database, such as mobile applications, enabling easy access by consumers and researchers (*Rossel et al., 2016*). The spectral signature was displayed as a reflectance graph for each MATAG variety identification. Creating a spectral library for MATAG in crop fields using the proposed mobile apps is an excellent technique to record spectral signatures for future reference.

5.5. Proposed System Architecture of IoT-Enhanced Smartphone Platform for MATAG Detection

The proposed platform describes IoT sensors as the primary spectral data collectors, with smartphones functioning as user interfaces and local processing units. Such an approach will integrate the smartphone accessibility with the precision of dedicated spectral sensors. The proposed mobile app design consists of two parts: system architecture (back-end) and menu design (graphical user interface), as illustrated in Table 2. The system architecture consists of three layers: presentation, logic, and data. The presentation layer allows users to view and interact with the app. The flow should be intuitive, with every menu having a specific objective. The logic layer serves as an API for farmers to obtain data from the database layer and send requests to the presentation layer. The data are then transmitted to the presentation layer. The data layer is the core of the proposed mobile application, where all data will be stored and retrieved. Each request for information in the presentation layer passes through the logic layer and then to the data layer before being displayed to the user in the presentation layer. Fig. 7 demonstrates the theoretical basis for creating a spectral signature graph to detect the MATAG variety that uses smartphones.

Table 2

List of main menus of the proposed mobile applications

Menu	Details Information
Location	Research site, crop-field area, and total number of plots used in the study
Planting schedule	Schedule of planting activities
UAV images	Spectral images
Field problems	Images showing field conditions and observed problems
Pest and disease	MATAG pest and disease categories, their spectral-signature graphs, and recommended control measures
Weather forecast	Weather conditions and forecasts for the field site
Yield	Quantity of harvested produce
Report	A function that allows farmers to prepare and submit reports on various MATAG characteristics

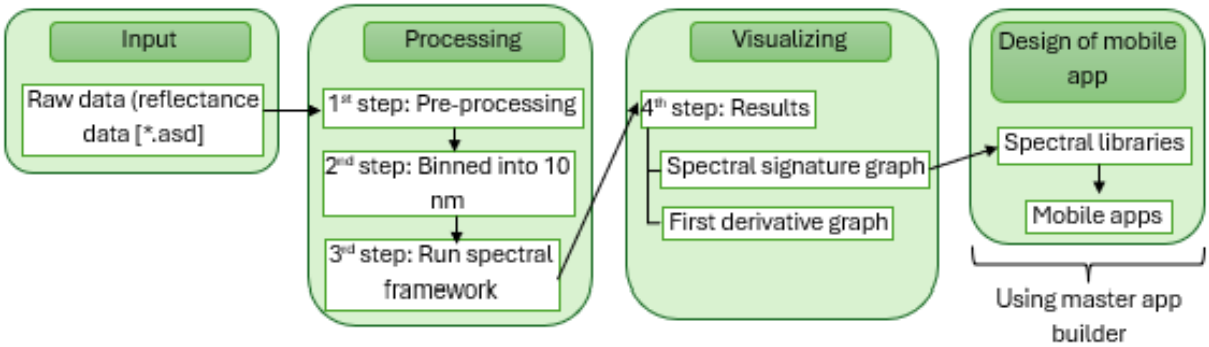


Fig. 7 - Theoretical framework for generating the spectral signature graph for detecting the MATAG variety using a smartphone

The spectral imaging module can be placed either on an aerial platform like a UAV or a stationary platform like a high pole, which keeps collecting data at regular intervals, which are determined by the type of MATAG and its characteristics. In the spectral imaging module, the data is sent directly to the cloud (*Inamdar et al., 2021*). Following the use of image-to-map geometric rectification techniques to coincide the image data with the actual map coordinates, the image is preprocessed before the spectral response is extracted from it. The processing involves applying suitable smoothing filters to the image to remove any outliers or incorrect data.

The next step involves the use of the Internet of Things (IoT), which enables the storage of farm data over the cloud to be utilised for data analytics and pattern recognition. Fig. 8 shows the overall system. The data that were obtained from the seedlings is collected and transmitted by the sensor nodes. These data are given to the Sink node, which transforms them into IP packets that can be transmitted to the cloud. The spectral Image Module captures the spectral image and sends it to the cloud on its own. The cloud then processes the data before being sent to the user. The cloud platform is accessible to farmers, who can access the dataset and its output (*Esther et al., 2019*).

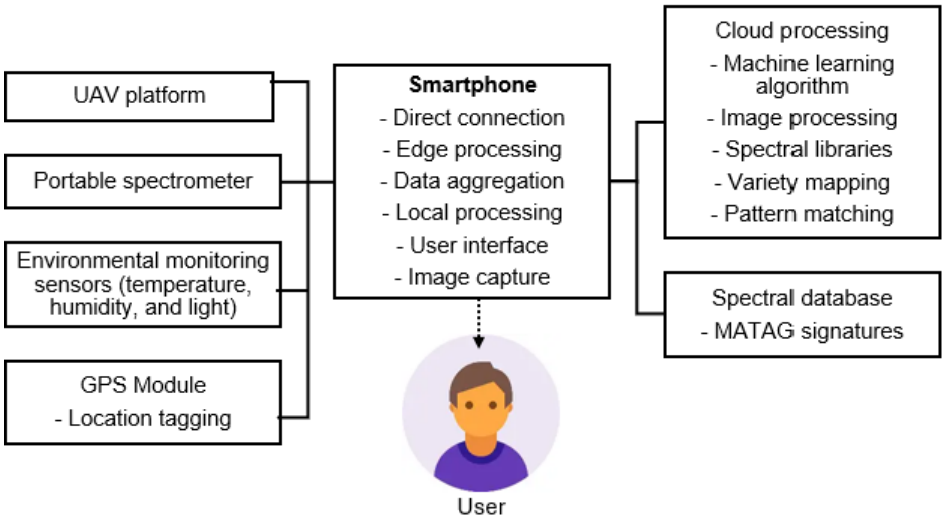


Fig. 8 - IoT-Enhanced Smartphone Platform

The spectral response of an image is then extracted. The sensor module's sensitivity to various wavelengths of optical radiation is determined by its spectral response. Therefore, the farmer can obtain information about the MATAG variety based on the number of different wavelengths. For example, the necessary parameters are estimated using the NDVI value as a standard. Data collected from the sensor node will be buried in the ground through the sink node stored in the cloud alongside the processed data. The data from these two sources are compared and processed per the MATAG's needs and the parameters estimated from the data collected (*Mohanty et al., 2022*). A proposed procedure for the development of intelligent MATAG coconut seedling identification using spectral signature analysis is presented in Fig. 9.

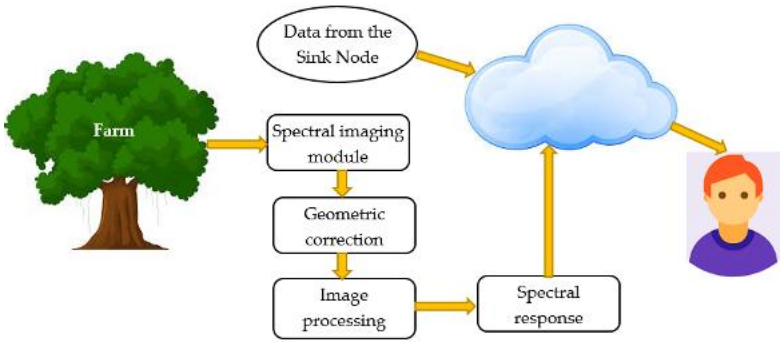


Fig. 9 - Spectral imaging with IoT

Finally, the future MATAG detection apps can provide a health assessment based on the spectral signature analysis based on healthy, stressed, or diseased categories that can improve interpretation and decision making. The app may provide recommendations for interventions, such as fertiliser application, pest control measures, or watering schedules. Regular monitoring and data collection are essential. The app can be used periodically to capture new data and update the health status of the MATAG trees. In short, tools will be involved in developing apps that involve the smartphone with a camera and GPS (to capture images and geotagging), mobile applications (software that performs spectral analysis), cloud services (to store data and perform complex computations), and machine learning models (to analyse spectral data and predict health conditions).

As a summary, the integrated workflow begins with UAV-mounted sensors collecting canopy-scale reflectance data, complemented by IoT devices monitoring soil and environmental parameters. In the meantime, smartphones are used by farmers to capture close-up seedling images. All data streams are integrated via a centralised platform, where analysis is performed, and the processed results are then returned to the farmer's smartphone for decision-making. Each technology complements the others to ensure continuous monitoring from planting to maturity.

6. CASE STUDIES AND TESTIMONIALS FROM FARMERS ON HOW SMARTPHONE HAVE REVOLUTIONISED CROP MONITORING PRACTICES

Three case studies reported the application of spectral signature analysis for coconut variety detection and monitoring using smartphones, which could be applied to MATAG studies in the future. First, an article published in the Journal of Agricultural Technology monitors health and detects diseases in coconut palms using spectral signature analysis. The researchers built a mobile app that uses a smartphone camera to capture images of coconut leaves. The app processes the images to extract spectral signatures, mainly focusing on specific wavelengths that relate to chlorophyll content and other indicators of plant health. Data collected by the app is analysed to determine stress indicators, including nutrient deficiencies or the presence of pests and diseases (*Singh et al., 2021*).

Second, an article published in the International Journal of Remote Sensing predicts the yield of coconut trees using spectral data collected. The researchers developed a mobile app to capture images of the coconut canopy. The app used machine learning algorithms to analyse the spectral data and predict crop production. Normalised Difference Vegetation Index (NDVI) was used to assess the health and productivity of the trees. The mobile app provided accurate yield predictions with a high association between predicted and actual yields (*Hebbar et al., 2022*).

Third, an article published in the Plantation Management Journal improves plantation management practices by monitoring coconut tree growth and health using spectral data. The app collected spectral data from the leaves and processed it to provide insights into the overall health of the plantation. Parameters such as leaf area index (LAI) and chlorophyll content were generated from the spectral signatures. Farmers reported improved management practices, such as optimised irrigation and fertilisation, based on the data provided from the app (*Samarakoon et al., 2025*).

However, none of the above studies detect the MATAG variety or even crop species based on the spectral signature analysis using a smartphone. Hence, this review mentions an app that found the weed species, which could be adopted for the identification of MATAG species in the future. For example, *Roslin et al. (2021)* generated a spectral signature graph of weeds and created a mobile app for spectral signature analysis of weeds. Using Master AppsBuilder, all spectral signatures were saved in a spectral database and illustrated on smartphones. Fig. 10 displays the website's main menu, which includes a list of applications, while Fig. 11 provides the content of menus, images, description, the control technique, and a spectral signature graph of MATAG. The main menu consists of information, spectral signatures, and recommendations for weed control. Users can download the mobile app on their devices. Besides the case study, this study also identified the testimonials from farmers on crop monitoring practices that were extracted from Google search, as shown in Fig. 12.

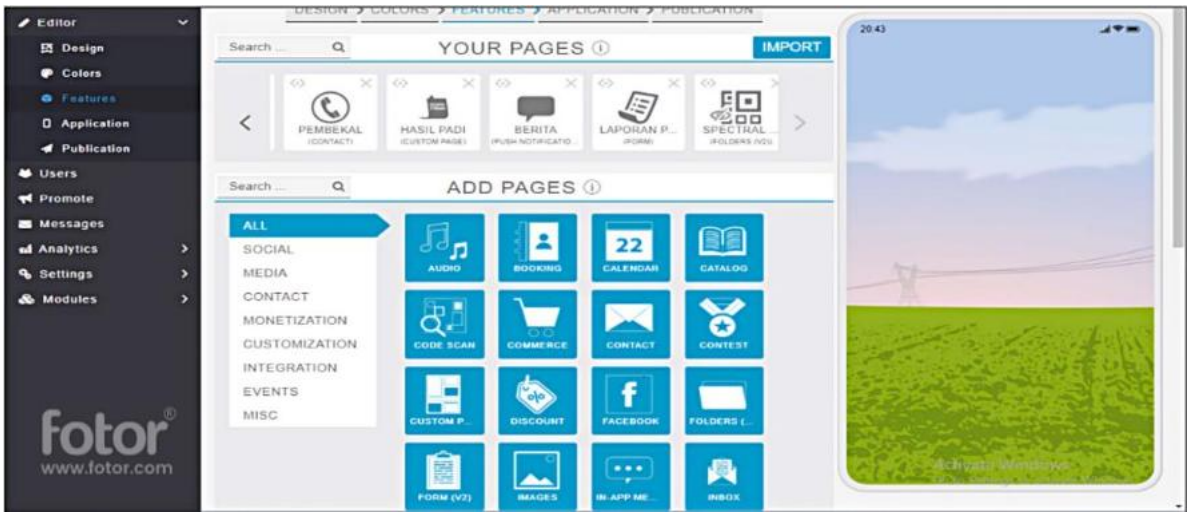


Fig. 10 - The application Editor tool and Feature menu in the MasterAppBuilder Application. (PEMBEKAL: SUPPLIER, HASIL PADI: RICE YIELD, BERITA: NEWS, LAPORAN: FORM)

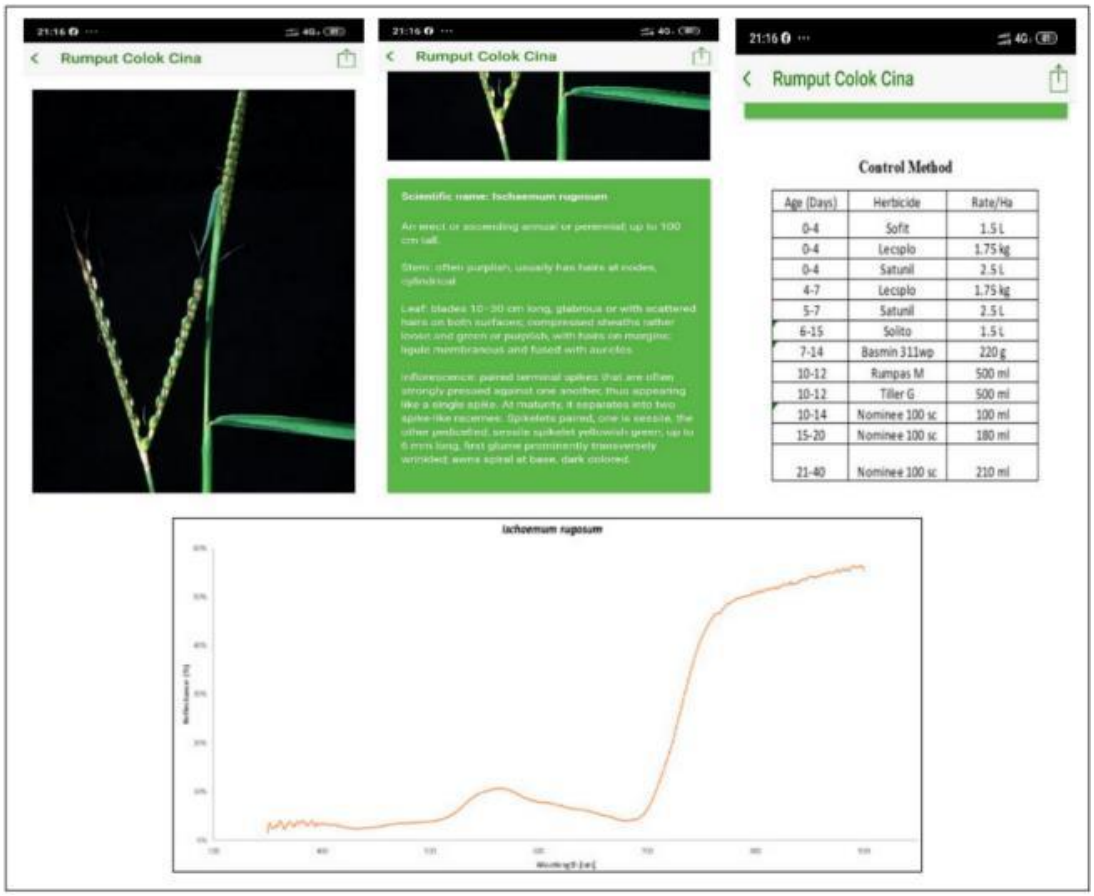


Fig. 11 - The content of menus, pictures, description, control method, and spectral signature graph of MATAG

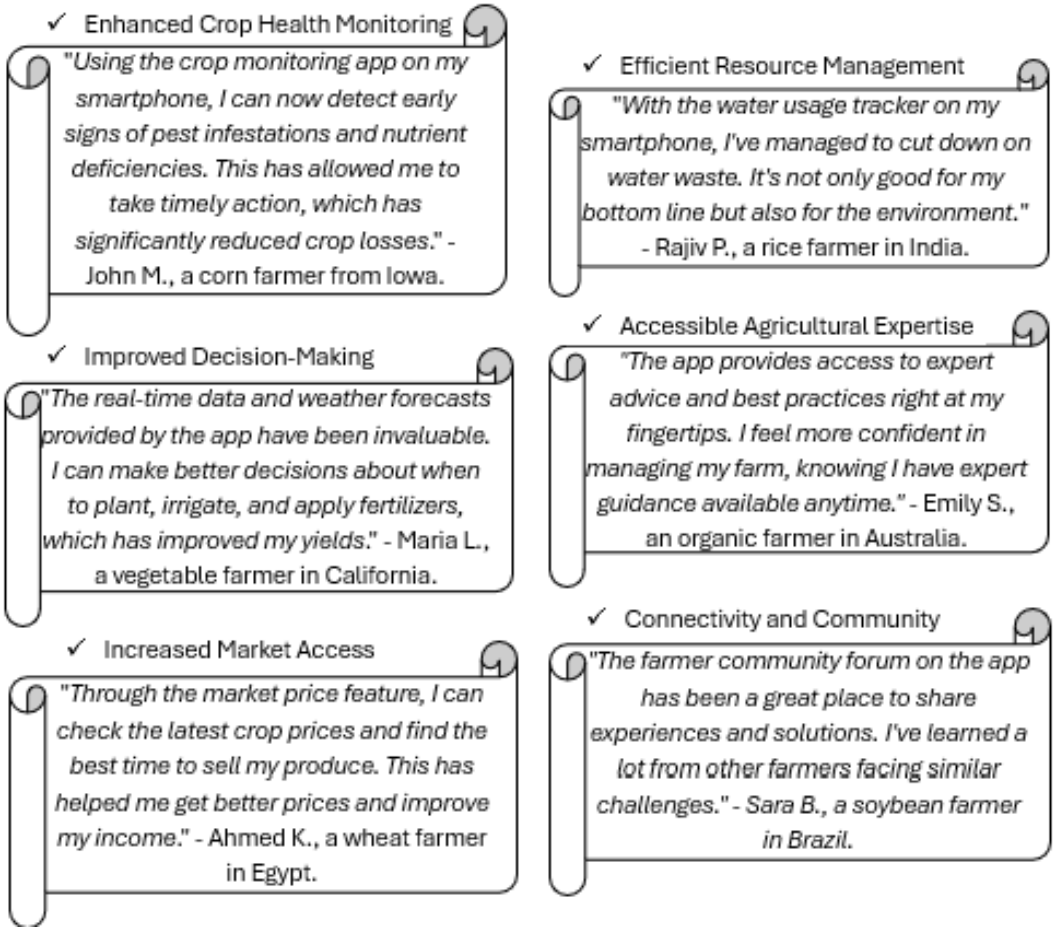


Fig. 12 - Testimonials from Farmers

7. POTENTIAL BENEFIT OF USING SMARTPHONE DEVICES TO THE AGRICULTURAL INDUSTRY

This section presents potential benefits and future perspectives for integrating smartphone-based spectral signatures into MATAG detection rather than established conclusions. While smartphones and spectral technologies show promise for MATAG identification, further field validation and multi-location trials are required before widespread adoption. Studies suggest that using smartphones for crop monitoring may have potential advantages for farm management. First, farmers can use a smartphone to identify early signs of crop stress, nutrient deficiencies, and disease outbreaks through real-time image-based monitoring, enabling timely and site-specific interventions (*Nyakuri et al., 2025*). This feature enables earlier mitigation measures to be implemented, lowering the chance of crop loss while increasing yield. Early intervention also saves resources through preventing expensive chemical treatments. Second, smartphones could help farmers to effectively monitor soil moisture levels, allowing them to change irrigation schedules based on crop needs. This feature assures that crops get enough moisture without wasting water, lowering water costs. Previous research demonstrates that images captured by smartphone sensors (under controlled lighting) can predict soil moisture with moderate accuracy (i.e., MAE = 0.35, RMSE = 0.15, $R^2 \approx 0.60$), confirming the feasibility of image-based soil moisture estimation (Riaz Hasib Hossain and Ashad Kabir, 2023). Third, farmers who have access to precise data on soil moisture, meteorological, and crop growth patterns can maximise resource allocation, including water, fertilisers, and pesticides (*Mansoor et al., 2025*). It ends up with a minimised environmental impact.

Fourth, farmers can use data-driven insights and practical alternatives to reduce risks, increase productivity, and improve overall farm management. This informed decision-making aspect eliminates the need for expensive trial-and-error procedures (*Mishra and Mishra, 2024*). Fifth, smartphones automate data gathering and analysis, reducing the need for human record-keeping and data entry. This characteristic not only saves time but also reduces the possibility of errors or anomalies in the handling of data (*Payero et al., 2021*). Farmers can concentrate more on their main farming tasks, leading to improved operational efficiency. Sixth, online monitoring using sensors might decrease agricultural maintenance expenditures. Such monitoring is crucial for small and medium-sized farms, where resources are limited. It can cut maintenance costs by up to 30% by enabling online monitoring via sensors. Real-time data on crop status improves production efficiency and resource utilisation (*Aarif et al., 2025*). Seventh, a smartphone should be compatible with existing farm management systems and interface with other farm-related devices. This compatibility implies seamless exchange of data while reducing the need for extra hardware or software investments (*Choudhary et al., 2025*).

Eighth, a smartphone may automate tasks including data collection and processing, freeing up staff for other important farming tasks. This automation lessens labour expenses and improves overall efficiency (*Mumuni and Mumuni, 2025*). Ninth, smartphone use imagines recognition technology to detect pests and diseases that potentially impact crops. Farmers can immediately identify and solve these problems, avoiding the need for costly chemical treatments and related expenditures. Tenth, smartphones allow farmers to precisely monitor soil moisture levels, ensuring that crops receive enough moisture without wasting water resources. IoT-based soil moisture monitoring systems integrated with smartphone alerts enabled real-time irrigation decisions, resulting in up to 30% water savings compared to conventional methods (*Dong et al., 2024*). Eleventh, a smartphone can help farmers optimise their energy consumption by providing real-time data. This optimisation facilitates them to regulate their energy use patterns, lowering energy expenses and environmental impact (*Ahmed and Shakoor, 2025*).

Twelfth, smartphones automate collection and analysis, reducing the need for human record-keeping and data entry. Such automation lowers labour expenses involved with data management, allowing farmers to concentrate on primary farming activities (*Resti et al., 2024*). Thirteenth, smartphones automate data administration, which reduces the probability of errors or discrepancies. This feature indicates that the data is correct and reliable, which reduces the need for costly adjustments (*Kumar, 2024*). Fourteenth, smartphones offer farmers data-driven insights and useful guidance, allowing them to improve their operations. Such a feature leads to increased agricultural yields and greater farm profitability. The global market for smart agriculture is predicted to expand from $12.4 billion in 2020 to $34.1 billion by 2026, indicating the enormous economic potential of implementing these technologies (*Techspian, 2024*). Farmers can use these economic benefits to reduce crop monitoring and management costs, resulting in enhanced efficiency and profitability. Overall, smartphones offer an effective and accessible platform for integrating spectral data into MATAG identification. However, successful adoption will depend on addressing technological limitations, farmer training, and validation in diverse environments.

8. CHALLENGES IN DETECTING THE MATAG VARIETY USING A SMARTPHONE

There are a few challenges in developing future MATAG detection apps for detecting MATAG using spectral signature analysis. The processing capacity, i.e., the operating time of mobile apps, is one of the main challenges. There is also a need to transfer the data to be processed to a remote server. Besides, some locations may not have an Internet connection, which loses its ability the operation time and could cause a delay because it can only be used when there is access to the Internet. When facing a weak Internet connection, the user needs to bring the apps to other nearby locations to ensure that the device is connected to the Internet, which is inefficient in practice (*Mendes et al., 2020*).

Another limitation is the size of the smartphone's screen. The small size of smartphones could result in changing geometric relationships between the user's face and the phone screen and low-resolution frontal cameras. Instead of purchasing a computer that has a bigger screen size, farmers should be able to use their smartphone simply. Although almost all smartphones today have sizable screens, there are some with smaller screens; hence features of the applications must be designed to be user-friendly across screen sizes.

Smartphone keyboards have much smaller buttons or touch spaces than standard desktop or PC keyboards. Therefore, incorrect touches could frequently happen. In addition, when using a capacitive touchscreen interface, there is a problem with dirt on the screen that is caused by fingerprints and finger sweat. Therefore, touch interfaces cannot be used as smartphone interfaces are not disabled-friendly or it is less functional when both hands are carrying something or doing some activities. Moreover, such mobile devices have an integrated camera as the default configuration.

There is also another issue that needs to be considered when developing apps for smartphones. The problem is the skill of the manpower to use the device, such as farmers. They primarily work in the field, are elderly, and do not particularly adapt to such technology. As a result, the future MATAG detection apps must be as simple, intuitive, and handy to use in their daily farming activities (*Abdullahi et al., 2021*). Consequently, user behaviour in using smartphones differs across community backgrounds. For instance, rural farmers in low-income countries may be restricted by low literacy and a lack of exposure to device interfaces. Therefore, they require highly intuitive interfaces, in which using too much text as an interface may be incomprehensible or difficult to use.

Other constraints were the high cost of buying smartphones, maintenance, lack of encouragement, and usage awareness. As a result, some farmers prefer to use the conventional method, which results in low participation of farmers. Moreover, it is not that easy to insert and update the information into the apps (*Abdullahi et al., 2021*). Therefore, smartphone application developers must solve this limitation by creating an interface design that is handy for multiple users.

9. FUTURE RESEARCH OPPORTUNITIES OF MATAG VARIETY DETECTION USING A SMARTPHONE

Many apps are being used in the public domain in the agricultural field, and not just by licensed users. However, most farmers who use these applications have little or no knowledge of the device attributes. Therefore, the future MATAG detection apps need to be designed in a simple way and be efficient to use promptly. However, as a new generation of farmers gains proficiency in using these apps, this issue will be addressed over time.

More apps that involve IoT in their farming practices are being developed, but users will only need a little IT knowledge to use the device. In addition, the developer will design criteria and usability standards so that the apps must consider work tools rather than just applications for enthusiasts or entertainment. It is also projected that software that currently operates on smartphones will progressively shift to larger devices such as tablets, tab, and iPads.

To increase smartphone processing capabilities, apps are likely to use deep learning, machine learning, or artificial intelligence techniques on the smartphone. This approach avoids the inability to use apps in remote areas where Internet access may be unavailable or limited. Instead, the apps are expected to be able to be used offline and then transfer data to a remote server that will be accessible via various devices.

Future developments in smartphone spectral signature technology are anticipated to focus on both hardware and software advancements. Developing equipment with image sensors capable of acquiring wavelengths outside of the visible spectrum is also anticipated to open up new alternatives for this type of application. Smartphones equipped with cameras capable of capturing the spectrum in the near-infrared and infrared zones will allow the implementation of vegetative vigour determination applications, such as creating spectral signature graphs of the MATAG variety in coconut nurseries.

More precise detection of physiological and varietal variations will be made possible by developments in smartphone cameras, such as the incorporation of multispectral and hyperspectral sensors or the use of

affordable clip-on spectrometers. Smartphones with powerful processors will be able to conduct on-device spectral analysis without exclusively depending on desktop or lab computers.

The combination of cloud computing and artificial intelligence will be equally significant. Real-time data analysis is feasible with AI algorithms implemented through mobile applications, providing farmers with fast decision support. It will also be essential to create open, standardised spectral libraries for coconut varieties so that farmers and researchers may access reliable reference data. Participatory collection of data, in which farmers help create extensive spectral repositories, could be used to develop these databases.

Smartphones will probably serve as hubs in larger digital agriculture ecosystems in the future, connecting cloud platforms, IoT field sensors, and UAV-based imaging. This integration will facilitate yield forecast, crop health monitoring, and MATAG hybrid identification. Future studies must focus on user accessibility, cost, and training in addition to policy assistance to promote digital agriculture solutions in coconut-producing countries to ensure successful adoption.

10. CONCLUSIONS

This article reviewed the potential of integrating smartphones with spectral signature analysis for detecting the MATAG hybrid. Key topics discussed consist of the morphological challenges of identifying MATAG varieties, the utilisation of spectral reflectance data and derivative analysis, the role of spectral signature libraries, and the comparison of smartphone-based methods with traditional approaches. The spectral signature graph was displayed as a reference to detect various species of MATAG more efficiently. The review emphasises that spectral libraries generated in mobile applications, when combined with external sensors and spectral databases attached to the smartphone, could provide a promising and affordable platform for intelligent MATAG seedling identification. Future research should focus on field validation, farmer adoption strategies, and the development of user-friendly applications tailored to plantation conditions.

11. ACKNOWLEDGEMENT

The authors delegate our thanks to the Department of Agriculture, Jorak (Johor) and Lekir (Perak) for providing the sample of MATAG species in this project and the Ministry of Higher Education, Malaysia under the Long-term Research Grant Scheme (LRGS) for the program titled “Precision Management of Coconut Nursery for Production of High Quality Seedlings”- LRGS/1/2020/UPM/01/2 (Vote No: 5545202) for the funding.

12. REFERENCES

[1] Aarif K.O., M., Alam, A., & Hotak, Y. (2025). Smart sensor technologies shaping the future of precision agriculture: recent advances and future outlooks. *Journal of Sensors*, 2025(1), 2460098. https://doi.org/10.1155/js/2460098

[2] Abdullahi, K.A., Oladele, O.I., & Akinyemi, M. (2021). Attitude, knowledge and constraints associated with the use of mobile phone applications by farmers in North West Nigeria. *Journal of Agriculture and Food Research*, 6, 100212. https://doi.org/10.1016/j.jafr.2021.100212

[3] Adam, S.N. (2012). *Design and development of an interactive digital spectral library* [Master thesis, Universiti Putra Malaysia]. Universiti Putra Malaysia Institutional Repository. http://psasir.upm.edu.my/id/eprint/67024/

[4] Agostini, A., Bína, D., Barcytė, D., Bortolus, M., Eliáš, M., Carbonera, D., & Litvín, R. (2024). Eustigmatophyte model of red-shifted chlorophyll a absorption in light-harvesting complexes. *Communications Biology*, 7(1), 1406. https://doi.org/10.1038/s42003-024-07101-9

[5] Ahansal, Y., Bouziani, M., Yaagoubi, R., Sebari, I., Sebari, K., & Kenny, L. (2022). Towards smart irrigation: a literature review on the use of geospatial technologies and machine learning in the management of water resources in arboriculture. *Agronomy*, 12(2), 297. https://doi.org/10.3390/agronomy12020297

[6] Ahmed, N., & Shakoor, N. (2025). Advancing agriculture through IoT, big data, and AI: a review of smart technologies enabling sustainability. *Smart Agricultural Technology*, 10, 100848. https://doi.org/10.1016/j.atech.2025.100848

[7] Arumugam, T., & Md Hatta, M.A. (2022). Improving coconut using modern breeding technologies: challenges and opportunities. *Plants*, 11(24), 3414. https://doi.org/10.3390/plants11243414

[8] Ballado, A., Lazaro, J., Avendano, G., De Claro, C.A.R.M., Sandoval, G.K., & Viloria, R.A. (2017, December). Characterisation using spectral signature of tropical plants through Fast Fourier Transform. In 2017 IEEE 9th International Conference on Humanoid, Nanotechnology, Information Technology, Communication and Control, Environment and Management (HNICEM) (pp. 1-6). IEEE. https://doi.org/10.1109/HNICEM.2017.8269552

[9] Bisi, R.B., Albrecht, U., & Bowman, K.D. (2020). Seed and seedling nursery characteristics for 10 USDA citrus rootstocks. *HortScience*, 55(4), 528-532. https://doi.org/10.21273/HORTSCI14598-19

[10] Borraz-Martínez, S., Simo, J., Gras, A., Mestre, M., Boqué, R., & Tarrés, F. (2022). Combining computer vision and deep learning to classify varieties of Prunus dulcis for the nursery plant industry. *Journal of Chemometrics*, *36*(2), e3388. https://doi.org/10.1002/cem.3388

[11] Buddenbaum, H., Watt, M.S., Scholten, R.C., & Hill, J. (2019). Preprocessing ground-based visible/near infrared imaging spectroscopy data affected by smile effects. *Sensors*, *19*(7), 1543. https://doi.org/10.3390/s19071543

[12] Che'Ya, N.N., Mohidem, N.A., Tarmidi, Z., Sarifudin, M.S.A., & Shah, J.A. (2022a, July). Mobile application devices for MATAG coconut variety detection based on spectral signature analysis: A review. *In IOP Conference Series: Earth and Environmental Science* (Vol. 1064, No. 1, p. 012039). IOP Publishing. https://doi.org/10.1088/1755-1315/1064/1/012039

[13] Che'Ya, N.N. (2016). Site-specific weed management using remote sensing. [Doctoral thesis, University of Queensland]. https://www.researchgate.net/publication/340133433_Site-Specific_Weed_Management_Using_Remote_Sensing

[14] Che'Ya, N.N., Mohidem, N.A., Roslin, N.A., Saberioon, M., Tarmidi, M.Z., Arif Shah, J., Fazlil Ilahi, W.F. & Man, N. (2022c). Mobile computing for pest and disease management using spectral signature analysis: A review. *Agronomy*, *12*(4), 967. https://doi.org/10.3390/agronomy12040967

[15] Department of Agriculture (DoA) Sarawak, 2022. Available online: https://doa.sarawak.gov.my/modules/web/pages.php?lang=bm&mod=webpage&sub=page&id=139 (accessed on 10th September 2022)

[16] Choudhary, V., Guha, P., Pau, G., & Mishra, S. (2025). An overview of smart agriculture using Internet of Things (IoT) and web services. *Environmental and Sustainability Indicators*, 26, 100607. https://doi.org/10.1016/j.indic.2025.100607

[17] Chu, T., Zha, H., Wang, Y., Yao, Z., Wang, X., Wu, C., & Liao, J. (2025). MaizeStar-YOLO: Precise detection and localization of seedling-stage maize. *Agronomy*, 15(8), 1788. https://doi.org/10.3390/agronomy15081788

[18] Dong, Y., Werling, B., Cao, Z., & Li, G. (2024). Implementation of an in-field IoT system for precision irrigation management. *Frontiers in Water*, 6, 1353597. https://doi.org/10.3389/frwa.2024.1353597

[19] Esther, G.M., Ahila, S.S., & Kumar, P.H. (2019, November). Coronary heart disease (CAD) monitoring system based on wireless sensors. In Journal of Physics: Conference Series (Vol. 1362, No. 1, p. 012045). IOP Publishing. https://doi:10.1088/1742-6596/1362/1/012045

[20] Franco, B., Clarisse, L., Stavrakou, T., Müller, J.F., Van Damme, M., Whitburn, S., Hadji-Lazaro, J., Hurtmans, D., Taraborrelli, D., Clerbaux, C. & Coheur, P. F. (2018). A general framework for global retrievals of trace gases from IASI: Application to methanol, formic acid, and PAN. *Journal of Geophysical Research*: *Atmospheres*, 123(24), 13-963. https://doi.org/10.1029/2018JD029633

[21] Golhani, K., Balasundram, S.K., Vadamalai, G., & Pradhan, B. (2018). A review of neural networks in plant disease detection using hyperspectral data. *Information Processing in Agriculture*, *5*(3), 354-371. https://doi.org/10.1016/j.inpa.2018.05.002

[22] Halim, H.H., Williams Dee, E., Pak Dek, M.S., Hamid, A.A., Ngalim, A., Saari, N., & Jaafar, A.H. (2018). Ergogenic attributes of young and mature coconut (*Cocos nucifera L.*) water based on physical properties, sugars and electrolytes contents. *International Journal of Food Properties*, *21*(1), 2378-2389. https://doi.org/10.1080/10942912.2018.1522329

[23] Hassan, A., Balachandran, P., & Khamis, K.R. (2021). Early root development of *Eucalyptus pellita F.* Muell. seedlings from seed and stem cutting propagation methods at nursery stage. *International Journal of Forestry Research*, 2021, 1-10. https://doi.org/10.1155/2021/6624266

[24] Hebbar, R., Ravishankar, H. M., Trivedi, S., Subramoniam, S. R., Uday, R., & Dadhwal, V. K. (2014). Object oriented classification of high resolution data for inventory of horticultural crops. *The International Archives of the Photogrammetry, Remote Sensing and Spatial Information Sciences*, *40*, 745-749. https://doi.org/10.5194/isprsarchives-XL-8-745-2014

[25] Hebbar, K.B., Abhin, P.S., Sanjo Jose, V., Neethu, P., Santhosh, A., Shil, S., & Prasad, P.V. (2022). Predicting the potential suitable climate for coconut (*Cocos nucifera L.*) cultivation in India under climate change scenarios using the MaxEnt model. *Plants*, *11*(6), 731. https://doi.org/10.3390/plants11060731

[26] Heim, R.H., Okole, N., Steppe, K., Van Labeke, M.C., Geedicke, I., & Maes, W.H. (2024). An applied framework to unlocking multi-angular UAV reflectance data: a case study for classification of plant parameters in maize (zea mays). *Precision Agriculture*, 25(3), 1751-1775. https://doi.org/10.1007/s11119-024-10133-0

[27] Ibrahim, A.S., Mohsen, S., Selim, I.M., Alroobaea, R., Alsafyani, M., Baqasah, A.M., & Eassa, M. (2025). AI-IoT based smart agriculture pivot for plant diseases detection and treatment. *Scientific Reports*, 15(1), 16576. https://doi.org/10.1038/s41598-025-98454-6

[28] Imanian, K., Pourdarbani, R., Sabzi, S., García-Mateos, G., Arribas, J.I., & Molina-Martínez, J.M. (2021). Identification of internal defects in potato using spectroscopy and computational intelligence based on majority voting techniques. *Foods*, 10(5), 982. https://doi.org/10.3390/foods10050982

[29] Inamdar, D., Kalacska, M., Arroyo-Mora, J.P., & Leblanc, G. (2021). The directly-georeferenced hyperspectral point cloud: preserving the integrity of hyperspectral imaging data. *Frontiers in Remote Sensing*, 9. https://doi.org/10.3389/frsen.2021.675323

[30] Jafarbiglu, H., & Pourreza, A. (2023). Impact of sun-view geometry on canopy spectral reflectance variability. *ISPRS Journal of Photogrammetry and Remote Sensing*, 196, 270-286. https://doi.org/10.1016/j.isprsjprs.2022.12.002

[31] Kingimi, M., Mohamad Zaki, N.A., Naharudin, N.S., Sinniah, U.R., Ahmad Hamdani, M.S., & Sulaiman, Z. (2023). Population structure of tagnanan coconut (*cocos nucifera l.*) and correlation among fruit yield and quality traits. *Climate Change Impact on the Sustainability of Agriculture, Forestry and Plantation*, 183, 204-213. http://psasir.upm.edu.my/id/eprint/110170/

[32] Kokaly, R.F., Clark, R.N., Swayze, G.A., Livo, K.E., Hoefen, T.M., Pearson, N.C., Wise, R.A., Benzel, W.M., Lowers, H.A., Driscoll, R.L., & Klein, A.J. (2017). *USGS spectral library version 7 data: US Geological Survey data release*. United States Geological Survey (USGS). https://doi.org/10.3133/ds1035

[33] Kreppel, K.S., Brinkel, J., & Sauli, E. (2023). Digital technologies to enhance infectious disease surveillance in Tanzania: a scoping review. *Healthcare*, 11(4), 470. https://doi.org/10.3390/healthcare11040470

[34] Kumar, D. (2024). AI-driven automation in administrative processes: Enhancing efficiency and accuracy. *International Journal of Engineering Science and Humanities*, 14(1), 256-265. https://doi.org/10.62904/qg004437

[35] Kutser, T., Hedley, J., Giardino, C., Roelfsema, C., & Brando, V.E. (2020). Remote sensing of shallow waters – A 50 year retrospective and future directions. *Remote Sensing of Environment*, 240, 111619. https://doi.org/10.1016/j.rse.2019.111619

[36] Lazaro Jr, J.B., Ballado Jr, A.H., Deriquito, J.P.P., Lamod, S.M.L., Mendez, B.A.Q., & Caya, M.V.C. (2019). Portable spectrometer device for Mapua-Phil-Lidar2 using charged coupled device array. *International Journal of Electrical and Electronic Engineering and Telecommunications*, *8*(2), 113-118. https://doi.org/10.18178/ijeetc.8.2.113-118

[37] Li, Y., Luo, J., Liu, Z., Wu, D., & Zhang, C. (2023). A personalized and smart flowerpot enabled by 3D printing and cloud technology for ornamental horticulture. *Sensors*, *23*(13), 6116. https://doi.org/10.3390/s23136116

[38] Liu, J., & Van Iersel, M. W. (2021). Photosynthetic physiology of blue, green, and red light: Light intensity effects and underlying mechanisms. *Frontiers in Plant Science*, 12, 328. https://doi.org/10.3389/fpls.2021.619987

[39] Liu, Q., Zhang, Y., Chen, J., Sun, C., Huang, M., Che, M., Li, C. & Lin, S. (2023). An improved Deeplab V3+ network based coconut CT image segmentation method. *Frontiers in Plant Science*, *14*, 1139666. https://doi.org/10.3389/fpls.2023.1139666

[40] Mahant, V., & Pal, P. (2025). Seeding the future: a review of artificial intelligence's pivotal role in seed technology. *Journal of Crop Science and Biotechnology*, 1-14. https://doi.org/10.1007/s12892-025-00284-5

[41] Manganiello, G., Nicastro, N., Caputo, M., Zaccardelli, M., Cardi, T., & Pane, C. (2021). Functional hyperspectral imaging by high-related vegetation indices to track the wide-spectrum Trichoderma

biocontrol activity against soil-borne diseases of baby-leaf vegetables. *Frontiers in Plant Science*, 12. https://doi.org/10.3389/fpls.2021.630059

[42] Man, N., & Shah, J.A. (2020). Acceptance of new coconut seed MATAG among coconut growers in Bagan Datoh, Perak and Bachok, Kelantan. *International Journal of Academic Research in Business and Social Sciences*, *10*(16), 1-26. http://dx.doi.org/10.6007/IJARBSS/v10-i16/8286

[43] Mansoor, S., Iqbal, S., Popescu, S.M., Kim, S.L., Chung, Y.S., & Baek, J.H. (2025). Integration of smart sensors and IOT in precision agriculture: trends, challenges and future prospectives. *Frontiers in Plant Science*, 16, 1587869. https://doi.org/10.3389/fpls.2025.1587869

[44] Mendes, J., Pinho, T.M., Neves dos Santos, F., Sousa, J.J., Peres, E., Boaventura-Cunha, J., Cunha, M. & Morais, R. (2020). Smartphone applications targeting precision agriculture practices—A systematic review. *Agronomy*, 10(6), 855. https://doi.org/10.3390/agronomy10060855

[45] Meerdink, S., Roberts, D., Hulley, G., Gader, P., Pisek, J., Adamson, K., King, J. & Hook, S.J. (2019). Plant species' spectral emissivity and temperature using the hyperspectral thermal emission spectrometer (HyTES) sensor. *Remote Sensing of Environment*, 224, 421-435. https://doi.org/10.1016/j.rse.2019.02.009

[46] Mimma, N.E.A., Ahmed, S., Rahman, T., & Khan, R. (2022). Fruits classification and detection application using deep learning. *Scientific Programming*, *2022*(1), 4194874. https://doi.org/10.1155/2022/4194874

[47] Mohanty, P., Valagadri, V., & Ramya, S. (2022). *Smart farming enabled by IoT and spectral imaging. In Journal of Physics*: Conference Series (Vol. 2161, No. 1, p. 012044). IOP Publishing. https://doi.org/10.1088/1742-6596/2161/1/012044

[48] Mihrete, T.B., & Mihretu, F.B. (2025). Crop diversification for ensuring sustainable agriculture, risk management and food security. *Global Challenges*, 9(2), 2400267. https://doi.org/10.1002/gch2.202400267

[49] Mishra, H., & Mishra, D. (2024). AI for data-driven decision-making in smart agriculture: From field to farm management. *In Artificial Intelligence Techniques in Smart Agriculture* (pp. 173-193). Singapore: Springer Nature Singapore. https://doi.org/10.1007/978-981-97-5878-4_11

[50] Mumuni, A., & Mumuni, F. (2025). Automated data processing and feature engineering for deep learning and big data applications: a survey. *Journal of Information and Intelligence*, 3(2), 113-153. https://doi.org/10.1016/j.jiixd.2024.01.002

[51] Musiolková, M., Huszár, P., Navrátil, M., & Špunda, V. (2021). Impact of season, cloud cover, and air pollution on different spectral regions of ultraviolet and visible incident solar radiation at the surface. *Quarterly Journal of the Royal Meteorological Society*, 147(738), 2834-2849. https://doi.org/10.1002/qj.4102

[52] Nyakuri, JP., Nkundineza, C., Gatera, O., Nkurikiyeyezu, K., & Mwitende, G. (2025). AI and IoT-powered edge device optimized for crop pest and disease detection. *Scientific Reports*, 15(1), 22905. https://doi.org/10.1038/s41598-025-06452-5

[53] Nesarajan, D., Kunalan, L., Logeswaran, M., Kasthuriarachchi, S., & Lungalage, D. (2020, December). Coconut disease prediction system using image processing and deep learning techniques. In 2020 IEEE 4th International Conference on Image Processing, Applications and Systems (IPAS) (pp. 212-217). IEEE. https://doi.org/10.1109/IPAS50080.2020.9334934

[54] Noor Azmi, A.N., Bejo, S.K., Jahari, M., Muharam, F.M., Yule, I., & Husin, N.A. (2020). Early detection of Ganoderma boninense in oil palm seedlings using support vector machines. *Remote Sensing*, 12(23), 3920. https://doi.org/10.3390/rs12233920

[55] OUC, 2018. *An app for monitoring crops by phone that reduces costs by 30%*. UOC researchers are developing low-cost apps for less productive sectors. Retrieved from https://www.uoc.edu/en/news/2018/102-digital-agriculture

[56] Padhiary, M., Kumar, A., & Sethi, L.N. (2025). Emerging technologies for smart and sustainable precision agriculture. *Discover Robotics*, *1*(1), 6. https://doi.org/10.1007/s44430-025-00006-0

[57] Paringit, C., Fabila, J.L., Ilagan, M.J., Cruz, C., & Samalburo, S. (2014). Spectral characterization of coconut scale insect (CSI) from field spectroradiometric measurements and high-resolution superspectral imagery. http://a-a-r-s.org/acrs/administrator/components/com_jresearch/files/publications/OS-032%20Paper%20-%20ACRS%202014%20Paringit%20et%20al.pdf

[58] Payero, J.O., Marshall, M.W., Farmaha, B.S., Davis, R.H., & Nafchi, A.M. (2021). Development and application of cell-phone-based Internet of Things (IoT) systems for soil moisture monitoring. *Agricultural Sciences*, 12(5), 549-564. https://doi.org/10.4236/as.2021.125035

[59] Pressreader. (2016). Hybrid coconut: Its potential to help overcome poverty. Retrieved from https://www.pressreader.com/philippines/

[60] Raj, D.M., Perumal, K., Balakrishnan, K., & Subramaniam, S. (2024). Revitalizing Cocos nucifera. L var matag: unravelling new horizons in clonal propagation through organogenesis and LED illumination. *Plant Cell, Tissue and Organ Culture (PCTOC)*, *158*(2), 36. https://doi.org/10.1007/s11240-024-02834-1

[61] Riaz Hasib Hossain, M., & Ashad Kabir, M. (2023). Machine learning techniques for estimating soil moisture from mobile captured images. *arXiv e-prints*, arXiv-2303. https://doi.org/10.48550/arXiv.2303.11527

[62] Rodríguez Machado, E., Luís Soca Muñoz, J., Hernández Santana, L., Aday Díaz, O.D.L.C., & Orozco Morales, R. (2020). Spectral signature of brown rust and orange rust in sugarcane, 96, 9-20. https://doi.org/10.17533/udea.redin.20191042

[63] Resti, Y., Reynoso, G.G., Probst, L., Indriasari, S., Mindara, G.P., Hakim, A., & Wurzinger, M. (2024). A review of on-farm recording tools for smallholder dairy farming in developing countries. *Tropical Animal Health and Production*, 56(5), 168. https://doi.org/10.1007/s11250-024-04024-9

[64] Rosle, R., Norasma, C.Y.N., Roslin, N.A., Halip, R.M., & Ismail, M.R. (2019). Monitoring early stage of rice crops growth using normalized difference vegetation index generated from UAV. In IOP Conference Series: Earth and Environmental Science (Vol. 355, No. 1, p. 012066). IOP Publishing. https://doi.org/10.1088/1755-1315/355/1/012066

[65] Roslin, N.A., Che'Ya, N.N., Sulaiman, N., Nor Alahyadi, L.A., & Ismail, M.R. (2021). Mobile application development for spectral signature of weed species in rice farming. *Pertanika Journal of Science & Technology*, *29*(4). https://doi.org/10.47836/pjst.29.4.01

[66] Rossel, R.V., Behrens, T., Ben-Dor, E., Brown, D.J., Demattê, J.A.M., Shepherd, K.D., ... & Ji, W. (2016). A global spectral library to characterize the world's soil. *Earth-Science Reviews*, *155*, 198-230. https://doi.org/10.1016/j.earscirev.2016.01.012

[67] Samarakoon, S.M.A.B.K., Rupasinghe, C.P., & Seneweera, S. (2025). Coconut leaf nitrogen measurement using different vegetative indices and multispectral images. *Smart Agricultural Technology*, 10, 100672. https://doi.org/10.1016/j.atech.2024.100672

[68] Schlemitz, A., & Mezhuyev, V. (2024). Approaches for data collection and process standardization in smart manufacturing: systematic literature review. *Journal of Industrial Information Integration*, 38, 100578. https://doi.org/10.1016/j.jii.2024.100578

[69] Singh, P., Verma, A., & Alex, J.S.R. (2021). Disease and pest infection detection in coconut tree through deep learning techniques. *Computers and Electronics in Agriculture*, *182*, 105986. https://doi.org/10.1016/j.compag.2021.105986

[70] Soca-Muñoz, J. L., Rodríguez-Machado, E., Aday-Díaz, O., Hernández-Santana, L., & Orozco-Morales, R. (2020). Spectral signature of brown rust and orange rust in sugarcane. *Revista Facultad de Ingeniería Universidad de Antioquia*, (96), 9-20. http://doi.org/10.17533/udea.redin.20191042

[71] Specchio, A Spectral Information System. Available online: http://specchio.ch (accessed on 2 January 2022).

[72] Strauss, A., Mold, L., Ercan, H.U., Bos, C., Peyerl, M., Zitek, A., & Hinterstoisser, B. (2021). Spectral signatures of concrete for the curing performance assessment. *In Life-Cycle Civil Engineering: Innovation, Theory and Practice* (pp. 1659-1665). CRC Press. https://doi.org/10.1201/9780429343292-226

[73] Systems Ecology Laboratory, Vegetation Spectral Library. Available online: http://spectrallibrary.utep.edu (accessed on 3 January 2017).

[74] Techspian (2024). Leveraging mobile apps for precision agriculture and crop monitoring. Retrieved from https://www.techspian.com/leveraging-mobile-apps-for-precision-agriculture-crop-monitoring/

[75] Torresani, M., Rossi, C., Perrone, M., Hauser, L.T., Féret, J.B., Moudrý, V., Simova, P., Ricotta, C., Foody, G.M., Kacic, P., Feilhauer, H., Malavasi, M., Tognetti, R. & Rocchini, D. (2024). Reviewing the spectral variation hypothesis: twenty years in the tumultuous sea of biodiversity estimation by remote sensing. *Ecological Informatics*, 82, 102702. https://doi.org/10.1016/j.ecoinf.2024.102702

[76] Virtanen, O., Constantinidou, E., & Tyystjärvi, E. (2022). Chlorophyll does not reflect green light–how to correct a misconception. *Journal of Biological Education*, *56*(5), 552-559. https://doi.org/10.1080/00219266.2020.1858930

[77] Yusuf, N., Nassir, N.N.M., Azmi, W.A., & Zakeri, H.A. (2017). Early oxidative stress responses in coconut (Cocos nucifera) stem of MATAG and PANDAN cultivars due to red palm weevil. https://www.researchgate.net/publication/322297687_Early_oxidative_stress_responses_in_coconut_Cocos_nucifera_stem_of_matag_and_pandan_cultivars_due_to_red_palm_weevil_Rhynchophorus_ferrugineus_olivier_infestation

[78] Mohamad Zaki, N.A., Kingimi, M., Naharudin, N.S., Jusoh, M., Ghazali, M.N., & Sinniah, U.R. (2023). Variability of fruit morphology, yield, and quality in the tagnanan population as MATAG pollen source. *Climate Change Impact on the Sustainability of Agriculture, Forestry and Plantation*, 55, 197-203. https://ijafp.org/wp-content/uploads/2023/12/IJAFP-Vol.13_046.pdf

[79] Zhang, C., Kerner, H., Wang, S., Hao, P., Li, Z., Hunt, K.A., Abernethy, J., Zhao, H., Gao F., Di, L., Guo, C., Liu, Z., Yang, Z., Mueller, R., Boryan, C., Chen, Q., Beeson, P.C., Zhang, H.K. & Shen, Y. (2025). Remote sensing for crop mapping: A perspective on current and future crop-specific land cover data products. *Remote Sensing of Environment*, 330, 114995. https://doi.org/10.1016/j.rse.2025.114995

[80] Zhang, Y., Liu, Q., Chen, J., Sun, C., Lin, S., Cao, H., Xiao, Z. & Huang, M. (2023). Developing non-invasive 3D quantificational imaging for intelligent coconut analysis system with x-ray. *Plant Methods*, *19*(1), 24. https://doi.org/10.1186/s13007-023-01002-4

DEEP LEARNING-BASED TARGET RECOGNITION AND LOCALIZATION IN CITRUS PICKING ROBOT
/
基于深度学习的柑橘采摘机器人目标识别与定位方法研究

Yu YANG*[1)], Linhui WANG[1)], Shuwei DENG[1)], Zhengqi ZHOU[1)], Zhizhuang LIU[1)]
[1)] Hunan Institute of Science and Engineering, Yongzhou, Hunan 425199, China
E-mail: u7e840@yeah.net
DOI: https://doi.org/10.35633/inmateh-79-44

Keywords: *deep learning, citrus, target recognition, depth camera*

ABSTRACT
Target recognition and localization of picking robots are very important in orchard environments. This paper analyzed the You Only Look Once version 8 normal (YOLOv8n) method in deep learning for citrus picking robots, introduced FasterNet, efficient multi-scale attention (EMA) mechanism, and Wise Intersection over Union (WIoU) loss function, developed an improved YOLOv8n method, and collected a citrus fruit dataset to analyze the recognition and positioning effects of the proposed methods. The selected FasterNet, EMA, and WIoU were all superior to the other types compared, and the improved YOLOv8n method achieved an accuracy of 0.893, a recall rate of 0.894, and a mean average percentage (mAP) of 0.895 for citrus recognition, outperforming other recognition methods. In terms of citrus localization, the average errors on X, Y, and Z axes were 3.56 mm, 3.54 mm, and 4.74 mm, respectively. The findings demonstrate the reliability of the proposed model, and it can be applied to actual citrus picking robots.

摘要
在果园环境下，采摘机器人的目标识别与定位十分重要。本文针对柑橘采摘机器人，分析了深度学习中的 YOLOv8n 方法，引入 FasterNet、EMA 注意力机制以及 WIoU 损失函数，设计了一种改进 YOLOv8n，并采集柑橘果实数据集，对所提方法的识别和定位效果进行了分析。结果发现，所选择的 FasterNet、EMA 以及 WIoU 均优于所比较的其他类型，改进 YOLOv8n 在柑橘识别上获得了 0.893 的准确率、0.894 的召回率和 0.895 的 mAP，优于其他识别方法。在柑橘定位上，在 、Y、Z 上的平均误差分别为 3.56mm、3.54mm 和 4. 4mm。结果证明了所提方法的可靠性，可以在实际的柑橘采摘机器人中进行应用。

INTRODUCTION
With the advancement of technologies such as intelligent control and mechanized equipment, the agricultural industry has also undergone tremendous changes. In the fruit industry, due to the limitations of planting patterns and terrain conditions, the degree of mechanization in orchards is still relatively low. Especially in fruit picking, as the seasonal intensity is high and the picking environment is complex, the labor cost is constantly rising. The high labor cost poses a huge challenge to the development of the fruit industry. The research, development, and application of intelligent picking equipment have become an important aspect of the development of the forest and fruit industry. The picking robot is a type of robot used to complete the picking of fruits and vegetables (*Wang et al., 2024*), and it is an important part of the current research on agricultural intelligence. The machine vision system is the perceptual core of a picking robot, and its target recognition accuracy, real-time inference speed, and three-dimensional positioning accuracy can directly affect the picking success rate and operation stability of the robot. In recent years, deep learning provides new technologies for visual perception in complex agricultural environments with its excellent feature extraction and autonomous learning abilities. *Chen et al.* (*2025*) designed a method for target recognition of agricultural picking robots in low-light conditions using template matching, achieving a maximum recognition accuracy of 98.56%, which enables efficient picking in low-light conditions. *Rong et al.* (*2024*) designed a tomato-picking robot system, and field trials showed that the robot had a harvesting success rate of over 50% and an average harvesting cycle of 24 seconds. *Zhao* (*2024*) developed a You Only Look Once version 5 (YOLOv5)-RACF algorithm for the problem of automatic apple picking, with an average detection accuracy of 98.748% and a time of 0.13 seconds to calculate the diameter of one apple. *Zhu et al.* (*2025*) designed an improved You Only Look Once version 7 (YOLOv7) network for the detection of Agaricus bisporus, and the experiment found that the acquisition success rate of this method was 80%, which could achieve automated acquisition.

Matache et al. (2026) designed a greenhouse tomato harvesting system that uses a hybrid vision framework that integrates convolutional neural networks (CNNs) and watershed-based segmentation to detect and position fruits. This system achieved a fruit detection precision of 96.9%. Citrus is a kind of fruit with high yield and demand at present. In the research of citrus-picking robots, *Lin et al.* (*2019*) designed an algorithm based on red-green-blue-depth (RGB-D) image analysis to detect and localize citrus. They conducted experiments on a dataset of 506 RGB-D images and found that the proposed algorithm was robust, with an F1 score of 0.9197. *Yin et al.* (*2023*) proposed an integrated citrus-harvesting robot solution, which adopted a multi-sensor-based fused simultaneous localization and mapping algorithm to achieve positioning and navigation for the orchard robot. Its overall success rate was 87.2%, and the average picking time was 10.9 seconds per fruit. *Zhang et al.* (*2025*) selected YOLOv5 for citrus object detection and achieved an accuracy of 92.3%, a recall of 79.1%, and a mean average percentage (mAP) of 88.5%, which verifies that this network is capable of handling detection tasks in real environments. *Hou et al.* (*2024*) combined a convolutional block attention module (CBAM) with the backbone network of a Mask region-based convolutional neural network (R-CNN). They found that the mean absolute error and relative error of citrus picking point localization was 8.63 mm and 2.76%, respectively, providing a valid solution for the accurate detection and localization of citrus picking points for harvesting robots.

In the current research, the main deficiencies are as follows. Firstly, most of the existing high-precision algorithms rely on deep and heavy network structures, which have a large number of parameters and high computational requirements, resulting in high hardware deployment costs and making it difficult to meet the real-time operation requirements of picking robots. Secondly, the training and performance verification of most models rely on small-scale and single-scene datasets, leading to insufficient robustness. Thirdly, most existing models have problems such as insufficient feature extraction, weak ability to recognize difficult samples, and low boundary regression accuracy, which limit the practical application of citrus picking robots. In response to the above research status and deficiencies, this paper aimed at high precision and strong robustness and took You Only Look Once version 8 normal (YOLOv8n), which has few parameters and is suitable for embedded devices, as the basic model for design. The effectiveness of the proposed method was verified through training with multi-scene datasets and laboratory positioning experiments, providing theoretical support for the design and application of citrus picking robots.

MATERIALS AND METHODS

Citrus identification model based on YOLOv8

In actual orchards, the robot first needs to accurately identify the target fruit, a process usually accomplished using object detection techniques. Conventional object detection techniques-including R-CNN and its improved variant, Faster R-CNN-have a slower detection speed and are not suitable for citrus picking tasks that require rapid object detection. CNNs are a typical method in deep learning and have shown excellent performance in visual information processing (*Shao et al., 2023*). You Only Look Once (YOLO) is a CNN-based object detection method that can classify and locate images through a single neural network and perform object detection better and faster. Currently, the YOLO series of methods have good applications in many fields such as pedestrian detection and equipment fault identification.

You Only Look Once version 8 (YOLOv) is one of the highly flexible and scalable models in the YOLO series and has been utilized in various domains such as medicine and agriculture (*Jraba et al., 2025*). Among them, YOLOv8n has the characteristics of fewer parameters and smaller size, which is more suitable for resource-constrained environments and has higher real-time performance. Therefore, this paper selected YOLOv8n to develop a citrus recognition model. The main current flaws of YOLOv8n are as follows.

(1) Convolutional mapping operations in the backbone network result in a large computational load for the model;

(2) The influence of overlapping citrus fruits and light intensity in the orchard environment results in the loss of target feature information, and more attention should be paid to key target areas;

(3) The original loss function may cause significant deviations in scenarios such as occlusion, density, and light variations.

Therefore, in order to achieve better results in citrus recognition and enhance the picking performance of robots, improvements need to be made based on the YOLOv8n.

Citrus recognition model based on YOLOv8n

The backbone network of YOLOv8n was improved by introducing FasterNet to reduce computational complexity. FasterNet is a model based on partial convolution (PConv). PConv refers to performing the convolution operation only on some channels of the input feature map while keeping the remaining channels unaltered, thereby reducing the computational load without compromising feature expression ability.

The FasterNet module is shown in Figure 1.

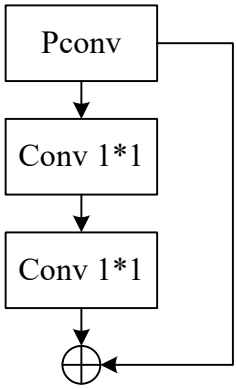


Fig. 1 - FasterNet module

The bottleneck module in the C2f module in the YOLOvn8 backbone network is substituted by the FasterNet module, thereby reducing the computational burden of the model while maintaining high feature expression ability.

By introducing the attention mechanism, the model can focus on information more relevant to citrus recognition among the numerous input information, thereby improving the performance of citrus recognition. Efficient multi-scale attention (EMA) is a mechanism that does not require dimensionality reduction, which significantly reduces computational costs while effectively preserving the integrity of feature channel information. Integrating it into citrus recognition models can enable the models to achieve better performance. The main structure of EMA is shown in Figure 2. EMA is combined with the C2f module to strengthen the model's capability to extract citrus features.

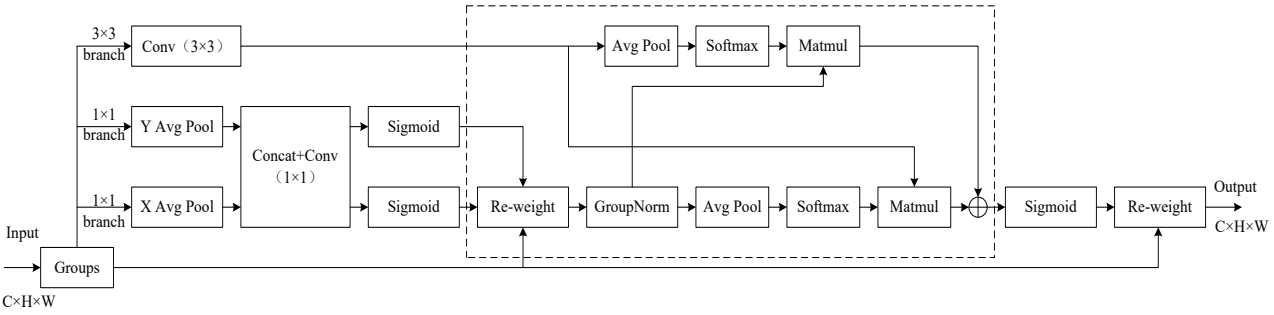


Fig. 2 - EMA mechanism

Finally, Wise Intersection Over Union (WIoU) replaces the Complete Intersection over Union loss (CIoU) function in the original YOLOv8n model.

$WIoU$ is defined as:

$$WIoU=\frac{\sum_{i=1}^{n} w_i IoU(b_i,g_i)}{\sum_{i=1}^{n} w_i} \quad (1)$$

where:

n denotes the number of ground-truth boxes, b_i is the coordinates of the i-th ground-truth box, and g_i is the coordinates of the ground-truth annotation box of the i-th object.

Combining the above three parts, the structure of the improved YOLOv8n is presented in Figure 3.

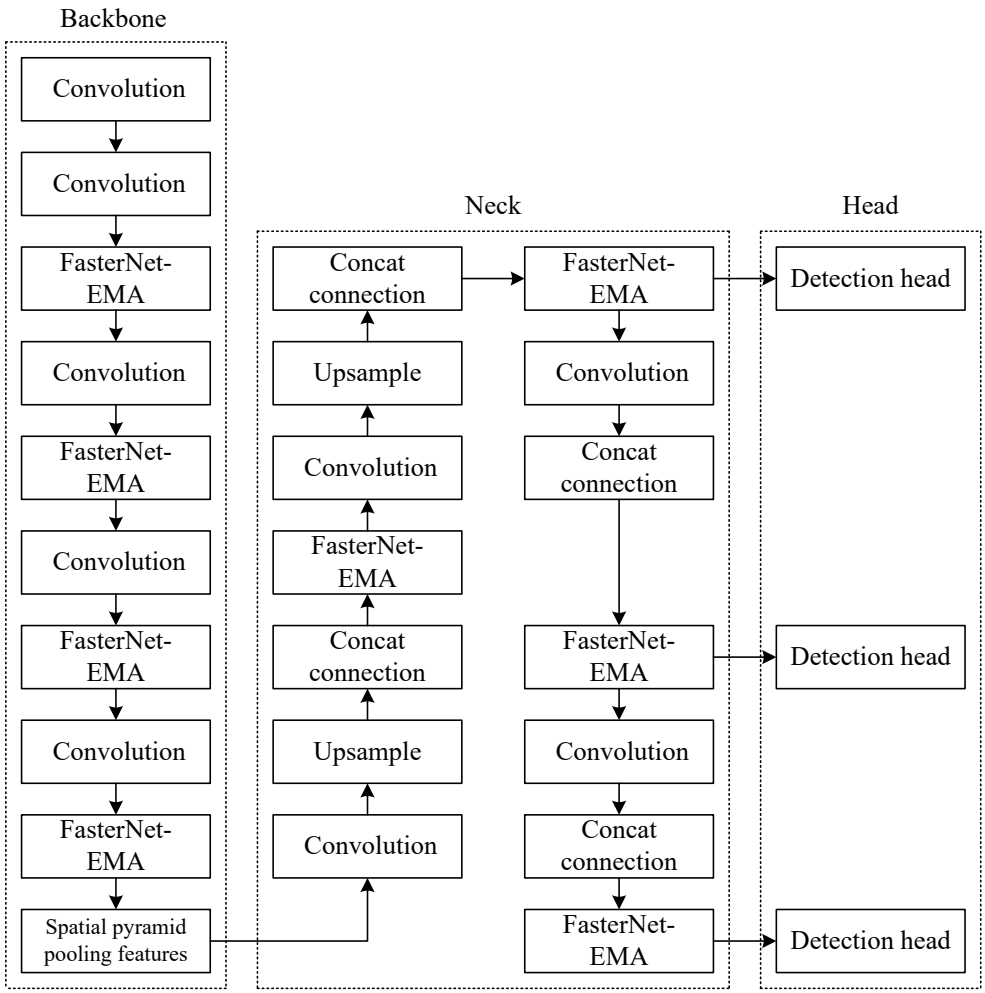


Fig. 3 - The structure of the improved YOLOv8n

Citrus positioning model

During the visual positioning process of the picking robot, a series of coordinate transformations are required to achieve three-dimensional positioning of the recognized fruit. The improved YOLOv8n outputs the rectangular detection box of a citrus target, extracts the pixel coordinates (u, v) of the center point of the box, and then obtains the relationship between the world coordinate system and the pixel coordinate system through coordinate transformation.

First, it is the conversion from the world coordinate system (X_W, Y_W, Z_W) to the camera coordinate system (X_C, Y_C, Z_C):

$$\begin{bmatrix} X_C \\ Y_C \\ Z_C \\ 1 \end{bmatrix} = \begin{bmatrix} R_{3\times3} & t_{3\times1} \\ 0 & 1 \end{bmatrix} \begin{bmatrix} X_W \\ Y_W \\ Z_W \\ 1 \end{bmatrix} \tag{2}$$

where R refers to a rotation matrix and t is a translation vector.

Then, (X_C, Y_C, Z_C) is converted to the image coordinate system (x, y):

$$\begin{cases} x = \frac{f}{Z_C} x_c \\ y = \frac{f}{Z_C} y_c \end{cases} \tag{3}$$

Ignoring image distortion, point P in the pixel coordinate system is (u, v), and the correspondence with (x, y) is:

$$\begin{cases} u = \frac{x}{dx} + u_0 \\ v = \frac{y}{dy} + v_0 \end{cases} \tag{4}$$

where (u_0, v_0) is the projection coordinate of the optical center in the image coordinate system, dx and dy are scaling factors.

When shooting, this article used the Astra Pro depth camera with parameters shown in Table 1.

Table 1

1Astra Pro depth camera parameters

	Parameter
Depth range	0.6-8 m
Relative accuracy	1 m ± 3 mm
Resolution	19,220 × 1,080
Frame rate	30 frames per second
Support operating system	Android/Windows/Linux

For the calibration method, the currently widely used Zhang Dingyou calibration method (*Zhang, 2000*) was used, and Table 2 presents the results of camera calibration.

Table 2

Results of camera calibration

	Calibration result
Internal parameter matrix	$\begin{bmatrix} 784.1254 & 0 & 0 \\ -0.1524 & 784.5524 & 0 \\ 947.5268 & 486.2145 & 1 \end{bmatrix}$
Radial distortion matrix	$[0.1325 \quad 0.4425 \quad -1.0547]$
Tangential distortion matrix	$[0.0063 \quad -0.0026]$

Laboratory experiment

In a laboratory environment, the measurement accuracy of the localization method proposed in this paper for citrus fruits was verified. A depth camera was fixed on the camera support, and a simulated citrus tree model was used to mimic the canopy structure of a real citrus tree. Several citrus fruits were randomly placed on the tree to simulate the picking scenario in an orchard. The laboratory lighting was kept stable to avoid the interference of external light changes. An aurora rangefinder was employed to detect the actual depth values of the fruits, and a spirit level was used to measure the actual coordinates of the fruits. Figure 4 shows the experimental setup.



Fig. 4 - Localization experiment

RESULTS

Dataset establishment

A dataset of citrus fruits was collected in an actual orchard environment to simulate the harvesting scenario of a picking robot. Images were taken in scenarios such as overlapping, dense, and occluded under different environments like front light, backlight, sunny days, and cloudy days. The distance between the camera and the outer edge of the canopy layer was 0.5-1.5 m, depending on the size of the fruit tree, and ultimately 1,186 images were taken. The dataset was divided into training, validation, and testing subsets (80%, 10%, and 10%).

The collected citrus fruit images were labeled using GitHub open-source labeling tool LabelImg (*Du et al., 2024*) to obtain xml format files, and Mosaic data augmentation technique was employed to expand the dataset, yielding a training set of 2,846 images, a validation set of 356 images, and a test set of 356 images.

Experimental setup

The experimental environment and software configurations are presented in Table 3.

Table 3

Experimental environment and software configurations

	Version
Central processing unit	Intel (R) Core i5-13500HX@4.70GHz
Graphics processing unit	RTX4060
Deep learning framework	PyTorch 1.8.1
Python	Python 3.10
Compute Unified Device Architecture (CUDA)	CUDA 11.3

During training, the stochastic gradient descent (SGD) optimizer was used, the epoch was set to 300, the initial learning rate was set to 0.01, the number of weight decay times was 0.005, and the batch size was 32.

Analysis of citrus recognition results

In the improved YOLOv8n model, FasterNet replaced the original backbone network. The recognition results of FastNet and several other models after replacing the YOLOv8n backbone network were compared (Table 4).

Table 4

Comparison of various backbone networks

	Accuracy	Recall	mAP@0.5-0.95
Original bottleneck	0.863	0.847	0.872
efficientViT *(Mu et al., 2025)*	0.871	0.853	0.875
MobileNetV4 *(Qin et al., 2017)*	0.868	0.836	0.874
HGNetV2 *(Deng et al., 2025)*	0.864	0.851	0.876
FasterNet	0.874	0.857	0.884

According to Table 4, when using FasterNet, the accuracy was 0.874, showing an increase of 1.27% compared to the original bottleneck, the recall rate was 0.857, showing an increase of 1.18%, and the mAP was 0.884, showing an increase of 1.37%. Among the comparisons with other models, FasterNet still performed the best. The results suggest that FasterNet's improvements to YOLOv8n is effective.

The recognition effects of various attention mechanisms were compared.

Table 5

Comparison of various attention mechanisms

	Accuracy	Recall	mAP@0.5-0.95
None	0.863	0.847	0.872
SENet (*Du et al., 2025*)	0.874	0.843	0.874
Convolutional Block Attention Module (CBAM)	0.872	0.845	0.875
EMA	0.876	0.855	0.881

According to Table 5, the performance of the model was enhanced to varying degrees after introducing the attention mechanism to YOLOv8n. Specifically, it was found that compared with SENet and CBAM, EMA was the best choice. Compared with the original YOLOv8n, accuracy was enhanced by 1.51%, recall rate by 0.94%, and mAP by 1.03%. The simultaneous improvement in accuracy and recall rate was achieved, suggesting the best performance in citrus recognition. The finding demonstrates the reliability of combining EMA with YOLOv8n.

The recognition outcomes of various loss functions were compared.

Table 6

Comparison of various loss functions

	Accuracy	Recall	mAP@0.5-0.95
CIoU	0.863	0.847	0.872
Distance Intersection over Union (DIoU) (*Huo et al., 2023*)	0.867	0.851	0.875
Efficient Intersection over Union (EIoU) (*Kumar & Dhanalakshmi, 2024*)	0.862	0.845	0.873
WIoU	0.871	0.849	0.882

According to Table 6, the recognition effect of the CIoU used in the original YOLOv8n was relatively poor. WIoU achieved a 0.93% enhancement in accuracy, a 0.24% enhancement in recall rate, and a 1.15% enhancement in mAP compared to CIoU, indicating that using WIoU as the loss function in YOLOv8n can achieve better citrus recognition results.

Finally, the improved YOLOv8n model was compared with some of the current popular deep learning-based detection methods.

Table 7

Comparison of various detection methods

	Accuracy	Recall	mAP@0.5-0.95
Faster R-CNN	0.836	0.826	0.846
YOLOv5n	0.851	0.843	0.867
YOLOv8n	0.863	0.847	0.872
Improved YOLOv8n	0.893	0.894	0.895

According to Table 7, Faster R-CNN performed poorly in citrus recognition, with a mAP as low as 0.846, indicating poor usability of the method in citrus recognition. The comparison between YOLOv5n and YOLOv8n showed that the recognition effect of YOLOv8n was better, demonstrating the reliability of the improvement to YOLOv8n. Finally, the improved YOLOv8n model achieved a mAP of 0.895 for citrus recognition, which can satisfy the recognition needs of the robot.

Analysis of citrus localization results

A total of ten sets of coordinate samples were counted, and the actual coordinates and positioning coordinates of citrus fruits were compared.

According to Table 8, the average errors in the X, Y, and Z directions for citrus positioning were 3.56 mm, 3.54 mm, and 4.74 mm respectively, indicating a relatively small overall positioning error. These errors may come from camera calibration errors and system hardware errors. But overall, the average error of the positioning results was within 5 mm, which can satisfy the positioning needs of robots in the actual citrus orchard environment.

Table 8

Analysis of citrus location results

	Actual coordinates/mm	Positioning coordinates/mm	Error value/mm
1	(352.18, 214.37, 1526.42)	(348.57, 217.94, 1522.11)	(3.61, 3.57, 4.31)
2	(487.62, 189.25, 1468.37)	(491.18, 185.73, 1463.89)	(3.56, 3.52, 4.48)
3	(296.73, 256.48, 1583.65)	(300.24, 252.95, 1578.84)	(3.51, 3.53, 4.81)
4	(415.89, 172.64, 1427.83)	(412.37, 176.28, 1423.26)	(3.52, 3.64, 4.57)
5	(371.52, 238.76, 1542.19)	(367.98, 242.33, 1537.92)	(3.54, 3.57, 4.27)
6	(523.47, 165.38, 1396.24)	(519.89, 168.92, 1391.73)	(3.58, 3.54, 4.51)
7	(284.35, 269.52, 1624.78)	(287.93, 265.96, 1620.07)	(3.58, 3.56, 4.71)
8	(438.71, 157.93, 1375.46)	(442.32, 154.46, 1371.18)	(3.61, 3.47, 4.28)
9	(309.64, 247.25, 1563.82)	(306.07, 250.78, 1559.33)	(3.57, 3.53, 4.49)
10	(466.28, 181.37, 1448.59)	(469.83, 177.86, 1444.28)	(3.55, 3.51, 4.31)

2

CONCLUSIONS

In this study, an optimized YOLOv8n model was developed for the recognition and localization of citrus fruits by citrus-picking robots. Through the analysis of a series of performance indicators, it was found that after replacing YOLOv8n backbone network with FasterNet, the recognition accuracy and FPS were improved. This indicates that the design of partial convolutions effectively reduces the memory access cost while maintaining the feature expression ability. In the comparison of attention mechanisms, EMA did not adopt the dimensionality reduction operation, which avoided the loss caused by channel information compression. Meanwhile, its parallel multi-scale structure fully utilized the parallel computing power of the GPU, hardly increasing parameter quantity and the computational burden. The comparison of loss functions demonstrated that WIoU exhibited good accuracy and mAP. This may be because WIoU assigns dynamic weights to samples of different qualities, forcing the model to focus more on the boundary regression of low-quality samples, such as those with severe occlusion and overlap, during training. According to the outcomes of the indoor positioning experiment, the positioning error of the proposed method for citrus fruits was within 5 mm.

Although the research has achieved certain results, there are two limitations.

(1) Dataset scale: The collected data is limited to a single orchard. The generalization ability of the model in more extensive scenarios (different production areas, fruit maturity levels, and tree shapes) needs to be verified.

(2) Lack of actual picking experiments: The positioning experiments were performed in a simulated laboratory environment, using model trees and artificially arranged citrus fruits. The picking situation in a real orchard environment was not involved.

Based on the limitations, future research will expand the dataset by collecting image data of different varieties, at different maturity stages, and under different weather conditions in multiple citrus-producing areas to construct a larger-scale and more representative citrus fruit dataset, build a complete prototype system of citrus picking robots to conduct end-to-end picking experiments in actual orchards, and study the task allocation and path planning methods for multiple picking robots in large-scale citrus orchards to achieve intelligent and clustered harvesting management of orchards.

In summary, the citrus recognition and localization method based on the improved YOLOv8n performs excellently in terms of recognition accuracy, inference speed, and positioning error, providing effective technical support for citrus picking robots. Although there are certain limitations in aspects such as the dataset scale, this study verifies the basic feasibility and advantages of the method.

ACKNOWLEDGEMENT

This work was supported by the Scientific Research Project of Hunan Provincial Department of Education, China (Grant No. 23B0761).

REFERENCES

[1] Chen, H., Zhang, Z., Luo, Q., Chen, R., & Zhao, Y. (2025). A Target Image Recognition Method of Agricultural Harvesting Robot using Template Matching in Low Light Environment. *Pakistan Journal of Agricultural Sciences*, *62*(1), 79-90. https://doi.org/10.21162/PAKJAS/25.66

[2] Deng, L., Miao, Z., Zhao, X., Yang, S., Gao, Y., Zhai, C., & Zhao, C. (2025). HAD-YOLO: An Accurate and Effective Weed Detection Model Based on Improved YOLOV5 Network. *Agronomy*, *15*(1), 57. https://doi.org/10.3390/agronomy15010057

[3] Du, Q., Tang, L., & Li, Y. (2024). SCB-YOLOv5: a lightweight intelligent detection model for athletes' normative movements. *Scientific Reports*, *14*(1), 1-11. https://doi.org/10.1038/s41598-024-59218-w

[4] Du, W., Yu, X., Guo, Z., Wang, H., Pu, Z., & Li, C. (2025). Squeeze-and-excitation attention residual learning of propulsion fault features for diagnosing autonomous underwater vehicles. *Journal of Field Robotics*, 42(1), 169-179. https://doi.org/10.1002/rob.22405

[5] Hou, C., Xu, J., & Fang, M. (2024). Detection and localization of citrus picking points based on binocular vision. *Precision Agriculture*, *25*(5), 2321-2355. https://doi.org/10.1007/s11119-024-10169-2

[6] Huo, C., Ma, J., & Tong, Z. (2023). Research on Pedestrian Crossing Intention Prediction Based on Deep Learning. *Proceedings of the 2023 7th International Conference on Electronic Information Technology and Computer Engineering*, 282-287. https://doi.org/10.1145/3650400.3650446

[7] Jraba, S., Elleuch, M., Ltifi, H., & Kherallah, M. (2025). Enhanced YOLOv8 Framework for Early Detection of Alzheimer's Disease Using MRI Scans. *Proceedings of the 17th International Conference on Agents and Artificial Intelligence*, 1229-1237. https://doi.org/10.5220/0013315300003890

[8] Kumar, A., & Dhanalakshmi, R. (2024). EYE-YOLO: a multi-spatial pyramid pooling and Focal-EIOU loss inspired tiny YOLOv7 for fundus eye disease detection. *International Journal of Intelligent Computing and Cybernetics*, *2024*(3), 503-522. https://doi.org/10.1108/ijicc-02-2024-0077

[9] Lin, G., Tang, Y., Zou, X., Li, J., & Xiong, J. (2019). In-field citrus detection and localisation based on RGB-D image analysis. *Biosystems Engineering*, 186:34-44. https://doi.org/10.1016/j.biosystemseng.2019.06.019

[10] Matache, M.G., Marin, F.B., Persu, C.I., Cristea, R.D., Nenciu, F., & Atanasov, A.Z. (2026). Autonomous Tomato Harvesting System Integrating AI-Controlled Robotics in Greenhouses. *Agriculture*, *16*(8), 1-28. https://doi.org/10.3390/agriculture16080847

[11] Mu, G., Zhang, H., Fei, Z., Gao, G., & Zhang, H. (2025). Defect detection method of Chinese mitten crab based on improved EfficientVit. *International Journal of Simulation and Process Modelling*, *22*(1-2), 47-59. https://doi.org/10.1504/IJSPM.2025.148289

[12] Qin, D., Leichner, C., Delakis, M., Fornoni, M., Luo, S., Yang, F., Wang, W., Banbury, C., Ye, C., Akin, B., Aggarwal, V., Zhu, T., Moro, D., & Howard, A. (2017). MobileNetV4: Universal Models for the Mobile Ecosystem. *18th European Conference*, 78-96. https://doi.org/10.1007/978-3-031-73661-2_5

[13] Rong, J., Hu, L., Zhou, H., Dai, G., Yuan, T., & Wang, P. (2024). A selective harvesting robot for cherry tomatoes: Design, development, field evaluation analysis. *Journal of Field Robotics*, *41*(8), 2564-2582. https://doi.org/10.1002/rob.22377

[14] Shao, G., Sun, Q., Gao, Y., Zhu, Q., Gao, F., & Zhang, J. (2023). Sub-Pixel Convolutional Neural Network for Image Super-Resolution Reconstruction. Electronics, 12(17), 3572. https://doi.org/10.3390/electronics12173572

[15] Wang, L. C., Chu, Y. C., Huang, Y., & Lian, F. L. (2024). Enhancement on Target-Gripper Alignment: A Tomato Harvesting Robot with Dual-Camera Image-Based Visual Servoing. 2024 IEEE International Conference on Robotics and Automation (ICRA), 13611-13617. https://doi.org/10.1109/icra57147.2024.10610772

[16] Yin, H., Sun, Q., Ren, X., Guo, J., Yang, Y., Wei, Y., Huang, B., Chai, X., & Zhong, M. (2023). Development, integration, and field evaluation of an autonomous citrus-harvesting robot. *Journal of Field Robotics*, *40*(6), 1363-1387. https://doi.org/10.1002/rob.22178

[17] Zhang, G, Li, L., Zhang, Y., Liang, J, & Chun, C. (2025). Citrus pose estimation under complex orchard environment for robotic harvesting. *European Journal of Agronomy*, *162*, 1-11. https://doi.org/10.1016/j.eja.2024.127418

[18] Zhang, Z. (2000). A Flexible New Technique for Camera Calibration. IEEE Transactions on Pattern Analysis and Machine Intelligence, 22(11), 1330-1334. https://doi.org/10.1109/34.888718

[19] Zhu, F., Zhang, W., Li, Z., Gao, T., & Zhao, Q. (2025). A YOLOv7-based robotic harvesting system for Agaricus bisporus using a depth camera. *Turkish Journal of Agriculture & Forestry*, *49*(2), 380-396. https://doi.org/10.55730/1300-011X.3272

[20] Zhu, F., Zhang, W., Wang, S., Jiang, B., Feng, X., & Zhao, Q. (2024). Apple-Harvesting Robot Based on the YOLOv5-RACF Model. *Biomimetics*, *9*(8), 1-24. https://doi.org/10.3390/biomimetics9080495

A COUPLED CFD–DEM NUMERICAL STUDY OF THE AERODYNAMIC SORTING OF *ZANTHOXYLUM BUNGEANUM* SHELLS AND SEED-BEARING PARTICLES
/
基于 CFD-DEM 耦合的红花椒果壳与带籽椒粒气动分选数值模拟研究

Ruiqiang XU [1], Zhongbin LIU *[1], Hongwei XIAO [2], Chunglim LAW [3], Fengkui XIONG *[1, 2]
[1] College of Mechanical Engineering, Sichuan University of Science and Engineering, Yibin, Sichuan 644000, P. R China;
[2] College of Engineering, China Agricultural University, Beijing 100080, P. R. China;
[3] Taylor's University, Subang Jaya, 47500, Malaysia.
Corresponding author: Zhongbin Liu; E-mail: liuzb@suse.edu.cn; Fengkui Xiong; E-mail: xfk763101899@126.com
DOI: https://doi.org/10.35633/inmateh-79-45

Keywords: *Zanthoxylum bungeanum, aerodynamic sorting, computational fluid dynamics, discrete element method*

ABSTRACT
This study presents a particle-scale coupled CFD–DEM numerical approach for elucidating aerodynamic sorting mechanisms and optimizing process parameters. Non-spherical particle models were developed to represent the geometric and physical differences between shells and seed-bearing particles. The Stokes number, which characterizes the balance between aerodynamic drag and particle inertia, was identified as the primary determinant of sorting performance. Under the optimized conditions, a primary airflow velocity of 8.4 m/s, a secondary airflow velocity of 7.85 m/s, and a feed mass flow rate of 80 g/s, the system achieved a shell purity of 95.3% and a recovery rate of 58.2% when processing feedstock with an initial shell content of 5%. The results further revealed an inherent trade-off between purity and recovery. These findings provide a theoretical and numerical basis for the design and optimization of aerodynamic sorting equipment.

摘要
本研究提出了一种基于颗粒尺度的 CFD-DEM 耦合数值模拟方法，旨在阐明气动分选机制并优化工艺参数。建立了非球体模型，以表征果壳与种子团聚体之间的几何和物理差异。研究发现，表征气动阻力与惯性平衡的斯托克斯数是分选性能的核心决定因素。在最优条件下（主气流速度 8.4 m/s，副气流速度 7.85 m/s，进料速率 80 g/s），以初始纯度为 5%的原料为进料，可获得 95.3%的壳体纯度和 58.2%的回收率。研究揭示了纯度与回收率之间固有的权衡关系，为分选设备的设计与优化提供了理论和数据支持。

INTRODUCTION
Zanthoxylum bungeanum serves as a vital spice and economic crop in China, celebrated for its unique pungent and numbing flavor, which primarily derives from the volatile oils and alkyl amides found in its pericarp *(Shi et al., 2025)*. Post-harvest processing typically results in a mixture of hollow shells and seed-bearing particles after threshing. Given the significant differences in flavor profiles, economic value, and suitability for downstream processing between the shells and seed-bearing particles, efficient separation is essential for improving product purity and market value *(Mutinda et al., 2023)*. Conventional sieving methods are ineffective due to the overlapping size and density ranges of these components. However, the distinct shapes and aerodynamic properties of the shells and seed-bearing particles offer a promising opportunity for separation through airflow classification, a precise sorting technique well-suited for this fine separation task *(Stepanenko et al., 2022).*

Aerodynamic sorting is a clean, efficient technology widely used for cleaning and grading agricultural materials. Its effectiveness depends on the interaction between material properties (size, shape, density, terminal velocity) and airflow parameters *(Zhu et al., 2021).* Particle shape significantly influences aerodynamic behavior; non-spherical particles behave differently from spherical ones *(Ulusoy et al., 2023). Zanthoxylum bungeanum* shells and seed-bearing particles are typical non-spherical granules. Their separation involves complex gas-solid interactions that traditional empirical design methods fail to adequately explain at the particle scale. In recent years, coupled CFD–DEM has become a robust tool for investigating complex multiphase flows. DEM effectively captures the geometry, contact mechanics, and motion of non-spherical particles *(Ma et al., 2022).*

Representative applications include: safflower petal cleaning, where high-fidelity shape models visualized trajectory separation driven by mass and aerodynamic differences *(Hu et al., 2021)*; sunflower seed shell-kernel separation, optimizing air channel parameters *(Guan et al., 2025);* rice cleaning, using multi-sphere models to study airflow velocity and inclination angle effects on impurity and loss rates *(Ma et al., 2020)*.

Accurate CFD–DEM simulations rely on precise particle models and contact parameters. Foundational studies have established the fundamental physical properties of *Zanthoxylum bungeanum* particles and their contact parameters with common engineering materials via experiments and calibration *(Wang et al., 2023; Zhang et al., 2022)*, providing a reliable particle-scale mechanical basis. For non-spherical particles, the parametric function method offers a flexible, efficient approach to construct complex non-convex geometries, especially suitable for biological particles with concave features *(Zhao et al., 2021)*. Despite advancements, systematic CFD–DEM studies on the motion, separation dynamics, and mechanisms of *Zanthoxylum bungeanum* shell-seed mixtures in tailored airflow fields remain lacking. To address this gap, the present study employs parametric proxy models based on superquadric surfaces *(Xu et al., 2025)* to capture critical geometric differences between shells and seed-bearing particles. High-fidelity discrete–element simulations are achieved by three-dimensional modeling in SolidWorks and subsequently importing them into rocky DEM software.

MATERIAL AND METHODS

GOVERNING EQUATIONS AND NUMERICAL METHODOLOGY

In the simulation herein, air was simply modelled as an incompressible ideal gas *(Xiao et al., 2022)*. The overall initial conditions of the system assumed homogeneous air distribution, neglecting other secondary factors such as dust generation, particle shrinkage, and chemical reactions. The gas phase was treated as a single continuous medium, with its flow governed by the continuity and momentum equations solved within a standard Eulerian framework. Momentum exchange between the gas and solid phases was incorporated through appropriate interphase momentum exchange terms *(Wu et al., 2025)*. Utilizing the widely adopted fluent-rocky coupled strategy, this model employed the Eulerian multiphase model in commercial fluent to resolve gas flow, while simultaneously the Discrete Element Method (DEM) in rocky was used to track the motion of individual particles. This robust integrated approach facilitated a high-fidelity coupled simulation of the gas-solid two-phase system.

The mass conservation equation is expressed as:

$$\frac{\partial}{\partial t}\left(\rho_g \theta_g\right) + \nabla \cdot \left(\rho_g \theta_g u_g\right) = 0 \tag{1}$$

where: u_g is the fluid velocity vector, m/s; ρ_g is the gas-phase density, kg/m^3; θ_g is the gas phase volume fraction, %.

The momentum conservation equation is:

$$\frac{\partial}{\partial t}\left(\rho_g \theta_g u_g\right) + \nabla \cdot \left(\rho_g \theta_g u_g u_g\right) = -\nabla P + \nabla \cdot \left(\theta_g \tau_g\right) + \rho_g \theta_g g + M \tag{2}$$

where: P is the static pressure, Pa; τ_g is the gas-phase viscous stress tensor, Pa; g is the gravitational acceleration vector, m/s²; M is the gas-solid interphase momentum exchange rate per unit volume, N/m³.

For a Newtonian fluid, the viscous stress tensor can be expressed as:

$$\tau_g = \mu_g \left[\nabla u_g + \left(\nabla u_g\right)^T\right] - \frac{2}{3}\mu_g \left(\nabla \cdot u_g\right) I \tag{3}$$

where: u_g is the gas dynamic viscosity.

The interphase momentum exchange rate is given by the following equation:

$$M = -\frac{1}{V_{cell}} \sum_{l=1}^{n} F_{d,l} \tag{4}$$

where: $F_{d,l}$ is the drag force acting on particle i, N; V_{cell} is the computational cell volume, m^3.

In multiphase flow systems, the motion of the particulate phase can be described using a probability distribution function in conjunction with the Liouville equation *(Domínguez-Vázquez et al., 2024)*. For the particulate phase of *Zanthoxylum bungeanum*, a distribution function $f\left(x, u_p, p_p, V_p, t\right)$ is defined, where x, u_p, p_p, V_p and t represent the particle's spatial position, velocity vector, density, volume, and time. This function fully defines the probabilistic distribution state of the particles in phase space, and the system is closed by solving the following Liouville equation:

$$\frac{\partial f}{\partial t} + \nabla_x \cdot (f u_p) + \nabla_{u_p} \cdot (f a_p) = 0 \quad (5)$$

where: a_p is the particle acceleration, m/s², determined by the net force acting on the particle according to Newton's second law.

In the simulation, air enters the chamber and penetrates the porous particle layer. Confined by walls and outlet geometry, fully developed turbulence forms. Due to short inlet–outlet distance and narrow flow gaps, a complex flow structure with recirculation and vortices emerges *(Echendu et al., 2011)*. To simulate this turbulence, the Realizable k-ε model *(Gong et al., 2025)* is used to close the Reynolds-averaged Navier-Stokes equations. This model computes turbulent viscosity by solving transport equations for turbulent kinetic energy (k) and dissipation rate (ε).

$$\mu_t = \rho_g C_\mu \frac{\kappa^2}{\epsilon} \quad (6)$$

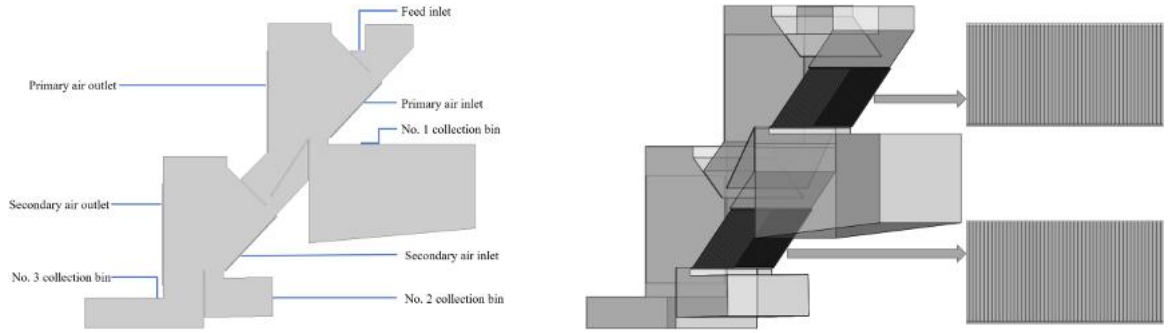
where: C_μ is no longer a constant. The empirical constants in the model take the following standard values: $C_{1\epsilon}$=1.44, C_2=1.9, σ_k=1.0, σ_ϵ=1.2.

SIMULATION SETUP

Computational Model and Parameter Specification

To investigate the motion patterns of particles during air-classification, a model of the classification apparatus measuring 397 mm in length, 110 mm in width and 309 mm in height was constructed; the apparatus is equipped with one feed inlet, two air inlets, two air outlets, three collection chambers and two classification stages (Fig. 1a). The two air inlets, with a combined length of 110 mm and a width of 76 mm, are inclined at an angle of 46.7° relative to the horizontal plane. They consist of a series of slotted inlets, each 2 mm wide and spaced 0.1 mm apart (Fig. 1b). They are made of the same material as the apparatus casing, and the width of the inlets is smaller than that of the *Zanthoxylum bungeanum* grains.

During the sorting process, the particles fall under the influence of gravity along a deflector plate inclined at an angle of 45° to the horizontal. The first stage performs preliminary separation, increasing the shell proportion entering the second stage. After first-stage separation, most seed-bearing particles and a few shells enter Collection Bin 1. The remaining mixture proceeds to the second stage for fine sorting. Ultimately, Collection Bin 3 yields predominantly shells, while Bin 2 contains a mixture.



(a) general schematic diagram *(b) close-up*

Fig. 1 - Schematic of the sorting device model

ANSYS Fluent was used to establish a continuous-phase flow field; *Zanthoxylum bungeanum* particles were generated using the 3D modelling software SolidWorks and imported into Rocky for DEM simulation. In the numerical simulation, the continuous-phase CFD calculations were performed on a 12th-generation Intel® Core™ i5-12490F processor with 16 GB of system memory. The discrete-phase DEM calculations were performed on an NVIDIA GeForce RTX 4060 graphics card with 8 GB of dedicated GDDR6 video memory. The CFD simulation for the gas phase took approximately 10 minutes, using the 'Automatic' time-step method, a time scaling factor of 0.1, and 200 iterations; the DEM simulation for the solid phase took approximately 74 hours, with a simulation duration of 4 s, with a time interval of 0.01 s. Since the volume fraction of the particulate phase is 0.068%, constituting a dilute gas-solid two-phase flow, and given the simulation time constraints, the gas-phase separation process was simulated using the Fluent-Rocky unidirectional coupling method *(Guan et al., 2025; Luo et al., 2020)*. The gas-phase governing equations are discretized by the finite volume method with the SIMPLE algorithm and second-order upwind scheme, and the realizable k-ε model is used for turbulence closure. For the discrete particle phase, the soft-sphere contact model is applied to calculate inter-particle and particle-wall contact forces, and particle kinematics are updated by an explicit time integration scheme in the Lagrangian framework.

The coefficient of restitution, coefficient of static friction and coefficient of rolling friction between *Zanthoxylum bungeanum* particles are 0.378, 0.56 and 0.0143, respectively. As the rolling coefficient of friction between *Zanthoxylum bungeanum* particles and galvanized steel sheet is relatively low (0.168) *(Zhang et al., 2022)*, this material was selected for the device walls. In this simulation, the density of the *Zanthoxylum bungeanum* was set at 997 kg/m³, with a Poisson's coefficient of 0.168 and a Young's modulus of 1.568×10^7 Pa *(Wang et al., 2023)*. The density of galvanized steel was 7,850 kg/m³, with a Poisson's coefficient of 0.3 and a Young's modulus of 206 GPa *(Gu et al., 2024)*.

Rationale and Parameterization of Particle Geometry Simplification

This study investigates the sorting process of *Zanthoxylum bungeanum* shells and seed-bearing particles. The total feed mass is 50 g, and the initial shell mass fraction is 5%. The material enters via the feed inlet at the top of the apparatus, with a total mass flow rate of 50 g/s to 120 g/s; the feed falls freely without any initial velocity. Air enters through two air inlets at a velocity of 6.85 m/s to 8.85 m/s, which corresponds to a volumetric flow rate of 206.16 m³/h to 266.35 m³/h. In the coupled CFD–DEM simulations, physics-oriented proxy models are used to balance computational efficiency and fidelity *(Ma et al., 2022)*.

Geometry is simplified based on dominant aerodynamic sorting mechanisms to capture the separation of shells from seed-bearing particles. Despite similar density, shells and seed-bearing particles behave differently due to geometry-induced forces. In transverse flow, trajectory reflects the Stokes number (drag vs. inertia), set by the volume-to-mass ratio linking geometry to dynamics *(Zhao et al., 2024)*. Based on mechanistic analysis, the volume-to-mass ratio is identified as the dominant parameter controlling shell–seed separation. To capture this difference in the model, two critical geometric features are abstracted: (1) the hollow, thin-walled shell structure, which causes the mass difference; (2) the aperture size, which affects the maximum projected area and thus the drag coefficient. Guided by this analysis, parametric proxy models are established *(Michaelides et al., 2023)*: pepper shells are modeled as hollow, thin-walled structures with large apertures to achieve a high volume-to-mass ratio; seed-bearing particles are modeled as composite structures with small apertures and internal spherical seed fillings to obtain a low volume-to-mass ratio. Geometric parameters are determined via sensitivity analysis from a preliminary study to maximize the difference in dynamic behavior.

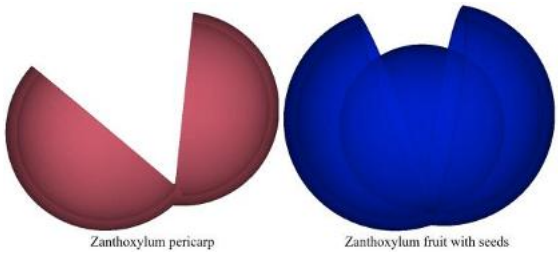


Fig. 2 - Geometric models of the particles

RESULTS AND DISCUSSION

Particle Distribution and Separation Mechanism

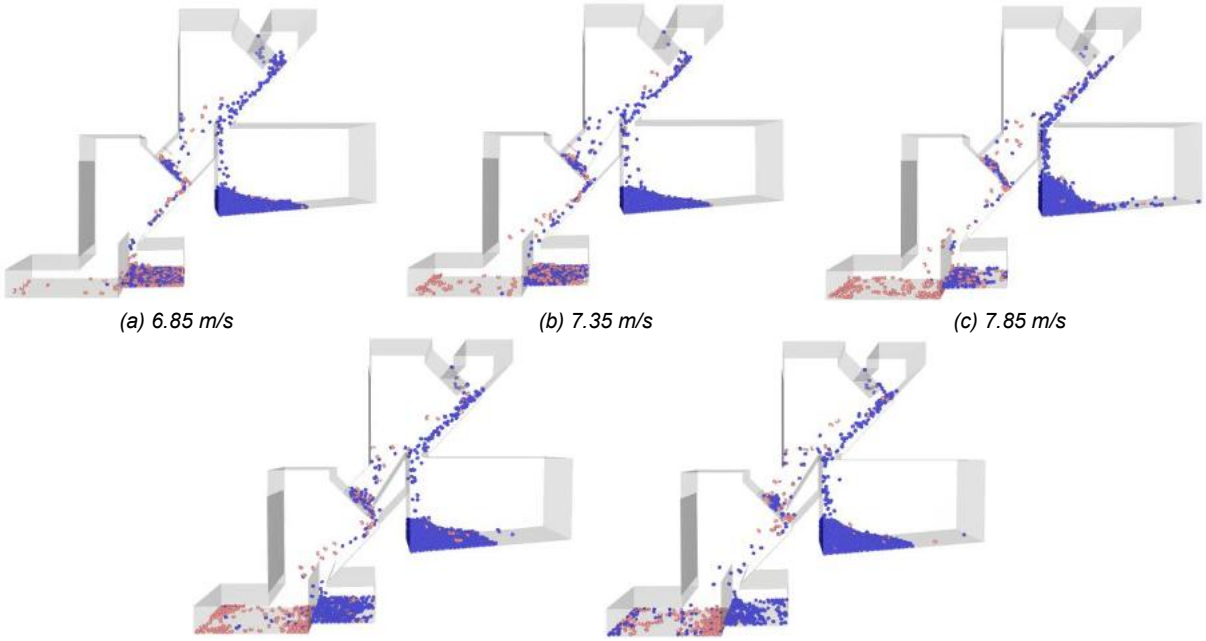
Recovery and purity are in conflict *(Lundin et al., 2024)*; for *Zanthoxylum bungeanum*, high purity is demanded. We thus maximize shell recovery in Bin 3 at >90% purity, acknowledging that relaxing purity boosts yield. To separate shells from seed-bearing particles, simulations employed distinct particle sizes/shapes *(Li et al., 2024)*. Despite similar density, volume/mass differences cause distinct free-fall behaviors. In airflow, particles experience gravity, drag, and inertia. Shells have a high volume-to-mass ratio and are easily entrained; seed-bearing particles have a low ratio, leading to stronger sedimentation and shorter migration *(Zhou et al., 2023)*. Adjusting airflow velocity amplifies this ratio's effect on trajectories, achieving separation. CFD–DEM validation clarifies sorting physics, enabling rational parameter selection over empirical optimization.

Effect of Secondary Airflow Velocity on Sorting Performance

Secondary airflow velocity was a key parameter governing both the flow-field characteristics and separation performance within the second-stage classification zone. By analyzing the flow-field contour maps (Fig. 4) and particle-distribution patterns (Fig. 3) at different airflow velocities, the underlying separation mechanism was clarified.

At low velocities (6.85–7.35 m/s), the low-velocity regions (cool colors) was uniform with a gentle gradient and lacks a high-speed core, indicating insufficient kinetic energy to penetrate the particle bed. At the optimal velocity (7.85 m/s), a stable, well-defined high-speed pathway formed without recirculation or vortices, concentrating flow energy along the separation path for highly selective sorting. At higher velocities (8.35–8.85 m/s), the flow became chaotic, with localized high-speed patches and recirculation vortices, where excess

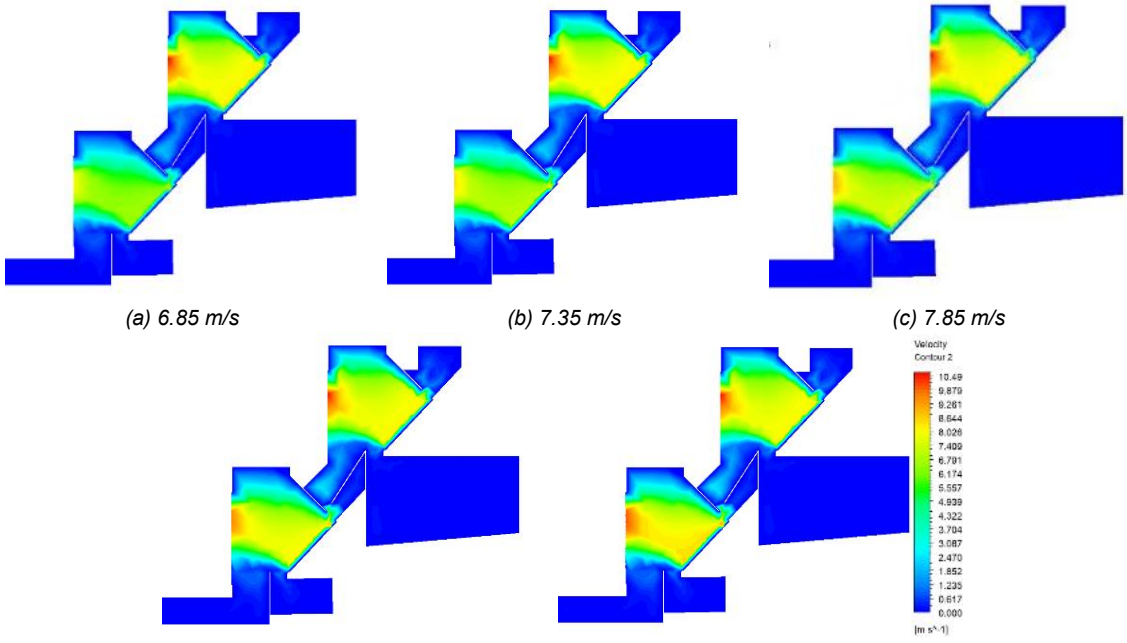
kinetic energy caused instability, dissipation, and flow separation. At low velocities, insufficient drag yielded high Stk; particle motion was inertia-dominated. Shells were not conveyed to Bin 3, causing low recovery; seed-bearing particles settled normally. Bin 3 purity remained acceptable, but the efficiency was poor. At the optimal velocity (7.85 m/s), drag and inertia were balanced: shells were carried into Bin 3, while seed-bearing particles settled into Bin 1, achieving separation. At high velocities, excessive drag caused an “over-bearing” effect, entraining seed-bearing particles into Bin 3 and reducing its purity to 52.5%. The Stokes number difference between the two particle types diminished; their dynamic responses converge, and separation selectivity was lost. Thus, secondary airflow velocity governed particle trajectories via the Stokes number by modulating flow-field structure and gas-solid momentum transfer.



(a) 6.85 m/s *(b) 7.35 m/s* *(c) 7.85 m/s*

(d) 8.35 m/s *(e) 8.85 m/s*

Fig. 3 - Distribution Patterns of Pepper Particles



(a) 6.85 m/s *(b) 7.35 m/s* *(c) 7.85 m/s*

(d) 8.35 m/s *(e) 8.85 m/s*

Fig. 4 - Contour of secondary airflow velocity

As shown in Fig. 5, with increasing secondary airflow velocity, shell purity in Bin 3 first rose then declined (with a sharper drop at high speeds), while purity in Bin 2 decreased continuously. Although excessively low airflow velocity helped prevent heavier seed-bearing particles from entering Bin 3, it also reduced the overall inflow of pepper shells, resulting in low shell purity in this bin.

Notably, seed-bearing particles had a larger mass and settling velocity, and even a small amount of their potential contamination could markedly reduce the purity of pepper shells. Notably, Bin 2 purity remained below 30%, whereas Bin 3 consistently exceeded 50%, confirming effective enrichment by the secondary airflow stream. At an airflow velocity of 7.35 m/s, the shell purity in Bin 3 reached a maximum of 96.6%, whereas the recovery rate was only 25.7% (Fig. 6). When the airflow velocity increased to 7.85 m/s, purity decreased slightly to 91.8%, while recovery increased substantially to 59.7%. These results clearly demonstrate the inherent trade-off between purity and recovery, indicating that system optimization must balance these competing objectives. The findings are consistent with the fundamental principles of aerodynamic classification and provide previously unavailable particle-scale mechanistic insights into the separation behavior of *Zanthoxylum bungeanum*. The validated CFD–DEM framework therefore offers a robust tool for the rational design and optimization of sorting equipment for similarly complex agricultural materials.

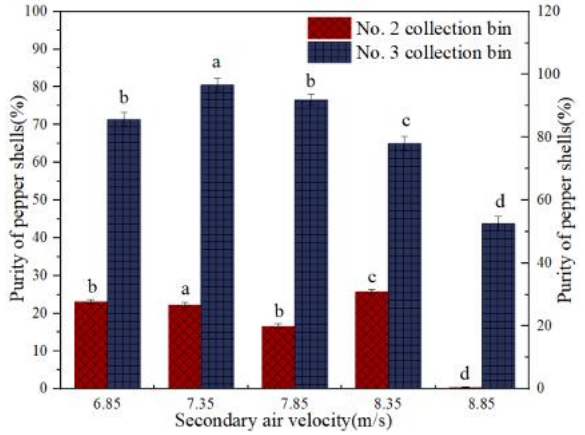


Fig. 5 - Purity of Pepper Shells in Different Collection Bins

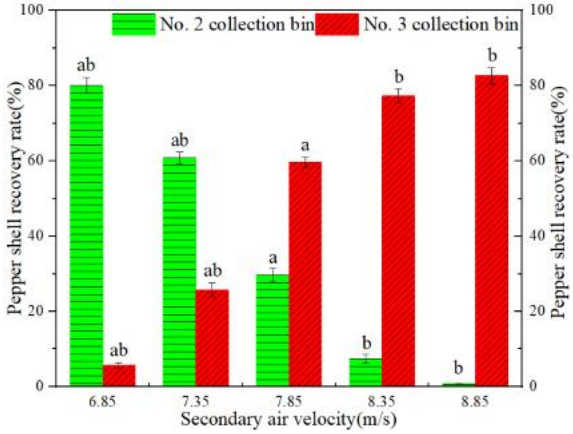


Fig. 6 - Recovery Rate of Pepper Shells in Different Collection Bins

As shown in Fig. 6, Bin 2 achieved the highest shell recovery at an airflow velocity of 6.85 m/s, reaching 80.1%, although shell purity remained below 25%. At 8.85 m/s, shell recovery in Bin 3 increased to 82.7%; however, the entrainment of seed-bearing particles reduced shell purity to a minimum of 52.5%. These results indicate that increasing airflow velocity enhances shell recovery but may simultaneously reduce product purity because of greater carryover of non-target particles. Figs. 5 and 6 further quantify the effect of secondary airflow velocity. Increasing the velocity from 7.35 to 7.85 m/s reduced shell purity in Bin 3 from 96.6% to 91.8%, while markedly increasing recovery from 25.7% to 59.7%, resulting in a more favorable overall separation performance at 7.85 m/s. This behavior can be interpreted in terms of Stokes number (Stk) optimization *(Farooq et al., 2023)*. At 7.85 m/s, Stk for the shells was much less than 1, indicating fluid-dominated motion, whereas Stk for the seed-bearing particles was close to or greater than 1, indicating inertia-dominated motion. Maximizing the difference in Stk between the two particle groups therefore promotes efficient aerodynamic separation.

At an airflow velocity of 8.85 m/s, shell recovery increased to 82.7%, whereas purity decreased sharply to 52.5%. This indicates that excessive airflow velocity reduces the difference in Stokes number between the two particle groups, thereby weakening separation selectivity. Accordingly, 7.85 m/s was identified as the optimal velocity for balancing recovery and purity. Under this condition, Bin 3 achieved a shell recovery of 59.7% and a purity of 91.8%. Aerodynamic drag enabled highly selective separation while minimizing the carryover of seed-bearing particles. The less-than-maximum recovery may be attributed to shells with aerodynamic characteristics close to the separation threshold, as well as particle losses caused by interparticle collisions and unfavorable initial positions. These limitations could be addressed in future studies through multistage cascade separation or improved flow-field uniformity.

By achieving a purity of 91.8% and a recovery of 59.7%, the separation of *Zanthoxylum bungeanum* shells from seed-bearing particles was successfully accomplished, despite their similar physical properties. This result outperforms traditional sieving processes (which are prone to blockages and are inefficient), demonstrating the feasibility and superiority of aerodynamic sorting in this application. The CFD–DEM framework elucidates the mechanisms at the particle scale and provides a predictive tool for optimizing the sorting of other complex agricultural products. A limitation of this study is its focus on single-stage optimization; future research could explore dynamic control or multi-stage integration to further enhance the upper limits of purity and recovery.

Effect of Primary Airflow Velocity on Sorting Performance

The primary airflow provides the initial momentum and performs pre-classification for the entire sorting process. With the secondary airflow velocity fixed at the optimal 7.85 m/s, the influence of the primary airflow velocity was systematically investigated. As shown in Fig. 7, increasing the primary airflow velocity led to a gradual decrease in the purity of pepper shells collected in Bin 3. The underlying cause of this trend can be attributed to a chain reaction in the dynamics: an excessively high primary velocity imparts substantial horizontal initial kinetic energy to the particles, reducing their effective residence time in the first-stage classification zone. The resulting high-energy, high-concentration particle stream then enters the stabilized flow field of the secondary classification zone, where it substantially increases the frequency of interparticle collisions. These interactions promote dynamic agglomeration and ultimately impair separation performance. Therefore, the objective of primary-airflow optimization is not to maximize preliminary separation, but rather to deliver a uniformly distributed feed with moderate kinetic energy to the secondary stage. This is an essential prerequisite for effective fine classification. Unlike studies that evaluate airflow parameters independently, the present analysis reveals the coupling between successive classification stages and highlights the importance of coordinated parameter optimization for overall system performance.

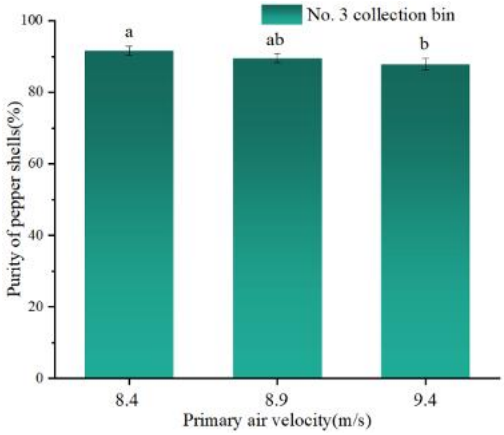


Fig. 7 - Purity of Pepper Shells in Collection Bin 3

Effect of Feed Mass Flow Rate on Sorting Efficiency

Under the optimal airflow conditions, the feed mass flow rate exhibited a trade-off between processing capacity and separation performance. As the feed mass flow rate increased from 64 to 80 g/s (Figs. 8 and 9), shell purity in Bin 3 increased from 91.8% to 95.3%, while recovery decreased slightly from 59.7% to 58.2%. This behavior may be attributed to the higher solid-to-gas ratio at the increased feed rate.

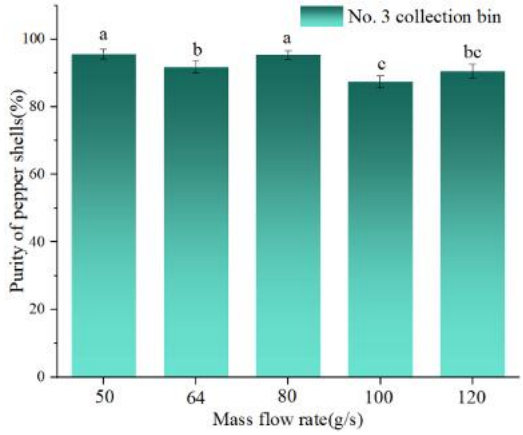


Fig. 8 - Purity of Pepper Shells in Collection Bin 3

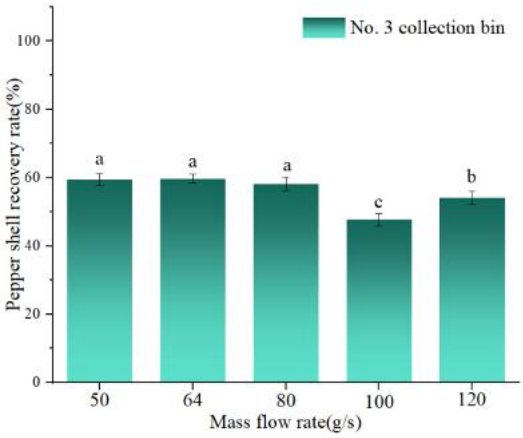


Fig. 9 - Recovery Rate of Pepper Shells in Collection Bin 3

The greater particle concentration intensified interparticle interactions and reduced the average aerodynamic drag acting on individual particles. The consistently high purity observed over the tested range indicates that the fundamental separation mechanism remained effective. Increasing the feed mass flow rate to 80 g/s produced a 25% increase in throughput with only a minor reduction in recovery, representing a

favorable engineering compromise. Considering purity, recovery, and processing capacity together, 80 g/s was identified as the optimal feed mass flow rate, yielding a shell purity of 95.3%, a recovery of 58.2%, and the highest throughput tested. In practical applications, overall system performance is more important than maximizing any single indicator. The recovery of 58.2%, achieved without compromising shell purity, represents a balanced and practically relevant operating condition for potential industrial scale-up. These findings demonstrate the value of multi-objective optimization over isolated parameter adjustment and provide a transferable approach for designing sorting systems for similarly complex agricultural materials.

Effect of Feedstock Shell Purity on Sorting Performance

Under the optimal operating conditions—a primary airflow velocity of 8.4 m/s, a secondary airflow velocity of 7.85 m/s, and a feed mass flow rate of 80 g/s—increasing the shell content of the feedstock from 5% to 80% progressively increased shell purity in Collection Bin 3 from 95.3% to 99.5% (Fig. 10). This strong positive relationship demonstrates the substantial influence of particle composition on separation selectivity.

The increase in Bin 3 purity may be explained by changes in the internal particle-flow structure. At a low feedstock shell content of 5%, the target shell fraction is dispersed within a dense background of seed-bearing particles. Although the aerodynamic drag acting on individual shells may be sufficient for separation, frequent collisions with the more abundant seed-bearing particles disturb shell trajectories, preventing some shells from reaching Bin 3 and limiting purity to 95.3%. At higher feedstock shell contents of 60–80%, the particle stream becomes shell-dominated. This collective flow structure may reduce random particle motion, strengthen momentum coupling among shells, and promote more coherent migration of the particle cloud toward Bin 3. Consequently, shell purity approaches 99.5%.

However, increasing the feedstock shell content from 5% to 80% reduced shell recovery in Bin 3 from 58.2% to 49.2% (Fig. 11), revealing an inherent trade-off between purity and recovery. For applications requiring extremely high product purity, a feedstock shell content of at least 60% may be selected, yielding up to 99.5% purity while accepting a recovery of approximately 49.2%. By contrast, when higher recovery is prioritized, a feedstock shell content of 5% provides approximately 95.3% purity and 58.2% recovery. These relationships provide a basis for selecting operating conditions according to different production objectives.

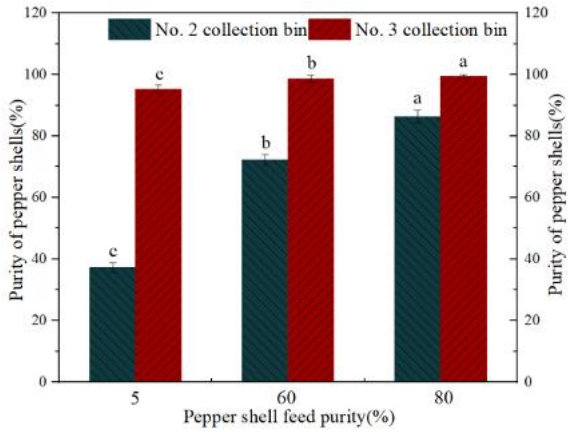


Fig. 10 - Purity of Pepper Shells in Different Collection Bins

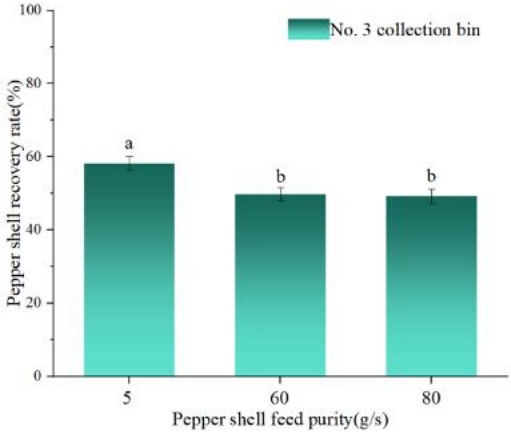


Fig 11 - Recovery Rate of Pepper Shells in Collection Bin 3

CONCLUSIONS

This study elucidated the fundamental mechanism governing the aerodynamic separation of *Zanthoxylum bungeanum* shells from seed-bearing particles. The results demonstrated that separation is primarily controlled by the balance between aerodynamic drag and particle inertia, as characterized by the Stokes number. The substantial difference in Stk between the two particle types, arising from their distinct volume-to-mass ratios and aerodynamic responses, enabled effective segregation.

Systematic parameter analysis showed that the secondary airflow velocity was the most influential factor affecting separation selectivity. At 7.85 m/s, the secondary airflow established a stable flow field in which aerodynamic drag and particle inertia were favorably balanced. The primary airflow mainly conditioned and distributed the incoming particle stream, whereas an excessively high primary airflow velocity disrupted secondary classification. A feed mass flow rate of 80 g/s provided a favorable compromise between throughput and separation performance.

Under the optimized operating conditions of a primary airflow velocity of 8.4 m/s, a secondary airflow velocity of 7.85 m/s, and a feed mass flow rate of 80 g/s, the device processed feedstock containing 5% shells and produced a shell fraction in Collection Bin 3 with a purity of 95.3% and a recovery rate of 58.2%. These results validated the proposed aerodynamic separation mechanism. The study also quantified the inherent trade-off between purity and recovery, thereby providing practical guidance for selecting operating conditions according to different downstream requirements.

Feedstock composition strongly influenced the internal particle-flow regime. Feedstock with a high shell content promoted a shell-dominated flow structure and enhanced collective particle migration toward Collection Bin 3, resulting in shell purities exceeding 99%. However, this improvement was accompanied by a lower recovery rate, indicating that feedstock composition should be considered in the design of upstream pre-sorting processes.

The integrated framework combining physics-based proxy modeling with CFD–DEM simulation successfully reproduced the aerodynamic separation of a non-spherical, multicomponent particle mixture. By linking particle-scale mechanics with system-scale separation performance, the framework provides a reliable basis for the design and optimization of sorting equipment for similarly complex agricultural materials.

ACKNOWLEDGEMENT

This research was funded by the National Natural Science Foundation of China [51876109]; the Sichuan University of Science & Engineering talent introduction project [2025RCZ066] and the Sichuan University of Science & Engineering Innovation Team [SUSE652A010].

REFERENCES

[1] Domínguez-Vázquez, D., Castiblanco-Ballesteros, S. A., Jacobs, G. B., & Tartakovsky, D. M. (2024). High-order Lagrangian algorithms for Liouville models of particle-laden flows. *Journal of Computational Physics*, 515, N.PAG. https://doi.org/10.1016/j.jcp.2024.113281.

[2] Echendu, S. O. S., Belblidia, F., Tamaddon-Jahromi, H. R., & Webster, M. F. (2011). Modelling with viscous and viscoplastic materials under combining and separating flow configurations. *Mechanics of Time-Dependent Materials*, 15(4), 407–428. https://doi.org/10.1007/s11043-011-9161-x.

[3] Elreafay, A. M., Salem, K. M., Abumandour, R. M., Dawood, A. S., & Al Nuaimi, S. (2025). Effect of particle diameter and void fraction on gas–solid two-phase flow: a numerical investigation using the Eulerian–Eulerian approach. *Computational Particle Mechanics*, 12(1), 289–311. https://doi.org/10.1007/s40571-024-00798-9.

[4] Farooq, U., Riaz, H. H., Munir, A., Tariq, A., Zhao, M., & Islam, M. S. (2023). Application of heliox for optimized drug delivery through respiratory tract. *Physics of Fluids*, 35(10). https://doi.org/10.1063/5.0169934.

[5] Gong, M., & Shen, Y. (2025). Study on heat flow decay in vertical jet of aircraft deicing fluid based on phase field and realizable k-ε turbulence model. *Thermal Science and Engineering Progress,* 60. https://doi.org/10.1016/j.tsep.2025.103446.

[6] Gu, M., Wang, H., Chen, G., Yu, A., Dang, W., & Ling, X. (2024). Experimental and numerical study on explosion resistance of polyurea-coated shelter in petrochemical industry. *Scientific Reports, 14*(1), 20643. https://doi.org/10.1038/s41598-024-71339-w.

[7] Guan, R., Gu, J., Li, Y., Yang, C., Zhang, B., Yao, X., Zhu, R., Wang, Q., Dong, W., & Huang, Y. (2025). Simulation and experimental study of shell-kernel separation device for household sunflower based on CFD-DEM coupling. *Scientific Reports,* 15(1), 9209. https://doi.org/10.1038/s41598-025-93459-7.

[8] Hu, Z., Zeng, H., Ge, Y., Wang, W., & Wang, J. (2021). Simulation and experiment of gas-solid flow in a safflower sorting device based on the CFD-DEM coupling method. *Processes,* 9(7). https://doi.org/10.3390/pr9071239.

[9] Li, H., Niu, H., Zhang, H., & Zhang, M. (2024). Performance evaluation and parameter optimization of a walnut shell–kernel winnowing device. *Journal of Food Process Engineering,* 47(1), e14498. https://doi.org/10.1111/jfpe.14498.

[10] Lundin, S.-T. B., Ikeda, A., & Hasegawa, Y. (2024). On the Maximum Obtainable Purity and Resultant Maximum Useful Membrane Selectivity of a Membrane Separator. *Membranes,* 14(6), 143. https://doi.org/10.3390/membranes14060143.

[11] Luo, W., Jiang, D., Wu, T., Guo, C., Wang, C., Deng, R., & Dai, S. (2020). Numerical simulation of an ice-strengthened bulk carrier in brash ice channel. *Ocean Engineering, 196*, N.PAG.

https://doi.org/10.1016/j.oceaneng.2019.106830.

[12] Ma, H., Zhou, L., Liu, Z., Chen, M., Xia, X., & Zhao, Y. (2022). A review of recent development for the CFD-DEM investigations of non-spherical particles. *Powder Technology,* 412. https://doi.org/10.1016/j.powtec.2022.117972.

[13] Ma, X., Zhao, L., Guo, B., & Dang, H. (2020). Simulation and experiment of rice cleaning in air-separation device based on DEM-CFD coupling method. *INTERNATIONAL JOURNAL OF AGRICULTURAL AND BIOLOGICAL ENGINEERING,* 13(5), 226–233. https://doi.org/10.25165/j.ijabe.20201305.5225.

[14] Michaelides, E. E., & Feng, Z. (2023). Review-Drag Coefficients of Non-Spherical and Irregularly Shaped Particles. *JOURNAL OF FLUIDS ENGINEERING-TRANSACTIONS OF THE ASME,* 145(6), 060801. https://doi.org/10.1115/1.4057019.

[15] Mutinda, E. S., Kimutai, F., Mkala, E. M., Waswa, E. N., Odago, W. O., Nanjala, C., Ndungu, C. N., Gichua, M. K., Njire, M. M., Gituru, R. W., & Hu, G.-W. (2023). Ethnobotanical uses, phytochemistry and pharmacology of pantropical genus Zanthoxylum L. (Rutaceae): An update. *Journal of Ethnopharmacology,* 303. https://doi.org/10.1016/j.jep.2022.115895.

[16] Shi, W.-J., Chai, T., Lv, C.-M., Wang, X.-R., Zhang, X.-R., Qiang, Y., Wang, W.-F., & Yang, J.-L. (2025). Research progress on the main flavor components and detection methods of Zanthoxylum bungeanum Maxim. *Journal of Food Composition and Analysis,* 144. https://doi.org/10.1016/j.jfca.2025.107658.

[17] Stepanenko, S., Kuzmych, A., Shvydia, V., Kotov, B., Kalinichenko, R., Kharchenko, S., Shchur, T., Kocira, S., Kwaśniewski, D., & Dziki, D. (2022). To the Theory of Grain Motion in an Uneven Air Flow in a Vertical Pneumatic Separation Channel with an Annular Cross Section. *Processes,* 10(10). https://doi.org/10.3390/pr10101929.

[18] Ulusoy, U. (2023). A Review of Particle Shape Effects on Material Properties for Various Engineering Applications: From Macro to Nanoscale. *MINERALS,* 13(1), 91. https://doi.org/10.3390/min13010091

[19] Wang, J., Chen, L., Tang, Y., Chen, Z., Wu, Q., & Han, D. (2023). Calibration and experiment of discrete element model parameters of Zanthoxylum bungeanum. *Frontiers in Mechanical Engineering,* 9. https://doi.org/10.3389/fmech.2023.1204659.

[20] Wu, Y., Zheng, Q., Yang, L., & Yu, A. (2025). Coupled CFD-FEM approach for dense particle-fluid flows. *International Journal of Mechanical Sciences,* 308, N.PAG. https://doi.org/10.1016/j.ijmecsci.2025.110985.

[21] Xiao, B., Wang, P., Wu, J., Zhu, H., Liu, M., Liu, Y., & Long, G. (2022). A Novel Fractal Model for Gas Diffusion Coefficient in Dry Porous Media Embedded with a Damaged Tree-Like Branching Network. *Fractals,* 30(7), 1–15. https://doi.org/10.1142/S0218348X2250150X.

[22] Xu, D., Xie, Z., & Shen, Y. (2025). Coarse-grained superquadric DEM-CFD model for gas–solid flow with non-spherical particles. *Chemical Engineering Science,* 315, N.PAG. https://doi.org/10.1016/j.ces.2025.121838.

[23] Zhang, J., Xie, C., Cao, L., Zhou, H., Li, C., & Wang, L. (2022). Determination of physical and interaction parameters of green pepper (Zanthoxylum armatum): Investigation of the mechanism of significant factors against the repose angle. *LWT - Food Science & Technology,* 162, N.PAG. https://doi.org/10.1016/j.lwt.2022.113409.

[24] Zhao, B., Shi, K., He, M., & Wang, J. (2024). Hydrodynamics of polydisperse gas-solid flows: Kinetic theory and multifluid simulation. *Chemical Engineering Science,* 287. https://doi.org/10.1016/j.ces.2024.119740.

[25] Zhao, C., Gao, Q., Chen, Y., & Li, C. (2021). Application of parametric function in construction of particle shape and discrete element simulation. *Powder Technology,* 387, 481–493. https://doi.org/10.1016/j.powtec.2021.04.054.

[26] Zhou, L., Zhao, Z., Li, W., Bai, L., & Agarwal, R. K. (2023). Influence mechanism of particle density in a gas-solid fluidized bed. *PHYSICS OF FLUIDS,* 35(12), 123345. https://doi.org/10.1063/5.0180227.

[27] Zhu, X., Zhang, C., Feng, P., Yang, X., & Yang, X. (2021). A novel pulsated pneumatic separation with variable-diameter structure and its application in the recycling spent lithium-ion batteries. *Waste Management,* 131, 20–30. https://doi.org/10.1016/j.wasman.2021.05.027.

DESIGN AND EXPERIMENT OF AN INTEGRATED AUTOMATIC TRANSPLANTING SYSTEM WITH A FLEXIBLE END-EFFECTOR FOR PLUG SEEDLINGS
/
基于柔性末端执行器的钵苗全自动移栽系统的设计与试验

Chao HE [1,2], Tian JIAO [1], Tie YE [1], Mingyuan WEI [3], Wanrui SONG *[4]
[1] School of Intelligent Manufacturing and Electrical Engineering, Nanyang Normal University / China;
[2] Collaborative Innovation Center of Intelligent Explosion-proof Equipment, Henan Province / China;
[3] College of Engineering, China Agricultural University / China
[4] Nanyang Vocational College of Agriculture, Nanyang 473061, China
*Corresponding author: Wanrui SONG. E-mail: song147@126.com
DOI: https://doi.org/10.35633/inmateh-79-46

Keywords: *Integrated Transplanting System, Manipulator, Flexible End-Effector, Performance Evaluation*

ABSTRACT
Automatic transplanting of plug seedlings is critical for improving agricultural efficiency. However, existing systems often suffer from functional fragmentation and use rigid end-effectors prone to damaging seedlings. This study presents a fully integrated automatic transplanting system that uniquely combines multi-tray storage and conveying, precise step-moving, manipulator-based picking and placing with a novel flexible end-effector, and automatic tray collection. In experiments using pepper seedlings, conducted over repeated trials (n=5) with 576 seedlings per trial, the integrated system achieved a picking success rate of 93.24% and a damage rate of 1.43%, with a maximum conveying positioning deviation of 1.79 mm. Compared with previously reported transplanting systems, the proposed system achieves a superior success rate while delivering a substantially lower seedling damage rate. This research provides a practical, highly integrated solution for small-to-medium scale nurseries.

摘要
全自动穴盘苗移栽对于提高农业效率至关重要。然而，现有系统常存在功能碎片化问题，且使用易损伤幼苗的刚性末端执行器。本研究提出了一种全自动移栽系统，创新地集成了多盘存储与输送、精确步进定位、基于机械手的移栽（配备新型柔性末端执行器）以及空盘自动收集。在以辣椒幼苗为对象的重复试验中（n=5，每次 576 株），该集成系统的取苗成功率达 93.24%，损伤率为 1.43%，最大输送定位偏差为 1.79 mm。与已有文献报道的移栽系统相比，本系统在达到更优异的取苗成功率的同时，实现了更低的幼苗损伤率。本研究提供了一种实用、高度集成的解决方案，适用于中小型苗圃。

INTRODUCTION
Seedling transplanting techniques are extensively used in the cultivation of major crops such as vegetables and rapeseed in China *(Liu et al., 2023)*. Compared with direct seeding, transplanting can shorten the field growth period of crops, enhance their resistance to natural disasters, and significantly increase yield per unit area *(Sharma and Khar, 2022)*. As labor shortages and rising costs become more pronounced, the development of efficient and reliable automatic transplanting machines is crucial *(Yang et al., 2020)*.

Currently, seedling transplanting in China still predominantly relies on semi-automatic transplanters *(Han et al., 2019; Jin et al., 2021)*. Their operational efficiency and quality are limited by the speed of manual seedling picking, resulting in low productivity, operator fatigue, and inconsistent plant spacing *(Wen et al., 2021; Zhang et al., 2024)*. To overcome these bottlenecks, developing fully automatic transplanting mechanisms has become a key research focus *(Khadatkar et al., 2021; Liu et al., 2022)*.

In European and American countries, fully automatic transplanters have reached an advanced level, such as the FUTURA from Ferrari and the GR-2700 from Visser *(Shao et al., 2021)*. However, such machines are typically large, costly, and designed for standardized trays, making them difficult to adapt to the small-to-medium scale and diversified operation modes in China *(Tian et al., 2022)*.

Chinese researchers have focused on the core seedling picking device, developing various technical approaches. *Shang et al. (2026)* developed an automatic seedling picking and placing manipulator for tobacco

Chao He, Ph.D. Eng.; Tian Jiao, Ph.D. Eng.; Tie Ye, Ph.D. Agr.; Mingyuan Wei, Ph.D. Eng.; Wanrui Song, Ph.D. Agr.

seedling transplanting machines, and conducted kinematics analysis and optimization. While their study did not address the integration of the manipulator with upstream seedling feeding and downstream tray handling, leaving the overall workflow discontinuous. *Jin et al. (2018)* designed a single-row automatic transplanting device for tomato plug seedlings, although the device demonstrated feasibility, the use of rigid picking fingers caused noticeable damage to seedling roots during clamping.

Han et al. (2023) developed a simplified automatic transplanting device equipped with a multi-needle gripper. However, the multi-needle design exerted concentrated stress on the substrate surface, leading to local breakage of the soil plug in approximately 2.69% of the seedlings tested. *Ye et al. (2020)* proposed a rotary seedling pick-up mechanism that improved picking speed, yet the rotating motion generated considerable inertial forces that compromised positioning accuracy at higher operating speeds. *Zhou et al. (2024)* combined pneumatic and mechanical technologies to design a dual-row seedling pick-up transplanter, but the complex pneumatic circuit and multiple actuators increased system cost and maintenance complexity.

In terms of functional integration, *Zhao et al. (2022)* designed a multi-functional transplanting system integrating sorting, transplanting, and replanting. Despite its innovative integration, the system relied on a vision module that significantly increased processing time, reducing overall throughput. *Zhu et al. (2025)* put forward automated equipment for vegetable seedling transplanting, which enables intermittent seedling feeding, precise seedling picking and rapid seedling planting. Nevertheless, their system still employed rigid end-effectors without passive compliance, and the upstream/downstream tray logistics were not fully automated.

A critical review of the existing literature indicates that several key challenges and research gaps persist. Firstly, most seedling pick-up mechanisms utilize rigid fingers that can damage the root system *(Bai et al., 2022)*. This issue is particularly acute in the designs of *Jin et al. (2018)*, *Han et al. (2023)*, and *Zhu et al. (2025)*, where concentrated clamping forces directly injured seedlings. Secondly, mechanisms with multiple simultaneously operating end-effectors can generate significant inertial impact, affecting precision and stability, as observed in the rotary mechanism of *Ye et al. (2020)* and the pneumatic system of *Zhou et al. (2024)*. Thirdly, and most critically, at the system level, existing research often focuses narrowly on picking and placing, neglecting upstream processes of tray storage and conveying, and downstream empty tray collection. This functional fragmentation limits overall automation and operational continuity.

To address these challenges, the present study puts forward the following innovations: (1) A novel flexible end-effector with a passive compliance mechanism is developed, integrating a spring-buffering and hinge-sliding composite structure that effectively decouples actuation force from clamping force, thereby reducing clamping impact and minimizing seedling injury. (2) An integrated automatic transplanting system is established, combining multi-tray storage and conveying, step-by-step positioning, manipulator-based picking and placing, and automatic tray collection. Our integrated design achieves a continuous and fully automated process from full-tray input to empty-tray stacking, eliminating intermediate manual interventions.

The overarching objective of this study is to provide a practical, highly integrated, and low-damage automatic transplanting solution suitable for small-to-medium scale nurseries in China. Through the integrated design and flexible end-effector, this research offers a feasible technical pathway for automated plug seedling transplanting, and serves as an important reference for developing next-generation automatic transplanting equipment.

MATERIALS AND METHODS

Overall Design of the Integrated Automatic Transplanting System

The automatic transplanting system consists of a frame, plug trays, a multi-tray storage and conveying unit, a tray step-moving unit, a seedling picking and placing unit, and a tray collecting unit (Fig. 1). The key technical specifications of the developed automatic transplanting system are summarized in Table 1.

The system workflow is as follows: eight 72-cell plug trays (cell center distance 42 mm) are placed on the storage unit. A geared motor drives them vertically to the picking station. An electric push rod pushes the tray onto the step-moving unit, which uses a dual-axis linear module to move the tray step by step (42 mm each time) along an S-shaped path. After the tray step-moving unit completes precise tray positioning, a cam in the seedling picking and placing unit ejects the seedling from the tray. Subsequently, a manipulator equipped with the flexible end-effector completes the seedling picking, lifting, transferring, and releasing operations. When all seedlings in one tray are transplanted, the empty tray is pushed to the collection unit, where it is lifted by cams and supported by electric push rods for stacking. Simultaneously, the multi-tray storage and conveying unit pushes the next tray filled with seedlings onto the step-moving unit, allowing the seedling picking and placing unit to begin a new transplanting cycle, achieving continuous operation.

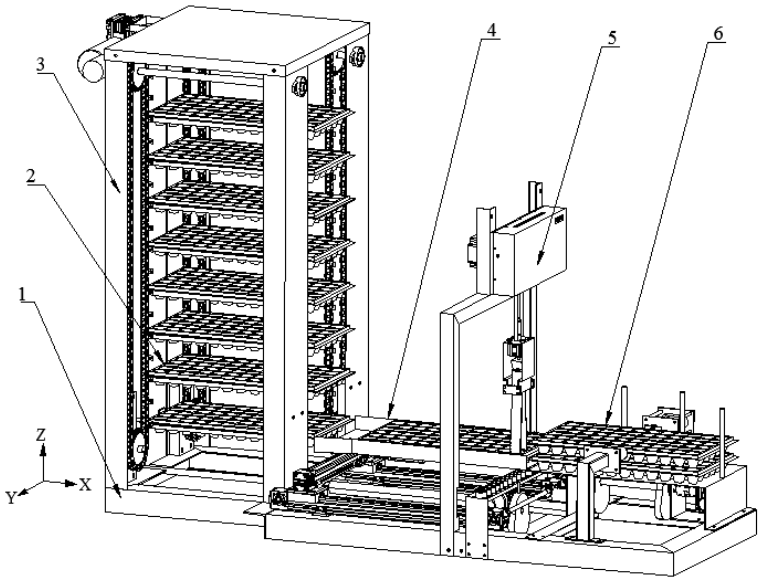


Fig. 1 - Overall structure of the integrated automatic transplanting system

1 - Frame; 2 - Plug tray; 3 - Multi-tray storage and conveying unit; 4 - Tray step-moving unit; 5 - Seedling picking and placing unit; 6 - Tray collecting unit

Table 1

Key technical specifications of the integrated automatic transplanting system

Parameter	Value / Specification
Overall dimensions (L × W × H)	2140 × 705 × 1265 mm
Total weight	273 kg
Total installed power	approximately 1.0 kW
Power supply	220V AC
Manipulator X/Y repeatability	±0.03 mm
Manipulator Z repeatability	±0.2 mm
Minimum motion cycle	0.8 s
Maximum operating speed	approximately 600 mm/s
Rated load (at min. cycle)	200 g
Transplanting efficiency	60 plants/min/row

Design of the Seedling Picking and Placing Unit

The seedling picking and placing unit mainly consists of a manipulator device and a seedling ejection device. The ejecting device pushes the seedling out of the tray, and the manipulator device then picks, transports, and releases the ejected seedling.

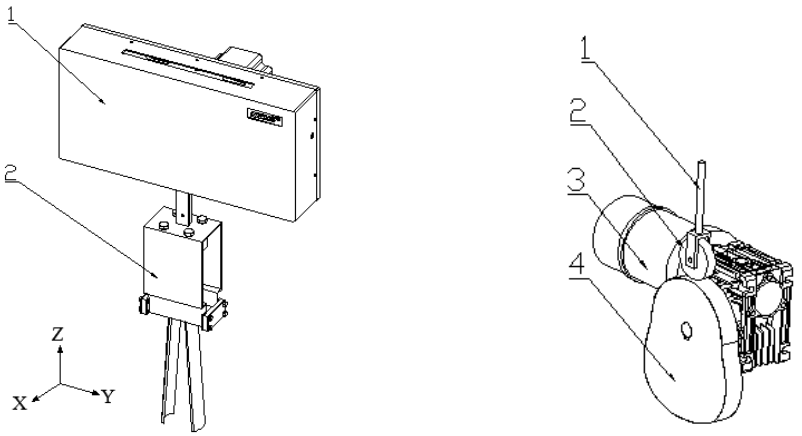


Fig. 2 - Seedling picking and placing unit

(a) Manipulator device

1 - Manipulator controller; 2 - Flexible end-effector

(b) The seedling ejection device

1 - Ejector rod; 2 - Roller; 3 - Geared motor; 4 - Cam

The manipulator device is primarily composed of a manipulator controller and a flexible end-effector (Fig. 2a). The flexible end-effector, which can perform clamping and splaying motions, is mainly responsible for seedling picking and releasing. The manipulator controller drives the flexible end-effector to lift, translate, and lower, thereby transporting the seedling.

The seedling ejection device mainly consists of a geared motor, a cam, an ejector rod, and a roller (Fig. 2b). When the geared motor is not working, the cam's near-dwell section contacts the roller. When the geared motor runs, the cam enters the lift phase, causing the roller to raise the ejector rod, which pushes the seedling out through the ventilation hole at the bottom of the tray cell. As the manipulator device picks the seedling, the geared motor continues to rotate, and then the ejector rod descends back to its initial position, waiting to eject the next seedling.

The complete picking and placing sequence (descending → gripping → lifting → releasing) is illustrated in Fig. 3. In process (a), the manipulator moves to the initial picking position while the end-effector remains open and the ejector rod stays in its lower position. In process (b), the ejecting motor rotates the cam, driving the ejector rod upward to push the seedling out of the tray cell. In process (c), the end-effector closes to grasp the ejected seedling. In process (d), the manipulator lifts the end-effector and moves rightward; simultaneously, the ejecting motor continues rotating, causing the cam to retract the ejector pin back to its initial lower position. In process (e), upon reaching the rightmost limit, the manipulator descends to its lowest position. In process (f), the end-effector opens, allowing the seedling to fall under gravity into the planter for soil insertion. After process (f), the seedling tray shifts one cell to the left, and the manipulator returns the end-effector to the initial position (a) to repeat the cycle.

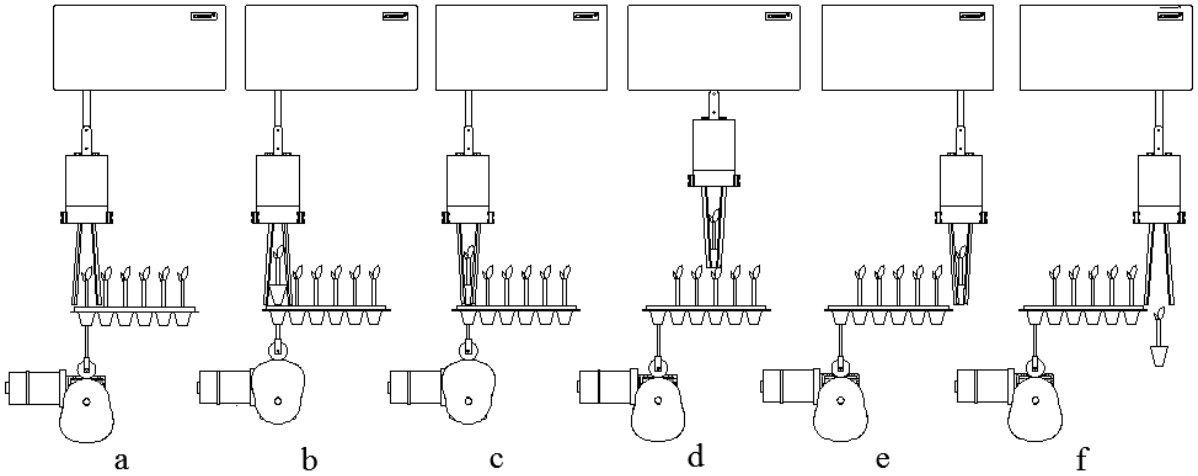


Fig. 3 - The process of picking and placing seedlings

Flexible End-Effector Design

The flexible end-effector developed in this study is of the finger-clamp type, specifically designed to pick the soil plug of the seedling, with an emphasis on flexibility. Recognizing that rigid fingers could potentially damage the delicate substrate, a spring buffer mechanism was integrated into the mechanical structure to significantly reduce the clamping impact on the soil plug, thereby minimizing the risk of root damage. The overall structure of this flexible end-effector is illustrated in Fig. 4.

The finger material was 20# stainless steel with a density of 7.85 g/cm^3, while the cone block was made of aluminum alloy (density 2.70 g/cm^3) to reduce inertial mass. The coefficient of friction between the steel fingers and the seedling substrate was taken as μ = 0.6, based on design calculations for reliable gripping. Both the tension springs and buffer springs were fabricated from stainless steel with a shear modulus of 71000 MPa.

The working principle of this flexible end-effector is as follows: When the electric cylinder piston extends, the cone block moves downward. As the cone block descends, the bearings following its inclined surfaces cause the fingers to rotate inward around their hinge points, transitioning from an open to a clamped position. When the fingers contact and pick the soil plug of the seedling, any excessive clamping force is absorbed by the buffer springs through lateral displacement of the hinges within their supports. This spring-based design effectively decouples the actuation force from the clamping force, allowing the fingers to prevent damage to the root system, and fit variations in plug size and shape.

To substantiate the force-decoupling effect, a mechanical model was established. The clamping force F_c is governed by the buffer spring preload F_0 and its compression x_s:

$$F_c = F_0 + k_s \cdot x_s \quad (1)$$

where K_s = 2.5 N/mm is the total spring stiffness. The springs are preloaded to F_0 = 20 N/mm, and the maximum hinge displacement is limited by a mechanical slot to x_s = 6 mm, yielding a maximum clamping force of:

$$F_{c,\max} = 20 + 2.5 \times 6 = 35\text{N} \quad (2)$$

This value is deliberately designed to remain below the substrate's allowable limit. Preliminary unconfined compression tests on seedling plugs (n=10) determined a compressive strength of 0.12MPa. With an effective finger-plug contact area of 400 mm^2, the maximum permissible clamping force is:

$$F_{\text{allow}} = 0.12 \times 400 = 48\text{N} \quad (3)$$

Thus, $F_{c,\max}$ = 35 N < 48 N, confirming that the spring-buffering mechanism effectively prevents over-clamping. Without this buffering, direct actuation would produce a theoretical clamping force of approximately 68 N (calculated from the cone block geometry with α=15°), which would exceed the substrate tolerance and cause damage. This quantitative analysis validates that the design decouples actuation force from clamping force, ensuring reliable gripping with minimal seedling injury.

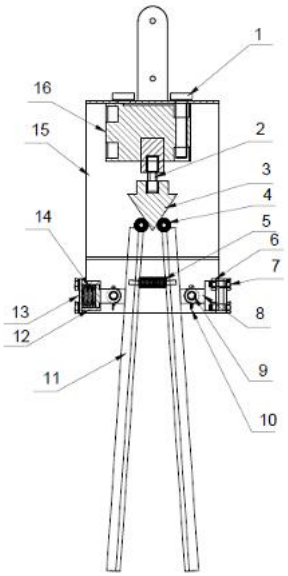


Fig. 4 - Overall structure of the flexible end-effector

1 - Hexagon bolt; 2 - Double-ended stud; 3 - Cone block; 4 - Bearing and circlip; 5 - Tension spring; 6 - Hexagon nut; 7 - Round head bolt; 8 - Hinge; 9 - Shaft pin; 10 - Cotter pin; 11 - Finger; 12 - Hinge support; 13 - Spring baffle; 14 - Buffer spring; 15 - Support frame; 16 - Electric cylinder

Seedling Ejection Device Design

The seedling ejection device employs a disk cam with a roller follower and an ejector rod (Fig. 2b). Its function is to push the plug seedling out of the tray cell through the bottom ventilation hole. Based on the seedling height and tray structure, the ejector rod stroke was set to 30 mm, which pushes the soil plug (plug height ≈ 40 mm) upward sufficiently for the end-effector fingers to grip its lower portion. The cam base circle radius (30 mm) was chosen to fit the available under-tray space while maintaining a pressure angle below 30° for smooth force transmission, as verified by ADAMS simulation (Fig. 6). The cam rotational speed (30 r/min) was synchronized with the 1.0 s manipulator cycle to ensure continuous workflow without idle waiting, and matches the tray conveying motor speed for simplified control. To ensure smooth movement with minimal impact, the lift phase was designed using a constant acceleration-deceleration motion, while the return phase adopted simple harmonic motion (cosine acceleration), achieving zero velocity at start and end points to avoid rigid impact.

With the cam rotation center as the origin, a polar coordinate system was established. The relationship between the ejector rod displacement s and the cam rotation angle δ was determined in segments (lift phase: $0 \le \delta \le \pi/2$; upper dwell: $\pi/2 \le \delta \le \pi$; return phase: $\pi \le \delta \le 3\pi/2$; lower dwell: $3\pi/2 \le \delta \le 2\pi$). Substituting the displacement expressions for each segment into the cam profile equations (4) and (5), the coordinates (x and y) of points on the theoretical cam profile were yielded:

$$x = (s_0 + s)\sin\delta + e\cos\delta \quad (4)$$

$$y = (s_0 + s)\cos\delta - e\sin\delta \quad (5)$$

where s is the ejector rod displacement, mm; δ is the cam rotation angle, °; e is the offset distance, mm; and $s_0 = \sqrt{r_0^2 - e^2}$. Since the designed cam mechanism is an in-line type, e = 0 and $s_0 = r_0$.

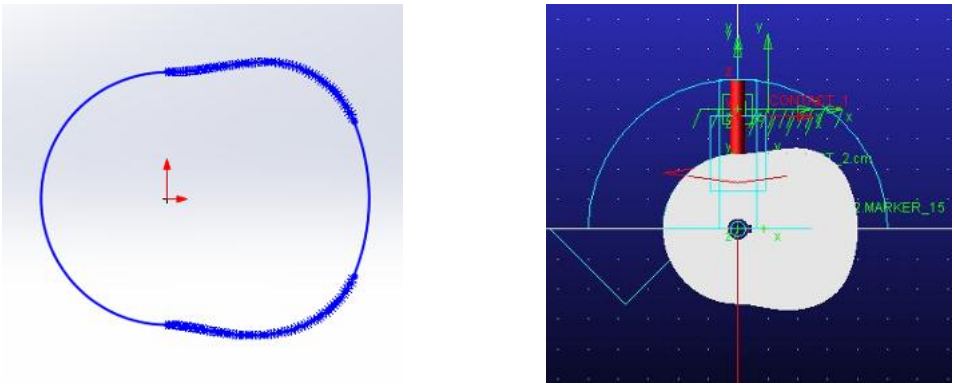
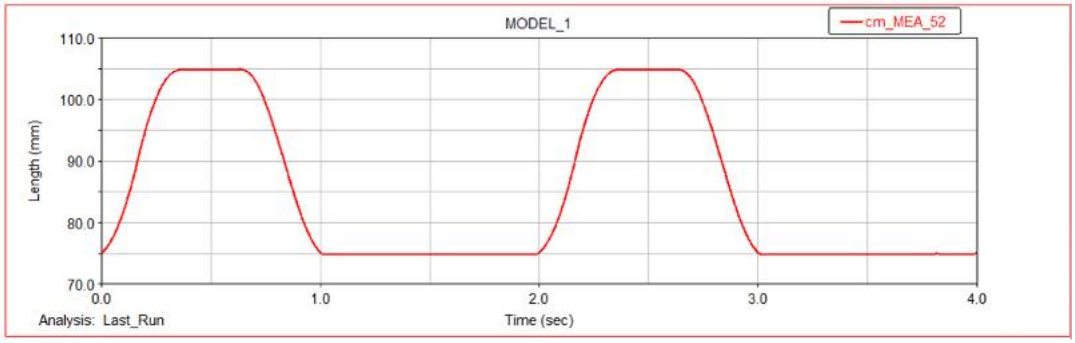


Fig. 5 - Cam design

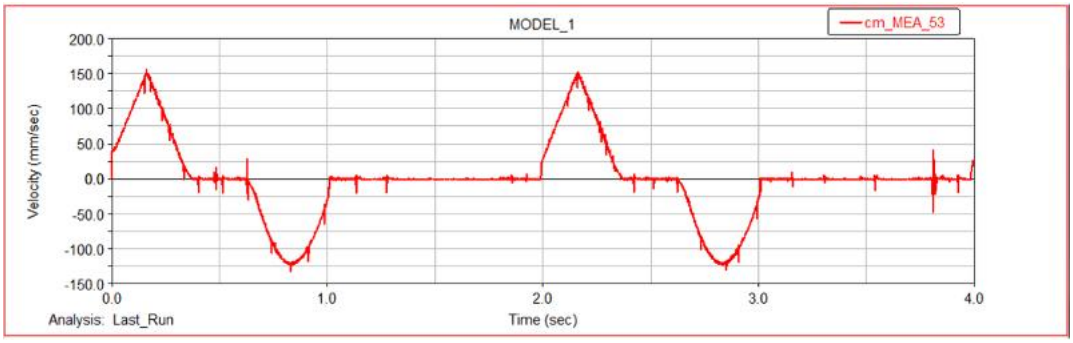
(a) Cam profile curve **(b) ADAMS simulation model**

A program was written in MATLAB software to calculate the coordinates at 1° intervals. The coordinate data were imported into SolidWorks software to generate the cam profile curve (Fig. 5a) and create a three-dimensional model of the cam.

To verify the rationality of the cam profile, the model was imported into ADAMS/View for motion simulation (Fig. 5b). A revolute joint was established between the cam and ground, and a translational joint between the ejector rod and ground. Contact forces were defined, and a driver with a rotational speed of 30 r/min was applied. Simulation results (Fig. 6) show that the displacement curve is smooth and the velocity curve is continuous without abrupt changes, confirming that the cam design meets the requirements for seedling ejection with smooth motion and no rigid impact.



(a) Displacement curve



(b) Velocity curve

Fig. 6 - Simulation results

Design of the Tray Step-Moving and Collecting Units

The tray step-moving unit (Fig.7) consists of a pallet and a dual-axis linear module that moves the tray in step increments of 42 mm (due to tray cell center distance 42 mm) with a positioning repeatability of ±0.05 mm. The tray collecting unit (Fig.8) uses a dual-cam mechanism and electric push rods to automatically stack empty trays. The cam profile was optimized to ensure the tray is lifted horizontally, following the same design methodology used for the seedling ejection device cam.

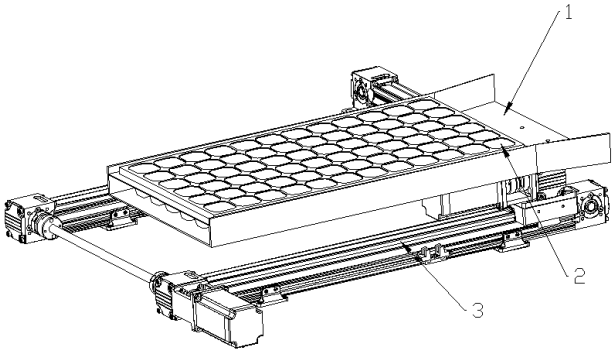


Fig. 7 - Structure of the tray step-moving unit

1 - Pallet; 2 - Tray; 3 - Linear module

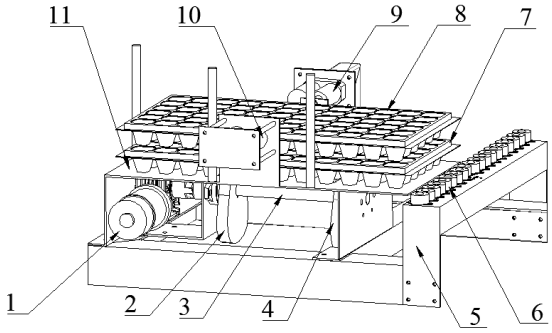


Fig. 8 - Structure of the tray collecting unit

1 - Geared motor; 2 - Cam 1; 3 - Transmission shaft; 4 - Cam 2; 5 - Universal ball support plate; 6 - Universal ball; 7 - Empty tray waiting for collection; 8 - Collected empty trays; 9 - Electric push rod 1; 10 - Electric push rod 2; 11 - Tray collection plate

Control System Design

The control system is built around a Delta DVP40ES200T Programmable Logic Controller (PLC). It controls three stepper motors (manipulator, X-axis, Y-axis), three geared motors (tray conveying, seedling ejecting, tray lifting), and nine relays (for electric push rods). The system operates in manual and automatic modes. In automatic mode, the PLC coordinates sequential actions for initialization, tray conveying and positioning, the seedling picking cycle (including step positioning, ejection, picking, transport, release, and return), and empty tray collection.

Experimental Design

Following the design methodology described above, a prototype of the integrated automatic transplanting system was developed, as shown in Fig. 9. To verify the performance of the developed system, pepper seedlings cultivated in 72-cell plug trays were used as test material (Fig. 10). The pepper seedlings had an average plant height of 150 mm, individual plant weight ranging from 20 to 50 g, and a substrate moisture content of 55%-60%.

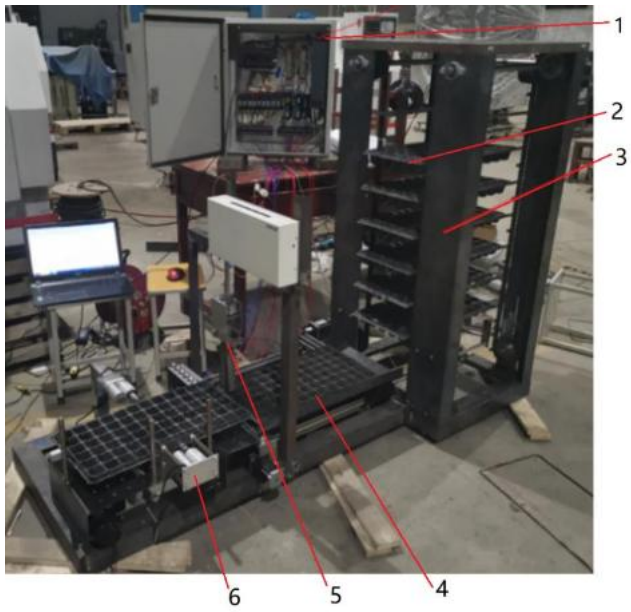


Fig. 9 - Prototype of the developed automatic transplanting system

1 - Control system; 2 - Plug tray; 3 - Multi-tray storage and conveying unit; 4 - Tray step-moving unit; 5 - Seedling picking and placing unit; 6 - Tray collecting unit

The experiments were conducted in three parts:

(1) Tray conveying accuracy test: Eight full plug trays were sequentially pushed from the storage unit to the step-moving unit. The deviation between the center of tray cell and the corresponding hole center on the pallet was measured, and the maximum and average deviation values were recorded.

(2) Standalone seedling-picking performance test: To evaluate the picking reliability of the flexible end-effector itself and eliminate potential interference from the ejecting device, seedlings were manually pre-positioned at the picking point in this test. The PLC independently controlled the manipulator and flexible end-effector to complete the full action cycle of descending, picking, lifting, translating, and releasing. Each group consisted of 72 seedlings, and the test was repeated five times. The numbers of damaged seedlings N_d, missed seedlings N_m, and successfully picked seedlings N_s were recorded.

(3) Integrated seedling-picking system performance test: The system was operated automatically at a transplanting rate of 60 plants per minute per row, corresponding to a manipulator motion cycle of 1 s (determined through preliminary debugging to ensure smooth operation). Each group consisted of 8 trays (72 seedlings per tray), and the test was repeated five times. The same indicators as above were recorded.

The seedling picking success rate S_s, damage rate S_d, and miss rate S_m were calculated using the following formulas:

$$S_s = \frac{N_s}{N_0} \times 100\% \quad (6)$$

$$S_d = \frac{N_d}{N_0} \times 100\% \quad (7)$$

$$S_m = \frac{N_m}{N_0} \times 100\% \quad (8)$$

where N_0 is the total number of seedlings, N_s is the number of successfully picked seedlings, N_d is the number of damaged seedlings, and N_m is the number of missed seedlings.



Fig. 10 - Pepper seedlings used in the experiment

Statistical Analysis

All experiments were conducted with five independent replications for each test condition. Data are presented as mean ± standard deviation (SD). To compare the seedling picking performance between standalone control and integrated system conditions, an independent-samples t-test was performed using SPSS software (version 22.0). The null hypothesis (H_0) was that there is no significant difference in the performance indicators (success rate, damage rate, and miss rate) between the two test conditions, while the alternative hypothesis (H_1) was that a significant difference exists. A two-sided *p*-value < 0.05 was considered statistically significant. In addition, 95% confidence intervals (CIs) for the mean differences between the two conditions were calculated to quantify the magnitude of the observed effects.

RESULTS

Tray Conveying Accuracy

The results of tray conveying accuracy are shown in Table 2. The deviations for the eight trays ranged from 1.12 mm to 1.79 mm, with an average deviation of 1.60 mm (SD = 0.24 mm, n = 8) and a maximum deviation of 1.79 mm. These deviations were primarily caused by vibrations during the conveying process.

Since the design tolerance for the holes on the pallet bottom was 2 mm, the maximum observed deviation of 1.79 mm remained within this tolerance. Therefore, the conveying accuracy meets the positioning requirements for seedling picking.

Table 2

Accuracy of tray conveying to the step-moving unit

Tray No.	Deviation (mm)	Maximum Deviation (mm)	Average Deviation (mm)
1	1.65	1.79	1.60 ± 0.24
2	1.63		
3	1.76		
4	1.79		
5	1.12		
6	1.39		
7	1.79		
8	1.70		

Seedling Picking Performance

(1) Standalone Control Test

Under standalone control of the manipulator device, without considering the influence of the ejecting device, the seedling picking performance indicators are shown in Table 3. The average success rate of seedling picking was 97.14%, with an average damage rate of 1.21% and an average miss rate of 1.65%. The low damage rate indicates the flexible end-effector verified reliable performance. Fig. 11 showed that the flexible end-effector securely holds the substrate without causing visible damage to the soil plug or root system, demonstrating the effectiveness of the spring-buffered finger-clamp mechanism.



Fig. 11 - Multi-angle photographs of the flexible end-effector gripping the seedling soil plug

Table 3

Seedling picking performance under separate control

Test Group	Success Rate S_s (%)	Damage Rate S_d (%)	Miss Rate S_m (%)
1	97.65	0.93	1.42
2	96.73	1.38	1.89
3	97.21	1.56	1.23
4	97.13	0.78	2.13
5	96.98	1.40	1.58
Mean ± SD	97.14 ± 0.35	1.21 ± 0.32	1.65 ± 0.35

(2) Integrated System Test

The seedling picking performance of the fully automated transplanting system is shown in Table 4. The average success rate of seedling picking was 93.24%, with an average damage rate of 1.43% and an average miss rate of 5.33%. Compared with the standalone control test, the damage rate showed no significant change, but the miss rate increased substantially, leading to a decrease in the success rate.

Observations during the experiment revealed that the primary cause of the increased miss rate was the clearance between the ejector rod and its linear bearing. The ejector rod was fitted with a linear bearing with a radial clearance of approximately 0.02 mm (standard fit tolerance). Under dynamic operation, this clearance caused a lateral deflection at the rod tip of approximately 1–3 mm, corresponding to an angular deviation of 1.5°–2.5° from the vertical axis. This deviation occasionally tilted the seedlings as they were pushed out of the tray cells, causing the flexible end-effector to miss the target and resulting in the increased miss rate.

Table 4

Seedling picking performance of the integrated system

Test Group	Success Rate S_s (%)	Damage Rate S_d (%)	Miss Rate S_m (%)
1	93.34	1.24	5.45
2	93.44	1.67	4.89
3	93.31	0.93	5.76
4	93.02	1.85	5.10
5	93.09	1.46	5.45
Mean ± SD	93.24 ± 0.18	1.43 ± 0.37	5.33 ± 0.33

Transplanting Efficiency

The transplanting efficiency was primarily influenced by the manipulator device in the seedling picking and placing unit. The movement speed of the manipulator was controlled by adjusting the input pulse frequency of its stepper motor via the PLC. Through repeated debugging trials (n = 5), it was determined that a manipulator motion cycle of 1.0 s (SD = 0.05 s) yielded the smoothest operation of the flexible end-effector, corresponding to a transplanting efficiency of 60 plants per minute per row. To further increase the efficiency, a high-speed manipulator with a shorter motion cycle would be required.

Tray Collection Performance

Observation of the tray collecting unit showed that the empty trays were stacked neatly according to the design requirements, as illustrated in Fig. 12. This confirms the reliability of the collection unit design.



Fig. 12 - Successfully collected empty trays

Discussion

Statistical comparison between the standalone control and integrated system tests revealed no significant difference in damage rate (1.21 ± 0.32% vs. 1.43 ± 0.37%; mean difference = 0.22 percentage points; 95% CI: -0.29 to 0.73; independent-samples t-test, *t* = 1.02, *p* = 0.34 > 0.05), indicating that the flexible end-effector maintained consistent clamping performance even when integrated with the ejection and conveying units. The 95% confidence interval contains zero, which further confirms the lack of statistical significance and supports the null hypothesis that the damage rate does not differ between the two conditions. However, the miss rate increased significantly in the integrated system (1.65 ± 0.35% vs. 5.33 ± 0.33%; mean difference = 3.68 percentage points; 95% CI: 2.86 to 4.50; *t* = 16.78, *p* < 0.001), which was the primary cause of the reduced overall success rate (97.14 ± 0.35% vs. 93.24 ± 0.18%; mean difference = 3.90 percentage points; 95% CI: 3.50 to 4.30; *t* = 22.04, *p* < 0.001). The confidence intervals for both miss rate and success rate do not contain zero, providing strong evidence against the null hypothesis. These statistically significant differences confirm that the ejection device, rather than the end-effector itself, was the limiting factor in system performance.

Compared with existing technologies, the main advantage of this study lies in the integration of multiple functions into a complete system, reducing manual intervention and improving operational continuity. The experimental results demonstrate that the developed automatic transplanting system performs reliably. Under standalone control, the flexible end-effector achieved a seedling picking success rate of 97.14%, which is higher than the 92.59% reported by *Jin et al. (2018)* and comparable to the 96.3% reported by *Ye et al. (2020)*. The seedling damage rate of 1.21% is lower than the 2.69% reported by *Han et al. (2023)* and 1.59% reported by *Zhou et al. (2024)*. The lower damage rate observed in this study can be attributed to the spring buffer mechanism incorporated into the finger-clamp design, which effectively reduces impact forces during clamping and accommodates variations in plug size and shape.

The transplanting efficiency of 60 plants per minute per row is higher than the 40 plants/min reported by *Han et al. (2018)* and the 48 plants/min achieved by *Jin et al. (2018)*, while it is lower than that of advanced international machines such as the Ferrari FUTURA *(Shao et al., 2021)*. Selecting a manipulator with a shorter motion cycle or increasing the number of end-effectors operating in parallel could improve efficiency, but may also increase mechanical complexity and cost. For small-to-medium scale nurseries in China, cost-effectiveness and adaptability may be more critical than achieving maximum possible speed. Tray conveying accuracy, with a maximum deviation of 1.79 mm, remained within the 2 mm design tolerance, comparable to results reported by *Yue et al. (2024)* and *Zhou et al. (2024)*.

Despite these promising results, several limitations of the present study should be acknowledged. First, the experiments were conducted exclusively with pepper seedlings, and the system's adaptability to other crop species (e.g., tomato, eggplant, or tobacco) with different plug sizes remains untested. Second, the transplanting efficiency of 60 plants/min/row, while outperforming several domestic counterparts, is lower than that of advanced international machines. Third, the clearance-induced wobble of the ejector rod (0.02 mm radial clearance resulting in approximately 1–3 mm tip deflection) remains a weak point of the current design. Fourth, all performance evaluations were conducted under relatively ideal laboratory conditions; the system's reliability under real field conditions have yet to be verified.

CONCLUSIONS

This study developed an automatic transplanting system for plug seedlings, integrating multi-tray storage and conveying, step-by-step positioning, manipulator-based picking and placing, and automatic empty tray collection. Through theoretical analysis, simulation optimization, and prototype experiments, the following conclusions were drawn:

(1) The system achieves fully automated operation from tray input to empty tray stacking, addressing functional fragmentation and reducing manual intervention.

(2) A finger-type flexible end-effector with a spring buffer mechanism was designed. Under standalone control, it achieved a picking success rate of 97.14% and a damage rate of 1.21%.

(3) Experiments with pepper seedlings showed that the integrated system achieved a success rate of 93.24% with a damage rate of 1.43%; tray conveying accuracy had a maximum deviation of 1.79 mm; and the tray collecting unit successfully stacked empty trays. The results demonstrate the feasibility of low-damage, fully automated transplanting for small-to-medium nurseries.

(4) Future work will focus on three aspects: (i) evaluating the system's adaptability to other crop species to broaden its applicability; (ii) refining the ejection mechanism by replacing linear bearings with precision guide rails to reduce wobble; (iii) integrating machine vision for seedling quality detection and exploring high-speed manipulators to further improve system performance; and (iv) evaluating the system's reliability and stability under actual field conditions, including uneven terrain and varying environmental factors.

ACKNOWLEDGEMENT

This work was supported by Natural Science Foundation of Henan Province in China (Grant Number: 252300423440, 252300420062, 262300420057 and 262300420372), Doctoral Special Project of Nanyang Normal University (Grant Number: 2024ZX030) and Henan Provincial Science and Technology Tackling Project (No. 262102310472).

REFERENCES

[1] Bai, H., Li, X., Zeng, F., Cui, J., Zhang, Y. (2022). Study on the impact damage characteristics of transplanting seedlings based on pressure distribution measurement system. *Horticulturae*, *8*(11), 1080.

[2] Han, C., Xu, Y., You, J., Zhang, J., Yuan, P. (2019). Parameter optimization of opener of semi-automatic

transplanter for watermelon seedlings raised on compression substrate. *Transactions of the CSAE*, *35*, 48-56.

[3] Han, L., Mao, H., Kumi, F., Hu, J. (2018). Development of a multi-task robotic transplanting workcell for greenhouse seedlings. *Applied Engineering in Agriculture*, *34*(2), 335-342.

[4] Han, L., Xiang, D., Xu, Q., Du, X., Ma, G., Mao, H. (2023). Development of Simplified Seedling Transplanting Device for Supporting Efficient Production of Vegetable Raw Materials. *Applied Sciences-Basel*, *13*(18), 10022.

[5] Jin, X., Li, D., Ma, H., Ji, J., Pang, J. (2018). Development of single row automatic transplanting device for potted vegetable seedlings. *International Journal of Agricultural and Biological Engineering*, *11*(3), 67-75.

[6] Jin, Y., Liu, J., Xu, Z., Yuan, S., Li, P., Wang, J. (2021). Development status and trend of agricultural robot technology. *International Journal of Agricultural and Biological Engineering*, *14*(3), 1-19.

[7] Khadatkar, A., Mathur, S., Dubey, K., Bhusana Babu, V. (2021). Development of embedded automatic transplanting system in seedling transplanters for precision agriculture. *Artificial Intelligence in Agriculture*, *5*, 175-184.

[8] Liu, D., Gu, M., Yang, M., Chen, X., Wang, G., Zhang, X. (2022). Design and experiment of key part of 2ZXS-2 cantaloupe transplanter. *INMATEH - Agricultural Engineering*, *68*(3), 367-372.

[9] Liu, W., Tian, S., Wang, Q., Jiang, H. (2023). Key technologies of plug tray seedling transplanters in protected agriculture: A review. *Agriculture*, *13*(8), 1488.

[10] Shang, Z.W., Liang, Y.X., Chen, J.H., et al. (2026). Kinematics analysis and optimization of automatic seedling picking and placing manipulator for tobacco seedling transplanting machine *(烟苗移栽机自动取投苗机械手运动学分析与优化)*. *Journal of Agricultural Mechanization Research*, *48* (04), 148-154.

[11] Shao, Y., Han, X., Xuan, G., Liu, Y., Gao, C., Wang, G., Hu, Z. (2021). Development of a multi-adaptive feeding device for automated plug seedling transplanter. *International Journal of Agricultural and Biological Engineering*, *14*(1), 91-96.

[12] Sharma, A., Khar, S. (2022). Current developments in vegetable transplanters in developing countries: a comprehensive review. *International Journal of Vegetable Science*, *28*(5), 417-440.

[13] Tian, Z., Ma, W., Yang, Q., Yao, S., Zhang, M., Duan, F., Xu, H. (2022). Research status and problem analysis of plug seedling transplanter in greenhouse *(温室穴盘苗移栽机械研究现状及问题分析)*. *Journal of China Agricultural University*, *27*(7), 22-38.

[14] Wen, Y., Zhang, J., Tian, J., Duan, D., Zhang, Y., Tan, Y., Yuan, T., Li, X. (2021). Design of a traction double-row fully automatic transplanter for vegetable plug seedlings. *Computers and Electronics in Agriculture*, *182*, 106017.

[15] Yang, Q., Huang, G., Shi, X., He, M., Ahmad, I., Zhao, X., Addy, M. (2020). Design of a control system for a mini-automatic transplanting machine of plug seedling. *Computers and Electronics in Agriculture*, *169*, 105226.

[16] Ye, B., Zeng, G., Deng, B., Yang, C., Liu, J., Yu, G. (2020). Design and tests of a rotary plug seedling pick-up mechanism for vegetable automatic transplanter. *International Journal of Agricultural and Biological Engineering*, *13*(3), 70-78.

[17] Yue, R., Yao, M., Zhang, T., Shi, J., Zhou, J., Hu, J. (2024). Design and experiment of dual-row seedling pick-up device for high-speed automatic transplanting machine. *Agriculture*, *14*(6), 942.

[18] Zhang, B., Wen, X., Wen, Y., Wang, X., Zhu, H., Pan, Z., Yang, Z. (2024). Design and testing of a closed multi-channel air-blowing seedling pick-up device for an automatic vegetable transplanter. *Agriculture*, *14*(10), 1688.

[19] Zhao, S., Liu, J., Jin, Y., Bai, Z., Liu, J., Zhou, X. (2022). Design and testing of an intelligent multi-functional seedling transplanting system. *Agronomy*, *12*(11), 2683.

[20] Zhou, B., Miao, H., Guan, C., Ji, X., Wang, X. (2024). Design and test of seedling-picking mechanism of fully automatic transplanting machine. *Applied Sciences*, *14*(24), 9235.

[21] Zhu, T.Y., Li, H.S., Wang, H.H., & Zhang, X.X. (2025). Design and study on the self-propelled fully automatic vegetable transplanting machine *(自走式全自动蔬菜移栽机的设计与研究)*. *Journal of Machine Design*, *42* (S2), 36-43.

CITRUS FLOWER, FRUIT, AND SHOOT RECOGNITION BASED ON IMPROVED YOLOv10
/
基于改进 YOLOv10 的柑橘花果梢识别

Wenfeng GUO*[1)], ZhiFang BI[1)], Linjuan WANG[1)], Qinqin WU[2)], Han WANG[3)]
[1)] Department of Basic Science, Shanxi Agricultural University, Taigu, Shanxi / China;
[2)] School of Mega Data, Jiangxi Institute of Fashion Technology, Nanchang, Jiangxi / China;
[3)] College of Information Science and Engineering, Shanxi Agricultural University, Taigu, Shanxi / China;
Corresponding Authors: Wenfeng Guo; E-mail: wenfengguo@sxau.edu.cn
DOI: https://doi.org/10.35633/inmateh-79-47

Keywords: *YOLOv10; deep learning; Citrus; BAM; GIoU*

ABSTRACT
In the process of agricultural intelligence, precise detection of plant organs serves as the foundation for core tasks such as crop phenotyping analysis and yield prediction. However, in complex field environments, small targets such as citrus flowers and shoots face challenges including scale variation, background interference, and dense occlusion, which severely impact detection accuracy. This study improves the YOLOv10 model by introducing the BAM (Bottleneck Attention Module) attention mechanism and GIoU (Generalized Intersection over Union) loss function, constructing a YOLOv10s-BAM-GIoU model suitable for citrus flower, fruit, and shoot recognition. The BAM attention mechanism enhances the model's feature extraction capability for small target organs under complex backgrounds through parallel channel and spatial attention branches; the GIoU loss function improves the localization accuracy of densely occluded targets by optimizing the geometric alignment between predicted and ground-truth boxes. Validation experiments were conducted on a self-constructed dataset. The experimental results show that the improved YOLOv10s achieves significant advantages in comprehensive detection accuracy, with an mAP50 of 89.1%, representing an improvement of 2.9%~9.5% over the original YOLOv10s and other comparative models. In fine-grained category detection, the model achieves mAP50 of 91.2%, 83.6%, and 92.5% for shoots, flowers, and fruits, respectively. Furthermore, while maintaining high detection accuracy, the model achieves a detection speed of 23.6 ms per frame, meeting real-time detection requirements. The research results demonstrate that the improved YOLOv10s model integrating the BAM attention mechanism and GIoU loss function achieves an optimal balance between accuracy and speed in citrus organ detection tasks, providing a preferred solution for field real-time detection systems.

摘要
在农业智能化进程中，植物器官精准检测是作物表型分析、产量预测等核心任务的基础。然而，田间复杂环境下柑橘花、梢等小目标存在尺度多变、背景干扰及密集遮挡等问题，严重影响检测精度。本研究基于 YOLOv10 模型，通过引入 BAM 注意力机制和 GIoU 损失函数对其进行改进，构建了适用于柑橘花果梢识别的 YOLOv10s-BAM-GIoU 模型。其中，BAM 注意力机制通过通道与空间的并行注意力分支，增强模型对复杂背景下小目标器官的特征提取能力；GIoU 损失函数则通过优化预测框与真实框的几何对齐，提升模型对密集遮挡目标的定位精度。在本研究自建数据集上进行验证，实验结果显示，改进后的 YOLOv10s 在综合检测精度上展现显著优势，其 mAP50 达到 89.1%，较原始 YOLOv10s 及其他对比模型提升 2.9%~9.5%。在细分类别检测中，该模型对梢（shoot）、花（flower）、果实（fruit）的 mAP50 分别达到 91.2%、83.6%、92.5%。此外，模型在保持较高检测精度的同时，检测速度达到 23.6ms/帧，满足实时检测需求。研究结果表明，融合 BAM 注意力机制与 GIoU 损失函数的改进 YOLOv10s 模型在柑橘器官检测任务中实现了精度与速度的最佳平衡，为田间实时检测系统提供了优选方案。

INTRODUCTION
The citrus industry is a vital component of agricultural economy. However, traditional cultivation management relies on manual experience, making it difficult to precisely regulate the proportion of flowers and fruits, leading to significant yield fluctuations and inconsistent fruit quality. Accurate identification of the number of flowers, fruits, and shoots is a prerequisite for implementing precision management measures such as flower and fruit thinning and scientific pruning.

Nevertheless, citrus flowers, fruits, and shoots share similar morphology and color and are often distributed in clusters. Traditional manual counting methods are inefficient and highly subjective, failing to meet the refined requirements of modern smart agriculture. The precise recognition of citrus flowers, fruits, and shoots enables scientific regulation of flower and fruit loads, thereby enhancing citrus quality and promoting the digital transformation of the industry.

Addressing the challenges of refined recognition that traditional methods struggle to solve, researchers have conducted extensive studies based on deep learning technologies in recent years, achieving significant progress. Huang et al. proposed ORD-YOLO, an enhanced YOLOv8-based model for citrus maturity detection. The key innovations of their approach include the incorporation of ODConv for robust feature extraction, RepGFPN for multi-scale feature fusion, and a Dynamic Head for adaptive key feature perception (*Huang et al., 2025*).

Lin et al. enhanced YOLOv5s by incorporating CBAM and Contextual Transformer modules into its backbone network and substituting GIoU with SIoU as the loss function. These modifications improved the average recognition accuracy for citrus fruits by 3.51% compared to the original algorithm (*Lin et al., 2023*).

For accurate assessment of citrus fruit ripeness (unripe and fully ripe), *Ünal et al.* proposed a lightweight deep learning model featuring an optimized YOLO12n-Seg backbone. By embedding a GhostConv module into the neck to minimize parameter overhead and applying a Global Attention Mechanism (GAM) to enhance feature discrimination, the model effectively reduces background clutter while maintaining high detection fidelity (*Ünal and Eceoğlu, 2025*). To accurately and immediately recognize mature citrus, *Xu et al.* proposed a novel method based on the Otsu adaptive threshold method and on the improved random ring method (*Xu et al., 2020*).

Lyu et al. achieved precise detection of green citrus fruits in natural scenes by proposing the YOLO-GC model incorporating GhostNet and GAM attention mechanisms, achieving a model mAP of 97.8%, yet missed detections occurred in densely overlapped fruit areas (*Lyu et al., 2024*).

El Akrouchi et al. broke whole-tree high-resolution images of small green citrus fruits into smaller patches to capture finer details, and employed a model combining Multiscale Vision Transformer version 2 (MViTv2) with Cascade Mask R-CNN for fruit detection (*El Akrouchi et al., 2025*).

Xiao et al. achieved high-precision citrus recognition in orchard environments by proposing the AC-YOLO model with a self-attention mechanism, attaining an average precision of 97.27%, though recognition performance for severely occluded fruits remained suboptimal (*Xiao et al., 2024*). A yield prediction scheme was proposed by *Qin et al*., which employs both Faster R-CNN and SSD to detect citrus fruits on the tree and subsequently computes fruit size based on the short diameter measurement (*Qin et al., 2021*).

Subeesh et al. used unmanned aerial vehicles (UAVs) to capture images of citrus fruits, and employed multiple deep learning algorithms such as YOLOv7 to detect two categories of fruits, "harvest-ready" and "unripe," from canopy images, thereby enabling orchard yield estimation (*Subeesh et al., 2024*). Based on the mask regional convolutional neural network (Mask R-CNN) and a branch segment merging algorithm, an integrated system was developed to simultaneously detect and measure citrus fruits and branches (*Yang et al., 2020*).

Qiu et al. achieved automatic segmentation and phenotypic quantification of citrus floral organs by independently developing the CF-ASPM model, enabling fine segmentation of seven organ types including petals, styles, and ovaries (*Qiu et al., 2025*). To estimate citrus flower quantities in natural orchards, *Lu et al.* proposed a lightweight recognition model based on an improved YOLOv4 architecture. To reduce model complexity, they employed MobileNetV3 as the backbone feature extractor and incorporated depthwise separable convolutions to accelerate inference (*Lu et al. 2021*).

Li et al. achieved citrus fruit-stem segmentation and precise picking point localization by improving the YOLOv8n-seg model and integrating the CBAM attention mechanism, attaining fruit-stem segmentation accuracy of 97.12%, though generalizability across different varieties remains unverified (*Li et al., 2025*). *Liu et al.* enhanced the YOLOv5s model with the BiFormer attention mechanism to achieve precise detection of citrus spring shoots, identifying 14-4 days before full bloom as the optimal phenological detection window, with a model mAP of 89.6% (*Liu et al., 2025*).

Yin et al. achieved intelligent recognition of citrus shoot growth by improving the YOLOX-Nano algorithm with multi-attention mechanisms, attaining a model mAP of 88.07% and successfully deploying it on mobile terminals, though detection accuracy for fine targets at the germination stage still requires improvement (*Yin et al., 2022*).

In summary, current research on citrus flower, fruit, and shoot recognition has achieved significant progress in technical methodologies. Improved YOLO series models combined with attention mechanisms have effectively enhanced recognition accuracy in complex scenes, research targets have expanded from single organs to multi-phenological dynamic monitoring, and model lightweighting has laid the foundation for real-time orchard applications. However, existing research still faces the following critical challenges. First, current research on citrus target detection predominantly focuses on a single category, such as detecting fruits, flowers, or shoots separately, while comprehensive methods that simultaneously encompass all three categories remain scarce. Second, the adaptability of existing models to complex environments, which are characterized by drastic illumination changes and severe occlusion, still requires further improvement. Third, the lack of standardized datasets hinders horizontal comparison among different studies and impedes the reproducibility verification of research results.

To address the aforementioned limitations, this study performs a targeted expansion of the existing citrus dataset on the PaddlePaddle platform, with particular emphasis on enhancing sample coverage under drastic illumination changes and severe occlusion. Furthermore, a multi-target detection model is constructed to simultaneously encompass three categories: fruits, flowers, and shoots. Specifically, this model introduces the BAM attention mechanism into the neck network of YOLOv10 to enhance feature extraction capability for small-target objects under complex backgrounds, while replacing the original CIoU loss function with the GIoU loss function to improve localization accuracy for densely occluded targets by optimizing geometric alignment between predicted and ground-truth boxes. This improvement scheme aims to enhance the model's simultaneous detection capability for flowers, fruits, and shoots in complex orchard environments through synergistic optimization of feature representation and localization loss, while improving its adaptability to challenging scenarios such as illumination variations and occlusion interference. Furthermore, by constructing a standardized dataset covering multiple phenological stages and varieties, this research provides a foundation for horizontal comparison and reproducibility verification in subsequent studies, thereby promoting the development of citrus organ detection technology toward practical and standardized applications.

MATERIALS AND METHODS

Image dataset

The recognition of citrus flowers, fruits, and shoots is of great significance for cultivation monitoring and yield estimation. The generalization ability and stability of the model heavily rely on citrus datasets covering different growth periods, lighting conditions, and occlusion scenarios. To ensure the effective application of the model under actual agricultural production conditions, the citrus dataset should include images of varying sizes and resolutions, as well as diverse scenarios such as overlap, complex backgrounds, and varying lighting conditions. This study adopts the following combined dataset:

Public dataset: A citrus flower, fruit, and shoot dataset provided by the PaddlePaddle platform, consisting of 420 JPG format images with a resolution of 608×608 pixels. The dataset includes annotation files in YOLO format, covering images from different growth stages that closely resemble real orchard scenes.

Self-constructed dataset: A citrus flower, fruit, and shoot dataset constructed through field photography using a commercial smartphone with a 64MP autofocus camera. This dataset comprises 380 JPG format images with a resolution of 640×640 pixels, encompassing citrus flowers, fruits, and shoots under various lighting conditions, occlusion, overlap, and different levels of background complexity. Sample images are shown in Figure 1.



a. Front lighting b. Back lighting c. Overlap d. Branch occlusion

Fig. 1 - Sample images from the dataset

To simulate the photometric and geometric distortions commonly observed in field operations, data augmentation techniques were applied to the dataset, including horizontal flipping, rotation, cropping, and brightness transformation. Ultimately, the number of sample images was increased to 1,000. The effect of data augmentation is shown in Figure 2.



a. Original image b. Mirror flip c. Rotation d. Cropping e. Brightness

Fig. 2 - Results of data augmentation

To ensure scientific training and testing of the model, the dataset consisting of 1,000 images was divided into training set and test set at a ratio of 8:2. To maintain an equal number of categories in both the training set and test set, stratified sampling was adopted. The number of labels for citrus flowers, fruits, and shoots in the dataset was statistically analyzed, and the label composition is shown in Table 1.

Table 1

Dataset Composition

Type	Data set	Flower	Fruit	Shoot
Train set	800	1813	1929	1351
Test set	200	465	483	338
Sum	1000	2278	2412	1689

Field Deployment and On-site Validation Pipeline

The proposed model was deployed on a handheld mobile terminal integrated with a monocular RGB camera, simulating a real-time in-field detection scenario. The system was calibrated under varying natural illumination conditions between 9:00 AM and 4:00 PM to cover extreme backlighting and shading conditions across different growth stages of citrus. Validation was conducted in a commercial citrus orchard located in Shanxi Juxin Modern Agricultural Demonstration Park. To ensure diversity, samples (fruits, flowers, and shoots) were collected from peripheral (outer canopy) and inner canopy layers, as well as from low-hanging and upper branches, to represent the occlusion complexity in real harvesting environments. Images were captured at a resolution of 1920 × 1080 with a fixed working distance of 0.5 m to 1.5 m. A total of 200 images were collected, consisting of 52 images of flowers, 57 images of fruits, and 99 images of shoots. Due to the difficulty of manual labeling in dynamic outdoor backgrounds, a pre-labeling correction strategy was adopted: initial bounding boxes were generated by the model and then manually corrected by three expert agronomists using LabelImg to establish the high-confidence ground truth for the validation set.

Improved YOLOv10 Model

YOLOv10 is a new generation real-time object detection model proposed by the research team at Tsinghua University in 2024 (*Wang et al., 2024*). Building upon the classic "backbone-neck-head" three-stage architecture inherited from the YOLO series, it achieves breakthroughs in detection performance and computational efficiency through two core innovations.

First, YOLOv10 proposes a consistent dual label assignment strategy, deploying both a one-to-many head (providing rich supervision signals) and a one-to-one head (simulating inference output) during training, while retaining only the latter during inference.

This fundamentally eliminates the reliance on non-maximum suppression (NMS) post-processing, significantly reducing inference latency and simplifying the deployment process. Second, it systematically optimizes the architecture from both efficiency and accuracy perspectives. In terms of efficiency, it adopts lightweight classification heads, spatially-channel decoupled downsampling, and rank-guided module design to reduce computational redundancy. In terms of accuracy, it introduces large-kernel depthwise convolutions in deeper stages to expand the receptive field, and designs a partial self-attention mechanism to enhance global feature representation capability at minimal computational cost. Based on these designs, YOLOv10 achieves industry-leading detection performance while significantly reducing inference latency and computational overhead. The network structure is shown in Figure 3.

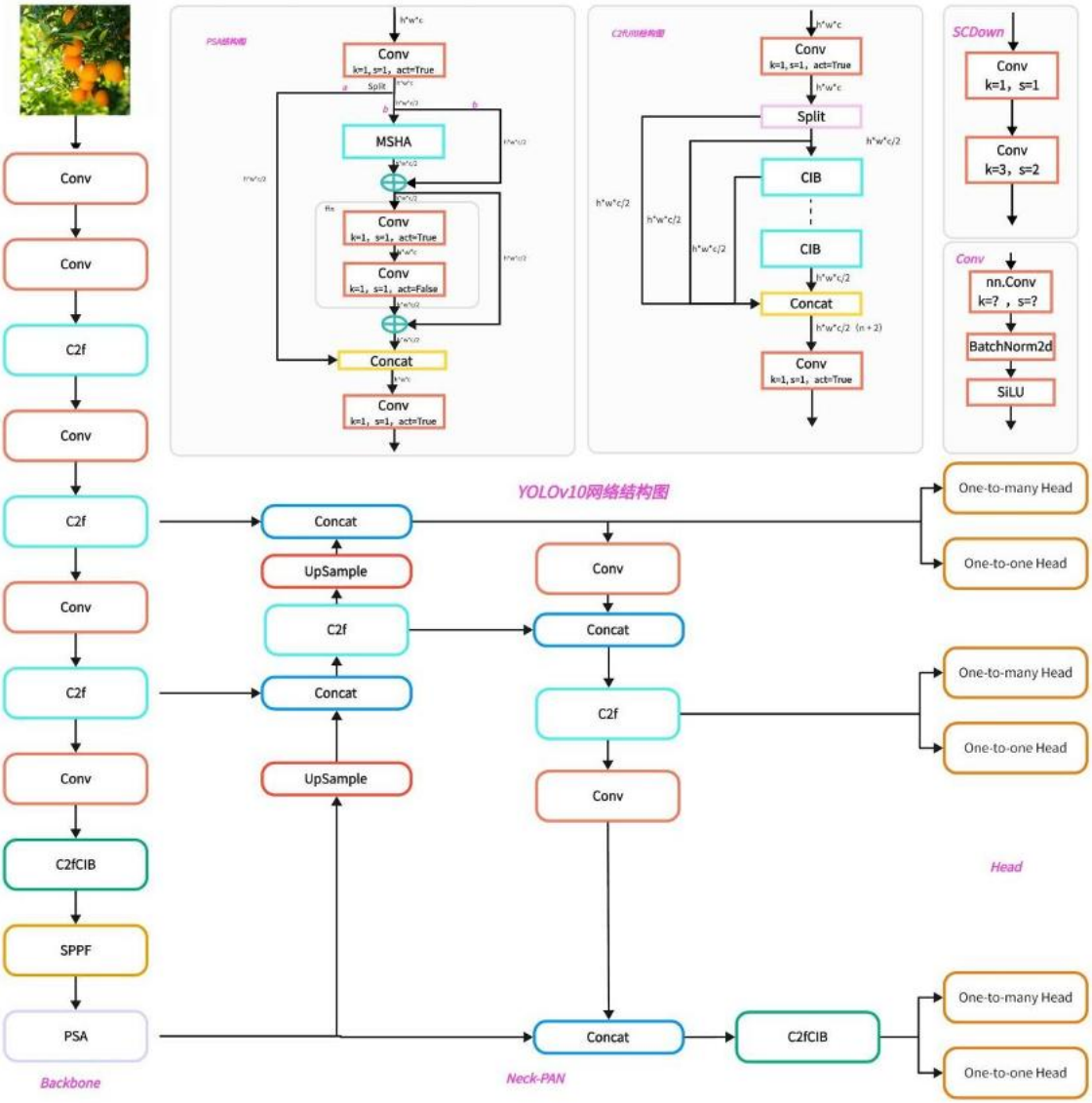


Fig. 3 - Structure of the YOLOv10 network

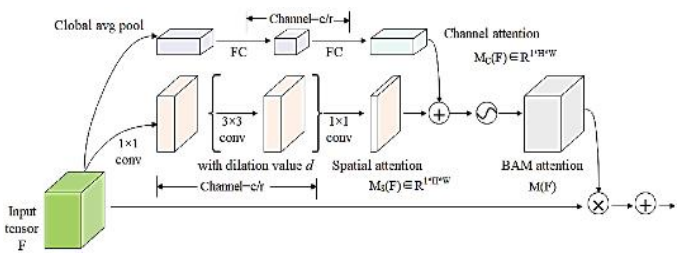


Fig. 4 - BAM Calculation mode

In this paper, the BAM (Bottleneck Attention Module) attention mechanism is incorporated into the neck network of the YOLOv10 model. BAM is an attention mechanism that combines both spatial and channel dimensions(*Park et al., 2020*). For a given feature map, this module processes it through channel attention and spatial attention branches separately to generate a 3D attention map. The specific workflow and structure are illustrated in Figure 4.

The BAM attention module can be integrated with any convolutional neural network, inferring attention maps along both spatial and channel dimensions to generate a 3D attention map that emphasizes important elements. This module combines two attention branches to reduce computational cost and parameter count, while employing residual learning to facilitate gradient flow.

In object detection tasks, IoU is used to measure the overlap between the predicted and ground truth box. Generalized Intersection over Union (GIoU) (*Rezatofighi et al., 2019*) is a loss calculation method for bounding boxes prediction derived from IoU that is scale-invariant. Compared with IoU Loss optimization part is: adding the influence of non-overlapping regions (in the prediction bounding box and the ground truth box there is no overlap part can also reflect the distance between the two boxes), can better measure to the degree of overlap, has a faster convergence speed. The formula is shown below:

$$GIoU = IoU - \frac{A^c - u}{A^c} \tag{1}$$

$$L_{GIoU} = 1 - GIoU \tag{2}$$

As can be seen from the formula, the final result of calculating GIoU Loss is returned as 1-GIoU. Since the value of 1-GIoU is in the range of [0,2] and has a certain “distance” property, i.e., the larger the overlap area between the predicted bounding box and ground truth box, the smaller the loss, and vice versa, the larger it is; and it can avoid the influence of the target shape size and more accurately reflect the interrelationships of the boxes, and possesses scale invariance.

Evaluation metrics

To evaluate the effectiveness of the proposed method, this experiment selects evaluation metrics from multiple dimensions. For model performance evaluation, precision (P), recall (R), mean average precision at IoU threshold 0.5 (mAP50), mean average precision averaged over IoU thresholds ranging from 0.5 to 0.95 with a step size of 0.05 (mAP50-95), and the harmonic mean of precision and recall (F1-score) are adopted. For performance efficiency evaluation, floating point operations (FLOPs), number of parameters (Parameters), and weight model memory size (weights size) are included. The specific formulas for each metric are as follows:

$$\text{Presicion} = \frac{\text{TP}}{\text{TP}+\text{FP}} \tag{3}$$

$$\text{Recall} = \frac{\text{TP}}{\text{TP}+\text{FN}} \tag{4}$$

$$\text{Accuracy} = \frac{\text{TP}+\text{TN}}{\text{TP}+\text{FP}+\text{TN}+\text{FN}} \tag{5}$$

$$\text{F1-score} = \frac{2 \bullet \text{Presicion} \bullet \text{Recall}}{\text{Presicion}+\text{Recall}} \tag{6}$$

In the formulas, TP (True Positive) represents the number of correctly predicted targets (both prediction and ground truth are positive), FP (False Positive) represents the number of incorrectly predicted targets (ground truth is negative but prediction is positive), TN (True Negative) represents the number of non-target regions correctly detected as non-targets (both prediction and ground truth are negative), and FN (False Negative) represents the number of missed targets (ground truth is positive but prediction is negative). The F1-score is the harmonic mean of precision and recall.

RESULTS

To comprehensively compare the performance of YOLOv10 models in citrus flower, fruit, and shoot detection, this study selected four models—YOLOv5s (*Jocher et al., 2021*), YOLOv7s (*Wang et al., 2023*), YOLOv8s (*Jocher et al., 2023*), and YOLOv10s—along with the improved YOLOv10s model for comparative experiments. Each model was trained and evaluated on the same dataset with identical training parameters, ensuring the comparability of test results. The baseline detection performance of each model is presented in Table 2.

Table 2

Comparison of Efficiency Performance Among Different Models

model	Params/M	FLOPs/G	VRAM/MB	F1-Score
YOLOv5s	7.0	15.8	159	0.797
YOLOv7s	13.0	33.1	180	0.831
YOLOv8s	11.1	28.4	145	0.793
YOLOv10s	8.0	24.5	127	0.814
YOLOv10s-BAM	8.2	25.2	127	0.827
YOLOv10s-BAM-GIoU	8.2	25.8	127	0.842

To comprehensively evaluate the effectiveness of the improvement strategy, this study conducted a quantitative comparative analysis of the detection performance of different models. In terms of model complexity, the original YOLOv10s has 8.0M parameters, 24.5G FLOPs, and 127MB VRAM usage, while the improved YOLOv10s-BAM-GIoU model has 8.2M parameters, 25.8G FLOPs, and maintains 127MB VRAM usage, indicating that the introduction of the BAM attention mechanism and GIoU loss function brings only minimal computational overhead without imposing additional burden on VRAM usage. In terms of detection accuracy, the original YOLOv10s achieves an F1-score of 0.814, outperforming YOLOv5s (0.797) and YOLOv8s (0.793), but lower than YOLOv7s (0.831). After introducing the BAM attention mechanism, the F1-score of YOLOv10s-BAM increases to 0.827. With the further integration of the GIoU loss function, the F1-score of YOLOv10s-BAM-GIoU reaches 0.842, representing a 2.8 percentage point improvement over the original YOLOv10s and a 1.1 percentage point improvement over YOLOv7s, achieving the optimal performance among all compared models. These results demonstrate that the BAM attention mechanism effectively enhances the model's feature extraction capability for small target organs under complex backgrounds, while the GIoU loss function improves the localization accuracy of densely occluded targets by optimizing the geometric alignment between predicted and ground-truth boxes. The synergistic effect of these two improvements enables the YOLOv10s-BAM-GIoU model to achieve significant detection accuracy gains with minimal computational overhead, validating the effectiveness and superiority of the proposed improvement strategy in complex agricultural scenarios.

To comprehensively evaluate the effectiveness of the proposed improvement strategy, comparative experiments were conducted on six models using a self-constructed citrus flower, fruit, and shoot dataset, with mAP@0.5, mAP@0.5-0.95, and per-class average precision as evaluation metrics. The comparison results of accuracy metrics are shown in Table 3.

Table 3

Comparison of Accuracy Performance Among Different Models

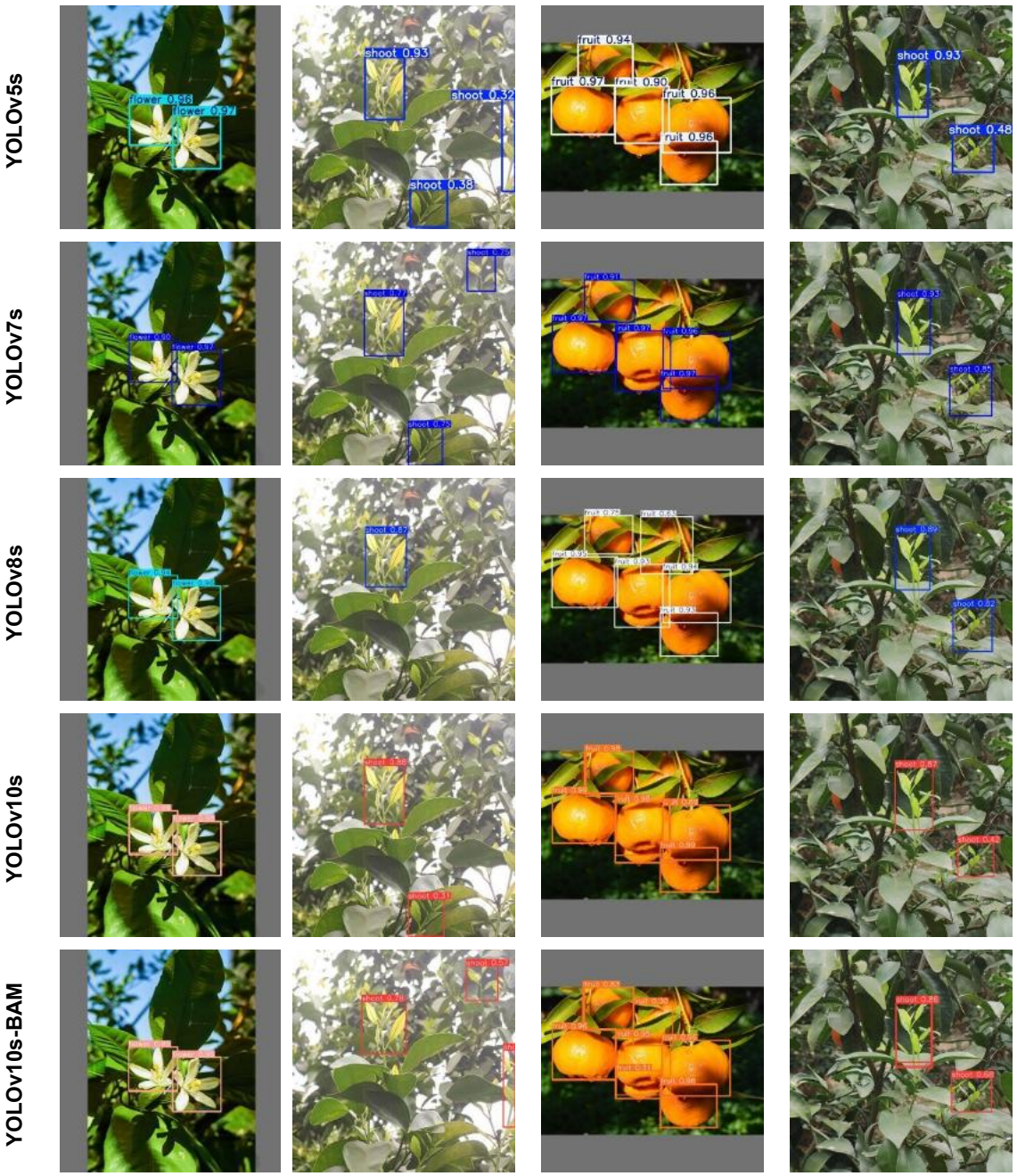
Model	mAP@0.5	mAP@0.5-0.95	Flower	Fruit	Shoot
YOLOv5s	0.831	0.521	0.806	0.782	0.904
YOLOv7s	0.862	0.541	0.864	0.81	0.912
YOLOv8s	0.842	0.539	0.839	0.779	0.909
YOLOv10s	0.796	0.483	0.810	0.724	0.853
YOLOv10s-BAM	0.854	0.539	0.849	0.804	0.908
YOLOv10s-BAM-GIoU	0.891	0.576	0.912	0.836	0.925

The original YOLOv10s achieved mAP@0.5 of 79.6% and mAP@0.5-0.95 of 48.3%, underperforming compared to YOLOv5s (83.1%/52.1%) and YOLOv7s (86.2%/54.1%), likely due to its lightweight design limiting feature capture capability for small targets in complex agricultural scenes. After introducing the BAM attention mechanism, YOLOv10s-BAM achieved mAP@0.5 of 85.4% (a 5.8 percentage point improvement) and mAP@0.5-0.95 of 53.9% (a 5.6 percentage point improvement), demonstrating that the BAM module enhances feature extraction for small target organs under complex backgrounds through parallel channel-spatial attention. With the further integration of the GIoU loss function, YOLOv10s-BAM-GIoU achieved optimal performance among all compared models, with mAP@0.5 reaching 89.1% (a 3.7 percentage point improvement over YOLOv10s-BAM) and mAP@0.5-0.95 reaching 57.6% (a 3.7 percentage point improvement). Compared to the original YOLOv10s, mAP@0.5 improved by 9.5 percentage points and mAP@0.5-0.95 by 9.3 percentage points; compared to the baseline optimal model YOLOv7s, improvements of 2.9 and 3.5 percentage points were achieved, respectively.

In terms of per-class detection accuracy, the original YOLOv10s achieved 81.0%, 72.4%, and 85.3% for flowers, fruits, and shoots, respectively, with relatively lower accuracy for fruits possibly due to dense overlap and similar color to the background. After introducing the BAM attention mechanism, detection accuracy for the three categories improved to 84.9%, 80.4%, and 90.8%, respectively.

With the further integration of the GIoU loss function, YOLOv10s-BAM-GIoU achieved 91.2%, 83.6%, and 92.5% for flowers, fruits, and shoots, representing improvements of 10.2, 11.2, and 7.2 percentage points over the original YOLOv10s, and 4.8, 2.6, and 1.3 percentage points over YOLOv7s, respectively. Notably, the most significant improvements were observed for small targets (flowers and fruits), validating the effectiveness of the proposed improvement strategy for small target recognition in complex scenes. These results demonstrate that while the original YOLOv10s has certain limitations in complex agricultural scenarios, the introduction of the BAM attention mechanism and GIoU loss function effectively compensates for these shortcomings. The synergistic effect of BAM enhancing feature representation for small target organs and GIoU optimizing localization accuracy enables YOLOv10s-BAM-GIoU to achieve significant detection performance improvements with minimal increases in parameters and computational overhead, validating the effectiveness and superiority of the proposed improvement strategy for citrus flower, fruit, and shoot recognition tasks.

To validate the effectiveness of the proposed model in complex environments, the six models in this study were visualized under front-lighting, back-lighting, occlusion, and background interference conditions respectively. The comparison results are show in Figure 5.





front-lighting back-lighting occlusion background interference

Fig. 5 - Visualization of model recognition results under different scenes

In the comprehensive detection task of citrus flower, fruit, and shoot recognition, the detection performance of each model under different lighting and occlusion conditions showed significant differences. Under front-lighting conditions, YOLOv5s, YOLOv7s, YOLOv8s, YOLOv10s, YOLOv10s-BAM, and YOLOv10s-BAM-GIoU all demonstrated good detection performance, accurately identifying various citrus organs. Under back-lighting conditions, although YOLOv5s, YOLOv8s, and YOLOv10s could capture citrus shoots at image edges, they exhibited varying degrees of missed detection for small targets; YOLOv7s and YOLOv10s-BAM-GIoU showed stronger small-target recognition capabilities, though missed detections still occurred for targets at image boundaries.

Detection results under occlusion conditions further revealed performance differences among the models. For scenarios with partial leaf occlusion and large-area fruit occlusion, YOLOv5s, YOLOv7s, and YOLOv10s all exhibited varying degrees of missed detection; YOLOv8s performed poorly only under large-area occlusion; YOLOv10s-BAM detected all targets, but annotation completeness required improvement; YOLOv10s-BAM-GIoU performed optimally under occlusion scenarios, achieving the highest detection rate and better annotation accuracy. Under complex background interference conditions, all models demonstrated relatively stable detection performance.

To evaluate model applicability under real agricultural conditions, YOLOv10s and YOLOv10s-BAM-GIoU were validated using 200 unaugmented images from Shanxi Juxin Park, covering backlighting, occlusion, fruit overlap, and tiny shoots without augmentation. The results are presented in Table 4.

Table 4

Validation Results of YOLOv10s and YOLOv10s-BAM-GIoU on The Field Dataset

Model	mAP@0.5	mAP@0.5-0.95	Flower	Fruit	Shoot
YOLOv10s	0.790	0.498	0.741	0.883	0.746
YOLOv10s-BAM-GIoU	0.812	0.519	0.771	0.907	0.757

The proposed YOLOv10s-BAM-GIoU achieves a mAP@0.5 of 81.2% on the challenging field dataset, representing a 2.2% absolute improvement over the standard YOLOv10s (79.0%). Moreover, the proposed model demonstrates its most substantial improvement over YOLOv10s on the "Flower" category (a 3.0 percentage points improvement, from 74.1% to 77.1%), followed by "Fruit" (a 2.4 percentage points improvement) and "Shoot" (a 1.1 percentage points improvement). These enhancements confirm that the integration of the BAM attention mechanism and GIoU loss function effectively mitigates environmental disturbances, particularly in scenarios with complex backgrounds and variable illumination. An unexpected yet insightful finding from the field validation is the superior detection performance for ''Fruit'' (AP = 90.7%) compared to ''Flower'' (77.1%) and ''Shoot'' (75.7%). This contrasts with the common assumption that fruits, being larger and more prone to occlusion, would exhibit the greatest performance degradation. This phenomenon is attributed to two principal factors: (i) the spherical shape and distinctive orange coloration of citrus fruits generate strong contrast against the green foliage background, facilitating robust feature extraction even under variable illumination; and (ii) the field validation images predominantly captured fruits at mid-to-late developmental phases with prominent visual saliency, whereas flowers and shoots presented comparatively greater scale- and color-ambiguity challenges. These findings underscore the importance of category-specific optimization in agricultural vision systems, particularly for enhancing small-target and low-contrast detection.

Comprehensive test results indicate that YOLOv10s-BAM-GIoU achieved the highest detection accuracy and annotation completeness under the most challenging back-lighting and occlusion scenarios. This model not only accurately identifies small targets but also possesses robust capabilities for handling occluded targets, demonstrating its advanced nature in complex agricultural production scenarios.

In conclusion, YOLOv10s-BAM-GIoU can be considered the optimal choice for citrus flower, fruit, and shoot recognition tasks, particularly suitable for complex environmental scenarios commonly encountered in agricultural production.

CONCLUSIONS

This study proposed an improved YOLOv10s model incorporating the BAM attention mechanism and GIoU loss function for the accurate recognition of citrus flowers, fruits, and shoots in complex orchard environments. The experimental results demonstrate that the proposed YOLOv10s-BAM-GIoU model achieves superior detection performance, with an mAP50 of 89.1%, representing improvements of 2.9%~9.5% over the original YOLOv10s and other comparative models. In fine-grained category detection, the model attains mAP50 of 91.2%, 83.6%, and 92.5% for shoots, flowers, and fruits, respectively. The BAM attention mechanism enhances feature extraction capability for small target organs under complex backgrounds through parallel channel-spatial attention branches, while the GIoU loss function improves localization accuracy for densely occluded targets by optimizing geometric alignment between predicted and ground-truth boxes. The synergistic effect of these two improvements enables significant detection accuracy gains with minimal computational overhead, as evidenced by the model's parameter count of 8.2M, computational load of 25.8G FLOPs, and detection speed of 23.6 ms per frame, meeting real-time detection requirements for agricultural applications.

The comparative analysis of six models under varying environmental conditions further validates the robustness and practical applicability of the proposed approach. Under challenging scenarios such as back-lighting and severe occlusion, YOLOv10s-BAM-GIoU consistently outperformed other models, achieving the highest detection rates and annotation accuracy. While YOLOv5s, YOLOv7s, YOLOv8s, and the original YOLOv10s exhibited varying degrees of missed detections for small targets and occluded objects, the improved model demonstrated reliable performance in detecting targets at image boundaries, handling partial and large-area occlusion, and maintaining accuracy under complex background interference. These results confirm that the integration of attention mechanisms and optimized loss functions effectively addresses the key challenges in agricultural target detection, including scale variation, background clutter, and dense occlusion, thereby providing a robust solution for real-world orchard monitoring applications.

The field validation results confirm the model's robustness under realistic orchard conditions, achieving a mAP@0.5 of 81.2% with consistent improvements over the baseline YOLOv10s across all categories, with gains of 3.0 percentage points for "Flower", 2.4 percentage points for "Fruit", and 1.1 percentage points for "Shoot". Notably, an unexpected finding emerged: "Fruit" achieved the highest detection accuracy (AP = 90.7%), substantially surpassing "Flower" (77.1%) and "Shoot" (75.7%). The superior performance of "Fruit" is likely attributable to its higher visual saliency in field images, offering valuable insights for the design of practical agricultural vision systems.

In conclusion, this research contributes to the advancement of precision agriculture by presenting an efficient and accurate deep learning model for citrus organ detection. The YOLOv10s-BAM-GIoU model achieves an optimal balance between detection accuracy and computational efficiency, making it suitable for deployment in field real-time detection systems. The findings highlight the importance of synergistic architectural improvements—combining attention mechanisms for enhanced feature representation with optimized loss functions for precise localization—in addressing the specific challenges of agricultural computer vision tasks. Although the accuracy is somewhat reduced due to the field environment, the system still demonstrates sufficient robustness in specific scenarios, providing a practical reference for the subsequent intelligent management of citrus orchards. Future work could focus on expanding the dataset to include more diverse citrus varieties and growing regions, further optimizing the model for edge device deployment, and extending the approach to other fruit crops and phenological stages. Additionally, integrating the detection system with automated agricultural equipment for precision management practices such as targeted spraying, thinning, and harvesting could realize the full potential of this technology in smart agriculture applications.

ACKNOWLEDGEMENT

This work was supported by Fundamental Research Program of Shanxi Province (Grant No. 202303021212120).

REFERENCES

[1] El Akrouchi, M., Mhada, M., Bayad, M., Hawkesford, M. J., & Gérard, B. (2025). AI-based framework for early detection and segmentation of green citrus fruits in orchards. *Smart Agricultural Technology*, 10, 100834.

[2] Huang, Z., Li, X., Fan, S., Liu, Y., Zou, H., He, X., Xu, S., Zhao, J., & Li, W. (2025). ORD-YOLO: A Ripeness Recognition Method for Citrus Fruits in Complex Environments. *Agriculture*, 15(15), 1711.

[3] Jocher, G., Chaurasia, A., & Qiu, J. (2023). YOLO by Ultralytics (Version 8.0.0) [*Computer software*]. https://github.com/ultralytics/ultralytics.

[4] Jocher, G., Stoken, A., Borovec, J., et al. (2021). ultralytics/yolov5: v6.0 - YOLOv5n 'Nano' models, Roboflow integration, TensorFlow export, OpenCV DNN support. *Zenodo*.

[5] Li, H., Yin, Z., Zuo, Z., Pan, L., & Zhang, J. (2025). Precision citrus segmentation and stem picking point localization using improved YOLOv8n-seg algorithm. *Frontiers in Plant Science*, 16, 1655093.

[6] Lin, Y., Hu, W., Zheng, Z., & Xiong, J. (2023). Citrus identification and counting algorithm based on improved YOLOv5s and DeepSort. *Agronomy*, 13(7), 1674.

[7] Liu, W. H., Jian, C., Zhang, S. A., Cong, G. X., Wang, H. B., Li, J. Y., & Zheng, Y. Q. (2025). Enhanced YOLOv5s with BiFormer attention for citrus spring shoot detection: Optimized phenological period and cross-regional application. *Smart Agricultural Technology*, 101446.

[8] Lu, J., Lin, W., Chen, P., Lan, Y., Deng, X., Niu, H., ... Luo, S., (2021). Research on lightweight citrus flowering rate statistical model combined with anchor frame clustering optimization. *Sensors*, 21(23), 7929.

[9] Lyu, Q., Lin, G., Jiang, J., Wang, M., Zhang, H., & Yi, S. (2024). Detecting green citrus fruit in natural scenes using improved YOLOv5s model. *Transactions of the Chinese Society of Agricultural Engineering*, 40(18), 147-154.

[10] Park, J., Woo, S., Lee, J. Y., & Kweon, I. S. (2020). A simple and light-weight attention module for convolutional neural networks. *International Journal of Computer Vision, 128*(4), 783-798.

[11] Qin, X., Huang, R., & Hua, B. (2021, March). Research and implementation of yield recognition of Citrus reticulata based on target detection. In *Journal of physics: conference series.* Vol. 1820, No.1, p.012128). IOP Publishing.

[12] Qiu, X., Zhu, F., Huang, P., Chen, H., Li, Y., Pu, C., & Wang, S. (2025). Quantifying high-temperature-induced reproductive growth imbalance in citrus at anthesis: Insights from the CF-ASPM model. *Computers and Electronics in Agriculture*, 236, 110421.

[13] Rezatofighi, H., Tsoi, N., Gwak, J., Sadeghian, A., Reid, I., & Savarese, S. (2019). Generalized intersection over union: A metric and a loss for bounding box regression. *In Proceedings of the IEEE/CVF conference on computer vision and pattern recognition*. pp. 658-666.

[14] Subeesh, A., Kumar, S. P., Chakraborty, S. K., Upendar, K., Chandel, N. S., Jat, D., ... Khan, M. M., (2024). UAV imagery coupled deep learning approach for the development of an adaptive in-house web-based application for yield estimation in citrus orchard. *Measurement*, 234, 114786.

[15] Ünal, İ., Eceoğlu, O., (2025). A Lightweight Instance Segmentation Model for Simultaneous Detection of Citrus Fruit Ripeness and Red Scale (Aonidiella aurantii) Pest Damage. *Applied Sciences*, 15(17), 9742.

[16] Wang, A., Chen, H., Liu, L., Chen, K., Lin, Z., Han, J., & Ding, G. (2024). Yolov10: Real-time end-to-end object detection. *Advances in neural information processing systems*, 37, 107984-108011.

[17] Wang, C. Y., Bochkovskiy, A., & Liao, H. Y. M. (2023). YOLOv7: Trainable bag-of-freebies sets new state-of-the-art for real-time object detectors. *In Proceedings of the IEEE/CVF conference on computer vision and pattern recognition* (pp. 7464-7475).

[18] Xiao, X., Wang, Y., Jiang, Y., Wu, H., Zhang, Z., & Wang, R. (2024). AC-YOLO: citrus detection in the natural environment of orchards. *Journal of Agricultural Engineering*, 55(4).

[19] Xu, L., Zhu, S., Chen, X., Wang, Y., Kang, Z., Huang, P., & Peng, Y. (2020). Citrus recognition in real scenarios based on machine vision. *DYNA-Ingeniería e Industria*, 95(1).

[20] Yang, C. H., Xiong, L. Y., Wang, Z., Wang, Y., Shi, G., Kuremot, T., ... & Yang, Y. (2020). Integrated detection of citrus fruits and branches using a convolutional neural network. *Computers and Electronics in Agriculture*, 174, 105469.

[21] Yin, X. B., Deng, X. L., Lan, Y. B., & Chen, X. (2022). Intelligent recognition of citrus shoot growth based on improved YOLOX-Nano algorithm. *Journal of South China Agricultural University*, 44(1), 142-150.

DESIGN AND PERFORMANCE EVALUATION OF A TOBACCO-CLIP LOADING AND UNLOADING DEVICE FOR BULK-CURING BARNS

/

密集烤房烟夹装卸装置设计及性能试验

Qingqing LÜ[1)], Yunlan MAO[1)], Ruixue LIU[1)], Kun ZHAO[1)], Xiaodong LIU[1)], Guangxi LI[1)], Liquan YANG[1,2*)], Guangyu YIN[2*)]

[1)] Henan Province Engineering Research Centre of Ultrasonic Technology Application, Pingdingshan University, Pingdingshan 467000, China;

[2)] Pingdingshan Company, Henan Tobacco Company, Pingdingshan 467033, China;

***** *Corresponding author: Liquan YANG, Guangyu YIN*

Tel: +8618339975718; E-mail: 2695@pdsu.edu.cn, 17703758110@163.com

DOI: https://doi.org/10.35633/inmateh-79-48

Keywords: *tobacco bulk-curing barn; tobacco-leaf loading and unloading; semi-automatic auxiliary platform; scissor-lift mechanism; belt-scale control*

ABSTRACT

To address the high labour intensity, low operating efficiency, and safety risks associated with loading and unloading flue-cured tobacco leaves in bulk-curing barns, a tobacco-clip loading and unloading device suitable for the confined barn environment was developed. The device integrates a powered platform, a two-stage scissor-lift mechanism, and an online weighing and conveying system. Mechanical modeling and finite element analysis were conducted to verify the structural strength and overturning stability of the lifting mechanism under a rated load of 350 kg and a maximum lifting height of 3 m. The resulting overturning stability coefficient was approximately 2.9. Within an inclination range of 0°–25°, the mass-measurement error of the conveying system did not exceed 0.40%. Field performance tests showed that the maximum conveying rate reached one tobacco clip every 2.7 s. The loading time for a single bulk-curing barn was reduced from 4 h to 1.5 h, while the required labour force decreased from four workers to two. Overall operating efficiency increased by 4.33 times, and the mean time between failures met the requirements for continuous operation during the tobacco-curing season. The developed device enables efficient, low-cost, and reliable loading and unloading of flue-cured tobacco leaves and provides technical support for improving the quality and efficiency of flue-cured tobacco production.

摘要

针对密集烤房烟叶装卸作业中存在的劳动强度大、作业效率低、安全隐患突出等问题，研究设计了一种适配密集烤房环境的烤房烟夹装卸装置。该装置集成了动力平台、二级剪叉式升降机构、在线称重输送系统，以适应烤房狭小空间。通过力学建模与有限元分析，验证了升降装置在额定载荷 350 kg、最大升降高度 3 m 条件下的结构强度与抗倾覆稳定性，抗倾覆系数 K≈2.9；输送系统在 0°–25°倾斜范围内的质量检测误差率不超过 0.40%；现场性能测试表明，装置单夹运输时间最短为 2.7 s，每烤房装烟时间由人工的 4 小时缩短至 1.5 小时，用工由 4 人减少至 2 人，作业效率提升了 4.33 倍，平均无故障运行时间满足烤烟季连续作业要求。该装置实现了烟叶装卸的高效低成本与高可靠性，为烤烟生产的提质增效提供了技术支撑。

INTRODUCTION

China is one of the world's major producers of flue-cured tobacco, and most of the crop is now cured in bulk-curing barns *(Liu, 2024)*. Over the past two decades, field operations from transplanting to stalk removal have become increasingly mechanized; however, tobacco loading and unloading are still performed manually. High labour costs, heavy workloads, and a low level of operational standardization remain the main challenges at this stage. Together, these constraints have hindered the tobacco industry's transition toward more efficient, large-scale, and intensive production.

Curing quality depends on two things: how the fans and heat exchangers hold airflow, temperature and humidity, and how the sticks are stacked on the racks (*Liang et al., 2014*). The heat side has moved faster. Ge et al. optimised a tobacco-drying heat pump that recovers waste heat from a nearby data centre, cutting the primary energy input while keeping drying temperatures within target (*Ge et al., 2024*). Wang et al. took a related route, integrating dehumidification into an air-source heat pump and reporting an average COP of 2.85 across a full curing cycle (*Wang et al., 2025*).

Both gains assume that the sticks are already stacked evenly and that the load per rack is known. Neither condition can be checked by the barn operator in the field today.

Zhang built a toppling-rotary rig that swings sticks from a horizontal frame onto the vertical racks (*Zhang, 2023*), and Jiao followed with an inclination stage that lets the loaded rack tilt into position (*Jiao, 2025*). *Lin et al*. and *Ai et al*. took a different route, using a side-mounted chain to hoist the sticks along the barn wall, which gives a smaller footprint and lower peak power (*Ai et al., 2025; Lin et al., 2021*). What none of these prototypes offers is a lift geometry sized to the door and rack layout of a Chinese curing barn, or an on-line record of the weight loaded onto each rack.

Guo et al. reported a mast-lift loading machine for dense curing barns, raising sticks to 1.3–3.6 m and tilting them by 0–32° through staggered linear modules; field trials returned a loading success rate above 90% at 2.89–4.60 times the throughput of manual work (*Guo et al., 2026*). However, this prototype does not record the weight loaded onto each rack, nor is it sized as a station platform placed at the barn door. These are the two functions that determine whether uneven rack loading can be detected before firing begins.

Islam et al. used a bond-graph model to predict the dynamic response of a scissor lift under load (*Islam et al., 2014*). Their study did not extend to static structural strength or anti-tipping stability under an off-centre agricultural payload. These are the conditions a barn-door platform must survive when a fully loaded rack is lifted to 3 m. For on-line weighing during the handling cycle, *Cveticanin, (2003),* proposed a walking-speed model that keeps the weighing error low while the payload moves on a horizontal belt. The accuracy of that approach on a tilted belt has not been reported. The present work addresses both gaps: FEA-based static and anti-tipping verification and belt-scale calibration over a 0°-25° tilt range.

This study designs and tests a loading and unloading device for cured tobacco, sized to the operating conditions inside a dense curing barn. The working environment and the load requirements were analysed first, and the overall layout of the power platform, the two-stage scissor lift, the conveying system and the control unit was drawn up on that basis. The strength and stability of the key parts were then checked by mechanical calculations and finite element analysis. A prototype was built and taken to a working barn, where its efficiency, safety and reliability were measured. The goal is a compact and easy-to-operate machine that lowers the physical load on operators, raises loading throughput, and supports the mechanisation and large-scale operation of tobacco curing.

MATERIALS AND METHODS

Overall structural design of the loading and unloading device for tobacco clips

The loading and unloading device for tobacco clips comprises a power platform, lifting device, conveying system, and control system. The power platform includes a power system and walking mechanism (*Li and Kang, 2020*). The walking mechanism adopts a four-wheel-drive design and is driven by an electrically remote-controlled chassis. The lifting device is a core component of the system. It uses a compact and highly load-resistant two-stage scissor-type lifting mechanism, which is driven by a hydraulic system to adapt to the maximum height of the tobacco rack in the curing barn. The conveying platform adopts a chain roller-driven conveyor belt structure with an adjustable inclination to improve conveying efficiency. The control system integrates weighing sensors, speed sensors, and proximity switches to achieve automatic control. The overall structure of the device is shown in Figure 1, and the main parameters are listed in Table 1.

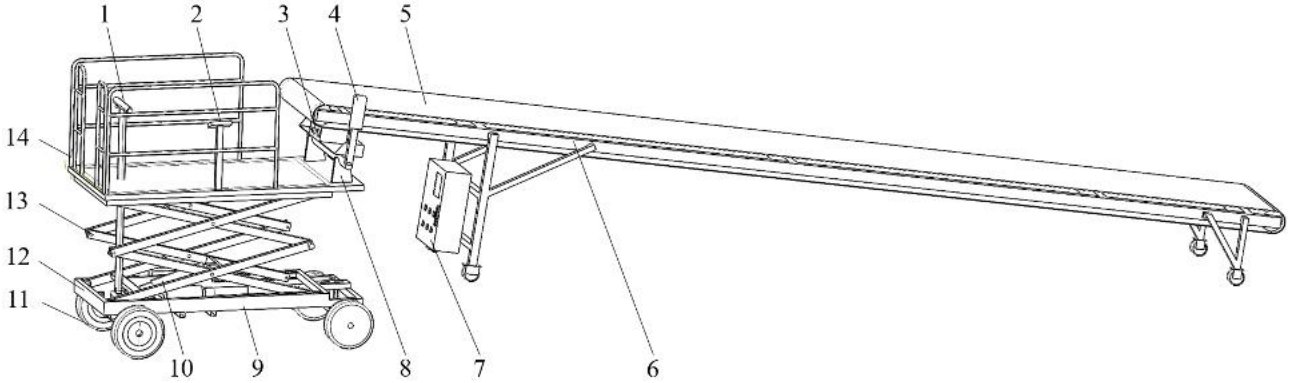


Fig. 1 - Structure diagram of the loading and unloading device for tobacco racks in the curing barn

(1) Steering handle; (2) Remote control panel; (3) Start button; (4) Proximity switch; (5) Conveyor belt; (6) Truss-type steel structure frame; (7) Control cabinet; (8) Front fork; (9) Remote-controlled electric chassis; (10) Hydraulic cylinder; (11) Walking wheels; (12) Battery box; (13) Scissor mechanism; (14) Fence

Table 1

Main Parameters of the Tobacco-Rack Loading and Unloading Device

Parameter	Value
Overall dimensions [mm]	8000×1000×3000
Rated platform load [kg]	350
Rated conveyor load [kg]	150
Power supply [V]	AC 220, DC 48
Power [W]	AC 375, DC 1000
Belt speed [m/min]	22
Adjustable inclination angle [°]	0–25
Number of operators	2

Design of the Lifting Device

Overall design of the lifting device

As the core component of the device, the lifting mechanism directly determines the efficiency and safety of the loading and unloading process. The scissor mechanism is the core component of the lifting device, and its design parameters affect the lifting performance (*Paramasivam et al., 2021*). *Huy et al. (2022)* used the MARCOS multi-criteria decision-making method to optimise the choice of scissor mechanism. Following their approach, and taking the working conditions and design requirements into account, a two-stage scissor mechanism was adopted here.

The structure is illustrated in Figure 2.

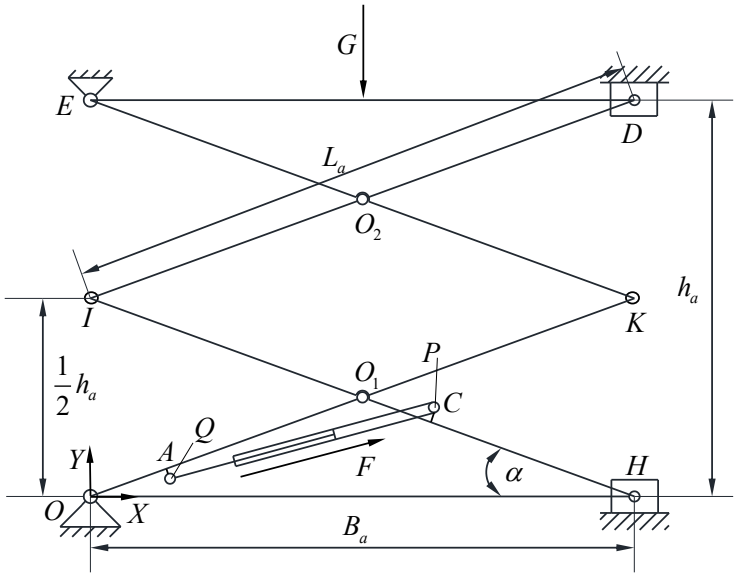


Fig. 2 - Schematic of the scissor-lift mechanism

As shown in Figure 2, O is the origin of the lifting structure coordinate system, DE is the worktable, AC is the lifting hydraulic cylinder, and B_a is the distance between O and H. EK, KO, DI, and IH are the scissor arms; L_a is the length of the scissor arm; O_1O, O_1H, O_1K, O_1I, O_2I, O_2K, O_2D, and O_2E have the same length; P and Q are the connection points between the upper and lower ends of the lifting hydraulic cylinder and scissor arms; O is the hinge point between the scissor arm and frame; E is the hinge point between the scissor arm and worktable; O_1 and O_2 are the hinge points of the two scissor arms; h_a is the lifting height of the worktable; G is the total weight of the worktable and load; α is the angle between the scissor arm and horizontal plane; and F is the thrust of the lifting hydraulic cylinder (*Yu, 2021*).

Optimisation of the hydraulic cylinder therefore focused on three factors: the maximum load, the stroke, and the movement speed. The force conditions of the scissors-lifting mechanism during the lifting process are illustrated in Figure 3.

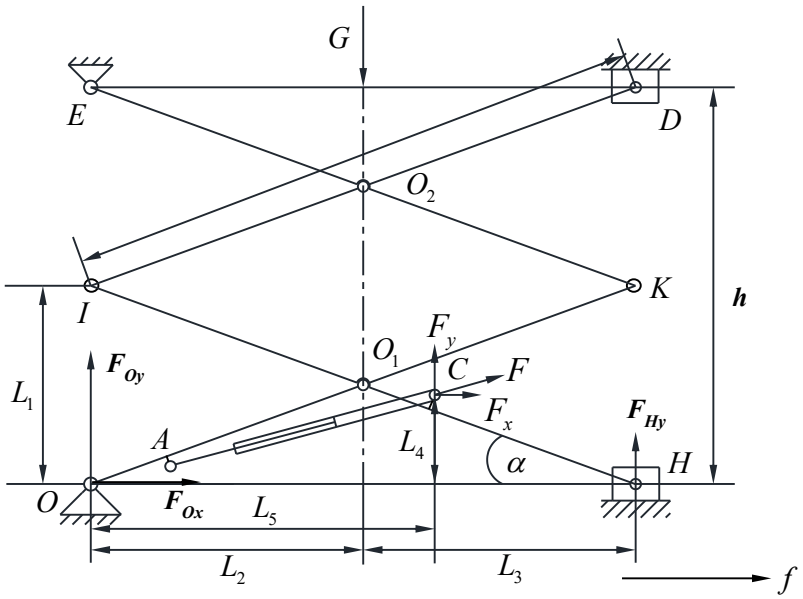


Fig. 3 - Force analysis of the scissor-lift mechanism

As shown in Figure 3, F_{Ox} and F_{Oy} are the horizontal and vertical restraining forces of the fixed hinge support O point on the mechanism, respectively; F_x and F_y are the horizontal and vertical components of the hydraulic cylinder thrust F, respectively; F_{Hy} is the vertical supporting force of the sliding hinge support H on the mechanism; f is the sliding friction force generated between the sliding hinge support H and the guide rail; L_1 is the vertical distance from the fixed hinge support O point to the hinge point I; L_2 is the horizontal distance from the fixed hinge support O point to the symmetry centre line of the mechanism; L_3 is the horizontal distance from the sliding hinge support H to the symmetry centre line of the mechanism; L_4 is the vertical distance from the force point C of the hydraulic cylinder to OH; and L_5 is the horizontal distance from the fixed hinge support O point to the force point C of the hydraulic cylinder. According to Figure 3, the equilibrium equation is listed as follows:

$$F_x = F\cos\alpha \tag{1}$$

$$F_y = F\sin\alpha \tag{2}$$

$$F_{O_x} + F_x + f = 0 \tag{3}$$

$$F_{O_y} + F_{H_y} + F_y - G = 0 \tag{4}$$

$$f = F_{H_y} \times \mu \tag{5}$$

At point O, list the torque equilibrium equation

$$G \cdot L_2 + F_{H_y} \cdot (L_2 + L_1) + F_x \cdot L_4 + F_y \cdot L_5 = 0 \tag{6}$$

It is assumed that the hydraulic cylinder drives the scissor-lifting mechanism at a constant speed under the thrust force. The vertical height at which the centre of mass rises per unit time is h, the vertical distances moved by the two ends of the hydraulic cylinder are h_1 and h_2, and the distance moved at point H is s. According to the law of conservation of energy:

$$F \cdot h_1 + F_1 \cdot h_2 = G \cdot h + f \cdot s \tag{7}$$

$$F + F_1 = 0 \tag{8}$$

From Eq. (7) and (8),

$$F = \frac{G \cdot h + f \cdot s}{h_1 - h_2} \tag{9}$$

The above analysis determines the quantitative relationship between the thrust, external load, and frictional resistance of the hydraulic cylinder and the vertical displacement of the hydraulic cylinder. This inclined-cylinder layout gives good space use, a reliable structure and a compact arrangement, and was

therefore adopted (*Liu, 2022*).

The lifting device is composed of a scissor arm assembly, hydraulic cylinders, guiding mechanism, platform frame, and limit switches, and can achieve safe and reliable lifting. Considering the working conditions of the tobacco rack in the curing barn with a height of 3.6 m, the maximum lifting height of the device was determined to be 3 m. When the machine is fully lowered, the height is 0.5 m, which meets the requirements for free movement within the curing barn. A dedicated wireless remote control (Fonda electronic power unit) provides precise control of chassis movement. The structure of the lifting device is shown in Figure 4, and the design parameters are listed in Table 2.

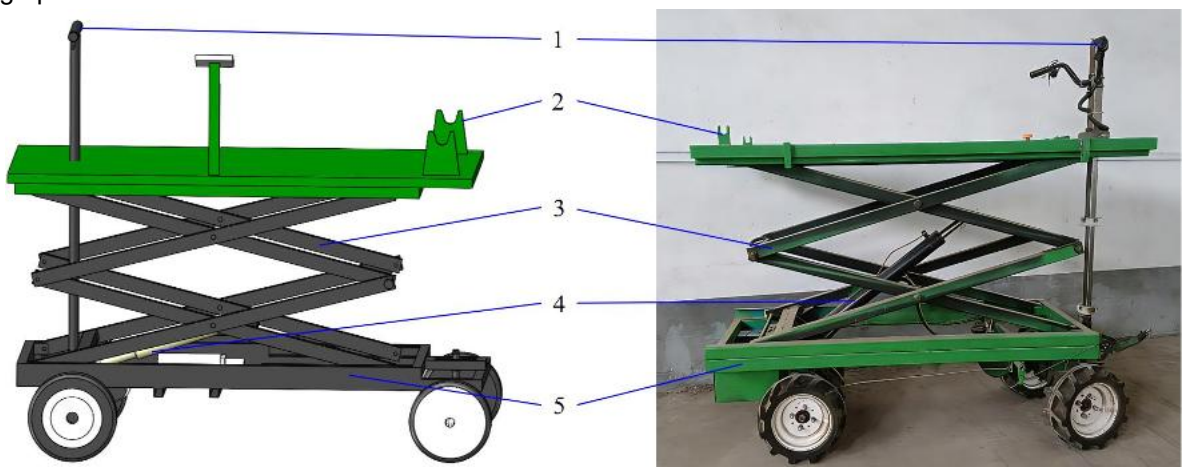


Fig. 4 - Structure of the lifting device

(1) Steering handle; (2) Front fork; (3) Scissor-lift mechanism; (4) Hydraulic cylinder; (5) Remote-controlled electric chassis

Table 2

Design Parameters of the Lifting Device

Parameter	Value
Lifting-height range [m]	0.5-3
Platform dimensions [mm]	2000×1000
Rated load [kg]	350
Lifting speed [m/s]	0.1-0.3

Design of the Hydraulic System for the lifting device

The stability of the hydraulic system is a key guarantee for the safe operation of aerial work platforms (*Liu et al., 2020*). The hydraulic system adopts a stroke-segmental speed-regulating hydraulic cylinder (Luo, 2022). The non-hydraulic end of the cylinder is equipped with two independent oil ports, and the distance between the two oil ports matches the length of the piston-sealing section. This design provides a structural basis for the regulation of segmental speed. The basic configuration of the circuit is illustrated in Figure 5.

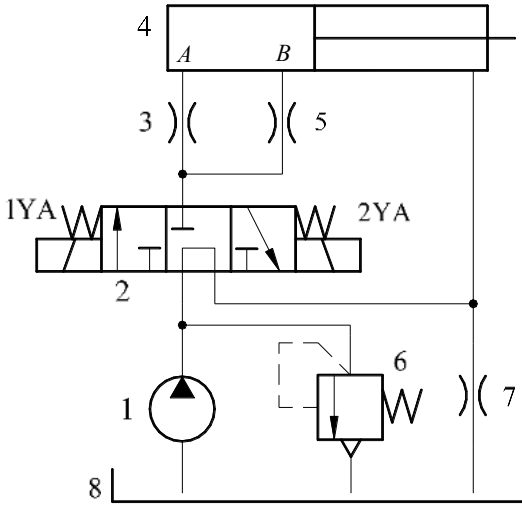


Fig. 5 - Schematic of the basic hydraulic system

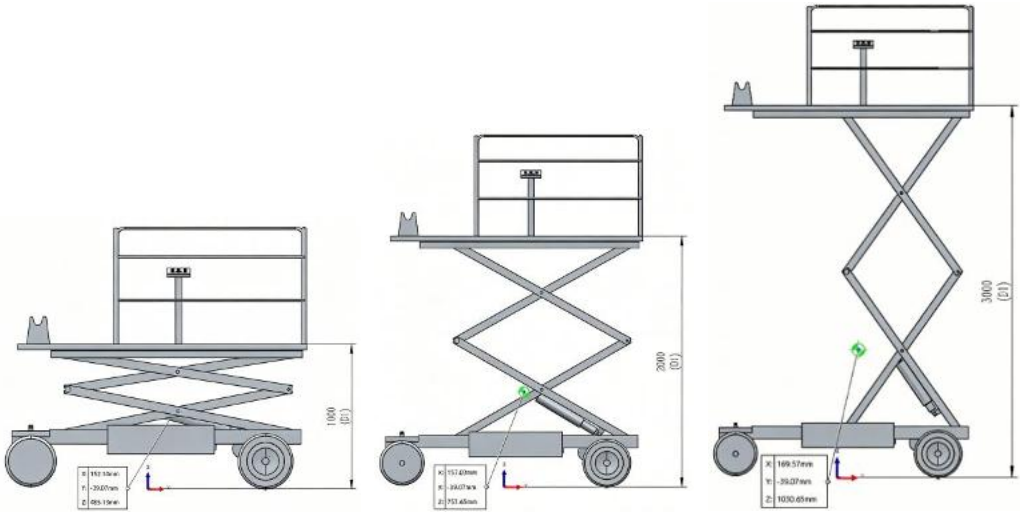
(1) hydraulic pump; (2) 3-position 3-way solenoid-operated directional control valve; (3) throttle valve; (4) hydraulic cylinder; (5) flow-control valve; (6) pressure-relief valve; (7) return-line throttle valve; (8) hydraulic oil tank

During the lifting stage of the workbench, after 1YA is energised, the hydraulic pump starts to operate, and the main directional control valve switches to the left position. The high-pressure oil is sent to the left chamber of the hydraulic cylinder through throttle valve 3, and the piston rod is moved to the right. When the piston is between points A and B, the piston rod moves at a lower velocity. After the piston rod passes point B, it accelerates and reduces the lifting time of the work platform.

During the descent stage of the work platform, when the 2YA is energised, the main reversing valve switches to the right position. Under the influence of the self-weight of the scissor mechanism, the hydraulic cylinder gradually retracts. The oil in the non-hydraulic cylinder chamber flows synchronously through throttle valves 3 and 5 in both directions and exits the chamber. The scissor-lifting platform then descends rapidly to the ground. When the piston moves to the left and passes point B, the movement speed of the hydraulic cylinder decreases. The scissor-lifting platform then falls back to the initial position at a lower speed, reducing the impact and ensuring smooth descent (*Yu et al., 2021*).

Analysis of the force on the lifting device

The centre of gravity of the lifting device directly determines the stability of the lifting process. Inside the narrow space of a curing barn, precise calculation and verification are needed to make sure the machine does not tip over under static or overload conditions. This analysis centres on a two-stage scissor-lift device. A Cartesian coordinate system was set up in SolidWorks. The plane containing the bottom of the scissor mechanism was taken as the reference plane, and the centre of that bottom as the origin. The centre of gravity coordinate points were obtained within the 1-3 m lifting range, as shown in Figure 6.



(a) Height 1000 mm *(b) Height 2000 mm* *(c) Height 3000 mm*

Fig. 6 - Point sampling process diagram

Based on the centre of gravity coordinate points, the overturning and restoring moments of the device were calculated and analysed. According to the rated load of 350 kg, the load force F = 350 × 9.8 = 3430 N. The mass of the device itself is 1046.494 kg, and its gravity G = 1046.494 × 9.8 = 10255.6412 N. The dimensions of the lifting platform are 2000 mm × 1000 mm, and the maximum lifting height is 3 m. At the maximum height, the Z-axis coordinate of the weight of the device was 1030.65 mm. The overturning moment calculation formula is shown in Eq. (10), and the restoring moment formula is presented in Eq. (11).

$$M_r = F \cdot h \tag{10}$$

where M_r is the overturning moment [N·m]; F is the load force [N]; and h is the centre of gravity height [m].

$$M_o = G \cdot d \tag{11}$$

where M_o is the restoring moment [N·m]; G is the gravity of the device [N]; and d is half the platform length.

The overturning moments at different elevations were calculated, and the results are shown in Figure 7.

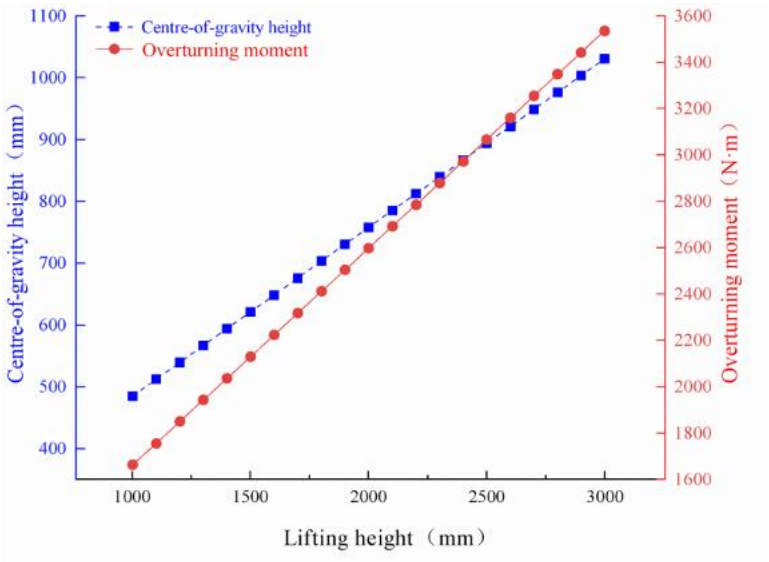


Fig. 7 - Variation in centre-of-gravity height and overturning moment with lifting height

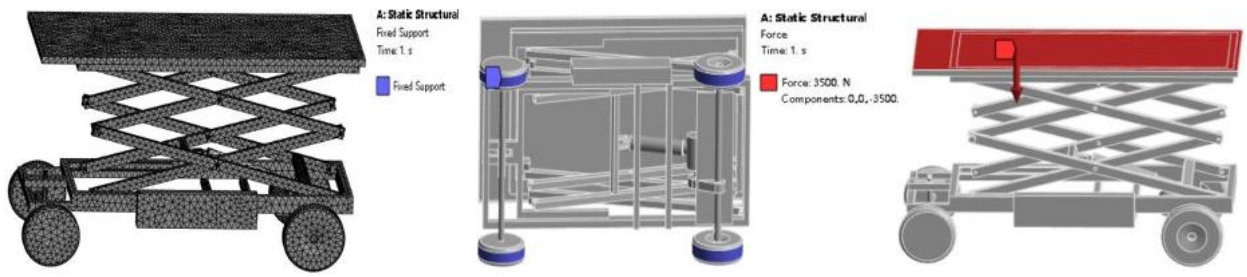
To further verify the overturning resistance capability of the device, the overturning coefficient K was introduced as an evaluation parameter. The overturning coefficient K must be determined. According to industry standards, K should be ≥ 1.5. The overturning moment at the highest point M_r = 3430 × 1.03065 = 3535.1295 N·m, and the restoring moment M_o = 10255.6412 × 1 = 10255.6412 N·m. The overturning coefficient is calculated using Eq. (12).

$$K = \frac{M_O}{M_r} = \frac{10255.6412}{3535.1295} \approx 2.9 \tag{12}$$

The results show that under the working condition of a maximum lifting height of 3 m and a rated load of 350 kg, the restoring coefficient K is approximately 2.9, which is higher than the safety limit value of 1.5 stipulated by the industry standards. This proves that the stability of the lifting device meets the design requirements set by industry standards (*Pan et al., 2017*).

Analysis of the Load-bearing Capacity of the Lifting Device

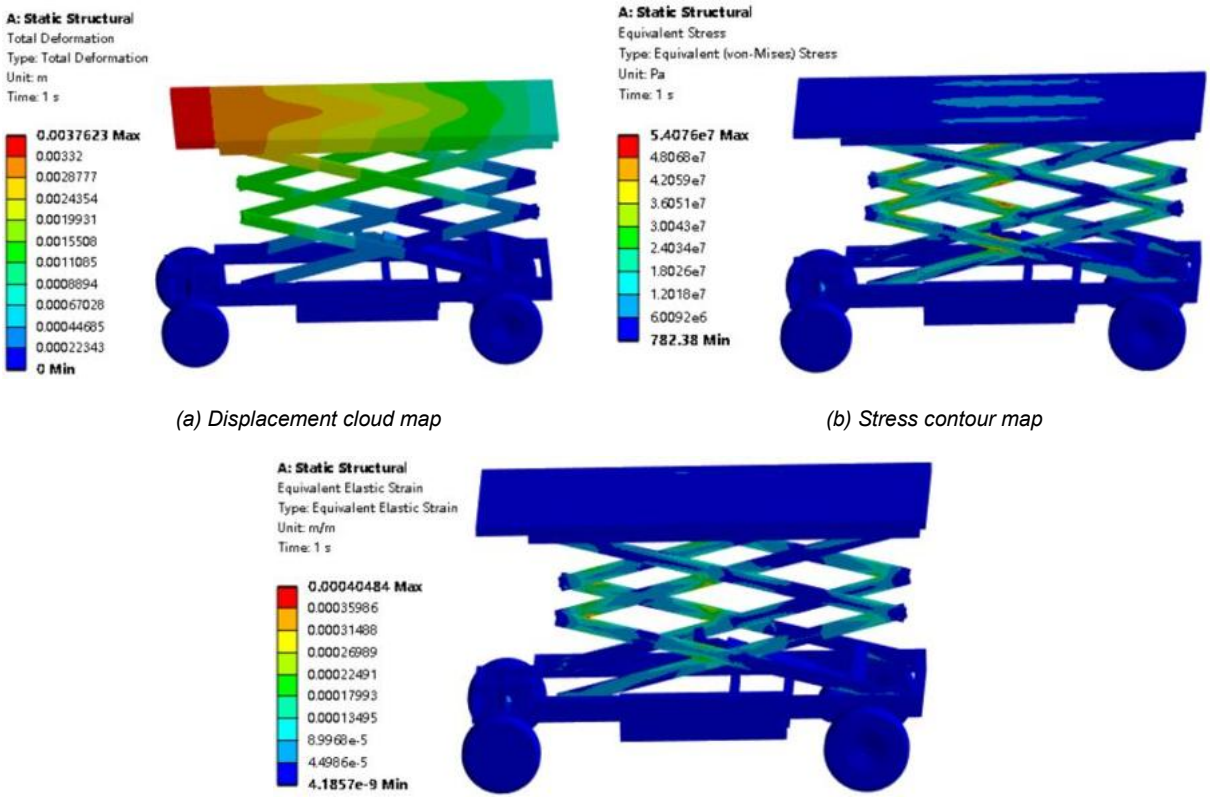
Finite element analysis is used to verify the structural strength and stiffness of scissor mechanisms. *Dengiz et al.* obtained key parameters such as the stress distribution, deformation, and safety factor of the scissor mechanism through a SolidWorks simulation (*Dengiz et al., 2018*). Ugwuoke et al. analysed the mechanical responses of each connection point of a scissor platform using CAD simulation (*Ugwuoke and Olushola, 2023*). In this study, ANSYS Workbench was used to conduct a static analysis of the lifting device, and in accordance with the usage requirement of the platform to carry out work by two people, to ensure a sufficient safety margin, a uniformly distributed load of approximately 350 kg was applied on the working platform, which is equivalent to the load condition of four adults. A process diagram is shown in Figure 8.



(a) Mesh generation *(b) Application of constraints* *(c) Application of the load*

Fig. 8 – Finite element analysis procedure

The finite element analysis results for the lifting device are presented in Figure 9.



(a) Displacement cloud map *(b) Stress contour map*

(c) Strain map

Fig. 9 - Lifting device stress contour plot

Figure 9 shows the displacement, stress distribution, and equivalent elastic strain of the lifting device under the rated load condition. The displacement distribution indicates that the platform frame has the maximum vertical downward displacement at the leftmost position, with a value of 3.7623 mm. This displacement is within the allowable engineering range and does not affect the normal operation of the equipment. The stress distribution shows that the stress concentration of the scissor mechanism mainly occurs at the movable hinge, with a maximum stress value of 54.076 MPa, which is less than the yield strength of the material and meets the strength requirements (*Shang et al., 2024; Zhao et al., 2022*). The finite element analysis results show that the scissor mechanism has good structural performance under the rated load, which is consistent with previous research results (*Bembenek et al., 2026; Ogbemhe et al., 2024*).

RESULTS

Design and Testing of Conveying Device

Overall Design of the Conveying Device

The conveying device is the core component of the tobacco clip loading and unloading system in a curing barn. It adopts a wear-resistant and anti-slip rubber conveyor belt, a high-strength and lightweight truss steel structure, an elastic adjustment device with a monitoring function (*Li, 2025*), and a control system with monitoring capabilities (*Ming and Qin, 2026*). Through the rotation of the rollers, the tobacco clips are directly borne and moved, achieving the continuous and automated conveying of the tobacco clips (*Tian, 2020*). The structural form of the conveying device is shown in Figure 10, and the design parameters are listed in Table 3.

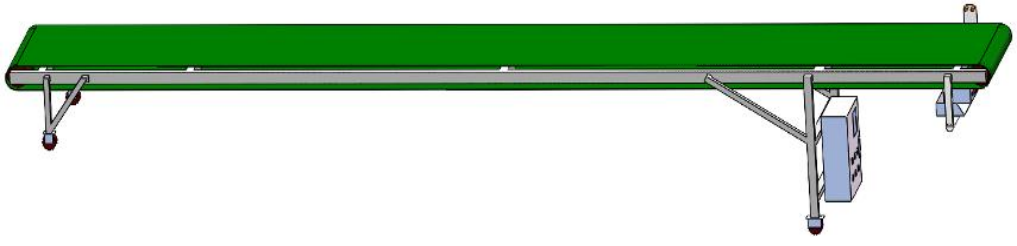


Fig. 10 - Conveyor structure

Table 3

Design parameters of the conveying device

Parameter	Value
Conveyor-belt width [mm]	920
Conveyor-belt length [mm]	7000
Conveying speed [m/min]	22
Maximum load capacity [kg]	150

Quality of Conveying Device - Correlation Test of Inclination Angle

The conveying device is prone to exhibit various tilt postures during actual operation in a curing barn. The tilt angle directly affects the quality detection accuracy and measurement stability of the belt scale. To quantify the correlation between the angle and detection quality and to optimise the system calibration parameters to ensure the reliability of the weighing data throughout the entire process, it is necessary to conduct a test on the correlation between the quality of the conveying device and tilt angle. The on-line weighing of the conveyor belt used the PSD-X3U model of the PUSHTON high-precision weighing sensor with a range of 50 kg, as shown in Figure 11.



Fig. 11 - High-precision weighing sensor

The test was conducted on the loading and unloading devices in the curing barn. The angle adjustment component and lifting device were used to achieve inclination angle regulation with an accuracy of ±0.5°. Four standard weights (5, 10, 15, and 20 kg) were used for the test. The independent variable of the test was the inclination angle of the conveyor belt, with six gradients set at 0° (horizontal reference group), 5°, 10°, 15°, 20°, and 25°, covering the travel range of the lifting device. The dependent variables were the detected mass values and detection error rates of the belt scale. The control variables included the standard weights of the conveyor belt, and running speed of the conveyor belt to ensure the reliability of the results.

Before the test, the conveyor belt was set to a 0° horizontal position and the belt scale was calibrated. The detection error should be within ±1% in the horizontal state. During the formal test, the target angle was adjusted and stabilised for 3 min. Different specifications of standard weights were placed steadily at the centre of the conveyor belt, and the conveyor belt was then started. The data were recorded after the weights completely passed through the detection zone. Each combination of angle and weight was tested three times and reset to avoid cumulative errors. The relationship between the conveyor belt inclination angle and the error rate of quality detection is shown in Figure 12.

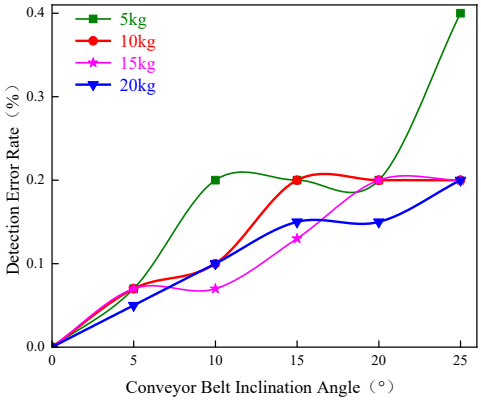


Fig. 12 - Relationship between conveyor belt inclination angle and detection error rate for different standard weights

The detection error rate rose with the belt inclination, showing a positive correlation. Under the horizontal reference state of 0°, the detection error rate for each standard weight was 0.00%. This verified the accuracy of the equipment calibration before the test and complied with the design specifications. As the inclination angle increased from 5° to 25°, the detection error rate for each standard weight gradually increased. Among them, the error rate of the 5 kg standard weight reached a maximum value of 0.40% at 25°, and the error rates of the other weights were controlled within 0.20%.

Design of the Device Control System

Considering the environment of the curing barn and the requirements of tobacco leaf handling operations, this control system features a high-precision measurement accuracy of 0.2 level, customisable interfaces, and MODBUS bus expansion. It adopts incremental digital PID control and can adapt to complex operating conditions. The automatic lifting control is set by the touchscreen to the target height and combined with limit switches to achieve deceleration when approaching the target height, ensuring stable and reliable operation. The control panel is shown in Figure 13.



(a) Control system front panel *(b) The rear panel of the control system*

Fig. 13 - The control panel

The setting of the key parameters of the control system directly determines the measurement accuracy and the control performance. The specific configuration of each parameter is as follows: the belt speed is 22 m/min, the length of the weighing section is 1 m, the speed measurement specification is 1000 P/m, the PID proportional coefficient is 8.0%, the integration time is 0.5 s, the control cycle is 50 ms, the rated load capacity of the system is 350 kg, the overload protection threshold is 110% of the rated load capacity, the belt speed deviation threshold is ±20% of the set value, the MODBUS address can be set within the range of 1 to 255, the baud rate supports 2400, 4800, 9600, and 19200 bps options, the data bit is 8 bits, the stop bit is 1 bit, and the check bit supports no check, odd check, and even check modes.

Loading and unloading measurement control is the core function of this system, which includes two processes: loading and unloading tobacco. During loading, the tobacco clip is placed on the conveyor belt, which is then started. The controller calculates the instantaneous flow rate in real time from the weight and speed sensors. When the clip reaches the end and triggers the proximity switch, the conveyor belt stops. After manual mounting and resetting, the next cycle is initiated. After the curing process is completed, the conveyor belt runs in reverse during unloading, and the measurement system accumulates the weight of the unloaded tobacco. To improve the control accuracy and response speed and reduce the adjustment fluctuations, the system adopts an incremental PID algorithm for closed-loop control. The error calculation and output correction are completed according to the PID control algorithm formula, as shown in Eq. (13).

$$\Delta u(k) = K_P\left[e(k) - e(k-1)\right] + K_i \cdot e(k) + K_d\left[e(k) - 2e(k-1) + e(k-2)\right] \quad (13)$$

where $\Delta u(k)$ is the increment of the kth output, K_P is the proportional coefficient, K_i is the integration coefficient, K_d is the differential coefficient, and $e(k)$ is the kth deviation.

The corresponding PID parameter adjustment strategy, adapted from established tuning rules (*Zhou, 2026*), is as follows: when adjusting the proportional coefficient (K_P), increasing K_P can enhance the system

response speed, but it may lead to overshoot if it is too large; when adjusting the integral coefficient (K_i), increasing K_i can reduce the steady-state error, but it may cause integral saturation if it is too large; when adjusting the derivative coefficient (K_d), increasing K_d can improve the system dynamic characteristics and suppress overshoot.

System calibration is crucial for ensuring measurement accuracy. Zero-point calibration is used to eliminate the drift. After the load is stable, the system automatically collects and saves the zero-point value. It must be calibrated before the first use and is usually performed once a week. Range calibration is accomplished using standard weights at 50–80% of the full range to correct the coefficient. It is calibrated before the first use and is typically performed once a month. It should be recalibrated after the key components are replaced.

Overall Performance Test

Tobacco Loading and Unloading Test

The device was manufactured, assembled and commissioned according to the above design, as shown in Figure 14. The test site was the dense curing barn of the Pingdingshan Modern Tobacco Agricultural Science Park in Li Kou Town, Jia County, Henan. The curing barn was 8 m long, 3 m wide, and 4.5 m high, which meets the general standards for dense-curing barns in China. The number of layers of the tobacco racks inside the curing barn was three, with a spacing of 1.2 m per layer, and the average length and width of the test tobacco clips were 1.5 m and 0.2 m, respectively.



Fig. 14 - Photograph of the Curing Oven Tobacco Clip Loading and Unloading Device

The basic performance tests included load capacity and positioning accuracy tests. The load test was conducted by applying 200, 300, and 350 kg loads to the lifting platforms. Under each load condition, the platform was raised to a height of 3 m and maintained for 10 min to observe any sinking or deformation of the platform. Simultaneously, 100 kg and 150 kg loads were applied to the conveying device to check whether the conveyor belt slipped or had an abnormal speed. The positioning test involved raising the platform to heights of 1, 2, and 3 m, as illustrated in Figure 15.







Fig. 15 - Experimental process

The test results show that this device can stably and efficiently complete operations such as lifting and lowering tobacco leaves, transportation, and loading into curing racks. It can adapt well to the curing barn environment and significantly improve operational efficiency.

Loading and Unloading Efficiency Test

To test the efficiency of the device for loading and unloading, a comparative test was conducted using a traditional manual method. The loading and unloading operations were performed separately in the same dense tobacco curing barn, and the operation time, number of workers, efficiency, and labour cost were recorded. The results showed that it took four hours and four workers to manually load tobacco into each curing barn. After adopting the tobacco curing barn tobacco clip loading and unloading device, the loading time for each curing barn was reduced to 1.5 h, and only two workers were needed to operate it. The comparison results indicated that the operation time was shortened from 4 h to 1.5 h, saving 62.5%; the number of workers was reduced from 4 to 2, and the labour cost decreased by 50%. The overall efficiency increased by 4.33 times.

CONCLUSIONS

This study addresses the problems in China's tobacco curing process, such as the reliance on manual operations for loading and unloading of tobacco leaves in curing barns, high labour intensity, low efficiency, and significant safety hazards. The design, analysis, manufacturing, and test verification of a loading and unloading device for tobacco leaves in curing barns were completed, and a technical solution suitable for dense curing barns was developed. The main conclusions are as follows:

(1) The device integrates a four-wheel-drive power platform, a two-stage scissor-type lifting mechanism, an on-line weighing and conveying system, and an incremental-PID control loop into a single barn-door station. The rated load is 350 kg and the lifting range is 0.5–3 m, meeting the requirements for loading tobacco in dense curing barns.

(2) A method combining mechanical modelling with finite element analysis provided a scientific basis for design verification of the scissor mechanism. Under the rated load, the maximum deformation was 3.7623 mm and the maximum stress was 54.076 MPa, both within the strength and stiffness limits. At the 3 m maximum lift and 350 kg rated load, the restoring coefficient K was approximately 2.9, well above the industry safety limit of 1.5.

(3) The conveying device adopted a truss-type steel structure with a rubber conveyor belt. Weighing tests over the 0°–25° inclination range gave a maximum error rate of ≤ 0.40 %, clarifying the influence of belt inclination on weighing accuracy and ensuring accurate weight detection across the full operating angle.

Field trials showed that the shortest transportation time per clip was 2.7 s, the loading time per curing barn was reduced from 4 h under manual operation to 1.5 h, and the number of operators was decreased from four to two, giving a 4.33-fold gain in overall efficiency. The fault-free working time met the requirements for continuous operation during the tobacco-curing season. Compared with manual loading, the device lowers labour intensity and improves the consistency of the loading and unloading process. Compared with hand loading, the device reduces manual intervention, lowers the physical demand on operators, removes the variability of hand loading, and improves the accuracy and stability of the loading and unloading process.

The main scientific contributions of this work are threefold. First, it presents a barn-door station platform that integrates power transfer, scissor lifting and on-line belt weighing into a single mobile unit, moving the loading task from inside the barn to a controlled workstation at the barn door. Second, it provides a quantitative restoring envelope for a two-stage scissor lift under an off-centre agricultural payload, with an restoring coefficient of K ≈ 2.9 at a lifting height of 3 m and a rated load of 350 kg. Third, it reports a measured error envelope of ≤ 0.40 % for on-line belt weighing across the 0°–25° tilt range, filling the gap in tilt-dependent weighing accuracy for agricultural conveyors. Together, these results supply reusable design data for the mechanised loading stage of dense-curing barns.

The field trial covered a single curing season, one site and one tobacco variety. Multi-region and multi-variety trials will be undertaken to verify adaptability across leaf moisture levels and barn geometries. The belt-scale weighing was validated only within a 0°-25° tilt range and under uniform loading. The model will be extended to wider tilt angles, higher loading rates and non-uniform leaf distribution. Integration with machine-vision leaf grading and IoT-based curing monitoring will also be explored to enable closed-loop optimisation of the curing chain.

ACKNOWLEDGEMENT

This research was funded by the Henan Science and Technology R&D Program Joint Fund (Industrial Category) (grant No. 202324119, 20250104); Henan Key Research and Development and Promotion Special Project (Science and Technology Tackling) (grant No. 262102231017, 262102231018, 252103810171), and Henan Province Tobacco Company Pingdingshan Company Science and Technology Project (PYKJ202204).

REFERENCES

[1] Ai, Y., Wen, Y., Sun, H., Zhou, X., Zheng, L., Zhang, F., Liu, G., Su, C., (2025). Design and experiment of chain side-lifting tobacco loading machine (链条侧举升式装烟上炕机设计与试验). *Agricultural Engineering*, Vol.*15*, no.3. Beijing/China. https://doi.org/10.19998/j.cnki.2095-1795.202503318

[2] Bembenek, M., Nurkusheva, S., Mykhailiuk, V., Deineha, R., Slabyi, O., Kowalski, Ł., Osyra, M., (2026). Lightweight Design and Safety Optimization of Scissor Lift Components Using FEM. *System Safety: Human-Technical Facility-Environment*, Vol.8, no.1, pp.58-69. Warsaw / Poland. https://doi.org/10.2478/czoto-2026-0006

[3] Cveticanin, D., (2003). New Approach to the Dynamic Weighing of Livestock. *Biosystems Engineering*, Vol.*86*, no.2, pp.247-252. Amsterdam/Netherlands. https://doi.org/10.1016/S1537-5110(03)00116-8

[4] Dengiz, C., Şenel, M., Yıldızlı, K., Koç, E., (2018). Design and Analysis of Scissor Lifting System by Using Finite Elements Method. *Universal Journal of Materials Science*, Vol.*6*, no.2, pp.58-63. San Jose/USA. https://doi.org/10.13189/ujms.2018.060202

[5] Ge, Z., Zhou, Y., Li, J., Zhang, X., Xu, J., Yang, F., (2024). Multi-objective optimization and benefit evaluation of heat pump system for tobacco drying using waste heat from data center. *Journal of Cleaner Production*, Vol.*448*, pp.141623. Amsterdam/Netherlands. https://doi.org/10.1016/j.jclepro.2024.141623

[6] Guo, T., Tang, H., Li, M., Liu, C., Chen, C., Wang, L., (2026). Design and experiment of transfer and loading machine for tobacco poles in bulk curing barn scenario. *Frontiers in Plant Science*, Vol.17 - 2026. Lausanne/Switzerland. https://doi.org/10.3389/fpls.2026.1801854

[7] Huy, T. Q., Liem, N. B., Hau, T. Q., Cuong, D. Q., Danh, T. H., Nga, N. T. T., Pi, V. N., Thieu, N. N., (2022). Application of MARCOS Method for Selecting the Best Schema of Scissors Mechanism. *Lecture Notes in Networks and Systems Advances in Engineering Research and Application (ICERA 2022)*, Vol.602, pp.234-243, Cham/Switzerland. https://doi.org/10.1007/978-3-031-22200-9_25

[8] Islam, M. T., Yin, C., Jian, S., Rolland, L., (2014). Dynamic analysis of Scissor Lift mechanism through bond graph modeling. *IEEE/ASME International Conference on Advanced Intelligent Mechatronics*, pp.1393-1399. Besançon/France. https://doi.org/10.1109/AIM.2014.6878277

[9] Jiao, T., (2025). *Design and Test of Rotary Inclined Automatic Tobacco Loader (旋转倾斜式自动装烟机设计与试验)* Master's Thesis, Northwest A&F University, Shaanxi/China. https://link.cnki.net/doi/10.27409/d.cnki.gxbnu.2025.000600

[10] Li, Q., (2025). Design of Automatic Tensioning Device for Mining Belt Conveyor (矿用带式输送机自动张紧装置设计). *Rock Drilling Machinery & Pneumatic Tools*, Vol.51, no.5, pp.48-50. Gansu/China. https://doi.org/10.19449/j.cnki.2095-6282.2025.05.016

[11] Li, W., Kang, F., (2020). Design and Analysis of Steering and Lifting Mechanisms for Forestry Vehicle Chassis. *Mathematical Problems in Engineering*, Vol.2020, no.1, pp.5971746. London/UK https://doi.org/10.1155/2020/5971746

[12] Liang, R., He, Z., Wen, J., Zhang, Y., Qiu, M., Huang, L., (2014). Study on effect of different loading tobacco leaf methods on curing in bulk curing barn (密集烤房不同装烟方式烘烤效果研究). *Guangdong Agricultural Sciences*, Vol.41, no.3, pp.33-35+40. Guangdong/China. https://doi.org/10.16768/j.issn.1004-874x.2014.03.012

[13] Lin, J., Gao, L., Lin, Y., Lin, Q., Lu, Y., (2021). Design and Experiment of Chain Lifting Type Tobacco Loading Machine (链条举升式装烟机的设计与试验). *China Southern Agricultural Machinery*, Vol.*52*, no.18, pp.72-74+104. Jiangxi/China. https://kns.cnki.net/kcms2/article/abstract?v=f9AMVDUgxC-xhxyX_2RLHnQKIrKW1A0UUl3Qfo2T1KXrgbU5KozKHQwCacgjdc2DDtEwdXVRsi34uE_z9Yjt5zqn8p6HQQSq3tjq5zLQ-JMNyb_LVCYA8MhJfUSA-97nE2t5gp_rziytURMqiyrflLqplsjWq-yOXwJqu2TM2JKNfgY8gOTwekUXIFuIipWy&uniplatform=NZKPT&language=CHS

[14] Liu, K., (2024,12-23). Sichuan Liangshan: "Golden Leaves" Spread Out a Road to Rural Revitalization, Consumption Daily (四川凉山：片片“金叶”铺就乡村振兴路). *Consumption Daily*. https://www.xfrb.com.cn/article/zx/17253189217091.html

[15] Liu, W., (2022). *Structure optimization design and stability research of caterpillar orchard working platform (履带式果园作业平台结构优化设计与稳定性研究)* Master's Thesis, Hebei Agricultural University, Hebei/China. https://link.cnki.net/doi/10.27109/d.cnki.ghbnu.2022.000733

[16] Liu, Z., Ji, A., Zhang, L., Wang, H., Zhao, Z., (2020). Stability analysis of hydraulic system on scissor type aerial work platform (剪叉式高空作业平台上车液压系统的稳定性研究). *Journal of Mechanical & Electrical Engineering*, Vol.37, no.6, pp.600-606. Zhejiang/China. https://kns.cnki.net/kcms2/article/abstract?v=f9AMVDUgxC9uZtCkCORIKcAQqNREDpocsmJFBe-dVDkiCPPuxbErSKfUn9KDdRNgZ10-bdaZ6mp98uJlvUW1t61FazzuhFvh2zYnCo9nZFvjhnA99ZcvNHk0Ng6cXc8JrnSlXcBSKPlSqo7904GQ2tHd_-mx2E2gGR_F-bnLs-6LVC2vpexyNepyWVzlk-Lo&uniplatform=NZKPT&language=CHS

[17] Luo, N., (2022). Design and Simulation of Hydraulic System in Scissor Lifting Platform (剪叉式液压升降台速度控制方法及仿真分析). *Mechanical Engineer*, no.4, pp.88-90+93. Heilongjiang/China. https://kns.cnki.net/kcms2/article/abstract?v=f9AMVDUgxC_2YjagfGqpkC9F0_EJ-UhD9BuWyS2Bc5FpZE6htxSLkU1Hy_9auvR1yIfcN7abuhLQhLTjphWbeN6iB_0jqY4Wq94uRgmiQDAQn3TmDrE12_An9FwFzuyGz2FPV5b6JNsZdcbY62Tiam9_2HMJwwqGJmzBMGRyxIT-6XN-m2nyaJLQ9u5NtA7B&uniplatform=NZKPT&language=CHS

[18] Ming, Z., Qin, X., (2026). Design and Implementation of Intelligent Conveyor Belt Control System (智能传送带控制系统设计与实现). *Modern Manufacturing Technology and Equipment*, Vol.62, no.2, pp.210-212. Shandong/China. https://doi.org/10.16107/j.cnki.mmte.2026.0129

[19] Ogbemhe, J., Ramatsetse, B., Mpofu, K., George, O. A., (2024). Multi-Physical Modelling and Simulation of a Planar Translational Scissor Lift Mechanism for Maintenance of Rail Transmission Lines. *Procedia CIRP*, Vol.121, pp.174-179. Amsterdam/Netherlands. https://doi.org/10.1016/j.procir.2023.09.246

[20] Pan, C. S., Chiou, S. S., Kau, T.-Y., Wimer, B. M., Ning, X., Keane, P., (2017). Evaluation of postural sway and impact forces during ingress and egress of scissor lifts at elevations. *Applied Ergonomics*, Vol.65, pp.152-162. Oxford/UK. https://doi.org/10.1016/j.apergo.2017.06.009

[21] Paramasivam, V., Tilahun, S., kerebih Jembere, A., Selvaraj, S. K., (2021). Analytical investigation of hydraulic scissor lift for modular industrial plants in ethiopia. *Materials Today: Proceedings*, Vol.46,

pp.7596-7601. Amsterdam/Netherlands. https://doi.org/10.1016/j.matpr.2021.01.838

[22] Shang, H., Li, X., Zhang, C., Xu, C., Hou, Y., Jia, M., (2024). Optimization design and experiment of automatic leveling system for orchard operating platform in hilly and mountainous areas. *INMATEH - Agricultural Engineering*, Vol.73, no.2, pp.364-374. Bucharest/Romania. https://doi.org/10.35633/inmateh-73-30

[23] Tian, Y., (2020). On the Design of Simulation Control System for Tobacco Logistics Storage Conveyor Belt Device (论烟草物流仓储传送带装置模拟控制系统设计). *Hebei Agricultural Machinery*, no.4, pp.73. Hebei/China. https://doi.org/10.15989/j.cnki.hbnjzzs.2020.04.056

[24] Ugwuoke, I. C., Olushola, T. O., (2023). Development of a 120kg Load Lifting Capacity Scissor Elevator Platform. *International Journal of Engineering and Manufacturing (IJEM)*, Vol.13, no.6, pp.38-52. Hong Kong/China. https://doi.org/10.5815/ijem.2023.06.04

[25] Wang, J., Ruan, X., Li, P., Song, Y., Liu, X., Jia, L., Yang, Z., Duan, W., (2025). Integrated crew for heating and dehumidification of air-source heat pump for tobacco curing. *Scientific Reports*, Vol.15, no.1, pp.38062. London/UK. https://doi.org/10.1038/s41598-025-21816-7

[26] Yu, Y., (2021). *Design and Test of High-Position and Automatic Leveling Work Platform in Orchard (果园高位自动调平作业平台设计与试验)* Master's Thesis, Beijing Forestry University, Beijing/China. https://link.cnki.net/doi/10.26949/d.cnki.gblyu.2021.000356

[27] Yu, Y., Kang, F., Zheng, Y., Lü, H., Wang, Y., (2021). Design and simulation of the automatic-leveling high-position platform in orchards (果园高位自动调平作业平台设计及仿真). *Journal of Beijing Forestry University*, Vol.43, no.2, pp.150-159. Beijing/China. https://kns.cnki.net/kcms2/article/abstract?v=f9AMVDUgxC8AWEyHq55bU0R931yn3Gw4e9RN87RpoX3CZ6OnLukcoHdrMuTxH3qY_fC8v8OUt8DQxdVam_Jb4oEqHJtr6lgfSV4IO_cZeRwCsVCmnZ4MYvRN0iwISGyO--e2puxZAQSdovigNHF3y3k9ebAHPPkMWTTouNGcJXlpMcHSBM8j1kjn3OBzeeJ8&uniplatform=NZKPT&language=CHS

[28] Zhang, X., (2023). *Design and experiment of toppling rotary tobacco loading machine in Bulk Curing Barn (密集烤房倾倒旋转式装烟机设计与试验)* Master's Thesis, Southwest University, Chongqing/China. https://link.cnki.net/doi/10.27684/d.cnki.gxndx.2023.001903

[29] Zhao, G., Liu, Y., Ye, N., (2022). An improved fatigue accumulation damage model based on load interaction and strength degradation. *International Journal of Fatigue*, Vol.156, pp.106636. Oxford/UK. https://doi.org/10.1016/j.ijfatigue.2021.106636

[30] Zhou, W., (2026). A speed control system design based on fuzzy-PID controller (一种基于模糊-PID 控制器的调速系统设计). *Science and Technology & Innovation*, no.2, pp.88-91. Shanxi/China. https://doi.org/10.15913/j.cnki.kjycx.2026.02.024

MECHANISM AND EFFICACY EVALUATION OF ATMOSPHERIC PRESSURE DBD PLASMA TREATMENT FOR FORAGE GRASS SEEDS
/
面向牧草种子应用的常压 DBD 等离子体种子处理机制与效能评估

Jun-hui XI[1)], Xiao-juan ZHAO[2)], Xiang-yang WU[3)], Zhen-hua WANG[3)], Jia-jia SU[2)], Yun-ting HUI*[1,2)], Yan-ying GUO[1)], Yang-yang LIAO[3)], De-cheng WANG*[1)]

[1)] College of Engineering, China Agricultural University, Beijing / China;
[2)] Hohhot Branch of Chinese Academy of Agricultural Mechanization Sciences Co., Ltd., Hohhot/ China;
[3)] Chinese Academy of Agricultural Mechanization Sciences Group Co., Ltd., Beijing / China
Tel: 18800125567; E-mail: hyt@cau.edu.cn
Correspondent author: Yun-ting Hui, De-cheng Wang
DOI: https://doi.org/10.35633/inmateh-79-49

Keywords: *Plasma Agriculture; Dielectric Barrier Discharge; Surface Modification; Electrical Conductivity; Dosage Effect*

ABSTRACT
To overcome the problems of low germination rate and irregular emergence caused by dense surface structure, poor water permeability, and dormancy of forage seeds, this study screened the optimal plasma generation mode suitable for continuous treatment of forage seeds under atmospheric pressure and evaluated its efficacy and mechanism. Through a comparative analysis of the uniformity and stability of corona, spark, gliding arc, and dielectric barrier discharge (DBD), the results showed that DBD can generate large-area, low-temperature, and uniform plasma in atmospheric air. Taking Leymus chinensis seeds as the research object, the effects of different treatment voltages (0–16 kV) on the glume microstructure and the electrical conductivity of the leachate were investigated. Scanning electron microscopy (SEM) observations indicated that DBD treatment with appropriate parameters caused significant etching on the seed glume surface, forming micropores and fissures, and removing impurities. The electrical conductivity measurements further revealed a "dosage effect": moderate voltage helped maintain the integrity of the membrane system, whereas excessive voltage led to severe damage to the glume and leakage of intracellular contents. The study confirmed that atmospheric pressure DBD plasma, through physical etching and surface modification, can effectively improve the water absorption channels and physiological activity of Leymus chinensis seeds, and an optimal parameter window exists. These findings provide a technical basis for the development of continuous plasma seed treatment equipment.

摘要
为克服牧草种子因表面结构致密、透水性差及休眠特性导致的萌发率低、出苗不齐等问题，本研究筛选适用于常压条件下牧草种子连续处理的最佳等离子体发生方式，并评估其效能与作用机制。通过对比电晕、火花、滑动电弧及介质阻挡放电（DBD）的均匀性与稳定性，结果显示，DBD 可在常压空气中产生大面积、低温、均匀等离子体。以羊草种子为对象，探究不同电压（0–16 ）处理对其颖壳微观结构及浸提液电导率的影响。扫描电镜观察表明，适宜参数的 DBD 处理可使种子颖壳表面产生显著刻蚀，形成微孔与裂隙，并清除杂质；电导率测定结果进一步揭示了"剂量效应"：中低电压有助于维持膜系统完整性，过高电压则导致颖壳过度损伤及内含物外渗。研究证实，常压 DBD 等离子体通过物理刻蚀与表面改性，可有效改善羊草种子的吸水通道与生理活性，且存在最优处理参数窗口。研究结果为开发连续式等离子体种子处理装备提供了技术依据。

INTRODUCTION
Superior forage seeds constitute the material basis for ecological restoration, pasture management, and urban greening (*Fekete et al., 2024*). However, a substantial number of dominant grass species are characterized by inherent physiological defects, such as hard and dense seed coats, poor water and air permeability, and deep dormancy. These characteristics inevitably lead to slow germination, irregular seedling emergence, and low seedling rates under natural conditions, thereby severely restricting their efficient utilization (*Harrison et al., 2025*). Although traditional physical or chemical treatment methods—such as mechanical scarification, concentrated sulfuric acid treatment, and hormone soaking—have demonstrated certain efficacy, they are associated with significant drawbacks.

These include uneven treatment, potential damage to the embryonic body, chemical residue pollution, and difficulties in scaling up. Consequently, these conventional approaches fail to fundamentally meet the new requirements for high efficiency, safety, and environmental protection demanded by modern green agriculture and ecological construction.

In recent years, various physical pre-sowing treatments have been explored to overcome seed dormancy and improve germination. For instance, pulsed electric fields (*Evrendilek et al., 2021*; *Hou et al., 2023*; *Song et al., 2025*) and electromagnetic treatment (*Ganeva et al., 2015; Pentoś et al., 2024*) have been reported to enhance seed germination and stress tolerance by affecting membrane potential and ion transport. However, these methods primarily rely on electric or magnetic forces without altering the seed coat's physical structure or surface chemistry. As a modern physical agricultural high-technology, low-temperature plasma has been introduced within the rapidly developing field of Plasma Agriculture, offering distinct advantages (*Waskow et al., 2021*; *Hui et al., 2025*). Research indicates that reactive species and ultraviolet radiation from plasma can etch seed coats, enhance hydrophilicity, and induce biostimulation (*Attri et al., 2023*; *Benabderrahim et al., 2025*). Various plasma technologies have been applied to seed treatment: corona discharge on alfalfa seeds reduced contact angle and increased water absorption (*Xu et al., 2021*); cold plasma jet on oat seeds improved germination under salt stress (*Zhang et al., 2024*); transient spark discharge restored germination of fungus-infected wheat seeds (*Doshi et al., 2024*); gliding arc discharge inactivated pathogens on Astragalus seeds while increasing germination rate (*Liu et al., 2021*).

Despite these confirmations, a systematic comparison of different atmospheric plasma generation modes for forage seed treatment is still lacking. Most studies focus on single technologies without evaluating their uniformity, continuity, and suitability for large-scale, continuous seed processing. Therefore, the research gap addressed by this paper is the need to identify the optimal plasma generation mode for continuous, non-damaging treatment of forage seeds under atmospheric pressure.

To address this gap, this study provides a side-by-side comparison of corona, spark, gliding arc, and DBD for seed treatment, identifies DBD as the preferred mode for continuous processing, and systematically evaluates the dosage effect on seed coat microstructure and membrane integrity, thereby establishing a technical basis for equipment development. Accordingly, the core hypothesis is that under atmospheric pressure, DBD plasma represents the optimal technical route for overcoming the inherent defects of grass seeds and achieving efficient continuous treatment.

MATERIALS AND METHODS

1 Comparative Experiment on Atmospheric Pressure Plasma Generation Modes

Based on the different configurations of electrodes, gas discharge generates plasma in various forms. Common discharge modes include corona discharge, spark discharge, glow discharge, Dielectric Barrier Discharge (DBD), and gliding arc discharge (*Wang et al., 2025*). To screen for an atmospheric pressure plasma generation mode suitable for continuous seed treatment, experimental test benches corresponding to each discharge principle were established. The experiments were conducted under ambient temperature and pressure conditions using seeds as the treatment object. By directly observing the discharge phenomena and seed status, the plasma generation modes were qualitatively evaluated from the perspectives of discharge uniformity and continuity, the stability of the discharge state upon seed introduction, thermal effects within the discharge region, and the risk of physical damage to the seeds (*Mazandarani et al., 2020*).

2 Evaluation Experiment of Plasma Treatment on Seed Performance

Upon determining the optimal atmospheric pressure plasma generation mode, an integrated plasma forage seed treatment prototype was developed based on the experimental setup to verify the feasibility of continuous treatment. Wild *Leymus chinensis* seeds, a typical gramineous forage, were selected as the experimental material and processed using this prototype.

2.1 Experimental Design for Plasma Seed Treatment

The DBD device used a plate-to-plate electrode configuration with a quartz glass dielectric barrier. The discharge gap was fixed at 6 mm, and the dimensions of each electrode plate were 150 mm × 150 mm. The power supply (CTP-2000K) operated at an AC frequency of 1–100 kHz (adjustable) and provided an output voltage from 0 to 30 kV.

Six discharge voltage levels were applied: 0 (control), 3, 6, 10, 13, and 16 kV. These values were selected to cover a wide range from weak to intense discharge, based on the adjustable capability of the power supply and preliminary observations of discharge stability. A fixed treatment time of 20 s was chosen for voltage effect tests, as suggested by preliminary experiments and prior work (*Tang et al., 2017*).

2.2 Assessment of Plasma Seed Treatment Performance

(1) Scanning Electron Microscopy (SEM) Test

To systematically elucidate the plasma seed treatment mechanism, specifically the physical etching and surface modification effects of DBD plasma on the seed coat of *Leymus chinensis*, high-resolution morphological observations were conducted using a scanning electron microscope (SU3500, Hitachi High-Tech Corporation). Samples were taken from untreated seeds and seeds treated with plasma at different voltages (3, 6, 10, 13, and 16 kV). The seeds were positioned at various orientations on the sample stage to facilitate the observation of different morphological features. For *Leymus chinensis* seeds, observations were required for the central protrusion, depressions, and edge bristles. The smooth surfaces and awns were observed at magnifications of 300x and 500x, respectively. The changes in surface particles, cracks, gaps, pores, and impurity contaminants on the seed coat were focused on and recorded to visualize the structural alterations under different discharge voltages.

(2) Electrical Conductivity Test

Electrical conductivity measurement was utilized to analyze the ion permeability of the seed leachate. Seeds treated at different voltages (0, 3, 6, 10, 13, and 16 kV) were divided into groups, with 40 seeds per group, and placed in beakers containing 50 mL of deionized water to ensure complete immersion. At a room temperature of 25°C, the electrical conductivity of the leachate was measured every 2 hours using a conductivity meter for a continuous duration of 24 hours. The experimental group was repeated 5 times to obtain the average value. By comparing the variation trends of conductivity over time among different treatment groups, the influence of plasma treatment on seed coat membrane permeability and the leakage of endogenous substances was analyzed, thereby revealing the potential dosage effect.

RESULTS AND DISCUSSION

1 Screening Results and Analysis of Plasma Generation Modes

The mode of plasma generation constitutes the core of the design for the seed pre-sowing treatment device, as the characteristics of plasma generated by different gas discharge forms and their effects on seeds vary significantly. Therefore, based on the fundamental principles of various gas discharges, corresponding test benches were designed. By positioning seeds within different forms of electric fields and regulating voltage and current parameters, the differences in discharge phenomena before and after the addition of seeds were systematically compared. The focus was placed on the uniformity and continuity of the discharge under atmospheric pressure, as well as its adaptability to seeds, to screen out the plasma generation mode most suitable for batch and continuous seed treatment in plasma agriculture.

1.1 Gliding Arc Discharge Seed Treatment

Based on the principle of gliding arc discharge, a seed treatment test bench was designed (Fig. 1). The apparatus primarily consists of a radio frequency (RF) power supply, a voltage regulator, an oscilloscope, a fan, electrodes, and a seed treatment section. The discharge component is composed of two high-voltage metal plate electrodes with a phase difference of 180°, mounted on an aluminum alloy frame. A fan is installed directly above the electrodes, while the seed treatment chamber is positioned directly below, with a discharge voltage range of 0–50 kV.

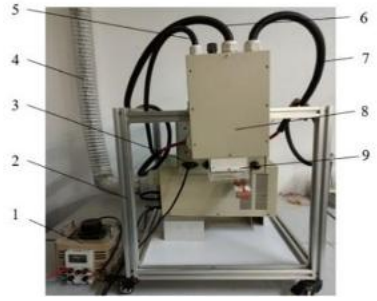


Fig. 1 - Gliding arc discharge seed treatment test bench

1. Voltage regulator; 2. Frame; 3. Discharge power supply; 4. Exhaust pipe; 5. Fan power cable; 6. High-voltage cable A; 7. High-voltage cable B; 8. Fan and electrode; 9. Seed treatment chamber

Observations of the discharge phenomena were conducted by placing different types of seeds in the gliding arc electric field and adjusting the discharge voltage via the regulator. The complete process from generation to extinction of the gliding arc was demonstrated: upon activating the power supply and fan, the gas between the electrodes was broken down, forming an initial arc (Fig. 2a).

Driven by the airflow generated by the fan, the arc moved along the electrode towards the other end and gradually elongated (Fig. 2b and c). When the supplied energy was insufficient to maintain arc propagation and compensate for thermal diffusion losses, the arc was extinguished and subsequently regenerated at the electrode throat, thereby entering the next discharge cycle (Fig. 2d). The discharge process after the addition of alfalfa seeds is shown in Fig. 3. The results indicated that due to the limited action area of the arc and the susceptibility of small-sized seeds to dispersion by strong airflow, this method is difficult to implement for the high-efficiency treatment of large batches of small seeds. Additionally, the high local temperature of the arc is prone to causing thermal damage to the structure of the treatment chamber.

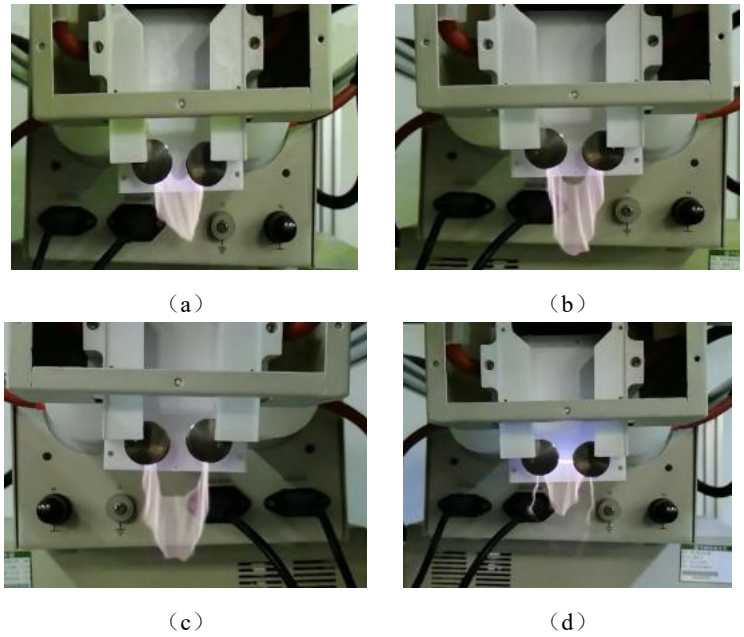


Fig. 2 - Generation process of gliding arc discharge

Note: (a), (b), (c) The process of arc diffusion; (d) The phenomenon of the previous arc extinguishing and the subsequent arc generating.



Fig. 3 - Phenomenon of gliding arc discharge seed treatment

1.2 Corona Discharge Seed Treatment

Based on the principle of corona discharge, a needle-to-plate corona discharge seed treatment test bench was designed, as illustrated in Fig. 4. The test bench is primarily composed of a radio frequency (RF) power supply, a voltage regulator, and a seed treatment chamber. The discharge component includes a high-voltage electrode and a grounded electrode. Specifically, the high-voltage electrode consists of a needle electrode fabricated from a conductive screw, whereas the grounded electrode is a flat metal plate. The overall frame structure is constructed using aluminum alloy profiles.

The working principle of the corona discharge test apparatus is described as follows: During the experiment, seeds were spread flat on the grounded electrode plate, and the distance between the needle and plate electrodes was adjusted via a lifting knob. The high-voltage and grounded electrodes were connected to the corresponding terminals of the power supply, respectively. By regulating the voltage parameters of the power supply, the corona discharge phenomena and the state of plasma wrapping around the seeds under different voltages were observed, thereby evaluating the applicability of this discharge form for seed treatment.

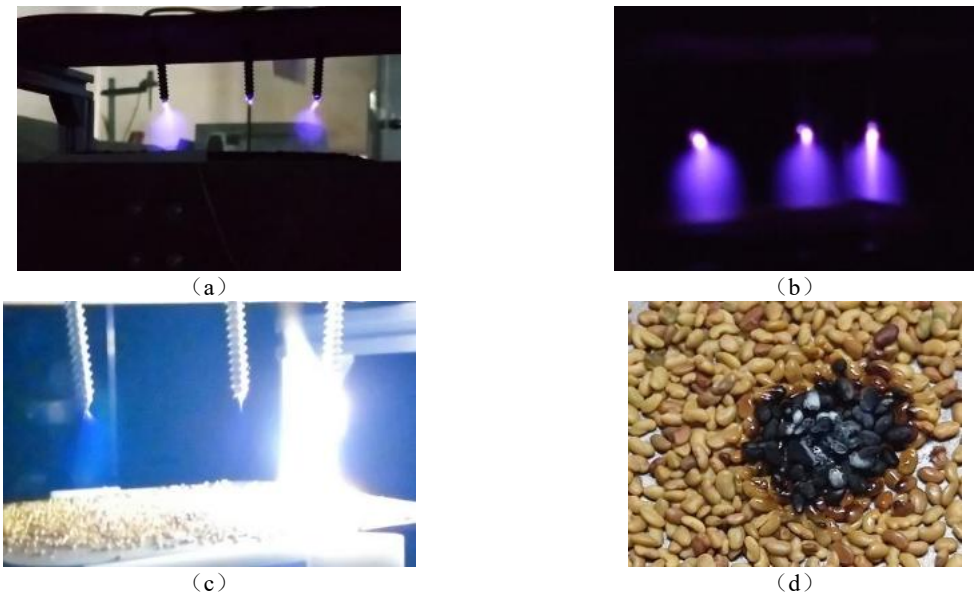


Fig. 4 - Corona discharge seed treatment

Note: (a), (b), (c) Discharge phenomena with gradually increasing discharge voltage; (d) Treatment effect on the seeds at maximum discharge voltage.

At the initial discharge stage, a glow accompanied by a "hissing" sound appeared around the needle electrode, with the current concentrated locally at the needle tip (Fig. 4a). As the voltage increased, localized discharge and halo phenomena emerged (Fig. 4b). When the voltage was further increased (Fig. 4c), significant damage was observed on the seed surface (Fig. 4d). The experiments demonstrated that the current density in corona discharge is highly concentrated at the needle tip, resulting in uneven charge distribution and poor electric field uniformity. Consequently, achieving a uniform plasma wrapping effect on the seed surface was difficult. Furthermore, this mode is prone to breakdown and high discharge temperatures, easily leading to seed scorching.

1.3 Spark and Glow Discharge

Spark discharge is mechanistically distinct from other forms, characterized by high current requirements and accompanying flashes and cracking sounds in charged regions with high potential differences. Although the voltage between the poles is high during discharge, the power supply is limited; once discharge occurs, the channel resistance drops sharply, causing the voltage to fall and the discharge to interrupt temporarily. This results in an intermittent process. Thus, despite its high intensity, the discontinuity of spark discharge limits its application in continuous seed treatment.

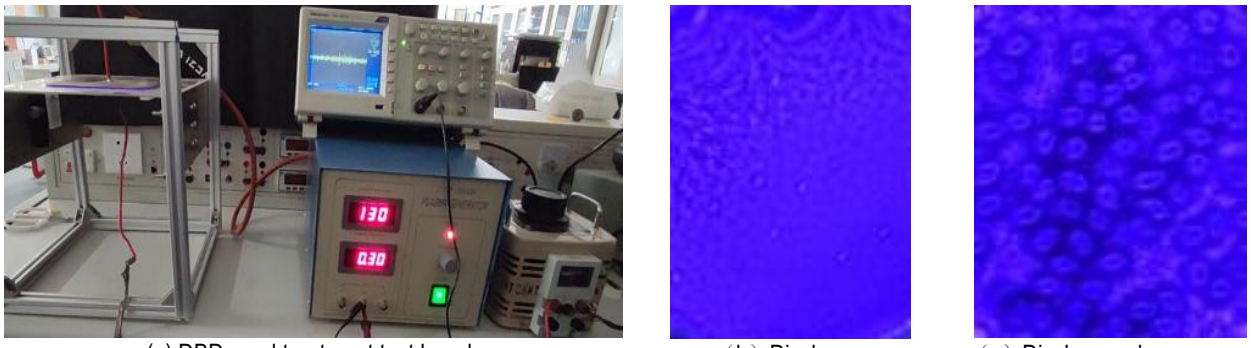
Glow discharge is a self-sustaining discharge phenomenon typically generated under low-pressure conditions (thin gas) and usually requires a sealed environment to maintain the plasma. Currently, this technology is mainly applied in the manufacturing of precision devices. However, in atmospheric, open-type agricultural scenarios, its applicability is limited due to the requirement for vacuum systems and the difficulty in achieving large-volume uniform discharge.

1.4 Dielectric Barrier Discharge (DBD) Seed Treatment

Based on the principle of Dielectric Barrier Discharge (DBD), a plate-to-plate seed treatment test bench was designed to investigate the discharge characteristics under different seed types and voltage parameters, as shown in Fig. 5(a) . The apparatus was primarily composed of a radio frequency (RF) power supply, a voltage regulator, an oscilloscope, and a seed treatment section. The discharge component of the test bench consisted of a high-voltage electrode and a grounded electrode. The dielectric barrier was constructed from quartz glass, while the high-voltage electrode plate was made of metal, and the frame was fabricated from aluminum alloy profiles.

The working principle of the Dielectric Barrier Discharge apparatus is described as follows: The height of the grounded electrode plate was adjusted via a screw rod. Seeds were spread flat on the grounded electrode, which was then elevated to an appropriate height. The high-voltage and grounded electrode plates were connected to the corresponding terminals of the power supply via wires. By regulating the voltage parameters of the power supply, the discharge phenomena of the device were observed and recorded.

Fig. 5 (b) and 5(c) illustrate the significant disparity in discharge phenomena with and without the presence of seeds under identical voltage conditions. It was observed that in the absence of seeds, atmospheric pressure DBD exhibited a filamentary discharge pattern. However, under the same conditions, the introduction of seeds caused the filamentary discharge to transition into a uniform discharge. The seed surfaces were uniformly wrapped by low-temperature plasma streamers, and the luminous intensity above the seeds was significantly higher than that in the interstitial regions. This indicates a dense distribution of low-temperature plasma over the seeds, whereas the regions between adjacent seeds exhibited weak luminescence and a lower plasma density. This phenomenon suggests that the introduction of seeds altered the electric field distribution between the plates and the transport behaviour of charged particles. This is likely due to the dielectric properties of the seed surface enhancing the local electric field, thereby promoting discharge uniformity and stability. Consequently, this result provides a critical basis for achieving continuous and uniform plasma treatment of seeds under atmospheric pressure.



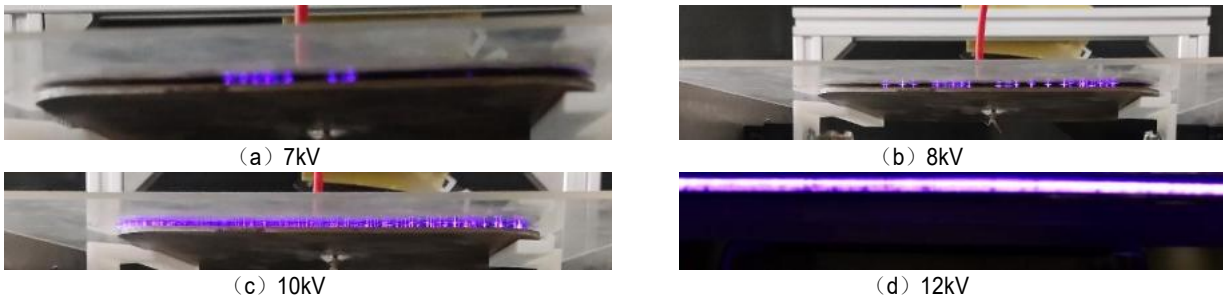
(a) DBD seed treatment test bench

（b）Discharge phenomenon without seeds

（c）Discharge phenomenon with seeds

Fig. 5 Dielectric barrier discharge seed treatment test bench

Medicago sativa (alfalfa) seeds were placed in the discharge test bench, and varying voltages (0–15 kV) were applied, resulting in the discharge phenomena shown in Fig. 6. As the discharge voltage was regulated and increased to 7 kV, discharge initiated at the locations of the seeds. With a further increase in voltage, the discharge intensity enhanced, the discharge area expanded, and discharge occurred in most of the air gap locations. As the voltage continued to rise, a large number of filamentary discharges began to appear in the air gap. When the voltage reached 10 kV, the alfalfa seeds were wrapped in low-temperature plasma. Upon the applied power supply voltage amplitude reaching 12 kV, the interior of the discharge device exhibited a complete and uniform discharge. Through these discharge tests, it was found that with the increase of discharge voltage, the Dielectric Barrier Discharge developed from filamentary discharge to uniform discharge. Under appropriate voltage conditions, DBD achieved uniform discharge, with low-temperature plasma wrapping the seeds, thereby subjecting them to uniform treatment.



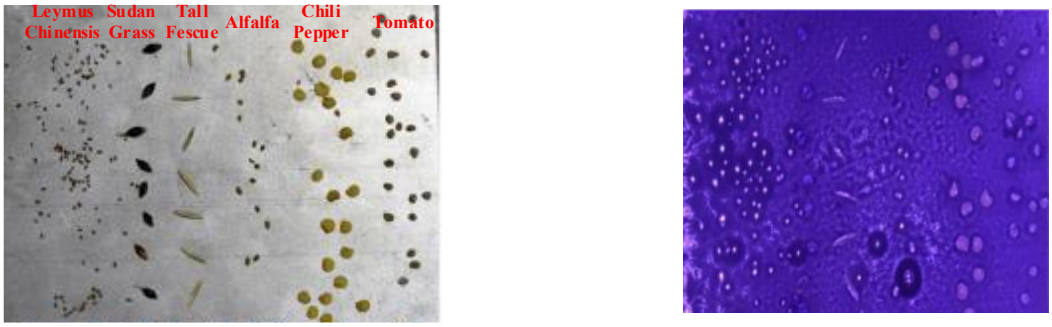
（a）7kV （b）8kV

（c）10kV （d）12kV

Fig. 6 - Discharge phenomena of plasma treatment on alfalfa seeds under different voltages

To investigate the influence of seed physical characteristics on the dielectric barrier discharge process, various typical forage and crop seeds—including *Leymus chinensis*, Sudan grass, tall fescue, alfalfa, chili, and tomato—were selected. These were simultaneously placed within the same DBD electric field, and the power supply voltage was regulated within the range of 0–20 kV to systematically observe their discharge behaviour, as shown in Fig. 7. The results indicated distinct differences in the discharge inception voltage for different seeds within the same electric field.

As the voltage gradually increased, the locations occupied by the thicker alfalfa seeds were the first to induce discharge, followed sequentially by chili, tomato, and tall fescue seeds. When the voltage rose to 16 kV, all seeds were uniformly wrapped by plasma, and the electric field achieved complete and uniform discharge coverage. It was experimentally determined that seed thickness is negatively correlated with the required discharge voltage. The mechanism is inferred to be that an increase in seed thickness reduces the equivalent discharge gap between the seed surface and the upper electrode plate. This leads to a reduction in the number of initial electrons in the air gap of that region, which in turn lowers the reverse potential in the area above the seed (*Liu et al., 2023*). Therefore, under the same applied voltage, the actual electric field strength in the air gap surrounding thicker seeds is higher, making it easier to reach the discharge threshold and thereby preferentially inducing plasma discharge (*Judée and Dufour, 2020*). This phenomenon reveals the significant regulatory role of seed geometric characteristics in the DBD process.



(a) Different seed types (b) Seeds fully wrapped by plasma

Fig. 7 – Discharge phenomena of different seed types in an electric field

As discussed in sections 1.1–1.3, the other discharge modes exhibit intrinsic limitations for continuous seed treatment. Corona discharge suffers from localized current concentration at the needle tip, leading to uneven charge distribution and a high risk of seed scorching (Fig. 4a–c).

Spark discharge is inherently intermittent due to its rapid breakdown and extinction cycle, making continuous uniform treatment unattainable. Despite reports demonstrating its efficacy in water sterilization and seed germination enhancement — for example, spark dielectric barrier discharge (SDBD) plasma achieved complete inactivation of E. coli and S. aureus after 8 min of treatment, increased coriander seed germination rate from 23.3% to 46.6% after 5 min, and reduced water contact angle from 105.65° to 57.19° owing to surface hydrophilization (*Dhakal et al., 2023*) — the intrinsic intermittency and discontinuity of spark discharge fundamentally preclude its application in continuous, large-scale seed processing. Gliding arc discharge, while capable of generating plasma at atmospheric pressure, produces a high-temperature arc zone that can thermally deform seeds and is further complicated by the tendency of small seeds to be dispersed by the required airflow (Fig. 2a–d, Fig. 3).

Glow discharge, though uniform and low in temperature, typically requires low-pressure (vacuum) conditions, which are impractical for large-scale, open-environment agricultural processing. Although large-volume atmospheric pressure glow discharge has been successfully demonstrated for Moringa oleifera seed treatment, achieving fungal disinfection and enhanced germination at low energy doses (2.46–4.35 mJ), it operates in a pulsed mode and still faces challenges in scaling to continuous seed flow (*Ouf et al., 2022*).

The requirement for precise gap control and the risk of arc transition at higher doses further limit its applicability for continuous, high-throughput processing. In contrast, Dielectric Barrier Discharge (DBD) overcomes all these drawbacks. Under the same atmospheric conditions, DBD generates a large-area, low-temperature, and remarkably uniform plasma. More importantly, the introduction of seeds into the DBD gap does not disrupt the discharge; instead, it promotes the transition from filamentary to uniform discharge (Fig. 5c), with the seeds being evenly wrapped by low-temperature plasma streamers (Fig. 6d, Fig. 7b). This unique behavior, attributed to the dielectric properties of the seed surface enhancing the local electric field (as described in section 1.4), enables continuous, non-thermal, and scalable treatment.

A systematic comparison of all five discharge modes based on experimental observations and literature evidence is provided in Table 1. Therefore, DBD is identified as the preferred discharge mode for developing continuous plasma seed treatment equipment for forage grasses under atmospheric pressure.

Table 1

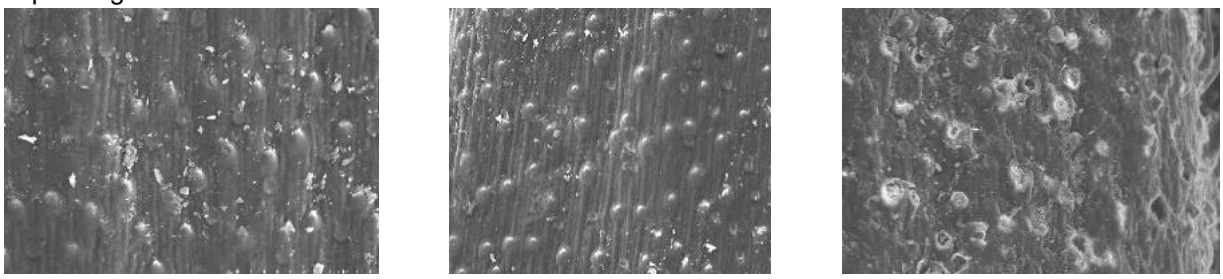
Comparison of different atmospheric pressure plasma generation modes

Discharge Mode	Uniformity & Continuity	Thermal Effect	Seed Damage Risk	Suitability for Continuous Treatment
Corona	Localized at needle tip (Fig. 4a–c)	Local temperature rise	Scorching at high voltage (Fig. 4d)	Low
Spark	Intermittent, flashes/cracking (*Dhakal et al., 2023*)	High (~1754 K)	Not directly observed	Very Low
Gliding Arc	Arc moves, small area (Fig. 2a–d)	High local temperature	Possible thermal deformation (Fig. 3)	Moderate
Glow	Uniform but requires low-pressure/vacuum; pulsed at atm. pressure (*Ouf et al., 2022*)	Low (~310 K)	Low at low doses, harmful at high doses	Low
DBD (This work)	Uniform, stable, large-area (Fig. 5c, 6d, 7b)	Room temperature, no charring	Controlled etching, no thermal damage (Fig. 8b, 9b)	**High**

2 Performance Evaluation Test Results

2.1 SEM Results and Analysis

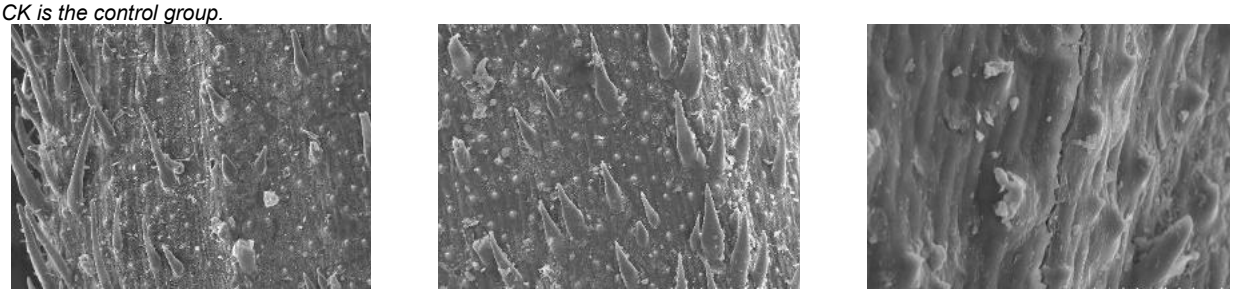
The constructed test bench was employed to conduct experiments for the treatment of *Leymus chinensis* seeds. To observe the microstructural changes of the seed coat following treatment at different voltages, Scanning Electron Microscopy (SEM) was utilized. A specific quantity of seeds was randomly selected from both untreated and treated batches, and the seeds were positioned in various orientations on the sample stage for observation.



（a）CK （b）10 kV （c）16 kV

Fig. 8 - Microstructural changes of *Leymus chinensis* seed coat before and after plasma treatment（×300）

Note: CK is the control group.



（a）CK （b）10 kV （c）16 kV

Fig. 9 - Microstructural changes of *Leymus chinensis* seed coat before and after plasma treatment（×500）

Note: CK is the control group.

Fig. 8 and 9 display the SEM micrographs of the *Leymus chinensis* seed coat surface under different treatment conditions. As shown in Fig. 8 (a) and Fig. 9(a), the surface of untreated seeds presented two typical morphologies: one side exhibited relatively uniform, smooth, granular protrusions, while the other side featured distinct long awn structures, with a certain amount of impurity contaminants attached to the surface. In contrast, the plasma-treated seeds, as shown in Fig. 8 (b-c) and Fig. 9 (b-c), exhibited significant surface modification. Distinct micropores and micro-cracks appeared on the surface. Furthermore, as the discharge voltage increased, surface contaminants were gradually reduced, pore sizes expanded, and the crack structures became more defined. This phenomenon is consistent with results reported in the literature (*Luchian et al., 2025*). The formation of these microstructures is conducive to enhancing the water absorption capacity of the seeds and promoting internal material exchange, thereby facilitating the breaking of seed dormancy.

These results further indicate that plasma treatment not only alters the seed coat structure through physical etching but may also indirectly regulate the physiological state of the seed by affecting the distribution of local active substances. The synergistic alteration of the aforementioned microstructure and composition provides direct evidence for explaining the plasma seed treatment mechanism regarding the enhancement of seed germination ability and stress resistance.

2.2 Analysis of the Effect of Plasma Treatment on Seed Electrical Conductivity

To comprehensively elucidate the mechanism of plasma treatment on seed physiology, quantitative verification was conducted using mechanistic data reflecting physiological functions, combined with the structural changes observed via SEM. The seed coat not only wraps and protects internal substances from external stress but also plays a key role in regulating material exchange between the embryo and the external environment. Changes in the structure and function of the seed coat can be indirectly reflected by variations in its permeability. Electrical conductivity serves as one of the indicators for evaluating seed vigor, as its value can sensitively reflect the integrity and permeability changes of the seed coat membrane system (*Ara˙jo et al., 2022*). Seeds were placed in deionized water, and as the intracellular contents leaked out, the ion concentration of the leachate changed. This weak variation was quantitatively detected using a precision conductivity meter, providing critical data support for revealing the regulatory mechanism of plasma treatment on the seed physiological state.

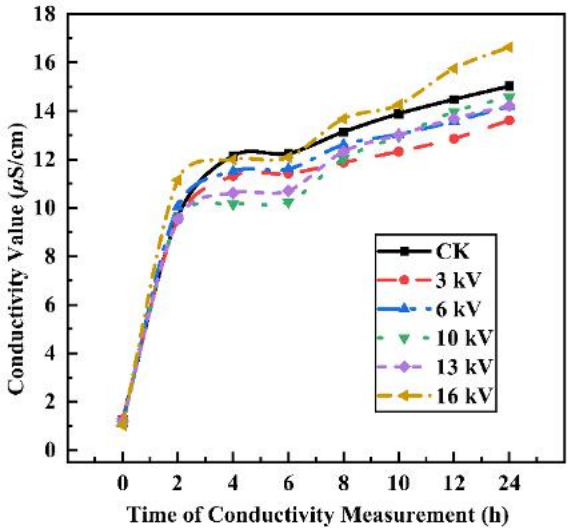


Fig. 10 - Changes in electrical conductivity of Leymus chinensis seeds before and after dielectric barrier discharge treatment

The measurement results of electrical conductivity revealed a distinct dosage effect of plasma treatment on *Leymus chinensis* seeds. As shown in Fig. 10, the conductivity data indicated a significant surge within 0 h to 2 h after immersion, primarily attributed to rapid water absorption by the awn structures of this gramineous seed. After 2 h, water absorption reached saturation and the conductivity change flattened.

Quantitative analysis of the 24 h conductivity values further elucidated the dosage effect. Compared to the control group (CK, 15.02 μS/cm), the 10 kV treatment reduced the final conductivity to 14.56 μS/cm, a decrease of approximately 3.1%, indicating enhanced membrane integrity and reduced ion leakage. In contrast, the 16 kV treatment increased the conductivity to 16.63 μS/cm, a 10.7% increase relative to CK, confirming that excessive energy input causes over-etching and loss of intracellular contents. This voltage-dependent biphasic response is consistent with previous reports on DBD treatment of wheat seeds (*Amado et al., 2025*) and alfalfa seeds (*Tang et al., 2015*), where moderate energy input improved surface wettability while excessive input led to over-etching. However, our findings extend these observations by directly correlating the conductivity surge with specific microstructural damage — notably, the formation of micropores and fissures at 16 kV (Fig. 8c, 9c) — which has not been quantitatively reported for gramineous forage seeds like *Leymus chinensis*.

Critically, unlike corona or gliding arc treatments reported for other species (*Xu et al., 2021*; *Liu et al., 2021*), the DBD configuration employed here enabled uniform treatment across the seed surface without localized overheating, as evidenced by the absence of charring or melting in SEM images. This confirms DBD's superior suitability for continuous, non-thermal processing of small-seeded forages.

In summary, Dielectric Barrier Discharge (DBD) plasma treatment can significantly alter the epidermal structure of *Leymus chinensis* seeds, but its effect is voltage-dependent; only an appropriate treatment voltage (e.g., 10–13 kV) can effectively enhance seed performance. These findings provide a quantitative basis for optimizing plasma treatment parameters in forage seed processing.

CONCLUSIONS

Through a systematic comparison and performance evaluation of different atmospheric pressure plasma generation modes, the efficacy of Dielectric Barrier Discharge (DBD) as the preferred technical path for continuous forage seed treatment was verified. The main conclusions obtained are as follows:

(1) Dielectric Barrier Discharge (DBD) was identified as the ideal generation mode for atmospheric pressure plasma. In contrast to the locality of corona discharge, the high temperature of gliding arc discharge, the intermittency of spark discharge, and the dependence of glow discharge on low-pressure environments, DBD is capable of generating large-area, uniform, and stable low-temperature plasma in atmospheric air. Consequently, it possesses superior adaptability for applications in plasma agriculture.

(2) The plate-type electrode configuration adopted by DBD facilitates integration into continuous conveying systems. This structure provides an ideal technical foundation for achieving large-scale, non-thermal damage treatment of forage seeds, thereby verifying the engineering feasibility of this technology for continuous agricultural production scenarios.

(3) The DBD plasma treatment exhibited a distinct dosage effect, and an optimal processing parameter window was identified. Experiments conducted on *Leymus chinensis* seeds demonstrated that treatment with appropriate parameters (e.g., 10–13 kV) induced surface modification, forming controllable micron-scale micropores and fissures on the glume surface, which effectively improved water and air permeability. Electrical conductivity kinetic analysis further confirmed at the physiological level that moderate treatment maintained cell membrane integrity while cleaning the surface. However, excessive energy input (e.g., 16 kV) led to excessive damage to the glume and the leakage of intracellular contents, thereby inhibiting seed vigor.

In conclusion, proceeding from principle verification and equipment realization to mechanism elucidation, this study systematically demonstrated the feasibility and application potential of atmospheric pressure DBD plasma treatment technology in overcoming germination obstacles in forage seeds. These findings provide a critical theoretical basis and design foundation for the development of green and efficient physical seed treatment equipment.

ACKNOWLEDGEMENT

This work was supported by Natural Science Foundation of Inner Mongolia Autonomous Region of China (Grant No. 2024MS03037).

REFERENCES

[1] Amado, C., Reyes, P. G., Gómez, A., Torres, C., Martínez, H., Vergara, J. Martínez López, J. C., (2025). Enhancement of wheat seed germination using double dielectric barrier discharges with electrodes immersed in a conductive liquid. *Scientific Reports*, 15(1), 44448. http://doi.org/10.1038/s41598-025-28066-7.

[2] Ara˙jo, J. D. O., Dias, D. C. F. D., Miranda, R. M. D.Nascimento, W. M., (2022). Adjustment of the electrical conductivity test to evaluate the seed vigor of chickpea (cicer arietinum l.). *Journal of Seed Science*, 44. http://doi.org/10.1590/2317-1545v44258666.

[3] Attri, P., Okumura, T., Takeuchi, N., Razzokov, J., Zhang, Q., Kamataki, K., Shiratani, M. Koga, K., (2023). Role of direct plasma irradiation, plasma-activated liquid, and plasma-treated soil in plasma agriculture. *Plasma Medicine*, 13(3), 33-52.

[4] Bakeev, I. Y., Klimov, A. S., Oks, E. M.Zenin, A. A., (2022). Hollow cathode glow discharge initiation in a fore-vacuum plasma–cathode electron source. *IEEE Transactions on Plasma Science*, 50(12), 4860-4864. http://doi.org/10.1109/TPS.2022.3219051.

[5] Benabderrahim, M. A., Bettaieb, I.Rejili, M., (2025). Boosting seed performance with cold plasma. *Applied Sciences*, 15(20), 10996. http://doi.org/10.3390/app152010996.

[6] Cai, Z., Zhang, H., Liu, K., Chen, Y.Yu, Q., (2020). Experimental investigation and mechanism analysis on rock damage by high voltage spark discharge in water: effect of electrical conductivity. *Energies*, 13(20), 5432. http://doi.org/10.3390/en13205432.

[7] Dhakal, O. B., Dahal, R., Acharya, T. R., Lamichhane, P., Gautam, S., Lama, B., Khanal, R., Kaushik, N. K., Choi, E. H., Chalise, R. (2023). Effects of spark dielectric barrier discharge plasma on water sterilization and seed germination. *Journal of Water Process Engineering*, 54, 103849. https://doi.org/10.1016/j.jwpe.2023.103849.

[8] Doshi, P., Scholtz, V., Oplíštilová, A., Khun, J., Klenivskyi, M., Julák, J., Aerý, M. Aerá, B., (2024). Effect of transient spark discharge and plasma activated water treatments against *fusarium graminearum* infected wheat grains under laboratory conditions. *Plasma Chemistry and Plasma Processing*, 44(4), 1689-1712. http://doi.org/10.1007/s11090-024-10479-3.

[9] Evrendilek, G.A., Atmaca, B., Bulut, N., Uzuner, S., (2021). Development of pulsed electric fields treatment unit to treat wheat grains: Improvement of seed vigour and stress tolerance. *Computers and Electronics in Agriculture*, 185, 106129. https://doi.org/10.1016/j.compag.2021.106129.

[10] Fekete, R., Valkó, O., Fischer, L.K., Deák, B., Klaus, V.H., (2024). Ecological restoration and biodiversity-friendly management of urban grasslands – a global review on the current state of knowledge. *Journal of Environmental Management*, 368, 122220. http://doi.org/10.1016/j.jenvman.2024.122220.

[11] Ganeva, D., Sirakov, K., Mihov, M., Zahariev, S., Palov, I., (2015). Influence of pre-sowing electromagnetic treatments and duration of storage on germination energy and laboratory germination of seeds from Bulgarian tomato varieties. *INMATEH - Agricultural Engineering*, 45(1), 47-54.

[12] Harrison, R. J., Howieson, J. G., Yates, R. J., Norman, H. C., O Hara, G. W. Jaganathan, G. K., (2025). The impact of agricultural intensification on legume seeds with physical dormancy in sustainable farming systems. A review. *Agronomy for Sustainable Development*, 45(6). http://doi.org/10.1007/s13593-025-01058-7.

[13] Hou, T.G., Wang, Z.Y., Zhao, M.C., Liu, C.H., Xin, M.J., Wu, L.Y., Zhang, B.H., (2023). Effects of low-frequency high-voltage pulsed electric fields on germination characteristics of aged rice seeds. *INMATEH - Agricultural Engineering*, 70(2), 517-526. https://doi.org/10.35633/inmateh-70-50.

[14] Hui, Y., Xi, J., Wang, J., Wang, S., Shao, G., Li, B., Huang, C. Wang, D., (2025). Design and Experiment of a Uniform Distribution System for Plasma Treatment of Alfalfa Seeds (面向等离子体首蓿种子处理的均匀布料系统设计与试验). *Transactions of the Chinese Society for Agricultural Machinery*, 56, 184-193. https://doi.org/10.6041/j.issn.1000-1298.2025.11.017.

[15] Jia, P., Gao, K., Zhou, S., Chen, J., Wu, J., Wu, K. Li, X., (2021). Morphology evolution of an atmospheric pressure glow discharge initiated in the air gap between a liquid cathode and a needle anode. *Plasma Sources Science and Technology*, 30(9), 95021.

[16] Judée, F. Dufour, T. (2020)., Seed-packed dielectric barrier device for plasma agriculture: understanding its electrical properties through an equivalent electrical model. *Journal of Applied Physics*, 128(4), 44901. http://doi.org/10.1063/1.5139889.

[17] Li, W., Long, H., Xu, W., Xue, H., Cao, W., Li, Z.Pu, L., (2023). Effects of contact glow discharge plasm a on lycium barbarum seed germination and seed treatment methodology (接触辉光放电等离子体对枸杞种子萌发的促进作用及其处理工艺). *Journal of Radiation Research and Radiation Processing*, 41(1), 83-93. http://doi.org/10.11889/j.1000-3436.2022-0103.

[18] Li, Z., Yang, L., Liu, X., Wang, J., Liu, Y.Li, C., (2015). Bactericidal kinetics and mechanisms of low temperature glow discharge plasma (辉光放电低温等离子体技术对微生物的杀菌动力学及杀菌机制). *Food Science*, 36(11), 167-171. http://doi.org/10.7506/spkx1002-6630-201511032.

[19] Liu, C., Cui, J., Zhang, D., Tang, H., Gong, B., Zu, S., Zhong, C., (2021). Decontamination of infected plant seeds utilizing atmospheric gliding arc discharge plasma treatment. *Plasma Science and Technol ogy*, 23(10), 105501. http://doi.org/10.1088/2058-6272/ac0e1f.

[20] Liu, K., Fang, Z. Dai, D., (2023). Numerical study on uniformity of atmospheric helium gas dielectric ba rrier discharge on non-smooth surface regulated by sinusoidal clipping voltage (正弦削波电压调控大气压氦气非平滑表面介质阻挡放电均匀性的仿真研究). *Acta Physica Sinica*, 72(13), 112-125. http://doi.org /10.7498/aps.72.20230385.

[21] Luchian, C. E., Lungoci, C., Ciolan, M., Rimbu, C., Miron, L. D. Motrescu, I., (2025). Changes induced in seeds as a result of non-thermal plasma treatment in plasma agriculture applications. *Applied Scien ces*, 15(19), 10366. http://doi.org/10.3390/app151910366.

[22] Mazandarani, A., Goudarzi, S., Ghafoorifard, H. Eskandari, A., (2020). Evaluation of DBD plasma effects on barley seed germination and seedling growth. *IEEE Transactions on Plasma Science*, 48(9), 3115-3121. http://doi.org/10.1109/TPS.2020.3012909.

[23] Ouf, S. A., Almarashi, J. Q. M., & Mohamed, A.-A. H. (2022). Characterization and evaluation of cold atmospheric plasma as seedborne fungal disinfectant and promoting mediator for physico-chemical characteristics of Moringa oleifera seedlings. *Scientific Reports*, 12, 15812. https://doi.org/10.1038/s41598-022-18768-7.

[24] Pentoś, K., Wondołowska-Grabowska, A., Gajda, G., Babij, M., Chohura, P., Zaleski, A., Szpunar-Krok, E., Jobczyk, W., Romaniuk, A., Gajda, D., (2022). The effect on the germination vigour of cucumber seeds after receiving magnetic field treatment pre-sowing. *Applied Sciences*, 12(11), 5490. https://doi.org/10.3390/app12115490.

[25] Sirakov, K., Álvarez, J., Muhova, A., (2021). Evaluation of the effect of electromagnetic treatment on the sowing qualities of triticale seeds. *Bulgarian Journal of Agricultural Science*, 27(4), 699-711.

[26] Song, Y.B., Su, Z.X., Shi, X.J., Shen, H.J., Zhao, W.Y., Liu, Z.Y., (2025). Effects of PEF on drought stress response of Scutellaria baicalensis seeds and its physiological mechanism. *INMATEH - Agricultural Engineering*, 77(3), 409-418. https://doi.org/10.35633/inmateh-77-33.

[27] Tang, X., Liang, F., Zhao, L., Zhang, L., Shu, J., Zheng, H., Qin, X., Shao, C., Feng, J., Du, K., (2015). Stimulating Effect of Low-Temperature Plasma (LTP) on the Germination Rate and Vigor of Alfalfa Seed (Medicago Sativa L.). In: Li, D., Li, Z. (Eds.), *Computer and Computing Technologies in Agriculture IX*, IFIP Advances in Information and Communication Technology, Vol. 479, Springer, Cham, pp. 522-529. https://doi.org/10.1007/978-3-319-48354-2_53.

[28] Wang, D., Li, S., You, Y., Hui, Y., Ma, P., Xi, J., Yan, C., Zhou, X., Hu, Y.Wang, Z., (2025). Review and prospect of full-process mechanization technology in forage production and processing (饲草生产与加工机械化技术研究现状与展望). *Transactions of the Chinese Society for Agricultural Machinery*, 56(11), 1-20. http://doi.org/10.6041/j.issn.1000-1298.2025.11.001.

[29] Waskow, A., Howling, A., Furno, I., (2021). Mechanisms of Plasma-Seed Treatments as a Potential Seed Processing Technology. *Frontiers in Physics*, 9, 617345. https://doi.org/10.3389/fphy.2021.617345.

[30] Xu, W., Luan, X., Li, Y., Chen, H., Ding, C. Song, Z., (2021). Effects of corona discharge plasma radiation on alfalfa seeds (电晕放电等离子体辐射对紫花苜蓿种子的影响). Journal of Radiation Research and Radiation Processing, 39(2), 45-54. http://doi.org/10.11889/j.1000-3436.2021.rrj.39.020401.

[31] Zhang, Q., Lv, X., Bao, J., (2024). Effect of cold plasma treatment on seed germination and seedling growth of oats under salt stress (冷等离子体处理对盐胁迫下燕麦种子萌发及幼苗生长的影响). Current Biotechnology, 14(3), 413-421. http://doi.org/10.19586/j.2095-2341.2023.0167.

OPTIMIZATION OF FUZZY PID CONTROL USING AN IMPROVED SPARROW SEARCH ALGORITHM FOR SOYBEAN FOLIAR FERTILIZER SPRAYING

/

基于改进麻雀搜索算法的大豆叶面肥喷施模糊 PID 控制优化研究

Yue CHEN[1)], Hailiang GONG[1)], Weidong ZHUANG*[1)]
College of Engineering, Heilongjiang Bayi Agricultural University, Daqing, Heilongjiang, 163319, China
Tel: 13836962853; E-mail: 81nd@163.com
DOI: https://doi.org/10.35633/inmateh-79-50

***Keywords**: Variable-rate application; Hydraulic actuator; Sparrow search algorithm; Dynamic response; Precision agriculture*

ABSTRACT

To address the low control precision caused by the high nonlinearity and pure time-delay of hydraulic pipelines in variable-rate soybean foliar fertilization, this study developed an automatic variable-rate control system for boom sprayers. Based on Fluent dynamic mesh simulations, the throttling characteristics of the electric control valve were revealed, and a second-order transfer function model with pure time-delay was accurately identified for the actuator. To overcome the reliance of conventional fuzzy controllers on expert experience, an improved Sparrow Search Algorithm-optimized Fuzzy PID (ISSA-Fuzzy PID) control strategy was proposed. By integrating optimized population initialization and adaptive global search, this improvement mechanism effectively avoids premature convergence during dynamic parameter tuning. Simulation results indicate that the proposed algorithm compresses the rise time to 0.35 s, limits the overshoot to within 20%, and achieves steady-state convergence within 1.0 s. Bench tests verified that the average detection errors for system flow rate and pressure were merely 2.14% and 2.34%, respectively. Under the working pressure of 250–350 kPa, dynamic pressure regulations were completed stably within 1.9 s without significant overshoot, exhibiting improved regulation precision under high-flow conditions. This research effectively overcomes the lag bottleneck of actuating mechanisms, providing an integrated control solution with high dynamic response and steady-state precision for variable-rate applications. Practically, this optimized system ensures rapid dosage correction and pressure stability, providing technical support for improving the operational timeliness and fertilizer-use efficiency of field spraying operations.

摘 要

针对大豆叶面肥变量喷施中液压管路高非线性与纯滞后导致的控制精度低等问题，本文开发了一套喷杆喷雾机变量自动控制系统。基于 Fluent 动网格仿真揭示了电控阀节流特性，并精确辨识出执行机构的二阶带纯滞后传递函数模型。为克服模糊控制器高度依赖专家经验的局限，提出改进麻雀搜索算法优化模糊 PID（ISSA-Fuzzy PID）控制策略。该改进机制通过融合优化的种群初始化与自适应全局搜索策略，有效避免了动态参数寻优过程中的早熟收敛问题。仿真表明，该算法将上升时间缩短至 0.35 s，超调量控制在 20% 以内，并在 1.0 s 内实现稳态收敛。台架试验验证：系统流量与压力的平均误差仅为 2.14% 和 2.34%；在 250~350 kPa 工作压力下，动态调节可在 1.9 s 内无显著超调地切入稳态，且大流量工况下调节精度更优。本研究有效突破了执行机构的滞后瓶颈，为高精度变量施药提供了兼具高动态响应与稳态精度的集成控制方案。在实际应用中，该系统能够确保施药量的快速修正与压力稳定，从而显著提升田间喷施作业的响应及时性与肥料利用率。

INTRODUCTION

The integration of base fertilizer application and precision foliar spraying represents a transformative shift in modern agricultural development (*Farooque et al., 2023*). Foliar fertilization enhances nutrient utilization efficiency, directly influencing crop physiological development, yield, and grain quality. Despite these benefits, traditional uniform spraying methods fail to account for spatial heterogeneities in soil fertility and crop nutrient requirements. Consequently, excessive application leads to environmental degradation, whereas under-application limits yield potential. To mitigate these issues, transitioning from uniform application to high-precision, variable-rate application (VRA) is imperative for sustainable agricultural production (*Yuxuan et al., 2025*).

Historically, VRA systems have relied heavily on pre-generated prescription maps. Although these maps support the optimization of spatial input distribution, their generation is labor-intensive, and their static nature prevents adaptation to dynamic field conditions in real time *(Pawase et al., 2023; Dong et al., 2025)*. This limitation has catalyzed a research trend toward real-time sensor-based feedback loops and advanced control algorithms. Extensive reviews on intelligent variable-rate spray technologies confirm that multi-variable coupling decision-making models and real-time execution remain the core direction of global agricultural engineering (*Jiao et al., 2025*). Among existing controllers, PID remains a standard, yet its performance is frequently compromised by system nonlinearities and time lags inherent in hydraulic sprayers. To overcome these deficiencies, recent studies have successfully utilized single-neuron architectures (*Su et al., 2022*) and intelligent optimization methods, such as incremental PID for side-deep fertilization (*Xie et al., 2026*) and PSO-based Fuzzy-PID for real-time regulation (*Xu et al., 2025*).

However, a critical comparison of recent AI-based control strategies reveals significant trade-offs regarding their suitability for low-cost agricultural machinery. Advanced machine learning policies typically necessitate extensive interaction data and high computational power, posing implementation challenges for embedded spraying terminals (*Dhanya et al., 2022*). Similarly, while neural-network PID tuning improves nonlinear approximation, these models often lack interpretability, complicating maintenance when hydraulic components degrade *(Zhu et al., 2023*). In contrast, Swarm-Intelligence-optimized Fuzzy PID control offers a pragmatic compromise: it maintains rule-based interpretability and low computational cost while leveraging global search capabilities for parameter optimization. This approach is heavily validated in the latest precision agricultural research. For example, recent works have demonstrated superior self-correcting fuzzy PID control for integrated water-fertilizer irrigation (*Zhang et al., 2025*), and Tuna Swarm Optimization (TSO) combined with Fuzzy PID has been reported to improve remote fertilization flow control and reduce overshoot (*Wu et al., 2026*).

Despite these advancements, rapid, stable, and precise real-time control tailored for soybean foliar fertilization remains elusive. Existing systems are frequently hindered by a combination of technical bottlenecks: prescription-map latency, nonlinear valve throttling, pure time-delay in long hydraulic pipelines, pressure pulsation from diaphragm pumps, and insufficient controller robustness under fluctuating flow demands. Therefore, this study tests the hypothesis that an improved Sparrow Search Algorithm (SSA) *(Xu et al., 2025*) optimized Fuzzy PID controller can significantly reduce transient response times and suppress overshoot compared to conventional PID and manually tuned controllers. To validate this, we propose an automatic boom sprayer control system integrating an improved SSA with a fuzzy PID strategy. To validate this approach, an automatic boom-sprayer control system integrating an improved SSA with a fuzzy PID control strategy is developed. By utilizing a GreenSeeker spectral sensor for real-time monitoring of crop growth status (*Patle et al., 2025*), the system facilitates immediate variable-rate topdressing, bypassing map latency and enhancing the precision of foliar fertilization practices.

MATERIALS AND METHODS

Structure and Principle of the Automatic Spraying Control System

The automatic spraying control system utilizes a spectral sensor at the front end to collect soybean NDVI data, which are transmitted via the CAN bus to an upper computer for analysis, thereby assisting the intelligent control terminal in making spraying decisions. At the rear end, an electronically controlled regulating valve is employed as the control component to achieve the regulation of pipeline pressure and flow rate. Upon receiving commands from the onboard intelligent control terminal, the motion controller outputs an analog voltage signal to regulate the electronically controlled valve. This adjusts the valve spool position, thereby modulating the opening degree of the valve. Changes in flow rate and pressure within the system pipeline are monitored by a flow sensor and a pressure transmitter, respectively, with the recorded data transmitted to the control terminal. The electronically controlled regulating valve continuously modulates the flow rate and pressure within the pipeline. Meanwhile, the motion controller collects signals from the sensors and receives commands from the upper computer to control the valve's on/off state and opening degree. The system structure schematic is shown in Fig. 1.

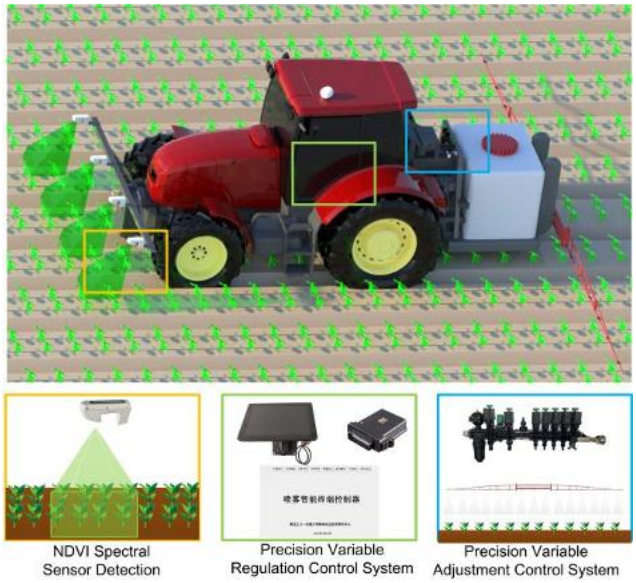
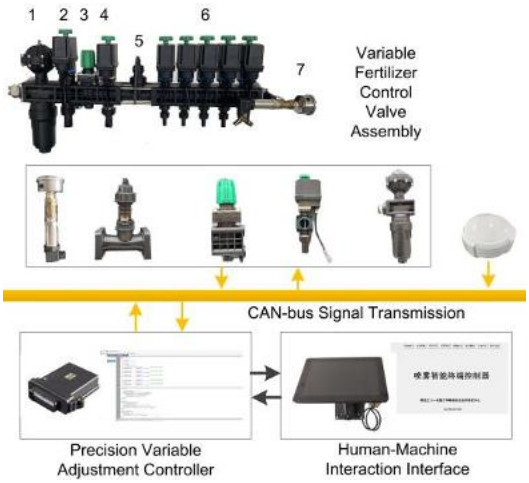


Fig. 1 - Schematic diagram of the system structure



1.Pressure Regulator Filter; 2. Electric Main Valve; 3. Manual Pressure Regulating Valve; 4. Electronic Control Valve; 5. Flow Sensor; 6. Electronic Control Branch Valve; 7. Pressure Sensor

Fig. 2 - Control valve assembly of the spraying system

Test Equipment

The control valve assembly of the automatic system utilized a product manufactured by Ningbo Licheng Agricultural Spraying Technology Co., Ltd., China (Fig. 2). This assembly ensures stable sprayer operation by integrating pressure stabilization, filtration, regulation, and pipeline flow distribution. In this system, the motion controller adjusts the spool opening of the electric control valve based on target commands. This alters the pressure within the flow channel, modulating the flow velocity to achieve precise variable-rate spraying.

Simulation of automatic spraying control system

To investigate the flow velocity and pressure fields within the flow channel and analyze the energy loss caused by the valve's intrinsic structural characteristics, ANSYS Fluent computational fluid dynamics (CFD) simulation was employed. This analysis provides a theoretical foundation for subsequent system adjustments and algorithm calibration.

3D modeling and mesh generation

Based on the structural parameters of the electronically controlled regulating valve, a 3D model was constructed in UG (Fig. 3), and its fluid domain was extracted and meshed for fluid dynamics analysis (Fig. 4). During operation, the foliar fertilizer enters through the valve inlet, is modulated by the valve spool, and exits via the outlet. A motor drives the spool vertically to a predetermined opening angle, altering the annular gap between the guiding spool and the valve body.



Fig. 3 - Three-dimensional model of the electronic control valve



Fig. 4 - Fluid domain mesh division

Given that the foliar fertilizer liquid is incompressible, a pressure-based solver was adopted. The inlet of the valve was defined as a pressure inlet, the outlet as a pressure outlet, and a no-slip condition was applied to all internal pipe walls.

For reproducibility, the CFD workflow was supplemented as follows. The valve fluid domain was discretized with an unstructured tetrahedral mesh and local refinement near the valve-core throttling region and wall boundary layers. Three mesh densities were compared during mesh-independence checking, and the final grid was selected when the outlet-flow variation between two adjacent refinements was below 2 %. The final model contained approximately 3.2 × 10^5 cells, the minimum orthogonal quality was greater than 0.20, and the maximum skewness was less than 0.85. The SIMPLE pressure-velocity coupling scheme and second-order upwind discretization were used, and each operating condition was iterated until scaled residuals for continuity and momentum were below 1.0 × 10^{-5} and the outlet-flow monitor became stable.

Turbulence modeling and dynamic mesh

The flow regime of the liquid is determined by the Reynolds number (Re), defined as:

$$Re = \frac{\rho v D}{\mu} \tag{1}$$

where ρ represents the fluid density, v is the fluid velocity, D is the pipe diameter, and μ is the fluid dynamic viscosity.

Calculations yielded an Re of 9726. Because $Re \geq 8000$, the fluid flow transitions to a fully turbulent state, necessitating the standard k-ε turbulence model for calculations. The standard k-ε model is a fully turbulent computational model that disregards the influence of molecular viscosity. By coupling turbulent kinetic energy and dissipation rate, it determines the distribution of velocity, pressure, and energy, enabling precise simulation of turbulent flow at intermediate-to-high Reynolds numbers. Furthermore, to simulate the continuous adjustment of the electric control valve, a dynamic grid method utilizing a dynamic layering approach (cell size of 0.002 m) was employed at the rigid interface, while all other variables were set to their default values.

Design of the ISSA-Fuzzy PID Control Algorithm

In the operational process of the variable-rate spray system, inherent pure time-delay and nonlinear characteristics emerge due to the response latency of the electric control valve, pressure regulation dynamics, and flow stabilization time. Conventional proportional-integral-derivative (PID) controllers struggle to handle such time-delay systems effectively, often resulting in severe overshoot and poor robustness (*Karimi et al., 2004*). To eliminate the hysteresis effect and enhance the dynamic precision of the spraying control system, this study proposes an advanced Sparrow Search Algorithm optimized Fuzzy PID (ISSA-Fuzzy PID) control strategy.

System Identification of the Actuator

Establishing an accurate mathematical model is a prerequisite for robust control system design. In this study, system identification was employed to derive the equivalent transfer function of the electric control valve. Fluent computational fluid dynamics (CFD) simulations, combined with dynamic mesh techniques, were conducted on the core components of the variable-rate system (*Kumar et al., 2021*). Analyzing the simulated transient response data revealed that the actuator exhibits second-order dynamic characteristics.

Consequently, a second-order transfer function structure was selected for the spraying automatic control system. The System Identification Toolbox in MATLAB 2020 was utilized for offline parameter identification. The input-output data pairs from the Fluent simulations were imported into the MATLAB workspace, with the transfer function order set to 2 and the number of zeros set to 0. Based on the CFD simulation data, the identified continuous-time transfer function is expressed as Eq. (2):

$$G_{sim}(s) = \frac{K_{sim}}{T_1 s^2 + T_2 s + 1} e^{-\tau_{sim} s} \tag{2}$$

where $G_{sim}(s)$ represents the simulated transfer function of the actuator; K_{sim} is the system gain derived from the simulation; T_1 and T_2 denote the time constants of the second-order system; τ_{sim} represents the pure time delay reflecting the response latency; and s is the Laplace complex variable.

Model validation through MATLAB demonstrated a fitting accuracy of 89.91%, verifying the reliability of the identification. Furthermore, utilizing the actual input-output data acquired from the physical performance tests, an empirical system identification was conducted to derive the practical transfer function, as shown in Eq. (3):

$$G_{\exp}(s) = \frac{K_{\exp}}{T_3 s^2 + T_4 s + 1} e^{-\tau_{\exp} s} \tag{3}$$

where $G_{\exp}(s)$ is the empirical transfer function obtained from physical experiments; $K_{\exp}$ represents the actual system gain; T_3 and T_4 are the experimental time constants; and $\tau_{\exp}$ is the actual pure time delay of the hardware system.

Conventional PID Control Model

The PID controller regulates the system output by calculating the proportion (P), integral (I), and derivative (D) of the error between the measured output and the desired target value (*Zhu et al., 2023*). The schematic diagram of the control system is shown in Fig. 5.

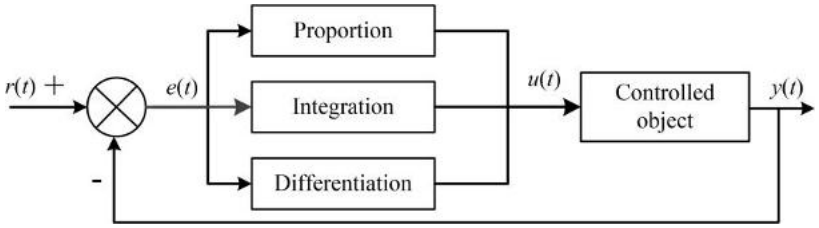


Fig. 5 - Schematic diagram of the PID control system

The error signal $e(t)$ between the system reference input $r(t)$ and the actual output $y(t)$ is defined in Eq. (4):

$$e(t) = r(t) - y(t) \tag{4}$$

The standard position PID control law, which continuously minimizes the error $e(t)$ to achieve the system's control objective, is expressed in Eq. (5):

$$u(t) = K_p \left[e(t) + \frac{1}{T_i} \int_0^t e(\tau) d\tau + T_d \frac{de(t)}{dt} \right] \tag{5}$$

where $u(t)$ represents the control output signal; K_p is the proportional gain; T_i denotes the integral time constant; and T_d represents the derivative time constant.

Sparrow Search Algorithm Optimized Fuzzy PID Control

The Sparrow Search Algorithm (SSA) is a swarm intelligence optimization technique inspired by the foraging and anti-predation behaviors of sparrows (*Xue and Shen, 2020*). By simulating these behaviors, the algorithm treats the solution space of the optimization problem as a foraging area, skillfully balancing global exploration with local exploitation. The population is divided into three functional roles: producers, scroungers, and scouts. Producers are responsible for locating optimal food sources and guiding the population. Scroungers follow the producers to exploit resources while monitoring environmental changes. Simultaneously, scouts act as an early-warning mechanism; upon detecting a predator, they issue alarm signals, prompting the population to evacuate. This division of labor endows the SSA with rapid convergence, strong adaptability, and exceptional global search capabilities.

The primary mission of the producers is to provide orientation and indicate food sources for the entire population. The position update rule for producers is given by Eq. (6):

$$X_{i,j}^{t+1} = \begin{cases} X_{i,j}^{t} \exp\left(-\frac{i}{\alpha iter_{\max}}\right), R_2 < ST \\ X_{i,j}^{t} + Q \cdot L, \qquad\qquad R_2 \geq ST \end{cases} \tag{6}$$

where $X_{i,j}$ denotes the position of the i-th sparrow in the j-th dimension; t represents the current iteration; $iter_{\max}$ is the maximum number of iterations; α is a uniformly distributed random number in $(0,1]$; $R_2 \in [0,1]$ represents the alarm value; $ST \in [0.5,1]$ is the safety threshold; Q is a random number generated from a normal distribution; and L is a $1 \times d$ matrix with all elements equal to 1. When $R_2 < ST$, the environment is safe, and producers conduct an extensive search; when $R_2 \geq ST$, danger is detected, and the population immediately relocates to a safe area.

The position update for the scroungers is defined by Eq. (7):

$$X_{i,j}^{t+1} = \begin{cases} Q \cdot \exp\left(\frac{X_{worst}^{t} - X_{i,j}^{t}}{i^2}\right), & i > \frac{n}{2} \\ X_{best}^{t+1} + \left|X_{i,j}^{t+1} - X_{best}^{t+1}\right| \cdot A^{+} \cdot L, & i \leq \frac{n}{2} \end{cases} \tag{7}$$

where X_{worst} denotes the global worst position in the current iteration; X_{best} represents the optimal position occupied by the producers; A is a multi-dimensional row matrix with elements randomly assigned 1 or -1, satisfying $A^{+} = A^{T}(AA^{T})^{-1}$; and n denotes the population size. When $i > n/2$, it indicates that the scrounger is in a poor location and must forage elsewhere.

The position update for the scouts is given by Eq. (8):

$$X_{ij}^{t+1} = \begin{cases} X_{best}^{t} + \beta \cdot \left| X_{ij}^{t} - X_{best}^{t} \right|, & f_i > f_g \\ X_{ij}^{t} + K \cdot \left(\frac{|X_{ij}^{t} - X_{worst}^{t}|}{f_i - f_w + \varepsilon} \right), & f_i = f_g \end{cases} \quad (8)$$

where β is a step control parameter following a standard normal distribution; X_{best} denotes the current global optimal position; $K \in [-1,1]$ is a random step parameter specifying the direction of movement; f_i is the fitness value of the i-th sparrow; and f_g and f_w are the current global best and worst fitness values, respectively. ε is a negligible constant to prevent division by zero.

In conventional fuzzy PID control, the formulation of fuzzy rules and scaling factors relies heavily on expert experience, which introduces subjectivity and limits real-time adaptability (*Xu et al., 2025*). This often leads to sub-optimal tuning of PID parameters, slowing down the system response and making it inadequate for the highly dynamic variable-rate spraying system. To overcome this, the SSA is employed to dynamically optimize the quantization factors (K_{E}, K_{EC}) and the PID parameters (K_p, K_i, K_d) within the fuzzy controller. The principle of the ISSA-Fuzzy PID controller is illustrated in Fig. 6.

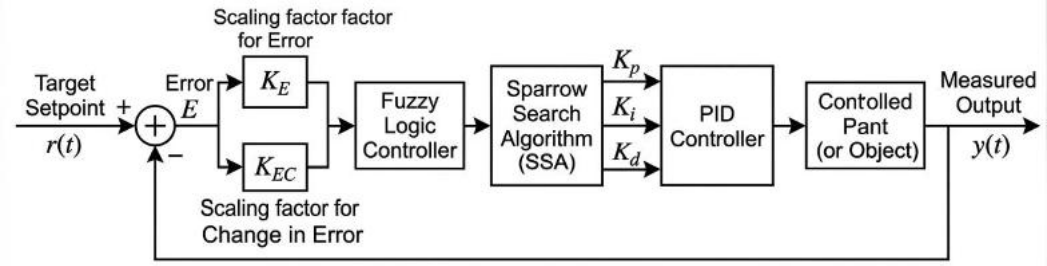


Fig. 6 - Schematic diagram of the Sparrow Search optimized fuzzy PID controller

To evaluate the optimization process, an integral objective function is defined. To prevent excessive control amplitudes and actuator saturation, the objective function integrates the absolute error and the control signal $u(t)$, as shown in Eq. (9):

$$J_1 = \int_0^{\infty} (w_1 \cdot t|e(t)| + w_2 \cdot u^2(t) + w_3 \cdot |e(t)|)\, dt \quad (9)$$

where w_1, w_2, w_3 denote the assigned parameter weight values used to balance the tracking performance and energy consumption.

Fuzzy Logic Design and SSA Optimization Parameters

The fuzzy controller utilizes the system error e and the error change rate ec as input variables. The input signals undergo a fuzzification process, followed by fuzzy inference based on established control rules. Finally, the centroid method is employed for defuzzification to output the precise PID parameter compensation increments: $\Delta \mathrm{K_p}, \Delta \mathrm{K_i}, \text{and } \Delta \mathrm{K_d}$.

The fuzzy input universe of discourse for both the system error and the error change rate is defined as [-2, 2], while the fuzzy output universe for K_p, K_i, and K_d is constrained to [-1, 1]. Both input and output variables are partitioned into seven fuzzy subsets (linguistic variables): Negative Big (NB), Negative Medium (NM), Negative Small (NS), Zero (ZO), Positive Small (PS), Positive Medium (PM), and Positive Big (PB). To ensure the sensitivity and computational efficiency of the control system, triangular membership functions with high distinguishability are universally adopted across the entire universe of discourse. Fig. 7 and Fig. 8 illustrate the membership functions for the input and output variables, respectively.

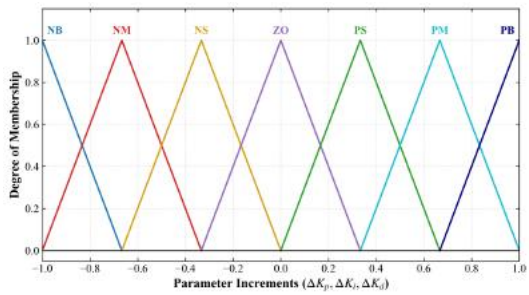


Fig. 7 - Membership functions of input variables

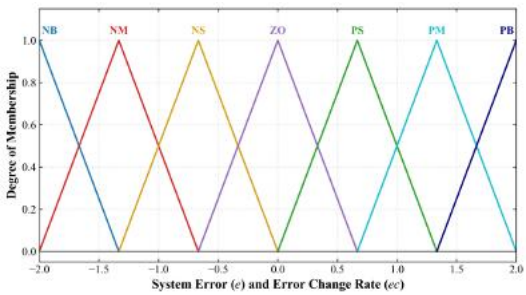


Fig. 8 - Membership functions of output variables

Fuzzy control rules form the core of the fuzzy inference mechanism, directly determining the dynamic performance of the control system. Rational rule configuration effectively enhances system stability, minimizes overshoot, and reduces the settling time. Tailored to the direct current (DC) motor-driven actuator, 49 IF-THEN fuzzy control rules were extracted based on expert experience, as detailed in Table 1.

Table 1

Fuzzy rule base for PID parameter increments

E \ EC	NB	NM	NS	ZO	PS	PM	PB
NB	PB/NB/PS	PB/NB/NS	PM/NM/NB	PM/NM/NB	PS/NS/NB	ZO/ZO/NM	ZO/ZO/PS
NM	PB/NB/PS	PB/NB/NS	PM/NM/NB	PS/NS/NM	PS/NS/NM	ZO/ZO/NS	NS/ZO/ZO
NS	PM/NB/ZO	PM/NM/NS	PM/NS/NM	PS/NS/NM	ZO/ZO/NS	NS/PS/NS	NS/PS/ZO
ZO	PM/NM/ZO	PM/NM/NS	PS/NS/NS	ZO/ZO/NS	NS/PS/NS	NM/PM/NS	NM/PM/ZO
PS	PS/NM/ZO	PS/NS/ZO	ZO/ZO/ZO	NS/PS/ZO	NS/PS/ZO	NM/PM/ZO	NM/PB/ZO
PM	PS/ZO/PB	ZO/ZO/NS	NS/PS/PS	NM/PM/PS	NM/PM/PS	NM/PB/PS	NB/PB/PB
PB	ZO/ZO/PB	ZO/ZO/PM	NM/PS/PM	NM/PM/PM	NM/PB/PS	NB/PB/PS	NB/PB/PB

To achieve global parameter optimization, the Sparrow Search Algorithm (SSA) is employed to optimize the scaling factors and the baseline PID parameters of the fuzzy controller. The specific hyperparameters of the algorithm are configured as follows: the population size is set to 30, and the maximum number of iterations is 100. The proportions of producers, scroungers, and scouts within the population are set to 20%, 70%, and 10%, respectively, with the safety threshold (ST) set to 0.8. Candidate solutions are initialized using a uniform distribution within the predefined parameter boundaries. Following a position update, if an individual exceeds the boundary limits, it is forcibly constrained to the nearest feasible boundary. The optimization process is terminated, satisfying the convergence criteria, when the algorithm reaches the maximum number of iterations or if the change in the best fitness value remains below 1.0×10^{-6} for 10 consecutive iterations. The configuration of these hyperparameters is based on a combination of standard SSA recommendations and preliminary experimental results, aiming to balance the global exploration capability and local convergence efficiency of the algorithm.

RESULTS

Simulation Data Analysis

Internal Flow Field Analysis of the Valve

By employing Fluent computational fluid dynamics (CFD) to simulate the operational behavior of the electric control valve, a deeper understanding of its hydrodynamic performance at various valve openings can be achieved. For a comprehensive assessment, simulations were conducted at effective valve openings of 15% and 30%, specifically analyzing the pressure and velocity fields. By comparing the dynamic simulation results under these two states, and integrating the precise application requirements of boom sprayers, the control valve's opening can be flexibly modulated to achieve an optimal balance between spray performance and energy efficiency.

Fluent was utilized to model the actual working conditions of the electric control valve, extracting the internal pressure field to elucidate the static pressure distribution. The correlation between the internal pressure gradients during operation and the overall macroscopic system performance was thoroughly investigated based on these simulations. Fig. 9 and Fig. 10 illustrate the pressure contours on the symmetrical cross-sections of the valve.

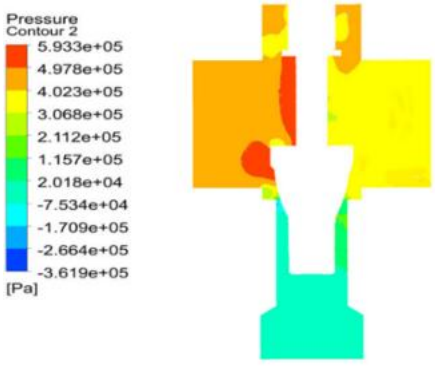


Fig. 9 - Pressure cloud map at 15% valve opening

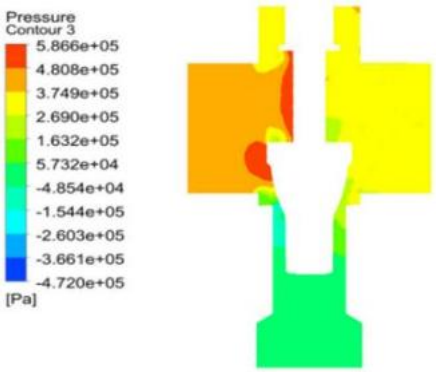


Fig. 10 - Pressure cloud map at 30% valve opening

Upon entering the valve body, the fluid pressure exhibits a highly stable state. This indicates an optimized inlet geometry design that ensures smooth fluid ingress without inducing significant pressure fluctuations, which is a critical prerequisite for the stable operation of the entire spraying system. However, as the fluid navigates through the valve core, the hydrodynamic conditions alter significantly. The physical presence of the valve core acts as a throttling obstruction, leading to a localized stagnation point and a subsequent pressure increase in the immediate vicinity of the core. This phenomenon is consistent with theoretical expectations, as the internal structure is engineered to dynamically throttle flow rate and pressure. Although this localized pressure rise is distinct, it serves as a crucial indicator of the valve's throttling efficacy. As the fluid continues its trajectory towards the outlet, it undergoes a sudden expansion, resulting in a rapid pressure drop. This continuous process functions as a "pressure dissipation" mechanism, ensuring fluid stabilization post-throttling. Once discharged from the lower outlet, the pressure profile reverts to a stable and uniform distribution.

Analysis of the Velocity Field

The velocity field characterizes the spatial distribution of fluid velocities, encompassing both the magnitude and trajectory of the flow, serving as an essential metric for describing fluid kinematics. In precision hydraulic systems, the uniformity of the velocity field directly dictates the stability of the volumetric flow rate. By thoroughly analyzing the velocity contours, the system's capability to achieve the desired flow control targets can be evaluated, thereby facilitating the optimization of the overall spraying performance. Fig. 11 and Fig. 12 present the velocity contours across the symmetrical cross-sections. It is observed that upon entering the valve body, the velocity profile exhibits a non-uniform distribution, characterized by a high-velocity core region and relatively lower velocities adjacent to the inner walls due to boundary layer friction. This initial non-uniformity induces localized turbulent vortices within the upstream chamber. However, following the flow velocity regulation at the constricted valve port, the downstream fluid velocity profile homogenizes significantly.

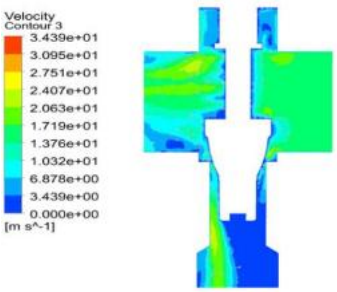


Fig. 11 - Velocity cloud map at 15% valve opening

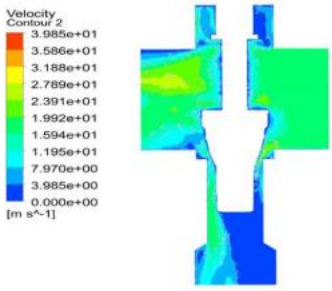


Fig. 12 - Velocity cloud map at 30% valve opening

Control System Simulation

To validate the proposed algorithms, a comprehensive simulation model of the variable-rate foliar fertilizer spraying control system was constructed using the Simulink environment in MATLAB, as shown in Fig. 13. For the transient response analysis of the automatic spraying control system, the simulation duration was set to 8.0 seconds. Based on the observed response curves and heuristic tuning, the three baseline proportional-integral-derivative parameters (K_p, K_i, K_d) were initially determined. Hardware-in-the-loop test results indicated that the intrinsic time delay— from control-signal transmission to the corresponding physical change in output flow rate—was approximately 1.0 second. Accordingly, the transport-delay block in the Simulink model was set to 1.0 seconds.

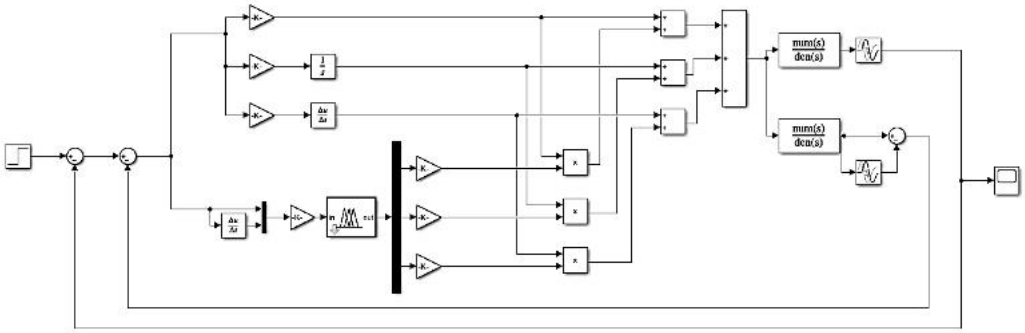


Fig. 13 - Simulink model of the variable-rate spraying control system

For the intelligent adaptive mechanism, the fuzzy controller utilizes the system error and the error change rate as input variables. The input universe of discourse was defined as [-2, 2], while the output universe of discourse for the parameter increments was constrained to [-1, 1]. Based on the fuzzy inference rules delineated in the previous section, the system quantization factors and scaling gains were strictly parameterized to satisfy the specific input-output mapping requirements of the actuator. Incorporating the empirical mathematical model derived from the Fluent CFD identification (Eq. 2), the initial baseline PID parameters were tuned to (K_p=2, K_i=10, K_d=0.5). To demonstrate the improved of the proposed algorithm, a comparative transient analysis was conducted among the conventional PID, Fuzzy PID, and the proposed ISSA-Fuzzy PID control strategies. The unit step response curves of the spraying control system under these three strategies are juxtaposed in Fig. 14.

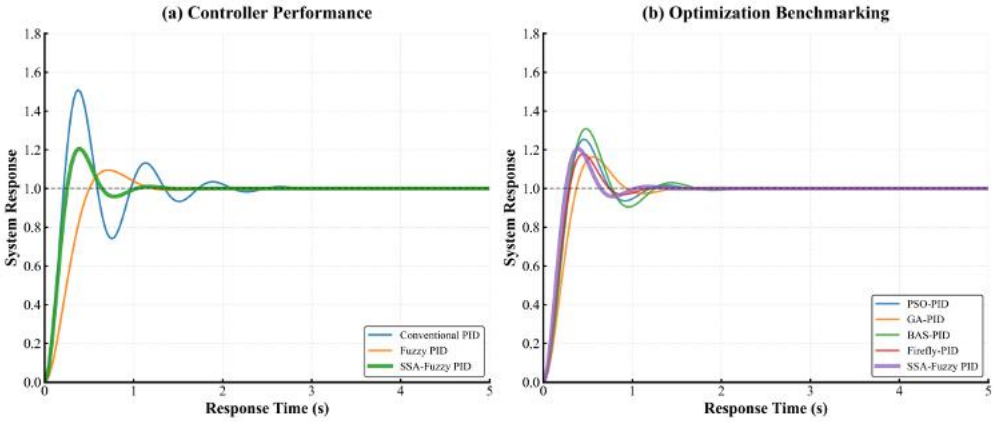


Fig. 14 - Unit step response curves of the spraying control system under different algorithms

Simulation results highlight significant performance disparities among the control strategies evaluated for the delayed second-order system (Fig. 14). As shown in the basic controller performance comparison (Fig. 14a), the conventional PID controller exhibits severe underdamped oscillations, with approximately 50% overshoot and a prolonged 2.2 s settling time, exposing its inadequacy for nonlinear hydraulic systems with pure time delays. The Fuzzy PID controller improves robustness by suppressing overshoot to 10% and reducing settling time to 1.2 s, but compromises transient speed with a slower 0.45 s rise time. Ultimately, the proposed ISSA-Fuzzy PID controller achieves the optimal dynamic balance, delivering the fastest rise time (0.35 s), an acceptable overshoot (20%), and a rapid settling time (1.0 s).

To further evaluate the performance of the Sparrow Search Algorithm, the proposed controller was benchmarked against representative swarm intelligence optimization algorithms, including PSO-PID, GA-PID, BAS-PID, and Firefly-PID (Fig. 14b). The benchmarking results demonstrate that while all intelligent algorithms mitigate the severe oscillations of the conventional PID, they exhibit varying degrees of dynamic trade-offs. BAS-PID and PSO-PID generate higher overshoots of approximately 30% and 25%, respectively. GA-PID effectively suppresses overshoot but suffers from a prolonged settling phase. Firefly-PID closely trails the proposed method; however, the ISSA-Fuzzy PID consistently demonstrates tighter overshoot control (under 20%) and the fastest convergence to the steady state.

Beyond transient response metrics, the structural advantages of the Sparrow Search Algorithm present distinct robustness benefits. While GA and PSO are prone to premature convergence in highly nonlinear hydraulic systems, and BAS struggles with multi-dimensional parameter tuning, the SSA's unique producer-scrounger-scout architecture prevents local optima trapping. This topological advantage translates into enhanced stability against sudden pressure disturbances. Furthermore, considering the limited computational resources of embedded agricultural terminals, the ISSA-Fuzzy PID algorithm provides a highly efficient alternative to advanced but computationally heavy strategies like Reinforcement Learning or Adaptive Model Predictive Control (MPC). By decoupling the global offline parameter optimization (handled by SSA) from the low-latency online adjustments (executed by the fuzzy inference engine), the real-time computational burden is reduced, supporting low-latency online execution suitable for CAN-bus-based tractor terminals. To confirm that the performance improvements observed were not due to random chance, a one-way analysis of variance (ANOVA) was performed on the settling time and overshoot data collected from the comparative tests. These results indicate that the ISSA-Fuzzy PID controller achieved the best overall balance among the tested methods, with faster convergence and tighter overshoot control than the conventional PID and the other swarm-intelligence-based controllers.

Bench Performance Tests

System Flow Rate Detection Precision Test and Data Analysis

The control accuracy of the variable-rate spraying system relies fundamentally on the measurement precision of the flow rate sensor. A bench test was conducted to calibrate the flow rate detection accuracy, ensuring that the intrinsic system error remains within permissible limits. During the experimental procedure, target flow values were transmitted via the intelligent control terminal. Simultaneously, the flow rate sensor continuously logged the dynamic flow data under operational conditions, displaying the real-time actual values on the terminal interface. To minimize random errors, the test was repeated three times. By comparing the preset target values with the actual measured values, the relative errors were calculated. The acquired data points were subsequently fitted to generate the scatter plot shown in Fig.15.

The regression analysis presented in Fig.15 reveals a coefficient of determination (R^2) of 0.995, indicating a highly significant linear correlation between the actual flow rates and the sensor-detected values. To evaluate the measurement precision and repeatability of the flow rate sensor, the experimental procedure was conducted with $n=3$ replicates for each setpoint. Statistical analysis of the absolute relative error yielded a mean of 2.14% ± 0.48%, with a 95% confidence interval (CI) of [1.62%, 2.66%]. This confined error margin and the narrow confidence interval demonstrate that the flow rate sensor provides highly reliable feedback, which exerts a minimal and statistically acceptable impact on the overall execution performance of the variable spraying control system.

System Pressure Detection Precision Test and Data Analysis

Dynamic pressure fluctuations within the hydraulic circuit can induce measurement deviations in sensor data. Consequently, the automatic spraying control system was evaluated under stable pressure environments. Pressure transmitters were installed to monitor the inlet and outlet pressures, with target values incrementally set between 200 kPa and 360 kPa. Nine distinct pressure setpoints were tested. The target setpoints and the corresponding measured values were subjected to linear regression fitting, yielding the scatter plot illustrated in Fig.16.

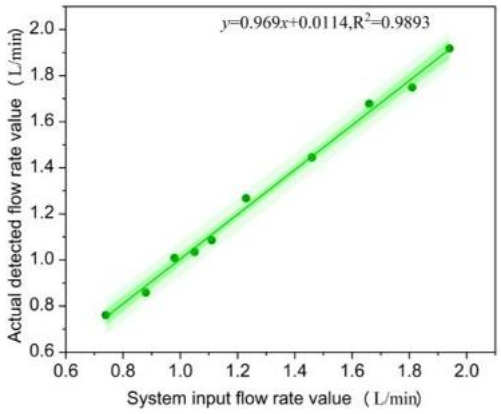


Fig. 15 - Scatter plot of flow rate detection

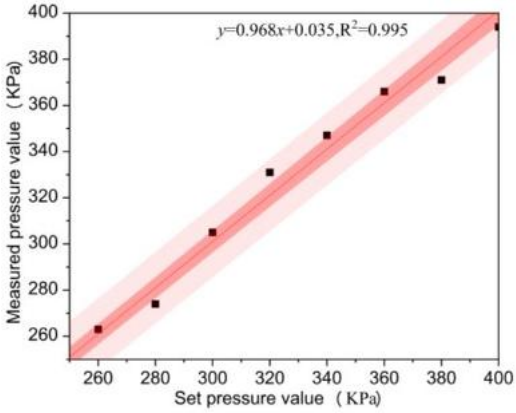


Fig. 16 - Scatter plot of pressure detection

As shown in Fig. 16, the fitted curve exhibits an (R^2) value of 0.989. To ensure repeatability, statistical analysis of the absolute relative error yielded a mean of 2.34% ± 0.52%, with a 95% confidence interval (CI) of [1.80%, 2.88%]. This acceptable and narrowly bounded pressure measurement deviation confirms that the pressure monitoring module possesses sufficient precision to support the robust operation of the spraying control system.

Electric Control Valve Core Adjustment Test and Data Analysis

During variable-rate spraying operations, the performance of the electric control valve is influenced by coupled factors, including its inherent flow regulation characteristics, sensor feedback accuracy, and the execution efficiency of the controller algorithms. These factors collectively contribute to the steady-state error between the actual applied spray volume and the target setpoint. To systematically address this, extensive adjustment tests were conducted to quantify the actuation accuracy. A metric defined as the "quantitative spraying error" was introduced, representing the arithmetic difference between the actual flow rate and the target flow rate. This error exhibits non-linear variations across different target spray flows; the specific quantitative data are detailed in Table 2.

Table 2

Quantitative spraying errors under different target spraying rates

Adjustment Direction	Set Spraying Volume (L/min)	Actual Spraying Volume (L/min)	Quantitative Spraying Error (L/min)	Relative Error (%)
Increase Spraying Flow	0.7	0.684	-0.016	-2.29
	1.0	1.021	0.021	2.10
	1.3	1.321	0.021	1.62
	1.6	1.623	0.023	1.44
	1.9	1.881	-0.019	-1.00
Decrease Spraying Flow	1.9	1.915	0.015	0.79
	1.6	1.625	0.025	1.56
	1.3	1.276	-0.024	-1.85
	1.0	1.019	0.019	1.90
	0.7	0.685	-0.015	-2.14

Furthermore, the transient relationship between the dynamic valve adjustment process and the system output flow was established. Time-domain response curves for stepwise increasing and decreasing flow rates were plotted, as shown in Fig. 17 and Fig. 18.

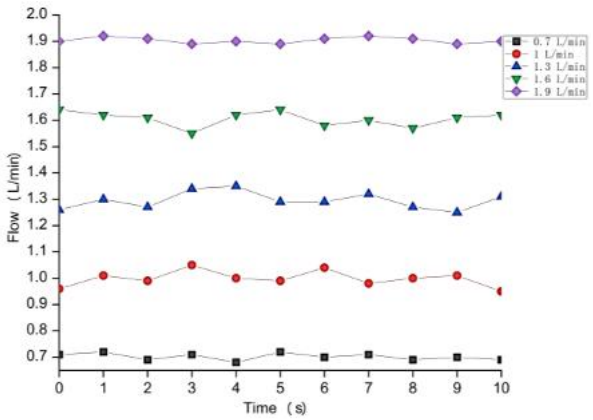


Fig. 17 - Time-domain response curve for increasing flow rate

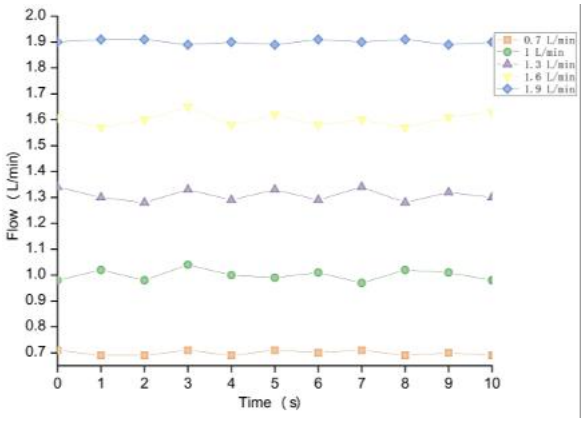


Fig. 18 - Time-domain response curve for decreasing flow rate

The transient profiles in Fig. 17 and Fig. 18 suggest that the pulsatile pressure application from the diaphragm pump inherently influences the output flow rate and pipeline pressure. Time-series data analysis confirms that the flow rate output fluctuates synchronously with periodic pressure pulsations. When the electric valve opening is small, the elevated hydraulic resistance dampens these pulsations, minimizing output flow fluctuations. Conversely, when the valve is fully open, the flow resistance is minimized, allowing the fluid to stabilize quickly, thereby achieving a stable high-flow output state.

ISSA-Fuzzy PID Control Algorithm Test and Data Analysis

The automatic spraying control system exhibits inherent time-delay and overshoot characteristics, which strictly compromise the precision of variable-rate field operations. To overcome this engineering bottleneck, the ISSA-Fuzzy PID control algorithm is deployed to counteract the pure lag effect, integrating a fuzzy inference module to diminish the system's sensitivity to external parameter variations, thereby achieving real-time, robust, and stable flow control.

To empirically evaluate the response stability of the hardware system driven by the ISSA-Fuzzy PID algorithm, pressure disturbance tests were executed. The reference system pressures were explicitly set to 250 kPa, 300 kPa, and 350 kPa. During the tests, the dynamic feedback data were continuously logged and exported via a CAN bus monitoring software. Data analysis corroborates that the system rapidly attains steady-state convergence under all three pressure conditions. The comparative dynamic characteristic curves are illustrated in Fig. 19.

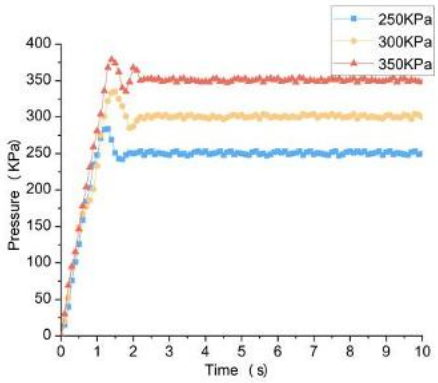


Fig. 19 - Dynamic response curves under different reference pressures

In summary, the ISSA-Fuzzy PID control algorithm demonstrates adaptive performance capabilities across varying operational pressures. At a target pressure of 250 kPa, the system exhibited a restrained overshoot of 7.12% coupled with a swift rise time of 1.1 seconds. Upon increasing the set pressure to 300 kPa, the overshoot optimally decreased to 6.67%, while the rise time slightly extended to 1.3 seconds. At the maximum tested pressure of 350 kPa, the overshoot further narrowed to 6.29%, maintaining a consistent rise time of 1.3 seconds. These empirical findings indicate that the ISSA-Fuzzy PID control architecture effectively suppresses overshoot while ensuring improved transient response rapidity across a broad spectrum of pressure settings, significantly enhancing both the steady-state stability and dynamic efficiency of the automated spraying system.

To further quantify the robustness of the ISSA-Fuzzy PID controller, performance metrics (overshoot and rise time) were evaluated across 10 independent simulation trials under stochastic pressure disturbances. The ISSA-Fuzzy PID controller achieved a mean overshoot of 6.69% with a 95% confidence interval (CI) of [6.40, 6.98] %. Compared to conventional PID, the ISSA-Fuzzy PID showed a significantly shorter mean settling time ($p < 0.05$ via one-way ANOVA), confirming that the proposed algorithm significantly improves control consistency and reliability for agricultural actuating systems.

While these bench experiments validate the hardware integration and algorithmic precision, several limitations inherent to laboratory environments must be acknowledged. The current evaluations were conducted under stable ambient temperatures utilizing homogeneous fluid properties. In practical field operations, soybean foliar fertilizers exhibit varying viscosities, and fluctuating ambient temperatures can alter hydraulic fluid dynamics. Additionally, real-world field conditions introduce mechanical vibrations from the tractor, irregular power take-off (PTO) speeds, and sensor noise induced by canopy shading or sloped terrain. Therefore, although the 1.9 s dynamic pressure regulation achieved in this study demonstrates strong technical feasibility at the bench scale, the comprehensive agronomic benefits—specifically regarding canopy fertilizer deposition, nutrient uptake efficiency, and ultimate yield improvements—require extensive multi-year field trials under complex, unstructured agricultural environments.

CONCLUSIONS

To address control-precision limitations in soybean foliar-fertilizer variable-rate spraying, this study designed an automatic real-time variable-rate control system. Based on CFD simulation, controller modeling, and bench-scale validation, the following conclusions are drawn:

(1) A second-order transfer function of the electric control valve was derived through system identification via CFD dynamic mesh simulations. Hydrodynamic analyses at 15% and 30% openings characterized the internal throttling behavior. An ISSA-Fuzzy PID control strategy was proposed to mitigate system time-delay; MATLAB/Simulink simulations verified that, under modeled bench conditions, this algorithm improved transient response, overshoot suppression, and stability compared with conventional PID and standard Fuzzy PID controllers.

(2) Bench tests validated hardware integration accuracy, with average relative errors of 2.14% and 2.34% for flow-rate and pressure detection, respectively. Hardware validation confirmed that the ISSA-Fuzzy PID algorithm achieved dynamic target-pressure regulation within 1.9 s. While these results demonstrate the technical feasibility of the proposed system at a bench scale, the performance of the system in terms of field-scale spraying stability, actual fertilizer-use efficiency, and agronomic yield impacts remains to be validated in future on-farm trials.

ACKNOWLEDGEMENT

This work was supported by the 2023 Key Research and Development Program of Heilongjiang Province under Grant No. 2023ZXJ07B02.

REFERENCES

[1] Dhanya, V.G., Subeesh, A., Kushwaha, N.L., Vishwakarma, D.K., Nagesh Kumar, T., Ritika, G., Singh, A.N. (2022). Deep learning based computer vision approaches for smart agricultural applications. *Artificial intelligence in agriculture* 6, 211-229.

[2] Dong, X., Li, R., Wang, M., Zhang, X., Yu, S., Xue, J. (2025). Design and research of variable fertilization system for rice based on bilinear interpolation. *INMATEH-Agricultural Engineering*. Vol.77(3), 1519-1531.

[3] Farooque, A.A., Hussain, N., Schumann, A.W., Abbas, F., Afzaal, H., McKenzie-Gopsill, A., Esau, T., Zaman, Q., Wang, X. (2023). Field evaluation of a deep learning-based smart variable-rate sprayer for targeted application of agrochemicals. *Smart agricultural technology,* 3, 100073.

[4] Jiao, Y., Zhang, S., Jin, Y., Cui, L., Chang, C., Ding, S., Sun, Z., Xue, X. (2025). Research progress on intelligent variable-rate spray technology for precision agriculture. *Agronomy-Basel,* 15(6), 1431.

[5] Karimi, A., Garcia, D., Longchamp, R., (2004). Pid controller tuning using Bode's integrals. *IEEE Trans. Control Syst. Technol*. 11(6), 812-821.

[6] Kumar, S., Tewari, V.K., Bharti, C.K., Ranjan, A. (2021). Modeling, simulation and experimental validation of flow rate of electro-hydraulic hitch control valve of agricultural tractor. *Flow Meas. Instrum*. 82, 102070.

[7] Patle, R., Kavitha, R., Surendrakumar, A., Sahni, R.K., Suthakar, B., Kannan, B., Maragatham, S. (2025). Development of a sensor-based embedded system for on-the-go variable-rate fertilizer applicator in maize crop. *Results Eng*. 28, 107852.

[8] Pawase, P.P., Nalawade, S.M., Bhanage, G.B., Walunj, A.A., Kadam, P.B., Durgude, A.G., Patil, M.R. (2023). Variable rate fertilizer application technology for nutrient management: a review. *Int. J. Agric. Biol. Eng*. 16(4), 11-19.

[9] Su, D., Yao, W., Yu, F., Liu, Y., Zheng, Z., Wang, Y., Xu, T., Chen, C. (2022). Single-neuron PID UAV variable fertilizer application control system based on a weighted coefficient learning correction. *Agriculture*-Basel 12(7), 1019.

[10] Wu, X., Zhang, L., Zhao, J., Hu, X. (2026). Control system based on tuna swarm optimization, fuzzy PID, and MQTT protocol for remote fertilization. *Agriculture* 16(11), 1206.

[11] Xie, L., Mao, W., Zhang, X., Du, Y., Fang, X., Zhou, C. (2026). Study on the variable side - deep fertilization control system for rice based on soil electrical conductivity. *Front. Plant Sci*. 17, 1748101.

[12] Xu, C., Xie, F., Tian, Z., Zhao, Z., Chen, Z., Li, Y. (2025). Fuzzy PID control strategy optimised by sparrow search algorithm for digital proportional valve with differential control of dual high-speed on/off valves. *Int. J. Hydromechatron*. 8(4), 444-467.

[13] Xu, Y., Jin, Y., Sun, Z., Xue, X. (2025). Pso-based system identification and fuzzy-PID control for EC real-time regulation in fertilizer mixing system. *Agronomy*-Basel 15(5), 1259.

[14] Xue, J., Shen, B. (2020). A novel swarm intelligence optimization approach: sparrow search algorithm. *Syst. Sci. Control Eng*. 8(1), 22-34.

[15] Yuxuan, J., Zhu, S., Yongkui, J., Longfei, C., Zhang, X., Wang, S., Songchao, Z., Chang, C., Suming, D., Xinyu, X., (2025). Current status and future prospects of key technologies in variable-rate spray. *Agriculture* 15(20), 2111.

[16] Zhang, W., Tong, J., Zhang, F., Zhang, W., Zhang, J., Zhang, J., Zhang, J., Sun, H., Northwood, D.O., Waters, K.E., Ma, H., (2025). Integrated irrigation of water and fertilizer with superior self-correcting fuzzy PID control system. *Plos One,* 20(5), e324448.

[17] Zhu, F., Zhang, L., Hu, X., Zhao, J., Meng, Z., Zheng, Y., (2023). Research and design of hybrid optimized backpropagation (BP) neural network PID algorithm for integrated water and fertilizer precision fertilization control system for field crops. *Agronomy*, 13(5), 1423.

COMPARATIVE ASSESSMENT OF RANDOM FOREST, XGBOOST AND MLP MODELS FOR PREDICTIVE GREENHOUSE CONTROL USING WIRELESS SENSOR NETWORK DATA

/

EVALUAREA COMPARATIVĂ A MODELELOR RANDOM FOREST, XGBOOST ȘI MLP PENTRU CONTROLUL PREDICTIV AL UNEI SERE, FOLOSIND DATE DINTR-O REȚEA DE SENZORI WIRELESS

Mihai Gabriel MATACHE[1)], Carmen BĂLȚATU[*1)], Dragoș SĂCĂLEANU[2)], Adrian IOSIF[2)], Tudor Adrian ENE[3)], Cristina Mihaela DOBRE[4)]

[1)] INMA Bucharest/ Romania;

[2)] National University for Science and Technology POLITEHNICA Bucharest, Romania;

[3)] ICDP Brașov; [4)] Beia Consult International SRL

E-mail: carmen.vasilachi@gmail.com

DOI: https://doi.org/10.35633/inmateh-79-51

Keywords: *greenhouse control, wireless sensor network, predictive control, machine learning, Random Forest, XGBoost, multilayer perceptron.*

ABSTRACT

Control of greenhouse microclimate requires the interpretation of several environmental and substrate-related parameters, including air temperature, relative humidity, light intensity, carbon dioxide concentration and soil moisture. This paper compares three machine learning models, Random Forest, Extreme Gradient Boosting (XGBoost) and a multilayer perceptron (MLP), for 30-minute-ahead prediction of irrigation, ventilation and shading states in a greenhouse. The models were trained using data collected from a wireless sensor network (WSN) with four sensor nodes installed in the protected cultivation area. After preprocessing, scaling, error removal, temporal synchronization and resampling at 10-minute intervals, a structured dataset of 7063 records was obtained. Individual sensor readings, spatially aggregated variables, time-related features, rolling averages and short-term differences were used to describe both the current and recent evolution of the greenhouse environment. The dataset was split chronologically into training, validation and test subsets, corresponding to 70%, 15% and 15% of the records, respectively, while preserving the temporal order of the measurements. The best average performance was obtained by XGBoost, with a mean F1-score of 0.9237, followed by Random Forest with 0.9045 and MLP with 0.5862. Random Forest achieved the best results for irrigation and ventilation control, with F1-scores of 0.9630 and 0.9611, respectively, while XGBoost achieved the best result for shading control, with an F1-score of 0.8571. XGBoost also achieved the highest mean accuracy, 0.9506, and mean balanced accuracy, 0.8904. The results indicate that tree-based ensemble models are more suitable than the tested MLP architecture for predictive greenhouse control based on multi-sensor WSN data. The proposed framework supports the selection of a final control model according to prediction performance, stability and interpretability.

REZUMAT

Controlul microclimatului din seră necesită interpretarea mai multor parametri de mediu și de substrat, inclusiv temperatura aerului, umiditatea relativă, intensitatea luminoasă, concentrația de dioxid de carbon și umiditatea solului. Această lucrare compară trei modele de învățare automată, Random Forest, Extreme Gradient Boosting (XGBoost) și perceptron multistrat (MLP), pentru predicția la 30 de minute a stărilor de irigare, ventilație și umbrire într-o seră. Modelele au fost antrenate folosind date colectate de la o rețea de senzori wireless (WSN) cu patru noduri instalate în spațiul protejat. După preprocesare, scalare, eliminarea erorilor, sincronizare temporală și reeșantionare la intervale de 10 minute, a fost obținut un set de date structurat, cu 7063 de înregistrări. Valorile individuale ale senzorilor, variabilele agregate spațial, variabilele temporale, mediile mobile și diferențele pe termen scurt au fost utilizate pentru a descrie atât starea curentă, cât și evoluția recentă a mediului din seră. Setul de date a fost împărțit cronologic în subseturi de antrenare, validare și testare, reprezentând 70%, 15% și, respectiv, 15% din înregistrări, cu păstrarea ordinii temporale a măsurătorilor. Cea mai bună performanță medie a fost obținută de XGBoost, cu un F1-score mediu de 0.9237, urmat de Random Forest, cu 0.9045, și MLP, cu 0.5862. Random Forest a obținut cele mai bune rezultate pentru controlul irigării și ventilației, cu F1-score-uri de 0.9630 și 0.9611, în timp ce XGBoost a obținut cel mai bun rezultat pentru controlul umbririi, cu un F1-score de 0.8571.

XGBoost a obținut, de asemenea, cea mai mare acuratețe medie, de 0.9506, și cea mai mare acuratețe echilibrată medie, de 0.8904. Rezultatele indică faptul că modelele ensemble bazate pe arbori sunt mai potrivite decât arhitectura MLP testată pentru controlul predictiv al serelor pe baza datelor multi-senzor WSN. Cadrul propus susține selectarea unui model final de control în funcție de performanța de predicție, stabilitate și interpretabilitate.

INTRODUCTION

Greenhouse cultivation allows a higher degree of control over plant growth conditions than open-field agriculture, but this advantage depends on the continuous regulation of several interacting environmental parameters. Air temperature, relative humidity, soil moisture, light intensity and carbon dioxide concentration influence plant development, water consumption, photosynthetic activity and thermal stress. If these parameters are not monitored and controlled properly, the greenhouse may consume excessive water and energy or may expose plants to unfavourable microclimate conditions.

Traditional greenhouse control systems are often based on fixed threshold rules. Such systems are simple and easy to implement, for example by activating irrigation when soil moisture drops below a predefined limit or by starting ventilation when air temperature or CO2 concentration exceeds a threshold. However, the greenhouse microclimate is dynamic and nonlinear. The need for irrigation, ventilation or shading may depend not only on one variable, but on the combined effect of temperature, humidity, radiation, CO2 concentration, soil moisture, time of day and recent trends in the measured data. Therefore, fixed rules may become insufficient when environmental variables interact or when borderline conditions occur. For this reason, modern greenhouse management increasingly relies on sensor-based monitoring, automatic data acquisition and decision support systems (*Dhanaraju et al., 2022; Săcăleanu et al., 2024*). Decision support systems have already shown practical value in horticultural irrigation management. For example, *Buono et al. (2022)* field-tested the Bluleaf DSS for kiwifruit irrigation management in Italy and reported water savings of approximately 20-25% compared with current farm management, without negative effects on yield and fruit quality. In this view, Wireless Sensor Networks (WSNs) are well suited for greenhouse monitoring and control applications because they allow the distributed measurement of environmental and substrate-related variables in different points of the protected cultivation area. Compared with single-point monitoring, multiple sensor nodes can capture spatial variability inside the greenhouse, which is important for irrigation, ventilation and shading decisions. Previous studies have shown that WSN-based systems can support real-time greenhouse monitoring, data aggregation and decision support, but also that the correct integration of sensing, communication, data processing and control remains a key challenge (*Kochhar and Kumar, 2019; Săcăleanu et al., 2024*).

IoT-based greenhouse control studies have emphasized the need for data-driven and optimization-based approaches able to improve climate regulation and resource efficiency (*Ullah et al., 2022; Chen et al., 2025*). *Ardiansah et al. (2022)* presented an IoT-enabled device for real-time monitoring and control of greenhouse irrigation water quality, using pH, TDS, EC, temperature and turbidity sensors. *Tan et al. (2021)* developed an intelligent irrigation system for a jujube orchard, consisting of a field control terminal and a remote client connected through a 4G network. The system monitored air temperature, relative humidity, light intensity, soil temperature and soil water content, and automatically controlled irrigation using lower and upper soil water content thresholds. Recent field studies have confirmed the importance of sensor-based and model-based irrigation strategies under increasing climatic variability. *Fˆ ll et al. (2026)* evaluated irrigation strategies in apple orchards over three years in Germany, comparing soil water tension-based irrigation, a web-based soil water balance model, interval irrigation and a non-irrigated control. Their results showed that sensor- and model-based irrigation strategies can improve water use efficiency compared with conventional interval irrigation.

Machine learning offers a practical alternative for transforming heterogeneous sensor data into control decisions. Tree-based ensemble models are particularly attractive for this type of application because they can handle nonlinear relationships, noisy measurements and mixed groups of input variables. A recent review focused on digital soil evaluation likewise identified Random Forest and boosting algorithms such as XGBoost as robust options for heterogeneous and multi-source agricultural datasets, while also emphasizing the associated trade-offs involving computational cost, hyperparameter sensitivity and model interpretability (*Nenciu et al., 2026*). Random Forest combines multiple decision trees in order to improve robustness and reduce overfitting, while also providing feature importance values that can be interpreted from an agronomic point of view (*Breiman, 2001*).

Recent studies in precision horticulture have also shown the value of integrating environmental monitoring, sensor fusion and machine learning for crop and fruit quality prediction. *Wang et al. (2026)* combined X-ray computed tomography, environmental data and machine learning models, including Random Forest and XGBoost, to analyse preharvest apple growth dynamics. Their results showed that environmental factors, especially temperature, can be used as relevant predictors in data-driven fruit quality modelling. Although their work focused on orchard fruit quality rather than greenhouse actuator control, it supports the broader use of multi-source sensor data and machine learning for predictive decision-making in horticultural system. XGBoost extends the tree-based approach through gradient boosting, where trees are added sequentially to correct previous errors, often leading to high predictive performance on structured tabular datasets (*Chen and Guestrin, 2016*).

Several studies have already demonstrated the potential of machine learning for greenhouse-related prediction tasks. *Cai et al. (2022)* developed a greenhouse temperature prediction model based on LightGBM using five years of environmental, control and temporal data collected from a Venlo-type greenhouse. Their comparison with BP neural network, RNN, XGBoost and stochastic gradient boosting showed that LightGBM achieved the best predictive performance, with an RMSE of 0.645 °C on the testing dataset and an average relative error below 2%. XGBoost also performed well, with an RMSE of 0.679 °C, confirming the suitability of gradient-boosted tree models for greenhouse microclimate prediction and real-time predictive control. *Tsai et al. (2020)* combined weather forecast data, numerical models and machine learning methods, including Random Forest, to predict soil temperature and volumetric water content in a greenhouse. Such results support the use of data-driven models in protected cultivation, especially when environmental variables are measured continuously and must be translated into management decisions. However, many studies focus on predicting individual environmental parameters, while fewer works address the direct prediction of control states for irrigation, ventilation and shading using multi-sensor greenhouse data (*Tsai et al., 2020*). *Wang et al. (2025)* compared several machine learning models for greenhouse cherry tomato irrigation prediction, including MLR, Ridge Regression, SVM, Random Forest, XGBoost, GRU, LSTM and Transformer. Their results showed that XGBoost provided the best performance when maximum and average values of temperature, relative humidity and light intensity were used as input variables. The model achieved R^2= 0.820 during the vegetative growth stage and R^2=0.840 during the reproductive growth stage. After deployment through a cloud platform and STM32-based irrigation control system, the model increased single fruit weight by 17.8% and improved water use efficiency by 20.7% compared with conventional irrigation management. *Mohammadi et al. (2024)* used IoT sensor data and machine learning for greenhouse water management in tomato production under water-limited conditions in Afghanistan. The authors collected real sensor data from a simulated greenhouse between June and August 2022 and compared six machine learning models. XGBoost achieved the best and most balanced classification performance among the tested models, indicating its suitability for predicting irrigation needs and avoiding excessive water use in greenhouse tomato production. The study also included an IoT-based visualization interface for farmers, supporting real-time supervision of greenhouse conditions and timely irrigation decisions. Another study compared several machine learning models, including Random Forest, XGBoost, LightGBM and MLP, for short-term greenhouse microclimate forecasting (*Cebolla-Alemany et al., 2026*). This study used temporal feature engineering, including lag variables and rolling statistics, and showed that tree-based ensemble models were highly suitable for predictive greenhouse control. In their case, LightGBM achieved the best temperature forecasting performance, with R^2 values above 0.99 for 5, 10 and 15-minute horizons, while XGBoost and Random Forest obtained comparable results. The integration of the forecasting model into a fuzzy predictive controller also reduced energy-related control costs by more than 60% compared with a conventional threshold-based strategy. Forecast-driven greenhouse control has also been investigated using time-series neural networks. *Elvanidi and Katsoulas (2023)* used microclimate and crop physiological data to detect tomato crop stress in greenhouses. Their Gradient Boosting classifier achieved 91% accuracy and 92% F1-score on the test set, while MLP reached 89% accuracy and 89% F1-score, supporting the use of ML models for greenhouse decision support. *Aborujilah et al. (2025)* developed an LSTM-based framework for smart greenhouse climate control, using multivariate environmental and actuator data to forecast temperature, relative humidity and CO_2 concentration. Their model achieved high prediction accuracy, with R^2=0.9835, and was used to generate actuator recommendations for heating, ventilation and lighting. *Ait Oussous et al. (2025)* compared several deep learning models for greenhouse internal temperature prediction and reported the best performance for PLSTM, with R^2=0.9999, RMSE = 0.0220 and MAE = 0.0160.

In this context, the present paper addresses the development of several machine learning-based decision models for greenhouse control using real data collected from a WSN installed in a protected cultivation environment. The monitored variables include air temperature, relative humidity, light intensity, CO2 concentration, atmospheric pressure, soil moisture and auxiliary diagnostic parameters collected from four distributed sensor nodes. The control problem is formulated as a supervised classification task, where the models estimate the future state of three greenhouse subsystems: irrigation, ventilation and shading.

The main objective of this study is to compare Random Forest, XGBoost and a multilayer perceptron neural network under the same experimental conditions and to identify the most suitable model for predictive greenhouse control. Unlike a same-time classification approach, where sensor values and actuator states correspond to the same timestamp, the final evaluation is formulated as a 30-minute-ahead prediction problem. In this formulation, the sensor-derived variables recorded at time t are used to estimate the control states at t+30 minutes. This approach is more relevant for practical greenhouse automation, because it evaluates the ability of the models to anticipate future control requirements rather than only reproduce the current state of the system.

MATERIALS AND METHODS

Experimental dataset and greenhouse monitoring system

The dataset used in this study was obtained from a wireless sensor network installed in a greenhouse environment. The monitoring system consisted of four distributed sensor nodes, identified as node_1, node_2, node_3 and node_4. Each node recorded several environmental and substrate-related parameters, allowing the characterization of the spatial variability of the greenhouse microclimate.

The raw dataset contained 1222305 individual sensor records stored in long format, where each row corresponded to one measurement from one sensor at a given timestamp. After cleaning, scaling, temporal synchronization and resampling at 10-minute intervals, the data were transformed into a wide-format dataset containing 7063 synchronized time steps. Each time step described the greenhouse state using 216 variables, including original sensor measurements, spatially aggregated microclimate indicators, temporal features, rolling statistics and the recorded control status variables.

Measured variables

The four WSN nodes included similar groups of sensors. The monitored variables covered the main physical quantities required for greenhouse control: air temperature, relative humidity, light intensity, carbon dioxide concentration, atmospheric pressure, soil moisture, local temperature measurements and battery voltage.

The following groups of variables were identified in the processed dataset:

Table 1

Types of process variables

Sensor group	Number of columns	Role in the control model
Air temperature	8	ventilation and shading control
Air relative humidity	8	ventilation control
Light intensity	4	shading control
CO2 concentration	4	ventilation control
Soil moisture	12	irrigation control

The air temperature group included measurements from HTS221 and SHT31 sensors installed on the four nodes. The air humidity group included the corresponding relative humidity measurements from the same sensor families. Light intensity was measured using TEMT6000 sensors, while CO2 concentration was measured using SCD41 sensors. Soil moisture was monitored using both tensiometer-based and capacitive sensors, providing several measurements per node. Besides these main variables, the dataset also included atmospheric pressure, UVA and UVB radiation, DS18B20 temperature measurements and battery voltage. These variables were retained in the processed dataset when their data quality was acceptable, but the main control decisions were based on the variables most directly related to greenhouse irrigation, ventilation and shading.

Raw data scaling

The raw sensor values were stored using an integer-based format. Therefore, a scaling operation was required before the data could be interpreted as physical measurements. The measured values were converted using the following relation:

$$x_{scaled} = \frac{x_{raw}}{10^6} \quad (1)$$

where x_{raw} is the original stored value and x_{scaled} is the corresponding physical or sensor-scale value used in the processed dataset.

This scaling step was applied uniformly to all measured values before the physical plausibility filters were applied.

Data cleaning and removal of erroneous values

The raw dataset contained abnormal values caused by sensor errors, communication issues or invalid readings. These values were removed or marked as missing before the temporal synchronization step. The cleaning process included:

- removal of missing timestamps, sensor identifiers and measurement values;
- conversion of timestamps to a standard datetime format;
- application of the scaling factor;
- identification of sensor-specific abnormal values;
- removal of physically impossible measurements;
- filtering of columns with excessive missing values.

Several physically based rules were applied according to the type of sensor. For example, air temperature values outside the plausible greenhouse range were removed, relative humidity values outside 0-100% were considered invalid, and CO2 values outside the expected measurement interval were discarded. Negative light intensity values were also removed. Similar checks were applied to atmospheric pressure, UV measurements and battery voltage.

Columns with a high proportion of missing values were removed from the final dataset. In the implemented preprocessing pipeline, a column was retained only if its missing data ratio was below the established threshold. This step reduced the risk of training models on unreliable variables.

The final report still indicated that some node-specific variables had relatively high missing ratios, especially for node 4 and for some UV-related measurements. For example, several node 4 variables had missing ratios around 0.54-0.58, while UVB and UVA measurements also showed notable missing data percentages. These variables were not used as primary control indicators.

Temporal synchronization

The raw WSN data were not directly synchronized, because the individual sensors and nodes did not necessarily transmit measurements at exactly the same timestamp. For machine learning, all input variables must refer to the same temporal state of the greenhouse. Therefore, the measurements were resampled using a fixed time interval.

A time step of 10 minutes was selected for the processed dataset. This interval provided a compromise between temporal resolution and data stability. It was short enough to capture relevant microclimate changes and long enough to reduce the effect of short-term noise or communication irregularities.

For each 10-minute interval, sensor measurements belonging to the same variable were aggregated using the mean value. The result was a wide-format dataset in which each row represented the greenhouse state at a specific time step, and each column represented one sensor-derived variable.

Interpolation of short data gaps

After temporal resampling, some missing values remained because not all sensors reported data in every 10-minute interval. Short gaps were filled using time-based interpolation. The interpolation was limited to a small number of consecutive missing intervals in order to avoid generating artificial data over long periods. In this study, interpolation was limited to three consecutive time steps. Since the sampling interval was 10 minutes, this corresponds to a maximum interpolated gap of approximately 30 minutes. Longer gaps were left as missing values and handled during the subsequent modelling stage.

This approach preserves the continuity of the dataset without overestimating the reliability of intervals where sensor information was not available.

Transformation from long format to machine learning format

The original dataset was stored in long format because of wireless communication optimization: **timestamp – sensor_id-value**

For machine learning, this format was transformed into a wide tabular structure:

timestamp	node_1_temp	node_1_rh	node_1_light	node_2_temp	...	control variables

This transformation allowed the models to receive, at each time step, a complete description of the greenhouse state. The final dataset retained the measurements from the individual nodes, so that the models could use spatial differences between measurement points. In figure 1 is presented a representative 3-day evolution of raw greenhouse variables recorded by node 1. The figure shows air and soil temperature, air humidity, soil moisture index and light intensity. The light intensity curve highlights the day-night alternation during the selected period The raw capacitive soil moisture signal was converted into a soil moisture index ranging from 0 to 100 using robust normalization based on the 5th and 95th percentiles calculated over the full monitoring period of the selected node. This index was used only for graphical representation and does not represent calibrated volumetric soil water content.

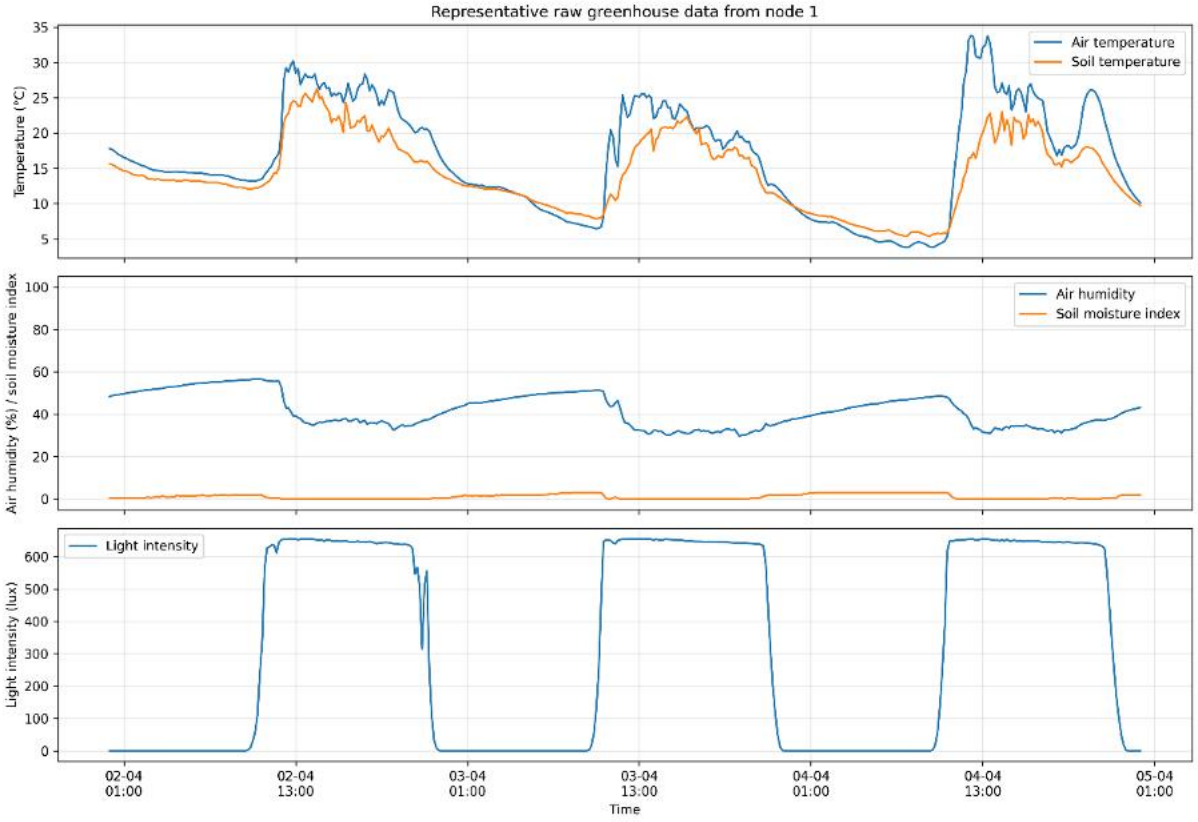


Fig.1 - Representative 3-day evolution of raw greenhouse variables recorded by node 1

Spatial aggregation of sensor data

Since the greenhouse was monitored using four WSN nodes, the dataset contains spatial information. The nodes were not treated as four independent control zones. Instead, they were used to describe the spatial variability of the greenhouse microclimate.

The control strategy considered in this study is a global control strategy:

4 WSN nodes→1 irrigation command, 1 ventilation command, 1 shading command

Therefore, in addition to the individual node measurements, aggregated variables were generated for each sensor group. For air temperature, air humidity, light intensity, CO2 concentration and soil moisture, the following statistics were calculated: x_{median}, x_{mean}, x_{min} , x_{max}, x_{range}, x_{std} , where:

$$x_{range} = x_{max} - x_{min} \quad (2)$$

Temporal feature generation

In addition to sensor measurements, time-related variables were generated. These variables help the machine learning models account for daily and seasonal patterns.

The following temporal variables were included:

- hour of the day;
- month;
- day of the year;
- sine and cosine encoding of hour;
- sine and cosine encoding of day of year.

Cyclic encoding was used for the hour of the day and the day of year in order to represent the daily and seasonal periodicity of greenhouse microclimate conditions. This transformation avoids the artificial discontinuity introduced by simple numerical encoding. For example, 23:00 and 00:00 are temporally close, although their numerical values are distant if the hour is represented as an integer. The cyclic representation allows the models to use time-related patterns associated with solar radiation, temperature evolution, ventilation demand and shading activation. The cyclic representation was calculated as:

$$\begin{cases} hour_{sin} = sin\left(2\pi \frac{hour}{24}\right) \\ hour_{cos} = cos\left(2\pi \frac{hour}{24}\right) \end{cases} \quad (3)$$

and similarly for the day of year.

Rolling and dynamic features

Greenhouse control decisions depend not only on the current measured values, but also on their recent evolution. Rolling and dynamic features were generated in order to describe the recent evolution of the greenhouse microclimate, not only its instantaneous state. For selected sensor variables, rolling means over 30 and 60 minutes were calculated, together with the difference from the previous time step. Since the dataset was resampled at 10-minute intervals, the 30-minute rolling mean used three consecutive samples, while the 60-minute rolling mean used six consecutive samples. These variables allow the models to capture short-term trends, such as increasing air temperature, decreasing soil moisture or rapid changes in light intensity, which are relevant for anticipating irrigation, ventilation and shading decisions at the 30-minute prediction horizon.

This feature engineering step was particularly important because the final modelling task was formulated as a 30-minute-ahead prediction problem. Therefore, the models had to use both the current state and the recent trend of the greenhouse environment to estimate future actuator states.

Control status variables

The final dataset included three binary control status variables: irrigation_control (OFF/ON), ventilation_control (OFF/ON) and shading_control (OFF/ON). In the methodological framework of this paper, these variables were treated as measured control status values associated with the greenhouse control system. They represent the observed operating state of the irrigation, ventilation and shading subsystems at each synchronized time step.

The distribution of the control status variables in the final dataset was:

Table 2

Control variables allocation

Control variable	OFF	ON
irrigation_control	5469	1594
ventilation_control	1213	5850
shading_control	5560	1503

This distribution shows that irrigation and shading were active in fewer time steps than they were inactive, while ventilation was active in most of the synchronized records. Because of this class imbalance, the training procedure used classification metrics that are suitable for imbalanced datasets. Precision, recall, F1-score and confusion matrices were used for each control variable.

Final dataset for machine learning

After preprocessing, the dataset was suitable for supervised machine learning. Each row represented one synchronized 10-minute greenhouse state, while the columns included:

1. individual sensor measurements from the four WSN nodes;
2. aggregated variables for each sensor group;
3. time-based features;
4. rolling and differential features;
5. reference control states for irrigation, ventilation and shading.

Agronomic operating limits were used only to interpret the control philosophy and to discuss model behaviour. They were not used as input variables and were not used to generate the target labels. The target variables were the recorded actuator states for irrigation, ventilation and shading.

Control philosophy

The control strategy adopted in this study was based on a greenhouse-wide decision model. The four WSN nodes captured the spatial variability of the greenhouse environment, whereas the control output represented the overall actuation state of each subsystem. The model did not assign separate irrigation, ventilation, or shading commands to individual sensor nodes. Instead, measurements from all nodes were combined to determine whether irrigation, ventilation, shading, or a combination of these operations was required.

The control philosophy was defined in relation to agronomic operating limits previously considered for greenhouse management: air temperature in the range of 18-35 °C, relative humidity between 45-85%, soil moisture between 20-60%, CO2 concentration between 400-1200 ppm and light intensity between 500-20000 lux. In addition, reference control thresholds such as low soil moisture for irrigation, high air temperature or CO2 concentration for ventilation and high light intensity for shading were used only as interpretative limits

Three algorithms were selected to cover complementary machine learning approaches suitable for tabular greenhouse sensor data. Random Forest was used as a robust and interpretable ensemble baseline, able to handle nonlinear relationships and noisy sensor measurements. XGBoost was included as a more advanced gradient boosting method, commonly effective on structured datasets and capable of improving predictive performance through sequential error correction. Multilayer perceptron was used to evaluate whether a neural network model could capture more complex interactions between microclimate variables and actuator states. This comparison allowed the final control model to be selected not only according to classification performance, but also according to stability and interpretability.

Random Forest was configured with 500 trees in order to reduce the variance of individual decision trees and improve prediction stability, while the maximum tree depth was limited to 15 to reduce excessive model complexity. The Gini criterion was used as a standard splitting rule, and balanced class weights were applied because the OFF and ON states were not equally represented for all control variables.

For XGBoost, a binary logistic objective was used because each control target was formulated as a binary classification problem. The number of boosting estimators was set to 500, with a learning rate of 0.05, in order to allow gradual error correction during training. The maximum tree depth was limited to 4 to control model complexity and reduce overfitting. Row and feature subsampling were both set to 0.8, providing additional regularization and improving generalization on the test subset.

The MLP architecture was kept relatively compact, with three hidden layers of 128, 64 and 32 neurons, in order to evaluate a neural network alternative without introducing an excessively large model for the available dataset size. The ReLU activation function and Adam optimizer were selected because they are widely used for tabular supervised learning problems. Input features were standardized before training, and early stopping was applied to reduce overfitting. The same chronological train-validation-test split and the same input feature set were used for all three models, allowing the comparison to reflect model behaviour rather than differences in data preparation.

The selected configurations should therefore be interpreted as controlled baseline settings suitable for comparative evaluation. Further hyperparameter optimization may improve individual model performance, but this was outside the scope of the present study.

Each algorithm was evaluated separately for irrigation, ventilation and shading control. The final model was selected according to prediction performance, stability and interpretability. Feature importance analysis was used for the tree-based models to identify the most relevant variables involved in each control decision.

To avoid direct reproduction of threshold-like actuator states, the machine learning models were trained to predict the control status at a future decision horizon of 30 minutes. The input vector at time t was therefore mapped to the actuator state at time t+30 min. In addition, the most direct aggregated control indicators, such as maximum air temperature, maximum CO2 concentration, maximum light intensity and minimum soil moisture, were removed from the input feature set. This reduced the risk of data leakage and

provided a more realistic evaluation of the ability of the models to anticipate irrigation, ventilation and shading states from multi-sensor data.

Random Forest, XGBoost and MLP were trained under identical experimental conditions. The same predictive dataset was used for all models, where sensor-derived variables recorded at time t were mapped to actuator states at t+30 minutes. The dataset was split chronologically into training, validation and test subsets, corresponding to 70%, 15% and 15% of the records, respectively. This approach preserved the temporal structure of the greenhouse data and prevented future information from being included in the training phase. The same evaluation metrics were then computed for each model and each control target, allowing a direct comparison of their predictive performance.

Software implementation

The experiments were conducted on a workstation running Windows 10 Pro 64-bit, equipped with an Intel Core i9-9900K processor at 3.60 GHz, 64 GB of RAM and an NVIDIA Quadro P4000 GPU with 8 GB of dedicated memory. All data preprocessing, feature engineering, model training and evaluation were performed using Python 3.9.13. Data handling and numerical operations were carried out using pandas 2.3.3 and NumPy 2.0.2. Data standardization, Random Forest and MLP implementation, and calculation of the evaluation metrics were performed using scikit-learn 1.6.1. The Random Forest and MLP models were executed on the CPU, whereas GPU acceleration was enabled for XGBoost by setting device="cuda" in XGBoost 2.1.4. Matplotlib 3.9.4 was used to generate the graphical representations of the results.

Evaluation metrics

The performance of the machine learning models was evaluated using accuracy, balanced accuracy, precision, recall, F1-score and ROC-AUC. These metrics were selected because the control states of the greenhouse subsystems were not equally distributed between the OFF and ON classes, especially for irrigation and shading. Therefore, the evaluation could not rely only on overall accuracy.

Accuracy represents the proportion of all correctly classified samples. It provides a general indication of model performance, but it can be misleading when one class is much more frequent than the other. For example, if the OFF state is dominant, a model may obtain high accuracy by mostly predicting OFF, while still failing to detect important ON events.

Balanced accuracy was used to provide a more reliable evaluation under class imbalance. Unlike standard accuracy, it considers the classification performance for both classes and gives equal importance to the OFF and ON states. This is important in greenhouse control, because missing an ON command for irrigation, ventilation or shading may have practical consequences even if the overall number of errors is small. Precision indicates how reliable the positive predictions are. In this study, it shows how many of the predicted ON states were actually correct. A high precision value means that the model does not frequently activate a control subsystem when it is not required. This is relevant for reducing unnecessary water use, energy consumption or shading activation.

Recall indicates how well the model detects the actual ON states. It shows whether the model correctly identifies the moments when irrigation, ventilation or shading should be active. A high recall value is important because failing to detect an ON state may lead to water stress, excessive temperature, high humidity, high CO2 concentration or excessive solar radiation inside the greenhouse.

The F1-score combines precision and recall into a single performance indicator. It is especially useful when the dataset is imbalanced, because it reflects both the reliability of ON predictions and the ability to detect actual ON events. For this reason, F1-score was used as one of the main criteria for comparing the models.

ROC-AUC was used to evaluate the ability of each model to distinguish between the OFF and ON classes over different decision thresholds. A high ROC-AUC value indicates that the model assigns higher probabilities to true ON cases than to OFF cases, even before a final classification threshold is applied. This metric is useful for assessing the separability of the two control states.

In this study, the final model selection was based mainly on F1-score, balanced accuracy and recall, rather than accuracy alone. This approach was adopted because the practical objective of the control system is not only to maximize the total number of correct predictions, but also to reliably identify the moments when each actuator should be activated.

RESULTS

An initial same-time classification test was first performed, in which the sensor-derived variables and the actuator states corresponded to the same timestamp. This evaluation produced very high scores, with several F1-

score values close to or equal to 1.00. Although this confirmed that the models could reproduce the observed actuator states from the available sensor data, the results were considered overly optimistic for a practical control application. In such a configuration, the model may learn relationships that are too close to the current control logic, especially when aggregated variables directly related to control decisions are present in the input dataset. Therefore, the final evaluation was reformulated as a predictive task, where the sensor data recorded at time t were used to estimate the actuator states at t+30 minutes. This second configuration was considered more relevant for real greenhouse control, because it evaluates the ability of the models to anticipate future irrigation, ventilation and shading requirements. In addition, the most direct aggregated control indicators, including maximum air temperature, maximum relative humidity, maximum CO2 concentration, maximum light intensity and minimum soil moisture, were removed from the input dataset to reduce the risk of direct threshold reproduction.

Random Forest classifier achieved strong predictive performance for irrigation and ventilation control. For irrigation, the model reached an F1-score of 0.9630, with a precision of 0.9811 and a recall of 0.9455. This indicates that the model was able to detect most future irrigation activation events while keeping false positive predictions low. Ventilation control also showed high performance, with an F1-score of 0.9611 and a recall of 0.9934, showing that most future ventilation ON states were correctly identified. Shading control was more difficult to predict, with an F1-score of 0.7894, mainly due to the lower recall of 0.6772 for the ON class. This suggests that Random Forest was conservative in predicting future shading activation, producing relatively reliable ON predictions but missing some actual shading events.

Table 3

Metrics for Random Forest classifier

Control	Accuracy	Balanced accuracy	Precision	Recall	F1-score	ROC-AUC
Irrigation	0.9962	0.9722	0.9811	0.9455	0.9630	0.9971
Ventilation	0.9311	0.7734	0.9309	0.9934	0.9611	0.9744
Shading	0.9027	0.8315	0.9461	0.6772	0.7894	0.9772

XGBoost classifier achieved high predictive performance on the 30-minute horizon dataset. For irrigation control, the model obtained an F1-score of 0.9533, with high precision and recall. For ventilation, the F1-score was 0.9606, very close to the Random Forest result. The best XGBoost result was obtained for shading control, where the model reached an F1-score of 0.8571, outperforming both Random Forest and MLP. This suggests that XGBoost captured more effectively the nonlinear relationships involved in shading decisions, especially those related to light intensity, temperature evolution and spatial variability within the greenhouse.

Table 4

Metrics for XGBoost classifier

Control	Accuracy	Balanced accuracy	Precision	Recall	F1-score	ROC-AUC
Irrigation	0.9953	0.9631	0.9808	0.9273	0.9533	0.9790
Ventilation	0.9311	0.8123	0.9437	0.9780	0.9606	0.9622
Shading	0.9254	0.8958	0.8843	0.8316	0.8571	0.9789

MLP model showed mixed performance. It achieved acceptable results for ventilation and shading, with F1-scores of 0.9455 and 0.8132, respectively. However, it failed to detect irrigation activation, obtaining an F1-score of 0.0000 for irrigation despite an accuracy of 0.9481. This indicates that the model mainly predicted the majority class for irrigation and did not correctly identify the ON state. The result confirms that accuracy alone is not sufficient for evaluating greenhouse control models when the class distribution is imbalanced. Balanced accuracy, recall and F1-score are more informative for this application.

Table 5

Metrics for MLP classifier

Control	Accuracy	Balanced accuracy	Precision	Recall	F1-score	ROC-AUC
Irrigation	0.9481	0.5000	0.0000	0.0000	0.0000	0.0444
Ventilation	0.9056	0.7836	0.9373	0.9538	0.9455	0.9187
Shading	0.8876	0.8943	0.7358	0.9088	0.8132	0.9480

The comparative evaluation was performed using the predictive dataset, where the sensor-derived variables recorded at time t were used to estimate the irrigation, ventilation and shading states at t+30 minutes.

This formulation provided a more realistic evaluation of the models for greenhouse control, since the objective was to anticipate future actuator states rather than reproduce the current control status. This result does not necessarily indicate that neural networks are unsuitable for greenhouse control in general, but that the tested MLP configuration was not robust enough for the irrigation target under the available dataset size and class distribution.

Table 6

Comparative results for the three investigated classifiers

Model	Accuracy mean	Balanced accuracy mean	Precision mean	Recall mean	F1-score mean	ROC-AUC mean
Random Forest	0.9433	0.8590	0.9527	0.8720	0.9045	0.9829
XGBoost	0.9506	0.8904	0.9363	0.9123	0.9237	0.9734
MLP	0.9138	0.7260	0.5577	0.6209	0.5862	0.6370

The predominance of tree-based ensemble models in the present study agrees with recent greenhouse research. *Mohammadi et al. (2024)* also reported XGBoost as the most balanced classifier for predicting greenhouse irrigation needs, while *Cebolla-Alemany et al. (2026)* found gradient-boosted tree models effective for short-term greenhouse microclimate forecasting. *Elvanidi and Katsoulas (2023)* obtained 91% accuracy and a 0.92 F1-score with Gradient Boosting, compared with 89% for both metrics with MLP, for greenhouse crop-stress detection. In the present study, XGBoost achieved a mean accuracy of 0.9506 and a mean F1-score of 0.9237 across the three actuator targets, whereas the tested MLP reached 0.9138 and 0.5862, respectively. These values should not be interpreted as a direct ranking across studies because the prediction targets, forecast horizons, datasets and validation protocols differ. The specific contribution of the present study is the direct 30-minute-ahead prediction of irrigation, ventilation and shading states from a distributed WSN, using a chronological data split and excluding the most direct aggregated control indicators to reduce data leakage.

To provide a more practical interpretation of the classification results, the predicted and actual actuator states were also compared over five days for a representative interval from the test dataset. The following figures show the 30-minute-ahead predicted states for the recommended model of each subsystem: Random Forest for ventilation, and XGBoost for irrigation and shading. The temporal representation confirms that the models generally followed the actual control transitions, especially for irrigation and ventilation. Shading control showed more deviations, which is consistent with the lower F1-score obtained for this subsystem and indicates that shading activation is more difficult to anticipate from the available sensor-derived variables.

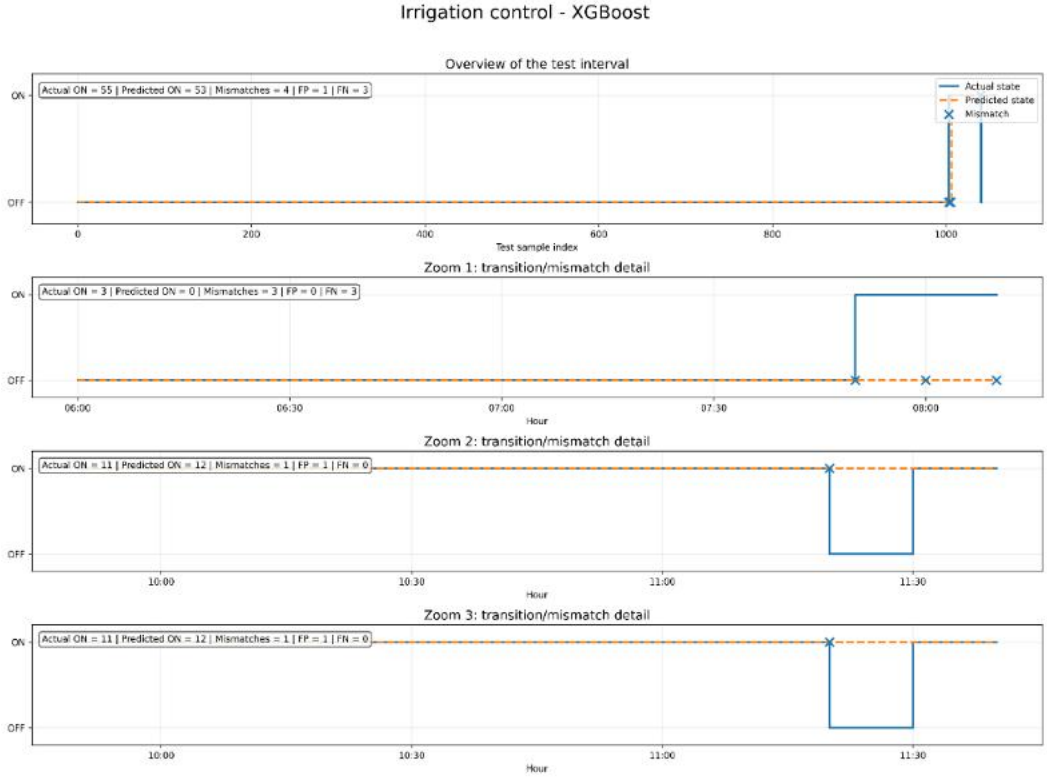


Fig. 2 - Temporal comparison between actual and predicted irrigation control states using the XGBoost model

Because irrigation control events were sparse and concentrated in a limited number of transition periods, a direct full-window visualization was not sufficiently informative. Therefore, the irrigation results were presented using an overview panel together with zoomed transition windows highlighting the agreement between actual and predicted states and the few mismatch cases. The upper panel provides an overview of the test interval, while the lower panels show zoomed details around transition and mismatch events.

For irrigation control, the temporal representation was adapted to the sparse occurrence of ON states. Therefore, an overview of the full test interval was combined with zoomed views around transition and mismatch events. The XGBoost model produced 53 predicted ON states compared with 55 actual ON states, with only four mismatches in the test interval. Most errors occurred near transition moments, indicating that the model captured the dominant irrigation state but remained sensitive to the exact timing of ON/OFF changes.

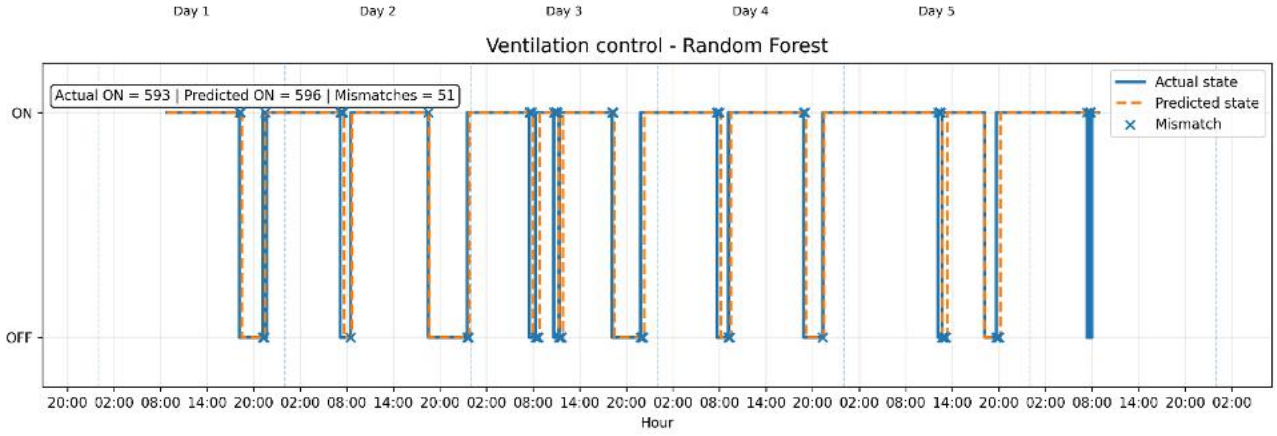


Fig. 3 - Actual and predicted ventilation control states obtained with the Random Forest model over a representative five-day test interval

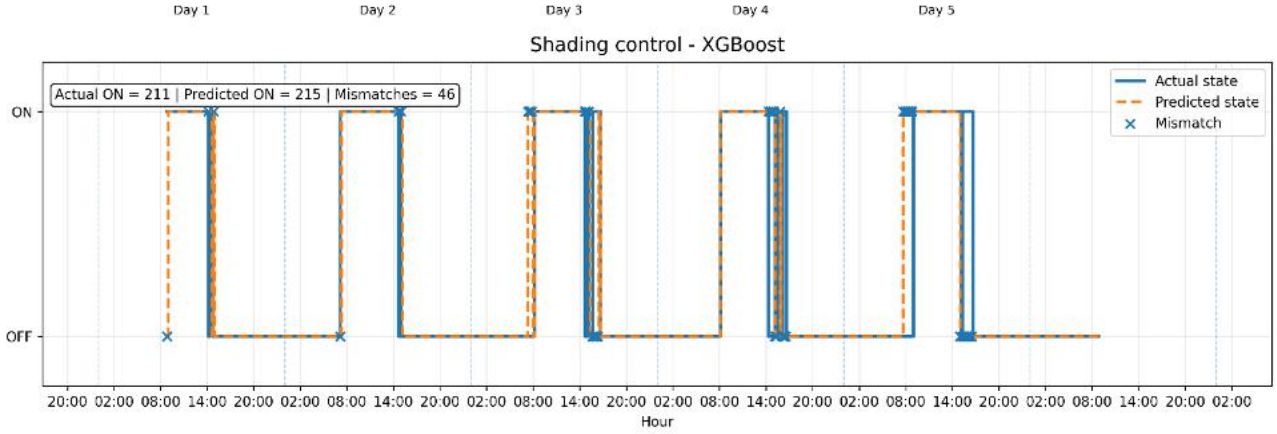


Fig. 4 - Actual and predicted shading control states obtained with the XGBoost model over a representative five-day test interval

The temporal comparison shows that the predicted states generally followed the actual actuator states. Most mismatches occurred close to OFF/ON or ON/OFF transitions, indicating that the main difficulty was not the identification of the dominant control state, but the exact timing of state changes in the 30-minute-ahead prediction task. This behaviour is particularly visible for shading control, where activation depends on rapidly changing light and temperature conditions.

Although Random Forest obtained a slightly higher F1-score for irrigation, XGBoost was retained as the recommended irrigation model because it provided a high and balanced performance and is consistent with the single-model implementation scenario.

Table 7

Recommended classifier for each investigated process

Control	Recommended model	F1-score	Balanced accuracy
Irrigation	XGBoost	0.9533	0.9631
Ventilation	Random Forest	0.9611	0.7734
Shading	XGBoost	0.8571	0.8958

Overall, XGBoost provided the best average predictive performance, while Random Forest offered the best performance for ventilation and remained highly interpretable. For a single-model implementation, XGBoost can be selected due to its highest average F1-score and balanced accuracy. For a subsystem-specific implementation, Random Forest is recommended for irrigation and ventilation control, while XGBoost is recommended for shading control.

CONCLUSIONS

This paper presented a machine learning-based decision model for greenhouse irrigation, ventilation and shading control using multi-sensor data collected from four WSN nodes. The raw dataset was cleaned, scaled, synchronized and transformed into a structured dataset suitable for supervised learning. To obtain a more realistic control formulation, the final evaluation was performed as a 30-minute-ahead prediction task, where sensor-derived variables recorded at time t were used to estimate the future control states at t+30 minutes.

The comparative evaluation showed that tree-based ensemble models were better suited to the processed greenhouse dataset than the tested MLP neural network. Random Forest remains a robust and interpretable alternative, with very strong results for irrigation and ventilation control. XGBoost achieved the highest average predictive performance and the best result for shading control, with an F1-score of 0.8571. The MLP model performed reasonably for ventilation and shading, but failed to detect irrigation activation, confirming that accuracy alone is not sufficient for evaluating imbalanced greenhouse control data.

Future work will first validate the selected model in shadow mode after integration with the actuator nodes, followed by supervised and closed-loop greenhouse trials. These experiments will assess control latency, false activations, missed activation events, robustness to sensor faults and seasonal distribution shifts, as well as the effects of predictive control on water and energy use. Model recalibration across crop cycles and greenhouse operating conditions will also be investigated.

ACKNOWLEDGEMENT

This work was supported by a grant of the Ministry of Education and Research, CCCDI - UEFISCDI, project number PN-IV-P7-7.1-PTE-2024-0359, within PNCDI IV.

REFERENCES

[1] Aborujilah, A., Al-Sarem, M., Abu-Zanona, M.A., 2025. Forecast-driven climate control for smart greenhouses: Energy optimization using LSTM model. *Energies*, 18(21), article 5821. DOI: https://doi.org/10.3390/en18215821

[2] Ait Oussous, S., Lail, D.M., El Bouayadi, R., Amine, A., 2025. Deep learning innovations for greenhouse climate prediction: insights from a Spanish case study. *IEEE Access*, 13, pp. 64810-64821. DOI: https://doi.org/10.1109/ACCESS.2025.3559232

[3] Ardiansah, I., Calibra, R.G., Bafdal, N., Bono, A., Suryadi, E., Nurhasanah, S., 2022. An IoT-enabled design for real-time water quality monitoring and control of greenhouse irrigation systems. *INMATEH – Agricultural Engineering*, 68(3), pp. 417-426. DOI: https://doi.org/10.35633/inmateh-69-39

[4] Buono, V., Mastroleo, M., Lucchi, C., D'Amato, G., Manfrini, L., Morandi, B., 2022. Field-testing of a decision support system (DSS) to optimize irrigation management of kiwifruit in Italy: a comparison with current farm management. *Acta Horticulturae*, 1335, pp. 355-362. DOI: https://doi.org/10.17660/ActaHortic.2022.1335.44

[5] Breiman, L., 2001. Random forests. *Machine Learning*, 45(1), pp. 5-32. DOI: https://doi.org/10.1023/A:1010933404324

[6] Cai, W., Wei, R., Xu, L., Ding, X., 2022. A method for modelling greenhouse temperature using gradient boost decision tree. *Information Processing in Agriculture*, 9(3), pp. 343-354. DOI: https://doi.org/10.1016/j.inpa.2021.08.004

[7] Cebolla-Alemany, J., Cheng, Y., Pinto-Espín, L., Albano, M., Macarulla, M., Gasso-Domingo, S., 2026. Short-term forecasting and predictive control of rooftop greenhouse microclimate using multi-horizon machine learning models. *Smart Agricultural Technology*, 13, article 101733. DOI: https://doi.org/10.1016/j.atech.2025.101733

[8] Chen, S., Yang, D., Tang, Y., Chen, X., Li, Y., 2025. A review of environmental control strategies and models for greenhouses. *Sensors*, 25(5), article 1388. DOI: https://doi.org/10.3390/s25051388

[9] Chen, T., Guestrin, C., 2016. XGBoost: A scalable tree boosting system. *Proceedings of the 22nd ACM SIGKDD International Conference on Knowledge Discovery and Data Mining*, pp. 785-794. DOI: https://doi.org/10.1145/2939672.2939785

[10] Dhanaraju, M., Chenniappan, P., Ramalingam, K., Pazhanivelan, S., Kaliaperumal, R., 2022. Smart farming: Internet of Things (IoT)-based sustainable agriculture. *Agriculture*, 12(10), article 1745. DOI: https://doi.org/10.3390/agriculture12101745

[11] Elvanidi, A., Katsoulas, N., 2023. Machine learning-based crop stress detection in greenhouses. *Plants*, 12(1), article 52. DOI: https://doi.org/10.3390/plants12010052

[12] Föll, S., McCormick, R.J., Biegert, K., 2026. Three-year evaluation of irrigation strategies on apple yield and quality in Germany. *Scientia Horticulturae*, 359, article 114764. DOI: https://doi.org/10.1016/j.scienta.2026.114764

[13] Kochhar, A., Kumar, N., 2019. Wireless sensor networks for greenhouses: An end-to-end review. *Computers and Electronics in Agriculture*, 163, article 104877. DOI: https://doi.org/10.1016/j.compag.2019.104877

[14] Mohammadi, M.N., Takahara, T., Sokout, H., 2024. Optimizing water consumption and improving productivity in Afghanistan's greenhouses through IoT and machine learning. *Proceedings of the 2024 11th International Conference on Internet of Things: Systems, Management and Security (IOTSMS)*, Malmö, Sweden, pp. 185-191. DOI: https://doi.org/10.1109/IOTSMS62296.2024.10710304

[15] Nenciu, F., Matache, M.G., Gageanu, I., Persu, I.C., Marin, F.B., Voicea, I.F., 2026. Emerging technologies for soil evaluation using spectrometry sensing, Internet of Things and machine learning. *Applied Sciences*, 16(9), article 4559. DOI: https://doi.org/10.3390/app16094559

[16] Săcăleanu, D.-I., Matache, M.-G., Roșu, Ș.-G., Florea, B.-C., Manciu, I.-P., Perișoară, L.-A., 2024. IoT-enhanced decision support system for real-time greenhouse microclimate monitoring and control. *Technologies*, 12(11), article 230. DOI: https://doi.org/10.3390/technologies12110230

[17] Tan, K., Sun, S., Du, L., Zhou, S., 2021. Design of an intelligent irrigation system for a jujube orchard based on IoT. *INMATEH – Agricultural Engineering*, 63(1), pp. 189-198. DOI: https://doi.org/10.35633/inmateh-63-19

[18] Tsai, Y.-Z., Hsu, K.-S., Wu, H.-Y., Lin, S.-I., Yu, H.-L., Huang, K.-T., Hu, M.-C., Hsu, S.-Y., 2020. Application of Random Forest and ICON models combined with weather forecasts to predict soil temperature and water content in a greenhouse. *Water*, 12(4), article 1176. DOI: https://doi.org/10.3390/w12041176

[19] Ullah, I., Fayaz, M., Aman, M., Kim, D., 2022. An optimization scheme for IoT based smart greenhouse climate control with efficient energy consumption. *Computing*, 104(2), pp. 433-457. DOI: https://doi.org/10.1007/s00607-021-00963-5

[20] Wang, W., Mengoli, D., Sun, S., Manfrini, L., 2026. Integration of X-Ray CT, Sensor Fusion, and Machine Learning for Advanced Modeling of Preharvest Apple Growth Dynamics. *Sensors*, 26(2), article 623. DOI: https://doi.org/10.3390/s26020623

[21] Wang, Z., Liu, Z., Yuan, M., Yin, W., Zhang, C., Zhang, Z., Hu, X., 2025. A machine learning-based irrigation prediction model for cherry tomatoes in greenhouses: Leveraging optimal growth data for precision irrigation. *Computers and Electronics in Agriculture*, 237, article 110558. DOI: https://doi.org/10.1016/j.compag.2025.110558

AN EFFICIENT RICE PEST DETECTION METHOD BASED ON YOLOv11N
/
基于 YOLOv11n 的高效水稻害虫检测方法

Xiaoke WANG, Zhichao ZHAO, Qiuyang HU, Jiyu LAI, Tiefeng WU*
School of Information and Control Engineering, Qingdao University of Technology, Qingdao 266520 / China
Tel: +86-15653723323; *E-mail: 791479558@qq.com*
DOI: https://doi.org/10.35633/inmateh-79-52

Keywords: *Rice pest detection, YOLOv11n, Detail-Preserving Contextual Fusion, Multi-cognitive Visual Adapter, Edge-device deployment*

ABSTRACT
Accurate and efficient rice-pest detection is essential for field scouting, early warning and precision control. This study presents a lightweight YOLOv11n-based framework for accurate edge deployment. It integrates a Multi-cognitive Visual Adapter (Mona), a Detail-Preserving Contextual Fusion module (DPCF) and Wise-IoU-based non-maximum suppression (Wise-IoU-NMS). Mona improves multi-scale feature representation with limited overhead; DPCF preserves fine-grained pest details during contextual fusion; and Wise-IoU-NMS stabilizes localization of overlapping and densely distributed targets. On a public dataset of 5,212 images from six near-balanced rice-pest classes, divided 8:1:1 for training, validation and testing, the proposed model achieved 95.4% mAP@50, 94.8% precision and 94.7% recall with 2.65 M parameters and 6.5 GFLOPs. The F1-confidence curve identified 0.476 as the alarm threshold. Deployment on Jetson Nano using ONNX and frame-level logging demonstrated a practical workflow for real-time monitoring and selective spraying.

摘要
水稻害虫的快速、准确检测对于田间巡检、虫情预警和精准防控具有重要意义。本文提出一种面向边缘端高精度部署的轻量化 YOLOv11n 检测框架，融合多认知视觉适配器（Multi-cognitive Visual Adapter, Mona）、细节保留型上下文融合模块（Detail-Preserving Contextual Fusion, DPCF）和基于 Wise-IoU 的非极大值抑制策略（Wise-IoU-NMS）。Mona 以较低开销增强多尺度特征表达，DPCF 在上下文融合中保留细粒度虫体信息，Wise-IoU-NMS 则提高重叠及密集目标的定位稳定性。在包含 5,212 张图像、6 类近均衡水稻害虫并按 8:1:1 划分训练集、验证集和测试集的公开数据集上，所提出模型取得 95.4% 的 mAP@50、94.8% 的精确率和 94.7% 的召回率，参数量为 2.65 M，计算量为 6.5 GFLOPs。F1-confidence 曲线确定 0.476 为报警阈值；基于 ONNX 的 Jetson Nano 部署及逐帧记录验证了该方法用于实时监测和选择性施药的可行流程。

INTRODUCTION

Rice is one of the most important staple crops worldwide, and pest outbreaks during the growing season directly affect yield, grain quality and pesticide-use decisions. Field scouting still relies heavily on visual inspection and manual counting, which are labor-intensive, subjective and difficult to scale across large planting areas. A practical rice-pest detection system therefore needs not only high recognition accuracy, but also real-time inference, stable performance under occlusion and illumination variation, and compatibility with low-power edge devices used in field monitoring or selective spraying.

Deep-learning-based object detection has become an important tool for agricultural pest monitoring. Two-stage detectors such as Faster R-CNN generally provide strong localization ability but require relatively high computational cost, whereas one-stage detectors represented by the YOLO series offer a better accuracy-speed trade-off for real-time applications. Recent studies on rice or field pest identification, including MobileNet-CA-YOLO, AgriPest-YOLO and transformer-based rice-pest detectors, have improved detection accuracy by introducing lightweight backbones, attention mechanisms or multi-scale feature fusion (*Jia et al., 2023; Zhang et al., 2023; Wang et al., 2025*). Complementary international studies have broadened both the sensing scenarios and the task definitions used for rice-pest identification. Hassan et al. combined remote-sensing imagery with a modified YO-CNN to identify major rice pests and demonstrated the potential of wide-area automated scouting *(Hassan et al., 2023)*.

Saufi and Suharjito developed a trap-image CNN for white rice stem borer detection and population counting, but reported that inference still depended on server resources rather than direct processing on the field device *(Saufi and Suharjito, 2024)*. Quach et al. released an expert-reviewed rice-pest dataset assembled from heterogeneous sources, highlighting the importance of data diversity and standardized preprocessing for smart-farming systems *(Quach et al., 2024)*. In parallel, RP-DETR used an end-to-end Transformer architecture to strengthen long-range feature interaction and multi-scale fusion for rice-pest recognition, thereby providing a complementary alternative to convolution-dominated detectors *(Wang et al., 2025)*.

Taken together, these model families address different operational needs. Image-level CNN systems are relatively simple and effective in controlled trap or aerial scenes, but they do not always localize several neighboring pests in a single field image and may require remote-server support *(Hassan et al., 2023; Saufi and Suharjito, 2024)*. Lightweight YOLO detectors generally offer a favorable accuracy-speed balance for edge deployment *(Jia et al., 2023; Zhang et al., 2023; Xiong et al., 2024)*; however, performance remains sensitive to the loss of fine-grained cues during downsampling and to small, dense or overlapping target layouts *(Sunkara and Luo, 2023; Wang et al., 2025)*. Transformer-based detectors capture longer-range dependencies and provide an end-to-end alternative for multi-scale rice-pest detection *(Wang et al., 2025)*. Moreover, headline accuracy values should not be compared directly across studies because pest categories, acquisition platforms, annotation protocols and test sets differ *(Quach et al., 2024; Xiong et al., 2024)*. Collectively, these observations indicate that field-oriented rice-pest detection should be treated as a coupled problem of fine-grained visual representation, reliable localization in dense or occluded scenes, and resource-efficient inference, rather than as an isolated improvement to one network component. Accordingly, the present study develops an integrated lightweight detection framework that coordinates feature representation, multi-scale information interaction and prediction refinement within a unified pipeline. The framework is intended to retain weak boundary and texture cues of very small pests, use broader contextual information to distinguish visually similar categories, reduce missed and duplicate detections in overlapping infestations, and maintain an accuracy-latency balance suitable for edge deployment. Its practical relevance is assessed through class-wise PR/F1 analysis, confidence-threshold selection and Jetson Nano validation at an average inference speed of 36 FPS.

However, several research gaps remain. First, small rice pests are often densely clustered or partially occluded, resulting in increased missed detections and duplicate bounding boxes. Second, many studies focus primarily on benchmark accuracy while providing limited analysis of class-specific errors, confidence-threshold selection, and practical alarm criteria. Third, the deployment performance of improved models on resource-constrained edge devices has often not been sufficiently validated. To address these gaps, this study developed a lightweight YOLOv11n-based detector integrating Mona, DPCF, and Wise-IoU-NMS. The proposed model was evaluated through ablation experiments, cross-model comparisons, class-wise precision–recall and F1-score analyses, and a deployment protocol designed for the Jetson Nano.

MATERIALS AND METHODS

DATA SOURCES AND PREPROCESSING

Because publicly available rice-pest datasets with uniform annotation standards remain limited, this study constructed a rice-pest image dataset from open-source images and expert-reviewed annotations. The dataset contains six target categories: green leafhopper, brown planthopper, rice bug, leaf folder, stem borer and whorl maggot. Representative images from the dataset are shown in Fig. 1.



Fig. 1 - Representative images from the dataset

The dataset used in this study was sourced from publicly available pest images collected from multiple online platforms (Fig. 1).

Before inclusion, the images were manually screened to remove duplicates, irrelevant samples and low-quality records, and the copyright and usage conditions of the source images were checked. Each retained image was annotated with pest category labels and bounding boxes under the guidance of agricultural experts and authoritative entomological references, thereby improving annotation reliability and domain consistency.

A total of 5,212 high-resolution images were collected, covering six rice-pest categories and diverse visual conditions, including occlusion, deformation, complex backgrounds and illumination variation. The dataset was divided into training, validation and test sets at a ratio of 8:1:1, with 4,170, 521 and 521 images, respectively. The six pest categories were arranged in a near-balanced manner: each class contained 868-869 images, corresponding to 16.65-16.67% of the dataset. This distribution reduces class-prior bias and allows the precision, recall and F1-score curves to be interpreted as class-comparable evidence rather than being dominated by one abundant pest category. To improve model generalization and reduce imbalance-related bias, data augmentation was applied, including random rotation, brightness adjustment, horizontal flip, translation, local occlusion and Gaussian noise.

Table 1

Class-wise composition of the rice-pest dataset

Pest class	Chinese name	Total images	Proportion (%)	Train/Val/Test
green-leafhopper	绿叶蝉	869	16.67	695 / 87 / 87
brown-planthopper	褐飞虱	869	16.67	695 / 87 / 87
rice-bug	稻蝽	869	16.67	695 / 87 / 87
leaf-folder	卷叶螟	869	16.67	695 / 87 / 87
stem-borer	螟虫	868	16.65	695 / 87 / 86
whorl-maggot	稻瘿蚊	868	16.65	695 / 86 / 87
Total	-	5,212	100.00	4,170 / 521 / 521

Note: *The dataset was organized as a near-balanced six-class rice-pest dataset. The train/validation/test split follows the 8:1:1 protocol.*

EXPERIMENTAL ENVIRONMENT AND PARAMETER CONFIGURATION

Experimental Environment Configuration

Model training was conducted in Python 3.8 using the PyTorch deep-learning framework. The training workstation ran Ubuntu 22.04.3 with CUDA 12.2 acceleration and used an Intel(R) Core(TM) i5-8300H CPU @ 2.30 GHz and an NVIDIA A100 GPU with 40 GB memory. This environment was used for model development, parameter optimization and benchmark comparison, whereas the edge-device validation was conducted separately on Jetson Nano as described below.

Experimental Parameter Configuration

YOLOv11n was used as the baseline model. All models were trained with an input resolution of 640 x 640 pixels. Stochastic Gradient Descent (SGD) was used for optimization with an initial learning rate of 0.01, momentum of 0.937 and cosine annealing for learning-rate scheduling. The batch size was set to 16 and the maximum number of epochs was 300. The same training and testing configuration was maintained across ablation and comparison experiments to ensure fair evaluation of the proposed modules.

EDGE-DEVICE VALIDATION PROTOCOL

To address the requirement for real-life validation, the final YOLOv11n-Mona-DPCF-Wise-IoU model was prepared for deployment on an NVIDIA Jetson Nano B01 (4 GB). The edge-device workflow included model export to ONNX, graph simplification, TensorRT FP32 engine conversion and local inference on 640 x 640 input frames. The deployment interface integrates image, video and camera-stream input, real-time visualization of bounding boxes and confidence scores, and result logging for subsequent pest occurrence analysis.

In practical use, detections with confidence scores above 0.476, the threshold selected from the F1-confidence curve, are treated as valid pest alarms. Each alarm record includes the pest category, confidence score, bounding-box coordinates and frame information. This design allows the system to support field

scouting, multi-class pest monitoring, pest-density recording and future integration with selective spraying equipment.

ALGORITHM IMPROVEMENT

YOLOv11n Algorithm

This study focuses on YOLOv11n as the baseline detector because of its lightweight structure and real-time potential. The YOLOv11n network consists of four major components: the input layer, backbone, neck feature-fusion network and detection head. The overall network structure is shown in Fig. 2.

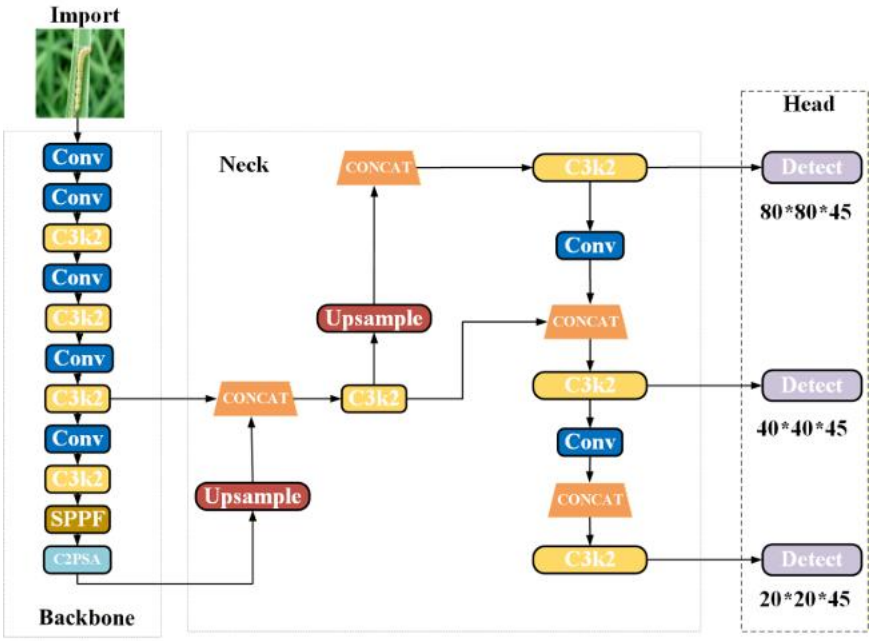


Fig. 2 - Architecture of the YOLOv11n network model

Multi-cognitive Visual Adapter

To address efficient and accurate pest detection under complex visual conditions, Mona (Multi-cognitive Visual Adapter) is introduced as a lightweight feature adaptation module (Fig. 3). Mona is designed to strengthen visual knowledge transfer without substantially increasing trainable parameters. It contains scaled layer normalization and a multi-branch depthwise convolutional filtering module. The scaled LayerNorm uses learnable weights to balance normalized and original features, improving the stability of transferred representations. The convolutional branches use 3 x 3, 5 x 5 and 7 x 7 depthwise kernels to capture pest features at different receptive fields, followed by pointwise convolution and GeLU activation. Residual connections maintain gradient flow and semantic consistency. This design improves fine-grained pest feature representation while preserving the lightweight nature of YOLOv11n.

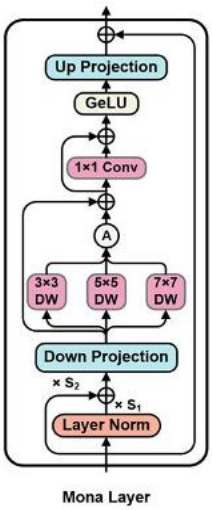


Fig. 3 - Architecture of the Multi-cognitive Visual Adapter

Detail-Preserving Contextual Fusion

To enhance feature fusion for rice-pest detection, the DPCF module is incorporated into the neck architecture (Fig. 4). DPCF addresses the limitations of static fusion schemes such as simple concatenation or summation, which may not sufficiently adapt to multi-scale pests, background interference and partial occlusion. Instead, DPCF performs content-adaptive fusion of hierarchical feature maps, enabling the model to preserve local details while incorporating broader contextual information.

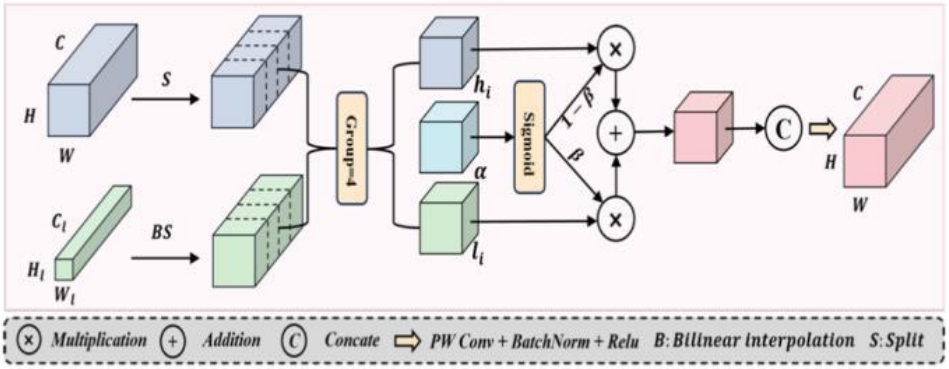


Fig. 4 - Architecture of the Detail-Preserving Contextual Fusion module

Structurally, DPCF is composed of two key components: Depthwise Separable Pyramid Convolution (DSPC) and Channel-wise Dynamic Fusion (CDF). DSPC applies a set of depthwise separable convolutions with multiple receptive fields (3×3, 5×5, 7×7) to enhance contextual representation at each scale. The outputs are then passed through the CDF module, which generates dynamic fusion weights across feature channels using attention mechanisms. These weights allow the model to selectively emphasize semantically relevant features while suppressing noisy or redundant ones. Residual connections are employed to preserve gradient stability and retain original semantic pathways.

Compared to conventional PANet-style feature aggregation, DPCF dynamically learns spatial-semantic relationships, yielding a more adaptive fusion process that is sensitive to local structure and global context. This is particularly advantageous for pest detection, where the targets are often small, densely distributed, and partially occluded. By modeling scale-aware and position-sensitive features, DPCF significantly improves the model's ability to discriminate subtle pest contours from noisy backgrounds.

Wise-IoU-NMS Non-Maximum Suppression Algorithm

The original YOLOv11n adopts conventional non-maximum suppression (NMS). When the Intersection over Union (IoU) between a candidate box and the highest-confidence box exceeds a predefined threshold, the candidate box is removed or heavily suppressed. This strategy may discard valid boxes in overlapping pest scenes and can therefore reduce recall. To alleviate this problem, this study adopts a Wise-IoU-based NMS strategy. The method adjusts suppression weights according to overlap and localization quality, so that boxes are retained or suppressed more adaptively rather than being removed only by a fixed IoU threshold. This improves localization stability for dense and partially occluded pest targets.

In this strategy, M denotes the detection box with the highest confidence score, B_i denotes the i-th candidate box, epsilon denotes the NMS threshold, s_i denotes the classification confidence score and IoU(B_i, M) denotes the overlap between the candidate box and M. The adjusted confidence score is used to determine whether the candidate box should be retained. This design reduces false suppression of valid pest boxes and mitigates duplicate detections caused by multiple high-confidence boxes corresponding to the same target.

For bounding-box regression, h and w denote the height and width of the minimum enclosing box, respectively, while x and y denote the center coordinates of the predicted and ground-truth boxes. The Wise-IoU formulation dynamically adjusts localization weights according to box quality, allowing the model to focus more effectively on difficult samples. The schematic representation is shown in Fig. 5.

Compared with traditional NMS, Wise-IoU-NMS considers overlap, center distance and localization quality jointly. This mechanism is particularly useful for small rice pests that appear close to one another or are partially occluded by leaves and stems. By reducing unnecessary suppression and duplicate alarm boxes, Wise-IoU-NMS improves practical detection reliability in complex field images.

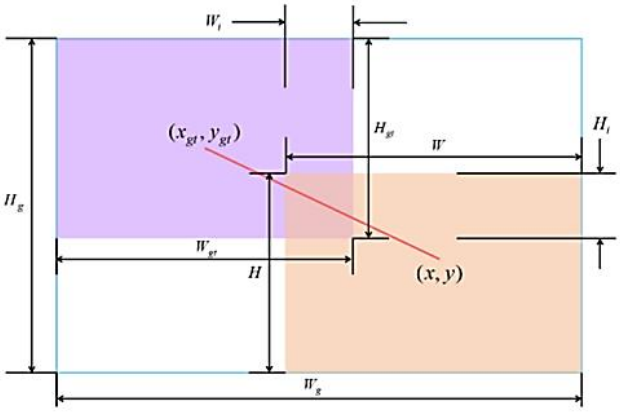


Fig. 5 - The architecture of the Wise-IoU

Overall Improved Network Architecture

This study introduces three key improvements to the YOLOv11n algorithm: Mona for lightweight feature adaptation, DPCF for detail-preserving contextual fusion and Wise-IoU-NMS for refined box suppression. The refined network architecture, denoted as YOLOv11n-Mona-DPCF-Wise-IoU, is depicted in Fig. 6.

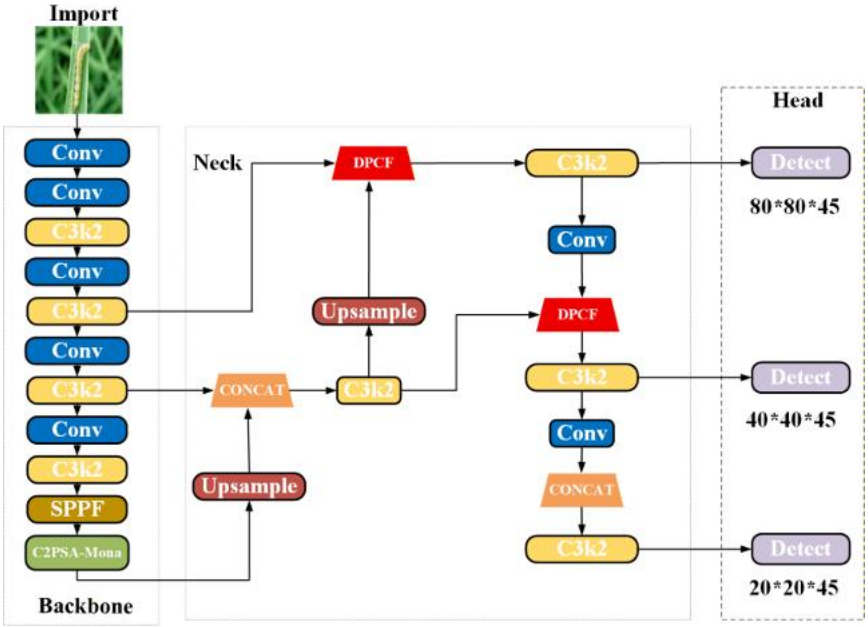


Fig. 6 - Improved YOLOv11n structure

RESULTS

A. Ablation Experiment

To evaluate the contribution of each module to detection accuracy and model complexity, a series of ablation experiments were conducted under identical training and testing conditions. Mona, DPCF and Wise-IoU-NMS were incrementally added to the YOLOv11n baseline. The results on the test set are summarized in Table 2.

Table 2

Ablation results of the proposed model on the test set

Model	Params (M)	GFLOPs	mAP@50
YOLOv11n	2.58	6.3	0.94
YOLOv11n-Mona	2.63	6.4	0.948
YOLOv11n-Mona-DPCF	2.65	6.5	0.952
YOLOv11n-Mona-DPCF-Wise-IoU	2.65	6.5	0.954

The ablation results demonstrate the effectiveness of the proposed components. The baseline YOLOv11n achieved 94.0% mAP@50 with 2.58 M parameters and 6.3 GFLOPs. After introducing Mona, mAP@50 increased to 94.8%, while the parameter count and computational cost only rose slightly to 2.63 M and 6.4 GFLOPs. Adding DPCF further improved mAP@50 to 95.2%, indicating that detail-preserving contextual fusion strengthened multi-scale pest representation. Finally, the complete YOLOv11n-Mona-DPCF-Wise-IoU model achieved the best mAP@50 of 95.4% with 2.65 M parameters and 6.5 GFLOPs. These results show that the proposed modules improve accuracy with limited additional cost, which is important for practical edge deployment.

Figure 7 illustrates the class-wise Precision-Recall (PR) curves of four YOLOv11n variants, corresponding to the baseline and each stage of the proposed incremental enhancements. Subfigure (a) represents the baseline YOLOv11n, which achieved an mAP@0.5 of 0.940. Although the baseline performed well for stem borer (0.979) and whorl maggot (0.974), it showed weaker performance for brown planthopper (0.847), indicating class-specific sensitivity. After Mona was introduced, mAP@0.5 increased to 0.948, with improved precision-recall balance for visually similar pest classes. Incorporating DPCF further improved mAP@0.5 to 0.952 by strengthening multi-scale feature aggregation. The complete YOLOv11n-Mona-DPCF-Wise-IoU model achieved the highest mAP@0.5 of 0.954 and produced more stable PR curves across categories. This confirms that the proposed modules progressively improve class-wise detection reliability, as summarized in Table 2.

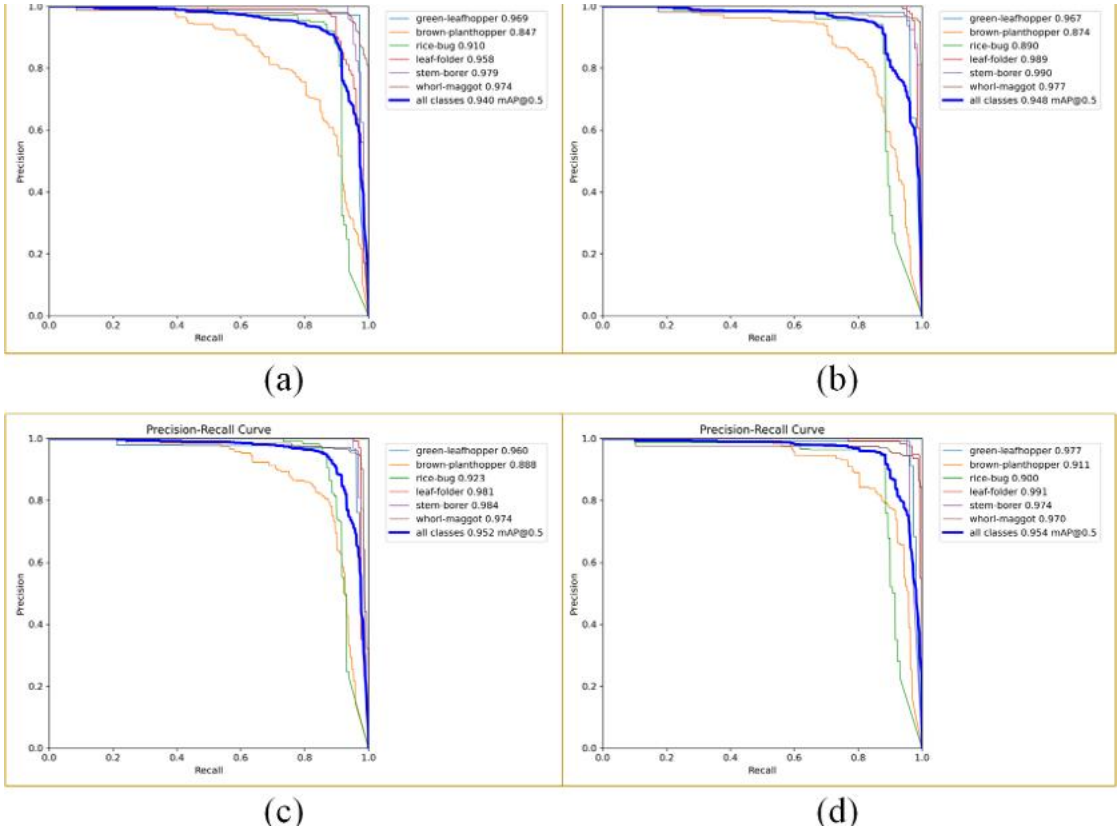


Fig. 7 - Precision-Recall (PR) curves

Figure 8 presents the F1-confidence curves of four sequentially enhanced YOLOv11n models, providing insight into classification robustness and the selection of practical alarm thresholds.

The baseline YOLOv11n reached a peak macro-average F1 score of 0.91 at a confidence threshold of 0.472, but its F1 values were lower for brown planthopper and rice bug, reflecting the difficulty caused by class imbalance and inter-class similarity. After Mona was introduced, the peak F1 score increased to 0.93 at a threshold of 0.437. Adding DPCF further stabilized the curves, with a macro F1 score of 0.93 at 0.452. The complete YOLOv11n-Mona-DPCF-Wise-IoU model maintained the highest F1 score of 0.93 and achieved it at a confidence threshold of 0.476. Therefore, 0.476 was selected as the recommended operating threshold for practical pest alerts in the deployment experiment. Detections with confidence scores above this threshold were treated as valid alarm events, while lower-confidence predictions were retained only for diagnostic review.

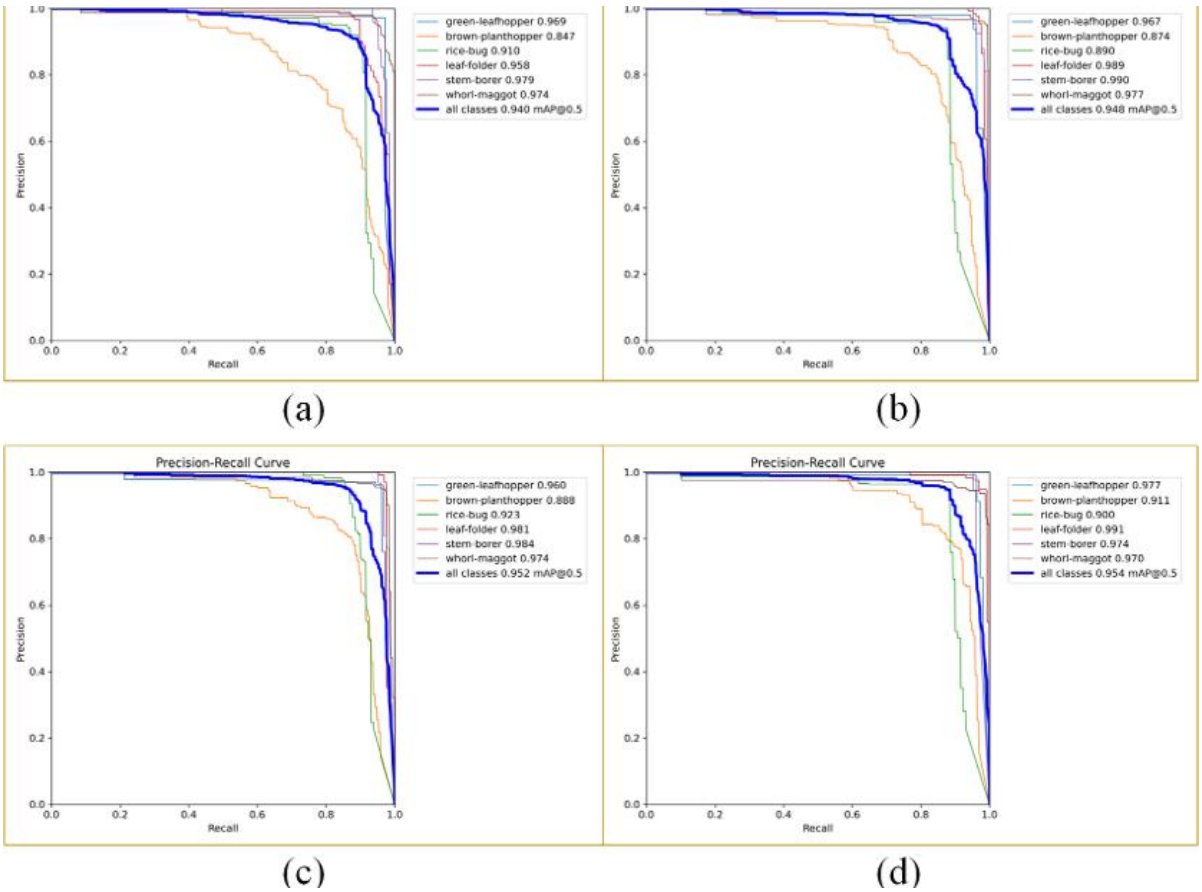


Fig. 8 - F1-Confidence curves

B. Comparative Experiment

To comprehensively evaluate the performance of the enhanced model, this study conducted comparative experiments between the proposed algorithm, YOLOv11n-Mona-DPCF-Wise-IoU, and several other prominent object detection algorithms, including SSD, Faster R-CNN, YOLOv10n, YOLOv12n, TPH-YOLOv5, RT-DETR, and DEIM. The results of these comparative experiments are summarized in Table 3.

Table 3

Comparison results with mainstream object-detection models

Model	Params (M)	GFLOPs	P	R	mAP@50	FPS
SSD	34.3	45.8	0.863	0.807	0.829	78
Faster R-CNN	69.2	217.8	0.894	0.917	0.858	84
YOLOv10n	2.69	8.2	0.911	0.904	0.933	106
YOLOv12n	2.50	5.8	0.931	0.914	0.939	117
TPH-YOLOv5	45.37	260.2	0.928	0.909	0.935	101
RT-DETR	31.99	103.3	0.933	0.921	0.937	95
DEIM	4.0	7.0	0.921	0.916	0.924	105
YOLOv11n	2.58	6.3	0.935	0.925	0.940	112
YOLOv11n-Mona-DPCF-Wise-IoU	2.65	6.5	0.948	0.947	0.954	109

The comparative results in Table 3 show that classical detectors such as SSD and Faster R-CNN obtained lower mAP@50 values of 82.9% and 85.8%, respectively, while requiring higher computational costs. YOLOv10n and YOLOv12n achieved 93.3% and 93.9% mAP@50 with high inference speeds, but their precision and recall were lower than those of the proposed method. The baseline YOLOv11n achieved 94.0% mAP@50 with 2.58 M parameters and 6.3 GFLOPs, demonstrating a strong lightweight baseline for rice-pest detection.

The proposed YOLOv11n-Mona-DPCF-Wise-IoU model achieved the best overall performance, with 95.4% mAP@50, 94.8% precision and 94.7% recall. It retained a compact model size of 2.65 M parameters and 6.5 GFLOPs and maintained high inference speed in the workstation test. Compared with the baseline, the proposed method improved mAP@50 by 1.4 percentage points while adding only 0.07 M parameters and 0.2 GFLOPs. These results indicate that the proposed architecture provides a more favorable balance between accuracy, robustness and computational efficiency than the compared detectors.

Figure 9 shows the mAP@50 convergence curves of the baseline YOLOv11n and the proposed YOLOv11n-Mona-DPCF-Wise-IoU model over 200 training epochs. The improved model converged faster in the early training stage and maintained a stable performance advantage throughout training, ultimately approaching an mAP@50 of 0.954. This indicates that Mona, DPCF and Wise-IoU-NMS not only improve detection accuracy but also enhance training stability.

Figure 10 visually compares the detection performance of YOLOv10n, YOLOv12n, YOLOv11n and the proposed YOLOv11n-Mona-DPCF-Wise-IoU model on three representative pest images. Across the samples, the improved model produced tighter bounding boxes and higher confidence scores.

In the first image, the proposed model localized the pest with a confidence score of 0.84, higher than the compared models (0.71-0.79). In the second image, which contained overlapping pests, the proposed model detected two targets with confidence scores of 0.87 and 0.83, whereas other models missed one target or produced lower-confidence detections. In the third image, which had high brightness and a complex background, the proposed model still detected the target with a confidence score of 0.88. These four valid detections all exceeded the recommended alarm threshold of 0.476, supporting the feasibility of threshold-based pest warning in practical monitoring.

Overall, the results demonstrate that Mona, DPCF and Wise-IoU-NMS improve both localization precision and detection stability, particularly under small-target, occlusion and illumination-challenging conditions. The remaining practical requirement is to verify whether this accuracy-efficiency balance can be maintained on low-power edge hardware; therefore, a Jetson Nano deployment validation was added in the following section.

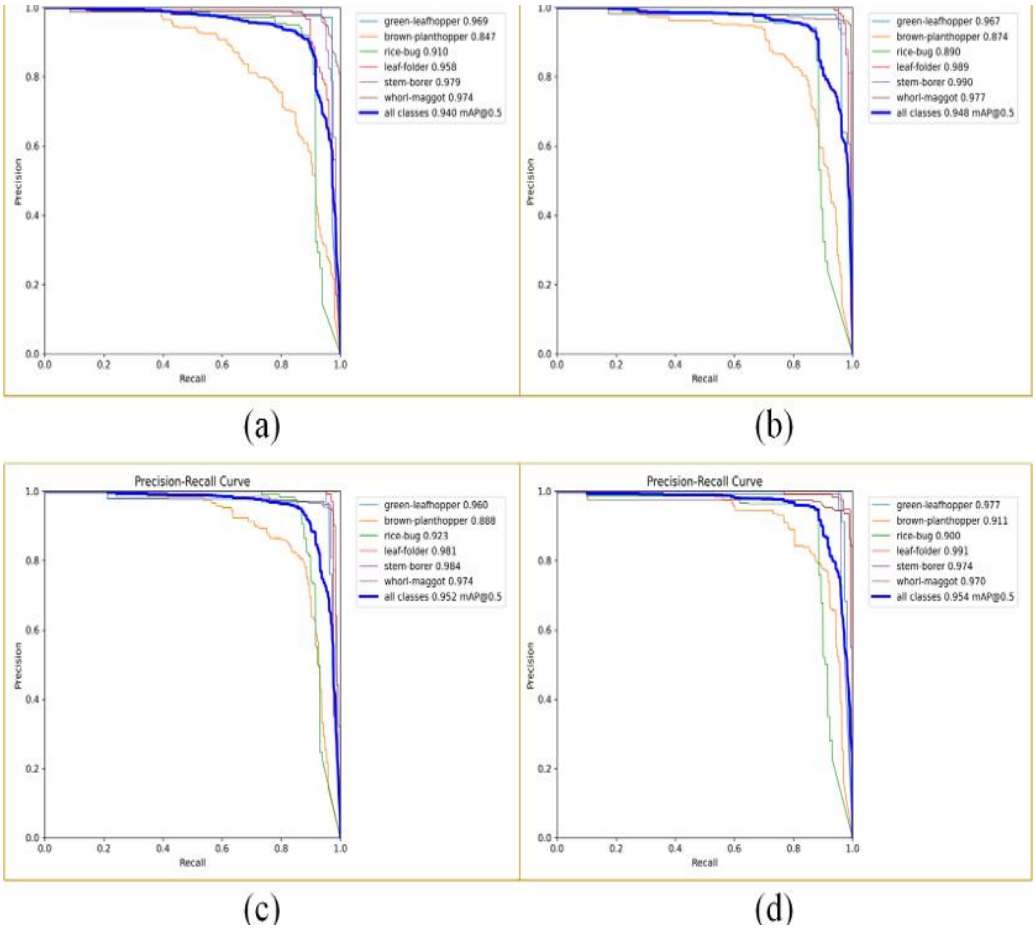


Fig. 9 - mAP@50 convergence curves

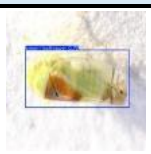
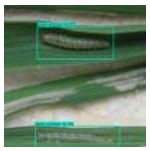
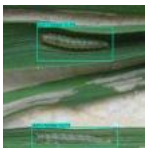
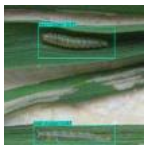
Image	1	2	3
YOLOv10n			
YOLOv12n			
YOLOv11n			
YOLOv11n-Mona-DPCF-Wise-IoU			

Fig. 10 - Comparison of model detection performance

C. Edge-Device Deployment and Practical Application Validation

To further clarify the engineering application scenario requested by the reviewer, the proposed model was deployed on Jetson Nano for rice-field pest monitoring (Fig. 11). The interface provides functions for opening images, videos and camera streams, starting or stopping detection and saving detection results. During operation, the model identifies six rice-pest categories, namely green leafhopper, brown planthopper, rice bug, leaf folder, stem borer and whorl maggot, and displays the predicted class, confidence score and bounding box in real time.

The deployment result demonstrates that the lightweight YOLOv11n-based model can be transferred from workstation evaluation to an embedded monitoring terminal. In field or greenhouse patrol scenarios, the confidence threshold can be used as an alarm rule: targets above the threshold are recorded as pest occurrences, while repeated frame records can be aggregated to estimate pest density. When connected to a fixed camera, mobile inspection platform or selective sprayer, the system can provide timely multi-class pest warnings and location-aware decision support for precision pest management.



Fig. 11 - Jetson Nano deployment interface of the rice-pest detection system

CONCLUSIONS

This study developed a lightweight rice-pest detector by integrating Mona, DPCF and Wise-IoU-NMS with YOLOv11n. The model achieved 95.4% mAP@50, 94.8% precision and 94.7% recall with 2.65 M parameters and 6.5 GFLOPs. Ablation and comparative experiments confirmed improved accuracy with limited computational overhead, particularly for small, occluded and complex-background targets. The Jetson Nano workflow further demonstrated the feasibility of embedded monitoring and threshold-based alarms. Future work should quantify long-term field robustness and end-to-end latency under varying environmental conditions.

ACKNOWLEDGEMENT

This study was funded by the Key Research and Development Program of Shandong Province (No. 2024RZB0202) and the Shandong Provincial Natural Science Foundation (No. ZR2025QC600).

REFERENCES

[1] Ahmad, I., Yang, Y., Yue, Y., Ye, C., Hassan, M., Cheng, X., Wu, Y., Zhang, Y. (2022). Deep Learning Based Detector YOLOv5 for Identifying Insect Pests (基于深度学习的 YOLOv5 检测器用于识别昆虫害虫). *Appl. Sci.*, Vol.12, 10167.

[2] Böckmann, E., Pfaff, A., Schirrmann, M., Pflanz, M. (2021). Rapid and low-cost insect detection for analysing species trapped on yellow sticky traps (用于分析黄色粘虫板上诱集物种的快速低成本昆虫检测方法). *Sci. Rep.*, Vol.11, 12854.

[3] Deserno, M., Briassouli, A. (2021). Faster R-CNN and EfficientNet for Accurate Insect Identification in a Relabeled Yellow Sticky Traps Dataset (基于 Faster R-CNN 和 EfficientNet 的重标注黄色粘虫板数据集昆虫 精准识别方法). In Proceedings of the 2021 IEEE International Workshop on Metrology for Agriculture and Forestry (MetroAgriFor), Trento-Bolzano, Italy, 3 November 2021; pp.209–214.

[4] Di, Y., Phung, S., Van Den Berg, J., Clissold, J., Bouzerdoum, A. (2023). TP-YOLO: A Lightweight Attention-Based Architecture for Tiny Pest Detection (TP-YOLO:一种用于微小害虫检测的轻量级注意力架构). In *Proceedings of the 2023 IEEE International Conference on Image Processing (ICIP)*, Kuala Lumpur, Malaysia, 8 October 2023; pp.3394–3398.

[5] Gutierrez, A., Ansuategi, A., Susperregi, L., Tubío, C., Rankic, I., Lenža, L. (2019). A Benchmarking of Learning Strategies for Pest Detection and Identification on Tomato Plants for Autonomous Scouting Robots Using Internal Databases (基于内部数据库的自主侦察机器人番茄植株害虫检测与识别学习策略基准测试). *Sensors*, 2019, 5219471.

[6] Guan, S., Lin, Y., Lin, G., Su, P., Huang, S., Meng, X., Liu, P., Yan, J. (2024). Real-Time Detection and Counting of Wheat Spikes Based on Improved YOLOv10 (基于改进 YOLOv10 的小麦穗实时检测与计数). *Agronomy*, Vol.14, 1936.

[7] Huang, J., Huang, Y., Huang, H., Zhu, W., Zhang, J., Zhou, X. (2022). An Improved YOLOX Algorithm for Forest Insect Pest Detection (一种用于森林害虫检测的改进 YOLOX 算法). *Comput. Intell. Neurosci.*, 2022, 5787554. [PubMed]

[8] Jia, L., Wang, T., Chen, Y., Zang, Y., Li, X., Shi, H., Gao, L. (2023). MobileNet-CA-YOLO: An Improved YOLOv7 Based on the MobileNetV3 and Attention Mechanism for Rice Pests and Diseases Detection (MobileNet-CA-YOLO：基于 MobileNetV3 和注意力机制的改进 YOLOv7 用于水稻病虫害检测). *Agriculture*, Vol.13, 1285.

[9] Khalid, S., Oqaibi, H., Aqib, M., Hafeez, Y. (2023). Small Pests Detection in Field Crops Using Deep Learning Object Detection (基于深度学习目标检测的田间作物微小害虫检测). *Sustainability*, Vol.15, 6815.

[10] Liu, J., Wang, X. (2020). Tomato Diseases and Pests Detection Based on Improved Yolo V3 Convolutional Neural Network (基于改进 Yolo V3 卷积神经网络的番茄病虫害检测). *Front. Plant Sci.*, Vol.11, 898.

[11] Pinto-Zevallos, D., Vänninen, I. (2013). Yellow sticky traps for decision-making in whitefly management: What has been achieved? (用于粉虱管理决策的黄色粘虫板：取得了哪些成果？). *Crop Prot.*, Vol.47, pp.74–84.

[12] Ramalingam, B., Mohan, R., Pookkuttath, S., Gómez, B., Borusu, C., Teng, T., Tamilselvam, Y. (2020). Remote Insects Trap Monitoring System Using Deep Learning Framework and IoT (基于深度学习框架和物联网的远程昆虫诱捕监测系统). *Sensors*, Vol.20, 5280. [PubMed]

[13] Sunkara, R., Luo, T. (2023). No More Strided Convolutions or Pooling: A New CNN Building Block for Low-Resolution Images and Small Objects (摒弃步幅卷积或池化：一种用于低分辨率图像和小目标的新型 CNN 构建模块). Springer, Berlin/Heidelberg, Vol.13715, pp.443–459.

[14] Tan, L., Liu, S., Gao, J., Liu, X., Chu, L., Jiang, H. (2024). Enhanced Self-Checkout System for Retail Based on Improved YOLOv10 (基于改进 YOLOv10 的零售增强自助结账系统). J. Imaging, Vol.10, 248.

[15] Wen, C., Chen, H., Ma, Z., Zhang, T., Yang, C., Su, H., Chen, H. (2022). Pest-YOLO: A model for large-scale multi-class dense and tiny pest detection and counting (Pest-YOLO：一种用于大规模多类别密集微小害虫检测与计数的模型). *Front. Plant Sci.*, Vol.13, 973985.

[16] Wang, A., Chen, H., Liu, L., Chen, K., Lin, Z., Han, J., Ding, G. (2024). YOLOv10: Real-Time End-to-End Object Detection (YOLOv10：实时端到端目标检测). arXiv, 2024, arXiv:2405.14458.

[17] Xia, D., Chen, P., Wang, B., Zhang, J., Xie, C. (2018). Insect Detection and Classification Based on an Improved Convolutional Neural Network (基于改进卷积神经网络的昆虫检测与分类). *Sensors*, Vol.18, 4169.

[18] Yang, S., Zhou, G., Feng, Y., Zhang, J., Jia, Z. (2024). SRNet-YOLO: A model for detecting tiny and very tiny pests… (SRNet-YOLO：一种用于检测微小及极微小害虫的模型…). *Front. Plant Sci.*, Vol.15, 1416940.

[19] Zhang, W., Huang, H., Sun, Y., Wu, X. (2023). AgriPest-YOLO: A rapid light-trap agricultural pest detection method based on deep learning (AgriPest-YOLO：一种基于深度学习的快速灯光诱集农业害虫检测方法). *Front. Plant Sci.*, Vol.13, 1079384.

[20] Zhang, L., Zhao, C., Feng, Y., Li, D. (2023). Pests Identification of IP102 by YOLOv5 Embedded with the Novel Lightweight Module (嵌入新型轻量级模块的 YOLOv5 用于 IP102 害虫识别). *Agronomy*, Vol.13, 1583.

DESIGN AND EXPERIMENT OF A SMALL SELF-PROPELLED LIQUID-FERTILIZER INJECTOR
/
小型自走式液肥注射机设计与试验

Ting GUO[1)], Xi XIAO[1)], Ming LIU[2)], Chengsong LI[2)], Linji LI[1)], Lin ZHU[1)], Wanneng LI[*2)]
[1)] Hunan Provincial Tobacco Company, Chenzhou City Company, Hunan / China
[2)] College of Engineering and Technology, Southwest University, Chongqing / China
Tel: +86 13102054853; E-mail: 19822514833@163.com
Corresponding author: Wanneng Li
DOI: https://doi.org/10.35633/inmateh-79-53

Keywords: *Liquid fertilizer, Precision deep fertilization, Crank-slider injection mechanism, Computational fluid dynamics*

ABSTRACT
To address the limited maneuverability and terrain adaptability of conventional liquid-fertilizer injection equipment in hilly and small-plot farmland, a compact self-propelled injector integrating a narrow-track four-wheel-drive chassis, an angle-adjustable injection unit, and a crank-slider penetration mechanism was developed. Unlike large tractor-mounted or fixed-orientation systems, the proposed machine integrates inter-row movement, posture adjustment, needle penetration, and timed point injection on a lightweight platform. The discharge characteristics of the injection needle were investigated using computational fluid dynamics, and a three-factor, three-level Box–Behnken design was employed to optimize injection duration, inlet pressure, and outlet-hole number, with fertilizer volume per injection as the response. Response surface optimization identified an injection duration of 1 s, an inlet pressure of 0.45 MPa, and six outlet holes as the preferred parameter combination. Field validation yielded a measured fertilizer volume of 675.4 mL per injection, compared with the predicted value of 700 mL, corresponding to a relative difference of 3.51%. The results demonstrate the feasibility of controllable deep point placement under the tested conditions and provide a lightweight equipment solution for liquid-fertilizer application in hilly and small-plot farmland.

摘要
针对传统液肥注射施肥装备在丘陵山区及小地块农田中机动性和地形适应性不足的问题，研制了一种集窄距四轮驱动底盘、角度可调式注射单元和曲柄滑块入土机构于一体的小型自走式液肥注射机。与大型拖拉机悬挂式或固定姿态作业系统相比，该机可在轻量化平台上实现行间行走、姿态调节、施肥针入土及定时定点注肥。采用计算流体动力学方法分析施肥针排液特性，并以单次注肥体积为响应值，开展三因素三水平 Box–Behnken 响应面试验，对注肥时间、入口压力和出液孔数进行优化。响应面优化得到较优参数组合为注肥时间 1 s、入口压力 0.45 MPa 和出液孔数 6 个。田间验证中，单次注肥体积实测值为 675.4 mL，模型预测值为 700 mL，相对误差为 3.51%。结果表明，所研制机具在试验条件下能够实现可控的液肥定点深施，可为丘陵山区及小地块农田液肥机械化施用提供轻量化装备方案。

INTRODUCTION
In agricultural production, fertilizers are mainly applied in solid and liquid forms. Solid fertilizers are widely used, but their slow nutrient release and prolonged crop uptake often result in low utilization efficiency and considerable nutrient loss. In contrast, liquid fertilizers have the advantages of rapid nutrient release, high absorption efficiency and low application cost, making them suitable for crop topdressing *(Zhou et al., 2023)*. However, surface or shallow application of liquid fertilizer is prone to volatilization and nutrient loss, which reduces fertilization efficiency and limits crop yield improvement *(Hu et al., 2016)*. Previous studies have shown that deep point placement of liquid fertilizer can reduce nutrient loss, improve fertilizer use efficiency, mitigate environmental pollution and promote crop yield *(Li et al., 2018)*.

Liquid fertilizer is commonly applied through drip irrigation, foliar spraying and subsurface placement. Among subsurface application methods, band placement and point placement are the two main modes. Deep-placement technology for liquid fertilizer has been investigated relatively early in other countries and various dedicated applicators have been developed to improve application accuracy and fertilizer utilization.

For example, a soil-punching liquid-fertilizer applicator was developed to keep the injection needle vertical during soil penetration and withdrawal, thereby enabling fixed-point injection *(da Silva et al., 2017)*. An injection dosing system for site-specific liquid-fertilizer management was also designed by synchronizing soil punching and liquid-fertilizer injection to improve placement accuracy *(da Silva and Magalhães, 2019)*. In addition, precision injection of dairy sludge in no-till silage corn was reported to improve nutrient uptake under injection placement *(Hunt and Bittman, 2021)*. More recently, a liquid-manure point-injection system was designed and tested under field conditions, showing that subsurface injection could reduce nitrogen losses *(Hesar et al., 2025).*

In China, considerable efforts have also been made to develop liquid-fertilizer deep-placement equipment. The 3SFBQ-500 pneumatic blasting soil-loosening and fertilization machine can achieve fixed-point fertilization at depths of 200–500 mm in orchard hard soil through the coordinated operation of a drilling rod and a fertilizer injection unit *(Xi et al., 2017; Xi, 2018)*. Several liquid-fertilizer point-application devices have been developed, including the 1YJ-140 deep-placement applicator, in which the punching component was driven by a crank-rocker mechanism and the transmission system was improved to enhance operating efficiency *(Wang et al., 2016, 2017, 2018)*. Nevertheless, severe vibration still occurred under high-frequency operating conditions *(Feng et al., 2017; Liu et al., 2016)*. A liquid-fertilizer applicator for maize topdressing was also developed to improve fertilization efficiency and field adaptability by using multiple injection needles and a ground-clearance adjustment mechanism *(Xing, 2019)*.

Although substantial progress has been made in quantitative deep placement of liquid fertilizer, existing equipment still has several limitations, including large machine size, inconvenient transport, and poor adaptability to complex terrain. These limitations restrict its application in hilly areas and small plots, where low mass, flexible mobility, posture adjustment, and stable needle penetration are required *(Sun, 2024)*. Moreover, previous studies have focused mainly on tractor-mounted or fixed-orientation systems, whereas integrated solutions that combine terrain adaptation, injection-posture adjustment, and intermittent point application on a lightweight self-propelled platform remain limited.

The main methodological contribution of this study is the integration of CFD-based internal-flow analysis with Box–Behnken response surface optimization to quantify the individual and interactive effects of injection duration, inlet pressure, and outlet-hole number on fertilizer volume per injection. The principal engineering contribution is the integration of a four-wheel-drive narrow-track chassis, a rotary–tilting posture-adjustment platform, and a crank-slider injection mechanism into a compact 45 kg machine. Structural design, mechanical analysis, CFD simulation, parameter optimization, and field validation were combined to evaluate the feasibility of controllable deep point placement in hilly and fragmented farmland.

MATERIALS AND METHODS

Structural design and working principle

The overall structure of the small self-propelled liquid-fertilizer injector is shown in Fig. 1. The machine mainly consists of a narrow-track chassis, an adjustable tilting platform, a rotary adjustment platform, a crank-slider injection mechanism, a guide support mechanism, and a liquid-fertilizer delivery system.

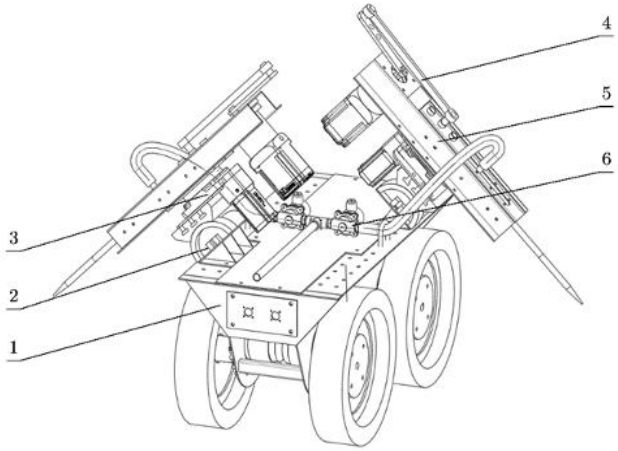
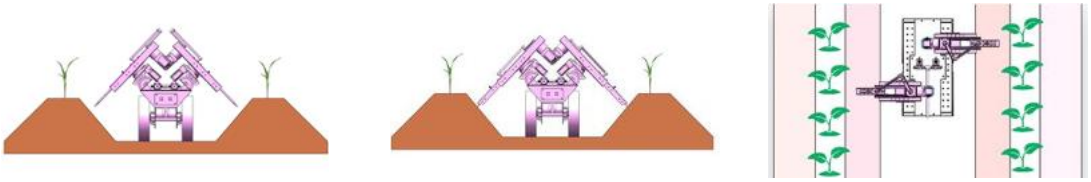


Fig. 1 - Overall structure of the small self-propelled liquid-fertilizer injector

1 - Narrow-track chassis; 2 - Adjustable tilting platform; 3 - Rotary adjustment platform
4 - Crank-slider injection mechanism; 5 - Guide support mechanism; 6 – Liquid-fertilizer delivery system

During operation, the injector is remotely guided into the inter-row space, and the liquid-fertilizer pipeline is connected to the pump. After automatic mode is activated, the machine moves to the preset fertilization position, where the rotary adjustment platform turns through 90 degrees to orient the injection unit perpendicular to the ridge slope (Fig. 2a). The stepper motor then drives the crank-slider mechanism, causing the injection needle to penetrate the soil to the preset depth (Fig. 2b). Once the needle reaches the target position, the solenoid valve opens, and pressurized liquid fertilizer is delivered through the needle into the soil. The needle then retracts, and the machine advances to the next position (Fig. 2c). Repetition of this sequence enables fixed-point deep placement of liquid fertilizer.



a) *b)* *c)*

Fig. 2 - Operating process of the small self-propelled liquid-fertilizer injector

Table 1

Main technical parameters of the machine

Item	Technical parameters
Overall dimensions / mm	810 × 430 × 500
Machine mass / kg	45
Narrow-track chassis motor / N·m	0.98
Holding torque of crank drive motor / N·m	80
Driving torque of rotary platform motor / N·m	2.2
Number of injection needles	2
Injection depth / mm	100–200

Design of key components and mechanical analysis

Narrow-track chassis

To improve passability and driving stability on wet, muddy and uneven terrain, the narrow-track chassis was equipped with a four-wheel electric drive system. Compared with a conventional two-wheel-drive configuration, four-wheel drive provides greater traction and improved terrain adaptability, thereby enhancing machine stability under complex field conditions *(Jiang et al., 2025)*. As shown in Fig. 3, the chassis mainly consists of an anti-collision beam, motor reducers, drive motors, a socket plate, triangular inclined plates, waterproof plates, a frame, wheels and flanges.

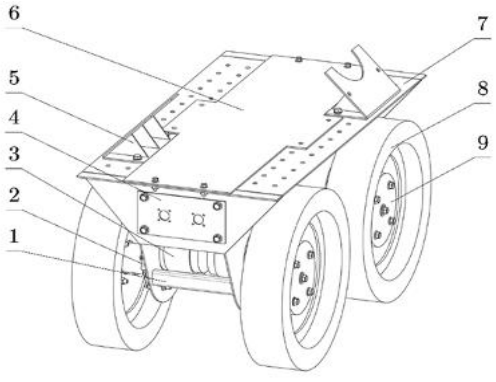


Fig. 3 – Structure of the narrow-track chassis

1 – Anti-collision beam; 2 – Motor reducer; 3 – Drive motor; 4 - Socket plate; 5 – Triangular inclined plate; 6 – Waterproof plate; 7 – Frame; 8 – Wheel; 9 – Flanges

According to China's third national land survey, farmland slopes generally range from 0 to 15 degrees *(People's Daily, 2021)*. Based on the operating conditions of tobacco fields in Guiyang County, Hunan Province, the design slope was set to 10°. The chassis was therefore required to climb a 10-degree slope steadily at 2 km·h^{-1}. A brushed DC motor was selected as the chassis power source, and its principal parameters are listed in Table 2.

Table 2

Main technical parameters of the motor

Item	Parameter
Rated power / kW	0.25
Rated torque / N·m	0.64–0.98
Rated speed / r/min	2400–3700
Maximum speed / r/min	3700
Rated current / A	13.4
Motor efficiency / %	70

Angle-adjustable injection unit

The angle-adjustable injection unit is the core component of the small self-propelled liquid-fertilizer injector, and its structure and operating parameters directly affect injection performance. As shown in Fig. 4, the unit mainly consists of an injection needle, sliding rail, crank-slider mechanism, drive motor, rotary adjustment platform and adjustable tilting platform. Needles with different lengths and diameters can be selected according to crop requirements, while the combined use of the rotary adjustment platform and adjustable tilting platform enables deep placement under different terrain and angular conditions.

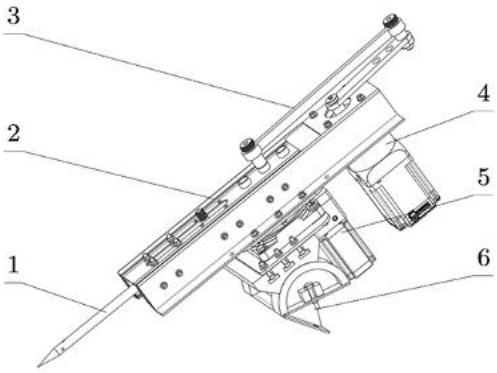


Fig. 4 - Structure of the angle-adjustable injection unit

1 - Injection needle; 2 - Sliding rail; 3 - Crank-slider injection mechanism; 4 - Drive motor; 5 - Rotary adjustment platform; 6 - Adjustable tilting platform

The injection needle directly affects fertilizer discharge through its internal flow channel and outlet geometry, particularly the number and diameter of the outlet holes. The required discharge performance was therefore evaluated through theoretical analysis and CFD simulation to provide a basis for needle design and parameter optimization. For each operating condition, the mean discharge rate of one injection needle was calculated from the injection duration and fertilizer volume as follows:

$$Q_{needle} = \frac{V}{t} \tag{1}$$

where:

Q_{needle} is the mean discharge flow rate of one injection needle (mL/s), V is *the fertilizer volume* delivered during one injection cycle (mL), and t is the injection duration (s).

Under steady-flow conditions, the discharge from each outlet hole is governed mainly by the pressure difference and effective flow area. Therefore, a theoretical discharge relation was established based on the Bernoulli equation as follows:

$$Q = C_d \bullet A \bullet \sqrt{\frac{2\triangle P}{\rho}} \tag{2}$$

where:

Q is the instantaneous flow rate through one outlet hole (m^3/s), C_d is the discharge coefficient, A is the outlet-hole area (m^2), ΔP is pressure difference between the needle inlet and outlets (Pa), and ρ is the density of the liquid fertilizer, taken as 1085 kg/m^3.

To ensure stable soil penetration of the injection needle under field conditions, the soil properties and loading characteristics were analyzed. Soil samples were collected from tobacco fields in Guiyang County, Chenzhou City, Hunan Province, China. Field measurements showed that the soil firmness ranged from 125 to 145 PSI, corresponding to approximately 0.86–1.00 MPa, indicating a relatively compact tillage layer.

During needle penetration, the soil resistance is mainly composed of cohesion, compressive resistance, frictional resistance and adhesion. These components jointly determine the total penetration resistance that must be overcome by the injection needle. Based on the force and failure characteristics of soil during penetration, the resistance model of the injection needle was established as follows *(You et al., 2017)*:

$$P = N + T + C_a + C \tag{3}$$

where: N is the compressive component of soil resistance, T is the frictional component, C_a is the adhesive component and C is the cohesive component of soil resistance.

In Fig. 5, P is the insertion force, which is equal in magnitude to the penetration resistance of the injection needle. N_1, T_1 and Ca_1 represent the normal force, frictional force and tangential adhesion acting on the needle tip, respectively, while N_2, T_2 and Ca_2 are the corresponding forces acting on the needle wall. C is the soil cohesive force.

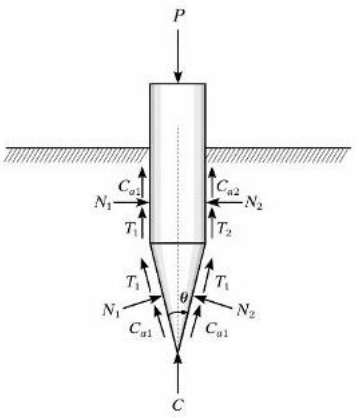


Fig. 5 - Force analysis of the injection needle during soil penetration

The penetration resistance analysis showed that the injection needle must overcome considerable soil resistance during insertion. Therefore, the injection mechanism should provide sufficient driving force while ensuring stable reciprocating motion at the required depth. In this study, an in-line crank-slider mechanism was adopted for the injection unit, as shown in Fig. 6. The mechanism has a simple structure, reliable transmission and good motion stability, and can convert the continuous rotary motion of the motor into the reciprocating linear motion of the injection needle, which is suitable for intermittent liquid-fertilizer deep placement.

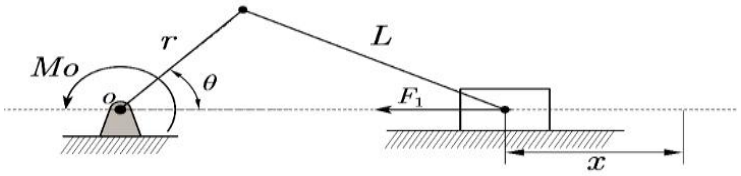


Fig. 6 - Crank-slider injection mechanism

The crank-slider injection mechanism mainly consists of a motor, reducer, crank, connecting rod, slider, and guide rail. According to the agronomic requirements and field operating conditions, the penetration depth of the injection needle was designed as 100–200 mm. To avoid interference between the needle and surface crops or mulch before soil entry, an idle-travel segment was included in the motion path. Therefore, the total slider stroke was designed to be no less than 300 mm, including 100 mm of idle travel and 100–200 mm of effective penetration depth. For the crank-slider mechanism, the slider stroke is determined by the crank radius and can be expressed as follows:

$$S = 2r \tag{4}$$

where: S is the slider stroke (mm) and r is the crank radius (mm).

According to the stroke requirement, the crank radius r was set to 160 mm, corresponding to a theoretical slider stroke of 320 mm. The connecting-rod length L was selected as 315 mm to achieve a compact layout and stable reciprocating motion.

Taking the crank center *O* as the coordinate origin, the horizontal and vertical directions were defined as the x- and y-axes, respectively. During needle penetration, the soil reaction force acting on the slider is transmitted to the crank through the connecting rod, thereby determining the torque requirement of the drive motor. The maximum penetration resistance calculated from the soil resistance model was taken as the design load. Based on the geometric constraints and static equilibrium of the crank-slider mechanism, the relationship among the required crank torque M_0, the penetration resistance F_1 and the connecting rod length L was established as follows:

$$M_0 = F_1 \bullet L \bullet \sin\theta \tag{5}$$

Control system

Due to the limited clearance of narrow ridge furrows and the uneven terrain in hilly areas, inter-row operation requires accurate positioning, stable motion, and safe control. Liquid-fertilizer deep placement also requires coordinated control of vehicle movement, injection-unit posture adjustment, needle penetration, and timed fertilizer injection. Therefore, an electronic control system based on a microcontroller unit (MCU) was developed for the small self-propelled liquid-fertilizer injector. The system forms a control chain comprising command input, signal processing, actuator driving, and status protection. As shown in Fig.7, it mainly consists of a remote controller, signal receiver, main control module, motor drivers, drive motors, solenoid valve, relays, and a 24 V battery.

Wireless remote control was adopted for human–machine interaction. Operator commands were transmitted to the MCU through the signal receiver, and the controller generated output signals according to the selected operating mode and preset logic. The travelling subsystem controlled the drive motors through motor drivers to achieve start–stop, steering, and speed regulation. The injection subsystem controlled the crank-slider drive motor and rotary stepper motor to complete posture adjustment and needle reciprocating motion. During injection, the relay actuated the solenoid valve according to the preset timing sequence, thereby enabling coordinated on–off control of liquid-fertilizer delivery.

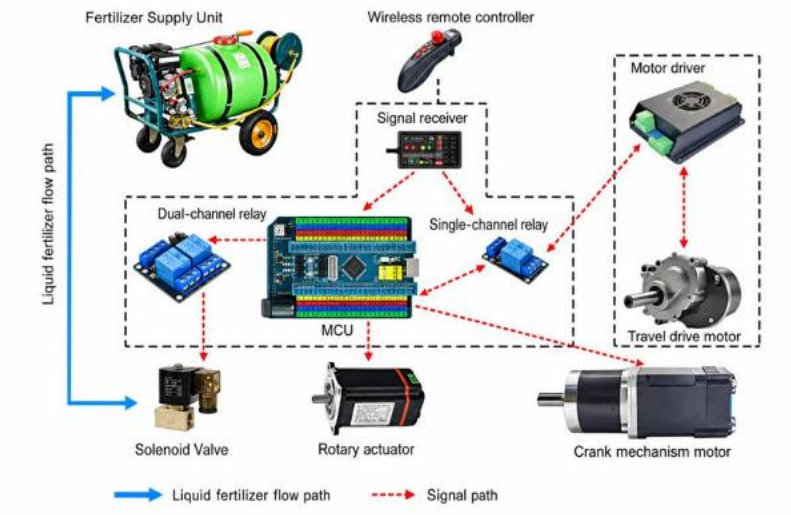


Fig. 7 - Hardware architecture of the control system

CFD simulation analysis of key components

To evaluate the discharge performance of the injection needle and quantify the effects of operating parameters on fertilizer volume per injection, a CFD model was established in ANSYS Fluent 2022 R1 *(Zawawi et al., 2018)*. The steady volumetric flow rate was obtained from the simulated outlet velocity field, and the fertilizer volume corresponding to a specified injection duration was calculated during post-processing using Eq. 7.

The liquid fertilizer was assumed to be an incompressible, single-phase Newtonian fluid uniformly supplied at the needle inlet. The internal flow was treated as steady, and gas–liquid interaction, evaporation, and particle transport were neglected. Under these assumptions, the flow was governed by the Reynolds-averaged continuity and momentum equations for an incompressible fluid.

$$\frac{\partial u}{\partial t}+(u\bullet\nabla)u=-\frac{1}{\rho}\nabla p+v\nabla^2 u \quad (6)$$

As shown in Fig.8, a three-dimensional model of the injection needle was created in SolidWorks 2021 and imported into ANSYS SpaceClaim and DesignModeler for geometry cleanup and internal flow-domain extraction. The computational domain was discretized using polyhedral cells in Fluent Meshing, with local refinement applied at the inlet and outlet-hole regions to resolve the relatively large velocity gradients near these boundaries.

A three-level mesh-independence test was conducted to assess the influence of mesh resolution on the numerical results. The four-outlet injection-needle model was evaluated at an inlet gauge pressure of 0.4 MPa, with all outlets maintained at 1 atm. Global mesh refinement was applied throughout the computational domain, while additional local refinement was imposed at the inlet and outlet regions to better resolve the flow gradients near these boundaries. The total volumetric flow rate through the four outlet holes was selected as the monitoring parameter. Except for the global and local mesh sizes and the resulting cell numbers, the geometry, fluid properties, boundary conditions, turbulence model, numerical schemes, and convergence criteria were kept unchanged. Therefore, differences in the calculated outlet flow rate were attributed solely to mesh refinement.

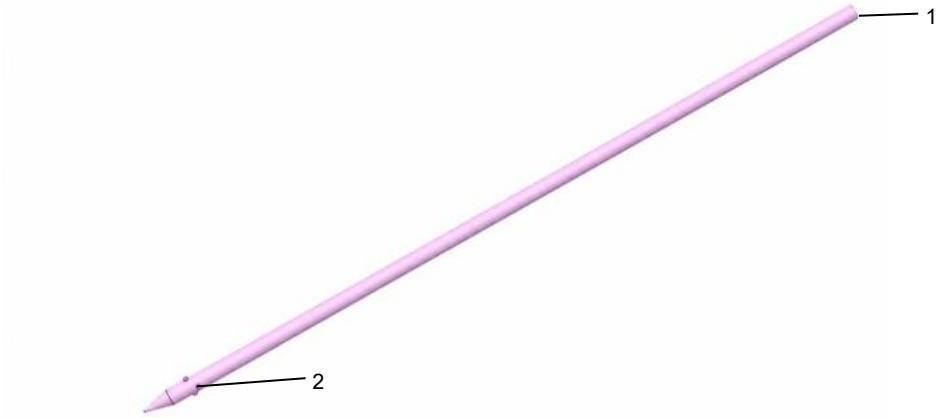


Fig. 8 - Three-dimensional model of the injection-needle flow domain

1 - inlet; 2 - outlet

Table 3

Mesh-independence assessment for the injection-needle internal-flow model

Mesh level	Global mesh size / mm	Local mesh size at the inlet and outlets / mm	Number of cells	Total outlet flow rate / (mL•s^{-1})
Coarse	0.60	0.07	550548	492.36
Medium	0.45	0.05	1565727	520.20
Fine	0.30	0.03	3495430	522.86

The total outlet flow rate increased from 492.36 mL·s-1 for the coarse mesh to 520.20 and 522.86 mL·s^{-1} for the medium and fine meshes, respectively. The relative difference between successive mesh levels decreased from 5.35% for the coarse-to-medium refinement to only 0.51% for the medium-to-fine refinement, demonstrating that further mesh refinement had a negligible influence on the predicted discharge performance. Accordingly, the medium mesh, with a global mesh size of 0.45 mm and a local mesh size of 0.05 mm at the inlet and outlet regions, was selected for subsequent simulations to achieve an appropriate balance between numerical accuracy and computational cost. The selected mesh comprised 1565727 polyhedral cells and 7322916 nodes.

The principal boundary conditions, fluid properties, and numerical settings used in the simulations are summarized in Table 4. In the Fluent post-processing stage, the fluid velocity at the outlet holes was used to calculate the volume as follows:

$$V = Q_v \bullet t = A \bullet v \bullet t \quad (7)$$

where: Q_v is the volumetric flow rate (m^3/s), A is the cross-sectional area through which fluid passes (m^2) and v is the fluid average velocity (m/s).

Table 4

Boundary conditions and numerical settings used in the CFD simulations

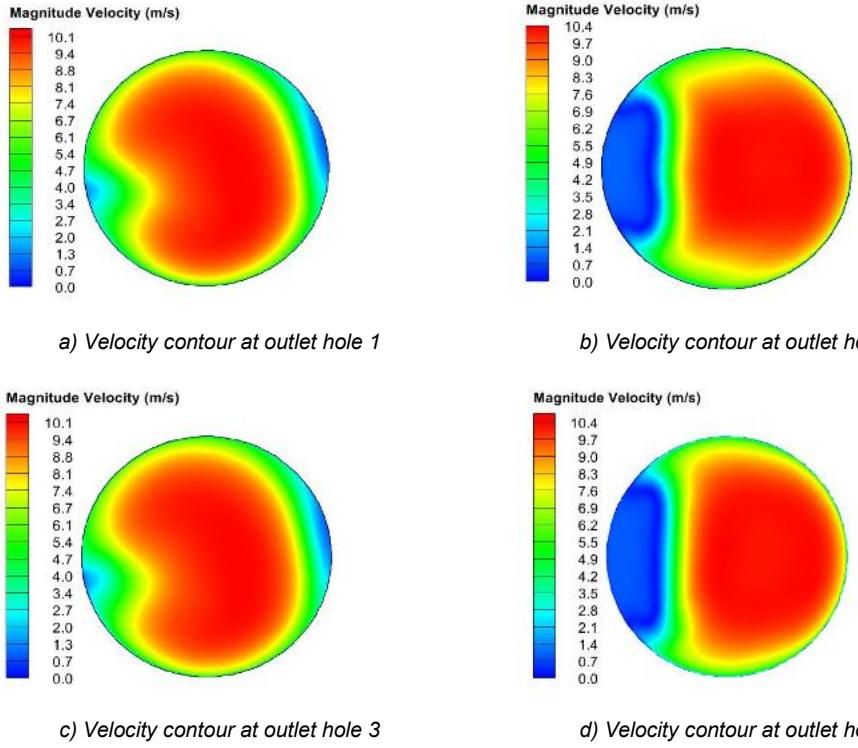
Item	Setting
Mesh	Polyhedral cells, global: 0.45 mm, inlet and outlet: 0.05 mm
Solver	Pressure-based, steady-state
Near-wall treatment	Standard wall functions
Turbulence model	Realizable *k-ε*
Pressure–velocity coupling	Coupled algorithm
Boundary conditions	Inlet: 0.2 - 0.6 MPa, outlet: 1 atm, no-slip walls
Fluid properties	ρ=1085 kg/m³, μ=1.05 × 10^{-3} Pa·s *(Zhang et al., 2018)*
Initialization	Standard initialization
Convergence criterion	Scaled residuals < 1 × 10^{-6}

A three-factor, three-level Box–Behnken design was generated using Design-Expert 13. Fertilizer volume per injection (Y_1) was taken as the evaluation index, while injection duration (X_1), injection pressure (X_2), and outlet-hole number (X_3) were selected as experimental factors. The factors and levels are listed in Table 5. In addition, velocity contours at the outlet holes under different working conditions were extracted to characterize the flow-field distribution in the outlet region. As an example, Fig. 9 shows the velocity contours obtained at an inlet pressure of 0.2 MPa with four outlet holes.

Table 5

Factors and levels for Box–Behnken design

Levels	Injection duration X_1 / (s)	Inlet pressure X_2 / (MPa)	Outlet-hole number X_3
-1	1	0.2	4
0	1.5	0.4	5
1	2	0.6	6



a) Velocity contour at outlet hole 1 *b) Velocity contour at outlet hole 2*

c) Velocity contour at outlet hole 3 *d) Velocity contour at outlet hole 4*

Fig. 9 - Outlet velocity contours of the injection needle at 0.2 MPa with four outlet holes

RESULTS

Simulation results and analysis of variance

The Box–Behnken factor combinations and corresponding CFD responses are presented in Table 6.

Table 6

Box–Behnken design matrix and simulated responses

Run	X_1	X_2	X_3	Y_1
1	1.5	0.4	5	778.3
2	2.0	0.6	5	1640.3
3	1.5	0.6	4	1473.1
4	2.0	0.2	5	465.3
5	1.5	0.2	6	400.3
6	1.5	0.4	5	785.2
7	1.5	0.6	6	1220.3
8	1.0	0.4	4	520.2
9	1.5	0.4	5	853.3
10	1.5	0.4	5	815.9
11	1.0	0.6	5	1095.4
12	1.0	0.4	6	626.9
13	2.0	0.4	4	958.2
14	2.0	0.4	6	976.4
15	1.0	0.2	5	188.2
16	1.5	0.4	5	848.2
17	1.5	0.2	4	192.3

Design-Expert 13 was used to fit a quadratic polynomial model to Y_1 and perform analysis of variance. Injection duration (X_1), inlet pressure (X_2), and the interactions X_1X_2 and X_2X_3 had highly significant effects on fertilizer volume per injection, while the quadratic term X_2^2 was significant. The remaining terms were not significant, as shown in Table 7.

Table 7

ANOVA results for the fitted regression model of fertilizer volume per injection

Source	Sum of Squares	Df	Mean Square	F-value	*p*-value
Model	2.60E+06	9	2.89E+05	235.18	< 0.0001**
X_1	3.24E+05	1	3.24E+05	263.91	< 0.0001**
X_2	2.19E+06	1	2.19E+06	1782.58	< 0.0001**
X_3	802.4	1	802.4	0.654	0.4453
X_1X_2	17929.21	1	17929.21	14.61	0.0065**
X_1X_3	1958.06	1	1958.06	1.6	0.2469
X_2X_3	53088.77	1	53088.77	43.27	0.0003**
X_1^2	419.37	1	419.37	0.3418	0.5771
X_2^2	7112.46	1	7112.46	5.8	0.0469*
X_3^2	5388.84	1	5388.84	4.39	0.0743
Residual	8588.75	7	1226.96		
Lack of fit	3790.85	3	1263.62	1.05	0.4611
Pure error	4797.91	4	1199.48		
Cor total	2.61E+06	16			

Note: * indicates significance at $p < 0.05$; ** indicates significance at $p < 0.01$.

From the analysis of variance of the regression model, the second-order response regression equation for Y_1 was obtained as follows:

$$Y_1 = 816.18 + 201.19X_1 + 522.87X_2 + 10.01X_3 + 66.95X_1X_2 - 22.13X_1X_3 - 115.2X_2X_3 - 9.98X_1^2 + 41.1X_2^2 - 35.77X_3^2 \quad (8)$$

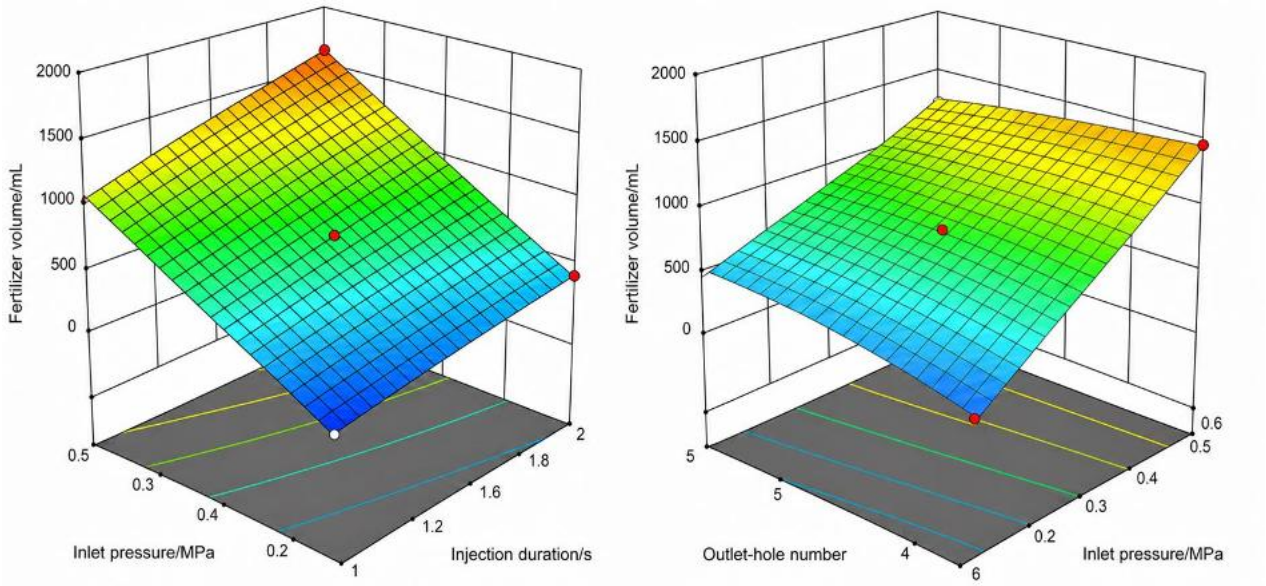
The model was highly significant, with a p-value below 0.01, an R^2 of 0.9967, an R^2_{adj} of 0.9925 and a CV of 4.30%, indicating an adequate fit for response-surface analysis and parameter optimization.

Response surface analysis

As shown in Table 7, the interaction terms X_1X_2 and X_2X_3 significantly affected fertilizer volume per injection, whereas X_1X_3 was not significant. Because X_2X_3 had the larger F-value, the response-surface analysis focused on the X_1X_2 and X_2X_3 interactions.

Figure 10a shows the interaction between injection duration and inlet pressure at a fixed outlet-hole number. Fertilizer volume per injection increased as both duration and pressure increased. The highest response occurred at the upper levels of both factors, whereas the lowest response occurred at the lower levels.

Figure 10b shows the interaction between inlet pressure and outlet-hole number at a fixed injection duration. Fertilizer volume per injection generally increased with inlet pressure, while the effect of outlet-hole number depended on the pressure level, consistent with the significant X_2X_3 interaction in Table 7.



a) Response surface of the effects of X_1X_2 on Y_1 *b) Response surface of the effects of X_2X_3 on Y_1*

Fig. 10 - Interactive effects of the experimental factors on the evaluation indicator

For tobacco transplanting, the target fertilizer volume per injection was set at 700 mL, while injection duration was minimized to improve operating efficiency. Numerical optimization was performed in Design-Expert 13, with Y_1 set to a target value of 700 mL, X_1 minimized and X_2 and X_3 constrained within their respective design ranges. The resulting preferred parameter combination consisted of an injection duration of 1 s, an inlet pressure of 0.45 MPa, and six outlet holes.

Field test

To evaluate the field feasibility of the optimized parameter combination and compare the measured response with the model prediction, a field validation test was conducted in March 2025 at the Fangyuan Tobacco Research Base in Guiyang County, Chenzhou City, Hunan Province, China. The test object was flue-cured tobacco at the transplanting stage, as shown in Fig. 11. The test was carried out according to GB/T 43908-2024 Water and Fertilizer Integrated Equipment *(SAC/TC 201, 2024)*. During the test, the ambient temperature was 19.2–25.3°C, soil moisture was 24.3%–27.9%, soil pH was 6.05–6.23, and soil firmness was 0.827–0.965 MPa.

One tobacco row was randomly selected for field validation. The plant spacing, ridge-top width, ridge-bottom width, and ridge height were 450, 450, 750, and 300 mm, respectively. The injection direction was perpendicular to the ridge surface, and the injection depth was fixed at 150 mm.

The optimized settings consisted of an injection duration of 1 s, an inlet pressure of 0.45 MPa, and six outlet holes. Five independent injections were performed at spatially separated positions along the selected row. Fertilizer volume per injection was measured using a flowmeter, and the mean value was compared with the model prediction.



Fig. 11 - Field test

The measured fertilizer volume per injection was 675.4 mL, compared with the model prediction of 700 mL, corresponding to a relative error of 3.51%. The agreement between measured and predicted values verified the predictive accuracy of the response surface model under the tested field conditions.

DISCUSSION

Effects of operating parameters and model applicability

The dominant effect of inlet pressure was consistent with the Bernoulli-based discharge relation, according to which the outlet flow rate increases approximately with the square root of the pressure difference. At a given steady volumetric flow rate, fertilizer volume per injection increased approximately linearly with injection duration. Although outlet-hole number alone was not significant within the investigated range, its interaction with inlet pressure was highly significant. Because the diameter of each outlet hole was kept constant, increasing the number of holes increased the total discharge area. However, it also redistributed the internal pressure and altered the local hydraulic losses among the outlets. Therefore, the effect of outlet-hole number cannot be evaluated independently of inlet pressure. This result demonstrates the importance of multi-factor optimization rather than simply selecting the maximum level of each operating parameter.

The relative difference of 3.51% between the predicted and measured fertilizer volumes was probably associated with the response delay of the solenoid valve, transient pressure fluctuations during valve opening and closing, and pressure losses in the pipeline and connectors. These dynamic effects were simplified in the steady-state CFD model. Therefore, the present model provided an acceptable estimate of average discharge under the tested operating condition, but it did not fully characterize the transient start–stop injection process. Future work should incorporate transient CFD analysis and synchronized measurements of pressure and flow rate to improve the description of the dynamic fertilizer-delivery process.

Comparison with previously reported liquid-fertilizer applicators

Previous liquid-fertilizer applicators have mainly focused on soil-punching mechanisms, site-specific fertilizer dosing, injection-trajectory optimization, and subsurface placement under particular cropping systems. The soil-punching system developed by da Silva et al. *(2017)* maintained the injection needle in a nearly vertical orientation to achieve fixed-point application, whereas da Silva and Magalhães *(2019)* synchronized soil punching and fertilizer delivery for site-specific dosing. The mechanisms reported by Wang et al. *(2016, 2017, 2018)* improved punching trajectories and operating efficiency, although vibration remained a concern under high-frequency operation *(Feng et al., 2017; Liu et al., 2016)*. In comparison, the present injector was specifically configured for inter-row operation in hilly and fragmented farmland by integrating a 45 kg narrow-track self-propelled chassis, a rotary–tilting posture-adjustment platform, and a crank-slider injection mechanism.

Table 8

Comparison of the proposed injector with previously reported liquid-fertilizer applicators

Study	Application mode	Primary contribution	Application context
da Silva et al. *(2017)*	Soil punching	Fixed-point placement	Sugarcane fields
da Silva and Magalhães *(2019)*	Site-specific injection	Variable-rate dosing	Site-specific management
Wang et al. *(2016, 2017, 2018)*	Mechanical punching	Trajectory optimization	Mechanized field operation
Zhou et al. *(2023)*	Targeted deep application	Delivery control	Field crop production
Present study	Self-propelled point injection	Posture-adjustable placement	Hilly and small plots

Overall, the comparison shows that the principal distinction of the proposed injector lies in the integration of lightweight self-propelled mobility, posture adjustment, and controllable point injection for hilly and fragmented farmland. Unlike previous studies that mainly emphasized punching trajectories, dosing control, or application performance under specific cropping systems, the present design gives greater consideration to machine maneuverability and injection orientation. However, because the reported systems were evaluated using different crops, operating conditions, and performance indicators, Table 8 provides a qualitative comparison rather than a direct performance ranking.

Limitations and generalizability

Field validation was conducted at a single tobacco research site under a limited range of soil moisture, pH, and penetration resistance. The results therefore demonstrate feasibility under the reported conditions but should not be generalized directly to sandy, highly cohesive, stony, or waterlogged soils. Soil texture, moisture content, bulk density, and compaction may affect needle penetration, liquid distribution in soil, and machine traction. Multi-site experiments covering different soil types, slope gradients, and moisture conditions are required to establish broader applicability. Future studies should also evaluate long-term durability, energy consumption, leakage, operational reliability, and crop-response benefits.

CONCLUSIONS

(1) A lightweight self-propelled liquid-fertilizer injector integrating a four-wheel-drive narrow-track chassis, a rotary–tilting posture-adjustment platform, and a crank-slider injection mechanism was developed for hilly and small-plot farmland. The compact configuration enabled controllable needle penetration and timed point injection while supporting inter-row maneuverability and terrain adaptation.

(2) The combined CFD-based discharge analysis and Box–Behnken response surface optimization quantified the individual and interactive effects of injection duration, inlet pressure, and outlet-hole number on fertilizer volume per injection. Inlet pressure and injection duration were identified as the dominant factors. Field validation under the tested condition showed satisfactory agreement between the predicted and measured fertilizer volumes.

(3) The developed injector provides an engineering reference for lightweight precision deep-placement equipment in fragmented hilly farmland and may support the development of similar systems for tobacco and other row crops. Because validation was limited to one site and one soil condition, further studies should evaluate machine performance under different soil textures, moisture contents, and slope conditions.

ACKNOWLEDGEMENT

This research was funded by the Chenzhou Tobacco Company of Hunan Province under the project Development of a Lightweight Tobacco Ridging Machine for the Nanling Hilly Region (CZYC2022JS05).

REFERENCES

[1] da Silva M.J., Franco H.C.J., Magalhães P.S.G., (2017), Liquid fertilizer application to ratoon cane using a soil punching method, Soil and Tillage Research, vol.165, pp.279-285. DOI: https://doi.org/10.1016/j.still.2016.08.020

[2] da Silva M.J., Magalhães P.S.G., (2019), Modeling and design of an injection dosing system for site-specific management using liquid fertilizer, Precision Agriculture, vol.20, no.4, pp.649-662. DOI: https://doi.org/10.1007/s11119-018-9602-5

[3] Feng J.L., Wang J.W., Zhou W.Q., Tang H., Liu C.X., (2017), Design and optimization of operating parameters for a punching mechanism with deformed elliptical gears (变形椭圆齿轮式扎穴机构设计与工作参数试验优化), Transactions of the Chinese Society for Agricultural Machinery, vol.48, no.4, pp.90-96. DOI: https://doi.org/10.6041/j.issn.1000-1298.2017.04.011

[4] Hesar L.G., İnce A., Ekinci K., Gücüm H., (2025), Design and effectiveness of an injection system for the application of liquid manure (slurry) to soil, Journal of Agricultural Engineering, vol.57, no.1. DOI: https://doi.org/10.4081/jae.2025.1912

[5] Hu H., Zhang Y.F., Chen W.Z., Zhao H.B., (2016), Current status and future prospects of maize topdressing machinery in China (我国玉米追肥机械发展现状与前景展望), Journal of Maize Sciences, vol.24, no.3, pp.147-152. DOI: https://doi.org/10.13597/j.cnki.maize.science.20160323

[6] Hunt D.E., Bittman S., (2021), Precision injection of dairy sludge on crop yield and N and P uptake in juvenile and mature no-till silage corn, Agronomy, vol.11, no.2, article 370. DOI: https://doi.org/10.3390/agronomy11020370

[7] Jiang Y., Wang R., Ding R., Sun Z., Jiang Y., Liu W., (2025), Research review of agricultural machinery power chassis in hilly and mountainous areas, Agriculture, vol.15, no.11, article 1158. DOI: https://doi.org/10.3390/agriculture15111158

[8] Li X., Wu X.M., Zhang F.G., Fu D.L., He H.L., Nie Y., (2018), Design and experiment of a two-row deep fertilizer applicator for one ridge (一垄双行深施肥机的设计与试验), Journal of Agricultural Mechanization Research, vol.40, no.4, pp.110-115. DOI: https://doi.org/10.13427/j.cnki.njyi.2018.04.021

[9] Liu C.X., Wang J.W., Tang H., Zhou W.Q., Wang Q., Yang W.P., (2016), Dynamic analysis and experiment of a liquid fertilizer hole-punching mechanism based on a Bézier curve (基于贝塞尔曲线的液肥扎穴机构动力学分析与试验), Transactions of the Chinese Society for Agricultural Machinery, vol.47, no.5, pp.115-122. DOI: https://doi.org/10.6041/j.issn.1000-1298.2016.05.016

[10] Sun Q.H., (2024), Effects of integrated water and fertilizer management on tobacco yield and quality in the tobacco-growing area of southern Henan Province (豫南烟区水肥一体化施肥对烟草产量及品质的影响), MSc Thesis, Henan Agricultural University, Zhengzhou/China. DOI: https://doi.org/10.27117/d.cnki.ghenu.2024.000391

[11] Wang J.W., Zhang C.F., Zhou W.Q., Pan Z.W., Tang H., Duo T.Y., (2016), Optimization design of an irregular gear planetary punching mechanism based on MATLAB simulation (基于 MATLAB 仿真的非规则齿轮行星系扎穴机构的优化设计), Transactions of the Chinese Society of Agricultural Engineering, vol.32, no.3, pp.22-28. DOI: https://doi.org/10.11975/j.issn.1002-6819.2016.03.004

[12] Wang J.W., Zhou W.Q., Li X., Feng J.L., Jiang D.X., Wang J.F., (2018), Design and experiment of a variable-speed punching mechanism based on an oval-circular gear planetary train (卵形-全正圆齿轮行星系变速扎穴机构设计与试验), Transactions of the Chinese Society for Agricultural Machinery, vol.49, no.5, pp.136-142. DOI: https://doi.org/10.6041/j.issn.1000-1298.2018.05.015

[13] Wang J.W., Zhou W.Q., Wang X., Li X., Wang J.L., Li S.W., (2017), Study on an inclined punching mechanism based on trajectory fitting using a cubic Lagrange curve (基于三次拉格朗日曲线拟合轨迹的斜置式扎穴机构研究), Transactions of the Chinese Society for Agricultural Machinery, vol.48, no.5, pp.79-85. DOI: https://doi.org/10.6041/j.issn.1000-1298.2017.05.009

[14] Xi X.B., (2018), Research on pneumatic blasting soil loosening and fertilizer injection methods and equipment (气爆松土注肥方法及装备研究), PhD dissertation, Yangzhou University, Yangzhou/China.

[15] Xi X.B., Zhang R.H., Shan X., Jin Y.F., Zhang J.F., (2017), Optimization design and experiment of the 3SFBQ-500 orchard pneumatic blasting soil-loosening and fertilization machine (3SFBQ-500 型果园气爆松土注肥机的优化设计与试验), Transactions of the Chinese Society of Agricultural Engineering, vol.33, no.24, pp.35-43. DOI: https://doi.org/10.11975/j.issn.1002-6819.2017.24.005

[16] Xing X., (2019), Design of a liquid fertilizer applicator for maize (玉米液肥施肥机设计), MSc Thesis, Hebei Agricultural University, Baoding/China. DOI: https://doi.org/10.27109/d.cnki.ghbnu.2019.000047

[17] You Y., He C.B., Wang D.C., Wang G.H., (2017), Study on the interaction between extremely narrow tillage teeth and soil (土壤耕作部件极窄刀齿与土壤作用关系研究), Transactions of the Chinese Society for Agricultural Machinery, vol.48, no.6, pp.50-58. DOI: https://doi.org/10.6041/j.issn.1000-1298.2017.06.006

[18] Zawawi M.H., Saleha A., Salwa A., Hassan N.H., Zahari N.M., Ramli M.Z., Muda Z.C., (2018), A review: Fundamentals of computational fluid dynamics (CFD), AIP Conference Proceedings, vol.2030, no.1, article 020252. DOI: https://doi.org/10.1063/1.5066893

[19] Zhang X.H., Luo W.Y., Yang Y.J., Chen J.R., Yang Y.B., (2018), Effects of different nitrate nitrogen and ammonium nitrogen ratios on the yield and main chemical components of flue-cured tobacco (不同硝态氮和铵态氮配比对烤烟产量、主要化学成分的影响), Jiangxi Agriculture, no.24, pp.30-32. DOI: https://doi.org/10.19394/j.cnki.issn1674-4179.2018.24.028

[20] Zhou W., An T., Wang J., Fu Q., Wen N., Sun X., Wang Q., Liu Z., (2023), Design and experiment of a targeted variable fertilization control system for deep application of liquid fertilizer, Agronomy, vol.13, no.7, article 1687. DOI: https://doi.org/10.3390/agronomy13071687

[21] *** People's Daily, (2021), Release of the main data results of the third national land survey (第三次全国国土调查主要数据成果发布), People's Daily, p.17.

[22] *** SAC/TC 201, (2024), GB/T 43908-2024 Water and fertilizer integrated equipment, National Technical Committee for Agricultural Machinery Standardization, State Administration for Market Regulation and Standardization Administration of China, Beijing/China.

PERFORMANCE ANALYSIS AND TESTING OF A CONICAL DEFLECTOR-TYPE SEED-METERING DEVICE UNDER VIBRATION
/
振动工况下锥面导流式排种器性能分析与试验

Jianxin DONG[1)], Hui QU*[1)], Wenxue DONG[1)], Shilin ZHANG[2)], Xiaojun GAO[3)], Zuoli FU[4)] , Lei WANG[5)]**
[1)] College of Mechanical and Electrical Engineering, Inner Mongolia Agricultural University, Huhhot 010018, China;
[2)] Mechanical and Electrical Engineering College, Gansu Agricultural University, Lanzhou 730070, China;
[3)] College of Engineering, Nanjing Agricultural University, Nanjing 210031, China;
[4)] College of Mechanical and Electronic Engineering, Northwest A&F University, Yangling 712100, China;
[5)] National Technology Innovation Center for Prataculture, Huhhot 010070, China;
Tel: +86 18402938247; E-mail: quhui333333@imau.edu.cn
DOI: https://doi.org/10.35633/inmateh-79-54

Keywords: *Discrete element, precision metering device, Model, Test, Vibration*

ABSTRACT
To address the deterioration in the seed-metering performance of mechanical seed-metering devices caused by vibration during field operation, a conical deflector-type seed meter was selected as the research object. A vibration-system model of the seed meter under field operating conditions was established, and the principal operating parameters affecting seed-metering performance were determined. The seed-metering process under vibration was then simulated using the discrete element method to investigate changes in the working angle of the seed population and its dynamic characteristics. In addition, vibration bench tests were conducted to evaluate the effects of vibration on seed-metering performance. The main results were as follows: (1) seed-filling efficiency, seed-clearing efficiency, and horizontal seed-throwing displacement were significantly affected by operating speed, vibration acceleration, and vibration frequency; (2) the adverse effect of vibration on seed-metering performance increased with increasing vibration acceleration but decreased with increasing operating speed or vibration frequency; and (3) when the vibration acceleration was below 0.63 g and the vibration frequency exceeded 4.28 Hz, the qualified-seed rate was greater than 95%, and the coefficient of variation of seed spacing was less than 20%. This study clarified the effects of vibration parameters on seed-metering performance and identified appropriate operating ranges, thereby providing theoretical support for the vibration-resistant design and optimization of mechanical seed meters.

ABSTRACT
针对机械式排种器在田间作业过程中易受振动影响导致排种性能下降的问题，选取锥面导流式排种器为研究对象，建立了排种器田间作业振动系统模型，推导出对排种性能产生影响的主要工况参数。运用离散元法对排种器振动工况下工作过程进行仿真试验，研究种群工作角度和动力学特性的变化规律，并通过振动台架试验测试了排种性能受到的影响。结果表明：1）排种器的充、清种效率及水平方向投种位移均受到作业速度、振动加速度和振动频率的显著影响；2）排种性能受到的负面影响随振动加速度的提升而增大，随作业速度和振动频率的提升而减小；3）当振动加速度小于 0.63 ，振动频率大于 4.28H 时，排种器的合格率高于 95%，粒距均匀性变异系数低于 20%。研究阐明了振动参数对排种性能的影响规律及其合理范围，为机械式排种器的抗振设计改进提供了理论支撑。

INTRODUCTION
High-speed precision seeding technology has become the development direction and trend of modern seeding technology due to its outstanding advantages, such as cost-saving, efficiency enhancement, and wide application (*Cujbescu et al., 2021; Emrah et al., 2021; Cay A. et al., 2018; Hijam J.S. et al., 2016*). As one of the carriers to realize high-speed and precision seeding technology, the mechanical precision metering device is still widely used in many countries because of its simple structure, low cost and easy maintenance (*Ibrahim et al., 2022; Shen et al., 2021; Karayel et al., 2022*).

By virtue of its inclined conical surface that guides seeds into the compound holes with reduced orientation requirements and randomness, the conical deflector-type seed-metering device enhances filling efficiency and thus qualifies as a high-speed precision mechanical seed-metering device for soybean planting.

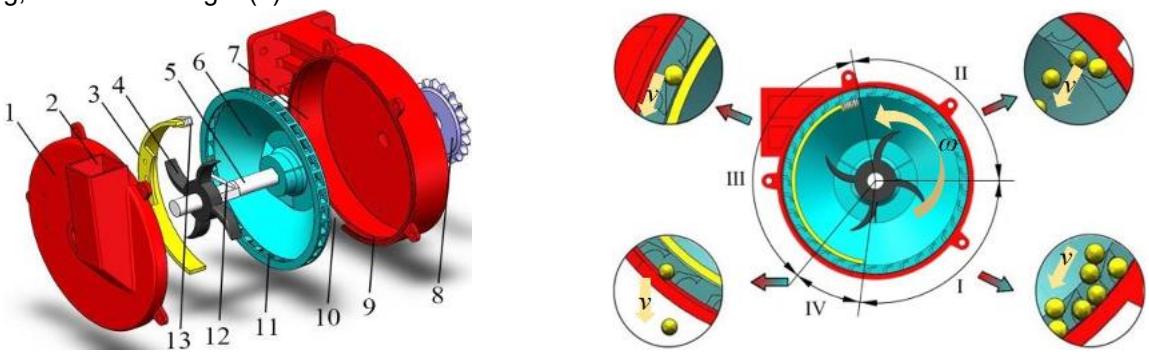
Through the design and optimization of its structure, the optimal structure of the seed-metering device is obtained, and verifies its excellent seed metering performance under the high-speed operation conditions through indoor bench test. Its qualified rate is higher than 97% when the operation speed is 6-12km/h (*Dong, 2021*). At present, studies had shown that the operation of seed-metering device suffers vibrations loads when the planter was working at high speed in the field (*Ku et al., 2021; Muhammad et al., 2021*). In this case, the working performance of the seed-metering device will be seriously affected, which may result in the deterioration of its working quality (*Zhang et al., 2016; Hao et al., 2017*). In order to improve the field operation performance of the planter, it is necessary to further research the influence of vibration on seed-metering device.

However, most studies on seed-metering devices have focused primarily on structural optimization, the effects of structural parameters on seed motion, and seed-metering performance under ideal laboratory conditions *(Chen et al., 2021; Liu et al., 2021; Zhao et al., 2026)*. By contrast, the motion state of seeds and their interaction with the seed-pickup mechanism under high-speed and vibrational operating conditions remain insufficiently understood. Consequently, the effects of vibration on the seed-metering process and performance have not yet been clearly established. Therefore, this study investigates the variation in seed-group motion and seed-metering performance under vibration.

MATERIALS AND METHODS

Conical deflector-type seed-metering device

The conical deflector-type seed-metering device mainly consisted of a seed-metering disc, rotating shaft, deflector, seed baffle, housing, and seed-feed tube, as shown in Fig. 1(a). The seed-metering disc, deflector, and rotating shaft were assembled as an integrated rotating unit driven by an external power source. The operating cycle comprised four stages: I, seed filling; II, seed clearing; III, seed carrying; and IV, seed throwing, as shown in Fig. 1(b).



a. Components of the seed-metering device *b. Operating principle of the seed-metering device*

Fig. 1 - Structure and operating principle of the conical deflector-type seed-metering device

1. Front housing 2. Seed-feed tube 3. Seed buffle 4. Deflector 5. Rotating shaft 6. Seed-metering disc 7. Rear housing 8. Sprocket 9. Arc-shaped guide rail 10. Seed outlet 11. Compound hole 12. Pin 13. Brush Ⅰ-Seed filling, Ⅱ-Seed clearing, Ⅲ-Seed carrying, and Ⅳ-Seed throwing

Vibration-system model of the seed-metering device

During field operation, the planter is subjected primarily to random vertical vibration loads *(Liu, 2016; Huang, 2018)*. Assuming that the excitation caused by tillage-surface unevenness can be represented by a sinusoidal waveform and that the planter remains in continuous contact with the ground during operation, the spring stiffness k and viscous damping coefficient c were treated as linear parameters *(Gao et al., 2021)*. Based on these assumptions, the field vibration model of the seed-metering device was simplified, as shown in Fig.2.

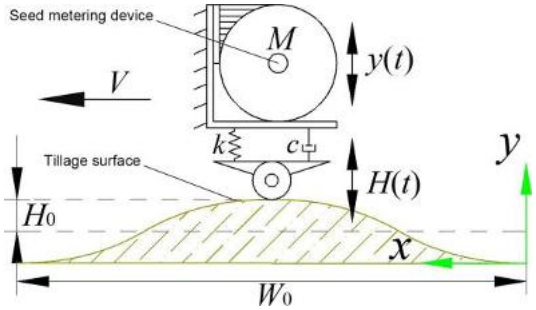


Fig. 2 - Field vibration-system model of the seed-metering device

As shown in Fig.2, the instantaneous displacement excitation in the vertical direction of the planter frame is expressed as follows:

$$H(t)=H_0 \sin \omega_0 t \tag{1}$$

where: ω_0 is the frequency of displacement excitation in the vertical direction (Hz), H_0 is the undulation amplitude of the cross section of the tillage surface compared with the reference plane (m).

Based on Eq. (1) the second derivative can be obtained, the acceleration excitation in the vertical direction of the planter frame is as follows:

$$H''(t) = \left| \frac{d^2 H(t)}{dt^2} \right| = H_0 \omega_0^2 \sin \omega_0 t \tag{2}$$

According to Eq. (2), the dynamic equilibrium equation of the vibration system of the seed-metering device is as follows:

$$M \frac{d^2 y(t)}{dt^2} + c \frac{dy(t)}{dt} + ky = MH_0 \omega_0^2 \sin \omega_0 t^2 \tag{3}$$

where: M is mass of seed metering system (kg).

From Eq. (3), the following expression is obtained:

$$\frac{d^2 y(t)}{dt^2} + 2\zeta \omega_n \frac{dy(t)}{dt} + \omega_n^2 y = \omega_n^2 H_0 \omega_0^2 \sin \omega_0 t \tag{4}$$

where: ω_n is natural frequency of seed metering system (Hz), ζ is the viscous damping ratio of the system.

By solving the steady-state response equation of sinusoidal excitation with frequency ω (4), a specific solution Eq. (5) is obtained, where the amplitude A and phase φ are given by the standard forced vibration amplitude / phase expression.

$$\begin{cases} \omega_0 = 2\pi V / W_0 \\ y(t) = A \sin(\omega_0 t + \varphi_0) \\ A = \dfrac{H_0 \omega_0^2}{\omega_n^2 \sqrt{(1 - \dfrac{\omega_0^2}{\omega_n^2})^2 + (2\zeta \dfrac{\omega_0}{\omega_n})^2}} \\ \varphi_0 = \arctan \dfrac{2\zeta \omega_0 \cdot \omega_n}{\omega_n^2 - \omega_0^2} \end{cases} \tag{5}$$

where: A is system displacement response amplitude (m), and φ_0 is phase difference of system displacement response (rad), V is operating speed of planter (km/h), and W_0 is wavelength of tillage surface section (m).

From Eq. (5):

$$\begin{cases} V_z(t) = \left| \dfrac{dy(t)}{dt} \right| = A\omega_0 \sin(\omega_0 t + \varphi_0) \\ a_z(t) = \left| \dfrac{d^2 y(t)}{dt^2} \right| = A\omega_0^2 \sin(\omega_0 t + \varphi_0) \end{cases} \tag{6}$$

where: $V_z(t)$ is the inertial velocity generated by vibration (m/s), and $a_z(t)$ is the inertial acceleration generated by vibration (m/s^2).

From Eq. (5) and (6), it can be concluded that the seed-metering device was mainly affected by vibration acceleration, vibration frequency and operating speed in the field working environment.

Simulation test

Simulation model and parameter setting

During the vibration process of the seed-metering device, the particle motion characteristics cannot be directly measured. The discrete element method is one of the methods to observe the seed motion characteristics during the vibration process. Therefore, the discrete element method is used in this study. To analyze the influence of vibration condition parameters on different working processes of seed-metering device, a 3D model of seed-metering device was established by using CAD software, and imported into EDEM software for simulation (Fig. 3).

The physical parameters and interaction parameters among the simulation model, the seed model and the material were consistent with the result of the previous research (*Dong, 2021*).

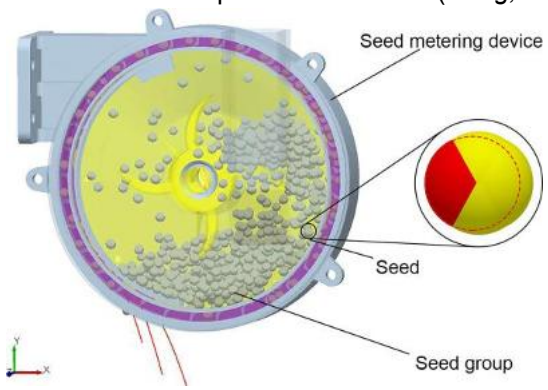


Fig. 3 - Simulation model of seed-metering device

Test method

According to the preliminary experimental results, the simulation was carried out at the speed of 6, 8, 10 and 12km/h (8km/h and above were classified as high-speed operation conditions), and the corresponding rotation speeds were 31.6, 40.8, 50.5, and 60.6r/min, respectively. The parameter value range of acceleration and frequency under vibration conditions were selected (*Wang et al., 2019; Zhang et al., 2016; Liu et al., 2016*). A total of 300 particles were generated in the simulation. The total simulation time was 3 s, and the data were recorded every 0.01 s.

Table 1

Simulation condition parameters

Working parameters	Numerical value	Fixed value
Operating speed [km·h^{-1}]	6; 8; 10; 12	10
Vibration acceleration [*g*]	0.3; 0.5; 0.7; 0.9;1.1	0.7
Vibration frequency [Hz]	3; 5; 7; 9; 11	7

The operating process of the seed-metering device under different vibration conditions was simulated using DEM software, and the velocity vectors of the seed particles were obtained, as shown in Fig.4.

In this study, a smaller seed-filling angle, θ (defined as the angle between the vertical direction and the position at which a seed is about to enter the compound hole) indicated higher seed-filling efficiency. Similarly, a larger seed-clearing angle, φ (defined as the angle between the vertical direction and the position at which the seed to be cleared leaves the compound hole) indicated higher seed-clearing efficiency. A larger seed-throwing angle, δ (defined as the angle between the position at which the seed completely leaves the compound hole and the edge of the seed outlet) indicated a greater horizontal seed-throwing distance.

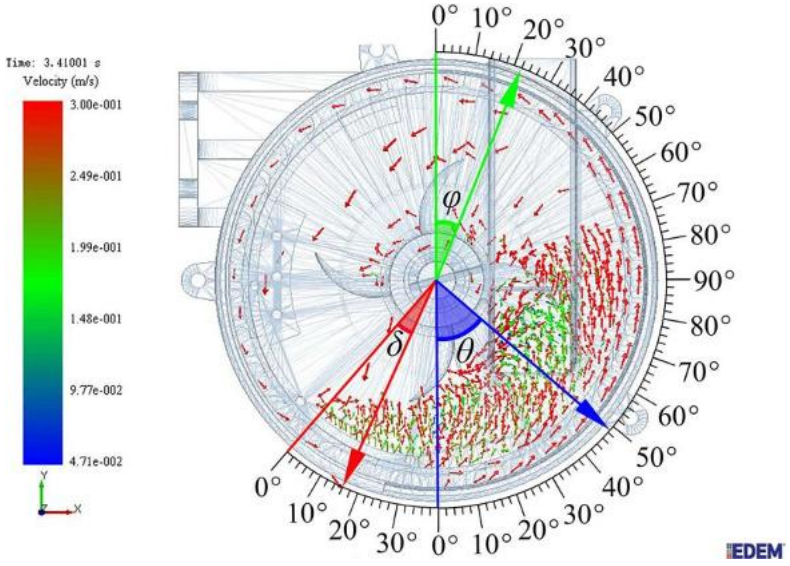


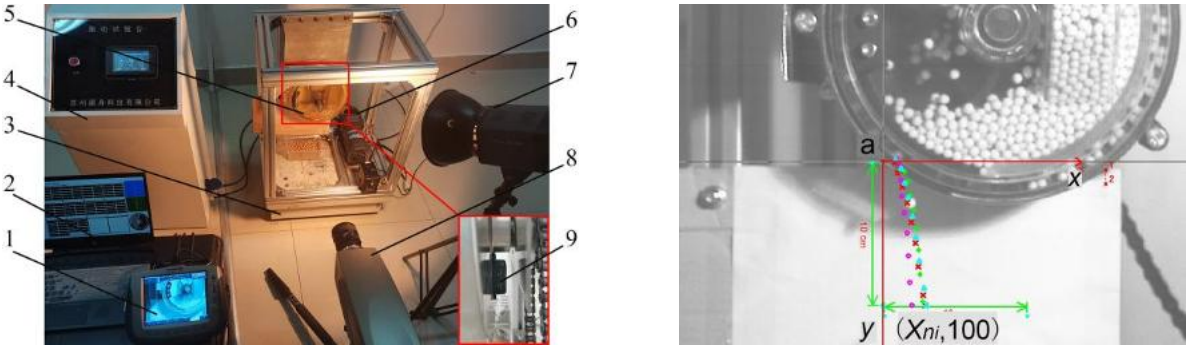
Fig. 4 - Working-angle distributions of seed particles under vibration

Vibration bench test

Test condition

To investigate the effects of vibration conditions on seed-metering performance, a vibration test bench was established in the Agricultural Machinery Laboratory at Northwest A&F University.

The vibration test bench consisted of a conical deflector-type seed-metering device, a mounting frame, a speed-control system, a vibration-excitation system, and an image-acquisition system, as shown in Fig. 5. The speed-control system comprised a 120 W variable-speed motor with an output torque of 8.5 N·m, a planetary gear reducer with a reduction ratio of 1:15, and a motor controller. The vibration-excitation system comprised a variable-frequency electromagnetic vibration table, a vibration-signal controller with a sinusoidal frequency range of 1-2000 Hz, and a vibration sensor equipped with Bluetooth 5.0 wireless transmission, a triaxial acceleration range of ±16 g, a frequency range of 0.2-200 Hz, and an output error not exceeding 1%. The image-acquisition system comprised a high-speed camera (Olympus i-SPEED 3), a computer running i-SPEED Suite software, a spatial grid panel, and a marker pen. Soybean seeds of the cultivar 'Suinong 26' were used in the tests. The thousand-seed mass was 0.21 kg, and the seed density was 1.267 g/cm^3.



a. Vibration test bench *b. Seed-position coordinate measurement*

Fig. 5 - Vibration bench test of the conical deflector-type seed-metering device

1. Image-acquisition unit; 2. Monitoring computer; 3. Vibration table; 4. Vibration-signal controller; 5. Conical deflector-type seed-metering device; 6. Drive unit; 7. High-intensity lam; 8. High-speed camera; 9. Vibration sensor

Test method

To evaluate the effects of the selected factors on seed-metering performance, a three-factor, three-level Box-Behnken design was employed. The seed-metering performance under different combinations of factor levels was measured using the vibration test bench for the seed-metering device. The factor levels were selected based on the significance of each factor observed in the simulation analysis of the different operating stages of the seed-metering device, as shown in Table 2. Each experimental treatment was repeated three times, and the mean value was used for analysis.

Table 2

Coded levels of the test factors

Level	Test factors		
	Rotational speed X1 [r·min^{-1}]	Vibration acceleration [*g*]	Vibration frequency [Hz]
-1	31.6	0.7	6
0	46.1	1.1	9
1	60.6	1.5	12

The response variables were the qualified-seed rate, Y_1, and the coefficient of variation of seed spacing, Y_2, as defined in Eq. (7). In the high-speed image-processing software, point "a" at the seed outlet was set as the coordinate origin, and the theoretical seed-throwing height was set to 100 mm. A seed i was classified as qualified when its spacing, X_i, ranged from 5 to 15 cm. The values of Y_1 and Y_2 were then calculated accordingly *(Shen et al., 2021)*.

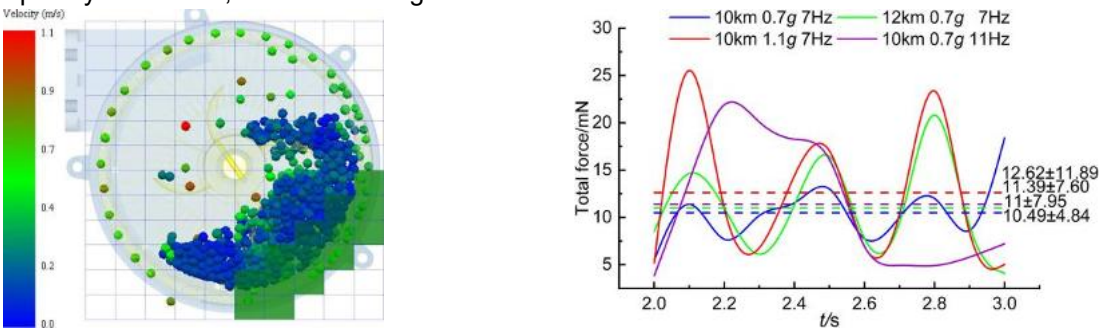
$$\begin{cases} Y_1 = \dfrac{N_1}{N} \times 100\% \\ X_i = X_{Ni} - X_{Ni\text{-}1} + S \\ \bar{X} = \dfrac{1}{N} \sum_{i=1}^{N+1} X_i \\ Y_2 = \dfrac{\sqrt{\dfrac{1}{N} \sum_{i=1}^{N} \left(X_i - \bar{X} \right)^2}}{\bar{X}} \times 100\% \end{cases} \quad (7)$$

where: Y_1 is the qualified-seed rate (%), $\bar{X}$ is the mean seed spacing (mm), Y_2 is the coefficient of variation of seed spacing (%), N_1 is the number of qualified seeds, N is the total number of seeds included in the statistical analysis, X_{Ni} is the abscissa of the i-th recorded seed, $X_{Ni\text{-}1}$ is the abscissa of the preceding recorded seed, S is the theoretical seed spacing, equal to 100 mm, and X_i is seed spacing of qualified seeds (mm).

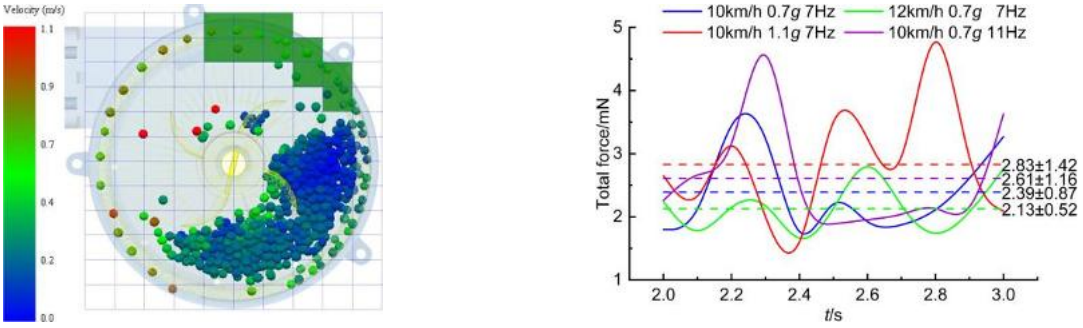
RESULTS AND DISCUSSION

Simulation results

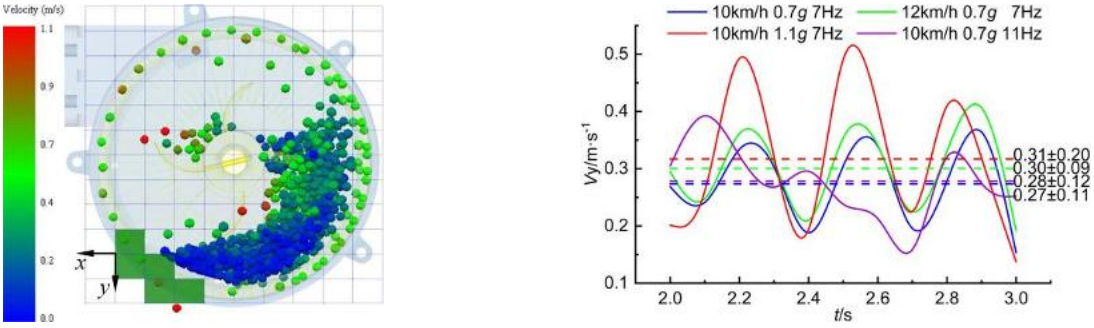
During post-processing of the simulation data, the external forces acting on the seeds in the seed-filling and seed-clearing zones and the downward vertical velocities of the seeds in the seed-throwing zone were statistically analyzed over the 2–3 s interval, as shown in Fig.6. For each simulation run, the seed-filling angle θ, seed-clearing angle φ, and seed-throwing angle δ were recorded from 1 to 5 s at intervals of 0.05 s. At each sampling time, the maximum value of each angle was selected, and the corresponding mean values were subsequently calculated, as shown in Fig.7.



a. Total force acting on the seed group in the seed-filling zone



b. Total force acting on the seed group in the seed-clearing zone



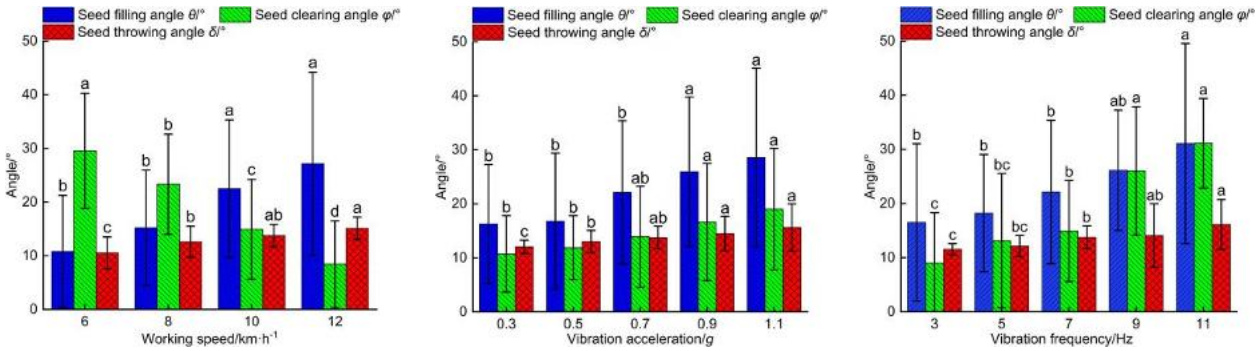
c. Vertical velocity of the seed group in the seed-throwing zone

Fig. 6 - Effects of vibration on seed-group dynamics

As vibration acceleration, vibration frequency, or operating speed increased, the fluctuations in the resultant force acting on the seeds in the seed-filling zone became more pronounced, and the seed-filling zone expanded, as shown in Fig. 6(a). Meanwhile, the mean seed-filling angle, θ, increased, as shown in Fig.7.

Increasing the vibration acceleration or vibration frequency intensified the fluctuations in the resultant force acting on the seeds in the seed-clearing zone and expanded this zone, as shown in Fig. 6(b). Correspondingly, the mean seed-clearing angle, φ, increased, as shown in Fig. 7(b) and (c), indicating improved seed-clearing efficiency. By contrast, increasing the operating speed reduced the force fluctuations and narrowed the seed-clearing zone. The mean value of φ also decreased, as shown in Fig. 7(a), indicating a reduction in seed-clearing efficiency. The vertical seed velocity, Vy, generally increased with operating speed, as shown in Fig. 6(c). The horizontal velocity, Vx, also increased, resulting in a larger mean seed-throwing angle, δ, and greater horizontal seed-throwing displacement, as shown in Fig. 7.

Overall, seed-filling efficiency, seed-clearing efficiency, and horizontal seed-throwing displacement were significantly affected by operating speed, vibration acceleration, and vibration frequency. Increasing any of these three factors reduced seed-filling efficiency and increased horizontal seed-throwing displacement. However, their effects on seed-clearing efficiency differed: increasing vibration acceleration or vibration frequency improved seed-clearing efficiency, whereas increasing operating speed reduced it.



a. Operating speed *b. Vibration acceleration* *c. Vibration frequency*

Fig. 7 - Effects of operating conditions on the seed-filling, seed-clearing, and seed-throwing angles

Bench test result

Establishment of regression model

The experimental results presented in Table 3 were subjected to analysis of variance (ANOVA), and the results are summarized in Table 4. As shown in Table 4, the model *P*-values for both Y_1 and Y_2 were less than 0.01, whereas the lack-of-fit *P*-values were greater than 0.05. These results indicate that the regression models were highly significant and that the lack of fit was not significant. The coded regression equations relating Y_1 and Y_2 to the test factors were established as follows:

$$Y_1 = 73.17 + 11.20X_1 - 18.68X_2 + 10.99X_3 + 6.22X_1X_2 - 4.16X_1X_3 + 9.09X_2X_3 - 1.62{X_1}^2 + 4.76{X_2}^2 + 2.49{X_3}^2 \quad (8)$$

$$Y_2 = 24.01 - 3.81X_1 + 6.29X_2 - 1.09X_3 - 4.44X_1X_2 + 3.11X_1X_3 - 0.89X_2X_3 - 0.87{X_1}^2 - 0.19{X_2}^2 + 0.36{X_3}^2 \quad (9)$$

Based on the *F*-values of the individual factors, their effects on both Y_1 and Y_2 were ranked in descending order as follows: vibration acceleration, operating speed, and vibration frequency.

Test result **Table 3**

Test number	Factors			Y_1[%]	Y_2[%]
	X_1[r·min^{-1}]	X_2[g]	X_3[Hz]		
1	-1	-1	0	91.33	14.47
2	1	-1	0	99.47	18.35
3	-1	1	0	40.7	36.42
4	1	1	0	73.73	33.73
5	-1	0	-1	44.27	22.56
6	1	0	-1	76.8	17.28

Test number	Factors			Y_1[%]	Y_2[%]
	X_1[r·min^{-1}]	X_2[g]	X_3[Hz]		
7	-1	0	1	79.6	23.5
8	1	0	1	95.5	23.48
9	0	-1	-1	99.3	18.42
10	0	1	-1	44.6	31.28
11	0	-1	1	98.07	17.84
12	0	1	1	79.73	29.15
13	0	0	0	72.93	26.78
14	0	0	0	74.13	19.23
15	0	0	0	75.6	27.61
16	0	0	0	72.27	18.61
17	0	0	0	70.93	21.81

Table 4

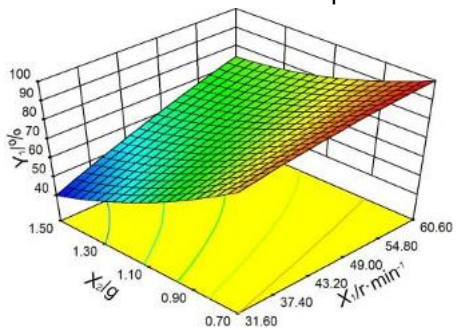
Variance analysis

Source	Y_1[%]				Y_2[%]			
	df	Mean Square	F	P	df	Mean Square	F	P
Model	9	605.38	59.40	<0.0001	9	62.92	7.24	0.0081
X_1	1	1003.52	98.47	<0.0001	1	115.90	13.33	0.0082
X_2	1	2790.42	273.81	<0.0001	1	316.64	36.41	0.0005
X_3	1	966.46	94.83	<0.0001	1	9.55	1.10	0.3295
$X_1 X_2$	1	154.88	15.20	0.0059	1	78.68	9.05	0.0197
$X_1 X_3$	1	69.14	6.78	0.0352	1	38.63	4.44	0.0730
$X_2 X_3$	1	330.51	32.43	0.0007	1	3.15	0.36	0.5662
X_{12}	1	11.10	1.09	0.3314	1	3.16	0.36	0.5656
X_{22}	1	95.36	9.36	0.0184	1	0.15	0.018	0.8977
X_{32}	1	26.19	2.57	0.1530	1	0.53	0.061	0.8115
Lack of fit	3	19.54	6.15	0.0559	3	62.92	0.70	0.5995
Pure error	4	3.18			4	6.98		

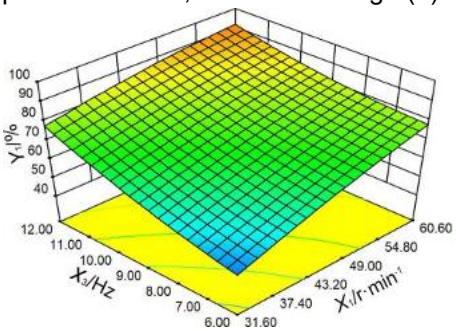
Values of P less than 0.05 indicate model terms are significant.

Response surface analysis

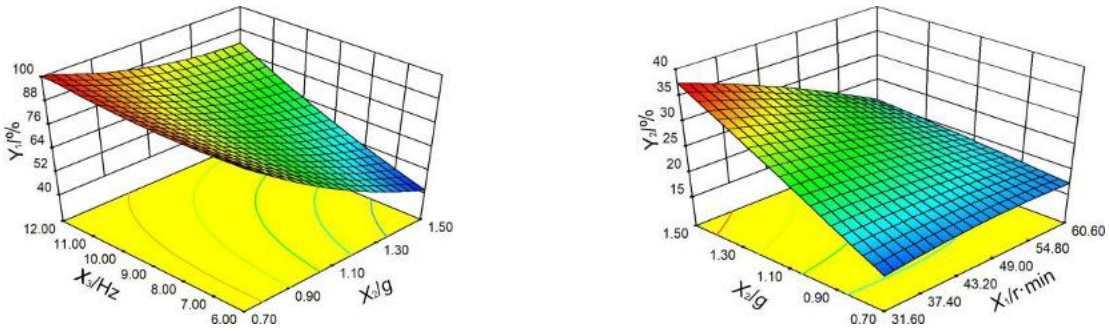
Design-Expert software was used to generate response surfaces illustrating the interactions between pairs of factors, as shown in Fig.8. The qualified-seed rate decreased with increasing vibration acceleration, although this decline became less pronounced as rotational speed increased, as shown in Fig.8(a). The qualified-seed rate increased with increasing vibration frequency, but the rate of increase decreased as rotational speed increased, as shown in Fig. 8(b). Similarly, the qualified-seed rate decreased with increasing vibration acceleration, while the magnitude of this decrease was reduced at higher vibration frequencies, as shown in Fig.8(c). The coefficient of variation of seed spacing increased with increasing vibration acceleration, although this increase became less pronounced as rotational speed increased, as shown in Fig.8(d).



a. $Y_1 = f(X_1, X_2, 9)$



b. $Y_1 = f(X_1, 1.1, X_3)$



c. $Y_1=f(46.9, X_2, X_3)$ *d.* $Y_2=f(X_1, X_2, 9)$

Fig. 8 - Response surfaces showing the effects of factor interactions on the response variables

The analysis indicated that increasing vibration acceleration intensified fluctuations in the external forces acting on the seeds and increased radial runout. During seed clearing, these effects promoted premature seed removal and increased variability in the seed-throwing trajectories. By contrast, increasing rotational speed or vibration frequency mitigated these effects.

Accordingly, the adverse effect of vibration on seed-metering performance increased with increasing vibration acceleration but decreased with increasing operating speed or vibration frequency.

To ensure satisfactory seed-metering performance over the tested range of operating speeds, the regression models were subjected to multi-objective optimization using a qualified-seed rate, Y_1, greater than 95% and a coefficient of variation of seed spacing, Y_2, less than 20% as constraints. The objective function is given in Eq. (10):

$$\begin{cases} Y_1(X_1, X_2, X_3) \geq 95\% \\ Y_2(X_1, X_2, X_3) \leq 20\% \\ 31.6\text{r/ min} \leq X_1 \leq 60.6\text{r/ min} \\ \max X_2(X_2 \leq 1.5\text{g}) \\ \min X_3(X_3 \leq 12\text{Hz}) \end{cases} \quad (10)$$

According to Eq. (10), the optimal parameter ranges were X_2<0.63 g and X_3>4.28 Hz. To verify the reliability of the optimization results, validation tests were conducted at rotational speeds (X_1) of 31.6, 46.1, and 60.6 r·min^{-1}. The qualified-seed rate, Y_1, exceeded 98.8%, while the coefficient of variation of seed spacing, Y_2, remained below 17.31%. These results satisfied the optimization objectives.

CONCLUSIONS

This study quantified the relationships between field vibration parameters and the performance of a mechanical conical deflector-type seed-metering device, a device type whose vibration behavior has received limited attention compared with pneumatic and finger-type seed meters. By linking seed-scale DEM simulations with bench-test measurements, the combined effects of vibration acceleration, vibration frequency, and operating speed on the seed-filling, seed-clearing, and seed-throwing processes were determined, and threshold conditions for acceptable seed-metering performance were identified.

1. Seed-filling efficiency, seed-clearing efficiency, and horizontal seed-throwing displacement were significantly affected by operating speed, vibration acceleration, and vibration frequency. Increasing any of these three factors reduced seed-filling efficiency and increased horizontal seed-throwing displacement. Increasing operating speed also reduced seed-clearing efficiency.

2. Based on the *F*-values of the main-effect terms, the effects of the factors on the qualified-seed rate and the coefficient of variation of seed spacing were ranked in descending order as follows: vibration acceleration, operating speed, and vibration frequency. The adverse effect on seed-metering performance increased with increasing vibration acceleration but decreased with increasing operating speed or vibration frequency.

3. Multi-objective optimization showed that when the vibration acceleration was below 0.63 g and the vibration frequency exceeded 4.28 Hz, the qualified-seed rate was greater than 95%, and the coefficient of variation of seed spacing was less than 20%.

ACKNOWLEDGEMENT

This work was supported by the National Technology Innovation Center for Prataculture Special fund for innovation platform construction (Grant No. CCPTZX2024GJ14).

REFERENCES

[1] Cay, A., Kocabiyik, H. & May, S. (2018). Development of an electro-mechanic control system for seed-metering unit of single-seed corn planters: Part II: Field performance. *Computers and Electronics in Agriculture*., 145, 11-17. https://doi.org/10.1016/j.compag.2017.12.021.

[2] Cujbescu, D., Găgeanu, I., Persu, C. et al. (2021). Simulation of Sowing Precision in Laboratory Conditions. *Appl. Sci.* 11, 6264. https://doi.org/10.3390/app11146264.

[3] Dong, J. (2021). *Design and experiment of cone diversion type soybean high speed precision seed-metering device*. [Master Dissertation]. Northwest A&F University.

[4] Emrah, K. (2021). Field-scale evaluation of parameters affecting planter vibration in single seed planting. *Measurement*. 184,109959. DOI:10.1016/J.MEASUREMENT.2021.109959.

[5] Gao, W., Lin, J., Li, B., Wang, W. & Gu, S. (2021). Vibration characteristics analysis and structural optimization of straw deep bury and returning machine. *Journal of Jilin University*, 1-11[2021-08-04].

[6] Hao, Y., Cui, T., Bora, G., Zhang, D., Wei, J., He, X., & Yang, L. (2017). Development of an instrument to measure planter seed meter performance. *Applied Engineering in Agriculture*. 33(1), 31-40. https://doi.org/10.13031/aea.11974.

[7] Hijam, J. S., Dipankar, D., & Pramod, K. S., (2014). Development and evaluation of metering mechanism for multi-crop planter for hilly regions. *Poljoprivredna Tehnika*, 39(4), 21-33.

[8] Huang, X. (2018). *Research on the vibration characteristics of seeding apparatus for corn no-tillage planter*. [Master Dissertation]. Jilin Agriculture University.

[9] Ibrahim, E.J., Elfadil, A.D., Abdallah, A.D. (2022). Laboratory and Field Investigation Comparison for Seed Distribution Accuracy of a Multi-Rows Pneumatic Plate Metering Device. *Asian Journal of Agriculture and Food Sciences*. Volume 10-Issue 2. DOI:10.24203/ajafs.v10i2.6942.

[10] Karayel, D., Güngör, O., Šarauskis E. (2022). Estimation of Optimum Vacuum Pressure of Air-Suction Seed-Metering Device of Precision Seeders Using Artificial Neural Network Models. *Agronomy* 12,1600. https://doi.org/10.3390/agronomy12071600.

[11] Ku, S.E. (2021). Field-scale evaluation of parameters affecting planter vibration in single seed planting. *Measurement*. 184,109959. DOI:10.1016/J.MEASUREMENT.2021.109959.

[12] Liu, F., Lin, Z., Li, D., & Zhang, T. (2021). Design optimization and performance test of magnetic pickup finger seed metering device. *INMATEH-Agricultural Engineering*, 63(1).

[13] Liu, Y., Liu, F., Zhao, M., Dong, S., & Zhang, X. (2016). Vibration test and vibration theoretical analysis of air suction no tillage planter. *Journal of China Agricultural University*, 21 (10), 109-116.

[14] Liu, Y., Zhao, M., Liu, F., Yang, T., Zhang, T. & Li, F. (2016). Simulation and optimization of working parameters of air Suction metering device based on discrete element. *Transactions of the CSAM*. 2016, 47(7): 65-73.

[15] Mao, X., Yi, S., Tao, G., Yang, L., Liu, H., & Ma, Y. (2015). Experimental study on seed-filling performance of maize bowl-tray precision seeder, *International Journal of Agricultural and Biological Engineering*, vol.8, issue 2, pp.31-38; https://doi.org/10.3965/j.ijabe.20150802.1809.

[16] Muhammad, D., Rozzaq H.A., Makbul H. (2021). Multiobjective Optimization of Vibro-Pneumatic Separator Using Full Factorial Design. *Advances in Biological Sciences Research*. 19, 380-386. Doi:10.2991/absr.k.220305.059.

[17] Shen, H., Zhang, J., Chen, X., Dong, J., Huang, Y. & Shi, J. (2021). Development of a guiding-groove precision metering device for high-speed planting of soybean. *Transactions of the ASABE*. 64.3: 1113-1122. https://doi.org/10.13031/trans.14307.

[18] Yulong, C., Meng, Z., Zeqi, L., Yubin, L., Lili, Y., Pengqiang, J., & Xiang, Y. (2021). Design and experiment of seed agitator for vertical disk seed metering device. *INMATEH-Agricultural Engineering*, *63*(1), pp.179-188. DOI: https://doi.org/10.35633/inmateh-63-18.

[19] Zhang, T., Liu, F., Zhao, M., Liu, Y., Li, F., Chen, C., Zhang, Y. (2016). Movement law of maize population in seed room of seed metering device based on discrete element method. *Transactions of the CSAE*. 32(22): 27-35.

SOIL–AIR THERMAL ENVIRONMENT IN CHINESE SOLAR GREENHOUSES WITH EARTHEN WALLS
/
中国土墙日光温室土壤-空气热环境研究

Kaixiao CHENG[2)], Hong YANG[1*)], Weiwei CHENG[1)]
[1)] Shanxi Agricultural University, College of Urban and Rural Construction, Taigu / China
[2)] Shanxi Agricultural University, College of Agricultural Engineering, Taigu / China
Tel: +86-0354-6287420; E-mail: 17735460705@163.com
Corresponding author: Hong Yang
DOI: https://doi.org/10.35633/inmateh-79-55

Keywords: *solar greenhouse with earthen walls; air temperature; soil temperature; synergy patterns*

ABSTRACT
Chinese solar greenhouses with earthen walls can provide a suitable environment for crop production during winter. In this study, air and soil temperatures inside solar greenhouses in Shanxi Province, China, were monitored from January 1 to March 31, 2024. The results showed that, during nighttime, vertical air-temperature variation among the measurement points was greater than horizontal variation. Zones with approximately equal soil temperatures were also identified among the measurement points. The onset of the increase in weighted mean soil temperature occurred 4 h later than that of the weighted mean air temperature, whereas the onset of the decrease in weighted mean soil temperature occurred 5 h later. These findings provide a data-based foundation for regulating the thermal environment inside Chinese solar greenhouses with earthen walls.

摘要
中国土墙日光温室在冬季期间可为作物提供适宜的生长环境,本研究在 2024 年 1 月 1 日-2024 年 3 月 31 日期间对中国山西地区日光温室内空气温度与土壤温度进行测定，其结果显示：在夜间沿测点温度沿竖向的变化速率大于其沿横向的变化速率；土壤测点温度存在近似相等的区域；土壤加权温度升高界点比空气加权温度升高界点滞后 4 个小时，土壤加权温度下降界点比空气加权温度下降界点滞后 5 个小时。该研究可为日光温室内热环境调控提供数据支撑。

INTRODUCTION

Chinese solar greenhouse (CSG) are widely used for winter vegetable production in northern China, where solar energy collection, enclosure insulation and thermal storage help maintain a suitable crop-growing microclimate *(Wang et al., 2026; Sun et al., 2025; Liu et al., 2023)*. Their winter thermal environment is jointly affected by outdoor weather, covering materials, north walls, indoor air, crops and soil. Physical and transient models have shown that greenhouse air temperature is controlled by radiation, convection, conduction, ventilation or infiltration, ground heat exchange and heat storage processes *(Sun et al., 2026; Zhao et al., 2023; Xu et al., 2017; Joudi et al., 2015;)*. Therefore, understanding the internal thermal response of CSG remains important for winter environmental regulation and low-temperature risk management.

Indoor air and soil are two key thermal components with different functions. Air temperature directly affects the canopy-level environment, while soil temperature determines root-zone thermal conditions and influences root activity, water uptake and crop stress. Because greenhouse soil absorbs heat during the daytime and releases part of it during cooling periods, the air-soil temperature relationship is affected by heat storage and thermal inertia. Previous studies have reported significant air-soil temperature correlations *(Chang et al., 2010)* soil-temperature hysteresis under different moisture and fertilizer conditions *(Lin et al., 2010)* and the influence of soil moisture on soil thermal conductivity and heat capacity *(Al-Kayssi et al., 2010)*. Thus, this relationship should be viewed as a dynamic response rather than a simple synchronous correlation.

Kaixiao Cheng, Lecturer M.S.Eng.; Hong Yang, Lecturer M.S.Arc; Weiwei Cheng, Associate Professor. PhD. Eng.

Recent studies have shown that greenhouse soil temperature varies with depth and spatial position: fluctuations generally weaken with depth, peak or valley times may be delayed, and marginal effects or structural asymmetry can produce horizontal differences *(Jiao et al., 2025; Cheng et al., 2024; Cheng et al., 2014)*. Studies on ground thermal storage, soil-wall-air thermal environment and soil heat loss have further emphasized the role of soil in greenhouse heat exchange *(Li et al., 2024; Zhang et al., 2025; Luo et al.,2025)*. Meanwhile, mechanistic, transient and temperature-wave models have described CSG heat transfer processes *(Zhang et al., 2023)* and data-driven models such as LSTM, Attention-LSTM, RF-XGBoost and Transformer-BiLSTM have improved greenhouse air or soil temperature prediction *(Li et al., 2024; Liu et al., 2026; Yu et al., 2025)*. However, most studies still focus on distribution, zoning, heat-loss evaluation or prediction accuracy, with limited explanation of how indoor air temperature fluctuations propagate into multi-depth soil through time lag, phase delay, amplitude attenuation and hysteresis.

Although previous studies provide an important foundation, several issues remain insufficiently addressed. First, the time lag between indoor air temperature changes and soil-temperature responses at different depths is still not clearly quantified. Second, amplitude attenuation, phase delay and thermal hysteresis are often discussed separately or only qualitatively. Third, the effects of spatial position, soil depth, soil moisture and weather condition on air-soil thermal response have not been systematically compared. These gaps limit our understanding of how air temperature waves propagate into greenhouse soil.

In summary, existing research has provided an important foundation for understanding soil temperature distribution, heat transfer processes in greenhouses and temperature forecasting; however, there is still a lack of clear quantification of the patterns of co-variation between indoor air temperature fluctuations and soil temperatures at different depths. In light of the above issues, this paper utilises field-measured air temperature and soil temperature data from solar greenhouses across different spans to analyse the dynamic coupling relationship between indoor air temperature and soil temperature at multiple depths, thereby providing a reference for the analysis of air–soil thermal responses in solar greenhouses and for the management of root-zone temperatures during winter.

Soil temperature, compared with air temperature, exhibited time lags and complexity. Even a difference of just 1°C can have a significant impact on crop growth and development *(Sypka et al., 2016)*. The novelty of this study lies in the quantitative analysis of the thermal lag between indoor air and soil temperatures using multi-point measurements in a Chinese solar greenhouse with earthen walls. The obtained results provide engineering guidance for greenhouse thermal management, energy-saving strategies and intelligent environmental control.

MATERIALS AND METHODS

In this experiment, soil and air temperatures in the greenhouse were measured between 1 January 2024 and 30 March 2024, with measurements taken at 30-minute intervals.

Experimental Greenhouse

This experiment was conducted in the Taigu area of Jinzhong City, Shanxi Province, at 112.50° east longitude and 37.37° north latitude. The experimental greenhouse was a sun-heated structure with earthen walls; the southern side was covered with plastic sheeting, whilst the eastern, western and northern sides consisted of earthen walls. There were 1-metre-wide walkways along the southern and northern edges of the greenhouse, providing access for pedestrians and space for the laying of pipes. The sun-heated greenhouse faced south, with a length of 100 metres, a span of 10 metres and a ridge height of 4.5 metres.

Test Equipment

Indoor and outdoor air temperature: Measurements were taken using the RC-5 USB temperature logger manufactured by Jingchuang Electric Co., Ltd. (as shown in Figure 2.a). The instrument has a measurement range of –30 °C to 70 °C; within the range of –20 °C to 40 °C, the measurement accuracy is ±0.5 °C; outside this range, it is ±1 °C. The data-recording interval was set to 30 min.

Soil temperature and humidity: The Jingchuang GSP-6 was selected as the measuring instrument. The instrument has a temperature measurement range of –40 °C to 85 °C; within the temperature range of –20 °C to +40 °C, the temperature accuracy is ±0.5 °C; for other temperature ranges, the accuracy is ±1.0 °C. Data were recorded at 30-minute intervals.



a) RC-5 Temperature Logger *b) GSP-6 Temperature and Humidity Logger*

Fig. 1- Testing Equipment

Layout of measurement points

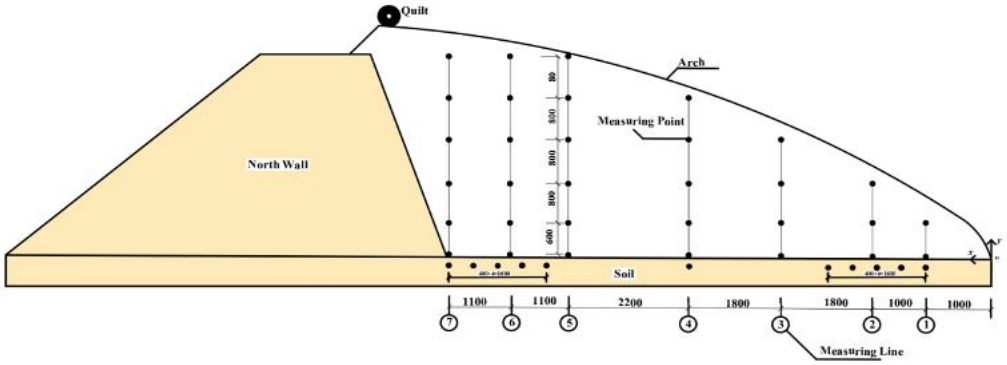


Fig. 2 - Layout of Testing Points

Soil measurement point layout: all measurement points situated at y = −150 mm and z = 0 mm; five measurement points arranged uniformly along the transverse direction at x = 1000–2600 mm and y = 8400–10000 mm, spaced 400 mm apart; a measurement point situated at x = 5600 mm in the centre of the greenhouse.

Table 1

Coordinates for Soil Measurement point Layout

Measurement point number	S1	S2	S3	S4	S5	S6	S7	S8	S9	S10	S11
x	1.0	1.4	1.8	2.2	2.6	5.6	8.4	8.8	9.2	9.6	10.0
y	-0.15	-0.15	-0.15	-0.15	-0.15	-0.15	-0.15	-0.15	-0.15	-0.15	-0.15

Air sampling point layout: at RC-5, in an open outdoor area, at a height of 1.5 m, to record the outdoor air temperature. Indoor sampling points are as shown in Table 2.

Table 2

Air Measurement point Layout Coordinate Table (m)

Measuring line number			1	2	3	4	5	6	7
x			1.0	2.0	3.800	5.6	7.8	8.9	10.0
Measurement point number	1	y	0.0	0.0	0.0	0.0	0.0	0.0	0.0
	2		0.6	0.6	0.6	0.6	0.6	0.6	0.6
	3			1.4	1.4	1.4	1.4	1.4	1.4
	4				2.2	2.2	2.2	2.2	2.2
	5					3.0	3.0	3.0	3.0
	6						3.8	3.8	3.8

RESULTS

As January was the coldest month of the year in Taigu, Jinzhong, Shanxi, in order to investigate the patterns of variation in air and soil temperatures during January and their mutual influence, the temperatures recorded at all monitoring stations in January 2024 were averaged on an hourly basis, and the hourly averages for all stations over the month were then calculated.

Variation in air temperature

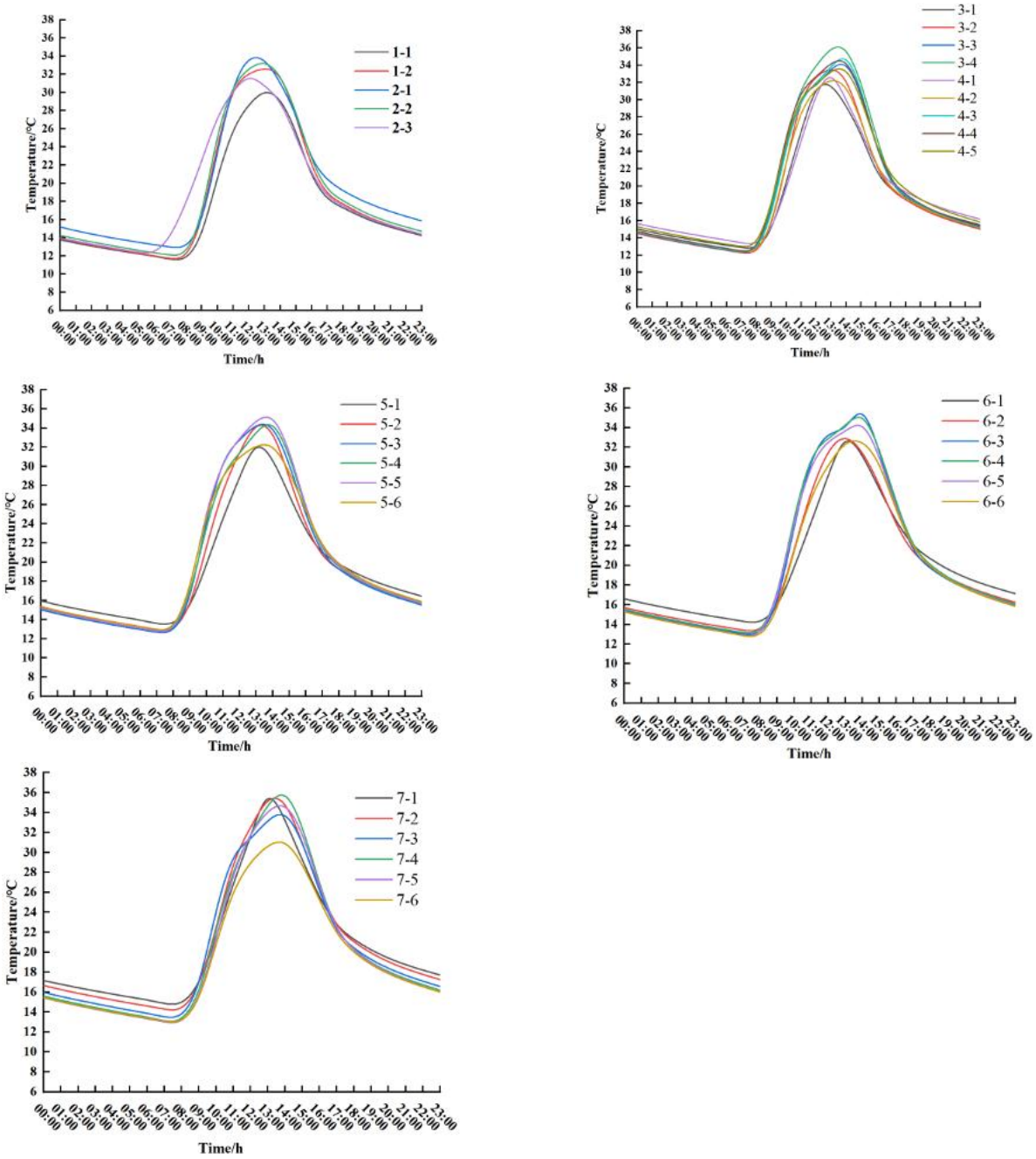


Fig. 3 - Graph of hourly averages at different measurement points in January 2024

As shown in Table 3, at all measurement points in January, temperatures gradually decreased over time during the night-time periods of 00:00–06:00 and 19:00–23:00, exhibiting a seasonal pattern. The average temperatures at all measurement points in January were above 10 °C; overall, the air temperatures at all measurement points met the requirements for plant growth. An analysis of the coldest days in January revealed that at measurement points 1 and 2—which were furthest from the wall and furthest from the soil, respectively—temperatures fell below 10 °C, with the lowest recorded temperature being 7.9 °C; these conditions still met the air temperature requirements for crop growth.

Between 0:00 and 6:00, temperatures were higher at measurement points closer to the ground. Excluding measurement point No. 1 from each measurement line, the maximum temperature difference among measurement points on the same line was 0.29 °C on measurement line No. 2, with a vertical distance of 600 mm; on measurement line No. 3, the maximum temperature difference was 0.18 °C, with a vertical distance of 1,600 mm; the maximum temperature difference between measurement points on Line 4 was 0.63 °C, with a vertical distance of 2,400 mm; on Line 5, the maximum temperature difference was 0.28 °C, with a vertical distance of 800 mm; on Line 6, the maximum temperature difference was 0.58 °C, with a

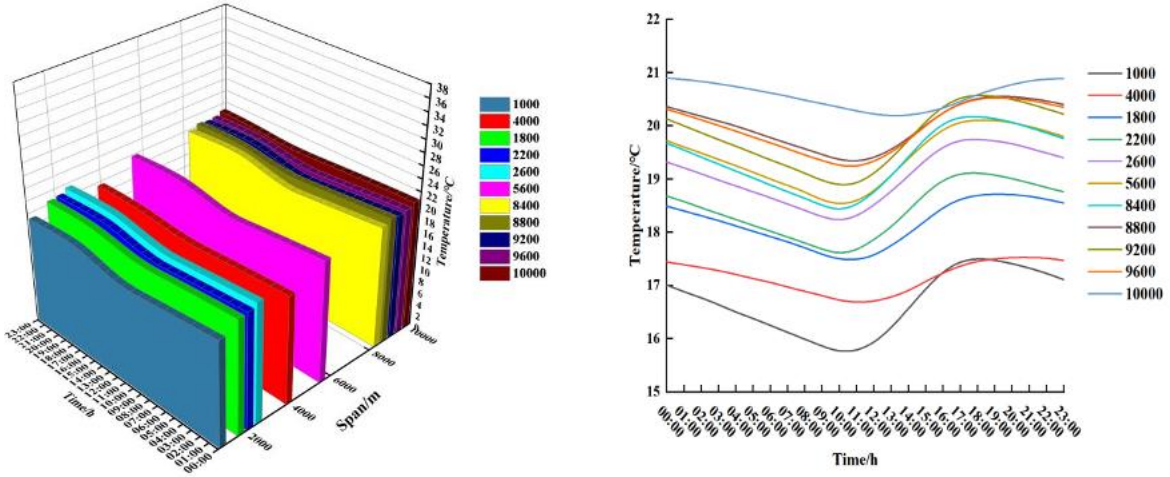
vertical distance of 2,400 mm; the maximum temperature difference on measurement line 7 was 1.29 °C, with a vertical distance of 1,600 mm. Therefore, during the period from 00:00 to 06:00, the maximum rate of change in temperature difference across the same span at different heights was 0.81 °C/m, and the minimum rate of change was 0.11 °C/m.

During the period from 0:00 to 6:00, across different spans, the maximum temperature difference at Measurement Point 1 on each transect was 3.37 °C, with a horizontal distance of 9,000 mm; the maximum temperature difference at Measurement Point 2 on each transect was 2.74 °C, with a horizontal distance of 9,000 mm; and the maximum temperature difference at Measurement Point 3 on each transect was 1.99 °C, with a horizontal distance of 8,000 mm; the maximum temperature difference at measurement point 4 on each transect was 0.91 °C, with a horizontal distance of 6,200 mm. Therefore, within the growth height of the crop layer, the maximum rate of variation in temperature difference across the transects was 0.37 °C/m, and the minimum rate was 0.15 °C/m.

Between 06:00 and 18:00, temperatures at each measurement point rose gradually in a curvilinear pattern from 06:00 to 14:00, and fell gradually in a curvilinear pattern from 14:00 to 18:00. Between 06:00 and 14:00, temperatures rose gradually; measurement points near the greenhouse film showed a greater increase in temperature, whilst the peak values at points 6 and 7 were lower than those at the central measurement points due to the obstruction caused by the cotton blankets. Measurement line 1 recorded a maximum temperature rise of 20.26 °C; measurement line 2, 19.71 °C; measurement line 3, 23.6 °C; measurement line 4, 22.84 °C; measurement line 5, 22.48 °C; measurement line 6, 23.35 °C; and measurement line 7, 23.04 °C. Between 14:00 and 18:00, temperatures gradually decreased, with a more pronounced drop observed at measurement points close to the greenhouse film. Measurement line 1 recorded a maximum temperature decrease of 14.55 °C; measurement line 2, 11.7 °C; measurement line 3, 17.38 °C; measurement line 4, 15.86 °C; measurement line 5, 16 °C; measurement line 6, 15.84 °C; and measurement line 7, 16.33 °C.

Consequently, at night, the rate of vertical temperature variation at the measurement points is higher than the rate of horizontal variation; during the daytime, when maintaining the thermal environment in a solar greenhouse, attention should be paid to heat absorption in the morning and heat dissipation in the afternoon. Within the crop growth range, equipment can be used to absorb heat from the greenhouse, thereby maintaining the thermal conditions of the solar greenhouse at night. The pattern of air temperature variation was consistent with the findings of *Cheng et al. (2024)*, with relatively marked vertical variations in temperature.

The pattern of soil temperature variation



a) Figure of soil temperature variation with span and time

b) *Graph of soil temperature over time for different span*

Fig. 4 - Soil temperature at measurement points over time and across different span

As can be seen from Figure 4, the temperatures at each measurement point in the soil gradually decreased over time during the periods from 00:00 to 12:00 and from 18:00 to 23:00, whereas they gradually increased over time during the period from 12:00 to 18:00. During the 00:00–12:00 period, the temperature decreased by 1.09 °C, 0.74 °C, 0.93 °C, 0.82 °C, 0.81 °C, 0.95 °C, 0.92 °C, 0.96 °C, 1.03 °C, 0.98 °C and 0.68°C at measurement points S1 to S11, respectively. During the period from 12:00 to 18:00, the

temperature at the measurement points increased by 1.59 °C, 0.76 °C, 1.14 °C, 1.26 °C, 1.24 °C, 1.34 °C, 1.43 °C, 1.14 °C, 1.48 °C, 1.18 °C and 0.37 °C respectively. During the period from 18:00 to 23:00, the temperature decreased at measurement points 1–11 by 0.4 °C, 0.01 °C, 0.15 °C, 0.36 °C, 0.35 °C, 0.31 °C, 0.42 °C, 0.12 °C, 0.36 °C, 0.16 °C and 0.3 °C respectively. Therefore, during January 2024, excluding the temperature at the measurement point at the base of the north wall (i.e. at y = 10,000 mm), the temperature decreased by approximately 1 °C between 00:00 and 12:00, whilst it increased by approximately 1.2 °C between 12:00 and 18:00, and a decrease of approximately 0.3°C between 18:00 and 23:00; the total temperature rise and fall over the course of the day were thus approximately equal.

At the same time, the temperature at each measurement point gradually increased with the span; compared with the temperature at measurement point S1 at y = 1000 mm, the maximum temperature difference between measurement points S2–S11 and S1 during the period from 00:00 to 12:00 was 0.97 °C , 1.74 °C, 1.94 °C, 2.59 °C, 2.85 °C, 2.83 °C, 3.61 °C, 3.18 °C, 3.5 °C and 4.6 °C; the maximum temperature differences between measurement points S2–S11 and S1 during the period from 12:00 to 18:00 were 0.58 °C, 1.55 °C, 1.90 °C, 2.57 °C, 2.87 °C, 2.86 °C, 3.35 °C, 3.19 °C, 3.3 °C and 3.99 °C; The maximum temperature differences between the S2–S11 measurement points and S1 during the period from 18:00 to 23:00 were 0.36 °C, 1.44 °C, 1.65 °C, 2.29 °C, 2.69 °C, 2.66 °C, 3.29 °C, 3.11 °C, 3.24 °C and 3.78 °C. It can therefore be seen that the temperatures at the soil measurement points are approximately equal. The variations in soil temperature were consistent with those reported in previous studies (*Li et al., 2024; Zhang et al., 2025*). Building on this prior research, the present study defined soil temperature ranges for different span lengths. Further research should be conducted on soil temperatures in solar greenhouses of different structural types and span lengths, in order to investigate the effects of span length and arch height on soil temperature.

The relationship between air temperature and soil temperature

As can be seen from Figure 3 and Figure 4, there was a certain temperature difference between air temperature and soil temperature. Air temperature gradually decreased over time between 18:00 and 06:00 the following day, and between 14:00 and 18:00, whilst it gradually increased between 06:00 and 14:00; soil temperature, on the other hand, gradually decreased with the passage of time between 18:00 and 12:00 the following day, whilst it gradually increased with the passage of time between 12:00 and 18:00. There was a certain discrepancy between the points at which soil temperature and air temperature began to rise. To investigate the relationship between air temperature at the measurement points and soil temperature, coordinate-weighted calculations were performed on the air temperatures from all measurement points in January and on the soil temperatures, and the two temperature series were analysed. The formulas for the coordinate-weighted soil temperature and the coordinate-weighted air temperature were as follows: $T = \frac{\sum T_i x_i y_i}{x_i y_i}$, where T is the weighted temperature, x_i,y_i was the coordinate value, and T_i is the temperature at the i-th measurement point.

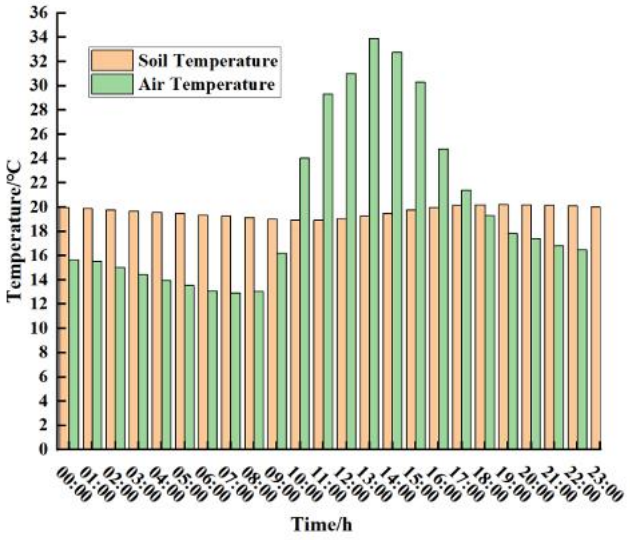


Fig. 5 - Curve of the ratio of air-weighted temperature to soil-weighted temperature in a solar greenhouse at the same time

As can be seen from Figure 5, the soil-weighted temperature gradually decreases between 00:00 and 11:00, whilst the air temperature gradually decreases between 00:00 and 07:00 and gradually increases between 07:00 and 13:00. Between 00:00 and 07:00, the air-weighted temperature was lower than the soil-weighted temperature, with an initial temperature difference of 4.3 °C; at 07:00, the difference between the soil-weighted temperature and the air-weighted temperature was 6.33 °C. At some point between 09:00 and 10:00, the weighted air temperature gradually equalled the weighted soil temperature, and between 10:00 and 14:00, the weighted air temperature was gradually higher than the weighted soil temperature. Between 09:00 and 14:00, the difference between the air-weighted temperature and the soil-weighted temperature gradually increased, reaching a maximum of 14.66 °C at 13:00. Between 14:00 and 19:00, the soil temperature gradually increased while the air temperature gradually decreased; between 17:00 and 18:00, the air-weighted temperature gradually decreased until it equalled the soil-weighted temperature. Consequently, there was a certain lag effect in the transition points for the rise and fall of the air-weighted temperature and the soil-weighted temperature in the solar greenhouse: the transition point for the rise in soil-weighted temperature lagged behind that for the rise in air-weighted temperature by four hours, whilst the transition point for the fall in soil-weighted temperature lagged behind that for the fall in air-weighted temperature by five hours.

At 11:00, the soil temperature only began to rise gradually when the difference between the air-weighted temperature and the soil-weighted temperature was 10.38 °C; at 19:00, the soil temperature only began to fall gradually when the difference between the air-weighted temperature and the soil-weighted temperature was 2.39 °C. Consequently, for the soil-weighted temperature to rise in the morning, there must be a significant difference between the air-weighted temperature and the soil-weighted temperature; similarly, for the soil temperature to fall in the afternoon, there must be a small difference between the air-weighted temperature and the soil-weighted temperature.

Previous studies have examined the factors influencing soil temperature (*Tana et al., 2022*). However, there has been limited research on the lag times and temperature differences between air temperature and soil temperature. This section examines the lag times of air-weighted temperature and soil-weighted temperature in solar greenhouses. The correlation between air-weighted temperature and soil-weighted temperature, as measured by the Spearman coefficient, was low, with an R^2 value of less than 0.1.

CONCLUSIONS

This paper employed experimental equipment to measure air and soil temperatures in a solar greenhouse, and analysed the patterns of variation and interrelationships between air and soil temperatures. The main conclusions were as follows:

(1) During the night, the rate of vertical temperature variation at each measurement point was greater than the rate of horizontal variation; during the daytime, the maintenance of the thermal environment within the solar greenhouse should take into account heat absorption in the morning and heat dissipation in the afternoon; within the crop growth range, equipment can be used to absorb heat from the greenhouse, thereby maintaining the thermal environment of the solar greenhouse at night

(2) Soil temperatures at all measurement points gradually decreased over time between 00:00 and 12:00 and between 18:00 and 23:00, whilst they gradually increased over time between 12:00 and 18:00; there were areas where soil temperatures at the various measurement points were approximately equal.

(3) There was a certain lag effect in the transition points for the rise and fall of the weighted air temperature and weighted soil temperature within the solar greenhouse; the transition point for the rise in weighted soil temperature lagged behind that of the weighted air temperature by 4 hours, whilst the transition point for the fall in weighted soil temperature lagged behind that of the weighted air temperature by 5 hours. Heat can be stored during the day using equipment and thermal storage media to harness the high air temperatures, and then released at night using the same equipment, thereby raising the air temperature in solar greenhouses during winter nights.

ACKOWLEDGEMENT

This research was supported by the Shanxi Province Youth Basic Research Programme in China (202403021222106) and the Innovation Programme for Higher Education Institutions in Shanxi Province (2024L059) in China.

REFERENCES

[1] Al-Kayssi, A.W., Al-Karaghouli, A.A., Hasson, A.M., Beker, S. (1990). Influence of soil moisture content on soil temperature and heat storage under greenhouse conditions. *Journal of Agricultural Engineering Research.* Vol.45, pp.241-252, Baghdad/Iraq.

[2] Chang, L., Zhang, L. (2010). Correlation analysis of air and soil temperature in solar greenhouse. *Journal of Shandong Jianzhu University*. Vol.4525(6), pp.595-598, Shandong/China.

[3] Cheng, W., Wang, C., Wang, Y., Hao, L., Liu, Z., Cui, Q. (2024). Soil marginal effect and LSTM model in Chinese solar greenhouse. Sensors 24, Shanxi/China.

[4] Cheng, W., Wang, C., Wang, Y., Chen, M., Qiao, P., Liu, Z. (2024). Study of the thermal environment and marginal effects of a sunken solar greenhouse. *Engenharia Agricola*. Vol.4544, e20230168, Shanxi/China.

[5] Jiao, Y., Chen, C., Li, J., Li, G., Lan, H., Han, F., Zhao, T. (2025). Study on soil temperature distribution and cold/heat zoning method of solar greenhouse based on thermal superposition principle. *Energy.* Vol.45314, pp.134222, Beijing/China.

[6] Li, Y., Jian, Y., Wang, S., Liu, X., Li, W., Arici, M., Zhang, L., Li, W., Cao, Y. (2024). Spatial temperature distribution and ground thermal storage in the plastic greenhouse: An experimental and modeling study. *Journal of Energy Storage*. Vol.4577, Sichuan/China.

[7] Li, X., Zhang, L., Wang, X., Liang, B. (2024). Forecasting greenhouse air and soil temperatures: A multi-step time series approach employing attention-based LSTM network. *Computers and Electronics in Agriculture*. Vol.45217, pp.108602, Beijing/China.

[8] Liu, X., Wu, X., Shi, W., Zhang, R., Wang, T., Zhang, F., Xu, Z., Wang, C. (2026). A hybrid RF-XGBoost model for soil temperature prediction in solar greenhouses. *Agriculture*. Vol.4516(7), Shenyang/China.

[9] Liu Yanhua, Wang Xiaoqian, Wang Cong, Zhang Feng (2023). Static analysis and optimization of slip-cover solar greenhouse structure (滑盖式节能日光温室结构静力分析及优化). *Journal of Shenyang Agricultural University*, Vol. 54(1), pp.112-120, Shenyang /China.

[10] Luo, Q., Guo, Y., Dai, A., Li, Y., Cheng, J., Wang, P., Zhao, S. (2025). Research on the evaluation model of soil heat loss in solar greenhouses. *Energy*. Vol. 322, Beijing /China.

[11] Lin, X.J., Liang, Y.-L., Wei, Z.X. (2011). Hysteresis of soil temperature under different soil moisture and fertilizer in solar greenhouse conditions. *African Journal of Biotechnology*. Vol. 10(63), pp.13729-13734, Shanxi /China.

[12] Joudi, K.A., Farhan, A.A. (2015). A dynamic model and an experimental study for the internal air and soil temperatures in an innovative greenhouse. *Energy Conversion and Management*. Vol. 91, pp.76-82, Baghdad/Iraq.

[13] Sun, W., Lu, C., Coules, A., Wei, X., Zheng, W. (2026). A full-scale climate model of the Chinese solar greenhouse. *Computers and Electronics in Agriculture.* Vol. 252, Beijing /China.

[14] Sun Yan, Yuan Yixin, Ge Hengjun, Jiang Feifei, Zou Ming, Chen Fu (2025). Spatial pattern and evolutionary trends of agricultural greenhouse facilities in China from 2010 to 2022(2010—2022 年中国农业温室设施空间格局及变化趋势). *Transactions of the Chinese Society of Agricultural Engineering*, Vol. 41(18), pp.341-349, Nanjing /China

[15] Sypka P., Kucza J., Starzak R.（2016）. Assumptions for Fourier-based modelling of diurnal temperature variations in the top soil layer under Istebna spruce stands. Agricultural & Forest Meteorology, Vol. 222, pp. 71-86, Kraków/Poland.

[16] Wang Yaoqi, Liu Yuexin, Wang Junlin, Zhang Wei, Zhao Shuli, Guo Hua (2026). Stability and critical span of Y-type braced multi-form arch solar greenhouses (Y 型支撑不同形式拱架日光温室稳定性与临界跨度). *Transactions of the Chinese Society of Agricultural Engineering*, Vol. 42(11), pp.1-8, Hebei/China.

[17] Xu, H., Zhang, Y., Li, T., Wang, R. (2017). Simplified numerical modeling of energy distribution in a Chinese solar greenhouse. *Applied Engineering in Agriculture*. Vol. 33(3), pp.291-304, Shenyang/China.

[18] Yu Jingxin, Zhao Jingpeng, Sun Congcong, Zhang Ruochen, Zheng Wenggang, Xu Linlin (2025). A dual deep learning approach for winter temperature prediction in solar greenhouses in Northern China. *Computers and Electronics in Agriculture*. Vol. 229, Beijing/China

[19] Zhang, Y., Xu, L., Zhu, X., He, B., Chen, Y. (2023). Thermal environment model construction of Chinese solar greenhouse based on temperature-wave interaction theory. *Energy and Buildings*. Vol. 279, Yangling/China

[20] Zhang, Z., Li, Y., Wang, L., Cheng, W., Liu, Z. (2025). A study of the soil-wall-indoor air thermal environment in a solar greenhouse. *Sensors*. Vol. 25, Shanxi /China

[21] Zhang X, Tana, Zhen Q, et al (2022). Soil hydrothermal experiment and simulation of different insulation structures on the south side of double-film solar greenhouse in cold and arid area (寒旱区日光温室南侧土壤保温衬砌低导热材料的水热试验与模拟). Journal of China Agricultural University, Vol.27, pp.175-185, Neimenggu /China

[22] Zhao, L., Lu, L., Liu, H., Li, Y., Sun, Z., Liu, X., Li, T. (2023). A one-dimensional transient temperature prediction model for Chinese assembled solar greenhouses. *Computers and Electronics in Agriculture.* Vol. 215, Liaoning /China

ARTIFICIAL INTELLIGENCE–BASED ANALYSIS OF DISCOURSES ON SUSTAINABLE AGRICULTURE
/
SÜRDÜRÜLEBILIR TARIM SÖYLEMLERININ YAPAY ZEKA TABANLI ANALIZI

Mehmet KAYAKUŞ[1)], Onder KABAS [2,*)], Valentin VLADUT [3,*)], Aylin KABAS [4)]

[1)] Department of Biomedical Engineering, Faculty of Engineering, Akdeniz University, 07058 Antalya, Türkiye; mehmetkayakus@akdeniz.edu.tr

[2)] Department of Machine, Technical Science Vocational School, Akdeniz University, 07070 Antalya, Türkiye; okabas@akdeniz.edu.tr

[3)] National Institute of Research—Development for Machines and Installations Designed for Agriculture and Food Industry—INMA Bucharest, 013813 Bucharest, Romania

[4)] Department of Organic Farming, Manavgat Vocational School, Akdeniz University, 07070 Antalya, Türkiye

Tel: +90-505-514-59-61; E-mail: okabas@akdeniz.edu.tr (O.K.)

Tel: +40-748-283-409; E-mail: vladut@inma.ro (V.V.)

DOI: https://doi.org/10.35633/inmateh-79-56

Keywords: *sustainable agriculture; social media analysis; artificial intelligence; text mining; sentiment analysis; topic modeling*

ABSTRACT

This study aims to investigate how sustainable agriculture is represented in the digital public sphere by examining technology-driven agricultural systems through artificial intelligence–based text analytics. A dataset of 13,354 English posts collected from the X platform during January 2026 was used, with 10,782 posts retained after preprocessing. The methodology integrates text mining, TF-IDF keyword extraction, BERT-based sentiment analysis, and LDA topic modelling. The optimal number of LDA topics was determined using coherence score evaluation to ensure statistical robustness and thematic interpretability. This study integrates text mining, BERT-based sentiment analysis, and LDA topic modelling within a unified artificial intelligence framework to provide a comprehensive analysis of sustainable agriculture discourse on social media. The results show predominantly neutral discourse (65.27%), reflecting informational content, while positive discourse (33.17%) highlights smart farming and innovation. Negative discourse (1.56%) primarily addresses structural challenges. Three dominant themes emerged: climate-oriented sustainability, community-based practices, and technology-driven agriculture, emphasizing the role of digital technologies in shaping sustainable agricultural systems. The findings provide practical insights for policymakers, agricultural stakeholders, and researchers by supporting evidence-based communication strategies and technology-oriented sustainability policies.

ÖZET

Bu çalışma, yapay zekâ tabanlı metin analitiği yöntemlerini kullanarak sürdürülebilir tarımın dijital kamusal alanda nasıl temsil edildiğini ve teknoloji odaklı tarımsal sistemlere ilişkin söylemin temel duygu ve konu yapılarını ortaya koymayı amaçlamaktadır. Ocak 2026 dönemine ait X platformundan 13.354 İngilizce paylaşım toplanmış, ön işleme sonrası 10.782 paylaşım analiz edilmiştir. Yöntemde metin madenciliği, TF-IDF anahtar kelime analizi, BERT tabanlı duygu analizi ve LDA konu modelleme kullanılmıştır. LDA için en uygun konu sayısı, istatistiksel güvenilirlik ve tematik yorumlanabilirlik dikkate alınarak coherence (uyumluluk) skoru yardımıyla belirlenmiştir. Bu çalışma, metin madenciliği, BERT tabanlı duygu analizi ve LDA konu modellemeyi bütünleşik bir yapay zekâ çerçevesinde bir araya getirerek sürdürülebilir tarım söylemine kapsamlı bir bakış sunmaktadır. Bulgular, söylemin ağırlıklı olarak nötr (%65,27) olduğunu, pozitif söylemin (%33,17) akıllı tarım ve inovasyonu vurguladığını göstermektedir. Negatif söylem (%1,56) ise ağırlıklı olarak yapısal sorunlara odaklanmaktadır. Analiz sonucunda üç temel tema belirlenmiştir: iklim odaklı sürdürülebilirlik, topluluk temelli uygulamalar ve teknoloji odaklı tarım. Elde edilen bulgular, sürdürülebilir tarım politikalarının geliştirilmesi, kanıta dayalı dijital iletişim stratejilerinin oluşturulması ve teknoloji odaklı sürdürülebilirlik uygulamalarının desteklenmesi açısından politika yapıcılara, sektör paydaşlarına ve araştırmacılara uygulamaya yönelik katkılar sunmaktadır.

INTRODUCTION

Sustainable agriculture has emerged as a critical framework for addressing the complex and interrelated challenges of global food security, climate change, and natural resource depletion. As agricultural systems are increasingly expected to produce more with fewer inputs, the transition toward sustainability requires not only ecological and economic adjustments but also the integration of innovative technologies and data-driven approaches. In this regard, the transformation of agriculture through digitalization and artificial intelligence has become a defining feature of contemporary agri-food systems.

In recent years, the convergence of sustainability principles with smart farming technologies—such as precision agriculture, artificial intelligence, Internet of Things (IoT), and data analytics—has reshaped the way agricultural production is managed and optimized. These developments align closely with the thematic focus of this special issue, which emphasizes the role of technological innovation in enhancing agricultural sustainability, efficiency, and resilience. Smart agriculture systems enable real-time monitoring, predictive analytics, and optimized resource allocation, thereby contributing to reduced environmental impact and improved productivity.

However, while the technological dimension of sustainable agriculture has been extensively explored, there remains a critical need to understand how these transformations are perceived, communicated, and socially constructed within the digital public sphere. Public discourse plays a vital role in shaping the adoption, legitimacy, and policy direction of sustainable agricultural practices. In this context, social media platforms function as dynamic environments where diverse stakeholders—including farmers, institutions, companies, and individuals—engage in discussions, share knowledge and construct narratives around sustainability and agricultural innovation.

The X platform provides a large-scale, real-time, and user-generated data environment for analyzing public discourse on sustainable agriculture. Unlike traditional data sources, social media data reflect immediate reactions, emerging trends, and multi-actor interactions, making them highly valuable for analyzing the societal dimension of agricultural transformation. Despite this potential, the integration of artificial intelligence–based text analytics into the study of sustainable agriculture discourse remains relatively underdeveloped in the literature.

Addressing this gap, the present study adopts a comprehensive artificial intelligence–based analytical framework to investigate social media discourse on sustainable agriculture. By combining text mining techniques, TF-IDF-based word frequency analysis, BERT-based sentiment analysis, and Latent Dirichlet Allocation (LDA) topic modeling, the study systematically examines large-scale Twitter data to uncover dominant sentiment patterns and thematic structures. This approach not only aligns with the technological orientation of the special issue but also extends it by incorporating the socio-discursive dimension of sustainability.

The contribution of this study is twofold. First, it provides empirical insights into how sustainable agriculture is framed in the digital public sphere, revealing the interplay between technology, sustainability narratives, and stakeholder perceptions. Second, it bridges the gap between artificial intelligence applications and sustainability research by demonstrating how advanced natural language processing methods can be employed to analyze complex, unstructured social media data in the agricultural domain.

LITERATURE REVIEW

Sustainable agriculture has evolved into a comprehensive and multidimensional framework that integrates environmental sustainability, economic viability, and social equity within agricultural systems. Early conceptualizations defined sustainable agriculture as a system capable of maintaining long-term productivity while minimizing environmental degradation and ensuring efficient use of natural resources *(Hobbs et al., 2008; Reganold et al., 1990*). Over time, this perspective has been expanded to include broader ecological and socio-economic dimensions, emphasizing the importance of soil health, biodiversity conservation, and integrated resource management *(Botero-Valencia et al., 2025; Brodt et al., 2011; Kumari et al., 2025; Velten et al., 2015*). Despite these advancements, the practical implementation of sustainable agriculture remains complex, as it requires balancing productivity with environmental protection and socio-economic inclusiveness across diverse regional and institutional contexts.

In recent years, sustainable agriculture has undergone a profound transformation driven by rapid technological advancements. The emergence of artificial intelligence (AI), machine learning, and digital agriculture has redefined traditional farming practices and introduced new opportunities for enhancing

efficiency and sustainability. Studies indicate that AI-based systems can significantly improve decision-making processes, optimize resource allocation, and support climate-resilient agricultural practices *(Rejeb et al., 2025; Xu et al., 2024*). In addition, machine learning applications have been widely adopted in agricultural supply chains, enabling predictive analytics, yield optimization, and risk management (*Anggoro & Sari, 2025*). Bibliometric analyses further confirm that technological innovation has become a central theme in contemporary sustainable agriculture research, reflecting a shift toward data-driven and precision-based farming systems (*Liu & Wan, 2024; Tucciarone et al., 2024*).

However, while existing literature strongly emphasizes the technological dimension of sustainable agriculture, it often adopts a predominantly system-oriented or engineering-focused perspective. These studies typically prioritize efficiency, productivity, and optimization, while paying limited attention to how sustainability is perceived, communicated, and socially constructed by different stakeholders. This indicates a critical gap in literature, as the success of sustainable agriculture depends not only on technological advancement but also on societal acceptance, awareness, and engagement.

Parallel to these technological developments, social media has emerged as a significant platform for information exchange, knowledge dissemination, and stakeholder interaction in agricultural systems. Social media platforms enable farmers, policymakers, institutions, and the public to share information, express opinions, and construct narratives about agricultural practices and sustainability. Studies suggest that social media plays an important role in agricultural development by facilitating knowledge sharing and influencing farmers' decision-making processes (*Chowdhury et al., 2024*). Furthermore, research focusing on precision agriculture highlights that social media discourse reflects both opportunities and challenges associated with digital transformation, including issues related to accessibility, adoption barriers, and institutional constraints (*Sharma et al., 2023*).

Nevertheless, existing studies on social media in agriculture tend to focus primarily on functional or adoption-related aspects rather than examining the discursive and perceptual dimensions of sustainability. In other words, while these studies explore how social media contributes to agricultural development, they do not sufficiently address how sustainable agriculture is framed, interpreted, and communicated within digital discourse. This limitation restricts the understanding of the broader socio-cultural dynamics that shape sustainability narratives in the agricultural domain.

In addition to social media research, computational approaches such as text mining, bibliometric analysis, and topic modeling have gained increasing attention in recent years. These methods allow researchers to analyze large-scale textual datasets and identify underlying patterns, themes, and research trends (*Chiangnangam et al., 2024; Panda & Sinha, 2023*). Topic modeling techniques, particularly Latent Dirichlet Allocation (LDA), have been widely used to uncover latent thematic structures within agricultural and sustainability-related datasets (*Ofori & El-Gayar, 2021*). These approaches provide valuable insights into the evolution of research topics and thematic priorities, contributing to a more systematic understanding of agricultural knowledge production.

However, despite their analytical strengths, most computational studies remain limited in scope, as they often focus on either thematic structures or research trends without incorporating the emotional and perceptual dimensions of discourse. In particular, the integration of advanced sentiment analysis techniques with topic modeling remains underexplored in agricultural research. While sentiment analysis has been applied in various domains to capture user attitudes and emotional responses (*Driscoll & Walker, 2014*), its combined use with topic modeling to analyze agricultural discourse—especially in the context of social media—remains relatively limited.

This gap becomes particularly significant in the context of sustainable agriculture, where public perception, stakeholder attitudes, and narrative framing play a crucial role in shaping policy development, technological adoption, and long-term sustainability outcomes. Understanding not only what is being discussed but also how it is perceived and emotionally framed is essential for developing a comprehensive understanding of agricultural transformation in the digital age.

Although previous studies have investigated sustainable agriculture, social media, or artificial intelligence separately, limited research has integrated text mining, transformer-based sentiment analysis, and topic modelling within a unified analytical framework to examine sustainable agriculture discourse. Consequently, there remains a need for a comprehensive artificial intelligence–based approach capable of simultaneously identifying both the thematic structure and sentiment dynamics of digital sustainability discussions.

Addressing this gap, the present study adopts an integrated analytical framework that combines text mining, TF-IDF-based keyword analysis, BERT-based sentiment analysis, and LDA topic modeling. This approach enables a comprehensive examination of both the thematic and emotional dimensions of sustainable agriculture discourse on social media. Unlike previous studies, which typically focus on isolated analytical dimensions, this research provides a multidimensional and data-driven perspective on how sustainable agriculture is constructed, interpreted, and communicated within the digital public sphere.

The originality of this study lies in integrating text mining, BERT-based sentiment analysis, and LDA topic modelling within a unified artificial intelligence framework to investigate sustainable agriculture discourse on social media. Methodologically, the study demonstrates the applicability of advanced natural language processing techniques to agricultural communication research. Empirically, it provides evidence on how sustainable agriculture is represented, interpreted, and discussed in the digital public sphere, thereby contributing to both artificial intelligence applications and sustainability research.

Based on the identified research gap, this study addresses the following research questions:

RQ1. How is sustainable agriculture represented in social media discourse on the X platform?

RQ2. What are the dominant sentiment patterns associated with sustainable agriculture discourse?

RQ3. What are the major thematic structures underlying sustainable agriculture discussions identified through LDA topic modelling?

Given the exploratory nature of this study and its objective of identifying thematic and sentiment patterns rather than testing causal relationships, no formal research hypotheses were proposed.

MATERIALS AND METHODS

This study utilized a dataset comprising 13,354 English posts exchanged between January 1 and January 31, 2026, to analyze social media discourse on sustainable agriculture. After cleaning the data and preparing the text (removing duplicate content, cleaning URLs and special characters, changing everything to lowercase, removing stop words, and lemmatizing), 10,782 posts were ready for analysis. The study utilized TF-IDF-based word frequency analysis as a text mining technique, employing a pre-trained BERT model for sentiment classification. Additionally, Latent Dirichlet Allocation (LDA) was used for topic modelling to find hidden themes in the conversation about sustainable agriculture. Word clouds, density maps, and keyword co-occurrence networks were used to show the results. The Python programming language was employed for all data processing and analysis tasks.

All analyses were conducted using Python 3.14.6. The main libraries included pandas 3.0.5, NumPy 2.5, NLTK 3.13, scikit-learn 1.9, transformers 5.14.1, gensim 4.4.0, matplotlib 3.11, NetworkX 3.6.1, and WordCloud 1.9.6.

Dataset

The dataset for this study was generated using the keyword 'sustainable agriculture' to examine the contemporary digital discourse surrounding sustainable agriculture. This keyword was selected as it represents the most prevalent and all-encompassing articulation of the concept of sustainable agriculture in the literature, thereby facilitating access to a wide array of content that includes environmental, economic, and social dimensions (*Liu & Wan, 2024; Sharma et al., 2023*). The X platform was selected as the data source due to its widespread use in academic research. It shows real-time public reactions, policy discussions, project announcements, and individual opinions in an open data format (*Driscoll & Walker, 2014; Naskar et al., 2020*). X's official Application Programming Interface (API) infrastructure was utilized to retrieve the data. This approach ensures the scientific reliability of the data in terms of accuracy, integrity, and reproducibility *(Das et al., 2024*).

The data collection process lasts from January 1 to January 31, 2026. This time frame was chosen because it reflects current discourse, minimizes temporal fluctuations by providing a homogeneous single-month period, and allows for the observation of intensive content production on the topic of sustainable agriculture. During the specified time, 13,354 posts were collected. After text preprocessing and cleaning, 10,782 of these posts were used for analysis. In social media–based text mining studies, datasets exceeding ten thousand observations are generally considered sufficient to reliably model thematic structures and sentiment distributions. In this context, the acquired dataset is sufficiently large for statistical and analytical examination of the thematic and sentimental framework of the discourse on sustainable agriculture.

Text Mining

This study employed text mining techniques to facilitate the systematic and quantifiable examination of social media content related to sustainable agriculture. Text mining is an analytical method based on natural language processing (NLP) that tries to find useful patterns, themes, and statistical relationships in unstructured text data (*Lan, 2026*). Because social media data is inconsistent, short, and changes depending on the situation, it needs to be standardized before it can be analyzed (*Zucco et al., 2020*).

In this case, text preprocessing was done first. Text preprocessing was performed to improve data quality and ensure reliable subsequent analyses (*Chai, 2023*). First, duplicate posts were removed to eliminate repeated content. URLs, user mentions, hashtags, punctuation marks, numbers, and other non-textual characters were then removed to reduce noise. Subsequently, all text was converted to lowercase to ensure consistent word representation. Common stop words that did not contribute meaningful semantic information were removed using the NLTK stop-word list (*Mubarak et al., 2023*). Finally, lemmatization was applied to reduce words to their base forms while preserving their semantic meaning. These preprocessing steps reduced the dataset from 13,354 to 10,782 posts, resulting in a cleaner and more consistent corpus for text mining, sentiment analysis, and topic modelling.

Word frequency analysis is one of the most important methods used in text mining. Word frequency refers to the number of occurrences of a term within a dataset. It is used to figure out which ideas are most important in the conversation (*Yeomans et al., 2023*). Nevertheless, raw frequency values may underscore excessively repetitive general concepts, resulting in words with low distinctiveness appearing predominant in the analysis. This study also used the Term Frequency–Inverse Document Frequency (TF-IDF) method for this reason.

TF-IDF is a weighting scheme that quantifies the importance of a term within a document relative to the entire corpus (*Liu et al., 2022*). "Term Frequency (TF)" counts how many times a word shows up in a single document (*Mohammed & Rashid, 2023*), while "Inverse Document Frequency (IDF)" counts how many times the word shows up in all the documents (*Yulita et al., 2023*). The IDF value of a word goes down if it is used a lot in many documents (*Mee et al., 2021*). If it is only used in a few documents, the IDF value goes up. The TF-IDF score, which is the product of these two numbers, helps you find more meaningful keywords by looking at both their local frequency and their global distinctiveness (*Xiao et al., 2024*). Therefore, ideas that are different from each other in the discussion of sustainable agriculture have come to the fore.

Sentiment Analysis

Sentiment analysis is a way to use natural language processing to figure out what someone's attitude and sentimental state (positive, negative, or neutral) is based on text data (*Nandwani & Verma, 2021*). It is commonly employed to methodically categorize users' opinions, expectations, and criticisms based on social media data(*Chakraborty et al., 2020*). This study used a supervised machine learning methodology and employed a pre-trained deep learning model to analyze the sentiment distribution of posts regarding sustainable agriculture.

The pretrained transformer model cardiffnlp/twitter-roberta-base-sentiment-latest, based on the RoBERTa architecture, was used for sentiment classification (*Acheampong et al., 2021*). RoBERTa is an optimized variant of BERT that builds on the Transformer architecture and has demonstrated high performance in sentiment analysis tasks, particularly for short and context-dependent texts such as social media posts *(Pota et al., 2020; Mars, 2022*). Its bidirectional contextual representation enables more accurate interpretation of word meanings by considering both preceding and following contexts, thereby improving classification performance.

The BERT model is trained on big text datasets ahead of time, and it can be fine-tuned to work on a specific task (*Qasim et al., 2022*). The model was used in this study to categorize Twitter texts into positive, negative, and neutral classifications (*Acheampong et al., 2021*). The model breaks the text down into tokens, turning each word into a vector representation. It then learns how words are related to each other through Transformer layers and gives a probabilistic classification output in the last layer *(Rodrawangpai & Daungjaiboon, 2022*). This made it possible to find sentiment orientation in conversations about sustainable agriculture with outstanding accuracy.

Topic Modelling

Topic modelling is a statistical method for analyzing text that tries to find hidden topics in large sets of text (*Vayansky & Kumar, 2020*). This method uses probabilities to model how documents are spread out around certain topic clusters and what words make up each topic (*Churchill & Singh, 2022*). In unstructured datasets with a wide range of content, like social media, topic modelling techniques are a keyway to systematically show the thematic structure (*Laureate et al., 2023*). In this research, topic modelling was used to discern the prevailing themes in the discourse surrounding sustainable agriculture.

In this study, the Latent Dirichlet Allocation (LDA) algorithm was used for topic modelling. The primary reason for selecting LDA is its ability to model texts as encompassing multiple topics, delineating each topic through a distinct word probability distribution (*Li et al., 2024*). Social media texts usually have multidimensional content, LDA's flexible and probabilistic structure makes it a good way to analyze these kinds of data *(Neijzen & Lunter, 2023*). LDA was selected due to its prevalence in social science literature and its capacity to generate interpretable results.

The LDA model posits that each document (in this study, each post) comprises a blend of various topics in designated proportions (*Qiang et al., 2020*). The model works by using two main distributions: (1) the word distribution for each topic and (2) the topic distribution for each document (*Chauhan & Shah, 2021*). The algorithm figures out how likely it is that words belong to certain topics by repeating the process repeatedly (*Churchill & Singh, 2022*). Over time, it finds the most consistent topic-word structures. Therefore, keywords that frequently appear together represent each topic. This has made it possible to systematically and statistically find the main themes of sustainable agriculture conversation.

RESULTS

This part shows the results of the analysis for the dataset that was collected from January 1 to January 31, 2026. After the text pre-processing stage, it was cut down to 10,782 posts. The researchers employed text mining, word frequency analysis, BERT-based sentiment analysis, LDA topic modelling, and diverse data visualization techniques. The Python programming language was employed for all analysis stages. Libraries such as pandas, NLTK, scikit-learn, transformers, gensim, and matplotlib were utilized for data cleaning, natural language processing, modeling, and visualization. The results show, through a comprehensive approach, the themes and sentiment frameworks that shape the conversation about sustainable agriculture on social media. Table 1 shows the framework of sentiment that social media users are using to talk about agriculture.

Table 1

Distribution of sentiment categories in sustainable agriculture discourse on the X platform

Positive	Negative	Neutral
3.576	168	7.038

As presented in Table 1, of the 10,782 posts analyzed, 3,576 (33.17%) were classified as positive, 168 (1.56%) as negative, and 7,038 (65.27%) as neutral. The results suggest that neutral and informative content primarily influences the conversation about sustainable agriculture on social media. The fact that most of the content is neutral shows that the topic is mostly talked about in the context of policy announcements, project sharing, corporate statements, and research-based content.

The fact that 33.17% of posts are positive compared to negative content shows that sustainable agriculture is usually linked to a vision of the future that is hopeful, innovative, and solution orientated. On the other hand, the very low level of negative content (1.56%) shows that criticism is limited but focused on specific implementation problems and structural deficiencies.

These findings indicate that sustainable agriculture doesn't see it as a controversial crisis area but rather as an informative and somewhat positive topic of change and growth.

Qualitative Evaluation of Sample Posts

In this part, a qualitative evaluation was done by picking the three posts with the most likes, reposts, and comments in each sentiment category from the posts that BERT-based sentiment analysis said were positive, negative, or neutral. The goal is to go beyond just looking at the numbers and find out which narrative frameworks, thematic emphasis, and social sensitivities shape the conversation about sustainable agriculture.

The chosen posts exemplify the sentiment category and illustrate the discourse formats that yield the highest visibility and engagement among social media users. In this context, the analysis seeks to elucidate the perceptual and discursive aspects of sustainable agriculture within the digital public sphere with greater depth.

Positive Post Examples

Post 1: "Innovative sustainable farming systems are the future of global food security. Supporting farmers with smart technology will drive real growth and long-term resilience.

This post frames sustainable agriculture as a future-oriented and innovation-driven process, emphasizing the role of smart technologies in enhancing productivity and resilience. The reference to supporting farmers highlights the central role of producers in sustainable transformation.

Post 2: "New agricultural projects are empowering rural communities through sustainable solutions and economic development."

This post presents sustainable agriculture as a multidimensional development tool, linking environmental sustainability with economic growth and rural empowerment. It reflects a project-based and solution-oriented perspective.

Post 3: "Smart agriculture and innovative crop systems are transforming food production for a more sustainable and secure future."

This post emphasizes transformation and modernization, framing sustainable agriculture as a pathway toward a secure and resilient future through technological innovation.

Negative Post Examples

Post 1: "Excessive pesticide use and poor land management are harming sustainable farming efforts."

This post highlights the gap between sustainability discourse and actual practices, emphasizing environmental risks associated with excessive chemical use and poor management.

Post 2: "Small farmers still struggle with limited land and low production despite sustainable farming promises."

This post reflects structural inequalities in agricultural systems, particularly the challenges faced by small-scale farmers in achieving sustainable production.

Post 3: "Food waste and inefficient management systems undermine sustainable agriculture goals."

This post underscores inefficiencies in resource management, indicating that sustainability goals are undermined by waste and systemic limitations.

Neutral Post Examples

Post 1: "National research on sustainable agriculture focuses on food security, rural development and climate resilience."

This post reflects a policy-oriented and research-driven perspective, focusing on food security and climate resilience without evaluative judgment.

Post 2: "Sustainable agriculture initiatives support rural communities and strengthen global food systems."

This post presents sustainable agriculture within an institutional and systems-based framework, emphasizing its role in strengthening global food systems.

Post 3: "Agricultural development strategies address soil health, water management and long-term security."

This post highlights a technical and strategic perspective, focusing on resource management and long-term agricultural planning.

Word Frequency Analysis

This part did a word frequency analysis to find the main ideas that were talked about in the conversation about sustainable agriculture. The analysis process used both raw frequency values and the TF-IDF (Term Frequency–Inverse Document Frequency) method. The primary rationale for selecting TF-IDF is to mitigate the influence of common words that are excessively repetitive yet possess low distinctiveness (e.g., agriculture' or 'sustainable') within the dataset, thereby highlighting more unique and elucidative concepts related to specific sentiment categories or text clusters. This method evaluates both the frequency of terms and their distinctiveness across the corpus. The analysis aims to reveal a more substantial and thematically

cohesive conceptual framework, free from superficial redundancies in the discourse on sustainable agriculture. Table 2 shows the words and frequency distributions that stand out by sentiment category.

Table 2

TF-IDF-based keyword distribution across sentiment categories

Positive	Negative	Neutral
Future	Waste	Agriculture
Innovative	Management	Sustainable
Growth	Small	Development
Project	Less	Security
Systems	Land	Rural
Support	Production	Research
Supporting	Nutrition	National
Solutions	Sustainable farming	World
Technology	Need	Health
Economic	Kerala	Resilience

The results indicate that positive discourse is strongly associated with future-oriented, innovation-driven, and solution-focused narratives. Keywords such as “innovation”, “technology”, and “growth” suggest that sustainable agriculture is framed as a driver of economic development and technological transformation, emphasizing systemic change rather than individual practices.

Negative discourse is primarily associated with structural and operational challenges, including resource inefficiency, inadequate management practices, and constraints faced by small-scale producers. These findings highlight a discrepancy between sustainability narratives and their practical implementation.

Neutral discourse is predominantly informational and institutional, characterized by terms related to policy, research, and development. This indicates that sustainable agriculture is largely framed within a technical and governance-oriented context rather than an evaluative one.

Topic Modelling Analysis

This section employed topic modelling analysis to uncover the underlying thematic structure of the discourse on sustainable agriculture (*Hussain et al., 2026*). The Latent Dirichlet Allocation (LDA) algorithm was used for the topical modelling process. The primary rationale for selecting LDA is its assumption that documents within extensive text datasets may probabilistically pertain to multiple themes, modelling each theme according to the distributions of co-occurring words (*De La Hoz-M et al., 2026*). This is a strong and well-known way to find hidden themes in datasets with multidimensional and mixed content structures, like social media. In addition, LDA makes it easier to analyze social science studies by giving them topical keyword outputs that are easy to understand (*Cheng et al., 2023*).

To identify the optimal topic structure, candidate LDA models with topic numbers ranging from 2 to 10 were evaluated using coherence scores. The corresponding coherence values are presented in Table 3.

Table 3

Coherence scores of candidate LDA models

Number of Topics	Coherence Score
2	0.3462
3	0.4710
4	0.3618
5	0.4526
6	0.4212
7	0.4315
8	0.4403
9	0.3376
10	0.4682

As shown in Table 3, the coherence scores ranged from 0.3376 to 0.4710 across the tested models. The three-topic model achieved the highest coherence score (0.4710), while the ten-topic model produced a very similar value (0.4682). However, qualitative examination indicated that the ten-topic solution generated fragmented and overlapping themes, whereas the three-topic model provided clearer thematic separation and greater interpretability. Models with fewer topics produced overly broad themes, while models with more topics resulted in increasingly fragmented topic structures. Therefore, considering both the quantitative coherence scores and the qualitative interpretability of the extracted topics, the three-topic model was selected for the subsequent analyses.

The findings of the topic modelling analysis are summarized in Table 4, which presents the extracted topics and their corresponding keyword distributions.

Table 4

Identified topics, prevalence, and representative keywords from LDA topic modelling

Topic N	Mean Topic Probability	Prevalence	Topmost co-occurring words
1	0.3900	40.18%	food, farming, systems, 2026, growth, security, innovation, support, farmers, future, development, today, climate, global, health, organic, agricultural, real, new
3	0.3102	30.11%	project, food, pulses, farmers, water, farming, security, innovative, Veera, on Veera, future, soil, communities, irrigation, world, practices, livelihoods, women, day, approach
2	0.2998	29.72%	farmers, farming, development, new, growth, energy, solutions, water, tech, production, land, food, ai, global, climate, farm, 2026, Kenya, soil

The table presents the dominant thematic structures identified through LDA, including topic prevalence and the most representative co-occurring terms.

Topic 1: The Future Vision of Sustainable Agriculture in the Context of Food Security and Climate

The fact that Topic 1 is the most common topic (40.18% of the time, with a mean topic probability of 0.3900) shows that posts about sustainable agriculture are most often about food security and future-orientated change. The words "food", "security", "climate", "global", "health", "organic", "innovation", "farmers", "future", and "development" often appear together. This shows that sustainable agriculture is linked to more than just production efficiency; it is also linked to a larger social agenda that includes healthy eating, fighting the climate crisis, global risks, and organic farming. The focus on "systems" and "innovation" shows that users see agriculture as more than just one thing; they see it as an agriculture-food system. The words "support" and "farmers" together suggest that producers are at the heart of the change. In terms of discourse, this topic sets up a framework that sees sustainable agriculture to build the future and deal with crises. It gives people hope and direction by saying, "Today's problem is tomorrow's solution.

Topic 3: Water, Soil and Community-Based Resilience: Innovative Projects and Sustainable Practices

Topic 3 (Prevalence: 30.11%; Mean Topic Probability: 0.3102) has a narrative that is more focused on projects and applications. Words like "project", "innovative", "practices", and "approach" suggest that sustainable agriculture is being talked about in terms of field applications and projects rather than as an abstract ideal. The three words "water, irrigation, and soil" are the main ideas of this theme. They stress that managing water and keeping soil healthy are important parts of sustainability. Words like "communities", "livelihoods", and "women" show that the conversation isn't just about the technical side of things. It also talks about sustainable agriculture in the context of rural livelihoods, social inclusion, and especially the role of women in agriculture. The language used in this topic supports the ideas of "solution-building" and "transformation". It shows that sustainable agriculture is seen as a practical way to develop that makes communities stronger, gives them more power, and helps them manage their resources better.

Topic 2: Efficient Production with Technology and Artificial Intelligence: Smart Agriculture in the Water-Energy-Food Nexus

Topic 2 (Prevalence: 29.72%; Mean Topic Probability: 0.2998) clearly moves the sustainable agriculture agenda toward technology and digitalization. The words "tech", "solutions", "AI", "energy", and

"production" show that people are talking about sustainability goals through smart farming, AI-supported decision systems, and technology-based solutions. The inclusion of "energy" alongside "water, land, soil" signifies a growing public comprehension of sustainable agriculture through the lens of the water-energy-food (WEF nexus) paradigm, emphasizing the interrelations among resources. Also, the words "Kenya" and "global" show that the conversation has moved beyond being about a local production problem and is now being talked about in a way that compares it to examples from around the world and different country contexts. This topic frames sustainable agriculture as "producing smarter and more resource-efficiently" instead of "producing more". It focuses on the language of efficiency, optimization, and innovation, and it also connects these ideas to climate and food security issues, making technology an "accelerator" of sustainability.

Data visualization

This section employs diverse data visualization techniques to enhance the clarity and interpretability of findings pertaining to discourse on sustainable agriculture. Word clouds, density maps, and keyword co-occurrence networks were used to illustrate the prominent concepts based on sentiment categories and the underlying thematic clustering structures. The visualization process was done with the Python programming language, and the structural relationships of the text mining results were shown in a graph. This method backs up the results of the quantitative analysis and gives us a chance to look at the main ideas and the relational network structure of the sustainable agriculture discourse in a more complete way.

Word cloud analysis

The word cloud was made with the WordCloud library in Python. This library automatically looks at how often words appear in the text and makes images that are proportional to how often they occur *(Trejo, 2025*). The pandas and NLTK libraries were used for data pre-processing, and the matplotlib library was used to organize the graphical output. This combination made it possible to show word density both in numbers and in pictures. Figure 1 shows the positive word cloud, which shows how the ideas in the positive sentiment category are spread out visually.



Fig. 1 - Positive word cloud

The word cloud analysis indicates that positive discourse on sustainable agriculture is dominated by terms related to innovation, productivity, and sustainability. Keywords such as “innovation”, “technology”, and “development” highlight a strong association with future-oriented and solution-driven narratives. In addition, the presence of terms such as “climate”, “water”, and “soil” reflects the integration of environmental sustainability within this positive framing. The prominence of words such as “farmers” and “communities” further suggests a producer-centered and socially inclusive perspective. Overall, the results demonstrate that sustainable agriculture is constructed in positive discourse as a transformative and development-oriented process.



Fig. 2 - Negative word cloud

The negative word cloud highlights that critical discourse is primarily centered on environmental and structural challenges. Terms such as “pesticide”, “waste”, and “management” indicate concerns related to resource inefficiency and unsustainable practices. Additionally, the presence of words associated with climate and resource constraints reflects the perceived risks and limitations in the implementation of sustainable agriculture. Overall, negative discourse emphasizes the gap between sustainability goals and practical challenges.



Fig. 3 - Neutral word cloud

The neutral word cloud reflects an informational and institutional discourse structure, dominated by terms related to policy, research, and development. Keywords such as “agriculture”, “development”, and “research” suggest that sustainable agriculture is primarily discussed within a technical and governance-oriented framework. This indicates that a significant portion of the discourse is descriptive rather than evaluative.

Density visualization

The density visualization was made to show how closely related and clustered concepts are in the discourse of sustainable agriculture (*Dabare et al., 2025*). For this analysis, words that often appeared together were placed on a two-dimensional plane to find areas of conceptual density. This made it possible to see which themes were at the center and which concepts were more strongly connected. This method has given us a more complete view of the main themes and environmental groups in sustainable agriculture conversation.

Figure 4 shows the density map that shows how concepts are grouped based on how similar their meanings are.

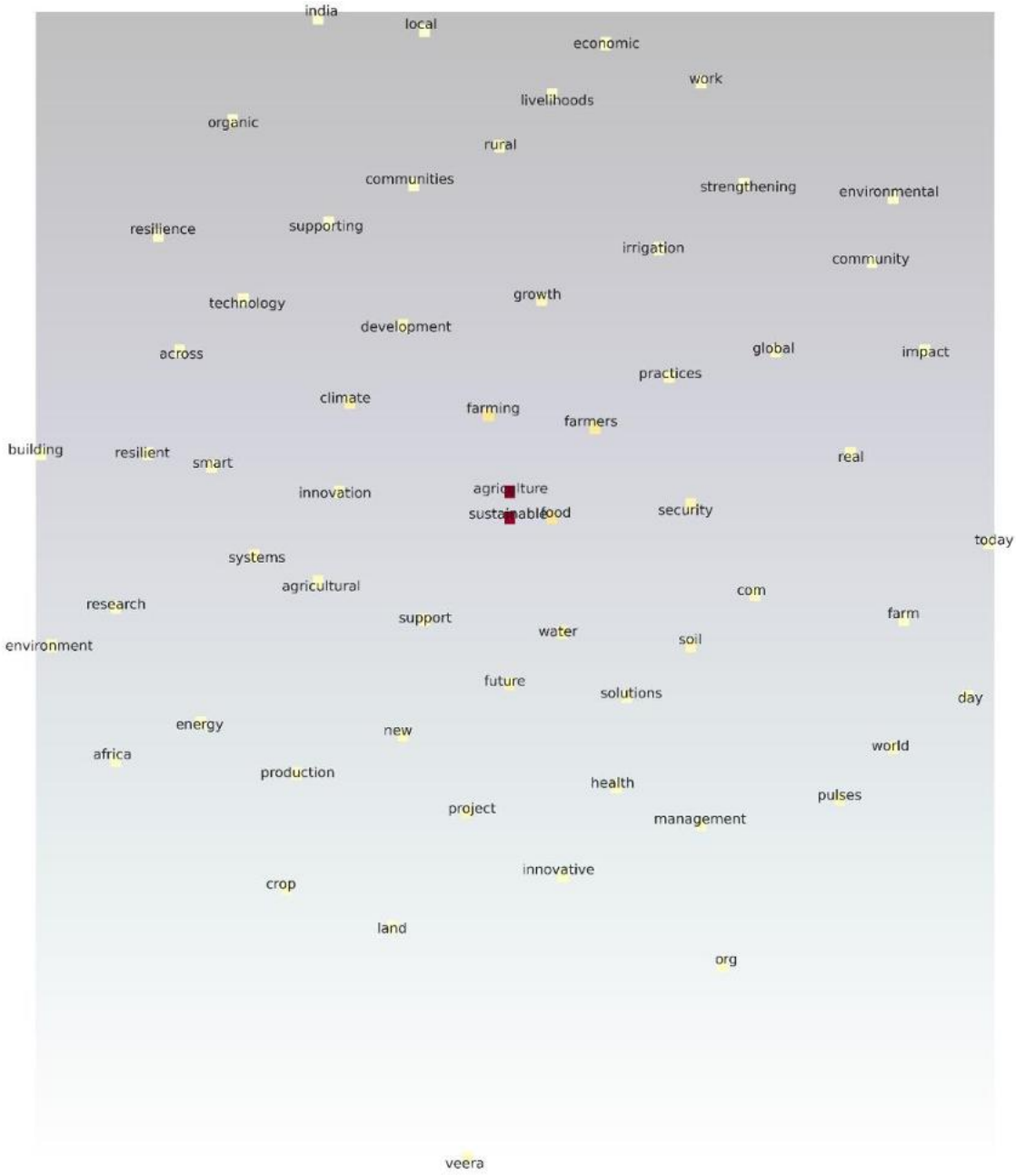


Fig. 4 - Density visualization

The density visualization reveals a clustered conceptual structure centered around key terms such as agriculture, food, and sustainability. This pattern reflects a multi-dimensional discourse shaped by environmental, economic, and social factors.

Keyword Co-occurrence Network

Keyword co-occurrence network analysis was conducted to examine how the concepts used together in the discourse on sustainable agriculture are interconnected. This approach used a node and edge structure to model words that co-occurred in the same post, facilitating an analysis of the connection density between concepts (*Yuan et al., 2022*). In this way, the main ideas that were talked about and the subthemes that went along with them were looked at in a visual network structure (*Yang et al., 2023*). The analysis took place in Python. The word 'co-occurrence matrix' was made first, then the NetworkX library was used to model the network structure, and finally Matplotlib was used to show the results. This method shows not only the ideas that shape the conversation about sustainable agriculture but also how these ideas fit together to make a whole. Figure 5 shows the keyword co-occurrence network, which demonstrates how keywords are related to each other and how the network is structured visually.

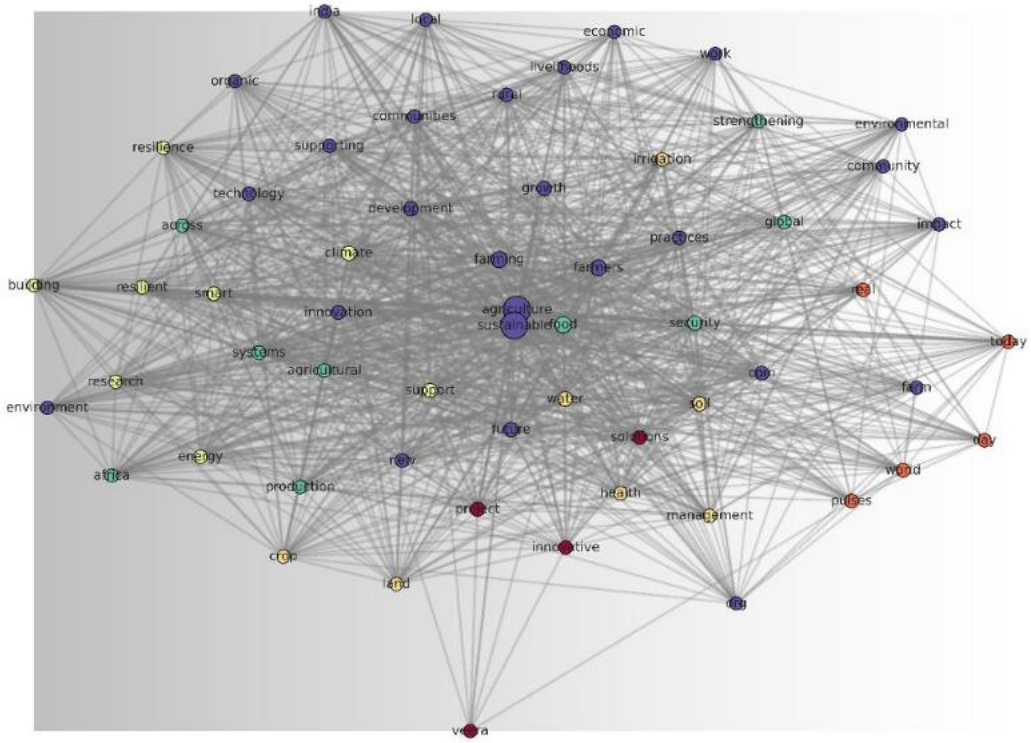


Fig. 5 - Keyword co-occurrence network

The keyword co-occurrence network demonstrates strong interconnections between sustainability, food systems, and technological innovation, indicating a highly integrated and systemic discourse structure.

CONCLUSIONS

This study provides a comprehensive analysis of sustainable agriculture discourse in the digital public sphere by integrating artificial intelligence–based methods with large-scale social media data. The findings reveal that discussions on sustainable agriculture are predominantly neutral and informational, largely shaped by institutional communication, policy-oriented content, and project-based narratives. At the same time, the significant presence of positive sentiment indicates that sustainable agriculture is strongly associated with innovation, technological advancement, and future-oriented development. In contrast, negative discourse remains limited and is primarily related to structural challenges such as resource inefficiency, management limitations, and the constraints faced by small-scale producers.

These findings are consistent with existing literature emphasizing the transformative role of artificial intelligence and digital technologies in sustainable agriculture (*Botero-Valencia et al., 2025; Kumari et al., 2025*). The prominence of themes such as food security, climate resilience, and smart farming aligns with studies highlighting the integration of technological innovation into sustainability frameworks (*Xu et al., 2024*). Furthermore, the dominance of informational discourse supports prior research suggesting that social media functions as both a communication and knowledge dissemination platform in agricultural systems *(Ofori & El-Gayar, 2021; Panda & Sinha, 2023*). However, unlike previous studies that primarily focus on technological applications or bibliometric patterns, this study demonstrates that sustainable agriculture is framed in digital discourse more as a narrative of transformation and opportunity rather than crisis. This shift toward solution-oriented and future-focused narratives represents a notable contribution to literature.

The originality of this study lies in its integration of artificial intelligence–based analytical methods with social media discourse analysis to examine sustainable agriculture from a socio-discursive perspective. By combining text mining, TF-IDF, BERT-based sentiment analysis, and LDA topic modelling, the study provides a multidimensional understanding of both the emotional and thematic structures of digital discourse. This integrative approach extends existing research by bridging the gap between technological innovation and public perception in the context of sustainable agriculture.

Despite these contributions, the study has several limitations. First, the analysis is based solely on data collected from the X platform, which may limit the generalizability of the findings across different digital environments. Second, the dataset was generated using the single keyword "sustainable agriculture," which

may have excluded relevant discussions expressed through alternative keywords or hashtags. Third, only English-language posts were analyzed, limiting the representation of multilingual perspectives on sustainable agriculture. In addition, although standard text preprocessing techniques were applied to improve data quality, these procedures may have removed contextual information and linguistic nuances. Furthermore, despite the use of a pretrained transformer-based sentiment classification model, contextual ambiguity and occasional misclassification may still occur, particularly in short and informal social media posts. Therefore, the findings should be interpreted within the scope of the analyzed dataset and should not be generalized to all online discussions on sustainable agriculture.

Future research can build on this study by incorporating multilingual datasets and cross-platform data sources, including Facebook, Instagram, Reddit, and YouTube, to achieve a more comprehensive understanding of digital agricultural discourse. Longitudinal analyses could also be conducted to examine how perceptions of sustainable agriculture evolve over time. Furthermore, multimodal approaches integrating text, images, and videos may provide richer insights into online discourse. Future studies may also compare alternative topic modelling techniques, such as BERTopic, Non-negative Matrix Factorization (NMF), and Dynamic Topic Models, together with different sentiment analysis models, to further improve the robustness and interpretability of artificial intelligence–based discourse analysis.

This study highlights the importance of integrating artificial intelligence and social media analytics into sustainability research, offering new insights into how agricultural transformation is perceived, constructed, and communicated in the digital age. These findings provide valuable implications for policymakers, practitioners, and researchers, emphasizing the need for inclusive communication strategies, technology-driven solutions, and policy frameworks that address both innovation and structural challenges in sustainable agriculture.

REFERENCES

[1] Acheampong, F. A., Nunoo-Mensah, H., & Chen, W. (2021). Transformer models for text-based emotion detection: a review of BERT-based approaches. *Artificial Intelligence Review*, 54(8), 5789-5829.

[2] Anggoro, M. R. L., & Sari, C. A. (2025). Harnessing artificial intelligence and machine learning for sustainable agriculture in Asia: insights from a bibliometric review. *2025 IEEE Conference on Technologies for Sustainability (SusTech)*, Santa Ana, California, United States.

[3] Botero-Valencia, J., García-Pineda, V., Valencia-Arias, A., Valencia, J., Reyes-Vera, E., Mejia-Herrera, M., & Hernández-García, R. (2025). Machine learning in sustainable agriculture: systematic review and research perspectives. *Agriculture*, 15(4), 377.

[4] Brodt, S., Six, J., Feenstra, G., Ingels, C., & Campbell, D. (2011). *Sustainable Agriculture, Nature Education Knowledge*, 2. In.

[5] Chai, C. P. (2023). Comparison of text preprocessing methods. Natural language engineering, 29(3), 509-553.

[6] Chakraborty, K., Bhattacharyya, S., & Bag, R. (2020). A survey of sentiment analysis from social media data. *IEEE Transactions on Computational Social Systems*, 7(2), 450-464.

[7] Chauhan, U., & Shah, A. (2021). Topic modeling using latent Dirichlet allocation: A survey. *ACM Computing Surveys (CSUR)*, 54(7), 1-35.

[8] Cheng, X., Zhao, Y., & Liao, S. S. (2023). Key topics in social science research on COVID-19: An automated literature analysis. *Health Information & Libraries Journal*, 40(4), 343-358.

[9] Chiangnangam, S., Manorom, P., & Chansanam, W. (2024). Analyzing Research Trends in Organic Agriculture and Entrepreneurship: A Topic Modeling Approach Using Latent Dirichlet Allocation (LDA). *Journal of Computational Analysis & Applications*, 33(5).

[10] Chowdhury, S. R., Ghosh, D., & Rao, T. J. (2024). Sentiment and success potential of farmers' producer organizations: A systematic literature review. *Local Economy*, 39(1-2), 92-104.

[11] Churchill, R., & Singh, L. (2022). The evolution of topic modeling. *ACM Computing Surveys*, 54(10s), 1-35.

[12] Dabare, S., Rajapaksha, S., & Munaweera, I. (2025). Exploring the intersection of innovation management and nanotechnology in sustainable agriculture. *International Journal of Innovation Science*, 1-37.

[13] Das, N., Sadhukhan, B., Bhakta, S. S., & Chakrabarti, S. (2024). Integrating EEMD and ensemble CNN with X (Twitter) sentiment for enhanced stock price predictions. *Social Network Analysis and Mining*, 14(1), 29.
[14] De La Hoz-M, J., Montes-Escobar, K., Salas-Macias, C. A., Fors, M., & Ballaz, S. J. (2026). Using Latent Dirichlet Allocation Topic Modeling to Uncover Latent Research Topics and Trends in Renal Cell Carcinoma: Bibliometric Review. *JMIR Cancer*, 12(1), e78797.
[15] Driscoll, K., & Walker, S. (2014). Big data, big questions| working within a black box: Transparency in the collection and production of big twitter data. *International Journal of Communication*, 8, 20-20.
[16] Hobbs, P. R., Sayre, K., & Gupta, R. (2008). The role of conservation agriculture in sustainable agriculture. *Philosophical Transactions of the Royal Society B: Biological Sciences*, 363(1491), 543-555.
[17] Hussain, M. R., Hannoun, O., Kovács, S., Mátyás, S., Orbán, S., & Szabados, G. N. (2026). Topic modelling and thematic analysis of research gaps and methodological innovations in rural sociology: A systematic review. *Social Sciences & Humanities Open*, 13, 102354.
[18] Kumari, K., Mirzakhani Nafchi, A., Mirzaee, S., & Abdalla, A. (2025). AI-driven future farming: achieving climate-smart and sustainable agriculture. *AgriEngineering*, 7(3), 89.
[19] Lan, M. (2026). Natural language processing and text mining. *In Artificial Intelligence for Drug Design* (pp. 189-215). Springer.
[20] Laureate, C. D. P., Buntine, W., & Linger, H. (2023). A systematic review of the use of topic models for short text social media analysis. *Artificial Intelligence Review*, 56(12), 14223-14255.
[21] Li, D., Wu, K., & Lei, V. L. (2024). Applying topic modeling to literary analysis: A review. *Digital Studies in Language and Literature*, 1(1-2), 113-141.
[22] Liu, H., Chen, X., & Liu, X. (2022). A study of the application of weight distributing method combining sentiment dictionary and TF-IDF for text sentiment analysis. *IEEE Access*, 10, 32280-32289.
[23] Liu, Y., & Wan, F. (2024). Unveiling temporal and spatial research trends in precision agriculture: A BERTopic text mining approach. *Heliyon*, 10(17).
[24] Mars, M. (2022). From word embeddings to pre-trained language models: A state-of-the-art walkthrough. *Applied Sciences*, 12(17), 8805.
[25] Mee, A., Homapour, E., Chiclana, F., & Engel, O. (2021). Sentiment analysis using TF–IDF weighting of UK MPs' tweets on Brexit. *Knowledge-Based Systems*, 228, 107238.
[26] Mohammed, M. T., & Rashid, O. F. (2023). Document retrieval using term frequency inverse sentence frequency weighting scheme. *Indonesian Journal of Electrical Engineering and Computer Science*, 31(3), 1478.
[27] Mubarak, H., Abdaljalil, S., Nassar, A., & Alam, F. (2023). Detecting and identifying the reasons for deleted tweets before they are posted. *Frontiers in Artificial Intelligence*, 6, 1219767.
[28] Nandwani, P., & Verma, R. (2021). A review on sentiment analysis and emotion detection from text. *Social Network Analysis and Mining*, 11(1), 81.
[29] Naskar, D., Singh, S. R., Kumar, D., Nandi, S., & Rivaherrera, E. O. d. l. (2020). Emotion dynamics of public opinions on twitter. *ACM Transactions on Information Systems (TOIS)*, 38(2), 1-24.
[30] Neijzen, D., & Lunter, G. (2023). Unsupervised learning for medical data: A review of probabilistic factorization methods. *Statistics in Medicine*, 42(30), 5541-5554.
[31] Ofori, M., & El-Gayar, O. (2021). Drivers and challenges of precision agriculture: a social media perspective. *Precision Agriculture*, 22(3), 1019-1044.
[32] Panda, R., & Sinha, B. (2023). An exploratory study on impact of social media on agriculture development from farmers growth perspective. *The Online Journal of Distance Education and e-Learning*, 11(2), 1966-1973.
[33] Pota, M., Ventura, M., Catelli, R., & Esposito, M. (2020). An effective BERT-based pipeline for Twitter sentiment analysis: A case study in Italian. *Sensors*, 21(1), 133.
[34] Qasim, R., Bangyal, W. H., Alqarni, M. A., & Ali Almazroi, A. (2022). A fine-tuned BERT-based transfer learning approach for text classification. *Journal of Healthcare Engineering*, 2022(1), 3498123.
[35] Qiang, J., Qian, Z., Li, Y., Yuan, Y., & Wu, X. (2020). Short text topic modeling techniques, applications, and performance: a survey. *IEEE Transactions on Knowledge and Data Engineering*, 34(3), 1427-1445.
[36] Reganold, J. P., Papendick, R. I., & Parr, J. F. (1990). Sustainable agriculture. *Scientific American*, 262(6), 112-121.

[37] Rejeb, A., Rejeb, K., & Hassoun, A. (2025). The impact of machine learning applications in agricultural supply chain: a topic modeling-based review. *Discover Food*, 5(1), 141.
[38] Rodrawangpai, B., & Daungjaiboon, W. (2022). Improving text classification with transformers and layer normalization. *Machine Learning with Applications*, 10, 100403.
[39] Sharma, S., Sharma, C., Asenso, E., & Sharma, K. (2023). Research constituents and trends in smart farming: an analytical retrospection from the lens of text mining. *Journal of Sensors*, 2023(1), 6916213.
[40] Trejo, J. A. O. (2025). Basic Uses of Python for Research in Our Laboratory: Examples of Data Analysis, and Processing of Histological Samples Based on the Special Graduate Lecture for Postgraduate Students Presented on January 2025. *Juntendo Medical Journal*, 71(4), 231-237.
[41] Tucciarone, I., Secci, G., Contiero, B., & Parisi, G. (2024). Sustainable aquaculture over the last 30 years: An analysis of the scientific literature by the Text Mining approach. *Reviews in Aquaculture*, 16(4), 2064-2076.
[42] Vayansky, I., & Kumar, S. A. (2020). A review of topic modeling methods. *Information Systems*, 94, 101582.
[43] Velten, S., Leventon, J., Jager, N., & Newig, J. (2015). What is sustainable agriculture? A systematic review. *Sustainability*, 7(6), 7833-7865.
[44] Xiao, L., Li, Q., Ma, Q., Shen, J., Yang, Y., & Li, D. (2024). Text classification algorithm of tourist attractions subcategories with modified TF-IDF and Word2Vec. *PloS One*, 19(10), e0305095.
[45] Xu, J., Li, Y., Zhang, M., & Zhang, S. (2024). Sustainable agriculture in the digital era: Past, present, and future trends by bibliometric analysis. *Heliyon*, 10(14).
[46] Yang, K., Lu, J., Duan, L., Tang, H., Bao, Z., Liu, Y., & Jiang, X. (2023). Research hotspots and theme trends in post-traumatic growth: A co-word analysis based on keywords. *International Journal of Nursing Sciences*, 10(2), 268-275.
[47] Yeomans, M., Boland, F. K., Collins, H. K., Abi-Esber, N., & Brooks, A. W. (2023). A practical guide to conversation research: How to study what people say to each other. *Advances in Methods and Practices in Psychological Science*, 6(4), 25152459231183919.
[48] Yuan, C., Li, G., Kamarthi, S., Jin, X., & Moghaddam, M. (2022). Trends in intelligent manufacturing research: a keyword co-occurrence network based review. *Journal of intelligent manufacturing*, 33(2), 425-439.
[49] Yulita, W., Untoro, M. C., Praseptiawan, M., Ashari, I. F., Afriansyah, A., & Pee, A. B. C. (2023). Automatic Scoring Using Term Frequency Inverse Document Frequency Document Frequency and Cosine Similarity. *Sci. J. Informatics*, 10(2), 93-104.
[50] Zucco, C., Calabrese, B., Agapito, G., Guzzi, P. H., & Cannataro, M. (2020). Sentiment analysis for mining texts and social networks data: Methods and tools. *Wiley Interdisciplinary Reviews: Data Mining and Knowledge Discovery*, 10(1), e1333.

PATH PLANNING FOR AGRICULTURAL PICKING MANIPULATORS USING A GRID-NUMBER-GUIDED IMPROVED RRT ALGORITHM
/
基于栅格编号引导的改进 RRT 算法的农业采摘机械臂路径规划

Wei ZHAO*[1)], Yang PAN[1)], Bangbo LIU[1)], Xi XU[1)], Tianle SHI[1)], Weijian SU[1)], Xiaobiao SHANG[1)], Hao PENG[1)], Hongfu ZHANG*[1)]
College of Mechanical and Electrical Engineering, Yunnan Agricultural University, Kunming, Yunnan / China
Tel: +86 184 8716 6782; E-mail: ynau_jd@163.com
Corresponding authors: Hongfu ZHANG
DOI: https://doi.org/10.35633/inmateh-79-57

Keywords: *picking manipulator; path planning; Optimized-RRT; grid-number-guided sampling; dynamic sampling region; trajectory smoothing*

ABSTRACT
Irregular branches in agricultural picking environments require rapid collision-free path planning and smooth manipulator motion. This study developed an improved RRT algorithm guided by grid numbering, termed Optimized-RRT, based on a unified indexed-set representation of numbered primary and backup free-grid regions. Within this framework, dynamic region adjustment, target biasing, node occupancy, and local burst expansion jointly guide the search, while greedy pruning and quintic polynomial interpolation are applied to post-process the resulting path. Unlike geometric-region-based methods that generate coordinate samples within an updated sampling window, Optimized-RRT selects a valid grid number from the active set and maps it directly to the corresponding state. Compared with RRT, GB-RRT, and Informed-RRT*, the complete algorithm reduced planning time, the number of iterations, and the final number of path nodes by 40.61%–94.32%, 57.51%–88.66%, and 89.29%–94.59%, respectively, in two-dimensional scenarios, and by 88.95%–98.92%, 79.26%–94.67%, and 67.31%–90.83%, respectively, in three-dimensional scenarios. The reduction in the number of nodes resulted from the combined effects of guided search and path pruning. Manipulator simulations and a demonstration on a single experimental platform confirmed the executability of the generated trajectories under the tested conditions.*

摘要
农业采摘环境中的不规则枝条要求机械臂快速生成无碰撞路径并实现平稳运动。本文提出基于统一索引集合表示的栅格编号引导改进 RRT 算法（Optimized-RRT），将主、备用自由栅格区域表示为可直接寻址的编号集合。在这一表示下，动态区域调整、目标偏置、节点占用和局部突发扩展协同引导搜索，贪心剪枝和五次多项式插值用于所得路径的后处理。不同于在更新后的几何区域中生成坐标样本的方法，Optimized-RRT 从当前活动集合中选择有效栅格编号，并将其直接映射为相应状态。相较于 RRT、B-RRT 和 Informed-RRT，完整算法流程在二维场景中将规划时间、迭代次数和最终路径节点数分别降低 40.61%-94.32%、5.51%-88.66%和 89.29%-94.59%，在三维场景中分别降低 88.95%-98.92%、9.26%-94.6%和 6.31%-90.83%。节点数的降低源于引导搜索与剪枝的共同作用。机械臂仿真和单一平台演示验证了测试条件下轨迹的可执行性。

INTRODUCTION
Labor shortages and the need for consistent harvesting efficiency have accelerated the development of agricultural robots and autonomous fruit- and vegetable-picking systems *(Cheng et al., 2023; Chen et al., 2024)*. In orchards and greenhouses, irregular branches and canopy structures form unstructured obstacles that complicate manipulator motion *(Karim et al., 2025)*. A picking manipulator must therefore generate a collision-free path to the target pose with sufficient planning speed and motion smoothness.

Deterministic graph-search methods such as A* and D* can become computationally demanding as the state dimension and map complexity increase *(Xuan et al., 2025)*, whereas population-based optimization may converge too slowly for online planning *(Zhu and Pan, 2024)*. Sampling-based motion planners avoid exhaustive state-space enumeration and are therefore well suited to complex, high-dimensional planning problems *(Orthey et al., 2024*). In agricultural applications, improved RRT variants have been used for grape-picking manipulators *(Hu et al., 2024)*, adaptive-step planning of tea-picking arms *(Li et al., 2024)*, and RGB-D-assisted Bi-RRT planning for orchard harvesting manipulators *(Liu et al., 2024)*.

These studies establish the application relevance of RRT-based planning, while conventional RRT still remains affected by random exploration, repeated expansion, and non-smooth paths.

Region-restricted and goal-guided sampling methods are the closest prior work to the present study. RRT* established parent reselection and rewiring as a foundation for asymptotically optimal sampling-based planning *(Karaman and Frazzoli, 2011)*, while Informed-RRT* restricts post-solution sampling to an admissible ellipsoidal subset *(Gammell et al., 2014)*. *Feng et al. (2023)* combined map-dependent step size and bias probability with dynamic sampling-region updates, sampling-point optimization, and node reconnection. For manipulators, *Shang et al. (2024)* developed the RRT*-DR algorithm for obstacle-avoidance planning, and *Xiao et al. (2024)* proposed FBi-RRT with heuristic node expansion. *He et al. (2025)* further combined ellipsoidal subset sampling and goal-biased sampling with adaptive step size, node rejection, pruning, and spline smoothing. These representative methods improve efficiency by restricting the geometric sampling domain, biasing expansion toward promising states, optimizing tree connections, or combining these mechanisms.

However, geometric-region restriction and target bias do not by themselves provide a common representation for active-region membership, alternative-region switching, and repeated-cell suppression. A target-biased planner changes how often the goal is selected, but its remaining samples still require a defined sampling domain. Likewise, a dynamically updated geometric window identifies where coordinates may be generated but does not necessarily make the valid free states directly addressable. The remaining engineering need is therefore a representation that coordinates region restriction and sampling control without presenting these established strategies as individually new.

Optimized-RRT addresses this need by representing the free cells of the main and backup regions as disjoint, directly addressable sets of grid numbers. A non-goal sample is obtained by selecting a number from the active set and mapping it directly to the corresponding cell-center state; dynamic restriction is implemented by set intersection, backup-region switching preserves an alternative sampling source, and node occupancy suppresses revisits at the selected grid resolution. Target bias therefore operates within the indexed-set representation rather than replacing region management. This differs from methods that primarily update a continuous sampling window or modify the probability or direction of goal-oriented sampling.

Accordingly, the primary contribution of this study lies in the indexed-set representation and the coordinated search mechanisms that it enables, rather than in the individual application of dynamic region adjustment, target biasing, pruning, or interpolation. The proposed representation supports direct grid-number-to-state mapping generalized to *d*-dimensional spaces and is integrated with local burst expansion, greedy pruning, and quintic polynomial interpolation within a unified search-to-trajectory pipeline for agricultural picking manipulators. The evaluation included repeated 2D and 3D simulations, sensitivity and ablation analyses, manipulator simulations, and a platform-based feasibility demonstration. No new results concerning asymptotic optimality or probabilistic completeness are claimed.

MATERIALS AND METHODS

Kinematic Modeling of the Picking Manipulator

Model of the Picking Manipulator and Modified D–H Parameters

A six-axis collaborative manipulator was used. Its model and modified D–H coordinate system are shown in Fig. 1, and the corresponding parameters are listed in Table 1.



a) *b)*

Fig. 1 – Six-axis collaborative manipulator: (a) manipulator model; (b) modified D–H coordinate system

Table 1

Modified D–H parameters of the manipulator

i	α_{i-1} [°]	a_{i-1} [m]	Joint variable θ_i	d_i [m]
1	0	0	θ_1	0.187
2	90	0	θ_2	0.006
3	0	0.210	θ_3	0
4	-90	0	θ_4	0.2105
5	90	0	θ_5	0
6	-90	0	θ_6	0.1593

Based on the modified D–H convention, the homogeneous transformation matrix from frame i to frame $i-1$ is expressed as:

$$\mathbf{T}_i^{i-1} = \begin{bmatrix} c_{\theta_i} & -s_{\theta_i} & 0 & a_{i-1} \\ s_{\theta_i}c_{\alpha_{i-1}} & c_{\theta_i}c_{\alpha_{i-1}} & -s_{\alpha_{i-1}} & -d_i s_{\alpha_{i-1}} \\ s_{\theta_i}s_{\alpha_{i-1}} & c_{\theta_i}s_{\alpha_{i-1}} & c_{\alpha_{i-1}} & d_i c_{\alpha_{i-1}} \\ 0 & 0 & 0 & 1 \end{bmatrix} \quad (1)$$

In Eq. (1), $c_{\theta_i} = \cos\theta_i$ and $s_{\theta_i} = \sin\theta_i$; the same notation applies to α_{i-1}. The end-effector pose relative to the base frame is obtained by successively multiplying the six adjacent-frame transformation matrices:

$$\mathbf{T}_6^0 = \mathbf{T}_1^0\mathbf{T}_2^1\mathbf{T}_3^2\mathbf{T}_4^3\mathbf{T}_5^4\mathbf{T}_6^5 = \prod_{i=1}^{6}\mathbf{T}_i^{i-1} \quad (2)$$

Collision Detection Modeling

For efficient collision checking, manipulator links were approximated by cylinders and irregular obstacles by spherical envelopes *(Jiang L. et al., 2022; Shi et al., 2022; Wang H. et al., 2025)*. As shown in Fig. 2, the link radius, obstacle radius, and an additional safety margin were combined into a conservative collision radius.

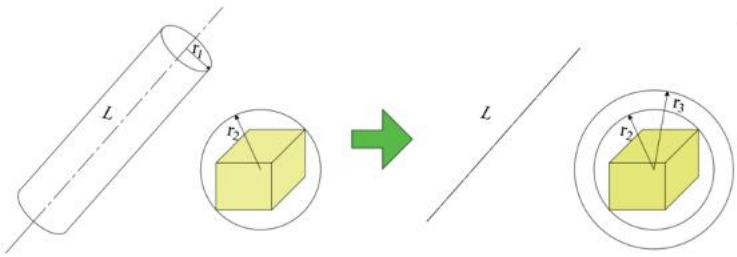


Fig. 2 – Conservative geometric simplification for collision detection

As shown in Fig. 3, each link segment was discretized into N equal subintervals. The point locations, point-to-obstacle distances, conservative collision radius, and collision criterion are defined as:

$$\begin{gathered} \mathbf{P}_i = \mathbf{P}_s + \frac{i}{N}(\mathbf{P}_e - \mathbf{P}_s), \quad i = 0,1,\ldots,N \\ d_i = \|\mathbf{P}_i - \mathbf{C}_o\|_2 = \sqrt{(x_i - x_c)^2 + (y_i - y_c)^2 + (z_i - z_c)^2} \\ r_c = r_l + r_o + \delta_s \\ \min_{0\le i\le N} d_i \le r_c \end{gathered} \quad (3)$$

In Eq. (3), $\mathbf{P}_s$ and $\mathbf{P}_e$ are the start and end points of the link segment, $\mathbf{P}_i$ is its i-th discrete point, and N is the number of equal subintervals. $\mathbf{C}_o = (x_c, y_c, z_c)^{\mathrm{T}}$ is the obstacle-center coordinate, while r_l, r_o, and δ_s denote the link-envelope radius, obstacle-envelope radius, and additional safety margin, respectively.

A collision was identified when the minimum discrete-point distance was not greater than the conservative collision radius. N was selected link-wise to keep adjacent checking points close relative to the conservative envelope. This discrete approximation improves efficiency but does not constitute certified continuous-time clearance; the safety margin represents modeling and localization uncertainty rather than a measured minimum clearance.

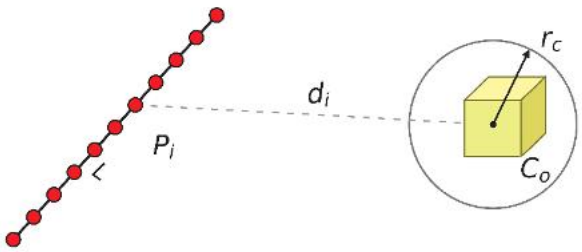


Fig. 3 – Discrete point-to-sphere collision detection along a link segment

Strategy of the Proposed Optimized-RRT Algorithm

Grid Map Construction

The planning map was discretized into fixed cells. A cell was marked as occupied when it intersected an obstacle; otherwise, it was treated as free. The complete grid set is defined as:

$$\mathcal{C} = \{c_{ij} \mid i = 1,2,\dots,n_r;\ j = 1,2,\dots,n_c\}, \qquad N_g = n_r n_c \tag{4}$$

In Eq. (4), c_{ij} denotes the cell in row i and column j, n_r and n_c are the numbers of rows and columns, and $N_g = n_r n_c$ is the total number of grid cells. The obstacle set is defined as:

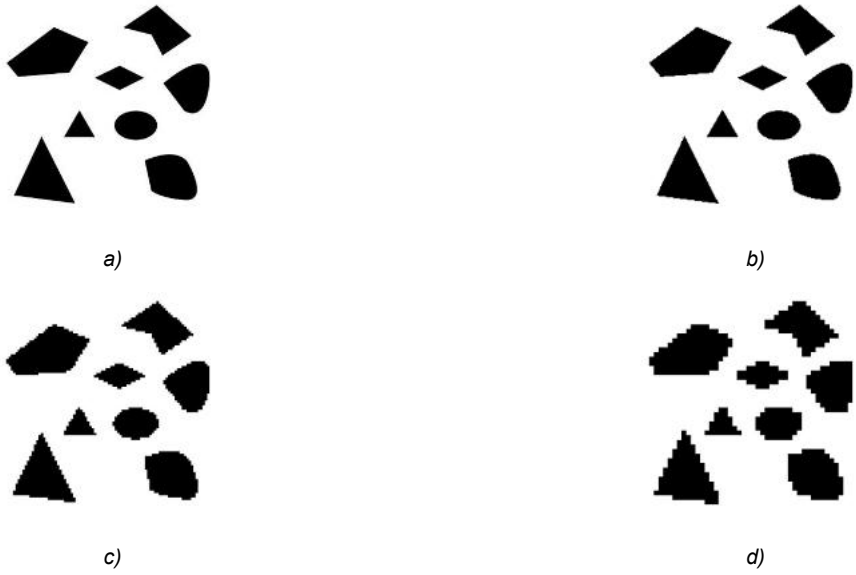
$$\mathcal{O} = \{o_k \mid k = 1,2,\dots,N_o\} \tag{5}$$

In Eq. (5), o_k denotes the k-th obstacle and N_o is the total number of obstacles. The occupancy state of each grid cell is described by the Boolean function:

$$\begin{aligned} f(c_{ij}) &= 1, \quad \text{if } \exists\, o_k \in \mathcal{O}:\ \Omega(c_{ij}) \cap \Omega(o_k) \neq \varnothing \\ f(c_{ij}) &= 0, \quad \text{otherwise} \end{aligned} \tag{6}$$

In Eq. (6), $\Omega(c_{ij})$ and $\Omega(o_k)$ denote the physical regions occupied by grid cell c_{ij} and obstacle o_k, respectively. A value of $f(c_{ij}) = 1$ identifies an obstacle cell, whereas $f(c_{ij}) = 0$ identifies a free cell.

Grid resolution controls the trade-off between obstacle-boundary fidelity and computational cost: smaller cells preserve geometry more accurately but increase storage and processing requirements. Fig. 4 compares side lengths of 2, 5, and 10 pixels. The precision retention ratio is the original obstacle area divided by the occupied grid-cell area; lower values indicate greater obstacle expansion after discretization.



a) *b)*

c) *d)*

Fig. 4 – Grid discretization at different resolutions: (a) original image; (b) 2 pixels; (c) 5 pixels; (d) 10 pixels

Table 2

Grid discretization data at different cell sizes

Grid side length [pixels]	Time [s]	Precision retention ratio
2	0.0509	0.97
5	0.0087	0.90
10	0.0027	0.77

As the grid side length increased from 2 to 10 pixels, processing time decreased from 0.0509 to 0.0027 s, while the precision retention ratio decreased from 0.97 to 0.77 (Table 2). The image-based example in Fig. 4 and Table 2 illustrates the general trade-off between grid resolution and processing efficiency. In the subsequent path-planning experiments, a grid side length of 10 mm was adopted as the baseline setting.

Grid-Number-Guided Sampling

Conventional restricted-region sampling defines a geometric domain and then generates coordinates within it; depending on the representation, samples may still fall outside the active free subset or revisit previously explored cells *(Oh et al., 2025; He et al., 2025).* Optimized-RRT instead divides the free workspace into a main sampling region and a backup sampling region (Fig. 5) and represents both regions using disjoint sets of valid grid numbers. The main set concentrates non-goal sampling toward the target, whereas the backup set preserves alternative routes when expansion in the main region becomes inefficient. Target-biased samples are introduced within this set-based region-management framework.

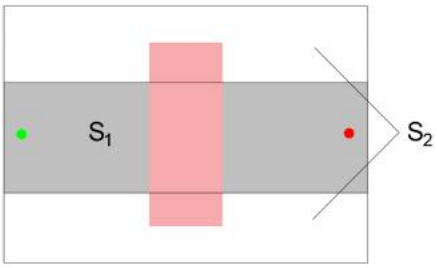


Fig. 5 – Division of the main and backup sampling regions

Each grid cell is assigned a unique number (Fig. 6). Sampling is performed by selecting a number from the active region set and mapping that number to the corresponding cell-center coordinate.

1	8	15	22	29	36	43	50	57	64
2	9	16	23	30	37	44	51	58	65
3	10	17	24	31	38	45	52	59	66
4	11	18	25	32	39	46	53	60	67
5	12	19	26	33	40	47	54	61	68
6	13	20	27	34	41	48	55	62	69
7	14	21	28	35	42	49	56	63	70

Fig. 6 – Grid numbering used for region-guided sampling

Using column-major numbering, each grid cell is assigned a unique number and the free-grid sampling set is defined as:

$$g_{ij} = (j-1)n_r + i, \qquad \mathcal{G}_f = \{g_{ij} \mid f(c_{ij}) = 0\} \tag{7}$$

In Eq. (7), $g_{ij} = (j-1)n_r + i$ is the unique number of the cell in row i and column j, and $\mathcal{G}_f$ contains only free-grid numbers. The main and backup sampling sets are defined as:

$$\begin{gathered} \mathcal{A} = \{g \in \mathcal{G}_f \mid \mathbf{x}(g) \in \Omega_{\text{main}}\} \\ \mathcal{B} = \{g \in \mathcal{G}_f \mid \mathbf{x}(g) \in \Omega_{\text{backup}}\} \\ \mathcal{A} \cup \mathcal{B} = \mathcal{G}_f, \qquad \mathcal{A} \cap \mathcal{B} = \varnothing \end{gathered} \tag{8}$$

In Eq. (8), $\mathbf{x}(g)$ maps grid number g to its cell-center coordinate, while Ω_{main} and Ω_{backup} denote the main and backup spatial regions. The two sets form a disjoint partition of $\mathcal{G}_f$, so direct number selection always produces a sample in the active free-grid region.

The following switching rule determines the active sampling region:

$$\begin{aligned} S_{k+1} &= S_2, \quad S_k = S_1, \quad \frac{N_1^{\text{succ}}}{\max\left(N_1^{\text{fail}}, 1\right)} < T_{\text{eff}} \\ S_{k+1} &= S_1, \quad S_k = S_2, \quad N_2^{\text{succ}} > \text{floor}\left(\frac{L}{10\Delta}\right) \\ S_{k+1} &= S_k \end{aligned} \tag{9}$$

In Eq. (9), S_k is the active region before the k-th switching decision. N_1^{succ} and N_1^{fail} are the numbers of successful and failed node-generation attempts in the main region S_1, respectively. T_{eff} is the region-switching threshold. N_2^{succ} is the number of valid nodes generated in the backup region S_2, L is the start-to-target distance, and Δ is the fixed expansion step.

After each switch, the counters are reset to avoid overly frequent alternation. When the valid-to-invalid expansion ratio in S_1 falls below T_{eff}, sampling is transferred to S_2; after sufficient valid expansion in S_2, the algorithm returns to S_1.

Local Burst Expansion Sampling Strategy

Local burst expansion provides two candidate samples in one iteration. The first is the center of a randomly selected grid; the second is generated within its neighboring-grid region (Fig. 7).



a) b)

Fig. 7 – Local burst expansion: (a) primary grid selection; (b) neighboring-grid sampling region

If the primary candidate fails to generate a valid node, a second candidate is sampled from the neighboring-grid region defined by:

$$\mathcal{R}_{\text{local}} = \{(x, y) \in \Omega_{\text{free}} \mid |x - x_c| \le d,\ |y - y_c| \le d\} \tag{10}$$

In Eq. (10), (x_c, y_c) is the center of the primary grid and d is the neighborhood half-width. For a one-cell neighborhood, d equals the grid side length. The second candidate reduces iterations lost when the first candidate is invalid.

Dynamic Sampling Region Strategy

The active sampling region is dynamically narrowed as the tree approaches the target. When a newly generated node is closer to the target than all existing nodes, its grid number and the target grid number define the updated sampling interval. A narrowly updated region may stagnate near an obstacle (Fig. 8(a)). The interval is therefore expanded on both sides to preserve alternative search directions (Fig. 8(b)).



a) b)

Fig. 8 – Dynamic sampling region: (a) narrowed region; (b) expanded region

The dynamically expanded free-grid interval is defined as:

$$g_{\min} = \max(1, \min(u, v) - fn_r)$$
$$g_{\max} = \min(N_g, \max(u, v) + fn_r) \quad (11)$$
$$\mathcal{G}' = \{g \in \mathcal{G}_f \mid g_{\min} \le g \le g_{\max}\}$$

In Eq. (11), u and v are the grid numbers of the target and the current node closest to the target, respectively; f is the number of columns added on each side; n_r is the number of grid cells per column; and N_g is the total number of grid cells. The operators $\min(u, v)$ and $\max(u, v)$ ensure that the interval remains valid regardless of the numbering direction. The partition sets are then updated as:

$$\mathcal{A}' = \mathcal{A} \cap \mathcal{G}', \qquad \mathcal{B}' = \mathcal{B} \cap \mathcal{G}' \quad (12)$$

Equation (12) intersects the original main and backup sets with the dynamically expanded free-grid set. This preserves the original spatial partition while removing grid numbers outside the active interval.

Extension to Three-Dimensional and Joint Spaces

For a d-dimensional state $\mathbf{q} = (q_1, \ldots, q_d)$, let $q_{k,\min}$ and $q_{k,\max}$ be the bounds of dimension k, h_k its cell width, n_k the number of cells, and $i_k = \lfloor \frac{q_k - q_{k,\min}}{h_k} \rfloor$ its zero-based index. The mixed-radix grid number is $g(\mathbf{q}) = 1 + \sum_{k=1}^{d} i_k \prod_{j=1}^{k-1} n_j$; the inverse state is recovered by integer division and remainder operations followed by cell-center mapping. Equation (7) is the $d = 2$ case; $d = 3$ was used for Cartesian simulation and $d = 6$ for the manipulator configuration space, with joint bounds obtained from the URDF model.

Main and backup sets contain free grid numbers whose centers satisfy the corresponding region definitions, and a local neighborhood satisfies $|i_k - i_{k,c}| \le r_k$ in every dimension. Number/state mapping costs $O(d)$, whereas the potential grid count $\prod_{k=1}^{d} n_k$ grows exponentially with dimension, so memory and behavior depend on resolution. Node occupancy suppresses revisits at cell resolution but may discard distinct configurations within one cell. Accordingly, no probabilistic-completeness or resolution-independent scalability claim is made.

Node occupancy Strategy

Each accepted node marks its grid cell as occupied (Fig. 9). A candidate falling in an occupied cell is discarded, reducing repeated visits and redundant computation.

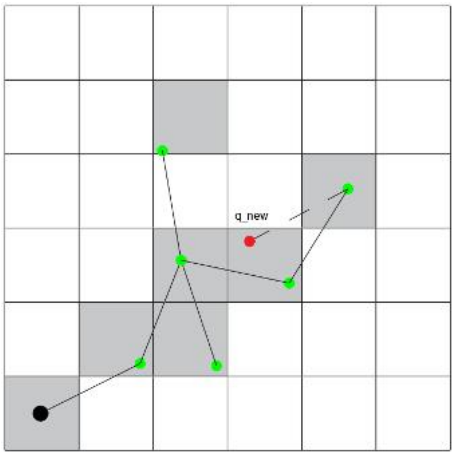


Fig. 9 – Node occupancy strategy

Target-Biased Sampling Strategy

Target-biased sampling improves the directional efficiency of tree expansion. The sampling rule is defined as follows:

$$\mathbf{x}_{\text{sample}} = \mathbf{x}_{\text{goal}}, \quad \xi \le p_g$$
$$\mathbf{x}_{\text{sample}} = \mathbf{x}(g), \quad \xi > p_g, \quad g \sim U(\mathcal{G}_{\text{active}}) \quad (13)$$
$$\xi \sim U(0,1)$$

In Eq. (13), ξ is uniformly distributed over $[0,1]$, p_g is the target-bias probability, $\mathcal{G}_{\text{active}}$ is the currently active grid-number set, and $\mathbf{x}(g)$ maps a selected grid number to its cell-center coordinate.

Greedy Pruning Strategy

The raw path may contain redundant intermediate nodes. Greedy pruning tests direct collision-free connections from the current node to later nodes and removes all bypassed nodes (Fig. 10).



a) b)

Fig. 10 – Greedy pruning: (a) raw path; (b) pruned path

Quintic Polynomial Interpolation for Trajectory Smoothing

A quintic polynomial was applied independently to each joint and each consecutive pruned path segment to obtain continuous joint position, velocity, and acceleration under specified endpoint conditions *(Xu et al., 2023)*:

$$\theta_j^{(s)}(t) = a_{0,j}^{(s)} + a_{1,j}^{(s)}t + a_{2,j}^{(s)}t^2 + a_{3,j}^{(s)}t^3 + a_{4,j}^{(s)}t^4 + a_{5,j}^{(s)}t^5, \quad 0 \le t \le T_s \tag{14}$$

For segment s, the start and end positions are defined by consecutive joint-space waypoints, while the endpoint velocity and acceleration are set to zero. The polynomial coefficients are obtained from:

$$\mathbf{a}_j^{(s)} = \mathbf{M}(T_s)^{-1}\mathbf{b}_j^{(s)}$$

$$\mathbf{M}(T_s) = \begin{bmatrix} 1 & 0 & 0 & 0 & 0 & 0 \\ 0 & 1 & 0 & 0 & 0 & 0 \\ 0 & 0 & 2 & 0 & 0 & 0 \\ 1 & T_s & T_s^2 & T_s^3 & T_s^4 & T_s^5 \\ 0 & 1 & 2T_s & 3T_s^2 & 4T_s^3 & 5T_s^4 \\ 0 & 0 & 2 & 6T_s & 12T_s^2 & 20T_s^3 \end{bmatrix} \tag{15}$$

$$\mathbf{b}_j^{(s)} = \left[\theta_j^{(s)}(0) \quad \dot{\theta}_j^{(s)}(0) \quad \ddot{\theta}_j^{(s)}(0) \quad \theta_j^{(s)}(T_s) \quad \dot{\theta}_j^{(s)}(T_s) \quad \ddot{\theta}_j^{(s)}(T_s)\right]^{\mathrm{T}}$$

In Eq. (15), $\mathbf{a}_j^{(s)} = \left[a_{0,j}^{(s)}, a_{1,j}^{(s)}, \ldots, a_{5,j}^{(s)}\right]^{\mathrm{T}}$ is the coefficient vector for joint j in segment s, T_s is the segment duration, and $\mathbf{b}_j^{(s)}$ contains the prescribed endpoint position, velocity, and acceleration. In this study, the endpoint velocities and accelerations were set to zero.

Quintic interpolation was applied segment by segment after pruning to produce the final executable joint trajectory.

Workflow of Optimized-RRT

Fig. 11 summarizes the complete pipeline: initialization and d-dimensional grid numbering are followed by region-set construction, grid-number sampling, collision and occupation checks, tree extension, region updating, path backtracking, greedy pruning, and quintic interpolation.

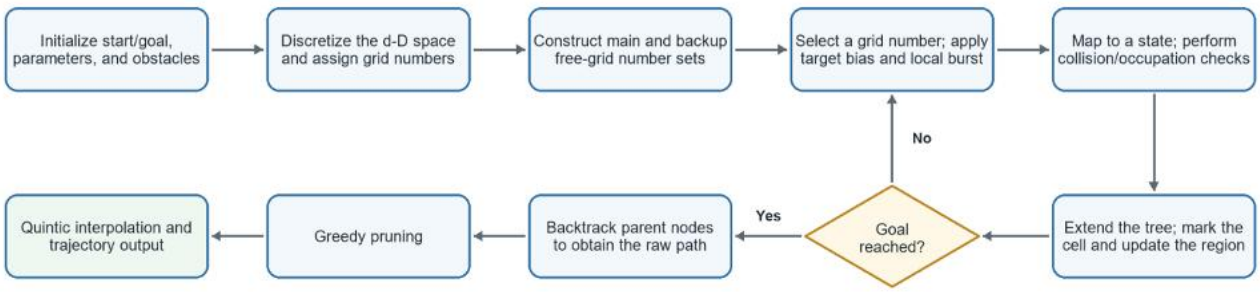


Fig. 11 – Workflow of Optimized-RRT

RESULTS

Simulation Experiments and Analysis of the Algorithm

RRT, goal-biased RRT* (GB-RRT*), Informed-RRT*, and Optimized-RRT were compared as practical time-to-feasible-path planners in 2D, 3D, and manipulator scenarios. Within each scenario, they used the same map, start/target states, obstacle model, collision criterion, computing environment, and expansion settings where applicable. Each implementation retained its own search and rewiring logic and stopped when it returned a feasible path; the comparison therefore concerns the implemented pipelines rather than asymptotic RRT* optimality.

For each algorithm and scenario, 100 independent simulations with random seeds were conducted in MATLAB 2022b on 64-bit Windows 11 Enterprise with an Intel Core i5-13500H processor. The tables report descriptive mean ± standard deviation for planning time, iterations, and path length, and the mean final node count. Greedy pruning was part of the Optimized-RRT pipeline and was not retrofitted to every baseline; consequently, final-node reductions represent the complete pipelines and cannot be attributed solely to sampling. The archived results were aggregate summaries, so no post hoc significance test or success-rate reconstruction was added, and no claim of statistical significance is made.

Two-Dimensional Simulation in a Narrow Agricultural Environment

The basic parameters of the four algorithms were kept consistent in the typical two-dimensional narrow and complex scenario. The simulation map was $1000\ \mathrm{mm} \times 1000\ \mathrm{mm}$, and each grid cell was $10\ \mathrm{mm} \times 10\ \mathrm{mm}$. The start and target points were $(35{,}35)\ \mathrm{mm}$ and $(900{,}900)\ \mathrm{mm}$, respectively, and the fixed expansion step was $\Delta = 20\ \mathrm{mm}$. The target-bias probability of both Optimized-RRT and GB-RRT* was set to $p_g = 0.05$. For Optimized-RRT, the number of expanded columns was $f = 10$, and the region-switching threshold was $T_{\mathrm{eff}} = 0.16$.

Fig. 12 shows the exploration trees and collision-free paths. Green and red circles denote the start and target, black areas denote obstacles, green lines denote the search tree, and the red line denotes the final path. In Fig. 12(d), the area between the blue boundaries is the main sampling region. Across 100 runs, Optimized-RRT reduced mean planning time by 40.61%–94.32%, iterations by 57.51%–88.66%, and final path-node count by 89.29%–94.59% relative to the three baselines (Table 3). Fig. 12 also shows a more concentrated search tree, with fewer repeated expansions near obstacles.

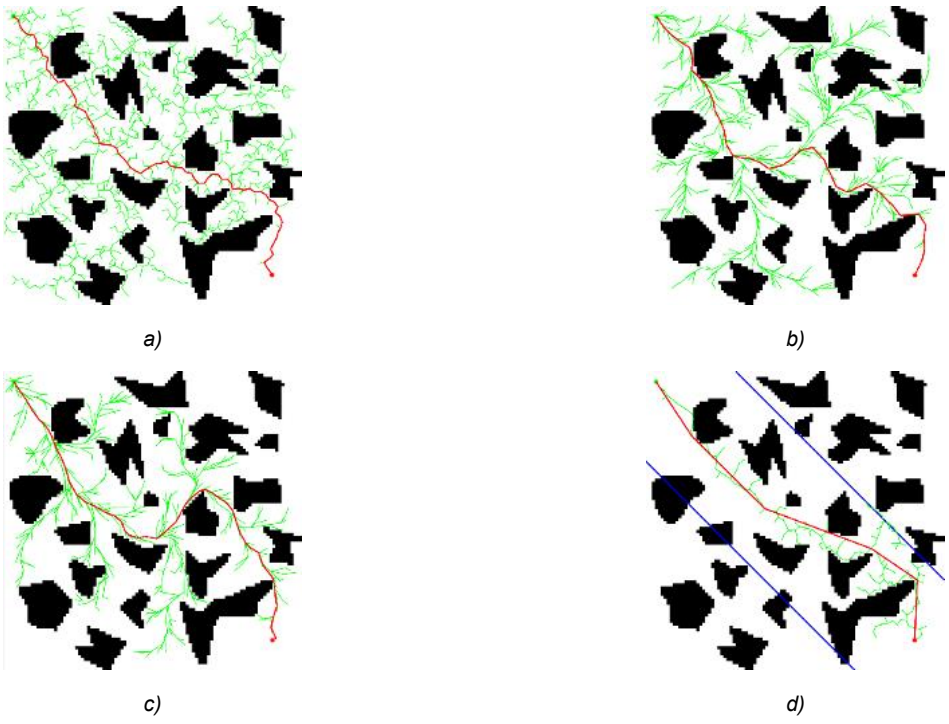


Fig. 12 – Two-dimensional planning results: (a) RRT; (b) GB-RRT*; (c) Informed-RRT*; (d) Optimized-RRT

Table 3

Performance comparison in the two-dimensional scenario (descriptive statistics)

Algorithm	Planning time [s]	Number of iterations	Path length [mm]	Final path nodes
RRT	0.097 ± 0.121	1144.1 ± 641.5	1674.990 ± 89.525	85.04
GB-RRT*	0.049 ± 0.026	662.3 ± 178.0	1448.045 ± 77.170	42.93
Informed-RRT*	0.512 ± 0.654	2480.7 ± 1127.6	1451.024 ± 74.337	43.07
Optimized-RRT	0.029 ± 0.011	281.4 ± 82.0	1291.823 ± 40.641	4.60

Three-Dimensional Simulation

The parameters of the four algorithms were kept consistent in the typical three-dimensional case. The simulation space was $500\,\mathrm{mm} \times 500\,\mathrm{mm} \times 500\,\mathrm{mm}$, and each grid cell was $10\,\mathrm{mm} \times 10\,\mathrm{mm} \times 10\,\mathrm{mm}$. The start and target points were $(10,10,10)\,\mathrm{mm}$ and $(460,460,460)\,\mathrm{mm}$, respectively, and the fixed expansion step was $\Delta = 20\,\mathrm{mm}$. For Optimized-RRT, $f = 10$ and $T_{\mathrm{eff}} = 0.16$.

In the three-dimensional scenario, Optimized-RRT reduced planning time by 88.95%–98.92%, iterations by 79.26%–94.67%, and final path-node count by 67.31%–90.83% relative to the baselines (Table 4). Figs. 13 and 14 show that Optimized-RRT generated a sparser exploration tree and a path with fewer turns. Grid-number-guided sampling concentrated expansion within the active region, while region switching preserved obstacle-bypassing alternatives and pruning simplified the final path.

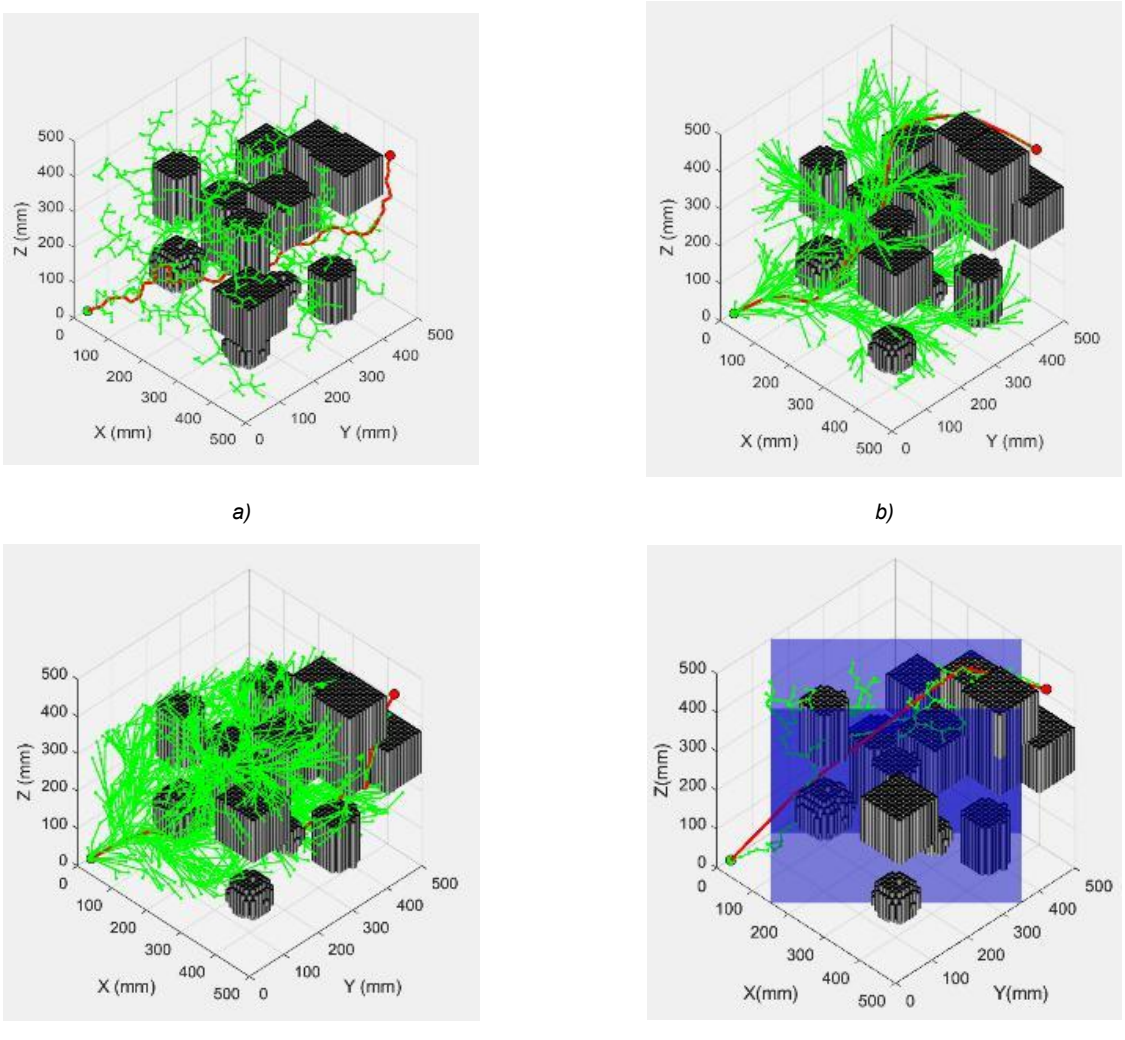


Fig. 13 – Three-dimensional exploration trees: (a) RRT; (b) GB-RRT*; (c) Informed-RRT*; (d) Optimized-RRT

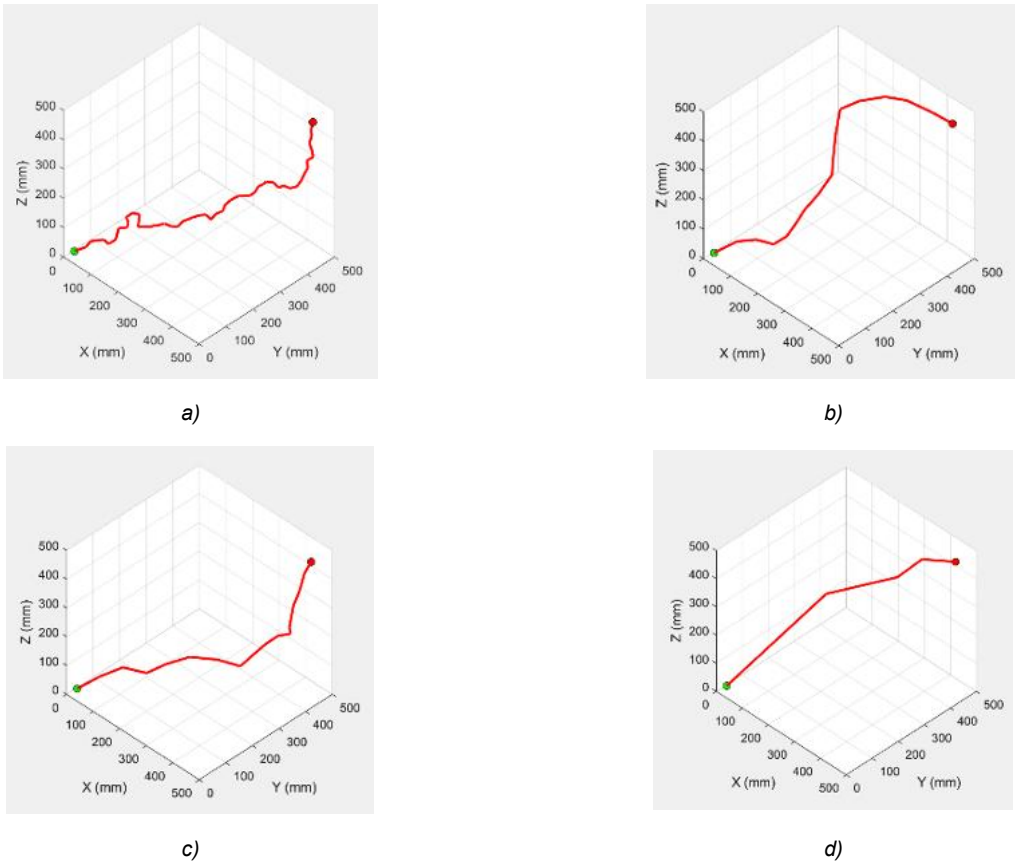


Fig. 14 – Three-dimensional final paths: (a) RRT; (b) GB-RRT*; (c) Informed-RRT*; (d) Optimized-RRT

Table 4

Performance comparison in the three-dimensional scenario (descriptive statistics)

Algorithm	Planning time [s]	Number of iterations	Path length [mm]	Final path nodes
RRT	0.662 ± 0.559	2400.9 ± 931.7	1239.371 ± 93.277	62.89
GB-RRT*	0.376 ± 0.421	1272.1 ± 650.1	932.245 ± 44.793	17.65
Informed-RRT*	3.825 ± 1.824	4948.0 ± 1383.4	947.552 ± 41.742	17.70
Optimized-RRT	0.041 ± 0.017	263.9 ± 81.1	858.918 ± 24.036	5.77

Parameter Sensitivity Analysis

A one-factor-at-a-time sensitivity analysis was conducted in the two-dimensional scenario. Grid side length was set to 5, 10, and 20 mm; expansion step Δ to 10, 20, and 30 mm; target-bias probability p_g to 0.02, 0.05, and 0.10; and region-switching threshold T_{eff} to 0.10, 0.16, and 0.25. Each level used 50 independent simulations with the other parameters fixed at their baseline values.

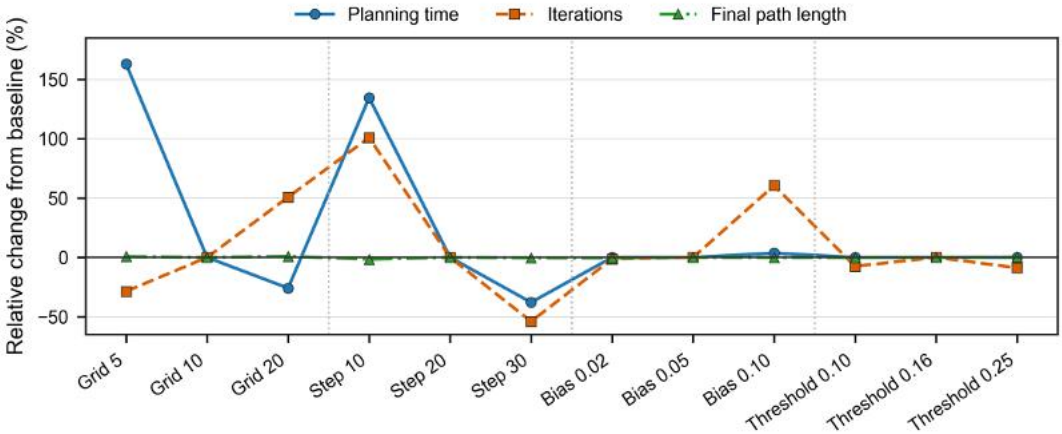


Fig. 15 – Parameter sensitivity analysis relative to the baseline settings

Fig. 15 shows that grid size and step size had the largest effects on planning time and iterations, whereas the final path length varied less. Smaller grids improved representation but increased numbering and search overhead; larger steps reduced expansion count but weakened local adjustment. Target-bias probability and the region-switching threshold had limited influence within the tested ranges. The baseline values—a 10-mm grid, $\Delta = 20\,\mathrm{mm}$, $p_g = 0.05$, and $T_{\mathrm{eff}} = 0.16$—provided a balanced combination of planning efficiency and path quality.

Ablation Experiment on Optimization Strategies

Ablation variants were created by disabling one strategy at a time: dynamic sampling-region adjustment (No-DSD), local burst expansion (No-LBES), node occupancy (No-NOP), target-biased sampling (No-GBS), or greedy pruning (No-GP). All variants used the same map, planning parameters, and random-seed sequence.

Planning time, iterations, original and final path lengths, and original and final node counts were recorded. All variants except No-GP used the same pruning procedure; No-GP retained the raw tree path.

Fig. 16 reports relative changes after each strategy was disabled; positive values indicate increases in time, iterations, or path length. The ablation results show a dimension-dependent trade-off rather than uniform benefit. Removing dynamic region adjustment reduced 2D planning time by approximately 50%, and disabling node occupancy or target bias also produced small 2D time reductions, indicating that set maintenance can outweigh guidance in a simple space. In 3D, dynamic adjustment and target bias produced clearer efficiency benefits, while local burst expansion reduced iterations in both spaces. Greedy pruning dominated final path reduction. Because Fig. 16 contains relative aggregate changes without uncertainty intervals, these effects are interpreted directionally rather than as statistically established module contributions.

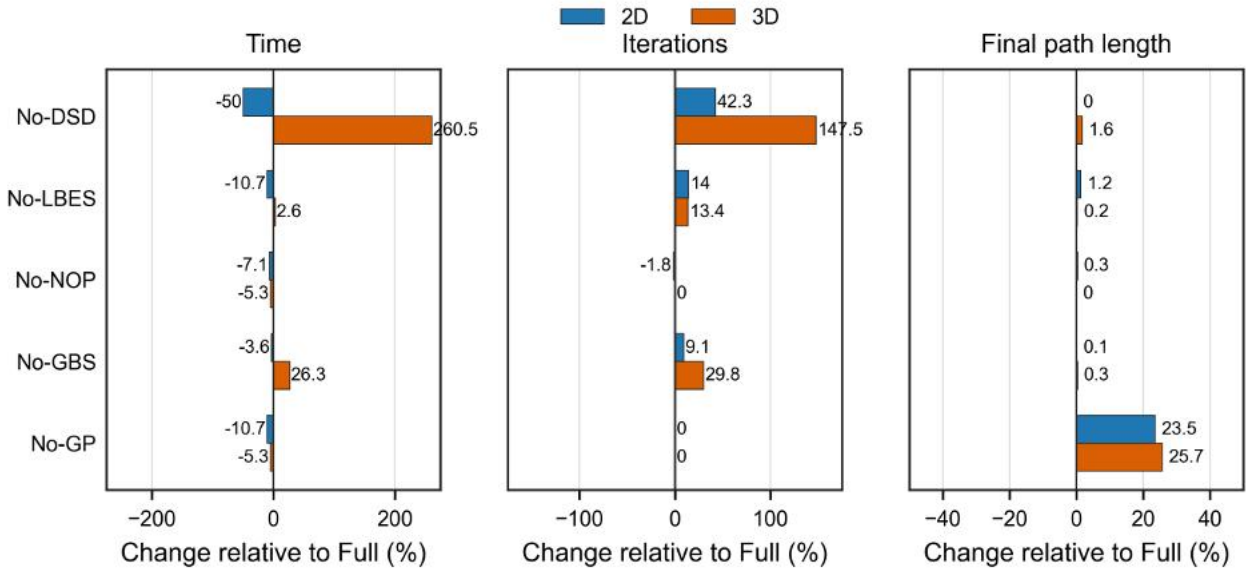
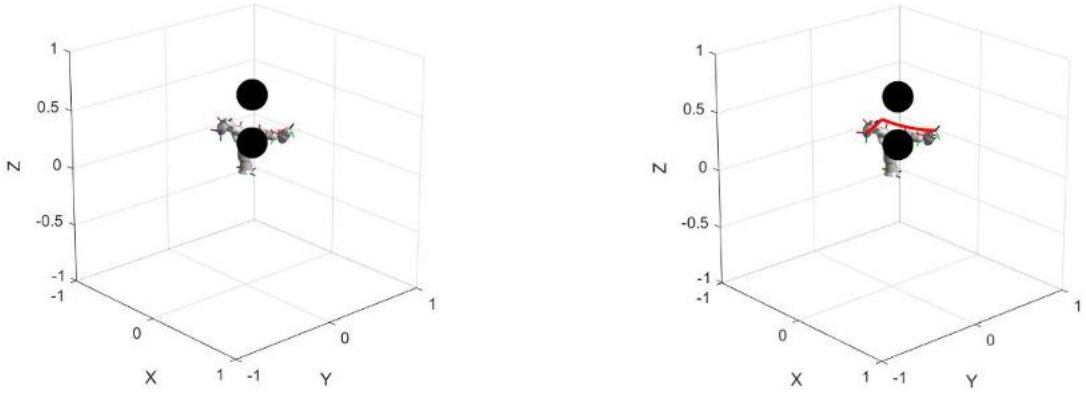


Fig. 16 – Ablation results relative to the complete Optimized-RRT

Simulation Experiment on Path Planning for the Picking Manipulator

A MATLAB 2022b manipulator simulation used the URDF model, the initial and target postures shown in Fig. 17, and two spherical obstacles centered at (0.33, −0.23, 0.40) m and (0.33, −0.23, 0.80) m (Fig. 17(a)).

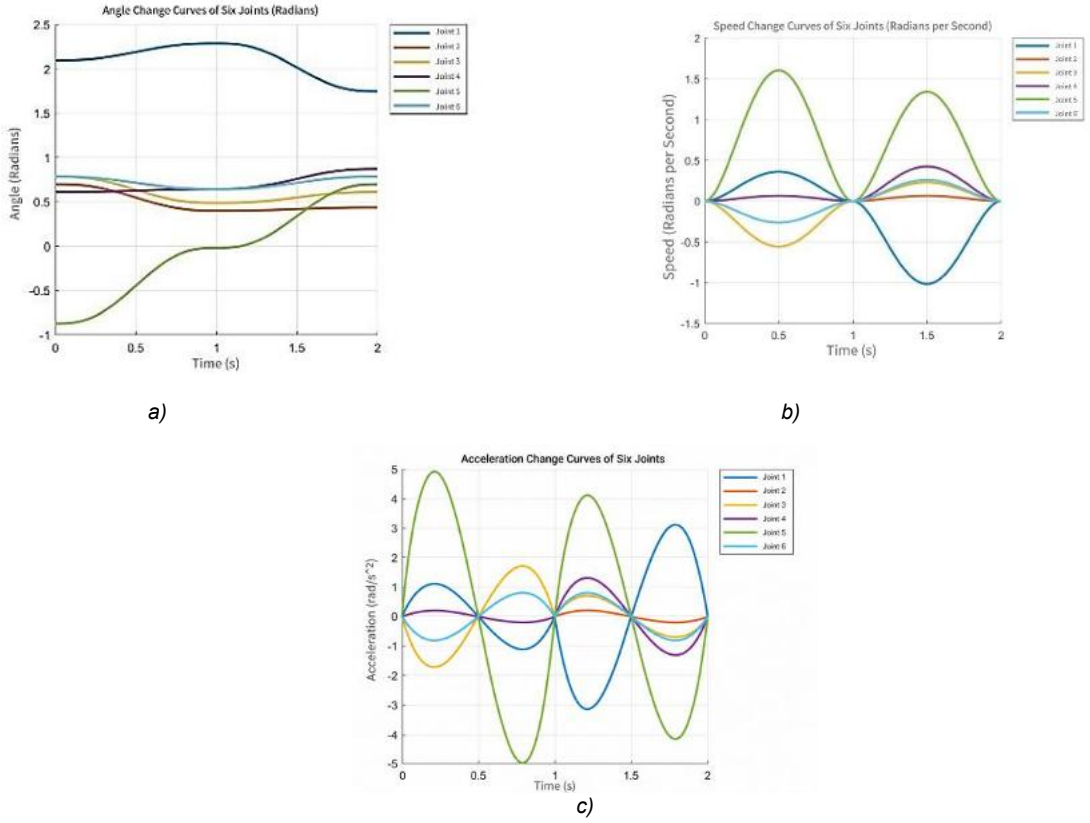
Planning was performed in the six-dimensional joint space using the URDF joint limits and joint-specific grid indices described above. The pruned path was smoothed by quintic interpolation, and the resulting end-effector trajectory is shown in Fig. 17(b).



a) b)

Fig. 17 – Manipulator planning: (a) simulation environment; (b) end-effector trajectory

Fig. 18 shows continuous joint-angle, velocity, and acceleration profiles with the prescribed zero endpoint conditions. These curves demonstrate interpolation continuity, but they were not optimized against measured hardware velocity, acceleration, or jerk limits and should not be interpreted as a time-optimality or actuator-margin assessment.



a) b)

c)

Fig. 18 – Joint trajectory profiles: (a) joint angle; (b) joint velocity; (c) joint acceleration

Real-Platform Feasibility Demonstration in an Agricultural Picking Environment

A single-case feasibility demonstration used a picking platform comprising a six-degree-of-freedom collaborative manipulator, depth camera, flexible end-effector, robot controller, and ROS upper computer; joint commands were transmitted via Gigabit Ethernet. GB-RRT* and Optimized-RRT used the same target, obstacle distribution, and initial posture. Execution time denotes total platform motion/task time rather than isolated planning computation time; joint-space path length and final node count were also recorded. In this arrangement, Optimized-RRT reduced total execution time from 23.1 to 16.5 s (28.57%), joint-space path length from 3.12 to 2.61 rad (16.35%), and final path nodes from 36 to 4 (88.89%) relative to GB-RRT* (Table 5), demonstrating executability and lower path redundancy for this case but not repeatability, statistical superiority, or robustness across greenhouse conditions.

Table 5

Single-case real-platform execution results

Algorithm / optimization rate	Total execution time [s]	Path length [rad]	Final path nodes
GB-RRT*	23.1	3.12	36
Optimized-RRT	16.5	2.61	4
Optimization rate [%]	28.57	16.35	88.89



a) b) c) d) e)

Fig. 19 – Platform sequence: (a) initial; (b–d) obstacle avoidance; (e) completed grasp

DISCUSSION AND LIMITATIONS

The indexed-set representation coordinated active-region restriction, backup-region switching, and repeated-cell suppression through a common sampling structure, but the benefits of its component strategies were dimension dependent. Grid-number guidance produced larger 3D gains while incurring 2D bookkeeping overhead. Planning time and iterations reflect sampling, extension, and switching, whereas node and path reductions depend strongly on pruning. Because baseline post-processing differed and only aggregate results were retained, comparisons are pipeline-level and establish neither module-level causality nor statistical significance. The single platform trial demonstrates feasibility, not robustness; discrete checking, uncalibrated clearance, and fixed endpoints limit safety conclusions. Future work should retain run-level data, harmonize post-processing, verify actuator and collision limits, and test varying branch density, occlusion, and localization error.

CONCLUSIONS

Optimized-RRT is built on a unified indexed-set representation of numbered main and backup free-grid regions. Within this representation, dynamic restriction, region switching, node occupancy, target bias, and local burst expansion coordinate the search, while greedy pruning and quintic interpolation post-process the path. In 2D, planning time, iterations, and final nodes decreased by 40.61%-94.32%, 57.51%-88.66%, and 89.29%-94.59%; in 3D, they decreased by 88.95%-98.92%, 79.26%-94.67%, and 67.31%-90.83%. The results support the value of the complete representation-and-processing pipeline rather than demonstrating that every component is uniformly beneficial: guided sampling improved search efficiency, whereas pruning dominated node reduction. Simulation yielded continuous trajectories, and the single platform case reduced total execution time, joint-space path length, and final nodes by 28.57%, 16.35%, and 88.89%, respectively. Repeatability, calibrated clearance, hardware-limit compliance, and robustness to branch density, occlusion, localization error, and fruit-tree geometry require further evaluation.

ACKNOWLEDGMENTS

This work was supported by the Yunnan Science and Technology Major Project under Grant No. 202602AE090051 and the China Central Fund for Guiding Development of Local Science and Technology under Grant No. 202407AB110010.

REFERENCES

[1] Chen Z., Lei X., Yuan Q., Qi Y., Ma Z., Qian S., Lyu X., (2024), Key technologies for autonomous fruit- and vegetable-picking robots: A review. *Agronomy*, vol.14, 2233. DOI:10.3390/agronomy14102233

[2] Cheng C., Fu J., Su H., Ren L., (2023), Recent advancements in agriculture robots: Benefits and challenges. *Machines*, vol.11, 48. DOI:10.3390/machines11010048

[3] Feng Y., Zhou Z., Shen Y., Wang L., (2023), Obstacle avoidance path planning based on an improved RRT algorithm (基于改进 RRT 算法的避障路径规划). *Chinese Journal of Engineering Design*, vol.30, 707–716. DOI:10.3785/j.issn.1006-754X.2024.03.141

[4] Gammell J.D., Srinivasa S.S., Barfoot T.D., (2014), Informed RRT*: Optimal sampling-based path planning focused via direct sampling of an admissible ellipsoidal heuristic. *Proceedings of the 2014 IEEE/RSJ International Conference on Intelligent Robots and Systems (IROS 2014)*, 2997–3004, Chicago/USA. DOI:10.1109/IROS.2014.6942976

[5] He X., Zhou Y., Liu H., Shang W., (2025), Improved RRT*-Connect manipulator path planning in a multi-obstacle narrow environment. *Sensors*, vol.25, 2364. DOI:10.3390/s25082364

[6] Hu Y., Qin J., Wang L., Chen X., Zhao Y., (2024), Path planning research on grape picking robotic arm based on improved RRT algorithm. *INMATEH-Agricultural Engineering*, vol.74, 833–844, Bucharest/Romania. DOI:10.35633/inmateh-74-73

[7] Jiang L., Liu S., Cui Y., Jiang H., (2022), Path planning for robotic manipulator in complex multi-obstacle environment based on improved RRT. *IEEE/ASME Transactions on Mechatronics*, vol.27, 4774–4785. DOI:10.1109/TMECH.2022.3165845

[8] Karaman S., Frazzoli E., (2011), Sampling-based algorithms for optimal motion planning. *The International Journal of Robotics Research*, vol.30, 846–894. DOI:10.1177/0278364911406761

[9] Karim M.R., Ahmed S., Reza M.N., Lee K.-H., Sung J., Chung S.-O., (2025), Geometric feature characterization of apple trees from 3D LiDAR point cloud data. *Journal of Imaging*, vol.11, 5. DOI:10.3390/jimaging11010005

[10] Li X., Yang J., Wang X., Fu L., Li S., (2024), Adaptive step RRT*-based method for path planning of a tea-picking robotic arm. *Sensors*, vol.24, 7759. DOI:10.3390/s24237759

[11] Liu Z., Sampurno R.M., Abeyrathna R.M.R.D., Nakaguchi V.M., Ahamed T., (2024), Development of a collision-free path planning method for a 6-DoF orchard harvesting manipulator using RGB-D camera and Bi-RRT algorithm. *Sensors*, vol.24, 8113. DOI:10.3390/s24248113

[12] Oh T., Won Y.-J., Lee S., (2025), TA-RRT*: Adaptive sampling-based path planning using terrain analysis. *Applied Sciences*, vol.15, 2287. DOI:10.3390/app15052287

[13] Orthey A., Chamzas C., Kavraki L.E., (2024), Sampling-based motion planning: A comparative review. *Annual Review of Control, Robotics, and Autonomous Systems*, vol.7, 285–310. DOI:10.1146/annurev-control-061623-094742

[14] Shang D., Wang J., Fan H., Suo S., (2024), Obstacle avoidance path planning for manipulators based on the RRT*-DR algorithm (基于 RRT*-DR 算法的机械臂避障路径规划). *Computer Integrated Manufacturing Systems*, vol.30, no.3, 1149–1160. DOI:10.13196/j.cims.2022.0902

[15] Shi W., Wang K., Zhao C., Tian M., (2022), Obstacle avoidance path planning for the dual-arm robot based on an improved RRT algorithm. *Applied Sciences*, vol.12, 4087. DOI:10.3390/app12084087

[16] Wang H., Zhao A., Zhong Y., Zhang G., Wu F., Zou X., (2025), Enhanced visual detection and path planning for robotic arms using YOLOv10n-SSE and hybrid algorithms. *Agronomy*, vol.15, 1924. DOI:10.3390/agronomy15081924

[17] Xiao G., Zhang L., Wu T., Han Y., Ding Y., Han C., (2024), FBi-RRT: A path planning algorithm for manipulators with heuristic node expansion. *Robotica*, vol.42, 644–659. DOI:10.1017/S0263574723001674

[18] Xu J., Ren C., Chang X., (2023), Robot time-optimal trajectory planning based on quintic polynomial interpolation and improved Harris hawks algorithm. *Axioms*, vol.12, 245. DOI:10.3390/axioms12030245

[19] Xuan D.T., Hung N.T., Thang V.T., (2025), A comprehensive review of improved A* path planning algorithms and their hybrid integrations. *Automation*, vol.6, 52. DOI:10.3390/automation6040052

[20] Zhu J., Pan D., (2024), Improved genetic algorithm for solving robot path planning based on grid maps. *Mathematics*, vol.12, 4017. DOI:10.3390/math12244017

RESEARCH PROGRESS ON MECHANICAL-TYPE AND PNEUMATIC-TYPE PRECISION SEED METERING DEVICES: A REVIEW

/

机械式与气力式精量排种器研究进展综述

Wenting JIN [1,2], Jinhui ZHAO [2], Jie WANG [1], Yunfei LV *[1], Wenpeng LI [1]
[1] Hebei Petroleum University of Technology, Chengde / P.R. China;
[2] State Key Laboratory of Agricultural Equipment Technology, Beijing / P.R. China
Tel: +86-15145498846; E-mail: 225071@hebpu.edu.cn
DOI: https://doi.org/10.35633/inmateh-79-58

Keywords: *precision seed metering, mechanical seeding, pneumatic seeding, high-speed seeding, seed filling mechanism, structural optimization*

ABSTRACT

The seed metering device was identified as the core actuating component of precision seeding equipment, directly determining seeding accuracy, seed spacing uniformity, seedling emergence rate, and crop yield. This review systematically examined the technological evolution and research status of mechanical-type and pneumatic-type precision seed metering devices. The identified limitations of mechanical-type devices included low seed filling efficiency, poor seed clearing performance, insufficient operational stability at high speeds, and significant interference from field vibrations. Pneumatic-type devices were found to face technical bottlenecks including difficulties in precision seeding of small-sized seeds, high air pressure loss, poor airtightness, and susceptibility to hole clogging. Recent advances in structural innovation, mechanism analysis, parameter optimization, and performance improvement were summarized. A comparative analysis was conducted on the technical advantages and applicable scenarios of the two mainstream seed metering device types. Future development trends were envisioned towards high-speed and high-efficiency operation, universal adaptability, intelligent monitoring, and low-damage energy saving, providing a reference for the optimal design and technological upgrade of precision seeding equipment.

摘要

排种器是精量播种装备的核心执行部件，其工作性能直接决定播种精度、粒距均匀性、种子出苗率与作物产量。为系统梳理精量排种器技术演进与研究现状，本文针对机械式精量排种器存在的充种效率低、清种效果差、高速作业稳定性不足及田间振动干扰显著等问题，以及气力式精量排种器面临的小籽粒精量播种困难、风压损耗大、气密性与型孔易堵塞等技术瓶颈，分别综述结构创新、机理分析、参数优化与性能提升的最新研究进展；对比分析两类主流排种器的技术优势与适用场景，展望了精量排种器向高速高效、通用适配、智能监测、低损节能方向的发展趋势，为精量播种装备优化设计与技术升级提供了参考。

INTRODUCTION

Precision seeding is a key technology for precision agriculture to save costs, increase efficiency, and ensure uniform seedling emergence. It enables single-grain precision sowing, quantitative positioning, reduced production costs, and significantly improved land utilization and crop yield (*Liao et al., 2025*). As the core functional component of a precision seeder, the seed metering device undertakes the processes of seed storage, seed filling, seed clearing, seed carrying, and seed delivery. Its structural design, working mechanism, and dynamic performance directly affect seeding quality and operational reliability (*Singh et al., 2020*). Precision seed metering devices can be classified into three types based on power source and working principle: mechanical, pneumatic, and electric. Among them, the mechanical and pneumatic types are currently the mainstream applications, while the electric type is still in the experimental and gradual promotion stage (*Ren et al., 2021; Li et al., 2026*). As the present review focuses on the two dominant categories for which sufficient field performance data are available in the published literature, electric-driven seed metering devices were not systematically covered.

---

[1] Wenting JIN, *Ph.D., Lecturer*; Yunfei LV*, *Associate Professor*; Jie WANG, *Lecturer*; Wenpeng LI, *Junior college student*;

[2] Jinhui ZHAO, *Senior Engineer*;

As precision agriculture advances toward higher operational speeds and intelligent control, conventional seed metering devices have progressively failed to satisfy modern agronomic demands, particularly in terms of high-speed adaptability, seed versatility, small-seed precision, vibration resistance, and energy efficiency (*Ren et al., 2026; Li et al., 2026*).

Recent system-level syntheses have identified the speed–precision paradox as a coupled phenomenon in which placement accuracy degrades non-linearly beyond architecture-specific thresholds. A three-regime model was proposed: Regime 1 (<10 km/h) where metering-stage singulation quality governs precision; Regime 2 (10–14 km/h) where delivery-stage instabilities are amplified; and Regime 3 (>14 km/h) where vibration, control latency, and soil–machine interactions dominate system-level breakdown (*Hussain et al., 2026*). This framework provides a unified reference for interpreting speed-dependent performance across mechanical and pneumatic architectures.

In recent years, researchers worldwide have conducted extensive studies on seed filling mechanisms, seed clearing and damage prevention, airflow field optimization, vibration suppression, and intelligent detection of seed metering devices, achieving a series of innovative results *(Liu et al., 2026; Li et al., 2026)*. This review was conducted by searching Web of Science, CNKI, and Scopus databases using keywords "precision seed metering", "mechanical seed metering", and "pneumatic seed metering" for publications from 2000 to 2026. A total of 162 papers were initially identified, of which 80 were selected based on relevance to structural design and performance evaluation. For the quantitative comparison tables (Tables 2, 4, and 5), performance ranges were synthesized from the reviewed literature. The reported values represent representative intervals compiled from reported experimental results, reflecting typical operating conditions across multiple studies. These ranges are intended for comparative illustration rather than absolute performance benchmarking. This paper reviews the technical bottlenecks, solutions, and research progress of mechanical and pneumatic precision seed metering devices, clarifies existing problems and breakthrough paths, and discusses future development trends, aiming to provide a theoretical basis and technical reference for the design optimization, performance improvement, and engineering application of precision seed metering devices.

RESEARCH STATUS OF MECHANICAL-TYPE SEED METERING DEVICES

Mechanical-type seed metering devices rely on mechanical structure differentiation and the combination of gravity and mechanical force to complete seed filling, seed clearing, and seed delivery, without the need for air source assistance *(Li et al., 2020)*. They offer advantages such as simple structure, low manufacturing cost, stable operation, and convenient maintenance, and are widely used in small and medium-sized fields and hilly mountainous areas in China.

Research on precision seeding technology in China began in the 1970s. After stages of structural imitation, independent innovation, and performance optimization, mature structures such as disc type (*Li et al., 2022*), wheel-scoop type (*Su et al., 2022*), chain-scoop type (*Zhang et al., 2023; Dun et al., 2022*), indented wheel type (*Lu et al., 2023; Liu et al., 2016*), and finger-clip type (*Wang et al., 2015*) have been developed, which are suitable for sowing corn, soybean, wheat, coarse cereals, and small-seeded cash crops.

Overseas research on precision seeding technology began in the 1940s, with Germany and the United States as representative countries (*Lai et al., 2022*). The focus was on developing highly reliable structures such as the finger-clip type and the inclined disc type, which have significant advantages in high-speed seeding of large-seeded crops (*Barut et al., 2004*). To address the drawbacks of the finger-clip type precision seed metering device, the German company Schmotzer developed an inclined disc type precision seed metering device. This type of metering device is installed obliquely at the bottom of the seed box. Seeds rely on their own gravity to enter the holes laterally to complete seed filling, and then fall into the seed furrow as the disc rotates. This metering device has a simple structure and low seed damage rate. It is suitable for seeds with regular shape and good flowability, and has strong adaptability to round seeds such as soybean and peanut. However, flat seeds have poor flowability and are prone to jamming, leading to miss-seeding. Based on this type of metering device, *Anantachar et al. (2011)* used an artificial neural network to optimize the seeding performance parameters of the inclined disc type metering device, establishing a relationship model among seeding speed, vegetable seed spacing, and seed damage rate. *Yadachi et al. (2013)* investigated the relationship between the continuous seed filling capacity of carrot seeds and the inclined disc angle. Through comparative experimental analysis, they determined that an inclination angle of 50° was most suitable for seeding carrot seeds.

Grewal et al. (2015) studied the seeding performance of an inclined disc onion seeder under different rotational speeds and different numbers of grooves/holes, evaluating the machine using the qualified seeding index, multiple-seeding index, and miss-seeding index, and obtained satisfactory results. *Van Loon et al. (2020)* conducted a cross-continental comparative study of ten mechanical maize seed metering devices from Latin America, Sub-Saharan Africa, and Asia, identifying 20 RPM as the optimal rotational speed across device types and demonstrating that adjustable-hole metering devices consistently outperformed fixed-hole designs in terms of seeding quality and operational flexibility.

Table 1

Mechanical-type precision seed metering devices: types, features and representative crops

(Synthesized from Geng et al., 2016, 2018; Su et al., 2022; Li et al., 2022; Lu et al., 2023; Liu et al., 2016; Wang et al., 2015; Dun et al., 2022)

Type	Main Features	Representative Crops
Disc type	Hole shape determines seed size; hole spacing, together with travel speed, plate rotational speed, transmission ratio, seed bounce, and delivery dynamics, collectively determines plant spacing. Simple structure but limited versatility.	Corn, soybean
Wheel-scoop type	Simple and durable structure, but requires changing the seed scoop to adapt to different seeds.	Sorghum, *Pinellia ternata* (banxia), potato
Indented wheel type	Strong power adaptability but poor seed adaptability. Generally used for seeds with relatively spherical shape and high roundness.	Soybean, rapeseed
Finger-clip type	Relatively stable operational performance, but complex structure and limited versatility.	Corn, *Cyperus esculentus* (tiger nut)

Note: Structural schematic diagrams have been omitted for brevity. For detailed structural illustrations, please refer to the original cited references.

Mechanical-type seed metering devices have the advantages of simple structure, low cost, and reliable operation, but they still suffer from the following problems:

(1) Limited seed filling efficiency: The hole shape must closely match the seed geometry. Under high-speed operation, seed filling is insufficient, leading to an increased miss-seeding rate.

(2) Prominent seed clearing contradiction: Relying on gravity for seed clearing tends to cause multiple-seeding, while relying on rigid components for seed clearing tends to cause seed damage and jamming.

(3) Poor high-speed and vibration resistance: When the operating speed reaches 6 km/h or higher, seed spacing uniformity deteriorates, and field vertical vibration significantly interferes with seeding stability. However, this threshold is device-specific; for example, in a finger-clip type corn seed metering device, seed spacing uniformity was found to deteriorate significantly when operating speed exceeded 6 km/h (*Wang et al., 2019*), whereas newer designs with disturbance-assisted mechanisms have extended this limit substantially.

Rapid seed filling and stable seed delivery

To address the problems of insufficient seed filling and disordered seed delivery under high-speed operation, domestic and overseas scholars have improved performance through structural improvement, mechanical modeling, and parameter optimization. *Huang et al. (2022)* added a guide plate and a lateral double-fixing structure, which shortened the seed delivery path and achieved a qualified seeding rate of >95.27% at operating speeds of 4–14 km/h. *Liu et al. (2016)* proposed an opposed swash plate structure, established a seed filling mechanical model, and determined that the seed filling effect for soybean was optimal at an inclination angle of 20°. *Li et al. (2018)* designed a cone-disc centrifugal pushing structure, which reduced the miss-seeding rate by 2.52% at operating speeds of 7–13 km/h. *Correia et al. (2016)* showed through experiments that moderately increasing the inclination angle of the seed metering device and increasing the working rotational speed could reduce seed accumulation in the chamber and improve the stability of seed filling and seed delivery.

Dong et al. (2025) introduced a posture-adjusting seed metering device for high-speed maize planting, in which seed-filling posture was adjusted and the seed group was fluidized through groove-type structures. EDEM simulation and bench testing demonstrated that the optimized device achieved pass, repeat, and miss rates of 94.8%, 1.3%, and 3.9%, respectively.

Within the speed range of 8–14 km/h, the pass rate consistently exceeded 94%, with repeat rate below 2.1% and miss rate below 3.9%, substantially outperforming devices without posture-adjusting mechanisms.

For rice mechanical seeding, *Zhang et al. (2025)* calibrated DEM contact parameters using a multi-sphere rice model, achieving prediction errors of less than 0.13% for miss-seeding, qualified, and re-seeding rates, demonstrating the effectiveness of DEM-based virtual design for non-spherical seeds. *Zheng et al. (2025)* designed a screw-guided posture-adjusting and filling-promoting precision seed metering device for wheat, establishing a mechanical model of seed posture adjustment under the combined action of spiral guidance and gravity. The device achieved a qualified seeding rate exceeding 90% within a working speed range of 30–70 r/min, providing an effective solution for precision seeding of small-sized cereal seeds.

Poor performance of the seed clearing zone

The seed clearing stage is key to reducing multiple-seeding and minimizing seed damage. *Zhang et al. (2021)* determined through force analysis that the minimum clearance of 1.47 mm in a dual-chamber vertical disc metering device is the critical damage threshold for cotton seeds, with damage occurring when the clearance was less than this threshold, whereas no significant damage was observed above this value under the tested conditions. The study clarified the order of influence of rotational speed, clearance, and installation angle on the damage rate. *Zhang et al. (2014)* replaced the seed guard plate with flexible rubber, reducing the seed damage rate by 0.6%. *Zhou et al. (2018)* established a shear damage model and reduced the breakage rate by constraining the hole length to avoid the shear zone. *Ryu and Kim (1988)* employed methods such as brush clearing and flexible scraping to reduce mechanical damage while ensuring clearing effectiveness.

Effect of vibration on seed metering performance

When a seeder operates in the field, random vibrations are generated due to factors such as soil structure and surface unevenness. Among these, the vertical vibration during forward motion is particularly significant, leading to reduced seeding performance and affecting subsequent crop growth and yield. *Wang et al. (2019)* established a vibration model of a finger-clip type seed metering device and confirmed that vibration has a significant effect on the qualified seeding rate and the coefficient of variation of seed spacing. Vibration experiments were conducted at frequencies of 5–20 Hz and amplitudes of 2–10 mm, based on field measurements from tillage operations. *Li (2022)* combined high-speed photography with trajectory equations to identify the key vibration parameters affecting seed delivery uniformity. *Huang et al. (2021)* revealed the coupled effects of vibration amplitude, frequency, and operating speed on the wheel-scoop type seed metering device, providing a theoretical basis for anti-vibration design. The interaction between vibration and seed metering performance has been further quantified through DEM-based sensitivity analysis. *Zhang et al. (2025)* identified inter-particle static and rolling friction coefficients as the dominant DEM contact parameters affecting rice seed metering, with optimal values of 0.445 and 0.059, respectively. The validation tests confirmed that errors between simulation and bench tests remained below 1.4% for seed number frequency per seeding hole, providing a calibrated modeling approach for evaluating vibration-induced performance degradation.

Table 2

Quantitative comparison of mechanical-type seed metering device performance across key metrics

(Synthesized from Anantachar et al., 2011; Barut and Özmerzi, 2004; Correia et al., 2016; Dong et al., 2025; Dun et al., 2022; Geng et al., 2016, 2018; Grewal et al., 2015; Huang et al., 2021, 2022; Kachman and Smith, 1995; Karayel, 2009; Li et al., 2018, 2020, 2022; Liu et al., 2016; Ryu and Kim, 1988; Su et al., 2022; Van Loon et al., 2020; Wang et al., 2015, 2019; Zhang et al., 2014, 2021, 2025; Zheng et al., 2025; Zhou et al., 2018)

Performance Metric	Disc Type	Wheel-Scoop Type	Indented Wheel Type	Finger-Clip Type
Typical operating speed	4–8 km/h	4–7 km/h	5–9 km/h	6–10 km/h
Qualified index	88–93%	85–90%	90–95%	92–96%
Miss index	3–7%	5–10%	2–5%	2–4%
Multiple index	3–6%	3–8%	2–5%	2–5%
Seed damage rate	0.5–1.5%	0.3–1.0%	0.3–0.8%	0.4–2.0%

Performance Metric	Disc Type	Wheel-Scoop Type	Indented Wheel Type	Finger-Clip Type
Seed adaptability	Poor	Medium	Poor	Medium
Structural complexity	Low	Low	Medium	High
Manufacturing cost	Low	Low	Medium	High

Note: Values represent representative ranges compiled from the cited references based on the authors' synthesis of reported experimental results. The ranges reflect typical operating conditions reported across multiple studies and are intended for comparative illustration rather than absolute performance benchmarking. Specific performance may vary with seed type, rotational speed, operating pressure, and other conditions.

RESEARCH STATUS OF PNEUMATIC-TYPE SEED METERING DEVICES

Pneumatic-type seed metering devices use positive/negative pressure generated by a fan to achieve seed suction, seed carrying, and seed delivery. They have low requirements on seed shape and size, low seed damage rate, high operating speed, and wide adaptability to seed varieties. They are the mainstream configuration for large and medium-sized high-speed precision seeders, and are mainly divided into four categories: air-suction type, air-blowing type, positive/negative pressure combined type, and central pneumatic delivery type.

Bustos-Gaytán et al. (2025) systematically reviewed experimental and numerical simulation approaches for pneumatic seed-metering devices, finding that 86% of studies focused on air-vacuum systems while only 14% addressed air-blowing systems. Numerical tools including CFD, DEM, and coupled CFD–DEM were identified as crucial for optimizing air chamber geometry, seed plate hole shapes, and seed-cleaning device designs. However, fewer studies have focused on seed-cleaning and anti-blocking devices, indicating a research gap.

With the development of mechanical-type seed metering devices, in the 1950s, many overseas scholars combined mechanical structure theory with fluid mechanics to investigate the effects of airflow pressure and direction on the various states of materials within mechanical structures, leading to the invention of pneumatic-type precision seed metering devices. By the 1960s, pneumatic-type precision seed metering devices had begun to be used and promoted, and countries with advanced agricultural systems, such as the United States and Germany, had developed various types of pneumatic seeders. In the 1980s, the new concept of pneumatic precision seeding reached international consensus. After years of development, operating speed and seeding quality have continuously improved, but still cannot meet the ever-increasing agronomic requirements, prompting European and American countries to vigorously develop precision seeding technology, thus leading to the widespread application of pneumatic-type precision seed metering devices. With technological advancement, precision seeding technology has become increasingly mature and is moving towards the direction of precision, high speed, automation, and intelligence, offering advantages such as compact structure and excellent performance (*Karayel, 2009*). Overseas pneumatic-type precision seed metering devices are mainly used for crops such as corn, soybean, and rice, while also serving vegetable seeding. Compared with mechanical-type seed metering devices, pneumatic-type precision seed metering devices have the advantages of less seed damage, wide adaptability, high operating speed, and good seeding performance. They have developed relatively quickly and gradually occupied a mainstream position. At present, pneumatic-type precision seed metering devices are relatively well-developed abroad, but their adaptability to small-sized vegetable seeds still needs improvement.

Table 3

Pneumatic-type precision seed metering devices: types, features and representative crops

(Synthesized from Bustos-Gaytán et al., 2025; Fang et al., 2024; Gao et al., 2022; Guo et al., 2024; Karayel, 2009; Li et al., 2023; Liu et al., 2022; Sun et al., 2025; Wang et al., 2019, 2026; Yan et al., 2017; Yang et al., 2022; Yatskul et al., 2017; Yi et al., 2021; Zha et al., 2024; Zhang et al., 2019)

Type	Main Features	Representative Crops
Air-suction type	Moderate seed adaptability (excellent for large seeds, challenging for seeds <3 mm); high requirements on airtightness; high fan power consumption (depending on system scale and operating pressure); capable of high-speed seeding. Typical negative pressure: 3–6 kPa.	Corn, soybean, vegetables

Type	Main Features	Representative Crops
Air-blowing type	Simple and durable structure; uses positive pressure airflow to assist seed filling and clearing; seed adaptability is improved by adjusting air pressure rather than changing mechanical components. Typical positive pressure: 2–4 kPa.	Sorghum, *Panax notoginseng*
Positive/negative pressure combined type	Generates lower air pressure than the air-suction type; low seed damage rate; good versatility; operating speed ≤8 km/h. Typical negative pressure: 2–4 kPa; positive pressure: 1–2 kPa.	Rapeseed, pak choi
Central pneumatic delivery type	Strong seed adaptability and easy seed filling, suitable for a wide range of crop types including cereals, rapeseed, and other small-to-medium seeds; high miss-seeding index at medium and high speeds requires further optimization.	Cereals, rapeseed, small-to-medium seeds

Note: Structural schematic diagrams have been omitted for brevity. For detailed structural illustrations, please refer to the original cited references.

Pneumatic-type precision seed metering devices are widely used on large and medium-sized seeding equipment in large-scale planting areas due to their low requirements on seed shape and size, good seeding quality, and high operating speed. *Guo et al. (2024)* systematically analysed four key technologies limiting the operational speed improvement of pneumatic seed metering devices: high-speed seed filling technology, stable seed clearing technology, smooth seed delivery control technology, and stable driving technology of the metering device, identifying stable filling, effective clearing, and smooth delivery as the core measures for effectively improving the qualified seeding rate and reducing the coefficient of variation at high speeds. However, they still have some problems:

(1) Multiple-seeding and miss-seeding: High-speed operation leads to airtightness fluctuations, hole clogging, and seed population dragging, resulting in reduced stability *(Zhang et al., 2019)*.

(2) Difficulty in seeding small seeds: Seeds with a particle size of less than 3 mm are light in weight and sensitive to negative pressure, requiring stringent hole geometry and air pressure parameters.

(3) Large air pressure loss: Seal wear and air leakage between chambers lead to increased energy consumption and degradation of metering performance.

Control of multiple-seeding and miss-seeding

To address the problems of multiple-seeding and miss-seeding caused by internal airtightness fluctuations, hole clogging during seed filling and seed clearing, and seed population dragging in pneumatic-type precision seed metering devices during high-speed operation, *Önal et a*l. *(2012)* optimized the airtightness of the air chamber using fluid mechanics and aerodynamics, effectively solving the issue of unstable airflow fields during seed filling for cotton and corn seeds. *Jia et al. (2018)* adopted an air-suction mechanical composite picking mechanism to reduce the interference of sudden negative pressure drops on soybean seeding. *Li et al. (2010)* proposed a seeding frequency method to detect hole clogging in a pneumatic-type precision seed metering device for rapeseed. *Yang (2020)* added grooves and seed disturbing teeth on the suction plate to suppress rapeseed population dragging and reduce miss-seeding. *Wang et al. (2019)* designed a flexible vibrating seed metering belt to achieve high-speed single-seed suction for soybean, and obtained the optimal operating parameters of the metering device through experiments.

Sun et al. (2025) designed a progressive seed-cleaning mechanism for an air-pressure maize precision seed metering device, establishing mechanical models for excess seeds entering the cleaning zone. Through single-factor and multi-factor experiments, the optimal parameter combination was determined as: seed-clearing angle of 0.024°, operating speed of 10 km/h, and positive pressure of 6.0 kPa. Under these conditions, the qualified index reached 98.11%, multiple index 1.44%, and miss index 0.45%. Comparative experiments demonstrated that the device with the seed-cleaning mechanism improved the qualified index by approximately 2.3 percentage points compared to the device without the mechanism. *Wang et al. (2026)* designed and optimized a combined seed cleaning mechanism for an air-suction seed metering device for small-seed crops with multi-seed hill, achieving significantly improved cleaning performance through structural optimization.

Zhang et al. (2019) conducted optimal design and experiments on a double-disc air-suction precision seed metering device with variable hole diameter, demonstrating that the device successfully adapted to six types of vegetable seeds by rotating and combining to produce different hole diameters under negative pressure conditions.

Precision seeding technology for small-sized seeds

For small-sized seeds such as sesame, millet, rapeseed, and vegetables, technologies including negative pressure suction combined with positive pressure seed delivery, variable-diameter holes, and photoelectric detection have been adopted both domestically and internationally. *Yi et a*l. *(2021)* and *Gao et al. (2022)* each designed pneumatic-type precision seed metering devices for millet and rapeseed, respectively, using the principle of negative pressure suction and positive pressure seed delivery. *Li et al. (2018)* proposed a beam-blocking method to detect insufficient filling and hole clogging in pneumatic-type precision seed metering devices, achieving precision seeding detection for white radish, rapeseed, and Shanghai bok choy seeds. *Li (2019)* designed a precision seed metering device capable of rotating and combining to produce different hole diameters under negative pressure conditions, adapting to six types of vegetable seeds. *Liao et al. (2018)* investigated the factors affecting the suction effect of spherical small-sized seeds such as rapeseed and Chinese cabbage, established a critical pressure model for seed suction, and clarified the coupling relationship among thousand-seed weight, hole diameter, and negative pressure.

For rice seeding, *Zha et al. (2024)* developed a branched air-chamber pneumatic seed metering device capable of adjusting seeding quantity from 1–3 to 5–8 seeds per hill by controlling the branched air chamber casing. Bench tests showed optimal qualification rates of 85.81% for 1–3 seeds/hole and 87.27% for 5–8 seeds/hole. *Fang et al. (2024)* integrated image recognition and orientation technology into an air-suction garlic seed metering device, achieving single-seed rates of 95.98%–96.23% under optimized parameters including negative pressure of 11.85–13.21 kPa and rotational speed of 6.85–7.25 r/min. *Zhao et al. (2024)* provided a comprehensive analysis of rice precision direct seeder seed metering devices, identifying the improvement path for air-suction precision: improving seed flowability, stabilizing negative pressure, and adjusting seed posture to enhance singulation accuracy. *Li et al. (2023)* optimized design parameters for a pneumatic hill-drop rapeseed metering device, determining that optimal performance was achieved at hole velocity of 30–70 r/min and negative pressure of –2.5 to –1.5 kPa, with miss-seeding rate consistently below 3%.

Suppression of air pressure loss

The susceptibility to wear of the sealing gasket between the seed plate and the negative pressure chamber of an air-suction type precision seed metering device is the main cause of air pressure loss *Yan et al. (2017)*. *Yan et al. (2017)* and Kverneland AS have both adopted a design where the seed plate and the negative pressure chamber rotate synchronously, thereby reducing sealing gasket wear, decreasing air pressure loss, and ensuring metering performance. On this basis, *Yan et al. (2017)* modified the seed plate into an annular frustum shape, achieving lower air pressure demand and energy consumption compared to Kverneland's design. To address the issue of significant air pressure loss caused by multiple seeding units sharing a common air chamber in air-suction type precision seed metering devices, *Li et al. (2023)* designed an independent grooved airway disc, enabling independent air supply to each row and reducing cross-leakage losses. *Wang et al. (2022)* analysed the mixing device of a central pneumatic delivery type seed metering device and indicated that the greater the amount of seeds being conveyed and the higher the seed-to-airflow ratio, the larger the air pressure loss in the mixing component.

Mechanical-pneumatic hybrid systems

Hao et al. (2026) designed and validated a mechanical-pneumatic hybrid metering device for mixed seeding of forage seeds, combining the simplicity of mechanical seed picking with the conveying capability of pneumatic assistance. The device achieved relative seeding errors of 6.81%–7.49% for mixed forage seed applications, demonstrating the feasibility of hybrid architectures for multi-species seeding operations where seed geometry and physical properties vary significantly among species. *Tang et al. (2023)* designed a high-speed precision seed metering device with air-assisted seed guide (inside-filling air-blowing type), achieving improved seed trajectory stability and placement accuracy through controlled airflow guidance.

Table 4

Quantitative comparison of pneumatic-type seed metering device performance across key metrics

(Synthesized from Bustos-Gaytán et al., 2025; Fang et al., 2024; Gao et al., 2022; Guo et al., 2024; Hussain et al., 2026; Jia et al., 2018; Li et al., 2010, 2023; Liu et al., 2022; Maleki et al., 2006; Önal et al., 2012; Sun et al., 2025; Wang et al., 2019, 2022, 2026; Yan et al., 2017; Yang et al., 2022; Yatskul et al., 2017; Yi et al., 2021; Zha et al., 2024; Zhang et al., 2019)

Performance Metric	Air-Suction Type	Air-Blowing Type	Positive/Negative Pressure Combined Type	Central Pneumatic Delivery Type
Typical operating speed	8–14 km/h	6–10 km/h	≤8 km/h	6–12 km/h
Qualified index	95–98%	90–95%	92–96%	88–93%
Miss index	2–5%	3–7%	2–5%	5–10%
Multiple index	2–5%	3–6%	2–4%	3–8%
Seed damage rate	＜0.5%	＜0.5%	＜0.3%	1–3%
Seed adaptability	Excellent	Good	Good	Excellent
Air pressure loss	High	Medium	Low	High
Fan power consumption	High (depending on system scale and operating pressure)	Medium (2–3 kW/row)	Low (1–2 kW/row)	High

Note: Values represent representative ranges compiled from the cited references based on the authors' synthesis of reported experimental results. The ranges reflect typical operating conditions reported across multiple studies and are intended for comparative illustration rather than absolute performance benchmarking. Specific performance may vary with seed type, rotational speed, operating pressure, and other conditions.

Table 5

Cross-type comparative analysis of mechanical versus pneumatic seed metering devices

(Synthesized from Bustos-Gaytán et al., 2025; Dong et al., 2025; Guo et al., 2024; Hussain et al., 2026; Karayel, 2009; Van Loon et al., 2020; Wang et al., 2019; Yang et al., 2022; Zhang et al., 2019)

Comparison Dimension	Mechanical Type	Pneumatic Type
Maximum stable operating speed	6–10 km/h	8–14 km/h
Qualified index (typical)	85–96%	88–98%
Seed adaptability	Poor–Medium	Good–Excellent
Seed damage rate	0.3–2.0%	<0.5%
Unit energy consumption (relative)	Low (~90 kJ/ha)	High (~6,400 kJ/ha for full pneumatic)
Centrifugal vs. pneumatic power ratio	—	1:71 (centrifugal consumes 1/71 of pneumatic)
Structural complexity	Simple	Complex
Manufacturing cost	Low	High
Operating speed increase trend	Optimized designs reaching 13–14 km/h with >94% qualified index	Clear speed–precision trade-off beyond 14 km/h
Suitable operation scale	Small-to-medium fields, hilly terrain	Large-scale plain farming
Vibration sensitivity	High	Medium
Airtightness requirement	None	Critical

Note: Values represent representative ranges compiled from the cited references based on the authors' synthesis of reported experimental results. The ranges reflect typical operating conditions reported across multiple studies and are intended for comparative illustration rather than absolute performance benchmarking. Specific performance may vary with seed type, rotational speed, operating pressure, and other conditions.

The cross-type comparison presented in Table 5 is intended to illustrate general performance trends and architectural trade-offs rather than to establish precise performance rankings. The reported ranges are compiled from multiple studies with varying experimental conditions. Actual performance comparisons should be interpreted with consideration of operating parameters and test standards.

DEVELOPMENT TRENDS

Mechanism-based and precision-oriented

Deepen the research on the multi-field coupling mechanism of seed–structure–airflow–vibration, and establish a full-cycle dynamic model. Employ simulation tools such as EDEM and CFD to achieve multi-objective optimization of structural and operating parameters. *Bustos-Gaytán et al. (2025)* confirmed that CFD-DEM coupling has become the essential tool for optimizing pneumatic metering components, yet seed-clearing and anti-blocking devices remain understudied. Develop a unified performance evaluation system to enhance the standardization level of seed metering device design, testing, and application. The speed–precision paradox framework provides a quantitative basis for defining architecture-specific performance envelopes and identifying optimal operating windows for different device types.

Lightweight and adaptable

For scenarios such as hilly and mountainous areas and facility agriculture, develop lightweight, miniaturized, and modular seed metering devices to improve adaptability to mountainous regions and small plots. Optimize structural materials and manufacturing processes to reduce cost, extend service life, and simplify maintenance. Promote the integration of mechanical and pneumatic technologies, combining the reliability of mechanical structures with the versatility of pneumatic systems, to form low-cost, high-performance composite seed metering technology. The mechanical-pneumatic hybrid approach demonstrated by *Hao et al. (2026)* offers a promising pathway for multi-species and mixed-seeding applications where seed physical properties vary considerably.

Intelligent and visualized

Integrate machine vision, photoelectric sensing, microcontroller, and virtual instrument technologies to achieve online monitoring of the seeding process, real-time alarming for miss-seeding, clogging, and multiple-seeding, and automatic adjustment of seeding rate. Build a digital twin system for seeding performance to enable visualized simulation and prediction of seed filling, seed clearing, airflow field, and vibration response. *Guo and Zhao* (*2026*) systematically reviewed edge-intelligent precision seeding monitoring and control technologies, identifying photoelectric, fibre-optic, and infrared-based methods as relatively mature in engineering applications. Capacitive, piezoelectric, near-infrared, laser-based, and machine vision methods offer advantages in detection accuracy and information richness, yet face challenges in system complexity, edge-side deployment, and long-term robustness. Future intelligent precision seeding technology was projected to develop toward multi-source heterogeneous information fusion, low-latency closed-loop control, standardized data sharing, and farm-level quality evaluation. Develop fault self-diagnosis and parameter self-optimization systems to enhance the reliability of the entire seeding process.

CONCLUSIONS

This systematic review of mechanical-type and pneumatic-type precision seed metering devices yielded the following synthesized findings.

Mechanical-type seed metering devices, including disc, wheel-scoop, indented wheel, and finger-clip types, offer advantages of simple structure, low manufacturing cost, and high reliability, making them suitable for small-to-medium sized fields and hilly terrain. However, their performance is constrained by architecture-specific thresholds: seed filling efficiency decreases significantly when operating speed exceeds 6–8 km/h, and seed spacing uniformity deteriorates under field vibration. Recent innovations, including disturbance-assisted filling mechanisms, screw-guided posture adjustment, and posture-adjusting metering devices, have extended stable operation to 13 km/h with qualified rates exceeding 94%. Cross-continental comparative testing has demonstrated that adjustable-hole metering devices consistently outperform fixed-hole designs, providing a practical pathway for improving mechanical device versatility.

Pneumatic-type seed metering devices, comprising air-suction, air-blowing, positive/negative pressure combined, and central pneumatic delivery types, demonstrate superior seed adaptability and high-speed capability. Nevertheless, 86% of research has focused on air-suction systems, while seed-cleaning and anti-blocking devices remain understudied. Key challenges include small-seed (<3 mm) precision seeding, air pressure loss from seal wear, and hole clogging at elevated speeds. Recent advances in progressive seed-cleaning mechanisms and branched air-chamber designs have substantially improved performance, with qualified indices exceeding 98% achieved under optimized conditions.

Table 6

Comparative decision framework for selecting seed metering device types

Operating Condition	Recommended Type	Rationale
Speed ≤8 km/h, uniform seed geometry, cost-sensitive	Mechanical	Lower cost, sufficient accuracy, simple maintenance
Speed ≥8 km/h, irregular seed shapes, large-scale	Pneumatic	Higher speed capability, better seed adaptability
Multi-species mixed seeding	Hybrid (mechanical-pneumatic)	Combines picking simplicity with conveying versatility
Small seeds (<3 mm), high precision requirement	Pneumatic with optimized hole/negative pressure	Superior singulation when properly tuned

Quantitative conclusions indicate that pneumatic systems typically achieve qualified indices 5–10 percentage points higher than mechanical types at speeds >8 km/h, at the cost of substantially higher energy consumption. Notably, recent system-level analysis reported that centrifugal metering systems consume approximately 71 times less power than full pneumatic systems under comparable single-row operating conditions. However, this comparison is based on a specific system configuration and operating point; the actual power ratio depends on factors including system scale, operating pressure, number of rows, and seed characteristics. The reported value should be interpreted as an indicative comparison for a reference operating condition rather than a universal constant.

The speed–precision paradox follows a three-stage pattern: Regime 1 (<10 km/h) where metering-stage singulation quality governs precision; Regime 2 (10–14 km/h) where delivery-stage instabilities are amplified; and Regime 3 (>14 km/h) where vibration, control latency, and soil–machine interactions dominate system-level breakdown.

Limitations of this review include: (1) electric-driven seed metering devices were not systematically covered due to limited published field data; (2) quantitative comparative analysis was constrained by inconsistent reporting of performance parameters across studies; and (3) the review primarily focused on English and Chinese language publications, potentially omitting relevant studies in other languages, although English-translated titles were provided for all Chinese references to ensure accessibility. Future research should deepen multi-field coupling mechanisms and integrate mechatronic technologies to promote high-efficiency, adaptive, and intelligent development of precision seed meters for modern agriculture.

ACKNOWLEDGEMENT

This work was supported by the Youth Science and Technology Fund of China National Machinery Industry Corporation (No. QNJJ - PY - 2022 - 05).

REFERENCES

[1] Anantachar M., Kumarb G.V.P., & Guruswamy T. (2011). Development of artificial neural network models for the performance prediction of an inclined plate seed metering device. *Applied Soft Computing*, 11(4), 3753-3763, Amsterdam/Netherlands. DOI: https://doi.org/10.1016/j.asoc.2011.02.006

[2] Barut Z.B. & Özmerzi A. (2004). Effect of different operating parameters on seed holding in the single seed metering unit of a pneumatic planter. *Turkish Journal of Agriculture and Forestry*, 28(6), 435-441, Ankara/Turkey.

[3] Bustos-Gaytán A., Saldaña-Robles N., Joya-Cárdenas D.R., Gutiérrez-Vaca C., Alfaro-Ayala J.A., Barco-Burgos J., & Saldaña-Robles A. (2025). Advancements in pneumatic seed-metering devices: A review of numerical and experimental approaches. *Results in Engineering*, 26, 105626, Amsterdam/Netherlands. DOI: 10.1016/j.rineng.2025.105626

[4] Correia T.P., Sousa S.F.G.D.E., & Silva P.R.A. (2016). Sowing performance by a metering mechanism of continuous flow in different slope conditions. *Engenharia Agrícola*, 36, 839-845, Jaboticabal/Brazil. DOI: 10.1590/1809-4430-Eng.Agric.v36n5p839-845/2016

[5] Dong J.X., Gao X.J., Zheng Z.Z., Zhao P.F., Bi Y.B., & Huang Y.X. (2025). Design and testing of a posture-adjusting precision metering device for high-speed maize planting. *Frontiers in Plant Science*, 16, 1458597, Lausanne/Switzerland. DOI: https://doi.org/10.3389/fpls.2025.1458597

[6] Du X., & Liu C.L. (2023). Design and testing of the filling-plate of inner-filling positive pressure high-speed seed-metering device for maize. *Biosystems Engineering*, 228, 1-17, Amsterdam/Netherlands. DOI: https://doi.org/10.1016/j.biosystemseng.2023.02.008

[7] Dun G.Q., Mao N., Gao Z.Y., Wu X.P., Liu W.H., & Zhou C. (2022). Model construction of soybean average diameter and hole parameters of seed-metering wheel based on DEM. *International Journal of Agricultural and Biological Engineering*, 15(1), 101-110, Beijing/China. DOI: 10.25165/j.ijabe.20221501.5914

[8] Fang F.H., Song J.L., Wang Z., Li K.Q., Zhang Y.Z., Zhou L., & Li C. (2024). Design and experiment of air-suction precision seed-metering device for garlic. *INMATEH Agricultural Engineering*, 74(3), 721-731, Bucharest/Romania. DOI : https://doi.org/10.35633/inmateh-74-64

[9] Gao L.P., Shi B.B., Liao Q.X., Zhang B.X., Zheng J., & Liao Y.T. (2022). Seed metering performance of cone hole plate of positive and negative air pressure combined rapeseed precision seed metering device (正负气压组合油菜精量排种器锥孔盘排种性能). *Transactions of the Chinese Society of Agricultural Engineering*, 38(6), 22-33, Beijing/China. DOI: 10.11975/j.issn.1002-6819.2022.06.003

[10] Geng D.Y., Li Y.H., Meng P.X., Du R.C., & Meng F.H. (2016). Design and Experiment of Corn Retractable Finger-Clip Type Seed Metering Device (玉米伸缩指夹式排种器设计与试验). *Transactions of the Chinese Society for Agricultural Machinery*, 47(5), 38-45, Beijing/China. DOI: 10.6041/j.issn.1000-1298.2016.05.006

[11] Geng D.Y., Zhang M.Y., He K., Li Y.H., Xie C.J., & Jin C.Q . (2018). Design and Experiment of Inclined Double-Ring Hole Disc Type Corn Seed Metering Device (倾斜双圆环型孔圆盘式玉米排种器设计与试验). *Transactions of the Chinese Society for Agricultural Machinery*, 49(1), 68-76, Beijing/China. DOI: 10.6041/j.issn.1000-1298.2018.01.008

[12] Grewal R.S., Khurana R., & Manes G.S. (2015). Development of a tractor operated planter for direct sowing of onion crop. *Agricultural Engineering International:* CIGR Journal, 17(2), 31-38, Beijing/China.

[13] Guo M.Z. & Zhao J.L. (2026). Research progress on edge-intelligent precision seeding monitoring and control technologies for smart farms. *Journal of South China Agricultural University*, 47(4), 560-572, Guangzhou/China. DOI: 10.7671/j.issn.1001-411X.202604023

[14] Guo W.Q., Zhang W.Y., Qi B., Yuan J.Y., Wang Y.X., & Xia Q.Q. (2024). Research status and prospect of pneumatic high-speed precision seed metering device (气力式高速精量排种器研究现状及展望). *Chinese Journal of Agricultural Mechanization*,45(3), 31-37, Nanjing/China. DOI: 10.13733/j.jcam.issn.2095-5553.2024.03.005

[15] Hao S.H., Zhu C.T., Wang Y.W., Liu C.L., You Y., Xu J.T., Guo S.B., & Huo J.X. (2026). Design and validation of mechanical-pneumatic metering device for mixed seeding of forage seeds. *Biosystems Engineering*, 267, 104485, Amsterdam/Netherlands. DOI: https://doi.org/10.1016/j.biosystemseng.2026.104485

[16] Huang Y.X., Han D.D., Han Z., Huang J.L., Chen P., He B., & Zhang L.H. (2021). Effect of Vibration on Metering Performance of Scoop Wheel Seed Metering Device (振动对勺轮式排种器排种性能的影响试验). *Journal of Henan Agricultural University*, 55(5), 896-905, Zhengzhou/China. DOI: 10.16445/j.cnki.1000-2340.20210629.001

[17] Huang Y.X., Li P., Dong J.X., Chen X.H., Zhang S.L., & Liu Y. (2022). Design and Experiment of Side-Guided Precision Seed Metering Device for High-Speed Soybean Seeder

(大豆高速播种机侧置导引式精量排种器设计与试验). *Transactions of the Chinese Society for Agricultural Machinery*, 53(10),44-53+75, Beijing/China. DOI: 10.6041/j.issn.1000-1298.2022.10.005

[18] Hussain S., Rui Z.Y., He J.Y., Zhang Z., Mhamed M., Faheem M., Javidan S.M., Farid M.U., Saeed A., & Abdelhamid M.A. (2026). The speed–precision paradox in seeding technology: a system-level review of regime transitions, validation gaps, and energy trade-offs. *Computers and Electronics in Agriculture*, 251, 112023, Amsterdam / Netherlands. DOI: 10.1016/j.compag.2026.112023

[19] Jia H.L., Chen Y.L., Zhao J.L., Wang J.X., Guo M.Z., & Zhang J. (2018). Design and Experiment of Air-Suction Mechanical Combined Precision Soybean Seed Metering Device (气吸机械复合式大豆精密排种器设计与试验). *Transactions of the Chinese Society for Agricultural Machinery*, 49(4), 75-86+139, Beijing/China. DOI: 10.6041/j.issn.1000-1298.2018.04.009

[20] Kachman S.D., & Smith J.A. (1995). Alternative measures of accuracy in plant spacing for planters using single seed metering. *Transactions of the ASAE*, 38(2), 379-387, St. Joseph/USA.

[21] Karayel D.A.V.U.T. (2009). Performance of a modified precision vacuum seeder for no-till sowing of maize and soybean. *Soil and Tillage Research*, 104(1), 121-125, Amsterdam/Netherlands. DOI: 10.1016/j.still.2009.02.001

[22] Karayel D.A.V.U.T., Wiesehoff M., Özmerzi A., & Müller J. (2006). Laboratory measurement of seed drill seed spacing and velocity of fall of seeds using high-speed camera system. *Computers and electronics in agriculture*, 50(2), 89-96, Amsterdam/Netherlands. DOI: 10.1016/j.compag.2005.05.005

[23] Lai Q.H., Xie G.F., Su W., Zhang J.W., Sun W.Q., & Chen Z.Y. (2022). Design and Experiment of Chain-Scoop Turnover-Cleaning Type Precision Seed Metering Device for Broad Bean (链勺翻转清种式蚕豆精密排种器设计与试验). *Transactions of the Chinese Society for Agricultural Machinery*, 53(8), 82-92, Beijing/China. DOI: 710.6041/j.issn.1000-1298.2022.08.009

[24] Li F.L., Chen J.H., Liu K.Y., Zhang J., Zhang Y.O., Yin J.C., Liu F., & Zhao M.Q. (2024). Design and experiment of precision seed metering plate for edible sunflower by adding seed guide bar. *INMATEH Agricultural Engineering*, 72(1), 162-172, Bucharest/Romania. DOI: https://doi.org/10.35633/inmateh-72-15

[25] Li H.Q., Zhao J., Liu E.G., & Liu C.X. (2022). Simulation Test of Indented Wheel Type Wheat Precision Seed Metering Device Based on EDEM (基于EDEM的窝眼轮小麦精量排种器排种仿真试验). *Jiangsu Agricultural Sciences*, 50(10), 188-193, Nanjing/China. DOI: 10.15889/j.issn.1002-1302.2022.10.030

[26] Li J.F. (2019). Design and Experimental Study of Air-Suction Precision Seed Metering Device for Small-Sized Vegetable Seeds (小粒径蔬菜种子气吸式精密排种器的设计与试验研究). Master dissertation, *Shandong Agricultural University*, Tai'an/China.

[27] Li M., Ding Y.C., & Liao Q.X. (2010). Field detection method for miss-seeding of pneumatic rapeseed precision metering device (气力式油菜精量排种器田间漏播检测方法). *Transactions of the Chinese Society of Agricultural Engineering*, 26(S1), 27-31, Beijing/China.

[28] Li M.T., Li T.Y., Guan X.D., Zhao G.K., & Zhou F.J. (2018). Structural Design of Centrifugal Pushing Device for Cone-Disc Seed Metering Device and Analysis of Seed Filling Mechanism (锥盘排种器离心推送结构设计与充种机理分析). *Transactions of the Chinese Society for Agricultural Machinery*, 49(3), 77-85, Beijing/China. DOI: 10.6041/j.issn.1000-1298.2018.03.009

[29] Li M.Y., Li H., Qi X.D., Meng Y.B., & Zhang X. (2026). Design and Experiment of Key Components of Air-Suction Type Garlic Seeder (气吸式大蒜播种机关键部件设计与试验). *Journal of Agricultural Mechanization Research*, 48(8), 65-73, Harbin/China. DOI: 10.13427/j.issn.1003-188X.2026.08.009

[30] Li P. (2022). Design and Experimental Study of Side-Guided High-Speed Precision Seed Metering Device for Soybean (侧置导引式大豆高速精量排种器设计与试验研究). Master dissertation, *Northwest A&F University*, Yangling/China.

[31] Li S.F., Mao X., Wang S., Wang G.Y., Yi S.J., Tao G.X., & Li Y.F. (2026). Design and Experiment of Control System of Belt-type High-speed Seed Guiding Device for Corn (带式玉米高速导种装置控制系统的设计与试验). *Journal of Agricultural Mechanization Research*, 48(2),

235-242, Harbin/China. DOI: 10.13427/j.issn.1003-188X.2026.02.028
[32] Li S.Q., Wang Y.B., Li W., Yang T., Zhang Z.S., & Yan X. (2022). Design and EDEM Simulation Test of Horizontal Disc Type Seed Metering Device for Mountainous Areas (山地水平圆盘式排种器设计及EDEM仿真试验). *Jiangsu Agricultural Sciences*, 50(14), 183-190, Nanjing/China. DOI: 10.15889/j.issn.1002-1302.2022.14.026
[33] Li X., Li X.H., Yang C., Xu Z.X., & Lu Z.H. (2026). Design and Experiment of Seed Scraping Mechanism for Air-Suction Type Seed Metering Device in Wheat Community Plot (小麦小区气吸式排种器刮种机构设计与试验). *Journal of Agricultural Mechanization Research*, 48(5), 27-34, Harbin/China. DOI: 10.13427/j.issn.1003-188X.2026.05.004
[34] Li X.R., Zhang Y.P., Diao P.S., Xie Z.G., & Cui Z.C. (2023). Optimal Design and Experiment of Pneumatic Vegetable Precision Seed Metering Device (气力式蔬菜精量排种器优化设计与试验). *Journal of Agricultural Mechanization Research*, 45(5), 88-92, Harbin/China. DOI: 10.13427/j.cnki.njyi.2023.05.043
[35] Li Y.H., Chu S., Jiao R.Z., Li B.G., Liu Z.M., Song Q., & He X.W. (2026). Design and Experiment of Double-Side Wheel-Type Seed Clearing Mechanism for Air-Suction Type High-Speed Precision Seed Metering Device (气吸式高速精量排种器双侧轮式清种机构的设计与试验). *Journal of Agricultural Mechanization Research*, 48(8), 82-89. Harbin/China. DOI: 10.13427/j.issn.1003-188X.2026.08.011
[36] Li Y.H., Zhang Z.L., Li T.H., Wu Y.Q., Niu Z.R., & Hou J.L. (2020). Design and Experiment of Wheel-Scoop Type Single-Seed Taking Device for Garlic (轮勺式大蒜单粒取种装置设计与试验). Transactions of the Chinese Society for Agricultural Machinery, 51,(3), 61-68, Beijing/China. DOI: 10.6041/j.issn.1000-1298.2020.03.007
[37] Li Z.D., Sun Y.N., Yang W.C., Wang W.W., Zhang T., & Chen L.Q. (2018). Synchronous Detection System of Miss-Filling and Hole Clogging for Small-Seed Vegetable Based on Beam-Blocking Method (光束阻断式小粒蔬菜种子漏充与堵孔同步检测系统研究). *Transactions of the Chinese Society for Agricultural Machinery*, 49(8), 119-126, Beijing/China. DOI: 10.6041/j.issn.1000-1298.2018.08.014
[38] Li Z.D., Wu J.J., Du J.H., Duan D.L., Zhang T., & Chen Y.X. (2023). Experimenting and optimizing design parameters for a pneumatic hill-drop rapeseed metering device. *Agronomy*, 13(1), 141, Basel/Switzerland. DOI: 10.3390/agronomy13010141
[39] Liao Y.T., Liao Q.X., Wang L., Zheng J., & Gao L.P. (2018). Factors Affecting Seed Suction Effect of Pneumatic Precision Metering Device for Small-Sized Seeds (气力式小粒径种子精量排种器吸种效果影响因素研究). *Transactions of the Chinese Society of Agricultural Engineering*, 34(24), 10-17, Beijing/China. DOI: 10.11975/j.issn.1002-6819.2018.24.002
[40] Liao Y.T., Tan Y., Liao Q.X., Zheng J., Wang L.S., & Zhang Q.S. (2025). Research Progress and Development Trends in Precision Seeding Technologies for Major Grain and Oil Crops (主要粮油作物精量播种技术与装备研究进展). *Transactions of the Chinese Society for Agricultural Machinery*, 56(9), 1-19, Beijing/China. DOI: 10.6041/j.issn.1000-1298.2025.09.001
[41] Liu H., Liao Y.T., Wang L., Wang B.S., Du Z., & Liao Q.X. (2022). Design and Experiment of Positive and Negative Air Pressure Combined Precision Seed Metering Device for Pak Choi (小白菜正负气压组合式精量排种器设计与试验). *Transactions of the Chinese Society for Agricultural Machinery*, 53(10), 54-65, Beijing/China. DOI: 10.6041/j.issn.1000-1298.2022.10.006
[42] Liu H.X., Liu J.X., Tang S.F., & Xu X.M. (2016). Design and Seed Filling Mechanism Analysis of Opposed Swash Plate High-Speed Precision Soybean Seed Metering Device (对置斜盘高速精密大豆排种器设计与充种机理分析). *Transactions of the Chinese Society of Agricultural Engineering*, 32(20), 24-31, Beijing/China. DOI: 10.11975/j.issn.1002-6819.2016.20.003
[43] Liu L., Liu D.Q., Sun Q.T., Qian K., Wang D.W., Sun W.X., & Li X.J. (2026). Design and Experiment of Chain-Scoop Type Double-Seed Precision Seed Metering Device for Peanut with Single Scoop and Double Holes (链勺式单勺双型孔花生双粒精量排种器设计与试验). *Journal of Agricultural Mechanization Research*, 48(5), 57-64, Harbin/China. DOI: 10.13427/j.issn.1003-188X.2026.05.008
[44] Liu R., Liu Z.J., Liu L.J., & Li Y.H. (2022). Design and Experiment of High-Speed Air-Suction Seed

Metering Device with Disturbance-Assisted Seed Filling for Corn (玉米扰动辅助充种高速气吸式排种器设计与试验). *Transactions of the Chinese Society for Agricultural Machinery*, 53(9), 50-59, Beijing/China. DOI: 10.6041/j.issn.1000-1298.2022.09.005

[45] Liu S., Lai Q.H., Dong J.Y., & Cao X.L. (2019). Simulation and Experiment of Filling Performance of Air-Blowing Type Precision Seed Metering Device for Panax notoginseng (气吹式三七精密排种器充填性能的仿真与试验). *Journal of South China Agricultural University*, 40(3), 125-132, Guangzhou/China.

[46] Liu Z.J., Liu L.J., Yang X.J., Zhao Z.B., & Liu X.Q. (2016). Design and Experiment of Finger-Clip Type No-Till Precision Seeder for Corn (指夹式玉米免耕精密播种机的设计与试验). *Transactions of the Chinese Society of Agricultural Engineering*, 32(S2), 1-6, Beijing/China. DOI: 10.11975/j.issn.1002-6819.2016.z2.001

[47] Lu Y.L., Jiang J.T., He X.N., Wang D.Q., & Zheng X.S. (2023). Design and Experiment of Indented Wheel Type Seed Metering Device for Cyperus esculentus (油莎豆窝眼轮式排种器设计与试验). *Journal of Agricultural Mechanization Research*, 45(2), 156-163, Harbin/China. DOI: 10.13427/j.cnki.njyi.2023.02.013

[48] Önal İ., Değirmencioğlu A., & Yazgi A. (2012). An evaluation of seed spacing accuracy of a vacuum type precision metering unit based on theoretical considerations and experiments. *Turkish Journal of Agriculture and Forestry*, 36(2), 133-144, Ankara/Turkey. DOI: 10.3906/tar-1010-1316

[49] Panning J.W., Kocher M.F., Smith J.A., & Kachman S.D. (2000). Laboratory and field testing of seed spacing uniformity for sugarbeet planters. *Applied Engineering in Agriculture*, 16(1), 7-13, St. Joseph/USA. DOI: 10.13031/2013.4985

[50] Ren J.D., (2021). Design and Experiment of Swing Finger-Clip Type Corn Seed Metering Device (摆动指夹式玉米排种器设计与试验). Master dissertation, *Northeast Agricultural University*, Harbin/China.

[51] Ren Y.X., Zhao X.C., Dong W.X., & Zhao J. (2026). Research Status and Development Trend of Precision Seed Metering Devices (精量排种器研究现状与发展趋势). *Southern Agricultural Machinery*, 57(6), 17-20+25, Nanning/China.

[52] Ryu I.H. & Kim K.U. (1998). Design of roller type metering device for precision planting. *Transactions of the ASAE*, 41(4), 923-930, St. Joseph/USA. DOI: 10.13031/2013.17249

[53] Singh I., Gautam A., Dixit A.K., & Manes G.S. (2020). Development and Evaluation of Inclined Plate Metering Mechanism for the Sowing of Maize (*Zea mays L*) Seed. *Current Journal of Applied Science and Technology*, 39(13), 118-128, London/UK. DOI: 10.9734/CJAST/2020/v39i1330689

[54] Su W., Chen Z.W., Lai Q.H., Jia G.X., Lv Q., & Tian B.N. (2022). Design and Experiment of Wheel-Scoop Type Precision Seed Metering Device for Pinellia ternata (轮勺式半夏精密排种器设计与试验). *Transactions of the Chinese Society for Agricultural Machinery*, 53(9), 60-71, Beijing/China. DOI: 10.6041/j.issn.1000-1298.2022.09.006

[55] Sun W.S., Yi S.J., Qi H.L., Li Y.F., Dai Z.B., Zhang Y.P., Yuan J.S., & Wang S. (2025). Design and optimization of air-assisted spiral seed-supply device for high-speed dense planting maize seeder. *INMATEH Agricultural Engineering*, 75(1), 13-25, Bucharest/Romania. DOI: https://doi.org/10.35633/inmateh-75-01

[56] Tang H., Xu F.D., Xu C.S., Zhao J.L., & Wang Y.J. (2023). The influence of a seed drop tube of the inside-filling air-blowing precision seed-metering device on seeding quality. *Computers and Electronics in Agriculture*, 204, 107555, Amsterdam/Netherlands. DOI: 10.1016/j.compag.2022.107555

[57] Van Loon J., Krupnik T.J., López-Gómez J.A., Timsina J., & Govaerts B. (2020). A standard methodology for evaluation of mechanical maize seed meters for smallholder farmers comparing devices from Latin America, Sub-Saharan Africa, and Asia. *Agronomy*, 10(8), 1091, Basel/Switzerland. DOI: https://doi.org/10.3390/agronomy10081091

[58] Wang J.W., Tang H., Zhou W.Q., Yang W.P., & Wang Q. (2015). Improved Design and Experiment of Finger-Clip Type Precision Corn Seed Metering Device (指夹式精量玉米排种器改进设计与试验). *Transactions of the Chinese Society for Agricultural Machinery*, 46(9), 68-76, Beijing/China. DOI:

10.6041/j.issn.1000-1298.2015.09.010
[59] Wang L., Liao Y.T., Wan X.Y., Wang B.S., Hu Q.L., & Liao Q.X. (2022). Design and Experiment of Mixing Device of Air-Assisted Central Metering System for Rapeseed and Wheat (油麦兼用型气送式集排器混种部件设计与试验). *Transactions of the Chinese Society for Agricultural Machinery*, 53(2), 68-79+97, Beijing/China. DOI: 10.6041/j.issn.1000-1298.2022.02.007
[60] Wang Q., Zhu L.T., Li M.W., Huang D.Y., Jia H.L., & Zhuang J. (2019). Vibration Characteristics of Finger-Clip Type No-Till Precision Seeder for Corn and Its Effect on Metering Performance (指夹式玉米免耕精密播种机振动特性及对排种性能的影响). *Transactions of the Chinese Society of Agricultural Engineering*, 35(9), 9-18, Beijing/China. DOI: 10.11975/j.issn.1002-6819.2019.09.002
[61] Wang Y.C., Sun H., Li B.Q., Han X., & Chen H.T. (2019). Design and Experiment of Soybean Gather-Belt Type Seed Metering Device (大豆集排带式排种器设计与试验). *Transactions of the Chinese Society for Agricultural Machinery*, 50(7), 74-83, Beijing/China. DOI: 10.6041/j.issn.1000-1298.2019.07.007
[62] Wang Z.W., Chen Y., Adilet S., Wei N.S., Zhou J.G., Zhang D.Y., Jiang Y.W., Fan Y.L., Zhang W., & Chen J. (2026). Design and Optimization of a Combined Seed Cleaning Mechanism for an Air-Suction Seed Metering Device for Small-Seed Crops with Multi-Seed Hill. *Sustainability*, 18(9), 4274, Basel/Switzerland. DOI: https://doi.org/10.3390/su18094274
[63] Xu G.L., Yang F.Z., Li Y.H., Peng Z.H., Shen X.T., & Cao B. (2026). Design and Experiment of Air-Suction Type Precision Seed Metering Device for Choy Sum (气吸式菜心精量排种器的设计与试验). *Journal of Agricultural Mechanization Research*, 48(6), 237-243+293, Harbin/China. DOI: 10.13427/j.issn.1003-188X.2026.06.030
[64] Yadachi S., Mani I., Kalra M.S., Kumar A., & Sahoo P.K. (2013). Development and evaluation of inclined plate metering mechanism for carrot seed. *Journal of Agricultural Engineering*, 50(2), 10, New Delhi/India. DOI: 10.52151/jae2013502.1508
[65] Yan B.X., Zhang D.X., Cui T., He C.T., Ding Y.Q., & Yang L (2017). Design of Air-Suction Corn Precision Seed Metering Device with Synchronous Rotation of Seed Plate and Negative Pressure Chamber (排种盘和负压腔室同步旋转气吸式玉米精量排种器设计). *Transactions of the Chinese Society of Agricultural Engineering*, 33(23), 15-23, Beijing/China. DOI: 10.11975/j.issn.1002-6819.2017.23.003
[66] Yang S., Zhai C.Y., Gao Y.Y., Dou H.J., Zhao X.G., He Y.K., & Wang X. (2022). Planting uniformity performance of motor-driven maize precision seeding systems. *International Journal of Agricultural and Biological Engineering*, 15(5), 101-108, Beijing/China. DOI: 10.25165/j.ijabe.20221505.5911
[67] Yang W C. (2020). Design and Experiment of Pneumatic Groove-Tooth Disc Type Precision Seed Metering Device for Rapeseed (油菜气力槽齿盘式精量排种器设计与试验). Master dissertation, *Anhui Agricultural University*, Hefei/China.
[68] Yatskul A., Lemiere J.P., & Cointault F. (2017). Influence of the divider head functioning conditions and geometry on the seed's distribution accuracy of the air-seeder. *Biosystems Engineering*, 161, 120-134, Amsterdam/Netherlands. DOI: https://doi.org/10.1016/j.biosystemseng.2017.06.015
[69] Yazgi A. & Degirmencioglu A. (2007). Optimisation of the seed spacing uniformity performance of a vacuum-type precision seeder using response surface methodology. *Biosystems engineering*, 97(3), 347-356, Amsterdam/Netherlands. DOI: https://doi.org/10.1016/j.biosystemseng.2007.03.013
[70] Yi S.J., Chen T., Li Y.F., TAO G.X., & MAO X. (2021). Design and Experiment of Positive-Negative Pressure-Combined Hole Wheel Type Hill-Seeding Metering Device for Millet (正负气压-型孔轮组合式谷子穴播排种器设计与试验). *Transactions of the Chinese Society for Agricultural Machinery*, 52(6), 83-94, Beijing/China. DOI: 10.6041/j.issn.1000-1298.2021.06.009
[71] Yi S.J., Zhang Y., Dai Z., Kong L., Sun W., & Xu L. (2025). Design and experiment of positive pressure airflow guide groove seed guiding device for maize double-row high-speed precision seeder (玉米品字形高速精量播种机正压气流导槽式导种装置设计与试验). *Transactions of the Chinese Society for Agricultural Machinery*, 56(2), 261-274, Beijing/China. DOI: 10.6041/j.issn.1000-1298.2025.02.025
[72] Zha X.T., Chen L., Chen D.Q., He Y.P., & Yang R.B. (2024). Design and Testing of a Branched Air-

Chamber Type Pneumatic Seed Metering Device for Rice. *Agriculture*, 14(11), 1934, Basel/ Switzerland. DOI: https://doi.org/10.3390/agriculture14111934

[73] Zhang K.X., Li J.F., Song Z.H., Liu X.X., & Liu L. (2019). Optimal Design and Experiment of Double-Disc Air-Suction Precision Seed Metering Device with Variable Hole Diameter (变粒径双圆盘气吸式精量排种器优化设计与试验). *Transactions of the Chinese Society for Agricultural Machinery*, 50(6), 52-63, Beijing/China. DOI: 10.6041/j.issn.1000-1298.2019.06.006

[74] Zhang M., Li X.Y., Wang L., Lai Q.H., & Yin Y.C. (2026). Effect of disturbed seeds on performance of centrifugal mechanical maize high-speed precision seed metering device (种群扰动对离心机械式玉米高速精量排种器性能的影响). *Transactions of the Chinese Society for Agricultural Machinery*, 57(8), 44-54, Beijing/China. DOI: 10.6041/j.issn.1000-1298.2026.08.005

[75] Zhang S., Cai Z.Y., He H.L., Kuang F.M., Xiong W., Zhu D.Q., Li Z.D., & Tekeste M.Z. (2025). DEM contact parameters of rice seed for mechanical seeding performance analysis. *Biosystems Engineering*, 260, 104298, Amsterdam/Netherlands. DOI: https://doi.org/10.1016/j.biosystemseng.2025.104298

[76] Zhang X., Yang R.B., & Shang S.Q. (2014). Design of Anti-Damage Device for Inside-Filling Disc Seed Metering Device (内侧充种圆盘排种器防伤种装置的设计). *Journal of Agricultural Mechanization Research*, 36(10), 75-78+83, Harbin/China. DOI: 10.13427/j.cnki.njyi.2014.10.018

[77] Zhang X.J., Chen Y., Shi Z.L., Jin W., Zhang H.T., Fu H., & Wang D.J. (2021). Design and Experiment of Dual-Chamber Turntable Type Cotton Vertical Disc Hole-Planting Seed Metering Device (双仓转盘式棉花竖直圆盘穴播排种器设计与试验). *Transactions of the Chinese Society of Agricultural Engineering*, 37(19), 27-36, Beijing/China. DOI: 10.11975/j.issn.1002-6819.2021.19.004

[78] Zhao S., Yang F.Z., Li Y.H., Song Q., Sui X.B., Yang Y., & Liu C.W. (2024). Research progress of precision direct seeder for rice (水稻精量直播排种器研究进展). *Jiangsu Agricultural Sciences*, 52(13), 13-21, Nanjing/China. DOI: 10.15889/j.issn.1002-1302.2024.13.002

[79] Zheng Z.Q., Ju X.T., Zhao P.F., Dong J.X., Yang P.K., Feng T., & Huang Y.X. (2025). Design and experiment of screw-guided posture-adjusting and filling-promoting precision seed metering device for wheat (螺旋引导调姿促充式小麦精量排种器设计与试验). *Transactions of the Chinese Society for Agricultural Machinery*, 56(9), 117-128, Beijing/China. DOI: 10.6041/j.issn.1000-1298.2025.09.010

[80] Zhou Y., Hu M.J., Xia J.F., Zhang G.Z., Xu Z.Y., Feng C.C., Tang N.R., & Liu D.Z. (2018). Design and Experiment of Adjustable Precision Seed Metering Device with Combined Holes for Cotton (内充种组合型孔式播量可调棉花精量排种器设计与试验). *Transactions of the Chinese Society of Agricultural Engineering*, 34(18), 59-67, Beijing/China. DOI: 10.11975/j.issn.1002-6819.2018.18.008

DESIGN AND EXPERIMENTAL STUDY OF FURROW OPENER FOR SELF-PROPELLED CODONOPSIS PILOSULA TRANSPLANTER BASED ON DISCRETE ELEMENT METHOD

/

基于离散元的自走式党参移栽机开沟器设计与试验研究

Qingxu YU[1,2,3], Ying LANG[1], Yan GONG[1] *, Xiao ZHANG[1], Jianling HU[1], Dehuan ZHOU[1],

[1] Nanjing Institute of agricultural mechanization, Ministry of agriculture and rural areas, Nanjing, China;

[2] Key Laboratory of Modern Agricultural Equipment, Ministry of Agriculture and Rural Affairs, Nanjing, China;

[3] Institute of Western Agriculture, Chinese Academy of Agricultural Science, Changji, China

E-mail: yqx5205@163.com;

** Correspondent authors: Yan Gong*

DOI: https://doi.org/10.35633/inmateh-79-59

Keywords: *Codonopsis pilosula transplantation; resistance reducing furrow opener; soil transport characteristics; discrete element simulation; optimal parameter combination*

ABSTRACT

Furrow opening is a critical operation in the transplantation of Codonopsis pilosula using the seedlings-with-exposed-heads-and-film-covered-bodies (HEBCF) method. The considerable resistance generated during furrow opening results in high power consumption, making resistance reduction an important research objective. Although furrow openers have been widely studied, this study focused on the furrow opener of a self-propelled HEBCF transplanter for C. pilosula. The interaction mechanism between the furrow opener and the soil was investigated through force analysis and the development of models describing soil transport patterns and particle velocities. A discrete element simulation model of the furrow-opening process was established using EDEM to evaluate the effects of the main structural parameters on furrow-opening resistance. A three-factor five-level Box–Behnken response surface experiment was conducted, and regression models for furrow-opening resistance and soil-particle velocity were developed based on the simulation results. The structural parameters were then optimized. The optimal parameter combination consisted of a chisel-tip angle of 65°, a clearance angle of 10°, and an oblique angle of 90°. Under these conditions, furrow-opening resistance was reduced by 30.82%, while the agronomic requirements of a furrow depth of 10 cm and a furrow width of 50 cm were satisfied. These results provide a technical basis for the development and optimization of self-propelled HEBCF transplanters for C. pilosula.

摘要

开种植沟作业为党参露头覆膜移栽流程的关键环节，移栽机在执行开沟作业时会产生较大阻力，进而消耗大量动力，因此减阻开沟技术成为当前研究的首要方向。国内外研究机构针对开沟装置开展了较多研究，本文针对自走式党参露头覆膜移栽机的开沟装置，研究开沟装置与土壤的互作机理，对开沟器进行受力分析，研究土壤运移规律和速度模型；借助 EDEM 软件构建开沟仿真试验模型，全面研究相关因素对开沟阻力的影响，采用 Bo -Behn en 响应曲面法设计三因素五水平的仿真试验，通过开沟性能仿真试验研究，得到开沟阻力模型和土壤颗粒速度模型，进行结构参数优化，最终确定开沟器的铲尖角 65°、隙角 10°和斜切角 90°的最优参数组合，开沟作业阻力降低 30.82%，同时满足党参移栽的开沟深度 10cm、开沟宽度 50cm 的农艺要求，为自走式党参露头覆膜移栽机研发提供支撑。

INTRODUCTION

In recent years, the market for traditional Chinese medicinal herbs has maintained a growth trend, presenting both new challenges and opportunities for the development of the related planting industry *(Wang et al., 2023)*. *Codonopsis pilosula* is one of the major traditional Chinese medicinal herbs in China, known for its effects in tonifying the middle energizer, strengthening qi, invigorating the spleen, and benefiting the lungs, earning it the reputation of "small ginseng" *(Xie et al., 2020; He et al., 2021*).

[1] *Qingxu YU, Ph. D. Assistant Researcher; Ying Lang, Master Candidate; Yan GONG, Researcher.; Xiao Zhang, Assistant Researcher; Hu Jianling, intern researcher; Dehuan Zhou, Associate Researcher;*

The genuine production areas of *Codonopsis pilosula* are mainly distributed in the arid and semi-arid regions of Northwest China. The "*seedlings-with-exposed-heads-and-film-covered-bodies*" (HEBCF) transplanting technique is a high-quality, high-yield, and high-efficiency planting method in these arid areas. It facilitates later field management and mechanized harvesting, thereby promoting the development of full-scale mechanization *(Liu et al., 2023)*. Currently, the HEBCF transplanting process for *Codonopsis pilosula* faces the problem of a "lack of available machinery" and relies entirely on manual transplantation, which is labor-intensive, time-consuming, and incurs high costs for auxiliary workers. With the rapid development of the *Codonopsis pilosula* planting industry, the demand for specialized HEBCF transplanting machines has become increasingly urgent *(Yu et al., 2025)*. Furrow opening is the first step in the *Codonopsis pilosula* transplantation process. The considerable resistance generated during furrow opening results in high power consumption; therefore, reducing furrow-opening resistance is a major research objective. The furrow opener, one of the core components of the transplanting machine, must ensure uniform furrow depth, a neat furrow shape, and minimal soil disturbance. Its performance directly affects seedling placement posture, transplanting uniformity, and plant growth, thereby influencing the yield and quality of the crops *(Chen et al., 1961)*. Currently, there are various types of furrow openers, which can be divided into two major categories: rolling and mobile types *(Li et al., 2020)*. The rolling type includes double-disc, single-disc, axial-rotating, vertical-rotating, and chain types, while the mobile type includes core-spade, sliding knife, and boat types.

Extensive research on furrow-opening devices has been conducted both domestically and internationally, focusing primarily on the resistance reduction design of furrow-opening components, soil-component interactions, and the effects of the physical and mechanical properties of soil on furrow-opening performance *(Aikins et al., 2023)*. The forces exerted by soil on furrow openers mainly include reaction force and frictional force, which are influenced by soil shear strength, cohesion, and internal and external friction angles. Additionally, soil adhesion increases operational resistance and energy consumption. Due to the complexity of soil composition and structural heterogeneity, existing theoretical models are limited and associated calculations remain cumbersome *(Gill et al., 1983)*. To optimize the design of furrow opening components and reduce operational resistance, researchers have employed bionic design, simulation models, and field experiments to investigate the effects of structural and working parameters on soil displacement distance and traction resistance, ultimately optimizing furrow opener design *(Liu et al., 2021; Shmulevich et al., 2007; Wang et al., 2024)*. Domestic scholars have conducted extensive research on furrow openers for medicinal herb transplanters. *Wang et al., (2023),* designed a furrow opener suitable for transplanting Panax notoginseng seedlings based on the agronomic parameters of under-forest cultivation, and performed simulation analysis and experimental validation. *Chen et al., (2023),* designed a moldboard furrow opener suitable for transplanting Astragalus membranaceus. This type of furrow opener features a simple structure, ease of manufacture, and good soil penetration performance. A simulation experiment was conducted using the radius of curvature of the ridge line, the oblique angle, and the clearance angle as experimental factors, with furrow opening resistance and the coefficient of variation of furrow width as evaluation indicators. *Wang et al., (2021),* designed a sharp-angled long-wing furrow opener based on the planting pattern of long-rooted medicinal herbs in the arid regions of Northwest China, aiming to address issues such as soil accumulation and seedling exposure observed in existing medicinal herb transplanters. They simulated the operation process of the furrow opener using EDEM software, and the results demonstrated satisfactory soil covering and backfilling effects. Field experiments indicated that the performance indicators of the furrow opener met the requirements of agricultural industry standards.

Furrow opening is a critical step in the transplanting process of *Codonopsis pilosula*. During operation, the transplanting machine generates substantial resistance, leading to high power consumption. Consequently, resistance reduction technology for furrow opening has become a key research focus. Numerous research institutions worldwide have conducted extensive studies on furrow openers, and domestic scholars have also carried out relevant research on furrow openers for medicinal herb transplanters *(Feng et al., 2025; Wang et al., 2017)*. Research on furrow opening resistance reduction primarily focuses on the resistance reduction design of furrow opening components, the interaction between soil and components, and the influence of soil physical and mechanical properties on furrow opening performance—including reaction forces and friction exerted by soil on the furrow opener, soil shear strength, cohesion, and internal and external friction angles. Additionally, soil adhesion increases operational resistance and power consumption.

Due to the complex composition and structural heterogeneity of soil, existing theoretical models have limitations, and the associated calculations remain relatively complex *(Yu et al., 2009; Pan et al., 2015; Zhang et al., 2024)*. This paper focuses on the furrow opener of a Codonopsis pilosula HEBCF transplanter. It investigates the interaction mechanism between the furrow opener and the soil, analyzes the forces acting on the furrow opener, and examines soil transport patterns and velocity models. Using EDEM software, a simulation test model for furrow opening was developed to comprehensively study the effects of relevant factors on furrow opening resistance. The Box-Behnken response surface method was employed to design a three-factor, five-level simulation experiment. Through the furrow opening performance simulation, a furrow opening resistance model and a soil particle velocity model were obtained, and the structural parameters were optimized. Finally, the optimal combination of chisel tip angle, clearance angle, and oblique angle for the furrow opener was determined.

MATERIALS AND METHODS

Structural design of the furrow opener

Based on the agronomic requirements for HEBCF transplanting of *Codonopsis pilosula*, and considering the topographic characteristics of hilly and mountainous regions in Northwest China as well as the properties of cultivated soils, this study presents the design of a self-propelled HEBCF *Codonopsis pilosula* transplanter. To facilitate turning and maneuverability during transplanting operations, as well as transport and transfer, a diesel powered tracked chassis was selected as the power platform. The machine is equipped with a furrow opener, a directional transplanting device, and a soil covering and film mulching device. It is capable of performing integrated operations, including furrow opening for planting, HEBCF transplanting of *Codonopsis pilosula* seedlings, soil covering, film mulching, and edge covering. The overall structure of the transplanter is schematically shown in Figure 1.

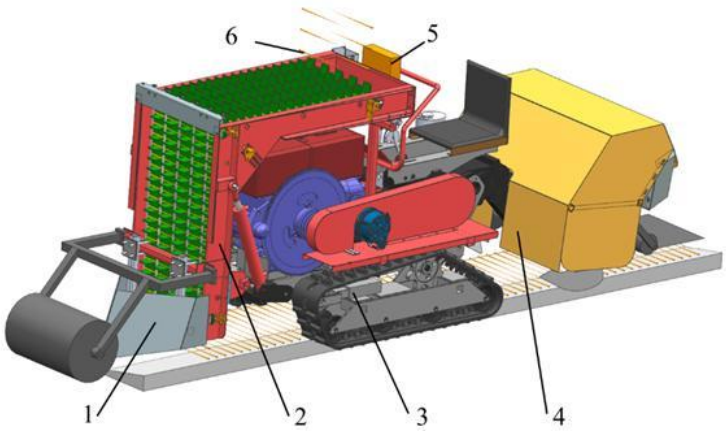


Fig. 1 - Schematic diagram of the overall structure of a transplanter

1. Ditching device, 2. Transplanting device, 3. Tracks chassis; 4. Soil covering and film covering device, 5. Transplanting electronic control system, 6. Codonopsis seedlings

The furrow opener is a key component of the HEBCF *Codonopsis pilosula* transplanting equipment. It is required to form a "V"-shaped planting furrow with a depth of 10–15 cm and a width of approximately 50 cm, with seedlings uniformly placed on one side slope of the furrow. Consistent planting depth and furrow configuration further enhance the survival rate, quality, and yield of *Codonopsis pilosula*. The furrow opener primarily consists of a furrow opener and a support wheel for furrow depth adjustment, as illustrated in Fig. 2.

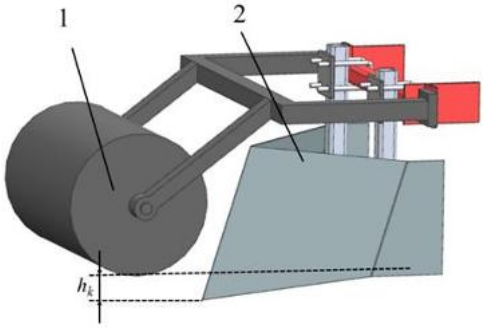


Fig. 2 - Schematic diagram of trenching unit

1. Front support wheel; 2. Furrowing device

By adjusting the mounting height of the furrow opener connecting rod, the relative height between the front support wheel and the furrow opener can be varied, thereby enabling adjustment of the furrow depth h_k. The support wheel ensures uniform furrow depth throughout the operation.

Key structural parameters of the furrow opener

Designed to satisfy agronomic requirements, the furrow opener is shown in Figure 3. Its key structural parameters are opener width (W_k), length(L_k), height (H_k), chisel tip angle (γ), clearance angle (β), and oblique cutting angle (ε). Soil on both sides backflows during trenching, so the opener width must exceed the target furrow width of 50 cm, and (W_k) is set as 52 cm in this study. The dimensions and profile of the opener depend mainly on γ, β and ε, which also affect trenching resistance and furrow cross-section shape. The chisel tip angle γ ranges 45°–75°, penetration clearance angle β is generally below 15°, and oblique cutting angle ε varies 60°–120°.

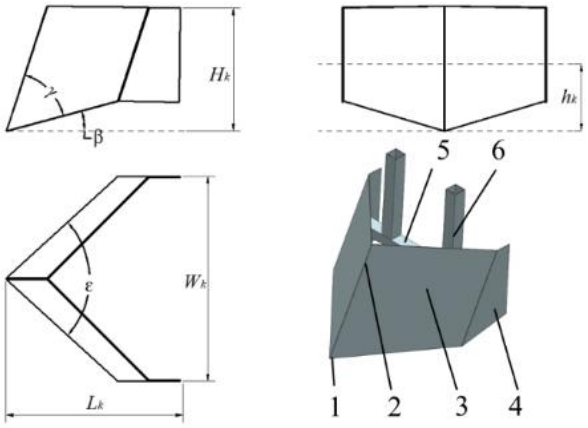


Fig. 3 - Structural diagram of a trenching opener

1. Chisel tip; 2. Cutting edge; 3. Furrow plate; 4. Side plate; 5. Supporting beam; 6. Connecting rod;

Soil characteristics of the main Codonopsis pilosula production area

Soil physical properties are a key indicator for mechanical operations and directly influence furrow opening resistance and furrow quality. In this study, soil samples were collected from the *Codonopsis pilosula* genuine producing area in Weiyuan County, Gansu Province. The soil type is sandy loam. Soil compactness was measured using a TYD-2 soil hardness tester, yielding an average value of 231.5 kPa. Measurements were also conducted in cultivated transplanting plots designated for HEBCF transplantation. The transplanting test plots were divided into six sampling areas, with random equal-volume sampling performed in each area. Surface soil samples from a depth of 0–20 cm were collected for testing, and the average moisture content of the soil samples was 16.32%. The soil samples were sieved using a standard sieve, and the proportion of particles larger than 10 mm exceeded 67.6%.

Force analysis of the furrow opener

During operation, the total force F_{Nk} acting on the furrow opener can be decomposed into the lateral force F_X along the X-axis, the forward resistance F_Y along the Y-axis, and the vertical downward force F_Z along the Z-axis. Due to the symmetrical structure of the furrow opener, the lateral forces on the left and right sides along the X-axis cancel each other out. The vertical force along the Z-axis creates a tendency for the furrow opener to penetrate the soil automatically. The power consumption of the furrow opener is primarily influenced by the force along the Y-axis. A schematic diagram of the forces acting on the furrow opener is shown in Fig.4.

During the furrow opening process, a cutting force F_T is generated at the cutting edge. After the soil undergoes shear failure, it slides backward along the furrow opener plate. The soil then exerts a normal load force F_N, tangential adhesion resistance F_S, and sliding friction force F_f on the two side plates. Subsequently, the displaced soil disperses to both sides of the furrow opener under its own gravity, resulting in relative sliding between the soil and the side plates, thereby generating a sliding friction resistance F_{Cf} on the side plates. Additionally, as the furrow opener advances, relative sliding also occurs between its bottom and the ground, causing the ground to exert a sliding friction force F_{Df} on the bottom of the furrow opener.

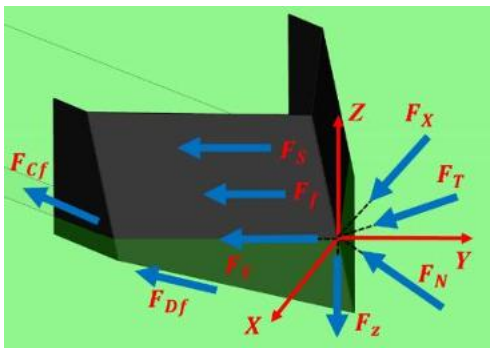


Fig. 4 - Schematic diagram of interaction between furrow opener and soil

Based on the force diagram of the furrow opener shown in Figure 5, the resistance model of the furrow opener can be derived as:

$$\begin{cases} F_X=0 \\ F_Y=F_T \sin(\gamma+\beta)+2F_N \sin(\gamma+\beta)\sin(\varepsilon/2)+2(F_s+F_f)\cos(\varepsilon/2)+2F_{Cf}+F_{Df} \\ F_Z=F_T \cos(\gamma+\beta)+2F_N \cos(\gamma+\beta)+G_k \end{cases} \quad (1)$$

where: G_k— Gravitational force of the furrow opener, N.

The normal load force F_N acting furrow opener plate is expressed as:

$$F_N=K_d S_{XZ} \quad (2)$$

where:

K_d — Resistance coefficient (N/cm²), the value of which is closely related to factors such as the structural parameters of the furrow opener plate, furrow depth, forward speed, self-weight of the furrow opener, and soil properties.

S_{XZ} — Normal cross-sectional area of soil cutting, cm².

The tangential adhesion resistance F_S on the furrow opener plate is given by:

$$F_s=N_n\mu_n+\tau_n \quad (3)$$

where:

N_n — Normal adhesion force on the furrow opener plate, N;

μ_n — Adhesion coefficient, which depends on soil properties and other factors;

τ_n — Tangential adhesion force on the furrow opener plate, N.

The friction force F_f on the furrow opener plate is expressed as:

$$F_f=F_N\mu_m \quad (4)$$

where:

μ_m — Sliding friction coefficient of the furrow opener plate, which depends on soil properties and other factors.

The friction force F_{Cf} on the side plates is given by:

$$F_{Cf}=2S_{YZ}\left(C_a+\frac{1}{2}K_0\rho_t d\tan\varphi+K_0 q\tan\varphi\right) \quad (5)$$

where:

S_{YZ} — Tangential cross-sectional area of soil cutting, cm²;

K_0 — Static earth pressure coefficient, related to soil properties and other factors;

C_a — Soil cohesion coefficient, related to soil properties and other factors;

q — Additional soil load, N;

φ — Soil internal friction angle, °;

ρ_t — Soil density, kg/m³.

The friction force F_{Df} on the bottom surface of the furrow opener is expressed as:

$$F_{Df}=F_Z \cos\beta\,\mu_m \tag{6}$$

Combining Equations (1) through (6), the furrow opening resistance model can be obtained as:

$$\begin{cases} F_X=0 \\ F_Y=F_T \sin(\gamma+\beta)+2K_d S_{XZ} \sin(\gamma+\beta) \sin\ （\varepsilon/2）+2\left(N_n\mu_n+\tau_n+F_N\mu_m\right) \cos\ （\varepsilon/2）+ \\ \&2S_{YZ}\left(C_a+\frac{1}{2}K_0\rho_t d \tan\varphi+K_0 q \tan\varphi\right)+F_Z \cos\beta\,\mu_m \\ F_Z=F_T \cos(\gamma+\beta)+2K_d S_{XZ} \cos(\gamma+\beta)+G_k \end{cases} \tag{7}$$

Analysis of soil particle dynamics

During the HEBCF transplanting operation of *Codonopsis pilosula*, the side plates must prevent premature soil backfilling into the planting furrow, thereby preserving the furrow cross-sectional shape and bottom flatness, and creating a stable and effective space for seedling placement. After the seedlings are deposited, appropriate soil backfilling helps secure the seedling tops to maintain their posture and minimize soil disturbance. Therefore, the length of the furrow opener side plates must be rationally designed, as it significantly influences both the furrow opening quality and the overall effectiveness of subsequent *Codonopsis pilosula* planting. An excessively long side plate increases furrow opening resistance, whereas an insufficiently long side plate leads to premature soil backfilling, resulting in suboptimal planting depth, furrow width, and bottom flatness, thereby compromising furrow opening quality. To further investigate the relevant parameters of the furrow opener side plates, a detailed analysis of soil particle motion characteristics on the furrow opener surface was conducted. Soil particles were assumed to be rigid granular materials that neither deform nor adhere. A specific point on the contact interface between the soil particles and the furrow opener was selected for analysis. A schematic diagram of the forces acting on the soil particles is shown in Figure 5.

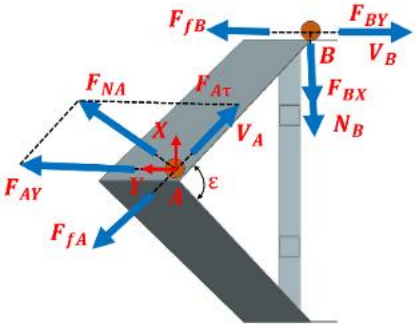


Fig. 5 - Schematic diagram of forces acting on soil particles

Assuming the soil particle is located at point A, it is subjected to a reaction force F_{NA} from the furrow opener plate and a friction force F_{fA}. The reaction force F_{NA} is first decomposed into a component F_{AY} in the forward direction (Y-axis) and a tangential component F_{At} along the furrow opener plate. The force analysis of the particle at point A yields the following equation:

$$\begin{cases} F_{AY}=\dfrac{F_{NA}}{\sin\ （\varepsilon/2）} \\ F_{A\tau}=\dfrac{F_{NA}}{\tan\ （\varepsilon/2）} \\ F_{fA}=F_{NA}\mu_m \\ F_{NA}=M_t g \cos(\gamma+\beta) \end{cases} \tag{8}$$

where:

M_t——mass of soil particles, kg;

g——gravitational acceleration, m/s².

Assuming the initial velocity of the soil particle is zero, if the tangential component F_{AT} of the force acting on the soil particle at point A exceeds the friction force F_{fA}, the soil particle will slide at point A on the furrow opener plate. Its equation of motion can be expressed as:

$$M_t a_A = F_{A\tau} - F_{fA} \tag{9}$$

where:

a_A——acceleration of the soil particles, m/s².

Combining and rearranging Equations (8) and (9) yields:

$$M_t a_A = M_t g \cos(\gamma+\beta)\left(\frac{1}{\tan(\varepsilon/2)} - \mu_m\right) \tag{10}$$

Given that the distance from point A to point B is L_{AB}, the acceleration a_A and velocity V_A of the soil particles during its motion from point A to point B are given by:

$$\begin{cases} a_A = g\cos(\gamma+\beta)\left(\frac{1}{\tan(\varepsilon/2)} - \mu_m\right) \\ V_A = \sqrt{2g\cos(\gamma+\beta)\left(\frac{1}{\tan(\varepsilon/2)} - \mu_m\right)L_{AB}} \end{cases} \tag{11}$$

Soil particles initiate movement from point A and accelerate from rest until they reach point B at the edge of the furrow opener. Subsequently, they collide with the soil at the planting furrow edge, rebound, and continue to move along the side plate. Assuming no energy loss during this process, the interaction between the soil at the furrow edge and the moving soil particles is analyzed. The reaction force exerted by the furrow edge soil on the moving particles can be decomposed into two components in the coordinate system: the force along the X-direction, F_{BX}, and the force along the Y-direction, F_{BY}. In addition, the unmoved soil particles on both sides, characterized by the repose angle α_t, exert a normal load N_B on the moving soil particles, and the side plate exerts a friction force F_{fB} on the particles. As shown in Figure 6, based on the force analysis of the soil particles at point B, the following mechanical model can be derived:

$$\begin{cases} F_{BX} = M_t a_A \sin(\varepsilon/2) \\ F_{BY} = M_t a_A \cos(\varepsilon/2) \\ N_B = M_t g \tan\alpha_t \\ F_{fB} = (N_B + F_{BX})\mu_m \end{cases} \tag{12}$$

The differential equation of motion for the soil particle at point B along the Y-direction is:

$$M\frac{d^2y}{dt^2} = F_{BY} - F_{fB} \tag{13}$$

Combining and rearranging Equations (12) and (13) yields:

$$M_t\frac{d^2y}{dt^2} = M_t a_A \cos(\varepsilon/2) - \left(M_t g\tan\alpha_t + M_t a_A \sin(\varepsilon/2)\right)\mu_m \tag{14}$$

During the soil particle migration process, it is assumed that after moving from point A to point B, the soil particles begin to move along the side plate. Given that the length of the side plate is S, the instantaneous velocity V_B of the soil particles when they detach from the side plate can be derived as:

$$V_B = \sqrt{\left(V_A\cos(\varepsilon/2)\right)^2 + 2\left[a_A\cos(\varepsilon/2) - \left(g\tan\alpha_t + a_A\sin(\varepsilon/2)\right)\mu_m\right]S} \tag{15}$$

EXPERIMENTAL STUDY ON FURROW OPENING PERFORMANCE BASED ON DISCRETE ELEMENT METHOD

Under the condition of maintaining consistent furrow width, furrow depth, and furrow cross-sectional shape, lower furrow opening resistance corresponds to reduced power consumption. The factors directly influencing the resistance of the furrow opener include the chisel tip angle γ, clearance angle β, oblique angle ε, furrow opener width W_k, and furrow opener length L_k, as well as inherent soil properties such as adhesion and density. Among these, the furrow opener width W_k and soil adhesion are considered fixed values and are therefore not treated as experimental factors in this study. The interaction among the chisel tip angle γ, clearance angle β, and oblique angle ε affects the furrow opener length L_k, which directly influences the forward resistance in the Y-direction and the vertical penetration force in the Z-direction. Additionally, it affects the volume of backfilled soil during the furrow opening process, ultimately determining the post-furrowing

cross-sectional shape. Consequently, the chisel tip angle γ, clearance angle β, and oblique angle ε are identified as key parameters and are selected as the main experimental factors.

At a given working depth, the cross-sectional area of furrow opening resistance varies with changes in the chisel tip angle γ, clearance angle β, and oblique angle ε. In this study, the furrow opening resistance per unit area, denoted as P_Y, was adopted as the evaluation index and calculated using the following equation:

$$P_Y = \frac{F_Y}{S_1} \tag{16}$$

where:

F_Y — forward resistance of the ditching tool in the Y direction, N;

S_1 — Cross-sectional area of furrow opening resistance, m².

Simulation test model and experimental scheme for furrow opening

To further investigate the factors influencing furrow opening resistance, a simulation experiment on furrow opening performance was conducted using EDEM software. The soil bin in the simulation measured 1500 mm × 4000 mm × 300 mm. Single spheres were used to simulate soil particles, with a particle radius of 5 mm. The Material Block module was employed to rapidly generate soil particles, and the Hertz–Mindlin (no-slip) contact model was adopted. Extensive research has been conducted by various scholars on the sandy loam soil of Northwest China *(Dai et al., 2019)*. The relevant soil parameters for the simulation test are presented in Table 1. After the soil particles in the simulation soil bin had stabilized, the three-dimensional model of the furrow opener was imported into the simulation model. The furrow opening depth was set to 10 cm, the furrow width to 52 cm, and the forward speed to 0.18 km/h. The furrow opening performance simulation experiment is illustrated in Figure 6. Experimental data on the furrow opening resistance per unit area in the Y-direction (P_Y) were collected from the stable operation zone.

Table 1

Parameters used in the simulation experiments

Material	Parameter	Value
Soil	Poisson's ratio	0.3
	Shear modulus / Pa	5×10^7
	Density (kg·m^{-3})	2600
Steel plate	Poisson's ratio	0.3
	Shear modulus / Pa	7.9×10^{10}
	Density (kg·m^{-3})	7865
Soil-soil	Coefficient of restitution	0.21
	Coefficient of static friction	0.68
	Coefficient of rolling friction	0.27
Soil-steel plate	Coefficient of restitution	0.54
	Coefficient of static friction	0.31
	Coefficient of rolling friction	0.13

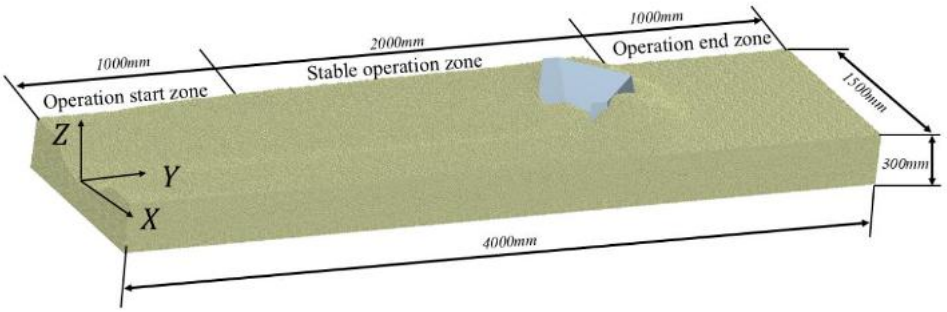


Fig. 6 - Simulation test of furrow opening performance

Through EDEM simulation experiments on furrow opening, the optimal parameter combination for the furrow opener was determined. In this study, the chisel tip angle γ, clearance angle β, and oblique angle ε were selected as experimental factors, while the furrow opening resistance per unit area in the Y-direction (P_Y) was used as evaluation indicators. A three-factor, second-order regression orthogonal rotational combination experiment was conducted to thoroughly investigate the influence of relevant factors on furrow opening performance. The coding of the simulation experiment factors is presented in Table 2, where the coded values correspond to the chisel tip angle γ, clearance angle β, and oblique angle ε, respectively. The design scheme and results of the simulation experiment are shown in Table 3, with the experimental results including the furrow opening resistance per unit area in the Y-direction (P_Y).

Table 2

Factor coding for simulation experiment

Level	Test factors		
	γ (°)	β (°)	ε (°)
1.682	75	15	120
1	69	13	108
0	60	10	90
-1	51	7	72
1.682	45	5	60

Table 3

Experimental scheme and results

Number	Test factors			Test Indicators
	γ (°)	β (°)	ε (°)	P_Y (Pa)
1	51	7	72	1685.13
2	69	7	72	1962.80
3	51	13	72	1598.33
4	69	13	72	1885.00
5	51	7	108	2161.24
6	69	7	108	2499.07
7	51	13	108	2058.64
8	69	13	108	2631.56
9	45	10	90	1772.11
10	75	10	90	2407.08
11	60	5	90	2106.61
12	60	15	90	2021.84
13	60	10	60	1632.93
14	60	10	120	2471.46
15	60	10	90	2023.67
16	60	10	90	2067.62
17	60	10	90	1945.05
18	60	10	90	2050.62
19	60	10	90	2023.67
20	60	10	90	1966.32

RESULTS AND ANALYSIS

Establishment of regression model and significance analysis

Multiple regression analysis was performed on the experimental data presented in Table 4. The regression equations relating the chisel tip angle (γ), clearance angle (β), and oblique angle (ε) to the furrow opening resistance per unit area in the Y-direction (P_Y) was obtained as follows:

$$P_Y=3643.983-52.3\gamma-152.593\beta-12.476\varepsilon+1.151\gamma\beta+0.272\gamma\varepsilon+0.458\beta\varepsilon+0.31\gamma^2+1.773\beta^2+0.036\varepsilon^2 \quad (17)$$

Table 4 presents the significance test results for the regression equations. The p-values for both the P_Y models are less than 0.01, indicating that the goodness of fit is highly significant and that the established models are reliable. The effects of γ, ε, and their interaction γ,ε on P_Y are highly significant ($p< 0.01$), while the effects of other factors on P_Y are not significant.

Table 4

Analysis of variance for the regression model

Source	P_Y - Experimental Results				
	Sum of squares	Degree of freedom	Mean Square	*F*-value	*P*-value
model	1483083.5	9	164787.06	77.82	<0.0001**
γ	473514.8	1	473514.83	223.62	<0.0001**
β	5629.2	1	5629.22	2.66	0.1341
ε	964577.0	1	964576.95	455.53	<0.0001**
$\gamma\beta$	7447.7	1	7447.74	3.52	0.0902
$\gamma\varepsilon$	14999.0	1	14998.96	7.08	0.0238**
$\beta\varepsilon$	4727.9	1	4727.90	2.23	0.1660
γ^2	8753.1	1	8753.13	4.13	0.0694
β^2	3540.9	1	3540.92	1.67	0.2250
ε^2	1879.9	1	1879.87	0.89	0.3683
Residual	21174.8	10	2117.48		
Lack of fit	9752.1	5	1950.43	0.85	0.5668
Pure error	11422.6	5	2284.52		
Total	1504258.3	19			

*Note: * indicates significant effect (P<0.05), ** indicates high significant effect (P<0.01)*

The coefficients of determination (R^2) for the regression equations are 0.9859 and 0.9771, respectively, both close to 1, indicating that the deviations between the predicted values and the actual values are minimal and nearly coincident. This demonstrates that the models accurately capture the relationship between the experimental factors and the response indicators. For the furrow opening resistance per unit area in the Y-direction (P_Y), the predicted R^2 and adjusted R^2 are both 0.9332, with a difference of less than 0.2. This indicates that the model exhibits excellent explanatory and predictive capabilities, and the high consistency between the two suggests that the model is not overfitted.

Figures 7(a) present the residual versus predicted value plots for the furrow opening resistance per unit area in the Y-direction (P_Y), respectively. The residual points for P_Y are randomly distributed with no discernible systematic pattern, indicating that the model fitting does not exhibit significant bias. Additionally, the residuals do not display a funnel-shaped pattern and are randomly scattered within the range of ±3 standard deviations (indicated by the red lines), suggesting the absence of significant outliers. Furthermore, the influence of individual data points on the estimation of model parameters is controllable, which further enhances the reliability of the established models.

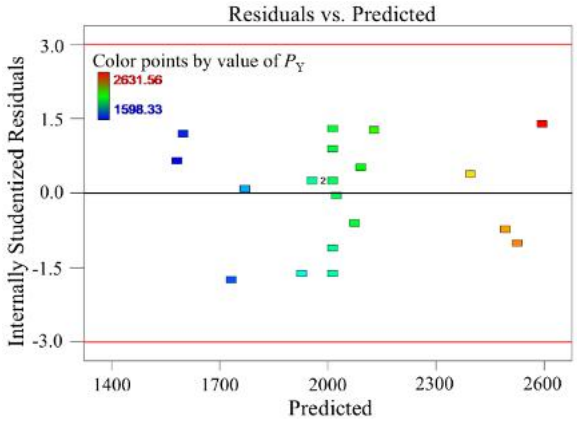


Fig. 7 - Residuals-versus-predicted plot for P_Y

Analysis of Furrowing Resistance per Unit Area in the Y-Direction (P_Y)

Box plots enable a rapid comparison of response distributions across different factor levels, facilitate the identification of outliers and data dispersion characteristics, and assist in evaluating the main effects and potential interactions of factors. To investigate the individual effects of the chisel tip angle (γ), clearance angle (β), and oblique angle (ε) on the furrow opening resistance per unit area in the Y-direction (P_Y), box plots were constructed for each factor against P_Y, as shown in Figure 8.

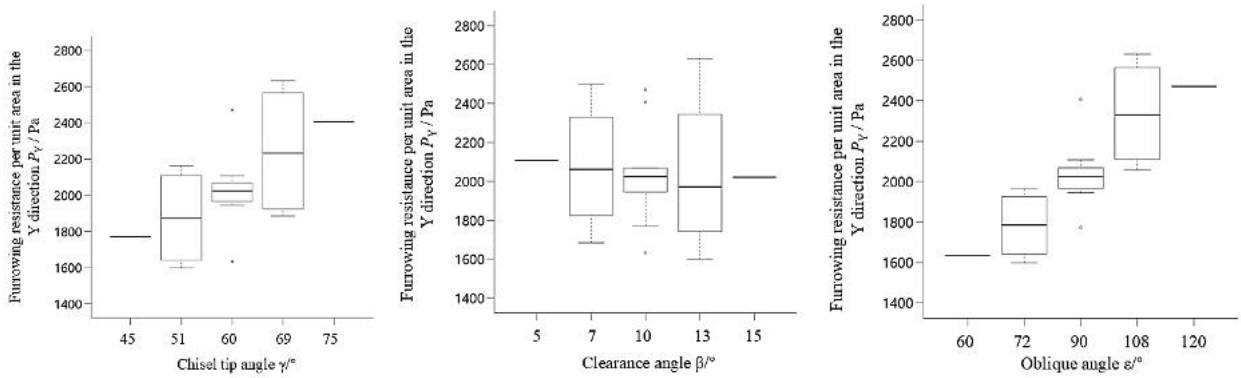


Fig. 8 - Box plot of P_Y

As shown in Figure 8(a), when the chisel tip angle (γ) is at levels −1, 0, and 1, the median values of the furrow opening resistance per unit area in the Y-direction (P_Y) are 1871.88, 2023.67, and 2230.93, respectively. P_Y exhibits a generally rapid increasing trend with increasing γ. At level 1 of γ, the box height is the largest, indicating the highest dispersion of P_Y data, which may lead to greater result variability and reduced data stability. To minimize P_Y, a low level of γ is preferable. As shown in Figure 8(b), when the clearance angle (β) is at levels −1, 0, and 1, the median values of P_Y are 2062.02, 2067.62, and 1971.82, respectively. P_Y initially shows a slight decreasing trend followed by a marginal increase as β increases. An optimal range for minimizing P_Y exists near level 1 of β. However, at level 1 of β, the box height is the largest and the whiskers are longer, indicating high dispersion of P_Y data, necessitating further collaborative optimization analysis considering other factors. As shown in Figure 8(c), when the oblique angle (ε) is at levels −1, 0, and 1, the median values of P_Y are 1785.07, 2023.67, and 2330.15, respectively. P_Y generally exhibits a rapid increasing trend with increasing ε. To minimize P_Y, a low level of ε is preferable.

To further investigate the interactive effects of the chisel tip angle (γ), clearance angle (β), and oblique angle (ε) on the furrow opening resistance per unit area in the Y-direction (P_Y), the influence of factor interactions on P_Y is illustrated in Figure 9.

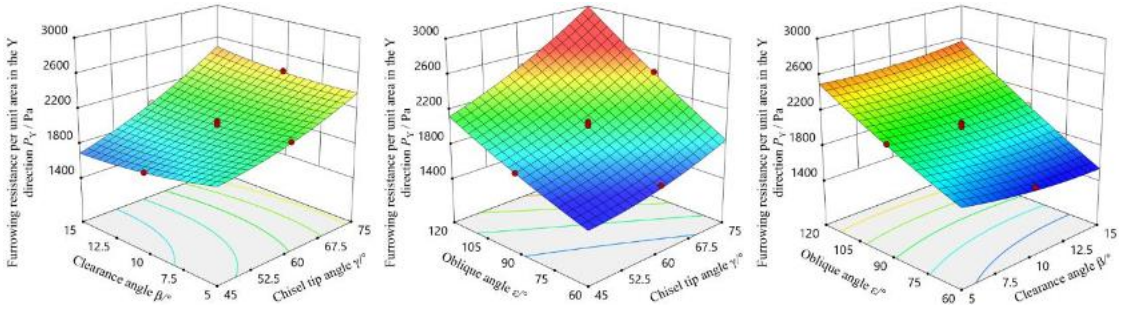


Fig. 9 - The interaction effects of various factors on P_Y

As shown in Figure 9(a), when the chisel tip angle (γ) is small, the furrow opening resistance per unit area in the Y-direction (P_Y) gradually decreases with increasing clearance angle (β); conversely, when γ is large, P_Y gradually increases with increasing β. When β is within the range of 5° to 15°, an increase in γ consistently leads to an increase in P_Y. Therefore, a combination of a smaller γ and a larger β yields a lower P_Y. As shown in Figure 9(b), when the oblique angle (ε) is within the range of 60° to 120°, an increase in γ results in an increase in P_Y. Similarly, when γ is within the range of 45° to 75°, an increase in ε also leads to an increase in P_Y. Both γ and ε exhibit a positive linear relationship with P_Y. Accordingly, a parameter combination of a smaller γ and a smaller ε yields a lower P_Y. As shown in Figure 9(c), when β is within the range of 5° to 15°, an increase in ε consistently leads to an increase in P_Y. When ε is small, P_Y gradually decreases with increasing β; when ε is large, P_Y gradually increases with increasing β. Under these conditions, a combination of a larger β and a smaller ε yields a lower P_Y.

Parameter optimization and simulation performance verification

Based on the established regression models, the influence patterns of the chisel tip angle (γ), clearance angle (β), and oblique angle (ε) on the furrow opening resistance per unit area in the Y-direction (P_Y) was obtained, facilitating an in-depth analysis of the mechanistic effects of these factors on resistance during the furrow opening process. The furrow opening resistance is closely related to γ, β, and ε. In this study, the optimization module of Design-Expert software was employed, with the optimization objectives set as minimizing P_Y, thereby ensuring low and stable furrow opening resistance. A multi-objective optimization mathematical model was established to determine the optimal parameter combination. The objective functions and constraint equations are as follows:

$$\begin{cases} min\ P_Y(\gamma,\ \beta,\ \varepsilon) \\ s.t.\begin{cases} 45 \le \gamma \le 75 \\ 5 \le \beta \le 15 \\ 60 \le \varepsilon \le 120 \end{cases} \end{cases} \tag{19}$$

Multiple sets of optimal parameter combinations were obtained. An increase in the oblique angle (ε) increases furrow opening resistance but also facilitates soil penetration. Considering manufacturability, furrow opener length, and the overall machine layout, the oblique angle ε was selected as 70°, with the optimized chisel tip angle γ = 55° and clearance angle β = 15°. The resistance-reducing furrow opener with the optimal parameter combination is shown in Figure 10. Under these conditions, the furrow opening resistance per unit area in the Y-direction (P_Y) is relatively low, and the penetration force acts in the negative Z-direction, which is conducive to soil penetration during furrow opening operations.



(a) 3D model (b) Physical object

Fig. 10 - Resistance-reducing furrow opener

To further verify the performance of the furrow opener with the optimal parameter combination in actual furrow opening operations, a simulation performance verification was conducted. The furrow opening resistance curve obtained from the simulation test is shown in Figure 11, which illustrates the variation of furrow opening resistance of the optimized furrow opener in the simulated environment, providing an important basis for further in-depth investigation of its performance characteristics. The measured furrow opening resistance in the Y-direction was 500.55 N, the furrow opening resistance per unit area in the Y-direction (P_Y) was 1587.30 Pa. Compared with the initial furrow opener (γ = 65°, β = 10°, ε = 90°), the furrow opening resistance in the Y-direction was reduced by 228.92 N, corresponding to a reduction rate of 30.82%.

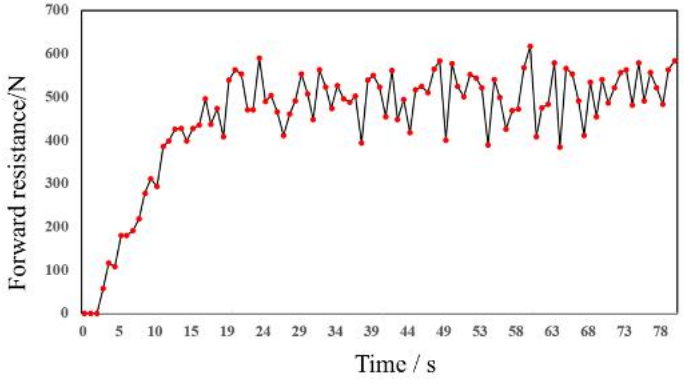


Fig. 11 - Simulation performance test trench resistance curve

Bench test verification of the furrow opener

Verification analysis of furrow opening resistance

A furrow opening resistance verification test was conducted at the research base of Gansu Agricultural University. The soil used in the test was collected from a genuine production area of *Codonopsis pilosula* in Northwest China. The soil moisture content was measured as 15.0% using an LHS16-A halogen moisture meter. Prior to the test, the soil was rotary tilled to simulate the actual transplanting environment. A furrow opener prototype with a chisel tip angle (γ) of 55°, oblique angle (ε) of 70°, clearance angle (β) of 15°, and width (W_k) of 52 cm was mounted on the traction frame of the furrow opener above the soil bin. After each test, the soil in the bin was rotary tilled again, as shown in Figure 12.



Fig. 12 - Bench test for trenching performance

As shown in Figure 13, the results obtained from the EDEM simulation were highly consistent with the actual operation of the furrow opener. The furrow profile predicted by the EDEM simulation closely matched the width, depth, and shape of the planting furrow formed during actual operation. Regarding soil flow direction, the EDEM simulation accurately reproduced the flow path and distribution of soil during the furrow opening process, demonstrating strong agreement with the actual soil flow observed under field conditions. To a considerable extent, the EDEM simulation method reflected the real working conditions of the furrow opener, providing a powerful tool for in-depth investigation of its operating principles and performance characteristics. It enabled the optimization and adjustment of structural and working parameters within a simulated environment and allowed for the prediction of furrow opener performance in advance. Consequently, this approach reduced the number and cost of physical experiments, thereby improving the efficiency and quality of the design and optimization process for the furrow opener.

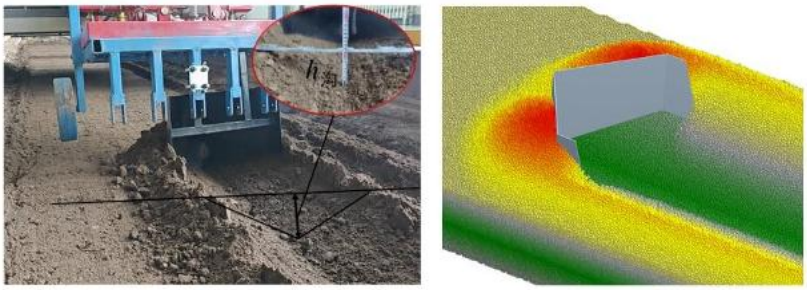


Fig. 13 - Comparative test between simulation and bench trenching operations

The test bench utilized an electric variable-frequency four-wheel-drive soil bin test vehicle as the power source, with the furrow opener attached via a three-point hitch for furrow opening operations. The test bench was equipped with an automated measurement system capable of simultaneously recording forward resistance and vertical resistance, with a data acquisition frequency set to 10 Hz. The operating parameters were consistent with those used in the simulation performance test: the furrow opening depth was set to h_k = 10 cm, the forward speed to 0.18 km/h, and each test run had a length of at least 3 m. The acquired data were processed using a moving average algorithm, and a curve of furrow opening resistance over time was plotted. The furrow opening resistance curve obtained from the bench performance test is shown in Figure 17. As shown in Figure 14, the average forward furrow opening resistance obtained from the bench test was 552.64N, with a relative error of 9.43% compared to the simulation result. Comparison between the simulated and experimental values indicates that the error in forward furrow opening resistance is relatively small, suggesting that the simulation results can reliably reflect the actual forward resistance of the furrow opener.

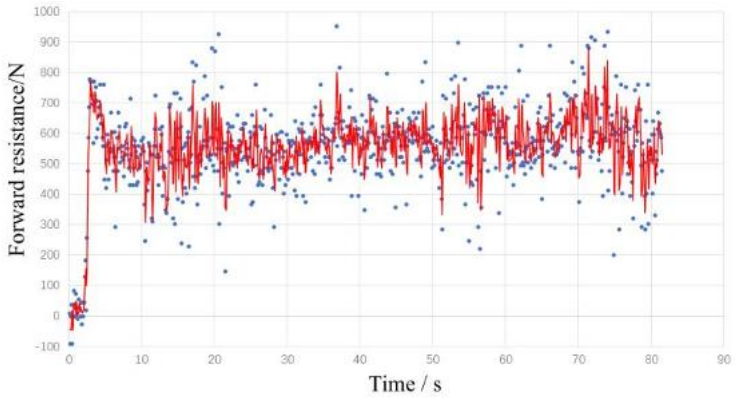


Fig. 14 - Trench resistance curve for bench performance test

CONCLUSIONS AND DISCUSSION

(1) The interaction between the furrow opener and the soil was investigated theoretically to address the high furrow-opening resistance encountered in the sandy loam soils of the main *Codonopsis pilosula* production region. The forces acting on the furrow opener and the soil during furrow opening were analyzed, and a resistance model for the furrow opener was established. The relationships among furrow-opening resistance, the intrinsic properties of the soil, the furrow cross-sectional area, and the structural parameters of the furrow opener were examined. The dynamic behavior of the soil particles during furrow opening was also investigated, and a mathematical model describing the particle velocity at detachment from the side plate was derived. This velocity was related to structural parameters such as the chisel-tip angle. The theoretical analysis indicated that, under fixed soil conditions, the chisel-tip angle, clearance angle, and oblique angle are the principal structural factors affecting furrow-opener performance.

(2) Furrow-opening performance was evaluated through discrete element simulations conducted using EDEM. A three-factor simulation experiment was designed using response surface methodology. Evaluation indicators, including furrow-opening resistance per unit area and penetration force, were defined, and a virtual soil-bin test platform was developed. Multiple regression analysis and analysis of variance were performed on the simulation results, yielding a highly significant regression model for the furrow-opening resistance per unit area in the *Y*-direction, P_Y. Residual analysis and box-plot analysis supported the adequacy and reliability of the model for optimizing the structural parameters of the furrow opener. The results showed that the chisel-tip angle was positively correlated with furrow-opening resistance. The clearance angle exhibited a positive linear relationship with penetration force but had only a limited effect on furrow-opening resistance, whereas the oblique angle significantly affected the evaluated performance indicators.

(3) Multiobjective optimization was conducted to determine the preferred structural parameter combination. An optimization model was established with the objective of minimizing the furrow-opening resistance per unit area in the *Y*-direction, P_Y. The selected optimal combination consisted of an oblique angle of 70°, a chisel-tip angle of 55°, and a clearance angle of 15°. Simulation verification showed that, after optimization, the furrow-opening resistance in the *Y*-direction was 500.55 N and P_Y was 1587.30 Pa, corresponding to a resistance reduction of 30.82%. Bench tests were subsequently conducted to validate the simulation results. The mean forward resistance measured in the bench tests was 552.64 N, resulting in a relative error of 9.43% compared with the simulated value. This level of agreement indicates that the simulation model can provide a useful basis for the structural optimization of resistance-reducing furrow openers for *C. pilosula* transplanting.

ACKNOWLEDGEMENT

We would like to thank all colleagues for their advice and support throughout the research process.

REFERENCES

[1] Aikins, K. A., Ucgul, M., Barr, J. B., Awuah, E., Antille, D. L., Jensen, T. A., Dwsbiolles, J. M. E. (2023). Review of discrete element method simulations of soil tillage and furrow opening. *Agriculture*, Vol. 13(3), Switzerland.

[2] Chen, E. (1961). Plowing Depth and the Layered Development of the Plow Layer (耕翻深度与耕层的层次发育), *Chinese Agricultural Science*, Vol. 2(12), PP. 1-6, Beijing/China.

[3] Chen, H., Qi, W., Wang, J., Zhang, J., Ma, A. (2023). Design of Moldboard Plow Openers Based on Discrete Element Method and Response Surface Method (基于离散元法和响应面法的铧式开沟器设计), *Mechanical Design*, Vol. 40(1), pp. 65-71, Tianjin/China.

[4] Dai, F., Song, X., Zhao, W., Zhang, F., Ma, A., Ma, M. (2019). Simulative Calibration on Contact Parameters of Discrete Elements for Covering Soil on Whole Plastic Film Mulching on Double Ridges (全膜双垄沟覆膜土壤离散元接触参数仿真标定), *Transactions of the Chinese Society for Agricultural Machinery*, Vol. 50(2), pp. 49-56,77, Beijing/China.

[5] Feng, B., Shi, L., Xin, S., Wang, G., Sun, W., Wang, J., Wang, S. (2025). Optimization and Experiment of Ditcher Parameters for Astragalus membranaceus Transplanter (黄芪移栽机开沟器参数优化与试验). *Journal of Agricultural Mechanization Research*, Vol. 47(10), pp. 189-196, Haerbin/Heilongjiang

[6] He, R., Jin, Z., Ma, R., Hu, F., Dai, J. Network pharmacology unveils spleen-fortifying effect of Codonopsis Radix on different gastric diseases based on theory of "same treatment for different diseases" in traditional Chinese medicine. *China Herbal Medicines*, Vol. 13(2), pp. 189-201, Tianjin/China.

[7] Li, B. (2020). Agricultural Mechanization (农业机械学). *China Agriculture Press*, Beijing/China.

[8] Liu, J., Li, Q., Zheng, X., Wang, Z. (2021). Research Status of Drag Reduction Technology for Soil Tillage Components (土壤耕作部件减阻技术研究现状). *Xinjiang Agricultural Mechanization,* pp. 25-28,37, Wulumuqi/Xinjiang.

[9] Liu, J., Zhang, J. (2023). A Brief Analysis of the Fully Mechanized Cultivation Technology of Dangshen with Mulching in Semi-Arid Mountain Areas (浅析半干旱山区党参露头覆膜全程机械化种植技术). *Agricultural Machinery*, pp. 57-59,62, Haerbin/Heilongjiang.

[10] Pan, S. (2015). Research on the Optimization Design and the Experiment of the Core Ploughshare Furrow Opener Based on the Discrete Element Method (基于离散元法的芯铧式开沟器优化设计与试验研究). *Jilin University,* Changchun/Jilin.

[11] Shmulevich, I., Asaf, Z. (2007). Rubinstein D. Interaction between soil and a wide cutting blade using the discrete element method. *Soil & Tillage Research*, Vol. 97(1), pp. 37-50, Netherland.

[12] Wang, F., Chen, S., Liu, Y., Chen, H., Hu, Y., Li, S., Chen, L. (2023). Advances and Prospects of Chinese Herbal Medicine Planting Industry in China (我国中药材种植产业进展与展望). *Mod Chin Med*, Vol. 25(6), pp. 1163-1171, Beijing/China.

[13] Wang, J. (2023). Optimized design and research of trenching components for panax notoginseng transplanting (三七移栽开沟部件的优化设计与研究). *Kunming: Yunnan Agricultural University*, Kunming/Yunnan.

[14] Wang, J., Sun, W., Wang, H., Zhang, H., Liu, X. (2021). Research of Long Wing and Sharp Angle Opener (尖角长翼型开沟器的研究). *Agricultural Mechanization Research*, Vol. 43(11), pp. 64-70, Haerbin/Heilongjiang.

[15] Wang, L., Zhou, B., Wan, C., Zhou, L. (2024). Structural parameter optimization of a furrow opener based on EDEM software. *International Journal of Agricultural & Biological Engineering*, Vol. 17(3), pp. 115-120, Beijing/China.

[16] Wang, X. (2017). Design and experimental study of key components for inclined licorice transplanting (甘草倾斜移栽关键部件设计与试验研究). *China Agricultural University*, Beijing/China.

[17] W. R. Gill., G,.E, VandenBerg. (1983). Tillage and Traction Soil Dynamics (耕作和牵引土壤动力学). *China Agricultural Machinery Press*, Beijing/China.

[18] Xie, Q., Sun, Y., Cao, L., Chen, L., Chen, J., Cheng, X., Wang, C. (2020). Antifatigue and antihypoxia activities of oligosaccharides and polysaccharides from *Codonopsis pilosula* in mice. *Food Funct*, Vol. 11(7), pp. 6352-6362, United Kingdom.

[19] Yu, J., Qian, L., Yu, W., Pan, S., Fang, Y., Fu, H. (2009). Analysis of the Resistances Applied on Furrow Openers (开沟器工作阻力的离散元法仿真分析). *Transactions of the Chinese Society for Agricultural Machinery*, Vol. 40(06), pp. 53-57, Beijing/China.

[20] Yu, Q., Li, R., Gong, Y., Ma, Y., Chen, X., Hu, J. (2025). Research status and development trends of mechanized transplanting of *Codonopsis pilosula* (党参移栽机械化研究现状与发展趋势). *Journal of Chinese Agricultural Mechanization*, Vol. 46(05), pp. 34-42, Nanjing/Jiangsu.

[21] Zhang, B., Yang, X., Zhu, Y. (2024). Design and Simulation of a Combined Trencher for Transverse Sugarcane Planter. *Agriculture*, Vol. 14(8), pp. 1416-1416, Netherland.

DESIGN AND INSERTION PERFORMANCE OPTIMISATION OF A COMPOSITE INSERTION PIN FOR A CORN STALK SAND BARRIER LAYING DEVICE
/
玉米秸秆沙障铺设装置复合插针设计及插入性能优化

Qidong SUN, Weiqiang ZHENG*), Liping ZHANG, Bolin LI, Zhiqiang FENG, Senyu NIU, Chengqian XIE
College of Mechanical Engineering, Xinjiang University, Urumqi 830046 / China
Tel: +86-17733853240; E-mail: xjzwq@xju.edu.cn
DOI: https://doi.org/10.35633/inmateh-79-60

Keywords: *Axial insertion, composite insertion pin, corn stalk, discrete element method, insertion force stiffness, response surface methodology*

ABSTRACT
To address the problems of unstable posture, end crushing, and poor release during conventional press-in sand barrier laying caused by the large diameter, rigid internodes, pronounced nodes, and heterogeneous structure of corn stalks, a smooth composite insertion pin consisting of a front steel pin and a rear sleeve was designed. Based on the structural characteristics of the corn stalk rind, pith, and nodes, a layered discrete element model was established to analyze pith compression, sidewall friction, and local failure during axial insertion. The sleeve contact-segment diameter, steel pin diameter, and sleeve front transition angle were selected as experimental factors, and insertion force stiffness was adopted as the evaluation index. A Box-Behnken response surface design was employed for parameter optimization, followed by internodal validation, finite element analysis, nodal insertion tests, and release tests. The results showed that the sleeve contact-segment diameter had the greatest influence on insertion force stiffness, while the steel pin diameter and transition angle also had significant effects. The regression model exhibited a good fit, and the lack-of-fit was not significant. Considering machining feasibility and structural stability, the optimal structural parameters were a sleeve contact-segment diameter of 5.5 mm, a steel pin diameter of 2.0 mm, and a sleeve front transition angle of 160°, corresponding to a predicted insertion force stiffness of 1.15 N/mm. The validation results agreed well with the model predictions. Although the insertion force increased substantially in the nodal region, the optimized composite insertion pin successfully achieved axial insertion through the nodes and enabled smooth release in both the internodal and nodal regions.

摘要
针对玉米秸秆直径大、节间硬、结节明显及组织非均质导致传统压入式沙障铺设中姿态不稳、端部压溃和脱落不畅等问题，设计了由前端钢针和后部套筒组成的光滑复合插针。基于玉米秸秆表皮、内瓤和结节的结构特征，建立分层复合离散元模型，分析轴向插入过程中的内瓤压缩、侧壁摩擦和局部破坏行为。以套筒接触段直径、钢针直径和套筒前端变径角为试验因素，以插入力刚度为评价指标，开展 Bo －Behn en 响应面优化，并通过普通节间验证、有限元分析、结节插入试验和脱落试验进行验证。结果表明，套筒接触段直径影响最显著，钢针直径和变径角也具有显著影响；模型拟合良好，失拟项不显著。综合考虑加工可行性和结构稳定性，推荐参数分别为 5.5 ㎜、2.0 ㎜ 和 160°，预测插入力刚度约为 1.15 N/㎜。普通节间验证结果表明，实测值与预测值吻合良好；虽然结节处插入力明显增大，但优化后的复合插针仍可完成结节处轴向插入，并能在普通节间和结节位置顺利脱落。

INTRODUCTION
Sand barrier laying is an important engineering measure for desertification control, wind-sand protection and ecological restoration in sandy areas (*Chen et al., 2024*). Its laying quality directly affects near-surface wind-speed reduction, sand-transport flux, surface stability and vegetation recovery. Among different sand-control measures, straw checkerboard sand barriers have been widely used in mobile sandy land, railway and highway protection, and ecological restoration projects because of their accessible materials, simple structure and stable sand-fixing effect. Previous studies have shown that sand barriers improve windbreak and sand-fixation performance by increasing surface roughness, modifying the near-surface airflow structure and weakening aeolian sand transport capacity (*Zhao et al., 2016; Wang et al., 2018; Zhang et al., 2018; Fang et al., 2023; Sun et al., 2024*). Semi-buried sand barriers, plate-type barriers, mesh barriers and porous sand-fixing components have also been developed to improve protective performance.

Their structural size, porosity, arrangement pattern and spacing can significantly affect wind-speed distribution, sediment deposition and sand-blocking efficiency (*Zhao et al., 2016; Wang et al., 2018; Fang et al., 2023; Sun et al., 2024; Xu et al., 2021; Zhang et al., 2021; Wang et al., 2024; Liu et al., 2025*).

With the development of wind-sand control engineering from manual construction towards mechanized, equipment-based and efficient operation, improving the laying quality and working efficiency of sand barriers has become an important research direction in desertification-control equipment (*Qu et al., 2019; Xu et al., 2020; Zhang et al., 2022*).

At present, most sand barrier laying machines have been developed for slender and flexible straw materials, such as wheat straw and reed straw. Conventional laying devices usually use inserting blades, pressing wheels, pressing discs or feeding–guiding mechanisms to press straw into sandy soil, forming sand barrier structures with a certain buried depth and exposed height. Related studies have shown that the mechanism type, feeding mode, pressing depth, working speed and straw feeding uniformity affect the forming quality of sand barriers and the straw mass per unit length (*An et al., 2025; Qi et al., 2025*). However, most existing machines are designed for flexible straw, and their working principle mainly depends on straw bending and overall pressing. For corn stalks with larger diameters, more rigid internodes and pronounced nodes, direct use of the conventional press-in method may easily cause unstable bending, poor posture control, end crushing, local splitting and poor release. Therefore, designing a key end-effector suitable for axial insertion and directional conveying according to the structural characteristics of corn stalks is fundamental for realizing mechanized laying of corn stalk sand barriers.

Corn stalk is a typical heterogeneous biological material consisting of nodes and internodes. Its cross-section includes a dense outer rind, vascular bundles and loose inner pith. Its mechanical properties are strongly affected by loading direction, moisture content, sampling position and stalk posture. Previous studies have shown that the corn stalk rind has relatively high tensile strength and stiffness, whereas the pith is loose and prone to compression, shearing and local failure (*Zhang et al., 2016; Chen and Qu, 2017; Zhang et al., 2020*). In addition, probe geometry, cross-sectional geometry and flexural stiffness affect puncture resistance, failure location and load-bearing capacity of corn stalks (*Robertson et al., 2016; Cook et al., 2020; Stubbs et al., 2022*). These studies provide a basis for understanding the mechanical behavior of corn stalks. Nevertheless, most of them focus on tension, bending, puncture, shearing or lodging, while limited attention has been paid to axial insertion, compression, friction and release of corn stalks during sand barrier laying.

During axial insertion of corn stalks, complex contact interactions occur between the insertion pin and the stalk pith. The front end of the pin first penetrates and compresses the loose pith. Subsequently, the pith is continuously squeezed and sheared. As the insertion depth increases, the contact length between the sidewall of the insertion pin and the pith increases, resulting in increased frictional resistance. When the insertion pin approaches a node, the dense tissue and transverse diaphragm increase local puncture, compression and shear resistance, causing obvious fluctuations or peaks in the insertion force curve. If the insertion pin diameter is too large, pith compression and sidewall friction increase significantly. If the diameter is too small, the supporting and guiding effects of the insertion pin are insufficient, leading to unstable stalk posture. Therefore, the structural parameters of the insertion pin should be optimized by comprehensively considering low-resistance insertion, stable holding and smooth release.

The discrete element method (DEM) can describe the contact, bonding, failure and motion processes of particulate materials, and has been increasingly applied to plant-material modelling, straw crushing, conveying and contact behavior analysis in recent years (*Coetzee, 2017; Zhang et al., 2020*). Meanwhile, response surface methodology is suitable for analyzing coupled effects among multiple factors and establishing regression relationships between structural parameters and performance indicators, and has been applied in the structural parameter optimization of agricultural equipment (*Myers et al., 2016; Montgomery, 2017; An et al., 2025; Qi et al., 2025*).

Based on this, a smooth composite insertion pin consisting of a front steel pin and a rear sleeve was designed for a corn stalk sand barrier laying device. The structural characteristics of corn stalks and the failure mechanism during axial insertion were analyzed, and a layered composite DEM model and an axial force model of the composite insertion pin were established. Then, the sleeve contact-segment diameter, steel pin diameter and sleeve front transition angle were selected as the main factors, and insertion force stiffness was used as the response value for Box-Behnken response surface optimization. Finally, direct internodal insertion validation, finite element analysis, nodal insertion tests and release verification tests were conducted to evaluate the prediction accuracy, structural stability and functional adaptability of the optimized structure.

MATERIALS AND METHODS

STRUCTURAL CHARACTERISTICS OF CORN STALK AND FAILURE MECHANISM DURING AXIAL INSERTION

Structural characteristics of corn stalk

Corn stalks are composed of nodes and internodes. The node is characterized by annular protrusions and contains a transverse diaphragm, with relatively dense tissue, whereas the internode is approximately cylindrical. In the cross-section, the stalk consists of a dense outer rind, vascular bundles and loose pith from the outside to the inside. The vascular bundles gradually become sparser from the outer region toward the center, forming a heterogeneous structure with a dense outer layer and a loose inner core, as shown in Figure 1.

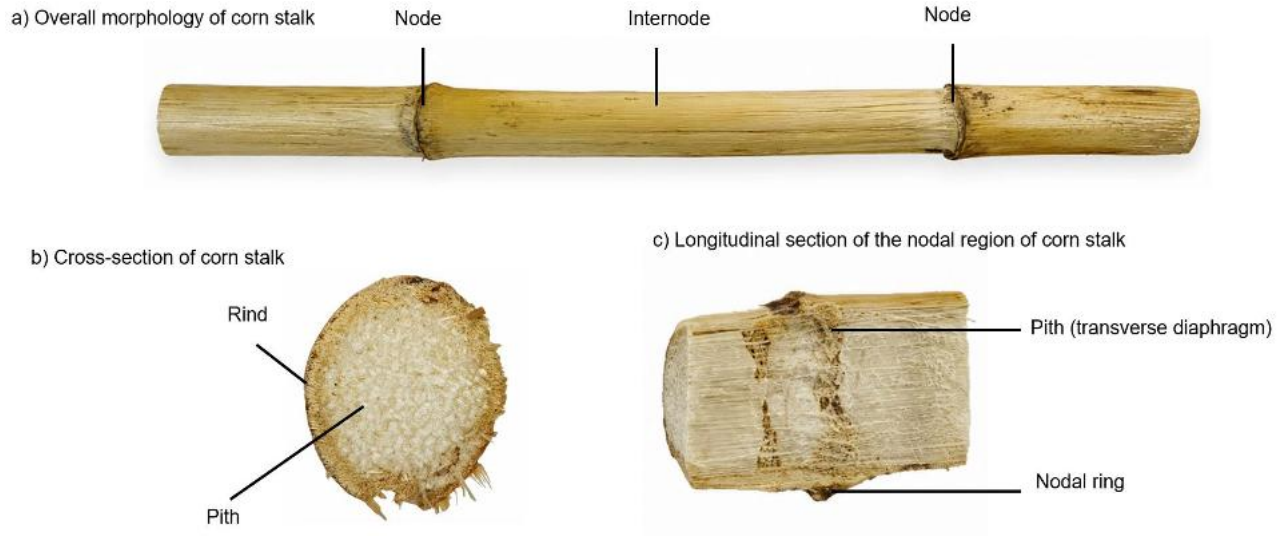


Fig. 1 - Morphological structure and nodal tissue characteristics of corn stalk

Discrete element representation of the layered structure of corn stalk

According to the structural differences among the rind, pith and nodal tissues, corresponding particle units were constructed and assigned material parameters and inter-particle bonding parameters for different regions, thereby forming a layered composite corn stalk model. The discrete element method (DEM) can describe inter-particle contact force transmission and local failure processes, and has been widely used to simulate the mechanical behavior of agricultural materials (Cundall and Strack, 1979; Tsuji et al., 1992). In recent years, many studies have optimized DEM parameter calibration and particle contact models, improving the simulation accuracy of plant materials (*Zhu et al., 2007*). In addition, DEM parameter calibration methods and model reliability evaluation have been systematically investigated (*Coetzee, 2017*). The model established in this study was used to characterize the structural differences between internodes and nodes, as well as local compression and failure behavior during insertion. The modelling process is shown in Figure 2.

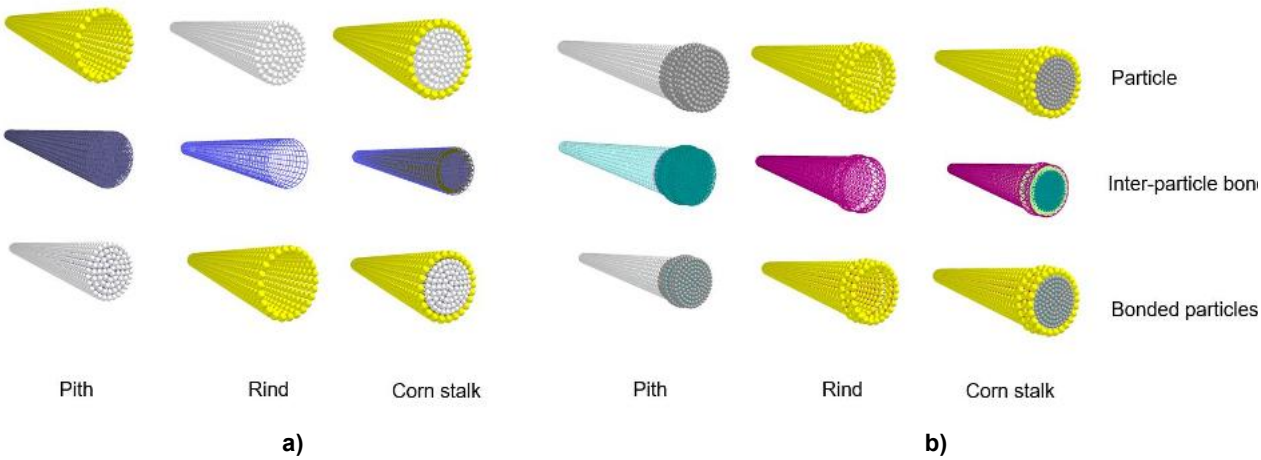
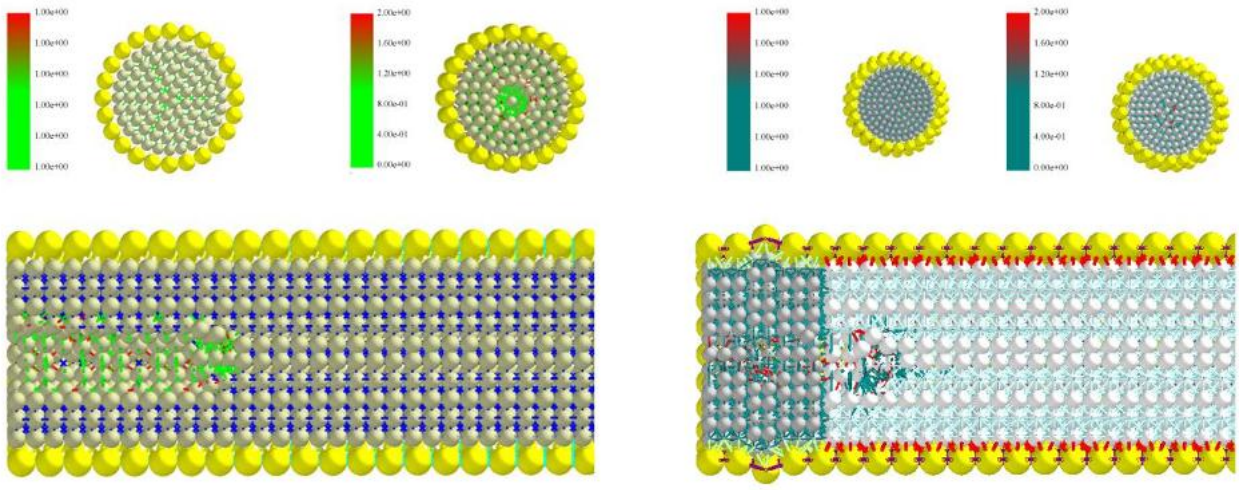


Fig. 2 - Construction process of the corn stalk discrete element model
a) internode model; b) nodal model

Analysis of insertion-induced failure modes

During axial insertion of corn stalks, the main failure modes include end crushing, pith compression, fiber shearing and nodal obstruction. The insertion pin first compresses the loose pith. Subsequently, the pith is continuously squeezed and sheared, while the sidewall friction increases with the contact length. When the pin approaches a node, the dense tissue and transverse diaphragm increase the local puncture and shear resistance, causing fluctuations or peaks in the insertion force curve. A typical process is shown in Figure 3. Therefore, the composite insertion pin should be designed to reduce the front penetration resistance and sleeve frictional resistance, while ensuring bending stability under lateral eccentric loading.



a) b)

Fig. 3 - Compression and failure characteristics of corn stalk pith during axial insertion
a) failure characteristics of internode; b) failure characteristics of nodal region

STRUCTURAL DESIGN OF THE INSERTION PIN

Design of the smooth composite insertion pin

The composite insertion pin was designed to realize axial insertion and directional conveying of corn stalks. Its design should ensure low-resistance penetration, stable holding and smooth release. In this study, a structure consisting of a front steel pin and a rear sleeve was adopted. The steel pin was used to penetrate and compress the pith and provide axial support, while the sleeve was used to fix the steel pin and connect it to the conveying mechanism. A gradual diameter transition was arranged between the two parts to reduce abrupt changes in contact resistance and improve the smoothness of load transmission. As shown in Figure 4, the corn stalk was sleeved along the axial direction of the insertion pin under the action of the push block. The thrust of the push block mainly overcame pith compression, local shearing and sidewall friction resistance. In addition, uneven stalk ends and non-uniform internal tissues may cause lateral eccentric loading.

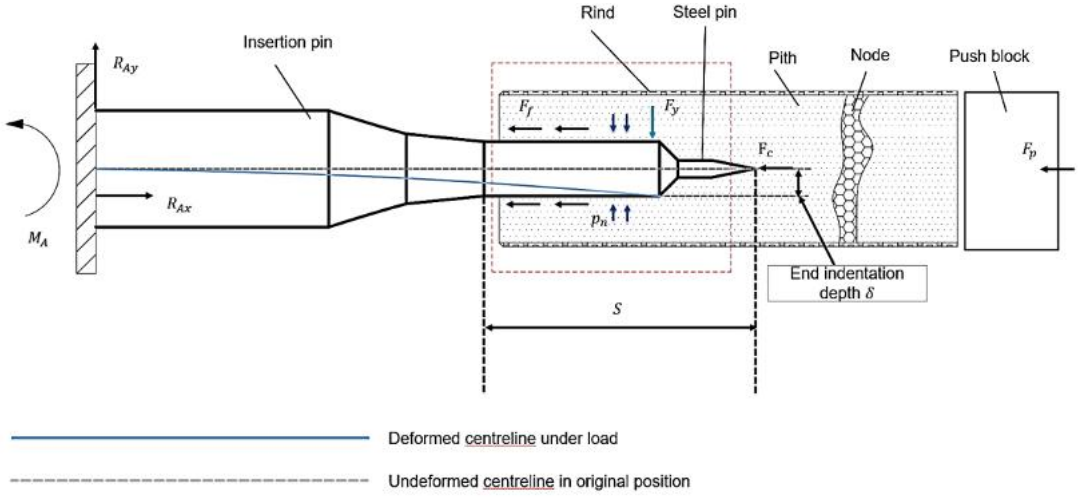


Fig. 4 - Force analysis of the composite insertion pin

In Figure 4, F_p represents the thrust of the push block; F_c represents the resistance caused by compression, squeezing and local shearing of the corn stalk pith; F_f represents the frictional resistance between the sidewall of the insertion pin and the stalk pith; P_n represents the radial normal pressure; and S represents the insertion depth of the stalk. R_{Ay}, R_{Ax}, M_A and F_y denote the vertical reaction force, axial reaction force, bending moment at the fixed end, and lateral force caused by eccentric loading, respectively, which are used to describe the possible non-axial loads during insertion.

Determination of key structural parameters of the composite insertion pin

According to the structural form of the composite insertion pin and the actual insertion process of corn stalks, the main structural parameters included the sleeve contact-segment diameter d_1, steel pin working-segment diameter d_2, sleeve front transition angle α, first transition angle β, second transition angle γ, and actual stalk insertion depth S. The structural annotations are shown in Figure 5.

Among these parameters, d_1 and d_2 jointly affect the compression degree of the stalk pith, sidewall friction and holding stability. When the diameters are small, pith squeezing and friction are reduced, which is beneficial for decreasing the insertion force; however, the supporting effect of the insertion pin on the stalk is also weakened. When the diameters are large, the supporting effect is enhanced, but pith compression and contact friction increase accordingly, resulting in higher thrust of the push block.

The sleeve front transition angle α determines the smoothness of the transition when the sleeve enters the pith, directly affecting contact resistance and sudden changes in thrust. The first transition angle β and second transition angle γ mainly affect the structural transition and load transmission between different diameter sections of the sleeve. The insertion depth S represents the total length of the stalk sleeved onto the composite insertion pin along the axial direction. The parameters and their functions are listed in Table 1.

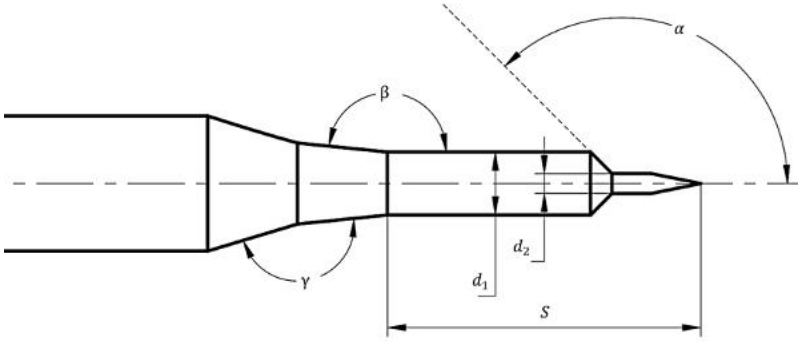


Fig. 5 - Structural parameters of the composite insertion pin

Table 1

Main structural parameters and functions of the composite insertion pin

Parameter	Symbol	Main function
Sleeve contact-segment diameter	d_1	Affects sleeve support stability and sidewall friction resistance
Steel pin working-segment diameter	d_2	Affects penetration resistance, compression resistance and insertion stability
Sleeve front transition angle	α	Affects the contact resistance and thrust fluctuation when the sleeve initially enters the stalk pith
First transition angle	β	Affects load transmission and structural transition at the variable-diameter section
Second transition angle	γ	Affects the structural transition and assembly stability of the rear connecting section
Actual stalk insertion depth	S	Represents the total depth of the stalk sleeved onto the composite insertion pin

Overall force model of the composite insertion pin

Under the action of an external axial load, the corn stalk moved along the axial direction of the insertion pin and was successively sleeved onto the steel pin working segment and the sleeve contact segment. Since the penetration of the steel pin into the stalk pith occurred simultaneously with local pith compression, these two effects were difficult to separate strictly. Therefore, they were collectively regarded as compression resistance. The total axial resistance acting on the composite insertion pin can be expressed by Eq. (1).

$$F_i = F_c + F_f \quad (1)$$

where $\boldsymbol{F_i}$ is the resultant axial force exerted by the stalk on the insertion pin, $\boldsymbol{F_c}$ is the compression resistance, and $\boldsymbol{F_f}$ is the sidewall friction force.

The sidewall friction force is related to the contact state between the insertion pin and the stalk pith and can be simplified by Eq. (2).

$$F_f = \mu p_n A_c \quad (2)$$

where $\boldsymbol{\mu}$ is the equivalent friction coefficient, $\boldsymbol{p_n}$ is the equivalent radial normal pressure, and $\boldsymbol{A_c}$ is the equivalent contact area between the insertion pin and the stalk pith. This equation indicates that increases in the pin diameter and contact length increase the sidewall friction force, thereby increasing the axial resistance during insertion.

During the actual insertion process, lateral force $\boldsymbol{F_y}$ may be generated by uneven stalk ends, non-uniform pith tissue distribution and eccentric loading. In this case, the vertical reaction force at the fixed end can be expressed by Eq. (3).

$$R_{Ay} = F_y \quad (3)$$

The bending moment at the fixed end can be calculated using Eq. (4).

$$M_A = F_i e + F_y l_y \quad (4)$$

where $\boldsymbol{e}$ is the eccentric distance of the resultant axial force relative to the centreline of the insertion pin, and $\boldsymbol{l_y}$ is the distance from the action point of the lateral force to the fixed end. Therefore, although the load mainly acts on the insertion region, its mechanical effect is transmitted to the entire composite insertion pin. The fixed end and the variable-diameter section are the key positions for structural verification.

Analysis of stalk release conditions

After the stalk is sleeved onto the insertion pin, smooth release should be ensured. Since the insertion pin has a smooth structure, the release process mainly needs to overcome the frictional resistance between the sidewall of the insertion pin and the stalk pith. Therefore, the release resistance can be approximated by Eq. (5).

$$F_d \approx F_f \quad (5)$$

To ensure smooth release of the stalk, the condition given in Eq. (6) should be satisfied.

$$F_r > F_d \quad (6)$$

where F_r is the release driving force, and F_d is the release resistance.

Optimization method for structural parameters of the composite insertion pin

To reduce the growth rate of insertion force while considering holding and release performance, the parameters of the composite insertion pin were determined using a procedure of "preliminary tests for range determination–Box-Behnken response surface optimization". Response surface methodology is suitable for analyzing the coupled effects of multiple factors, and the Box-Behnken design can establish a quadratic regression model and evaluate factor significance with fewer tests (*Box and Behnken, 1960; Myers et al., 2016; Montgomery, 2017*). In this study, the sleeve contact-segment diameter $\boldsymbol{d_1}$, steel pin diameter $\boldsymbol{d_2}$, and sleeve front transition angle $\boldsymbol{\alpha}$ were selected as factors, and the insertion force stiffness $\boldsymbol{K_F}$ was used as the response value. The factor levels were first determined through single-factor preliminary tests, and then modelling and optimization were performed using Design-Expert 13.

Insertion force stiffness $\boldsymbol{K_F}$ was selected as the continuous response because it directly characterizes the growth rate of insertion resistance. Holding stability and release performance were treated as functional constraints rather than continuous regression responses. Holding was considered successful when the stalk remained stably sleeved without obvious slipping after insertion, whereas release was considered successful when the stalk was completely detached without jamming, overall end splitting or visible bending of the insertion pin.

PARAMETER OPTIMISATION AND PERFORMANCE VERIFICATION OF THE COMPOSITE INSERTION PIN

Preliminary test design and determination of factor levels

Air-dried corn stalks with an average moisture content of 5.2% and diameters of 20–24 mm were used. Nine preliminary tests and 17 Box–Behnken tests were conducted independently, with a new stalk used in each test. The test system consisted of a screw-driven push block, composite insertion pin, support frame, RP-C30-ST resistive force sensor, voltage-conversion module and data-acquisition unit. The sensor had a nominal range of approximately 0.20–196 N and a sensing-area diameter of 25 mm.

RESULTS

Before testing, the sensor was calibrated, and its output was converted into force according to the calibration relationship. Force and displacement were recorded at 40 Hz during insertion to a depth of 30 mm at a speed of 0.1 m/s. The maximum insertion force $F_{p,max}$ was extracted from each force–displacement curve, and K_F was calculated using Eq. (7).

Table 2

Preliminary test results of structural parameters of the composite insertion pin

Test No.	d_1/mm	d_2/mm	α /(°)	Test purpose	K_F/(N/mm)
1	6	2	155	Centre point	1.17
2	5	2	155	Low level of d_1	1.11
3	7	2	155	High level of d_1	1.66
4	6	1	155	Low level of d_2	1.28
5	6	3	155	High level of d_2	1.50
6	6	2	145	Low level of α	1.57
7	6	2	165	High level of α	1.21
8	6	2	155	Centre point replicate	1.13
9	6	2	155	Centre point replicate	1.18

The preliminary test results showed that the repeated center-point values were 1.17, 1.13 and 1.18 N/mm, indicating good repeatability. As d_1 increased, the insertion force stiffness increased markedly. K_F also showed an increasing trend with the increase in d_2, but the increment was smaller than that caused by d_1. In contrast, K_F decreased as α increased, indicating that a larger transition angle helped reduce the concentrated squeezing of the pith by the front end of the sleeve. These results show that the selected factor levels can be used for the subsequent response surface tests.

Evaluation index of insertion force stiffness

To quantitatively characterize the growth rate of insertion force with displacement, the insertion force stiffness K_F was introduced. Considering that the initial contact stage is strongly affected by uneven stalk ends and local compaction, whereas pith crushing, fiber failure or sudden changes in friction may occur near the peak force, the stable rising interval from $0.1F_{p,max}$ to $0.8F_{p,max}$ was selected for calculating K_F (*Mohsenin, 1986; Bourne, 2002; Rivera et al., 2022*). Accordingly, K_F was calculated using Eq. (7):

$$K_F = \frac{0.8F_{p,\max} - 0.1F_{p,\max}}{s_{0.8} - s_{0.1}} \quad (7)$$

where K_F (N/mm) is the insertion force stiffness; $F_{p,max}$ (N) is the maximum insertion force; and $s_{0.1}$ and $s_{0.8}$ (mm) are the insertion displacements corresponding to $0.1F_{p,max}$ and $0.8F_{p,max}$, respectively.

Response surface test design

A three-factor and three-level response surface test was conducted using the Box-Behnken design in Design-Expert 13, with d_1, d_2 and α selected as the test factors. The insertion depth was fixed at 30 mm, and the push block speed was fixed at 0.1 m/s. The factor levels are listed in Table 3, and the test scheme and results are shown in Table 4.

Table 3

Factors and levels of the response surface test

Factor	Parameter	Low level -1	Centre level 0	High level +1
A	Sleeve contact-segment diameter d_1 / mm	5	6	7
B	Steel pin diameter d_2 / mm	1	2	3
C	Sleeve front transition angle α / °	145	155	165

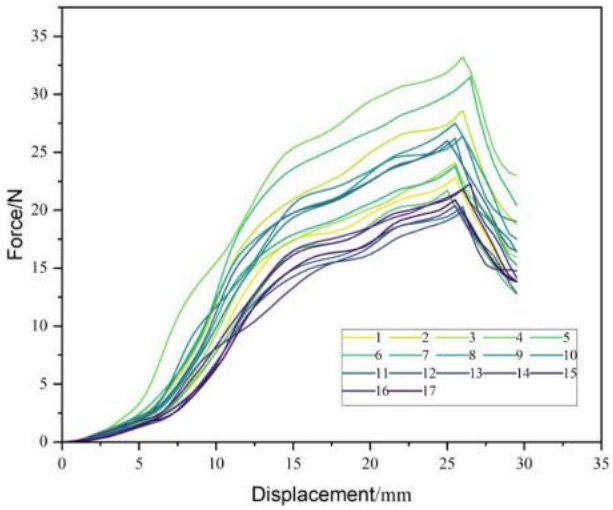


Fig. 6 - Force–displacement curves under different test groups

Table 4

Box-Behnken experimental design and results

Test No	A	B	C	K_F/(N/mm)
1	-1	-1	0	1.34
2	1	-1	0	1.65
3	-1	1	0	1.41
4	1	1	0	1.95
5	-1	0	-1	1.24
6	1	0	-1	1.86
7	-1	0	1	1.41
8	1	0	1	1.51
9	0	-1	-1	1.62
10	0	1	-1	1.55
11	0	-1	1	1.15
12	0	1	1	1.57
13	0	0	0	1.09
14	0	0	0	1.08
15	0	0	0	1.27
16	0	0	0	1.26
17	0	0	0	1.15

Among the 17 test groups, K_F ranged from 1.08 to 1.95 N/mm, indicating that the structural parameters had a significant effect on the growth rate of insertion force. The highest $\boldsymbol{K_F}$ value was 1.95 N/mm in test No. 4 ($\boldsymbol{d_1} = 7$ mm, $\boldsymbol{d_2} = 3$ mm and $\boldsymbol{\alpha} = 155°$). The repeated center-point values ranged from 1.08 to 1.27 N/mm, indicating a relatively small test error. Overall, $\mathbf{K_F}$ was lower near the center region and under some low-level parameter combinations, whereas it increased markedly under high-diameter combinations.

Regression model establishment and analysis of variance

Design-Expert 13 was used to conduct analysis of variance on the insertion force stiffness results, and the quadratic polynomial regression equation was obtained as follows: $\boldsymbol{K_F = 1.17 + 0.1963A + 0.09B - 0.0788C + 0.0575AB - 0.13AC + 0.1225BC + 0.225A^2 + 0.1925B^2 + 0.11C^2}$.

The regression equation shows that the coefficients of the linear terms $\boldsymbol{A}$ and $\boldsymbol{B}$ are positive, indicating that increases in $\boldsymbol{d_1}$ and $\boldsymbol{d_2}$ both increase the insertion force stiffness. The coefficient of $\boldsymbol{C}$ is negative, indicating that an appropriate increase in the transition angle is beneficial for reducing the insertion force stiffness. The quadratic terms $\boldsymbol{A^2}$, $\boldsymbol{B^2}$and $\boldsymbol{C^2}$are all positive, suggesting obvious nonlinear effects of the factors on $\boldsymbol{K_F}$. Therefore, a lower optimization region exists in the response surface.

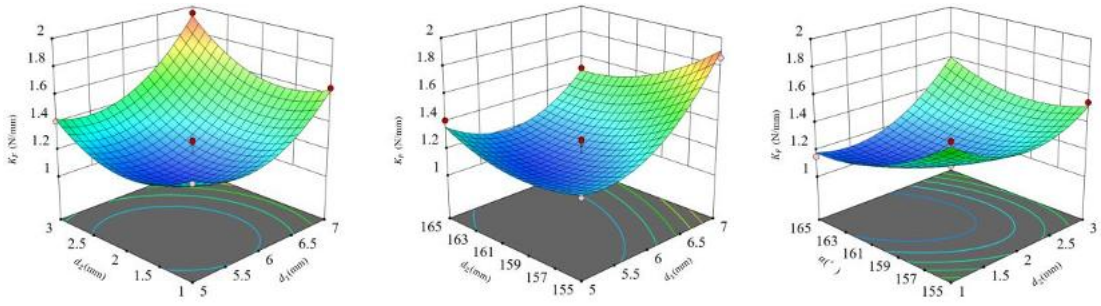
Table 5

Analysis of variance for the regression model

Source	Sum of squares	df	Mean square	F-value	p-value	Significance
Model	1.03	9	0.1142	18.06	0.0005	**
A	0.3081	1	0.3081	48.71	0.0002	**
B	0.0648	1	0.0648	10.25	0.0150	*
C	0.0496	1	0.0496	7.84	0.0265	*
AB	0.0132	1	0.0132	2.09	0.1914	
AC	0.0676	1	0.0676	10.69	0.0137	*
BC	0.0600	1	0.0600	9.49	0.0178	*
A^2	0.2132	1	0.2132	33.70	0.0007	**
B^2	0.1560	1	0.1560	24.67	0.0016	**
C^2	0.0509	1	0.0509	8.05	0.0251	*
Residual	0.0443	7	0.0063			
Lack of fit	0.0113	3	0.0038	0.4556	0.7278	
Pure error	0.0330	4	0.0083			
Total	1.07	16				
R^2	0.9587					
R^2_{Adj}	0.9056					

Note: * indicates significant difference at $\boldsymbol{P} < 0.05$; ** indicates highly significant difference at $\boldsymbol{P} < 0.01$.

The analysis of variance showed that the model was highly significant, with $\boldsymbol{P} = 0.0005 < 0.01$. The lack-of-fit term was not significant ($\boldsymbol{P} = 0.7278 > 0.05$), indicating that the model fitted the test data well. The values of $\boldsymbol{R^2}$ and $\boldsymbol{R^2_{adj}}$ were 0.9587 and 0.9056, respectively, further confirming the good fitting performance of the model. Factor $\boldsymbol{A}$ had a highly significant effect on $\boldsymbol{K_F}$, while factors $\boldsymbol{B}$ and $\boldsymbol{C}$ also had significant effects. This indicates that the sleeve contact-segment diameter had the greatest influence on $\boldsymbol{K_F}$, followed by the steel pin diameter and the sleeve front transition angle. Among the interaction terms, $\boldsymbol{AC}$ and $\boldsymbol{BC}$ were significant.



a) A-B b) A-C c) B-C

Fig. 7 - Effects of response surface interactions on insertion force stiffness

a) A-B; b) A-C; c) B-C

Parameter optimization and engineering recommended values

The regression model showed that the theoretical optimal parameter region was approximately $\boldsymbol{d_1} = \boldsymbol{5.70}$ mm, $\boldsymbol{d_2} = \boldsymbol{1.70}$ mm and $\boldsymbol{\alpha} = \boldsymbol{158.5}°$, with a predicted insertion force stiffness of about 1.11 N/mm. Considering practical machining requirements, $\boldsymbol{d_1} = 5.5$ mm, $\boldsymbol{d_2} = 2.0$ mm and $\boldsymbol{\alpha} = 160°$ were finally selected as the engineering recommended parameter combination. Under this combination, the predicted insertion force stiffness was approximately 1.15 N/mm. Its prediction accuracy was subsequently evaluated through internodal insertion tests, whereas nodal insertion and release tests were conducted to assess high-resistance adaptability and functional reliability.

According to the axial force model in Section 3, the insertion force mainly consisted of pith compression resistance and sidewall friction resistance. The steel pin diameter, sleeve contact-segment diameter and sleeve front transition angle affected pith compression, sidewall friction and guided compression, respectively. The response surface results were consistent with the theoretical analysis, indicating that the established model can provide a basis for structural parameter optimization of the composite insertion pin.

It should be noted that the response surface optimization was mainly used to obtain a low-resistance parameter combination under regular axial insertion conditions. Since the nodal region has denser tissue and a transverse diaphragm, stronger local resistance fluctuations occur during insertion. Therefore, nodal insertion was used as a high-resistance adaptability verification of the recommended parameter combination, rather than to evaluate the prediction accuracy of the response surface regression model.

PERFORMANCE VERIFICATION OF THE COMPOSITE INSERTION PIN

Finite element analysis of bending resistance of the composite insertion pin

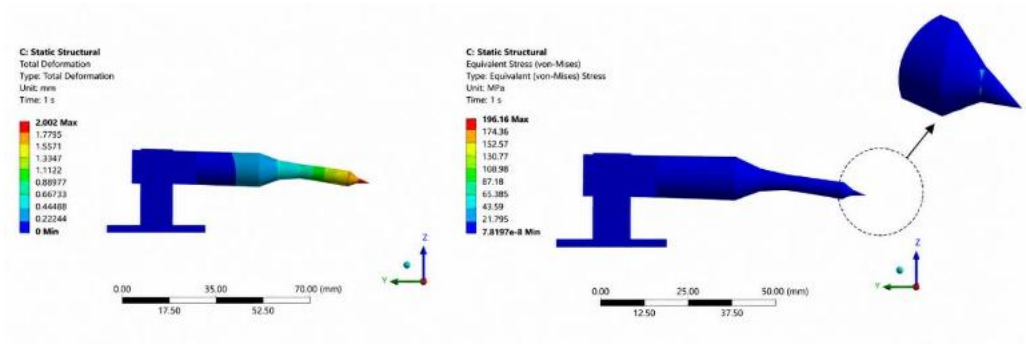
Static structural analysis was conducted in ANSYS Workbench to evaluate the bending stability of the optimized composite insertion pin. Bonded contacts were defined at the interfaces among the steel pin, steel shaft, PETG sleeve and support. The PETG support base was fixed to represent its frame connection, and a lateral load of 20 N was applied at the pin tip.

Table 6

Mesh convergence results

Element size /mm	Nodes	Elements	Deformation /mm	Average stress /MPa
0.30	1,256,239	730,860	1.9039	1.6589
0.25	1,818,875	1,060,416	2.0224	1.7260
0.20	2,838,580	1,658,786	2.0020	1.7159

The differences between the 0.25 and 0.20 mm meshes were 1.02% for maximum deformation and 0.59% for area-averaged equivalent stress; therefore, the 0.20 mm mesh was adopted. As shown in Figure 8, the maximum deformation was 2.00 mm, while the maximum equivalent stresses of the whole model and PETG sleeve were 196.2 and 36.09 MPa, respectively. Based on yield strengths of 355 MPa for steel and 45 MPa for PETG, the corresponding safety factors were 1.81 and 1.25, indicating that no yielding was predicted under the applied load.



a) **b)**

Fig. 8 - Finite element analysis results of the bending resistance of the composite insertion pin

a) total deformation contour; b) equivalent stress contour

The PETG transition region could be strengthened by increasing the fillet radius and wall thickness, while its mechanical properties could also be improved by optimizing the printing parameters (*Szykiedans et al., 2017; Özen et al., 2021; Tunçel et al., 2024*).

Internodal and nodal insertion verification tests

To directly validate the recommended parameter combination under regular internodal insertion conditions and evaluate its adaptability to the nodal region, five independent internodal and five independent nodal axial insertion tests were conducted. The composite insertion pin with $\boldsymbol{d_1} = 5.5$ mm, $\boldsymbol{d_2} = 2.0$ mm and $\boldsymbol{\alpha} = 160°$ was used. The insertion depth was 30 mm, and the force–displacement curve, maximum insertion force, insertion force stiffness and end failure condition were recorded.

Table 7

Verification test results of axial insertion in the internodal and nodal regions

Test No	Insertion depth /mm	Internodal $F_{p,\max}/N$	Internodal K_F/(N/mm)	Nodal $F_{p,\max}/N$	Nodal K_F/(N/mm)
1	30	39.2	1.12	68.7	2.12
2	30	40.1	1.16	70.1	2.18
3	30	38.7	1.15	71.4	2.25
4	30	41.0	1.19	69.3	2.16
5	30	39.6	1.14	72.0	2.31



a) b) c)

Fig. 9 - Verification tests of axial insertion in the internodal and nodal regions
a) insertion test device and initial state; b) axial insertion process in the internodal region; c) state after insertion in the nodal region

Table 7 and Figure 9 show that the optimized composite insertion pin completed 30 mm axial insertion in all internodal and nodal tests. Under regular internodal insertion, the measured K_F was 1.15 ± 0.03 N/mm, with a relative error of 0.17% from the predicted value of 1.15 N/mm, confirming the prediction accuracy of the response surface model. In the nodal region, $F_{p,\max}$ and K_F increased to 70.3 ± 1.4N and 2.20 ± 0.08 N/mm, respectively, owing to the dense tissue and transverse diaphragm. Nevertheless, no obvious bending of the insertion pin, overall splitting of the stalk or interruption of the insertion process was observed.

Stalk release function verification

To evaluate the holding stability and release performance of the optimized composite insertion pin, repeated release tests were conducted using stalks pre-sleeved in the internodal and nodal regions. The composite insertion pin with $d_1 = 5.5$ mm, $d_2 = 2.0$ mm and $\alpha = 160°$ was used. After being pre-sleeved to a depth of 30 mm, each stalk was axially released by the release mechanism. Holding was considered successful when the stalk remained stably sleeved without visible slipping, whereas release was considered successful when the stalk was completely detached without jamming, overall end splitting or visible bending of the insertion pin. The holding state, release state and possible failure phenomena were recorded.



Fig. 10 - Stalk release verification test results

As shown in Figure 10, stable holding and complete release were achieved in both the internodal and nodal tests. No visible slipping, jamming, overall end splitting, bending of the insertion pin or structural damage was observed. Although the local contact resistance was higher in the nodal region, complete release was still achieved, indicating that the optimized composite insertion pin satisfied the requirements for stable holding and smooth release after axial insertion.

CONCLUSIONS

This study designed and optimized a smooth composite insertion pin consisting of a front steel pin and a rear sleeve to solve the problems of high resistance, obvious force fluctuation near nodes and poor release during axial insertion of corn stalks. The main conclusions are as follows:

(1) A smooth composite insertion pin consisting of a front steel pin and a rear sleeve was designed according to the heterogeneous structural characteristics of corn stalks. The structure enabled axial insertion, stable sleeving and subsequent release while reducing end crushing and overall stalk splitting.

(2) The axial insertion force was mainly composed of pith compression resistance and sidewall friction. The sleeve contact-segment diameter $\boldsymbol{d_1}$, steel pin diameter $\boldsymbol{d_2}$ and sleeve front transition angle $\boldsymbol{\alpha}$ affected sidewall friction, pith compression and guided compression, respectively, providing a theoretical basis for parameter optimization.

(3) The Box–Behnken regression model was highly significant, whereas the lack-of-fit term was not significant, with $\boldsymbol{R^2} = 0.9587$ and $\boldsymbol{R^2_{adj}} = 0.9056$. The sleeve contact-segment diameter had the greatest effect on $\boldsymbol{K_F}$, while the steel pin diameter and transition angle also had significant effects.

(4) Considering response surface optimization, machining feasibility and structural stability, the engineering parameters were determined as $\boldsymbol{d_1} = 5.5$ mm, $\boldsymbol{d_2} = 2.0$ mm and $\boldsymbol{\alpha} = 160°$, with a predicted $\boldsymbol{K_F}$ of approximately 1.15 N/mm. Five internodal validation tests gave a measured $\boldsymbol{K_F}$ of 1.15 ± 0.03 N/mm, with a relative prediction error of 0.17%, indicating good agreement between the measured and predicted results.

(5) Finite element analysis showed that the optimized structure maintained acceptable bending stability under the applied lateral load. In nodal insertion tests, the maximum insertion force increased to approximately 70 N, but no obvious bending, overall stalk splitting or insertion interruption occurred. Holding and release tests further confirmed stable sleeving and complete release in both internodal and nodal regions. However, the present study was limited to laboratory tests over a narrow moisture-content and diameter range, and dynamic impact and fatigue during continuous field operation were not considered. Future work will focus on multi-condition field tests and continuous-operation verification.

ACKNOWLEDGEMENT

The authors were funded for this project by the National Natural Science Foundation of China (NSFC), Grant/Award Number: 52265039.

REFERENCES

[1] An R., Ge Y., Zheng Y.J., Cheng J.J., Zeng X.Y., Jin M.Y., (2025), Transverse intermittent straw-pressing mechanism of the paving machine for reed straw checkerboard. *Transactions of the Chinese Society of Agricultural Engineering*, Vol.41(7), pp.36-46.

[2] Bourne M.C., (2002), *Food Texture and Viscosity: Concept and Measurement*, 2nd ed., Academic Press, San Diego/USA.

[3] Box G.E.P., Behnken D.W., (1960), Some new three level designs for the study of quantitative variables. *Technometrics*, Vol.2(4), pp.455-475.

[4] Chen Y.F., Wang F., Pan X.B., Zhang F.M., Ren G.Y., Li Q., (2024), 150-year shift of potential geographical distribution of desertification in China: Past, present and future (中国荒漠化潜在发生区域 150 年变迁: 过去、现在和未来), *Chinese Science Bulletin*, Vol.69(31), pp.4637-4650.

[5] Chen Z., Qu G., (2017), Shearing characteristics of corn stalk pith for separation. *BioResources*, Vol.12(2), pp.2296-2309.

[6] Coetzee C.J., (2017), Review: Calibration of the discrete element method. *Powder Technology*, Vol.310, pp.104-142.

[7] Cook D.D., Meehan K., Asatiani L., Robertson D.J., (2020), The effect of probe geometry on rind puncture resistance testing of maize stalks. *Plant Methods*, Vol.16, pp.65.

[8] Cundall P.A., Strack O.D.L., (1979), A discrete numerical model for granular assemblies. *Géotechnique*, Vol.29(1), pp.47-65.
[9] Fang W., Li S.X., Jiang Y.J., Dong W.J., (2023), Research on the effect of sand barriers on highways in desert areas on sand control. *Sustainability*, Vol.15, pp.13906.
[10] Liu Y.N., Li Y.X., Han X.Q., Yang Q.W., Yang D.M., Tao H.J., (2025), Analysis of the effectiveness of four types of banded sand barriers in the Ulan Buh Desert (乌兰布和沙漠 4 种带状沙障建设成效分析), *Journal of Inner Mongolia Forestry Science & Technology*, Vol.51(1), pp.1-6.
[11] Mohsenin N.N., (1986), *Physical Properties of Plant and Animal Materials*, 2nd ed., Gordon and Breach Science Publishers, New York/USA.
[12] Montgomery D.C., (2017), *Design and Analysis of Experiments*, 9th ed., John Wiley & Sons, Hoboken/USA.
[13] Myers R.H., Montgomery D.C., Anderson-Cook C.M., (2016), *Response Surface Methodology: Process and Product Optimization Using Designed Experiments*, 4th ed., John Wiley & Sons, Hoboken/USA.
[14] Özen A., Auhl D., Völlmecke C., Kiendl J., Abali B.E., (2021), Optimization of Manufacturing Parameters and Tensile Specimen Geometry for Fused Deposition Modeling (FDM) 3D-Printed PETG. *Materials*, Vol.14(10), pp.2556.
[15] Qi Y., Kong D., Zhang P., Zhang Y., Zheng X., Su Y., Ma X., Sun B., (2025), Design and Optimization of a Compact Machine for Laying and Pressing Straw Checkerboard Sand Barriers in Desert Areas. *Agriculture*, Vol.15(17), pp.1818.
[16] Qu J.J., Ling Y.Q., Liu B.J., Chen G.T., Wang T., Dong Z.B., (2019), Research status and development trend of wind-blown sand control engineering in China (我国风沙防治工程研究现状及发展趋势). Advances in Earth Science, Vol.34(3), pp.225-231.
[17] Rivera S., Giongo L., Cappai F., Kerckhoffs H., Sofkova-Bobcheva S., Hutchins D., East A., (2022), Blueberry firmness: A review of the textural and mechanical properties used in quality evaluations. *Postharvest Biology and Technology*, Vol.192, pp.112016.
[18] Robertson D.J., Julias M., Lee S.Y., Cook D.D., (2016), Maize stalk lodging: flexural stiffness predicts strength. *Crop Science*, Vol.56(4), pp.1711-1718.
[19] Stubbs C.J., McMahan C.S., Tabaracci K., Kunduru B., Sekhon R.S., Robertson D.J., (2022), Cross-sectional geometry predicts failure location in maize stalks. *Plant Methods*, Vol.18, Article 56.
[20] Sun J., Shen W., Li Y.Z., Ma J.J., Huang J.Z., Wang J., Chen P., Li H.B., Zhang B.Y., Li Y., (2024), Experimental study on a combined sand barrier: Integration of porous mesh plate and novel porous sand-fixing bricks. *Journal of Wind Engineering & Industrial Aerodynamics*, Vol.251, pp.105809.
[21] Szykiedans K., Credo W., Osiński D., (2017), Selected mechanical properties of PETG 3-D prints. *Procedia Engineering*, Vol.177, pp.455-461.
[22] Tsuji Y., Tanaka T., Ishida T., (1992), Lagrangian numerical simulation of plug flow of cohesionless particles in a horizontal pipe. *Powder Technology*, Vol.71(3), pp.239-250.
[23] Tunçel O., Kahya Ç., Tüfekci K., (2024), Optimization of Flexural Performance of PETG Samples Produced by Fused Filament Fabrication with Response Surface Method. *Polymers*, Vol.16(14), pp.2020.
[24] Wang T., Qu J.J., Ling Y.Q., Liu B.L., Xiao J.H., (2018), Shelter effect efficacy of sand fences: A comparison of systems in a wind tunnel. *Aeolian Research*, Vol.30, pp.32-40.
[25] Wang Y., Jiang A.F., Jiang J.Z., (2024), Numerical Simulation and Parameter Optimization of a New Slant Insertion-Opening Combination Sand Fence. *Sustainability*, Vol.16, pp.8651.
[26] Xu G.W., He N., Zhang J., Dong H.C., (2021), Investigations into the design of sand control fence for Gobi buildings. *Aeolian Research*, Vol.49, pp.100662.
[27] Xu X.Y., Zhao P., Tang J.N., Ji Y.F., Ma X.B., (2020), Research and development status and prospect of sand control machinery in China (我国治沙机械研发现状与展望). Forestry and Grassland Machinery, Vol.1(2), pp.21-25.
[28] Zhang K., Zhang P.W., Zhang J.C., Zhang X.X., (2021), Protective effect of multi-row HDPE board sand fences: A wind tunnel study. *International Soil and Water Conservation Research*, Vol.9(1), pp.103-115.
[29] Zhang L., Sun B.G., Zhang K.P., Zhang P., Qi Y., Kong D.R., (2022), Research status and prospect of sand control machines in China (我国治沙机器的研究现状与展望). Forestry Machinery & Woodworking Equipment, Vol.50(12), pp.4-8.

[30] Zhang L., Yang Z., Zhang Q., Guo H., (2016), Tensile properties of maize stalk rind. *BioResources*, Vol.11(3), pp.6151-6161.
[31] Zhang S., Ding G.D., Yu M.H., Gao G.L., Zhao Y.Y., Wu G.H., Wang L., (2018), Effect of straw checkerboards on wind proofing, sand fixation, and ecological restoration in shifting sandy land. *International Journal of Environmental Research and Public Health*, Vol.15(10), pp.2184.
[32] Zhang T., Zhao M.Q., Liu F., Tian H.Q., Wulan T., Yue Y., Li D.P., (2020), A discrete element method model of corn stalk and its mechanical characteristic parameters. *BioResources*, Vol.15(4), pp.9337-9350.
[33] Zhao C.L., Li Q., Zhou N., Zhang J.Q., Kang L.Q., Shen Y.P., Jia W.R., (2016), Field observations of wind profiles and sand fluxes above the windward slope of a sand dune before and after the establishment of semi-buried straw checkerboard barriers. *Aeolian Research*, Vol.20, pp.59-70.
[34] Zhu H.P., Zhou Z.Y., Yang R.Y., Yu A.B., (2007), Discrete particle simulation of particulate systems: Theoretical developments. *Chemical Engineering Science*, Vol.62(13), pp.3378-3396.

DESIGN AND EXPERIMENTAL EVALUATION OF A DIRECT-INJECTION WINGED SHOVEL FOR A DEEP STRAW INCORPORATION MACHINE

/

秸秆深埋还田机直注翼铲设计与试验评价

Sicheng YANG[1)], Lihua WEI*[1)], Fanbowen MENG[1)], Deshuai LI[1)], Jiantian LI[2)], Zhengqing WANG[1)],Ruili WANG*[1)]

[1)]College of Engineering, Shenyang Agricultural University, Shenyang / China;

[2)]Fengcheng Caohe Machinery Manufacturing Co., Ltd., Dandong / China.

Corresponding authors. Lihua Wei; Tel: +86 13386825657; E-mail: weilihua@syau.edu.cn;

Ruili Wang, Tel: +86 17702424189; E-mail: wangruili@syau.edu.cn.

DOI: https://doi.org/10.35633/inmateh-79-61

Keywords: *straw deep burial machine, soil-direct-injection wing shovel interaction, Box-Behnken design, soil coverage rate, response surface methodology*

ABSTRACT

Conventional deep-burial devices typically employ a split structure consisting of a furrowing shovel and a soil-covering plate. During field operation, vibrations can cause relative displacement between these components, resulting in unstable soil coverage. Such devices may also exhibit structural redundancy, insufficient tillage depth, and high energy consumption. In this study, theoretical analysis and numerical simulation based on mechanical and soil-dynamics models were conducted to elucidate the soil–tool interaction mechanism of a direct-injection winged shovel and determine its key structural parameters. Using an EDEM-based soil–tool interaction model, a single-factor Box–Behnken experimental design was conducted with penetration angle, operating speed, and wing depth as the experimental factors and soil coverage rate and tillage resistance as the response variables. The optimal parameter combination consisted of a shovel-tip penetration angle of 25°, a wing depth of 150 mm, and an operating speed of 1.4 m·s⁻¹. Under these conditions, the direct-injection winged shovel achieved low tillage resistance, a high soil coverage rate, stable operation, and consistent furrow width. Field tests showed that all measured performance indicators met the requirements of the applicable Chinese national standards. The developed shovel exhibited stable and consistent performance during deep straw incorporation, thereby effectively improving operational quality.

摘要

传统深埋部件多采用开沟铲与覆土板分体装配结构，田间作业过程中易受振动发生相对偏移，造成覆土稳定性较差，同时存在结构冗余、耕深不足、作业能耗偏高等问题，为此本文创新设计一体化开沟覆土直注翼铲，单一部件可同步完成开沟、覆土、秸秆深埋、深松复合作业。采用理论分析与数值模拟相结合的方法，通过力学和土壤动力学分析模型，阐明直注翼铲与土壤的相互作用机制，确定直注翼铲主要结构参数。基于 EDEM 土壤耕作仿真模型，采用单因素试验 Box-Behnken 组合试验设计，以入土角、耕作速度、尾翼深度为试验因素，以覆土率、耕作阻力为核心评价指标，结果确定直注翼铲较优参数为铲尖入土角 25°、铲体尾翼深度 150 mm、耕作速度 1.4 m·s-1，该组参数下耕作阻力较小，自动覆土率高，作业稳定性与开沟宽度一致性较好。田间试验结构表明，该直注翼铲各项作业指标均符合国家标准要求，在秸秆还田作业中表现出良好的稳定性与一致性，能够有效提升作业质量。

INTRODUCTION

China is a major agricultural country with extremely abundant crop straw resources, accounting for nearly one-fifth of the global total (*Zhang et al., 2025*). Among them, the production of corn straw ranks first in the country, which is attributed to the continuous development of agricultural mechanization and has now become a necessary support condition for sustainable agricultural development (*Fang et al., 2021; Liu et al., 2025; Awachat et al., 2024; Wang et al., 2023)*. The deep straw incorporation machine buries postharvest crop residues in the subsoil, enabling their efficient incorporation at the required depth. The structural design and operational performance of its furrow-opening and soil-covering components directly affect the quality of straw burial *(Barr et al., 2020; Madhusudan et al., 2024)*.

Most straw incorporation machines currently available in China are designed only to pulverize and scatter straw or apply it as surface mulch, whereas only a limited number of models can incorporate crushed straw deep into the soil *(Shen et al., 2022)*.

This deep-burial device typically employs a split assembly structure comprising a furrowing shovel and a soil covering plate. Due to soil impact and machine vibration, component positions tend to deviate, leading to issues such as uneven soil coverage and insufficient backfilling. The separate connection components introduce structural redundancy, resulting in excessive tillage resistance for the entire unit. Current research lacks an integrated design capable of simultaneously performing furrowing, soil guidance, return flow, and directional soil covering, making it difficult to fundamentally address soil instability caused by positional deviations in the modular assembly (*Aikins et al., 2020*). In contrast, straw incorporation equipment developed in other countries offers greater automation and operational precision, together with compact designs and integrated functions. It can simultaneously perform multiple processes including straw pulverization, soil mixing, and deep burial, offering high operational efficiency and automation*(Lin et al., 2022; Xu et al., 2022)*. Such machine can adapt to various field cultivation needs. However, when applied domestically, these machines face challenges such as high costs, substantial maintenance expenses, and difficulty in adapting to local working conditions.

To address challenges in deep straw incorporation such as unstable soil coverage and high tillage resistance, this study developed a direct-injection wing shovel with the dual functions of furrowing and automatic soil covering, while optimizing its core structure and operational parameters. The effects of key structural parameters, including the penetration angle and tail-wing depth, on soil–tool interactions were analyzed. The physical and mechanical properties of the soil and the requirements for deep straw incorporation were then incorporated into a performance-optimization model. Based on theoretical analysis, an EDEM discrete element simulation was employed to construct a shovel-soil interaction model, identifying the optimal structural and operational parameter combination. Field trials were conducted to validate the shovel's operational efficiency.

MATERIALS AND METHODS

Structure and Working Principle

The deep straw incorporation machine shown in Fig. 1 consists of a three-point hitch frame, chain-drive system, main frame, soil-lifting and covering device, straw-crushing device, flow-guiding device, and transmission system. The machine is mounted on the rear three-point hitch of the tractor, and its transmission system is connected to the tractor power take-off (PTO) shaft through a universal joint *(Cedik et al., 2024)*. During operation, the shovel tip penetrates to a depth of 30 cm below the soil surface. Symmetrically arranged side blades driven by the chain-drive system further crush the preprocessed straw, reducing its particle size. The processed straw is conveyed by airflow through the fan outlet to the flow-guiding device, which collects it and directs it into the feeding tube. The tube then delivers the straw directly into the cavity created by the direct-injection winged shovel as it lifts and displaces the soil. The displaced soil subsequently falls back automatically, covering the accumulated straw at a depth of approximately 30 cm within the subsoil layer. This process enables the concentrated placement and deep incorporation of straw. By promoting straw decomposition and increasing the organic matter returned to the soil, this method can improve soil structure and create favorable conditions for subsequent crop growth.

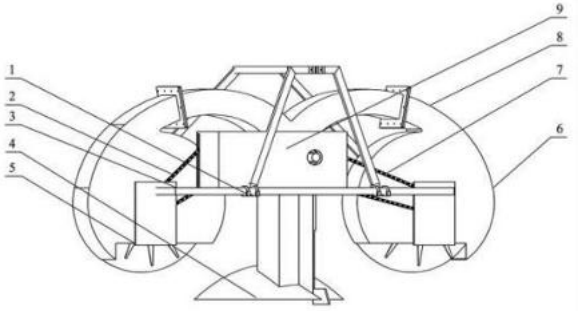


Fig. 1 - Structural schematic of the deep straw incorporation machine

1. Three-point hitch frame; 2. Left chain-drive system; 3. Main frame; 4. Soil-lifting and covering device; 5. Straw-crushing device; 6. Fan housing; 7. Right chain-drive system; 8. Flow-guiding device; 9. Transmission system.

Design of the direct-injection winged shovel for furrow opening and soil covering

The direct-injection winged shovel shown in Fig. 2 consists of a shovel body, feeding tube, support plate, and soil-guiding rails.

The device delivers crushed straw beneath the cultivated soil layer, while its structural configuration promotes the automatic return of displaced soil, thereby ensuring uniform straw burial and restoration of the soil profile. During operation, the wing-shaped shovel body lifts and displaces the soil, forming a subsurface cavity for deep straw placement. The coordinated design of the feeding tube and shovel body allows the crushed straw to pass smoothly into this cavity. As the shovel advances, the displaced soil falls back over the deposited straw, ensuring deep burial while maintaining a relatively level soil surface and a stable soil profile. The shovel also disrupts the compacted layer beneath the cultivated soil, increasing soil porosity and potentially improving soil aeration, water infiltration, and root development.

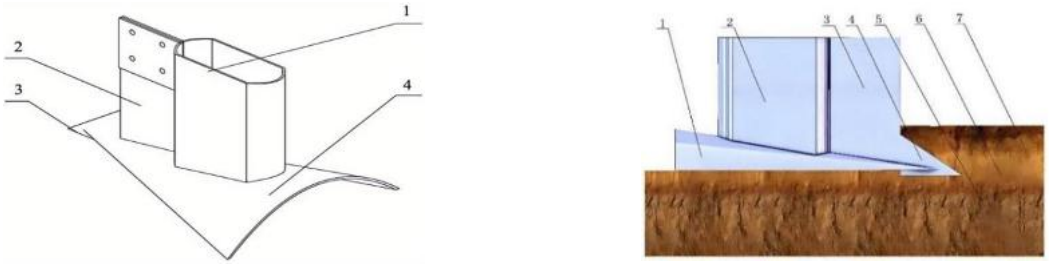


Fig. 2 - Structural schematic of the direct-injection winged shovel and its position within the soil profile

1. feeding tube; 2. shovel body; 3. support plate; 4. soil-guiding rail; 5. tillage layer; 6. plough pan; 7. subsoil

Analysis of the Operating Process

The following assumptions were adopted to establish the analytical model: (1) the shovel moves forward at a constant velocity, and acceleration during startup and stopping is neglected; (2) the soil is regarded as a homogeneous elastoplastic medium; (3) stones, crop residues, and other randomly distributed inclusions are excluded; and (4) only the soil stress state under steady-state cutting conditions is considered. Figure 3 illustrates the forces acting on the soil during operation of the direct-injection winged shovel. The soil–tool interaction process is divided into three regions: AB, BC, and BD. In region AB, the soil is primarily subjected to its weight G_1, the friction force f generated by relative motion along the contact surface, and the normal force F_1 exerted by the shovel tip. The weight G_1 acts vertically downward, f acts tangentially to the upper surface of the shovel tip, and F_1 exerted by the shovel tip acts perpendicular to the shovel-tip surface. In region BC, the support plate acts on the soil, which is subjected to its weight G_2 and the contact force F_2 exerted by the plate. This interaction compresses, shears, and fractures the soil, resulting in structural deformation. In region BD, the shovel body interacts with the soil, which is subjected to its weight G_3, the normal force F_3 exerted by the side surface of the shovel body, and the longitudinal compressive force F_4, acting in the direction of travel.

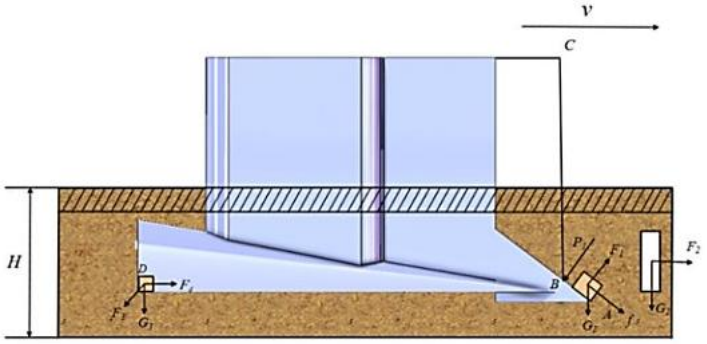


Fig. 3 - Diagram of soil forces

Force analysis during the earth-breaking process

During operation of the direct injection wing shovel, the wedge-shaped soil mass formed ahead of its working area is lifted and subsequently fragmented, preventing soil overturning. As the shovel advances, its blade continuously cuts through the soil while encountering horizontal tillage resistance. The combined traction resistance P generated by the blade tip and handle during soil cutting is calculated as:

$$P = k_1 l_1 + k_2 l_2 \quad (1)$$

In the formula: k_1 and k_2 represent the components of resistance in the direction of movement per unit length; l_1 and l_2 denote the lengths of the blade tip and handle blade, respectively (mm).

Analysis of Soil cutting failure motion

During cultivation, the shovel blades compress the soil, causing shear damage. The horizontal component of the force acting on the shovel blades is the traction resistance T:

$$T = N\sin\alpha + F\cos\alpha = N(\sin\alpha + f\cos\alpha) \quad (2)$$

where N is the normal pressure, F is the friction force of the soil on the shovel tip, and θ is the penetration angle of the direct-injection winged shovel.

The normal stress level of soil is the correlation coefficient of soil. Assuming that the working area of the straight injection wing shovel is A, then the normal pressure N is:

$$N = A \cdot \xi \cdot \delta\Delta t \quad (3)$$

Furthermore:

$$f = tan\,\phi \quad (4)$$

where φ denotes the soil's friction angle.

The traction resistance T is given by:

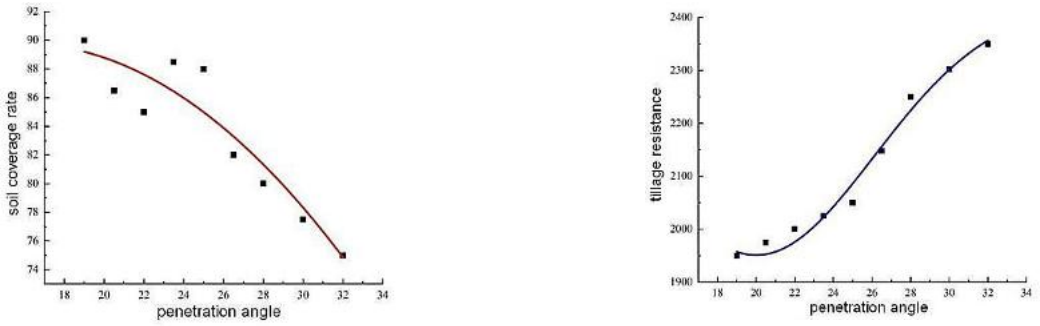
$$T = A \cdot \xi \cdot \delta(sin\,\alpha + f\,cos\,\alpha) = A \cdot \xi \cdot \delta(sin\,\alpha + tan\,\phi\,cos\,\alpha) \quad (5)$$

This set of mechanical equations establishes the theoretical relationship among the penetration angle, contact area, and traction resistance, thereby determining the appropriate range for the penetration angle and providing a theoretical basis for selecting factor levels in subsequent Box-Behnken experiments, while establishing an intrinsic connection between the theoretical model and the experimental design.

Structural Optimization

Single-factor experiment

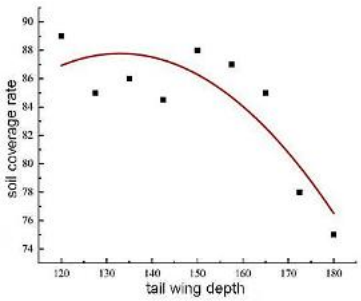
As shown in Figure 4(a), when the penetration angle of the direct-injection wing shovel falls within the range of 19-28°, the soil coverage rate decreases gradually with increasing penetration angle; whereas within the range of 28-32°, the coverage rate exhibits a negative correlation with the penetration angle. Figure 4(b) demonstrates that for penetration angles between 19° and 25°, tillage resistance increases steadily and slowly with increasing angle, while for angles between 25° and 32°, tillage resistance shows an inverse relationship with the penetration angle. Considering the optimization of both soil coverage rate and tillage resistance, an optimal penetration angle range of 22-25° is identified as achieving both significantly improved soil coverage efficiency and effective reduction of tillage resistance.



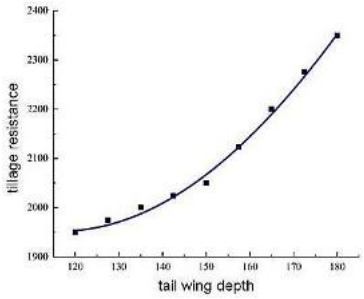
(a) Soil coverage rate at different penetration angles *(b) Tillage resistance at different penetration angles*

Fig. 4 - Effects of shovel tip penetration angle on test indicators

As the depth of the plow body tail wing increases, the soil coverage rate remains generally stable; however, a turning point occurs at a tail wing depth of 150 mm, where the decline rate accelerates significantly. An optimal tail wing depth helps reduce tillage resistance and lower operational energy consumption. Considering the combined effects of tail wing depth on both soil coverage rate and tillage resistance, an ideal range of 120-150 mm is identified, which yields high soil coverage while minimizing tillage resistance.



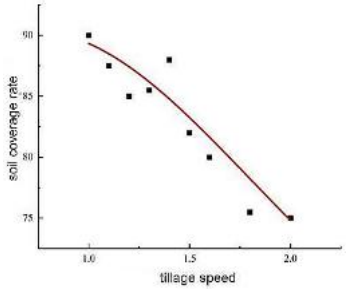
(a) Soil coverage rate at different tail wing depths



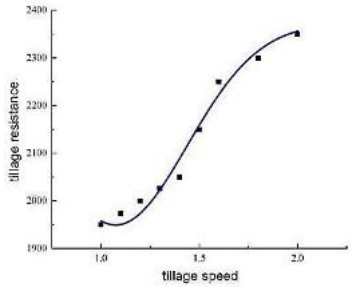
(b) Tillage resistance at different tail wing depths

Fig. 5 - Effects of shovel body tail wing depth on test indicators

The effects of different tillage speeds on soil coverage rate and tillage resistance are illustrated in Figure 6. The experimental results demonstrate that tillage speed significantly influences both coverage rate and tillage resistance. The coverage rate generally decreases with increasing tillage speed, whereas the trend for tillage resistance is opposite. This relationship remains stable within the speed range of 1.2-1.6 m/s. Within this range, an optimal tillage speed can be identified—one that maintains adequate soil coverage by the direct-injection wing shovel while effectively reducing tillage resistance.



(a) Soil coverage rate at different tillage speeds



(b) Tillage resistance at different tillage speeds

Fig. 6 - Effects of tillage speed on test indicators

Establishment of the simulation model

The direct-injection winged shovel consists of a shovel body, feeding tube, support plate, and soil-guiding rail, as shown in Fig. 3. A 3D model of the shovel was developed in SolidWorks, exported in IGS format, and imported into EDEM. The material properties, contact parameters, and mechanical parameters required for the discrete element method (DEM) simulation were then defined. The parameters used in the simulation are presented in Table 1.

Table 1

Parameter	Numeric value
Poisson's ratio of the direct-injection winged shovel (45 steel)	0.25
Shear modulus of the direct-injection winged shovel (45 steel) (Pa)	8.21×10^{10}
Density of the direct-injection winged shovel (45 steel) (kg·m^{-3})	7900
Shear modulus of the cultivated-layer soil (Pa)	1×10^{6}
Density of the cultivated-layer soil (kg·m^{-3})	1440
Bond stiffness of the cultivated-layer soil (km·m^{-3})	5×10^{7}
Bond strength of the cultivated-layer soil (Pa)	2×10^{4}
Coefficient of friction of the cultivated-layer soil	0.333
Poisson's ratio of the plow-pan soil	0.36
Shear modulus of the plow-pan soil (Pa)	1.1×10^{6}
Density of the plow-pan soil (kg·m^{-3})	1500
Bond stiffness of the plow-pan soil (km·m^{-3})	5×10^{7}
Bond strength of the plow-pan soil (Pa)	3×10^{4}
Coefficient of friction of the plow-pan soil	0.282
Poisson's ratio of the subsoil	0.36
Shear modulus of the subsoil (Pa)	1.2×10^{6}
Density of the subsoil (kg·m^{-3})	1540
Bond stiffness of the subsoil (km·m^{-3})	5×10^{7}
Bond strength of the subsoil (Pa)	4×10^{4}
Coefficient of friction of the subsoil	0.224

The contact model is a fundamental component of the discrete element method (DEM), as it describes the forces and deformations generated by particle–particle and particle–boundary interactions *(Liu et al., 2025)*. Commonly used contact models include Hertz–Mindlin with JKR, the Parallel Bond Model, and Hertz–Mindlin with Bonding. The Hertz–Mindlin with JKR model accounts for adhesive forces at particle contacts but does not explicitly represent the fracture of cemented bonds. The Parallel Bond Model is widely used to simulate the fracture of brittle bonded materials, such as rock, but may require extensive calibration for soil applications. Considering both simulation accuracy and computational efficiency, the Hertz–Mindlin with Bonding model was selected in this study.

By allowing bonds between particles to break when prescribed strength criteria are exceeded, this model can represent soil cracking, shear failure, and the separation and movement of soil layers during tillage. It was therefore considered suitable for simulating the interaction between the direct-injection winged shovel and the soil.

The soil in this experimental area is sandy loam, with the plow pan extending from the surface to a depth of 150 mm. Soil physical analysis reveals that this layer exhibits high porosity and soft texture, primarily composed of granular and columnar soil particles. Below 150 mm lies the shovel subsoil, which shows significantly increased compaction and greater hardness, with soil particles consisting of individual grains and clumps. The core soil layer below 300 mm is classified as the non-plow pan, mainly composed of large-sized kernel-like particles.

For numerical simulations of deep loosening operations, a scaled virtual soil tank was developed with dimensions of 2000 mm × 1200 mm × 450 mm, designed to mitigate boundary effects. Soil parameters were stratified across three layers: 0–150 mm, 150–300 mm, and 300–450 mm, corresponding to the tillage, shovel, and core soil layers, respectively *(Wei et al., 2025)*. A discretized soil particle model was then constructed to balance computational efficiency and the representation of soil structural characteristics, as presented in Fig.7.

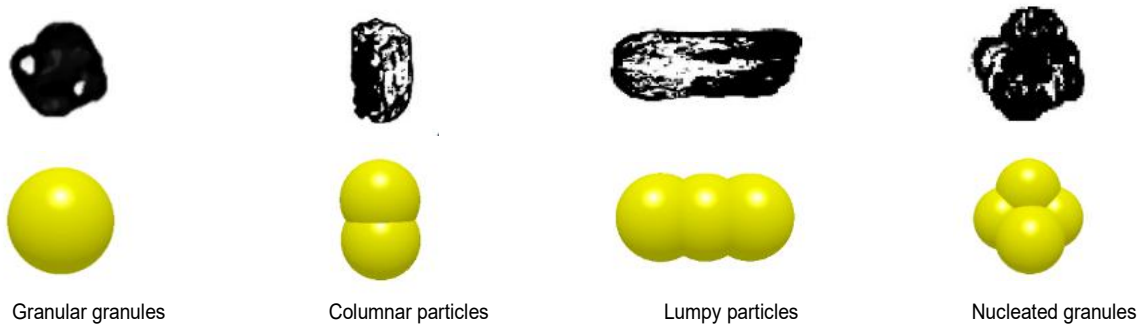


Fig. 7 - Soil particle model

Simulation test analysis

Based on the parameter ranges determined through preliminary single-factor experiments, a Box–Behnken experimental design was developed using Design-Expert 13. The experimental factors and their coded levels are presented in Table 2.

Table 2

Table of factor level coding

Level	Factor		
	Penetration angle *A* / (°)	Tail wing depth *B* / mm	Tillage speed *C* / (m·s^{-1})
-1	22	135	1.2
0	25	150	1.4
1	28	165	1.6

RESULTS

Analysis of variance of the simulation results

A Box–Behnken experimental design was developed using Design-Expert 13, and the simulations were performed according to the resulting design matrix. The design comprised 17 runs, including five replicates at the center point, to estimate experimental error and assess model adequacy. The objective was to determine the effects of three factors—the penetration angle (A), tail-wing depth (B), and operating speed (C)—on the soil coverage rate and tillage resistance of the direct-injection winged shovel. The design matrix and simulation results are presented in Table 3.

Table 3

Experimental design and simulation results

Run	Penetration angle A / [°]	Tail wing depth B / [mm]	Tillage speed C / [min]	Soil coverage rate Y_1 / [%]	Tillage resistance Y_2 / [N]
1	25	150	1.4	88.79	2060.33
2	22	150	1.6	82.43	2073.33
3	25	165	1.2	79.83	2065.09
4	25	135	1.6	79.23	2282.48
5	22	135	1.4	79.70	2233.33
6	28	135	1.4	77.43	2370.38
7	28	165	1.4	80.43	2160.92
8	28	150	1.2	79.77	2153.73
9	25	150	1.4	87.99	2055.33
10	25	165	1.6	82.23	2162.54
11	25	150	1.4	88.23	2051.33
12	22	165	1.4	81.70	2083.33
13	28	150	1.6	78.17	2280.69
14	25	135	1.2	78.83	2295.91
15	25	150	1.4	88.03	2049.33
16	22	150	1.2	80.03	2136.33
17	25	150	1.4	88.43	2099.33

Significance analysis of soil coverage rate Y_1 and tillage resistance Y_2 with direct injection wing shovel

A variance analysis and regression coefficient significance test were performed on the regression model of soil coverage rate Y_1 for direct injection wing shovels, with detailed results presented in Table 4. The regression equation for soil coverage rate Y_1 is as follows:

$$\hat{Y}_1 = 88.29\text{-}1.01A + 1.12B + 0.45C + 0.25AB - AC + 0.5BC - 4.2A^2 - 4.27B^2 - 3.99C^2 \quad (5)$$

A model is considered significant when its F-value reaches 177.94. In this context, a P-value below 0.0500 indicates a statistically significant model term, while a P-value below 0.01 signifies extremely significant. The specific P-values are: A (0.0002), B (0.0001), C (0.0172), AC (0.0018), BC (0.0448), A^2 (0.0001), and B^2 (0.0001). Therefore, terms A, B, C, AC, A^2, B^2, and C^2 are all statistically significant. The out-of-fit term shows an F-value of 2.3 with a P-value of 0.2189, indicating that the out-of-fit term is not significant. This suggests the model fits well and the data is reliable.

Table 4

Analysis of variance of coverage rate

Source of variation	Sum of square	Degree of freedom	Mean square	F value	P value	Significance
Model	269.20	9	29.91	177.94	< 0.000 1	**
A	8.12	1	8.12	48.31	0.0002	**
B	10.12	1	10.12	60.23	0.0001	**
C	1.62	1	1.62	9.64	0.0172	*
AB	0.2500	1	0.2500	1.49	0.2621	
AC	4.00	1	4.00	23.80	0.0018	**
BC	1.0000	1	1.0000	5.95	0.0448	*
A^2	74.44	1	74.44	442.87	< 0.0001	**
B^2	76.94	1	76.94	457.73	< 0.0001	**
AB^2	67.03	1	67.03	398.73	< 0.0001	**
Residual	1.18	7	0.1681			
Lack of Fit	0.7450	3	0.2483	2.30	0.2189	
Pure Error	0.4316	4	0.1079			
Sum	270.37	16				

Note: $p \leq 0.01$ means highly significant (**); $0.01 < p \leq 0.05$ means significant (*); $p > 0.05$ means not significant.

The regression model for tillage resistance Y_2 of direct injection wing shovels was constructed. Through analysis of variance and regression coefficient significance test, the results are shown in Table 5. The regression equation for tillage resistance Y_2 is:

$$\hat{Y}_2 = 2063.13 + 54.93A - 88.78B + 18.5C - 14.87AB + 47.49AC + 27.72BC + 54.19A^2 + 94.67B^2 - 43.7C^2 \quad (6)$$

As shown in Table 5, A, B, and C represent the penetration angle, tail-wing depth, and operating speed, respectively, and tillage resistance is the response variable. The model F-value of 72.86 indicates statistical significance. A P-value below 0.0500 signifies a significant model term, while a P-value below 0.01 denotes extremely significant terms.

Specifically, the P-values for A and B are both <0.0001, C is 0.0135, AC is 0.1046, BC is 0.0103, A^2 is 0.0002, B^2 is <0.0001, and C^2 is 0.0008. Thus, A, B, C, AC, BC, A^2, B^2, and C^2 are significant model terms. The out-of-fit term has an F-value of 0.0566 and a P-value of 0.9799, indicating no significant out-of-fit term, suggesting good model fit and reliable data.

Table 5

Analysis of variance of tillage resistance

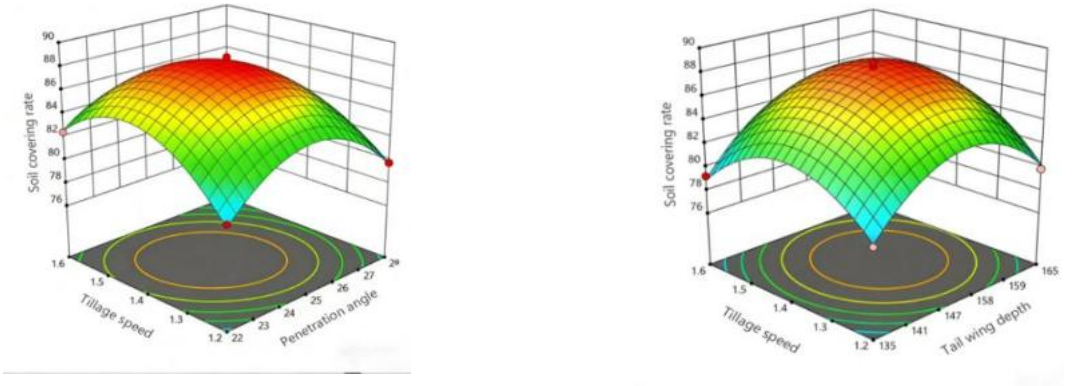
Source of variation	Sum of square	Degree of freedom	Mean square	F value	P value	Significance
Model	1.669×10^5	9	18540.22	72.86	< 0.000 1	**
A	24134.05	1	24134.05	94.84	< 0.0001	**
B	63051.56	1	63051.56	247.78	< 0.000 1	**
C	2737.26	1	2737.26	10.76	0.0135	*
AB	883.87	1	883.87	3.47	0.1046	*
AC	9021.20	1	9021.20	35.45	0.0006	**
BC	3073.59	1	3073.59	12.08	0.0103	*
A^2	12363.15	1	12363.15	48.58	0.0002	**
B^2	37738.19	1	37738.19	148.30	< 0.0001	**
AB^2	8041.60	1	8041.60	31.60	0.0008	**
Residual	1781.28	7	893.33			
Lack of Fit	72.56	3	24.19	0.0566	0.9799	
Pure Error	1708.72	4	427.18			

Response surface analysis

The response surface analysis method was employed to analyze the test data, aiming to investigate the intrinsic relationship between the core performance indicators and key influencing factors of the direct injection wing shovel. Based on the data analysis results, response surface plots of each factor with respect to the soil coverage rate were generated. These plots visually illustrate the specific impact of each influencing factor on the performance evaluation index of the direct injection wing shovel, as well as how these factors interact and jointly influence the evaluation index.

Effects of the experimental factors on soil coverage rate

Response surface analysis was used to evaluate the effects of penetration angle, tail-wing depth, and operating speed on the soil coverage rate of the direct-injection winged shovel. The response surface plots shown in Fig. 8 illustrate the effects of pairs of factors and their interactions on soil coverage rate while the third factor is held at its center level. These plots show the direction and magnitude of the factor effects and reveal how their interactions influence soil coverage performance.



(a) Interaction between penetration angle and tillage speed (b) interaction between tail-wing depth and tillage speed

Fig. 8 - Effects of factor interactions on the soil coverage rate of the direct-injection winged shovel

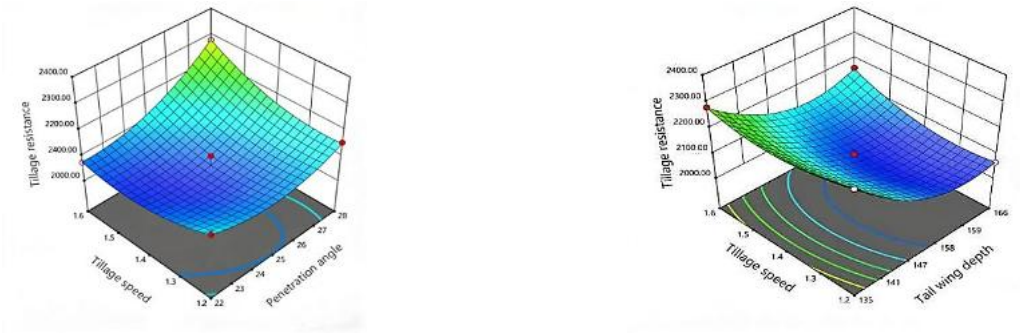
As shown in Fig. 8(a), under the interactive influence of the penetration angle and the tillage speed, as both the tillage speed and the soil penetration angle increase, the soil coverage rate overall exhibits a trend of first increasing and then decreasing.

The magnitudes of change in the soil coverage rate with respect to the increase and decrease of the tillage speed are approximately equal, and the change pattern is relatively uniform. The soil coverage rate reaches its peak when the tillage speed is approximately 1.5 m·s^{-1}. The overall response surface is convex.

As can be seen from Fig. 8(b), under the interactive influence of the tillage speed and the tail wing depth, the slope of the tangent plane of the response surface first gradually decreases and then becomes steeper, with the tangent slope also first decreasing and then increasing. The influence trends of the two factors are relatively similar, and the soil coverage rate is more significantly affected by the tail wing depth than by the tillage speed.

The influence on the tillage resistance of the direct injection wing shovel

Response surface methodology was applied to analyze the experimental data, with a comprehensive investigation into the interactive effects of key influencing factors—penetration angle, tail wing depth and tillage speed—on the tillage resistance, a critical performance index of the direct injection wing shovel. Data analysis further enabled the generation of response surface plots illustrating the relationship between each individual factor and tillage resistance, which are presented in Fig.9.



(a) Interaction between penetration angle and operating speed (b) Interaction between tail-wing depth and operating speed

Fig. 9 - Effects of factor interactions on the tillage resistance of the direct-injection winged shovel

As shown in Fig. 9(a), under the interactive influence of the penetration angle and the tillage speed, the resistance overall exhibits a trend of first decreasing and then increasing as both the tillage speed and the penetration angle increase. When the tillage speed is approximately 1.5 m·s^{-1}, the resistance reaches its minimum value, and the overall response surface is concave.

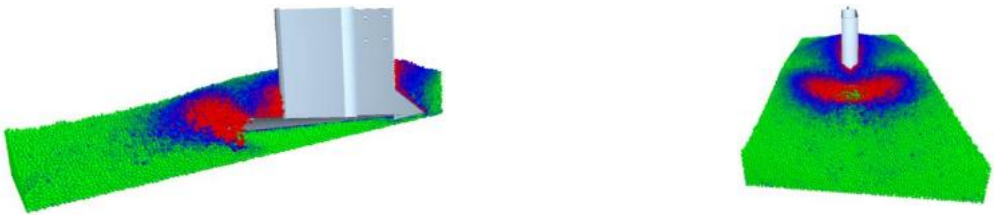
As can be seen from Fig. 9(b), under the interactive influence of the tillage speed and the tail wing depth, the resistance is significantly more affected by the tail wing depth than by the tillage speed, and this significant influence is completely opposite to the influence on the soil coverage rate.

Simulation Results for Soil Movement

As shown in Fig. 10, when the direct-injection winged shovel is fully engaged with the soil, its tip penetrates the plow pan and loosens the compacted soil layer. As the shovel advances, the shovel tip cuts and lifts the soil, causing soil particles to move upward. The winged shovel body then displaces the lifted soil laterally, creating a furrow. After the shovel passes, the displaced soil falls back into the furrow behind the shovel, thereby completing the furrow-opening and soil-covering process.



(a) Soil movement at 2.2 seconds



(b) Soil movement at 2.8 seconds

Fig. 10 - Soil displacement dynamics during operation of direct injection winged shovel

Field trial

Test conditions

The test equipment comprised a deep straw incorporation machine equipped with the direct-injection winged shovel, a draft-force measurement system, measuring tapes, straightedges, marker poles, and sampling shovels. Field tests were conducted after the autumn harvest to evaluate the operational performance of the shovel and validate the simulation results. Before testing, the dimensions of the designated test plots were measured with a tape measure, and their boundaries were marked with poles in accordance with NY/T 500–2002, *Operating Quality of Straw-Returning Machines*. The selected field was continuous and uniform, with a stated length of more than 1,500 m. The test area was divided into a principal test plot and reserve plots. If abnormal conditions invalidated a test in the principal plot, a comparable reserve plot was used. Field topography and soil conditions were considered when selecting the plots to ensure comparable and representative testing conditions.

Performance Test

The performance evaluation of the direct-injection winged shovel focused on its furrow-opening and soil-covering performance. The selected evaluation indicators were furrow-depth stability, furrow-width consistency, and soil coverage rate.

To measure furrow depth, loose soil was carefully removed from the furrow edges and bottom to expose the original soil surface and furrow bottom. A straightedge was placed across the furrow, and the vertical distance from the straightedge to the furrow bottom was measured as the furrow depth. Before measuring furrow width, naturally collapsed soil was removed. Width measurements were taken at longitudinal positions of 0, 150, and 300 mm, and their mean was calculated as the furrow width. The soil coverage rate was determined within a 100 × 300 mm sampling area. The masses of soil displaced outside the furrow and soil that naturally fell back into the furrow were measured separately. The soil coverage rate was calculated as the mass of soil returned to the furrow divided by the total mass of displaced soil.

As shown in Table 6, the mean furrow depths obtained in five consecutive test runs were 305, 302, 301, 298, and 299 mm, respectively. The furrow-depth stability coefficient exceeded 94% in all runs, indicating that the direct-injection winged shovel maintained consistent operating depth across repeated field tests.

Table 6

Field test results for furrow depth

Parameters		First run	Second run	Third run	Fourth run	Fifth run
Furrow depth	Maximum/mm	308	307	311	306	310
	Minimum/mm	291	297	286	294	297
	Average value/mm	305	302	301	298	299
	Range/mm	17	10	25	12	13
	Stability coefficient	94.75	98.34	94.17	95.48	95.32

To determine the backfilling rate of the direct injection wing shovel, the furrow depth must first be precisely measured *(Bao et al., 2017; Du et al., 2025).* Specifically, soil accumulated both inside and outside the furrow was thoroughly cleared using shovels to ensure the original ground surface and furrow bottom were fully exposed. Next, a straightedge was placed between the furrow walls to measure the vertical height from the furrow bottom to the ground surface.

As shown in Table 7, the average furrow width of the direct injection wing shovel across five consecutive operations was 1008 mm,1004 mm,1005 mm,1003 mm, and 1009 mm, respectively. The maximum deviation in furrow width during each operation never exceeded 20 mm.

Moreover, the furrow-width consistency coefficient exceeded 95% in all five test runs, indicating that the shovel maintained a consistent furrow width. These results demonstrate stable furrow-opening performance over different operating distances.

Table 7

Field test results for furrow width

Parameters		**First run**	**Second run**	**Third run**	**Fourth run**	**Fifth run**
Furrow width	Maximum/mm	1017	1011	1014	1010	1016
	Minimum/mm	1002	995	994	994	998
	Average value/mm	1008	1004	1005	1003	1009
	Range/mm	15	16	20	16	18
	Consistency coefficient	95.39	95.44	96.43	96.32	96.52



Fig. 11 - Operating process of the direct-injection winged shovel during furrow opening and soil covering

During operation, the shovel tip and body penetrate and lift the soil. The displaced soil moves rearward along the shovel body and subsequently falls into the cavity formed behind the shovel. As shown in Fig.11, this cavity provides space for straw placement. After the straw is guided into the cavity, the displaced soil falls back and covers it, thereby completing the deep straw incorporation process. Field tests confirmed that the direct-injection winged shovel performed its intended functions during deep straw incorporation *(Gao et al., 2022)*.

As shown in Table 8, the mean soil coverage rates recorded in five consecutive test runs were 87.45%, 88.05%, 87.55%, 86.75%, and 87.55%, respectively. The small variation among the five mean values indicates that the shovel maintained relatively consistent soil-covering performance across repeated tests.

Table 8

Experimental results of soil coverage rate

Parameters		First run	Second run	Third run	Fourth run	Fifth run
Soil coverage rate	Maximum/mm	88.7	89.3	88.9	92.1	89.4
	Minimum/mm	83.5	85.5	83.2	85.4	83.7
	Average value/mm	87.45	88.05	87.55	86.75	87.55
	Range/%	5.2	4.7	5.7	6.5	5.7

Experimental Comparative Verification

As shown in Table 9, the variation patterns of simulation results and field experiment results are largely consistent, with relative errors for both indicators below 3%, indicating high agreement. The minor discrepancies mainly stem from the following factors: the simulation model simplifies soil as a homogeneous medium, neglecting random variables such as straw residues and local moisture fluctuation; additionally, slight systematic errors exist in soil contact parameter calibration, leading to minor deviations between simulation and measured results. Standard deviation and 95% confidence interval analyses demonstrate that field experiment data exhibit low dispersion and good repeatability, confirming that this discrete element model meets the accuracy requirements for simulation analysis.

Table 9

Evaluating indicator	Experimental Mean value	Simulation mean	Relative error	Standard deviation	Confidence interval
Tillage resistance	2121.00	2063.13	2.73	24.73	[2089.81,2152.19]
Soil coverage rate	87.47	88.29	0.94	0.47	[86.89,88.05]

CONCLUSIONS

To address the insufficient operating depth, limited soil-backfilling capability, and high tillage resistance of conventional furrow-opening and soil-covering components, an integrated direct-injection winged shovel was developed. The effects of its structural and operating parameters on soil coverage and tillage resistance were investigated through theoretical analysis, discrete element simulation, and field testing. The main conclusions are as follows:

(1) The soil properties varied with depth. Moisture content ranged from 15.99% to 22.04%, while bulk density increased from 1.41 to 1.54 g/cm³ from the cultivated layer to the subsoil. The shear strength of the plow pan was 30.43 kPa, which was higher than the 23.30 kPa measured in the cultivated layer. These data provided the basis for designing the direct-injection winged shovel and calibrating the soil model.

(2) EDEM simulation results showed that the direct-injection winged shovel effectively disrupted the plow pan and promoted automatic soil backfilling, with a soil coverage rate of 88.45% and a tillage resistance of 2048.78 N, achieving lower energy consumption than traditional two-step operations.

(3) The optimal parameter combination comprised a shovel-tip penetration angle of 25°, a tail-wing depth of 150 mm, and an operating speed of 1.4 m/s. Under these conditions, the predicted soil coverage rate exceeded 88%, while the tillage resistance remained below 2050 N.

(4) Field tests confirmed that the direct-injection winged shovel performed its intended functions during deep straw incorporation. The reported furrow-depth stability, furrow-width consistency, and soil coverage values were 94.65%, 96.06%, and 87.47%, respectively. The measured performance indicators met the requirements of the applicable Chinese agricultural machinery standard, demonstrating stable furrow opening and soil covering under the tested field conditions.

（5）This study has several limitations. In the discrete element model, each soil layer was treated as a homogeneous medium, and field-scale soil heterogeneity, stones, and crop residues were not represented. These simplifications may have contributed to differences between the simulated and measured results. Moreover, the field tests were conducted only in relatively loose black soil in Northeast China. The performance of the shovel in compacted loess, cohesive paddy soil, and sandy loam therefore remains unknown. Hard soil may accelerate component wear, cohesive soil may adhere to the shovel and obstruct straw delivery, and loose sandy soil may not provide stable soil coverage. In addition, the integrated curved tail-wing structure results in a relatively large overall width, potentially limiting maneuverability in narrow-row fields. Future research should optimize the tail-wing profile to reduce the transverse dimensions, conduct comparative tests in different soil types, and develop a DEM model that accounts for spatial soil heterogeneity. These improvements would enhance simulation accuracy and broaden the applicability of the device.

ACKNOWLEDGEMENT

This research was supported by General Program of Natural Science Foundation of Liaoning Provincial Science and Technology Plan Joint Funds (2025-MSLH-613) and Shenyang Science and Technology Plan Project (24-216-2-10).

REFERENCES

[1] Awachat, S., & Sharma, D. (2024). A Review on Impact of Agricultural Mechanization on Farm Productivity and Factors Facilitating the Growth of Mechanization, *Institute of Electrical and Electronics Engineers Inc*.pp. 1163–1166. DOI:10.1109/ICDICI62993.2024.10810850.

[2] Aikins, K.A., Barr, J.B., Ucgul, M., Ucgul, M., Jensen, T.A., Antille, D.L., & Desbiolles, J.M. (2020). No-tillage furrow opener performance: A review of tool geometry, settings and interactions with soil and crop residue, *Soil Research*, Vol.58, pp. 603–621. DOI:10.1071/SR19153.

[3] Bao, P., Wu, M., Guan, C., Luo, H., He, Y., & Xiang, W. (2017). Design of plow-rotary style ditching and ridging device for rapeseed seeding (犁旋组合式油菜播种开沟起垄装置设计). *Transactions of the Chinese Society of Agricultural Engineering*, Vol. 33, pp. 23–31. DOI: 10.11975/j.issn.1002-6819.2017.20.003.

[4] Barr, J., Desbiolles, J., Ucgul, M., & Fielke, J. (2020). Bentleg furrow opener performance analysis using the discrete element method. *Biosystems Engineering*, Vol.189, pp.99-115. DOI: 10.1016/j.biosystemseng.2019.11.008.

[5] Cedik, J., Praan, R., Leger, V., Havlicek, M., Lopot, F., Rybansky, M., & Pexa, M. (2024). three-point hitch dynamometer for measuring tractor-implement forces, *Applied Engineering in Agriculture*, Vol. 40, pp. 303–310. DOI: 10.13031/aea.15731.

[6] Du, W., Lin, J., Li, X., Li, L., Zhang, Q., & Liao, Q. (2025). Design and Experiments of the shallow plow for the high-speed strip micro-ridge combined direct seeding machine for rapeseed (油菜高速带状微垄联合播种机浅犁设计与试验). *Transactions of the Chinese Society of Agricultural Engineering*, Vol. 41, pp. 38–48. DOI:10.11975/j.issn.1002-6819.202411157.

[7] Fang, L., Wang, Y., Deng, D., Yuan, S., & Wang, Z. (2021). Research Status and Development Trend Of Mechanized Straw Returning Technology. *INMATEH - Agricultural Engineering*, Vol. 65, pp. 465–475. DOI: 10.35633/inmateh-65-48.

[8] Gao, W.-Y., Lin, J., Li, B., Wang, W., & Gu, S. (2022). Vibration characteristics analysis and structural optimization of straw deep bury and returning machine (秸秆深埋还田机振动特性分析与结构优化). *Transactions of the Journal of Jilin University*, Vol. 52, pp. 970–980. DOI: 10.13229/j.cnki.jdxbgxb20200882.

[9] Jin, F., Liu, D., Zhong, C., Yao, K., Tong, J., & Jiang, Z. (2024). Parameter calibration and discrete element model of highland barley stem based on EDEM. *INMATEH - Agricultural Engineering*, Vol. 72, pp. 363–373. DOI: 10.35633/inmateh-72-33

[10] Liu, G., Wang, K., Chen, X., Gong, J., Deng, Z., & Li, B. (2025). Research on contact parameter calibration and experiment of discrete element simulation model for rice straw. *INMATEH - Agricultural Engineering*, Vol.77, pp. 215–226. DOI: 10.35633/inmateh-77-17

[11] Lin, H., He, J., Li, H., Wang, Q., & Lu, C. (2022). Design and Experiment of a Reciprocating Intermittent Chopping Device for Maize Straw Returning, Agriculture-Basel, Vol.12(2). DOI: 10.3390/agriculture12020220.

[12] Lu, F., Meng, J., & Cheng, B. (2024). How does improving agricultural mechanization affect the green development of agriculture? Evidence from China. *Journal of Cleaner Production*, Vol. 472. DOI: 10.1016/j.jclepro.2024.143298.

[13] Madhusudan, B. S., Kushwaha, H. L., Kumar, A., & Mattar, M. A. (2024). Critical assessment of furrow openers and operational parameters for optimum performance under conservation tillage, Scientific Reports, Vol.14(1). DOI:10.1038/s41598-024-70569-2.

[14] Si, Y., He, M., Chen, S., Liu, Z., Li, Y., Yao, F., & Lu, J (2025). Effects of Deep Plowing and Returning Straw on Corn Yield and Black Soil Fertility under Corn-Soybean Rotation in the Northeast Black Soil Region (东北黑土区玉米-大豆轮作下秸秆深翻还田对玉米产量及黑土肥力的影响). *Transactions of the Corn Science*, Vol. 33(11), pp. 98–105. DOI: 10.13597/j.cnki.maize.science.20251112.

[15] Shen, T., Liu, H., Wu, X., & Sun, X. (2022). Research Status and Prospect of Straw Mechanization and Returning Technology and Equipment（秸秆机械化还田技术及装备研究现状与展望). *Transactions of the Jiangsu Agricultural. DOI:10.15889/j.issn.1002-1302.2022.15.001.*

[16] Wang, R., Li, D., LI, P., Bai, X., Wang, T ., Wang, W., & Zhao, Y. (2023). Optimum design for breaking device with double roller based EDEM. *INMATEH - Agricultural Engineering*, Vol. 70, pp. 570–582. DOI: 10.35633/inmateh-70-55.

[17] Wang, S., Huang, H., Zhang, Y., Yin, C., & Richel, A. (2021). The effect of corn straw return on corn production in Northeast China: An integrated regional evaluation with meta-analysis and system dynamics. Resources, *Conservation and Recycling*, Vol. 167. DOI: 10.1016/j.resconrec.2021.105402.

[18] WEI, L., LI, J., Meng, X., & Li, L. (2025). Design and experiment of subsoiling shovel with offset column and curved surface based on discrete element method (基于离散元法的偏柱式曲面深松铲设计与试验).*Transactions of Shenyang Agricultural University*, vol. 56(5), pp. 135-146. DOI:10.3969/j.issn.1000-1700.2025.05.015

[19] Xu, S.-C., Tao, G., Yi, S., Wang, S., & San, Y. (2025). Design and testing of bionic winged deep-loosening shovel for a strip tillage deep-loosening fertilization machine. *INMATEH - Agricultural Engineering*, Vol.77, pp. 550–562. DOI:10.35633/inmateh-77-45.

[20] Xu, G., Xie, Y., Liang, L., Ding, Q., Xie, H., & Wang, J. (2022). Straw-Soil-Rotary Blade Interaction: Interactive Effects of Multiple Operation Parameters on the Straw Movement, *Agronomy*-Basel, Vol.12(4). DOI:10.3390/agronomy12040847.

[21] Zhang, N., Bai, L., Wei, X., Li, T., Tang, Y., Zeng, X., Lei, Z., Wen, J., & Su, S. (2025). Promoted decomposition in straw return to double-cropped rice fields controls soil acidity, increases soil fertility and improves rice yield. *Chemical Engineering Journal*, Vol. 509. DOI:10.1016/j.cej.2025.161309.

PARAMETER CALIBRATION OF THE DISCRETE ELEMENT MODEL FOR THE AGRICULTURAL MACHINERY-LATERITIC SOIL-PANAX NOTOGINSENG INTERACTION DURING THE TRANSPLANTING PROCESS

/

三七移栽过程机具-红土-三七交互离散元模型参数标定

Wei SU[1)], Yi ZENG [1)], Qingxu YU*[2)], Congcong LIAO[1)], Qinghui LAI[1)], Cantong SU[1)]

[1)]University of Science and Technology Kunming, Kunming 650093, China;

[2)]Nanjing Institute of Agricultural Mechanization, Ministry of Agriculture and Rural Affairs, Nanjing 210014, China;

E-mail: yqx5205@163.com

** Correspondent authors: Qing xu YU*

DOI: https://doi.org/10.35633/inmateh-79-62

Keywords: *Discrete element method; Parameter calibration; Notoginseng; laterite soil; JKR contact model*

ABSTRACT

This study calibrated key contact parameters for discrete element simulations of interactions among Panax notoginseng seedlings, lateritic soil, and 65Mn steel to address the lack of systematic multi-media parameter calibration methods. The researchers investigated three core contact interfaces using EDEM software, focusing on JKR surface energy, restitution coefficient, static friction coefficient, and rolling friction coefficient. They employed angle of repose tests, mixture collapse tests, and inclined plane rolling tests, combined with orthogonal design and response surface methodology, to establish correlation models between simulation and physical results. Through analysis of variance and multi-objective optimization, the team identified significant parameters and their optimal combinations for each interface. Validation showed that the optimized model exhibited relative errors below 7.5% across all tests, with prediction accuracy improved by over 30%. Field experiments further confirmed the model's reliability, providing theoretical support for structural optimization of Panax notoginseng transplanters.

摘要

为解决农业机械—红壤—作物相互作用离散元模拟中多介质接触参数缺乏系统标定方法的问题，本研究针对三七种苗—红壤、红壤—红壤、红壤—65Mn 钢三个核心接触界面，采用 EDEM 软件开展了关键接触参数标定优化研究。研究团队以 JKR 表面能、恢复系数、静摩擦系数和滚动摩擦系数为标定参数，采用休止角、混合坍塌、斜面滚动等物理试验，结合正交设计和响应面法，建立了模拟与物理试验的关联模型。通过方差分析和多目标优化，确定了各界面的显著参数及其最优组合。验证表明，优化后模型各项试验相对误差均低于 7.5%，预测精度提高 30% 以上。田间试验进一步证实了模型的可靠性，为三七移栽机结构优化提供了理论支撑。

INTRODUCTION

Panax notoginseng is a rare and valuable medicinal plant endemic to China, primarily cultivated in the southwestern regions including Yunnan, Guangxi, and Guizhou *(Liu et al., 2017; Yang et al., 2019*). Its dried roots and rhizomes have notable therapeutic effects. However, *P. notoginseng* transplantation faces challenges: tender seedlings are easily damaged during mechanical operations, reducing survival rates and yields. The cultivation soil for *P. notoginseng* is a cohesive lateritic soil characterized by poor workability, high moisture content, heavy texture, and high specific resistance (*Shao et al., 2006; Xing et al., 2020*). Such soil causes excessive resistance and severe adhesion, hindering Yunnan's *P. notoginseng* industry and mechanized transplantation development.

Discrete element method (*DEM*) simulation serves as a critical approach for investigating the coupled motion characteristics of the agricultural machinery–soil–seedling system, while accurate and reliable DEM parameters constitute the fundamental basis and prerequisite for studying the interaction characteristics of the agricultural machinery–lateritic soil–*P. notoginseng* system *(Aikins et al., 2021; Zeng et al., 2021*).

[1] *Wei SU, Ph. D. Professor; Qingxu YU, Ph. D. Assistant Researcher; Qinghui LAI, Ph. D. Professor; Yi ZENG, Master Candidate; Congcong LIAO, Master Candidate; Cantong SU, Master Candidate.*

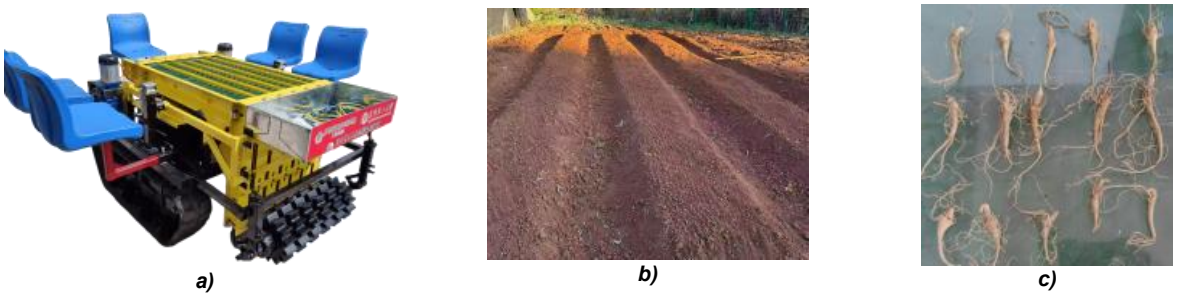
Parameter calibration is a pivotal step in DEM simulations, as its accuracy directly governs the reliability of simulation results. The Johnson-Kendall-Roberts (*JKR*) contact model, capable of precisely characterizing cohesive interactions between particles, has been widely adopted in DEM modeling of cohesive soils. To date, researchers worldwide have conducted systematic studies on seedling–soil contact parameter calibration targeting crops such as corn, potato, and ginseng. *Tian Xinliang et al., (2021*) provided theoretical references for the discrete element simulation of corn straw–soil mixtures in black soil regions. *Xiang Wei et al., (2019*), based on soil accumulation tests, adopted the Hertz-Mindlin with JKR contact model to construct a discrete element simulation model of southern clayey soil. *Li Junwei et al., (2019)*, utilized the Hertz-Mindlin with JKR cohesion contact model in EDEM to calibrate clayey black soil with varying moisture contents in Northeast China, providing references for agricultural machinery operations under different moisture conditions. *Bahrami et al., (2020)*, employed the hysteretic spring–linear cohesion contact model to conduct DEM simulations of plate sinkage tests on cohesive soils with varying moisture contents, elucidating the influence of key parameters on sinkage characteristics. *Adajar et al., (2021)*, performed calibration of the residue–soil friction coefficient and restitution coefficient using the discrete element method, specifically targeting the crop residue–soil contact interface, thereby providing key parameter foundations for modeling soil–crop interactions under straw mulching conditions.

Although substantial progress has been achieved in agricultural DEM parameter calibration, a significant research gap remains regarding the systematic investigation of the distinctive tool–lateritic soil – *P. notoginseng* ternary system. This study focuses on *P. notoginseng* seedlings, southwestern lateritic soil, and 65Mn steel tools, with the primary objective of improving discrete element simulation accuracy. Adopting a methodology that couples physical experiments with simulation modeling, parameter calibration was conducted using three types of tests: angle of repose test, mixture collapse test, and inclined plane rolling test, to acquire fundamental physical data for multiple contact interfaces. A discrete element model was developed using EDEM software, and the JKR contact model was selected to characterize interparticle cohesion and friction behaviors. By integrating orthogonal experimental design with response surface methodology, correlation models between simulation outputs and physical test results were established. Iterative optimization was performed to determine the optimal values of JKR surface energy, coefficient of restitution, coefficient of static friction, and coefficient of rolling friction for all contact interfaces. The reliability of the calibrated model was ultimately validated through experimental verification. The research outcomes provide critical parameter support and theoretical foundations for optimizing the structural design of *P. notoginseng* transplanting machinery and precisely matching operational parameters, while simultaneously establishing a transferable technical framework for DEM parameter calibration in characteristic medicinal plant–regional soil systems.

MATERIALS AND METHODS

Material selection

Lateritic soil samples were collected from the core cultivation area of *P. notoginseng* in Wenshan Prefecture, Yunnan Province, which features typical lateritic soil well-suited for *P. notoginseng* cultivation (*You et al., 2022*). *P. notoginseng* seedling samples were obtained from a cultivation base in Wenshan. In accordance with the DB53/T 055.3-2020 standard for *P. notoginseng* seedlings (*Yunnan Provincial Administration for Market Regulation, 2020*), 30 robust and undamaged first-grade annual seedlings were selected.



a) b) c)

Fig. 1 – Experimental materials

a) P. notoginseng Transplanting Machine; b) Experimental laterite soil; C) P. notoginseng Seedlings for Experiment

Physical test determination of contact parameters

The mechanical behavior and motion characteristics involved in *P. notoginseng* transplantation are governed primarily by the contact parameters for soil–soil, soil–implement, and soil – *P. notoginseng* interactions. Therefore, these contact parameters were initially determined through physical experiments.

The coefficient of restitution (C_R) was determined in this study using the free-fall impact method (*Shi et al., 2020*), as illustrated in Figure 2.

$$C_R = \frac{V_1}{V_0} \tag{1}$$

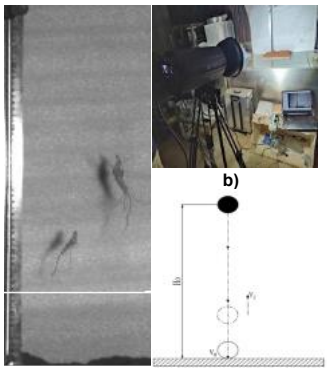


Fig. 2 – Measurement of the coefficient of restitution

a) High-speed photography; b) High-speed photographic setup; c) Schematic diagram of the coefficient of restitution (C_R)

The coefficient of *static friction (S_F)* was determined using the inclined plane method (*Aikins et al., 2021*), as shown in Figure 3.

$$S_F = \frac{F_1}{N_1} = \frac{G_1 \sin\theta_1}{G_1 \cos\theta_1} = \tan\theta_1 \tag{2}$$

where: F_1 is the friction force acting on the material specimen, *N;*

N_1 is the normal support force exerted on the specimen, *N;*

G_1 is the weight of the material specimen, *N;*

θ_1 is the inclination angle at which sliding begins, (°).

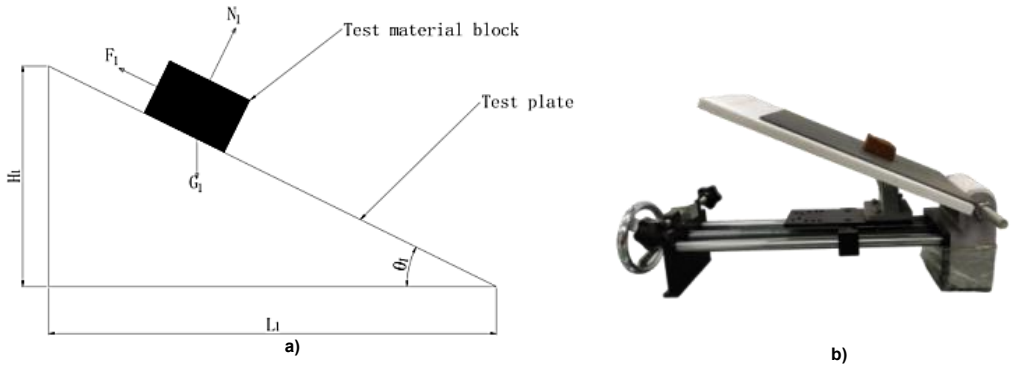


Fig. 3 – Measurement of the coefficient of static friction

a) Principle of static friction coefficient testing; b) Static friction coefficient test bench

The rolling friction coefficient (R_F) was determined using an angle adjustment device based on the principle of energy conservation (*Zhang et al., 2022*), as shown in Figure 4.

$$G_2 H_2 = R_F G_2 (G_2 \cos\theta_2 + L_2) \tag{3}$$

where: G_2 is the weight of the material sphere, *N;*

H_2 is the vertical distance between the material sphere and the horizontal plane, *mm;*

L_2 is the distance traveled by the material sphere along the horizontal plate, *mm.*

θ_2 is the angle between the two test platforms, (°)

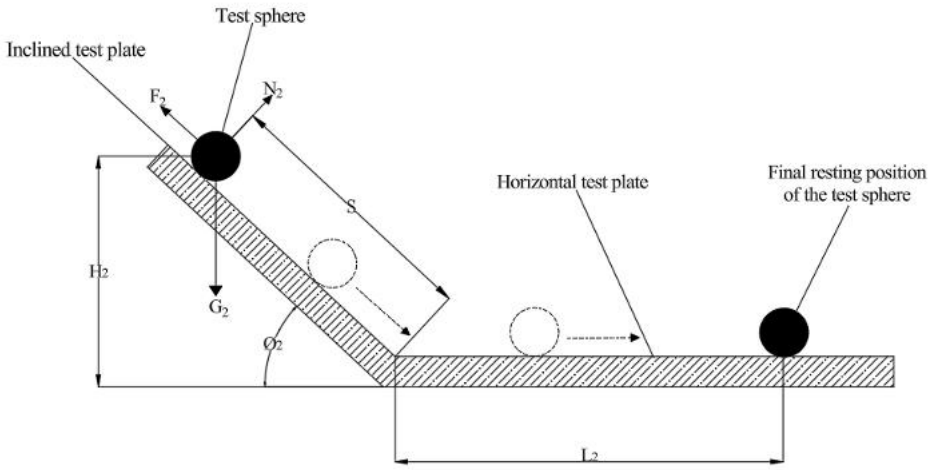


Fig. 4 – Principle of measuring the coefficient of rolling friction

Construction of the Discrete Element Model

Discrete Element Model of Lateritic Soil

Particle size distribution was determined using the standard sieve analysis method. The test equipment consisted of a set of standard sieves (with aperture sizes of 0.15 mm, 0.5 mm, 1 mm, 2 mm, and 3.5 mm) and an electronic balance (accuracy: 0.01 g). Sieve analysis was performed with a consistent shaking duration of 10 minutes. After shaking, the lateritic soil particles retained on each sieve were weighed. The test was repeated three times, with measurements recorded to an accuracy of 0.1 g. The lateritic soil particles after sieving are shown in Figure 5.

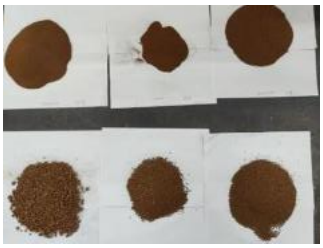


Fig. 5 – Particles after sieving

Based on the fundamental theory of the discrete element method (*DEM*) and the assumption of medium continuity, the macroscopic mechanical behavior of a granular system is essentially governed by the microscopic contact network and interaction forces between particles (*Cundall P.A. et al., 1979*). Through dimensional analysis and similarity principles, an upscaled model can equivalently reproduce macroscopic rheological and mechanical properties while reducing particle count and enhancing simulation feasibility. Currently, there is no unified standard for soil particle modeling based on the discrete element method (*DEM*). Spherical particles with diameters of 4–6 mm are commonly employed in studies (*Hang et al., 2018; Ucgul et al., 2015*). To balance efficiency and authenticity, this study adopts a five-fold coarse-graining technique and generates particles proportionally by mass fraction to ensure consistent particle size distribution. The corresponding mass fraction settings are shown in Table 1.

Table 1

Diameter and Mass Distribution of EDEM-Simulated Red Clay Particles

Actual particle size [mm]	Simulated particle diameter [mm]	Mass fraction [%]
≤0.25	0.625	22.4
0.25-0.5	1.875	11.8
0.5-1	3.250	19.4
1-2	7.500	19.8
2-3	12.500	20.6
≥3	15.000	6.0

Considering both simulation accuracy and modeling efficiency, particles were appropriately scaled up and then consolidated in shape. For particles smaller than 0.5 mm, the default spherical model in EDEM was adopted; for particles ranging from 0.5 mm to 2 mm, a two-ball model in EDEM was employed; and for particles larger than 2 mm, a three-ball model in EDEM was used. The established model is shown in Fig. 6.

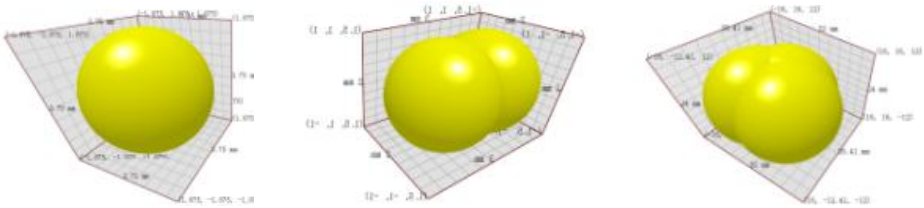


Fig. 6 – Establishment of Simulated Red Clay Particles

Discrete Element Model of Panax notoginseng (DEM)

The key physical parameters of *P. notoginseng* seedlings were determined for construction of the DEM. The morphological structure and principal dimensions of a representative seedling are shown in Fig. 7.

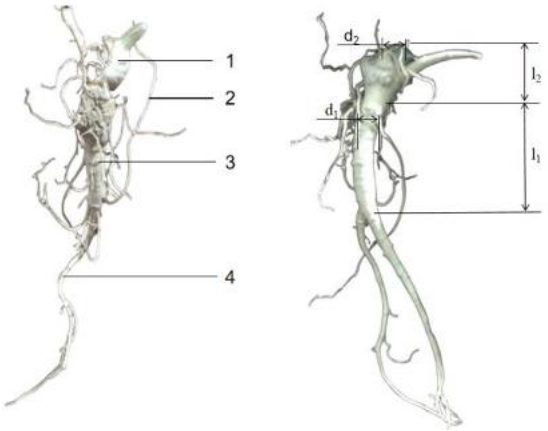


Fig. 7 – *P. notoginseng* seedling

1.dormant bud (rhizome head) 2. lateral root 3. main root 4. fibrous root

Two hundred *P. notoginseng* seedlings were selected for measurement, and their dimensional parameters are presented in Table 2.

Table 2

Dimensional parameters of *P. notoginseng* seedlings

Parameter	Main root length l_1[mm]	Main root diameter d_1[mm]	Dormant bud length l_2[mm]	Dormant bud diameter d_2[mm]
maximum value	26.12	15.68	17.74	8.89
minimum value	17.50	9.08	8.38	4.35
average value	22.42	12.64	13.28	6.15

High-precision point cloud data of *P. notoginseng* seedlings were acquired using the Wiiboox Reeyee 3D scanner, and a digital twin model with realistic topological structure was constructed through reverse engineering technology, overcoming the limitations of traditional contact measurement methods in characterizing the geometric features of complex biological samples (*Tang et al., 2023; Zhao et al., 2023*), as shown in Figure 8.



Fig. 8 – Wiiboox Reeyee 3D scanner

The model was imported into Creo Parametric 2.0, where the biologically characteristic surfaces were mathematically reconstructed by optimizing the control points and imposing surface-continuity constraints. To reduce the computational burden and simulation time, the *P. notoginseng* seedling model was simplified by retaining only the main root structure. The modeling procedure and resulting model are shown in Fig. 9.



Fig. 9 – Modeling process of *P. notoginseng* seedling
a) 3D Scanning File; b) Simplified Contour Model; c) Seedling Simulation Model

Experiment and Simulation

Determination of Simulation Parameters

In the EDEM simulation of interaction processes, the contact parameters include the coefficient of restitution (C_R), coefficient of static friction (S_F), coefficient of rolling friction ($R_{F)}$, and surface energy (S_E) between materials. This study focused on the contact parameters of the implement–lateritic soil – *P. notoginseng* interaction system during transplantation. These parameters included the following: for lateritic soil–lateritic soil, the coefficient of restitution (C_{R1}), static friction coefficient (S_{F1}), rolling friction coefficient (R_{F1}), and surface energy (S_{E1}); for lateritic soil–*P. notoginseng*, the coefficient of restitution (C_{R2}), coefficient of static friction (S_{F2}), coefficient of rolling friction (R_{F2}), and surface energy (S_{E2}); and for lateritic soil–65Mn steel, the coefficient of restitution (C_{R3}), coefficient of static friction (S_{F3}), coefficient of rolling friction (R_{F3}), and surface energy (S_{E3}). The intrinsic parameters and contact parameters were obtained through physical experiments and relevant literature (*Yu et al., 2020; Zhang et al., 2025; Liu et al., 2025*), as listed in Table 3.

Table 3

Ranges of intrinsic material properties and contact parameters

Parameter	Lateritic soil	*P. notoginseng*	65Mn
Density [kg/m^3]	1900	1050	7865
Young's modulus [Pa]	7.8e+06	2.29e+06	7.27e+10
Poisson's Ratio	0.370	0.402	0.35
Coefficient of restitution with lateritic soil	0.06-0.15	0.1-0.5	0.2-0.6
Coefficient of static friction with lateritic soil	0.1-0.6	0.2-0.6	0.1-0.55
Coefficient of rolling friction with lateritic soil	0.05-0.3	0.1-0.5	0.04-0.12
JKR surface energy with lateritic soil [J/m²]	2-8	2-5	1-5

Development of Calibration Experiments for the Discrete Element Simulation

Calibration experiments for the lateritic soil–lateritic soil contact parameters were conducted using a Box–Behnken design. The mean natural angle of repose of the lateritic soil, denoted as C_{S1} was selected as the response variable to evaluate the effects and statistical significance of the four factors C_{R1}, S_{F1}, R_{F1}, and S_{E1}. After each simulation, images of the soil pile were captured from the ±*X* and ±*Y* directions, as shown in Figure 10.

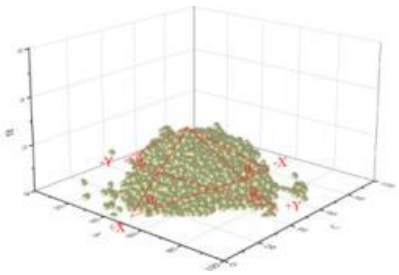


Fig. 10 - Cross-section selection

Calibration simulations for the lateritic soil–*P. notoginseng* contact parameters were conducted using

a Box–Behnken design. The angle of repose of the lateritic soil–*P. notoginseng* mixture, denoted as C_{S2} was selected as the response variable to evaluate the effects and statistical significance of C_{R2}, S_{F2}, R_{F2}, and S_{E2}. As shown in Fig. 11, the mixture was placed in the test container, after which the bottom support plate was withdrawn. Once the material had stabilized, image processing and linear fitting were performed to determine the angle of repose. The mean measured angle was used as the simulation response.

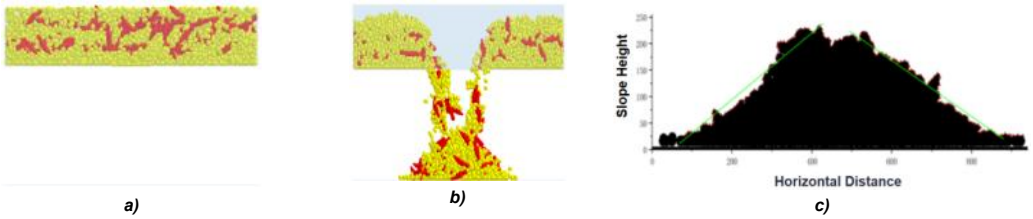


Fig. 11 – Mixture Collapsing Test

a) Laterite-P. notoginseng mixture uniformly distributed; b) Mixture Collapsing; c) Experimental Image Processing

The calibration test for simulation parameters between lateritic soil and 65Mn steel was conducted using an inclined plane simulation with a Box-Behnken design, as shown in Figure 12. A particle factory was set parallel to the inclined plane to generate a 15 mm-diameter soil sphere, which was initialized tangent to the surface with zero initial velocity and allowed to slide naturally, with its sliding distance on the horizontal plane (C_{S3}) recorded as the response value to investigate the effects and significance of the coefficient of restitution (C_{R3}), coefficient of static friction (S_{F3}), coefficient of rolling friction (R_{F3}), and surface energy (S_{E3}).

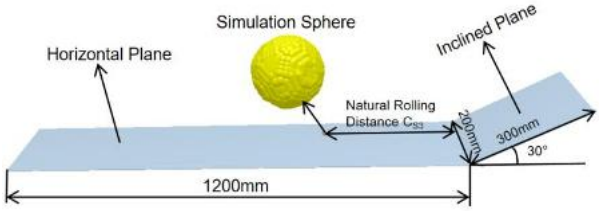


Fig. 12 – Inclined Plane Simulation

Results of Box-Behnken Simulation Calibration Experiments

Analysis of variance (*ANOVA*) was performed on the Box-Behnken experimental results for the lateritic soil–lateritic soil contact parameters, as shown in Table 4. After removing the non-significant terms with P > 0.05 from the ANOVA, the final predictive model for the response value under the lateritic soil–lateritic soil contact parameters was obtained as follows:

$$C_{S1} = 39.9 + 1.51R_{F1} + 7.63S_{E1} + 0.475C_{R1}S_{E1} + 2.18S_{F1}S_{E1} + 3.37C_{R1}^2 - 1.08C_{R1}S_{F1} - 0.725R_{F1}S_{E1} - 0.6417S_{F1}^2 - 0.9917R_{F1}^2 + 0.5708S_{E1}^2 \quad (4)$$

Table 4

Analysis of variance (ANOVA) for Laterite—Laterite parameter experiments

Source of Variance	Sum of Squares (SS)	Degrees of Freedom (df)	Mean Square (MS)	F	P
Model	861.69	14	61.55	295.34	< 0.0001
C_{R1}	0.0000	1	0.0000	0.0000	1.0000
S_{F1}	0.5208	1	0.5208	2.50	0.1399
R_{F1}	27.30	1	27.30	131.00	< 0.0001
S_{E1}	699.21	1	699.21	3355.1	< 0.0001
$C_{R1}S_{F1}$	4.62	1	4.62	22.18	0.0005
$C_{R1}R_{F1}$	0.9025	1	0.9025	4.33	0.0595
$C_{R1}S_{E1}$	10.24	1	10.24	49.14	< 0.0001
$S_{F1}R_{F1}$	0.3025	1	0.3025	1.45	0.2515
$S_{F1}S_{E1}$	18.92	1	18.92	90.80	< 0.0001
$R_{F1}S_{E1}$	2.10	1	2.10	10.09	0.0080
C_{R1}^2	60.60	1	60.60	290.78	< 0.0001
S_{F1}^2	2.20	1	2.20	10.54	0.0070
R_{F1}^2	5.24	1	5.24	25.17	0.0003
S_{E1}^2	1.74	1	1.74	8.34	0.0136
Lack of Fit	2.36	10	0.2361	3.37	0.2503
Total	864.19	26			

Analysis of variance (*ANOVA*) was conducted on the Box-Behnken experimental results for the lateritic

soil–*P. notoginseng* contact parameters, and the results are presented in Table 5. After removing non-significant terms with P > 0.05 from the analysis, the final prediction model for the natural collapse coefficient C_{S2} under the lateritic soil–*P. notoginseng* contact parameters was obtained as follows:

$$C_{S2} = 37.97 + 3.78S_{F2} + 4.7R_{F2} + 3.08S_{E2} + 0.85R_{F2}S_{E2} + 0.475{S_{F2}}^2 - 0.3125{S_{E2}}^2 \quad (5)$$

Table 5

Analysis of variance (ANOVA) for Laterite-*P. notoginseng* parameter experiments

Source of Variance	Sum of Squares (SS)	Degrees of Freedom (df)	Mean Square (MS)	F	P
Model	556.81	14	39.77	422.05	< 0.0001
C_{R2}	0.1408	1	0.1408	1.49	0.245
S_{F2}	171.01	1	171.01	1814.67	< 0.0001
R_{F2}	265.08	1	265.08	2812.93	< 0.0001
S_{E2}	114.08	1	114.08	1210.61	< 0.0001
$C_{R2}S_{F2}$	0.4225	1	0.4225	4.48	0.0558
$C_{R2}R_{F2}$	0.09	1	0.09	0.955	0.3477
$C_{R2}S_{E2}$	0.01	1	0.01	0.1061	0.7502
$S_{F2}R_{F2}$	0.04	1	0.04	0.4245	0.527
$S_{F2}S_{E2}$	0.01	1	0.01	0.1061	0.7502
$R_{F2}S_{E2}$	2.89	1	2.89	30.67	0.0001
C_{R2}^2	0.4033	1	0.4033	4.28	0.0608
S_{F2}^2	1.2	1	1.2	12.77	0.0038
R_{F2}^2	0.0208	1	0.0208	0.2211	0.6467
S_{E2}^2	0.5208	1	0.5208	5.53	0.0367
Lack of Fit	0.9242	10	0.0924	0.8944	0.6354
Total	557.94	26			

Analysis of variance (*ANOVA*) was conducted on the Box-Behnken experimental results for the lateritic soil–65Mn steel contact parameters, and the results are presented in Table 6. After removing non-significant terms with P > 0.05 from the analysis, the final prediction model for the sliding distance C_{S3} under the lateritic soil–65Mn steel contact parameters was obtained as follows:

$$C_{S3} = 407 - 3.5S_{F3} - 162.42R_{F3} - 80.08S_{E3} - 33.5S_{F3}R_{F3} - 27.5R_{F3}S_{E3} + 34.38{R_{F3}}^2 + 27.63{S_{E3}}^2 \quad (6)$$

Table 6

Experimental design and results for Laterite—65Mn contact parameter calibration

Source of Variance	Sum of Squares (SS)	Degrees of Freedom (df)	Mean Square (MS)	F	P
Model	4.12E+05	14	29395.45	1014.36	< 0.0001
C_{R3}	65.33	1	65.33	2.25	0.1591
S_{F3}	147	1	147.00	5.07	0.0438
R_{F3}	3.17E+05	1	3.17E+05	10923.3	< 0.0001
S_{E3}	76960.08	1	76960.08	2655.7	< 0.0001
$C_{R3}S_{F3}$	1.0000	1	1.0000	0.0345	0.8557
$C_{R3}R_{F3}$	12.25	1	12.25	0.4227	0.5278
$C_{R3}S_{E3}$	6.25	1	6.25	0.2157	0.6507
$S_{F3}R_{F3}$	4489	1	4489	154.9	< 0.0001
$S_{F3}S_{E3}$	9.0000	1	9.0000	0.3106	0.5876
$R_{F3}S_{E3}$	3025	1	3025	104.39	< 0.0001
C_{R3}^2	0.3333	1	0.3333	0.0115	0.9164
S_{F3}^2	3.0000	1	3.0000	0.1035	0.7532
R_{F3}^2	6302.08	1	6302.08	217.47	< 0.0001
S_{E3}^2	4070.08	1	4070.08	140.45	< 0.0001
Lack of Fit	291.75	10	29.18	1.04	0.5844
Total	4.12E+05	26			

Analysis of Simulation Results and Optimal Combination of Contact Parameters

Quadratic multiple regression fitting and analysis of variance (*ANOVA*) were performed on the experimental data of the three contact interfaces using Design-Expert software. The ANOVA results revealed significant interaction effects among the factors, and 3D response surfaces were plotted for the factors with significant interactions, as shown in Figure 13.

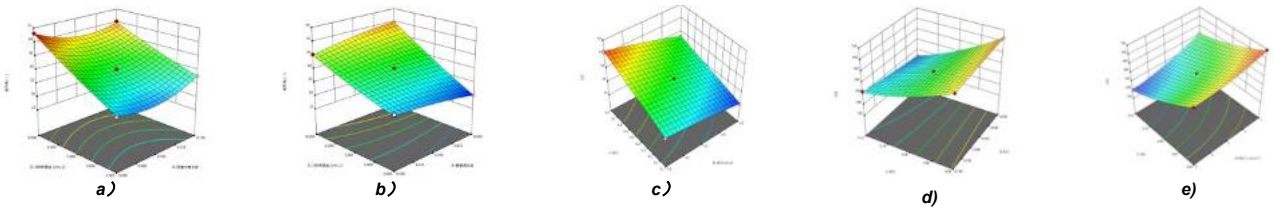


Fig. 13 – 3D response surface of significant factors on C_S

The regression models were solved via Design-Expert optimization, targeting the experimental values: a lateritic soil angle of repose of 41.2°, a mixture collapse angle of 45.2°, and a natural sliding distance of 423 mm. After simulation verification (Figure 14), the parameter combinations closest to the measured data were selected as optimal solutions. For the lateritic soil–lateritic soil interface, the optimal parameters were a rolling friction coefficient of 0.287 and a JKR surface energy of 5.302 J/m², with non-significant factors (static friction coefficient 0.575, coefficient of restitution 0.11) set to average experimental values. For the lateritic soil–*P. notoginseng* interface, the optimal parameters were: coefficient of restitution 0.157, coefficient of static friction 0.482, coefficient of rolling friction 0.124, and JKR surface energy 4.101 J/m². For the lateritic soil–65Mn steel interface, the optimal parameters were a coefficient of static friction of 0.42, a coefficient of rolling friction of 0.09, and a JKR surface energy of 3.806 J/m², with the non-significant coefficient of restitution set to 0.13.

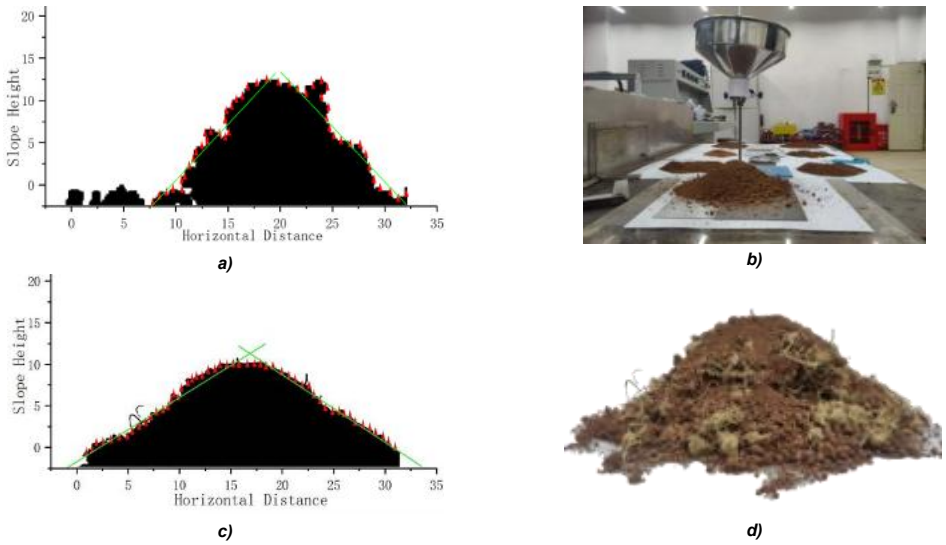


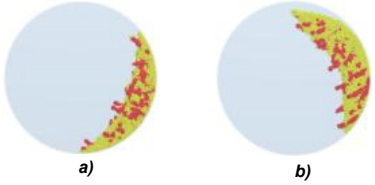
Fig. 14 – Comparison between Simulation Results and Physical Experimental Results

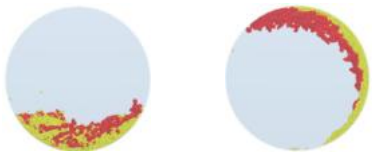
a) Binarization Processing of Simulation Results; b) Physical Experiment of Laterite Accumulation; c) Binarization Processing of Physical Collapsing Test; d) Mixture Collapsing Test

Interactive Simulation Validation

Dynamic Bench-Test Validation

A drum-test simulation based on the discrete element method (DEM) was conducted using EDEM. As shown in Fig. 15, the 65Mn steel drum had a diameter of 300 mm and a height of 80 mm and was uniformly filled with a mixture of *P. notoginseng* and lateritic soil. Three comparative tests were conducted at drum rotational speeds of 60, 90, and 120 r/min, with rotational speed as the only variable. After each simulation, four representative stages were compared: initial material lifting, critical slippage, the first complete circulation cycle, and stable dynamic flow. The analysis included measuring the tangential angle between the material bed and the inner drum wall at the three-quarter lifting position; recording the time from initial lifting to critical slippage; comparing the binarized contours obtained during the first circulation cycle with those from the physical test at the corresponding time point; and measuring the material-distribution length during stable flow to compare it with the stratification observed in the physical tests.





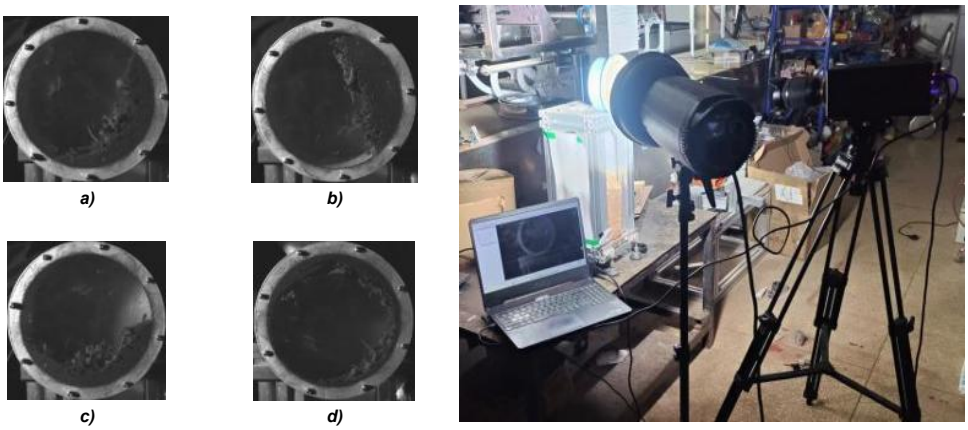
c) d)

Fig. 15 – Four key moments of the mixture

a) initial material lifting; b) critical slippage; c) the first complete accumulation cycle; d) stable dynamic flow

The motion of the materials inside the drum was recorded using a high-speed imaging system, as shown in Fig. 16. The drum dimensions and material properties were consistent with those used in the simulation model.

Tests were conducted at drum rotational speeds of 60, 90, and 120 r/min. Images of the material behavior at four representative stages were captured, and a quantitative comparison between the physical tests and simulation results is presented in Table 12. The relative error in the initial material-lifting angle was 4.33%, the relative error in the time from initial lifting to critical slippage was 4.06%, the contour-overlap rate during the first circulation cycle was 93.3%, and the relative error in the material-distribution length during the stable-flow stage was 2.79%.



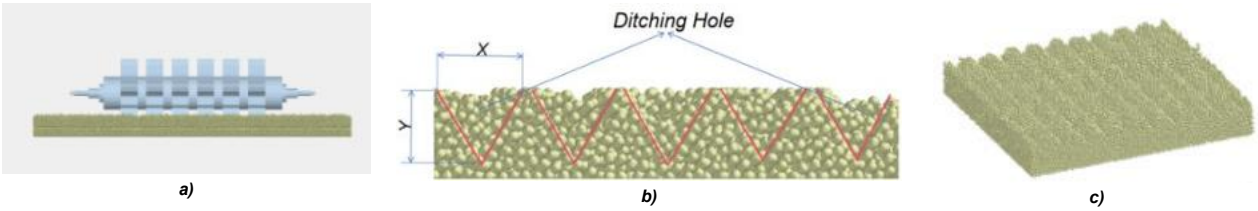
a) b) c) d) e)

Fig. 16 – Physical rotary-drum experiment

a) initial material lifting; b) critical slippage; c) first complete accumulation cycle; d) stable dynamic flow; e) high-speed image acquisition

Field validation test

A discrete element simulation of the ditching operation was conducted using EDEM, as shown in Fig. 17. The soil bin measured 2.0 m in length, 1.5 m in width, and 0.4 m in height. With the forward speed of the ditching tool as the only variable, three comparative simulations were conducted at 3, 9, and 15 m/min. The simulation used the optimized physical properties of the lateritic soil and the tool–soil contact parameters determined in the preceding study. After each simulation, the top diameter of the ditching hole, *x*, and the hole depth, *y*, were measured consistently.



a) b) c)

Fig. 17 – Ditching Simulation

a) Ditching Simulation; b) Simulation Results and Measurement Principle; c) Soil Mass After Ditching

A field ditching test was conducted using a pitting roller with a length of 842 mm, a shaft diameter of 220 mm, and a tooth height of 50 mm, as shown in Fig. 18.



a) b)

Fig. 18–Results of Field Experiment

a) Field ditching result; b) Field test

The forward speed of the implement was set at three levels: 3, 9, and 15 m/min. After each test, the top diameter of the pit, *x*, and the pit depth, *y*, were measured at five randomly selected locations, and the mean values were calculated. The mean relative errors between the simulated and field-measured values were 3.52% for the pit-top diameter and 4.28% for the pit depth. The comparison between the simulation and physical-test results is presented in Table 7.

Table 7

Comparison of simulation and physical-test results

Operating condition	Evaluation parameter	Simulated result	Measured result	Relative error
Drum speed at 60 r/min; implement speed at 3 m/min.	Initial material-lifting angle [°]	42.8	44.7	4.27%
	Time to critical slippage [ms]	124	128	3.13%
	Material-distribution length during stable flow [mm]	565	550	2.72%
	First complete accumulation stage [mm]	-	-	7.23%
	Pit-top diameter [mm]	36.6	34.3	3.79%
	Pit depth [mm]	41.8	40.2	3.98%
Drum speed at 90 r/min; implement speed at 6 m/min.	Initial material-lifting angle [°]	40.3	42.2	4.50%
	Time to critical slippage [ms]	179	187	4.28%
	Material-distribution length during stable flow [mm]	659	642	2.65%
	First complete accumulation stage	-	-	6.18%
	Pit-top diameter [mm]	36.2	34.5	2.86%
	Pit depth [mm]	40.8	39.2	4.08%
Drum speed at 120 r/min; implement speed at 9 m/min.	Initial material-lifting angle [°]	36.3	37.9	4.22%
	Time to critical slippage [ms]	198	208	4.76%
	Material-distribution length during stable flow [mm]	754	732	3.00%
	First complete accumulation stage	-	-	6.68%
	Pit-top diameter [mm]	34.6	33.3	3.90%
	Pit depth [mm]	38.4	36.6	4.79%

CONCLUSIONS

Three Box-Behnken experiments were conducted to systematically evaluate the relationships between contact parameters and the response variables (C_{S1}, C_{S2}, C_{S3}). The significant factors were identified as follows: R_{F1} and S_{E1} for C_{S1}; S_{F2}, R_{F2}, and S_{E2} for C_{S2}; and R_{F3} and S_{E3} for C_{S3}.

Response surface analysis was then performed using C_{S1}, C_{S2}, and C_{S3} as the response variables to optimize the significant contact parameters associated with each response. The nonsignificant parameters were assigned the mean values obtained from the physical experiments. The optimal parameter combinations were determined as follows: S_{E1}=5.302 J/m², R_{F1}=0.287; S_{E2}=4.101 J/m², S_{F2}=0.482, R_{F2}=0.124; S_{E3}=3.806 J/m², S_{F3}=0.42, R_{F3}=0.09. The corresponding nonsignificant parameters were set to: C_{R1}=0.11, S_{F1}=0.575; C_{R2}=0.157; C_{R3}=0.13.

Comparison of the simulation and physical-test results showed a high degree of agreement under all test conditions, including different drum rotational speeds and implement forward speeds. The relative errors for all evaluated indicators, including pit depth and mixture behavior at four representative stages, were below 7.5%, with a maximum value of 7.23%. This close agreement confirmed the accuracy and reliability of the calibrated parameters used in the discrete element interaction model. The resulting model therefore provides a reliable parameter basis for subsequent simulation and optimization of the operating process of the *P. notoginseng* transplanting machine.

REFERENCES

[1] Aikins, K.A., Ucgul, M., Barr, J.B. (2021). Determination of discrete element model parameters for a cohesive soil and validation through narrow point opener performance analysis. *Soil and Tillage Research*, Vol 213, pp. 105123.

[2] Adajar, J.B., Alfaro, M., Desses, P. (2021). Calibration of discrete element parameters of crop residues and their interfaces with soil. *Computers and Electronics in Agriculture*, Vol 188, pp. 106340.

[3] Aikins, K. A., Ucgul, M., Barr, J. B. (2021). Determination of discrete element model parameters for a cohesive soil and validation through narrow point opener performance analysis. *Soil and Tillage Research*, Vol 213, pp. 105123.

[4] Bahrami, M., Naderi - Boldaji, M., Ghanbarian, D., Ucgul, M., Keller, T. (2020). Simulation of plate sinkage in soil using discrete element modelling: calibration of model parameters and experimental validation. *Soil and Tillage Research*, Vol 203, pp. 104700.

[5] Cundall, P.A., Strack, O.D.L. (1979). A discrete numerical model for granular assemblies. *Geotechnique*, Vol 29(1), pp. 47 - 65.

[6] Hang, C., Gao, X., Yuan, M.L. (2018). Discrete element simulations and experiments of soil disturbance as affected by the tine spacing of subsoiler. *Biosystems Engineering*, Vol 168, pp. 73 - 82.

[7] Liu, L. H., Liu, Y., Wang, F., Liu, S.L., Hu, H.Z., Zhang, W.S., Xin, W.F. (2017). Current situation and development suggestions of the Panax notoginseng industry in Yunnan (云南三七产业发展现状及发展建议). *China Journal of Modern Chinese Medicine*, Vol 19, pp. 1331 - 1335.

[8] Li, J. W., Tong, J., Hu, B., Wang, H.B., Mao, C.Y., Ma, Y.H. (2019). Calibration of discrete element simulation parameters for the interaction between heavy clay black soil with different moisture contents and soil - contacting components (不同含水率黏重黑土与触土部件互作的离散元仿真参数标定). *Transactions of the Chinese Society of Agricultural Engineering*, Vol 35(6), pp. 130 - 140.

[9] Liu, W. Z., Huang, X. J., Xu, Y., Li, H. L., Wan, J. L. (2025). Research on the cumulative deformation law and control of compacted red clay under dynamic wetting (动力湿化作用下压实红黏土累积变形规律与控制研究). *Chinese Journal of Geotechnical Engineering*, Vol 47(03), pp. 535 - 547.

[10] Shao, M. A., Wang, Q. J., Huang, M. B. (2006). Soil Physics (土壤物理学). *Beijing: Higher Education Press.*

[11] Shi, R.J., Dai, F., Zhao, W.Y., Zhang, F., Shi, L., Guo, J. (2022). Establishment of a discrete element flexible model for flax stalks and experimental verification of contact parameters (胡麻茎秆离散元柔性模型建立与接触参数试验验证). *Transactions of the Chinese Society for Agricultural Machinery*, Vol 53(10), pp. 146 - 155.

[12] Tang, J. (2023). The shape parameters of coal and gangue particles derived from 3D scanning. *Scientific Data*, Vol 10(1), pp. 1 - 7.

[13] Tian, X. L., Cong, X., Qi, J. T., Guo, H., Li, M., Fan, X. H. (2021). Parameter calibration of the discrete element model for corn straw - soil mixture in black soil area (黑土区玉米秸秆 - 土壤混料离散元模型参数标定). *Transactions of the Chinese Society for Agricultural Machinery*, Vol 52(10), pp. 100 - 108 + 242.

[14] Ucgul, M., Fielke, J. M., Saunders, C. (2015). Three - dimensional discrete element modelling (DEM) of tillage: accounting for soil cohesion and adhesion. *Biosystems Engineering*, Vol 129, pp. 298 - 306.

[15] Xing, J. J., Zhang, R., Wu, P., Zhang, X., Dong, X., Chen, Y., Ru, S. (2020). Parameter calibration of discrete element simulation model for latosol particles in Hainan tropical area (海南热区砖红壤颗粒离散元仿真模型参数标定). *Transactions of the Chinese Society of Agricultural Engineering*, Vol 36(5), pp. 158 - 166.

[16] Xiang, W., Wu, M. L., Lü, J. N., Quan, W., Ma, Lan, Liu, J. J. (2019). Calibration of simulation physical parameters of cohesive loam based on stacking test (基于堆积试验的黏壤土仿真物理参数标定). *Transactions of the Chinese Society of Agricultural Engineering*, Vol 35(12), pp. 116 - 123.

[17] Yang, K., Yang, L., Fan, W. (2019). Illumina - based transcriptomic analysis on recalcitrant seeds of Panax notoginseng for the dormancy release during the after - ripening process. *Physiologia Plantarum*, Vol 167(4), pp. 597 - 612.

[18] You, Q., Yang, Q. L. (2022). Effects of different drainage bodies on the growth of Panax notoginseng, soil nutrients and soil microorganisms in the root zone (不同排水体对三七生长、土壤养分及根区土壤微生物的影响). *Journal of Drainage and Irrigation Machinery Engineering*, Vol 40(9), pp. 959 - 965.

[19] Yunnan Provincial Administration for Market Regulation. (2020). DB53/T 055.3 - 2020 Panax notoginseng seedlings (三七种苗). *Kunming: Yunnan Provincial Administration for Market Regulation*.

[20] Yu, Q. X., Liu, Y., Chen, X. B., Sun, K., Lai, Q. H. (2020). Calibration and experiment of simulation parameters for Panax notoginseng seeds based on the discrete element method (基于离散元的三七种子仿真参数标定与试验). *Transactions of the Chinese Society for Agricultural Machinery*, Vol 51(02), pp. 123 - 132.

[21] Zeng, Z.W., Ma, X., Cao, X.L., Li, Z., Luo, X.. (2021). Application status and prospects of the discrete element method in agricultural engineering research (离散元法在农业工程研究中的应用现状和展望). *Transactions of the Chinese Society for Agricultural Machinery*, Vol 52(4), pp. 1 - 20.

[22] Zhang, R. F., Zhou, J. L., Liu, H., Shi, S., Wei, G. J., & He, T. F. (2022). Research on the calibration method of discrete element simulation parameters for the corn particle bonding model (玉米颗粒粘结模型离散元仿真参数标定方法研究). *Transactions of the Chinese Society for Agricultural Machinery*, Vol 53(Suppl 1), pp. 69 - 77.

[23] Zhao, J. W. (2022). Design and experiment of a pneumatic directional transplanting device for Panax notoginseng seedlings (气力式三七种苗定向移栽装置设计与试验). *Kunming University of Science and Technology.*

[24] Zhang, H.D., Tang, Z.X., Zhang, L.Y. (2025). Optimization of Discrete Elemental Simulation Parameters for Forest Panax pseudoginseng Plantation Red Soil Based on GA - BP - GA. *Journal of Agricultural Science and Technology*, Vol 27(9), pp. 120 - 130.

BODY CONDITION SCORING METHOD FOR JERSEY CATTLE BASED ON ME-POINTNEXT
/
基于 ME-PointNeXt 的娟姗奶牛体况评分方法

Zhenwei YU [1,2], Xiaolong SHI [1], Baotong LI [1], CI-Ren DUOJI [3], Ji ZHANG [1], Fuyang TIAN [*1,2]
[1] College of Mechanical and Electronic Engineering, Shandong Agricultural University, 271018, Tai'an/ China;
[2] Shandong Engineering Research Centre of Agricultural Equipment Intelligentization, 271018, Tai'an/ China;
[3] Tibet Nianxiongziji Animal Husbandry Co., Ltd., 857000 Rikaze/China
Tel:+86-15653812560; E-mail: fytian@sdau.edu.cn
Corresponding author: Fuyang Tian
DOI: https://doi.org/10.35633/inmateh-79-63

Keywords: *Jersey cattle; Body condition score; Segmentation model; Point cloud*

ABSTRACT
To address the impact of changes in dairy cow posture on intelligent body condition scoring, this study proposes a dairy cow body condition scoring model (ME-PointNeXt). Based on PointNeXt, this model incorporates a dynamic graph convolutional module at the global feature level; furthermore, a selective sequence block is added to the encoder's upper layers, improving the SA-FP architecture and enhancing the model's overall understanding of the structure. Using this model to segment the hindquarters of dairy cows, principal component analysis is performed via eigenvalue decomposition of the local neighbourhood covariance matrix. This enables the determination of edge point normal vectors and the calculation of surface curvature, thereby enabling the scoring of the cows' body condition. Experimental results show that the ME-PointNeXt model achieved an overall accuracy, mean precision, mean recall, and mean F1 score of 91.43%, 84.33%, 87.92%, and 90.74%, respectively, on the test set. Compared with PointNeXt, the ME-PointNeXt model achieved improvements of 2.72, 3.65, 4.13, and 4.19 percentage points in overall accuracy, average precision, average recall, and average F1 score, respectively. This study has significantly improved the efficiency of dairy cow body condition scoring, ensuring accuracy whilst reducing the workload, and can provide technical support for non-contact dairy cow body condition scoring.

摘要
为解决奶牛姿态变化对体况智能评分的影响，本研究提出了一种奶牛体况评分模型（ME-PointNeXt）。该模型基于 PointNeXt，在全局特征层加入一个动态图卷积模块；并且在编码器高层中加入一个选择性序列块，改进了 SA-FP 结构，增强整体对结构的理解。利用该模型对奶牛尻部进行分割，通过计算局部邻域协方差矩阵的特征值分解实现主成分分析，进而确定边缘点法向量并计算表面曲率，对奶牛体况进行评分。试验结果表明，ME-PointNeXt 模型在测试集上的总体准确率、平均交互比、平均准确率与平均 F1 分数分别达到 91.43%、84.33%、87.92%和 90.74%。相较于 PointNeXt，ME-PointNeXt 的总体准确率、平均交互比、平均准确率与平均F1 分数分别提升了2.72、3.65、4.13 和4.19 个百分点。本研究显著的提高了奶牛体况的评分效率，在降低工作量的同时保证了精度，可为非接触式奶牛体况评分提供技术支持。

INTRODUCTION
As the scale of dairy cattle farming in China continues to expand *(Zhang et al., 2024)*, the sector is undergoing a transition towards grain-saving and high-efficiency practices, facing significant challenges. Body condition score is a key indicator for assessing animal welfare and herd management; it is closely linked to the health *(Zhao et al., 2025)* and metabolic status *(Sadiq et al., 2017)* of dairy cattle, and provides a reliable basis for formulating feed rations *(Yu et al., 2026).* Body condition scores enable the identification of cows that are either overweight or underweight; formulating rations based on these scores ensures that cows of different body conditions receive appropriate diets. Consequently, body condition assessment is an indispensable part of the dairy farming industry *(Tian et al., 2025)*.

Currently, body condition scoring in dairy cattle is primarily carried out manually; however, due to the subjectivity of human assessment *(Feng et al., 2025)*, the reliability of the results is poor, and the evaluation process is time-consuming and labour-intensive, relying heavily on the assessor's experience *(Huang et al., 2024)*.

Furthermore, the assessment process can induce stress responses in the cattle *(Li et al., 2025)*, making measurement difficult and leading to significant errors *(Fan et al., 2020)*. With the gradual adoption of machine vision and deep learning technologies in the livestock industry *(Qi et al., 2023)*, it is now possible to utilise visual detection techniques to capture conformation characteristics and establish intelligent assessment models linking these to body condition *(Sun et al., 2025)*. Practical evidence indicates that machine vision has already achieved significant success in detecting dairy cow conformation characteristics and behaviour *(Xie et al., 2022)*, offering a new direction for research into dairy cow body condition scoring. *Zhao et al., 2021,* used EfficientNet to identify the structural features of dairy cows and assess their body condition; EfficientNet achieved a recognition accuracy of 73.12% and an average recognition speed of 3.441 s/f, outperforming models such as MobileNet-V2, XceptionNet, and LeNet-5. *Jiang et al., 2025,* incorporated the GSConv module into the YOLOv8s model to enable automatic localisation and detection of the dorsal region of dairy cows, thereby facilitating body condition scoring and individual identification. The improved model achieved accuracy rates of 93.9% and 92.2% for body condition scoring and individual identification, respectively, representing increases of 1.9 and 4.5 percentage points compared to single-task models. *Shi et al., 2023,* proposed a method for body condition scoring in dairy cows based on attention-guided 3D point cloud feature extraction, which incorporates an attention-guidance mechanism into PointNet. This scoring model achieved accuracy rates of 0.49, 0.80, and 0.96 within point deviation ranges of 0, 0.25, and 0.50, respectively, yielding satisfactory estimation results. *Wei et al., 2025,* utilised 3D reconstruction to recreate the spatial morphology of sheep, followed by training a PointNet++ model, achieving relative errors of 3.63%, 1.14%, and 3.57% for chest width, rump height, and body length, respectively. The aforementioned methods all localise the target's entire torso; however, the target's posture and movement can influence the shooting angle, leading to the loss of some key information.

To address the aforementioned issues, this study segments the hindquarters of dairy cows based on 3D point cloud imagery, extracting key regions within a small area to obtain accurate body condition scores. This study proposes the ME-PointNeXt model for dairy cow body condition scoring, which primarily builds upon the PointNeXt model by incorporating a dynamic convolutional module to enhance local edge detection capabilities; simultaneously, selective sequence blocks are introduced at the higher layers of PointNeXt to strengthen the model's global consistency. Finally, the curvature is calculated based on the edge points segmented by the ME-PointNeXt model, and a body condition score is derived.

MATERIALS AND METHODS

Dataset construction

Design of a Contactless Data Collection Device for Cattle

This study developed a non-contact point cloud data acquisition device for dairy cows. From the moment a cow enters the acquisition channel until it exits, the device can capture three-dimensional point cloud data from two different rear angles, thereby enabling intelligent body condition scoring. The system comprises a depth camera (Azure Kinect DK), a power supply, a motion controller, and a measurement channel. To capture depth images of the cow's back and hindquarters, the Arzue Kinect DK depth camera is positioned 2.6 m above the ground and at a 45° downward angle 2.4 m above the ground, respectively. This study employs a single-channel data acquisition design to prevent crowding and congestion of cows within the channel, ensuring that cows maintain a normal standing posture, thereby guaranteeing the validity and reliability of the collected data. The structure of the data acquisition system is shown in Figure 1.



Fig. 1 - Data Acquisition Structure

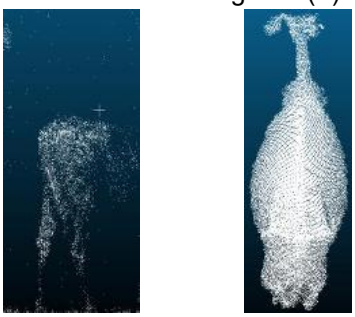
1 – Rear-facing Azure Kinect DK depth camera; 2 – Top Azure Kinect DK depth camera; 3 – Drive shaft; 4 – Steel wire

Test data acquisition

Data collection took place from 25 July to 1 August 2025 at Tibet Nianxiongziji Livestock Co., Ltd. in Zaxi Village, Gadong Town, Bailang County, Shigatse City, Tibet Autonomous Region. The test subjects were Jersey cows with a lactation period of 100 to 300 days. To minimise stress reactions in the cows and their impact on milk yield, data collection commenced after milking. Collection took place between 10:00 and 14:00, and between 15:00 and 19:00. A total of 2,280 point cloud datasets were collected from 104 cows; after removing highly similar datasets, 342 point cloud datasets remained.

Dataset creation

By comparing the point cloud images captured at the tail root and on the back, it was found that the point cloud image at the tail root contained a significant amount of noise and failed to capture key information in full. Consequently, the point cloud image from the back was ultimately selected as the dataset and divided into training, test and validation sets in a ratio of 8:1:1. The point cloud image at the tail root is shown in Figure 2(a), whilst the point cloud image of the back is shown in Figure 2(b).



(a) (b)

Fig. 2 - Point cloud image of the cow's back and hindquarters

The criteria for assessing a dairy cow's body condition are typically based on body fat reserves. These reserves are primarily evident in the area between the hip bones and the ischial tuberosities, with the rump being the most distinctive feature; the degree of contour variation in this region is useful for assessing the cow's fat reserves and health status. The region of interest is shown in Figure 3.

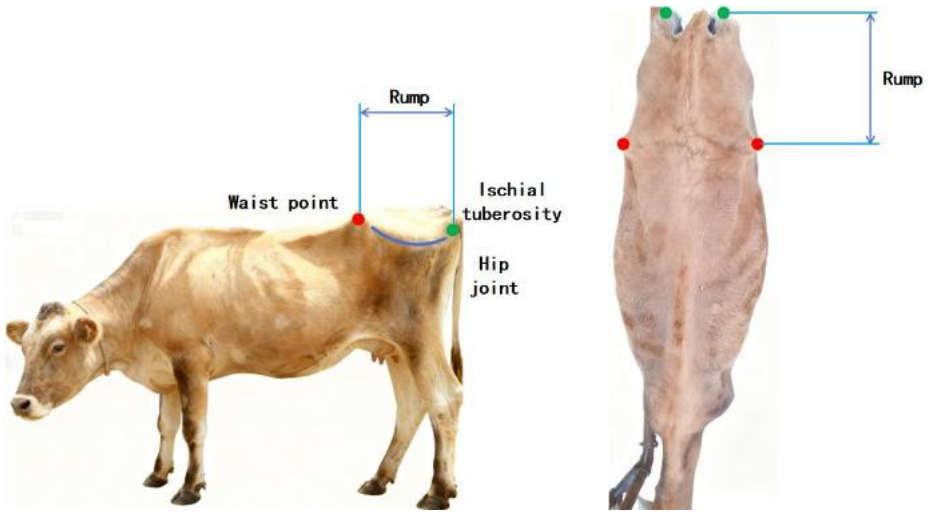
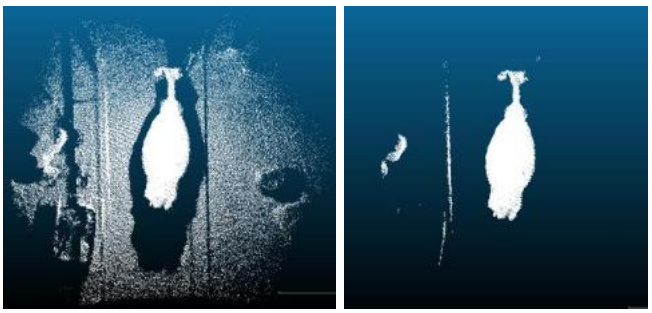


Fig. 3 - Region of interest

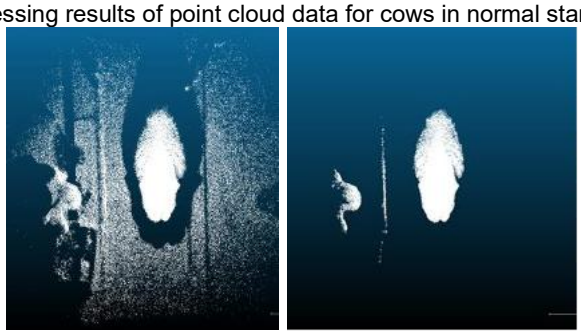
When processing the dataset, CloudCompare was selected to perform radius filtering and statistical filtering as pre-processing steps, followed by manual segmentation and annotation of the filtered dataset. The results of the point cloud data pre-processing are shown in Figure 4.

(1) Statistical filtering. By setting a 30-neighbour radius and a threshold of 1.0 based on the density of the point cloud data, high-frequency noise can be effectively reduced whilst retaining key structural information.

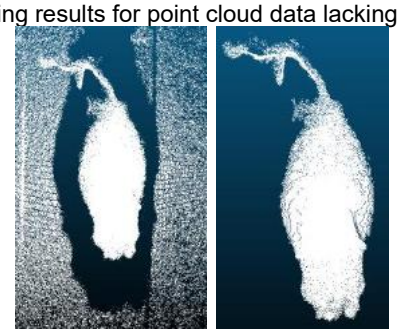
(2) Radius filtering: The radius was set to 15, requiring at least five neighbouring points within the radius. Points where the density within the neighbourhood fell below a specific threshold were treated as outliers and removed. This approach ensures the density of the point cloud after downsampling whilst maximising the retention of the basic features of the cows' hindquarters, and also improves the speed of data processing.



(a) Pre-processing results of point cloud data for cows in normal standing posture



(b) Preprocessing results for point cloud data lacking the cow's head



(c) Pre-processing results of point cloud data from the head of an abnormally standing dairy cow

Fig. 4 - Pre-processing results of point cloud data

Following the removal of duplicates and filtering, manual segmentation and annotation were carried out using CloudCompare. The body part annotated was the rear end of the cow, labelled as “back”; this label is automatically generated once each point cloud image has been annotated. The results of the manual segmentation are shown in Figure 5. To prevent data leakage and overestimation of performance, random noise points were added to the point cloud images during the division of the dataset.

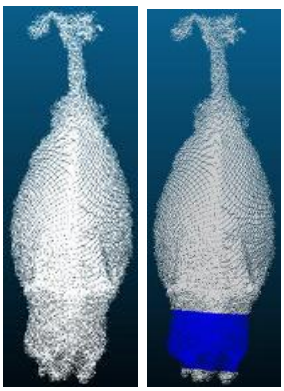


Fig. 5 - Manual segmentation results

Cattle Body Condition Scoring Model

Compared to PointNet, PointNeXt *(Qian et al., 2020)* modifies the training strategy by adopting a hierarchical multi-scale architecture and utilising a feature pyramid, whilst applying local neighbourhood aggregation to the edge features on the cow’s back; this is more conducive to improving the accuracy of the cow’s body condition score. The model applied scaling and rotation enhancements to the data; jittering and randomised data point removal were employed to enhance the model’s generalisation ability.

By introducing slight variations or omissions, the training data was made more diverse, thereby reducing the model's overfitting to data details.

However, due to the model's lack of sensitivity to edge details and its inability to interact with global information, it proved insensitive to information regarding the cows' backs and exhibited low feature utilisation, rendering it incapable of intelligently scoring the cows' body condition. Consequently, a dynamic graph convolutional module *(Wang et al., 2019)* and a sequence block *(Ding et al., 2023)* were incorporated into PointNeXt to enhance edge point perception and global information interaction, ensuring the model could capture structural changes between points and edge features.

ME-PointNeXt

ME-PointNeXt consists of an input head, an encoder, a global feature layer, a decoder and an output head. To address PointNeXt's limited perception of local edge information, a dynamic graph convolutional module is introduced in the global feature layer. By determining the convolutional receptive field through dynamic neighbourhood configuration and constructing geometric convolutional inputs via differential edge features, this enhances the perception of surface curvature changes and boundary details on the cow's hindquarters. The neighbourhood is shifted from geometric proximity to semantic proximity, thereby improving the ability to represent local structures. Furthermore, to mitigate the attenuation and fragmentation of high-level semantic information during multi-level propagation, selective sequence blocks are introduced as global feature interaction modules in the 3rd and 4th Set Abstraction stages following downsampling in the encoder. Relevant selective parameters are generated via point-level linear projection, and state recursion is employed to model long-range dependencies in the sequence dimension, thereby enhancing the global consistency of high-level features in the encoder. The structure of the ME-PointNeXt model is shown in Figure 6.

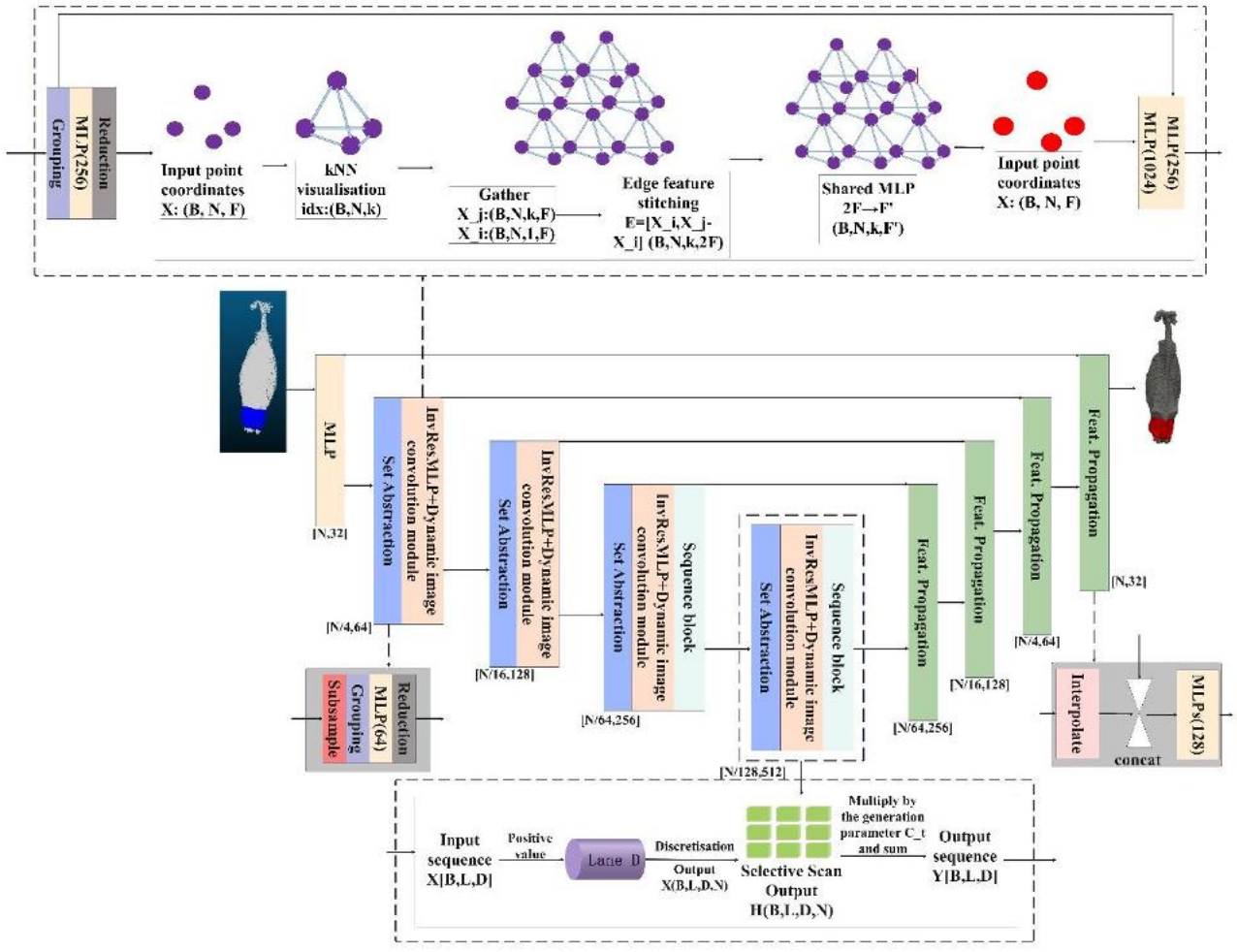


Fig. 6 - ME-PointNeXt Model Architecture

Dynamic image convolution module

To enhance the model's ability to capture global structure and cross-region semantic consistency in the point cloud of a dairy cow's hindquarters, a Dynamic Graph CNN (DGCNN) module has been introduced into the global feature layer of PointNeXt. This module constructs a k-NN dynamic adjacency graph in the feature space to strengthen global semantic representation and robustness. Whilst maintaining the translation invariance of the hindquarters point cloud, the dynamic graph convolutional module effectively mitigates feature instability in the hindquarters region caused by pose variations, sparse sampling or noise interference, thereby improving the consistency of the overall segmentation results and the ability to distinguish boundaries.

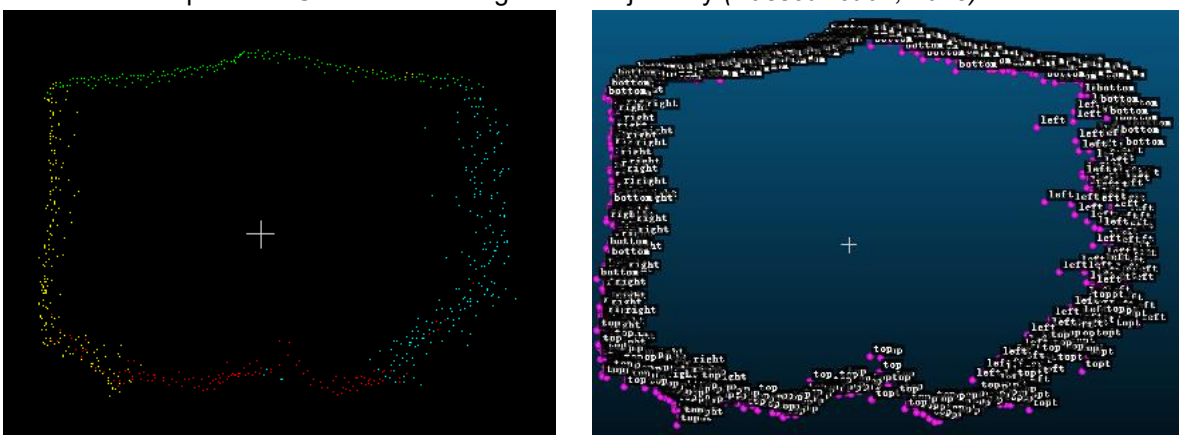
Sequence block

To enhance the model's ability to globally fuse point clouds of dairy cows' hindquarters across multiple scales and its adaptability to complex morphological variations, selective sequence blocks are introduced in the third and fourth Set Abstraction layers of PointNeXt. These sequence blocks establish inter-point relationships through projection and employ grouped vector attention to apply weighted groupings to feature channels, thereby facilitating more accurate capture of morphological contours and boundary transition features in the large receptive field stage. The model can strengthen feature interactions and contextual consistency at a higher semantic level, improving robustness against noise, occlusion, and variations in point density, and consequently enhancing the performance of rump segmentation.

Curvature calculation

In this study, a computational programme was developed to perform principal component analysis on edge feature points on the hindquarters of dairy cows. For each point in the point cloud of a dairy cow's rump, the method calculates the three-dimensional covariance matrix of its k nearest neighbours and performs an eigenvalue decomposition using the formula $k = \frac{\lambda 1}{\sum \lambda}$. Through this eigenvalue decomposition, the eigenvector corresponding to the smallest eigenvalue is defined as the surface normal vector of the rump, and the spatial curvature of the rump's edge is calculated. These quantitative geometric features, which are insensitive to changes in posture, provide robust input data for the subsequent development of an objective and efficient body condition scoring model for dairy cows. The body condition score is calculated using the formula $BCS = -15.0 \times K + 3.55$, where *K* represents the spatial curvature of the rump edge points. These quantitative geometric features are unaffected by changes in body posture, providing reliable input data for the subsequent development of an objective and efficient body condition scoring model for dairy cows. Figure 7 illustrates the process of extracting edge points and calculating normal vectors.

Manual scoring involves professional and experienced assessors conducting body condition scoring on the same dairy cows. Whilst the Juan Shan cows are being assessed using the scoring equipment, five assessors also carry out manual body condition scoring on the cows at close range. Where the maximum difference in scores between assessors does not exceed 0.50 points, the arithmetic mean of the individual assessors' scores is taken as the cow's manual reference body condition score; where the maximum difference exceeds 0.50 points, the Juan-Shan cow is re-assessed and the final result is determined through consultation amongst the assessors. For this type of classification analysis, where the category intervals are 0.25 points, the mean is rounded to the nearest 0.25 points. When BCS is treated as a continuous variable, the intraclass correlation coefficient (ICC) can be calculated; when treated as an ordered scale, the weighted Kappa coefficient can be reported. BCS involves a degree of subjectivity *(Vasseur et al., 2013)*.



(a) Edge point extraction (b) Edge Point Normal Vector Calculation

Fig. 7 - Edge Point Extraction and Normal Vector Calculation

Evaluation criteria

To evaluate the algorithm's performance in segmenting different body parts, this study employed mean Intersection over Union (mIoU), mean Accuracy (mAcc), Overall Accuracy (OA) and mean F1 (mF1) as evaluation metrics. Acc stands for Accuracy, which reflects whether the points predicted by the model for each label fall within the cow's hindquarters; IoU stands for Intersection over Union, which reflects the accuracy of semantic segmentation for each label; after calculating the Intersection over Union (IoU) and accuracy for each label, the mean Intersection over Union (mIoU) and mean Accuracy (mAcc) are obtained; Overall Accuracy (OA) refers to the proportion of correctly predicted samples out of the total number of samples; mF1 refers to the average of the F1 scores across all categories.

RESULTS

In a study examining the contour of a dairy cow's hindquarters, the characteristics of point cloud data were utilised to calculate the average curvature of the hindquarter point cloud, thereby assessing the contour of the hindquarters. A five-point scale is widely used for body condition scoring, with increments of 0.25 points. A score of 1.0 is the lowest, indicating that the cow is excessively thin, whilst a score of 5.0 is the highest, indicating that the cow is excessively fat.

Point cloud segmentation results

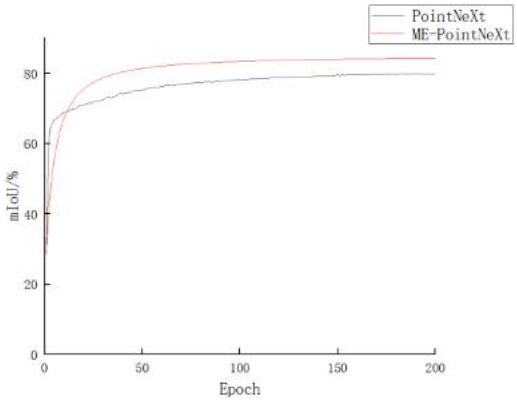
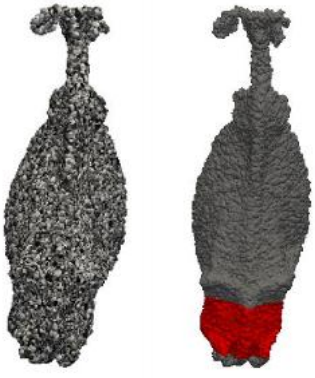


Fig. 8 - Curve depicting the mIoU of the ME-PointNeXt model on the validation set for dorsal segmentation of dairy cows as a function of iteration count

Figure 8 illustrates the trend in the mIoU on the validation set as the number of training iterations increases during the training of the ME-PointNeXt model. In the initial stage, the mIoU increases rapidly with the number of training iterations, indicating that the model is effectively learning the most fundamental and significant patterns from the data. Finally, around 150 iterations, the mIoU levels off and stabilises at approximately 84.33 per cent, suggesting that the model's performance is gradually converging. After 200 iterations, the model converges, and the mIoU on the validation set remains virtually unchanged.

Figure 9 presents a comparison of the model's segmentation results: (a) shows the unlabelled point cloud predicted by the ME-PointNeXt model, and (b) shows the point cloud labelled by the ME-PointNeXt model. The point cloud results demonstrate that incorporating the dynamic convolutional module and selective sequence blocks into PointNeXt enhances the model's ability to extract edge features. The red areas indicate where the rump should be cut. Figure 10 displays the contour map of edge points extracted from the rear of a cow.



(a) (b)

Fig. 9 - Comparison of Model Segmentation Results

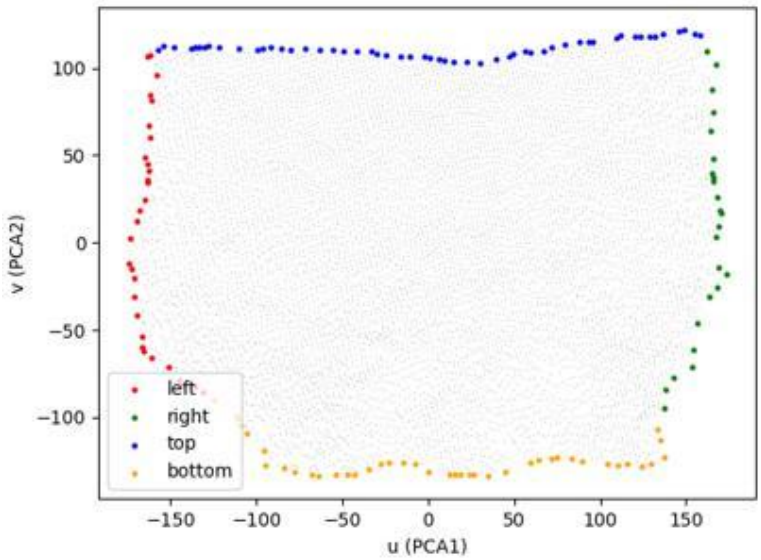


Fig. 10 - Contour diagram extracted from the edge of the cow's hindquarters

A statistical analysis of the segmentation results was conducted using Overall Accuracy (OA), Mean Intersection over Union (mIoU), Mean Accuracy (mAcc), and Mean F1 score as evaluation metrics. The segmentation results for the dorsal region of dairy cows are shown in Table 1.

Table 1

Comparison of partitioning results across test sets for different models

Method	OA/%	mIoU/%	mAcc/%	mF1/%
PointNet	79.65	56.83	69.72	66.49
PointNet++	88.77	80.37	82.83	81.90
PointNeXt	88.71	80.68	83.79	85.55
ME-PointNeXt	91.43	84.33	87.92	89.74

Table 1 presents the quantitative comparison results for PointNet, PointNet++, PointNeXt and ME-PointNeXt on the segmentation task using the test set. As shown in Table 1, because PointNet relies primarily on global feature aggregation, its ability to capture local geometric details and boundaries is limited, resulting in an mIoU of only 56.83%. Following the introduction of hierarchical local neighbourhood modelling, PointNet++ demonstrated a significant improvement in segmentation performance (OA 88.77%, mIoU 80.37%, mF1 81.90%), indicating that local structural features are crucial for this task. Building upon this, PointNeXt further optimises the backbone network and feature extraction methods, achieving further improvements in metrics such as mIoU and mF1 (mIoU 80.68%, mF1 85.55%). In contrast, ME-PointNeXt achieves the best performance across all evaluation metrics, with OA, mIoU, mAcc, and mF1 reaching 91.43%, 84.33%, 87.92%, and 89.74%, respectively. Compared to PointNeXt, ME-PointNeXt's OA, mIoU, mAcc, and mF1 improved by 2.72, 3.65, 4.13, and 4.19 percentage points, respectively, indicating that the proposed improvements effectively enhance the model's ability to recognise key regions and improve prediction consistency, thereby significantly increasing overall segmentation accuracy.

Ablation Test

To verify the impact of different improvement methods on model performance, ablation experiments were designed using PointNeXt as the baseline model. The effectiveness of the improvement methods was assessed using different modules; the experimental results are shown in Table 2.

Table 2

Melting test results

PointNeXt	Dynamic image convolution module	Sequence block	OA/%	mIoU/%	mAcc/%	mF1/%
√			88.71	80.68	83.79	85.55
√	√		89.35	84.72	87.10	89.40
√		√	88.89	82.44	85.83	88.20
√	√	√	91.43	84.33	87.92	89.74

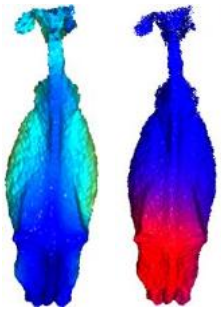
Nota: "√" indicates the adoption of this module; "×" indicates not using this module

As shown in Table 2, adding dynamic graph convolutions to the baseline network effectively improved the model's recognition performance, with the overall accuracy, average precision, average recall, and average F1 score increasing by 0.64, 4.04, 3.31, and 2.85 percentage points, respectively.

This indicates that the use of this convolutional module effectively enhances the model's ability to detect local edge points, helping the network to extract key information from the rear of the cow more effectively. Following the incorporation of the selective sequence block, the overall accuracy, mIoU, average precision and average F1 score increased by 0.18, 1.76, 2.04 and 1.65 percentage points respectively. This indicates that the use of this sequence block helps to enhance global consistency and mitigate the fragmentation of local predictions. Building upon PointNeXt, by incorporating a dynamic graph convolutional module into the global feature layer and adding a selective sequence block to the downsampling layer of the encoder, results in increases of 2.72, 3.65, 4.13, and 4.19 percentage points in overall accuracy, average interaction ratio, average precision, and average F1 score, respectively. This indicates that the simultaneous incorporation of these two modules alongside the sequence block not only enhances sensitivity to curvature changes and boundary regions but also strengthens cross-regional semantic consistency and the ability to model long-range dependencies.

Heatmap visualization

Given the complex nature of the environment in which dairy cows are photographed, heatmaps were selected to visualise the model's recognition performance. A comparison of the heatmaps for the model before and after improvement is shown in Figure 11. As can be seen from Figure 11a, the heatmap of the pre-improvement model shows a relatively dispersed distribution when recognising the rear end of a dairy cow, focusing not only on the key area but also on the middle of the torso and the abdomen. Figure 11b, on the other hand, displays the heatmap visualisation results of the ME-PointNeXt model, which is an improvement based on the PointNeXt model. Following the improvement, the high-response areas are highly concentrated in the hindquarters region, whilst thermal responses in non-target areas are significantly suppressed, markedly reducing activation responses in irrelevant regions.



(a) (b)

Fig. 11 - Heatmap of the model before and after improvement

Discussion

This study employs a method combining 3D data acquisition with deep learning technology to propose a body condition scoring method for dairy cows based on point cloud segmentation. As shown by the comparative results in Figure 12, the improved model is able to accurately capture the rump region of the cow, with a small prediction error. However, the accuracy of the segmentation model has a certain impact on the accuracy of the body condition scoring. Deviations in the segmentation model, particularly segmentation errors in the hindquarters of dairy cows, can lead to prediction errors and inaccuracies in curvature calculations, resulting in significant discrepancies between automatic and manual body condition scores. For example, the incorrect prediction of the critical hindquarter region in Figure 13 led to an erroneous body condition score, thereby reducing the model's reliability. Although the segmentation model proposed in this study has seen a significant improvement in accuracy, it still has shortcomings and considerable room for optimisation. Future work could focus on refining the neural network architecture to improve segmentation accuracy, thereby providing reliable data support for the formulation of dairy cow feed.

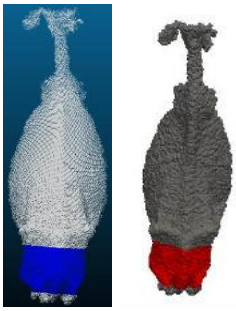


Fig. 12 - Comparison of Manual Point Cloud Annotation and ME-PointNeXt Model Segmentation

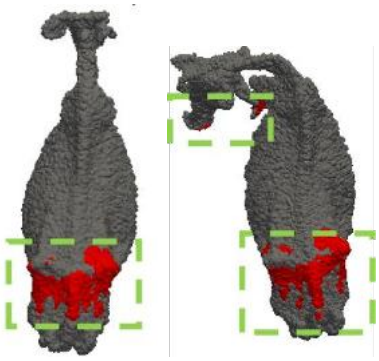


Fig. 13 - Typical Examples of Segmentation Errors

Table 3 presents data on the correlation between the ME-PointNeXt model's automated scores and manual scores. With ten Jersey cows assessed simultaneously, the discrepancy between the automated and manual scores was minimal, with inconsistencies observed in only two cows. This indicates that the method is suitable for assessing the body condition scores of dairy cows and validates the effectiveness of incorporating dynamic convolutional modules and selective sequence blocks into the PointNeXt model.

Table 3

Model scoring versus human scoring error

Cow number	Physical Condition Score	
	Smart Scoring	Manual scoring
20200314	3.25	3.25
20200722	4.00	4.00
20201105	3.25	**3.50**
20210130	3.50	3.50
20210518	4.25	4.25
20210909	3.75	3.75
20211224	4.00	**3.75**
20220214	4.25	4.25
20220607	3.75	3.75
20221031	3.50	3.50

To ensure the accuracy of the model for assessing the body condition score of dairy cows, this study employed the Mean Absolute Error (MAE), Root Mean Square Error (RMSE) and correlation coefficient (r) as performance metrics. For the same cattle shed, both manual scoring and model-based scoring were conducted simultaneously, with the results shown in Table 4. The mean absolute error, root mean square error and correlation coefficient were 0.15, 0.22 and 0.80 respectively, all of which indicate that the model-based scores show a high degree of consistency with the manual scores and are capable of accurately reflecting the actual body condition of the dairy cows.

$$MAE = \frac{1}{n}\sum_{i=1}^{n}\left|y_i - \hat{y}_i\right| \tag{1}$$

$$RMSE = \sqrt{\frac{1}{n}\sum_{i=1}^{n}\left(y_i - \hat{y}_i\right)^2} \tag{2}$$

$$r = \frac{\sum\left(y_i - \bar{y}\right)\left(\hat{y}_i - \bar{\hat{y}}\right)}{\sqrt{\sum\left(y_i - \bar{y}\right)^2 \sum\left(\hat{y}_i - \bar{\hat{y}}\right)^2}} \tag{3}$$

Here, n denotes the total number of samples; is the observed value for the *i-th* sample; is the predicted value for the *i-th* sample; is the arithmetic mean of all observed values; and is the arithmetic mean of all predicted values.

Table 4

Quantitative Error Analysis

Model	MAE	RMSE	r
E-PointNeXt	0.14	0.22	0.79

CONCLUSIONS

(1) By incorporating a dynamic convolutional module into the PointNeXt model, a point cloud segmentation model was proposed. Experimental results demonstrated that this model achieved higher overall accuracy and precision than the PointNeXt model when segmenting local point cloud data from the backs of dairy cows, thereby improving the segmentation accuracy of point cloud data from this region.

(2) By incorporating sequence blocks into the PointNeXt model, experiments have verified that this model demonstrates improved global interaction capabilities when extracting point cloud information from the rear of dairy cows, resulting in more accurate predicted point cloud edges. Compared to the PointNeXt model, this approach has improved the model's prediction accuracy.

(3) Building upon the point cloud segmentation results of the ME-PointNeXt model for the cow's back, an intelligent scoring system was applied to assess the cow's body condition, achieving high accuracy with minimal error. This validated the capability of the segmented point cloud data for body condition scoring.

ACKNOWLEDGEMENT

This study was funded by the Research Projects under the Shigatse Municipal Science and Technology Programme (RKZ2024ZY-03).

REFERENCES

[1] Ding, H., Dong, W., Mao, Q. (2023). Keyword Mamba: Spoken keyword spotting with state space models. *Computer Speech and Language*. Vol. 99, pp. 1-12.

[2] Fan, B., Xue, X., Li, M., Li, C. (2020). Production layout optimization of dairy farming in China: An empirical analysis based on comparative advantage (中国奶牛养殖生产布局优化研究——基于比较优势的实证分析). *Research of Agricultural Modernization*, Vol. 41, pp. 331-340.

[3] Feng, R., Li, C. (2025). Research on the level measurement and evolution characteristics of the green development of the dairy farming industry (奶牛养殖业绿色发展水平测度与演进特征研究). *Research of Agricultural Modernization*, Vol. 46, pp. 1-12.

[4] Guo, R. (2023). Effects of different dietary composition on the lactation performance and milk quality of perinatal cows. (不同日粮组成对围产期奶牛泌乳性能和如品质的影响). *Animal Breeding and Feed*, Vol.22, p. 8.

[5] Huang, J., Li, Y., Zhang, K., Zhang, J., Li, C., Meng, H. (2024). Leg tracking and lameness intelligent detection method for dairy cows based on occlusion environment (基于遮挡环境下的奶牛腿部跟踪与跛行智能检测方法). *Chinese Society of Agricultural Engineering*, Vol. 40, pp. 179-189.

[6] Jiang, H., Li, J., Fa, R., Zhang, G., Mao, W., Qiao, Y. (2025). Multi-task Learning-based Method for Simultaneous Dairy Cow Body Condition Scoring and Individual Identification (基于多任务学习的同步奶牛体况评分和个体识别方法). *Chinese Society for Agricultural Machinery*, Vol. 56, pp. 581-589.

[7] Li, Z., Sun H., Guo, Q., Zhang, H., Liu, H. (2025). Research progress on machine vision technology for non-contact body measurement of large livestock (机器视觉技术在大体型家畜无接触体尺测量中的研究进展). *Chinese Society of Agricultural Engineering*. Vol. 41, pp. 1-12.

[8] Qi, Y., Jiao, J., Bao, T., Wang, Z., Du, X. (2023). Cattle face detection algorithm in complex scenes using adaptive attention mechanism (基于自适应注意力机制的复杂场景下牛脸检测算法). *Chinese Society of Agricultural Engineering*, Vol. 39, pp.173-183.

[9] Qian, G., Li, Y., Peng, H., Mai, J., Hammoud, H. A. A. K., Elhoseiny, M., Ghanem, B. (2022). PointNeXt: Revisiting PointNet++ with Improved Training and Scaling Strategies. *Advances in neural information processing systems*, Vol. 35, pp. 1-13.

[10] Sadiq, M. B., Ramanoon, S. Z., Mossadeq, W. M. S., Mansor, R., SyedHussain, S. S. (2017). Association between Lameness and Indicators of Dairy Cow Welfare Based on Locomotion Scoring, Body and Hock Condition, Leg Hygiene and Lying Behavior. *Animals*, Vol. 7, p. 79.

[11] Shi, W., Dai, B., Shen, W., Sun, Y., Zhao, K., Zhang, Y. (2023). Automatic estimation of dairy cow body condition score based on attention-guided 3D point cloud feature extraction. *Computers & Electronics in Agriculture*, Vol. 206, p. 107666.

[12] Sun, S., Sun, X., Wang, C., Yuan, W., Wang, F. (2025). Sheep peripartum behavior recognition method based on improved YOLOv8n-pose (基于改进 YOLOv8n-Pose 的羊只围产期行为识别方法). *Chinese Society of Agricultural Engineering*, Vol, 41, pp. 258-268.

[13] Tian, F., Zhang, L, Zhang, J, Zhang, S., Soomro, S. A., Xiong, B., Shen, W., Song, Z., Yan, Y., Yu, Z. (2025). Cattle-ES3D: A spatiotemporal feature fusion method for detecting tachypnea and salivation behaviors in beef cattle. *Computers and Electronics in Agriculture*, Vol. 239, pp. 1-12.

[14] Vasseur, E., Gibbons, J., Rushen, J., Passillé de A.M. (2013) Development and implementation of a training program to ensure high repeatability of body condition scoring of dairy cows. *Journal of Dairy Science*, Vol. 96, pp. 4725-4737.

[15] Wang, Y., Sun, Y., Liu, Z., E, S. S. (2019). Dynamic Graph CNN for Learning on Point Clouds. *ACM Transactions on Graphics*, Vol. 38(5), p. 146.

[16] Wei, Y., Zhang, L., Yang, F., Jiang, X., Zhang, J., Zhu, L., Yu, M., Gong, M. (2025). Automatic measurement method of sheep body size based on 3D reconstruction and point cloud segmentation. *Computers and Electronics in Agriculture*, Vol. 239, pp. 1-15.

[17] Xie, Q., Zhou, H., Bao, J., Li, Q. (2022). Review on Machine Vision-based Weight Assessment for Livestock and Poultry (基于机器视觉的畜禽体质量评估研究进展). *Chinese Society for Agricultural Machinery*, Vol. 53, pp. 1-15.

[18] Zhao, K., Liu, X., Ji, J. (2021). Automatic Body Condition Scoring Method for Dairy Cows Based on EfficientNet and Convex Hull Feature of Point Cloud (基于 EfficientNet 与点云凸包特征的奶牛体况自动评分). *Chinese Society for Agricultural Machinery*, Vol. 52, pp. 192-201.

[19] Zhao, W., Du, X., Shi, Z. (2025) Driving mechanism for the sustainable development of dairy farming in China (中国奶牛养殖业可持续发展的驱动机制). *Journal of China Agricultural University*, Vol. 30, pp. 241-253.

[20] Zhang, L., Zhang, J., Yang, Q., Li, Y., Yu, Z., Tian, F., Yu, S. (2024). Detection of dairy cow feeding behavior based on video and BCE-YOLO model (基于视频和 BCE-YOLO 模型的奶牛采食行为检测). *Journal of South China Agricultural University*, Vol. 45, pp. 782-792.

DESIGN AND EXPERIMENTAL EVALUATION OF A CELL-WHEEL SEED-METERING DEVICE FOR RAPESEED BLANKET SEEDLING PRODUCTION

/

窝眼轮式油菜毯状苗育苗排种器的设计与试验

Yaodong WU[1)], Jing LUO[2)], Qing TANG[1,2)], Jixuan WANG[2)], Qun LI[1)], Meng BAI[2)] , Jinhui CHEN[2], Tong WU[1)]

[1)] Jiangsu Yunma Agricultural Machinery Manufacturing Co., Ltd., Yancheng, 224100, China

[2)]Nanjing Institute of Agricultural Mechanization, Ministry of Agriculture and Rural Affairs, Nanjing, 210014, China;

Corresponding author: Qing TANG

Tel: +86.15366092914; E-mail: tangqing01@caas.cn

DOI: https://doi.org/10.35633/inmateh-79-64

***Keywords**: rapeseed blanket seedlings; cell-wheel seed-metering device; seed-filling mechanics; response surface optimization; qualified seed-metering rate*

ABSTRACT

To address the low operating efficiency and uneven seeding associated with conventional seedling-production seeders, a cell-wheel seed-metering device was developed specifically for rapeseed blanket seedling production. The key components of the device were designed, and its seed-filling and seed-metering characteristics were analyzed. Using 'Ningza 1838' rapeseed as the test material, single-factor tests and multifactor response surface experiments were conducted. Seed-metering wheel rotational speed, seedling-tray conveying speed, and seed-box opening size were selected as the test factors, while the qualified seed-metering rate and missed-hill rate were used as the performance indicators. The results showed that the factors influencing the performance indicators, in descending order, were seed-box opening size, seedling-tray conveying speed, and seed-metering wheel rotational speed. The optimal parameter combination consisted of a seed-metering wheel rotational speed of 9.16 r·min^{-1}, a seedling-tray conveying speed of 0.45 m·s^{-1}, and a seed-box opening size of 22.80 mm. Under these conditions, the bench test yielded a qualified seed-metering rate of 94.41% and a missed-hill rate of 1.49%. These values were consistent with the predicted results, with deviations of less than 0.5 percentage points.

摘要

针对现有油菜育苗排种器作业效率低、播种均匀性差等问题，设计了一种窝眼轮式油菜育苗排种器，分析了充种与排种过程的力学特性与影响因素。以宁杂 1838 油菜种子为试验材料，以排种轮转速、秧盘输送速度、种箱开度为试验因素，以播种合格率及空穴率为性能评价指标，开展单因素和多因素响应面试验。结果表明：影响评价指标的主次顺序为种箱开度、秧盘输送速度和排种轮转速，最优参数组合为排种轮转速 9.16r·min^{-1}，秧盘输送速度 0.45m·s^{-1}，种箱开度 22.80 mm，在最优参数下的该条件下台架试验播种合格率为 94.41%，空穴率为 1.49%，与预测值误差小于 0.5 个百分点。

INTRODUCTION

Rapeseed is an important oil crop in China, with a planting area of more than 6.5 million hm² (*Wu et al., 2024; Deng.,2023)*. Its cultivation includes seedling transplanting and direct seeding. Compared with direct seeding, seedling transplanting can shorten the growth period in the field and effectively alleviate the contradiction of crop rotation, so it has been widely valued (*Lin et al.,2023*). Cultivating qualified and robust rapeseed blanket seedlings is the prerequisite for high-quality transplanting, and the quality of seedling sowing is crucial. The seed-metering device is the core component of the seedling-production system, and its performance directly influences seedling quality (*Wang et al.,2023*). Due to the characteristics of small size, light weight and large particle size variation of rapeseed seeds, problems such as missed seeding, multiple seeding, off-center seed placement and localized seed accumulation can readily occur during operation (*Cong J., 2014*), leading to an increase in the empty-cell rate and a decrease in the qualified rate. Therefore, developing a precision seeding device suitable for rapeseed blanket seedling production is important for improving seedling quality and, ultimately, rapeseed yield.

Seeding devices can be divided into pneumatic and mechanical types. Pneumatic precision seeders usually realize seed filling and metering by negative pressure adsorption or positive pressure ejection. They are characterized by strong single-seed separation ability and good adaptability to seed shape differences, and can theoretically maintain high precision at a relatively high operating speed (*Cao et al., 2021; Li et al., 2020*). Most studies focus on the optimization of seed-airflow dynamics.

Singh R.C et al. (2006) optimized the structure and operating parameters of pneumatic seeders for sowing different seeds such as mustard and peanut. *Albasheer et al. (2024)* designed a cylindrical pneumatic centralized seed metering device, which was suitable for rice, wheat and rapeseed through a double-cell wheel structure, with a field emergence rate of 88% and a coefficient of variation of 3.44%. *Akhalaya et al. (2021)* adopted a synchronous staggered double-disc and double-nozzle seed cleaning structure to solve the contradiction between seed adhesion and missed seeding, enabling compact double-row sowing. *Liao et al. (2018)* explored the influencing factors of seed suction performance of pneumatic precision seeders for small-sized seeds through seed suction and migration tests. *Li et al. (2019)* used EDEM numerical simulation to study the influence laws of various factors on seed population disturbance. *Gao et al. (2022)* proposed a conical hole seed disc, which was verified by theory, simulation and experiments to improve the performance of rapeseed precision seeders, significantly increasing the qualification index and reducing the rates of repeated and missed seeding.

However, despite these advances, pneumatic systems still face inherent limitations: the whole machine structure is complex, manufacturing and maintenance costs remain high, and the small size of rapeseed grains makes seeding consistency susceptible to air pressure fluctuations. Moreover, pneumatic seeders require dedicated air supply and vacuum systems, which increase energy consumption and limit their application in small-scale and hilly farming operations. Mechanical precision seeders generally achieve seed filling and metering through mechanical force. Typical types include grooved wheel, finger clamp, disc, hole wheel, and cell wheel type (*Liu Y et al., 2019; Wang et al., 2022; Li et al., 2025*). Most studies focus on device structure innovation and size optimization. *Maleki et al. (2006)* studied and evaluated the seed distribution uniformity of a multi-screw conveyor as a seeding device for grain drills, and found that its performance was superior to that of the traditional fluted roller device. *Karayel et al. (2022)* established a model between seed physical properties and optimal vacuum degree based on artificial neural network, with a prediction accuracy $R^2 > 0.99$, providing a basis for pressure regulation on demand. *Singh et al. (2005)* took cotton seeds as the object and obtained that the combination of 120° conical holes, 2 kPa vacuum degree and 0.42 m/s linear velocity could achieve a single-seed rate of 94.7%, providing a reference for the optimization of small seed seeders. *Lei et al. (2020)* analyzed the influences of cell length, cross-section size and cell depth on rapeseed filling performance through simulation, and proposed involute-shaped cells suitable for 1–3 seeds per hill of rapeseed. *Zhang et al. (2020)* analyzed the working process of the seeder, determined the spoon-wheel combination and the main parameters such as the size, installation number, installation inclination angle of the spoon-type cells and the rotating speed of the spoon wheel, and designed a rapeseed precision hill-seeding metering device with notched rectangular spoon-type cells. *Xing et al. (2019)* proposed a structure with staggered double circles of cells for rapeseed and three circles for wheat, as well as oblique conical cells by establishing a mechanical model of the sowing process. Among mechanical seeders, the cell wheel type stands out for its simple structure, ease of processing, and convenient seed cleaning, making it particularly suitable for small-seed crops like rapeseed.

However, a critical review of the existing literature reveals a significant scientific gap: most studies on cell wheel seeders for rapeseed have focused either on conventional direct seeding applications or on generalized seed metering for multiple crop types, with limited attention to the specific requirements of blanket seedling nursery production. The nursery seeding process imposes distinct demands—including precise control of 2–3 seeds per cell, compatibility with high-speed seedling tray conveying, and stable performance under continuous operation—that are not adequately addressed by existing designs. Furthermore, systematic investigations into the interactive effects of key operational parameters (metering wheel speed, tray conveying speed, and seed box opening) on seeding performance for blanket seedling applications remain scarce, and the underlying seed-filling mechanics have not been fully characterized for this specific context.

To address this gap, this study developed a novel cell-wheel seed-metering device specifically for rapeseed blanket seedling production. The cylindrical cell structure is simple, easy to manufacture, and convenient to clean. Although its seed-guiding performance is slightly inferior to that of conical or hemispherical cells, reliable seed filling and low seed damage can be achieved by optimizing the cell depth-to-diameter ratio. The principal innovations of the proposed device are threefold: (1) it is the first cell-wheel seed-metering device to be systematically designed and optimized for the nursery seeding stage of rapeseed blanket seedling production, with the cell geometry and arrangement tailored to the agronomic requirement of 2–3 seeds per tray cell; (2) it incorporates a synchronized seed-cleaning brush and seed-cleaning blade, enabling continuous removal of excess seeds without causing seed damage or cell blockage and thereby addressing a common failure mode in mechanical metering devices for small seeds; and (3) through comprehensive mechanical analyses of the seed-filling and seed-discharging processes, it establishes a theoretical basis for parameter optimization by directly linking operating parameters to seed-metering performance indices.

The specific objectives of this study were: (i) to design and fabricate a cell-wheel seed-metering device for rapeseed blanket seedling production, with the key structural parameters determined through theoretical analyses of the seed-filling and seed-metering processes; (ii) to investigate the effects of seed-metering wheel rotational speed, seedling-tray conveying speed, and seed-box opening size on the qualified seed-metering rate and empty-cell rate through single-factor and response surface experiments; and (iii) to determine the optimal combination of operating parameters through multi-objective optimization and validate the results through bench tests. The findings provide a reference for the structural optimization and parameter matching of seed-metering devices for rapeseed blanket seedling production and offer technical support for the development of precision seeding equipment for other small-seeded crops.

MATERIALS AND METHODS

Structure and Operating Principle of the Seed-Metering Device

The principal components of the rapeseed blanket-seedling seed-metering device include a cell-wheel seed meter, seed-cleaning brush, seed box, seed-guide plate, seed-box opening adjustment plate, seed-retaining plate, seed-cleaning blade, and continuously variable-speed motor (Fig. 1). The main technical parameters are listed in Table 1. The operating principle is as follows. Under the action of gravity, rapeseed seeds in the seed box pass through the seed outlet and enter the seed-filling zone under the guidance of the seed-guide plate. Driven by the motor, the seed-metering wheel and seed-cleaning brush rotate synchronously. Seeds enter the cells of the metering wheel under the combined effects of gravity and pressure from the seed mass. As the seed-metering wheel rotates, the seeds retained in the cells pass through the seed-retaining zone. The seed-cleaning brush continuously removes excess seeds from the cells and returns them to the seed-filling zone. The retained seeds continue to rotate with the metering wheel while being held in place by the seed-retaining plate. When the cells reach the seed-discharging zone, the seeds are no longer constrained by the seed-retaining plate and are discharged under the combined effects of gravity and the seed-cleaning blade. They then fall uniformly into the cells of the seedling tray carried by the conveyor belt, thereby completing the seed-metering process.

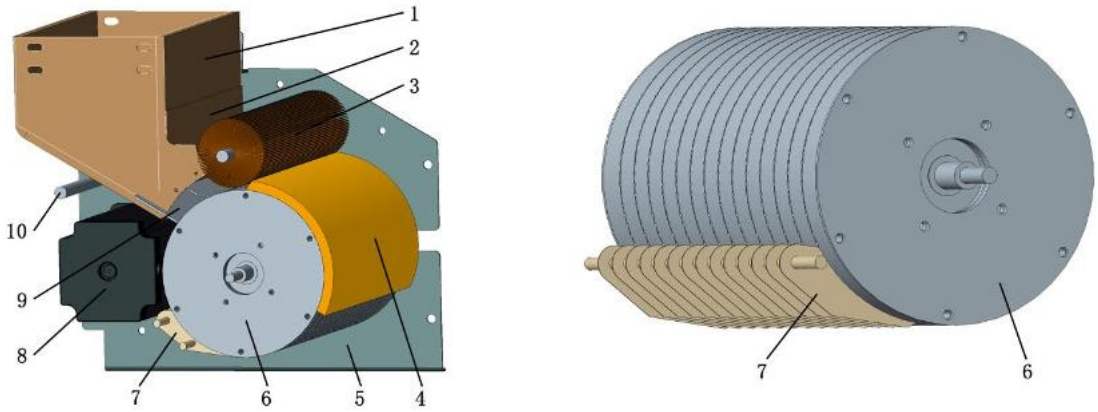


Fig. 1 - Structure of the cell-wheel seed-metering device

a) Seed-metering device assembly; b) Cell-wheel

1.Seed box; 2. Seed-box opening adjustment plate; 3. Seed-cleaning brush; 4. Seed-retaining plate; 5. Housing; 6. Cell-wheel; 7. Seed-cleaning blade; 8. Continuously variable-speed motor; 9. Seed-guide plate; 10. Support rod

Table 1

Main parameters of the seed-metering device

No.	Parameter	Value
1	Seed-metering device type	Cell-wheel type
2	Cell shape	Cylindrical
3	Number of cells per circumferential row	90
4	Cell diameter [mm]	3
5	Cell depth [mm]	5
6	Center-to-center spacing between adjacent cells [mm]	20
7	Seed-metering wheel diameter [mm]	160
8	Seed-metering wheel circumference [mm]	512
9	Seed-metering wheel width [mm]	303
10	Number of axial cell rows	14

No.	Parameter	Value
11	Seeding rate [g·tray^{-1}]	3.28 ~ 5.33
12	Seeding rate adjustment method	Stepless adjustment

Figure 2 shows the cell arrangement on the developed surface of the seed-metering wheel, with the principal dimensions defined in Table 1. In Fig. 2, a is the circumferential spacing between adjacent cells, b is the axial center-to-center spacing between adjacent cells, c is the cell diameter, d is the width of the seed-cleaning groove, e is the depth of the seed-cleaning groove, and f is the cell depth. The number of axial cell rows was set to 14 based on the seedling-pickup cycle of the rapeseed blanket seedling transplanter *(Jiang et al., 2024; Wu et al., 2020)*.

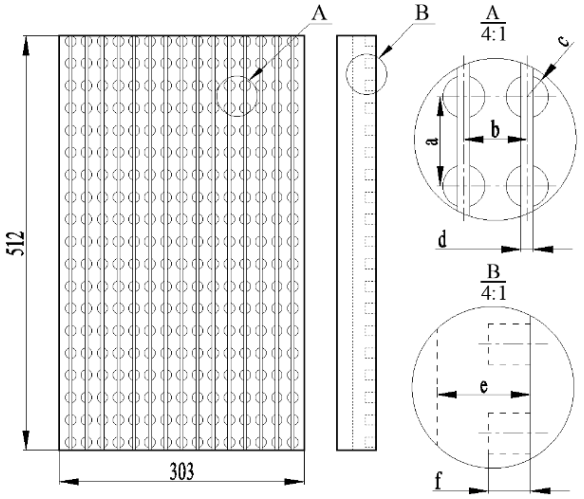


Fig. 2 - Cell arrangement on the developed surface of the seed-metering wheel

Analysis of the Seed-Filling Process of the Seed-Metering Device

Cell geometry is a critical design parameter that directly affects seed filling, retention, and cleaning performance. In this study, cylindrical cells were selected based on the physical properties of rapeseed, manufacturing feasibility, and operational requirements. Rapeseed seeds are approximately spherical, with diameters of 2–3 mm and relatively smooth surfaces. The axisymmetric geometry of a cylindrical cell therefore provides uniform radial clearance around the seeds, facilitating entry into the cell and stable retention during wheel rotation. Compared with conical or hemispherical cells, cylindrical cells offer several advantages.

First, their simple geometry facilitates conventional machining or injection molding, helping ensure dimensional consistency and reduce manufacturing costs. Second, the straight cell walls reduce the wedging effect that may occur in tapered cells when slightly oversized seeds enter the cavity, thereby decreasing the risk of seed damage and cell blockage. Third, the uniform cross-section throughout the cell depth supports stable filling with the agronomically required 2–3 seeds per cell. The seeds can stack naturally within the cylindrical cavity rather than being forced into a narrowing space. Spoon-shaped or elliptical cells may improve single-seed metering in precision direct-seeding applications.

However, their irregular inlet geometry may restrict seed entry, while localized dead zones may retain seed dust and debris, potentially increasing the missed-seeding rate during continuous nursery operation. Cylindrical cells also facilitate seed cleaning. The seed-cleaning brush can sweep smoothly across the flat cell openings without snagging, while the seed-cleaning blade can dislodge seeds that remain partially retained in the cells. These functions may be less reliable with non-axisymmetric cell geometries. The selected cell diameter of 3 mm and depth of 5 mm were determined according to the rapeseed diameter of 2–3 mm, the target seeding rate, and the design requirements of cell-wheel seed-metering devices. This combination provides sufficient cell volume to accommodate 2–3 seeds while reducing the empty-cell rate and limiting excessive multiple seeding beyond the agronomic requirement.

When the cell wheel rotates into the seed-filling zone, rapeseed seeds enter the cells, thereby completing the seed-filling process, as shown in Fig. 3(a). The time available for seeds to enter the cells is a key factor affecting the filling performance of the seed-metering wheel. Therefore, to analyze the seed-filling process and optimize filling performance, the forces acting on an individual rapeseed seed were analyzed, and the required filling time was subsequently calculated.

Rapeseed seeds were simplified as spherical particles with uniform mass distribution and regular arrangement. The vertical pressure acting on a seed was assumed to result only from the weight of the overlying seed layer; lateral pressure, vibration, and other disturbances were neglected. During seed filling, a seed is mainly subjected to its weight G, centrifugal force F_2, Coriolis force F_3, the compressive force exerted by adjacent seeds F_1, the normal reaction force of the cell wall N, the friction force between the seed and the cell wall f_2, and the interseed friction force f_1. A coordinate system was established with the seed center as the origin, the direction normal to the cross-section of the seed-metering wheel as the x-axis, and the tangential direction as the y-axis, as shown in Fig. 3(b). The equations of motion are expressed as follows:

$$\begin{cases} ma_x = (F_1 + G)cos\,\theta + f_1 sin\,\theta - F_3 - F_2 - N \\ ma_y = f_2 + f_1 cos\,\theta - (F_1 + G) f_1 sin\,\theta \\ F_2 = mr\varpi^2 \\ F_3 = 2mv_r\varpi \\ f_1 = \mu_1 F_1 \\ f_2 = \mu_2 F_2 \\ G = mg \end{cases} \quad (1)$$

where: m is mass of a single seed, [kg]; θ is the acute angle between the direction of the centrifugal force acting on the seed and the vertical direction, [rad]; a_x is the normal acceleration of the seed, [m/s²]; a_y is the tangential acceleration of the seed, [m/s²]; r is the distance from the seed centroid to the center of the seed-metering wheel, [m]; ω is the angular velocity of the seed-metering wheel, [rad/s]; μ_1 is the coefficient of friction between seeds; μ_2 is the coefficient of friction between the seed and the cell wall.

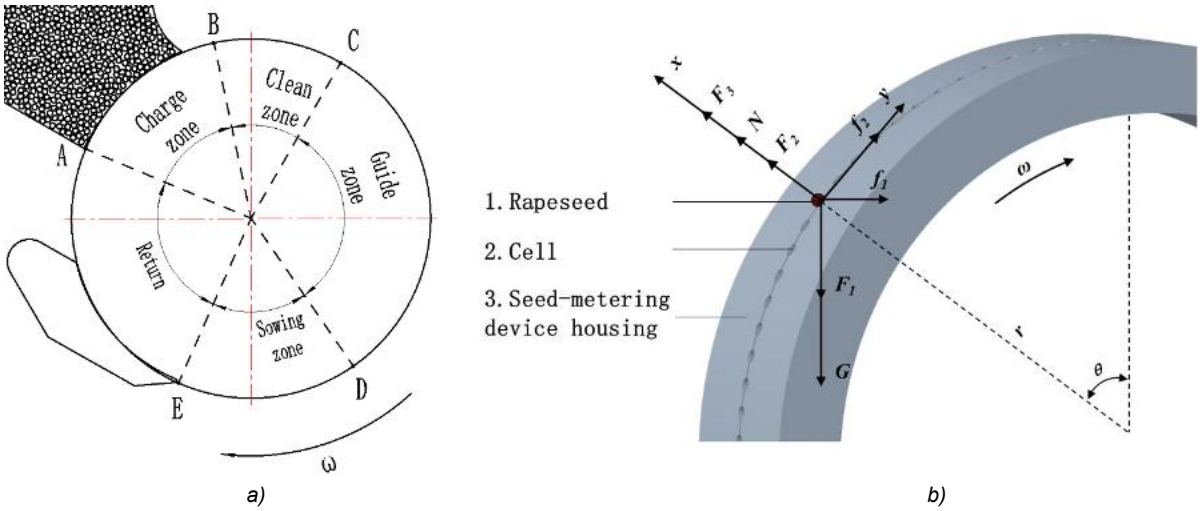


Fig. 3 - Seed-filling process and force analysis

a) Schematic of the seed-filling process; b) Free-body diagram of a single seed during seed filling

Rearranging Equation (1) yields:

$$\begin{cases} a_x = \frac{(mg+F_1)cos\,\theta + \mu_1 F_1 sin\,\theta - N}{m} - 2v_r\varpi - r\varpi^2 \\ a_y = \frac{\mu_2 F_2 + \mu_1 F_1 cos\,\theta - (F_1 + mg)sin\,\theta}{m} \end{cases} \quad (2)$$

According to the analysis of the seed filling process of a single seed, the following relationship exists between the normal displacement h of the seed centroid along the cross-section of the seed metering wheel (i.e., the hole depth) and its tangential acceleration a_x: According to the force analysis of a single seed during the filling process, the normal displacement h of the seed centroid along the cross-section of the seed-metering wheel, corresponding to the cell depth, is related to the normal acceleration a_x as follows:

$$h = \frac{1}{2} a_x t^2 \quad (3)$$

where: t is the time required for the seed to enter the cell, [s].

Combining Equations (2) and (3), the seed-filling time t *(s)* is obtained as:

$$t = \sqrt{\frac{2hm}{(mg+F_1)\cos\theta + \mu_1 F_1 \sin\theta - N - 2v_r\varpi m - mr\varpi^2}} \quad (4)$$

To improve seed-filling performance, the time required for seeds to enter the cells should be minimized. Because the angular range θ of the seed-filling zone is fixed, Equation (4) indicates that the filling time t is primarily affected by parameters such as seed mass m, cell depth h, and the interseed friction coefficient μ_1. The diameter of seeds from common rapeseed cultivars is approximately 2.5 mm. Based on the design criteria for cell-wheel seed-metering devices *(Cong, 2014)*, the cell diameter was set to 3 mm and the cell depth h to 5 mm.

Analysis of the Seed-Discharging Process of the Seed-Metering Device

After entering the seed-discharging zone, the seeds are no longer constrained by the cells or the seed-retaining plate. Under the action of gravity, they leave the cells with an initial velocity determined by the rotational motion of the seed-metering wheel and subsequently undergo projectile motion. The seed-discharge trajectory is shown in Fig. 4.

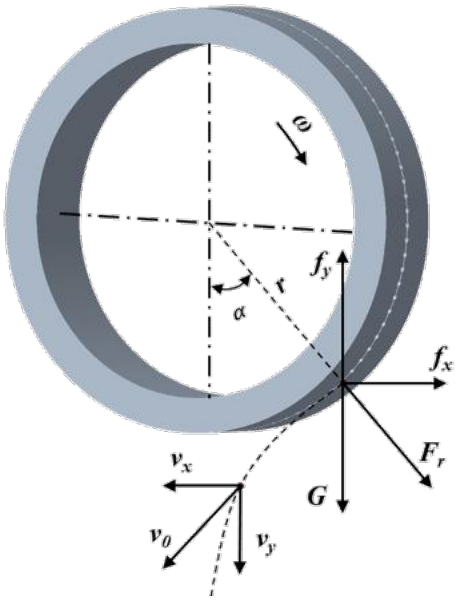


Fig. 4 - Force analysis of a seed during discharge

The initial velocity v_0 of the seed when it leaves the hole can be decomposed into horizontal and vertical components v_x and v_y. During the subsequent falling process, the seed is subjected to the combined action of gravity G, centrifugal force F_r and aerodynamic drag f. The gravity components along the x-axis and y-axis are expressed as ma_x and ma_y respectively, and the aerodynamic drag f is also decomposed into f_x and f_y accordingly. Thus, the equilibrium equations are obtained as follows:

$$\begin{cases} ma_x = -f_x - F_r \sin\alpha \\ ma_y = -F_r \cos\alpha - f_y \\ F_r = m\omega^2 r \end{cases} \quad (5)$$

where: m is the mass of a single seed, [kg]; α is angle between centrifugal direction of a single seed and vertical direction, [rad]; a_x is tangential acceleration of a single seed, [m/s²]; a_y is normal acceleration of a single seed, [m/s²]; r is distance from seed centroid to center of seed metering wheel, [m]; ω is angular velocity of seed metering wheel, [rad/s].

Rapeseed grains are small in size, light in weight, and fall over a short distance, so the effect of the drag force can be neglected. The movement of seeds during the seeding stage can be simplified as projectile motion. Decompose the movement into horizontal displacement x and vertical displacement y, the total displacement is denoted by Z, and the time elapsed during the seeding process is denoted by t.

The relationship among them can be expressed as follows:

$$\begin{cases} Z = \sqrt{x^2 + y^2} \\ v_0 = \omega r \\ v_x = v_0 \cos\alpha \\ x = v_x t \\ y = \frac{1}{2} g t^2 \end{cases} \quad (6)$$

From Equation (6):

$$Z = \sqrt{(\omega r t)^2 + \frac{1}{4} g^2 t^4} \quad (7)$$

According to Equation (7), the movement path of seeds depends on the angular velocity ω and the rotating radius r. Since the seed diameter is much smaller than the radius of the seed metering wheel, r can be approximated as the radius of the seed metering wheel. Reducing the values of ω and r can shorten the movement distance of seeds, thereby reducing the time required in the seed-dropping stage. With reference to the design of other cell-wheel seed-metering devices *(Cong, 2014)*, the radius of the seed-metering wheel was set to 80 mm. Because the angular velocity ω affects the seed-discharge speed, it should be kept as low as possible while still ensuring the required operating efficiency.

Experimental Conditions

The experiment was conducted at the test site of Yunma Agricultural Machinery Manufacturing Co., Ltd. in Yancheng, Jiangsu Province. The rapeseed cultivar used was Ningza 1838, with a seed diameter of 2–3 mm and a 1,000-seed weight of 4.1 g. The developed precision rapeseed seed-metering device was installed in place of the original precision rice seed-metering device on a 2BLY-280B rice seedling-production line (Fig. 6). Rigid plastic trays with overall dimensions of 560 mm × 280 mm × 30 mm (length × width × height) were used. To facilitate clearer counting of the rapeseed seeds during the experiment, quicklime powder was used in place of the seedling substrate employed in actual production.

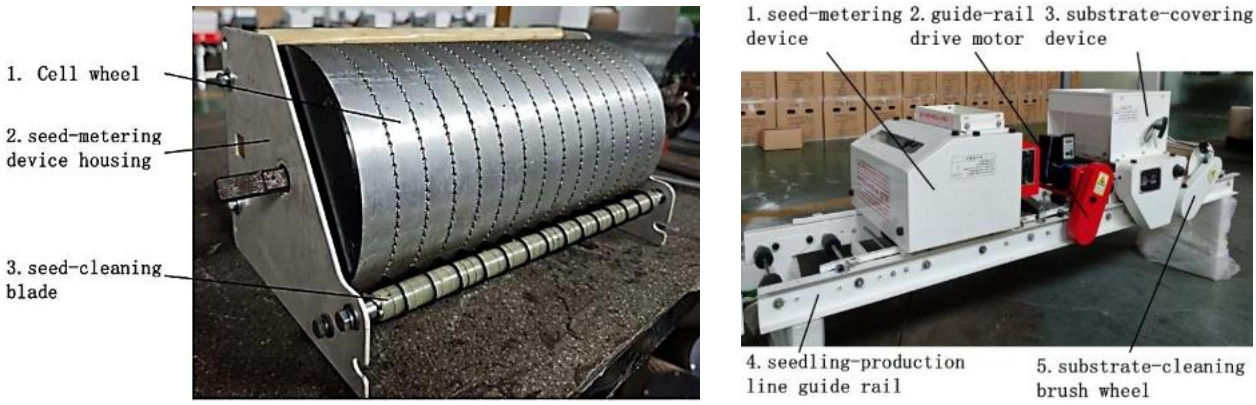


Fig. 5 - Seeder bench-test setup

According to the agronomic requirements for rapeseed mat-type seedling production *(National Technical Committee for Agricultural Machinery Standardization, 2021)*, 2–3 seeds per tray cell are considered appropriate. With reference to the relevant promotion and evaluation guidelines *(Ministry of Agriculture and Rural Affairs of the People's Republic of China, 2024)*, the qualified seed-metering rate and empty-cell rate were calculated using Equation (7). During each test, the operating parameters were adjusted and 10 consecutive trays were sown. After stable operation was achieved, the middle five trays were selected for evaluation. For each tray, five sampling areas were selected using the five-point sampling method, with 20 cells examined in each area, resulting in a total of 100 cells per tray.

The sampling method is shown in Figure 6.

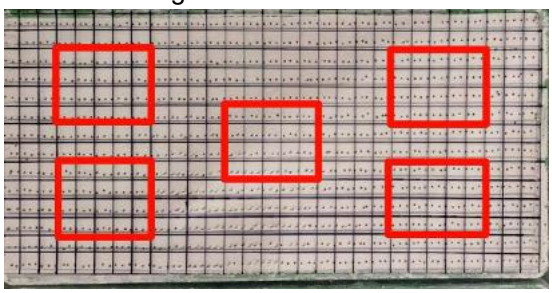


Fig. 6 - Sampling areas for seed counting in the seedling tray

The seed-metering performance indices were calculated as follows:

$$\begin{cases} R_j(\%) = \frac{H_j}{Z_j} \times 100 \\ R_K(\%) = \frac{N_k}{Z_k} \times 100 \end{cases} \quad (8)$$

where:

R_j is the qualified seed-metering rate, [%]; H_j is the number of qualified cells; Z_j is the total number of cells evaluated; R_k is the empty-cell rate, [%];N_k is the number of empty cells; Z_k is the total number of cells evaluated.

Single-factor experimental design

Based on previous studies *(Liu et al., 2025; Yu et al., 2025; Zhou et al., 2016)*, the rotational speed of the seed-metering wheel, the conveying speed of the seedling tray, and the seed-box opening size were selected as the experimental factors. Their effects on the qualified seed-metering rate and empty-cell rate were investigated. Each test was repeated five times, and the mean value was used for analysis. (1) With the seedling-tray conveying speed fixed at 0.45 $\mathrm{m \cdot s^{-1}}$ and the seed-box opening size fixed at 17 mm, the rotational speed of the seed-metering wheel was set to 7.6, 8.4, 9.2, 10.0, and 10.8 r·min⁻¹. The qualified seed-metering rate and empty-cell rate were then measured. (2) With the rotational speed of the seed-metering wheel fixed at 9.2 r·min⁻¹ and the seed-box opening size fixed at 17 mm, the seedling-tray conveying speed was set to 0.35, 0.40, 0.45, 0.50, and 0.55 m·s⁻¹ to evaluate its effect on seed-metering performance. (3) With the rotational speed of the seed-metering wheel fixed at 9.2 r·min⁻¹ and the seedling-tray conveying speed fixed at 0.45 m·s⁻¹, the seed-box opening size was set to 10, 13.5, 17, 20.5, and 24 mm for testing.

Effects of Seed-Metering Wheel Speed on Seeding Performance

As shown in Fig. 7, as the rotational speed of the seed-metering wheel increased, the qualified seed-metering rate initially increased and then decreased, whereas the empty-cell rate showed the opposite trend. This was mainly because an increase in rotational speed enhanced the mobility of the seed mass and strengthened the entrainment effect of the seed-metering wheel on the seeds, thereby facilitating seed entry into the cells and significantly reducing the empty-cell rate. The resulting improvement in seed-filling efficiency also increased the qualified seed-metering rate, indicating the presence of a relatively stable seed-filling range at intermediate rotational speeds. However, an excessively high rotational speed shortened the effective contact time between the seeds and the cells. Consequently, the seed-filling process could not be completed before the seeds were carried away from the seed bed. At the same time, the centrifugal effect became more pronounced, causing some seeds to leave the cells because of inertia. This resulted in insufficient filling, an increase in the empty-cell rate, and a decrease in the qualified seed-metering rate. Therefore, to maintain a qualified seed-metering rate above 90% while keeping the empty-cell rate within an acceptable range, the rotational speed of the seed-metering wheel should be set to 8.4–10 r·min⁻¹.

Effects of Seedling-Tray Conveying Speed on Seed-Metering Performance

As shown in Fig. 8, as the seedling-tray conveying speed increased, the qualified seed-metering rate initially increased and then decreased, whereas the empty-cell rate showed the opposite trend. Within the low-to-medium speed range, an increase in conveying speed improved the coordination between seed discharge

and tray movement, allowing the discharged seeds to enter the tray cells more accurately. This reduced missed seeding, sharply decreased the empty-cell rate, improved seed-distribution uniformity, and significantly increased the qualified seed-metering rate. When the conveying speed exceeded the critical value of 0.45 m·s^{-1}, two adverse effects occurred. First, the impact velocity of the seeds upon contact with the substrate in the seedling tray increased, resulting in seed bouncing and scattering and thereby reducing seeding uniformity. Second, the time interval during which each tray cell passed beneath the seed-discharge position became too short for the seeds to settle stably in the cells, leading to an increase in the empty-cell rate. Therefore, considering both seed-metering performance and production efficiency, a seedling-tray conveying speed of 0.40–0.50 m·s^{-1} was considered appropriate.

Effects of Seed-Box Opening Size on Seed-Metering Performance

As shown in Fig. 9, the qualified seed-metering rate decreased when the seed-box opening size increased from 10 to 13.5 mm, increased when the opening size increased from 13.5 to 17 mm, and then gradually decreased when the opening size exceeded 17 mm. The rate of decrease became smaller when the opening size exceeded 20.5 mm. The empty-cell rate initially decreased and then increased. As the seed-box opening size increased, the quantity of seeds entering the seed-filling zone also increased, producing two beneficial effects. First, increased interseed friction reduced the mobility of the seed mass and limited seed bouncing during the seed-filling process. Second, the increased pressure within the seed mass promoted more complete filling of the cells. However, when the opening size exceeded the critical value of 17 mm, excessive seed accumulation increased interseed compression and friction, potentially causing seed jamming and disrupting seed-metering uniformity. In addition, excessive seed accumulation in the seed passage prevented some cells from being completely filled. Therefore, the seed-box opening size was selected within the range of 10–24 mm.

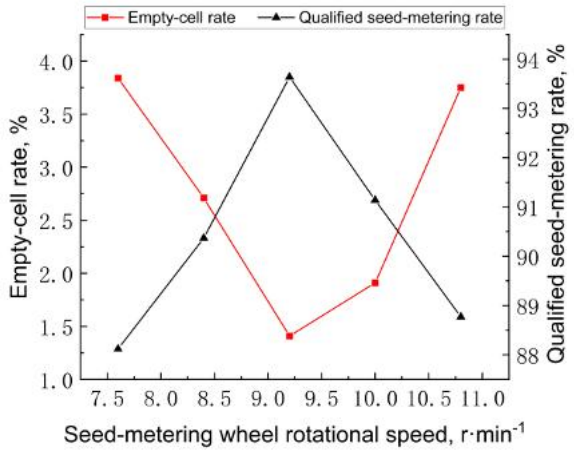


Fig. 7 - Effects of seed-metering wheel rotational speed on seed-metering performance

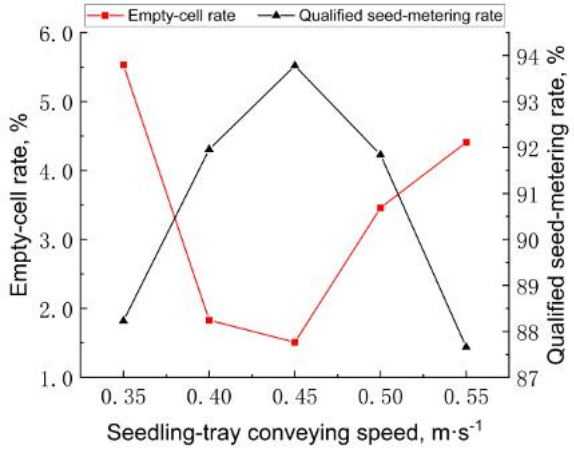


Fig. 8 - Effects of seedling-tray conveying speed on seed-metering performance

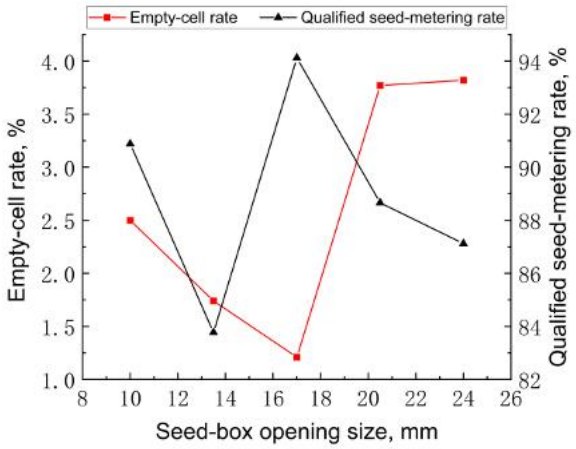


Fig. 9 - Effects of seed-box opening size on seed-metering performance

Experimental design

Based on the factor ranges determined from the single-factor experiments, a three-factor, three-level orthogonal experiment was conducted using the qualified seed-metering rate (R_j) and empty-cell rate (R_k) as the evaluation indices. The experimental factors and their levels are listed in Table 2. X_1, X_2 and X_3 represent the coded values of the seed-metering wheel rotational speed, seedling-tray conveying speed, and seed-box opening size, respectively. A total of 17 experimental runs were performed. Each run was repeated three times, and the mean value was used for analysis. The experimental results are presented in Table 3.

Table 2

Experimental factors and levels

Level	Seed-metering wheel rotational speed X_1 [r·min^{-1}]	Seedling-tray conveying speed X_2 [m·s^{-1}]	Seed-box opening size X_3 [mm]
-1	8.4	0.4	10
0	9.2	0.45	17
1	10	0.5	24

RESULTS

The experimental results are presented in Table 3. Regression analysis of the experimental data was performed using Design-Expert 13.0, and the following regression equations were obtained:

$$R_j = 93.78 - 0.39X_1 + 0.2662X_2 + 1.63X_3 - 0.75X_1X_2 + 0.04X_1X_3 + 0.7075X_2X_3 - 2.21X_1^2 - 2.86X_2^2 - 1.35X_3^2 \quad (9)$$

$$R_k = 1.58 + 0.9963X_1 - 0.345X_2 - 0.7138X_3 - 0.49X_1X_2 + 0.3025X_1X_3 + 0.295X_2X_3 + 1.22X_1^2 + 0.8123X_2^2 + 0.1847X_3^2 \quad (10)$$

The analysis of variance presented in Table 4 showed that both regression models were highly significant ($P < 0.01$), whereas the lack-of-fit terms were not significant ($P > 0.05$), indicating that the models adequately fitted the experimental data. The coefficients of determination, R^2, were 0.9985 and 0.9821 for the qualified seed-metering rate and empty-cell rate models, respectively. The corresponding adjusted R^2 values were 0.9966 and 0.9591, and the predicted R^2 values were 0.9942 and 0.7657. The coefficients of variation were 0.1571% and 9.64%, respectively. These results indicate good agreement between the predicted and experimental values. The order of influence of the experimental factors on seed-metering performance was seed-box opening size, followed by seedling-tray conveying speed and seed-metering wheel rotational speed.

Table 3

Results of the response-surface experiment

Test No.	Seedling-tray conveying speed X_2 [m·s^{-1}]	Seed-metering wheel rotational speed X_1 [r·min^{-1}]	Seed-box opening size X_3 [mm]	Empty-cell rate R_k [%]	Qualified seed-metering rate R_j [%]
1	0.45	8.4	10	3.82	88.31
2	0.4	8.4	17	2.42	88.09
3	0.5	9.2	24	3.41	91.45
4	0.45	8.4	24	1.78	90.27
5	0.45	9.2	17	1.54	93.97
6	0.45	9.2	17	1.82	93.51
7	0.45	10	10	2.78	87.44
8	0.4	9.2	10	3.17	89.07
9	0.45	9.2	17	1.42	93.75
10	0.4	9.2	24	1.16	92.15
11	0.5	9.2	10	4.21	88.21
12	0.45	10	24	1.92	92.23
13	0.45	9.2	17	1.51	93.81
14	0.5	10	17	3.83	87.83
15	0.4	10	17	2.47	90.11
16	0.5	8.4	17	5.74	88.81
17	0.45	9.2	17	1.6	93.87

Note: *Each treatment was replicated three times, and the reported values are the means.*

The analysis of variance indicated interaction effects among the seed-metering wheel rotational speed, seedling-tray conveying speed, and seed-box opening size. The corresponding response surfaces are shown in Fig.10.

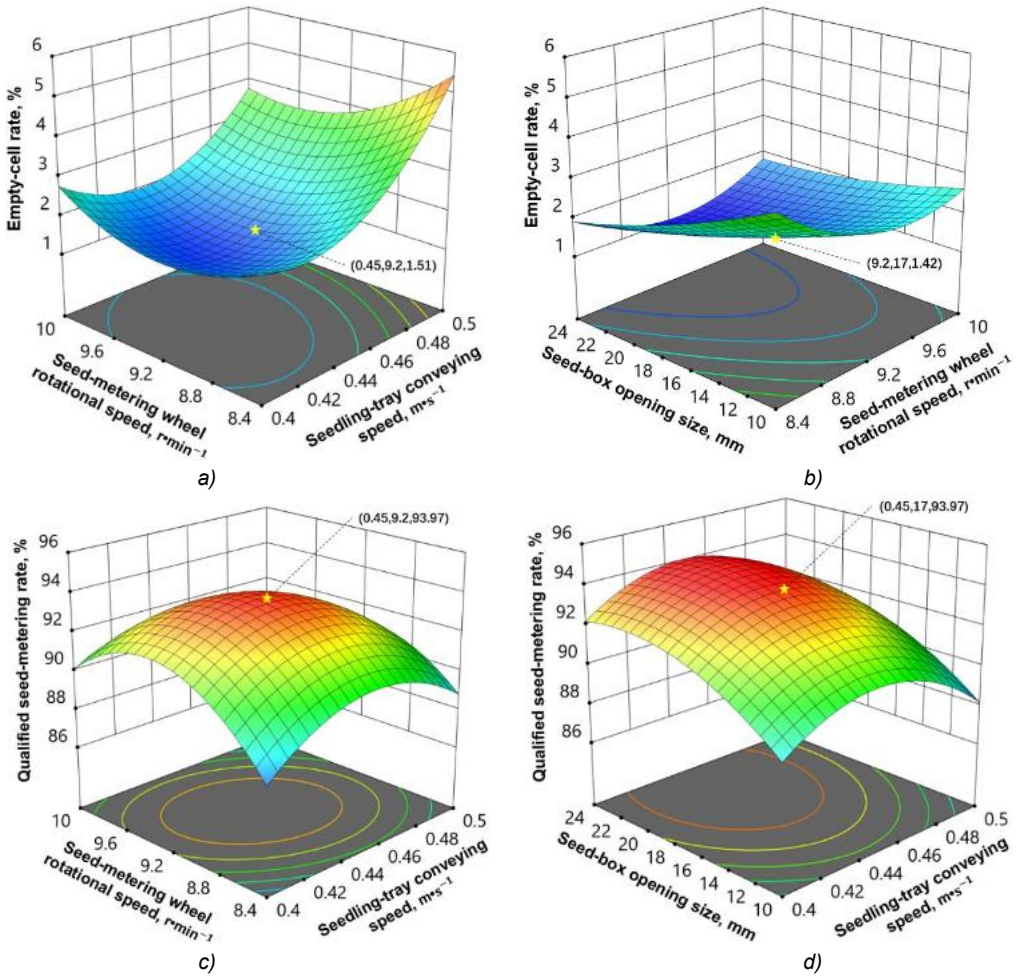


Fig. 10 - Response surfaces showing the interactive effects of seed-metering wheel rotational speed, seedling-tray conveying speed, and seed-box opening size on the qualified seed-metering rate and empty-cell rate

The interaction between X_1 and X_2 reflects the temporal and spatial coordination between the seed-discharge frequency and the rate at which tray cells pass beneath the discharge position (Figs. 10a and 10b). At low values of both X_1 and X_2, seed agitation and circulation in the filling zone are relatively weak, resulting in insufficient cell filling (Eq. 2). Meanwhile, the low rotational speed of the seed-metering wheel produces a low initial seed-release velocity, and the horizontal displacement of the seed during flight, (Eq. 6), remains relatively small. As both factors increase toward their intermediate levels, the seed-discharge frequency becomes better matched to the tray-cell passing frequency, allowing the seeds to land more accurately in the tray cells. This region therefore represents the optimal synchronization range, in which the qualified seed-metering rate reaches its maximum. When X_2 is high while X_1 remains low, the seed supply rate per unit time may be insufficient relative to the number of tray cells passing beneath the discharge position, resulting in a marked increase in the empty-cell rate. This represents a temporal mismatch between seed supply and tray-cell demand. Conversely, when X_1 is high while X_2 is low, seeds are discharged with greater initial velocity ($v_y = gt$) and may undergo increased bouncing or scattering after striking the substrate, thereby reducing the qualified seed-metering rate even when the seed supply is sufficient. The deterioration in performance at the highest combination of the two factors is attributed to the excessive rotational speed of the seed-metering wheel ($Fc > mg$), which may cause seeds to detach prematurely from the cells before reaching the optimal discharge position (Eq. 5). This leads to irregular landing positions and a sharp increase in the empty-cell rate. The interaction between X_1 and X_3 reflects the balance between the available seed-filling time and the pressure exerted by the seed mass at the cell entrance (Figs. 10c and 10d). At a small seed-box opening size (low X_3), the quantity of seeds entering the filling zone is limited, and the pressure exerted by the seed layer above the cells is relatively low. As X_1 increases, the effective seed-filling time decreases proportionally (Eq. 4), making it more difficult for seeds to enter the cells completely. Consequently, the qualified seed-metering rate decreases rapidly at small opening sizes. Increasing X_3 increases the amount of seed in the filling zone and enhances both interseed contact and the pressure exerted by the upper seed layer. Within an appropriate range, this promotes seed entry into the cells and improves the qualified seed-metering rate. However, when the opening size exceeds a critical value, approximately 17 mm according to the response-surface results, excessive seed accumulation may increase interseed compression and restrict the mobility of the seed mass. This can promote bridging or arching near the cell entrances, thereby obstructing seed flow and reducing the effective filling rate. The ridge observed in the response surface therefore indicates that an optimal combination of rotational speed and seed-box opening size is required: sufficient seed pressure is needed to promote filling, but excessive accumulation should be avoided to prevent flow obstruction. The gradual decline observed when the opening size exceeded 20.5 mm in the single-factor experiment shown in Fig. 9 may also be associated with this reduced seed mobility and localized bridging. Although the X_2X_3 interaction term was not significant for the qualified seed-metering rate (P=0.5922 , Table 4), it was significant for the empty-cell rate (P=0.0480). The seedling-tray conveying speed X_2 affects the relative horizontal position between the falling seeds and the moving tray cells, whereas the seed-box opening size X_3 influences the quantity of seeds supplied to the discharge zone. At a high conveying speed, the available time for each tray cell to pass beneath the discharge position is reduced, increasing the likelihood of positional misalignment. A larger seed-box opening size increases the seed flow rate and may intensify interseed collisions, bouncing, and scattering during discharge. Therefore, at higher conveying speeds, a moderately smaller opening size may help limit excessive seed flow and reduce collision-induced scattering. This interpretation is consistent with the slight shift in the optimal region observed in the response surface as X_2 increased from 0.4 to 0.5 m·s^{-1}.

Table 4

Analysis of variance for the regression models

Source of variance	Analysis of Variance of Void Rate				Analysis of Variance of Qualified Rate			
	Sum of squares	Degree of freedom	F	P	Sum of squares	Degree of freedom	F	P
Model	24.58	9	42.69	<0.0001	96.77	9	528.91	<0.0001
X_2	7.94	1	124.12	<0.0001	1.22	1	59.85	0.0001
X_1	0.9522	1	14.88	0.0062	0.5671	1	27.90	0.0011
X_3	4.08	1	63.71	<0.0001	21.35	1	1050.36	<0.0001
X_2X_1	0.9604	1	15.01	0.0061	2.25	1	110.68	<0.0001
X_2X_3	0.3660	1	5.72	0.0480	0.0064	1	0.3148	0.5922

Source of variance	Analysis of Variance of Void Rate				Analysis of Variance of Qualified Rate			
	Sum of squares	Degree of freedom	F	P	Sum of squares	Degree of freedom	F	P
$X_1 X_3$	0.3481	1	5.44	0.0524	2.00	1	98.49	<0.0001
X_2^2	6.32	1	98.73	<0.0001	20.51	1	1009.06	<0.0001
X_1^2	2.78	1	43.42	0.0003	34.55	1	1699.76	<0.0001
X_3^2	0.1437	1	2.25	0.1776	7.73	1	380.13	<0.0001
Residual	0.4478	7			0.1423	7		
Lack of fit	0.3577	3	5.29	0.0706	0.0234	3	0.2627	0.8495
Pure error	0.0901	4			0.1189	4		
Total	25.03	16			96.91	16		

Note: P ≤ 0.01 indicates the model is highly significant, 0.01 < P ≤ 0.05 indicates the model is significant, and P > 0.05 indicates the model is not significant.

Each response surface was constructed using the mean of three replicate measurements for each treatment combination listed in Table 3. The red asterisk (★) in each subfigure indicates the optimal operating point identified through multi-objective optimization.

Optimization and Verification

Using the optimization module in Design-Expert 13.0, multi-objective optimization was performed to minimize the empty-cell rate and maximize the qualified seed-metering rate. During the numerical optimization, the seedling-tray conveying speed (X_2) was fixed at 0.45 m·s⁻¹ for the following reasons: (i) this value corresponded to the optimal performance range identified in the single-factor experiment (Fig. 8) and was also consistent with the standard operating speed of commercial seedling-production lines, thereby ensuring compatibility with upstream and downstream operations; (ii) in practical production, the conveying speed is determined by the overall cycle time of the production line and is rarely adjusted during operation, whereas the seed-metering wheel rotational speed and seed-box opening size are the main parameters adjusted by operators to improve seed-metering quality; and (iii) fixing X_2 at its optimal value allowed the optimization to focus on the two most influential and practically adjustable factors, X_1 *and* X_3, thereby producing results that could be applied directly without changing the operating speed of the entire production line. Accordingly, the optimization objectives and constraints were defined as follows:

$$\begin{cases} minY_1(x1, x2, x3) \\ maxY_2(x1, x2, x3) \\ s.t. \begin{cases} 8.4 \leqslant x_1 \leqslant 10 \\ x_2 = 0.45 \\ 10 \leqslant x_3 \leqslant 24 \end{cases} \end{cases} \quad (10)$$

The optimal parameter combination obtained through numerical optimization was a seed-metering wheel rotational speed of 9.16 r·min⁻¹, a seedling-tray conveying speed of 0.45 m·s⁻¹, and a seed-box opening size of 22.80 mm. Under these conditions, the predicted qualified seed-metering rate and empty-cell rate were 94.15% and 1.12%, respectively. Three replicate bench verification tests were conducted using the optimal parameter combination. The measured mean qualified seed-metering rate was 94.41%, with a standard deviation of 0.23 percentage points and a 95% confidence interval of 93.85%–94.97%. The measured mean empty-cell rate was 1.49%, with a standard deviation of 0.036 percentage points and a 95% confidence interval of 1.40%–1.58%. The predicted qualified seed-metering rate of 94.15% and empty-cell rate of 1.12% both fell within the corresponding 95% confidence intervals of the measured values. The absolute deviations between the predicted and measured values were 0.26 and 0.37 percentage points, respectively, both of which were below the engineering tolerance threshold of 0.5 percentage points. The optimal parameter combination obtained through optimization was a seed-metering wheel rotational speed of 9.16 r·min⁻¹, a seedling-tray conveying speed of 0.45 m·s⁻¹, and a seed-box opening size of 22.80 mm. The predicted qualified seed-metering rate was 94.15%, and the predicted empty-cell rate was 1.12%. Subsequently, a bench verification experiment was conducted using this parameter combination. The experiment was repeated five times, and the mean qualified seed-metering rate and empty-cell rate were 94.41% and 1.49%, respectively. These results demonstrate that the regression models provide adequate predictive accuracy and reliability for practical operation.

CONCLUSIONS

(1) This study extends beyond parameter optimization by clarifying the underlying seed-filling and seed-discharge mechanisms of a cell-wheel seed-metering device designed for rapeseed blanket seedling production. Seed-metering performance was governed by three interacting mechanisms: the competition between the available seed-filling time and premature seed release, which was mainly affected by the seed-metering wheel rotational speed; the transition between pressure-assisted filling and seed bridging, which was mainly affected by the seed-box opening size; and the trade-off between landing accuracy and seed bouncing, which was mainly affected by the seedling-tray conveying speed. The cylindrical cells, with a diameter of 3 mm and a depth of 5 mm, together with the coordinated action of the seed-cleaning brush and blade, reduced cell blockage and seed damage and enabled stable metering of 2–3 seeds per tray cell.

(2) The validated regression models provided reliable predictions of seed-metering performance, with R^2 values of 0.9985 for the qualified seed-metering rate and 0.9821 for the empty-cell rate. The absolute deviations between the predicted and measured values were below 0.5 percentage points. The optimal parameter combination consisted of a seed-metering wheel rotational speed of 9.16 $r \cdot min^{-1}$, a seedling-tray conveying speed of 0.45 $m \cdot s^{-1}$, and a seed-box opening size of 22.80 mm. Because the optimization was conducted at the standard operating speed of the seedling-production line, the resulting parameter combination can be applied directly in practical operation. Factor significance order was: seed box opening > tray speed > metering wheel speed.

(3) This study has three main limitations. First, quicklime powder was used instead of the actual seedling substrate during the bench tests, which may have affected seed landing and bouncing behavior. Second, only the Ningza 1838 rapeseed cultivar was evaluated; therefore, other cultivars may require recalibration of the operating parameters. Third, the seedling-tray conveying speed was fixed during numerical optimization, and adaptive adjustment of the conveying speed was not investigated. Future research should include production-scale or field validation using actual seedling substrate, testing of multiple rapeseed cultivars, and the development of a closed-loop control system for adaptive parameter adjustment.

ACKNOWLEDGEMENT

The authors were funded for this project by the national key R & D project, 2023YFD2001001 and China Agriculture Research System of MOF and MARA（CARS-12）.

REFERENCES

[1] Albasheer A.H., Liao Q., Wang L., Anas D. A., Lin J., (2024). Design and preliminary evaluation of a precision cylindrical air-assisted drill sowing device for rapeseed, wheat, and rice. *Agriculture*, Vol. 14, no. 12, pp.2355, Switzerland. DOI: https://doi.org/10.3390/agriculture14122355

[2] Akhalaya B.K., Shogenov Y.K., Starovoitova S.I., (2021). Effect of design changes in pneumatic seeding devices on quality indicators of seeding. *Russian Agricultural Sciences*, Vol. 47, no.1, pp.93–98, Moscow/Russia. DOI: https://doi.org/10.3103/S106836742101002X

[3] Cong J., (2014). *Study on Seeding System and Mechanism of Pneumatic Precision Metering Device for Wheat & Rapeseed (油菜小麦兼用型气力式精量排种系统及其机理研究)*. PhD dissertation, Huazhong Agricultural University, Wuhan/China.

[4] Cao X., Ma X., Li H., Wen Z., Li Z., Wang X., (2021). Design and experiments of pneumatic roller type precision seed-metering device for rapeseed plug seedlings (气吸滚筒式油菜穴盘育苗精密排种器设计与试验). *Transactions of the Chinese Society of Agricultural Engineering*, Vol. 37, no. 2, pp. 51-60, Beijing/China. DOI: https://doi.org/10.11975/j.issn.1002-6819.2021.2.007

[5] Chinese Academy of Agricultural Mechanization Sciences., (2007). *Agricultural Machinery Design Manual,* Vol 1 & Vol 2, Agricultural Science and Technology Press, ISBN9787802333352, Beijing/China.

[6] Deng C., (2023). *Development and Testing of a Centralized Rapeseed Seeding and Fertilizing Device (集排式油菜播种施肥装置研制与试验)*. Msc Thesis, Southwest University, Chongqing/China.

[7] Gao L., Shi B., Liao Q., Zhang B., Zheng J., Liao Y., (2022). Seeding performance of conical-hole seeding plate of the positive and negative pressure combination precision seed metering device for rapeseed (正负气压组合油菜精量排种器锥孔盘排种性能). *Transactions of the Chinese Society of*

Agricultural Engineering, Vol. 38, no. 6, pp. 22-33, Beijing/China. DOI: https://doi.org/10.11975/j.issn.1002-6819.2022.06.003

[8] Jiang L., Zhu T., Tang Q., Wu J., Jiang D., Huang M., (2024). Mechanical Characteristics Testing and Parameter Optimization of Rapeseed Blanket Seedling Conveying for Transplanters. *Agriculture*, Vol 14, no.5, pp. 699, Switzerland. DOI: https://doi.org/10.3390/agriculture14050699

[9] Karayel D., Güngör O., Šarauskis E., (2022). Estimation of optimum vacuum pressure of air-suction seed-metering device of precision seeders using artificial neural network models. *Agronomy*, Vol. 12, no. 7, pp. 1600, Switzerland. DOI: https://doi.org/10.3390/agronomy12071600

[10] Lin G., Wang L., Li J., Qian C., Li Y., Zheng J., You J., Zuo Q., (2023). Research progress on mechanized transplantation technology of rapeseed blanket seedlings (油菜毯苗机械化移栽技术研究进展). *Jiangsu Agricultural Sciences*, Vol. 51, no. 18, pp. 20-27, Nanjing/China. DOI: https://doi.org/10.15889/j.issn.1002-1302.2023.18.003

[11] Li Z., Yang W., Wu Y.Y., He S., Wang W., Chen L., (2020). Performance analysis and experiments of seed filling assisted by groove-tooth of pneumatic disc precision metering device for rapeseed (油菜气力盘式精量排种器槽齿辅助充种性能分析与试验). *Transactions of the Chinese Society of Agricultural Engineering*, Vol. 36, no. 20, pp. 57-66, Beijing/China. DOI: https://doi.org/10.11975/j.issn.1002-6819.2020.20.008

[12] Liao Y., Liao Q., Wang L., Zheng J., Gao L.P., (2018). Investigation on vacuum singulating effect influencing factors of pneumatic precision seed metering device for small particle size of seeds (气力式小粒径种子精量排种器吸种效果影响因素研究). *Transactions of the Chinese Society of Agricultural Engineering*, Vol. 34, no. 24, pp.10-17, Beijing/China. DOI: https://doi.org/10.11975/j.issn.1002-6819.2018.24.002

[13] Li Z., Yang W., Zhang T., Wang W., Zhang S, Chen L., (2019). Design and suction performance test of sucking-seed plate combined with groove-tooth structure on high speed precision metering device of rapeseed (油菜高速精量排种器槽齿组合式吸种盘设计与吸附性能试验). *Transactions of the Chinese Society of Agricultural Engineering*, Vol. 35, no. 1, pp. 12-22, Beijing/China. DOI: https://doi.org/10.11975/j.issn.1002-6819.2019.01.002

[14] Li P., Gu Y., Zhang T., Feng W., Ren G., Zhou X., Wu M., (2025). Design and Experiment of Inclined Disc Precision Seeding Apparatus for Rape (倾斜圆盘式油菜精密排种器设计与试验). *Journal of Agricultural Mechanization Research*, Vol. 47, no. 09, pp. 178-186, Haerbin/China. DOI: https://doi.org/10.13427/j/issn.1003-188x.2025.09.024

[15] Liu Y., Wu Z., Nie Y., Liu F., Wu M., (2019). Seeding performance of double hole-wheel seeder for rapeseed based on EDEM (基于 EDEM 的双排型孔轮式油菜排种器的排种性能分析). *Journal of Hunan Agricultural University (Natural Sciences)*, Vol. 45, no. 2, pp. 554-559, Changsha/China. DOI: https://doi.org/10.13331/j.cnki.jhau.2019.05.018

[16] Liu D., Qin F., Wang Z., Xie F., Li X., Gong M., (2025). Optimization design and experiment of herringbone groove seed metering unit for rice seedling raising (人字纹斜槽式水稻育秧播种排种器优化设计与试验). *Journal of Shenyang Agricultural University*, Vol. 56, no. 2, pp. 99-109, Shenyang/ China. DOI: https://doi.org/10.3969/j.issn.1000-1700.2025.02.011

[17] Lei X., Yang W., Yang L., Liu L., Liao Q., Ren W., (2020). Design and Experiment of Seed Hill-seeding Centralized Metering Device for Rapeseed (油菜精量穴播集中排种装置设计与试验). *Transactions of the Chinese Society for Agricultural Machinery*, Vol. 51, no. 2, pp. 54-64, Beijing/ China. DOI: https://doi.org/10.6041/j.issn.1000-1298.2020.02.007

[18] Ministry of Agriculture and Rural Affairs of the People's Republic of China., (2024). *Complete sets of equipment for seedling tray seeding,* DG/T 074—2024, Beijing/ China.

[19] Maleki M.R., Jafari J.F., Raufat M.H., Baerdemaeker D., (2006). Evaluation of seed distribution uniformity of a multi-flight auger as a grain drill metering device. *Biosystems Engineering*, Vol. 94, no. 4, pp. 535-543, San Diego/USA. DOI: https://doi.org/10.1016/j.biosystemseng.2006.04.003

[20] National Technical Committee for Agricultural Machinery Standardization., (2021). *Operating quality of rapeseed blanket seedling transplanter,* NY/T 3887-2021, Beijing/China.

[21] Singh R.C., Singh G., Saraswat D.C., (2006). Optimisation of design and operational parameters of a pneumatic seed metering device for planting mustard seeds. *International Agriculture Engineering Journal*, Vol. 15, no. 2, pp. 31-41, Beijing/China.

[22] Singh R.C., Singh G., Saraswat D.C., (2007). Optimisation of design and operational parameters of a pneumatic seed metering device for planting of groundnut (Arcahis hypogaea) seeds. *Indian Journal of Agricultural Sciences*, Vol. 77, no. 1, pp. 40-42, New Delhi/India.

[23] Singh R.C., Singh G., Saraswat D.C., (2005). Optimisation of design and operational parameters of a pneumatic seed metering device for planting cottonseeds. *Biosystems Engineering*, Vol. 92, no. 4, pp. 429–438, San Diego/USA.DOI: https://doi.org/10.1016/j.biosystemseng.2005.07.002

[24] Wu C., Wang J., Yang Y., Li D., Li X., Yan R., (2024). Analysis of the development status and mechanization trends of economic crop industry in China (我国经济作物产业发展现状与机械化趋势分析). *Journal of Chinese Agricultural Mechanization*, Vol. 45, no.1, pp. 01-13, Nanjing/China. DOI: https://doi.org/10.13733/j.jcam.issn.2095-5553.2024.01.001

[25] Wang Z., Leng S., Zhang Y., Zhou X., Gong C., Zuo Q., Yang G., (2023). Research progress on seedling transplanting technology of rapeseed blanket-like seedlings (油菜毯状苗育苗移栽技术研究进展). *Jiangsu Journal of Agricultural Sciences*, Vol.39, no. 5, pp. 1247-1255, Nanjing/China. DOI: https://doi.org/10.3969/j.issn.1000-4440.2023.05.018

[26] Wang B., Wang L., Liao Y., Wu C., Cao M., Liao Q., (2022). Design and Test of Seeding Wheels of Precision Hole-seeding Centralized Metering Device for Small Particle Size Seeds (小粒径种子精量穴播集排器型孔轮设计与试验). *Transactions of the Chinese Society for Agricultural Machinery*, Vol. 53, no. 11, pp. 64-75, 119, Beijing/China. DOI: https://doi.org/10.6041/j.issn.1000-1298.2022.11.007

[27] Wu J., Yu W., Zhang M., Wu C., Jiang L., Tang Q., (2020). Design and Test of 2ZY-6 Rapeseed Carpet Seedling Transplanter (2ZY-6 型油菜毯状苗移栽机设计与试验). *Transactions of the Chinese Society for Agricultural Machinery*, Vol 51, no. 12, pp. 95-102, 275, Beijing/China. DOI: https://doi.org/10.6041/j.issn.1000-1298.2020.12.010

[28] Xing H., Liao Q., Wang L., Wang D., Liao Y., Wang D., Yu Q., (2019). Design and test of oblique taper hole-type wheel centralized metering device for rapeseed and wheat (油麦兼用斜锥型孔轮式集排器设计与试验). *Journal of Huazhong Agricultural University*, Vol. 38, no. 5, pp. 143-151, Wuhan/China. DOI: https://doi.org/10.13300/j.cnki.hnlkxb.20190701.003

[29] Yu Y., Pan Y., Wang T., Wang Y., Luo T., (2025). Design and Test of Drum Seed Metering Device for Drill Seeding of Rice Blanket Seedlings (播量可调式水稻毯苗条播机滚筒排种器设计与试验). *Transactions of the Chinese Society for Agricultural Machinery*, Vol. 56, no. 10, pp. 310-320, Beijing/China. DOI: https://doi.org/10.6041/j.issn.1000-1298.2025.10.026

[30] Zhang Q., Yu Q., Wang L., Liao Y., Wang D., Liao Q., (2020). Design and Experiment of Scoop-type Precision Hole Metering Device for Rapeseed (油菜勺式精量穴播排种器设计与试验). *Transactions of the Chinese Society for Agricultural Machinery*, Vol. 51, no. 6, pp. 47-54, 64, Beijing/ China. DOI: https://doi.org/10.6041/j.issn.1000-1298.2020.06.005

[31] Zhou H., Liang Q., Wei T., Ma X., Jiao C., (2016). Design and Experiment of Quantitative Seed Supply Device with Fluted Roller Used for Double-vibrating Precision Seed Meter (双级振动精密排种器外槽轮式定量供种装置设计与试验). *Transactions of the Chinese Society for Agricultural Machinery*, Vol. 47, no. s1, pp. 57-61, Beijing/China. DOI: https://doi.org/10.6041/j.issn.1000-1298.2016.S0.009

INTELLIGENT ANIMAL FEEDING SYSTEM BASED ON MULTISOURCE INFORMATION ACQUISITION

/

基于多源信息采集的动物智能饲喂系统

Linwei Li[1,7], Jie Bai[2], Xinyu Zhao[1], Guanzhen Li[3], Yuanrong Tian[4], Peng Cheng[5], Dongyao Liu[6], Zhenyu Liu[8,9], Senhao Yang[1], Tao Zhao[2], Xiaoping Ji*[4]

[1] College of Information Science and Engineering, Shanxi Agricultural University, Taigu 030801, Shanxi/China;
[2] Department of Big Data and Intelligent Engineering, Shanxi Institute of Technology, Yangquan 045000, Shanxi/China;
[3] College of Computer Science and Software Engineering, Hohai University, Nanjing 211100, Jiangsu/China;
[4] Faculty of Software Technologies, Shanxi Agricultural University, Taigu 030801, Shanxi/China;
[5] Combat Support Academy, Rocket Force University of Engineering, Xi'an 710025, Shanxi/China;
[6] Department of Mechanical Engineering, Shanxi Institute of Technology, Yangquan 045000, Shanxi/China;
[7] Key Laboratory of Equipment and Informatization in Environment Controlled Agriculture, Ministry of Agriculture and Rural Affairs, Hangzhou 310058, Zhejiang/China;
[8] Dryland Farm Machinery Key Technology and Equipment Key Laboratory of Shanxi Province, Taigu 030801, Shanxi/China;
[9] College of Agricultural Engineering, Shanxi Agricultural University, Taigu 030801, Shanxi/China;
Tel: 0354-6288587; E-mail: jixiaoping@sxau.edu.cn
Corresponding author: Ji Xiaoping
DOI: https://doi.org/10.35633/inmateh-79-65

Keywords: *intelligent animal feeding system; multisource information acquisition; audio–video assisted localization; RFID-based identity verification; weight-based arrival confirmation*

ABSTRACT

With the increasing refinement of livestock feeding management, conventional manual feeding and record-keeping methods often fail to ensure reliable confirmation of individual animal arrival and accurate identity matching. This may result in ineffective feeding, feed misdelivery, missed feeding, and deviations from the prescribed feed amount. To address these limitations, an intelligent animal feeding system based on multisource information acquisition was developed. The system integrates camera-based monitoring with microphone-array sound-source localization to support target positioning and combines radio-frequency identification (RFID)-based identity verification with weight-based arrival confirmation to enable individualized feeding while minimizing animal–target mismatches. The system also collects body weight and environmental data to generate traceable individual records and supports data transmission and command delivery through an ESP8266 module using the Message Queuing Telemetry Transport (MQTT) protocol. A WeChat mini-program is integrated into the platform to provide remote control, feeding-plan configuration, and data visualization, as well as AI-assisted recognition and question-answering functions. Experimental results demonstrated that the proposed system successfully integrates intelligent feeding with multisource information acquisition. Under the combined audio–visual configuration, the target-positioning success rate reached 92.67%, while the combined RFID–weight configuration achieved a trigger accuracy of 93.33%. These results indicate that the system can support refined feeding management and improve process traceability.

摘要

随着饲喂管理逐步向精细化发展，传统人工饲喂与记录的方式难以保证个体到位确认与身份匹配，易出现无效投喂、误投漏投与饲喂量偏差等问题。为此，本文构建基于多源信息采集的动物智能饲喂系统。系统通过摄像头监测与麦克风阵列声源方位数据辅助定位，并结合 Radio Frequency Identification（RFID）身份确认与称重到位判定，实现个体化饲喂，避免对象错配；系统同步采集体重与环境参数，形成可追溯的个体记录，通过 ESP8266 与 Message Queuing Telemetry Transport（MQTT）实现数据上报与指令下发；微信小程序与平台对接，提供远端控制、方案配置与数据可视化，并集成 AI 辅助识别与问答服务。实验结果表明，本系统能够实现智能饲喂与信息采集的一体化运行，在音频与视频联合配置下，指向成功率为 92.67%；在 RFID 与称重联合配置下，触发准确率为 93.33%。上述结果可为精细化饲喂管理与过程溯源提供参考依据。

INTRODUCTION

Feeding is very important for both feed supply and animal observation. Relevant information is collected during the feeding process, and this information can help adjust feeding plans when the condition of the animals changes *(Kavlak et al., 2023; Gauthier et al., 2022)*. Traditional feeding methods mainly rely on manual operation and record keeping. Prolonged use of such practices may result in inconsistent feed allocation and fragmented records that are difficult to maintain continuously. Poor data continuity also limits timely adjustment of feeding plans and may reduce the effectiveness of long-term management *(Bhaskaran et al., 2024)*. Therefore, intelligent feeding systems generally need to support individualized feeding, continuous acquisition of key state information, and remote cloud-platform management simultaneously (*Leliveld et al., 2024; McCarthy et al., 2023*).

Although sensing and automation modules have been increasingly adopted in animal feeding management, existing solutions are mostly designed independently for single tasks. As a result, process fragmentation and non-uniform interfaces often arise during on-site integration and maintenance, and data and control interactions across modules are difficult to standardize, making it difficult to establish a unified workflow for feeding management *(Nyamuryekung'e et al., 2024)*. Existing intelligent feeding-related devices are typically used for individual functions such as feeding equipment control, RFID-based individual identification, weight acquisition, environmental monitoring, and audio-video behavior recognition. Representative examples include data cleansing for electronic feeding station data *(Garrido-Izard et al., 2022)*, individualized ration supply and precision-feeding strategy validation based on automatic feeders (*Ribas et al., 2024; Spinler et al., 2024; Durand et al., 2023*), behavior-oriented audio-video multimodal recognition *(Yang et al., 2025)*, and association analysis between environmental factors and health/behavior indicators (*Bus et al., 2025*). Furthermore, *Funk et al. (2024)* developed an online monitoring and abnormality warning method for individual feeding behavior based on a low-frequency RFID electronic feeding system, achieving abnormal decline detection in 2,826 finishing pigs, identifying 55.7% of stockperson-diagnosed events, and providing warnings 2.8 days in advance on average. *Decarie et al. (2025*) also proposed and validated a walk-over dynamic weighing system in commercial pig farms, enabling non-invasive automatic body weight estimation while pigs walked through the device and demonstrating the engineering feasibility of a standalone weight-acquisition device. However, because modules are often triggered independently by different hardware and software devices, feeding triggering and execution are easily affected by group-housing behavior, equipment layout, and communication conditions, resulting in missed triggers or record gaps. Data gathered from different sources cannot always be matched reliably, noise and missing data entries are also fairly common, and this raises the amount of work needed for follow-up data cleaning and system maintenance.

In animal feeding, a trigger based on only one signal is easily affected by occlusion, changes in animal posture, and surrounding conditions. These factors can cause false activation and inconsistent data acquisition. When visual information alone is used to control feeding activation, an animal may be detected before reaching the feeding position or before completing the arrival process. Premature detection may therefore lead to invalid triggering *(Scaillierez et al., 2024; Han et al., 2023)*. Weight-only triggering also lacks sufficient reliability. An animal may not stand completely inside the weighing area or may continue moving during measurement. The resulting variation in weight readings can reduce the reliability of the trigger decision *(Zhang et al., 2025)*. Time-based strategies are likewise difficult to align with the actual arrival time of individuals, because the arrival of a preset time point does not necessarily imply arrival at the feeding position, which may lead to empty feeding or repeated triggering *(Bus et al., 2024; Bus et al., 2023; Wallgren et al., 2025; Lagoda et al., 2025)*. Therefore, an organization method based on a controllable on-site process is required to improve the reliability of feeding execution *(Gaillard et al., 2022)* and to provide a stable event entry for multisource information acquisition.

To address these issues, this study designed and implemented an intelligent animal feeding system based on multisource information acquisition. The system uses a single feeding event as the basic operational unit and integrates audio-visual-assisted monitoring, RFID-based individual identification, weight-based arrival confirmation, feeding execution, environmental parameter acquisition, and remote data interaction into a unified workflow. This design establishes continuous associations among target confirmation, trigger decision-making, execution control, and process recording. The camera and microphone array provide visual positional feedback and acoustic directional assistance, respectively. RFID and weight information are jointly used for individual identity verification and arrival confirmation. The acquired body weight, environmental parameters, and device operating status are synchronously uploaded to a mini-program for record retrieval, trend visualization, feeding-plan configuration, and remote management. The system uses OpenMV and a K210 microphone array to support low-cost on-site deployment, local real-time processing, and direct integration

with the pan-tilt control system. A DHT11 sensor records the basic temperature and humidity conditions associated with feeding events and provides the environmental information required for functional validation of the prototype rather than high-precision environmental regulation.

On this basis, the study evaluates whether the proposed multisource information coordination mechanism can improve the reliability of target pointing and feeding triggering while supporting continuous process recording and traceability. Based on the complementary roles of different information sources in the feeding workflow, acoustic directional information is expected to assist target reorientation when visual tracking becomes temporarily unstable or is lost. Visual information is expected to provide more accurate positional feedback once the target enters the field of view. Their coordinated use is therefore expected to improve the continuity and stability of target pointing. When RFID identity confirmation is combined with weight measurement to confirm arrival, this method is likely to make the activation of feeding more reliable, but the system needs to wait until the weight reading is stable, and this may make the trigger time longer.

MATERIALS AND METHODS

Overall System Architecture

To achieve multisource information acquisition, this study develops an intelligent animal feeding system, which is mainly composed of two components: a feeding device and a WeChat mini-program. The STM32F103ZET6 microcontroller is employed to implement system control and task scheduling, and coordinate the operation of modules including audio-video assisted target monitoring, animal identity recognition, automatic feeding, and IoT-based environmental data acquisition. Information on animal identity, arrival status, body weight, environmental conditions and feeding execution status is correlated within the system and stored in a structured form. The ESP8266 module is adopted for wireless communication, MQTT supports bidirectional transmission of data and control commands, and the cloud server undertakes storage and forwarding of the relevant data. The WeChat mini-program allows users to view historical records and collected data, set feeding plans, and perform remote control of the system. Additionally, the platform supports centralized storage, remote access, and system maintenance. Figure 1 presents the overall architecture of the system.

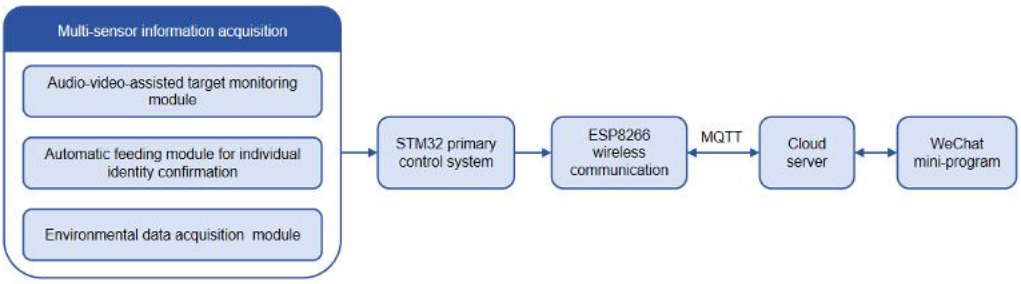


Fig. 1 - Structure diagram of system

Experimental Protocol

The prototype was tested in an indoor nursery pig house. Three weaned piglets were chosen for this experiment. Each piglet was equipped with an RFID ear tag. Their ages were between 21 and 28 days, and their body weight was around 6 to 8 kg. The whole test lasted for three straight days. During the test with combined audio and video for target pointing, a blue visual marker assisted the OpenMV camera with target tracking work, and it also provided support for the control of pan and tilt. Throughout the whole test process, the surrounding temperature stayed between 26 and 30℃, and the relative humidity was within the range of 50% to 65%. The feeding device, RFID reader, weighing platform, OpenMV camera, and K210 microphone array were installed around the feeding port. All devices were calibrated before formal testing.

A complete system operation was defined as a single event-level trial. Consecutive video frames and individual sensor readings were not treated as independent replicates. The audio–visual pointing test comprised a visual-only group, an acoustic-only group, and a combined audio–visual group. The feeding-trigger test comprised an RFID-only group, a weight-only group, and a combined RFID–weight group. Each group included 300 event-level trials, and cases of target loss, feed misdelivery, and missed feeding were included in the statistical analysis. The three piglets were used primarily to establish a representative on-site feeding scenario. Accordingly, the repetitions represented system-event-level replicates rather than animal-level biological replicates. The results were used solely to evaluate the feasibility and operational reliability of the prototype system and were not intended to support inferences regarding population-level production performance or behavioral patterns.

Hardware Design of the Animal Feeding Device

Primary control system

The system adopts STM32F103ZET6 as the main control chip, which is a 32-bit microcontroller manufactured by STMicroelectronics. Under the control and scheduling of the main control system, each subsystem cooperates closely to acquire parameter information from surrounding sensors and connect to the STM32 through GPIO and other interfaces, where local data encapsulation and state management are completed. Subsequently, data are uploaded to the cloud server through the WLAN subsystem, where storage and forwarding are performed and synchronized to the mini-program platform, facilitating real-time access to breeding information and remote management.

The process of the main control system based on STM32F103ZET6 is shown in Figure 2.

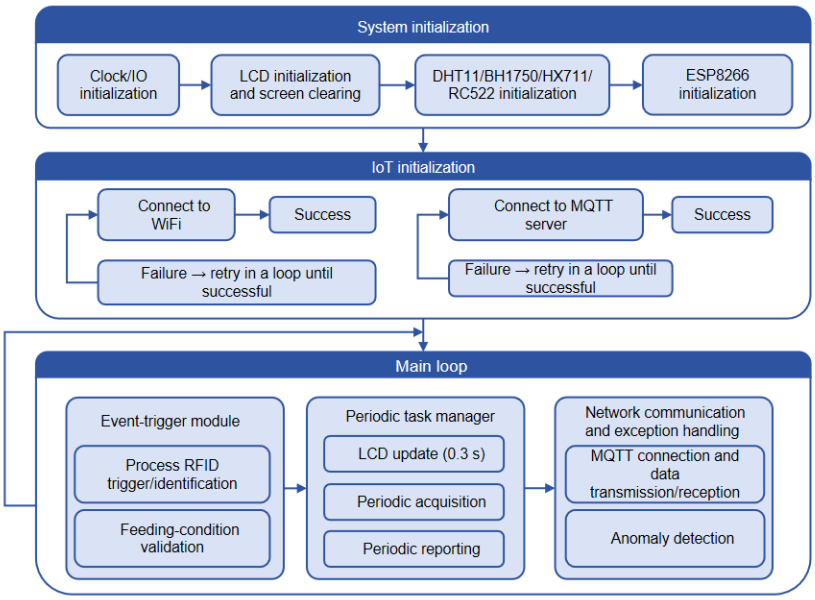


Fig. 2 - Flowchart of the Main Controller

Audio-Visual Assisted Target Monitoring Module

The target monitoring module combines an OpenMV camera with a K210 microphone array to continuously monitor animal targets in the feeding area and provide directional guidance. Visual and acoustic information is collected in parallel. When illumination is weak, the target is occluded, or image quality becomes unstable, the estimated sound direction provides an additional reference for target orientation. The combined sensing approach improves monitoring stability and increases the adaptability of the system under complex environmental conditions.

Target Tracking Based on Image Information

The image-based tracking unit uses an OpenMV module equipped with an OV7725 camera. An animal that enters the feeding range and carries a blue marker is regarded as the current target. OpenMV reads the video stream frame by frame and segments the blue region in the LAB color space using a preset threshold. The centroid offset relative to the image center is then calculated. A PID controller converts the offset into servo control signals and adjusts the pan and tilt angles. During the control process, the target is slowly moved back toward the center of the visual field. Real-time tracking state is maintained all the time. Meanwhile, the identity information of the animal is collected by the RFID reader and writer module. The main controller connects the RFID number with the target position sent back by the camera. The connected information is then used to make feeding records. It also offers support for data tracing work. The functional introduction of the OpenMV module is shown in Table 1.

Table 1

Functional Description of the OpenMV Module

Module Pin	Main Controller Pin	Specific Function
GND	GND	Ground
VIN(3.6-5)	VIN	Power input
UART1_RX	P0	UART receive
UART1_TX	P1	UART transmit

Module Pin	Main Controller Pin	Specific Function
CAN2_TX	P2	CAN bus transmit
CAN2_RX	P3	CAN bus receive
UART3_TX	P4	UART transmit
UART3_RX	P5	UART receive
P6	P6	Reserved analog output or general-purpose I/O
P7	P7	Servo control signal output (pan / horizontal)
P8	P8	Servo control signal output (tilt / pitch)
P9	P9	Reserved general-purpose I/O pin
BOOT0	BOOT	Boot mode selection
FRAMESYNC	SYN	Frame synchronization signal interface
3V3_OUT	3.3V	3.3 V power output
RESET	RST	Reset signal input

OpenMV initializes the camera and acquires image frames through the sensor module. Camera initialization includes sensor reset and configuration of the pixel format and image size. Automatic white balance is disabled to reduce the effect of color drift on detection based on preset thresholds. After initialization, OpenMV continuously captures frames in the main loop. Color blob detection and servo angle updates are performed on each frame to achieve pan and tilt tracking control. Table 2 lists the pixel format, image resolution, and frame skipping setting used during the warm-up stage of image acquisition.

Table 2

Image Acquisition and Operating Parameters

Parameter	Setting Value
Pixel format	RGB565
Image size	QQVGA 160 × 120
Frame-skipping warm-up	10frames
Automatic white balance	Disabled

Color blob detection is carried out on every single frame by the system after a steady image stream is acquired, and the pre-set LAB color threshold is applied in this process. Pixels are screened by the find_blobs() function based on the given threshold, connected regions that meet the detection condition are sorted into different groups. A group of candidate blobs is formed by the obtained regions. Candidate blobs are represented by bounding rectangles, and their centroid coordinates are output as position observations; the pixel discrimination rule is expressed in Equation (1).

To reduce target drift when multiple candidates are present, the system determines the primary target blob using the maximum bounding-rectangle area criterion, as shown in Equation (2), where w_k and h_k denote the width and height of the bounding rectangle of the k-th candidate blob, respectively.

$$M(x,y) = \begin{cases} 1, t_1 \le L(x,y) \le t_2, t_3 \le a(x,y) \le t_4, t_5 \le b(x,y) \le t_6 \\ 0, otherwise \end{cases} \quad (1)$$

Let $L(x,y)$, $a(x,y)$, and $b(x,y)$ denote the values of the three LAB color channels at pixel (x,y). The intervals (t_1,t_2), (t_3,t_4), and (t_5,t_6) represent the calibrated threshold ranges for the L, a, and b channels, respectively.

$$k^* = \underset{k}{\operatorname{argmax}} S_k, S_k = w_k \cdot h_k \quad (2)$$

After the individual target is determined, the system outputs the bounding rectangle and centroid coordinates as tracking results. The bounding rectangle is represented by the four-tuple (x,y,w,h), and conversion between the top-left and bottom-right coordinates is given in Equation (3). The centroid coordinates are obtained from color blob object processing and are used to characterize the target position in the current frame.

$$(x_1,y_1) = (x,y), (x_2,y_2) = (x+w, y+h) \quad (3)$$

To keep the target animal near the center of the field of view, the centroid deviation is calculated with the image center as the reference point. The control signal is then obtained through PID computation. The pitch error is defined as positive upward. The control signal is used to update the pan and tilt servo angles, thereby driving the pan-tilt unit to adjust and gradually return the target to the image center region, as defined in Equation (4). Here, c_x and c_y denote the centroid coordinates of the target, W and H are the image width and height, and w and h represent the width and height of the target bounding rectangle.

$$e_{pan} = c_x - \frac{W}{2}, e_{tilt} = c_y - \frac{H}{2} \quad (4)$$

In the single-target tracking scenario, the system selects the connected region with the largest area among the candidate blobs in each frame as the target marker and outputs its bounding rectangle and centroid coordinates. For visualization and debugging, the circular marker is enclosed by a bounding rectangle in each frame, and a cross marker is drawn at the centroid position to visualize detection and tracking status. The detection and annotation effects are shown in Figure 3.



Fig. 3 - Example of color blob detection with centroid visualization

Target Tracking Based on Audio Information

The system uses a K210 microphone array module as the acoustic sensing unit. The module receives audio information from the feeding area and the surrounding space and determines the direction of the sound source. The main controller is connected to the microphone array through the I^2S digital audio interface. A multichannel synchronous sampling path is built through this connection. Audio signals from different spatial positions can be received at the same time in this way. Multichannel synchronous sampling also provides basic support for sound source direction judgment. The directional information obtained from this process helps realize stable rough target positioning. It works under the conditions of weak light, blocked targets, or incomplete field of view information.

Two main functions are fulfilled by the K210 microphone array in this system. Multi-channel audio signals are collected by this module. The sound source direction of the target animal is calculated based on these signals. This direction information can reflect the position changes of the target's activity area. It provides early direction reference for the rotation of the camera and pan-tilt. The cost of video data collection is reduced in this way. The continuity of monitoring work is improved at the same time. Sound events can also reflect the activity state of the target animal. These events mainly include animal calls and collision noises generated during the feeding process. All kinds of related data are recorded by the system within the same feeding window. These data cover audio direction data, individual identity, body weight and environmental parameters. These records enrich the description of the animal's feeding state. They also provide reference for research on feeding quantity adjustment and related management applications.

The reproducibility of system integration needs to be guaranteed. For this purpose, the interface connections between the K210 microphone array module and the main controller are listed in Table 3. In addition to the I^2S audio signal lines, the module contains LED data and clock lines for directional display and on-site debugging.

Table 3

Pin Connections of the K210 Microphone Array Module

Module Pin	K210 Pin	Function Description
GND	GND	Ground
5V	5V	5 V power supply
BCLK	MIC_CK	I^2S bit clock
WS	MIC_WS	I^2S word select / frame sync
D0	MIC_D0	I^2S serial data output (Channels 0 and 1)
D1	MIC_D1	I^2S serial data output (Channels 2 and 3)
D2	MIC_D2	I^2S serial data output (Channels 4 and 5)
D3	MIC_D3	I^2S serial data output (center microphone channel)
LED_DA	LED_DA	LED data line
LED_CK	LED_CK	LED clock line

To obtain directional information from target animal sounds near the feeding area, the system calls the MIC_ARRAY function of the microphone array for multichannel audio acquisition. Real-time calculations are then performed on the K210. During operation, the system first obtains response intensities from different directions. The dominant direction of the sound source is displayed by the ring LED. Angle and operating status information are also displayed for on-site debugging and parameter calibration. Acoustic processing runs simultaneously with video acquisition, which allows sound and image information to be collected in parallel.

The sound source direction is calculated at fixed angular intervals of 30°. A threshold is first applied to the directional response intensities to remove directions with weak responses and reduce the effect of background noise. The reserved directional components are weighted and combined first. The main azimuth of the sound source is obtained through this step. Smoothing processing is performed afterwards. This step helps improve the stability of the output. Jitter during intermediate calculations is suppressed by recursive filtering. A moving average is used to process the final angle sequence. These two filtering operations prevent the output angle from changing frequently. These changes are caused by intermittent vocalizations or impulsive noise. The real-time response intensity in each angle range is used as the reference. The ring LED indicates the direction based on this reference. Continuous pointing toward the sound source is maintained. The smoothed azimuth angle is adopted as the servo steering input for this purpose. Approximate estimation of the sound source distance is required when distance reference information is needed. This work is completed with the installation calibration constant OneD_Distance. Relative changes of distance are reflected by the estimated distance. This estimated value is applied to reference display and steering control. This distance estimation is not suitable for high-precision ranging.

Servo Control

Some difficulties are caused by insufficient light or unstable target capture by the camera. To deal with these difficulties, the system applies the K210 microphone array to calculate the sound source direction. The calculated result is taken as the control input of the pan-tilt servo. The K210 acquires array audio signals through the I^2S interface and calculates the directional vector of the sound source in the horizontal plane based on directional energy distribution, thereby obtaining the azimuth angle. In addition, to suppress directional jitter caused by noise, recursive smoothing is applied to the directional vector components, and window averaging is applied to the output angle sequence to improve the stability of control inputs.

At the execution level, two servo control signals are configured as PWM outputs. The K210 timer generates control pulses on GPIO pins to drive the two degrees of freedom (pan and tilt) of the gimbal, enabling real-time pointing and maintenance toward the sound source direction. The system simultaneously outputs current directional information on the display and supports operating-mode switching via buttons. The servo PWM control flow is shown in Figure 4.

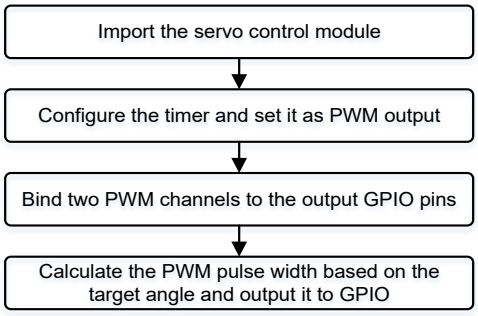


Fig. 4 - Servo control flow based on PWM

Automatic Feeding Module for Individual Identification

The intelligent feeding system is designed for large-scale captive breeding scenarios. Through a closed-loop process including individual identity confirmation, weight and status acquisition, feeding execution, and record uploading, the system realizes scheduled feeding at the individual level. Compared with manual feeding, this scheme can reduce human intervention and feeding errors and provide data support for subsequent growth assessment and traceable management.

Individual Information Acquisition Module

An RFID reader/writer module is installed near the feeding port to trigger identity recognition when an animal enters the feeding area. After obtaining the unique ear-tag number, the reader/writer uses it as an

individual index and binds it with acquired body weight, feeding status, and other information. These data are sent to the main controller or server through the wireless network, and feeding records as well as traceability data for multiple individuals are formed in the end.

Body Weight Information Acquisition Module

Body weight collection work is finished by the weighing module, and this module makes use of a load cell and a 24-bit A/D conversion chip (HX711) in the process. The load cell typically outputs a weak differential signal in the form of a Wheatstone bridge, while the HX711 performs high-gain amplification and high-resolution sampling and outputs digital values. During operation, the main controller reads sampled results at a fixed interval. To eliminate the dead weight of the scale body and installation bias, a tare operation is performed during initialization to record the no-load baseline value. During operation, the real-time sample value is differenced from the no-load baseline, and linear conversion is completed using a pre-calibrated proportional coefficient to obtain the current body weight. The final body weight result is bound to the RFID number read at the same moment and uploaded via the wireless network to the main controller or server for growth recording and feeding control.

Intelligent Feeder Module



(a) Structural diagram of the feeding device *(b) Detail view of the trough structure*

Fig. 5 - Structural diagram of the feeding device and trough

The feeding device and trough are illustrated in Figure 5. The device includes a storage hopper, a feed drop channel, a valve plate assembly, and a trough. An actuator rotates the valve plate so that the valve opening aligns with the feed outlet and the trough inlet at different operating stages. The position alignment controls the switching between feed discharge and closure. The valve changes the way of continuous manual material adding. The process becomes a set of adjustable opening and closing movements. The system uses identity checking and weighing results. It changes feeding ways for different individual situations.

For every single feeding event, the feeding parameters are figured out by the main controller based on the identified individual number and current body weight, and the computed result is changed into a valve plate angle command or an equivalent opening duration. The valve plate is adjusted and reset by the actuator as required by the control instruction. The controlled positioning process makes the feeding amount and feeding time repeatable. The valve plate is rotated in separate stages by the drive motor, and this action adjusts the feed output and pushes the whole feeding process forward. The angle control of the valve plate follows the alignment restrictions between the valve plate and the openings.

Environmental Data Acquisition Module

Light, temperature and humidity in the feeding region can affect animal activity and feeding status. Sensors for light, temperature and humidity are installed around the feeding place. These sensors are used to keep records of these environmental conditions. These sensors test light intensity, air temperature and air humidity at fixed time intervals. After the system begins to work, the main control device gets the sensors ready. It collects data from these sensors at regular periods. The system checks and changes the gathered data first. Then the data are shown on local equipment or sent through the communication device.

Light intensity is measured by the system using a BH1750 digital light sensor, and the collected data are sent through the I^2C bus. During initialization, the system configures the I^2C pins and the operating mode of the sensor. During data acquisition, the main controller first checks the device acknowledgment to confirm normal bus communication. The measurement result is then read and converted into a light intensity value that represents the illumination condition of the feeding area. The DHT11 sensor is used to collect temperature and

humidity data, and the whole collection process follows a single-wire timing protocol. During sampling, the main controller first sends a start signal. The data frame is then read according to the specified timing and checked for validity. When verification is successful, the temperature and humidity values are parsed. The sensor should be installed away from heating elements to reduce the effects of local heat sources and structural heat dissipation. Adequate air circulation should also be maintained around the sensor. The installation arrangement improves the stability and representativeness of the measurements. Figure 6 shows the flowchart of the light acquisition module, while Figure 7 shows the flowchart of the temperature and humidity acquisition module.

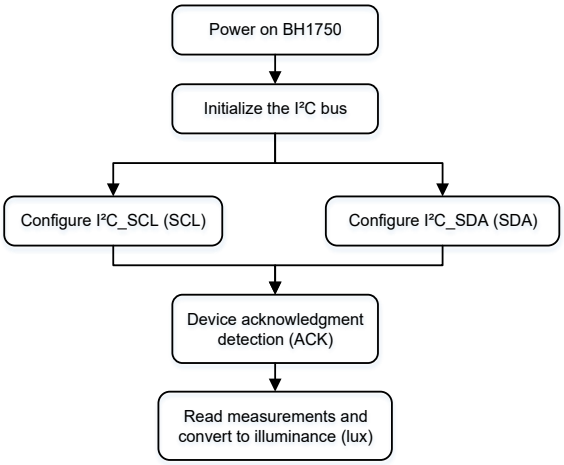


Fig.6 - Flowchart of the Light Control Module

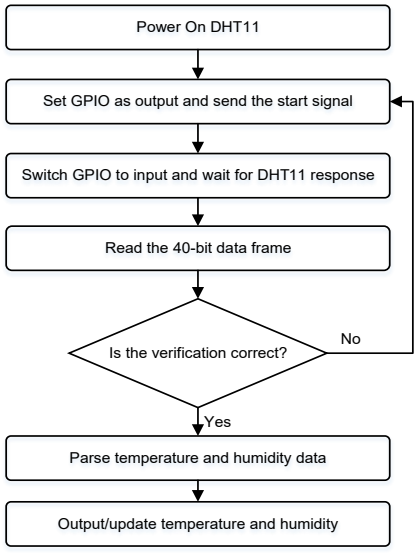


Fig. 7 - Temperature-Humidity Sensor Module Flowchart

Remote monitoring and control of the feeding device are implemented through an ESP8266 wireless communication module. The ESP8266 connects to the main control board through a serial interface and accesses the local area network in the feeding area. After startup, the module completes network access and establishes an MQTT connection with the IoT platform through the TCP-based MQTT protocol. The system publishes environmental parameters and other operating data to upstream topics at fixed intervals. The platform receives the published data for storage and interface display. The device also subscribes to downstream topics and receives control commands from the mini-program. The received commands support remote control and parameter configuration. Uploaded data are organized into structured fields. The fields include key environmental parameters such as temperature, humidity, and illumination. Device operating status fields may also be included. The structured format facilitates data parsing, storage, and trend visualization on the platform. The mini-program sends control messages to the device through the platform. After receiving a message, the device parses the command and performs the corresponding action or parameter update. Basic exception handling is included to support stable field operation. The communication module retries the connection after a connection failure and reconnects after a disconnection. The retry and reconnection mechanisms maintain the availability of data reporting and control links during network fluctuations.

Software Design of the Feeding System

The WeChat mini-program is taken as the interface for information aggregation and user interaction in this system. This platform offers centralized data display and remote control for livestock breeding, and it supports the combined workflow of production and marketing. For the hardware part, data from multiple sensors are collected by the STM32, and the operation of devices is also controlled by it. Wireless network connection and data transmission are supported by the ESP8266. The collected data are shown on the WeChat mini-program, and related control functions are also provided on it. Feeding information, body weight data, images and environmental data collected in the feeding area are sent to the mini-program at the same time. The information can be viewed and managed by users in real time. This integrated data flow helps realize precise feeding, and it also cuts down the waste of feed.

The device connects to a router or mobile hotspot through the ESP8266 and establishes an MQTT connection over TCP. The hardware publishes sensor data and device status to the pcTopic topic. The cloud server mqtt1tbtb.xyz forwards the published messages. The WeChat mini-program subscribes to pcTopic to receive and display the data. The mini-program also sends MQTT control commands for the remote operation of devices such as buzzers and lighting LEDs.

Client Side

The client interface is available to users and provides a unified entry point for product selection, intelligent services, and reservation services. The mini-program contains five pages, namely Home, Category, Recognition, Reservation, and Personal Center. The Home page brings together the main functions of the platform, including the animal encyclopedia, animal feeding, video monitoring, AI animal recognition, and AI-powered question answering. Users can quickly access remote feeding, status viewing, image recognition, and health service functions from the Home page. The Category page uses a layout with categories on the left and item lists on the right to display animals and related supplies. Users can add items to the shopping cart and complete checkout, forming a complete process from product browsing to order placement. The Recognition page allows users to upload an image by taking a photograph or selecting one from the album. The page then returns the pet recognition result and corresponding basic information. The Reservation page provides access to medical consultation and home service appointments. Users can complete and submit reservation information and review previous reservation records. The Personal Center provides the login entry and includes order viewing, About Us, online customer service, and sharing functions. Figure 8 presents the functional structure of the client interface.

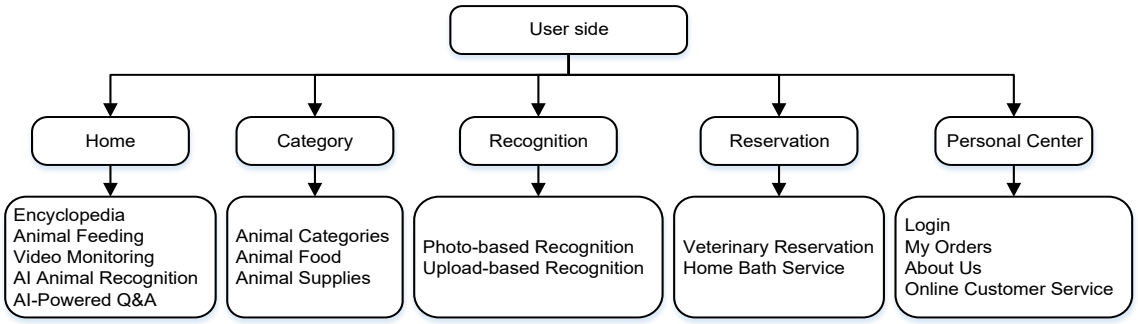


Fig. 8 - Functions of the client-side app

Deployment Side

This module serves to monitor and manage feeding work and surrounding environment in large-scale breeding sites in a unified way. A variety of sensing devices and video shooting devices are set up around feeding zones. These devices can work nonstop to gather various data. The collected information includes temperature, moisture, light intensity, animal weight and other related breeding indicators. Individual data and environmental data for each animal are aggregated using individual identifiers as indices, enabling feeding personnel to grasp group status in real time and providing a basis for subsequent intelligent feeding decisions and data analysis.

After data association is established between the mini-program and field devices, device acquisition results are synchronously transmitted to the mini-program for display. Uploaded data mainly include feeding information, body weight information, environmental information, and image information captured by the camera. Users can centrally view and compare state changes on the page, thereby assisting in feeding amount adjustment and management strategy optimization, reducing feed waste, and improving management efficiency. The deployment-side data acquisition and classification architecture is shown in Figure 9.

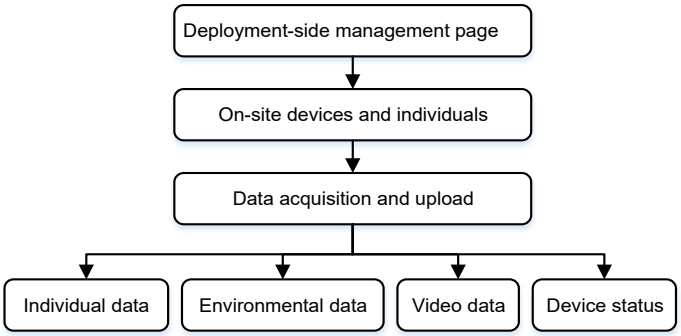


Fig. 9 - Deployment-Side Data Acquisition and Classification Architecture

On the deployment-side interface, users can centrally view individual and environmental data and remotely control lower-level actuators. The system establishes a wireless network connection through ESP8266, allowing the lower-level device to access the cloud message service as an MQTT client. The device uploads collected temperature, humidity, illumination, body weight, and device operational status to the cloud at the configured interval, and the cloud forwards the data through fixed data channels. After the mini-program connects to the cloud, it continuously listens to the data channel and receives new data in real time to refresh the page display.

For the control link, operations such as turning on the buzzer and turning off lighting are sent by the mini-program to the cloud control channel. The lower-level device continuously listens to the control channel and, after receiving control content, determines the required action according to predefined control fields, then drives actuators such as the buzzer and LED to respond. After execution, the lower-level device can upload the latest status again for synchronization on the mini-program interface. The mini-program control flow for the lower-level device is shown in Figure 10.

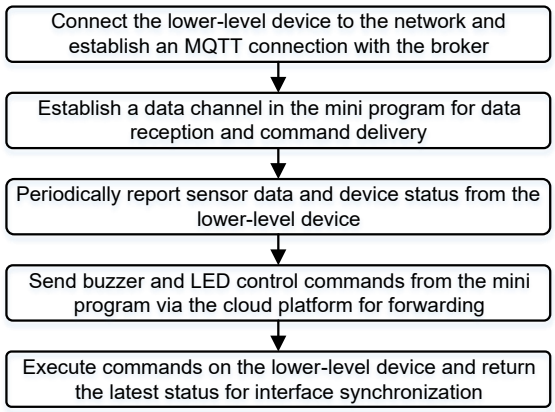


Fig. 10 - Mini-Program Control Flowchart for the Device Side

RESULTS

Test Results and Analysis

To verify the availability and trigger reliability of the system in practical feeding scenarios, comparative tests were conducted for (i) audio-video pointing and observation performance and (ii) feeding target confirmation and triggering performance. For the audio-video comparison, three experimental groups were set: video, audio, and audio and video. For the feeding trigger comparison, three experimental groups were set: RFID, weight, and RFID and weight. Each experimental group included 300 event-level trials. The final results were sorted and summed up based on the indexes shown in Table 4 and Table 5.

Table 4

Comparison Results of Audio-Video Pointing

Group	Configuration	Pointing Success Rate (%)	Loss Rate (%)	Mean Re-stabilization Time (ms)
A	Video	78.33	21.67	230
B	Audio	66.00	34.00	310
C	Audio and Video	92.67	7.33	145

The share of test runs with stable pointing is called pointing success rate. The stable state is kept during the whole fixed observation period. The loss rate describes the percentage of test cases. These cases include target loss or obvious direction error in pointing. The mean re-stabilization time refers to the average time required to restore stable pointing after target loss. It is used to rebuild stable pointing after the target is lost. Three hundred event-level test runs were arranged in each experimental group.

Three key indexes of the three test schemes are shown in Table 4. They are pointing success rate, loss rate and average re-stabilization time. For the video test group, the pointing success rate reached 78.33%. The loss rate of this group was 21.67%. The average re-stabilization time was 230 ms. For the audio test group, the pointing success rate was 66.00%. This rate was lower than the video group. The loss rate of the audio group reached 34.00%. This rate was higher than the video group. The average re-stabilization time was 310 ms. It was also longer than the video group. The test result of the audio group shows that only sound direction cues cannot offer enough stability. They cannot support stable pointing and continuous observation well. The test group using both audio and video got the best test effect. Its pointing success rate rose to 92.67%. The loss rate fell to 7.33%. The average re-stabilization time was reduced to 145 ms. When the target cannot be seen for a short time, or the pointing direction goes wrong, audio information can offer direction guidance. It helps to make the re-stabilization time shorter. After the target comes into the view range, video information provides clearer position feedback. It helps to keep pointing more stable. Using audio and video together obviously reduces the loss rate. It also increases the proportion of stable pointing. This improved performance makes on-site observation and debugging more continuous.

Table 5

Comparison Results of Feeding Target Confirmation and Triggering

Group	Decision Method	Trigger Accuracy (%)	Misdelivery Rate (%)	Missed-feeding rate (%)	Mean Trigger Delay (ms)
A	RFID	92.00	2.00	6.00	300
B	Weight	82.33	6.67	11.00	2500
C	RFID and Weight	93.33	2.00	4.67	2200

Trigger accuracy is defined as the proportion of cases in which the system successfully executes feeding when the target animal has arrived and the RFID identity matches. The misdelivery rate is defined as the proportion of cases in which feeding is still executed when the target has not arrived or the RFID identity does not match. The missed-feeding rate is defined as the proportion of cases in which the target animal has arrived and the identity matches, but the system does not execute feeding. Trigger delay is defined as the average time from the moment the animal arrives and is successfully recognized to the start of feeding execution. For the weight group, the trigger condition was that the weight reading exceeded a threshold and satisfied a stability-window condition. Identity matching was used only for statistical evaluation, with RFID used as the ground-truth label, and RFID did not participate in trigger decision-making for the weight group. Each experimental group included 300 event-level trials.

Table 5 reports the trigger accuracy, misdelivery rate, missed-feeding rate, and mean trigger delay for the three decision methods. For the RFID test group, the correct trigger rate was 92.00%. The wrong feeding rate was 2.00%. The missed feeding rate was 6.00%. The average trigger delay time was 300 ms. These test data show that RFID can finish target confirmation quickly. However, missed feeding may still occur. This situation appears when the animal does not stay in a stable position. It also happens when RFID signal reading conditions are influenced. For the weight test group, the correct trigger rate was 82.33%. The wrong feeding rate reached 6.67%. The missed feeding rate was 11.00%. The average trigger delay time was 2500 ms. The trigger delay time increased obviously. Both the wrong feeding rate and the missed feeding rate remained at relatively high levels. The unstable body posture of animals causes fluctuations in weight reading values. For this reason, the judgment method that only uses weight threshold has clear shortcomings. It has difficulty balancing trigger speed and trigger correctness. For the test group using both RFID and weight detection, the correct trigger rate rose to 93.33%. The wrong feeding rate fell to 2.00%. The missed feeding rate dropped to 4.67%. The average trigger delay time was 2200 ms. The results of the combined test show that RFID confirmation works effectively. It can reduce the risk of wrong feeding caused by target matching errors. Weight information improves the reliability of arrival determination. Although the joint decision sacrifices some triggering speed, it significantly improves trigger accuracy and feeding reliability and is therefore more suitable for long-term field operation.

Taken together, the two sets of comparative results indicate that the combined audio and video configuration improves the continuity of pointing and observation, reduces loss, and shortens re-stabilization time, whereas the combined RFID and weight decision improves feeding trigger accuracy and reduces misdelivery and missed delivery. These findings demonstrate that the system has good engineering usability under field conditions and can support target confirmation, information acquisition, and feeding execution during the feeding process.

Each of the 300 tests in every group was treated as one complete system event. After each event, the current decision state was cleared to minimize carryover between successive tests. Therefore, the results represent repeated observations at the system event level. The higher pointing success rate and shorter re-stabilization time obtained with the combined audio and video configuration may be explained by the complementary roles of the two information sources under different observation conditions. Visual information provides relatively accurate positional feedback when the target is clearly visible. Acoustic information is not used for precise localization. Instead, it provides a directional reference for pan-tilt reorientation when visual tracking is temporarily degraded or the target is lost. Previous studies have shown that variations in illumination, animal posture, and environmental conditions can affect the stability and generalization of visual monitoring systems in pigs *(Scaillierez et al., 2024; Han et al., 2023)*. The present results further show that acoustic directional information can provide supplementary cues when visual observations are limited, thereby improving monitoring continuity. This finding is consistent with previous studies on the complementary use of audio and visual information in animal monitoring *(Yang et al., 2025)*. In the feeding trigger process, RFID and weight information correspond to identity verification and arrival confirmation, respectively. Previous studies have commonly used RFID-based systems for individual identification and feeding behavior recording *(Funk et al., 2024)* or weighing devices to acquire body weight information *(Decarie et al., 2025)*. In the present system, both signals are incorporated into the same trigger decision. Feeding execution is therefore constrained by both individual identity and physical arrival at the feeding position. This approach was associated with improved trigger reliability in the present tests, although the stability check for the weight signal also increased trigger delay. Overall, the results indicate that the multisource information coordination mechanism improved monitoring continuity and feeding trigger reliability, thereby supporting the feasibility and operational reliability of the prototype system.

CONCLUSIONS

To meet the requirements of refined feeding and traceable management, this study designed and implemented an intelligent animal feeding system based on multisource information acquisition. The system uses STM32F103ZET6 as the control core, incorporates visual and audio sensing units, and integrates RFID-based identity recognition, weighing, and environmental parameter acquisition modules. When an animal enters the feeding area, the system can perform target monitoring and localization, individual identity confirmation, and acquisition of body weight and environmental parameters, and can upload the acquired results together with feeding execution status to form multi-target feeding records and a remote management link, thereby providing a feasible data basis for subsequent physiological assessment and traceability applications.

(1) The system uses an OpenMV camera to detect color blobs with preset color thresholds and to control pan and tilt tracking. A K210 microphone array provides directional information about the sound source. The acoustic direction is used to maintain target pointing when illumination is weak or camera observations are unstable. The combined sensing method improves continuous monitoring under complex lighting and occlusion conditions. Under the combined audio and video configuration, the pointing success rate was 92.67%, the loss rate was 7.33%, and the mean re-stabilization time was 145 ms.

(2) In multi-target feeding scenarios, an RFID reader and writer module at the feeding port obtains each animal's unique ear tag number, while an HX711-based weighing unit collects body weight information. Identity and body weight are then synchronously associated as key variables for each feeding event. The system also controls the feeding mechanism for individualized feeding. This changes feeding from a manual, experience-based process into one that is controllable, recordable, and reproducible. The workflow provides an implementation path for individualized and differentiated feeding. Under the combined RFID and weight configuration, the trigger accuracy was 93.33%, the misdelivery rate was 2.00%, the missed-feeding rate was 4.67%, and the mean trigger delay was 2200 ms.

(3) Different kinds of environmental data like temperature, humidity and light are collected by this system. Network connections are built through the ESP8266 device. MQTT is used to finish uploading data and sending commands. The WeChat mini-program serves as the information aggregation and interaction interface, enabling visualization of feeding records and body weight/environment trends, and supporting remote control and parameter configuration. Through multisource data acquisition and interaction, the system enables end-to-end monitoring and management.

Future work may introduce target tracking and re-identification algorithms to maintain continuous individual tracking in multi-target scenarios, reduce identity interruption caused by occlusion and interaction, and preserve individual identity as much as possible during unstable card reading or short-term occlusion. To enrich animal state information, non-contact sensors such as infrared and radar can be added to the existing device and aligned/fused with existing video and audio data to form more complete multi-target datasets. Based on continuously accumulated multisource data, animal health status can be predicted, health anomaly detection and risk alerts can be performed, and feeding adjustment recommendations can be generated, thereby further improving the level of refined management.

ACKNOWLEDGEMENT

The authors would like to thank all the funding projects for their support in this study:

Project No. CXGC2025076, "Scientific and Technological Innovation Enhancement Project" of Shanxi Agricultural University.

Project No. 2011NYZD2202, Open Program Foundation of the Key Laboratory of Equipment and Informatization in Environment Controlled Agriculture, Ministry of Agriculture and Rural Affairs of China.

Project No. 202302010101002, Key R&D Program of Shanxi Province.

Project No. 2023-092, Shanxi Scholarship Council of China.

REFERENCES

[1] Bhaskaran, H. S., Gordon, M., & Neethirajan, S. (2024). Development of a cloud-based IoT system for livestock health monitoring using AWS and python. *Smart Agricultural Technology*, 9, 100524.

[2] Bus, J. D., Boumans, I. J., te Beest, D. E., Webb, L. E., Bolhuis, J. E., & Bokkers, E. A. (2024). Understanding the feeding strategies of growing-finishing pigs: Exploring links with pig characteristics and behaviour. *Applied Animal Behaviour Science*, 272, 106208.

[3] Bus, J. D., Boumans, I. J., Engel, J., Te Beest, D. E., Webb, L. E., & Bokkers, E. A. (2023). Circadian rhythms and diurnal patterns in the feed intake behaviour of growing-finishing pigs. *Scientific reports*, 13(1), 16021.

[4] Bus, J. D., Franchi, G. A., Boumans, I. J., Te Beest, D. E., Webb, L. E., Jensen, M. B., Pedersen, L. J., & Bokkers, E. A. (2025). Short-term associations between ambient ammonia concentrations and growing-finishing pig performance and health. *Preventive Veterinary Medicine*, 242, 106555.

[5] Decarie, F., Grant, C., & Dallago, G. (2025). Weighing finishing pigs in motion: A walk-over scale for accurate weight estimation. *Computers and Electronics in Agriculture*, 232, 110019.

[6] Durand, M., Largouët, C., De Beaufort, L. B., Dourmad, J. Y., & Gaillard, C. (2023). Prediction of the daily nutrient requirements of gestating sows based on sensor data and machine-learning algorithms. *Journal of Animal Science*, 101, skad337.

[7] Funk, T. H., Rohrer, G. A., Brown-Brandl, T. M., & Keel, B. N. (2024). Online feeding behavior monitoring of individual group-housed grow-finish pigs using a low-frequency RFID electronic feeding system. *Translational Animal Science*, 8, txae051.

[8] Gaillard, C., & Dourmad, J. Y. (2022). Application of a precision feeding strategy for gestating sows. *Animal Feed Science and Technology*, 287, 115280.

[9] Garrido-Izard, M., Correa, E. C., Requejo, J. M., Villarroel, M., & Diezma, B. (2022). Cleansing data from an electronic feeding station to improve estimation of feed efficiency. *Biosystems Engineering*, 224, 361-369.

[10] Gauthier, R., Largouët, C., Bussières, D., Martineau, J. P., & Dourmad, J. Y. (2022). Precision feeding of lactating sows: implementation and evaluation of a decision support system in farm conditions. *Journal of Animal Science*, 100(9), skac222.

[11] Han, J., Siegford, J., Colbry, D., Lesiyon, R., Bosgraaf, A., Chen, C., Norten, T., & Steibel, J. P. (2023). Evaluation of computer vision for detecting agonistic behavior of pigs in a single-space feeding stall through blocked cross-validation strategies. *Computers and Electronics in Agriculture*, 204, 107520.

[12] Kavlak, A. T., Pastell, M., & Uimari, P. (2023). Disease detection in pigs based on feeding behaviour traits using machine learning. *biosystems engineering*, 226, 132-143.
[13] Lagoda, M. E., Boyle, L. A., Marchewka, J., & O'Driscoll, K. (2025). Welfare implications of non-nutritive visits to an electronic feeder by pregnant gilts. *Applied Animal Behaviour Science*, 106758.
[14] Leliveld, L. M., Brandolese, C., Grotto, M., Marinucci, A., Fossati, N., Lovarelli, D., Riva, E., & Provolo, G. (2024). Real-time automatic integrated monitoring of barn environment and dairy cattle behaviour: Technical implementation and evaluation on three commercial farms. *Computers and Electronics in Agriculture*, 216, 108499.
[15] McCarthy, K. L., Underdahl, S. R., Undi, M., & Dahlen, C. R. (2023). Using precision tools to manage and evaluate the effects of mineral and protein/energy supplements fed to grazing beef heifers. *Translational Animal Science*, 7(1), txad013.
[16] Nyamuryekung'e, S. (2024). Transforming ranching: Precision livestock management in the Internet of Things era. *Rangelands*, 46(1), 13-22.
[17] Ribas, C., Quiniou, N., & Gaillard, C. (2024). On farm precision feeding of gestating sows based on energy and amino acids on farrowing performances and feeding behavior over 3 consecutive gestations. *Journal of Animal Science*, 102, skae201.
[18] Scaillierez, A. J., Izquierdo García-Faria, T., Broers, H., van Nieuwamerongen-De Koning, S. E., Van Der Tol, R. P., Bokkers, E. A., & Boumans, I. J. (2024). Determining the posture and location of pigs using an object detection model under different lighting conditions. *Translational Animal Science*, 8, txae167.
[19] Spinler, M. S., Woodworth, J. C., Tokach, M. D., Goodband, R. D., DeRouchey, J. M., Frobose, H. L., Uitermarkt, A., & Gebhardt, J. T. (2024). Evaluation of precision feeding standardized ileal digestible lysine and other amino acids to determine and meet the lactating sow's requirement estimates. *Journal of Animal Science*, 102, skae285.
[20] Wallgren, P., Johansson, S. E., Kirk, M., Mattsson, P., Lindahl, L., & Zoric, M. (2025). Varied residential options for gestating sows ensured welfare and productivity. *Porcine Health Management*, 11(1), 63.
[21] Yang, Y., Xu, C., Hou, W., McElligott, A. G., Liu, K., & Xue, Y. (2025). Transformer-based audio-visual multimodal fusion for fine-grained recognition of individual sow nursing behaviour. *Artificial Intelligence in Agriculture*, 15(3), 363-376.
[22] Zhang, S., Peng, J., Huang, Q., Li, Z., & Yin, L. (2025). Pig body weight prediction based on weight waveform graph. *Computers and Electronics in Agriculture*, 236, 110412.

RESEARCH PROGRESS AND DEVELOPMENT TRENDS OF KEY TECHNOLOGIES FOR ELECTRIC TRACTORS
/
纯电动拖拉机关键技术研究进展与发展趋势

Xiaodong LV[1)], Zhaoyue LIU[1)], Jikang XU[*1)], Jinliang LI[2)]
[1)] Qingdao Agricultural University, Qingdao / China;
[2)] Long Agricultural Equipment Co., Ltd., Linyi, Shandong, China.
Tel: 15275289164; E-mail: xujikang@qau.edu.cn
Corresponding author: Jikang Xu
DOI: https://doi.org/10.35633/inmateh-79-66

Keywords: *Electric tractor, powertrain, energy management, intelligent control, system simulation, technology readiness*

ABSTRACT
Research on electric tractors has expanded rapidly; however, previous reviews have generally examined energy sources, powertrains, intelligent control, and supporting infrastructure separately. This narrative review establishes an integrated technology-chain framework encompassing energy supply, electric drive systems, energy management, power take-off (PTO) and hitch control, autonomous operation, simulation, standardization, and industrial deployment. The available evidence was synthesized and compared in terms of system performance, advantages, limitations, and technological maturity. The results indicate that battery-electric systems can reduce energy consumption and life-cycle environmental impacts but remain constrained by limited operating endurance, high battery costs, thermal-safety risks, and insufficient charging capacity. Hybrid and fuel-cell powertrains offer greater adaptability to varying operating conditions but introduce additional system complexity. Future research should prioritize standardized duty cycles, integrated simulation frameworks, modular energy-replenishment systems, reliability testing, and interoperability standards.

摘要
电动拖拉机研究发展迅速，但既有综述通常将能源来源、动力系统、智能控制和配套基础设施割裂讨论。本研究采用叙述性综述方法，建立了涵盖能源供给、电力驱动、能量管理、动力输出轴与悬挂控制、自主作业、系统仿真、标准体系及产业化应用的技术链框架，并从性能、优势、局限和成熟度等方面比较相关证据。结果表明，纯电动系统能够降低能源需求和全生命周期环境影响，但仍受续航能力、电池成本、热安全与充电能力制约；混合动力和燃料电池路线可提高工况适应性，却增加系统复杂性。未来应重点推进标准化作业循环、集成仿真、模块化能源补给、可靠性测试及互操作标准。

INTRODUCTION

Agricultural tractors must deliver high tractive power and power take-off (PTO) output under strongly variable loads, while reducing fossil-fuel use, local air pollutants, and greenhouse-gas emissions. Electric powertrains offer high conversion efficiency and precise torque control, but their benefits depend on the electricity mix, battery manufacture, duty cycle, and charging strategy. Life-cycle studies have reported substantial reductions in climate and resource impacts for battery-electric field systems, while also identifying battery production, purchase cost, mass, and operating range as important trade-offs *(Lagnelˆ v et al., 2021; Mousazadeh et al., 2011; Vogt et al., 2021)*.

This review used a structured narrative-synthesis protocol. Peer-reviewed English- and Chinese-language studies were identified in Web of Science Core Collection, Scopus, and CNKI using terms related to electric and hybrid tractors, batteries, electric drives, energy management, PTO/hitch control, autonomous navigation, and simulation. Searches prioritized 2015-2026 publications; earlier landmark prototypes, control methods, and life-cycle assessments were retained, and backward citation searching supplemented the results.

Studies were included when they addressed tractor-specific architecture, components, modeling, control, field testing, environmental performance, or deployment economics and supplied sufficient evidence for comparison. Because tasks, power classes, and metrics were heterogeneous, the evidence was grouped by technology chain and compared using reported indicators, advantages, limitations, and maturity rather than pooled statistically.

Unlike previous reviews focusing on individual subsystems or the status of domestic technological development *(Liu et al., 2022; Liu H.L. et al., 2024; Wang L. et al., 2025)*, this study links component-level advances to whole-vehicle integration and deployment readiness. It compares powertrain architectures; evaluates batteries, electric drives, energy management, PTO and hitch control, autonomous navigation, and simulation methods; and identifies cross-cutting bottlenecks to establish a staged research agenda. The proposed framework distinguishes laboratory-scale advances from field-ready capabilities.

Table 1

Literature retrieval and screening framework

Review stage	Database / source	Search topic	Selection criteria	Analytical use
Database retrieval	Web of Science Core Collection; Scopus; CNKI	Electric and hybrid tractors; batteries; electric drives; energy management; PTO/hitch control; autonomous navigation; simulation	Peer-reviewed English- or Chinese-language studies; priority period 2015–2026	Identify tractor-specific technical, environmental, and deployment evidence
Supplementary retrieval	Backward citation searching	Landmark prototypes, control methods, and life-cycle assessments	Earlier studies retained only when foundational to technological evolution	Trace development stages and preserve seminal evidence
Eligibility screening	Title, abstract, and full-text review	Architecture, components, modeling, control, field testing, environmental performance, and economics	Tractor-specific scope and sufficient quantitative or qualitative evidence for comparison	Exclude non-tractor studies and records with insufficient comparative evidence
Evidence synthesis	Included studies	Reported performance, advantages, limitations, and indicative maturity	Grouped by technology chain; no statistical pooling because tasks and metrics were heterogeneous	Support comparative tables, bottleneck analysis, and the staged research agenda

Although electric tractors have achieved notable advances in diversified power supply and intelligent control, they still face practical challenges in operational adaptability, high manufacturing costs, and large-scale industrial promotion. Focusing on key common technologies, core industry bottlenecks, and actual agricultural production needs, this study aims to advance the industrialization and practical application of electric tractors. The main research contents are as follows.

(1) Development overview: The technological evolution of electric tractors is reviewed across three generations, with emphasis on their technical configurations, characteristics, and limitations. Domestic and international development models are compared, and diversified powertrain and energy-supply technologies, including hybrid and solar-energy systems, are evaluated. This analysis clarifies the evolution of electric tractor technologies and provides a basis for improving operating endurance and adaptability to different applications, thereby supporting a differentiated development strategy for China's electric tractor industry.

(2) Core power technologies: Optimization strategies and technological advances in traction batteries, electric drive systems, energy management, and power coordination are examined to establish an integrated pathway for powertrain development.

(3) Intelligent control: Electric power steering, active suspension, autonomous navigation, and system simulation are reviewed to improve adaptability to field conditions and operational performance.

(4) Standard system and industrialization: Bottlenecks related to technologies, key components, standards, and supporting infrastructure are identified, and pathways toward industrialization are proposed to facilitate large-scale adoption.

Overall, this review supports technological innovation and industrial upgrading in the electric tractor sector, thereby contributing to the mechanized, intelligent, and environmentally sustainable development of agriculture in China.

TECHNOLOGICAL EVOLUTION AND POWER-SUPPLY CONFIGURATIONS

Development history and representative tractor models

The development of electric tractors falls into three stages. From the early 20th century to the 1970s was the wired power supply stage: Harbin Songjiang Tractor Factory developed China's first "Dianiu 28" electric tractor, powered by transmission lines with a 28 kW rated output, pioneering domestic research *(Yu et al., 2024a)* but not widely used due to grid limitations. From the 1970s to the early 21st century, it shifted from wired power to on-board batteries, enabling wheel driving and power take-off shaft control, with initial promotion driven by energy storage technology. Since the early 21st century, high-density battery technology has supported long-time light-load operation; intelligent functions and unmanned driving based on path planning have matured. Electric tractors covering a wide range of power ratings are currently being developed by numerous manufacturers *(Han, 2023)*.

International research has progressed from solar-assisted and battery-powered prototypes to autonomous platforms, hybrid powertrains, and farm-level energy planning. In addition to the life-cycle and farm-system analyses summarized above, prototype- and system-level studies have investigated tractor electrification, autonomous field robots, parallel-hybrid control strategies, hardware-in-the-loop validation, and series-hybrid powertrain sizing *(Dalboni et al., 2019; Estevez et al., 2024; Ghobadpour et al., 2021; Ghobadpour et al., 2022; Grimstad and From, 2017; Mocera and Somà, 2020; Mocera, 2021; Pedersen et al., 2006; Rosales et al., 2022; Ueka et al., 2013)*. Collectively, these studies demonstrate the technical feasibility of electric agricultural machinery; however, operating endurance under field conditions, implement integration, charging logistics, and economic viability remain dependent on the specific application.

Research and product development in China have pursued battery-electric, diesel-electric hybrid, and hydrogen fuel-cell technologies in parallel. High-power hybrid prototypes have focused on sustained operation under heavy loads, whereas smaller battery-electric tractors have been developed primarily for greenhouse, orchard, and transport applications. Representative projects have advanced dual-motor power coupling, electronically controlled continuously variable transmissions, distributed drive systems, and tractor-specific energy-management strategies *(Feng et al., 2023; Li et al., 2023; Wen et al., 2025)*. A major advantage is the ability to leverage the existing agricultural-machinery supply chain for rapid technological development. However, validation across diverse operating conditions remains limited, some high-end components still depend on imports, and charging and maintenance infrastructure is unevenly developed. Representative products are presented in Fig. 1.



(a) X-Tractor *(b) CNH concept tractor* *(c) MK-V* *(d) E-Power*

(e) HB2204 *(f) E3404-8H* *(g) ET14100* *(h) E904i*

Fig. 1 - Representative electric tractor models developed in China and other countries

The comparison indicates that powertrain selection depends primarily on the duty cycle rather than following a uniform geographical pattern. Battery-electric systems are the most technologically mature option for low- and medium-power tasks with predictable daily energy requirements. Hybrid systems retain an advantage in prolonged, high-load operations, whereas hydrogen fuel-cell systems remain at the prototype or early demonstration stage because their potential vehicle-level benefits must be weighed against the challenges associated with hydrogen production, storage, and distribution.

Accordingly, Table 2 compares representative tractor platforms in terms of powertrain type, reported performance, advantages, limitations, and suitable applications.

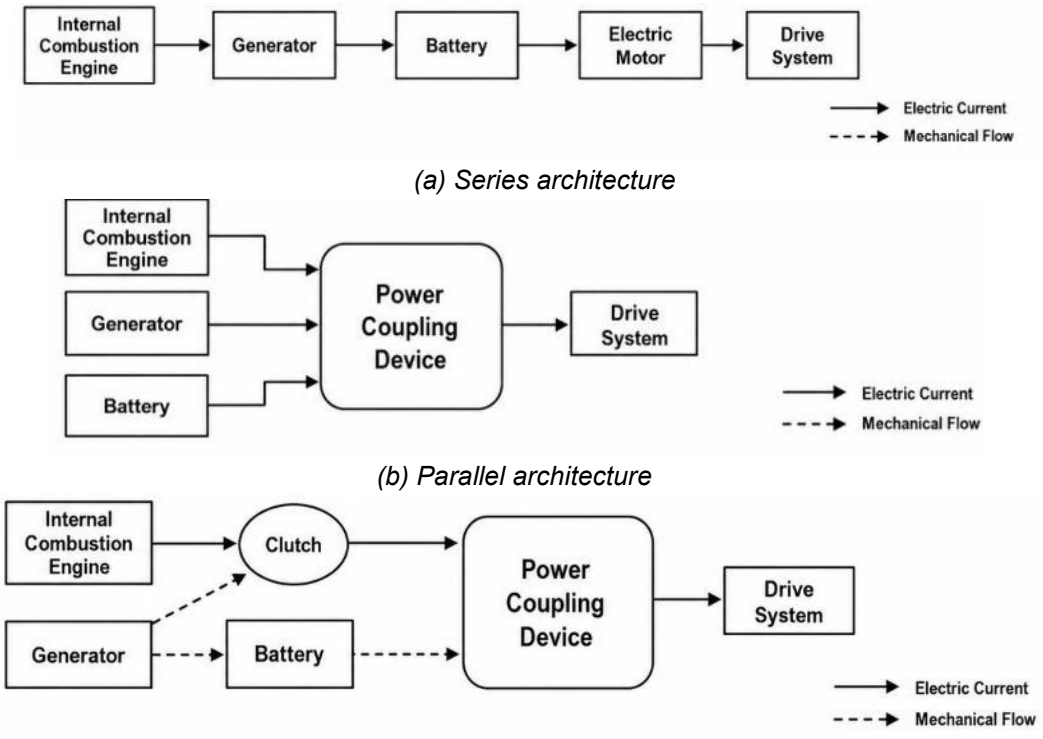
Table 2

Representative electric tractor platforms and their application characteristics

Representative platform	Power train or energy-supply type	Reported performance	Main advantage	Main limitation	Suitable application	Technology maturity
Dianiu 28 *(Yu et al., 2024a)*	Cable-powered electric	Rated power: 28 kW	Continuous power supply	Grid and cable restriction	Fixed-area work	Historical prototype
Solar-assisted prototype *(Mousazadeh et al., 2011)*	Solar-assisted battery-electric	≈14 t CO_2-eq annual reduction in case study	Lower life-cycle impact	Cost, mass and range	Light duty / demonstration	Prototype
Unmanned platform *(Chen et al., 2022)*	Battery electric; dual motor	2 × 7.5 kW; ≥3.5 h	Compact autonomous operation	Low power and endurance	Orchards / protected farming	Field prototype
Autonomous fleet *(Lagnelˆv et al., 2021)*	Battery-electric fleet	102 vs 293 kg CO_2-eq ha^{-1} y^{-1}	Life-cycle benefit	Charging coordination	Predictable field schedules	System simulation / pilot evidence
Terrain-aware platform *(Luo et al., 2024)*	Battery electric	Speed stability +45.09%; energy −9.51%	Terrain adaptation	Single test setting	Variable-soil traction	Field prototype
Field charging / exchange *(Wallander et al., 2025)*	Battery-electric farm system	Process time +5%; energy 37.5% of diesel	Near-diesel work rate	Grid and logistics sensitivity	Large coordinated farms	Farm-system modeling

Comparative assessment of diversified powertrain technologies

Electric tractor development in China currently integrates diverse powertrain and energy-supply technologies, including battery-electric, diesel-electric hybrid, biomass-based, solar-powered, and fuel-cell systems. These technologies are being explored to overcome the limitations of battery-electric tractors in terms of operating endurance and adaptability to different applications, and substantial progress has been achieved. However, the available technological options differ considerably in power performance, economic viability, environmental adaptability, and technological and industrial maturity.



(a) Series architecture

(b) Parallel architecture

(c) Power-split architecture

Fig. 2 - Architectures of hybrid electric powertrains

Diesel-electric hybrid systems can reduce engine transients and extend endurance while retaining rapid refueling. Series architectures simplify mechanical transmission and permit flexible engine operation; parallel and power-split layouts can achieve higher peak efficiency but require more complex coordination. Recent studies have used life-cycle-cost analysis, dynamic programming, model-predictive control, fuzzy following control, and hardware-in-the-loop testing to compare architectures and operating strategies *(Beligoj et al., 2022; Mocera, 2021; Zhang et al., 2023; Yan et al., 2024; Zhao et al., 2024a, 2024b; Pascuzzi et al., 2024)*.

The evidence is promising but remains dominated by prototypes, simulations, or individual duty cycles rather than multi-season commercial operation.

Solar energy is more viable as an auxiliary or farm-level energy source than as the sole source of traction power. Vehicle-mounted photovoltaic panels can supply low-power auxiliary systems and extend operating time, whereas rooftop or field-edge photovoltaic installations can provide electricity for battery charging or swapping stations. A solar-assisted plug-in hybrid tractor prototype achieved lower annual life-cycle emissions but remained constrained by battery weight and limited operating range *(Mousazadeh et al., 2011)*. Farm-system simulations further indicate that coordinated charging and battery swapping can maintain operational work rates while reducing energy consumption *(Wallander et al., 2025)*. Table 3 summarizes the advantages, limitations, and technological maturity of these solar-energy integration configurations.

Table 3

Comparison and technological maturity of solar-energy integration configurations

Integration configuration	Energy-system configuration	Reported performance	Main advantage	Main limitation	Technology maturity
Vehicle-mounted PV	PV + traction battery	Contribution to auxiliary power; tractor-specific field data remain limited	Utilizes otherwise unused vehicle surfaces	Area, shading, dust and mass	Concept / prototype
Solar-powered charging station	PV + stationary storage + charger	Output depends on solar irradiance and the sizing of the storage and charging systems	Separates solar-energy collection from the vehicle's available surface area	Land requirements and capital costs	Pilot / early deployment
Integrated farm-energy system	PV + grid + storage + fleet scheduling	Operational work rate depends on grid capacity, battery size, and logistical coordination	Supports multiple machines and peak-load management	Complex planning and seasonal use	System modeling / pilot

Biomass-derived fuels can utilize locally available agricultural residues and may reduce net fossil-carbon consumption. However, their relevance to electric tractors lies primarily in range-extender generators, farm microgrids, and hydrogen production rather than in the direct replacement of traction batteries. Studies of biodiesel, biomass gasification, and integrated biomass–solar systems have demonstrated the potential of locally sourced energy supplies *(Jing et al., 2025; Liu H., 2024; Sun et al., 2025; Wang D.G. et al., 2024)*. Nevertheless, feedstock logistics, gas-cleaning requirements, conversion efficiency, and seasonal feedstock availability limit their broader applicability. These technologies should therefore be evaluated at the farm-system level through comprehensive energy, emissions, and cost assessments.

Fuel-cell electric tractors offer fast refueling and high gravimetric energy density, but stack durability, hydrogen storage, thermal management, and fuel infrastructure remain decisive.

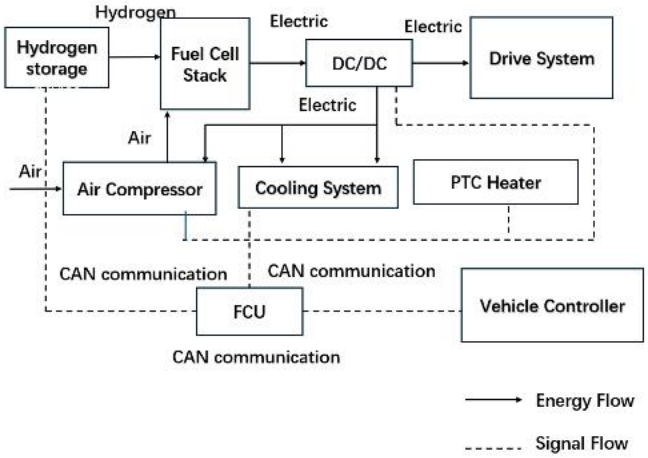


Fig. 3 - Fuel-cell electric tractor system architecture

Integrated electromechanical-hydraulic modeling has shown that optimized energy management can reduce hydrogen consumption and state-of-charge fluctuation under plowing and transport cycles *(Liu et al., 2023; Yu et al., 2024c; Zhang M. et al., 2025)*. Predictive control validated on a fuel-cell powertrain testbed also reduced damaging load cycling without sacrificing efficiency across three agricultural duty cycles *(Varlese et al., 2024)*. These results move the technology beyond concept analysis, but whole-tractor durability and farm-scale hydrogen supply still require field demonstration.

POWERTRAIN AND ENERGY MANAGEMENT TECHNOLOGIES

Battery systems and management

The power battery determines vehicle mass, available power, continuous operating time, thermal risk, and total cost. Lead-acid and nickel-metal hydride batteries retain niche advantages in cost or robustness, but lithium-ion chemistries dominate new electric-tractor designs because of their higher specific energy and cycle efficiency. Lithium iron phosphate prioritizes thermal stability and cycle life, whereas nickel-rich chemistries prioritize gravimetric energy density. Fig. 4 compares the principal performance trade-offs; the appropriate chemistry must be selected using task-level energy and peak-power demand, ambient temperature, packaging, and maintenance constraints rather than energy density alone.

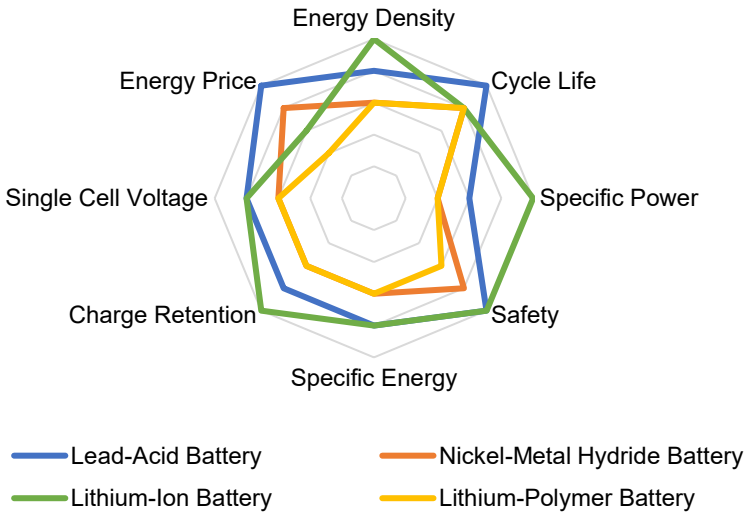


Fig. 4 - Comparison of battery technologies

Lithium-ion systems remain the practical baseline for current electric tractors. LFP cells are attractive for heavy-duty and harsh-environment applications because safety and cycle life are prioritized, while higher-energy chemistries can reduce pack mass for orchard, horticultural, and transport tasks. Battery sizing should also account for auxiliary hydraulic and PTO loads, which are often underrepresented when capacity is derived only from traction demand. Research on high-specific-energy systems and lithium-sulfur batteries indicates potential for future mass reduction, but field durability, cost, and safety validation remain incomplete *(Zhang et al., 2014; Wen et al., 2025)*.

Solid-state and sodium-ion batteries may eventually widen the feasible operating-temperature and cost envelope, but published tractor-specific evidence remains limited. Claims based on cell-level energy density cannot be transferred directly to pack or vehicle performance because structural protection, thermal management, state estimation, and power electronics add mass and losses. A defensible technology comparison therefore requires pack-level specific energy, usable depth of discharge, cycle life under pulsating loads, safety testing, and end-of-life recovery.

A tractor battery-management system must estimate state of charge and health, supervise voltage and temperature, balance cells, and enforce charge-discharge limits under rapidly changing traction, hydraulic, and PTO loads. The central challenge is not monitoring alone but reliable state estimation when current profiles, temperature, aging, and vibration differ markedly from standard road-vehicle cycles. Magneto-thermal coupling models have also been used to characterize battery temperature fields under dynamic loads *(Yang J.Q. et al., 2023)*.

Recent studies have combined filtering, power-frequency decomposition, condition recognition, and communication-network design to reduce battery peaks and improve energy allocation *(Xu et al., 2025; Xue et al., 2023; Zhang Q.H. et al., 2025)*. Data-driven estimators and digital twins can improve prediction, but they require representative field data, uncertainty bounds, and fail-safe behavior. Future validation should therefore report estimation error, computational load, aging sensitivity, and performance across multiple agricultural operations rather than a single simulated cycle.

Electric-drive architectures and control

Centralized drives preserve a conventional transmission path and therefore offer lower redesign cost, mature sealing and cooling, and straightforward maintenance. Their disadvantages are mechanical losses, limited independent wheel control, and reduced packaging flexibility. Distributed or wheel-side drives shorten the transmission path and enable independent torque allocation, but increase unsprung mass, sealing and thermal-management demands, controller coordination, and exposure to impact and mud.

For medium- and high-power tractors, dual-motor coupling provides an intermediate powertrain configuration that shifts motor operating points toward high-efficiency regions while maintaining mechanical robustness. Studies on the optimization of distributed-drive and coupled-drive systems have reported improvements in transmission efficiency and coverage of the operating range *(Li et al., 2023; Li et al., 2022)*. However, these comparisons are often based on different operating tasks and boundary conditions; therefore, the reported percentage improvements should not be considered directly transferable across systems or applications.

Motor selection must be matched to the actual low-speed, high-torque duty distribution. *Kwon et al. (2024)* found up to 7.9% difference in plowing energy consumption among motors with identical ratings but different efficiency-map distributions. This demonstrates that rated power alone is insufficient; frequent tasks, cooling limits, field-weakening operation, inverter losses, and gearbox ratios must be optimized jointly.

Distributed drive is therefore a promising architecture for precision traction and autonomous operation, but its present maturity is mainly prototype to early field-demonstration level. Centralized and coupled drives are more mature for near-term commercialization, especially where serviceability and component protection dominate the design decision.

Electric-drive control must maintain speed and traction while limiting wheel slip and energy loss under changing soil resistance. Rule-based and PID methods remain attractive for reliability and low computational demand, whereas fuzzy, observer-based, predictive, and learning-based controllers offer better adaptation at the cost of calibration, model, and validation burden.

Terrain-aware control provides a useful bridge between theoretical optimization and field operation. *Luo et al. (2024)* combined terrain-parameter identification, a sliding-mode observer, and optimal-slip control; hardware-in-the-loop and vehicle tests improved operating-speed stability by 45.09% and reduced total energy consumption by 9.51%. Other fuzzy and neural-network controllers have improved disturbance compensation, shift quality, and fault diagnosis *(Li Y. et al., 2024; Wang C.Y. et al., 2024; Yu et al., 2023; Yu et al., 2024b)*.

The main evidence gap is generalization. Many algorithms are evaluated on one soil, speed, implement, or simulated load. Future studies should disclose baseline controllers, sampling and computational requirements, uncertainty, and independent field validation across soil moisture, slopes, tire inflation, ballast, and PTO disturbances.

Hybrid power supply and energy management

A battery-supercapacitor hybrid energy-storage system separates energy demand from short-duration peak power. Passive topologies are simple but provide little control; semi-active topologies balance controllability, cost, and converter loss; fully active topologies provide the greatest power-allocation freedom but require two converters and more complex protection. Table 4 summarizes the functions, representative methods, benefits, limitations, and research priorities of key electric-tractor components and control systems.

Capacity sizing and control must be optimized together. Semi-active systems using fuzzy thresholds and genetic algorithms have reduced hourly power cost, while multi-objective allocation has reduced battery power fluctuation *(Li L.Q. et al., 2024a, 2024b; Xu et al., 2024)*. Deep-reinforcement-learning and predictive methods can further adapt power split to recognized agricultural conditions, but their robustness outside the training distribution remains a concern.

Table 4

Key electric-tractor components, control strategies, and research priorities

Component / strategy	Representative method	Reported indicator / advantage	Main limitation	Indicative maturity	Research priority
Battery and BMS	SOC/SOH estimation, balancing, thermal supervision	Reduces peak stress; safeguards usable energy	Aging, heat and limited field datasets	Commercial components; tractor validation developing	Pack-level safety and multi-season aging
Electric drive	Dual-motor coupling, terrain identification, slip control	Up to 7.9% motor-dependent plowing-energy difference; energy −9.51% in one terrain-aware test	Single-condition evidence and drivetrain complexity	Prototype to early field validation	Cross-soil and thermal validation
Hybrid storage	Semi-active DC/DC; fuzzy, optimization or predictive control	Buffers transient peak power and reduces battery fluctuation	Converter loss and sizing sensitivity	Laboratory / simulation to prototype	Joint sizing, aging and fault tolerance
PTO and hitch	Load following, force-position and fuzzy-PID control	Improves response and tillage-depth stability; metrics are not standardized	Impact loads and coupled dynamics	Prototype / subsystem field tests	Integrated standardized duty-cycle tests
Autonomous navigation	RTK-GNSS, sensor fusion, MPC and learning control	Centimeter-level guidance reported in controlled field studies	Perception uncertainty and functional safety	Field prototype; limited supervised deployment	Intervention, safety and energy metrics
Simulation / digital twin	Multi-domain models and HIL	Earlier controller verification and fault detection	Model fidelity and data interoperability	HIL established; digital twins emerging	Reusable models and parameter traceability

Semi-active topology is currently the most balanced research and prototype solution. Fully active systems may be justified for high-power tractors with severe load transients, whereas passive systems remain suitable only when cost and simplicity outweigh control performance. Technology selection should be supported by full-life-cycle converter loss, component aging, fault tolerance, and maintenance analysis.

Regenerative braking converts kinetic energy into electrical energy during deceleration, but tractor recovery potential is lower and more variable than in road vehicles because field speed is low, tire-soil adhesion is uncertain, and PTO or hydraulic loads may dominate the energy balance. Recovery control must therefore coordinate motor torque, friction braking, battery limits, wheel slip, and implement safety rather than maximize recovered energy alone. Fig. 5 summarizes the principal energy-management classes.

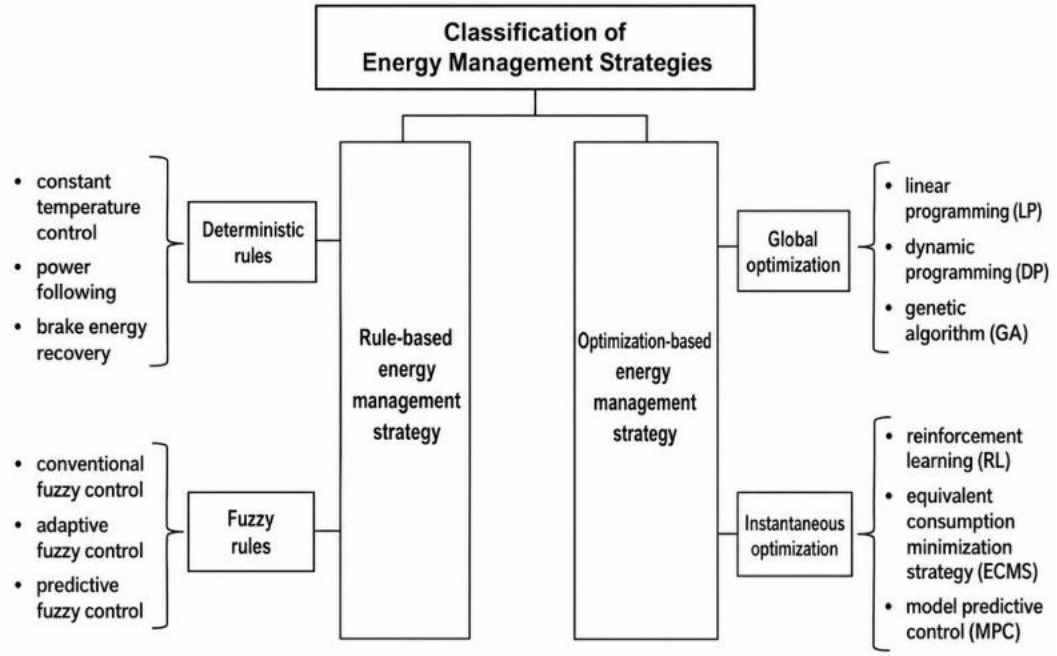


Fig. 5 - Classification of energy-management strategies

Rule-based strategies have low computational demand and predictable safety behavior, while model-predictive and learning-based methods can exploit load forecasts and repeated field patterns. International studies on off-road plug-in hybrids and parallel or series hybrid tractors report progress from offline global optimization toward operation recognition, predictive control, and real-time validation *(Ghobadpour et al., 2021; Mocera, 2021; Zhang et al., 2023; Yan et al., 2024; Zhao et al., 2024a)*. However, reported gains are not directly comparable because duty cycles, SOC boundaries, component maps, and baseline controllers differ.

Accordingly, advanced energy management should be evaluated against a transparent baseline using energy consumption, battery aging, hydrogen or fuel use, tracking error, computational time, and safety constraints. A numerical improvement obtained in one cycle is not sufficient evidence of technology readiness without real-time implementation and multi-condition field validation.

Current bottlenecks include weak adaptation to low-adhesion roads, saturation of battery charge acceptance during long descents, limited coordination among traction, hydraulic, hitch, and PTO subsystems, and the absence of standardized agricultural duty cycles. These gaps explain why many high-performing simulation strategies remain at laboratory or prototype maturity.

Agricultural operations require different combinations of vehicle speed, PTO speed, draft force, and hydraulic power. Adaptive strategies have improved cruising range, disturbance suppression, and PTO response *(Ding et al., 2024; Liao et al., 2024; Zhang et al., 2024; Zhou et al., 2024)*. Future controllers should identify the current operation and soil-load state online, but they must remain computationally lightweight and retain a validated fallback mode.

Power-output and PTO coordination

Electric tractors must divide available power among traction, PTO, hydraulic, and auxiliary loads. Mechanical coupling provides a direct and robust path for power splitting, whereas multi-motor architectures provide flexible electronic allocation. The latter can shift motor operating points and decouple traction from PTO speed, but increases inverter count, calibration effort, and fault-management requirements. A representative architecture is shown in Fig. 6.

Dual-motor coupling has expanded operating-mode coverage and improved plowing efficiency, but mechanical complexity and cost increase with the number of clutches and gear paths. Power-allocation strategies based on dynamic programming, Pontryagin's minimum principle, stochastic optimization, and load following have reduced equivalent fuel or energy consumption in specific tasks *(Li et al., 2019; Li T.H. et al., 2024; Zhang et al., 2023)*.

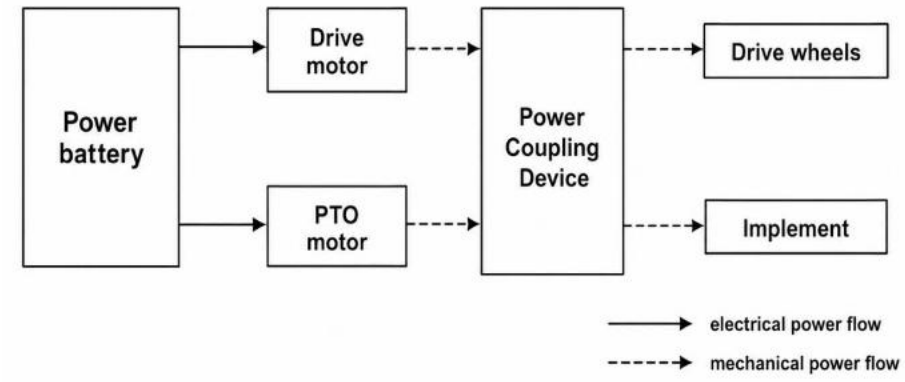


Fig. 6 - Power transmission system of the electric tractor

A key research priority is the integrated management of electrical, mechanical, hydraulic, and thermal systems, together with the development of standardized implement interfaces. Controller performance should be evaluated under simultaneous traction and PTO transients rather than only under steady-state loads. Evaluations should report torque reserve, PTO speed deviation, energy consumption, response time, and fault-recovery performance.

Load-following control is suitable for conventional operations involving variable draft; tractor–implement attitude coordination is required when working depth and posture determine agronomic quality; and multisource coupling is appropriate for high-power combined operations. These control modes are complementary rather than mutually exclusive. A field-ready system should switch between or blend them based on task recognition while maintaining slip, PTO speed, hitch position, and energy consumption within prescribed limits *(Xie et al., 2023; Yang F.Z. et al., 2023)*.

INTELLIGENT CONTROL AND DIGITAL DEVELOPMENT

Electric power steering replaces continuously driven hydraulic assistance with motor torque commanded from steering torque, angle, and vehicle-state signals. It improves controllability and enables automatic guidance, but agricultural deployment also requires high shock-load tolerance, sealing, redundancy, and safe manual fallback. Performance should be compared using steering effort, tracking error, response time, returnability, energy use, and fault behavior rather than road-feel metrics alone.

An electric hitch can regulate implement position and draft without continuous hydraulic throttling. Position, draft, and attitude feedback permit precise depth control, but motor and reduction mechanisms must withstand impact loads and contamination. Recent work has combined inclination sensing, force-position feedback, and fuzzy-PID coordination to improve body-implement attitude and tillage-depth stability *(Xie et al., 2024; Yang F.Z. et al., 2023; Zhang et al., 2022)*.

The main design trade-off is between the energy efficiency and controllability of electromechanical actuation and the overload capacity of hydraulics. Hybrid electro-hydraulic solutions may therefore remain preferable for high-power implements until compact actuators, impact protection, and thermal performance are validated.

Field evaluation should report depth error, draft-force fluctuation, settling time, energy consumption, mechanical temperature, and failure response across soil types and travel speeds. Without these common metrics, algorithm comparisons remain predominantly qualitative.

Autonomous navigation integrates GNSS/RTK, inertial sensing, perception, localization, path planning, and steering control. Early single-sensor guidance established the feasibility of automatic tractor steering, whereas later agricultural-robot studies emphasized modular platforms, sensor fusion, safety, task planning, and whole-farm economics *(Thuilot et al., 2002; Pedersen et al., 2006; Slaughter et al., 2008; Bechar and Vigneault, 2016; Grimstad and From, 2017; Shamshiri et al., 2018; Fountas et al., 2020; Lowenberg-DeBoer et al., 2020)*. For electric tractors, navigation accuracy must therefore be assessed together with energy use, implement performance, intervention frequency, and functional safety.

Linear, PID, optimal, model-predictive, and learning-based controllers provide different balances of computation, robustness, and curvature tracking. Recent tractor studies have used multi-body simulation, BeiDou/RTK, 5G monitoring, and resistance-adaptive control *(Jeon et al., 2023; Luo et al., 2025; Tian et al., 2024; Wang Q. et al., 2025)*. Commercial maturity is limited by obstacle perception, functional safety, remote supervision, and validation under dust, vibration, crop occlusion, and intermittent communication.

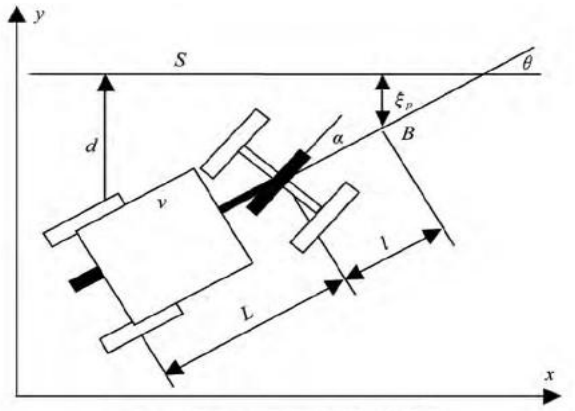


Fig. 7 - Tractor dynamic model

IoT integration can connect tractor, implement, operator, and service platform for condition monitoring and scheduling *(Wen and Wang, 2022; Zhao et al., 2023)*. However, interoperability, cybersecurity, data ownership, and degraded-mode operation must be treated as engineering requirements rather than later software additions.

System simulation and digital twins. General-purpose platforms such as MATLAB/Simulink, AMESim, ADAMS, AVL-Cruise, and multi-body tools support subsystem and vehicle development, but the literature still relies heavily on isolated models. Hardware-in-the-loop and model-based design have improved controller verification before field trials *(Mocera, 2021)*, while digital agricultural-robot platforms demonstrate the value of modular hardware and reusable software *(Grimstad and From, 2017)*. A tractor digital twin should link battery aging and thermal behavior with traction, PTO, hitch, hydraulics, navigation, and task-level energy demand, and should retain parameter provenance for reproducibility.

BOTTLENECKS AND DEVELOPMENT PRIORITIES

Technical, component, and infrastructure bottlenecks

First, continuous high-power operation remains constrained by pack mass, usable energy, thermal limits, and charging time. The relevant requirement is task energy per hectare or per workday, including PTO and hydraulic demand, rather than nominal vehicle range. Modular batteries, field charging, and exchange can reduce downtime, but require compatible interfaces and farm-level power planning *(Wallander et al., 2025)*.

Second, battery, motor, inverter, transmission, hydraulic, and PTO systems are still frequently optimized separately. Integrated optimization is needed to avoid response lag, oversizing, and energy transfer among subsystems. The absence of standardized agricultural duty cycles makes reported efficiency and endurance difficult to compare across studies.

Third, reliability evidence is weaker than performance evidence. Batteries, connectors, sensors, inverters, and distributed drives must tolerate dust, mud, water, chemicals, vibration, impact, and wide temperature ranges. Accelerated laboratory tests should be correlated with multi-season field data and accompanied by maintainability and fault-recovery analysis.

Components and standards. Tractor-specific component and interface standards remain incomplete. Communication, high-voltage safety, charging, battery exchange, electric implements, and diagnostic interfaces should be harmonized while permitting multiple power classes. Domestic localization should focus not only on nominal performance but also on consistency, sealing, thermal design, and service life.

Infrastructure and economics. Sparse rural charging, limited grid capacity, seasonal utilization, and insufficient service networks can offset powertrain advantages. Techno-economic and life-cycle studies show that outcomes are highly sensitive to annual use, electricity supply, battery replacement, charging strategy, and fleet logistics *(Mousazadeh et al., 2011; Lagnelˆ v et al., 2021; Vogt et al., 2021; Beligoj et al., 2022; Wallander et al., 2025; Ali et al., 2025)*. Broader automation studies likewise show that machine utilization, scale, labor substitution, and timeliness determine economic feasibility *(Pedersen et al., 2006; Lowenberg-DeBoer et al., 2020)*. Deployment assessments should therefore report scenario assumptions and sensitivity ranges rather than a single payback value.

Development priorities and research agenda

Technology and validation. Near-term research should prioritize validated tractor-specific batteries, high-efficiency low-speed motors, robust power electronics, and integrated traction-PTO-hitch control. Shared duty cycles and reporting metrics should be established for plowing, rotary tillage, seeding, transport, and mixed operations. These benchmarks should include energy per hectare, work rate, slip, PTO-speed error, component temperature, degradation, and failure response.

System integration and industrialization. Medium-term development should combine reusable multi-domain models, digital twins, condition-aware energy management, and modular charging or battery exchange. Long-term industrialization requires interoperable interfaces, functional-safety and cybersecurity requirements, recycling and second-life pathways, rural energy infrastructure, and total-cost and life-cycle assessment. A staged progression from simulation to hardware-in-the-loop, prototype, multi-condition field test, and multi-season demonstration would make maturity claims transparent and comparable.

CONCLUSIONS

Electric tractors have evolved from isolated prototypes into integrated battery-electric, hybrid, fuel-cell, and autonomous systems. The available evidence does not support a universally applicable powertrain architecture. Battery-electric systems are best suited to predictable low- and medium-power operations, hybrid systems remain practical for prolonged heavy-load operations, and fuel-cell systems offer rapid refueling but continue to be constrained by durability limitations and insufficient hydrogen infrastructure. Across all architectures, representative duty-cycle characterization and whole-system integration are more important than nominal component ratings.

A major limitation of the existing literature is its reliance on single-condition simulations and subsystem-level testing. Reported improvements are difficult to compare because studies differ in tractor power class, soil conditions, implements, reference systems, and evaluation metrics. International studies have demonstrated meaningful reductions in life-cycle environmental impacts and operating energy consumption. However, battery manufacturing, annual equipment utilization, charging logistics, and the electricity-generation mix can substantially influence these benefits. Performance claims should therefore be supported by uncertainty analyses and evidence concerning reliability, economic viability, and life-cycle impacts.

The highest research priorities include standardized agricultural duty cycles; pack-level safety and aging validation; integrated energy management for traction, PTO, and hitch systems; reusable multidomain models; modular field energy-replenishment systems; and interoperable standards for high-voltage systems and communication protocols. Technological progress should be demonstrated through a traceable validation sequence extending from simulation and hardware-in-the-loop testing to field trials conducted under multiple operating conditions and over multiple seasons. Such an evidence chain is essential for transforming promising algorithms and prototypes into reliable, economically viable, and scalable electric tractor systems.

ACKNOWLEDGEMENT

This work was supported by the following projects:

- Shandong Province Integrated Pilot Project for Agricultural Machinery R&D, Manufacturing, Promotion and Application, Grant No. **SDNJYTH-202507**.
- Key Research and Development Program of Shandong Province, Grant No. **2024TSGC0754**.
- Anhui Province Integrated Pilot Project for Agricultural Machinery R&D, Manufacturing, Promotion and Application, Grant No. **201**.

REFERENCES

[1] Ali D., de Castro R., Ehsani R., Vougioukas S., Wei P., (2025). Unlocking the potential of electric and hybrid tractors via sensitivity and techno-economic analysis. *Applied Energy*, vol.377, article no.124545. DOI: https://doi.org/10.1016/j.apenergy.2024.124545

[2] Bechar A., Vigneault C., (2016). Agricultural robots for field operations: Concepts and components. *Biosystems Engineering*, vol. 149, pp. 94–111. DOI: https://doi.org/10.1016/j.biosystemseng.2016.06.014

[3] Beligoj M., Scolaro E., Alberti L., (2022). Feasibility evaluation of hybrid electric agricultural tractors based on life cycle cost analysis. *IEEE Access*, vol.10, pp.28853-28867. DOI: https://doi.org/10.1109/ACCESS.2022.3157635

[4] Chen Y.-C., Chen L.-W., Chang M.-Y., (2022). A design of an unmanned electric tractor platform. *Agriculture*, vol.12, no.1, p.112. DOI: https://doi.org/10.3390/agriculture12010112

[5] Dalboni M., Santarelli P., Patroncini P., Soldati A., Concari C., Lusignani D., (2019). Electrification of a compact agricultural tractor: A successful case study. *2019 IEEE Transportation Electrification Conference and Expo (ITEC)*, pp.1–6.

[6] Ding W.M., Zhang Q., Li J., (2024). Research on SDP adaptive energy management strategy for electric tractor PTO system (in Chinese). *Transactions of the Chinese Society of Agricultural Engineering*, vol.40, no.18, pp.198–206.

[7] Estevez M.A.P., Frigola J.M., Llobet J.A., Alberti L., Renzi M., (2024). Optimal design of a series hybrid powertrain for an agricultural tractor. *Energy Conversion and Management: X*, vol.24, article no.100789. DOI: https://doi.org/10.1016/j.ecmx.2024.100789

[8] Feng R.G., Wang M.J., Niu X.S., (2023). Development status and key technology analysis of electric tractors (in Chinese). *Tractor & Farm Transporter*, vol.50, no.5, pp.16–19.

[9] Fountas S., Mylonas N., Malounas I., Rodias E., Santos C.H., Pekkeriet E., (2020). Agricultural robotics for field operations. *Sensors*, vol.20, no.9, article no.2672. DOI: https://doi.org/10.3390/s20092672

[10] Ghobadpour A., Mousazadeh H., Kelouwani S., Zioui N., Kandidayeni M., Boulon L., (2021). An intelligent energy management strategy for an off-road plug-in hybrid electric tractor based on farm operation recognition. *IET Electrical Systems in Transportation*, vol.11, no.4, pp.333–347. DOI: https://doi.org/10.1049/els2.12029

[11] Ghobadpour A., Mousazadeh H., Kelouwani S., Zioui N., Kandidayeni M., Boulon L., (2022). Off-road electric vehicles and autonomous robots in agricultural sector: Trends, challenges, and opportunities. *Vehicles*, vol.4, no.3, pp.843–864. DOI: https://doi.org/10.3390/vehicles4030047

[12] Grimstad L., From P.J., (2017). The Thorvald II agricultural robotic system. *Robotics*, vol.6, no.4, article no.24. DOI: https://doi.org/10.3390/robotics6040024

[13] Han H.B., (2023). Recognition of Zoomlion new energy pure electric tractor (in Chinese). *Agricultural Machinery Market*, no.9, p.40.

[14] Jeon H.H., Baek S.Y., et al., (2023). Development and performance evaluation of lateral control simulation-based multi-body dynamics model for autonomous agricultural tractor. *Korean Journal of Agricultural Science*, vol.50, no.4, pp.773–784.

[15] Jing C.H., Zheng Z.M., Hou H.J., (2025). Planning of rural energy system with biomass coupled solar energy considering electric substitution of agricultural machinery (in Chinese). *Transactions of the Chinese Society for Agricultural Machinery*, vol.56, no.5, pp.560–568.
[16] Kwon D., Ahn D.-V., Kim J.-G., Park Y.-J., (2024). Effect analysis of motor power characteristics on the energy consumption of dual motor driven powertrain for electric tractor. *Journal of Biosystems Engineering*, vol.49, pp.465-475. DOI: https://doi.org/10.1007/s42853-024-00245-w
[17] Lagnelöv O., Larsson G., Larsolle A., Hansson P.-A., (2021). Life cycle assessment of autonomous electric field tractors in Swedish agriculture. *Sustainability*, vol.13, no.20, article no.11285. DOI: https://doi.org/10.3390/su132011285
[18] Li G., Zhang M.Z., Liu M.N., Xu L.Y., Yan X.H., (2023). Optimal design and experiment of distributed drive system for electric tractor based on multi-island genetic algorithm (in Chinese). *Transactions of the Chinese Society for Agricultural Machinery*, vol.54, no.12, pp.1–12.
[19] Li H.B., (2024). Research on multi-parameter cooperative control of agricultural machinery based on fuzzy control and BP neural network (in Chinese). *Transactions of the Chinese Society of Agricultural Engineering*, vol.40, no.20, pp.201–210.
[20] Li L., Xie B., Zhang M., (2022). Research on application of dual-motor power coupling drive system in heavy-duty tractor (in Chinese). *Transactions of the Chinese Society of Agricultural Engineering*, vol.38, no.16, pp.213–221.
[21] Li L.Q., Ran G.W., Gao Z.Y., (2024b). Topology optimization and capacity configuration of semi-active hybrid power supply for electric tractor (in Chinese). *Transactions of the Chinese Society for Agricultural Machinery*, vol.55, no.8, pp.38–47.
[22] Li L.Q., Ran G.W., Gao Z.Y., et al., (2024a). Adaptive energy management and capacity configuration of composite power supply system for pure electric tractor (in Chinese). *Transactions of the Chinese Society of Agricultural Engineering*, vol.40, no.22, pp.81–89.
[23] Li T.H., Wang H., Zhang L., (2024). Energy management strategy of dual-motor multi-mode power coupling drive system for pure electric tractor (in Chinese). *Transactions of the Chinese Society for Agricultural Machinery*, vol.55, no.6, pp.32–40.
[24] Li T.H., Xu L.Y., Wang H., (2019). Research on power distribution strategy of dual-motor coupling drive tractor (in Chinese). *Transactions of the Chinese Society for Agricultural Machinery*, vol.50, no.7, pp.34–42.
[25] Li Y., Liu K., Yu Q., Zhang M., (2024). Application of deep learning network with attention mechanism in fault diagnosis of tractor power shift (in Chinese). *Transactions of the Chinese Society for Agricultural Machinery*, vol.55, no.10, pp.45–53.
[26] Liao Q.X., Wang L., Zhang Q.H., (2024). Optimization of electronically controlled PTO system for tractor based on four-motor dual coupling (in Chinese). *Journal of Huazhong Agricultural University (Natural Science Edition)*, vol.43, no.5, pp.189–197.
[27] Liu H., (2024). *Numerical simulation and device research on hydrogen production from bio-methanol reforming for agricultural vehicles (in Chinese)*, MSc thesis, Henan Agricultural University.
[28] Liu H.L., Shen C., Hu L.L., (2024). Research progress and development trend of electric agricultural equipment (in Chinese). *Transactions of the Chinese Society of Agricultural Engineering*, vol.40, no.23, pp.39–51.
[29] Liu M., Li Y., Xu L., Wang Y., Zhao J., (2023). General modeling and energy management optimization for the fuel cell electric tractor with mechanical shunt type. *Computers and Electronics in Agriculture*, vol.213, article no.108178. DOI: https://doi.org/10.1016/j.compag.2023.108178
[30] Liu M.N., Lei S.H., Zhao J.H., et al., (2022). Review on development process and research status of electric tractor. *Transactions of the Chinese Society for Agricultural Machinery*, vol.53, no.S1, pp.348–364.
[31] Lowenberg-DeBoer J., Huang I.Y., Grigoriadis V., Blackmore S., (2020). Economics of robots and automation in field crop production. *Precision Agriculture*, vol.21, pp.278–299. DOI: https://doi.org/10.1007/s11119-019-09667-x
[32] Luo X.W., He J., Feng D.W., (2025). Research on precision operation technology of unmanned tractor supported by Beidou navigation (in Chinese). *Transactions of the Chinese Society of Agricultural Engineering*, vol.41, no.22, pp.1–9.

[33] Luo Z.-H., Xie B., Tong Y.-K., Zhao Z.-H., Zheng B.-W., Chen Z.-Y., Wen C.-K., (2024). Energy-saving drive control strategy for electric tractors based on terrain parameter identification. *Applied Energy*, vol.376, article no.124230. DOI: https://doi.org/10.1016/j.apenergy.2024.124230

[34] Mocera F., (2021). A model-based design approach for a parallel hybrid electric tractor energy management strategy using hardware in the loop technique. *Vehicles*, vol.3, no.1, pp.1–19. DOI: https://doi.org/10.3390/vehicles3010001

[35] Mocera F., Somà A., (2020). Analysis of a parallel hybrid electric tractor for agricultural applications. *Energies*, vol.13, no.12, article no.3055. DOI: https://doi.org/10.3390/en13123055

[36] Mousazadeh H., Keyhani A., Javadi A., Mobli H., Abrinia K., Sharifi A., (2011). Life-cycle assessment of a solar assist plug-in hybrid electric tractor in comparison with a conventional tractor. *Energy Conversion and Management*, vol.52, no.3, pp.1700-1710. DOI: https://doi.org/10.1016/j.enconman.2010.10.033

[37] Pascuzzi S., Anifantis A.S., Blanco I., Mugnozza G.S., (2024). Sustainability evaluation of hybrid agriculture-tractor powertrains. *Sustainability*, vol.16, no.3, article no.1184. DOI: https://doi.org/10.3390/su16031184

[38] Pedersen S.M., Fountas S., Have H., Blackmore B.S., (2006). Agricultural robots—system analysis and economic feasibility. *Precision Agriculture*, vol.7, pp.295–308. DOI: https://doi.org/10.1007/s11119-006-9014-9

[39] Rosales J.C., Machado R.L.T., Machado A.L.T., Andrade H.G., Kroessin L., (2022). Design specifications of an autonomous electric vehicle for use in family farm units. *Engenharia Agrícola*, vol.42, no.3, article no.e20210220. DOI: https://doi.org/10.1590/1809-4430-Eng.Agric.v42n3e20210220/2022

[40] Shamshiri R.R., Weltzien C., Hameed I.A., Yule I.J., Grift T.E., Balasundram S.K., Pitonakova L., Ahmad D., Chowdhary G., (2018). Research and development in agricultural robotics: A perspective of digital farming. *International Journal of Agricultural and Biological Engineering*, vol.11, no.4, pp.1–14. DOI: https://doi.org/10.25165/j.ijabe.20181104.4278

[41] Slaughter D.C., Giles D.K., Downey D., (2008). Autonomous robotic weed control systems for specialty crops: A review. *Computers and Electronics in Agriculture*, vol.61, no.1, pp.63–78. DOI: https://doi.org/10.1016/j.compag.2007.05.008

[42] Sun J.K., Wang X.H., Zhang Y., (2025). Application and benefit analysis of biomass gasification power generation system in energy supply of electric agricultural machinery (in Chinese). *Journal of Agricultural Mechanization Research*, vol.47, no.3, pp.230–236.

[43] Thuilot B., Cariou C., Martinet P., Berducat M., (2002). Automatic guidance of a farm tractor relying on a single CP-DGPS. *Autonomous Robots*, vol.13, pp.53-71. DOI: https://doi.org/10.1023/A:1015678121948

[44] Tian Y.W., Chen J., Wang Y.P., (2024). Design of unmanned monitoring system for electric tractor based on 5G and Beidou RTK (in Chinese). *Transactions of the Chinese Society for Agricultural Machinery*, vol.55, no.2, pp.15–22.

[45] Ueka Y., Yamashita J., Sato K., Doi Y., (2013). Study on the development of the electric tractor: Specifications and traveling and tilling performance of a prototype electric tractor. *Engineering in Agriculture, Environment and Food*, vol.6, no.4, pp.160–164. DOI: https://doi.org/10.1016/S1881-8366(13)80003-1

[46] Varlese C., Ferrara A., Hametner C., Hofmann P., (2024). Experimental validation of a predictive energy management strategy for agricultural fuel cell electric tractors. *International Journal of Hydrogen Energy*, vol.77, pp.1-14. DOI: https://doi.org/10.1016/j.ijhydene.2024.06.097

[47] Vogt H.H., de Melo R.R., Daher S., Schmuelling B., Antunes F.L.M., dos Santos P.A., Albiero D., (2021). Electric tractor system for family farming: Increased autonomy and economic feasibility for an energy transition. *Journal of Energy Storage*, vol.40, article no.102744. DOI: https://doi.org/10.1016/j.est.2021.102744

[48] Wallander E., Frank B., Alaküla M., Márquez-Fernández F.J., (2025). Full electric farming with on-field energy replenishment. *Applied Energy*, vol.377, article no.124416. DOI: https://doi.org/10.1016/j.apenergy.2024.124416

[49] Wang C.Y., Li G., Zhang M.Z., (2024). Research on fault diagnosis of agricultural machinery based on random forest and support vector machine integrated algorithm (in Chinese). *Journal of Jiangsu University (Natural Science Edition)*, vol.45, no.4.

[50] Wang D.G., Li R., Yang M., (2024). Performance and emission characteristics of agricultural diesel engine with B20 biodiesel blended fuel at high altitude (in Chinese). *Transactions of the Chinese Society of Agricultural Engineering*, vol.40, no.8, pp.48–56.
[51] Wang L., Yang M., Deng X.T., (2025). Review on key technologies of hybrid electric tractors (in Chinese). *Transactions of the Chinese Society for Agricultural Machinery*, vol.56, no.12, pp.1–18.
[52] Wang Q., Wang X.D., Wang W., (2025). Research on resistance adaptive operation control of electric tractor ploughing unit (in Chinese). *Journal of Agricultural Mechanization Research*, no.4, pp.224–229.
[53] Wen C.K., Xie B., Song Z.H., (2025). Research status and development suggestions of agricultural new energy power equipment (in Chinese). *Transactions of the Chinese Society for Agricultural Machinery*, vol.56, no.12, pp.1–18.
[54] Wen X., Wang X., (2022). Research on OneNet remote monitoring system based on agricultural machinery CAN bus (in Chinese). *Journal of Chinese Agricultural Mechanization*, vol.43, no.1, pp.116–121.
[55] Xie B., Li L., Wang H., (2023). Drive torque management strategy of tractor with load following based on slip ratio control (in Chinese). *Transactions of the Chinese Society of Agricultural Engineering*, vol.39, no.8, pp.192–200.
[56] Xie B., Zhang M., Li L., (2024). Automatic measurement and attitude optimization of tillage depth of suspended unit based on inclination sensor (in Chinese). *Journal of Agricultural Mechanization Research*, vol.46, no.3, pp.187–192.
[57] Xu L.Y., Shang Y.C., Lei S.H., (2025). Design and experiment of communication network for autonomous hydrogen fuel cell tractor (in Chinese). *Transactions of the Chinese Society for Agricultural Machinery*, vol.56, no.12, pp.69–77.
[58] Xu Z.C., Zhang L., Wang H., (2024). Optimization of power distribution for hybrid power supply of dual-source electric tractor (in Chinese). *Power Supply Technologies and Applications*, vol.48, no.6, pp.789–794.
[59] Xue S.S., Cai Z.P., Li Q., et al., (2023). Research and experiment on hybrid power supply system of electric mini-tiller based on super capacitor auxiliary energy (in Chinese). *Journal of Southwest University (Natural Science Edition)*, vol.45, no.2, pp.179–191.
[60] Yan X., Li X., Du Y., Zhang M., (2024). Research on energy management strategy for series diesel–electric hybrid tractors based on dynamic programming. *World Electric Vehicle Journal*, vol.15, no.4, article no.156. DOI: https://doi.org/10.3390/wevj15040156
[61] Yang F.Z., Zhao W., Li J., (2023). Cooperative control of tractor body and implement attitude based on double closed-loop fuzzy PID (in Chinese). *Transactions of the Chinese Society for Agricultural Machinery*, vol.54, no.11, pp.234–242.
[62] Yang H., Zhang M., Liu M., Xu L., (2022). Research on energy management strategy of fuel cell hybrid tractor. *Energies*, vol.15, no.17, article no.6389. DOI: https://doi.org/10.3390/en15176389
[63] Yang J.Q., Wang L., Zhang Q.H., (2023). Magneto-thermal bidirectional coupling model and multi-objective optimization of deceleration wheel-side drive motor (in Chinese). *Energy Storage Science and Technology*, vol.12, no.10, pp.3124–3132.
[64] Yang S.M., Zhang L., Wang H., (2023). Path planning and energy consumption optimization of agricultural machinery based on hybrid model of reinforcement learning and genetic algorithm (in Chinese). *Journal of Northwest A&F University (Natural Science Edition)*, vol.51, no.8, pp.158–166.
[65] Yu Q., Fu Y.P., Niu P.H., (2024a). Research status of electric tractor application in agricultural field (in Chinese). *Agricultural Machinery Technology Extension*, no.1, pp.36–38, 60.
[66] Yu Q., Wang P., Zhang M., (2024b). Optimization of electronically controlled shift for tractor based on dynamic programming and BP neural network (in Chinese). *Journal of Chinese Agricultural Mechanization*, vol.45, no.5, pp.167–174.
[67] Yu Q., Zhang M., et al., (2024c). Application of fuel cell dual-source cooperative energy management in tractor electronic control system (in Chinese). *Transactions of the Chinese Society for Agricultural Machinery*, vol.55, no.9, pp.54–62.
[68] Yu Q., Zhang M., Li J., (2023). Disturbance compensation research on electric control system of electric tractor based on fuzzy PID compensation algorithm (in Chinese). *Journal of Chinese Agricultural Mechanization*, vol.44, no.8, pp.156–163.
[69] Zhang H., Li J.L., Hui D., (2014). Key technologies and development of high specific energy lithium-sulfur batteries (in Chinese). *Energy Storage Science and Technology*, vol.3, no.4, pp.351–358.

[70] Zhang J., Li J., Wang P., (2024). Research on dual-source cooperative energy management control strategy of fuel cell tractor (in Chinese). *Transactions of the Chinese Society of Agricultural Engineering*, vol.40, no.16, pp.220–228.
[71] Zhang J., Wang H., Li X., (2023). Research on global optimal energy management strategy of an agricultural hybrid tractor based on dynamic programming. *World Electric Vehicle Journal*, vol.14, no.5, article no.127. DOI: https://doi.org/10.3390/wevj14050127
[72] Zhang J.J., Feng G.H., Xu L.Y., (2023). Energy-saving control of hybrid tractor based on Pontryagin's minimum principle (in Chinese). *Transactions of the Chinese Society for Agricultural Machinery*, vol.54, no.5, pp.396–406.
[73] Zhang M., Li X., Han D., Shang L., Xu L., (2025). Energy management strategy for fuel cell hybrid tractor considering demand power frequency characteristic compensation (in Chinese). *International Journal of Hydrogen Energy*, vol.50, no.34, pp.15678–15691.
[74] Zhang Q.H., Wang Q., Li G., (2025). Research progress of new power supply technology for electric agricultural equipment (in Chinese). *Transactions of the Chinese Society of Agricultural Engineering*, vol.41, no.18, pp.1–12.
[75] Zhang W., Liu M.N., Xu L.Y., (2022). Design and simulation of hydraulic suspension system for electric tractor (in Chinese). *Machine Tool & Hydraulics*, vol.50, no.2, pp.93–98.
[76] Zhao J., Wang Q., Liu Y., (2023). Remote monitoring and intelligent scheduling system of agricultural machinery based on Internet of Things (in Chinese). *Agricultural Engineering*, vol.13, no.8, pp.78–84.
[77] Zhao X., Zhang M., Liu M., Xu L., (2024a). Study and verification of a fuzzy-following energy management strategy for a hybrid tractor. *World Electric Vehicle Journal*, vol.16, no.1, article no.18. DOI: https://doi.org/10.3390/wevj16010018
[78] Zhao Y., Li X., Zhang M., Xu L., (2024b). Research on energy management strategy for hybrid tractors based on DP-MPC. *Energies*, vol.17, no.16, article no.3924. DOI: https://doi.org/10.3390/en17163924
[79] Zhou R., Zhang M., Xu L., (2024). Research on energy distribution strategy of tandem hybrid tractors. *Agriculture*, vol.14, no.3, article no.440. DOI: https://doi.org/10.3390/agriculture14030440
[80] Zhou X.Y., Wu Y.Z., Zhang L., Yang X.N., (2024). Complex disturbance compensation control strategy of VLF-PM motor under PTO system of electric tractor (in Chinese). *Transactions of the Chinese Society of Agricultural Engineering*, vol.40, no.12, pp.211–219.

A REVIEW ON RESEARCH OF MECHANIZED RESIDUAL FILM RECOVERY TECHNOLOGIES AND EQUIPMENT
/
机械化残膜回收技术与装备研究综述

Hongjian ZHANG*[1)], Junyi LU[1)], Yufeng LI[1)], Linlong JING[1)], Shuo KANG[1)], Jinxing WANG[1)]
[1)]School of Mechanical and Electronic Engineering, Shandong Agricultural University, Shandong/China
Corresponding author: Hongjian ZHANG
Tel: +8618805488951; E-mail: zhanghongji_an@163.com
DOI: https://doi.org/10.35633/inmateh-79-67

Keywords: *agricultural residual film, mechanized recovery, mechanized film-impurity separation, resource utilization of residual film*

ABSTRACT
Agricultural plastic mulch films have significantly increased crop yields but have also caused severe residual film pollution. This review summarizes the research progress in residual film recovery machinery, intelligent monitoring systems, film–impurity separation technologies, and resource utilization methods, while analyzing the advantages, limitations, and development trends of different technologies. Post-harvest recovery equipment has been widely applied due to its strong adaptability and broad application range, whereas seedling-stage and pre-sowing recovery technologies still require improvements in automation and environmental adaptability. Intelligent monitoring technologies can enhance the evaluation of recovery processes, but their application is restricted by complex field environments. Vibrating, pneumatic, and water-washing separation technologies exhibit advantages in processing capacity, film purity, and impurity removal, respectively. Recycled pelletizing and wood–plastic composites are important resource utilization pathways, but they still face challenges related to cost and performance. In the future, residual film management will develop toward intelligent, efficient, and high-value utilization.

摘要
农业塑料覆盖膜提高了作物产量，但也造成严重的残膜污染。本综述总结了残膜回收机械、智能监测系统、膜杂分离技术及资源利用方法的研究进展，并分析了不同技术的优势、局限性和发展趋势。收获后回收设备因适应性强、应用范围广而得到广泛应用，而苗期和播前回收技术仍需提升自动化和环境适应能力。智能监测技术可提高回收过程评价水平，但复杂田间环境限制其应用。振动、气力和水洗分离技术分别在处理能力、膜纯度和杂质去除方面具有优势。再生造粒和木塑复合材料是重要资源化途径，但仍面临成本和性能挑战。未来残膜治理将向智能化、高效化和高值化方向发展。

INTRODUCTION
In the 20th century, with the rise of the plastics industry, plastic mulch cultivation technology emerged and gradually developed *(Wang et al., 2018; Briassoulis et al., 2013; Wei et al., 2019)*. Japan conducted relatively early research on plastic mulch technology, which greatly promoted crop production. Plastic mulches are widely used in vegetable and fruit production systems across Europe, particularly in Mediterranean countries such as Spain and Italy. Plasticulture is widely adopted in North America for the production of high-value crops such as strawberries, tomatoes and melons. China has a history of about 40 years in the application of plastic mulch cultivation. Among them, the plastic mulch coverage rate of cotton in Xinjiang is 96.6%, and that of peanut and tobacco in Shandong and Hubei reaches 100% *(Chen et al., 2020)*. However, with extensive use and large amounts of plastic mulch left in farmland after harvest (Fig.1(c)), mulch mainly made of polyethylene is difficult to decompose naturally. Inadequate post-treatment by farmers has led to soil and environmental pollution, reducing water infiltration, ventilation and moisture content, hindering water and nutrient transport, causing soil compaction, and inhibiting crop root growth *(Filipe et al., 2023)*. To date, 7.4 million tons of agricultural plastic films are consumed globally each year. Just 10% are recycled and 14% incinerated, while 76% enter landfills or the environment, creating major risks to ecosystems and human health (Fig.1(a)). In Europe, approximately 0.6 million tons of agricultural plastic waste are generated annually, of which about 24% are recycled *(Martín et al., 2018)*.

The U.S. has implemented plastic recycling initiatives, waste mulch film recycling is low (*Sarpong et al., 2024*). Soil residues account for 60%–80% of film mass, so recycling costs exceed regeneration benefits. Farmers use on-farm storage, paid landfilling or open burning, which emits heavy metals and dioxins and pollutes the environment *(Montoya et al., 2018).* The average residual mulch film content in long-term mulched farmland soils of China ranges from 60 to 90 kg/hm². A residual film concentration of 58.5 kg/hm² significantly inhibits crop root growth and hinders water and nutrient transport. (*Li et a., 2023*).

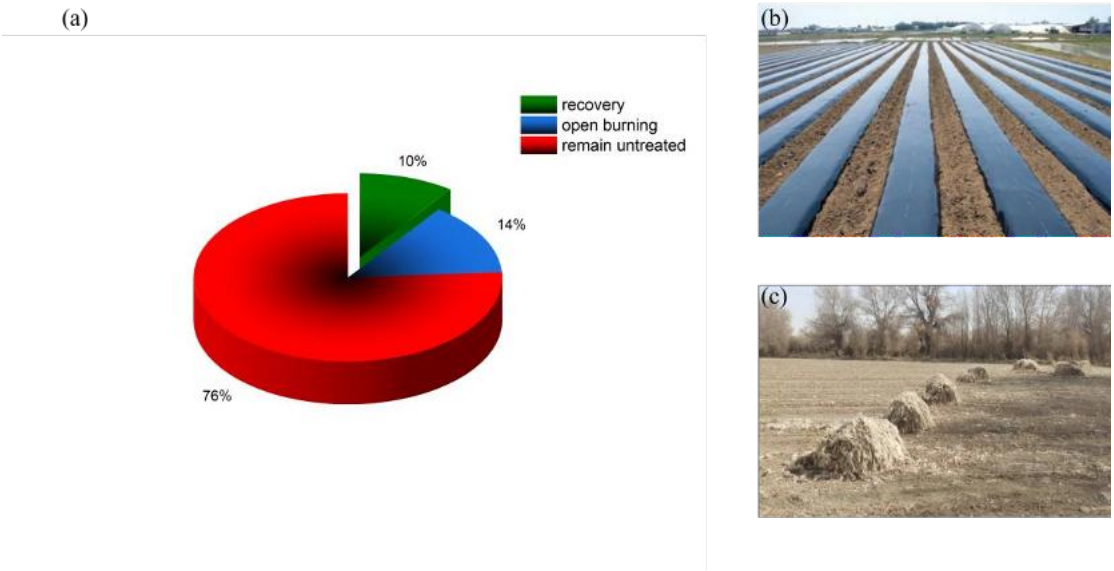


Fig. 1 – Usage of Agricultural Plastic Mulch

(a) The proportions of disposal approaches for waste agricultural plastic films worldwide; (b) Farmland Mulching; (c) Residual Mulch Accumulation in Farmland

Many reviews have discussed agricultural plastic films regarding their application, degradation, ecological risks and recycling technologies. Some analyzed plastic environmental behavior, while others evaluated residual film recovery machinery. Nevertheless, existing reviews focus merely on pollution assessment or general waste management. Comprehensive summaries of mechanized residual film recovery, intelligent detection, separation and resource utilization are scarce. The integration of recovery machinery with intelligent sensing and automation lacks systematic analysis *(Li et al., 2020; Wang et al., 2026; Yang et al., 2024)*.

This paper focuses on the core technical chain of residual film pollution control and systematically reviews related technologies, including recycling machine classification, intelligent systems, membrane-impurity separation, and resource utilization. It covers the whole-process system of mechanized recovery, intelligent monitoring, impurity separation, and resource regeneration, providing a research basis for technical optimization and equipment development. Systematic literature searches to identify research on agricultural residue film recovery, separation technologies, intelligent monitoring systems, and resource utilization pathways. Literature retrieval was conducted using Web of Science Core Collections, Scopus, ScienceDirect, SpringerLink, and Google Scholar databases. The search strategy combines keywords, including "agricultural plastic film," "residual film," "plastic cover film recycling," "film recycling equipment," "machine vision," "intelligent detection," "plastic separation," and "resource utilization." This review covers studies published between 2000 and 2026. After removing duplicate records, the retrieved articles are filtered according to the title, abstract, and full text, following preset inclusion and exclusion criteria. Subsequently, the selected studies were analyzed to summarize the findings.

KEY LINKS IN MECHANIZED RECYCLING OF RESIDUAL FILM

Farmland residual plastic film mainly includes two types: surface residual film and subsurface tillage layer residual film. Among them, surface residual film is classified into relatively intact film and fragmented film according to its morphology, while residual film in the tillage layer is entirely fragmented. Due to the short laying period and low degree of mechanical property degradation, relatively intact plastic film is relatively easy to recover. In contrast, fragmented residual film is scattered and exhibits severe mechanical property degradation, making it difficult to recover. Thus, fragmented residual film is the main target for residual film recovery.

Based on current practical recovery conditions, residual film collection and operation evaluation, film-impurity separation, and residual film processing and utilization are the key links in mechanized residual film recovery. In terms of mechanized residual film collection, residual film recovery equipment at different stages is used to lift and pick up residual film from both the surface and tillage layer, then transport it to a baling unit to complete baling and recovery *(Zhang et al., 2008a)*. During recovery evaluation, residual film image recognition, machine operation status monitoring, and operation area monitoring are adopted to identify residual film, monitor key components in real time, and detect picked, missed, and repeated areas in the field. In mechanized processing, baled residual film is first separated from straw and sand by film-impurity separation equipment *(Guo et al., 2011c)*, and then made into high-purity raw materials for plastic products through regenerative granulation technology, as shown in Fig. 2.

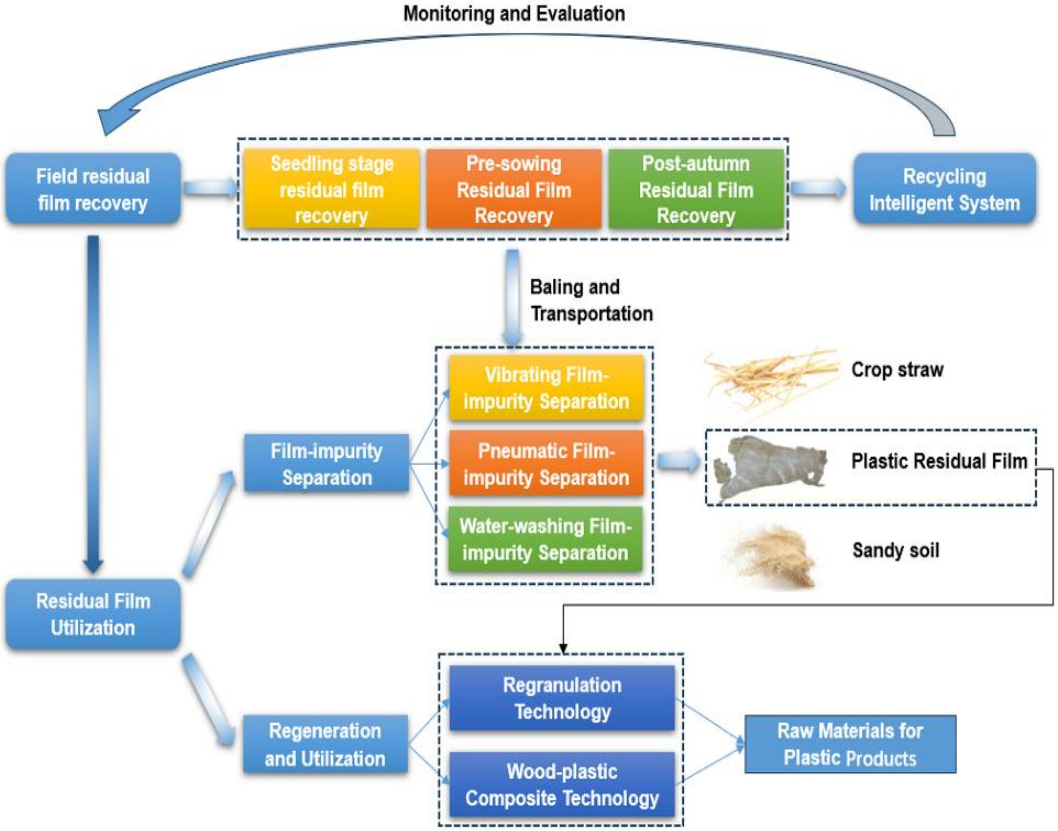


Fig. 2 – Key Processes of Mechanized Residual Film Recovery

MECHANIZED RECOVERY TECHNOLOGY, EQUIPMENT AND INTELLIGENT SYSTEM

In the early 20th century, some developed countries began research on residual film recovery machinery. Since the plastic film they used was generally thicker than 0.20 mm, film-soil separation was mainly achieved by relying on the relatively high tensile strength of the film itself, with research focused on winding mechanisms. Relevant research in China started in the 1980s. Affected by factors such as thin film thickness, low strength and easy damage, research has mainly focused on key components including film lifting and film collection *(Cheng et al., 2023)*. Due to regional agronomic differences, China has various residual film recovery machines, which can be categorized by operating period into seedling-stage, post-harvest and pre-sowing types, with post-harvest machines being the most widely applied. Accordingly, residual film recovery equipment is gradually integrating intelligent technologies, developing monitoring systems for field operation and recovery performance to realize intelligent upgrading *(Kou et al., 2023; Jin et al., 2023a)*.

Seedling-stage Residual Film Recovery Technology and Equipment

In China, residual plastic film is mainly recovered at the seedling stage before the first irrigation, as the film is relatively intact and easy to collect. The mainstream film rolling technology uses the inherent strength of plastic film to meet tension needs during film-soil separation, and is widely used for vegetable film recovery abroad and seedling-stage residual film recovery in China.

Early seedling-stage residual plastic film collectors were mostly semi-automatic, composed of frame, ground wheels, cutting blades, film lifters and cutoff discs *(Liu et al., 2024; Yang et al., 2010; Hu et al., 2016)*. They cut weeds first, lifted the film, and relied on manual pickup, leading to low efficiency. Accordingly, researchers worldwide developed fully automatic machines that wind residual film with rolling rollers and separate it from the soil using the film's inherent tensile force, offering higher efficiency and better adaptability for seedling-stage film recovery, Typical seedling-stage residual film recovery machines from various countries and their operating parameters are listed in Table 1.

Table 1

Representative Seedling-stage Residual Film Recovery Machines and Operating Parameters

Brand	Country	Picture	Operating speed	Working width	Advantages	Disadvantages
PS610 In-Season Plastic-Film Recovery Machine	USA		3–4 km/h	1.5m	It enables efficient pre-recycling with less residual film, intact mulch film, and continuous mechanized operation.	Recovery efficiency decreases under severe film fragmentation or soil embedding conditions.
ROCCA PMR-01 Plastic Mulch Retriever	USA		2–5 km/h	1.5–1.8 m	High-efficiency continuous collection with preliminary film–impurity separation.	Sensitive to film fragmentation and soil adhesion; limited adaptability and high cost.
MSM-3 type seedling-stage residual film recovery machine	CHN		2–3 km/h	1.2-1.8m	It features a compact design, high recovery efficiency, reduced soil contamination, and multi-row operation.	Affected by field conditions, with limited recovery of buried and fragmented film and limited adaptability.
Mulch film winding/recovery device	JPN		0.72–2.88km/h	0.9–1.2 m	Reduces film damage, improving recovery quality and resource-use efficiency.	Poor soil-film separation, low fragmented-film adaptability, low throughput, not for large-scale use.
Jaulent Industrie DTR	FRA		4–8km/h	1.5m	Simple structure, high efficiency, suitable for European vegetable fields, and capable of recovering film and drip lines.	Designed mainly for intact mulch films, with poor adaptability to fragmented films and limited film–soil separation capability.

However, the film-rolling seedling-stage residual film recovery equipment still relies on manual film guiding and unloading, with high labor intensity, low efficiency and insufficient tension control that easily causes film tearing, breaking or residue. To solve this, the floating synchronous film-rolling machine adopts a special mechanism to dynamically adjust the roller's speed and pressure according to real-time film conditions, ensuring uniform film stress and avoiding tearing or breaking *(Zhou et al., 2019)*.

Existing studies show that seedling-stage residual film recovery is mainly suitable for crops like corn with little need for later soil warming. The method varies with crop type, agronomy and production conditions. However, such recovery may increase water demand and soil compaction, especially in arid areas using under-film irrigation. Relevant technologies and equipment remain limited.

Autumn residual film recovery technologies and equipment

Post-harvest residual film recovery refers to the recovery operation conducted after crop harvest and before tillage, mainly targeting the plastic film used in the current season. As this operation is independent of crop harvesting, it avoids impacts on harvesting efficiency and crop quality, making it a widely applied method. However, plastic film is severely aged after harvest and disturbed by straw coverage, increasing operational difficulty.

Dense root stubbles after straw returning also cause fine residual film to hook and adhere, further complicating recovery *(Wang et al., 2017; Wu et al., 2025)*. In response, research institutions have developed corresponding equipment.

Current post-harvest recovery mainly includes two categories: one is single recovery dominated by drum-type devices, and the other is combined recovery integrating film collection, straw crushing and film baling.

1. Drum-type residual film recycler

Drum-type residual film recovery technology uses a toothed drum to collect residual film. As the drum rotates, residual film in the shallow tilled layer is hooked and attached to the teeth, then removed and collected by mechanical stripping or air blowing. According to the relative motion between the pick-up teeth and the drum, such recyclers are divided into concentric drum type and eccentric drum type *(Hu,2021; Zhang et al., 2023a)*.

Figure 4(a) shows the pick-up drum of a concentric drum-type residual film recycler. Its characteristic is that the elastic pick-up teeth are rigidly fixed to the drum body, with no relative movement between them during operation, and their rotational axes remain concentric. The residual film pick-up drum and the film stripping drum rotate in opposite directions. The elastic pick-up teeth on the pick-up drum pick up and clamp residual film from the tilled layer, then convey it to the stripping zone. Under the relative motion of the two drums, residual film attached to the pick-up teeth is effectively stripped by the stripping drum, and finally delivered to the residual film collection device, realizing continuous operations of film pick-up, conveyance, stripping and collection. Figure 4(d) shows the pick-up drum of an eccentric drum-type residual film recycler. Unlike the concentric type, the film pick-up teeth and the roller of the eccentric type can produce controllable relative movement. During operation, the pick-up teeth and the roller undergo periodic radial relative displacement to grasp, carry and separate residual film in the field. When the elastic pick-up teeth are fully extended, they fully contact residual film and complete the grasping operation. As the elastic teeth gradually retract, the grasped residual film moves with the teeth away from the working surface and then returns to the roller surface, creating conditions for subsequent film separation and cleaning.



Fig. 4 – Drum-type residual film recovery machine

(a) Concentric drum pickup structure (Zhang, 2023b). (b) Comb-tooth lifting and pneumatic stripping residual film recovery machine for tillage layer (Liu et al., 2021). (c) FEM-SPH Coupled Roller-Type Residual Film Recovery Machine (Zhang et al., 2024b). (d) Eccentric drum pickup structure (Niu et al., 2023). (e) Eccentric drum pickup structure (Shi et al., 2023). (f) Collecting and Separating Device for Strip Plastic Film Baler (Niu et al., 2017).

2. Combined residual film recovery machine

Combined residual film recovery machines can be divided into combined straw crushing and returning machines with residual film recovery, and combined residual film recovery and film block baling machines. Compared with single residual film recovery, the combined operation mode integrates and optimizes processes, which can effectively reduce field operation times and the interference of straw on film recovery. Meanwhile, it realizes baling of residual film, significantly improves operation stability and simplifies subsequent treatment. Therefore, Chinese researchers have developed various combined residual film recovery machines *(He et al.,2013; Yu et al; 2016; He et al., 2023)*. As shown in Figure 5(c), the 4JMLQ-210 combined straw returning and residual film recovery machine is a tractor-mounted unit with front straw crushing and rear film recovery. During operation, high-speed rotating parts crush straw, break stubbles and level the field, preparing for film recovery. Residual film is then collected by film lifting, pickup and separation mechanisms.

One-pass operation achieves both straw returning and film pollution control. Figure 5(e) shows the MJY-1500 residual film picking and baling machine. It uses three sets of vertical hydraulic cylinders to compact film into square bales. This baler forms bales quickly with a high baling rate. Compared with conventional collection boxes, hydraulic compression greatly increases film density, easing transport and preventing secondary pollution. The structure is simple and reliable.



Fig. 5 – Combined Residual Film Recovery Machine

(a) 4JSM-2200 Combined Straw Returning and Residual Film Recovery Machine (Luo et al., 2024). (b) Second stage chain plate straw crushing and plastic film recycling combined operation machine (Wen et al., 2021). (c) Model 4JMLQ-210 Combined Operation Machine for Straw Returning and Residual Film Recovery (Liu et al., 2024). (d) Cotton Field Mulch Film Recovery Baler (Shi et al., 2025). (e) Model MJY-1500 Residual Film Collecting and Baler Combined Machine (Zhan et al., 2017). (f) Self-propelled Combined Machine for Cotton Stalk Baling and Residual Film Packing (Li et al., 2025)

Technology and Equipment for Pre-sowing Residual Film Recovery

Pre-sowing residual film recovery is performed after tillage and land leveling but before sowing *(Wang et al., 2017)*. It can effectively increase the seedling emergence rate. At this stage, most residual film exists as fragments in the plough layer, making recovery difficult, so the windrowing method is mainly used *(Shen et al., 2024)*. As shown in Figure 6, the machine mainly used is a closely arranged spring-tooth residual film recovery machine. As the key working component, the spring teeth are usually made of manganese alloy materials such as No.60 or No.65 manganese steel, with an arc-shaped structure. During operation, the elastic teeth can pierce the residual film in the field, quickly hook and attach it to the tooth surface, thus completing residual film picking. When the machine reaches the end of the field, the collected residual film is then unloaded. However, most spring-tooth residual film recovery machines only pierce and pick up film, and unloading depends on manual work, which limits efficiency. To solve this problem, researchers have added a film unloading mechanism to the machine, as shown in Figure 6(c), realizing the integration of film picking, stripping and unloading, and effectively improving the automation and recovery efficiency. Compared with other film recovery machines, the spring-tooth type has a low recovery rate of only about 50% and high impurity content. Still, due to its simple structure, low cost and high efficiency, it has been widely used and promoted in northern China such as Xinjiang, Gansu and Inner Mongolia.



Fig. 6 – Closely Arranged Spring-Tooth Residual Film Recovery Machine

(a) Structure of TM-120 Residual Film Recovery Machine (Song et al., 2023).
(b) Standing cotton stalks raking-film machine with wide folding and monomer profiling (Wang, 2018).
(c) Raking-Type Residual Film Recovery Machine with Rotary Film Stripping (Zheng, 2020).

Residual film recycling machines have different application characteristics at different operation stages. Seedling-stage, autumn, and pre-sowing machines are designed for different residual film conditions, but challenges remain in adaptability, separation efficiency, and intelligent operation.

The characteristics, advantages, disadvantages, and development trends of different types of residual film recycling machines are summarized in Table 2.

Table 2

Characteristics and Future Development Trends of Residual Film Recycling Machines at Different Operation Stages

Type	Operation period	Residual film state	Advantages	Disadvantages	Future development directions
Seedling stage residual film recycling machine	Crop seedling stage	Relatively intact film	The residual film can be recovered timely with high film integrity, which reduces subsequent pollution.	Poor adaptability to fragmented film and soil-contaminated film; restricted by seedling crops	Adaptable mechanisms for diverse crops, planting systems, and film conditions.
Autumn residual film recycling machine	Crop postharvest stage	High fragmentation degree with obvious soil adhesion	It adapts well to fragmented and soil-contaminated films, supports large-scale operations, and is the most widely used residual film recovery equipment.	Fragmented and soil-contaminated films are difficult to separate, and complex structures increase energy consumption and reduce adaptability.	Enhanced separation, efficient fragmented film recovery, and multifunctional development.
Pre-sowing residual film recycling machine	Pre-sowing stage	Severe fragmentation and increased burial depth	Enables intact film recovery, simplifies film–soil separation, and improves field conditions for subsequent operations.	Complex structure, high energy consumption, and limited field adaptability.	Efficient fragmented film recovery, intelligent operation, and multifunctional development.

Intelligent System for Residual Film Recovery

The intelligent monitoring system for residual film recovery is an integrated intelligent system that integrates sensing, identification, positioning, computing and communication technologies. It mainly fulfills two functions: real-time monitoring of the operating status of key components during the operation of residual film recovery machines, and accurate monitoring of the effective operating area and recovery quality of the equipment.

1. Monitoring System for Key Components of Residual Film Recovery Machines

During operation, key components of residual film recovery machines often suffer from abnormal speed and damage due to entanglement by film and straw. Drive shaft speed directly affects recovery efficiency and quality. Proper speed ensures effective film picking and conveying, while abnormal speed reduces recovery performance. Thus, real-time speed monitoring of rotating parts is essential *(Xu, 2014; Jaumann et al., 2022)*. As shown in Figure 7, mature commercial intelligent monitoring systems from CASE, Massey Ferguson and Precision Planting enable key component monitoring, warning and fault diagnosis for residual film recovery machines, providing important references for China's research. Research on intelligent monitoring for residual film recovery machines in China started late and remains mostly in small-scale experiments. Using the 11FMJ toothed-chain residual film recovery machine, Chinese researchers developed a monitoring system that increased speed monitoring accuracy by 0.25%. They also proposed an STM32F103-based scheme to realize multi-parameter synchronous monitoring for drum-type machines, filling relevant technological gaps *(Ke et al., 2023; Xue et al., 2024)*.

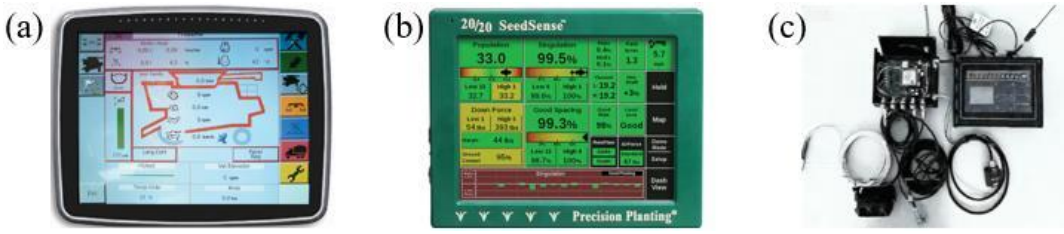


Fig. 7 – Key Component Monitoring System for Residual Film Recovery Machines

(a) FieldStar System (Coena et al., 2008) (b) 20/20 SeedSense System (Ding et al., 2018)
(c) Monitoring System for Key Components of Domestic Residual Film Recovery Machines

2. Residual Film Recovery Machine Operation Effect Monitoring System

The operation performance monitoring system for residual film recovery machines comprises two parts: an effective operation area monitoring system and a residual film image recognition system. Some countries have developed GPS-based agricultural machinery operation area monitoring methods *(Reid et al., 2000; Hamada et al., 2009)*, but these often suffer from overlapping tracks and poor boundary positioning accuracy *(Ji et al., 2012; Zhang et al., 2018)*. China's BeiDou Navigation Satellite System (BDS) has broken the technological monopoly. Its high-precision positioning provides key technical support for accurate monitoring of residual film recovery operation area. Based on BDS, Chinese researchers have developed an effective operation area monitoring system for residual film recovery machines, enabling precise calculation of effective operation area and resolving ineffective operation issues *(Zhao et Al., 2018; Zhang et al., 2020; Wang et al., 2025; Song et al., 2009)*. The residual film image recognition system detects residual films via image capture and computer vision algorithms, allowing quantitative evaluation of recovery performance. Image noise in complex fields greatly reduces model accuracy and robustness. With advances in artificial intelligence, residual film recognition has evolved from traditional machine learning to deep learning. Chinese scholars have developed lightweight detection models that achieve accurate segmentation of residual films in complex field environments while maintaining precision *(Liu et al., 2022; Ding et al., 2024; Zhang et al., 2021c; Zhai et al., 2022; Meng et al., 2025; Lu et al., 2025)*.

3. Challenges of intelligent monitoring systems under field conditions

Although deep learning-based intelligent recognition methods have achieved high detection accuracy under experimental conditions, their practical performance is still significantly affected by complex field environments. First, variations in weather conditions, solar elevation angles, and shadows caused by crops and agricultural machinery lead to constantly changing illumination conditions, thereby affecting image acquisition quality and target feature extraction. This issue is particularly significant for plastic mulch film with strong reflective properties, which is prone to local overexposure and feature loss *(Silwal et al., 2021)*. In addition, after long-term exposure to field environments, residual film surfaces are often covered with dust and soil particles, resulting in changes in their visual and spectral characteristics. These changes reduce the difference between residual film and the surrounding soil background, increasing the difficulty of image segmentation and target recognition. Meanwhile, residual film recovery operations are often accompanied by large amounts of straw and plant residues, which may overlap with residual film in images, causing false detections and missed detections and reducing the reliability of recognition systems *(Milioto et al., 2018)*. Furthermore, residual films partially buried in soil generally exhibit incomplete shapes, limited visible areas, and weak visual features, making it difficult for traditional image-based methods to achieve accurate recognition. Therefore, although intelligent monitoring technologies provide a new technical pathway for automated residual film recovery, complex and unstructured field environments remain a major factor restricting their large-scale application *(Murad et al., 2023)*.

Future research should focus on developing recognition models with stronger environmental adaptability and robustness. By integrating multi-source information, including RGB images, hyperspectral data, and environmental sensing data, the accuracy and stability of residual film detection under complex scenarios can be improved. Meanwhile, lightweight deep learning algorithms combined with edge computing technologies should be employed to achieve real-time target recognition. Furthermore, the deep integration of intelligent monitoring systems with automated residual film recovery equipment should be promoted to enable intelligent and autonomous residual film management, as illustrated in Fig. 8.

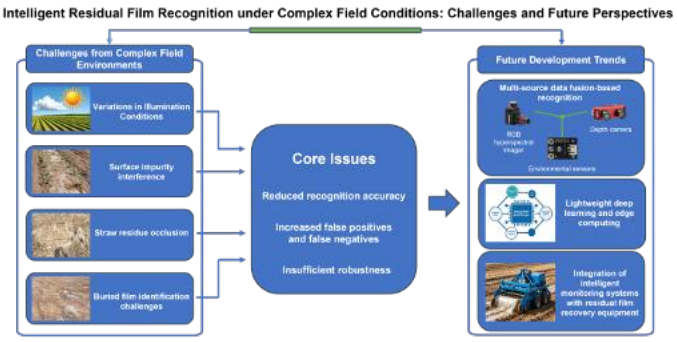


Fig. 8 – Intelligent Residual Film Recognition under Complex Field Conditions: Challenges and Future Perspectives

FILM-IMPURITY SEPARATION AND RESOURCE UTILIZATION

Although there are many types of residual film recovery machines, the recovered film mixtures have similar compositions, mainly consisting of strip or sheet old films, straw and soil clods, with varying proportions of each component. Severe entanglement between straw and residual film makes resource utilization difficult, and manual separation is inefficient and labor-intensive. Meanwhile, random stacking, burying and incineration of recovered residual film cause serious secondary pollution. Therefore, developing high-performance equipment for film-impurity separation and resource utilization is key to solving recycling challenges and achieving comprehensive control of farmland residual film *(Zhang et al., 2018)*.

Film-Impurity Separation Technology and Equipment

China has made initial progress in film-impurity separation technologies and equipment. Based on different power and working media, these technologies are mainly divided into three types: vibrating, pneumatic and water-washing *(Jiang et al., 2026)*.

1. Vibrating Film-Impurity Separation Technology and Equipment

Vibrating separation uses mechanical vibration to generate periodic oscillations, so that residual film and impurities are repeatedly thrown, bounced and slid during vibration. Based on differences in physical properties between film and impurities, they show different motion trajectories, thus achieving effective separation *(Zhang et al., 2022; Wei et al., 2018; Ruj et al., 2015)*. After mechanical recovery of farmland plastic film, the collected film-impurity mixture is complex, containing not only residual film, straw and gravel but also large amounts of soil, with severe soil wrapping on the film being especially prominent *(Guo et al., 2018b; Lubongo et al., 2022)*.To solve the resulting separation difficulties, Chinese scholars have carried out extensive research to improve separation efficiency *(You et al., 2018a; You et al.,2017b; Zhang et al., 2007d; Zhang et al., 2013)*. Figure 9(a) shows a vibrating film-soil separation device for residual film. After natural drying, the film-soil mixture collected from the field is conveyed by a belt to squeeze rollers for pre-compaction. Rotary cutters in the crushing unit then break up entangled straw and soil clods. Finally, the resulting mixture passes through a vibrating screen, which separates the residual plastic film from the soil.

Vibrating separators provide good separation and can effectively sort film from soil and stubble. They are stable, reliable and suitable for large-scale recovery. However, small and fine film pieces easily fall through the screen, lowering purity. They also adapt poorly to clay soil, where screens clog easily and reduce working efficiency.

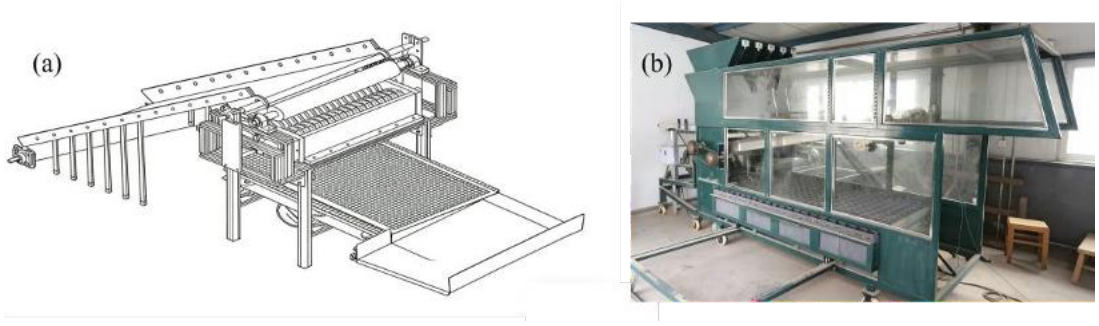


Fig. 9 – Vibrating film-impurity separation equipment

(a) Film-soil separation device (Liu et al., 2025) (b) Staggered Multi-Screen Film-Impurity Soil Removal Device (Peng, 2021)

2. Pneumatic Film-Impurity Separation Technology and Equipment

Pneumatic separation is based on the different responses of materials to airflow. Residual film has low density and low suspension velocity and is easily carried by airflow. In contrast, soil and straw have higher density and higher suspension velocity, so they tend to fall under gravity (*Anchieta e Silva; Shapiro et al., 2005*). By adjusting airflow path and velocity, film can be conveyed to a specific zone and separated *(Ma, 2024; Xie et al., 2024b)*. As shown in Figure 10(a), a pneumatic film-impurity separation device mainly consists of a fan, a rotary drum sieve, blades, a housing, a motor, and a film collection box. During operation, the fan generates airflow while the drum sieve rotates slowly. The residual film mixture (Figure 10(b)) enters the sieve through the inlet and is thrown as the sieve rotates, loosening the film. Due to the different air settling characteristics of residual film and impurities, the film is carried by airflow to the end of the sieve and into the film collection box (Figure 10(c)), while cotton stalks (Figure 10(d)) are pushed by blades to the discharge outlet, completing separation.

However, pneumatic separation requires continuous and sufficient air pressure to produce separating airflow, resulting in high power consumption, especially high energy costs for large-area operations. Restricted by environmental conditions, in humid environments, residual film adheres to impurities, reducing separation accuracy *(Kang et al., 2020; Guo et al., 2020a; Jin et al., 2022b)*.

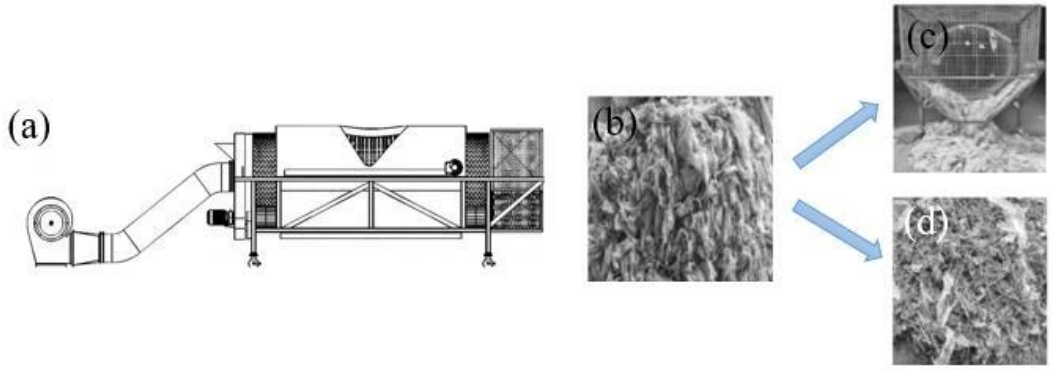


Fig. 10 – Pneumatic residual film-impurity separation device

3. Water-washing film-impurity separation technology and equipment

Water-washing separation uses the large differences in floating and settling behavior of flexible film, straw and soil particles in water. Under water flow impact and agitation, they show different trajectories and settling speeds, realizing efficient film-impurity separation *(Feng et al., 2026)*.

Water-washing separation has unique advantages in film-impurity separation, and researchers have conducted systematic research on relevant equipment. The impeller-driven water-washing separator (Fig. 11(a)) consists of a stalk collection box, stalk collection plate, water level sensor, separation tank, nozzles and water pump. During operation, cotton stalks float, residual film suspends in the middle layer, and soil settles at the bottom under water spraying. The impeller driven by the motor produces spiral thrust to enhance separation efficiency. Stalks and film are collected separately, and water is recycled through the pump. The countercurrent hook-type washing separator (Fig. 11(b)) effectively separates residual film from straw and soil. It overcomes the high soil content of air-separated film and the high energy and water consumption of ordinary washing devices *(Carvalho et al., 2010).* However, manual removal of film from the hooks reduces separation efficiency.

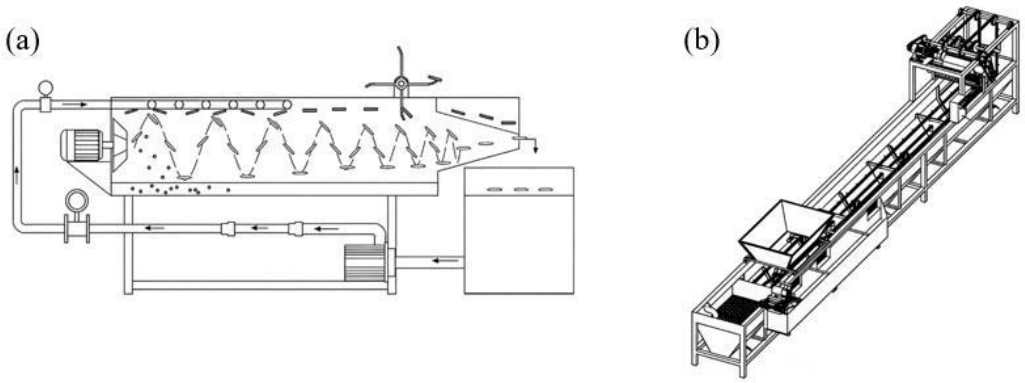


Fig. 11 – Water-washing film-impurity separation device

(a) Impeller-driven water-washing separator for mechanically harvested residual film (He et al., 2020) (b) Countercurrent hook-type washing and separating device for residual film mixture (Xie et al., 2025a)

4. Comparison of Different Film-Impurity Separation Technologies

Table 3

Comparison of different film-impurity separation technologies

Separation technology	Advantages	Limitations	Applicable conditions
Vibrating separation	Simple structure, low energy consumption, high processing capacity, no water requirement	Limited removal ability for fine soil particles and strongly adhered impurities; affected by moisture content	Suitable for preliminary separation and large-scale treatment of relatively clean residual film

Separation technology	Advantages	Limitations	Applicable conditions
Pneumatic separation	High film purity; effective separation of lightweight impurities based on aerodynamic differences	High energy consumption; separation performance affected by material moisture and particle size	Suitable for removing lightweight impurities and improving recovered film purity
Water-washing separation	High separation efficiency; excellent removal of soil and organic impurities	High water consumption; requires wastewater treatment; high operating cost	Suitable for heavily contaminated residual film requiring high-quality recycling

Overall, vibrating separation is characterized by simple structure, low energy consumption, and high processing capacity, while pneumatic separation can improve recovered film purity through airflow classification. Water-washing separation provides superior impurity removal performance but requires considerable water resources and increases treatment costs. Future development of film-impurity separation technologies will focus on improving separation efficiency while reducing energy and resource consumption. Hybrid separation systems integrating vibrating screening, pneumatic classification, and water-assisted cleaning are expected to become a promising approach for handling complex residual film mixtures and achieving efficient, sustainable, and resource-oriented recycling.

Technology and equipment for resource utilization of residual film

Waste agricultural films obtained after film-impurity separation are mainly disposed of through reuse, landfilling, incineration, and resource recycling. Although several pathways have been developed for residual film utilization, their environmental benefits and technical feasibility vary considerably. Direct reuse has the lowest processing requirement and environmental burden, but it requires relatively intact and clean films, limiting its application for highly fragmented agricultural residues. Landfill and incineration can rapidly reduce waste volume; however, landfill may cause long-term environmental risks, while incineration requires strict emission control to avoid secondary pollution. In contrast, recycling and regeneration align with the concepts of sustainable agricultural development and circular economy, making it an ideal disposal method, but they require effective impurity removal and film purification because soil particles and organic residues can deteriorate processing stability and product quality. Wood-plastic composites offer an alternative pathway for low-quality residual films, although the influence of residual soil, additives, and polymer degradation on composite mechanical properties remains a major challenge. Currently, the treatment of waste agricultural films worldwide is gradually shifting toward resource utilization. The core technologies include regenerative granulation technology and wood-plastic composite technology, as shown in Figure 12. *(Zhang et al., 2017; Hu et al., 2019; Madrid et al., 2022).*

Regenerative granulation is a core technology for residual film recycling due to its high efficiency and simple process, which is mainly divided into dry and wet methods. Wet granulation is the mainstream process, using water for cleaning. It achieves high impurity removal and high-quality recycled pellets through crushing, washing, drying, melting and pelletizing, but consumes large amounts of water, requires wastewater treatment, and has high costs, making it suitable for large-scale projects with sufficient water. Dry granulation is water-free and removes impurities via mechanical crushing, friction screening and air separation. It features low energy consumption, low investment and potentially lower environmental impacts, suitable for water-scarce regions *(Lamtai et al., 2023)*, table 4 summarizes the comparison of the two technologies.

Table 4

Comparison between wet and dry granulation technologies for residual film recycling

Technique	Water consumption	Energy consumption	Impurity removal capacity	Product purity
Wet granulation	It requires a large amount of water as the medium and features high water consumption.	The drying step consumes a certain amount of energy.	Impurities can be further eliminated by water washing and centrifugation, and a favorable impurity removal effect can be obtained.	A large proportion of surface impurities can be removed, achieving high product purity.
Dry granulation	It requires no or minimal water, with extremely low water consumption.	It requires relatively high pressure or temperature, leading to high energy consumption.	Surface impurities tend to remain, resulting in inferior impurity removal performance.	Considerable surface impurities remain, leading to low product purity.

Residual film wood-plastic composite technology takes recycled agricultural film as the matrix, blends it with straw, wood chips and additives, and forms products via melt extrusion. The composite material combines plastic's water and corrosion resistance with wood-like appearance, and can be made into garden walkways, pallets, guardrails and building formworks *(Xia et al., 2020; Huang et al., 2021; Nukala et al., 2022)*.

Despite its potential, the application of residual film in wood-plastic composites faces several challenges. Residual soil particles and impurities can interfere with polymer–wood bonding, resulting in reduced mechanical strength and poor processing stability *(Turku et al., 2017; Ribeiro et al., 2023)*. In addition, repeated recycling may cause polymer chain degradation, which decreases tensile strength and impact resistance of composite products. Furthermore, the end-of-life management of wood-plastic composites containing recycled agricultural films remains challenging because their mixed polymer–biomass structure complicates further recycling. Future studies should focus on improving purification technologies, interface modification methods, and circular recycling strategies.

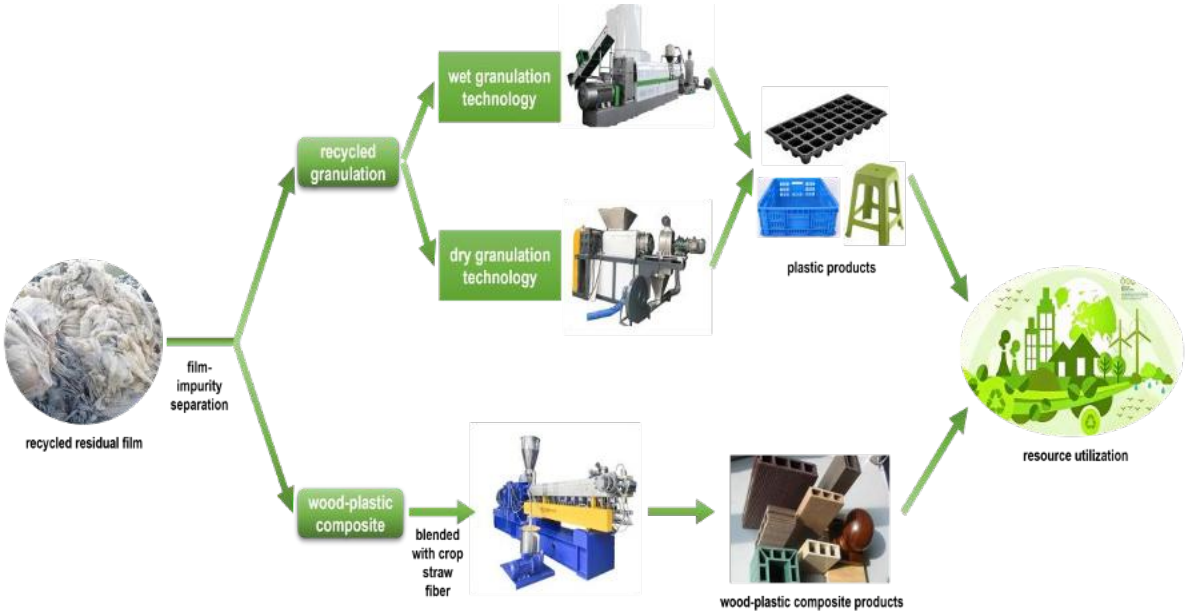


Fig. 12 – Resource utilization technology of residual film

SUMMARY AND OUTLOOK

This paper systematically reviews the core research progress throughout the entire process of farmland residual plastic film pollution control. Based on relevant research and application practices, the main conclusions are as follows: Mechanized recovery of residual film is the core link of pollution control, and an equipment system has been formed covering three key operation periods: seedling stage, post-harvest stage, and pre-sowing stage. Among them, post-harvest recovery is the most widely applied; seedling-stage recovery is developing toward automation; and pre-sowing recovery machinery is extensively used in arid agricultural areas of northern China, yet its recovery rate and automation level need to be improved. The intelligent system for residual film recovery has developed two core monitoring modules, enabling fault early warning, area measurement, and residual film identification. However, it remains in the experimental stage in China, lagging behind the commercialization level of foreign products. Membrane-impurity separation is a prerequisite for the resource utilization of residual film, and three existing types of equipment—vibratory, pneumatic, and water-washing separation—each have their advantages and disadvantages. The core technologies for the resource utilization of residual film are recycled granulation and wood-plastic composite technology, among which wood-plastic composite technology represents an important direction for the high-value utilization of residual film. At present, a full-process technical system has been established and is developing steadily with multi-stakeholder collaboration. Nevertheless, several bottlenecks still exist, restricting its large-scale and efficient application.

In view of the current technical bottlenecks in residual film pollution control and the demand for green and sustainable agriculture, future technologies and equipment will develop toward intelligence, high efficiency, coordination, and high value-added utilization. Key efforts include upgrading mechanized recovery equipment, developing new pickup mechanisms to improve the recovery rate of fragmented residual film, and optimizing combined machines and regionally adapted equipment.

Supported by Beidou navigation, AI and IoT, intelligent recovery technologies will be industrialized, with integrated management platforms and optimized algorithms to promote large-scale application. Membrane-impurity separation technologies and composite equipment will be optimized to solve existing problems, along with water-saving washing technologies to reduce costs. Resource utilization paths will be expanded by optimizing related processes, developing modification technologies, and exploring coordinated utilization with other agricultural solid wastes. Relevant standards and industrial chain mechanisms will be improved to form a sound cycle with government guidance, enterprise leadership and farmer participation, ultimately achieving "reduction, resource utilization and harmless treatment" to support green agriculture and plastic pollution control.

ACKNOWLEDGEMENT

The authors were funded for this project by the Shandong Provincial Key Research and Development Program (2024CXGC010903), the China Agriculture Research System (CARS-27), the Shandong Youth Talent Promotion Program (SDAST2024QTA050), and the Youth Innovation Team Program of Universities in Shandong Province (2023KJ160).

REFERENCES

[1] Anchieta e Silva, F., Cartaxo, A. D. S., Esmeraldo, A. D. D. S. R., Senra, E. M., & Pinto, J. C. (2026). Advancements in plastic waste sorting: A review of techniques and applications. *Processes*. 14(7):1144.

[2] Briassoulis D., Hiskakis, M., Babou, E., (2013). Technical specifications for mechanical recycling of agricultural plastic waste, *Waste Management*, 33(6), 1516-1530.

[3] Cheng, F. P., Tuo, H. Z., Yi, W. Y., Wang, P., Yang, C. M., Zhan, B. T. (2023). Research status and development trend of residual film recycling machinery in cotton field (棉田残膜回收机械研究现状及发展趋势). *Journal of Chinese Agricultural Mechanization.* 44(02):200-207.

[4] Coena, T., Saeysa, W., Missottenb, B., De Baerdemaeker, J. (2008). Cruise control on a combine harvester using model-based predictive control. *Biosystems Engineering,* 106(02),47-55.

[5] Carvalho, T., Durão, F., Ferreira, C. (2010). Separation of packaging plastics by froth flotation in a continuous pilot plant. *Waste Management*. 30:2209-2215.

[6] Ding, Y. C., Zhang, L. L., Yang, J. Q., Zhu, K. (2018). Sensing device improvement and communication design on sowing monitoring system of precision planter for rapeseed (油菜精量直播机播种监测系统传感装置改进及通信设计). *Transactions of the Chinese Society of Agricultural Engineering.* 34(14):19-26.

[7] Ding, Y. J., Yang, W. T., Zhao, Y. L. (2024). Apple Leaf Spot Segmentation Model Based on Consistency Semi-supervised Learning (基于一致性半监督学习的苹果叶片病斑分割模型研究). *Transactions of the Chinese Society for Agricultural Machinery.* 55(12):314-321.

[8] Feng, Z., Kan, Z., Wu, G. D., Peng, H. J., Meng, H. W., Zhang, B. C. (2026). Numerical Simulation and Experiment of Turbulent Flow Membrane Debris Separation Device (扰流式碎后膜杂分离装置数值模拟与试验). *Transactions of the Chinese Society for Agricultural Machinery.* 57(04):257-267.

[9] Filipe, S.; Mourão, P.M.; Couto, N.; Tranchida, D. (2023). Towards a Sustainable Future: Advancing an Integrated Approach for the Recycling and Valorization of Agricultural Plastics. *Polymers*, 15(23), 4529.

[10] Guo, W. S., He, X. W., Wang, L., Zhao, P. F., Hu, C., Hou, S. L., Wang, X. F. (2020). Development of a comb tooth loosening and pneumatic stripping ploughlayer residual film recovery machine (梳齿松土气力脱膜式耕层残膜回收机研制). *Transactions of the Chinese Society of Agricultural Engineering.* 36(18):1-10.

[11] Guo, W. S., Jian, J. M., San, Y. L., Li, G., Gao, M. Q., Hou, S. L. (2018). Design and Experimental Optimization of 4CML-1000 Type Chain Rake Film Recycling Machine (4CML-1000 型链耙式残膜回收机设计与试验优化). *Transactions of the Chinese Society for Agricultural Machinery.* 49(02):66-73.

[12] Guo, W. S., Kan, Z., Zhang, R. Y., Guo, S. X., An, H. L., Cong, T. D. (2011). Analysis of material character based on mesh roller-type cotton and film remnant separator (基于网式滚筒棉秆残膜分离装置的物料特性分析). *Transactions of the Chinese Society of Agricultural Engineering.* 27(S2):1-5.

[13] Hamada, Y., Matsuo, Y., Yamashita, T. (2009). Agricultural vehicle navigation system: Development of a guidance information display. *Japan Agricultural Research Quarterly.* 43(3):187-192.

[14] He, H. M., Hu, B., Li, J. H., Cai, H., Luo, X. (2020). Research and Experiment of the Machine Collecting Residual Film in the Impeller-driven Washing Separation Device (叶轮驱动式水洗分离装置残膜回收机的研究与试验). *Journal of Agricultural Mechanization Research.* 42(09):151-155.

[15] He, Y. C., Wang, X. J., Wang, J. L., Cao, S. L., Wang, M., Liu, Y. (2013). Research and Design of Cotton Plastic Film Collector&Field Straw Chopper Combined Machine after Autumn (棉花秋后残膜回收与茎秆粉碎联合作业机设计). *Acta Agriculture Boreali-occidentalis Sinica.* 22(08):199-204.

[16] He, Y. Z., Lu, Y. T., Wang, M., Ying, Y. K., Wang, J. L., Qin, C. M., Xue, L. (2023). Development and test of 4MKJ residual film recycling and straw crushing integrated machine (4MKJ 残膜回收打捆与秸秆粉碎联合作业机的研制与试验). *Xinjiang Agricultural Mechanization.* (02):7-8+22.

[17] Hu, B. Q., Zhu, D. G., Yang, Y. F. (2018). Design of the Main Structure of Plastic Film Collector for Toabcco at Seedling Stage (苗期烟草残膜回收机主要结构设计). *Journal of Anhui Agricultural Sciences.* 44(10):251-253.

[18] Hu, C., Wang, X. F., Chen, X. G., Tang, X. Y., Zhao, Y., Yan, C. R. (2019). Current situation and control strategies of residual film pollution in Xinjiang (新疆农田残膜污染现状及防控策略). *Transactions of the Chinese Society of Agricultural Engineering.* 35(24):223-234.

[19] Hu, G. F. (2021). Design of Farmland Residual Film Recycling Machine and Parameter Optimization of Key Components (农田残膜回收机设计与关键部件的参数优化). [Master's thesis]. Hunan Agricultural University.

[20] Huang, X. Y., Pan, L. W., Tan, L., Wang, H. (2021). Study on Reuse Techniques of Hot Air Melting of Waste Plastics (热风熔融废旧塑料再生利用技术研究中国塑料). *China Plastics*. 35(08):195-199.

[21] Ji, B. B., Li, J., Yang, Y. P., Zhang, S. (2012). A Real-time Measurement Based on GPS Which Was Designed for Calculating the Harvest Area of Combine (基于 GPS 的联合收割机作业面积实时测算装置设计). *Journal of Chinese Agricultural Mechanization.* (06):89-92.

[22] Jiang, S. Q., Zhang, H. D., Hua, Y. J. (2016). Research on location of residual plastic film based on machine vision (基于机器视觉的残膜定位方法研究). *Journal of Chinese Agricultural Mechanization.* 37(11):150-154.

[23] Jiang, W. J., Du, Y. K., Fang, W. Q. (2026). Research progress and prospects of cotton field residue film recycling machines (棉田残膜回收机械研究进展与展望). *Journal of Chinese Agricultural Mechanization.* 47(02):14-20.

[24] Jin, W., Ding, Y. C., Nong, F., Zhang, X. J., Bai, S. H. (2023). Design and Test of Excavating and Conveying Device with Vibrating Chain Tooth and Bar for Residual Film-Soil-Straw (振动链齿杆式残膜-土-秸秆挖掘输送装置设计与试验). *Transactions of the Chinese Society for Agricultural Machinery.* 54(11):71-82.

[25] Jin, W., Zhang, X. J., Ding, Y. C., Bai, S. H., Liu, W. P., Zhou, X. C. (2022). Experiment on Suspension Separation of Residual Film and Impurity Based on EDEM-Fluent Coupling (基于 EDEM-Fluent 耦合的残膜-杂质悬浮分离试验). *Transactions of the Chinese Society for Agricultural Machinery.* 53(04):89-98.

[26] Jaumann, M., Olcay, E., & Oksanen, T. (2022). Condition monitoring using convolutional neural network in agricultural machinery-use case: disc mower. *IFAC-PapersOnLine.* 55(32):235-240.

[27] Kang, J. M., Zhang, H., Zhang, G. H., Du, H. Y., Peng, Q. J., Song, Y. M. (2020). Aerodynamic characteristics of residual film materials and test of membrane separation device (残膜物料气动特性及膜杂分离装置试验). *Journal of Chinese Agricultural Mechanization.* 41(01):167-172.

[28] Ke, Z. R. (2023). Design of on-line monitoring system for field operations of the tooth chain type residual film recovery machine (齿链式残膜回收机田间作业在线监测系统设计). [Master's thesis]. Ningxia University.

[29] Kou, J. L., Wang, J. K., Wang, L., Zhao, Y. M. (2023). Integrating clamping finger-chain residual film recycling and straw crushing return to cotton field (棉田夹指链式残膜回收-秸秆粉碎还田联合作业装置). *Transactions of the Chinese Society of Agricultural Engineering.* 39(23):14-22.

[30] Li, D., Zhao, W. Y., Xin, S. L., Liu, X. L., Qu. H., Xu, Y. (2020). Current situation and prospect of recycling technology of farmland residual film (农田残膜回收技术研究现状与展望). *Journal of Chinese Agricultural Mechanization.* 41(05):204-209.

[31] Li, K. K. (2023). *Theoretical Analysis and Experimental Research on the Stripping and Impurity Removal Device for Spring-Tooth Residual Plastic Film Collector (弹齿式残膜回收机脱膜除杂装置理论分析与试验研究).* [Master's thesis]. Shandong University of Technology.

[32] Li, T., Zhang, H. C., Wang, X. Y., Wang, X. X., Liu, X. F., Liu, C.H., Kang, J. M., Li, G. M. (2025). Development of Self-propelled Combined Operation Machine for Cotton Stalk Baling and Residual Film Packing (自走式棉秆打捆-残膜打包联合作业机研制). *Transactions of the Chinese Society for Agricultural Machinery.* 56(07):424-433.

[33] Liu, E. S. (2021). *Optimal Design of Residual Film Recovery Machine with Comb-Tooth Film Lifting and Pneumatic Film Stripping (梳齿起膜-气吹脱膜式残膜回收机优化设计).* [Master's thesis]. Tarim University.
[34] Liu, J. H., Quan, L. Z. (2025). Design and experiment of a vibratory separation device for residual plastic film and soil (残膜-土壤振动分离装置设计与试验). *Agricultural Engineering and Equipment.* 52(03):1-4.
[35] Liu, X. H., Tian, X. L., Zhao, Y., Li, Y. C., Ma, H. Z. (2024). Research on Film Collection Device of Residual Film Recycling Machine (残膜回收机集膜装置研究). *Agricultural Engineering.* 14(01):5-14.
[36] Liu, Y. L., Zhang, T. Y., Jiang, M., Li, B., Song, J, L. (2022). Review on Non-destructive Detection Methods of Grape Quality Based on Machine Vision (基于机器视觉的葡萄品质无损检测方法综述). *Transactions of the Chinese Society for Agricultural Machinery.* 53(S1):299-308.
[37] Lu, J. D., Zhai, Z. Q., Meng, Q. J., Miao, L. P., Chen, Y. Zhang, R. Y. (2025). Surface Residual Film Recognition Method Based on Vehicle-mounted Imaging and Deep Convolutional Neural Networks (基于车载成像与深度卷积神经网络的地表残膜识别方法). *Transactions of the Chinese Society for Agricultural Machinery.* 56(05):26-37+70.
[38] Luo, W. J., Zhang, H. C., Liu, X. F., Zhang, L., Zhou, X. (2024). Research of combined operation machine for secondary throwing straw crushing and residual film recovery (二次抛送式秸秆粉碎残膜回收联合作业机研究). *Xinjiang Agricultural Sciences.* 61(S1):142-146.
[39] Lamtai, A., Elkoun, S., Robert, M., Mighri, F., & Diez, C. (2023). Mechanical recycling of thermoplastics: A review of key issues. *Waste*. 1(4):860-883.
[40] Lubongo, C., Alexandridis, P. (2022). Assessment of performance and challenges in use of commercial automated sorting technology for plastic waste. *Recycling*. 7(2):11.
[41] Ma, Z. (2024). *Design and test of wind power-vibration type residual film-impurity (风振式残膜杂质分离装置设计与试验)*. [Master's thesis]. Shenyang Agricultural University.
[42] Meng, Q. J., Zhai, Z. Q., Zhang, L. P., Lu, J. D., Wang, H. T., Zhang, R. Y. (2025). Recognition Method of Cotton Field Surface Residual Film Based on Improved YOLO 11 (基于改进 YOLO11 的棉田地表残膜识别方法). *Transactions of the Chinese Society for Agricultural Machinery.* 56(05):17-25+48.
[43] Milioto, A., Lottes, P., & Stachniss, C. (2018). Real-time semantic segmentation of crop and weed for precision agriculture robots leveraging background knowledge in CNNs. *IEEE International Conference on Robotics and Automation (ICRA)*, 2229-2235.
[44] Murad, N. Y., Mahmood, T., Forkan, A. R. M., Morshed, A., Jayaraman, P. P., & Siddiqui, M. S. (2023). Weed detection using deep learning: A systematic literature review. *Sensors.* 23(7): 3670.
[45] Madrid, B., Wortman, S., Hayes, D. G., DeBruyn, J. M., Miles, C., Flury, M. (2022). End-of-life management options for agricultural mulch films in the United States—a review. *Frontiers in Sustainable Food Systems*. 6:921496.
[46] Martín Martín, A., Orduna-Malea, E., Thelwall, M. (2018). Google Scholar, Web of Science, and Scopus: A systematic comparison of citations in 252 subject categories. *Scientometrics*. 116: 1-30.
[47] Montoya, F. G., Alcayde, A., Baños, R., et al. (2018). A fast method for identifying worldwide scientific collaborations using the Scopus database. *Telematics and Informatics*. 35(1): 168-185.
[48] Niu, A., Wu J., Zhao X. (2023). Infrared Spectrum Analysis of Degradation Characteristics of PPC Plastic Film Under Different Covering Methods (不同覆盖方式下 PPC 地膜降解特性红外光谱分析). *Spectroscopy and Spectral Analysis.* 43(02):533-540.
[49] Niu, Q., Ji, C., Zhao, Y., Chen, X., Zheng, X., Li, H. (2017). Design and Experiment on Collecting and Separating Device for Strip Plastic Film Baler (条状残膜打捆机集膜分离装置设计与试验). *Transactions of the Chinese Society for Agricultural Machinery.* 48(05):101-107.
[50] Nukala, S. G., Kong, I., Kakarla, A. B., Kong, W., & Kong, W. (2022). Development of wood polymer composites from recycled wood and plastic waste: thermal and mechanical properties. *Journal of Composites Science*. 6(7):194.
[51] Peng, X. B. (2021). *Design and experiment of alternated multi-sieve device with function of separating soil from residual film mixture (交替多筛式残膜混合物土膜分离装置设计与试验).* [Master's thesis]. Shihezi University.
[52] Reid, J. F., Zhang, Q., Noguchi, N., Diskin, M. D. (2000). Agricultural automatic guidance research in North America. *Computers and Electronics in Agriculture.* 25(1-2):155-167.
[53] Ribeiro, L. S., Stolz, C. M., Amario, M., Silva, A. L. N. D., & Haddad, A. N. (2023). Use of post-consumer plastics in the production of wood-plastic composites for building components: a systematic review. *Energies*. 16(18):6549.

[54] Ruj, B., Pandey, V., Jash, P., & Srivastava, V. K. (2015). Sorting of plastic waste for effective recycling. *International Journal of Applied Science and Engineering Research.* 4(4):564-571.

[55] Shen, S. L., Zhang, J. X., Jiang, Y. X., Wang, Y. C., Liu, X. F., Li, J. M., Dong, W. H. (2024). Tensile Properties of Residual Film in Tillage Layer Based on Discrete Element Method (基于离散元法的耕层残膜拉伸性能研究). *Transactions of the Chinese Society for Agricultural Machinery.* 55(07):132-141.

[56] Shi, M. W., Wang, M. G., Wang, W., Li, Z. G., Wang, L., Zhang, H. J. (2025). Design and Experiment of Integrated Machine for Cotton Stalk Crushing and Residual Film Recycling and Baling (棉秆粉碎-残膜回收打捆一体机设计与试验). *Transactions of the Chinese Society for Agricultural Machinery.* 56(12):397-406.

[57] Shi, Z., Zhang, X., Cheng, J., Zhou, X., Zhang, C. (2023). Design and test of film transfer and unloading device of vertical double-row chain residual film recycling machine (垂直双排链式残膜回收机输膜卸膜装置设计与试验). *Agricultural Research in the Arid Areas.* 41(03):257-265.

[58] Song, J. H., Zhao, L. Y., Wu, M. Q. (2009). Research and Design of Intelligent Operation Area Measurement System for Agricultural Machinery (农机智能作业面积测量系统研究与设计). *Farm Machinery.* (11):92-94.

[59] Song, Z. T., Guo, J. J., Wen, H. J. (2023). Design and test of film-hanging conveyor belt of rotary-tooth residual film recycling machine (旋齿式残膜回收机挂膜输送带设计与试验). *Xinjiang Agricultural Mechanization.* (04):34-37.

[60] Silwal, A., Parhar, T., Yandun, F., Baweja, H., & Kantor, G. (2021). A robust illumination-invariant camera system for agricultural applications. *IEEE/RSJ International Conference on Intelligent Robots and Systems (IROS)*, 3292-3298.

[61] Sarpong KA, Adesina FA, DeVetter LW, Zhang K, DeWhitt K, et al. (2024). Recycling agricultural plastic mulch: limitations and opportunities in the United States. *Circular Agricultural Systems* 4: e005.

[62] Shapiro, M., Galperin, V. (2005). Air classification of solid particles: a review. *Chemical Engineering and Processing: Process Intensification.* 44(2):279-285.

[63] Turku, I., Keskisaari, A., Kärki, T., Puurtinen, A., & Marttila, P. (2017). Characterization of wood plastic composites manufactured from recycled plastic blends. *Composite Structures*. 161:469-476.

[64] Wang, D. Y., Zhang, R. Y., Duan, H. W., Zhai, Z. Q., Fu, Y. X., Meng, Q. J. (2024). Design and Research of Effective Working Area Monitoring System for Residual Film Recycling Machine (残膜回收机有效作业面积监测系统设计研究). *Journal of Agricultural Mechanization Research.* 47(01):54-60.

[65] Wang, G., Wang, Q., Tian, Z. H., Ji, D., Liu, F. B. (2026). Research Progress of Farmland Plastic Film Recycling Device (农田残膜回收装置研究进展). *Journal of Agricultural Mechanization Research.* 1-8[2026-03-30].

[66] Wang, J., Ghimire, R., Fu, X., Sainju, U. M. Liu, W. Z. (2018). Straw mulching increases precipitation storage rather than water use efficiency and dryland winter wheat yield. *Agricultural Water Management.* 206:95-101.

[67] Wang, K. (2018). *Design and study on standing cotton stalks raking-film machine with wide folding and monomer profiling (宽幅折叠单体仿形直立棉秆搂膜机设计与研究).* [Master's thesis]. Shihezi University.

[68] Wang, P. Z., Wu, X. M., Zhang, F. G., Huang, H. G., Yu, L. H., Nie, Y. (2017). Design and performance test of comb-type automatic profiling residual film collecting machine (梳齿式自动仿形残膜捡拾机设计及性能试验). *Acta Tabacaria Sinica.* 23(03):56-62.

[69] Wang, X., Zhang, T., Li, S. J., Sun, W., Wang, L. J. (2017). Experimental study on increasing yield and efficiency of mechanical potato planting with whole black film mulching technology (黑色全膜覆盖马铃薯机械种植增产增效试验研究). *Journal of Chinese Agricultural Mechanization.* 38(06):89-93.

[70] Wei, B. Q., Shan, Z. H. (2019). Types of Mulch and Research Progress (地膜类型及研究进展). *West Leather.* 41(17):53-55.

[71] Wei, Z. C., Li, H. W., Sun, C. Z., Li, X. Q., Liu, W. Z., Su, G. L., Wang. F. M. (2018). Improvement of potato harvester with two segment of vibration and wave separation (振动与波浪二级分离马铃薯收获机改进). *Transactions of the Chinese Society of Agricultural Engineering.,* 34(12):42-52.

[72] Wen, H., Gou H., Chen X. (2021). Development of a two-stage chain-plate combined machine for straw crushing and plastic-film recovery (二阶链板式秸秆粉碎地膜回收联合作业机的研制). *Agricultural Development & Equipment,* 235(07):40-41.

[73] Wu, Z. X., Ma, S. H., Ren, W., Han, X. J., Wang, K. L., Lan, W. Q. (2025). Research status and prospects of domestic residual film recycling machine pickup device (国内残膜回收机捡拾装置研究现状及展望). *Xinjiang Agricultural Mechanization.* (04):40-44+49.

[74] Xia, Y., Liu, Z. Y., Zhu, C. (2020). Mechanical Properties Repair Method and Processing Technology of Waste Plastic Regeneration Granulation (废旧塑料再生造粒力学性能修复方法及加工工艺). *China Resources Comprehensive Utilization.* 38(03):96-98.

[75] Xie, J. H., Liu, W., Cao, S. L., Huang, W. R., Zhang, J., Li, Y. Z., Meng, Q. H. (2025). Design and Test of Countercurrent Hook-type Residual Film Mixture Cleaning and Separation Device (逆流钩拽式残膜混合物清洗分离装置设计与试验). *Transactions of the Chinese Society for Agricultural Machinery.* 56(06):397-408.

[76] Xie, J. H., Li, Y. Z., Liu, Y. C., Zhang, J., Du, Y. K., Shi, X. (2024). Design and Test of Segmented Drum Pneumatically Assisted Potosia brevitarsis Larva Residual Film Mixture Separation Device (分段滚筒式气力辅助白星花金龟幼虫转化残膜混合物分离装置设计与试验). *Transactions of the Chinese Society for Agricultural Machinery.* 55(11):329-341+428.

[77] Xu, B. (2014). *Research on Real-time Measurement of Torque and Speed of Transmission Shaft of Micro Combine (微型联合收割机传动轴转矩转速实时测量装置的研究).* [Master dissertation]. Southwest University.

[78] Xue, D. Q., Dong, Z. S., Zhang, J. X. (2024). Design and Experiment of Stress and Strain Monitoring System for Key Components of Drum Film Recovery Machine (滚筒式残膜回收机关键部件应力应变监测系统设计与实验). *Journal of Nanyang Institute of Technology*. 04.009.

[79] Yang, L., Liu, J., Zhang, D. X., Hou, S. L., Xu, F. (2010). Cotton seedling-stage mulch film recycler (棉花苗期地膜回收机设计与试验). *Transactions of the Chinese Society for Agricultural Machinery.* 41(S1):73-77.

[80] You, Z. Y., Hu, Z. C., Wu, H. C., Zhang, Y. P., Yan, J. C., Yan, W., Zhou, X. X. (2017). Design and experiment of 1MCDS-100A typed shovel-sieve residual film recovery machine (1MCDS-100A 型铲筛式残膜回收机的设计与试验). *Transactions of the Chinese Society of Agricultural Engineering.* 33(09):10-18.

[81] You, Z. Y., Wu, H. C., Chen, Y. Q., Hu, Z. C., Tan, L. K., Peng, B. L., Zhang, J. L. (2018). Design and experiment on double-sieve-driving apparatus for film-soil separation and transportation (双筛体驱振式膜土分离与输送装置设计与试验). *Journal of Chinese Agricultural Mechanization.* 39(11):4-11.

[82] Yu, Y. H., Chen, X. G., Wen, H. J. (2016). Development and experiment of straw chopping and plastic filmstrip-collection combined machine (秸秆粉碎与残膜集条联合作业机的研制与试验). *Transactions of the Chinese Society of Agricultural Engineering.* 32(24):1-8.

[83] Yang, S. M., Wang, B. X., Ru, S. F., Chen, X. G., Yan, L. M., & Wu, J. L. (2024). Review of agricultural plastic film recycling equipment from China (中国农田农膜回收装备综述). *INMATEH-Agricultural Engineering*. 74(3):683-698.

[84] Zhai, Z. Q., Chen, X. G., Qiu, F. S., Meng, Q. J., Wang, H. Y., Zhang, R. Y. (2022). Detecting surface residual film coverage rate in pre-sowing cotton fields using pixel block and machine learning (基于像素块和机器学习的播前棉田地表残膜覆盖率检测). *Transactions of the Chinese Society of Agricultural Engineering.* 38(06):140-147.

[85] Zhan, Y., Zheng, X., Chen, X. G., Niu, Q., Ji, C., Zhou, D. X. (2017). Design and test of CMJY-1500 type plastic film residue collecting and balling machine (CMJY-1500 型农田残膜捡拾打包联合作业机设计与试验). *Transactions of the Chinese Society of Agricultural Engineering.* 33(05):1-9.

[86] Zhang, D. H., Ma, Y. H., Guan, F., Wang, Q., Zheng, T. (2018). Agricultural Machinery Operation Area and Track Monitoring Management System Based on GPS (基于 GPS 的农机作业面积与轨迹监测管理系统). *Geospatial Information.* 16(02):68-70+11.

[87] Zhang, D., Liu, H. B., Ma, Z. M., Tang, W. X., Wei, T., Yang, H. D., Li, J. G., Wang, H. Y. (2017). Effect of Residual Plastic Film on Soil Nutrient Contents and Microbial Characteristics in the Farmland (残膜对农田土壤养分含量及微生物特征的影响). *Agricultural Engineering Technology.* 39(14):49-50.

[88] Zhang, J., Yang, W. Z., Xie, X. Y., Mu, D. H., Zhang, J. (2013). Design and Experimental Research on Separating Used Plastic Film from Soil and Transporting Used Plastic Film Mechanism (膜土分离与输送装置的设计及试验研究). *Agricultural Science & Technology and Equipment.* (02):29-30+33.

[89] Zhang, L., Wu, B. T., Xie, J. X., Zhang, H. D., Huang, J. Q., Li, M. (2020). Design and test on agricultural machinery operation area management system of Beidou navigation (北斗导航农机作业面积管理系统设计与试验). *Journal of Chinese Agricultural Mechanization.* 41(12):139-146.

[90] Zhang, X. J., G, L., Shi, Z. L., Yan, J. S., Liu, X. P., Zhang, C. S., Liu, L. (2024). Structural optimization and test of the roll type tillage residual film recovery components using FEM-SPH coupling (基于 FEM-SPH 耦合的卷辊式耕层残膜回收部件结构优化与试验). *Transactions of the Chinese Society of Agricultural Engineering (Transactions of the CSAE).* 40(10): 55-65.

[91] Zhang, X. J., Huang, S., Jin, W., Yan, J. S., Shi, Z. L., Zhou, X. C., Zhang, C. S. (2021). Identification Method of Agricultural Film Residue Based on Improved Faster R-CNN (基于改进 Faster R-CNN 的农田残膜识别方法). *Journal of Hunan University (Natural Sciences).* 48(08):161-168.

[92] Zhang, X. J., Wu, C. W., Wang, W., Ma, S. H., Wang, X. F. (2008). Design and Experiment on the Zigzag Scraper Transportation Device for Remnant Plastic Film and Stubble (锯齿刮板式残膜根茬输送装置设计与试验). *Transactions of the Chinese Society for Agricultural Machinery.* (09):49-51.

[93] Zhang, X. J., Wu, C. W., Wang, X. D., Ma, S. H., Wang, X. F. (2007). Motion simulation and analysis of separating sieve mechanism for scrap plastic film (残膜分离筛机构的运动仿真与分析). *Transactions of the Chinese Society of Agricultural Engineering.* (07):113-116.

[94] Zhang, Y. M., Shen, L. X. (2018). Pollution of Residual Film in Farmland Soil and Countermeasures (农田土壤残膜污染及防治对策). *Tianjin Agricultural Sciences.* 24(02):86-90.

[95] Zhang, Z. (2023). *Study on the mechanism of picking up and recovering the residual film of sowing layer based on arc-shaped nail-tooth roller (基于弧钉齿滚筒的播种层残膜捡拾回收机理研究).* [Doctoral dissertation]. Shihezi University.

[96] Zhang, Z., Li J., Wang X., Zhao Y., Xue S., Su Z., Liang J. (2023). Design and test of 1SMB-3600A type fragmented mulch film collector for sowing layer soil (1SMB-3600A 型播种层碎膜捡拾机设计与试验). *Soil and Tillage Research.* 225:105555.

[97] Zhao, Y. D., Tu, J. Y. (2018). Intelligent Surveying and Mapping System of Forest Inspection Based on Beidou Satellite (基于北斗卫星的林业巡检智能测绘系统). *Transactions of the Chinese Society for Agricultural Machinery.* 49(07):177-185.

[98] Zheng, S. Q. (2020). *Design and experiment of spring tooth type rotary unloading mulch film residue collector (弹齿式旋卸残膜捡拾机设计与试验).* [Master's thesis]. Shihezi University.

[99] Zhou, L., Tang, W., Xie, J. H. (2019). Present Research Situation and Existing Problems of Residue Film Collectors (残膜捡拾机研究现状及存在问题). *Xinjiang Agricultural Mechanization.* (05):13-15+32.

YOUNG APPLE FRUIT DETECTION METHOD FOR ENTIRE DWARF AND DENSELY PLANTED APPLE TREES BASED ON CHUNKING STRATEGY
/
基于分块策略的矮砧密植苹果整株果树幼果识别方法研究

Yu YANG[1)], Xingchen QIAO[1)], Huijun ZHAO[2)], Yicheng YANG[1)], Zhaohui ZHENG[3)], Gang ZHANG[4)], Xiaole WANG[1)], Zhenchao WU*[1)]

[1)]School of Engineering, Anhui Agricultural University, Hefei, Anhui 230036, China;
[2)] Himile Industrial Park, Economic Development Zone, Weifang, Shandong 261500, China
[3)] College of Mechanical and Electrical Engineering, Shihezi University, Shihezi 832000, China
[4)] School of Intelligent Manufacturing, Anhui Science and Technology University, Chuzhou 239000, China
Corresponding author: Zhenchao Wu
Tel: +8613204655989; E-mail: wuzhenchao@ahau.edu.cn
DOI: https://doi.org/10.35633/inmateh-79-68

Keywords: *Chunking strategy, Apple fruitlets, Branch-leaf occlusion, YOLOv12n, Small-target detection*

ABSTRACT

A chunking strategy based on YOLOv12n has been proposed in this study to address challenges of young fruit detection for entire trees in dwarf and densely planted apple orchards, such as small young fruit volume, high similarity between fruit skin color and surrounding young leaves. This strategy divides an image into sub-images before feeding them into the network for training. Experimental results show that, compared with using only the YOLOv12n model for whole-image recognition, the chunking strategy achieved a precision of 85.57% and a recall of 62.54% in young fruit detection. In contrast, the YOLOv12n model alone, due to ineffective small-target capture and missing edge features, achieved a detection precision of less than 1% for young fruits, making effective detection nearly impossible. The introduction of the chunking strategy achieved a qualitative leap in young fruit detection performance. This strategy provides technical support for precise young fruit counting, subsequent accurate thinning, and growth dynamic monitoring in dwarf and densely planted orchards, and also offers a new implementation approach for small-target detection scenarios in orchards.

摘要

本研究提出了一种基于 YOLOv12n 的分块策略，以解决矮化密植苹果园整树幼果检测的难题，如幼果体积小、果皮颜色与周围幼叶高度相似等。该策略通过将图像分割为子图像后输入网络进行训练。试验结果表明，与仅使用 YOLOv12n 模型进行整图识别，分块策略的使用在幼果识别的准确率上达到 85.57%，召回率达到 62.54%，而单独使用 YOLOv12n 模型则因小目标捕捉失效、边缘特征遗漏，对幼果的检测准确率不足 1%，几乎无法完成有效检测，分块策略的引入实现了幼果识别性能的质的飞跃。该策略为矮砧密植果园幼果精准计数、后续精准疏果及生长动态监测等环节提供了技术支撑，也为果园小目标检测场景提供了新的实现思路。

1. INTRODUCTION

The development of intelligent and precise thinning devices is of great significance for improving the efficiency of the apple industry, reducing production costs, and achieving refined orchard management. Thinning is a key link in apple tree management *(Pawikhum et al., 2025)*. Proper thinning can improve fruit size and quality, maintain tree vigor, and extend the productive lifespan of trees *(Patiyal et al., 2024; Tang et al., 2023)*. Currently, the mainstream thinning methods include manual thinning, chemical thinning, and mechanical thinning. Although manual thinning allows precise control of fruit load, its efficiency is low and labor costs are high *(Du et al., 2024)*. Chemical thinning, while low in cost and simple to operate, is easily affected by climatic conditions, leading to unstable results *(Hussain et al., 2023)*. Mechanical thinning greatly improves efficiency and reduces labor input, but suffers from inaccurate young fruit detection and a tendency to damage fruits *(Hua et al., 2025)*. Therefore, the development of automated intelligent thinning devices is a direction for solving existing problems and promoting industrial upgrading *(Wang et al., 2025)*. The prerequisite for achieving such high-performance devices is the provision of a precise visual perception foundation for apple fruitlets, i.e., reliable detection and localization of young fruits, which directly affects the operational performance and practical value of the device.

Performance improvement of the visual perception module is inseparable from the technical support of deep learning in computer vision fields such as object detection *(Borugadda et al., 2026; Oba et al., 2025)*. Currently, some researchers have applied deep learning networks to fruit detection in complex scenes to enhance the adaptability of the vision module to field environments. *Fu et al. (2020)* improved ZFNet and VGG16 models based on Faster R-CNN for apple detection in dense-foliage fruit trees, achieving average precision improvements to 89.3% and 80.5% for the VGG16 and ZFNet models, respectively, with an average processing time of 0.181 seconds per image for VGG16, indicating almost no impact on processing speed. To quickly and accurately predict the positions of key points such as fruit picking points in complex field environments, *Ma et al. (2025)* proposed a joint detection model for strawberry targets and key points, STRAW-YOLO, based on the YOLOv8-pose network. The improved network achieved a keypoint detection precision of 91.6% and an average precision of 96.0%. *Zheng et al. (2021)* proposed a multi-scale feature fusion network, YOLO-BP, to recognize green citrus, achieving an average precision of 91.55%, but missed detections and false detections occurred in some partially occluded and overlapping fruit scenes. *Liu et al. (2024)* proposed a lightweight algorithm, Faster-YOLO-AP, to detect orchard apples, achieving an average precision of 85.3% for large targets but only 65.6% for small targets. Despite these good results in fruit detection, few studies have captured entire trees for fruit detection in the context of dense small targets such as apple fruitlets in dwarf and densely planted orchards *(Chen et al., 2024)*, to better meet the high precision and high reliability requirements of practical applications.

Compared with deep learning network improvements, the chunking strategy has potential to achieve better small-target detection performance in orchard scene images. Although object detection has developed rapidly, small-target detection remains a major challenge due to the small proportion of pixels occupied by small targets, limited semantic information, susceptibility to complex scene interference, and ease of clustering and occlusion *(Feng et al., 2024; Zhang et al.,2022; Hou et al., 2025)*. The dwarf and densely planted cultivation mode makes small-target detection scenes even more complex, as dense planting causes severe overlap of branches, leaves, and fruits, blurring target boundaries. The color and texture of fruits and leaves converge, and contrast decreases under complex lighting *(Gao et al., 2024)*. However, current small-target detection methods mainly focus on modifying widely used deep learning network architectures *(Wu et al., 2024; Liang et al., 2025)*. Although local performance is improved, effective features are severely attenuated after standard resize operations, and network customization for specific objects limits generalization capability *(Chen et al., 2025)*. In contrast, the chunking strategy preserves the original features of small targets directly through local high-resolution processing, while effectively increasing the number of datasets, avoiding insufficient feature learning during model training due to small dataset sizes, thus opening up a better solution for building a universal detection framework.

The potential of the chunking strategy in young apple fruit detection in large-field-of-view complex scenes is significant, but its practical application still faces multiple key challenges. Currently, limitations of the chunking strategy often lead to missed detections of small targets, such as ignoring dense small fruitlets when chunks are too large, or computational redundancy when chunks are too small *(Dang et al., 2025; Jiang et al., 2023)*. Therefore, it is necessary to determine the optimal chunk size and overlap rate to balance detection accuracy and computational efficiency while avoiding cutting of young fruits. It is also necessary to reduce the destruction of contextual information from the original image during chunking and minimize feature loss caused by local fragmentation. An efficient chunking result recombination strategy needs to be designed to eliminate duplicate detections or missed detection errors at boundaries. These issues have not been fully explored in current immature apple detection research. Therefore, the scientific design and optimization of the chunking strategy is the core prerequisite and implementation path for achieving efficient, high-precision, and large-scale detection of apple fruitlets under the dwarf and densely planted mode.

This study aims to address the key challenges in applying the chunking strategy to young apple fruit detection in dwarf and densely planted orchards. Through scientific chunking strategy design, the problems in young apple fruit detection are solved, and the ability to extract and classify fruit features in complex and diverse environments is enhanced. The chunking strategy is integrated with the YOLOv12n model to achieve accurate detection of dense, occluded apple fruitlets.

2. MATERIALS AND METHODS

This method includes six main processes. First, a mobile phone camera was used to collect images of young apple fruits.

The young apple fruits were annotated to establish a dataset of young apple fruits in dwarf and densely planted orchards. The dataset was divided into training and validation sets through data processing operations. Then, model training was carried out according to three different training strategies, and finally, detection results of young apple fruits in the dwarf and densely planted orchard environment were obtained. An overall schematic diagram of this method is shown in Fig. 1.

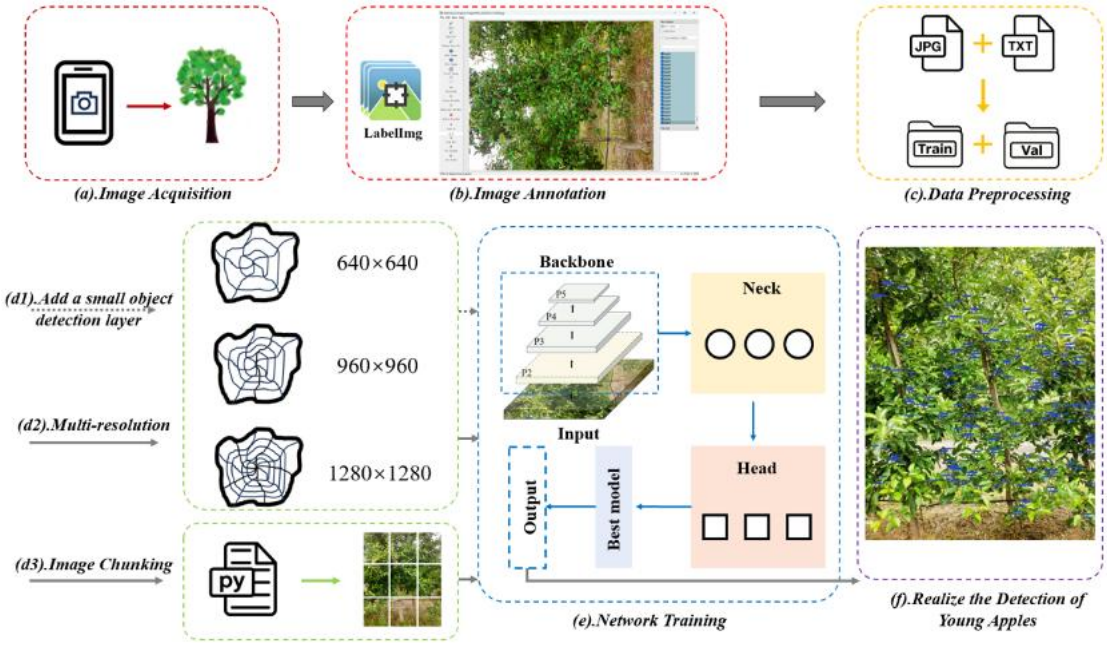


Fig. 1 - Schematic diagram of the overall workflow

2.1 Dataset

2.1.1 Image Acquisition of Young Apple Fruits

On May 16, 2025, images of "Gala" apples were collected at Xinyuan Fruit Industry Group Co., Ltd. in Weihai City, Shandong Province. The planting pattern of the studied apple trees was dwarf and densely planted *(Yuan et al., 2025; Ma et al., 2025)*, without bagging, with a row spacing of 3.5 meters and a plant spacing of 1 meter. The tree age was 7 years, and the length of the tree rows ranged from 30 to 240 meters. A mobile phone camera (Xiaomi Mix 2S) was used to collect images of young apple fruits at a distance of 2.6 meters from the tree row. The image resolution was 4032 × 3024 pixels. A total of 200 original images were collected and saved in JPG format. The acquisition scene is shown in Fig. 2.



Fig. 2 - Apple tree planting pattern and image acquisition method

2.1.2 Image Annotation and Data Preprocessing

Annotation of the young apple fruit dataset was completed using the labeling software LabelImg. The annotation box size was the bounding rectangle of the young fruit. After annotation, the resulting annotation file information was saved as .XML files, which contained key data such as the filename of the young fruit image, the coordinates of the four corners of the annotated rectangular region, and the target classification label. After annotation, the image dataset was split and augmented for training. The 200 images in the dataset were randomly divided into a training set of 160 images and a validation set of 40 images, a ratio of 8:2. After processing with the chunking strategy, the dataset was augmented, expanding the training set from 160 images to 5,600 images. Examples of images in the young apple fruit dataset and the scenes they contain are shown in Fig. 3, including various scenes such as dark lighting, normal lighting, leaf occlusion, and fruit stacking.

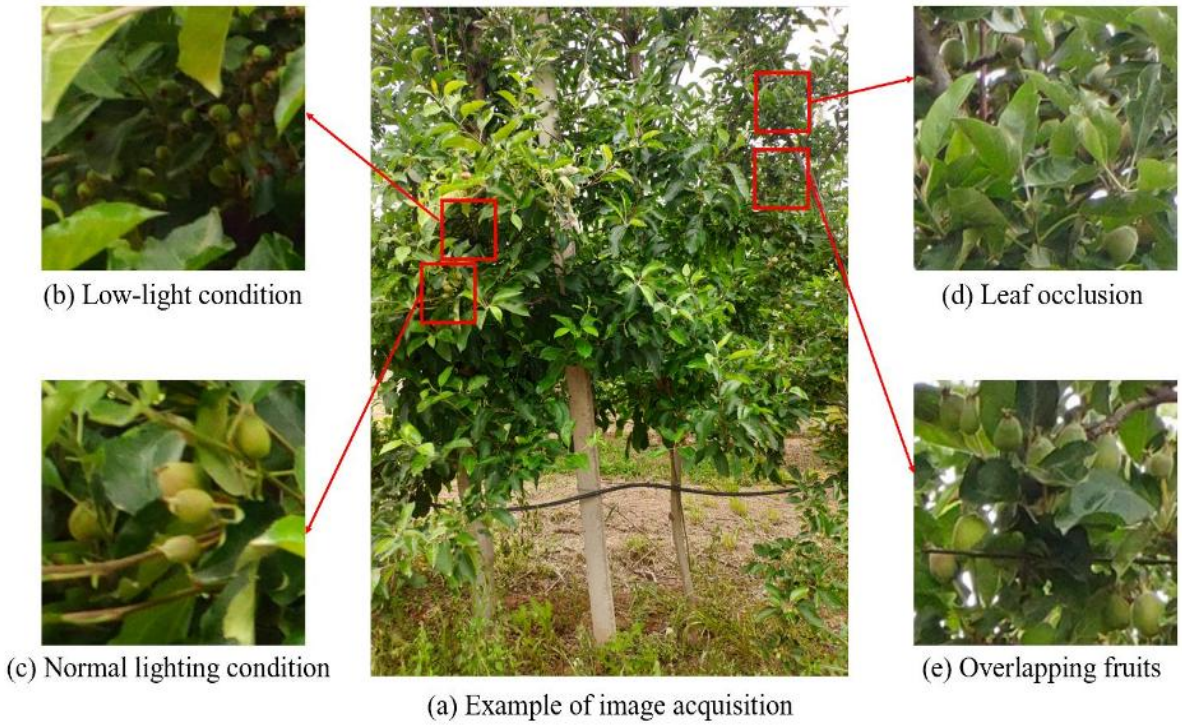


Fig. 3 - Apple samples from a dwarf and densely planted orchard

2.2 Methods

2.2.1 Multi-Resolution Strategy

YOLOv12n is an efficient lightweight model designed for general object detection tasks, with a model structure that includes a small-target detection mechanism suitable for real-time detection scenarios *(Zhang et al., 2025)*. Multiple studies have shown that its innovative region attention mechanism significantly improves the feature extraction efficiency of tiny targets by dynamically dividing feature maps and focusing on local regions. At the same time, the optimized multi-scale feature fusion architecture strengthens the retention of shallow, high-resolution details, effectively solving the problem of information loss of small targets in deep networks. Combined with lightweight design and position-aware enhancement technology, this model has significant advantages in high-precision small-target detection scenarios. Based on its breakthrough performance in balancing accuracy and efficiency, YOLOv12n was used to detect young apple fruits, and the resize parameters were set to 640 × 640, 960 × 960, and 1280 × 1280 to examine their impact on young apple fruit detection.

2.2.2 Adding a Small-Target Detection Layer Strategy

The detection head of YOLOv12n includes three detection layers: P3, P4, and P5 detection heads. Among them, the P3 detection head, which has the largest output feature map, is suitable for detecting small targets due to its smallest global receptive field and high spatial resolution, making it the small-target detection layer *(Wei et al., 2024; Jing et al., 2024)*. Similarly, the P5 detection head with the smallest output feature map is the large-target detection layer, and P4 is the medium-target detection head. Before chunking, the number of small targets was 26,558; after chunking, the number of small targets was 24,315, as shown in Table 1.

Table 1

Statistics of instance counts

Dataset	Images	Instances	Objects		
			Small Objects	Medium Objects	Large Objects
Training Set (Non-chunked)	160	20456	20455	1	0
Validation Set (Non-chunked)	40	6103	6103	0	0
Training Set (Chunked)	5600	22595	18655	3594	346
Validation Set (Chunked)	1400	6685	5660	901	124

Small targets accounted for a large proportion of the overall samples, placing higher demands on the performance of the small-target detection layer. Moreover, due to the small target size of young fruits in the images, their feature information was easily lost during detection, leading to missed detections. In this study, a newly added P2 detection head was set to detect tiny targets approximately 4×4 to 8×8 pixels in size to detect even smaller young apple fruits. The network structure diagram is shown in Fig. 4. Through a series of operations such as convolution, upsampling, and concatenation, feature maps suitable for tiny target detection were generated, thereby improving the detection accuracy of small young fruit targets. Similarly, this strategy was also evaluated at three resolutions, and both strategies were jointly used to comprehensively examine the effect of resolution changes on detection performance.

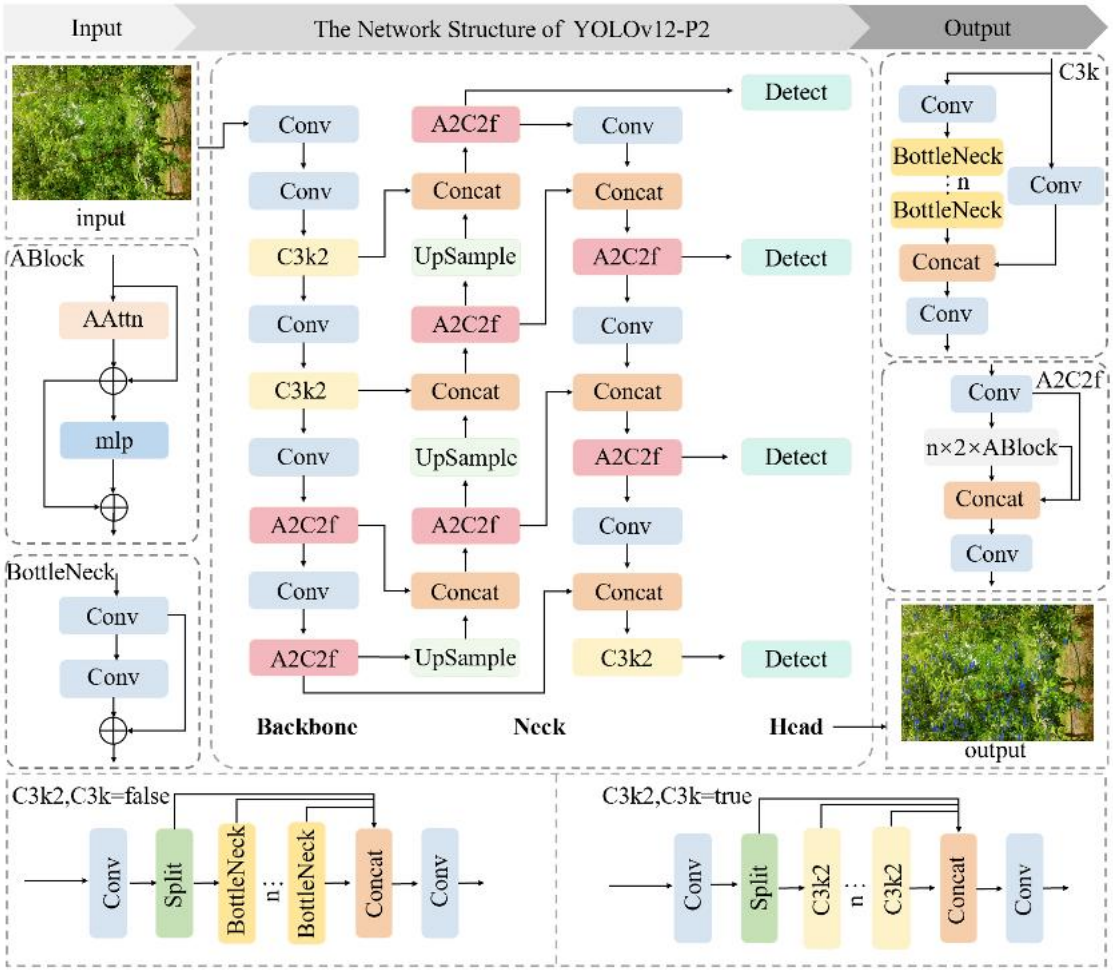


Fig. 4 - Network structure diagram of YOLOv12n-P2

2.2.3 Chunking Strategy

Young apple fruits occupy a very small proportion of pixels in the original image, which poses a challenge to current object detection models based on deep learning networks. Therefore, a chunking strategy was proposed to augment the data and increase the proportion of young apple fruit pixels in the image.

This algorithm started from the upper left corner of the image and progressively moved to the lower right, decomposing the originally large image into multiple small segmented images, each with a pixel size that met the input specifications of the training network. Some segmented images might contain no young apple fruits, while others had an increased proportion of young apple fruits. The traditional chunking method sequentially divides an image based on pixels. When a target crosses chunk boundaries or is unevenly distributed, it easily leads to feature fragmentation and loss of contextual information, affecting detection or counting accuracy. Therefore, a certain overlap was set between adjacent chunks to prevent missing young fruit information at the edges of the images due to chunking. As shown in Fig. 5, three black rectangular boxes represent three adjacent partitions, and the blue area represents the overlapping area between the three partitions.

The overlap length was calculated using formulas (1) and (2).

$$overlap = \frac{x'}{2x - x'} \tag{1}$$

$$overlap = \frac{y'}{2y - y'} \tag{2}$$

where:

$overlap$ is the overlap rate of the chunking strategy, [%]; x is the width of the chunked image on the horizontal axis, [pixel]; y is the height of the chunked image on the vertical axis, [pixel]; x' is the length of the overlapping part on the horizontal axis, [pixel]; y' is the length of the overlapping part on the vertical axis, [pixel].

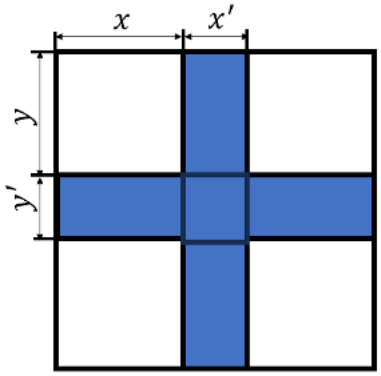


Fig. 5 - Examples of overlap rate setting and overlap region

After the overlap rate was set, the image information was read, and the number of chunks along the horizontal and vertical axes was calculated. The formulas for calculating the number of image chunks required are shown in formulas (3) and (4).

$$a = 1 + \left[\frac{w - x}{x - x'} \right] \tag{3}$$

$$b = 1 + \left[\frac{h - y}{y - y'} \right] \tag{4}$$

where:

a is the number of chunked images required on the horizontal axis; w is the width of the original image, [pixel]; b is the number of chunked images required on the vertical axis; h is the height of the original image, [pixel].

At the same time, to ensure that all young fruit information in the image could be detected, the results were rounded up. However, rounding up caused the relative coordinates of the edge images to exceed the original image during chunking, resulting in blank areas in the chunked images. To avoid this, the relative coordinates were shifted. An example of chunked image shifting is shown in Fig. 6.

The yellow box represents the original calculated partition position of the image, and the red box represents the corrected partition position of the image.



Fig. 6 - Example of chunked image shifting

The segmented small images were set to 640 × 640 pixels in this study to fit the network input size. The chunking strategy was also used to partition the XML annotation files and original label files to avoid re-labeling the label files after image chunking. The relative coordinate calculation formulas are shown in formulas (5) and (6).

$$x'_{\min} = x_{\min} - x_0 \tag{5}$$

$$y'_{\min} = y_{\min} - y_0 \tag{6}$$

where:

$x'_{\min}$ is the relative horizontal coordinate of the bounding box with respect to the chunked image, [pixel]; $y'_{\min}$ is the relative vertical coordinate of the bounding box with respect to the chunked image, [pixel]; $x_{\min}$ is the original horizontal coordinate of the bounding box with respect to the whole image, [pixel]; $y_{\min}$ is the original vertical coordinate of the bounding box with respect to the whole image, [pixel]; x_0 is the horizontal coordinate of the top-left corner of the chunked image, [pixel]; y_0 is the vertical coordinate of the top-left corner of the chunked image, [pixel].

The image to be detected was divided into regions as shown in Fig. 7. The black boxes indicate the chunk positions after setting the overlap rate, the red boxes indicate the chunk positions after shifting, and the blue boxes indicate the chunk positions for the last image. Finally, the detected chunked images were merged to restore their original size.

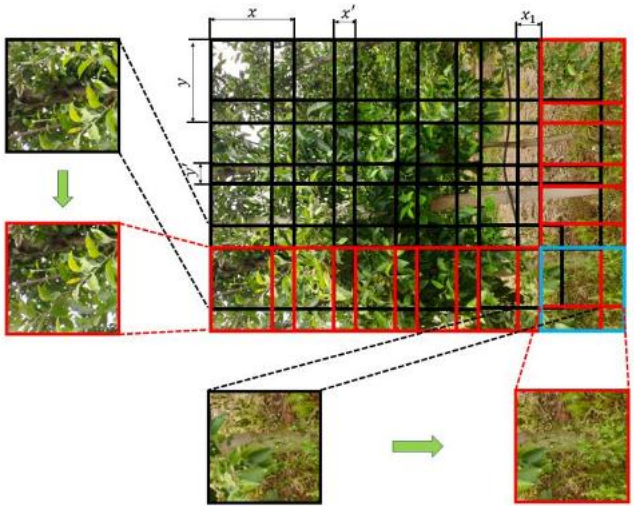


Fig. 7 - Chunk region division of the image to be detected

2.3 Experimental Platform and Training Parameters

The experimental model training platform used an NVIDIA GeForce RTX 4050 graphics card, a 13th Gen Intel(R) Core(TM) i7-13620H processor, and 6 GB of video memory. The network model was trained using the Windows 11 operating system, PyTorch 2.0.0 framework, CUDA 11.8, PyCharm editor, and Python 3.12 programming language. Stochastic gradient descent was used for training, with a momentum of 0.937 and a weight decay of 0.0005. The initial learning rate of the network was set to 0.01, and the number of network training epochs was 300.

2.4 Evaluation Metrics

To evaluate the performance of different strategies in recognizing young apple fruits, the following metrics were used: *Precision (P), Recall (R),* and *Average Precision (AP)*. *AP* is the area under the *P-R* curve and was used as a comprehensive metric reflecting network performance. The calculation formulas for P, R, and AP are shown in formulas (7), (8), and (9).

$$P = \frac{TP}{TP + FP} \times 100\% \tag{7}$$

$$R = \frac{TP}{TP + FN} \times 100\% \tag{8}$$

$$AP_i = \int_0^1 P_i(R_i) dR_i \tag{9}$$

where: TP (*True Positive*) is the number of correctly detected young apple fruits; *FP (False Positive)* is the number of incorrectly detected young apple fruits; *FN (False Negative)* is the number of young apple fruits that were not detected.

3. RESULTS

3.1 Comparison of Different Detection Models

To systematically evaluate the detection difficulty of this dataset and exclude performance anomalies caused by specific model implementations or training settings, four mainstream lightweight object detection models, YOLOv5n, YOLOv8n, YOLOv11n, and the baseline YOLOv12n, were selected to detect young apple fruits in the dwarf and densely planted orchard environment. The experimental results are shown in Table 2. The P values of YOLOv5n, YOLOv8n, and YOLOv11n on this dataset were only 0.10%, 0.29%, and 0.23%, respectively, and their *P* and *R* values were also below 1%. This result was highly consistent with the baseline performance of YOLOv12n used in this study, indicating that the extremely small size, dense distribution, severe leaf occlusion, and fruit stacking of young apple fruits in this dataset made it nearly impossible for current mainstream object detection models to learn effective young fruit features. These results together confirmed that the baseline model *AP* below 1% was not caused by specific code defects or training errors, but was an objective reflection of the extreme challenge of this dataset.

Table 2

Performance comparison of different detection models on the young apple fruit dataset

Model	Different resolutions	P (%)	R (%)	AP (%)
YOLOv5n	640×640	0.10	0.20	0.05
YOLOv8n	640×640	0.29	0.57	0.17
YOLOv11n	640×640	0.23	0.44	0.36
YOLOv12n	640×640	0.24	0.48	0.12

3.2 Comparison of Three Detection Methods

The performance of three methods in object detection tasks was compared. The experimental results are shown in Table 3. The chunking strategy significantly outperformed the other two methods, achieving an *AP* as high as 77.50%, an *R* of 62.54%, and a *P* of 85.57%, indicating that this method maintained high detection stability and accuracy even in complex scenes. Particularly in environments with many small targets and heavy occlusion, the chunking strategy effectively improved target detection and localization through local enhancement processing. As shown in Fig. 8e, the chunking strategy was the only method among the three that effectively recognized young fruits.

Table 3

Performance comparison of the three detection methods

Strategies	Different resolutions	P (%)	R (%)	AP (%)
YOLOv12n	640×640	0.38	0.75	0.20
	960×960	0.28	0.54	0.24
	1280×1280	0.31	0.61	0.20
YOLOv12n-P2	640×640	0.29	0.57	0.16
	960×960	0.24	0.48	0.13
	1280×1280	0.29	0.57	0.15
YOLOv12n-chunking	640×640	85.57	62.54	77.50

In contrast, the multi-resolution training and the small-target detection layer addition methods performed poorly in this experiment. The highest AP achieved by the multi-resolution training method was only 0.24%, and the highest R was only 0.75%, indicating that this method failed to effectively capture target features, possibly due to insufficient model training in adapting to scale variations. The method of adding a small-target detection layer also failed to significantly improve performance, with the highest AP reaching only 0.16% and the highest R only 0.57%, indicating that simply increasing network depth or the number of detection layers cannot fundamentally solve the problems of semantic loss and feature weakening in small-target detection. Although the multi-resolution training and small-target detection layer addition methods showed slight numerical improvements in P, R, and AP, their extremely low values indicated that these methods were practically unable to detect real targets, with severe missed detections. As shown in Figure 8, methods other than the chunking strategy produced almost no detection boxes.



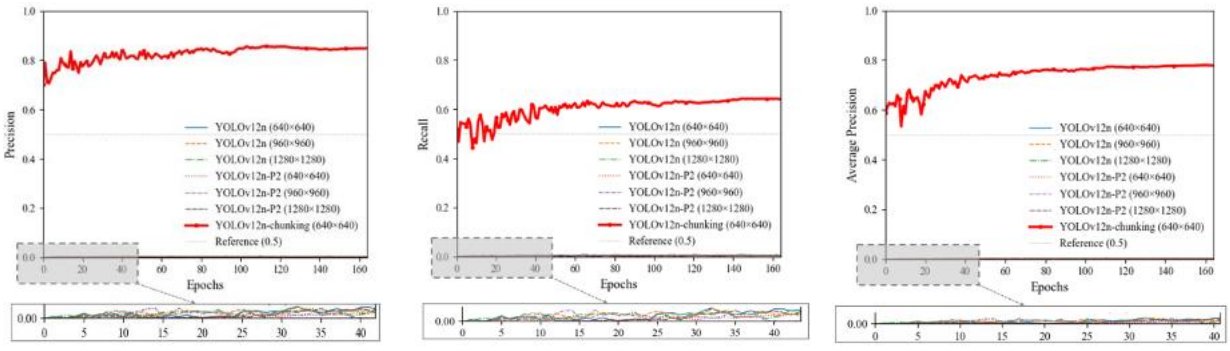
Fig. 8 - Detection effects of the three strategies

The superior performance of the chunking strategy was closely related to the growth characteristics of young apple fruits. Young fruits are typically small in the early stage, highly similar in color to leaves, and often occluded by branches and leaves, making detection extremely challenging *(Liu et al., 2023; Xu et al., 2024)*. When the network needs to process images containing many such tiny, highly similar targets, its receptive field and feature extraction capacity easily reach a bottleneck *(Lin et al., 2025)*. The chunking strategy physically increases the relative size and feature richness of each young fruit in the sub-images by dividing the high-resolution image into smaller sub-images, greatly alleviating the problem of weak small-target feature signals in the original image and enabling the network to capture key discriminative features more clearly. In contrast, although the other two methods enhanced small-target perception to some extent, they did not fundamentally change the proportional relationship between the target and the entire image, thus still suffering from many missed detections and false detections in complex backgrounds.

For small targets such as young apple fruits, a more complex network structure does not necessarily yield better results. Sometimes, a relatively simple and direct method, such as changing the input strategy, can bring more significant performance improvements. This finding is not entirely consistent with the conclusion of *Chutichaimaytar et al. (2025)*, who suggested increasing model depth and complexity to improve small-target detection accuracy. This discrepancy indicates that the optimal detection strategy may vary depending on the specific detection object and its environmental background. For objects with tiny features and complex backgrounds, ensuring that key features are fully represented is more effective than designing complex networks for difficult discrimination.

3.3 Effectiveness Analysis of Each Method

As shown in Figure 9, the performance curves of the three strategies indicate that the model performance achieved a breakthrough improvement after adopting the chunking strategy. The *AP* value significantly increased from less than 1.00% to 77.50%, and *R* and *P* reached 62.54% and 85.57%, respectively. The superior performance of this strategy stemmed from the physical partitioning of the image, which fundamentally increased the relative size of young fruits in the sub-images, allowing the network to capture clearer and richer feature information, thus effectively solving the fundamental problem of extremely weak small-target feature signals *(Wu et al., 2024)*. However, the main cost of this strategy was reduced computational efficiency. Because more sub-images needed to be processed and results fused, the detection time per image was several times that of the end-to-end model. Nevertheless, in offline high-precision analysis scenarios such as young apple fruit yield prediction, trading computation time for unparalleled detection accuracy is a necessary and acceptable trade-off.



(a) (b) (c)

Fig. 9 - Performance curve comparison of the three methods

(a) Comparison of precision curves of the three methods; (b) Comparison of recall curves of the three methods; (c) Comparison of average precision curves of the three methods.

The multi-resolution training strategy achieved AP values below 1% at different resolutions. The intention of this strategy was to enhance the scale invariance of the model, but its failure in young apple fruit detection was attributed to the fact that downsampling operations destroyed the already weak features of young fruits, while upsampling to higher resolutions could not create effective details but instead amplified image noise, interfering with model judgment *(Ma et al., 2022)*. Similar to the detection layer addition strategy, this method was lightweight but did not change the proportional relationship between the target and the entire image, thus having limited effect in addressing the specific difficulties of this study.

As a model enhancement method, the addition of a small-target detection layer aimed to improve small-target perception by introducing a shallower detection head. However, the experimental results did not meet expectations, with the highest AP reaching only 0.16%. The root cause of its failure was that the feature extraction bottleneck occurred in the early stage of the network. The extremely small size of young fruits meant that after several downsampling operations during feature extraction in the backbone network, the effective signal had severely attenuated or been lost. Subsequently, even with the introduction of a detection layer specifically designed for small targets, key information could not be recovered from the already confused feature maps. This strategy had negligible detection effects in the extremely challenging scenario of this study, characterized by extremely small targets and high-background similarity, and was only suitable for general detection tasks with relatively more prominent targets.

In contrast, the failure of the multi-resolution training and small-target detection layer addition strategies highlighted the particularity and challenges of young apple fruit detection. For targets with extremely small features and very low signal-to-noise ratios, traditional methods aimed at enhancing model perception may have limited effect. The most effective strategy is to start from the input side and fundamentally change the relationship between the target and the image scale through physical methods such as chunking, ensuring that the original features of the target are completely captured by the model. The results of this study provide important insights for the detection of similar small targets in agriculture: when the target is small to a certain extent, optimizing the data input strategy should take priority over designing complex models.

3.4 Performance Demonstration and Analysis of the Chunking Strategy

The overall detection effect showed that in real orchard environments with uneven lighting and cluttered backgrounds, the chunking strategy demonstrated excellent overall performance. The model successfully located and recognized tiny young fruit targets with high prediction confidence, as shown in Figure 10. This indicates that the strategy of enhancing local feature representation through chunking processing fundamentally solved the feature loss and receptive field mismatch problems in the baseline method, achieving extremely high recall and precision.



Fig. 10 - Overall detection effect of the chunking strategy and enlarged views of local areas

The enlarged local areas show the model's detailed performance in scenes with partial occlusion, boundary blur, extreme occlusion, and dense targets. While affirming the model's strengths, these examples also reflect its shortcomings and directions for improvement. In Fig.10a, a fruit with approximately 30%–40% leaf occlusion is shown. The model was able to effectively infer and recognize the fruit based on its visible features, providing a reasonable confidence level. This demonstrates the model's ability to complete features and reason under moderate occlusion. However, when the occlusion proportion increases further or the occlusion pattern becomes more complex, the model may still show decreased confidence or missed detections, indicating that its occlusion reasoning mechanism is not yet fully robust. In the future, adversarial occlusion training or structure-aware reasoning modules could be introduced to enhance adaptability to diverse occlusion patterns. In Fig.10b, the chunking strategy significantly improved the distinction between adjacent targets by enhancing local feature resolution. The model generated prediction boxes with accurate spatial positions and clear boundaries in this region, demonstrating excellent discrimination ability for highly overlapping targets. Nevertheless, when target edges are highly fused with the background, the model may still show boundary localization errors, suggesting that the current edge perception mechanism still has room for optimization. Subsequent work could incorporate edge enhancement operators or introduce boundary-aware loss functions to further improve localization accuracy. Fig.10c presents a boundary case of the current method. When a target is severely occluded or presents only very small local features, detection confidence decreases. In the future, introducing attention-based contextual reasoning modules *(Xu et al., 2023)* could allow the model to better utilize surrounding environmental information to infer the presence of extremely occluded targets. Fig.10d shows the model's excellent ability to distinguish dense targets. For closely clustered young fruit groups, the model did not incorrectly merge them into a single detection target but generated multiple independent and accurately bounded prediction boxes. However, when target spacing is extremely small and targets are heavily adhered to each other, the model may still suffer from duplicate detections or missed detections, indicating that its instance separation capability in extremely dense scenes needs strengthening. This demonstrates that the high-resolution local contextual information provided by the chunking strategy is crucial for distinguishing spatially adjacent targets with similar appearances.

4. CONCLUSIONS

This study addressed the problems of extremely small young apple fruit targets and high detection difficulty in dwarf and densely planted orchard environments by proposing a detection method based on the YOLOv12n-chunking strategy. Compared with methods such as multi-resolution training and adding a small-target detection layer, the chunking strategy adopted in this study achieved significant improvements in detection performance, with an *AP* of 77.50%, while the *AP* values of the multi-resolution training and small-target detection layer addition methods were both below 1%. The chunking strategy enhanced local feature expression through image preprocessing, effectively overcoming the detection bottlenecks caused by extremely small target scales and complex backgrounds, providing an effective solution for small-target agricultural detection in large-field-of-view orchard images. However, the current detection accuracy of 77.50% still has room for improvement. In the future, the dataset will be expanded with multi-season, multi-variety, and multi-weather-condition images, and lightweight design and advanced algorithms will be integrated to further improve the model's generalization ability and deployment suitability.

5. ACKNOWLEDGEMENT

This work was supported by National Natural Science Foundation of China Youth Program (32501768); Anhui Provincial Natural Science Foundation of Youth Program (2508085QC086), Scientific Research Project of Anhui Education Department (2025AHGXZK40673), Scientific Research Start-up Foundation of Anhui Agricultural University (rc412405).

6. REFERENCES

[1] Borugadda P., Kalluri H.K., (2026). A comprehensive analysis of artificial intelligence, machine learning, deep learning and computer vision in food science, *Journal of Future Foods*, vol.6, no.6, pp.971-987, Beijing/China. DOI: https://doi.org/10.1016/j.jfutfo.2025.07.002

[2] Chen L.-H., Bampis C.G., Li Z., Krasula L., Bovik A.C., (2025). Estimating the resize parameter in end-to-end learned image compression, *Signal Processing: Image Communication*, vol.135, article no.117277, Amsterdam/Netherlands. DOI: https://doi.org/10.1016/j.image.2025.117277

[3] Chen Y., Niu Y., Cheng W., Zheng L., Sun D., (2024). Apple detection method in the natural environment based on improved YOLOv5 (自然环境下基于改进 YOLOv5 的苹果检测方法), *INMATEH Agricultural Engineering*, vol.72, no.1, pp.183-192, Bucharest/Romania. DOI: https://doi.org/10.35633/inmateh-72-17

[4] Chutichaimaytar P., Zhang Z., Kaewtrakulpong K., Ahamed T., (2025). An improved small object detection CTB-YOLO model for early detection of tip-burn and powdery mildew symptoms in coriander (Coriandrum sativum) for indoor environment using an edge device, *Smart Agricultural Technology*, vol.12, article no.101142, Amsterdam/Netherlands. DOI: https://doi.org/10.1016/j.atech.2025.101142

[5] Dang H., He L., Shi Y., Janneh L.L., Liu X., Chen C., Li R., Ye H., Chen J., Majeed Y., Kou X., Fu L., (2025). Growth characteristics based multi-class kiwifruit bud detection with overlap-partitioning algorithm for robotic thinning, *Computers and Electronics in Agriculture*, vol.229, article no.109715, Amsterdam/Netherlands. DOI: https://doi.org/10.1016/j.compag.2024.109715

[6] Du Y., Han Y., Su Y., Wang J., (2024). A lightweight model based on you only look once for pomegranate before fruit thinning in complex environment, *Engineering Applications of Artificial Intelligence*, vol.137, Part A, article no. 109123, Amsterdam / Netherlands. DOI: https://doi.org/10.1016/j.engappai.2024.109123

[7] Feng L., Liu Y., Yang H., Jia Z., Guan J., Zhu H., Hou Y., (2024). Detection of apple leaf diseases target based on improved YOLOv7 (基于改进 YOLOv7 的苹果叶片病害目标检测), *INMATEH Agricultural Engineering*, vol.72, no.1, pp.280-290, Bucharest/Romania. DOI: https://doi.org/10.35633/inmateh-72-26

[8] Fu L., Majeed Y., Zhang X., Karkee M., Zhang Q., (2020). Faster R–CNN–based apple detection in dense-foliage fruiting-wall trees using RGB and depth features for robotic harvesting, *Biosystems Engineering*, vol.197, pp.245-256, London/United Kingdom. DOI: https://doi.org/10.1016/j.biosystemseng.2020.07.007

[9] Gao A., Tian Z., Ma W., Song Y., Ren L., Feng Y., Qian J., Xu L. (2024). Fruits hidden by green: an improved YOLOV8n for detection of young citrus in lush citrus trees, *Frontiers in Plant Science*, vol.15, article no.1375118, Lausanne/Switzerland. DOI: https://doi.org/10.3389/fpls.2024.1375118

[10] Hou S., Pang Y., Wang J., Hou J., Wang B., (2025). RS-YOLO: A highly accurate real-time detection model for small-target pest, *Smart Agricultural Technology*, vol.12, article no.101212, Amsterdam/Netherlands. DOI: https://doi.org/10.1016/j.atech.2025.101212

[11] Hua W., Zhang Z., Zhang W., Liu X., Hu C., He Y., Mhamed M., Li X., Dong H., Saha C.K., Khan W.U., Abid F., Abdelhamid M.A., (2025). Key technologies in apple harvesting robot for standardized orchards: A comprehensive review of innovations, challenges, and future directions, *Computers and Electronics in Agriculture*, vol.235, article no.110343, Amsterdam/Netherlands. DOI: https://doi.org/10.1016/j.compag.2025.110343

[12] Hussain M., He L., Schupp J., Lyons D., Heinemann P., (2023). Green fruit segmentation and orientation estimation for robotic green fruit thinning of apples, *Computers and Electronics in Agriculture*, vol.207, article no.107734, Amsterdam/Netherlands. DOI: https://doi.org/10.1016/j.compag.2023.107734

[13] Jiang H., Sun X., Fang W., Fu L., Li R., Cheein F.A., Majeed Y., (2023). Thin wire segmentation and reconstruction based on a novel image overlap-partitioning and stitching algorithm in apple fruiting wall architecture for robotic picking, *Computers and Electronics in Agriculture*, vol.209, article no.107840, Amsterdam/Netherlands. DOI: https://doi.org/10.1016/j.compag.2023.107840

[14] Jing R., Zhang W., Liu Y., Li W., Li Y., Liu C., (2024). An effective method for small object detection in low-resolution images, *Engineering Applications of Artificial Intelligence*, vol.127, Part A, article no.107206, Amsterdam/Netherlands. DOI: https://doi.org/10.1016/j.engappai.2023.107206

[15] Liang X., Xiang J., Qin S., Xiao Y., Chen L., Zou D., Ma H., Huang D., Huang Y., Wei W., (2025). Small target detection algorithm based on SAHI-improved-YOLOv8 for UAV imagery: A case study of tree pit detection, *Smart Agricultural Technology*, vol.12, article no.101181, Amsterdam/Netherlands. DOI: https://doi.org/10.1016/j.atech.2025.101181

[16] Lin C., Jiang W., Zhao W., Zou L., Xue Z., (2025). DPD-YOLO: dense pineapple fruit target detection algorithm in complex environments based on YOLOv8 combined with attention mechanism, *Frontiers in Plant Science*, vol.16, article no.1523552, Lausanne/Switzerland. DOI: https://doi.org/10.3389/fpls.2025.1523552

[17] Liu P., Yin H., (2023). YOLOv7-Peach: An algorithm for immature small yellow peaches detection in complex natural environments, *Sensors*, vol.23, no.11, article no.5096, Basel/Switzerland. DOI: https://doi.org/10.3390/s23115096

[18] Liu Z., Abeyrathna R.M.R.D., Sampurno R.M., Nakaguchi V.M., Ahamed T., (2024). Faster-YOLO-AP: A lightweight apple detection algorithm based on improved YOLOv8 with a new efficient PDWConv in orchard, *Computers and Electronics in Agriculture*, vol.223, article no.109118, Amsterdam/Netherlands. DOI: https://doi.org/10.1016/j.compag.2024.109118

[19] Ma J., Han X., Zhang X., Li Z., (2022). MLWAN: multi-scale learning wavelet attention module network for image super resolution, *Sensors*, vol.22, no.23, article no.9110, Basel/Switzerland. DOI: https://doi.org/10.3390/s22239110

[20] Ma W., Ma Z., Hou Y., Lu S., Liang G., Mao J., Chen B., (2025). The 'green code' in fruit cultivation: research progress and prospects of rootstock control tree dwarfing, *Plant, Cell & Environment*, vol.48, no.12, pp.8860-8872, Oxford/United Kingdom. DOI: https://doi.org/10.1111/pce.70151

[21] Ma Z., Dong N., Gu J., Cheng H., Meng Z., Du X., (2025). STRAW-YOLO: A detection method for strawberry fruits targets and key points, *Computers and Electronics in Agriculture*, vol.230, article no.109853, Amsterdam/Netherlands. DOI: https://doi.org/10.1016/j.compag.2024.109853

[22] Oba Y., Doi H., (2025). Accelerating ecosystem monitoring through computer vision with deep metric learning, *Ecological Complexity*, vol.62, article no.101124, Amsterdam/Netherlands. DOI: https://doi.org/10.1016/j.ecocom.2025.101124

[23] Patiyal V., Rana V.S., Rana N., Hashem A., Abd Allah E.F., Sharma S., (2024). Appraisal of extended cane length and fruit thinning strategies on the performance of growth yield and quality of kiwifruit, *Heliyon*, vol.10, no.8, article no.e29546, Amsterdam/Netherlands. DOI: https://doi.org/10.1016/j.heliyon.2024.e29546

[24] Pawikhum K., Yang Y., He L., Heinemann P., (2025). Development of a machine vision system for apple bud thinning in precision crop load management, *Computers and Electronics in Agriculture*, vol.236, article no.110479, Amsterdam/Netherlands. DOI: https://doi.org/10.1016/j.compag.2025.110479

[25] Tang Y., Qiu J., Zhang Y., Wu D., Cao Y., Zhao K., Zhu L., (2023). Optimization strategies of fruit detection to overcome the challenge of unstructured background in field orchard environment: a review, *Precision Agriculture*, vol.24, no.4, pp.1183-1219, Dordrecht/Netherlands. DOI: https://doi.org/10.1007/s11119-023-10009-9

[26] Wang X., Yang T., Chen Z., Liu J., He Y., (2025). NLDETR-YOLO: A decision-making method for apple thinning period, *Scientia Horticulturae*, vol.341, article no.113991, Amsterdam/Netherlands. DOI: https://doi.org/10.1016/j.scienta.2025.113991

[27] Wei W., Cheng Y., He J., Zhu X., (2024). A review of small object detection based on deep learning, *Neural Computing and Applications*, vol.36, no.12, pp.6283-6303, London/United Kingdom. DOI: https://doi.org/10.1007/s00521-024-09422-6

[28] Wu S., Lu X., Guo C., Guo H., (2024). Accurate UAV small object detection based on HRFPN and EfficentVMamba, *Sensors*, vol.24, no.15, article no.4966, Basel/Switzerland. DOI: https://doi.org/10.3390/s24154966

[29] Wu Z., Wang X., Jia M., Liu M., Sun C., Wu C., Wang J., (2024). Dense object detection methods in RAW UAV imagery based on YOLOv8, *Scientific Reports*, vol.14, no.1, article no.18019, London/United Kingdom. DOI: https://doi.org/10.1038/s41598-024-69106-y

[30] Xu D., Xiong H., Liao Y., Wang H., Yuan Z., Yin H., (2024). EMA-YOLO: A novel target-detection algorithm for immature yellow peach based on YOLOv8, *Sensors*, vol.24, no.12, article no.3783, Basel/Switzerland. DOI: https://doi.org/10.3390/s24123783

[31] Xu W., Xu T., Thomasson J.A., Chen W., Karthikeyan R., Tian G., Shi Y., Ji C., Su Q., (2023). A lightweight SSV2-YOLO based model for detection of sugarcane aphids in unstructured natural environments, *Computers and Electronics in Agriculture*, vol.211, article no.107961, Amsterdam/Netherlands. DOI: https://doi.org/10.1016/j.compag.2023.107961

[32] Yuan B., Zhang H., Li Y., Cao X., Sun L., Jing L., Xue L., Liu C., Fan G., Wang J., (2025). Design and experimental evaluation of a two-stage domain-segmented harvesting device for densely planted dwarf apple orchards, *AgriEngineering*, vol.7, no.5, article no.135, Basel/Switzerland. DOI: https://doi.org/10.3390/agriengineering7050135

[33] Zhang C., Kang F., Wang Y., (2022). An improved apple object detection method based on lightweight YOLOv4 in complex backgrounds, *Remote Sensing*, vol.14, no.17, article no.4150, Basel/Switzerland. DOI: https://doi.org/10.3390/rs14174150

[34] Zhang J., Zhang C., Xu L., Mao B., Chen Z., (2025). DBA-YOLO: a mamba-incorporated dual-branch axial feature enhancement network for small object detection in traffic scenarios, *Signal, Image and Video Processing*, vol.19, article no.991, London/United Kingdom. DOI: https://doi.org/10.1007/s11760-025-04572-z

[35] Zheng Z., Xiong J., Lin H., Han Y., Sun B., Xie Z., Yang Z., Wang C., (2021). A method of green citrus detection in natural environments using a deep convolutional neural network, *Frontiers in Plant Science*, vol.12, article no.705737, Lausanne/Switzerland. DOI: https://doi.org/10.3389/fpls.2021.705737

EXPERIMENTAL EVALUATION OF BUCKWHEAT DEHULLING USING A NOVEL DEHULLING DEVICE WITH A ROTATING DRUM AND A SHAPE-ADAPTIVE PRESSURE DECK

/

Эргэх хүрд ба сагаг будааны хэлбэрт тохируулсан шинэ хийцийн шахах дектэй хальслах төхөөрөмжөөр сагаг будааг хальсалсан туршилтын үр дүн

Amartuvshin OIDOV [1)]; Baatarkhuu DORJSUREN[1*)] ; Dovchinvanchig MAASHAA[2*)]
[1)] School of Engineering and Technology, Mongolian University of Life Sciences, Ulaanbaatar 17024, Mongolia
[2)] School of Applied Sciences, Mongolian University of Life Sciences, Ulaanbaatar 17024, Mongolia
**Corresponding author, E-mail: dovchinvanchig@muls.edu.mn*
elec_eng@muls.edu.mn
DOI: https://doi.org/10.35633/inmateh-79-69

Keywords: *Buckwheat; dehulling; rotating drum; pressure deck; elastic contact surface; rotatable central composite design.*

ABSTRACT

A novel buckwheat dehulling device consisting of a rotating drum and a pressure deck with an elastic contact surface was developed to eliminate the need for grain size classification prior to dehulling. The geometry of the pressure deck was designed to match the shape of buckwheat grains, ensuring stable contact and effective dehulling across the commercial grain size range of 3–5 mm. The performance of the device was experimentally evaluated using a three-factor rotatable central composite design. The effects of drum rotational speed, working gap, and grain moisture content on the dehulling degree were investigated, and a quadratic regression model was established. The results showed that the maximum dehulling degree of 66.08% was achieved at a drum rotational speed of 846 rpm, a working gap of 4.2 mm, and a grain moisture content of 13.86%. The developed device demonstrates that optimizing the geometry and elastic properties of the pressure deck can significantly improve buckwheat dehulling efficiency while eliminating the need for prior grain size classification.

ХУРААНГУЙ

Сагаг будааг хэмжээний ангилалгүйгээр хальслах зорилгоор эргэх хүрд болон уян харимхай ажлын гадаргуутай, сагаг үрийн хэлбэрт тохируулан хийцлэгдсэн шахах декээс бүрдэх шинэ төрлийн хальслах төхөөрөмжийг боловсруулав. Шахах декний геометр хэлбэрийг сагаг үрийн хэлбэрт тохируулснаар 3–5 мм хэмжээтэй үрийг тогтвортой шахаж, үрийн гадаргууг жигд хальслах нөхцөлийг бүрдүүлсэн. Төхөөрөмжийн ажиллагааг гурван хүчин зүйлт төвийн зохиомжит ротатабель төлөвлөлтийн аргаар туршиж, хүрдний эргэлтийн давтамж, ажлын завсар, үрийн чийгийн агууламжийн хальслалтын зэрэгт үзүүлэх нөлөөг судлан шугаман бус регрессийн математик загвар байгуулсан. Туршилтын үр дүнгээр хүрдний эргэлтийн давтамж 846 эрг/мин, ажлын завсар 4.2 мм, үрийн чийгийн агууламж 13.86% байх үед хальслалтын зэрэг 66.08%-д хүрсэн. Судалгааны үр дүнгээс үзэхэд шахах декний геометр хэлбэр болон уян харимхай шинж чанарыг оновчтой сонгосноор сагаг будааг хэмжээний ангилалгүйгээр үр ашигтай хальслах боломжтой болохыг тогтоов.

INTRODUCTION

Various types of dehulling machines have been developed for cereal grain processing because differences in the anatomical structure and physical–mechanical properties of grains require different dehulling mechanisms. Grain shape, the adhesion strength between the hull and kernel, differences in the mechanical properties of the hull and kernel, and the elastic behavior of the grain determine the type and magnitude of the mechanical forces required during dehulling. Consequently, dehulling machines have been developed based on different operating principles to satisfy these technological requirements (*Chebotarev et al., 2004; Egorov et al., 2005; Tarasenko et al., 2017; Kent et al., 2018)*. Experimental studies on roller-type dehulling machines have been reported by *Kamst et al. (2002)*, *Adisa et al. (2016, 2020)*, *Mar'in et al. (2020)*, *Itodo et al. (2023)*, and *Cheng et al. (2026)*.

According to their operating principles, dehulling machines can be classified as compression–friction, compression–impact, impact–inertia, and combined systems. Based on the mode of operation, they are categorized as mechanical, aerodynamic, or combined machines. According to the characteristics of the working surfaces, they are further classified into rigid, elastic, abrasive, and fluid- or gas-assisted types *(Chebotarev et al., 2004; Egorov et al., 2005; Tarasenko et al., 2017).*

Previous experimental studies have shown that dehulling machines operating on the principles of compression, friction, and impact provide high processing efficiency while being relatively simple to control and adjust *(Itodo et al., 2023; Kamst et al., 2002; Mar'in et al., 2020; Oidov et al., 2025; Shitanda et al., 2001; Solanki et al., 2018; Upreti et al., 2022; Zhang et al., 2025)*. Consequently, these machines are widely used in industrial buckwheat processing.

Despite their effectiveness, conventional buckwheat dehulling machines require the grains to be classified into several size fractions before processing. Typically, buckwheat is separated into six size fractions (4.5, 4.2, 4.0, 3.8, 3.6, and 3.3 mm), and each fraction is processed using a different working clearance. Although this approach improves dehulling efficiency, it increases processing time, equipment complexity, energy consumption, and production costs.

To overcome these limitations, a new dehulling device has been developed that is capable of processing unsorted buckwheat within the commercial size range of 3–5 mm without preliminary size classification. The device consists of a rotating drum and a newly designed pressure deck whose geometry is adapted to the shape of buckwheat grains. During operation, the elastic contact surface of the pressure deck continuously presses the grains into the rotating drum while accommodating variations in grain size. The abrasive surface of the rotating drum then removes the hull without causing excessive grain breakage.

The successful operation of this device depends primarily on the elastic properties of the pressure deck material. If its elastic stiffness is lower than that required to generate sufficient contact pressure, larger grains cannot be properly compressed and effective dehulling cannot be achieved. Therefore, selecting an appropriate elastic material for the pressure deck makes it possible to maintain stable contact between grains and the rotating drum over a wide range of grain sizes, thereby eliminating the need for preliminary size classification.

The objective of this study was to experimentally evaluate the dehulling performance of the newly developed rotating drum–pressure deck device and to determine its optimal operating conditions using a three-factor rotatable central composite design. The effects of drum rotational speed, working gap, and grain moisture content on the degree of dehulling were investigated, and a quadratic regression model describing the dehulling process was established.

MATERIALS AND METHODS

The objective of this experimental study was to verify the theoretical model previously developed by the authors *(Oidov et al., 2025).* Under practical operating conditions and to evaluate the dehulling performance of unsorted buckwheat using a newly designed dehulling device consisting of a rotating drum and a pressure deck with an elastic contact surface (elastic coefficient ($k_m \approx 10\ N/mm$)). The study focused on identifying the operating conditions that maximize the degree of dehulling while preventing excessive grain damage.

Based on the theoretical analysis and previous studies, three operating parameters were selected as the main independent variables because they have the greatest influence on the dehulling process: drum rotational speed (X_1), working gap between the rotating drum and the pressure deck (X_2), and buckwheat moisture content (X_3). The response variable was the degree of dehulling (y), which was used as the optimization criterion.

The experimental material consisted of common buckwheat (*Fagopyrum esculentum* Moench) with a moisture content ranging from 9 to 16% (wet basis) and a grain size ranging from 3.2 to 5.0 mm. The selection of the experimental material and evaluation of its physical and mechanical properties were based on the methods and the engineering principles reported by *(Bonafaccia et al., 2003; Mohsenin., 1986; Altuntas et al., 2007; Rao et al., 2005).* The upper limit of 5 mm was used as the equivalent grain diameter in the design calculations because it represents the largest grain fraction processed by the machine and therefore corresponds to the most critical operating condition. The experimental apparatus consisted of a rotating drum and a newly developed pressure deck with an elastic contact surface, as illustrated in Fig. 1.

To investigate the combined effects of the selected factors while minimizing the number of experiments, a three-factor, second-order Central Composite Rotatable Design (CCRD) was employed. This experimental design enables the development of a quadratic regression model describing the relationship between the operating parameters and the degree of dehulling, while also allowing evaluation of interaction and quadratic effects. The design matrix comprised 20 experimental runs, including factorial, axial, and center points. For each experimental run, a sample of 100 buckwheat grains was processed, and the degree of dehulling was determined experimentally. The resulting data were subsequently analyzed using regression analysis and analysis of variance to determine the optimum operating conditions.

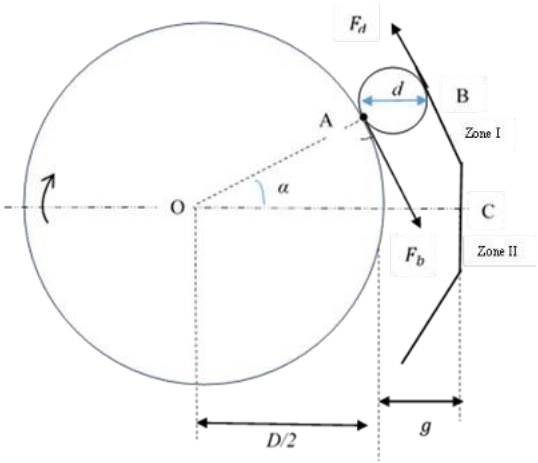


Fig. 1 - Schematic diagram of the rotating drum-pressure deck dehulling system and force analysis of a buckwheat grain

O - drum center; A – contact point between the drum and grain; B – contact point between the pressure deck and grain; F_b– friction force between the drum and grain; F_d – friction force between the pressure deck and grain; d_{eq}- equivalent grain diameter; D- drum diameter; g-working gap, α – grain position angle (measured from the horizontal centerline of the rotating drum).

Calculation of the Rotating Drum Diameter and Pressure Deck Length

The geometric parameters of the experimental dehulling device were determined from the kinematic conditions governing the entry of a buckwheat grain into the working gap between the rotating drum and the pressure deck Fig. 1. At contact point **A**, the rotating drum exerts a friction force F_b on the grain, whereas at contact point **B**, the pressure deck exerts a friction force F_d. In addition, normal reaction forces are generated at both contact points due to the elastic deformation of the grain. Owing the tetrahedral geometry of buckwheat grains, their rotational motion during feeding was assumed to be negligible, and the grains were therefore considered to undergo pure translational motion. This assumption is consistent with the principles of contact mechanics described by *Johnson., (1985),* and with the mechanical behaviors of biological materials reported by *Mohsenin., (1986).*

For the grain to be drawn into the working gap, the friction force generated by the rotating drum must exceed that generated by the pressure deck:

$$F_b > F_d \tag{1}$$

where F_b is the friction force between the rotating drum and the grain, and F_d is the friction force between the pressure deck and the grain.

The condition for grain entry can also be expressed in terms of the nip angle:

$$\tan\alpha < (f_b - f_d) \tag{2}$$

where α is the grain position angle, f_b is the coefficient of friction between the rotating drum and the grain, and f_d is the coefficient of friction between the pressure deck and the grain.

The friction coefficients were experimentally determined using the inclined-plane method described in our previous study *(Oidov et al., 2025)*. The measured values were $f_b = 0.47$ for the rotating drum and $f_d = 0.36$ for the pressure deck.

From the geometric relationship between the drum, grain, and working gap, the minimum drum diameter is determined by

$$D = \frac{d_{eq}cos\alpha - g}{(1 - cos\alpha)} \tag{3}$$

where D is the drum diameter, d_{eq} is equivalent diameter of the buckwheat grain, g is the working gap.

The equivalent diameter of the buckwheat grain was experimentally determined in our previous study *(Oidov et al., 2025)* by measuring the grain height of 100 randomly selected grains and converting it to the equivalent diameter using $d_{eq} = 4h/3$. Statistical analysis yielded an average equivalent diameter of $5.00 \pm 0.48\ mm$. The equivalent diameter is widely used for the engineering characterization of agricultural processing equipment because it provides a representative geometric for irregularly shaped biological materials (*Mohsenin, 1986; Rao et al., 2005*). Since the experimental material included grains with equivalent diameters of up to 5.0 mm, this value was adopted in the present design calculations as the representative grain size corresponding to the most critical operating condition for determining the minimum drum diameter. The working gap was selected as $g = 4$ mm.

Substituting these values into Equation (2),

$$\tan\alpha < (0.47 - 0.36) = 0.11$$

thus,

$$\alpha = \arctan(0.11) = 6.3^0$$

Using Equation (3),

$$D_{min} = \frac{5 \cdot cos(6.3^0) - 4}{1 - cos(6.3^0)} = 95 \text{ mm}$$

Accordingly, the selected drum diameter of 152 mm satisfies the design requirement: $D_{min} < D = 152\ mm$

The drum width was selected as 60 mm.

The minimum length of the pressure deck (working gap) is calculated from:

$$\alpha = arccos\frac{D_{min}+\delta}{D_{min}+d} \quad (4)$$

and

$$L_{min} = 2 \cdot \frac{\pi D_{min}}{360} \cdot \alpha \quad (5)$$

Substituting $D_{min} = 95\ mm$

$$\alpha = arccos\frac{95+4}{95+5} = 8.1^0;$$

$$L_{min} = 13.4\ mm$$

For the selected drum diameter $D = 152\ mm$,

$$L_{min} = 13.26\ mm$$

For the selected drum diameter of $D = 152\ mm$, the calculated minimum working gap length was $L_{min} = 13.26\ mm$. To ensure complete contact between the buckwheat grain and the abrasive surface during dehulling, the working section of the pressure deck was designed with a length of 15 mm. Based on these calculations, the experimental dehulling device was constructed with a drum diameter of 152 mm, a drum width of 60 mm, a working gap of 4 mm, and a pressure deck working length of 15 mm. These parameters were adopted in all subsequent experiments.

Mathematical Processing of Experimental Data

To evaluate the performance of the proposed dehulling device, the experiments were conducted according to a three-factor central composite rotatable design (CCRD). This design enables the effects of the main operating factors and their interactions to be evaluated efficiently while providing a quadratic regression model suitable for process optimization.

The response variable was the degree of dehulling (%), which was used as the optimization criterion. Based on previous studies *(Itodo et al., 2023; Kamst et al., 2002; Mar'in et al., 2020; Oidov et al., 2025; Shitanda et al., 2001; Solanki et al., 2018; Upreti et al., 2022; Zhang et al., 2025; Zhen et al., 2022)* and the theoretical analysis presented in this work, three independent variables were selected:

- $\boldsymbol{X_1}$ – drum rotational speed, n (rpm);
- $\boldsymbol{X_2}$ – working gap between the rotating drum and the pressure deck, g (mm);
- $\boldsymbol{X_3}$ – buckwheat grain moisture content, w (%).

The coded and actual levels of the experimental factors are presented in Table 1, while the corresponding experimental design matrix is given in Table 2.

Table 1

Experiment factors and their coded levels

№	Real factors and units of measurement	Marking	The rate at which factors change					
			-1	**0**	**+1**	**Δ**	**+1,68**	**-1,68**
1	Drum rotational speed, n *(rpm)*	X_1	700	800	900	100	968	632
2	Working gap between the rotating drum and pressure deck, g *(mm)*	X_2	3	3.8	4.6	0.8	5.14	2.5
3	Buckwheat grain moisture content, w *(%)*	X_3	11	13	15	2	16.36	9.64

Table 2

Central composite rotatable design matrix and experimental results

Experimental types	№	X_1	X_2	X_3	X_1X_2	X_1X_3	X_2X_3	X_1X_1	X_2X_2	X_3X_3	y_i
Full factorial experiment	1	1	1	1	1	1	1	1	1	1	65
	2	1	1	-1	1	-1	-1	1	1	1	62
	3	1	-1	1	-1	1	-1	1	1	1	61
	4	1	-1	-1	-1	-1	1	1	1	1	60
	5	-1	1	1	-1	-1	1	1	1	1	64
	6	-1	1	-1	-1	1	-1	1	1	1	61
	7	-1	-1	1	1	-1	-1	1	1	1	60
	8	-1	-1	-1	1	1	1	1	1	1	58
Experiment on star points	9	1.68	0	0	0	0	0	2.8224	0	0	65
	10	-1.68	0	0	0	0	0	2.8224	0	0	56
	11	0	1.68	0	0	0	0	0	2.8224	0	64
	12	0	-1.68	0	0	0	0	0	2.8224	0	55
	13	0	0	1.68	0	0	0	0	0	2.8224	64
	14	0	0	-1.68	0	0	0	0	0	2.8224	56
Experiment on the planning center	15	0	0	0	0	0	0	0	0	0	64
	16	0	0	0	0	0	0	0	0	0	60
	17	0	0	0	0	0	0	0	0	0	61
	18	0	0	0	0	0	0	0	0	0	62
	19	0	0	0	0	0	0	0	0	0	58
	20	0	0	0	0	0	0	0	0	0	63

The experimental data were analyzed using response surface methodology (RSM). A second-order polynomial regression model was developed to describe the relationship between the degree of dehulling and the operating factors. The homogeneity of the experimental variance was evaluated using Cochran's test, the statistical significance of the regression coefficients was determined using Student's t-test, and the adequacy of the regression model was verified using Fisher's F-test.

To homogeneity of variance was evaluated from six replicated experiments performed at the center point of the design.

$$G_t = \frac{max{S_i}^2}{\sum_i^n {s_i}^2} \quad (6)$$

where, G_t is the calculated Cochran statistic, ${S_i}^2$ is the variance obtained from the $i-th$ replicated experiment, $max{S_i}^2$ is the maximum variance among all experimental conditions, n is the number of replicated experiments.

The experimental variance at the center point was determined from

$$S_i^2 = \frac{\sum_i^{N_0}(y_i-\bar{y})^2}{N_0-1} \quad (7)$$

where S_i^2 is the experimental variance, N_0 is the number of replicated center-point experiments, y_i is the measured degree of dehulling, and $\bar{y}$ is the mean response.

The constants required for calculating the regression coefficients are presented in Table 3.

Table 3

Determinants and Constants for Rotatable Central Composite Design

Parameter	Symbol / Description	Value
Number of factors	n	3
Total number of experiments	N	20
Number of center-point experiments	N_0	6
Calculation constant	A	0.4537037
Calculation constant	B	0.8571429
Calculation constant	C	1.4285714

The auxiliary sums used for estimating the regression coefficients were calculated as

$$S_0 = \sum_{i=1}^{n} y_i \quad (8)$$

$$S_i = \sum_{i=1}^{n} (X_{\boldsymbol{i}} \cdot y_i) \quad (9)$$

$$S_{ij} = \sum_{i=1}^{n} (X_{\boldsymbol{ij}} \cdot X_{\boldsymbol{ji}} \cdot y_i), \qquad (i \neq j) \quad (10)$$

$$S_{ii} = \sum_{i=1}^{n} (X_{ii}^2 \cdot y_i) \quad (11)$$

where, S_0 is the sum of the response values, S_i is the weighted sum for the linear terms, S_{ij} is the weighted sum for the interaction terms, S_{ii} is the weighted sum for the quadratic terms.

The regression coefficients were calculated using Equations (12) - (15).

$$b_0 = \frac{2AB}{N}\left[S_0 B(n+2) - C\sum_{i=1}^{n} S_i\right] \quad (12)$$

$$b_i = \frac{CS_i}{N} \quad (13)$$

$$b_{ij} = \frac{C^2 S_{ij}}{BN} \quad (14)$$

$$b_{ii} = \frac{AC}{N}\left[S_{ii} C[B(n+2-n) + C(1-B)\sum_{i=1}^{n} S_{ii} - 2BS_0\right] \quad (15)$$

The variances of the regression coefficients were calculated using Equations (16) - (19).

$$s_{b_0}^2 = \frac{2AB(n+2)}{N} \cdot S_y^2 \quad (16)$$

$$s_{b_i}^2 = \frac{S_y^2}{N - N_0} \quad (17)$$

$$s_{b_{ij}}^2 = \frac{C^2}{N} \cdot S_y^2 \quad (18)$$

$$s_{b_{ii}}^2 = \frac{AC^2}{N}[B(n+1) - (n-1)] \cdot S_y^2 \quad (19)$$

The statistical significance of the regression coefficients was evaluated using Student's *t*-test.

RESULTS AND DISCUSSION

Statistical Analysis of the Regression Model

The calculated Cochran statistic was:

$$G_t = 0.47,$$

whereas the critical value was:

$$G_{cr} = 0.616.$$

Since:

$$G_t < G_{cr},$$

the experimental variances were considered homogeneous, confirming the reproducibility of the experimental data.

The calculated center-point variance was:

$$S_y^2 = 4.67$$

The results of the variance calculations are presented in Table 4.

Table 4

Evaluation of Variance at the Center Point of the Design

№	y_i	$(y_i - \bar{y})$	$(y_i - \bar{y})^2$	S_i^2
15	64	2.67	7.11	3.55
16	60	-1,33	1.78	0.89

№	y_i	$(y_i - \bar{y})$	$(y_i - \bar{y})^2$	S_i^2
17	61	-0.33	0.11	0.05
18	62	0.67	0.44	0.22
19	58	-3.33	11.11	**5.55**
20	63	1,67	1.78	1.39
	61.33		23.33	11.67

The statistical significance of the regression coefficients is presented in Table 5. Only statistically significant were retained in the final regression equation.

Table 5

Significance of Regression Coefficients

$\|b_i\|$	$b_i =$	t-criterion	Significant (Yes/No)
$\|b_0\|$	64.88	2.45	Y
$\|b_1\|$	1.58	1.48	Y
$\|b_2\|$	2	1.48	Y
$\|b_3\|$	1.6	1.48	Y
$\|b_{12}\|$	0.12	1.77	N
$\|b_{13}\|$	0.12	1.77	N
$\|b_{23}\|$	0.36	1.77	N
$\|b_{11}\|$	1.71	1.43	Y
$\|b_{22}\|$	2.04	1.43	Y
$\|b_{33}\|$	1.87	1.43	Y

The adequacy variance of the regression equation was calculated from

$$S_{ad}^2 = \frac{\sum_{i=1}^{n}(y_i - y_i^t)^2 - S_y^2(N_0 - 1)}{N - \frac{(n+2)(n+1)}{2} - (N_0 - 1)} \quad (20)$$

where, S_{ad}^2 is the adequacy variance, y_i is the experimental value, y_i^t is the value predicted by the regression model.

The Fisher criterion was determined as:

$$F_p = \frac{S_{ad}^2}{S_y^2} \quad (21)$$

The calculated value was:

$$F_p = 4.70$$

whereas the critical value was:

$$F_{cr} = 5.05$$

Since:

$$F_p < F_{cr}$$

the developed regression model was considered statistically adequate for describing the buckwheat dehulling process.

The comparison between the experimental and predicted values is presented in the Table 6.

Table 6

Variance Evaluation of the Regression Equation

№	Output parameter		$(y_i - y_i^t)^2$	№	Output parameter		$(y_i - y_i^t)^2$
	Experimental, y_i	Calculation, y_i^t			Experimental , y_i	Calculation, y_i^t	
1	65	64.45487	0.297168	11	64	61.49649	2.260531
2	62	61.24915	0.563769	12	55	55.74769	0.559046
3	61	60.43773	0.316152	13	64	62.28906	2.927326
4	60	57.23201	7.66176	14	56	56.90346	0.816235

№	Output parameter		$(y_i - y_i^t)^2$	№	Output parameter		$(y_i - y_i^t)^2$
	Experimental, y_i	Calculation, y_i^t			Experimental , y_i	Calculation, y_i^t	
5	64	61.29487	7.317736	15	64	64.18	0.0324
6	61	58.08915	8.473022	16	60	64.18	17.4724
7	60	57.27773	7.410776	17	61	64.18	10.1124
8	58	54.07201	15.42909	18	62	64.18	4.7524
9	65	61.72482	5.176442	19	58	64.18	38.1924
10	56	57.41602	2.005114	20	63	64.18	1.3924
Σ					1219	1216.465	133.1686

Based on the experimental data, a second-order regression model describing the relationship between the degree of buckwheat dehulling and the operating parameters of the developed dehulling device was obtained:

$$y = 64.88 + 1.58X_1 + 2X_2 + 1.6X_3 - 1.71X_1^2 - 2.04X_2^2 - 1.87X_3^2. \quad (22)$$

The adequacy of the developed model was confirmed by Fisher's test ($F_{\text{p}} = 4.70 < F_{cr} = 5.05$), indicating that the regression equation provides adequately descries the experimental data. The maximum predicted degree of dehulling was $66.08\ \%$, obtained at the coded factor levels of $X_1 = 0.46, X_2 = 0.49$ and $X_3 = 0.43$. These values correspond to a drum rotational speed of 846 rpm, a working gap of 4.2 mm, and a buckwheat moisture content of 13.86%.

The optimum moisture content obtained in this study (13.86%) is consistent with the moisture range reported by *(Solanki et al., 2018)* for efficient buckwheat dehulling and is also in agreement with the experimental findings of *(Upreti et al., 2022)*. Although *(Zhang et al., 2025)* employed a grinding-disc dehuller operating on a different mechanical principle, they similarly reported that grain moisture content significantly influences dehulling performance.

The results further demonstrate that the dehulling efficiency is governed by the combined influence of drum rotational speed, working gap, and grain moisture content. The optimum operating conditions were located near the center of the experimental region rather than at its boundaries, indicating that excessive or insufficient values of the operating parameters reduce the degree of dehulling. Similar relationships between operating parameters and dehulling efficiency have also been reported for roller-type rice hullers *(Shitanda et al., 2001; Cheng et al., 2026)* and buckwheat dehulling machines *(Zhen et al., 2022)*.

Response Surface Analysis

The influence of the operating factors was further analyzed using response surface and contour plots generated from the regression model.

To illustrate the interaction between factors, one variable was fixed at its central coded level while the remaining two variables were varied.

Fig. 2, shows the response surface for the combined effect of drum rotational speed (X_1) and working gap (X_2) at the central moisture content ($X_3 = 0$).

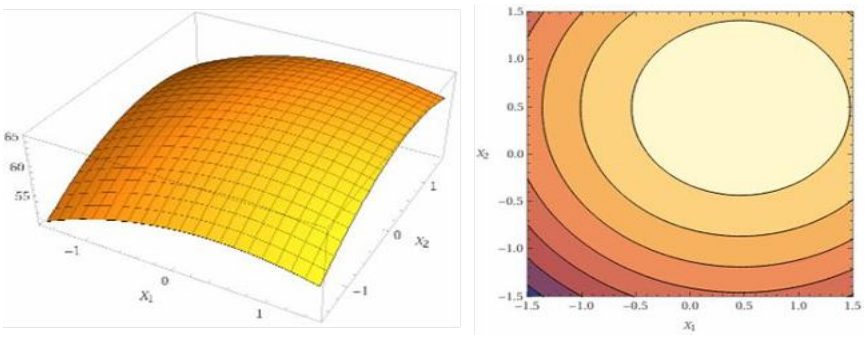


Fig. 2 - Response surface and contour plot of the degree of dehulling as a function of drum rotational speed and working gap ($X_3 = 0$)

Fig. 3, illustrates the interaction between drum rotational speed (X_1) and grain moisture content (X_3) while maintaining the working gap at its central level ($X_2 = 0$).

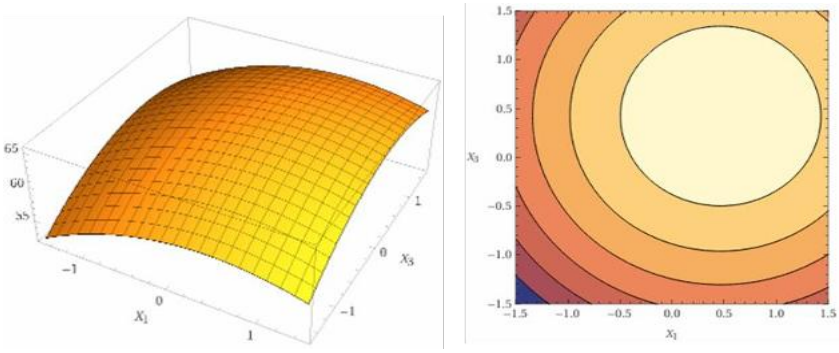


Fig. 3 - Response surface and contour plot of the degree of dehulling as a function of drum rotational speed and grain moisture content ($X_2 = 0$)

Fig. 4, presents the combined influence of working gap (X_2) and grain moisture content (X_3) at the central drum speed ($X_1 = 0$).

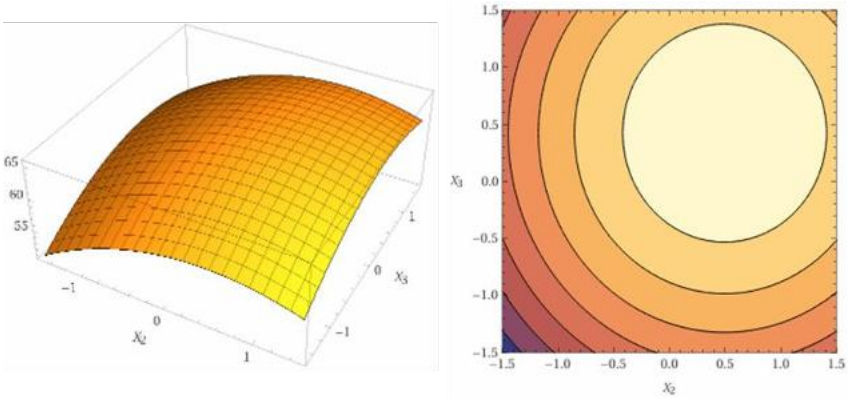


Fig. 4 - Response surface and contour plot of the degree of dehulling as a function of working gap and grain moisture content ($X_1 = 0$)

The response surface analysis demonstrated that drum rotational speed, working gap, and grain moisture content all had significant effects on the degree of buckwheat dehulling. The response surface indicate that the dehulling degree is governed by the combined interaction of these operating parameters, with the highest values occurring in the vicinity of the optimum conditions predicted by the regression model. Similar relationships between operating parameters and dehulling efficiency have been reported for roller-type rice hullers (*Shitanda et al., 2001; Cheng et al., 2026*) and buckwheat dehulling machines (*Solanki et al., 2018; Zhen et al., 2022*). The agreement between the response surface analysis and statistical optimization results confirms the reliability of the developed regression model for predicting the operating conditions that maximize the degree of dehulling.

Compared with conventional rubber-roll and impeller-type hullers reported by *(Shitanda et al., 2001*; *Solanki et al., 2018; Upreti et al., 2022),* the proposed rotating drum-pressure deck system achieves comparable dehulling performance while eliminating the need for preliminary grain size classification.

CONCLUSIONS

Experimental investigations of buckwheat dehulling using the developed dehulling device consisting of a rotating drum and a pressure deck with an elastic contact surface ($k_m \approx 10\ N/mm$) were successfully carried out using a three-factor central composite rotatable experimental design.

The main conclusions are as follows:

1. A statistically adequate second-order regression model describing the influence of drum rotational speed, working gap, and grain moisture content on the degree of buckwheat dehulling was developed and verified using Cochran's, Student's, and Fisher's statistical tests.
2. The optimum operating conditions predicted by the regression model were:
   - drum rotational speed: 846 rpm;
   - working gap: 4.2 mm;
   - buckwheat moisture content: 13.86%.

3. Under these operating conditions, the maximum predicted degree of dehulling reached 66.08**%**.
4. Response surface analysis demonstrated that the interaction of the operating factors significantly affects the dehulling performance. The use of an elastic pressure deck enables effective dehulling of buckwheat grains over the investigated size range without preliminary size classification.
5. The obtained results confirm the feasibility of the proposed dehulling principle and provide a basis for further optimization of the mechanical properties of the elastic pressure deck and the operating parameters of the dehulling device.

REFERENCES

[1] Adisa, A. F., Eberendu, O. N., Aderinlewo, A. O., & Kuye, I. S. (2016). Effectiveness of Teflon as roller material for a prototype rice processing machine. *Agricultural Engineering International: CIGR Journal*, Vol. 18(4)**,** 107–118**.**

[2] Adisa, A. F., Mamah, K. C., Aderinlewo, A. A., & Ismaila, S. O. (2020). Effectiveness of industrial rubber as roller material for rice processing machine. *Agriculture and Natural Resources*, Vol. 54(1)**,** 98–104.

[3] Altuntas, E., & Demirtola, H. (2007). Effect of moisture content on physical properties of some grain legume seeds. Journal of Food Engineering, Vol. 73(3), 315–322, Netherlands.

[4] Berk, Z. (2018). *Food Process Engineering and Technology*. 3rd ed. Academic Press, New York, United States.

[5] Bonafaccia, G., Marocchini, M., & Kreft, I. (2003). Composition and technological properties of buckwheat. *Journal of Cereal Science*, Vol. 37(1), 1–6, United Kingdom.

[6] Chebotarev, O. N., Shazzo, A. Y., & Martynenko, Y.F. (2004). *Technology of Flour, Cereals and Compound Feeds*. Moscow, Russia.

[7] Cheng, M., Zhou, S., Pan, Y., Meng, H., Wang, X., & Cao, X. (2026). Effects of abnormal paddy feeding states on the contact mechanical properties of rubber rollers in rice hullers. *International Journal of Agricultural and Biological Engineering*, Vol. 19(1), 251–262, China.

[8] Egorov, G. A. (2005). *Technology of Flour*. Cereal Technology. Moscow, Russia.

[9] Johnson, K. L., (1985). *Contact Mechanics. Cambridge University Press*, Cambridge, United Kingdom.

[10] Kamst, G., Bonazzi, C., & Vasseur, J. (2002). Effect of deformation rate and moisture content on the mechanical properties of rice grains. *Transactions of the ASAE*, Vol. 45(1), 145–151, United States.

[11] Mar'in, V., Vereshchagin, A., & Ivanov, A. (2020). Application of visco-elastic deck in decorticating buckwheat grains. *Foods and Raw Materials*, Vol. 8(1), 87–95, Russia.

[12] Mohsenin, N. N., (1986). *Physical Properties of Plant and Animal Materials: Structure, Physical Characteristics and Mechanical Properties*. 2nd ed. Gordon and Breach Science Publishers, New York, United States.

[13] Oidov, A., & Maashaa, D. (2025). Research on the process of peeling buckwheat grain on roller equipment with new design decks. *Key Engineering Materials*, Vol. 1030, 101–109, Switzerland.

[14] Rao, M. A., Rizvi, S. S. H., & Datta, A. K. (2005). *Engineering Properties of Foods*. 3rd ed. CRC Press, Boca Raton, United States.

[15] Shitanda, D., Nishiyama, Y., & Koide, S. (2001). Performance analysis of impeller and rubber roll husker using different varieties of rice. *CIGR Journal*, Vol. 3, Manuscript FP 01 001, China.

[16] Solanki, C., Mridula, D., & Gupta, R. K. (2018). Buckwheat dehuller and optimization of dehulling parameters. *International Journal of Current Microbiology and Applied Sciences*, Vol. 7(11), 1041–1052, India.

[17] Tarasenko, S. S., & Vladimirov, N. P. (2017). *Technology of Cereal Production. Part I. Theoretical Foundations of Cereal Technology*. Orenburg State University, Orenburg, Russia.

[18] Upreti, M., Norbu, K., & Tshering, D. (2022). AMC-made impeller-type buckwheat dehuller and optimization of impeller speed. *Bhutanese Journal of Agriculture*, Vol. 5(1), 172–182, Bhutan.

[19] Zhang, N., Li, W., Li, L., & Zheng, D. (2025). Design and experimental analysis of a grinding disc buckwheat dehulling machine. *Agriculture*, Vol. 15(16), 1793, Switzerland.

[20] Zhen, J., Chen, W., & Gao, H. (2022). Study on hulling characteristics of buckwheat huller. *INMATEH – Agricultural Engineering*, Vol. 66(1), 239–246, Romania.

TRAJECTORY TRACKING APPROACH FOR ORCHARD INSPECTION VEHICLE BASED ON IMM-EKF AND IMPROVED STANLEY CONTROLLER

/

基于 IMM-EKF 与改进 STANLEY 的果园巡检车轨迹跟踪方法

Junling HU [1)], Xiaofan LIU [2)], Meixia JIA [1,*)]

[1)] Chongqing Jianzhu College, School of Intelligent Manufacturing, Chongqing, China

[2)] Communication University of China, School of Economics and Management, Beijing, China;

Tel: +86 13637821418; E-mail: jiameixia23@163.com

Corresponding author: Meixia JIA

DOI: https://doi.org/10.35633/inmateh-79-70

Keywords: *orchard inspection vehicle; IMM-EKF; pose correction; trajectory tracking*

ABSTRACT

To address the instability of trajectory tracking in unmanned orchard inspection vehicles caused by satellite navigation signal attenuation and track slippage, an integrated control method based on pose correction and an improved Stanley controller was proposed. First, a pose-correction algorithm based on the interacting multiple-model extended Kalman filter (IMM-EKF) was developed. By incorporating the nonlinear dynamic characteristics of tracked vehicles, the algorithm improved the robustness of pose estimation under varying motion states and measurement conditions. Second, an improved Stanley trajectory-tracking controller incorporating feedforward control and dynamic parameter adjustment was designed based on the corrected pose estimates. By accounting for path curvature in advance, the controller optimized the control commands and reduced lateral and heading errors. Simulations conducted using the Robot Operating System (ROS) platform and field tests performed in an actual vineyard were used to evaluate the proposed method. At a representative operating speed of 1.0 m/s, the mean lateral error during continuous multi-route trajectory tracking was 0.019 m, and the mean root-mean-square error (RMSE) was 0.021 m. These results demonstrate that the proposed method can improve trajectory-tracking accuracy, stability, and smoothness under the tested orchard conditions.

摘要

针对果园复杂环境下卫星导航信号衰减与履带滑移引起的无人巡检车轨迹跟踪不稳定问题，本文提出了一种基于位姿修正与改进 Stanle 算法的综合控制方法。首先，构建了基于交互式多模型扩展卡尔曼滤波（IMM-E F）的位姿修正算法。该算法结合履带车辆非线性动力学特征，提高了车辆在运动状态和观测条件变化下的位姿估计鲁棒性。其次，基于修正后的位姿数据，设计了一种融合前馈控制策略与动态参数调整的改进 Stanle 轨迹跟踪控制器。该控制器通过提前考虑路径曲率信息，对轨迹跟踪控制指令进行优化，从而减小横向误差与航向误差。基于机器人操作系统（Ro ot O erat n S stem, ROS）平台的仿真分析与真实葡萄园环境下的实车试验结果表明，在 1 m/s 的典型作业速度下，车辆在多路线连续轨迹跟踪中的平均横向误差为 0.019 m，平均均方根误差（RMSE）为 0.021 m。结果表明，所提方法在测试果园条件下能够提高车辆轨迹跟踪的精度、稳定性与平顺性。

INTRODUCTION

As Chinese agricultural transformation and upgrading progresses, the automation and intelligentisation of orchard operations have become key means of alleviating labour shortages and reducing production costs (*Gao et al., 2021*). However, orchard environments are highly complex and unstructured, featuring undulating terrain, canopy obstruction and variable soil physicochemical properties, which pose a significant challenge to the autonomous navigation capabilities of unmanned inspection vehicles *(Xue et al., 2023)*. Recent studies from different agricultural regions have shown that orchard rows and dense tree canopies can seriously affect satellite-based navigation. Dense orchard canopies may prevent the reliable use of GPS signals *(Durand-Petiteville et al., 2018)*, and accurate robot localisation with respect to orchard row centre lines remains challenging because satellite signals are often obstructed by foliage *(Fei et al., 2022)*. Intermittent GNSS dropout in orchards can also significantly degrade navigation accuracy and requires auxiliary localisation methods such as LiDAR or INS *(Li et al., 2024)*. Particularly in complex orchard terrain, Global Navigation Satellite System (GNSS) signals are often attenuated or interrupted due to vegetation cover; coupled with the inherent slippage of tracked chassis when travelling on unpaved surfaces, this makes it difficult for traditional

navigation systems to provide continuous, high-precision position and attitude data, thereby leading to system oscillations and instability in trajectory tracking control.

For tracked and wheeled agricultural vehicles, track–soil and wheel–soil slip represent important sources of motion uncertainty. Slip estimation has been shown to be essential for the path-tracking control of autonomous agricultural vehicles operating on wet and deformable soils *(Han et al., 2019)*. In addition, kinematic models incorporating both translational slip and rotational slippage have been developed for trajectory prediction in tracked agricultural robots *(Zhao et al., 2024)*. These findings indicate that pose estimation, slip modelling, and trajectory tracking should be considered jointly when developing autonomous navigation systems for orchard inspection vehicles.

Stable, high-precision pose estimation is the cornerstone of autonomous navigation *(Zhou et al., 2021*). At present, autonomous navigation systems commonly employ data fusion techniques combining GNSS and Inertial Navigation Systems (INS) to compensate for the limitations of single GNSS signals; however, due to cost constraints on orchard operation vehicles, low-to-medium accuracy INS systems are highly prone to accumulating drift errors during prolonged signal blockage, making it difficult to meet high-precision positioning requirements *(Lv et al., 2025)*. In terms of filtering algorithms, the Extended Kalman Filter (EKF) is widely used for state estimation and noise filtering in non-linear systems; however, filters based on a single motion model struggle to accurately capture the complex non-linear dynamic behaviour of a vehicle under variable road conditions *(Zhang et al., 2014)*. To this end, the Interactive Multi-Model (IMM) algorithm demonstrates excellent adaptability to system behaviour, thanks to its ability to dynamically switch between multiple motion hypotheses *(Nie et al., 2021)*. The deep integration of IMM with the Extended Kalman Filter (EKF) enables effective addressing of the challenge of high-precision pose estimation for orchard operation vehicles under complex constraints.

In the field of trajectory tracking control, the Stanley algorithm is widely used for lateral control in autonomous vehicles due to its geometric intuitiveness and computational efficiency *(Thrun et al., 2006).* In response to the time-varying and uncertain nature of agricultural scenarios, many researchers have introduced improved geometric control, fuzzy control, optimisation algorithms and model predictive control (MPC) to enhance the tracking performance of agricultural vehicles *(Kayacan et al., 2015; Plessen and Bemporad, 2017; Wang et al., 2022; Xu et al., 2022).* For example, improved Stanley controllers have been used to reduce path-tracking errors of autonomous tractors, while MPC-based methods have been adopted to handle actuator constraints and improve tracking stability in agricultural machinery. However, the narrow row spacing, uneven terrain and frequent curved sections within orchards require the control system to be more proactive and robust. Existing improved methods still have limitations in terms of transient smoothness, adaptability to variable ground conditions, and tracking accuracy on curved paths *(AbdElmoniem et al., 2020; Wang et al., 2022).*

To address navigation challenges in complex orchards, this study proposes an integrated control framework combining IMM-EKF for precise pose correction and an improved feedforward Stanley algorithm. The proposed method uses IMM-EKF to reduce pose fluctuation caused by GNSS signal degradation and vehicle motion uncertainty, and introduces curvature feedforward into the Stanley controller to improve tracking response on curved paths. Simulations and field trials verify that this method can improve the accuracy, smoothness, and reliability of vehicle trajectory tracking under the tested orchard conditions.

To address navigation challenges in complex orchards, this study proposes an integrated control framework combining IMM-EKF for precise pose correction and an improved feedforward Stanley algorithm. Simulations and field trials verify that this method significantly enhances the accuracy, smoothness, and reliability of the vehicle trajectory tracking.

MATERIALS AND METHODS

Using dual-antenna GNSS-RTK positioning technology, the vehicle is able to determine its global position through absolute positioning. However, in real-world orchards, vehicles often need to operate in complex environments characterised by uncertainty and dynamic changes *(Zhou et al., 2014)*. For example, signal instability or unavailability caused by tree cover may affect the accuracy and reliability of absolute positioning. To overcome these challenges, this study introduces an attitude correction technique based on the Interactive Multiple Model Extended Kalman Filter (IMM-EKF). The IMM framework provides an adaptive state-estimation strategy for systems with switching motion modes or time-varying uncertainty by combining multiple model hypotheses according to their posterior probabilities (*Blom and Bar-Shalom, 1988; Li and Jilkov, 2005*). By integrating the IMM framework with the estimation capability of the EKF in nonlinear systems, the IMM-EKF can improve the robustness of vehicle pose estimation under varying motion and measurement

conditions (*Jwo et al., 2013*). Specifically, at each time step, the IMM-EKF first calculates the mixed initial state of each model based on the model transition probability and the state estimate from the previous time step. Then, each EKF sub-filter performs state prediction and measurement update. Finally, the posterior probability of each model is updated according to the measurement likelihood, and the EKF estimates are weighted and combined to obtain the integrated state estimate at the current time. The architecture of the IMM-EKF algorithm is shown in Figure 1.

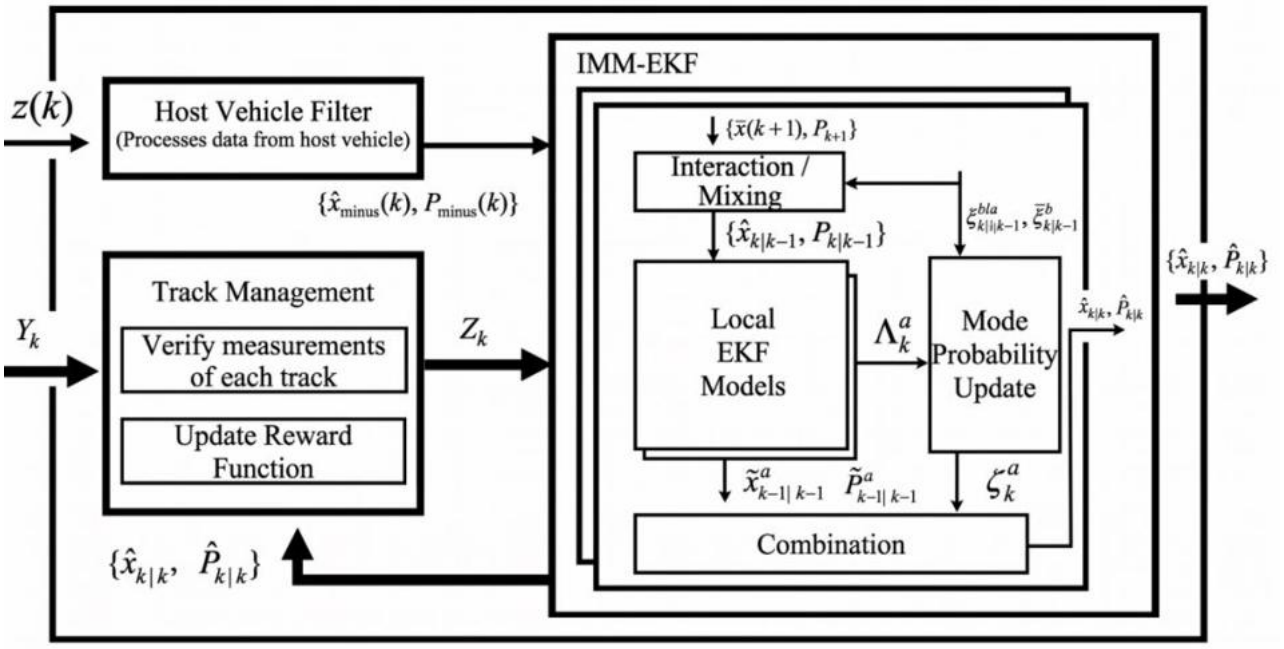


Fig. 1 - IMM-EKF algorithm architecture

This study employs a dual-antenna GNSS-RTK (Global Navigation Satellite System-Real Time Kinematic) system to obtain the vehicle's global position and attitude data. The system is based on real-time dynamic carrier phase differential technology. By calculating the relative positions of the master and slave antennas, it is capable of outputting high-precision global coordinates (longitude, latitude and altitude) as well as the vehicle's three-dimensional attitude angles (heading, pitch and roll) in real time *(Zhang et al., 2022)*.

To meet the requirements for subsequent non-linear dynamic modelling and trajectory tracking control, the system uses a standard Direction Cosine Matrix (DCM) to map the geodetic Cartesian coordinate system data obtained from GNSS-RTK to the local horizontal coordinate system *(Shan et al., 2018)*. Following the coordinate transformation, the absolute coordinates (x, y) and heading angle θ of the orchard operation vehicle in the planar coordinate system are extracted. These three state variables will serve directly as the initial observation inputs for the subsequent Interactive Multi-Model Extended Kalman Filter (IMM-EKF), which is designed to address signal attenuation and noise interference in environments where the signal is obscured by orchard canopies *(Wu et al., 2021)*.

The vehicle pose in the local planar coordinate frame is selected as the system state. The angular velocities of the left and right drive sprockets are treated as the control inputs, whereas the corresponding slip ratios and the vehicle slip angle are regarded as time-varying model parameters. These variables are used to characterize the effects of track slip on the vehicle motion *(Yang et al., 2022)*.

At discrete time step *k*, the longitudinal position, lateral position, and yaw angle of the tracked inspection vehicle are combined into the state vector:

$$\mathbf{x}_k = \begin{bmatrix} x_k \\ y_k \\ \theta_k \end{bmatrix} \quad (1)$$

where x_k and y_k denote the global longitudinal and lateral coordinates of the vehicle, respectively, in m, and θ_k denotes the vehicle yaw angle in rad, measured counterclockwise from the positive direction of the global *X*-axis.

The control input $\mathbf{u}_k$ (comprising the angular velocities of the left and right drive sprockets) and the slip-related parameter vector $\boldsymbol{\eta}_k$ are respectively defined as:

$$\mathbf{u}_k = \begin{bmatrix} \omega_{l,k} \\ \omega_{r,k} \end{bmatrix}, \boldsymbol{\eta}_k = \begin{bmatrix} i_{l,k} \\ i_{r,k} \\ \alpha_k \end{bmatrix} \quad (2)$$

Here, $i_{l,k}$ and $i_{r,k}$ are the real-time slip ratios of the left and right tracks, respectively, and α_k is the vehicle slip angle. Accordingly, the discrete-time nonlinear state equation is written as:

$$\mathbf{x}_{k+1} = f(\mathbf{x}_k, \mathbf{u}_k, \boldsymbol{\eta}_k) + \mathbf{w}_k \quad (3)$$

where $\mathbf{w}_k$ denotes the process noise.

Since the GNSS-RTK system directly measures the vehicle pose (x_k, y_k, θ_k), the observation model is linear, and its Jacobian is given by:

$$\mathbf{H}_k = \left.\frac{\partial h(\mathbf{x})}{\partial \mathbf{x}}\right|_{\mathbf{x}=\mathbf{x}_{k|k-1}} = \mathbf{I}_3 = \begin{bmatrix} 1 & 0 & 0 \\ 0 & 1 & 0 \\ 0 & 0 & 1 \end{bmatrix} \quad (4)$$

Since the standard prediction and measurement-update equations of the EKF are well established, they are not repeated here. In this study, the system nonlinearity mainly arises from the state-transition model $f(\cdot)$ whereas the observation model is linear, with H_k=I_3. Therefore, the following discussion focuses on the covariance prediction and the Jacobian matrix of the nonlinear state-transition model *(Yang et al., 2015)*.

On this basis, in order to quantify the uncertainty in the forecast, the process of updating the forecast state covariance P requires the introduction of a process noise covariance matrix, the calculation of which can be expressed as:

$$P_{k+1} = A_k P_k A_k^T + Q_k \quad (5)$$

Here, A_k is the Jacobian matrix of the system's dynamic model based on the current state estimate, reflecting how minute changes in the system's state variables affect the evolution of the system's overall state.

$$A_k = \begin{bmatrix} 1 & 0 & A_{K13} \\ 0 & 1 & A_{K23} \\ 0 & 0 & 1 \end{bmatrix} \quad (6)$$

$$A_{K13} = -\frac{r\left(\left(1-i_l\right)w_l + \left(1-i_r\right)w_r\right)(\sin(\theta) + \cos(\theta)\tan(\alpha))}{2} \quad (7)$$

$$A_{K23} = \frac{r\left(\left(1-i_l\right)w_l + \left(1-i_r\right)w_r\right)(\cos(\theta) - \sin(\theta)\tan(\alpha))}{2} \quad (8)$$

In particular, A_{K13} and A_{K23} are based on a vehicle kinematic model, taking into account the effects of slip ratio and wheel speed on changes in vehicle direction, and reveal the complexity of the interactions between state variables in a non-linear dynamic system.

$$Q_k = \begin{bmatrix} \sigma_{w_l}^2 & 0 & 0 \\ 0 & \sigma_{w_r}^2 & 0 \\ 0 & 0 & \sigma_\theta^2 \end{bmatrix} \quad (9)$$

$$P_k = \begin{bmatrix} \sigma_x^2 & 0 & 0 \\ 0 & \sigma_y^2 & 0 \\ 0 & 0 & \sigma_\theta^2 \end{bmatrix} \quad (10)$$

The process noise covariance accounts for the influence of random noise from various sources in real-world driving conditions—such as wheel speed noise and steering noise—on state estimation.

Based on the standard IMM framework, the weights of each motion model are dynamically updated using the model transition probability matrix, and the posterior probability is calculated using the likelihood function, ultimately outputting the fused optimal state estimate and covariance matrix.

In order to precisely control the vehicle movement along the desired path whilst performing a path-tracking task, it is essential to accurately calculate the path-tracking error, including lateral and heading errors. These errors serve as key indicators of the deviation between the vehicle's current state and its desired trajectory, and are crucial for designing effective control strategies.

Lateral error refers to the perpendicular distance between the vehicle's current position and the nearest point on the intended path. Let the actual position of the vehicle be denoted by (x_v, y_v), and determine the projection point (x_p, y_p) of the vehicle's current position onto the desired path, as shown in Figure 2.

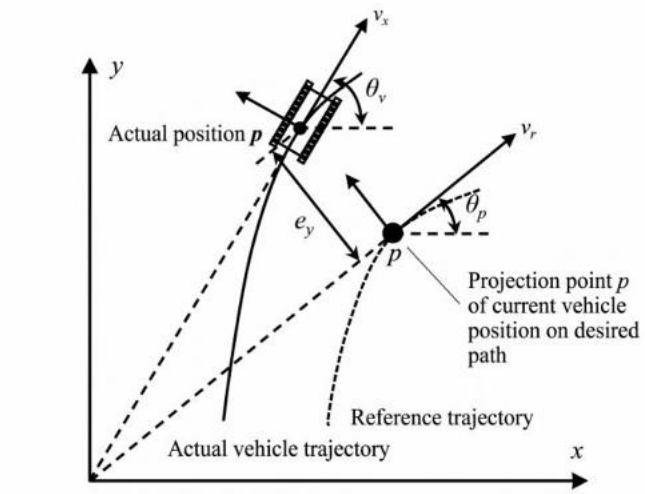


Fig. 2 - The correlation between the actual driving trajectory and the reference trajectory of the vehicle.

The lateral error e_y is given by the distance between the vehicle's actual position and its projected position on the desired path; the mathematical expression is:

$$e_y = \sqrt{(x_v - x_p)^2 + (y_v - y_p)^2} \cdot \mathrm{sgn}(y_v - f(x_v)) \quad (11)$$

Here, $\mathrm{sgn}(\cdot)$ is a sign function used to determine the direction of the error (whether the vehicle is to the left or right of the desired path). Heading error refers to the angular difference between the vehicle's current heading and the tangent direction of the desired path at its projection point. Let θ_v be the vehicle's actual heading angle; the tangent angle θ_p at the projection point (x_p, y_p) on the desired path can be obtained by differentiating $f'(x_p)$:

$$\theta_p = \arctan(f'(x_p)) \quad (12)$$

The course error e_θ can then be calculated as:

$$e_\theta = \theta_v - \theta_p, \quad e_\theta \in (-\pi, \pi] \quad (13)$$

The pose compensation module calculates the deviation between the actual trajectory and the desired trajectory, and adjusts the control inputs accordingly to achieve more precise trajectory tracking.

The expected trajectory can be expressed as a function:

$$y_r = f(x_r) \quad (14)$$

(x_r, y_r) denotes a point on the desired trajectory. The lateral error e_y and heading error e_θ between the vehicle's actual position and its desired position are defined as:

$$e_y = y - f(x) \quad (15)$$

$$e_\theta = \theta - \tan^{-1}(f'(x)) \quad (16)$$

Here, $f'(x)$ is the derivative of the expected trajectory at x, representing the direction of the tangent line to the trajectory.

Based on the findings of the above study, the pose estimates provided by the IMM-EKF are used to calculate the corrected lateral error $\hat{e}_y$ and heading error $\hat{e}_\theta$:

$$\hat{e}_y = \hat{y} - f(\hat{x}) \quad (17)$$

$$\hat{e}_\theta = \hat{\theta} - \tan^{-1}(f'(\hat{x})) \quad (18)$$

Using these corrected errors, a pose compensation module is designed to adjust the vehicle's control inputs in order to minimise these errors. The control input δ for pose compensation—namely, the vehicle's steering angle—can be adjusted using the following control law:

$$\delta = k_1 \cdot \hat{e}_y + k_2 \cdot \hat{e}_\theta \quad (19)$$

In this context, k_1 and k_2 are the control gains.

In order to further enhance the accuracy and stability of path tracking, the Stanley controller requires optimisation and refinement. Building upon the traditional Stanley method, the improved controller must not only accurately calculate path tracking errors but also adapt more flexibly to a variety of driving conditions, including different speeds, curvatures and changes in the external environment.

The improved Stanley control law is as follows:

$$\delta(t) = \arctan\left(\frac{k_e \cdot e_y(t)}{v(t)}\right) + k_\theta \cdot e_\theta(t) + \psi(t) \quad (20)$$

where: $e_y(t)$ - the lateral error at time t; $e_\theta(t)$ - the heading error at time t; $v(t)$ - the vehicle's speed; k_e - the adjustment coefficient for the lateral error; k_θ - the adjustment coefficient for the heading error.

Here, $\psi(t)$ represents the feedforward control term, which is expressed as follows:

$$\psi(t) = \arctan(k_\psi \cdot \frac{1}{g(t)}) \quad (21)$$

where: k_ψ — the feedforward control coefficient; $g(t)$ — the radius of curvature of the path at time t.

This control law responds directly to the current lateral and heading errors via the feedback term, whilst anticipating upcoming path changes via the feedforward term.

When designing a trajectory tracking control algorithm based on Stanley, the stability of the system must also be taken into account.

Given that the controller minimises the lateral error $\hat{e}_y$ and the yaw error $\hat{e}_\varphi$ by controlling the input δ, a Lyapunov function can be constructed to reflect these two errors, expressed as follows:

$$L = \frac{1}{2}(k_1 \hat{e}_y^2 + k_2 \hat{e}_\theta^2) \quad (22)$$

This function satisfies the condition that $L > 0$ holds for all $\hat{e}_y \neq 0$ or $\hat{e}_\varphi \neq 0$, and $L(0,0) = 0$, thereby fulfilling the first condition for a Lyapunov function.

Next, it is necessary to calculate $\dot{L}$, that is, the derivative of L with respect to time:

$$\dot{L} = k_1 \hat{e}_y \dot{\hat{e}}_y + k_2 \hat{e}_\theta \dot{\hat{e}}_\theta \quad (23)$$

Based on the system dynamics, $\dot{\hat{e}}_y$ and $\dot{\hat{e}}_\theta$ are determined by the vehicle's dynamic model and the control input δ; $\dot{\hat{e}}_y$ can be regarded as a function of lateral velocity, whilst $\dot{\hat{e}}_\theta$ can be regarded as a function of angular velocity.

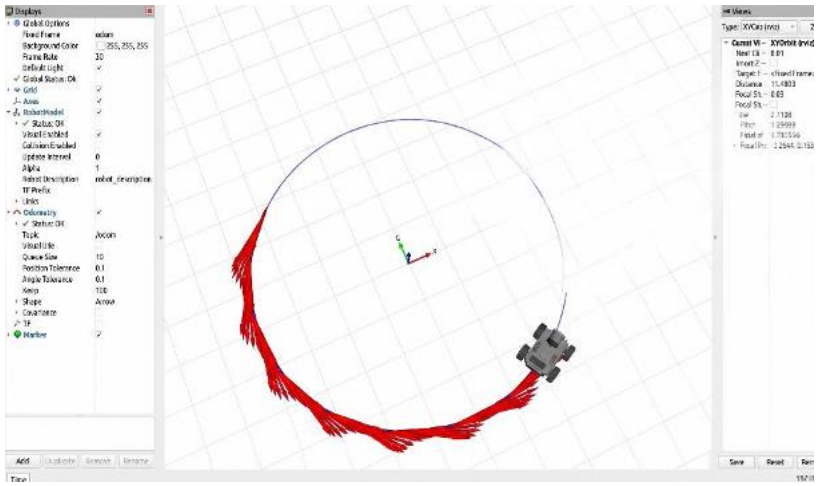
Incorporating the control law into the analysis, the control input δ is designed to minimise $\hat{e}_y$ and $\hat{e}_\theta$. Stability analysis based on the Lyapunov function—namely, the expressions for $\dot{\hat{e}}_y$ and $\dot{\hat{e}}_\theta$—reveals a trend whereby the lateral and yaw errors decrease over time, thereby ensuring that the system converges within a specified error margin.

RESULTS

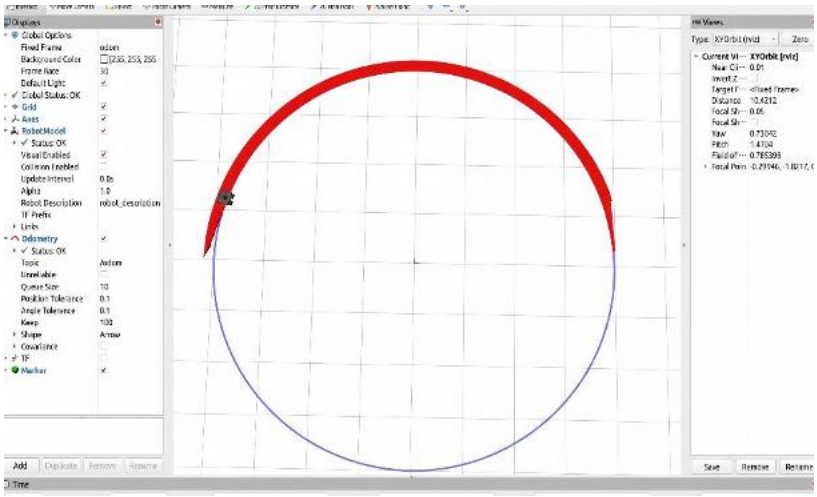
Precise trajectory tracking is the cornerstone of autonomous tracked vehicles, and this requires powerful and efficient algorithms.

To validate the performance and robustness of the proposed method, two simulation experiments were conducted: one involving straight-line path tracking control, and the other involving circular trajectory control.

A simulated orchard environment containing tree obstacles was created using ROS and Gazebo. A three-dimensional vehicle model with realistic physical and dynamic properties was then imported, and the sensor parameters were configured. Subsequently, a multimodel extended Kalman filter (EKF) framework was developed to fuse multisensor data. The framework dynamically updated the probability assigned to each motion model based on the observations and performed weighted fusion of the corresponding state estimates to obtain an optimal estimate of the vehicle pose. At the control level, a Stanley controller node was deployed to calculate the lateral tracking error by combining the predefined reference trajectory with the EKF-based state estimate. The controller then generated steering commands that enabled the vehicle to follow the prescribed path. Finally, RViz was used to visualize the planned and actual trajectories and the sensor outputs, as shown in Fig. 3(a). The controller and filter parameters were subsequently tuned to improve path-tracking stability, as shown in Fig. 3(b).



(a)



(b)

Fig. 3 - Trajectory tracking simulation experiment

To evaluate the performance of the control algorithm, different trajectory types, including straight and curved paths, were defined, and the vehicle's tracking accuracy, path-convergence rate, and robustness were assessed. The relevant state and control data were recorded by logging ROS topics during the simulation runs.

The simulation parameters were selected to reproduce real-world operating conditions as closely as possible. The vehicle's initial heading angle was set to 0.02 rad to represent the small initial orientation errors commonly encountered in practical applications. To reflect the physical constraints of an actual tracked vehicle, the maximum steering angular velocity was limited to 0.2 rad/s. In addition, the vehicle speed was set to 1.0 m/s to represent the typical low-speed operating conditions of tracked vehicles in the field.

The simulation results showed that the vehicle rapidly converged to the predefined reference path and subsequently followed it with high accuracy. However, an evaluation based solely on the mean error and standard deviation would provide an incomplete statistical characterization of tracking performance. Additional information, including the simulation duration, number of repeated runs, and confidence intervals, is required to quantify tracking stability more comprehensively.

For the straight-line path-tracking simulation shown in Fig. 4, the vehicle travelled at a constant speed of 1.0 m/s. Each simulation run lasted 120 s, and 20 independent trials were conducted to reduce the influence of random variability. The statistical results aggregated across the 20 trials were as follows: the mean lateral tracking error was 0.014 m, with a standard deviation of 0.0057 m and a 95% confidence interval of 0.0116–0.0164 m; the mean heading error was 0.002 rad, with a standard deviation of 0.0008 rad and a 95% confidence interval of 0.0017–0.0023 rad.

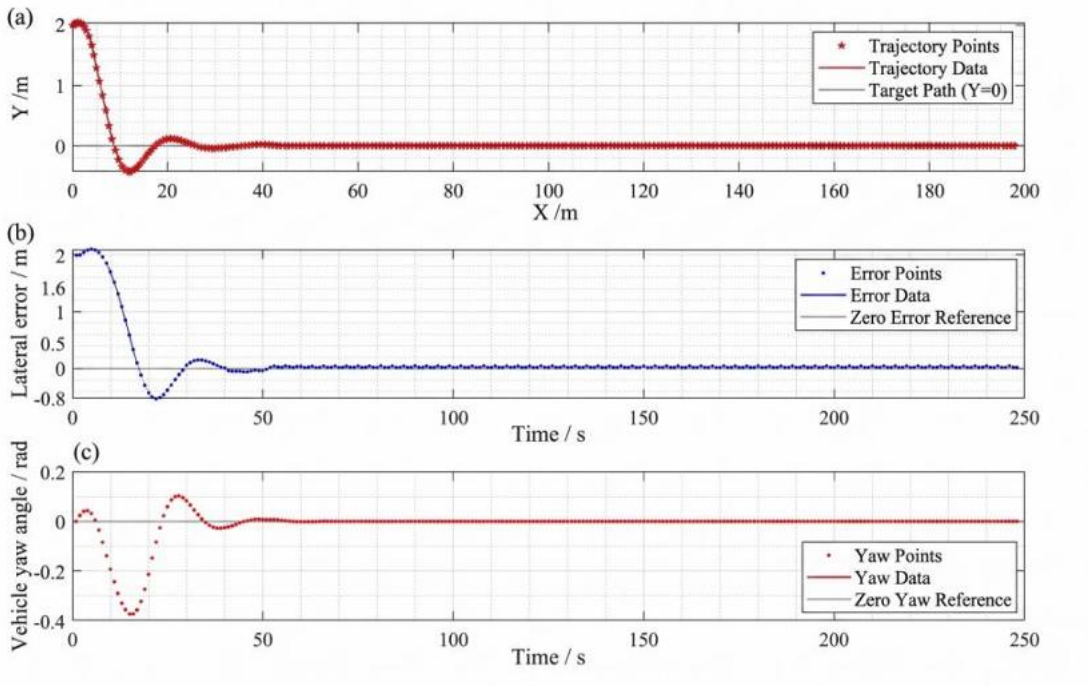


Fig. 4 - Straight-line path-tracking simulation and error.

As shown in Fig. 5, the circular trajectory-tracking simulation yielded a mean lateral error of 0.023 m, with a standard deviation of 0.0086 m, and a mean heading error of 0.033 rad, with a standard deviation of 0.021 rad. These results demonstrate that the proposed algorithm achieved accurate and stable trajectory tracking along a curved reference path.

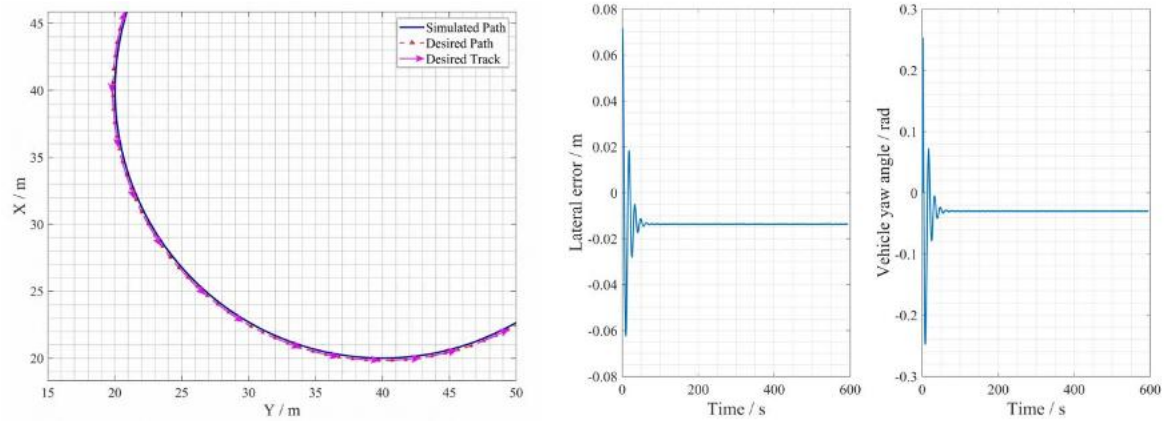


Fig. 5 - Simulated circular path-tracking error

To evaluate the effectiveness of the proposed path-tracking algorithm under real operating conditions, field experiments were conducted in a vineyard. Fig. 6 shows the test site, which featured uneven terrain and inter-row weeds. Each vine row was 100 m long, and the row spacing ranged from 3.5 to 4.0 m.



Fig. 6 - Vineyard real-field scenario

Two field tests were conducted using the tracked orchard inspection vehicle: constant-speed straight-line trajectory tracking at 1.0 m/s and continuous trajectory tracking along multiple routes. Each test condition was repeated six times to improve the statistical reliability of the results. The straight test route was 100 m long, whereas the total length of the continuous multi-route trajectory was 480 m. Standardized initial conditions were applied, with nominal position and heading offsets set to zero. Before data recording, the maximum allowable initial position and heading deviations were limited to 0.03 m and 1.5°, respectively. Data acquisition began only after the GNSS-RTK positioning solution had remained stable for 3 s at the starting point and ended when the vehicle entered the predefined coordinate threshold at the endpoint. A GNSS-RTK receiver operating at 10 Hz recorded the vehicle's real-time position and heading. The relative deviation was defined as the ratio of the instantaneous lateral tracking error to the maximum allowable lateral offset from the reference trajectory. This dimensionless metric was calculated and statistically analysed across all repeated trials.

Fig. 7 shows the continuous multi-route trajectory-tracking trials conducted in the vineyard under operating conditions representative of autonomous orchard vehicles. The reference trajectories were generated and measured using a clearly defined procedure. Discrete waypoints were manually surveyed by static GNSS-RTK measurements at the row boundaries and turning zones, and a minimum turning radius of 2.5 m was applied to all inter-row turns. Cubic B-spline interpolation was then used to convert the discrete waypoints into smooth, continuously differentiable trajectories. All trajectory data were expressed in a local horizontal Cartesian coordinate system transformed from geodetic coordinates. Before the vehicle tests, the ground-truth reference trajectories were fully surveyed using static RTK measurements. The tracked vehicle followed the preplanned smooth trajectories stably across multiple vine rows, and the recorded trajectory curves demonstrated reliable tracking accuracy over uneven vineyard terrain.

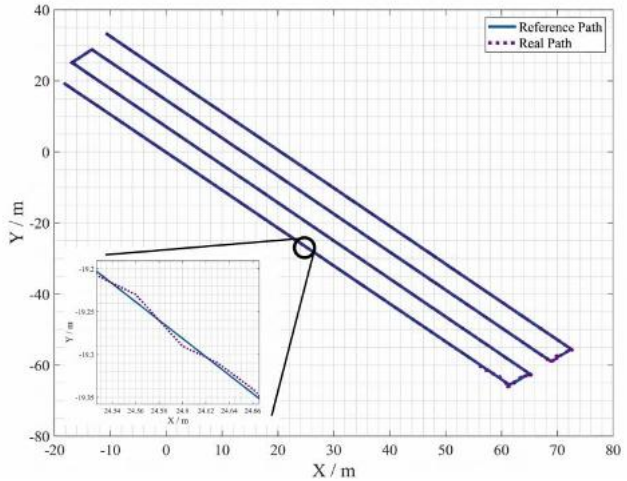
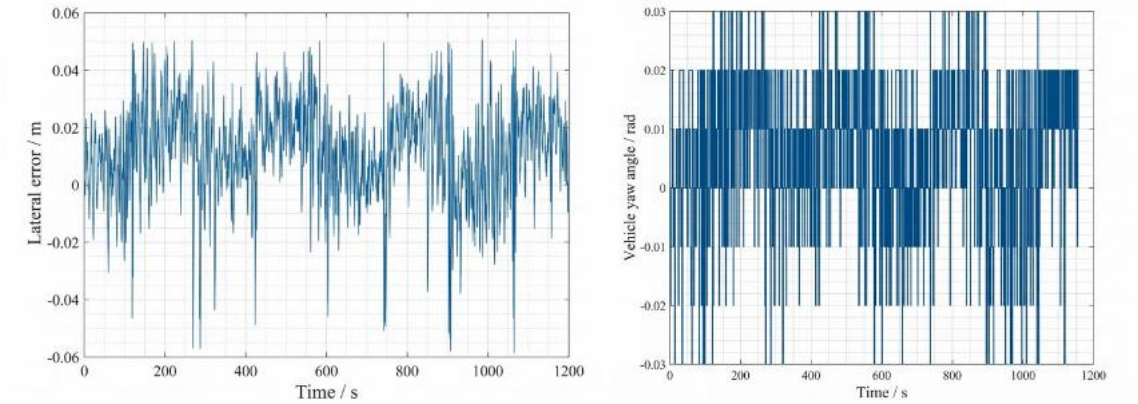


Fig. 7 - Continuous multi-route trajectory-tracking test

Fig. 8(a) shows the variation in lateral tracking error over time. The lateral error remained within 0.06 m throughout the test and exhibited increasingly stable fluctuations as the test progressed, with an apparent periodic pattern. Fig. 8(b) shows the variation in heading error over time. The heading error remained below 0.03 rad (approximately 1.72°) throughout the tracking process, indicating that the vehicle maintained stable heading alignment with the reference trajectory.



(a) Lateral tracking error over time (b) Vehicle yaw angle over time

Fig. 8 - Experimental results for continuous multi-route trajectory tracking

Analysis of the multi-route test data shown in Fig. 8 was used to quantify the tracking performance of the proposed algorithm. Across six repeated vineyard trials, the mean lateral RMSE was 0.021 m, while the steady-state heading error remained within ±0.03 rad. Compared with the baseline method combining a standard single-model EKF with the original Stanley controller, the proposed method reduced the mean lateral RMSE by 42.7% under identical vineyard conditions. The tracked vehicle maintained stable alignment with the reference trajectory and limited both lateral and heading errors to relatively low levels, demonstrating the applicability of the proposed method to vineyard navigation. Nevertheless, this study has several limitations. Only the low-speed operating condition of 1.0 m/s was evaluated, and tracking performance under severe slip or on steep terrain was not investigated.

Table 1

Statistical results for the absolute lateral tracking error during continuous multi-route trajectory tracking (Unit: meter)

Test	Maximum	Minimum	Mean	Standard deviation	RMSE
1	0.042	0.0000016	0.019	0.016	0.021
2	0.078	0.0000077	0.022	0.023	0.027
3	0.015	0.0000008	0.020	0.018	0.023
4	0.075	0.0000016	0.019	0.018	0.021
5	0.128	0.0000026	0.017	0.016	0.019
6	0.055	0.0000019	0.014	0.011	0.017

The data presented in Table 1 is derived from multiple repeated trials conducted along the planned route shown in Figure 8. To simulate real-world conditions, these trials were carried out on different dates. This approach aims to ensure that, whilst the route remains consistent, the appearance of the soil changes in the real world due to human activity and environmental influences, and that external noise, such as weather conditions, is also constantly varying.

Table 1 presents the absolute lateral-error statistics obtained from six repeated multi-route trajectory-tracking trials. An audit of the raw data identified two important inconsistencies. First, Trial 3 reported a maximum absolute lateral error of 0.015 m, together with a mean absolute error of 0.020 m and an RMSE of 0.023 m. These values are mathematically inconsistent because, for a set of non-negative absolute errors, neither the mean nor the RMSE can exceed the maximum observed value. The Trial 3 statistics were therefore recalculated.

Second, the reported minimum errors, including values such as 0.0000016 m, were below the practical measurement capability of the field GNSS-RTK system and were considered numerical noise rather than physically meaningful measurements. Accordingly, the minimum-error values were reported to a practical precision of 0.001 m.

After recalculating the trial statistics and standardizing the raw data, the aggregated results from the six tests were as follows. The mean maximum lateral error was 0.066 m, and the mean minimum detectable error, rounded to three decimal places, was 0.001 m. The overall mean absolute lateral error was 0.019 m, with a standard deviation of 0.017 m. The RMSE values for the individual trials ranged from 0.017 to 0.027 m, with a mean of 0.021 m. For every trial, the RMSE was lower than the corresponding maximum lateral error after calibration. These calibrated metrics characterize the lateral-error distribution of the proposed Stanley controller enhanced with IMM-EKF under uneven vineyard conditions and demonstrate its ability to limit lateral tracking deviations under canopy-induced signal attenuation and track-slip disturbances.

CONCLUSIONS

This study developed an integrated navigation framework combining IMM-EKF-based multimodel pose correction with a feedforward-enhanced Stanley controller for tracked orchard inspection vehicles operating under GNSS signal attenuation and track-slip disturbances. Simulations and vineyard field tests demonstrated measurable improvements in trajectory-tracking performance. At a constant speed of 1.0 m/s, the straight-line simulation achieved a mean lateral error of 0.014 m, while the multi-route field trials produced a mean lateral RMSE of 0.021 m. Compared with the baseline method combining a single-model EKF with the original Stanley controller, the proposed method reduced the mean lateral RMSE by 42.7% under identical orchard conditions.

This study nevertheless has several limitations. Only one low operating speed, 1.0 m/s, was evaluated, and all field experiments were conducted in a single vineyard with relatively mild terrain irregularities. Performance under more demanding conditions, including steep slopes and severe track slip, was not investigated, and the method was not cross-validated using different vehicle chassis. Future work will therefore focus on extending the method to variable-speed operation, conducting additional tests on sloped and highly slippery orchard terrain, integrating LiDAR- and vision-based positioning to reduce long-term localization drift, and evaluating the generalizability of the framework across different types of tracked agricultural vehicles. Overall, the proposed method provides experimentally supported guidance for centimetre-level autonomous trajectory tracking by unmanned orchard vehicles.

ACKNOWLEDGEMENT

This work was supported by the Science and Technology Research Project of Chongqing Municipal Education Commission (Grant No. KJQN202504305).

REFERENCES

[1] Abd Elmoniem, Osama A., Abdelaziz M., Maged S. A. (2020). A path-tracking algorithm using predictive Stanley lateral controller. *International Journal of Advanced Robotic Systems*, vol. 17, no. 6. DOI: 10.1177/1729881420974852.

[2] Bar-Shalom Y., Li X. R., Kirubarajan T. (2001). Estimation with Applications to Tracking and Navigation: Theory, Algorithms and Software. *John Wiley & Sons.* DOI: 10.1002/0471221279.

[3] Blom H. A. P., Bar-Shalom Y. (1988). The interacting multiple model algorithm for systems with Markovian switching coefficients. *IEEE Transactions on Automatic Control*, vol. 33, no. 8, pp. 780–783. DOI: 10.1109/9.1299.

[4] Durand-Petiteville A., Le Flecher E., Cadenat V., Sentenac T., Vougioukas S. (2018). Tree detection with low-cost three-dimensional sensors for autonomous navigation in orchards. *IEEE Robotics and Automation Letters*, vol. 3, no. 4, pp. 3876–3883. DOI: 10.1109/LRA.2018.2857005.

[5] Fei Z., Vougioukas S. (2022). Row-sensing templates: A generic 3D sensor-based approach to robot localization with respect to orchard row centerlines. *Journal of Field Robotics*, vol. 39, pp. 712–738. DOI: 10.1002/rob.22072.

[6] Gao P., Jiang J., Song J., Xie F., Bai Y., Fu Y., Wang Z., Zheng X., Xie S., Li B. (2021). Fruit Tree Model Reconstruction Method for Robotic Canopy Volume Measurement in Orchards. *IEEE Access*, vol. 9, pp. 156246–156259. DOI: 10.1109/ACCESS.2021.3127566.

[7] Grewal M. S., Andrews A. P., Bartone C. G. (2020). Global Navigation Satellite Systems, *Inertial Navigation, and Integration. 4th Edition. John Wiley & Sons.* DOI: 10.1002/9781119547860.

[8] Han X., Kim H. J., Jeon C. W., Yi S. Y., Moon H. C., Kim J. H. (2019). Application of a 3D tractor-driving simulator for slip estimation-based path-tracking control of auto-guided tillage operation. *Biosystems Engineering*, vol. 178, pp. 70–85. DOI: 10.1016/j.biosystemseng.2018.11.003.

[9] Jwo D. J., Chung F. C., Yu K. L. (2013). GPS/INS integration accuracy enhancement using the interacting multiple model nonlinear filters. *Journal of Applied Research and Technology*, vol. 11, no. 4, pp. 496–509. DOI: 10.1016/S1665-6423(13)71557-8.

[10] Kayacan E., Kayacan E., Ramon H., Saeys W. (2015). Towards agrobots: Identification of the yaw dynamics and trajectory tracking of an autonomous tractor. *Computers and Electronics in Agriculture*, vol. 115, pp. 78–87. DOI: 10.1016/j.compag.2015.05.012.

[11] Li X. R., Jilkov V. P. (2005). Survey of maneuvering target tracking. Part V: Multiple-model methods. *IEEE Transactions on Aerospace and Electronic Systems*, vol. 41, no. 4, pp. 1255–1321. DOI: 10.1109/TAES.2005.1561886.

[12] Li Y., Feng Q., Ji C., Sun J., Sun Y. (2024). GNSS and LiDAR integrated navigation method in orchards with intermittent GNSS dropout. *Applied Sciences*, vol. 14, no. 8, Article 3231. DOI: 10.3390/app14083231.

[13] Plessen M. M. G., Bemporad A. (2017). Reference trajectory planning under constraints and path tracking using linear time-varying model predictive control for agricultural machines. *Biosystems Engineering*, vol. 153, pp. 28–41. DOI: 10.1016/j.biosystemseng.2016.10.019.

[14] Shan T., Englot B. (2018). LeGO-LOAM: Lightweight and ground-optimized LiDAR odometry and mapping on variable terrain. Proceedings of the *2018 IEEE/RSJ International Conference on Intelligent Robots and Systems (IROS), Madrid, Spain*, pp. 4758–4765. DOI: 10.1109/IROS.2018.8594299.

[15] Thrun S., Montemerlo M., Dahlkamp H., Stavens D., Aron A., Diebel J., Fong P., Gale J., Halpenny M., Hoffmann G., Lau K., Oakley C., Palatucci M., Pratt V., Strohband S., Dupont C., Jendrossek L. E., Koelen C., Markey C., Rummel C., van Niekerk J., Jensen E., Alessandrini P., Bradski G., Davies B., Ettinger S., Kaehler A., Nefian A., Mahoney P. (2006). Stanley: The robot that won the DARPA Grand Challenge. *Journal of Field Robotics*, vol. 23, no. 9, pp. 661–692. DOI: 10.1002/rob.20147.

[16] Wang L., Zhai Z., Zhu Z., Mao E. (2022). Path tracking control of an autonomous tractor using improved Stanley controller optimized with multiple-population genetic algorithm. *Actuators*, vol. 11, no. 1, Article 22. DOI: 10.3390/act11010022.

[17] Wu J., Ma X., Peng T., Wang H. (2021). An improved timed elastic band (TEB) algorithm of autonomous ground vehicle (AGV) in complex environment. *Sensors*, vol. 21, no. 24, Article 8312. DOI: 10.3390/s21248312.

[18] Xu J., Lai J., Guo R., Lu X., Xu L. (2022). Efficiency-oriented MPC algorithm for path tracking in autonomous agricultural machinery. *Agronomy*, vol. 12, no. 7, Article 1662. DOI: 10.3390/agronomy12071662.

[19] Xue G., Li R., Zhang Z., Liu R. (2023). State-of-the-art and tendency of SLAM algorithms based on 3D LiDAR. *Information and Control*, vol. 52, no. 1, pp. 18–36. DOI: 10.13976/j.cnki.xk.2023.2254.

[20] Yang J., Chung S. J., Hutchinson S., Johnson D., Kise M. (2015). Omnidirectional-vision-based estimation for containment detection of a robotic mower. Proceedings of the *2015 IEEE International Conference on Robotics and Automation (ICRA)*, Seattle, USA, pp. 6344–6351. DOI: 10.1109/ICRA.2015.7140090.

[21] Yang L., Xu Y., Liang Y., Qin J., Li Y., Wang X., Zhai W., Wen L., Chen Z., Wu C. (2022). Extraction of straight field roads between farmlands based on agricultural vehicle-mounted LiDAR. *International Journal of Agricultural and Biological Engineering*, vol. 15, no. 5, pp. 155–162. DOI: 10.25165/j.ijabe.20221505.6933.

[22] Zhang X., Zhu T., Du L., Hu Y., Liu H. (2022). Local path planning of autonomous vehicle based on an improved heuristic Bi-RRT algorithm in dynamic obstacle avoidance environment. *Sensors*, vol. 22, no. 20, Article 7968. DOI: 10.3390/s22207968.

[23] Zhao X., Lu E., Tang Z., Luo C., Xu L., Wang H. (2024). Trajectory prediction method for agricultural tracked robots based on slip parameter estimation. *Computers and Electronics in Agriculture*, vol. 222, Article 109057. DOI: 10.1016/j.compag.2024.109057.

[24] Zhou K., Leck Jensen A., Sørensen C. G., Busato P., Bochtis D. D. (2014). Agricultural operations planning in fields with multiple obstacle areas. *Computers and Electronics in Agriculture*, vol. 109, pp. 12–22. DOI: 10.1016/j.compag.2014.08.013.

[25] Zhou Q., Zhang H., Li Y., Li Z. (2015). An adaptive low-cost GNSS/MEMS-IMU tightly-coupled integration system with aiding measurement in a GNSS signal-challenged environment. *Sensors*, vol. 15, no. 9, pp. 23953–23982. DOI: 10.3390/s150923953.

BGE-YOLOv11: A LIGHTWEIGHT MODEL FOR DETECTING MAIN STEM NODES IN SOYBEAN
/
基于大豆主茎节点检测的 BGE-YOLOv11 轻量化模型研究

Hao BI, Xiuying XU*)[1], Yiting LIU, Yanxu JIAO, Lingfeng ZHU

College of Engineering, Heilongjiang Bayi Agricultural University, Daqing/ China;
Tel: +86 13945925608; E-mail: xuxiuying@byau.edu.cn
Corresponding author: Xiuying Xu
DOI: https://doi.org/10.35633/inmateh-79-71

Keywords: *soybean main stem node detection; BGE-YOLOv11; lightweight model; deep learning*

ABSTRACT

The number of main stem nodes in soybean is an important phenotypic trait for evaluating plant growth, varietal characteristics, and breeding potential. However, automatically detecting soybean main stem nodes under field conditions remains challenging because of plant occlusion, variations in illumination, and complex backgrounds, while manual counting is inefficient for large-scale phenotypic data acquisition. Therefore, this study proposes BGE-YOLOv11, a lightweight model for detecting soybean main stem nodes in complex field environments. Using an image dataset of soybean main stem nodes collected under field conditions, the model was developed by integrating a bidirectional feature pyramid network (BiFPN), Global–Local Self-Attention (GLSA), and EfficientHead into the YOLOv11n baseline to enhance multiscale feature representation and detection performance. The proposed model was evaluated in terms of precision, recall, mean average precision at an intersection over union threshold of 0.5 (mAP50), and model complexity. BGE-YOLOv11 achieved a precision of 94.9%, recall of 92.9%, and mAP50 of 97.6%, representing improvements of 3.9, 4.0, and 3.0 percentage points, respectively, over the YOLOv11n baseline. Moreover, the model contained only 1.87 million parameters, required 5.6 GFLOPs, had a memory footprint of 8.0 MB, and achieved an inference time of 3.0 ms. These results demonstrate that BGE-YOLOv11 improves detection performance while retaining a lightweight architecture. Nevertheless, its performance may be affected by severe occlusion and highly variable field conditions. Future research will focus on expanding the dataset and further improving the model's generalization ability. This study provides an effective method for the automated counting of soybean main stem nodes and the analysis of phenotypic traits.

摘要

大豆主茎节点数量是反映植株生长状态、品种特征和育种潜力的重要表型性状。然而，在实际田间环境中，由于植株遮挡、光照变化以及复杂背景干扰等因素，大豆主茎节点的自动检测仍面临挑战，而人工计数方法难以满足大规模表型数据获取需求。针对复杂田间环境下大豆主茎节点快速检测问题，本文提出了一种轻量化 BGE-YOLOv11 检测模型。基于田间采集的大豆主茎节点图像数据集，在 YOLOv11n 基础模型上引入 BiFPN、全局局部自注意力（GLSA）模块和 EfficientHead 检测头，以增强多尺度特征表达能力并提升节点检测性能。采用 Precision、Recall、mAP50 以及模型复杂度指标对所提出模型进行综合评价。结果表明，BGE-YOLOv11 模型的 Precision、Recall 和 mAP50 分别达到 94.9%、92.9%和 97.6%，相比 YOLOv11n 分别提升 3.9、4.0 和 3.0 个百分点。同时，该模型参数量降低至 1.87 M，浮点计算量仅为 5.6 G，模型大小为 8.0 MB，推理时间为 3.0 ms。结果表明，BGE-YOLOv11 在提高检测性能的同时保持了良好的轻量化特性。然而，在极端遮挡和复杂多变田间环境下，模型性能仍可能受到一定影响。未来研究将进一步扩充数据集规模，提高模型泛化能力。本研究为大豆主茎节点自动计数和表型性状分析提供了一种有效方法。

INTRODUCTION

At present, China is actively developing soybean varieties with high yield, superior quality, and strong adaptability to mechanized production (*Qu et al., 2022*). Heilongjiang Province, one of China's major soybean-producing regions, primarily cultivates determinate soybean varieties.

[1] *Hao Bi, currently pursuing a master's degree; Yiting Liu, currently pursuing a master's degree; Yanxu Jiao, currently pursuing a master's degree; Lingfeng Zhu, currently pursuing a master's degree; Xiuying Xu, Associate Professor, Doctor of Engineering.*

During soybean breeding and variety evaluation, accurate acquisition of plant phenotypic traits is essential for characterizing varieties and selecting superior breeding materials. The number of main stem nodes is an important agronomic trait reflecting soybean plant architecture. It affects plant height, stem structure, lodging resistance, and pod spatial distribution, and is closely associated with yield formation. Therefore, it serves as an important indicator for evaluating soybean growth status and yield potential (*Qiu et al., 2006*). However, under field conditions, soybean main stem node detection is affected by inter-plant occlusion, illumination variations, and complex backgrounds, resulting in inefficient and labor-intensive manual measurements that cannot satisfy the requirements of large-scale phenotypic data acquisition in breeding programs (*Liu et al., 2026*). Therefore, computer vision-based automatic detection of soybean main stem nodes is of great significance for improving phenotyping efficiency. With the development of high-throughput plant phenotyping technologies, automated acquisition of crop structural parameters and genetic evaluation has provided new approaches for intelligent breeding (*Fiorani & Schurr, 2013*).

With the rapid development of computer vision and deep learning, image-based crop phenotyping has become an important research direction in intelligent breeding and has been widely applied in agricultural object detection, disease recognition, and phenotypic parameter extraction (*McCarthy & Raine, 2022; Kamilaris & Prenafeta-Bold´, 2018*). For soybean main stem node detection, several deep learning methods have been explored. *Zhu et al. (2020)* improved the Mask-RCNN-plus network for soybean main stem phenotyping and achieved pixel-level segmentation and node counting. However, this method requires extensive pixel-level annotation and has high training costs and slow inference speed. *Yang et al. (2026)* proposed a YOLOv8_obb-based rotated object detection method to address field occlusion, scale variation, and small-object detection problems. By incorporating attention mechanisms and multi-scale feature fusion, the method improved node localization and achieved an average precision of 89.45%. Nevertheless, its relatively large model size limits its application in resource-constrained computing environments.

Besides CNN-based approaches, Transformer-based detectors, multi-model fusion methods, and three-dimensional vision techniques have also been investigated for soybean phenotyping. *Sun et al. (2026)* proposed an RT-DETR-based Transformer detection model with wavelet feature enhancement, achieving an average precision of 91.10%. However, its high computational complexity requires substantial hardware resources. *Zhou et al. (2023)* developed an SPP-extractor framework by combining YOLOv5s and U²-Net for soybean phenotypic information extraction under dense planting conditions, but the cascaded multi-model structure increased system complexity and inference time. *Cui et al. (2025)* applied three-dimensional point cloud technology for non-destructive soybean node measurement; however, this method relies on specialized acquisition equipment, resulting in high cost and operational complexity, which limits its application in rapid field phenotyping.

To overcome these limitations, researchers have conducted extensive studies on YOLO-based agricultural object detection models by introducing attention mechanisms, multi-scale feature fusion strategies, and lightweight network architectures (*Guo et al., 2021; Zhang et al., 2024*). However, many high-performance detection models still suffer from large parameter sizes, high computational complexity, and strong hardware requirements, restricting their application in resource-limited environments. Lightweight methods, including lightweight network design (*Vijayakanthan et al., 2026*), model pruning (*Ahsaei et al., 2026*), and knowledge distillation (*Jisan et al., 2026*), can effectively reduce computational costs. Nevertheless, achieving a balance among detection accuracy, inference speed, and model complexity remains challenging in agricultural intelligent detection. YOLOv11 provides strong feature extraction capability and efficient inference performance, making it a suitable baseline for soybean main stem node detection under complex field conditions (*Khanam & Hussain, 2024*).

Based on the above analysis, this study proposes a lightweight soybean main stem node detection model, BGE-YOLOv11, based on YOLOv11n. To address small-object characteristics, complex background interference, and insufficient feature representation in field environments, BiFPN-based weighted bidirectional feature fusion is introduced to enhance multi-scale feature interaction. A Global-Local Self-Attention (GLSA) module is incorporated to strengthen node feature representation and suppress background noise. Furthermore, the original detection head is replaced with the EfficientHead lightweight detection head to reduce model complexity while maintaining detection performance. This study aims to develop a lightweight detection model that achieves a balance between accuracy and computational efficiency, providing technical support for automated soybean phenotyping, breeding material selection, and intelligent breeding applications.

MATERIALS AND METHODS

Dataset Acquisition

To construct a field soybean main stem node detection dataset at the maturity stage, field experiments were conducted at the Anda Agricultural Science and Technology Park of Heilongjiang Bayi Agricultural University, Anda City, Heilongjiang Province, China. The determinate soybean cultivar Qinnong 13 was selected and planted using a single-row ridge planting pattern.

During image acquisition, field conditions involved inter-plant occlusion, interference from basal branches and senescent leaves, and complex soil backgrounds, resulting in unclear boundaries of some main stem nodes and increased annotation difficulty. To improve annotation accuracy, a local background-assisted acquisition strategy was adopted. A dark background curtain was placed behind the plants while retaining the natural soil environment at the plant base, reducing background interference while preserving field plant characteristics.

Soybean images were captured at the maturity stage using a Sony A7M3 full-frame camera. Images were collected at a fixed distance using a fixed-scale imaging protocol to ensure consistency. A total of 680 soybean plant images were obtained, with an original resolution of 4000 × 6000 pixels. All images were stored in JPEG format for subsequent annotation and model training.

Dataset Construction and Preprocessing

The collected soybean plant images were manually annotated using LabelImg. The main stem node was defined as the target category with the class name “Node”. Bounding box information, including center coordinates (x, y), width, and height, was recorded, and annotation files were generated in XML format for model training.

To prevent potential data leakage caused by augmentation, the original dataset was randomly divided into training, validation, and test sets at a ratio of 8:1:1 before data augmentation. The training set contained 544 images, while the validation and test sets each contained 68 images. Data augmentation was applied only to the training set, including brightness adjustment, rotation, horizontal flipping, vertical flipping, Cutout, random cropping, and translation. After augmentation, the training set was expanded to 1,408 images, resulting in a final soybean main stem node detection dataset containing 1,544 images. The validation and test sets maintained the original data distribution and were used for model optimization and final performance evaluation, respectively. Examples of augmented images are shown in Fig. 1.



Fig. 1 – Data augmentation examples for soybean plant images

BGE-YOLOv11 Model

To improve the performance of YOLOv11 for mature soybean main stem node detection under field conditions, a lightweight detection model named BGE-YOLOv11 was proposed to address challenges including inter-plant occlusion, weak small-object feature representation, and model complexity. Based on YOLOv11n, the proposed model incorporates improvements in feature fusion, attention mechanism, and detection head design. Specifically, BiFPN, a Global-Local Self-Attention (GLSA) module, and an EfficientHead detection head were introduced to enhance multi-scale feature representation and reduce computational complexity while maintaining detection accuracy. The overall architecture of BGE-YOLOv11 is shown in Fig. 2.

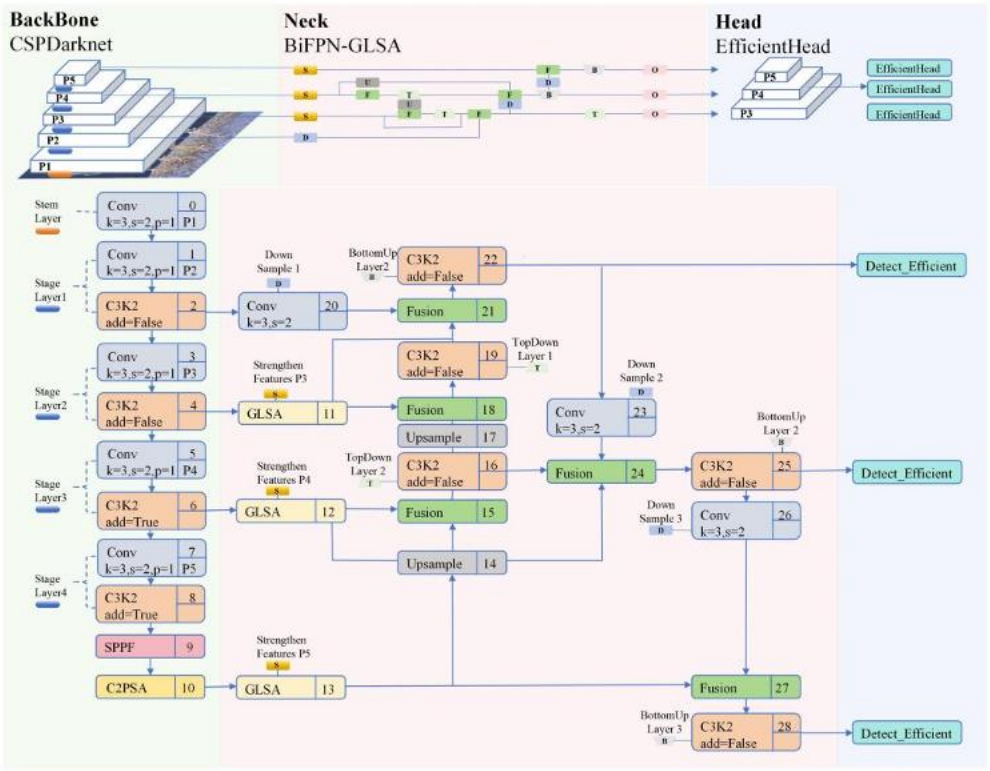


Fig. 2 – The improved BGE-YOLOv11 model structure

BiFPN Weighted Bidirectional Feature Pyramid Network

Inter-plant occlusion is a major challenge in mature soybean plants under field conditions, which may weaken multi-scale node features. The original PANet structure in YOLOv11 adopts a unidirectional feature aggregation strategy with fixed-weight feature fusion, limiting its ability to adaptively enhance occluded target features. This may result in insufficient cross-scale feature interaction and weak representation of small soybean main stem nodes.

To improve these limitations, a weighted bidirectional feature pyramid network (BiFPN) was introduced to replace the original PANet structure, forming an efficient multi-scale feature fusion module with enhanced occlusion robustness. The detailed architecture is shown in Fig. 3 (Doherty et al.,2025). By constructing bidirectional cross-scale connections and removing redundant feature nodes, BiFPN enables effective information exchange among different feature levels. Meanwhile, the learnable weighting mechanism adaptively adjusts the contribution of features from different scales, facilitating the fusion of high-level semantic information and low-level spatial details.

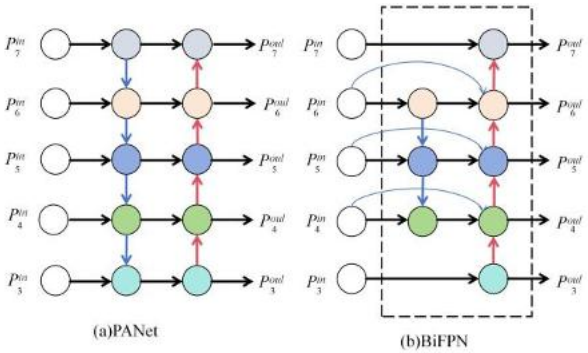


Fig. 3 – The network model structure diagram of PANet and BiFPN

During feature fusion, BiFPN adopts top-down and bottom-up pathways to achieve bidirectional information flow. Fast normalized weighted fusion is applied to reduce instability caused by feature weight differences. Compared with PANet, BiFPN improves multi-scale feature fusion quality with limited additional computational cost, thereby enhancing the feature representation of small and occluded soybean main stem nodes and improving detection performance under complex field conditions.

GLSA Global Local Self-Attention Module

Field-grown soybean plants often contain soil particles, senescent leaves, and scattered branches around the plant base, resulting in complex background interference. Meanwhile, the weak feature representation of small soybean main stem nodes makes accurate detection challenging. To enhance feature representation and suppress background noise while maintaining lightweight characteristics, a Global-Local Self-Attention (GLSA) module was embedded at the input of the neck feature pyramid.

Conventional convolutional neural networks have limited capability in modeling long-range dependencies and global contextual information, whereas standard self-attention mechanisms usually introduce high computational costs. Therefore, GLSA was adopted to improve global feature modeling capability under lightweight constraints (*Jia et al., 2026*). As shown in Fig. 4, GLSA employs a dual-branch parallel architecture. The local branch uses depthwise separable convolution to extract local detail features and preserve sensitivity to node edge and texture information. The global branch applies region-based self-attention to establish long-range dependencies among different regions with low computational overhead.

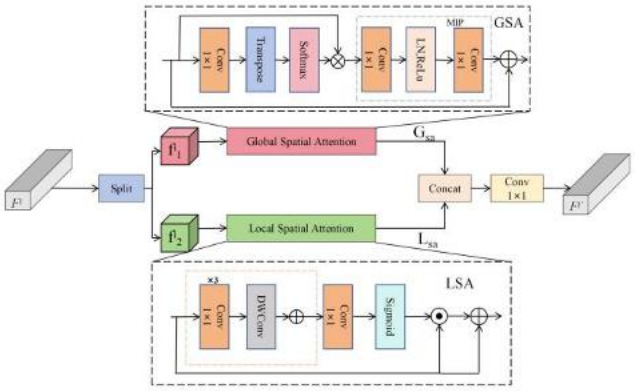


Fig. 4 – GLSA structure diagram

By embedding GLSA into the P3, P4, and P5 multi-scale feature layers before feature fusion, the model enhances target feature representation and reduces interference from complex field backgrounds. This design strengthens the feature responses of small soybean main stem nodes and provides more discriminative features for subsequent multi-scale feature fusion.

EfficientHead Lightweight Detection Head

The original YOLOv11 detection head has limited multi-scale feature alignment capability and inefficient channel information utilization, which may affect feature representation and localization performance. To improve detection performance while maintaining lightweight characteristics, an EfficientHead lightweight detection head was introduced to replace the original structure (Fig. 5) (*Jiang et al., 2025*).

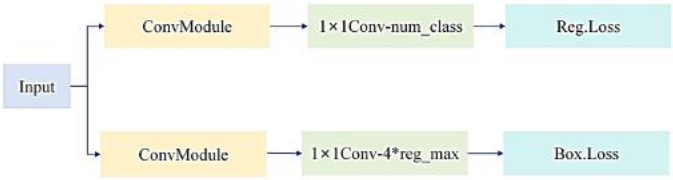


Fig. 5 – EfficientHead structure diagram

The proposed detection head integrates multi-scale feature alignment, lightweight channel attention, and dynamic localization decoding mechanisms. These designs enhance feature fusion, strengthen important soybean main stem node features, and suppress background interference. Without significantly increasing computational cost, EfficientHead improves the detection capability of weak-texture and occluded soybean main stem nodes while maintaining model lightweight characteristics.

Experimental Environment

The experiments were conducted using the PyTorch deep learning framework. The operating system was Windows 10, with an Intel® Core™ i7-14700HX CPU and an NVIDIA GeForce RTX 4060 Laptop GPU. The system was equipped with 16 GB of RAM and 8 GB of GPU memory. The software environment included Python 3.9, PyTorch 2.2.0, and CUDA 12.6. During model training, the input image size was set to 640 × 640 pixels, with a batch size of 16 and 200 training epochs.

The stochastic gradient descent (SGD) optimizer was adopted, with an initial learning rate of 0.01. Pre-trained weights were used for all models, and Mosaic augmentation was disabled during the final 10 epochs.

Model-Evaluation Index

For soybean main stem node detection, precision (P), recall (R), average precision (AP), mean average precision (mAP), and inference time were adopted to evaluate model performance. The corresponding calculation formulas are as follows:

$$P = \frac{TP}{TP+FP} \tag{1}$$

$$R = \frac{TP}{TP+FN} \tag{2}$$

$$AP = \sum_{i=1}^{N} P(i)\Delta R(i) \tag{3}$$

$$mAP = \frac{\sum_{i=1}^{k} AP_i}{k} \tag{4}$$

where TP, FP, and FN represent the numbers of true positive, false positive, and false negative detections of soybean main stem nodes, respectively. N denotes the number of samples, and k represents the number of categories.

To further evaluate the node counting performance of the proposed model, mean absolute error (MAE), root mean square error (RMSE), mean bias (Bias), and coefficient of determination (R^2) were introduced for quantitative analysis. The calculation formulas are as follows:

$$MAE = \frac{1}{N}\sum_{i=1}^{N} |y_i - \hat{y}_i| \tag{5}$$

$$RMSE = \sqrt{\frac{1}{N}\sum_{i=1}^{N} (y_i - \hat{y}_i)^2} \tag{6}$$

$$Bias = \frac{1}{N}\sum_{i=1}^{N} (\hat{y}_i - y_i) \tag{7}$$

$$R^2 = 1 - \frac{\sum_{i=1}^{N}(y_i - \hat{y}_i)^2}{\sum_{i=1}^{N}(y_i - \bar{y})^2} \tag{8}$$

where $y_i$represents the manually counted number of soybean main stem nodes, $\hat{y}_i$ denotes the number of nodes predicted by the model, and N represents the number of samples.

RESULTS AND ANALYSIS

Comparison of Detection Performance of Basic Detection Network

To validate the effectiveness of BGE-YOLOv11, it was compared with representative object detection models, including YOLOv5n, YOLOv6n, YOLOv7n, YOLOv8n, YOLOv9t, YOLOv10n, YOLOv11n, YOLOv12n, and RT-DETR-L. All models were trained and tested on the same soybean main stem node dataset. FLOPs, number of parameters, precision (P), recall (R), average precision (AP), memory footprint, and inference time were selected as evaluation metrics. The results are shown in Table 1.

Table 1

Comparison of different object detection models for soybean main stem node detection

Model	FLOPs [G]	Params [M]	P [%]	R [%]	mAP50 [%]	Memory footprint [MB]	Inference time [ms]
YOLOv5n	5.8	2.18	90.80	88.70	94.30	9.1	1.4
YOLOv6n	11.5	4.15	90.30	88.20	94.00	16.9	1.5
YOLOv8n	6.8	2.68	90.90	89.20	94.60	11.1	2.3
YOLOv9t	6.4	1.73	90.50	89.00	94.30	7.8	3.5
YOLOv10n	6.5	2.26	91.70	87.50	94.30	11.3	2.5

Model	FLOPs [G]	Params [M]	P [%]	R [%]	mAP50 [%]	Memory footprint [MB]	Inference time [ms]
YOLOv11n	6.3	2.58	91.00	88.90	94.60	10.7	2.7
YOLOv12n	7.80	2.50	91.30	88.10	94.30	10.6	3.7
RTDETR-L	100.6	28.44	87.00	84.10	89.20	117.8	16.3
BGE-YOLOv11	5.6	1.87	94.90	92.90	97.60	8.0	3.0

As shown in Table 1, BGE-YOLOv11 achieved a precision of 94.9%, a recall of 92.9%, and an mAP50 of 97.6%, providing superior detection performance among the compared models. In terms of lightweight characteristics, BGE-YOLOv11 required only 5.6 G FLOPs, 1.87 M parameters, and 8.0 MB memory footprint. Meanwhile, its inference time was lower than YOLOv9t, YOLOv10n, YOLOv12n, and RT-DETR-L.

Compared with the baseline YOLOv11n, BGE-YOLOv11 improved precision, recall, and mAP50 by 3.9, 4.0, and 3.0 percentage points, respectively, while reducing FLOPs by 0.7 G and parameters by 0.71 M. These results demonstrate that BGE-YOLOv11 achieves an effective balance between detection accuracy and model lightweight characteristics.

Ablation Test

An ablation study was conducted to evaluate the contribution of each improvement module to the YOLOv11n-based soybean main stem node detection model. Based on the constructed soybean main stem node dataset, different model variants were compared to verify the effectiveness of each module. The results are shown in Table 2.

Table 2

Ablation test results

Model	BiFPN	GLSA	EfficientHead	FLOPs[G]	Params[M]	P[%]	R[%]	mAP50[%]	Memory footprint [MB]	Inference time[ms]
YOLOv11n	-	-	-	6.3	2.58	91.00	88.90	94.60	10.7	2.7
B-YOLOv11	✓	-	-	6.3	1.92	92.00	89.20	95.10	8.1	2.1
G-YOLOv11	-	✓	-	8.6	3.73	91.80	90.40	95.50	15.5	3.1
E-YOLOv11	-	-	✓	5.1	2.31	92.20	89.90	95.60	9.6	2.0
BG-YOLOv11	✓	✓	-	6.7	2.07	91.30	90.10	95.20	8.8	2.8
BE-YOLOv11	✓	-	✓	5.2	1.73	91.80	89.90	95.10	7.3	2.3
GE-YOLOv11	-	✓	✓	7.4	3.48	91.50	89.00	94.60	14.4	3.2
BGE-YOLOv11	✓	✓	✓	5.6	1.87	94.90	92.90	97.60	8.0	3.0

Note: ✓ indicates that the module is used; - indicates that the module is not used.

To investigate the contribution of each module in BGE-YOLOv11, BiFPN, GLSA, and EfficientHead were individually incorporated into the YOLOv11n baseline model. The ablation results are shown in Table 2.

The single-module experiments indicate that all three modules improved model performance to different degrees. After introducing BiFPN, the mAP50 increased to 95.10%, while the parameters decreased from 2.58 M to 1.92 M, demonstrating improved feature fusion capability with reduced model complexity. The integration of GLSA increased recall and mAP50 by 1.5 and 0.9 percentage points, respectively, indicating enhanced feature representation under complex field backgrounds. With EfficientHead, the mAP50 increased to 95.60%, while FLOPs and inference time decreased to 5.1 G and 2.0 ms, respectively, showing that this module effectively reduces computational cost while maintaining detection accuracy.

When all three modules were combined, BGE-YOLOv11 achieved the best overall performance. Compared with YOLOv11n, BGE-YOLOv11 improved precision, recall, and mAP50 by 3.9, 4.0, and 3.0 percentage points, reaching 94.90%, 92.90%, and 97.60%, respectively. Meanwhile, the parameters were reduced from 2.58 M to 1.87 M, FLOPs decreased from 6.3 G to 5.6 G, and memory footprint decreased from 10.7 MB to 8.0 MB, with only a 0.3 ms increase in inference time. These results demonstrate that BGE-YOLOv11 enhances detection accuracy while reducing model complexity, achieving an effective balance between detection performance and lightweight characteristics.

Model Recognition Results

Based on the model comparison results, YOLOv8n, YOLOv11n, YOLOv12n, and the proposed BGE-YOLOv11 were selected for soybean main stem node detection experiments. Quantitative performance evaluation and visual comparison experiments were conducted to further analyze the detection capability of different models. Three representative field scenarios were considered, including fully visible soybean plants, interference from senescent leaves and branches near the plant base, and inter-plant occlusion. The samples used for both visualization analysis and quantitative node counting evaluation were collected from field experiments. All models were evaluated using the same detection settings, with a confidence threshold of 0.5 and an IoU matching threshold of 0.45.

Quantitative Performance Statistical Test

To further evaluate the soybean main stem node counting capability of the proposed model under practical field conditions, an independent node counting validation dataset was constructed. The dataset contained 44 field-collected images, including 108 soybean plants and 1,384 main stem nodes. The node numbers were manually counted and recorded as ground truth for comparison with model predictions. This dataset was not involved in model training and was only used to assess the node recognition and counting performance under field conditions.

It should be noted that the Precision, Recall, and mAP50 values in Table 1 were calculated from the model test set and used to evaluate overall object detection performance. In contrast, the evaluation metrics in Table 3 were obtained from the independent field counting validation dataset and were used to assess the practical node counting capability of the models. Since these two evaluations represent different tasks and experimental scenarios, their results should not be directly compared.

Table 3

Quantitative evaluation of soybean main stem node counting performance

Model	TP	FN	FP	Total Ground-Truth Nodes	Detection Success Rate	Miss Rate	False Alarm Rate
BGE-YOLOv11	1333	51	149	1384	96.32%	3.69%	10.05%
YOLOv11n	1312	72	171	1384	94.80%	5.20%	11.52%
YOLOv8n	1312	72	166	1384	94.80%	5.20%	11.22%
YOLOv12n	1297	87	136	1384	93.71%	6.29%	9.50%

Note: TP, FN, and FP represent correctly detected, missed, and falsely detected nodes, respectively. Total ground-truth nodes = TP + FN. Detection success rate = TP/(TP+FN), miss rate = FN/(TP+FN), and false alarm rate = FP/(TP+FP).

As shown in Table 3, BGE-YOLOv11 achieved superior performance in soybean main stem node counting. The proposed model correctly detected 1,333 nodes, with a detection success rate of 96.32% and a miss rate of 3.69%. Compared with YOLOv11n, YOLOv8n, and YOLOv12n, BGE-YOLOv11 increased the number of correctly detected nodes by 21, 21, and 36, respectively, while improving the detection success rate by 1.52, 1.52, and 2.61 percentage points and reducing the miss rate by 1.51, 1.51, and 2.60 percentage points.

Regarding false detection control, BGE-YOLOv11 achieved a false alarm rate of 10.05%, which was lower than YOLOv11n and YOLOv8n but slightly higher than YOLOv12n. This result indicates that the proposed model improves feature extraction and node recognition under complex field conditions, achieving a better balance between detection accuracy and false detection control.

Visualization Effect Comparison Test

To further evaluate the detection performance of the proposed model under complex field conditions, the results under different scenarios were visualized and compared, as shown in Fig. 6. Green bounding boxes indicate correctly detected targets, blue bounding boxes represent missed targets, and red bounding boxes denote false detections.

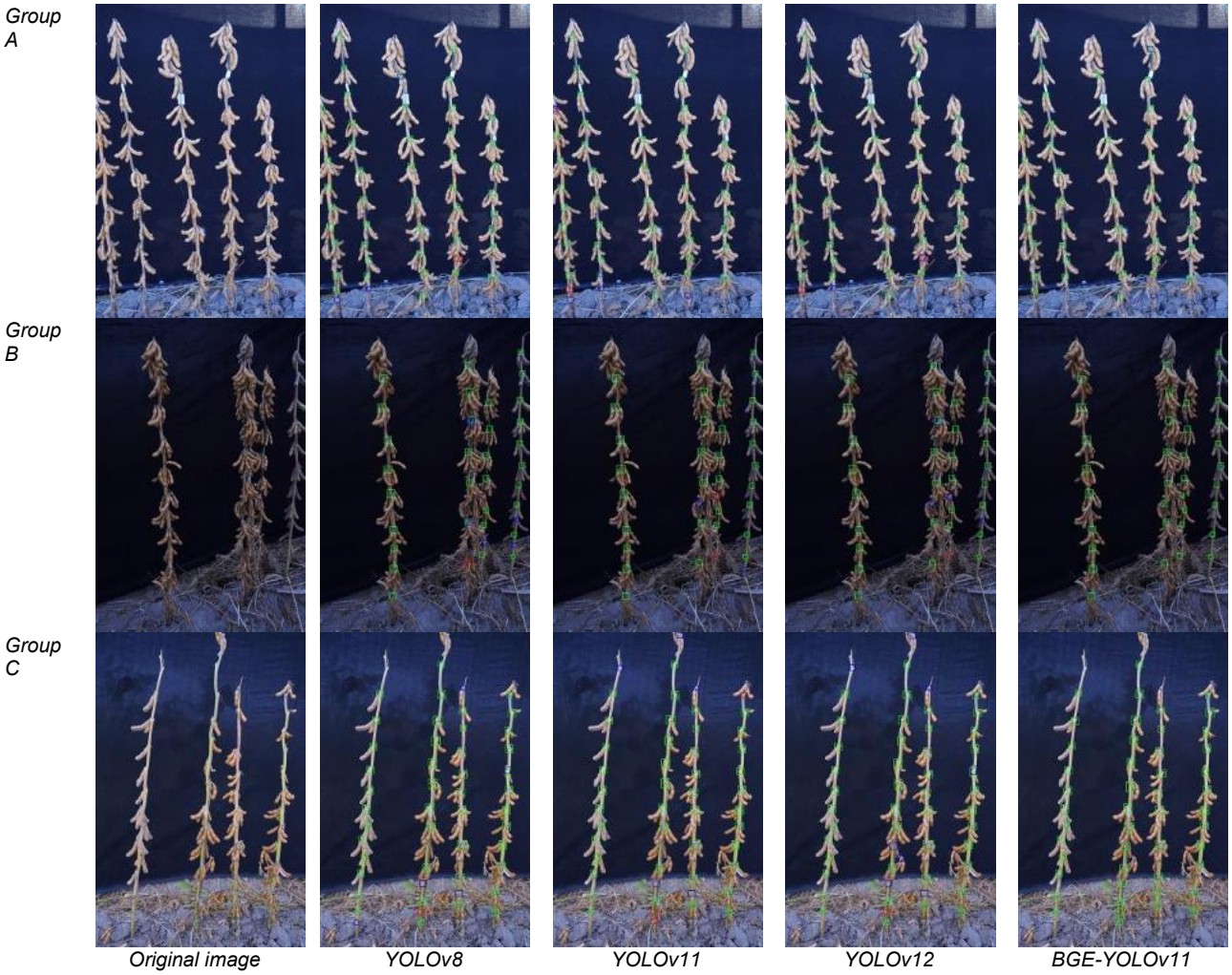
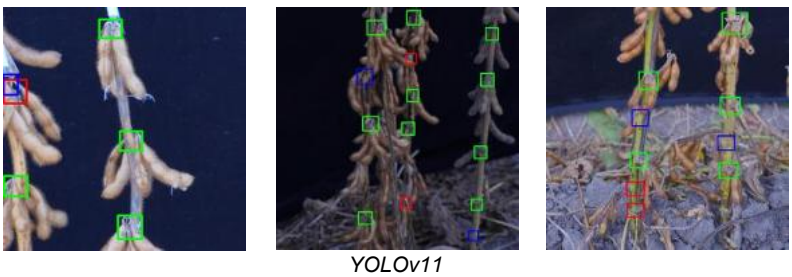


Fig. 6–Comparison of detection effects of four network models

As shown in Fig. 6, in Group A, YOLOv11n produced missed and false detections when soybean main stem nodes were located near image boundaries. YOLOv8n and YOLOv12n showed two or more detection errors, whereas BGE-YOLOv11 generated only one false detection at the basal stem region, demonstrating better boundary localization capability.

Under the severe occlusion conditions in Group B, BGE-YOLOv11 maintained relatively stable detection performance despite strong inter-plant overlap. However, missed detections still occurred in areas with densely distributed pods, while the baseline models exhibited more missed and false detections. In Group C, complex background interference from senescent leaves and scattered branches affected detection performance. Nevertheless, BGE-YOLOv11 achieved more reliable detection results, whereas the baseline models showed obvious false and missed detections.

Furthermore, BGE-YOLOv11 generally produced higher confidence scores than the baseline models, indicating improved feature extraction capability and more reliable node detection. Figure 7 shows enlarged views of the false and missed detection regions in Fig. 6. Compared with YOLOv11n, BGE-YOLOv11 improves node feature representation through enhanced feature extraction and multi-scale feature fusion, reducing missed detections under complex field conditions and achieving a better balance between detection accuracy and false detection control.



YOLOv11



BGE-YOLOv11

Fig. 7 – Partial detection results of partial amplification schematic diagram

Prediction Error Evaluation of Soybean Main Stem Node Number

To further evaluate the soybean main stem node counting capability of the proposed model under field conditions, an independent dataset containing 44 field-collected images was used for node number estimation experiments. This dataset was not involved in model training or parameter optimization. The manually counted node numbers were used as ground truth, and MAE, RMSE, Bias, and R^2 were adopted to evaluate the estimation performance of YOLOv11n and BGE-YOLOv11. The results are presented in Table 4.

Table 4

Comparison of soybean main stem node number estimation performance among different models

Model	MAE	RMSE	Bias	R^2
BGE-YOLOv11	2.09	2.82	-0.86	0.96343
YOLOv11n	3.07	3.71	-2.57	0.93895

As shown in Table 4, BGE-YOLOv11 achieved better performance in soybean main stem node number estimation. Compared with YOLOv11n, BGE-YOLOv11 reduced MAE and RMSE by 0.98 and 0.89, respectively, and its Bias value was closer to zero, indicating lower estimation error and higher prediction stability. Meanwhile, the R^2 value of BGE-YOLOv11 increased from 0.93895 to 0.96343, demonstrating a stronger agreement between the estimated node numbers and the manually counted ground-truth values.

CONCLUSIONS

In this study, YOLOv11n was selected as the baseline model. By introducing the BiFPN module to enhance multi-scale feature fusion, incorporating the GLSA global-local self-attention module to improve small-object feature representation, and adopting the EfficientHead lightweight detection head to reduce computational cost, a lightweight BGE-YOLOv11 model was developed for soybean main stem node detection and counting. Experimental results demonstrated that the proposed model achieved an mAP50 of 97.6% under complex field conditions, with only 1.87 M parameters and an inference time of 3.0 ms. It improved detection accuracy while maintaining favorable lightweight characteristics, providing technical support for the automated acquisition of soybean phenotypic information.

Currently, this study mainly focuses on main stem node detection in mature soybean plants. In future work, the proposed method will be further extended to other phenotypic parameters, such as stem diameter and plant height, as well as different growth stages. Moreover, correlation models between phenotypic traits and yield-related characteristics will be established to provide data support for precision breeding.

ACKNOWLEDGEMENT

This work was supported by the Doctoral Research Startup Fund Project of Heilongjiang Bayi Agricultural University [grant number XDB202501].

REFERENCES

[1] Ahsaei, S., Raji, M., & Ghavami, B. (2026). RAP: A reliability-aware pruning framework for deep neural networks. *Journal of Systems Architecture, 176*, 103829. https://doi.org/10.1016/j.sysarc.2026.103829

[2] Cui, D. H. (2025). *Research on extraction methods of mature soybean plant phenotypic parameters based on point cloud data* [Master's thesis, Northeast Agricultural University]. https://doi.org/10.27010/d.cnki.gdbnu.2025.000329

[3] Doherty, J., Gardiner, B., Kerr, E., & Siddique, N. (2025). BiFPN-YOLO: One-stage object detection integrating bi-Directional feature pyramid networks. *Pattern Recognition, 160*, 111209. https://doi.org/10.1016/j.patcog.2024.111209

[4] Fiorani, F., & Schurr, U. (2013). Future scenarios for plant phenotyping. *Annual Review of Plant Biology, 64*, 267–291. https://doi.org/10.1146/annurev-arplant-050312-120137

[5] Guo, R., Yu, C. Y., He, H., Zhao, Y. J., Yu, H., & Feng, X. Z. (2021). Detection method for pod number of single soybean plant using improved YOLOv4 algorithm. *Transactions of the Chinese Society of Agricultural Engineering, 37*(18), 179–187.

[6] Jia, B., Wang, X. C., Shi, Y. Y., Zhang, X. L., Xu, Z., Wang, J. H., Yang, H. H., & Qian, D. W. (2026). Efficient and lightweight model for detecting juvenile fish feeding behavior using feed pellet key point analysis. *Computers and Electronics in Agriculture, 240*, 111141. https://doi.org/10.1016/j.compag.2025.111141

[7] Jiang, T. T., Li, L., Zhang, Z., Yu, X., Zhu, Y. Q., Li, L. M., Liu, Y. D., Bai, Y. L., Tang, Z. Q., Liu, S. B., Zhang, Y., Duan, Z., Yin, D. M., & Jin, X. L. (2026). YOLO-light-pruned: A lightweight model for monitoring maize seedling count and leaf age using near-ground and UAV RGB images. *Artificial Intelligence in Agriculture, 16*, 164–186. https://doi.org/10.1016/j.aiia.2025.10.002

[8] Jisan, M. K., Hoque, K. E., Azhar, T., & Newton, M. H. (2026). Rice leaf disease classification using resource-efficient deep learning models via response-based knowledge distillation. *Applied Soft Computing, 199*, 115356. https://doi.org/10.1016/j.asoc.2026.115356

[9] Kamilaris, A., & Prenafeta-Bold˙ , F.X. (2018). Deep learning in agriculture: A survey. *Computers and Electronics in Agriculture, 147*, 70–90. https://doi.org/10.1016/j.compag.2018.02.016

[10] Khanam, R., & Hussain, M. (2024). YOLOv11: An overview of the key architectural enhancements. *arXiv*. https://doi.org/10.48550/arXiv.2410.17725

[11] Liu, F., Wu, Q., Han, Z., Zhao, L., Pang, S., & Wang, S. (2026). Automatic stem phenotyping in soybean using keypoint detection. *Engineering Applications of Artificial Intelligence, 165*, 113300. https://doi.org/10.1016/j.engappai.2025.113300

[12] McCarthy, A., & Raine, S. (2022). Automated variety trial plot growth and flowering detection for maize and soybean using machine vision. *Computers and Electronics in Agriculture, 194*, 106727. https://doi.org/10.1016/j.compag.2022.106727

[13] Qiu, L. J., Chang, R. Z., Wang, K. J., Wang, X. M., Guan, R. X., Li, Y. H., Yang, T., Zhang, B., Zhao, L. M., Hao, C. Y., Yuan, C. P., Guo, Y., & Dong, Y. S. (2006). *Descriptors and data standard for soybean germplasm resources*. China Agriculture Press.

[14] Qu, H. L., Jiang, Z., Li, J., & Zhao, L. (2022). Development status of global soybean industry and suggestions for China's soybean industry development. *Soybean Science & Technology*, (5), 28–33, 39.

[15] Sun, L. Q., Zhang, Q. Y., He, Y. H., Guo, K., Yang, C., Su, W. H., & Tian, Z. X. (2026). Multi-phenotype measurement and yield prediction of soybean plants based on RT-DETR. *Transactions of the Chinese Society of Agricultural Engineering, 42*(3), 192–200.

[16] Vijayakanthan, G., Nasser, M., Algbear, A. F., Alosaimi, H. M., Ibrahim, A. O., & Ravi, V. (2026). Explainable and lightweight deep learning models for tea leaf disease detection: A systematic review. *Smart Agricultural Technology, 14*, 102042. https://doi.org/10.1016/j.atech.2026.102042

[17] Yang, Y. X., Li, J. Y., Shi, W. Q., Qi, L. Q., & Zhang, W. (2026). Research on soybean main stem node recognition based on improved YOLOv8-obb. *Journal of Chinese Agricultural Mechanization, 47*(1), 79–86. https://doi.org/10.13733/j.jcam.issn.2095-5553.2026.01.012

[18] Zhang, Q.Y., Fan, K. J., Tian, Z., Guo, K., & Su, W. H. (2024). High-precision automated soybean phenotypic feature extraction based on deep learning and computer vision. *Plants, 13*(18), 2613.

[19] Zhou, W., Chen, Y. J., Li, W. H., Zhang, C., Xiong, Y. J., Zhan, W., Huang, L., Wang, J., & Qiu, L. J. (2023). SPP-extractor: Automatic phenotype extraction for densely grown soybean plants. *The Crop Journal, 11*(5), 1569–1578.

[20] Zhu, R. S., Li, S., Yan, X. H., Yan, Z. Z., Yu, J. L., Shi, J., Su, X. Y., Cao, Y. Y., Xin, D. W., Li, Y., Jiang, H. W., Zhao, Z. Q., Zhang, Z. G., & Chen, Q. S. (2020). Automatic precise acquisition of soybean main stem phenotypes based on semantic segmentation and its application in introgression line selection. *Chinese Journal of Oil Crop Sciences, 42*(1), 61–70. https://doi.org/10.19802/j.issn.1007-9084.2020028

DISCRETE ELEMENT MODELING AND PARAMETER CALIBRATION OF THE WHEAT ROOT–SOIL COMPOSITE
/
小麦根土复合体离散元模型建立与标定试验

Chengcheng GUO[1)], Zhiping YANG*[1)], Junchang ZHANG[2)], Huiyan YIN[1)], Cui LI[1)]
[1)]College of Agricultural Machinery and Automotive Engineering, Gansu Polytechnic College of Animal Husbandry & Engineering, Wuwei 733006/ China;
[2)]College of Mechanical and Electronic Engineering, Northwest A&F University, Yangling 712100/ China;
Tel: +86 18729219567; E-mail: 1091257144@qq.com

DOI: https://doi.org/10.35633/inmateh-79-72

Keywords: *root-soil composite, conservation tillage, discrete element method, shear test, parameter calibration*

ABSTRACT

Due to the anisotropy and small size of wheat roots, as well as the neglect of shear process effects on mechanical properties in existing wheat root-soil composite (WRSC) models, the establishment and parameter calibration of WRSC models remain inaccurate, hindering the precise analysis of the microscopic effects of furrow openers on WRSC during no-till sowing. This study aimed to develop an accurate and reliable WRSC model based on the discrete element method (DEM) using rapid particle filling and the Hertz-Mindlin with bonding contact model. Plackett-Burman tests identified particle shear modulus, inter-particle bonding radius, and bonding stiffness as significant factors affecting the ultimate shear force of wheat roots. Steepest ascent tests narrowed the optimal parameter ranges, and Box-Behnken test results were used to establish a quadratic regression model, leading to the optimal parameter combination: particle shear modulus of 7.96 MPa, inter-particle bonding stiffness of 4.13 GN/m³, and bonding radius of 0.32 mm. Actual and simulated shear tests on WRSC were conducted, and key parameters between wheat roots and soil particles were calibrated via steepest ascent tests with the ultimate shear force on the cutter as the target value: static friction coefficient of 0.8, bonding stiffness of 11 MN/m³, and critical stress of 11 MPa. Validation showed a relative error of 7.35% between simulated and actual shear resistance, indicating that the proposed WRSC model and parameters can effectively simulate field operations such as furrowing and rotary tillage.

摘要

针对玉米免耕播种时前茬小麦根系与开沟器相互作用过程分析复杂，且小麦根系的各向异性和直径较小等特点，现有根土复合体模型忽略小麦根系对对剪切过程力学特性的影响导致标定参数不准确的问题，该研究基于离散元法采用颗粒快速填充和 Hertz-Mindlin with bonding 粘结模型建立了一种准确性和可靠性较高的小麦根-土复合体模型。基于 Hertz-Mindlin bonding 粘结模型，采用颗粒快速填充的方法，构建小麦根系模型。通过 Plackett-Burman 试验发现颗粒剪切模量和颗粒间粘结半径、粘结刚度对小麦根系极限剪力有显著影响。通过最陡爬坡试验确定显著性影响参数最优区间的基础上，根据 Box-Behnken 试验结果建立了根系极限剪力与显著性影响参数的二阶回归模型并对其进行优化，得到显著性参数的最佳组合为：颗粒剪切模量 7.96 MPa、颗粒间粘结刚度 4.13 GN/m3、粘结半径 0.32 mm。其次，采用最陡爬坡试验方法，标定了小麦根-土间的关键参数。以切刀受到的极限剪力为目标值，基于小麦根-土复合体进行实际剪切和仿真剪切试验结果，标定得到小麦根系与土壤颗粒间的静摩擦系数为 0.8、粘结刚度为 11 MN/m3、临界应力为 11 MPa。最后，验证标定后的根-土复合体模型，结果显示仿真剪切阻力与实际剪切阻力间相对误差为 7.35%，表明基于离散元法建立的小麦根-土复合体模型可以用于模拟田间实际土壤环境。

INTRODUCTION

Conservation tillage is an important agricultural technology for improving soil quality, conserving water and moisture, and enhancing economic benefits. As a key link in conservation tillage, no-till and reduced-till sowing imposes higher requirements on the performance of furrow openers.

In the double cropping area of Guanzhong, Shaanxi Province, corn no-till sowing is carried out immediately after wheat harvest. Undecomposed wheat roots in the soil are closely bonded with soil particles, significantly increasing the working resistance of furrow openers and intensifying soil disturbance.

Traditional soil bin tests fail to reflect the actual field operating environment due to the absence of root factors, while the discrete element method provides an effective means to simulate complex root-soil interactions.

Yang et al. (1996) first explicitly proposed the concept of "soil-root composite" in their study on herbaceous plant roots. Since roots are tightly attached to soil, they reinforce soil structure and improve water absorption capacity. The combination of crop roots and soil is termed the root-soil composite, and it is assumed to partially satisfy the Mohr-Coulomb law. Currently, experimental methods are mainly used to study the shear resistance of root-soil composites. However, numerous factors influence shear resistance, broadly categorized into soil-related and plant root-related factors *(Chen et al., 2026)*, each encompassing multiple sub-factors. Consequently, experimental studies on composite shear resistance are labor-intensive and time-consuming. The discrete element method is a numerical computation technique for analyzing complex dynamic discrete systems, with distinct advantages in agricultural machinery research. With advancements in computer hardware and DEM theory, numerical simulation has been increasingly applied to study root-soil interactions due to its higher efficiency, season independence, and low cost *(Ji et al., 2012; Yang et al., 2014; Ji et al., 2014; Tian et al., 2015)*. Yang et al. established a soil model using DEM and a rigid lettuce root model via SolidWorks. However, their pull-out simulations failed to account for root deformation and bending, leading to significant discrepancies between simulated and actual results. *Lenaerts et al. (2014)*, *Li et al. (2016)*, and *Gao et al. (2020)* respectively established slender straw models using DEM, but the minimum particle units employed prevented cutting and separation. *Li et al. (2020)* and *Liu et al. (2018)* successfully developed flexible corn and spinach root models capable of bending and fracture using the Hertz-Mindlin with bonding model and rapid particle filling. To date, no literature has been published on the establishment of a wheat root-soil composite DEM model. Wheat roots differ significantly from corn and spinach roots in diameter and mechanical properties, necessitating the development of a dedicated DEM model for wheat root-soil composites.

To address the aforementioned issues, this study determined the morphological dimensions of wheat root models by analyzing the actual growth state of wheat roots in post-harvest soil, and constructed a complete flexible wheat root model using EDEM. Parameters of wheat roots, soil, and their interactions were calibrated through comparative validation of actual and simulated tests, aiming to improve the accuracy of the wheat root-soil composite DEM model. This research provides a foundation and reference for the establishment of DEM models for wheat root-soil composites and similar agricultural materials.

MATERIALS AND METHODS

Physical Properties of Materials

Physical Parameters of Wheat Roots

Roots of the wheat cultivar "Xinong 511" were sampled from the experimental field of Northwest A&F University on June 2, 2025. The experimental field was regularly fertilized prior to planting, meeting standard cultivation conditions, with manual weeding performed during the growing period before harvest the following year. A wheat-growing area of 1.5 m × 1.3 m (6 rows) was selected for statistical counting. Field investigations revealed that wheat grows in clusters with an inter-cluster spacing of 30 mm (Fig. 1).



Fig. 1 - Wheat growth status

Five clusters of wheat roots were collected using the five-point sampling method (Fig. 2a). Each cluster contained an average of 20 roots, which were twisted into a knot with a radius of approximately 6 mm at the upper end. Roots were densely distributed in the upper soil layer and sparsely in the lower layer (*Liu, 2008*) (Fig. 2c). Under actual field conditions, wheat roots are tightly bonded to the soil, functioning to reinforce the soil structure. Wheat possesses a fibrous root system consisting of primary and secondary roots (Fig. 2b), with negligible differences in diameter and ultimate shear force between the two root types. Considering computational efficiency and simulation speed, primary and secondary roots were modeled as a single root type (*Guo, 2008*).



（a）Wheat root samples *（b）Morphological structure of wheat roots*

Fig. 2 - Wheat root system sample and morphological structure

Ten roots were randomly selected from each cluster to measure physical parameters. The average length, diameter, and mass of wheat roots were 87.2 mm, 0.31 mm, and 0.521 g, respectively, with a mass per unit length of 1.195×10^{-4} g/mm.

Due to the anisotropy and small diameter of wheat roots, constructing a DEM model capable of both bending and fracture is challenging, resulting in limited research in this area. Drawing on previous studies (Liu, 2018) and combining physical parameters of wheat roots, a wheat root model was established using rapid filling with particles of 0.15 mm in diameter. The Hertz-Mindlin with bonding contact model was selected for inter-particle interactions.

To calibrate the particle density for root model filling in DEM, the particle density was iteratively adjusted until the mass per unit length of the simulated root model matched that of actual roots, as described by Eq. (1). The calibrated particle density was 87.6 kg/m³.

$$\frac{m_R}{l_R} = \frac{m_r}{l_r} \quad (1)$$

where: m_R, m_r—mass of actual and simulated roots, g;

l_R, l_r—length of actual and simulated roots, mm.

Basic Physical Parameters of Soil

Soil samples were collected after wheat harvest, with an average bulk density of 1.41 g/cm³ and soil compaction of 2.88 MPa. To realistically simulate soil particle fracture and breakage, the Hertz-Mindlin with bonding contact model was adopted based on the soil type of the experimental field. Simulation time decreases geometrically with increasing soil particle radius. Referring to previous studies on soil-tool interactions, spherical soil particles with a radius of 8 mm were used (*Ucgul et al., 2017; Ding et al., 2017; Zheng et al., 2016*). Soil material and contact parameters were determined through experimental measurements and literature review (*Ding et al., 2018; Guo et al., 2017; Wang et al., 2017*), as presented in Table 1.

Table 1

Basic parameters of soil discrete element model

Parameter	Value
Soil density/(kg·m^{-3})	1410
Soil Poisson's ratio	0.4
Soil shear modulus/(Pa)	6×10^{7}
Inter-soil dynamic friction coefficient	0.4
Inter-soil static friction coefficient	0.34
Inter-soil restitution coefficient	0.6
Inter-soil bonding radius/(mm)	8.5
Inter-soil bonding stiffness/(N·m^{-3})	2.4×10^{6}
Inter-soil critical stress/(Pa)	235000

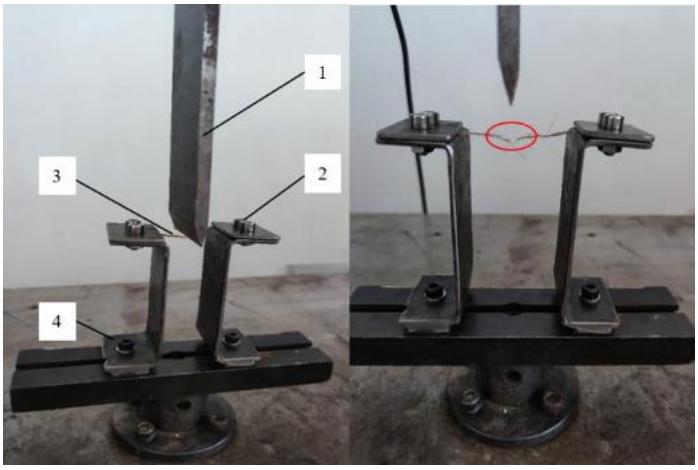
Establishment of Discrete Element Model and Parameter Calibration Method

Wheat Roots

Actual shear tests were conducted on wheat roots to measure the ultimate shear force at root breakage. A DEM model of wheat roots was then established for shear simulations, and the ultimate shear force of the simulated model was obtained. Full-level tests were performed on key model parameters using the actual root ultimate shear force as the target value to establish a response equation and calibrate the key parameters.

Actual Shear Test of Wheat Roots

Referring to relevant shear test standards (*Lenaerts et al., 2014; Yuan, 2019*), actual shear tests were conducted to measure the ultimate shear force of roots (Fig. 3a). To prevent root breakage and slippage at the clamping points during testing, custom fixtures were fabricated, and both ends of the roots were wrapped in 16 mm-thick sponges in their natural state. Twenty wheat roots with consistent length and diameter were sheared at a speed of 4 mm/s using a DDL10 universal testing machine. Sixteen samples where root breakage occurred at the midpoint were selected to ensure fracture was induced by the cutter rather than clamping forces. The average ultimate shear force at root breakage was 3.7 N, with the fracture position shown in Fig.3b.



（a）Shear test *（b）Root fracture*

Fig. 3 - Actual root shear test

1.Cutter; 2.Custom fixture; 3.Wheat root; 4.Base

Simulation Model and Parameters of Wheat Roots

A DEM model of wheat roots consistent with the actual shear test was constructed in EDEM (Fig. 4). Assuming no relative sliding between root-filling particles, both static and dynamic friction coefficients between root particles were set to 1. The geometric models of the fixture and cutter were made of 65Mn steel. Material and contact parameters of wheat roots and 65Mn were determined through literature review (*Boac et al., 2014; Pan, 2012*). The density, Poisson's ratio, and shear modulus of 65Mn were 7865 kg/m³, 0.3, and 7.9×10^{11} MPa, respectively.

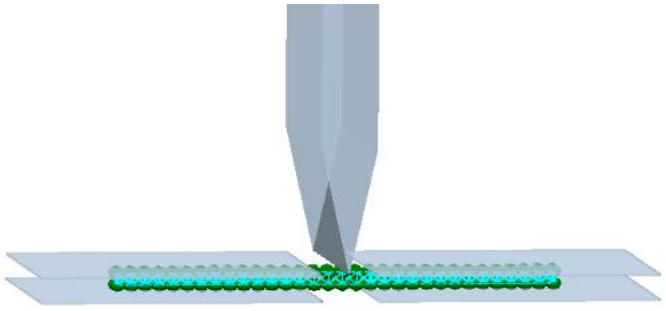


Fig. 4 - Shear simulation model

As determined earlier, the Hertz-Mindlin with bonding contact model was used for inter-particle interactions in wheat roots. Key parameters of this model include shear modulus, normal and tangential bonding stiffness, and bonding radius (*Ding et al., 2017; Zhang, 2012*). Since root-filling particles are randomly bonded, normal and tangential bonding parameters were set to be identical. Initial ranges of root particle model parameters were obtained through literature review and extensive shear simulation debugging, as listed in Table 2.

Table 2

Basic parameters of root model particles

Category	Simulation parameter	Value
Material parameters	Root density/(kg·m⁻³)	87.6
	Root Poisson's ratio	0.2-0.3a
	Root shear modulus/(MPa)	6-10a
Contact parameters	Root restitution coefficient	0.6-0.8a
	Root static friction coefficient	1
	Root dynamic friction coefficient	1
	Root-steel restitution coefficient	0.6-1a
	Root-steel static friction coefficient	0.35-0.6a
	Root-steel dynamic friction coefficient	0-0.02a
Bonding parameters	Bonding stiffness/(GN·m⁻³)	1-10a
	Critical stress/(MPa)	1-1.5a
	Bonding radius/(mm)	0.25-0.5a

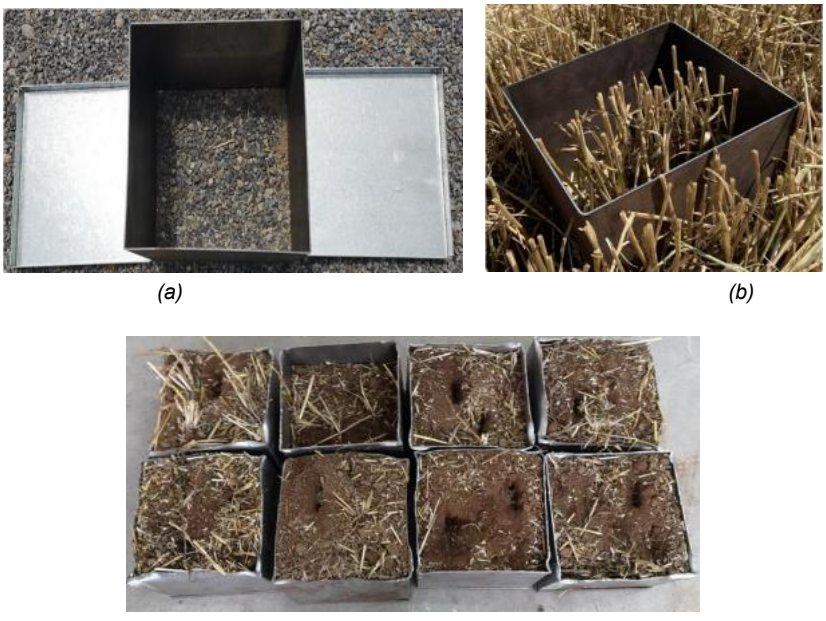
Note: "a" indicates parameters to be screened.

Parameter Calibration Method for Wheat Root-Soil Complex Based on Ultimate Shear Force

Ultimate shear force is a key reference characteristic for calibrating WRSC models (*Yuan et al., 2020*). To obtain accurate contact and bonding parameters at the wheat root-soil interface, actual shear tests on WRSC were conducted following relevant literature methods (*Mak et al., 2012; Jiang et al., 2018; Zhao et al., 2019; Zheng et al., 2017*) to measure the ultimate shear force. Shear simulations of the WRSC model were then performed, and key parameters such as static and dynamic friction coefficients, bonding stiffness, and critical stress of the Hertz-Mindlin with bonding contact model at the root-soil interface were calibrated using the steepest ascent method.

Sampling of Wheat Root-Soil Complex

On the day after wheat harvest, areas with uniform soil conditions were selected in the middle of the field. Taking the center of wheat stubble as the sampling point, WRSC samples were collected using an uncovered iron box of 250 mm × 250 mm × 200 mm (Fig. 5a). The sampling process involved slowly driving the iron box into the soil with a hammer, excavating the soil around the box, and removing the box together with the WRSC. Sampling was repeated 8 times (Fig. 5b). To exclude the influence of stubble during modeling, above-ground stubble was cut off, retaining only the underlying wheat roots. The collected WRSC samples are shown in Fig. 5c. During storage and transportation, samples were wrapped in sponges to prevent fragmentation due to vibration.



(a) *(b)*

(c)

Fig. 5 - Root-soil complex field sampling (b) with iron box (a) and the sample (c)

Sampling of Wheat Root-Soil Complex

Shear tests on WRSC samples were conducted using a universal testing machine in the mechanical laboratory (Fig. 6) to measure the ultimate shear force when the cutter sheared the midpoint of wheat roots. To prevent cutter deviation during shearing, the shear speed was set to 2 mm/s (*Liu, 2018*). Each shear test was repeated 8 times, and the average ultimate shear force was 445 N.

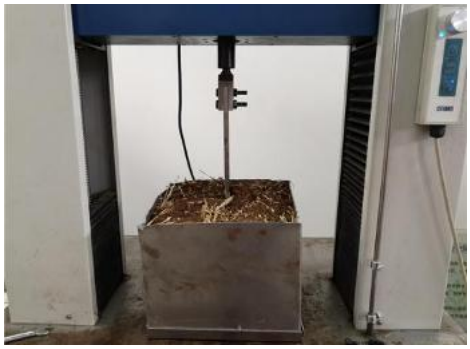


Fig. 6 - Shear test of root-soil complex

Previous studies by *Liu (2018)* and *Sun (2011)* indicated that friction and bonding forces between roots and soil are key factors contributing to the increased ultimate shear force of the complex. The Hertz-Mindlin with bonding contact model was therefore adopted for root-soil interactions. To reduce the number of parameters to be calibrated, the restitution coefficient and bonding stiffness at the root-soil interface were set to 0.6 and 1×10^{7} N/m³, respectively, based on literature review (*Asaf et al., 2007; Zheng et al., 2016*). The bonding radius between wheat roots and soil was determined to be 4 mm through DEM simulation debugging.

RESULTS AND DISCUSSION

Calibration Test Results and Analysis of Wheat Roots

As shown in Table 2, 9 parameters need to be determined for wheat root shear simulations. However, the influence of each parameter on root shear resistance varies (*Liu et al., 2016*). To screen parameters with significant effects on the ultimate shear force of the root model, Plackett-Burman test design was performed using Design-Expert software. Significance analysis of the 9 undetermined parameters was conducted through root shear simulation tests. Each parameter was set at two levels (high and low), encoded as +1 and -1, respectively. According to Plackett-Burman test design requirements, 3 sets of zero-level tests were included, resulting in a total of 15 shear simulation tests with different parameter combinations. The shear speed was set to 4 mm/s. Test parameters, levels, and simulation results are presented in Tables 3 and 4, respectively.

Table 3

Placket-Burman test parameter list

Parameter	Parameter No.	Parameter level	
		Low level (-1)	High level (+1)
Root Poisson's ratio	X1	0.2	0.3
Root shear modulus/(MPa)	X2	6	10
Root restitution coefficient	X3	0.6	0.8
Root-steel restitution coefficient	X4	0.6	1
Root-steel static friction coefficient	X5	0.35	0.6
Root-steel dynamic friction coefficient	X6	0	0.02
Bonding stiffness/(GN·m^{-3})	X7	1	10
Critical stress/(MPa)	X8	1	1.5
Bonding radius/(mm)	X9	0.25	0.5

Table 4

Placket-Burman experimental design and results

No.	X_1	X_2	X_3	X_4	X_5	X_6	X_7	X_8	X_9	Ultimate shear force/(N)
1	0	0	0	0	0	0	0	0	0	4.956
2	1	1	1	-1	-1	-1	-1	-1	1	7.165
3	1	1	-1	1	1	1	-1	-1	-1	1.403
4	-1	1	1	1	-1	-1	-1	1	-1	1.347
5	-1	-1	-1	1	-1	1	1	-1	1	4.273
6	1	-1	1	1	1	-1	-1	-1	1	4.085
7	0	0	0	0	0	0	0	0	0	4.956
8	-1	-1	1	-1	1	1	-1	1	1	4.119

No.	X_1	X_2	X_3	X_4	X_5	X_6	X_7	X_8	X_9	Ultimate shear force/(N)
9	-1	1	-1	1	1	-1	1	1	1	9.069
10	0	0	0	0	0	0	0	0	0	4.956
11	1	-1	1	1	-1	1	1	1	-1	3.491
12	-1	-1	-1	-1	-1	-1	-1	-1	-1	1.362
13	1	1	-1	-1	-1	1	-1	1	1	3.795
14	1	-1		-1	1	-1	1	1	-1	2.889
15	-1	1	1	-1	1	1	1	-1	-1	2.888

Analysis of variance (ANOVA) of simulation results was performed using Design-Expert software, and the effects of each parameter on ultimate shear force are presented in Table 5. Bonding radius, bonding stiffness, and root shear modulus were found to have significant effects on ultimate shear force, while other parameters had minimal impacts. Therefore, only these three parameters were considered in subsequent steepest ascent and screening tests.

Table 5

Placket-Burman significance analysis of test parameters

Parameter	Parameter No.	Effect	Sum of squares	Influence rate/%	Significance ranking
Root Poisson's ratio	X1	-0.038	4.408×10-3	6.090×10-3	9
Root shear modulus/(MPa)	X2	0.91	2.47	4.07	3
Root restitution coefficient	X3	0.051	2.95	0.011	8
Root-steel restitution coefficient	X4	0.24	0.18	0.24	7
Root-steel static friction coefficient	X5	0.50	0.76	1.05	6
Root-steel dynamic friction coefficient	X6	-0.99	7.701×10-3	3.42	4
Bonding stiffness/(GN·m^{-3})	X7	2.28	15.56	21.49	2
Critical stress/(MPa)	X8	0.59	1.04	1.44	5
Bonding radius/(mm)	X9	3.19	30.48	42.11	1

To further narrow the ranges of root shear modulus (G), bonding stiffness (K), and bonding radius (Rb), steepest ascent tests were conducted. Subsequently, Box-Behnken tests were performed to establish a response equation through regression analysis of these three parameters. Taking the actual root ultimate shear force as the target value, the optimal values of G, K, and Rb were obtained using Design-Expert software. The factor levels and simulation results of the steepest ascent tests are presented in Table 6.

Table 6

Steepest climbing test and results

No.	Shear modulus G (X_2)/(MPa)	Bonding stiffness K (X_7)/(GN·m^{-3})	Bonding radius Rb (X_9)/(mm)	Ultimate shear force F_R/(N)	Relative error/%
1	6	2	0.25	1.86	49.73
2	7	4	0.3	3.34	9.73
3	8	6	0.35	4.48	21.08
4	9	8	0.4	5.21	41.81
5	10	10	0.45	7.27	96.49

As shown in Table 6, relatively small relative errors were observed at levels 2 and 3. These levels were therefore selected as the low (-1) and high (+1) levels for Box-Behnken tests. The factor levels, test design, and results are presented in Tables 7 and 8, respectively. Quadratic polynomial ANOVA of simulation results was performed using Design-Expert software.

Table7

Box-Behnken test factor level table

Factor	Level		
	Low (-1)	Medium (0)	High (+1)
Shear modulus/(MPa)	7	7.5	8
Bonding stiffness/(GN·m^{-3})	4	5	6
Bonding radius/(mm)	0.3	0.325	0.35

Table 8

Steepest climbing test and results

No.	Shear modulus/(MPa)	Bonding stiffness/(GN·m⁻³)	Bonding radius/(mm)	Ultimate shear force F_R/(N)
1	7.5	5	0.325	3.55
2	7.5	6	0.35	4.36
3	7.5	4	0.3	3.42
4	7	5	0.3	3.18
5	8	6	0.325	3.56
6	7	4	0.325	3.64
7	7.5	5	0.325	3.55
8	8	5	0.35	4.02
9	8	4	0.325	3.82
10	7	5	0.35	3.92
11	8	5	0.3	3.25
12	7.5	5	0.325	3.55
13	7.5	5	0.325	3.55
14	7.5	5	0.325	3.55
15	7.5	4	0.35	4.74
16	7.5	6	0.3	3.05
17	7	6	0.325	3.94

Non-significant terms were eliminated to optimize the regression model while ensuring model significance and non-significant lack of fit. The ANOVA results of the optimized model are presented in Table 9.

Table 9

The Box-Behnken results of quadratic polynomial variance analysis after experimental optimization

Source of variation	Sum of squares	Degrees of freedom	Mean square	P-value
Model	3.36	6	0.49	< 0.0001**
Shear modulus G	0.090	1	0.090	0.0196*
Bonding stiffness K	0.078	1	0.078	0.0269*
Bonding radius Rb	2.83	1	2.83	< 0.0001**
G×Rb	0.16	1	0.16	0.0047**
K²	0.062	1	0.062	0.0433*
Rb²	0.14	1	0.14	0.0071**
Residual	0.10	9	0.011	
Lack of fit	0.10	5	0.020	
Pure error	0.000	4	0.000	
Total	3.50	16		

Fit statistics: R^2=0.9711; Adjusted R^2=0.9486; Coefficient of variation (CV)=2.85%; Adequate precision=21.786

Note: ** indicates extremely significant difference ($P < 0.01$); * indicates significant difference ($P < 0.05$).

As shown in Table 9, bonding radius (Rb), the interaction term of shear modulus and bonding radius (G×Rb), and the quadratic term of bonding radius (Rb^2) had extremely significant effects on the ultimate shear force of wheat roots. Shear modulus (G), bonding stiffness (K), and the quadratic term of bonding stiffness (K^2) had significant effects. The model exhibited high significance ($P < 0.01$), good reliability (CV=2.85%), excellent fit (R^2=0.9711, Adjusted R^2=0.9486 > 0.8), and high precision (adequate precision=21.786). The optimized regression equation is as follows:

$$F_R = 3.58 - 0.11 \times G + 0.60 \times R_b - 0.14 \times G \times K - 0.20 \times G \times R_b + 0.12 \times K^2 + 0.18 \times R_b^2 \quad (2)$$

To minimize the difference between simulated and actual ultimate shear forces of wheat roots, parameter optimization was performed using the optimization module of Design-Expert software. The optimal values were determined as follows: shear modulus of 7.96 MPa, bonding stiffness of 4.13 GN/m³, and bonding radius of 0.32 mm. Three repeated simulations were conducted with these optimal parameters, yielding ultimate shear forces of 3.725 N, 3.72 N, and 3.74 N, with relative errors of 0.68%, 0.54%, and 1.08%, respectively. The small relative errors indicate that the calibrated wheat root model exhibits shear resistance consistent with actual roots and can be used as a substitute for mechanical simulations.

Calibration Results and Analysis of Wheat Root-Soil Complex Parameters Based on Ultimate Shear Force

Establishment of the WRSC DEM model requires determining parameters such as static and rolling friction coefficients at the root-soil interface, as well as bonding stiffness, bonding stress, and bonding radius of the Hertz-Mindlin with bonding contact model. Based on the actual ultimate shear force of the WRSC, shear simulations of the WRSC model were performed to calibrate these key parameters (Fig. 7). The shear speed in simulations was consistent with that in actual tests. Referring to relevant literature (Lenaerts et al., 2014; Liu, 2018), the dynamic friction coefficient was set to 0.3. The effective ranges of the static friction coefficient, particle bonding stiffness, and particle bonding stress at the root-soil interface were determined as 0.3~0.9, 1~13 MN/m³, and 1~13 MPa, respectively.

Steepest ascent tests were conducted within the determined parameter ranges to simulate shear of the WRSC model. The factor levels and simulation results are presented in Table 10. At test No. 6, the shear resistance was 453 N with a relative error of 1.80% (< 5%). Thus, the calibrated parameters at the wheat root-soil interface were determined as follows: static friction coefficient of 0.8, bonding stiffness of 11 MN/m³, and critical stress of 11 MPa.

Table 10

Horizontal design of the steepest climbing test factors and shear simulation results

No.	Static friction coefficient f_{r-s}	Bonding stiffness τ_{r-s}/(MN·m^{-3})	Critical stress σ_{r-s}/(MPa)	Shear resistance/(N)	Relative error/%
1	0.3	1	1	322	27.64
2	0.4	3	3	346	22.25
3	0.5	5	5	361	18.88
4	0.6	7	7	383	13.93
5	0.7	9	9	410	7.87
6	0.8	11	11	453	1.80
7	0.9	13	13	506	13.71

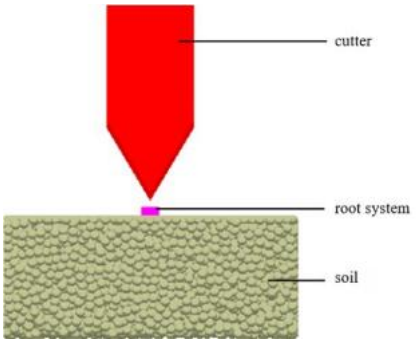


Fig. 7 - Shear simulation of root-soil complex

The calibrated static friction coefficient, bonding stiffness, and critical stress at the wheat root-soil interface were reconfigured in EDEM. Shear tests on the WRSC were then performed at the midpoint of wheat roots, and the cutter resistance-vertical displacement curve was exported after simulation (Fig. 8). The simulated shear resistance curve was found to be in good agreement with the actual curve. Within the depth range of 30-100 mm, the relative error between simulated and actual shear resistance was 7.32%, indicating that the calibrated WRSC DEM model can accurately simulate actual field soil conditions.

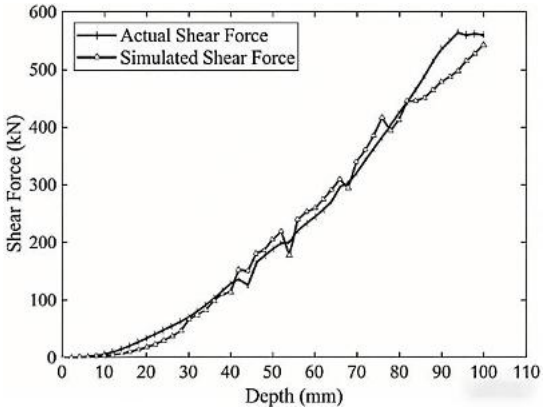


Fig. 8 - After parameter calibration, simulation and test cutter resistance-displacement curve

CONCLUSIONS

(1) A wheat root model was constructed using rapid particle filling and the Hertz-Mindlin with bonding contact model. Through Plackett-Burman screening tests and steepest ascent tests, inter-particle bonding radius, bonding stiffness, and particle shear modulus were identified as the significant parameters affecting the ultimate shear force of wheat roots. Using Box-Behnken design with ultimate shear force as the target value, the optimal parameters were calibrated as follows: root shear modulus of 7.96 MPa, inter-particle bonding stiffness of 4.13 GN/m³, and bonding radius of 0.32 mm.

(2) Actual and simulated shear tests were conducted on the WRSC. With the ultimate shear force on the cutter as the target value, key parameters at the root-soil interface were calibrated: static friction coefficient of 0.8, bonding stiffness of 11 MN/m³, and critical stress of 11 MPa.

(3) Validation of the WRSC model showed a relative error of 7.35% between the ultimate shear force of the calibrated model and the actual value, indicating that the DEM-based WRSC model can be used to simulate actual field soil environments.

REFERENCES

[1] Barr, J., Desbiolles, J., Ucgul, M., Fielke, J.M., (2020). Bentleg furrow opener performance analysis using the discrete element method. *Biosystems Engineering, Vol.* 189, pp. 99-115, United States.

[2] Barr, J.B., Desbiolles, J.M.A., Fielke, J.M., (2016). Minimising soil disturbance and reaction forces for high speed sowing using bentleg furrow openers. *Biosystems Engineering*, Vol. 151, pp. 53-64, USA.

[3] Chen, Y., Munkholm, L.J., Nyord, T., (2013). A discrete element model for soil–sweep interaction in three different soils. *Soil and Tillage Research*, Vol. 126, pp. 34-41, Netherlands.

[4] Chen W.Q., (2026). Analysis Of The Operational Performance Of Straw Baler Pickup Device Based On Edem And Adams. *INMATEH Agriculture Engineering*, Vol. 78, No. 1, Romania.

[5] Ding, S., Bai, L., Yao, Y., Yue, B., Fu, Z., Zheng, Z., Huang, Y., (2018). Discrete element modelling (DEM) of fertilizer dual-banding with adjustable rates. *Computers and Electronics in Agriculture*, Vol. 152, pp. 32-39, Netherlands.

[6] Hang, C., Gao, X., Yuan, M., Huang, Y., Zhu, R., (2018). Discrete element simulations and experiments of soil disturbance as affected by the tine spacing of subsoiler. *Biosystems Engineering*, Vol. 168, pp. 73-82, United States.

[7] Li, S.B., Huan, X.L., Wang, T.Y., (2024). Biomechanical properties and discrete element modeling of PSR stalks during silage harvest. *Computers and Electronics in Agriculture*, Vol.217: 108644, Netherlands.

[8] Solhjou, A., Desbiolles, J.M.A., Fielke, J.M., (2013). Soil translocation by narrow openers with various blade face geometries. *Biosystems Engineering*, Vol.114, pp. 259-266, United States.

[9] Solhjou, A., Fielke, J.M., Desbiolles, J.M.A., (2012). Soil translocation by narrow openers with various rake angles. *Biosystems Engineering*, Vol. 112, pp. 65-73, United States.

[10] Solhjou, A., Fielke, J.M., Desbiolles, J.M.A., Saunders, C., (2014). Soil translocation by narrow openers with various bent leg geometries. *Biosystems Engineering*, Vol. 127, pp. 41-49, United States.

[11] Tanaka, H., Momozu, M., Oida, A., Yamazaki, M., (2000). Simulation of soil deformation and resistance at bar penetration by the Distinct Element Method. *Journal of Terramechanics*, Vol. 37, pp. 41-56, UK.

[12] Ucgul, M., Fielke, J.M., Saunders, C., (2014). 3D DEM tillage simulation: Validation of a hysteretic spring (plastic) contact model for a sweep tool operating in a cohesionless soil. *Soil and Tillage Research*, Vol. 144, pp. 220-227, Netherlands.

[13] Yang, L., Wu,P, Zuo, Z.,(2024). E Roots: a three-dimensional dynamic growth model of rice roots coupled with soil. *Biosystems Engineering*, Vol. 244, pp. 122-133, United States.

[14] Cao, X.D., (2018). Structural optimization and experimental study of core share furrow opener (芯铧式开沟器结构优化及试验研究). *Northwest A&F University*, Yangling/China.

[15] Fang, H.M., Ji, C.Y., Chandio, F.A., Guo, J., Zhang, Q.Y., Arslan, C., (2016a). Discrete element method analysis of soil movement behavior during rotary tillage (基于离散元法的旋耕过程土壤运动行为分析). *Transactions of the Chinese Society for Agricultural Machinery*, Vol. 47, pp. 22-28, Beijing/China.

[16] Fang, H.M., Ji, C.Y., Tagar, A.A., Zhang, Q.Y., Guo, J., (2016b). Simulation analysis of straw displacement in straw-soil-rotary blade system (秸秆-土壤-旋耕刀系统中秸秆位移仿真分析). *Transactions of the Chinese Society for Agricultural Machinery*, Vol. 47, pp. 60-67 (in Chinese with English abstract).

[17] He, J., Li, H.W., Chen, H.T., Lu, C.Y., Wang, Q.J., (2018). Research progress on conservation tillage technologies and implements (保护性耕作技术与机具研究进展). *Transactions of the Chinese Society for Agricultural Machinery*, Vol. 49, pp. 1-19, Beijing/China.

[18] Huang, Y.X., Hang, C.G., Yuan, M.C., Wang, B.T., Zhu, R.X., (2016). Discrete element simulation and experiment of subsoiling soil disturbance behavior (深松土壤扰动行为的离散元仿真与试验). *Transactions of the Chinese Society for Agricultural Machinery*, Vol. 47, pp. 80-88, Beijing/China.

[19] Jia, H.L., Zheng, J.X., Yuan, H.F., Guo, M.Z., Wang, W.J., Jiang, X.M., (2017). Design and experiment of profiling sliding knife furrow opener (仿形滑刀式开沟器设计与试验). *Transactions of the Chinese Society of Agricultural Engineering*, Vol. 33, pp. 16-24, Beijing/China.

[20] Li, G.H., (2018). Structural design and experimental study of cross-slot furrow opener (十字槽开沟器结构设计及试验研究). *Northwest A&F University*, Yangling/China.

[21] Wang, X.Z., Yue, B., Gao, X.J., Zheng, Z.Q., Zhu, R.X., Huang, Y.X., (2018). Simulation and experiment of soil disturbance behavior with different wing shovel installation heights of subsoiler (深松铲不同翼铲安装高度时土壤扰动行为仿真与试验). *Transactions of the Chinese Society for Agricultural Machinery*, Vol. 49, pp. 124-136, Beijing/China.

[22] Yang, Y.L., (2015). Experimental study of core share furrow opener based on discrete element method (基于离散元法的芯铧式开沟器试验研究). *Jilin Agricultural University*, Changchun/China.

[23] Yu, J.Q., Qian, L.B., Yu, W.J., Pan, S.Q., Fang, Y., Fu, H., (2009). Discrete element method simulation analysis of furrow opener working resistance (开沟器工作阻力的离散元法仿真分析). *Transactions of the Chinese Society for Agricultural Machinery*, Vol. 40, pp. 53-57, Beijing/China.

[24] Zhai, L.X., Ji, C.Y., (2008). Establishment of soil mechanical contact model based on discrete element method (基于离散单元法的土壤力学接触模型的建立). *Jiangxi Agricultural Journal*, Vol. 20, pp. 108-111, Jiangxi/China.

[25] Zhang, J.C., Yan, X.L., Li, G.H., Cao, X.D., Liu, N., Sun, L.W., Tong, M., (2019). Design of cross-slot furrow opener for separate application of seed and fertilizer and stratified fertilization (十字槽种肥分施及分层施肥开沟器设计). *Journal of Agricultural Mechanization Research*, Vol. 41, pp. 86-90, Heilongjiang/China.

[26] Zhang, J.C., Yan, X.L., Lin, Z.K., Zhu, R.X., (2016). Design and experiment of self-excited vibration subsoiling and land preparation machine (自激式振动深松整地机设计与试验). *Transactions of the Chinese Society for Agricultural Machinery*, Vol. 47, pp. 44-49+72, Beijing/China.

[27] Zhao, S.H., Liu, H.J., Tan, H.W., Cao, X.Z., Zhang, X.M., Yang, Y.Q., (2017). Design and performance test of furrow opener imitating sailfish head curve (仿旗鱼头部曲线型开沟器设计与性能试验). *Transactions of the Chinese Society of Agricultural Engineering*, Vol. 33, pp. 32-39, Beijing/China.

STUDY OF THE MOTION STABILITY AND OPERATIONAL SMOOTHNESS OF AN AGRICULTURAL ROBOTIC PLATFORM

/

ԳՅՈՒՂԱՏՆՏԵՍԱԿԱՆ ՆՇԱՆԱԿՈՒԹՅԱՆ ՌՈԲՈՏ-ՀԱՐԹԱԿԻ ՇԱՐԺՄԱՆ ԿԱՅՈՒՆՈՒԹՅԱՆ ԵՎ ԸՆԹԱՑՔԻ ՍԱՀՈՒՆՈՒԹՅԱՆ ՈՒՍՈՒՄՆԱՍԻՐՈՒԹՅՈՒՆ

Arshaluys TARVERDYAN[1)], Aghavard KHACHATRYAN[2)], Artur ALTUNYAN[1*)], Sergey PAPYAN[1)], Albert GRIGORYAN[1)]

[1)]Scientific Research Institute for Agricultural Mechanization and Automation, Armenian National Agrarian University, Yerevan, Armenia

[2)]Chair of Higher Mathematics and Physics, Armenian National Agrarian University, Yerevan, Armenia

Tel: +37455327325; E-mail: arturaltunyan@gmail.com

Corresponding author: Artur Altunyan

DOI: https://doi.org/10.35633/inmateh-79-73

Keywords: *movement smoothness, oscillation characteristics, robotic platform, stability on slopes, vehicle stability*

ABSTRACT

This study focuses on the development of a multifunctional agricultural robotic platform. Previous articles in this series established the need for such a platform based on the specific soil and climatic conditions of the Republic of Armenia. Tests of a laboratory prototype indicated the need for further investigation of the platform's dynamic behavior, particularly during operation in orchards and agricultural fields on sloping terrain, which is common in Armenia. Particular attention was given to changes in platform inclination during turning maneuvers on slopes and to the yaw moment generated about the vertical axis in four-wheeled robotic platforms with independently controlled wheels. Based on a mathematical model of the chassis incorporating elastic elements (springs) and damping elements (shock absorbers), the differential equation governing the motion of the platform's center of mass was formulated, together with moment equations about the transverse and longitudinal axes passing through the center of mass. Analysis of these equations yielded the differential equations governing the platform's vertical oscillations. Expressions were subsequently derived for the displacement, velocity, acceleration, and jerk associated with the platform's free oscillations. These equations can be used to evaluate ride smoothness and determine the spring stiffness and shock-absorber damping coefficient required to achieve the desired suspension performance.

ԱՄՓՈՓԱԳԻՐ

Ներկայացվող հոդվածը նվիրված է գյուղատնտեսական բազմաֆունկցիոնալ ռոբոտ-հարթակի մշակման խնդրին: Շարքի նախորդ հոդվածներում հիմնավորվել է այդպիսի ռոբոտ-հարթակի մշակման անհրաժեշտությունը ելնելով հանրապետության հողակլիմայական պայմանների առանձնահատկություններից: Մշակվող ռոբոտ-հարթակի լաբորատոր փորձանմուշի փորձարկումները ցույց տվեցին, որ անհրաժեշտ է իրականացնել լրացուցիչ հետազոտություններ, որոնք հնարավորություն կտան բացահայտելու ռոբոտ-հարթակի շարժման դինամիկան հատկապես թեքություններում տեղակայված այգիներում ու դաշտերում, որոնք բնութագրական են Հայաստանի Հանրապետության հողատեսքերի համար: Հաշվի են առնվել թեքություններում շրջադարձի ընթացքում տեղի ունեցող թեքության անկյան տրանսֆորմացիան, և որ չափազանց կարևոր է, միայն քառանիվ, իրարից անկախ կառավարվող անիվներով ռոբոտ-հարթակներին ներհատուկ, ուղղաձիգ առանցքի շուրջ առաջացող պտտող մոմենտը, որը էական ազդեցություն է թողնում կայունության վրա: Ընթացքային մասի, առաձգական էլեմենտ (զսպանակ) և մարիչ (ամորտիզատոր) պարունակող հաշվարկային սխեմայի համար կազմվել են ռոբոտ-հարթակի մասսաների կենտրոնի շարժման դիֆերենցիալ հավասարումը, ծանրության կենտրոնով անցնող լայնական ու երկայնական սիմետրիայի առանցքների նկատմամբ մոմենտների հավասարումները, դրանց վերլուծության արդյունքում ստացվել են հարթակի ուղղաձիգ տատանումների դիֆերենցիալ հավասարումները: Արդյունքում ստացվել են հարթակի սեփական տատանումների ընթացքում առաջացող տեղափոխությունների, արագությունների, արագացումների և արագացումների փոփոխության որոշման հավասարումները, որոնք հնարավորություն են տալիս գնահատելու ընթացքի սահունությունը և որոշելու դրա ապահովման համար անահրաժեշտ կախոցի համակարգի զսպանակի անհրաժեշտ կոշտությունն ու ամորտիզատորի դիմադրության գործակիցը:

INTRODUCTION

In all countries ensuring food security has always been, and remains, one of the most pressing challenges facing agricultural production. The solving of this problem must involve the conservation and improvement of land resources, meeting environmental requirements, increasing production volumes, the production of environmentally friendly food products, full mechanization of agricultural production, and, particularly importantly, reducing of the energy intensity of these processes. It is evident that the stated problem is multidimensional, and its complete solution using existing technologies and technical means is objectively limited (*Abrosimov and Raykov, 2022; Bak and Jakobsen, 2004; Fontani et al., 2025; O'Meara, 2019; Ritchie, 2024*).

For this reason, two key trends have recently become central to agricultural production technological processes (*Abrosimov and Raykov, 2022; Markets and Markets, 2025; Navone et al., 2025; Tarverdyan et al., 2025*).

First, one of the fastest growing areas in recent years in agricultural production is precision and digital technologies in crop and livestock production.

Second, the direction without which it is impossible to effectively utilize and implement the information obtained through the above-mentioned technologies is the organization of robot-assisted agricultural production. This implies that the development and large-scale implementation of robotics play a central role in addressing the stated problem (*Abrosimov and Raykov, 2022; Navone et al., 2025; O'Meara, 2019; Ritchie, H., 2024)*.

Although the global agricultural robotics market is developing at an unprecedented rate (over the last five years alone, its volume has increased approximately 20-fold) (*Bak and Jakobsen, 2004; MarketsandMarkets, 2025*), the application of such systems in the agricultural sector of the Republic of Armenia remains highly limited. This is primarily due to their relatively high market price, making them inaccessible to the majority of local producers, and second, to their structural characteristics, which result in low operational reliability under the soil conditions of the Republic of Armenia (*Tarverdyan et al., 2025*).

It follows that the problem can be addressed through two approaches: either partial structural modifications should be made to existing robots, or a new universal robotic platform should be developed that is better adapted to the country's soil conditions (presence of stones of various sizes, fragmented terrain) and, importantly, is cost-effective.

For all mobile agricultural robots, the mobile platform is a critical component that plays a key role in the overall system performance of the system. It is therefore not surprising that researchers in this field have devoted significant efforts to the development of high-performance mobile platforms for agricultural robots, as well as to improving their control and positioning accuracy, since these issues are of crucial importance in precision agriculture (*Amin et al., 2025; Bayar et al., 2015; Lipiński et al., 2016; Qiu et al., 2018; Zagazezheva and Berbekova, 2021*).

The operational practice of agricultural robotic platforms over the last 20–25 years, as well as the results of numerous research studies, lead to a clear conclusion: from the perspective of accurate perception and response to external influences during agro-technological processes, minimal energy consumption, minimal soil damage, and high maneuverability, four-wheeled robotic platforms are preferred (*Akimov, 2017; Blasco et al., 2002; Cho et al., 2002*).

In addition, four-wheeled robotic platforms with independently controlled wheels provide high maneuverability and enable parallel motion of the vehicle during turning, allowing positional accuracy and orientation accuracy to be controlled independently (*Bak and Jakobsen, 2004; Cho et al., 2002; Orebäck and Christensen, 2003; Tarverdyan et al., 2025*).

Research on robotic platforms is primarily driven by the shortcomings and challenges identified during their operation. Current studies place significant emphasis on optimal control, stability, and ensuring smooth motion. In this regard, the studies conducted by a group of researchers are of particular interest *(Blasco et al., 2002; Fountas et al., 2020; Zakaria et al., 2024*), in which the authors demonstrate that integrated control systems (ICS)—such as combined steering and wheel torque control, suspension and wheel torque coordination, as well as the integration of steering control systems with suspension—provide superior performance characteristics for multi-axle mobile devices (Multi-axle Vehicles, MAV) compared with skid-steering control systems (SCS). In this optimal distribution approach, the target vehicle forces and yaw torque are distributed among the individual tire forces (*Ali et al., 2017; Li and Shi, 2017; Zakaria et al., 2024*).

Another group of researchers has approached the problem from the perspective of determining the critical speed and its more accurate estimation for a two-axle dynamic model. A 4×2-wheel configuration was

adopted as the vehicle model, and the acting forces and other lateral dynamic parameters were calculated for this model. The problem was analyzed in terms of the forces acting on the vehicle during turning and on inclined surfaces to ensure stability, taking into account the redistribution of reaction forces and variations in the tire–surface adhesion coefficient (*Ivanov et al., 2025*).

In a previous study devoted to this problem (*Tarverdyan et al., 2025*), the kinematic parameters of the motion subsystem of a robotic platform were examined in detail. In particular, the relationships between four independently steerable wheels, steering angles, and their angular velocities were established. Lateral forces arising during turning on a horizontal plane were also partially analyzed.

The present article is devoted to the investigation of the stability of robotic platform motion and conditions of lateral slip on sloped terrain, as well as to the assessment of motion smoothness based on the proposed model.

MATERIALS AND METHODS

Stability of Robotic Platform Motion on Inclined Surfaces

As previously noted, for robotic platforms intended to perform agro-technological operations, the four-wheel configuration with independently controlled wheels is considered preferable. The ability of the platform to perform parallel translational motion, in some cases without rotational turning, provides high maneuverability.

Independent control of all four wheels minimizes lateral slip, thereby reducing not only soil disturbance but also the wear of drivetrain components (*Bak and Jakobsen, 2004; Torii, 2000*).

Although the dynamics of a four-wheeled independently controlled system are inherently nonlinear and control is not straightforward, relatively simple control systems can still be effective at low operational speeds (2–6 km/h), (*Cho et al., 2002; MarketsandMarkets, 2025; Tarverdyan et al.,2025*). The conceptual scheme of the proposed robotic platform is presented in Figure 1. It consists of a platform frame (1), on which various agro-technological implements and devices are mounted; four drive wheels with independent actuation (2); a wheel steering control unit (3); and a wheel steering mechanism (4).

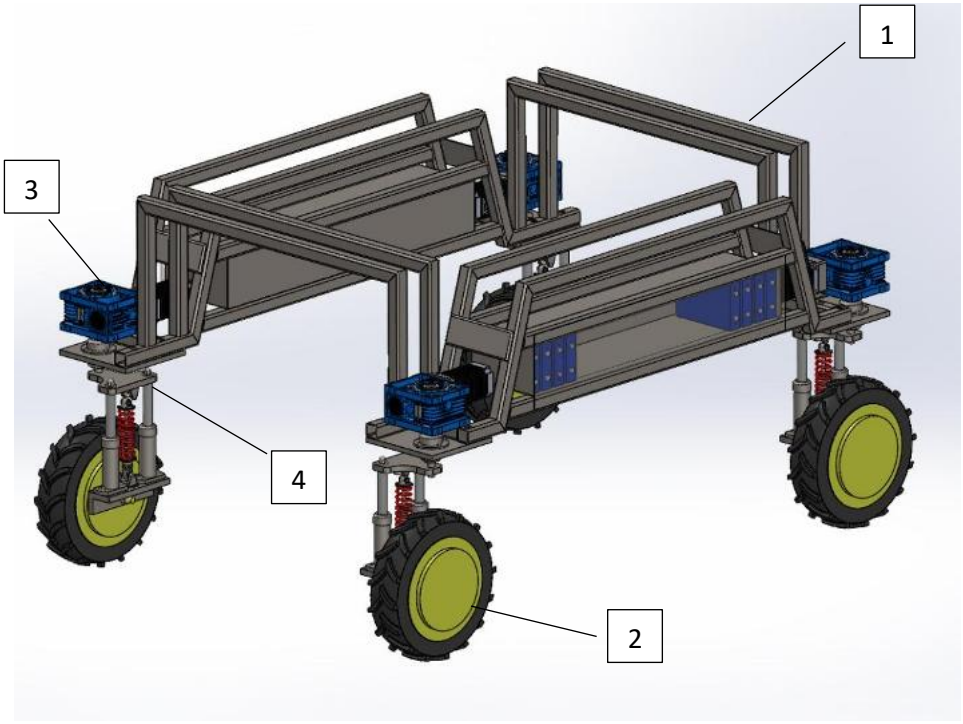


Fig. 1 - 3D model of the developed robotic platform

A detailed kinematic analysis of the locomotion subsystem of the developed robotic platform (*Tarverdyan et al., 2025*) yielded equations that make it possible to determine and refine the parameters used as the basis for programming the platform's turning motion on a horizontal surface.

As a result of the dynamic analysis, precise equations for determining lateral slip forces were obtained. These equations enable the development of a robotic platform drivetrain in which wheel slip during turning is minimized, thereby minimizing soil damage while ensuring operational reliability and durability (*Tarverdyan et al., 2025*).

An agricultural robotic platform can also perform agro-technological operations in fields located on sloped terrain, which is particularly characteristic of the Republic of Armenia. Under such conditions, during the development of the robotic platform, the issue of motion stability, especially during turning, becomes a key subject of analysis.

Assume that the robotic platform performs a turning maneuver on a planar slope inclined at an angle *β* where the rotation axis OO' is perpendicular to the inclined plane and is positioned upslope relative to the robotic platform (Figure 2). The geometric dimensions of the platform are – width B and length L. Since the goal is to develop a structure that is as symmetric as possible in terms of both geometry and mass distribution, it can be assumed that the center of mass coincides with point O_1', located at the intersection of the longitudinal (x_2) and transverse (y_2) symmetry axes of the platform. In this case $a = \frac{L}{2}, b = \frac{B}{2}$. Let the distance of the center of mass from the supporting plane CDEF be denoted by h, and the turning radius of the center of mass by R_0. The steering angles of the wheels are $\theta_1, \theta_2, \theta_3, \theta_4$, while the corresponding turning radii are R_1, R_2, R_3, R_4.

Let consider the turning motion of the robotic platform with a constant turning radius on a slope inclined at an angle β (Figures 2 and 3). Before determining the forces and reactions acting on the platform, it is necessary to account for the transformation of the slope inclination during rotational motion, since it directly affects the magnitude of the force components involved. Let the coordinate system xoy (Figure 3) be fixed to the inclined plane, where the y-axis is aligned with the transverse direction of the slope and the x -axis with the longitudinal direction, with the origin located at the center of rotation. When the rotation angle is φ = 0 (position $\mathcal{A}$ of the robotic platform), the transverse symmetry axis $y_1$of the robotic platform coincides with the y -axis, the longitudinal axis (x_1) inclination angle is β.

When φ = 90°, the axis x_1 becomes parallel to the y-axis $x_1 \parallel y$, while y_1 coincides with the x-axis and is inclined at angle β (Figure 2). When φ = 180°, the configuration becomes symmetric to position $\mathcal{A}$. For all intermediate positions (e.g., position B), the inclination of the robotic platform is characterized by angles β_1 and β_2, which are determined as follows:

$$\begin{cases} sin\beta_1 = sin\beta \cdot sin\varphi, \\ sin\beta_2 = sin\beta \cdot cos\varphi. \end{cases} \quad (1)$$

Let consider the analysis of the forces acting on the robotic platform during turning motion at an arbitrary intermediate position B within the range $0 \leq \varphi \leq 90^0$ (Figure 3) (within the interval $90 - 180^0$, the configuration is repeated symmetrically).

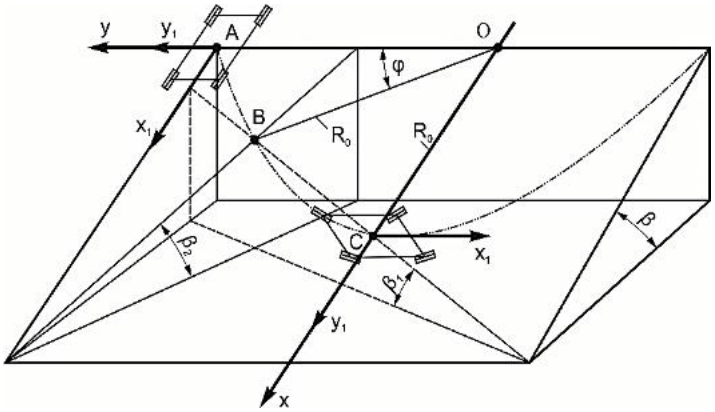


Fig. 2 - Schematic diagram of tilt-angle transformation during the turning motion of the robotic platform

At the specified position, the following forces and torques act on the robotic platform:

The gravitational force G acts at the center of mass and has three components: $G_x = G\cos\beta_1 \cdot sin\beta_2$, directed along the x_2 axis, $G_y = G sin\beta_1$ - directed along the y_2 axis, $G_z = G\cos\beta_1 \cdot \cos\beta_2$ – perpendicular to the inclined plane.

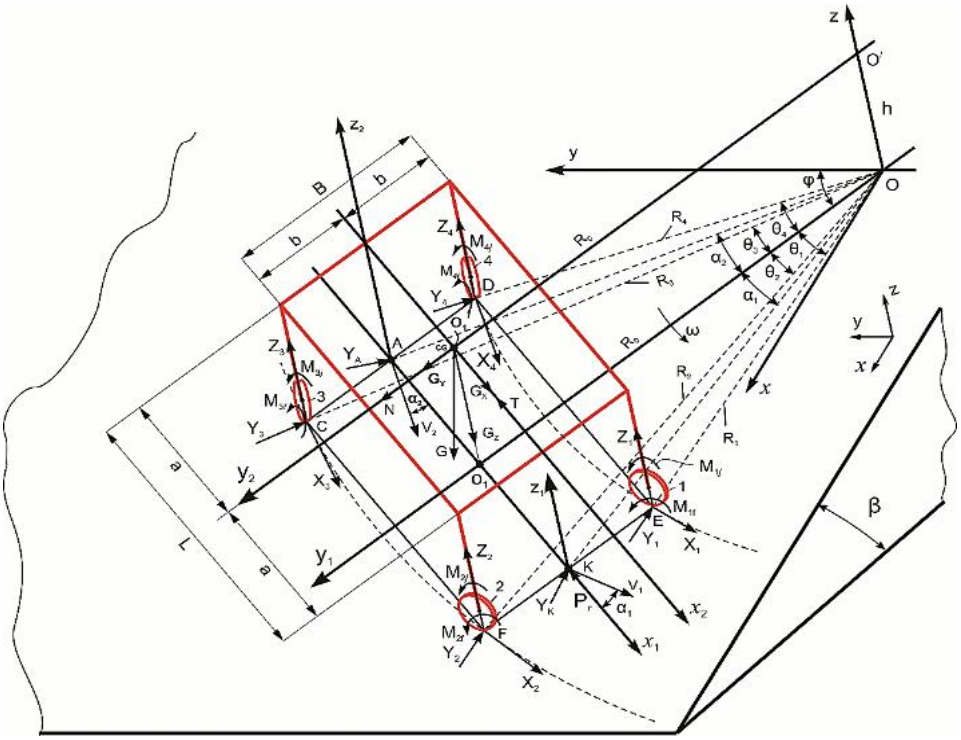


Fig. 3 - Kinematic and dynamic analysis scheme of the turning motion of the robotic platform on an inclined surface

At the wheel–ground contact surfaces, the support reactions Z_i, act normal to the supporting surface. The driving (tractive/tangential) forces $\mathrm{X_i}$ act at the wheel contact surfaces and are perpendicular both to the wheel radii (r_w) and to the turning radii R_i associated with rotation about point *O*. The lateral slip resistance forces Y_i, also act at the wheel–ground contact surfaces and are directed along the turning radii (R_i). In the general case, the wheels are also subjected to a torque of the rolling resistance (M_{if}).

The robotic platform is additionally subjected to inertial force factors. At the center of mass (O_1'), the longitudinal inertial force T acts along the x_2 axis, with its direction determined by the nature of the motion (acceleration or deceleration). The centrifugal force N associated with curvilinear motion acts along the y_2 axis. The wheels are also subjected to inertial torques (M_{ij}), as well as the inertial torque of the robotic platform associated with curvilinear motion about the z-axis, denoted by M_{j} (*Litvinov, 1971; Qiu et al., 2018; Zinoviev, 1975*).

To solve the problem of lateral slip of the robotic platform, it is first necessary to determine the support reactions at the wheel–ground contact surfaces, namely Z_1, Z_2, Z_3 *and* Z_4. By formulating the equilibrium equations with respect to the axes passing through the wheel support points ($\mathcal{CD}$, EF, CF and DE) and performing the corresponding transformations, the following equations are obtained:

$$\mathrm{Z}_1 + \mathrm{Z}_2 = \frac{\mathrm{G_z}}{2} + \frac{\mathrm{G}_x \cdot \mathrm{h}}{2a} - \frac{T \cdot \mathrm{h}}{2a} - \frac{4M_{\mathrm{ij}}}{2a} \tag{2}$$

$$\mathrm{Z}_3 + \mathrm{Z}_4 = \frac{\mathrm{G_z}}{2} - \frac{\mathrm{G}_x \cdot \mathrm{h}}{2a} + \frac{T \cdot \mathrm{h}}{2a} + \frac{4M_{\mathrm{ij}}}{2a} \tag{3}$$

$$\mathrm{Z}_1 + \mathrm{Z}_4 = \frac{\mathrm{G_z}}{2} + \frac{\mathrm{G_y} \cdot \mathrm{h}}{2b} - \frac{N \cdot \mathrm{h}}{2b} \tag{4}$$

$$\mathrm{Z}_2 + \mathrm{Z}_3 = \frac{\mathrm{G_z}}{2} + \frac{\mathrm{G_y} \cdot \mathrm{h}}{2b} + \frac{N \cdot \mathrm{h}}{2b} \tag{5}$$

Besides:

$$\mathrm{Z}_1 + \mathrm{Z}_2 + \mathrm{Z}_3 + \mathrm{Z}_4 = \mathrm{G_z} \tag{6}$$

Let's also introduce the following denotations:

$$\begin{cases} \mathrm{Z}_1 + \mathrm{Z}_2 = \mathcal{A} \\ \mathrm{Z}_3 + \mathrm{Z}_4 = B \\ \mathrm{Z}_1 + \mathrm{Z}_4 = C \\ \mathrm{Z}_2 + \mathrm{Z}_3 = \mathcal{D}. \end{cases} \Rightarrow \mathcal{A} + B = C + \mathcal{D} \tag{7}$$

Let us denote: $Z_1 = S$, where S is an arbitrary parameter. Then:

$$\begin{cases} Z_1 = S \\ Z_2 = \mathcal{A} - S \\ Z_3 = B - C + S = \mathcal{D} + S \\ Z_4 = C - S. \end{cases} \quad (8)$$

The parameter S characterizes the redistribution of the load among the supports, which does not alter the quantities $(Z_1 + Z_2)$, $(Z_1 + Z_4)$, $(Z_3 + Z_4)$ and $(Z_2 + Z_3)$, in other words, equilibrium is preserved, and the model is self-balancing (*Buchholz, 2023; Ilarionov, 2013; Litvinov, 1971*).

Using Equations (2), (3), (4), and (5), together with relations (6) and (8), and considering that $G_x = G\cos\beta_1 \cdot sin\beta_2$, $G_y = G sin\beta_1$, $G_z = G\cos\beta_1 \cdot \cos\beta_2$, where the angles β_1 and β_2 are determined from Equation (1), $N = \frac{G}{g}\omega^2 R_0$, $T = \frac{G}{g} \cdot \frac{dv}{dt}$, $M_{ij} = J_w \cdot \frac{d\omega_w}{dt}$ (J_w is the wheel torque of inertia, and $\frac{d\omega_w}{dt}$ is the angular acceleration of the wheel), and taking into account that uniform motion of the robotic platform is considered, the following equations are obtained for the support reactions:

$$\left.\begin{aligned} Z_1 &= \frac{G}{4}cos\beta_1 \cdot cos\beta_2 - \frac{h \cdot G}{2L} \cdot sin\beta_1 + \frac{G \cdot h}{2B}cos\beta_1 \cdot sin\beta_2 - \frac{G \cdot h \cdot \omega^2 R_0}{g \cdot L} \\ Z_2 &= \frac{G}{4}cos\beta_1 \cdot cos\beta_2 + \frac{G \cdot h}{2L} \cdot sin\beta_1 + \frac{G \cdot h}{2B}cos\beta_1 \cdot sin\beta_2 + \frac{G \cdot h \cdot \omega^2 R_0}{g \cdot L} \\ Z_3 &= \frac{G}{4}cos\beta_1 \cdot cos\beta_2 + \frac{G \cdot h}{2L} \cdot sin\beta_1 - \frac{G \cdot h}{2B}cos\beta_1 \cdot sin\beta_2 + \frac{G \cdot h \cdot \omega^2 R_0}{g \cdot L} \\ Z_4 &= \frac{G}{4}cos\beta_1 \cdot cos\beta_2 - \frac{G \cdot h}{2L} \cdot sin\beta_1 - \frac{G \cdot h}{2B}cos\beta_1 \cdot sin\beta_2 - \frac{G \cdot h \cdot \omega^2 R_0}{g \cdot L} \end{aligned}\right\}. \quad (9)$$

It should be noted that the obtained solutions satisfy condition (7) and correctly reflect the physical nature of the problem.

Assessment and improvement of the Motion Smoothness of the Robotic Platform

Ensuring the smooth motion of the developed robotic platform is an important issue, since it directly determines the accurate execution of agro-technical processes, the operational reliability and durability of its components—particularly the suspension system—and the reliable performance of the orientation and control system.

Figure 4. shows the schematic diagram of the suspension system of the developed robotic platform, which includes an elastic element (spring) (1), a coaxially mounted hydraulic damper (shock absorber) (2), pneumatic wheels (3) each equipped with an independent electric hub motors, and an independent wheel steering control unit (4).

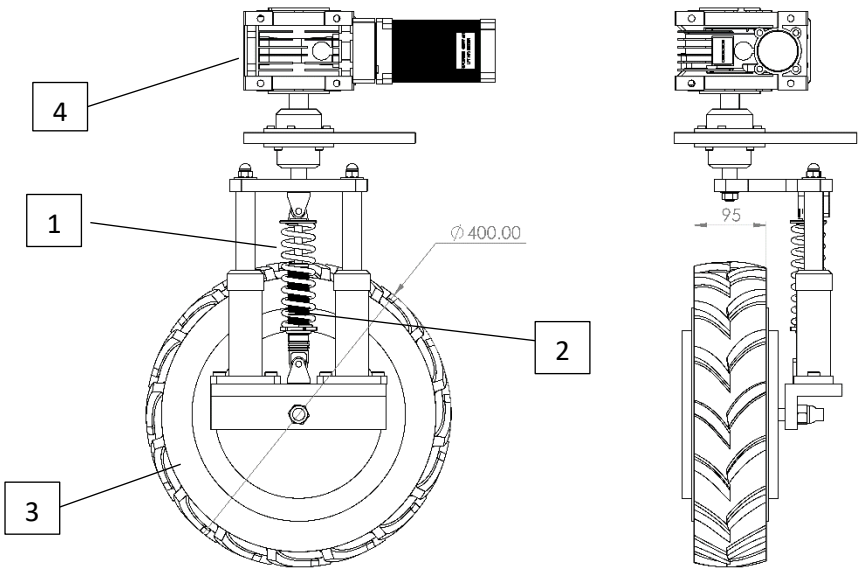


Fig. 4 - Schematic diagram of the suspension system of the robotic platform (all dimensions in *mm*)

It should be noted that, based on the presented suspension system configuration, from an application standpoint it is important to analyze the vertical translational oscillations of the platform, as well as the angular oscillations in the longitudinal and transverse symmetry planes.

The computational scheme of the problem is presented in Figure 5.

The data required for solving the problem are as follows:

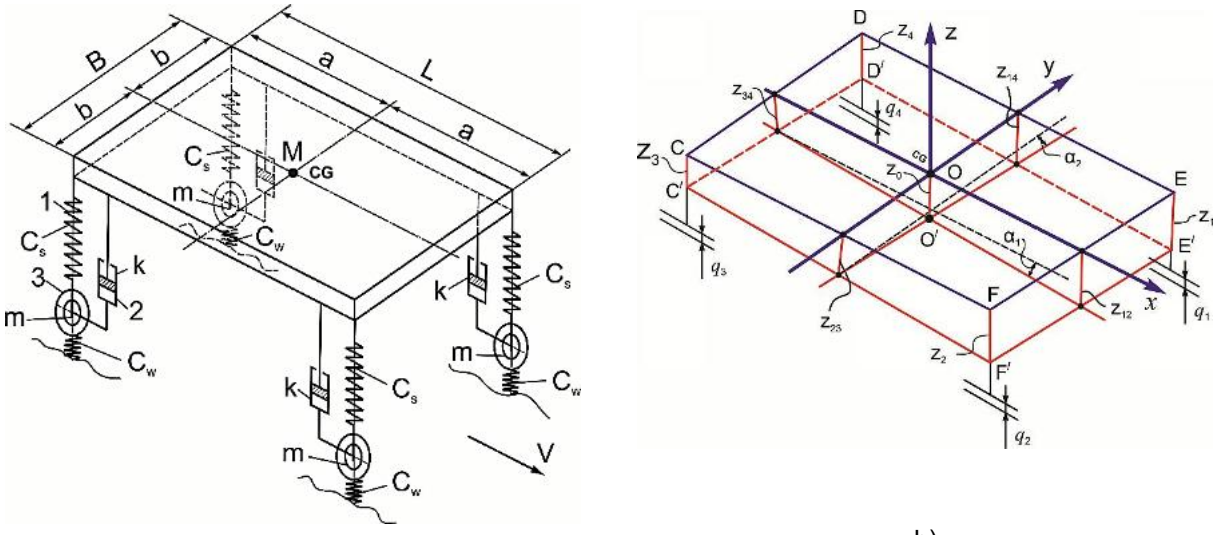
- the overall dimensions of the robot platform: length L, width B;
- the identical stiffness of all four suspension springs c_s;
- wheel stiffness c_w;
- the sprung mass of the robotic platform M;
- the mass of the assemblies located below the springs (unsprung mass) m;
- the damping coefficient of the shock absorbers *k*. Since the two elastic elements the suspension spring and the wheel are connected in series, their combined stiffness can be represented by a single equivalent stiffness coefficient (*Ilarionov, 2013; Litvinov, 1971*).

$$c = \frac{c_s \cdot c_w}{c_s + c_w}.$$

Several assumptions were adopted in solving the problem, which considerably simplify the analysis while having no significant influence on the results.

It is assumed that the robotic platform moves uniformly across field surface irregularities, with the wheels continuously rolling over them while maintaining uninterrupted contact with the ground. Under these conditions, the wheel axles undergo vertical displacements (q_i).

The self-weight of the robotic platform and the loads mounted on it are assumed to be distributed symmetrically with respect to the *x* and *y* axes, such that the center of gravity of the total mass coincides with the origin of the coordinate system (Figure 5).



a) b)

Fig. 5 - Scheme for determining the driving/motion smoothness of the robotic platform:

a) schematic diagram of the suspension system,

b) computational scheme of the platform vertical displacements

In addition, the following notations were adopted:

z_0- vertical displacement of the platform's center of mass caused by oscillations;

z_1; z_2; z_3; z_4- vertical displacements of points C; D; E and F respectively located above the wheel axles;

α_1; α_2 – rotational angles of the platform in the longitudinal and transverse planes of symmetry, respectively;

a - distances from the front (conventionally defined) and rear wheel axles to the y-axis of symmetry passing through the center of mass (a=L/2, since the robotic platform is designed to have a symmetric structure);

b- distance from the wheel suspension attachment points to the x-axis of symmetry passing through the center of mass ($b = \frac{B}{2}$);

ρ_1- radius of inertia of the robotic platform with respect to the y-axis;

ρ_2- radius of inertia of the robotic platform with respect to the x-axis.

It is evident that the solution of the problem involves six unknowns: z_1; z_2; z_3; z_4; z_0 and α_1 (in one case) and α_2 (in the other case). In such situations, it is useful to establish relationships among these unknowns. Considering the sprung part of the robotic platform as a rigid horizontal plate CDEF (Figure 5), as a result of its vertical linear oscillations, at an arbitrary instant it will occupy the position C′ D′ E′ F′ while remaining planar. In the general case of oscillations, it is assumed that the displacements at the indicated points above the wheel axles are different, namely z_1; z_2; z_3; z_4. Under these conditions, geometric relationships exist between these displacements, making it possible to simplify the solution of the problem. In the longitudinal plane of symmetry of the robotic platform (along the x-axis), the displacements of the front edge points, as the midlines of the corresponding rectangles, are expressed as $z_{12} = \frac{z_1+z_2}{2}, z_{34} = \frac{z_3+z_4}{2}$. From the scheme shown in Figure 5, it follows that:

$$z_{12} = z_0 + a_1 \mathrm{a}\,, \qquad z_{34} = z_0 - a_1 \mathrm{a} \tag{11}$$

From which:

$$a_1 = \frac{z_{12} - z_{34}}{L} = \frac{z_1 + z_2 - z_3 - z_4}{2L}\,.$$

Similarly, in the plane of lateral symmetry (along the y-axis), the displacements and the rotation angle of the platform are given by:

$$z_{14} = z_0 + a_2 \cdot \mathrm{b};\; z_{23} = z_0 - a_2 \cdot \mathrm{b} \tag{12}$$

$$a_2 = \frac{z_{14} - z_{23}}{B} = \frac{z_1 + z_4 - z_2 - z_3}{2B}. \tag{13}$$

From the scheme, the following relationships also hold: $z_0 = \frac{z_1+z_3}{2}$, $z_0 = \frac{z_2+z_4}{2}$, from which it follows that:

$$\left.\begin{aligned} z_2 + z_3 &= z_2 + z_4 \\ z_0 &= \frac{z_1 + z_2 + z_3 + z_4}{4} \end{aligned}\right\} \tag{14}$$

To formulate the equations of motions for the considered problem, the principles of rigid-body dynamics are applied (*Biderman, 1980; Buchholz, 2023; Zinoviev, 1975*).

Since in this stage the task is to study only the free oscillations of the robotic platform, the forces caused by terrain irregularities, which include terms proportional to q_i, can be neglected as external excitations. In this case, the differential equation of motion of the platform's center of inertia can be written in the following form:

$$M\frac{d^2 z_0}{dt^2} = \mathrm{k}\left(\frac{dz_1}{dt} + \frac{dz_2}{dt} + \frac{dz_3}{dt} + \frac{dz_4}{dt}\right) + c(z_1 + z_2 + z_3 + z_4) = 0. \tag{15}$$

The torque equations about the x and y axes passing through the center of inertia will be:

$$\mathrm{M}\rho_1^2\frac{d^2\alpha_1}{dt^2} + \mathrm{ka}\left(\frac{dz_1}{dt} - \frac{dz_2}{dt} - \frac{dz_3}{dt} + \frac{dz_4}{dt}\right) + c(z_1 - z_2 - z_3 + z_4) = 0, \tag{16}$$

$$\mathrm{M}\rho_2^2\frac{d^2\alpha_2}{dt^2} + \mathrm{k}b\left(\frac{dz_1}{dt} + \frac{dz_2}{dt} - \frac{dz_3}{dt} - \frac{dz_4}{dt}\right) + cb(z_1 + z_2 - z_3 - z_4) = 0. \tag{17}$$

By inserting the values of $\alpha_1, \alpha_2\ and\ z_0$ from the Equations of (11); (13) and (14) in the Equations of (15); (16) and (17), the following is obtained:

$$\mathrm{M}\cdot\frac{1}{4}\left(\frac{d^2 z_1}{dt^2} + \frac{d^2 z_2}{dt^2} + \frac{d^2 z_3}{dt^2} + \frac{d^2 z_4}{dt^2}\right) + \mathrm{k}\left(\frac{dz_1}{dt} + \frac{dz_2}{dt} + \frac{dz_3}{dt} + \frac{dz_4}{dt}\right) + C(z_1 + z_2 + z_3 + z_4) = 0, \tag{18}$$

$$\frac{\mathrm{M}\rho_1^2}{2L}\cdot\left(\frac{d^2 z_1}{dt^2} + \frac{d^2 z_2}{dt^2} - \frac{d^2 z_3}{dt^2} - \frac{d^2 z_4}{dt^2}\right) + \mathrm{ka}\left(\frac{dz_1}{dt} - \frac{dz_2}{dt} - \frac{dz_3}{dt} + \frac{dz_4}{dt}\right) + ca(z_1 - z_2 - z_3 + z_4) = 0, \tag{19}$$

$$\frac{\mathrm{M}\rho_2^2}{2B}\cdot\left(\frac{d^2 z_1}{dt^2} + \frac{d^2 z_4}{dt^2} - \frac{d^2 z_2}{dt^2} - \frac{d^2 z_3}{dt^2}\right) + \mathrm{k}b\left(\frac{dz_1}{dt} + \frac{dz_2}{dt} - \frac{dz_3}{dt} - \frac{dz_4}{dt}\right) + cb(z_1 + z_2 - z_3 - z_4) = 0. \tag{20}$$

To establish the relationships between Equations (18) and (19), (18) and (20) Equation (18) is multiplied by a and is added to (19), then (18) is multiplied by a and (19) is subtracted. In both cases, the resulting equations are divided by L. Similarly, Equation (18) is multiplied by *b* and added to Equation (20), and the resulting equation is divided by *B*. Equation (18) is then multiplied by *b* and Equation (20) is subtracted from the result, after which the resulting equation is divided by B. Considering the symmetry of the system, such that L=2a and B=2b, the following equations are obtained:

$$\mathrm{M}\left(\frac{\mathrm{a}^2+\rho_1^2}{2L^2}\right)\left(\frac{d^2z_1}{dt^2}+\frac{d^2z_2}{dt^2}\right)+\mathrm{M}\left(\frac{\mathrm{a}^2-\rho_1^2}{2L^2}\right)\cdot\left(\frac{d^2z_3}{dt^2}+\frac{d^2z_4}{dt^2}\right)+\mathrm{k}\left(\frac{dz_1}{dt}+\frac{dz_4}{dt}\right)+c(z_1+z_4)=0, \quad (21)$$

$$\mathrm{M}\left(\frac{\mathrm{a}^2-\rho_1^2}{2L^2}\right)\left(\frac{d^2z_1}{dt^2}+\frac{d^2z_2}{dt^2}\right)+\mathrm{M}\left(\frac{\mathrm{a}^2+\rho_1^2}{2L^2}\right)\cdot\left(\frac{d^2z_3}{dt^2}+\frac{d^2z_4}{dt^2}\right)+\mathrm{k}\left(\frac{dz_1}{dt}+\frac{dz_3}{dt}\right)+c(z_1+z_3)=0, \quad (22)$$

$$\mathrm{M}\left(\frac{\mathrm{b}^2+\rho_2^2}{2B^2}\right)\left(\frac{d^2z_1}{dt^2}+\frac{d^2z_4}{dt^2}\right)+\mathrm{M}\left(\frac{\mathrm{b}^2-\rho_2^2}{2B^2}\right)\cdot\left(\frac{d^2z_2}{dt^2}+\frac{d^2z_3}{dt^2}\right)+\mathrm{k}\left(\frac{dz_1}{dt}+\frac{dz_2}{dt}\right)+c(z_1+z_2)=0, \quad (23)$$

$$\mathrm{M}\left(\frac{\mathrm{b}^2-\rho_2^2}{2B^2}\right)\left(\frac{d^2z_1}{dt}+\frac{d^2z_4}{dt^2}\right)+\mathrm{M}\left(\frac{\mathrm{b}^2+\rho_2^2}{2B^2}\right)\cdot\left(\frac{d^2z_2}{dt^2}+\frac{d^2z_3}{dt^2}\right)+\mathrm{k}\left(\frac{dz_3}{dt}+\frac{dz_4}{dt}\right)+c(z_3+z_4)=0. \quad (24)$$

The Equations (21)–(22) and (23)–(24) are pairwise interrelated through their first and second terms Even in the particular case where $\mathrm{a}=\rho_1$ and $\mathrm{b}=\rho_2$, these interrelations are preserved. This indicates that the vertical oscillations of the considered robotic platform, characterized by the coordinates z_1; z_2; z_3 and z_4 are mutually coupled.

The following notation is introduced:

$$\mathrm{M}\left(\frac{\mathrm{a}^2+\rho_1^2}{2L^2}\right)=\mathrm{M}_1;\ \ \mathrm{M}\left(\frac{\mathrm{a}^2-\rho_1^2}{2L^2}\right)=\mathrm{M}_2;\ \mathrm{M}\left(\frac{\mathrm{b}^2+\rho_2^2}{2\mathrm{B}^2}\right)=\mathrm{M}_3;\ \ \mathrm{M}\left(\frac{\mathrm{b}^2-\rho_2^2}{2\mathrm{B}^2}\right)=\mathrm{M}_4.$$

The Equations (21) (22); (23) and (24) will take the following form:

$$\mathrm{M}_1\left(\frac{d^2z_1}{dt^2}+\frac{d^2z_2}{dt^2}\right)+\mathrm{M}_2\left(\frac{d^2z_3}{dt^2}+\frac{d^2z_4}{dt^2}\right)+k\left(\frac{d^2z_1}{dt}+\frac{d^2z_4}{dt}\right)+c(z_1+z_4)=0, \quad (25)$$

$$\mathrm{M}_2\left(\frac{d^2z_1}{dt^2}+\frac{d^2z_2}{dt^2}\right)+\mathrm{M}_1\left(\frac{d^2z_3}{dt^2}+\frac{d^2z_4}{dt^2}\right)+k\left(\frac{dz_2}{dt}+\frac{dz_3}{dt}\right)+c(z_2+z_3)=0, \quad (26)$$

$$\mathrm{M}_3\left(\frac{d^2z_1}{dt^2}+\frac{d^2z_4}{dt^2}\right)+\mathrm{M}_4\left(\frac{d^2z_2}{dt^2}+\frac{d^2z_3}{dt^2}\right)+k\left(\frac{dz_1}{dt}+\frac{dz_2}{dt}\right)+c(z_1+z_2)=0, \quad (27)$$

$$\mathrm{M}_4\left(\frac{d^2z_1}{dt}+\frac{d^2z_4}{dt^2}\right)+\mathrm{M}_3\left(\frac{d^2z_2}{dt^2}+\frac{d^2z_3}{dt^2}\right)+k\left(\frac{dz_3}{dt}+\frac{dz_4}{dt}\right)+c(z_3+z_4)=0. \quad (28)$$

The obtained equations enable to study the free oscillations of the robotic platform and also serve as a basis for the further investigation of its forced vibrations.

RESULTS AND ANALYSIS

Stability Conditions of the Robotic Platform Motion on Slopes

For the initial parameters of the developed robotic platform (L = 1.6m, B = 1.2m, G = 5000 N, h = 0.6m, ω = 0.278 s^{-1}, R_0 = 5m, β = 10^0) the following results are obtained for three characteristic positions using the derived equations:

when $\varphi=0^0$, $sin\beta_1=0$, $\beta_1=0$, $sin\beta_2=sin\beta$, $\beta_2=\beta$, $\mathrm{G_z}=\mathrm{G}\cos\beta_1\cdot\cos\beta_2=5000\cdot0.9848=4925\ N$;

when $\varphi=45^0$, $sin\beta_1=sin\beta\cdot sin\varphi=0.1222$, $sin\beta_2=sin\beta\cdot cos\varphi=0.1222$, $cos\beta_1=cos\beta_2=0.9925$, $\mathrm{G_z}=\mathrm{G}\cos\beta_1\cdot\cos\beta_2=5000\cdot0.9925=4962.5\ N$;

when $\varphi=90^0$, $sin\beta_1=sin\beta\cdot sin\varphi$, $\beta_1=\beta$, $\beta_2=0$, $G_z=G\cos\beta_1\cdot\cos\beta_2=5000\cdot0.9848=4925\ N$;

Substituting the numerical values into Equations (9), the following values are obtained for the support reactions:

when $\varphi=0^0$, $\mathrm{Z}_1=1355\ N$; $\mathrm{Z}_2=1515\ N$; $\mathrm{Z}_3=1095\ N$; $\mathrm{Z}_4=960\ N$, verification: $\mathrm{Z}_1+\mathrm{Z}_2+\mathrm{Z}_3+\mathrm{Z}_4=4925\ N=\mathrm{G_z}$;

when $\varphi=45^0$, $\mathrm{Z}_1=1195\ N$; $\mathrm{Z}_2=1562.5\ N$; $\mathrm{Z}_3=1265\ N$; $\mathrm{Z}_4=940\ N$, verification: $\mathrm{Z}_1+\mathrm{Z}_2+\mathrm{Z}_3+\mathrm{Z}_4=4962.5\ N=\mathrm{G_z}$;

when $\varphi=90^0$, $\mathrm{Z}_1=1004.5\ N$; $\mathrm{Z}_2=1458\ N$; $\mathrm{Z}_3=1458\ N$; $\mathrm{Z}_4=1004.5\ N$, verification: $\mathrm{Z}_1+\mathrm{Z}_2+\mathrm{Z}_3+\mathrm{Z}_4=4925\ N=\mathrm{G_z}$.

The discussion of the robotic platform overturning problem is of little practical significance, since its operational speeds (3 – 6 km/h) and field slope angles (up to 7^0) cannot create a situation in which, even in the most unfavorable position ($\varphi=90^0$) the support reactions Z_1 and Z_4 become equal to 0. In this regard, the analysis of lateral skidding is of primary importance.

To determine the resistance forces against lateral skidding, it is first necessary to determine the tangential reactions (X_i) developed at all driving wheels during rolling motion. It is known that these reaction forces are determined as follows:

$$X_i = P - f\mathrm{Z}_i$$

where P is the circumferential force acting on each driving wheel, f is the rolling resistance coefficient, for various soils $f = 0{,}10 \div 0{,}25$ (*Cho et al., 2002; Litvinov, 1971*), while for cultivated soils $f = 0{,}25$; Z_i is the reaction force at the wheel–ground contact surface. For the considered case:

$$P = \frac{M_m \cdot i \cdot \eta}{r_w} - \mathrm{J}_w \cdot \frac{d\omega_w}{dt} \cdot \frac{1}{r_w}$$

where; r – wheel diameter, M_m - a torque developed by the electric motor, i – a transmission ratio of the motor–wheel drivetrain, η – a drivetrain efficiency, J – a wheel moment of inertia, $d\omega_w$ – an angular acceleration of the wheel

Taking into account that, $\frac{d\omega_w}{dt} = \frac{1}{r_w} \cdot \frac{dv}{dt}$ the following expression is obtained:

$$X_i = \frac{M_m \cdot i \cdot \eta}{r_w} - \mathrm{J}_w \cdot \frac{1}{r_w^2} \cdot \frac{dv}{dt} - f\mathrm{Z}_i \quad (29)$$

Under uniform motion conditions $\frac{dv}{dt} = 0$, therefore:

$$X_i = \frac{M_w}{r_w} - f\mathrm{Z}_i \quad (30)$$

In the case under consideration, where all four wheels are driving wheels and are independently controlled, the tangential (reaction) forces are not equal in either magnitude and direction. As a result, a torque M_z is generated, causing the robotic platform to rotate in the plane of motion. This torque significantly affects lateral skidding.

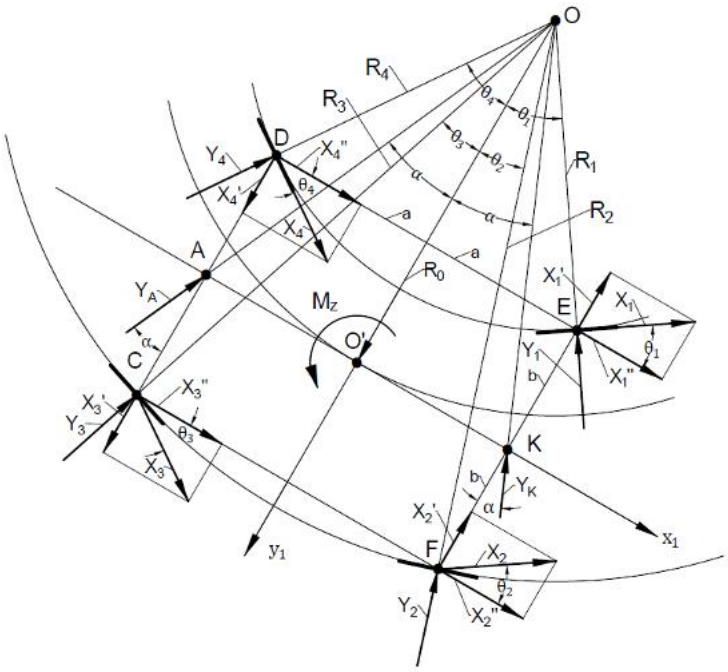


Fig. 6 - Schematic diagram for determining the torque about the vertical axis of the robotic platform

The value/magnitude of this torque is determined according to the scheme shown in Figure 6 as follows:

$$M_z = X_4' \cdot a + X_3' \cdot a + X_2' \cdot a + X_1' \cdot a - X_1'' \cdot b + X_2'' \cdot b + X_3'' \cdot b - X_4'' \cdot b,$$

$$M_z = (X_1 sin\theta_1 + X_2 sin\theta_2 + X_3 sin\theta_3 + X_4 sin\theta_4)a + (X_2 cos\theta_2 + X_3 cos\theta_3)b - (X_1 cos\theta_1 + X_4 cos\theta_4)b; \quad (31)$$

Taking into account that in the considered case $\theta_1 = \theta_4$; $\theta_2 = \theta_3$, for M_z Equation (32) becomes:

$$M_z = (X_1 + X_4)a \cdot sin\theta_1 + (X_2 + X_3)a \cdot sin\theta_2 + (X_2 + X_3)b \cdot cos\theta_2 - (X_1 + X_4)b \cdot cos\theta_1. \quad (32)$$

In the final equation, the forces X_1; X_2; X_3 and X_4 are determined by Equations (29) or (30). The problem of determining θ_1 and θ_2 as well as establishing the relationship between them, is comprehensively discussed in the work of *Tarverdyan et al. (2025)*. Therefore, the torque M_z is determined and for the indicated direction, it is always positive and at least equal to the sum of the first two terms of the equation.

After determining the force factors Z_i; X_i and M_z the lateral resistance (reaction) forces Y_1, Y_2, Y_3 and Y_4 can be determined. Naturally, these forces may be obtained from the dynamic equilibrium conditions of the robot platform; however, it should be emphasized that, in the analysis of the lateral drift phenomenon, the individual determination of these forces is not essential, since lateral skidding is caused by the pairwise combined lateral slip of the conventionally defined front and rear wheels. Proceeding from this consideration, the problem of determining the resultant forces $(Y_3 + Y_4)$ and $(Y_1 + Y_2)$ was examined.

Let the resultant force $(Y_1 + Y_2)$ be transferred to point K on the longitudinal axis of symmetry (x_2), and denote it by Y_K. Similarly, let the resultant $(Y_3 + Y_4) = Y_{\mathcal{A}}$ be applied at point $\mathcal{A}$. It should be noted that this transfer does not alter the mechanical effect of the force system, since the forces Y_1 and Y_2; Y_3 and Y_4 form pairwise concurrent force systems. Since a symmetric system is considered, $Y_{\mathcal{A}}$ and Y_K are inclined relative to the $y_1 - \text{axis}$ by the same angle α, where $tg\alpha = \frac{a}{R_0}$.

Considering the equilibrium condition of the torque of the forces acting on system with respect to the axes Z_1 and Z_2 passing through points $\mathcal{A}$ and K respectively, and using the schematic diagrams shown in Figures 3 and 6, the following equations are obtained:

$$\sum M_{Z_1} = 0; \quad -Y_{\mathcal{A}} cos\alpha \cdot 2a + M_z + M_j + G_y \cdot a + N \cdot a = 0;$$

$$\sum M_{Z_2} = 0; \quad Y_K cos\alpha \cdot 2a + M_z + M_j - G_y \cdot a - N \cdot a = 0; \quad \text{or}$$

$$Y_{\mathcal{A}} = \frac{M_z + M_j + G_y \cdot a + N \cdot a}{2a \cdot cos\alpha} \tag{33}$$

$$Y_K = \frac{N \cdot a + G_y \cdot a - M_z - M_j}{2a \cdot cos\alpha} \tag{34}$$

In these equations, the torque M_z is determined from Equation (32). The inertial torque M_j is determined as follows:

$$M_j = m\rho^2 \frac{d\omega}{dt},$$

where: m is the total loaded mass of the robot platform, ρ is the radius of inertia of the mass m with respect to Z axis perpendicular to the xoy plane and passing through the center of mass; $\frac{d\omega}{dt}$ is the angular acceleration of the rotational motion of the robot platform during turning (for uniform motion $\frac{d\omega}{dt} = 0$). G_y is the component of the gravitational force directed along the transverse axis of symmetry (y_2) of the platform:

$$G_y = G \cdot sin\beta \cdot sin\varphi.$$

N is the centrifugal force generated during turning motion:

$$N = m\omega^2 R_0.$$

Let us determine the magnitude of the lateral drift forces for the adopted initial numerical values, when $\varphi = 90^0$ and G_y attains its maximum value:

$$G_y = G \cdot sin\beta.$$

The numerical data are the same as in the previous example; in this case, the following additional data are also required:

$M_m = 150N \cdot m$; $\eta = 0.9$; $r_w = 0.2m$; $Z_1 = 1004N$; $Z_2 = 1458N$; $Z_3 = 1458N$; $Z_4 = 1004N$; $\theta_1 = 12^0$; $\theta_2 = 9^0$; $\alpha = 10^0$;

For these values, Equation (30) yields the following values for X_i. (assuming that the motion of the robot platform is uniform):

$X_1 = 349.0N$; $X_2 = 236.0N$; $X_3 = 236.0N$; $X_4 = 349.0N$.

Using Equation (32), the following value is obtained for M_z : $M_z = 46.3N \cdot m$; $G_y = 868N$; $N = 193.25N$ (as noted earlier, in the considered case it is assumed that $M_j = 0$).

Using Equations (33) and (34), the lateral drift forces ($Y_{\mathcal{A}}$ and Y_K) of the rear and front axles of the robotic platforms are obtained as:

$$Y_{\mathcal{A}} = 568.0\ N; Y_K = 508.8\ N.$$

For these values of lateral forces, lateral skidding will not occur provided that $(Z_3 + Z_4) \cdot \mu > Y_{\mathcal{A}}$ and $(Z_1 + Z_2) \cdot \mu > Y_K$, where μ is the coefficient of adhesion between the wheel and the supporting surface. For cultivated soil types $\mu = 0{,}4 \div 0{,}45$ (*Litvinov, 1971; Sineokov and Panov, 1977*). For the considered example:

$$(1004 + 1452) \cdot 0.45 > Y_{\mathcal{A}}.$$

$982.4\ N > 568.0\ N$, moreover,

$$982.4\ N > 508.8\ N.$$

Therefore, the condition excluding lateral skidding is satisfied.

Evaluating and Ensuring the Smooth Motion of the Robot Platform

It is well established that, for mobile vehicles—including the robot platform considered and analyzed in this study—the maximum smoothness of motion is ensured when $a = \rho_1$, and in the present case, also when $b = \rho_2$ (*Litvinov,1971; Tarverdyan et al., 2025; Zinoviev, 1975*). Under these conditions, $M_2 = 0$; $M_4 = 0$ and therefore, Equations (25), (26), (27), (28) take the following form:

$$M_1\left(\frac{d^2z_1}{dt^2}+\frac{d^2z_2}{dt^2}\right)+k\left(\frac{dz_1}{dt}+\frac{dz_4}{dt}\right)+c(z_1+z_4)=0, \quad (35)$$

$$M_1\left(\frac{d^2z_3}{dt^2}+\frac{d^2z_4}{dt^2}\right)+k\left(\frac{dz_2}{dt}+\frac{dz_3}{dt}\right)+c(z_2+z_3)=0, \quad (36)$$

$$M_3\left(\frac{d^2z_1}{dt^2}+\frac{d^2z_4}{dt^2}\right)+k\left(\frac{dz_1}{dt}+\frac{dz_2}{dt}\right)+c(z_1+z_2)=0, \quad (37)$$

$$M_3\left(\frac{d^2z_2}{dt^2}+\frac{d^2z_3}{dt^2}\right)+k\left(\frac{dz_3}{dt}+\frac{dz_4}{dt}\right)+c(z_3+z_4)=0. \quad (38)$$

The following notations are introduced:

$$\left.\begin{array}{l} z_1+z_2=R; \\ z_1+z_4=Q; \\ z_3+z_4=F; \\ z_2+z_3=N; \end{array}\right\} \quad \text{and also note that } R+F=Q+N \quad (39)$$

Then, combining Equations (35) and (37) yields:

$$\begin{cases} \dfrac{d^2R}{dt^2}+\dfrac{k}{M_1}\cdot\dfrac{dQ}{dt}+\dfrac{c}{M_1}\cdot Q=0; \\ \dfrac{d^2Q}{dt^2}+\dfrac{k}{M_1}\cdot\dfrac{dR}{dt}+\dfrac{c}{M_1}\cdot R=0. \end{cases} \quad (40)$$

Similarly, from Equations (36) and (38):

$$\begin{cases} \dfrac{d^2F}{dt^2}+\dfrac{k}{M_1}\cdot\dfrac{dN}{dt}+\dfrac{c}{M_1}\cdot N=0; \\ \dfrac{d^2N}{dt^2}+\dfrac{k}{M_3}\cdot\dfrac{dF}{dt}+\dfrac{c}{M_3}\cdot F=0. \end{cases} \quad (41)$$

It follows from the latter equations that systems (40) and (41) are identical, i.e., $F = R$; $N = Q$. Therefore, it is sufficient to solve only system (40).

The following substitutions are introduced:

$$X=\sqrt{M_1}\cdot R;\quad Y=\sqrt{M_3}\cdot Q \quad (42)$$

$$\alpha=\frac{k}{\sqrt{M_1\cdot M_3}};\quad \gamma=\frac{c}{\sqrt{M_1\cdot M_3}}. \quad (43)$$

The system of equations in Equation (40) can then be written as:

$$\begin{cases} X''+\alpha Y'+\gamma Y=0; \\ Y''+\alpha X'+\gamma Y=0. \end{cases} \quad (44)$$

The following notation is introduced:

$$X+Y=U;\quad X-Y=V \quad (45)$$

Adding and subtracting the equations in system (44) yields:

$$U''+\alpha U'+\gamma U=0; \quad (46)$$

$$V''-\alpha V'-\gamma Y=0. \quad (47)$$

The characteristic equation associated with Equation (46) will be:

$\varepsilon^2+\alpha\varepsilon+\gamma=0$; whose roots are:

$\varepsilon_{1,2}=\frac{-\alpha\pm\sqrt{\alpha^2-4\gamma}}{2}=\frac{-\alpha\pm i\sqrt{4\gamma-\alpha^2}}{2}=-\frac{\alpha}{2}\pm\frac{i\omega}{2}$, where $\omega=\sqrt{4\gamma-\alpha^2}$.

Since $4\gamma>\alpha^2$, the general solution of Equation (46) will be:

$$U(t)=e^{-\frac{\alpha t}{2}}\left(A_1 cos\frac{\omega}{2}t+A_2 sin\frac{\omega}{2}t\right). \quad (48)$$

The characteristic equation associated with Equation (47) is: $\xi^2-\alpha\xi-\gamma=0$, which has two real roots:

$\varepsilon_{1,2}=\frac{\alpha\pm\sqrt{\alpha^2+4\gamma}}{2}$, besides $\varepsilon_1=\frac{\alpha+\sqrt{\alpha^2+4\gamma}}{2}>0$.

The general solution of Equation (47) is therefore:

$$V(t)=A_3e^{\varepsilon_1 t}+A_4e^{\varepsilon_2 t}. \quad (49)$$

Because an exponentially increasing solution has no physical meaning in this context, the following condition $A_3 = 0$ is imposed.

Returning to the original functions R and Q and using Equations (42) and (45), the following is obtained:

$$R = \frac{U+V}{2\sqrt{M_1}}; Q = \frac{U-V}{2\sqrt{M_3}}, \text{ or}$$

$$R(t) = \frac{1}{2\sqrt{M_1}}\left[e^{-\frac{\alpha t}{2}}\left(A_1 cos\frac{\omega}{2}t + A_2 sin\frac{\omega}{2}t\right) + A_4 e^{\varepsilon_2 t}\right]; \quad (50)$$

$$Q(t) = \frac{1}{2\sqrt{M_3}}\left[e^{-\frac{\alpha t}{2}}\left(A_1 cos\frac{\omega}{2}t + A_2 sin\frac{\omega}{2}t\right) - A_4 e^{\varepsilon_2 t}\right]. \quad (51)$$

The solution to system (39) is now considered. Taking into account that $R + F = Q + N; \Rightarrow R = Q$, the solution can be expressed as:

$$z_1 = Q - z_4; \quad z_2 = R - Q + z_4; \quad z_3 = F - z_4.$$

where z_4 is an arbitrary function.

Using the geometric relationship among the vertical linear displacements given by Equation (14), the following expression is obtained:

$Q - z_4 + F - z_4 = R - Q + z_4 + z_4$, from which it follows that:

$$z_4 = \frac{2Q}{4} = \frac{Q}{2} = \frac{R}{2}.$$

Thus: $z_1 = z_2 = z_3 = z_4 = \frac{R}{2}$.

The initial conditions are: $\begin{cases} z_{i(0)} = \delta, & i = 1,2,3,4 \\ \dot{z}_{i(0)} = 0, & i = 1,2,3,4. \end{cases}$

Where δ is the static deflection of the elastic element (spring) of the suspension system under the static load.

$$\left.\begin{aligned} z_{1(0)} = \frac{R(0)}{2} = \delta \Rightarrow \frac{1}{4\sqrt{M_1}}(A_1 + A_4) \\ z_{2(0)} = \frac{Q(0)}{2} = \delta \Rightarrow \frac{1}{4\sqrt{M_3}}(A_1 - A_4) \end{aligned}\right\}, \text{ wherefrom}$$

$$\left.\begin{aligned} A_1 = 2\delta\left(\sqrt{M_1} + \sqrt{M_3}\right) \\ A_4 = 2\delta\left(\sqrt{M_1} - \sqrt{M_3}\right) \end{aligned}\right\} \quad (52)$$

The following condition is now applied: $\dot{z}_{i(0)} = 0$, $\dot{z}_{1(0)} = 0 = \frac{\dot{R}(0)}{2} = \frac{1}{4\sqrt{M_1}}\left(-\frac{\alpha}{2}A_1 + A_2\frac{\omega}{2} + A_4\varepsilon_2\right)$,

$$\dot{z}_{2(0)} = 0 = \frac{\dot{Q}(0)}{2} = \frac{1}{4\sqrt{M_3}}\left(-\frac{\alpha}{2}A_1 + A_2\frac{\omega}{2} - A_4\xi_2\right),$$

From the latter equations it follows that:

$$\begin{cases} A_2\frac{\omega}{2} = \frac{\alpha}{2}A_1 - A_4\varepsilon_2, \\ A_2\frac{\omega}{2} = A_4\varepsilon_2 + \frac{\alpha}{2}A_1, \end{cases}$$

from which it follows that:

$$A_4 = 0, \quad A_2 = \frac{\alpha A_1}{\omega} = \frac{2\delta\alpha}{\omega}\left(\sqrt{M_1} + \sqrt{M_3}\right). \quad (53)$$

From the condition $A_4 = 0$, it becomes evident that $\sqrt{M_1} = \sqrt{M_3}$, $M_1 = M_3$.

Thus, taking into account Equations (50), (51), (52) and (53), the following equation is obtained for the linear displacements of oscillation:

$$z_1 = z_2 = z_3 = z_4 = \frac{1}{4\sqrt{M_1}} \cdot e^{-\frac{\alpha t}{2}}\left(4\delta\sqrt{M_1} \cdot cos\frac{\omega t}{2} + \frac{4\delta\alpha}{\omega} \cdot \sqrt{M_1} sin\frac{\omega t}{2}\right).$$

Or, in final form:

$$z_{i(t)} = \delta e^{-\frac{\alpha t}{2}} \cdot \left(cos\frac{\omega t}{2} + \frac{\alpha}{\omega} \cdot sin\frac{\omega t}{2}\right) \quad (54)$$

Based on the analysis of the free oscillations of the robotic platform, the derived equations make it possible to determine the key oscillation parameters included in the characteristic performance indicators of the suspension system, namely the oscillation frequency, amplitude, and period, which determine the smoothness of motion (*Biderman, 1980; Ilarionov, 2013; Zinoviev,1975*). In addition, the final Equation (54) makes it possible to determine the oscillation velocity: $\left(\frac{dz}{dt}\right)$

The acceleration: $\left(\frac{d^2z}{dt^2}\right)$ and the rate of acceleration change, which is an important characteristic parameter in problems of this type: $\left(\frac{d^3z}{dt^3}\right)$.

Based on Equation (54), the equations derived from it, and the initial parameters of the robotic platform being developed, the following values were adopted: L=1,60 m; B=1,20 m; a=0,8 m; b=0,6 m; $\rho_1 = 0{,}8\ m$; $\rho_2 = 0{,}6\ m$; M=500 kg. Under these conditions: $M_1 = M_2 = M_3 = M_4 = 125$ kg, the equivalent stiffness coefficient of the suspension system is: $c_b = 66.65 \cdot 10^3 \frac{N}{m} = 66.65 \cdot 10^3 \frac{kg}{s^2}$, the average value of the resistance coefficient of a shock absorber: $k = 420 \frac{N \cdot s}{m} = 420 \frac{kg}{s}$, the vertical static deflection: $\delta = 0.01\ m$, and with calculated values:

$\alpha = \frac{k}{M_1} = \frac{420}{125} = 3.36\ s^{-1}$, $\frac{\alpha}{2} = 1.68\ s^{-1}$, $\omega = \sqrt{\frac{4c}{M_1} - \alpha^2} = \sqrt{\frac{4 \cdot 66.65 \cdot 10^3}{125} - (3.36)^2} = 46.06 s^{-1}$, the graphs of the obtained functions are presented in Figure 7.

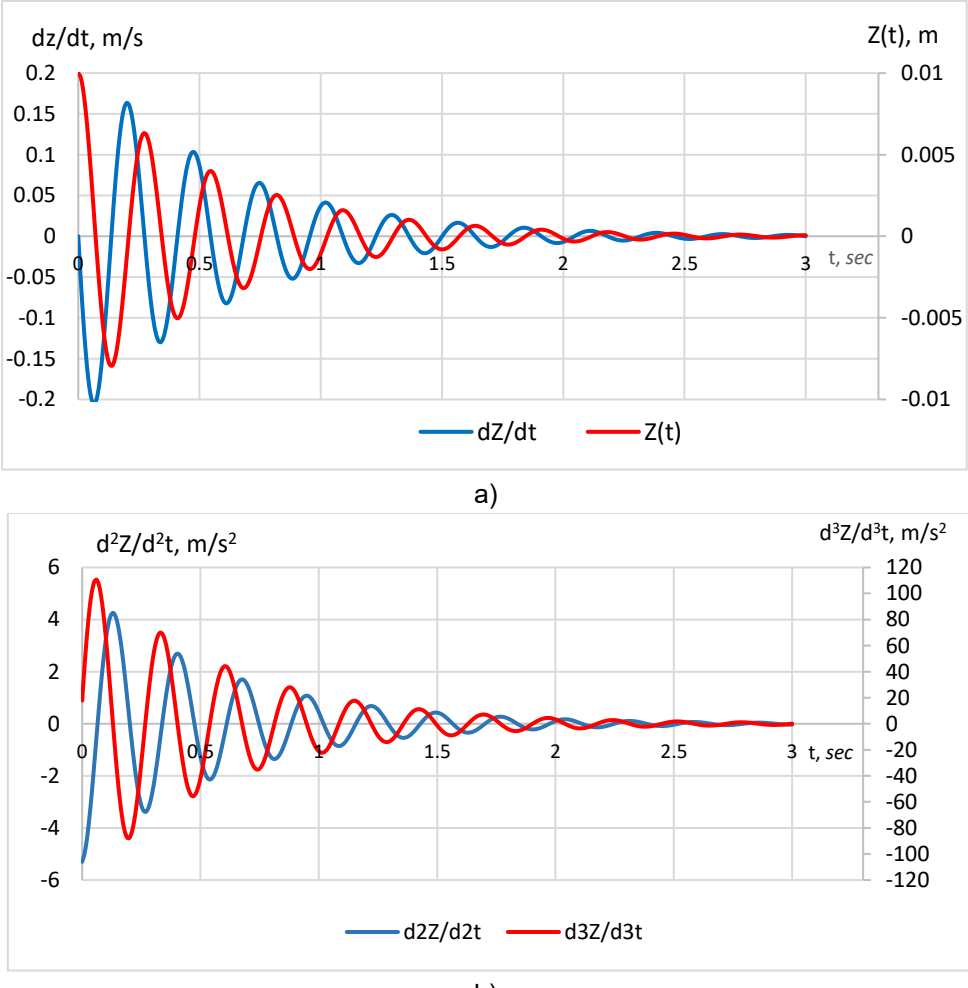


Fig. 7 - Graphs of the free oscillations of the robot platform

a) vertical displacements and velocities; b) velocities and accelerations.

The obtained analytical equations make it possible to select such stiffness values (c) for the elastic elements of the suspension system and such a damping coefficient (k), for the shock absorber (damper) that the required programmed parameters of the oscillatory motion are ensured.

Furthermore, the presented results and derived equations provide the basis for the next stage of the research, namely the investigation of the forced oscillations of the robotic platform.

CONCLUSIONS

As a result of the stability analysis of the developed agricultural robotic platform equipped with four driven and self-steering wheels operating on slopes, analytical equations were obtained that make it possible to determine the conditions of rollover and sideslip during turning motion, as well as the threshold values of the slope angle and the linear velocity of turning motion.

The magnitude of the torque about the vertical axis, which is characteristic particularly of four-wheeled robotic platforms with self-steering wheels operating on slopes and has a significant influence on skidding phenomenon, was determined.

Based on the analysis of the differential equation describing the motion of the robotic platform's center of mass and the torque equations with respect to the platform's transverse and longitudinal symmetry axes, the equations of the robotic platform's free oscillations were derived. The derived equations make it possible to determine the vertical displacements, velocities, accelerations, and variations of acceleration of the oscillatory motion, as well as choosing the stiffness of the shock absorber (damper) required to ensure smooth motion of the platform.

The obtained results are of considerable significance and provide a foundation for further investigations into the forced vibration behavior of the robotic platform.

REFERENCES

[1] Abrosimov, V.K., Raykov, A.N. (2022). Intelligent Agricultural Robots (*Интеллектуальные сельскохозяйственные роботы*). Career Press (*Карьера Пррес*), Moscow, 512p.

[2] Akimov, A.V. (2017). Robotics and labor-saving technologies: perspectives of impact on socio-economic development (*Робототехника и трудосберегающие технологии: перспективы воздействия на социально-экономическое развитие*). Historical psychology and sociology (*Историческая психология и социология истории*). - No 1. - pp. 173-192.

[3] Ali, M.A., Kim, C., Kim, S. Khan A.M., Iqbal J, Khalil M.Z., Lim D. and Han Ch. (2017) Lateral acceleration potential field function control for rollover safety of multi-wheel military vehicle with in-wheel-motors. *Int. J. Control Autom. Syst.* 15, 837–847. https://doi.org/10.1007/s12555-014-0573-7

[4] Amin, A., Wang, X., Chen, Y., Guoxiang, S., Xuekai, H., Rottok, L.T., Sayed, H.A.A., Okasha, M. and Hassanien, R.H.E. (2025), Enhancing Greenhouse Performance Through Robotic Roof Cleaning Solutions: A Review. Journal of Field Robotics, 42: 1401-1426. https://doi.org/10.1002/rob.22459

[5] Bak T., Jakobsen H. (2004). Agricultural Robotic Platform with Four Wheel Steering for Weed Detection. *Biosystems Engineering* 87(2), 125-136, DOI:10.1016/j.biosystemseng.2003.10.009.

[6] Bayar, G., Bergerman, M., Koku, A. B., & Ilhan, Konukseven, E. (2015). Localization and control of an autonomous orchard vehicle, *Computers and Electronics in Agriculture*, Volume 115, , Pages 118-128, https://doi.org/10.1016/j.compag.2015.05.015

[7] Biderman V.A.(1980). Theory of Mechanical Oscillations (*Теория механических колебаний*), Mashinostroenie (*Машиностроение*), Moscow.

[8] Blasco, J., Aleixos, N., Rojer, J. M., Rabatal, G., Molto, E. (2002). Robotic weed control using machine vision. *Biosystems Engineering*, 83(2), 149-157.

[9] Buchholz N.N. (2023). Basic Course of Theoretical Mechanics, Part 1 and 2 (*Основной курс теоретической механики, часть 1 и 2*), Lomonosov Moscow State University Publishing House (*Издательство МГУ им. Ломоносова*), Moscow.

[10] Cho, S. I., Kim, Y.Y., An, K.J. (2002). Development of a three-degrees-of-freedom robot for harvesting lettuce using machine vision and fuzzy logic control. *Biosystems Engineering*, 82(2), 143-149.

[11] Fontani, M., Luglio, S. M., Gagliardi, L., Peruzzi, A., Frasconi, C., Raffaelli, M., & Fontanelli, M. (2025). A Systematic Review of 59 Field Robots for Agricultural Tasks: Applications, Trends, and Future Directions. *Agronomy*, 15(9), 2185. https://doi.org/10.3390/agronomy15092185

[12] Fountas, S., Mylonas, N., Malounas, I., Rodias, E., Hellmann Santos, C., & Pekkeriet, E., (2020). Agricultural Robotics for Field Operations. *Sensors*, *20*(9), 2672. https://doi.org/10.3390/s20092672

[13] Ilarionov V.A. (2013). Theory of Automobile (*Теория автомобиля*), NSTU Publishing House, (*Издателтство НГТУ*), Nizhny Novgorod.

[14] Ivanov R., Ivanova D., Kadikyanov G., Staneva G., Minkovska L. (2025) Theoretical study of the stability of a two-axle vehicle with a dynamic model. *Transport Problems,* 20(3):229-241. http://doi.org/10.20858/tp.2025.20.3.18

[15] Li Zhipeng, Shi Songzhuo (2017) Stability of eps system of agricultural vehicles under vibration environment. *INMATEH-Agricultural Engineering*, Vol.51, No.1, 101-110

[16] Lipiński Adam J., Markowski P., Lipiński S., Pyra P., (2016). Precision of tractor operations with soil cultivation implements using manual and automatic steering modes, *Biosystems Engineering,* Volume 145, Pages 22-28, ISSN 1537-5110, https://doi.org/10.1016/j.biosystemseng.2016.02.008.

[17] Litvinov, A.S. (1971). Automobile Controllability and Stability (*Управляемость и устойчивость автомобиля*). Mashinostroenie (*Машиностроение*). Moscow, - 416p.

[18] MarketsandMarkets. (2025, November 7). *Agricultural robots market by robot type, application, offering, end use, farming environment, farm size, and region – global forecast to 2030*. https://www.marketsandmarkets.com/Market-Reports/agricultural-robot-market-173601759.html

[19] Navone A., Martini M., Chiaberge M., (2025). Autonomous robotic pruning in orchards and vineyards: A review, *Smart Agricultural Technology*, Volume 12, 101283, ISSN 2772-3755, https://doi.org/10.1016/j.atech.2025.101283.

[20] O'Meara P. (2019). The ageing farming workforce and the health and sustainability of agricultural communities: A narrative review. *Aust J Rural Health*; 27: 281–289. https://doi.org/10.1111/ajr.12543

[21] Orebäck A; Christensen, H. I. (2003). Evaluation of architectures for mobile robotics. *Autonomous Robots*, 14(1), 33-49.

[22] Qiu Q., Fan Z., Meng Zh., Zhang Q., Cong Y., Li B., Wang N., Zhao Ch., (2018). Extended Ackerman Steering Principle for the coordinated movement control of a four wheel drive agricultural mobile robot, *Computers and Electronics in Agriculture*, Volume 152, Pages 40-50, ISSN 0168-1699, https://doi.org/10.1016/j.compag.2018.06.036.

[23] Ritchie H. (2019). Food production is responsible for one-quarter of the world's greenhouse gas emissions, *Published online at OurWorldinData.org. Retrieved from: https://archive.ourworldindata.org/20251125-173858/food-ghg-emissions.html [Online Resource] (archived on November 25, 2025).*

[24] Sineokov G.N., Panov I.M., (1977) *Theory and calculation of tillage machines (Теория и расчет почвообрабатывающих машин)*, Mashinostroenie (Машиностроение), Moscow -322 p.

[25] Tarverdyan, A., Altunyan, A., Grigoryan, A., (2025). Justification of the Kinematic Parameters of the Running Gear of a Horticultural Robot Platform. "*Agriscience and Technology*", International scientific journal, Armenian National Agrarian University, - №2(90), - pp. 112-119. https://doi.org/10.52276/25792822-2025.2-112

[26] Torii, T. (2000). Research in autonomous agriculture vehicles in Japan. *Computers and Electronics in Agriculture*, 25 (1-2),-pp. 133-153. https://doi.org/0.1016/S0168-1699(99)00060-5

[27] Zagazezheva, O.Z., Berbekova, M.M. (2021). The main trends in the development of robotic technologies in agriculture. *News of the Kabardino-Balkarian Scientific Center of RAS*. - No.5 (103), - pp. 11-20. https://doi.org/10.35330/1991-6639-2021-5-103-11-20.

[28] Zakaria, M.S.M., Singh, A.S.P. and Aras, M.S.M. (2024) "Integrated Chassis Control for Multi-Axle Vehicles: A Comprehensive Review", *International Journal of Automotive and Mechanical Engineering*, 21(3), pp. 11663–11681. doi:10.15282/ijame.21.3.2024.17.0900.

[29] Zinoviev V.A. (1975). *Theory of Mechanisms and Machines* (*Теория механизмов и машин*), Nauka (*Наука*), Moscow.

STUDY OF THE MOTION STABILITY AND OPERATIONAL SMOOTHNESS OF AN AGRICULTURAL ROBOTIC PLATFORM

/

ԳՅՈՒՂԱՏՆՏԵՍԱԿԱՆ ՆՇԱՆԱԿՈՒԹՅԱՆ ՌՈԲՈՏ-ՀԱՐԹԱԿԻ ՇԱՐԺՄԱՆ ԿԱՅՈՒՆՈՒԹՅԱՆ ԵՎ ԸՆԹԱՑՔԻ ՍԱՀՈՒՆՈՒԹՅԱՆ ՈՒՍՈՒՄՆԱՍԻՐՈՒԹՅՈՒՆ

Arshaluys TARVERDYAN[1)], Aghavard KHACHATRYAN[2)], Artur ALTUNYAN[1*)], Sergey PAPYAN[1)], Albert GRIGORYAN[1)]

[1)]Scientific Research Institute for Agricultural Mechanization and Automation, Armenian National Agrarian University, Yerevan, Armenia

[2)]Chair of Higher Mathematics and Physics, Armenian National Agrarian University, Yerevan, Armenia

Tel: +37455327325; E-mail: arturaltunyan@gmail.com

Corresponding author: Artur Altunyan

DOI: https://doi.org/10.35633/inmateh-79-73

Keywords: *movement smoothness, oscillation characteristics, robotic platform, stability on slopes, vehicle stability*

ABSTRACT

This study focuses on the development of a multifunctional agricultural robotic platform. Previous articles in this series established the need for such a platform based on the specific soil and climatic conditions of the Republic of Armenia. Tests of a laboratory prototype indicated the need for further investigation of the platform's dynamic behavior, particularly during operation in orchards and agricultural fields on sloping terrain, which is common in Armenia. Particular attention was given to changes in platform inclination during turning maneuvers on slopes and to the yaw moment generated about the vertical axis in four-wheeled robotic platforms with independently controlled wheels. Based on a mathematical model of the chassis incorporating elastic elements (springs) and damping elements (shock absorbers), the differential equation governing the motion of the platform's center of mass was formulated, together with moment equations about the transverse and longitudinal axes passing through the center of mass. Analysis of these equations yielded the differential equations governing the platform's vertical oscillations. Expressions were subsequently derived for the displacement, velocity, acceleration, and jerk associated with the platform's free oscillations. These equations can be used to evaluate ride smoothness and determine the spring stiffness and shock-absorber damping coefficient required to achieve the desired suspension performance.

ԱՄՓՈՓԱԳԻՐ

Ներկայացվող հոդվածը նվիրված է գյուղատնտեսական բազմաֆունկցիոնալ ռոբոտ-հարթակի մշակման խնդրին: Շարքի նախորդ հոդվածներում հիմնավորվել է այդպիսի ռոբոտ-հարթակի մշակման անհրաժեշտությունը ելնելով հանրապետության հողակլիմայական պայմանների առանձնահատկություններից: Մշակվող ռոբոտ-հարթակի լաբորատոր փորձանմուշի փորձարկումները ցույց տվեցին, որ անհրաժեշտ է իրականացնել լրացուցիչ հետազոտություններ, որոնք հնարավորություն կտան բացահայտելու ռոբոտ-հարթակի շարժման դինամիկան հատկապես թեքություններում տեղակայված այգիներում ու դաշտերում, որոնք բնութագրական են Հայաստանի Հանրապետության հողատեսքերի համար: Հաշվի են առնվել թեքություններում շրջադարձի ընթացքում տեղի ունեցող թեքության անկյան տրանսֆորմացիան, և որ չափազանց կարևոր է, միայն քառանիվ, իրարից անկախ կառավարվող անիվներով ռոբոտ-հարթակներին ներհատուկ, ուղղաձիգ առանցքի շուրջ առաջացող պտտող մոմենտը, որը էական ազդեցություն է թողնում կայունության վրա: Ընթացքային մասի, առաձգական էլեմենտ (զսպանակ) և մարիչ (ամորտիզատոր) պարունակող հաշվարկային սխեմայի համար կազմվել են ռոբոտ-հարթակի մասսաների կենտրոնի շարժման դիֆերենցիալ հավասարումը, ծանրության կենտրոնով անցնող լայնական ու երկայնական սիմետրիայի առանցքների նկատմամբ մոմենտների հավասարումները, դրանց վերլուծության արդյունքում ստացվել են հարթակի ուղղաձիգ տատանումների դիֆերենցիալ հավասարումները: Արդյունքում ստացվել են հարթակի սեփական տատանումների ընթացքում առաջացող տեղափոխությունների, արագությունների, արագացումների և արագացումների փոփոխության որոշման հավասարումները, որոնք հնարավորություն են տալիս գնահատելու ընթացքի սահունությունը և որոշելու դրա ապահովման համար անահրաժեշտ կախոցի համակարգի զսպանակի անհրաժեշտ կոշտությունն ու ամորտիզատորի դիմադրության գործակիցը:

INTRODUCTION

In all countries ensuring food security has always been, and remains, one of the most pressing challenges facing agricultural production. The solving of this problem must involve the conservation and improvement of land resources, meeting environmental requirements, increasing production volumes, the production of environmentally friendly food products, full mechanization of agricultural production, and, particularly importantly, reducing of the energy intensity of these processes. It is evident that the stated problem is multidimensional, and its complete solution using existing technologies and technical means is objectively limited (*Abrosimov and Raykov, 2022; Bak and Jakobsen, 2004; Fontani et al., 2025; O'Meara, 2019; Ritchie, 2024*).

For this reason, two key trends have recently become central to agricultural production technological processes (*Abrosimov and Raykov, 2022; Markets and Markets, 2025; Navone et al., 2025; Tarverdyan et al., 2025*).

First, one of the fastest growing areas in recent years in agricultural production is precision and digital technologies in crop and livestock production.

Second, the direction without which it is impossible to effectively utilize and implement the information obtained through the above-mentioned technologies is the organization of robot-assisted agricultural production. This implies that the development and large-scale implementation of robotics play a central role in addressing the stated problem (*Abrosimov and Raykov, 2022; Navone et al., 2025; O'Meara, 2019; Ritchie, H., 2024)*.

Although the global agricultural robotics market is developing at an unprecedented rate (over the last five years alone, its volume has increased approximately 20-fold) (*Bak and Jakobsen, 2004; MarketsandMarkets, 2025*), the application of such systems in the agricultural sector of the Republic of Armenia remains highly limited. This is primarily due to their relatively high market price, making them inaccessible to the majority of local producers, and second, to their structural characteristics, which result in low operational reliability under the soil conditions of the Republic of Armenia (*Tarverdyan et al., 2025*).

It follows that the problem can be addressed through two approaches: either partial structural modifications should be made to existing robots, or a new universal robotic platform should be developed that is better adapted to the country's soil conditions (presence of stones of various sizes, fragmented terrain) and, importantly, is cost-effective.

For all mobile agricultural robots, the mobile platform is a critical component that plays a key role in the overall system performance of the system. It is therefore not surprising that researchers in this field have devoted significant efforts to the development of high-performance mobile platforms for agricultural robots, as well as to improving their control and positioning accuracy, since these issues are of crucial importance in precision agriculture (*Amin et al., 2025; Bayar et al., 2015; Lipiński et al., 2016; Qiu et al., 2018; Zagazezheva and Berbekova, 2021*).

The operational practice of agricultural robotic platforms over the last 20–25 years, as well as the results of numerous research studies, lead to a clear conclusion: from the perspective of accurate perception and response to external influences during agro-technological processes, minimal energy consumption, minimal soil damage, and high maneuverability, four-wheeled robotic platforms are preferred (*Akimov, 2017; Blasco et al., 2002; Cho et al., 2002*).

In addition, four-wheeled robotic platforms with independently controlled wheels provide high maneuverability and enable parallel motion of the vehicle during turning, allowing positional accuracy and orientation accuracy to be controlled independently (*Bak and Jakobsen, 2004; Cho et al., 2002; Orebäck and Christensen, 2003; Tarverdyan et al., 2025*).

Research on robotic platforms is primarily driven by the shortcomings and challenges identified during their operation. Current studies place significant emphasis on optimal control, stability, and ensuring smooth motion. In this regard, the studies conducted by a group of researchers are of particular interest *(Blasco et al., 2002; Fountas et al., 2020; Zakaria et al., 2024*), in which the authors demonstrate that integrated control systems (ICS)—such as combined steering and wheel torque control, suspension and wheel torque coordination, as well as the integration of steering control systems with suspension—provide superior performance characteristics for multi-axle mobile devices (Multi-axle Vehicles, MAV) compared with skid-steering control systems (SCS). In this optimal distribution approach, the target vehicle forces and yaw torque are distributed among the individual tire forces (*Ali et al., 2017; Li and Shi, 2017; Zakaria et al., 2024*).

Another group of researchers has approached the problem from the perspective of determining the critical speed and its more accurate estimation for a two-axle dynamic model. A 4×2-wheel configuration was

adopted as the vehicle model, and the acting forces and other lateral dynamic parameters were calculated for this model. The problem was analyzed in terms of the forces acting on the vehicle during turning and on inclined surfaces to ensure stability, taking into account the redistribution of reaction forces and variations in the tire–surface adhesion coefficient (*Ivanov et al., 2025*).

In a previous study devoted to this problem (*Tarverdyan et al., 2025*), the kinematic parameters of the motion subsystem of a robotic platform were examined in detail. In particular, the relationships between four independently steerable wheels, steering angles, and their angular velocities were established. Lateral forces arising during turning on a horizontal plane were also partially analyzed.

The present article is devoted to the investigation of the stability of robotic platform motion and conditions of lateral slip on sloped terrain, as well as to the assessment of motion smoothness based on the proposed model.

MATERIALS AND METHODS

Stability of Robotic Platform Motion on Inclined Surfaces

As previously noted, for robotic platforms intended to perform agro-technological operations, the four-wheel configuration with independently controlled wheels is considered preferable. The ability of the platform to perform parallel translational motion, in some cases without rotational turning, provides high maneuverability.

Independent control of all four wheels minimizes lateral slip, thereby reducing not only soil disturbance but also the wear of drivetrain components (*Bak and Jakobsen, 2004; Torii, 2000*).

Although the dynamics of a four-wheeled independently controlled system are inherently nonlinear and control is not straightforward, relatively simple control systems can still be effective at low operational speeds (2–6 km/h), (*Cho et al., 2002; MarketsandMarkets, 2025; Tarverdyan et al.,2025*). The conceptual scheme of the proposed robotic platform is presented in Figure 1. It consists of a platform frame (1), on which various agro-technological implements and devices are mounted; four drive wheels with independent actuation (2); a wheel steering control unit (3); and a wheel steering mechanism (4).

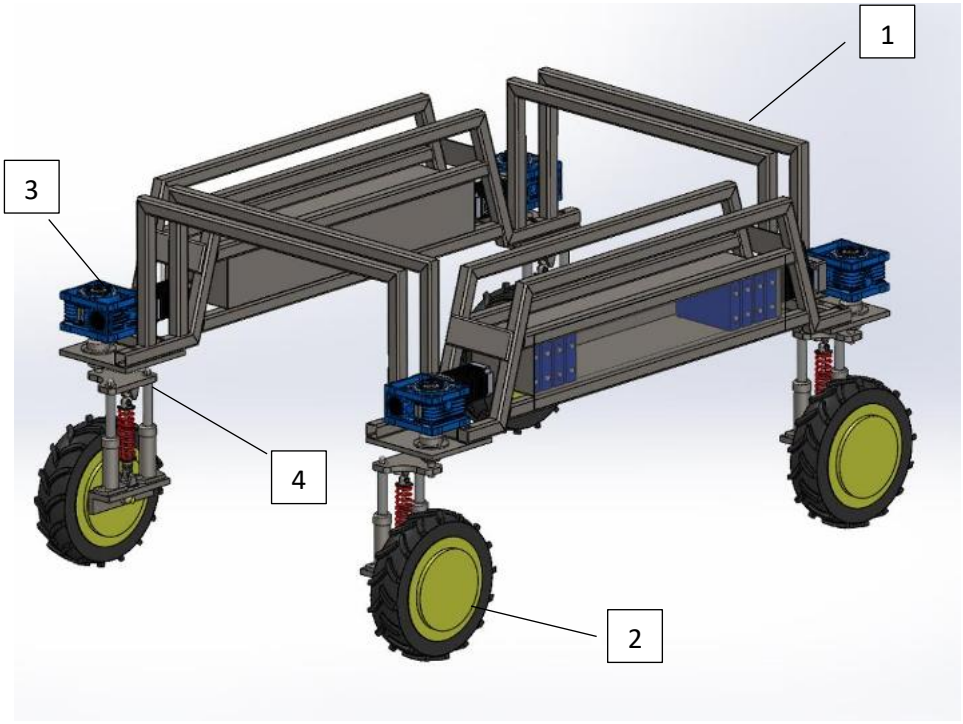


Fig. 1 - 3D model of the developed robotic platform

A detailed kinematic analysis of the locomotion subsystem of the developed robotic platform (*Tarverdyan et al., 2025*) yielded equations that make it possible to determine and refine the parameters used as the basis for programming the platform's turning motion on a horizontal surface.

As a result of the dynamic analysis, precise equations for determining lateral slip forces were obtained. These equations enable the development of a robotic platform drivetrain in which wheel slip during turning is minimized, thereby minimizing soil damage while ensuring operational reliability and durability (*Tarverdyan et al., 2025*).

An agricultural robotic platform can also perform agro-technological operations in fields located on sloped terrain, which is particularly characteristic of the Republic of Armenia. Under such conditions, during the development of the robotic platform, the issue of motion stability, especially during turning, becomes a key subject of analysis.

Assume that the robotic platform performs a turning maneuver on a planar slope inclined at an angle *β* where the rotation axis OO' is perpendicular to the inclined plane and is positioned upslope relative to the robotic platform (Figure 2). The geometric dimensions of the platform are – width B and length L. Since the goal is to develop a structure that is as symmetric as possible in terms of both geometry and mass distribution, it can be assumed that the center of mass coincides with point O_1', located at the intersection of the longitudinal (x_2) and transverse (y_2) symmetry axes of the platform. In this case $a = \frac{L}{2}, b = \frac{B}{2}$. Let the distance of the center of mass from the supporting plane CDEF be denoted by h, and the turning radius of the center of mass by R_0. The steering angles of the wheels are $\theta_1, \theta_2, \theta_3, \theta_4$, while the corresponding turning radii are R_1, R_2, R_3, R_4.

Let consider the turning motion of the robotic platform with a constant turning radius on a slope inclined at an angle β (Figures 2 and 3). Before determining the forces and reactions acting on the platform, it is necessary to account for the transformation of the slope inclination during rotational motion, since it directly affects the magnitude of the force components involved. Let the coordinate system xoy (Figure 3) be fixed to the inclined plane, where the y-axis is aligned with the transverse direction of the slope and the x -axis with the longitudinal direction, with the origin located at the center of rotation. When the rotation angle is φ = 0 (position $\mathcal{A}$ of the robotic platform), the transverse symmetry axis $y_1$of the robotic platform coincides with the y -axis, the longitudinal axis (x_1) inclination angle is β.

When φ = 90°, the axis x_1 becomes parallel to the y-axis $x_1 \parallel y$, while y_1 coincides with the x-axis and is inclined at angle β (Figure 2). When φ = 180°, the configuration becomes symmetric to position $\mathcal{A}$. For all intermediate positions (e.g., position B), the inclination of the robotic platform is characterized by angles β_1 and β_2, which are determined as follows:

$$\begin{cases} sin\beta_1 = sin\beta \cdot sin\varphi, \\ sin\beta_2 = sin\beta \cdot cos\varphi. \end{cases} \quad (1)$$

Let consider the analysis of the forces acting on the robotic platform during turning motion at an arbitrary intermediate position B within the range $0 \leq \varphi \leq 90^0$ (Figure 3) (within the interval $90 - 180^0$, the configuration is repeated symmetrically).

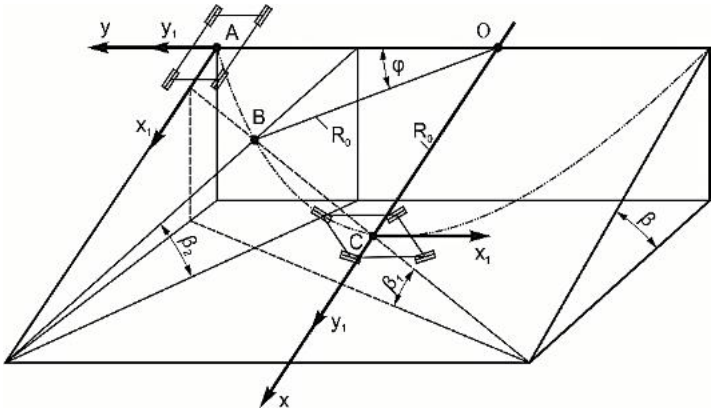


Fig. 2 - Schematic diagram of tilt-angle transformation during the turning motion of the robotic platform

At the specified position, the following forces and torques act on the robotic platform:

The gravitational force G acts at the center of mass and has three components: $G_x = G\cos\beta_1 \cdot sin\beta_2$, directed along the x_2 axis, $G_y = G sin\beta_1$ - directed along the y_2 axis, $G_z = G\cos\beta_1 \cdot \cos\beta_2$ – perpendicular to the inclined plane.

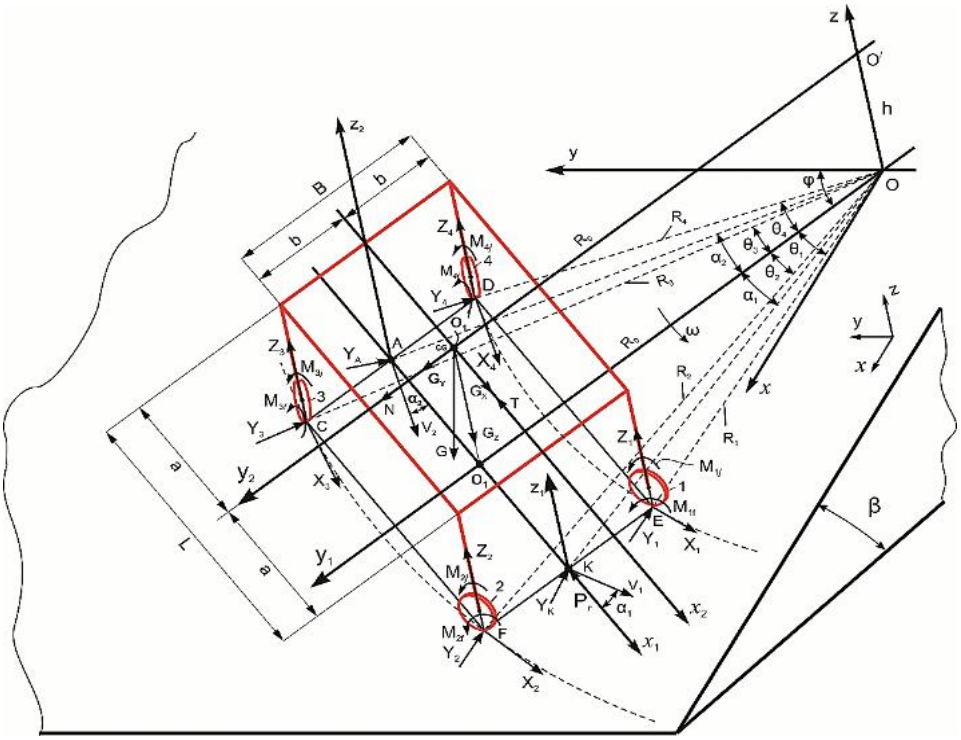


Fig. 3 - Kinematic and dynamic analysis scheme of the turning motion of the robotic platform on an inclined surface

At the wheel–ground contact surfaces, the support reactions Z_i, act normal to the supporting surface. The driving (tractive/tangential) forces X_i act at the wheel contact surfaces and are perpendicular both to the wheel radii (r_w) and to the turning radii R_i associated with rotation about point *O*. The lateral slip resistance forces Y_i, also act at the wheel–ground contact surfaces and are directed along the turning radii (R_i). In the general case, the wheels are also subjected to a torque of the rolling resistance (M_{if}).

The robotic platform is additionally subjected to inertial force factors. At the center of mass (O_1'), the longitudinal inertial force T acts along the x_2 axis, with its direction determined by the nature of the motion (acceleration or deceleration). The centrifugal force N associated with curvilinear motion acts along the y_2 axis. The wheels are also subjected to inertial torques (M_{ij}), as well as the inertial torque of the robotic platform associated with curvilinear motion about the z-axis, denoted by M_{j} (*Litvinov, 1971; Qiu et al., 2018; Zinoviev, 1975*).

To solve the problem of lateral slip of the robotic platform, it is first necessary to determine the support reactions at the wheel–ground contact surfaces, namely Z_1, Z_2, Z_3 *and* Z_4. By formulating the equilibrium equations with respect to the axes passing through the wheel support points ($\mathcal{CD}$, EF, CF and DE) and performing the corresponding transformations, the following equations are obtained:

$$\mathrm{Z}_1 + \mathrm{Z}_2 = \frac{\mathrm{G}_\mathrm{z}}{2} + \frac{\mathrm{G}_x \cdot \mathrm{h}}{2a} - \frac{T \cdot \mathrm{h}}{2a} - \frac{4M_{\mathrm{ij}}}{2a} \tag{2}$$

$$\mathrm{Z}_3 + \mathrm{Z}_4 = \frac{\mathrm{G}_\mathrm{z}}{2} - \frac{\mathrm{G}_x \cdot \mathrm{h}}{2a} + \frac{T \cdot \mathrm{h}}{2a} + \frac{4M_{\mathrm{ij}}}{2a} \tag{3}$$

$$\mathrm{Z}_1 + \mathrm{Z}_4 = \frac{\mathrm{G}_\mathrm{z}}{2} + \frac{\mathrm{G}_\mathrm{y} \cdot \mathrm{h}}{2b} - \frac{N \cdot \mathrm{h}}{2b} \tag{4}$$

$$\mathrm{Z}_2 + \mathrm{Z}_3 = \frac{\mathrm{G}_\mathrm{z}}{2} + \frac{\mathrm{G}_\mathrm{y} \cdot \mathrm{h}}{2b} + \frac{N \cdot \mathrm{h}}{2b} \tag{5}$$

Besides:

$$\mathrm{Z}_1 + \mathrm{Z}_2 + \mathrm{Z}_3 + \mathrm{Z}_4 = \mathrm{G}_\mathrm{z} \tag{6}$$

Let's also introduce the following denotations:

$$\begin{cases} \mathrm{Z}_1 + \mathrm{Z}_2 = \mathcal{A} \\ \mathrm{Z}_3 + \mathrm{Z}_4 = B \\ \mathrm{Z}_1 + \mathrm{Z}_4 = C \\ \mathrm{Z}_2 + \mathrm{Z}_3 = \mathcal{D}. \end{cases} \Rightarrow \mathcal{A} + B = C + \mathcal{D} \tag{7}$$

Let us denote: $Z_1 = S$, where S is an arbitrary parameter. Then:

$$\begin{cases} Z_1 = S \\ Z_2 = \mathcal{A} - S \\ Z_3 = B - C + S = \mathcal{D} + S \\ Z_4 = C - S. \end{cases} \quad (8)$$

The parameter S characterizes the redistribution of the load among the supports, which does not alter the quantities $(Z_1 + Z_2)$, $(Z_1 + Z_4)$, $(Z_3 + Z_4)$ and $(Z_2 + Z_3)$, in other words, equilibrium is preserved, and the model is self-balancing (*Buchholz, 2023; Ilarionov, 2013; Litvinov, 1971*).

Using Equations (2), (3), (4), and (5), together with relations (6) and (8), and considering that $G_x = G\cos\beta_1 \cdot sin\beta_2$, $G_y = G sin\beta_1$, $G_z = G\cos\beta_1 \cdot \cos\beta_2$, where the angles β_1 and β_2 are determined from Equation (1), $N = \frac{G}{g}\omega^2 R_0$, $T = \frac{G}{g} \cdot \frac{dv}{dt}$, $M_{ij} = J_w \cdot \frac{d\omega_w}{dt}$ (J_w is the wheel torque of inertia, and $\frac{d\omega_w}{dt}$ is the angular acceleration of the wheel), and taking into account that uniform motion of the robotic platform is considered, the following equations are obtained for the support reactions:

$$\left.\begin{aligned} Z_1 &= \frac{G}{4}cos\beta_1 \cdot cos\beta_2 - \frac{h \cdot G}{2L} \cdot sin\beta_1 + \frac{G \cdot h}{2B}cos\beta_1 \cdot sin\beta_2 - \frac{G \cdot h \cdot \omega^2 R_0}{g \cdot L} \\ Z_2 &= \frac{G}{4}cos\beta_1 \cdot cos\beta_2 + \frac{G \cdot h}{2L} \cdot sin\beta_1 + \frac{G \cdot h}{2B}cos\beta_1 \cdot sin\beta_2 + \frac{G \cdot h \cdot \omega^2 R_0}{g \cdot L} \\ Z_3 &= \frac{G}{4}cos\beta_1 \cdot cos\beta_2 + \frac{G \cdot h}{2L} \cdot sin\beta_1 - \frac{G \cdot h}{2B}cos\beta_1 \cdot sin\beta_2 + \frac{G \cdot h \cdot \omega^2 R_0}{g \cdot L} \\ Z_4 &= \frac{G}{4}cos\beta_1 \cdot cos\beta_2 - \frac{G \cdot h}{2L} \cdot sin\beta_1 - \frac{G \cdot h}{2B}cos\beta_1 \cdot sin\beta_2 - \frac{G \cdot h \cdot \omega^2 R_0}{g \cdot L} \end{aligned}\right\}. \quad (9)$$

It should be noted that the obtained solutions satisfy condition (7) and correctly reflect the physical nature of the problem.

Assessment and improvement of the Motion Smoothness of the Robotic Platform

Ensuring the smooth motion of the developed robotic platform is an important issue, since it directly determines the accurate execution of agro-technical processes, the operational reliability and durability of its components—particularly the suspension system—and the reliable performance of the orientation and control system.

Figure 4. shows the schematic diagram of the suspension system of the developed robotic platform, which includes an elastic element (spring) (1), a coaxially mounted hydraulic damper (shock absorber) (2), pneumatic wheels (3) each equipped with an independent electric hub motors, and an independent wheel steering control unit (4).

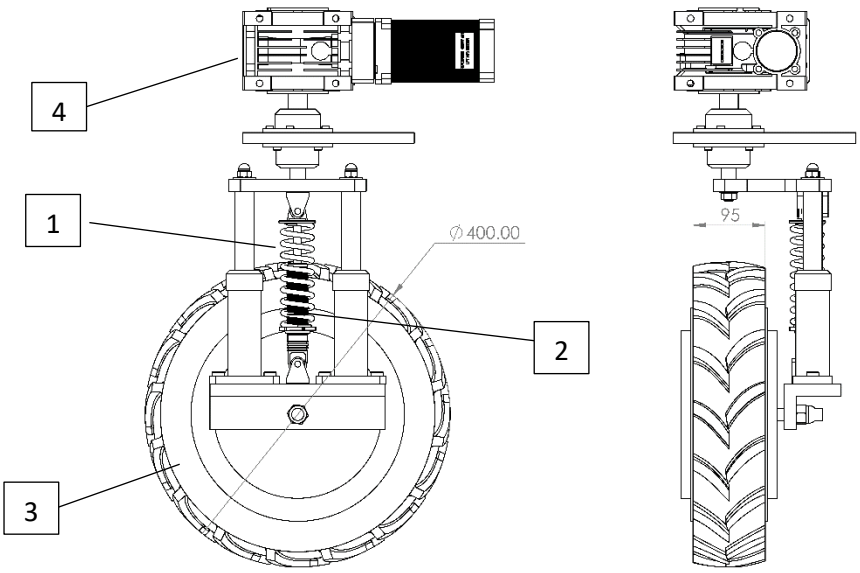


Fig. 4 - Schematic diagram of the suspension system of the robotic platform (all dimensions in *mm*)

It should be noted that, based on the presented suspension system configuration, from an application standpoint it is important to analyze the vertical translational oscillations of the platform, as well as the angular oscillations in the longitudinal and transverse symmetry planes.

The computational scheme of the problem is presented in Figure 5.

The data required for solving the problem are as follows:

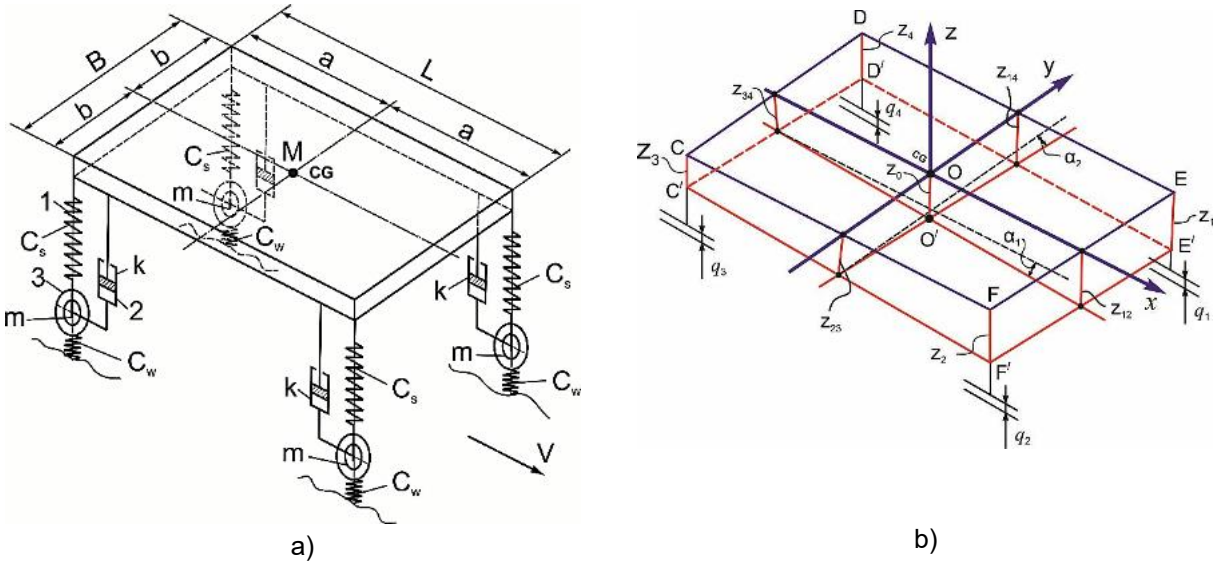
- the overall dimensions of the robot platform: length L, width B;
- the identical stiffness of all four suspension springs c_s;
- wheel stiffness c_w;
- the sprung mass of the robotic platform M;
- the mass of the assemblies located below the springs (unsprung mass) m;
- the damping coefficient of the shock absorbers *k*. Since the two elastic elements the suspension spring and the wheel are connected in series, their combined stiffness can be represented by a single equivalent stiffness coefficient (*Ilarionov, 2013; Litvinov, 1971*).

$$c = \frac{c_s \cdot c_w}{c_s + c_w}.$$

Several assumptions were adopted in solving the problem, which considerably simplify the analysis while having no significant influence on the results.

It is assumed that the robotic platform moves uniformly across field surface irregularities, with the wheels continuously rolling over them while maintaining uninterrupted contact with the ground. Under these conditions, the wheel axles undergo vertical displacements (q_i).

The self-weight of the robotic platform and the loads mounted on it are assumed to be distributed symmetrically with respect to the *x* and *y* axes, such that the center of gravity of the total mass coincides with the origin of the coordinate system (Figure 5).



a) b)

Fig. 5 - Scheme for determining the driving/motion smoothness of the robotic platform:

a) schematic diagram of the suspension system,

b) computational scheme of the platform vertical displacements

In addition, the following notations were adopted:

z_0- vertical displacement of the platform's center of mass caused by oscillations;

z_1; z_2; z_3; z_4- vertical displacements of points C; D; E and F respectively located above the wheel axles;

α_1; α_2 – rotational angles of the platform in the longitudinal and transverse planes of symmetry, respectively;

a - distances from the front (conventionally defined) and rear wheel axles to the y-axis of symmetry passing through the center of mass (a=L/2, since the robotic platform is designed to have a symmetric structure);

b- distance from the wheel suspension attachment points to the x-axis of symmetry passing through the center of mass ($b = \frac{B}{2}$);

ρ_1- radius of inertia of the robotic platform with respect to the y-axis;

ρ_2- radius of inertia of the robotic platform with respect to the x-axis.

It is evident that the solution of the problem involves six unknowns: z_1; z_2; z_3; z_4; z_0 and α_1 (in one case) and α_2 (in the other case). In such situations, it is useful to establish relationships among these unknowns. Considering the sprung part of the robotic platform as a rigid horizontal plate CDEF (Figure 5), as a result of its vertical linear oscillations, at an arbitrary instant it will occupy the position C′ D′ E′ F′ while remaining planar. In the general case of oscillations, it is assumed that the displacements at the indicated points above the wheel axles are different, namely z_1; z_2; z_3; z_4. Under these conditions, geometric relationships exist between these displacements, making it possible to simplify the solution of the problem. In the longitudinal plane of symmetry of the robotic platform (along the x-axis), the displacements of the front edge points, as the midlines of the corresponding rectangles, are expressed as $z_{12} = \frac{z_1+z_2}{2}, z_{34} = \frac{z_3+z_4}{2}$. From the scheme shown in Figure 5, it follows that:

$$z_{12} = z_0 + a_1 \mathrm{a}\,, \qquad z_{34} = z_0 - a_1 \mathrm{a} \tag{11}$$

From which:

$$a_1 = \frac{z_{12} - z_{34}}{L} = \frac{z_1 + z_2 - z_3 - z_4}{2L}\,.$$

Similarly, in the plane of lateral symmetry (along the y-axis), the displacements and the rotation angle of the platform are given by:

$$z_{14} = z_0 + a_2 \cdot \mathrm{b};\; z_{23} = z_0 - a_2 \cdot \mathrm{b} \tag{12}$$

$$a_2 = \frac{z_{14} - z_{23}}{B} = \frac{z_1 + z_4 - z_2 - z_3}{2B}. \tag{13}$$

From the scheme, the following relationships also hold: $z_0 = \frac{z_1+z_3}{2}$, $z_0 = \frac{z_2+z_4}{2}$, from which it follows that:

$$\left.\begin{aligned} z_2 + z_3 &= z_2 + z_4 \\ z_0 &= \frac{z_1 + z_2 + z_3 + z_4}{4} \end{aligned}\right\} \tag{14}$$

To formulate the equations of motions for the considered problem, the principles of rigid-body dynamics are applied (*Biderman, 1980; Buchholz, 2023; Zinoviev, 1975*).

Since in this stage the task is to study only the free oscillations of the robotic platform, the forces caused by terrain irregularities, which include terms proportional to q_i, can be neglected as external excitations. In this case, the differential equation of motion of the platform's center of inertia can be written in the following form:

$$M\frac{d^2 z_0}{dt^2} = \mathrm{k}\left(\frac{dz_1}{dt} + \frac{dz_2}{dt} + \frac{dz_3}{dt} + \frac{dz_4}{dt}\right) + c(z_1 + z_2 + z_3 + z_4) = 0. \tag{15}$$

The torque equations about the x and y axes passing through the center of inertia will be:

$$\mathrm{M}\rho_1^2\frac{d^2\alpha_1}{dt^2} + \mathrm{ka}\left(\frac{dz_1}{dt} - \frac{dz_2}{dt} - \frac{dz_3}{dt} + \frac{dz_4}{dt}\right) + c(z_1 - z_2 - z_3 + z_4) = 0, \tag{16}$$

$$\mathrm{M}\rho_2^2\frac{d^2\alpha_2}{dt^2} + \mathrm{k}b\left(\frac{dz_1}{dt} + \frac{dz_2}{dt} - \frac{dz_3}{dt} - \frac{dz_4}{dt}\right) + cb(z_1 + z_2 - z_3 - z_4) = 0. \tag{17}$$

By inserting the values of $\alpha_1, \alpha_2\ and\ z_0$ from the Equations of (11); (13) and (14) in the Equations of (15); (16) and (17), the following is obtained:

$$\mathrm{M}\cdot\frac{1}{4}\left(\frac{d^2 z_1}{dt^2} + \frac{d^2 z_2}{dt^2} + \frac{d^2 z_3}{dt^2} + \frac{d^2 z_4}{dt^2}\right) + \mathrm{k}\left(\frac{dz_1}{dt} + \frac{dz_2}{dt} + \frac{dz_3}{dt} + \frac{dz_4}{dt}\right) + C(z_1 + z_2 + z_3 + z_4) = 0, \tag{18}$$

$$\frac{\mathrm{M}\rho_1^2}{2L}\cdot\left(\frac{d^2 z_1}{dt^2} + \frac{d^2 z_2}{dt^2} - \frac{d^2 z_3}{dt^2} - \frac{d^2 z_4}{dt^2}\right) + \mathrm{ka}\left(\frac{dz_1}{dt} - \frac{dz_2}{dt} - \frac{dz_3}{dt} + \frac{dz_4}{dt}\right) + ca(z_1 - z_2 - z_3 + z_4) = 0, \tag{19}$$

$$\frac{\mathrm{M}\rho_2^2}{2B}\cdot\left(\frac{d^2 z_1}{dt^2} + \frac{d^2 z_4}{dt^2} - \frac{d^2 z_2}{dt^2} - \frac{d^2 z_3}{dt^2}\right) + \mathrm{k}b\left(\frac{dz_1}{dt} + \frac{dz_2}{dt} - \frac{dz_3}{dt} - \frac{dz_4}{dt}\right) + cb(z_1 + z_2 - z_3 - z_4) = 0. \tag{20}$$

To establish the relationships between Equations (18) and (19), (18) and (20) Equation (18) is multiplied by a and is added to (19), then (18) is multiplied by a and (19) is subtracted. In both cases, the resulting equations are divided by L. Similarly, Equation (18) is multiplied by *b* and added to Equation (20), and the resulting equation is divided by *B*. Equation (18) is then multiplied by *b* and Equation (20) is subtracted from the result, after which the resulting equation is divided by B. Considering the symmetry of the system, such that L=2a and B=2b, the following equations are obtained:

$$M\left(\frac{a^2+\rho_1^2}{2L^2}\right)\left(\frac{d^2z_1}{dt^2}+\frac{d^2z_2}{dt^2}\right)+M\left(\frac{a^2-\rho_1^2}{2L^2}\right)\cdot\left(\frac{d^2z_3}{dt^2}+\frac{d^2z_4}{dt^2}\right)+k\left(\frac{dz_1}{dt}+\frac{dz_4}{dt}\right)+c(z_1+z_4)=0, \quad (21)$$

$$M\left(\frac{a^2-\rho_1^2}{2L^2}\right)\left(\frac{d^2z_1}{dt^2}+\frac{d^2z_2}{dt^2}\right)+M\left(\frac{a^2+\rho_1^2}{2L^2}\right)\cdot\left(\frac{d^2z_3}{dt^2}+\frac{d^2z_4}{dt^2}\right)+k\left(\frac{dz_1}{dt}+\frac{dz_3}{dt}\right)+c(z_1+z_3)=0, \quad (22)$$

$$M\left(\frac{b^2+\rho_2^2}{2B^2}\right)\left(\frac{d^2z_1}{dt^2}+\frac{d^2z_4}{dt^2}\right)+M\left(\frac{b^2-\rho_2^2}{2B^2}\right)\cdot\left(\frac{d^2z_2}{dt^2}+\frac{d^2z_3}{dt^2}\right)+k\left(\frac{dz_1}{dt}+\frac{dz_2}{dt}\right)+c(z_1+z_2)=0, \quad (23)$$

$$M\left(\frac{b^2-\rho_2^2}{2B^2}\right)\left(\frac{d^2z_1}{dt}+\frac{d^2z_4}{dt^2}\right)+M\left(\frac{b^2+\rho_2^2}{2B^2}\right)\cdot\left(\frac{d^2z_2}{dt^2}+\frac{d^2z_3}{dt^2}\right)+k\left(\frac{dz_3}{dt}+\frac{dz_4}{dt}\right)+c(z_3+z_4)=0. \quad (24)$$

The Equations (21)–(22) and (23)–(24) are pairwise interrelated through their first and second terms Even in the particular case where $a=\rho_1$ and $b=\rho_2$, these interrelations are preserved. This indicates that the vertical oscillations of the considered robotic platform, characterized by the coordinates z_1; z_2; z_3 and z_4 are mutually coupled.

The following notation is introduced:

$$M\left(\frac{a^2+\rho_1^2}{2L^2}\right)=M_1;\ M\left(\frac{a^2-\rho_1^2}{2L^2}\right)=M_2;\ M\left(\frac{b^2+\rho_2^2}{2B^2}\right)=M_3;\ M\left(\frac{b^2-\rho_2^2}{2B^2}\right)=M_4.$$

The Equations (21) (22); (23) and (24) will take the following form:

$$M_1\left(\frac{d^2z_1}{dt^2}+\frac{d^2z_2}{dt^2}\right)+M_2\left(\frac{d^2z_3}{dt^2}+\frac{d^2z_4}{dt^2}\right)+k\left(\frac{d^2z_1}{dt}+\frac{d^2z_4}{dt}\right)+c(z_1+z_4)=0, \quad (25)$$

$$M_2\left(\frac{d^2z_1}{dt^2}+\frac{d^2z_2}{dt^2}\right)+M_1\left(\frac{d^2z_3}{dt^2}+\frac{d^2z_4}{dt^2}\right)+k\left(\frac{dz_2}{dt}+\frac{dz_3}{dt}\right)+c(z_2+z_3)=0, \quad (26)$$

$$M_3\left(\frac{d^2z_1}{dt^2}+\frac{d^2z_4}{dt^2}\right)+M_4\left(\frac{d^2z_2}{dt^2}+\frac{d^2z_3}{dt^2}\right)+k\left(\frac{dz_1}{dt}+\frac{dz_2}{dt}\right)+c(z_1+z_2)=0, \quad (27)$$

$$M_4\left(\frac{d^2z_1}{dt}+\frac{d^2z_4}{dt^2}\right)+M_3\left(\frac{d^2z_2}{dt^2}+\frac{d^2z_3}{dt^2}\right)+k\left(\frac{dz_3}{dt}+\frac{dz_4}{dt}\right)+c(z_3+z_4)=0. \quad (28)$$

The obtained equations enable to study the free oscillations of the robotic platform and also serve as a basis for the further investigation of its forced vibrations.

RESULTS AND ANALYSIS

Stability Conditions of the Robotic Platform Motion on Slopes

For the initial parameters of the developed robotic platform (L = 1.6m, B = 1.2m, G = 5000 N, h = 0.6m, ω = 0.278 s^{-1}, R_0 = 5m, β = 10^0) the following results are obtained for three characteristic positions using the derived equations:

when $\varphi=0^0$, $sin\beta_1=0$, $\beta_1=0$, $sin\beta_2=sin\beta$, $\beta_2=\beta$, $G_z=G\cos\beta_1\cdot\cos\beta_2=5000\cdot0.9848=4925\ N$;

when $\varphi=45^0$, $sin\beta_1=sin\beta\cdot sin\varphi=0.1222$, $sin\beta_2=sin\beta\cdot cos\varphi=0.1222$, $cos\beta_1=cos\beta_2=0.9925$, $G_z=G\cos\beta_1\cdot\cos\beta_2=5000\cdot0.9925=4962.5\ N$;

when $\varphi=90^0$, $sin\beta_1=sin\beta\cdot sin\varphi$, $\beta_1=\beta$, $\beta_2=0$, $G_z=G\cos\beta_1\cdot\cos\beta_2=5000\cdot0.9848=4925\ N$;

Substituting the numerical values into Equations (9), the following values are obtained for the support reactions:

when $\varphi=0^0$, $Z_1=1355\ N$; $Z_2=1515\ N$; $Z_3=1095\ N$; $Z_4=960\ N$, verification: $Z_1+Z_2+Z_3+Z_4=4925\ N=G_z$;

when $\varphi=45^0$, $Z_1=1195\ N$; $Z_2=1562.5\ N$; $Z_3=1265\ N$; $Z_4=940\ N$, verification: $Z_1+Z_2+Z_3+Z_4=4962.5\ N=G_z$;

when $\varphi=90^0$, $Z_1=1004.5\ N$; $Z_2=1458\ N$; $Z_3=1458\ N$; $Z_4=1004.5\ N$, verification: $Z_1+Z_2+Z_3+Z_4=4925\ N=G_z$.

The discussion of the robotic platform overturning problem is of little practical significance, since its operational speeds (3 – 6 km/h) and field slope angles (up to 7^0) cannot create a situation in which, even in the most unfavorable position ($\varphi=90^0$) the support reactions Z_1 and Z_4 become equal to 0. In this regard, the analysis of lateral skidding is of primary importance.

To determine the resistance forces against lateral skidding, it is first necessary to determine the tangential reactions (X_i) developed at all driving wheels during rolling motion. It is known that these reaction forces are determined as follows:

$$X_i = P - f\mathrm{Z}_i$$

where P is the circumferential force acting on each driving wheel, f is the rolling resistance coefficient, for various soils $f = 0{,}10 \div 0{,}25$ (*Cho et al., 2002; Litvinov, 1971*), while for cultivated soils $f = 0{,}25$; Z_i is the reaction force at the wheel–ground contact surface. For the considered case:

$$P = \frac{M_m \cdot i \cdot \eta}{r_w} - \mathrm{J}_w \cdot \frac{d\omega_w}{dt} \cdot \frac{1}{r_w}$$

where; r – wheel diameter, M_m - a torque developed by the electric motor, i – a transmission ratio of the motor–wheel drivetrain, η – a drivetrain efficiency, J – a wheel moment of inertia, $d\omega_w$ – an angular acceleration of the wheel

Taking into account that, $\frac{d\omega_w}{dt} = \frac{1}{r_w} \cdot \frac{dv}{dt}$ the following expression is obtained:

$$X_i = \frac{M_m \cdot i \cdot \eta}{r_w} - \mathrm{J}_w \cdot \frac{1}{r_w^2} \cdot \frac{dv}{dt} - f\mathrm{Z}_i \quad (29)$$

Under uniform motion conditions $\frac{dv}{dt} = 0$, therefore:

$$X_i = \frac{M_w}{r_w} - f\mathrm{Z}_i \quad (30)$$

In the case under consideration, where all four wheels are driving wheels and are independently controlled, the tangential (reaction) forces are not equal in either magnitude and direction. As a result, a torque M_z is generated, causing the robotic platform to rotate in the plane of motion. This torque significantly affects lateral skidding.

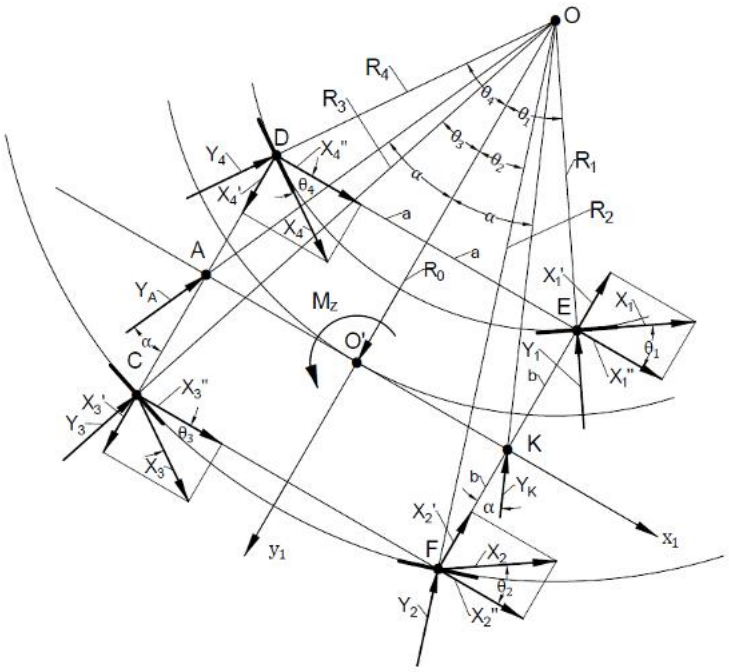


Fig. 6 - Schematic diagram for determining the torque about the vertical axis of the robotic platform

The value/magnitude of this torque is determined according to the scheme shown in Figure 6 as follows:

$$M_z = X_4' \cdot a + X_3' \cdot a + X_2' \cdot a + X_1' \cdot a - X_1'' \cdot b + X_2'' \cdot b + X_3'' \cdot b - X_4'' \cdot b,$$

$$M_z = (X_1 sin\theta_1 + X_2 sin\theta_2 + X_3 sin\theta_3 + X_4 sin\theta_4)a + (X_2 cos\theta_2 + X_3 cos\theta_3)b - (X_1 cos\theta_1 + X_4 cos\theta_4)b; \quad (31)$$

Taking into account that in the considered case $\theta_1 = \theta_4$; $\theta_2 = \theta_3$, for M_z Equation (32) becomes:

$$M_z = (X_1 + X_4)a \cdot sin\theta_1 + (X_2 + X_3)a \cdot sin\theta_2 + (X_2 + X_3)b \cdot cos\theta_2 - (X_1 + X_4)b \cdot cos\theta_1. \quad (32)$$

In the final equation, the forces X_1; X_2; X_3 and X_4 are determined by Equations (29) or (30). The problem of determining θ_1 and θ_2 as well as establishing the relationship between them, is comprehensively discussed in the work of *Tarverdyan et al. (2025)*. Therefore, the torque M_z is determined and for the indicated direction, it is always positive and at least equal to the sum of the first two terms of the equation.

After determining the force factors Z_i; X_i and M_z the lateral resistance (reaction) forces Y_1, Y_2, Y_3 and Y_4 can be determined. Naturally, these forces may be obtained from the dynamic equilibrium conditions of the robot platform; however, it should be emphasized that, in the analysis of the lateral drift phenomenon, the individual determination of these forces is not essential, since lateral skidding is caused by the pairwise combined lateral slip of the conventionally defined front and rear wheels. Proceeding from this consideration, the problem of determining the resultant forces $(Y_3 + Y_4)$ and $(Y_1 + Y_2)$ was examined.

Let the resultant force $(Y_1 + Y_2)$ be transferred to point K on the longitudinal axis of symmetry (x_2), and denote it by Y_K. Similarly, let the resultant $(Y_3 + Y_4) = Y_{\mathcal{A}}$ be applied at point $\mathcal{A}$. It should be noted that this transfer does not alter the mechanical effect of the force system, since the forces Y_1 and Y_2; Y_3 and Y_4 form pairwise concurrent force systems. Since a symmetric system is considered, $Y_{\mathcal{A}}$ and Y_K are inclined relative to the $y_1 - \text{axis}$ by the same angle α, where $tg\alpha = \frac{a}{R_0}$.

Considering the equilibrium condition of the torque of the forces acting on system with respect to the axes Z_1 and Z_2 passing through points $\mathcal{A}$ and K respectively, and using the schematic diagrams shown in Figures 3 and 6, the following equations are obtained:

$$\sum M_{Z_1} = 0; \quad -Y_{\mathcal{A}} cos\alpha \cdot 2a + M_z + M_j + G_y \cdot a + N \cdot a = 0;$$

$$\sum M_{Z_2} = 0; \quad Y_K cos\alpha \cdot 2a + M_z + M_j - G_y \cdot a - N \cdot a = 0; \quad \text{or}$$

$$Y_{\mathcal{A}} = \frac{M_z + M_j + G_y \cdot a + N \cdot a}{2a \cdot cos\alpha} \tag{33}$$

$$Y_K = \frac{N \cdot a + G_y \cdot a - M_z - M_j}{2a \cdot cos\alpha} \tag{34}$$

In these equations, the torque M_z is determined from Equation (32). The inertial torque M_j is determined as follows:

$$M_j = m\rho^2 \frac{d\omega}{dt},$$

where: m is the total loaded mass of the robot platform, ρ is the radius of inertia of the mass m with respect to Z axis perpendicular to the xoy plane and passing through the center of mass; $\frac{d\omega}{dt}$ is the angular acceleration of the rotational motion of the robot platform during turning (for uniform motion $\frac{d\omega}{dt} = 0$). G_y is the component of the gravitational force directed along the transverse axis of symmetry (y_2) of the platform:

$$G_y = G \cdot sin\beta \cdot sin\varphi.$$

N is the centrifugal force generated during turning motion:

$$N = m\omega^2 R_0.$$

Let us determine the magnitude of the lateral drift forces for the adopted initial numerical values, when $\varphi = 90^0$ and G_y attains its maximum value:

$$G_y = G \cdot sin\beta.$$

The numerical data are the same as in the previous example; in this case, the following additional data are also required:

$M_m = 150N \cdot m$; $\eta = 0.9$; $r_w = 0.2m$; $Z_1 = 1004N$; $Z_2 = 1458N$; $Z_3 = 1458N$; $Z_4 = 1004N$; $\theta_1 = 12^0$; $\theta_2 = 9^0$; $\alpha = 10^0$;

For these values, Equation (30) yields the following values for X_i. (assuming that the motion of the robot platform is uniform):

$X_1 = 349.0N$; $X_2 = 236.0N$; $X_3 = 236.0N$; $X_4 = 349.0N$.

Using Equation (32), the following value is obtained for M_z : $M_z = 46.3N \cdot m$; $G_y = 868N$; $N = 193.25N$ (as noted earlier, in the considered case it is assumed that $M_j = 0$).

Using Equations (33) and (34), the lateral drift forces ($Y_{\mathcal{A}}$ and Y_K) of the rear and front axles of the robotic platforms are obtained as:

$$Y_{\mathcal{A}} = 568.0\ N; Y_K = 508.8\ N.$$

For these values of lateral forces, lateral skidding will not occur provided that $(Z_3 + Z_4) \cdot \mu > Y_{\mathcal{A}}$ and $(Z_1 + Z_2) \cdot \mu > Y_K$, where μ is the coefficient of adhesion between the wheel and the supporting surface. For cultivated soil types $\mu = 0{,}4 \div 0{,}45$ (*Litvinov, 1971; Sineokov and Panov, 1977*). For the considered example:

$$(1004 + 1452) \cdot 0.45 > Y_{\mathcal{A}}.$$

$982.4\ N > 568.0\ N$, moreover,

$$982.4\ N > 508.8\ N.$$

Therefore, the condition excluding lateral skidding is satisfied.

Evaluating and Ensuring the Smooth Motion of the Robot Platform

It is well established that, for mobile vehicles—including the robot platform considered and analyzed in this study—the maximum smoothness of motion is ensured when $a = \rho_1$, and in the present case, also when $b = \rho_2$ (*Litvinov,1971; Tarverdyan et al., 2025; Zinoviev, 1975*). Under these conditions, $M_2 = 0$; $M_4 = 0$ and therefore, Equations (25), (26), (27), (28) take the following form:

$$M_1\left(\frac{d^2z_1}{dt^2}+\frac{d^2z_2}{dt^2}\right)+k\left(\frac{dz_1}{dt}+\frac{dz_4}{dt}\right)+c(z_1+z_4)=0, \quad (35)$$

$$M_1\left(\frac{d^2z_3}{dt^2}+\frac{d^2z_4}{dt^2}\right)+k\left(\frac{dz_2}{dt}+\frac{dz_3}{dt}\right)+c(z_2+z_3)=0, \quad (36)$$

$$M_3\left(\frac{d^2z_1}{dt^2}+\frac{d^2z_4}{dt^2}\right)+k\left(\frac{dz_1}{dt}+\frac{dz_2}{dt}\right)+c(z_1+z_2)=0, \quad (37)$$

$$M_3\left(\frac{d^2z_2}{dt^2}+\frac{d^2z_3}{dt^2}\right)+k\left(\frac{dz_3}{dt}+\frac{dz_4}{dt}\right)+c(z_3+z_4)=0. \quad (38)$$

The following notations are introduced:

$$\left.\begin{array}{l} z_1+z_2=R; \\ z_1+z_4=Q; \\ z_3+z_4=F; \\ z_2+z_3=N; \end{array}\right\} \quad \text{and also note that } R+F=Q+N \quad (39)$$

Then, combining Equations (35) and (37) yields:

$$\begin{cases} \dfrac{d^2R}{dt^2}+\dfrac{k}{M_1}\cdot\dfrac{dQ}{dt}+\dfrac{c}{M_1}\cdot Q=0; \\ \dfrac{d^2Q}{dt^2}+\dfrac{k}{M_1}\cdot\dfrac{dR}{dt}+\dfrac{c}{M_1}\cdot R=0. \end{cases} \quad (40)$$

Similarly, from Equations (36) and (38):

$$\begin{cases} \dfrac{d^2F}{dt^2}+\dfrac{k}{M_1}\cdot\dfrac{dN}{dt}+\dfrac{c}{M_1}\cdot N=0; \\ \dfrac{d^2N}{dt^2}+\dfrac{k}{M_3}\cdot\dfrac{dF}{dt}+\dfrac{c}{M_3}\cdot F=0. \end{cases} \quad (41)$$

It follows from the latter equations that systems (40) and (41) are identical, i.e., $F = R$; $N = Q$. Therefore, it is sufficient to solve only system (40).

The following substitutions are introduced:

$$X=\sqrt{M_1}\cdot R;\quad Y=\sqrt{M_3}\cdot Q \quad (42)$$

$$\alpha=\frac{k}{\sqrt{M_1\cdot M_3}};\quad \gamma=\frac{c}{\sqrt{M_1\cdot M_3}}. \quad (43)$$

The system of equations in Equation (40) can then be written as:

$$\begin{cases} X''+\alpha Y'+\gamma Y=0; \\ Y''+\alpha X'+\gamma Y=0. \end{cases} \quad (44)$$

The following notation is introduced:

$$X+Y=U;\quad X-Y=V \quad (45)$$

Adding and subtracting the equations in system (44) yields:

$$U''+\alpha U'+\gamma U=0; \quad (46)$$

$$V''-\alpha V'-\gamma Y=0. \quad (47)$$

The characteristic equation associated with Equation (46) will be:

$\varepsilon^2+\alpha\varepsilon+\gamma=0$; whose roots are:

$\varepsilon_{1,2}=\frac{-\alpha\pm\sqrt{\alpha^2-4\gamma}}{2}=\frac{-\alpha\pm i\sqrt{4\gamma-\alpha^2}}{2}=-\frac{\alpha}{2}\pm\frac{i\omega}{2}$, where $\omega=\sqrt{4\gamma-\alpha^2}$.

Since $4\gamma>\alpha^2$, the general solution of Equation (46) will be:

$$U(t)=e^{-\frac{\alpha t}{2}}\left(A_1 cos\frac{\omega}{2}t+A_2 sin\frac{\omega}{2}t\right). \quad (48)$$

The characteristic equation associated with Equation (47) is: $\xi^2-\alpha\xi-\gamma=0$, which has two real roots:

$\varepsilon_{1,2}=\frac{\alpha\pm\sqrt{\alpha^2+4\gamma}}{2}$, besides $\varepsilon_1=\frac{\alpha+\sqrt{\alpha^2+4\gamma}}{2}>0$.

The general solution of Equation (47) is therefore:

$$V(t)=A_3e^{\varepsilon_1 t}+A_4e^{\varepsilon_2 t}. \quad (49)$$

Because an exponentially increasing solution has no physical meaning in this context, the following condition $A_3 = 0$ is imposed.

Returning to the original functions R and Q and using Equations (42) and (45), the following is obtained:

$$R = \frac{U+V}{2\sqrt{M_1}}; Q = \frac{U-V}{2\sqrt{M_3}}, \text{ or}$$

$$R(t) = \frac{1}{2\sqrt{M_1}}\left[e^{-\frac{\alpha t}{2}}\left(A_1 cos\frac{\omega}{2}t + A_2 sin\frac{\omega}{2}t\right) + A_4 e^{\varepsilon_2 t}\right]; \quad (50)$$

$$Q(t) = \frac{1}{2\sqrt{M_3}}\left[e^{-\frac{\alpha t}{2}}\left(A_1 cos\frac{\omega}{2}t + A_2 sin\frac{\omega}{2}t\right) - A_4 e^{\varepsilon_2 t}\right]. \quad (51)$$

The solution to system (39) is now considered. Taking into account that $R + F = Q + N; \Rightarrow R = Q$, the solution can be expressed as:

$$z_1 = Q - z_4; \quad z_2 = R - Q + z_4; \quad z_3 = F - z_4.$$

where z_4 is an arbitrary function.

Using the geometric relationship among the vertical linear displacements given by Equation (14), the following expression is obtained:

$Q - z_4 + F - z_4 = R - Q + z_4 + z_4$, from which it follows that:

$$z_4 = \frac{2Q}{4} = \frac{Q}{2} = \frac{R}{2}.$$

Thus: $z_1 = z_2 = z_3 = z_4 = \frac{R}{2}$.

The initial conditions are: $\begin{cases} z_{i(0)} = \delta, & i = 1,2,3,4 \\ \dot{z}_{i(0)} = 0, & i = 1,2,3,4. \end{cases}$

Where δ is the static deflection of the elastic element (spring) of the suspension system under the static load.

$$\left.\begin{aligned} z_{1(0)} = \frac{R(0)}{2} = \delta \Rightarrow \frac{1}{4\sqrt{M_1}}(A_1 + A_4) \\ z_{2(0)} = \frac{Q(0)}{2} = \delta \Rightarrow \frac{1}{4\sqrt{M_3}}(A_1 - A_4) \end{aligned}\right\}, \text{ wherefrom}$$

$$\left.\begin{aligned} A_1 = 2\delta\left(\sqrt{M_1} + \sqrt{M_3}\right) \\ A_4 = 2\delta\left(\sqrt{M_1} - \sqrt{M_3}\right) \end{aligned}\right\} \quad (52)$$

The following condition is now applied: $\dot{z}_{i(0)} = 0$, $\dot{z}_{1(0)} = 0 = \frac{\dot{R}(0)}{2} = \frac{1}{4\sqrt{M_1}}\left(-\frac{\alpha}{2}A_1 + A_2\frac{\omega}{2} + A_4\varepsilon_2\right)$,

$$\dot{z}_{2(0)} = 0 = \frac{\dot{Q}(0)}{2} = \frac{1}{4\sqrt{M_3}}\left(-\frac{\alpha}{2}A_1 + A_2\frac{\omega}{2} - A_4\xi_2\right),$$

From the latter equations it follows that:

$$\begin{cases} A_2\frac{\omega}{2} = \frac{\alpha}{2}A_1 - A_4\varepsilon_2, \\ A_2\frac{\omega}{2} = A_4\varepsilon_2 + \frac{\alpha}{2}A_1, \end{cases}$$

from which it follows that:

$$A_4 = 0, \quad A_2 = \frac{\alpha A_1}{\omega} = \frac{2\delta\alpha}{\omega}\left(\sqrt{M_1} + \sqrt{M_3}\right). \quad (53)$$

From the condition $A_4 = 0$, it becomes evident that $\sqrt{M_1} = \sqrt{M_3}$, $M_1 = M_3$.

Thus, taking into account Equations (50), (51), (52) and (53), the following equation is obtained for the linear displacements of oscillation:

$$z_1 = z_2 = z_3 = z_4 = \frac{1}{4\sqrt{M_1}} \cdot e^{-\frac{\alpha t}{2}}\left(4\delta\sqrt{M_1} \cdot cos\frac{\omega t}{2} + \frac{4\delta\alpha}{\omega} \cdot \sqrt{M_1} sin\frac{\omega t}{2}\right).$$

Or, in final form:

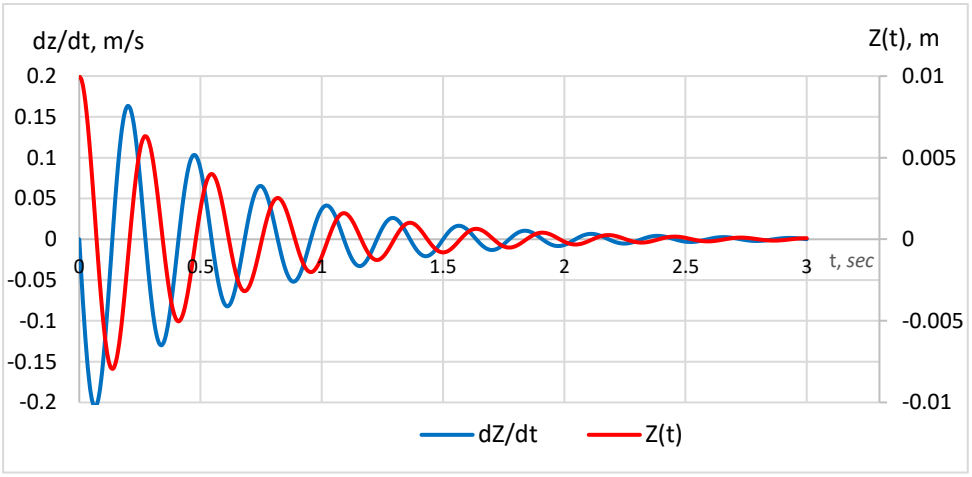
$$z_{i(t)} = \delta e^{-\frac{\alpha t}{2}} \cdot \left(cos\frac{\omega t}{2} + \frac{\alpha}{\omega} \cdot sin\frac{\omega t}{2}\right) \quad (54)$$

Based on the analysis of the free oscillations of the robotic platform, the derived equations make it possible to determine the key oscillation parameters included in the characteristic performance indicators of the suspension system, namely the oscillation frequency, amplitude, and period, which determine the smoothness of motion (*Biderman, 1980; Ilarionov, 2013; Zinoviev,1975*). In addition, the final Equation (54) makes it possible to determine the oscillation velocity: $\left(\frac{dz}{dt}\right)$

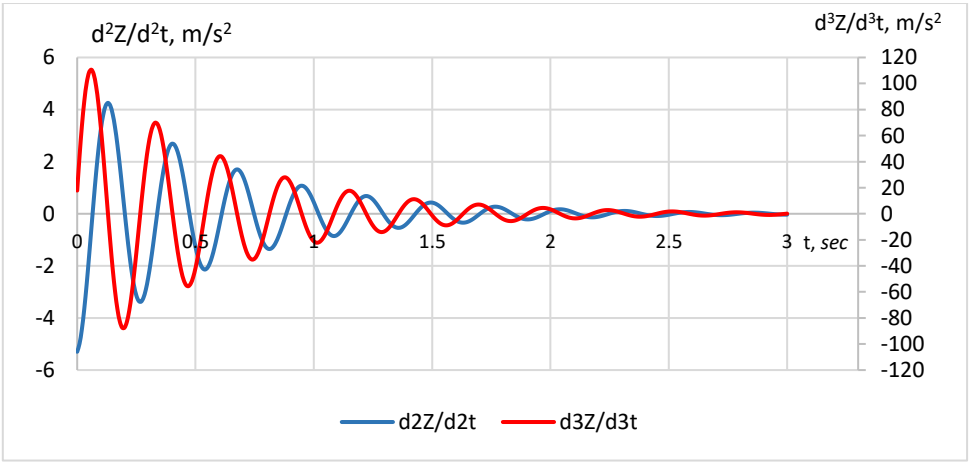
The acceleration: $\left(\frac{d^2z}{dt^2}\right)$ and the rate of acceleration change, which is an important characteristic parameter in problems of this type: $\left(\frac{d^3z}{dt^3}\right)$.

Based on Equation (54), the equations derived from it, and the initial parameters of the robotic platform being developed, the following values were adopted: L=1,60 m; B=1,20 m; a=0,8 m; b=0,6 m; $\rho_1 = 0{,}8\ m$; $\rho_2 = 0{,}6\ m$; M=500 kg. Under these conditions: $M_1 = M_2 = M_3 = M_4 = 125$ kg, the equivalent stiffness coefficient of the suspension system is: $c_b = 66.65 \cdot 10^3 \frac{N}{m} = 66.65 \cdot 10^3 \frac{kg}{s^2}$, the average value of the resistance coefficient of a shock absorber: $k = 420 \frac{N \cdot s}{m} = 420 \frac{kg}{s}$, the vertical static deflection: $\delta = 0.01\ m$, and with calculated values:

$\alpha = \frac{k}{M_1} = \frac{420}{125} = 3.36\ s^{-1}$, $\frac{\alpha}{2} = 1.68\ s^{-1}$, $\omega = \sqrt{\frac{4c}{M_1} - \alpha^2} = \sqrt{\frac{4 \cdot 66.65 \cdot 10^3}{125} - (3.36)^2} = 46.06 s^{-1}$, the graphs of the obtained functions are presented in Figure 7.



a)



b)

Fig. 7 - Graphs of the free oscillations of the robot platform

a) vertical displacements and velocities; b) velocities and accelerations.

The obtained analytical equations make it possible to select such stiffness values (c) for the elastic elements of the suspension system and such a damping coefficient (k), for the shock absorber (damper) that the required programmed parameters of the oscillatory motion are ensured.

Furthermore, the presented results and derived equations provide the basis for the next stage of the research, namely the investigation of the forced oscillations of the robotic platform.

CONCLUSIONS

As a result of the stability analysis of the developed agricultural robotic platform equipped with four driven and self-steering wheels operating on slopes, analytical equations were obtained that make it possible to determine the conditions of rollover and sideslip during turning motion, as well as the threshold values of the slope angle and the linear velocity of turning motion.

The magnitude of the torque about the vertical axis, which is characteristic particularly of four-wheeled robotic platforms with self-steering wheels operating on slopes and has a significant influence on skidding phenomenon, was determined.

Based on the analysis of the differential equation describing the motion of the robotic platform's center of mass and the torque equations with respect to the platform's transverse and longitudinal symmetry axes, the equations of the robotic platform's free oscillations were derived. The derived equations make it possible to determine the vertical displacements, velocities, accelerations, and variations of acceleration of the oscillatory motion, as well as choosing the stiffness of the shock absorber (damper) required to ensure smooth motion of the platform.

The obtained results are of considerable significance and provide a foundation for further investigations into the forced vibration behavior of the robotic platform.

REFERENCES

[1] Abrosimov, V.K., Raykov, A.N. (2022). Intelligent Agricultural Robots (*Интеллектуальные сельскохозяйственные роботы*). Career Press (*Карьера Пррес*), Moscow, 512p.

[2] Akimov, A.V. (2017). Robotics and labor-saving technologies: perspectives of impact on socio-economic development (*Робототехника и трудосберегающие технологии: перспективы воздействия на социально-экономическое развитие*). Historical psychology and sociology (*Историческая психология и социология истории*). - No 1. - pp. 173-192.

[3] Ali, M.A., Kim, C., Kim, S. Khan A.M., Iqbal J, Khalil M.Z., Lim D. and Han Ch. (2017) Lateral acceleration potential field function control for rollover safety of multi-wheel military vehicle with in-wheel-motors. *Int. J. Control Autom. Syst.* 15, 837–847. https://doi.org/10.1007/s12555-014-0573-7

[4] Amin, A., Wang, X., Chen, Y., Guoxiang, S., Xuekai, H., Rottok, L.T., Sayed, H.A.A., Okasha, M. and Hassanien, R.H.E. (2025), Enhancing Greenhouse Performance Through Robotic Roof Cleaning Solutions: A Review. Journal of Field Robotics, 42: 1401-1426. https://doi.org/10.1002/rob.22459

[5] Bak T., Jakobsen H. (2004). Agricultural Robotic Platform with Four Wheel Steering for Weed Detection. *Biosystems Engineering* 87(2), 125-136, DOI:10.1016/j.biosystemseng.2003.10.009.

[6] Bayar, G., Bergerman, M., Koku, A. B., & Ilhan, Konukseven, E. (2015). Localization and control of an autonomous orchard vehicle, *Computers and Electronics in Agriculture*, Volume 115, , Pages 118-128, https://doi.org/10.1016/j.compag.2015.05.015

[7] Biderman V.A.(1980). Theory of Mechanical Oscillations (*Теория механических колебаний*), Mashinostroenie (*Машиностроение*), Moscow.

[8] Blasco, J., Aleixos, N., Rojer, J. M., Rabatal, G., Molto, E. (2002). Robotic weed control using machine vision. *Biosystems Engineering*, 83(2), 149-157.

[9] Buchholz N.N. (2023). Basic Course of Theoretical Mechanics, Part 1 and 2 (*Основной курс теоретической механики, часть 1 и 2*), Lomonosov Moscow State University Publishing House (*Издательство МГУ им. Ломоносова*), Moscow.

[10] Cho, S. I., Kim, Y.Y., An, K.J. (2002). Development of a three-degrees-of-freedom robot for harvesting lettuce using machine vision and fuzzy logic control. *Biosystems Engineering*, 82(2), 143-149.

[11] Fontani, M., Luglio, S. M., Gagliardi, L., Peruzzi, A., Frasconi, C., Raffaelli, M., & Fontanelli, M. (2025). A Systematic Review of 59 Field Robots for Agricultural Tasks: Applications, Trends, and Future Directions. *Agronomy*, 15(9), 2185. https://doi.org/10.3390/agronomy15092185

[12] Fountas, S., Mylonas, N., Malounas, I., Rodias, E., Hellmann Santos, C., & Pekkeriet, E., (2020). Agricultural Robotics for Field Operations. *Sensors*, *20*(9), 2672. https://doi.org/10.3390/s20092672

[13] Ilarionov V.A. (2013). Theory of Automobile (*Теория автомобиля*), NSTU Publishing House, (*Издателтство НГТУ*), Nizhny Novgorod.

[14] Ivanov R., Ivanova D., Kadikyanov G., Staneva G., Minkovska L. (2025) Theoretical study of the stability of a two-axle vehicle with a dynamic model. *Transport Problems,* 20(3):229-241. http://doi.org/10.20858/tp.2025.20.3.18

[15] Li Zhipeng, Shi Songzhuo (2017) Stability of eps system of agricultural vehicles under vibration environment. *INMATEH-Agricultural Engineering*, Vol.51, No.1, 101-110

[16] Lipiński Adam J., Markowski P., Lipiński S., Pyra P., (2016). Precision of tractor operations with soil cultivation implements using manual and automatic steering modes, *Biosystems Engineering,* Volume 145, Pages 22-28, ISSN 1537-5110, https://doi.org/10.1016/j.biosystemseng.2016.02.008.

[17] Litvinov, A.S. (1971). Automobile Controllability and Stability (*Управляемость и устойчивость автомобиля*). Mashinostroenie (*Машиностроение*). Moscow, - 416p.

[18] MarketsandMarkets. (2025, November 7). *Agricultural robots market by robot type, application, offering, end use, farming environment, farm size, and region – global forecast to 2030*. https://www.marketsandmarkets.com/Market-Reports/agricultural-robot-market-173601759.html

[19] Navone A., Martini M., Chiaberge M., (2025). Autonomous robotic pruning in orchards and vineyards: A review, *Smart Agricultural Technology*, Volume 12, 101283, ISSN 2772-3755, https://doi.org/10.1016/j.atech.2025.101283.

[20] O'Meara P. (2019). The ageing farming workforce and the health and sustainability of agricultural communities: A narrative review. *Aust J Rural Health*; 27: 281–289. https://doi.org/10.1111/ajr.12543

[21] Orebäck A; Christensen, H. I. (2003). Evaluation of architectures for mobile robotics. *Autonomous Robots*, 14(1), 33-49.

[22] Qiu Q., Fan Z., Meng Zh., Zhang Q., Cong Y., Li B., Wang N., Zhao Ch., (2018). Extended Ackerman Steering Principle for the coordinated movement control of a four wheel drive agricultural mobile robot, *Computers and Electronics in Agriculture*, Volume 152, Pages 40-50, ISSN 0168-1699, https://doi.org/10.1016/j.compag.2018.06.036.

[23] Ritchie H. (2019). Food production is responsible for one-quarter of the world's greenhouse gas emissions, *Published online at OurWorldinData.org. Retrieved from: https://archive.ourworldindata.org/20251125-173858/food-ghg-emissions.html [Online Resource] (archived on November 25, 2025).*

[24] Sineokov G.N., Panov I.M., (1977) *Theory and calculation of tillage machines (Теория и расчет почвообрабатывающих машин)*, Mashinostroenie (Машиностроение), Moscow -322 p.

[25] Tarverdyan, A., Altunyan, A., Grigoryan, A., (2025). Justification of the Kinematic Parameters of the Running Gear of a Horticultural Robot Platform. "*Agriscience and Technology*", International scientific journal, Armenian National Agrarian University, - №2(90), - pp. 112-119. https://doi.org/10.52276/25792822-2025.2-112

[26] Torii, T. (2000). Research in autonomous agriculture vehicles in Japan. *Computers and Electronics in Agriculture*, 25 (1-2),-pp. 133-153. https://doi.org/0.1016/S0168-1699(99)00060-5

[27] Zagazezheva, O.Z., Berbekova, M.M. (2021). The main trends in the development of robotic technologies in agriculture. *News of the Kabardino-Balkarian Scientific Center of RAS*. - No.5 (103), - pp. 11-20. https://doi.org/10.35330/1991-6639-2021-5-103-11-20.

[28] Zakaria, M.S.M., Singh, A.S.P. and Aras, M.S.M. (2024) "Integrated Chassis Control for Multi-Axle Vehicles: A Comprehensive Review", *International Journal of Automotive and Mechanical Engineering*, 21(3), pp. 11663–11681. doi:10.15282/ijame.21.3.2024.17.0900.

[29] Zinoviev V.A. (1975). *Theory of Mechanisms and Machines* (*Теория механизмов и машин*), Nauka (*Наука*), Moscow.

SIMULATION ANALYSIS AND PARAMETER OPTIMIZATION OF A TWIN-ROLL SOIL-CRUSHING DEVICE FOR A POTATO HARVESTER

马铃薯收获机对辊式碎土装置仿真分析与参数优化

Yangbiao HUANG[1)], Song CHEN[1)], Zihao OU[1)], Qingmiao XIANG[1)], Bei WU*[1,2)], Bang JI[1,2)], Zhichao FANG[1,2)], Fangping XIE[1,2)]

[1)] Hunan Agricultural University, College of Mechanical and Electrical Engineering, Changsha / China;
[2)] Hunan Key Laboratory of Intelligent Agricultural Machinery and Equipment, Changsha / China
Tel: +86 15802521582; E-mail: wubei@hunau.edu.cn
Corresponding author: Bei Wu
DOI: https://doi.org/10.35633/inmateh-79-74

Keywords: *Potato harvester; Roller-type Soil Crushing Device; Potato-soil separation device; EDEM; Heavy clay soil*

ABSTRACT

Winter potato cultivation in paddy fields in southern China can improve land-use efficiency and increase farmers' incomes. However, compared with those in northern China, paddy soils in southern China are generally heavy, cohesive, and compacted, resulting in poor mechanized potato-harvesting performance and restricting the development of the potato industry. To improve potato-soil separation efficiency under heavy clay soil conditions, a twin-roll soil-crushing device was installed ahead of a conventional chain-and-rod potato-soil separation device based on the characteristics of clayey soils in southern China. This configuration formed a two-stage separation process involving soil crushing followed by screening. The soil-crushing process was theoretically analyzed, a discrete element model of the soil-crushing and screening device was established, and the soil-crushing and potato–soil separation processes were numerically simulated. Response surface simulation experiments were conducted using rib height, number of ribs, and twin-roll rotational speed as the experimental factors, with soil-screening efficiency and the maximum force acting on the potato tubers as the response variables. The results showed that the twin-roll soil-crushing device effectively disturbed and crushed the soil during operation. Increasing the rib height and twin-roll rotational speed enhanced the soil-disturbance and crushing effects. The optimal structural and operating parameters of the twin-roll soil-crushing device were a rib height of 30 mm, three ribs, and a twin-roll rotational speed of 323.70 r/min. A simulation verification test conducted using these optimal parameters yielded a soil-screening efficiency of 72.80% and a maximum force acting on the potato tubers of 15.45 N. Field-test results showed that the potato harvester equipped with the soil-crushing device achieved a tuber damage rate of 0.285%, a skin-damage rate of 2.38%, and a tuber loss rate of 3.18%, thereby meeting the requirements of the applicable national standards. These findings provide a reference and technical support for the development of potato-harvesting machinery suitable for heavy clay soil conditions.

摘要

中国南方水稻田冬种马铃薯能提高土地利用率，促进农民增收，相较于北方，南方水稻田土壤黏重板结，常见马铃薯机械化收获作业效果不佳，制约了产业的发展。为了提高黏重土壤下薯土分离效率，本研究针对中国南方黏土土壤特点，在传统链杆式薯土分离装置前设计了对辊式碎土装置，形成“先破碎、后筛分”两级分离流程，提高薯土分离效率，对碎土过程进行了理论分析，构建了碎土筛分装置离散元模型并对土壤破碎和薯土分离过程进行了数值模拟。以碎土装置的凸棱高度、凸棱数量、对辊转速为试验因素，以土壤筛分效率和薯块最大受力为评价指标，开展了响应面仿真试验，结果表明，对辊式碎土装置在工作时对土壤起到了扰动和破碎作用，增加凸棱高度和提高对辊转速能够增加碎土装置对土壤的扰动和破碎作用。对辊式碎土装置的最优结构运行参数为凸棱高度 30 mm，凸棱数量为 3 个，对辊转速 323.0 r/m n，以此最优参数开展仿真验证试验，土壤筛分效率为 2.80%，薯块最大受力为15.45N。田间试验结果表明，配置有碎装置的马铃薯收获机伤薯率为0.285%，破皮率为2.38%，损失率为3.18%，满足国家标准要求。研究结果能为黏重土壤条件下马铃薯收获机具的研发提供参考和支撑。

Yangbiao Hunag, Ms. Stud.; Song Chen, Ms. Stud.; Zihao Ou, Ms. Stud.; Qingmiao Xiang, Ms. Stud.; Bei Wu, Lect. Ph.D.; Bang JI, Prof. Ph.D. Zhichao Fang Lect. Ph.D. Pingfang Xie Prof. Ph.D.

INTRODUCTION

The annual potato planting area in China exceeds 6 million hectares, making the potato industry a vital pillar for promoting rural revitalization and ensuring national food security *(Li et al., 2022*). In the southern regions, cultivating potatoes in winter-idle rice fields enhances land-use efficiency and complements the market supply season, offering broad development prospects. However, potato-growing areas in the south are predominantly located in hilly and mountainous regions characterized by heavy, compact clay soils. Furthermore, the harvest season often coincides with the rainy season, leading to high soil moisture content. These harsh conditions pose severe challenges for mechanized harvesting (*Jiang et al., 2016*). Existing harvesting machinery, primarily designed for the loose, sandy soils of the north, struggles to adapt to southern clay soils, resulting in low soil-tuber separation efficiency and a low rate of exposed tubers (*Bei et al., 2021; Li et al., 2022; Lv et al., 2017*). Therefore, designing potato harvesting machinery tailored to heavy clay soil and hilly terrain is of great significance for the southern winter potato industry (*Wang et al., 2021; Zhang et al., 2021; Zhongcai et al., 2019; Zhou et al., 2021*).

To achieve efficient, low-loss potato harvesting in heavy clay soils, existing research has primarily explored mechanical structure innovations and operational parameter optimizations. In terms of mechanical structures, various separation mechanisms have been developed. For instance, digging devices with vibration functions have been designed to reduce digging resistance in sticky soils (*Lv et al., 2015*). Multi-stage chain-and-rod screening devices and concave-bar structures have been implemented to increase soil disturbance and enhance separation efficiency (*Xiaoxuan et al., 2024; Qingmiao et al., 2024*). Additionally, roller structures with staggered rod arrangements *(Shi et al., 2012)* and flexible rotary-vibration systems *(Xiang et al., 2020)* have been developed to reduce clogging and mechanical damage. Regarding operational parameters, studies have demonstrated that matching a "high frequency and low amplitude" vibration with appropriate linear velocities can improve the soil crushing rate and minimize tuber damage (*CAAMS, 2007; Li et al., 2016; Li et al., 2021*). Furthermore, recent studies have continuously emphasized the importance of optimizing machine-soil interaction mechanisms through Discrete Element Method (DEM) simulations to improve separation and digging performance in complex agricultural terrains (*Fu et al., 2023; Ge et al., 2025*).

Despite these advancements in screening structures and kinematics, a critical research gap remains: existing separation mechanisms are primarily designed to sieve pre-loosened soil rather than actively break hard, cohesive clods. Practical experiments indicate that severe soil compaction and high viscosity are the fundamental causes of incomplete soil-tuber separation in southern fields. Under such conditions, standard chain-and-rod or vibrating separation devices lack the initial mechanical impact required to shatter the compacted clay structure. Consequently, large, wet soil clods carry the tubers over the sieves without separating, rendering the subsequent screening stages ineffective. To overcome this bottleneck, it is imperative to introduce a robust, active soil-breaking mechanism prior to the main screening device to destroy the compacted soil structure at the earliest stage.

To address this gap, a twin-roll soil-crushing device was installed ahead of a conventional chain-and-rod separation conveyor. The protruding ribs on the rolls exert impact and shear forces on compacted clay clods, thereby promoting their fragmentation. Based on a theoretical kinematic analysis, a discrete element model of the soil-crushing and screening device was established to simulate the potato–soil separation process. A response surface methodology (RSM) simulation experiment was conducted using rib height, number of ribs, and twin-roll rotational speed as the experimental factors, with soil-screening efficiency and the maximum force acting on the potato tubers as the response variables. This study aimed to optimize the structural and operating parameters of the twin-roll soil-crushing device and provide a theoretical basis and technical reference for the development of efficient potato-harvesting machinery suitable for heavy clay soils.

MATERIALS AND METHODS

Structure of the twin-roll soil crushing device

The potato harvester equipped with a twin-roll soil-crushing device was designed for operation in the heavy clay soils of southern China. As shown in Fig. 1, the machine mainly comprises a digging shovel, disc coulters, a transmission system, a lateral conveying device, a debris-removal device, a potato–soil separation device, and a soil-crushing device. According to the *Agricultural Machinery Design Manual* (CAAMS, 2007), the potato–soil separation device was designed with a length of 1.75 m, and the chain-and-rod conveyor was inclined at an angle of 30° to the horizontal *(Ma et al., 2012; Zhou et al., 2021)*.

To facilitate the fragmentation of heavy, cohesive soil and improve the screening efficiency of the potato–soil separation device, the twin-roll soil-crushing device was installed between the digging shovel and the potato–soil separation device. The device consists of two rolls rotating in the same direction, with three to five protruding ribs arranged on the surface of each roll. During operation, the twin-roll soil-crushing device rotates rearward and conveys the potato–soil mixture toward the separation device. Simultaneously, the protruding ribs exert bending forces on the soil clods, causing them to fracture.

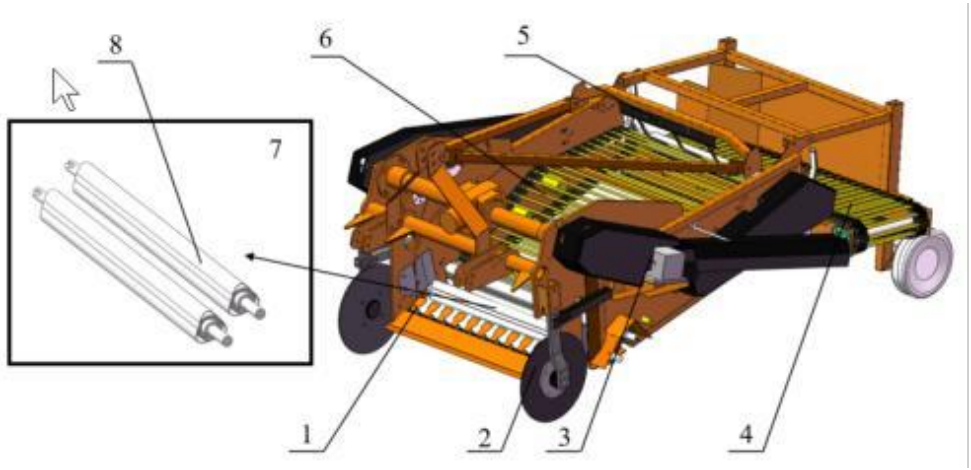


Fig. 1 - Structural schematic of the potato harvester and twin-roll soil-crushing device

1. Digging shovel; 2. Disc coulter; 3. Transmission system; 4. Lateral conveying device; 5. Debris removal device; 6. Potato-soil separation device; 7. Twin-roll soil-crushing device; 8. Protruding rib

Development of the Simulation Model

Development of the Potato Tuber and Soil Models

During potato-harvester operation, the interactions among the potato tubers, soil, and soil-crushing device are highly complex. Soil clods undergo fragmentation under external excitation, whereas the crushing rolls can be regarded as rigid bodies. EDEM software was used to simulate the interactions among the potato tubers, soil, and soil-crushing device and thereby evaluate the performance of the device.

The particle model of the potato tuber is shown in Fig. 3. A multisphere clump model was used to represent the potato tuber *(Qingmiao et al., 2024)*, with its three principal dimensions set to 62 mm × 52 mm × 52 mm. The Hertz–Mindlin (no slip) contact model was applied to tuber-tuber, tuber-soil, and tuber-machine interactions. The soil particles were modeled as spheres with a radius of 3 mm. Considering the characteristics of heavy clay soils in southern China *(Bei et al., 2021; Ren et al., 2017)*, the Hertz–Mindlin with Bonding V2 contact model was used to simulate interparticle bonding within the soil. Based on the moisture-content range of heavy clay soils in southern China, the contact radius of the soil particles was set to 3.75 mm. The simulation parameters of the potato tubers and soil particles are presented in Table 1 *(Qingmiao et al., 2024; Xie et al., 2020)*. Some parameters for the soil-particle and metal-component models were obtained from the literature *(Minzhang et al., 2024; Linrong et al., 2018; Wei et al., 2019; Zhongcai et al., 2020)*, whereas the remaining parameters, including those of the potato-tuber model, were determined experimentally.

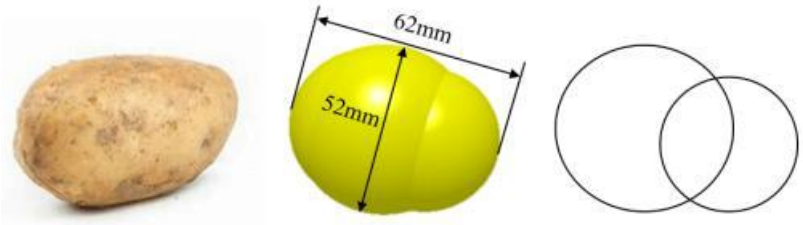


Fig. 2 - Multisphere particle model of a potato tuber

Table 1

Parameters of the Discrete Element Model

Parameter	Numerical value	Parameter	Numerical value
Poisson's ratio of potato tubers	0.5	Coefficient of static friction between potato tubers and rods	0.4
Shear modulus of potato tubers / MPa	1.366	Coefficient of rolling friction between potato tubers and rods	0.1
Potato-tuber density / (kg·m^{-3})	1100	Normal stiffness between soil particles / (N·m^{-1})	1.4 × 10^{6}
Coefficient of restitution between potato tubers	0.79	Maximum normal stress between soil particles / MPa	0.235
Coefficient of static friction between potato tubers	0.5	Tangential stiffness between soil particles / (N·m^{-1})	1 × 10^{6}
Coefficient of rolling friction between potato tubers	0.024	Poisson's ratio of the rod material	0. 3
Poisson's ratio of soil	0.38	Shear modulus of the rod material / MPa	3. 1 × 10^{5}
Shear modulus of soil / MPa	1	Density of the rod material / (kg·m^{-3})	7 800
Soil-particle density / (kg·m^{-3})	2670	Coefficient of restitution between soil particles and rods	0.16
Coefficient of restitution between soil particles	0.37	Coefficient of static friction between soil particles and rods	0.6
Coefficient of static friction between soil particles	0.6	Coefficient of rolling friction between soil particles and rods	0.35
Coefficient of rolling friction between soil particles	0.26	Coefficient of restitution between potato tubers and rods	0.5
Coefficient of restitution between potato tubers and soil particles	0.06	Coefficient of static friction between potato tubers and soil particles	0.5

Development of the Simulation Model of the Soil-Crushing and Screening Device

The geometric model of the soil-crushing and screening device is shown in Fig. 4. A particle factory measuring 1,100 mm × 1,000 mm × 600 mm was established at the front of the model to generate soil and potato-tuber particles. Below the particle factory, a conveyor belt was created using the moving-plane tool in EDEM to convey the potato–soil mixture rearward. The conveyor-belt speed was set to 1 m/s, corresponding to the forward speed of the potato harvester. A soil-compaction plate was positioned above the conveyor belt to compact the potato–soil mixture before it entered the harvesting components, thereby simulating compacted clay soil. The machine model consisted of a digging shovel, a twin-roll soil-crushing device, and a chain-and-rod potato–soil separation device, all of which were modeled as steel components. The rolls of the soil-crushing device were set to rotate rearward. The chain-and-rod separation device comprised 69 rods, each of which was assigned linear and circular motion cycles. A fixed time interval was applied between the motions of adjacent rods to simulate the continuous operation of the chain-and-rod device. In the model, the rod diameter was 11 mm *(Sun et al., 2019)*, the linear speed was 1.7 m/s, and the center-to-center spacing between adjacent rods was 50 mm. Accordingly, the time interval between the motions of adjacent rods was calculated to be 0.02941 s. Based on the dimensions and linear speed of the chain-and-rod separation device, the angular velocity of the rods in the circular-motion section was calculated to be 20.98765 rad/s, and the time required for one complete circulation was 2.64706 s. At the position of the shaking device, a sinusoidal translational motion perpendicular to the screening surface was applied to each rod at a frequency of 5 Hz to simulate the vibrational action of the device. A potato-and-soil collection bin was positioned behind the separation device to collect and quantify the residual soil and potato tubers discharged from the screening surface, thereby allowing the potato–soil separation performance to be evaluated.

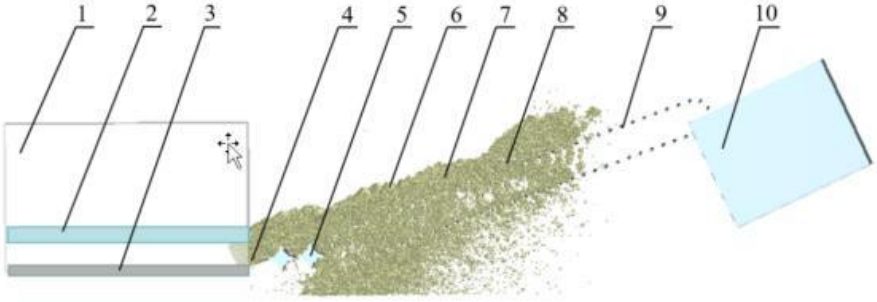


Fig. 3 - Simulation model of the potato–soil separation device

1. Particle Factory; 2. Soil Compaction Plate; 3. Conveyor Belt; 4. Digging Shovel; 5. Twin-roll soil-crushing device; 6. Potato Tuber Particles; 7. Soil Particles; 8. Shaking Device; 9. Chain-and-rod separation device; 10. Potato-and-soil collection bin

Simulation Process and Parameter Settings

Before the simulation, a mixture of soil and potato-tuber particles was generated. A total of 600,000 soil particles forming the lower soil layer were generated between 0 and 0.8 s. The generation of 20 potato-tuber particles began at 0.5 s. Subsequently, 1,300,000 soil particles forming the upper soil layer were generated over a period of 0.4 s, beginning at 0.8 s. After all particles had been generated, the soil-compaction plate moved downward to compact the soil, forming a 180-mm-thick soil–potato–soil layered mixture. The conveyor belt was activated at 1.6 s and transported the potato–soil mixture rearward into the twin-roll soil-crushing device and the chain-and-rod potato–soil separation device. The total simulation duration was 6 s. The simulation time step was set to 20% of the Rayleigh time step, which was 1.037×10^{-4} s, and the data-saving interval was set to 0.1 s.

Simulation Test Method

Experimental Design

During operation, the structural and operating parameters of the twin-roll soil-crushing device affect both soil-screening efficiency and the likelihood of potato-tuber damage. To determine the optimal parameters of the soil-crushing device, a three-factor, three-level Box–Behnken response surface design was developed using Design-Expert software. Rib height h, number of ribs q, and twin-roll rotational speed n were selected as the experimental factors. The factor levels are presented in Table 2, and the experimental design is presented in Table 3. Simulation tests were then performed using the model described above, and the resulting data were used to optimize the parameters of the twin-roll soil-crushing device.

Table 2

Experimental factors and levels

Level	Factor		
	Rib height *h* / mm	Number of ribs *q* / pieces	Twin-roll rotational speed *n* / (r/min)
1	20	3	200
2	25	4	300
3	30	5	400

Measurement of Response Variables

Soil-screening efficiency *E* and the mean maximum force acting on the potato tubers *E* were selected as the response variables in the response surface experiment. Soil-screening efficiency was used to evaluate the combined soil-crushing and screening performance of the twin-roll soil-crushing device and the chain-and-rod separation device. In each simulation test, EDEM was used to determine the mass of residual soil collected in the potato-and-soil collection bin and the total mass of soil generated. Soil-screening efficiency was calculated as follows *(Sun et al., 2019)*:

$$E=1-\frac{M_r}{M_t}\times100\% \quad (1)$$

where, *E* is the soil-screening efficiency M_r is the mass of residual soil collected in the potato-and-soil collection bin, [kg]; M_t is the total mass of soil generated, [kg].

The force acting on the potato tubers was used as an indicator of their risk of mechanical damage during conveying and screening. EDEM was used to determine the maximum force experienced by each of the 20 potato tubers during each simulation test. The mean of these individual maximum values was then calculated and used as the force response variable.

RESULTS

Analysis of Soil Disturbance

The motion of the potato–soil mixture above the twin-roll soil-crushing device was visualized using the EDEM post-processing module. The soil particles were color-coded according to their velocity. Particles approaching red had higher velocities, indicating greater soil disturbance, whereas particles approaching blue-green had lower velocities and were subjected to less disturbance. The soil-particle disturbance produced by the twin-roll soil-crushing device is shown in Fig. 5.

As shown in Fig. 5, a distinct red region formed among the soil particles above the twin-roll soil-crushing device, indicating that the device effectively disturbed the soil and promoted clod fragmentation. As rib height *h* and twin-roll rotational speed *n* increased, the red region expanded, indicating enhanced soil disturbance and crushing. By contrast, when the number of ribs *q* increased from three to five, no marked change in the size of the red region was observed, suggesting that the number of ribs had a limited effect on soil disturbance within the investigated range.

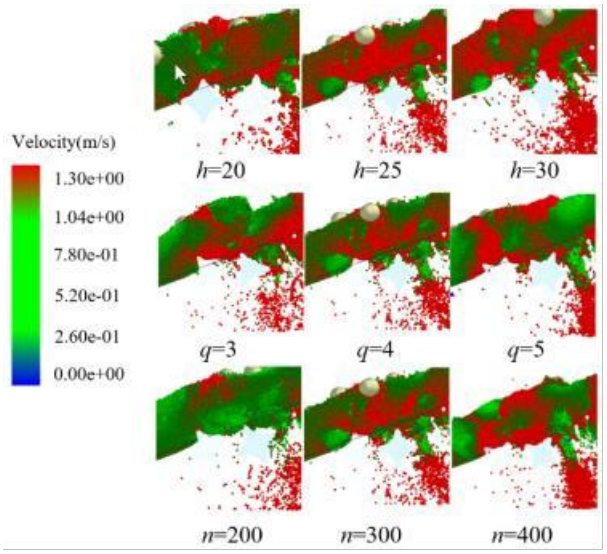


Fig. 5 - Soil-disturbance patterns under different operating conditions

Analysis of Response Surface Experiment Results

The response surface experiment results are presented in Table 3. Regression analysis and analysis of variance (ANOVA) were performed using Design-Expert software, and the results are presented in Table 4. The P-values of the regression models for soil-screening efficiency and the maximum force acting on the potato tubers were both less than 0.05, whereas the P-values of the lack-of-fit terms were greater than 0.05. Thus, both regression models were statistically significant and adequately fitted the experimental data. After removing nonsignificant terms with P-values greater than 0.10, the regression equations for soil-screening efficiency and the maximum force acting on the potato tubers were obtained, as given in Eqs. (2) and (3), respectively.

$$E = 69.14888 - 0.025552n - 12.22375q + 2.65918h + 0.003305nh + 0.344500qh - 0.000072n^2 - 0.089574h^2 \quad (2)$$

$$F = +63.94900 - 0.298455n - 24.2665q + 4.2125h - 0.0193nq + 0.00397nh + 0.000416n^2 + 4.0005q^2 - 0.11398005h^2 \quad (3)$$

Table 3

Response surface experimental design and results

Run number	Factor			Experimental result	
	Rib height *h* / mm	Number of ribs *q* / pieces	Twin-roll rotational speed *n* / (r/min)	Soil screening efficiency *E* / %	Mean maximum force acting on potato tubers *F* / N
1	200	3	25	77.38	25.27
2	400	3	25	79.13	24.48
3	200	5	25	69.78	34.58
4	400	5	25	73.11	26.07
5	200	4	20	70.98	27.81
6	400	4	20	70.64	17.66
7	200	4	30	72.29	19.87
8	400	4	30	78.56	17.66
9	300	3	20	75.68	19.28
10	300	5	20	64.6	23.85

Run number	Factor			Experimental result	
	Rib height *h* / mm	Number of ribs *q* / pieces	Twin-roll rotational speed *n* / (r/min)	Soil screening efficiency *E* / %	Mean maximum force acting on potato tubers *F* / N
11	300	3	30	78.62	19.57
12	300	5	30	74.43	19.68
13	300	4	25	76.15	19.46
14	300	4	25	75.41	19.77
15	300	4	25	76.67	20.74
16	300	4	25	76.01	17.79
17	300	4	25	75.9	19.46

Table 4

Analysis of variance for the response surface regression models

Source of variation	Soil screening efficiency *E* / %				Source of variation	Mean maximum force exerted on the potato mass *F* / N			
	Sum of squares	df	F-value	P-value		Sum of squares	df	F-value	P-value
model	0.0229	9	63.02	< 0.0001	**model**	314.21	9	19.35	0.0004
n	0.0015	1	37.62	0.0005	***n***	58.64	1	32.49	0.0007
q	0.0104	1	258.78	< 0.0001	***q***	30.32	1	16.80	0.0046
h	0.006	1	150.05	< 0.0001	***h***	17.46	1	9.68	0.0171
nq	0.0001	1	1.55	0.2535	***nq***	14.95	1	8.28	0.0237
nh	0.0011	1	27.17	0.0012	***nh***	15.78	1	8.75	0.0212
qh	0.0012	1	29.52	0.001	***qh***	4.96	1	2.75	0.1414
n^2	0.0002	1	5.07	0.059	n^2	72.64	1	40.25	0.0004
q^2	0.0001	1	2.44	0.1626	q^2	67.40	1	37.35	0.0005
h^2	0.0021	1	51.19	0.0002	h^2	34.15	1	18.92	0.0034
residual	0.0003	7			**residual**	12.63	7		
Lack of fit	0.0002	3	3.25	0.1424	**Lack of fit**	8.09	3	2.37	0.2113
Pure error	0.0001	4			**Pure error**	4.54	4		
Cor total	0.0231	16			**Cor total**	326.84	16		

Parameter Optimization and Validation

Based on the regression Eqs. (2) and (3), numerical parameter optimization was performed using the optimization module in Design-Expert. The objective functions and constraints were defined as follows:

$$\begin{cases} \max E(n,\ q,\ h) \\ \min F(n,\ q,\ h) \\ 20\text{mm} \le A \le 30\text{mm} \\ B \in \{3,\ 4,\ 5\} \\ 200\text{r/min} \le C \le 400\text{r/min} \end{cases} \tag{4}$$

The optimal structural and operating parameters of the twin-roll soil-crushing device were a rib height h of 30.00 mm, three ribs (q =3), and a twin-roll rotational speed n of 323.70 r/min. The simulation model was configured using this optimal parameter combination, and a verification simulation was subsequently conducted. The resulting soil-screening efficiency was 72.80%, and the mean maximum force acting on the potato tubers was 15.45 N.

Verification Test

Based on the optimal structural and operating parameters determined above, a prototype of the twin-roll soil-crushing device was manufactured and installed on a 4U-1100 side-discharging potato harvester. Field tests were subsequently conducted in a paddy field in Liuyang City, Hunan Province, China. The potatoes, cultivar Xingjia No. 2, were grown using ridge cultivation, and the soil moisture content at the time of testing was 16.3%. The ridge height, ridge-top width, ridge-base width, and furrow width were 300, 700, 1,100, and 400 mm, respectively. The field-test conditions are shown in Fig. 6, and the results are presented in Table 5. The tuber damage rate, skin-damage rate, and tuber loss rate of the potato harvester equipped with the twin-roll soil-crushing device satisfied the requirements of the agricultural industry standard NY/T 648-2015 *(MOA, 2015)*.



Fig. 6 - Field verification test

Table 5

Test Results of Field Experiment

Evaluation criterion	Tuber damage rate/%	Skin-damage rate/%	Tuber loss rate/%
Government standard	≤2	≤3	≤4
Measured value	0.285	2.38	3.18

CONCLUSIONS

To improve potato–soil separation under heavy clay soil conditions, a twin-roll soil-crushing device was installed ahead of a conventional chain-and-rod potato–soil separation device. The soil-crushing process was theoretically analyzed, a discrete element model of the soil-crushing and potato–soil separation system was developed, and the corresponding processes were simulated. The main conclusions are as follows:

（1） The twin-roll soil-crushing device effectively disturbed the soil and promoted clod fragmentation during operation. Increasing the rib height and twin-roll rotational speed enhanced the soil-disturbance and crushing effects. By contrast, the number of ribs had no marked effect on the observed soil-disturbance pattern within the investigated range.

（2） The response surface simulation results indicated that the optimal structural and operating parameters of the twin-roll soil-crushing device were a rib height of 30 mm, three ribs, and a twin-roll rotational speed of 323.70 r/min. A verification simulation conducted using this optimal parameter combination yielded a soil-screening efficiency of 72.80% and a mean maximum force of 15.45 N acting on the potato tubers.

（3） Field-test results showed that the potato harvester equipped with the twin-roll soil-crushing device achieved a tuber damage rate of 0.285%, a skin-damage rate of 2.38%, and a tuber loss rate of 3.18%. All three performance indicators satisfied the requirements of the national standards.

ACKNOWLEDGEMENT

This research was supported by the Hunan Provincial Natural Science Foundation of China (2024JJ5194) and the Hunan Agriculture Research System (HARS-02).

REFERENCES

[1] Bei W. Tianci H., Xuanxuan Q., Tianlin Z., Xiushan W., Fangping X., (2021), Design and experimental study of potato-soil separation device for sticky soils condition. *Applied Sciences*, vol. 11, no. 22, pp. 10959. Basel / Switzerland.

[2] Chinese Academy of Agricultural Mechanization Sciences (CAAMS). (2007). *Design Handbook of Agricultural Machinery* (农业机械设计手册), vol.1, China Agricultural Science and Technology Press, pp.1086-1088. ISBN: 9787802333352. Beijing / China.

[3] Fu Y., Ren S., Tang P., Leng Y., Chen X., Tu X., Lv X., (2023). Design and simulation test of digging device for small potato harvester. *INMATEH-Agricultural Engineering*, vol. 69, no. 1. Bucharest/Romania.

[4] Ge J., Zhu X., Cao C., Fang L., Sun Y., Lu J., Qin K., (2025). Experimental and DEM-based analysis of lateral stress and soil particle displacement under the action of a subsoiler. *INMATEH-Agricultural Engineering*, vol. 76, no. 2, pp. 862-871. Bucharest / Romania.

[5] Jiang L., Ma X., Wu T., Chen X., Sun G., Tan Y., Lu F., Chen G., (2016). Application status and research prospect of southern winter planting potato harvesting machine(南方冬种马铃薯收获机的应用现状与研究展望), *Journal of Agricultural Mechanization Research*, vol.38, no.07, pp. 263-268. Heilongjiang/China.

[6] Li Z., Jiang J., Zhan C., Yue Q., Sui X., (2016). Design and experimental study on the conveying chain soil cleaning device of potato harvester (薯类收获机输送链条清土装置的设计和试验研究). *Journal of Agricultural Mechanization Research*, vol. 38, no. 02, pp. 123-127. Heilongjiang/China.

[7] Li Y., Zhang Z., Wang Y., Wang H., Pang Y., Zhang Z., (2021). Design and experiment of multistage conveying and separating device for potato harvester (马铃薯收获机多级输送分离装置设计与试验). *Journal of Shenyang Agricultural University*, vol.52, no.06, pp.758-768. Shenyang/China.

[8] Li J., Lü Y., Sun Y., Lin Y., (2022). Design and experiment of separating and lifting device of potato harvester based on equivalent radius method (马铃薯收获机分离升运装置设计与试验—基于当量半径法), *Journal of Agricultural Mechanization Research*, vol.44, no.12, pp. 199-206+256. Heilongjiang/China.

[9] Wei X., Mingliang W., Jiangnan L., Wei Q., Lan M., Jiajie L., (2019). Calibration of simulation physical parameters of clay loam based on soil accumulation test (基于堆积试验的黏壤土仿真物理参数标定), *Transactions of the Chinese Society of Agricultural Engineering*, vol.35, no.12, pp.116-123, Beijing/China.

[10] Lv J., Tian Z., Wu J., Yang Y., Shang Q., Wang Y., Liu Z., (2015). Design and experiment of 4U1Z vibrating potato digger (4U1Z 型振动式马铃薯挖掘机的设计与试验). *Transactions of the Chinese Society of Agricultural Engineering*, vol. 31, no. 12, pp.39-47. Beijing/China.

[11] Lv J., Sun H., Dui H., Peng M., Yu J., (2017). Design and experiment on conveyor separation device of potato digger under heavy soil condition (粘重土壤下马铃薯挖掘机分离输送装置改进设计与试验). *Transactions of the Chinese Society for Agricultural Machinery*, vol. 48, no. 11, pp. 146-155. Beijing/China.

[12] Ma L., Chu X., Zhang L., Yan Z., Wu H., He S., (2012). Modal analysis of potato separating device based on ANSYS workbench (马铃薯土薯分离装置模态分析—基于 ANSYS Workbench). *Journal of Agricultural Mechanization Research*, vol. 34, no. 10, pp. 62-65. Heilongjiang/China.

[13] Ministry of Agriculture of the People's Republic of China (MOA), (2015). *Technical specification of quality evaluation for potato harvesters NY/T 648-2015* (马铃薯收获机质量评价技术规范: NY/T648-2015), Standards Press of China, Beijing/China.

[14] Minzhang L., Fangping X., Dawei L., Xiushan W., (2024). Analysis and experiment of the power of blade roller in reverse-rotary ditching machine based on the granular scale effect (基于颗粒放尺效应的逆旋开沟机刀辊功耗分析与试验), *Transactions of the Chinese Society of Agricultural Engineering*, vol.40, no.7, pp.83-92, Beijing/China.

[15] Qingmiao X., Bei W., Fangping X., Zhichao F., Huaiyuan Q., Zhuo L., (2024). Simulation analysis and optimization of concave bar potato-soil separation device. *INMATEH-Agricultural Engineering*, vol. 74, no. 3, pp. 460-472. Bucharest/Romania.

[16] Ren J., (2017). *Research on the mechanism of subsoiling in paddy soil using DEM* (*基于离散元法的水稻土深松耕作机理研究*). MSc Thesis, Nanjing Agricultural University, Nanjing/China.

[17] Shi, L., Wu, J., Zhao, W., Sun, W., Wang, D., Li, H., Liu, Q., (2012). Development and experiment of disc-grid type potato digger (圆盘栅式马铃薯挖掘机的研制与试验). *Transactions of the Chinese Society of Agricultural Engineering*, vol. 28, no. 24, pp. 15-21. Beijing/China.

[18] Sun H., (2019). *Design and experimental research on transporting and separating device of lifting chain potato digger (升运链式马铃薯挖掘机输送分离装置的设计与试验研究)*. MSc Thesis, Northeast Agricultural University, Haerbin/China.

[19] Wang H., (2021) . *Mountain self-propelled potato combine harvester design and experiment (山地自走式马铃薯联合收获机设计与试验)*. MSc Thesis, Kunming University of Science and Technology, Kunming /China.

[20] Linrong S., Wei S., Wuyun Z., Xiaoping Y., Bin F., (2018). Parameter determination and validation of discrete element model of seed potato mechanical seeding (马铃薯种薯机械排种离散元仿真模型参数确定及验证), Transactions of the Chinese Society of Agricultural Engineering, vol.34, no.6, pp.35-42, Beijing/China.

[21] Xiang J., (2020). *Research and experiment of clay potato separation device for potato harvester (适用于粘土的马铃薯收获机土薯分离装置的设计与试验)*. MSc Thesis, Sichuan Agricultural University, Yaan/China.

[22] Xiaoxuan, Z., Jin L., Chenglin Z., Yueyun Z., Xinwu D., (2024). Design and experimentation of small potato harvester for heavy soil in hilly and mountainous areas. *Agronomy*, vol.14, no.9, pp. 2131. Basel/ Switzerland.

[23] Xie F., Wu Z., Wang X., Liu D., Wu B., Zhang Z., (2020). Calibration of discrete element parameters of soils based on unconfined compressive strength test (基于无侧限抗压强度试验的土壤离散元参数标定). *Transactions of the Chinese Society of Agricultural Engineering*, vol.36, no.13, pp. 39-47. Beijing/China.

[24] Zhang T., Pang Y., Song S., Wu Y., Pan L., Shao W., Yang M., Tang X., Wang Y., Li X., (2021). Design of small potato combine harvester under heavy soil (黏重土壤下小型马铃薯联合收获机设计). *South China Agriculture*, vol. 15, no. 16, pp. 98-101+115. Chongqing/China.

[25] Zhongcai W., Hongwen L., Guangzhu S., Guoliang S., Wenzheng L., Xueqiang L., (2019). Experiments and analysis of a conveying device for soil separation and clod-crushing for a potato harvester. *Applied Engineering in Agriculture*, vol. 35, no.6. pp. 987-996. United States.

[26] Zhongcai W., Guoliang S., Xueqiang L., Faming W., Chuanzhu S., Pengxiang M., (2020)Parameter Optimization and Test of Potato Harvester Wavy Sieve Based on EDEM (基于离散元的马铃薯收获机波浪形筛面参数优化与试验). *Transactions of the Chinese Society of Agricultural Engineering*, vol.51, no.10, pp.35-42, Beijing/China.

[27] Zhou J., Yang S., Li M., Chen Z., Zhou J., Gao Z., Chen J., (2021). Design and experiment of a self-propelled crawler-potato harvester for hilly and mountainous areas. *INMATEH-Agricultural Engineering*, vol. 64, no. 2, pp. 1-8. Bucharest/Romania.

ARTIFICIAL NEURAL NETWORK FOR OPTIMIZING THE CONVECTIVE DRYING PROCESS OF PEAR SLICES / *REȚEA NEURALĂ ARTIFICIALĂ PENTRU OPTIMIZAREA PROCESUL DE USCARE CONVECTIVĂ A FELIILOR DE PERE*

Alexandru-Polifron CHIRIȚĂ[*1)], Vitali VIȘANU[2)], Radu RĂDOI[1)], Victor POPESCU[2)], Gabriela MATACHE[1)], Mihail BALAN[2)], Gheorghe ȘOVĂIALĂ[1)], Mihail MELENCIUC[2)]

[1)] National Institute of Research & Development for Optoelectronics / INOE 2000, Subsidiary Hydraulics and Pneumatics Research Institute / IHP / Romania.

[2)] Technical University of Moldova, Department of Mechanical Engineering / Republic of Moldova

[*]*E-mail: chirita.ihp@fluidas.ro*

DOI: https://doi.org/10.35633/inmateh-79-75

Keywords: *ANN, optimization, convective drying process, pear slices.*

ABSTRACT

This study develops an artificial neural network (ANN) model to optimize the convective drying process of pear slices. Experimental data from drying at 50°C, 60°C, and 70°C were used to train an ANN with three hidden layers. The model predicted drying rate with high accuracy (98.823% validation fidelity), capturing the nonlinear relationship between moisture content, time, and drying rate. Results demonstrated that higher temperatures accelerated drying but required careful control to maintain quality. The ANN effectively identified optimal drying parameters, balancing energy efficiency and product quality preservation, providing a valuable tool for industrial drying process optimization.

REZUMAT

Acest studiu dezvoltă un model de rețea neurală artificială (ANN) pentru optimizarea uscării convective a feliilor de pere. Date experimentale de la uscarea la 50°C, 60°C și 70°C au fost folosite pentru antrenarea unei ANN cu trei straturi ascunse. Modelul a prezis viteza de uscare cu precizie ridicată (98,823% fidelitate de validare), capturând relația neliniară dintre umiditate, timp și viteză. Rezultatele au arătat că temperaturile mai mari accelerează uscarea, dar necesită control atent. ANN-ul a identificat parametrii optimi, echilibrând eficiența energetică și calitatea produsului, oferind un instrument valoros pentru optimizarea procesului industrial de uscare.

INTRODUCTION

Convective drying remains one of the most extensively utilized preservation techniques in the global food industry, particularly for perishable commodities like fruits and vegetables, which are subject to significant seasonal and geographical production constraints *(Sagar and Kumar, 2010)*. The core objective of this process is the controlled removal of moisture to a level that ensures microbial stability, thereby extending the product's shelf life. However, the challenge extends far beyond simple dehydration; it is equally critical to preserve the nutritional composition, color, texture, and overall sensory quality of the final product *(Sablani, 2006, Calín-Sánchez et al., 2022)*. Traditional approaches to optimizing the drying process have historically relied on empirical models and first-principles physics-based formulations. While these methods provide a foundational understanding, they often fall short in capturing the highly complex, non-linear, and dynamic relationships that exist between key process parameters such as air temperature, velocity, and humidity and the evolving physical and chemical properties of the biological material *(Erbay and Icier, 2010)*.

The inherent heterogeneity of biological matrices like pear slices, combined with the intricate interplay of heat and mass transfer phenomena during drying, creates a formidable barrier to developing universally applicable mathematical models *(Khan et al., 2022, Farid, 2019)*. These classical models, often based on Fick's law of diffusion or other simplified assumptions, struggle to accurately predict drying behavior across diverse fruit and vegetable types and under varying operational conditions *(Kalantari et al., 2022)*. This limitation has driven the search for more robust and flexible modeling tools capable of learning directly from experimental data without being constrained by a priori assumptions about the underlying physical mechanisms (*Lenart, 1996*).

In this context, Artificial Neural Networks (ANNs) have emerged as a powerful and versatile computational paradigm for modeling complex systems in food engineering *(Francik et al., 2024).* ANNs are data-driven, non-linear mapping functions inspired by the human brain's structure, which can learn intricate patterns and relationships from a set of input-output data pairs *(El-Mesery et al., 2025).* By leveraging experimental drying data, ANNs can effectively model the non-linear dynamics of the drying process, making them exceptionally well-suited for food drying applications where multiple interacting factors influence the final product quality *(Selvi et al., 2022).* The application of ANNs in convective drying offers significant potential for improving process efficiency, reducing energy consumption, and enhancing product quality through more precise prediction and control capabilities *(Đaković et al., 2023).*

One of the most immediate and valuable applications of ANNs in fruit drying is the accurate prediction of moisture content as a function of time, temperature, and other process variables. A well-trained ANN model would allow processors to anticipate the exact moisture content at any point during the drying cycle in real-time, without the need for disruptive and time-consuming offline measurements *(Tepe, 2024).* This capability is crucial for targeting specific, critical moisture levels required for optimal product stability, as different fruits have varying thresholds for microbial safety and quality preservation. Furthermore, ANNs can be used to model the instantaneous drying rate as a function of the current moisture content and process temperature, providing insights into the transition points between the constant-rate and falling-rate drying phases *(Kalsi et al., 2023).* This knowledge enables the development of more sophisticated, adaptive control strategies that can dynamically adjust process parameters to match the changing drying kinetics throughout the process, thereby preventing quality degradation from excessive heat exposure in the later stages.

The predictive power of ANNs extends to critical operational planning tasks. For instance, these models can reliably estimate the total drying time required to achieve a target moisture content at a specified set of drying conditions, which is essential for production scheduling and resource allocation in commercial operations *(Nguyen et al., 2025).* Conversely, they can also be used in an inverse manner to determine the optimal drying temperature and air velocity needed to reach a desired final moisture content within a predefined time frame, a common industry challenge that requires balancing throughput demands with stringent quality requirements *(Demir et al., 2023).* A particularly sophisticated application involves using ANNs to predict the critical moisture content, the point at which the drying rate begins its significant decline which is not a fixed value but varies with temperature and the specific physical structure of the fruit or vegetable being processed *(Das et al., 2018).*

Beyond basic process parameters, the true potential of ANNs lies in their ability to integrate moisture removal kinetics with final product quality outcomes. Advanced ANN models can be developed to predict key quality indicators-such as vitamin C retention, color change (ΔE), or textural hardness, based on the entire drying history *(Khan et al., 2022).* While such comprehensive models require a rich dataset that includes both drying kinetics and post-process quality analyses, they represent a paradigm shift from traditional time or energy – oriented optimization toward a holistic, quality driven process design optimization *(Asrate et al., 2025).* This approach is especially important for high-value fruits like pears, where even minor quality degradation during drying can significantly impact market value and consumer acceptance.

The ability of ANNs to interpolate accurately between tested experimental conditions and to modestly extrapolate to untested but approximate parameter ranges offers substantial practical and economic benefits for food processors *(Ming et al., 2021).* Rather than conducting extensive and costly new experiments for every new product variant or slight change in processing conditions, manufacturers can leverage validated ANN models to predict drying behavior for similar fruits and vegetables, drastically reducing product development time and resource expenditure *(Hossan et al., 2023).* This capability is increasingly valuable in a global food industry facing intense pressure to innovate, develop new dried products with optimized nutritional and sensory profiles, and simultaneously minimize energy consumption and environmental impact *(Spagnuolo et al., 2023).*

Ultimately, the integration of robust ANN based models into modern drying process control systems represents a clear pathway toward more intelligent, adaptive, and efficient food processing operations *(El-Mesery et al., 2025).* By enabling real-time prediction and dynamic adjustment of process parameters based on the current state of the product – which is also the aim of our study, these AI-driven models can help achieve the dual, and often competing, objectives of energy efficiency and superior product quality preservation that are central to the future of sustainable food manufacturing *(Yao et al., 2023).*

MATERIALS AND METHODS

To generate a robust experimental dataset for training the artificial neural network (ANN), a systematic series of convective drying experiments was conducted using the GUNT CE130 drying apparatus (GUNT Hamburg, Germany) as part of a structured research internship. The experimental protocol involved drying 1000 g batches of fresh pear slices (Pyrus communis L.), pre-cut to a uniform thickness of 3.0 mm using a precision slicer, as illustrated in Fig. 1. This standardization of slice thickness and initial mass ensured consistent starting conditions, a critical prerequisite for capturing reproducible drying kinetics and minimizing variability in the dataset. The CE130 convective drying system was configured with advanced process control and monitoring capabilities to ensure precise experimental conditions. Key components included a proportional-integral-derivative (PID) controller for maintaining channel temperature within ±0.5°C of the setpoint, an adjustable axial fan system for airflow regulation, and integrated sensors for real-time monitoring of channel temperature (accuracy: ±0.5°C) and relative humidity (accuracy: ±3% RH). A high-precision digital scale (KERN 440, Germany; resolution: 0.1 g) was located above the drying channel to continuously record mass loss of the pear samples, enabling detailed quantification of moisture ratio dynamics. All experimental parameters were controlled and logged via the manufacturer's proprietary software (CE130 v.16.1.3.4), which facilitated automated data acquisition at 5-minute intervals, thereby capturing high-resolution temporal profiles of the drying process.



Fig. 1 - Experimental setup of the GUNT CE130 convective dryer, including sample preparation, instrumentation, and data acquisition system

The experimental design incorporated three drying temperatures (50, 60, and 70 °C) at a constant hot air velocity of 2.0 m/s, selected to represent a range of industrially relevant conditions while elucidating the nonlinear thermal behavior of pear tissue. Each temperature condition was replicated several times to assess data reproducibility and statistical reliability. Prior to each trial, the drying channel was preheated to the target temperature, and ambient conditions (initial temperature: 22 ± 1 °C; relative humidity: 45 ± 5%) were recorded to account for environmental variability. The drying process was terminated when the pear slices reached a moisture content slightly below 15% (dry basis), a threshold determined through preliminary trials to balance product quality retention and energy efficiency.

Artificial neural network development training and validation. An artificial neural network (ANN) was developed and trained within Simcenter Amesim V2310 (Siemens Digital Industries Software) to model and optimize the convective drying kinetics of pear slices. The experimental dataset, acquired from the GUNT CE130 drying apparatus, was systematically partitioned into six subsets: three training datasets (TD_cd50C, TD_cd60C, TD_cd70C) and three validation datasets (VD_cd50C, VD_cd60C, VD_cd70C), corresponding to

the three drying temperatures (50, 60, and 70 °C). Each dataset comprised time-resolved measurements of drying time [min], moisture content (u) [%], and drying rate (du/dt) [%/min], with the latter derived from numerical differentiation of moisture loss profiles. These variables were selected as critical inputs and outputs to capture the transient behavior of the drying process, where du/dt [%/min] serves as a direct indicator of process efficiency.

Data preprocessing and model ANN configuration. The training and validation subsets were imported into Simcenter Amesim via a structured file directory, ensuring traceability and reproducibility of data handling (Fig. 2). The ANN architecture was configured with three hidden layers (30, 20, and 10 neurons), each employing hyperbolic tangent (tanh) activation functions to model the nonlinear relationships between input variables and drying rate. This configuration was selected through iterative hyperparameter tuning to balance model complexity and generalization capability, minimizing overfitting while retaining sufficient capacity to capture the intricate dynamics of moisture diffusion and heat transfer in pear tissue.

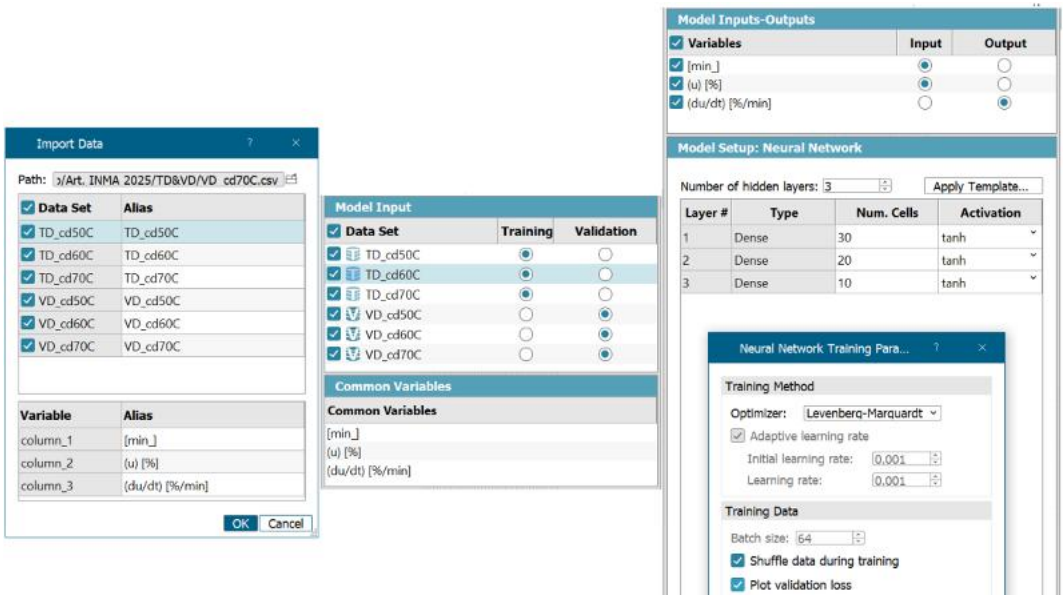


Fig. 2 - Software interface for ANN configuration, data partitioning, and training parameters in convective drying process optimization

Left: Data import and variable mapping for training (TD) and validation (VD) datasets (center) across 50°C, 60°C, and 70°C drying conditions. Right: ANN architecture (3 hidden layers with 30, 20, and 10 neurons) and input-output configuration (drying time and moisture content as inputs; drying rate as output). Right: Training parameters, including Levenberg-Marquardt optimization, adaptive learning rate, and batch size settings.

Training methodology and validation. The network was trained using the Levenberg-Marquardt (LM) optimizer, a robust algorithm well-suited for small-to-medium-sized datasets due to its rapid convergence and low computational overhead. Key training parameters included: adaptive learning rate (initial value: 0.001), dynamically adjusted during training to stabilize convergence; batch size: 64 samples, selected to balance gradient accuracy and training speed; data shuffling prior to each epoch to eliminate sequence bias; validation loss monitoring to prevent overfitting (Fig. 2, right panel).

ANN model design. The choice of du/dt as the primary output variable reflects its critical role in process optimization, as it directly quantifies the rate of moisture removal, a key metric for energy efficiency and product quality preservation. By focusing on this parameter, the ANN enables real-time prediction of drying dynamics, facilitating the identification of optimal operating parameters (e.g., temperature, airflow) that minimize energy consumption while avoiding thermal degradation of the fruit. The inclusion of drying time and moisture content as inputs ensures the model accounts for both temporal and state-dependent effects, providing a comprehensive representation of the drying process.

RESULTS

The experimental results of the convective drying process kinetics of pear slices across three temperature regimes (50°C, 60°C, and 70°C), establishing the empirical foundation for the artificial neural network model development. These systematic measurements capture the time-dependent moisture removal behavior and drying rate dynamics essential for understanding the physical mechanisms governing the drying

process. The data reveals clear temperature-dependent patterns that demonstrate the trade-off between processing speed and potential quality implications, providing critical insights for subsequent optimization of the drying parameters. This characterization serves as the basis for training the ANN model that will ultimately identify the optimal drying conditions while preserving product quality.

Fig. 3 illustrate the temperature-dependent moisture content evolution during convective drying, with 70°C achieving 14.5% moisture content at 180 minutes compared to 260 minutes at 50°C. The sigmoidal drying curves (with 3 slopes) reveal the characteristic heating period followed by active drying and approach to equilibrium moisture content, with higher temperatures accelerating the entire process.

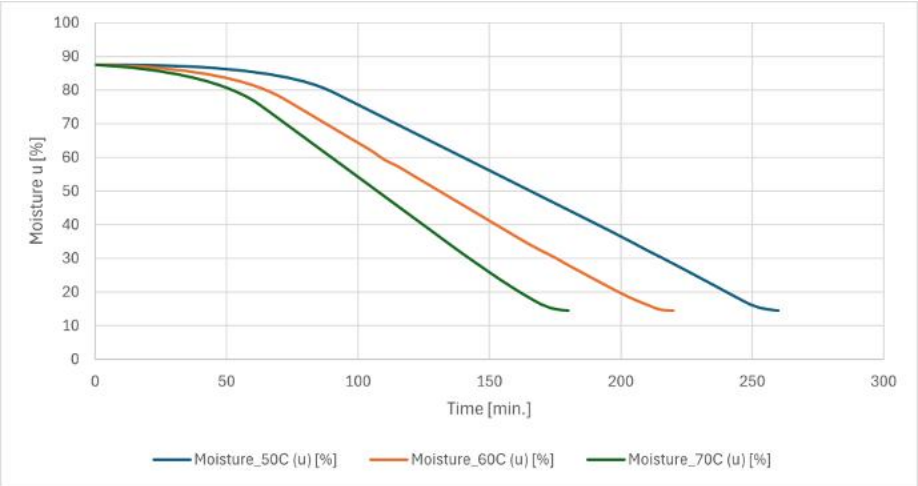


Fig. 3 - Moisture content evolution during convection drying of pear slices at 50°C, 60°C, and 70°C.

Fig. 4 presents the drying rate profiles showing temperature-dependent maximum rates of 0.57 %/min (70°C), 0.46 %/min (60°C), and 0.40 %/min (50°C), with first peak drying rate occurring progressively later as temperature decreases (70 minutes at 70°C, 75 minutes at 60°C and 95 minutes at 50°C). The curves exhibit the expected pattern of initial rate increase followed by a sharp decline, with higher temperatures reaching their maximum drying rates earlier and showing more pronounced falling rate periods. This information is essential for identifying the transition points between drying phases and optimizing energy input timing during the process.

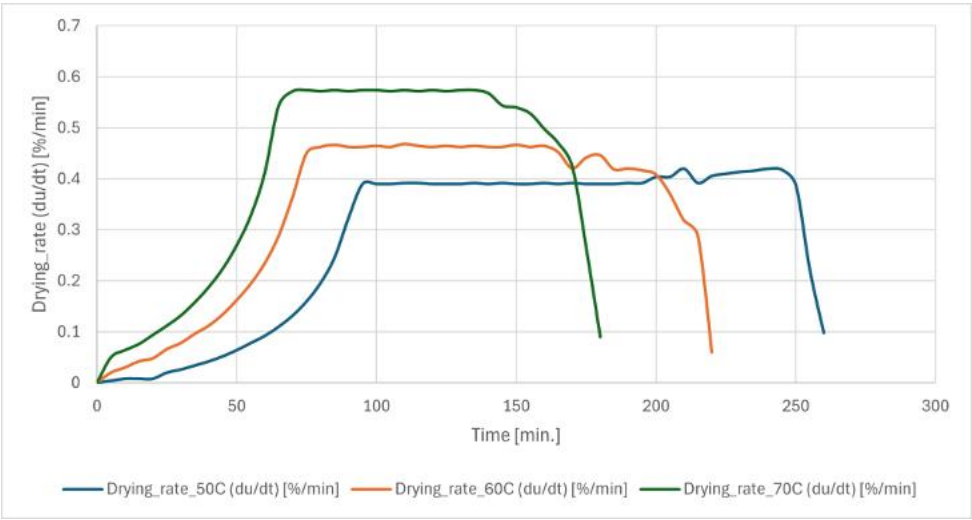


Fig. 4 - Drying rate profiles during convection drying of pear slices at 50°C, 60°C, and 70°C

Fig. 5 reveals the relationship between moisture content and drying rate, showing that maximum drying rates occur at different moisture contents: 74% (70°C), 76% (60°C), and 77% (50°C), with higher temperatures consistently demonstrating greater drying rates at equivalent moisture levels. The approximately linear decline during the falling rate period confirms diffusion-controlled drying behavior, with the steeper slopes at higher temperatures indicating enhanced moisture diffusivity. This relationship provides the critical basis for modeling drying kinetics and determining optimal operating parameters that balance process efficiency with product quality requirements.

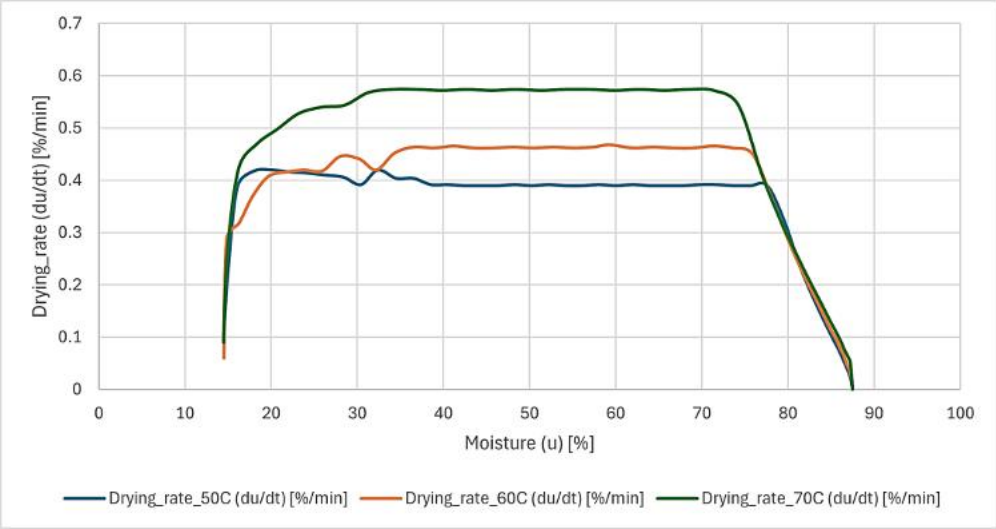


Fig. 5 - Relationship between moisture content and drying rate during convection drying of pear slices

The three trays presented in Fig. 6 display the final product appearance after completing the convective drying process at different temperature conditions, with the left tray representing the 50°C treatment, the middle tray the 60°C treatment, and the right tray the 70°C treatment. Visual examination reveals distinct but subtle differences in color, texture, and structural integrity among the samples, demonstrating the critical relationship between drying temperature and product quality. The 70°C treatment shows the most pronounced browning and edge curling, with some slices exhibiting significant shrinkage and deformation due to rapid moisture removal. The 50°C treatment maintains the most uniform light color and structural integrity, preserving the original shape of the pear slices with minimal deformation and shrinkage. The 60°C treatment demonstrates an intermediate quality profile, showing moderate color change while maintaining reasonable structural integrity. These visual differences align with the drying kinetics data presented in Figures 3-5, where higher temperatures accelerated moisture removal but potentially at the cost of quality degradation. The observed variations underscore the importance of temperature optimization for balancing process efficiency with product quality attributes such as color retention, texture, and visual appearance - factors that directly impact consumer acceptance and market value.



Fig. 6 - Final product quality of dried pear slices following convective drying at 50°C, 60°C, and 70°C

Fig. 7 presents the comprehensive performance evaluation of the trained ANN, demonstrating its capability to accurately predict drying behavior and establish a foundation for process optimization. Fig. 7 presents a comprehensive assessment of the ANN's predictive capability for drying rate (du/dt) in pear slice convective drying at 60°C. The top-left plot demonstrates successful training convergence, with training and validation losses both stabilizing below or around 0.01 after approximately 1,000 epochs, indicating effective learning without significant overfitting. The top-right plot reveals exceptional correlation between predicted and reference drying rate values ($R^2 > 0.99$), confirming the model's high prediction accuracy for this critical process parameter.

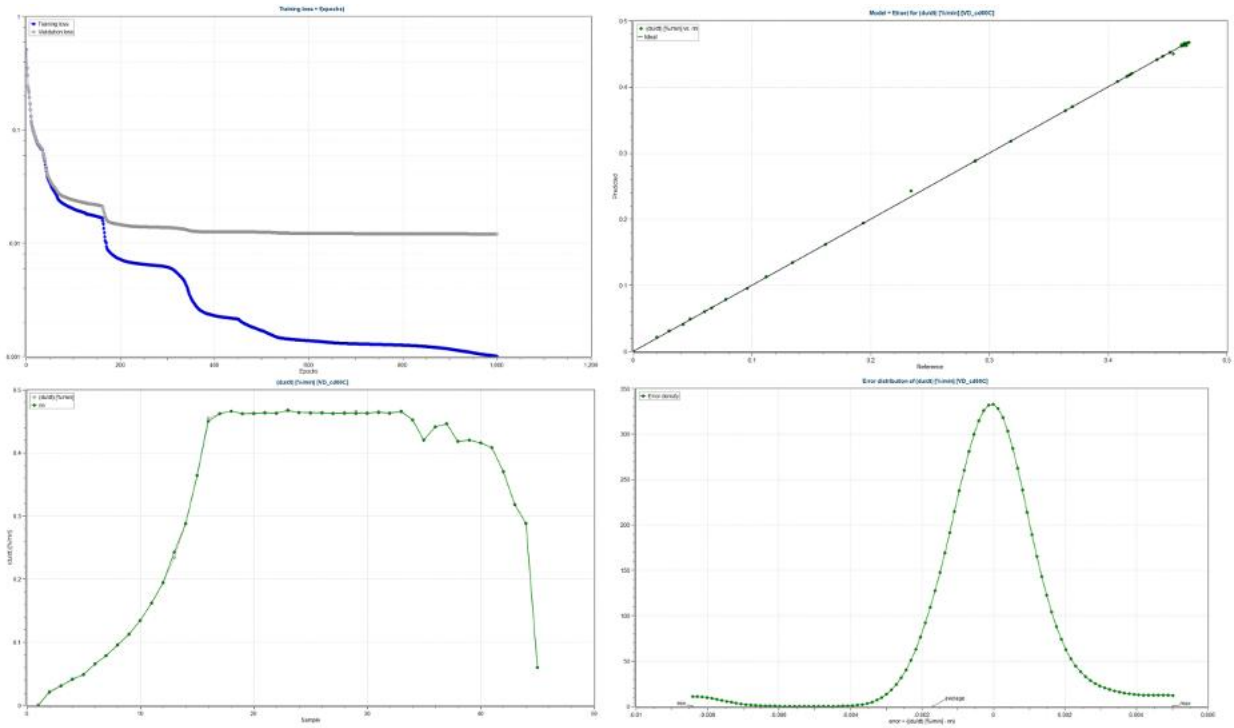


Fig. 7 - Performance evaluation of the artificial neural network model for predicting moisture loss rate during convective drying of pear slices

The bottom-left plot (from Fig. 7) illustrates how the ANN successfully captures the characteristic drying rate pattern, including the initial increase to maximum rate (reaching approximately 0.46-0.47 %/min) followed by the gradual decline during the falling rate period. The bottom-right error distribution follows a near-normal curve centered at zero with minimal deviation (average error < 0.002 %/min), demonstrating the model's reliability and absence of systematic bias. This high-precision drying rate prediction capability directly supports the ANN's application in dynamically adjusting drying parameters based on current process conditions, potentially optimizing energy consumption while maintaining product quality. As noted in the experimental results, understanding these drying rate patterns is crucial for identifying the critical moisture content where the drying rate begins to decline significantly, which is essential for determining when internal moisture diffusion becomes the rate-limiting step in the process.

Fig. 8. presents the detailed configuration and performance metrics of the artificial neural network developed for predicting drying rate (du/dt) in the convective drying of pear slices. The model demonstrates exceptional performance with a training fidelity of 99.881% and validation fidelity of 98.823%, confirming its robustness and generalization capability across the three temperature conditions. The high validation fidelity (98.823%) indicates the model's reliability in predicting the critical drying rate parameter, which is essential for understanding the transition from constant rate period to falling rate period at different temperatures. This predictive capability directly supports the optimization framework by enabling precise determination of when internal moisture diffusion becomes the rate-limiting step, allowing processors to dynamically adjust drying parameters for optimal energy efficiency while maintaining product quality.

Model Details

Models: nn Sorting: None

	nn
Type of model	Neural Network
Training fidelity [%]	99.881
Validation fidelity [%]	98.823
Total trained epochs	1000
Number of layers	3
Layer types	Dense Dense Dense
Number of cells	30 20 10
Activation types	tanh tanh tanh
Training method	Levenberg-Marquardt
Learning rate	N/A
Batch size	N/A
Adaptive learning	N/A
Data shuffling	Yes
Input variables	[min_] (u) [%]
Output variables	(du/dt) [%/min]
Training duration [s]	262

Fig. 8 - Neural network architecture and performance metrics for drying rate prediction model

CONCLUSIONS

The present study successfully developed and validated an artificial neural network (ANN) model for optimizing the convective drying process of pear slices, demonstrating exceptional predictive capability for drying rate dynamics with 98.823% validation fidelity. The model accurately captured the complex nonlinear relationships between moisture content, drying time, and drying rate across three temperature regimes (50°C, 60°C, and 70°C), providing valuable insights into the drying kinetics of pear slices. Experimental results revealed that higher temperatures significantly accelerated the drying process, with 70°C achieving target moisture content (14.5 %) in 180 minutes compared to 260 minutes at 50°C, while also producing higher maximum drying rates (0.57 %/min at 70°C versus 0.40 %/min at 50°C).

The ANN model successfully identified the critical moisture content thresholds (74% at 70°C, 76% at 60°C, and 77% at 50°C) where the drying rate begins to decline significantly, enabling precise determination of when internal moisture diffusion becomes the rate-limiting step. This capability is essential for implementing adaptive control strategies that dynamically adjust drying parameters to balance energy efficiency with product quality preservation.

This research demonstrates that artificial neural networks represent a powerful tool for optimizing convective drying processes in the food industry, offering substantial advantages over traditional empirical models. The developed ANN model provides processors with the ability to predict drying behavior accurately, identify optimal operating conditions, and minimize energy consumption while maintaining critical quality parameters.

Future work should focus on expanding the model to incorporate additional quality indicators (such as color change, texture, and nutrient retention) and testing its applicability across different fruit varieties and drying configurations. The integration of such models into industrial control systems presents a promising pathway toward more intelligent, adaptive, and sustainable food processing operations that simultaneously optimize energy efficiency and product quality.

ACKNOWLEDGEMENT

The experimental data presented in this article were obtained during the project MC 336/30.11.2024 – Mobilities, code PN-IV-P2-2.2-MC-2024-0905, during the period 20.11.2024 - 29.11.2024, project whose theme was "Choosing the optimal technical drying parameters in the fruit dehydration process". This work was supported by a grant of the Ministry of Research, Innovation and Digitization (National Research Authority), CCCDI - UEFISCDI, project number PN-IV-P7-7.1-PTE-2024-0039, within PNCDI IV.

REFERENCES

[1] Asrate D.A., Ali A.N., (2025), Review on the recent trends of food dryer technologies and optimization of drying parameters, *Applied Food Research,* vol.5, no.1, 100927, Amsterdam/Netherlands. DOI: https://doi.org/10.1016/j.afres.2025.100927

[2] Calín-Sánchez Á., Lipan L., Cano-Lamadrid M., Kharaghani A., Masztalerz K., Carbonell-Barrachina Á.A., Figiel A., (2020), Comparison of Traditional and Novel Drying Techniques for Fruits, Vegetables, and Aromatic Herbs, Vegetables and Aromatic Herbs, *Foods,* vol.9, no.9, 1261, Basel/Switzerland. DOI: https://doi.org/10.3390/foods9091261

[3] Das M., Akpinar E.K., (2018), Investigation of Pear Drying Performance by Different Solar Dryers, *Applied Sciences,* vol.8, no.2, 215, Basel/Switzerland. DOI: https://doi.org/10.3390/app8020215

[4] Demir H., Demir H., Lončar B., Pezo L., Brandić I., Voća N., Yilmaz F., (2023), Optimization of Caper Drying Using Response Surface Methodology and Artificial Neural Network, *Energies,* vol.16, no.4, 1687, Basel/Switzerland. DOI: https://doi.org/10.3390/en16041687

[5] Đaković D., Kljajić M., Milivojević N., Doder Đ., Anđelković A.S., (2023), Review of Energy-Related Machine Learning Applications in Food Drying, *Energies,* vol.17, no.1, 224, Basel/Switzerland. DOI: https://doi.org/10.3390/en17010224

[6] El-Mesery H.S., Qenawy M., ElMesiry A.H., Ali M., Adelusi O.A., Hu Z., Salem A., (2025), Application of experimental, numerical, and machine learning techniques to improve drying performance and decrease energy consumption infrared continuous dryer, *Case Studies in Thermal Engineering,* vol.69, 106025, Amsterdam/Netherlands. DOI: https://doi.org/10.1016/j.csite.2025.106025

[7] Erbay Z., Icier F., (2010), A Review of Thin Layer Drying of Foods: Theory, Modeling, and Experimental Results, *Critical Reviews in Food Science and Nutrition,* vol.50, no.5, pp.441-464, London/UK. DOI: https://doi.org/10.1080/10408390802437063

[8] Farid M., (2019), Chapter 17 - Heat and Mass Transfer in Food Processing, in *Handbook of Farm, Dairy and Food Machinery Engineering*, 3rd ed., Academic Press, ISBN 978-0-12-814803-7, New York/USA. DOI: https://doi.org/10.1016/B978-0-12-814803-7.00017-8

[9] Francik S., Łapczyńska-Kordon B., Hajos M., Basista G., Zawiślak A., Francik R., (2024), Modeling the Drying Process of Onion Slices Using Artificial Neural Networks, *Energies,* vol.17, no.13, 3199, Basel/Switzerland. DOI: https://doi.org/10.3390/en17133199

[10] Hossan S., Wasim S., Yiasmin M.N., Saqib M.N., Easdani M., Liu S., (2023), Advanced Research Progress of Food Drying Technology, *North American Academic Research,* vol.6, no.9, pp.18-47, Genève/Switzerland. DOI: https://doi.org/10.5281/zenodo.8415214

[11] Kalantari D., Naji-Tabasi S., Kaveh M., Azadbakht M., Majnooni M., Khorshidi Y., Asghari A., Khalife E., (2022), Drying kinetics and shrinkage rate of thin-sliced pears in different drying stages, *Journal of Food Process Engineering*, vol.46 no.3, e14264, Hoboken/USA. DOI: https://doi.org/10.1111/jfpe.14264

[12] Kalsi B.S., Singh S., Alam M.S., Sidhu G.K., (2023), Comparison of ANN and ANFIS modeling for predicting drying kinetics of Stevia rebaudiana leaves in a hot-air dryer and characterization of dried powder, *International Journal of Food Properties*, vol.26, no.2, pp.3356-3375, London/UK. DOI: https://doi.org/10.1080/10942912.2023.2283380

[13] Khan Md.I.H., Sablani S.S., Joardder M.U.H., Karim M.A., (2022), Application of machine learning-based approach in food drying: opportunities and challenges, *Drying Technology*, vol.40, no.6, 1051-1067, London/UK. DOI: https://doi.org/10.1080/07373937.2020.1853152

[14] Lenart A., (1996), Osmo-convective drying of fruits and vegetables: technology and application, *Drying Technology*, vol.14, no.6, pp.391-413, London/UK. DOI: https://doi.org/10.1080/07373939608917104

[15] Ming J.L.K., Anuar M.S., How M.S., Noor S.B.M., Abdullah Z., Taip F.S., (2021), Development of an Artificial Neural Network Utilizing Particle Swarm Optimization for Modeling the Spray Drying of Coconut Milk, *Foods,* vol.10, no.11, 2708, Basel/Switzerland. DOI: https://doi.org/10.3390/foods10112708

[16] Nguyen T.D., Thai T.Q., Bui H.M., (2025), Application of Machine Learning Models for Hot Air Dryer Design in Food Drying Process, *Journal of Food Processing and Preservation*, vol.2025, 5594122, Hoboken/USA. DOI: https://doi.org/10.1155/jfpp/5594122

[17] Sablani S.S., (2006), Drying of Fruits and Vegetables: Retention of Nutritional/Functional Quality, *Drying Technology*, vol.24, no.2, pp.123–135, London/UK. DOI: https://doi.org/10.1080/07373930600558904

[18] Sagar V.R., Kumar P.S., (2010), Recent advances in drying and dehydration of fruits and vegetables: a review, *Journal of Food Science and Technology*, vol.47, pp.15-26, Berlin/Germany. DOI: https://doi.org/10.1007/s13197-010-0010-8

[19] Selvi K.Ç., Alkhaled A.Y., Yıldız T., (2022), Application of Artificial Neural Network for Predicting the Drying Kinetics and Chemical Attributes of Linden (Tilia platyphyllos Scop.) during the Infrared Drying Process, *Processes,* vol.10, no.10, 2069, Basel/Switzerland. DOI: https://doi.org/10.3390/pr10102069

[20] Spagnuolo A., Vetromile C., Masiello A., De Santo G., Suriano M., Mercuri G., Pellegrino M., Piccolo G., Lubritto C., Di Cicco M.R., (2023), Industrial Drying of Fruit and Vegetable Products: Customized Smart Monitoring and Analytical Characterization of Process Variables in the OTTORTO Project, *Processes*, vol.11, no.6, 1635, Basel/Switzerland. DOI: https://doi.org/10.3390/pr11061635

[21] Tepe T.K., (2024), Improvement of pear slices drying by pretreatments and microwave-assisted convective drying method: drying characteristics, modeling of artificial neural network, principal component analysis of quality parameters, *Journal of Thermal Analysis and Calorimetry*, vol.149, pp.7313–7328, Berlin/Germany. DOI: https://doi.org/10.1007/s10973-024-13280-8

[22] Yao J., Chen W., Fan K., (2023), Novel Efficient Physical Technologies for Enhancing Freeze Drying of Fruits and Vegetables: A Review, *Foods,* vol.12, no.23, 4321, Basel/Switzerland. DOI: https://doi.org/10.3390/foods12234321

NUMERICAL SIMULATION STUDY ON FALLING-FILM EVAPORATION OF MOLASSES ETHANOL WASTEWATER

/

甘蔗糖蜜酒精废水降膜蒸发的数值模拟研究

Liang WANG[1,3#] Mingzhe HU[2#] Xiaole WANG[2*]

[1)]College of Energy and Architectural Engineering, Shandong Huayu University of Technology, Dezhou 253023, China;
[2)]School of Thermal Engineering, Shandong Jianzhu University, Jinan, Shandong 250101, China;
[3)]Shandong Engineering Research Center of Low-Carbon Energy Internet of Things Technology, Dezhou, 253023, China;
Tel:13406930176; E-mail: Wang24215@163.com

DOI: https://doi.org/10.35633/inmateh-79-76

Keywords: *Falling-film evaporation, molasses ethanol wastewater, VOF method, Lee phase-change model, Liquid film thickness, Heat transfer coefficient*

ABSTRACT

To investigate the concentration of molasses ethanol wastewater, a two-dimensional numerical model of falling-film evaporation over horizontal tubes was developed. The model used the Volume of Fluid (VOF) method to capture the liquid-gas interface and was coupled with the Lee phase-change model. The model was validated by comparing the predicted liquid-film thickness and average heat-transfer coefficient with experimental data reported in the literature. The validated model was then used to systematically investigate the effects of spray density (0.10 ~ 0.30 kg/(m·s)) and heat-transfer temperature difference (2 ~ 8 °C) on the falling-film flow and evaporation performance of molasses ethanol wastewater. The results showed that the liquid-film thickness initially decreased and subsequently increased along the circumferential direction, reaching a minimum within the angular range of 90° ~ 120°. Increasing the spray density produced a thicker liquid film; nevertheless, the average heat-transfer coefficient increased monotonically by 23.0% ~ 27.2%, whereas the mass-transfer rate decreased by 19.3% ~ 25.1%. Increasing the heat-transfer temperature difference increased both the average heat-transfer coefficient and the mass-transfer rate. When the temperature difference increased from 2 to 8 °C, the mass-transfer rate increased 2.84 ~ 3.07-fold, and its effect on evaporation performance was substantially greater than that of spray density. Therefore, where operating conditions permit, a lower spray density combined with a higher heat-transfer temperature difference is recommended for the falling-film evaporative concentration of molasses ethanol wastewater.

摘要

为了处理糖蜜酒精废液的浓缩问题，基于流体体积法（VOF）和 Lee 相变模型，针对水平管外的降膜蒸发过程建立了一个二维数值模型。首先，通过将模拟得到的液膜厚度和平均传热系数与文献实验数据对比，验证了模型的可靠性。随后，利用已验证的模型系统研究了喷淋密度（0.10 ~ 0.30 kg/(m·s)）和传热温差（2~8 ℃）对糖蜜酒精废液降膜流动与蒸发性能的影响。结果表明：液膜厚度沿周向先减小后增大，在 90°~120°的圆周角范围内达到最小值。喷淋密度增大使液膜变厚，但平均传热系数单调上升（增幅为 23.0% ~ 27.2%），而质量传递速率则下降了 19.3% ~ 25.1%。提高传热温差同时增大了平均传热系数和质量传递速率。值得注意的是，当温差从 2℃升至 8 ℃时，质量传递速率增大了 2.84 ~ 3.07 倍，其对蒸发效率的影响远超喷雾密度。因此，建议在糖蜜酒厂废水的降膜蒸发浓缩过程中，在条件允许的情况下，可以采用低喷雾密度与高温差相结合的操作策略。

INTRODUCTION

Molasses ethanol wastewater is a high-strength organic effluent discharged during the fermentation of sugarcane molasses for alcohol production.

It is principally characterized by exceedingly high chemical oxygen demand, pronounced viscosity, intense coloration, and an abundance of suspended solids and dissolved organic matter (*Li et al., 2022*).

Liang Wang and Mingzhe Hu contributed equally to this work

In China, the cane molasses alcohol industry generates millions of tons of such wastewater annually, which, if discharged directly without adequate treatment, would provoke severe ecological consequences, such as eutrophication of water bodies and soil acidification accompanied by compaction, while concurrently representing a colossal waste of organic resources (*Chowdhary et al., 2018*). Among the various concentration techniques, falling-film evaporation is regarded as a comparatively definitive treatment strategy, owing to its small driving temperature difference, high heat transfer coefficient, compact equipment footprint, and compatibility with low-temperature heat sources (*Wang et al., 2026*).

A considerable body of research has examined the distribution of liquid film thickness during the falling-film process (*Wang et al., 2026*). Although increasing the tube spacing promotes falling-film evaporation, an excessively large spacing adversely affected the overall volume of the falling-film evaporator; therefore, elucidating the influence of tube spacing on film thickness could contribute to enhancing evaporator compactness while preserving its thermal performance (*Tahir et al., 2019*). *Ibrahim et al.* (*2020*) reported that, at a Reynolds number of 574, increasing the tube spacing from 10 mm to 40 mm reduced the film thickness by 26%. Moreover, investigations have revealed that the liquid film was circumferentially non-uniform. Nusselt (1916) indicated that the film thickness is symmetric about the circumferential angle of 90° and followed a trend of initially decreasing and subsequently increasing along the circumferential direction. For circumferential angles between 0° and 90°, the resultant tangential component of gravity consistently outweighed the viscous force, causing the film flow velocity to rise and the film thickness to diminish with increasing circumferential angle (*Qiu et al., 2015*). As the circumferential angle further increased, the viscous force progressively intensified, whereas the combined contribution of the tangential gravity component and the inertial force gradually diminished (*Zhao et al., 2018*). Within the circumferential angle range of 90° to 120°, the tangential gravity component, the inertial force, and the viscous force attained mutual equilibrium. Under these conditions, the circumferential film thickness reached its minimum (*Zhang et al., 2020*).

Relevant scholars have noted that, in horizontal-tube falling-film evaporators, the falling-film heat transfer coefficient is merely 50%–80% of the in-tube condensation heat transfer coefficient (*Dai et al., 2022*); consequently, augmenting the falling-film heat transfer coefficient constitutes the key to intensifying falling-film evaporator performance. Under convection-dominated regimes, three distinct academic viewpoints have emerged concerning the effect of spray density on horizontal-tube falling-film evaporation (*Ubara et al., 2021*): (1) The heat transfer coefficient increased with rising spray density (*Qi et al., 2010*). For example, *Chen et al. (1997)* experimentally demonstrated that the average Nusselt number increased with the Reynolds number over the range 800 < Re < 4000. (2) As the spray density increased, the heat transfer coefficient initially decreased and then increased (*Su and Ouyang, 2019*). (3) No clear correlation was observed between the heat-transfer coefficient and spray density (*Gong, 2017*).

Considerable research has also investigated the effects of fluid properties on heat transfer during falling-film evaporation. However, most studies have focused on applications such as seawater desalination, alcohol concentration, refrigeration, and air conditioning, and have primarily measured falling-film heat-transfer coefficients for fluids such as pure water *(Liu et al., 2021)*, brine *(Gong et al., 2016)*, and halocarbon refrigerants *(Jin et al., 2019)*. Consequently, systematic investigations on high-viscosity, complex organic fluids such as molasses distillery wastewater remain scarce, and their falling-film flow and heat transfer behaviors are poorly understood. To fill this knowledge gap, the present study adopted molasses ethanol wastewater as the working fluid. The Volume of Fluid (VOF) method was introduced to track the gas-liquid interface and was coupled with the Lee evaporation phase-change model, thereby establishing a mathematical framework for the falling-film evaporation of molasses ethanol wastewater. The reliability of the numerical model was verified by comparing the predicted liquid film thickness and heat transfer coefficient with experimental data reported in the published literature (*Jia, 2025; Parken et al., 1990*), rather than through experiments conducted in the present study. The local distributions of the liquid film thickness and the heat transfer coefficient during the evaporation of this high-viscosity fluid were analyzed, and the variation patterns of the Nusselt number together with local and average heat transfer coefficients were systematically examined. The findings were anticipated to provide both a theoretical basis and a numerical predictive tool for the design of falling-film evaporators intended for molasses ethanol wastewater, while simultaneously enriching the numerical research methodology applicable to the evaporation and concentration of high-viscosity, complex liquid feeds.

MATERIAL AND METHODS

Physical model and meshing

Molasses ethanol wastewater was uniformly sprayed onto the outer surface of a horizontal tube through a liquid distributor, forming a thin and even liquid film. As the film spreads, it absorbs the latent heat released by the condensation of steam inside the horizontal tube and subsequently evaporates (*Jia, 2025*). Due to the symmetry of the horizontal tube structure, only the half-tube region between adjacent dropping points is modeled to reduce the computational cost. Considering that the two-dimensional model requires only 1.7% of the mesh count of a three-dimensional model to accurately capture the gas-liquid interface distribution, the two-dimensional model is adopted to simulate the falling-film flow process. The geometric dimensions of the physical model depicted in Fig. 1 were as follows: the diameter of the liquid distribution opening at the top was 1 mm, and the distance from this opening to the first horizontal tube was 10 mm. To eliminate the influence of the distributor height on the falling-film behavior of the molasses ethanol wastewater, the upper one of the two horizontal tubes (with a diameter of 25.4 mm) was designated as the distribution tube, while the lower one served as the object of simulation.

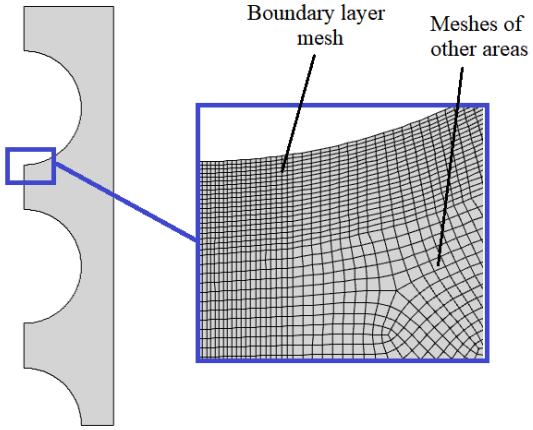


Fig. 1 - Physical model and meshing

As illustrated in Fig. 1, the physical model featured a relatively simple geometry, which was well suited for high-precision structured grids. As the contour of the molasses ethanol wastewater needed to be captured, boundary-layer grids were refined in the near-wall region of the horizontal tubes. The boundary layer comprised 20 layers; the thickness of the first layer was 0.2 mm, and each subsequent layer was 1.15 times as thick as the preceding one. The grid size in the remaining regions was set to 4 mm.

Governing equations

Before establishing the mathematical model, the following assumptions were made regarding the falling-film evaporation of molasses ethanol wastewater *(Wang, 2025)*: (1) the liquid film completely wets the tube surface; (2) only liquid-film flow over the outer surface of the horizontal tube is considered, and the tube wall thickness is neglected; (3) the tube wall temperature is uniform; and (4) the temperature dependence of the thermophysical properties of the molasses ethanol wastewater is neglected.

A numerical model of the falling-film evaporation process was established within an Eulerian framework using the Volume of Fluid (VOF) method. The liquid and gas phases were treated as a single fluid mixture sharing common velocity and pressure fields, and the liquid-gas interface was captured using the phase-volume fraction *(Jia et al., 2026)*.

The transport equation for the liquid-phase volume fraction (α_l), used to capture the liquid-gas interface is expressed as:

$$\frac{\partial \alpha_l}{\partial t} + \nabla \cdot \left(\alpha_l \vec{u}\right) = -\frac{\dot{m}}{\rho_l} \tag{1}$$

The vapor-phase volume fraction (α_v) is given by:

$$\alpha_v = 1 - \alpha_l \tag{2}$$

where: t is the time, s; $\vec{u}$ is the velocity vector, m/s; ρ_l is the density of the molasses ethanol wastewater, kg/m^3; $\dot{m}$ is the volumetric mass-source term associated with evaporation, (kg/(m·s)).

The mixture continuity equation is obtained by summing the mass-conservation equations for the liquid and gas phases *(Jia et al., 2026)*:

$$\frac{\partial \rho}{\partial t} + \nabla \cdot \left(\rho \vec{u}\right) = 0 \tag{3}$$

The density of the fluid mixture (ρ) is calculated as follows:

$$\rho = \alpha_l \rho_l + \alpha_v \rho_v \tag{4}$$

The momentum equation used in the model is given as follows (*Wang, 2025*):

$$\frac{\partial \left(\rho \vec{u}\right)}{\partial t} + \nabla \cdot \left(\rho \vec{u}\vec{u}\right) = -\nabla p + \nabla \cdot \left[\mu\left(\nabla \vec{u} + (\nabla u)^T\right)\right] + \rho g + F_\sigma \tag{5}$$

where: p is the pressure, Pa; g is the acceleration due to gravity, m/s^2; μ is the dynamic viscosity of the fluid mixture, Pa·s; F_σ is the surface-tension force per unit volume, N/m^3.

The dynamic viscosity of the fluid mixture is calculated using Eq. (6).

$$\mu = \alpha_l u_l + \alpha_v \mu_v \tag{6}$$

The energy equation is expressed as follows (*Jia et al., 2026*):

$$\frac{\partial \left(\rho c_p T\right)}{\partial t} + \nabla \cdot \left(\rho c_p \vec{u} T\right) = \nabla \cdot \left(\lambda \nabla T\right) - \dot{m} h_v \tag{7}$$

where: c_p is the specific heat capacity of the fluid mixture, J/(kg·K); T is the temperature, K; λ is the thermal conductivity of the fluid mixture, W/(m^2·K); $\dot{m}$ is the mass-transfer rate per unit volume (kg/(m^3·s)); h_v is the latent heat of vaporization, (J/kg).

c_p and μ are calculated using Eqs. (8) and (9).

$$c_p = \alpha_l c_{p,l} + \alpha_v c_{p,v} \tag{8}$$

The phase-change mass-source term is determined using the Lee model:

$$\dot{m} = r_e \alpha_l \rho_l \frac{T - T_{sat}}{T_{sat}} \tag{9}$$

where: r_e is the evaporation relaxation factor, s^{-1}; T_{sat} is the saturation temperature of the molasses ethanol wastewater, ℃;

F_σ in Eq. (5) is calculated using the continuum surface force model proposed by Brackbill (*Yang et al., 2024*):

$$F_\sigma = \sigma \left[\nabla \cdot \left(\frac{\nabla \alpha_l}{|\nabla \alpha_l|}\right)\right] \tag{10}$$

where σ is the surface-tension coefficient at the liquid-gas interface, N/m. The effect of the wall contact angle is incorporated by correcting the interface normal vector near the wall.

The thermophysical properties used in the governing equations are presented in Table 1.

Table 1

Thermal properties parameters

Name	Density / kg/m3	Specific heat capacity/ J/(kg·K)	Thermal conductivity W/(m·K)	Dynamic viscosity / Pa·s
Molasses ethanol wastewater	1096.7	3709	0.58	0.00851
Vapor	0.5542	2014	0.0261	1.34×10-5

Boundary conditions and Simulation Settings

The liquid distribution inlet on the upper side of the horizontal tube is set as a velocity inlet boundary condition, with the velocity set to 0.23 ~ 0.137 m/s to ensure that the spray density remains within the range of 0.010 ~ 0.030 kg/(m·s). The bottom of the horizontal tube is set as a pressure outlet boundary condition with a reference pressure of 0 Pa. The horizontal tube is set as a wall boundary condition, with a constant temperature of 62℃, 64℃, 66℃, and 68℃, respectively, and a contact angle of 60°.

Based on the spray density, the calculated Reynolds number indicates that the investigated Re ranges from 2 to 14, which is far below the turbulent threshold; therefore, in this study, the molasses alcohol waste liquid is considered to exhibit laminar flow.

The numerical simulation is performed using ANSYS Fluent 18.0 software. The pressure and velocity are solved using the Pressure-Implicit with Splitting of Operators (PISO) algorithm. The pressure term is spatially discretized using the PRESTO! scheme, while both the temporal term and the momentum term are discretized using the second-order upwind scheme. In the dynamic time-stepping settings, the maximum Courant number is 0.25.

Evaluations

In falling-film evaporation, the film thickness constituted the dominant thermal resistance during the evaporation process. The degree of uniformity in the film thickness distribution markedly influenced the evaporation rate of the descending liquid film; therefore, it was imperative to examine the film thickness of molasses ethanol wastewater during falling-film evaporation.

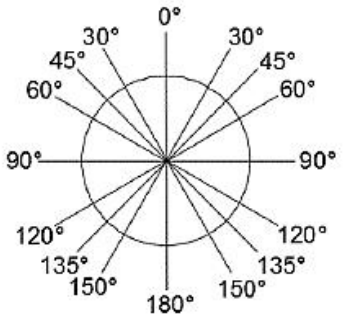


Fig. 2 - Local film thickness measurement method

As illustrated in Fig. 2, with the center of the horizontal tube taken as the origin and the vertically upward direction designated as 0°, straight lines were drawn at circumferential angles of 15°, 30°, 45°, 60°, 75°, 90°, 105°, 120°, 135°, and 150°. The length occupied by the liquid phase along each of these ten lines was extracted directly from Fluent, and this length was defined as the film thickness at the corresponding circumferential angle.

The average heat transfer coefficient served as a pivotal indicator for quantifying the heat transfer rate during the falling-film evaporation of molasses ethanol wastewater, and was determined as follows:

$$h_{ave} = \frac{q}{\Delta T} \tag{11}$$

where: h_{ave} was the average heat transfer coefficient, W/(m²·K); q was heat flux of the horizontal tube, W/m²; ΔT was the temperature difference, ℃.

RESULTS AND DISCUSSIONS

Verification

To ensure the relevance of the validation, the experimental cases cited from the literature were selected to closely match the key physical features of the present simulation, including the horizontal tube geometry (D = 25.4 mm), laminar falling-film flow regime, and constant wall-temperature thermal boundary condition. Although the working fluid in the referenced experiments was pure water, the present study focuses on molasses ethanol wastewater, the two fluids have comparable density and surface tension, though the viscosity of the wastewater is moderately higher. This viscosity difference is explicitly accounted for in the present model through the mixture property equations (Eq. (6)). Therefore, the validation results provide meaningful support for the reliability of the present model. Fig.3 presented a comparison between the simulated local film thickness and the experimental ones documented in the literature (*Jia, 2025*). It is evident from Fig.3 that the simulated film thickness conformed to the literature values, both exhibiting an initial thinning followed by a subsequent thickening, with a relative deviation of less than 5%. The falling-film evaporation process constituted a complex heat and mass transfer phenomenon characterized by dynamic coupling between the liquid and gas phases. To further substantiate the validity of the established model, it was necessary to verify its heat transfer characteristics.

Fig. 4 presents the simulated heat transfer coefficient for a smooth tube with the experimental data of *Parken et al.* (*1990*). As clearly observed from Fig. 4, the simulated heat transfer coefficient was in favorable agreement with the values reported in the literature, the relative deviation being below 5%. A synthesis of the analyses in Fig. 3 and Fig. 4 revealed that the developed mathematical model was capable of effectively capturing the physical trends and thermal performance characteristics of molasses ethanol wastewater during falling-film evaporation. It should be noted that, since the validation was performed against external literature data rather than experimental results obtained from the specific molasses ethanol wastewater under identical conditions, the numerical predictions of absolute values may bear inherent uncertainties. Nevertheless, the model demonstrates high reliability in capturing the underlying physical mechanisms and performance trends.

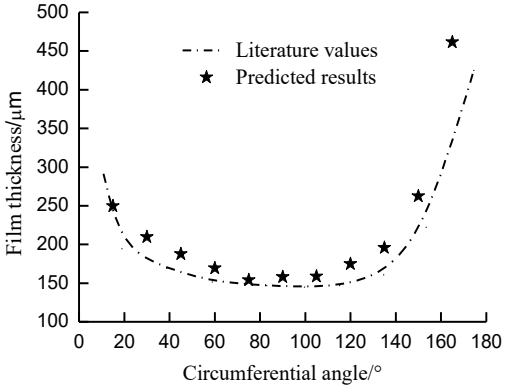


Fig. 3 - Comparison of the reported and simulated film thickness

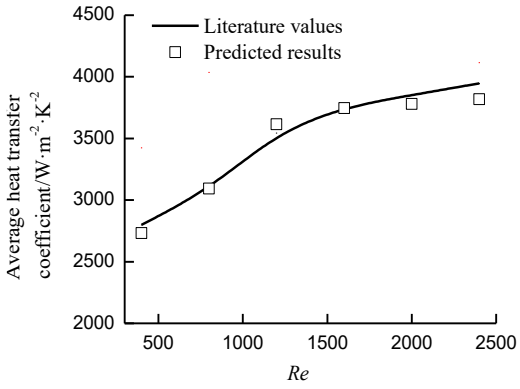


Fig. 4 - Comparison of the reported and simulated average heat transfer coefficient

To ensure the reliability of the numerical results, a systematic mesh-independence study was conducted before the main simulations. Three structured grids were generated with different refinement levels: a coarse mesh (13475 cells), a medium mesh (26669 cells), and a fine mesh (39863 cells). The average heat transfer coefficient and the minimum film thickness at 105° were selected as the evaluation criteria, using a typical operating condition (Γ = 0.20 kg/(m·s), ΔT = 6 °C). The average falling-film heat transfer coefficient decreased from 1724.84 W/(m²·K) for the medium mesh to 1703.72 W/(m²·K) for the finer mesh, with a reduction of only 1.22%. Therefore, the medium mesh can be considered an appropriate meshing scheme.

The effect of spray density

Fig. 5 shows the variation in local liquid film thickness with circumferential angle at spray densities ranging from 0.10 to 0.25 kg/(m·s). Despite differences in spray density, the circumferential distributions of the local film thickness exhibited similar trends. Specifically, as the circumferential angle increased, the film thickness initially decreased, attained its minimum within the circumferential angle of 90° ~ 120°, and subsequently increased.

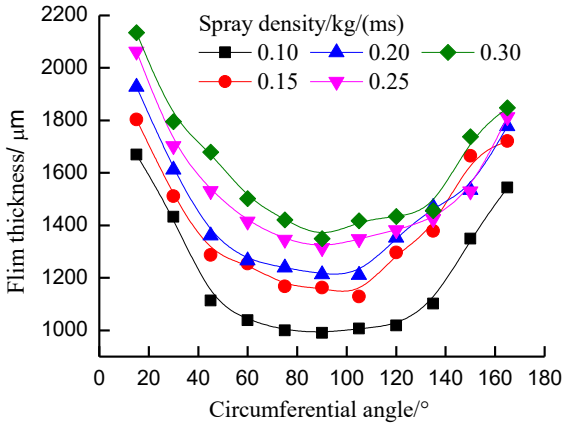


Fig. 5 - Local liquid film thickness at different spray densities

The change behavior of the local film thickness with respect to the circumferential angle conformed to the theoretical prediction derived from Nusselt's classical analysis. Furthermore, it was evident that the local film thickness progressively increased with rising spray density.

The reason was that under gravity, to maintain a steady laminar falling-film, the liquid film had to enlarge its cross-sectional area to handle a greater volumetric flow. An examination of the extent of this influence revealed that when the spray density was augmented from 0.10 to 0.15 kg/(m·s), the film thickness thickened by 16.66%, whereas an increase from 0.25 to 0.30 kg/(m·s) resulted in a mere 5.39% thickening. In accordance with the classical Nusselt laminar falling-film theory, the film thickness scaled with the spray density to the one-third power. Hence, when the spray density already resided within a high baseline range, an identical absolute increment (e.g., 0.05 kg/(m·s)) inevitably induced a pronounced attenuation in the relative increase of the film thickness.

The effect of spray density on the average heat-transfer coefficient is shown in Fig. 6. The average heat transfer coefficient increased monotonically as the spray density increased from 0.10 to 0.30 kg/(m·s), with a relative increase of 23.0% ~ 27.2%. When considered together with the results in Fig. 5, these findings indicate that although increasing the spray density produced a thicker liquid film and consequently increased conductive thermal resistance, the accompanying increase in flow rate raised the film velocity. This enhanced mixing within the liquid film and intensified interfacial disturbances, thereby reducing the thermal-boundary-layer resistance. These results are consistent with those of *Chen et al. (1997)*, who reported an increase in the Nusselt number with increasing film Reynolds number.

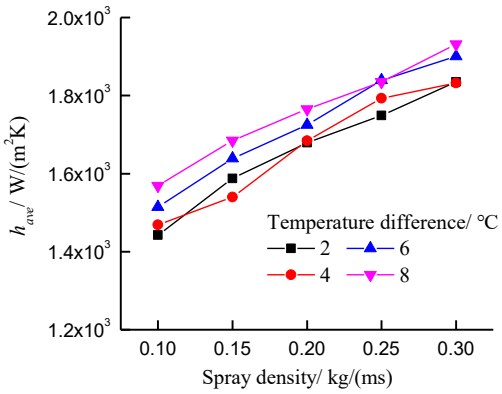


Fig. 6 - Average heat transfer coefficient with spray densities

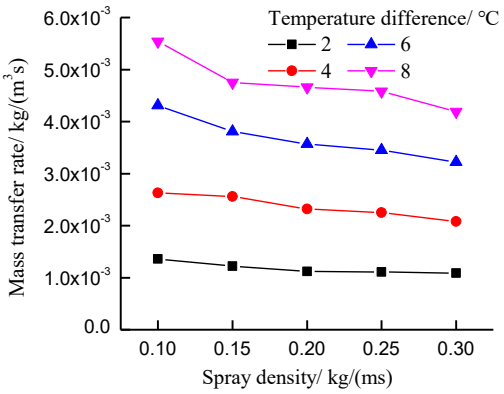


Fig. 7 - Mass volume rate with spray densities

Fig. 7 shows the variation in mass transfer rate with spray density during the falling-film evaporation of molasses ethanol wastewater. The mass transfer rate decreased progressively as the spray density increased. When the spray density increased from 0.10 to 0.30 kg/(m·s), the mass-transfer rate decreased by 19.3% ~ 25.1%. Although the higher flow rate enhanced convective heat transfer, as shown in Fig. 6, the corresponding increase in liquid-film thickness (Fig. 5) increased the heat-transfer distance between the tube wall and the liquid-gas interface. Consequently, the heat supplied at the wall was distributed over a larger liquid volume, reducing the heat available for evaporation per unit volume and thereby decreasing the volumetric mass-transfer rate. Therefore, a relatively low spray density is recommended for enhancing evaporation, provided that complete and stable wetting of the tube surface is maintained.

The effect of temperature difference

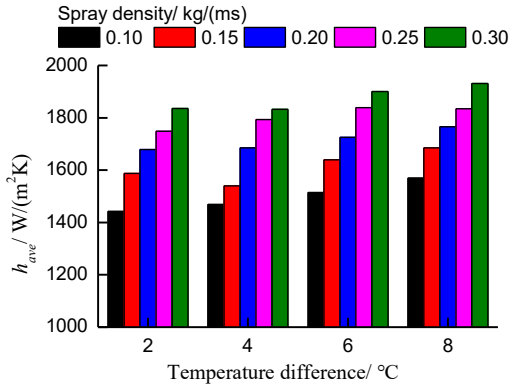


Fig. 8 - Average heat transfer coefficient with temperature difference

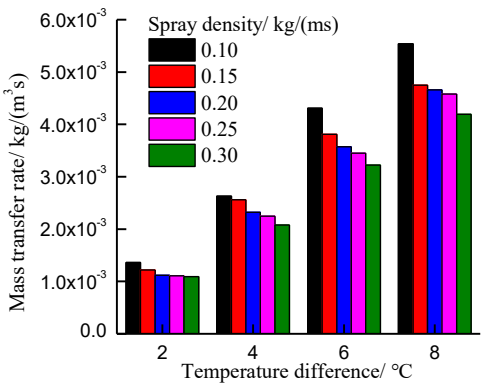


Fig. 9 - Mass volume rate with temperature difference

In addition to spray density, the heat-transfer temperature difference, which is the primary driving force for heat transfer and phase change during falling-film evaporation, requires systematic investigation. Figs. 8 and 9 show the variations in the average heat-transfer coefficient and mass-transfer rate, respectively, during the falling-film evaporation of molasses ethanol wastewater at temperature differences of 2, 4, 6, and 8 °C.

As shown in Fig. 8, the average heat-transfer coefficient increased with increasing temperature difference. At a spray density of 0.10 kg/(m·s), increasing the temperature difference from 2 to 8 °C increased the average heat-transfer coefficient from 1,442.48 to 1,569.14 W/(m²·K), corresponding to a relative increase of 8.8%. The larger temperature difference increased the wall-normal temperature gradient and intensified heat transfer from the inner region of the liquid film toward the liquid–gas interface. The resulting enhancement of evaporation and interfacial disturbance further promoted heat transfer through the liquid film.

As shown in Fig. 9, at a spray density of 0.10 kg/(m·s), increasing the temperature difference from 2 to 8 °C increased the mass-transfer rate from 1.36×10^{-3} kg/(m³·s) to 5.54×10^{-3} kg/(m³·s), with an amplification by a factor of 3.07. Even at the higher spray density of 0.30 kg/(m·s), at which the lowest mass-transfer rates were obtained, the value increased from 1.09×10^{-3} to 4.19×10^{-3} kg/(m³·s), registering a 2.84-fold increase. According to the Lee phase-change model (Eq. (9)), the phase-change mass-source term is positively related to the degree of superheat. As the temperature difference increased, the heat flux from the tube wall to the liquid film increased, allowing the wastewater near the liquid-gas interface to absorb sufficient latent heat and undergo evaporation. These results demonstrate that, within the investigated parameter ranges, increasing the heat-transfer temperature difference was more effective than varying the spray density in enhancing the instantaneous water-removal rate.

To quantitatively compare the relative effects of the two operating parameters, a normalized sensitivity index was defined as $S = (\varphi_{max} - \varphi_{min})/\varphi$. Over the investigated parameter ranges, $S_{\Delta T} = 1.24$, whereas $S_{\Gamma} = 0.11$, indicating that the effect of the heat-transfer temperature difference was approximately 11 times greater than that of spray density. This difference arises because the phase-change mass-transfer rate is directly related to the degree of superheat, whereas spray density affects mass transfer indirectly by altering liquid-film thickness, flow characteristics, and heat-transfer resistance.

CONCLUSIONS

A two-dimensional numerical model of the falling-film evaporation of molasses ethanol wastewater over the outer surface of a horizontal tube was developed using the Volume of Fluid (VOF) method coupled with the Lee phase-change model. The effects of spray density and heat-transfer temperature difference on heat- and mass-transfer performance were systematically investigated. The main conclusions are as follows:

(1) The developed model satisfactorily predicted the liquid-film thickness distribution and heat-transfer characteristics. The simulation results agreed well with experimental data reported in the literature, with relative deviations of less than 5%.

(2) The circumferential distribution of liquid-film thickness was consistent with classical Nusselt theory. As the circumferential angle increased, the film initially became thinner and subsequently thickened, reaching its minimum thickness within the angular range of 90° ~ 120°. Increasing the spray density increased the local film thickness. However, because laminar falling-film thickness is proportional to the cube root of spray density, the rate of film thickening gradually decreased as spray density increased.

(3) Within the spray-density range of 0.10 ~ 0.30 kg/(m·s), the average heat-transfer coefficient increased monotonically with spray density. By contrast, the volumetric mass-transfer rate decreased because the thicker liquid film distributed the supplied heat over a larger liquid volume. Increasing the heat-transfer temperature difference enhanced the thermal driving force, resulting in a moderate increase in the average heat-transfer coefficient and a pronounced increase in the mass-transfer rate. Sensitivity analysis indicated that the effect of temperature difference on the mass-transfer rate was more than one order of magnitude greater than that of spray density.

(4) Within the investigated ranges of spray density (0.10 ~ 0.30 kg/(m·s)) and heat-transfer temperature difference (2 ~ 8 °C), combining a relatively low spray density with a relatively high temperature difference is recommended for the falling-film evaporative concentration of molasses ethanol wastewater. However, the spray density should remain above the critical wetting rate to prevent dry-patch formation. Although a higher temperature difference substantially enhances evaporation, practical applications must also consider heat-source energy consumption and the increased risks of fouling and thermal degradation or carbonization of high-viscosity wastewater on the heated tube surface. Therefore, operating parameters should be comprehensively optimized together with equipment-cleaning intervals.

ACKNOWLEDGMENTS

This work was supported by the Doctoral Research Fund of Shandong Huayu University of Technology and the Shandong Engineering Research Center of Low-Carbon Energy Internet of Things Technology (PT2025KJS004).

REFERENCES

[1] Chen, H., & Jebson, R. S. (1997). Factors affecting heat transfer in falling film evaporators. *Food and Bioproducts Processing*, Vol. 75(2), pp. 111-116, New Zealand.

[2] Chowdhary, P., Raj, A., Bharagava, R.N. (2018). Environmental pollution and health hazards from distillery wastewater and treatment approaches to combat the environmental threats: A review. *Chemosphere*, Vol. 194, pp. 229-246, India.

[3] Dai, Z., Zhang, Y., Wang, S., Nawaz, K., & Jacobi, A. (2022). Falling-film heat exchangers used in desalination systems: A review. *International Journal of Heat and Mass Transfer*, Vol. 185, 122407, Shanghai/ China.

[4] Gong, L. (2017). *Thermal Performance and Parameters Distribution of Large-scale Horizontal-tube Falling Film Evaporators (大型水平管降膜蒸发器热力性能和参数分布特性研究).* PhD dissertation, Dalian University of Technology, Dalian/ China.

[5] Gong, L., Shen, S., Liu, H. (2016). Parametric distributions of a horizontal-tube falling film evaporator for desalination. *Desalination and Water Treatment*, Vol. 57(25), pp. 11699-11711, Dalian/China.

[6] Ibrahim A., Fath H., Ibrahim M., (2020), Numerical simulation for falling film thickness around horizontal tube in MVC and MED evaporators, *Proceedings of the Materials Science Forum*, pp.139-150, Egypt.

[7] Jia, B. (2025). *Heat Transfer Mechanisms of Droplet Falling Film Evaporation on Nano-structured Surfaces and its Application in Building Wastewater Treatment (纳米结构表面滴状流降膜蒸发传热机理及其在建筑废水处理中的应用).* Doctoral dissertation, Shandong Jianzhu University, Jinan/China. https://doi.org/10.27273/d.cnki.gsajc.2025.000002

[8] Jia, B., Zhao, Z., Wang, X., Chen, C., Ma, X., Wu, J., Yang, L., Politaeva, N. (2026). Local film thickness in relation to the droplet topological structure of droplet falling film on micro-nano structured horizontal tubes. *Case Studies in Thermal Engineering*, 108125, Dezhou/China.

[9] Jin, P. H., Zhang, Z., Mostafa, I., Zhao, C., Ji, W., Tao, W. (2019). Heat transfer correlations of refrigerant falling film evaporation on a single horizontal smooth tube. *International Journal of Heat and Mass Transfer*, Vol. 133, pp. 96-106, Dalian/China.

[10] Li, J., Xu, J., Ma, N., Tan, C., Xia, Z., Zuo, J. (2022). Research progress on recovery of sugarcane molasses alcohol wastewater (甘蔗糖蜜酒精废液的回收利用研究进展). *Modern Chemical Industry*, Vol. 42(7), pp. 79, Harbin/China. https://doi.org/10.16606/j.cnki.issn0253-4320.2022.07.017.

[11] Liu, S., Mu, X., Shen, S., Li, C., Wang, B. (2021). Experimental study on the distribution of local heat transfer coefficient of falling film heat transfer outside horizontal tube. *International Journal of Heat and Mass Transfer*, Vol. 170, 121031, Dalian/China.

[12] Nusselt, W. (1916). Die Oberflächenkondensation des Wasserdampfes. *Zeitschrift des Vereines Deutscher Ingenieure*, Vol. 60(3), pp. 541-546, 556, Germany.

[13] Parken, W. H., Fletcher, L. S., Sernas, V., Han, J. (1990). Heat transfer through falling film evaporation and boiling on horizontal tubes. *Journal of Heat Transfer*, Vol. 112, pp. 744-750, USA.

[14] Qi, L., Ma, H., Li, C., Luo, Z. (2010). Experimental research on heat transfer performance of falling film evaporation on horizontal tubes (水平管外降膜蒸发传热性能实验研究). *Journal of University of Shanghai for Science and Technology*, Vol. 32(1), pp. 27-30, Shanghai/China. https://doi.org/10.13255/j.cnki.jusst.2010.01.014.

[15] Qiu, Q., Jiang, W., Shen, S., Zhu, X., Mu, X. (2015). Numerical investigation on characteristics of falling film in horizontal-tube falling film evaporator. *Desalination and Water Treatment*, Vol. 55(12), pp. 3247-3252, Dalian/China.

[16] Su, X., & Ouyang, X. (2019). Experimental Study of Falling Film Evaporation Heat Transfer Performance of R410A, R404A and R407C in Horizontal T Type Fin Inner Thread Tube (R410A/R404A/R407C 在 T 型翅内螺纹水平管外的降膜蒸发换热研究). *Journal of Engineering for Thermal Energy and Power*, Vol. 34(2), pp. 88-93, Shanghai/China. https://doi.org/10.16146/j.cnki.rndlgc.2019.02.013

[17] Tahir, F., Mabrouk, A., Koc, M. (2019). Review on CFD analysis of horizontal falling film evaporators in multi effect desalination plants. *Desalination and Water Treatment*, Vol. 166, pp. 296-320, Qatar.

[18] Ubara, T., Asano, H., Sugimoto, K. (2021). Falling film evaporation and pool boiling heat transfer of R1233zd (E) on thermal spray coated tube. *Applied Thermal Engineering*, Vol. 196, 117329, Shanghai/ China.

[19] Wang, D., Shen, S., Pan, B., & Guo, Y. (2026). Numerical study on liquid column deflection and liquid film thickness characteristics of falling film on horizontal tubes under cross-flow steam. *Desalination*, 119884, Dalian/China.

[20] Wang, L. (2025). Numerical simulation on liquid film flow turbulence characteristics of corrugated baffle-type plate under high Reynolds number. *Chemical Engineering and Processing-Process Intensification*, 110511, Shanghai/China.

[21] Wang, L., Huang, X., Wang, Y., Yu, G. (2026). Study on falling film in large-diameter tube and co-current gas-liquid heat transfer under high temperature and velocity of gas flow. *Chemical Engineering Research and Design*, Vol. 225, pp. 230-244, Shanghai/China.

[22] Yang, L., Jia, B., Zhang, Q., Zhou, Z. (2024). Effect of dynamic contact angle behavior on droplet topological structure and film thickness evolutions in droplet mode. *Desalination*, Vol. 576, 117359, Jinan/China.

[23] Zhang, Y., Wang, D., Liu, Y., Tang, M., Zhang, S. (2020). Distribution characteristics of falling film thickness around a horizontal corrugated tube [J]. *International Journal of Heat and Mass Transfer*, 154: 119773, Tianjin/China.

[24] Zhao, C., Ji, W., Jin, P., Zhong, Y, Tao, W. (2018). Hydrodynamic behaviors of the falling film flow on a horizontal tube and construction of new film thickness correlation. *International Journal of Heat and Mass Transfer*, Vol. 119, pp. 564-576, Hangzhou/China.

LIGHTWEIGHT DETECTION OF EGG SURFACE DEFECTS UNDER CONVEYOR-BELT CONDITIONS USING YOLOv11N-DAL

/

传送带条件下基于 YOLOv11n-DAL 的鸡蛋外观缺陷轻量化检测

Xianyong MENG[1,2)], Haoran GUO[1,2)], Jun YAN[1,2)], Qimiao WANG[1,2,*)], Qinyou SUN[1,2,*)]

[1)] School of Information Science and Engineering, Shandong Agricultural University, Taian 271018, China;

[2)] Key Laboratory of Huanghuaihai Smart Agricultural Technology, Ministry of Agriculture and Rural Affairs, Taian 271018, China;

** Corresponding author: E-mail: 15753837976@163.com;2024121207@sdau.edu.cn*

DOI: https://doi.org/10.35633/inmateh-79-77

Keywords: *egg surface defects; lightweight detection; YOLOv11n-DAL; conveyor-belt sorting; machine vision*

ABSTRACT

Egg appearance defect detection in conveyor-belt environments is challenged by irregular defect morphology, illumination variations, and the limited computational resources of intelligent sorting equipment, making it difficult to simultaneously achieve high detection accuracy and lightweight deployment. In this study, a lightweight detection model, termed YOLOv11n-DAL, is proposed to improve egg defect detection performance while reducing computational complexity. The proposed model integrates C3k2_DCNv4, ADown, and Detect_LSDECD modules into the YOLOv11n framework to enhance defect feature representation, improve effective information retention during downsampling, and reduce computational redundancy in the prediction stage. A conveyor-belt egg image dataset containing three categories, namely damaged, dirty, and good, was constructed. The dataset consisted of 1,730 original images, and the training set was expanded to 4,152 images through data augmentation. Comparative experiments and ablation studies were conducted to validate the effectiveness of the proposed model. The experimental results demonstrated that YOLOv11n-DAL achieved 95.2% Precision, 94.5% Recall, 94.8% F1-score, 96.7% mAP@0.5, and 95.8% mAP@0.5:0.95. Compared with the original YOLOv11n model, YOLOv11n-DAL reduced the number of parameters from 2.6 M to 1.7 M, GFLOPs from 6.3 to 4.8, and model size from 5.2 MB to 3.8 MB, while maintaining superior detection performance. The results indicate that YOLOv11n-DAL achieves an effective balance between detection accuracy and computational efficiency, providing a lightweight and practical solution for intelligent egg sorting systems in conveyor-belt environments.

摘要

传送带环境下鸡蛋外观缺陷检测受到缺陷形态不规则、光照变化以及智能分拣设备计算资源有限等因素影响，难以同时满足检测精度和轻量化部署需求。本文提出一种轻量化检测模型 YOLOv11n-DAL，在降低计算复杂度的同时提升鸡蛋缺陷检测性能。该模型将 C3k2_DCNv4、ADown 和 Detect_LSDECD 融合至 YOLOv11n 框架中，以增强缺陷特征表达能力、提高下采样过程中的有效信息保留能力，并降低预测阶段的计算冗余。本文构建了包含 damaged、dirty 和 good 三类的传送带鸡蛋图像数据集，包括 1730 张原始图像，训练集经数据增强后扩展至 4152 张。通过对比实验和消融实验对模型性能进行验证。实验结果表明，YOLOv11n-DAL 模型的 Precision、Recall、F1-score、mAP@0.5 和 mAP@0.5:0.95 分别达到 95.2%、94.5%、94.8%、96.7%和 95.8%。相比 YOLOv11n，所提出模型将参数量由 2.6 M 降低至 1.7 M，GFLOPs 由 6.3 降低至 4.8，模型大小由 5.2 MB 降低至 3.8 MB，同时保持更高检测性能。研究结果表明，YOLOv11n-DAL 能够在检测精度和计算效率之间取得良好平衡，为传送带鸡蛋智能分拣系统提供了一种轻量化解决方案。

INTRODUCTION

Eggs are important poultry products with high nutritional and economic value, and their external quality directly affects commercial grading, storage stability, transportation safety, and consumer acceptance. During collection, conveying, grading, and packaging, eggs are easily affected by mechanical impact, collision, and environmental contamination, resulting in defects such as cracks, shell breakage, and surface dirt. These defects not only reduce product value but may also increase potential food safety risks. Therefore, rapid, accurate, and non-destructive external-defect detection is essential for automated egg sorting and intelligent quality control in modern poultry processing systems (*Gautron et al., 2021; So and Kim, 2022; Yang et al., 2023; Atwa et al., 2024; Yu et al., 2025*).

Traditional manual inspection methods are still widely used in some egg-processing facilities. However, manual inspection is highly dependent on operator experience and is affected by fatigue, subjective judgment, and low efficiency, making it difficult to satisfy the requirements of high-speed industrial sorting. With the development of intelligent agricultural equipment, machine vision and deep learning technologies have gradually become effective solutions for agricultural product quality evaluation due to their advantages of rapid image acquisition, objective decision-making, and automated operation. In recent years, deep learning-based visual methods have been successfully applied to egg defect classification, eggshell crack detection, freshness evaluation, and online quality monitoring (*Turkoglu, 2021; Botta et al., 2022; Chen et al., 2023; Huang et al., 2023; Zhao et al., 2023; Yin et al., 2024; Çengel et al., 2025; Wu et al., 2025*).

Among deep learning-based object detection algorithms, the YOLO series has attracted extensive attention in agricultural visual applications because of its excellent balance between detection accuracy and computational efficiency (*Kanna et al., 2024; Gupta et al., 2025*). Compared with image classification methods, object detection algorithms can simultaneously achieve target localization and category recognition, making them more suitable for continuous conveyor-belt inspection scenarios. Recent studies have demonstrated that improved YOLO models can effectively enhance detection performance under complex agricultural environments. *Tang et al., (2026),* proposed an improved RT-DETR model for defective egg detection in edge-computing environments, demonstrating the effectiveness of advanced detection architectures for intelligent egg sorting applications. *Ma et al*., *(2025),* developed YOLO-TRS based on YOLO11 for tomato fruit ripeness and stem detection, demonstrating the effectiveness of YOLO11-based lightweight models in agricultural vision tasks. *Shi et al., (2025),* proposed an improved YOLOv11n-based model for missing-seed detection and counting, further confirming the potential of lightweight networks for intelligent agricultural equipment deployment. In addition, *Bing et al., (2025),* introduced improved feature extraction strategies into YOLOv8s for apple leaf lesion detection under complex backgrounds, indicating that feature enhancement is important for small-object detection tasks.

However, practical application of deep learning-based egg inspection systems still faces several challenges. First, egg defects such as small cracks, irregular damaged regions, and weak dirty spots usually exhibit unclear boundaries and low contrast, making them easily confused with eggshell texture, illumination variation, and conveyor-belt background interference. Second, some existing methods rely on image classification or specialized imaging systems, which limits their application in low-cost and high-speed sorting lines. Although hyperspectral and other advanced imaging technologies can improve defect visibility, their high equipment cost and complex configuration restrict large-scale industrial deployment. Third, large-scale detection networks generally require considerable computational resources, making them difficult to deploy on embedded devices and edge-computing platforms. YOLO11 provides a lightweight backbone-neck-head structure with improved computational efficiency; however, its original architecture still has limitations for fine-grained egg external-defect detection, since redundant feature fusion and repeated prediction-head operations increase computational overhead without proportionally improving sensitivity to irregular defect boundaries *(Jocher et al., 2024*).

In recent years, feature-enhancement and computational-optimization strategies for lightweight object detection networks have provided new research directions for addressing these problems. Deformable convolution was first introduced by *Dai et al. (2017)* to achieve flexible kernel deformation by learning content-adaptive sampling offsets, and was later refined into the more efficient DCNv4 by *Xiong et al. (2024)*; DCNv4-based modules have already been applied to irregular-target detection tasks outside agriculture, such as steel surface defect detection (*Zhu et al., 2025*). For efficient downsampling, *Wang et al. (2024)* proposed the ADown module in YOLOv9, which has since been used in YOLOv11-based agricultural detection models to preserve small-target features under complex backgrounds (*Wang et al., 2026*). For the detection head, Detail-Enhanced Convolution (DEConv), proposed by *Chen et al. (2024)* for image dehazing, enhances fine-detail representation without additional inference cost when combined with a lightweight shared convolutional head. Although each of these modules has been individually validated, their joint application to egg external-defect detection under conveyor-belt conditions has not yet been reported.

Based on the above, this study proposes a lightweight detection model, YOLOv11n-DAL, for egg external-defect detection under conveyor-belt conditions, in which three modules are jointly designed to improve detection accuracy while reducing model parameters and computational cost. Specifically, DCNv4 is introduced into the C3k2 structure of YOLOv11n to construct the C3k2_DCNv4 module, enhancing the representation of irregular defect features; ADown replaces the original downsampling convolution, reducing model size while improving feature preservation; and Detect_LSDECD combines a lightweight shared

convolutional structure with DEConv to reduce redundant prediction-head computation while enhancing detail sensitivity. Together, these modules achieve both improved accuracy and reduced model complexity, offering a feasible solution for resource-constrained conveyor-belt sorting equipment. A conveyor-belt egg image dataset containing the damaged, dirty, and good categories was constructed, and the proposed method was comprehensively evaluated.

MATERIALS AND METHODS

Data Collection and Dataset Construction

Egg images were collected from a conveyor belt located in Jining City, Shandong Province, China, from February 8 to February 10, 2026, using an iPhone 17 Pro Max. To reduce motion blur and improve image quality, the conveyor belt was temporarily stopped during image acquisition. A top-view imaging configuration was adopted, where the smartphone camera was positioned vertically above the conveyor belt and kept parallel to its surface. The shooting distance was approximately 10–60 cm, and the original image resolution was 3072 × 4096 pixels. The data collection environment involved a combination of natural light and indoor illumination conditions to simulate the lighting variations that may occur in practical egg inspection scenarios. Each egg was captured from only a single viewpoint to prevent potential data leakage caused by the same instance appearing across different subsets.

A total of 1730 original JPG images were retained. The category labels were determined according to the overall appearance characteristics of each egg. Eggs with cracks, shell breakage, or holes were labeled as damaged. Eggs exhibiting surface contamination, such as feces, blood stains, or mud stains, but without structural damage were labeled as dirty. Eggs without apparent defects were labeled as good. When an egg simultaneously exhibited both structural damage and surface contamination, it was consistently assigned to the damaged category, since structural defects represent more severe quality issues. Representative samples of the three categories are shown in Fig. 1.

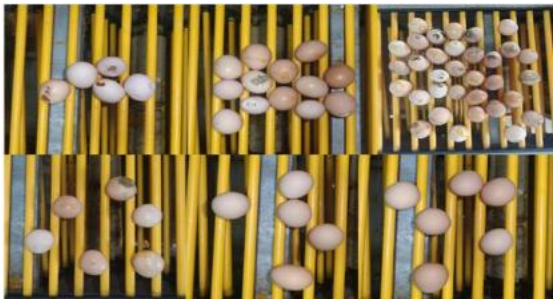


Fig. 1 - Representative images of the good, damaged, and dirty egg classes collected under conveyor-belt conditions

Dataset Annotation and Data Augmentation

The dataset was randomly divided into training, validation, and testing subsets at a ratio of 8:1:1, resulting in 1384, 173, and 173 images, respectively. Image annotation was manually performed using the Roboflow platform. Rectangular bounding boxes were generated to enclose the entire egg region. Data augmentation was applied only to the training set, including horizontal flipping, vertical flipping, ±90° rotation, ±10° random rotation, ±10° shearing, ±25% saturation adjustment, ±15% brightness adjustment, and noise injection with a maximum intensity of 2.24% pixels. For each original training image, three augmented images were generated, expanding the training set to 4152 images (Fig. 2).

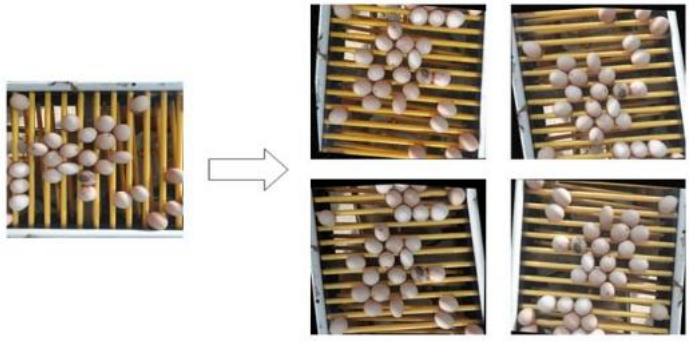


Fig. 2 - Examples of data augmentation effects

The final dataset contained 28,893 egg object instances in total. The numbers of instances belonging to the damaged, dirty, and good categories are summarized in Table 1.

Table 1

Distribution of annotated egg instances in the complete dataset.

Egg category	Annotated instances	Proportion (%)
damaged	8582	29.7
dirty	9449	32.7
good	10862	37.6
Total	28893	100.0

YOLOv11n-DAL Network Architecture and Improvement Methods

YOLOv11n was selected as the baseline because of its compact one-stage backbone–neck–head architecture and P3–P5 multi-scale prediction. To improve its sensitivity to small and irregular eggshell defects without increasing model complexity, YOLOv11n-DAL replaces the original C3k2 blocks with C3k2_DCNv4, adopts ADown for downsampling, and uses Detect_LSDECD as the prediction head. The overall architecture is shown in Fig. 3.

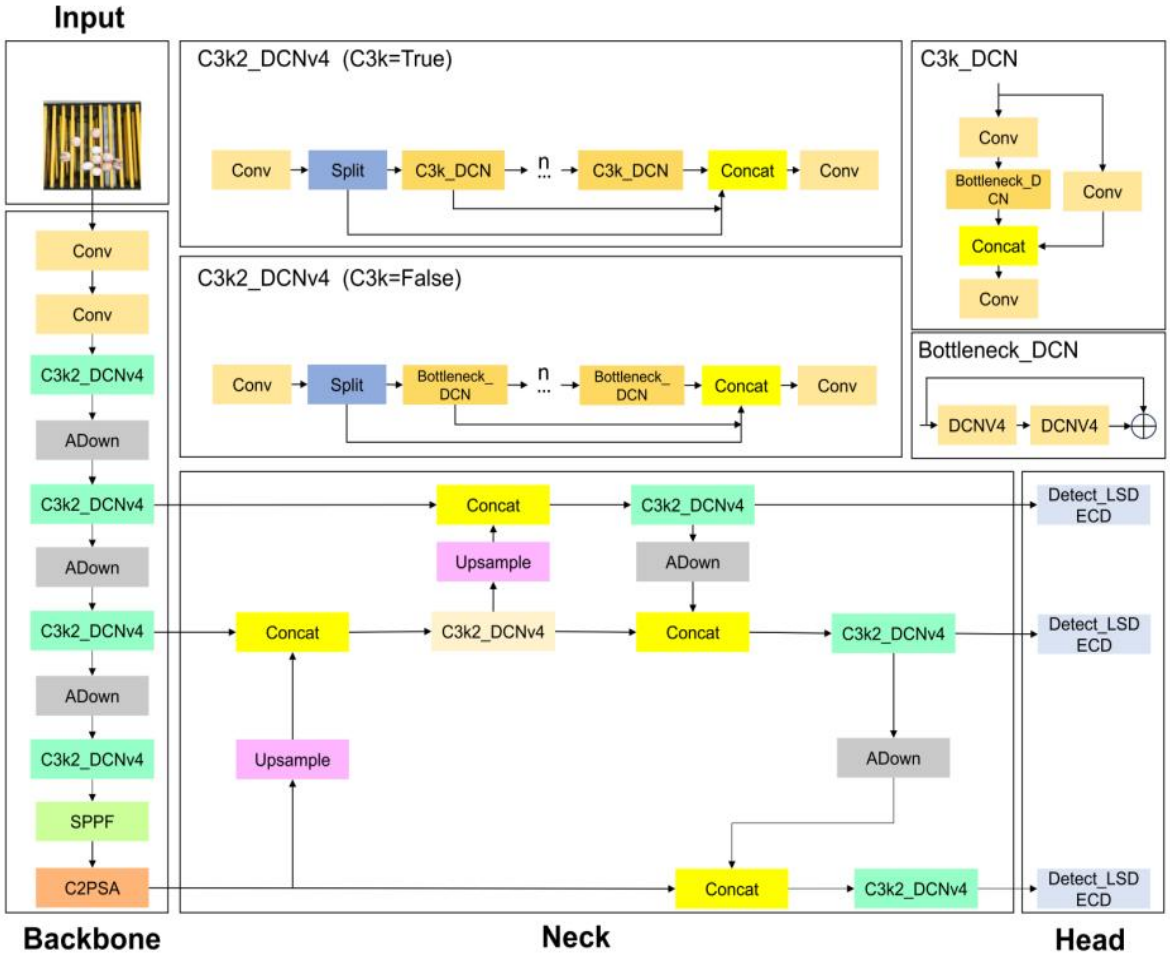


Fig. 3 - Overall architecture of the proposed YOLOv11n-DAL model for egg surface defect detection

C3k2_DCNv4 and ADown are deployed in the backbone and neck for adaptive feature extraction and efficient multi-scale transmission. Detect_LSDECD receives the P3, P4, and P5 feature maps and predicts the damaged, dirty, and good categories. The structures of the three improved modules are summarized in Fig. 4.

C3k2_DCNv4 Feature Extraction Module

C3k2_DCNv4 integrates deformable convolution into the C3k2 framework. As shown in Fig. 3, the input undergoes a 1×1 convolution, then splits into two branches.

One branch passes through *n* stacked C3k_DCN (or Bottleneck_DCN) blocks, while the other serves as a shortcut. The two branches are concatenated and fused by another 1×1 convolution. Each C3k_DCN block contains two DCNv4 layers with residual connections. DCN [Fig. 4(a)] learns offset fields to sample adaptively from irregular positions, improving the model's ability to handle geometric variations while maintaining efficiency.

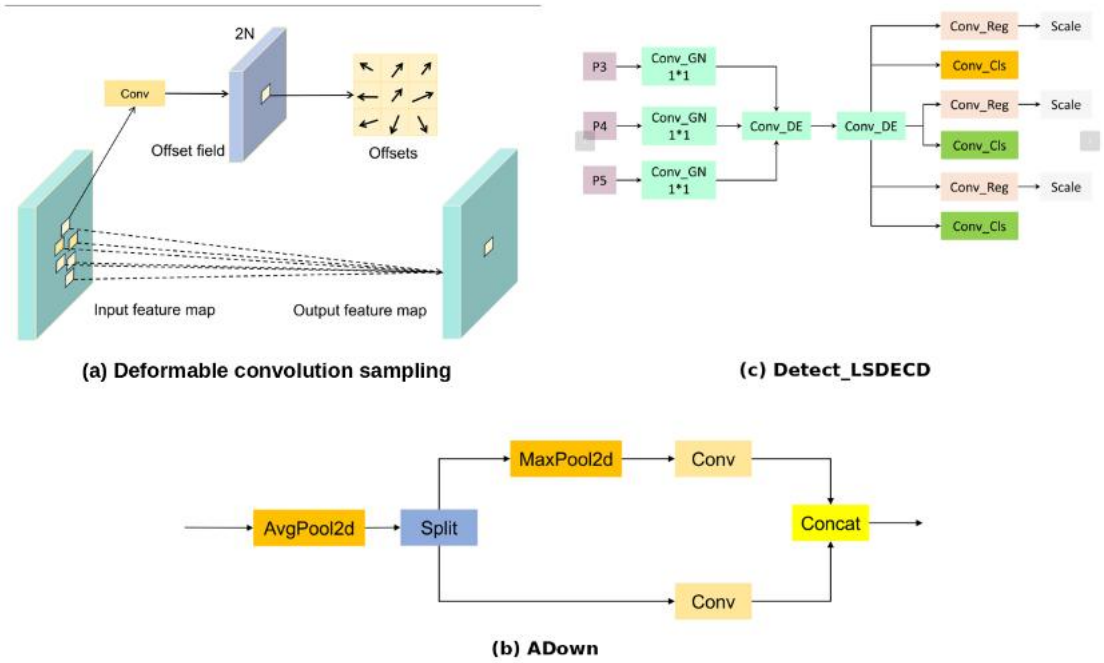


Fig. 4 - Structures of the improved modules in YOLOv11n-DAL
(a) Deformable convolution sampling; (b) ADown; (c) Detect_LSDECD

Unlike fixed-grid convolution, DCNv4 learns offsets according to target geometry:

$$y(p_0) = \sum_{k=1}^{K} w_k \; x(p_0 + p_k + \Delta p_k) \tag{1}$$

where x and y denote the input and output feature maps, p_0 is the current position, p_k is the regular sampling position, Δp_k is the learnable offset, and w_k is the convolution weight. This adaptive sampling is suitable for cracks, holes, broken-shell regions, and contaminants with irregular boundaries.

ADown Downsampling Module

ADown first applies average pooling and channel splitting. One branch uses a 3 × 3 stride-2 convolution, while the other uses max pooling followed by a 1 × 1 convolution; the two outputs are concatenated (Fig. 4(b)).

$$X_1, X_2 = \mathrm{Split}\big(\mathrm{AvgPool}(X)\big) \tag{2}$$

$$Y = \mathrm{Concat}(Y_1, Y_2) \tag{3}$$

where X is the input feature map, X_1 and X_2 are the two channel branches, $Y_1 = Conv_{3\times3,s=2}(X_1)$, $Y_2 = Conv_{1\times1}(MaxPool(X_2))$, and Y is the concatenated output. The dual-branch strategy combines average and maximum responses, helping preserve edge and texture information during downsampling.

Detect_LSDECD Detection Head

Detect_LSDECD first maps multi-scale features to a unified hidden dimension and then applies shared detail-enhanced convolutions, reducing repeated operations across detection layers (Fig. 4(c)).

$$F_i' = H_{\mathrm{shared}}\big(\mathrm{Conv}_{1\times1}(F_i)\big) \tag{4}$$

where F_i is the input of the i-th scale, $Conv_{1\times1}$ performs channel adjustment, H_{shared} denotes the shared feature extractor, and F_i' is the refined feature map.

$$B_i = \mathrm{DFL}(R_i), \quad C_i = \sigma(S_i) \tag{5}$$

where B_i and C_i are the predicted box and class probability, R_i and S_i denote the regression and classification outputs obtained from F_i', DFL denotes distribution-based box regression, and σ is the sigmoid function. Separate branches retain prediction quality while the shared extractor reduces head redundancy.

Training Environment and Parameter Settings

All models were trained and evaluated under the same experimental conditions to ensure a fair comparison. The hardware platform was equipped with an NVIDIA A10G GPU, and the software environment included Python 3.10.16, PyTorch 2.2.2, CUDA 12.1, and Ultralytics 8.3.9. The same training strategy and hyperparameter settings were applied to YOLOv11n-DAL and all comparison models. The main training hyperparameters are summarized in Table 2.

Table 2

Main training hyperparameter settings

Parameter	Value
Image size	640 × 640
Epochs	200
Batch size	16
Optimizer	SGD
Initial learning rate	0.01
Workers	10
close_mosaic	10

Model Performance Evaluation Indicators

Precision, Recall, F1-score, mAP@0.5, and mAP@0.5:0.95 were used to evaluate detection accuracy. Parameters, GFLOPs, and model size reflected model complexity. Inference speed was measured in FPS on a single GPU with batch size 1 and input size 640×640, including preprocessing, forward pass, and post-processing, Precision, Recall, and F1-score were calculated as follows:

$$\text{Precision} = \frac{TP}{TP + FP} \times 100\% \tag{6}$$

$$\text{Recall} = \frac{TP}{TP + FN} \times 100\% \tag{7}$$

where TP, FP, and FN denote true positives, false positives, and false negatives, respectively; P and R in Eq. (8) denote Precision and Recall.

$$F_1 = \frac{2PR}{P + R} \times 100\% \tag{8}$$

The mean Average Precision over N egg categories was calculated as:

$$mAP = \frac{1}{N}\sum_{i=1}^{N} AP_i \times 100\% \tag{9}$$

where AP_i is the Average Precision of the i-th category. $mAP@0.5$ uses an IoU threshold of 0.5, whereas $mAP@0.5{:}0.95$ averages thresholds from 0.5 to 0.95 in steps of 0.05.

Human Baseline Validation on the Test Set

To further evaluate the performance of YOLOv11n-DAL in practical egg appearance defect detection scenarios, a comparative experiment between manual inspection and model-based detection was conducted using 173 original images from the test set. Two inspectors with more than three years of experience in egg quality inspection were invited to participate in the experiment.

The two inspectors independently performed defect classification on the egg targets in each test image without communication or discussion. Each egg sample was categorized into one of three classes: damaged, dirty, or good. Precision, recall, and F1-score were calculated separately based on the independent annotations of the two inspectors, and the arithmetic mean of these metrics was used as the baseline performance of manual inspection.

Subsequently, YOLOv11n-DAL was evaluated on the same test set using identical evaluation metrics and calculation procedures. By comparing the Precision, Recall, and F1-score between the proposed model and the manual inspection baseline, the performance differences between YOLOv11n-DAL and experienced quality inspectors in egg appearance defect recognition were analyzed.

RESULTS

YOLOv11n-DAL Model Performance Analysis

To comprehensively evaluate the detection performance of the improved model, Precision, Recall, mAP@50, and mAP@50:95 were adopted as evaluation metrics to analyze the model's performance across different categories. Table 3 presents the per-class results. As shown, the mAP@50 values for the damaged, dirty, and good categories reached 97.9%, 95.2%, and 97.0%, respectively. The overall Precision, Recall, mAP@50, and mAP@50:95 of the model were 95.2%, 94.5%, 96.7%, and 95.8%, respectively.

Table 3

Performance comparison of the YOLOv11n-DAL model on different egg categories

Class	P (%)	R (%)	F1 (%)	mAP50 (%)	mAP50–95 (%)
damaged	96.6	95.3	96.0	97.9	97.7
dirty	94.6	91.4	93.0	95.2	94.3
good	95.2	97.0	95.6	97.0	95.3
all	95.2	94.5	94.8	96.7	95.8

The normalized confusion matrix and visualization results are presented in Fig. 5. Fig. 5(a) compares heatmaps generated by YOLOv11n and YOLOv11n-DAL. The proposed model produces more concentrated activations on egg and defect regions, with weaker responses on conveyor rollers. Fig. 5(c) also demonstrates more complete target coverage for densely distributed, partially occluded, and visually ambiguous eggs, corroborating the quantitative improvements.

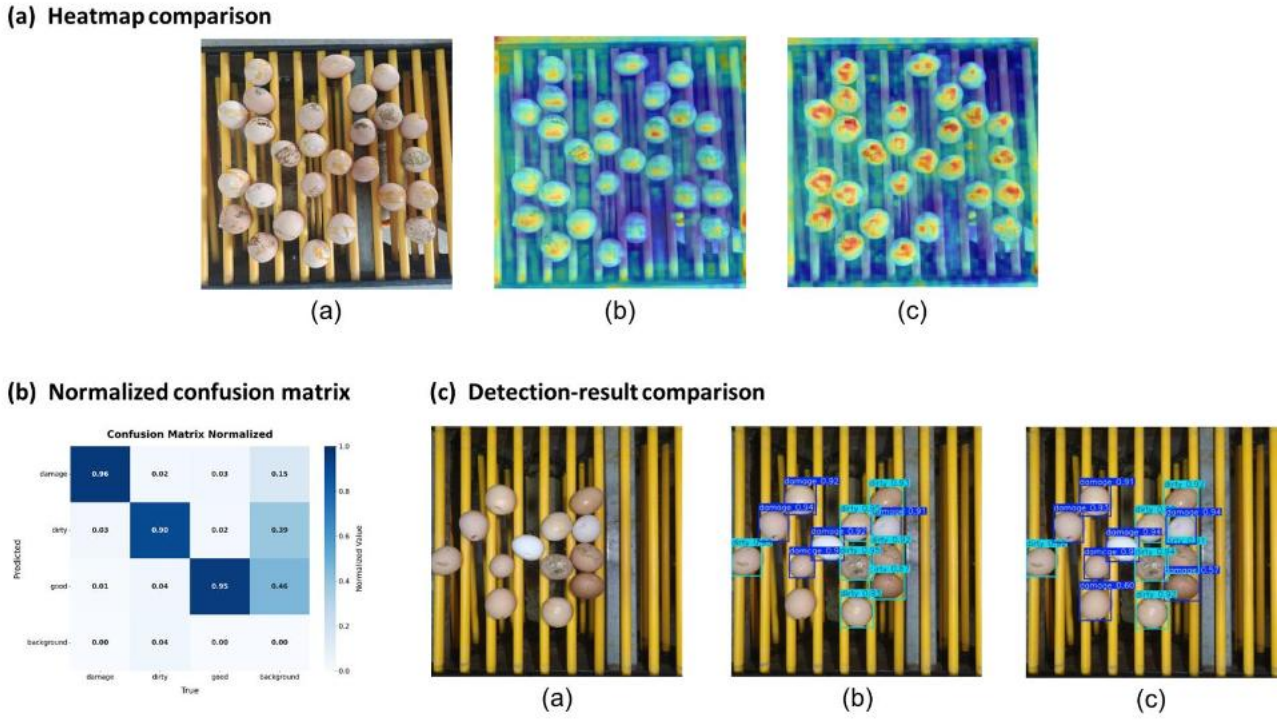


Fig. 5 - Visualization comparison between YOLOv11n and YOLOv11n-DAL: heatmaps (upper), normalized confusion matrix of YOLOv11n-DAL (lower left), and detection-result comparison (lower right)

The row-normalized confusion matrix in Fig. 5(b) shows class-wise recall of 96%, 90%, and 95% for damaged, dirty, and good, respectively. The dirty category remains comparatively more challenging, as slight stains, natural eggshell spots, shadows, and illumination-induced dark regions can appear visually similar. Some background false positives persist, indicating that weak defects and complex textures are the primary sources of missed or incorrect detections.

Ablation Experiments

To verify the effectiveness of the improved modules, ablation experiments were conducted using YOLOv11n as the baseline model. The effects of ADown, C3k2_DCNv4, and Detect_LSDECD were evaluated separately and jointly, and the results are shown in Table 4.

Table 4

Ablation study results of YOLOv11n-DAL

Exp.	ADown	DCNv4	LSDECD	P (%)	R (%)	F1 (%)	mAP50 (%)	mAP50–95 (%)	Params (M)	GFLOPs	Size (MB)
1	×	×	×	93.5	93.5	93.5	95.8	94.8	2.6	6.3	5.2
2	√	×	×	95.8	92.6	94.2	96.1	94.8	2.0	5.3	4.1
3	×	√	×	95.5	92.2	93.8	96.3	95.4	2.5	6.2	5.1
4	×	×	√	95.5	92.9	94.2	96.9	95.6	2.3	6.0	5.0
5	√	√	×	94.9	93.1	94.0	96.2	95.3	2.0	5.1	4.1
6	√	×	√	93.4	95.3	94.3	96.9	96.0	1.8	5.0	4.1
7	×	√	√	95.5	93.8	94.6	96.4	95.4	2.1	5.8	4.7
8	√	√	√	95.2	94.5	94.8	96.7	95.8	1.7	4.8	3.8

Note: AD denotes ADown, DCNv4 denotes C3k2_DCNv4, and LSDECD denotes Detect_LSDECD; √ indicates that a module is included, whereas × indicates that it is excluded; bold values indicate the best result for each metric.

Compared with the baseline model, incorporating ADown reduced the number of parameters, computational complexity, and model size from 2.6 M, 6.3 GFLOPs, and 5.2 MB to 2.0 M, 5.3 GFLOPs, and 4.1 MB, respectively, while maintaining comparable detection performance. When introduced individually, C3k2_DCNv4 and Detect_LSDECD increased mAP@0.5:0.95 from 94.8% to 95.4% and 95.6%, respectively, indicating their effectiveness in enhancing feature extraction and localization performance.

Furthermore, the combinations of ADown + C3k2_DCNv4 (Exp. 5), ADown + Detect_LSDECD (Exp. 6), and C3k2_DCNv4 + Detect_LSDECD (Exp. 7) were evaluated to investigate the complementary effects of the proposed modules. By integrating all three modules, the resulting YOLOv11n-DAL achieved the best overall performance, obtaining a precision of 95.2%, recall of 94.5%, F1-score of 94.8%, mAP@0.5 of 96.7%, and mAP@0.5:0.95 of 95.8%. Meanwhile, the model size was reduced to 1.7 M parameters, 4.8 GFLOPs, and 3.8 MB. These results indicate that the proposed modules simultaneously enhance detection accuracy while reducing computational cost and model size, demonstrating the effectiveness of YOLOv11n-DAL for lightweight object detection.

Comparison with Different Detection Models

To further evaluate the comprehensive performance of YOLOv11n-DAL, several representative detection models were selected for comparison, including YOLOv6, YOLOv8, YOLOv10, YOLOv11n, YOLO12n, YOLO26n, Hyper-YOLO, and RT-DETR-R18. All models were trained and tested under the same experimental conditions, and the results are shown in Table 5.

Table 5

Performance comparison results of different detection models

Model	P (%)	R (%)	F1 (%)	mAP50 (%)	mAP50–95 (%)	Params (M)	GFLOPs	Size (MB)	FPS
YOLOv6n	94.2	91.3	92.7	95.9	95.2	4.2	11.4	8.2	146.5
YOLOv8n	93.0	93.9	93.4	96.2	95.2	2.7	6.8	5.4	138.5
YOLOv10n	94.0	91.4	92.7	95.3	94.1	2.3	6.5	5.5	127.9
YOLOv11n	93.5	93.5	93.5	95.8	94.8	2.6	6.3	5.2	96.7
YOLO12n	95.0	94.0	94.5	96.7	95.8	2.5	6.3	5.3	78.5
YOLO26n	92.4	91.3	91.8	95.5	93.6	2.5	5.2	5.2	89.6
Hyper-YOLO	96.3	92.4	94.3	96.6	95.7	3.6	9.5	7.3	88.9
RT-DETR-R18	95.2	95.4	95.3	95.1	93.9	19.9	56.9	307.3	100.1
YOLOv11n-DAL	95.2	94.5	94.8	96.7	95.8	1.7	4.8	3.8	61.0

Note: Model size refers to the saved weight-file size generated by the corresponding implementation.

YOLOv11n-DAL achieves a precision of 95.2%, recall of 94.5%, F1-score of 94.8%, mAP@0.5 of 96.7%, and mAP@0.5:0.95 of 95.8%. It achieves the highest mAP@0.5 (96.7%) among all methods, tied with YOLO12n, while surpassing the baseline YOLOv11n by 0.7% in mAP@0.5 and 0.9% in mAP@0.5:0.95.

More importantly, these gains are achieved with only 1.7 M parameters, 4.8 GFLOPs, and 3.8 MB model size—a 34.6% reduction in parameters and 23.8% reduction in GFLOPs compared to the baseline. In contrast, RT-DETR-R18 requires 19.9 M parameters and 56.9 GFLOPs, and Hyper-YOLO requires 3.6 M parameters and 9.5 GFLOPs.

Inference speed is 61.0 FPS, lower than the baseline 96.7 FPS due to DCNv4-based feature fusion, but still well above the 30 FPS real-time requirement for industrial inspection. The compact model size (3.8 MB) also alleviates edge-device memory constraints, making YOLOv11n-DAL a more practical solution for edge deployment.

Comparison with Human Inspectors

To further evaluate the practical applicability of the proposed YOLOv11n-DAL, its performance was compared with that of human inspectors, as shown in Table 6.

Table 6

Detection performance of YOLOv11n-DAL vs. human inspectors on the test set

Method	P (%)	R (%)	F1 (%)
Inspector 1	91.3	91.3	91.0
Inspector 2	88.6	88.4	88.0
Average of manual inspectors	89.9	89.8	89.5
YOLOv11n-DAL	95.2	94.5	94.8

As shown in Table 6, the two inspectors achieved precision values of 91.3% and 88.6%, recall values of 91.3% and 88.4%, and F1-scores of 91.0% and 88.0%, respectively. The corresponding average values for manual inspection were 89.9%, 89.8%, and 89.5%, respectively. In comparison, YOLOv11n-DAL achieved a precision of 95.2%, recall of 94.5%, and F1-score of 94.8%, representing improvements of 5.3, 4.7, and 5.3 percentage points, respectively, over the average manual inspection performance.

These results indicate that YOLOv11n-DAL provides superior overall detection performance compared with manual inspection under conveyor-belt operating conditions. Moreover, the differences between the two inspectors indicate a certain degree of variability in manual inspection, which may be attributed to subjective judgment and differences in visual perception. In contrast, YOLOv11n-DAL provides a more consistent and automated detection process. Therefore, the proposed model demonstrates good potential for automated egg defect detection in conveyor-belt inspection scenarios.

Training Stability Analysis

To evaluate the robustness of YOLOv11n-DAL against training randomness, both YOLOv11n and YOLOv11n-DAL were independently trained five times using different random seeds (0–4), while maintaining the same dataset split, training strategy, and hyperparameter settings. The mean ± standard deviation of the five runs, together with paired t-test results and effect sizes, are summarized in Table 7.

Table 7

Training stability comparison between YOLOv11n and YOLOv11n-DAL over five runs

Metric	YOLOv11n (Mean ± SD)	YOLOv11n-DAL (Mean ± SD)	Δ	p-value	Cohen's d_z
P (%)	94.4 ± 0.7	94.9 ± 0.7	+0.5	0.373	0.5
R (%)	93.3 ± 0.2	94.1 ± 1.0	+0.8	0.187	0.7
F1 (%)	93.8 ± 0.4	94.5 ± 0.4	+0.7	0.047	1.3
mAP50 (%)	96.0 ± 0.2	96.8 ± 0.2	+0.7	0.010	2.0
mAP50–95 (%)	94.9 ± 0.2	95.6 ± 0.4	+0.7	0.028	1.5

Note: Values are presented as mean ± standard deviation over five independent runs with different random seeds (0–4).
Δ represents the performance improvement of YOLOv11n-DAL compared with YOLOv11n.
Statistical significance was evaluated using paired t-tests.
Cohen's dz represents the paired effect size.

As shown in Table 7, YOLOv11n-DAL achieved higher average performance than YOLOv11n across all evaluation metrics. Specifically, the proposed model improved Precision, Recall, F1-score, mAP@0.5, and mAP@0.5:0.95 by 0.5, 0.8, 0.7, 0.7, and 0.7 percentage points, respectively. The relatively small standard deviations (<1.1%) across repeated experiments indicate that both models exhibited stable training behavior.

The paired t-test results showed that the improvements in F1-score, mAP@0.5, and mAP@0.5:0.95 achieved statistical significance in the five repeated runs, with relatively large effect sizes. Although Precision and Recall improvements did not reach statistical significance, they remained consistently higher than the baseline model. Overall, the repeated experiments demonstrate that the performance gains of YOLOv11n-DAL are reproducible and not caused by a single random training process.

DISCUSSION

The experiments show that YOLOv11n-DAL improves detection accuracy while reducing model complexity rather than relying on a larger network. ADown contributes mainly to computational reduction, C3k2_DCNv4 strengthens the representation of irregular shell defects, and Detect_LSDECD reduces redundant prediction operations while enhancing fine-grained feature extraction. Their complementary effects explain the simultaneous improvements in F1-score and mAP and the reductions in parameters, GFLOPs, and model size.

It is noteworthy that the difference between mAP@0.5 and mAP@0.5:0.95 is relatively small in this study. For YOLOv11n-DAL, the gap between the two metrics was only 0.9 percentage points (96.7% vs. 95.8%), indicating that the model maintained stable localization performance under stricter IoU thresholds. This phenomenon is mainly attributed to the characteristics of the proposed dataset and annotation strategy. Unlike defect-region detection tasks that require precise localization of irregular crack or stain areas, the bounding boxes in this study were annotated for complete egg regions. Since eggs exhibit relatively regular elliptical shapes and clear boundaries from the background, the localization difficulty is relatively low, allowing the model to maintain high IoU overlap even under stricter evaluation criteria. In addition, the C3k2_DCNv4 module improves structural feature modeling through adaptive sampling, which further contributes to accurate object localization.

The dirty category remained more difficult than damaged and good because slight stains, natural eggshell spots, shadows, and illumination-induced dark regions may share similar visual characteristics. Partial occlusion and single-view acquisition also limit the visibility of some defects. Moreover, the dataset was collected using one device within a limited region and period, which may affect the generalization ability under different acquisition conditions. Therefore, further validation using multi-source datasets and diverse imaging conditions is required before large-scale deployment. In addition, the statistical analysis was conducted based on five repeated training runs (n=5), and the limited sample size may reduce the statistical power of significance tests. Moreover, no correction for multiple comparisons was applied; therefore, the statistical results should be interpreted as supportive evidence rather than definitive proof of superiority.

CONCLUSIONS

This study proposed YOLOv11n-DAL, a lightweight detection framework for egg external-defect inspection under conveyor-belt conditions. By integrating C3k2_DCNv4, ADown, and Detect_LSDECD into YOLOv11n, the proposed model enhanced irregular defect feature representation, improved feature preservation during downsampling, and reduced redundant prediction computation.

Compared with the baseline YOLOv11n, YOLOv11n-DAL achieved improved detection accuracy while reducing model complexity, with the parameters, GFLOPs, and model size reduced from 2.6 M, 6.3 GFLOPs, and 5.2 MB to 1.7 M, 4.8 GFLOPs, and 3.8 MB, respectively. The ablation experiments, comparative evaluations, and stability analysis demonstrated the effectiveness and reproducibility of the proposed optimization strategy.

The proposed model provides a feasible lightweight solution for automated egg external-defect detection in resource-constrained conveyor-belt sorting scenarios. Future work will focus on validating the model under more diverse acquisition conditions and conducting deployment tests on practical edge devices.

REFERENCES

[1] Atwa, E. M., Xu, S., Rashwan, A. K., Abdelshafy, A. M., ElMasry, G., Al-Rejaie, S., Xu, H., Lin, H., Pan, J., (2024). Advances in emerging non-destructive technologies for detecting raw egg freshness: a comprehensive review, *Foods*, vol.13, no.22, 3563, Switzerland. https://doi.org/10.3390/foods13223563

[2] Botta, B., Gattam, S. S. R., Datta, A. K., (2022). Eggshell crack detection using deep convolutional neural networks, *Journal of Food Engineering*, vol.315, 110798, United Kingdom. https://doi.org/10.1016/j.jfoodeng.2021.110798
[3] Bing, Y., Yu, X., Lin, Z., Yu, F., (2025). PAME-YOLO: A model for apple leaf lesion detection in complex environments based on improved YOLOv8s, *INMATEH - Agricultural Engineering*, vol.75, no.1, pp.1179–1192, Romania. https://doi.org/10.35633/inmateh-75-97
[4] Chen, S. Y., Hsu, S. H., Ko, C. Y., Hsu, K. H., (2023). Real-time defect and freshness inspection on chicken eggs using hyperspectral imaging, *Food Control*, vol.150, 109716, United Kingdom. https://doi.org/10.1016/j.foodcont.2023.109716
[5] Çengel, T. A., Gencturk, B., Yasin, E. T., Yildiz, M. B., Cinar, I., Koklu, M., (2025). Automating egg damage detection for improved quality control in the food industry using deep learning, *Journal of Food Science*, vol.90, no.1, e17553, United States. https://doi.org/10.1111/1750-3841.17553
[6] Chen, Z., He, Z., Lu, Z. M., (2024). DEA-Net: single image dehazing based on detail-enhanced convolution and content-guided attention, *IEEE Transactions on Image Processing*, vol.33, pp.1002–1015, United States. https://doi.org/10.1109/TIP.2024.3354108
[7] Dai, J., Qi, H., Xiong, Y., Li, Y., Zhang, G., Hu, H., Wei, Y., (2017). Deformable convolutional networks, Proceedings of the IEEE International Conference on Computer Vision (ICCV), pp.764–773, Italy. https://doi.org/10.1109/ICCV.2017.89
[8] Gautron, J., Stapane, L., Le Roy, N., Nys, Y., Rodriguez-Navarro, A. B., Hincke, M. T., (2021). Avian eggshell biomineralization: an update on its structure, mineralogy and protein tool kit, *BMC Molecular and Cell Biology*, vol.22, 11, United Kingdom. https://doi.org/10.1186/s12860-021-00350-0
[9] Gupta, C., Gill, N. S., Gulia, P., Duhan, S., Alduaiji, N., Shukla, P. K., Dwivedi, A., (2025). Deep vision in agriculture: assessing the function of YOLO in the classification of plant leaf diseases, *BioData Mining*, vol.18, 91, United Kingdom. https://doi.org/10.1186/s13040-025-00497-y
[10] Huang, Y., Luo, Y., Cao, Y., Lin, X., Wei, H., Wu, M., Yang, X., Zhao, Z., (2023). Damage detection of unwashed eggs through video and deep learning, *Foods*, vol.12, no.11, 2179, Switzerland. https://doi.org/10.3390/foods12112179
[11] Jocher, G., Chaurasia, A., Qiu, J., (2024). Ultralytics YOLO11, *Ultralytics software documentation*, United States. Available at: https://docs.ultralytics.com/models/yolo11/
[12] Kanna, S. K., Ramalingam, K., Pazhanivelan, P., Jagadeeswaran, R., Prabu, P. C., (2024). YOLO deep learning algorithm for object detection in agriculture: a review, *Journal of Agricultural Engineering*, vol.55, no.4, 1641, Italy. https://doi.org/10.4081/jae.2024.1641
[13] Ma, F., Li, S., Tan, J., Li, Y., (2025). YOLO-TRS: An improved YOLO11 for tomato fruit ripeness and stem detection, *INMATEH - Agricultural Engineering*, vol.77, no.3, pp.1131–1144, Romania. https://doi.org/10.35633/inmateh-77-91
[14] Shi, W., Zhang, D., Wei, N., Ge, Y., Chen, J., Huang, T., Chen, Y., Zhang, S., Hong, B., Yuan, W., Zhang, B., (2025). An improved YOLOv11n-based GENET model for vision-based missing-seed detection and counting in an oblique hook-shaped spoon-type small precision seed metering device, *INMATEH - Agricultural Engineering*, vol.77, no.3, pp.490–501, Romania. https://doi.org/10.35633/inmateh-77-40
[15] So, J. H., Kim, H. S., (2022). Current advances in detection of abnormal egg: a review, *Journal of Animal Science and Technology*, vol.64, no.5, pp.813–829, Korea. https://doi.org/10.5187/jast.2022.e52
[16] Tang, F., Zhang, Y., Zhang, Y., Yang, L., (2026). An improved RT-DETR for stable and real-time defective egg detection in edge computing environments, *INMATEH - Agricultural Engineering*, vol.78, no.1, pp.644–655, Romania. https://doi.org/10.35633/inmateh-78-52
[17] Turkoglu, M., (2021). Defective egg detection based on deep features and Bidirectional Long-Short-Term-Memory, *Computers and Electronics in Agriculture*, vol.185, 106152, Netherlands. https://doi.org/10.1016/j.compag.2021.106152
[18] Wu, Z., Zhang, H., Fang, C., (2025). Research on machine vision online monitoring system for egg production and quality in cage environment, *Poultry Science*, vol.104, 104552, United States. https://doi.org/10.1016/j.psj.2024.104552
[19] Wang, C. Y., Yeh, I. H., Liao, H. Y. M., (2024). YOLOv9: learning what you want to learn using programmable gradient information, Proceedings of the European Conference on Computer Vision (ECCV), pp.1–21, Italy. https://doi.org/10.1007/978-3-031-72751-1_1

[20] Wang, P., Li, C., Wei, L., Li, Y., Guo, L., (2026). Improved YOLOv11 for lightweight and accurate detection of flax diseases and pests in complex field environments, *Agriculture*, vol.16, no.7, 741, Switzerland. https://doi.org/10.3390/agriculture16070741

[21] Xiong, Y., Li, Z., Chen, Y., Wang, F., Zhu, X., Luo, J., Wang, W., Lu, T., Li, H., Qiao, Y., Lu, L., Zhou, J., Dai, J., (2024). Efficient deformable convnets: Rethinking dynamic and sparse operator for vision applications, Proceedings of the IEEE/CVF Conference on Computer Vision and Pattern Recognition (CVPR), pp.5652–5661. https://doi.org/10.1109/CVPR52733.2024.00540.

[22] Yang, X., Bist, R. B., Subedi, S., Chai, L., (2023). A computer vision-based automatic system for egg grading and defect detection, *Animals*, vol.13, no.14, 2354, Switzerland. https://doi.org/10.3390/ani13142354

[23] Yin, J. J., Kang, J. Q., Xiao, D. Q., (2024). Lightweight detection algorithm for duck egg cracks based on improved YOLOv5l, *Transactions of the Chinese Society of Agricultural Engineering*, vol.40, no.5, pp.216–223, China. https://doi.org/10.11975/j.issn.1002-6819.202307259

[24] Yu, P., Shen, C., Cheng, J., Yin, X., Liu, C., Yu, Z., (2025). Advances in nondestructive technologies for external eggshell quality evaluation, *Sensors*, vol.25, no.18, 5796, Switzerland. https://doi.org/10.3390/s25185796

[25] Zhao, Z. X., Wei, H. F., Huang, Y., Huang, X. P., Mi, Y. L., Luo, Y. F., (2023). Online real-time detection system for broken shell eggs based on improved YOLOv7, *Transactions of the Chinese Society of Agricultural Engineering*, vol.39, no.20, pp.255–265, China. https://doi.org/10.11975/j.issn.1002-6819.202305228

[26] Zhu, G., Qi, H., Lv, K., (2025). DGYOLOv8: an enhanced model for steel surface defect detection based on YOLOv8, *Mathematics*, vol.13, no.5, 831, Switzerland. https://doi.org/10.3390/math13050831

DESIGN AND TESTING OF AN AUTOMATIC SEEDLING-LOADING SYSTEM FOR A HIGH-SPEED RIDE-ON RICE TRANSPLANTER

/

高速乘坐式插秧机自动装秧系统设计与试验

Fengpeng NING, Jinping CAI, Yihan ZHOU, Qilong ZHANG, Xianhao DUAN, Zhaopeng LIU, Muhua LIU, Xiongfei CHEN, Peng XU *

Jiangxi Provincial Key Laboratory of Modern Agricultural Equipment.
College of Engineering Jiangxi Agricultural University, Nanchang 33045, China

DOI: https://doi.org/10.35633/inmateh-79-78

Keywords: *STM32 control system, response surface methodology, parameter optimization, lateral positioning; bench test, mat-type seedlings*

ABSTRACT

Seedling replenishment during the operation of high-speed ride-on rice transplanters still relies heavily on manual labor, thereby limiting the level of operational automation. To address this limitation, an automatic seedling-loading system comprising a longitudinal conveying mechanism, a lateral drive mechanism, and a tracking compensation mechanism was developed. Based on an STM32 embedded platform, a control strategy for detecting seedling shortages and performing precise seedling-loading operations was developed, enabling automatic shortage detection, lateral positioning, and targeted seedling replenishment. The main operating parameters—conveyor belt speed, lateral offset distance, and fore-aft tilt angle—were first investigated individually to determine their appropriate ranges. Subsequently, a second-order, three-factor, five-level rotatable orthogonal experiment was conducted. Seedling-loading success rate was used as the evaluation index, and a multifactor regression model was established to analyze the interactions among the factors. Bench tests were conducted to optimize the system parameters and determine the optimal parameter combination. Subsequent field trials confirmed the operational reliability of the system, with an average seedling-loading success rate of 90.67% over five batches of tests. The proposed system shows considerable potential for replacing manual loading of mat-type rice seedlings and provides a practical solution for advancing the full-process automation of rice transplanting operations.

摘要

在高速乘坐式插秧机作业过程中，补秧环节依赖人工、自动化程度不足。本文构建了由纵向输送装置、横向移动装置与随动装置组成的自动装秧系统，基于 STM32 嵌入式平台设计缺秧检测与执行机构控制逻辑，实现缺秧检测、横向定位与定点补秧。以输送带速度、横向偏移距离与前后倾斜角度为试验因素，开展单因素试验确定因素取值范围；采用三因素五水平二次旋转正交组合试验，以装秧成功率为评价指标建立多因素回归模型并分析各因素及其交互作用。通过台架试验优化关键参数。田间试验结果表明，系统完成 5 批次自动装秧任务，平均成功率为 90.67%。所研制的自动装秧系统能够实现毯状苗机插从缺秧识别到定点补秧的自动补秧作业，降低了补秧过程的人工依赖，可为水稻种植全程自动化提供技术支持。

INTRODUCTION

The development of agricultural machinery is steadily advancing toward full automation and intelligent operation *(Liu C.L. et al., 2020; Zhao C.J. et al., 2021*). Among various mechanized systems, rice transplanters have become a central component due to their widespread use and their role as key carriers of smart agricultural technologies *(Wang X., 2022)*. In recent years, the deployment of unmanned driving systems in rice transplanters has become increasingly common in China (*Liu X.W. et al., 2021; Yin Y.X. et al., 2022*). However, research on automatic seedling-loading systems specifically designed for high-speed ride-on rice transplanters remains limited. Consequently, the seedling-loading process continues to rely heavily on manual labor, which limits the realization of fully autonomous transplanter operations. Enhancing automation at this stage is thus critical for the practical implementation of unmanned rice farming systems. Studies on automatic seedling delivery have primarily focused on the mechanical design and technical development of systems that ensure the accurate transfer of mat-type or pot seedlings (*Liu M.H. et al., 2021; Deng G. et al., 2022; Liu M.H. et al., 2024; Xiao L.P. et al., 2018*). *Yu G.H. et al., (2024),* proposed a dual-belt longitudinal conveyor system integrated with lateral translation to realize automatic tray replenishment.

Wang X.F. et al., (2021), developed a push-type seedling delivery box that generates a dispensing opening through the relative motion of the box and its base, thereby improving replenishment reliability. *Fan Y.J. et al., (2016),* and *Yin C.et al., (2025),* introduced automated systems based on sliding-rail pushing and multi-layer tray delivery structures, aiming to reduce manual involvement through modular designs. These studies improved the efficiency and reliability of seedling replenishment through synchronized tray repositioning, push-type seedling delivery, and multi-layer tray conveying, respectively. However, relatively limited attention has been paid to seedling shortage detection, target positioning, and coordinated control of the seedling carrying platform. Despite these efforts, many of the existing devices remain at the conceptual or prototyping stage. In particular, performance issues such as poor vibration resistance under complex paddy field conditions and the lack of high-precision one-to-many seedling alignment persist. Robotic manipulation technologies may offer solutions in this regard (*Shen J.J. et al., 2023; Fountas S. et al., 2020; Bechar A. et al., 2017*).

Currently, multi-degree-of-freedom robotic systems have been widely applied in transplanting operations for crops like vegetables, corn, and tobacco. *Wang Z.Z. et al., (2017)*, employed a servo-driven module under PLC control to achieve accurate grasping and delivery of vegetable seedlings; *Shi T., (2015),* developed a fully automated corn transplanter with integrated seedling-picking and vertical delivery mechanisms; and *Chen B et al., (2024)*, used a staggered dual-disc configuration to improve the efficiency of a tobacco seedling feeding system. These studies demonstrate that Cartesian robotic systems, when combined with high-precision sensing technologies, can effectively address the challenges of automatic material handling in unstructured environments. Such insights provide valuable reference points for the design and control strategies of automatic seedling-loading systems tailored for paddy field operations (*Wu W.J. et al., 2016; Wang Z.Z. et al., 2019; Zhao C.L. et al., 2027*). However, existing systems still fall short in terms of operational stability, delivery precision, and system integration when exposed to real-world field disturbances. Developing a robust and adaptive automatic seedling-loading system remains a key technical challenge in advancing rice transplanter intelligence.

This study addresses the challenges posed by the distributed arrangement of multiple seedling-holding columns on high-speed ride-on rice transplanters, the difficulty in accurately aligning the conveying mechanism with the column requiring replenishment, and changes in their relative positions caused by the reciprocating lateral and vertical movements of the seedling-carrying platform. Based on a one-to-many seedling-replenishment concept, an automatic seedling-loading system comprising a longitudinal conveying mechanism, a lateral drive mechanism, and a tracking mechanism was developed. The lateral drive mechanism allows a single longitudinal conveying mechanism to move among multiple seedling-holding columns and align with the target column. The tracking mechanism accommodates the reciprocating lateral and vertical movements of the seedling-carrying platform, thereby reducing the relative positional deviation between the conveyor outlet and the target seedling-holding column. An STM32-based control system integrates seedling-shortage detection, lateral position feedback, and coordinated control of the lateral drive and conveyor motors, thus enabling the complete operational sequence of seedling-shortage detection, lateral positioning, and targeted seedling replenishment. The study focuses on developing and evaluating an automatic loading system for mat-type rice seedlings. To evaluate and optimize system performance, bench tests were conducted using three key operating factors: conveyor belt speed, lateral offset distance, and fore-aft tilt angle. The effects of these factors on the seedling-loading success rate were investigated, and their optimal combination was determined. The study ultimately aimed to establish a complete technical process—from seedling shortage detection to precise automatic replenishment—and provide a technical basis for structural optimization and overall performance improvement of automatic seedling-loading systems.

MATERIALS AND METHODS

Structure composition and working principle

In Fig. 1, the automatic seedling-loading system of the high-speed ride-on rice transplanter comprises four main components: ① a tracking mechanism, ② a lateral drive mechanism, ③ a longitudinal conveying mechanism, and ④ a lateral oscillation mechanism.

The front end of the mechanism is attached to the transplanter main body via the swing mechanism, which compensates for variations in machine posture and provides a stable front fulcrum for the loading structure. The rear end is connected to the seedling-carrying platform through a joint within the tracking mechanism, enabling synchronized moving with the carrier platform. The lateral drive mechanism, comprising a slide rail and rack-and-pinion assembly, is mounted at the rear of the rice transplanter body and drives the longitudinal conveying mechanism laterally.

The longitudinal conveying mechanism is mounted on the upper crossbeam of the sliding platform and conveys the seedlings longitudinally after alignment with the target seedling-holding column.

During automatic seedling loading, the operator manually places the seedling mats onto the belt of the longitudinal conveying mechanism. To initiate detection, the seedling mats must remain in firm contact with the detection switches mounted on the side baffles. Each seedling-holding column of the seedling platform is equipped with a seedling-shortage sensor. When a shortage is detected in any column, the control system activates the lateral drive mechanism, which moves the longitudinal conveying mechanism laterally toward the corresponding target position. Once the pull-wire displacement sensor confirms that the target position has been reached, the control system activates the conveyor drive motor to deliver the seedling mat to the column requiring replenishment. After leaving the conveyor belt, the seedling mat slides under gravity along the chute and into the target column, thereby eliminating the shortage and clearing the corresponding alarm signal. Upon completion of the replenishment operation, the longitudinal conveying mechanism automatically returns to its initial loading position and waits for the next seedling-shortage signal.

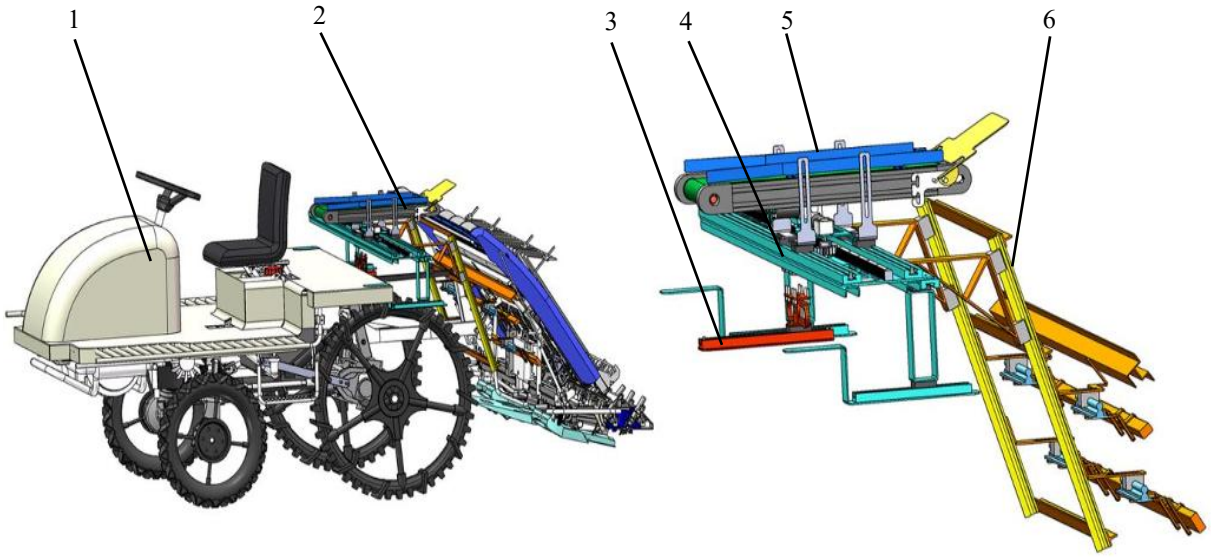


Fig. 1 - Schematic of the automatic seedling-loading system for a high-speed ride-on rice transplanter

1. Rice transplanter main body; 2. Automatic seedling-loading system (overall structure); 3. Tracking mechanism; 4. Lateral drive mechanism; 5. Longitudinal conveying mechanism; 6. Lateral oscillation mechanism

Key component design

(1) Longitudinal Conveying Mechanism

As shown in Fig. 2, the longitudinal conveying mechanism transports mat-type rice seedlings to replenish seedling shortages in the target columns of the seedling platform. It mainly comprises ① a connecting mechanism, ② a conveyor belt mechanism, ③ side baffles, ④ a support platform, ⑤ a drive unit, ⑥ a concave-convex roller assembly, and ⑦ a master-slave roller assembly. The conveyor belt mechanism is located at the top of the device and is supported by four structural members mounted on the support platform. The connecting mechanism is located at the rear of the conveyor belt mechanism, while the side baffles are installed on both sides of the conveyor belt to guide the seedling mats during loading and conveyance. The drive unit is located at the bottom of the device and transmits power to the conveyor system through a belt drive. The master-slave roller assembly consists of an intermediate drive shaft coupled to an external nylon roller. The assembly is mounted in bearing supports to prevent relative slippage between the nylon roller and the conveyor belt, thereby ensuring stable and reliable seedling conveyance. An MY5840-31ZY worm-geared DC motor is used to drive the longitudinal conveying mechanism. Under loaded conditions, the maximum torque required at the conveyor drive shaft was measured using a torque wrench and found to be 12.8 kgf·cm. The selected motor has a rated torque of 16 kgf·cm and a maximum load torque of 38 kgf·cm, thus satisfying the torque requirements of the longitudinal conveying mechanism. Based on the calculated transmission parameters, the conveyor belt can reach a maximum operating speed of 0.4 m/s, which meets the speed requirement for seedling replenishment.

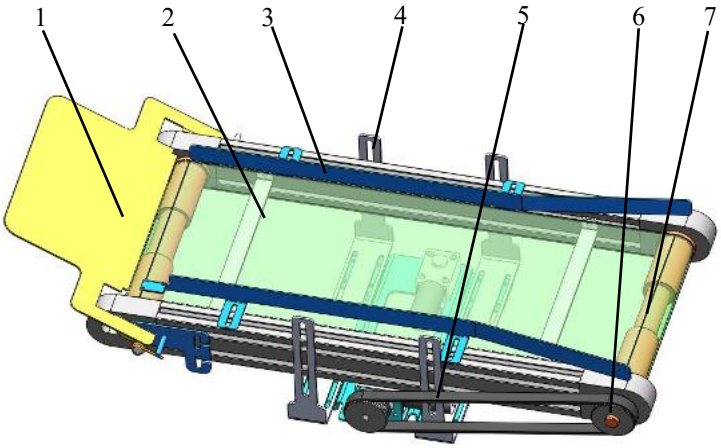


Fig. 2 - Schematic of the longitudinal conveying mechanism

1. Connecting mechanism; 2. Conveyor belt mechanism; 3. Side baffle; 4. Support platform; 5. Drive unit; 6. Concave-convex roller assembly; 7. Master-slave roller assembly

(2) Tracking mechanism

As shown in Fig. 3, the tracking mechanism is designed to accommodate the multidirectional motion of the seedling platform during operation. While awaiting a seedling-replenishment operation, the mechanism remains stationary relative to the seedling platform, thereby accommodating both lateral displacement and vertical offset. The mechanism mainly comprises ① a vertical slide rail, ② a horizontally movable beam, ③ an upper beam, ④ a horizontal slide rail, and ⑤ a lower beam. It is connected to the base plate through the lower beam and forms a sliding connection with the seedling platform. Its primary function is to enable the automatic seedling-loading system to move laterally in synchrony with the seedling platform while maintaining a stable relative height when the platform undergoes lifting, pitching, or swaying motions. To verify the structural feasibility of the conveying and positioning mechanisms, a SolidWorks interference check was performed for the longitudinal conveying mechanism throughout the full travel range of the lateral guide rail. The results showed no structural interference between the longitudinal conveying mechanism and the seedling platform. Furthermore, the position of the longitudinal conveying mechanism at the end of the lateral guide rail was selected as the worst-case operating condition, and a static deformation analysis was conducted on the 5-mm-thick aluminum-alloy base plate. The maximum displacement at the end of the base plate was less than 8 mm, indicating that the structure satisfied the basic positioning and conveying requirements of the automatic seedling-loading system.

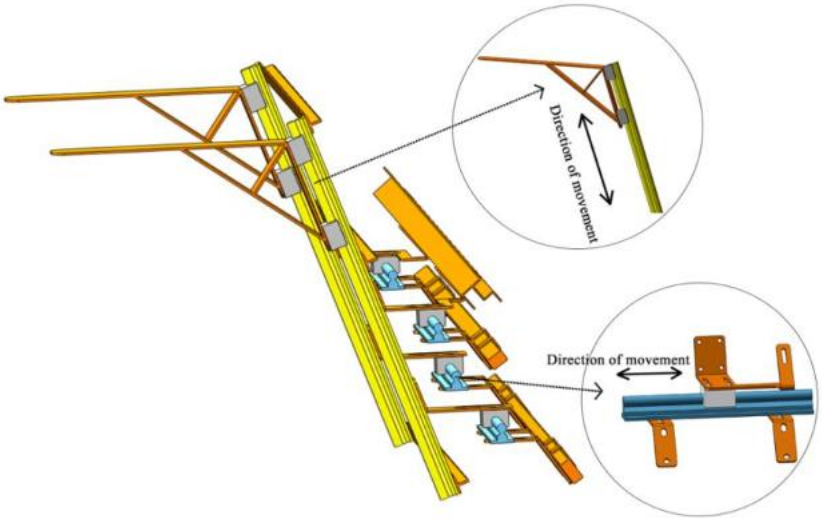


Fig. 3. Schematic of the vertical and horizontal slide-rail mechanisms

1. Vertical slide rail; 2. Horizontally movable beam; 3. Upper beam; 4. Horizontal slide rail; 5. Lower beam

Control system design

To achieve full automation of the rice seedling loading process, a dedicated control system was developed. In Fig. 4, the system uses the seedling shortage alarm signal from the high-speed ride-on rice transplanter as its input and employs an STM32-M3 microcontroller as the central processing unit.

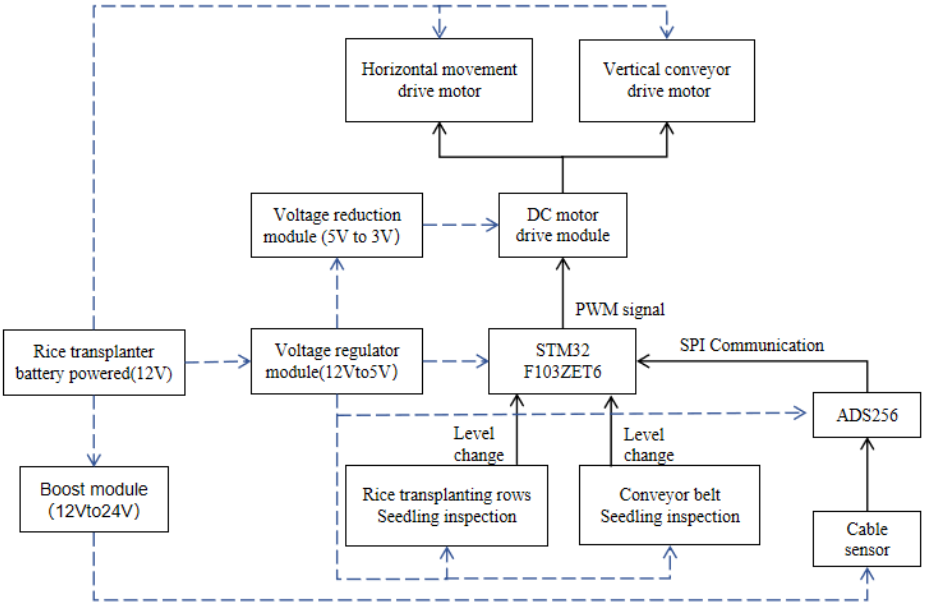


Fig. 4. System architecture of the automatic seedling-loading system

Note: The seedling-shortage switches detect the presence or absence of seedlings on the conveyor belt and in each seedling-holding column. The pull-wire displacement sensor measures the position of the laterally movable platform, and its signal is transmitted through the ADS1256 converter. Based on the detected seedling status and lateral-position feedback, the STM32 controller drives the lateral motor to align the longitudinal conveying mechanism with the target column and then activates the conveyor drive motor to complete the seedling-replenishment operation. Solid lines indicate control-signal or drive relationships, whereas dashed lines indicate power-supply connections.

The control architecture comprises four functional modules: ① seedling status detection, ② lateral position detection, ③ drive control, and ④ power management. A seedling-shortage switch installed on the rice transplanter detects the presence or absence of seedlings in each seedling-holding column of the seedling platform and determines whether the longitudinal conveying mechanism is ready to perform a replenishment operation.

An MPS-S-2500-V1-F pull-wire displacement sensor, used in conjunction with an ADS1256 analog-to-digital (A/D) converter, acquires real-time positional data from the laterally movable platform. The sensor has an output voltage range of 0–5 V, a linearity of ±0.15%, a repeatability of ±0.02%, a maximum operating speed of 1 m/s, and an IP65 ingress protection rating. The sensor output is acquired using the 24-bit ADS1256 A/D converter. Before the tests, the longitudinal conveying mechanism was sequentially aligned with the center of each seedling-holding column, and the corresponding digital output values were recorded as the calibrated target-position values for the respective columns.

Seedling shortage detection was performed using mechanically actuated switch sensors. When a seedling pressed the sensor lever, the corresponding controller input changed from a high level to a low level, and the system determined that seedlings were present at that position. When the lever was released, the system identified a seedling shortage. The shortage detection signal was assigned a relatively high interrupt priority to ensure timely recognition.

After identifying the seedling-holding column requiring replenishment and its corresponding lateral position, the STM32 controller employed a closed-loop control method based on position error and velocity feedback to regulate the PWM signal of the lateral drive motor, thereby moving the longitudinal conveying mechanism to the target shortage column. Once positioning was completed, the longitudinal conveyor motor was activated to perform point-specific seedling replenishment. The controller used a position-control cycle of 50 ms, during which the lateral positions measured by the pull-wire displacement sensor at the current and previous sampling instants were acquired.

The lateral velocity was then calculated from the difference between the two sampled positions:

$$V_k = \frac{x_k - x_{k-1}}{T_s} \quad (1)$$

where the two position variables denote the lateral positions at the current and previous sampling instants, respectively, and the sampling period is set to 50 ms. The controller considers both the distance between the target and current positions and the lateral velocity, and controls the lateral drive motor by adjusting the PWM duty cycle. As the mechanism approaches the target position, the PWM output is reduced to ensure that it stops smoothly at the seedling-holding column requiring replenishment. The conveyor belt of the longitudinal seedling conveying mechanism is then actuated to transport the seedlings and complete the replenishment operation, thereby enabling precise control of both the lateral moving mechanism and the conveyor belt mechanism.

The hardware configuration of the control system is shown in Fig. 5. It consists of the following components: ① a motor drive module, ② a main control unit, ③ an STM32F103ZET6 core board, ④ an A/D acquisition module, and ⑤ a boost module. The control system and the autonomous-driving controller are housed together in a sealed control box. To ensure reliable operation under field conditions, the control box is mounted within a protective frame that provides additional protection against water ingress, solar radiation, and mechanical vibration.

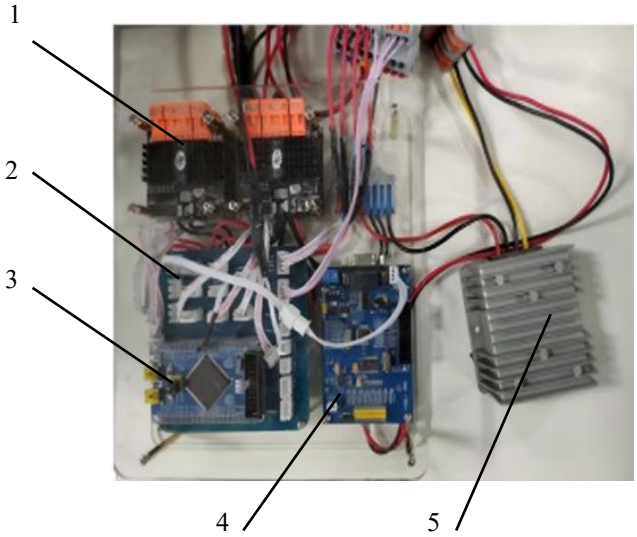


Fig. 5 - Component layout of controller unit

1. Motor driver module; 2. Main control unit; 3. STM32F103ZET6 core board; 4. AD acquisition module; 5. Boost module

In terms of software design, the system's logical workflow is illustrated in Fig. 6

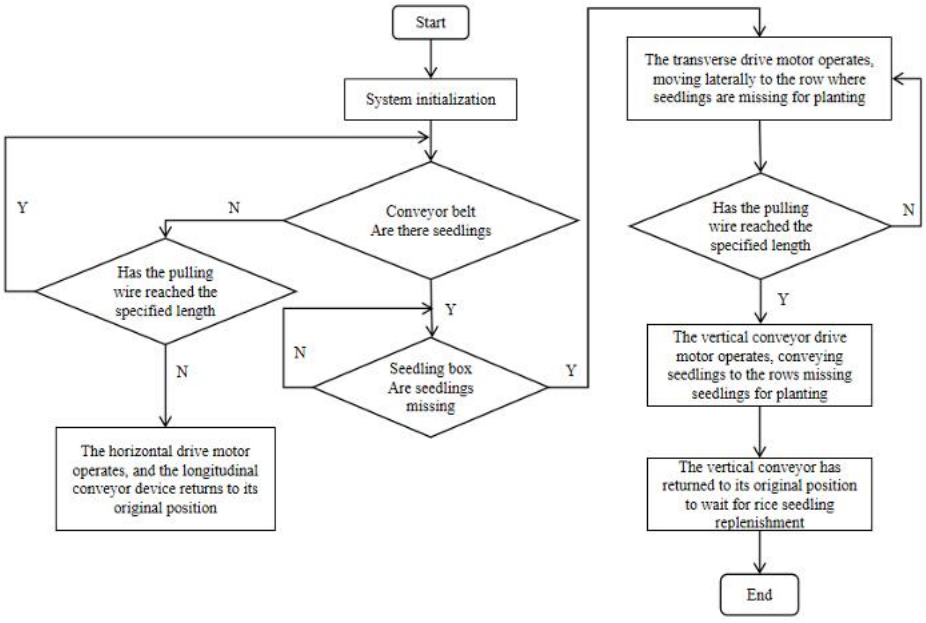


Fig. 6 - System flowchart of automatic seedling loading process

After the system is powered on, an initial self-check is performed, followed by the start of the replanting cycle. The control system continuously monitors the status of each seedling column in real time. When a missing seedling column is detected, the drive mechanism moves to the corresponding target position, and the conveying mechanism is activated to carry out the replanting operation. Upon completion of the replanting task, the system halts the conveyor motor and resets the mechanism to its initial position. It then proceeds to the next round of detection, thus enabling a closed-loop control process for fully automated seedling replenishment.

Bench test

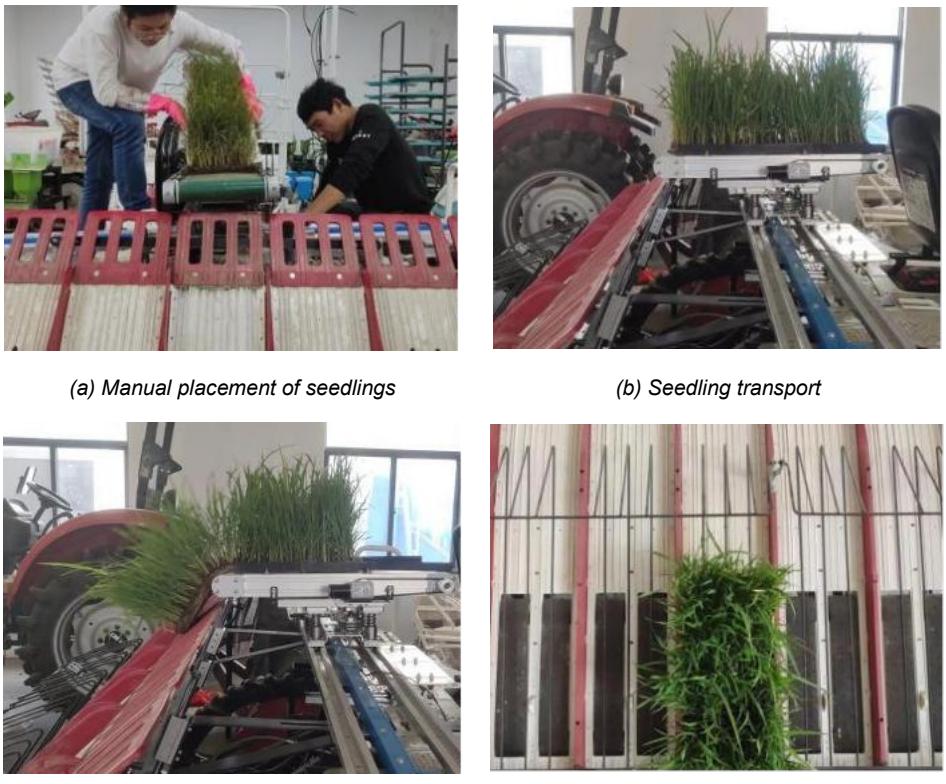
(1) Single-factor experiment

Preliminary experiments verified the reliability of the seedling delivery device, demonstrating its ability to move synchronously with the transplanting platform. However, several key parameters were found to significantly influence the seedling loading success rate, including the conveyor belt speed, the lateral offset distance between the conveyor belt and the seedling column, the left-right tilt angle deviation between the conveyor belt and the seedling platform, the fore-aft tilt angle of the conveyor mechanism, and the height difference between the conveyor belt and the seedling platform. To determine the optimal value range for each factor and improve seedling loading performance, single-factor bench tests were carried out. The seedling loading success rate (C) was used as the evaluation index. A loading operation was considered successful if the result was comparable to manual loading and did not interfere with the transplanter's normal seedling grasping process; otherwise, it was classified as failed loading.

$$C=\frac{R}{Z}\times 100\% \quad (2)$$

where: R is the number of seedling trays successfully loaded (trays) and Z is the total number of seedling trays loaded (trays).

In Fig.7a, seedlings are manually placed onto the conveyor belt. The drive motor is then activated to initiate seedling transportation (Fig.7b). The motor speed is regulated via a speed controller, ensuring controlled moving of the seedlings. As the seedlings reach the end of the conveyor, they detach and drop into the seedling loading column, thereby completing the loading process (Fig. 7c and 7d).



(a) Manual placement of seedlings *(b) Seedling transport*

(c) Seedlings falling into seedling platform *(d) Completion of seedling loading*

Fig. 7 - Bench test process for seedling loading

(2) Multifactor experimental design

Based on the results of the single-factor experiments, the structure of the longitudinal conveying mechanism was optimized. Limit stops were installed to restrict the left-right tilt angle to within ±12°. By adjusting the longitudinal conveying mechanism along the vertical slide rail, the height difference between the conveyor belt and the seedling platform was maintained within 80 mm. Based on these modifications, the factor levels and coded values were determined from the ranges that yielded a seedling-loading success rate of 100% in the single-factor experiments. The selected factors were conveyor belt speed, lateral offset distance, and fore-aft tilt angle (Table 1).

Table 1

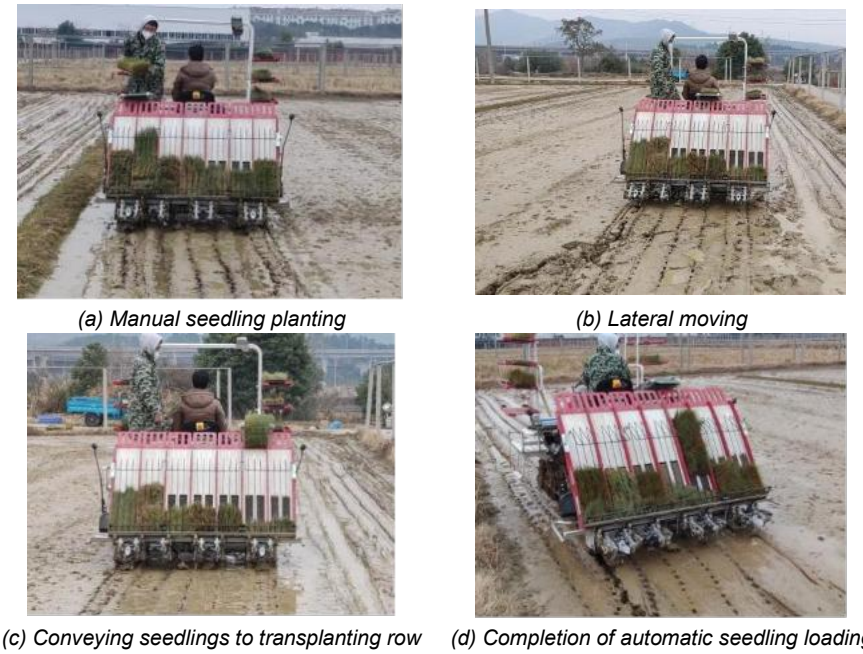
Factor level coding for experimental design

Encoded values	A: Conveyor belt speed (m/s)	B: Lateral offset distance (mm)	C: Fore-aft tilt angle (°)
−1.682	0.1	−17	−38
−1	0.2	−8.5	−24
0	0.3	0	−10
1	0.4	8.5	4
1.682	0.5	17	18
Horizontal interval value	0.1	8.5	14

Field verification experiment

To further evaluate the overall performance of the automatic rice seedling-loading system, field tests were conducted using the optimal combination of operating parameters obtained from the bench experiments. These tests aimed to verify the system's accuracy, stability, and reliability under actual field operating conditions.

On October 8, 2024, a field trial was conducted at the experimental field of Jiangxi Agricultural University. The experimental material consisted of 7-inch mat-type seedling trays, with seedlings aged 28 days, an average height of 15 cm, and a substrate moisture content of 28%. The seedlings were in healthy condition and met the agronomic requirements for mechanized rice transplanting. The automatic seedling loading process was divided into four stages (Fig. 9). Seedlings were firstly manually placed onto the longitudinal conveyor while the system awaited a seedling shortage signal. Once the seedling shortage detection system identified a column requiring replenishment, the longitudinal conveying mechanism was laterally positioned using the lateral moving device. The longitudinal conveyor belt was then activated to transport seedlings to the corresponding shortage column until the loading process was complete. A total of five batches of automatic seedling loading operations were performed, with 30 loading cycles per batch, successfully completing the loading of 150 seedling trays.



(a) Manual seedling planting *(b) Lateral moving*

(c) Conveying seedlings to transplanting row *(d) Completion of automatic seedling loading*

Fig. 9 - Field operation process of automatic rice seedling-loading system

RESULTS AND ANALYSIS

Bench test results

(1) Single-factor experiment results

During the experiment, the conveyor belt speed was varied across 0.1, 0.2, 0.3, 0.4, 0.5, and 0.6 m/s; the lateral offset distance between the conveyor belt and the seedling carrier was set at 12, 13, 14, 15, 16, 17, and 18 mm; the left-right tilt angle deviation between the conveyor belt and the seedling carrier ranged from 0°, 2°, 4°, 6°, 8°, 10°, 12°, to 14°; the fore-aft tilt angle of the conveyor belt mechanism was tested at −35°, −30°, −25°, −20°, −15°, −10°, −5°, 0°, 5°, 10°, 15°, and 20°; and the height difference between the conveyor belt and the seedling carrier was set at 30, 40, 50, 60, 70, and 80 mm.

The statistical values corresponding to seedling loading success rates exceeding 60% were recorded, and their respective ranges are summarized in Table 2. Notably, a 100% success rate was achieved when the left-right tilt angle deviation reached ±12°, and the height difference ranged from 0 to 80 mm.

Table 2

Value ranges of key influencing factors for seedling loading performance

Category	Conveyor belt speed (m/s)	Lateral offset distance (mm)	Left/right tilt angle (°)	Fore-aft tilt angle (°)	Height difference (mm)
Upper limit	0.5	17	−12	18	80
Lower limit	0	−17	12	−38	0

(2) Results of the multifactor experiment

A three-factor, five-level quadratic rotatable orthogonal composite design was employed. The design comprised 20 experimental runs, including six replicates at the center point to evaluate experimental repeatability. Each run consisted of 10 seedling-loading trials, from which the seedling-loading success rate was calculated. The experimental results are presented in Table 3.

To evaluate the repeatability of the automatic seedling-loading system under identical parameter settings, the results of the six center-point runs were statistically analyzed. The center-point settings were a conveyor-belt speed of 0.3 m/s, a lateral offset distance of 0 mm, and a fore-aft tilt angle of −10°. The seedling-loading success rates obtained from the six center-point runs were 90%, 90%, 90%, 80%, 90%, and 90%, respectively. The mean success rate was 88.33%, with a standard deviation of 4.08 percentage points, a 95% confidence interval for the mean of 84.05%–92.62%, and a coefficient of variation of 4.62%. These results demonstrate that the automatic seedling-loading system exhibited good repeatability under identical bench-test conditions and operating parameters.

$$CV = \frac{S}{\bar{Y}} \times 100\% \quad (3)$$

where CV is the coefficient of variation, [%]; S is the standard deviation of the center-point results, [percentage points]; and $\bar{Y}$ is their mean value, [%].

Table 3

Test design and results for seedling loading success rate

Test No.	A: Conveyor belt speed (m/s)	B: Lateral offset distance (mm)	C: Fore-aft tilt angle (°)	Y: Seedling-loading success rate (%)
1	0	0	0	90
2	−1	−1	1	80
3	1.682	0	0	60
4	0	0	−1.682	70
5	0	0	0	90
6	1	1	−1	70
7	0	0	0	90
8	−1	1	1	70
9	0	−1.682	0	60
10	1	−1	1	60
11	−1	−1	−1	90
12	−1	1	−1	90
13	0	0	0	80
14	0	0	0	90

Test No.	A: Conveyor belt speed (m/s)	B: Lateral offset distance (mm)	C: Fore-aft tilt angle (°)	Y: Seedling-loading success rate (%)
15	0	1.682	0	80
16	0	0	1.682	50
17	1	1	1	60
18	0	0	0	90
19	1	−1	−1	70
20	−1.682	0	0	90

The experimental data were analyzed using Design-Expert software, and the corresponding results are outlined in Table 4.

Table 4

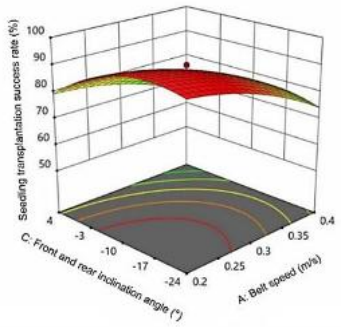
ANOVA for factors influencing seedling loading success rate

Sources of variance	Sum of squares	Degrees of freedom	Mean square	F-value	P-value
Model	3189.66	9	354.41	13.36	0.0002
A	1056.25	1	1056.25	39.81	< 0.0001
B	56.25	1	56.25	2.12	0.1761
C	506.25	1	506.25	19.08	0.0014
AB	12.5	1	12.5	0.4711	0.5081
AC	12.5	1	12.5	0.4711	0.5081
BC	12.5	1	12.5	0.4711	0.5081
A^2	273.05	1	273.05	10.29	0.0094
B^2	519.48	1	519.48	19.58	0.0013
C^2	1248.05	1	1248.05	47.04	< 0.0001
Residual	265.34	10	26.53		
Misfit	182.01	5	36.4	2.18	0.2057
Error	83.33	5	16.67		
Total	3455	19			
R^2	0.9232				
Adjusted R^2	0.8541				
Signal-to-noise ratio	5.15				
Coefficient of variation	6.73%				

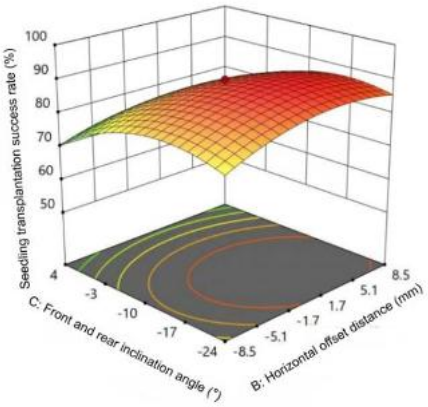
Note: P < 0.01 indicates highly significant and P < 0.05 indicates significant.

Analysis of variance indicated that the model's lack of fit was not significant (P > 0.05), suggesting that no unaccounted factors had a substantial influence on the rice seedling loading success rate. The coefficient of determination (R^2 = 0.9232) demonstrated an excellent model fit, reflecting high reliability and strong predictive capability. The overall model was statistically significant, and A, C, A^2, B^2, and C^2 had highly significant effects on the seedling loading success rate. Using Design-Expert software, the relationship between the multifactor response values and coded variables was analyzed, and a fitted regression equation was derived accordingly.

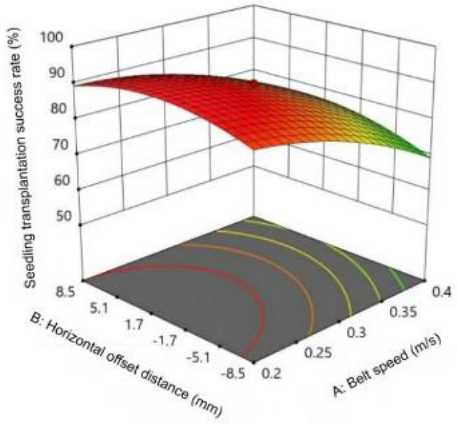
$$Y=88.41-8.13A+1.88B-5.63C+1.25AB+1.15AC-1.25BC-3.3A^2-4.55B^2-7.05C^2 \quad (2)$$



(a) Interaction between conveyor belt speed and fore-aft tilt angle



(b) Interaction between lateral offset distance and fore-aft tilt angle



(c) Interaction between conveyor belt speed and lateral offset distance

Fig. 8 - The influence of various factors on seedling loading success rate

Note: A denotes the conveyor belt speed, B denotes the lateral offset, and C denotes the fore-aft tilt angle. In (a), B was fixed at 0 mm; in (b), A was fixed at 0.3 m/s; and in (c), C was fixed at −10°. The response surfaces and contour plots were generated from the quadratic regression model of the seedling loading success rate and represent the model-predicted success rate under the combined variation of two factors.

The contour plots and response surface analyses of various factors affecting the rice seedling loading success rate were performed using MATLAB (Fig. 8). In Fig. 8a, when the lateral offset distance is 0 mm, the success rate exhibits a "first increase, then decrease" trend with increasing conveyor belt speed and fore-aft tilt angle. Moreover, fluctuations in success rate caused by changes in conveyor belt speed are more pronounced, indicating that conveyor belt speed has a stronger influence on the response variable than the fore-aft tilt angle. In Fig. 8b, when the conveyor belt speed is fixed at 0.3 m/s, the combined effects of lateral offset distance and fore-aft tilt angle on the success rate follow a "large first, then small" trend. The magnitude of variation caused by changes in lateral offset distance is more substantial, suggesting its greater impact relative to the tilt angle. In Fig. 8c, when the fore-aft tilt angle is −10°, the combined effect of conveyor belt speed and lateral offset distance still follows the "large first, then small" pattern. Additionally, significant fluctuations in the success rate are observed with changes in conveyor belt speed, reinforcing that this factor exerts a greater influence than lateral offset distance.

Based on optimization analysis conducted in Design-Expert, the optimal parameter combination for maximizing the rice seedling loading success rate was determined to be a conveyor belt speed of 0.238 m/s, a lateral offset distance of 2.261 mm, and a fore-aft tilt angle of −11.643°, yielding a predicted success rate of 93.39%. For ease of parameter adjustment, a validation experiment was conducted using rounded values: conveyor belt speed of 0.25 m/s, lateral offset distance of 2 mm, and fore-aft tilt angle of −11°. The experiment was repeated 20 times, resulting in 19 successful loadings and an actual success rate of 95%. The 95% confidence interval for the seedling loading success rate, calculated using the Wilson method, was 76.39%–99.11%. The relative error between the experimental result and the model prediction was 1.72%, confirming the accuracy of the regression model and the reliability of the optimized parameter combination.

Results of the field verification tests

The seedling-loading success rates for the individual batches are presented in Table 5. The second and third batches achieved the highest success rate of 100%, whereas the first and fifth batches had the lowest success rate of 83.3%. The mean success rate across the five batches was 90.67%, with a standard deviation of 8.64 percentage points and a range of 83.3%–100%. Based on the 150 field trials, the 95% Wilson confidence interval for the overall seedling-loading success rate was 84.94%–94.36%.

Table 5

Seedling-loading success rates obtained in the field trials

Trial batch	First	Second	Third	Fourth	Fifth
Seedling-loading success rate (%)	83.3%	100%	100%	86.7%	83.3%

Based on field observations and an analysis of the operating mechanism, the main factors contributing to the reduced seedling-loading success rate were identified as follows:

1) The lateral tilt and vertical displacement of the seedling platform significantly affected the seedling-loading success rate. Owing to uneven terrain, variations in mud depth, and other field conditions, irregular and uncontrollable torsional displacement occurred between the rice transplanter main body and the seedling platform. When the longitudinal conveying mechanism moved laterally to the end of the guide rail, its large lateral overhang, combined with the structural flexibility of the system, amplified this torsional displacement. Consequently, the conveyor outlet fell below the reference height of the seedling platform, hindering the effective delivery of the seedling mat into the target seedling-holding column.

2) Structural constraints and contact interference between the seedling mats and the seedling platform during loading adversely affected placement stability. When the seedling mats collided with the side baffles of the seedling platform, they tended to curl or become entangled with the retaining strips. Consequently, they could not settle properly at the bottom of the seedling-holding column, thereby reducing the seedling-loading success rate.

3) Lateral vibration of the rice transplanter reduced the measurement accuracy of the pull-wire displacement sensor, thereby affecting the alignment accuracy between the conveyor belt and the target seedling-holding column. This vibration caused deviations between the actual and target lateral positions of the longitudinal conveying mechanism, preventing accurate alignment with the column requiring replenishment.

Performance comparison of automatic seedling-handling systems

To evaluate the operating performance of the developed automatic seedling-loading system, representative automatic seedling-picking, feeding, and transplanting systems for which success-rate data were clearly reported were selected for comparison (Table 6). Under the optimized test conditions, the developed system achieved a seedling-loading success rate of 95.00%. This value was 6.77, 4.00, 5.00, and 0.83 percentage points higher than those reported by *Jin et al. (2018), Khadatkar et al. (2024), Han et al. (2019),* and *Chen et al. (2025)*, respectively, but 3.00 percentage points lower than that reported by *Kumar and Raheman (2012)*. The results indicate that the longitudinal conveying, lateral positioning, and seedling-shortage detection and control components operated cooperatively to achieve the automatic loading of mat-type rice seedlings. Because the studies differed in seedling type, stage of automated operation, experimental conditions, and criteria used to define success, the reported values should be interpreted only as indicators of system performance under the respective test conditions.

Table 6

Performance comparison of similar automatic seedling-handling systems

Study	Seedling type	Success rate (%)
Jin X. et al., (2018)	Pepper plug seedlings	88.23
Khadatkar A. et al., (2024)	Pepper and tomato plug seedlings	91.00
Kumar G.V.P. et al., (2012)	Vegetable paper-pot seedlings	98.00
Han L.H et al., (2019)	Vegetable plug seedlings	90.00
Chen M. et al., (2025)	Pepper plug seedlings	94.17
Present study	Mat-type rice seedlings	95.00

CONCLUSIONS

1) An automatic seedling-loading system for high-speed ride-on rice transplanters was developed. The system comprises a longitudinal conveying mechanism, a lateral drive mechanism, and a tracking mechanism. Based on an STM32 embedded platform, the control system integrates seedling-shortage detection, position acquisition, and actuator-control modules, enabling the coordinated execution of seedling-shortage detection, lateral positioning, and targeted seedling replenishment. The developed system successfully performed the automatic loading of mat-type rice seedlings.

2) Single-factor bench tests were conducted using conveyor-belt speed, lateral offset distance, and fore-aft tilt angle as the experimental factors to determine their appropriate ranges. Subsequently, a three-factor, five-level quadratic rotatable orthogonal composite design was employed, and a multifactor regression model of the seedling-loading success rate was established (R^2 = 0.9232). The overall regression model was statistically significant. Twenty verification tests were conducted using the optimized parameter settings of approximately 0.24 m/s, 2 mm, and −11°, resulting in a mean success rate of 95.00%. The overall success rate obtained in the field tests was 90.67%, demonstrating that the system could perform automatic seedling loading under actual paddy-field conditions. However, its performance was lower than that achieved under controlled bench-test conditions, indicating that complex field disturbances remain an important factor limiting stable system operation.

3) The triggering of the mechanical seedling-shortage switches was affected by the morphology of the seedling mats and their contact positions. The output signal of the pull-wire displacement sensor fluctuated owing to lateral oscillation and vibration of the rice transplanter main body. The tracking mechanism accommodated the normal lateral reciprocating and vertical movements of the seedling platform; however, its ability to compensate for irregular lateral oscillation, torsional displacement, and height variations at the ends of the guide rail remained limited. Therefore, the field adaptability of the current system requires further improvement. Future work will focus on improving the seedling-shortage detection method, vibration resistance of the position sensor, support structure at the guide-rail ends, and structural design of the tracking mechanism.

4) The field validation comprised five batches and a total of 150 automatic seedling-loading operations. These tests primarily demonstrated the short-term feasibility of the prototype under specific field conditions but were insufficient to fully assess its long-term operational reliability. Further multi-site, multi-season, and long-duration continuous-operation tests are required, with particular emphasis on evaluating wear of the mechanical connections and transmission components, conveyor-belt tension, sensor drift, motor temperature rise, and adaptability to muddy and waterlogged field conditions. In addition, the attitude of the seedling platform, vibration of the rice transplanter main body, and lateral-positioning error should be measured simultaneously to facilitate further optimization of the tracking mechanism, position-detection method, and control strategy.

REFERENCES

[1] Bechar A., & Vigneault C. (2017). Agricultural robots for field operations. Part 2: Operations and systems. *Biosystems Engineering*, 153, 110–128. https://doi.org/10.1016/j.biosystemseng.2016.11.004

[2] Chen B., Zou X., He Y., Yu B., Xiang P.H., & Xiao M.T. (2024). Design and testing of a double-tray symmetrical staggered automatic seedling extraction device for tobacco pot seedlings (烟草钵苗双盘对称交错式自动取苗装置设计与试验). *Journal of Chinese Agricultural Mechanization*, 45(7), 22–27. https://doi.org/10.13733/j.jcam.issn.2095-5553.2024.07.004

[3] Chen M., Xu Y., Han C.J., Li D.S., Yang B.N., Qiu S.L., Luo Y., Mao H.P., & Ma X. (2025). Design and testing of miniaturized electrically driven plug seedling transplanter. *Agriculture*, 15(15), 1589. https://doi.org/10.3390/agriculture15151589

[4] Deng G., He J., Zhang J., Ju L., Yao R.W., Duan X.B., Chai N., Wang J.L., Lv J.X., Zhao Q., & Xu C.B. (2022). *A complete automatic seedling feeding device for rice mat seedlings (一种成套型的水稻毯状自动上苗装置)*. Patent. No. CN217779800U. China.

[5] Fan Y.J., Ma R.J., Huang Q., Huang M.S., & Zhang Y.L. (2016). Design and experiment of automatic feeding seedling mechanism and control system for rice pot seedlings (穴盘水稻钵苗自动送秧机构及控制系统设计与试验). *Journal of South China Agricultural University*, 37(4), 117–123. https://doi.org/10.7671/j.issn.1001-411X.2016.04.019

[6] Fountas S., Mylonas N., Malounas I., Rodias E., Hellmann Santos C., & Pekkeriet E. (2020). Agricultural robotics for field operations. *Sensors*, 20(9), 2672. https://doi.org/10.3390/s20092672

[7] Han L.H., Mao H.P., Hu J.P., & Kumi F. (2019). Development of a riding-type fully automatic transplanter for vegetable plug seedlings. *Spanish Journal of Agricultural Research*, 17(3), e0205. https://doi.org/10.5424/sjar/2019173-15358

[8] Jin X., Zhao K.X., Ji J.T., Du X.W., Ma H., & Qiu Z.M. (2018). Design and implementation of intelligent transplanting system based on photoelectric sensor and PLC. *Future Generation Computer Systems*, 88, 127–139. https://doi.org/10.1016/j.future.2018.05.034

[9] Khadatkar A., Magar A.P., Sawant C.P., & Modi R.U. (2024). Development and testing of automatic seedling extractor in robotic transplanter using mechatronics for nursery seedlings. *Discover Applied Sciences*, 6, 51. https://doi.org/10.1007/s42452-024-05670-2

[10] Kumar G.V.P., & Raheman H. (2012). Automatic feeding mechanism of a vegetable transplanter. International *Journal of Agricultural and Biological Engineering*, 5(2), 20–27. https://doi.org/10.3965/j.ijabe.20120502.003

[11] Liu C.L., Lin H.Z., Li Y.M., Gong L., & Miao Z.H. (2020). Analysis on status and development trend of intelligent control technology for agricultural equipment (农业装备智能控制技术研究现状与发展趋势分析). *Transactions of the Chinese Society for Agricultural Machinery*, 51(1), 1–18. https://doi.org/10.6041/j.issn.1000-1298.2020.01.001

[12] Liu M.H., Hou W.M., Liu Z.P., Xiao Y., Chen X.F., Huang J.X., Duan X.H., Gu J.M., & Xu H.C. (2021*). An auxiliary seedling loading device and rice transplanter (一种辅助装秧装置及插秧机).* Patent. No. CN113597853A. China.

[13] Liu M.H., Liu Z.X., Chen X.F., Yu J.J., Liu J.A., Liu Z.P., Li H.L., & Peng Y.F. (2024). *A crank-arm-type seedling tray positioning and conveying mechanism (一种曲柄臂式秧盘定位输送机构).* Patent. No. CN111264149B. China.

[14] Luo X.W., Liao J., Hu L., Zhou Z.Y., Zhang Z.G., Zang Y., Wang P., & He J. (2021). Research progress of intelligent agricultural machinery and practice of unmanned farm in China (我国智能农机的研究进展与无人农场的实践). *Journal of South China Agricultural University*, 42(6), 8–17.

[15] Shen J.J. (2023). Research on industrial robot technology based on intelligent manufacturing (基于智能制造的工业机器人技术研究*). Development & Innovation of Machinery & Electrical Products*, 36(4), 96–98.

[16] Shi T. (2015). Development and test of automatic corn seedling transplanter (全自动玉米秧苗移栽机的研制与试验). *Transactions of the Chinese Society of Agricultural Engineering*, 31(3), 23–30.

[17] Wang X. (2022). Analysis on current research status and development trend of agricultural machinery navigation technology (农业机械导航技术研究现状与发展趋势分析). *Journal of Agricultural Mechanization Research*, 44(1), 1–10.

[18] Wang X.F., Zhu M., Zhang J., Wang J.B., Qi J.Y., Wu D., & Yao Y. (2021). *Seedling feeding device, rice transplanter with seedling feeding device and automatic seedling feeding method (送秧装置、带送秧装置的插秧机及自动送秧方法)*. Patent. No. CN112655328A. China.

[19] Wang Z.Z., Zhang J.M., & Li W. (2019). Research on pot making and conveying device of automatic vegetable plug pot machine (自动蔬菜穴盘钵机制钵和输送装置的研究). *Wen Yuan*, (6), 313.

[20] Wang Z.Z., Zhu W.Q., & Li W. (2017). Research on pot making and conveying device of automatic vegetable plug pot machine based on PLC (基于PLC的自动蔬菜穴盘钵机制钵和输送装置研究). *Journal of Agricultural Mechanization Research*, 39(4), 229–233.

[21] Wu W.J. (2016). *Automatic seedling feeding peanut picker (自动送秧花生摘果机)*. Patent. No. CN205040268U. China.

[22] Xiao L.P., Ye Y.Y., Cai J.P., Liu M.H., Pu C., Huang L.L., & Deng F.Q. (2018). *A seedling conveying device for a new type of rice pot seedling transplanter (一种新型水稻钵苗移栽机的输秧装置).* Patent. No. CN208029413U. China.

[23] Yin C., Li B., & Jin Y. (2025). Design of an automatic seedling tray conveying device for seedling throwing machine (一种抛秧机秧苗盘自动输送装置的设计). *Mechanical Engineer*, (10), 80–82, 88.

[24] Yin Y.X., Meng Z.J., Zhao C.J., Wang H., Wen C.K., Chen J.P., Li L.W., Du J.W., Wang P., An X.F., Shang Y.H., Zhang A.Q., Yan B.X., & Wu G.W. (2022). State-of-the-art and prospect of research on key technologies for unmanned farms of field crops. *Smart Agriculture*, 4(4), 1–25. https://doi.org/10.12133/j.smartag.SA202212005

[25] Yu G.H., Shan H.Q., Su C.M., Wu T.H., Fang Z.C., & Wang L. (2024). *An automatic seedling feeding device and its feeding method for a four-row rice mat seedling transplanter (用于水稻毯苗四行插秧机的自动送秧装置及其送秧方法)*. Patent. No. CN118679916A. China.

[26] Zhao C.J. (2021). Current situations and prospects of smart agriculture (智慧农业的发展现状与未来展望). *Journal of South China Agricultural University*, 42(6), 1–7.

[27] Zhao C.L. (2017). *Design of full-automatic vegetable transplanter (全自动蔬菜移栽机设计)* [Master's thesis]. Jiamusi University.

STUDY ON ORTHOGONAL STRAIN CHARACTERISTICS OF BRASSICA NAPUS STEMS DURING TENSILE PROCESS BASED ON DIGITAL IMAGE CORRELATION
/
基于 DIC 的油菜茎秆拉伸过程正交应变特性试验研究

Guangchao ZHAN[1)], Yi YANG[1)], Guodang LIAN[*2)], Peng ZHANG[1)], Wangyuan ZONG[3)]
[1)] School of Electromechanical and Intelligent Manufacturing, Huanggang Normal University, Huanggang 438000, Hubei, China
[2)] School of Mechanical and Electrical Engineering, Lanzhou University of Technology, Lanzhou 730050, Gansu; China
[3)]College of Engineering, Huazhong Agricultural University, Wuhan 430070, Hubei, China
Tel: +86-180-8650-1301; E-mail: guangchaozhan@hgnu.edu.cn
DOI: https://doi.org/10.35633/inmateh-79-79

Keywords: *Brassica napus; stem biomechanics; orthogonal strain; digital image correlation*

ABSTRACT
The key challenge in Brassica napus combine harvesting is achieving a balance between threshing rate and impurity rate, both of which are strongly influenced by stem breakage. This study investigated the breakage characteristics and static mechanical properties of Brassica napus stems from the middle and lower reaches of the Yangtze River using axial tensile tests combined with digital image correlation (DIC). The results showed that the fiber layer area of rapeseed *stems increased with stem diameter, and stem breaking force was significantly positively correlated with stem diameter. For stem diameters ranging from 7 to 16 mm, the breaking force ranged from 166.82 to 970.82 N and was described by the relationship* $F_b=42.064d_{x1}-92.894$. *The tensile strength of rapeseed stems ranged from 25.1 to 64.6 MPa, and a quadratic response surface model relating tensile strength to stem diameter and moisture content was established. DIC measurements of strain in the radial and axial orthogonal directions showed that axial deformation was substantially smaller than radial deformation, with an average axial strain of* $\varepsilon_y=4.22\pm2.23\times10^{-3}$ *and an average radial strain of* $\varepsilon_x=3.84\pm2.17\times10^{-2}$. *These findings improve the understanding of the mechanical response of rapeseed stems under tensile loading and provide a theoretical basis for optimizing threshing devices for efficient, low-damage rapeseed harvesting.*

摘要
油菜联合收割中的核心挑战是平衡物料的脱净率与破碎率，而这直接受到茎秆破碎程度的影响。本研究针对长江中下游地区的油菜植株，通过轴向拉伸试验配合数字图像相关技术，深入探讨茎秆的破碎条件和静态特性。研究结果显示，油菜茎秆的纤维层的面积随着茎秆直径的增大而增大，茎秆的拉断力和茎秆直径呈显著正相关。在直径为 7 至 16 mm 的油菜茎秆中，拉断力介于 166.82 N 到 970.82 N 之间，其与直径的关系表达为：$F_b=42.064d_{x1}-92.894$*。油菜茎秆的抗拉强度范围为 25.1 MPa 至 64.6 MPa，并建立了油菜茎秆的抗拉强度与油菜茎秆直径及含水率的二次响应面模型。使用数字图像技术对径向和轴向两个正交方向的应变进行测量，结果表明轴向变形显著小于径向变形，平均轴向应变为* $\varepsilon_y=4.22\pm2.23\times10^{-3}$，*径向应变为* $\varepsilon_x=3.84\pm2.17\times10^{-2}$。*这些结果不仅揭示了茎秆在受力过程中的机械响应规律，还为优化脱粒装置以实现高效低损伤的油菜籽收割提供了重要的理论依据。*

INTRODUCTION

Brassica napus is a predominant oil crop in China, playing a pivotal role in ensuring the supply of edible vegetable oil and enhancing farmers' economic returns (*Sun et al., 2026; Guo et al., 2024; Mazzilli et al., 2024*). With the transformation of rapeseed production from merely establishing crop acreage to achieving high-quality harvesting, combine harvesting technology has emerged as a critical factor in enhancing production efficiency and reducing labor costs (*Li et al., 2025; Shu et al., 2025*). In a rapeseed combine harvester, the threshing device is the core component that directly processes the crop mixture consisting of seeds, pods, and stems. Its operating performance directly affects harvest loss, breakage rate, and the load on the cleaning system (*Zhang et al., 2025*).

Guangchao Zhan, Lecture, Ph.D.; Yi Yang, Lecture, Ph.D.; Guodang Lian, Associate Professor, Ph.D.; Peng Zhang, Lecture, Ph.D.; Wangyuan Zong, Professor, Ph.D.

Extensive research indicates that grain loss and cleaning burden during mechanized rapeseed harvesting are intrinsically linked to the mechanical properties and fracture behavior of plant organs such as stems and pods (*Qing et al., 2021*). However, the majority of existing studies have prioritized the optimization of threshing parameters and the evaluation of overall machine performance, while the biomechanical responses of the rapeseed stem itself under typical loading conditions have received comparatively less attention.

During the threshing process of rapeseed combine harvesting, the drum and concave apply repeated beating, rubbing, and compression actions on the material. Consequently, the stems are subjected not only to axial tension, bending, and shear loads but also to complex stress states coupled with transverse compression (*Vlădut et al., 2023; Zhan et al., 2025*). Insufficient stem breakage often leads to the entrapment of pods and grains, thereby reducing threshing and separation efficiency. Conversely, excessive stem fragmentation generates substantial quantities of short segments and fine fibers, significantly increasing the separation burden on the cleaning system, degrading the airflow field and screening conditions, and ultimately resulting in increased cleaning losses and energy consumption (*Zhou et al., 2025; Yuan et al., 2024*). Therefore, a systematic investigation into the deformation and failure laws of rapeseed stems under typical loads, such as tension, from a plant biomechanics perspective is essential. Acquiring a comprehensive understanding of their critical fracture conditions and anisotropic mechanical properties holds significant theoretical value and engineering utility for the structural design and parameter matching of threshing devices (*Tang et al., 2024; Cujbescu et al., 2021; Vlăduț et al., 2022*).

Currently, research regarding the mechanical properties of rapeseed plants primarily concentrates on overall flexural strength, bending modulus, and parameter calibration based on Discrete Element Method simulations (*Guo et al., 2024; Guan et al., 2022; Hu et al., 2025*). In the context of mechanized harvesting conditions, scholars have analyzed stem breaking forces, pod threshing forces, and grain damage mechanisms by combining experimental and simulation approaches (*Sun et al., 2025; Han et al., 2024; Shan et al., 2024*). Some studies have explored the viscoelastic properties and constitutive relationships of rapeseed stems, demonstrating that their mechanical performance is significantly influenced by factors such as variety, moisture content, and nodal structure (*Ren et al., 2014; Lian et al., 2022; Sikorska et al., 2023*). However, these studies predominantly rely on traditional loading and measurement techniques or simulation model assumptions. Consequently, the strain data obtained are typically limited to single-point or local measurements, rendering it challenging to elucidate the full-field deformation characteristics and strain distribution patterns of rapeseed stems, which are heterogeneous and anisotropic biomaterials, under complex loading conditions.

Digital Image Correlation is a non-contact full-field displacement and strain measurement method based on grayscale image matching, distinguished by high measurement precision, broad material applicability, and flexible experimental configuration. In recent years, DIC technology has been widely applied in mechanical testing of materials such as steel and composites, capable of acquiring full-field strain information on specimen surfaces under tensile, compressive, and fatigue loads (*Fang et al., 2026; Wang et al., 2023*). By analyzing speckle images on a material's surface, this method can effectively capture local strain concentrations and damage evolution during deformation, offering a novel technical approach for investigating the deformation and damage of heterogeneous materials like plant stems.

It is noteworthy that reports on the orthogonal strain characteristics of rapeseed stems during uniaxial tensile processes such as axial-radial strain response, cross-sectional anisotropy, and the coupling effects of hollow structures remain scarce. On one hand, rapeseed stems possess hollow, multi-layered tissue structures with distinct fiber orientations, exhibiting significant orthotropic anisotropic deformation characteristics under tensile loads (*Xiao et al., 2026; Han et al., 2024; Parvin et al., 2021*). On the other hand, traditional measurement methods face limitations in simultaneously acquiring full-field strain data in both axial and radial directions during the stretching process, thereby restricting quantitative in-depth analysis of orthogonal strain characteristics and failure mechanisms. Full-field strain measurement based on DIC allows for the synchronous observation and quantitative characterization of axial and radial strains in rapeseed stems during stretching without altering the force boundary conditions of the specimen, providing an effective means to reveal these orthogonal strain properties.

In summary, in light of the significant impact of stem crushing behavior on threshing and cleaning performance during rapeseed combine harvesting, and addressing the current lack of research on orthogonal strain characteristics under tensile conditions, this study aims to employ DIC technology to conduct full-field measurement and analysis of the axial and radial strains of rapeseed stems during the tensile process.

This research seeks to explore the laws governing orthotropic anisotropic deformation and their relationship with structural parameters, thereby providing a theoretical basis and experimental support for understanding the working mechanisms of rapeseed threshing devices and optimizing their design parameters.

MATERIALS AND METHODS

Test Materials and Equipment

Observation of the internal structure of *Brassica napus* plants showed that the rapeseed stem is mainly composed of an outer fiber layer and an inner pith. The rapeseed stem is approximately cylindrical with neatly arranged fiber layers, as shown in figure 1. Assuming that the mechanical parameters in all radial directions (representing the bonding force between fiber layers) are equal, and the axial mechanical parameters primarily consist of the tensile strength of the fibers, the rapeseed stem can be regarded as an orthotropic material similar to wood and bamboo. Therefore, this paper investigates the axial and radial mechanical properties of rapeseed stem respectively.

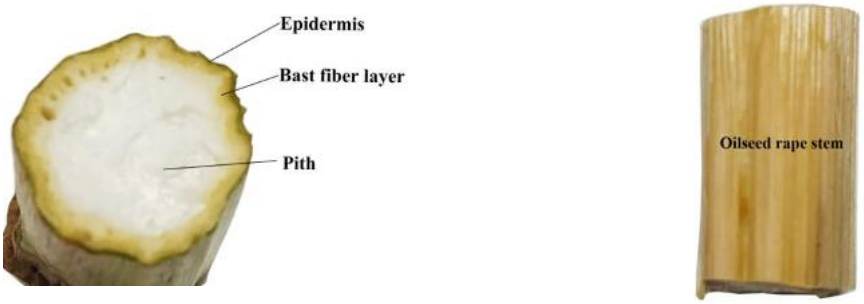


Fig.1 - Structure of rape stem

The test materials were mechanically precision-sown *Brassica napus* plants from the experimental field of Huazhong Agricultural University. The variety was *Brassica napus L*. 'Huayouza 62'. Three plots were randomly selected, and 12 rape plants were chosen from each plot. Healthy plants showing vigorous growth and free from pests or diseases were manually harvested. After harvesting, the rape stems were sectioned to obtain 200 mm segments below the first branch, with diameters ranging from 7 to 16 mm, to serve as the materials for tensile testing. To prevent moisture loss, the collected samples are stored in sealed bags.

Tensile tests were conducted on the rapeseed stems to determine their axial breaking force, tensile strength, and axial and radial deformation. The main equipment used during the testing process included: a universal material testing machine, a Kinect v2 camera, a laptop computer, a vernier caliper, a marker pen, label paper, an OHAUS moisture analyzer (drying method), sealing bags, and scissors. Key instrument parameters are listed in Table 1.

Table 1

Parameters of the equipment

Equipment	Parameters	Values
RGM-3005 Universal Testing Machine	Maximum Load	5 KN
	Test Speed	0.001~500 mm/min
	Accuracy	±0.5 %
Kinect v2 Camera	Resolution	1920×1080 32bits
	Frame Rate	30 fps
OHAUS Moisture Analyzer	Heating Source	Halogen lamp
	Maximum Capacity	90 g
	Accuracy	0.001 g

Test Methods

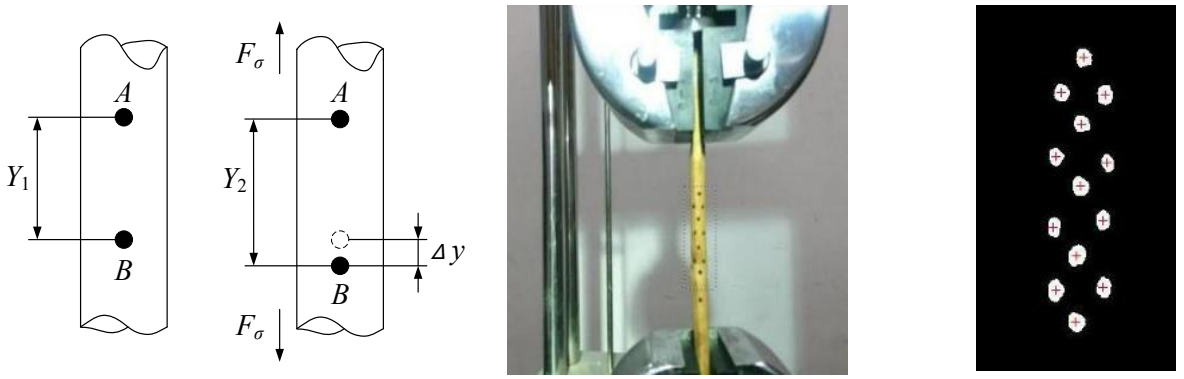
During the tensile test, the stem diameter was first measured in two perpendicular directions using a vernier caliper, and the average was taken as the stem diameter. Excluding data on significant slippage and uneven stem cracks during the stretching process, a total of 36 sets of data were recorded in the experiment. Several feature points were marked with a marker pen within a 50 mm gauge section in the middle of the 200 mm long stem. Images of these points were recorded with a camera during stretching for subsequent extraction of axial and radial strains. During the test, the stem was clamped in self-tightening wedge grips to prevent slippage. A universal testing machine was used to apply the load at a constant speed of 20 mm/min.

F_b represents the maximum breaking force endured by the stem at break. This maximum breaking force was monitored in real-time by the universal testing machine and could be read immediately after the test concluded. The moisture content of each numbered stem was measured after testing.

In this experiment, image recognition technology is employed to measure the deformation per unit length of a rapeseed stem. A camera captures images of the stem, which are marked with distinct points for precise tracking. Using MATLAB, these marked points, A and B, are digitally identified to obtain their coordinates. The axial distance between these points before the application of stress is denoted as Y_1. When the stem is stretched to its breaking force, Fb, the new distance is recorded as Y_2. Thus, the axial deformation ε_y can be calculated. Since strain is the relative deformation per unit length of the stem, the spacing between feature points does not need to be converted to actual length, only the pixel changes between feature points in the image are used to calculate. Similarly, radial deformation, ε_x can also be calculated using identified coordinates. As shown in formula (1).

$$\begin{cases} \varepsilon_y = \dfrac{Y_2 - Y_1}{Y_1} \\ \varepsilon_x = \dfrac{X_2 - X_1}{X_1} \end{cases} \quad (1)$$

Prior to the experiment, each stem is marked using a marker to assist in subsequent image recognition, as depicted in figure 2. The setup involves connecting a Kinect v2 camera to a computer, ensuring that the camera is aligned directly with the marked points on the stem.



a. Axial deformation of stem b. Feature point marking c. Obtain the coordinates

Fig. 2 - Measuring orthogonal strain by digital image correlation

A caliper is employed to measure the diameter of each stem before testing. During the tensile test, the Kinect v2 camera is used continuously until the stems break, while the maximum breaking force is noted. Each broken stem is catalogued and sealed in a bag for moisture content measurement after the test. Post-experimentation, images captured by the Kinect v2 camera, both before stretching and at the point of breaking, are analyzed using image processing to calculate the radial and axial deformations of the stem. The experimental setup is illustrated in Figure 3.



Fig. 3 - Field of stem tensile test

In the tensile fracture test of rapeseed stems, significant differences were observed in the fracture modes, which can be categorized into three main types: a. Edge fracture; b. Central fracture; c. Tearing, as illustrated in figure 4.

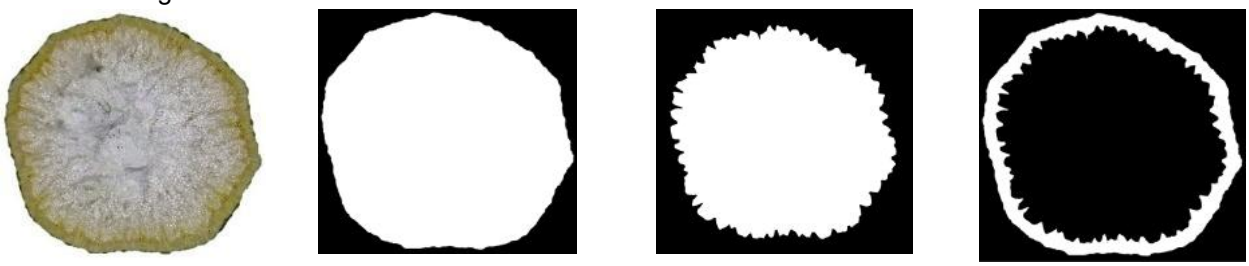
To ensure the accuracy and comparability of experimental data, this study defines stems that exhibit a clean break through the center as the standard mode of fracture. This selection criterion is essential for excluding variations caused by edge effects or asymmetric tearing, thereby ensuring the data reflect the intrinsic tensile properties of the material.



a. Edge fracture b. Central fracture c. Tearing

Fig. 4 - Images of stem before and after tensile stress

The tensile strength of rapeseed stems is primarily governed by the fiber layer, whereas the contribution of the pith layer to the tensile strength is negligible compared with that of the fiber layer. Therefore, the connected domain of the fiber layer in the cross-section of rapeseed stems was extracted through image processing to calculate the area fraction of the fiber layer. Using a standard correction version with a known side length of 1 cm as a reference, convert the pixel area to the actual area. The processing workflow is illustrated in Figure 5.



a. Rapeseed stem cross-section b. Connected domain in the cross-section c. Connected domain of the pith d. Connected domain of the fiber layer

Fig. 5 – Image processing workflow for a rapeseed stem cross-section.

The tensile strength σ_b of rapeseed stems was calculated using the following equation:

$$\sigma_b = \frac{F_b}{S} \quad (2)$$

In Equation (2), F_b is the tensile breaking force of the stem, and S is the area of the fiber layer.

$$S = S_1 - S_2 \quad (3)$$

The area of the fiber layer can be calculated using Equation (3), where S_1 is the total area of the stem cross-section and S_2 is the area of the pith layer.

RESULTS

As shown in figure 5, the tensile breaking force of stems increases with stem diameter. For rapeseed stems with diameters ranging from 7 to 16 mm, the minimum breaking force is 166.82 N and the maximum breaking force is 970.82 N. The functional relationship between stem breaking force and stem diameter d_{x1} is given in equation 4.

$$F_b = 42.064 d_{x1} - 92.894 \quad (4)$$

Figure 6 illustrates the tensile strain of rapeseed stems with different diameters. Analysis indicates that the tensile strain of the stems shows no significant correlation with stem diameter. After removing outlier data points, the average values for radial and axial strain were calculated. The average axial strain was ε_y=4.22±2.23×10^{-3}, and the average radial strain was ε_x=3.84±2.17×10^{-2}. Comparing radial strain with axial strain in stems reveals that axial deformation is significantly smaller than radial deformation. This difference is mainly attributable to the longitudinal orientation of the fiber bundles in rapeseed stems, which provides greater resistance to axial deformation. Conversely, the hollow radial structure of rapeseed stems, when subjected to axial tension, facilitates greater contraction toward the center. Therefore, to thoroughly investigate the mechanical properties of rapeseed stems, their structural characteristics must be fully accounted for. This necessitates separate studies of stem mechanical behavior along both the axial and radial directions.

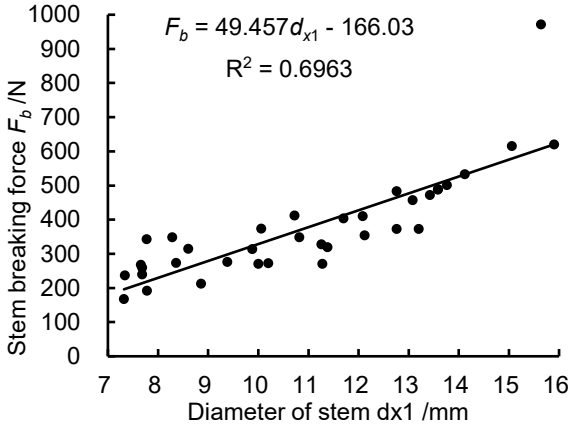


Fig. 5 - Effect of diameter on breaking force

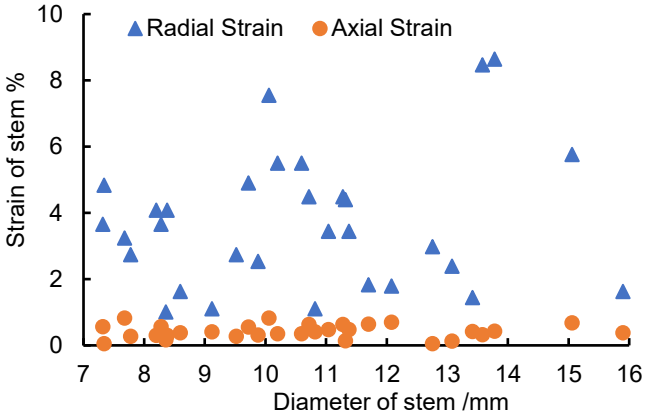


Fig. 6 - Effect of diameter on tensile strain

As shown in figure 7, the area of the rapeseed fiber layer increases with the increase of the diameter of the rapeseed stem, and an R-squared value of 0.9355 indicates a significant correlation between the area of the fiber layer and the size of the diameter. Figure 8 shows the relationship between the diameter of rapeseed stems and their tensile strength. It can be seen from the figure that the tensile strength of rapeseed stems decreases with the increase of stem diameter. The functional relationship between fiber area layer S and stem diameter d_{x1} is given in Equation 5.

$$S = 2.363d_{x1} - 13.135 \quad (5)$$

Figure 8 shows the relationship between the diameter of rapeseed stems and their tensile strength. It can be seen from the figure that the tensile strength of rapeseed stems decreases with the increase of stem diameter. The R value of 0.6617 indicates that the trend is not very obvious, and it is difficult to maintain consistent stem moisture content during the experiment. Therefore, it is necessary to add moisture content as an influencing factor to further analyze the tensile strength of the stem.

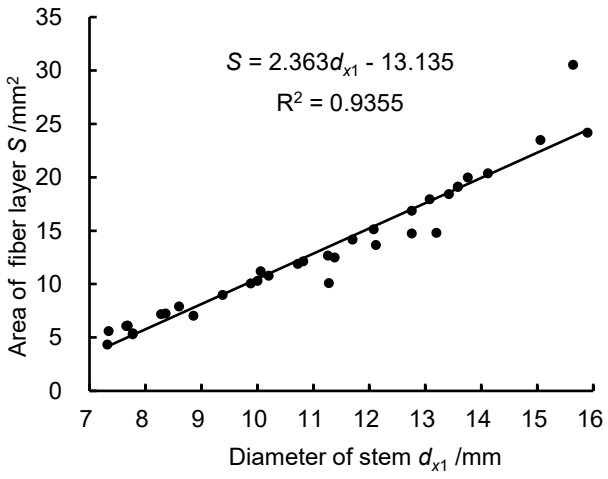


Fig. 7 - Effect of diameter on fiber area

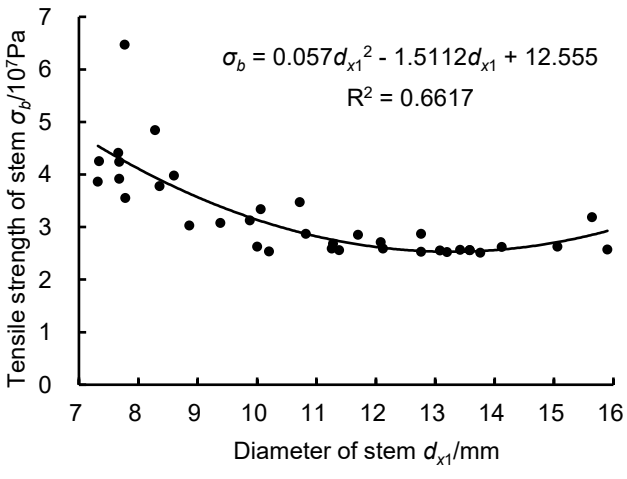


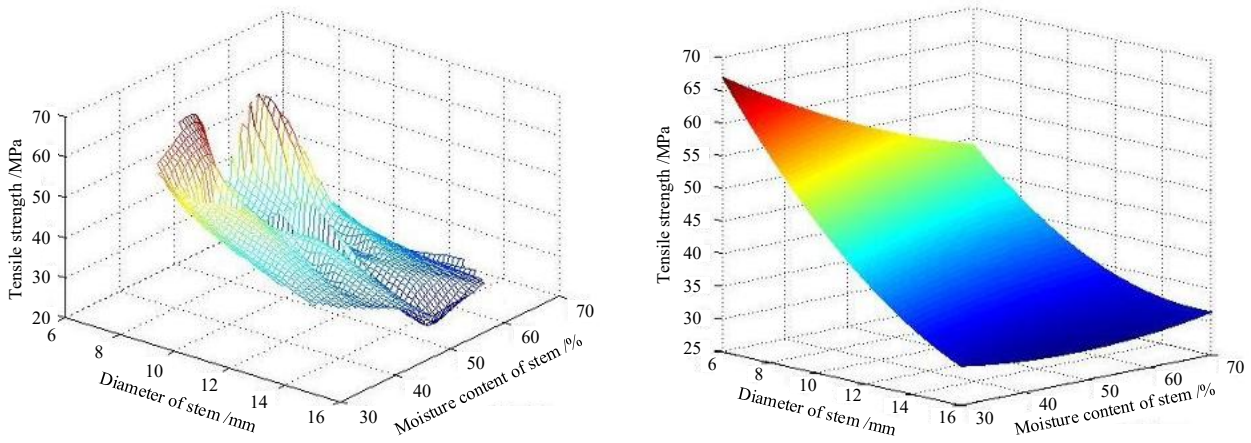
Fig. 8 - Effect of diameter on tensile strength

To investigate the combined effects of stem diameter and moisture content on tensile strength, tensile strength was measured for stems with different diameters and moisture contents, as shown in Table 2. To more clearly visualize the combined effects of stem diameter and moisture content on tensile strength, the measured data were fitted using the least-squares method to construct a three-dimensional response surface. The resulting surface plot, illustrating the relationship among stem diameter, moisture content, and tensile strength over the tested range, is presented in Figure 9.

Experimental Data from Rapeseed Stem Tensile Tests **Table 2**

Number	Mass (g)	Diameter (mm)	Tensile Breaking Force (N)	Moisture Content (%)	Tensile strength (MPa)
1	2.354	8.60	313.73	44.10	39.8
2	2.233	8.86	212.08	47.33	30.3
3	1.856	7.32	166.82	50.57	38.6
4	2.904	10.00	269.60	49.97	26.3
5	3.445	10.20	272.25	50.33	25.3
6	3.770	9.38	275.27	48.70	30.8
7	4.202	11.38	318.43	47.94	25.6
8	3.585	10.72	411.73	42.40	34.7
9	4.456	13.20	372.34	41.10	25.2
10	2.935	13.76	500.52	42.24	25.1
11	5.973	12.76	483.00	43.86	28.7
12	5.280	13.42	471.82	37.65	25.6
13	4.321	7.34	236.64	52.51	42.5
14	1.858	7.68	258.67	37.57	42.4
15	2.065	8.36	272.93	38.97	37.7
16	2.360	7.77	341.97	37.09	64.6
17	3.363	9.88	313.42	45.75	31.2
18	3.810	10.06	372.84	41.84	33.3
19	5.250	13.08	456.53	42.78	25.5
20	4.823	11.70	403.26	44.55	28.5
21	4.856	12.08	409.45	44.92	27.1
22	6.140	13.58	487.82	43.24	25.6
23	5.972	15.06	614.99	40.63	26.2
24	9.483	15.90	619.92	46.37	25.7
25	2.494	7.68	238.90	52.00	39.2
26	3.082	8.28	347.50	54.40	48.4
27	2.580	7.78	190.82	57.39	35.5
28	3.465	7.66	267.44	51.59	44.1
29	3.945	10.82	347.35	56.93	28.7
30	3.273	11.26	327.47	50.91	25.9
31	5.107	11.28	269.89	57.67	26.8
32	5.631	12.12	352.97	60.76	25.9
33	6.321	12.76	372.16	53.68	25.3
34	8.156	13.58	487.90	52.94	25.6
35	10.577	15.64	970.82	60.60	31.8
36	8.265	14.12	532.60	60.59	26.2

As shown in Figure 9, the tensile strength of rapeseed stems generally decreases with increasing stem diameter. Within the tested stem diameter range of 7–16 mm, the tensile strength exhibits considerable variability, with a minimum value of 25.1 MPa and a maximum of up to 64.6 MPa. In addition, Figure 9 comprehensively presents the combined influence of stem moisture content and diameter on tensile strength. It can be observed that changes in moisture content also alter the mechanical response of the stem material. Generally, as moisture content increases, the binding strength of hydrogen bonds between fibers and the lignin–hemicellulose matrix within the stem may weaken, leading to a decrease in tensile strength. However, the extent to which moisture content reduces tensile strength is not entirely consistent across different diameter classes; stems with larger diameters, owing to their greater structural redundancy, may be relatively less sensitive to changes in moisture content.



a. Mesh plot of the experimental data b. Regression equation surface plot

Fig. 9 - Effect of stem moisture content and diameter on tensile strength

Analysis indicates that both stem moisture content and diameter exert a significant influence. The experimental data were entered into EViews for optimization analysis of regression equation, where dx1 represents rapeseed stem diameter, dx_2 represents stem moisture content, and C denotes the constant term. The correlation test results of variables are shown in Table 3, the results show that the correlation coefficients between d_{x1} d_{x2} and d_{x1}, as well as between d_{x1}^2 d_{x2}^2 and d_{x1}, are all greater than 0.8, indicating strong collinearity. Therefore, the interaction term is not included in the regression model. The results of the analysis of variance for the experimental data are presented in Table 4.

Table 3

Correlation test results of variables

Variable	d_{x1}	d_{x2}	d_{x1}^2	d_{x2}^2	d_{x1} d_{x2}	d_{x1}^2 d_{x2}^2
d_{x1}	1.0000	0.0278	0.9944	0.0404	0.8419	0.7963
d_{x2}	0.0278	1.0000	0.0323	0.9975	0.5478	0.5591
d_{x1}^2	0.9944	0.0323	1.0000	0.0463	0.8408	0.8063
d_{x2}^2	0.0404	0.9975	0.0463	1.0000	0.5614	0.5793
d_{x1} d_{x2}	0.8419	0.5478	0.8408	0.5614	1.0000	0.9849
d_{x1}^2 d_{x2}^2	0.7963	0.5591	0.8063	0.5793	0.9849	1.0000

Table 4

Regression analysis of experimental data

Variable	Coefficient	Std. Error	t-Statistic	Prob.
C	23.9645	4.1115	5.8287	0.0000
d_{x1}	-1.3803	0.2942	-4.6921	0.0001
d_{x1}^2	0.0505	0.01315	3.8367	0.0006
d_{x2}	-0.4815	0.1679	-2.8684	0.0074
d_{x2}^2	0.0047	0.0018	2.7564	0.0097
R2	0.7483	Mean dependent var		3.1924
Adjusted R2	0.7158	S.D. dependent var		0.8628
S.E of regression	0.4600	Akaike info criterion		1.4130
Sum squared resid	6.5593	Schwarz criterion		1.6329
F-statistic	23.0361	Hannan-Quinn criterion		1.4898
Prob(F-statistic)	0.0000	Durbin-Watson stat		2.3786

The experimental data were processed using stem diameter d_{x1} and stem moisture content d_{x2} as variables to perform a quadratic polynomial regression analysis on tensile strength σ_b, yielding the regression equation 6.

$$\sigma_b = -1.3803d_{x1} - 0.4815d_{x2} + 0.0505{d_{x1}}^2 + 0.0047{d_{x2}}^2 + 23.9645 \quad (6)$$

CONCLUSIONS

Axial tensile tests combined with digital image correlation (DIC) systematically revealed the fundamental relationships among stem diameter, moisture content, and the fracture behavior of tensile strength. The breaking force exhibited a strong linear increase with stem diameter, whereas the tensile strength was well described by a quadratic response surface model as a function of both stem diameter and moisture content. Most notably, DIC strain measurements demonstrated pronounced mechanical anisotropy: the radial strain was approximately an order of magnitude larger than the axial strain, strongly indicating a lateral-dominated deformation mechanism prior to failure. Nevertheless, it should be emphasized that these quantitative results are subject to inevitable measurement uncertainties. Primary sources of error include the inherent biological variability among specimens, micro-slippage at the clamping interfaces, local moisture gradients within the stem tissue, and intrinsic noise in the DIC strain computation. Consequently, although the reported trends are considered physically meaningful, the absolute force and strain values should be applied with due caution when high precision is required.

Despite the above limitations, the strongly anisotropic strain behavior suggests that threshing elements designed to induce multi-axial stress states—such as combined bending, shear, and compression—rather than simple uniaxial tension, could more effectively suppress uncontrolled stem fracture, potentially contributing to reduced grain loss and improved seed cleanliness, pending further validation under dynamic and field conditions. These findings thus establish a critical bridge between the biomechanical properties of oilseed rape stems and the engineering optimization of combine harvester threshing units. Future work should progress beyond the quasi-static conditions employed here to dynamic loading regimes that better replicate the complex impact and bending actions encountered inside a threshing chamber. A systematic investigation of additional influential factors—including varietal differences, the maturity gradient along the stem, and internode position—is essential to enhance the generality and predictive power of the developed models. Furthermore, integrating the experimentally measured mechanical parameters into finite element simulations of the stem–threshing element interaction will enable virtual prototyping and parametric optimization. Coupling such simulations with field validation and real-time sensing of stem diameter and moisture content could lay the foundation for adaptive control strategies that autonomously regulate threshing parameters. Ultimately, this integrated approach holds great promise for achieving more efficient and cleaner rapeseed combine harvesting.

ACKNOWLEDGEMENT

The authors gratefully acknowledge the support of the affiliated institution and the technical assistance provided during the research. Appreciation is also extended to the research group members for their valuable discussions. This project was funded by the Hubei Natural Science Foundation of China (2025AFB006).

REFERENCES

[1] Cujbescu, D., Găgeanu, I., & Iosif, A. (2021). Mathematical modeling of ear grain separation process depending on the length of the axial low threshing apparatus. *INMATEH–Agricultural Engineering*. 65, 101–110.

[2] Fang, Z., Yu, J., Yang, F., Sheng, Y., Rao, J., & Zheng, Z. (2026). Tensile and fatigue tests of steel specimens based on digital image correlation. *Progress in Steel Building Structures*, 1-10.

[3] Guan, Z., Mu, S., Li, H., Jiang, T., Zhang, M., & Wu, C. (2022). Flexible DEM model development and parameter calibration for rape stem. *Applied Sciences*, 12(17), 8394.

[4] Guo, H., Guo, L., Li, H., Dong, Y., Zhou, W., & Han, J. (2024). Calibration and experiment of the discrete element simulation parameters for rapeseed stems during the suitable harvest period. *Transactions of the Chinese Society of Agricultural Engineering*, 40(24), 20-29.

[5] Han, M., Li, M., Duan, H., Xu, K., & Yu, K. (2024). Rigid-flexible coupling simulation and experiment of plant stem clamping device based on ADAMS. *Transactions of the Chinese Society for Agricultural Machinery*, 55(2), 109-118.

[6] Hu, Y., Javed, H., Liu, L., Alabdallah, N., Ghaffor, K., & Liu, Y., Luo, Y., Gulzar, F., Peng, X., & Wu, Y. (2025). Evaluate the sensitivity of rapeseed lodging under low light: a field study on the biomechanics of stem and root lodging in rapeseed (*Brassica napus l.*). *Field Crops Research*, 327.

[7] Li, Z., Luo, H., Wang, X., Li, Y., Zhang, S., & Tong, X. (2025). Design and optimization of transverse differential speed conveying device for horizontal rapeseed windrower. *Journal of Jiangxi Agricultural University*, 47(2), 486-504.

[8] Lian, G., Wei, X., Ma, L., Zhou, G., & Zong, W. (2022). Design and experiments of the axial-flow spiral-drum threshing device for the edible sunflower. *Transactions of the Chinese Society of Agricultural Engineering*, 38(17), 42–51.

[9] Mazzilli, SR., & Verocai, M. (2024). A comparative study of yield components and their trade-off in oilseed crops (*Brassica napus l*. and brassica carinata a. braun). *European Journal of Agronomy*.

[10] Parvin, A., Rahman, M., & Cattani, DJ. (2021). The effect of stem diameter on the *Brassica napus* (type: canola) (cultivar: HYHEAR 3) fiber quality. *World Journal of Engineering and Technology*, 09(3):458-481.

[11] Qing, Y., Li, Y., Xu, L., & Ma, Z. (2021). Study on the rape pod shatter resistance suitable for low-loss harvesting of harvester reel. *INMATEH–Agricultural Engineering*, 63(1).

[12] Ren, S., Wu, M., Xie, F., & Guan, C. (2014). Study on viscoelastic properties of rapeseed stem and the constitutive relationship. *Journal of Anhui Agricultural Sciences*, 42(35), 12749-12751.

[13] Shan, Y., Liao, Q., Yuan, J., Wan, X., & Liao, Y. (2024). Effects of cutting parameters on the shearing properties of oilseed rape (*Brassica Napus L*.) shoots in harvesting. *Applied Engineering in Agriculture*, 40(3):339-349.

[14] Shu, C., Yi, P., Wu, C., Wan, X., Liao, Q., & Yuan, J. (2025). Design and experiment of lightweight and simple threshing machine in hilly areas for rapeseed. *Transactions of the Chinese Society of Agricultural Engineering*, 41(19), 54-64.

[15] Sikorska, A., Gugaa, M., Zarzecka, K., Mystkowska, I., Ginter, A., Findura, P., & Pristavka, M. (2023). Biometric characteristics of winter rape plants (*Brassica napus l*.) before harvest in the soil and climatic conditions of north-eastern Poland. PLoS ONE (v.1;2006), 023, 18(8):14.

[16] Sun, X., Zong, W., Ma, L., & Wan, X. (2025). Design and test of the dual-airduct cleaning device for oilseed rape harvesters in hilly and mountainous areas. *Transactions of the Chinese Society of Agricultural Engineering,* 41(13), 72-82.

[17] Sun, Y., Jiao, Z., Huang, J., Dai, L., Sun, R., Hu, X., Liang, Z., Xue, Y., & Xu, Z. (2026). Current status and research progress in the utilization of oilseed rape straw as feed in China. *Chinese Journal of Oil Crop Sciences*, 1-7.

[18] Tang, Q., Jiang, L., Yu, W., Wu, J., & Wang, G. (2024). Design and experiment of high moisture corn threshing device with low damage. *INMATEH–Agricultural Engineering*, 74(3), 172-183.

[19] Vlăduț, N., Biriş, S., Cârdei, P., Găgeanu, I., Cujbescu, D., Ungureanu, N., Popa, L., Perişoară, L., Matei, G., & Teliban, G. (2022). Contributions to the mathematical modeling of the threshing and separation process in an axial flow combine. *Agriculture*, *12*, 1520.

[20] Vlădut, N., Ungureanu, N., Biris, S., Voicea, I., Nenciu, F., Găgeanu, I., Cujbescu, D., Popa, L., Boruz, S., Matei, G., Ekielski, A., & Teliban, G. (2023). Research on the identification of some optimal threshing and separation regimes in the axial flow apparatus. *Agriculture*, 13(4), 838.

[21] Wang, C., Wang, S., Xie, L., Liu, Y., Deng, J., & He, W. (2023). Fatigue crack growth behavior of marine steel under variable amplitude loading-combining DIC technique and SEM observation. *International Journal of Fatigue*, 170, 107508.

[22] Xiao, R., Su, H., Liao, Y., Wang, H., Sheng, Y., Rao, J., & Zheng, Z. (2026). Study on MOE and MOR of bamboo-wood composite panels with different core materials. *Journal of Central South University of Forestry & Technology*, 1-9.

[23] Yuan, J., Liao, Q., Wan, X., Yang, J., & Shu, C. (2024). Parameter matching and experiment of the combined cyclone separation and cylinder sieve cleaning system for rape combine harvester. *International Journal of Agricultural & Biological Engineering*, 17(1), 128–136.

[24] Zhan, G., Liu, W., & Zhang, P. (2025). Study on the movement characteristics of rapeseed threshing materials based on dem simulation and high-speed imaging. *INMATEH–Agricultural Engineering*, 76(2), 1279-1288.

[25] Zhang, M., Xu, C., Li, C., Wang, G., Yang, Y., & Jiang, T. (2025). Parameter optimization and experiment of a single longitudinal axial flow full-circumference separation threshing device for rapeseed harvester. *INMATEH – Agricultural Engineering*, 76(2), 1231-1243.

[26] Zhou, J., Liao, Q., Wan, X., Yuan, J., Li, J., & Qin, Y. (2025). Discrete element simulation of grain crushing and optimization of chopping and throwing device for rapeseed combine harvester. *Journal of Huazhong Agricultural University*, 44(1), 265-275.

SUSTAINABLE CONTROL OF *BOTRYTIS CINEREA* IN VITICULTURE USING BIOACTIVE PLANT EXTRACTS OBTAINED BY HYBRID ULTRASOUND-PERCOLATION TECHNOLOGY

/

CONTROLUL SUSTENABIL AL FUNGULUI BOTRYTIS CINEREA ÎN VITICULTURĂ UTILIZÂND EXTRACTE BIOACTIVE DIN PLANTE OBȚINUTE PRIN TEHNOLOGIA HIBRIDĂ ULTRASUNETE-PERCOLARE

Ana-Maria TĂBĂRAȘU[1)], Florin NENCIU*[1)], Cristina FĂTU[2)], Lorena-Diana POPA *[3)], Nicolae-Valentin VLĂDUȚ[1)], Iuliana GĂGEANU[1)], Teofil-Alin ONCESCU[1)], Diana COCÂRȚĂ[4)], Dragoș-Nicolae ANGHELACHE[1)], Andra-Maria LĂCUREANU[4)], Iulian VOICEA[1)], Elena-Valeria VLĂDUȚ[4)]

[1)]INMA Bucharest / Romania; [2)] Research Development Institute for Plant Protection / Romania;
[3)] Agricultural Research and Development Station Secuieni / Romania;
[4)] National University of Science and Technology POLITEHNICA Bucharest / Romania
E-mail: florin.nenciu@inma.ro; dy.hemp420@gmail.com
DOI: https://doi.org/10.35633/inmateh-79-80

Keywords: *botrytis cinerea control, green extraction, ultrasound-assisted percolation, bioactive polyphenols, botanical fungicides, sustainable viticulture*

ABSTRACT

Sustainable management of gray mold (Botrytis cinerea) in viticulture necessitates eco-friendly alternatives to synthetic fungicides to alleviate chemical residue risks and combat emerging pathogen resistance. This study evaluated the biocontrol potential of botanical extracts derived from Allium sativum, Lavandula angustifolia, Salvia officinalis, Cannabis sativa, and Melissa officinalis, obtained via an optimized hybrid ultrasound-assisted percolation process. The optimal extraction parameters were determined to be a particle size of 30 mm, a solid-to-liquid ratio of 1:30, a system pressure of 7 bar, and an ultrasound power of 120 W over a 120-minute extraction duration, achieving high polyphenolic yields while maintaining process energy efficiency. In vitro antifungal screening via the poisoned food technique revealed that A. sativum extract exhibited the most potent inhibition against B. cinerea (78.62% on day 2 and 39.84% on day 7 at a 50% v/v concentration), followed by L. angustifolia (69.62% on day 2). In vivo evaluations on Vitis vinifera L. corroborated a concentration-dependent reduction in disease incidence following post-inoculation application. However, a progressive temporal decline in antifungal efficacy was observed across all crude extracts, highlighting the critical need for microencapsulation strategies or condensed application intervals (3–5 days) under field conditions. Overall, hybrid ultrasound-assisted percolation represents a highly efficient green extraction platform for recovering bioactive compounds suitable for integration into sustainable vineyard crop protection regimes.

REZUMAT

Managementul sustenabil al putregaiului cenușiu (Botrytis cinerea) în viticultură necesită identificarea unor alternative ecologice la fungicidele de sinteză, cu scopul de a diminua riscurile legate de reziduurile chimice și de a combate fenomenul de rezistență al patogenilor. Acest studiu a evaluat potențialul de biocontrol al extractelor botanice obținute din Allium sativum, Lavandula angustifolia, Salvia officinalis, Cannabis sativa și Melissa officinalis, procesate printr-o tehnologie optimizată de percolare hibridă asistată de ultrasunete. Parametrii optimi de extracție au fost stabiliți la o dimensiune a particulelor de material vegetal de 30 mm, un raport solid-lichid de 1:30, o presiune de 7 bar și o putere a ultrasunetelor de 120 W pe o durată de 120 de minute, obținându-se randamente ridicate de compuși polifenolici cu menținerea eficienței energetice a procesului. Evaluarea in vitro a activității antifungice prin metoda Mediului Toxic (Poisoned Food Technique) a arătat că extractul de A. sativum a prezentat cea mai puternică inhibiție împotriva B. cinerea (78.62% în ziua 2 și 39.84% în ziua 7 la o concentrație de 50% v/v), urmat de cel de L. angustifolia (69.62% în ziua 2). Testele in vivo efectuate pe Vitis vinifera L. au confirmat o reducere dependentă de concentrație a incidenței bolii în urma aplicării post-inoculare. Cu toate acestea, s-a observat o scădere progresivă în timp a eficacității antifungice pentru toate extractele brute, ceea ce subliniază necesitatea dezvoltării unor formulări microincapsulate sau a scurtării intervalelor de aplicare (3–5 zile) în condiții de câmp. În ansamblu, percolarea hibridă asistată de ultrasunete se dovedește a fi o platformă ecologică de extracție extrem de eficientă pentru recuperarea compușilor bioactivi capabili să fie integrați în strategii durabile de protecție a culturilor de viță-de-vie.

INTRODUCTION

Grapevine (*Vitis vinifera L.*) is one of the most economically important horticultural crops worldwide, with global grape production exceeding 77 million tons annually (*Ohana-Levi and Netzer, 2025; Butiuc-Keul and Coste, 2023*). However, grape yield and quality can be significantly affected by numerous phytopathogenic agents, among which *Botrytis cinerea*, the causal agent of gray mold, is one of the most important fungal pathogens of grapevine. Infection can cause berry deterioration and decay, with negative effects on grape yield, quality, and commercial value. Disease development is particularly favored by high-humidity conditions, while the difficulties associated with its control justify the interest in identifying effective and sustainable prevention and management methods (*Rahman et al., 2024; Jiang et al., 2023; De Simone et al., 2020; Jacometti et al., 2010*).

Under certain controlled conditions, *Botrytis cinerea* can contribute positively to wine quality through the phenomenon known as “noble rot” (*Hegyi et al., 2022*; *Negri et al., 2017*). *Azzolini et al., (2013),* showed that the controlled inoculation of grapes intended for passito wine production with selected *B. cinerea* strains can modify the aromatic profile, promoting the accumulation of volatile and terpenic compounds associated with the complex aromas of sweet wines. In the study (*Kelly et al., 2022*), the use of a 10% proportion of infected grapes in appassimento-style red wines resulted in only minor chemical and aromatic changes, without significantly affecting consumer acceptance. The article (*Thakur et al., 2018*) mentions *Tokaji Asz´* , *Sauternes, Beerenauslese*, and *Trockenbeerenauslese* among the best-known wines produced through “noble rot”. Botrytization promotes sugar concentration and the accumulation of compounds such as glycerol and gluconic acid, while also contributing to the development of characteristic honey, caramel, and dried-fruit notes typical of premium botrytized wines.

The control of *B. cinerea* relies largely on the use of synthetic fungicides. However, repeated use of chemical products may favor the selection of resistant pathogen populations, while concerns regarding the reduction of the environmental impact of plant protection products have stimulated research aimed at identifying alternative control methods (*Hahn, 2014; Sofianos et al., 2023; Tăbăraşu et al., 2025a; Nenciu et al., 2023)*. In this context, extracts obtained from medicinal and aromatic plants are of interest due to the diversity of bioactive compounds they contain and may represent natural sources of substances with antifungal activity (*Dėnė and Valiuškaitė, 2021; Oprescu et al., 2023*).

Several studies have highlighted the potential of garlic (*Allium sativum L.*) extracts for the control of *Botrytis cinerea*. Aqueous and ethanolic extracts have demonstrated the ability to inhibit both mycelial growth and conidial germination, with the effect being concentration-dependent and potentially reaching complete inhibition (*Daniel et al., 2015*). Furthermore, volatile compounds derived from garlic have proved effective in limiting disease development, highlighting the contribution of sulfur-containing compounds to the antifungal activity of this species (*Campa-Siqueiros et al., 2017*). Antifungal activity has also been demonstrated for extracts obtained from garlic peels, for which inhibition of *B. cinerea* mycelial growth of up to 57.57% was reported, together with a reduction in disease development in *in vivo* tests on strawberries (*Carreón-Delgado et al., 2023*).

Antifungal activity against *B. cinerea* has also been reported for sage extracts. *Rabilu et al., (2021),* evaluated aqueous extracts obtained from *Salvia officinalis subsp. lavandulifolia* and *Salvia officinalis subsp. major*, reporting inhibition of the pathogen’s mycelial growth. Efficacy depended on the extract concentration and the harvesting period of the plant material, with the maximum reported inhibition reaching 59.34%.

The antifungal potential of lavender and lemon balm extracts was evaluated by (*Kasmi et al., 2017)*, who assessed aqueous extracts of *Lavandula officinalis* and *Melissa officinalis* against *B. cinerea*. Under *in vitro* conditions, both extracts affected pathogen development, with the effects being concentration-dependent and varying according to the developmental stage of the fungus. Lavender extract exhibited particularly pronounced activity against spore germination, resulting in 79.65% inhibition at a concentration of 1 mg/mL, whereas lemon balm extract showed lower antifungal activity. In *in vivo* tests, the effects of both extracts were considerably weaker, indicating that the efficacy observed *in vitro* is not necessarily maintained under more complex biological conditions.

Compared with other plant species, the antifungal potential of hemp extracts against *Botrytis cinerea* has been less extensively studied, and the available literature in this field remains limited. In this context, *Kursa et al., (2024)*, highlighted the antifungal potential of extracts obtained from *Cannabis sativa L.* inflorescences against several phytopathogenic fungi. In the case of *B. cinerea*, antifungal activity was concentration-dependent, with the most pronounced effect observed for the 20% extract, for which inhibition values ranging from 45.00 to 75.42% were reported.

The available literature thus highlights the potential of plant extracts to inhibit *B. cinerea*, while also showing considerable variability in their efficacy depending on the plant species, concentration used, and experimental conditions. Moreover, existing studies have predominantly focused on individual plant species or employed different experimental conditions, thereby limiting direct comparisons of their efficacy. In this context, evaluating several plant extracts under the same experimental conditions may contribute to identifying the species with the greatest antifungal potential.

Therefore, the present study aimed to comparatively evaluate the antifungal activity of lavender (*Lavandula angustifolia*), lemon balm (*Melissa officinalis*), sage (*Salvia officinalis*), garlic (*Allium sativum*), and hemp (*Cannabis sativa*) extracts against *Botrytis cinerea* isolated from grapes, in order to determine their ability to inhibit pathogen development and to identify extracts with potential for the development of alternative methods for gray mold control.

MATERIALS AND METHODS

Plant material and preparation

The plant material of *Lavandula angustifolia* Mill., *Melissa officinalis* L., *Salvia officinalis* L., and *Allium sativum* L. was obtained from experimental crops established at the National Institute of Research–Development for Machines and Installations Designed for Agriculture and Food Industry (INMA Bucharest, Romania). Lavender, lemon balm, and sage were harvested between May and June by cutting the aerial parts approximately 10–15 cm above the soil surface. Garlic plants were manually harvested by removing the entire plants from the soil, and the whole plant was used for extract preparation. For *Cannabis sativa* L., the monoecious industrial cultivar '*Marideea*', developed at the Agricultural Research and Development Station Secuieni (ARDS Secuieni, Romania), was used. The buds and inflorescences were used for extract preparation.

After harvesting, the plant materials were sorted and cleaned to remove impurities and damaged tissues and subsequently cut into fragments of 8, 10, 20, and 30 mm. The plant materials were dried in a UFE 500 Model 100–800 laboratory oven (Memmert, Germany) at 40 °C until a final moisture content of 8–10% was reached.



Cannabis sativa L. *Lavandula angustifolia* *Melissa officinalis* *Salvia officinalis* *Allium sativum* L.

Fig. 1 - Dried plant materials prepared for shredding and processing using the hybrid ultrasound-assisted percolation

Preparation of plant extract

The plant extracts were obtained separately from dried and ground material of *Lavandula angustifolia*, *Melissa officinalis*, *Salvia officinalis*, *Allium sativum*, and *Cannabis sativa* using the hybrid ultrasound-assisted pressurized percolation extraction method previously described by (*Tăbărașu et al. 2024b, Tăbărașu et al., 2025c*). For each extraction batch, 400 g of plant material and 12 L of water were used, corresponding to a solid-to-liquid ratio of 1:30 (g/mL). An additional 7 L of water was used as a buffer solvent to fill the pipelines and auxiliary components of the extraction system, thereby ensuring proper system operation.

The extractions were performed using a hybrid extraction system consisting of a TIMATIC Duo percolator (Tecnolab SRL, Spello, Italy), adapted to operate with a single 12 L extraction chamber, and an UP400St ultrasonic generator (Hielscher Ultrasonics GmbH, Teltow, Germany) (Figure 2). The plant material was placed in permeable bags inside the extraction chamber, and water was used as the extraction solvent. The operating conditions were selected based on the results of previous studies (*Tăbărașu et al., 2024b; Tăbărașu et al., 2025c*), which identified the most efficient extraction parameters as an extraction time of 120 min, a pressure of 7 bar, and an ultrasonic power of 120 W. Pressurized percolation and ultrasonic treatment were applied simultaneously throughout the entire extraction process.



(a) (b)

Fig. 2 - Hybrid extraction equipment: (a) front view of the TIMATIC Duo extraction system; (b) rear view showing the Hielscher UP400St ultrasonic generator

At the end of the extraction process, the aqueous extracts obtained from each plant species were collected separately, filtered, and stored at 4 °C until further use in antifungal assays against *Botrytis cinerea*.



a) b) c) d) e)

Fig. 3 - Aqueous plant extracts obtained by ultrasound-assisted pressurized percolation

Based on previous studies, an extraction time of 120 min, a pressure of 7 bar, and an ultrasound power of 120 W were maintained as constant operating parameters. In the present study, the influence of plant material particle size was further evaluated using four fragmentation levels (8, 10, 20, and 30 mm), with 30 mm included as a reference condition based on its favorable performance in previous experiments.

Table 1

Experimental parameters used for the preparation of plant extracts

Parameter	Evaluated / selected values	Experimental approach
Plant material particle size	8, 10, 20, 30 mm	Variable
Extraction time	40, 60, 120 min	Variable
Extraction pressure	7 bar	Constant
Extraction power	120 W	Constant
Plant material	400 g	Constant
Solvent volume	12 L	Constant
Solvent	Water	Constant
Solid-to-liquid ratio	1:30 (w/v)	Constant

***Botrytis cinerea* isolation and culture conditions**

The *Botrytis cinerea* strain (ICDPP-BC-02) was obtained from the Microorganism Collection of the Bioproducts Laboratory for Plant Protection, Research and Development Institute for Plant Protection (ICDPP, Bucharest, Romania), and was originally isolated from grapes of the *Fetească albă* cultivar. Fungal identity was confirmed based on macroscopic and microscopic characteristics, together with phenotypic analysis of the metabolic profile using the Biolog Gen III MicroPlate™ system.

The pathogenicity of the isolate was confirmed prior to the antifungal assays by inoculating healthy grape berries and monitoring the development of characteristic gray mold symptoms. The fungal culture was maintained on Potato Dextrose Agar (PDA) at 4°C and periodically subcultured to preserve viability. For inoculum preparation, conidia were harvested from actively growing cultures and suspended in sterile distilled water containing 0.01% Tween 80.

In vitro antifungal activity of plant extracts

Antifungal effect of the plant extracts evaluated by the poisoned food method

Poisoned Food Technique is a standard *in vitro* microbiological method widely used to evaluate the antifungal activity of bioactive plant extracts or synthetic compounds against phytopathogenic fungi such as *Botrytis cinerea*. The method is based on the homogeneous incorporation of a defined concentration of the test extract into a sterile, melted agar growth medium, followed by solidification of the medium. Subsequently, a mycelial plug of *B. cinerea* is placed at the center of the Petri dish and incubated under controlled conditions. Antifungal activity is quantified by measuring the radial mycelial growth of the treated colonies and comparing it with that of the untreated control, with the percentage of mycelial growth inhibition calculated accordingly.

The plant extracts were tested at final concentrations of 10% and 20%. To prepare the experimental treatments, the appropriate amount of each extract was incorporated into 100 mL of Potato Dextrose Agar (PDA) previously cooled to approximately 45–50 °C. After addition of the extracts, the medium was thoroughly homogenized and aseptically poured into 90-mm-diameter Petri dishes, using 20 mL per plate. Five replicates were prepared for each extract and concentration, while PDA medium without plant extract served as the negative control. Approximately 1 h after medium solidification, each plate was aseptically inoculated at the center with a 5.5-mm-diameter mycelial disc, excised using a sterile cork-borer from the actively growing peripheral region of a 7-day-old *B. cinerea* colony. The inoculum discs were transferred using a sterile inoculating loop. The plates were subsequently sealed with Parafilm and incubated under a natural photoperiod at 22 ± 1 °C.

Antifungal activity was evaluated at 2, 5, and 7 days after inoculation by determining the mycelial growth of *B. cinerea*. The diameter of each colony was measured using a digital caliper along two perpendicular axes, and the mean of the two measurements was used for subsequent calculations. The initial diameter of the inoculum disc (5.5 mm) was subtracted from the measured colony diameter prior to calculating mycelial growth and the percentage of inhibition.

The percentage of mycelial growth inhibition (MGI) was calculated relative to the negative control using the following equation 1:

$$ICM(\%) = \frac{D_m - D_p}{D_m} * 100 \quad (1)$$

where:

D_m represents the mycelial growth diameter in the negative control, and D_p represents the mycelial growth diameter in the treatment containing the plant extract.

In vivo antifungal activity of the hydroalcoholic solutions on grape berries

The *in vivo* antifungal activity of the plant extracts against *Botrytis cinerea* was evaluated on grape berries of the Romanian wine grape cultivar *Fetească albă* (*Vitis vinifera* L. cv.). Healthy berries uniform in size and color, with no mechanical damage or visible symptoms of infection, were selected for the experiment.

Prior to inoculation, the berries were surface-disinfected by immersion in a 1% sodium hypochlorite solution for 2 min, followed by three consecutive rinses with sterile distilled water and drying under aseptic conditions. To verify the effectiveness of the disinfection procedure, a subset of surface-disinfected berries was maintained under the same experimental conditions without artificial inoculation with *B. cinerea*.

For controlled inoculation, each berry was superficially wounded to a depth of approximately 1 mm using a sterile needle. A 10 µL aliquot of a *B. cinerea* conidial suspension, adjusted to a concentration of 1×10^5 conidia/mL using a Thoma counting chamber, was applied to the wounded area. At 2 h after inoculation, aqueous extracts of *Lavandula angustifolia*, *Melissa officinalis*, *Salvia officinalis*, and *Allium sativum* were uniformly applied by spraying. Each extract was evaluated individually at concentrations of 5%, 10%, 15%, and 30%. The control treatment consisted of berries inoculated with *B. cinerea* and left untreated with plant extracts.

The experiment was conducted using a completely randomized design. Each treatment consisted of three biological replicates, with 30 grape berries per replicate, resulting in a total of 90 berries per treatment. After treatment application, the berries were maintained in closed plastic containers to ensure a high relative humidity of approximately 90–95% and incubated in the dark at 20 °C for 14 days. Gray mold development was evaluated 14 days after inoculation by determining disease incidence, expressed as the percentage of grape berries showing visible symptoms of *B. cinerea* infection relative to the total number of berries evaluated for each experimental treatment.

Disease incidence was calculated using the following equation 2:

$$DI(\%) = \frac{N_i}{N_t} * 100 \quad (2)$$

where DI represents disease incidence (%),N_i represents the number of grape berries showing visible gray mold symptoms, and N_t represents the total number of grape berries evaluated.

The treatment groups were structured as follows:

- Control: *Botrytis cinerea* inoculation, then after 4 hours sterile water;
- A1: *Botrytis cinerea* + 5% bio-solution in sterile water;
- A2: *Botrytis cinerea* + 10% bio-solution in sterile water;
- A3: *Botrytis cinerea* + 15% bio-solution in distilled water;
- A4: *Botrytis cinerea* + 30% bio-solution in distilled water.

Statistical analysis

Experimental data was analyzed using three-way Analysis of Variance (ANOVA). For the extraction experiment, extraction time, plant material particle size, and plant species were considered as fixed factors, and total polyphenol content was used as the response variable. For the in vitro antifungal assay, botanical extract type, treatment concentration, and incubation time were considered as fixed factors, and mycelial growth inhibition was used as the response variable. Main effects and all two-way and three-way interactions were evaluated. Prior to analysis, data normality and homogeneity of variance were verified. When significant effects were detected, mean comparisons were performed using Tukey's Honestly Significant Difference (HSD) post-hoc test at a significance level of α = 0.05.

RESULTS

Three-way analysis of variance (ANOVA) was performed to evaluate the effects of extraction time, plant material particle size, and plant species on the total polyphenol content obtained by hybrid ultrasound-assisted percolation. The analysis revealed highly significant effects of extraction time ($F_{2,120}$ = 14152.33, p < 0.001), particle size ($F_{3,120}$ = 32.75, p < 0.001), and plant species ($F_{4,120}$ = 1289.40, p < 0.001). Significant interactions were also observed between extraction time and particle size ($F_{6,120}$ = 30.50, p < 0.001), extraction time and plant species ($F_{8,120}$ = 122.62, p < 0.001), and particle size and plant species ($F_{12,120}$ = 2.82, p = 0.0019). Furthermore, the three-way interaction between extraction time, particle size, and plant species was significant ($F_{24,120}$ = 3.87, p < 0.001), indicating that the effect of particle size on polyphenol recovery depended simultaneously on extraction duration and plant species.

Tukey's HSD post-hoc analysis (α = 0.05) showed significant differences among all three extraction times (p < 0.001). The mean total polyphenol content increased from 11.46 mg GAE/100 g after 40 min to 18.45 mg GAE/100 g after 60 min and 29.22 mg GAE/100 g after 120 min, demonstrating the strong influence of extraction duration on polyphenol recovery under the experimental conditions.

Table 2

Extraction method improvement for hybrid ultrasound-assisted percolation technology

Extraction time (min)	Particle size (mm)	Pressure (bar)	Ultrasound power (W)	TPC *Cannabis sativa* (mg GAE/100g)	TPC *Lavandula angustifolia* (mg GAE/100g)	TPC *Melissa officinalis* (mg GAE/100g)	TPC *Salvia officinalis* (mg GAE/100g)	TPC *Allium sativum* (mg GAE/100g)
40	8	7	120	9.67±0.665	10.16±0.290	10.29±0.619	14.57±0.661	10.32±0.481
40	10	7	120	10.13±0.670	10.68±0.310	10.67±0.583	15.03±0.620	9.76±0.488
40	20	7	120	10.92±0.597	11.22±0.321	11.34±0.550	16.11±0.601	8.83±0.479
40	30	7	120	11.29±0.601	11.85±0.387	11.97±0.545	17.18±0.599	7.18±0.471
60	8	7	120	17.73±0.663	18.96±0.670	19.32±0.619	27.33±0.661	13.01±0.480
60	10	7	120	17.10±0.594	17.85±0.559	18.98±0.603	26.84±0.645	12.72±0.472
60	20	7	120	16.78±0.669	17.03±0.576	18.30±0.608	26.11±0.653	12.19±0.483
60	30	7	120	15.83±0.663	17.93±0.598	17.10±0.619	25.90±0.661	11.89±0.480
120	8	7	120	27.15±0.559	33.11±0.631	29.65±0.596	34.79±0.760	27.82±0.465
120	10	7	120	26.43±0.551	32.28±0.631	28.84±0.611	34.18±0.754	27.06±0.454
120	20	7	120	25.71±0.563	31.24±0.562	28.06±0.599	33.25±0.767	26.58±0.470
120	30	7	120	24.03±0.559	30.46±0.549	26.47±0.596	31.92±0.760	25.34±0.465

*TPC – Total polyphenol content

Significant differences were also observed among the plant species evaluated. Across all experimental conditions, *Salvia officinalis* exhibited the highest mean total polyphenol content (25.27 mg GAE/100 g), followed by *Lavandula angustifolia* (20.23 mg GAE/100 g), *Melissa officinalis* (19.25 mg GAE/100 g), *Cannabis sativa* (17.73 mg GAE/100 g), and *Allium sativum* (16.06 mg GAE/100 g). Tukey's HSD test indicated significant differences among all pairwise species comparisons ($p < 0.001$).

Particle size also significantly influenced polyphenol recovery. The overall mean values were 20.26, 19.90, 19.58, and 19.09 mg GAE/100 g for particle sizes of 8, 10, 20, and 30 mm, respectively. Tukey's HSD test indicated significant differences among the particle-size levels ($p < 0.05$). However, because significant interactions involving particle size were detected, particularly the significant three-way interaction, these overall means should be interpreted cautiously, as the magnitude and direction of the particle-size effect depended on both extraction time and plant species.

At the shorter extraction time of 40 min, the influence of particle size varied among plant species, whereas at 120 min smaller particle sizes generally resulted in higher polyphenol recovery. At 120 min, the differences between 8 and 30 mm were approximately 3.12, 2.65, 3.18, 2.87, and 2.48 mg GAE/100 g for *Cannabis sativa, Lavandula angustifolia*, *Melissa officinalis, Salvia officinalis*, and *Allium sativum*, respectively. Although reducing particle size increased polyphenol recovery at the longest extraction time, the additional gain obtained by reducing the material from 30 to 8 mm remained relatively limited compared with the additional energy requirements associated with intensive size reduction.

Overall, the statistical results demonstrate that extraction time exerted a major influence on polyphenol recovery, while the effect of particle size varied according to both extraction duration and plant species. Under the experimental conditions, the combination of a 120 min extraction time, 7 bar pressure, 120 W ultrasound power, and a 30-mm particle size therefore represents a practical technological compromise between polyphenol recovery and process efficiency.

In Vitro Antifungal Efficacy of Selected Essential Oils Against Botrytis cinerea

To address the need for sustainable crop protection solutions, this study evaluated the *in vitro* antifungal efficacy of selected essential oils against *Botrytis cinerea*, systematically characterizing the interaction between oil selection, working concentration, and time-dependent bioactivity retention to support the development of novel botanical formulations.

Table 3

Mycelial growth and growth inhibition of *Botrytis cinerea* in response to hydroalcoholic extract treatments determined by the Poisoned Food technique at 2, 5 and 7 days after inoculation

Hydroalcoholic extract	Concentration (%)	Growth inhibition (%)		
		2 days	*5 days*	*7 days*
Lavandula angustifolia	10	39.84±4.72	25.26 ± 3.91	15.84 ± 3.46
	20	47.14±4.15	32.18 ± 3.67	22.52 ± 3.21
	50	69.62±2.23	44.37 ± 2.84	30.26 ± 2.71
Salvia officinalis	10	40.47±4.75	25.82 ± 4.12	15.46 ± 3.74
	20	48.66±3.36	32.71 ± 3.18	22.12 ± 2.86
	50	58.05±1.53	42.46 ± 1.76	28.27 ± 1.82
Melisa officinalis	10	38.79±3.81	24.74 ± 3.52	14.63 ± 3.17
	20	43.06±0.58	28.47 ± 0.81	18.16 ± 0.94
	50	51.15±1.64	35.38 ± 1.73	23.27 ± 1.69
Allium sativum	10	37.12±0.87	29.85 ± 1.14	20.17 ± 1.26
	20	53.14±4.15	39.72 ± 3.68	28.18 ± 3.51
	50	78.62±2.23	60.36 ± 2.41	39.84 ± 2.63
Cannabis sativa	10	36.22±0.51	23.58 ± 0.73	14.41 ± 0.86
	20	46.24±1.9	31.52 ± 1.83	20.68 ± 1.79
	50	51.31±2.17	34.14 ± 2.08	22.26 ± 2.02
Control (water)	-	0	0	0

Hydroalcoholic extract	Concentration (%)	Growth inhibition (%)		
		2 days	*5 days*	*7 days*
Control (alcohol 6%)	-	3.84 ± 0.72	2.71 ± 0.68	1.96 ± 0.61
Control (chemical)	-	92.10 ± 1.84	94.76 ± 1.42	96.18 ± 1.17

Three-way analysis of variance (ANOVA) showed that mycelial growth inhibition of *Botrytis cinerea* was significantly affected by extract type, concentration, and incubation time ($p < 0.001$ for all three main effects). Incubation time had the largest effect ($F_{2,180} = 1808.64$, $p < 0.001$), followed by extract concentration ($F_{2,180} = 795.32$, $p < 0.001$) and extract type ($F_{4,180} = 145.49$, $p < 0.001$). Significant interactions were also detected between extract type and concentration ($F_{8,180} = 38.68$, $p < 0.001$), extract type and incubation time ($F_{8,180} = 2.59$, $p = 0.010$), and concentration and incubation time ($F_{4,180} = 24.87$, $p < 0.001$). Importantly, the three-way interaction among extract type, concentration, and incubation time was also significant ($F_{16,180} = 3.23$, $p < 0.001$), indicating that the effect of extract concentration on fungal growth inhibition varied according to both botanical species and incubation period.

Tukey's HSD post-hoc test ($\alpha = 0.05$) confirmed significant differences among several extract–concentration combinations at each evaluation time. At 2 days after inoculation, *Allium sativum* extract at 50% produced the highest mycelial growth inhibition (78.62 ± 2.23%), significantly exceeding all other botanical treatments. *Lavandula angustifolia* at 50% showed the second-highest inhibition (69.62 ± 2.23%) and was significantly more effective than the remaining botanical treatments, whereas Salvia officinalis at 50% produced an intermediate inhibition of 58.05 ± 1.53%. The 50% treatments of M*elissa officinalis and Cannabis sativa* showed statistically comparable inhibition values (51.15 ± 1.64% and 51.31 ± 2.17%, respectively).

A similar statistical pattern was observed after 5 days of incubation. The 50% A. sativum treatment remained significantly more effective than the other botanical treatments, with an inhibition of 60.36 ± 2.41%. *L. angustifolia* (44.37 ± 2.84%) and S. officinalis (42.46 ± 1.76%) formed an intermediate efficacy group and did not differ significantly from each other, while *M. officinalis* (35.38 ± 1.73%) and *C. sativa* (34.14 ± 2.08%) showed statistically comparable lower inhibition levels.

After 7 days, A. sativum at 50% continued to exhibit the highest inhibition (39.84 ± 2.63%) and remained significantly superior to all other botanical treatments. *L. angustifolia* (30.26 ± 2.71%) and S. officinalis (28.27 ± 1.82%) showed statistically similar intermediate activity, whereas *M. officinalis* (23.27 ± 1.69%) and *C. sativa* (22.26 ± 2.02%) exhibited the lowest inhibition among the 50% botanical treatments and did not differ significantly from each other.

Tukey's HSD analysis further indicated that the three incubation periods differed significantly within each extract–concentration combination ($p < 0.05$), confirming a progressive reduction in antifungal efficacy between days 2, 5, and 7. Overall, the statistical analysis demonstrates that the antifungal activity of the tested botanical extracts was concentration-dependent but progressively decreased with incubation time, with A. sativum showing the strongest and most persistent inhibitory effect, followed by *L. angustifolia* and *S. officinalis*. The significant three-way interaction indicates that the magnitude of these concentration- and time-dependent effects was specific to the botanical extract evaluated.

A general trend observed across all botanical extracts is the regressive dynamic of inhibition over time. The maximum efficacy recorded on day 2 was followed by a progressive decline in fungistatic effect on days 5 and 7. This phenomenon can be attributed to the gradual volatilization of bioactive compounds or the metabolic capability of the fungus to degrade plant secondary metabolites during advanced stages of mycelial growth. The analysis of experimental controls confirms that the suppressive effect is exclusively attributable to plant biosynthesizes; the 6% alcohol control variant recorded negligible inhibition (ranging between 3.84% and 1.96%), contrasting sharply with the synthetic chemical control, which exhibited persistent and near-total pathogen suppression, increasing from 92.10% on day 2 to 96.18% on day 7.

From an applied perspective, the findings suggest that while botanical extracts—particularly garlic and lavender—represent promising eco-friendly alternatives for mitigating *Botrytis cinerea* infestation, their limited persistence necessitates technological optimization.

To achieve plant protection comparable to synthetic chemical fungicides, higher application concentrations, microencapsulation of bioactive compounds, or repeated applications at short intervals of 3–5 days are recommended.

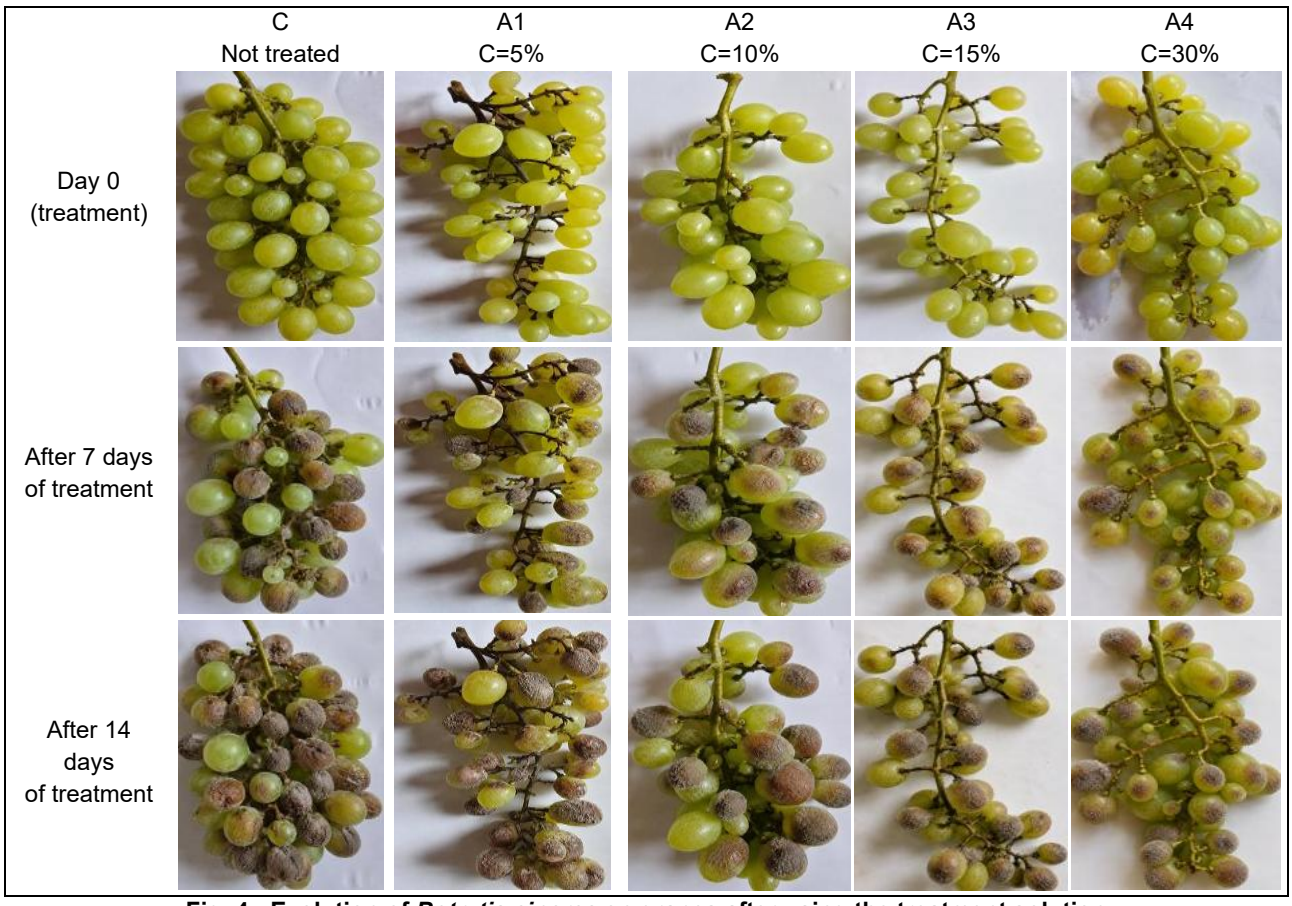


Fig. 4 - Evolution of *Botrytis cinerea* on grapes after using the treatment solution at different concentrations and time periods

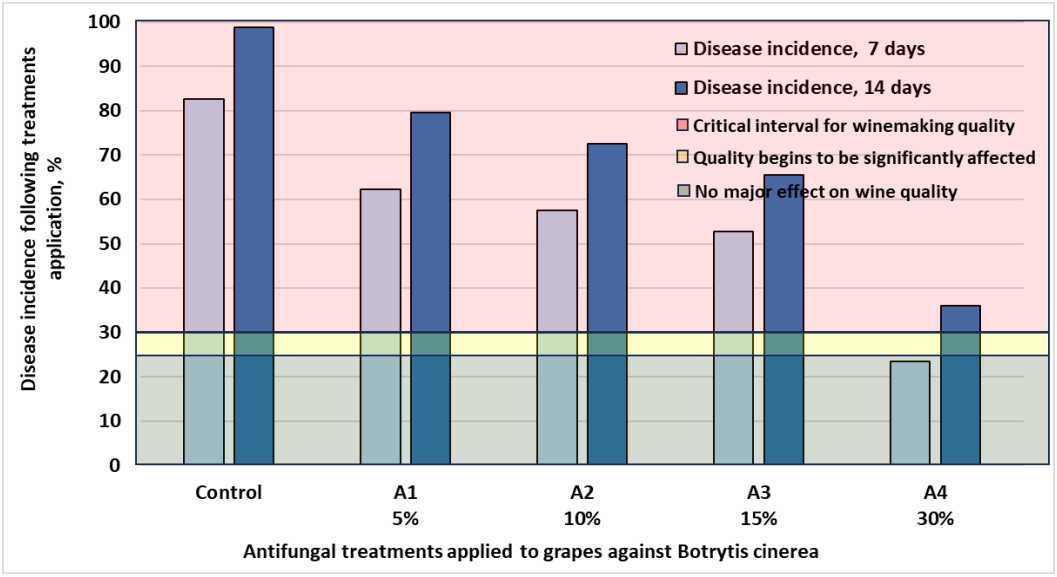


Fig. 5 - Impact of hydroalcoholic plant extracts on *Botrytis cinerea* incidence in grape clusters

The figure 5 demonstrates a clear concentration-dependent antifungal effect, with the incidence of *Botrytis cinerea* progressively decreasing as the concentration of the hydroalcoholic extracts increased. In the control, disease incidence increased from approximately 83% at 7 days to nearly 100% at 14 days, whereas treatments at 5–15% progressively limited infection development, although they were insufficient to maintain disease incidence below the thresholds associated with preserving grape quality. The 30% concentration showed the highest efficacy, reducing disease incidence to approximately 24% after 7 days and 36% after 14 days. The increase in incidence between the two assessment times indicates that the treatment did not completely suppress the infection but rather delayed and limited its progression, with the strongest effect observed at the highest concentration tested.

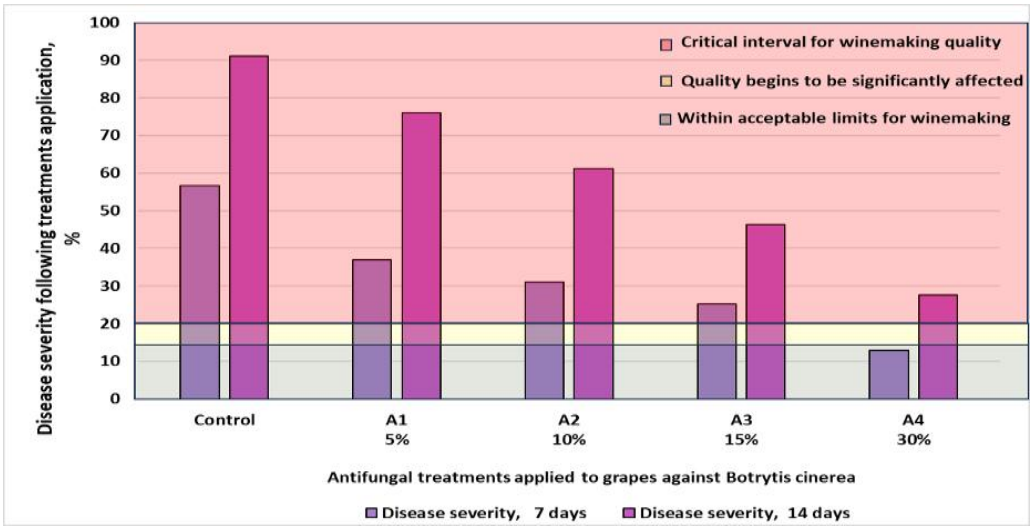


Fig. 6 - Impact of hydroalcoholic plant extracts on *Botrytis cinerea* disease severity in grape clusters

The figure 6 shows a progressive, concentration-dependent reduction in the severity of *Botrytis cinerea* infection. In the control, disease severity increased from approximately 57% after 7 days to 91% after 14 days, confirming the rapid progression of infection. Treatment with hydroalcoholic extracts limited disease development, with severity progressively decreasing as extract concentration increased, reaching approximately 13% at 7 days and 28% at 14 days for A4 (30%). The 30% concentration showed the highest efficacy, being the only treatment that maintained disease severity below 20% after 7 days and substantially limited its progression at 14 days. These results indicate that, although the extracts did not completely prevent disease progression over time, they exerted a clear concentration-dependent protective effect, with the greatest reduction in disease severity observed at the highest concentration tested.

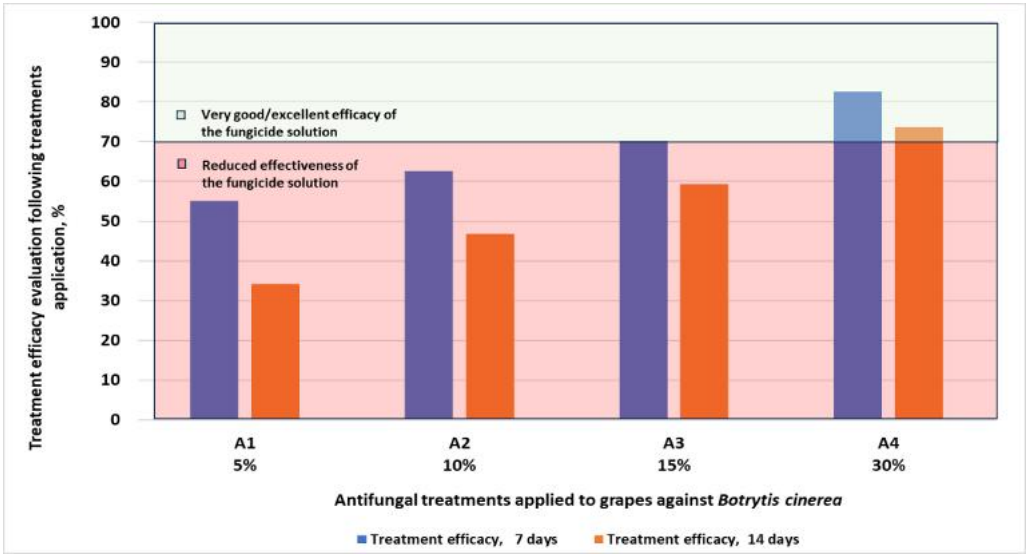


Fig. 7 - Treatment efficiency evaluation on antifungal treatment applied against *Botrytis cinerea* fungus

The figure 7 demonstrates a clear concentration-dependent increase in treatment efficacy against *Botrytis cinerea*. At 5% (A1), efficacy reached approximately 55% after 7 days but decreased to 34% after 14 days, indicating limited persistence of the antifungal effect. Increasing the concentration progressively improved treatment performance, with A2 (10%) and A3 (15%) reaching approximately 62% and 70% efficacy at 7 days, respectively. The highest efficacy was obtained with A4 (30%), reaching approximately 83% after 7 days and remaining at about 74% after 14 days, thus exceeding the 70% threshold associated with very good/excellent efficacy. Although efficacy decreased between 7 and 14 days for all treatments, the results indicate that the 30% concentration provided the strongest and most persistent antifungal effect, confirming the concentration-dependent response of *B. cinerea* to the hydroalcoholic extract treatment.

CONCLUSIONS

The findings of this study demonstrate that hybrid ultrasound-assisted percolation is a highly efficient green technology for recovering bioactive compounds from medicinal and aromatic plants, delivering rich polyphenolic profiles while preserving their structural integrity. Across the in vitro assays, the botanical extracts exhibited clear concentration-dependent antifungal efficacy against *Botrytis cinerea*. Among the single-plant treatments, garlic (*Allium sativum*) and hemp (*Cannabis sativa*) hydroalcoholic extracts achieved the most prominent inhibition of mycelial growth, effectively suppressing fungal development at elevated concentrations. Furthermore, the multi-extract formulation showed enhanced antifungal activity compared to individual extracts, indicating a synergistic action among diverse phytochemicals—such as organosulfur compounds, terpenes, and polyphenols—in disrupting fungal cell membranes and physiological pathways.

When evaluating these results against alternative botanical biopesticides, essential oils derived from aromatic species (e.g., *Lavandula angustifolia* or *Salvia officinalis*) often exhibit superior localized antifungal potency due to their high concentration of volatile lipophilic monoterpenes and sesquiterpenes (*Nenciu et al., 2026*). These volatile fractions penetrate fungal cell walls and disrupt membrane permeability more rapidly than hydroalcoholic extracts. However, pure essential oils present significant operational challenges, including high volatility, rapid photodegradation under field conditions, low extraction yields, and elevated production costs. Hydroalcoholic and aqueous extracts, by contrast, offer a broader spectrum of polar and non-polar phytocompounds, higher extraction yields, better environmental stability, and simpler, cost-effective scalability for bio-fungicide formulations.

Despite these promising biological properties, several practical limitations must be addressed before large-scale adoption. Hydroalcoholic extracts display lower physical persistence on plant tissue post-application, requiring frequent re-application during periods of high disease pressure. Additionally, batch-to-batch variation in secondary metabolite profiles—driven by environmental factors, harvest timing, and raw plant material quality—can result in inconsistent field efficacy.

Future research should focus on optimizing stability through eco-friendly nano-encapsulation or micro-emulsion delivery systems to protect volatile and sensitive polyphenolic compounds from solar degradation. Furthermore, extensive in vivo field trials on grapevine (*Vitis vinifera*) and horticultural crops are required to evaluate phytotoxicity, systemic host defense induction, optimal application timing, and long-term compatibility within integrated pest management (IPM) frameworks.

ACKNOWLEDGEMENT

This research was supported by Project ADER 16.1.1 /29.01.2024 Research on the potential for superior exploitation of the *Cannabis sativa* species for food purposes, funded by Ministry of Agriculture and Rural Development.

REFERENCES

[1] Azzolini, M., Tosi, E., Faccio, S., Lorenzini, M., Torriani, S., Zapparoli, G. (2013). Selection of *Botrytis cinerea* and *Saccharomyces cerevisiae* strains for the improvement and valorization of Italian passito style wines. *FEMS Yeast Res*, 13, 540–552, DOI:10.1111/1567-1364.12054.

[2] Butiuc-Keul, A., Coste, A. (2023). Biotechnologies and Strategies for Grapevine Improvement. *Horticulturae*, 9, 62. https://doi.org/10.3390/horticulturae9010062.

[3] Campa-Siqueiros, P., Vallejo-Cohen, S., Corrales-Maldonado, C., Martínez-Téllez, M.Á., Vargas-Arispuro, I. (2017). Reduction in the incidence of grey mold in table grapes due to the volatile effect of a garlic extract. *Revista Mexicana de Fitopatología*, 35(3): 494-508. DOI: 10.18781/R.MEX.FIT.1707-1.

[4] Carreón-Delgado, D.F., Hernández-Montesinos, I.Y., Rivera-Hernández, K.N., del Sugeyrol Villa-Ramírez, M., Ochoa-Velasco, C.E., Ramírez-López, C. (2023). Evaluation of Pretreatments and Extraction Conditions on the Antifungal and Antioxidant Effects of Garlic (*Allium sativum*) Peel Extracts. *Plants*, 12, 217. https://doi.org/ 10.3390/plants12010217.

[5] Daniel, C.K., Lennox, C.L., Vries, F.A. (2015). In-vitro effects of garlic extracts on pathogenic fungi *Botrytis cinerea, Penicillium expansum* and *Neofabraea alba*. *S Afr J Sci*., 111(7/8). http://dx.doi.org/10.17159/ sajs.2015/20140240.

[6] De Simone, N., Pace, B., Grieco, F., Chimienti, M., Tyibilika, V., Santoro, V., Capozzi, V., Colelli, G., Spano, G., Russo, P. (2020). *Botrytis cinerea* and Table Grapes: A Review of the Main Physical, Chemical, and Bio-Based Control Treatments in Post-Harvest. *Foods*, 9, 1138; doi:10.3390/foods9091138.

[7] Dènè, L., Valiuškaitè, A. (2021). Sensitivity of *Botrytis cinerea* Isolates Complex to Plant Extracts. *Molecules*, 26, 4595. https://doi.org/ 10.3390/molecules26154595.

[8] Hahn, M. (2014). The rising threat of fungicide resistance in plant pathogenic fungi: *Botrytis* as a case study. *J. Chem. Biol.*, 7:133-141, DOI 10.1007/s12154-014-0113-1.

[9] Hegyi, Á.I., Otto, M., Geml, J., Hegyi-Kaló, J., Kun, J., Gyenesei, A., Pierneef, R., Váczy, K.Z. (2022). Metatranscriptomic Analyses Reveal the Functional Role of *Botrytis cinerea* in Biochemical and Textural Changes during Noble Rot of Grapevines. *J. Fungi*, 8, 378. https://doi.org/10.3390/jof8040378.

[10] Jacometti, M.A., Wratten, S.D., Walter, M. (2010). Review: Alternatives to synthetic fungicides for *Botrytis cinerea* management in vineyards. *Australian Journal of Grape and Wine Research*, 16, 154–172, doi: 10.1111/j.1755-0238.2009.0067.x.

[11] Jiang, L., Qiu, Y., Dumlao, M.C., Donald, W.A., Steel, C.C., Schmidtke, L.M. (2023). Detection and prediction of *Botrytis cinerea* infection levels in wine grapes using volatile analysis. *Food Chemistry*, 421, https://doi.org/10.1016/j.foodchem.2023.136120.

[12] Kasmi, M., Aourach, M., El Boukari, M., Barrijal, S., Essalmani, H. (2017). Effectiveness of aqueous extracts of aromatic and medicinal plants against tomato grey mould in Morocco. *C.R. Biologies, 340*, 386-393, http://dx.doi.org/10.1016/j.crvi.2017.07.010.

[13] Kelly, J., Inglis, D., Dowling, L., Pickering, G. (2022). Impact of *Botrytis cinerea*-infected grapes on quality parameters of red wine made from withered grapes. *Australian Journal of Grape and Wine Research*, 28, 439–449, doi: 10.1111/ajgw.12545.

[14] Kursa, W., Jamiołkowska, A., Wyrostek, J., Kowalski, R. (2024). Attempts to Use Hemp (*Cannabis sativa* L. var. sativa) Inflorescence Extract to Limit the Growth of Fungi Occurring in Agricultural Crops. *Appl. Sci.*, 14, 1680. https://doi.org/10.3390/ app14041680.

[15] Negri, S., Lovato, A., Boscaini, F., Salvetti, E., Torriani, S., Commisso, M., Danzi, R., Ugliano, M., Polverari, A., Tornielli, G.B., Guzzo, F. (2017). The Induction of Noble Rot (*Botrytis cinerea*) Infection during Postharvest Withering Changes the Metabolome of Grapevine Berries (*Vitis vinifera* L., cv. Garganega). *Front. Plant Sci*. 8:1002. doi: 10.3389/fpls.2017.01002.

[16] Nenciu, F., Fatu, V., Arsenoaia, V., Persu, C., Voicea, I., Vladut, N-V., Matache, M.G., Gageanu, I., Marin, E., Biris, S.S., Ungureanu, N. (2023). Bioactive Compounds Extraction Using a Hybrid Ultrasound and High-Pressure Technology for Sustainable Farming Systems. *Agriculture*, 13(4), https://doi.org/10.3390/agriculture13040899.

[17] Nenciu, F., Tăbărașu, A.-M., Fătu, C., Vlăduț, N.-V., Voicea, I., & Dinu, S. (2026). Ultrasound-Assisted Hydrodistillation of Essential Oils for Eco-Friendly Biocontrol of *Botrytis cinerea* in Grapevines. *Horticulturae*, *12*(9), 1054. https://doi.org/10.3390/horticulturae12091054.

[18] Ohana-Levi, N., Netzer, Y. (2025). Long-Term Global Trends in Vineyard Coverage and Fresh Grape Production. *Agriculture*, 15, 1976. https://doi.org/10.3390/ agriculture15181976.

[19] Oprescu, M. R., Biris, S.-S., & Nenciu, F. (2023). Novel Furrow Diking Equipment-Design Aimed at Increasing Water Consumption Efficiency in Vineyards. *Sustainability*, *15*(4), 2861. https://doi.org/10.3390/su15042861.

[20] Rabilu, S.A., Agyemang, E.D., Farkas, B. (2021). Antifungal activity of *Salvia officinalis* subsp. l*avandulifolia* and *Salvia officinalis* subsp. *major* aqueous extracts against *Botrytis cinerea*. *Journal of Central European Agriculture*, 22(2), p.420-428. DOI: /10.5513/JCEA01/22.2.3104.

[21] Rahman, M.U., Liu, X., Wang, X., Fan, B. (2024). Grapevine gray mold disease: infection, defense and management. *Horticulture Research*, 11, https://doi.org/10.1093/hr/uhae182.

[22] Sofianos, G., Samaras, A., Karaoglanidis, G. (2023). Multiple and multidrug resistance in *Botrytis cinerea*: molecular mechanisms of MLR/MDR strains in Greece and effects of co-existence of different resistance mechanisms on fungicide sensitivity. *Front. Plant Sci.*, 14:1273193. doi: 10.3389/fpls.2023.1273193.

[23] Tăbărașu, A-M., Vlăduț, N-V., Găgeanu, I., Nenciu, F., Cismau, E-M., Oncescu, T-A., Gheorghe, G.V., Harabagiu, A., Anghelache, D-N., Cujbescu, D., Voicea, I. (2025a). Extraction and valorization of active principles from medicinal plants – A perspective for the sustainable development of farms in Romania. *INMATEH-Agricultural Engineering*, vol. 77, no. 3, DOI: https://doi.org/10.35633/inmateh-77-10.

[24] Tăbărașu, A.-M., Nenciu, F., Anghelache, D.-N., Vlăduț, V.-N., Găgeanu, I. (2024b). Hybrid Percolation Ultrasound Method for Extracting Bioactive Compounds from *Urtica dioica* and *Salvia officinalis*. *Agriculture*, 14, 1561. https://doi.org/ 10.3390/agriculture14091561.

[25] Tăbărașu, A.-M., Vlăduț, N.-V., Nenciu, F., Cârdei, P., Găgeanu, I., Catană, L., Begea, M., Matache, M.-G., Anghelache, D.-N., Persu, I.-C., et al. (2025c). Improved Hybrid Percolation–Ultrasound Extraction of Bioactive Compounds and Their Application as Nettle and Sage-Derived Biostimulants in Tomato and Pepper Crops. *Foods*, 14, 3900. https://doi.org/10.3390/ foods14223900.

[26] Thakur, N.S.; Thakur, A.; Joschi, V.K.; Sharma, S.K. Botrytized Wines: A Review. *Intl. J. Food. Ferment. Technol.*, 2018, 8(1): 01-13, DOI: 10.30954/2277-9396.01.2018.1.

STUDY ON KEY PARAMETERS AND FERTILIZATION PERFORMANCE OF A FLUTED-WHEEL FERTILIZER METERING DEVICE BASED ON EDEM
/
基于 EDEM 的外槽轮式排肥器关键参数和施肥性能研究

Chang WAN[1,2,3], Jiajun ZHANG[1], Zhihui QI[1], Zilun ZHOU[1], Yu WANG[1], Qingqing FAN[4], Ling ZHOU*[1,2,3]
[1] College of Mechanical and Electrical Engineering, Tarim University, Alar, Xinjiang / China
[2] Key Laboratory of Modern Agricultural Engineering of Xinjiang Uygur Autonomous Region, Alar, Xinjiang / China
[3] Xinjiang Production and Construction Corps (XPCC) Key Laboratory of Utilization and Equipment of Special Agricultural and Forestry Products in Southern Xinjiang, Alar, Xinjiang / China
[4] Alar Runong Modern Agricultural Technology Co., Ltd., Alar, Xinjiang / China
Correspondence author: Ling ZHOU
Tel: +8609974683855; *E-mail: zhoul-007@163.com*
DOI: https://doi.org/10.35633/inmateh-79-81

Keywords: *granular organic fertilizer, DEM calibration, fluted-wheel fertilizer metering device, fertilization uniformity, discrete element method, response surface methodology*

ABSTRACT
To address parameter optimization and fertilization uniformity of a fluted-wheel fertilizer metering device for granular organic fertilizer, a 3D-scanned fertilizer model was constructed, and an EDEM fertilization simulation model was established. The Poisson's ratio and elastic modulus of the fertilizer were determined using a texture analyzer. Drop tests were conducted to determine the coefficients of restitution between fertilizer particles and between the fertilizer and PA, PC, and PLA. Inclined-plane rolling tests were conducted to determine the rolling friction coefficients between the fertilizer and PA, PC, and PLA. A cylinder-lifting test for measuring the angle of repose, combined with EDEM simulations and a Design-Expert experimental design, was used to determine the static and rolling friction coefficients between fertilizer particles, as well as the static friction coefficients between the fertilizer and PA, PC, and PLA. By combining the discrete element method (DEM) with response surface methodology, the effects of the parameters on fertilization uniformity were ranked as follows: fluted-wheel inscribed-circle diameter > fluted-wheel lead angle > number of grooves; fertilizer-metering shaft rotational speed > fertilizer-discharge flap angle > effective working length of the fluted wheel. The optimal parameter combination was determined to be a fluted-wheel inscribed-circle diameter of 37 mm, 7 grooves, a fluted-wheel lead angle of 63°, an effective working length of the fluted wheel of 31 mm, a fertilizer-metering shaft rotational speed of 28 rpm, and a fertilizer-discharge flap angle of −1°. Soil-bin tests using 3D-printed fluted wheels with different structural parameters produced results that were generally consistent with the simulation results, providing a reference for the DEM-based optimization and design of fluted-wheel fertilizer metering devices.

摘要
针对外槽轮式排肥器施用颗粒有机肥参数优化与施肥均匀性问题，构建肥料 3D 扫描模型，建立施肥 EDEM 仿真模型。通过质构仪，获得肥料泊松比和弹性模量；通过下落试验，获得肥料与肥料、PA、PC、PLA 的碰撞恢复系数；通过斜面滚动试验，获得肥料与 PA、PC、PLA 的滚动摩擦系数；通过休止角圆筒提升试验、EDEM 仿真，结合 Design-Expert 试验设计，测定肥料与肥料静摩擦系数、滚动摩擦系数，肥料与 PA、PC、PLA 的静摩擦系数。结合离散元法（DEM）与响应面法，获得参数对施肥均匀性的影响排序分别为：槽轮内接圆直径>槽轮升角>凹槽个数；排肥轴转速>排肥舌角度>槽轮有效工作长度。最优参数组合是：槽轮内接圆直径为37mm，凹槽数量为7，槽轮升角为63°，槽轮有效工作长度为31mm，排肥轴转速为28RPM，排肥舌角度为-1°。采用 3D 打印不同结构参数槽轮，土槽试验结果与仿真基本一致，为排肥器离散元优化设计提供参考

INTRODUCTION
Discrete Element Method (DEM) can simulate fertilizer and other discontinuous agricultural materials. EDEM is a simulation software based on DEM. It comprises a pre-processor for creating and initializing discrete element models, a solver for simulation and calculation, and a post-processing module for displaying and analyzing simulation results.

Published studies have primarily focused on the calibration of discrete element parameters for fertilizers, including intrinsic parameters, basic contact parameters, and contact model parameters; parameter optimization of fertilizer metering devices; and the optimization and design of fertilizer applicators based on EDEM simulations.

The accuracy of the fertilizer particle model, the fertilizer metering device model, and the discrete element parameters forms the basis for reliable EDEM simulations. Most fertilizer particle modeling methods have used single-sphere or multi-sphere models to approximate the actual particle geometry (*Adilet et al., 2021; Xie et al., 2021; Bivainis et al., 2023; Ma et al., 2025*). Experimental designs generated using Design-Expert software, physical angle of repose tests, and discrete element simulations have been used to calibrate the contact model parameters (*Adilet et al., 2021; Xie et al., 2021; Nouh et al., 2024; Ma et al., 2025*).

EDEM was used to simulate the fertilizer discharge process, determine optimal structural and operating parameters and evaluate fertilization performance. In order to enhance the uniformity of fertilizer application, EDEM simulation of a centrifugal fertilizer spreader with two shutter holes was employed to optimize the shutter hole position (*Hwang et al., 2021*). EDEM simulations were used to conduct single-factor and orthogonal tests on the inner diameter, pitch, outlet spacing, and number of screw starts of a blocking-wheel-type screw fertilizer metering device to determine the optimal structural parameters (*Zha et al., 2021*). EDEM simulation was used to establish a simulation model of a centrifugal spreader and evaluated the lateral uniformity of a granular cylindrical organic fertilizer application (*Zinkevičienė et al., 2021*). The structural design and parameters of outer groove wheel fertilizer metering device were studied according to fertilization performance simulated using discrete element modeling (*Zeng, et al., 2020; Wang, J. F. et al., 2023*). Focusing on optimizing the spreading uniformity of a vertical spiral rotor organic fertilizer applicator, EDEM simulations were employed to investigate the effects of rotor speed and rotor inclination angle (*Ștefan et al., 2025*).

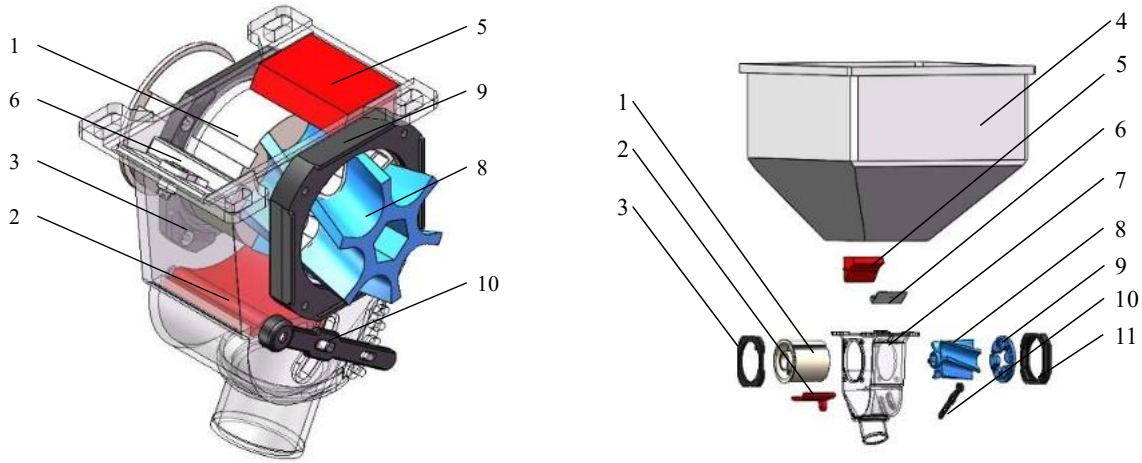
Using the coefficient of variation of fertilization uniformity as the evaluation criterion, this study proposed a DEM parameter calibration procedure and an EDEM simulation method to optimize the key parameters of a fluted-wheel fertilizer metering device for granular organic fertilizer. The DEM contact parameters between the fertilizer and three materials used in the metering device (PA, PC, and PLA) were determined. Three structural parameters (the fluted-wheel inscribed-circle diameter, number of grooves, and fluted-wheel lead angle) and three operating parameters (the effective working length of the fluted wheel, fertilizer-metering shaft rotational speed, and fertilizer-discharge flap angle) were optimized. Soil bin tests were conducted to validate the performance of the optimized parameter combination.

MATERIALS AND METHODS

Simulation model and key parameters

Model and materials of fertilizer metering device

As shown in Fig. 1(a), the fluted wheel is the core component of the fertilizer metering device, with a mounting-hole diameter of 70 mm.



(a) Fluted-wheel fertilizer metering device (b) Exploded view of the fertilizer metering device

Fig. 1 - 3D model of the fertilizer metering device

1. blocking wheel; 2. fertilizer discharge flap; 3. blocking-wheel fixing ring; 4. fertilizer hopper; 5. baffle; 6. brush; 7. fertilizer metering device housing; 8. fluted wheel; 9. fluted-wheel retaining ring; 10. fertilizer-discharge flap adjusting handle; 11. fluted-wheel fixing ring

Table 1 details the materials used for different components of the fertilizer metering device, including PA, PC, and PLA.

Table 1

Materials of different components of the fertilizer metering device

No.	Component	Material
1	Blocking wheel	Polyamide (PA)
2	Fertilizer metering device housing	Polycarbonate (PC)
3	Fluted wheel	Polylactic acid (PLA)
4	Fertilizer discharge flap	Polyamide (PA)
5	Baffle	Polyamide (PA)

Key parameters of fertilizer metering device

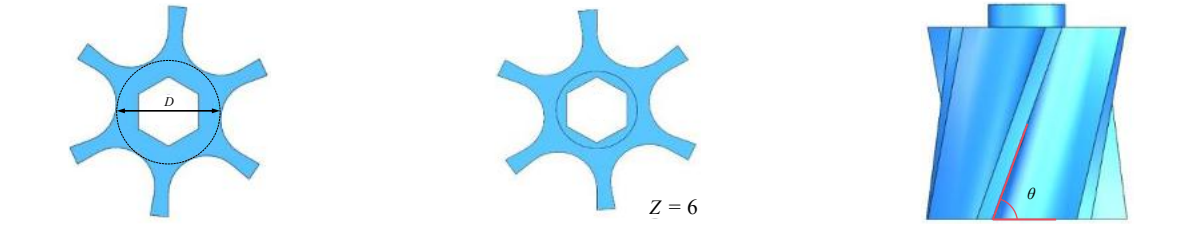
Consistent with previous literatures (*Zeng et al. 2020; Wang Y. et al. 2023*), the fertilizing amount per circle *q* and the total fertilizing amount *Q* of a fluted-wheel fertilizer metering device can be calculated by:

$$q = L\,\gamma\,S\,\psi\,Z \tag{1}$$

$$Q = q\,n\,t \tag{2}$$

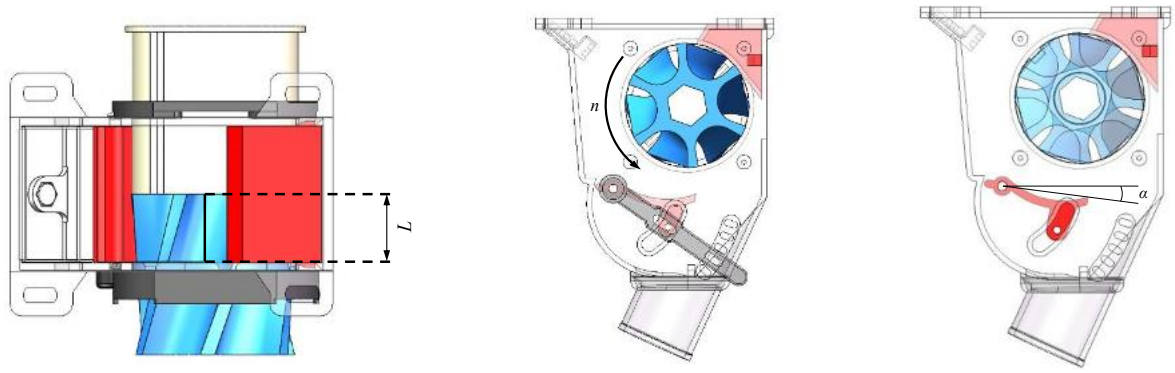
where, L is the effective working length of fluted wheel, cm; γ is the density of fertilizer, g/cm^3; S is the cross-sectional area of a single flute, cm^2; ψ is the filling coefficient of the groove; Z is the number of grooves; n is the fertilizer-metering shaft rotational speed, RPM; t is the time of fertilizer discharge, minute.

Fig. 2 shows the fluted-wheel inscribed-circle diameter D, the number of grooves Z, and the fluted-wheel lead angle θ. Fig. 3 shows the adjustable operating parameters, namely the effective working length L of the fluted wheel, the fertilizer-metering shaft rotational speed n, and the fertilizer-discharge flap angle α. According to Eqs. (1) and (2) and previous studies (*Zeng et al., 2020; Wang Y. et al., 2023; Wang J. F. et al., 2023*), these key parameters may affect the variables involved in the equations and thereby influence fertilization uniformity.



(a) fluted-wheel inscribed-circle diameter *D* (b) number of grooves *Z* (c) fluted-wheel lead angle *θ*

Fig. 2 - Structural parameters of the fluted wheel



(a) effective working length *L* of the fluted wheel (b) fertilizer-metering shaft rotational speed *n* (c) fertilizer discharge flap angle *α*

Fig. 3 - Operating parameters of the fertilizer metering device

Fertilizer simulation model

This study used an amino acid organic fertilizer (China agricultural industry standard for organic fertilizer, NY525-2012), organic matter ≥ 45%, and total nutrient ($N+P_2O_5+K_2O$) ≥ 10%. The 100 fertilizer particles were randomly selected and measured using a digital display vernier caliper (DL 91200 with an accuracy of 0.01 mm) to obtain the fertilizer's average length, width, and thickness.

$$D = \sqrt[3]{LWT} \tag{3}$$

$$\phi = \frac{D}{L} \tag{4}$$

where: D is the equivalent diameter (mm); L is the average length (mm); W is the average width (mm); T is the average thickness (mm); Φ is the sphericity. The equivalent diameter D of the fertilizer was 4.29 mm, and the sphericity Φ was 97%. The proportion of particles in three intervals of large (D ≥ 5 mm), medium (4 mm < D < 5 mm), and small (D < 4 mm) were 15%, 80%, and 5%, respectively.

As shown in Fig. 4(a), the fertilizer particle was sprayed with a contrast enhancer (imaging agent), and was scanned using a 3D scanner (G5-630 with a scanning accuracy of 0.02 mm). To improve the accuracy of three-dimensional model of the fertilizer particle, the turntable was rotated approximately every 10 degrees to scan the particles, capturing surface characteristic data each time. As illustrated in Fig. 4(b), the completeness of the particle model was monitored in the software to ensure all surface feature data were acquired. After scanning, the 3D shell model of the fertilizer particle underwent noise removal and defect correction.

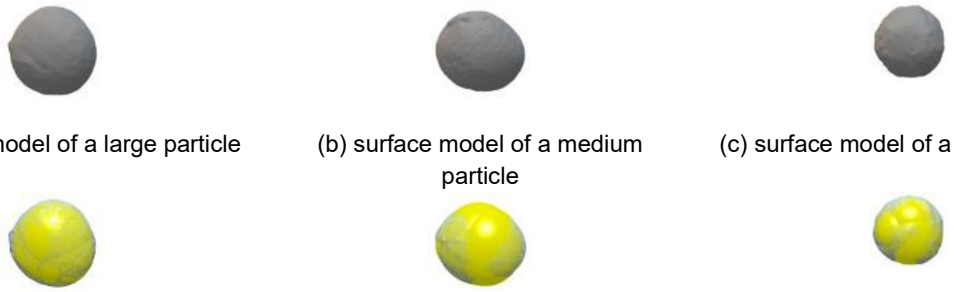


(a) fertilizer particle scanning process (b) interface of the scanning software

Fig. 4 - Fertilizer particle scanning and processing

(a) 1. fertilizer granule; 2. tripod turntable; 3. 3D scanner (b) 1. editing area; 2. surface model of the fertilizer granule

Figs. 5(a), 5(b), and 5(c) show three surface models obtained by 3D scanning representative large, medium, and small fertilizer granules. As shown in Figs. 5(d), 5(e), the surface models were imported into EDEM 2022 and filled with spheres to generate the corresponding DEM particle models.



(a) surface model of a large particle (b) surface model of a medium particle (c) surface model of a small particle

(d) sphere-filled model of a large particle (e) sphere-filled model of a medium particle (f) sphere-filled model of a small particle

Fig. 5 - Three-dimensional model of fertilizer particles

DEM parameter calibration method

Poisson's ratio of the fertilizer

As shown in Fig. 6, a fertilizer particle was placed at the center of the platform of a texture analyzer (TA.XTplusC, force measurement accuracy: 0.0001 N). The particle was compressed using a rigid probe at a loading rate of 5 mm/min, with an initial trigger force of 0.375 N. Loading was stopped when the fertilizer particle fractured. The transverse and longitudinal dimensions of the particle were then measured after compression.

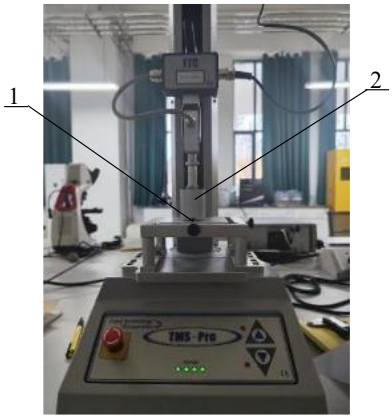


Fig. 6 - Measurement procedure using the texture analyzer

1. fertilizer particle, 2. probe

Poisson's ratio was calculated using Eq. (5). The test was repeated five times, and the mean value was used as the final result.

$$\mu = \frac{\varepsilon_T}{\varepsilon_L} = \frac{\Delta l / l}{\Delta d / d} \tag{5}$$

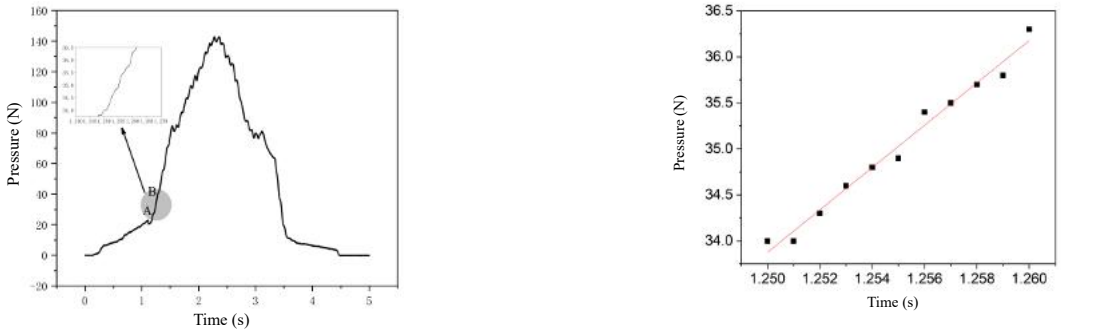
where: μ is the Poisson's ratio, ε_T is the transverse strain of the fertilizer particle, ε_L is the longitudinal strain of the fertilizer particle, Δl is the transverse deformation of the fertilizer particle (mm), l is the initial transverse dimension of the fertilizer particle (mm); Δd is the longitudinal deformation of the fertilizer particle (mm); d is the initial longitudinal dimension of the fertilizer particle (mm).

Elastic modulus of the fertilizer

The elastic modulus reflects a material's resistance to elastic deformation and was measured using a texture analyzer. Large fertilizer particles were selected and polished with sandpaper into cylindrical specimens. The prepared specimens were placed at the center of the loading platform and compressed using a rigid probe at a loading rate of 5 mm/min. The initial trigger force was set to 0.375 N. Fig. 7(a) shows the force–time curve, while Fig. 7(b) shows the force–time curve corresponding to the elastic deformation region. The elastic modulus was calculated using Eq. (6). The test was repeated five times, and the mean value was taken as the final result.

$$E = \frac{\sigma}{\varepsilon} = \frac{\Delta F / A}{v \cdot \Delta t / h} = \frac{h}{vA} \cdot \frac{\Delta F}{\Delta t} = \frac{kh}{vA} \tag{6}$$

where: E is the elastic modulus of the fertilizer (Pa), σ is the stress within the elastic limit, ε is the strain within the elastic limit, A is the cross-sectional area of the fertilizer specimen (mm²), ΔF is the force increment within the elastic deformation region (N), v is the loading speed of the texture analyzer (mm/s), h is the height of the fertilizer specimen (mm), k is the slope of the elastic deformation region of the force–time curve.



(a) force-time curve (b) linear fit of the elastic deformation region

Fig. 7 - Force–time characteristics of a fertilizer particle

Coefficient of restitution of the fertilizer

The coefficient of restitution characterizes the degree of energy loss during a collision and can be expressed as follows:

$$e = \sqrt{\frac{l_2}{l_1}} \tag{7}$$

where: l_1 is the initial drop height (m) and l_2 is the rebound height (m).

As shown in Fig. 8, the complete rebound and subsequent falling process of the fertilizer particles was recorded during the free-fall test. The rebound height of the fertilizer particles was measured, and the test was repeated five times to obtain the mean value.



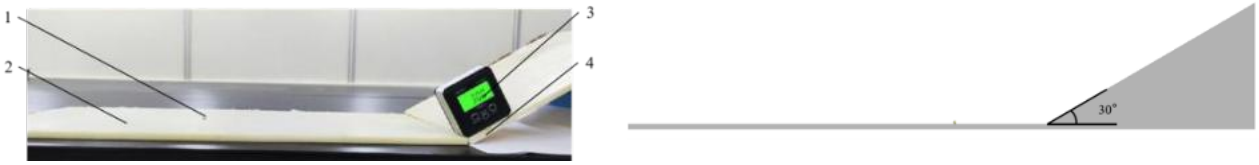
(a) coefficient of restitution test setup (b) slow-motion image of the rebound process

Fig. 8 - Coefficient of restitution test

1. ruler, 2. fertilizer granules, 3. background plate, 4. impact plate

Rolling friction coefficients between the fertilizer and PA, PC, and PLA

Fig. 9(a) shows the inclined-plane rolling test used in this study. Two plates made of the same material as the corresponding components of the fertilizer metering device were used. One plate was placed horizontally, while the other was inclined at 30° to the horizontal. Fertilizer granules were released from a position 100 mm above the horizontal plate and moved down the inclined plate under gravity. The rolling distance of the fertilizer granules on the horizontal plate was recorded, as shown in Table 2. The test was repeated five times, and the mean value was calculated. Fig. 9(b) shows the corresponding EDEM simulation of the fertilizer particle rolling test. As shown in Table 3, the rolling friction coefficient was varied within the range of 0.1-0.2 in the simulation tests. Each test condition was repeated five times, and the mean value was calculated.



(a) inclined-plane rolling test (b) EDEM simulation test

Fig. 9 - Calibration test for the rolling friction coefficient

1. fertilizer granule, 2. horizontal nylon plate, 3. digital inclinometer, 4. inclined nylon plate

Table 2

Results of the inclined-plane rolling test

Material pair	Mean rolling distance [mm]
Fertilizer - PA	212.09
Fertilizer - PC	244.09
Fertilizer - PLA	230.36

Table 3

Simulation results of the rolling test

Rolling friction coefficient / Material pair	0.10	0.12	0.14	0.16	0.18	0.20
Fertilizer - PA [mm]	357.21	276.33	232.41	195.63	152.67	136.89
Fertilizer - PC[mm]	389.47	311.96	263.25	226.34	179.35	146.23
Fertilizer - PLA[mm]	372.89	308.37	253.12	210.39	177.45	149.20

As shown in Table 4, Origin software was used to perform linear regression on the simulation data, and a fitting equation was obtained for each material pair. In the fitting equations, *y* represents the rolling distance of the fertilizer granules, and *x* represents the rolling friction coefficient. As shown in Table 5, the rolling friction coefficients between the fertilizer and PA, PC, and PLA were determined by substituting the experimentally measured rolling distances into the corresponding fitting equations.

Table 4

Fitting equations for the rolling friction coefficients

Material pair	Fitting equation
Fertilizer - PA	y=−2154.20x+548.26
Fertilizer - PC	y=−2358.49x+606.54
Fertilizer - PLA	y=−2219.91x+578.22

Table 5

Coefficient of rolling friction between fertilizer and materials

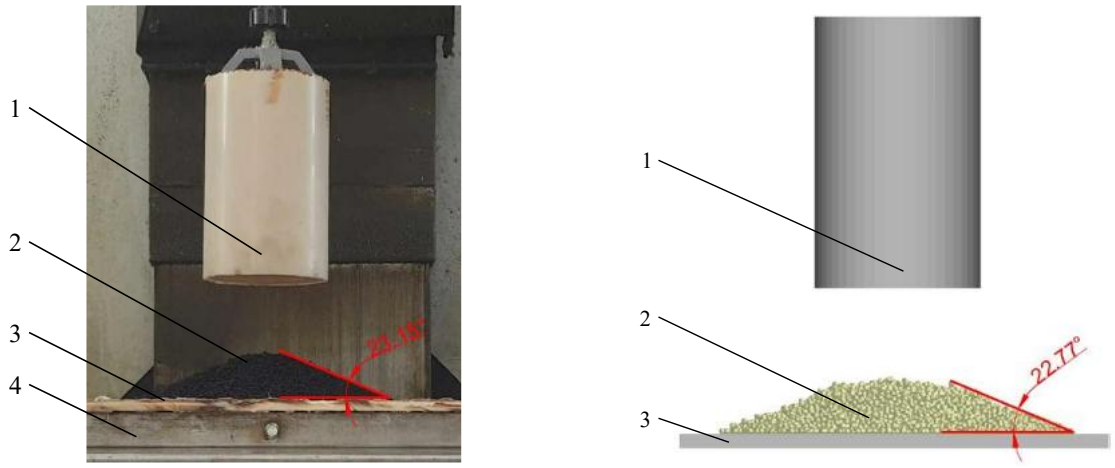
Material pair	Rolling friction coefficient
Fertilizer - PA	0.156
Fertilizer - PC	0.154
Fertilizer - PLA	0.157

Contact parameter calibration method based on the angle of repose

Due to space limitations, this section describes the calibration procedure using polyamide (PA) as an example. The calibration procedures for the other two materials, PC and PLA, were similar.

Cylinder-lifting test for the angle of repose

Fig. 10(a) shows the physical angle-of-repose test conducted using a PA cylinder. The cylinder had an inner diameter of 100 mm and a height of 200 mm. It was clamped in the chuck of a CNC milling machine, and fertilizer granules were poured into the cylinder until it was approximately 60% full. The cylinder was then lifted vertically at a speed of 1000 mm/min. After lifting, an approximately conical fertilizer pile formed on the bottom plate. Images of the fertilizer pile were imported into AutoCAD 2021, and the angle measurement tool was used to determine the angle of repose. The test was repeated five times, and the mean value was calculated. The measured angle of repose of the fertilizer granules on PA was 22.57°.



(a) physical angle of repose test using a PA cylinder (b) EDEM simulation of the angle of repose test

Fig. 10 – Angle of repose test for fertilizer granules

1. bottomless cylinder, 2. fertilizer particle pile, 3. bottom plate, 4. CNC milling machine table

Discrete element simulation of the angle of repose

As shown in Fig. 10(b), the bottomless cylinder was placed in close contact with the bottom plate. The particle factory generated fertilizer particles until the cylinder was approximately 60% full, corresponding to about 1000 g, at a generation rate of 2000 g/s. The cylinder was then lifted vertically at the same speed used in the physical test (1000 mm/min) until a stable fertilizer pile was formed. A screenshot of the final particle pile was imported into AutoCAD®, and the angle measurement tool was used to determine the angle of repose.

Plackett-Burman test

Table 6 lists the factors used in the Plackett-Burman design generated using Design-Expert 13 software. Eight parameters were selected, with each parameter assigned a high level (+1) and a low level (−1). A center point was also included in the simulation design.

Table 6

Factors and levels of the Plackett-Burman design

Parameter	Factor	Low level (-1)	High level (+1)
X_1	Poisson's ratio of the fertilizer	0.1	0.5
X_2	Shear modulus of the fertilizer	1×10^6	1×10^7
X_3	Fertilizer–fertilizer coefficient of restitution	0.1	0.7
X_4	Fertilizer–fertilizer static friction coefficient	0.1	0.9
X_5	Fertilizer–fertilizer rolling friction coefficient	0.05	0.55
X_6	Fertilizer–PA coefficient of restitution	0.1	0.7
X_7	Fertilizer–PA static friction coefficient	0.1	0.9
X_8	Fertilizer–PA rolling friction coefficient	0.05	0.55

Table 7 presents the Plackett-Burman experimental design generated using Design-Expert 13 software. EDEM simulations were then conducted to determine the angle of repose for each test combination.

Table 7

Plackett–Burman experimental design and results

No.	X_1	X_2	X_3	X_4	X_5	X_6	X_7	X_8	Angle of repose [°]
1	0.1	1×10^7	0.7	0.1	0.55	0.7	0.9	0.05	17.41
2	0.1	1×10^6	0.1	0.1	0.05	0.1	0.1	0.05	0.66
3	0.5	1×10^6	0.7	0.9	0.05	0.7	0.9	0.55	25.42
4	0.3	5.5×10^6	0.4	0.5	0.3	0.4	0.5	0.3	46.89
5	0.5	1×10^6	0.1	0.1	0.55	0.1	0.9	0.55	17.61
6	0.5	1×10^7	0.7	0.1	0.05	0.1	0.9	0.05	10.96
7	0.5	1×10^6	0.7	0.9	0.55	0.1	0.1	0.05	28.05
8	0.1	1×10^7	0.1	0.9	0.55	0.1	0.9	0.55	43.15
9	0.1	1×10^6	0.7	0.1	0.55	0.7	0.1	0.55	0.82
10	0.5	1×10^7	0.1	0.1	0.05	0.7	0.1	0.55	2.49
11	0.1	1×10^6	0.1	0.9	0.05	0.7	0.9	0.05	25.13
12	0.1	1×10^7	0.7	0.9	0.05	0.1	0.1	0.55	5.41
13	0.5	1×10^7	0.1	0.9	0.55	0.7	0.1	0.05	35.19

Table 8 shows that the fertilizer-fertilizer static friction coefficient (X_4), fertilizer-fertilizer rolling friction coefficient (X_5), and fertilizer-PA static friction coefficient (X_7) significantly affected the angle of repose of the fertilizer. The effects of the remaining factors were not significant. Therefore, these three significant factors were selected for further analysis using the steepest ascent test and the Box-Behnken design.

Table 8

Significance analysis of the Plackett-Burman design

Factor	Effect	Sum of squares	F-value	*p*-value	Significance ranking
X_1	4.52	61.38	2.05	0.23	5
X_2	2.82	23.86	0.80	0.42	7
X_3	-6.03	108.96	3.65	0.14	4
X_4	18.73	1052.81	35.22	0.01	1
X_5	12.03	433.92	14.52	0.03	2
X_6	0.10	0.03	0.0011	0.97	8

Factor	Effect	Sum of squares	F-value	*p*-value	Significance ranking
X_7	11.18	374.75	12.54	0.03	3
X_8	-3.75	42.19	1.41	0.30	6

Steepest ascent test

Table 9 presents the results of the steepest ascent test for the three significant factors. The relative error was minimized at test No. 2, indicating that the optimum region was located near this factor combination. Therefore, the factor levels corresponding to test No. 2 were selected as the center levels for the subsequent response surface design, with the adjacent lower and higher levels used as the low and high levels, respectively.

Table 9

Results of the steepest ascent test

No.	Fertilizer-fertilizer static friction coefficient (X_4)	Fertilizer-fertilizer rolling friction coefficient (X_5)	Fertilizer-PA static friction coefficient (X_7)	Angle of repose	Relative error
				[°]	[%]
1	0.1	0.1	0.05	1.08	95.21
2	0.3	0.3	0.175	25.37	12.41
3	0.5	0.5	0.3	33.22	47.19
4	0.7	0.7	0.425	38.65	71.25
5	0.9	0.9	0.55	44.56	97.43

Box-Behnken test

Table 10 presents the levels of the three significant factors used in the Box-Behnken design. A total of 15 test combinations were conducted, including three replicates at the center point.

Table 10

Box–Behnken design and test results

No.	Fertilizer-fertilizer static friction coefficient (X_4)	Fertilizer-fertilizer rolling friction coefficient (X_5)	Fertilizer-PA static friction coefficient (X_7)	Angle of repose
				[°]
1	0.1	0.05	0.3	16.75
2	0.5	0.05	0.3	25.5
3	0.1	0.3	0.3	16.1
4	0.5	0.3	0.3	42.57
5	0.1	0.175	0.1	1.72
6	0.5	0.175	0.1	7.57
7	0.1	0.175	0.5	22.37
8	0.5	0.175	0.5	41.61
9	0.3	0.05	0.1	1.5
10	0.3	0.3	0.1	5.32
11	0.3	0.05	0.5	23.97
12	0.3	0.3	0.5	34.97
13	0.3	0.175	0.3	31.78
14	0.3	0.175	0.3	30.25
15	0.3	0.175	0.3	32.64

In Table 11, the model *p*-value was less than 0.0001, indicating that the regression model was highly significant. The *p*-value for lack of fit was 0.2485, which was greater than 0.05, indicating that the lack of fit was not significant and that the model adequately fitted the experimental data. The coefficient of determination (R^2) and adjusted coefficient of determination (R^2_{adj}) were 0.9936 and 0.9821, respectively, indicating a good agreement between the predicted and experimental values. The coefficient of variation (*CV*) was 8.24%, indicating acceptable experimental reproducibility. The adequate precision value was 27.8298, which was substantially greater than 4, indicating an adequate signal-to-noise ratio.

In Eq. (8), *A* (fertilizer–fertilizer static friction coefficient), *B* (fertilizer–PA static friction coefficient), *C* (fertilizer–fertilizer rolling friction coefficient), *AB* (interaction between the fertilizer–fertilizer static friction coefficient and the fertilizer–PA static friction coefficient), B^2 (quadratic term of the fertilizer–PA static friction coefficient), and C^2 (quadratic term of the fertilizer–fertilizer rolling friction coefficient) had highly significant effects on the angle of repose *θ*. The interaction term *AC* (interaction between the fertilizer–fertilizer static friction coefficient and the fertilizer–fertilizer rolling friction coefficient) had a significant effect on the angle of repose. The quadratic polynomial regression equation is expressed as follows:

$$\theta = 31.56 + 7.54A + 3.90B + 13.35C + 4.43AB + 3.35AC + 1.79BC - 2.22A^2 - 4.10B^2 - 11.01C^2 \quad (8)$$

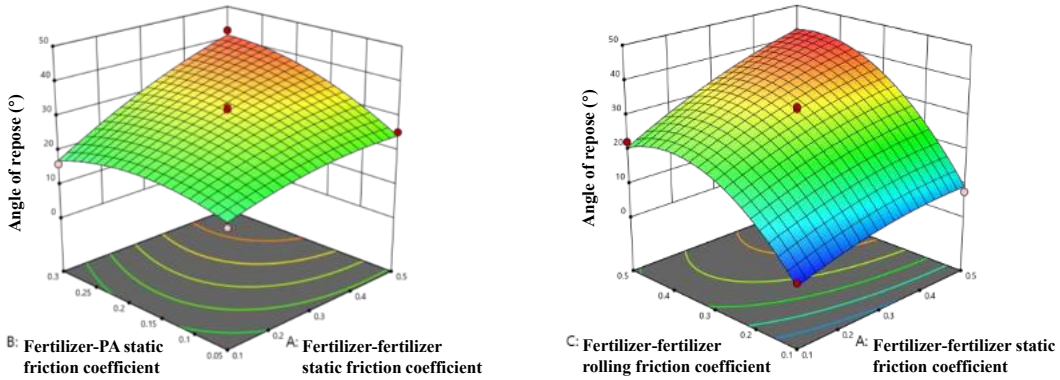
Table 11

ANOVA for the quadratic polynomial model of the Box–Behnken design

Item	Mean square	Degrees of freedom	Sum of squares	*p*-value
Model	2631.11	9	292.35	<0.0001
A	454.66	1	454.66	<0.0001
B	121.99	1	121.99	0.0018
C	1426.05	1	1426.05	<0.0001
AB	78.50	1	78.50	0.0048
AC	44.82	1	44.82	0.0149
BC	12.89	1	12.89	0.1083
A^2	18.27	1	18.27	0.0676
B^2	62.13	1	62.13	0.0078
C^2	447.95	1	447.95	<0.0001
Residual	16.90	5	3.38	
Lack of fit	13.97	3	4.66	0.2485
Pure error	2.93	2	1.47	
Total	2648.01	14		
R^2 = 0.9936, R^2_{adj} = 0.9821, *CV* = 8.24%, degree of precision = 27.8298				

Note: "P < 0.01" indicates a highly significant effect, "0.01 < P < 0.05" indicates a significant effect, and P > 0.05 indicates a nonsignificant effect.

The angle of repose measured in the physical tests was used as the target value. As shown in Fig. 11, Design-Expert 13 software was used to optimize the three parameters and generate the response surface plots.



(a) fertilizer-PA static friction coefficient and fertilizer–fertilizer static friction coefficient

(b) fertilizer-fertilizer rolling friction coefficient and fertilizer-fertilizer static friction coefficient

Fig. 11 - Response surfaces of the interaction effects

The fertilizer–fertilizer static friction coefficient (*A*) was 0.402, the fertilizer–PA static friction coefficient (*B*) was 0.276, and the fertilizer–fertilizer rolling friction coefficient (*C*) was 0.177. The center values were used for the remaining parameters: the Poisson's ratio of the fertilizer was 0.3, the shear modulus of the fertilizer was 5.5×10^6 P_a, the fertilizer–fertilizer coefficient of restitution was 0.4, the fertilizer–PA coefficient of restitution was 0.4, and the fertilizer–PA rolling friction coefficient was 0.3. Three EDEM simulations of the angle of repose were conducted, yielding values of 22.10°, 22.34°, and 22.77°, respectively. The results were analyzed using a *t*-test, and $t = -1.442 < t_{0.05/2} = 2.776$, indicating that there was no significant difference between the simulated and experimentally measured angles of repose.

Contact parameter calibration results

The contact parameters between the fertilizer and the other materials (PC and PLA) were calibrated using the same procedure described above. As shown in Table 12, the calibrated fertilizer-fertilizer static and rolling friction coefficients obtained for the three material-based calibration tests were similar. Therefore, the mean fertilizer-fertilizer static friction coefficient and rolling friction coefficient were calculated as 0.413 and 0.181, respectively.

Table 12

Calibration results of fertilizer contact parameters

Contact parameter / Material pair	Fertilizer-material static friction coefficient	Fertilizer-fertilizer static friction coefficient	Fertilizer-fertilizer rolling friction coefficient
Fertilizer and PA	0.276	0.402	0.177
Fertilizer and PC	0.266	0.424	0.180
Fertilizer and PLA	0.173	0.412	0.187
Mean value		0.413	0.181

Fertilization EDEM simulation method

Coefficient of variation of fertilization uniformity

According to Chinese agricultural industry standard for technical specifications of quality evaluation for fertilizing machinery (*NY/T1003-2006, 2006*) and literature review (Bangu*ra et al., 2020; Ștefan et al., 2025*), coefficient of variation of fertilization uniformity (CVFU) was calculated using Equations (9), (10), and (11).

$$\bar{m} = \frac{1}{n}\sum m_i \tag{9}$$

$$s = \sqrt{\frac{\sum (m_i - \bar{m})^2}{n-1}} \tag{10}$$

$$\sigma = \frac{s}{m} \times 100\% \tag{11}$$

where: $\bar{m}$ is average mass of fertilizer of grid cell (g); m_i is fertilizer mass of the i-th experiment (g); n is number of experiments; s is standard deviation of n fertilizer discharge measurements; and σ is CVFU(%).

DEM parameter settings

As shown in Table 13, the fertilizer density was determined using the water displacement method, whereas the Poisson's ratio, density, and shear modulus of PA, PC, and PLA were obtained from the literature (*Zhang et al., 2019*). The remaining simulation parameters were obtained using the DEM parameter calibration procedures described above. Because the moisture content of the fertilizer granules was low, interparticle adhesion was considered negligible. The Hertz-Mindlin (no slip) model was therefore adopted as the contact model in the simulations.

Table 13

Discrete element parameters

Simulation parameter	Value	Simulation parameter	Value
Poisson's ratio of the fertilizer	0.314	Fertilizer-fertilizer coefficient of restitution	0.421
Poisson's ratio of PA	0.34	Fertilizer-PA coefficient of restitution	0.422
Poisson's ratio of PC	0.39	Fertilizer-PC coefficient of restitution	0.436
Poisson's ratio of PLA	0.43	Fertilizer-PLA coefficient of restitution	0.426
Fertilizer density (g/cm^3)	1.580	Fertilizer-fertilizer static friction coefficient	0.413
PA density (g/cm^3)	1.130	Fertilizer-PA static friction coefficient	0.276
PC density (g/cm^3)	1.200	Fertilizer-PC static friction coefficient	0.266
PLA density (g/cm^3)	1.240	Fertilizer-PLA static friction coefficient	0.173
Fertilizer elastic modulus (Pa)	9.8×10^7	Fertilizer-fertilizer rolling friction coefficient	0.181
PA shear modulus (Pa)	9.7×10^8	Fertilizer-PA rolling friction coefficient	0.156
PC shear modulus (Pa)	8.62×10^8	Fertilizer-PC rolling friction coefficient	0.154
PLA shear modulus (Pa)	1.3×10^9	Fertilizer-PLA rolling friction coefficient	0.157

EDEM simulation model

As shown in Fig. 12, Granule factory was set on fertilizer box. Total amount of fertilizer particles was 2 kg, and generation speed was 5 kg/s. Generation proportion of large, medium, and small fertilizer particles was 15%, 80%, and 5%, respectively. Forward speed of the fertilizer metering device was 1m/s. Grid bin group module was adopted, and 1000 mm was set as sampling area, divided into five areas on average (each cell size 200 mm x 1000 mm x 200 mm). Fertilizer quality of each cell was statistically analyzed. Coefficient of variation of fertilization uniformity was calculated using Equation (9), (10), and (11).

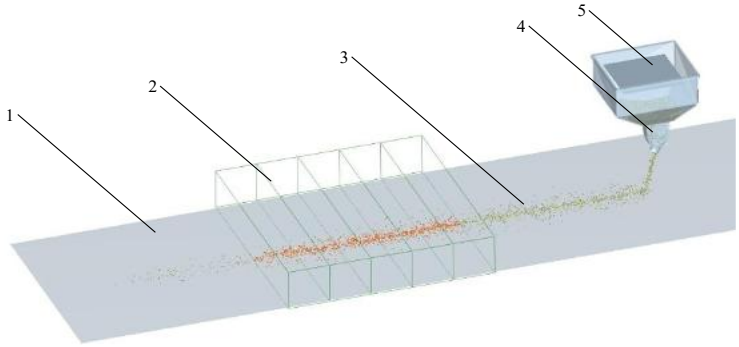
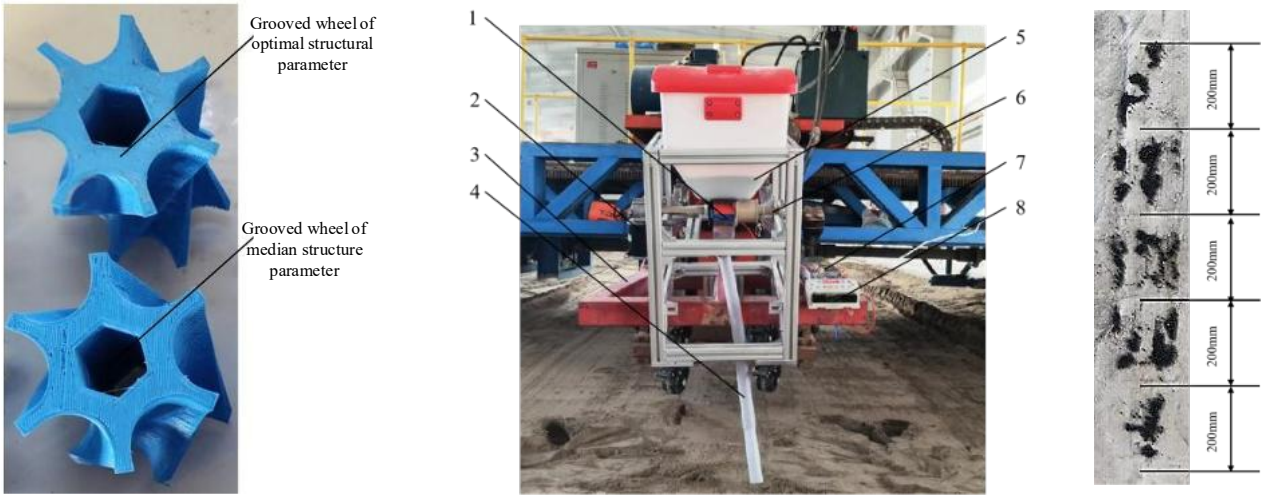


Fig. 12 - Discrete element simulation model of the fertilizer metering device

1. ground surface, 2. sampling area, 3. fertilizer particles, 4. fertilizer metering device, 5. particle factory

Soil bin test validation method



(a) 3D-printed fluted wheels (b) test apparatus (c) sampling grids

Fig. 13 - Soil bin test

1. fluted-wheel fertilizer metering device, 2. DC motor, 3. three-point hitch frame, 4. fertilizer delivery tube, 5. fertilizer hopper, 6. fertilizer-metering shaft, 7. power supply, 8. DC motor controller

Fig. 13(a) shows the two 3D-printed fluted wheels used in the test. As shown in Fig. 13(b), the test apparatus was connected to the soil-bin tractor through a three-point hitch frame. The sampling grids shown in Fig. 13(c) were consistent with those used in the simulation described above. The sampling length was 1 m and was divided into five 200 mm sections. The forward speed of the soil-bin tractor was set to 1 m/s. A DC motor drove the fluted-wheel fertilizer metering device through the fertilizer-metering shaft, and the fertilizer granules were discharged through the fertilizer delivery tube onto the sampling grids. The mass of fertilizer collected in each grid was recorded. The coefficient of variation of fertilization uniformity (CVFU) was calculated using Eqs. (9)–(11). Five sections of the fertilizer strip were randomly selected as sampling intervals.

RESULTS

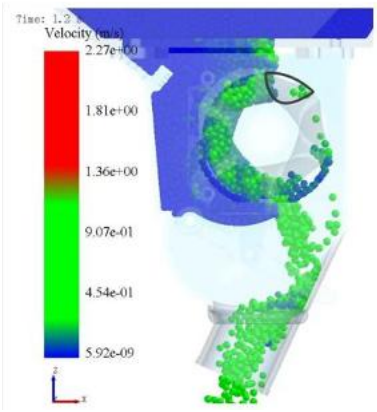
EDEM simulation of the fertilization process

Operation of the fertilizer metering device

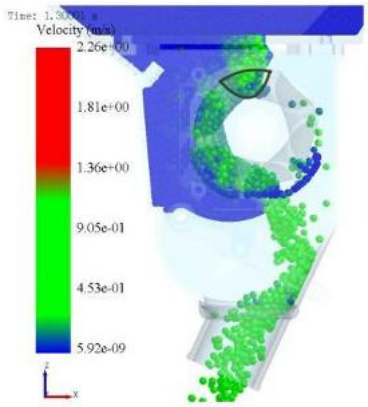
Fig. 14 shows a sectional view of the fluted-wheel fertilizer metering device, with particle velocity represented by the color scale. The structural parameters were as follows: fluted-wheel inscribed-circle diameter (D) of 38 mm, number of grooves (Z) of 6, and fluted-wheel lead angle (θ) of 65°.

The operating parameters were an effective working length of the fluted wheel (*L*) of 35 mm, a fertilizer-metering shaft rotational speed (*n*) of 35 rpm, and a fertilizer-discharge flap angle (*α*) of 0°.

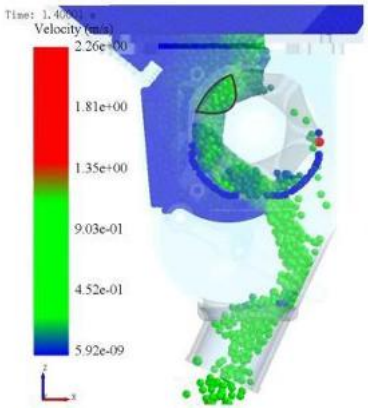
In Fig. 14, the groove outlined in black is used as an example. As the fluted wheel rotates counterclockwise, the interval from 1.2 to 1.3 s represents the fertilizer filling stage, during which fertilizer enters the groove under gravity and the action of the fluted wheel. The interval from 1.4 to 1.7 s represents the fertilizer conveying stage, whereas the interval from 1.8 to 1.9 s represents the fertilizer discharge stage. The particle velocities in the forcing layer were markedly higher than those in the driving layer. A distinct boundary between the forcing and driving layers, together with consistent groove filling, contributed to improved fertilization uniformity.



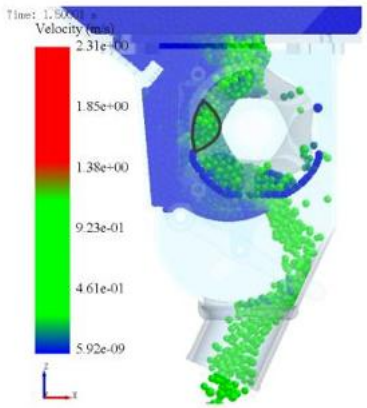
(a) 1.2s



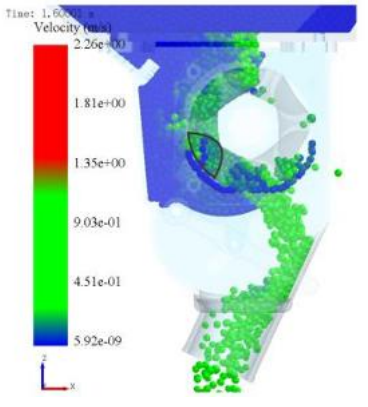
(b) 1.3s



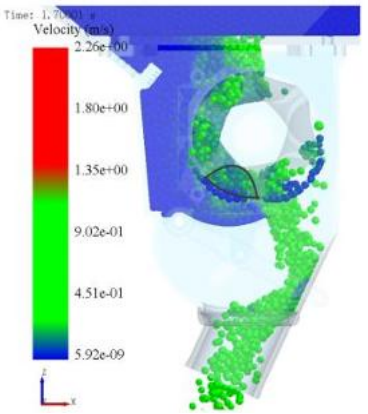
(c) 1.4s



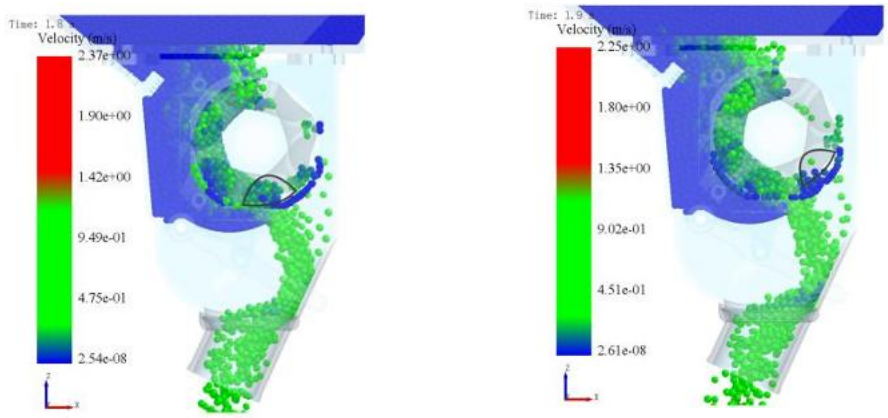
(d) 1.5s



(e) 1.6s



(f) 1.7s

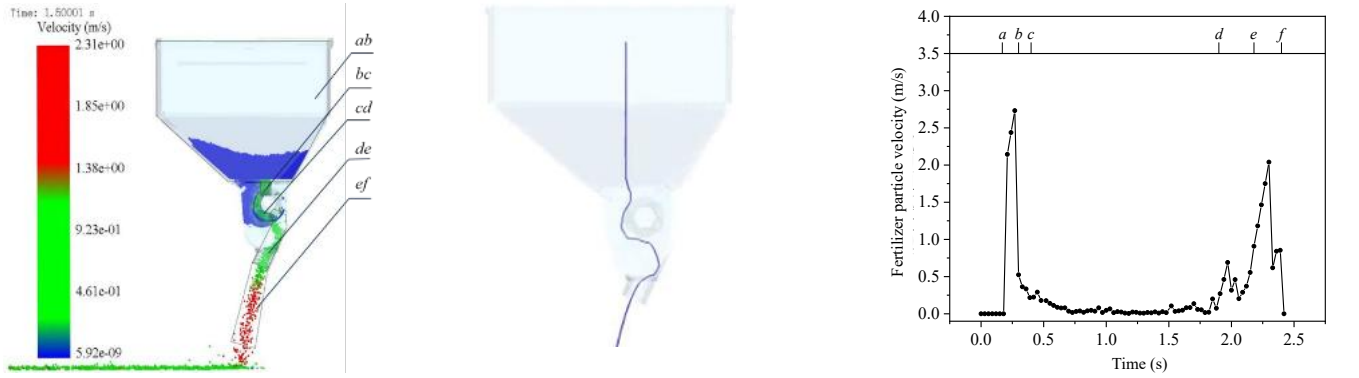


(g) 1.8s (h) 1.9s

Fig. 14 - Movement of fertilizer particles within the fertilizer metering device

Fertilizer motion during the fertilization process

Fig. 15(a) shows the velocity distribution of fertilizer particles within the fertilizer metering device. Fig. 15(b) shows the trajectory of a single fertilizer particle, and Fig. 15(c) shows the variation in particle velocity with time. Region *ab* corresponds to the particle generation stage. The particle velocity initially increases and then decreases after the particle reaches the bottom of the fertilizer hopper. Region *bc* corresponds to the fertilizer filling stage, during which the particle velocity gradually decreases from its maximum value to its minimum value. In region *cd*, the particle moves together with the fluted wheel, and its velocity remains relatively stable. Region *de* corresponds to the discharge stage from the fluted wheel, during which interaction with the fertilizer-discharge flap causes substantial fluctuations in particle velocity. Region *ef* corresponds to the final fertilizer discharge stage, in which the particle velocity increases to 2.04 m/s before impact with the ground and then decreases.



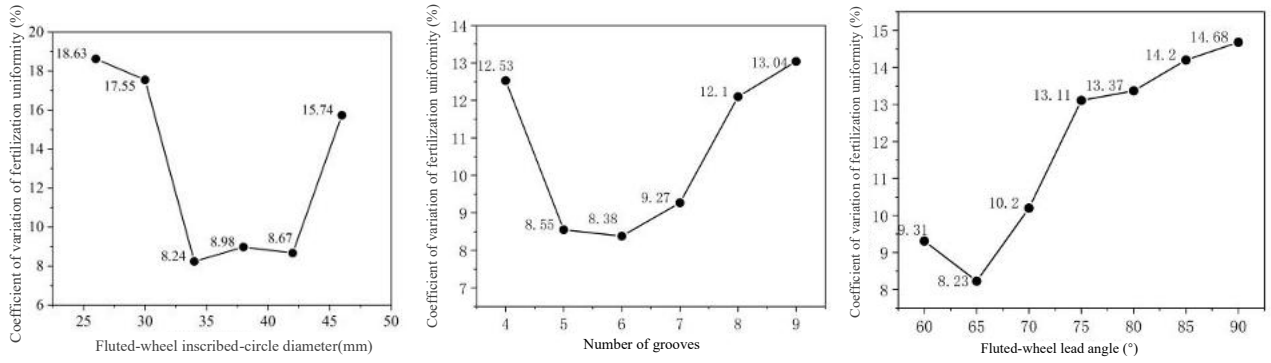
(a) fertilizer particle velocity distribution (b) trajectory of a fertilizer particle (c) variation in fertilizer particle velocity with time

Fig. 15 - Motion characteristics of fertilizer particles in the fertilizer metering device

Single-factor simulation test

Structural parameters

Fig. 16 shows that the CVFU generally decreased initially and then increased with changes in the structural parameters. The fluted-wheel inscribed-circle diameters of 34, 38, and 42 mm yielded the best results. Similarly, 5, 6, and 7 grooves produced better fertilization uniformity, while fluted-wheel lead angles of 60°, 65°, and 70° yielded the best results. Therefore, these parameter levels were selected for the subsequent multifactor tests.



(a) fluted-wheel inscribed-circle diameter (b) number of grooves (c) fluted-wheel lead angle

Fig. 16 - Single-factor tests of the structural parameters

Operating parameters

Fig. 17 shows that the coefficient of variation of fertilization uniformity generally decreased initially and then increased as the operating parameters changed. Effective working lengths of the fluted wheel of 20, 30, and 40 mm yielded the best results. Fertilizer-metering shaft rotational speeds of 25, 35, and 45 rpm also produced better performance, while fertilizer-discharge flap angles of −5°, 0°, and 5° gave the best results. Therefore, these operating parameter levels were selected for the subsequent multifactor tests.

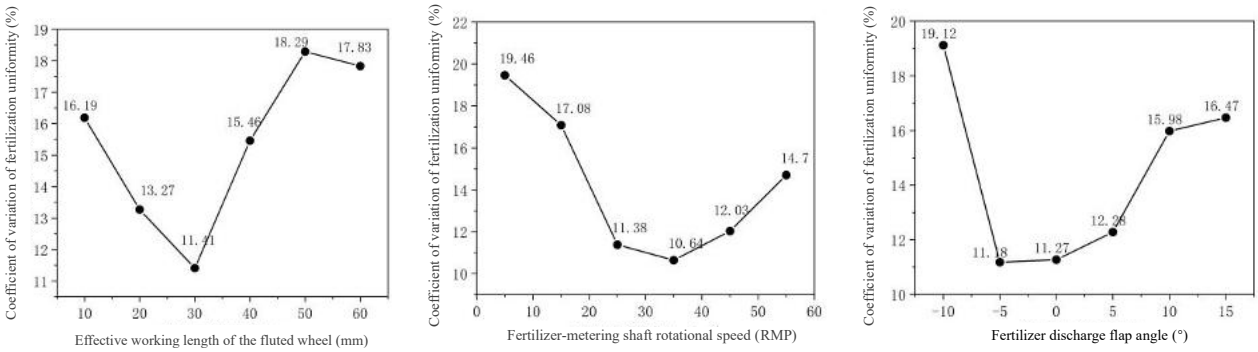


Fig. 17 - Single-factor tests of the operating parameters

Multifactor simulation test

Factor coding

Table 14

Factor levels and coding for the structural parameters

Coded level	Experimental factor		
	Fluted-wheel inscribed-circle diameter	Number of grooves	Fluted-wheel lead angle
	[mm]		[°]
-1	34	5	60
0	38	6	65
1	42	7	70

Table 15

Factor levels and coding for the operating parameters

Coded level	Experimental factor		
	Effective working length of the fluted wheel	Fertilizer-metering shaft rotational speed	Fertilizer discharge flap angle
	[mm]	[RPM]	[°]
-1	20	25	-5
0	30	35	0
1	40	45	5

Optimization of structural parameters

The operating parameters were set to the center levels listed in Table 15. The simulation design and results for different combinations of structural parameters are presented in Table 16.

Table 16

Simulation design and results for structural parameter optimization

No.	Fluted-wheel inscribed-circle diameter	Number of grooves	Fluted wheel lead angle	Coefficient of variation of fertilization uniformity
	[mm]		[degree]	[%]
1	34	5	65	9.74
2	42	5	65	11.25
3	34	7	65	10.55
4	42	7	65	12.33
5	34	6	60	10.34
6	42	6	60	14.18
7	34	6	70	13.53
8	42	6	70	14.24
9	38	5	60	11.34
10	38	7	60	8.21
11	38	5	70	8.95
12	38	7	70	13.34
13	38	6	65	8.43
14	38	6	65	8.57
15	38	6	65	9.23
16	38	6	65	8.53
17	38	6	65	8.56

An analysis of variance (ANOVA) was performed on the regression model relating the structural parameters to the coefficient of variation of fertilization uniformity (CVFU), based on the results presented in Table 17. As shown in Table 17, the model was highly significant ($p < 0.01$). The structural parameters affected CVFU in the following order: fluted-wheel inscribed-circle diameter (A) > fluted-wheel lead angle (C) > number of grooves (B). The lack of fit was not significant, and the coefficient of determination (R^2) was 0.9907, indicating a good fit of the regression model.

Table 17

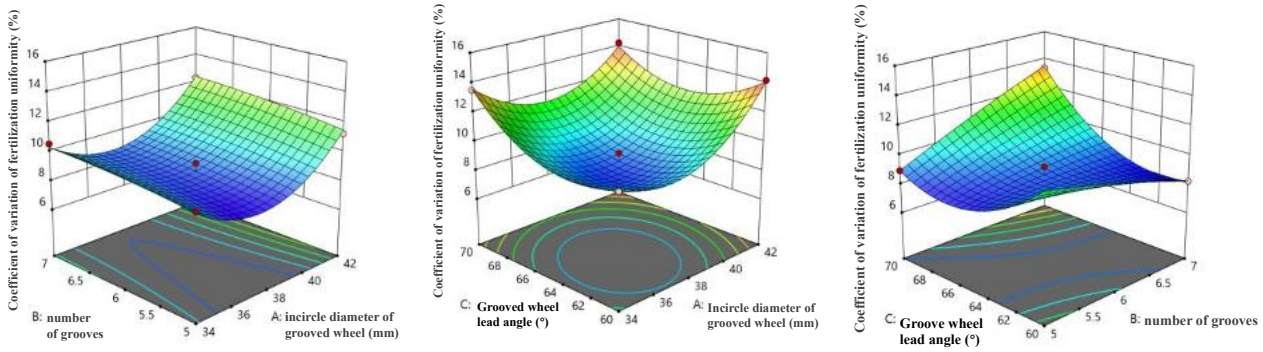
ANOVA of the regression model for structural parameters and CVFU

Source	Mean square	Degrees of freedom	*F* value	*p*-value	Significance
Model	73.75	9	82.74	< 0.0001	**
A	7.68	1	77.58	< 0.0001	**
B	1.24	1	12.52	0.0095	**
C	4.49	1	45.28	0.0003	**
AB	0.0182	1	0.184	0.6808	
AC	2.45	1	24.73	0.0016	**
BC	14.14	1	142.74	< 0.0001	**
A^2	25.44	1	256.85	< 0.0001	**
B^2	0.1005	1	1.01	0.3473	
C^2	16.02	1	161.74	< 0.0001	**
Lack of fit	0.2806	3	0.9064	0.5127	

*Note: ** indicates a highly significant effect ($p < 0.01$), and * indicates a significant effect ($0.01 < p < 0.05$).*

Fig. 18(a) shows that, when the fluted-wheel lead angle was fixed at 65° (center level), the coefficient of variation of fertilization uniformity first decreased and then increased as the fluted-wheel inscribed-circle diameter increased from 34 to 42 mm. When the fluted-wheel inscribed-circle diameter was fixed, the coefficient of variation of fertilization uniformity gradually increased as the number of grooves increased from 5 to 7. Fig. 18(b) shows that, when the number of grooves was fixed at 6 (center level), the coefficient of variation of fertilization uniformity first decreased and then increased as the fluted-wheel inscribed-circle diameter increased from 34 to 42 mm.

When the fluted-wheel inscribed-circle diameter was fixed, the coefficient of variation of fertilization uniformity first decreased and then increased as the fluted-wheel lead angle increased from 60° to 70°. Fig. 18(c) shows that, when the fluted-wheel inscribed-circle diameter was fixed at 38 mm (center level), the coefficient of variation of fertilization uniformity gradually decreased as the number of grooves increased from 5 to 7. When the number of grooves was fixed, the coefficient of variation of fertilization uniformity first decreased and then increased as the fluted-wheel lead angle increased from 60° to 70°.



(a) fluted wheel incircle diameter and number of grooves

(b) fluted wheel incircle diameter and lead angle

(c) number of grooves and fluted wheel lead angle

Fig. 18 - Response surface diagram of the structural parameters

The regression equation relating the coefficient of variation of fertilization uniformity (σ) to A, B, and C was obtained based on the statistical analysis, as follows:

$$\sigma = 8.66 + 0.98A + 0.3938B + 0.7487C + 0.0675AB - 0.7825AC + 1.88BC + 2.46A^2 - 0.1545B^2 + 1.95C^2 \quad (12)$$

$$\begin{cases} \min \sigma(A,B,C) \\ A \in [34,42] \\ B \in [5,7] \\ C \in [60,70] \end{cases} \quad (13)$$

Eq. (13) presents the objective function and constraints used to optimize the structural parameters of the fluted-wheel fertilizer metering device. In Eqs. (12) and (13), σ is the coefficient of variation of fertilization uniformity [%], A is the fluted-wheel inscribed-circle diameter [mm], B is the number of grooves, and C is the fluted-wheel lead angle [°]. The numerical optimization module in Design-Expert software was used to solve the optimization problem. The optimal structural parameter combination was a fluted-wheel inscribed-circle diameter of 37 mm, 7 grooves, and a fluted-wheel lead angle of 63°, corresponding to a minimum predicted coefficient of variation of fertilization uniformity of 7.95%.

Optimization of operating parameters

The structural parameters were set to the center levels listed in Table 14, and the coefficient of variation of fertilization uniformity was used as the evaluation index. The simulation design and results are presented in Table 18.

Table 18

Simulation design and results for operating parameter optimization

No.	Effective working length of the fluted wheel	Fertilizer-metering shaft rotational speed	Fertilizer-discharge flap angle	Coefficient of variation of fertilization uniformity
	[mm]	[rpm]	[°]	[%]
1	20	25	0	11.35
2	40	25	0	13.37
3	20	45	0	16.87

No.	Effective working length of the fluted wheel	Fertilizer-metering shaft rotational speed	Fertilizer-discharge flap angle	Coefficient of variation of fertilization uniformity
	[mm]	[rpm]	[°]	[%]
4	40	45	0	23.67
5	20	35	-5	13.25
6	40	35	-5	18.76
7	20	35	5	18.53
8	40	35	5	22.71
9	30	25	-5	10.76
10	30	45	-5	17.94
11	30	25	5	15.35
12	30	45	5	25.96
13	30	35	0	13.09
14	30	35	0	12.08
15	30	35	0	12.81
16	30	35	0	13.36
17	30	35	0	13.32

As shown in Table 19, an analysis of variance (ANOVA) was performed on the regression model relating the operating parameters to the coefficient of variation of fertilization uniformity (CVFU), based on the simulation results presented in Table 18. The model was highly significant ($p < 0.01$). The operating parameters affected CVFU in the following order: fertilizer-metering shaft rotational speed (B) > fertilizer-discharge flap angle (C) > effective working length of the fluted wheel (A). The lack of fit was not significant, and the coefficient of determination (R^2) was 0.9907, indicating a good fit of the regression model.

Table 19

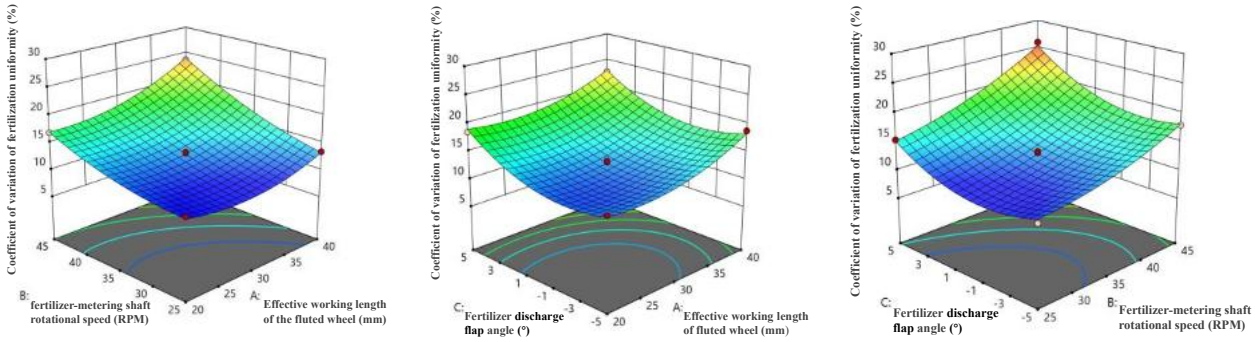
ANOVA of the regression model for operating parameters and CVFU

Source	Mean square	Degree of freedom	*F*-value	*p*-value	Significance
Model	330.55	9	82.74	< 0.0001	**
A	42.83	1	96.48	< 0.0001	**
B	141.2	1	318.1	< 0.0001	**
C	59.62	1	134.32	< 0.0001	**
AB	5.71	1	12.87	0.0089	**
AC	0.4422	1	0.9962	0.3515	
BC	2.94	1	6.63	0.0368	*
A2	18.51	1	41.69	0.0003	**
B2	6.97	1	15.7	0.0054	**
C2	45.41	1	102.3	< 0.0001	**
Lack of fit	2.01	3	2.43	0.2049	

*Note: ** indicates a highly significant effect ($p < 0.01$), * indicates a significant effect ($0.01 < p < 0.05$).*

Fig. 19(a) shows that, when the fertilizer-discharge flap angle was fixed at 0° (center level), the coefficient of variation of fertilization uniformity first decreased and then increased as the effective working length of the fluted wheel increased from 20 to 40 mm. When the effective working length of the fluted wheel was fixed, the coefficient of variation of fertilization uniformity gradually increased as the fertilizer-metering shaft rotational speed increased from 25 to 45 rpm. Fig. 19(b) shows that, when the fertilizer-metering shaft rotational speed was fixed at 35 rpm (center level), the coefficient of variation of fertilization uniformity first decreased and then increased as the effective working length of the fluted wheel increased from 20 to 40 mm. When the effective working length of the fluted wheel was fixed, the coefficient of variation of fertilization uniformity first decreased and then increased as the fertilizer-discharge flap angle increased from −5° to 5°. Fig. 19(c) shows that, when the effective working length of the fluted wheel was fixed at 30 mm (center level), the coefficient of variation of fertilization uniformity gradually increased as the fertilizer-metering shaft rotational speed increased from 25 to 45 rpm. When the fertilizer-metering shaft rotational speed was fixed, the coefficient of variation of fertilization uniformity first decreased and then increased as the fertilizer-discharge flap angle increased from −5° to 5°.

The simulation results indicate that the fertilizer-metering shaft rotational speed and the effective working length of the fluted wheel affect the fertilizer filling process, which is consistent with previous findings (*Wang J. F. et al., 2023*), whereas the fertilizer-discharge flap angle affects the fertilizer discharge process.



(a) effective working length of fluted wheel and fertilizer-metering shaft rotational speed

(b) effective working length of fluted wheel and fertilizer discharge flap angle

(c) fertilizer-metering shaft rotational speed and fertilizer discharge flap angle

Fig. 19 - Response surfaces of the operating parameters

The regression equation relating the coefficient of variation of fertilization uniformity (σ) to *A*, *B*, and *C*, derived from the statistical analysis, is given in Eq. (14). The objective function and constraints for optimization of the operating parameters of the fluted-wheel fertilizer metering device are expressed in Eq. (15).

$$\sigma = 12.93 + 2.31A + 4.20B + 1.2C - 0.3325AB + 0.8575BC + 2.10A^2 + 1.29B^2 + 3.28C^2 \quad (14)$$

$$\begin{cases} \min \sigma(A,B,C) \\ A \in [20,40] \\ B \in [25,45] \\ C \in [-5,5] \end{cases} \quad (15)$$

where σ is the coefficient of variation of fertilization uniformity (%); *A* is effective working length of fluted wheel [mm]; *B* is the fertilizer-metering shaft rotational speed [rpm]; and *C* is the fertilizer discharge flap angle [°]. The numerical optimization module in Design-Expert software was used to determine the optimal solution. When the effective working length of the fluted wheel was 31 mm, the fertilizer-metering shaft rotational speed was 28 rpm, and the fertilizer-discharge flap angle was −1°, the minimum predicted coefficient of variation of fertilization uniformity was 10.33%.

Soil bin test results

Optimal structural parameter

As shown in Fig. 13(a), the test of the optimal structural parameters used a 3D-printed fluted wheel with the optimal structural parameter combination obtained from the simulation: a fluted-wheel inscribed-circle diameter of 37 mm, 7 grooves, and a fluted-wheel lead angle of 63°. The center levels listed in Table 15 (an effective working length of the fluted wheel of 30 mm, a fertilizer-metering shaft rotational speed of 35 rpm, and a fertilizer-discharge flap angle of 0°) were used as the operating parameters. As shown in Table 20, the mean CVFU was 8.68%. Compared with the simulated value of 7.95%, the relative error was 12.19%. This result is generally consistent with the ranges of the coefficient of variation reported in previous studies (*Wang Y. et al., 2023*).

Table 20

Soil-bin test results for the optimal structural parameters

No.	Fertilizer mass in grid 1	Fertilizer mass in grid 2	Fertilizer mass in grid 3	Fertilizer mass in grid 4	Fertilizer mass in grid 5	Coefficient of variation of fertilization uniformity
	[g]	[g]	[g]	[g]	[g]	[%]
1	25.13	21.09	19.65	22.54	21.08	8.48
2	22.03	25.14	20.36	22.54	25.31	8.22
3	20.78	18.66	24.08	18.96	22.04	9.62
4	21.57	23.21	22.28	19.05	20.11	7.03
5	20.69	24.43	18.22	19.51	20.37	10.06
Mean value						**8.68**

Optimal operating parameters

As shown in Fig. 13(a), the test of the optimal operating parameters used a 3D-printed fluted wheel with the center-level structural parameters listed in Table 14: a fluted-wheel inscribed-circle diameter of 38 mm, 6 grooves, and a fluted-wheel lead angle of 65°. The fluted-wheel fertilizer metering device was set to the optimal operating parameters: an effective working length of the fluted wheel of 31 mm, a fertilizer-metering shaft rotational speed of 28 rpm, and a fertilizer-discharge flap angle of −1°. As shown in Table 21, the mean CVFU was 10.61%. Compared with the simulated value of 10.33%, the relative error was 2.71%.

Table 21

Soil-bin test results for the optimal operating parameters

No.	Fertilizer mass in grid 1	Fertilizer mass in grid 2	Fertilizer mass in grid 3	Fertilizer mass in grid 4	Fertilizer mass in grid 5	Coefficient of variation of fertilization uniformity
	[g]	[g]	[g]	[g]	[g]	[%]
1	25.66	19.71	18.49	22.09	24.33	12.23
2	21.05	22.95	19.65	19.2	24.63	9.49
3	22.91	21.46	25.98	20.75	19.50	10.05
4	21.06	26.85	19.25	22.32	24.58	11.67
5	22.63	24.19	18.47	23.54	20.55	9.6
Mean value						**10.61**

CONCLUSIONS

(1) This study proposed a calibration method for the discrete element simulation parameters of a granular organic fertilizer metering device. Measurements using a texture analyzer showed that the Poisson's ratio and elastic modulus of the fertilizer were 0.314 and 9.8×10^7 Pa, respectively. Coefficient of restitution tests showed that the fertilizer-fertilizer coefficient of restitution and the coefficients of restitution between the fertilizer and PA, PC, and PLA were 0.421, 0.422, 0.436, and 0.426, respectively. Rolling friction calibration tests showed that the rolling friction coefficients between the fertilizer and PA, PC, and PLA were 0.156, 0.154, and 0.157, respectively. The contact parameters between the fertilizer and the metering device materials were calibrated using a cylinder-lifting angle of repose test combined with EDEM simulations and a Design-Expert experimental design. The fertilizer-fertilizer static and rolling friction coefficients were 0.413 and 0.181, respectively, while the static friction coefficients between the fertilizer and PA, PC, and PLA were 0.276, 0.266, and 0.173, respectively.

(2) A discrete element simulation method was proposed to optimize the key parameters of a fluted-wheel fertilizer metering device. The coefficient of variation of fertilization uniformity was used as the evaluation index of fertilization performance. By combining the discrete element method (DEM) with response surface methodology, the effects of the parameters on fertilization uniformity were ranked as follows: fluted-wheel inscribed-circle diameter > fluted-wheel lead angle > number of grooves; fertilizer-metering shaft rotational speed > fertilizer-discharge flap angle > effective working length of the fluted wheel. Fluted wheels with the optimal and center-level structural parameters were fabricated by 3D printing and tested in a soil bin to validate the simulation results. The simulation and soil-bin tests identified two optimal parameter combinations: (1) a fluted-wheel inscribed-circle diameter of 37 mm, 7 grooves, and a fluted-wheel lead angle of 63°; and (2) an effective working length of the fluted wheel of 31 mm, a fertilizer-metering shaft rotational speed of 28 rpm, and a fertilizer-discharge flap angle of −1°.

ACKNOWLEDGEMENT

This paper was supported by the Xinjiang Provincial Key Project Fund (Ling ZHOU, No. 2025AB005), the Key Core Technology Research Project of Agriculture in Xinjiang Production and Construction Corps, China (Ling ZHOU, research on resource utilization model of livestock and poultry manure, development & integrated demonstration of production processes, grant number: [2023] No. 11 by Agriculture Bureau of Xinjiang Production and Construction Corps), the Project of the Innovation and Development Support Plan for Key Industries in Southern Xinjiang of China (Chang WAN, No. 2020DB003-04), the postgraduate research innovation project of Tarim University (Zilun ZHOU, No. TDGRI202347).

REFERENCES

[1] Adilet, S., Zhao, J., Sayakhat, N., Chen, J., Nikolay, Z., Bu, L., Sugirbayeva, Z., Hu, G., Marat, M., & Wang, Z. (2021). Calibration strategy to determine the interaction properties of fertilizer particles using two laboratory tests and DEM. *Agriculture*, 11(7), 592. https://doi.org/10.3390/agriculture11070592

[2] Bangura, K., Gong, H., Deng, R., Tao, M., Liu, C., Cai, Y., Liao, K. Liu, J. & Qi L. (2020). Simulation analysis of fertilizer discharge process using the Discrete Element Method (DEM). *PLoS ONE*, 15(7): e0235872. https://doi.org/10.1371/journal.pone.0235872

[3] Bivainis, V., Jotautienė, E., Lekavičienė, K., Mieldažys, R., & Juodišius, G. (2023). Theoretical and experimental verification of organic granular fertilizer spreading. *Agriculture*, 13(6), 1135. https://doi.org/10.3390/agriculture13061135

[4] Hwang, S.-J., & Nam J.-S. (2021). DEM simulation model to optimise shutter hole position of a centrifugal fertiliser distributor for precise application. *Biosystems Engineering*, 204, 326-345. https://doi.org/10.1016/j.biosystemseng.2021.02.004

[5] Ma, X., You, Y., Yang, D., Wang, D. & Hu,i Y. (2025). Discrete element parameter calibration of compound fertilizer used in Camellia oleifera planting areas. *Journal of Mechanical Science & Technology*, 39(10), 5997–6009. https://doi.org/10.1007/s12206-025-0830-0

[6] Nouh, S. A., Kushaari, K. Z., Keong, L. K., & Samsuri, S. (2024). Material characterization and inter/intra-particle validation for DEM simulation of urea coating process. *Particuology*, 88, 32-48. https://doi.org/10.1016/j.partic.2023.09.010

[7] Ștefan, V., Popa, L., Harabagiu, A., Ciupercă, R., Zaica, A., & Vișan, A. (2025). Optimization of organic fertilizer distribution using EDEM simulation analysis. *INMATEH - Agricultural Engineering*, 76(2), 1217-1230. https://doi.org/10.35633/inmateh-76-102

[8] Wang, J. F., Wang, R. D., Ju, J. Y., Song, Y. L., Fu, Z. D., Lin, T. H., Chen, G. Q., Jiang, R., & Wang, Z. (2023). Study on the influence of grooved-wheel operating parameters on fertilizer emission performance and parameter optimization. *Agronomy*, 13(11), 2779. https://doi.org/10.3390/agronomy13112779

[9] Wang, Y., Tan, Y. P., Wei, S. L., Liao, M.M.，Zang, Y. & Zeng, S. (2023). Design and experimental study of the fertilizer applicator with vertical spiral fluted roller. *International Journal of Agricultural and Biological Engineering*, 17(3), 102–112. https://doi.org/10.25165/j.ijabe.20231605.7555

[10] Xie, C., Yang, J., Wang, B., Zhuo, P., Li, C., & Wang, L. (2021). Parameter calibration for the discrete element simulation model of commercial organic fertilizer. *International Agrophysics*, 35(01), 107-117. https://doi.org/10.31545/intagr/134141

[11] Zeng, S., Tan, Y. P., Wang, Y., Luo, X. W., Yao, L. M., Huang, D. P., & Mo, Z. W.（2020）Structural design and parameter determination for fluted-roller fertilizer applicator. *International Journal of Agricultural and Biological Engineering*, 13(2): 101–110. https://doi.org/10.25165/j.ijabe.20201302.4999

[12] Zha, X., Zhang, G., Han, Y., Salem, A. E., Fu, J., & Zhou, Y. (2021). Structural optimization and performance evaluation of blocking wheel-type screw fertilizer metering device. *Agriculture*, 11(3), 248. https://doi.org/10.3390/agriculture11030248

[13] Zhang, Y. L., Li, P., Shi, L., & Zhang, W. D. (2019). *Practical engineering plastics handbook (实用工程塑料手册)*, Second Edition, China Machine Press, Beijing / China, ISBN: 9787111620792.

[14] Zinkevičienė, R., Jotautienė, E., Juostas, A., Comparetti, A., & Vaiciukevičius, E. (2021). Simulation of granular organic fertilizer application by centrifugal spreader. *Agronomy*, 11(2), 247. https://doi.org/10.3390/agronomy11020247

OPERATIONAL RELIABILITY OF UAV-BASED WASTE SITE DETECTION FOR ENVIRONMENTAL MONITORING

/

FIABILITATEA OPERAȚIONALĂ A IDENTIFICĂRII ZONELOR CU DEȘEURI UTILIZÂND UAV-URI ÎN MONITORIZAREA MEDIULUI

Adrian IOSIF [1)], Edmond MAICAN[1)], Sorin-Ștefan BIRIȘ[1)], Gabriel-Alexandru CONSTANTIN[1)], Mihai-Gabriel MATACHE[2)]

[1)]Department of Biotechnical Systems, Faculty of Biotechnical Systems Engineering, National University of Science and Technology Politehnica Bucharest, 060042 Bucharest, Romania

[2)]INMA Bucharest/Romania

Tel.: 0723700628; Email: aiosif@yahoo.com

DOI: https://doi.org/10.35633/inmateh-79-82

Keywords: *environmental monitoring; illegal dumping detection; UAV inspection; change detection; deep learning; operational reliability.*

ABSTRACT

Illegal dumping in peri-urban and natural environments poses persistent challenges for environmental authorities, particularly when large areas must be inspected with limited personnel and budget. Reliable and scalable monitoring approaches are essential for practical environmental management. Unmanned Aerial Vehicles (UAVs) offer rapid spatial coverage, yet it remains unclear how complex the analysis must be to reliably detect waste sites in practice. This controlled pilot study evaluated the operational reliability of three UAV-based image analysis approaches (global statistical screening, classical change detection with colour filtering, and deep learning object recognition) under controlled field conditions. The field experiment used controlled contamination conditions so that the evaluation reflected practical detection reliability rather than algorithm benchmarking. The statistical method could not reliably identify localised waste, while change detection achieved moderate reliability (~72%; 29 of 40 evaluated acquisitions) but required reference imagery. The deep learning model achieved the highest site detection reliability (~93%; 37 of 40 evaluated acquisitions) and worked without baseline images. Its main advantage was improved object completeness rather than better identification of contaminated areas. These observations showed that monitoring workflow design matters more than increasing algorithmic complexity. A tiered strategy that combines broad screening with focused high-accuracy analysis can reduce inspection effort without compromising the results of inspection. The evaluated pilot framework supported the selection of monitoring approaches according to available resources, and the findings apply to the controlled, low-altitude field conditions (15 m above ground level, single test site) examined here rather than to fully validated multi-site operation.

REZUMAT

Depozitarea ilegală a deșeurilor în zone periurbane și în mediul natural reprezintă o provocare continuă pentru autoritățile de mediu, în special atunci când trebuie inspectate suprafețe extinse cu personal și bugete limitate. În acest scop, sunt necesare metode de monitorizare fiabile și scalabile pentru o gestionare practică a mediului. Vehiculele aeriene fără pilot (UAV) oferă o acoperire spațială rapidă, însă rămâne încă neclar cât de complexă trebuie să fie analiza pentru a detecta în mod fiabil siturile de deșeuri. Acest studiu-pilot, desfășurat în condiții controlate, a evaluat fiabilitatea operațională a trei abordări de analiză a imaginilor bazate pe UAV (analiza statistică globală, detecția clasică a schimbărilor cu filtrare de culoare și recunoașterea obiectelor prin învățare profundă) în condiții de teren controlate. Experimentul a utilizat condiții de contaminare controlate, astfel încât evaluarea să reflecte fiabilitatea practică a detecției, și nu performanța algoritmilor în sine. Metoda statistică nu a putut identifica în mod fiabil deșeurile localizate, în timp ce analiza detecției schimbărilor a atins o fiabilitate moderată (~72%; 29 din 40 de achiziții evaluate), dar a necesitat imagini de referință. Modelul de învățare profundă a obținut cea mai ridicată fiabilitate în detectarea siturilor cu deșeuri (~93%; 37 din 40 de achiziții evaluate) și a funcționat fără imagini de referință. Principalul său avantaj a fost îmbunătățirea prin completare a setului de obiecte detectate, mai degrabă decât o identificare mai bună a zonelor contaminate. Aceste observații arată că proiectarea fluxului de monitorizare este mai importantă decât creșterea complexității algoritmice. O strategie pe niveluri, care combină o analiză generală cu o analiză focalizată pe obținerea unei acurateți mai mari, poate reduce efortul de inspecție fără a compromite rezultatele inspecției.

Cadrul de lucru evaluat sprijină selectarea metodelor de monitorizare în funcție de resursele disponibile, iar rezultatele sunt valabile pentru condițiile de teren controlate, la altitudine redusă (15 m deasupra solului, un singur amplasament de test), examinate în acest studiu-pilot.

INTRODUCTION

Illegal dumping in peri-urban areas, waterways, agricultural fields, and natural reserves remains a common environmental problem. Ground-based inspections are labour-intensive, time-consuming, and often provide limited spatial coverage.

Illegal dumping affects soil, groundwater, biodiversity, and public health and is regulated within several European and international policy frameworks. The European Union Waste Framework Directive (Directive 2008/98/EC) establishes the legal basis for waste prevention, monitoring, and remediation obligations within Member States. Locating illegal disposal sites is required for regulatory compliance and enforcement. Waste monitoring is also aligned with the United Nations Sustainable Development Goals, particularly SDG 11 (Sustainable Cities and Communities) and SDG 12 (Responsible Consumption and Production), which promote environmentally sound waste management. Scalable and cost-efficient inspection methods therefore support environmental governance and sustainable urban management (*European Parliament and Council Directive, 2008; United Nations, 2015*).

UAV surveys combined with machine learning provide a practical alternative to ground inspections by enabling rapid coverage and automatic identification of potential waste hotspots. UAVs offer high spatial resolution and have become an established tool in environmental monitoring (*Manfreda et al., 2018*). However, their effectiveness depends not only on detection algorithms but also on acquisition strategy and survey design (*Torresan et al., 2017*). Recent studies have explored deep learning approaches for waste detection from aerial imagery. Reported results show promising detection accuracy but also reveal practical limitations such as dataset size requirements, variability of acquisition conditions, and lack of standardized datasets (*Youme et al., 2021; Sliusar et al., 2022; Mei et al., 2023; Wang et al., 2024*).

Experimental applications further illustrate these constraints. Deep neural networks have been used for marine litter detection and coastal debris mapping, where performance depends strongly on spatial resolution and scene complexity (*Fallati et al., 2019; Moy et al., 2018*). Other studies focus on spatial distribution mapping rather than individual object identification, highlighting the role of UAV surveys in environmental assessment workflows (*Gonçalves et al., 2020*).

Beyond object detection, UAVs have also been used for volumetric estimation and structural monitoring of waste sites. Applications include landfill volume modelling, settlement analysis, and combined UAV–terrestrial laser scanning workflows for improved topographic characterisation (*Filkin et al., 2022; Baiocchi et al., 2019; Son et al., 2020*).

Plastic waste detection has received particular attention across aquatic and terrestrial environments. Approaches range from deep semantic segmentation and hyperspectral discrimination to multisensor fusion and thermal infrared imaging (*Jakovljevic et al., 2020; Balsi et al., 2021; Maharjan et al., 2022; Topouzelis et al., 2019; Goddijn-Murphy et al., 2022; Yang et al., 2019*). These studies demonstrate that detection performance is influenced not only by algorithm choice but also by sensor characteristics, spatial resolution, and acquisition conditions. In UAV-based environmental applications, spatial resolution and acquisition geometry must be matched to the monitoring objective. Ground sampling distance and revisit frequency directly affect detectability, particularly for small or partially reflective objects such as plastic waste (*Pîrjol, 2018*).

Although UAV and AI tools are increasingly used, authorities still face uncertainty regarding how much analytical complexity is actually required in routine monitoring. In many situations, simpler approaches may already provide sufficient information, particularly when inspection resources are limited (*Gheres et al., 2025*).

This study therefore examines monitoring methodology rather than proposing a new detection algorithm. Three levels of analysis are compared in an operational context: basic statistical screening, change detection using classical computer vision techniques, and deep learning–based object recognition. The aim is to determine the minimum level of analysis needed for reliable site identification and to support the selection of appropriate monitoring strategies.

The main novelty of this work is therefore twofold and is stated here explicitly. First, the study provides an operational comparison of three distinct levels of image analysis (global statistical screening, classical change detection with colour filtering, and deep learning object recognition) applied to the same imagery, acquired with the same flight parameters and assessed with the same decision criterion, instead of comparing values reported on different benchmark datasets.

Second, the study separates two performance concepts that are usually reported together: site-level inspection triggering, that is, whether a survey correctly decides that a field inspection is needed, and object-level detection performance, that is, how completely the individual waste items are identified. This separation is what allows the minimum sufficient level of analysis to be identified for a given monitoring objective, and it is the element that distinguishes the present work from conventional algorithm benchmarking.

The dataset is used as a calibration scenario rather than a large training corpus. Controlled contamination conditions allow consistent comparison between methods while minimizing environmental variability.

MATERIALS AND METHODS

UAV Platform and Image Acquisition

The UAV system used in this study is a DJI Mini 2 (SZ DJI Technology Co., Ltd., Shenzhen, China), a lightweight quadrotor platform weighing 249 g, equipped with a 1/2.3" CMOS sensor capable of capturing 12 MP still images and 4K video.



Fig. 1 - DJI Mini 2 UAV platform used for image acquisition in this study

All imagery was acquired over the orchard garden of the Faculty of Biotechnical Systems Engineering, National University of Science and Technology Politehnica Bucharest. The drone was operated at a maximum altitude of 15 m above ground level (AGL), providing a spatial resolution of approximately 0.5 cm per pixel. Two reference images were captured: one depicting the undisturbed scene (baseline) and one after controlled placement of PET bottles and aluminium cans of varying sizes, colours, and shapes. This controlled setup enables direct verification of detection outputs across the three evaluated methods.

Colour-Based Image Representation. RGB Colour Model

The RGB colour space was used for initial statistical screening based on channel histogram comparison. Due to its sensitivity to illumination variation, RGB alone is not suitable for reliable outdoor segmentation but serves as a baseline reference for global scene changes (*Stan et al., 2025*).

The statistical screening criterion was defined as follows. For each of the three red–green–blue (RGB) channels the 256-bin histogram was normalised and compared between the baseline and the post-contamination image with the OpenCV correlation metric (cv2.HISTCMP_CORREL). A scene was flagged as changed when the correlation coefficient of at least one channel fell below 0.98. This threshold was derived from the data and not assumed: 15 repeated acquisitions of the undisturbed scene produced baseline-to-baseline channel correlations between 0.962 and 0.998 (mean 0.987), so 0.98 corresponds approximately to the lower quartile of the natural, illumination-driven variability of the site. The correlation criterion was preferred over histogram intersection or the chi-square distance because it is normalized, dimensionless and directly comparable between the three channels, which is the property required for a single global screening decision. These 15 undisturbed acquisitions are the same frames that form the uncontaminated part of the 40-frame evaluation set defined in the Experimental Setup subsection. The 0.98 correlation threshold was therefore calibrated on the evaluation imagery itself and not on an independent image set, and this is taken into account when the corresponding results are interpreted.

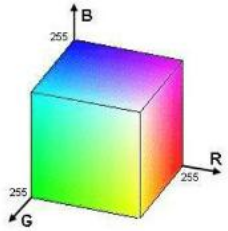


Fig. 2 - Conceptual illustration of RGB channel composition used as baseline reference for histogram comparison

HSV and HSL Colour Representations

The HSV and HSL colour representations were evaluated for colour-based segmentation of plastic waste. Both separate chromatic information from intensity, reducing sensitivity to illumination variations in outdoor scenes. In practice, HSV provided more stable threshold intervals for the tested objects, while HSL produced less consistent separation under shadow and reflective conditions. Consequently, HSV was selected for the segmentation stage.

The numerical hue–saturation–value (HSV) intervals applied in the segmentation stage were derived empirically from the acquired imagery rather than assumed. A total of 120 regions of interest containing polyethylene terephthalate (PET) bottles or aluminium cans and 120 regions of interest containing only vegetation, bare soil or shadow were sampled manually from the post-contamination frames. For the waste regions of interest, the 5th - 95th percentile range of the hue, saturation and value channels was computed (OpenCV convention, hue in the range 0-179) and rounded, which produced the two intervals used later for validation: dark blue (H 70-130, S 40-255, V 30-255) and cyan or light blue (H 50-100, S 40-255, V 100-255). The lower saturation bound of 40 removes desaturated soil and dry vegetation and the lower value bounds remove deep shadow pixels; these two classes were the dominant sources of false colour matches in the sampled background regions of interest. The 240 regions of interest were sampled from frames that also belong to the 40-frame evaluation set, so the hue–saturation–value intervals and the 5% coverage criterion were likewise calibrated on the evaluation imagery rather than on independent data. It should also be stated explicitly that these two intervals deliberately target only the blue and cyan chromatic cues that dominate the staged polyethylene terephthalate bottles: the validation stage was never intended to cover the complete range of colours and material classes placed in the scene, and it is applied as a colour-consistency filter on candidate regions rather than as a general waste classifier.

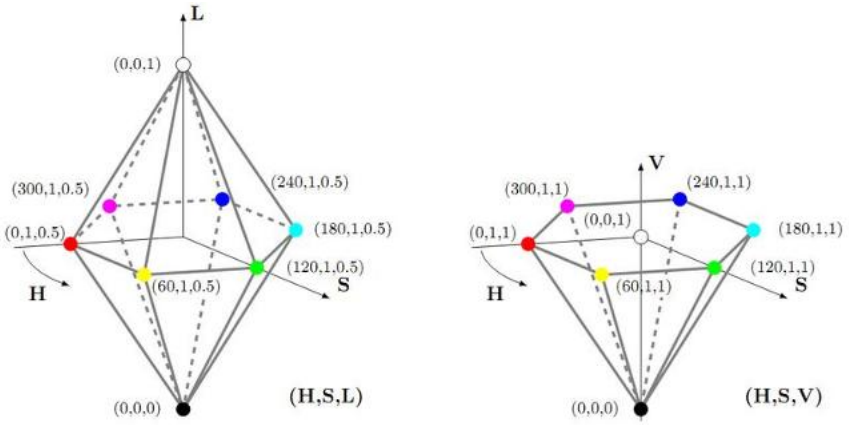


Fig. 3 - Comparison of HSL and HSV representations used during segmentation testing. HSV showed more stable threshold behaviour under field conditions
(original figure, produced by the authors)

Neural Network Architecture: YOLOv8

A YOLOv8 single-stage object detection model was used to evaluate deep learning–based recognition performance. The model was retrained on a domain-specific dataset to detect PET bottles and aluminium cans under field conditions.

The pretrained YOLOv8 model (COCO dataset, 80 classes) does not include PET bottles or aluminium cans as dedicated categories. Retraining was therefore required to adapt the detector to the specific waste classes considered in this study. The YOLOv8s (small) variant was selected as a balance between detection performance and computational efficiency.

Dataset Preparation for YOLOv8 Retraining

A dedicated dataset was constructed consisting of 1130 images of PET bottles and aluminium cans placed in natural outdoor settings representative of field inspection conditions. Objects covered multiple brands, sizes, colours, and deformation states. Images were captured at varying distances (0.5–3 m), viewing angles, and illumination conditions to introduce intra-class variability while maintaining controlled environmental context. Annotations were created in YOLO format using Roboflow with two classes: *pet_bottle* and *aluminium_can*. Data augmentation included horizontal and vertical flips, HSV variation (±15%), and mosaic augmentation.

The dataset was split image-wise into 791 training images (70%), 226 validation images (20%) and 113 test images (10%), with no scene and no physical object appearing in more than one subset, and it was used to calibrate the detection workflow rather than to train a general-purpose detector. Diverse backgrounds, lighting conditions, and object appearances were intentionally included.



Fig. 4 - Selection of field-collected PET bottle and aluminium can images used for YOLOv8 retraining
(original images, acquired by the authors)

Retraining was performed for 100 epochs using the YOLOv8s (small) variant with a batch size of 16 and an initial learning rate of 0.01 reduced through cosine annealing. Training was executed on an NVIDIA T4 GPU (Google Colab). The model checkpoint with the highest validation mAP@0.5 was used for inference.

The validation subset was used exclusively for checkpoint selection (highest validation mean average precision at an intersection-over-union of 0.5, reached at epoch 87 of 100), and the 113-image test subset was processed only once, after the final checkpoint had been fixed, giving a mean average precision at an intersection-over-union of 0.5 of 0.83. The 40 unmanned aerial vehicle frames used for the operational evaluation reported in the Results section were fully independent from model training and from model selection: they were acquired in a separate flight session at 15 m above ground level in nadir orientation, whereas all 1130 dataset images were acquired at close range (0.5–3 m) on different dates and in different parts of the site. No evaluation frame, and no crop derived from an evaluation frame, was used at any stage of training, augmentation, validation or checkpoint selection.

The experimental site was selected to ensure controlled environmental conditions rather than geographic representativeness. The orchard contains mixed vegetation, variable illumination, and reflective surfaces typical of peri-urban dumping areas. Using a single controlled location isolates detection behaviour from geographic variability and is consistent with pilot validation procedures prior to multi-site deployment.

Experimental Setup

In environmental inspection scenarios, detection performance is evaluated in terms of operational reliability rather than pure computer vision accuracy. The objective is to determine whether a method can reliably trigger a site inspection when waste is present, not to optimize object-level classification metrics. Accuracy values are therefore interpreted as indicators of inspection reliability.

Site-level detection reliability was defined as the correct classification of a monitored area as contaminated or uncontaminated. A detection was considered successful if at least one waste object was correctly identified within the contaminated scene, triggering an inspection flag. To reduce random variability, each scenario was repeated with slight UAV repositioning (±0.5 m lateral shift). Each waste layout was captured 5 times and the undisturbed condition was captured 15 times, all within short temporal intervals and with identical flight parameters.

The evaluation set was identical for the three methods and consisted of 40 unmanned aerial vehicle frames acquired in the same session: 25 frames of the contaminated area (5 distinct spatial layouts of the waste objects, each captured 5 times) and 15 frames of the undisturbed area. Each method was therefore applied 40 times, which gives 40 site-level decisions per method and 120 site-level decisions in total.

For the change detection method, which requires a reference, each of the 25 contaminated frames was paired with a baseline frame from the same session, and the 15 undisturbed frames were processed as baseline-to-baseline pairs so that false alarms could be counted under identical processing conditions.

Site-level detection reliability R was computed as the proportion of correct site-level decisions over the complete evaluation set: R = (TPsite + TNsite) / Ntotal, with Ntotal = 40. Here TPsite is the number of contaminated frames (out of 25) in which at least one waste object was correctly localised, thereby raising the inspection flag, and TNsite is the number of undisturbed frames (out of 15) in which no inspection flag was raised. The denominator is therefore the total number of evaluated acquisitions and not the number of waste objects present in the scene; object counts are used only for the object-level metrics reported separately in the subsection Object-Level Detection Metrics.

Concerning the independence of the data used for threshold selection, the three methods were not evaluated under exactly the same conditions, and this difference should be clearly acknowledged. For the two classical approaches, the decision thresholds (the 0.98 histogram-correlation threshold, the two hue–saturation–value (HSV) ranges, and the 5% coverage criterion) were established using frames and regions of interest from the same 40-frame dataset used for evaluation. No separate calibration flight was carried out. Therefore, the reliability values reported below for the RGB histogram comparison and the OpenCV change-detection method with HSV filtering should be regarded as calibration-scenario results rather than as performance obtained on an independent test set. In contrast, the retrained YOLOv8 model was evaluated under fully independent conditions. Its training and validation data, as well as the data used for checkpoint selection, consisted of close-range images acquired during separate sessions, as described in the Dataset Preparation subsection. This difference in the evaluation procedure actually gives the classical methods an advantage. Consequently, the better performance of the deep learning approach reported in the Results section can be considered a conservative result rather than one caused by a more favourable evaluation setup. At the same time, this experimental design reflects a realistic operational situation, since threshold-based methods are commonly adjusted to the specific conditions of a site before deployment.

All experiments were conducted in the orchard garden of the Faculty of Biotechnical Systems Engineering. Following the baseline image acquisition, PET bottles (ranging from 0.5 L to 2 L, in transparent, blue, green, and branded varieties) and aluminium cans (330 mL, assorted brands) were distributed across a defined ground area. The UAV was repositioned using identical flight parameters (15 m AGL, nadir orientation) for post-contamination acquisition.



Fig. 5 - Baseline UAV image acquired at 15 m AGL over the experimental site (no waste present)

(original image, acquired by the authors)



Fig. 6 - Post-contamination UAV image showing PET bottles and aluminium cans distributed across the test area. Waste objects appear as reflective elements contrasting with the surrounding vegetation

(original image, acquired by the authors)

RESULTS

Method 1: RGB Histogram Channel Comparison

RGB channel histograms were computed using OpenCV (256 intensity bins per channel) and compared between baseline and contaminated scenes to assess global distribution shifts.

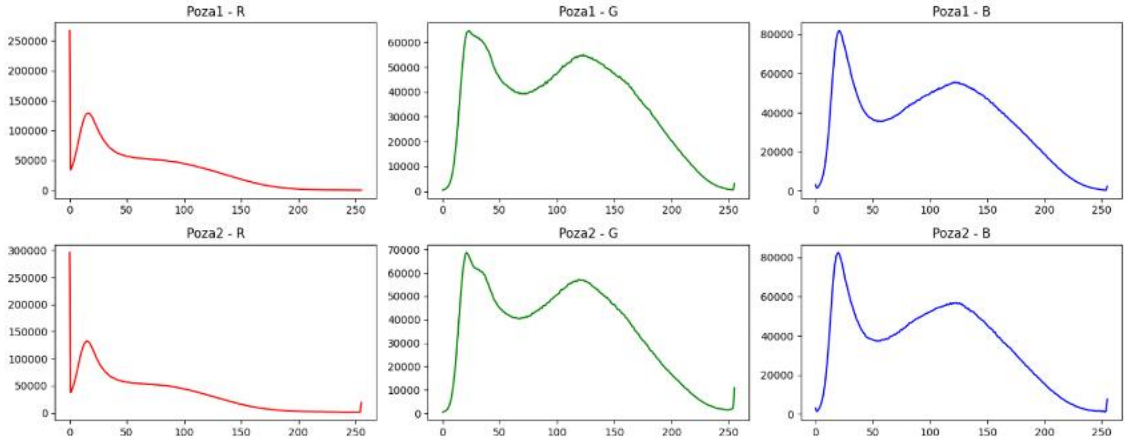


Fig. 7 - RGB channel histograms for the baseline image (Row 1) and contaminated image (Row 2). The distributions are nearly identical, indicating limited sensitivity to localised waste objects

(Original figure, produced by the authors)

The histogram pairs (Fig. 7) show minimal differences between the two scenes. This reflects the small spatial footprint of the waste objects relative to the full image and the reflective or semi-transparent nature of PET bottles, which blend with surrounding vegetation. As a result, global RGB statistics were insufficient for detecting localised contamination under these conditions and serve primarily as a baseline reference for comparison with more advanced methods.

Expressed in the terms defined in the Experimental Setup subsection, the correlation criterion flagged none of the 25 contaminated frames (0 of 25) and correctly classified 11 of the 15 undisturbed frames as unchanged, so the site-level reliability was (0 + 11) / 40 = 11/40 = 27.5%. The waste objects covered only 0.4-0.6% of the frame area, and the mean channel correlation between a baseline frame and its contaminated counterpart was 0.994, that is, higher than the correlation observed between two repeated captures of the undisturbed scene (0.962–0.998). This is the direct numerical reason why the global statistical approach is non-conclusive rather than merely imprecise: the signal produced by the waste is smaller than the natural variability of the scene. As stated in the Experimental Setup subsection, the 0.98 threshold was calibrated on these same frames, so this value describes calibration-scenario performance and not an independent test; a threshold transferred from another site would not be expected to perform better.

Method 2: OpenCV Change Detection with HSV Filtering

The second method combines temporal change detection (pixel-level image differencing) with spatial object filtering based on HSV colour masking, a classical approach used in environmental and surveillance monitoring (*Radke et al., 2005*). Similar threshold-based segmentation strategies have been applied in UAV imagery analysis for vegetation detection (*Torres-Sánchez et al., 2015*).

The processing steps were as follows:

Step 1 – Image alignment and differencing. The two images were resized to identical dimensions and the absolute pixel-wise difference was computed using cv2.absdiff(), producing a map highlighting changed regions.

Geometric alignment was obtained in two stages. First, both acquisitions were taken from the same programmed waypoint with the aircraft in hover-hold, at 15 m above ground level and with the gimbal oriented nadir, so that the residual horizontal displacement logged by the onboard global navigation satellite system and vision positioning remained within ±0.5 m; frames whose logged attitude deviated by more than 2° in pitch or roll from the baseline frame were discarded before processing. Second, the post-contamination frame was resized to the baseline dimensions and shifted by an integer pixel offset obtained by maximising the normalised cross-correlation of the two grayscale images over a ±30-pixel search window, computed only on the outer 15% of the frame, a border region that contains no waste objects. The residual misalignment after this correction was 1–2 pixels, that is, approximately 0.5–1 cm on the ground, which is smaller than the smallest object footprint considered. Only a translational correction was applied; sub-pixel and rotational residuals were not compensated, which is why feature-point registration is proposed as an improvement in the final part of

this section. The ±0.5 m quoted above is the position-hold envelope specified for the platform and not the displacement actually observed; at the stated ground sampling distance it would correspond to about 100 pixels, whereas the correlation search window of ±30 pixels covers approximately ±15 cm. The two values are reconciled by the acceptance procedure applied to the frames: the residual translational offset measured between each post-contamination frame and its baseline, before correction, was 6–24 pixels (approximately 3–12 cm on the ground) with a mean of 13 pixels (approximately 6.5 cm), so every accepted pair lay inside the search window. Three acquisitions exceeded the ±30-pixel window and were rejected and re-flown before the evaluation set was assembled; consequently all 40 frames used in the evaluation satisfy this criterion, and the search window was sized on the measured offsets rather than on the worst-case positioning specification.

Step 2 – Noise reduction and binarisation. The difference map was converted to grayscale and smoothed with a Gaussian blur (kernel 5×5, σ=10) to reduce high-frequency noise and minor registration artifacts. A fixed threshold (T=60) generated a binary mask in which values above the threshold corresponded to significant changes.

Step 3 – Contour extraction and filtering. External contours were extracted using cv2.findContours(). Contours with bounding box areas smaller than 1000 pixels were discarded. At the tested resolution of approximately 0.5 cm per pixel this threshold corresponds to a ground footprint of about 250 cm² and was set to suppress the small change blobs produced by vegetation movement between the two acquisitions. As a direct consequence, an isolated 330 mL aluminium can, whose bounding box covers approximately 310 pixels, falls below the threshold and is retained only when it merges with an adjacent object into a larger change region; this is one of the identified causes of the moderate object-level recall reported below.

Step 4 – HSV colour validation. For each candidate bounding box, the corresponding Region of Interest (ROI) was converted to HSV. Two mask intervals targeted typical waste colours: dark blue (H:70-130, S:40-255, V:30-255) and cyan/light blue (H:50-100, S:40-255, V:100-255). If more than 5% of ROI pixels satisfied either mask, the object was classified as PET waste and marked with a bounding box. The 5% coverage value was determined from the same sampled regions of interest used to derive the HSV intervals: true waste regions showed between 12% and 48% of pixels inside the two masks, whereas vegetation, soil and shadow regions remained below 2%, so any value between 3% and 10% separates the two populations; 5% was retained as the midpoint of that interval. This validation stage is intentionally restricted to blue and cyan colour cues and is not intended to detect the complete range of waste colours and classes staged in the experiment. Candidate regions corresponding to transparent, green or metallic objects are consequently rejected here even when the differencing step localised them correctly, which is a further identified cause of the moderate object-level completeness discussed below.



Fig. 8 - Output of the OpenCV change detection pipeline. Overlapping bounding boxes are visible due to the absence of Non-Maximum Suppression (NMS). Detection reliability under controlled conditions was approximately 72% (29 of 40 evaluated acquisitions)

(original figure, produced by the authors)

The method localised the main waste cluster and most individual objects, performing substantially better than the histogram-based approach. However, several limitations were observed. Illumination changes between acquisitions (e.g., sun angle or cloud cover) affected chromatic consistency and reduced stability.

The absence of Non-Maximum Suppression produced overlapping bounding boxes in partially occluded areas. False positives occurred when non-waste blue objects were present. In addition, the approach requires a clean baseline image of the same scene, limiting its use to monitoring scenarios where prior reference imagery exists.

In numerical terms, the change detection pipeline raised a correct inspection flag in 21 of the 25 contaminated frames and correctly returned no flag in 8 of the 15 undisturbed frames, which gives a site-level reliability of (21 + 8) / 40 = 29/40 = 72.5%, reported throughout as approximately 72%. The 7 false alarms on undisturbed frames were produced by illumination changes on reflective leaf surfaces between the two acquisitions of a pair, and the 4 missed contaminated frames corresponded to layouts containing only small isolated cans, which fall below the contour area threshold defined in Step 3. This value is likewise a calibration-scenario result, since the hue–saturation–value intervals and the coverage criterion were derived from the same imagery.

Method 3: Custom-Retrained YOLOv8 Neural Network

YOLOv8 was retrained on the 1130-image PET and aluminium can dataset described in Section 2.4. Inference was performed using the Ultralytics Python API with a confidence threshold of 0.3 and an Intersection-over-Union threshold of 0.7 for duplicate suppression. Detected objects were annotated with bounding boxes and saved to folder runs/detect/predict/.

Under the tested conditions, the retrained YOLOv8 reached approximately 93% site detection reliability (23 of the 25 contaminated frames were correctly flagged and 14 of the 15 undisturbed frames correctly returned no flag, that is (23 + 14) / 40 = 37/40 = 92.5%), representing the highest reliability among the evaluated methods. The model remained stable in the presence of partial occlusion, varied object orientations, and reflective surfaces that reduced the performance of the colour-based methods.

PET bottles of different sizes and colours were correctly identified in the test scene. The built-in NMS mechanism within the YOLO inference pipeline prevented duplicate bounding boxes. A representative detection example under field conditions is presented in Fig. 9.

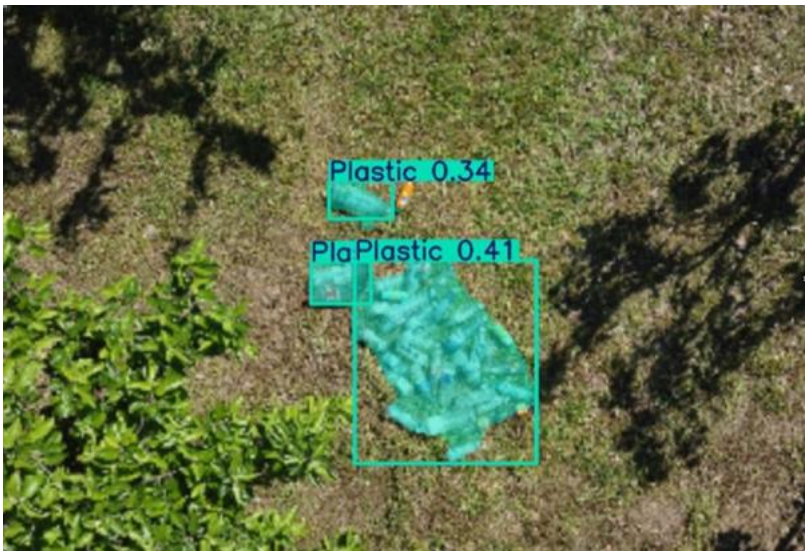


Fig. 9 - Site-level detection result obtained with the retrained YOLOv8 model. All but one waste object were identified, sufficient to trigger a positive inspection flag under the defined reliability criteria
(original figure, produced by the authors)

Unlike the change-detection approach, YOLOv8 does not require a reference image. Detection can therefore be performed on single acquisitions, which is relevant for surveys in areas without prior coverage. However, the approach requires dedicated computational resources for training, and its performance depends on the diversity and representativeness of the training dataset.

Object-Level Detection Metrics

Beyond site-level reliability, object-level detection was assessed using standard object detection metrics. The retrained YOLOv8 model reached a precision of approximately 0.90 and a recall of approximately 0.75, resulting in an F1-score of about 0.82. Mean average precision was approximately mAP@0.5≈0.80 and mAP@0.5:0.95≈0.52. These metrics were computed over the 25 contaminated evaluation frames, which contain 168 annotated waste objects in total (112 PET bottles and 56 aluminium cans).

The model returned 140 detections above the confidence threshold, of which 126 were true positives and 14 false positives, while 42 annotated objects were not detected; this gives a precision of 126/140 = 0.90, a recall of 126/168 = 0.75 and an F1-score of 0.82. Recall was lower than site-level reliability because small, partially occluded, or highly reflective objects were not always individually detected, even when the contaminated area was correctly classified. Such behaviour is consistent with monitoring tasks where confirming contamination presence is more relevant than detecting every individual item.

To evaluate robustness, inference was repeated under identical flight parameters using multiple image captures acquired within short temporal intervals. Variability in detection performance remained within ±3-5% for precision and recall (computed as the range of the precision and recall values across the five repeated captures of each of the five waste layouts), indicating stable behaviour under consistent environmental conditions. While the study does not address multi-site generalisation, the limited variability indicates stable performance under the tested conditions.

Comparative Performance Summary

Table 1 summarizes the key characteristics and operational monitoring characteristics of the three methods evaluated in this study. The site-level reliability values of the two classical methods are calibration-scenario values in the sense defined in the Experimental Setup subsection, whereas the YOLOv8 value was obtained with a model trained, validated and selected on independent imagery.

Table 1

Comparative summary of the three waste detection methods

Method	Core Technique	Site Detection Reliability	Baseline Required	Operational Processing Feasibility
RGB Histogram	Global colour distribution comparison	<30% (non-conclusive)	Yes	Yes
OpenCV Change Detection + HSV	Pixel differencing + HSV colour masking	~72%	Yes	Partially
YOLOv8 (retrained)	Custom deep learning detector	~93%	No	Yes

Note: the column Operational Processing Feasibility was rated with two criteria measured on the evaluation set: (a) the mean processing time per frame on the field configuration used in this study, a laptop with an Intel Core i7 processor, 16 GB of memory and no dedicated graphics card, and (b) the need for additional inputs or manual tuning during processing. The rating Yes means under 30 s per frame with no manual intervention (RGB histogram comparison, 0.8 s per frame; YOLOv8 inference, 2.1 s per frame on the processor and 0.35 s per frame on the NVIDIA T4 graphics card). The rating Partially means that the processing chain completes but requires a co-registered reference frame and manual re-tuning of the HSV intervals whenever object colours or illumination change (OpenCV change detection, 4.2 s per frame in addition to the alignment step). To ensure that the same definition is applied consistently to all three methods, the need for a reference image is not included in this rating. Instead, this requirement is reported separately in the *Baseline Required* column. The rating therefore considers only the requirements of the processing chain once the input images are available. Based on this definition, the RGB histogram comparison is rated *Yes*. Although it uses a reference frame, it compares global histograms and therefore does not require geometric co-registration or parameter adjustment during operation. The OpenCV change-detection method is rated *Partially*, not because it requires a reference image, but because the two images must be accurately aligned before comparison. In addition, the HSV intervals may need to be manually adjusted when object colours or illumination conditions change. YOLOv8 is rated *Yes* because it processes a single frame using fixed model parameters. Thus, the three ratings are based on the same criteria: processing time, co-registration effort, and the need for manual parameter tuning. This makes the ratings directly comparable across the three methods.

The contrast between object-level metrics and site-level reliability highlights the distinction between algorithm benchmarking and practical inspection needs. Missing individual items has limited impact on operational decisions if contamination presence is correctly identified. In this context, the combination of high precision and moderate recall is appropriate for screening scenarios in which UAV surveys are followed by targeted ground verification.

The subsections above report the direct experimental findings of the study. The subsections that follow (Analysis of Method Limitations, Toward Improved Waste Detection Systems, Environmental Monitoring Implications and Study Scope and Generalizability) contain the interpretation of those findings, the limitations of the experimental design and the directions proposed for future work, and are grouped here so that they remain clearly separated from the measured results.

Analysis of Method Limitations

The RGB histogram analysis method failed primarily due to the optical properties of the waste material. Transparent PET bottles at 15 m altitude act as highly reflective surfaces, reflecting the surrounding vegetation's spectral signature, thus making their contribution to the global colour histogram negligible. *Balsi et al. (2021)* reported similar challenges with transparent plastics in hyperspectral marine remote sensing, and the acquisition-dependent behaviour described by *Honkavaara et al. (2013)* suggests that global colour statistics are insufficient for localised waste mapping regardless of spectral resolution.

The OpenCV change detection pipeline overcomes the transparency problem by exploiting temporal changes (the appearance of new objects) rather than absolute colour. However, the method inherits the fundamental limitation of requiring a clean baseline image, which is unavailable in many operational contexts (e.g., post-event disaster assessments, areas with no prior UAV coverage). The fixed HSV threshold intervals are also susceptible to limitation when waste colours deviate from the assumed blue/cyan range – as would occur with red, yellow, or transparent bottles, or at different altitudes where atmospheric scattering modifies apparent hue. The absence of NMS is a practical limitation producing visually cluttered output; this could readily be addressed by applying cv2.dnn.NMSBoxes() to the detected bounding box list.

The retrained YOLOv8 model showed higher reliability than the classical methods but requires a domain-specific training corpus. Although the dataset contains 1130 training images, it remains limited in environmental diversity, as acquisitions were performed in a single site under controlled conditions. The model may struggle with out-of-distribution waste types (unusual colours, highly degraded bottles, dense overlapping clusters). Scale variation between training (ground-level photography) and inference (15 m AGL aerial) may also introduce domain shift, which was partially mitigated by including perspective-augmented crops in the dataset. Similar limitations have been widely reported for small object detection tasks, where limited pixel footprint and complex backgrounds reduce detection recall (*Ren et al., 2018; Kellenberger et al., 2018*). In operational monitoring, avoiding false alarms is often more critical than detecting every individual item. High precision reduces unnecessary field interventions, while moderate recall remains acceptable when aerial screening is followed by ground verification (*Gheorghe et al., 2024*).

The baseline-referenced approach is better suited to targeted surveillance contexts, such as periodically inspected protected areas, riverbanks, or infrastructure corridors. In these cases, reference imagery is typically available from previous inspection flights, making change-based detection a practical operational strategy.

While the experimental validation was conducted in a single controlled site, the environmental characteristics of the orchard – heterogeneous vegetation, variable illumination, reflective surfaces, and partial occlusion – represent common features of peri-urban dumping locations, which are known challenges in UAV-based remote sensing due to varying acquisition geometry and illumination conditions (*Honkavaara et al., 2013*). Detection performance mainly depends on ground sampling distance (GSD) and object size in pixels rather than on location (*Torresan et al., 2017*). At the tested altitude (15 m AGL, ~0.5 cm per pixel), standard PET bottles occupy sufficient pixel area to ensure detectability. Performance would likely decrease at higher altitudes or in dense vegetation. This relationship can be approximated from the ratio between object size and pixel size. The results should therefore be considered applicable to similar low-altitude UAV surveys.

Toward Improved Waste Detection Systems

Several improvements could further strengthen the proposed framework. Expanding the YOLOv8 training dataset beyond the current 1130 images to include aerial imagery acquired at multiple altitudes and additional waste classes (e.g., glass, cardboard, textiles) would improve generalisation. Instance segmentation models such as YOLOv8-seg could also enable pixel-level delineation and more precise estimation of contaminated surface area. The OpenCV pipeline could be refined through feature-point-based image registration (e.g., ORB with RANSAC homography) to reduce misalignment artifacts that occasionally generate spurious detections.

Multispectral or hyperspectral sensing may further enhance discrimination by exploiting the spectral contrast between plastics and natural materials, as previously reported by *Balsi et al. (2021)*.

From an operational perspective, deployment on embedded platforms such as NVIDIA Jetson devices could enable near real-time onboard inference during flight, reducing post-processing delays.

The proposed framework may support municipal dump site monitoring, GIS-based documentation of illegal dumping, emergency response assessments, and other environmental surveys using comparable UAV workflows.

Environmental Monitoring Implications

Environmental authorities rarely require exhaustive object inventories during initial inspections; instead, rapid identification of suspicious locations is typically sufficient to trigger field intervention, similar to zone-based environmental risk mapping approaches used in remote sensing (*Rozario et al., 2018*). The present results indicate that moderate-complexity approaches can detect contamination presence reliably, while deep learning mainly improves object-level completeness rather than site classification.

In practice, environmental surveillance programs may benefit from a tiered monitoring structure: wide-area screening using lower-cost detection followed by targeted high-accuracy analysis only where needed. This approach aligns with adaptive monitoring strategies discussed in environmental management literature (*Nichols and Williams, 2006*) and can reduce inspection effort and operational time. UAV imagery also provides georeferenced visual documentation that may support inspection reporting and enforcement procedures. Such tiered structures are consistent with established environmental decision-support practice (*Matthies et al., 2007*).

Study Scope and Generalizability

The dataset size reflects the methodological focus of the study rather than an attempt at statistical generalisation. While large datasets are necessary for training broadly transferable detectors, pilot environmental monitoring studies typically aim to evaluate workflow feasibility, acquisition constraints, and detection behaviour under realistic field conditions. The results should therefore be interpreted within the context of controlled validation rather than multi-site generalisation.

CONCLUSIONS

This study examined the feasibility of UAV-assisted waste monitoring workflows rather than benchmarking artificial intelligence performance. Inspection reliability was found to depend more on operational design – such as baseline availability, inspection objectives, and intervention criteria – than on algorithmic complexity alone. All results reported here were obtained under controlled, low-altitude field conditions (a single orchard site, 15 m above ground level, nadir acquisition, a ground sampling distance of approximately 0.5 cm per pixel and deliberately placed PET bottles and aluminium cans) and the conclusions are limited to that scope.

RGB histogram comparison was ineffective for detecting transparent PET waste against vegetation. OpenCV-based change detection with HSV filtering reached approximately 72% detection reliability under controlled conditions (29 of 40 evaluated acquisitions), a calibration-scenario value obtained with thresholds tuned on the same imagery, and proved useful when reference imagery was available, although sensitive to illumination variability and colour assumptions. The retrained YOLOv8 model achieved the highest site-level reliability (~93%; 37 of 40 evaluated acquisitions) and remained stable under occlusion, reflection, and colour variability without requiring a baseline image.

The main outcome of the study is an evaluated pilot monitoring framework linking analytical complexity to inspection reliability under the controlled conditions tested. The findings offer practical guidance for structuring UAV-based waste monitoring systems and may support decision-support workflows in which rapid aerial screening informs targeted field intervention.

Future developments may include expanding the dataset, exploring onboard inference, and integrating multispectral sensing. Overall, while higher analytical complexity improves object-level completeness, reliable contamination detection can already be achieved at moderate complexity levels under the conditions tested here, depending on operational objectives. Method selection should therefore follow monitoring needs rather than detection accuracy alone.

REFERENCES

[1] Baiocchi, V., Napoleoni, Q., Tesei, M., Servodio, G., Alicandro, M., Costantino, D. (2019). UAV for monitoring the settlement of a landfill. *European Journal of Remote Sensing*, 52(sup1), 41–52. https://doi.org/10.1080/22797254.2019.1683471

[2] Balsi, M., Moroni, M., Chiarabini, V., Tanda, G. (2021). High-resolution aerial detection of marine plastic litter by hyperspectral sensing. *Remote Sensing*, 13(8), 1557. https://doi.org/10.3390/rs13081557

[3] European Parliament and Council (2008). Directive 2008/98/EC of the European Parliament and of the Council of 19 November 2008 on Waste and Repealing Certain Directives. *Official Journal of the European Union*, L312, 3–30.

[4] Fallati, L., Polidori, A., Salvatore, C., Saponari, L., Savini, A., Galli, P. (2019). Anthropogenic Marine Debris assessment with Unmanned Aerial Vehicle imagery and deep learning: A case study along the beaches of the Republic of Maldives. *Science of the Total Environment*, 693, 133581. https://doi.org/10.1016/j.scitotenv.2019.133581

[5] Filkin, T., Sliusar, N., Huber-Humer, M., Ritzkowski, M., Korotaev, V. (2022). Estimation of Dump and Landfill Waste Volumes Using Unmanned Aerial Systems. *Waste Management*, 139, 301–308. https://doi.org/10.1016/j.wasman.2021.12.029

[6] Gheorghe, G.-V., Dumitru D.-N., Ciupercă, R., Mateescu M., Mantovani S.-A., Prisacariu E., Harabagiu A. (2024). Advancing Precision Agriculture with UAV'S: Innovations in Fertilization. *INMATEH - Agricultural Engineering*, 74(3). https://doi.org/10.35633/inmateh-74-89

[7] Gheres, M.-I., Mariasiu, F., Csato, A., Sechel, I.-C. (2025). Main Directions of Application of Artificial Intelligence in Agriculture: A Review. *INMATEH - Agricultural Engineering*, 77(3). https://doi.org/10.35633/inmateh-77-52

[8] Goddijn-Murphy, L., Williamson, B.J., McIlvenny, J., Corradi, P. (2022). Using a UAV Thermal Infrared Camera for Monitoring Floating Marine Plastic Litter. *Remote Sensing*, 14(13), 3179. https://doi.org/10.3390/rs14133179

[9] Gonçalves, G., Andriolo, U., Pinto, L., Bessa, F. (2020). Mapping Marine Litter Using UAS on a Beach-Dune System: a Multidisciplinary Approach, *Science of the Total Environment*, 706, 135742. https://doi.org/10.1016/j.scitotenv.2019.135742

[10] Honkavaara, E., Saari, H., Kaivosoja, J., Pölönen, I., Hakala, T., Litkey, P., Mäkynen, J., Pesonen, L. (2013). Processing and Assessment of Spectrometric, Stereoscopic Imagery Collected Using a Lightweight UAV Spectral Camera for Precision Agriculture. *Remote Sensing*, 5(10), 5006–5039. https://doi.org/10.3390/rs5105006

[11] Jakovljevic, G., Govedarica, M., Alvarez-Taboada, F. (2020). A Deep Learning Model for Automatic Plastic Mapping Using Unmanned Aerial Vehicle (UAV) Data. *Remote Sensing*, 12(9), 1515. https://doi.org/10.3390/rs12091515

[12] Kellenberger, B., Marcos, D., Tuia, D. (2018). Detecting Mammals in UAV Imagery: Best Practices to Address a Substantially Imbalanced Dataset with Deep Learning. *Remote Sensing of Environment*, 216, 139–153. https://doi.org/10.1016/j.rse.2018.06.028

[13] Maharjan, N., Miyazaki, H., Pati, B.M., Dailey, M.N., Nakamura, T., Shrestha S., Yoshida, Y. (2022). Detection of River Plastic Using UAV Sensor Data and Deep Learning. *Remote Sensing*, 14(13), 3049. https://doi.org/10.3390/rs14133049

[14] Manfreda, S., McCabe, M.F., Miller, P.E., Lucas, R., Pajuelo Madrigal, V., Mallinis, G., Ben Dor, E., Helman, D., Estes, L., Ciraolo, G., et al. (2018). On the Use of Unmanned Aerial Systems for Environmental Monitoring. *Remote Sensing*, 10(4), 641. https://doi.org/10.3390/rs10040641

[15] Matthies, M., Giupponi, C., Ostendorf, B. (2007). Environmental decision support systems: Current issues, methods and tools. *Environmental Modelling & Software*, 22(2), 123–127. https://doi.org/10.1016/j.envsoft.2005.09.005

[16] Mei, A., Baiocchi, V., Mattei, S., Zampetti, E., Pai, H.-J., Tratzi, P., Ragazzo, A.V., Cuzzucoli, A., Mancuso, A., Bearzotti, A., Fontinovo, G., Grosso, M., Chu, C.-Y., Bianconi, D. (2023). Conceptualization of a Satellite, UAS and UGV Downscaling Approach for Abandoned Waste Detection and Waste to Energy Prospects. *The International Archives of the Photogrammetry, Remote Sensing and Spatial Information Sciences*, XLVIII-1/W1-2023, 287–293. https://doi.org/10.5194/isprs-archives-XLVIII-1-W1-2023-287-2023

[17] Moy, K., Neilson, B., Chung, A., Meadows, A., Castrence, M., Ambagis, S., Davidson, K. (2018). Mapping Coastal Marine Debris Using Aerial Imagery and Spatial Analysis. *Marine Pollution Bulletin*, 132, 52–59. https://doi.org/10.1016/j.marpolbul.2017.11.045

[18] Nichols, J.D., Williams, B.K. (2006). Monitoring for Conservation. *Trends in Ecology & Evolution*, 21(12), 668–673. https://doi.org/10.1016/j.tree.2006.08.007

[19] Pȏol, P. (2018). Aspects Regarding the Use of Remote Sensing in Air Surveillance Missions. *Buletinul Universității Naționale de Apărare "Carol I"*, pp. 31–37.
[20] Radke, R.J., Andra, S., Al-Kofahi, O., Roysam, B. (2005). Image Change Detection Algorithms: A Systematic Survey. *IEEE Transactions on Image Processing*, 14(3), 294–307. https://doi.org/10.1109/TIP.2004.838698
[21] Ren, Y., Zhu, C., Xiao, S. (2018). Small Object Detection in Optical Remote Sensing Images via Modified Faster R-CNN. *Applied Sciences*, 8(5), 813. https://doi.org/10.3390/app8050813
[22] Rozario, P.F., Madurapperuma, B.D., Wang, Y. (2018). Remote Sensing Approach to Detect Burn Severity Risk Zones in Palo Verde National Park, Costa Rica. *Remote Sensing*, 10(9), 1427. https://doi.org/10.3390/rs10091427
[23] Sliusar, N., Filkin, T., Huber-Humer, M., Ritzkowski, M. (2022). Drone Technology in Municipal Solid Waste Management and Landfilling: A Comprehensive Review. *Waste Management*, 139, 1–16. https://doi.org/10.1016/j.wasman.2021.12.006
[24] Son, S.W., Kim, D.W., Sung, W.G., Yu, J.J. (2020). Integrating UAV and TLS Approaches for Environmental Management: A Case Study of a Waste Stockpile Area. *Remote Sensing*, 12(10), 1615. https://doi.org/10.3390/rs12101615
[25] Stan, A., Bănică, C.-K., Gândescu, C.-H., Simion, C., Cotorobai, D.-M., Simion, V., Muraru-Ionel, C. (2025). Design and Experiment of Multi-Purpose and Modular Sensor Robotic Platform for Real-Time Assessing and Monitoring of Cea Farms Using Point Cloud, LIDAR, RGB and Thermal Imaging. *INMATEH - Agricultural Engineering*, 77(3). https://doi.org/10.35633/inmateh-77-01
[26] Topouzelis, K., Papakonstantinou, A., Garaba, S.P. (2019). Detection of Floating Plastics from Satellite and Unmanned Aerial Systems. *International Journal of Applied Earth Observation and Geoinformation*, 79, 175–183. https://doi.org/10.1016/j.jag.2019.03.011
[27] Torresan, C., Berton, A., Carotenuto, F., Di Gennaro, S. F., Gioli, B., Matese, A., Wallace, L. (2017). Forestry Applications of UAVs in Europe: A Review. *International Journal of Remote Sensing*, 38(8–10), 2427–2447. https://doi.org/10.1080/01431161.2016.1252477
[28] Torres-Sánchez, J., López-Granados, F., Peña, J.M. (2015). An Automatic Object-based Method for Optimal Thresholding in UAV Images: Application for Vegetation Detection in Herbaceous Crops. *Computers and Electronics in Agriculture*, 114, 43–52. https://doi.org/10.1016/j.compag.2015.03.019
[29] United Nations (2015). Transforming Our World: The 2030 Agenda for Sustainable Development. United Nations General Assembly Resolution A/RES/70/1, New York.
[30] Wang, B., Xing, Y., Wang, N., Chen, C.L.P. (2024). Monitoring Waste from Uncrewed Aerial Vehicles and Satellite Imagery Using Deep Learning Techniques: A Review. *IEEE Journal of Selected Topics in Applied Earth Observations and Remote Sensing*, 17, 20064–20079. https://doi.org/10.1109/JSTARS.2024.3488056
[31] Yang, Q., Liu, M., Zhang, Z., Yang, S., Ning, J., Han, W. (2019). Mapping Plastic Mulched Farmland for High Resolution Images of Unmanned Aerial Vehicle Using Deep Semantic Segmentation. *Remote Sensing*, 11(17), 2008. https://doi.org/10.3390/rs11172008
[32] Youme, O., Bayet, T., Dembele, J.M., Cambier, C. (2021). Deep Learning and Remote Sensing: Detection of Dumping Waste Using UAV. *Procedia Computer Science*, 184, 197–204. https://doi.org/10.1016/j.procs.2021.05.037

PERFORMANCE EVALUATION OF MOBILE AND STATIONARY FISH SMOKING TECHNOLOGIES

/

የተንቀሳቃሽ እና የቋሚ የዓሣ ማጨሻ ቴክኖሎጂዎች የአፈጻጸም ማምገማ

Amanuel ERCHAFO[1*)], Maney AYALEW[1)]

[1)] Ethiopian Institute of Agricultural Research, Melkassa Agricultural Research Centre, Department of Agricultural Engineering, P.O. Box 436, Adama, Ethiopia

Corresponding author; E-mail: amanbaaman40@gmail.com; ORCID: https://orcid.org/0009-0002-2436-430.

DOI: https://doi.org/10.35633/inmateh-79-83

Keywords: *Drying rate, Fish, Moisture content reduction, Smoking technology, Smoking temperature*

ABSTRACT

A study was carried out to evaluate the performance of mobile and stationary fish smoking technologies. The experiment was conducted using a randomized block factorial design, with smoking temperature as a blocking factor. According to the investigation findings, at a smoking temperature of 90℃ and a smoking time of 4 hours, the maximum moisture content reduction of 81.4% was noted. In contrast, at a smoking temperature of 70 ℃ and a smoking time of 2 hours, the minimum moisture content reduction of 57.6% was noted for the electric fish smoker. Based on the test results of the electric fish smoker, at 90 ℃ of smoking temperature and 4 h of smoking time, the maximum drying rate of 0.69 kg h^{-1} was obtained. The findings verified that the maximum thermal efficiency of 69.8% was recorded at a smoking temperature of 90 ℃, and a smoking time of 2 h for the electric fish smoker. Based on comparative evaluation results, the moisture content reduction, drying rate, fuel consumption and thermal efficiency for the fuelwood fish smoker were found to be 66.17%, 0.38 kg h^{-1}, 4.8 kg kg^{-1} fish, and 37.9%, respectively. The study demonstrated that electric fish smoking technology significantly outperformed fuelwood smoking technology across all evaluated parameters. This study revealed that the electric fish smoking technology is strongly recommended for demonstration and scaling up to end users, particularly in areas where traditional fish smoking methods remain dominant.

አጎፅሮተ-ጥናት

በሞባይል እና በቋሚ የዓሣ ማጨስ ቴክኖሎጂዎች የአፈጻጸም ግምገማ ለማድረግ ጥናት ተካሂዷል። ሙከራው የተከናወነው የተደራጀ የቡድን ፋክቶሪያል ዲዛይን በመጠቀም ሲሆን የማጨስ ሙቀት እንደ ቡድን መከፋፈያ ተወስዷል። እንደ ምርመራው ውጤቶች መሠረት፣ በ90 ℃ የማጨስ ሙቀት እና በ4 ሰዓት የማጨስ ጊዜ ከፍተኛው 81.4% የእርጥበት መቀነስ ተመዝግቧል፤ በ70 ℃ የማጨስ ሙቀት እና በ2 ሰዓት የማጨስ ጊዜ ግን ዝቅተኛው 57.6% የእርጥበት መቀነስ ለኤሌክትሪክ የዓሣ ማጨሻ ተመዝግቧል። የኤሌክትሪክ የዓሣ ማጨሻ የፈተና ውጤቶች መሠረት፣ በ90 ℃ የማጨስ ሙቀት እና በ4 ሰዓት የማጨስ ጊዜ ከፍተኛው 0.69 kg h^{-1} የማድረቅ ፍጥነት ተገኝቷል፤ በ70 ℃ እና በ2 ሰዓት የማጨስ ጊዜ ግን ዝቅተኛው 0.47 kg h^{-1} ተመዝግቧል። ውጤቶቹ በ90 ℃ የማጨስ ሙቀት እና በ2 ሰዓት የማጨስ ጊዜ ከፍተኛው 69.8% የሙቀት ብቃት መመዝገቡን አሳይተዋል፤ በ70 ℃ የማጨስ ሙቀት እና በ4 ሰዓት የማጨስ ጊዜ ግን ዝቅተኛው 45.6% የሙቀት ብቃት ለኤሌክትሪክ የዓሣ ማጨሻ ተመዝግቧል። የንጽጽር ግምገማ ውጤቶች መሠረት፣ ለየእንጨት ነዳጅ የዓሣ ማጨሻ ግን 66.17%፣ 0.38 kg h^{-1}፣ 4.8 kg kg^{-1} ዓሣ እና 37.9% ተመዝግበዋል። ጥናቱ ኤሌክትሪክ የዓሣ ማጨስ ቴክኖሎጂ ከእንጨት ነዳጅ ማጨስ ቴክኖሎጂ ጋር ሲነጻጸር በሁሉም የተገመገሙ መለኪያዎች ላይ ከፍተኛ አፈጻጸም እንዳሳየ አረጋግጧል።በተለይም በባህላዊ የዓሣ ማጨስ ቴክኖሎጂ በሚበዛባቸው አካባቢዎች ለመስራት እና ለማስፋፋት ኤሌክትሪክ የዓሣ ማጨስ ቴክኖሎጂ በጥብቅ ይመከራል።

INTRODUCTION

Fish is one of the most important sources of high-quality animal protein, essential fatty acids, vitamins, and minerals for billions of people worldwide. It contributes approximately 17% of the global population's intake of animal protein and provides essential nutrients, including omega-3 fatty acids, vitamins A and D, calcium, phosphorus, iron, and iodine (*Badoni et al., 2021*). Fish is generally ranked as the third largest source of animal protein in the world (*Tacon et al., 2025*). It is one of the most essential renewable natural resources and a key component of global food security. Over three billion people rely on fish as their primary source of protein (*Boyd et al., 2022*).

In addition to nutrition, fish play an important role in income generation, employment, industrial production (fish oil, fish meal, and animal feed), recreation, and ecological balance (*Bakhsh et al., 2023*).

According to *Bhujel (2024)*, global total fish production was approximately 193.7 million tons, of which 92.3 million tons came from capture fisheries and 101.4 million tons from aquaculture. In developing countries, fish contribute more than 50% of animal protein intake among coastal and rural populations (*Akpalu & Okyere, 2023)*. Ethiopia's annual fish production was estimated at 29,000 metric tons, mainly from lakes, rivers, reservoirs, and emerging aquaculture systems. However, the country has a much higher production potential under improved management and commercial aquaculture expansion (*Lakew, 2025*).

Despite its importance, fish is highly perishable due to its high moisture content (70–80%), which accelerates microbial growth and enzymatic spoilage (*Ali et al., 2022*). Under tropical conditions, fresh fish may spoil within 8–12 hours if not properly preserved. This rapid deterioration leads to significant post-harvest losses, especially in regions with limited cold storage facilities (*Abbas et al., 2024*). Globally, it is estimated that 20–35% of harvested fish is lost annually due to inadequate preservation, poor handling, and limited processing technologies (*Abelti & Teka, 2024*). These losses reduce food availability, lower market value, and negatively affect income generation for fish processors and traders.

To reduce these losses, various preservation methods such as drying, salting, fermentation, and smoking are widely used. Among these, smoking is one of the most important methods because it combines drying, heating, and chemical preservation effects, reducing moisture content from about 75–80% to 10–20%, thereby extending shelf life from hours to weeks or months (*Adeyeye, 2019*). Smoking also improves sensory qualities such as flavor, aroma, and texture, increasing consumer acceptability (*Puke & Galoburda, 2020*).

Traditional fish smoking systems, commonly made from mud, clay, metal drums, or open-fire structures using firewood, are widely used due to low cost and simplicity *(Idris et al., 2025*). However, they suffer from low thermal efficiency (10–20%), high fuel consumption (2.5–4.0 kg of wood per kg of fish), and uneven temperature distribution, which leads to inconsistent product quality and high operational costs (*Bujas et al., 2022*).

These limitations have encouraged the development of improved fish smoking technologies such as chorkor kilns, cabinet smokers, solar-assisted systems, and hybrid dryers (*Abiodun et al., 2021*). These technologies aim to improve heat transfer, airflow, fuel efficiency, and product quality. For example, solar integration can reduce fuelwood consumption by 35–60% (*Manaye et al., 2022*). One of the improved technologies is the electric fish smoking system, which reduces fuel consumption, processing time, and smoke contamination while enhancing drying rate, moisture reduction, thermal efficiency, and final product safety (*Tahir et al., 2020*). It is suitable for both small-scale and commercial processing due to better control of smoking conditions and improved product quality *(Akande & Adeyemi, 2016*).

As a research gap, there is still limited comparative evidence on the performance of mobile and stationary fish smoking technologies under similar operating conditions in Ethiopia. Most existing studies have focused either on traditional smoking methods or on single improved technologies, without adequately evaluating key performance indicators such as fuel efficiency, drying rate, thermal efficiency, processing time, product quality, and moisture reduction in a comparative framework (*Oyewole et al., 2025*). In addition, context-specific data on how these technologies perform under local fish processing conditions remains insufficient, particularly in developing regions where adoption decisions depend on cost, accessibility, and operational efficiency (*Shittu et al., 2021*). This lack of comprehensive, quantitative comparison creates a knowledge gap that limits informed selection and scaling of the most efficient and sustainable fish smoking system.

Continuous research is necessary to develop and evaluate efficient, low-cost, and environmentally sustainable fish smoking systems. The quantitative evaluation of moisture reduction, thermal efficiency, fuel utilization, drying characteristics, and product quality provides scientific evidence for selecting appropriate technologies and improving processing performance. Technology is critically important in fish processing because it drives improvements in productivity, processing, efficiency, and sustainability.

The main objective of this study is to investigate the key performance parameters of fish smoking technologies in terms of thermal efficiency, fuel consumption, moisture content reduction, product quality, and drying rate in order to improve fish preservation efficiency and reduce post-harvest losses. Therefore, this study aimed to evaluate the performance of mobile (electric) and stationary (fuelwood) tilapia fish species smoking technologies to generate performance metrics information for fish producers in Ethiopia.

MATERIALS AND METHODS

Study area

The study was conducted in Sebeta and Melkassa, two major agricultural research-oriented areas in central Ethiopia, which were selected for their contrasting agro-climatic conditions and suitability for evaluating fish smoking technologies. Sebeta, located approximately 25 km southwest of Addis Ababa at an altitude of about 2,200 m above sea level, experiences a subtropical highland climate with mean annual temperatures ranging from 10°C to 25°C and annual rainfall between 900 and 1,200 mm. Melkassa, situated in the East Shewa Zone of the Oromiya Region about 107 km southeast of Addis Ababa along the main road to Adama, lies at an altitude of approximately 1,550 m above sea level and has a semi-arid climate with mean annual temperatures ranging from 14°C to 32°C and annual rainfall of about 700–850 mm. Therefore, the selection of Sebeta and Melkassa enabled the study to evaluate fish smoking technologies under diverse environmental and operational conditions, thereby improving the reliability and applicability of the research findings.

Description of fish smoking technologies

The fish smoking technologies are widely used for fish preservation through moisture reduction and smoke treatment. Electric smoking technology uses electrically generated heat with controlled temperature and uniform drying conditions, resulting in higher thermal efficiency, faster processing time, improved product quality, and reduced environmental pollution. In contrast, fuelwood smoking relies on burning wood to produce heat and smoke, making it less efficient due to uneven heating, higher fuel consumption, longer drying time, and increased smoke emissions. Overall, electric fish smoking technology provides a cleaner, more efficient, and environmentally sustainable alternative to fuelwood smoking systems.

Mobile or electric fish smoking technology

The mobile or electric fish smoking technology shown in Figure 1 uses electrical energy as the primary heat source to smoke fish under controlled temperature and airflow conditions. The main components of the electric fish smoking technology include an electric heating element, which converts electrical energy into thermal energy for smoking fish; a smoking chamber, which is an insulated enclosure where fish are placed to ensure uniform heat and smoke distribution; and fish trays made of stainless steel to properly arrange fish for effective drying and smoking. A temperature control system, consisting of thermostats, controllers, or sensors, is used to regulate and maintain the desired smoking temperature, while a fan or air circulation system ensures even distribution of heat and smoke throughout the chamber. In addition, insulation materials surround the chamber to minimize heat loss and enhance thermal efficiency. The power supply system, including electrical wiring, switches, plugs, and control panels, provides and regulates electric power to the smoker. An exhaust outlet removes excess smoke, moisture and hot air while maintaining proper airflow, and an oil collector gathers fish oil, water droplets, and residues for improved hygiene and easier cleaning.

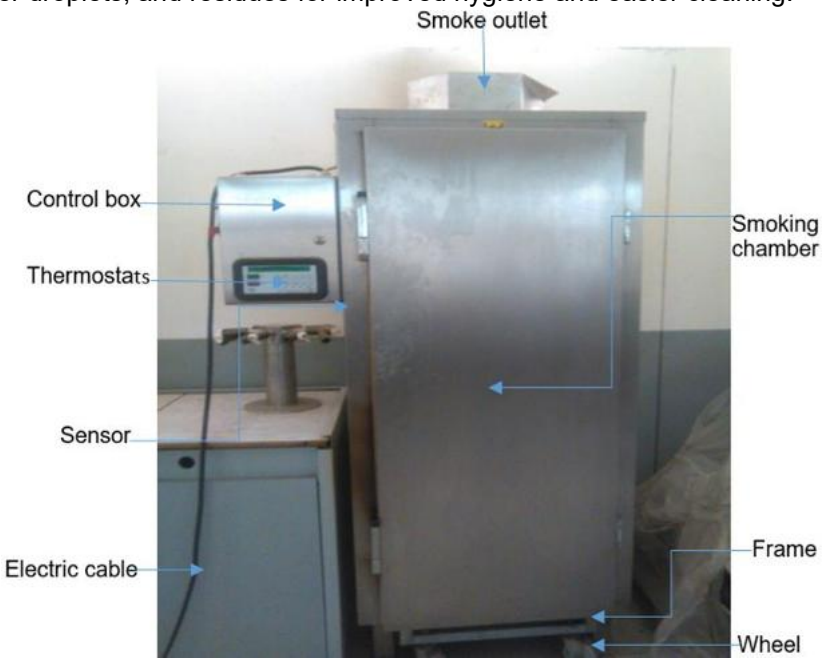


Fig. 1 - Mobile or electric fish smoking technology

This smoking chamber, as shown in Figure 1, has an overall length of 600 mm, height of 1400 mm, and width of 500 mm and is made from aluminum with a thickness of 3 mm to enhance fish quality, marketability, and acceptability. The outer part of the cabinet is made from mild steel with a length of 650 mm, height of 1500 mm, width of 550 mm, and a thickness of 1.5 mm, which covers the inner part of the chamber, and between them, there is an aluminum foil that minimizes heat loss. The developed smoker was portable; it moved from place to place, and the chamber was supported by a flexible frame.



Fig. 2 - Fish tray



Fig. 3 - Stove

Stationary or fuelwood fish smoking technology

The stationary or fuelwood fish smoking technology, as shown in Figure 4, uses firewood as the primary source of heat for smoking fish. In this system, fish are placed on trays inside a smoking chamber, where heat generated from burning wood removes moisture while smoke imparts desirable flavor, color, and preservative compounds. The main components of the fuelwood fish smoking technology include: the combustion chamber, where firewood is burned to produce heat and smoke; the smoking chamber, where fish are dried and smoked under controlled conditions; fish trays made of wire mesh, perforated metal, or wood for uniform arrangement and proper smoke circulation; a smoke outlet to regulate smoke flow and ventilation; firewood as the heat source; and insulated brick walls that retain heat and improve smoking efficiency.



Fig. 4 - Stationary or fuelwood fish smoking technology

The fish smoking mechanism in this system is hanged type and a laying type of fish smoking mechanism on a fish tray. The fish tray can hold smoking fish; it is constructed from wire mesh with a length of 950 mm, a width of 850 mm and a height of 300 mm. There are four trays; each tray contains 25 tilapia fish species, so that one hundred fish can be smoked at once a time. In the case of vertically smoking fish hung by a hook made from a rod. The fish are hung on the hanger with a crossed arrangement to optimize the smoke heat air contact. The heat transfers from the combustion chamber to the smoking chamber by convention with concrete pipe. This heat transfer occurs within the smoking cabinet, like a fish tray and a fish smoking chamber. The wood used for smoking fish in this case was Acacia (Girar). This smoking chamber uses wood as a source of energy. No burning of the smoker due to combustion from oil drops on the heat source because smoking & combustion chambers are developed separately.

Materials

The materials used in this study were selected to support the investigation of smoking technologies, ensure accurate performance evaluation, and maintain product safety and quality. The materials generally used in this research work were fish samples, controlled fuel sources, and precise measuring instruments, which enabled a comprehensive assessment of fish smoking performance under different operational conditions. The selection of materials was based on availability, durability, heat resistance, cost-effectiveness, and suitability for fish smoking operations under local conditions in Sebeta and Melkassa.

Fish material

The fresh tilapia fish species was the primary raw material used for the smoking experiments. The fish samples of uniform size and species were selected to minimize variability in processing outcomes. Typically, freshwater species commonly available in local waters were used. The fish were obtained immediately after harvesting to ensure freshness, with initial moisture content estimated at approximately 70–80% *(Sabu & Sasidharan, 2020*). Before smoking, the fish were washed thoroughly with clean water to remove dirt, slime, and blood residues, and then allowed to drain under hygienic conditions.



Fig. 5 - Experimental material; a) before adding salt, b) after adding salt

Fuel materials

The electrical energy and fuelwood were the main fuel sources used for generating heat and smoke in the mobile and stationary smoking technologies. The hardwood species were selected due to their higher calorific value and slower burning characteristics compared with softwoods in the case of a stationary smoker. The fuelwood was cut into uniform sizes to ensure consistent combustion rates.

Measurement device

The range of instruments was used to evaluate the performance of the fish smoking technologies quantitatively. These included a digital weighing balance for measuring fish weight before and after smoking. Moisture meter or oven-drying apparatus for determining moisture content reduction. Thermocouples and digital thermometers for monitoring temperature distribution inside smoking chambers. Stopwatch for recording processing time. A hygrometer for measuring relative humidity in the smoking environment. Calorimeter for estimating fuel energy value. These instruments were essential for ensuring accurate measurement of thermal efficiency, drying rate, and process consistency (*Nwakuba, 2016*).

Cleaning and hygiene materials

During experimentation, to ensure food safety and hygienic processing conditions, several cleaning materials were used during the preparation and handling of fish samples and equipment. These included clean water, food-grade detergents, disinfectants, and clean cloths. The proper sanitation practices were applied to reduce contamination risks during smoking (*Geraldo et al., 2024*).

Packaging and storage materials

After smoking, fish products were stored and evaluated using appropriate packaging materials. These included polyethylene bags, plastic containers, and aluminum foil packs to prevent moisture reabsorption and contamination. Storage materials were selected based on their ability to preserve product quality during short-term evaluation periods (*Nizio et al., 2023*).

Methods

The study employed an experimental and comparative approach to evaluate fish smoking technologies under controlled conditions. The key performance indicators, including thermal efficiency, fuel consumption, moisture content reduction, processing time, and sensory quality, were systematically measured. The methodology ensured reliable, quantitative, and reproducible assessment of smoking technologies suitable for improving fish preservation systems in rural and peri-urban processing environments.

Sample collection and preparation

Sample allocation to mobile smokers: A total of 270 Nile tilapia were used in the experiment. The fish were randomly assigned to mobile smoking technology. Each temperature treatment consisted of three replications, with 15 fish per replication, resulting in 45 fish per treatment. Therefore, the mobile smoker processed a total of 270 fish for the experiment.

Sample allocation to mobile and stationary smokers for comparative evaluation: A total of 90 Nile tilapia were used in the experiment. The fish were randomly allocated to two smoking treatments: a mobile electric smoker and a stationary fuelwood smoker. Each treatment was replicated three times, with 15 fish per replication, resulting in 45 fish per treatment. Thus, 45 fish were assigned to the mobile electric smoker and 45 fish to the stationary fuelwood smoker. Random allocation of fish to treatments and replications was used to minimize experimental bias.

Test conditions: Both the mobile electric smoker and the stationary fuelwood smoker were evaluated using the same sample load of 15 Nile tilapia per replication under identical experimental conditions. Fish of similar size and weight were used, and the smoking trials were conducted under the same ambient environmental conditions. The same smoking temperatures and processing durations were maintained for both technologies to ensure that any observed differences in performance were attributable to the smoking technology rather than variations in sample load or environmental conditions.

The fresh fish samples were collected immediately after harvest from the Sebeta research center. The tilapia fish species commonly available in the study areas were selected to reflect typical processing conditions. The fish were sorted based on uniform size and weight to minimize variability in smoking performance. Before smoking, the fish were washed thoroughly using clean water to remove slime, blood, and surface impurities. The fish were then drained for approximately 15–30 minutes under hygienic conditions (*Bedane et al., 2022*). The initial weight and moisture content were recorded before loading into the smoking chambers. The experimental fish were healthy Nile tilapia with an average initial body weight of 250 ± 20 g and an average total length of 26.0 ± 1.5 cm (mean ± standard deviation).



Fig. 6 - Dimension and weight measurement of the tilapia fish species

Smoking procedure

The smoking process was conducted separately for each smoking technology under similar environmental conditions. A predetermined quantity of fish was loaded into each smoking chamber for both technologies. The power supply system contained electrical wiring, switches, plugs, and control panels that provide and regulate electric power to the smoker. The fuelwood was ignited in the combustion chamber, and fire intensity was controlled to maintain a temperature range between 70°C and 90°C, which is optimal for fish smoking (*Alakali et al., 2017*). The temperature inside the smoking chamber was monitored using thermocouples placed at different locations to assess heat distribution. The smoking process continued until the fish reached the desired dryness level.

Measurement of performance parameters

Key performance parameters commonly evaluated include thermal efficiency, fuel consumption, drying rate, smoking time, moisture reduction, processing capacity, and sensory acceptability. Several quantitative parameters were measured to evaluate the performance of each smoking technology. After smoking, fish samples were removed and allowed to cool at ambient temperature before post-processing measurements were taken. The total smoking duration was recorded for each treatment.

Moisture content reduction

The moisture content was determined using the oven-drying method. Final moisture content was used to assess product stability and shelf life potential. The fish samples were weighed before and after drying to calculate moisture loss using Equation (1), the formula by *Ojotu et al. (2024)*.

$$\text{Moisture loss (\%)} = \frac{W1-W2}{W1} x100 \quad (1)$$

Drying rate

The drying rate was calculated using Equation (2), based on the reduction in moisture content over the smoking period (*Ojotu et al., 2024*).

$$\text{Drying rate (kg h}^{-1}) = \frac{\text{Moisture removed (kg)}}{\text{Time(h)}} \quad (2)$$

Fuel Consumption

The fuelwood consumption was measured by weighing the amount of wood used before and after each smoking session. The fuel consumption of an electric fish smoking technology is commonly expressed as the amount of electrical energy used during smoking relative to the quantity of fish processed or moisture removed. The total fuel consumed per kilogram of smoked fish was calculated using Equations (3) and (4) by *Sintali et al. (2023)*.

$$\text{Fuel consumption } (F_{cw}) = \frac{\text{Total fuel used (kg)}}{\text{Mass of smoked fish (kg)}} \quad (3)$$

$$\text{Fuel consumption } (F_{ce}) = \frac{E \times t}{Wf} \quad (4)$$

Electrical energy equivalent conversion

To enable comparison between the electric and fuelwood smoking technologies, the electrical energy consumed by the mobile electric smoker was converted to an equivalent fuelwood mass based on the energy content of the fuelwood. Electrical energy consumption was first recorded in kilowatt-hours (kWh) using an energy meter. This conversion was used solely to provide an energy-equivalent comparison between the mobile electric smoker and the stationary fuelwood smoker. The equivalent fuelwood consumption was then calculated using the lower heating value (LHV) of fuelwood according to the following Equations (5) and (6) by *Sintali et al. (2023)*.

$$\text{Equivalent fuelwood (kg)} = \frac{\text{Electrical energy (kWh)}}{\text{LHV of fuelwood (MJ kg}-1)} \text{x}3.6 \quad (5)$$

$$\text{Equivalent fuelwood consumption (kg kg}^{-1}\text{fish)} = \frac{\text{Equivalent fuelwood}}{\text{Mass of fish processed}} \quad (6)$$

where 3.6 is the conversion factor from 1 kWh to 3.6 MJ, and the LHV of air-dried fuelwood was assumed to be 16 MJ kg^{-1}, equivalent fuelwood in (kg), and mass of fish processed in (kg).

Determination of fuelwood calorific value: The calorific value of the fuelwood was not measured experimentally. Instead, the lower heating value (LHV) of air-dried fuelwood was obtained from literature. An LHV of 16 MJ kg^{-1} was used for the calculations, which is within the typical range reported for air-dried hardwood fuelwood. This value was used to estimate the energy equivalent of the fuelwood consumed during the smoking process.

Thermal efficiency

The thermal efficiency of each smoking technology was estimated using Equations (7) and (8) by comparing the useful energy utilized for moisture removal to the total energy content of the fuelwood and electricity. The thermal efficiency of an electric fish smoking technology is generally expressed as the ratio of the useful heat utilized for moisture evaporation from the fish to the total electrical energy supplied to the smoker formula by *Sintali et al. (2023)*.

$$\text{Thermal efficiency for fuelwood (\%)} = \frac{\text{Energy usd for drying}}{\text{Total fuel energy input}} \text{x}100 \quad (7)$$

$$\text{Thermal efficiency for electric (\%)} = \frac{Mw \times Lv}{Ein} \quad (8)$$

where, W_1 = initial weight of fresh fish, W_2 = final weight after smoking, F_c = fuel consumption (kWh kg^{-1} fish), E = electrical power rating of the smoker (kW), t = smoking time (hours), W_f = weight of fish processed (kg), ηth = thermal efficiency (%), Mw = mass of water evaporated from fish (kg), Lv = latent heat of vaporization of water (Kj kg^{-1}) (commonly 2257 Kj kg^{-1}), and Ein = total electrical energy supplied to the smoker (kJ).

Sensory evaluation

The sensory quality of smoked fish was evaluated using a semi-trained panel of 10–15 individuals familiar with fish products. The evaluation was conducted under controlled conditions to minimize bias. The attributes assessed included: color**,** aroma**,** texture**,** taste and overall acceptability. Panelists evaluated coded samples using a 9-point hedonic scale to ensure blind assessment. Mean sensory scores were calculated for each smoking technology (*Rossetto et al., 2024*).

Selection and training of sensory panelists: Sensory evaluation was conducted by semi-trained panelists selected from staff and food science experts familiar with fish and fish products. Panelists were selected based on their willingness to participate, good health, normal sensory perception (including taste, smell, and vision), and prior experience in food sensory evaluation. Before the evaluation, the panelists received a 30-minute training session on the evaluation procedure and the quality attributes to be assessed. During training, reference smoked fish samples were used to familiarize panelists with the evaluation criteria and to improve consistency among assessors. Drinking water was provided for palate cleansing between samples, and samples were presented in a randomized order using coded identifiers to minimize bias.

Ethical considerations: Before the sensory evaluation, all panelists were informed about the study's objectives and procedures. Written informed consent was obtained from each participant before participation. Participation was voluntary, and panelists were free to withdraw from the evaluation at any time without consequence. The sensory evaluation involved the consumption of smoked fish prepared under hygienic conditions and posed minimal risk to participants. All personal information and evaluation responses were kept confidential and used solely for research purposes. The study was conducted in accordance with institutional ethical guidelines for research involving human participants.



Fig. 7 - Sensory evaluation of smoked fish by the panelists

Experimental design

The experiment was carried out by randomized block factorial design with smoking temperature as a blocking factor and the levels of smoking temperature with smoking time taken as a treatment combination. Each experiment is to be replicated three times to ensure reliability and reduce experimental error, to have 18 experimental units (3×2×3 = 18). Quantitative data, including moisture content reduction, drying rate, fuel consumption, thermal efficiency, and sensory evaluation scores, were considered as experimental treatments. Each treatment consisted of 45 fish, with 15 fish allocated to each of three replications, resulting in a total of 270 fish for the six treatments. Random allocation of fish to treatments and replications was used to minimize experimental bias and ensure the reliability of the results.

Statistical data analysis

The collected data were analyzed using Statistix 8 software and Statistical Package for Social Sciences software (SPSS version 25.0). Confidence intervals of 95% was used to show the significant effect of the independent variable on the dependent variable. The mean separation between treatment means was conducted by least significance difference (LSD) at a 5% level. Comparative analysis between stationary and mobile smoking technologies was conducted. Descriptive statistics such as mean and standard deviation were computed for all measured parameters. The data were subjected to two-way analysis of variance (ANOVA) by following the appropriate procedure.

RESULTS AND DISCUSSION

Effects of smoking temperature and time on performance indicators

The results indicate that smoking temperature and smoking time have a significant influence on moisture content reduction, drying rate, energy consumption, and thermal efficiency of the electric or mobile fish smoking technology. The findings suggest that maintaining an optimal combination of smoking temperature and time is critical for achieving efficient drying performance, leading to a marked reduction in moisture content, lower fuel consumption, and higher thermal efficiency in electric fish smoking technology. The optimum operating conditions were generally observed within a smoking temperature range of 70–90°C and a smoking time of 2–4 hours. A similar trend was reported by *Adepoju et al. (2018)*. The electric or mobile fish smoking technology was evaluated at three smoking temperature levels (70, 80, and 90°C) and two smoking time levels (2 and 4 h) to assess its performance. The test results indicated that the electric smoker performed efficiently in fish smoking under controlled temperature and time conditions.

Effects of smoking temperature and time on moisture content reduction

Analysis of variance for the effects of smoking temperature, smoking time, and the interaction effect on the moisture content reduction of the mobile or electric fish smoking technology was presented in Table 1. The analysis of variance indicated that the main effects of smoking temperature, smoking time, and the interaction effect were significant at the 5% level (Table 1), as the P-values were less than 5%. The results revealed that the moisture content reduction of a fish smoking technology was influenced by smoking temperature, smoking time, and the interaction effect.

Table 1

Analysis of variance (ANOVA) for moisture content reduction

Sources	DF	SS	MS	F	P	
Replication	2	23.11	11.554			
Smoking temperature	2	1120.70	560.351	600.0	0.0000	*
Smoking time	1	80.22	80.222	85.90	0.0000	*
ST ×St	2	26.85	13.427	14.38	0.0011	*
Error	10	9.34	0.934			
Total	17	1260.22				

* = significant, ** = non-significant, P < 0.05, significant at 5 % level, P>0.05, non-significant at 5% level.

In accordance with the investigation findings, the moisture content reduction ranged from 57.6 % to 81.4 %, as illustrated in Figure 8.

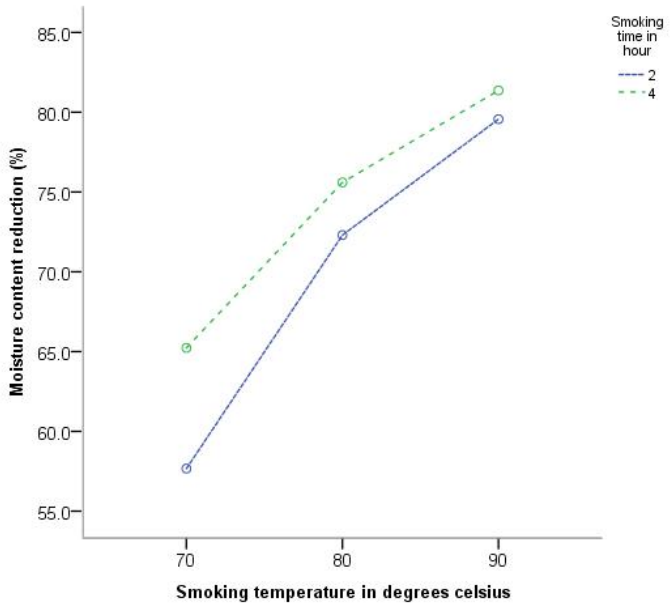


Fig. 8 - Effects of smoking temperature and time on moisture content reduction

The smoking technology moisture content reduction increased from 57.6 % to 81.4% when the smoking temperature increased from 70 to 90 ℃, whereas the smoking temperature increased, the moisture content reduction tended to rise; on the other hand, smoking time began to increase. Based on the result, the moisture content reduction was directly associated with the smoking time and also directly associated with the smoking temperature of the technology. From the investigation results, at 90 ℃ of smoking temperature and 4 h smoking time, the maximum moisture content reduction of 81.4% was noted; also, at 70 ℃ smoking temperature and 2 h smoking time, the minimum moisture content reduction was noted, as it was verified. It was observed that an increase in smoking temperature and time led to a marked reduction in moisture content, as higher thermal energy enhanced the evaporation and diffusion of water from fish tissues. This study's finding is related to the previous research findings conducted by *Toworfe et al. (2023).*

Effects of smoking temperature and time on drying rate

The analysis of variance for the main effects of smoking temperature, smoking time, and the interaction effect on the drying rate of the mobile fish smoking technology. Analysis of variance showed that the effect of smoking temperature and smoking time was significant at a 5% level because the value for P found in Table 2 was lower than 0.05, based on the result, and their interaction effect was also significant at a 5% level. As a result, the main effect of smoking temperature and smoking time could influence the drying rate of a smoking technology; also, the interaction effect did influence the drying rate.

Table 2

Analysis of variance (ANOVA) for drying rate

Sources	DF	SS	MS	F	P	
Replication	2	0.00163	0.00082			
Smoking temperature	2	0.10093	0.05047	5046.67	0.0000	*
Smoking time	1	0.00681	0.00681	680.56	0.0000	*
ST ×St	2	0.00018	0.00009	8.89	0.0060	*
Error	10	0.00010	0.00001			
Total	17	0.10965				

* = significant, ** = non-significant, P < 0.05, significant at 5 % level, P>0.05, non-significant at 5% level.

From the investigation outcomes, it was revealed that the smoking technology drying rate ranged from 0.47 to 0.69 kg h^{-1}, as demonstrated in Figure 9.

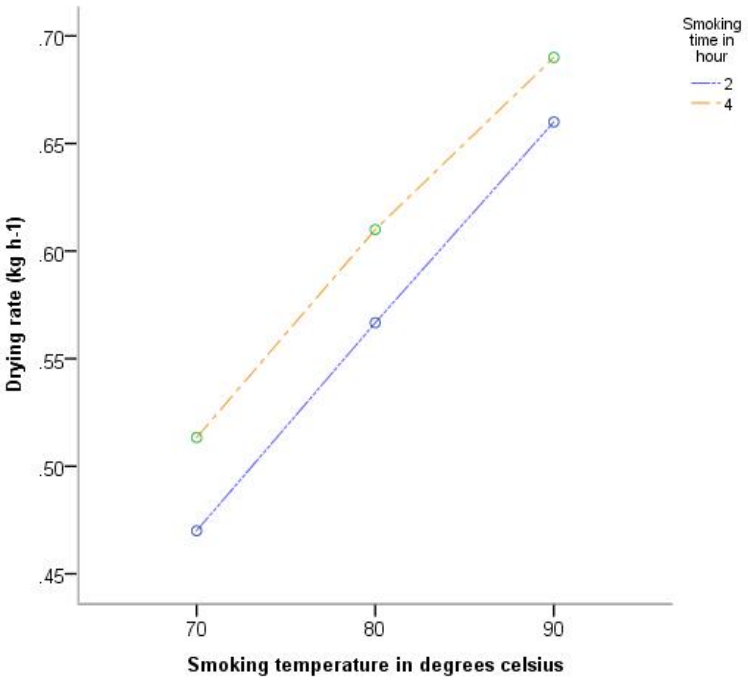


Fig. 9 - Effects of smoking temperature and time on drying rate

So, the drying rate increased from 0.47 to 0.69 kg h^{-1} as the smoking temperature increased from 70 to 90 ℃. The drying rate tends to increase as the smoking temperature and smoking time increase. It demonstrated that a direct association exists between the smoking temperature and smoking time of the drying rate. Generally, at 90 ℃ of smoking temperature and 4 h of smoking time, the maximum drying rate of 0.69 kg h^{-1} was obtained, whereas at 70 ℃ and 2 h smoking time, the minimum drying rate of 0.47 kg h^{-1} was obtained. The drying rate increased with rising temperature due to enhanced heat transfer and moisture migration; however, the rate gradually decreased over time as the moisture gradient between the fish surface and interior diminished. The previous studies in the literature relating results were reported by *Sintali et al. (2023a)*.

Effects of smoking temperature and time on fuel consumption

Analysis of variance for the effects of smoking temperature, smoking time, and the interaction effect on the fuel consumption of the mobile fish smoking technology was presented in Table 3. The analysis of variance indicated that (Table 3) the main effect of smoking temperature and smoking time was significant at a 5% level, depending on the result obtained, because the value for P found was less than 0.05, as well as the interaction effect was significant due to the value obtained for P was lower than 5% (P<5%). Depending on the findings, fuel consumption was impacted by the main effects, whereas it was also affected by the interaction effect.

Table 3

Analysis of variance (ANOVA) for fuel consumption

Sources	DF	SS	MS	F	P	
Replication	2	0.10858	0.05429			
Smoking temperature	2	8.82194	4.41097	754.16	0.0000	*
Smoking time	1	0.37267	0.37267	63.72	0.0000	*
ST ×St	2	0.19034	0.09517	16.27	0.0007	*
Error	10	0.05849	0.00585			
Total	17	9.55203				

* = significant, ** = non-significant, P < 0.05, significant at 5 % level, P>0.05, non-significant at 5% level.

Based on the investigation results, it was found that the fuel consumption ranged from 0.5 to 2.49 kg of fuel kg^{-1} smoked fish, as shown in Figure 10.

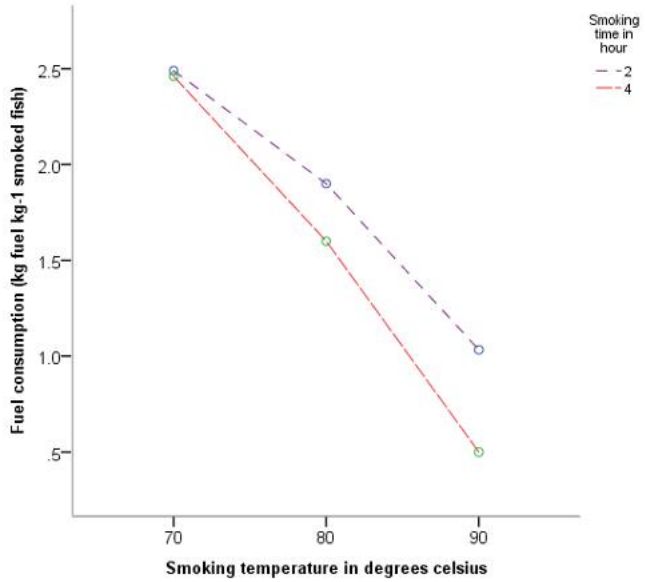


Fig. 10 - Effects of smoking temperature and time on fuel consumption

The fuel consumption reduced from 2.49 to 0.5 kg fuel kg^{-1} smoked fish as the smoking temperature rose from 70 to 90 ℃. By adjusting the smoking temperature and smoking time, fuel consumption was expected to decline as well. It demonstrated that the smoking temperature and smoking time had a reverse association with fuel consumption. According to the findings, at a smoking temperature of 90 ℃ and a smoking time of 4h, the smallest fuel consumption was observed at 0.5, whereas at a smoking temperature of 70℃ and a smoking time of 2 h, the highest fuel consumption was observed at 2.49 for the smoking technology.

Regarding fuel consumption, the results showed that higher temperatures and longer smoking durations increased total electrical energy use due to continuous heater operation and elevated power demand. A similar funding pattern for the smoker was reported by *Taherzadeh-Shalmaei et al. (2021)*.

Effects of smoking temperature and time on thermal efficiency

Analysis of variance for the effect of smoking temperature, smoking time, and interaction on the thermal efficiency of mobile fish smoking technology is presented (Table 4). Based on the findings, the analysis of variance revealed that the effect of smoking temperature and smoking time was significant at the level of five per cent due to the values for P obtained were lower than 0.05; however, the interaction effect was non-significant. According to the outcomes, the thermal efficiency was affected by smoking temperature and smoking time without their interaction effect.

Table 4

Analysis of variance (ANOVA) for thermal efficiency

Sources	DF	SS	MS	F	P	
Replication	2	9.45	4.727			
Smoking temperature	2	1361.56	680.780	1160.2	0.0000	*
Smoking time	1	58.32	58.320	99.41	0.0000	*
ST ×St	2	3.64	1.820	3.10	0.0895	**
Error	10	5.87	0.587			
Total	17	1438.84				

* = significant, ** = non-significant, P < 0.05, significant at 5 % level, P>0.05, non-significant at 5% level.

Based on the investigation results, the mean thermal efficiency of the mobile fish smoking technology varied from 45.6% to 69.8% with increasing smoking temperature from 70 to 90 ℃, whereas thermal efficiency increased from 45.6% to 69.8%. Figure 11 illustrates that the thermal efficiency of the technology tended to increase with the increase of smoking temperature and decreased with smoking time, which means thermal efficiency had a direct relationship to the smoking temperature and was inversely associated with smoking time.

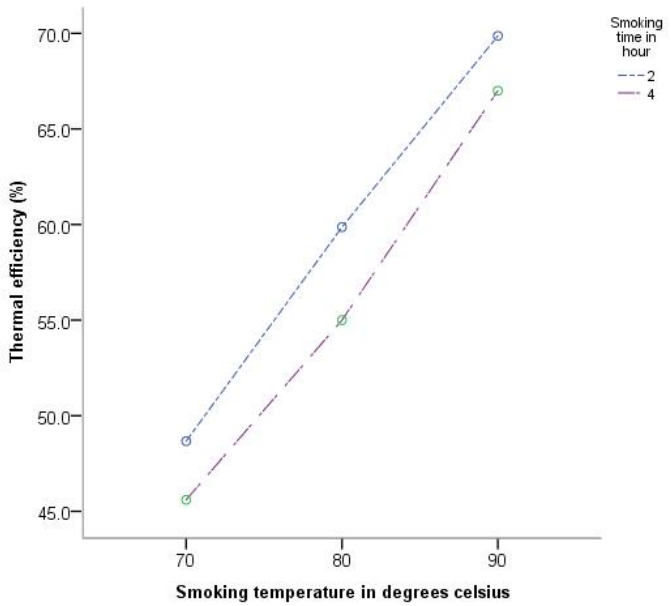


Fig. 11 - Effects of smoking temperature and time on thermal efficiency

The maximum thermal efficiency of 69.8% was recorded at a smoking temperature of 90 ℃, and a smoking time of 2 h, whereas the minimum thermal efficiency was 45.6 recorded at a smoking temperature of 70 ℃, and a smoking time of 4 h. It was found that thermal efficiency improved with controlled increases in temperature and proper smoking duration, as more input energy was effectively converted into useful heat for moisture removal. This study's finding result is similar to the previous research conducted by *Nwakuba et al. (2025)*.

Mean separations of treatment means

The least significance difference all pairwise comparisons test of moisture content reduction, drying rate, fuel consumption and thermal efficiency for mobile fish smoking technology were carried out for each treatment was given below in Table 5 then this analysis was subjected to the least significance difference all pairwise comparisons test of dependent variables for three levels of smoking temperature and two levels of smoking time to know significant differences among treatment means, So, the least significance difference all pairwise comparisons test showed (Table 5) that there were 6 groups (a, b, c, d, e and f) for test of moisture content reduction, drying rate and thermal efficiency for treatment, all 6 means are significantly different from one another but for test of fuel consumption for treatment, there are 4 groups (a, b, c, and d) in which the treatment means were not significantly different from one another at 5% level based on least significance difference all pairwise comparisons test.

Table 5

Comparisons between treatment means for the mobile fish smoking technology

No.	Treatment combination	Smoking temperature (℃)	Smoking time (h^{-1})	Moisture content reduction (%)	Drying rate (kg h^{-1})	Fuel consumption (kg kg^{-1})	Thermal efficiency (%)
1	S_T1S_t1	70	2	57.66^{f}	0.470^{f}	2.490^{a}	48.66^{e}
2	S_T1S_t2	70	4	65.23^{e}	0.513^{e}	2.460^{a}	45.60^{f}
3	S_T2S_t1	80	2	72.3^{d}	0.566^{d}	1.90^{b}	59.86^{c}
4	S_T2S_t2	80	4	75.6^{c}	0.610^{c}	1.60^{c}	55.0^{d}
5	S_T3S_t1	90	2	79.56^{b}	0.660^{b}	1.033^{d}	69.86^{a}
6	S_T3S_t2	90	4	81.37^{a}	0.690^{a}	0.50^{b}	67.0^{b}

S_T = Smoking temperature, S_t = Smoking time

Comparative evaluation of fish smoking technologies

This study demonstrated that electric fish smoking technology significantly outperformed fuelwood smoking systems across all evaluated parameters. The technology achieved an 81.4% improvement in moisture content reduction, reduced drying time by 0.69 kg h^{-1}, lowered fuel consumption by 2.49 kg kg^{-1} of fish smoked, increased thermal efficiency by 69.8%, and enhanced sensory acceptability by 48%. These findings confirm that electric fish smoking technology provides a more efficient, energy-saving, and high-quality fish processing method compared to fuelwood systems. The findings of this study demonstrate that both fish smoking technologies can significantly enhance fish preservation efficiency, improve product quality and safety, and reduce post-harvest losses.

Moisture content reduction

The moisture content of fish before and after smoking showed a clear difference between fuelwood and electric smoking technologies. Both systems reduced moisture significantly; however, the electric system achieved a greater reduction, resulting in safer storage conditions.

Table 6

Moisture content reduction in fish smoking technologies

Smoking technologies	Initial moisture (%)	Final moisture (%)	Moisture content reduction (%)
Stationary technology	78.05 ± 0.38	26.4 ± 0.2	66.17 ± 0.05
Mobile technology	78.1 ± 0.15	14.5 ± 0.22	81.4 ± 0.51

The electric smoking technology achieved a final moisture content of 14.5%, which is below the critical safe storage threshold of 15%. This level is ideal for long-term preservation and significantly reduces microbial growth risk. In contrast, the stationary smoker retained 26.4% moisture, which is insufficient for long-term storage and increases susceptibility to spoilage.

Drying rate

The drying rate varied significantly between smoking technologies as indicated in Table 7. The electric smoking technology increases drying rate by approximately 0.69 kg h^{-1}, which significantly increases the shelf life of fish. This faster drying is due to higher and more stable internal temperature (70–90°C), improved smoke circulation system, reduced moisture boundary layer resistance and enhanced energy transfer efficiency.

Table 7

Drying rate

Smoking technologies	Drying rate (kg h^{-1})	Total smoking time (h)	Smoking temperature (℃)
Stationary technology	0.38 ± 0.01	4	90
Mobile technology	0.69 ± 0.015	4	90

Thermal efficiency and fuel consumption

As indicated in Table 8, the thermal efficiency of electric fish smoking technology was higher, but the fuel usage was considerably lower in the electric smoking system.

Table 8

Thermal efficiency and fuel consumption

Smoking technologies	Thermal efficiency (%)	Fuel consumption (kg kg^{-1} fish)	Fuel saving
Stationary technology	37.9 ± 0.1	4.8 ± 0.05	low
Mobile technology	69.8 ± 0.78	2.49 ± 0.1	high

The electric fish smoking technology achieved approximately 69.8% of the maximizing of thermal efficiency due to an enclosed combustion chamber design, reduced heat leakage, efficient smoke recycling within the system and improved insulation materials. Fuelwood systems suffer from heat losses, leading to inefficient fuel use and higher operating costs. The electric smoker thus offers both environmental and economic benefits by reducing deforestation pressure and energy waste.

Based on the comparative evaluation of both electric and fuelwood fish smoking technologies, the results obtained for evaluation parameters in Figure 12 were higher in the case of electric fish smoking but lower in the fuelwood smoker, except for fuel consumption. The findings strongly support the adoption of electric fish smoking technologies in regions such as Sebeta and Melkassa, where traditional processing systems remain dominant.

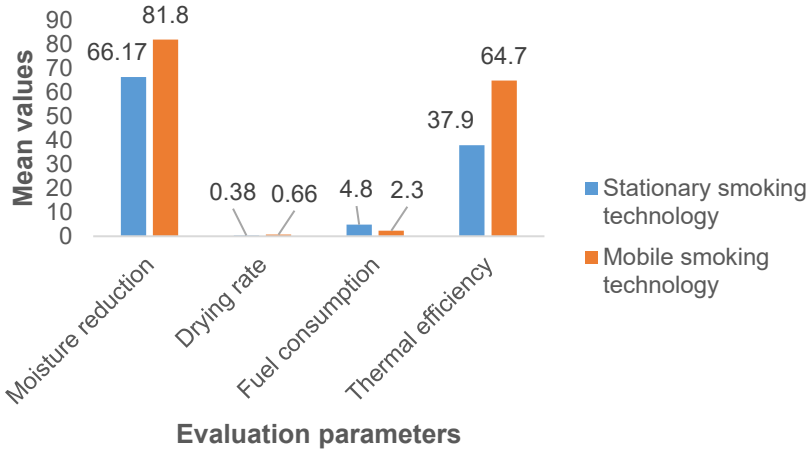


Fig. 12 - Comparative evaluation of smoking technologies

Sensory evaluation of smoked fish for the technologies

Sensory evaluation showed significantly higher acceptability scores for fish processed using improved technology.

Table 9

Sensory evaluation scores (9-point hedonic scale)

Attribute	Stationary smoking technology	Mobile smoking technology
Color	6.4 ± 0.049	8.8 ± 0.05
Aroma	6.7 ± 0.15	8.9 ± 0.06
Texture	6.3 ± 0.03	8.6 ± 0.03
Taste	6.5 ± 0.1	8.8 ± 0.05
Overall Acceptability	6.8 ± 0.17	8.7 ± 0.04

The results obtained in Figure 13 showed that the electric fish smoker consistently achieves higher sensory scores across all parameters. This improvement is due to uniform smoke penetration, controlled heating preventing burning, better moisture balance in the final product and reduced contamination from ash, but the fuelwood energy sourced smoker products showed darker coloration and slightly burnt flavor as well as reducing consumer preference. The same funding pattern for fish smoking technologies was reported by *Tahir et al. (2020).* This study was limited to tilapia fish, specific smoking conditions, and the experimental setup; therefore, the findings may not be directly applicable to other fish species or commercial-scale operations. Future studies should evaluate these technologies under diverse environmental conditions, processing parameters, and large-scale production systems.

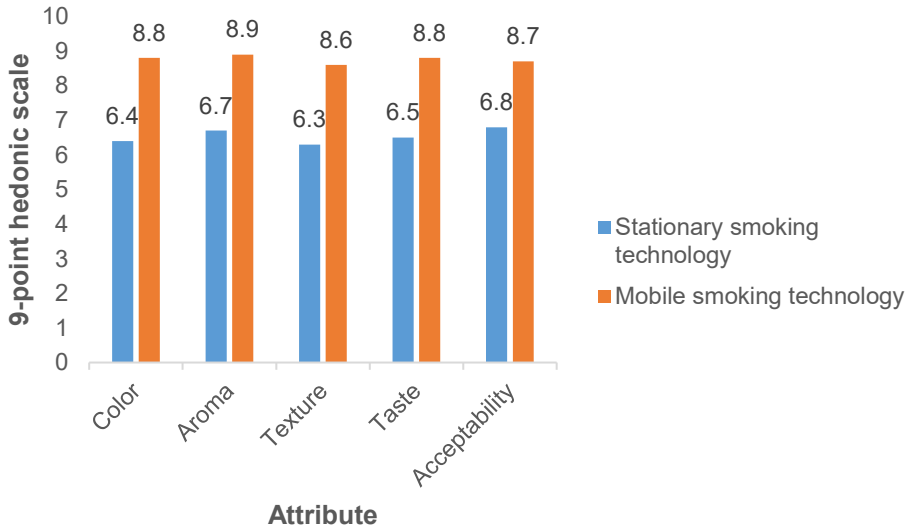


Fig. 13 - Sensor evaluation of smoked fish

CONCLUSIONS

The electric or mobile fish smoking technology was experimentally investigated at three levels of smoking temperature (70, 80, and 90°C) as well as two levels of smoking time (2 and 4 h) in terms of key performance indicators for the tilapia fish species. According to the investigation findings, with increasing smoking temperature from 70 °C to 90°C, the moisture content reduction increased from 57.6% to 81.4%; the drying rate increased from 0.47 kg h^{-1} to 0.69 kg h^{-1}, the thermal efficiency rose from 45.6% to 69.8%, and the fuel consumption reduced from 2.49% to 0.5%. Based on the analysis of variance results, the smoking temperature, smoking time and their interaction effects could influence the moisture content reduction, drying rate, fuel consumption, and thermal efficiency of an electric fish smoker; however, the combination effect did not influence thermal efficiency. The least significant difference all pairwise comparisons test revealed that the treatment means were significantly different from one another at 5% level, except for the test of fuel consumption for treatment based on the comparisons test. The comparative evaluation was carried out for electric and fuelwood fish smoking technologies with respect to key performance indicators. The study revealed that electric fish smoking technology significantly outperformed fuelwood smoking systems across all evaluated parameters. This study was limited to tilapia fish, specific smoking conditions, and the experimental setup; therefore, the findings may not be directly applicable to other fish species or commercial-scale operations. The study revealed that the electric fish smoking technology is strongly recommended for demonstration and scaling up to end users, particularly in areas where traditional smoking methods remain dominant.

REFERENCES

[1] Abbas, H., Zhao, L., Gong, X., Jiang, M., & Faiz, T. (2024). Environmental and economic influences of postharvest losses across the fish-food products supply chain in the developing regions. *Environment, Development and Sustainability*, *26*(11), 28335–28366.

[2] Abelti, A. L., & Teka, T. A. (2024). Intervening fish post-harvest losses to narrow the gap between demand and supply: A review on the magnitude of fish post-harvest losses in some Sub-Saharan African countries. *Aquaculture, Fish and Fisheries*, *4*(2), 3-15.

[3] Abiodun, M., Ida, O., Dare, S., Ida, O., & Bamidele, C. (2021). Impact of improved smoking kiln design on hygiene and timeliness of drying of smoked fish. *Turkish Journal of Agricultural Engineering Research (TURKAGER)*, *2*(1), 133–155.

[4] Adepoju, M. A., Omitoyin, B. O., Ajani, E. K., & Asha, K. (2018). Effect of smoking time and temperature on the proximate composition and quality of milkfish steaks. *Journal of Aquatic Food Product Technology*, *27*(3), 369–378.

[5] Adeyeye, S. A. O. (2019). Smoking of fish: A critical review. *Journal of Culinary Science & Technology*, *17*(6), 559–575.

[6] Akande, G. R., & Adeyemi, R. S. (2016). Performance of a biofuelled detachable fish smoking kiln. *Agricultural Engineering International: CIGR Journal*, *18*(3), 233–244.

[7] Akpalu, W., & Okyere, M. A. (2023). Fish protein transition in a coastal developing country. *Environmental and Resource Economics*, *84*(3), 825–843.

[8] Alakali, J. S., Adekoyeni, O. O., Alaka, I. C., Faasema, J., & Torvor, T. (2017). Fabrication and performance evaluation of a hybrid fish smoking kiln. *Journal of Food Processing and Preservation*, *41*(3), 2-6.

[9] Ali, A., Wei, S., Ali, A., Khan, I., Sun, Q., Xia, Q., Wang, Z., Han, Z., Liu, Y., & Liu, S. (2022). Research progress on nutritional value, preservation and processing of fish: A review. *Foods*, *11*(22), 3-24.

[10] Badoni, P., Nazir, I., Aier, M., Maity, P. B., Samanta, S., & Das, A. (2021). Significant role of fish nutrients with special emphasis on essential fatty acids in human nutrition. *Int. J. Curr. Microbiol. Appl. Sci.*, *10(2)*, 2034–2046.

[11] Bakhsh, M., Shehzad, A., Waqar, Z., Randhawa, N. K., Subhan, A., Ijaz, M., Kashif, M., Channo, A., Yar, M. K., & Ghazali, M. H. (2023). The role of fish in global food and nutrition security: Current aspects and future prospects. *Journal of Animal Sciences*, *7*(04), 23–35.

[12] Bedane, T. D., Agga, G. E., & Gutema, F. D. (2022). Hygienic assessment of fish handling practices along the production and supply chain and its public health implications in Central Oromia, Ethiopia. *Scientific Reports*, *12*(1), 1-11.

[13] Bhujel, R. C. (2024). Global aquatic food production. In *Aquatic Food Security*, 3(2), 99–126.

[14] Boyd, C. E., McNevin, A. A., & Davis, R. P. (2022). The contribution of fisheries and aquaculture to the global protein supply: Aquaculture and global protein. *Food Security*, *14*(3), 805–827.

[15] Bujas, T., Koričan, M., Vukić, M., Soldo, V., Vladimir, N., & Fan, A. (2022). Review of energy consumption by the fish farming and processing industry in Croatia and the potential for zero-emissions aquaculture. *Energies*, *15*(21), 1-26.

[16] Geraldo, V., Ampofo-Asiama, J., Adinortey, C. A., Okyere, I., Tulashie, S. K., Nuer, A. T. K., Nkansah, S. B., Omega, S., Seidu-Larry, S., & Kizzie-Hayford, N. (2024). Implementation of good manufacturing practices to improve the quality of smoked fish (Scomber colias). *Heliyon*, *10*(5), 1-14

[17] Idris, S., Adam, A. A., Sambo, M. U., Sambo, F., Abubakar, A., Chiroma, Y., & Rod, S. (2025). Design and fabrication of a modified drum smoking kiln for artisanal fish processors hitches. *International Journal of Fisheries and Aquatic Studies, 13*(5), 222–224.

[18] Lakew, A. (2025). Managing fisheries and aquaculture for sustainable food and nutrition security in Ethiopia. *Ethiopian Journal of Agricultural Sciences*, *35*(2), 84–105.

[19] Manaye, A., Amaha, S., Gufi, Y., Tesfamariam, B., Worku, A., & Abrha, H. (2022). Fuelwood use and carbon emission reduction of improved biomass cookstoves : Evidence from kitchen performance tests in Tigray, Ethiopia. *Energy, Sustainability and Society*, 12(1) 1–9. https://doi.org/10.1186/s13705-022-00355-3

[20] Nizio, E., Czwartkowski, K., & Niedbała, G. (2023). Impact of smoking technology on the quality of food products: Absorption of Polycyclic Aromatic Hydrocarbons (PAHs) by food products during smoking. *Sustainability*, *15*(24), 1-21.

[21] Nwakuba, N. R. (2016). Development of a hybrid fish smoker. *Umudike Journal of Engineering and Technology*, *2*(1), 34–45.

[22] Nwakuba, N. R., Ofojioha, O. M., Ikechukwu, K. U., Angela, N., Chikwue, M. I., Oham, P. N., & Okorie, C. E. (2025). Development and sustainability assessment of a fish-drying Kiln *: Eco-thermodynamic Insights*, 6(3), 65-68.

[23] Ojotu, M., Williams, O., Ikagu, M., Salaudeen, K. O., & Imoleayo, A. (2024). Drying kinetics of smoked catfish using an improved smoking kiln. *International Journal of Research in Engineering and Science (IJRES), 12*(3), 319–328.

[24] Oyewole, S.N., Ajao, T.O., Oyewole, O. S., Famakinwa, J.O., Afolabi, A.A., Ogundare, O.A., Ogungbemi, K., Shotonwa, A., & Ojo, O. A. (2025). Comparative evaluation of rotary and NSPRI model-B smoking kilns for quality assurance of smoked catfish. *Nigerian Journal of Post-Harvest Research, 3(1), 24- 32.*

[25] Puke, S., & Galoburda, R. (2020). Factors affecting smoked fish quality: A review. *Research for Rural Development*, *35*(1), 132–139.

[26] Rossetto, J.F., Rocha, J. D. M., da Cruz, M. C. S., da Silva, T. C., & Signor, A. (2024). Smoked fish salam: Development and sensory analysis. *Revista de Gestão Social e Ambiental*, *18*(11), 1–9.

[27] Sabu, S., & Sasidharan, A. (2020). Impact of fishing on freshness and quality of seafood. *International Journal of Fisheries and Aquatic Studies*, *8*(2), 193–198.

[28] Shittu, S. K., Ibrahim, B., Nalado, D. D., Lawan, I., & Jibril, A. N. (2021). Modification of an existing NSPRI fish smoking kiln. *Bayero Journal of Engineering and Technology*, *16*(1), 148–156.

[29] Sintali, I. S., Abioye, A. M., & Shuaibu, I. (2023a). Charcoal-fired fish smoking kiln. *Nigerian Journal of Tropical Engineering, 17*(1), 32–41. https://doi.org/10.59081/njte.17.1.004

[30] Sintali, I. S., Abioye, A. M., & Shuaibu, I. (2023b). Experimental performance evaluation of a charcoal-fired fish smoking kiln. *Nigerian Journal of Tropical Engineering*, *17*(1), 32–41.

[31] Tacon, A. G. J., Levy, J., Coelho, R., Machado, T. M., Neiva, C. R. P., & Lemos, D. E. L. (2025). Fish for health: Role of fish in global food and animal protein supply. *Reviews in Fisheries Science & Aquaculture*, *33*(2), 319–333.

[32] Taherzadeh-Shalmaei, N., Sharifi, M., Ghasemi-Mobtaker, H., & Kaab, A. (2021). Evaluating the energy use, economic and environmental sustainability for smoked fish production from a life cycle assessment point of view (case study: Guilan Province, Iran). *Environmental Science and Pollution Research*, *28*(38), 53833–53846.

[33] Tahir, M., Salengke, S., Mursalim, Metusalach, & Caesarendra, W. (2020). Performance of a smokehouse designed for smoking fish with the indirect method. *Processes*, *8*(2), 1-18.

[34] Toworfe, E. K., Osei, M. S., Sammah, G. A., & Darko, C. B. (2023). Effects of packaging & moisture content on the quality & shelf life of smoked catfish (Clarias Gariepinus). *Journal of Biosystems Engineering, 6(2), 64-72. http://dx.doi.org/10.2139/ssrn.5971935.*

MULTIBODY DYNAMICS SIMULATION AND TESTING OF A SMALL ELECTRONICALLY CONTROLLED TRACKED CHASSIS FOR HILLY AND MOUNTAINOUS TERRAIN

/

丘陵山地小型履带式电控底盘多体动力学仿真与试验

Xiaolian LÜ[1)], Jiankang HUANG[1)], Ruijuan SU[1)], Yang ZHANG[2)], Xiaorong LÜ*[2)]

[1)] College of Mechanical & Electrical Engineering, Chuzhou University, Chuzhou, 239000, China;

[2)] College of Machinery & Electronics, Sichuan Agricultural University, Yaan, 625014, China

** Corresponding author, E-mail: lxrxj2008@163.com*

DOI: https://doi.org/10.35633/inmateh-79-84

Keywords: *Track Chassis; Electronic Control; RecurDyn; Dynamical Model; Testing*

ABSTRACT

To meet the maneuverability and terrain-adaptability requirements of agricultural machinery operating in hilly and mountainous areas, an electronically controlled tracked chassis was designed and developed. Based on a theoretical analysis of chassis terrain-crossing capability and stability, a multibody dynamic model was established using RecurDyn to simulate the dynamic response of the chassis under typical operating conditions. The chassis trajectory and variations in dynamic stability were analyzed. A physical prototype was then manufactured and tested under multiple operating conditions on actual road surfaces. The chassis achieved a maximum straight-line travel speed of 4 km/h on level ground, a maximum uphill and downhill travel speed of 2 km/h, a maximum climbing angle of 18°, a maximum trench-crossing width of 500 mm, and a turning radius not exceeding 675 mm. The simulation and experimental results were in close agreement, with a maximum relative error of 11%, demonstrating the predictive accuracy of the multibody dynamic model. The developed chassis exhibited good terrain-crossing capability and operational stability. This study provides a theoretical basis and technical support for the development and application of small agricultural machinery in hilly and mountainous areas.

中文摘要

针对丘陵山地复杂地形对农机装备机动性与适应性的要求，本文设计开发了一款小型履带式电控底盘。基于多体动力学底盘通过性及稳定性理论分析，运用 RecurD n 仿真软件构建底盘动力学模型，模拟底盘在典型工况下的动态响应特性，并对其运动轨迹及系统稳定性变化规律进行仿真分析。对研制样机进行实际路况条件下多工况性能测试，当平地直行最大速度为 4 m/h，上下坡最大速度为 2 m/h 时，最大坡度角为 18°，跨越壕沟最大宽度为 500mm，最小转向半径小于 6 5mm。仿真与试验结果表明，构建的多体动力学模型具有较高的预测精度，底盘在复杂地形下具有良好的通过性与稳定性，相对误差均≤11%。研究为丘陵山地小型农机装备研发提供了可靠的理论依据与技术支撑。

INTRODUCTION

From the perspective of global agricultural development trends, the efficient utilization of agricultural resources in hilly and mountainous areas has become a crucial direction for countries to enhance comprehensive agricultural productivity and expand production boundaries. In regions with limited arable land and diverse topography, the mechanization of agriculture in hilly and mountainous areas is not only vital for local agricultural modernization but also a key component of national agricultural strategies *(HU et al., 2025; Jin et al., 2023; Jiang et al., 2025)*. Due to the complex terrain and insufficient agricultural infrastructure, the promotion and application of agricultural mechanization in hilly and mountainous areas lag far behind those in plain regions. Accelerating the modernization of agriculture have become urgent problems *(Sun et al., 2024; Xiong et al., 2023; Chen, 2025)*. The small tracked electronic control chassis, with its advantages of low ground pressure ratio and strong terrain adaptability, is conducive to the operation of mountainous mechanized equipment *(Ding et al., 2025; Buzunov et al., 2023; Belloni et al., 2024; Liu et al., 2025; Chen et al., 2024; Zemánek and Neruda, 2021)*.

Xiaolian LÜ, Prof.; Jiankang HUANG, B.S. Stud; Ruijuan SU, M.S. Stud; Yang ZHANG, M.S. Stud; Xiaorong LÜ,Prof.

As the core traveling and load-bearing component of agricultural machinery, the dynamic performance of the chassis is a key technical link that restricts the development of agricultural machinery equipment. Scholars have conducted extensive research on chassis, and obtained many achievements *(Archut et al., 2026; Baek et al., 2020; HIDALGO et al., 2015; Grazioso et al., 2023; Yun et al., 2023; Ugenti et al., 2023; HUANG et al., 2025)*. *Mirosław et al. (2025)* developed a model of an articulated UGV (unmanned ground vehicle), and studies on the influence of clearances in the steering and track systems on the directional stability of articulated tracked UGVs. *Dudzińskiand and Chołodowski (2021)* established an internal resistance model for the tracked chassis to optimize energy efficiency. *Pei et al. (2025)* examines the climbing performance of the crawler harvester chassis to solve the problems of running ability and stability of the chassis of the crawler combine harvester during mechanical operation. *Komissarov (2025)* developed a simulation model of a high speed tracked vehicle power train with step track gear boxes to be inserted as a subsystem into a highly computationally efficient model of the tracked vehicle curvilinear motion. Existing research mostly focuses on chassis structure design and conventional performance testing, and the study of chassis dynamic response laws under complex and variable working conditions in hilly and mountainous areas is still not deep enough. Traditional physical testing has high costs and long cycles, making it difficult to comprehensively and accurately obtain chassis dynamic characteristics. Dynamic simulation technology can effectively compensate for the shortcomings of testing. This article takes the self-designed electrically controlled tracked chassis in hilly and mountainous areas as the research object, systematically conducts dynamic theoretical analysis of chassis operating performance. The research provides technical support for promoting the mechanization and intelligence of agricultural equipment in hilly and mountainous areas.

MATERIALS AND METHODS

Overall Structure and Parameters

This article has completed the modular integrated design of an electronically controlled tracked chassis. The chassis consists of a frame, a track traveling mechanism, a steering system, a braking mechanism, an electric drive unit, a control system, and a power supply. The overall configuration is shown in Fig. 1. The basic technical parameters are shown in Table 1. The chassis uses STC89C52 microcontroller as the main control chip to build a remote wireless remote-control system. The system integrates modules such as speed display, Bluetooth communication, encoder, motor drive controller, drive motor, power battery, and data acquisition. The matching principles of various hardware parameters have been clarified, and the core control logic has been formulated. Implementing closed-loop regulation of driving speed and brake pressure threshold through PID algorithm is to achieve precise steering control. The designed chassis has a driving speed of 2-4 km/h, a maximum climbing ability of 20°, and a maximum crossing trenches width of 550 mm. The chassis has remote control and flexible steering characteristics, which can meet the needs of multi working conditions in hilly and mountainous areas.

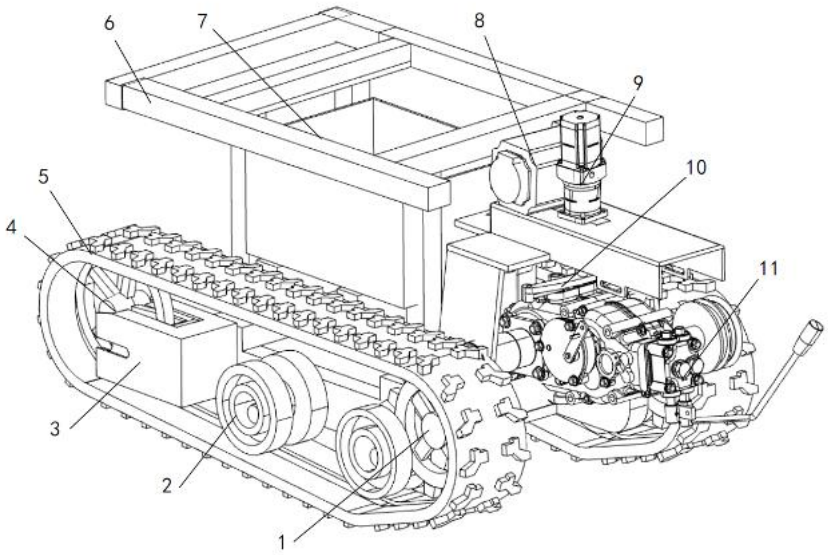


Fig. 1 - The structure diagram of the small tracked electronic control chassis
1 - Drive sprocket; 2 - Support wheel; 3 – Bracket; 4 - Guide wheel; 5 – Track; 6 – Frame; 7 – Controller; 8 - Travel motor; 9 - Steering motor; 10 - Steering mechanism; 11 – Transmission

Table 1

Track Chassis Parameters

Name	Parameter	Name	Parameter
Length × Width ×Height/mm	1000×650×200	Drive sprocket diameter /mm	210
Wheelbase /mm	860	Support wheel diameter /mm	150
Track gauge /mm	470	Guide wheel diameter /mm	190
Track ground-contact length /mm	680	Climbing angle /°	20
Track width /mm	150		

Overall Scheme of the Control System

To achieve wireless remote control and real-time monitoring of the tracked chassis, a measurement and control system was designed with the STC89C52 microcontroller as the main controller. The system primarily consists of a microcontroller minimal system, power module, motor drive module, wireless communication module, and speed monitoring and display module. The overall scheme is shown in Figure 2. The microcontroller minimal system serves as the core control unit, responsible for command reception, logical operations, signal parsing, and motion control. The power module uses a 48 V lithium battery as the primary power source, employing a voltage step-down regulation method to provide 5 V operating voltage for the microcontroller and output stable 24 V through a voltage step-down module, ensuring reliable and stable power supply for the encoder and stepper motor. The motor drive section adopts a dual-channel drive architecture, with the DC brushless motor using the ZM-6750A driver (Operating voltage range: DC32~60 V; Capable of handling peak currents below 50 A); the stepper motor employs the DM-542 driver (Operating voltage range: DC24~50 V; Output current range: 1.0~4.2 A). Wireless communication utilizes the HC-06 Bluetooth module to establish a stable communication link with the mobile app, ensuring reliable transmission of remote control commands and data interaction. Speed monitoring employs the Omron E6B2- CWZ1X rotary encoder, installed at the DC brushless motor shaft end, to collect real-time actual speed data of the driven wheels. The display module uses an LCD1602 screen (Operating voltage range: 4.8~5.2 V), and powered directly by the microcontroller, enabling real-time display of the chassis speed and visualizing the operational status. During system operation, Bluetooth serial assistant of the mobile phone sends control commands, which are transmitted via the Bluetooth module to the microcontroller. After signal parsing and computation, the microcontroller outputs corresponding drive signals to control the motor drivers, thereby enabling functions such as starting, stopping, steering, and speed adjustment of the tracked chassis, ensuring stable system operation, rapid response, and reliable control.

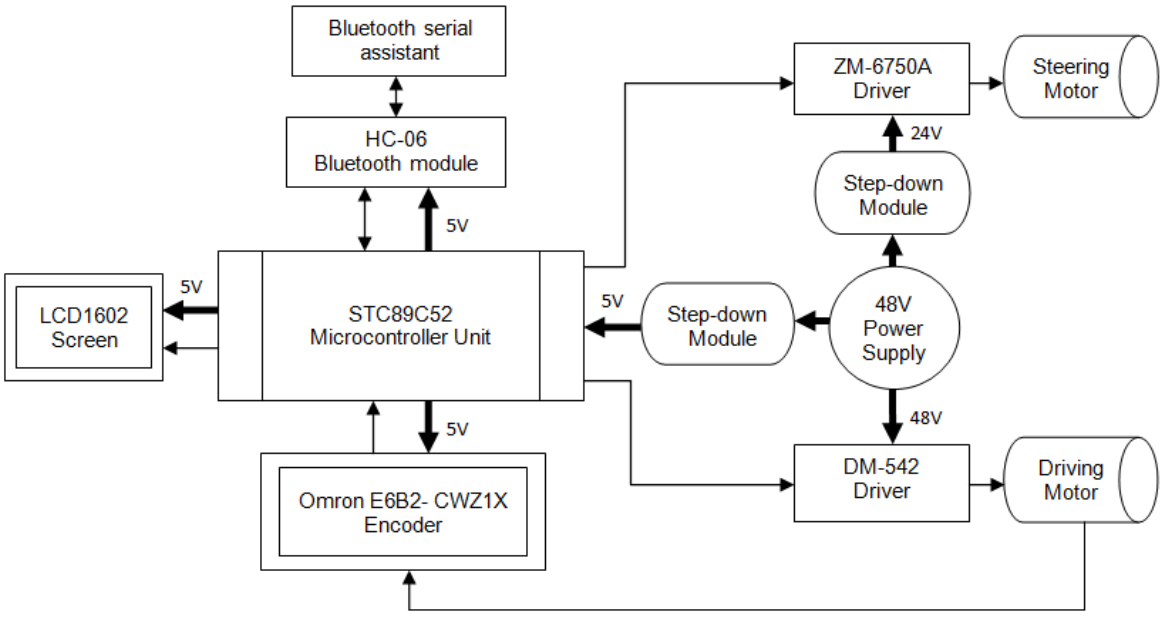
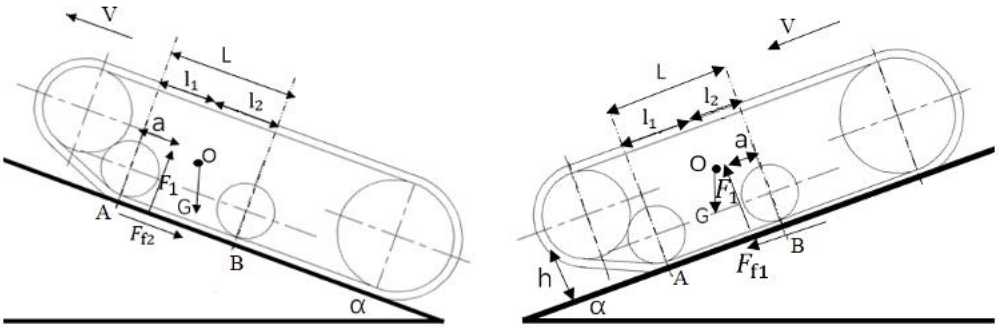


Fig. 2 - The Overall scheme block diagram of control system

Dynamic Performance Analysis of the Chassis

The climbing capability, trench-crossing performance, and steering characteristics of the tracked chassis are key indicators of its operational stability and adaptability to complex terrain. Under idealized operating conditions, mechanical modeling and force analysis of the chassis under different operating conditions provide a theoretical basis for structural design and parameter matching. The forces acting on the chassis during uphill and downhill travel are shown in Fig. 3.



(a) Uphill (b) Downhill

Fig. 3 - Force analysis diagram of the chassis climbing

V-Chassis forward speed, m/s; O-chassis center of mass; G-chassis gravity, N; α - slope, °; h-ground clearance of the center of mass, mm; F_1- ground support force of the chassis, N; a-distance between the support wheel and the support force, mm; L - distance between the support wheel A and the support wheel B, mm; l_1- distance between the support wheel A and the center of mass, mm; l_2- distance between the support wheel B and the center of mass, mm

When the chassis is stable uphill, the force on the vehicle body is balanced, and it can be obtained.

$$\begin{cases} F_1 a - G l_1 \cos\alpha - G h \sin\alpha = 0 \\ F_1 = G \cos\alpha \end{cases} \quad (1)$$

Thus, it can be obtained.

$$a = \frac{l_1 \cos\alpha + \mathrm{h} \sin\alpha}{\cos\alpha} \quad (2)$$

The critical condition for chassis overturning is $a = 0$.

The maximum uphill angle is:

$$\alpha_{max,\mathrm{up}} = \tan^{-1}\frac{l_1}{\mathrm{h}} = 25° \quad (3)$$

The maximum downhill angle is:

$$\alpha_{max,\mathrm{down}} = \tan^{-1}\frac{l_2}{\mathrm{h}} = 22° \quad (4)$$

When the chassis crosses the trench, the force distribution and key geometric parameters are shown in Fig. 4.

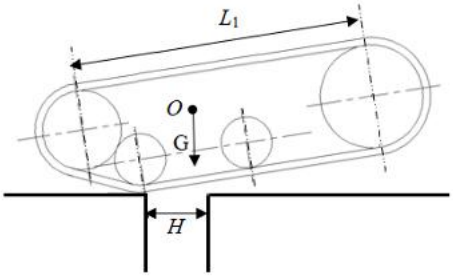


Fig. 4 - Force analysis diagram of tracked chassis crossing trenches

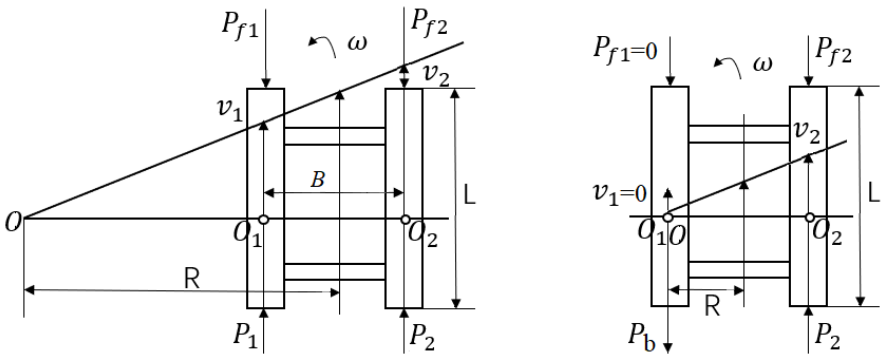
H - maximum width of the chassis crossing the trench, mm; L_1 - distance between the drive sprocket and the guide wheel, mm; O - the center of mass of the chassis; G - chassis gravity, N.

The theoretical maximum trench width of the chassis can be derived:

$$H = \sqrt{(\frac{L_1}{2})^2 + \mathrm{h_1}^2} + r = 581 \text{ mm} \quad (5)$$

where: r - drive sprocket radius, mm; h_1 - guide wheel height, mm.

Mechanical analysis of typical working conditions of chassis steering: the differential steering and unilateral braking steering. The force situation during chassis steering is shown in Fig. 5.



(a) Differential steering (b) Unilateral braking steering

Fig. 5 - Chassis steering performance analysis diagram

O - theoretical steering center of tracked chassis vehicles; O_1,O_2 - instantaneous turning center of the inner and outer track contact sections; v_1,v_2 - the inner and outer track line velocities, m/s; R - steering radius, m; L - the track ground-contact length, m; B - the track gauge, m; P_1,P_2 - the inner and outer track driving force, N; P_{f1},P_{f2} - inner and outer track rolling resistance, N; P_b - track braking force, N; ω - chassis angular velocity, rad/s.

During chassis steering, the following relationship can be obtained:

$$\begin{cases} \omega = \frac{v_2 - v_1}{B} \\ R = \frac{B}{2} \cdot \frac{v_2 + v_1}{v_2 - v_1} \end{cases} \quad (6)$$

where: ω - chassis angular velocity; v_1 - the inner track line velocities; v_2 - the outer track line velocities; B - the track gauge; R - steering radius.

The maximum adhesion of the left and right tracks is:

$$P_{\varphi 1} = P_{\varphi 2} = \frac{1}{2} G\varphi \quad (7)$$

where: $P_{\varphi 1}$ - the maximum adhesion of the left; $P_{\varphi 2}$ - the maximum adhesion of the right; G - the gravity of track chassis; φ - adhesion coefficient.

The rolling resistance of the left and right tracks is:

$$P_{f1} = P_{f2} = \frac{1}{2} G\, f \quad (8)$$

where: P_{f1} - the inner track rolling resistance; P_{f2} - the outer track rolling resistance; G - the gravity of track chassis; f - rolling resistance coefficient.

The steering resistance torque is:

$$M_f = \frac{\mu G L}{4} \quad (9)$$

where: M_f - the steering resistance torque; μ - the average resistance coefficient of steering; G - the gravity of track chassis; L - the track ground-contact length.

The steering torque is:

$$M_1 = \frac{B}{2} P_1 - \frac{B}{2} P_2 \quad (10)$$

where: B - the track gauge; P_1 - the inner track driving force; P_2 - the outer track driving force.

When $M_1 \gg M_f$, the following relationship can be obtained:

$$\frac{L}{B} \ll \frac{2(\varphi - f)}{\mu} \quad (11)$$

In this article, the L of the tracked chassis is designed to be 680 mm and B is 470 mm. The minimum turning radius of the tracked chassis is theoretically less than the sum of the wheelbase and track width. The radius of the chassis unilateral braking steering is 620 mm.

Development of the Multibody Dynamic Simulation Model

To balance dynamic-response fidelity and computational efficiency, the chassis model was simplified to include the main load-bearing frame and the track traveling mechanism. The track traveling mechanism was modeled using the dedicated Track/HM module in RecurDyn, and the constraint relationships among the components were defined, as shown in Fig. 6. The road surface was modeled using the built-in Ground module in RecurDyn. The main simulation parameters are presented in Table 2.

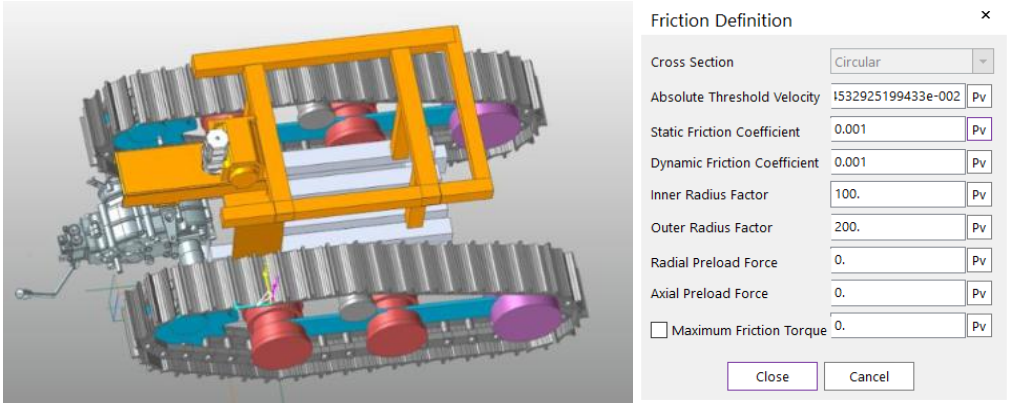


Fig. 6 - Development of the multibody dynamic model of the tracked chassis

Table 2

The road surface characteristic parameters

Parameter	Value
Cohesive deformation modulus of soil k / (N·$m^{-(n+1)}$)	0.417
Frictional deformation modulus of soil k_φ/(N · $m^{-(n+2)}$)	2.19×10^{-2}
Soil deformation exponent n	0.5
Soil cohesion c_i/ kPa	4.14×10^{-3}
Internal friction angle / (°)	13
Shear deformation modulus k_s	25
Sinkage ratio	0.05

Chassis performance was comprehensively evaluated in terms of driving stability, terrain-crossing capability, and steering maneuverability using the chassis pitch angle relative to the ground, center-of-mass displacement, center-of-mass velocity, steering angular acceleration, drive-sprocket angular velocity, and chassis angular displacement as evaluation indicators. The simulation conditions were as follows:

(1) Climbing-performance simulation: The slope angle was set to 20°, the travel speed to 2 km/h, and the drive-sprocket angular velocity to ω=5.32 rad/s. The simulation duration was 10 s, with 500 computational steps.

(2) Trench-crossing simulation: The travel speed was set to 3 km/h, and the drive-sprocket angular velocity was set to ω=7.93 rad/s. The STEP function was used to control the variation in drive-sprocket angular velocity STEP (TIME, 1,0,3, -7.93). The simulation duration and number of computational steps were the same as those used in the climbing simulation.

(3) Steering-performance simulation: Two steering modes — single-track braking and pivot steering — were simulated to determine the minimum turning radius. For single-track braking, the right track was braked while the left track continued to travel at 2 km/h, corresponding to a drive-sprocket angular velocity of ω=5.29 rad/s. The function expression for the right drive sprocket was STEP (TIME, 1,0,4,5.29) +STEP (TIME, 5,0,7, -5.29) +STEP (TIME, 8,0,9,5.29), and the speed function for the left drive sprocket was STEP (TIME, 1,0,4,5.29). When performing a Pivot steering, the driving speed was set to 1.5 km/h, the drive sprocket angular velocity ω=3.96 rad/s, the speed function of the right drive sprocket was STEP (TIME, 1,0,2,3.96), and the speed function of the left drive sprocket was STEP (TIME, 1,0,2, -3.96). Pivot steering was achieved by driving the two tracks at equal angular-velocity magnitudes in opposite directions, and the simulation duration and number of computational steps were the same as those used in the preceding simulations.

Field Performance Test Scheme

Test objective: The field tests were conducted to verify the accuracy of the chassis dynamic model, evaluate the dynamic performance of the chassis, and validate the structural design parameters and simulation results. The climbing, trench-crossing, and steering performance of the chassis was investigated.

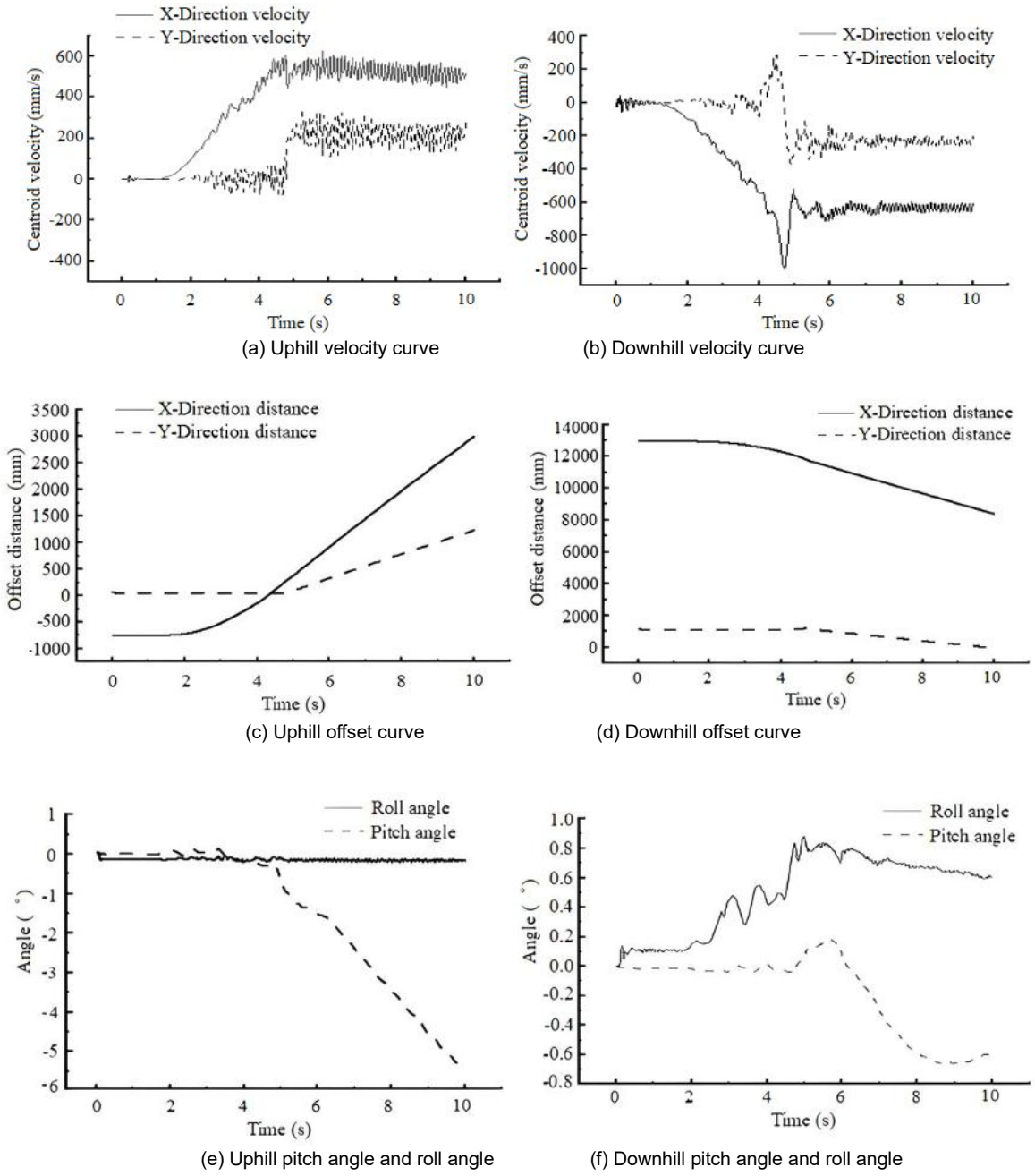
Test object and method: The test object was the independently developed electronically controlled tracked chassis, and the field-test conditions were consistent with the simulation conditions. Climbing performance was evaluated using the maximum stable climbing angle. The ability of the chassis to travel smoothly on slopes ranging from 5° to 20° was tested. Each operating condition was tested three times and was considered successful only if the chassis completed all three trials. Trench-crossing performance was evaluated using the maximum safe trench-crossing width, with trench widths ranging from 0.30 to 0.55 m.

Each trench width was tested three times and was considered successfully traversed only if all three trials were completed. Steering performance was evaluated using the turning radius during single-track braking. Four steering modes were tested: forward left turn, forward right turn, reverse left turn, and reverse right turn. The largest stable turning radius measured among the four steering modes was taken as the steering-performance value.

RESULTS AND DISCUSSION

Multibody Dynamic Simulation Results

The climbing-performance and trench-crossing simulation results are shown in Figs. 7 and 8, respectively, while the steering-performance results are presented in Fig. 9. Based on the actual steering mode of the chassis, the trajectory of its center of mass during single-track braking on a clay road surface was simulated, as shown in Fig. 10.

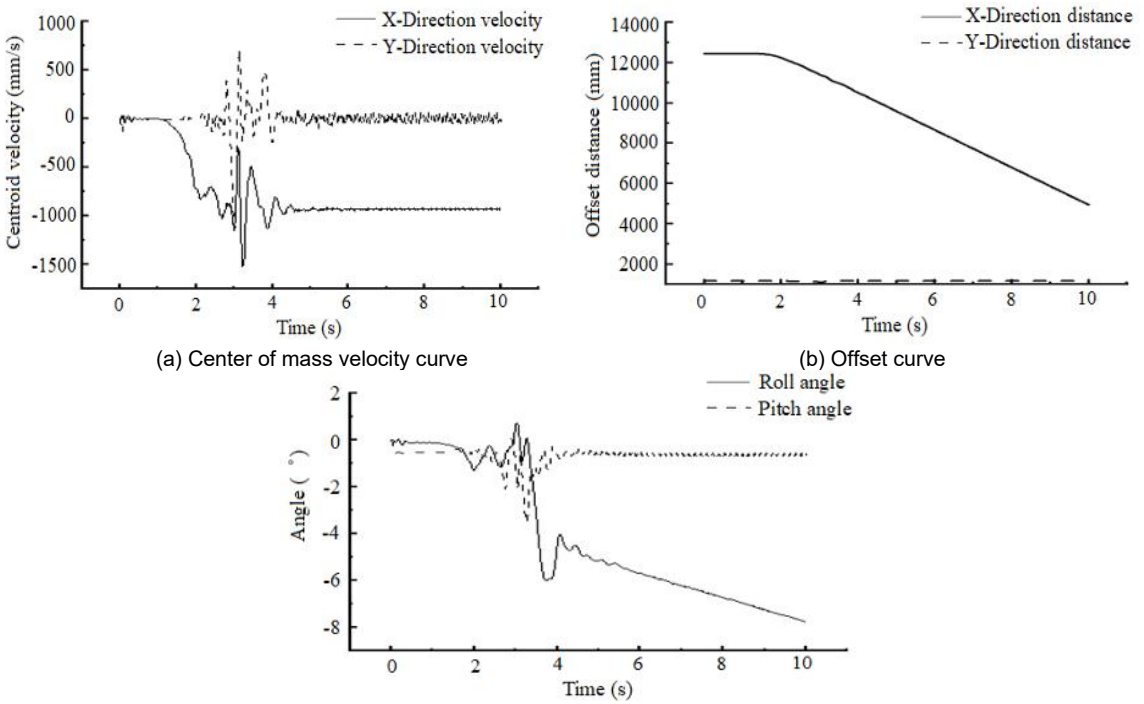


(a) Uphill velocity curve (b) Downhill velocity curve

(c) Uphill offset curve (d) Downhill offset curve

(e) Uphill pitch angle and roll angle (f) Downhill pitch angle and roll angle

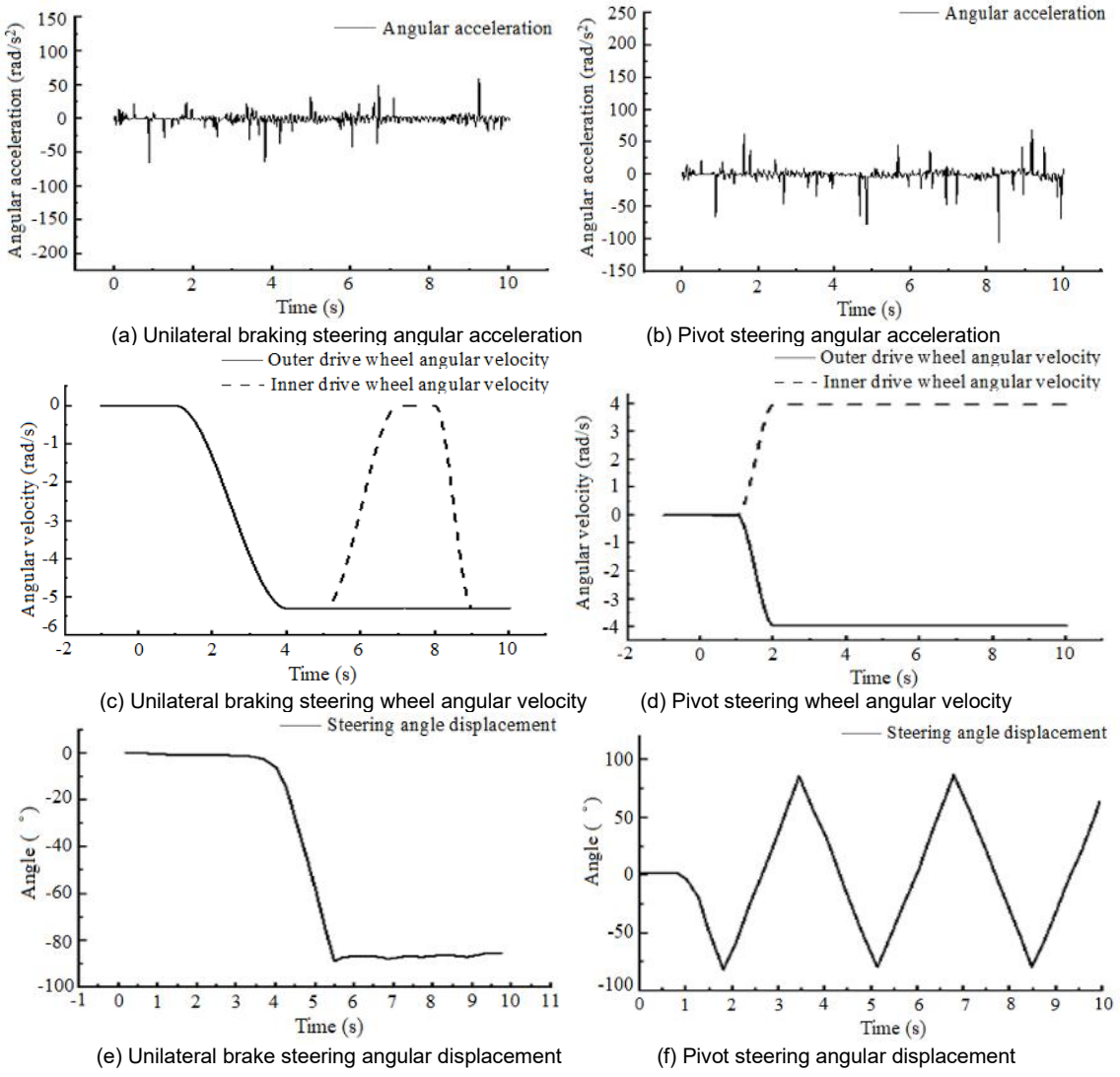
Fig. 7 - Dynamic simulation of chassis climbing



(a) Center of mass velocity curve (b) Offset curve

(c) Pitch angle and roll angle

Fig. 8 - Dynamic simulation of chassis trench crossing



(a) Unilateral braking steering angular acceleration (b) Pivot steering angular acceleration

(c) Unilateral braking steering wheel angular velocity (d) Pivot steering wheel angular velocity

(e) Unilateral brake steering angular displacement (f) Pivot steering angular displacement

Fig. 9 - Dynamic simulation of chassis steering

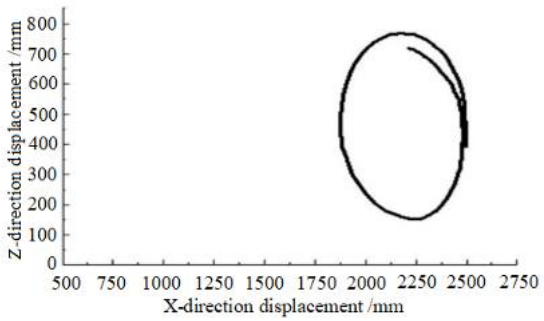
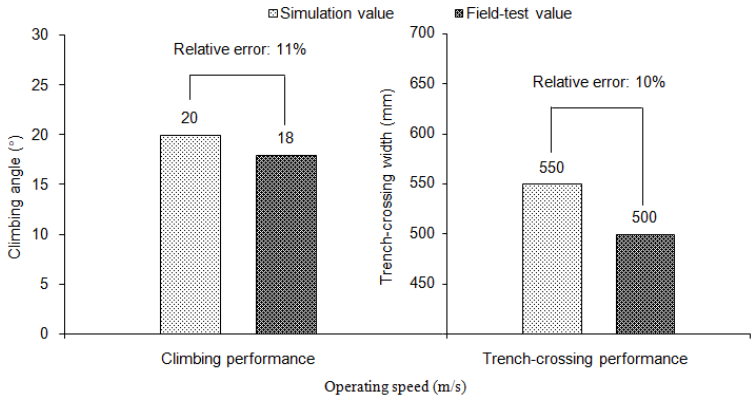


Fig. 10 - Simulated trajectory of the chassis center of mass during steering

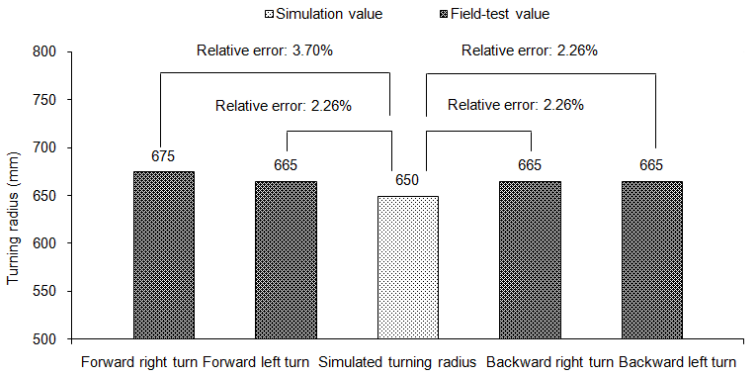
The simulation results were analyzed as follows. As shown in Figs. 7(a) and 7(b), during uphill travel, the mean values of *Vx* and *Vy* were 0.53 and approximately 0.23 m/s, respectively. During downhill travel, *Vx* remained relatively stable within the range of 0.5–0.6 m/s, while the mean *Vy* was 0.23 m/s. The simulated velocity of the chassis center of mass was consistent with the calculated value, supporting the validity of the dynamic model. As shown in Figs. 7(c) and 7(d), at approximately 4 s during both uphill and downhill travel, the displacement in the X-direction began to decrease gradually, while the center of mass exhibited considerable vertical displacement in the Y-direction. After the chassis had fully entered the slope, its center-of-mass displacement continued to increase approximately linearly with time, although the rate of increase decreased slightly. As shown in Figs. 7(e) and 7(f), the pitch and roll angles remained close to zero during most of the uphill process. Near the end of the climb, both angles increased slightly but remained below 6°. During downhill travel, the pitch and roll angles fluctuated more noticeably, with a maximum roll angle of 0.9°. As shown in Fig. 8(a), the center-of-mass velocity fluctuated considerably while the chassis crossed the trench between 2 and 4 s. After trench crossing was completed, the velocity rapidly stabilized, indicating effective drive-speed regulation. As shown in Fig. 8(b), the center-of-mass displacement in the Y-direction remained nearly constant, indicating negligible lateral deviation perpendicular to the direction of travel. The chassis began to enter the trench at 2 s, after which the corresponding vertical-displacement curve decreased approximately linearly. This behavior was consistent with the velocity fluctuations and load variations occurring during trench crossing. As shown in Fig. 8(c), the roll angle exhibited periodic oscillations during trench crossing, while the pitch angle remained below 8° throughout the process. As shown in Figs. 9(a) and 9(b), the angular acceleration varied smoothly during steering, indicating stable steering-power output without marked impact loading. As shown in Figs. 9(c) and 9(d), the single-track braking maneuver proceeded smoothly and steadily. As shown in Figs. 9(e) and 9(f), the chassis initially completed a 90° right turn and subsequently continued traveling in a straight line until the end of the simulation, producing a regular turning trajectory. During pivot steering, the chassis also exhibited a rapid steering response. The simulated trajectory of the chassis center of mass during single-track braking on a clay road surface is shown in Fig. 10. The maximum turning radius was 650 mm, corresponding to an error of 4.85% relative to the theoretical design value.

Field Performance Test Results

The field test results are shown in Figure 11.



(a) climbing and trench-crossing performance



(b) turning radius under different steering conditions

Fig. 11 - Analysis of performance test results for small electronically controlled tracked chassis

Analysis of the experimental results yielded the following findings: (1) The maximum climbing angle of the chassis was 18°, with a relative error of no more than 11% compared with the simulated value. These results validated the accuracy of the climbing dynamic model and demonstrated that the chassis could meet the climbing requirements of operations in hilly and mountainous areas. The deviation was mainly attributed to differences between the actual operating conditions and the idealized model, including track–ground adhesion, track characteristics, and chassis mass distribution. (2) The maximum trench-crossing width measured during the field tests was 500 mm, with a relative error of no more than 10% compared with the simulated value. The results confirmed the reliability of the trench-crossing dynamic model and indicated that the chassis structure could traverse common trench obstacles in hilly and mountainous areas. The deviation was mainly caused by differences in ground conditions, track–ground contact characteristics, chassis attitude, and load distribution between the field tests and the idealized model. (3) The single-track braking tests yielded a maximum turning radius of 675 mm under the different steering conditions, with a relative error of no more than 3.70% compared with the simulated value. The close agreement between the experimental and simulated results validated the developed dynamic model and theoretical analysis method. The steering flexibility and accuracy of the chassis met the requirements for operation in confined spaces in hilly and mountainous areas.

CONCLUSIONS

(1) The multibody dynamic model developed for the electronically controlled tracked chassis under typical operating conditions demonstrated adequate accuracy and applicability. The relative errors for climbing and trench-crossing performance were within 11%, while the relative error in turning radius under different steering conditions was within 3.70%. The model accurately represented the dynamic response of the chassis during operation in hilly and mountainous terrain, providing a reliable theoretical basis for evaluating chassis travel performance and optimizing the track traveling mechanism.

(2) The independently developed electronically controlled tracked chassis met the operational requirements for complex terrain in hilly and mountainous areas. Field-test results showed that the chassis achieved the design targets for climbing, trench crossing, and steering, while maintaining smooth and stable motion. The measured motion parameters under the different operating conditions agreed closely with the theoretical and simulation results. The chassis exhibited good adaptability to uneven terrain and complex ground conditions, thereby confirming the feasibility and practicality of the track traveling mechanism design.

ACKNOWLEDGEMENT

The study was supported by the Natural Science Research Projects of Universities in Anhui Province (2023AH040222), Chengdu Municipal Bureau of Science and Technology Project (2024-YF09-00035-SN), and the SichuanInnovationTeamofChineseNationalModernAgriculturalIndustryTechnologySystem (SCCXTD-2026-21(27)).

REFERENCES

[1] Archut, J. L., & Corves, B. (2026). Non-iterative implicit integration methods with linearization-based equations of motion approximation for real-time multibody vehicle dynamics simulation. *Mechanics Based Design of Structures and Machines, 54(1).* https://doi.org/10.1080/15397734.2026.2623082

[2] Baek, S.H., Shin, G.B., Lee, S.H., Yoo, M., & Chung, C.K. (2020). Evaluation of the slip sinkage and its effect on the compaction resistance of an off-road tracked vehicle. *Applied Sciences*, *10*(9), 317. https://doi.org/10.3390/app10093175

[3] Belloni, M., Vignati, M., & Sabbioni, E. (2024). Analyzing the Effect of Chassis Torsional Flexibility on the Rollover Threshold of a Multi-Purpose Agricultural Vehicle. *Vehicles*, *6*(1), 415-432. https://doi.org/10.3390/vehicles6010018

[4] Buzunov, N.V., Ivanenkov, V.V., Pirozhkov, R.D., Kositsyn, B.B., & Kotiev, G.O. (2023). The method of development of the electronic control system for curvilinear motion of a high-speed tracked vehicle with dual-flow transmission. *Tractors and Agricultural Machinery*, *90*(2), 133-147. https://doi.org/10.17816/0321-4443-312191

[5] Chen, F. (2025). Agricultural mechanization and service innovation in hilly and mountainous areas: An experimental study based on the construction of the Three-in-One demonstration zone in Jiangjin(山地丘陵地区农业机械化与服务创新——基于江津"三化"示范区建设的试验研究). *Journal of Chinese Agricultural Mechanization*, *46*(9), 72-80. https://doi.org/10.13733/j.jcam.issn.2095-5553.2025.09.010

[6] Chen, Y., Wang, Z., Zhang, H., Liu, X., Li, H., Sun, W., & Li, H. (2024). Investigation of the Traveling Performance of the Tracked Chassis of a Potato Combine Harvester in Hilly and Mountainous Areas. *Agriculture*, *14*(9), 1625. https://doi.org/10.3390/agriculture14091625

[7] Ding, R., Qi, X., Chen, X., Mei, Y., Li, A., Wang, R., & Guo, Z. (2025). Research on the Design of an Omnidirectional Leveling System and Adaptive Sliding Mode Control for Tracked Agricultural Chassis in Hilly and Mountainous Terrain. *Agriculture*, *15*(18), 1920. https://doi.org/10.3390/agriculture15181920

[8] Dudziński, P. A. & Chołodowski, J. (2021). A method for predicting the internal motion resistance of rubber-tracked undercarriages, Pt. 1: a review of the state-of-the-art methods for modeling the internal resistance of tracked vehicles. *Journal of Terrmechanics*, *96*, 81-100. https://doi.org/10.1016/j.jterra.2021.02.006

[9] Grazioso, A., Ugenti, A., Galati, R., Mantriota, G., & Reina, G. (2023). Modeling and validation of a novel tracked robot via multibody dynamics. *Robotica, 41*(10), 3211–3232. https://doi.org/10.1017/S0263574723000966

[10] Hidalgo A, García de Jalón J. (2015). Real-Time Dynamic Simulations of Large Road Vehicles Using Dense, Sparse, and Parallelization Techniques. *Journal of Computational and Nonlinear Dynamics, 10(3): 031005.* https://doi.org/10.1115/1.4028794

[11] Hu, Z., Zhang, M., Luo, W., Pang, Y., Lang, F., & Li, Q. (2025). Advancing agricultural mechanization in China's hilly and mountainous areas: Key strategies and technological focus(加快中国丘陵山区农机化发展的思考与对策). *Transactions of the Chinese Society of Agricultural Engineering*,*41*(14), 39-50. https://doi.org/10.11975/j.issn.1002-6819.202412206

[12] Huang, X., Shi, Y., Wang, X., Lin, L., Wang, Y., & Xu, L. (2025). Design and development of a fully electric weeding robot for hilly and mountainous orchards(丘陵山地果园纯电驱动除草机器人研制). *Transactions of the Chinese Society of Agricultural Engineering*, *41*(18), 28-41. https://doi.org/10.11975/j.issn.1002-6819.202412242

[13] Jiang, Y., Wang, R., Ding, R., Sun, Z., Jiang, Y., & Liu, W. (2025). Research Review of Agricultural Machinery Power Chassis in Hilly and Mountainous Areas. *Agriculture*, *15*(11), 1158. https://doi.org/10.3390/agriculture15111158

[14] Jin, W.C., Wang, O., Yang, M.Y. & Long, T.Y. (2023). The development strategy and path of China's agricultural mechanization under the goal of building a strong agricultural country(农业强国建设目标下的中国农业机械化发展战略与路径策). *Issues in Agricultural Economy*, *2023*(10), 13-21. https://doi.org/10.13246/j.cnki.iae.2023.10.007

[15] Komissarov, A.I. (2025). Simulation model of a high speed tracked vehicle powertrain with step track gear boxes. *Tractors and Agricultural Machinery*, *92*(1), 25-34. https://doi.org/10.17816/0321-4443-631516

[16] Liu, Q., Ji, Y.X., Yang, F.Z., Zhang, L.H., Du, Z.X., Liu, Z.J., & Zhu, X.Y. (2025). Development and Validation of Traction Performance for Mountain Tracked Chassis on Slopes(山地履带式底盘坡地牵引性能预测模型构建与试验). *Transactions of the Chinese Society for Agricultural Machinery*, *56*(5), 597-607. https://doi.org/10.6041/j.issn.1000-1298.2025.05.058

[17] Mirosław, P., Tomasz, M., & Karol, K. (2025). Simulation studies on the influence of clearances on the directional movement stability of articulated tracked unmanned ground vehicles. *Advances in Science*

and Technology Research Journal,*19*(1), 229-24. https://doi.org/10.12913/22998624/194887

[18] Pei, C.N., Dai, F., Shi, R.J., Zhao, W.Y., Zhao, Y.M., Chen, J.Z., Pan, H.F., & Deng, H. (2025). Simulation analysis and test of chassis climbing performance of hilly area crawler quinoa combine harvester(丘陵山地履带式藜麦联合收割机底盘爬坡性能仿真分析与试验). *Agricultural Research in the Arid Areas*, *43*(1), 287-298. https://doi.org/10.7606/j.issn.1000-7601.2025.01.30

[19] Sun, J.B., Zeng, L.K., Ying, J., Zhen, H., Sun, Q., & Meng, X.Z. (2024). Research Status and Prospect of Key Technologies of Agricultural Track Chassis(农业履带底盘关键技术研究现状与展望). *Transactions of the Chinese Society for Agricultural Machinery*, *55*(11), 202-220. https://doi.org/10.6041/j.issn.1000-1298.2024.11.022

[20] Ugenti, A., Galati, R., Mantriota, G., & Reina, G. (2023). Analysis of an all-terrain tracked robot with innovative suspension system, *Mechanism and Machine Theory*, *182*, 105237. https://doi.org/10.1016/j.mechmachtheory.2023.105237

[21] Xiong, Y.S., Si, J.Y., Xie, X.B., Ding, Z., Wang, J.S., & Zhang, L.H. (2023). Development of agricultural crawler traveling device(农用履带行走装置研制). *Journal of Chinese Agricultural Mechanization*, *44*(12), 87-91. https://doi.org/10.13733/j.jcam.issn.2095-5553.2023.12.014

[22] Yun, S., Lee, J., Jang, W., Kim, D., Choi, M., & Chung, J. (2023). Dynamic modeling and analysis of a driving passenger vehicle. *Applied Sciences, 13(10), 5903.* https://doi.org/10.3390/app13105903

[23] Zemánek, T., & Neruda, J. (2021). Impact on the Operation of a Forwarder with the Wheeled, Tracked-Wheel or Tracked Chassis on the Soil Surface. *Forests*, *12*(3), 336. https://doi.org/10.3390/f12030336

AUTOMATIC RADICLE LENGTH ESTIMATION OF GERMINATED CUCUMBER SEEDS BASED ON GERMHRNET

/

基于 GermHRNet 的发芽黄瓜种子胚根长度自动估测方法

Rui ZHAO[1)], Heng ZHAO[1)], Feng ZHANG[1)], Wenjie LI[2)], Bei WANG[2)], Qi WANG[4)], Yiting SU[1)], Qiulan WU[*1)], Bo ZHOU[*2,3)],

[1)]College of Information Science and Engineering, Shandong Agricultural University, Tai'an/China
[2)]College of Life Sciences, Shandong Agricultural University, Tai'an/China
[3)]Eukaryotic Biotechnology (Shandong) Co., Ltd., Tai'an/China
[4)]Yoheng Biotechnology (Ningbo) Co., Ltd., Ningbo/China
Corresponding author: Qiulan WU; Tel: +86 13181817575; E-mail: zxylsg@sdau.edu.cn
Bo ZHOU; Tel: +86 13562802798; E-mail: Zhoubo2798@163.com

DOI: https://doi.org/10.35633/inmateh-79-85

Keywords: *Cucumber seeds, Radicle length estimation, Keypoint detection, High-throughput plant phenotyping*

ABSTRACT

Radicle length is an important phenotypic trait for evaluating the growth-promoting effects of plant growth-promoting rhizobacteria on cucumber seeds. However, conventional manual measurement is time-consuming, labor-intensive, and prone to subjective errors, while existing radicle phenotyping systems still suffer from insufficient throughput. To address these limitations, this study proposes an automatic radicle length estimation method for germinated cucumber seeds based on GermHRNet. First, a YOLOv8-p2s model was used to automatically detect seed instances in Petri dish images. Subsequently, a GermHRNet keypoint detection network was developed to accurately localize radicle keypoints. A high-resolution cross-scale feature enhancement module and a dynamic coordinate feature enhancement module were introduced to improve feature representation and keypoint localization accuracy for slender and curved radicles. Finally, radicle length was estimated using a polyline-based pixel distance accumulation strategy according to the detected keypoint coordinates. Experimental results showed that the proposed method achieved an average precision, average recall, and percentage of correct keypoints of 90.6%, 92.2%, and 88.2%, respectively. The mean absolute error, root mean square error, normalized mean absolute error, normalized root mean square error, and coefficient of determination for radicle length estimation were 0.51 mm, 0.61 mm, 6.06%, 7.25%, and 0.98, respectively. Under a CPU-only environment without GPU acceleration, the proposed method achieved a throughput of 3.38 × 10^4 seeds/h. The proposed method enables rapid and accurate radicle length acquisition without specialized equipment and provides an efficient technical solution for large-scale microbial strain screening and seed phenotyping.

摘要

黄瓜种子胚根长度是评价植物促生根际菌促生效应的重要表型参数，但传统人工测量费时费力且主观性强，而现有胚根表型采集系统也存在通量不足的问题。为此，本研究提出一种基于 ermHRNet 的发芽黄瓜种子胚根长度自动估测方法。首先，利用 YOLOv8- 2s 模型实现培养皿中种子个体的自动检测。随后，构建 ermHRNet 关键点检测网络，实现胚根关键点的准确定位。通过引入高分辨率交叉特征增强模块和动态坐标特征增强模块，提高了细长弯曲胚根的特征表达与关键点定位精度。最后，基于关键点坐标采用多段折线像素距离累积方法实现胚根长度估测。结果表明：关键点检测的平均精度、平均召回率和正确关键点百分比分别达到 90.6%、92.2% 和 88.2%；长度估测的平均绝对误差、均方根误差、归一化平均绝对误差、归一化均方根误差和决定系数分别为 0.51 mm、0.61 mm、6.06%、 .25%和 0.98；在普通设备 CPU 推理且未启用 PU 加速的环境下，单机处理通量可达 3.38×10^4 粒/h。该方法无需专业设备即可实现发芽黄瓜种子胚根长度的准确、快速获取，可为大规模菌株筛选及种子表型分析提供高效技术支撑。

INTRODUCTION

Cucumber is widely used as a representative crop for investigating root development in plant physiology and plant–microbe interaction studies because of its short growth cycle, clear phenotypic characteristics, and high sensitivity to environmental changes *(Shaik et al., 2025).* In studies involving plant growth-promoting rhizobacteria (PGPR), cucumber seeds are commonly used as experimental materials to evaluate the growth-promoting potential of microbial strains and their combinations *(Fu et al., 2026).* Radicle length is one of the most important phenotypic indicators of early root development, as it directly reflects seed germination status and the regulatory effects of microbial metabolites on root growth. However, PGPR screening usually requires the evaluation of a large number of candidate strains, which places high demands on both the efficiency and accuracy of radicle length measurement. At present, radicle length measurement still largely depends on manual operation, which is time-consuming, labor-intensive, and susceptible to subjective errors. Although several automated seed phenotyping systems, such as TPN-Pheno-ZM1 *(Top Cloud-Agri Technology Co., Ltd., 2026)* and OpenPheno *(Hu et al., 2025)*, have been developed to improve measurement efficiency, their throughput for radicle length measurement remains limited. For example, the TPN-Pheno-ZM1 system can process only approximately 1,000 seeds within 2 h. Therefore, developing an accurate, efficient method for automatic radicle length estimation is of practical importance for high-throughput microbial screening and seed phenotyping.

To realize automatic radicle length estimation in germinated seeds, image semantic segmentation has been widely used to extract radicle regions and estimate length based on contour or skeleton information *(Wu et al., 2024; Zhao et al., 2025)*. However, segmentation-based methods are highly dependent on image quality and segmentation accuracy. When radicles are curved, slightly lifted from the filter paper, adherent to the background, or partially blurred, these methods are prone to structural discontinuities, boundary errors, and mis-segmentation, which may further affect length estimation. Compared with segmentation-based methods, keypoint detection provides a more structured representation by localizing critical anatomical or morphological positions of the target *(Li et al., 2026).* This strategy reduces the dependence on complete pixel-level segmentation and can provide a more robust representation of complex radicle morphology. In recent years, keypoint detection has been increasingly applied to agricultural phenotyping tasks. For example, *Chen et al. (2025)* developed an improved LTHRNet model for accurate localization and pose estimation of pineapple fruit keypoints. *Yuan et al. (2026)* proposed CLR-YOLO-Pose based on YOLO-Pose, which improved keypoint detection performance under complex scenarios and enabled high-precision measurement of peduncle length. *He et al. (2024)* introduced DEKR-SPrior based on a bottom-up keypoint detection framework for phenotypic analysis of soybean pods in complex field environments. *Pan et al. (2025)* developed the PFLO model to reconstruct plant skeletons from keypoints for high-precision maize phenotyping. *Wu et al. (2023)* improved HRNet by incorporating a Ghost module and developed a lightweight keypoint detection model for grape stem recognition in complex cluster structures. *Niu et al. (2025)* introduced an attention mechanism into YOLOv11-Pose to achieve whole-plant keypoint localization and phenotypic parameter extraction in maize. *Chen et al. (2024)* improved skeleton extraction and phenotypic parameter acquisition for individual rice tillers by integrating the CBAM module into a cascaded pyramid network. These studies demonstrate the potential of keypoint detection for plant phenotyping. However, most existing methods focus on relatively large plant organs, such as fruits, stems, pods, tillers, or whole plants, which usually have more distinct structural features. In contrast, germinated seed radicles are small, slender, curved, and sometimes structurally discontinuous in images. As a result, keypoint detection for germinated seed radicles remains insufficiently investigated, and a dedicated methodological framework is still lacking.

In summary, automatic radicle length estimation still faces two main challenges. First, existing measurement methods often rely on manual operation, specialized imaging devices, or low-throughput processing workflows, making them difficult to apply to large-scale microbial strain screening. Second, current keypoint detection methods have limited capability in preserving fine structural details of small and slender targets, which may lead to unstable or inaccurate keypoint localization when radicles show obvious curvature, complex poses, adhesion to the filter paper, or blurred root tips.

To address these challenges, this study proposes a GermHRNet-based automatic radicle length estimation method for germinated cucumber seeds. Based on the high-resolution network (HRNet), the proposed method enhances the keypoint detection framework to improve the representation of fine radicle structures and the localization stability of curved radicles. Specifically, YOLOv8-p2s is first used to detect individual seed instances in Petri dish images. Then, GermHRNet is constructed to localize radicle keypoints accurately.

To improve the representation of slender radicle structures, a high-resolution cross-scale feature enhancement strategy was introduced. In addition, a coordinate-aware dynamic feature enhancement strategy was further incorporated to enhance spatial coordinate awareness and reduce keypoint displacement caused by radicle curvature. Finally, radicle length is estimated using a polyline-based pixel-to-millimeter accumulation method. The proposed method aims to provide an accurate, rapid, and high-throughput technical solution for cucumber seed radicle phenotyping and large-scale PGPR screening.

The main contributions of this study are summarized as follows:

1) An automated radicle phenotyping framework integrating seed detection, keypoint localization, and radicle length estimation was developed for germinated cucumber seeds, providing an efficient technical solution for large-scale PGPR screening.

2) A GermHRNet-based keypoint detection model was proposed to improve the localization accuracy of small, slender, and curved radicles. The model enhances fine-grained structural representation and spatial coordinate perception for complex radicle morphology.

3) A polyline-based radicle length estimation strategy was established to achieve accurate radicle length quantification without relying on pixel-level segmentation, thereby improving robustness under curved and partially blurred radicle conditions.

4) The proposed framework achieved accurate and high-throughput radicle phenotyping under CPU-only deployment conditions, demonstrating its practical potential for low-cost agricultural phenotyping applications.

MATERIALS AND METHODS

Data Acquisition and Dataset Construction

High-Throughput Image Acquisition System

To satisfy the requirements for high-quality and large-scale image acquisition in radicle phenotyping, a high-throughput imaging system for germinated seeds was designed and developed in this study, as shown in Fig. 1. The system consisted of three main modules: image acquisition, image processing, and data management.



Fig. 1 - High-throughput image acquisition system for germinated seeds

For image acquisition, the system consisted of an industrial camera produced by Jierui Weitong Co., Ltd., China, an aluminum-alloy frame, and a standardized Petri dish holder. Images were acquired at a resolution of 1600 × 1200 pixels. During image acquisition, the vertical distance between the camera lens and the Petri dish plane was fixed at 42 cm to ensure consistent imaging conditions. The holder accommodated up to 12 Petri dishes with a diameter of 9 cm in a single acquisition, allowing batch image acquisition. A reference ruler was placed in the imaging plane for scale calibration, and the calibrated scale factor was approximately 6 pixels/mm. This scale factor was used to convert the estimated radicle length from pixel units to physical length.

For image processing, the system provided basic preprocessing functions. Original images containing multiple Petri dishes were automatically divided into individual dish images. In addition, image parameters such as brightness, sharpness, and resolution could be adjusted to improve image consistency and reduce quality differences among samples. These preprocessing procedures provided standardized data for subsequent seed detection, keypoint localization, and radicle length estimation.

For data management, the system supported centralized storage and standardized organization of acquired images and related experimental data. This facilitated dataset construction, sample retrieval, and subsequent model training and evaluation.

The developed imaging system provided a standardized and efficient platform for high-throughput radicle phenotyping of germinated cucumber seeds.

High-Throughput Image Acquisition

The cucumber seeds used in this study were from the cultivar Zhongnong No. 6 and were provided by the State Key Laboratory of Crop Biology at Shandong Agricultural University. Before the germination experiment, healthy, well-filled, and morphologically uniform seeds were manually selected to reduce the influence of seed quality variation on radicle phenotyping. The selected seeds were placed in standard Petri dishes with a diameter of 9 cm and incubated in a constant-temperature incubator at 25 °C under dark conditions for 48 h. After germination, seed images were acquired using the custom-built high-throughput image acquisition system shown in Fig. 1. Each original image contained 12 Petri dishes, as illustrated in Fig. 2, and the average acquisition time for one original image was approximately 0.35 s. A total of 220 original images were collected, including 2,640 Petri dishes and 34,793 germinated cucumber seeds. These images were used for subsequent seed detection, radicle keypoint annotation, model training, and radicle length estimation.

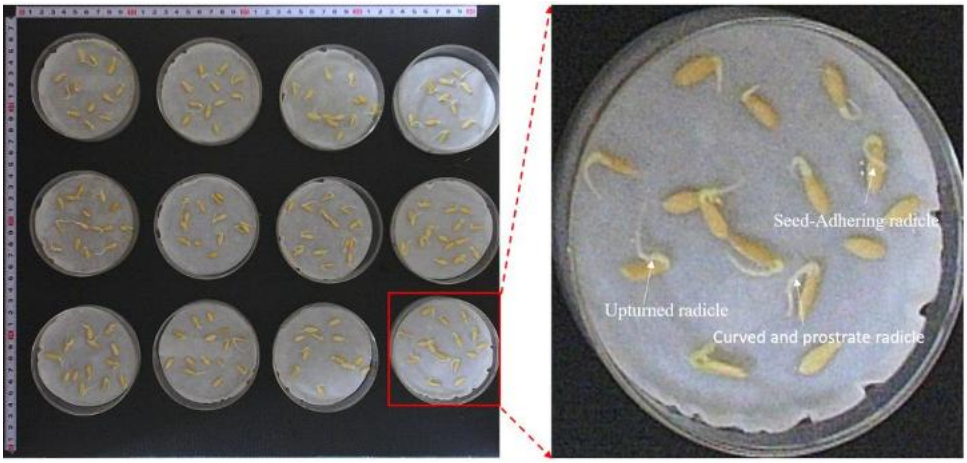


Fig. 2 - Images of germinated cucumber seeds

Dataset Construction

After image acquisition, the 220 original images were divided into two datasets: CucumberSeeds-1 and CucumberSeeds-2. CucumberSeeds-1 contained 100 original images with 15,653 seeds and was used for model training, validation and testing. The dataset was divided into training, validation and test sets at a ratio of 8:1:1. Since each original image contained 12 Petri dishes and a large number of seed instances, an automatic cropping procedure was used to convert the original multi-dish images into single-dish images. This operation increased the effective number of samples and provided clearer local image information for fine-grained radicle feature learning. After cropping, the dataset included 960 training images, 120 validation images and 120 test images. CucumberSeeds-2 contained 120 original images with 19,140 seeds and was used to evaluate the high-throughput phenotyping performance of the proposed method.

The LabelMe annotation tool was used to construct the radicle keypoint dataset. Each seed was annotated with a bounding box and four radicle keypoints, namely the radicle base, pre-bending point, post-bending point and root tip. As shown in Fig. 3, the four-keypoint annotation scheme was determined through preliminary experiments. When fewer than four keypoints were used, the curved morphology of the radicle could not be sufficiently represented, resulting in larger length estimation errors. When more than four keypoints were used, annotation complexity and computational cost increased, but the improvement in estimation accuracy was limited. Therefore, the four-keypoint strategy was adopted to balance length estimation accuracy, annotation efficiency and computational efficiency.

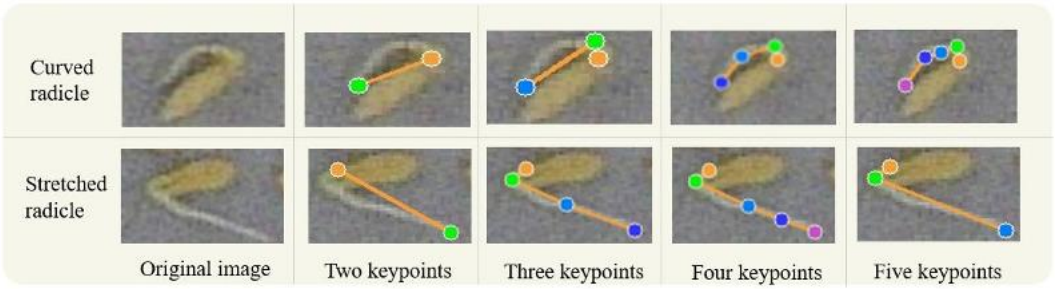


Fig. 3 - Keypoint annotation strategy

Automatic Detection of Individual Cucumber Seeds

To accurately localize individual cucumber seeds in densely distributed Petri dish images, an object detection framework was used as the first step of the proposed method. Germinated cucumber seeds are small and densely distributed, and overlap or partial occlusion may occur among adjacent seeds. Therefore, representative models from different object detection paradigms were selected for comparison, including one-stage detectors, SSD, YOLOv8-p2s, YOLOv8s and YOLO11s; the two-stage detector Faster R-CNN; and the Transformer-based detector DETR.

Each Petri dish image was input into the detection model to obtain the bounding box coordinates and confidence score of each seed instance. The detection results were then used to crop or constrain valid single-seed regions for subsequent radicle keypoint localization. By comparing the detection performance of different models in dense small-object scenarios, the model with the best overall performance was selected as the seed detection module. This step provided accurate spatial priors for radicle keypoint detection and reduced the interference caused by background regions, seed overlap and dense distribution.

Radicle Keypoint Detection Model for Cucumber Seeds

To accurately localize radicle keypoints of individual cucumber seeds, this study proposed a top-down keypoint detection network named GermHRNet. GermHRNet was developed based on HRNet and used HRNet-W32 as the backbone. By maintaining parallel multi-resolution branches throughout the network, the model preserved high-resolution feature representations during feature extraction, which is important for detecting small and slender radicle structures. The overall architecture of GermHRNet is shown in Fig. 4.

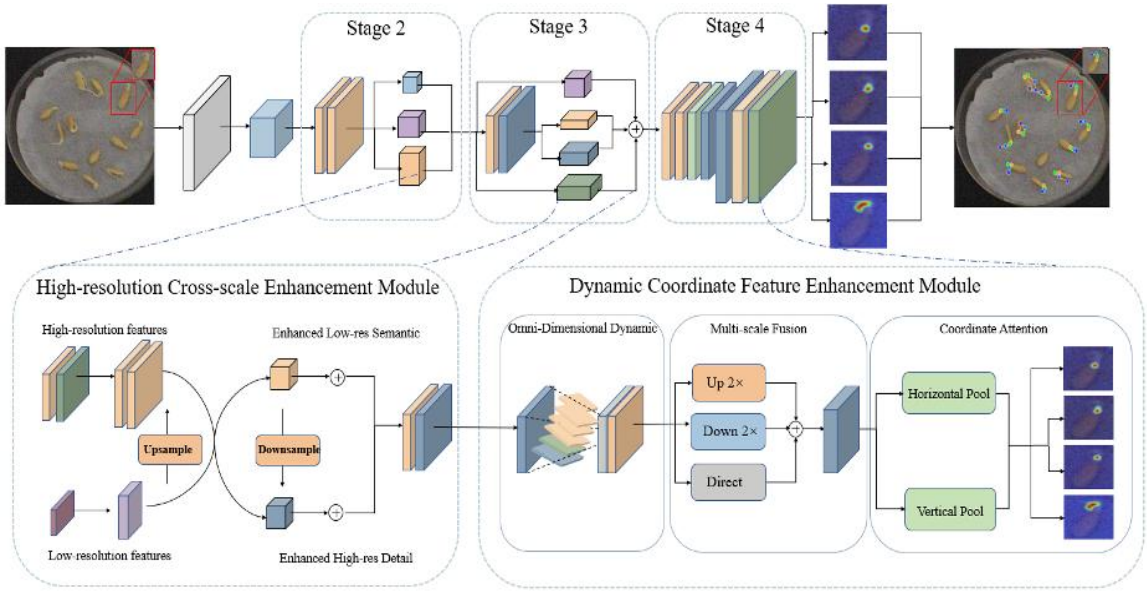


Fig. 4 - Architecture of GermHRNet

To reduce the loss of fine structural information in deeper layers, a High-resolution Cross-scale Enhancement Module (HCEM) was introduced before the multi-scale fusion stage in Stage 3. HCEM maintained the parallel multi-resolution structure of HRNet and established bidirectional cross-scale information pathways. This allowed high-resolution detail features and low-resolution semantic features to interact before fusion, thereby improving the representation of continuous radicle structures and reducing missed keypoint detections.

To further improve localization accuracy, a Dynamic Coordinate Feature Enhancement Module (DCFE) was incorporated into Stage 4. DCFE combined omni-dimensional dynamic convolution blocks, multi-scale feature fusion and coordinate attention. The dynamic convolution blocks adaptively enhanced feature representation according to radicle morphology, while the coordinate attention mechanism introduced directional positional information to guide the network toward key regions such as root tips and bending points. With these designs, the proposed network improved the stability and accuracy of keypoint localization for curved radicles and reduced localization errors caused by complex radicle poses.

High-Resolution Cross-Scale Enhancement Module (HCEM)

Built upon HRNet, a High-Resolution Cross-Scale Enhancement Module (HCEM) is introduced prior to the multi-scale fusion stage (Stage 3). The architecture of HCEM is shown in Fig. 5.

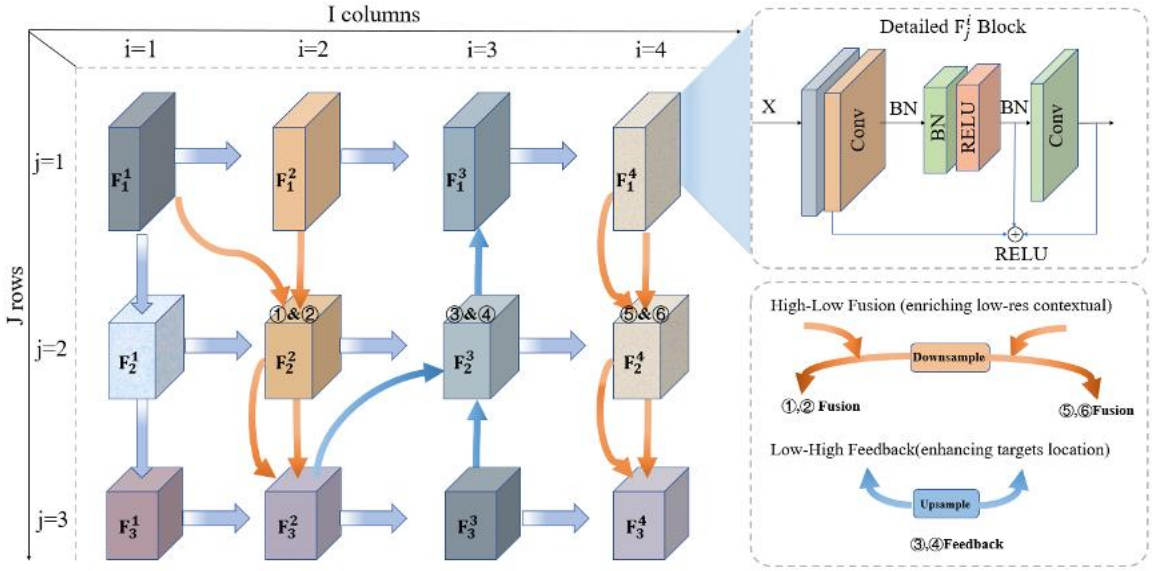


Fig. 5 - Architecture of the High-Resolution Cross-scale Enhancement Module

Considering that the slender and continuous radicle structure depends heavily on spatial resolution and fine-grained details, repeated downsampling leads to reduced spatial resolution and loss of fine-grained information *(Ni et al., 2025)*, thereby affecting the localization of critical radicle regions. Within a parallel multi-resolution framework, the module is organized as a grid-structured network composed of basic residual blocks arranged in i columns and j rows. For the output node F_i^j at the i-th column and j-th row, the computation is defined as follows.

$$F_i^j = X + ReLU\left(BN\left(Conv_2\left(ReLU(BN(Conv_1(X)))\right)\right)\right) \quad (1)$$

where X denotes the input feature map, $Conv_1$ and $Conv_2$ represent two consecutive convolutional layers, BN denotes batch normalization, and $ReLU$ represents the activation function. This structure employs two consecutive convolutional layers with a residual connection, enabling the extraction of discriminative local features while alleviating the vanishing-gradient problem and preserving spatial information.

To enhance feature interaction across different resolution branches, HCEM constructs a bidirectional cross-scale information flow. At even-column nodes, such as nodes ①, ②, ⑤ and ⑥, high-resolution features are downsampled using convolutional operators with a stride of 2 and injected into lower-resolution branches. This process introduces fine-grained spatial cues and alleviates localization ambiguity in low-resolution features caused by enlarged receptive fields. At odd-column nodes, such as nodes ③ and ④, global contextual information from low-resolution branches is upsampled using nearest-neighbor interpolation and propagated to high-resolution branches. This process provides global structural guidance, enabling the network to infer keypoint locations more accurately under radicle bending conditions.

Therefore, HCEM improves the complementarity between high-resolution spatial details and low-resolution semantic context, thereby enhancing the localization accuracy of slender and curved radicles.

Dynamic Coordinate Feature Enhancement Module (DCFE)

Based on HRNet, a Dynamic Coordinate Feature Enhancement Module (DCFE) was introduced in Stage 4. This module was designed to reduce keypoint displacement caused by morphological variations of radicles through joint feature enhancement across spatial, channel and scale dimensions. DCFE consists of three components: an Omni-dimensional Dynamic Block (OD Block), a multi-scale feature fusion module and a Coordinate Attention (CA) module. The overall structure is illustrated in Fig. 6.

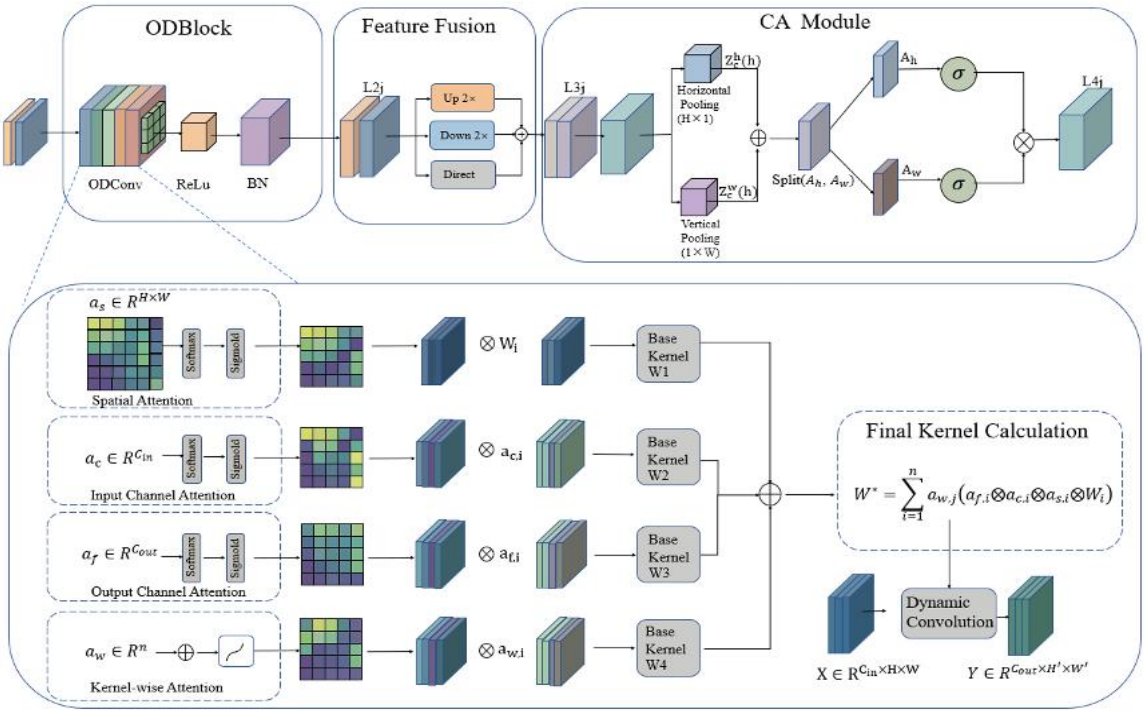


Fig. 6 - Architecture of the Dynamic Coordinate Feature Enhancement Module

The OD Block generates adaptively modulated dynamic convolution kernels based on the contextual information of the input feature map X, enabling the network to adjust feature responses according to radicle morphology. The output Y can be expressed as:

$$\mathrm{Y} = W^*(X) * X \tag{2}$$

where $W^*(X)$ denotes the dynamically generated convolution kernel conditioned on the input feature map X, and $*$ represents the convolution operation. This process performs weighted aggregation of a base kernel pool across four attention dimensions: spatial attention $\mathrm{a_s} \in \mathrm{R^{H\times W}}$ captures pixel-level features of local radicle morphology; input channel attention $\mathrm{a_c} \in \mathrm{R^{C_{in}}}$ and output channel attention $\mathrm{a_f} \in \mathrm{R^{C_{out}}}$ dynamically select the most relevant feature channels for keypoint localization; and kernel−wise attention $\mathrm{a_w} \in \mathrm{R^n}$ enables nonlinear combinations of base kernels. The resulting dynamic convolution kernel is calculated as follows:

$$W^* = \sum_{i=1}^{n} a_{w,i}\left(a_{f,i} \otimes a_{c,i} \otimes a_{s,i} \otimes W_i\right) \tag{3}$$

where W_i denotes the $i-\mathrm{th}$ base convolution kernel, n is the number of base kernels, and ⊗ multi-scale feature fusion module aligns features at different scales by applying upsampling and denotes element-wise multiplication with broadcasting when necessary. This omni-dimensional parameter modulation enables the network to adaptively adjust the receptive field and response intensity of convolutional operators according to different degrees of radicle curvature.

The multi-scale feature fusion module aligns features at different scales by applying upsampling and downsampling operations to the input feature $L_{2,j}$ followed by feature aggregation. This process combines fine-grained spatial details and semantic information, providing a more discriminative feature representation for radicle keypoint localization.

To further enhance spatial positional encoding, a coordinate attention mechanism was incorporated. First, pooling kernels with sizes of (H,1) and (1,W) were used to aggregate spatial information along the horizontal and vertical directions, respectively:

$$Z_c^h(h) = \frac{1}{W}\sum_{0\le i<W} X_c(h,i), Z_c^w(w) = \frac{1}{H}\sum_{0\le j<H} X_c(j,w) \quad (4)$$

where $Z_c^h(h)$ and $Z_c^w(w)$ denote the horizontal output at height h and the vertical output at width w for the $c-$th channel, respectively. The terms $\frac{1}{W}$ and $\frac{1}{H}$ are normalization factors representing averaging pooling. Specifically, $\sum X_c(h,i)$ represents accumulation along the width direction, compressing each row into a single value while preserving positional accuracy along the height dimension. Similarly, $\sum X_c(j,w)$ represents accumulation along the height direction, compressing each column into a single value while preserving positional information along the width dimension.

The aggregated feature maps are then concatenated, convolved, and split to generate two independent directional weights A_h and A_w. After Sigmoid activation, these weights are applied as attention masks to the feature map:

$$L_{4j} = X \otimes \sigma(A_h) \otimes \sigma(A_w) \quad (5)$$

where σ denotes the sigmoid activation function.

This module enhances the network's ability to capture keypoints in curved radicle regions and effectively reduces localization errors. By integrating dynamic convolution, multi-scale feature fusion and coordinate attention, DCFE strengthens spatial consistency in critical regions and improves the accuracy and robustness of keypoint localization.

Radicle Length Estimation and Validation Method

In the radicle length estimation stage, the two-dimensional pixel coordinates of the detected keypoints, including the radicle base, bending points and root tip, were first obtained from the keypoint detection results. These keypoints were then connected sequentially along the radicle growth direction to form a central path. The line segments between adjacent keypoints were regarded as piecewise linear approximations of the radicle structure *(Bagchi et al., 2025)*. The Euclidean distance of each segment was calculated to obtain its pixel length, and the total radicle length in pixels was estimated by cumulative summation. The calculation can be expressed as follows:

$$L_{pixel} = \sum_{k=1}^{m-1} \sqrt{(x_{k+1}-x_k)^2 + (y_{k+1}-y_k)^2}$$

where L_{pixel} is the radicle length in pixels, m is the number of detected keypoints, and (x_k, y_k) denotes the pixel coordinate of the $k-$th keypoint.

A pixel-to-millimeter scale factor was calibrated using the reference ruler in the image acquisition system. The radicle length in pixels was then converted into the actual physical length as follows:

$$L_{mm} = L_{pixel} \times S$$

where L_{mm} denotes the estimated radicle length in millimeters, and S represents the calibrated pixel-to-millimeter scale factor. Through this procedure, automatic radicle length estimation was achieved based on the predicted keypoint coordinates.

To validate the effectiveness of the proposed keypoint-based estimation method, the estimated radicle lengths were compared with manually measured ground-truth values. The manual measurements were used as reference values for accuracy evaluation. In addition, to evaluate the efficiency of automated radicle phenotyping, the total inference time of the complete pipeline, including object detection and keypoint detection, was recorded and analyzed. This evaluation was used to assess the high-throughput capability of the proposed method.

Experimental Parameter Settings

During the object detection training stage, the AdamW optimizer was used with an initial learning rate of 0.001 and a weight decay coefficient of 0.0005. The batch size was set to 16, and the model was trained for 300 epochs. Pretrained weights were used for network initialization to accelerate convergence and improve the initial training stability.

Table 1

Experimental environment configuration

Environment	Details
Programming Language	Python 3.10.15
Operating System	Windows 11

Environment	Details
Deep Learning Framework	PyTorch 2.2.2
CUDA Version	11.8
GPU	NVIDIA RTX 4090
CPU	Intel Core i9-14900KF

For keypoint detection training, the Adam optimizer was adopted with an initial learning rate of 0.0001. The batch size was also set to 16, and the model was trained for 300 epochs. Automatic mixed precision (AMP) training was implemented using NVIDIA Apex to accelerate training and reduce GPU memory consumption. The experimental environment is summarized in Table 1.

Evaluation Metrics

In the comparative experiments for seed instance detection, precision (P), recall (R) and mean average precision (mAP) were used as evaluation metrics *(Rana et al., 2026)*. Precision and recall were used to evaluate the correctness and completeness of seed detection, respectively. The mAP was calculated by first computing average precision (AP) at intersection over union (IoU) thresholds ranging from 0.50 to 0.95 in increments of 0.05 and then averaging the AP values across all thresholds. This metric provides a comprehensive assessment of the localization accuracy and detection performance of the object detection models.

In the radicle keypoint detection experiments, average precision (AP), average recall (AR) and percentage of correct keypoints (PCK) were adopted to evaluate model performance *(Duan et al., 2025)*. AP and AR were calculated according to the COCO (Common Objects in Context) keypoint evaluation protocol, with object keypoint similarity (OKS) used to quantify the similarity between predicted and ground-truth keypoints. Both metrics were averaged over OKS thresholds ranging from 0.50 to 0.95 in increments of 0.05 to characterize the overall accuracy and recall of keypoint detection. PCK was calculated using normalized Euclidean distance, with the longer side of the ground-truth bounding box of each target instance used as the normalization reference. The distance threshold coefficient α was set to 0.05 to evaluate keypoint localization accuracy.

In the radicle length estimation and validation experiments, mean absolute error (MAE), root mean square error (RMSE), coefficient of determination (R^2), normalized mean absolute error (nMAE), and normalized root mean square error (nRMSE) were used to quantitatively evaluate estimation accuracy *(Tan et al., 2025)*. MAE and RMSE were used to quantify the absolute errors between the estimated and ground-truth values, whereas R^2 was used to evaluate the goodness of fit between them. The nMAE and nRMSE were calculated by dividing MAE and RMSE, respectively, by the overall mean of the ground-truth radicle lengths and expressing the resulting ratios as percentages. These normalized metrics quantify the estimation errors relative to the actual radicle length.

In the high-throughput validation experiments, throughput (T) was used to evaluate the efficiency of radicle length acquisition *(Poorter et al., 2023)*. Throughput was defined as the number of seeds processed per hour.

RESULTS AND ANALYSIS

Comparative Experiment on Seed Instance Detection

To select the most suitable detector for cucumber seed localization, six object detection models, including YOLOv8-p2s, YOLOv8s, YOLO11s, Faster R-CNN, DETR and SSD, were compared. The quantitative results are shown in Table 2.

Table 2

Comparison of different object detection models

Model	P%	R%	mAP%
YOLOv8-p2s	98.2	97.9	98.3
YOLOv8s	97.4	97.4	97.8
YOLOv11s	98.0	97.7	97.7
Faster R-CNN	94.9	95.6	94.0
DETR	93.2	97.3	95.4
SSD	95.0	95.3	96.1

YOLOv8-p2s achieved the best overall performance, with precision, recall and mAP values of 98.2%, 97.9% and 98.3%, respectively. Compared with YOLOv8s and YOLO11s, the mAP of YOLOv8-p2s increased by 0.5 and 0.6 percentage points, respectively. It also outperformed SSD, DETR and Faster R-CNN by 2.2, 2.9 and 4.3 percentage points in mAP, respectively. These results indicate that YOLOv8-p2s has better localization accuracy and robustness for densely distributed cucumber seeds.

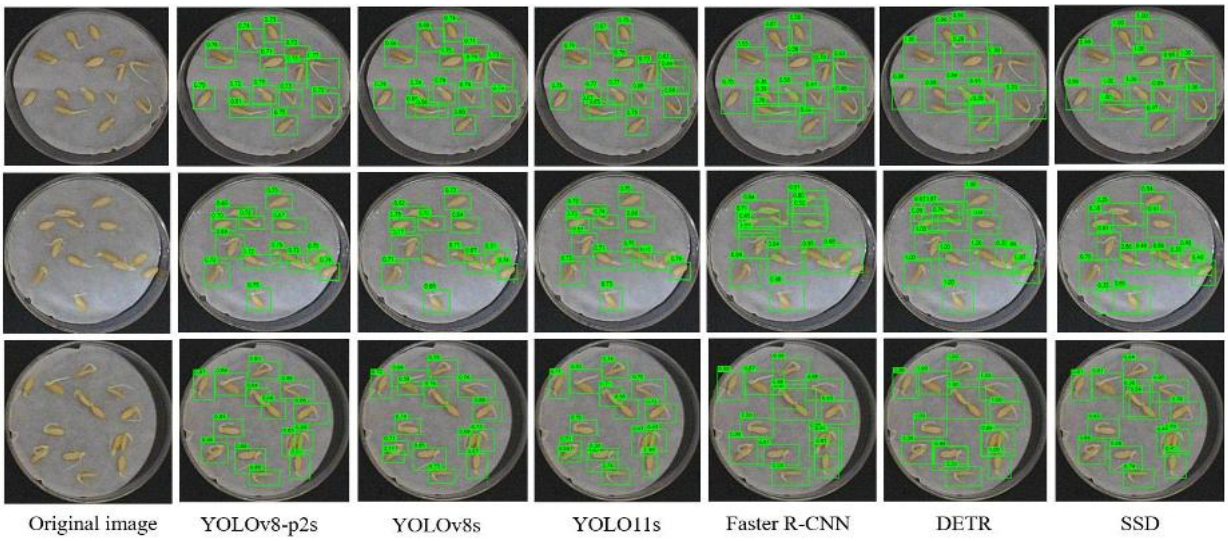


Fig. 7 - Visual comparison of seed instance detection results produced by different object detection models.

Representative detection results are shown in Fig. 7. Under dense small-object conditions, the compared models showed different types of errors, including missed detections, redundant detections and inaccurate localization. YOLOv8s and YOLO11s exhibited missed detections in densely distributed regions, which may be related to the loss of fine-grained features during downsampling. Faster R-CNN tended to generate redundant bounding boxes in crowded regions because of excessive proposal generation. DETR showed limited local detail perception for small targets, resulting in merged detections in clustered regions. SSD produced less accurate bounding boxes, mainly due to insufficient semantic representation in shallow feature maps. In comparison, YOLOv8-p2s produced more compact and accurate bounding boxes by introducing the high-resolution P2 feature layer, which improved the representation of small seed targets and reduced duplicate or missed detections.

Based on the quantitative results and visual comparisons, YOLOv8-p2s was selected as the seed detection model for subsequent radicle keypoint detection and length estimation.

Ablation Study of GermHRNet

To quantitatively evaluate the contributions of the proposed modules, ablation experiments were conducted on the High-resolution Cross-scale Enhancement Module (HCEM) and the Dynamic Coordinate Feature Enhancement Module (DCFE). The performance of each model configuration was evaluated using AP, AR and PCK, as summarized in Table 3.

Table 3

Comparison of ablation experiments with different improvements

Experiment No.	Improvement strategy		AP(%)	AR(%)	PCK(%)
	HCEM	DCFE			
1	×	×	87.5	89.8	86.7
2	√	×	89.6	91.2	87.7
3	×	√	88.7	90.4	87.9
4	√	√	90.6	92.2	88.2

Experiment 1 used the original HRNet as the baseline model, achieving AP, AR and PCK values of 87.5%, 89.8% and 86.7%, respectively. After introducing HCEM in Experiment 2, the AP, AR and PCK increased to 89.6%, 91.2% and 87.7%, respectively, indicating that HCEM enhanced cross-scale feature interaction and improved the structural representation of slender radicles.

In Experiment 3, only DCFE was added to the baseline model, achieving AP, AR and PCK values of 88.7%, 90.4% and 87.9%, respectively. The relatively higher PCK suggests that DCFE improved spatial localization accuracy by enhancing dynamic feature adaptation and coordinate-aware representation, especially for curved regions and root tips.

When both HCEM and DCFE were integrated in Experiment 4, GermHRNet achieved the best performance, with AP, AR and PCK values of 90.6%, 92.2% and 88.2%, respectively. These results show that HCEM and DCFE provide complementary improvements: HCEM strengthens multi-scale structural representation, while DCFE enhances keypoint localization accuracy. Their combination effectively improves the overall accuracy and robustness of radicle keypoint detection.

Comparative Experiment of GermHRNet

To comprehensively evaluate the effectiveness of the proposed GermHRNet, it was compared with five representative keypoint detection methods, namely HRNet, RTMPose, UDP, ViTPose and SimplePose. AP, AR and PCK were used as evaluation metrics, and the quantitative results are presented in Table 4.

Table 4

Comparison of different radicle keypoint detection models

Model	AP(%)	AR(%)	PCK(%)
GermHRNet	90.6	92.2	88.2
HRNet	87.5	89.8	86.7
RTMPose	88.1	90.2	85.0
ViTPose	87.4	90.0	85.4
UDP	86.7	89.3	86.1
SimplePose	86.0	89.2	86.4

As shown in Table 4, GermHRNet achieved the best performance across all evaluation metrics. Compared with the baseline HRNet, GermHRNet improved AP, AR and PCK by 3.1, 2.4 and 1.5 percentage points, respectively. Compared with other representative methods, GermHRNet also consistently outperformed RTMPose, ViTPose, UDP and SimplePose. Specifically, compared with RTMPose, GermHRNet improved AP, AR and PCK by 2.5, 2.0 and 3.2 percentage points, respectively. Compared with ViTPose, the corresponding improvements were 3.2, 2.2 and 2.8 percentage points. Compared with UDP, the improvements were 3.9, 2.9 and 2.1 percentage points. Compared with SimplePose, the improvements reached 4.6, 3.0 and 1.8 percentage points, respectively.

These consistent improvements across multiple metrics indicate that the proposed model has better keypoint detection performance for germinated cucumber seed radicles. In particular, the improvement in PCK suggests enhanced spatial localization accuracy, which is essential for accurately capturing complex radicle structures. Therefore, GermHRNet provided more accurate and stable keypoint localization, especially under challenging conditions involving curved radicles, blurred root tips and densely distributed seeds.

To further evaluate the qualitative performance of different methods, representative visualization results are shown in Fig. 8. Existing methods exhibited several types of errors, including keypoint displacement in curved regions, inaccurate localization of root tips, and redundant or missing detections in densely distributed seed regions. CNN-based methods, such as HRNet and SimplePose, showed localization deviations in some cases, which may be related to the loss of fine spatial details caused by repeated downsampling. ViTPose demonstrated strong global modeling capability, but it still showed limitations in capturing fine-grained local structures of slender radicles. RTMPose and UDP improved coordinate regression or decoding strategies; however, their feature representation ability was still insufficient for accurately modeling complex radicle morphology. In contrast, GermHRNet alleviated these problems by integrating cross-scale feature enhancement and dynamic coordinate-aware representation. The proposed HCEM improved structural continuity through bidirectional multi-scale feature interaction, while DCFE enhanced spatial localization accuracy through dynamic convolution and coordinate attention. As a result, GermHRNet produced keypoint predictions that were more consistent with the actual radicle morphology, particularly in challenging regions such as bending points and root tips.

Overall, both quantitative and qualitative results demonstrate that GermHRNet improves the accuracy and robustness of radicle keypoint localization, validating the effectiveness of the proposed architecture.

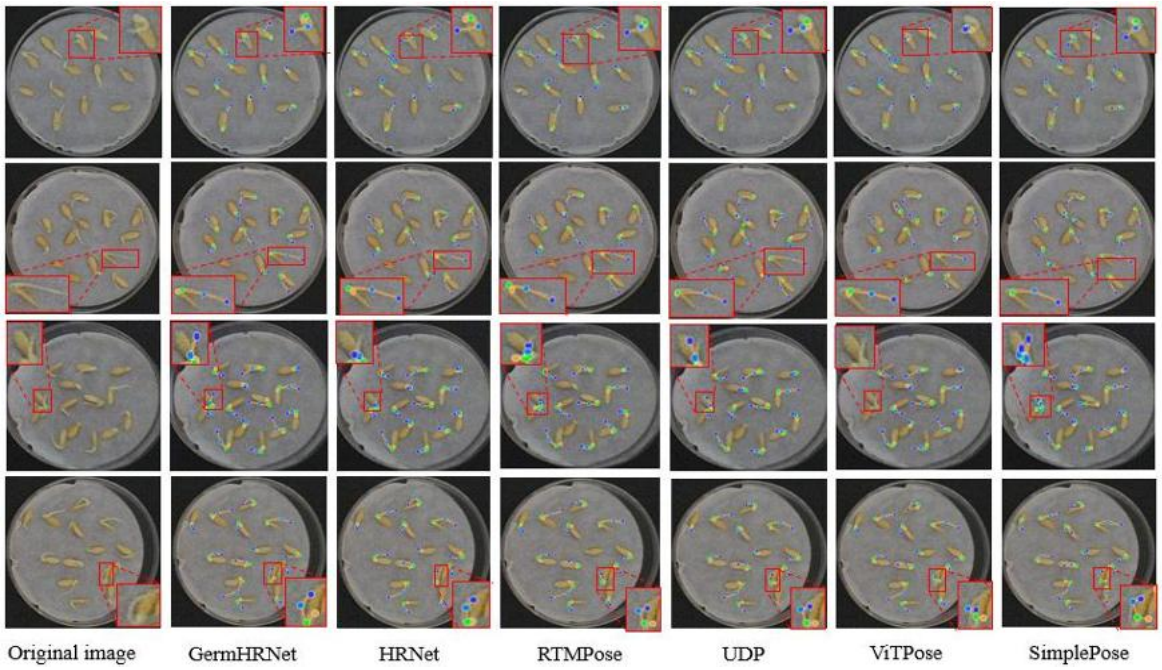


Fig. 8 - Keypoint detection results of germinated cucumber seeds using different models

Radicle Length Validation Experiment

To evaluate the accuracy of GermHRNet for automatic radicle length estimation, a quantitative validation experiment was conducted on all germinated seeds contained in the 120 test-set images. The ground-truth radicle lengths were obtained as follows. First, two experimenters manually measured the radicles corresponding to all seeds in the 120 images using a vernier caliper with a precision of 0.1 mm. Curved radicles were carefully straightened before measurement to obtain their full lengths. Subsequently, a third experimenter reviewed and confirmed all measurement results, and the final confirmed values were used as the ground-truth radicle lengths.

The distribution of the ground-truth radicle lengths in the test set was then statistically analyzed. The mean radicle length was 8.41 mm, with a standard deviation of 4.06 mm. The median was 7.92 mm, and the values ranged from 1.50 to 20.65 mm. This distribution included cucumber seed samples at different degrees of germination, indicating that the test set adequately represented variations in radicle growth during the germination process.

To comprehensively evaluate the overall estimation performance, the error metrics were subsequently calculated. The results showed that the MAE, RMSE, and R^2 were 0.51 mm, 0.61 mm, and 0.98, respectively. As shown in Fig. 9, the data points in the regression plot were closely distributed around the reference line (y=x), indicating strong agreement between the estimated and ground-truth values and a relatively low overall estimation error.

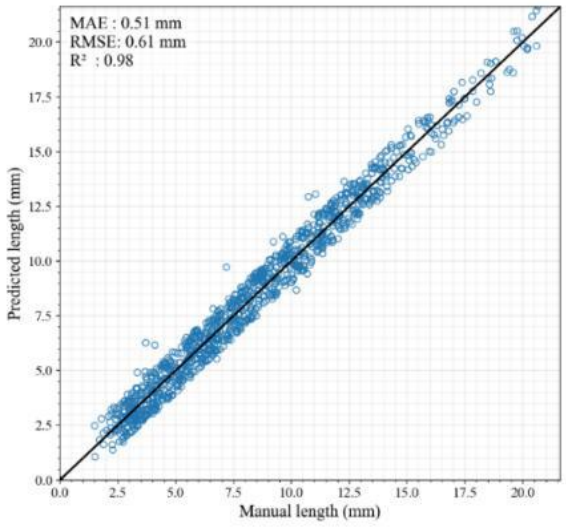


Fig. 9 - Regression analysis of predicted versus ground-truth radicle lengths

To further quantify the relative magnitude of the estimation errors, normalized error metrics were calculated using the mean ground-truth radicle length of 8.41 mm as the normalization reference. The nMAE and nRMSE were 6.06% and 7.25%, respectively. These results indicate that the estimation errors accounted for only a small proportion of the mean ground-truth radicle length, further demonstrating the high accuracy of GermHRNet for automatic radicle length estimation.

Throughput Validation Experiment

To validate the high-throughput processing capability and computational stability of the proposed radicle length estimation method, 120 original images from the CucumberSeeds-2 dataset were used for experimentation. These images contained a total of 19,140 germinated cucumber seeds. The dataset was randomly divided into 10 independent experimental groups, with each group containing 12 original images. All experiments were conducted on a CPU-only platform without GPU acceleration. The hardware configuration is shown in Table 5.

Table 5

Hardware configuration for CPU-only throughput validation

Environment	Details
Programming Language	Python 3.13.2
Operating System	Windows 64-bit (x64)
Memory (RAM)	16 GB
Processor (CPU)	AMD Ryzen 7 7435H (3.10 GHz)

The runtime statistics for the 10 experimental groups are presented in Table 6.

Table 6

Throughput evaluation results of the proposed method under CPU-only conditions

Group No	Seeds Per Original Image	Prep. [s]	Det. [s]	Kpt. [s]	Len [s]	Total [s]	T [seeds/s]
1	175	0.20	0.88	17.31	0.12	18.51	9.45
2	166	0.23	0.86	16.52	0.11	17.72	9.37
3	167	0.23	0.86	16.55	0.11	17.75	9.41
4	160	0.24	0.83	16.01	0.11	17.19	9.31
5	165	0.22	0.79	16.35	0.11	17.47	9.44
6	162	0.21	0.84	16.16	0.11	17.32	9.35
7	150	0.22	0.81	14.93	0.10	16.06	9.34
8	150	0.22	0.85	14.84	0.10	16.01	9.37
9	149	0.20	0.81	14.80	0.10	15.91	9.37
10	151	0.24	0.82	14.97	0.10	16.13	9.36

Each group contained 12 original images, and the reported time values were averaged per original image within each group. Abbreviations: Prep. = image preprocessing time; Det. = object detection time; Kpt. = keypoint detection time; Len. = radicle length estimation time; Total = total processing time per original image; T = throughput, expressed as seeds per second.

As shown in Table 6, the average processing time per original image ranged from 15.91 s to 18.51 s, with an overall mean of approximately 17.01 s. The relatively small variation in processing time indicates good computational stability of the entire pipeline under different seed densities. Among all processing steps, keypoint detection accounted for the largest proportion of the total processing time, whereas image preprocessing, object detection and length estimation required relatively short computation times.

Based on the average throughput across the 10 experimental groups, the proposed system achieved a processing capacity of approximately 3.38×10^4 seeds/h on a single machine. Compared with manual measurement, which processes approximately 120 seeds/h, the proposed method substantially improved radicle length acquisition efficiency. These results demonstrate that the proposed method has strong high-throughput processing capability and is suitable for large-scale cucumber seed phenotyping and microbial strain screening.

CONCLUSIONS

To address the limitations of low efficiency, subjective measurement errors and insufficient throughput in germination tests for plant growth-promoting rhizobacteria (PGPR) screening, this study proposed an automatic radicle length estimation method for germinated cucumber seeds based on GermHRNet. The proposed framework achieved automated analysis from seed localization and radicle keypoint detection to radicle length quantification. The main conclusions are as follows.

1) A GermHRNet-based keypoint detection network for germinated cucumber seed radicles was developed. To improve feature representation for slender and curved radicle structures, cross-scale feature enhancement and coordinate-aware dynamic feature modeling strategies were incorporated into the HRNet backbone. The proposed model achieved AP, AR and PCK values of 90.6%, 92.2% and 88.2%, respectively, outperforming the compared mainstream keypoint detection models. These results demonstrate that the proposed framework improved the accuracy and robustness of radicle keypoint localization under complex morphological conditions.

2) A polyline-based radicle length estimation strategy was proposed for curved radicle estimation. Based on the detected keypoint coordinates, radicle length was estimated through multi-segment polyline pixel accumulation. The proposed method achieved MAE, RMSE, nMAE, nRMSE, and R^2 values of 0.51 mm, 0.61 mm, 6.06%, 7.25%, and 0.98, respectively, showing strong agreement with manual measurements. These results indicate that the proposed method can satisfy the accuracy requirements of radicle phenotyping and seed vigor evaluation.

3) The proposed method demonstrated strong high-throughput processing capability. Throughput experiments showed that the proposed framework achieved a processing capacity of approximately 3.38×10^4 seeds/h on a CPU-only platform. Compared with manual measurement (~120 seeds/h), the proposed method improved radicle length acquisition efficiency by approximately 282-fold. These results demonstrate the practical potential of the proposed framework for large-scale cucumber seed phenotyping and PGPR screening applications.

Although GermHRNet achieved favorable performance in radicle keypoint detection and automatic length estimation for germinated cucumber seeds, several limitations remain. First, the experiments were limited to seeds from a single cucumber cultivar and a specific germination stage. Further investigation is therefore required to determine how variations in radicle morphology across different cultivars and germination stages affect keypoint detection and length estimation performance. Second, all experimental data were acquired using a single imaging system under controlled laboratory conditions. Consequently, the generalizability of the model across different imaging devices and illumination conditions has not yet been fully validated.

To address these limitations, future studies will conduct external validation using different cucumber cultivars, germination stages, and imaging conditions to further assess the robustness and applicability of the model. In addition, lightweight deployment and real-time integration of the proposed framework with image acquisition systems will be further investigated to improve computational efficiency and system stability, thereby providing a more efficient and reliable solution for high-throughput and standardized seed phenotyping.

ACKNOWLEDGEMENT

This research was funded by the Potato Innovation Program for the Chief Expert of Shandong Province (Grant No. SDAIT-16-01).

REFERENCES

[1] Bagchi, P., Seredin, O. S., Kopylov, A. V., Surkov, E. E., Mityugov, N. S., Tokarev, A. R., & Bhattacharjee, D. (2025). Skeletons distance evaluation for automated control of exercises in physical therapy. *The International Archives of the Photogrammetry, Remote Sensing and Spatial Information Sciences*, XLVIII-2/W9-2025, 33–38. https://doi.org/10.5194/isprs-archives-XLVIII-2-W9-2025-33-2025

[2] Chen, H., Song, Q., Chang, T., Zheng, L., Zhu, X., Zhang, M., et al. (2024). Extraction of single-tiller rice phenotypic parameters based on YOLOv5m and CBAM-CPN. *Transactions of the Chinese Society of Agricultural Engineering,* 40(2), 307–314. https://doi.org/10.11975/j.issn.1002-6819.202304126

[3] Chen, P., Yan, B., Deng, G., Li, G., Cui, Z., Zheng, S., et al. (2025). Pose detection and localization of pineapple fruit picking based on improved LiteHRNet. *Frontiers in Plant Science*, 16, 1577312. https://doi.org/10.3389/fpls.2025.1577312

[4] Duan, W., Wang, F., Li, H., et al. (2025). Lameness detection in dairy cows from overhead view: High-precision keypoint localization and multi-feature fusion classification. *Frontiers in Veterinary Science*, 12, 1675181. https://doi.org/10.3389/fvets.2025.1675181

[5] Fu, Y., Lin, K., Cheng, B., Qi, L., Zhang, Q., Li, H., Chen, X., & Zhang, C. (2026). Phosphate-solubilizing Bacillus subtilis Y31 promotes cucumber growth and yield: insights from rhizosphere microbiomics and bacterial genomics. *Frontiers in Microbiology*, 16, 1751005. https://doi.org/10.3389/fmicb.2025.1751005

[6] He, J., Weng, L., Xu, X., Chen, R., Peng, B., Li, N., et al. (2024). DEKR-SPrior: An efficient bottom-up keypoint detection model for accurate pod phenotyping in soybean. *Plant Phenomics,* 6, 0198. https://doi.org/10.34133/plantphenomics.0198

[7] Hu, T., Shen, P., Zhang, Y., et al. (2025). OpenPheno: An open-access, user-friendly, and smartphone-based software platform for instant plant phenotyping. *Plant Methods*, 21, 76. https://doi.org/10.1186/s13007-025-01395-4

[8] Li, J., Lu, J., Liu, L., & Wang, K. (2026). UAV-based high-throughput phenotyping of soybean using lightweight point detection for multi-organ trait extraction. *INMATEH-Agricultural Engineering*, 78(1), 410-421. https://doi.org/10.35633/inmateh-78-33

[9] Ni, R., et al. (2025). Point-to-point regression: Accurate infrared small target detection with single-point annotation. *IEEE Transactions on Geoscience and Remote Sensing*, 63, 5002719. https://doi.org/10.1109/TGRS.2025.3554025

[10] Niu, Z., & Qiu, Z. (2025). Extraction method of maize plant skeleton and phenotypic parameters based on improved YOLOv11-Pose. *Smart Agriculture,* 7(2), 95–105. https://doi.org/10.12133/j.smartag.SA202501001

[11] Pan, Y., Chang, J., Dong, Z., Liu, X., & Li, H. (2025). PFLO: A high-throughput pose estimation model for field maize based on YOLO architecture. *Plant Methods, 21*, 51. https://doi.org/10.1186/s13007-025-01369-6

[12] Poorter, H., Hummel, G. M., Nagel, K. A., Fiorani, F., von Gillhaussen, P., Virnich, O., Schurr, U., Postma, J. A., van de Zedde, R., & Wiese-Klinkenberg, A. (2023). Pitfalls and potential of high-throughput plant phenotyping platforms. *Frontiers in Plant Science, 14*, 1233794. https://doi.org/10.3389/fpls.2023.1233794

[13] Rana, A., & Vaidya, P. (2026). YOLO-based deep learning framework for real-time multi-class plant health monitoring in precision agriculture. *Scientific Reports, 16*(1), 197. https://doi.org/10.1038/s41598-025-29132-w

[14] Shaik, A., Karthikeyan, R., & Kousik, C. S. (2025). Growth stage-specific responses of cucumber to salinity stress: Germination, seedling establishment, and vegetative development. *Frontiers in Plant Science, 16*, 1617809. https://doi.org/10.3389/fpls.2025.1617809

[15] Tan, Z., Xiao, D., Liu, J., et al. (2025). Cascade vision-based weight estimation algorithm for monitoring fattening pig weight. *Computers and Electronics in Agriculture, 236*, 110384. https://doi.org/10.1016/j.compag.2025.110384

[16] Top Cloud-Agri Technology Co., Ltd. (2026). *TPN-Pheno-ZM1 in situ root phenotyping system for seed germination stage*. Retrieved April 23, 2026, from https://www.tpyn.net/productshow_615.html

[17] Wu, Y., Li, Z., Jiang, H., Li, Q., Qiao, J., Pan, F., Fu, X., & Guo, B. (2024). YOLOv8-segANDcal: Segmentation, extraction, and calculation of soybean radicle features. *Frontiers in Plant Science, 15*, 1425100. https://doi.org/10.3389/fpls.2024.1425100

[18] Wu, Z., Xia, F., Zhou, S., & Xu, D. (2023). A method for identifying grape stems using keypoints. *Computers and Electronics in Agriculture, 209*, 107825. https://doi.org/10.1016/j.compag.2023.107825

[19] Yuan, C., Zhao, Z., Huang, X., Hu, Z., & Chen, R. (2026). Phalaenopsis flower stem length measurement method based on keypoint detection. *Measurement, 271*, 120865. https://doi.org/10.1016/j.measurement.2026.120865

[20] Zhao, J., Hou, Z., Hua, H., Nie, Q., Pang, Y., Ma, Y., & Huang, X. (2025). LenRuler: A rice-centric method for automated radicle length measurement with multicrop validation. *Plant Phenomics,* 7(3), 100103. https://doi.org/10.1016/j.plaphe.2025.100103

DESIGN AND EXPERIMENTAL STUDY OF AN INCLINED SPOON-DISC MAIZE SEED-METERING DEVICE
/
倾斜勺盘式玉米排种器的设计与试验研究

Ziyu WANG[1]; Xingkang LIU[2]; Wentao LI[2]; Hongchao WANG*[2]; Junlei LIU[2]; Qinglong TANG[2]; Jiakai XU[2]; Xinying DONG[1]

[1] College of Information and Electrical Engineering, Heilongjiang Bayi Agricultural University, Daqing 163319, China
[2] College of Engineering, Heilongjiang Bayi Agricultural University, Daqing 163319, China
Tel: 16645548678; E-mail: 452713509@qq.com

DOI: https://doi.org/10.35633/inmateh-79-86

Keywords: *maize, inclined spoon-disc, seed-metering, parameter optimization*

ABSTRACT

To address the problems of multiple seeding, missed seeding, and insufficient operational stability commonly encountered during the operation of precision maize seed-metering devices, an inclined spoon-disc seed-metering device was designed in this study. The seed-metering process of maize kernels within the device was analysed, and the key components, including spoon wheel, partition plate, and seed-metering wheel, were structurally designed. Bench tests were conducted using a JPS-16 seed-metering device performance testing system. First, single-factor tests were performed to investigate the effects of metering-wheel rotational speed, overall inclination angle, and seed-layer height on the qualified index, multiple index, and miss index. Subsequently, a three-factor, five-level quadratic regression orthogonal rotational combination experiment was conducted using the metering-wheel rotational speed, overall inclination angle, and seed-layer height as the experimental factors. Optimization was performed with the objective of maximizing the qualified index. The optimal parameter combination was determined to be a seed-metering wheel rotational speed of 25 r·min^{-1}, an overall inclination angle of 27°, and a seed-layer height of 71.9 mm. Under these conditions, the model-predicted qualified index was 96.5%. In the verification tests, the average qualified index was 95.0%, with a relative error of 1.5% compared with the predicted value. The results can provide a reference for the structural design and operating-parameter optimization of inclined spoon-disc precision maize seed-metering devices.

摘要

针对玉米精量排种器在作业过程中易出现重播、漏播及排种稳定性不足的问题，本文设计了一种倾斜勺盘式排种器。分析玉米籽粒在排种器内的工作过程，并对排种勺轮、隔板及导种轮等关键部件进行了结构设计。在 JPS-16 排种器性能测试系统上开展台架试验。首先通过单因素试验分析排种轮转速、整体倾斜角和种层高度对合格率、重播率和漏播率的影响；在此基础上，以排种轮转速、整体倾斜角和种层高度为试验因素，开展三因素五水平二次回归正交旋转组合试验。以合格率最大为目标进行优化，得到较优参数组合为排种轮转速 25 r·min^{-1}、整体倾斜角 27°、种层高度 71.9 mm，模型预测合格率为 96.5%。验证试验中合格率平均值为 95.0%，与预测值的相对误差为 1.5%。研究结果可为倾斜勺盘式玉米精量排种器的结构设计和作业参数优化提供参考。

INTRODUCTION

Maize is one of the major grain crops in China and plays an important role in ensuring food security and maintaining stable agricultural production (*Chen et al., 2025*). With the continuous expansion of large-scale maize cultivation and the advancement of fully mechanized production, increasingly stringent requirements have been imposed on planting efficiency, consistency of plant spacing, and the quality of precision single-seed placement (*Baghooee et al., 2024*).

The quality of maize planting directly affects seedling emergence uniformity, crop population structure, and subsequent yield formation. As the core component of a precision planter, the seed-metering device largely determines planting performance. Therefore, improving the operational performance of the seed-metering device is of great significance for enhancing maize planting quality (*Ding et al., 2024*).

---

[1] *Ziyu Wang, master degree; Xinying Dong, bachelor degree.*

[2] *Xingkang Liu, bachelor degree; Wentao Li, bachelor degree; Hongchao Wang, Ph.D.; Junlei Liu, bachelor degree; Qinglong Tang, bachelor degree; Jiakai Xu, bachelor degree.*

Currently, precision maize seed-metering devices can be broadly classified into mechanical and pneumatic types. Pneumatic seed-metering devices use negative- or positive-pressure airflow to perform seed pickup, singulation, and seed release (*Bakirov et al., 2025*). They offer high metering accuracy and good adaptability to high-speed operation and have therefore been widely used in large precision planters. However, these devices generally require a fan, an air chamber, and a pneumatic circuit, and they impose stringent requirements on system airtightness and pressure stability (*Gao et al., 2023*). Consequently, the overall machine structure is relatively complex, and the manufacturing and maintenance costs are comparatively high. Common mechanical seed-metering devices include finger-pickup, cell-wheel, pocket-wheel, and spoon-disc types. Among them, spoon-disc seed-metering devices use seed spoons to directly scoop individual kernels from the seed mass, offering a straightforward seed-pickup mechanism, a compact structure, and good adaptability (*Li et al., 2024*).

The seed-metering performance of a spoon-wheel seed-metering device is jointly affected by several factors, including the spoon geometry, rotational speed of the metering wheel, installation inclination angle of the seed-metering device, seed-layer height, and physical properties of the seeds. When the rotational speed of the metering wheel is too low, the seed spoons remain in contact with the seed mass for a relatively long period and may carry multiple kernels simultaneously, thereby increasing the probability of multiple seeding (*Cortez et al., 2020*). By contrast, when the rotational speed is excessively high, the residence time of the seed spoons in the filling zone is shortened, making it difficult for kernels to enter the spoon cavities in time and remain stably retained, which can readily result in missed seeding. The inclination angle of the seed-metering device changes the gravitational components acting on the kernels and the accumulation state of the seed mass in the filling zone, thereby affecting the seed-filling and singulation processes. Seed-layer height directly influences the number of kernels near the seed spoons and the pressure exerted by the seed mass. An excessively low seed layer may lead to insufficient seed filling, whereas an excessively high seed layer may cause multiple-kernel filling and increase the difficulty of seed singulation (*Lin et al., 2026*). Therefore, analysis of a single factor alone cannot accurately reflect the actual operating state of the seed-metering device, and the interactions among these factors require further investigation (*Sun et al., 2025*).

Previous studies have optimized the cell dimensions, seed-spoon geometry, rotational speed of the metering disc, and installation angle of mechanical seed-metering devices through theoretical analysis, discrete element simulation, and bench testing, and satisfactory seed-metering performance has been achieved (*Koller et al., 2016*). However, some studies have focused primarily on individual structural parameters of the metering wheel or seed-pickup elements, while relatively limited attention has been paid to the continuity of kernel transfer from the seed spoons to the seed-metering wheel, as well as the seed-retaining and seed-release processes. In addition, interactions and mutual constraints may exist among the rotational speed of the metering wheel, overall inclination angle, and seed-layer height (*Wang et al., 2026*). Consequently, the optimum level of an individual factor may not correspond to the optimal parameter combination under the combined effects of multiple factors (*Yang et al., 2025*). It is therefore necessary to consider the entire seed-metering process, analyse the key operating parameters and their interactions, and establish a regression model capable of describing the variation in seed-metering performance (*Zhao et al., 2026*).

Based on the above considerations, an inclined spoon-disc precision maize seed-metering device was designed in this study. The device uses a spoon-type metering wheel to perform seed scooping and singulation. A partition plate is employed to achieve the directional transfer of kernels from the spoon cavities to the seed-metering wheel, while the seed-metering wheel and housing jointly complete the seed-retaining and seed-release processes. First, the key components, including spoon wheel, partition plate, and seed-metering wheel, were structurally designed, and the movement of maize kernels within the seed-metering device was analysed. Subsequently, single-factor tests were conducted using Zhengdan 958 maize kernels to investigate the effects of seed-metering wheel rotational speed, overall inclination angle, and seed-layer height. Finally, a three-factor, five-level quadratic regression orthogonal rotatable combination design was employed to analyse the effects of the individual factors and their interactions on the qualified index. The operating parameters were then optimized and verified through bench tests. This study aims to provide a theoretical and experimental basis for the structural improvement and operating-parameter selection of inclined spoon-disc seed-metering devices.

MATERIALS AND METHODS

Structure and Operating Principle of the Seed-Metering Device

The inclined spoon-disc seed-metering device mainly consists of front and rear seed-metering housings, a seed-metering shaft, a spoon wheel, a partition plate, a seed-metering wheel, a brush, two end covers, and

bearings, as shown in Fig. 1. The front and rear seed-metering housings are assembled to form the enclosed working chamber and provide support and positioning for the internal components. The spoon wheel and seed-metering wheel are driven by the same power source through a mechanical transmission system. They rotate synchronously in the same counterclockwise direction at a transmission ratio of 1:1. A fixed phase relationship is maintained between the spoon cavities and the corresponding U-shaped grooves of the seed-metering wheel, ensuring accurate seed transfer at the designed angular position.

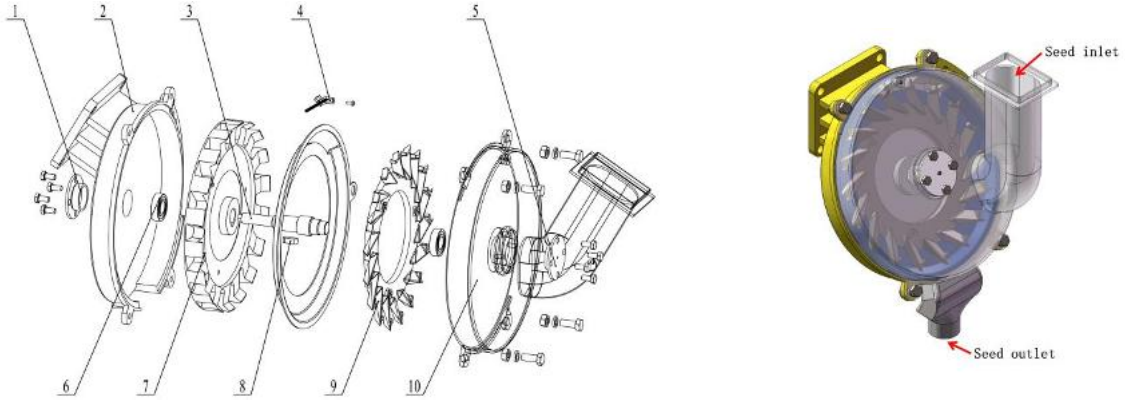


Fig. 1 - Structure of the inclined spoon-disc seed-metering device

1. Rear end cover; 2. Rear seed-metering housing; 3. Seed-metering shaft; 4. Brush; 5. Front end cover; 6. Deep-groove ball bearing; 7. seed-metering wheel; 8. Partition plate; 9. Spoon wheel; 10. Front seed-metering housing.

The movement of maize kernels within the seed-metering device consists of five successive stages: seed pickup, seed clearing, seed transfer, seed retention, and seed discharge, as shown in Fig. 2. During the seed-pickup stage, maize kernels enter the seed-filling zone at the bottom of the device and are captured by the spoon cavities. In the seed-clearing zone, excess kernels retained in unstable positions are removed under the combined effects of gravity, centrifugal force, and inter-kernel interactions, leaving one kernel in each spoon cavity. When the spoon reaches the seed-transfer zone, the retained kernel passes through the arc-shaped opening of the partition plate and enters the corresponding U-shaped groove of the seed-metering wheel.

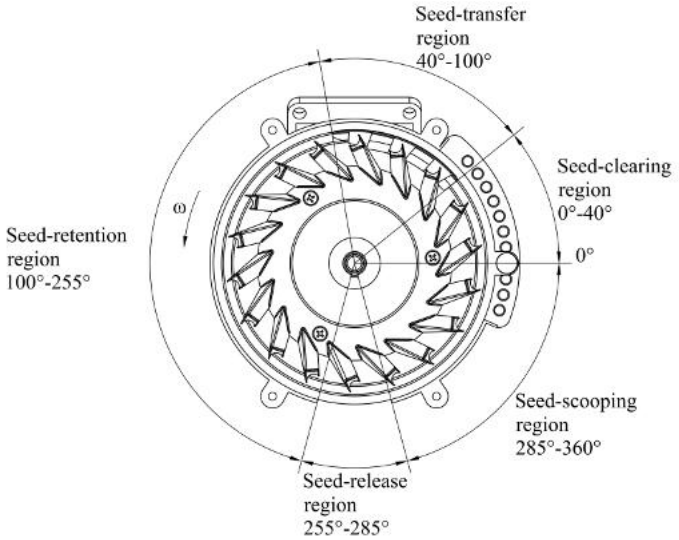


Fig. 2 - Operating process of the inclined spoon-disc seed-metering device

During the seed-retention stage, the kernel is constrained by the U-shaped groove and the seed-metering housing and is carried stably to the seed outlet. At the outlet, the structural constraint is removed, allowing the kernel to leave the groove under gravity and inertia and fall into the seed furrow. The proposed configuration reduces abnormal seed motion through the coordinated action of its components. The single-kernel spoon cavity and the seed-clearing process reduce multiple seed pickup.

The combined constraint of the U-shaped groove and the seed-metering housing prevents premature seed release. The dimensional matching among the spoon cavity, partition-plate opening, and U-shaped groove, together with an appropriate operating clearance, reduces kernel lodging and blockage. The arc-shaped transfer path and smooth structural transition reduce collision, squeezing, and seed damage.

Moreover, the fixed 1:1 transmission ratio and phase relationship between the spoon wheel and seed-metering wheel ensure that each spoon cavity aligns with the corresponding U-shaped groove at the designed transfer position, thereby preventing delayed seed transfer.

Design of spoon wheel

Because the device developed in this study is primarily intended for precision single-seed maize planting, the structural configuration, principal dimensions, and kinematic characteristics of spoon wheel must be appropriately designed and analysed. A schematic diagram of the spoon cavity in the spoon wheel is shown in Fig. 3.



Fig. 3. Schematic diagram of the spoon cavity in spoon wheel

Based on the operating principle of the seed-metering device, maize-kernel length was selected as the characteristic dimension for determining the spoon-cavity size. Kernel length was defined as the maximum dimension along the longitudinal axis of an individual maize kernel. To ensure that maize kernels can enter the spoon cavity smoothly, the cavity diameter should be slightly larger than the mean kernel length. Therefore, the dimensional relationship between the spoon cavity and the maize kernel was expressed as:

$$2R=L+\delta \quad (1)$$

where L is the mean length of the Zhengdan 958 maize kernels, mm; R is the radius of the cylindrical spoon cavity, mm; and δ is the diametral design allowance, mm.

In this study, the mean length of the Zhengdan 958 maize kernels was 12.0 mm. Considering variations in kernel dimensions, changes in kernel orientation during entry into the spoon cavity, and manufacturing errors of the spoon cavity, the reasonable range of the design allowance was determined to be 0.5–1.5 mm. To balance seed-filling reliability and single-seed pickup performance, the intermediate value of δ=1.0 mm was selected. The corresponding spoon-cavity radius was R=6.5 mm. The selected allowance provides sufficient clearance for reliable kernel entry while preventing excessive enlargement of the spoon cavity. Combined with the removal of unstable excess kernels in the seed-clearing zone, the selected cavity size facilitates single-seed pickup and reduces the probability of multiple seed pickup.

The main design parameters of the spoon disc also include the number of seed spoons (Z_1), the pitch-circle radius of the spoon disc (r_1), and the outer radius of spoon wheel (r_2). Among these parameters, A schematic diagram of spoon wheel designed in this study is shown in Fig. 4. The angle (θ_2) is defined as the central angle between two adjacent seed spoons.

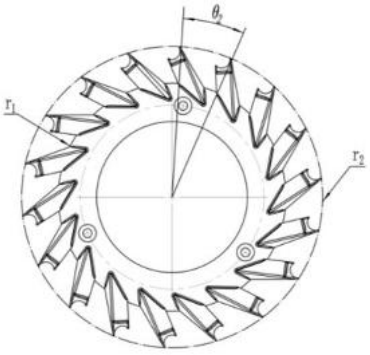


Fig. 4 - Structure of the spoon disc

According to Eq. (2), an increase in the number of seed spoons results in a decrease in the angular spacing between adjacent spoons. At a constant rotational speed of the seed-metering device, a greater number of kernels can therefore be discharged during each revolution of the spoon disc. When the required

plant spacing remains unchanged, increasing the number of seed spoons can increase the operating speed of the planter while maintaining the same seeding rate.

$$Z_1 = \frac{360°}{\theta_2} \tag{2}$$

Based on the practical requirements of this study, the number of seed spoons was set to (Z_1=18). Accordingly, the pitch-circle radius of the spoon disc was determined as (r_1=83) mm, and the outer radius of spoon wheel was (r_2=115) mm. In addition, three M6 through-holes were uniformly arranged on the spoon disc at angular intervals of 120°, enabling spoon wheel to be securely connected to the seed-metering wheel.

Structural Design of the Partition Plate

The partition plate has an annular disc-shaped structure and is installed between the seed-metering housing and the cover. It is secured by a positioning structure and remains stationary during operation. A schematic diagram of the partition plate is shown in Fig. 5. A sector-shaped seed-transfer opening is arranged in the upper part of the partition plate. The starting position of the opening is located 15° forward of the vertical direction, and its opening angle is set to 65°; therefore, the seed-transfer angle of the partition plate is θ_3 = 65°. When the partition plate is adjusted to its highest position, the starting point of the seed-transfer zone is located at the arc-shaped opening. The angle between the horizontal direction and the line connecting this point to the centre of the partition plate is defined as θ_4, while the endpoint of the seed-transfer zone is located at the terminal end of the arc-shaped groove.

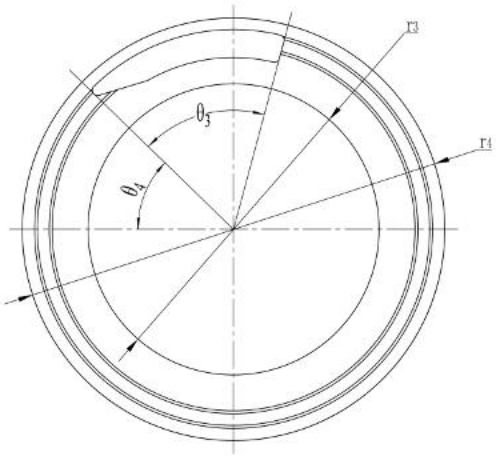


Fig. 5 - Structural schematic of the partition plate

Two positioning grooves are arranged along the lower outer edge of the partition plate. During assembly, the grooves are fitted into the seed-discharge opening at the lower part of the seed-metering device housing to restrict the rotation of the partition plate and prevent positional misalignment. Because the partition plate operates in coordination with the seed-metering spoon wheel and the seed-metering wheel, its structural dimensions should be determined according to the dimensions of these two components. Therefore, the following geometric relationships exist among the three components:

$$r_1 = r_3 \tag{3}$$

$$r_4 = r_5 \tag{4}$$

where r_3 is the inner radius of the partition plate, mm; r_4 is the outer radius of the partition plate, mm; and r_5 is the radius of the seed-metering wheel, mm.

Structural Design of the Seed-Metering Wheel

The seed-metering wheel is generally mounted on the main shaft of the seed-metering device and rotates synchronously with the spoon wheel. To ensure that the working circumferences of the two components coincide at the seed-transfer position, their working radii were designed to be equal, as expressed in Eq. (5). The seed-metering wheel has a cylindrical body with several uniformly distributed U-shaped seed grooves around its circumference. The number of seed grooves is equal to the number of spoon cavities on the spoon wheel, enabling the kernels delivered by the spoon wheel to be received smoothly. The spoon wheel and the

seed-metering wheel are axially separated by the partition plate, with an axial operating clearance of 0.5 mm. The manufacturing tolerance of both the spoon wheel and the seed-metering wheel was controlled within ±0.1 mm. A schematic diagram of the seed-metering wheel is shown in Fig. 6.

$$r_5 = r_2 = 115mm \tag{5}$$

$$\theta_5 = \frac{\theta_2}{2} = 10° \tag{6}$$

$$s_1 = d_1 \tag{7}$$

$$Z_2 = Z_1 = 18 \tag{8}$$

where (s_1) is the height of the seed-metering wheel, mm; (d_1) is the width of the seed outlet, mm; θ_5 is the angle of a single U-shaped groove, °; θ_2 is the angular spacing between two adjacent seed spoons on the spoon-type seed-metering wheel, °; and (Z_2) is the number of U-shaped seed grooves on the seed-metering wheel.

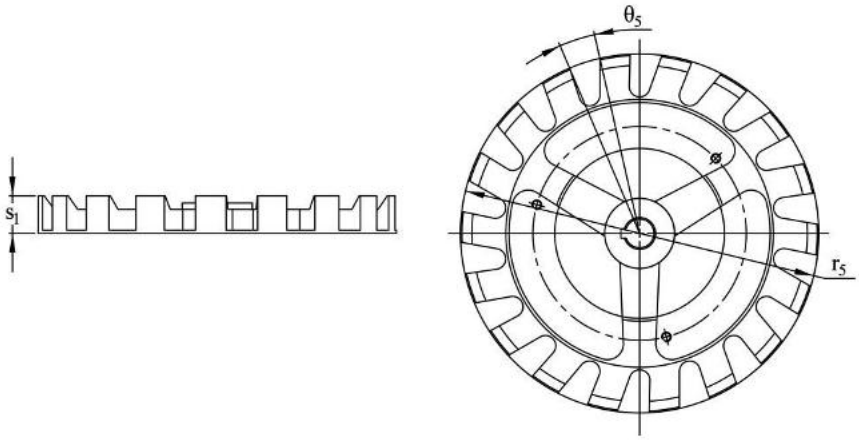


Fig. 6 - Schematic diagram of the seed-metering wheel

Bench Test

The bench tests were conducted using a JPS-16 seed-metering performance test system at the Key Laboratory of Intelligent Agricultural Machinery and Equipment, Heilongjiang Bayi Agricultural University. The system mainly consisted of a seed-metering-device mounting platform, a conveyor belt, an industrial camera, a control unit, an oil-applying and scraping device, and an illumination chamber. The conveyor belt was 0.9 m wide, and its speed was continuously adjustable from 0 to 16 km·h^{-1}. The seed-metering shaft speed ranged from 0 to 150 r·min^{-1}, with measurement and control accuracies of ±0.1% and ±0.5%, respectively. A computer-vision method was used to identify seed positions and calculate the spacing between adjacent seeds. The image-acquisition width was 400 mm, the acquisition frequency was 30–60 frames·s^{-1}, the seed-spacing resolution was 1 mm, and the mean measurement error was within ±2 mm. Before each test, the conveyor-belt speed, seed-metering shaft speed, and image-detection system were calibrated. The inclination angle was set and measured using the test system, with an accuracy of ±0.1°. The seed-layer height was measured using a steel ruler with 1-mm graduations, with an accuracy of ±1 mm. Data acquisition was initiated after the seed-metering device reached a stable operating state. Each test lasted 90 s, and 300 consecutive seed spacings were selected for statistical analysis. The tests were conducted at an ambient temperature of 20 ± 5 °C and a relative humidity of 40%–70%. Each treatment was repeated five times, and the mean value was used for subsequent analysis. Zhengdan 958 maize seeds were used in the experiments. The qualified index (A), multiple-seeding index (D), and miss-seeding index (M) were calculated using Eqs. (9)–(11), respectively (*Wang et al., 2026*).

$$A = \frac{n_1}{N} \times 100\% \tag{9}$$

$$D = \frac{n_2}{N} \times 100\% \tag{10}$$

$$M = \frac{n_3}{N} \times 100\% \tag{11}$$

Single-Factor Tests

To determine the effects of seed-metering wheel rotational speed, overall inclination angle, and seed-layer height on the performance of the inclined spoon-disc seed-metering device, three single-factor tests were conducted. The factor ranges were selected based on the operating range of the test system, preliminary tests, and the requirements of maize precision seeding. Maize kernels from the same cultivar, seed lot, and size grade were used throughout the tests. The treatment order within each single-factor test was randomized to reduce systematic errors. Except for the factor under investigation, all other operating and environmental conditions were kept constant. Each treatment was repeated five times, and 300 consecutive seed spacings were evaluated in each repetition. The arithmetic mean of the five repetitions was used as the final result. The qualified index, miss-seeding index, and multiple-seeding index were selected as the performance indicators, and the data were statistically analysed using IBM SPSS Statistics 26.0. To investigate the effect of seed-metering wheel rotational speed, the overall inclination angle and seed-layer height were maintained at 22.5° and 60 mm, respectively, while the rotational speed was set to 14, 17, 20, 23, 26, and 29 r·min^{-1}. To evaluate the effect of the overall inclination angle, the rotational speed and seed-layer height were maintained at 21 r·min^{-1} and 60 mm, respectively, while the inclination angle was set to 15°, 18°, 21°, 24°, 27°, and 30°. To examine the effect of seed-layer height, the rotational speed and overall inclination angle were maintained at 21 r·min^{-1} and 22.5°, respectively, while the seed-layer height was set to 40, 48, 56, 64, 72, and 80 mm.

Multi-Factor Test

Based on the single-factor test results, a three-factor, five-level central composite rotatable design was employed to investigate the individual and interaction effects of seed-metering wheel rotational speed, overall inclination angle, and seed-layer height on seed-metering performance. The qualified index, multiple-seeding index, and miss-seeding index were selected as the response variables. The experimental runs were conducted in a randomized order. Each run was repeated five times, and the response values were expressed as the mean ± standard deviation. The coded factor levels are presented in Table 1, and the experimental design and results are presented in Table 2.

Table 1

Coded levels of the experimental factors

Coded value	Factor		
	Seed-metering wheel rotational speed (r·min^{-1})	Overall inclination angle (°)	Seed-layer height (mm)
1.682	27.8	30	80
1	25	27	71.9
0	20.8	22.5	60
-1	16.7	18	48.1
-1.682	13.9	15	40

RESULTS AND DISCUSSIONS

Effect of Seed-Metering Wheel Rotational Speed on Seed-Metering Performance

Under an overall inclination angle of 22.5° and a seed-layer height of 60 mm, the effects of seed-metering wheel rotational speed on seed-metering performance are shown in Fig. 7. As the rotational speed of the seed-metering wheel increased from 14 to 23 r·min^{-1}, the qualified index increased from 85.1% to 96.3%, representing an increase of 11.2 percentage points. Meanwhile, the multiple-seeding index decreased from 9.6% to 1.6%, a reduction of 8.0 percentage points, and the miss-seeding index generally decreased from 4.1% to a relatively low level. When the rotational speed was further increased to 29 r·min^{-1}, the qualified index decreased to 87.4%, whereas the miss-seeding index increased markedly to 9.5%. In contrast, the multiple-seeding index increased only slightly to 2.3%. At a relatively low rotational speed, the seed spoons remained within the seed mass for a longer period, thereby increasing the likelihood of capturing multiple maize kernels simultaneously. Moreover, the relatively weak centrifugal effect acting on the kernels in the seed-clearing zone made it difficult for excess kernels located outside the spoon cavity to fall back into the seed mass in a timely manner, resulting in a relatively high multiple-seeding index. As the rotational speed increased, the disturbance exerted by the seed spoons on the seed mass became stronger. Consequently, excess kernels were more readily detached from the spoon cavities under the combined effects of gravity, centrifugal force, and inter-kernel collisions. This gradually reduced the multiple-seeding index and consequently increased the qualified index.

Table 2

The experimental design and results

Coded value	Factor			Qualified index y_1 (%)	multiple-seeding index y_2 (%)	miss-seeding index y_3 (%)
	Seed-metering wheel rotational speed (r·min⁻¹)	Overall inclination angle (°)	Seed-layer height (mm)			
1	25	27	71.9	96.6	4	2.2
2	25	27	48.1	94.2	2.2	4.3
3	25	18	71.9	94.2	2.4	5.8
4	25	18	48.1	92.6	0.4	7.9
5	16.7	27	71.9	93.9	4.3	3.7
6	16.7	27	48.1	91.3	2.9	6.5
7	16.7	18	71.9	93.2	2.6	4.3
8	16.7	18	48.1	93.9	1.9	4.6
9	27.8	22.5	60	93.7	1.6	6.1
10	13.9	22.5	60	91	2.5	6.6
11	20.8	30	60	94.4	3.4	2.6
12	20.8	15	60	93.6	2.7	4.1
13	20.8	22.5	80	92.9	3.9	3.2
14	20.8	22.5	40	92.1	2.2	6.1
15	20.8	22.5	60	95.3	2.4	1.5
16	20.8	22.5	60	93.6	1.7	1.6
17	20.8	22.5	60	95	1.2	3.4
18	20.8	22.5	60	95.2	2.1	2.3
19	20.8	22.5	60	95.1	2	3.6
20	20.8	22.5	60	94.2	1.4	3.8
21	20.8	22.5	60	94.8	2	3.7
22	20.8	22.5	60	94.9	2.7	1.5
23	20.8	22.5	60	95.3	1.2	4

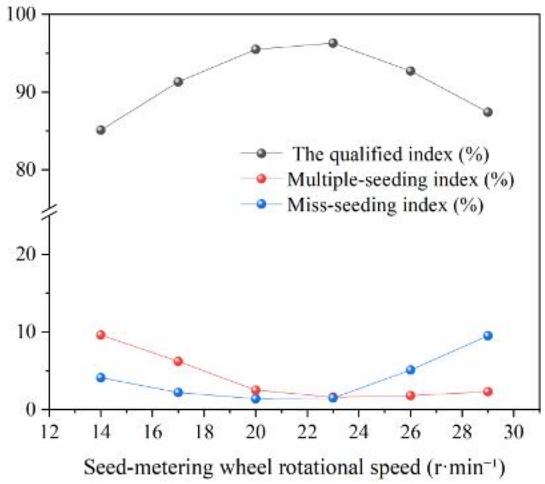


Fig. 7 - Effects of seed-metering wheel rotational speed on seed-metering performance

Effect of Overall Inclination Angle on Seed-Metering Performance

At a seed-metering wheel rotational speed of 21 r·min^{-1} and a seed-layer height of 60 mm, the effects of the overall inclination angle on seed-metering performance are shown in Fig. 8. As the overall inclination angle increased from 15° to 24°, the qualified index increased from 89.2% to 96.5%, corresponding to an increase of 7.3 percentage points. Meanwhile, the multiple-seeding index decreased from 3.1% to 1.7%, and the miss-seeding index decreased from 7.7% to 1.6%. When the inclination angle was further increased to 30°, the qualified index decreased to 91.7%, whereas the multiple-seeding index increased to 6.4% and the miss-seeding index increased slightly to 2.2%. At a relatively small overall inclination angle, the maize kernels were insufficiently concentrated in the seed-pickup zone under the action of gravity.

Consequently, the probability of effective contact between the seed spoons and the kernels was relatively low, making the spoon cavities more likely to remain unfilled and resulting in a higher miss-seeding index. As the inclination angle increased to an appropriate level, the component of gravitational force acting on the seed mass along the plane of the seed-metering disc increased. This promoted the movement of kernels

toward the seed-pickup zone and improved the filling conditions of the seed spoons, thereby reducing the miss-seeding index and increasing the qualified index.

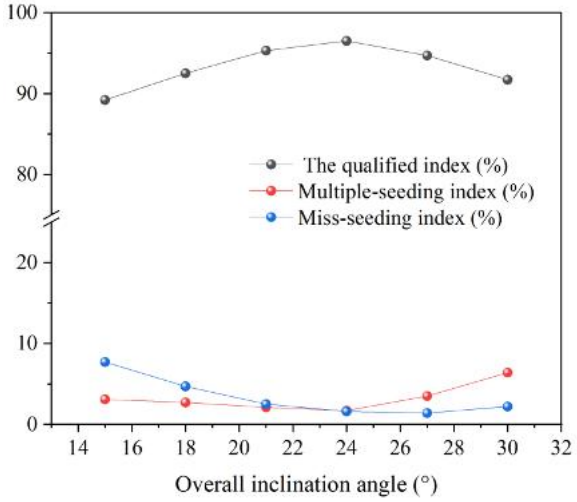


Fig. 8 - Effects of overall inclination angle on seed-metering performance

Effect of Seed-Layer Height on Seed-Metering Performance

At a seed-metering wheel rotational speed of 21 r·min^{-1} and an overall inclination angle of 22.5°, the effects of seed-layer height on seed-metering performance are shown in Fig. 9. As the seed-layer height increased from 40 to 64 mm, the qualified index increased from 88.6% to 96.4%, corresponding to an increase of 7.8 percentage points. Meanwhile, the miss-seeding index decreased from 9.2% to 0.9%, representing a reduction of 8.3 percentage points, whereas the multiple-seeding index increased only slightly from 2.1% to 2.6%. When the seed-layer height was further increased to 80 mm, the qualified index decreased to 90.5%, while the multiple-seeding index increased to 7.1% and the miss-seeding index increased to 2.3%. At a relatively low seed-layer height, fewer kernels were available for capture by the seed spoons within the seed-pickup zone. In addition, the contact pressure exerted by the seed mass on the seed spoons was insufficient, increasing the likelihood of unfilled spoon cavities and consequently resulting in a higher miss-seeding index. As the seed-layer height increased, both the number of kernels and the pressure exerted by the seed mass within the seed-pickup zone increased. This enhanced the probability of kernels entering the spoon cavities, thereby markedly reducing the miss-seeding index and gradually increasing the qualified index.

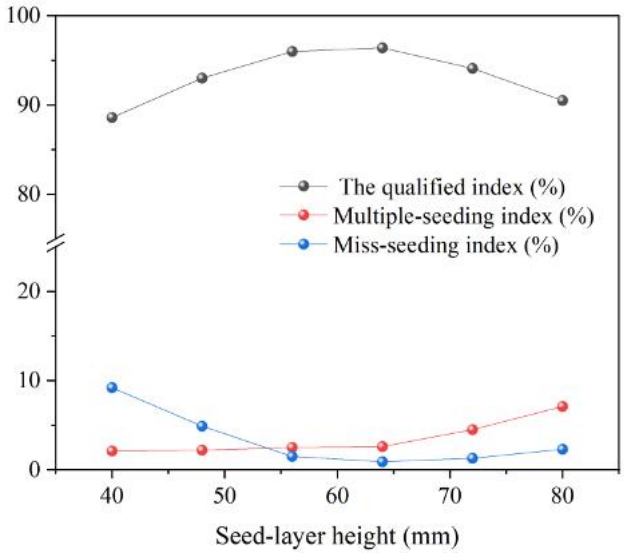


Fig. 9 - Effects of seed-layer height on seed-metering performance

Results and Analysis of the Central Composite Rotatable Design

The qualified index is an important indicator for evaluating the operating performance of the inclined spoon-disc seed-metering device. The analysis of variance for the regression model of the qualified index is presented in Table 3.

The model yielded an (F)-value of 6.88 with (P<0.01), indicating that the established quadratic regression model was highly significant. Significant regression relationships were observed between the qualified index and the rotational speed of the seed-metering wheel, the overall inclination angle, and the seed-layer height. The (P)-value for the lack-of-fit term was 0.1073, indicating that the lack of fit was not significant and that the model adequately described the relationships between the investigated factors and the qualified index. After eliminating the nonsignificant terms while retaining a significant overall model and a nonsignificant lack of fit, the regression equation for the qualified index in terms of coded variables was established as follows:

$$y_1 = 89.18 + 0.64x_1 - 1.11x_2 + -0.25x_3 + 0.03x_1x_2 + 0.005x_1x_3 + 0.009x_2x_3 - 0.04{x_1}^2 - 0.005{x_2}^2 - 0.004{x_3}^2 \quad (12)$$

where y_1 is the qualified index; x_1 is the coded value of the seed-metering wheel rotational speed; x_2 is the coded value of the overall inclination angle; and x_3 is the coded value of the seed-layer height.

Table 3

The results of the analysis of variance for the regression equations

Source of variance	Qualified index (%)			
	Square sum	Degrees of freedom	*F*	*P*
Model	32.74	9	6.88	0.0011**
x_1	7.12	1	13.47	0.0028**
x_2	0.89	1	1.69	0.2159
x_3	3.86	1	7.31	0.0181*
x_1x_2	4.35	1	8.23	0.0132*
x_1x_3	0.56	1	1.06	0.3214
x_2x_3	2.10	1	3.97	0.0676
${x_1}^2$	7.55	1	14.28	0.0023**
${x_2}^2$	0.16	1	0.30	0.5915
${x_3}^2$	6.38	1	12.06	0.0041**
Residual	6.87	13		
Lost proposal	4.28	5	2.64	0.1073
Errors	2.60	8		
Sum of all	39.62	22		

Note: * indicates significant (P < 0.05) and ** indicates highly significant (P < 0.01).

Interaction Effect of Metering-Wheel Rotational Speed and Overall Inclination Angle

When the seed-layer height was fixed at 60 mm, the combined effects of seed-metering wheel rotational speed and overall inclination angle on the qualified index are shown in Fig. 10. As the rotational speed of the seed-metering wheel increased, the qualified index generally exhibited an initial increase followed by a subsequent decrease. Variations in the overall inclination angle resulted in markedly different changes in the qualified index at different rotational speeds. At relatively low rotational speeds, the seed spoons remained within the seed mass for a longer period, increasing the likelihood of simultaneously capturing multiple maize kernels and consequently increasing the multiple-seeding index. As the rotational speed increased further, the time available for the seed spoons to pass through the seed-pickup zone was shortened, making it difficult for the kernels to enter the spoon cavities completely and remain stably retained. This increased the probability of missed seeding and ultimately reduced the qualified index. The overall inclination angle altered the accumulation pattern and force direction of the maize kernels within the seed-pickup zone. At a relatively small inclination angle, the kernels were insufficiently concentrated toward the seed-pickup zone, resulting in a lower probability of effective contact between the kernels and the seed spoons. An appropriate increase in the inclination angle improved kernel accumulation and contact conditions, thereby facilitating seed filling.

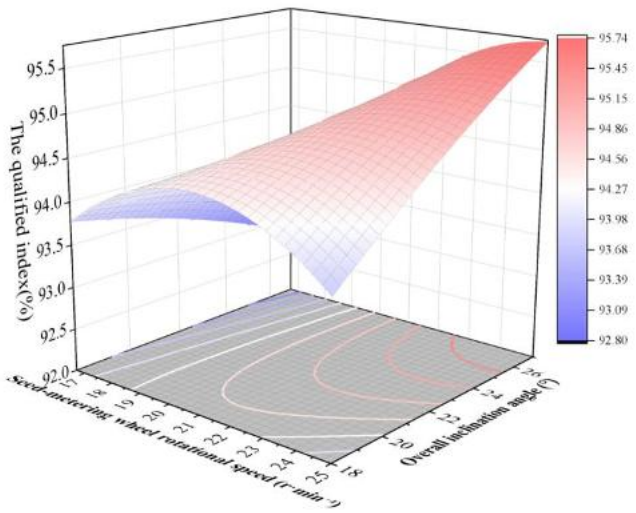


Fig. 10 - Effects of seed-metering wheel rotational speed and overall inclination angle on the qualified index

Interaction Effect of Seed-Metering Wheel Rotational Speed and Seed-Layer Height

When the overall inclination angle was fixed at 22.5°, the combined effects of seed-metering wheel rotational speed and seed-layer height on the qualified index are shown in Fig. 11. The response surface exhibited an arch-shaped profile, with a higher central region and lower peripheral regions, indicating that appropriate ranges existed for both the seed-metering wheel rotational speed and seed-layer height. As either the rotational speed or seed-layer height increased, the qualified index generally exhibited an initial increase followed by a decrease. At a relatively low seed-layer height, the number of kernels available for capture by the seed spoons in the seed-scooping region was limited. Moreover, the pressure exerted by the seed mass on the seed spoons was insufficient, increasing the likelihood of empty spoon cavities as the seed spoons passed through the seed mass and consequently increasing the miss-seeding index. An appropriate increase in seed-layer height enhanced the probability of contact between the kernels and seed spoons, improved the seed-filling conditions, and thereby increased the qualified index.

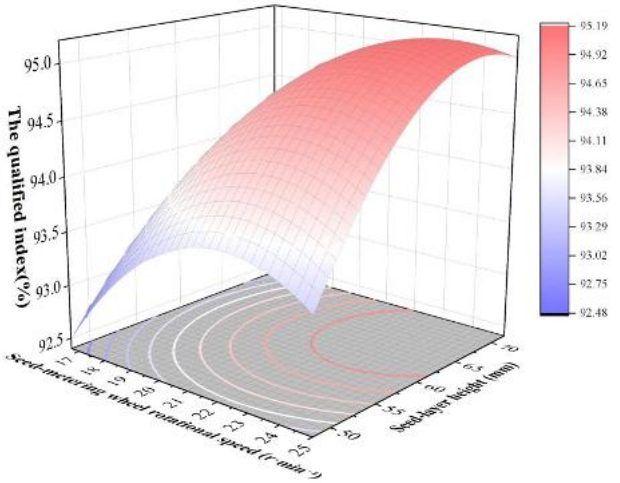


Fig. 11 - Effects of seed-metering wheel rotational speed and seed-layer height on the qualified index

Interaction Effect of Overall Inclination Angle and Seed-Layer Height

When the rotational speed of the seed-metering wheel was fixed at 20.85 r·min^{-1}, the combined effects of overall inclination angle and seed-layer height on the qualified index are shown in Fig. 12. The response surface exhibited more pronounced curvature along the seed-layer-height axis, whereas the variation along the overall-inclination-angle axis was relatively gradual. This indicated that seed-layer height had a greater effect on the qualified index than the overall inclination angle. As the seed-layer height increased, the qualified index initially increased and subsequently decreased. At a relatively low seed-layer height, an insufficient number of kernels were present around the seed spoons, increasing the likelihood of incomplete seed filling. As the seed-layer height increased, both the number of kernels and the pressure exerted by the seed mass in the seed-filling region increased, thereby enhancing the probability of kernel capture by the seed spoons.

However, with a further increase in seed-layer height, the probability of multiple kernels simultaneously entering a spoon cavity increased. Meanwhile, the intensified friction and compression among the kernels hindered the removal of surplus kernels, leading to an increase in the multiple-seeding index and a corresponding decrease in the qualified index.

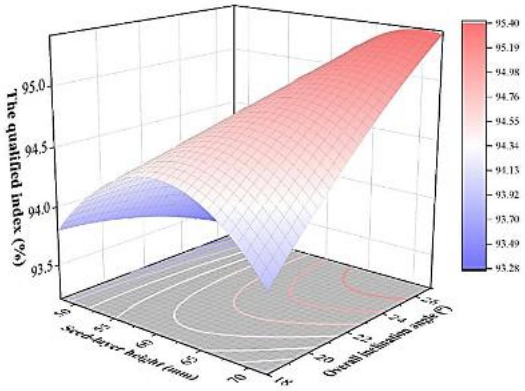


Fig. 12 - Effects of overall inclination angle and seed-layer height on the qualified index

To determine the optimal parameter combination, an optimization model was established within the factor ranges of the three-factor, five-level quadratic orthogonal rotatable design, with the qualified index maximized and the miss-seeding and multiple-seeding indices minimized as the optimization objectives, as shown in Eq.(13).

$$\begin{cases} \max y_1 \\ \min y_2 \\ \min\ y_3 \\ s.t. \begin{cases} 13.9 \le x_1 \le 27.8 \\ 15 \le x_2 \le 30 \\ 40 \le x_3 \le 80 \end{cases} \end{cases} \tag{13}$$

The numerical optimization module in Design-Expert software was used to solve the established regression model for the qualified index. Based on the fitting results obtained from the 23 experimental runs, the qualified index was set as the optimization objective to be maximized within the complete five-level ranges of the experimental factors. The theoretically optimal parameter combination was determined as follows: a seed-metering wheel rotational speed of 25 r·min^{-1}, an overall inclination angle of 27°, and a seed-layer height of approximately 71.9 mm. Under these conditions, the qualified index predicted by the regression model was approximately 96.5%. Bench validation tests were subsequently conducted using the optimized parameter combination, as shown in Fig. 13.

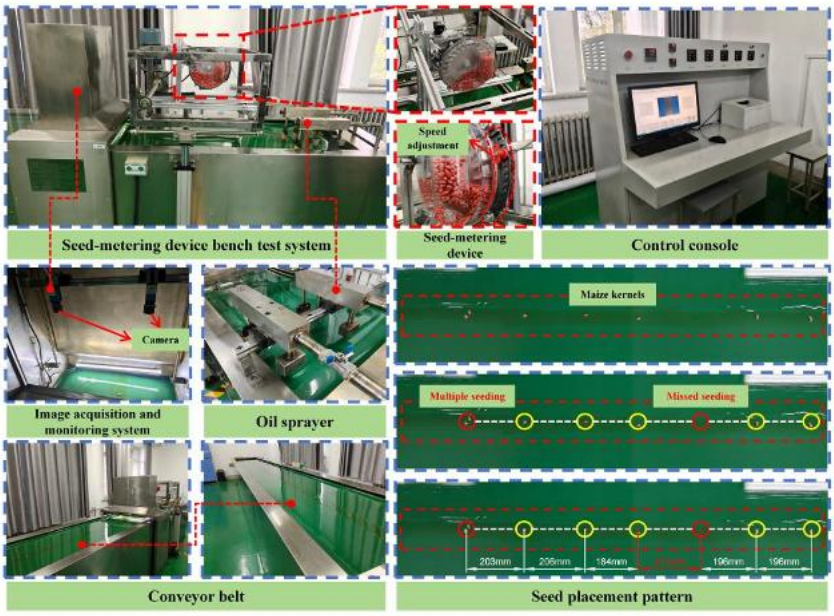


Fig. 13 - Results of the bench validation test under the optimized parameter combination

Three replicate tests were performed, and the mean qualified index was used as the validation result. The mean qualified index obtained experimentally was 95.0%, with a relative error of 1.5% compared with the model-predicted value. The experimental result was in good agreement with the predicted result, demonstrating that the established regression model had satisfactory predictive accuracy and that the optimized parameter combination was reasonable and reliable.

CONCLUSIONS

(1) An inclined spoon-disc seed-metering device was developed in this study. The spoon wheel and seed-metering wheel were driven synchronously at a transmission ratio of 1:1 and maintained a fixed phase relationship, ensuring that each spoon cavity was accurately aligned with the corresponding U-shaped groove at the designated seed-transfer position and thereby enabling precision maize seeding. In addition, the seed-metering wheel rotational speed, overall inclination angle, and seed-layer height exhibited pronounced nonlinear effects on seed-metering performance. Regression analysis showed that the rotational speed had the greatest effect on the qualified index, followed by the seed-layer height, whereas the main effect of the overall inclination angle was comparatively weak. A significant interaction was observed between the rotational speed and overall inclination angle, indicating that the appropriate inclination angle varied with rotational speed. These findings demonstrate that optimal seed-metering performance cannot be achieved by optimizing a single parameter independently; rather, the operating parameters must be properly coordinated.

(2) Multi-objective optimization identified the optimal parameter combination as a seed-metering wheel rotational speed of 25 r·min^{-1}, an overall inclination angle of 27°, and a seed-layer height of 71.9 mm. Under these conditions, the qualified index predicted by the regression model was 96.5%, whereas the mean qualified index obtained from the validation tests was 95.0%, corresponding to a relative error of 1.5%. The close agreement between the predicted and experimental results indicates that the established regression model can reliably describe and optimize the seed-metering performance within the investigated ranges. Future studies will assess the adaptability of the device to different maize cultivars, conduct high-speed and field validation tests, and further evaluate its seed-metering performance under a broader range of operating conditions.

ACKNOWLEDGEMENT

This work was supported by the Youth Science Fund Project of the Natural Science Foundation of Heilongjiang Province (QC2025C033), the China Postdoctoral Science Foundation (2024MD763975), the Daqing Municipal Directed Science and Technology Program (zd-2025-032), and the School Orientation Training Research Initiation Fund Program (XYB202307).

REFERENCES

[1] Baghooee, M., Karparvarfard, S. H., Azimi-Nejadian, H., Keramat-Jahromi, M., Balanian, H., & Sardarpour, F. (2023). DEM Simulation for Seeding Performance of a Slotted Roller Seed-Metering Device for Planting Maize in Laboratory Condition. *Journal of Biosystems Engineering*, *48*(4), 428-436. https://doi.rog/10.1007/s42853-023-00202-z

[2] Bakirov, A., Kostyuchenkov, N., Kostyuchenkova, O., Grishin, A., Omarbekova, A., & Zagainov, N. (2025). Application of Seed Miss Prevention System for a Spoon-Wheel Type Precision Seed Metering Device: Effectiveness and Limitations. *Agriculture - Basel*, *15*(13), 1363. https://doi.rog/10.3390/agriculture15131363

[3] Chen, J., Qi, S., Xu, F., Jia, P., Yuan, Z., Xi, D., & Wang, J. (2025). CFD-DEM-based simulation and performance analysis of key parameters in pneumatic high- speed precision maize seed-metering device. *Frontiers In Plant Science, 16*, 1700037. https://doi.rog/10.3389/fpls.2025.1700037

[4] Cortez, J. W., Anghinoni, M., & Arcoverde, S. N. S. (2020). Seed Metering Mechanisms and Tractor-Seeder Forward Speed on Corn Agronomic Components. *Engenharia Agrícola*, *40*(1), 61-68. https://doi.rog/10.1590/1809-4430-eng.agric.v40n1p61-68/2020

[5] Ding, L., Yuan, Y., Dou, Y., Li, C., He, Z., Guo, G., & Li, H. (2024). Design and Experiment of Air-Suction Maize Seed-Metering Device with Auxiliary Guide. *Agriculture-Basel, 14*(2), 169. https://doi.rog/10.3390/agriculture14020169

[6] Gao, X., Xie, G., Li, J., Shi, G., Lai, Q., & Huang, Y. (2023). Design and validation of a centrifugal variable-diameter pneumatic high-speed precision seed-metering device for maize. *Biosystems Engineering, 227*, 161-181. https://doi.rog/10.1016/j.biosystemseng.2023.02.004

[7] Koller, A. A., Taylor, R. K., Raun, W. B., Weckler, P. R., & Buser, M. D. (2016). Modelling and validation of maize seed orientation by pushing. *Biosystems Engineering*, *151*, 338-349. https://doi.rog/10.1016/j.biosystemseng.2016.09.011

[8] Li, C., Zhang, D., Yang, L., Cui, T., He, X., Li, Z., & Liang, J. (2024). Research on a centrifugal high-speed precision seed metering device for maize with airflow-assisted seed filling and cleaning. *Computers and Electronics in Agriculture, 226*, 109434. https://doi.rog/10.1016/j.compag.2024.109434

[9] Lin, C., Wang, H., Wu, J., Zhou, Y., Deng, J., & Liu, X. (2026). Design and Experiment of Potato Planter with Electric Chassis. *INMATEH - Agricultural Engineering, 78*(1), 1528-1537. https://doi.rog/10.35633/inmateh-78-120

[10] Sun, W., Yi, S., Qi, H., Li, Y., Dai, Z., Zhang, Y., & Wang, S. (2025). DEM-CFD coupling simulation and optimization of an air-pressure high-speed precision seed-metering device for maize delta-row dense plantings. *Powder Technology, 466*, 121481. https://doi.rog/10.1016/j.powtec.2025.121481

[11] Wang, Z., Wei, N., Zhang, D., Adilet, S., Jiang, Y., Zhou, J., & Chen, J. (2026). Theoretical Design and Bench Validation of an Air-Suction Precision Seed Metering Device for Multiple Seeds Per Hill of Small-Seed Crops. *INMATEH - Agricultural Engineering*, *78*(1), 1067-1078. https://doi.rog/10.35633/inmateh-78-83

[12] Yang, R., Shi, Y., Pan, Z., Zhang, H., Luo, X., Miao, Y., & Wu, H. (2025). Design and Experimental Evaluation of a High-Speed Spoon-Belt Potato Seed-Metering Device. *INMATEH-Agricultural Engineering*, *77*(3), 1555-1568 https://doi.rog/10.35633/inmateh-77-124

[13] Zhao, P., Song, Q., Bi, Y., Dong, J., Fu, Z., Huang, Y., & Zheng, Y. (2026). Interaction mechanisms of seed suction and cleaning negative pressure of an air-suction seed metering device for maize breeding plots. *Biosystems Engineering, 262*, 104368. https://doi.rog/10.1016/j.biosystemseng.2025.104368

CONSTRUCTION AND PARAMETER CALIBRATION OF A DISCRETE ELEMENT MODEL FOR SEED GINGER IN SOWING OPERATIONS
/
播种期生姜离散元模型构建与参数标定

Jinbiao ZHANG[1)], Jin CHENG*[1)], Lin LIU[1)], Jialin HOU[1)], Rui HOU[2)], Qiwei ZHAO[3)], Yuhua LI[1)]
[1)] Shandong Agricultural University, Tai'an / China;
[2)] Beijing University of Posts and Telecommunications, Beijing / China
[3)] Dezhou Chunming Agricultural Machinery Company Limited, Dezhou / China
Cheng Jin, Tel: +8615666763312; Email: ttcheng@163.com

DOI: https://doi.org/10.35633/inmateh-79-87

Keywords: *discrete element method, seed ginger, particle interaction, angle of repose, DEM parameter calibration*

ABSTRACT
To address the lack of contact parameters for seed ginger and the insufficient accuracy of existing discrete element models used in simulations of seed ginger machinery, a discrete element modeling and contact parameter calibration method for irregularly shaped seed ginger was proposed. A discrete element model of seed ginger was constructed using 3D laser scanning and an adaptive multi-sphere filling method. The contact parameters between seed ginger and steel were calibrated using free-fall collision tests, inclined-plane tests, and combined inclined-plane–horizontal-plane tests. Using the angle of repose as the response variable, the optimal parameter combination was determined through steepest ascent tests and response surface methodology. The relative error between the simulated angle of repose and the value measured in the bench test was 2.24%. The results provide a modeling basis for the optimization and design of key components of seed ginger machinery and for investigating the dynamic interaction mechanisms among seed ginger particles.

摘要
针对生姜播种机械仿真研究中姜种接触参数缺失、模型精度不足的问题，提出一种不规则姜种的离散元建模与接触参数标定方法。基于三维激光扫描与多球自适应填充方法构建姜种离散元模型；采用自由落体碰撞法、斜面法及斜面-平面组合法标定姜种与钢材间接触参数；并以休止角为响应指标，结合最陡爬坡试验与响应面试验，获得最优参数组合，仿真休止角与台架试验实测值的相对误差为2.24 %。研究结果可为生姜播种机械关键部件优化设计及颗粒群动态互作机理研究提供模型基础。

INTRODUCTION
Ginger is a vital specialty vegetable and medicinal crop in China, ranking first globally in both planting area and total yield, with stable and continuously growing market demand. Currently, ginger sowing operations face challenges such as labor shortages and low efficiency *(Yang et al., 2022)*. The irregular shape of seed ginger and their distinctive features like surface protrusions and nodes impose stringent requirements on single-seed picking and bud orientation during mechanized sowing. However, establishing a granular simulation model using the discrete element method enables precise analysis of microscopic force interactions, providing a crucial tool for the design verification and simulation optimization of key components in ginger sowing machinery *(Zhao et al., 2025)*. Accurate calibration of seed ginger-related contact parameters and the construction of discrete element models have become essential foundations for ensuring the rational design of core sowing machinery components and the accuracy of virtual simulations.

Currently, numerous researchers have conducted studies on the construction and parameter calibration of discrete element models for conventional crops. *Lu et al., (2023),* and others simulated the natural stacking and sowing processes of wheat seeds, effectively addressing the challenge of balancing simulation accuracy and computational time in the multi-sphere method. *Shi Linrong et al., (2018)* employed the slice modeling method to construct a potato seed model and validated the effectiveness of the stacking angle simulation parameters through physical experiments. *Lu Qi et al., (2023),* and others developed a soil-seed interaction model, determining contact parameter values using the response surface method.

[1] *Zhang Jinbiao[1], Ph.D. Stud.; Cheng Jin, * Ph.D.; Liu Lin, Ph.D.; Hou Jialin, Prof. Ph.D.; Hou Rui, Ph.D.; Zhou Qiwei.; Li Yuhua, Ph.D.*

Xia Junfang et al., (2024), *Liao Yitao et al., (2020)*, and *Shi Ruijie et al., (2022),* combined simulation with bench tests to accurately obtain contact parameters for rice straw, rapeseed stems, and sesame stems, providing foundational data for low-loss harvesting technologies. Other scholars have also conducted relevant research on the establishment of discrete element simulation model and parameter calibration of crops and products such as alfalfa (*Chen et al., 2023*), sunflower (*Guo et al., 2025*), tea (*Du et al., 2025*), quinoa (*Liu et al., 2020*), maize (*Jia et al., 2020*), coated cotton-seeds (*Wang et al., 2021*), sweet sorghum seeds (*Yang et al., 2026*) and millet threshing mixtures (*Huang et al., 2026*). These studies predominantly employed a combination of physical experiments and simulation to optimize parameters but primarily focused on regular-shaped, single-mechanical-property agricultural granular materials. Under external loading, seed ginger exhibits dynamic mechanical responses, including friction and collision, as well as asymmetric stacking behavior characterized by the angle of repose, which differ fundamentally from those of conventional crop materials.

To address the complex stacking behavior caused by the irregular shape of seed ginger, a parameter calibration optimization procedure was established based on steepest ascent tests and response surface methodology, providing a calibration approach suitable for irregular block-shaped seed materials. This study systematically reports key physical and mechanical properties of seed ginger during sowing, addressing a gap in the existing research and providing an accurate modeling basis for further investigation of dynamic interaction mechanisms in mechanical ginger sowing and for the optimized design of key components.

MATERIALS AND METHODS

Determination of physical properties of seed ginger

In order to obtain the basic physical characteristic parameters of seed ginger, this study selected "Laiwu Big Ginger" with intact scales after germination as the experimental object. This variety has strong growth potential and a yield of about 30 t/hm^2. It is the main cultivated variety in Shandong region and has certain representativeness. Regarding the shape of seed ginger Based on the principle of "moderate block size, typical shape, and full scale", seed ginger were randomly spread out on the open space due to their complex and irregular characteristics. Then, the five point sampling method (Fig.1) was used, with 40 seed ginger randomly taken from each sampling point, for a total of 200 seed ginger as the measurement samples. Using the AES-G5 electronic scale, the average mass of the sample monomer was 68.5 g. The volume was measured using the drainage method, and the average density of the seed ginger was calculated to be 1094.7 kg/m^3. The average moisture content of the seed ginger was determined to be 64.38% using the standard drying method. The external dimensional parameters of seed ginger were measured and statistically analyzed using a vernier caliper with an accuracy of 0.1 mm. Considering the typical irregular block structure of seed ginger, this study selected the maximum radial size of the main body of seed ginger at the thick end and the minimum radial size at the thin end as the external dimensional parameter indicators. The results are shown in Table 1.

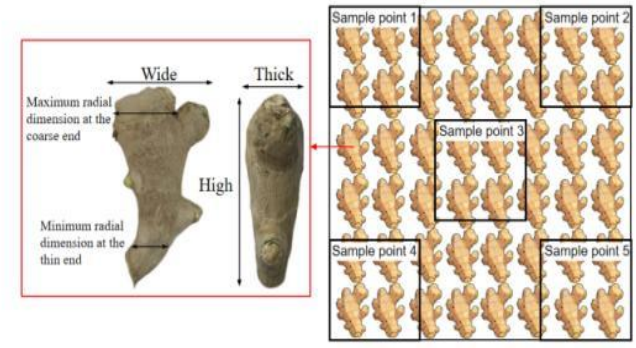


Fig. 1 - Five point sampling method

Table 1

Measurement results of external dimensions parameters of seed ginger during sowing period

Project	High[mm]	Width[mm]	Thickness [mm]	Maximum radial dimension at the coarse end[mm]	Minimum radial dimension at the thin end[mm]
Max	125.2	74.3	35.6	42.5	17.8
Min	72.7	52.6	24.9	35.4	12.4
Mean	93.8	63.7	31.7	37.8	14.7
Standard Deviation	13.7	9.3	5.8	2.9	3.1

The Poisson's ratio, elastic modulus, and shear modulus of seed ginger were determined through compression tests *(Sun et al., 2025)*. Cylindrical pulp specimens with a diameter of 10 mm and a length of 20 mm were prepared and placed on the lower compression platen of a TA-XT2i texture analyzer. The pre-compression speed of the upper platen was set to 60 mm/min, the compression speed to 5 mm/min, and the compression distance to 5 mm. Ten replicate compression tests were conducted. The radial dimensions of the specimens before and after compression were measured, and the mean Poisson's ratio μ of seed ginger was calculated using Eq. (1) as 0.46. Compression was then continued until the cylindrical specimen completely collapsed. The test was repeated ten times, and the maximum load *F* within the elastic deformation stage and the corresponding axial deformation ΔL were recorded. According to Eq. (2), the mean elastic modulus E of seed ginger was calculated as 2.97 MPa, as shown in Table 2. The shear modulus G was subsequently calculated using Eq. (3), yielding a mean value of 1.02 MPa.

$$\mu = \left|\frac{\varepsilon_t}{\varepsilon_a}\right| = \frac{\Delta d / d}{\Delta h / h} = \frac{\Delta dh}{\Delta hd} \tag{1}$$

$$E = \frac{Fh}{S\Delta L} \tag{2}$$

$$G = \frac{E}{2(1+\mu)} \tag{3}$$

where: μ is Poisson's ratio; ε_t is the radial deformation of the sample, [mm]; ε_a is the axial deformation of the sample, [mm]; Δd is the radial size change, [mm]; d is the radial original size, [mm]; Δh is the axial size change, [mm]; h is the axial original size, [mm]. E is the elastic modulus, [MPa]; F is the maximum load during the elastic stage, [N]; S is the compressive cross-sectional area, [mm^2]; ΔL is the compression deformation of the sample at the maximum load, [mm]; G is the shear modulus, [MPa].

Table 2

Determination results of compression test of seed ginger during sowing period

No.	Radial dimension after compression [mm]	variation[mm]	Poisson's ratio	maximum load/ [N]	Compression deformation amount [mm]	Elastic Modulus
1	11.05	1.05	0.42	92.10	8.20	2.86
2	11.13	1.13	0.45	94.92	8.25	2.93
3	11.20	1.20	0.48	97.46	8.30	2.99
4	11.25	1.25	0.50	100.94	8.40	3.06
5	11.00	1.00	0.40	92.49	8.15	2.89
6	11.23	1.23	0.49	97.39	8.35	2.97
7	11.15	1.15	0.46	98.52	8.28	3.03
8	11.28	1.28	0.51	93.93	8.22	2.91
9	11.08	1.08	0.43	102.54	8.45	3.09
10	11.18	1.18	0.47	97.04	8.32	2.97
Max	11.28	1.28	0.51	102.54	8.45	3.09
Min	11.00	1.00	0.40	92.10	8.15	2.86
Mean	11.16	1.16	0.46	96.73	8.29	2.97
Standard Deviation	0.09	0.09	0.036	3.44	0.09	0.075

Compare and analyze the mechanical properties of seed ginger with typical agricultural bulk materials *(Zhou et al., 2023; Cai et al., 2024; Zhang et al., 2025; Zhang et al., 2022)*, as shown in Table 3. Compared with high-stiffness particles such as wheat and beans, seed ginger exhibits markedly lower stiffness. Compared with root and tuber crops such as potatoes, water chestnuts, yams, and sweet potatoes, seed ginger has a higher Poisson's ratio.

The typical low stiffness and high deformation physical characteristics of ginger provide a reliable theoretical basis for the selection and parameter configuration of low stiffness contact models in subsequent

discrete element simulations, which result in high viscous resistance and asymmetric contact phenomena during dynamic collisions and natural accumulation processes.

Table 3

Comparison of mechanical properties of typical agricultural bulk materials

Name	Wheat	Soybean	Potato	Water Chestnut	Yam	Sweet Potato	Ginger
Type	Cereals	Legumes	Roots and Tubers	Roots and Tubers	Roots and Tubers	Roots and Tubers	Roots and Tubers
Elastic Modulus	37	180	5.65	5.433	3.92	3.22	2.97
Poisson's Ratio	0.30	0.40	0.42	0.395	0.4	0.28	0.46

Construction of Discrete Element Model

During the sowing period, seed ginger exhibit a significant irregular block structure, and it is difficult to accurately reflect their complex boundary contours using conventional single sphere or ellipsoid models. The multi-sphere adaptive filling model can flexibly approach the irregular block structure and angle characteristics by adjusting the number, radius and spatial arrangement of the constituent spheres, and also simplify the contact between particles with complex shapes as the interaction between spheres. This study utilized a high-precision 3D laser scanner (Accuracy: 0.02 mm; Resolution: 0.02 mm; Scanning speed: 2,800,000 points/s) to obtain 3D point cloud data on the surface of ginger samples, and imported it into Geomagic Studio software for reverse engineering processing. During the processing, the focus is on preserving the coarse and fine end contour features of seed ginger, and then using HyperMesh software for mesh partitioning and optimization to export high-precision 3D geometric models of seed ginger. The three-dimensional model was imported into EDEM software. Based on the multi-sphere combination method, a small ball with a radius of 2 mm was selected to discretize and fill the model. The smoothing value was set to 3, and the total number of spheres was 6988. The discrete element model of ginger seeds was constructed (Fig. 2).

Seed ginger is a kind of granular material with large size, and the particles will not adhere and agglomerate with each other due to the effect of water and chemical substances, the measured mechanical parameters of seed ginger were directly assigned in EDEM software, and the Hertz Mindlin (no slip) contact model was selected. This setting accurately reproduces the high viscosity resistance and asymmetric stacking behavior of seed ginger, laying the foundation for precise calibration of subsequent contact parameters.

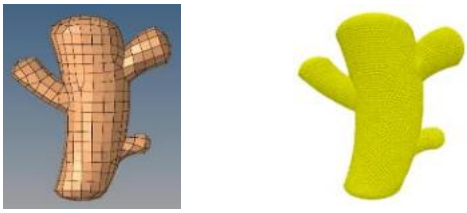


Fig. 2 - Seed ginger simulation model

Coefficient of restitution between seed ginger and steel

The coefficient of restitution is a dimensionless parameter that characterizes the ability of two colliding bodies to recover kinetic energy after impact *(Guo et al., 2023)*. In this study, the coefficient of restitution between seed ginger and a steel plate was measured using a free-fall collision test. A smooth steel plate was fixed horizontally on the base, and 30 seed ginger samples were randomly selected and released from rest from a vertical height of 200 mm. After impact with the steel plate, the samples rebounded. A 1 mm grid was placed in the background as a reference scale, and the rebound process was analyzed frame by frame using a high-speed camera. The mean maximum rebound height h_r was 38.6 mm. According to Eq. (4), the coefficient of restitution *e* between seed ginger and steel was calculated as 0.439. A corresponding simulation model was established in EDEM. The particle factory generated seed ginger particles with zero initial velocity, and the seed ginger–steel coefficient of restitution was set to 0.439. The particles were allowed to fall freely under gravity and collide with the steel plate. The simulation data storage interval was 0.01 s, the total simulation time was 20 s, and the time step was 4.501×10^{-7} s. Considering both computational accuracy and efficiency, the minimum fluid-grid porosity setting was specified such that the grid size was three times the particle diameter. The center-of-mass trajectories of the seed ginger particles were tracked using the post-processing tools. The mean maximum rebound height after impact was 34.9 mm, corresponding to a simulated coefficient of restitution of 0.418.

The relative error between the simulated coefficient of restitution and the bench-test value of 0.439 was 4.78%, indicating that the established discrete element model of seed ginger could adequately reproduce the actual collision characteristics. Therefore, the coefficient of restitution *e* between seed ginger and the steel plate was set to 0.439. The experimental setup and simulation process are shown in Fig. 3.

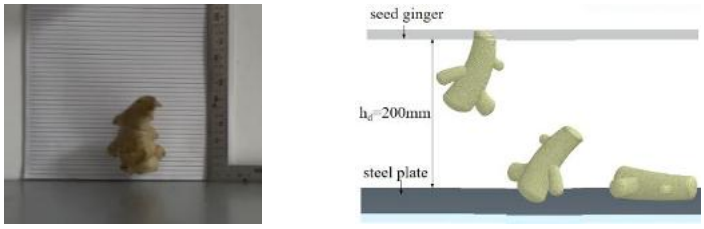


Fig. 3 - Calibration test for the coefficient of restitution between seed ginger and steel

$$e = \sqrt{\frac{h_r}{h_d}} \tag{4}$$

where: e is the coefficient of restitution; h_r is the maximum rebound height of the seed ginger, [mm].

Sliding friction coefficient between ginger and steel

The sliding friction coefficient between seed ginger and a steel plate was measured using the inclined-plane method *(Jiang et al., 2023)*. The longitudinal axis of the seed ginger was aligned parallel to the long side of the steel plate. A digital inclinometer was attached to one side of the plate, and one end of the plate was raised slowly and uniformly to increase the inclination angle. When the seed ginger was on the verge of sliding, the inclination angle was recorded as the critical sliding angle α_1. The test was repeated 30 times, yielding a mean critical sliding angle of 25.75°. According to Eq. (5), the sliding friction coefficient f_1 between seed ginger and the steel plate was calculated as 0.482. For simulation validation, the sliding friction coefficient between the discrete element model of seed ginger and the steel plate model was set to 0.482. A simulation model corresponding to the bench test was established, and the inclination angle of the plate was gradually increased until the seed ginger model began to slide. The critical sliding angle obtained from the simulation was 24.90°, corresponding to a simulated sliding friction coefficient of 0.464. The relative error between the simulated and experimentally measured values was 3.73%, indicating good agreement. Therefore, the sliding friction coefficient f_1 between seed ginger and the steel plate was set to 0.482. The bench-test and simulation procedures are shown in Fig. 4.

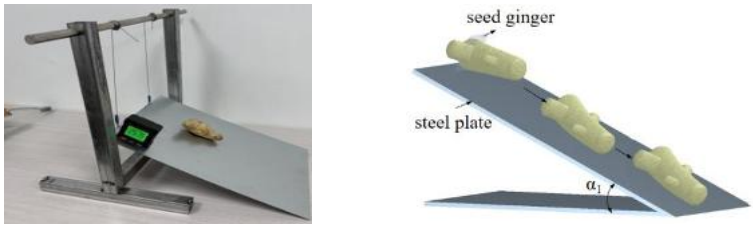


Fig. 4 - Calibration test for the sliding friction coefficient between seed ginger and steel

$$f_1 = \tan\alpha_1 \tag{5}$$

Rolling friction coefficient between seed ginger and steel

In this study, the rolling friction coefficient between seed ginger and steel was measured using a combined inclined-plane and horizontal-plane method. The seed ginger was placed on a steel plate inclined at an angle α_2 of 45°, with its longitudinal axis aligned with the long side of the plate, and was released from rest at a vertical height N of 200 mm above the horizontal plane. The seed ginger accelerated while rolling down the inclined plate and then transitioned smoothly onto the horizontal steel plate, where it decelerated under the action of rolling friction until coming to rest. The test was repeated 30 times, and the mean rolling distance M on the horizontal plate was 178 mm. According to Eqs. (6) and (7), the rolling friction coefficient f_2 between seed ginger and the steel plate was calculated as 0.308. A simulation model with the same dimensions was established in EDEM. The calibrated coefficient of restitution and sliding friction coefficient, together with the rolling friction coefficient to be validated, were assigned to the seed ginger particle model. A seed ginger particle with zero initial velocity was generated at a height of 200 mm. After 30 simulation runs, the mean horizontal rolling distance was 192 mm, corresponding to a simulated rolling friction coefficient of 0.324. The relative error between the simulated and experimentally measured values was 5.19%, indicating good agreement and supporting the validity of the calibrated parameter. Therefore, the rolling friction coefficient f_2 between seed ginger and the steel plate was set to 0.308. The bench-test and simulation procedures are shown in Fig. 5.

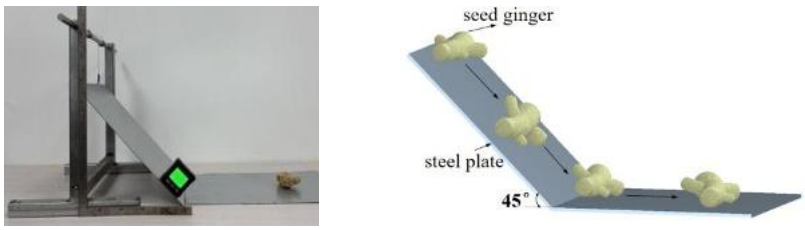


Fig. 5 - Calibration test for the rolling friction coefficient between seed ginger and steel

$$f_2\left(B+M\cos\alpha_2\right)=M\sin\alpha_2 \tag{6}$$

$$B=\frac{N}{\sin\alpha_2} \tag{7}$$

where: α_2 is the inclination angle of the steel plate, [°]; B is the rolling distance of the seed ginger along the inclined plane, [mm]; M is the horizontal rolling distance of the seed ginger, [mm].

Calibration of contact parameters between seed ginger particles

Given the complex and irregular shape of seed ginger, it is difficult to ensure the accuracy of directly measuring seed ginger–seed ginger contact parameters using bench tests alone. The angle of repose can reflect the combined effects of interparticle friction, collision, and asymmetric accumulation behavior. In this study, the experimentally measured angle of repose was used as the target response value. Based on the parameter ranges determined from the bench tests, the seed ginger–seed ginger coefficient of restitution, sliding friction coefficient, and rolling friction coefficient were selected as the experimental factors, and a three-factor, three-level orthogonal test was conducted to determine the optimal combination of contact parameters.

To determine the range of the seed ginger–seed ginger coefficient of restitution, a double-inclined-plane collision method was used *(Xia et al., 2019)*, as illustrated in Fig. 7. Two inclined planes, each set at an inclination angle of 45°, were fixed on the test bench. Seed ginger slices were closely arranged over the working surfaces of the inclined planes to form seed ginger–seed ginger collision layers. The vertical heights from the collision points on the two inclined planes to the horizontal plane were set to H_1 = 200 mm and H_2 = 500 mm, respectively. An intact seed ginger sample was released from rest from a vertical height K of 200 mm above the impact point on the inclined plane. After collision, the sample was projected from the inclined plane and eventually landed on a horizontal plane covered with coordinate paper. The corresponding horizontal travel distances Z_1 and Z_2 were recorded. The test was repeated 30 times, and the seed ginger–seed ginger coefficient of restitution e_1 was calculated using Eqs. (8)–(10). The preliminary range of e_1 was determined to be 0.15–0.65.

$$e_1=\frac{2\sqrt{V_X^2+V_Y^2}\cdot\cos\left[45^\circ+\arctan\left(\frac{V_Y}{V_X}\right)\right]}{\sqrt{0.8g}} \tag{8}$$

$$V_X=\sqrt{\frac{gZ_1Z_2\left(Z_1-Z_2\right)}{\left(0.4Z_2-Z_1\right)}} \tag{9}$$

$$V_Y=\frac{0.5V_X}{Z_2}-\frac{gZ_2}{2V_X} \tag{10}$$

where: Z_1 is the horizontal landing distance corresponding to the first inclined plane, [m]; Z_2 is the horizontal landing distance corresponding to the second inclined plane, [m]; V_X is the horizontal velocity component after collision with the inclined plane, [m/s]; V_Y is the vertical velocity component after collision with the inclined plane, [m/s]; g is the acceleration due to gravity, [m/s^2].

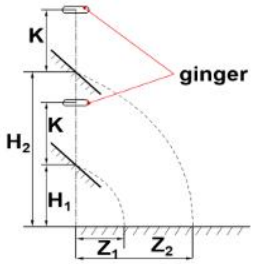


Fig. 6 - Schematic diagram of the bench test for measuring the coefficient of restitution between seed ginger samples

Sliding and rolling friction coefficients between seed ginger samples

In this study, a modified inclined-plane method and a combined inclined-plane and horizontal-plane method were used to determine the preliminary ranges of the seed ginger–seed ginger sliding and rolling friction coefficients. A representative seed ginger sample was cut longitudinally, and the cut pieces were closely arranged and fixed onto the surface of a steel plate to form a seed ginger friction surface. During the sliding test, an intact seed ginger sample was placed on the friction surface as the sliding body, with its longitudinal axis aligned parallel to that of the seed ginger pieces fixed to the plate. One end of the friction plate was raised slowly and uniformly, and the critical inclination angle at the onset of macroscopic sliding was recorded. Thirty seed ginger samples were tested, and the seed ginger–seed ginger sliding friction coefficient f_3 was calculated using Eq. (5), yielding a range of 0.37–0.87. For the rolling friction test, the inclination angle was fixed at 45°. A seed ginger sample was positioned at a vertical height D of 200 mm above the horizontal plane, with its transverse orientation perpendicular to the longitudinal direction of the seed ginger pieces on the friction surface. The sample rolled to the end of the inclined plate along an approximately curved trajectory and subsequently landed on the contact surface. The horizontal distance to the first landing point, Z_3, was recorded. Thirty seed ginger samples were tested, and the seed ginger–seed ginger rolling friction coefficient f_4 was calculated using Eq. (11), yielding a range of 0.32–0.82. The bench-test procedures are shown in Fig. 7.

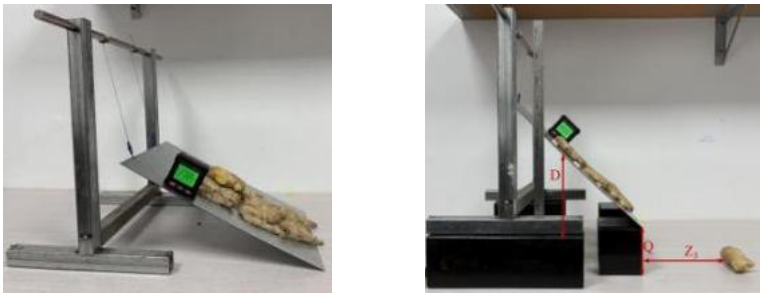


Fig. 7 - Bench tests for the sliding and rolling friction coefficients between seed ginger samples

$$f_4 = \frac{D - Z_3^{\,2}}{2(Q - Z_3)D} \tag{11}$$

where: Z_3 is the horizontal distance to the first landing point on the contact surface, [mm]; Q is the vertical height difference between the end of the inclined plate and the contact surface, [mm].

Physical angle of repose test

In this study, the bottomless-cylinder lifting method (*Zhang et al., 2022*) was used to determine the physical angle of repose of seed ginger. A cylindrical steel container with an inner diameter of 300 mm and a height of 900 mm was used for the test. Its relatively large diameter-to-height ratio helped reduce boundary effects during particle accumulation. Seed ginger samples were naturally filled into the cylinder, after which the cylinder was lifted vertically at a constant speed. Under gravity, the seed ginger mass collapsed and eventually formed a stable asymmetric pile. The angle between the natural slope of the pile and the horizontal surface was measured as the natural angle of repose θ of seed ginger.

To reduce errors associated with manual measurement, image processing was used to determine the angle of repose. After a frontal image of the pile was acquired, grayscale conversion and binarization were sequentially performed using a Python-based image-processing procedure, and the edge contour points were extracted from the binary image. The contour on one side of the pile was then fitted linearly using the least-squares method to obtain the slope of the fitted line, as shown in Fig. 8. After 30 repeated tests, the angle of repose θ of seed ginger was calculated using Eq. (12) as 28.60°.



Fig. 8 - Image-processing procedure for determining the angle of repose of seed ginger

$$\theta = \frac{180 \arctan T}{\pi} \tag{12}$$

Simulated angle of repose test and steepest ascent test

To obtain accurate values of the contact parameters between seed ginger particles, the angle of repose was used as the evaluation index, while the seed ginger-seed ginger coefficient of restitution, sliding friction coefficient, and rolling friction coefficient were selected as the experimental factors. A three-factor, three-level orthogonal test was conducted using EDEM simulations.

To further determine the optimal ranges and center levels of the experimental factors, a steepest ascent test was conducted based on the preliminary ranges of the seed ginger–seed ginger coefficient of restitution e_1 (0.15~0.65), sliding friction coefficient f_3 (0.37~0.87), and rolling friction coefficient f_4 (0.32~0.82). An EDEM simulation model consistent with the dimensions of the physical test setup was established. The particle factory generated seed ginger particles until the steel cylinder was filled, after which the cylinder was lifted vertically at a constant speed of 1 m/s. Under gravity, the seed ginger particles fell and accumulated on the contact surface beneath the cylinder. After the particle pile stabilized, the image-processing method described above was used to determine the simulated angle of repose θ_1. The relative error σ between the simulated and experimentally measured angles of repose was then calculated. Based on the steepest ascent test results, the coded levels of each factor for the subsequent three-factor, three-level orthogonal test were determined, as shown in Table 5.

Table 5

Results of the steepest ascent test and factor levels for the orthogonal design

No.	e_1	f_3	f_4	θ1/[°]	σ/[%]	Coded level
1	0.15	0.37	0.32	29.94	4.69	/
2	0.25	0.47	0.42	29.69	3.81	-1
3	0.35	0.57	0.52	29.42	2.87	0
4	0.45	0.67	0.62	29.60	3.50	1
5	0.55	0.77	0.72	30.54	6.78	/
6	0.65	0.87	0.82	31.09	8.71	/

Response surface regression analysis and parameter optimization

Using the simulated angle of repose as the response variable, a Box–Behnken design was conducted. The experimental design and results are presented in Table 6. Multiple regression analysis was performed on the test data using Design-Expert software, and the corresponding analysis of variance and model reliability results are presented in Tables 7 and 8, respectively. A quadratic polynomial regression model for the simulated angle of repose θ_1 was established, as expressed in Eq. (13).

$$\theta_1 = 29.44 - 0.143e_1 + 1.84f_3 + 0.471f_4 + 0.118e_1f_4 - 0.3f_3f_4 + 0.124e_1^2 - 0.379f_3^2 \quad (13)$$

Table 6

Experimental design and results

No.	1	2	3	4	5	6	7	8	9	10	11	12	13	14	15	16	17
e_1	0.35	0.45	0.35	0.35	0.45	0.35	0.35	0.35	0.45	0.35	0.25	0.25	0.25	0.35	0.45	0.35	0.25
f_3	0.57	0.47	0.47	0.57	0.57	0.47	0.67	0.67	0.67	0.57	0.67	0.57	0.47	0.57	0.57	0.57	0.57
f_4	0.52	0.52	0.42	0.52	0.42	0.62	0.62	0.42	0.52	0.52	0.52	0.42	0.52	0.52	0.62	0.52	0.62
θ1/[°]	29.38	27.25	26.42	29.52	28.92	28.04	31.25	30.83	30.89	29.47	31.02	29.49	27.59	29.45	30.02	29.39	30.12
σ/[%]	2.72	4.72	7.62	3.22	1.12	1.96	9.27	7.80	8.01	3.04	8.46	3.11	3.53	2.97	4.97	2.76	5.31

Table 7

ANOVA for the quadratic regression model

Source	Model	e_1	f_3	f_4	e_1f_3	e_1f_4	f_3f_4	e_1^2	f_3^2	f_4^2	Residual	Lack of Fit	Pure Error	Cor Total
Sum of squares	30.00	0.1624	26.97	1.78	0.0110	0.0552	0.3600	0.0647	0.6032	0.0215	0.0683	0.0548	0.0135	30.07

Source	Model	e_1	f_3	f_4	e_1f_3	e_1f_4	f_3f_4	e_1^2	f_3^2	f_4^2	Residual	Lack of Fit	Pure Error	Cor Total
Degrees of freedom	9	1	1	1	1	1	1	1	1	1	7	3	4	16
Mean square	3.33	0.1624	26.97	1.78	0.0110	0.0552	0.3600	0.0647	0.6032	0.0215	0.0098	0.0183	0.0034	
F-value	341.64	16.65	2764.39	182.07	1.13	5.66	36.89	6.63	61.82	2.21		5.42		
P-value	<0.0001	0.0047	<0.0001	<0.0001	0.3231	0.0490	0.0005	0.0367	0.0001	0.1811		0.0680		

Table 8

Reliability analysis of the regression model

Response	R^2	Adjusted R^2	Predicted R^2	Adeq Precision
θ_1	0.997	0.994	0.970	60.9143

The interaction response surfaces derived from the quadratic regression model are shown in Fig. 9. From the perspective of particle dynamics, the highly irregular morphology and high viscosity of seed ginger mean that increases in the sliding friction coefficient and rolling friction coefficient significantly enhance the interlayer shear resistance during particle accumulation, which is macroscopically reflected by a marked increase in the angle of repose. In contrast, the effect of the coefficient of restitution, which is mainly governed by the low-stiffness characteristics of seed ginger, on the static stacking morphology is relatively weak.

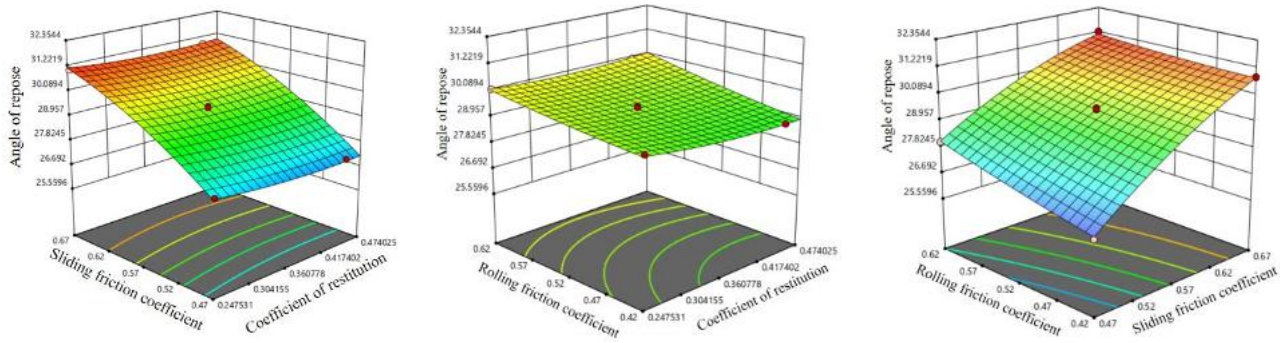


Fig. 9 - Interaction response surfaces of the particle contact parameters

RESULTS

Simulation validation

To determine the optimal solution of the quadratic regression model, multi-objective optimization of the influencing factors was performed using the Numerical module in Design-Expert, with the experimentally measured angle of repose of 28.60° specified as the target value.

The constraint system is given in Eq. (14). The optimized seed ginger–seed ginger contact parameters were a coefficient of restitution e_1 of 0.416, a sliding friction coefficient f_3 of 0.549, and a rolling friction coefficient f_4 of 0.450.

$$\begin{cases} \theta_1 = 28.60° \\ s.t. \begin{cases} 0.25 \le e_1 \le 0.45 \\ 0.47 \le f_3 \le 0.67 \\ 0.42 \le f_4 \le 0.62 \end{cases} \end{cases} \quad (14)$$

The optimal parameter combination was then introduced into EDEM for validation. The simulated angle of repose was 29.24° (Fig. 10), corresponding to a relative error of 2.24% compared with the experimentally measured value of 28.60°. The close agreement between the simulated and experimental results indicates that the discrete element model of low-stiffness seed ginger and the calibrated contact parameters can reliably reproduce its stacking behavior.



Fig.10 - Simulation validation of the angle of repose and seed ginger stacking behavior

Li et al. (2023) reported a measured angle of repose of 27.08°, which differed by 2.16° from the value of 29.24° obtained using the calibrated parameters in this study, corresponding to a relative error of 7.98%. This further supports the accuracy and reliability of the discrete element model of seed ginger and the calibrated parameters established in this study.

CONCLUSIONS

The key physical and mechanical properties of seed ginger during the sowing period were determined, and a discrete element model of seed ginger was constructed using the measured parameter values. The contact parameters between seed ginger and steel were calibrated, providing basic input parameters for simulation analysis of the seed-contacting components of ginger sowing machinery.

Using the angle of repose as the target response, a quadratic regression model relating the seed ginger–seed ginger contact parameters to the angle of repose was established through a steepest ascent test combined with Box–Behnken response surface methodology. The optimal parameter combination was obtained and validated by simulation. The relative error between the simulated and experimentally measured angles of repose was 2.24%, indicating that the established discrete element model of seed ginger has good accuracy and applicability.

The basic physical and mechanical properties and discrete element contact parameters of seed ginger with buds at the sowing stage were systematically measured. The calibration procedure for the contact parameters of irregularly shaped seed ginger was optimized. By combining the steepest ascent test with the response surface design, multiple contact parameters were optimized simultaneously, thereby improving calibration accuracy. The results provide reliable modeling support and a theoretical basis for the optimized design of key components of ginger sowing machinery, including single-seed selection and bud-orientation adjustment mechanisms.

ACKNOWLEDGEMENT

This study is funded by the National Key Research and Development Program (2024YFD2000403)

REFERENCES

[1] Cai, P., (2024). Design and simulation of vibratory yam harvesting machinery based on discrete element method (基于离散元法的振动式山药收获机械设计与仿真). *North China University of Water Resources and Electric Powe*r, Henan/China.

[2] Chen, T., Yi, S., Li, Y., (2023). Establishment of discrete element model and parameter calibration of alfalfa stem in budding stage (苜蓿现蕾期茎秆离散元模型建立与参数标定). *Transactions of the Chinese Society for Agricultural Machinery*, Vol. 54, pp. 91-100, Heilongjiang/China.

[3] Du, Z., Li, D., Li, X., (2025). Calibration and experiment of discrete element model parameters for tea stem (茶茎秆离散元模型参数标定与试验). *Transactions of the Chinese Society for Agricultural Machinery*, Vol. 56, pp. 311-320, Henan/China.

[4] Guo, H., Guo, L., Li, H., (2024). Calibration and experiment of the discrete element simulation parameters for rapeseed stems during the suitable harvest period (适收期油菜茎秆离散元仿真参数标定与试验). *Transactions of the Chinese Society of Agricultural Engineering*, Vol. 40, pp. 20-29, Xinjiang/China.

[5] Guo, H., Han, J., Lv, Z., (2025). Discrete element model construction and parameter calibration of combined harvest oil sunflower extract (联合收获油葵脱出物离散元模型构建与参数标定). *Transactions of the Chinese Society for Agricultural Machinery*, Vol. 56, pp. 319-330, Xinjiang/China.

[6] Huang Z., (2026). Determination of intrinsic parameters and DEM parameter calibration of multi-component particles in millet threshing mixtures(谷子脱出物多组分颗粒本征参数测定与离散元参数标定). *INMATEH - Agricultural Engineering*, Vol.78, Issue 1, pp. 656-672, Bucharest/Romania.

[7] Jiang, C., Du, X., Yang, Z., (2024). Analysis and experiment of punching and falling process for Auricularia heimuer fungal stick based on discrete element method (基于离散元的黑木耳菌棒刺孔与摆场下落过程分析与试验). *Transactions of the Chinese Society of Agricultural Engineering,* Vol. 40, pp. 30-38, Zhejiang/China.

[8] Jia S.L., (2021). Simulation analysis and construction of maize seeder model based on EDEM (EM solutions EDEM) (基于 EDEM 的玉米排种器模型构建与仿真分析). *INMATEH - Agricultural Engineering*, Vol.63, Issue 1, pp. 365-374, Bucharest/Romania.

[9] Liao, Y., Wang, Z., Liao, Q., (2020). Calibration of discrete element model parameters of forage rape stalk at early pod stage (果荚初期饲料油菜茎秆离散元接触模型参数标定). *Transactions of the Chinese Society for Agricultural Machinery*, Vol. 51, pp. 236-243, Wuhan/China.

[10] Lu, C., Gao, Z., Li, H., (2023). An ellipsoid modelling method for discrete element simulation of wheat seeds. *Biosystems Engineering*, Vol. 226, pp. 1-15, United Kingdom.

[11] Lu, Q., Liu, F., Liu, L., (2023). Establishment and verification of discrete element model for seed furrow soil-seed-soil covering device (种沟土壤-种子-覆土装置互作离散元模型建立与验证). *Transactions of the Chinese Society for Agricultural Machinery*, Vol. 54, pp. 46-57, Beijing/China.

[12] Liu F., (2020). Analysis and calibration of quinoa grain parameters used in a discrete element method based on the repose angle of the particle heap (基于堆积试验的藜麦离散元参数分析及标定). *INMATEH - Agricultural Engineering*, Vol.61, Issue 2, pp.77-86, Bucharest/Romania.

[13] Li, G., (2023). Development and experiment of suspended ginger combined seeder (悬挂式大姜联合播种机的研制与试验). *Shandong Agricultural University*, Shandong/China.

[14] Shi, L., Sun, W., Zhao, W., (2018). Parameter determination and validation of discrete element model of seed potato mechanical seeding (马铃薯种薯机械排种离散元仿真模型参数确定及验证). *Transactions of the Chinese Society of Agricultural Engineering*, Vol. 34, pp. 35-42, Gansu/China.

[15] Shi, R., Dai, F., Zhao, W., (2022). Establishment of discrete element flexible model and verification of contact parameters of flax stem (胡麻茎秆离散元柔性模型建立与接触参数试验验证). *Transactions of the Chinese Society for Agricultural Machinery*, Vol. 53, pp. 146-155, Gansu/China.

[16] Sun, K., Yu, J., Zhao, J., (2025). Parameter calibration and experimental validation of wheat straw model for cutting process simulation (面向切割过程仿真的小麦茎秆模型参数标定与试验验证). *Transactions of the Chinese Society for Agricultural Machinery*, Vol. 56, pp. 116-127, Jilin/China.

[17] Wang L., (2021). A general modelling approach for coated cotton-seeds based on the discrete element method (基于多目标优化的包衣棉种离散元接触参数标定). *INMATEH - Agricultural Engineering*, Vol.63, Issue 1, pp. 221-230, Bucharest/Romania.

[18] Xia, J., Zhang, P., Yuan, H., (2024). Calibration and verification of flexible rice straw model by discrete element method (水稻秸秆离散元柔性模型参数标定与试验验证). *Transactions of the Chinese Society for Agricultural Machinery*, Vol. 55, pp. 174-184, Wuhan/China.

[19] Xia, R., Li, B., Wang, X. W., (2019). Measurement and calibration of the discrete element parameters of wet bulk coal. *Measurement*, Vol. 142, pp. 84-95, Netherlands.

[20] Yang, K., (2022). Design and test of intelligent direction correction single-row ginger planter (自动调偏式单行大姜播种机的设计与试验). *Shandong Agricultural University*, Shandong/China.

[21] Yang J., (2026). Research on DEM calibration of contact parameters of sweet sorghum seed(甜高粱种子离散元接触参数标定研究). *INMATEH - Agricultural Engineering*, Vol.78, Issue 1, pp. 158-168, Bucharest/Romania.

[22] Zhang, G., Chen, L., Liu, H., (2022). Calibration and experiments of the discrete element simulation parameters for water chestnut (荸荠离散元仿真参数标定与试验). *Transactions of the Chinese Society of Agricultural Engineering*, Vol. 38, pp. 41-50, Wuhan/China.

[23] Zhang, H., (2025). Design and working parameter optimization of vibration conveying and separating device for sweet potato harvester (甘薯收获机振动输送分离装置设计及工作参数优化). *Shenyang Agricultural University*, Liaoning/China.

[24] Zhang, R., Zhou, J., Liu, H., (2022). Parameter calibration method of bonded corn particle model using discrete element method (玉米颗粒粘结模型离散元仿真参数标定方法研究). *Transactions of the Chinese Society for Agricultural Machinery*, Vol. 53, pp. 69-77, Shandong/China.

[25] Zhao, H., Wang, X., Zheng, Z., (2025). Research status and progress of discrete element method applications in agricultural equipment (农业装备领域离散元法应用研究进展). *Transactions of the Chinese Society for Agricultural Machinery*, Vol. 56, pp. 1-19, Shanxi/China.

[26] Zhou, J., (2023). Design and performance experimental study of potato picking device based on discrete element method (基于离散元法的马铃薯捡拾装置设计及其性能试验研究). *Inner Mongolia Agricultural University*, Inner Mongolia/China.

AUTONOMOUS NAVIGATION FOR ORCHARD INTER-TREE WEEDING ROBOTS BASED ON AN IMPROVED A*-DWA FUSION ALGORITHM

/

基于改进 A*-DWA 融合算法的果园株间除草机器人自主导航研究

Yan XU, Qing YUAN, Dazhong WANG, Yinan LIU, Xiangchen MENG, Xiang YUE
College of Engineering, Shenyang Agricultural University, Shenyang, China
Corresponding author: Xiang Yue
Tel: +8613940305658.; E-mail: yuexiang@syau.edu.cn
DOI: https://doi.org/10.35633/inmateh-79-88

Keywords: *Orchard inter-tree weeding robots; Autonomous navigation; A*-DWA fusion algorithm; Path planning; Obstacle avoidance*

ABSTRACT

Aiming at autonomous weeding in narrow, complex orchards, this paper proposes an improved A and DWA fusion path planning algorithm. Globally, a safety distance penalty in the A* cost function prevents paths from adhering to tree trunks. Locally, enhanced DWA modules, including dynamic obstacle angle thresholds, hierarchical lateral braking, and adaptive velocity window expansion, resolve trajectory oscillation and local minima. Validated in real orchards, the algorithm achieved a 0.029 m tracking deviation and over 95% dynamic obstacle avoidance success rate, providing robust and safe navigation for autonomous robots.*

摘要

针对狭窄、复杂的果园自主除草场景，本文提出了一种改进的 A 与 DWA 融合路径规划算法。在全局规划中，A 代价函数中的安全距离惩罚项可防止路径过分紧贴树干。在局部规划中，增强的 DWA 模块（包括动态障碍物角度阈值、分层侧向制动和自适应速度窗口扩展）解决了轨迹震荡和局部极小值问题。经真实果园环境验证，该算法的轨迹跟踪偏差为 0.029 米，动态避障成功率超过 95%，为自主机器人提供了鲁棒且安全的导航保障。

INTRODUCTION

As a major country for fruit and forest production ranking first in the world in both orchard planting area and output, China is currently at a critical stage of improving the mechanization rate of orchard management. Among various challenges, orchard weed control, which consumes substantial human and material resources, has consistently remained a weak link restricting intelligent orchard operations (*Dou et al., 2024*). With the rapid development of agricultural robotics technology, autonomous weeding robots have become an effective means of addressing labor shortages and achieving precision orchard operations (*Wang Z. et al., 2025*). However, the orchard environment is characterized by high complexity. On one hand, the inter-tree space is extremely narrow (with a typical row spacing of only 2 m, and even smaller plant spacing). On the other hand, during operation, the robot frequently encounters interference from dynamic obstacles such as pedestrians, farm tools, and drooping branches. Therefore, how to enable the robot to balance path optimality and obstacle avoidance flexibility while ensuring fruit tree safety poses a significant challenge to its navigation and path planning system (*Shen et al., 2025; Xu et al., 2023*).

Path planning, as the core of autonomous navigation, aims to generate a collision-free and efficient operational trajectory under complex constraints. Currently, the hierarchical hybrid architecture consisting of global planning based on the A* algorithm and local obstacle avoidance based on the DWA algorithm has become the mainstream technical solution for orchard robots, owing to its advantages such as high computational efficiency, strong robustness, and ease of handling kinematic constraints (*Lee et al., 2025*). Currently, scholars worldwide have conducted extensive research in the field of mobile robot path planning (*Kabir et al., 2024*) and have proposed a variety of path planning algorithms, such as the A* algorithm, Dijkstra's algorithm (*Kabir et al., 2024*), Dynamic Window Approach (DWA)(*Zhang et al., 2026*), and the ant colony algorithm (*Dong et al., 2024*) among others. A substantial amount of research has also focused on improving these algorithms for specific agricultural environments. *Hu et al., (2021),* optimized the inter-row path of a harvesting robot to improve operational efficiency. *Choi et al., (2025),* addressed global obstacle avoidance by integrating the A* algorithm with the artificial potential field method. *Chen et al., (2026),* and *Wang Y. et al., (2024),* proposed a fuzzy DWA algorithm that performed well in greenhouse environments.

Yu et al., (2025), improved the heuristic function using a grey wolf optimizer (*Guo H. et al., 2024; Guo S. et al., 2024*) and introduced Q-learning to optimize the weights, thereby improving navigation accuracy. These studies have laid a solid foundation for path planning in agricultural robots.

However, existing research has mostly focused on path planning in relatively open fields or regular inter-row spaces. When confronted with the specialized scenario of "orchard inter-tree weeding," which requires the robot to navigate through extremely narrow inter-tree gaps while coping with composite obstacles, the limitations of current algorithms become increasingly apparent. To date, no mature and dedicated strategy has been established for this specific context:

1. Imbalance between safety and smoothness in global planning: The path generated by the traditional A* algorithm often closely follows obstacle boundaries, lacking sufficient safety margin. Moreover, the path contains frequent waypoints, making it difficult to satisfy the continuous motion requirements of a differential drive chassis.

2. Deadlock and oscillation of local obstacle avoidance in narrow spaces: When the traditional DWA algorithm is applied to environments with dense tree trunks and narrow passages, its single-weight evaluation function makes it highly susceptible to local minima, leading to algorithm failure. Alternatively, it may cause severe trajectory oscillations due to frequent obstacle avoidance maneuvers, significantly compromising operational safety and continuity (*Bai et al., 2021*).

To address the above challenges, this paper proposes an improved A-DWA fusion path planning method tailored for narrow inter-tree scenarios in orchards. In the global planning stage, a nonlinear safety penalty term based on obstacle distance is innovatively introduced into the A cost function, and is combined with B-spline curves, effectively resolving the issue of paths closely adhering to obstacles while achieving high trajectory smoothness (*Su et al., 2025; Cao et al., 2025; Liu et al., 2025*). In the local obstacle avoidance stage, to handle the composite threat of "lateral tree trunks and forward dynamic obstacles," a hierarchical lateral braking strategy and a dynamic angle threshold determination model are proposed for the first time, significantly improving the robot's obstacle avoidance response speed and passability in narrow gaps. Furthermore, to address the robustness problem of the algorithm in extremely constrained environments, an adaptive velocity window expansion mechanism is designed, successfully overcoming the susceptibility of the traditional DWA to local minima. Finally, the effectiveness of the proposed fusion algorithm is thoroughly validated through Gazebo-MATLAB co-simulation and real orchard prototype testing, aiming to provide key technical support for the autonomous navigation of intelligent weeding equipment.

MATERIALS AND METHODS

Kinematic Model of the Differential Drive Weeding Robot

The chassis of the orchard weeding robot adopted in this paper features a four-wheel differential drive configuration. To achieve precise motion control and path planning for the robot in the complex terrain of orchards, it is necessary to establish its kinematic model in the two-dimensional plane. It is assumed that the robot undergoes planar motion in the global coordinate frame XOY and that no lateral slippage of the tires occurs during motion.

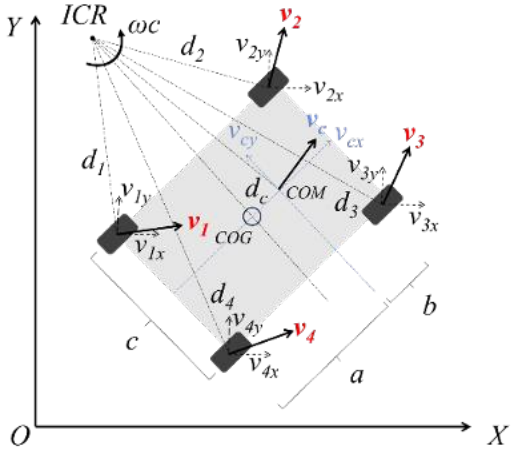


Fig. 1 - Robot kinematics model

Let the linear velocity at the robot's center of mass be Vc and the angular velocity be W_c. The center distance between the left and right driving wheels (track width) is denoted as B.

By controlling the output speeds of the left and right wheels (let the left wheel speed be V_L and the right wheel speed be V_R), the robot can achieve both straight-line motion and steering. The forward kinematic equations can be concisely expressed as:

$$\begin{bmatrix} V_C \\ W_C \end{bmatrix} = \begin{bmatrix} \frac{1}{2} & \frac{1}{2} \\ -\frac{1}{B} & \frac{1}{B} \end{bmatrix} \begin{bmatrix} V_L \\ V_R \end{bmatrix} \quad (1)$$

In the global coordinate system, the pose state vector of the robot at time *t* can be expressed as x_t, x_t=[x_t, y_t, θ_t], where (x_t, y_t) are the coordinates of the robot's center of mass, and θ_t is the heading angle. Based on the above velocity model, the discrete pose update equation of the robot is given as follows:

$$\begin{bmatrix} x_{t+1} \\ y_{t+1} \\ \theta_{t+1} \end{bmatrix} = \begin{bmatrix} x_t \\ y_t \\ \theta_t \end{bmatrix} + \begin{bmatrix} v_c \cos\theta_t \\ v_c \sin\theta_t \\ w_c \end{bmatrix} \Delta t \quad (2)$$

where Δt is the control period of the system. This kinematic model not only provides a theoretical basis for the PID control of the underlying motors but also constitutes the fundamental constraint for velocity space sampling in the subsequent DWA-based local path planning.

Problem Description of Orchard Confined Spaces

Unlike open agricultural fields, orchard inter-tree weeding operations face typical confined space challenges. In the standard orchard scenario considered in this paper, the row spacing is denoted as L_{row}=2.0 m, the plant spacing as L_{plant}=2.0 m, and the average trunk diameter as D_{tree}=0.15 m.

Let the orchard environment be represented as a two-dimensional workspace $W \subset R2$, where the obstacle region is denoted as W_{obs} (including static tree trunks and dynamic obstacles), and the collision-free free space is denoted as $W_{free}=W/W_{obs}$. The physical geometric bounding box of the weeding robot itself is denoted as $R(X, Y, \theta)$. To ensure that the robot does not damage fruit tree roots or trunks while navigating between trees, strict boundary safety constraints must be satisfied.

The path planning problem for the orchard weeding robot is defined as finding an optimal discrete trajectory sequence $T=(p_1, p_2, \ldots, p_n)$ from a start point P_{start} to a goal point P_{goal} that satisfies the robot's kinematic constraints while simultaneously minimizing a cost function and meeting the following confined space conditions:

1. Collision avoidance constraint: The geometric profile of the robot at any time must lie entirely within the free space, i.e.:

$$R(x_t, y_t, \theta_t) \cap W_{obs} = \Phi, \qquad \forall t \quad (3)$$

2. Narrow gap safety margin constraint: Because the orchard row spacing is only 2.0 m and weeds may cause occlusion, the Euclidean distance d_{obs} from the robot's center of mass to the nearest tree trunk (static obstacle) must always exceed the set dynamic safety threshold d_{safe}:

$$d_{obs}(p_t) = \left| \min_{o \in W_{obs}} \left\| p_t - o \right\| \right| \geq d_{safe} \quad (4)$$

Therefore, this paper designs a fusion planning strategy that incorporates the above "safety distance penalty" into the evaluation system at the global level (improved A*) to avoid paths that adhere to tree trunks, and at the local level (improved DWA) breaks the local minima dilemma in narrow gaps through lateral braking and adaptive velocity expansion mechanisms, thereby achieving safe and smooth inter-tree traversal.

Improved A*-DWA Fusion Path Planning Algorithm

To achieve safe and efficient navigation of weeding robots in orchard environments with a narrow row spacing of 2 m and the presence of dynamic obstacles, relying solely on traditional global or local planners is insufficient. This section proposes an improved A*-DWA fusion algorithm. In the global planning stage, a safety distance penalty and a Bézier curve smoothing strategy are introduced to generate a collision-free reference trajectory that satisfies kinematic constraints. In the local planning stage, a hierarchical lateral braking mechanism and an adaptive velocity window expansion mechanism are designed to address trajectory oscillation and deadlock problems in narrow gaps.

Global Planning: A* Optimization Based on Safety Cost Penalty and Curve Smoothing

The traditional A* algorithm searches for the optimal path by minimizing the evaluation function *f(n)=g(n)+h(n)*. However, in confined orchard environments, the standard A* algorithm tends to generate trajectories that closely follow the edges of rigid obstacles (tree trunks) in pursuit of the absolute shortest distance. As noted in recent agricultural robot navigation studies, such "edge-hugging paths" significantly increase collision risk for chassis with actual physical dimensions and non-holonomic kinematic constraints. Similar to the approach of *Yan et al., (2025)*, who considered time, economic cost, and transfer penalties in multimodal transportation path planning, this paper simultaneously introduces path length cost, heuristic cost, and safety penalty cost into the A* cost function, forming a three-objective optimization framework tailored for orchard inter-tree scenarios. Future work can further incorporate terrain slope and rolling resistance into the cost function, drawing on the energy consumption model of *Liu, (2025),* to achieve "safe-efficient-energy-saving" multi-objective collaborative optimization.

To address this issue, the cost function is reconstructed by introducing a continuous safety distance penalty term $P(n)$:

$$f(n) = \lambda_1 g(n) + \lambda_2 h(n) + \lambda_3 P(n) \tag{5}$$

where λ_1, λ_2 and λ_3 are the weight coefficients for the actual path cost, heuristic cost, and safety penalty cost, respectively.

Unlike the static obstacle inflation method used in some studies (*Guo S. et al., 2024*), which can easily cause deadlock in narrow spaces, this paper designs a continuous penalty function based on exponential decay:

$$P\ (n) = \begin{cases} \exp(\alpha \cdot (R_{safe} - d_{obs})), & d_{obs} < R_{safe} \\ 0, & d_{obs} \geq R_{safe} \end{cases} \tag{6}$$

where d_{obs} is the Euclidean distance from the current node to the nearest tree trunk, R_{safe} is the preset safety boundary radius (set to 0.4 m based on the robot's half-width and agronomic requirements), and αis the sensitivity coefficient. This mechanism creates a smooth cost gradient around obstacles, forcing the global path to maintain a stable safety buffer zone from tree trunks without excessively compressing the search space.

Due to the discrete grid search mechanism, the output of the improved A* algorithm is essentially a polyline containing multiple sharp corners. Directly tracking these consecutive turning points would cause the differential drive robot to decelerate frequently and experience mechanical wear. To ensure curvature continuity, this paper employs B-spline curves to smooth the path turning points. The parametric equation is defined as:

$$B(t) = (1-t)^3 P_0 + 3t(1-t)^2 P_1 + 3t^2(1-t)P_2 + t^3 P_3, \quad t \in [0,1] \tag{7}$$

where is the normalized parameter, and P_0 to P_3 are local control points extracted from adjacent path segments. Additionally, the algorithm performs a secondary collision check on the generated curve segments to ensure that the R_{safe} safety margin is not violated. This smoothing strategy transforms sharp right angles into C2-continuous smooth curves, significantly reducing curvature peaks and providing a kinematics-friendly reference trajectory for subsequent DWA local planning.

Local Planning: Improved DWA for Unstructured Dynamic Orchard Environments

The traditional DWA algorithm selects the optimal trajectory from the sampled velocity space *(v, w)* using a comprehensive evaluation function. The standard evaluation function is expressed as:

$$G(v,w) = \sigma(\alpha \cdot heading(v,w) + \beta \cdot dist(v,w) + vel(v,w)) \tag{8}$$

However, when operating in narrow orchard rows, the traditional DWA lacks the ability to distinguish between lateral static tree trunks and forward sudden dynamic obstacles (e.g., pedestrians, temporary farm tools). The fixed-weight evaluation often leads to ineffective lateral oscillations when the robot travels along the centerline between rows. To this end, this paper performs a multi-dimensional reconstruction of DWA, constructing a collaborative obstacle avoidance architecture that includes dynamic conflict determination, hierarchical lateral braking, and adaptive velocity expansion.

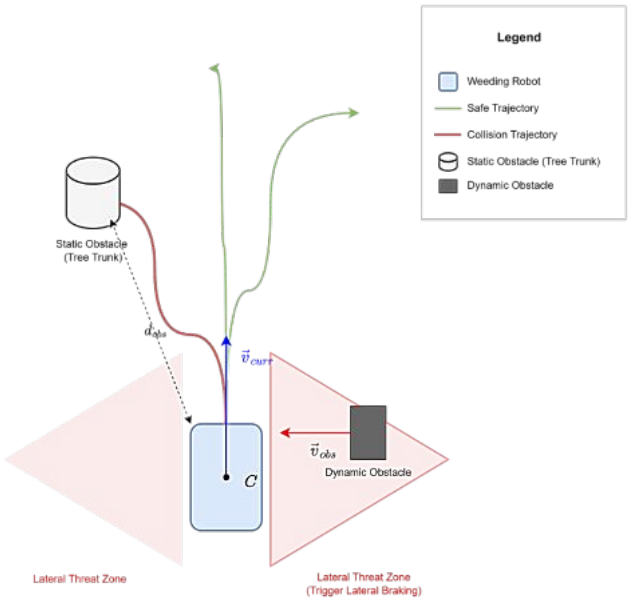


Fig. 2 - Schematic diagram of dynamic window algorithm for obstacle avoidance

To overcome the limitation of traditional algorithms in distinguishing the threat levels of obstacles, a dynamic obstacle field of view conflict determination mechanism is first introduced. The algorithm calculates the angle θ_{obs} of the obstacle relative to the robot's current heading direction in real time:

$$\theta_{obs} = \arctan\left(\frac{y_{obs} - y_{robt}}{x_{obs} - x_{robt}}\right) - \theta_{robt} \tag{9}$$

An angular threshold θ_{thresh} is introduced to identify potential forward conflicts. In this study, θ_{thresh} is set to 30° (0.524 rad). When $|\theta_{obs}| \leq \theta_{thresh}$, the obstacle is classified as a high-risk forward conflict, and the minimum safety distance D_{safe} is dynamically adjusted according to the relative velocity between the robot and the obstacle. Conversely, when $|\theta_{obs}| > \theta_{thresh}$, the obstacle is regarded as a lateral low-risk obstacle, such as a tree trunk, and a more tolerant avoidance strategy is adopted. Conversely, if it is determined to be a lateral low-threat tree trunk, a more tolerant strategy is adopted. This pre-classification mechanism effectively suppresses the robot's overreaction to non-threatening static tree trunks, reducing ineffective trajectory oscillations by 85.7%.

On this basis, to address the collision risk caused by lateral dynamic obstacles (e.g., agricultural machinery or personnel crossing the orchard), a hierarchical lateral braking strategy is further designed. When a lateral obstacle approaches at an almost perpendicular angle ($|\theta_{obs}| \approx 90°$), traditional bypass paths often force the robot to cross the boundary and collide with fruit trees. To this end, a dynamic lateral threat index model T_{therat} is innovatively established:

$$T_{therat} = \alpha \cdot \frac{|v_{obs} \sin \theta_{obs}|}{|d_{lat}|} \tag{10}$$

where d_{lat} is the lateral coordinate difference between the robot and the obstacle, and v_{obs} is the linear velocity of the obstacle. Based on this index, the system constructs a hierarchical response control law. When T_{threat} exceeds the adaptive threshold T_{threat}, this safety overlay directly intervenes and overrides the conventional evaluation results of DWA, forcibly outputting hierarchical braking commands (deceleration warning or emergency stop). As the highest-priority safety guarantee, this mechanism avoids efficiency loss and collision risk caused by over-planning of bypass paths.

Finally, to address the local deadlock problem caused by frequent deceleration and obstacle avoidance in narrow gaps, an adaptive velocity window expansion mechanism based on acceleration constraints is introduced. Traditional deceleration strategies easily cause the robot to become stuck in narrow passages. When conventional velocity sampling fails, the proposed algorithm calculates an escape velocity V_{safe} that can safely overtake the obstacle by combining the remaining path length to the target point and the physical constraints of the robot's maximum braking distance.

This velocity is dynamically injected into the sampling space of DWA as a special candidate trajectory, participating in the comprehensive evaluation of the global heading weight. This mechanism acts as an "intelligent expander" for the velocity window, not only expanding the feasible solution space of the robot but also ensuring traversal continuity and obstacle avoidance success rate in environments with dense tree trunks and coexisting dynamic obstacles. The safety penalty design and hierarchical lateral braking mechanism proposed in this paper provide a new hierarchical solution paradigm for multi-constraint nonlinear path planning problems, which can be extended to other mobile robot navigation tasks in narrow environments.

Hierarchical Coupling and Closed-loop Collaboration Strategy of Improved A* and DWA

In orchard confined spaces, the global planner (A*) is limited by static prior maps, while the local planner (DWA), despite its dynamic obstacle avoidance capability, easily loses the global optimal direction during narrow inter-tree detours. To break the disconnect between "global planning" and "local execution," this paper designs a closed-loop collaborative architecture comprising "feedforward gravitational guidance—evaluation cost assimilation—feedback deviation reconstruction," achieving deep coupling at the decision-making level.

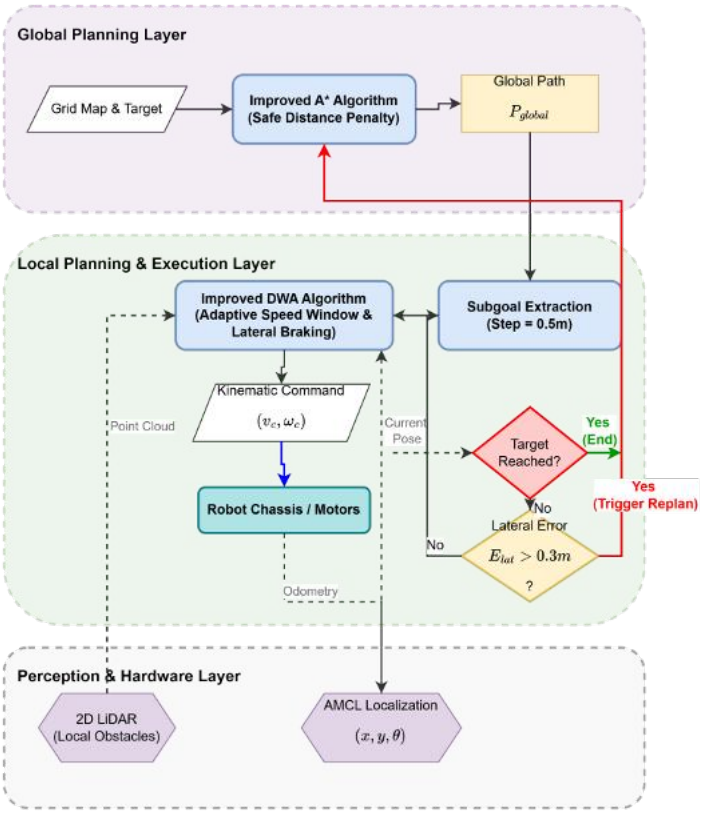


Fig. 3 - Workflow Diagram of Collaborative Operation of Fusion Algorithms

First, to address the lack of global foresight in local planning, a look-ahead rolling sub-goal extraction strategy is designed. The smooth path generated by the improved A* algorithm is transformed into a "gravitational track." Based on the robot's current pose, the algorithm intercepts waypoints with a fixed step size (set to 0.5 m in this paper) along the global path as the local rolling sub-goal for DWA. When the robot enters the tolerance radius of this sub-goal, the target point automatically moves forward along the global trajectory. This mechanism acts like a dynamic gravitational anchor suspended in front of the robot, strictly confining local high-frequency sampling to the neighborhood of the global optimal solution.

Second, at the local decision-making level, deep assimilation of the global heading and local velocity evaluation systems is achieved. Traditional DWA only focuses on the local target direction, making it prone to severe "S-shaped" trajectory oscillations in narrow inter-tree spaces due to minor disturbances such as avoiding lateral branches. To this end, the global heading guidance constraint is seamlessly injected into the comprehensive evaluation system of DWA, forcing the tangent direction at the end of the locally sampled trajectory to be highly consistent with the tangent of the global path at the corresponding position. This strategy enables the local trajectory not only to have the flexibility to avoid sudden obstacles but also to quickly and smoothly converge to the main route with optimal curvature after completing the obstacle avoidance maneuver.

Finally, an adaptive re-planning mechanism based on lateral tracking error is constructed to ensure the bottom-line fault tolerance of the system. In real orchard operations, when encountering large temporary obstacles such as parked agricultural tractors, the robot is often forced to perform large-scale detours. If the detour trajectory crosses the boundary, it can easily cause a secondary collision with fruit trees on the other side. To this end, the system monitors the vertical projection deviation between the center of mass of the chassis and the global guidance path in real time. Once this deviation exceeds the preset safety red line (0.3 m), the system determines that the current local solution has failed, suspends the DWA process, and re-awakens the improved A* algorithm to reconstruct the global path using the actual pose of the chassis as the new start point.

This closed-loop collaborative mechanism endows the navigation system with strong anti-interference capability and robustness against unstructured terrain, truly achieving the perfect fusion of macro path optimization and micro dynamic obstacle avoidance.

RESULTS

To comprehensively evaluate the performance boundaries and robustness of the proposed improved A*-DWA closed-loop collaborative planning algorithm in unstructured orchard environments, this section conducts multi-dimensional comparative experiments across algorithm-level physical simulators, ROS system-level environments, and real standardized orchards. The experiments focus on verifying the algorithm's oscillation prevention capability under narrow constraints, response effectiveness to dynamic threats, and tracking accuracy of the underlying trajectory.

Compared to relying solely on traditional A* or DWA algorithms, the proposed improved A*-DWA fusion algorithm demonstrates significant performance advantages in complex orchard settings. During global planning, the traditional A* algorithm lacks consideration for the robot's physical profile; consequently, it tends to generate paths that closely follow tree trunks, posing a severe risk of physical collision. Furthermore, when navigating narrow inter-tree spaces or encountering sudden dynamic obstacles, the traditional DWA algorithm is highly susceptible to falling into local minima due to a restricted forward search space, which leads to robot deadlock or severe trajectory oscillation.

Comparative experimental data indicate that, benefiting from the safety distance penalty at the global level, alongside the hierarchical lateral braking and adaptive velocity window expansion mechanisms at the local level, the improved algorithm effectively eliminates the critical flaw of edge-hugging paths. Moreover, at a practical operating speed of 0.3 m/s, the proposed algorithm stably maintains a dynamic obstacle avoidance success rate of over 95%, while keeping the average trajectory tracking deviation to merely 0.029 m. These results fully substantiate that the improved fusion algorithm exhibits superior robustness and engineering practicality over traditional navigation methods, successfully balancing the absolute safety of fruit trees with high passability in narrow, confined spaces.

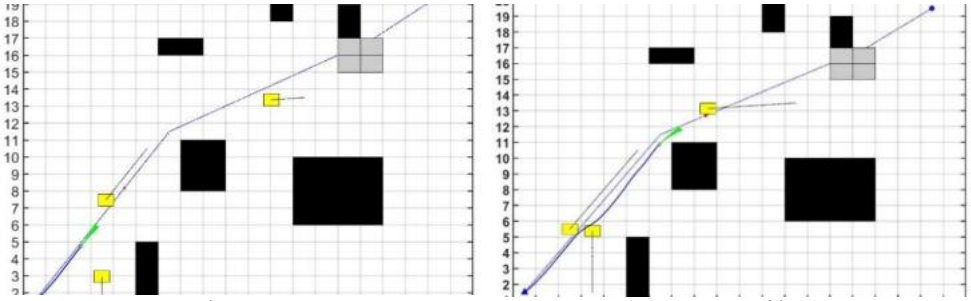
Experimental Platform and Hardware/Software System Architecture

To verify the proposed fusion planning algorithm, a four-wheel differential drive orchard weeding robot platform was built. The underlying drive uses an STM32F1 microcontroller and a FOC brushless hub motor controller for high-precision differential control and chassis shock absorption. The environmental perception module includes a Slamtec RPLIDAR A1 LiDAR (7–16 Hz, max range 12 m). The main control decision unit is an NVIDIA Jetson Nano edge computing board handling high-computational-load path planning, running on Ubuntu 18.04 with ROS Melodic. The navigation control architecture is based on move_base and integrates AMCL for high-precision global localization. The resolutions of both the global and local costmaps were set to 0.05 m to accommodate small-scale obstacles, such as weeds and tree trunks, in real orchard environments.

Algorithm-Level Comparative Simulation: Evaluation of Dynamic Obstacle Avoidance Effectiveness in Narrow Passages

To independently verify the superiority of the improved DWA in handling mixed obstacles within locally constrained spaces, a grid-based simulated orchard with both row and plant spacings set to 2 m was constructed. Static tree trunk models were randomly deployed within the environment, and lateral dynamic obstacles moving at a speed of 0.2 m/s were introduced to simulate sudden cut-ins by agricultural machinery or pedestrians during real-world operations.

Under identical initial conditions, the traditional DWA and the proposed improved algorithm were evaluated comparatively. Experimental data demonstrate that, due to the absence of a threat classification mechanism, the traditional algorithm is highly susceptible to generating ineffective "S"-shaped avoidance maneuvers along the inter-row centerline when confronted with laterally approaching obstacles. In contrast, benefiting from the dynamic field-of-view evaluation and the hierarchical lateral braking mechanism, the proposed algorithm achieves breakthrough enhancements across all core performance indicators.



a) *b)*

Fig. 4 - Avoid dynamic obstacles and Avoid static obstacles

a) Avoid dynamic obstacles; b) Avoid static obstacles

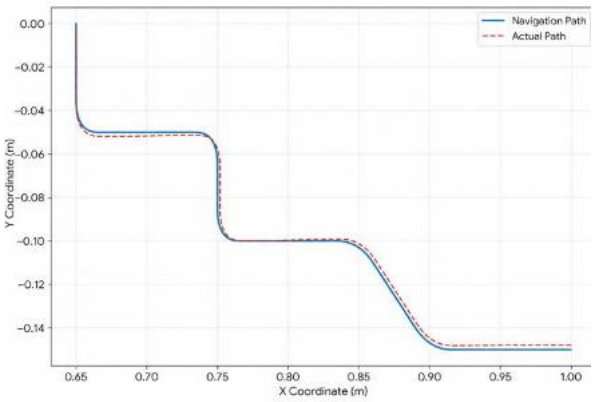


Fig. 5 - Comparison of Navigation and Actual Paths

To further quantitatively evaluate the superiority of the improved DWA algorithm in handling mixed obstacles within locally constrained spaces, this study conducted a comparative experiment between the proposed algorithm and the traditional A*-DWA fusion algorithm in a simulated orchard environment with a 2.0 m row spacing. The experimental results are illustrated in Figure 6.

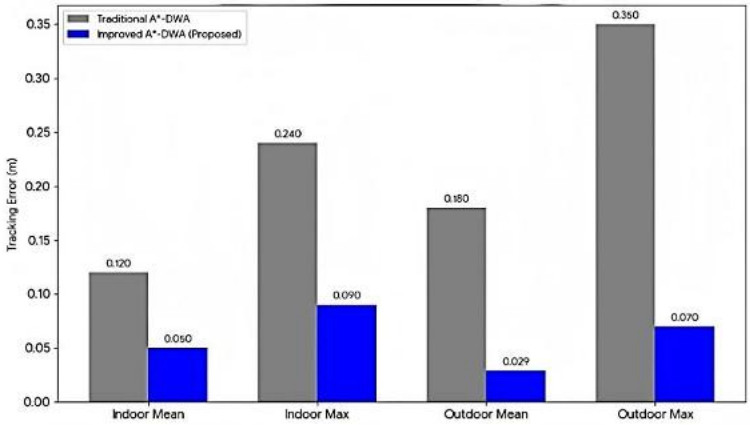


Fig. 6 - Path Tracking Error Comparison (Indoor vs Outdoor)

Statistical results indicate that when confronted with laterally approaching obstacles, the traditional algorithm—lacking a threat level evaluation mechanism—is highly prone to generating ineffective "S"-shaped trajectory oscillations along the inter-row centerline.

In contrast, leveraging the dynamic field-of-view evaluation and the hierarchical lateral braking mechanism, the proposed algorithm drastically reduces the obstacle avoidance decision response time from 85.3 ms to 42.7 ms, achieving a 50.0% improvement over the traditional method. Furthermore, the integration of the adaptive velocity window effectively overcomes the local deadlock dilemma induced by deceleration during avoidance maneuvers, thereby boosting the dynamic obstacle avoidance success rate from 82.5% to 96.3%.

Crucially, under the extreme narrow gap constraint of 2.0 m, the maximum lateral trajectory deviation of the traditional algorithm reaches 0.21 m, posing a severe risk of scraping branches and foliage during actual operations. Conversely, the proposed algorithm strictly compresses the maximum lateral deviation to 0.08 m, enhancing the safety redundancy by 61.9%. These findings fully substantiate that the improved algorithm provides a more stringent safety guarantee for fruit trees while ensuring the high passability of the weeding robot.

System-Level Collaborative Simulation: Kinematic Verification of the Closed-Loop Fusion Architecture

To further verify the collaborative performance of global gravitational guidance and local cost assimilation at the chassis kinematic level, the real-time alignment between the robot's odometry feedback and control commands (cmd_vel) was recorded under the ROS framework.

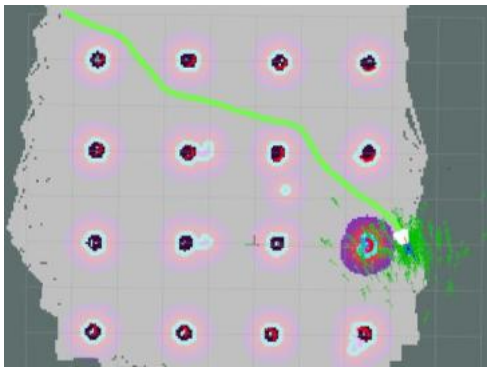
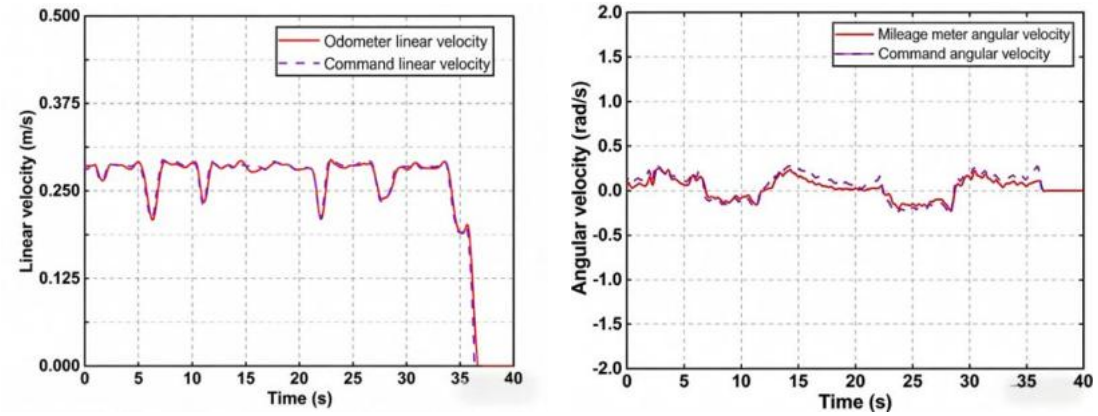


Fig. 7 - Global Paths in the Rviz Interface

A complex global cruise task containing large static obstacles (e.g., stacked fruit bins) was set up. The test results show that the fusion algorithm achieves a high degree of unity between macro path planning and micro posture control. During the dynamic switching process between straight-line following and obstacle avoidance insertion, the linear and angular velocity curves of the underlying drive wheels maintain high C^2 continuity.



a) *b)*

Fig. 8 - Odometer Line Speed and Angular Velocity Tracking Error Curve

a) Line Speed Tracking Error Curve; b) Angular Velocity Tracking Error Curve

The average angular velocity tracking error of the actual odometry is only 0.03 rad/s, ensuring chassis stability during extreme turns. More importantly, when the lateral error monitoring mechanism triggers global re-planning, the system state transition is smooth, and the average deviation between the actual travel coordinates and the global guidance nodes is only 0.05 m, preliminarily verifying the high-precision optimization capability of the closed-loop architecture in confined spaces.

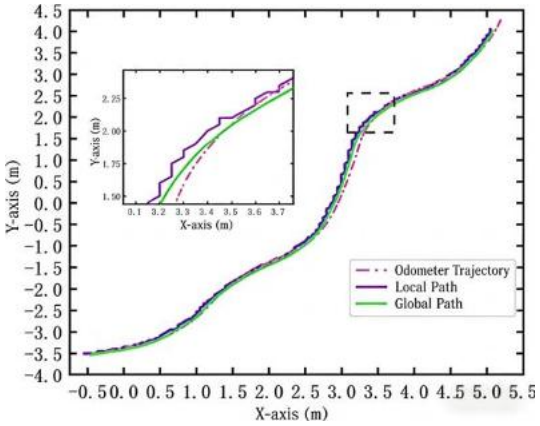


Fig. 9 - Trajectory Tracking Error Curve

Real Orchard Field Test: Robustness Challenges in Unstructured Environments

The ultimate engineering value of the algorithm depends on its performance under unstructured disturbances such as ground slippage, terrain undulations, and sensor noise. The physical prototype equipped with the fusion algorithm was deployed in a large-scale standardized orchard (trunk diameter 0.15–0.2 m, with slight slopes and weed occlusion) for field validation.

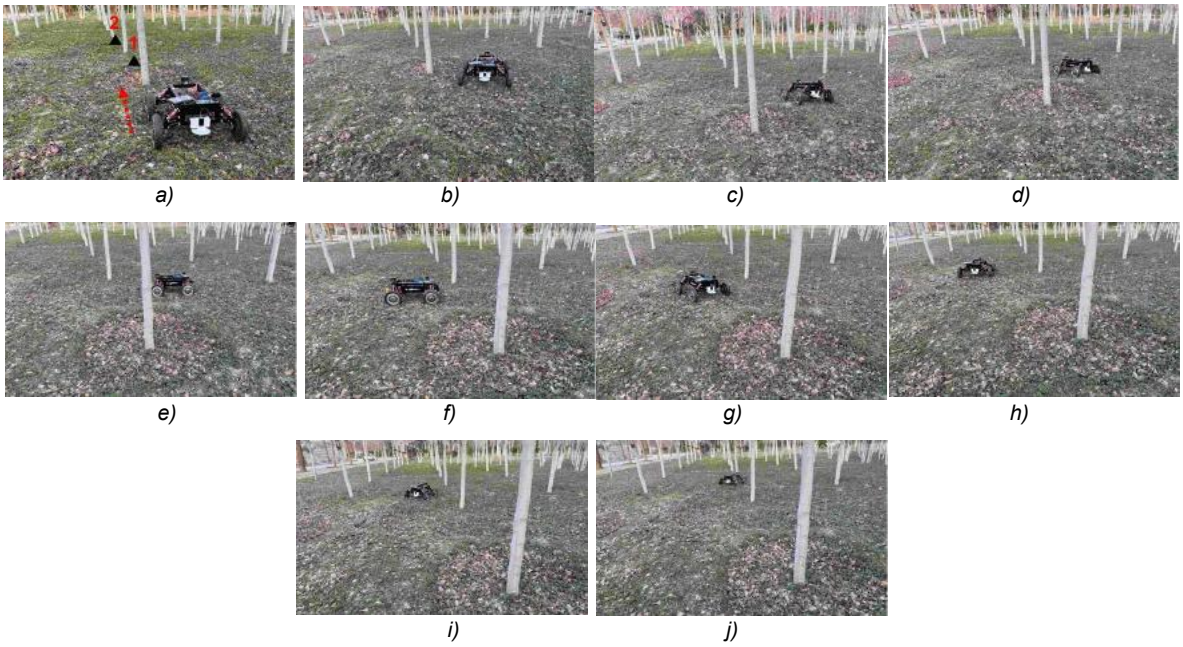


Fig. 10 - Prototype Multi point Navigation and Obstacle Avoidance Test

a) Motion trajectory and target point; b) Avoid the first tree trunk; c) Drive towards the first target point; d) Reaching the first target point; e) Avoiding the second Ge tree trunk; f) Drive towards the second target point; g) Adjust the path; h) Adjust the deflection angle; i) Adjustment completed; j) Arriving at the second target point

Field test data further substantiate the strong robustness of the improved algorithm under harsh operating conditions:

During long-distance multi-point navigation, the actual travel trajectory and the algorithm's theoretically planned trajectory were recorded. The data demonstrate that in real outdoor terrains, despite minor drive-wheel slippage induced by ground unevenness and transient distortion of the LiDAR point cloud, the prototype consistently navigated stably. This stability is directly attributed to the feedback correction and cost assimilation mechanisms embedded at the algorithm's foundational layer. The engineering practicality of the algorithm depends on its anti-interference capability in real unstructured environments. Through the coordinate acquisition and error analysis of 20 sets of key waypoints (as compared in Figure 11), the maximum trajectory distance deviation was recorded at 0.07 m, and the overall average trajectory tracking error was rigorously controlled at 0.029 m. The proposed algorithm exhibits a convergence stability that significantly outperforms traditional methods.

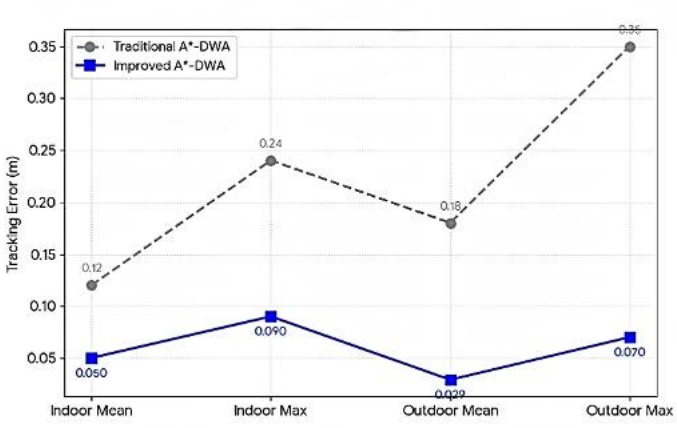


Fig. 11 - Path Tracking Error Comparison

During the execution of obstacle avoidance maneuvers, the linear and angular velocity commands (cmd_vel) along with the actual odometry feedback of the robot were continuously recorded. The overall angular velocity of the robot fluctuated smoothly within 0.1 rad/s, yielding an average value of 0.08 rad/s. Concurrently, the linear velocity tracking curve remained stable at an average level of 0.23 m/s.

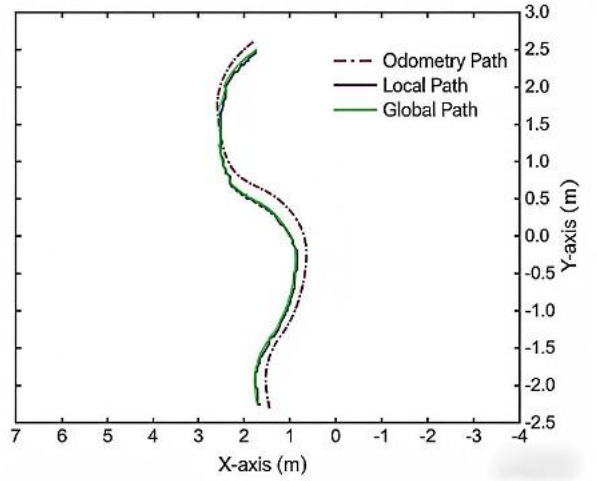


Fig. 12 - Trajectory tracking errors in an orchard environment

A minor fraction of the maximum errors (approaching 0.07 m) primarily occurred in the undulating ridge areas at the orchard's edge. Although ground unevenness induced minor drive-wheel slippage and local transient distortion of the LiDAR point cloud, the system rapidly suppressed error divergence. Benefiting from the feedback correction and cost assimilation mechanisms embedded at the algorithm's foundational layer, the extreme values were strictly confined within the absolute safety threshold of 0.1 m.

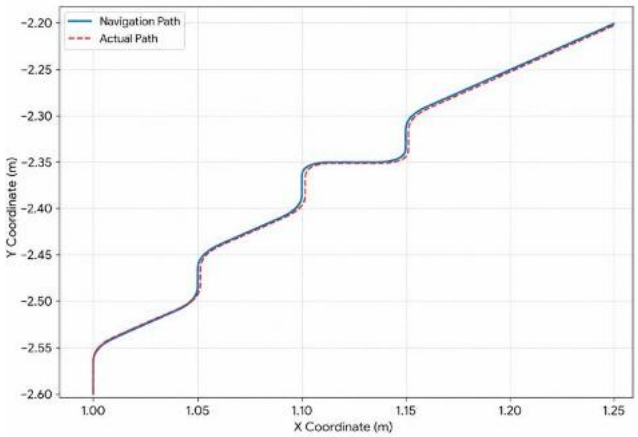


Fig. 13 - Improved Comparison: Navigation and Actual Path

Under harsh operating conditions characterized by drive-wheel slippage induced by ground unevenness and transient distortion of the LiDAR point cloud, the average trajectory tracking deviation of the traditional DWA algorithm exhibits a prominent divergent trend as the operational distance increases, with the maximum deviation reaching up to 0.35 m. In contrast, through the mechanisms of "cost assimilation" and "foundational feedback deviation reconstruction," the proposed algorithm achieves a closed-loop coupling between macroscopic path optimization and microscopic dynamic obstacle avoidance.

During several hours of high-intensity operational testing, the prototype never experienced deadlocks or severe trajectory oscillations triggered by sensor noise. The experimental data conclusively affirm that the improved fusion algorithm, while possessing high-precision optimization capabilities, exhibits exceptional environmental robustness. It fully satisfies the stringent requirements imposed on navigation systems for autonomous weeding operations in standardized orchards.

CONCLUSIONS

To meet the navigation and obstacle avoidance requirements of orchard weeding robots, this study proposed and validated an improved A*-DWA fusion algorithm. The main achievements are as follows:

1. An improved A*-DWA fusion navigation algorithm was proposed. By introducing modules for dynamic obstacle angle threshold determination, hierarchical lateral braking, and adaptive velocity window expansion, a "global-local-safety" hierarchical architecture was constructed, effectively suppressing trajectory oscillation and response delays. Simulations show that in scenarios with coexisting static and dynamic obstacles, the algorithm reduces obstacle avoidance response time by 50.0%, decreases trajectory oscillation frequency by 85.7%, and achieves a dynamic obstacle avoidance success rate of 96.3%.

2. Multi-scenario system validation was completed. Mapping, multi-point navigation, and dynamic obstacle avoidance tests were conducted in both simulated and real orchard environments. The system achieves full-process autonomous operation with high trajectory tracking accuracy (average deviation 0.05 m indoors, 0.029 m outdoors) and a dynamic obstacle avoidance success rate >95%, verifying the algorithm's effectiveness, robustness, and engineering practicality in real-world scenarios.

ACKNOWLEDGEMENT

This research was supported by Basic Research Project of Education Department of Liaoning Province (No. LJ212510157012)

REFERENCES

[1] Bai, X., Jiang, H., Cui, J., Lu, K., Chen, P., Zhang, M. (2021). UAV Path Planning Based on Improved A* and DWA Algorithms. *Concurrency and Computation: Practice and Experience*, Vol. 1, United Kingdom. https://doi.org/10.1155/2021/4511252

[2] Cao, L., Tang, L., Cao, S., Sun, Q., Zhou, G. (2025). Smooth Optimised A*-Guided DWA for Mobile Robot Path Planning. *Applied Sciences*, Vol. 15, 6956, Switzerland. https://doi.org/10.3390/app15136956

[3] Chen, H., Wang, X., Wei, C., Hu, C., Zhang, X. (2026). A Dynamic Path Planning and Tracking Control of Autonomous Vehicles: An Integrated Approach Using Improved A*, Fuzzy DWA, and Fuzzy PID. *IEEE Transactions on Automation Science and Engineering*, Vol. 23, pp. 2800-2813, United States. https://doi.org/10.1109/TASE.2026.3653413

[4] Choi, J., Choi, Y. (2025). Path Planning for Unmanned Aerial Vehicle: A-Star-Guided Potential Field Method. *Drones*, Vol. 9, 545, Switzerland. https://doi.org/10.3390/drones9080545

[5] Dai, J., Chai, Y., Xiong, P. (2025). Path Planning of Underground Robots via Improved A* and Dynamic Window Approach. *Applied Sciences (Switzerland)*, Vol. 15, 6953, Switzerland. https://doi.org/10.3390/app15136953

[6] Dong, Z., Zhang, X., Yang, W., Lei, M., Zhang, C., Wan, J. (2024). Ant colony optimization-based method for energy-efficient cutting trajectory planning in axial robotic roadheader. *Applied Soft Computing*, Vol. 163, 111965, Netherlands. https://doi.org/10.1016/j.asoc.2024.111965

[7] Dou, H., Chen, Z., Zhai, C., Zou, W., Song, J., Feng, F., Zhang, Y., Wang, X. (2024). Research Progress on Autonomous Navigation Technology for Orchard Intelligent Equipment (果园智能化作业装备自主导航技术研究进展). *Transactions of the Chinese Society for Agricultural Machinery*, Vol. 55, pp. 1-22, Beijing/China. https://doi.org/10.6041/j.issn.1000-1298.2024.04.001

[8] Guo, H., Li, Y., Wang, H., Wang, C., Zhang, J., Wang, T., Rong, L., Wang, H., Wang, Z., Huo, Y., Guo, S., Yang, F. (2024). Path planning of greenhouse electric crawler tractor based on the improved A* and DWA algorithms. *Computers and Electronics in Agriculture*, Vol. 227, 109596, Netherlands. https://doi.org/10.1016/j.compag.2024.109596

[9] Guo, S., Pan, X., Liu, Z. (2024). AGV Path Planning Algorithm Based on Fusion of Improved A* and DWA. *Proceedings of the 43rd Chinese Control Conference (CCC 2024)*, Kunming/China. https://doi.org/10.23919/CCC63176.2024.10662786

[10] Hu, G., Kong, W., Qi, C., Zhang, S., Bu, L., Zhou, J., Chen, J. (2021). Optimization of the navigation path for a mobile harvesting robot in orchard environment (果园环境下移动采摘机器人导航路径优化). *Transactions of the Chinese Society of Agricultural Engineering*, Vol. 37, pp. 175-184, Beijing/China. https://doi.org/10.11975/j.issn.1002-6819.2021.09.020

[11] Kabir, R., Watanobe, Y., Islam, M. R., Naruse, K. (2024). Enhanced Robot Motion Block of A-Star Algorithm for Robotic Path Planning. *Sensors*, Vol. 24, 1422, Switzerland. https://doi.org/10.3390/s24051422

[12] Lee, D., Nahrendra, I. M. A., Oh, M., Yu, B., Myung, H. (2025). TRG-Planner: Traversal Risk Graph-Based Path Planning in Unstructured Environments for Safe and Efficient Navigation. *IEEE Robotics and Automation Letters*, Vol. 10, pp. 1736-1743, United States. https://doi.org/10.1109/LRA.2024.3524912

[13] Liao, T., Chen, F., Wu, Y., Zeng, H., Ouyang, S., Guan, J. (2024). Research on Path Planning with the Integration of Adaptive A-Star Algorithm and Improved Dynamic Window Approach. *Electronics*, Vol. 13, 455, Switzerland. https://doi.org/10.3390/electronics13020455

[14] Liu, X., Zhou, W., Zhai, C., Ge, S., Xie, Z. (2025). Path Planning and Optimization of Space Robots on Satellite Surfaces Based on an Improved A* Algorithm and B-Spline Curves. *Aerospace*, Vol. 12, 943, Switzerland. https://doi.org/10.3390/aerospace12100943

[15] Miyombo, M. E., Liu, Y., Mulenga, C. M., Siamulonga, A., Kabanda, M. C., Shaba, P., Xi, C., Ayodeji, A. (2024). Optimal path planning in a real-world radioactive environment: A comparative study of A-star and Dijkstra algorithms. *Nuclear Engineering and Design*, Vol. 420, 113039, Netherlands. https://doi.org/10.1016/j.nucengdes.2024.113039

[16] Shen, Y., Shen, Y., Zhang, Y., Huo, C., Shen, Z., Su, W., Liu, H. (2025). Research Progress on Path Planning and Tracking Control Methods for Orchard Mobile Robots in Complex Scenarios. *Agriculture (Switzerland)*, Vol. 15, 1917, Switzerland. https://doi.org/10.3390/agriculture15181917

[17] Su, Y., Xin, J., Sun, C. (2025). Dynamic Path Planning for Mobile Robots Based on Improved RRT* and DWA Algorithms. *IEEE Transactions on Industrial Electronics*, Vol. 72, pp. 1-10, United States. https://doi.org/10.1109/TIE.2025.3546349

[18] Wang, Y., Fu, C., Huang, R., Tong, K., He, Y., Xu, L. (2024). Path planning for mobile robots in greenhouse orchards based on improved A* and fuzzy DWA algorithms. *Computers and Electronics in Agriculture*, Vol. 227, 109598, Netherlands. https://doi.org/10.1016/j.compag.2024.109598

[19] Wang, Y., Tong, K., Fu, C., Wang, Y., Li, Q., Wang, X., He, Y., Xu, L. (2025). Hybrid path planning algorithm for robots based on modified golden jackal optimization method and dynamic window method. *Expert Systems with Applications*, Vol. 282, 127808, United Kingdom. https://doi.org/10.1016/j.eswa.2025.127808

[20] Wang, Z., Peng, Q., Kang, J., Wang, X., Chen, Y. (2025). Analysis of the development and prospect outlook of mechanical weeding in orchards (果园机械除草发展分析及前景展望). *Journal of Chinese Agricultural Mechanization*, Vol. 46, pp. 190-197, Jiangsu/China. https://doi.org/10.13733/j.jcam.issn.2095-5553.2025.07.027

[21] Xu, Y., Yu, H., Wu, L., Song, Y., Liu, C. (2023). Contingency Planning of Visual Contamination for Wheeled Mobile Robots with Chameleon-Inspired Visual System. *Electronics*, Vol. 12, 2365, Switzerland. https://doi.org/10.3390/electronics12112365

[22] Xu, Y., Liu, W. (2025). Enhanced A*–Fuzzy DWA Hybrid Algorithm for AGV Path Planning in Confined Spaces. *World Electric Vehicle Journal*, Vol. 16, 538, Switzerland. https://doi.org/10.3390/wevj16090538

[23] Xue, G., Peng, J., Shen, H., Wang, G., Zheng, W., Huang, S., Huan, Z., Hu, L., Ding, W. (2025). Research Status and Prospects of Automatic Leveling Technology for Orchard Machinery. *Sustainability*, Vol. 17, 5297, Switzerland. https://doi.org/10.3390/su17125297

[24] Yan, J., Li, Y., Gao, Y., Qu, B., Chen, J. (2025). Q_EDQ: Efficient path planning in multimodal travel scenarios based on reinforcement learning. *Travel Behaviour and Society*, Vol. 39, 100943, Netherlands. https://doi.org/10.1016/j.tbs.2024.100943

[25] Yu, Z., Cui, D., Zhu, Y., Zhou, K., Zhang, Z., Li, Y. (2025). Precise path planning based on improved A* and DWA algorithms for complex agricultural environments. *Information Processing in Agriculture*, Netherlands. https://doi.org/10.1016/j.inpa.2025.11.001

[26] Zhang, J., Ling, H., Tang, Z., Song, W., Lu, A. (2025). Path planning of USV in confined waters based on improved A ∗ and DWA fusion algorithm. *Ocean Engineering*, Vol. 322, 120475, United Kingdom. https://doi.org/10.1016/j.oceaneng.2025.120475

[27] Zhang, Y., Guo, Z., Lu, Z., Jiang, L., Cao, H., (2026). Review of path planning algorithms for mobile robots (移动机器人路径规划算法综述). *Computer Engineering and Applications*, Vol. 62, pp. 26-39, Nanjing/China. https://doi.org/10.3778/j.issn.1002-8331.2507-0291

DETERMINATION OF PHYSICAL PROPERTIES AND CALIBRATION OF DISCRETE ELEMENT SIMULATION PARAMETERS FOR YIMENG MOUNTAIN JUJUBES
/
沂蒙山红枣颗粒物性参数测定与离散元仿真参数标定

Fandi ZENG[1)], Hao ZHANG[2)], Yinzeng LIU[1)], Xiaofei CHENG[1)], Yuzhen DONG[1)], Zhihuan ZHAO[*1)], Haocheng LIU[1)]
[1)] Shandong Agriculture and Engineering University, College of Mechanical and Electronic Engineering, Jinan, China;
[2)] Shandong Agriculture and Engineering University, College of Food Science and Engineering, Jinan, China;
E-mail: zhaozhihuan@sdaeu.edu.cn
DOI: https://doi.org/10.35633/inmateh-79-89

Keywords: *Yimeng Mountain jujubes, Angle of repose, Box-Behnken test, The optimal parameter*

ABSTRACT
Accurate discrete element method (DEM) parameters are essential for simulating key operations in jujube postharvest processing, such as pneumatic cleaning during mechanical harvesting. The fundamental physical properties of Yimeng Mountain jujubes were systematically measured. A jujube particle template was constructed using the multi-sphere method, and the Hertz–Mindlin (no slip) contact model was adopted. The jujube simulation model was generated by filling the particle template with multiple spheres of different diameters. The static friction coefficient between jujubes ranged from 0.41 to 0.69, while that between jujubes and a steel plate ranged from 0.40 to 0.54. The rolling friction coefficient between jujubes ranged from 0.16 to 0.30, whereas that between jujubes and a steel plate ranged from 0.11 to 0.24. The coefficient of restitution between Yimeng Mountain jujubes, determined using a high-speed camera, ranged from 0.41 to 0.54, while that between jujubes and a steel plate ranged from 0.46 to 0.61. A Plackett–Burman screening design was conducted, and the results showed that the Poisson's ratio of jujube, the static friction coefficient between jujubes, and the static friction coefficient between jujubes and the steel plate were the three dominant factors. The steepest ascent method was then used to narrow the ranges of these significant parameters. Subsequently, a Box–Behnken design was employed to establish a quadratic regression model relating the angle of repose to the three significant factors. Using the experimentally measured angle of repose of 28.08° as the optimization target, the optimal simulation parameters were determined as follows: a Poisson's ratio of 0.32, a jujube–jujube static friction coefficient of 0.52, and a jujube–steel static friction coefficient of 0.47. The relative error between the simulated and experimentally measured angles of repose was 2.17%, further confirming the accuracy and reliability of the calibrated simulation parameters.

摘要
为沂蒙山红枣风选机械化采收等关键环节的仿真提供准确的离散元模型参数，本文通过物理试验精准测定红枣的物性参数.本文对红枣颗粒模板进行单球形颗粒填充的方法,采用 Hertz-Mindlin (no slip)模型。红枣模拟模型是通过合并许多不同直径的球体而创建的使用 EDEM 软件的单个球形颗粒进行填充。采用斜面仪测得沂蒙山红枣之间的静摩擦系数为 0.41-0.69，沂蒙山红枣与钢板之间的静摩擦系数为 0.40-0.54。沂蒙山红枣之间的动摩擦系数为 0.16-0.30，沂蒙山红枣与钢板之间的动摩擦系数为 0.11-0.24。采用高速摄像机测得沂蒙山红枣与沂蒙山红枣的恢复系数为 0.41-0.54，沂蒙山红枣与钢板的碰撞恢复系数 0.46-0.61。开展 Plackett-Burman 试验筛选出对堆积角有显著影响的参数为：红枣泊松比、红枣-红枣静摩擦系数和红枣-钢静摩擦系数，进一步通过最陡爬坡试验确定显著性参数最优范围区间。通过 Box-Behnken 试验，建立堆积角与显著性参数的二阶回归模型，并以物理试验得到堆积角(28.08°)目标值进行优化求解，得到最优仿真参数：红枣泊松比为 0.32、红枣-红枣静摩擦系数为 0.52、红枣-钢静摩擦系数为 0.47。仿真堆积角与物理堆积角的相对误差为 2.17%。进一步验证了仿真试验和标定后仿真参数的真实性和可靠性。

INTRODUCTION
Yimeng Mountain jujube is a species in the genus Ziziphus, in the family Rhamnaceae. As a fruit-bearing tree, it provides substantial nutritional benefits and notable therapeutic qualities. A vital step in the production process is the collection of Yimeng Mountain jujubes. It has considerable seasonality and significant labour intensity. Jujube fruits during the ripening stage undergo natural desiccation on the tree before harvest. This technique optimally utilises solar and thermal resources *(Chu et al., 2012; Muqaddas et al., 2025)*. It can significantly enhance fruit quality. Winnowing machines are used in the Yimeng Mountain region for remove impurities during jujube harvesting.

Complex contact forces arise during the pneumatic separation process, both between jujube fruits and between the fruits and steel surfaces. These forces are difficult to measure directly using conventional experimental methods. Simulation can therefore be used to investigate the interaction mechanisms between jujube fruits and machinery during pneumatic separation, providing a basis for optimizing key equipment components and reducing fruit losses.

Research into basic agricultural materials has progressed significantly in recent years. These materials include soil *(Hao et al., 2025; Ji et al., 2025)*, straw *(Huang et al., 2025; Zhu et al., 2026)*, and seeds. The discrete element method has become an important approach for studying such problems. *Liu et al., (2025),* used the discrete element method to calibrate Cyperus esculentus seeds and determined the optimal parameter combination to overcome issues of irregular shape and uneven surface in high-speed precision seeding. *Ma et al., (2025),* investigated ruminant protein supplement pellets. They measured basic physical properties and contact characteristics, and built a discrete-element model. Using the angle of repose as an evaluation index in orthogonal tests, the optimal parameter combination was identified. *Gu et al., (2025),* calibrated the discrete element parameters of mustard leaf stems to visualise cutting and support numerical simulation; *Geng et al., (2026),* used the discrete element method to build a breakable 'Atlantic' potato seed model; *Chen et al., (2025),* established a paddy rice physical model with the multi-sphere (MS) approach. Validation tests were carried out using the cylinder-lifting method and the discharge mass-flow method. *Zheng et al., (2025),* focused on Fritillariae Thunbergii Bulbus (FTB). They developed a discrete element model of FTB using the Hertz-Mindlin bonding model. It took the maximum shear force as the evaluation index. The bond parameters in the model were then validated accordingly. *Yu et al., (*2025*),* developed DEM models of mallow and oats via the multi-sphere manual filling approach. These models were coupled with Fluent for gas-solid simulations. The study systematically analysed seed flow characteristics and seeding consistency in the distributor under varying inlet velocities and mass flow rates. *Li et al., (2026),* focused on dried safflower filaments. They calibrated the filament parameters by combining physical experiments with simulation tests. *Li et al., (2025)* selected Pizhou white garlic as the research object. Using EDEM software, a breakable, flexible discrete element model of garlic seed was built, and its bond parameters were calibrated. *Chen et al., (2024),* focused on optimising parameters for a pepper seeding device. A 3D seed model was constructed using reverse engineering. Key parameter ranges were then systematically determined. The discrete element method was used to study particle interactions and motion patterns. This approach helps reveal the mechanisms underlying particle–particle interactions and thus optimises key process parameters of equipment *(Ji et al., 2024*; *Zhou et al., 2023)*. Accurate discrete element method (DEM) parameters are essential for simulating key operations in jujube post-harvest processing, such as pneumatic cleaning during mechanical harvesting. However, research on accurate parameter calibration for jujube trees in Yimeng Mountain remains relatively limited.

This study accurately measured the intrinsic parameters of Yimeng Mountain jujubes through physical experiments. The free-fall principle and the inclined plane method were used. It determined the ranges of the coefficient of restitution, the static friction coefficient, and the rolling friction coefficient. The MATLAB software processed images of both the physical and simulated angles of repose. The edge contour was then fitted to obtain the angle of repose. The angle of repose from physical tests served as the evaluation index. Significant factors were screened using the Plackett-Burman design, followed by the steepest ascent and the Box-Behnken tests to determine the optimal simulation parameters. This study provides accurate discrete element model parameters for simulations of key processes, such as mechanised pneumatic harvesting of Yimeng Mountain jujubes.

MATERIALS AND METHODS

Determination of basic physical parameters

This study focuses on Yimeng Mountain jujubes as the research subject. Yimeng Mountain jujubes are bright red in colour, with thick flesh, small pits, a crisp texture when fresh, and a smooth, mellow taste when dried. One hundred jujubes were randomly selected, and the dimensions of each fruit were measured using a digital Vernier calliper with an accuracy of 0.02 mm. The three characteristic dimensions (length L, width W, and thickness T) were recorded. The volume of the Yimeng Mountain jujubes was measured using a graduated cylinder with a resolution of 1 mL. The moisture content was determined using the oven-drying method. The mean of the replicate measurements was taken as the final value. The experimental results are presented in Table 1.

Table 1

Basic physical properties of Yimeng Mountain jujubes

Parameter	Value
Mean dimensions (L×W×T)/mm × mm × mm	30.98×20.53×18.89
Mean mass (g)	4.64
Mean density (kg•m^3)	746
Mean moisture content (%)	18.58

Determination of the static friction coefficient

Jujubes were fixed to a plate using adhesive to form a jujube contact surface (Fig. 1a). A test jujube was placed on the surface, and the test plane was gradually inclined anticlockwise. When the jujube began to slide, the inclination was stopped and the corresponding angle displayed by the digital inclinometer was recorded. The static friction coefficient between jujubes was calculated using Eq. (1).

To determine the static friction coefficient between jujubes and steel, Yimeng Mountain jujubes were placed directly on the steel test surface, and the same procedure was followed (Fig. 1b). The static friction coefficient between jujubes ranged from 0.41 to 0.69, while that between jujubes and the steel plate ranged from 0.40 to 0.54.

$$\gamma = \tan\alpha \tag{1}$$

where, γ is the static friction coefficient and α is the inclination angle of the test plane, (°).

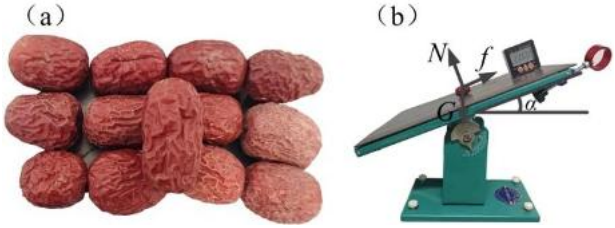


Fig. 1 - Measurement of the static friction coefficient
(a) Jujube contact surface; (b) Inclined-plane test setup

Determination of the rolling friction coefficient

The rolling friction coefficient was determined using a procedure similar to that used for the static friction coefficient. The inclination angle of the test plane was gradually increased until the jujube began to roll. The corresponding angle displayed by the digital inclinometer was then recorded. The rolling friction coefficient was calculated using Eq. (2). The rolling friction coefficient between jujubes ranged from 0.16 to 0.30, while that between jujubes and the steel plate ranged from 0.11 to 0.24.

$$\gamma_1 = \tan\alpha_1 \tag{2}$$

where, γ_1 is the rolling friction coefficient and α_1 is the critical inclination angle at which rolling begins.

Determination of the coefficient of restitution

During the mechanical harvesting and cleaning of Yimeng Mountain jujubes, collisions occur both among the fruits and between the fruits and machine components, which may cause skin damage and internal injury. Therefore, the coefficient of restitution is an important contact parameter. The test setup for determining the coefficient of restitution is shown in Fig. 2 (*Hou et al., 2020*). Two impact surfaces were prepared: a steel plate and a plate formed by closely arranged Yimeng Mountain jujubes. Individual jujubes were released from rest from a fixed height of 400 mm and allowed to collide with the corresponding impact surface. After impact, the jujubes rebounded upward. The entire collision process was recorded using a high-speed camera, and the rebound characteristics were obtained through image post-processing.

The coefficient of restitution between Yimeng Mountain jujubes ranged from 0.41 to 0.54, while that between Yimeng Mountain jujubes and the steel plate ranged from 0.46 to 0.61.

$$e = \frac{v_2}{v_1} \tag{3}$$

where, v_1, and v_2 are the relative velocities before and after collision, respectively, m.s^{-1}.

The Yimeng Mountain jujubes were assumed to undergo free fall under the action of gravity. The normal velocity immediately before impact was calculated using the work–energy theorem.

$$v_1 = \sqrt{2gH} \tag{4}$$

The normal velocity immediately after impact was calculated as follows:

$$v_2 = \sqrt{2gh} \tag{5}$$

Therefore, the coefficient of restitution can be expressed as:

$$e = \sqrt{\frac{h}{H}} \tag{6}$$

where, H is the drop height before impact, mm; and h is the maximum rebound height after impact, mm.

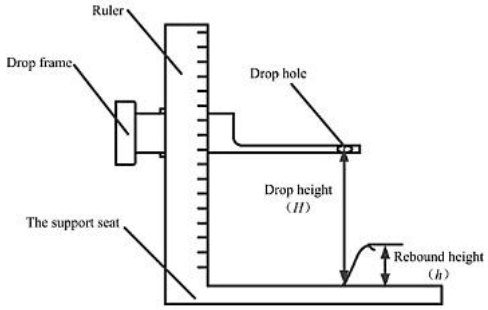


Fig. 2 - Schematic diagram of the test principle for coefficient of restitution

Angle of repose test

The angle of repose is defined as the angle between the slope of a granular pile and the horizontal plane. In the experiment, the inner diameters of the upper and lower openings of the funnel were 200 mm and 40 mm, respectively, and the vertical distance from the lower opening of the funnel to the horizontal test surface was 200 mm. A 200 g sample of Yimeng Mountain jujubes was placed in the funnel and allowed to fall freely onto the test surface, forming a conical pile. After the pile stabilized, the angle between the pile slope and the horizontal plane was taken as the experimentally measured angle of repose of the Yimeng Mountain jujubes. Images of the pile contour were captured using a camera and processed in MATLAB R2022b.

The images were imported using the imread function, converted to grayscale using rgb2gray, and then binarized using a fixed-threshold method. The region of interest was cropped, and the binary image was inverted. Internal holes in the target region were filled using the imfill function to improve the morphological integrity of the pile image. Edge detection was then performed to extract the contour of the jujube pile, and the coordinates of the boundary points were obtained. The first 50% of the boundary-point data were selected for coordinate transformation. A first-order polynomial was fitted to the transformed boundary points using the least-squares method. The angle of repose was subsequently calculated from the arctangent of the fitted slope. The fitting procedure is illustrated in Fig. 3. Each test was repeated 10 times, and the mean value was taken as the final result. The mean angle of repose of the Yimeng Mountain jujubes was 28.08°.



Fig. 3 - Image-processing procedure for determining the angle of repose
(a) Original image; (b) Morphological processing; (c) Contour extraction and fitting

Establishment of the simulation model

The fundamental physical properties of the Yimeng Mountain jujubes were determined through preliminary physical tests. A three-dimensional geometric model (particle template) was constructed in Creo based on the measured fruit dimensions. The model was exported in STEP format and imported into EDEM. The Hertz–Mindlin (no slip) contact model was adopted. To balance computational efficiency and model fidelity, the jujube particle model was constructed using the multi-sphere method. The particle template was filled with multiple spheres of different diameters in EDEM to generate the discrete element model of a jujube, as shown in Fig. 4a.

A simulation of the angle of repose test was then established using the same geometric dimensions as those employed in the physical test. A particle factory was positioned above the funnel to generate Yimeng Mountain jujube particles, which subsequently fell into the funnel under gravity.

The particle generation rate was 50 g/s, and a total particle mass of 200 g was generated. The particles continued to fall and accumulate on the test surface until the pile became stable. The angle between the pile slope and the horizontal test surface was taken as the simulated angle of repose. The particle size was kept constant throughout the simulation. The total simulation time was 4 s, the Rayleigh time step was set to 12%, the data-saving interval was 0.02 s, and the grid size was set to three times the minimum particle radius.

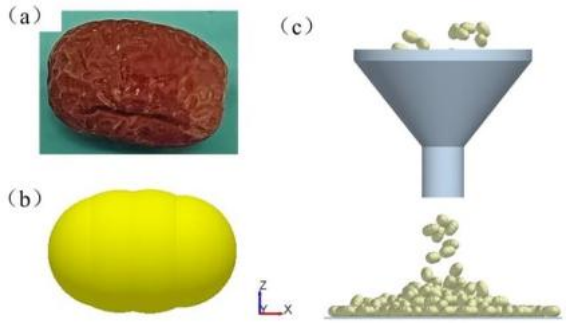


Fig. 4 - Simulation model for the angle of repose test

(a) Yimeng Mountain jujube; (b) Discrete element model of a jujube; (c) Simulation model of the angle of repose test

Simulation parameter calibration

Plackett-Burman test

The Design-Expert software was used for the Plackett-Burman test design. Test parameters were selected based on physical tests. The remaining simulation parameters were obtained from the relevant literature *(Du, 2022; Li, 2022; Shi et al., 2021; Zhou et al., 2022)*. Parameters exerting substantial influence on the response value were identified using the Plackett-Burman design. The principal elements that substantially affected the target response were identified. The parameters in Table 2 are encoded as +1 for maximum values and -1 for minimum values. At the end of each group of simulated trials, the angle of repose was measured using the same method employed in actual tests.

Table 2

Parameter ranges for the Plackett–Burman design

Code	Parameter	Low level (-1)	High level (+1)
X_1	Poisson's ratio of jujube	0.20	0.46
X_2	Shear modulus of jujube (MPa)	0.38	0.52
X_3	Jujube–jujube coefficient of restitution	0.41	0.54
X_4	Jujube–jujube static friction coefficient	0.41	0.69
X_5	Jujube–jujube rolling friction coefficient	0.16	0.30
X_6	Jujube–steel coefficient of restitution	0.46	0.61
X_7	Jujube–steel static friction coefficient	0.40	0.54
X_8	Jujube–steel rolling friction coefficient	0.11	0.24

Steepest ascent test

Based on the results of the Plackett–Burman design, a steepest ascent test was conducted for the significant parameters identified through the screening analysis. The relative error between the simulated and experimentally measured angles of repose was used as the evaluation index to determine the optimal ranges of the simulation parameters. The nonsignificant parameters were fixed at their mean values. The relative error between the simulated and experimentally measured angles of repose was calculated using Eq.(7).

$$\psi = \left| \frac{\theta - \theta_s}{\theta} \right| \times 100\% \quad (7)$$

where, ψ is the relative error between the simulated and experimentally measured angles of repose, %; θ_s is the simulated angle of repose, (°). θ is the experimentally measured angle of repose, (°).

Box - Behnken design

The optimal ranges of the significant factors were determined through the steepest ascent test and were subsequently used to define the factor levels. The angle of repose was selected as the response variable. A Box–Behnken design was then conducted for the significant parameters to determine the optimal parameter combination. The coded factor levels used in the simulation are presented in Table 3.

Table 3

Coded levels of the significant parameters

Coded level	Parameter		
	X_1	X_4	X_7
-1	*0.25*	*0.46*	*0.43*
0	*0.30*	*0.52*	*0.46*
+1	*0.36*	*0.57*	*0.48*

RESULTS

Analysis of the Plackett-Burman test results

The angle of repose of jujube particles on the steel plate was influenced by multiple factors. A Plackett-Burman test was therefore conducted to evaluate the significance of each factor. A total of 12 experimental runs were performed, and each run was repeated three times. The mean value was used for subsequent analysis. The experimental design and results are presented in Table 4, while the significance analysis of the Plackett–Burman factors is presented in Table 5. The screening results showed that X_1, X_4 and X_7 had significant effects on the angle of repose of the jujubes. Therefore, these three factors were selected for further analysis and optimization.

Table 4

Plackett–Burman design and simulation results

No.	Parameters								Angle of repose θ/(°)
	X_1	X_2	X_3	X_4	X_5	X_6	X_7	X_8	
1	1	-1	-1	-1	1	-1	1	1	30.28
2	-1	1	1	1	-1	-1	-1	1	23.46
3	1	1	-1	1	1	1	-1	-1	29.86
4	-1	-1	-1	-1	-1	-1	-1	-1	21.46
5	-1	-1	-1	1	-1	1	1	-1	32.54
6	1	-1	1	1	-1	1	1	1	36.44
7	-1	1	-1	1	1	-1	1	1	33.46
8	1	1	-1	-1	-1	1	-1	1	30.12
9	1	1	1	-1	-1	-1	1	-1	28.88
10	1	-1	1	1	1	-1	-1	-1	31.42
11	-1	-1	1	-1	1	1	-1	1	24.26
12	-1	1	1	-1	1	1	1	-1	32.46

Table 5

Significance analysis of the Plackett–Burman design

Parameters	Standardized effect	Sum of Squares	Contribution/(%)	Rank
X_1	3.23	31.23	14.49	3
X_2	0.31	0.28	0.13	6
X_3	-0.13	0.053	0.025	8
X_4	3.29	32.41	15.03	2
X_5	1.47	6.51	3.02	5
X_6	2.79	23.30	10.81	4
X_7	5.58	93.41	43.33	1
X_8	0.23	0.16	0.076	7

Analysis of the steepest ascent test results

The design and results of the steepest ascent test are presented in Table 6. As the Poisson's ratio of jujube and the jujube-jujube and jujube-steel static friction coefficients increased, the simulated angle of repose also increased. The relative error between the simulated and experimentally measured angles of repose first decreased and then increased. Run 3 produced the minimum relative error of 3.36%; therefore, its factor levels were selected as the centre point for the subsequent Box–Behnken design.

Table 6

Design and results of the steepest ascent test

No.	Parameters			Angle of repose (°)	Relative error (%)
	X_1	X_4	X_7		
1	0.20	0.41	0.40	21.34	24%
2	0.25	0.46	0.43	24.82	11.61%
3	0.30	0.52	0.46	27.06	3.36%
4	0.36	0.57	0.48	29.64	5.56%
5	0.41	0.63	0.51	32.44	15.53%
6	0.46	0.69	0.54	35.86	27.71%

Analysis of the Box–Behnken design results

The Box–Behnken experimental design and simulation results are presented in Table 7. Multiple regression analysis was performed on the simulation results, and a quadratic regression model for the simulated angle of repose was established as follows:

$$\theta = 27.43 - 0.72X_1 + 2.3X_4 + 1.33X_7 - 1.67X_1X_4 - 1.12X_1X_7 - 0.025X_4X_7 - 0.24X_1^2 + 2.05X_4^2 + 0.93X_7^2 \quad (8)$$

where, X_1 is the Poisson's ratio of jujube; X_4 is the jujube–jujube static friction coefficient; X_7 is the jujube–steel static friction coefficient.

The analysis of variance (ANOVA) for the quadratic regression model is presented in Table 8. X_1, X_4, X_7, X_1X_4, X_1X_7, X_4^2, X_7^2 had a significant impact on the angle of repose. The fitted angle of repose regression model had $P < 0.0001$. The lack-of fit term was $P=0.6438 > 0.05$. The model fit was good. The lack of fit was not significant. The coefficient of determination R^2 of the regression equation was 0.9898. The modified coefficient of determination R^2 was 0.9767, and the coefficient of variation CV was 1.33%. These results indicate that the regression model has good predictive ability and can be used to analyse and optimize the angle of repose.

Table 7

Box–Behnken design and simulation results

No.	Coding			Angle of repose (°)
	X_1	X_4	X_7	
1	0	0	0	26.88
2	1	0	1	27.34
3	0	-1	-1	26.66
4	0	0	0	28.04
5	1	-1	0	27.98
6	-1	-1	0	25.83
7	0	-1	1	29.66
8	0	0	0	27.36
9	0	0	0	27.54
10	-1	0	-1	26.68
11	0	1	-1	31.22
12	0	0	0	27.34
13	1	1	0	29.32
14	-1	0	1	31.26
15	1	0	-1	27.22
16	-1	1	0	33.85
17	0	1	1	34.12

Table 8

ANOVA for the quadratic regression model

Source of variance	Sum of squares	Degree of freedom	Mean square	*F*-value	*P*-value
Model	98.86	9	10.98	75.45	<0.0001**
X_1	4.15	1	4.15	28.49	0.0011**
X_4	42.23	1	42.23	290.05	<0.0001**
X_7	14.05	1	14.05	96.47	<0.0001**
X_1 X_4	11.16	1	11.16	76.62	<0.0001**
X_1 X_7	4.97	1	4.97	34.16	0.0006**
X_4 X_7	2.5E-003	1	2.5E-003	0.017	0.8994

Source of variance	Sum of squares	Degree of freedom	Mean square	*F*-value	*P*-value
X_1^2	0.24	1	0.24	1.65	0.2405
X_4^2	17.72	1	17.72	121.72	<0.0001**
X_7^2	3.65	1	3.65	25.09	0.0015**
Residual	1.02	7	0.15		
Lack of fit	0.32	3	0.11	0.61	0.6438
Pure error	0.7	4	0.17		
Cor total	99.88	16			

*Note: ** in Table 8 indicates that the impact is extremely significant(P<0.01), and * indicates that the impact is significant(P<0.05).*

Determination of the optimal parameters and experimental validation

The optimization objective was to minimize the difference between the simulated and experimentally measured angles of repose. The quadratic regression model was optimized using the experimentally measured angle of repose as the target value. Among the candidate solutions, the parameter combination closest to the mean values obtained from the physical measurements was selected. The optimal simulation parameters were determined as follows: Poisson's ratio, 0.32; jujube-jujube static friction coefficient, 0.52; and jujube-steel static friction coefficient, 0.47. To validate the calibrated discrete element parameters, the optimized parameter combination was used in EDEM simulations. Three repeated simulation tests were conducted, yielding angles of repose of 27.24°, 29.26°, and 29.58°. The mean simulated angle of repose was 28.69°, with a standard deviation of 1.04°. The relative error compared with the experimentally measured angle of repose of 28.08° was 2.17%. The close agreement between the simulated and experimental results further confirms the reliability and applicability of the calibrated simulation parameters.

DISCUSSION

In this study, the fundamental physical properties of Yimeng Mountain jujubes were systematically measured, and a three-dimensional geometric model incorporating their dimensional and morphological characteristics was established. A multi-sphere particle model was then developed in EDEM, in which the jujube geometry was represented by an assembly of spheres with different diameters. The coefficient of restitution, static friction coefficient, and rolling friction coefficient were determined using free-fall and inclined-plane tests. Images from both the physical and simulated angle-of-repose tests were processed in MATLAB, and the pile contours were fitted to determine the corresponding angles of repose. The experimentally measured angle of repose was used as the calibration target. Significant factors were identified using a Plackett–Burman design, followed by a steepest ascent test and Box–Behnken design to determine the optimal simulation parameters. Using the experimentally measured angle of repose as the optimization target, the calibrated parameters were determined as follows: Poisson's ratio of jujube, 0.32; jujube–jujube static friction coefficient, 0.52; and jujube–steel static friction coefficient, 0.47. The relative error between the simulated and experimentally measured angles of repose was 2.17%.

However, the calibration was conducted under ambient laboratory conditions, and the effects of variations in moisture content, temperature, and ripening stage on the contact parameters were not systematically investigated. Although the angle-of-repose test is widely used as a benchmark for evaluating bulk material behaviour, it represents only one quasi-static flow condition. Therefore, the calibrated parameters may not provide the same level of accuracy under highly dynamic conditions, such as high-velocity pneumatic conveying or rapid discharge. Validation using additional bulk-behaviour tests, such as shear-cell tests, hopper discharge tests, or direct shear tests, would further strengthen the general applicability of the calibrated parameter set. In addition, the present study focused primarily on jujube–jujube and jujube–steel contact parameters. Under actual harvesting and postharvest handling conditions, jujubes may also come into contact with materials such as rubber belts, plastic screens, and plant debris. Extending the calibration to these additional contact pairs would improve the practical applicability of the DEM model.

CONCLUSIONS

(1) The fundamental physical and contact parameters of Yimeng Mountain jujubes were determined through physical tests. The jujube–jujube static friction coefficient ranged from 0.41 to 0.69, while the jujube–steel static friction coefficient ranged from 0.40 to 0.54. The jujube–jujube rolling friction coefficient ranged from 0.16 to 0.30, whereas the jujube–steel rolling friction coefficient ranged from 0.11 to 0.24. The jujube–

jujube coefficient of restitution, determined using a high-speed camera, ranged from 0.41 to 0.54, while the jujube–steel coefficient of restitution ranged from 0.46 to 0.61.

(2) The measured physical and contact parameters were used to define the initial ranges of the DEM parameters. A Plackett–Burman design was conducted to screen the factors affecting the angle of repose. The Poisson's ratio of jujube, the jujube–jujube static friction coefficient, and the jujube–steel static friction coefficient were identified as the dominant factors. A steepest ascent test was then performed to further narrow the ranges of these parameters.

(3) A Box–Behnken design was subsequently employed to establish a quadratic regression model relating the angle of repose to the three dominant factors. Using the experimentally measured angle of repose of 28.08° as the optimization target, the optimal simulation parameters were determined as follows: Poisson's ratio of jujube, 0.32; jujube–jujube static friction coefficient, 0.52; and jujube–steel static friction coefficient, 0.47. The relative error between the simulated and experimentally measured angles of repose was 2.17%, indicating good agreement between the simulation and physical test results.

The calibrated parameters provide a basis for DEM simulations of key operations in the mechanical harvesting and postharvest handling of Yimeng Mountain jujubes, particularly pneumatic cleaning and separation processes, and can support further investigation of jujube motion and interaction behaviour during these operations. However, the present study adopted the Hertz–Mindlin (no slip) contact model, which is commonly used for dry, noncohesive particle systems in EDEM. Future work will consider more detailed contact and damage models, such as Bonding V2, to represent the skin and flesh of jujubes and to investigate fruit damage during harvesting. The effects of fruit morphology on DEM model accuracy will also be examined further.

ACKNOWLEDGEMENT

This project was funded by Shandong Agriculture and Engineering University Start-Up Fund for Talented Scholars (2024GCCZR-05). We also appreciate the work of the editors and the reviewers of the paper.

REFERENCES

[1] Chen, X. Y., Wang, X. Z., Bai, J., Fang, W. Q., Hong, T. Y., Zang, N. & Wang, G. L. (2024). Virtual parameter calibration of pod pepper seeds based on discrete element simulation. *Heliyon*, 10(11), e31686.

[2] Chen, Z. F., Che, G., Wan, L., Wang, H. C. & Zhang, K. (2025). Calibration and experimental validation of discrete element parameters for long-grain rice with different moisture contents based on angle of repose. *Agriculture*, 15(10), 1058.

[3] Chu, L., Wu, M.Y., Zhu, F.T., Zhao, Y., He, F.T., Ge, B.G. & Ma C. (2012). Industry Status and Development Proposal of Jujube in Xinjiang (新疆地区红枣产业现状及发展建议). *Academic Periodical of Farm Products Processing),* 4, 110–113.

[4] Du, X. (2022). Design and Experimental Research of Landing Red Jujube Harvesting Machinery (落地红枣收获机的设计与试验研究). Master's thesis. Xinjiang Agricultural University, Uumqi.

[5] Geng, H., Hu, J. M., Feng, Q., Sun, W., Yang, M., Wang, H. H., Qiao, W. H. & Wang, P. (2026). Calibration of V2 Discrete Element Model Parameters for Simulation of Atlantic Potato Slicing and Sorting. *Agriculture*, 16(4), 489.

[6] Gu, M., Shen, H. Y., Luo, W. W., Ling, J., Wang, B. K., Gu, F. W., Song, S. M., Pan, L. &Hu, Z. C. (2025). Calibration of Parameters for Leaf-Stem-Cutting Model of Tuber Mustard (Brassica juncea L.) Based on Discrete Element Method. *Agriculture*, 15(7), 773.

[7] Hao, B. E., Ma, X. J., Wang, L. X. & Tong, X. (2025). Discrete Element Method-Based Stratified Soil Modeling to Improve the Precision of Soil-Machine Interaction Simulations. *Agronomy*, 15(6), 1421.

[8] Hou, Z, F., Dai, N. Z., Chen, Z., Qiu, Y. & Zhang, X. W. (2020). Measurement and calibration of physical property parameters for Agropyron seeds in a discrete element simulation (冰草种子物性参数测定与离散元仿真参数标定). *Transactions of the Chinese Society of Agricultural Engineering*, 36(24), 46–54.

[9] Huang, H. N., Zhang, Y., Hou, G. Y., Su, B. H., Yin, H., Fu, Z. J., Zhuang, Y. F., Lv, Z. J., Tian, H. & Li, L. H. (2025). Establishment of Hollow Flexible Model with Two Types of Bonds and Calibration of the Contact Parameters for Wheat Straw. *Agriculture*, 15(15), 1686.

[10] Ji, C., Liu, W. R., Deng, Y. G., Wang, Y. Q., Chen, P. M. & Yan, B. (2025). Calibration of DEM Parameters and Microscopic Deformation Characteristics During Compression Process of Lateritic Soil with Different Moisture Contents. *Agriculture*, 15(14), 1548.

[11] Ji, J., Yu, L. H., Wu, X. M., Su, W., Xiao, Y. & Zhang, Z. (2024). Parameter Calibration of Discrete Element Simulation of Sorghum Seed for Wine Use (酒用高粱种子离散元仿真参数标定). *Journal of Agricultural Mechanization Research*, 46(09), 46–52.

[12] Li, H., Meng, Y. B., Qi, X. D., Wang, Y. J., Li, Y. Q. & Li, M. Y. (2025). Discrete Element Modelling Method and Parameter Calibration of Garlic Species Based on Bonding V2 Model (基于 Bonding V2 模型的蒜种离散元建模与参数标定). *Transactions of the chinese society for agricultural machinery*, 56(07), 150–157+169.

[13] Li, J. J. (2022). Design and experiment of picking up key components of self-propelled jujube harvester (自走式红枣收获机捡拾关键部件的设计与试验). Master's thesis. Tarim University, Tarim.

[14] Li, X. K., Xu, Y., Zhou, J. P., Wang, H. Y., Xu, X. & Zuo, J. W. (2026). Discrete elemental parameter calibration and experiments for mechanically harvested dried safflower filaments (机收干红花丝离散元参数标定与试验). *Transactions of the Chinese Society of Agricultural Engineering*, 42(04), 150–160.

[15] Liu, Z. Y., Yan, J. G., Liu, F. & Wang, L. J. (2025). Calibration and Testing of Discrete Element Simulation Parameters for the Presoaked Cyperus esculentus L. Rubber Interface Using EDEM. *Agronomy*, 15(10), 2440.

[16] Ma, G. Y., Zhang, S., Wang, H. F., Han, M. Y. & Sheng, S. Y. (2025). Calibration of contact parameters for ruminant protein supplement feed pellets based on the discrete element method. *INMATEH-Agricultural Engineering*, 77(3), 882–893.

[17] Muqaddas, Mengaya L., Ahmed M. M., Hamid S. M., Yanju X., Asim M. &Yunfeng P. (2025). Postharvest handling and storage strategies for preserving jujube (Ziziphus jujuba mill.) fruit quality: A review. *Foods*, 14(19), 3370.

[18] Shi, G. K., Li, J. B., Ding, L. P., Zhang, Z. Y., Ding, H. Z., Li, N. & Kan, Z. (2021). Calibration and tests for the discrete element simulation parameters of fallen jujube fruit. *Agriculture*, 12(1), 38.

[19] Yu, F., Wang, D. W., Wang, X. F., Wang, L., Hu, J. L., Chi, X. G. & Ji, M. (2025). Parameter Calibration and Experimentation of the Discrete Element Model for Mixed Seeds of Vetch (Vicia villosa) and Oat (Avena sativa) in a Pneumatic Seed Drilling System. *Applied Sciences*, 15(24), 13048.

[20] Zheng, H., Hu, Z. W., Xue, X. L., Ye, Y. X., Liu, T., Ren, N., Liu, F.Y. & Yu, G. H. (2025). Calibration and Experimental Validation of Discrete Element Parameters of Fritillariae Thunbergii Bulbus. *Applied Sciences*, 15(14), 7951.

[21] Zhou, J., Sun, W. T. & Liang, Z. A. (2023). Construction of Discrete Element Flexible Model for Jerusalem Artichoke Root-Tuber at Harvest Stage (收获期菊芋根-块茎离散元柔性模型研究). *Transactions of the chinese society for agricultural machinery*, 54(10), 124–132.

[22] Zhou, L., Li, J. B., Ding, L. P., Ding, H. Z. & Liang, J. P. (2022). Analysis and design of operating parameters of floor-standing jujube pickup device based on discrete element method. *Agriculture*, 12(11), 1904.

[23] Zhu, G.S., He, X. W., Wang, X. F., Shi J., Xing, J. F. & Wang, L. (2026). Physical properties and experimental study of cotton stalks from typical arid regions of southern Xinjiang based on DEM. *Agriculture*, 16(4), 427.

WIND-BLOWN SAND EROSION OF A POLYCARBONATE LAMP COVER FOR AGRICULTURAL MACHINERY AT DIFFERENT WIND SPEEDS AND YAW ANGLES
/
不同风速与偏航角下农用机械聚碳酸酯灯罩的风沙冲蚀特性

Sheng JIANG, Afang JIN*), Mengyao XU
College of Mechanical Engineering, Xinjiang University, Urumqi 830046/ China;
Tel: +86-17591715179; E-mail: jinaf3500_xju@xju.edu.cn
DOI: https://doi.org/10.35633/inmateh-79-90

Keywords: *agricultural-machinery lamp cover, wind-blown sand erosion, yaw angle, Eulerian–Lagrangian approach, polycarbonate*

ABSTRACT
Wind-blown sand erosion threatens agricultural-vehicle lamp covers, yet the effects of wind speed and yaw angle have not been sufficiently quantified. A one-way coupled Eulerian–Lagrangian CFD model of a full-scale isolated polycarbonate (PC) lamp cover was combined with gas-jet erosion tests on flat PC specimens for trend-level comparison. Wind speeds of 10–30 m/s and yaw angles of −30° to 30° were investigated, with erosion predicted using the Oka model. Erosion was concentrated near the windward leading edge and downstream surface, whereas the maximum pressure remained closer to the stagnation region. The mean and maximum erosion rates followed power-law relationships with exponents of 2.70 and 2.31, respectively. From −30° to 30°, the mean erosion rate increased by 28.3%, 57.0%, and 13.9% at 10, 20, and 30 m/s, respectively. At 30 m/s, the maximum erosion rate increased by 55.8% from 0° to 30°. At 20 m/s, the erosion concentration factors were 13.31, 5.45, and 9.54 at −30°, 0°, and 30°, respectively. Over the same yaw-angle range, the experimental mass loss increased by 212.5%, 115.4%, and 88.9%, while the surface roughness increased by 23.9%, 18.9%, and 20.1%. After normalization, the numerical and experimental indicators exhibited consistent yaw-angle-dependent trends (R^2 = 0.9481, RMSE = 0.0822, MAE = 0.0671). Within the investigated conditions, the model successfully captured the relative erosion trends, and the combined indicators supported the assessment of localized erosion risk.

摘要
风沙冲蚀对农用车辆灯罩的服役性能构成威胁，但风速与偏航角对其冲蚀特性的影响尚未得到充分量化。本文建立全尺寸孤立灯罩的单向耦合欧拉–拉格朗日 CFD 模型，并结合平板聚碳酸酯试样气固射流冲蚀试验进行趋势对比。研究考虑 10–30 m/s 的风速和−30°–30°的偏航角，并采用 Oka 模型预测冲蚀。结果表明，冲蚀主要集中于迎风前缘及其下游表面，而压力峰值更接近滞止区域。平均冲蚀率和最大冲蚀率均与风速呈幂律关系，其指数分别为 2.70 和 2.31。偏航角由−30°增至 30°时，10、20 和 30 m/s 下的平均冲蚀率分别增加 28.3%、57.0%和 13.9%。在 30 m/s 下，最大冲蚀率由 0°至 30°增加 55.8%。在 20 m/s 下，−30°、0°和 30°对应的冲蚀集中系数分别为 13.31、5.45 和 9.54。在相同偏航角范围内，试验质量损失分别增加 212.5%、115.4%和 88.9%，表面粗糙度分别增加 23.9%、18.9%和 20.1%。归一化后的数值与试验指标均呈现出一致的偏航角依赖变化规律。（R^2 = 0.9481，RMSE = 0.0822，MAE = 0.0671）。在本文研究条件下，该模型能够反映相对冲蚀变化趋势，综合指标可为局部冲蚀风险评估提供依据。

INTRODUCTION
Modern agricultural machinery is widely used for crop production, land reclamation, and material transport in arid, semi-arid, and desertified agricultural regions, where near-ground flows frequently contain wind-blown sand and dust particles *(Li et al., 2025; Yan et al., 2024)*. These particles are transported mainly through saltation and suspension, and their motion is governed by wind velocity, turbulence intensity, surface roughness, and particle inertia *(Kok et al., 2012; Shao and Lu, 2000)*. During field operation, vehicle motion and crosswinds may generate stagnation, acceleration, and flow-separation regions around frontal surfaces, thereby modifying particle trajectories, impact velocity, and local incidence conditions. Repeated particle impacts on exposed transparent components may consequently cause pits, scratches, material loss, and progressive optical degradation *(Zhao et al., 2021)*.

Solid-particle erosion is a surface-degradation process governed by particle kinetic energy, impact angle, and material response. Its principal damage modes include cutting, ploughing, plastic deformation, and localized fracture *(Bellman and Levy, 1981; Deng, 2025; Finnie, 1960; Hutchings, 1981; Sundararajan, 1991)*, while erosion severity is influenced by impact velocity, particle characteristics, and material toughness. For agricultural-machinery lamp covers, wind-blown sand erosion may lead to material removal, surface roughening, haze formation, and reduced light transmittance, thereby affecting illumination range and field-boundary recognition during night-time or dusty operation. Failure analyses of automotive headlamp lenses have also shown that surface degradation and cracking may compromise the functional integrity of transparent lighting components *(Ferreira and Lins, 2019)*. Polycarbonate (PC) is widely used for transparent vehicle components because of its optical transparency, low weight, and impact resistance *(Katsamberis et al., 1998)*. Its erosion response is closely associated with resilience, impact-energy absorption, and local deformation under repeated particle impacts *(Xie et al., 2019)*. The gradual accumulation of pits, grooves, and scratches may therefore alter both the surface condition and optical performance of PC lamp covers exposed to wind-blown sand.

Previous studies of wind-blown sand and solid-particle erosion have focused mainly on turbomachinery components and wind-turbine blades *(Alqallaf et al., 2020; Hamed et al., 2006; Wang et al., 2024)*. These studies show that wind velocity, particle mass flow rate, particle characteristics, and wall impact angle strongly influence erosion location and intensity, providing a basis for understanding particle transport and wall collision in gas–solid flows *(Deng, 2025)*. However, curved transparent components on agricultural machinery exhibit different geometrical boundaries and local flow conditions. Under yawed wind-blown sand inflow, changes in the incoming-flow direction redistribute the velocity field, pressure gradient, particle concentration, and impact-angle distribution around the lamp cover. The resulting variation in the position, intensity, and spatial concentration of high-erosion regions therefore requires further quantitative analysis.

Eulerian–Lagrangian and CFD–DEM approaches have been applied to gas–particle transport in agricultural equipment and aeolian-sand systems *(Bi et al., 2023; Chen et al., 2025; Li et al., 2025; Zhang et al., 2025)*. These methods enable particle trajectories, impact conditions, and erosion distributions to be evaluated under controlled operating conditions. However, mean erosion alone cannot fully characterize local peak damage, particularly when erosion becomes spatially concentrated under yawed inflow. Therefore, both overall erosion severity and localized erosion characteristics should be considered when assessing the erosion risk of exposed transparent components.

The objectives of this study are to: (1) establish a one-way coupled Eulerian–Lagrangian framework for predicting wind-blown sand transport and erosion on a full-scale isolated agricultural-machinery lamp cover; (2) quantify the effects of wind speed and yaw angle on the mean erosion rate, maximum erosion rate, and erosion concentration factor; (3) identify variations in erosion-prone regions and the spatial concentration of erosion under different operating conditions; and (4) conduct gas-jet erosion tests on flat PC coupons to determine whether mass loss, surface roughness, and surface morphology follow the parametric trends predicted numerically.

MATERIALS AND METHODS

Numerical simulation

Governing Equations and Numerical Models

A one-way coupled Eulerian–Lagrangian CFD model was developed to simulate air–sand two-phase flow around an agricultural-machinery lamp cover under wind-blown sand conditions. The airflow was solved as a continuous phase using the Reynolds-averaged Navier–Stokes equations, while sand-particle trajectories were tracked in a Lagrangian framework. Owing to the low particle volume fraction, particle feedback on the airflow was neglected *(Elghobashi, 1994)*. The SST k–ω model was adopted to account for adverse pressure gradients and flow separation near the curved lamp-cover surface *(Menter, 1994)*. Identical numerical schemes and convergence criteria were applied to all wind-speed and yaw-angle cases to ensure consistent comparison.

After convergence of the continuous-phase solution, the sand-particle trajectories were calculated. Interparticle collisions were neglected, and the particle equation of motion was formulated according to Newton's second law:

$$m_p \frac{d\mathbf{v}_p}{dt} = \mathbf{F}_D + m_p\mathbf{g} + \mathbf{F}_{other} \quad (1)$$

where m_p is the particle mass, $\boldsymbol{v}_p$ is the particle velocity vector, $\boldsymbol{F}_D$ is the drag force exerted by the fluid on the particle, and $\boldsymbol{F}_{\mathrm{other}}$ includes the pressure-gradient force and Saffman lift force. The drag force was determined from the local relative velocity, particle Reynolds number, and drag coefficient.

Material loss caused by particle impact was evaluated using the Oka erosion model *(Oka et al., 1997; Oka et al., 2005a; Oka and Yoshida, 2005b)*. In the model, the erosion ratio is determined by the particle impact angle, impact velocity, particle diameter, and material-related coefficients:

$$E(\alpha, V_p, d_p) = E_{\mathrm{ref}} g(\alpha) \left(\frac{V_p}{V_{\mathrm{ref}}}\right)^{k_v} \left(\frac{d_p}{d_{\mathrm{ref}}}\right)^{k_d} \quad (2)$$

The impact-angle correction function is expressed as:

$$g(\alpha) = (\sin\alpha)^{n_1}[1 + H_v(1 - \sin\alpha)]^{n_2} \quad (3)$$

where $E(\alpha, V_p, d_p)$ is the ratio of eroded material mass to incident particle mass; E_{ref} is the reference erosion ratio; $g(\alpha)$ is the impact-angle correction function; and α is the particle impact angle. V_p and d_p denote the particle velocity immediately before wall impact and the particle diameter, respectively, whereas V_{ref} and d_{ref} are the corresponding reference values. H_v is the hardness coefficient used in the Oka model, n_1 and n_2 are the impact-angle coefficients, and k_v and k_d are the velocity and diameter exponents, respectively.

The parameters used in the simulations are listed in Table 1. The reference erosion ratio was 2.141×10^{-4}, while the reference velocity and particle diameter were 104 m/s and 3.26×10^{-4}m, respectively. The hardness coefficient was 1.34, resulting in impact-angle coefficients $n_1 = 0.7397$ and $n_2 = 1.8228$. The velocity and diameter exponents were 2.3257 and 0.19, respectively. The same parameter set was applied to all wind-speed and yaw-angle conditions, without case-specific adjustment.

Table 1

Parameters used in the Oka erosion model

Parameter	Symbol	Value	Unit
Reference erosion ratio	E_{ref}	2.141×10^{-4}	-
Hardness coefficient	H_v	1.34	-
Impact-angle coefficient	n_1	0.7397	-
Impact-angle coefficient	n_2	1.8228	-
Reference velocity	V_{ref}	104	m/s
Velocity exponent	k_v	2.3257	-
Reference particle diameter	d_{ref}	326	μm
Diameter exponent	k_d	0.19	-

Note: *$d_{ref} = 326\ \mu m$ is the reference diameter in the Oka model, whereas the actual particle diameters followed a log-normal distribution within the specified particle-size range.*

The default Oka-model parameter set was used without independent calibration for the present quartz-sand–PC system. Therefore, the calculated erosion rates were used primarily to compare spatial distributions and relative variations among operating conditions rather than to predict absolute material loss.

The local erosion rate was calculated from the particle mass flow rates associated with the trajectories striking each wall-face cell:

$$\dot{m}''_{\mathrm{e},f} = \frac{1}{A_f} \sum_{j=1}^{N_f} E(\alpha_j) \dot{m}_{\mathrm{p},j} \quad (4)$$

where $\dot{m}''_{e,f}$ is the erosion rate of the f-th wall-face cell, A_f is the area of the cell, N_f is the number of particle trajectories striking the cell; and $\dot{m}_{p,j}$ is the mass flow rate represented by the j-th particle trajectory.

The mean and maximum erosion rates over the lamp-cover surface are defined as:

$$\dot{m}''_{e,\mathrm{avg}} = \frac{\sum_{f=1}^{N} \dot{m}''_{e,f} A_f}{\sum_{f=1}^{N} A_f}, \dot{m}''_{e,\max} = \max_{1\le f\le N} \left(\dot{m}''_{e,f}\right) \quad (5)$$

where $\dot{m}''_{e,\mathrm{avg}}$ and $\dot{m}''_{e,\max}$ denote the mean and maximum erosion rates, respectively, and N is the total number of wall-face cells on the agricultural vehicle lamp cover. The mean erosion rate characterizes the overall material loss from the lamp-cover surface, whereas the maximum erosion rate reflects the severity of localized erosion. These two parameters are used to evaluate the overall erosion level and local damage concentration under different wind-speed and yaw-angle conditions.

Geometric Model and Computational Domain

A three-dimensional model of a representative **PC lamp cover used on agricultural machinery** was constructed to investigate its wind-blown sand erosion characteristics. The external contour and curvature of the exposed lamp-cover surface were retained, whereas mounting structures and internal optical components

were omitted. The adjacent body panels, grille, bumper, and other surrounding vehicle structures were not included; therefore, the lamp cover was treated as an isolated component in the computational domain. The resulting model had overall dimensions of approximately 415 mm × 431 mm × 201 mm.

Because the surrounding vehicle body was excluded, the calculated results represent the aerodynamic and erosion responses of the isolated lamp cover and are primarily applicable to comparative analyses of wind speed and yaw angle.

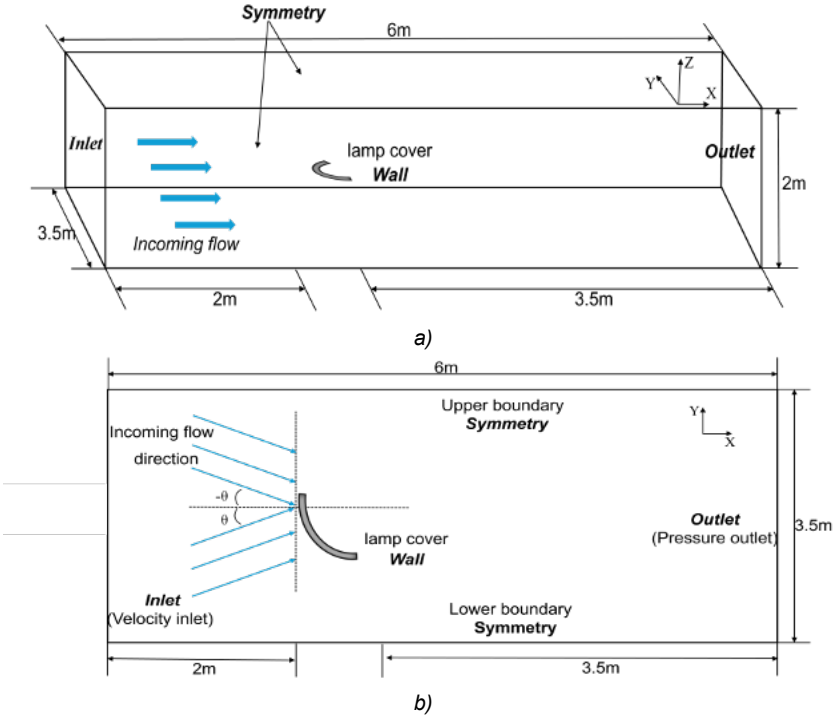


Fig. 1 - Schematic of the computational domain

a) three-dimensional computational domain; b) top view and definition of the yaw angle

As shown in Figure 1(a), the computational domain extended 2 m upstream and 3.5 m downstream of the lamp cover, with overall dimensions of 6 m × 3.5 m × 2 m. This arrangement limited the blockage ratio to less than 3% and reduced the influence of the outer boundaries on the flow around the lamp cover. The inlet and outlet were specified as a velocity inlet and a pressure outlet, respectively, while the remaining outer boundaries were treated as symmetry boundaries.

The yaw angle θ was defined as the angle between the incoming-flow direction and the central normal axis of the lamp cover, as illustrated in Figure 1(b). Five yaw-angle conditions, −30°, −15°, 0°, 15°, and 30°, were considered. A Cartesian coordinate system was adopted, with the X-axis aligned was aligned with the inflow direction at the 0° reference condition, the Y-axis oriented transversely, and the Z-axis directed vertically. Different yaw conditions were imposed by rotating the inlet velocity vector while keeping the computational domain unchanged.

Mesh Generation and Grid Sensitivity Verification

The computational domain was discretized using polyhedral cells, which are well suited to the curved lamp-cover surface and its surrounding flow field. Prism layers were generated along the lamp-cover wall to resolve the near-wall flow. The boundary-layer mesh consisted of 15 layers with a total thickness of 5 mm and a growth rate of 1.2. Local refinement was applied to the windward surface, regions of pronounced curvature, and areas expected to experience high erosion. This mesh arrangement provided sufficient resolution of the near-wall flow and particle impacts without imposing excessive computational cost.

Grid sensitivity was examined using three meshes under a wind speed of 20 m/s, a particle mass flow rate of 2 g·s^{-1}, and a yaw angle of 0°. As reported in Table 2, increasing the cell count from 0.68×10^6 to 1.24×10^6 changed the mean and maximum erosion rates by 2.22% and 2.37%, respectively. Further refinement to 1.83×10^6 cells reduced the corresponding changes to 0.72% and 1.04%. The medium and fine meshes therefore produced closely comparable results, with all variations remaining below 5%. Considering both numerical accuracy and computational cost, the mesh containing 1.24×10^6 cells was selected for the subsequent simulations.

Table 2

Results of the grid-independence study

Number of cells (10^6)	Mean erosion rate (10^{-9} kg·m^{-2}·s^{-1})	Variation (%)	Maximum erosion rate (10^{-9} kg·m^{-2}·s^{-1})	Variation (%)
0.68	1.35	--	7.58	--
1.24	1.38	2.22	7.76	2.37
1.83	1.39	0.72	7.84	1.04

Gas-Jet Sand Erosion Experiment

Gas-jet sand erosion tests were conducted to examine the effects of wind speed and specimen orientation on the mass loss, surface roughness, and surface morphology of PC coupons, and to compare the resulting parametric trends with the numerical predictions *(ASTM International, 2018)*. As shown in Figure 2(a), the test system comprised an air compressor, a pressure regulator, an abrasive feed unit, a nozzle, a specimen rotation stage, and a material recovery chamber. Compressed air entered the nozzle after pressure regulation, where quartz sand particles were entrained and accelerated by the high-speed airflow. The particles then struck the specimen at the prescribed velocity and orientation. The rotation stage controlled the specimen position and yaw angle, while the recovery chamber collected the particles after impact. Surface morphology and local roughness after erosion were examined using the digital microscope shown in Figure 2(b).



a) *b)*

Fig. 2 - Experimental instruments

a) wind–sand erosion test system; b) extended-depth-of-field imaging system.

To introduce an asymmetric reference orientation comparable with the installed lamp cover in its installed position, the specimen was mounted with an initial nozzle angle of α_0=15°. The distance from the nozzle outlet to the specimen center was fixed at $S = 200$ mm, as illustrated in Figure 3. The 0° yaw condition corresponded to the installation reference position rather than normal impact. With α_0 held constant, the specimen rotation stage was adjusted to obtain yaw angles of −30°, −15°, 0°, 15°, 30°. The same nominal yaw-angle range was used in the numerical and experimental cases to facilitate trend comparison.

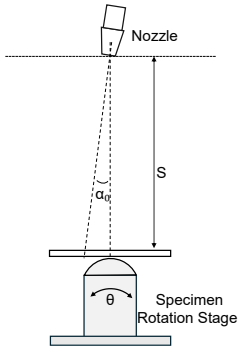


Fig. 3 - Initial nozzle orientation and definition of the specimen yaw angle

The principal test conditions are listed in Table 3. PC specimens were eroded by quartz sand at nominal nozzle-exit air velocity of 10, 20, and 30 m/s. Each test lasted 60 s and was independently repeated three times. Specimen mass was measured before and after erosion using an analytical balance with a resolution of 0.001 g. The measured mass loss, surface roughness, and surface morphology were used to compare the effects of wind speed and yaw angle with the corresponding numerical trends.

Table 3

Experimental conditions for gas-jet sand erosion tests

Parameter	Value
Specimen material	Polycarbonate (PC)
Specimen size	40 mm × 40 mm × 3 mm
Particle material	Quartz sand
Particle density	2650 kg/m^3
Particle size	50–250 μm
Nozzle inner diameter, D_n	6 mm
Sand mass flow rate, $\dot{m}_s$	2.5 g/s
Nominal air velocity	10, 20, and 30 m/s
Initial nozzle angle, α_0	15°
Yaw angle, θ	−30°, −15°, 0°, 15° and 30°
Nozzle–specimen distance, S	200 mm
Exposure time	60 s
Number of repetitions	3

RESULTS

Numerical simulation results and analysis

Effect of Yaw Angle on Surface Erosion and Pressure Distributions

Figure 4 compares the surface erosion-rate and pressure distributions on the agricultural-machinery lamp cover at 20 m/s under different yaw angles. As shown in Figure 4(a), erosion was mainly concentrated near the windward leading edge and the adjacent downstream surface, whereas the leeward region remained at a relatively low erosion level. As the yaw angle changed from −30° to 30°, the high-erosion region gradually expanded, while its main location remained near the windward leading edge. This distribution is associated with particle inertia in the curved flow. Because particles cannot instantaneously follow strongly turning streamlines, they may retain wall-directed momentum and impact the windward region. A similar dependence of wind-sand transport on local flow-field modification was reported by *Yan et al., (2024)*.

The pressure contours in Figure 4(b) show a maximum near the windward stagnation region, followed by a downstream decrease. Although the pressure and erosion distributions partially correspond, the erosion peak is located slightly downstream of the pressure maximum. This offset reflects the different dynamics of the gas and particle phases: pressure is governed by gas-phase stagnation, whereas erosion depends on particle impact velocity and angle. Particle inertia may therefore shift the strongest impact away from the pressure peak. This interpretation is consistent with *Oka et al., (2005a)*, who identified impact velocity and impact angle as key parameters controlling solid-particle erosion.

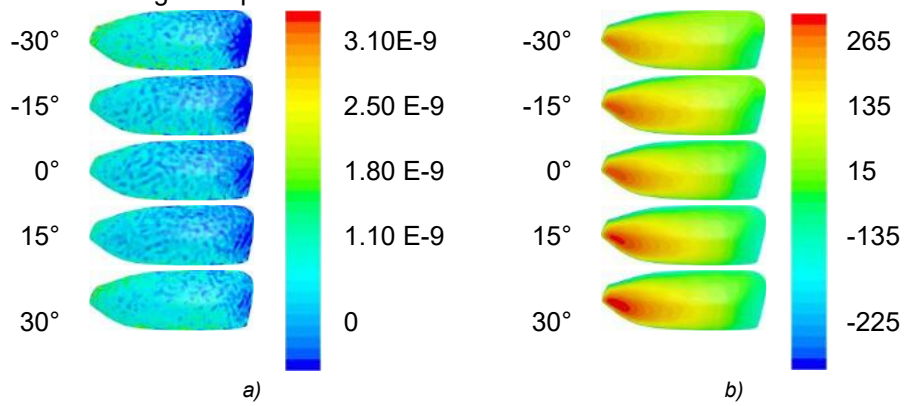


Fig. 4 - Surface erosion-rate and gauge-pressure distributions at 20 m/s under different yaw angles

a) Erosion rate distribution (kg·m^{-2}·s^{-1}); b) surface gauge-pressure distribution (Pa)

Effects of Wind Speed and Yaw Angle on Erosion Characteristics

Figure 5 shows that increasing wind speed markedly intensified surface erosion on the agricultural vehicle lamp cover, whereas yaw angle mainly changed the spatial distribution of erosion on the curved surface. As shown in Figure 5(a), the mean erosion rate generally increased as the yaw angle changed from −30° to 30° at the same wind speed, with increases of 28.3%, 57.0%, and 13.9% at 10, 20, and 30 m/s, respectively.

Higher wind speed increases particle impact velocity and energy transfer, thereby increasing the overall erosion magnitude, which reached its highest level at 30 m/s. In contrast, yaw modifies particle trajectories and incidence conditions, and its relative influence was most pronounced at 20 m/s. This non-monotonic yaw sensitivity may arise from the combined effects of particle-impact intensity and yaw-induced trajectory redistribution. This result is similar to *Li et al., (2025)*, who identified wind speed as a dominant factor in aeolian-particle transport.

As shown in Fig. 5(b), the mean erosion rate increased with wind speed according to a power-law relationship with an exponent of approximately 2.70. This velocity dependence is consistent with the Oka erosion model, indicating that the fitted exponent characterizes the velocity sensitivity of the present flow–particle–erosion system rather than representing an intrinsic material constant of PC.

In contrast to the mean erosion rate, Fig. 5(c) shows an approximately U-shaped variation in the maximum erosion rate with yaw angle. At 30 m/s, the maximum erosion rate increased from approximately 2.13×10^{-8} kg·m^{-2}·s^{-1} at 0° to 3.33×10^{-8} kg·m^{-2}·s^{-1} at 30°, corresponding to an increase of approximately 56%. Figure 5(d) further shows a power-law dependence on wind speed, with an exponent of approximately 2.31 and R^2=0.9704. The U-shaped response indicates that local peak erosion is more sensitive to spatial non-uniformity than the mean erosion. Yawed flow may normalize particle impacts within the windward region, increasing maximum erosion without a proportional increase in mean erosion.

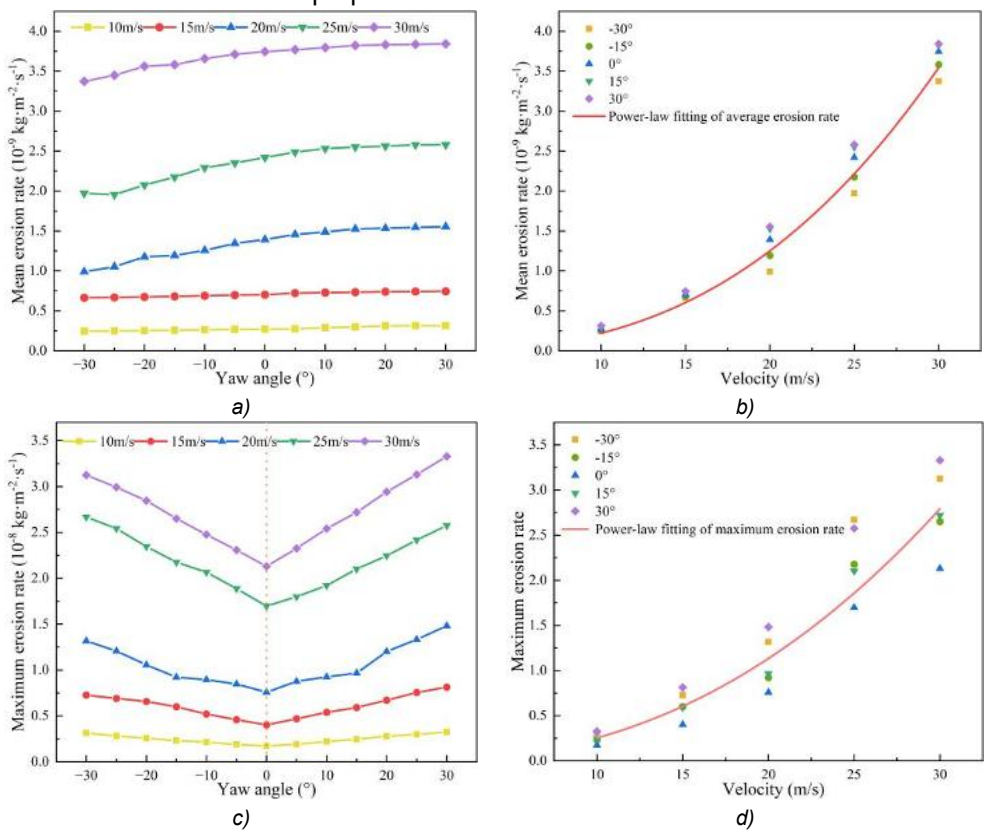


Fig. 5 – Erosion rate under different wind speeds and yaw angles

a) Mean erosion rate–yaw angle; b) Mean erosion rate–wind speed;
c) Maximum erosion rate–yaw angle; d) Maximum erosion rate–wind speed

To quantify the spatial concentration of erosion damage, the erosion concentration factor KCF was introduced as the ratio of the maximum erosion rate to the mean erosion rate:

$$KCF = \frac{E_{\max}}{E_{\text{avg}}} \tag{6}$$

where KCF is a dimensionless index describing the deviation of local peak erosion from the mean erosion level. $E_{\max}$ is the maximum erosion rate in the exposed region under the same condition, and E_{avg} is the corresponding mean erosion rate.

For clarity and to facilitate direct comparison with the experimental conditions, only the cases at 10, 20, and 30 m/s are presented in Figure 6. KCF was lowest near 0° and increased toward larger yaw angles; at 20 m/s, the values at −30°, 0°, and 30° were 13.31, 5.45, and 9.54, respectively. The variation in KCF primarily reflects changes in the spatial concentration of erosion rather than in the overall erosion intensity. Near 0°, particle impacts are distributed relatively broadly, reducing the difference between $E_{\max}$ and E_{avg}.

Under yawed conditions, asymmetric flow redistributes particle impacts and may increase their spatial concentration, causing the local peak to rise relative to the mean. This behaviour is physically analogous to the non-uniform particle-impact erosion discussed by *Hamed et al., (2006)*. Notably, the high KCF at −30°, despite a non-maximum E_{avg}, indicates that mean erosion alone may underestimate normalize damage. Therefore, E_{avg}, E_{max}, and KCF should be considered jointly to characterize both erosion severity and spatial concentration.

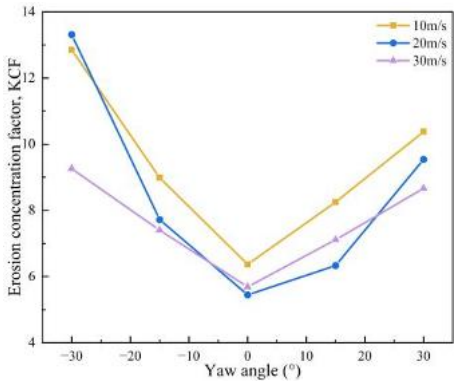
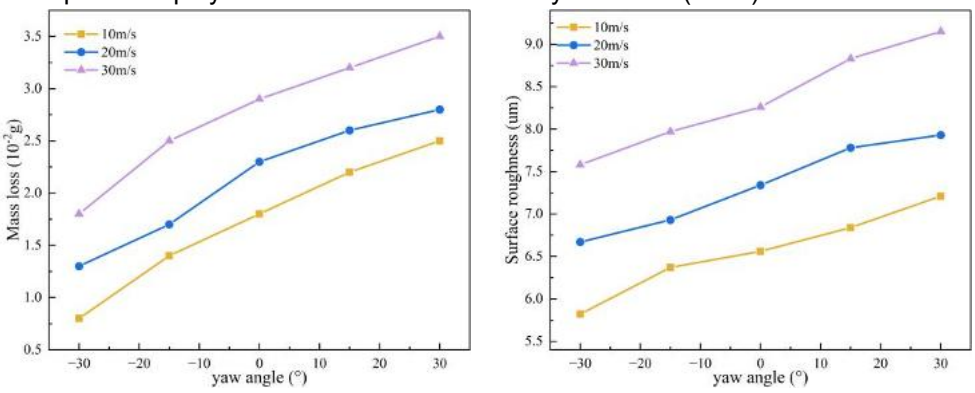


Fig. 6 – Variation of the KCF with yaw angle at different wind speeds

Erosion Damage and Surface Morphology Evolution of PC

Figure 7(a) shows that mass loss increased with both wind speed and yaw angle. From −30° to 30°, the mean mass loss increased by 212.5%, 115.4%, and 88.9% at 10, 20, and 30 m/s, respectively. The observed response is associated with changes in particle-impact momentum and incidence conditions. Higher wind speed increases particle momentum and impact energy, promoting local deformation and progressive material removal. Meanwhile, yaw modifies the relative normal and tangential impact components; the former favors indentation and deformation, whereas the latter promotes grooving and scratching. Their combined variation therefore alters the efficiency of material removal. In contrast, *Zhao et al., (2021),* reported a non-monotonic dependence of glass erosion on particle impact angle. This difference is physically reasonable because yaw angle is not equivalent to the local impact angle, which also depends on particle trajectory and surface orientation, while PC and glass exhibit different mechanical responses.

Surface roughness showed a similar overall trend in Figure 7(b). From −30° to 30°, the mean roughness increased from 5.82 to 7.21 μm, 6.67 to 7.93 μm, and 7.62 to 9.15 μm at 10, 20, and 30 m/s, representing increases of 23.9%, 18.9%, and 20.1%, respectively. The increase in surface roughness reflects the accumulation and overlap of pits, grooves, and displaced material. This result is similar to the deformation-related erosion response of polymeric materials discussed by Xie et al. (2019).



a) *b)*

Fig. 7 – Erosion characteristics of PC specimens

a) mass loss; b) surface roughness.

Figure 8 presents representative surface morphologies of PC specimens along a stepwise comparison path in which either yaw angle or wind speed was varied between adjacent conditions. At 10 m/s, increasing the yaw angle from −30° to −15° increased the density of isolated irregular defects, while relatively smooth regions remained visible. At a constant yaw angle of −15°, increasing the wind speed to 20 m/s enlarged the characteristic size of the defects and promoted local overlap. A further increase in yaw angle to 15° produced more densely distributed and partially interconnected damage features.

At the same yaw angle, increasing the wind speed to 30 m/s resulted in locally concentrated roughening, whereas increasing the yaw angle to 30° led to a more widespread and relatively continuous roughened surface. These changes are consistent with the increases in mass loss and surface roughness shown in Figure 7, indicating that enhanced material removal was accompanied by the accumulation, enlargement, and overlap of surface defects. Irregular local features may be associated with impact-induced deformation, while elongated and groove-like traces suggest the contribution of tangential abrasion. The observed surface degradation therefore reflects the combined effects of repeated particle impacts, local deformation, and abrasive material removal. The coexistence of impact-induced deformation and tangential abrasion is consistent with the combined deformation and cutting mechanisms reported in solid-particle erosion studies.

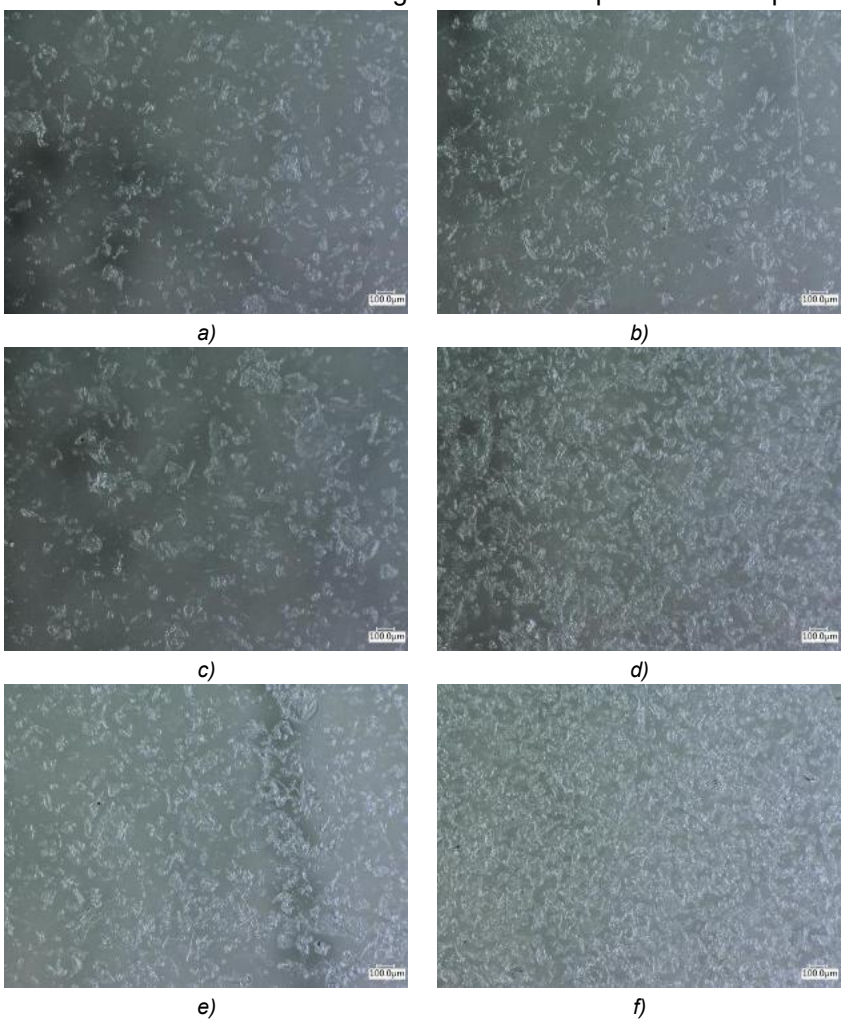


Fig. 8 – Surface Damage and Morphology Variation of PC Specimens

a) $v = 10$ *m/s,* $\theta = -30°$*; b)* $v = 10$ *m/s,* $\theta = -15°$*;*
c) $v = 20$ *m/s,* $\theta = -15°$*; d)* $v = 20$ *m/s,* $\theta = 15°$*;*
e) $v = 30$ *m/s,* $\theta = 15°$*; f)* $v = 30$ *m/s,* $\theta = 30°$

Comparison between Numerical and Experimental Erosion Trends

To eliminate the difference in magnitude and units between the simulated mean erosion rate and the experimental mass loss, the two indicators were independently normalized within each wind-speed group using min–max normalization:

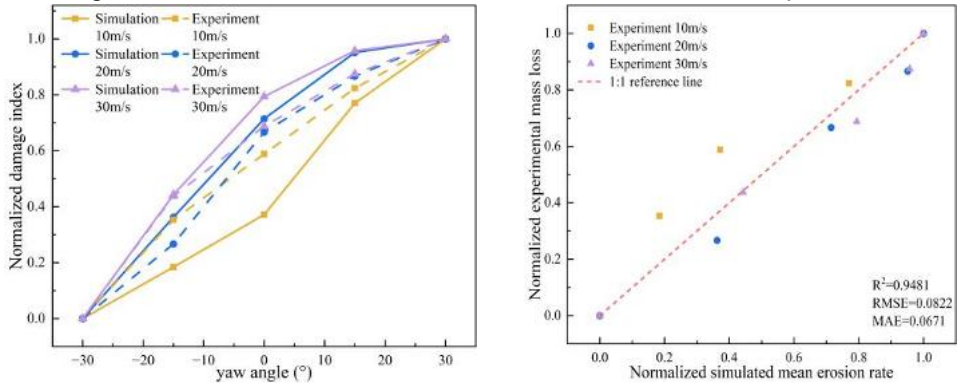
$$D_{i,j}^{*} = \frac{D_{i,j} - D_{min,j}}{D_{max,j} - D_{min,j}} \tag{7}$$

where $D_{i,j}^{*}$ is the normalized value of the i-th yaw-angle condition in the j-th wind-speed group; $D_{i,j}$ is the corresponding original value; and $D_{\min,j}$ and $D_{\max,j}$ are the minimum and maximum values of the same indicator within that wind-speed group, respectively. The simulated mean erosion rate and experimental mass loss were normalized separately using the same procedure. The resulting dimensionless indicators were used to compare their relative variations with yaw angle rather than their absolute magnitudes.

Figure 9(a) compares the normalized mean erosion rate with the normalized experimental mass loss. At all three wind speeds, both quantities generally increased as the yaw angle varied from −30° to 30°, indicating a consistent yaw-dependent response. This agreement can be attributed to the common dependence of both indicators on particle–surface interaction conditions. Variations in yaw alter the relative direction between the particle-laden flow and the exposed surface, thereby modifying particle trajectories, local incidence conditions, and the effective impact area. This result is similar to that reported by *Li et al. (2025)*, where numerical predictions and experimental measurements exhibited consistent variation trends in aeolian-particle transport. The remaining differences at intermediate yaw angles may be associated with the distinct geometrical and loading conditions of the two configurations of the two approaches: the simulation represents spatially averaged erosion over a curved lamp cover, whereas the experiment measures cumulative mass loss from a flat PC specimen subjected to jet impingement.

The correlation analysis in Figure 9(b) yielded R^2=0.9481, RMSE = 0.0822, and MAE = 0.0671, with most points distributed close to the 1:1 reference line. Because min–max normalization was performed separately within each wind-speed group, these statistics quantify similarity in the yaw-dependent variation rather than absolute predictive accuracy. The relatively high R^2 together with the low error metrics further indicate a consistent trend-level agreement between the numerical and experimental results, suggesting that both approaches capture the same variation pattern with respect to yaw angle.

The correlation analysis in Figure 9(b) yielded R^2=0.9481, RMSE = 0.0822, and MAE = 0.0671. Most data points were distributed near the 1:1 reference line, indicating close agreement between the relative variations of the numerical and experimental indicators. Because min–max normalization was performed independently within each wind-speed group, these statistics characterize similarity in the yaw-angle-dependent trends rather than absolute predictive accuracy. The high R^2 and relatively small errors therefore support trend-level agreement between the simulated mean erosion rate and experimental mass loss.



a) *b)*

Fig. 9 - Comparison between normalized numerical and experimental erosion indicators

a) Comparison of normalized simulation and experimental results;
b) Correlation between normalized simulation and experimental results

Fig.10 further quantifies the differences between the normalized numerical and experimental responses.

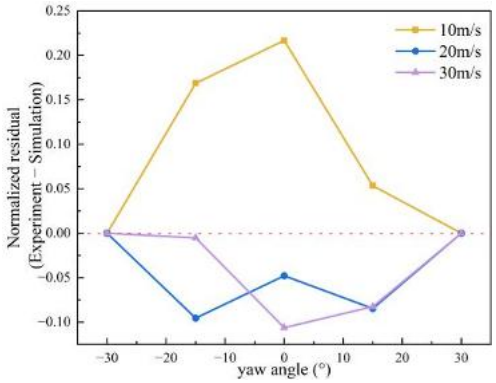


Fig. 10 - Residuals between normalized simulation and experimental results

Positive residuals occurred mainly at 10 m/s, indicating that the normalized experimental mass loss exceeded the corresponding normalized mean erosion rate at several intermediate yaw angles. At 20 and 30 m/s, negative residuals occurred more frequently at intermediate yaw angles, indicating comparatively higher

normalized numerical values. This change in residual sign is likely related to differences in particle incidence, near-wall velocity, dispersion, and effective impact area between the curved lamp cover and the flat PC specimen. Despite these local deviations, both indicators retained the same overall yaw-dependent tendency. This result is similar in validation outcome to *Yan et al., (2024)*, whose wind-tunnel experiments supported the reliability of CFD predictions for wind–sand flow. The residual analysis therefore supports comparative evaluation of erosion response across wind-speed and yaw-angle conditions rather than direct prediction of experimental mass loss.

CONCLUSIONS

The wind-blown sand erosion characteristics of a PC lamp cover for agricultural machinery were investigated using one-way coupled Eulerian–Lagrangian simulations and controlled gas-jet erosion tests. The main conclusions were as follows:

(1) Erosion concentrated near the windward leading edge and adjacent downstream surface, whereas the leeward region was weakly affected. The pressure maximum occurred in the stagnation region, but the erosion maximum shifted downstream, suggesting that the spatial separation between the pressure and erosion maxima was associated with the combined effects of particle impact velocity, impact angle, local particle flux, and the near-wall flow field.

(2) Wind speed strongly influenced erosion intensity within the investigated range. Mean and maximum erosion rates followed power laws with exponents of approximately 2.70 and 2.31. As yaw changed from negative to positive values, the mean erosion rate generally increased, while the maximum erosion rate showed a U-shaped variation with a minimum near 0°.

(3) The erosion concentration factor KCF reflected localized damage. At 20 m/s, its values at −30°, 0°, and 30° were 13.31, 5.45, and 9.54, respectively. The high value at −30° showed that a relatively low mean erosion rate could coexist with pronounced local erosion concentration. Mean erosion rate, maximum erosion rate, and KCF should therefore be considered together.

(4) The coupon tests showed increasing mass loss and surface roughness with wind speed and yaw angle, accompanied by an increase in the density and coverage of surface defects. The normalized mean erosion rate followed the experimental mass-loss trend (R^2 = 0.9481, RMSE = 0.0822, MAE = 0.0671). Because the numerical and experimental configurations differed, this agreement supports relative trend prediction rather than absolute quantitative validation of the full-scale lamp-cover model.

ACKNOWLEDGEMENT

The authors were funded for this project by the National Natural Sciences Foundation of China (NSFC), Grant/Award Number: 12362033.

REFERENCES

[1] Alqallaf J., Ali N., Teixeira J.A., & Addali A. (2020). Solid particle erosion behaviour and protective coatings for gas turbine compressor blades—A review. *Processes*, 8(8), 984. https://doi.org/10.3390/pr8080984

[2] *** ASTM International. (2018). *ASTM G76-18: Standard test method for conducting erosion tests by solid particle impingement using gas jets*. ASTM International, West Conshohocken, Pennsylvania, USA. https://doi.org/10.1520/G0076-18

[3] Bellman R., & Levy A. (1981). Erosion mechanism in ductile metals. *Wear*, 70(1), 1–27. https://doi.org/10.1016/0043-1648(81)90268-4

[4] Bi H., Jia P., Qin K., Yu L., Cao C., Xia D., Guo X., Liu Y., Chen B., Bi Y. (2023). Porous hot air tea de-enzyming and carding machine under gas–solid coupling conditions: Numerical simulations and performance testing. *INMATEH – Agricultural Engineering*, 71(3), 301–318. https://doi.org/10.35633/inmateh-71-26

[5] Chen G., Li F., Qu F., & Zhang C. (2025). Simulation study on soybean winnowing based on CFD–DEM coupling. *INMATEH – Agricultural Engineering*, 77(3), 362–372. https://doi.org/10.35633/inmateh-77-29

[6] Deng T. (2025). Erosive wear mechanisms of materials—A review of understanding and progresses. *Materials*, 18(7), 1615. https://doi.org/10.3390/ma18071615

[7] Elghobashi S. (1994). On predicting particle-laden turbulent flows. *Applied Scientific Research*, 52(4), 309–329. https://doi.org/10.1007/BF00936835

[8] Ferreira M.M., & Lins V.F.C. (2019). Failure in automobile headlight lenses. *Engineering Failure Analysis*, 104, 844–855. https://doi.org/10.1016/j.engfailanal.2019.06.051
[9] Finnie I. (1960). Erosion of surfaces by solid particles. *Wear*, 3(2), 87–103. https://doi.org/10.1016/0043-1648(60)90055-7
[10] Hamed A., Tabakoff W., & Wenglarz R. (2006). Erosion and deposition in turbomachinery. *Journal of Propulsion and Power*, 22(2), 350–360. https://doi.org/10.2514/1.18462
[11] Hutchings I.M. (1981). A model for the erosion of metals by spherical particles at normal incidence. *Wear*, 70(3), 269–281. https://doi.org/10.1016/0043-1648(81)90347-1
[12] Katsamberis D., Browall K., Iacovangelo C., Neumann M., & Morgner H. (1998). Highly durable coatings for automotive polycarbonate glazing. *Progress in Organic Coatings*, 34(1–4), 130–134. https://doi.org/10.1016/S0300-9440(98)00002-2
[13] Kok J.F., Parteli E.J.R., Michaels T.I., & Bou Karam D. (2012). The physics of wind-blown sand and dust. *Reports on Progress in Physics*, 75(10), 106901. https://doi.org/10.1088/0034-4885/75/10/106901
[14] Li F., Jin A., Yang B., Li J., & Yang J. (2025). CFD–DEM simulation of aeolian sand transport: Effects of wind speed and sand particle shape. *INMATEH – Agricultural Engineering*, 77(3), 1116–1130. https://doi.org/10.35633/inmateh-77-90
[15] Menter F.R. (1994). Two-equation eddy-viscosity turbulence models for engineering applications. *AIAA Journal*, 32(8), 1598–1605. https://doi.org/10.2514/3.12149
[16] Oka Y.I., Ohnogi H., Hosokawa T., & Matsumura M. (1997). The impact angle dependence of erosion damage caused by solid particle impact. *Wear*, 203–204, 573–579. https://doi.org/10.1016/S0043-1648(96)07430-3
[17] Oka Y.I., Okamura K., & Yoshida T. (2005a). Practical estimation of erosion damage caused by solid particle impact: Part 1—Effects of impact parameters on a predictive equation. *Wear*, 259(1–6), 95–101. https://doi.org/10.1016/j.wear.2005.01.039
[18] Oka Y.I., & Yoshida T. (2005b). Practical estimation of erosion damage caused by solid particle impact: Part 2—Mechanical properties of materials directly associated with erosion damage. *Wear*, 259(1–6), 102–109. https://doi.org/10.1016/j.wear.2005.01.040
[19] Shao Y., & Lu H. (2000). A simple expression for wind erosion threshold friction velocity. *Journal of Geophysical Research: Atmospheres*, 105(D17), 22437–22443. https://doi.org/10.1029/2000JD900304
[20] Sundararajan G. (1991). A comprehensive model for the solid particle erosion of ductile materials. *Wear*, 149(1–2), 111–127. https://doi.org/10.1016/0043-1648(91)90368-5
[21] Wang J., Gao J., Zhang Y., & Cui H. (2024). Analysis of the sand erosion effect and wear mechanism of wind turbine blade coating. *Energies*, 17(2), 413. https://doi.org/10.3390/en17020413
[22] Xie Y., Jiang J.J., & Islam M.A. (2019). Elastomers and plastics for resisting erosion attack of abrasive/erosive slurries. *Wear*, 426–427, 612–619. https://doi.org/10.1016/j.wear.2019.01.123
[23] Yan M., Jin A., & Gao W. (2024). Optimization of joint sand barrier spacing and characterization of wind-sand flow study based on CFD numerical simulation. *INMATEH – Agricultural Engineering*, 73(2), 855–869. https://doi.org/10.35633/inmateh-73-72
[24] Zhang D.M., Huang Z.Y., Yi S.J., Wang S., & Chen Y.F. (2025). Simulation and experimental study on the stability of airflow distribution above the screen in an air-screen millet cleaning device. *INMATEH – Agricultural Engineering*, 77(3), 326–339. https://doi.org/10.35633/inmateh-77-26
[25] Zhao Y., Liu R., Yan F., Zhang D., & Liu J. (2021). Windblown sand-induced degradation of glass panels in curtain walls. *Materials*, 14(3), 607. https://doi.org/10.3390/ma14030607

LIQUID SLOSHING SUPPRESSION EFFECT OF DOUBLE-LAYER ELASTICALLY CONSTRAINED FLOATING PLATE USED FOR PLANT PROTECTION UAVS
/
双层弹性约束浮板液体晃动抑制实验研究

Jizhou ZHENG[1),2)], Chengbin ZHANG[3)], Yixuan SUN[1)], Lin ZHU[1)], Yan ZHANG[*4,5)]
[1)] College of Mechanical and Electronic Engineering, Shandong Agricultural University, Taian 271018, China
[2)] Shandong Key Laboratory of Intelligent Production Technology and Equipment for Facility Horticulture, Taian 271018, China
[3)] Shandong Taikai Power Electronic CO. LTD, Taian 271018, China
[4)] College of Information Science and Engineering, Shandong Agricultural University, Taian 271018, China
[5)] Smart Agriculture Technology Laboratory of the Ministry of Agriculture and Rural Affairs, Taian 271018, China
Tel: 13954896475; E-mail: zhangyandxy@ sdau.edu.cn
DOI: https://doi.org/10.35633/inmateh-79-91

Keywords: *double-layer floating plate*, *liquid sloshing*, *pesticide tank*, *UAVs*

ABSTRACT
Liquid sloshing in pesticide tanks is a major factor affecting the stability of plant-protection unmanned aerial vehicles (UAVs). A double-layer floating plate was developed to improve sloshing suppression. A series of experiments was conducted to measure the sloshing-induced force under horizontal sinusoidal displacement excitation. The results showed that the double-layer floating plate provided superior sloshing suppression over a wider range of liquid depths. An intermediate-sized floating plate also significantly reduced the sloshing-induced force at specific liquid depths, making it suitable for installation within the limited space available inside pesticide tanks.

摘要
药箱内液体晃动是影响植保无人机飞行稳定性的重要因素之一。为提高液体晃动抑制性能设计了双层弹性约束浮板，并实验测量了水平正弦位移激励下的液体晃动力。结果表明双层浮板在更宽的液体深度范围内具有更优异的抑制晃动能力。同时，中等面积的浮板在某些液体深度也可以显著减小晃动力，从而方便布置于药箱的狭小空间。

INTRODUCTION
With the development of agricultural aviation technology, the use of unmanned aerial vehicles (UAVs) has quickly increased over past decade in China. Apart from agricultural information monitoring, fertilizing, seeding, and pest and disease monitoring, one important role of these UAVs are pesticide spraying for their efficient operation and minimal damage properties *(Kartal et al., 2025)*. For the plant protection UAVs, many studies have done such as path planning *(Huang et al., 2023)*, spraying systems design, spraying decisions, downwash airflow *(Fan et al., 2023)*, and droplet drift and deposition *(Kharim et al., 2019)*.

The attitude and velocity of the UAVs may change violently during the operation process involving of take-off, landing, turn around and barrier-avoidance. So, the liquid sloshing occurs almost inevitably in the pesticide tank. Sloshing is the motion of the free liquid surface. Most of the time during the pesticide spraying process, the pesticide container has a free liquid surface. So, the liquid sloshing is prone to occur when the attitude and velocity of the tank change. The fluid sloshing can introduce large complex disturbance forces and torques and the center of mass shifting, which affect the position and attitude stability of the UAVs. Not only is it difficult to ensure the accuracy of the trajectory and spraying, but also it endangers the safety of the drone. The liquid sloshing in plant protection UAVs has attracted the attention of many researchers *(Sun et al., 2024)*. Apart from the reasonable shape design of the container *(Ahmed et al., 2022)*, one effective way to suppress liquid sloshing is to install rigid or flexible bulkheads *(Liu et al., 2025; Park et al., 2025; Raja et al., 2023; Ren et al., 2023; Raja et al., 2023)*, grilles *(Li et al., 2017; Ru et al., 2023; Yu et al., 2020)*, perforated baffles *(Nimisha et al., 2022; Wang et al., 2023; Wang et al., 2026)*, and other similar structures inside the vessel.

Jizhou Zheng, associate professor; Chengbin Zhang, staff with master degree of engineering; Yixuan Sun, undergraduate student; Lin ZHU, postgraduate student; Yan Zhang, associate professor

To reduce liquid impact load induced by sloshing, moving baffles that contain a spring system were introduced *(Kim et al., 2018)*. A kind of floating baffle that can move up and down along two slide rails was adopted to reduce sloshing at different liquid levels *(Yu et al., 2017; Zhang et al., 2025)*.

Bulkheads or baffles that placed horizontally or vertically can suppress the liquid sloshing effectively, especially in the case of multilayer boards. However, the mass of these boards will definitely reduce the payload of the UAVs. For the multi-rotor electric drones that are widely used in plant protection operation, it's definitely something to keep in mind. Based on this consideration, the author used low-density foam to make the baffle and introduced an elastically constrained floating plate to suppress liquid sloshing in the pesticide tank of plant protection UAVs *(Zheng et al., 2023)*. The experimental results show that the liquid sloshing suppression capability is improved to some extents and the sloshing suppression effect depends on the relative location between the free surface and the floating plate.

Based on this discovery, the research is further extended and a double-layer elastically constrained floating plate is proposed in this article. A series of experiments are conducted to investigate the liquid sloshing suppression performance of this new structure, and the underlying physical mechanism is strived to explore.

MATERIALS AND METHODS

Experimental setup

The experiment is carried out on a 6-degree-of-freedom motion simulator that moves horizontally in a sinusoidal function form to drive the liquid in a rectangular tank to slosh, as shown in Fig. 1.

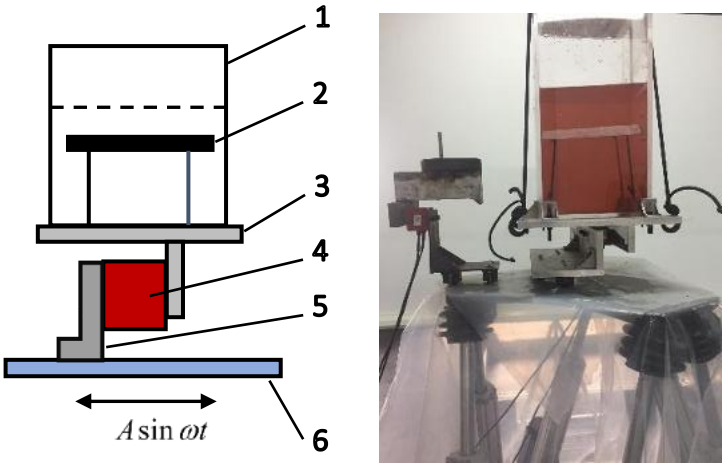


Fig. 1 - Schematic (left) and onsite photo (right) of experiment setup

1-tank; 2-elastically constrained floating plate; 3-T-shaped bracket; 4-force sensor; 5-L-shaped bracket; 6-movement simulator

The internal dimensions of the transparent acrylic rectangular tank are 230 × 220 × 400 mm (length× breadth× height), and the thickness of the walls is 10 mm.

The sloshing force is measured by a force sensor that based on the stress-strain relation and a corresponding dynamic strain instrument. The inertial force of the tank and the T-shaped bracket is synchronously measured by a specially designed mass block and another force sensor, and removed in following data processing procedure.

The square-shaped floating plate is made of foam material with a thickness of 20 mm. Three different side lengths of the square, i.e.,100, 150 and 200 mm, are adopted in different cases. Corresponding to these three lengths, the ratio of the area of the floating plate to the cross-sectional area of the tank is 20%, 45% and 79% respectively.

The floating plate is connected to the fixed point on the bottom of the tank with elastic rubber ropes. The elasticity recovery coefficient of the rope is determined as 67 N/m after undergoing tensile tests on a testing machine and fitting. The length of the rubber rope is set to 150 mm for the single-layer floating plate, and the lengths of the two rubber ropes are both 75 mm for the series-connected double-layer floating plate. In other words, the total length of the rope is the same for these two kinds of floating plate.

The liquid used in the experiment is tap water. Some paint is added in the water for the convenience of observation.

Experimental cases

Basic conditions

During the spraying process, the liquid inside the pesticide tank of the plant protection drone is constantly consumed, causing the liquid depth to change. To reflect the liquid sloshing suppression ability of the floating plate at different liquid depths, six liquid depths are considered, namely 100 mm, 150 mm, 200 mm, 250 mm, 300 mm and 350 mm.

The natural frequency of the liquid depends on the tank's length and the liquid depth that can be calculated according to the formula listed as follows *(Ibrahim, 2005)*.

$$\omega_n = \sqrt{g \frac{n\pi}{l} \tanh \frac{n\pi h}{l}} \tag{1}$$

where:

ω_n is the n-th order natural frequency of the liquid, [rad/s];

n is the order of the liquid sloshing frequency, n = 1,2,3….;

g is the acceleration due to gravity, [m/s^2], and g = 9.8 m/s^2;

l and h are is the tank length in the direction of excitation and the liquid depth respectively, [m].

The first-order natural frequency plays a critical role in liquid sloshing. So, experimental conditions focus on the vicinity of the first-order natural frequency in this article. The first-order natural frequency f in Hz is adopted in experiments for convenience. According to the formula (1), the first natural frequencies of six depths above-mentioned are 1.725 Hz, 1.811 Hz, 1.834 Hz, 1.839 Hz, 1.841 Hz and 1.841 Hz, respectively.

The horizontal displacement of the motion simulator, denoted by $x(t)$, is expressed as:

$$x(t) = A \sin(\omega t) \tag{2}$$

where:

A is the amplitude of the horizontal displacement, [m];

ω is the excitation frequency generated by the motion simulator, [rad/s];

t is the time of motion, [s].

After many trials, A = 5 mm is chosen as the excitation amplitude. Either small amplitude or violent sloshing can be got by changing excitation frequency at this amplitude. The duration time for each case is set to 60 seconds.

To get different amplitude sloshing, the excitation frequency is adopted as 0.5 f - 1.2 f (with an interval of 0.1 f). It should be noted that the sloshing phenomenon is more severe when approaching the first natural frequency, so two excitation frequencies are further introduced, i.e., 0.95 f and 1.05 f.

In the subsequent experiments, the liquid depth and excitation frequency are used as basic conditions. In other words, the sloshing forces at different liquid depth and excitation frequency will be measured for all kinds of floating plate. The number of floating plate layers and the area of the floating plates are the focus of this research, so they are served as control variables.

The number of layers

In previous studies *(Zheng et al., 2003)*, only one elastically contained floating plate is used which has been described in detail. Based on this layout, another floating plate and elastic ropes are added. Namely, two floating plates are used which connect with rubber ropes and arrange in a series form. Here, the former is called as a single-layer floating plate and the latter is named as a double-layer one. At this stage, the focus is on examining the impact of the number of floating board layers on the ability to suppress sloshing. So, the area of the floating plate keeps as same, and the area ratio of floating plate is 79% in both single-layer and double-layer floating plate.

To analyze the effect of the different floating plate arrangement on suppressing liquid sloshing, experiments were also conducted to measure the liquid sloshing force without any floating plate.

The areas of the double-layer floating plate

The cross-sections of the container may change at different position and there are accessories such as pumps and tubes in the pesticide tank of plant protection UAVs. It means that the space available may be limited for arranging the floating plate. Therefore, a smaller floating plate may be needed in practical applications.

Based on the first stage experiment, the floating plate with different sizes are used in the double-layer floating plate to analyze the influence of area on the sloshing suppression effect. In the first case, both the upper and the lower floating plate have the same area ratio. In other words, the areas of two floating plates change synchronously. Three area ratios are adopted, i.e., 20%, 45% and 79%. In the second case, the area ratio of the upper floating plate keeps as 79%, but the lower one has the area ratio of 20%, 45% and 79%, respectively.

RESULTS

The effect of the number of layers

At each liquid depth, horizontal displacement excitations with different frequencies were applied to the tank without any floating plate, with the single-layer floating plate, and with the double-layer floating plate. The liquid sloshing force was measured using the strain-type force sensors, and the results are shown in Fig. 2. Where, three configurations are indicated as 'without plate', ‘single-layer’ and ‘double-layer’, respectively.

The blue curve shown in the figure is the theorical liquid sloshing force in a rectangular tank that given in following formula *(Ibrahim, 2005)*

$$F = A\omega^2 \rho l w h \left\{ 1 + \sum_{n=1}^{\infty} \left[\frac{8 \tanh \frac{(2n-1)\pi h}{l}}{\frac{(2n-1)^3 \pi^3 h}{l}} \frac{\omega^2}{\omega_n^2 - \omega^2} \right] \right\} \tag{3}$$

where: F is the sloshing force, [N];

ρ is the density of the liquid, [kg/m^3], and the density of water is 1000 kg/m^3;

w is the liquid width, [m].

The other variables and values have already been given earlier.

It needs to be pointed that the theoretical sloshing force is given based on linear theory. The sloshing force tends towards infinity at the natural frequency, and it isn’t been fully drawn for clarity.

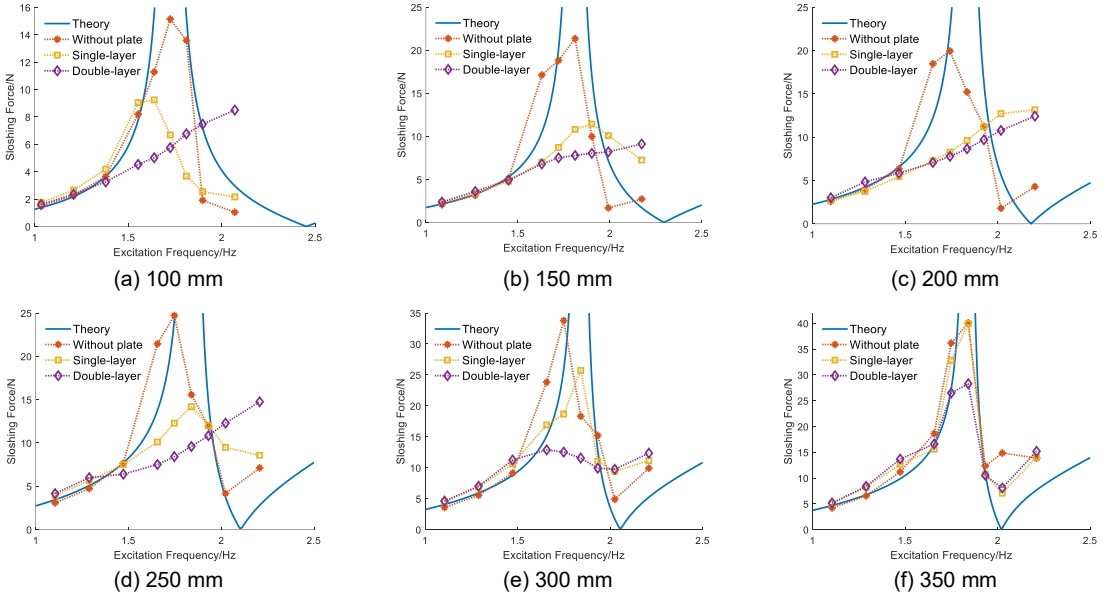


Fig. 2 - Liquid sloshing force at different liquid depths

It can be seen that the sloshing suppression effect of single-layer and double-layer floating plates varies at different liquid depths. Therefore, the following discussion will be based on the liquid depth.

When the excitation frequency is 0.6, 0.7, and 0.8 times the first-order natural frequency (i.e. 0.6 f, 0.7 f and 0.8 f), the experimental values agree well with the theoretical ones at all liquid depths, as shown in the figure. The reason is that the amplitude of liquid sloshing is relatively small at these excitation frequencies, meeting the small-amplitude sloshing assumption in formula (2). This also indicates that the sloshing force measurement system in this article is reasonable and reliable.

Moreover, it also can be seen that the sloshing force with a single-layer or double-layer floating board is not significantly different from that without any floating board at all liquid depths and these three excitation frequencies. This implies that the float plate is not very effective in suppressing slight movements of the liquid. Therefore, the main concerns are put on the large amplitude sloshing of the liquid near its natural frequency.

Fig. 2(a) shows the liquid sloshing force when the liquid depth is 100 mm. It can be seen that the sloshing force decreases from 11 N to 9 N and 5 N for without plate, single-layer and double-layer floating plate at 0.95 f. When the excitation frequency is equal to 1.0 f, the sloshing forces under these cases are 15N, 7N and 5N, respectively. The elastic rope length of the single-layer floating board is 150 mm, which is greater than the liquid depth. Therefore, the floating board remains in a floating state and cannot effectively suppress the movement of the liquid. However, the elastic rope length of the lower section of the double-layer floating plate is 75 mm, which is less than the depth of the liquid. The elastic rope is stretched by the buoyancy of the lower floating plate. On one hand, the lower floating plate rises to a position near the free liquid surface. On the other hand, the movement of the lower floating board is restricted by the elastic cord. As a result, neither the floating board nor the free liquid surface can move violently in the vertical direction. In other words, the liquid can hardly move freely, but only moves horizontally along with the tank. Therefore, the sloshing force for the double-layer floating plate exhibits characteristics of an inertial force that increases with the increase of the excitation frequency.

When the liquid depth equals the rope length of the single-layer floating plate, i.e., 150 mm, the elastic rope begins to bear the tension generated by the upwards movement of the plate. It means that the elastic rope can rebound to some extent if large amplitude liquid sloshing occurs. Therefore, it exhibits relatively good sloshing suppression effect near the natural frequency. As for the double-layer floating plate, the lower plate is completely submerged in the liquid and the lower elastic rope is fully stretched at this depth. So, the sloshing of the liquid below the lower plate is completely suppressed. Meanwhile, the small amount of liquid above the lower floating plate hardly moves vertically due to the suppression of the upper floating plate. Thus, the sloshing force still maintains the inertial force characteristics.

Both single-layer and double-layer floating plate are submerged below the free liquid surface when the liquid depth is 200 mm. The elastic rope is fully stretched for both cases so that the liquid sloshing is effectively suppressed. The sloshing force is about 8 N at 0.95 f, which is 40% of that without any plate. The sloshing forces for the two kinds of floating plate exhibit an inertial force characteristic and are almost the same except for a few frequencies.

When the depth is 250 mm, the sloshing forces exhibit characteristics similar to those at the liquid depth of 150 mm. However, the formation mechanism of the sloshing force for the single-layer floating plate is different. The floating plate is totally submerged and the elastic rope is fully stretched. Thus, the liquid below the plate moves with the tank and the sloshing force with inertial force characteristics generates. But the liquid on the floating plate (about 50 mm deep) can move freely. This part of the liquid will experience significant oscillation when the excitation frequency is close to the natural frequency, resulting in relatively large dynamic forces. For the double-layer floating plate, both segments of the elastic rope are fully stretched. The upper floating plate is closer to the free liquid surface, and all the liquid cannot move freely. Therefore, the sloshing force still remains in the form of the inertial force. As for the magnitude of the sloshing forces at natural frequency, they are 25 N, 14 N and 8 N for without plate, single-layer and double-layer floating plate, respectively. In other words, the sloshing force can be reduced about half or two-third by single-layer or double-layer floating plate.

When the liquid depth reaches 300 mm, the maximum sloshing forces for three cases are 33 N, 25 N and 12 N, respectively. The suppression strength and effective range of the double-layer plate are both greater than those of the single-layer plate.

The sloshing forces at all frequencies for the single-layer floating plate are basically the same as those without plate when the liquid depth is 350 mm. It implies that the sloshing suppression capability is almost completely lost. Although the double-layer floating plate still functions, the range is limited to a narrow frequency band. The reason is that the floating plate locates a deeper position below the free surface and the liquid on the floating plate is no longer restricted by the floating plate.

Overall, the double-layer floating plate has a wider effective range and better suppression capability than the single-layer floating plate. To intuitively understand the sloshing suppression effect of the floating plate, the typical waveforms of the free liquid surface under different excitation frequencies are shown in Fig.3.

Where, the liquid depth is 250 mm and the excitation frequency is 0.7 f, 0.8 f, 0.9 f, 1.0 f, 1.1 f, and 1.2 f, respectively.

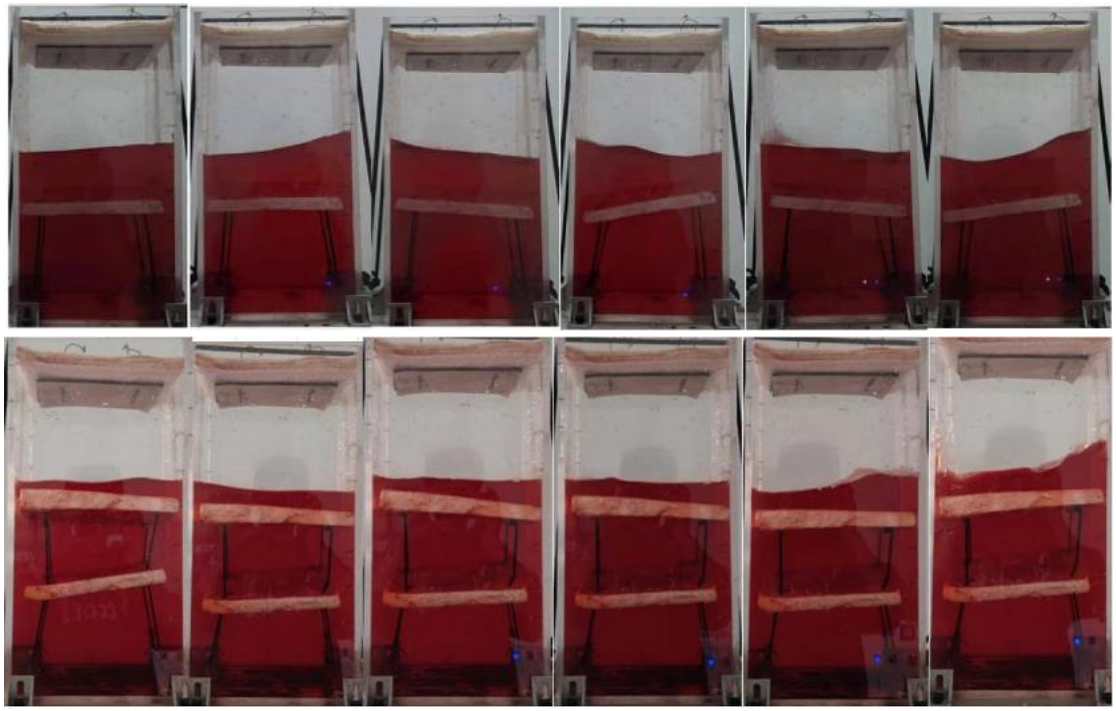
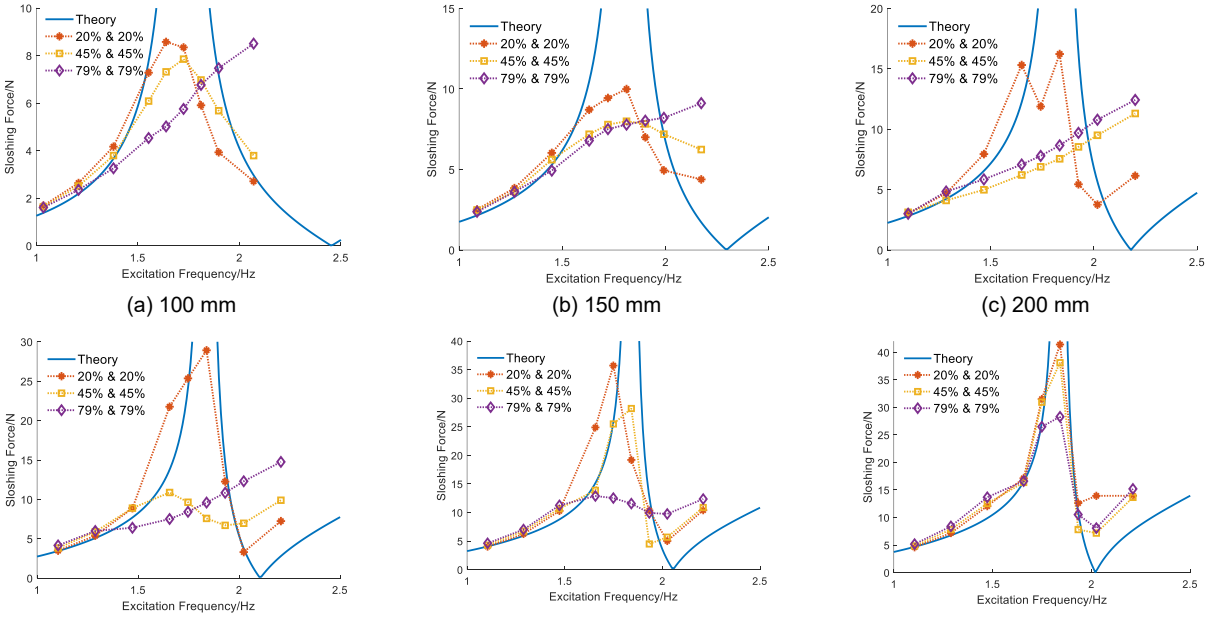


Fig. 3 - Snapshots of free surface (top: single-layer floating plate; bottom: double-layer floating plate; from left to right: 0.7 f, 0.8 f, 0.9 f, 1.0 f, 1.1 f, and 1.2 f)

It can be seen that the upper plate of the double-layer floating plate is closer to the free liquid surface than the single-layer floating plate because of larger buoyancy. The sloshing of the liquid above the floating plate can be suppressed by the floating plate and large amplitude sloshing hardly occurs even if at the natural frequency.

The effect of the areas of the floating plate

As mentioned earlier, the influence of the plate areas on the sloshing suppression effect of the double-layer floating plate is divided into two cases. The results under the first case are given here. The liquid sloshing force at different depth is shown in Fig. 4 when the areas of two plates change synchronously.



(a) 100 mm (b) 150 mm (c) 200 mm

(d) 250 mm (e) 300 mm (f) 350 mm

Fig. 4 - Liquid sloshing force at different liquid depths

Apart from the liquid depth of 350 mm, the double-layer floating plate with the largest area ratio (i.e. 79%) shows excellent sloshing suppression performance. Over a wide range of liquid depths, the sloshing force exhibits characteristics of inertial force because the movement of the upper part of liquid is almost completely suppressed by the floating plate.

Comparing the liquid sloshing forces with those of without any plate shown in Fig. 2, it can be got that the double-layer floating plate with the smallest area ratio (i.e. 20%) has good sloshing suppression capability at smaller liquid depths. At the liquid depth of 100 mm, 150 mm and 200 mm, the maximum sloshing force is about 9 N, 10 N and 16 N, reduced by about 40%, 52% and 20%, respectively. However, the sloshing suppression effect almost disappears totally at liquid depths higher than 250 mm. On one hand, smaller plate areas have less impact on the sloshing of the upper free liquid. On the other hand, smaller areas mean less buoyancy from the floating plates, and thus the position of the upper floating plate is lower than that of a larger floating plate. This also reduces the effect of the floating plate on the upper layer of liquid. Therefore, the double-layer floating plate with the smallest area ratio is more likely to fail under larger liquid depth conditions. In other words, the small area of the floating plate is a disadvantage for the liquid sloshing suppression. A larger area is preferred if there is enough space available in the container.

Compared with the floating plate that have the largest area ratio, the double-layer floating plate with the moderate area ratio (i.e. 45%) has relatively weaker liquid sloshing suppression performance when the liquid depth is equal to or greater than 300 mm. The difference of the liquid sloshing force is about 10 N-17 N near the natural frequency. The situation is similar when the liquid depth is 100 mm but the difference is not so significant. It is determined by the fact that the sloshing force of the liquid is relatively small at this depth. However, the situation changes obviously within the range of medium liquid depths (i.e. 150 mm – 250 mm). The sloshing force of medium-sized floating plate is not significantly different from that of large-sized floating plate, especially near the natural frequency. The maximum difference of the sloshing force is less than 5 N. It means that the double-layer floating plate can still effectively suppress liquid sloshing even if the area ratio is less than 50%. This makes it possible to arrange the double-layer floating plate within the limited space of the pesticide container.

The typical wave shapes of the free liquid surface for the double-layer floating plate with the smallest and medium area ratio are shown in Fig. 5. Where, the liquid depth is 250mm and the excitation frequency is also 0.7 f -1.2 f. The waveforms for the double-layer floating plate with the largest area have been shown in Fig. 3, so they are not given again.

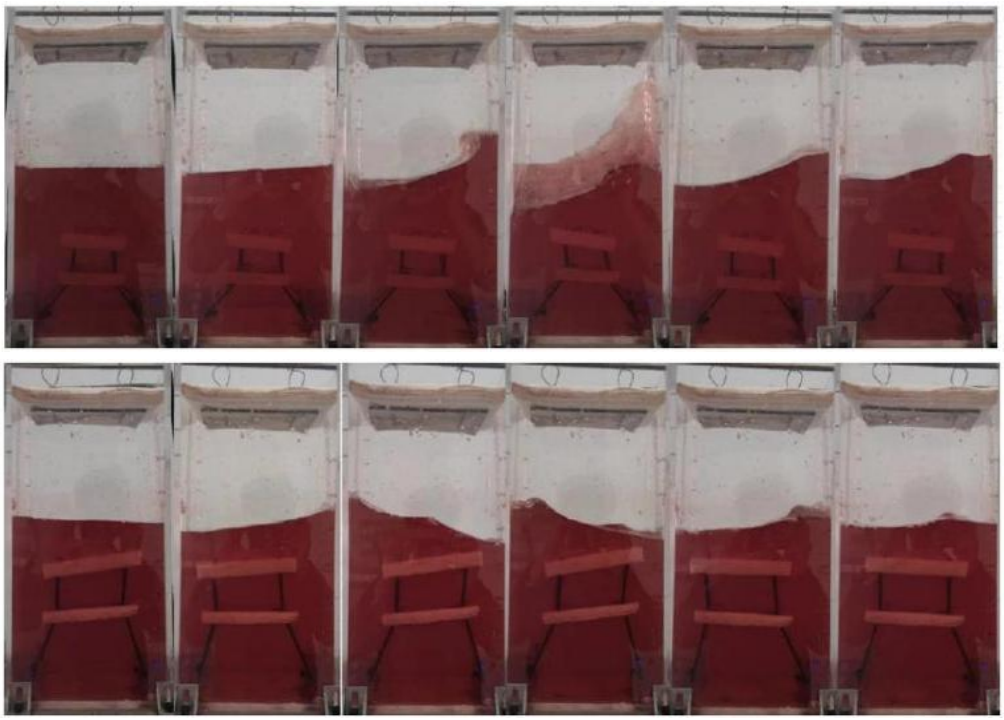


Fig. 5 - Snapshots of the liquid free surface (top: 20% and 20%; bottom: 45% and 45% from left to right: 0.7 f, 0.8 f, 0.9 f, 1.0 f, 1.1 f, and 1.2 f)

It can be seen that the double-layer floating plate with the smallest area ratio exhibits large amplitude sloshing near the natural frequency, which is similar to the case without any plate. However, the situation is much better for the double-layer floating plate with medium area ratio. Although the sloshing amplitude of the free surface is relatively large at $0.9f$ and $1.0f$, the sloshing force does not increase significantly.

According to the experimental results above mentioned, the size of the floating plate that is close to the free liquid surface seems to have a greater influence on the sloshing of the liquid. Therefore, the experiment under the second case were further carried out. That is, the upper floating plate keeps the largest area, and the lower floating plate is the smallest or medium area. The liquid sloshing forces at different depths are shown in Fig. 6 when only the area of lower plate changes.

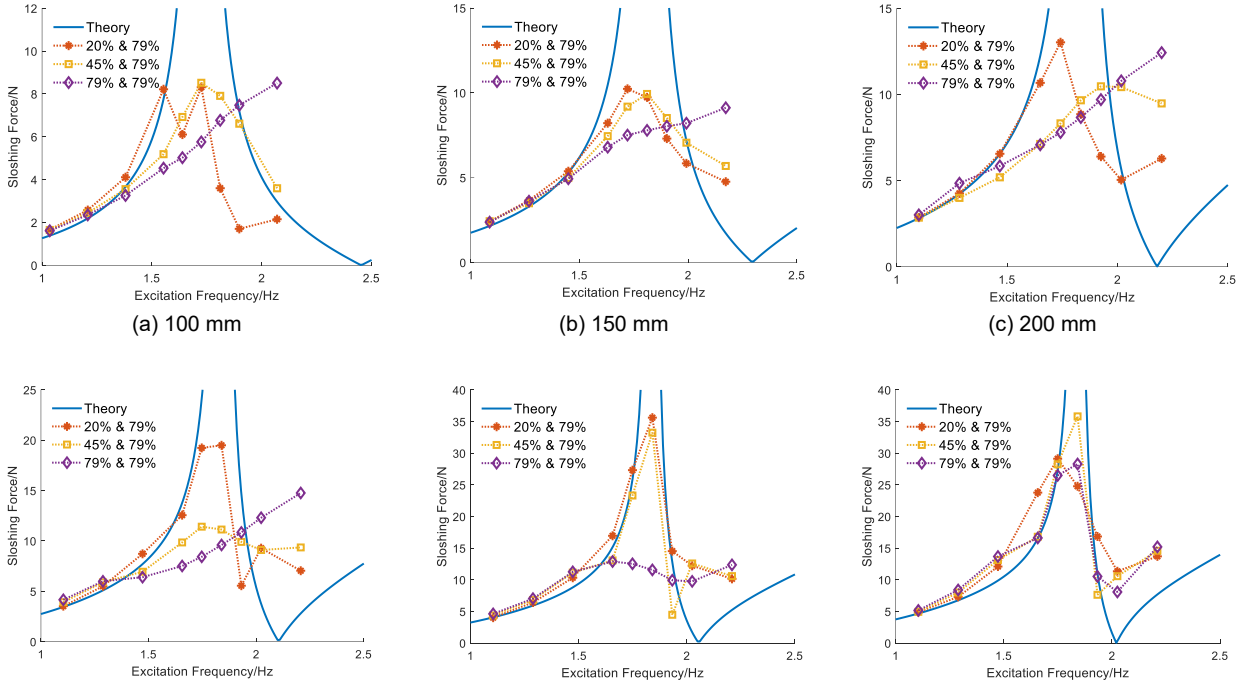


Fig. 6 - Liquid sloshing force at different liquid depths

When the liquid depth is equal to 100 mm and 150 mm, the maximum sloshing force for the smallest and medium area lower plate is about 8 N and10 N, respectively. The forces are almost equal to those of both floating plate with the same area. The reason is that only the lower floating plate functions at these liquid depths. The similar situation occurs at the liquid depth of 300 mm and 350 mm. The peak of the sloshing force near the natural frequency means that large amplitude liquid sloshing appears and the sloshing suppression performance of the floating plate decreases to some extent. The largest difference occurs at the liquid depth of 250 mm. The maximum sloshing force is 19 N for the double-layer floating plate composed of areas ratio of 20% (lower layer) and 79% (upper layer), while the maximum sloshing force is 28 N for the double-layer floating plate with the smallest area. This illustrates the role of the upper floating plate area in damping the motion of the upper liquid.

Overall, compared with configurations in which the area ratios of both floating plates were increased simultaneously, increasing only the area of the upper floating plate did not significantly reduce the sloshing-induced force. Moreover, the sloshing force exhibits some unusual changes at certain liquid depths and excitation frequencies. The reason may lie in the change of the direction of the tension of the upper elastic rope, which makes the interaction between the upper floating plate and the liquid more complex. It is necessary to further study its mechanism with the help of numerical simulations and other methods in order to apply the double-layer floating plate in complex situation.

The typical wave shape of the free surface is shown in Fig. 7 where the liquid depth is 250 mm.



Fig. 7 - Snapshots of the liquid free surface (top: 20% and 79%; bottom:45% and 79%; from left to right: 0.7 f, 0.8 f, 0.9 f, 1.0 f, 1.1 f, and 1.2 f)

It can be seen that large amplitude sloshing occurs near the natural frequency for the area combination of 20% and 79%, while the sloshing amplitude is relatively small for the area combination of 45% and 79%. It is consistent with the changes of the measured sloshing forces shown in Fig.6 (d).

CONCLUSIONS

To improve sloshing suppression in practical applications, a double-layer floating plate was developed based on the single-layer configuration. The effects of the structural parameters of the double-layer floating plate were investigated by measuring the sloshing-induced force at different liquid depths and excitation frequencies. The underlying sloshing-suppression mechanism was also preliminarily examined. The main conclusions are as follows:

(1) The double-layer floating plate provided superior sloshing suppression over a wider range of liquid depths and excitation frequencies.

(2) The medium-sized double-layer floating plate also exhibited effective sloshing suppression at specific liquid depths, indicating its suitability for installation within tanks with limited internal space.

(3) In this study, low- and high-amplitude sloshing conditions were generated by varying the excitation frequency. Both the sloshing-induced forces and the suppression performance of the floating plates were evaluated under steady-state excitation. During actual UAV operation, however, sudden changes in attitude or velocity may produce transient sloshing. Therefore, future work should develop a measurement and data-acquisition system incorporating strain gauges and a microcontroller to capture transient sloshing-induced forces and moments during flight.

ACKNOWLEDGEMENT

The research was supported by Shandong Province Key R&D Program Project (No. 2023TZXD033).

REFERENCES

[1] Ahmed S., Xin H., Faheem M., & Qiu B.J. (2022). Stability analysis of a sprayer UAV with a liquid tank with different outer shapes and inner structures. *Agriculture*, 12(3), 379-397.

[2] Fan G., Liu Z., Qin Y., Long B., Li H., & Li J. (2023). Airflow characteristics of rotorcraft plant protection UAV operating in rice fields. *Biosystem Engineering*, 226, 209-222.

[3] Huang J., Luo Y., Quan Q., Wang B., Xue X., & Zhang Y. (2023). An autonomous task assignment and decision-making method for coverage path planning of multiple pesticide spraying UAVs. *Computer and Electronics in Agriculture*, 212, 108128.
[4] Ibrahim R. A. (2005). *Liquid sloshing dynamics*. Cambridge University Press.
[5] Kartal M. R., Ignatyev D., & Zolotas A. (2025). Comprehensive review of agriculture spraying UAVs challenges and advances: modelling and control. *The Aeronautical Journal*. 129(1340): 2859-2879.
[6] Kharim M.N.A., Wayayok A., Shariff A.R.M., Abdullah A.F., & Husin E.M. (2019). Droplet deposition density of organic liquid fertilizer at low altitude UAV aerial spraying in rice cultivation. *Computer and Electronics in Agriculture*, 167, 105045.
[7] Kim S.P., Chung S.M., Shin W.J., Cho D.S., & Park J.C. (2018). Experimental study on sloshing reduction effects of baffles linked to a spring system. *Ocean Engineering*, 170,136-147.
[8] Li X., Zhang J., Qu F., Zhang W., Wang D., & Li W. (2017). Optimal design of anti-sway inner cavity structure of agricultural UAV pesticide tank（农用无人机药箱防晃内腔结构优化设计）. *Transactions of Chinese Society of Agricultural Engineering*, 33(18), 72-79.
[9] Liu D.X., Chang F.Y., & Chen Y.J. (2025). Experimental study of vertical baffle height on sloshing reduction effects in the rectangular tank. *Ocean Engineering*, 335, 121674.
[10] Nimisha P., Jayalekshmi B.R., & Venkataramana K. (2022). Effective configuration of perforated baffle plate for efficient slosh damping in liquid retaining tanks under lateral excitation. *Ocean Engineering*, 259, 111855.
[11] Park T., Park C., Lee J., & Kim Y. (2025). Experimental observation on violent sloshing flows inside rectangular tank with flexible baffles. *Applied Ocean Research*, 154, 104307.
[12] Raja V.R., & Palanisamy P. (2023). Numerical modelling of nonlinear baffles on sloshing suppression of rectangular tanks under horizontal excitation. *Ocean Engineering*, 267.
[13] Ren Y., Xue M.A., & Lin P. (2023). Experimental study of sloshing characteristics in a rectangular tank with elastic baffles. *Journal of Fluids and Structure*, 122, 103984.
[14] Ru Y., Xue J.K., Liu B., Fang S.P., Hu C.M., & Zhou J. (2023). Simulation and experiment of the anti-shake damping of liquid in helicopter application tank (直升机施药药箱药液阻尼防晃模拟及试验). *Transactions of Chinese Society of Agricultural Engineering*, 39(9), 55-63.
[15] Saghi R., Hirdaris S., & Saghi H. (2022). The influence of flexible fluid structure interactions on sway induced tank sloshing dynamics. *Engineering Analysis with Boundary Elements*, 131, 206-217.
[16] Sun X.B., Cai M.C., Niu L.H., Wang Q., Zhou W.Q., Tang H., & Wang J.W. (2024). Numerical simulation analysis and experimental research on liquid sloshing in herbicide tank of the plant protection UAV. *Computers and Electronics in Agriculture*, 227, 109532.
[17] Wang J.D., Liu X.Q., & Zhao S.Y. (2026). Mitigating liquid sloshing in cylindrical containers using rotationally adjustable elliptical-hole baffles. *Journal of Sound and Vibration*, 623, 119533.
[18] Wang S., Xu T., Shen K., Wang B., Dong G.H., & Wang T.Y. (2023). Numerical simulation of the interaction between nonlinear sloshing flow and side-mounted perforated baffles. *Physics of Fluids*, 35 (8), 083607.
[19] Yu L., Xue M.A., & Jiang Z., (2020). Experimental investigation of parametric sloshing in a tank with vertical baffles. *Ocean Engineering*, 213, 107783.
[20] Yu Y.M., Ma N., Fan S.M., & Gu X.C. (2017). Experimental and numerical studies on sloshing in a membrane-type LNG tank with two floating plates. *Ocean Engineering*, 129:217-227
[21] Zhang H.D., Chen J.S., Ahmed R., Shi G.J., & Mohamed E. (2025). Comparative study on sloshing suppression effectiveness between single and double floating composite baffles under horizontal resonant conditions. *Ocean Engineering*, 342, 123011.
[22] Zheng J.Z., Li Y.P., Lin Q.M., & Xue X.Y. (2023). Experimental investigation of liquid sloshing suppression in plant protection UAV based on floating plate structure (基于浮板结构的植保无人机药液晃动抑制试验). *Transactions of Chinese Society of Agricultural Machinery*, 54(6), 94-103.

FAILURE MECHANISMS IN REPAIRABLE AGRICULTURAL TRACTORS ACROSS ENGINE OPERATING-HOUR CLASSES
/
MECHANIZMY POWSTAWANIA USZKODZEŃ W CIĄGNIKACH ROLNICZYCH W ZALEŻNOŚCI OD CZASU PRACY SILNIKA

Karol DURCZAK[*1]; Tomasz ŻELAZIŃSKI[2]; Adam EKIELSKI[2]
[1] Department of Biosystems Engineering, Faculty of Environmental and Mechanical Engineering, Poznan University of Life Sciences, Poznań / Poland;
[2] Department of Production Engineering, Faculty of Production Engineering, University of Life Sciences in Warsaw, Warsaw / Poland
Tel.: +48 61 846 60 75; E-mail: karol.durczak@up.poznan.pl (corresponding author)

DOI: https://doi.org/10.35633/inmateh-79-92

Keywords: *agricultural tractor, failure mechanism, service record, engine operating hour, reliability, mechanical engineering*

ABSTRACT
Agricultural tractors are repairable mechanical systems whose service records can provide insight into how failure mechanisms evolve over their operating life. This study analysed 200 failure cases recorded for 75 Zetor tractors. Failure causes were classified into six mechanism categories and compared across four engine operating-hour classes. The relationship between operating-hour class and failure mechanism was evaluated using contingency tables, chi-square tests, Cramer's V, odds ratios, and correspondence analysis. Sealing-related failures predominated in the dataset, whereas material/manufacturing and electrical causes were more prevalent during the early stages of operation, and wear-, friction-, and fatigue-related mechanisms became more prominent at higher operating hours. The findings provide a basis for service planning and the assessment of tractor reliability.

STRESZCZENIE
Ciągniki rolnicze są naprawialnymi układami mechanicznymi, a dane serwisowe mogą wskazywać, jak mechanizmy uszkodzeń zmieniają się w trakcie eksploatacji. W pracy przeanalizowano 200 przypadków uszkodzeń zarejestrowanych dla 75 ciągników marki Zetor. Przyczyny uszkodzeń pogrupowano w sześć kategorii mechanizmów i porównano w czterech klasach motogodzin pracy silnika. Zastosowano tabele kontyngencji, statystykę chi-kwadrat, współczynnik V Cramera, ilorazy szans oraz analizę korespondencji. Największy udział w zbiorze danych miały mechanizmy uszczelnieniowe, natomiast wady materiałowo-wykonawcze i elektryczne częściej występowały we wczesnej fazie eksploatacji, a mechanizmy zużyciowo-tarciowe w późniejszych zapisach serwisowych.

INTRODUCTION

Agricultural tractors are complex repairable machines that combine mechanical, hydraulic, pneumatic, electrical and control subsystems. In the discipline of mechanical engineering, they can be treated as mobile technical systems exposed to variable loads, vibration, contamination, thermal cycles, lubricant ageing, environmental effects and operator-dependent usage patterns. Their failure behaviour is important because breakdowns may interrupt agrotechnical operations during short seasonal windows and can increase maintenance costs, downtime and logistic pressure on service networks.

Reliability engineering describes the performance of technical systems using concepts such as failure occurrence, maintainability, availability, lifetime distribution and risk of degradation during operation (*Birolini, 2017; Blischke and Murthy, 2000; O'Connor and Kleyner, 2012; Rausand and Hoyland, 2004*). In many repairable systems, the life cycle is often interpreted through early-life failures, random failures and wear-out failures. However, these phases should not be treated only as statistical intervals. From a mechanical engineering perspective, they should also be linked with loads, material response, contact conditions, lubrication, sealing quality, electrical continuity and structural integrity. This interpretation is consistent with failure-mechanism analysis, which connects observed failure symptoms with the physical processes that caused them (*Tinga, 2013; Zio, 2009*).

A complete lifetime dataset is required to estimate reliability functions, failure intensity or hazard rates with high confidence (*Birolini, 2017; Rausand and Hoyland, 2004*). In agricultural service practice, however, available data are often more limited. Service databases may include only failed cases, incomplete exposure histories, repair descriptions or non-standardised cause descriptions. Such data are not sufficient for estimating absolute failure probability in the whole tractor population, but they can still be useful for analysing the internal structure of recorded failures. This distinction is important because an incomplete service dataset may still indicate which physical mechanisms are more frequent at different stages of recorded operation.

The practical importance of maintenance and diagnostic data in agricultural machinery has been confirmed in several recent studies. Tractor maintenance planning, reliability support systems and replacement strategies have been analysed using field, service and decision-support approaches (*Atli, 2024; Kataev et al., 2024; Kolhe et al., 2024; Mishra and Satapathy, 2023*). Diagnostic and predictive-maintenance methods have also been applied to tractor transmission systems and agricultural machinery components (*da Silva et al., 2019; Jardine et al., 2006; Mobley, 2002; Moubray, 1997*). Other studies have examined failures and reliability models of farm tractors and working parts exposed to abrasive or variable operating conditions (*Durczak and Selech, 2022; Mikolajczak and Napiorkowski, 2016; Napiorkowski and Gonera, 2020; Paman et al., 2024*). These works show that service and field information can support engineering decisions, but they also indicate that the interpretation of failure records depends strongly on the quality and structure of the available data.

Recent developments in agricultural engineering additionally show that tractor operation can be described with increasing detail using mission profiles, CAN-BUS data, GNSS records, working cycles and operational analytics (*Angelucci and Mattetti, 2024; Gˆ tz et al., 2025; Mattetti et al., 2021*). These studies are important because they link machine use with real operating conditions. At the same time, many service organisations still rely on ordinary workshop records rather than continuous sensor-based monitoring. Therefore, there is a practical need for simple methods that can extract engineering information from historical service records, even when these records do not contain complete exposure data.

From a mechanical engineering viewpoint, the physical interpretation of the recorded cause is essential. A sealing failure may indicate a different technical problem than a short circuit, a material defect, a seized actuator, a fractured pipe or excessive wear of a transmission component. Therefore, the service cause can be transformed into a mechanism-oriented variable that supports feedback to design, manufacturing quality control, warranty analysis and maintenance planning. This interpretation is also consistent with contemporary agricultural engineering studies, where machine behaviour, material properties, reliability, operational data and environmental aspects are jointly analysed (*Angelucci and Mattetti, 2024; Kim and Kim, 2023; Lovarelli and Bacenetti, 2019; Mattetti et al., 2021; Scolaro et al., 2021; Zelazinski et al., 2023*).

Categorical-data methods are useful when service records are grouped into operating-time classes and mechanism categories. Contingency tables, the Pearson chi-square test, Cramer's V, odds ratios and correspondence analysis allow the researcher to describe associations between two categorical variables without assuming a continuous failure-time distribution (*Agresti, 2019; Friendly and Meyer, 2015; Greenacre, 2017; McHugh, 2013*). In the present context, these methods are not used to build a complete reliability model. They are used to determine whether the structure of recorded failure mechanisms changes across engine operating hour classes.

The research gap addressed in this paper is the limited use of ordinary service records for identifying operating-time-dependent failure mechanisms of agricultural tractors. Previous studies have often focused on failure frequency, maintenance planning, diagnostic methods or general reliability indicators, whereas fewer studies have transformed workshop failure causes into physical mechanism categories and analysed their distribution across operating-time classes. The objective of the study was therefore to analyse how recorded failure causes of Zetor tractors were distributed across engine operating hour classes. The working assumption was that early service records would contain a relatively higher contribution of material, manufacturing, assembly and electrical faults, whereas later records would show a higher contribution of wear-, friction- and fatigue-related mechanisms.

MATERIALS AND METHODS

The empirical material consisted of historical service failure records of Zetor agricultural tractors. The dataset contained 200 diagnostic service cases recorded for 75 unique vehicle identification numbers. Each record included the tractor model, engine operating hours (EOH; the source records used the Polish term motogodziny, abbreviated as “mth”), observed symptom, assembly group, damaged part, failure cause, labour

cost, parts cost and total repair cost. The dataset contained recorded failures only; therefore, it was not used to estimate failure probability, reliability function or hazard rate.

The operating time indicator was discretised into four classes: 0-250 EOH, 251-500 EOH, 501-750 EOH and more than 750 EOH. These intervals were used as practical stages of recorded operation: early operation, initial regular operation, intermediate operation and later recorded operation. The descriptive characteristics of the dataset are presented in Table 1.

Table 1

Characteristics of the analysed service failure dataset

Characteristic	Value
Number of service failure cases	200
Number of unique VIN identifiers	75
Minimum [EOH]	2
Maximum [EOH]	1498
Mean [EOH]	414.69
Median [EOH]	390
Number of EOH classes	4
Number of mechanism categories	6

The original service causes were translated from Polish service terminology and grouped into six failure-mechanism categories. The grouping was performed on the basis of the physical interpretation of the cause, not on the basis of the failed subsystem. This distinction is important because the same subsystem may fail through several mechanisms. For example, a pneumatic or hydraulic component may fail because of a sealing fault, material defect, contamination or wear. The taxonomy used in the analysis is shown in Table 2.

Table 2

Failure-cause taxonomy used for mechanism-based analysis

Failure-mechanism category	Original service causes included in the category
Sealing-related	damaged sealing surface; damaged sealing collar; damaged seals; damaged cylinder seal
Material/manufacturing	material defect; defective weld or soldering; inaccurate machining; defective thread; defective battery cell
Electrical	short circuit; burnout; no continuity; broken wire
Wear/friction/fatigue	seizure; excessive wear; excessive clearance; cracking
Assembly/structural	faulty assembly; unriveting; pipe fracture; bending; fracture
Other/contamination/joint	delamination; impurities; clogging; functional fault

Following general recommendations for categorical and count-data analysis (*Agresti, 2019; Friendly and Meyer, 2015*), three statistical measures were used to describe the association between operating-time class and failure-mechanism category. First, the Pearson chi-square statistic was calculated from the contingency table, as shown in Equation (1):

$$\chi^2 = \sum_{i=1}^{r} \sum_{j=1}^{c} \frac{(O_{ij} - E_{ij})^2}{E_{ij}} \quad (1)$$

where:

O_{ij} – observed frequency in row i and column j;

E_{ij} – expected frequency in row i and column j under the assumption of independence;

r – number of rows in the contingency table;

c – number of columns in the contingency table.

The strength of association was expressed using Cramer's V, as given in Equation (2):

$$V = \sqrt{\frac{\chi^2}{n \cdot min(r-1,\ c-1)}} \quad (2)$$

where: n – total number of observations included in the contingency table;

$min(r - 1, c - 1)$ – the smaller dimensional correction factor used to normalise the chi-square statistic.

For early-life comparison, the odds ratio for each failure-mechanism category was calculated using the 0-250 EOH class versus all later records, as shown in Equation (3):

$$OR = \frac{(a+0.5)(d+0.5)}{(b+0.5)(c+0.5)} \quad (3)$$

where:

OR – odds ratio for the occurrence of a given failure mechanism in early-life service cases compared with later service cases;

a – number of early-life cases with the analysed failure mechanism;

b – number of early-life cases without the analysed failure mechanism;

c – number of later service cases with the analysed failure mechanism;

d – number of later service cases without the analysed failure mechanism;

0.5 – Haldane–Anscombe continuity correction added to each cell to stabilise the odds-ratio estimate when sparse cells occur.

Finally, correspondence analysis was used as an exploratory graphical method to visualise associations between EOH classes and failure-mechanism categories. The map was not treated as a predictive model; it was used to support interpretation of the contingency structure.

RESULTS

The overall distribution of failure-mechanism categories is shown in Figure 1. The largest category was sealing-related failures, which included 90 service cases and represented 45.0% of the dataset. Material/manufacturing mechanisms accounted for 37 cases, electrical mechanisms for 32 cases and wear/friction/fatigue mechanisms for 23 cases. Assembly/structural and other/contamination/joint mechanisms were less frequent.

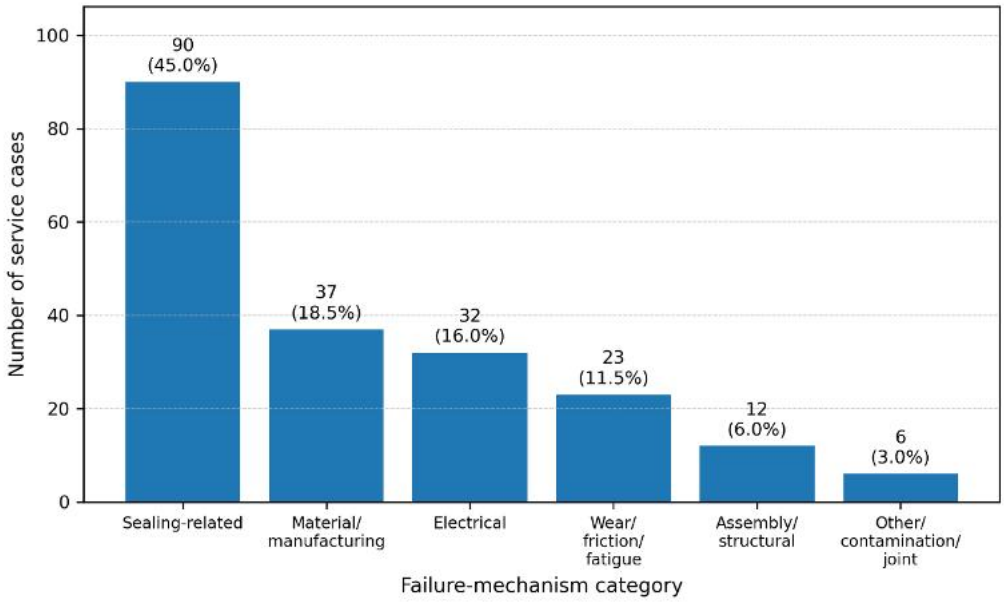


Fig. 1 - Distribution of failure-mechanism categories in the analysed service records

The predominance of sealing-related causes is mechanically meaningful. Many tractor assemblies operate with hydraulic oil, lubricants, compressed air or coolant, and their functional reliability depends on the integrity of seals, collars, sealing surfaces and joints. A sealing fault may therefore appear in different subsystems, but it represents one common physical mechanism that can be targeted by improved material selection, assembly control and early leakage inspection.

The cross-classification of EOH classes and failure-mechanism categories is presented in Table 3.

Table 3

Contingency table of engine operating hour class and failure-mechanism category

EOH class	Sealing-related	Material/ manufacturing	Electrical	Wear/ friction/ fatigue	Assembly/ structural	Other/ contamination/ joint	Total
0-250	18	14	11	2	3	4	52
251-500	38	16	8	10	4	2	78
501-750	29	7	10	5	4	0	55
>750	5	0	3	6	1	0	15
Total	90	37	32	23	12	6	200

The chi-square statistic calculated according to Equation (1) was 31.25, with 15 degrees of freedom and p = 0.008. Cramer's V calculated according to Equation (2) was 0.228. This indicates a weak-to-moderate but interpretable association between operating-time class and failure-mechanism category.

The percentage structure by EOH class is illustrated in Figure 2.

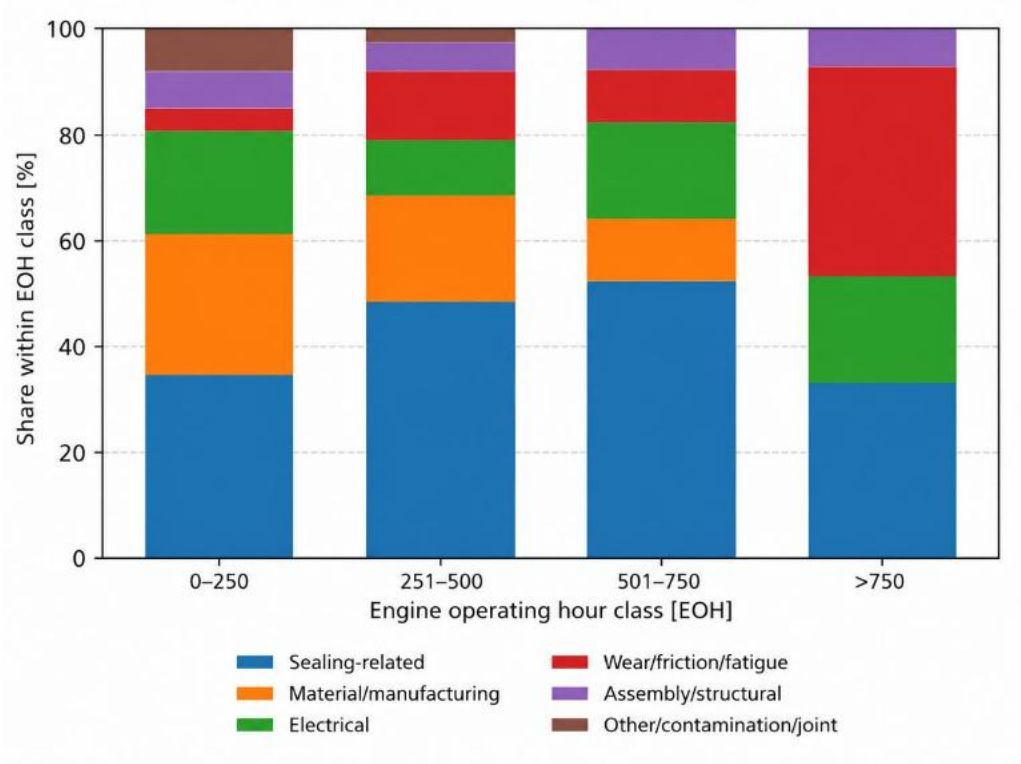


Fig. 2 - Failure-mechanism structure across engine operating hour classes

In the 0-250 EOH class, material/manufacturing and electrical mechanisms together accounted for 48.1% of records, while wear/friction/fatigue accounted for only 3.8%. In the >750 EOH class, wear/friction/fatigue represented 40.0% of recorded cases. Sealing-related mechanisms remained important in all classes, but they were particularly visible in the 251-500 and 501-750 EOH classes.

The early-life odds ratios calculated according to Equation (3) are presented in Table 4.

Table 4

Early-life odds ratios for failure-mechanism categories

Failure-mechanism category	0-250 EOH	>250 EOH	OR	95% CI
Sealing-related	18	72	0.57	0.30-1.08
Material/manufacturing	14	23	2.01	0.95-4.25
Electrical	11	21	1.64	0.74-3.65
Wear/friction/fatigue	2	21	0.29	0.08-1.13
Assembly/structural	3	9	1.04	0.29-3.69
Other/contamination/joint	4	2	5.44	1.12-26.39

Values above 1.0 indicate that the category was relatively more frequent in the 0-250 EOH group than in later records. Material/manufacturing mechanisms had an odds ratio of 2.01, while electrical mechanisms had an odds ratio of 1.64. Wear/friction/fatigue mechanisms had an odds ratio of 0.29, confirming their lower occurrence in early records and higher occurrence after 250 EOH.

The correspondence analysis map is presented in Figure 3.

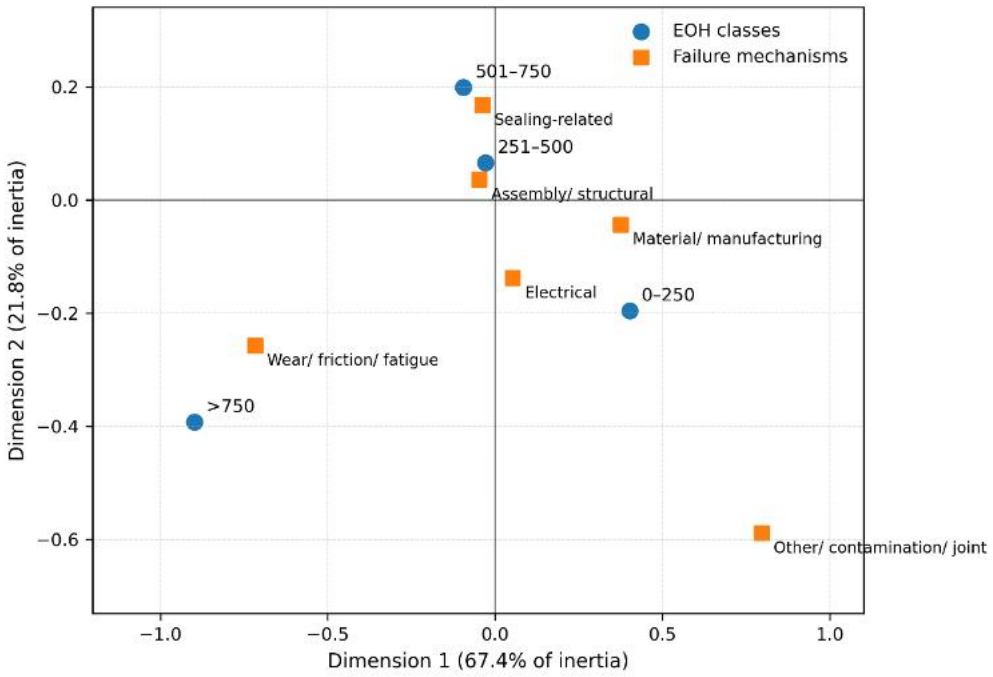


Fig. 3 - Correspondence analysis map of EOH classes and failure-mechanism categories

The first two dimensions explained 89.2% of the total inertia. The 0-250 EOH class was located closer to material/manufacturing, electrical and other/contamination/joint categories. The >750 EOH class was located closest to wear/friction/fatigue mechanisms. The 251-500 and 501-750 EOH classes were positioned nearer to sealing-related mechanisms, which reflects the high contribution of sealing faults in these operating ranges.

To connect the mechanism-oriented view with the mechanical structure of the tractor, the failure mechanisms were also compared across aggregated subsystem classes. The percentage structure is presented in Figure 4. Cabin/control failures were dominated by sealing-related causes associated mainly with gas springs, locks and cabin fittings. Electrical/starting failures were mostly electrical or material/manufacturing in nature. Engine/cooling and pneumatic/braking classes showed mixed mechanisms, which confirms that subsystem names alone do not fully explain the physical origin of the failure.

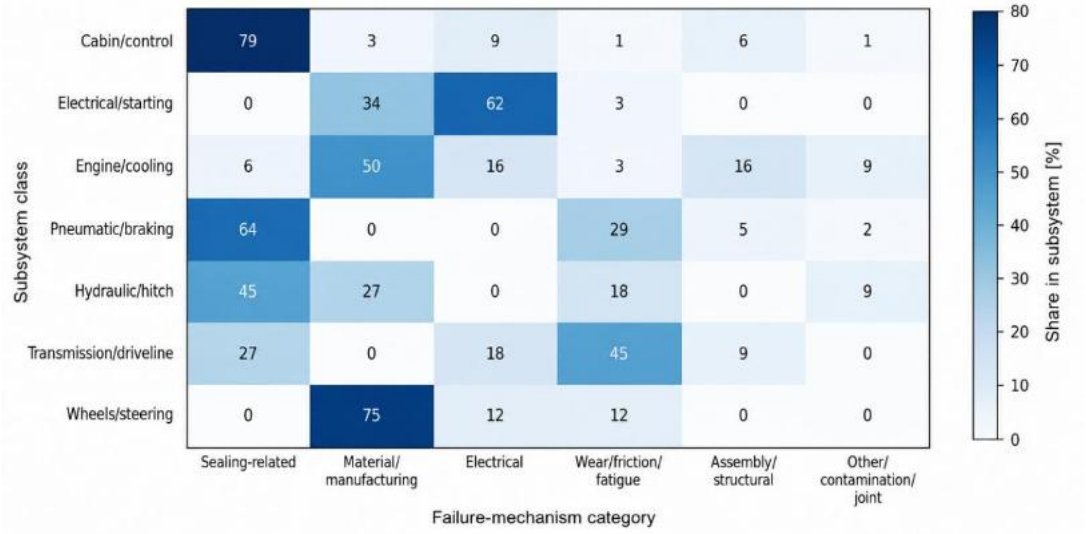


Fig. 4 - Failure-mechanism share within aggregated tractor subsystem classes

Values inside the cells represent shares of mechanism categories within a given subsystem class, [%].

Table 5 confirms that the mechanism-oriented approach adds information that is not visible in a subsystem-only classification.

Table 5

Dominant failure mechanism in each aggregated subsystem class

Subsystem class	Dominant mechanism	Share [%]	Secondary mechanism
Cabin/control	Sealing-related	79.1	Electrical
Electrical/starting	Electrical	62.1	Material/manufacturing
Engine/cooling	Material/manufacturing	50.0	Electrical
Pneumatic/braking	Sealing-related	64.3	Wear/friction/fatigue
Hydraulic/hitch	Sealing-related	45.5	Material/manufacturing
Transmission/driveline	Wear/friction/fatigue	45.5	Sealing-related
Wheels/steering	Material/manufacturing	75.0	Electrical

Cabin/control and pneumatic/braking were dominated by sealing-related mechanisms, whereas electrical/starting was dominated by electrical mechanisms. Hydraulic/hitch and transmission/driveline had more mixed patterns, which suggests that their maintenance cannot be reduced to a single inspection action. For these assemblies, a technician should consider leakage, wear, material condition and adjustment simultaneously.

Table 6 summarises the mechanical interpretation of the identified failure-mechanism categories and indicates their practical implications for tractor servicing, inspection planning and maintenance decision-making.

Table 6

Mechanical interpretation and practical service implications of failure-mechanism categories

Failure mechanism	Mechanical interpretation	Service implication
Sealing-related	Loss of tightness, damaged sealing surface, collar or elastomer element	Leakage inspection, cleanliness control, seal material and surface check
Material/manufacturing	Defect originating from material quality, machining, weld, thread or component manufacture	Quality feedback, incoming component control, warranty monitoring
Electrical	Short circuit, burnout, interrupted continuity or wiring defect	Connector, wiring, switch and protection-system inspection
Wear/friction/fatigue	Seizure, excessive wear, excessive clearance or cracking during operation	Lubrication, adjustment, clearance, load and friction-pair control
Assembly/structural	Faulty assembly, bending, fracture or loss of mechanical connection	Assembly procedure verification and structural inspection
Other/contamination/joint	Impurities, clogging, functional fault or joint degradation	Filtration, cleaning, fluid quality and functional testing

The mechanism-oriented interpretation presented in Table 6 expands the meaning of the numerical results. The high share of sealing-related failures indicates that tightness should be treated as one of the central reliability problems in the analysed tractor records. This category included failures of sealing surfaces, collars and seals, and it appeared in several subsystem classes. Therefore, the result should not be interpreted only as a problem of one assembly group. It rather indicates a cross-system mechanism associated with leakage, contact surface condition, elastomer quality, installation accuracy, contamination and pressure or temperature variation during operation.

The operating-time distribution of mechanisms also has a clear engineering meaning. In the 0-250 EOH class, material/manufacturing and electrical mechanisms were more visible than wear/friction/fatigue mechanisms. This pattern is consistent with the interpretation of early service records as a period in which hidden defects of manufacturing, assembly, component quality, wiring, connectors or protection systems may become visible. In this stage, inspection activities should therefore include targeted checks of sealing surfaces, threaded joints, welded or soldered parts, wiring continuity, connectors and hydraulic or pneumatic tightness. The early-life odds ratios support this interpretation because material/manufacturing and electrical categories had values above 1.0, whereas wear/friction/fatigue had a value below 1.0.

For later operation, especially above 750 EOH, the increasing contribution of wear/friction/fatigue mechanisms suggests a different service logic. In these cases, maintenance should pay more attention to lubrication quality, friction pairs, clearances, seizure risk, fatigue cracking and components exposed to cyclic loads.

This transition from quality-related and electrical mechanisms toward wear-related mechanisms is consistent with the general mechanical interpretation of repairable systems. However, the present dataset does not include non-failed tractors or complete exposure histories, so it cannot be used to estimate the absolute probability of failure or to construct a complete bathtub curve.

The subsystem-mechanism comparison confirms that a parts-based classification is not sufficient for engineering interpretation. Cabin/control and pneumatic/braking failures were dominated by sealing-related mechanisms, electrical/starting failures were mostly electrical or material/manufacturing in nature, whereas hydraulic/hitch and transmission/driveline groups showed more mixed patterns. This means that the same subsystem may require different corrective actions depending on the underlying physical mechanism. For example, a hydraulic failure may require leakage inspection, material-quality feedback, contamination control or wear assessment, depending on the coded cause.

From a service-management perspective, the results show that ordinary workshop records can support more than spare-parts logistics and can contribute to maintenance support systems and strategic maintenance management (*Kataev et al., 2024; Tsang, 2002*). If a record is coded only as a replacement of a component, it mainly supports inventory planning and repair-cost accounting. If the same record is additionally coded as sealing-related, electrical, material/manufacturing, assembly-related or wear-related, it becomes useful for design feedback, warranty monitoring and maintenance planning. This distinction is important in mechanical engineering because the same external symptom may result from different degradation processes and may require different preventive actions.

The obtained association between EOH class and failure-mechanism category was statistically significant but not strong. Cramer's V indicated a weak-to-moderate association, which is reasonable for field service data affected by variable tractor use, operator behaviour, maintenance history, environmental exposure and recording practices. Therefore, the results should be interpreted as evidence of an interpretable structure in the recorded service cases, not as a deterministic rule for all tractors. The value of the approach lies in its ability to organise incomplete service data into mechanically meaningful categories and to identify where targeted inspections may be most useful.

The practical recommendation is that warranty-period servicing should not be limited to routine replacement or adjustment. Early inspections should include quality-control-oriented checks of sealing elements, electrical connections, threads, welds, machined surfaces and hydraulic or pneumatic tightness. In contrast, later inspections should increasingly focus on lubrication, friction pairs, clearances, fatigue-sensitive elements and components exposed to cyclic or abrasive loading. Such a distinction can help service organisations adapt inspection priorities to the operating-time class of the tractor.

The study also has several limitations that should be considered when applying the findings to other service networks. The dataset covers a single tractor brand and a single historical set of service records. Information on non-failed tractors, the exact population at risk, and complete maintenance histories was unavailable. Therefore, the results characterize the distribution of recorded failure mechanisms rather than the failure probability of the entire tractor population in service. Future research should integrate failure-mechanism classification with cost data, downtime, warranty status, operating conditions, and complete exposure histories to develop more robust reliability and maintenance decision-support models.

CONCLUSIONS

1. The analysed service dataset contained enough information to distinguish six practical failure-mechanism categories of agricultural tractors: sealing-related, material/manufacturing, electrical, wear/friction/fatigue, assembly/structural and other/contamination/joint mechanisms.
2. The strongest group of recorded mechanisms was sealing-related failure, which represented 45.0% of all service cases. This confirms that sealing elements are a critical reliability area in repairable tractor systems.
3. The association between EOH class and failure-mechanism category was statistically visible. The chi-square test gave $p = 0.008$ and Cramer's V was 0.228, indicating a weak-to-moderate but interpretable structure in the service records.
4. Material/manufacturing and electrical mechanisms were relatively more visible in the 0-250 EOH class, whereas wear/friction/fatigue mechanisms were more visible in later records, especially above 750 EOH.
5. The same tractor subsystem may be affected by different physical mechanisms. Therefore, maintenance decisions should combine subsystem information with mechanism-oriented interpretation of the service cause.

6. For maintenance practice, early service inspections should emphasise sealing, electrical and quality-control-related defects, while later inspections should increasingly focus on wear, friction, fatigue, lubrication and clearance-related mechanisms.
7. The method supports mechanical reliability assessment from incomplete service records, but it should not be treated as a replacement for full lifetime reliability modelling based on complete exposure data and non-failed observations.

ACKNOWLEDGEMENT

This research received no external funding. The authors acknowledge that the analysis was based on historical service records of agricultural tractors. AI-assisted tools were used only to support language editing, formatting and checking of the manuscript; the authors verified all calculations, interpretations and references.

REFERENCES

[1] Agresti A., (2019). An Introduction to Categorical Data Analysis, 3rd ed., Wiley, Hoboken/USA. DOI: https://doi.org/10.1002/9781119405269

[2] Angelucci L., Mattetti M., (2024). The development of reference working cycles for agricultural tractors, *Biosystems Engineering*, vol.242, pp.29-37, London/United Kingdom. DOI: https://doi.org/10.1016/j.biosystemseng.2024.04.004

[3] Atli H.F., (2024). Safety of agricultural machinery and tractor maintenance planning with fuzzy logic and MCDM for agricultural productivity, *International Journal of Agriculture Environment and Food Sciences*, vol.8, no.1, pp.25-43, Turkey. DOI: https://doi.org/10.31015/jaefs.2024.1.4

[4] Birolini A., (2017). Reliability Engineering: *Theory and Practice*, 8th ed., Springer, Berlin/Germany. DOI: https://doi.org/10.1007/978-3-662-54209-5

[5] Blischke W.R., Murthy D.N.P., (2000). Reliability: Modeling, Prediction, and Optimization, Wiley, New York/USA. DOI: https://doi.org/10.1002/9781118150481

[6] da Silva C.A.G., Rodrigues de Sá J.L., Menegatti R., (2019). Diagnostic of failure in transmission system of agriculture tractors using predictive maintenance based software, *AgriEngineering*, vol.1, no.1, pp.132-144, Basel/Switzerland. DOI: https://doi.org/10.3390/agriengineering1010010

[7] Durczak K., Selech J., (2022). The quantification of operational reliability of agricultural tractors with the competing risks method, *Technical Gazette*, vol.29, no.2, pp.628-633, Croatia. DOI: https://doi.org/10.17559/TV-20201118115902

[8] Friendly M., Meyer D., (2015). Discrete Data Analysis with R: Visualization and Modeling Techniques for Categorical and Count Data, CRC Press, Boca Raton/USA. DOI: https://doi.org/10.1201/b19022

[9] Greenacre M., (2017). Correspondence Analysis in Practice, 3rd ed., CRC Press, Boca Raton/USA. DOI: https://doi.org/10.1201/9781315369983

[10] Götz K., Kusuma A., Dörfler A., Lienkamp M., (2025). Agricultural load cycles: tractor mission profiles from recorded GNSS and CAN bus data, *Data in Brief*, vol.60, article 111494, Amsterdam/Netherlands. DOI: https://doi.org/10.1016/j.dib.2025.111494

[11] Jardine A.K.S., Lin D., Banjevic D., (2006). A review on machinery diagnostics and prognostics implementing condition-based maintenance, *Mechanical Systems and Signal Processing*, vol.20, no.7, pp.1483-1510, London/United Kingdom. DOI: https://doi.org/10.1016/j.ymssp.2005.09.012

[12] Kataev Y., Malykha E., Gradov E., (2024). Maintaining the reliability of agricultural machinery in the complex of developing an engineering and technical system, BIO Web of Conferences, vol.141, article 04059, Les Ulis/France. DOI: https://doi.org/10.1051/bioconf/202414104059

[13] Kolhe K.P., Lemi D.G., Busse S.K., (2024). Studies of tractor maintenance and replacement strategies of Wonji Shoa Factory, Ethiopia, *Journal of Agricultural Engineering*, vol.55, no.1, article 1552, Pavia/Italy. DOI: https://doi.org/10.4081/jae.2024.1552

[14] Kim M.H., Kim S.M., (2023). Estimation of air pollutant emissions by tractor utilization in Korea, *Agriculture*, vol.13, no.9, article 1811, Basel/Switzerland. DOI: https://doi.org/10.3390/agriculture13091811

[15] Lovarelli D., Bacenetti J., (2019). Exhaust gases emissions from agricultural tractors: state of the art and future perspectives for machinery operators, *Biosystems Engineering*, vol.186, pp.204-213, London/United Kingdom. DOI: https://doi.org/10.1016/j.biosystemseng.2019.07.011

[16] Mattetti M., Maraldi M., Lenzini N., Fiorati S., Sereni E., Molari G., (2021). Outlining the mission profile of agricultural tractors through CAN-BUS data analytics, *Computers and Electronics in Agriculture*, vol.184, article 106078, Amsterdam/Netherlands. DOI: https://doi.org/10.1016/j.compag.2021.106078
[17] McHugh M.L., (2013). The chi-square test of independence, *Biochemia Medica*, vol.23, no.2, pp.143-149, Croatia. DOI: https://doi.org/10.11613/BM.2013.018
[18] Mikolajczak P., Napiorkowski J., (2016). Analysing the reliability of working parts operating in abrasive soil pulp taking into consideration confounding factors, *Eksploatacja i Niezawodnosc - Maintenance and Reliability*, vol.18, no.4, pp.544-551, Warsaw/Poland. DOI: https://doi.org/10.17531/ein.2016.4.9
[19] Mishra D., Satapathy S., (2023). Reliability and maintenance of agricultural machinery by MCDM approach, International Journal of System Assurance Engineering and Management, vol.14, no.1, pp.135-146, Singapore. DOI: https://doi.org/10.1007/s13198-021-01256-y
[20] Mobley R.K., (2002). An Introduction to Predictive Maintenance, 2nd ed., Butterworth-Heinemann, Oxford/United Kingdom.
[21] Moubray J., (1997). Reliability-Centered Maintenance, 2nd ed., Industrial Press, New York/USA.
[22] Napiorkowski J., Gonera J., (2020). Analysis of failures and reliability model of farm tractors, *Agricultural Engineering*, vol.24, no.2, pp.89-101, Krakow/Poland. DOI: https://doi.org/10.1515/agriceng-2020-0020
[23] O'Connor P.D.T., Kleyner A., (2012). Practical Reliability Engineering, 5th ed., Wiley, Chichester/United Kingdom. DOI: https://doi.org/10.1002/9781119961260
[24] Paman U., Khairizal, Sutriana S., (2024). Field investigation of component failures for selected farm machinery used in small rice farming operations, *Open Agriculture*, vol.9, no.1, article 20220292, Berlin/Germany. DOI: https://doi.org/10.1515/opag-2022-0292
[25] Rausand M., Hoyland A., (2004). System Reliability Theory: Models, Statistical Methods, and Applications, 2nd ed., Wiley, Hoboken/USA. DOI: https://doi.org/10.1002/9780470316900
[26] Scolaro E., Beligoj M., Estevez M.P., Alberti L., Renzi M., Mattetti M., (2021). Electrification of agricultural machinery: a review, *IEEE Access*, vol.9, pp.164520-164541, USA. DOI: https://doi.org/10.1109/ACCESS.2021.3135037
[27] Tinga T., (2013). Principles of Loads and Failure Mechanisms: Applications in Maintenance, *Reliability and Design*, Springer, London/United Kingdom. DOI: https://doi.org/10.1007/978-1-4471-4917-0
[28] Tsang A.H.C., (2002). Strategic dimensions of maintenance management, *Journal of Quality in Maintenance Engineering*, vol.8, no.1, pp.7-39, Bradford/United Kingdom. DOI: https://doi.org/10.1108/13552510210420577
[29] Zelazinski T., Ekielski A., Durczak K., Morawska M., (2023). Study on biodegradable materials from thermoplastic starch with the addition of nuts shell, *INMATEH - Agricultural Engineering*, vol.70, no.2, pp.201-210, Bucharest/Romania. DOI: https://doi.org/10.35633/inmateh-70-20
[30] Zio E., (2009). Reliability engineering: old problems and new challenges, *Reliability Engineering & System Safety*, vol.94, no.2, pp.125-141, Amsterdam/Netherlands. DOI: https://doi.org/10.1016/j.ress.2008.06.002

COMPUTER VISION-BASED CORN STALK IMAGE RECOGNITION RESEARCH
/
基于计算机视觉的玉米秆图像识别研究

Wenlong LI[1)], Ning DAI[*1),2)], Qiuyan LIANG[*1)], Liuxuan MA[1)], Lianyang WANG[1)]
[1)] School of Mechanical Engineering, Jiamusi University, Jiamusi, Heilongjiang, 154007;
[2)] The First Affiliated Hospital of Jiamusi University, Jiamusi, Heilongjiang, 154007
Tel: +86-13504771669; E-mail: lwl0408_jljl@163.com
Corresponding author: Ning Dai
DOI: https://doi.org/10.35633/inmateh-79-93

Keywords: *machine vision; image processing; identification of corn stalks; morphological processing*

ABSTRACT

The utilization of machine vision and image processing techniques enables the recognition of corn stalks in complex field conditions, thereby enhancing the efficiency and accuracy of corn stalk identification. Initially, images of corn stalks are captured using a camera, followed by Gaussian filtering to effectively reduce noise within the images. Subsequently, RGB and HSV color segmentation is applied to the corn stalk images to isolate the component V, which most distinctly differentiates the corn stalks from the background. Threshold segmentation is then conducted on component V, establishing a threshold range to identify and extract the corn stalks from the background. Morphological operations are employed to enhance the fullness of the image. Finally, grid division is performed, using the coverage area of the straw as a feature to assign density values to corn straw in various sub-regions, ultimately generating a distribution grade map of corn straw. The results indicate that when the straw coverage rate ranges from 25% to 80%, the discrepancy between the corn straw recognition rate obtained through threshold segmentation and the manually measured straw coverage rate is less than 5%, satisfying the requirements for subsequent real-time variable spraying of corn straw decomposition agents.

摘要

运用机器视觉和图像处理的方法可实现玉米秸秆田间复杂条件下的识别，提高玉米秸秆田间识别效率和精度。首先通过摄像头对田间玉米秸秆进行采集，将采集到的田间玉米秸秆图像进行高斯滤波处理，有效消除图像中的噪音；然后对玉米秸秆图像进行 RGB 和 HSV 颜色分割，找出玉米秸秆与背景区分最明显的分量 V；再对分量 V 进行阈值分割处理，设定阈值范围，将玉米秸秆从背景中识别提取出来，运用形态学运算，使图像更加饱满；最后进行网格划分，以秸秆覆盖率面积作为特征，将不同子区域内的玉米秸秆密度进行赋值，生成玉米秸秆的分布等级图。结果表明：秸秆覆盖率为 25%~80%时，通过阈值分割的玉米秸秆识别率与人工测量的秸秆覆盖率结果误差小于 5%，能够满足后续玉米秸秆腐解剂实时变量喷施作业要求。

INTRODUCTION

During the 14th Five-Year Plan period, several forward-looking research directions have been strategically identified to encourage the exploration and development of new concepts, theories, and methods. These efforts are intended to promote innovation in scientific research paradigms and interdisciplinary integration. With the rapid advancement of technology, machine vision has become increasingly important not only in industry but also in agriculture and forestry, placing higher demands on its application in complex environments. Currently, employing machine vision to identify various plants and fruits has emerged as a prominent research focus. In China, the vast grain output and abundant straw resources have led to traditional practices that primarily involve burning straw for fuel. This approach results in a low resource utilization rate and contributes significantly to environmental pollution *(Chang, 2022a; Chang, 2022b; Kurumayya, 2025)*.

In alignment with the priority development areas outlined in the National Natural Science Foundation of China's "14th Five-Year Plan" and the "Five-way Comprehensive Utilization of Straw" initiative, this study employs a treatment method that integrates machine vision technology with straw fertilization.

[1] *Wenlong LI, Lecturer; Qiuyan Liang*, Professor (Corresponding author); Liuxuan MA, Professor; Lianyang Wang, Professor;*
[2] *Ning Dai, Lecturer (Corresponding author);*

The application of variable spraying of decomposers facilitates the decomposition of corn straw and its subsequent return to the field, thereby improving the efficiency of straw resource utilization. *Su Boni et al*. employed median filtering, mean filtering, and Wiener filtering to address salt-and-pepper noise in strawberry images. Their findings indicated that median filtering provided the most effective denoising results. Jinli Diamond utilized 14 texture features for the identification and localization of cucumbers; however, this approach requires substantial computational resources, rendering it impractical. Consequently, ongoing enhancements are necessary *(Wang et al., 2021; Su et al., 2018; Gao, 2022; Yang et al., 2023; Niu et al., 2025)*.

Research on the identification of corn stalks remains incomplete and has yet to achieve full automation. This paper initiates an investigation into the identification of corn stalks. Initially, corn stalk images undergo processing through an image preprocessing method. Subsequently, a color space model, in conjunction with morphological processing operations, is employed to execute threshold segmentation, effectively isolating the corn stalks from the background. The variable spraying device is then regulated based on the percentage of the corn stalk coverage area, facilitating the decomposition and return of corn stalks to the field (*Niu et al.*, 2024; *Ding et al., 2022a; Ding et al., 2022b; Deng, Wang, & Zhang, 2020; Niu et al.*, *2024)*.

MATERIALS AND METHODS

Experimental conditions

The corn stalk images were collected in Heping Village, Xiangyang District, Jiamusi City, Heilongjiang Province. The data collection occurred from September to October 2022, between 09:00 and 15:00. A mobile phone was utilized for capturing the images, which were taken under natural light conditions. To enhance data diversity and improve the model's generalization ability, images of corn stalks were gathered under various environmental conditions and distribution scenarios. Subsequently, the collected images underwent manual screening, resulting in the selection of those with stalk distribution percentages of 20% to 33%, 33% to 50%, 50% to 66%, 66% to 80%, and 80% to 90%. The selected images are presented in Figure 1. To further enhance the model's recognition accuracy, additional corn stalk images were sourced from the internet and incorporated into the self-captured image set. The flowchart illustrating the research on the identification of corn stalks in the field soil background is depicted in Figure 2 *(Wang; Dongxiang MA, 2023; Yasin et al., 2025)*.



Fig. 1 - Image of corn straw collection

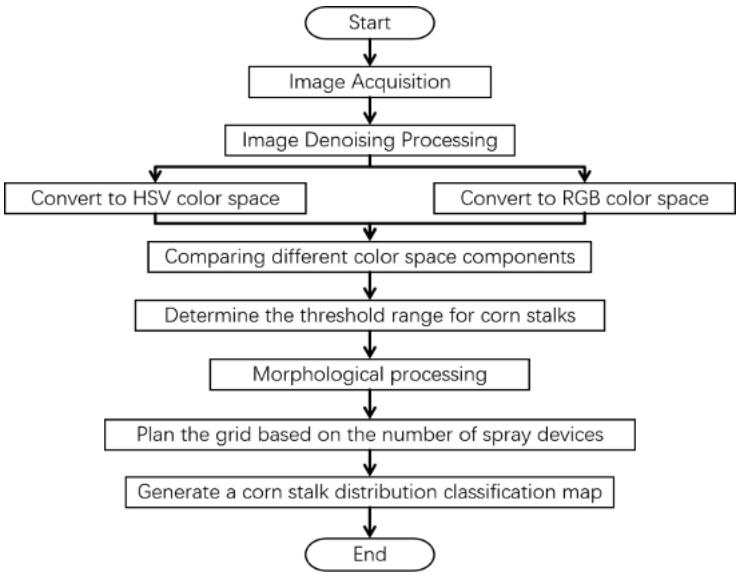


Fig. 2 - Flow chart of corn straw identification

Image color segmentation method

Images of corn stalks were captured using a camera. These images were subsequently analyzed and processed with PyThon-OpenCV, initially converting them into the RGB color space. Following this, the images were transformed into the HSV color space, allowing for a comparison with the RGB color space to identify the color component that provided the most effective separation between the corn stalks and the soil background. The corn stalks were isolated from the background using threshold segmentation, after which morphological processing techniques were employed to enhance the representation of the corn stalks *(Liu et al., 2024*).

Image filtering processing

This paper employs a denoising method that integrates Gaussian filtering with median filtering. Initially, Gaussian filtering is applied to the image prior to color space conversion. This technique utilizes the Gaussian function to smooth the image by computing the weighted average of pixels within a specified neighborhood around each pixel, thereby mitigating the impact of noise and effectively reducing high-frequency noise. The mathematical representation is provided in Equation (1), and the resulting image is illustrated in Figure 3. Subsequently, before the binarization process, median filtering is performed for further denoising. In this step, the median value of the pixel intensities within a defined area surrounding the central pixel replaces the original pixel value, effectively eliminating salt-and-pepper noise or impulse noise. The corresponding expression is detailed in Equation (2), and the processed image is depicted in Figure 4 *(Shah et al., 2022; Suneetha & Reddy, 2021; Latorre-Carmona, 2024)*.

$$(x)=\frac{1}{2\pi\sigma^2}e^{-\frac{x^2+y^2}{2\sigma^2}} \quad (1)$$

$$\hat{f}(x,y)=\underset{(i,j)\in S_{(x,y)}}{\text{median}}\{g(i,j)\} \quad (2)$$



Fig. 3 - Gaussian filter denoising process



Fig. 4 - Median filter denoising process

Color space model

The RGB color space is the most widely recognized method for representing colors, with its color space model illustrated in Figure 5. Any color F in a color image can be created by mixing the three primary colors: R (red), G (green), and B (blue) in varying proportions, as expressed in Equation (3) *(Togban & Ziou, 2025; Mengibar-Rodriguez & Chamorro-Martinez, 2022)*:

$$F=r[R]+g[G]+b[B] \quad (3)$$

where: R - red component; G - green component; B - blue component.

This color space accurately represents colors, as it has not been converted to other color spaces, resulting in minimal loss of image information. Following image processing, the image is subsequently processed through the RGB color space, with the outcome depicted in Fig. 6.

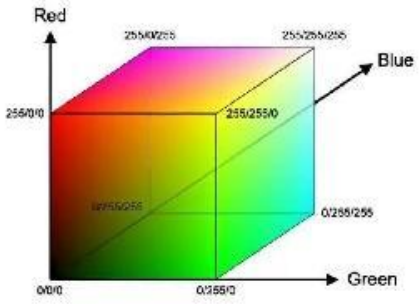
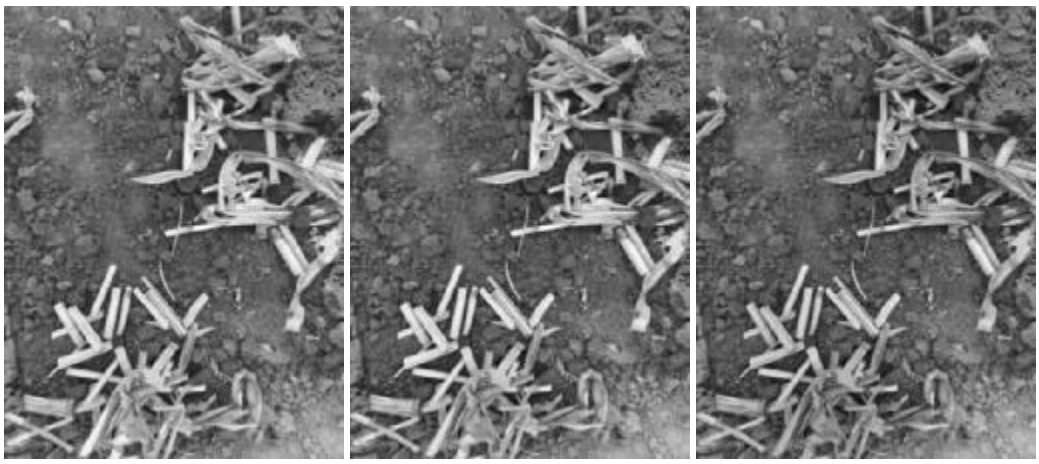


Fig. 5 - RGB color space model



(a) R component (b) G component (c) B component

Fig. 6 - RGB component map

The HSV color space is a color model defined by the attributes of Hue, Saturation, and Value, commonly referred to as a hexagonal cone model. The representation of this color space is illustrated in Fig. 7 *(Kamiyama & Taguchi, 2021; Yan, Li, & Hirota, 2021)*.

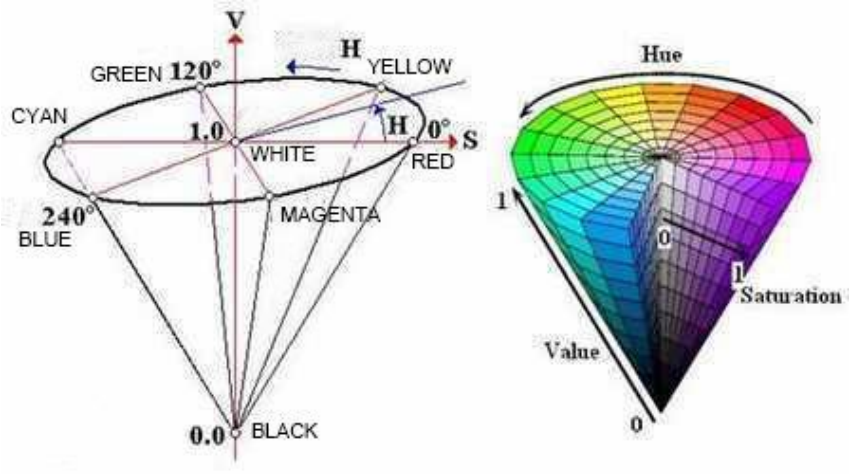


Fig. 7 - HSV color space model

The conversion relationship expression between this model and the RGB color space model is shown in Equation (4), that is:

$$H = \begin{cases} 0^{\circ}, & \text{if Max} = \text{Min} \\ 60^{\circ} \times \frac{G-B}{Max-Min} + 0^{\circ}, & \text{if Max} = R \text{ and } G > B \\ 60^{\circ} \times \frac{G-B}{Max-Min} + 360^{\circ}, & \text{if Max} = R \text{ and } G < B \\ 60^{\circ} \times \frac{G-B}{Max-Min} + 120^{\circ}, & \text{if Max} = G \\ 60^{\circ} \times \frac{G-B}{Max-Min} + 240^{\circ}, & \text{if Max} = B \end{cases} \quad (4)$$

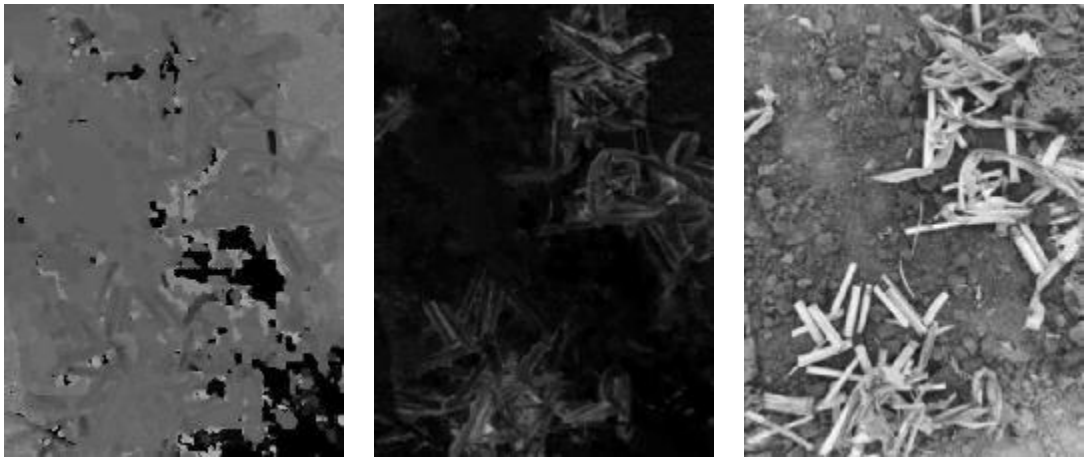
$$S = \begin{cases} 0, & \text{if Max} = 0 \\ \frac{Max-Min}{Max} = 1 - \frac{Min}{Max}, & \text{otherwise} \end{cases} \quad (5)$$

$$V = Max \quad (6)$$

where: Max - the maximum among R, G, and B;

Min - the minimum among R, G, and B

Subsequently, the preprocessed image undergoes processing in the HSV color space. A comparison is made between the components of the RGB color space model and those of the HSV color space model to identify the component that most effectively distinguishes corn stalks from the background. The diagram of the HSV color space components is presented in Fig. 8.



(a) H com onent ( ) S com onent (c) V com onent

Fig. 8 - HSV component map

By comparison, it can be seen that among the six components, the differences between the corn stalks and the soil background in component V are more obvious.

Research on recognition algorithms

As indicated in Section 2, the V component exhibits the most pronounced distinction effect. Consequently, threshold segmentation is applied to the V component, enabling the identification of corn stalks through this method.

The image acquisition process using industrial cameras is influenced by various unstable factors, including perspective, distance, light source, reflection, occlusion, and shadow, which can significantly affect image recognition outcomes. Additionally, noise interference may occur during both the acquisition and transmission of images. Consequently, preprocessing the images is essential to eliminate this noise and ensure the accuracy of subsequent results.

Image smoothing processing

To mitigate the effects of image noise generated during acquisition and transmission on image processing, it is essential to perform denoising prior to processing to enhance the resolution of image features. Image denoising involves applying filtering techniques to smooth the image, recalculating the value of each pixel to align it more closely with the values of neighboring pixels.

The commonly used image smoothing processing methods are as follows:

Mean filtering

Mean filtering is a linear filtering algorithm that employs a template to conduct convolution operations on the target image. This method replaces the value of each target pixel with the average pixel value of its surrounding neighborhood, thereby enhancing denoising effects and making the desired target more prominent.

$$(x,y)=\frac{1}{M}\sum_{(k,l)\square N} f(i,j) \quad (7)$$

Median filtering

Median filtering is a technique that employs a template to execute convolution operations on a target image. This process replaces the pixel value at a given point with the median of the pixel values within its neighborhood. Consequently, the surrounding pixel values are adjusted to approximate the true values, effectively eliminating isolated noise points.

$$\hat{f}(x,y)=\underset{(i,j)\in S_{(x,y)}}{\text{median}}\{g(i,j)\} \quad (8)$$

Gaussian filtering

Gaussian filtering involves the weighted averaging of the entire image. The value of each pixel is determined by the weighted average of its own value and those of neighboring pixels. When the mean μ is 0:

$$(x)=\frac{1}{2\pi\sigma^2}e^{-\frac{x^2+y^2}{2\sigma^2}} \quad (9)$$

In Gaussian filtering for denoising, the value of σ is crucial, as it dictates the dimensions of the filter template. A larger template results in increased blurring of the edge information of the particles. This article compares the denoising effects of three different templates $3\times3(\sigma=0.65)$, $5\times5(\sigma=1.43)$, $7\times7(\sigma=1.79)$, with the results illustrated in Figure 9.

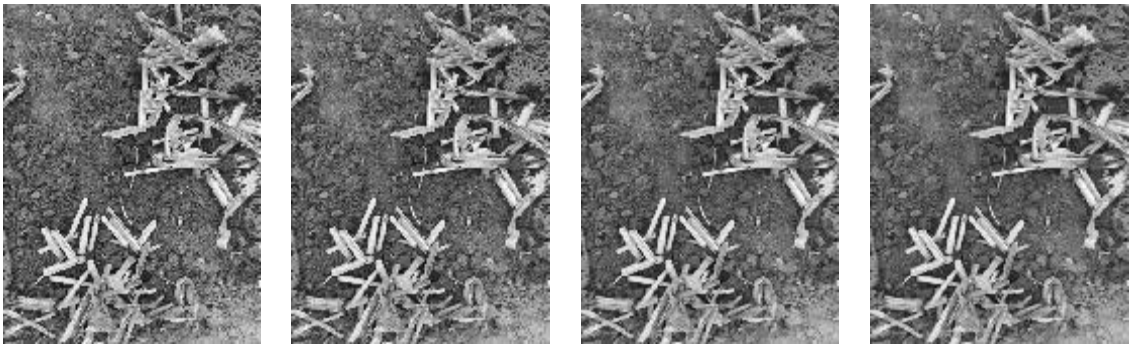


Fig. 9 - Gaussian filtering effect

Comparative analysis of the experimental effects of Gaussian filtering reveals that an increase in template weight significantly suppresses image noise. When utilizing templates of the same size, a comparison of various filtering processes demonstrates that $5\times5(\sigma=1.43)$ template Gaussian filtering effectively reduces noise while preserving edge information, resulting in favorable outcomes.

Image grayscale processing

The image data captured by industrial cameras is typically in color, comprising a combination of three channel vectors. For instance, in the RGB color model, each color channel ranges from 0 to 255. Consequently, color images require substantial storage space, which significantly impacts the speed of image processing. In contrast, grayscale images consist of a single channel without color, also ranging from 0 to 255. In the case of a binary grayscale image, white is represented by 255 and black by 0.

Common image grayscale conversion algorithms:

Single-channel component method

According to the requirements, one of the R, G, or B components in the color image is taken as the gray value of the image.

$$V_{gary1}=R \quad (10)$$

$$V_{gary2}=G \quad (11)$$

$$V_{gary3}=B \quad (12)$$

Maximum value method

The maximum brightness among the R, G, and B components in the color image is taken as the gray value of the grayscale image.

$$V_{gary}=\max(R, G, B) \quad (13)$$

Average value method

Take the average luminance of the R, G, and B components in the color image as a gray value.

$$V_{gary}=(R, G, B)/3 \quad (14)$$

Weighted average method

Based on their importance and other indicators, the three components are weighted and averaged with different weights.

$$V_{gary}=(\omega_r*R+\omega_g*G+\omega_b*B)/3 \quad (15)$$

where: $\omega_r, \omega_g, \omega_b$ - respectively the weights of R, G, and B.

Research shows that the grayscale effect of the image is the best when the following conditions are met. That is:

$$V_{gary} = 0.299 * R + 0.578 * G + 0.114 * B \quad (16)$$

The following figure is the grayscale image, as shown in Figure 10.



Fig. 10 - Image binarization

Image binarization processing

Color images captured by industrial cameras are converted into grayscale images. Following this, image binarization processing transforms the grayscale images into black-and-white images. Image binarization involves assigning pixel grayscale values of 0 or 255, thereby creating a pronounced black-and-white effect throughout the image and decreasing the overall data size.

A comparison of the preprocessing results presented in Figures 9 and 10 reveals that the application of image smoothing effectively removes target information while eliminating noise interference. The image processed through Gaussian filtering exhibits distinct edges, free from noise or artifacts, thereby facilitating subsequent image processing.

Morphological processing

Following the threshold segmentation of corn stalks, the desired outcome is frequently not attained. Consequently, morphological operations must be employed to enhance the completeness of the target. Morphology is among the most prevalent techniques in image processing. Its fundamental principle involves utilizing a specific structural element to measure or extract corresponding shapes or features from the input image, thereby facilitating further image analysis and target recognition. The commonly employed morphological processing methods are illustrated in Figure 11.

Image erosion

The erosion operation serves to "shrink" the selected area, effectively removing edges and speckles. It smooths the edges of the image area and reduces the number of pixels within that area; however, this process may result in the disconnection of adjacent components.

Image dilation

Dilation is the process of expanding a selected area, which smooths the edges of the image region, increases the pixel count within that region, and may connect previously unconnected components. However, regions that were originally separate will remain distinct and will not merge, despite any pixel overlap.

Open operation

The procedure for the opening operation involves initially executing the erosion operation, followed by the expansion operation. This sequence effectively eliminates isolated and small points, smooths rough edge lines, and ensures that the original area remains largely unchanged, akin to a "deburring" effect.

Closing operation

The procedure for the closed operation involves initially executing the expansion operation, followed by the erosion operation. This sequence effectively connects cavities within the area and merges isolated points outside into a single entity. The overall appearance and area of the region remain largely unchanged, akin to the effect of "filling the gaps."

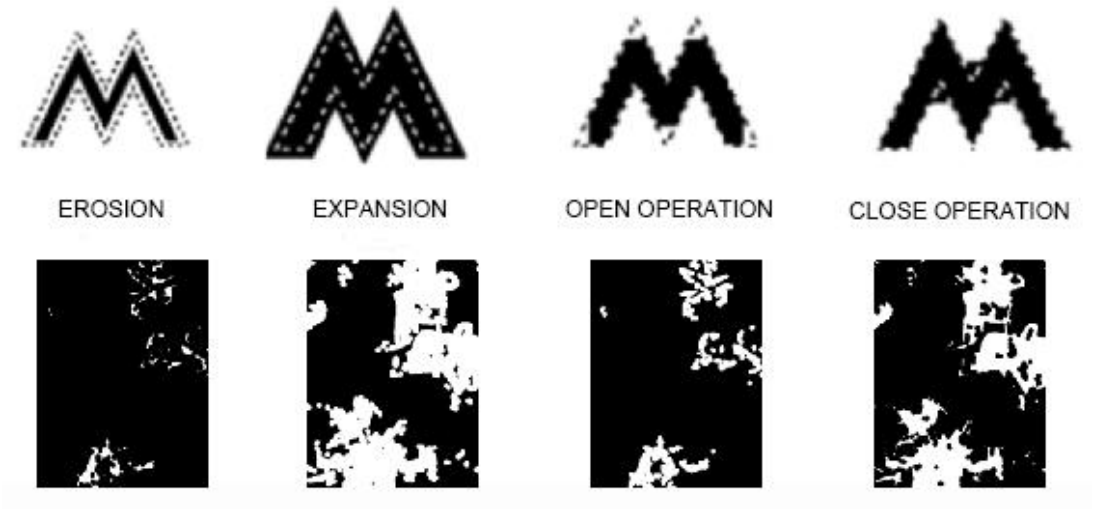


Fig. 11 - Morphological processing methods

This paper employs the closed operation method for image processing. This approach fills the gaps between corn stalks without thickening the edge contours, thereby connecting scattered targets within the image. As a result, the operational complexity is diminished, and efficiency is enhanced.

Image threshold segmentation method

The threshold is established based on specific requirements, incorporating various restrictive conditions to isolate the target from the image background. Threshold segmentation primarily relies on the disparity in gray values between the target and other objects within the background. This method filters the pixels in the image that satisfy the criteria determined by the gray values of the target pixels, thus enabling the segmentation of target features.

Fixed threshold segmentation

Fixed threshold segmentation represents the most basic and straightforward method of threshold segmentation. The underlying principle involves establishing a gray value, denoted as T. If the gray value of a pixel is less than T, it is assigned a value of 0 (i.e., black). Conversely, if the gray value exceeds T, it is assigned a value of 255 (i.e., white).

$$(x)=\begin{cases} 0, & x<T \\ 255, & x>T \end{cases} \quad (17)$$

Large law threshold segmentation

The OTSU method was introduced by Japanese researcher Nobuyuki Otsu in 1979. This method binarizes and segments images by identifying threshold pairs that maximize the inter-class variance between the foreground and background, thereby minimizing the likelihood of misclassification. However, the effectiveness of this segmentation diminishes when there is a substantial area difference between the target and the background, or when the gray levels of the target and background exhibit significant overlap.

Interval threshold segmentation

In a manner akin to fixed-threshold segmentation, the fixed threshold is modified to an interval threshold. If a pixel's threshold falls within this interval, its gray value is assigned a value of 255 (i.e., white). Conversely, if a pixel's threshold does not reside within the specified range, its gray value is designated as 0 (i.e., black).

The working environment described in this paper is complex, influenced by various factors, including light conditions, shooting angle, the presence of weeds, and the timing of straw collection, all of which affect straw color. Consequently, this study employs the interval threshold segmentation method to analyze the acquired images.

RESULTS

Experimental verification

Images of corn stalks in the field were captured using cameras. A total of fifteen images, representing varying coverage rates of corn stalks, were obtained and subsequently compared with the manually measured straw coverage rates.

Among the 15 selected images, the straw coverage rates were categorized into ranges: three images each for 20% - 33%, 33% - 50%, 50% - 66%, 66% - 80%, and 80% - 90%. The results of the two measurements are summarized in Figure 12. The figure illustrates that the corn stalk recognition algorithm developed in this study exhibits higher measurement accuracy within the straw coverage range of 25% to 80%, achieving an error of less than 5%.

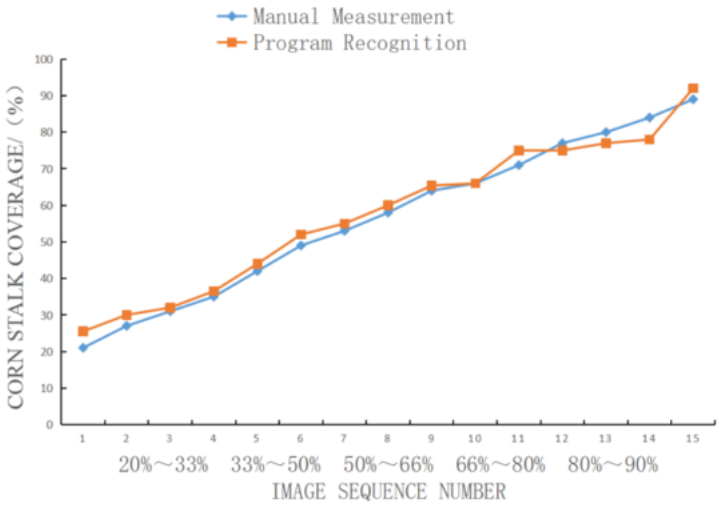


Fig. 12 - Straw cover comparison curve

Corn stalk identification

Heilongjiang Province, recognized as China's leading corn-growing and corn-producing region, generates a substantial quantity of corn stalks. Following the autumn harvest, a portion of these stalks is recycled and reused; however, a significant number are either burned or left to decay in the fields, representing a considerable waste of resources. Corn stalks are abundant in organic matter and contain various nutrients essential for plant growth. The effective utilization of these nutrients can significantly enhance soil fertility and decrease reliance on chemical fertilizers. Consequently, the decomposition and utilization of corn stalks hold considerable research significance.

Following the autumn harvest, corn stalks are crushed by harvesters and dispersed across the fields. The crushing is relatively uniform, resulting in a brownish-yellow color that contrasts markedly with the black soil characteristic of Northeast China. Consequently, this study employs color and area as the primary features for segmentation.

First, images of straw distribution in the field are captured using a camera. These images undergo several processing steps, including grayscale conversion, denoising, binarization, morphological processing, and grid division. Ultimately, a straw distribution grade map is generated, as illustrated in Figure 13.

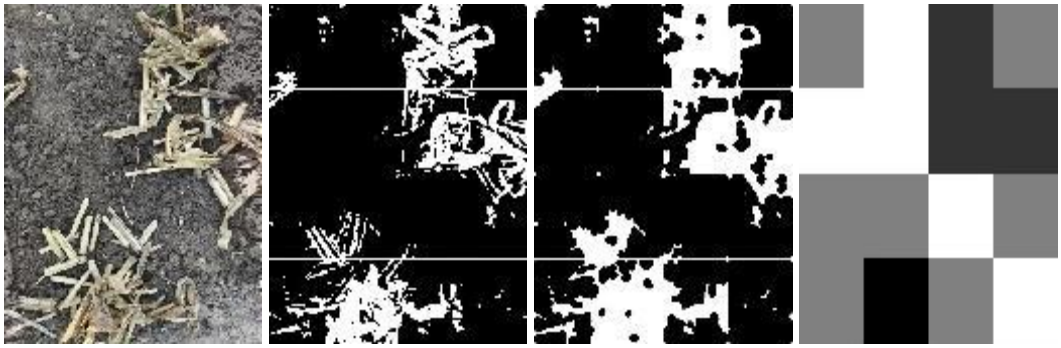


Fig. 13 - Corn straw identification

The figure illustrates that within each small cell, an increase in the area of straw corresponds to a progressively darker color of the cell. The classification is divided into four grades. If the straw area within a small cell is less than 5% of the total cell area, it is deemed to contain no straw. When the straw area comprises 5% to 33% of the cell area, it is categorized as level 1. If the straw area constitutes 33% to 66% of the cell area, it is classified as level 2. Finally, when the straw area exceeds 66% of the cell area, it is designated as level 3.

CONCLUSIONS

The HSV color space was chosen for this study after comparing three color models: RGB, HSV, and L*a*b*. Subsequently, the color images were converted to grayscale. To mitigate noise in the images, Gaussian filtering and median filtering techniques were employed. Among three threshold segmentation methods—fixed threshold, OTSU threshold, and interval threshold—the interval threshold method was selected based on its suitability for the actual working environment. The analysis focused on the color and shape characteristics of corn stalks, utilizing color as the segmentation feature to distinguish the stalks from the background. Area was then used as a feature to create a distribution grade map of the corn stalks. The corn stalk recognition algorithm, which relies on interval threshold segmentation, is straightforward and exhibits targeted effectiveness. When the straw coverage rate ranges from 25% to 80%, the recognition accuracy remains high, with an error margin of less than 5%.

ACKNOWLEDGEMENT

Project of Basic Scientific Research Business Expenses of the Heilongjiang Provincial Department of Education: "Research on a Variable-Rate Spray Device for Corn Stalk Decomposition Based on Machine Vision" (2024-KYYWF-0556).

REFERENCES

[1] Deng, L., Wang, Z., & Zhang, X. (2020). Application of agricultural insect pest detection and control map based on image processing analysis. *Journal of intelligent & fuzzy systems*. https://doi.org/10.3233/jifs-179413

[2] Ding, L., Hoover, A. N., Emerson, R. M., Lin, K.-T., Gruber, J. N., Donohoe, B. S., … Ray, A. E. (2022a). Image Analysis for Rapid Assessment and Quality-Based Sorting of Corn Stover. *Frontiers in Energy Research*, 10. https://doi.org/10.3389/fenrg.2022.837698

[3] Gao, Y. L. H. W. S. (2022). Farmland Aerial Images Fast-Stitching Method and Application Based on Improved SIFT Algorithm. *IEEE Access*. https://doi.org/10.1109/access.2022.3204657

[4] Kamiyama, M., & Taguchi, A. (2021). Color Conversion Formula with Saturation Correction from HSI Color Space to RGB Color Space. *IEICE Transactions on fundamentals of electronics communications and computer sciences*. https://doi.org/10.1587/transfun.2020eal2087

[5] Kurumayya, V. (2025). Cutting-edge computational approaches to plant phenotyping. *Plant molecular biology*, 115(2). https://doi.org/10.1007/s11103-025-01582-w

[6] Latorre-Carmona, K. A. M. (2024). Fuzzy Inference Systems to Fine-Tune a Local Eigenvector Image Smoothing Method. *Electronics*. https://doi.org/10.3390/electronics13061150

[7] Liu, X., Zhang, Z., Igathinathane, C., Flores, P., Zhang, M., Li, H., … Kim, H.-J. (2024). Infield corn kernel detection using image processing, machine learning, and deep learning methodologies under natural lighting. *Expert systems with applications*, 238, 122278. https://doi.org/10.1016/j.eswa.2023.122278

[8] Ma, D. X., Li, W. F., Li, S. F., Lu, F., & Li, L. L. (2023). Research on Maize Acreage Extraction and Growth Monitoring Based on a Machine Learning Algorithm and Multi-Source Remote Sensing Data. *Sustainability*. https://doi.org/10.3390/su152316343

[9] Mengibar-Rodriguez, M., & Chamorro-Martinez, J. (2022). An image-based approach for building fuzzy color spaces. *Information sciences*, 616, 592–577. https://doi.org/10.1016/j.ins.2022.10.130

[10] Niu, L.-T., Su, W.-H., Zhang, H.-Y., Wang, Q., Dong, B.-W., & Peng, Y. (2025). Development of intelligent equipment for weed identification and variable spraying in lettuce fields based on instance segmentation framework. *Engineering applications of artificial intelligence*, 159, 111634. https://doi.org/10.1016/j.engappai.2025.111634

[11] Niu, Shanwei, Nie, Zhigang, & Zhu, Wenyu. (2024). Multi-Altitude Corn Tassel Detection and Counting Based on UAV RGB Imagery and Deep Learning. *Drones*. https://doi.org/10.3390/drones8050198

[12] Shah, A., Bangash, J. I., Khan, A. W., Ahmed, I., Khan, A., Khan, A., & Khan, A. (2022). Comparative analysis of median filter and its variants for removal of impulse noise from gray scale images. *Journal of King Saud University-Computer and Information Sciences*, 34(3), 519–505. https://doi.org/10.1016/j.jksuci.2020.03.007

[13] Shin, J., Mahmud, M. S., Rehman, T. U., Ravichandran, P., Heung, B., & Chang, Y. K. (2023). Trends and Prospect of Machine Vision Technology for Stresses and Diseases Detection in Precision Agriculture. AgriEngineering, 5(1), 20-39. https://doi.org/10.3390/agriengineering5010003

[14] Su, B. N., Hua, X. Y. (2018). A Study on Strawberry Image Processing Based on Machine Vision. Journal of Capital Normal University (Natural Science Edition), 39(4): 42–45. DOI: 10.19789/j.1004-9398.2018.04.008.
[15] Suneetha, A., & Reddy, E. S. (2021). Enhanced statistical nearest neighbors with steerable pyramid transform for Gaussian noise removal in a color image. *Evolutionary Intelligence*, 15(3), 2139–2151. https://doi.org/10.1007/s12065-021-00627-5
[16] Togban, E., & Ziou, D. (2025). Improved image display by identifying the RGB family color space. *Displays*, 90, 103106. https://doi.org/10.1016/j.displa.2025.103106
[17] Wang, X., Wang, X. X., Geng, P., Yang, Q., Chen, K., Liu, N., … Han, X. R. (2021). Effects of different returning method combined with decomposer on decomposition of organic components of straw and soil fertility. Sci Rep 11, 15495. https://doi.org/10.1038/s41598-021-95015-5
[18] Yan, F., Li, N., & Hirota, K. (2021). QHSL: A quantum hue, saturation, and lightness color model. *Information sciences*, 577, 213–196. https://doi.org/10.1016/j.ins.2021.06.077
[19] Yang, G., Pan, H., Lei, H., Tong, W., Shi, L., & Chen, H. (2023). Dissolved organic matter evolution and straw decomposition rate characterization under different water and fertilizer conditions based on three-dimensional fluorescence spectrum and deep learning. *Journal of Environmental Management*, 344, 118537. https://doi.org/10.1016/j.jenvman.2023.118537
[20] Yasin, E. T., Ropelewska, E., Kursun, R., Cinar, I., Taspinar, Y. S., Yasar, A., … Koklu, M. (2025). Optimized feature selection using gray wolf and particle swarm algorithms for corn seed image classification. *Journal of food composition and analysis*, 145, 107738. https://doi.org/10.1016/j.jfca.2025.107738

A REVIEW OF INTELLIGENT TOBACCO TRANSPLANTERS: KEY TECHNOLOGIES AND DEVELOPMENT TRENDS

/

烟草智能化移栽机械关键技术演进与发展趋势综述

Lichang CHEN[1)], Guangliang LI[1)], Wuli DUAN[2*)], Xiaolei SONG[1)], Ran RAN[2)], Jianmin XU[3)], Wutai DONG[1)]

[1)] College of Mechanical and Electrical Engineering, Yunnan Agricultural University, Kunming 650201, Yunnan / China

[2)] Baoshan Branch of Yunnan Provincial Tobacco Company, Baoshan 678001, Yunnan / China

[3)] Yunnan Agricultural Machinery Research Institute Co., Ltd., Kunming 650224, Yunnan / China

Corresponding author: Wuli DUAN E-mail: 2845037784@qq.com

DOI: https://doi.org/10.35633/inmateh-79-94

Keywords: *tobacco transplanter; automatic seedling picking; planting mechanism; machine–soil–seedling interaction; machine vision; digital twin*

Abbreviations: *AI – artificial intelligence; CV – coefficient of variation; DEM – discrete element method; FPS – frames per second; GNSS – Global Navigation Satellite System; LCA – life-cycle assessment; LCC – life-cycle cost; MBD – multibody dynamics; MCU – microcontroller unit; MTBF – mean time between failures; MTTR – mean time to repair; PLC – programmable logic controller; RGB-D – red–green–blue plus depth; ROI – return on investment; UAV – unmanned aerial vehicle; YOLO – You Only Look Once.*

ABSTRACT

This review examines tobacco transplanting machinery, focusing on regional adaptation, automated seedling handling, planting mechanisms, coupled modeling, intelligent sensing, and field robustness. A narrative search covered English- and Chinese-language literature and standards through June 2026, selecting evidence by tobacco relevance or transferable similarity. High-throughput automation suits standardized production; hilly areas require compact, maneuverable, agronomically adaptable machines. Progress includes compliant seedling picking, buffered conveying, zero-relative-velocity planting, machine–soil–seedling modeling, machine vision, and digital twins. Constraints include seedling variability, adhesive soils, slope-induced disturbances, sensing degradation, and life-cycle cost. Future systems should integrate nursery standards, robust perception, decision-oriented digital twins, and modular electrification.

摘要

烟草移栽是连接育苗与大田生产的劳动密集型环节；丘陵碎片化地块、黏重红壤以及膜上移栽和井窖深栽等区域性农艺要求，进一步增加了装备适配难度。本文采用结构化叙述性检索，覆盖截至 2026 年 6 月的中英文文献与标准，并依据烟草相关性以及苗体形态、机构、土壤互作、感知任务或验证方法的可迁移性筛选证据。本文比较了不同区域的移栽装备技术路线，重点综述取苗、送苗、栽植、机-土-苗耦合建模以及感知与控制技术。研究表明，标准化平原或设施生产场景适宜采用高通量自动化装备，而丘陵烟区更需要小型化、模块化和高鲁棒性机具。现阶段的主要瓶颈包括钵苗一致性不足、高频作业与低损伤之间的矛盾、土壤黏附、传感器性能衰减以及较高的全寿命周期成本。未来应协同推进育苗标准化、柔性末端执行器、多模态感知、数字孪生和轻量化电动底盘的发展。

INTRODUCTION

Tobacco transplanting links nursery production to field establishment and directly affects plant spacing, planting depth, and early establishment. The global harvested area was approximately 3.2 million ha in 2023, with China accounting for roughly one third *(WHO, 2022; WHO, 2023a; WHO FCTC, 2025)*. Because the operation requires synchronized seedling separation, transport, soil or mulch penetration, placement, and covering, failure in one module can propagate through the entire cycle *(Jia et al., 2018; Wang X.B. et al., 2025; Yuan et al., 2023)*. Mechanization can reduce repetitive manual labor and improve spatial uniformity. Industry-wide fiscal data should not be interpreted as farm-level profitability, and labor-saving claims should still be considered alongside occupational and environmental costs *(IMTMA, 2024; WHO, 2023b)*. The present review therefore keeps these contextual issues concise and concentrates on the engineering problem.

These constraints are particularly acute in the hilly tobacco-growing regions of southwestern China, including Yunnan, Guizhou, and adjacent production areas. Fragmented plots, variable slopes, narrow access roads, and sticky red soils constrain machine dimensions and traction, while single-ridge, mulch-film, and well-cellar practices differ substantially from standardized vegetable transplanting. Historical national zoning data assigned 53.57% of tobacco planting area and 57.01% of commercial leaf volume to the Southwest tobacco-growing region *(Zhu, 2008)*. Because this regional classification is not equivalent to a slope-based definition and the data are historical, these percentages should not be interpreted as a current national share of 'hilly tobacco land'; no current nationally harmonized slope-class statistic was identified in authoritative public sources. Nevertheless, the historical concentration, together with continuing research on tobacco-specific crawler, electric, and well-cellar machines in these regions, demonstrates the engineering importance of hilly-area mechanization *(Bai et al., 2025; Wang B. et al., 2024; Xu L., 2024; Zhao Y., 2024)*. Consequently, a machine that performs well on level ground may lose planting-depth consistency, accumulate soil, or become difficult to maneuver on slopes.

Meanwhile, automated transplanting has progressed from purely mechanical mechanisms to compliant end-effectors, electromechanical control, machine vision, navigation, coupled simulation, and digital-twin-based quality monitoring. These advances create new opportunities but also reveal a persistent gap between laboratory performance and field reliability. High picking success obtained with uniform seedlings does not necessarily ensure stable operation when substrate moisture varies. Likewise, visual-detection accuracy may decline under dust, vibration, and rapidly changing illumination, and highly automated equipment may be economically unattractive when annual utilization is low *(Luo et al., 2022; Wang X.B. et al., 2025; Zhao Q. et al., 2026)*.

In this review, an intelligent transplanter is defined as a transplanting machine that uses sensing, state estimation, and/or programmable control to adapt seedling handling, mechanism timing, navigation, or quality decisions to observed conditions. Conventional and semi-automatic mechanisms are discussed as engineering baselines, compatible modules, or low-cost alternatives; they are not classified as intelligent unless they provide condition-aware or closed-loop functions. With this functional boundary established, the following paragraph explains how the evidence used to evaluate these machine functions was identified and screened.

The evidence base was assembled as a structured narrative review rather than a meta-analysis. Searches from database inception to 30 June 2026 covered Web of Science Core Collection, Scopus, Google Scholar, CNKI, and Wanfang, supplemented by citation tracing and publisher and standards websites. English and Chinese terms combined tobacco or plug seedling with transplanter, seedling picking or feeding, planting mechanism, well-cellar, vision or navigation, digital twin, DEM or MBD, field performance, safety, cost, and life cycle. Eligible records reported traceable evidence on mechanisms, modeling, sensing and control, safety, economics, or field performance; untraceable or engineering-irrelevant records were excluded.

Non-tobacco evidence was retained only when it shared an explicit engineering interface with tobacco: plug or root-block handling, planting trajectory, soil-tool interaction, sensing or control task, or validation method; crops are labeled in quantitative tables. Such evidence informs mechanisms, methods, and failure modes, not tobacco performance. Values are not treated as benchmarks unless crop, machine, seedling, soil, speed, and protocol are comparable.

Section 1 relates regional production conditions to machine architecture; Section 2 compares picking, conveying, and planting mechanisms; Section 3 evaluates coupled modeling, perception, AI, edge computing, and mechatronic integration; Section 4 examines deployment bottlenecks, safety, sustainability, and economics; Section 5 translates evidence gaps into short- and medium-term milestones; and the Conclusions summarize the review's principal contributions.

1. TECHNOLOGICAL ROUTES AND REGIONAL ADAPTATION

1.1 HIGH-THROUGHPUT AUTOMATION IN STANDARDIZED PRODUCTION

International tobacco-specific mechanization provides an important baseline. A U.S. self-feeding system handled cell-strand or bare-root material at about 100-140 plants/min under controlled conditions, while Japanese research developed a high-clearance mechanically fed tobacco transplanter *(Suggs et al., 1987; Asai and Miyake, 1989)*. European developments broadened this evidence base: an Italian DGNSS-RTK-assisted vine-cutting transplanter demonstrated automated georeferenced placement under different topographic conditions, and a precision three-row synchronized transplanter developed by Spanish/U.S. researchers addressed cross-row spatial and temporal coordination *(Mazzetto and Calcante, 2011; Pérez-*

Ruiz and Slaughter, 2021). These studies show that feeder reliability, positioning, and operator-machine coordination are system constraints. Robotic research subsequently established automated seedling-handling feasibility, with *Kutz et al. (1987)* representing an early milestone. Contemporary systems integrate perception, end effectors, and tray logistics: recent work used selective seedling assessment or plant-factory vision and automated tray handling *(Li M. et al., 2025; Liu W. et al., 2024b)*. The engineering question is whether the complete system can make reliable decisions at production speed.

High-throughput systems in protected horticulture commonly integrate tray indexing, parallel or multichannel handling, pneumatic assistance, and machine vision. Reviews of plug-seedling transplanting technologies indicate that protected-environment machines increase throughput by parallelizing picking and separating grading, transfer, and planting operations *(Habineza et al., 2023; Liu W. et al., 2023)*. Nevertheless, a higher nominal cycle frequency does not necessarily yield greater effective productivity. As seedling uniformity deteriorates, missed picks, substrate fragmentation, blockages, and operator interventions may increase rapidly. The appropriate design objective is therefore the maximum stable throughput sustained over an operating period, not the maximum instantaneous frequency.

The same principle applies to kinematic studies of dibbling and planting mechanisms. To control planting angle and uprightness, forward speed must be synchronized with the relative velocity between the planting component and the ground, the opening and closing phases of the planting element, and the instant of seedling release *(Iqbal et al., 2021)*. Compact, field-oriented automatic transplanters further demonstrate that robotic or mechanized picking can be integrated into multirow or mobile platforms. However, whole-machine performance continues to depend strongly on tray standardization, seedling mechanical properties, and reliable transfer between modules *(Ji D. et al., 2024; Khadatkar et al., 2023; Zhou et al., 2024)*.

1.2 COMPACT AND PRECISION-ORIENTED ROUTES FOR SMALL FIELDS

In East Asian production systems characterized by small, fragmented fields, equipment development places greater emphasis on compact dimensions, maneuverability, and repeatable mechanism timing. Compact electrically driven transplanters demonstrate how automatic conveying, picking, and planting can be integrated within a restricted machine width. Similarly, recent field tests of greenhouse cabbage equipment in Korea show that the capacities of the collection and transplanting modules must be coordinated at the system level *(Chen M. et al., 2025; Reza et al., 2025)*. Mechanical precision and compact integration remain attractive because they can reduce dependence on sensors; however, increased mechanism density makes accessibility, modularity, and maintainability more important.

Low-cost, manually assisted transplanters remain appropriate when farm scale, terrain, and service capacity do not justify full automation. Their engineering value lies in reducing repetitive bending, improving placement regularity, and increasing work rate without presuming that the most highly automated architecture is necessarily the most economical. In hilly tobacco-growing areas, semi-automatic guide-tube and duckbill machines may therefore remain competitive when they are lightweight, repairable, and tolerant of variable seedlings, even as fully automatic systems advance *(Jia et al., 2018; Wang X.B. et al., 2025)*. The relevant benchmark is the cost and quality per successfully transplanted area under local operating conditions, rather than the level of automation alone.

1.3 CHINA: FROM SEMI-AUTOMATIC MACHINES TO REGION-ADAPTED INTELLIGENT SYSTEMS

The development of Chinese tobacco transplanters has followed a region-adaptive pathway because production conditions differ markedly between the northern plains and the hilly southwest. Early integrated tobacco-machine designs established a foundation for mechanized transplanting *(Fei and Yan, 2018)*, while conventional guide-tube and duckbill machines remain useful where low cost and straightforward maintenance are priorities. Well-cellar production in hilly areas has stimulated the development of auger-type hole formers, electric drives, and tracked self-propelled platforms. Hydraulic and mechanical well-cellar systems, zero-relative-velocity planting concepts, and high-speed hole-forming devices have progressively addressed the requirements of deep planting and small mulch openings *(Fan et al., 2020a; Fan et al., 2020b; Jing, 2025; Wang L., 2025)*.

Automated seedling handling has advanced in parallel. Dual-tray staggered picking, compliant or pneumatic separation, multi-adaptive feeding, and low-cost motion-control architectures are intended to increase cycle frequency while limiting rigid contact with stems and substrate blocks *(Chen B. et al., 2024; Li G. et al., 2025; Shao et al., 2021; Zheng et al., 2025)*. Crawler platforms and microcontroller-based pneumatic control have lowered the entry barrier to field automation. Nevertheless, these field systems remain more

sensitive than semi-automatic machines to seedling variability and environmental disturbances *(Bai et al., 2025; Li H.M. et al., 2024; Xu L., 2024)*.

Perception and autonomous functions are increasingly being integrated into this hardware base. Fuzzy control for missed-plant prevention, deep-learning-based seedling grading, GNSS/vision navigation, machine-vision-assisted low-damage handling, and tobacco-transplant recognition illustrate the transition from preset mechanism timing to condition-aware control *(Jin X. et al., 2020; Li T. et al., 2023; Liu Z. et al., 2026; Xin et al., 2022; Zhang S. et al., 2026)*. Digital-twin-based online quality inspection extends this concept by linking physical signals to predicted spacing, uprightness, and operating quality *(Zhao Q. et al., 2026)*. The central question is whether these functions remain reliable after prolonged exposure to dust, vibration, occlusion, and field variability.

Figure 1 summarizes this regional design logic. The comparison is not intended as a ranking of technological sophistication; rather, it shows that the preferred architecture depends on nursery-system standardization, field scale, terrain, agronomic practices, and local service capacity.

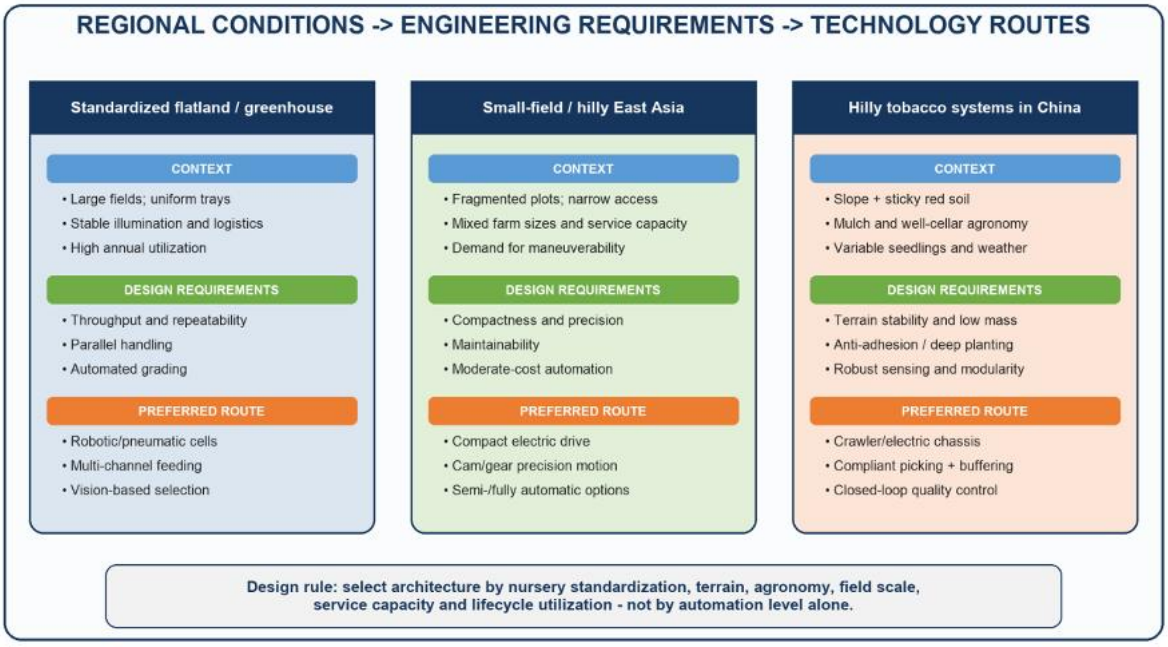


Fig. 1 - Regional production conditions and corresponding technological routes for transplanting machinery

Source: synthesized by the authors from the reviewed literature.

Table 1

Cross-regional comparison of transplanter development routes

Context / crop scope	Dominant objective	Typical technical route	Main strength	Key limitation for tobacco transfer
Protected systems vegetables; flowers	High stable throughput	Multi-channel robotic/pneumatic handling, vision grading	High cycle frequency and repeatability	Requires uniform trays/seedlings and stable environment
East Asia cabbage; vegetables	Mobility and precise motion	Compact chassis, gear/cam trajectories, moderate automation	Good maneuverability and mechanical repeatability	Complex transmissions; limited flexibility when agronomy changes
Low-capital systems tobacco; vegetables	Low cost and ergonomics	Manual or semi-automatic guide-tube/duckbill machines	Simple, repairable, low investment	Throughput limited by operator feeding
Hilly China tobacco	Agronomic adaptation and robustness	Crawler/electric chassis, well-cellar hole forming, flexible picking, sensing	Matches deep planting, mulch and slope constraints	Seedling inconsistency, soil adhesion and sensor reliability remain limiting

2. KEY MECHANISMS FOR AUTOMATIC TOBACCO TRANSPLANTING

2.1 SEEDLING PICKING: FROM RIGID GRIPPING TO FORCE-DECOUPLED EXTRACTION

Seedling picking is typically the first bottleneck encountered as the operating frequency of an automatic transplanter increases. Existing mechanisms can be classified broadly as direct-clamping or force-decoupled extraction systems. Direct clamping applies force to the stem or substrate block before removing the seedling from the tray. Although this approach offers a compact structure and short cycle time, its safe operating window depends on stem strength, root binding, substrate moisture, and adhesion between the substrate block and tray wall. Reviews and experimental studies consistently identify missed picks, stem damage, and substrate breakage as the principal failure modes *(Huang M. et al., 2023; Wang N. et al., 2021; Wang X. et al., 2023)*. Recent flexible multi-pin grippers further demonstrate that penetration geometry, squeezing force, and extraction speed must be optimized jointly rather than independently *(Han L. et al., 2025)*.

Trajectory and contact design can mitigate these failures. Oblique insertion followed by straight extraction, optimized cam paths, and whole-row mechanisms have been used to improve contact geometry and synchronize picking with downstream transfer *(Chen B. et al., 2024; Li Z., 2023; Xie et al., 2020)*. Coupled discrete-element and multibody simulations also allow mechanism–substrate interactions to be evaluated before physical prototyping *(Hou et al., 2023)*. A recent flexible gripper achieved reliable picking through oblique penetration, gradual squeezing, and vertical extraction, demonstrating the benefit of distributing contact through the substrate block rather than relying on a single rigid pull *(Han L. et al., 2025)*. Although reported success rates above 90% are encouraging, direct comparisons remain difficult because tray type, seedling age, substrate moisture, and even the definition of success are not standardized.

A second design strategy reduces stem loading by separating or redistributing the force required to detach the substrate block. Top-clamping-and-pulling, top-pushing/stem-clamping, and oblique multi-tine end-effectors either separate loosening from transport or distribute the extraction force across a larger root-block volume *(Hu J. et al., 2022; Liu W. et al., 2024a; Zhang N. et al., 2024; Zhang X.D. et al., 2023)*. For loose substrates, discrete-element calibration has been used to optimize an end-effector specifically for substrate mechanics, illustrating how material behavior can be incorporated directly into gripper design. Alternating dual-tray mechanisms can also reduce waiting time between operating cycles *(Liu C. et al., 2025)*. These benefits are obtained at the cost of a longer or more tightly coordinated action sequence and greater sensitivity to timing errors.

A notable shift in recent research is the use of plant and substrate mechanical properties instead of geometry alone. Studies of flexible multi-pin gripping, stem-damage modeling, and low-damage machine vision indicate that gripping force, penetration depth, impact acceleration, contact area, and substrate integrity should be treated as explicit design constraints *(Han L. et al., 2025; Xi et al., 2026; Xin et al., 2022)*. For tobacco seedlings, a useful next step would be to define a measurable damage envelope linking stem diameter, substrate moisture, root binding, and extraction resistance to allowable force and acceleration. Such an envelope would enable servo trajectories and compliant grippers to be tuned to the actual seedling batch rather than to a nominal specimen.

2.2 SEEDLING CONVEYING AND BUFFERING: DECOUPLING FAST PICKING FROM STABLE PLANTING

A high-frequency picking mechanism provides little benefit if seedlings reach the planter with an unstable orientation. Unconstrained free-fall transport can cause rolling and impact, whereas direct robot-to-soil placement assigns the manipulator responsibility for the entire cycle. Buffered or relay-type conveying offers a practical compromise by decoupling rapid tray-handling operations from the slower, near-zero-relative-velocity planting event. The buffer can absorb timing differences, correct orientation, and reduce the sensitivity of the planting mechanism to brief disturbances in seedling picking *(Fang et al., 2021; Shao et al., 2021)*.

Tray feeding and pre-loosening also require attention because high extraction resistance may dominate the failure rate. A rotary tray-feeding device that flexed the tray before picking reduced extraction resistance and improved picking success for rapeseed plug seedlings, illustrating how upstream tray mechanics can lessen the load on the end-effector *(Chen H. et al., 2025)*. Tobacco feeding devices based on structural guidance are intended to preserve seedling orientation during transfer, whereas compact automatic machines coordinate picking and feeding within a restricted spatial envelope *(Yan et al., 2020; Zhao X. et al., 2022)*. Flexible finger-and-chain conveying has produced similar benefits for fragile seedlings by reducing abrupt speed changes *(Ning et al., 2025)*.

Accordingly, the performance of a conveying system should be assessed using metrics broader than transport capacity alone. Relevant indicators include transfer success, orientation deviation at planter entry, residence-time variability, impact acceleration, and blockage probability over repeated cycles. This system-

level perspective is particularly important for tobacco because large leaves may interfere with guides even when the substrate block is transferred successfully.

2.3 PLANTING MECHANISMS: MATCHING TRAJECTORY TO SOIL, MULCH AND PLANTING DEPTH

Duckbill planters remain widely used because a single mechanism can open the soil or mulch, receive and release the seedling, and initiate soil closure. Their principal kinematic requirement is to minimize horizontal relative velocity at the lowest point of the trajectory. Early elliptical-gear planetary mechanisms established deterministic noncircular transmissions as a means of shaping planting trajectories *(Chen J. et al., 2012; Yu G. et al., 2011)*. Tobacco-transplanter studies and subsequent mechanism optimization have focused on phase synchronization and the relationship between forward speed and release timing *(Iqbal et al., 2021; Ji J. et al., 2015; Xiong, 2025)*. Inadequate compensation for forward motion can elongate the planting hole, enlarge the mulch opening, or tilt the seedling. However, a purely kinematic optimum cannot represent resistance from the soil, mulch, or substrate block.

In mulch-film transplanting, the design problem extends beyond kinematics because the planting component interacts simultaneously with the film, soil, and substrate block. Studies of tobacco and other mulched crops show that planter geometry, penetration angle, and release control determine both film-opening size and seedling uprightness *(Li Y. et al., 2025; Yang W., 2019; Zhang W. et al., 2024)*. European field evidence from central Italy further showed 95-99% transplant success for savoy cabbage, fennel, and lettuce with a modified transplanter operating in both tilled and no-till soils, while also revealing crop- and spacing-specific skip risk *(Frasconi et al., 2019)*. Coupled machine-soil-pot models confirm that soil resistance and pot posture can shift the actual trajectory away from the ideal path *(Jin X. et al., 2025)*. Similarly, machinery-plant-soil modeling in rice transplanting demonstrates the value of representing impact and soil interaction when analyzing seedling damage *(Xue et al., 2022)*. Collectively, these studies indicate that a planting mechanism should not be optimized solely in a multibody model without a calibrated representation of the working medium.

Guide-tube and cup-type planters are structurally simpler and well suited to semi-automatic machines. In these systems, the seedling descends by free or constrained fall; tube inclination, inner-wall friction, and the opener's relative position determine its final orientation. High-speed imaging and dynamic analysis have been used to replace disordered tumbling with more stable sliding, while timing studies coordinate guide-tube discharge with planter opening *(Wu et al., 2022; Yin D. et al., 2021)*. This simplicity is advantageous in hilly tobacco production, although throughput remains closely coupled to manual feeding or upstream automatic orientation.

Well-cellar planting imposes a different engineering requirement: the machine must form a deep, narrow, and stable hole while minimizing wall collapse and mulch damage. Tobacco-specific planter and hole-forming studies have investigated auger rotational speed, penetration rate, soil discharge, anti-blocking geometry, planting-element design, and modal vibration *(Fan et al., 2020a; Fan et al., 2020b; Jiang X. et al., 2024; Liu W., 2017; Peng, 2025; Shi Y., 2023; Xu S. et al., 2024; Zhang D. et al., 2021)*. Recent continuous zero-relative-velocity well-cellar systems and high-speed dual-hole-forming devices seek to maintain hole quality as field capacity increases *(Jing, 2025; Wang L., 2025; Yang Y., 2025)*. A major remaining need is to relate hole geometry and wall stability to soil moisture and texture instead of validating a mechanism at a single soil state.

Table 2

Engineering comparison of key mechanism families

Mechanism / crop scope	Principle	Reported engineering advantage	Primary failure modes	Best-fit conditions	Priority metric
Direct clamp tobacco; pepper; tomato	Grip stem or substrate and extract directly	Short action chain; high potential frequency	Stem damage, substrate breakage, missed picking	Uniform seedlings with sufficient root binding	Success + damage severity + force margin
Eject + gripper tobacco; vegetables	Loosen block from below, then grasp	Lower peak extraction load; wider tolerance	Longer cycle; timing and alignment errors	Variable tray adhesion; fragile blocks	Extraction resistance + timing error
Buffer/relay tobacco; rapeseed; vegetables	Temporary storage and controlled handover	Decouples pick frequency from planting event	Orientation drift, blockage, impact	Automatic systems with multi-stage timing	Entry-angle deviation + impact acceleration

Mechanism / crop scope	Principle	Reported engineering advantage	Primary failure modes	Best-fit conditions	Priority metric
Duckbill tobacco; pepper; tomato	Penetrate/open/release/close in one cycle	Compact integrated operation; mulch compatibility	Dragging, large film tear, tilted seedlings	Mulched or bare soil with controlled trajectory	Relative ground speed + uprightness
Guide-tube/cup tobacco; vegetables	Seedling slides/falls into opened furrow/hole	Simple, inexpensive, maintainable	Rolling, collision, timing dependence	Semi-automatic and low-cost systems	Orientation at outlet + missed planting
Well-cellar auger tobacco	Rotary or impact formation of deep narrow hole	Matches deep-planting tobacco agronomy	Soil adhesion, blockage, wall collapse	Hilly tobacco regions using well-cellar planting	Hole geometry + wall stability + power

3. ENABLING TECHNOLOGIES FOR INTELLIGENT TRANSPLANTERS

3.1 MACHINE–SOIL–SEEDLING COUPLED MODELING AND COMPLIANT DESIGN

Multibody dynamics and discrete-element modeling have become important tools for moving transplanter design beyond trial-and-error geometry. Mechanism models are well suited to trajectory, acceleration, and phase analyses, whereas DEM represents soil and substrate-block contact. Coupling these approaches enables designers to evaluate how resistance and impact alter a nominal motion path. Applications include picking devices, planter–soil interactions, and hole-forming systems *(Hou et al., 2023; Jin X. et al., 2025; Zhang Q. et al., 2025)*. These methods are most informative when their parameters are calibrated against physical measurements rather than selected solely for numerical convenience.

The same principle applies to adhesion reduction. Sticky red soil can increase draft, prevent complete duckbill closure, and disrupt hole geometry. Studies of bionic microtextured tillage surfaces demonstrate that surface morphology can modify soil adhesion and resistance, suggesting a transferable strategy for tobacco-contact components *(Wang Z. et al., 2026)*. Future transplanting studies should therefore combine contact-angle or adhesion measurements with soil-moisture and texture characterization so that anti-adhesion surfaces are designed for a defined operating envelope.

Table 3

Quantitative evidence for coupled machine-soil-seedling modeling

Study / crop or system	Model / task	Validation	Reported quantitative evidence	Computational reporting used in this review
Jin et al. (2025), dryland vegetable pot seedlings (species not specified)	EDEM-RecurDyn; soil-pot seedling-planting device	Field comparison	Mean errors: soil backflow 2.14%; soil disturbance 2.46%; verticality 1.86%	Not ranked: platforms and computational-cost units were not harmonized
Hou et al. (2023), pepper	DEM-MFBD; pepper picking/depositing	Bench validation after coupled optimization	Picking success 97.92%; substrate loss 2.21%; errors versus regression predictions 0.49% and 3.8%, respectively	Not ranked: platforms and computational-cost units were not harmonized
Xue et al. (2022), rice	Machine-plant-paddy-soil numerical coupling	Physical transplanting validation (abstract-level evidence)	No numerical value reproduced because the full text was not accessible during this review	Not ranked: platforms and computational-cost units were not harmonized

Note: Full texts were available and checked for 2 of the 3 studies (Jin et al., 2025; Hou et al., 2023). For Xue et al. (2022), only the publisher abstract and indexed record were accessible; therefore, no numerical validation value was transcribed. Crop, soil, calibration, response variables, solvers, and coupling frameworks differ, so neither accuracy nor computational cost is ranked. Table 3 reports study-level evidence; proposed system gates appear in Table 7.

Compliant end-effectors constitute the mechanical counterpart to this modeling approach. Pneumatic, elastomeric, and force-limited grippers can attenuate impact and accommodate a broader range of seedlings than rigid clamps. Their performance should be evaluated in terms of force–displacement behavior, fatigue life, and contamination tolerance rather than short-duration laboratory picking success alone. In field machinery, a compliant element that is difficult to clean or whose stiffness changes after repeated cycles may introduce a new reliability problem.

3.2 PERCEPTION, NAVIGATION AND ONLINE QUALITY INSPECTION

Machine vision is used for seedling grading, selective picking, low-damage handling, planting-posture assessment, and missed-plant detection. Improved YOLO-based methods can distinguish seedling condition or transplanting targets, while RGB-D data support three-dimensional positioning and obstacle avoidance *(Li T. et al., 2023; Xin et al., 2022; Zhang S. et al., 2026; Zhao S. et al., 2022)*. More recent systems extend vision beyond recognition: selective transplanting uses perceived condition to determine which seedling to pick, YOLO-RDS estimates post-transplant uprightness, and UAV imagery combined with detection and tracking quantifies missed tobacco transplants at field scale *(Jin X. et al., 2024; Li M. et al., 2025; Su et al., 2025)*. These applications move perception toward a closed operational quality loop rather than an isolated classification task.

Research integrating machine vision with GNSS suggests a pathway toward autonomous field navigation *(Liu Z. et al., 2026)*. Nevertheless, tobacco transplanting involves disturbances that are underrepresented in many benchmark datasets, including large flexible leaves, changing canopy appearance, soil splash, mulch reflections, dust, and chassis vibration. The UAV-based tobacco study by *Su et al. (2025)* is particularly informative because it achieved useful field-scale evaluation while identifying limited scenario coverage as an unresolved generalization issue. Consequently, models trained under one agronomic background may attain high test accuracy yet exhibit lower operational availability when transferred to different soils, mulch conditions, or regions. Datasets should therefore represent disturbance levels and failure cases, and field studies should report the proportion of operating time for which the perception module remains valid.

Digital-twin-based quality inspection provides a framework for integrating physical signals, machine states, and predicted operating quality. A plant-factory transplanting study combined vibration data with virtual equipment models for online monitoring *(Chen K. et al., 2023)*, while broader agricultural-machinery research has described digital twins as bidirectional physical–virtual frameworks for equipment life-cycle applications *(Guo et al., 2023)*. Tobacco-specific research has further linked field and machine information to online quality indicators *(Zhao Q. et al., 2026)*. These layers should remain conceptually distinct: coupled DEM–MBD or other numerical models explain mechanisms, sensing estimates the current state, and a digital twin becomes operationally meaningful only when updated information supports parameter adjustment, fault warnings, or maintenance decisions within a useful time horizon.

Table 4

Reported perception performance (task-specific; not a universal leaderboard)

Study / task	Model	Reported accuracy	Speed / size	Robustness / comparison boundary
Su et al. (2025), tobacco UAV missed-plant assessment	YOLOv5s	P 75.1%; R 75.4%; mAP 75.8%	16.8 ms/image; 14.1 MB	Same self-constructed dataset; direct baseline
Su et al. (2025), tobacco - same dataset	YOLOv8s	P 72.6%; R 72.2%; mAP 72.9%	51.0 ms/image; 42.7 MB	Directly comparable with YOLOv5s; newer family was not superior here
Su et al. (2025), tobacco - same dataset	YOLOv11s	P 74.9%; R 75.1%; mAP 75.2%	17.8 ms/image; 19.6 MB	Directly comparable; accuracy close to YOLOv5s
Su et al. (2025), tobacco - same dataset	Improved YOLOv5s	P 79.0%; R 79.6%; mAP 81.1%	17.2 ms/image; 14.2 MB	With DeepSORT on field videos: Mm 4.1%, Mf 9.1%, MOTA 78.5%, 19.9 FPS; no cross-region test

Study / task	Model	Reported accuracy	Speed / size	Robustness / comparison boundary
Jin et al. (2024), vegetable seedlings (species not specified)	YOLO-RDS	mAP 97%; field accuracy 92.56%; mean relative error 3.09%	22 FPS	Absolute angle error 0–3°; different task/data, so not comparable with UAV rows

Within the shared dataset of *Su et al. (2025)*, YOLOv5s exceeded YOLOv8s in both mAP (75.8% versus 72.9%) and latency (16.8 versus 51.0 ms/image), demonstrating that a newer detector family is not automatically superior for small UAV targets. The improved YOLOv5s–DeepSORT pipeline yielded a missed-detection rate of 4.1%, a false-detection rate of 9.1%, a multiple-object tracking accuracy of 78.5%, and 19.9 FPS on field videos, but the single-site dataset does not establish cross-region robustness. Target-hardware testing is equally important: UAM-YOLO reported more than 175 FPS on its development platform but 10.57 FPS on a Qualcomm QCS6490 edge platform, illustrating the desktop-to-edge performance gap *(Su et al., 2025; Wang X.R. et al., 2026)*. Edge-deployment choices should therefore be based on end-to-end latency, energy consumption, thermal headroom, and operating-time availability rather than mAP alone. Compact convolutional detectors and sensor-fusion pipelines currently provide a stronger basis for deterministic real-time control than large language models (LLMs). LLMs may assist with maintenance-information retrieval, log summarization, and operator interaction, but safety-critical motion should remain under verified deterministic control. Cloud dependence also introduces latency, connectivity, and data-governance risks.

3.3 LOW-COST MECHATRONIC INTEGRATION AND FIELD ROBUSTNESS

The transition from prototype mechanisms to deployable intelligent machines depends on a control architecture that connects sensors, actuators, seedling-handling modules, and the chassis. Studies on the motion control of whole-row or reciprocating picking mechanisms have shown that shaped velocity profiles and coordinated multiaxis timing can reduce vibration at higher operating frequencies *(Shi J. et al., 2025)*. Integrated robotic systems likewise show that vision, tray logistics, and end-effector motion must be synchronized as a single production cycle rather than optimized independently *(Liu W. et al., 2024b)*. Automatic separation, air-assisted picking, and flexible feeding impose the same requirement for pneumatic–mechanical coordination *(Shao et al., 2021; Zhang B. et al., 2024; Zheng et al., 2025)*.

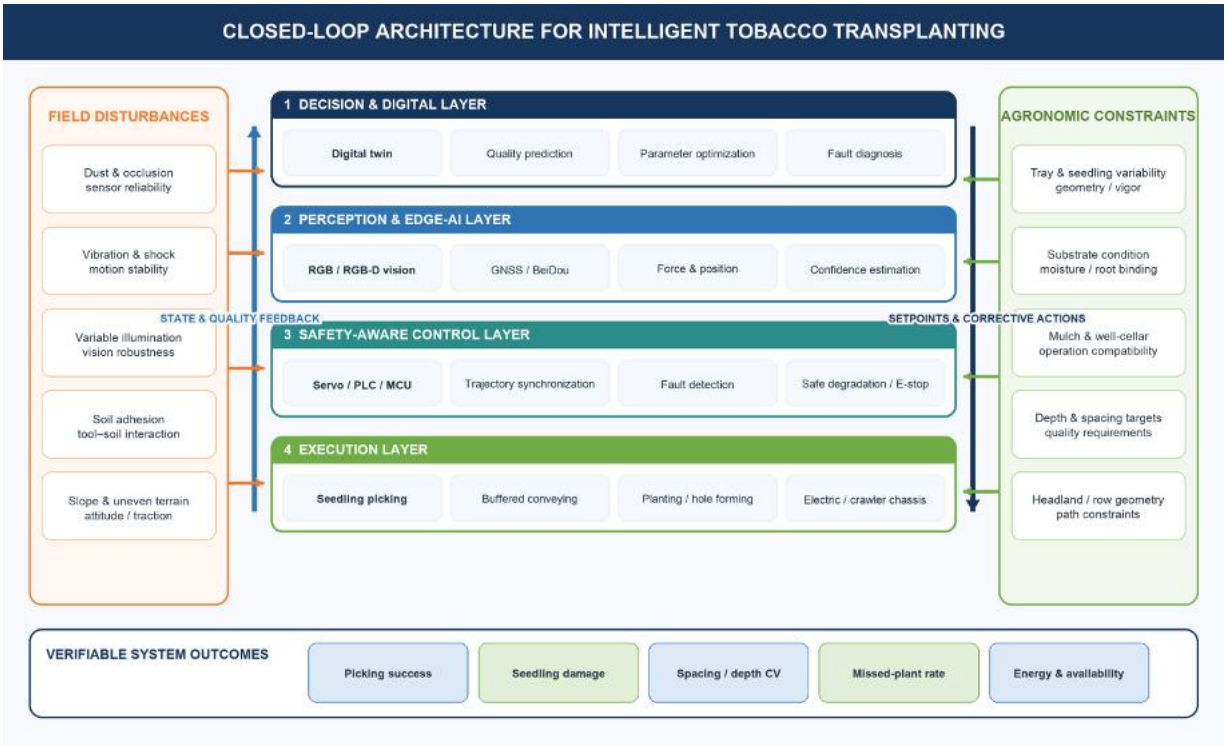


Fig. 2 - Closed-loop layered architecture, disturbance pathways, and performance feedback for intelligent tobacco transplanting

Source: synthesized by the authors from the reviewed literature.

For hilly tobacco production, control performance must be evaluated together with maintainability, energy consumption, and field availability. Industrial servos and PLCs may provide excellent laboratory control, but field machines must also tolerate dust, mud, voltage fluctuations, and maintenance by local service personnel. A miniaturized electrically driven plug-seedling transplanter demonstrated the practical advantages of compact electric actuation; however, its bench and field results also illustrate why module-level success should not be equated with whole-machine field performance *(Chen M. et al., 2025)*. Reviews of agricultural chassis for hilly and mountainous terrain further identify power, travel, steering, leveling, and navigation as coupled subsystems rather than independent design choices *(Jiang Y. et al., 2025)*. Lightweight electric tobacco platforms with microcontroller-based control should therefore be evaluated for slope stability, thermal load, battery endurance, contamination tolerance, and fault recovery over complete working days *(Bai et al., 2025; Li H.M. et al., 2024; Wang B. et al., 2024)*.

4. BOTTLENECKS FOR FIELD DEPLOYMENT

4.1 NURSERY–MACHINE MISMATCH AND AGRONOMIC DIVERSITY

The most fundamental barrier to fully automated transplanting often lies outside the machine itself. Seedling height, stem strength, root binding, substrate moisture, and tray geometry determine extraction resistance and the safe gripping window. When these properties vary, a mechanism optimized for one batch may cause missed picks or damage in another. Consequently, increasingly sophisticated end-effectors do not eliminate the need for nursery standardization *(Wang N. et al., 2021; Zhang X., 2021)*. A practical standard should specify not only nominal tray dimensions but also measurable tolerances for substrate integrity and seedling mechanical properties.

Agronomic diversity creates a second mismatch. Northern flatland tobacco may use ridge, row-spacing, and planting-depth configurations that differ from those used for well-cellar tobacco in the southwest. If the chassis, feeder, planter, hole former, and mulch-handling components are tightly integrated without standardized interfaces, a change in agronomic practice may require redesign of the entire machine. Modular connections, parameter-adjustable actuators, and software-defined timing can improve cross-regional reuse, provided that interface requirements are specified early in the design process.

4.2 HILLY TERRAIN AND ADHESIVE SOILS

Slope alters chassis attitude and, consequently, the penetration angle of the planting or hole-forming element. Wheel or track slip and shifts in the center of gravity can transform a well-tuned laboratory trajectory into an inclined hole or variable planting depth. Research on unmanned farms emphasizes that machine-friendly field infrastructure should be developed alongside autonomous equipment *(Luo et al., 2024)*. Similarly, a recent review of agricultural chassis for hilly and mountainous regions indicates that power, travel, steering, leveling, navigation, and path tracking must be designed as an integrated platform *(Jiang Y. et al., 2025)*. For hilly tobacco production, structural mass, track geometry, active or adaptive leveling, attitude sensing, and field accessibility should therefore be treated as system-level requirements rather than addressed by increasing traction power alone.

Sticky red soil imposes a direct tribological constraint. Soil accumulation on duckbills, press wheels, or augers increases resistance and may prevent complete opening or closing. Current well-cellar and hole-forming studies provide valuable kinematic and structural optimization, but field robustness must be validated across soil-moisture levels and repeated operating cycles *(Fan et al., 2020b; Jiang X. et al., 2024; Xu S. et al., 2024)*. Anti-adhesion microtextures, low-surface-energy coatings, and active cleaning devices are promising only if their durability, sensitivity to contamination, and effects on planting quality are quantified under representative red-soil conditions.

4.3 THE SPEED–DAMAGE–ROBUSTNESS TRADE-OFF

Increasing cycle frequency raises acceleration, inertial loading, and contact frequency, but the available literature quantifies speed–quality deterioration more often than direct plant injury. Direct injury evidence from rice seedling separation shows that the damaged stem-area ratio generally remained below 2% at 100–150 rpm, whereas at 300 rpm the median exceeded 8% for 40-day seedlings; maximum impact load and damaged-area ratio were strongly correlated ($\rho > 0.93$, $p < 0.001$) *(Xi et al., 2026)*. These results are seedling-age- and mechanism-specific and cannot be transferred quantitatively to tobacco. In a pepper transplanter, increasing the operating rate from 80 to 120 plants/min reduced overall transplanting success from 97.5% to 90.0% *(Chen M. et al., 2025)*. In a dryland tomato test, increasing the rate from 45 to 96 plants/min increased spacing CV from 6.6% to 8.9% and the missed-transplanting rate from 1.7% to 2.8% *(Wang Y.W. et al., 2018)*. Collectively,

these findings support a speed–damage or speed–quality trade-off across crop-specific mechanisms, but they do not establish a nonlinear speed–damage curve for tobacco. The nonlinear-threshold hypothesis therefore remains to be tested in tobacco using matched seedling batches and direct injury measurements *(Chen Z. et al., 2026; Xi et al., 2026)*.

A comparable trade-off exists in sensing. Additional cameras and sensors can improve observability, but they also increase the number of failure points, calibration demands, and power consumption. In dusty, vibration-prone fields, robustness may be improved more effectively by combining a limited number of complementary sensors with self-diagnostics and confidence estimation than by simply adding channels. Field-grade intelligent transplanters should therefore support graceful degradation: when a perception module becomes unreliable, the machine should transition to a reduced but safe operating mode rather than stop unnecessarily or continue issuing erroneous commands.

Table 5

Empirical evidence for speed–quality trade-offs and damage risk

Study / crop	Operating rate	Observed response	Boundary of inference
Chen et al. (2025), pepper	80 → 120 plants/min	Overall success 97.5% → 90.0%; at 120 plants/min, picking 95.83% and depositing 94.78%	Direct speed sweep, but physical damage was not reported separately
Wang Y.W. et al. (2018), dryland tomato	45 → 96 plants/min	Spacing CV 6.6% → 8.9%; missed rate 1.7% → 2.8%	Direct speed sweep; quality loss, not a tobacco damage curve
Karayel et al. (2023), tomato/watermelon	0.4 m/s in the reported field protocol	Spacing CV 3.52–5.55%; only disc type damaged >3%; survival >90%	Mechanism comparison; no within-machine speed sweep
Xi et al. (2026), rice seedling separation	100–150 rpm versus 300 rpm	Damaged stem-area ratio generally <2% at 100–150 rpm; median >8% for 40-day seedlings at 300 rpm; ρ(Fmax, damage) >0.93 ($p < 0.001$)	Direct internal stem-damage evidence, but crop, seedling age and separation mechanism differ from tobacco field transplanting

The available evidence supports a speed–quality trade-off but does not establish a universal speed–damage relationship for tobacco. A defensible experiment should test at least three speeds on the same machine and seedling batch, report confidence intervals, and simultaneously quantify damage severity, missed plants, spacing CV, and field capacity.

4.4 ECONOMICS, MAINTAINABILITY AND SERVICE CAPACITY

A technically advanced transplanter may fail commercially if its capital cost and seasonal utilization are mismatched with farm scale. Full automation adds servomotors, pneumatic components, controllers, cameras, and wiring, increasing both manufacturing cost and the expertise required for troubleshooting. In fragmented tobacco-production systems, financial viability may depend on cooperative ownership or professional contracting services rather than individual purchase. Accordingly, cost per successfully transplanted hectare and annual machine availability are more informative deployment metrics than purchase price alone.

Maintainability should be treated as a primary design variable. Sensors and actuators should be accessible; connectors should be protected from mud and vibration; diagnostic information should be intelligible to field technicians; and critical spare parts should be standardized. Remote fault diagnosis may reduce downtime, but it cannot compensate for an architecture that is inherently difficult to inspect or repair. Region-adapted intelligent machines should therefore combine automation with an explicit service and maintenance strategy.

Table 6

Transparent LCC and ROI framework for intelligent transplanter adoption

Component	Included variables	Minimum evidence	Reporting rule
Annualized ownership	Purchase, financing, depreciation, insurance, housing	Local quotations and accounting records	Report currency/base year and discount rate

Component	Included variables	Minimum evidence	Reporting rule
Operating	Energy/fuel, labor, consumables, transport	Metered energy + time-and-motion records	Include charging losses and operator/support labor
Reliability	Planned service, failures, spares, downtime	MTBF, MTTR and seasonal availability logs	Value lost field windows explicitly
Benefit	Labor displaced, timeliness, quality/yield effects, service revenue	Matched field comparison	Do not monetize unmeasured yield gains
Decision	LCC/ha = discounted total cost / successful area; ROI = (discounted benefits - costs)/costs	Sensitivity by annual hectares and service life	Report break-even utilization, not purchase price alone

Published studies of tobacco transplanters rarely report comparable purchase prices, maintenance records, or annual utilization, so a tobacco-specific currency ROI cannot yet be calculated without speculative assumptions. European system analysis of agricultural robotics likewise identifies vehicle capacity and positioning-system cost as major economic drivers *(Pedersen et al., 2006)*. Cross-crop cases further demonstrate the controlling effect of utilization. A survey of six U.S. greenhouse firms evaluated a USD 125,000 transplant robot: under the average scenario, automated cost was USD 0.010 per cutting versus USD 0.014 manually, ten-year NPV was USD 105,807, and discounted payback was 4.8 years *(Adegbola et al., 2019)*. An Indonesian rice-transplanter rental case reported a break-even use of 27.96 ha/year, B/C ratio of 1.02, IRR of 20.79%, and payback of 4.84 years; increasing annual working days shortened the reported payback *(Asmara et al., 2024)*. These values are not transferable cost estimates for hilly tobacco because crop, wage, currency/base year, machine duty, and service model differ. Their transferable lesson is methodological: annual throughput, utilization, labor substitution, and service organization must be included explicitly. Table 6 converts this evidence into a reproducible tobacco field-data requirement for comparing individual ownership, cooperative ownership, and contracting scenarios.

The gates in Table 7 are provisional engineering targets, not standards or pooled estimates. The ≥95% picking-success gate is set below the best reported values used in this review: 97.92% for pepper in *Hou et al. (2023)*, 97.5% overall success at 80 plants/min in *Chen M. et al. (2025)*, and 95-99% transplant success across three vegetable crops in Italian tilled/no-till field tests by *Frasconi et al. (2019)*. The ≤3% damage/miss screen is consistent with 2.21% substrate loss in *Hou et al. (2023)* and a 2.8% missed-transplanting rate in dryland tomato at 96 plants/min in *Wang Y.W. et al. (2018)*. The 5% CV screen is informed by, but is not equivalent to, the 3.52-5.55% spacing CV reported for tomato/watermelon by *Karayel et al. (2023)*; it is not a validated tobacco depth limit. Because the reviewed studies did not report comparable full-period perception availability, seasonal availability, or fouling duration, the ≥95%, ≥90%, and ≥1 h values are protocol-design targets rather than literature bests and require multi-site calibration.

Table 7

Field bottlenecks, engineering responses and proposed validation thresholds

Bottleneck	Engineering response	Recommended validation	Why it matters	Exploratory gate (basis explained in text; not a standard)
Variable plug seedlings	Nursery tolerances + compliant/force-limited end-effector	Success rate, damage severity, extraction-force distribution across batches	Separates mechanism quality from unusually uniform test seedlings	Picking success ≥95%; damage ≤3% over ≥3 seedling batches
Slope and chassis attitude	Lightweight crawler, attitude sensing, self-leveling or trajectory compensation	Depth CV, uprightness, slip rate and stability on defined slopes	Directly measures field adaptation	Depth CV ≤5%; missed plants ≤3%; report defined slope classes
Sticky red soil	Anti-adhesion geometry/material + active cleaning	Draft/torque, adhesion mass, hole-quality decay over repeated cycles	Captures progressive fouling, not just first-cycle performance	Hole dimensions within agronomic tolerance after ≥1 h continuous work

Bottleneck	Engineering response	Recommended validation	Why it matters	Exploratory gate (basis explained in text; not a standard)
Dust/vibration/ill umination	Multimodal sensing, confidence estimation, rugged mounting	Detection/navigation availability over full working period	Measures robustness rather than single-image accuracy	mAP plus ≥95% perception availability; safe fallback tested
High automation cost	Modular architecture and standardized components	Cost per hectare, annual utilization, MTBF/MTTR	Connects technical design with adoption feasibility	Seasonal availability ≥90%; MTBF/MTTR and LCC/ha reported

4.5 SAFETY, STANDARDIZATION AND HUMAN-MACHINE INTERACTION

Autonomous and electric transplanting introduces hazards beyond conventional guarding, including unintended motion, failure to detect people or obstacles, communication loss, battery thermal events, and unsafe recovery after sensor degradation. Internationally, ISO 18497 Parts 1–4:2024 address design principles, obstacle protection, autonomous operating zones, and verification for partially automated to autonomous agricultural machinery; ISO 25119 covers safety-related control systems; ISO 10975:2023 covers auto-guidance on operator-controlled machines; and IEC 62619:2022 addresses industrial lithium-battery safety *(ISO, 2024; ISO, 2019; ISO, 2023; IEC, 2022)*. In China, GB/T 39521-2020 covers agricultural auto-guidance but identically adopts the now-superseded ISO 10975:2009 edition, revealing an update gap relative to ISO 10975:2023. GB/T 16754-2021 specifies emergency-stop design principles, GB/T 41678.1-2022 covers higher-voltage electrical/electronic systems in agricultural machinery, and GB/T 46270-2025 specifies a BeiDou-based agricultural automatic-driving system. The mandatory general agricultural-machinery safety standard GB 10395.1-2025 has been published and is scheduled to take effect on 1 November 2026 *(SAC, 2020; SAC, 2021; SAC, 2022; SAC, 2025a; SAC, 2025b)*. A safety case for a tobacco transplanter should include accessible emergency stops, fail-safe stopping, guarded pinch points, battery isolation, ingress and thermal protection, audible and visual state indication, defined autonomous operating zones, obstacle detection, and documented residual risks. Compliance with general standards is necessary but not sufficient; machine-specific validation is still required on slopes, near workers, and during blockage clearing.

4.6 ENVIRONMENTAL SUSTAINABILITY AND LIFE-CYCLE BOUNDARIES

Electrification can eliminate machine-level tailpipe emissions and improve low-speed controllability, but its overall environmental benefit depends on the electricity mix, battery production and replacement, machine utilization, mass, service life, and end-of-life management. Consistent with ISO 14040 and ISO 14044, a comparative life-cycle assessment should state its goal and scope; define a functional unit, such as one successfully transplanted hectare; document inventory boundaries and data quality; and separate inventory results from impact assessment and interpretation *(ISO, 2006a; ISO, 2006b)*. The boundary should include embodied impacts of the machine and battery, energy supply and charging losses, maintenance, transport, interactions with mulch, and disposal, and should report both energy demand and greenhouse-gas emissions. Sensitivity analysis should vary battery life, annual utilization, electricity mix, and machine service life because these parameters can reverse comparisons between electric and combustion platforms. Design priorities include appropriately sized batteries, high-efficiency actuators, repairable modules, durable anti-adhesion surfaces, and battery take-back programs. These requirements prevent the label “electric” from being used as a sufficient proxy for sustainability.

5. RESEARCH PRIORITIES

First, nursery and machine design should be linked through measurable interface standards. Plug dimensions alone are insufficient; allowable ranges should also be specified for substrate moisture, root binding, stem diameter, seedling height, and extraction resistance. These specifications would allow end-effectors and feeding systems to be tested against representative variability rather than an idealized batch. Existing studies of picking, feeding, and damage provide a technical basis for developing such standards *(Wang X. et al., 2023; Xi et al., 2026; Zhang N. et al., 2024)*.

Second, compliant end-effectors should progress from passive flexibility to closed-loop interaction. Force or displacement sensing, elastic elements, and model-based motion profiles can regulate contact according to seedling and substrate conditions. Recent flexible multi-pin and DEM-optimized end-effectors provide useful starting points because they explicitly link geometry and operating parameters to root-block

mechanics *(Han L. et al., 2025; Liu W. et al., 2024a)*. The objective is not to minimize gripping force unconditionally, but to maintain a robust force margin that guarantees extraction without damage. Closed-loop compliance should also be designed for contamination tolerance, fatigue resistance, and ease of cleaning.

Third, field perception should be evaluated in terms of operational availability and generalizability. Multimodal vision, depth sensing, and GNSS can complement one another, but the system should also estimate confidence and detect sensor degradation. Datasets and experiments must represent dust, mud, leaf occlusion, variable illumination, mulch reflections, and vibration. Post-transplant uprightness monitoring and UAV-based missed-plant assessment demonstrate that quality can be measured after planting; however, cross-scenario validity must be demonstrated rather than assumed *(Jin X. et al., 2024; Su et al., 2025)*. Ultimately, online quality inspection should update machine parameters or trigger corrective actions instead of remaining a post-operation monitoring layer *(Zhao Q. et al., 2026)*.

Fourth, machine–soil–seedling models and digital twins should be linked to experimentally verifiable decisions. DEM, multibody dynamics, and other coupled numerical models can predict contact forces, soil resistance, impact, and trajectory deviations; machinery–plant–soil modeling provides a transferable example of how damage mechanisms can be analyzed beyond ideal kinematics *(Hou et al., 2023; Jin X. et al., 2025; Xue et al., 2022)*. Digital twins add value when physical measurements update the virtual model and the resulting state estimate supports a decision, as illustrated by monitoring of transplanting equipment and broader agricultural-machinery frameworks *(Chen K. et al., 2023; Guo et al., 2023; Zhao Q. et al., 2026)*. A meaningful closed loop should adjust penetration timing, motion profiles, cleaning intervals, or maintenance actions and subsequently demonstrate improved planting quality or a lower failure rate.

Fifth, platforms for hilly regions should prioritize lightweight, modular electrification. Electric drives simplify low-speed control and support distributed actuation, while modular planters, feeders, and hole-forming units allow one chassis to serve multiple agronomic configurations. Research on miniaturized electric transplanters and reviews of agricultural chassis for hilly terrain provide a practical basis for integrating electric drive, compact packaging, leveling, and navigation instead of treating electrification as battery substitution alone *(Chen M. et al., 2025; Jiang Y. et al., 2025)*. The engineering challenge is to balance energy capacity, slope safety, structural mass, and serviceability. Crawler and electric tobacco-transplanter studies provide a tobacco-specific basis for this development *(Bai et al., 2025; Wang B. et al., 2024; Zhao Y., 2024)*.

Finally, the field requires common reporting protocols. Studies of seedling picking should report seedling variability, picking success, damage, and force-related indicators. Planting studies should report depth, spacing, uprightness, missed-plant rate, and mulch damage under defined soil and speed conditions. Evaluations of intelligent functions should report full-period availability and recovery from faults in addition to algorithmic accuracy. Consistent reporting would help distinguish genuine technological advances from performance that depends on favorable test conditions.

Table 8 applies the same provisional gates as research milestones, not current tobacco standards; medium-term availability targets must be recalibrated from multi-region seasonal data.

Table 8

Measurable short- and medium-term research milestones

Priority	Short-term horizon	Short-term measurable milestone	Medium-term horizon	Medium-term measurable milestone
Nursery-machine interface	0-2 y	Measure extraction force, moisture, stem diameter and root binding across ≥3 batches	3-5 y	Inter-laboratory protocol and crop/region-specific tolerance bands
Closed-loop compliant picking	0-2 y	≥95% success and ≤3% damage across defined batch variability	3-5 y	Full-day field validation with fatigue/contamination and fault recovery
Robust perception/edge AI	0-2 y	Public disturbance-labeled dataset; latency, energy and availability reported	3-5 y	Cross-region validation with ≥95% operating-time availability and safe degradation
Models/digital twins	0-2 y	Report calibration, error, hardware and wall-clock cost	3-5 y	Online parameter or maintenance decision shown to improve field KPI

Priority	Short-term horizon	Short-term measurable milestone	Medium-term horizon	Medium-term measurable milestone
Electric/autonomous platform	0-2 y	Battery endurance, slope stability, emergency-stop and obstacle tests	3-5 y	Seasonal LCC/LCA plus standards-aligned autonomous-zone validation
Common reporting	0-2 y	Core KPI dictionary and minimum test metadata	3-5 y	Multi-site benchmark with shared protocols and uncertainty intervals

CONCLUSIONS

Tobacco transplanting machinery is evolving from mechanism-centered equipment into integrated systems that couple nursery quality, seedling handling, soil interaction, chassis motion, sensing, and control. The available international evidence indicates that no single transplanter architecture is universally superior: high-throughput automation is effective in standardized production, whereas hilly tobacco-growing areas require compact, maneuverable, and agronomically adaptable machines.

At the mechanism level, the most important transition is from rigid, single-action designs to force-decoupled picking, buffered conveying, and planting trajectories that explicitly account for soil and seedling interactions. Reported high success rates demonstrate technical feasibility, but field performance remains difficult to compare because seedling properties, soil conditions, and disturbance levels are not reported consistently.

For intelligent tobacco transplanters, the principal bottleneck is system robustness rather than the availability of individual algorithms. Vision, navigation, coupled simulation, and digital twins will have practical value only if they remain functional under dust, vibration, slope, and soil adhesion and if their outputs trigger corrective machine actions. The next generation of equipment should therefore integrate nursery standardization, compliant end-effectors, rugged multimodal sensing, decision-oriented digital twins, and lightweight modular electric chassis, while treating life-cycle cost and maintainability as explicit design objectives.

The key takeaways arising from these conclusions are:

(1) Machine architecture should be selected according to terrain, agronomic practice, nursery uniformity, service capacity, and annual utilization; automation level alone does not define a performance hierarchy.

(2) Cross-crop technology transfer is most defensible at the level of mechanisms, sensing methods, and validation protocols; tobacco-specific constraints associated with well-cellar planting, mulch, and hilly soils still require dedicated field tests.

(3) DEM–MBD models, perception systems, and digital twins are useful only when simulation error, computational cost, field availability, and decision benefit are reported together.

(4) Available evidence supports a speed–quality trade-off, but no universal speed–damage curve has been established for tobacco; matched, multispeed experiments should therefore be prioritized.

(5) Safety, LCC/ROI, and LCA should be treated as design inputs for electric and autonomous machines rather than as post hoc claims.

ACKNOWLEDGEMENT

This work was supported by the General Science and Technology Project of the Baoshan Tobacco Monopoly Bureau (Grant No. 2024530000242006); the Scientific Research Fund Project of the Yunnan Provincial Department of Education (Grant No. 2026Y0540); and the 18th Student Science and Technology Innovation and Entrepreneurship Action Fund Project of Yunnan Agricultural University (Grant No. 20250406008).

REFERENCES

[1] Adegbola Y.U., Fisher P.R., Hodges A.W., (2019), Economic evaluation of transplant robots for plant cuttings, *Scientia Horticulturae*, vol. 246, pp. 237-243. DOI: https://doi.org/10.1016/j.scienta.2018.10.070.

[2] Asai K., Miyake Y., (1989), High performance mechanically-fed transplanter for tobacco, *Tobacco Science*, vol.33, pp.26-30, USA.
[3] Asmara S., Mahesa K.M.D., Suharyatun S., Kuncoro S., (2024), Analisis ekonomi usaha jasa penyewaan transplanter [Economic analysis of a transplanter rental service], *Journal Agricultural Biosystem Engineering*, vol.3, no.2, pp.285-296 (in Indonesian). DOI: https://doi.org/10.23960/jabe.v3i2.9547.
[4] Bai Z., Yang W., Gu Y., Song D., Wang H., Wang W., (2025), Design of a crawler self-propelled fully automatic tobacco transplanter, *Journal of Henan Agricultural University*, vol.59, no.3, pp.497-507, Zhengzhou/China (in Chinese). DOI: https://doi.org/10.16445/j.cnki.1000-2340.20250422.001.
[5] Chen B., Zou X., He Y., Yu B., Xiang P.H., Xiao M.T., (2024), Design and experiment of a dual-tray symmetrically staggered automatic seedling-picking device for tobacco plug seedlings, *Journal of Chinese Agricultural Mechanization*, vol.45, no.7, pp.22-27, Nanjing/China (in Chinese). DOI: https://doi.org/10.13733/j.jcam.issn.2095-5553.2024.07.004.
[6] Chen H., Quan W., Shi F., Jiang X., Xiang Y., Wu M., (2025), Design and testing of rotary seedling tray conveying device for oilseed rape seedling transplanting machine, *Transactions of the Chinese Society of Agricultural Engineering*, vol.41, no.14, pp.61-70, Beijing/China (in Chinese). DOI: https://doi.org/10.11975/j.issn.1002-6819.202501009.
[7] Chen J., Huang Q., Wang Y., Zhang G., (2012), Kinematic modelling and analysis of an elliptical-gear planetary planting mechanism for plug-seedling transplanters, *Transactions of the Chinese Society of Agricultural Engineering*, vol.28, no.5, pp.6-12, Beijing/China (in Chinese).
[8] Chen K., Yuan Y., Zhao B., Zhou L., Niu K., Jin X., Gao S., Li R., Guo H., Zheng Y., (2023), Digital twins and data-driven in plant factory: an online monitoring method for vibration evaluation and transplanting quality analysis, *Agriculture*, vol.13, 1165. DOI: https://doi.org/10.3390/agriculture13061165.
[9] Chen M., Xu Y., Han C., Li D., Yang B., Qiu S., Luo Y., Mao H., Ma X., (2025), Design and testing of miniaturized electrically driven plug seedling transplanter, *Agriculture*, vol.15, 1589. DOI: https://doi.org/10.3390/agriculture15151589.
[10] Chen Z., Zeng T., Ren H., Chen Y., Yang L., Yang M., Zhang Y., (2026), Design and experiment of the dedicated robotic arm for picking-and-placing of pepper plug seedlings in transplanters, *Transactions of the Chinese Society of Agricultural Engineering*, vol.42, no.11, pp.151-161, Beijing/China (in Chinese). DOI: https://doi.org/10.11975/j.issn.1002-6819.202509113.
[11] Fan Y., Li J., Zhang C., (2020a), Design and hydraulic system simulation analysis of tobacco cellar-type transplanting machine, *Chinese Hydraulics & Pneumatics*, no.2, pp.146-150, Beijing/China (in Chinese). DOI: https://doi.org/10.11832/j.issn.1000-4858.2020.02.022.
[12] Fan Y., Zhang X., Li J., Wang D., (2020b), Design and experiment of a tobacco well-cellar transplanter, *Journal of Chinese Agricultural Mechanization*, vol.41, no.5, pp.40-46, Nanjing/China (in Chinese). DOI: https://doi.org/10.13733/j.jcam.issn.2095-5553.2020.05.007.
[13] Fang Q., Xiao M.T., Sun S.L., Liu Q., Chen B., (2021), Research status and prospects of automatic seedling-feeding devices for plug-seedling transplanters, *Agricultural Engineering and Equipment*, vol.48, no.1, pp.1-6,21, China (in Chinese).
[14] Fei Z., Yan Y., (2018), Design of the tobacco seedling transplanting machine, *IOP Conference Series: Materials Science and Engineering*, vol.398, 012027. DOI: https://doi.org/10.1088/1757-899X/398/1/012027.
[15] Frasconi C., Martelloni L., Raffaelli M., Fontanelli M., Abou Chehade L., Peruzzi A., Antichi D., (2019), A field vegetable transplanter for use in both tilled and no-till soils, *Transactions of the ASABE*, vol.62, no.3, pp.593-602, USA. DOI: https://doi.org/10.13031/trans.12896.
[16] Guo D., Du Y., Wu X., Hou S., Li X., Zhang Y., Chen D., (2023), Digital twin for agricultural machinery: from concept to application, *Smart Agriculture*, vol.5, no.2, pp.149-160, Beijing/China. DOI: https://doi.org/10.12133/j.smartag.SA202305007.
[17] Habineza E., Ali M., Reza M.N., Woo J.K., Chung S.O., Hou Y., (2023), Vegetable transplanters and kinematic analysis of major mechanisms: a review, *Korean Journal of Agricultural Science*, vol.50, no.1, pp.113-129, Republic of Korea. DOI: https://doi.org/10.7744/kjoas.20230007.
[18] Han L., Zhang M., Wang Y., Ma G., Yang Q., Liu Y., (2025), Design and tests of a large-opening flexible seedling pick-up gripper with multiple grasping pins, *Agronomy*, vol.15, 1634. DOI: https://doi.org/10.3390/agronomy15071634.

[19] Hou J., Zhang E., Zhang K., Li Y., (2023), Design and experiment of a pepper transplanter seedling picking and depositing device based on DEM-MFBD, *Transactions of the Chinese Society for Agricultural Machinery*, vol.54, no.12, pp.46-57,87, Beijing/China (in Chinese). DOI: https://doi.org/10.6041/j.issn.1000-1298.2023.12.004.

[20] Hu J., Liu Y., Liu W., Zhang S., Han L., Zeng T., (2022), Experimental study on a top-clamping-and-pulling combined seedling-picking device for an automatic vegetable transplanter, *Transactions of the Chinese Society for Agricultural Machinery*, vol.53, S1, pp.110-117,184, Beijing/China (in Chinese).

[21] Huang M., Tang Q., Song Z., Liu H., Wu Y., Zhu T., (2023), Development status and trends of seedling-picking mechanisms for dryland transplanting machinery, *Journal of Intelligent Agricultural Mechanization*, vol.4, no.4, pp.57-64, China (in Chinese). DOI: https://doi.org/10.12398/j.issn.2096-7217.2023.04.008.

[22] IEC, (2022), *IEC 62619:2022 Secondary cells and batteries containing alkaline or other non-acid electrolytes - Safety requirements for secondary lithium cells and batteries, for use in industrial applications*, International Electrotechnical Commission, Geneva/Switzerland.

[23] Inner Mongolia Tobacco Monopoly Administration (IMTMA), (2024), *China's tobacco industry achieved record-high taxes and profits in 2023*, Hohhot/China (in Chinese), source data from the State Tobacco Monopoly Administration, published 13 May 2024.

[24] Iqbal M.Z., Islam M.N., Chowdhury M., Islam S., Park T., Kim Y.J., Chung S.O., (2021), Working speed analysis of the gear-driven dibbling mechanism of a 2.6 kW walking-type automatic pepper transplanter, *Machines*, vol.9, 6. DOI: https://doi.org/10.3390/machines9010006.

[25] ISO, (2006a), *ISO 14040:2006. Environmental management - Life cycle assessment - Principles and framework*, International Organization for Standardization, Geneva/Switzerland.

[26] ISO, (2006b), *ISO 14044:2006. Environmental management - Life cycle assessment - Requirements and guidelines*, International Organization for Standardization, Geneva/Switzerland.

[27] ISO, (2019), *ISO 25119-1:2018, ISO 25119-2:2019, ISO 25119-3:2018 and ISO 25119-4:2018. Tractors and machinery for agriculture and forestry - Safety-related parts of control systems*, International Organization for Standardization, Geneva/Switzerland.

[28] ISO, (2023), *ISO 10975:2023. Agricultural machinery and tractors - Auto-guidance systems for operator-controlled tractors and self-propelled machines - Safety requirements*, International Organization for Standardization, Geneva/Switzerland.

[29] ISO, (2024), *ISO 18497-1:2024 to ISO 18497-4:2024. Agricultural machinery and tractors - Safety of partially automated, semi-autonomous and autonomous machinery*, International Organization for Standardization, Geneva/Switzerland.

[30] Ji D., Liu L., Zeng F., Zhang G., Liu Y., Diao H., Tian S., Zhao Z., (2024), Design and experimental study of a traction double-row automatic transplanter for Solanum lycopersicum seedlings, *Horticulturae*, vol.10, 692. DOI: https://doi.org/10.3390/horticulturae10070692.

[31] Ji J., Zheng Z., He Z., (2015), Design and motion simulation of a 2ZY-B1 tobacco transplanter, *Journal of Chinese Agricultural Mechanization*, vol.36, no.4, pp.22-25, Nanjing/China (in Chinese). DOI: https://doi.org/10.13733/j.jcam.issn.2095-5553.2015.04.006.

[32] Jia R., He Z., Zhu W., Liu F., Li X.J., Ye Y.Y., Yang Z., (2018), Research progress of transplanting mechanisms for tobacco transplanters, *Modern Agricultural Equipment*, no.4, pp.30-36, China.

[33] Jiang X., Jiang H., He X., (2024), Design and experiment of a transplanting hole-forming device for a self-propelled tobacco transplanter, *Journal of Qingdao Agricultural University (Natural Science)*, vol.41, no.4, pp.289-294, Qingdao/China (in Chinese). DOI: https://doi.org/10.3969/J.ISSN.1674-148X.2024.04.008.

[34] Jiang Y., Wang R., Ding R., Sun Z., Jiang Y., Liu W., (2025), Research review of agricultural machinery power chassis in hilly and mountainous areas, *Agriculture*, vol.15, 1158. DOI: https://doi.org/10.3390/agriculture15111158.

[35] Jin X., Yuan Y., Ji J., Zhao K., Li M., Chen K., (2020), Design and implementation of anti-leakage planting system for transplanting machine based on fuzzy information, *Computers and Electronics in Agriculture*, vol.169, 105204. DOI: https://doi.org/10.1016/j.compag.2019.105204.

[36] Jin X., Zhao G., Li M., Li S., Zhou L., Liang J., Xie X., Hou B., (2025), Optimization of transplanting mechanism working parameters based on a coupled machine-soil-pot seedling model, *Computers and Electronics in Agriculture*, vol.238, 110786. DOI: https://doi.org/10.1016/j.compag.2025.110786.

[37] Jin X., Zhu X., Xiao L., Li M., Li S., Zhao B., Ji J., (2024), YOLO-RDS: an efficient algorithm for monitoring the uprightness of seedling transplantation, *Computers and Electronics in Agriculture*, vol.218, 108654. DOI: https://doi.org/10.1016/j.compag.2024.108654.

[38] Jing W., (2025), *Optimization design and experiment of a continuous zero-velocity well-cellar hole-forming and planting device for tobacco transplanters*, MSc thesis, Henan Agricultural University, Zhengzhou/China (in Chinese). DOI: https://doi.org/10.27117/d.cnki.ghenu.2025.000339.

[39] Karayel D., Canakci M., Topakci M., Aktas A., Aytem H., Kriauciuniene Z., (2023), Technical evaluation of transplanters performance for potted seedlings, *Turkish Journal of Agriculture and Forestry*, vol.47, no.1, pp.116-123. DOI: https://doi.org/10.55730/1300-011X.3068.

[40] Khadatkar A., Pandirwar A.P., Paradkar V., (2023), Design, development and application of a compact robotic transplanter with automatic seedling picking mechanism for plug-type seedlings, *Scientific Reports*, vol.13, 1883. DOI: https://doi.org/10.1038/s41598-023-28760-4.

[41] Kutz L.J., Miles G.E., Hammer P.A., Krutz G.W., (1987), Robotic transplanting of bedding plants, *Transactions of the ASAE*, vol.30, no.3, pp.586-590, USA. DOI: https://doi.org/10.13031/2013.30443.

[42] Li G., Xu Y., Han C., Liang J., Cao G., (2025), Design and experiment of the follow-up seedling picking and depositing mechanism for the pepper plug seedling transplanter, *Agriculture*, vol.15, 2026. DOI: https://doi.org/10.3390/agriculture15192026.

[43] Li H., Ma X., Cao W., Li S., Zhou W., (2020), Design and experiment of a stem-clamping seedling-picking mechanism for tomato plug seedlings, *Transactions of the Chinese Society of Agricultural Engineering*, vol.36, no.21, pp.39-48, Beijing/China (in Chinese). DOI: https://doi.org/10.11975/j.issn.1002-6819.2020.21.005.

[44] Li H.M., Yang Y., Xu W., Dong A., Li P., Yuan Z., (2024), Design and experiment of a seedling picking and depositing device for a tobacco seedling transplanter, *Journal of Chinese Agricultural Mechanization*, vol.45, no.11, pp.42-47, Nanjing/China (in Chinese).

[45] Li M., Zhu X., Ji J., Jin X., Li B., Chen K., Zhang W., (2025), Visual perception enabled agriculture intelligence: a selective seedling picking transplanting robot, *Computers and Electronics in Agriculture*, vol.229, 109821. DOI: https://doi.org/10.1016/j.compag.2024.109821.

[46] Li T., Ren L., Hu B., Wang S., Zhao M., Zhang Y., Yang M., (2023), Grading detection of tomato plug seedlings using improved YOLOv5s and transfer learning, *Transactions of the Chinese Society of Agricultural Engineering*, vol.39, no.23, pp.174-184, Beijing/China (in Chinese). DOI: https://doi.org/10.11975/j.issn.1002-6819.202308078.

[47] Li Y., Li J., Du X., Xu L., Fu Z., Huang Y., Zheng Z., (2025), Design and experiment of a planting mechanism for a tobacco transplanter, *Agricultural Research in the Arid Areas*, vol.43, no.6, pp.317-328, China (in Chinese).

[48] Li Z., (2023), *Design and experiment of a stem-clamping seedling-picking mechanism for line-pepper plug seedlings*, MSc thesis, Jiangsu University, Zhenjiang/China (in Chinese). DOI: https://doi.org/10.27170/d.cnki.gjsuu.2023.002342.

[49] Liu C., Peng C., Zhou D., Xiang P., Xiao M., (2025), Design and experiment of an alternating dual-tray seedling picking and depositing device for pepper, *Journal of Chinese Agricultural Mechanization*, vol.46, no.7, pp.55-64, Nanjing/China (in Chinese). DOI: https://doi.org/10.13733/j.jcam.issn.2095-5553.2025.07.009.

[50] Liu W., (2017), *Research on seedling-picking method and planter design for flue-cured tobacco transplanters*, MSc thesis, Northeast Agricultural University, Harbin/China (in Chinese).

[51] Liu W., Tian S., Wang Q., Jiang H., (2023), Key technologies of plug tray seedling transplanters in protected agriculture: a review, *Agriculture*, vol.13, 1488. DOI: https://doi.org/10.3390/agriculture13081488.

[52] Liu W., Wang Q., Jiang H., (2024a), Design and optimisation of end effector for loose substrate grasping based on discrete element method, *Biosystems Engineering*, vol.241, pp.43-55. DOI: https://doi.org/10.1016/j.biosystemseng.2024.03.009.

[53] Liu W., Xu M., Jiang H., (2024b), Design, integration, and experiment of transplanting robot for early plug tray seedling in a plant factory, *AgriEngineering*, vol.6, pp.678-697. DOI: https://doi.org/10.3390/agriengineering6010040.

[54] Liu Z., Wu X., Gao W., Ning F., Zhang W., He J., Liu M., Chen X., Fang P., (2026), Research on a vision navigation system for rice transplanters based on machine vision fused with GNSS, *Biosystems Engineering*, vol.262, 104354. DOI: https://doi.org/10.1016/j.biosystemseng.2025.104354.
[55] Luo X., Hu L., He J., Zhang Z., Zhou Z., Zhang W., Liao J., Huang P., (2024), Key technologies and practice of unmanned farm in China, *Transactions of the Chinese Society of Agricultural Engineering*, vol.40, no.1, pp.1-16, Beijing/China (in Chinese). DOI: https://doi.org/10.11975/j.issn.1002-6819.202312126.
[56] Luo X., Liao J., Zang Y., Ou Y., Wang P., (2022), Developing from mechanized to smart agricultural production in China, *Strategic Study of CAE*, vol.24, no.1, pp.46-54, Beijing/China (in Chinese). DOI: https://doi.org/10.15302/J-SSCAE-2022.01.005.
[57] Mazzetto F., Calcante A., (2011), Highly automated vine cutting transplanter based on DGNSS-RTK technology integrated with hydraulic devices, *Computers and Electronics in Agriculture*, vol.79, no.1, pp.20-29. DOI: https://doi.org/10.1016/j.compag.2011.08.007.
[58] Ning M., Sun W., Luo J., Zhang L., (2025), Electric self-propelled double-row transplanter for Angelica sinensis seedlings, *Computers and Electronics in Agriculture*, vol.237, 110512. DOI: https://doi.org/10.1016/j.compag.2025.110512.
[59] Pedersen S.M., Fountas S., Have H., Blackmore S., (2006), Agricultural robots - system analysis and economic feasibility, *Precision Agriculture*, vol.7, no.4, pp.295-308. DOI: https://doi.org/10.1007/s11119-006-9014-9.
[60] Peng Y., (2025), *Design and experimental study of a planter for tobacco seedling transplanters*, MSc thesis, Fujian Agriculture and Forestry University, Fuzhou/China (in Chinese).
[61] Pérez-Ruiz M., Slaughter D.C., (2021), Development of a precision 3-row synchronised transplanter, *Biosystems Engineering*, vol.206, pp.67-78. DOI: https://doi.org/10.1016/j.biosystemseng.2021.03.014.
[62] Reza M.N., Karim M.R., Ali M.R., Lee K.H., Bicamumakuba E., Lee K.Y., Chung S.O., (2025), Field evaluation of a transplanter and a collector under development for Korean spring cabbage production in greenhouses, *AgriEngineering*, vol.7, 226. DOI: https://doi.org/10.3390/agriengineering7070226.
[63] Shao Y., Han X., Xuan G., Liu Y., Gao C., Wang G., Hu Z., (2021), Development of a multi-adaptive feeding device for automated plug seedling transplanter, *International Journal of Agricultural and Biological Engineering*, vol.14, pp.91-96. DOI: https://doi.org/10.25165/j.ijabe.20211402.6003.
[64] Shi J., Hu J., Liu W., Lv J., Jin Y., Yao M., Wang C., (2025), The design and experiment of a motion control system for the whole-row reciprocating seedling picking mechanism of an automatic transplanter, *Agriculture*, vol.15, 1423. DOI: https://doi.org/10.3390/agriculture15131423.
[65] Shi Y., (2023), *Design and experiment of a well-cellar hole-forming and transplanting device for tobacco*, MSc thesis, Shandong Agricultural University, Tai'an/China (in Chinese). DOI: https://doi.org/10.27277/d.cnki.gsdnu.2023.001254.
[66] Standardization Administration of China (SAC), (2020), *GB/T 39521-2020. Tractors and machinery for agriculture - Auto-guidance systems for operator-controlled tractors and self-propelled machines - Safety requirements*, Beijing/China (in Chinese).
[67] Standardization Administration of China (SAC), (2021), *GB/T 16754-2021. Safety of machinery - Emergency stop function - Principles for design*, Beijing/China (in Chinese).
[68] Standardization Administration of China (SAC), (2022), *GB/T 41678.1-2022. Agricultural machinery and tractors - Safety of higher-voltage electrical and electronic components and systems - Part 1: General requirements*, Beijing/China (in Chinese).
[69] Standardization Administration of China (SAC), (2025a), *GB 10395.1-2025. Agricultural machinery - Safety - Part 1: General requirements*, Beijing/China (in Chinese; effective 1 November 2026).
[70] Standardization Administration of China (SAC), (2025b), *GB/T 46270-2025. Agricultural machinery automatic driving system based on BDS*, Beijing/China (in Chinese).
[71] Su R., Yu B., Sun Y., Wang L., Gao L., Chen D., (2025), Missed transplanting rate evaluation method for tobacco seedling transplanter based on UAV imagery and improved YOLOv5s, *Frontiers in Plant Science*, vol.16, 1659559. DOI: https://doi.org/10.3389/fpls.2025.1659559.
[72] Suggs C.W., Thomas T.N., Eddington D.L., Peel H.B., Seaboch T.R., Gore J.W., (1987), Self-feeding transplanter for tobacco and vegetable crops, *Applied Engineering in Agriculture*, vol.3, no.2, pp.148-152, St. Joseph/USA. DOI: https://doi.org/10.13031/2013.26663.
[73] Wang B., Yuan K., Wang C., Zhang Y., Liu H., Deng S., (2024), Design and experiment of electric well-

cellar tobacco transplanting machine in hilly and mountainous areas, *Agricultural Engineering*, vol.14, no.4, pp.92-96, Beijing/China (in Chinese). DOI: https://doi.org/10.19998/j.cnki.2095-1795.2024.04.015.

[74] Wang L., (2025), *Design and parameter optimization of a high-speed cutting double-well-cellar one-step tobacco transplanter*, MSc thesis, Jiangsu University, Zhenjiang/China (in Chinese). DOI: https://doi.org/10.27170/d.cnki.gjsuu.2025.000471.

[75] Wang N., Ren L., Li J., Hu H., Wang B., Shang J., (2021), Research status and prospects of automatic seedling-picking technology for plug-seedling transplanters, *Journal of Chinese Agricultural Mechanization*, vol.42, no.1, pp.59-66, Nanjing/China (in Chinese). DOI: https://doi.org/10.13733/j.jcam.issn.2095-5553.2021.01.009.

[76] Wang X., Liu M., Zhai C., Han C., Yang S., Gao Y., (2023), Design and experiment of a stem-clamping seedling-picking device for vegetable transplanting, *Transactions of the Chinese Society for Agricultural Machinery*, vol.54, no.9, pp.122-132, Beijing/China (in Chinese). DOI: https://doi.org/10.6041/j.issn.1000-1298.2023.09.012.

[77] Wang X.B., Li D., He G., He Z., Zeng S., Yang W., (2025), Progress and prospect of tobacco transplanting technology in China, *Modern Agricultural Equipment*, vol.46, no.1, pp.10-22,68, China (in Chinese).

[78] Wang X.R., Guan X., Wan H., Zhu Z., Zheng Y., Zhou Z., (2026), UAM-YOLO: Lightweight obstacle detection algorithm for unmanned agricultural machinery with structure reparameterized YOLOv11-Nano, *Computers and Electronics in Agriculture*, vol.246, 111603. DOI: https://doi.org/10.1016/j.compag.2026.111603.

[79] Wang Y.W., He Z., Wang J., Wu C., Yu G., Tang Y., (2018), Experiment on transplanting performance of automatic vegetable pot seedling transplanter for dry land, *Transactions of the Chinese Society of Agricultural Engineering*, vol.34, no.3, pp.19-25, Beijing/China (in Chinese). DOI: https://doi.org/10.11975/j.issn.1002-6819.2018.03.003.

[80] Wang Z., Zhang Y., Xu H., Du H., Yang Z., Yang J., Mao Z., Wang H., (2026), Mechanism and optimization of adhesion and resistance reduction by bionic microtextured rotary tillage blades in soil-straw environment, *Agriculture*, vol.16, 437. DOI: https://doi.org/10.3390/agriculture16040437.

[81] WHO FCTC, (2025), *2025 Global Progress Report on Implementation of the WHO Framework Convention on Tobacco Control*, World Health Organization, Geneva/Switzerland.

[82] WHO, (2022), *Tobacco agriculture trade: China country profile*, World Health Organization, Geneva/Switzerland.

[83] WHO, (2023a), *World No Tobacco Day 2023 - Grow food, not tobacco: questions and answers*, World Health Organization, Geneva/Switzerland.

[84] WHO, (2023b), *Tobacco growing: myth buster*, World Health Organization, Geneva/Switzerland.

[85] Wu G., An X., Yan B., Li L., He Y., (2022), Design and experiment of an automatic bare-seedling sweet-potato transplanter based on pretreated seedling belts, *Transactions of the Chinese Society for Agricultural Machinery*, vol.53, S1, pp.99-109, Beijing/China (in Chinese). DOI: https://doi.org/10.6041/j.issn.1000-1298.2022.S1.011.

[86] Xi D., Que J., Shen R., Kuang F., Xiong W., Zhang S., Zhu D., (2026), Quantitative assessment and predictive modelling of stem damage during seedling separation in mechanical rice transplanting, *Biosystems Engineering*, vol.263, 104377. DOI: https://doi.org/10.1016/j.biosystemseng.2025.104377.

[87] Xie S., Yang S., Liu J., Song L., Xie Q., Duan T., (2020), Development of an oblique-insertion plug-clamping seedling picking and depositing device for vegetable transplanters, *Transactions of the Chinese Society of Agricultural Engineering*, vol.36, no.6, pp.1-10, Beijing/China (in Chinese). DOI: https://doi.org/10.11975/j.issn.1002-6819.2020.06.001.

[88] Xin J., Li R., Tang Q., Wu J., Jiang L., Wu C., (2022), Low-damage transplanting method for leafy vegetable seedlings based on machine vision, *Biosystems Engineering*, vol.220, pp.159-171. DOI: https://doi.org/10.1016/j.biosystemseng.2022.05.017.

[89] Xiong J., (2025), Design of key transmission components for a duckbill tobacco transplanter, *Modern Manufacturing Technology and Equipment*, vol.61, no.10, pp.46-48, China (in Chinese). DOI: https://doi.org/10.16107/j.cnki.mmte.2025.0645.

[90] Xu L., (2024), *Design research on a crawler self-propelled fully automatic tobacco transplanter*, MSc thesis, Henan Agricultural University, Zhengzhou/China (in Chinese). DOI: https://doi.org/10.27117/d.cnki.ghenu.2024.000498.

[91] Xu S., Shi D., Zhao C., (2024), Design of a well-cellar transplanting hole-forming drill bit, *Southern Agricultural Machinery*, vol.55, no.22, pp.27-30, China (in Chinese).
[92] Xue K., Gao K., Kuang F., Zhang S., Liao J., Zhu D., (2022), Machinery-plant-paddy soil coupling model based numerical simulation method of mechanical transplanting process of big rice seedling, *Computers and Electronics in Agriculture*, vol.198, 107053. DOI: https://doi.org/10.1016/j.compag.2022.107053.
[93] Yan Y., Qiao X., Zhang G., Chu Y., Zhang Y., Yang F., (2020), Design and experiment of a seedling-feeding device for a tobacco transplanter, *Journal of Chinese Agricultural Mechanization*, vol.41, no.4, pp.24-28, Nanjing/China (in Chinese). DOI: https://doi.org/10.13733/j.jcam.issn.2095-5553.2020.04.005.
[94] Yang W., (2019), *Research and development of key components of a mulch-film tobacco seedling transplanter*, MSc thesis, Kunming University of Science and Technology, Kunming/China (in Chinese). DOI: https://doi.org/10.27200/d.cnki.gkmlu.2019.000005.
[95] Yang Y., (2025), *Design and experiment of well-cellar forming components and a seedling-picking mechanism for transplanting machinery*, MSc thesis, Henan Agricultural University, Zhengzhou/China (in Chinese).
[96] Yin D., Chen F., Cao Y., (2021), Dynamic analysis and experiment of seedling receiving and dropping in the guide tube of a dryland plug-seedling transplanter, *Transactions of the Chinese Society of Agricultural Engineering*, vol.37, no.11, pp.27-36, Beijing/China (in Chinese).
[97] Yu G., Liu B., Zhao Y., Sun L., (2011), Motion mechanism analysis of an automatic vegetable plug-seedling transplanting mechanism with an elliptical-gear planetary train, *Transactions of the Chinese Society for Agricultural Machinery*, vol.42, no.4, pp.53-57, Beijing/China (in Chinese).
[98] Yuan C., Yang Y., Zhao G., (2023), Design and analysis of a tobacco seedling transplanter, *Forestry Machinery & Woodworking Equipment*, vol.51, no.12, pp.29-32, China (in Chinese). DOI: https://doi.org/10.13279/j.cnki.fmwe.20231220.007.
[99] Zhang B., Wen X., Wen Y., Wang X., Zhu H., Pan Z., Yang Z., (2024), Design and testing of a closed multi-channel air-blowing seedling pick-up device for an automatic vegetable transplanter, *Agriculture*, vol.14, 1688. DOI: https://doi.org/10.3390/agriculture14101688.
[100] Zhang D., Zhang Y., Zhang Y., Li Z., (2021), Design and motion characteristics of an intermittent moving tobacco-transplanter hole-forming mechanism, *Journal of Agricultural Mechanization Research*, vol.43, no.3, pp.106-112, Harbin/China (in Chinese). DOI: https://doi.org/10.13427/j.cnki.njyi.2021.03.017.
[101] Zhang N., Zhang G., Fu J., Liu W., Chen L., Tang N., (2024), Design and experiment of the seedling pick-up device with ejecting pot-clamping stem combination, *Transactions of the Chinese Society of Agricultural Engineering*, vol.40, no.3, pp.50-61, Beijing/China (in Chinese). DOI: https://doi.org/10.11975/j.issn.1002-6819.202309091.
[102] Zhang Q., Song J., Li X., Chen W., Chu J., Qi Z., Wang T., (2025), EDEM-based simulation of upright transplanting for a chain-clamping Paeonia lactiflora transplanter, *Journal of Agricultural Mechanization Research*, vol.47, no.11, pp.19-27, Harbin/China (in Chinese). DOI: https://doi.org/10.13427/j.issn.1003-188X.2025.11.003.
[103] Zhang S., Chen G., Peng Z., (2026), Design of a tobacco transplanting recognition system based on improved YOLOv8, *Agricultural Engineering*, vol.16, no.2, pp.17-23, Beijing/China (in Chinese). DOI: https://doi.org/10.19998/j.cnki.2095-1795.202508039.
[104] Zhang W., Zhu Q., Zhang T., Liu H., Mu G., (2024), Design and control of a side dense transplanting machine for sweet potato seedlings on mulch film, *Computers and Electronics in Agriculture*, vol.224, 109193. DOI: https://doi.org/10.1016/j.compag.2024.109193.
[105] Zhang X., (2021), *Design and experiment of a clamping seedling-picking and planting mechanism for tobacco plug seedlings*, MSc thesis, Northeast Agricultural University, Harbin/China (in Chinese). DOI: https://doi.org/10.27010/d.cnki.gdbnu.2021.000320.
[106] Zhang X.D., Liu L., Ning Y., Kong D., Liu Y., Wu H., (2023), Design and experiment of the end-effector of a top-clamping seedling-picking device for vegetable transplanters, *Transactions of the Chinese Society for Agricultural Machinery*, vol.54, S1, pp.115-124,134, Beijing/China (in Chinese). DOI: https://doi.org/10.6041/j.issn.1000-1298.2023.S1.013.
[107] Zhao Q., Ma E., Zhao J., You Z., Liu J., Zhao D., (2026), A digital twin-driven deep learning framework for online quality inspection in tobacco transplanting, *Frontiers in Plant Science*, vol.17, 1716046. DOI: https://doi.org/10.3389/fpls.2026.1716046.

[108] Zhao S., Liu J., Jin Y., Bai Z., Liu J., Zhou X., (2022), Design and testing of an intelligent multi-functional seedling transplanting system, *Agronomy*, vol.12, 2683. DOI: https://doi.org/10.3390/agronomy12112683.
[109] Zhao X., Yang Q., Huang G., He M., Mao H., (2022), Design and experiment of a seedling-picking mechanism for a small automatic plug-seedling transplanter, *Journal of Jiangsu University (Natural Science Edition)*, vol.43, no.1, pp.54-61, Zhenjiang/China (in Chinese). DOI: https://doi.org/10.3969/j.issn.1671-7775.2022.01.008.
[110] Zhao Y., (2024), *Design and experimental study of the planting mechanism of an electric tobacco transplanter*, MSc thesis, Kunming University of Science and Technology, Kunming/China (in Chinese). DOI: https://doi.org/10.27200/d.cnki.gkmlu.2024.001846.
[111] Zheng S., Li J., Dong Z., Wang J., Weng W., Cui Z., Wang C., Wu X., (2025), Design and experiments of automatic seedling separation device for vegetable substrate block seedling transplanter, *Agriculture*, vol.15, 428. DOI: https://doi.org/10.3390/agriculture15040428.
[112] Zhou B., Miao H., Guan C., Ji X., Wang X., (2024), Design and test of seedling-picking mechanism of fully automatic transplanting machine, *Applied Sciences*, vol.14, 9235. DOI: https://doi.org/10.3390/app14209235.
[113] Zhu Z., (2008), Current status and prospect of tobacco leaf production and research in China, *Acta Tabacaria Sinica*, vol.14, no.6, pp.70-72, China (in Chinese).

CONTRIBUTIONS TO THE INVESTIGATION OF THE MECHANICAL BEHAVIOUR OF ROSE HIP SEEDS UNDER COMPRESSION AND CREEP TESTS: EXPLORATORY UNSUPERVISED CLASSIFICATION OF COMPRESSION RESPONSES

/

CONTRIBUȚII LA CERCETAREA COMPORTAMENTULUI MECANIC AL SEMINȚELOR DE MĂCEȘE PRIN TESTE DE COMPRESIUNE ȘI FLUAJ: CLASIFICAREA EXPLORATORIE PRIN TEHNICI DE ÎNVĂȚARE AUTOMATĂ NESUPRAVEGHEATĂ A RĂSPUNSURILOR LA COMPRESIUNE

George IPATE*[1)], Iuliana GĂGEANU*[2)], Alina Corina DUMITRAŞCU[3)]
[1)]National University of Science and Technology Politehnica Bucharest / Romania;
[2)] National Institute of Agricultural Machinery, Bucharest, Romania
[3)] "Gheorghe Asachi" Technical University, Iasi, Romania
E-mail: iulia.gageanu@gmail.com, george.ipate@upb.ro
DOI: https://doi.org/10.35633/inmateh-79-95

Keywords: *rosehip seeds, physical properties, main components analysis, machine learning*

ABSTRACT

This study proposes an artificial intelligence-based method for the automatic identification of natural groups of mechanical behaviour in rose hip seeds (Rosa canina). The method combines compression testing with unsupervised machine learning techniques, namely Principal Component Analysis (PCA) and K-means clustering, while creep tests are analysed separately to assess the time-dependent mechanical behaviour of the seeds. This approach enables the identification of distinct mechanical patterns and the objective classification of samples according to their response to mechanical loading. The unsupervised multivariate analysis was performed using mechanical features extracted from compression tests conducted on 25 individual rose hip seeds (n = 25), with each individual compression test generating a force–displacement dataset comprising 934 experimental data points. Each cluster was analysed separately in terms of the experimentally determined mechanical parameters. For each group, the mean values of maximum compression force (F_{max}), displacement at maximum force (x_{max}), deformation energy, and initial stiffness were calculated. The results revealed the existence of two main categories of mechanical behaviour. The first group was characterized by an average maximum force of approximately 141 N and a displacement at maximum force of 0.73 mm, indicating seeds with high mechanical strength. The second group exhibited an average maximum force of approximately 75 N and a displacement at maximum force of 0.85 mm, corresponding to seeds that were more deformable and less resistant to compression. The seeds were tested at a moisture content of 2.79% (wet basis), determined thermo-gravimetrically. To validate cluster separation and reduce the dimensionality of the dataset, Principal Component Analysis (PCA) was applied. The quality of clustering was assessed using the silhouette index, which indicated a satisfactory separation of samples according to their mechanical response. PCA revealed that the main differences between clusters were associated with maximum force, absorbed energy, and initial stiffness values, confirming the existence of distinct categories of mechanical behaviour within the analysed seed batch.

REZUMAT

Lucrarea de fata propune o metodă bazată pe inteligența artificială pentru identificarea automată a unor categorii distincte de comportament mecanic al semințelor de măceș (Rosa canina). Metoda integrează încercările de compresiune cu tehnici de învățare automată nesupravegheată, respectiv Analiza Componentelor Principale (PCA) și algoritmul K-means, în timp ce testele de fluaj sunt analizate separat pentru caracterizarea răspunsului mecanic al semințelor în timp. Această abordare permite evidențierea și clasificarea obiectivă a diferitelor tipuri de răspuns mecanic la compresiune. Analiza multivariată nesupravegheată a fost realizată utilizând caracteristici mecanice extrase din testele de compresiune efectuate pe 25 de semințe individuale de măceș (n = 25), fiecare test individual de compresiune generând un set de date forță–deplasare alcătuit din 934 de puncte experimentale. Fiecare cluster a fost analizat separat din punctul de vedere al parametrilor mecanici determinați experimental. Pentru fiecare grup au fost calculate valorile medii ale forței maxime de compresiune (F_{max}), deplasării la forța maximă (x_{max}), energiei de deformare și rigidității inițiale. Rezultatele au evidențiat existența a două categorii principale de comportament mecanic. Primul grup a fost

caracterizat printr-o forță maximă medie de aproximativ 141 N și o deplasare la forța maximă de 0,73 mm, indicând semințe cu rezistență mecanică ridicată. Al doilea grup a prezentat o forță maximă medie de aproximativ 75 N și o deplasare la forța maximă de 0,85 mm, corespunzând unor semințe mai deformabile și cu o rezistență mai redusă la compresiune. Semințele au fost testate la un conținut de umiditate de 2,79% (bază umedă), determinat prin metoda termogravimetrică. Pentru validarea separării clusterelor și reducerea dimensionalității setului de date a fost aplicată Analiza Componentelor Principale (PCA). Calitatea grupării a fost evaluată utilizând indicele silhouette, care a indicat o separare satisfăcătoare a probelor în funcție de răspunsul lor mecanic. Analiza PCA a evidențiat faptul că principalele diferențe dintre clustere au fost asociate cu valorile forței maxime, energiei absorbite și rigidității inițiale, confirmând existența unor categorii distincte de comportament mecanic în cadrul lotului de semințe analizat.

INTRODUCTION

The need to identify and utilize new food resources with high nutritional and energy value, together with the continuous growth of the global population, has led to a significant increase in research efforts in this field worldwide. All available food resources can contribute, to a greater or lesser extent, to ensuring food security and meeting the nutritional requirements of the population. However, the efficiency of their utilization depends on their nutritional characteristics, availability, and the sustainability of production and valorisation processes (*Chen and Kates, 1994*) .

By combining state-of-the-art computational algorithms with the ability of modern computer systems to rapidly process very large volumes of data, researchers are now able to efficiently identify and evaluate solutions to complex problems whose direct experimental investigation may be costly, difficult, or time-consuming. In this way, optimized technical solutions can be obtained, capable of reproducing the behaviour of real physical phenomena with a high degree of accuracy within a reasonable time frame.

In this context, rose hip seeds (*Rosa canina*), derived from a perennial plant that is resistant to low temperatures, grows optimally in sunny or slightly shaded areas, and requires moderate irrigation, are of particular interest due to their nutritional and functional value (*Yildiz and Alpaslan, 2012*). The plant is characterized by delicate pale pink flowers followed by intensely red fruits (as shown in Fig. 1), which are well known for their high content of bioactive compounds, particularly vitamin C, polyphenols, and antioxidants (*Marmol et al., 2017*). Beyond its mechanical and technological relevance, *Rosa canina* has attracted considerable scientific interest due to the valuable chemical composition and diverse biological properties of its fruits and other plant components. *Demir and Özcan (2001)* highlighted the chemical and technological properties of wild rose fruits, while *Polumackanycz et al. (2020)* reported the rich phenolic composition and associated biological properties of dog rose fruits and leaves. The broader potential of *Rosa canina* has also been addressed through pharmacognostic investigations (*Oproshanska et al., 2021*) and through its use as a phytogenic source in animal nutrition (*Stătescu et al., 2025*). Collectively, these studies emphasize the considerable biological, nutritional, and technological value of *Rosa canina* and support continued research aimed at improving the characterization and valorisation of this plant and its derived materials.



a) b)

Fig. 1 – Rosa hip (rosa canina), wild: a) fruits; b) seeds

The mechanical behaviour and fracture resistance of agricultural seeds under compressive loading have been extensively investigated because of their relevance to handling, processing, grinding, and size-reduction operations. *Paulsen, (1978),* investigated the fracture resistance of soybeans subjected to compressive loading, while *Gupta and Das, (2000),* analysed the fracture resistance of sunflower seeds and kernels under compression.

Similar investigations were subsequently conducted by *Łysiak (2007),* who characterized the fracture toughness of pea seeds using Weibull analysis, and by *Khodabakhshian et al., (2010)*, who evaluated the mechanical properties of sunflower seeds and kernels under compressive loading. In addition to the intrinsic mechanical properties of the biological material, experimental factors such as moisture content, seed dimensions, loading rate, and loading orientation can substantially influence the force and energy associated with seed fracture, as investigated for cumin seeds by *Saiedirad et al., (2008).* The importance of specimen orientation and moisture level was also addressed by *Dowd et al., (2019),* in their study of cottonseed fracture resistance. These studies demonstrate that the mechanical response of seeds is strongly dependent on both material characteristics and testing conditions, emphasizing the importance of controlling moisture content, loading orientation, and compression conditions when evaluating fracture behaviour.

Ionescu et al., (2025), investigated the influence of grinding time on the particle size distribution of rose hip powder, highlighting its direct implications for various applications in the food and pharmaceutical industries. The authors emphasized that improvements in solubility, stability, and bioavailability form the basis for the development of new rose hip powder-based products tailored to the specific requirements of different industrial sectors. In addition, *Gokduman (2026)* conducted a comprehensive study on the main physical and mechanical characteristics of rose hip fruits, analysing parameters such as dimensions, mass, firmness, and the mechanical behaviour of the fruits under detachment and puncture loading conditions. Indentation techniques have also been extensively employed for the mechanical characterization of materials, with *Evans et al. (2013)* investigating nano-indentation methods for compliant materials and *Han et al. (2015)* analysing the factors influencing micro-indentation measurements.

The application of machine learning techniques for the characterization of elastic, viscoelastic, stress relaxation, and creep behaviour of agri-food materials has been addressed in numerous recent studies, including those conducted by *Xu (2020)*, *Biswas et al. (2020)*, *Li et al. (2021)*, and *Singh et al. (2026)*.

These studies propose and validate various predictive models based on machine learning algorithms that are capable of accurately estimating the characteristic parameters of creep and stress-relaxation phenomena. Their findings contribute to a deeper understanding and improved modelling of the rheological behaviour of agri-food materials.

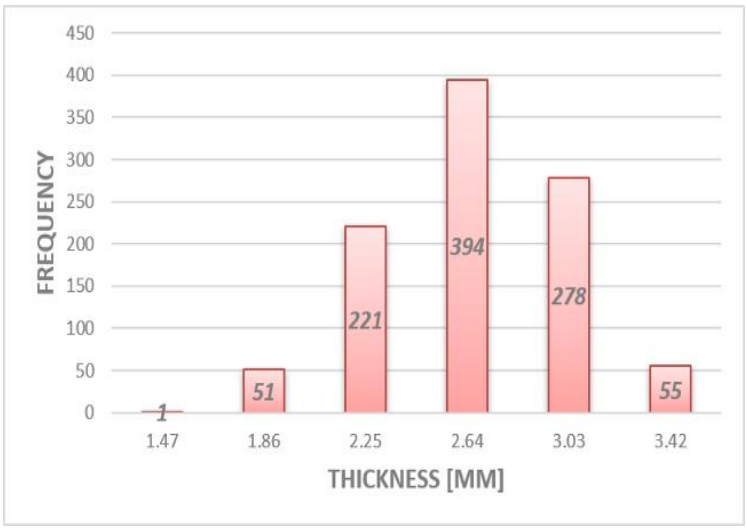
The main objective of the present study is the theoretical and experimental investigation of the mechanical behaviour of rose hip seeds subjected to compression and creep tests, as well as the identification of natural groups of mechanical response using unsupervised machine learning techniques. Mechanical features extracted from the force–displacement curves were analysed using Principal Component Analysis (PCA) and the K-means clustering algorithm in order to reveal distinct patterns of mechanical behaviour. The proposed approach enables an objective characterization of the mechanical response of the seeds and provides relevant insights into the mechanisms of deformation, energy absorption, and structural failure.

MATERIAL AND METHOD

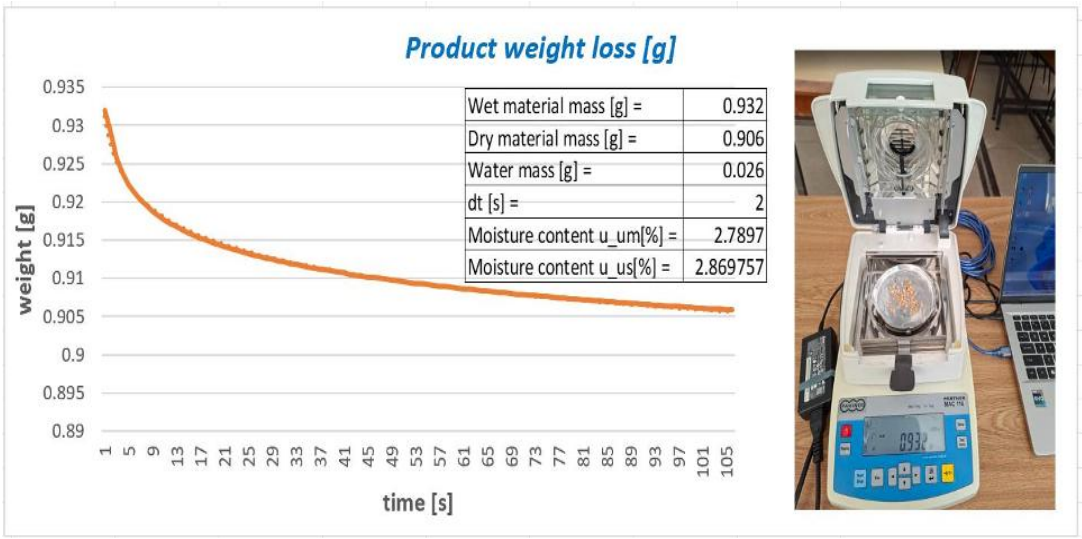
Rose hip seeds (*Rosa canina* L.) used in the experiments were obtained from mature fruits and cleaned prior to testing. The seeds were recovered after separation of the fruit pulp and subsequently dried until hygroscopic equilibrium was reached. Before mechanical testing, they were stored in plastic containers under laboratory conditions at a temperature of 22 ± 2 °C and a relative humidity of approximately 30%.

For the dimensional characterization of the experimental batch, 1,000 seeds were analysed and their thickness distribution was determined. The results revealed an approximately normal distribution, with most seeds exhibiting thickness values between 2.25 and 3.03 mm. The physical characterization of the rose hip seeds also included the determination of the thousand-seed weight (TSW), which was found to be 19.64 g. Together with the dimensional distribution presented in Figure 2a, this parameter indicates a relatively high degree of uniformity of the experimental batch used for the compression and creep tests. Seed dimensions were measured using a digital micrometre (measuring range: 0–25 mm, resolution: 0.001 mm, accuracy: ±0.001 mm; PR China). Seed mass was determined using the precision balance integrated into the PARTNER MAC 110 moisture analyser (RADWAG, Poland), with a maximum capacity of 110 g and a resolution of 1 mg. The same instrument was subsequently used for the thermo-gravimetric determination of seed moisture content. The moisture content of the rose hip seeds was determined thermo-gravimetrically using a PARTNER MAC 110 moisture analyser. The initial sample mass was 0.932 g and the final dry mass was 0.906 g, corresponding to a water loss of 0.026 g. The resulting moisture content was 2.79% on a wet basis, equivalent to 2.87% on a dry basis (Fig. 2b).

A unimodal distribution can be observed, with the highest frequency recorded for a thickness of 2.64 mm, corresponding to 394 seeds (39.4% of the total). An additional 278 seeds (27.8%) exhibited a thickness of approximately 3.03 mm, while 221 seeds (22.1%) had a thickness of approximately 2.25 mm. The results show that more than 89% of the analysed seeds had thickness values ranging from 2.25 to 3.03 mm, indicating a high degree of dimensional uniformity within the experimental batch. The small number of seeds with extreme thickness values, approximately 1.47 mm and 3.42 mm, suggests limited data dispersion and the absence of a significant number of outliers.



a)



b)

Fig. 2 – Physical characterization of rose hip (*Rosa canina L.*) seeds

(a) thickness distribution illustrating the dimensional uniformity of the experimental batch (N = 1000);
(b) thermo-gravimetric determination of seed moisture content using the PARTNER MAC 110 moisture analyser

Mechanical tests were performed using a Hounsfield 1K universal testing machine, equipped with a load cell appropriate for the investigated force range (0–1000 N) and controlled through QMat 5.50 software. Mechanical compression tests were performed using a Hounsfield 1K universal testing machine (Hounsfield Test Equipment Ltd., UK), equipped with a 1000 N load cell with a force measurement accuracy of 0.01 N and controlled through QMat 5.50 software. A crosshead speed of 15 mm/min was used for all specimens. Since this loading rate is higher than that commonly employed for strictly quasi-static testing of agricultural biological materials, its potential influence on the measured force–deformation response should be considered when interpreting the results. The experiments were carried out using a cylindrical indenter with a radius of 1.4 mm. Compression tests were conducted on 25 seeds randomly selected from the analysed population. Each specimen was tested only once, and the force–deformation data were continuously recorded throughout the loading process.

Stiffness was determined by calculating the slope of the linear portion of the force–deformation curve, while the fracture energy was calculated as the area under the curve up to the failure point. Similar mechanical evaluation procedures based on force–deformation curves have been reported for small fruits and other biological materials. (*Gageanu et al., 2021, Gˆ kduman, 2026*).

Compression tests were performed at a crosshead speed of 15 mm/min. For each of the 25 compression tests, representative mechanical features were extracted from the force–displacement curve, including maximum compression force, displacement at maximum force, deformation energy, initial stiffness, mean force, RMS force, fracture index, and number of force peaks (*Stryjecka et al., 2024*). These variables were standardized using z-score normalization and subsequently analysed using Principal Component Analysis (PCA) and K-means clustering.

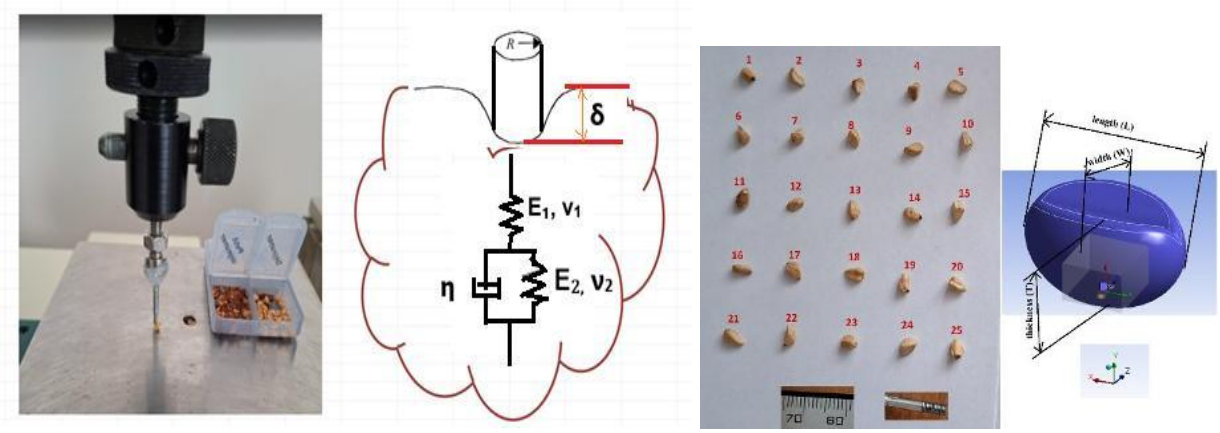
Creep tests were carried out by applying a constant load of 25 N for a period of 600 s. The evolution of deformation over time was continuously monitored, allowing the viscoelastic behaviour of the rose hip seeds to be evaluated. Data obtained from the creep tests were not included in the PCA or K-means analysis.

For the description of the creep behaviour of rose hip seeds, the Zener Standard Linear Solid (SLS) viscoelastic model, shown in Fig. 3, was employed. This model consists of an elastic element with modulus E_1, connected in series with a Kelvin–Voigt element composed of an elastic spring with modulus E_2 and a viscous dashpot characterized by the viscosity coefficient η. The Zener model is widely used to describe the viscoelastic behaviour of biological materials because it simultaneously represents the instantaneous elastic response and the time-dependent deformation. Within the model, the parameter E_1 characterizes the instantaneous elastic stiffness of the material, E_2 describes the delayed elastic component associated with relaxation and creep phenomena, while η represents the internal viscous resistance to deformation.

Data Analysis and Machine Learning.

Representative mechanical features were extracted from the force–displacement curves, including the maximum compression force, displacement at maximum force, deformation energy, initial stiffness, and the viscoelastic parameters determined using the Zener model (Fig. 3b).

To identify natural groups of mechanical behaviour, an unsupervised machine learning approach was employed. Dimensionality reduction of the dataset was performed using Principal Component Analysis (PCA), while sample clustering was carried out using the K-means algorithm. Figures 3c present the 25 seeds used for compression testing. The principal geometrical dimensions of the rose hip seed are defined in Figure 3d as length (L), width (W), and thickness (T). In the present experimental campaign, thickness was the dimension systematically measured and used for the dimensional characterization of the seed batch.



a) *b)* *c)* *d)*

Fig. 3 – Experimental system used for the mechanical characterization of rose hip seeds

(a) force sensor of the Hounsfield 1K universal testing machine employed for compression tests; (b) Standard Linear Solid (SLS) viscoelastic model, also known as the Zener model, used to describe the viscoelastic behaviour of the seeds; (c) rose hip seeds used in the compression tests (n = 25); (d) schematic representation of the principal seed dimensions: length (L), width (W), and thickness (T)

Before applying Principal Component Analysis (PCA), all mechanical features were standardized using the z-score normalization method in order to eliminate the influence of differences in scale among the variables. The normalization was performed according to the following equation:

$$z_{ij} = \frac{x_{ij} - \mu_j}{\sigma_j} \quad (1)$$

where x_{ij} is the original value of the variable, μ_j is the mean value of the variable, and σ_j is its standard deviation. The quality of the obtained clusters was evaluated using the silhouette index, calculated according to the following equation:

$$s(i) = \frac{b(i)-a(i)}{max[a(i),b(i)]} \quad (2)$$

where $a(i)$ represents the average distance between sample i and all other samples within the same cluster, while $b(i)$ represents the smallest average distance between sample i and the samples belonging to a different cluster.

The silhouette index ranges from −1 to 1. Values close to 1 indicate very good cluster separation, values close to 0 suggest overlap between clusters, whereas negative values indicate a possible misclassification of samples. In the present study, silhouette analysis was used to determine the optimal number of clusters and to evaluate the performance of the K-means algorithm.

RESULTS

The mechanical properties of rose hip seeds are essential for evaluating their behaviour during grinding processes and for optimizing powder production technologies. Similar mechanical assessments focused on compression, fracture, and fragmentation processes have also been reported for various medicinal and aromatic plants. In these studies, parameters such as maximum compression force, deformation energy, and stiffness have been identified as important indicators for the design and optimization of grinding and mechanical processing equipment for plant materials (*Yilmaz and Gökduman, 2015; Stan et al., 2014*).

Figure 4 shows the force–displacement curves obtained from compression tests performed on individual rose hip seeds. During the compression tests, the load was applied in the vertical direction, along the Y-axis, as illustrated in Figure 3d. The same loading configuration was maintained for all tested seeds.

A significant variability in the mechanical response can be observed, as evidenced by differences in the maximum force, displacement at failure, and overall curve shape. Some specimens exhibit a progressive increase in force followed by a sudden drop, associated with the fracture of the internal structure, whereas others display a more deformable behaviour characterized by gradual force increases and multiple successive fracture events. In some cases, the maximum force values exceed 200 N, indicating substantial differences in mechanical strength among the analysed seeds.

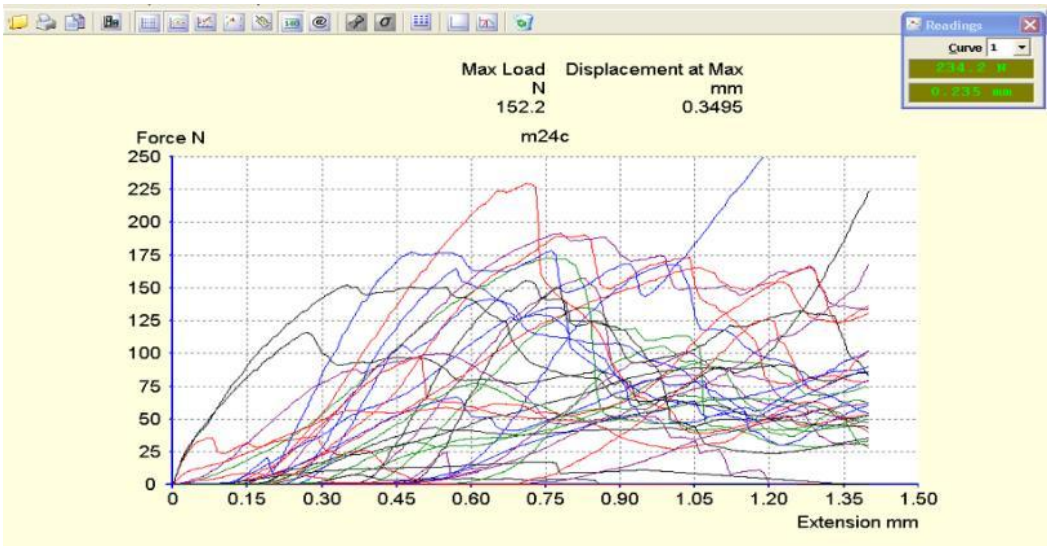
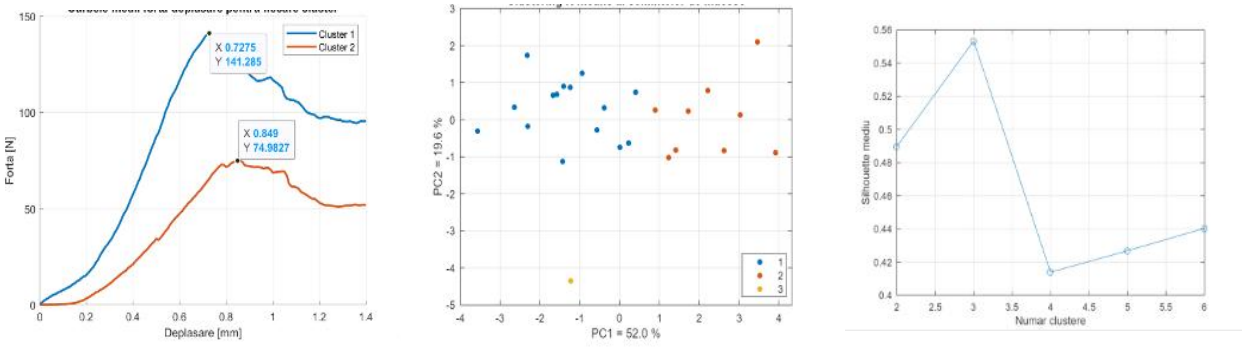


Fig. 4 – Force–displacement curves of rose hip seeds obtained from compression tests

In the absence of predefined classes, the force–displacement curves were analysed using unsupervised machine learning techniques to identify natural groups of mechanical behaviour among the rose hip seeds. Representative mechanical features were extracted from each force–displacement curve, including maximum force, displacement at maximum force, deformation energy, initial stiffness, mean force, RMS value, fracture index, and number of peaks. The data were standardized and analysed using Principal Component Analysis (PCA), while sample clustering was performed using the K-means algorithm.

Cluster analysis revealed the existence of two main categories of mechanical behaviour, shown in Fig. 5. Cluster analysis revealed two principal categories of compression behaviour. Cluster 1 was characterized by higher maximum force and deformation energy, indicating greater mechanical resistance. Cluster 2 exhibited lower maximum force and energy values and greater deformability, corresponding to a mechanically less resistant response.



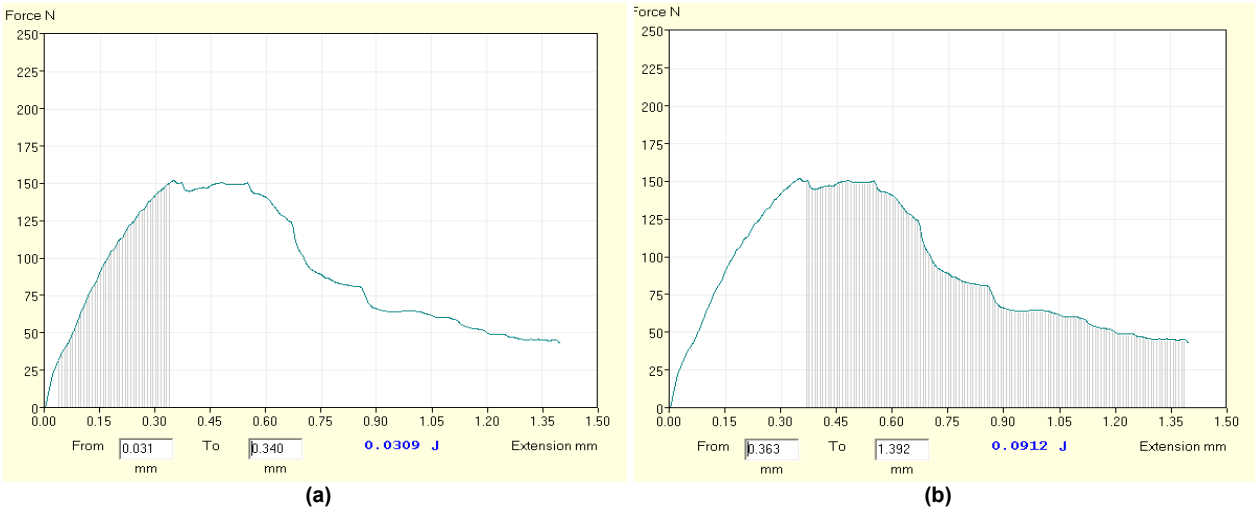
a) b) c)

Fig. 5 - Identification of the mechanical behaviour of rose hip seeds using unsupervised machine learning techniques

(a) mean force–displacement curves of the resulting clusters; (b) projection of samples in the PCA space (PC1–PC2); (c) evaluation of the optimal number of clusters using the silhouette index

The distribution of samples in the PCA space confirms the separation between the two groups. Furthermore, silhouette analysis indicates that the three-cluster solution provides the best mathematical separation of the data. However, one of the clusters is represented by a very small number of observations and can therefore be interpreted as an outlier group. Consequently, from a physical and mechanical perspective, the behaviour of the seeds can be adequately described by two principal categories of compression response. In Fig. 5b, Cluster 3 consists of a single point (or only a very small number of points). This indicates that the algorithm identifies this sample as a separate group because its mechanical characteristics differ substantially from those of the remaining data. Figure 5c shows the variation of the silhouette index as a function of the number of clusters.

Figure 6 presents a representative force–displacement curve obtained during the compression of a rose hip seed belonging to Cluster 1 (mechanically rigid/high-strength seeds). An initial increase in force can be observed up to approximately 150 N, followed by a resistance plateau associated with the redistribution of internal stresses. At a displacement of approximately 0.7 mm, a sudden drop in force occurs, indicating the primary fracture of the seed structure. Following this event, the mechanical response is characterized by a gradual decrease in force, which is typical of the progressive fragmentation and compaction of the resulting material.



(a) (b)

Fig. 6 - Representative force–displacement curve of a Cluster 1 seed (mechanically rigid/high-strength seeds)

(a) energy absorbed within the viscoelastic region and up to the yield point (E = 0.0309 J); (b) energy absorbed after exceeding the yield point and until the end of the compression process (E = 0.0912 J)

The energy value of 0.0309 J, determined between the point corresponding to the elastic limit at a displacement of 0.031 mm and the yield point at a displacement of 0.340 mm (Fig. 6a), highlights the ability of the seed to absorb mechanical energy before the onset of irreversible deformation. This value reflects the resistance of the internal structure to compression and suggests a relatively rigid mechanical behaviour, characterized by an initial stage of controlled deformation prior to the initiation of cracking or structural failure processes. Figure 6b presents the mechanical energy absorbed by the seed within the deformation range from 0.363 mm to 1.392 mm, determined by integrating the force–displacement curve. The obtained value, 0.0912 J, reflects the seed's capacity to absorb energy after reaching the yield point, including the processes of cracking, fracture, and progressive compaction of the resulting fragments. The energy absorbed during this stage is approximately three times greater than that accumulated within the viscoelastic region, highlighting a significant capacity for energy dissipation under compressive loading.

A comparative analysis of the two energy intervals shows that approximately 75% of the total absorbed energy is dissipated after the onset of irreversible deformation. This result suggests a progressive failure mechanism of the seed structure, characterized by the successive development of cracks and the gradual fragmentation of the material, rather than by a sudden and instantaneous fracture.

Figure 7 highlights the creep behaviour of rose hip seeds subjected to a constant load of 25 N for a duration of 600 s. The final creep deformation values were 0.018 mm, 0.027 mm, and 0.067 mm for the three analysed specimens, confirming the existence of significant variability in the viscoelastic response within the experimental batch. It can be observed that, although all specimens were tested under identical conditions, the deformation recorded after 600 s differed considerably, which may be attributed to structural and geometrical differences among the seeds. The observed behaviour confirms the viscoelastic nature of the biological material and its ability to develop progressive deformation under constant loading. Furthermore, the relatively low creep displacement values indicate good structural stiffness and high resistance to permanent deformation. The obtained results suggest that rose hip seeds are capable of withstanding long-term mechanical loading with limited deformation, an important aspect for handling, transportation, storage, and mechanical processing operations.

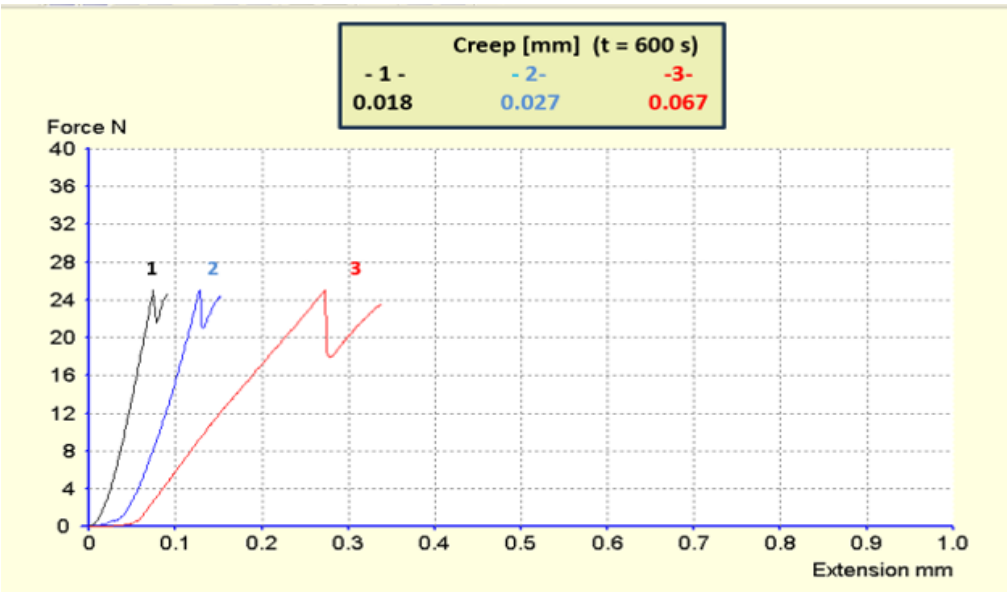


Fig. 7 – Creep behaviour of rose hip seeds under a constant load of 25 N for 600 s

Figure 8 presents the evolution of the applied force during the creep test for the three rose hip seed specimens. After reaching the maximum load of approximately 25 N, all specimens exhibited an initial decrease in the measured force, followed by a gradual increase throughout the 600 s creep period. The force increased from values ranging between 18–21.5 N to approximately 24–25 N at the end of the test. This behaviour suggests the occurrence of compaction and structural reorganization processes within the rose hip seeds, leading to a progressive increase in resistance to deformation under sustained loading. The observed response indicates that, following the initial accommodation phase, the internal structure becomes increasingly resistant to further deformation, resulting in the gradual recovery of the measured force toward the imposed load level.

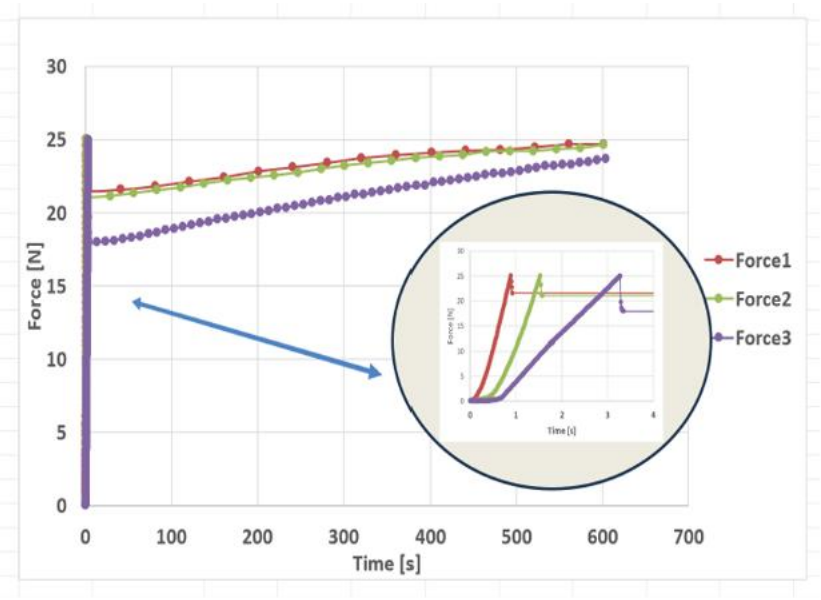


Fig. 8 – Variation of force with time during creep testing of rose hip seeds, showing the initial force decrease followed by a gradual recovery toward the imposed load of 25 N

From an experimental perspective, an interesting finding is that the force does not relax over time but instead tends to recover toward the initial value of 25 N, indicating a behaviour different from that of many conventional polymeric materials and characteristic of compact granular plant structures. After the initial compaction and local structural failure, the material does not continue to soften but rather exhibits a progressive increase in resistance to compression. This behaviour may be associated with material densification, a reduction in internal porosity, an increase in the contact surfaces between particles, and a redistribution of stresses within the seed structure. From the standpoint of granular material mechanics, the observed response resembles a strain-hardening phenomenon induced by compaction.

The force distribution over time confirms that all specimens were tested under similar loading conditions. Therefore, the differences subsequently observed in creep deformation can be attributed primarily to the specific viscoelastic properties of each seed rather than to variations in the applied load.

Figure 9 presents the variation of deformation as a function of time for the three rose hip seed specimens subjected to a constant load of 25 N for 600 s. A progressive increase in deformation can be observed for all specimens, which is characteristic of the creep behaviour of viscoelastic materials. During the initial stage of the test, an instantaneous deformation occurs, associated with the elastic component of the mechanical response, followed by a slow and continuous increase in deformation throughout the entire loading period.

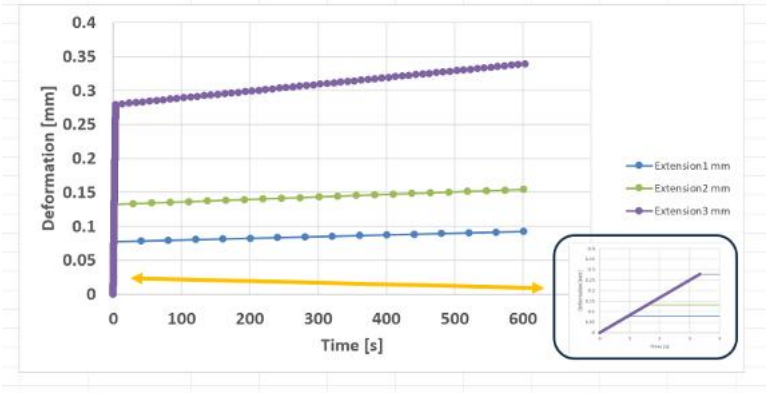


Fig. 9 - Time-dependent deformation (creep) of rose hip seeds under a constant compressive load of 25 N

Specimen 3 exhibited the highest deformation, increasing from approximately 0.28 mm to 0.34 mm after 600 s, indicating a greater susceptibility to time-dependent deformation. Specimen 2 displayed an intermediate behaviour, with deformation values ranging from approximately 0.14 mm to 0.16 mm, whereas Specimen 1

showed the lowest displacement values, approximately 0.08–0.09 mm. The differences observed among the three curves highlight the variability of the viscoelastic properties of the analysed seeds and suggest the existence of internal structural differences that influence their deformation capacity under long-term mechanical loading. Nevertheless, the relatively low slopes of the creep curves indicate good dimensional stability and high resistance to permanent deformation.

For the description of the creep behaviour of rose hip seeds, the Zener Standard Linear Solid (SLS) viscoelastic model was employed. The viscoelastic model parameters E_1, E_2, and η can be determined from the experimental creep data using the values of the initial deformation, final deformation, and deformation at an arbitrary time t. Thus, the instantaneous elastic modulus E_1 can be determined using the following relationship:

$$E_1 = \frac{3P0}{8R} \cdot \frac{1}{\delta(0)} \quad (3)$$

where $\delta(0)$ represents the initial penetration depth, or the instantaneous deformation, occurring immediately after the application of the constant load P_0.

The modulus E_2, associated with the delayed elastic component, can be determined using the following relationship:

$$E_2 = \frac{3P0}{8R} \cdot \frac{1}{\delta(\infty)-\delta(0)} \quad (4)$$

where $\delta(\infty)$ represents the asymptotic deformation reached at a very long time, corresponding to the equilibrium state of the creep process under the applied constant load.

The dynamic viscosity coefficient η can be calculated using the following relationship:

$$\eta = \frac{P0 \cdot t}{8R} \cdot \frac{1}{[\delta(\infty)-\delta(0)] \cdot \ln[\frac{\delta(\infty)-\delta(0)}{\delta(\infty)-\delta(t)}]} \quad (5)$$

Considering the applied load P_0 and the indenter radius R = 1.4 mm, the instantaneous elastic modulus E_1 and the delayed elastic modulus E_2 were determined using Eqs. (3) and (4). The viscosity coefficient η was calculated using Eq. (5) for a creep time of t = 300 s. The obtained values are summarized in Table 1.

Table 1

Experimental creep parameters and viscoelastic parameters determined using the Zener model for rose hip seeds

Sample	$P0$ [N]	$\delta(0)$ [mm]	$\delta(600)$ [mm]	E_1 [GPa]	E_2 [GPa]	η [GPa·s]
1	21.57	0.074	0.092	0.078	0.321	46.308
2	21.05	0.128	0.155	0.044	0.209	30.128
3	18.03	0.281	0.34	0.018	0.072	10.399

The results reveal a progressive decrease in the elastic moduli E_1 and E_2 from Specimen 1 to Specimen 3, indicating a reduction in structural stiffness and an increase in material deformability. Similarly, the viscosity coefficient η exhibits decreasing values, suggesting a lower resistance to time-dependent deformation. Specimen 1 displays the most rigid viscoelastic behaviour, whereas Specimen 3 is characterized by the greatest susceptibility to creep and progressive deformation under constant loading.

The literature indicates that cereal grains exhibit time-dependent and viscoelastic mechanical behaviour, although at low loads and short loading times the elastic response may become predominant and the load–deformation relationship remains approximately linear (*Mohsenin, 1966; Shelef and Mohsenin, 1967*). Similarly, the rose hip seeds investigated in the present study exhibited a time-dependent response under constant loading; however, the 600 s creep tests enabled the progressive deformation and associated viscoelastic behaviour to be clearly identified.

For biological materials considered nearly incompressible, the evolution of the penetration depth (deformation) over time can be expressed by the following relationship (*Cheng et al., 2000*):

$$\delta(t) = \frac{3P0}{8RE1}[-(\frac{E1}{E2})\, e^{-(\frac{E2}{3\eta})t} + (1+\frac{E1}{E2})] \quad (6)$$

Following the approach used by *Shelef and Mohsenin (1967)* for cereal grains, the influence of Poisson's ratio may be expressed through the correction factor $k = 1 / (1 - \nu^2)$, with $1 < k < 1.33$.

This range corresponds mathematically to $0 < \nu < 0.49$. Since Poisson's ratio was not independently determined for the rose hip seeds investigated in the present study, the calculated elastic parameters should be regarded as apparent, model-dependent values rather than intrinsic material constants.

The relatively limited number of compression specimens (n = 25) should be considered when interpreting the PCA/K-means results, which are therefore regarded as exploratory evidence of natural patterns within the investigated batch rather than as a definitive population-level classification. Regarding the creep experiments (n = 3), despite the limited number of specimens, a relatively consistent time-dependent response was observed under identical loading conditions, with the differences being mainly associated with seed dimensions. Considering this consistency and the relatively long duration of each individual test (600 s), the three experiments were considered adequate for a descriptive assessment of the creep phenomenon within the scope of the present study, without claiming statistical representativeness for the entire rose hip seed population.

A limitation of the present study is the crosshead speed of 15 mm/min used during compression testing, which is higher than the loading rates commonly employed for strictly quasi-static testing of agricultural biological materials. Therefore, a possible influence of the loading rate on the measured force–deformation response cannot be excluded. Future studies should investigate lower loading rates and systematically evaluate their effects on maximum compression force, stiffness, deformation energy, and fracture behaviour.

CONCLUSIONS

The exploratory application of unsupervised machine learning techniques (PCA and K-means) to the mechanical features extracted from the compression tests enabled the identification of natural groups of mechanical behaviour. The results revealed two main categories within the investigated seed batch: one group characterized by high mechanical strength and stiffness, and a second group exhibiting greater deformability and lower resistance to compression.

The Zener (SLS) viscoelastic model made it possible to determine the parameters E_1, E_2, and η, revealing differences in the time-dependent mechanical response of the tested specimens. The progressive decrease in the elastic moduli and viscosity coefficient was associated with increased deformability and reduced resistance to creep.

The proposed methodology, combining conventional mechanical testing with modern data analysis and unsupervised machine learning techniques, provides a useful approach for investigating the mechanical behaviour of rose hip seeds and may be extended to other biological materials used in the food and pharmaceutical industries.

REFERENCES

[1] Biswas, S., Fernandez Castellanos, D., Zaiser, M. (2020). *Prediction of creep failure time using machine learning*. Scientific Reports, 10(1), 16910, https://doi.org/10.1038/s41598-020-72969-6.

[2] Chen, R. S., Kates, R. W. (1994). World food security: prospects and trends. *Food Policy*, 19(2), pp. 192-208, https://doi.org/10.1016/0306-9192(94)90069-8.

[3] Cheng L., Xia X., Yu W., Scriven L. E., Gerberich W. W.(2000). Flat-punch indentation of viscoelastic material", *J. Polym. Sci. Part B Polym. Phys*., vol. 38, nr. 1, pp. 10–22, https://doi.org/10.1002/(SICI)1099-0488(20000101)38:1%3C10::AID-POLB2%3E3.0.CO;2-6.

[4] Demir, F., Özcan, M. (2001). Chemical and technological properties of rose (*Rosa canina L.*) fruits grown wild in Turkey. *Journal of food engineering*, 47(4), pp. 333-336, https://doi.org/10.1016/S0260-8774(00)00129-1.

[5] Dowd, M. K., Manandhar, R., Delhom, C. D. (2019). Effect of seed orientation, acid delinting, moisture level, and sample type on cottonseed fracture resistance. *Transactions of the ASABE*, 62(4), 1045-1053, https://doi.org/10.13031/trans.13109.

[6] Evans, D. W., Vavalle, N. A., DeVita, R., Rajagopalan, P., Sparks, J. L. (2013). Nano-indentation device for investigating the mechanics of compliant materials. *Experimental Mechanics*, 53(2), pp. 217-229, https://doi.org/10.1007/s11340-012-9618-0.

[7] Gageanu, I., Cujbescu, D., Persu, C., Tudor, P., Cardei, P., Matache, M., Ungureanu, N. (2021). Influence of input and control parameters on the process of pelleting powdered biomass. *Energies*, 14(14), 4104, https://doi.org/10.3390/en14144104.

[8] Gökduman, M. E. (2026). Evaluation of physico-mechanical properties of Rosehip (*Rosa canina L.*) fruits. *International Journal of Agriculture Environment and Food Sciences*, (Advanced Online

Publication), pp.77-85, https://doi.org/10.31015/jaefs.2026.1.9.
[9] Gupta, R. K., Das, S. K. (2000). Fracture resistance of sunflower seed and kernel to compressive loading. *Journal of food engineering*, 46(1), pp. 1-8, https://doi.org/10.1016/S0260-8774(00)00061-3.
[10] Han, Q., Chen, P., Ma, T. (2015). Influencing factor analysis of shale micro-indentation measurement. *Journal of Natural Gas Science and Engineering*, 27, pp. 641-650, https://doi.org/10.1016/j.jngse.2015.09.010.
[11] Ionescu, A. D., Voicu, G., Constantin, G. A., Ipate, G., Ştefan, E. M., Begea, M., Iordache, S. D. (2025). Research On The Influence Of Grinding Time On The Particle Size Distribution When Obtaining Rosehips Powder. *INMATEH-Agricultural Engineering*, 76(2), pp. 923-933, https://doi.org/10.35633/inmateh-76-79.
[12] Khodabakhshian, R., Emadi, B., Fard, M. A., Saiedirad, M. H. (2010). Mechanical properties of sunflower seed and its kernel, azargol variety as a case study, under compressive loading. *J. Agric. Sci. Technol*, 4(2), 34-40.
[13] Li, J., Zhang, L., Huang, G., Wang, H., Jiang, Y. (2021). Experimental study on creep properties prediction of reed bales based on SVR and MLP. *Plant Methods*, 17(1), 112, https://doi.org/10.1186/s13007-021-00814-6.
[14] Łysiak, G. (2007). Fracture toughness of pea: Weibull analysis. *Journal of Food Engineering*, 83(3), 436-443, https://doi.org/10.1016/j.jfoodeng.2007.03.034.
[15] Mármol, I., Sánchez-de-Diego, C., Jiménez-Moreno, N., Ancín-Azpilicueta, C., Rodríguez-Yoldi, M. J. (2017). Therapeutic applications of rose hips from different Rosa species. *International journal of molecular sciences*, 18(6), 1137, https://doi.org/10.3390/ijms18061137.
[16] Mohsenin, N.N. (1966). *Physical Properties of Plant and Animal Materials*. *Part I: Structure, Physical Characteristics and Rheological Properties*. Department of Agricultural Engineering, The Pennsylvania State University, University Park, PA.
[17] Oproshanska, T., Khvorost, O., Skrebtsova, K., Vitkevicius, K. (2021). Comparative pharmakognostical study of roots of *Rosa Majalis Herrm*. and *Rosa Canina L*. *ScienceRise: Pharmaceutical Science*, (5 (33)), 71-78, https://doi.org/10.15587/2519-4852.2021.243525.
[18] Paulsen, M. R. (1978). Fracture resistance of soybeans to compressive loading. *Transactions of the ASAE*, 21(6), 1210-1216, https://doi.org/10.13031/2013.35470.
[19] Polumackanycz, M., Kaszuba, M., Konopacka, A., Marzec-Wróblewska, U., Wesolowski, M., Waleron, K., Viapiana, A. (2020). Phenolic composition and biological properties of wild and commercial dog rose fruits and leaves. *Molecules*, *25*(22), 5272, https://doi.org/10.3390/molecules25225272.
[20] Saiedirad, M. H., Tabatabaeefar, A., Borghei, A., Mirsalehi, M., Badii, F., Varnamkhasti, M. G. (2008). Effects of moisture content, seed size, loading rate and seed orientation on force and energy required for fracturing cumin seed (Cuminum cyminum Linn.) under quasi-static loading. *Journal of food engineering*, 86(4), 565-572, https://doi.org/10.1016/j.jfoodeng.2007.11.021.
[21] Shelef, L., Mohsenin, N. N. (1967). Effect of moisture content on mechanical properties of shelled corn. *Cereal Chemistry*, 46(3), pp. 242-253.
[22] Singh, M. J., Borana, L., Hattab, M., Yin, J. H. (2026). Time-dependent compressibility characteristics of soil: Experimental and integrated machine learning framework. *Engineering Applications of Artificial Intelligence*, 163, 112809, https://doi.org/10.1016/j.engappai.2025.112809.
[23] Stan, C., Apostol, T., Paraschiv, G., Pásztai, Z. (2014). Two solutions for MSW treatment in view of landfill minimization and energy recovery maximization. *UPB Scientific Bulletin, Series D: Mechanical Engineering*, 76 (4), pp. 247-256.
[24] Stătescu, M., Petrescu, S. I., Pop, I. M., Boișteanu, P. C. (2025). Rosehip tea as a phytogenic additive in broilers drinking water-a review. *Animal & Food Sciences Journal* Iasi, Vol. 83 (7), pp. 189-194.
[25] Stryjecka, M., Kiełtyka-Dadasiewicz, A., Michalak, M. (2024). Physico-chemical characteristics of Rosa canina L. seeds and determining their potential use. *Applied Sciences*, 15(1), 168, https://doi.org/10.3390/app15010168.
[26] Xu, X. (2020). *Machine learning approach to characterize elastic, viscoelastic, relaxation and creep behavior of materials* (Doctoral dissertation, New York University Tandon School of Engineering).
[27] Yildiz, O., Alpaslan, M. (2012). Properties of rose hip marmalades. *Food Technology and Biotechnology*, 50(1), 98.
[28] Yılmaz, D., Gokduman, M. E. (2015). Determination of physico-mechanical properties of sage (*Salvia officinalis L.*) at different moisture contents, *Journal of Agriculture Faculty*, 10 (1), pp. 73-82.

TOBACCO COATED SEED RECOGNITION AND CLASSIFICATION METHOD BASED ON IMPROVED YOLOv10N

/

基于改进 YOLOv10n 的烟草包衣种子识别分类方法

Limin XIE[1,2], Xinghong ZOU[2,3], Bing FANG[1,2], Changling YIN[4], Zhihui LIN[4], Zhansheng JIANG[4*]
[1] College of Mechanical and Electrical Engineering, Fujian Agriculture and Forestry University, Fuzhou 350100, China
[2] Fujian Key Laboratory of Agricultural Information Sensing Technology, Fuzhou 350100, China
[3] College of Computer and Information Sciences, Fujian Agriculture and Forestry University, Fuzhou 350100, China)
[4] Fujian Tobacco Company Sanming Company
Corresponding e-mail: 447056391@qq.com

DOI: https://doi.org/10.35633/inmateh-79-96

Keywords: *tobacco seeds; coated seeds; YOLOv10; object detection; lightweight network*

ABSTRACT

Efficient classification of tobacco coated seeds is critical for seed quality assurance in the tobacco industry, yet the nearly identical appearance of coated seeds renders manual sorting labor-intensive and unreliable. Existing automated solutions either lack the precision required for distinguishing sub-millimeter size differences or are too computationally demanding for deployment on edge devices in seed processing facilities. To bridge this gap, this study proposes a lightweight classification model, EMC-YOLO, based on an improved YOLOv10n. This model optimizes YOLOv10n in three aspects: first, replacing the original backbone network with EfficientViT, balancing low computational requirements and global feature extraction capabilities; second, introducing an improved multi-scale spatial pyramid attention (MSPA) into the neck network, utilizing parallel dilated convolution to optimize feature fusion; third, employing the CARAFE operator for upsampling to enhance the edge restoration effect of small targets. Experiments show that the precision, recall, and mAP@0.5 of EMC-YOLO reach 95.12%, 91.20%, and 93.01%, respectively, representing improvements of 2.12, 1.20, and 1.01 percentage points over the original model. Simultaneously, the model reduces the number of parameters by 71%, computational load by 75%, and weight volume by 68.1%. This model achieves high-performance detection with low resource consumption, providing a technical reference for automated seed quality inspection. Validation on a designed seed detection platform under simulated production conditions yielded a coating qualification rate of 95.50%, meeting the 95% industrial benchmark, and confirming the practical feasibility of the proposed method for automated quality inspection in tobacco seed processing lines.

摘要

烟草包衣种子的精准分级对保障种子质量至关重要，然而包衣种子外观高度相似，人工分选劳动密集且易出错。现有自动化方案或精度不足以区分亚毫米级尺寸差异，或计算量过大难以部署于种子加工场景中的资源受限边缘设备。为此，本研究提出一种基于改进 YOLOv10n 的轻量级分类模型 EMC-YOLO。该模型通过三方面优化 YOLOv10n：第一，使用 EfficientViT 替换原主干网络，兼顾低计算量与全局特征提取能力；第二，在颈部网络引入改进的多尺度空间金字塔注意力（MSPA），利用并行空洞卷积优化特征融合；第三，采用 CARAFE 算子进行上采样，提升小目标的边缘恢复效果。实验显示，EMC-YOLO 的精确率、召回率及 mAP@0.5 分别达到 95.12%、91.20%和 93.01%，较原模型提升了 2.12、1.20 和 1.01 个百分点。同时，模型参数量减少 71%，计算量降低 75%，权重体积缩小 68.1%。该模型能在低资源消耗下实现高性能检测，为种子自动化质量检测提供了技术参考。在设计的种子检测平台上进行模拟生产条件下的验证，包衣合格率达 95.50%，超过 95%的行业基准，验证了所提方法在烟草种子自动化质量检测中的实际可行性。

INTRODUCTION

As a major economic crop in China, flue-cured tobacco leads global production in both scale and yield (*Han, 2025*). Seed coating improves seed quality and yield, driving growth in the tobacco industry (*Javed et al., 2022*). However, coated seeds share nearly identical shapes, sizes, and colors, making visual classification difficult (*Zinsmeister et al., 2020*). Manual sorting is slow, labor-intensive, and error-prone, creating a significant bottleneck in seed processing workflows. Given that China produces over 2 million tons of flue-cured tobacco annually, even a modest improvement in seed sorting efficiency can yield substantial economic benefits across

the industry. Thus, there is an urgent demand for efficient, automated sorting and quality control technologies deployable in tobacco seed processing lines.

Traditional image processing uses phenotypic features like size and shape (*Ozaktan et al., 2024*), but 2D visual data cannot capture internal properties, resulting in low accuracy. Other methods, such as chemical analysis or electronic noses (*Fu Jie, 2024*), require complex conditions and damage the samples. For small seeds, these traditional approaches often fail to extract enough features to distinguish subtle differences (*Reena S. et al., 2025*).

Deep learning has transformed image recognition by automatically capturing complex features through neural networks (*Yinglong Li, 2022*). This technology enables precise recognition in agriculture (*Feng Y. et al., 2023*) and handles large datasets effectively (*Wang D. et al., 2022*). Recent studies have optimized networks for small-target detection in agricultural contexts. For example, *Ye et al. (2022),* integrated additional micro-scale detection heads into YOLOv5 for densely-planted Chinese fir seedling identification, improving detection recall for small, overlapping targets but increasing model complexity. *Li J. et al., (2022),* developed Pineapple-Aerial-YOLO with a dedicated small-scale target enhancement framework, achieving improved localization at the expense of higher computational overhead. *Wu et al., (2023),* modified the YOLOv4 architecture with Res2block and depthwise separable convolutions for weed detection, reducing the parameter count of the originally heavy backbone while maintaining competitive detection accuracy.

Despite these advances, recognizing coated tobacco seeds remains challenging. Their sub-millimeter size variations and nearly identical surface morphology demand high detection precision, which typically requires deeper architectures with substantial parameter counts. Conversely, lightweight models designed for edge deployment in seed processing facilities often sacrifice fine-grained discrimination capability (*Li C. et al., 2021; Hamid et al., 2022*). To bridge this gap between detection accuracy and model efficiency, EMC-YOLO, an improved YOLOv10n model, is proposed. It replaces the backbone with EfficientViT, substantially reducing parameters while preserving global feature extraction; introduces a C2f_MSFA mechanism with parallel dilated convolution for adaptive multi-scale feature fusion; and employs CARAFE upsampling for content-aware edge recovery—thereby achieving high detection accuracy with substantially reduced computational requirements. This work contributes to the application of machine-vision-based detection methods in agricultural seed quality inspection, an increasingly important direction in agricultural engineering.

MATERIALS AND METHODS

Establishment of the dataset

Dataset

The dataset of coated tobacco seeds used in this study was independently collected and constructed. The seeds were provided and coated by the Sanming Branch of the Fujian Tobacco Agricultural Science Research Institute, while image acquisition was conducted in the laboratory of Fujian Agriculture and Forestry University. The acquisition equipment consisted of a Hikvision 20-megapixel MV-SC200 industrial camera and a 25-megapixel MVL-KF1224M industrial lens. The images were captured at a resolution of 5472 × 3648 pixels and saved in JPG format. To minimize background interference, black light-absorbing velvet was laid on the workbench. The coated seeds were scattered across the shooting area to simulate their natural distribution after output from a coating machine, ensuring each seed could be effectively captured. The image acquisition setup, consisting of the industrial camera, lens, black velvet-covered sample stage, and LED light source, is shown in Fig. 1

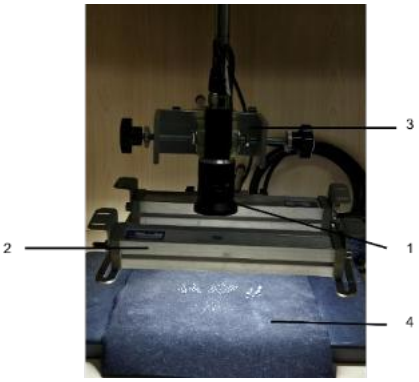


Fig. 1 – Image acquisition setup for coated tobacco seeds

1. industrial camera; 2. LED light source; 3. bracket; 4. black light-absorbing velvet

All collected images were manually annotated using the AnyLabeling tool. By drawing bounding boxes to precisely locate every coated seed, a dataset suitable for object detection tasks was constructed. Each seed instance is accompanied by bounding box annotation information to support deep learning model training. According to the national standard for tobacco seeds (GB/T 21138-2019, 2019), the coated seeds were categorized into four classes: qualified seeds (1.6mm–1.8mm), undersized seeds (< 1.6mm), oversized seeds (> 1.8mm), and damaged seeds (insufficient coating coverage with the seed clearly exposed). Considering that a single test batch contains 100 coated seeds, the number of seeds per image was controlled to under 200. All images were taken under indoor lighting supplemented by LED tubes, and a total of 320 original images were manually annotated using boxes tangent to the seed outlines. The types of coated tobacco seed samples are shown in Figure 2.

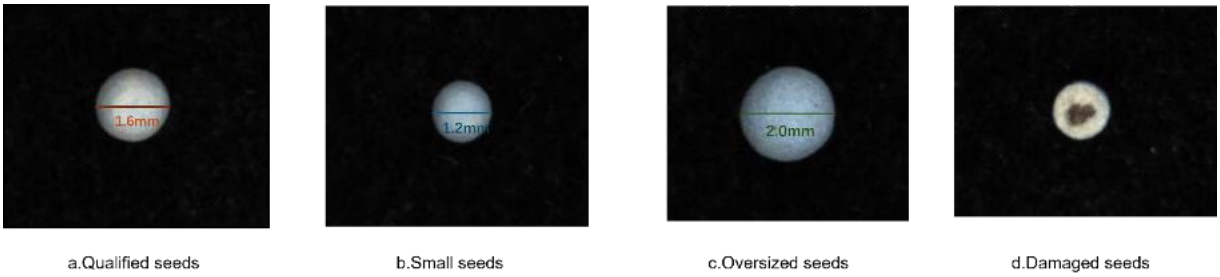


Fig. 2 – Type of coated seeds collected

Data augmentation

To enhance model generalization and environmental adaptability, a multi-dimensional data augmentation scheme was implemented. This approach effectively expands the parameter search space and simulates real-world factory conditions, such as lighting fluctuations, occlusion, and varied target postures. Specifically, the system integrates photometric and geometric transformations, including random rotation, horizontal flipping, brightness adjustments, and random cropping, each with a probability of 0.5.

The dataset was divided into training, validation, and test sets at an 8:1:1 ratio, comprising 1024, 128, and 128 images, respectively. By fusing these augmentation strategies, the spatial and visual diversity of the training data was significantly improved, effectively reducing overfitting and ensuring robust performance across diverse industrial scenarios.

Improvement of the tobacco coating seed detection model of YOLOv10n

To accurately detect small and densely distributed coated tobacco seeds, this study proposes an improved model, EMC-YOLO, based on the YOLOv10n architecture (*Wang et al., 2024*). While maintaining a lightweight design, the model optimizes feature extraction, fusion, and upsampling as shown in Figure 3.

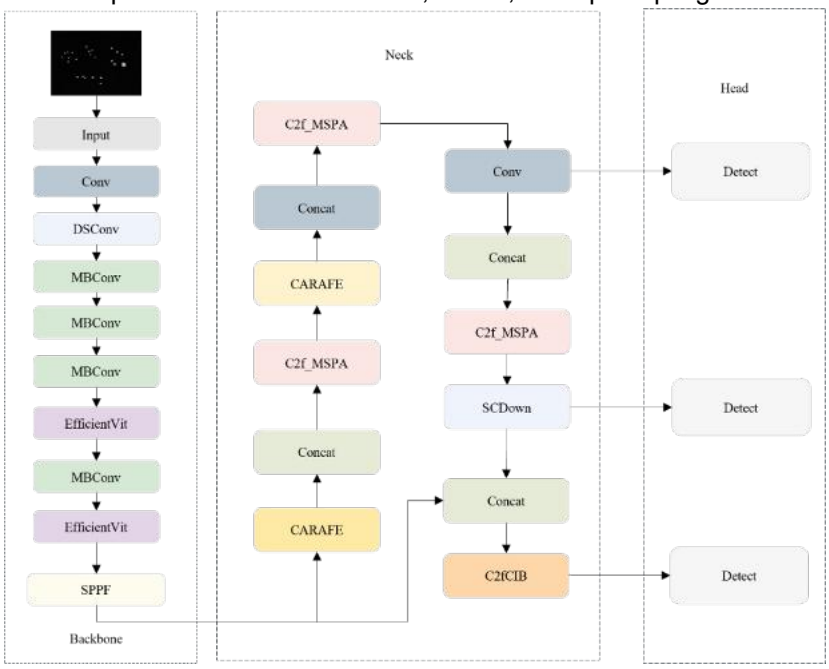


Fig. 3 – The network structure of EMC-YOLO

First, the original backbone is replaced with EfficientViT to enhance global modeling and fine-grained feature capture through grouped attention mechanisms while reducing parameters. Second, a Multi-Scale Spatial Attention (MSFA) module is introduced in the neck, utilizing multi-branch dilated convolutions and channel weighting for dynamic feature selection to better distinguish varying seed sizes. Finally, the CARAFE module replaces traditional upsampling to strengthen edge recovery and small-target detection through content-aware feature reorganization.

Efficient ViT backbone network

Due to the small diameter and subtle surface features of tobacco coated seeds, traditional backbones often lose discriminative textures during deep downsampling. To enhance feature extraction for tiny targets, this study introduces EfficientViT (*Liu X. et al., 2023*) to replace the original backbone, as shown in Fig. 4.

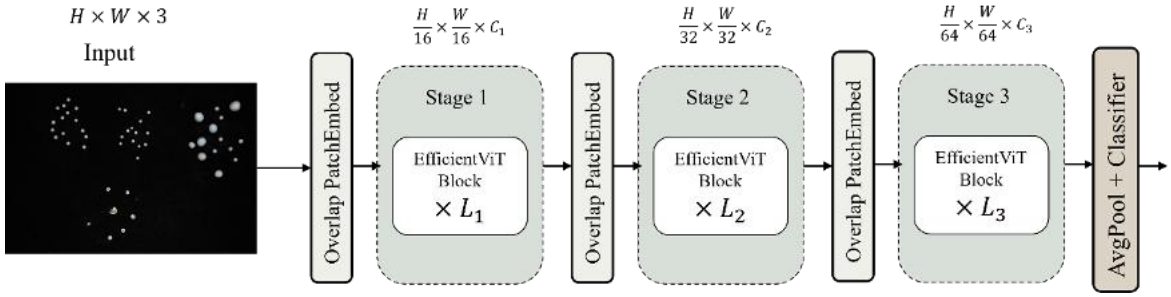


Fig. 4 – The network structure of EfficientViT

The advantage of EfficientViT lies in its core unit, the EfficientViT Block. As illustrated in Fig. 5, this unit features a unique FFN-CGA-FFN sandwich structure. Its operational mechanism utilizes the Cascaded Group Attention (CGA), which splits feature channels and transmits them layer-wise to create specialized attention heads. These heads focus on diverse features such as seed contours, coating integrity, and surface cracks. This hierarchical approach enables the model to accurately extract key semantics from complex reflections or background interference while minimizing computational redundancy.

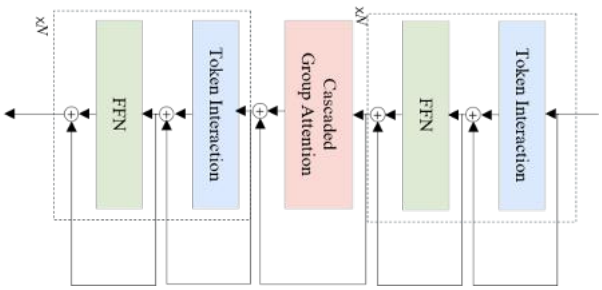


Fig. 5 – The structure of EfficientViT Block

Multi-scale spatial attention mechanism module

To address the continuous scale variation in the grain size of different varieties and batches of tobacco coated seeds, this study, inspired by the Multi-scale Spatial Pyramid Attention (MSPA) (*Yang Yu et al., 2024*), designed a Multi-scale Spatial Attention module (MSFA), whose detailed structure is shown in Fig. 6.

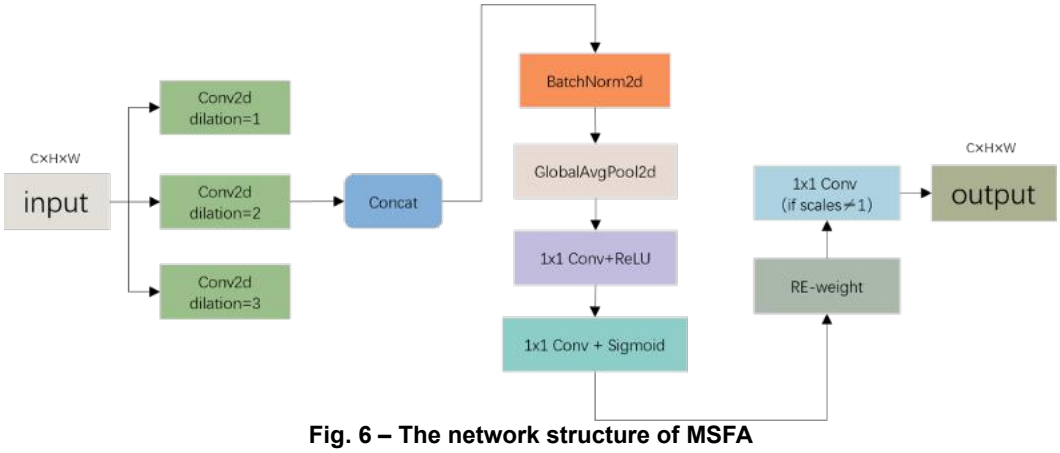


Fig. 6 – The network structure of MSFA

The original C2f module in YOLOv10 relies on fixed receptive fields *(Wang A. et al., 2024)*, which is sensitive to scale changes and lacks adaptive weighting, thus limiting the network to local information. To compensate, MSFA utilizes parallel dilated convolution branches to construct diverse receptive fields. Unlike the original MSPA, this study recalibrated the dilation rates and optimized spatial feature aggregation to suit the dense distribution of seeds. Through a dynamic feature selection mechanism, the module adaptively assigns higher weights to corresponding scale branches based on target size, simultaneously capturing local details and global context.

To further improve feature fusion, MSFA is integrated into the C2f structure to form the C2f_MSFA module (Fig. 7). This integration effectively addresses the limitations of the original C2f in processing scale-sensitive targets and enhances capture sensitivity during the feature fusion stage.

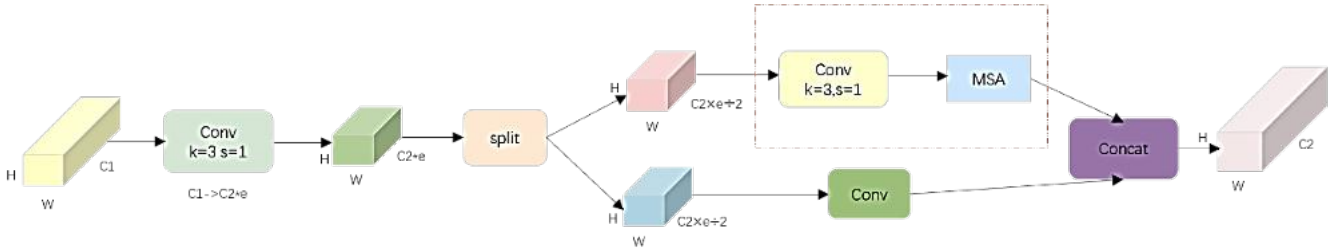


Fig. 7 – The network structure of C2f_MSFA

Sampling operator on CARAFE

In the upsampling stage, the original bilinear interpolation in YOLOv10 often ignores global semantic information (*Wang D. et al., 2022*), leading to blurring and artifacts at seed edges. Consequently, this study adopts the CARAFE content-aware upsampling module (*Wang J. et al., 2019*), with its structure shown in Fig. 8.

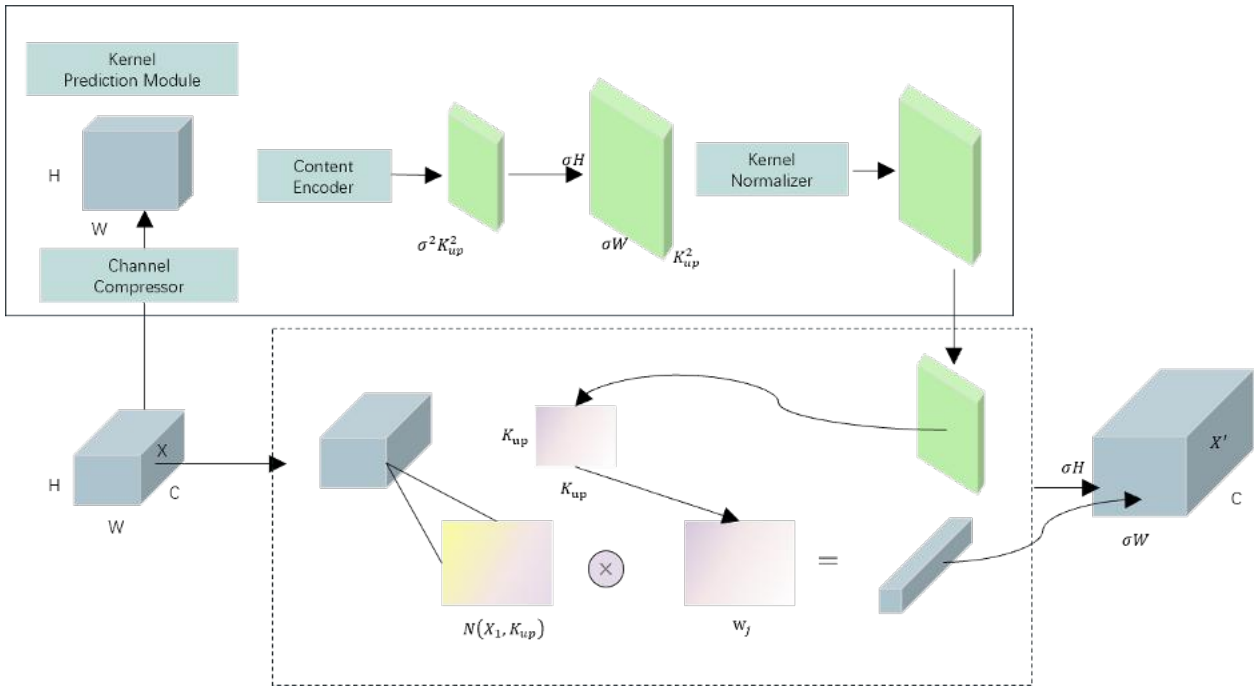


Fig. 8 – The network structure of CARAFE

Unlike traditional operators, CARAFE possesses content-aware capabilities. Its kernel prediction module dynamically generates exclusive kernels for each pixel by analyzing the local context between the seed and its surroundings. Subsequently, the reassembly module uses these adaptive kernels for dynamic feature aggregation. This mechanism allows the model to perceive boundary transitions and perform intelligent enhancement rather than mechanical pixel filling. Experimental results show that CARAFE effectively compensates for traditional interpolation deficiencies, significantly improving the recovery fidelity of tiny target edges and ensuring more precise localization.

RESULTS

Experimental results and analysis

Experimental indicators

To evaluate the performance of the tobacco seed classification model, core metrics such as Precision, Recall, and Mean Average Precision (mAP@0.5) are adopted. Specifically, mAP@0.5 reflects the model's detection stability when the Intersection over Union (IoU) threshold is set to 0.5. Regarding computational efficiency, resource consumption is quantified through the number of Parameters (Params) and Floating Point Operations (FLOPs). To better verify the effectiveness and robustness of the model, this study primarily selects mAP50 as the key evaluation metric.

Comparative experiment

To verify the effectiveness of the proposed EMC-YOLO model, it was compared with several lightweight object detection models, including NanoDet, YOLOv5n, YOLOv8n, and YOLOv10n. The results are summarized in Table 1.

Table1

Contrast test

Model	P/%	R/%	mAP@0.5/%	GFLOPs	Weights/MB
NanoDet	0.85	0.5	0.90	8.3	4.2
YOLOv5n	0.92	0.91	0.91	7.1	5.3
YOLO8n	0.93	0.91	0.92	8.1	6.3
YOLOv10n	0.93	0.90	0.92	63.4	33.5
EMC-YOLO	0.95	0.91	0.93	16.0	10.7

As seen in Table 1, EMC-YOLO outperforms the other lightweight models across all key accuracy metrics. Compared to NanoDet, YOLOv5n, YOLOv8n, and YOLOv10n, it achieves:

- +10.0%, +3.0%, +2.0%, and +2.0% improvement in Precision
- +41.0%, +0.0%, +0.0%, and +1.0% improvement in Recall
- +3.0%, +2.0%, +1.0%, and +1.0% improvement in mAP@0.5

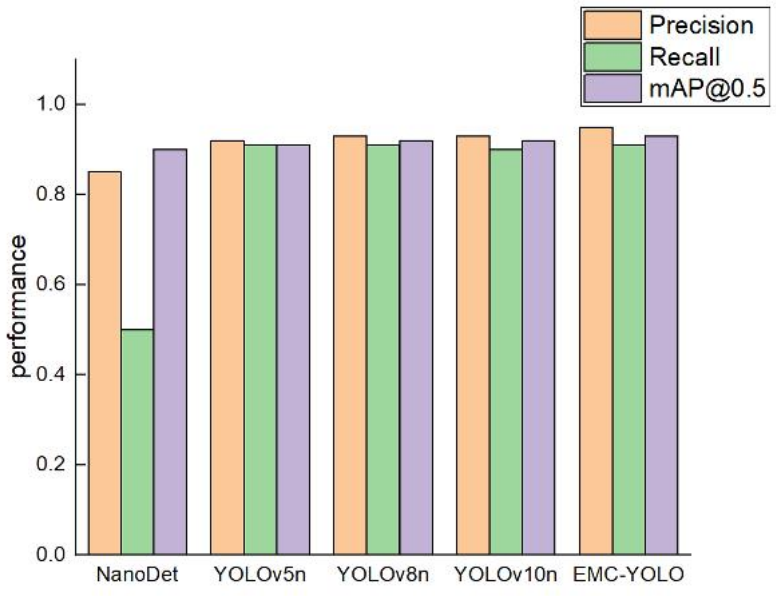


Fig. 9 – Comparison of detection performance of different models

As shown in Fig. 9, EMC-YOLO achieves the highest precision of 0.95 and the highest mAP@0.5 of 0.93 among the five models, which are 2 and 1 percentage points higher than those of YOLOv8n and YOLOv10n, respectively. The recall of EMC-YOLO is 0.91, similar to that of the other lightweight models.

EMC-YOLO achieves an optimal balance between performance and resource efficiency, reducing GFLOPs by 75% and weight size by 68.1% compared to YOLOv10n. These improvements enhance deployment flexibility and operational stability, making the model highly suitable for automated intelligent sorting of coated tobacco seeds.

Visualization of test results

To assess real-world robustness, a visual comparison between YOLOv10n and EMC-YOLO was conducted (Figure 10). The results show that EMC-YOLO provides superior localization with bounding boxes more accurately fitting seed boundaries. Notably, in small-size discrimination, EMC-YOLO correctly distinguished "undersized" from "qualified" seeds, whereas YOLOv10n missed 2 undersized and 4 qualified instances. Furthermore, EMC-YOLO eliminated the misclassification of 5 normal seeds as "oversized" and successfully detected damaged seeds missed by the baseline model. In dense regions, EMC-YOLO maintained high precision without the overlapping or missed detections observed in YOLOv10n. These results confirm that EMC-YOLO is significantly more robust for fine-grained classification, offering improved localization, fewer false positives, and higher recall under complex sorting conditions.

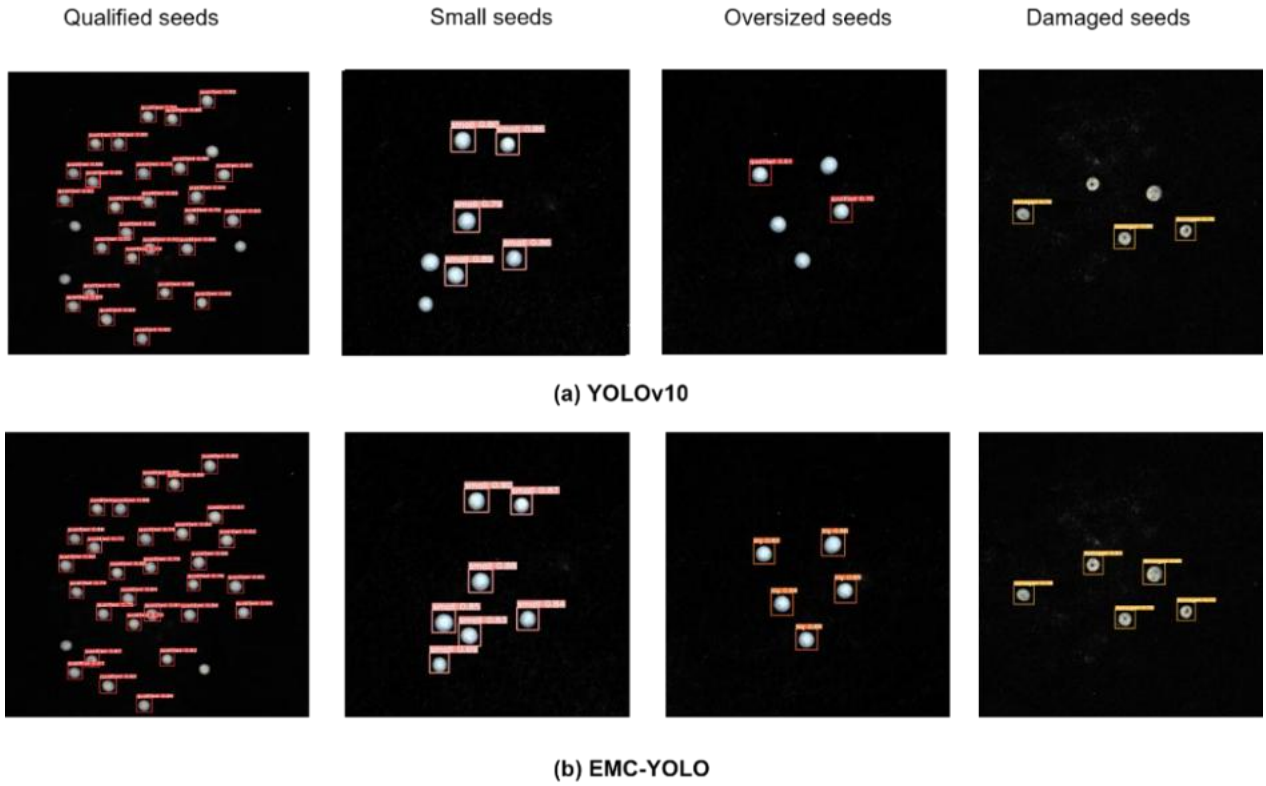


Fig. 10 – Comparison of different algorithm detect results

Ablation experiment

To evaluate the individual contribution of each improvement module, ablation experiments were conducted using YOLOv10n as the baseline. Modules tested include the EfficientViT, C2f_MSFA, and CARAFE mechanisms. All models were trained under identical conditions, and performance was evaluated using Precision (P), mAP@0.5, GFLOPs, and Parameters. The results are presented in Table 2.

The results show that:

- EfficientViT significantly reduced parameters from 16.5M to 4.9M and FLOPs by 75%, providing an efficient lightweight foundation for the model.
- C2f_MSFA improved mAP@0.5 to 0.91, effectively capturing fine-grained seed features through multi-scale modeling and dynamic weight allocation.
- CARAFE enhanced small-target localization and boundary detail recovery, further stabilizing detection performance.
- The final EMC-YOLO model, integrating all three modules, achieved a precision of 95% and mAP@0.5 of 0.93. Compared to the baseline, it achieved a 1% accuracy gain while reducing parameters by 71%, ensuring superior stability for industrial seed screening.

Table2

Ablation experiment

Number	EfficientViT	C2f_MSFA	CARAFE	P/%	R/%	mAP/%	Parameters/M	FLOPs/G	Model size/MB
1	×	×	×	0.93	0.90	0.92	16455016	63.4	33.5
2	√	×	×	0.88	0.58	0.68	4943528	8.9	10.9
3	×	√	×	0.91	0.88	0.91	2911751	9.1	6.2
4	×	×	√	0.90	0.86	0.90	2836080	8.5	6.1
5	×	√	√	0.91	0.88	0.91	3051855	9.3	6.5
6	√	×	√	0.95	0.90	0.92	4445608	14.9	9.9
7	√	√	×	0.94	0.91	0.92	4661380	15.8	10.4
8	√	√	√	0.95	0.91	0.93	4801484	16.0	10.7

Notes: "x" indicates not using this module; "√" indicates the adoption of this module; P is the precision rate; R is the recall rate; mAP is the average precision mean.

Practical application and validation

Design of the seed detection platform

To validate the practical applicability of the proposed EMC-YOLO model in a production-relevant environment, a tobacco coated seed detection platform was constructed in a factory setting, as shown in Fig. 11a. The platform mainly consists of an industrial camera, a camera stand, and a computer. The industrial camera is fixed above the sample stage by the camera stand to capture high-resolution images of the coated seeds, and the captured images are transmitted to the computer for real-time detection and classification using the EMC-YOLO model.

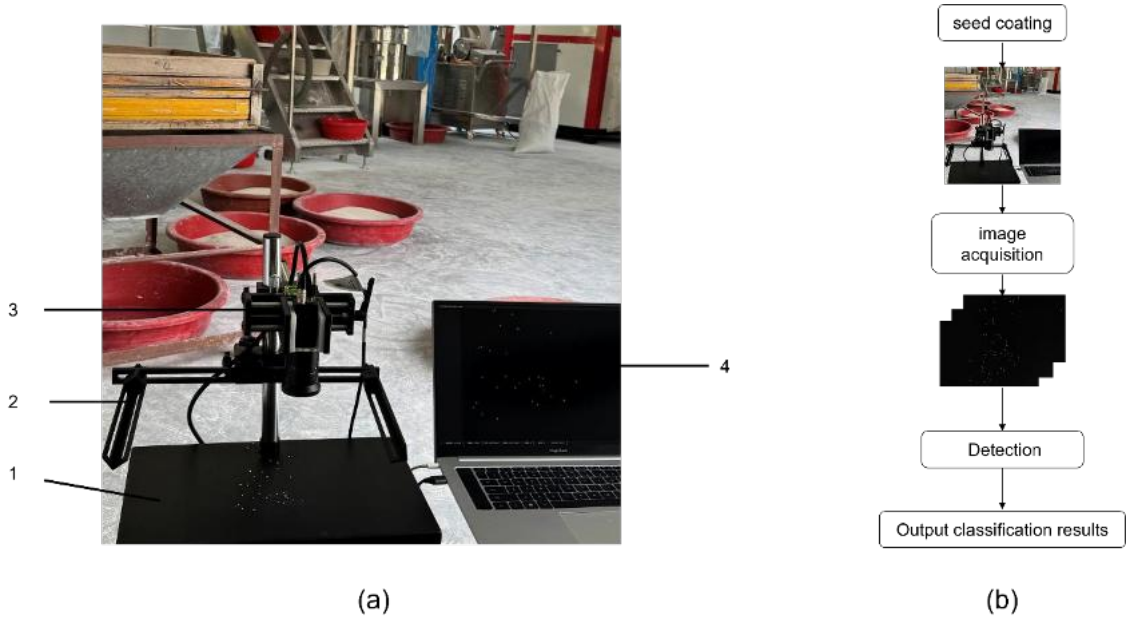


Fig.11 – Detection platform and workflow

a) detection platform: 1. camera bracket; 2. industrial camera; 3. outlet of coating machine; 4. Computer
b) workflow

Platform workflow

After the coating process is completed, the coated seeds are placed on the sample stage, and the industrial camera is triggered to capture images. The acquired high-resolution images are transmitted to the computer through a data interface, where the EMC-YOLO model performs real-time multi-class detection and classification, outputting the count and proportion of seeds in each category. The workflow of the detection process is shown in Fig. 11b. The platform serves as a quality inspection aid for the coating machine, enabling operators to quantitatively assess the performance of the coating process without requiring a physical seed sorting mechanism.

Coating quality validation experiment

To further verify the performance of the proposed model in the experimental device, EMC-YOLO was compared with YOLOv10n, YOLOv8n, and YOLOv5n in terms of detection results. YOLOv5n exhibited more missed detections; although YOLOv10n and YOLOv8n performed well in certain aspects, their detection accuracy was inferior to that of EMC-YOLO. This result further confirms the feasibility and practicability of the EMC-YOLO model in practical applications. The detection comparison is shown in Fig. 12.

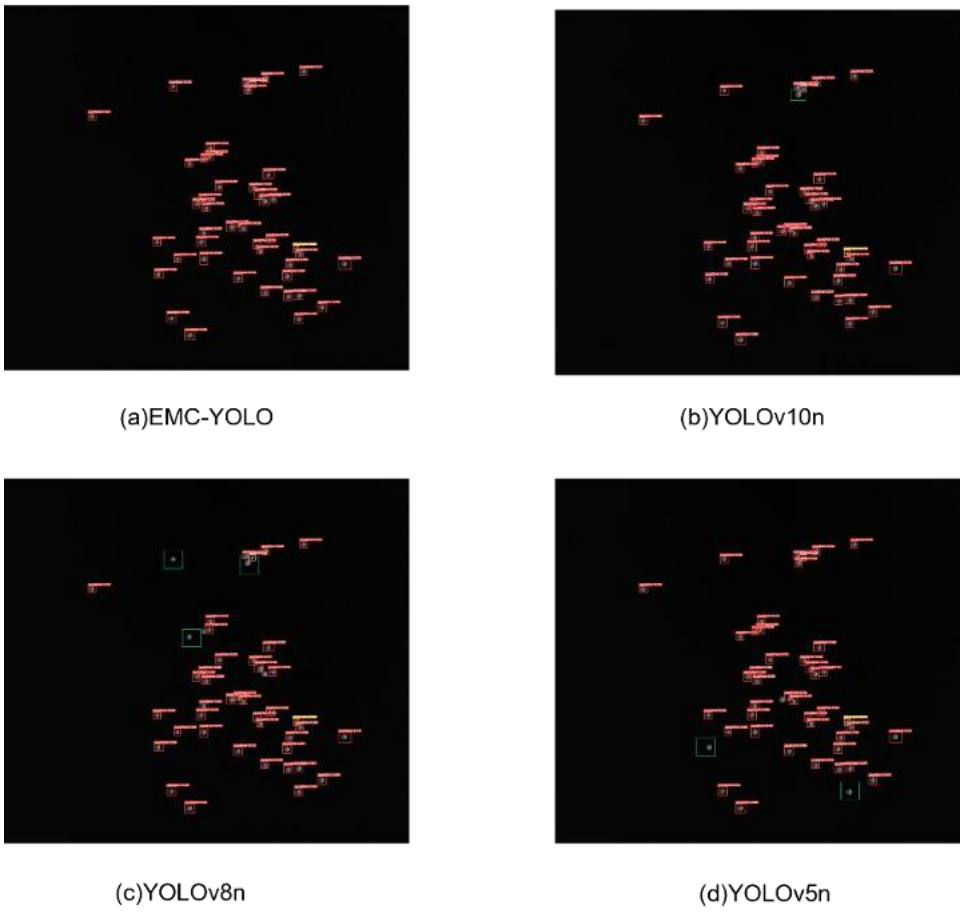


Fig. 12 – Comparison tests of device end models

To evaluate the coating quality of seeds produced by the coating machine, a batch validation experiment was conducted. A total of 200 tobacco coated seeds were directly collected from the coating machine output. The seeds were placed on the sample stage in four batches of approximately 50 seeds each, and each batch was independently imaged and classified by the EMC-YOLO model. The coating qualification rate was calculated as the ratio of qualified seeds (1.6–1.8 mm) to the total number of seeds tested. The classification results of the four batches are summarized in Table 3.

Table3

Coating quality validation

Batch	Total number	Number of qualified seeds	Particle size compliance/%
1	50	48	96.0
2	50	46	92.0
3	50	48	96.0
4	50	49	98.0

As shown in Table 3, a total of 200 tobacco coated seeds were tested in four batches. Among them, 191 seeds were determined to be qualified, with an overall coating qualification rate of 95.50%, reaching the 95% threshold specified by GB/T 21138-2019. The test results also indicated that this model could effectively distinguish between qualified and unqualified seeds. Overall, the designed platform meets the requirements of practical applications and provides a reliable solution for the automatic quality inspection of tobacco coated seeds during the coating process.

CONCLUSIONS

By optimizing the YOLOv10n architecture, this study developed the EMC-YOLO model for the intelligent recognition and classification of coated tobacco seeds. The main conclusions are as follows:

1. The EMC-YOLO model integrates EfficientViT, C2f_MSFA, and CARAFE to deal with the small target size and subtle size differences of coated tobacco seeds. The precision, recall, and mAP@0.5 reached 95.12%, 91.20%, and 93.01%, which are 2.12, 1.20, and 1.01 percentage points higher than those of YOLOv10n. The accuracy for undersized seeds improved by 15%. With only 4.8M parameters and a 10.7 MB weight size, the model is suitable for deployment on edge devices.

2. The three modules worked together to improve the model. EfficientViT reduced the computational cost while keeping the global features. C2f_MSFA improved multi-scale feature fusion through dynamic weighting. CARAFE recovered the edges of small targets. These changes reduced missed detections and false detections under complex conditions, such as reflective surfaces and dense seed distributions.

3. A detection platform was built in a factory to test the model. Compared with YOLOv10n, YOLOv8n, and YOLOv5n, EMC-YOLO showed fewer missed detections and higher accuracy. In the validation experiment, 200 coated seeds were tested in four batches, and 191 seeds were classified as qualified. The coating qualification rate was 95.50%, which meets the national standard. The platform can be used as a quality inspection tool for the coating machine. Future work will focus on deploying the platform in actual seed processing lines and extending it to more coated seed varieties. These efforts are expected to promote the wider application of machine-vision-based detection methods in agricultural seed processing.

ACKNOWLEDGEMENT

This study is supported by Science and Technology Project of Sanming Tobacco Company, Fujian Tobacco Company (2025YY004), Construction Project of Fujian Provincial Key Laboratory of Agricultural Information Perception Technology (KJG22052A), and Key Technical Innovation and Industrialization Project of Fujian Province (2024XQ010)

REFERENCES

[1] Feng Y., Liu C., Han J., Lu Q., Xing X., (2023), IRB-5-CA Net: A Lightweight, Deep Learning-Based Approach to Wheat Seed Identification, *IEEE Access*, vol. 11, pp. 119553, New York/USA. DOI: 10.1109/ACCESS.2023.3326824.

[2] Fu J., (2024), Rice variety authenticity identification based on polarization image features (基于偏振图像特征的大米品种真实性鉴别), PhD dissertation, Central South University of Forestry and Technology, Zhuzhou/China (Original in Chinese).

[3] GB/T 21138-2019, (2019), *Tobacco Seed* (烟草种子), National Market Supervision and Administration Bureau, Beijing/China (Original in Chinese).

[4] Hamid Y., Wani S., Soomro A.B., Alwan A.A., Gulzar Y., (2022), Smart Seed Classification System based on MobileNetV2 Architecture, *2022 2nd International Conference on Computing and Information Technology (ICCIT)*, pp. 217-222, Tabuk/Saudi Arabia. DOI: 10.1109/ICCIT52419.2022.9711662.

[5] Han J., (2025), Yield estimation of Xuchang tobacco leaves based on WOFOST model and remote sensing assimilation (基于 WOFOST 模型与遥感同化的许昌烟叶产量估测), PhD dissertation, Nanjing University of Information Science and Technology, Nanjing/China (Original in Chinese).

[6] Javed T., Afzal I., Shabbir R., Ikram K., Zaheer M.S., Faheem M., Ali H.H., Iqbal J., (2022), Seed coating technology: An innovative and sustainable approach for improving seed quality and crop performance, *Journal of the Saudi Society of Agricultural Sciences*, vol. 21, no. 8, pp. 536-545, Riyadh/Saudi Arabia. DOI: 10.1016/j.jssas.2022.03.003.

[7] Kong W.-B., Zhang Z.-F., Zhang T.-L., Wang L., Cheng Z.-Y., Zhou M., (2024), SMC-YOLO: Surface Defect Detection of PCB Based on Multi-Scale Features and Dual Loss Functions, *IEEE Access*, vol. 12, pp. 137667-137682, New York/USA. DOI: 10.1109/ACCESS.2024.3434559.

[8] Li C., Li H., Liu Z., Li B., Huang Y., (2021), SeedSortNet: a rapid and highly efficient lightweight CNN based on visual attention for seed sorting, *PeerJ Computer Science*, vol. 7, e639, London/UK. DOI: 10.7717/peerj-cs.639.

[9] Li J., Chen H., Lu J., Zeng S., Luo X., Chen P., Yang C., (2025), A small-scale target enhancement framework for aerial pineapple images on accurate agricultural information, *Computers and Electronics in Agriculture*, vol. 239, 110874, Amsterdam/Netherlands. DOI: 10.1016/j.compag.2025.110874.

[10] Li Y., (2022), Research and Application of Deep Learning in Image Recognition, *2022 IEEE 2nd International Conference on Power, Electronics and Computer Applications (ICPECA)*, pp. 994-999, Shenyang/China. DOI: 10.1109/ICPECA53709.2022.9718847.

[11] Liu X., Peng H., Zheng N., Yang Y., Hu H., Yuan Y., (2023), EfficientViT: Memory Efficient Vision Transformer with Cascaded Group Attention, *2023 IEEE/CVF Conference on Computer Vision and Pattern Recognition (CVPR)*, pp. 14420-14430, Vancouver/Canada. DOI: 10.1109/CVPR52729.2023.01386.

[12] Ozaktan H., Çetin N., Uzun S., Uzun O., Ciftci C.Y., (2024), Prediction of mass and discrimination of common bean by machine learning approaches, *Environment, Development and Sustainability*, vol. 26, no. 7, pp. 18139-18160, Dordrecht/Netherlands. DOI: 10.1007/s10668-023-03383-x.

[13] R.S, R.R., (2025), Effective Classification of Plant Diseases Using Blend Unity Resqueeze With ResNet Model, *CLEI Electronic Journal*, pp. 1-18, Montevideo/Uruguay. DOI: 10.19153/cleiej.28.4.10.

[14] Shen L., Lang B., Song Z., (2023), DS-YOLOv8-Based Object Detection Method for Remote Sensing Images, *IEEE Access*, vol. 11, pp. 125122-125137, New York/USA. DOI: 10.1109/ACCESS.2023.3330844.

[15] Wang A., Chen H., Liu L., Chen K., Lin Z., Han J., Ding G., (2024), YOLOv10: Real-Time End-to-End Object Detection, *ArXiv*, 14458, Ithaca/NY/USA. DOI: 10.48550/arXiv.2405.14458.

[16] Wang D., Cao W., Zhang F., Li Z., Xu S., Wu X., (2022), A Review of Deep Learning in Multiscale Agricultural Sensing, *Remote Sensing*, vol. 14, 559, Basel/Switzerland. DOI: 10.3390/rs14030559.

[17] Wang J., Chen K., Xu R., Liu Z., Loy C.C., Lin D., (2019), CARAFE: Content-Aware ReAssembly of FEatures, *2019 IEEE/CVF International Conference on Computer Vision (ICCV)*, pp. 3007-3016, Seoul/South Korea. DOI: 10.1109/ICCV.2019.00310.

[18] Wu H., Wang Y., Zhao P., Mengbo Q., (2023), Small-target weed-detection model based on YOLO-V4 with improved backbone and neck structures, *Precision Agriculture*, vol. 24, pp. 2149-2170, New York/USA. DOI: 10.1007/s11119-023-10035-7.

[19] Yang Yu, Yi Zhang, Zeyu Cheng, Zhe Song, Chengkai Tang, (2024), Multi-scale spatial pyramid attention mechanism for image recognition: An effective approach, *Engineering Applications of Artificial Intelligence*, vol. 133, 108261, Oxford/UK. DOI: 10.1016/j.engappai.2024.108261.

[20] Ye Z., Guo Q., et al., (2022), Recognition of terminal buds of densely-planted Chinese fir seedlings using improved YOLOv5 by integrating attention mechanism, *Frontiers in Plant Science*, vol. 13, 991929, Lausanne/Switzerland. DOI: 10.3389/fpls.2022.991929.

[21] Zinsmeister J., Leprince O., Buitink J., (2020), Molecular and environmental factors regulating seed longevity, *Biochemical Journal*, vol. 477, no. 2, pp. 305-323, London/UK. DOI: 10.1042/BCJ20190165.

COMPARATIVE EVALUATION OF AEROPONIC, HYDROPONIC AND CONVENTIONAL SYSTEMS FOR POTATO MINITUBER PRODUCTION

EVALUAREA COMPARATIVĂ A SISTEMELOR AEROPONICE, HIDROPONICE ȘI CONVENȚIONALE UTILIZATE PENTRU PRODUCEREA MINITUBERCULILOR DE CARTOF

Andreea TICAN*, Carmen CHELMEA, Mihaela CIOLOCA, Monica POPA
National Institute of Research and Development for Potato and Sugar Beet Brașov, Romania
E-mail: tican_andreea@yahoo.com)
DOI: https://doi.org/10.35633/inmateh-79-97

Keywords: *Biomass Accumulation, Controlled Environment, Genotype Adaptability, Nutrient Availability, Root-Zone Oxygenation, Soilless Cultivation, Tuberization.*

ABSTRACT

Aeroponic cultivation has emerged as a promising technology for improving potato minitubers production under controlled conditions. This study evaluated the effects of three cultivation systems (aeroponics, hydroponics, and conventional cultivation) and four potato genotypes (Azaria, Brasovia, Cosiana and Cezarina) on plant growth and minitubers production. Plant height, number of minitubers per plant and minitubers weight per plant were assessed. Analysis of variance reveals a statistically significant effect of the cultivation method on plant height at one month ($p < 0.01$) and a highly significant effect on plant height at two months, as well as on the number and weight of minitubers per plant ($p < 0.001$). The variety has a statistically significant effect on plant height at one month ($p < 0.01$) and a highly significant effect on the other parameters analyzed ($p < 0.001$). The interaction between cultivation method and variety is insignificant for plant height at one month ($p > 0.05$), but becomes highly significant for plant height at two months and for production traits ($p < 0.001$), indicating a differentiated response of the varieties to the conditions specific to each cultivation method. Hydroponic cultivation stimulated early plant growth one month after transplanting, whereas aeroponic cultivation resulted in the greatest plant height two months after transplanting. The aeroponic system also produced the highest number of minitubers (37.26 per plant) and the greatest minitubers weight (357.11 g per plant), significantly exceeding both hydroponic and conventional systems. Among the evaluated genotypes, Cosiana, Brasovia and Azaria showed superior minitubers production compared with control cultivar Cezarina. The results demonstrate the high potential of aeroponic cultivation for efficient potato minitubers production and support the implementation of advanced soilless technologies.

REZUMAT

Cultura aeroponică reprezintă o tehnologie promițătoare pentru îmbunătățirea producției de minituberculi de cartof în condiții controlate. Acest studiu a evaluat efectele a trei sisteme de cultură (aeroponică, hidroponică și cultura convențională) și a patru genotipuri de cartof (Azaria, Brasovia, Cosiana și Cezarina) asupra creșterii plantelor și producției de minituberculi. Au fost evaluate înălțimea plantei, numărul de minituberculi per plantă și greutatea minituberculilor per plantă. Analiza variației evidențiază un efect semnificativ statistic al metodei de cultură asupra înălțimii plantelor la o lună ($p < 0,01$) și un efect foarte semnificativ asupra înălțimii plantelor la două luni, precum și asupra numărului și greutății minituberculilor per plantă ($p < 0,001$). Soiul prezintă un efect semnificativ statistic asupra înălțimii plantelor la o lună ($p < 0,01$) și un efect foarte semnificativ asupra celorlalți parametri analizați ($p < 0,001$). Interacțiunea dintre metoda de cultură și soi este nesemnificativă pentru înălțimea plantelor la o lună ($p > 0,05$), dar devine foarte semnificativă statistică pentru înălțimea plantelor la două luni și pentru caracterele de producție ($p < 0,001$), indicând un răspuns diferențiat al soiurilor la condițiile specifice fiecărei metode de cultură. Cultura hidroponică a stimulat creșterea timpurie a plantei la o lună după transplantare, în timp ce cultura aeroponică a dus la cea mai mare înălțime a plantei la două luni după transplantare. Sistemul aeroponic a produs, de asemenea, cel mai mare număr de minituberculi (37,26 per plantă) și cea mai mare greutate a minituberculilor (357,11 g per plantă), depășind semnificativ atât sistemele hidroponice, cât și cele convenționale. Printre genotipurile evaluate, Cosiana, Brasovia și Azaria au prezentat o producție superioară de minituberculi în comparație cu cultivarul martor, Cezarina. Rezultatele demonstrează potențialul ridicat al culturii aeroponice pentru producția eficientă de minituberculi de cartof și susțin implementarea tehnologiilor avansate de cultivare fără sol în sistemele românești de producție a cartofului de sămânță.

INTRODUCTION

Feeding the expanded global population nutritiously and sustainably will require substantial improvements to the food system. The main challenge will be to produce more food using the same or fewer resources while reducing waste (*Devaux, 2021*). The increasing challenges associated with climate change, water scarcity, soil degradation, and the growing demand for high-quality planting material have stimulated the development of innovative crop production systems (*Tunio et al., 2020*; *Balasundram et al., 2023*; *Deguine, 2023*; *Salma and Kaushal, 2024*). Traditional seed potato production systems are characterized by a low multiplication rate (1:6) and a high risk of disease accumulation (*Sadawarti et al., 2026*). Controlled environment agriculture (CEA), including hydroponic and aeroponic cultivation systems, has gained increasing attention as a promising approach for improving productivity while reducing resource consumption and environmental constraints (*Benke and Tomkins, 2017*; *Eldridge et al., 2020*; *Kozai et al., 2020; Shamshiri et al., 2021; Cheema et al., 2024; Silva Filho et al., 2024; Wang, 2024*). Within this framework, soilless culture systems are increasingly adopted as a major technological component in the modern greenhouse industry (*Savvas and Gruda, 2018*). The technological innovations in solid and non-solid substrate cultivation have significantly improved the controllability of the root environment and the production stability (*Sharma et al., 2024*). Aeroponic cultivation has gained considerable attention in recent years due to its potential to enhance plant growth, nutrient-use efficiency. In aeroponic systems, plant roots are suspended in the air and periodically supplied with a nutrient-rich mist, improving root-zone oxygenation and nutrient availability (*Eldridge et al., 2020*). The aeroponic method is highly efficient (*Sinha, 2025*), requiring less space and less water than even the most optimized hydroponic systems (*Kumari and Kumar, 2019*). Compared with conventional cultivation, aeroponic cultivation considerably reduces water and substrate requirements (*Oljača et al., 2024; Hartinger et al., 2025*). Previous studies have demonstrated that aeroponics can substantially increase the multiplication rate of potato minitubers compared to conventional cultivation methods (*Ritter et al., 2001; Buckseth et al., 2016; Çalışkan et al., 2021*). Recent investigations have also highlighted the advantages of aeroponic systems for producing disease-free plantlets and improving minituber yield under controlled environmental conditions (*Tunio et al., 2020*; *Salma and Kaushal, 2024*). In addition, aeroponic systems allow successive harvesting during the vegetation period, thereby increasing multiplication efficiency (*Brocic et al., 2022*; *Buckseth et al., 2024*; *Oljača et al., 2024*). Multiple harvests not only increase the total number of tubers by 36%, but also improve tuber quality with adjustable tuber size and reduced the number of rotten tubers per plot (*Dianawati, 2025*). Research interest in aeroponic potato cultivation has intensified in recent years due to the possibility of integrating automated monitoring systems, sensors and controlled environmental conditions for optimizing plant growth and productivity. Recent studies have emphasized the importance of genotype, nutrient management and environmental control for maximizing minituber production efficiency under aeroponic conditions (*Cheema et al., 2024*; *Silva Filho et al., 2024*). *Farran and Mingo-Castel (2006)* demonstrated that both planting density and harvesting interval significantly influence minituber yield, with shorter harvesting intervals resulting in higher production efficiency. *Singh et al. (2025)* reported that in the aeroponic system for the production of potato minitubers, crop performance is significantly influenced by the interaction between cultivar, planting date and planting density. Studies conducted in an aeroponic system have demonstrated that this technology allows for the efficient differentiation of potato genotypes according to root system characters, nitrogen use efficiency and production capacity, providing a valuable tool for breeding programs oriented towards the efficient use of resources (*Tiwari et al., 2022*).

Although aeroponic cultivation has the potential to increase potato minituber production, its performance with local genotypes in Eastern Europe remains insufficiently studied. This study compares aeroponic, hydroponic, and conventional cultivation systems using four potato genotypes grown under controlled conditions in Romania. Plant growth, minituber number, and minituber weight were evaluated. It was hypothesized that improved root-zone aeration and nutrient availability in the aeroponic system would enhance productivity compared with the other cultivation systems. The findings contribute to the development of more sustainable potato minituber production systems in Romania.

MATERIALS AND METHODS

Experimental site and plant material

The experiment was conducted in 2025 at the National Institute of Research and Development for Potato and Sugar Beet (NIRDPSB) Brașov, Romania. Four potato (*Solanum tuberosum* L.) genotypes obtained through *in vitro* propagation were evaluated: Azaria, Brasovia, Cosiana, and Cezarina, the latter being

used as the control cultivar. Virus-free *in vitro* plantlets, belonging to the four cultivars, were transplanted and cultivated using three cultivation systems: hydroponic, aeroponic, and conventional systems.

Experimental design

The experiment was organized as a bifactorial trial in a completely randomized design with three replicates. Two experimental factors were studied: the cultivation system and the genotype. Factor A comprised three cultivation systems: hydroponics, aeroponics, and conventional cultivation (control), while Factor B consisted of four potato genotypes. Plant growth and minituber production parameters were evaluated throughout the experimental period.

Hydroponic and conventional cultivation systems

For the hydroponic and conventional cultivation systems, transplanting of the *in vitro* plantlets was carried out at the end of May 2025 in a conventional insect-proof greenhouse without temperature control. The nutrient solution pH was maintained at 5.8 ± 0.2, while electrical conductivity (EC) was set at 1.0 mS cm^{-1} during the first week after transplanting and gradually increased to 2.0 mS cm^{-1} over the following two weeks. In the hydroponic system, perlite was used as the growth substrate, and the nutrient solution was supplied daily each morning for 2 h, utilizing the same formulation as the aeroponic system. The conventional cultivation system served as the control and consisted of plants grown in a peat-based substrate under greenhouse conditions. Plants in this system were irrigated daily with water for 2 h to maintain adequate substrate moisture throughout the experimental period. No nutrient solution was supplied to the pots, as was done in the hydroponic and aeroponic systems. Instead, a foliar fertilizer was applied weekly to provide supplemental nutrients and support normal plant development. The conventional system was managed according to a substrate-based cultivation approach and was therefore intentionally maintained without continuous nutrient delivery through the irrigation water, in contrast to the hydroponic and aeroponic systems. This distinction was part of the experimental design and allowed the biological performance of the soilless hydroponic and aeroponic systems to be compared with a conventional substrate-based cultivation system under greenhouse conditions.

Aeroponic cultivation system

For the aeroponic system, transplanting was performed at the beginning of June 2025. Plants were cultivated under controlled environmental conditions using artificial lighting. The aeroponic system was installed in a growth room with temperature and humidity control. The aeroponic system developed at NIRDPSB Brașov was equipped with automated sensors for monitoring and controlling nutrient solution pH, electrical conductivity (EC), and temperature. Recent advances in digital agriculture have further increased the potential of aeroponic production systems. The integration of sensors, automated nutrient management, environmental monitoring, and data-driven decision support systems enables precise control of cultivation conditions and contributes to improved crop performance (*Balasundram et al., 2023; Wang, 2024*). Such technologies are particularly relevant for seed potato production, where uniformity, phytosanitary quality, and multiplication efficiency are critical factors determining the success of the production chain. Figure 1 illustrates images of minituber harvesting obtained via the aeroponic method.

The nutrient solution pH was maintained at 5.8 ± 0.2, while the EC was adjusted to 1.0 mS cm^{-1} during the first week after transplanting and gradually increased to 2.0 mS cm^{-1} over the following two weeks, remaining at this level until the end of the harvesting period. The chemical composition of the nutrient solution corresponded to the following ionic concentrations: macronutrients (in mg L^{-1}) - N: 104, P: 60.3, K: 148, Ca: 16 mg, Mg: 50.4, and S: 48; micronutrients (in mg L^{-1}) - Fe: 0.192, Mn: 0.080, Zn: 0.024, B: 0.016, Cu: 0.016, Mo: 0.006, and Co: 0.003. Plant roots were suspended inside the aeroponic chamber and sprayed with the nutrient solution for 20 seconds at 10-minute intervals, resulting in an automated delivery frequency of approximately 6 cycles per hour.

Air temperature was kept at 20 °C during the day and 18 °C during the night, while the relative humidity ranged between 65% and 70%. The nutrient solution temperature was regulated at 18 °C using a cooling system. The artificial photoperiod was adjusted according to the plant development stage as follows: 16 h of light during the first week after transplanting to reduce transplant stress, 15 h after one month, 14 h after six weeks, and 13 h after two months of cultivation.

The aeroponic cultivation unit used in this study represents a prototype system currently undergoing patent application procedures. Therefore, certain engineering details have been withheld due to ongoing

intellectual property protection requirements. However, all cultivation parameters relevant to plant growth and experimental reproducibility are fully detailed herein.



Fig. 1 - Visual aspects of the aeroponic cultivation system and minituber production: (top) root-zone development, stolon architecture, and manual sequential harvesting of potato minitubers inside the aeroponic chambers; (bottom) sorted potato minitubers demonstrating distinct phenotypic characteristics and size uniformity among the evaluated genotypes

Measurements

Plant height was measured one month and two months after transplanting, from the stem base to the top of the canopy. At harvest, the number of minitubers per plant and total minituber weight per plant were recorded for all experimental treatments. For minitubers from aeroponic culture, 8 sequential harvests were performed. For those from classical culture and hydroponic culture, only one harvest was performed. In the aeroponic system, only minitubers larger than 15 mm were included in the statistical analysis. In the hydroponic and conventional systems, no minitubers smaller than 15 mm were obtained. The study primarily focused on the biological performance of the cultivation systems in terms of plant growth and minituber production efficiency.

Statistical analysis

Experimental data were analyzed using two-way analysis of variance (ANOVA) to evaluate the effects of the cultivation system, genotype, and their interaction. Mean comparisons were performed using Duncan's multiple range test at $p < 0.05$. All statistical analyses were carried out using the POLYFACT software package (developed for polyfactorial agricultural experiments). Additionally, regression analysis was performed to evaluate the relationships between plant growth parameters and minituber yield components, with Microsoft Excel (Microsoft Corp., Redmond, WA, USA) utilized for regression modeling, coefficient of determination (R^2) calculation, and graphical representation

RESULTS

The present study demonstrated the clear superiority of aeroponic cultivation over hydroponic and conventional systems for potato minituber production under Romanian conditions. Aeroponics significantly increased plant growth, minituber number, and minituber biomass, indicating that optimized root-zone conditions can substantially improve potato productivity under controlled environments. Overall, the present results support the hypothesis that aeroponic cultivation provides a more favorable environment for potato growth and minituber production than hydroponic or conventional systems. The consistency of the observed responses with previous investigations (*Eldridge et al., 2020; Buckseth et al., 2024; Cheema et al., 2024; Oljača et al., 2024; Silva Filho et al., 2024; Hartinger et al., 2025*) strengthens the evidence supporting the adoption of aeroponic technologies for minituber potato production.

Local and general context

Aeroponic potato cultivation in Romania is currently primarily limited to research applications. Nevertheless, our findings demonstrate its strong potential for optimizing minituber production under controlled conditions. Aeroponics is mainly used in potato cultivation for the production of minitubers as high-quality planting material. This method enables the rapid production of a large number of healthy tubers, originating from pathogen-free plants obtained through in vitro techniques.

Technological advantages and limitations

Despite its obvious advantages, aeroponics also has certain limitations, including high initial costs for infrastructure and equipment, the need for continuous monitoring and advanced technological management,

dependence on stable energy sources for optimal system operation, and variability in response depending on cultivar and growing conditions. These aspects may limit large-scale adoption, especially in traditional agricultural systems. In Romania, previous research on the hydroponic method for potato cultivation has shown superior results compared to the conventional method (*Tican, 2018; Tican et al., 2018a*; *Tican et al., 2025*). While studies on aeroponic methods had also been carried out, early systems were inefficient and failed to yield results comparable to international standards (*Tican et al., 2018b*). More recently, *Tican et al. (2026)* presented results regarding minituber production using an aeroponic system across different cultivation periods.

Plant height

The cultivation system exerted a highly significant influence on plant height one month after transfer, indicating that the cultivation system strongly affected the early vegetative growth of potato plants. Furthermore, cultivar also had a very significant effect on plant height, confirming the important role of genotype in growth expression. By two months after transfer, the effect of the cultivation system became even more pronounced (Table 1). Similar observations regarding the influence of soilless systems on plant development were reported by *Ritter et al. (2001)*, who demonstrated that aeroponic and hydroponic systems stimulate vegetative growth compared to conventional cultivation. Consistent with these findings*, Buckseth et al. (2016)* and *Tunio et al. (2020*), emphasized the favorable effect of aeroponics on potato plant growth and physiological activity.

One month after transfer, the hydroponic system significantly stimulated the initial growth of the plants, while two months later, the aeroponic system ensured the most intense stem elongation (Table 2). At the second determination, aeroponics generated the highest mean plant height (89.77 cm), exceeding the conventional system by more than 50 cm. This was due to the superior oxygenation and nutrient availability inherent to the aeroponic system, which enhanced both stem elongation and plant vigor. Consistent results were presented by *Eldridge et al. (2020)*, who mentioned that hydroponic systems provide stable root-zone conditions during early plant development.

Table 1

Analysis of variance

Source of variation	Sum of squares	DF	Mean square	*F*
Analysis of variance for plant height 1 month after transfer				
Cultivation system (*a*)	172.02	2	86.01	20.45 **(6.94; 18.00)
Cultivar (*b*)	283.06	3	94.35	8.30 **(3.16; 5.09)
Cultivation system (*a*) x Cultivar (*b*)	50.27	6	8.38	0.73 ns (2.66; 4.01)
Analysis of variance for plant height 2 months after transfer				
Cultivation system (*a*)	17413.50	2	8706.75	135.86 **(6.94; 18.00)
Cultivar (*b*)	7482.23	3	2494.08	77.02 **(3.16; 5.09)
Cultivation system (*a*) x Cultivar (*b*)	2505.36	6	417.56	12.90 **(2.66; 4.01)

Note: DF, degrees of freedom; ** significant for $p < 0.01$. Values in parentheses represent the critical *F*-values ($F_{0.05}$; $F_{0.01}$)

The differences observed among cultivars demonstrate the strong influence of genotype on vegetative growth and adaptation to intensive cultivation systems. The Cosiana and Brasovia cultivars exhibited the highest values for plant height (Table 3), indicating a superior capacity to exploit favorable growth conditions.

The interaction between cultivation system and genotype significantly influenced plant height, particularly two months after transfer (Tables 4 and 5). At the first evaluation, differences among cultivation systems were less pronounced, although hydroponic cultivation stimulated early vegetative growth in certain cultivars, especially Cosiana and Brasovia. At the second evaluation, aeroponic cultivation markedly enhanced plant growth for all analyzed genotypes, with the highest values recorded for Cosiana and Brasovia.

Table 2

Influence of the cultivation system on plant height (cm) at 1 and 2 months after transfer

Cultivation system (*a*)	Plant height (cm) at 1 month		Diff. (cm)/Signif.	Plant height (cm) at 2 months		Diff. (cm)/Signif.
Hydroponic (a_1)	22.90	A	4.48 **	60.06	B	24.06 **
Aeroponic (a_2)	18.12	B	−0.30 ns	89.77	A	53.77 ***
Conventional (a_3) (Ct)	18.42	B	—	36.00	C	—
LSD ($p < 0.05$) = 2.33; ($p < 0.01$) = 3.85; ($p < 0.001$) = 7.21.				LSD ($p < 0.05$) = 9.09; ($p < 0.01$) = 15.03; ($p < 0.001$) = 28.14.		

Note: Means within the same column followed by the same letter do not differ significantly according to Duncan's multiple range test ($p < 0.05$).
ns = not significant; ** = significant at $p < 0.01$; *** = highly significant at $p < 0.001$; Ct = Control system

Table 3

Influence of cultivar on plant height (cm) at 1 month and 2 months after transfer

Cultivar	Plant height (cm) at 1 month		Diff. (cm)/Signif.	Plant height (cm) at 2 months		Diff. (cm)/Signif.
Azaria	18.24	BC	2.11 ns	64.93	B	26.62 ***
Brasovia	23.33	A	7.20 ***	67.25	B	28.94 ***
Cosiana	21.55	AB	5.42 **	77.29	A	38.99 ***
Cezarina (Ct)	16.13	C	−	38.31	C	—
LSD (p 0.05) = 3.34; (p 0.01) = 4.58; (p 0.001) = 6.23.				LSD (p 0.05) = 5.63; (p 0.01) = 7.73; (p 0.001) = 10.52.		

Note: Means within the same column followed by the same letter do not differ significantly according to Duncan's multiple range test ($p < 0.05$).
ns = not significant; ** = significant at $p < 0.01$; *** = highly significant at $p < 0.001$; Ct = Control cultivar.

Table 4

Combined influence of the cultivation system and cultivar on plant height (cm) 1 month after transfer

Cultivation system (a)/ Cultivar (b)	Hydroponic system (a_1)		Aeroponic system (a_2)		Conventional system (a_3) (Ct)		a_1-a_3 (cm)/ Signif.	a_2-a_3 (cm)/ Signif.
	Plant height (cm)	Diff. (cm)/ Signif.	Plant height (cm)	Diff. (cm)/ Signif.	Plant height (cm)	Diff. (cm)/ Signif.		
Azaria (b_1)	20.54	1.12 ns	16.00	1.36 ns	18.17	3.84 ns	2.37 ns	−2.17 ns
Brasovia (b_2)	25.23	5.81 *	21.27	6.63 *	23.50	9.17 **	1.73 ns	−2.23 ns
Cosiana (b_3)	26.41	6.99 *	20.58	5.95 *	17.67	3.34 ns	8.74 **	2.91 ns
Cezarina (b_4) (Ct)	19.42	—	14.64	—	14.33	—	5.09 ns	0.31 ns
LSD ($p < 0.05$) = 5.78; ($p < 0.01$) = 7.93; ($p < 0.001$) = 10.79.					LSD ($p < 0.05$) = 5.50; ($p < 0.01$) = 7.76; ($p < 0.001$) = 11.21.			

Note: ns = not significant; * = significant at $p < 0.05$; ** = significant at $p < 0.01$; Ct = Control.

Table 5

Combined influence of cultivation system and cultivar on plant height (cm) 2 months after transfer

Cultivation system (a)/ Cultivar (b)	Hydroponic system (a_1)		Aeroponic system (a_2)		Conventional system (a_3) (Ct)		a_1-a_3 (cm)/ Signif.	a_2-a_3 (cm)/ Signif.
	Plant height (cm)	Diff. (cm)/ Signif.	Plant height (cm)	Diff. (cm)/ Signif.	Plant height (cm)	Diff. (cm)/ Signif.		
Azaria (b_1)	60.61	21.86 ***	80.67	21.34 ***	53.50	36.67 ***	7.11 ns	27.17 **
Brasovia (b_2)	62.25	23.50 ***	107.83	48.50 ***	31.67	14.84 **	30.58 ***	76.17 ***
Cosiana (b_3)	78.61	39.86 ***	111.26	51.93 ***	42.00	25.17 ***	36.61 ***	69.26 ***
Cezarina (b_4) (Ct)	38.75	—	59.33	—	16.83	—	21.92 **	42.50 ***
LSD ($p < 0.05$) = 9.76; ($p < 0.01$) = 13.38; ($p < 0.001$) = 18.21.					LSD ($p < 0.05$) = 12.29; ($p < 0.01$) = 18.47; ($p < 0.001$) = 29.98.			

Note: ns = not significant; ** = significant at $p < 0.01$; *** = highly significant at $p < 0.001$; Ct = Control.

Minituber number and weight per plant

Analysis of variance revealed highly significant effects of the cultivation system, genotype, and their interaction on minituber number and weight per plant (Table 6). These results indicate that both technological factors and genetic background strongly influence the efficiency of minituber production under controlled cultivation environment. The significant effect of the cultivation system confirms the importance of root environment optimization for improving tuber initiation and biomass accumulation. The significant genotype effect suggests that potato varieties differ in their capacity to adapt to intensive soilless cultivation systems. In addition, the significant interaction between the cultivation system and genotype indicates that the varietal response depends on the cultivation environment, emphasizing the importance of selecting suitable genotypes for aeroponic production systems.

Aeroponic method led to highest number of minitubers/plant (37.26), the difference of 32.59 minitubers, compared to the classical method, being very statistically significant (Table 7). The hydroponic method achieved a mean number of 9.25 minitubers/plant, a value higher than the control, but the difference of 4.58 minitubers compared to the control method was not statistically significant. The results highlight the efficiency of the aeroponic method, by this method the number of minitubers increased by almost 7.97 times compared to the classical method and 4 times compared to the hydroponic method.

Table 6

Analysis of variance

Source of variation	Sum of squares	DF	Mean square	*F*
Analysis of variance for the number of minitubers per plant				
Cultivation system (*a*)	7472.54	2	3736.27	91.84 **(6.94; 18.00)
Cultivar (*b*)	1652.02	3	550.67	65.95 **(3.16; 5.09)
Cultivation system (*a*)*Cultivar (*b*)	2417.32	6	402.89	48.252 **(2.66; 4.01)
Analysis of variance for minituber weight/plant				
Cultivation system (*a*)	568810.50	2	284405.30	191.46 **(6.94; 18.00)
Cultivar (*b*)	247619.30	3	82539.77	56.95 **(3.16; 5.09)
Cultivation system (*a*)* Cultivar (*b*)	190533.80	6	31755.63	21.91 **(2.66; 4.01)

Note: DF, degrees of freedom; ** significant for p <0.01. Values in parentheses represent the critical *F*-values ($F_{0.05}$; $F_{0.01}$)

Table 7

Influence of cultivation system on the number of minitubers and their weight (g)/plant

Cultivation system (*a*)	Minitubers number per plant		Diff./ Signif.	Minituber weight per plant (g)		Diff. (g)/ Signif.
Hydroponic (a_1)	9.25	B	4.58 ns	111.85	B	38.57 ns
Aeroponic (a_2)	37.26	A	32.59 ***	357.11	A	283.83 ***
Conventional (a_3) (Ct)	4.67	B	—	73.28	B	—
LSD (p < 0.05) = 7.24; (p < 0.01) = 11.98; (p < 0.001) = 22.42.				LSD (p < 0.05) = 43.74; (p < 0.01) = 72.38; (p < 0.001) = 135.48.		

Note: Means within the same column followed by the same letter do not differ significantly according to Duncan's multiple range test (p <0.05). ns = not significant; *** = highly significant at (p < 0.001).

Table 8

Influence of cultivar on the number of minitubers and their weight (g) per plant

Cultivar (*b*)	Minituber number per plant		Diff./ Signif.	Minituber weight per plant (g)		Diff. (g) / Signif.
Azaria (b_1)	20.50	A	15.12***	227.67	A	190.43 ***
Brasovia (b_2)	20.38	A	15.00 ***	223.87	A	186.63 ***
Cosiana (b_3)	21.99	A	16.61 ***	234.20	A	196.96 ***
Cezarina (Ct) (b_4)	5.38	B	—	37.24	B	—
LSD (p <0.05) = 2.86; (p < 0.01) = 3.92; (p < 0.001) = 5.34				LSD (p <0.05) = 37.69 g; (p < 0.01) = 51.68 g; (p < 0.001) = 70.35 g.		

Note: Means within the same column followed by the same letter do not differ significantly according to Duncan's multiple range test (p <0.05). *** = highly significant at p < 0.001.

The analysis of cultivar influence (Table 8) highlights significant genetic differences regarding minituber formation and biomass accumulation. The highest values of minitubers number/plant were recorded for Cosiana (21.99 minitubers/plant), Azaria (20.50 minitubers/plant) and Brașovia (20.38 minitubers/plant) varieties with positive, highly statistically significant differences compared to the control variety Cezarina (5.38 minitubers/plant). Regarding the weight of minitubers/plant, the same trend is observed. Cosiana variety achieved the highest value (234.20 g), followed by Azaria (227.67 g/plant) and Brașovia (223.87 g), with very statistically significant differences (196.96 g, 190.43 g and 186.63 g), compared to the control variety Cezarina (37.24 g).

The aeroponic method led to an increase in the number of minitubers for the Azaria, Brasov and Cosiana varieties, obtaining very significant positive differences (41.56; 43.84; 44.28 minituber/plant) compared to the classical method (Table 9).

Table 9

Combined influence of cultivation system and cultivar on the mean number of minitubers per plant

Cultivation system (*a*)/ Cultivar (*b*)	Hydroponic system (a_1)		Aeroponic system (a_2)		Conventional system (a_3) (Ct)		a_1-a_3/ Signif.	a_2-a_3/ Signif.
	Minituber number per plant	Diff./ Signif.	Minituber number per plant	Diff./ Signif.	Minituber number per plant	Diff./ Signif.		
Azaria (b_1)	11.29	6.21 *	45.89	40.00 ***	4.33	−0.84 ns	6.96 ns	41.56 ***
Brasovia (b_2)	7.63	2.55 ns	48.67	42.78 ***	4.83	−0.34 ns	2.80 ns	43.84 ***
Cosiana (b_3)	13.01	7.93 **	48.61	42.72 ***	4.33	−0.84 ns	8.68 *	44.28 ***
Cezarina (b_4) (Ct)	5.08	—	5.89	—	5.17	−	−0.09 ns	0.72 ns
LSD (p <0.05) = 4.95; (p < 0.01) = 6.97; (p < 0.001) = 9.25.					LSD (p <0.05) = 8.34; (p < 0.01) = 13.06; (p < 0.001) = 22.58.			

Note: ns = not significant; * = significant at p <0.05; ** = significant at p < 0.01; *** = highly significant at p < 0.001.

Table 10

Combined influence of cultivation system and cultivar on mean weight of minitubers per plant

Cultivation system (*a*)/ Cultivar (*b*)	Hydroponic system (a_1)		Aeroponic system (a_2)		Conventional system (a_3) (Ct)		a_1-a_3 (g)/ Signif.	a_2-a_3 (g)/ Signif.
	Minituber weight (g) per plant	Diff. (g)/ Signif.	Minitub. weight (g) per plant	Diff. (g)/ Signif.	Minitub. weight (g) per plant	Diff. (g)/ Signif.		
Azaria (b_1)	180.74	140.99 ***	410.11	362.09 ***	92.17	68.23 *	88.57 *	317.94 ***
Brasovia (b_2)	85.78	46.03 ns	494.17	446.15 ***	91.67	67.73 *	−5.89 ns	402.5 ***
Cosiana (b_3)	141.13	101.38 **	476.14	428.12 ***	85.33	61.39 ns	55.80 ns	390.81 ***
Cezarina (b_4) (Ct)	39.75	—	48.02	—	23.94	—	15.81 ns	24.08 ns
LSD (p <0.05) = 65.27 g; (p < 0.01) = 89.52 g; (p < 0.001) = 121.85 g.					LSD (p <0.05) = 70.88 g; (p < 0.01) = 103.46 g; (p < 0.001) = 159.47 g.			

Note: ns = not significant; * = significant at $p < 0.05$; ** = significant at $p < 0.01$; *** = highly significant at $p < 0.001$.

The combined effect of the cultivation system and genotype (Table 10) further confirms the superiority of aeroponic systems in enhancing minituber biomass production, recording very significant positive differences compared to the classical method for Azaria, Brasovia, and Cosiana (317.94; 402.5; 390.81 g). All cultivars exhibited maximum minituber weight under aeroponic conditions, with Brasovia, Cosiana, and Azaria showing the most pronounced responses. Hydroponics produced intermediate values, while conventional cultivation resulted in the lowest biomass accumulation, reflecting the physical and physiological constraints of soil-based growth. The superior response recorded for the Cosiana, Brasovia, and Azaria cultivars indicates that genotype plays an essential role in the adaptation to intensive soilless systems. In addition to increasing the number of minitubers, aeroponic cultivation significantly enhanced minituber biomass accumulation. The greater minituber weight recorded under aeroponic conditions may reflect a more efficient allocation of assimilates toward tuber development resulting from optimal root development and continuous nutrient availability.

Regression analysis

Regression analysis revealed a strong positive correlation between plant height and the number of minitubers produced per plant (R = 0.81, p < 0.01), indicating that greater vegetative development was associated with increased minituber production (Figure 2). In the aeroponic system, where water and nutrients are continuously available, vegetative development is often an indicator of the plant's ability to support the tuberization process. The study by *Silva Filho et al.* (2024) confirms a direct correlation between early vegetative growth indicators measured 21 days after transplantation and the final production of minitubers in an aeroponic system, an aspect that is also strongly supported by the findings in this study.

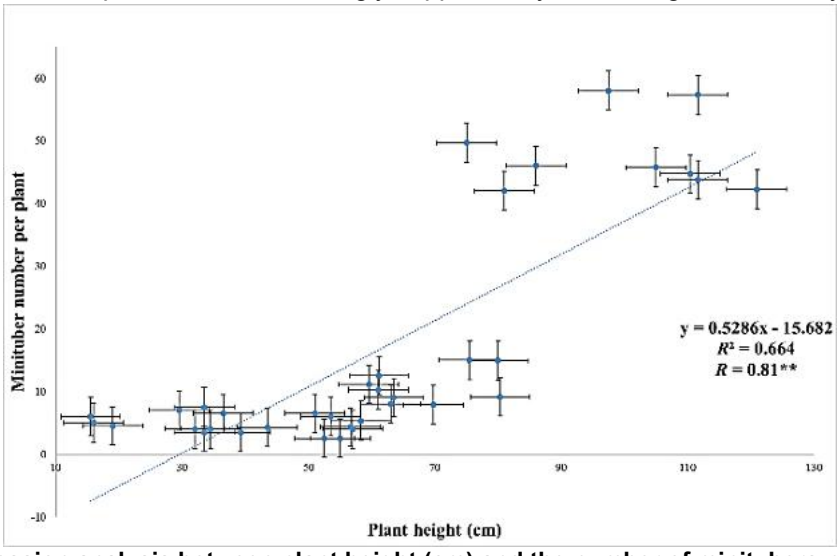


Fig. 2 - Linear regression analysis between plant height (cm) and the number of minitubers per plant across the evaluated potato genotypes and cultivation systems (** indicates significance at $p < 0.01$).

Limitations and practical implications

Although aeroponics requires a higher initial investment and careful technological management, its capacity to generate high yields of healthy planting material makes this technology promising for the modernization of potato minitubers production in Romania. However, the magnitude of the response differed among genotypes, suggesting that genetic factors strongly influence the ability of plants to exploit the favorable root environment provided by aeroponic systems. An alternative interpretation highlights that part of the observed differences stems not only from the independent cultivation system effects but also from the complex interaction between genotype and specific environmental conditions maintained during cultivation. Therefore, additional studies involving a larger number of genotypes, different nutrient management strategies, and multi-season evaluations would be valuable for confirming the stability of these responses.

Results and Discussions are recommended to be presented as a single section, using subheadings if needed. Be clear and easy to understand but complete and concise in stating and discussing the findings, comparing results with previous works and proposing explanation for the result obtained. All the data of this section must be accompanied by appropriate statistical analyses. Avoid comparisons or contrast which are not relevant to your findings. Avoid any type of speculation unsupported by the data obtained.

CONCLUSIONS

Aeroponic cultivation significantly improved potato plant growth, minituber number and weight compared to hydroponic and conventional cultivation systems. The superiority of the aeroponic system became more evident during advanced vegetation stages.

The aeroponic method leads to obtaining the largest number of minitubers (37.26/plant).

The number of minitubers was ~8 times higher than the classical method and ~4 times higher than the hydroponic method, highlighting the superior efficiency of the aeroponic system;

Among the analyzed genotypes, Cosiana, Brasovia, and Azaria showed superior adaptability to intensive soilless culture systems, recording the highest values for plant development and minituber production. The interaction between the cultivation system and genotype demonstrated that the varietal response plays an important role in the efficiency of minituber production.

The hydroponic method offered intermediate results, but the differences compared to the control were not statistically significant.

The obtained results confirm the potential of aeroponics as an efficient technology for the production of healthy potato planting material in Romania and support its future use in modern minitubers potato production systems.

ACKNOWLEDGEMENT

This research work was carried out with the support of National Institute of Research and Development for Potato and Sugar Beet Brașov and also was financed by Ministry of Research, Innovation and Digitalization, from PN 23 19 01 01 Project “Research on increasing the performance process of the potato minitubers production using an intelligent aeroponic system”, period 2023-2026. We mention that for aeroponic system we are in the process of filing patent applications.

REFERENCES

[1] Balasundram, S. K., Shamshiri, R. R., Sridhara, S., & Rizan, N. (2023). The Role of Digital Agriculture in Mitigating Climate Change and Ensuring Food Security. An Overview. *Sustainability 15(6*), 5325. DOI: https://doi.org/10.3390/su15065325

[2] Benke K., Tomkins B. (2017). Future food-production systems: vertical farming and controlled-environment agriculture. *Sustainability: Science, Practice and Policy 13(*1), 13–26. DOI: https://doi.org/10.1080/15487733.2017.1394054

[3] Brocic, Z., Oljaca, J., Pantelic, D., Rudic, J., Poštić, D., & Momčilović, I. (2022). Potato aeroponics: effects of cultivar and plant origin on minituber production. *Horticulturae 8(10),* 915. DOI: https://doi.org/10.3390/horticulturae8100915

[4] Buckseth, T., Sharma, A. K., Pandey, K. K., Singh, B. P., & Muthuraj, R. (2016). Methods of pre-basic seed potato production with special reference to aeroponics—A review. *Scientia Horticulturae* 204, 79-87. DOI: https://doi.org/10.1016/j.scienta.2016.03.041

[5] Buckseth, T., Sharma, S., Tiwari, J. K., Kuma, R V., Sharma, A. K., Challam, C., *et al*. (2024). Plant sources identify variations in potato production potential under aeroponics, *Potato Research 67*, 931–943. DOI: https://doi.org/10.1007/s11540-023-09670-4

[6] Çalışkan, M. E., Yavuz, C., Yağız, A. K., Demire, l U., & Çalışkan, S. (2021). Comparison of Aeroponics and Conventional Potato Mini Tuber Production Systems at Different Plant Densities. *Potato Research 64,* 41–53. DOI: https://doi.org/10.1007/s11540-020-09463-z

[7] Cheema, H. N., Ma, H., Wang, K. X., Tang M., Zhang, K., Jahandad, A., *et al.* (2024). Deciphering nitrogen dynamics in aeroponics: physio-biochemical and enzymatic responses influencing nitrogen use efficiency in contrasting potato genotypes. *Scientia Horticulturae* 338, 113768, ISSN 0304-4238. DOI: https://doi.org/10.1016/j.scienta.2024.113768

[8] Deguine, J. P., Aubertot, J. N., Bellon, S., Côte, F., Lauri, P. E., Lescourret, F., *et al.* (2023). Chapter One, Agroecological Crop Protection for Sustainable Agriculture. *Advances in Agronomy 178*, 1–59, ISSN 0065-2113. DOI: https://doi.org/10.1016/bs.agron.2022.11.002

[9] Devaux, A., Goffart, J. P., Kromann, P., Piedra, J. A., Polar, V., & Hareau, G. (2021). The Potato of the Future: Opportunities and Challenges in Sustainable Agri-food Systems. *Potato Research 64(4),* 681–720. DOI: https://doi.org/10.1007/s11540-021-09501-4

[10] Dianawati, M., Hamdani, K. K., Sulastrini, I., Susanto, B., Nurawan, A., Cartika, I., *et al.* (2025). Multiple versus single harvest comparison for two potato cultivars with an aeroponic system in Indonesia. *Chilean Journal of Agricultural Research 85(6),* 920-391. DOI: http://dx.doi.org/10.4067/s0718-58392025000600920

[11] Eldridge, B. M., Manzoni, L. R., Graham, C. A., Rodgers, B., Farmer, J. R., & Dodd A. N. (2020). Getting to the roots of aeroponic indoor farming. *New Phytol. 228(4),* 1183-1192. DOI: https://doi.org/10.1111/nph.16780

[12] Farran I., Mingo-Castel A. M. (2006). Potato minituber production using aeroponics: Effect of plant density and harvesting intervals. *American Journal of Potato Research 83(1),* 47–53. DOI: https://doi.org/10.1007/BF0286960

[13] Hartinger, S. C., de Matos, C. K., Moccellin, R., Faria, C. M. D. R., & Kawakami, J. (2025). Plant Growth Promoting Microorganisms: Performance of Potato Cultivars in Aeroponics. *Potato Research 68*, 1965-1984. DOI: https://doi.org/10.1007/s11540-024-09813-1

[14] Kozai, T., Niu, G., Takagaki, M. (2020). Plant Factory: An Indoor Vertical Farming System for Efficient Quality Food Production, 2nd ed.; Academic Press: Cambridge, MA, USA, ISBN: 978-0-12-816691-8

[15] Kumari, R., Kumar, R. (2019). Aeroponics: A review on modern agriculture technology. *Indian Farmer 6(4),* 286–292. DOI: https://indianfarmer.net/assets/archieves/2019/APRIL%202019.pdf

[16] Lakhiar, I. A., Gao, J., Syed, T. N., Chandio, F. A., & Buttar, N. A. (2018). Modern plant cultivation technologies in agriculture under controlled environment: A review on aeroponics. *Journal of Plant Interactions 13(1),* 338–352. DOI: https://doi.org/10.1080/17429145.2018.1472308

[17] Oljača, J. M., Broćić, Z. A., Pantelić, D. I., Rudić, J. J., Poštić, D. J., & Momčilović, I. D. (2024). Potato minituber production by aeroponics: effects of genotype and plant origin. *Journal of Agricultural Sciences 69(4),* 367-381. DOI: https://doi.org/10.2298/JAS2404367O

[18] Ritter, E., Angulo, B., Riga, P., Herran, C., Relloso, J., San Jose, M. (2001). Comparison of hydroponic and aeroponic cultivation systems for the production of potato minitubers. *Potato Research 44(2),*127-135. DOI: https://doi.org/10.1007/BF02410099

[19] Sadawarti, M. J., Singh, S. P., Buckseth, T., Kumar, V., Singh, R. K., Sharma, A. K., *et al.* (2026). Augmenting Seed Potato Production Through Integration of Aeroponics, Apical Rooted Cuttings and Sprout Cutting Techniques: A Comprehensive Review. *Agricultural Research*. DOI: https://doi.org/10.1007/s40003-026-00972-w

[20] Salma, S. B., Shubham, Kaushal S. (2024). Aeroponics: An emerging food growing system in sustainable agriculture for food security. International *Journal of Research in Agronomy* 7(11):93-97. DOI: https://www.doi.org/10.33545/2618060X.2024.v7.i11b.1947

[21] Savvas, D., Gruda N. (2018). Application of soilless culture technologies in the modern greenhouse industry – A review. *European Journal of Horticultural Science 83(5),* 280–293, ISSN 1611-442. DOI: https://doi.org/10.17660/eJHS.2018/83.5.2

[22] Shamshiri R. R., Hameed, I. A., Thorp, K. R., Balasundram, S. K., Shafian, S. Fatemieh, M., *et al*. (2021). Greenhouse Automation Using Wireless Sensors and IoT Instruments Integrated with Artificial

Intelligence. *Next-generation greenhouses for food security, IntechOpen*: London, UK, Chapter 1, ISBN 978-1-83968-075-5. DOI: https://www.intechopen.com/chapters/76695

[23] Sharma, A., Hazarika, M., Heisnam, P., Pandey, H., Devadas, V. S., & Wangsu, M. (2024). Controlled environment ecosystem: A plant growth system to combat climate change through soilless culture. *Crop Design 3(1),* 100044. DOI: https://doi.org/10.1016/j.cropd.2023.100044

[24] Silva, Filho, J. B., Fontes, P. C. R., Ferreira, J. Fd. S., Ceco, P. R., & Santosm, M. FSd. (2024). Best Morpho-Physiological Parameters to Characterize Seed-Potato Plant Growth under Aeroponics: A Pilot Study. *Agronomy 14(3),* 517. DOI: https://doi.org/10.3390/agronomy14030517

[25] Singh, P., Upadhyay, P., & Singh, S. K. (2025). Unlocking the Economic Potential of Potato Cultivars for Mini-tuber Production Under Aeroponic Culture. *Potato Research 68*, 2877–2900. DOI: https://doi.org/10.1007/s11540-025-09853-1

[26] Sinha, A., Solankey, S. S., Akhtar, S., & Patel, P. (2025). Advances in Potato Mini-tubers Production through Aeroponics and ARC Techniques. In: Solankey, S.S. (eds) *Advances in Research on Potato Production. Advances in Olericulture*. Springer, Cham, ISBN 978-3-031-82709-9. https://doi.org/10.1007/978-3-031-82710-5_7

[27] Tican, A. (2018). Experimenting hydroponic culture systems on different substrates to obtain potato minitubers. *Romanian Agricultural Research 35*, 147-153. DOI: https://doi.org/10.59665/rar3519

[28] Tican, A., Chiru, N., Cioloca ,M., & Bădărău, C. L. (2018a). Obtaining mini tubers by applying hydroponic culture. *Romanian Agricultural Research 35,* 141-146. DOI: https://doi.org/10.59665/rar3518

[29] Tican, A., Cioloca, M., Ștefan, M., & Bădărău, C. L. (2018b). Previous results on obtaining minitubers by aeroponic method applied at National Institute of Research and Development for Potato and Sugar Beet Brașov. *Journal of Horticulture, Forestry and Biotechnology*, *USAMVB Timișoara, Volume 22(4),* 136-139. DOI: https://journal-hfb.usab-tm.ro/2018/Volum%2022(4)%20PDF/25Tican%20Andreea.pdf

[30] Tican, A., Cioloca, M., & Popa, M. (2025). Study referring to potato mini tubers production using various culture systems. *Romanian Agricultural Research 42,* 133-139. DOI: https://doi.org/10.59665/rar4211

[31] Tican, A., Cioloca, M., & Chelmea, C. (2026). Obtaining potato minitubers using aeroponic methods under artificial conditions across different cultivation periods. *Romanian Agricultural Research 43:*445-457. DOI: https://incda-fundulea.ro/rar/nr43/rar43.39.pdf

[32] Tiwari, J. K., Buckseth, T., Singh, R. K., Zinta, R., Thakur, K., Bhardwaj, V., *et al.* (2022). Aeroponic evaluation identifies variation in Indian potato varieties for root morphology, nitrogen use efficiency parameters and yield traits. *Journal of Plant Nutrition 45(17):*2696–2709. DOI: https://doi.org/10.1080/01904167.2022.2046080

[33] Tunio, M.H., Gao, J., Shaikh, S. A., Lakhiar, I. A., Qureshi, W. A., Solangi, K. A., *et al.* (2020). Potato production in aeroponics: An emerging food growing system in sustainable agriculture for food security. *Chilean journal of agricultural research 80(1):*118-132. DOI: http://dx.doi.org/10.4067/S0718-58392020000100118

[34] Wang, C., Gong, J. (2024). Intelligent agricultural greenhouse control system based on internet of things and machine learning. *arXiv* preprint arXiv:2402.09488. DOI: https://arxiv.org/pdf/2402.09488

A STUDY OF THE QUALITY OF CARROT ROOT CLEANING WITH A SPIRAL CLEANER: SOIL SEPARATION AND MECHANICAL DAMAGE

/

ДОСЛІДЖЕННЯ ЯКОСТІ ОЧИЩЕННЯ КОРЕНЕПЛОДІВ МОРКВИ СПІРАЛЬНИМ ОЧИСНИКОМ: ВІДОКРЕМЛЕННЯ ҐРУНТУ ТА МЕХАНІЧНІ ПОШКОДЖЕННЯ

Volodymyr BULGAKOV[1)], Oleksandr MATSUIEV[2,*)], Lucretia POPA[3)], J. ri OLT[4)]

[1)] National University of Life and Environmental Sciences of Ukraine, Kyiv, Ukraine

[2)] Institute of Mechanics and Automation of Agroindustrial Production of the National Academy of Agrarian Sciences of Ukraine, Hlevakha, Ukraine

[3)] Research Institute for Agriculture Economy and Rural Development – ICEADR Bucharest, Romania

[4)] Estonian University of Life Sciences, Institute of Forestry and Engineering, Chair of Biosystems Engineering, Tartu, Estonia

Corresponding author: Oleksandr Matsuiev; e-mail: oleksandr.matsuiev@claas.com; ORCID: 0009-0000-9878-0591

DOI: https://doi.org/10.35633/inmateh-79-98

***Keywords:** carrot roots; spiral cleaner; soil separation; mechanical damage; angular velocity; entry orientation.*

ABSTRACT

This study combined two complementary criteria for evaluating a spiral cleaner for carrot roots: the spatial distribution of separated soil and the occurrence of mechanical damage. A laboratory test rig with a V-shaped cleaning trough formed by cantilevered spiral springs and driven brushes equipped with elastic rods was used. Nantes carrot roots were tested at cleaner-shaft angular velocities of 27.2, 31.4, and 35.6 rad·s^{-1} and in two entry orientations: tail-end-first and thicker-end-first. Separated soil was collected in three consecutive zones along the transport path. Mechanical damage was assessed immediately after cleaning and again after 24 h using samples of 100 roots. Zone I accounted for 38–48% of the separated soil, Zone II for 33–41%, and Zone III for 11–28%. Increasing the angular velocity shifted soil separation toward the inlet section. The proportion of undamaged roots decreased from 66% to 44% for the tail-end-first orientation and from 75% to 59% for the thicker-end-first orientation. The thicker-end-first orientation resulted in 9–15 percentage points more undamaged roots and reduced the combined proportion of cracks, broken tail ends, and impact bruises from 13–25% to 5–14%. Under the tested conditions, an angular velocity of 27.2 rad·s^{-1} with the thicker-end-first orientation was identified as the preferred low-damage operating condition. The results provide a basis for further multifactor optimization incorporating residual adhering soil, throughput, and energy consumption as additional evaluation criteria.

РЕЗЮМЕ

У дослідженні поєднано два взаємодоповнювальні критерії оцінювання спірального очисника коренеплодів моркви: просторовий розподіл відокремленого ґрунту та виникнення механічних пошкоджень. Використано лабораторну установку з V-подібним очисним руслом, утвореним консольними спіральними пружинами і приводними щітками з еластичними прутками. Коренеплоди моркви сорту «Нантська» досліджували за кутових швидкостей обертання валів 27,2; 31,4 і 35,6 рад·с$^{-1}$ та двох орієнтацій подавання: хвостовою або товстішою частиною вперед. Відокремлений ґрунт збирали у трьох послідовних зонах за довжиною транспортування. Механічні пошкодження оцінювали безпосередньо після очищення та повторно через 24 год у вибірках по 100 коренеплодів. У зоні I відокремлювалося 38-48% ґрунту, у зоні II – 33-41%, у зоні III – 11-28%. Зі збільшенням кутової швидкості процес зміщувався до початкової ділянки русла. Частка непошкоджених коренеплодів зменшилася з 66 до 44% за руху хвостовою частиною вперед і з 75 до 59% за руху товстішою частиною вперед. Друга орієнтація забезпечила на 9-15 відсоткових пунктів більше непошкоджених коренеплодів та зменшила сумарну частку тріщин, обламаних хвостових частин і плям від удару з 13-25 до 5-14%. За досліджених умов переважним малотравматичним режимом визначено режим, що відповідає 27,2 рад·с$^{-1}$ за подавання коренеплодів моркви товстішою частиною вперед.

INTRODUCTION

Cleaning the carrot-root heap after digging must simultaneously remove soil impurities and plant residues while preserving the marketable integrity of the produce. This task is complicated by the elongated shape of the roots, the small local contact area with the working elements, and differences in mechanical strength between the crown and tail sections.

Data on the geometric and mechanical properties of carrots indicate that impacts, local compression and bending may cause skin abrasions, cracks, internal bruising and tail-end breakage (*Jahanbakhshi et al., 2018; Nath et al., 2019; Stopa et al., 2017; Stopa et al., 2019; Xia et al., 2021*). Such damage impairs storability and reduces the proportion of marketable roots.

Modern carrot harvesters use digging shares, clamping-and-conveying belts, topping devices and cleaning units. Studies of these assemblies show that performance depends strongly on operating speed, working-element geometry and root orientation during interaction (*Jin et al., 2016; Jin et al., 2020; Rybacki et al., 2024; Wang et al., 2025a; Wang et al., 2025b; Yasmeen et al., 2023; Zeng et al., 2018; Zhao et al., 2024*). Machine-vision systems are also being developed for rapid defect detection; however, they do not eliminate the need for a mechanically gentle process (*Zhou et al., 2023*).

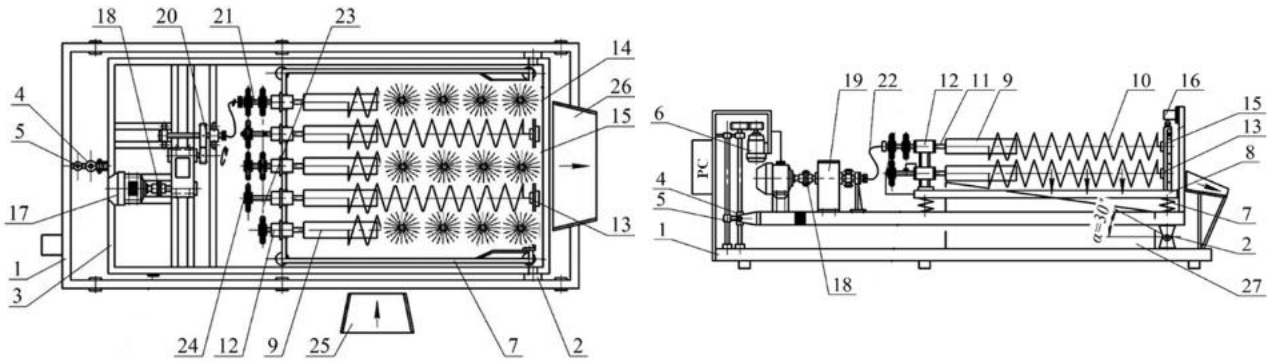
Spiral working elements are promising for separating heaps of root and tuber crops because they combine conveying, screening of fine impurities and self-cleaning from adhering moist soil. Scientific principles developed for potatoes and other root crops confirm that angular velocity, spiral geometry and the interaction scheme affect separation intensity and product damage (*Bulgakov et al., 2017; Bulgakov et al., 2018; Guo and Campanella, 2017; Hevko et al., 2020; Hoffmann et al., 2018; Issa et al., 2020*). However, direct transfer of such operating modes to carrots is inappropriate because of their elongated shape and the greater vulnerability of the tail end.

Recent studies on optimized conveying and separation systems for *Panax notoginseng* and potato have combined bench or field experiments with coupled simulation, while whole-machine studies on *Panax notoginseng* and white radish have emphasized the importance of controlling crop damage (*Chen et al., 2024; Pan et al., 2025; Wang et al., 2023; Xiao et al., 2023; Zhang et al., 2016*). These results provide useful quantitative benchmarks, but their operating modes and quality indices are not directly transferable to a dedicated carrot cleaner because carrot roots are elongated, orientation-sensitive and readily bruised.

In previous studies, soil separation and carrot damage were considered separately, preventing an integrated assessment of the technological trade-off between cleaning intensity and root preservation. The objective of this study was to determine the effects of spiral-cleaner shaft angular velocity and carrot-root entry orientation on the distribution of separated soil along the cleaning trough and on the pattern of mechanical damage, and to identify the preferred low-damage operating mode within the investigated factor range.

MATERIALS AND METHODS

Experimental studies were conducted using a laboratory spiral-cleaner test rig (Fig. 1). An intermediate frame 3 was attached to the main frame *1* by a hinge *2*; its inclination was adjusted by a screw mechanism *4* with a guide *5* and actuator *6*. A working-unit frame *8* was mounted on elastic supports *7*. Each spiral working element comprised a drum *9*, a cylindrical spring *10*, a shaft *11* and a bearing assembly *12*. The free end of each spiral rested, through bracket *13*, on a movable support *15* connected to vibrator *16*. Spiral springs *10* and driven cleaning brushes *14* formed a V-shaped cleaning trough.



a) b)

Fig. 1 – Schematic of the laboratory test rig:

a – top view; b – side view

1 - main frame; 2 - hinge; 3 - intermediate frame; 4 - screw mechanism; 5 - guide; 6 - actuator; 7 - elastic supports; 8 - working-unit frame; 9 - drum; 10 - cylindrical spring; 11 - shaft; 12 - bearing housing; 13 - bracket; 14 - cleaning brushes; 15 - movable support; 16 - vibrator; 17 - electric motor; 18 - coupling; 19 - continuously variable transmission; 20 - spur gear transmission; 21 - drive shaft; 22 - flexible shaft; 23, 24 - chain drives; 25 - feed chute; 26 - discharge chute; 27 - soil collection tray

The bottom and one side surface of the trough were formed by cantilevered spiral springs whose turns conveyed the material from the inlet towards the outlet. The opposite side surface was formed by flat driven brushes with elastic rods. Rotation of the spirals provided axial conveying and allowed soil to pass through the inter-turn gaps, while the brushes assisted root movement and removal of fine impurities. The mutual overlap of adjacent spirals promoted self-cleaning. General views of the test rig, working elements, cleaning trough and soil-collection zones are shown in Fig. 2.

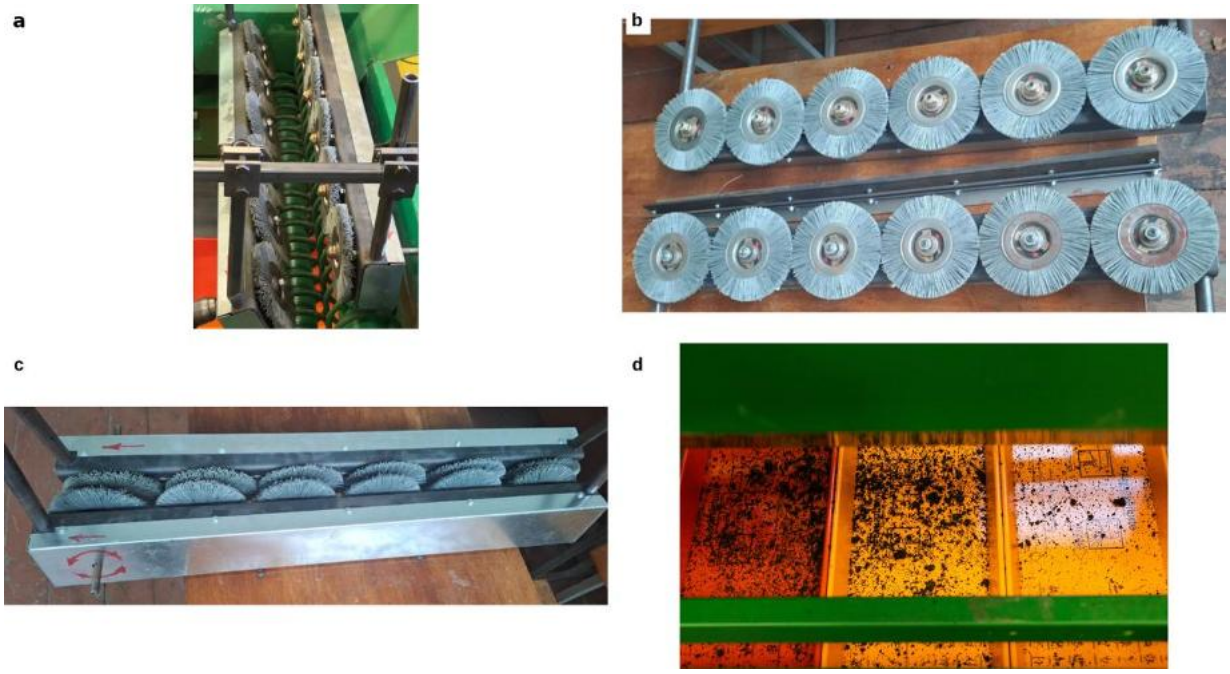


Fig. 2 – Components of the experimental test rig:
a – general view; b – frames with driven brushes; c – cleaning trough; d – trays for collecting soil by zone

Pre-dug roots of the Nantes carrot cultivar, predominantly elongated-cylindrical in shape, were used in the experiments. No cleaning elements were used during digging. Roots without initial mechanical damage were selected, transported separately and weighed on an electronic balance with 0.1 g resolution. The permissible mass deviation within each experimental group was ±5 g. For damage assessment, all adhering soil was removed from the roots beforehand so that surface defects would not be obscured.

Table 1

Factors and experimental conditions

Parameter or indicator	Levels / assessment procedure	Unit / note
Shaft angular velocity, ω	27.2; 31.4; 35.6	rad·s^{-1}
Entry orientation A	tail-end-first	–
Entry orientation B	thicker-end-first	–
Number of replicate soil-separation test series	3	for each operating mode
Damage-assessment sample size	100	roots per operating mode (600 total)
Assessment of latent impact damage	repeat inspection after 24	h

Experimental design and scope. Two complementary experimental series were performed for each of the six operating modes: (i) zonal collection of soil released from roots carrying adhering soil and (ii) mechanical-damage assessment using roots from which adhering soil had been removed before testing. The soil-separation series comprised three replicate test runs per mode with group masses matched to within ±5 g. The damage distribution was determined from 100 roots per mode (600 roots in total).

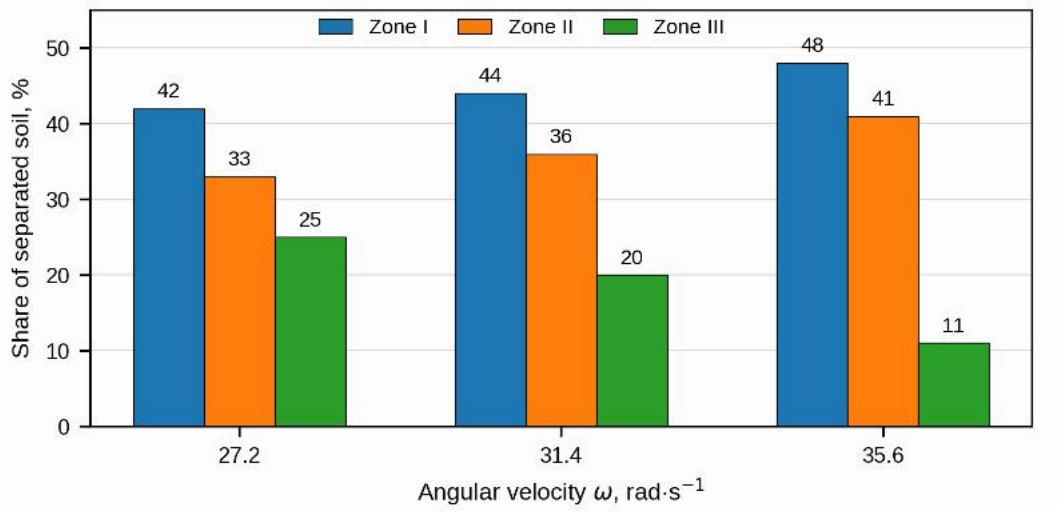
Along the transport direction, the cleaning trough was conventionally divided into three consecutive sections. Zone I represented the initial impact-separation interaction, Zone II the steady-state cleaning stage, and Zone III the completion of cleaning before discharge. Soil passing through the working surface was collected in three separate trays. The share attributed to each zone was calculated as the mass of soil in the corresponding tray divided by the total mass collected in all three trays and was expressed as a percentage.

After passing through the cleaning trough, each root was inspected in two stages. Immediately after the test, skin abrasions, scratches, cracks and tail-end breakage were recorded. A second inspection was performed after 24 h to detect darkened bruises resulting from impact or severe local compression. The dimensions of damaged areas were measured with a vernier caliper. For each operating mode, the percentage distribution among six categories was calculated: 1 – no damage; 2 – skin abrasions; 3 – scratches; 4 – cracks; 5 – broken tail end; 6 – impact bruise.

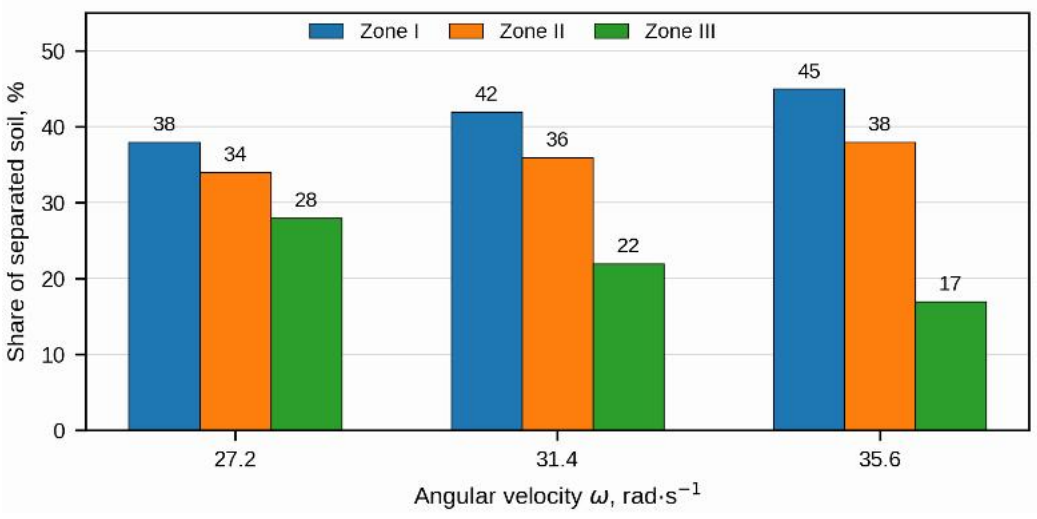
Statistical analysis. The primary damage endpoint was the proportion of undamaged roots. A secondary endpoint, termed severe damage, combined cracks, broken tail ends and impact bruises. Wilson 95% confidence intervals were calculated for both endpoints. The effect of entry orientation across the three angular-velocity strata was assessed with the Cochran-Mantel-Haenszel test, and ordered trends across angular velocity were tested with the Cochran-Armitage trend test. All tests were two-sided with $\alpha = 0.05$. Because the available zonal soil data consisted of mode-level shares that sum to 100%, the soil-separation distribution was analyzed descriptively; no ANOVA or claim of a global optimum was made.

RESULTS

Under all operating modes, the largest proportion of separated soil was collected at the beginning of the cleaning trough. In the tail-end-first orientation, Zone I accounted for 42, 44 and 48% of the separated soil at ω = 27.2, 31.4 and 35.6 rad·s^{-1}, respectively. The share in Zone III decreased from 25 to 11%. In the thicker-end-first orientation, the share in Zone I was 38-45%, whereas that in Zone III was 17-28% (Fig. 3).



a)



b)

Fig. 3 – Distribution of separated soil along the cleaning trough:
a – tail-end-first orientation; b – thicker-end-first orientation

Increasing angular velocity shifted the separation process towards Zone I in both entry orientations: its share increased by 6-7 percentage points, whereas the share in Zone III decreased by 11-14 percentage points. This indicated intensification of the initial interaction between the roots, spirals and brushes. With thicker-end-first feeding, the distribution along the trough was slightly more uniform: the Zone I share was 2-4 percentage points lower and the Zone III share 2-6 percentage points higher than with tail-end-first feeding.

Mechanical damage. Five types of defect were recorded: skin abrasions, scratches, cracks, broken tail ends and impact bruises, the last of which became clearly visible after 24 h (Fig. 4). The delayed appearance of impact bruises confirmed the need for two-stage inspection, because a single inspection immediately after cleaning would have underestimated the proportion of damaged roots. The delayed appearance of impact bruises confirmed the need for a two-stage inspection, as inspection conducted only immediately after cleaning would have underestimated the proportion of damaged roots.

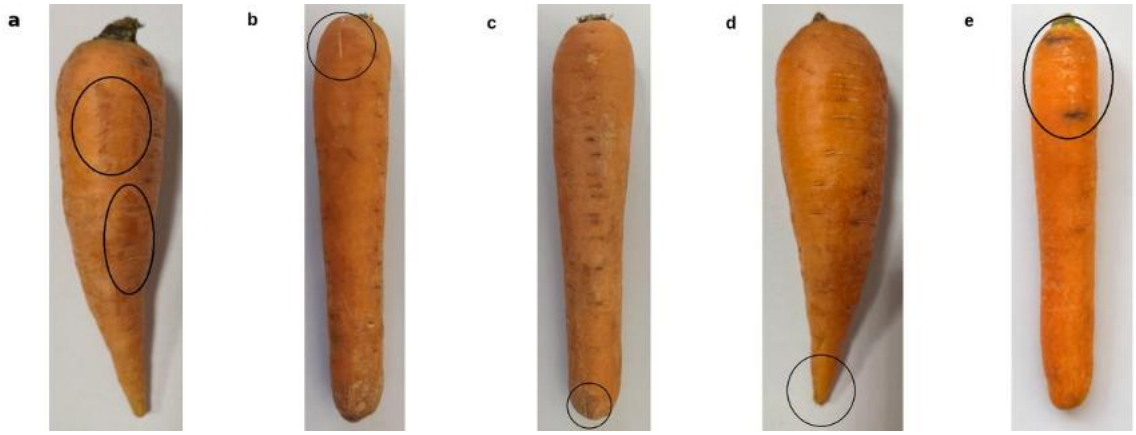


Fig. 4 – Types of mechanical damage to carrot roots:
a – skin abrasion; b – scratch; c – crack; d – broken tail end; e – impact bruise

In the tail-end-first orientation, the proportion of undamaged roots decreased from 66% at 27.2 rad·s^{-1} to 56% at 31.4 rad·s^{-1} and 44% at 35.6 rad·s^{-1}. All damage categories increased simultaneously: skin abrasions from 11 to 16%, scratches from 10 to 15%, cracks from 5 to 10%, broken tail ends from 5 to 8%, and impact bruises from 3 to 7% (Fig. 5a). Thus, increasing angular velocity intensified both superficial and structural defects.

In the thicker-end-first orientation, 75, 68 and 59% of roots remained undamaged at the three angular velocities, respectively (Fig. 5b). These values were 9, 12 and 15 percentage points higher than for the opposite orientation. The difference was particularly pronounced for more severe damage. The combined proportions of cracks, broken tail ends and impact bruises in the tail-end-first orientation were 13, 18 and 25%, compared with 5, 8 and 14% in the thicker-end-first orientation. Thus, the advantage of the thicker-end-first orientation increased with angular velocity.

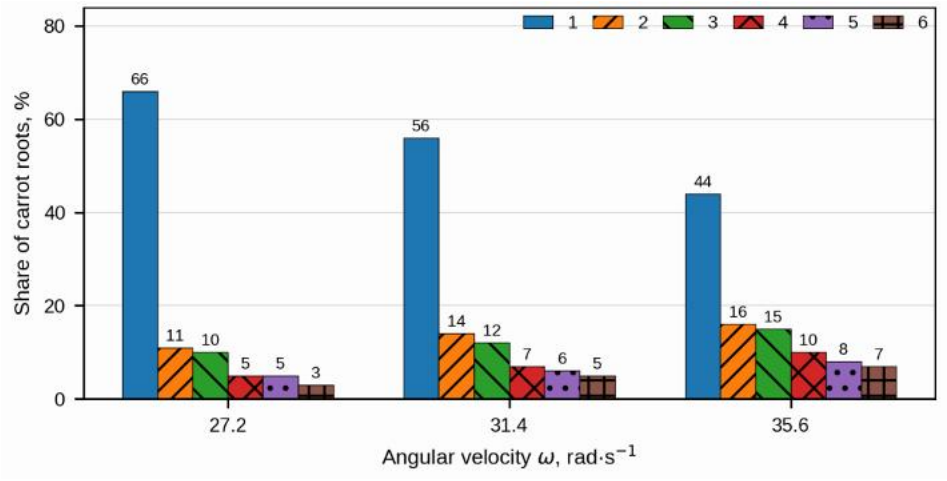
Table 2

Statistical summary of mechanical-damage endpoints (n = 100 roots per operating mode)

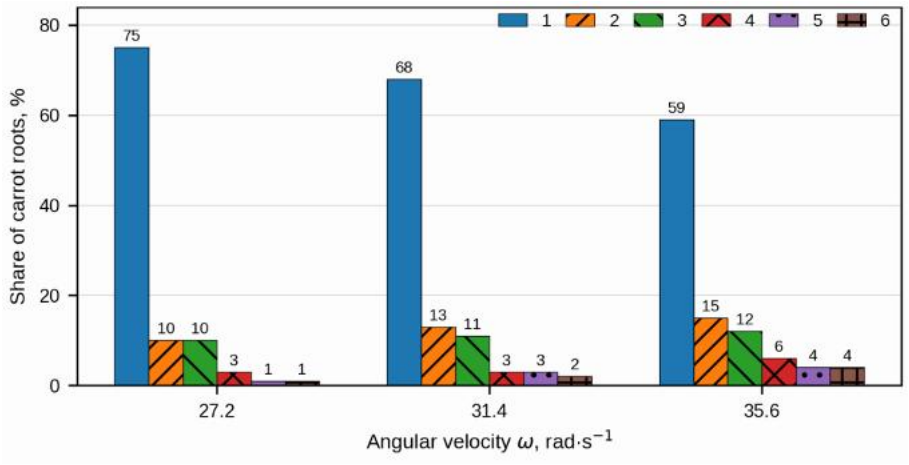
Entry orientation	Angular velocity, ω, rad·s^{-1}	Undamaged roots, % (95% CI)	Severe damage, % (95% CI)
tail-end-first	27.2	66 (56.3-74.5)	13 (7.8-21.0)
tail-end-first	31.4	56 (46.2-65.3)	18 (11.7-26.7)
tail-end-first	35.6	44 (34.7-53.8)	25 (17.5-34.3)
thicker-end-first	27.2	75 (65.7-82.5)	5 (2.2-11.2)
thicker-end-first	31.4	68 (58.3-76.3)	8 (4.1-15.0)
thicker-end-first	35.6	59 (49.2-68.1)	14 (8.5-22.1)

Note: severe damage = cracks + broken tail ends + impact bruises; confidence intervals are Wilson intervals.

Across angular-velocity strata, thicker-end-first feeding increased the odds that a root remained undamaged (common OR = 1.69, 95% CI 1.20-2.36; p = 0.002) and reduced the odds of severe damage (common OR = 0.42, 95% CI 0.26-0.70; p < 0.001). The proportion of undamaged roots decreased significantly with angular velocity for both tail-end-first (p = 0.002) and thicker-end-first (p = 0.016) feeding, whereas severe damage increased (p = 0.029 and p = 0.026, respectively).



a)



b)

Fig. 5 – Distribution of damage categories at different angular velocities: a – tail-end-first orientation; b – thicker-end-first orientation

1 – no damage; 2 – skin abrasions; 3 – scratches; 4 – cracks; 5 – broken tail end; 6 – impact bruise

DISCUSSION

Integrated assessment of operating modes. The two experimental components yielded a consistent mechanical interpretation. Thicker-end-first feeding resulted in a somewhat more even distribution of separated soil along the trough while reducing peak loading on the vulnerable tail end. The lowest damage level was obtained at ω = 27.2 rad·s^{-1} in the thicker-end-first orientation: 75% of roots had no visible defects, and the combined proportion of cracks, broken tail ends and impact bruises was 5%. However, the spatial distribution of separated soil is not equivalent to absolute cleaning efficiency because the available data did not include a complete balance of residual adhering soil for each operating mode. The identified mode should therefore be regarded as preferable according to the damage-minimization criterion, while final optimization for production conditions should consider a set of indicators: residual adhering soil, total separation, throughput, energy consumption and the proportion of mechanically damaged roots.

Comparison with published systems. A *Panax notoginseng* conveying-separating device achieved a separating rate of 93.60% and a screening rate of 92.64% under optimized bench conditions (*Wang et al., 2023*), while a self-propelled *Panax notoginseng* harvester reported a 96.8% net harvesting rate and 1.6% root damage (*Zhang et al., 2016*). Optimized potato separation systems reported 97.8% separation with 1.16% tuber damage (*Chen et al., 2024*) and 96% separation with 2% damage (*Pan et al., 2025*). A self-propelled white-radish combine reported 4.99% damage and 1.64% impurity (*Xiao et al., 2023*).

The 5% severe-damage proportion obtained here at 27.2 rad·s^{-1} with thicker-end-first feeding is close to the white-radish benchmark but higher than the 1.16-2% values reported for optimized Panax and potato systems. This comparison is indicative rather than direct: the cited studies evaluated whole harvesters or soil-crop complexes and used different damage thresholds, whereas the present protocol also counted superficial abrasions, scratches and bruises visible only after 24 h.

In addition, the present soil metric describes where separated soil was collected along the cleaner and is not an absolute separation efficiency or conveying rate. Consequently, the scientific contribution is the quantified effect of root orientation and angular velocity on the cleaning-damage trade-off.

In conclusion, it is particularly noteworthy that the movement of carrot roots within the cleaning channel of the newly developed soil-removal device differs substantially from that observed for other root crops. Furthermore, it's important to keep in mind that carrot roots themselves have specific shapes and sizes that are not comparable to those of potatoes, sugar beets, table beets, or fodder beets. This is particularly true for other root crops, such as *Panax notoginseng*, which cannot be effectively cleaned using the proposed device.

These two factors—the specific size and shape of carrot roots and the specialized design of the developed cleaner, which was specifically intended for cleaning carrot roots during harvesting—limit the relevance of direct comparisons with other root crops and cleaning devices. Consequently, the cleaning and damage results obtained in this study should not be directly compared with those reported for other root crops or cleaner designs. Moreover, the developed cleaner is unlikely to provide effective cleaning for root crops with substantially different morphological characteristics. The cleaning channel itself, consisting of spirals and a brush wall, was designed and manufactured solely for testing the cleaning of carrot roots from soil impurities using other types of cleaners and different types of root crops, is unlikely to be useful or relevant to scientists and designers.

Limitations and future work. The laboratory study used pre-dug Nantes roots, controlled entry orientation and a limited range of shaft speeds. Field-scale optimization should retain replicate-level tray masses and quantify residual adhering soil, total separation, throughput, energy consumption and random-orientation effects under varying soil moisture and root-size distributions. A future DEM-MBD model should be calibrated and validated against measured root trajectories, contact loads, zonal soil mass distributions and the observed damage categories; such a model was outside the scope of present experimental study.

CONCLUSIONS

1. An integrated method for evaluating the spiral cleaner was proposed, combining determination of the spatial distribution of separated soil in three cleaning-trough zones with two-stage inspection of mechanical damage to carrot roots.

2. Zone I accounted for 38-48% of the separated soil, Zone II for 33-41%, and Zone III for 11-28%. As angular velocity increased from 27.2 to 35.6 rad·s^{-1}, the Zone I share increased and the Zone III share decreased, indicating that intensive separation shifted towards the inlet of the trough.

3. The proportion of undamaged roots decreased from 66 to 44% in the tail-end-first orientation and from 75 to 59% in the thicker-end-first orientation. The latter orientation yielded 9-15 percentage points more undamaged roots and reduced the combined proportion of cracks, broken tail ends and impact bruises from 13-25% to 5-14%. Across all three angular-velocity strata, the common odds ratio for an undamaged root was 1.69 (95% CI 1.20-2.36; $p = 0.002$), while the odds of severe damage were reduced to 0.42 (95% CI 0.26-0.70; $p < 0.001$).

4. Under the tested conditions, $\omega = 27.2$ rad·s^{-1} in the thicker-end-first orientation was identified as the preferred operating mode according to the damage-minimization criterion. Establishing a global optimum will require a complete balance of residual adhering soil, together with measurements of throughput and energy consumption. Future work should also include field validation and development of a quantitatively validated DEM-MBD model.

REFERENCES

[1] Bulgakov V., Ivanovs S., Adamchuk V., Ihnatiev Y., (2017), Investigation of the influence of the parameters of the experimental spiral potato heap separator on the quality of work, *Agronomy Research*, vol. 15, no. 1, pp. 44-54.

[2] Bulgakov V., Nikolaenko S., Arak M., Holovach I., Ruzhylo Z., Olt J., (2018), Mathematical model of cleaning potatoes on surface of spiral separator, *Agronomy Research*, vol. 16, no. 4, pp. 1590-1606, DOI: 10.15159/AR.18.173.

[3] Chen M.D., Liu X.T., Hu P.X., Zhai X.T., Han Z.L., Shi Y.L., Zhu W.J., Wang D.W., He X.N., Shang S.Q., (2024), Study on rotor vibration potato-soil separation device for potato harvester using DEM-MBD coupling simulation, *Computers and Electronics in Agriculture*, vol. 218, article 108638, DOI: 10.1016/j.compag.2024.108638.

[4] Guo W., Campanella O.H., (2017), A relaxation model based on the application of fractional calculus for describing the viscoelastic behavior of potato tubers, *Transactions of the ASABE*, vol. 60, no. 1, pp. 259-264.
[5] Hevko R.B., Tkachenko I.G., Khomyk N.I., Gumeniuk Y.P., Flonts I.V., Gumeniuk O.O., (2020), Determination of technical-and-economic indices of root crop conveyer-separator during their motion on curved path, *INMATEH-Agricultural Engineering*, vol. 61, no. 2, pp. 175-182, DOI: 10.35633/inmateh-61-19.
[6] Hoffmann C., Engelhardt M., Gallmeier M., Gruber M., Märländer B., (2018), Importance of harvesting system and variety for storage losses of sugar beet, *Sugar Industry*, vol. 143, no. 8, pp. 474-484, DOI: 10.36961/si19782.
[7] Issa I.I.M., Zhang Z., El-Kolaly W., Yang X., Wang H., (2020), Design, ANSYS analysis and performance evaluation of potato digger harvester, *International Agricultural Engineering Journal*, vol. 29, no. 1, pp. 60-73.
[8] Jahanbakhshi A., Abbaspour-Gilandeh Y., Mesri Gundoshmian T., (2018), Determination of physical and mechanical properties of carrot in order to reduce waste during harvesting and post-harvesting, *Food Science & Nutrition*, vol. 6, no. 7, pp. 1898-1903, DOI: 10.1002/fsn3.760.
[9] Jin W., Xiang L., Peng G., Ming N., Qi W., Wen Z., (2020), Design and experiment of high-efficiency drag-reducing shovel for carrot combine harvester, *Transactions of the Chinese Society for Agricultural Machinery*, vol. 51, pp. 93-103 (in Chinese).
[10] Jin X., Du X., Wang S., Ji J., Dong X., Wang D., (2016), Design and experiment of stems cutting device for carrot harvester, *Transactions of the Chinese Society for Agricultural Machinery*, vol. 47, no. 3, pp. 82-89 (in Chinese).
[11] Nath S., Kumar A., Mani I., Singh J.K., Sureja A.K., (2019), Determination of physical and mechanical properties of carrot (Daucus carota) for designing combine harvesting mechanism, *The Indian Journal of Agricultural Sciences*, vol. 89, no. 6, pp. 1011-1016, DOI: 10.56093/ijas.v89i6.90825.
[12] Pan Y.F., Yang R.B., Zhang H., Zhang J., Zha X.T., Qiu Z.C., Wu M.S., (2025), Experiment and optimization of the potato-soil separation and conveying device for a harvester using RecurDyn-EDEM coupling simulation, *International Journal of Agricultural and Biological Engineering*, vol. 18, no. 4, pp. 149-156, DOI: 10.25165/j.ijabe.20251804.9219.
[13] Rybacki P., Przygodziński P., Osuch A., Osuch E., Kowalik I., (2024), Artificial neural network model for predicting carrot root yield loss in relation to mechanical heading, *Agriculture*, vol. 14, no. 10, article 1755, DOI: 10.3390/agriculture14101755.
[14] Stopa R., Komarnicki P., Szyjewicz D., Kuta Ł., (2017), Modeling of carrot root radial press process for different shapes of loading elements using the finite element method, *International Journal of Food Properties*, vol. 20, suppl. 1, pp. S340-S352, DOI: 10.1080/10942912.2017.1296862.
[15] Stopa R., Komarnicki P., Kuta Ł., Szyjewicz D., Słupska M., (2019), Modeling with the finite element method the influence of shaped elements of loading components on the surface pressure distribution of carrot roots, *Computers and Electronics in Agriculture*, vol. 167, article 105046, DOI: 10.1016/j.compag.2019.105046.
[16] Wang B., Hu Z., Gu F., Wu F., Cao M., Sun Y., (2025a), Analysis and evaluation of the experimental effect of double-disc knife-cutting device for carrot combine harvester, *Agriculture*, vol. 15, no. 7, article 682, DOI: 10.3390/agriculture15070682.
[17] Wang B., Hu Z., Wu F., Gu F., (2025b), Analysis and evaluation of harvest quality effectiveness of carrot clamping and conveying device, *Agriculture*, vol. 15, no. 3, article 275, DOI: 10.3390/agriculture15030275.
[18] Wang F.A., Wen B., Xie X.H., Jie K.T., Guo S.W., Zhang Z.G., (2023), Operation mechanism analysis and parameter optimization of conveying and separating device of Panax notoginseng harvester, *Transactions of the Chinese Society for Agricultural Machinery*, vol. 54, suppl. 1, pp. 201-211, 259 (in Chinese).
[19] Xia X., Xu Z., Yu C., Zhou Q., Chen J., (2021), Finite element analysis and experiment of the bruise behavior of carrot under impact loading, *Agriculture*, vol. 11, no. 6, article 471, DOI: 10.3390/agriculture11060471.
[20] Xiao X., Xie F.P., Zhao Z.Q., Liu D.W., Wang X.S., (2023), Design and experimentation of a self-propelled picking type white radish combine harvester, *Agriculture*, vol. 13, no. 8, article 1578, DOI: 10.3390/agriculture13081578.

[21] Yasmeen Z., Ashraf M., Ahmad S., Ahmad M., Sabir I., Shahzaib, (2023), Development and economic evaluation of carrot harvester cum trimmer, *Journal of Agricultural Research*, vol. 61, no. 1, pp. 65-76, DOI: 10.58475/2023.61.1.1837.
[22] Zeng G.J., Chen J.N., Xia X.D., (2018), Design and experiment on pull type of tassel-fruit separation for carrot, *Transactions of the Chinese Society for Agricultural Machinery*, vol. 49, pp. 73-79 (in Chinese).
[23] Zhang Z.G., Wang F., Zhang Y.C., Zhang D., Tian R., (2016), Design and experiment of self-propelled Panax notoginseng harvester, *Transactions of the Chinese Society for Agricultural Machinery*, vol. 47, suppl. 1, pp. 234-240 (in Chinese).
[24] Zhao Z.H., Wang J.S., Yang L.L., Shao Z.T., (2024), Optimal design of carrot digging shovel based on discrete element method, *Journal of Agricultural Mechanization Research*, vol. 46, pp. 139-145 (in Chinese).
[25] Zhou W., Song C., Song K., Wen N., Sun X., Gao P., (2023), Surface defect detection system for carrot combine harvest based on multi-stage knowledge distillation, *Foods*, vol. 12, no. 4, article 793, DOI: 10.3390/foods12040793.

DESIGN AND EXPERIMENTAL STUDY OF A SOIL PICKUP AND SEPARATION DEVICE FOR AN AUTOMATIC FLOWER TRANSPLANTER

/

花卉自动移栽机取分土装置设计与试验研究

Xiang ZOU[1)], Lihua WEI*[1,2)], Denghui ZHAO[1)], Jian KANG[1)], Xiaohu BAI[1,2)] and Subo TIAN*[1,2)]

[1)]College of Engineering, Shenyang Agricultural University, Shenyang/ China;

[2)]Key Laboratory of Agricultural Equipment for Horticultural Crops, Ministry of Agriculture and Rural Affairs, Shenyang/ China.

Corresponding authors: Lihua Wei, Tel:13386825657; E-mail: weilihua@syau.edu.cn;

Subo Tian, Tel:13940428180; E-mail: tiansubo@syau.edu.cn.

DOI: https://doi.org/10.35633/inmateh-79-99

Keywords: *flower transplanter; soil pickup and separation device; operating parameter optimization; discrete element simulation; Box-Behnken design; performance validation*

ABSTRACT

To enable automatic and precise flower transplanting, a soil pickup and separation device was designed for substrate filling in greenhouse flower transplanting operations. The soil-conveying mechanism of the soil pickup auger was analyzed through theoretical analysis and discrete element simulation. Taking the soil pickup quantity and its coefficient of variation as the evaluation indices, the effects of auger rotational speed, soil penetration depth, and pitch were investigated and optimized using Box-Behnken response surface methodology. The simulation results showed that the optimal operating parameters were an auger rotational speed of 115.7 rpm, a soil penetration depth of 39.28 mm, and a pitch of 149.26 mm. Based on the optimized parameters, a prototype was fabricated and field tests were conducted. The measured soil pickup quantity was 4.13 kg, and the corresponding coefficient of variation was 1.44%, with relative errors of 3.05% and 4.00%, respectively, compared with the simulation results. The validation results demonstrated that the device operated stably and could achieve accurate and efficient substrate filling.

摘要

为实现花卉移栽过程的自动化与精准化，针对温室环境下花卉自动移栽机的作业需求，本文设计了一种用于软质花盆基质填充的取分土装置。结合理论分析与离散元仿真明确取土搅龙推土机理，以取土量及变异系数为指标，用 Box-Behnken 响应面法优化转速、入土深度和螺距。仿真结果表明，当转速为 115.7 r·min⁻¹、入土深度为 39.28 mm、螺距为 149.26 mm 时，取土性能最优。基于优化结果试制样机并开展田间试验，实际取土量为 4.13 kg，变异系数为 1.44%，与仿真预测值的相对误差分别为 3.05%与 4.00%。试验结果表明，该装置结构合理、工作稳定，可实现花盆基质的精准高效填充。

INTRODUCTION

The floral industry is a high-value sector of global agricultural trade. Driven by emerging markets and consumption upgrades, global flower demand continues to grow—the market exceeded $51.16 billion in 2024. As a major producer and consumer, China's floral exports reached $516 million in 2024, a year-on-year increase of 17.78% *(Gu et al., 2025)*. Against this backdrop, the comprehensive mechanization of flower production is not only crucial for enhancing the competitiveness of the flower industry and supporting its sustainable development, but also a key step in promoting rural revitalization and achieving agricultural modernization *(Cheng et al., 2023)*.

Flower transplanting primarily involves two core steps: growing medium filling and seedling planting. Growing medium filling is a prerequisite that directly affects operational efficiency and quality. However, it remains largely manual in China, resulting in high labor intensity and inconsistent quality, and making it difficult to meet the demands of large-scale production *(Zhou et al., 2018)*. Although some studies have addressed matrix filling mechanisms *(Minglani et al., 2021, Xu et al., 2020, He et al.,2023)* and transplanting apparatus optimization *(Zhao et al., 2020, Zhao et al., 2022, Tian et al., 2022, Tian et al.,2023, Ji et al., 2022, Tong et al., 2024, Hu et al., 2022)*, most focus on single functional modules or theoretical simulation analyses. There is still a lack of integrated soil pickup and separation devices specifically designed for automatic transplanting on greenhouse ridges, as well as systematic experimental studies of their operating performance and parameter effects.

Moreover, existing soil pickup devices often perform poorly under variable field conditions, such as uneven ridge surfaces and differences in soil properties, resulting in fluctuations in soil pickup quantity and filling uniformity. To address these challenges, this study develops an integrated soil pickup and separation device, optimizes its operating parameters using EDEM simulation and response surface methodology, and validates its performance through field tests. The aim is to provide a reliable and precise soil-handling solution for automatic flower transplanting and to support the development of more efficient, stable, and intelligent transplanting equipment.

MATERIALS AND METHODS

Structure and Working Principle

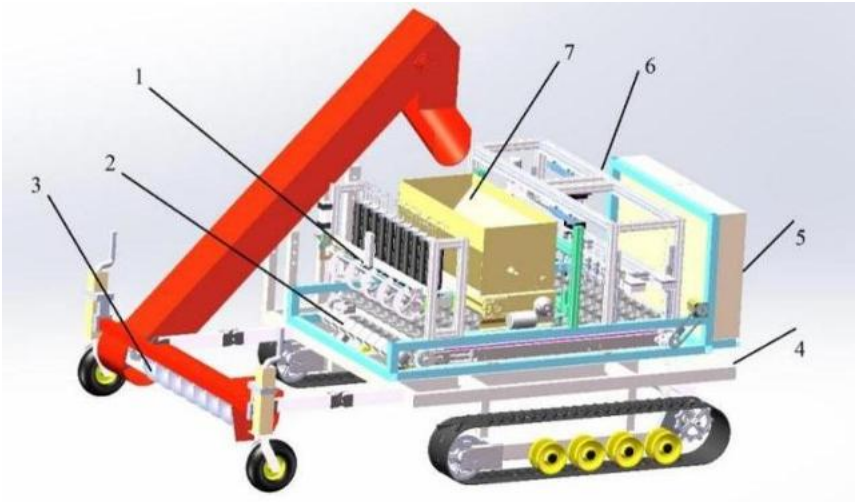


Fig.1 - Schematic diagram of the automatic flower transplanter

1-Soil sampling device; 2-Flowerpot Conveyor System; 3-Soil pickup Device; 4-Frame and Traveling Mechanism; 5-PLC Control Unit; 6-Seedling Transplanting Device; 7-Soil Storage Device

The automatic flower transplanter, shown in Fig. 1, integrates pot separation, substrate filling, hole punching, seedling transplanting, and ridge placement. It consists of a traveling mechanism, a PLC control system, and soil-handling units, enabling the fully automatic transfer of plug seedlings into cultivation pots.

The automatic flower transplanter is equipped with a tracked chassis to provide mobility, with a high-power DC motor serving as the drive unit. During operation, soil is collected and conveyed to the storage unit for uniform filling of soft nursery pots. The operating process is as follows: vacuum suction cups remove pots from stacked racks; the pots are conveyed individually for precise substrate filling; holes are vertically formed in the filled pots; seedlings are transplanted into the holes to ensure close root-soil contact; and finally, the pots are guided into the cultivation ridges through sequential guide plates, thereby achieving uniform placement along the ridges.

DESIGN OF SOIL PICKUP AND SEPARATION DEVICE

Design of Soil pickup and Lifting Unit

The soil pickup and lifting unit consists of a soil lifting box measuring approximately 2100 mm in length and 1800 mm in height after inclined installation, along with a housing, soil-lifting baffle, soil pickup auger, height adjustment mechanism, and soil discharge chute opening as shown in Fig. 2. The chain is positioned at a 40°angle to the ground, with four chain links between adjacent soil-lifting baffles at a pitch of 40 mm. Rotating shaft of the soil pickup auger has a length of 1100 mm and a diameter of 40 mm, while the helical blades feature an outer diameter of 150 mm and a thickness of 2 mm.

The soil pickup auger consists of a rotating shaft and helical blades (*Bulgakov et al., 2023*), while the soil-lifting baffles are composed of steel plates and rigid PVC strips, as shown in Fig. 3. During transplanting operations, the motor drives the auger to rotate and convey soil laterally beneath the baffles. The chain then drives the baffles upward, lifting the soil to the discharge opening.

The soil pickup quantity can be adjusted by changing the engagement length between the externally threaded rocker and the internally threaded square tube. Rotating the rocker outward moves the auger away from the ridge surface, thereby reducing soil pickup, whereas rotating it inward moves the auger closer to the ridge surface, thereby increasing soil pickup.

Design of the Soil Storage and Separation Unit

The soil storage and separation unit (*Li et al., 2019; Feng et al., 2022*) consists of a soil storage box, a conveyor-belt tensioning mechanism, a brushed DC motor, a soil separation quantity adjustment mechanism, a soil separation baffle, a conveyor belt, and a soil separation auger, as shown in Fig. 4. Soil discharged from the chute enters the storage box, is conveyed toward the separation baffle, and is then distributed uniformly into the flowerpots. The soil separation quantity adjustment mechanism, consisting of an adjustment knob, a gear set, and an adjustment plate, changes the gap between the adjustment plate and the conveyor belt by varying the meshing position of the gears, thereby enabling precise soil filling for 10 flowerpots per cycle. The conveyor-belt speed must also be properly adjusted: excessive speed may cause soil accumulation or clogging at the belt-baffle gap, whereas insufficient speed may result in inadequate filling.

Because of structural constraints, the soil discharge chute can only be installed on one side, which may cause soil accumulation near the discharge point. A soil separation auger is therefore used to improve soil conveying and distribution. The auger shaft is supported by F206 bearings and is provided with mounting holes at predetermined intervals, through which the blades are bolted. The shaft has a total length of 955 mm, including an 830 mm conveying section. The mounting holes have a diameter of 15 mm, the blade spacing is 40 mm, and 16 blades are arranged symmetrically around the shaft.

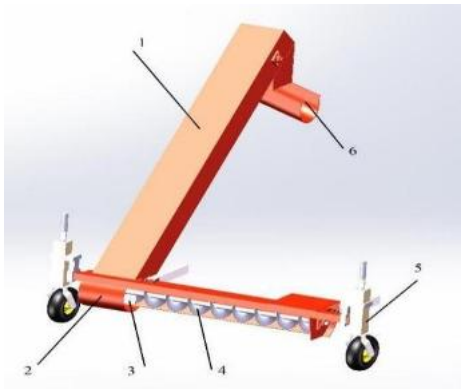


Fig. 2 - Schematic diagram of the soil pickup and lifting unit

1-Soil lifting box; 2-Housing; 3-Soil-lifting baffle; 4-Soil pickup auger; 5-Height adjustment mechanism; 6-Soil discharge chute opening

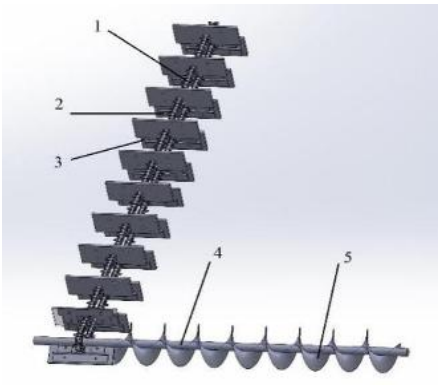


Fig. 3 - Schematic diagram of the soil pickup auger and soil-lifting baffle

1-Chain; 2-Steel plate; 3-Rigid PVC strips; 4-Rotating shaft; 5-Helical blade

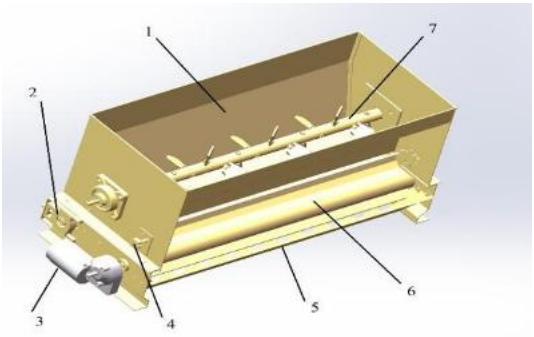


Fig. 4 - Schematic diagram of the soil storage and separation unit

1-Soil storage box; 2-Conveyor belt tensioning mechanism; 3-Brushed DC motor; 4-Soil separation quantity adjustment mechanism; 5-Soil separation baffle; 6-Conveyor belt; 7-Soil separation auger

Analysis of Soil Particle Conveying Characteristics

Soil particles conveyed by the helical blades of the soil separation auger undergo combined axial translation and circumferential rotation. To investigate this motion behavior in detail, the forces acting on individual soil particles and their velocity components during conveying were analyzed using a single-particle analysis method.

Dynamic Analysis

The resultant force F exerted by the helical blade on soil particle P can be decomposed into an axial component F_z along the auger axis and a tangential component F_t. At the same time, particle P is subjected to a normal force F_n from the helical surface and a tangential friction force f_1, as shown in Fig. 5.

Under the combined action of F_t and f_1, P tends to rotate around the auger axis. When F_t is moderate, this rotational tendency is restrained by the combined effects of gravity and the frictional force exerted by the housing. When F_t becomes excessively large, the tendency of particle P to roll increases, thereby reducing the axial conveying efficiency. The force balance of particle P can be expressed by Eq. (1).

$$\begin{cases} F_z = F\cos(\alpha+\beta) \\ F_t = F\sin(\alpha+\beta) \\ f_1 = \mu F_n = F_n \tan\alpha \end{cases} \quad (1)$$

For soil particles to move axially along the auger shaft, the axial driving force must exceed the axial resistance acting on the particles. This condition can be expressed by Eq. (2).

$$\begin{cases} F_n\cos\beta > f_1\sin\beta \\ F_n\cos\beta > F_n\tan\alpha\sin\beta \\ \alpha+\beta < 90^\circ \end{cases} \quad (2)$$

where F is the resultant force exerted by the helical surface on particle P, N; F_n is the normal force exerted by the helical surface N; f_1 is the tangential friction force along the helical surface N; F_z is the axial component of the resultant force along the auger shaft N; F_t is the circumferential component of the resultant force N; α is the friction angle of particle P, °; β is the helix angle of the soil pickup auger °; μ is the sliding friction coefficient between particle P and the helical surface; s is the pitch of the soil pickup auger [mm]; and r is the radial distance from particle P to the auger axis [mm].

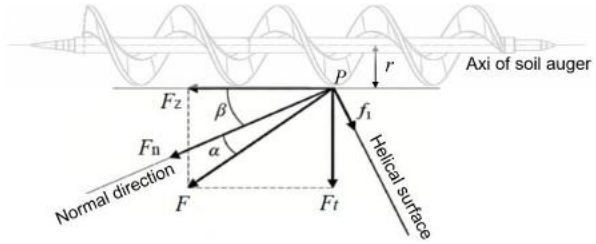


Fig. 5 - Force analysis of a soil particle under the action of the helical blade

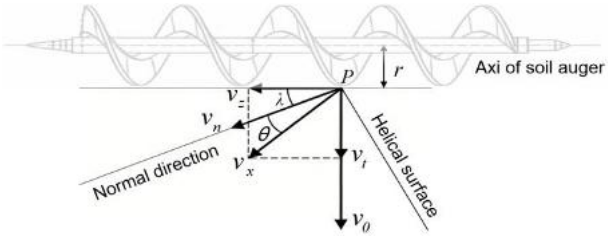


Fig. 6 - Velocity analysis of a soil particle during conveying by the helical blade

Kinematic Analysis

As shown in Fig. 6, the initial velocity of soil particle P is the circumferential velocity V_0 associated with the rotation of the helical blade. If the friction between the particle and the rotating blade is neglected, particle P moves with an absolute velocity V_n along the normal direction of the helical surface. In practice, however, friction causes the actual velocity of particle P to deviate from this direction, resulting in a velocity V_x. This velocity can be decomposed into an axial component V_z along the auger shaft and a circumferential component V_t. The velocity relationships of particle P are given in Eqs. (3) and (4).

$$\begin{cases} V_t = V_x\sin(\alpha+\beta) \\ V_z = V_x\cos(\alpha+\beta) \\ V_0 = wr = \dfrac{2\pi n}{60}r = \dfrac{ns}{60\tan\beta} \\ V_x = \dfrac{V_n}{\cos\alpha} = \dfrac{V_0\sin\beta}{\cos\alpha} = \dfrac{ns\cos\beta}{60\cos\alpha} \end{cases} \quad (3)$$

$$\begin{cases} V_z = \dfrac{ns}{60}(\cos^2\beta - \cos\beta\sin\beta\tan\alpha) \\ V_t = \dfrac{ns}{60}(\cos\beta\sin\beta + \cos^2\beta\tan\alpha) \end{cases} \quad (4)$$

where:

V_x is the actual velocity of particle P considering friction with the rotating blade m/s; V_n is the velocity of particle P along the normal direction of the helical surface m/s; V_0 is the circumferential velocity induced by auger rotation m/s; V_z is the axial velocity component along the auger shaft m/s; V_t is the circumferential velocity component m/s; and n is the rotational speed of the soil pickup auger , rpm.

PERFORMANCE SIMULATION AND OPTIMIZATION OF SOIL PICKUP DEVICE

Transplant Ridge Modeling

Soil samples of 200 g were collected from the ridge surface using the five-point sampling method. The particle size distribution was determined by sieve analysis, showing that particles of 0~1 mm, 1~2 mm, and >2 mm accounted for 70.8%, 14.2%, and 15.0%, respectively. A soil trough of 120 mm (length) × 1250 mm (width) × 200 mm (height) was established in EDEM to simulate the transplanting ridge. To balance simulation efficiency and accuracy, the simulated particle size was set to three times the actual average particle size. Spherical, columnar (three-sphere), and blocky (four-sphere) particles were constructed based on a single sphere with a radius of 3 mm, and generated in the trough according to the measured mass proportions *(Li et al., 2023, He et al., 2024, Huan et al., 2025, Han et al., 2025)*.

Motion Settings for the Soil-Lifting Baffles

A simplified simulation model of the soil pickup and separation device was established in SolidWorks 2022 and imported into EDEM 2023, as shown in Fig. 7. The chain was omitted, and the soil storage unit was simplified as an open box. To simulate the periodic motion of the baffles (*Zhao et al., 2020*), 21 baffles were generated at equal time intervals. Their motion was divided into the following cycle: inclined downward movement → rotation near the auger → inclined upward movement → rotation near the discharge opening → return to the initial position.

Simulation Parameter Settings

The 25s simulation included particle generation and soil filling (0~5.0s), followed by auger rotation and forward movement (5.0~25.0s) with sequential soil lifting. Motion parameters are in Table 1.

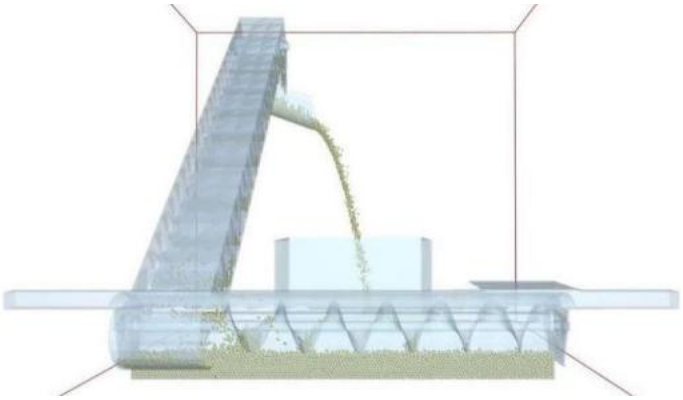


Fig. 7 - EDEM simulation model

Table 1

Motion parameters of the auger shaft and soil-lifting baffles

Auger shaft		Soil lifting baffle	
rotational angular velocity / rad.s^{-1}	13.8	duration of initial inclined descent/s	0.08
forward velocity / m.s^{-1}	0.02	duration of rotation near the auger/s	0.23
		duration of inclined ascent/s	1.56
		duration of rotation near the discharge opening/s	0.23
		duration of return inclined descent/s	1.48
		ascent/descent velocity/m/s	1.2
		rotational angular velocity/rad/s	13.8

Simulation Contact Model and Setting of Material Contact Parameters

Considering the moisture content and cohesiveness of the soil particles, the Hertz–Mindlin with JKR contact model was selected because it can represent the adhesive behavior of moist, cohesive particles under the actual operating conditions of the soil pickup and lifting device (*Han et al., 2023)*. The basic physical property parameters of various materials involved in the study are shown in Table 2, and the contact mechanical property parameters between different materials are presented in Table 3.

Table 2

Physical properties of the materials

Material	Density (kg/m³)	Elastic Modulus (Pa)	Shear Modulus (Pa)	Poisson's Ratio
Soil Particles	1526	2.808×10^{6}	1.080×10^{6}	0.30
Rigid PVC Sheet Strip	1282	1.056×10^{7}	4.000×10^{6}	0.32
Q235 Carbon Steel	7830	7.270×10^{10}	1.963×10^{11}	0.35

Table 3

Contact parameters between materials

Contact pair	Coefficient of Restitution	Coefficient of Static Friction	Coefficient of Rolling Friction
Soil Particles-Soil Particles	0.45	0.89	0.43
Soil Particles-Q235 Carbon Steel	0.20	0.30	0.03
Soil Particles-Rigid PVC Sheet Strip	0.50	0.50	0.01

Parametric Optimization Simulation Test

To obtain the optimal soil pickup and lifting performance of the device, the operating parameters of the soil pickup auger were optimized, including auger rotational speed, soil penetration depth, and pitch.

Optimization Test Design

To investigate the effects and interactions of the operating parameters of the soil pickup auger, a three-factor, three-level Box-Behnken response surface simulation design was conducted. The coded levels of the experimental factors are presented in Table 4.

Table 4

Coded levels of the experimental factors

Coded level	Test Factor		
	Rotational Speed X_1 (r.min^{-1})	Soil Penetration Depth X_2 (mm)	Pitch X_3 (mm)
-1	90	30	130
0	110	40	150
1	130	50	170

Evaluation Indexes of Optimization Test

The evaluation indices used in the optimization test were the soil lifting quantity, Y_1, and the coefficient of variation of the soil lifting quantity, Y_2. These indices were calculated using Eq. (5).

$$\begin{cases} Y_1 = \dfrac{\sum_{i=1}^{m} x_i}{\phi} \\ Y_2 = \dfrac{\sigma}{Y_1}\times 100\% \\ \sigma = \sqrt{\dfrac{\sum_{i=1}^{m}(x_i - Y_1)^2}{\phi - 1}} \end{cases} \quad (5)$$

where x_1 is the mass of soil in the soil storage box at the i-th measurement kg; ϕ is the number of measurements; σ is the standard deviation of the soil mass in the soil storage box during the simulation; Y_1 is the soil lifting quantity kg; and Y_2 is the coefficient of variation of the soil lifting quantity, %.

RESULTS

Results of Optimization Test

The simulation results of the optimization experiments are presented in Table 5, where X_1 and X_2 represent the coded values of the experimental factors. Multivariate regression fitting and analysis of variance (ANOVA) were conducted on the simulation results of the optimization experiments using Design-Expert 12.0 software, with the results shown in Table 6. The P-values of all models were less than 0.05, indicating that the models were significant and the ANOVA results had high reliability. In addition, the P-values of the lack-of-fit terms were all greater than 0.05, meaning the lack-of-fit terms were not significant and the ANOVA results had

a high degree of fitting. For the response surface model of soil lifting quantity, Y_1, the terms X_1, X_2, X_1X_2, X_1X_3, X_2^2 and X_3^2 had highly significant effects on the response, while X_3 and X_2X_3 had significant effects. For the response surface model of the coefficient of variation of soil lifting quantity Y_2, the terms X_1, X_2, X_3, X_1X_2, X_1X_3 and X_1^2 had highly significant effects, and X_3^2 had a significant effect.

Table 5

Box-Behnken design and simulation results

Serial Number	Test Factor			Evaluation Index	
	X_1	X_2	X_3	Y_1/kg	Y_2/%
1	-1	-1	0	2.73	1.16%
2	1	-1	0	4.31	1.77%
3	-1	1	0	4.85	1.27%
4	1	1	0	5.51	1.42%
5	-1	0	-1	4.05	1.30%
6	1	0	-1	4.52	1.85%
7	-1	0	1	3.52	1.17%
8	1	0	1	4.93	1.44%
9	0	-1	-1	3.78	1.72%
10	0	1	-1	5.65	1.55%
11	0	-1	1	3.75	1.46%
12	0	1	1	5.17	1.44%
13	0	0	0	4.18	1.50%
14	0	0	0	4.28	1.52%
15	0	0	0	4.13	1.44%
16	0	0	0	4.19	1.50%
17	0	0	0	4.23	1.49%

Table 6

ANOVA for the response surface models

Source of Variance	Soil Lifting Quantity				Coefficient of Variation of Soil Lifting Quantity			
	SS	df	F-Value	P-Value	SS	df	F-Value	P-Value
Model	8.49	9	137.48	< 0.0001**	0.0231	1	20.29	0.0028**
X_1	2.12	1	309.40	< 0.0001**	0.1035	1	90.86	< 0.0001**
X_2	5.46	1	796.39	< 0.0001**	0.0529	1	46.43	0.0002**
X_3	0.0496	1	7.23	0.0311*	0.0196	1	17.20	0.0043**
X_1X_2	0.2116	1	30.86	0.0009**	0.0056	1	4.94	0.0617
X_1X_3	0.2209	1	32.21	0.0008**	0.0370	1	32.48	0.0007**
X_2X_3	0.0506	1	7.38	0.0299*	0.0003	1	0.2830	0.6112
X_1^2	0.0358	1	5.22	0.0562	0.0081	1	7.07	0.0325*
X_2^2	0.2430	1	35.44	0.0006**	0.0231	1	20.29	0.0028**
X_3^2	0.0888	1	12.95	0.0088**	0.1035	1	90.86	< 0.0001**
Residual	0.0480	7			0.0080	7		
Lack of Fit	0.0353	3	3.71	0.1187	0.0044	3	1.62	0.3185
Pure error	0.0127	4			0.0036	4		
Total	8.53	16			0.5683	16		

Note: **: P<0.01 (indicates a highly significant effect); *: P<0.05 (indicates a significant effect); no symbol: *P*>0.05 (indicates not significant).

With the model significance guaranteed and the lack-of-fit terms confirmed to be non-significant, the non-significant terms for the response were eliminated, and the optimized regression equations for soil lifting quantity Y_1 and the coefficient of variation of soil lifting quantity Y_2 were obtained as follows:

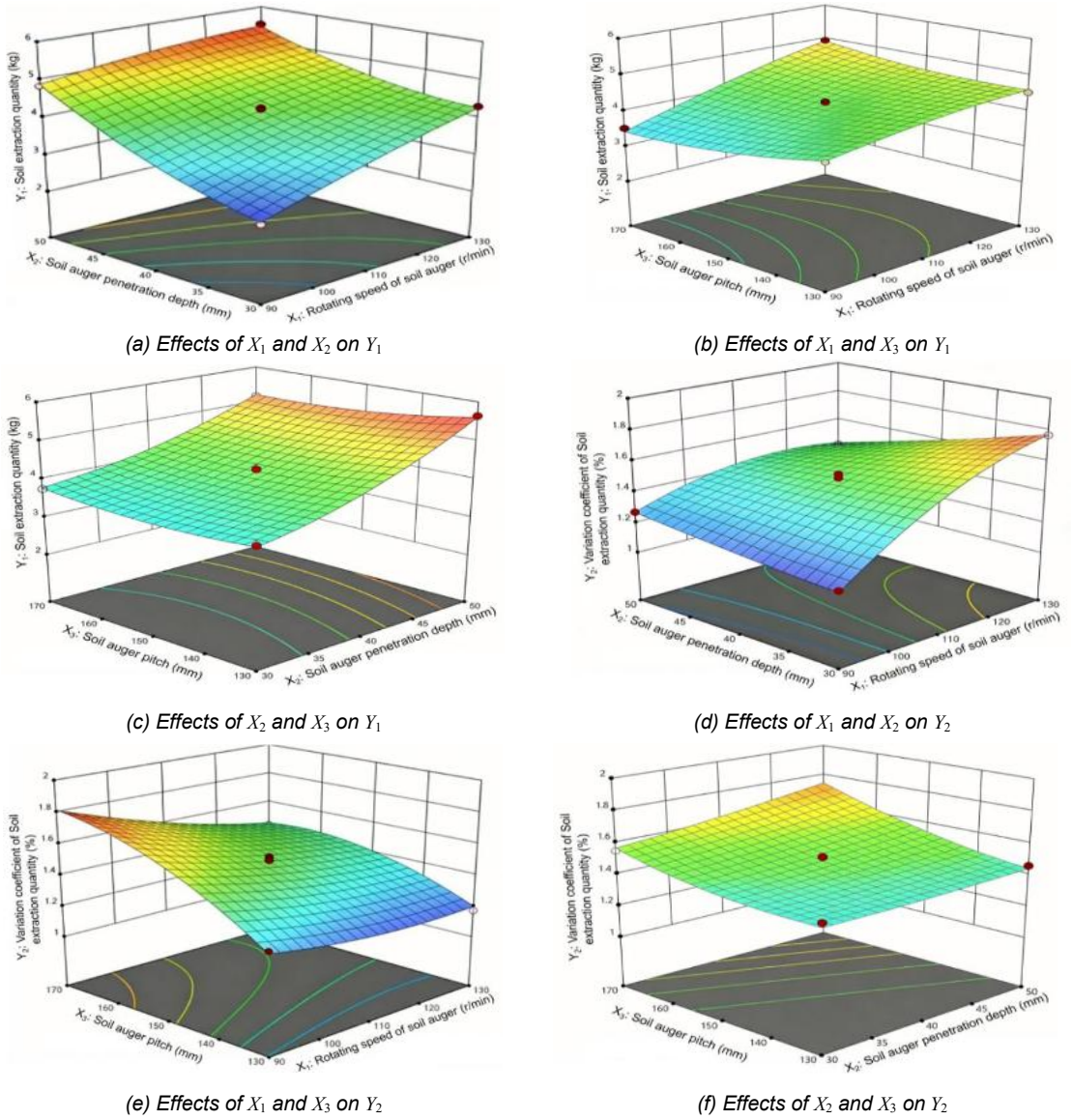
$$Y_1 = 7.70 + 0.5150x_1 + 0.8263x_2 - 0.0788x_3 - 0.2300x_1x_2 + 0.2350x_1x_3 - 0.1125x_2x_3 + 0.2402x_2^2 + 0.1453x_3^2 \quad (6)$$

$$Y_2 = 1.49 + 0.1975x_1 - 0.0538x_2 - 0.1138x_3 - 0.1150x_1x_2 - 0.0700x_1x_3 - 0.0937x_1^2 + 0.0437x_3^2 \quad (7)$$

The results of analysis of variance (ANOVA) indicated that the coefficients of determination (R_1^2=0.9944, R_2^2=0.9860) and adjusted coefficients of determination (R_1^2adj=0.9871, R_2^2adj=0.9679) of the fitted models all approached 1.00, which demonstrated that the regression models possessed an extremely high fitting accuracy and strong correlation.

Interaction Analysis of the Regression Models

To investigate the effects of the interaction between the experimental factors on the soil lifting quantity Y_1 and its coefficient of variation Y_2, response surface analysis was performed on the ANOVA results of the optimization experiments via Design-Expert 12, as shown in Fig. 8.



(a) Effects of X_1 and X_2 on Y_1

(b) Effects of X_1 and X_3 on Y_1

(c) Effects of X_2 and X_3 on Y_1

(d) Effects of X_1 and X_2 on Y_2

(e) Effects of X_1 and X_3 on Y_2

(f) Effects of X_2 and X_3 on Y_2

Fig. 8 - Effects of the experimental factors on soil lifting quantity and its coefficient of variation

As shown in Fig. 8(a), Y_1 increased gradually with increasing rotational speed and increased sharply with increasing soil penetration depth, indicating that soil penetration depth had the greater effect. As shown in Fig. 8(b), Y_1 increased continuously with increasing rotational speed, while changes in pitch had only a slight effect, indicating that rotational speed was the more influential factor. As shown in Fig. 8(c), Y_1 increased markedly with increasing soil penetration depth and changed only slightly with pitch, confirming that soil penetration depth had the greater effect. As shown in Fig. 8(d), Y_2 increased sharply with increasing rotational speed but only gradually with increasing soil penetration depth, indicating that rotational speed had the stronger effect. As shown in Fig. 8(e), Y_2 increased rapidly with increasing rotational speed and remained nearly unchanged with changes in pitch, indicating that rotational speed was the dominant factor.

As shown in Fig. 8(f), Y_2 decreased gradually with increasing soil penetration depth and also decreased with increasing pitch, indicating that soil penetration depth had the greater influence. Overall, the response surface analysis indicates that the interaction between rotational speed and soil penetration depth has an important effect on soil lifting performance, which is consistent with the ANOVA results.

Optimal Parameter Combination

To ensure that the soil lifting quantity met the requirements of practical operation while maximizing the stability of the soil lifting process, the operating parameters were optimized. The optimal parameter combination was an auger rotational speed of 116 rpm, a soil penetration depth of 40 mm, and a pitch of 150 mm. Three repeated simulation validation tests were conducted, and the mean values were used to evaluate the optimization results. The resulting soil lifting quantity, Y_1, was 4.26 kg, and the coefficient of variation of soil lifting quantity, Y_2, was 1.50%. These values were in good agreement with the predicted optimization results.

FIELD TRIALS

Test Conditions

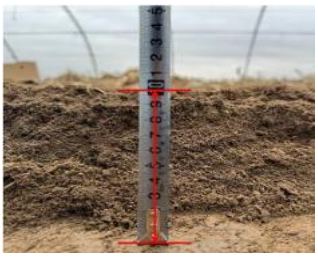
The field trials were conducted at the experimental field of Rongliang Ecological Agriculture Co., Ltd. in Heishan County. A laser tachometer was used to adjust the auger rotational speed, an electronic balance was used to measure the soil lifting quantity, and a tape measure was used to evaluate ridge flatness. The field test procedure is shown in Fig. 9(a).



(a) Soil Pickup Process



(b) Selection of Measurement Sections



(c)Surface Levelness Measurement

Fig. 9 - Field test

Test Methods and Content

The experimental design methodology and measurement procedures were based on the preceding simulation tests and relevant literature. To enhance the reliability of field trial data and comprehensively evaluate the performance of the soil pickup device, which the surface levelness Y_3 was measured. Manual measurement methods were employed, with a tape measure used to select one measurement section every 3 meters along the transplanted ridges. The vertical distance from the surface of randomly sampled points, which each measurement section to the reference plane was measured, it is shown in Figs. 9(b) and 9(c).

The primary evaluation metrics for the tests include soil lifting quantity, coefficient of variation for soil lifting quantity, and surface levelness. Each test group was replicated three times, with calculations performed according to Equations (8).

$$Y_3 = \sqrt{\frac{\sum_{j=1}^{n}(a_{kj}-a_k)^2}{n_k-1}} \tag{8}$$

where n_k represents number of test points in the k-th measurement; a_{kj} represents measure the vertical distance from the ground surface to the horizontal reference line before and after the k-th measurement at the j-th equidistant point, mm; a_k represents vertical distance from the ground surface to the horizontal reference line before and after the k-th soil pickup operation, mm; Y_3 represents surface levelness, mm.

Experimental Results and Analysis

Three suboptimal parameter combinations closely resembling the optimal operating parameter combination were selected from Table 5. Each combination underwent three replicate trials, with results averaged. The field trial outcomes are presented in Table 7.

Table 7

Field experiment results

Group Number	Rotational speed	Soil penetration depth	Pitch	Soil lifting quantity/ kg	Coefficient of variation of soil lifting quantity/ %	Surface levelness / mm
1	130	30	150	4.35	1.82	110
2	90	50	150	5.03	1.55	90
3	130	40	130	4.66	1.61	100
4	116	40	150	4.13	1.44	100

The field test results showed that, under the optimal operating parameter combination determined from the simulation, the soil lifting quantity, Y_1, was 4.13 kg and the coefficient of variation of soil lifting quantity, Y_2, was 1.44%. Compared with the simulation results, the relative errors were only 3.05% and 4.00%, respectively. Under the same parameter combination, the surface levelness, Y_3, was approximately 100 mm. The close agreement between the field test and simulation results verifies the accuracy and reliability of the numerical simulation model.

CONCLUSIONS

A soil pickup and separation device for an automatic flower transplanter was designed in this study. The structural parameters of the key components were determined, and the soil-conveying characteristics of the helical blades of the soil pickup auger were analyzed.

Through parameter optimization based on simulation, the optimal operating parameters were determined as follows: auger rotational speed of 116 rpm, soil penetration depth of 40 mm, and pitch of 150 mm. Under these conditions, the simulated soil lifting quantity, Y_1, was 4.26 kg, and the coefficient of variation of soil lifting quantity, Y_2, was 1.50%.

Field tests conducted under the optimal operating conditions yielded a soil lifting quantity of 4.13 kg and a coefficient of variation of 1.44%. The relative errors compared with the simulation results were 3.05% and 4.00%, respectively. The measured surface levelness, Y_3, was approximately 100 mm. The close agreement between the simulation and field test results indicates that the structural design and numerical model are reliable. The device can meet the soil-handling requirements of automatic flower transplanting operations and provides a basis for its further application in greenhouse production.

ACKNOWLEDGEMENT

This research was supported by Liaoning Provincial Department of Agriculture and Rural Affairs - “Xingliao Talent Program” Agricultural Expert Project (Grant No. XLYC2413011).

REFERENCES

[1] Bulgakov, V., Kaletnik H., Trokhaniak O., Lutkovska S., Klendii M., Ivanovs S., Popa L., Yaropud V. (2023). Investigation of the Energy Indicators for the Surface Treatment of Soil by a Harrow with a Screw-Type Working Body. *INMATEH--Agricultural Engineering*, 71(3), 818-833. DOI: 10.35633/inmateh-71-72.

[2] Cheng, T., Wang, J., Zheng, T., & Zhang, Q. (2023). From "Mother of Gardens" to "Beautiful China" (从“花园之母”到“美丽中国”). *Chinese Landscape Architecture*, 39 (6), 107-113.

[3] Feng, X., Chen, L., Li, M., & Xiang, J. (2022). Design and Test of Potato Soil Separation Device Based on Potato Harvester (基于土豆收获机的土壤分离装置的设计与测试). *ACM International Conference Proceeding Series*, 135-142.

[4] Gu, Z. (2025). China's seedling and flower enterprises achieve an annual output value exceeding 520 billion yuan (中国种苗花卉企业年产值超 5200 亿元). *People's Daily*, 03-22 (002).

[5] Han, D., Hu, J., Liu, H., Ren, L., Zhou, M., Yang, Q., Li, B., & Chen, X. (2025). Parameter calibration and experiment of the discrete element contact model of water-containing sandy soil particles (含水砂土颗粒离散元接触模型的参数校准与实验). *Nongye Gongcheng Xuebao/Transactions of the Chinese Society of Agricultural Engineering*, 41(8), 70-78. DOI: 10.11975/j.issn.1002-6819.202407112.

[6] He, L., Jiang, J., Li J., Zhang, F., Yi, S., Zheng, Y., & Lv, Q. (2023). Design and test of seedling pot filling and hole punching processing line for citrus (柑橘育苗钵装填成穴生产线的设计与试验). *Journal of Southwest University (Natural Science Edition)*, 45 (5), 108-121. DOI: 10.13718/j.cnki.xdzk.2023.05.011.

[7] He, X., Ma, S., Liu, Z., Wang, D., Shang, S., Li, G., & Li, H. (2024). Calibration and testing of saline soil parameters based on EDEM discrete element methodology (基于 EDEM 离散元方法的盐碱土壤参数标定与测试). *INMATEH - Agricultural Engineering*, 73(2), 822-833. DOI: 10.35633/inmateh-73-69.

[8] Hu, J., Liu, Y., Liu, W., et al. (2022). Experiment on Combined Seedling Picking Device with Top Clamping and Pulling (蔬菜自动移栽机顶夹拔组合式取苗装置试验研究). *Transactions of the Chinese Society for Agricultural Machinery*, v53, p110-117. DOI: 10.6041/j.issn.1000-1298.2022.S1.013.

[9] Huan, X., Feng, M., Wu, C., Jia, J., & Chen, J. (2025). Construction and Experiment of Discrete Element Model for Tea Garden Soil-Organic Fertilizer Mixture Based on EDEM (基于 EDEM 的茶园土壤-有机肥混合物离散元模型的构建与试验). *Nongye Jixie Xuebao / Transactions of the Chinese Society for Agricultural Machinery*, 56(12), 267-278. DOI: 10.60465/j.issn.1000-1298.2025.12.024.

[10] Ji, D., Hu, X., Zhe, X., Bia, X., Gong, Y., & Tian, S. (2022). Design and experiment of double row transplanting manipulator linkage high speed transplanting device (双排移栽机械手联动式高速移栽装置设计与试验). *Transactions of the Chinese Society for Agricultural Machinery*, 52 (12), 126-133, 146. DOI:10.6041/j.issn.1000-1298.2022.12.012.

[11] Li, B., & Gao, G. (2019). Research on parameter optimization of potato soil transportation separation mechanism (土豆土壤运输分离机构参数优化研究). *Proceedings - 2019 2nd World Conference on Mechanical Engineering and Intelligent Manufacturing*, WCMEIM 2019, 147-150.

[12] Li, S., Diao, P., Zhao, Y., Miao, H., Li, X., & Zhao, H. (2023). Calibration of discrete element parameter of soil in high-speed tillage (高速耕作条件下土壤离散元标定). *INMATEH - Agricultural Engineering*, 71(3), 248-258. DOI: 10.35633/inmateh-71-21.

[13] Minglani, D., Sharma, A., Pandey, H., Dayal, R., & Joshi, J. (2021). Analysis of flow behavior of size distributed spherical particles in screw feeder. *Powder Technology*, v382, p1-22. DOI: 10.1016/j.powtec.2020.12.041.

[14] Tian, S., Hu, X., Xie, T., Zhe, X., Li, B. & Sun, Z. (2022). Design and experimental study on automatic separation device for multiple stacked seeding bowls (多组叠摞营养钵同时自动分离装置设计与试验). *Journal of Shenyang Agricultural University*, 53 (01),103-109. DOI: 10.3969/j.issn.1000-1700.2022.01.013.

[15] Tian S., Xie, T., Wang H., Zhang, X., Zhang, K., Bai, X., & Sun, Z. (2023). Design and experiment of adjustable seedling-feeding device for vegetable transplanting machine (蔬菜移栽机可调式喂苗装置设计与试验). *Journal of South China Agricultural University*, 44 (3), 464-472. DOI: 10.7671/j.issn.1001-411X.202205012.

[16] Tong, J., Shang, K., Wang, X., Sun, L., Zhang, N., NORUPIRI, R., & Man, S. (2024). Design and Test of Spiral Rejection Mechanism for Inferior Bowl Seedlings (温室穴盘育苗劣质钵苗螺旋式剔除机构设计与试验). *Transactions of the Chinese Society for Agricultural Machinery*, 55 (9), 129-137. DOI: 10.60465/j.issn.1000-1298.2024.09.013.

[17] Xu, Q., Li, S., Zhang, Y., Meng, L., Lu, H., & Xie, L. (2020). Design and test of seedling pot filling and transporting machine for citrus (柑橘育苗钵装填转运机设计与试验). *Transactions of the CSAE*, 36 (18), 66-72. DOI: 10.11975/j.issn.1002-6819.2020.18.009.

[18] Zhao, R., Guo, L., Gao, W., & Xiao, X. (2022). Structure Optimization Design of Screw Conveyor based on EDEM (基于 EDEM 的螺旋输送机结构优化). *Journal of Physics: Conference Series*, 2200(1). DOI: 10.1088/1742-6596/2200/1/012002.

[19] Zhao, X., Guo, J., Li, K., Dai, L., & Chen, J. (2020). Optimal design and experiment of 2-DoF five-bar mechanism for flower seedling transplanting (花卉苗移栽二自由度五杆机构的优化设计与试验). *Computers and Electronics in Agriculture*, 178, 105746. DOI:10.1016/j.compag.2020.105746.

[20] Zhao, X., Zhang, X., Wu, Q., Dai, L., & Chen, J. (2020). Research and experiment of a novel flower transplanting device using hybrid-driven mechanism (基于混合驱动机构的新型花卉移栽装置研究与试验). *International Journal of Agricultural and Biological Engineering*,13 (2), 92-100. DOI: 10.25165/j.ijabe.20201302.5187.

[21] Zhou, M., Xu, J., Tong, J., Yu, G., Zhao, X., & Xie, J. (2018). Design and experiment of integrated automatic transplanting mechanism for taking and planting of flower plug seedlings (花卉穴盘苗取栽一体式自动移栽机构设计与试验). *Transactions of the CSAE*, 34 (20), 44-51. DOI: 10.11975/j.issn.1002-6819.2018.20.006.

KINEMATICS OF A ROTARY TILLER EQUIPPED WITH A TURNING MECHANISM FOR TREE-TRUNK BYPASS

/

ՇՐՋԱԴԱՐՁԱՅԻՆ ՄԵԽԱՆԻԶՄՈՎ ՀՈՂԱՄՇԱԿ ՖՐԵԶԻ ԿԻՆԵՄԱՏԻԿԱՆ ԾԱՌԱԲՆԵՐԻ ՇՐՋԱՆՑՄԱՆ ԺԱՄԱՆԱԿ

Albert GRIGORYAN, Artur ALTUNYAN*), Seryozha PAPYAN, Arman SIMONYAN, Aram MAZMANYAN, Arshaluys TARVERDYAN

Scientific Research Institute for Agricultural Mechanization and Automation, Armenian National Agrarian University, Yerevan, Armenia

Tel: +37455327325; E-mail: arturaltunyan@gmail.com

Corresponding author: Artur Altunyan

DOI: https://doi.org/10.35633/inmateh-79-100

Keywords: *rotary tiller, near-trunk zone, bypass kinematics, protection zone, untreated area, motion trajectory.*

ABSTRACT

To prevent mechanical damage to tree trunks during cultivation of orchard inter-row and near-trunk areas, agrotechnical requirements prescribe leaving a certain uncultivated soil area around each trunk as a plant protection zone. When the working unit is periodically displaced relative to the tree-row axis by forced motion, an additional untreated soil area remains outside the plant protection zone. Its size is influenced by several factors, including the diameters of the rotary tiller and tree trunk, the lengths of the swing arm carrying the tiller and the sensing probe that actuates the hydraulic system, the tractor travel speed, and the piston-rod velocities of the hydraulic cylinder. Among these factors, the present study considers the principal kinematic factor: the influence of the backward motion of the hydraulic-cylinder piston rod toward the inter-row space and its forward motion toward the tree row, which provide and regulate the transverse displacement of the tiller relative to the tree-row axis, on the size of the untreated soil area. Using a grapho-analytical method for drive mechanism analysis, the equations of motion of the vertical-axis rotary tiller during tree-trunk bypass were derived for the backward motion of the hydraulic-cylinder piston toward the inter-row space and the forward motion toward the tree row. The resulting motion trajectories are cycloids. To characterize them, the concept of a bypass kinematic parameter was introduced: $\Lambda = V_c/V_m$, representing the ratio of the circumferential velocity of the tiller's transverse-radial motion to the tractor forward velocity. The size, shape, and position of the untreated soil area outside the plant protection zone relative to the tree trunk are determined by the value of the bypass kinematic parameter, which, for a given tractor speed, depends on the backward and forward velocities of the hydraulic-cylinder piston rod. It was established that, for given structural and kinematic parameters of the tillage machine, regulating the volume of oil supplied to the hydraulic cylinder makes it possible to minimize the untreated soil area outside the plant protection zone around the tree trunk.

ԱՄՓՈՓԱԳԻՐ

Պտղատու այգիներում միջբնային և մերձբնային տարածությունների մշակման ընթացքում ծառաբների մեխանիկական վնասումը բացառելու նպատակով, ագրոտեխնիկական պայմաններով նախատեսված դրանց շուրջ թողնվում է որոշակի չափով անմշակ հողատարածք (բուսապաշտպան գոտի): Ծառաշարքի առանցքի նկատմամբ աշխատանքային օրգանի պարբերական տեղաշարժը հարկադրական իրականացնելու դեպքում բուսապաշտպան գոտուց դուրս մնում է որոշ չափի չմշակված հողամակերես: Դրա մեծության վրա ազդում են մի շարք գործոններ. ֆրեզի և ծառաբնի տրամագծերը, ֆրեզը տեղափոխող շարժաթևի և հիդրոհամակարգի գործարկման ազդանշանային շոշափոցի երկարությունները, տրակտորի արագությունը, հիդրոգլանի մխոցակոթի շարժման արագությունները: Նշված գործոններից դիտարկվել է հիմնական կինեմատիկական գործոնը՝ ծառաշարքի առանցքի նկատմամբ ֆրեզի լայնական տեղափոխություններն ապահովող և կարգավորող հիդրոգլանի մխոցակոթի հետընթաց (դեպի միջշարք) և առաջընթաց (դեպի ծառաշարք) շարժումների արագությունների ազդեցությունը չմշակված հողամակերեսի մեծության վրա:

Շարժաբեր մեխանիզմի գրաֆո-անալիտիկական վերլուծության եղանակով ստացվել են ծառաբների շրջանցման ընթացքում ուղղաձիգ առանցքով հողամշակ ֆրեզի շարժման հավասարումները հիդրոգլանի մխոցի հետընթաց (դեպի միջշարք) և առաջընթաց (դեպի ծառաշարք) շարժումների դեպքում: Շարժման հետագծերն իրենցից ներկայացնում են ցիկլոիդաներ, որոնց բնութագրման համար ներմուծել ենք շրջանցման կինեմատիկական պարամետր հասկացությունը՝ $\Lambda = V_c/V_m$, որն իրենից ներկայացնում է ֆրեզի լայնակի-շառավղային շարժման շրջագծային և տրակտորի համընթաց շարժման արագությունների հարաբերությունը: Բուսապաշտպան գոտուց դուրս չմշակված հողամակերեսի չափը, տեսքը և ծառաբնի նկատմամբ դիրքը պայմանավորված են շրջանցման կինեմատիկական պարամետրի արժեքներով, որը՝ տրակտորի տրված արագության դեպքում, կախված է հիդրոգլանի մխոցակոթի հետընթաց և առաջընթաց շարժումների արագություններից: Սահմանվել է, որ հողամշակ մեքենայի կառուցվածքային և կինեմատիկական տրված պարամետրերի դեպքում հիդրոգլան մղվող յուղի ծավալի կարգավորման միջոցով կարելի է ապահովել ծառաբնի շուրջ բուսապաշտպան գոտուց դուրս անմշակ հողամակերեսի նվազագույն մեծություն:

INTRODUCTION

The technological process of soil cultivation in the near-trunk and inter-trunk zones of orchards plays an important role in increasing fruit yield, its primary objectives being weed control and loosening of the upper soil layers *(Cabrera-Pérez et al., 2022; Manzone et al., 2020; Hanson et al., 2016).*

Despite the existence of various weed-control methods — including thermal, chemical, laser, and other techniques — mechanical weed control remains the most widely applied approach at present. This method is environmentally friendly, sustainable, and effective; it improves soil aeration and increases crop productivity, which explains its widespread application in horticulture *(Morin, 2020; Gagliardi et al., 2023; Gagliardi et al., 2024; Zawada et al., 2023; Parasca et al., 2024; Liu et al., 2023; Pergher et al., 2019)*.

It should be noted that one of the most important agrotechnical requirements for mechanical orchard maintenance is to prevent damage to the tree trunk and root system by the working unit during near-trunk cultivation. In particular, the risk of uprooting the tree must be completely eliminated (*Manayenkon et al., 2017*). To meet this requirement, a prescribed uncultivated area is maintained around the tree trunk, referred to as the *plant protection zone* (Fig. 1).

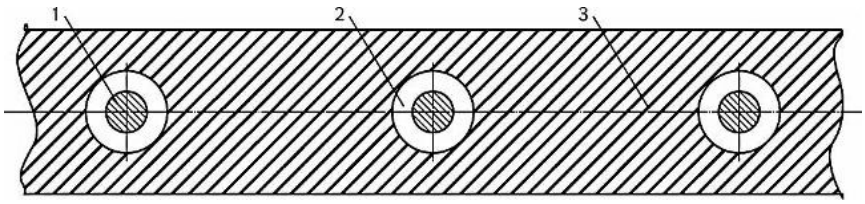


Fig. 1- Schematic representation of the inter-trunk and near-trunk cultivation areas in accordance with agrotechnical requirements

1- tree trunk, 2- plant protection zone, 3- cultivated area.

To implement the above-mentioned process, various types of tillage equipment operating on different principles may be used, including rotary tillers, harrows, sweep blades, and cultivators *(Kostandinov et al., 2016)*. Regardless of the tillage method and the type of technical equipment employed, the working units must be capable of performing periodic transverse displacements relative to the tree-row axis.

Among modern orchard tillage machines, rotary tiller units equipped with a turning section and a working body with a vertical axis of rotation have recently become widely used *(Rzaliev et al., 2025)*. As a rule, these machines cultivate both the inter-trunk and near-trunk zones in a single pass. Operational practice and experimental studies of currently used rotary tiller machines demonstrate that, during the cultivation of inter-trunk and near-trunk zones, an untreated soil area remains between the plant protection zone and the area cultivated by the working unit while bypassing the tree trunk *(Papyan & Harutyunyan, 2024; Inter-Row Machine, EP 3 824 708 A1, 2021; Wang et al., 2023)*.

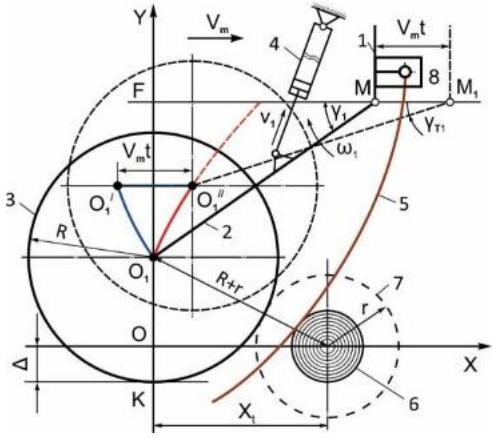
The objective of this study is to determine a trajectory of rotary tiller motion during tree-trunk bypass that prevents the tiller from entering the plant protection zone while simultaneously ensuring a minimum distance between the tiller contour and the plant protection zone boundary. It is evident that such an approach will also ensure the minimum possible area of untreated soil remaining outside the plant protection zone.

MATERIALS AND METHODS

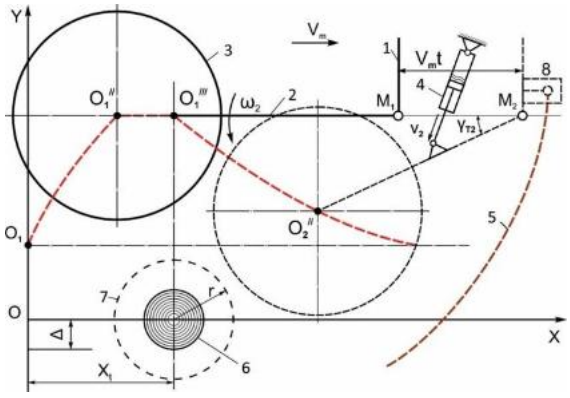
The object of the study was a rotary tiller machine with a vertical axis of rotation, intended for the cultivation of near-trunk and inter-trunk zones in intensive orchards and vineyards, was selected. Its structural and design schemes are presented in Fig. 2 a, b. According to the classification of automatic control systems, the machine may be categorized as an *astatic indirect-action system*, in which the automatic control system maintains the prescribed parameter independently of the magnitude of external disturbances. In the present case, there is no static correspondence between the mutual positions of the working unit and the sensing probe, while the extreme positions of the working unit are determined either by the full stroke of the hydraulic-cylinder piston or by external limiters.

The developed rotary tiller machine consists of a transverse frame (1), a swing arm rotating in the radial direction (2) mounted on the frame by means of a hinge joint, a rotary tiller with a vertical axis of rotation (3) fixed to the swing arm, a hydraulic cylinder (4) actuating the swing arm, the sensing probe (5) mounted on the frame, and an inductive sensor assembly (8).

The operating principle of the rotary tiller machine is as follows. Prior to contact with a tree trunk, the hydraulic cylinder (4) is in its extended (open) position, while the rotary tiller (3) mounted on the swing arm is located within the tree row. In order to ensure overlap between successive passes during field operation, the contour of the tiller is laterally offset from the tree-row axis by a value Δ (Fig. 2a,b).



a)



b)

Fig. 2- Schematics for deriving the equations of motion of the center of the vertical-axis rotary tiller during tree-trunk bypass:

a) backward motion of the hydraulic-cylinder piston; b) forward motion of the hydraulic-cylinder piston

The bypass of the tree trunk by the tiller is conventionally divided into two stages. Stage 1**:** from the moment the signal probe contacts the tree trunk until the end of contact and stage 2: after the probe–trunk contact is terminated, when the tiller, in the free state of the probe, returns again into the tree row. In the first stage, the signal probe (5), mounted on the frame (1), upon encountering the tree trunk (6), rotates and, via inductive sensors, transmits a signal to the electromagnetic hydraulic distributor. Due to the change in the position of the distributor spool, the direction of the oil flow supplied to the hydraulic cylinder is reversed. As a result, the piston of the hydraulic cylinder moves backward, and through the rotation of the swing arm about point M, the tiller is withdrawn from the tree row (Fig. 2a). In the second stage, when the contact between the probe and the tree trunk ceases, the probe returns to its initial position under the action of a spring. A reverse signal is transmitted from the inductive sensor to the hydraulic distributor, and the forward movement of the hydraulic-cylinder piston causes the tiller to re-enter the tree row (Fig. 2b).

During tree-trunk bypass, the turning section of the rotary tiller machine performs a complex motion, consisting of a rotation about point M with radius $L = |O_1M|$ and a translational motion with velocity V_m in the direction of tractor forward motion.

For deriving the equations of motion of the tiller center, the coordinate system is defined such that the X-axis is aligned with the longitudinal direction of the tree row, while the ordinate axis passes through the initial position of the tiller center O_1 .

During the withdrawal phase from the tree row (first stage), over a time interval t_1, the center O_1 of the tiller rotates about point M from its initial position by an angle of $\gamma_1 - \gamma_{т1}$. As a result, point O_1 moves to position O_1'. However, since during the same time interval t_1 the translational motion of the tractor with velocity V_m also occurs, point O_1' is further displaced by a distance $V_m t_1$ in the direction of motion, reaching position O_1'' . The coordinates of point O_1'' can be written as:

$$\begin{cases} x_1 = V_m t_1 + L(cos\gamma_1 - cos\gamma_{т1}) \\ y_1 = R - \Delta + L(sin\gamma_1 - sin\gamma_{т1}), \end{cases} \quad (1)$$

where:

V_m is the tractor forward (translational) velocity, $[m/s]$; t_1-is the time interval during which the tiller center O_1 rotates about point M through the angle $\gamma_1 - \gamma_{т1}$; $[s]$; γ_1-is the initial installation angle of the tiller relative to the direction of machine motion $(\angle O_1MF)$, $[deg]$; $\gamma_{т1}$ is the current bypass angle $(\angle O_1''M_1F)$, $\left(\gamma_{т1} \in [\gamma_1,\ 0]\middle|\begin{matrix}\gamma_{т1}^{max} = \gamma_1 \\ \gamma_{т1}^{min} = 0\end{matrix}\right)$, $[deg]$; L is the length of the swing arm of the tiller $(|O_1M|)$, $[m]$; R is the radius of the tiller, $[m]$; Δ is the overlap width/value between adjacent passes of the tiller, $[m]$.

At the end of the first stage of bypass, the position of the tiller relative to the tree trunk is determined by the length of the sensing probe. In the case of a long probe, the tiller begins entering the inter-tree zone relatively late, thereby increasing the area of untreated soil around the tree trunk. Conversely, if the probe is excessively short, the risk of the tiller entering the plant protection zone and damaging the tree trunks increases.

Assume that the first stage of tree-trunk bypass ends when the centers of the tiller and the tree trunk lie on the same line, i.e., when the contact between the tree trunk and the sensing probe terminates. This means that the extreme point of the probe will also be located on the line connecting the centers of the tree trunk and the tiller. Depending on the kinematic parameters of the technological process, situations may arise in which, after the tiller center O_1 has rotated through a prescribed angle about point M, contact between the probe and the tree trunk is still maintained. In this case, the tiller continues only its translational motion along the segment $|O_1''O_1'''||$ (Fig. 2b). Starting from point O$_1$"", the second stage of bypass begins through the forward motion of the hydraulic-cylinder piston, and the tiller is displaced back toward the tree row (Fig. 2b).

For the specified section, $|O_1'''O_2''|$, the equations of the tiller motion may be written in the following form:

$$\begin{cases} x_2 = x_1^{max} + V_m\ t_2 + L\left(cos_{\gamma_{т1}}^{min} - cos\gamma_{т2}\right) \\ y_2 = R - \Delta + L(sin\gamma_1 - sin\gamma_{т2}), \end{cases} \quad (2)$$

where: x_1^{max} is the abscissa of the tiller center at the end of the first stage of bypass, $[m]$; t_2 is the duration of the second stage of bypass, $[s]$; $\gamma_{т2}$ is the current bypass angle of the tiller during its motion toward the tree row $(\angle O_2''M_2F)$; $\left(\gamma_{т2} \in [0,\ \gamma_1,]\middle|\begin{matrix}\gamma_{т2}^{max} = \gamma_1 \\ \gamma_{т2}^{min} = 0\end{matrix}\right)$, $[deg]$;.

The actuation mechanism of the swing arm of the rotary tiller machine may be represented as a slotted-link mechanism with one degree of freedom, in which the rotation of the swing arm of length $L = |MO_1|$ about point M is determined by the variation of the distance $S = |DB|$ (forward and backward motions of the hydraulic-cylinder piston) *(Artobolevkiy, 1988; Smirnov, 2014)* (Fig. 3).

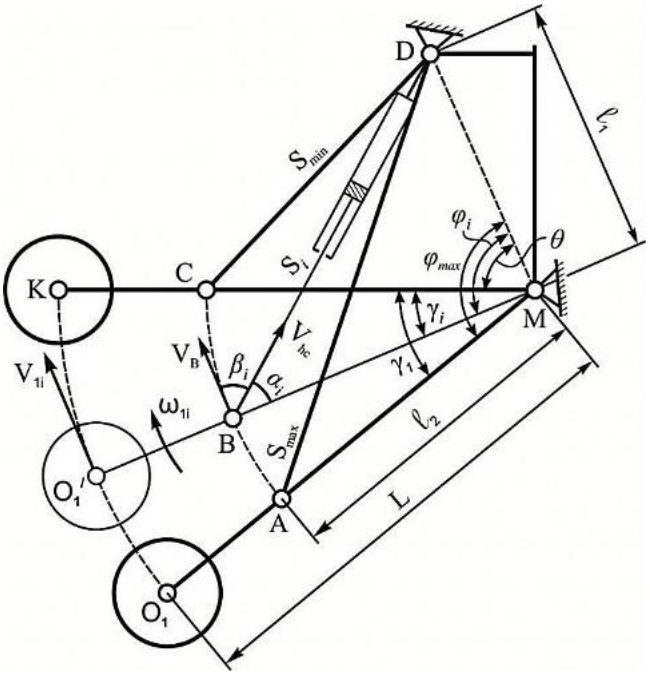


Fig. 3 - Scheme for determining the angular velocity of the swing arm

According to the scheme:

$$\gamma_i = \varphi_i - \theta, \tag{3}$$

where:

φ_i is the current angle formed between the swing arm and the line connecting the fixed kinematic pairs M and D, $(\angle AMD)$, $\left(\varphi_i \in [\varphi_{max}, \theta] \middle| \begin{matrix} \varphi_{max} = \gamma_1 + \theta \\ \varphi_{min} = \theta \end{matrix}\right)$, $[deg]$; θ is a structural parameter (constant geometric angle), $[deg]$.

The kinematic relationship between the rotation angle φ_i of the swing arm and the distance S_i may be expressed by the following equation for triangle (ΔDMB):

$$S_i^2 = l_1^2 + l_2^2 - 2l_1 l_2 cos\varphi_i, \tag{4}$$

from which:

$$\varphi_i = arccos\frac{l_1^2 + l_2^2 - S_i^2}{2l_1 l_2}, \tag{5}$$

where:

$S_i = S_{max(min)} \mp \Delta S$ - represents the current extension value of the hydraulic cylinder, $\left(S_i \in [S_{max},\ S_{min}] \middle| \begin{matrix} S_{max} = |AD| \\ S_{min} = |CD| \end{matrix}\right)$, $[m]$; $\Delta S = V \cdot t_i$- is the displacement of the hydraulic-cylinder piston per unit time, $[m]$; V is the velocity of the hydraulic-cylinder piston, $[m/s]$; l_1 is the length of the line connecting the fixed kinematic pairs M and D, $[m]$; l_2 is the distance from point M to point A, where the hydraulic cylinder is connected to the swing arm, $[m]$.

The angular velocity analogue of the swing arm is obtained by differentiating Eq. (5) with respect to S. Multiplying the resulting equation by the velocity of the driving link — namely, the hydraulic-cylinder piston velocity $\left(\frac{dS_i}{dt}\right)$, yields the angular velocity of the swing arm:

$$\omega_i = \frac{d\varphi_i}{dS} = \frac{S_i}{l_1 l_2} \cdot \frac{1}{\sqrt{1 - \left(\frac{l_1^2 + l_2^2 - S_i^2}{2 l_1 l_2}\right)^2}} \cdot \frac{dS_i}{dt}. \quad (6)$$

where:

ω_i is the angular velocity, [s^{-1}].

Because the backward velocity V_1 and the forward velocity V_2 of the hydraulic-cylinder piston are different, with $V_1 > V_2$, the angular velocities of the swing arm in the corresponding sections of motion also differ. Accordingly, for a swing arm of length $L = |MO_1|$, the angular velocities of the swing arm during the backward and forward motions of the hydraulic cylinder piston are given, respectively, by:

$$\omega_1 = \frac{S_{max} - \Delta S}{l_1 l_2} \cdot \frac{1}{\sqrt{1 - \left(\frac{l_1^2 + l_2^2 - (S_{max} - \Delta S)^2}{2 l_1 l_2}\right)^2}} \cdot \frac{d(S_{max} - \Delta S)}{dt} \quad (7)$$

$$\omega_2 = \frac{S_{min} + \Delta S}{l_1 l_2} \cdot \frac{1}{\sqrt{1 - \left(\frac{l_1^2 + l_2^2 - (S_{max} + \Delta S)}{2 l_1 l_2}\right)^2}} \cdot \frac{d(S_{min} + \Delta S)}{dt}, \quad (8)$$

where:

$V_1 = \frac{d(S_{max} - \Delta S)}{dt}$ is the backward velocity of the piston, $[m/s]$; $V_2 = \frac{d(S_{min} + \Delta S)}{dt}$ is the forward velocity of the piston, $[m/s]$.

Knowing the angular velocities of the swing arm in the corresponding sections, the respective circumferential velocities of the tiller center may be determined:

$$V_1 = L \cdot \omega_1 \quad (9)$$

$$V_2 = L \cdot \omega_2. \quad (10)$$

The backward and forward velocities of the hydraulic-cylinder piston are also determined by the following equation:

$$v_{1(2)} = \frac{Q \cdot \mu}{F_{1(2)} \cdot 60 \cdot 1000}, \quad (11)$$

where:

$F_{1(2)}$ are the effective piston areas in the rod-side and piston-side chambers of the hydraulic cylinder $[m^2]$; μ is the efficiency coefficient of the hydraulic system, $\mu = 0{,}85 - 0{,}95$.

The effective piston areas on the rod side and piston side of the hydraulic cylinder are, respectively:

$$F_1 = \pi \frac{(D^2 - d^2)}{4}, \quad F_2 = \pi \frac{D^2}{4},$$

where: D is the piston diameter, and d is the piston-rod diameter, $[m]$.

The objective of the study is to determine the optimal relationship between the tractor forward velocity and the circumferential velocity of the swing arm rotating about point M, such that the untreated soil area remaining outside the plant protection zone around the tree trunk is minimized.

RESULTS AND ANALYSIS

The ratio of the circumferential velocity of the tiller center about point M, i.e., the swing-arm mounting point, to the tractor forward velocity is defined as the *bypass kinematic parameter* and expressed as:

$$\Lambda_i = V_i / V_m, \tag{12}$$

where:

$V_i = L\omega_i$ is the circumferential velocity of the tiller center about point M (ω_i is the angular velocity of the swing arm).

During the first stage of tree-trunk bypass, corresponding to the backward motion of the hydraulic-cylinder piston, the angular velocity of the tiller center about point M is $\omega_1 = \frac{|\gamma_1 - \gamma_{T1}|}{t_1}$, whereas during the motion of the tiller toward the tree row, corresponding to the forward motion of the hydraulic-cylinder piston, the angular velocity is $\omega_2 = \frac{|\gamma_{T1}^{min} - \gamma_{T2}|}{t_2}$. These angular velocities may also be determined from Eqs (7) and (8). Substituting the relation $\Lambda = V_c / V_m$ into Eqs. (1) and (2), and taking into account that $V_c = \omega \cdot L$, the equations of motion of the tiller center O_1 for the backward and forward motions of the hydraulic-cylinder piston take the following form:

For the backward motion of the piston:

$$\begin{cases} x_2 = x_1^{max} + L\left(\dfrac{\left|\gamma_{T1}^{min} - \gamma_{T2}\right|}{\Lambda_2} + cos\gamma_{T1}^{min} - cos\gamma_{T2}\right) \\ y_2 = R - \Delta + L(sin\gamma_1 - sin\gamma_{T2}), \end{cases} \tag{13}$$

For the forward motion of the piston:

$$\begin{cases} x_2 = x_1^{max} + L\left(\dfrac{\left|\gamma_{T1}^{min} - \gamma_{T2}\right|}{\Lambda_2} + cos\gamma_{T1}^{min} - cos\gamma_{T2}\right) \\ y_2 = R - \Delta + L(sin\gamma_1 - sin\gamma_{T2}), \end{cases} \tag{14}$$

where:

$\Lambda_1 = \frac{\omega_1 t_1}{V_m}$ is the bypass kinematic parameter during the first stage of tree-trunk bypass (backward motion of the hydraulic-cylinder piston); $\Lambda_2 = \frac{\omega_2 t_2}{V_m}$ is the bypass kinematic parameter during the second stage of tree-trunk bypass (forward motion of the hydraulic-cylinder piston); x_1^{max} is the abscissa corresponding to the centers of the tiller and the tree trunk at the end of the first stage of bypass.

It is evident that the angles $|\gamma_1 - \gamma_{T1}|$ and $\left|\gamma_{T1}^{min} - \gamma_{T2}\right|$ vary over equal intervals, but at different rates, which is due to the difference between the forward and backward velocities of the hydraulic cylinder piston; specifically, the forward velocity is lower than the backward velocity.

From the equation defining the bypass kinematic parameter $\Lambda = V_c / V_m$, it follows that, at a constant tractor forward velocity, its value depends on the circumferential velocity of the rotary tiller's center relative to point *M*. This velocity, in turn, depends on the forward and backward velocities of the hydraulic-cylinder piston.

Since the piston velocities differ during the forward and backward motions of the hydraulic cylinder, the values of the bypass kinematic parameter also differ along the corresponding sections of the tree trunk bypass trajectory; moreover, $\Lambda_s < \Lambda_b$.

In order to prevent the rotary tiller from entering the plant protection zone and damaging the tree trunk and root system, it is necessary that the distance from any point of the tiller center trajectory to the center of the tree trunk be greater than or equal to the sum of the radii of the tiller and the plant protection zone: $R + r$ (Fig. 2).

Thus, for the trajectory section corresponding to the first stage of tree trunk bypass, Eq. (15) can be written as follows:

$$\sqrt{(x_1 - x_t)^2 + y_1^2} \geq R + r, \tag{15}$$

Similarly, for the trajectory section corresponding to the second stage of tree-trunk bypass, Eq. (16) can be written as follows:

$$\sqrt{(x_2 - x_t)^2 + y_2^2} \geq R + r, \tag{16}$$

where:

x_1 and y_1 are the current coordinates of the rotary tiller center during the first stage of bypassing; x_2 and y_2 are the current coordinates of the tiller's center during the second stage of bypassing; $x_t = \sqrt{2R(r+\Delta)}$ is the abscissa of the tree trunk center (Fig. 2a).

The problem is analyzed for a specific set of geometric and kinematic parameters of the rotary tiller.

Consider the kinematics of a rotary tiller with a vertical axis of rotation, equipped with rotary tiller of diameter $D = 0{,}35$ m and a swing arm length $L = 0{,}38$ m during tree trunk bypassing.

It is assumed that the tractor forward travel speed is $V_m = 0{,}75$ m/s, the overlap between adjacent passes of the rotary tiller is $\Delta = 0{,}05$ m, and the angular position of the tiller relative to the direction of the aggregate motion is $(\angle O_1MF)$ $\gamma_1 = 35^0$ (Fig. 2a). Therefore, during the first stage of tree-trunk bypass, the angle of rotation of the rotary tiller about point M varies from 35^0 to 0^0, while during the second stage, when returning to the tree row, it varies from $0^0$to 35^0. The maximum displacement of the rotary tiller center along the ordinate axis from the initial position is determined as $|O_1F| = |O_1M| \cdot sin\gamma_1 = 0{,}38 \cdot sin35 \approx 0{,}22$ m (Fig. 2a). The length of the line connecting the fixed kinematic pairs M and D is $l_1 = 0{,}3$ m, while the distance from point M to point A, where the hydraulic cylinder is connected to the swing arm, is $l_2 = 0{,}35$ m (Fig. 3).

The rotation angle of the sensing probe is adjusted so that the inductive sensors generate a signal for the backward motion of the hydraulic cylinder when the distance between the rotary tiller contour and the probe becomes equal to the width of the plant protection zone, i.e., 0.05 m.

To actuate the swing arm, a hydraulic cylinder of type 40-25-160 is selected, with the following principal parameters: piston diameter: $D = 0{,}04$ m, piston rod diameter: $d = 0{,}025$ m, stroke length: $h = 0{,}16$ m, $S_{max} = 0{,}51$ m, $S_{min} = 0{,}35$ m.

Table 1 presents the variation ranges of the swing-arm angular velocities calculated using Eqs. (7) and (8), the circumferential velocities of the rotary tiller center calculated using Eq. (9), and the bypass kinematic parameter calculated using Eq. (11), for the forward and backward motions of the hydraulic cylinder at different volumetric flow rates of oil supplied to the cylinder.

Table 1

Values of the rotary tiller center velocity and bypass kinematic parameter at different hydraulic oil flow rates ($V_m = 0,75$ m/s)

Oil flow rate, Q, L/min	Swing arm angular velocity, s^{-1}		Circumferential velocity of the rotary tiller center, m/s		Bypass kinematic parameter, Λ	
	Backward motion, ω_1 (7)	Forward motion, ω_2 (8)	Backward motion, V_1 (9)	Forward motion, V_2 (10)	Backward motion, Λ_1 (12)	Forward motion, Λ_2 (12)
10	1.025-0.76	0.46-0.63	0.39-0.29	0.17-0.24	0.52-0.38	0.23-0.32
15	1.54-1.14	0.7-0.94	0.58-0.43	0.27-0.36	0.77-0.57	0.36-0.48
20	2.05-1.51	0.93-1.26	0.78-0.57	0.35-0.48	1.04-0.76	0.47-0.64
30	3.08-2.28	1.39-1.89	1.17-0.87	0.53-0.72	1.56-1.16	0.7-0.96
40	4.1-3.03	1.86-2.51	1.56-1.15	0.71-0.95	2.08-1.53	0.94-1.28
50	5.13-3.8	2.3-3.14	1.95-1.44	0.87-1.19	2.6-1.92	1.16-1.61

Based on the system of Eqs. (13) and (14), as well as the data presented in Table 1, the trajectories of motion of the rotary tiller center were plotted for different values of the hydraulic oil flow rate supplied to the hydraulic cylinder and for different values of the bypass kinematic parameter (Fig. 4).

Among the trajectories shown in Fig. 4, the optimal one should be considered the trajectory in which the edge of the rotary tiller moves at the minimum possible distance from the plant protection zone, while simultaneously satisfying conditions (15) and (16). It is evident that, in this case, the uncultivated area outside the plant protection zone will also be minimal.

Fig. 5 shows the variation in the distance between the centers of the rotary tiller and the tree trunk as a function of the bypass kinematic parameter.

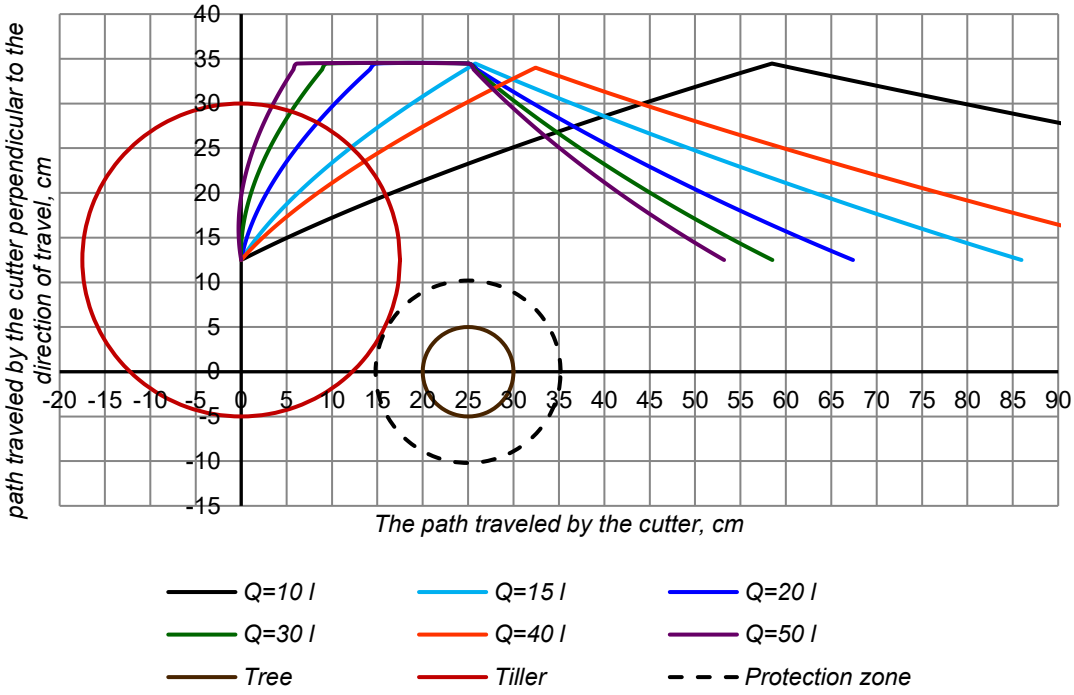


Fig. 4 - Trajectories of the rotary tiller center at different hydraulic oil flow rates, *Q*, and corresponding values of the bypass kinematic parameter, *Λ*

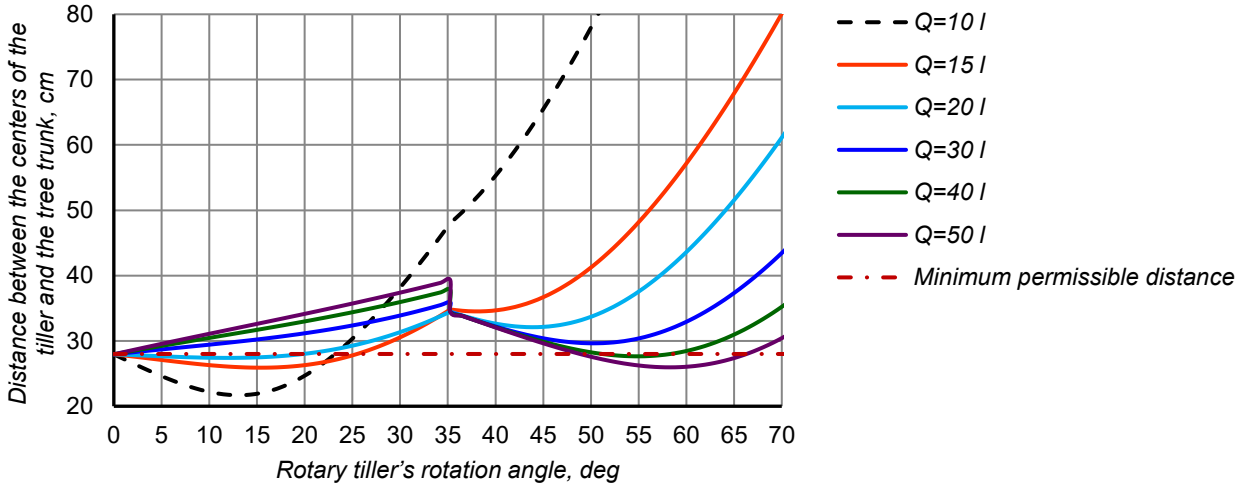
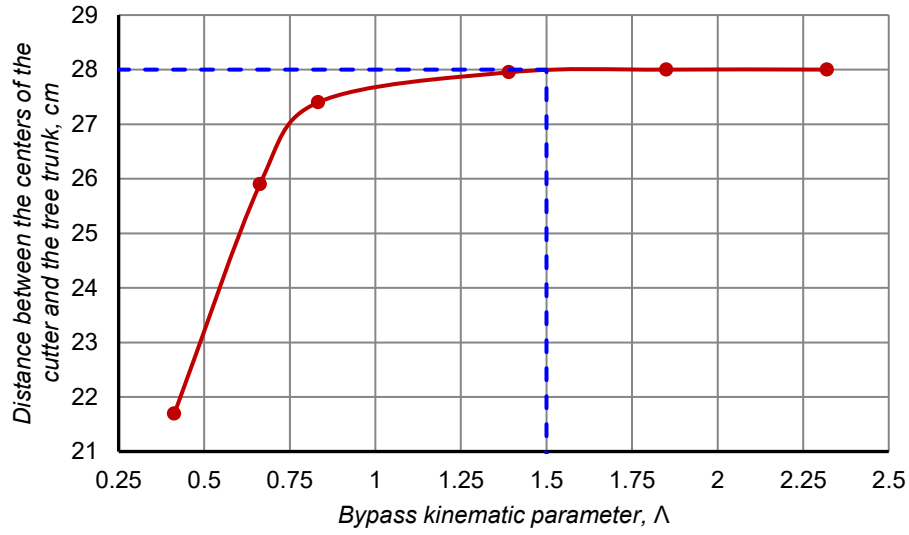
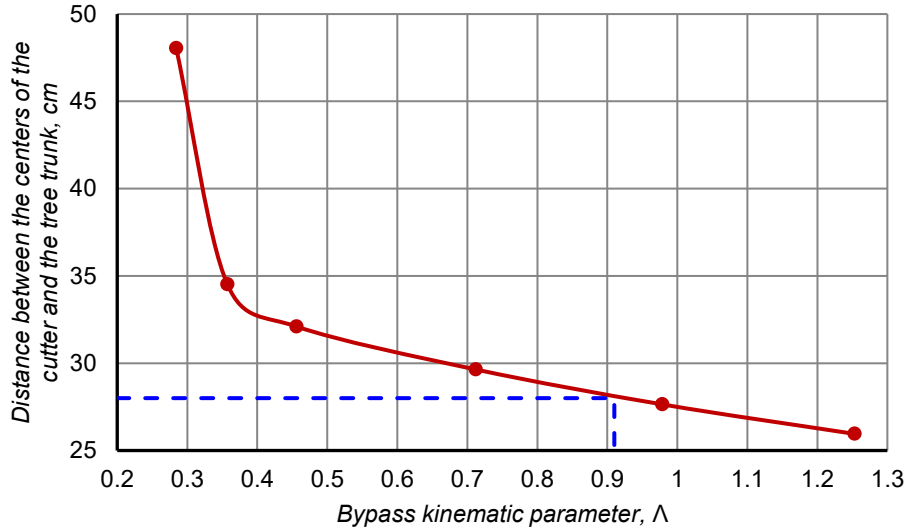


Fig. 5 - Variation in the distance between the centers of the rotary tiller and the tree trunk s a function of the bypass kinematic parameter

The graphs in Figs. 6a and 6b show the variation of the minimum values of the distance between the centers of the rotary tiller and the tree trunk during the first and second stages of tree trunk bypassing, respectively, for different values of the bypass kinematic parameter.



a)



b)

Fig. 6 - Variation in the minimum distance between the centers of the rotary tiller and the tree trunk for different values of the bypass kinematic parameter:
a) first stage, b) second stage

Analysis of the plotted trajectories shows that, during the first stage of tree trunk bypassing, the optimal value of the bypass kinematic parameter is $\Lambda_1 = 1{,}5$, while during the second stage the optimal value is $\Lambda_2 = 0{,}91$.

When selecting the hydraulic system parameters, the value of Λ_2, corresponding to the second stage of tree trunk bypassing, should be taken as the reference, from which the corresponding value of Λ_1 for the first stage is obtained.

In the example considered, the optimal value for the second stage is $\Lambda_2 = 0{,}91$, which corresponds to $\Lambda_1 = 1{,}16$ for the first stage. Therefore, for a machine travel speed of $V_m = 0{,}75$ m/s and the selected hydraulic cylinder of type 40-25-160 the specified values of the bypass kinematic parameters are achieved at a hydraulic oil flow rate of approximately $Q \approx 30$ l/min in the hydraulic cylinder (Table 1).

CONCLUSIONS

The study showed that, for automatically controlled working units operating on an astatic principle during cultivation of near-trunk and inter-trunk areas in vineyards and intensive orchards, the kinematic parameter based solely on the circumferential velocity of the rotary tiller is insufficient to determine the optimal tiller trajectory and minimize the untreated soil area outside the plant protection zone around tree trunks. Therefore, to more adequately characterize the rotary bypass motion, the concept of the *bypass kinematic parameter* was introduced. The analysis showed that this parameter more accurately reflects the kinematic characteristics of the rotary tiller during tree-trunk bypass.

It was established that, for given agrotechnical requirements, operating conditions, and known structural parameters of the machine, regulation of the hydraulic oil flow rate supplied to the hydraulic cylinder makes it possible to vary the forward and backward velocities of the piston and, consequently, the values of the bypass kinematic parameter. In this way, a tree-trunk bypass trajectory can be obtained that minimizes the untreated soil area outside the plant protection zone.

ACKNOWLEDGEMENT

This work was supported by the Higher Education and Science Committee of RA (research project № 25DD-2D022).

REFERENCES

[1] Artobolevsky I.I., (1988). *Theory of Mechanisms and Machines (Теория механизмов и машин),* Nauka (Наука), Moscow, 640 p.

[2] Cabrera-Pérez, C., Valencia-Gredilla, F., Royo-Esnal, A., Recasens, J. (2022). Organic Mulches as an Alternative to Conventional Under-Vine Weed Management in Mediterranean Irrigated Vineyards. *Plants*, 11, 2785. https://doi.org/10.3390/plants11202785

[3] Gagliardi, L., Fontanelli, M., Luglio, S., Frasconi, C., Peruzzi, A., Raffaelli, M. (2023). Evaluation of Sustainable Strategies for Mechanical Under-Row Weed Control in the Vineyard. *Agronomy* 13, 3005. https://doi.org/10.3390/agronomy13123005

[4] Gagliardi, L., Luglio, S., Peruzzi, A., Fontanelli, M., Frasconi, C., Raffaelli, M. (2024). Comparative Analysis of the Performance of a Chain Mower and Tools That Perform Under-Row Weed Control with Tillage in the Vineyard. *Agronomy* 2024, 14. https://doi.org/10.3390/agronomy14010206

[5] Hanson, B.D., Roncoroni, J., Hembree, K.J., Molinar, R., Elmore, C.L. (2016). Weed Control in Orchards and Vineyards. *Encyclopedia of Applied Plant Sciences*, New York, NY, USA, pp. 479–484. https://doi.org/10.1016/B978-0-12-394807-6.00032-0

[6] Inter-Row Machine, EP 3 824 708 A1, 26.05.2021. RINIERI, Nicola 47121 Forli', Frazione Collina (IT)

[7] Kostadinov G. D., G. Parkhomenko G. G., Tverdohlebov S. A., Ponomarev A. V., (2016). Systematization of Devices for Soil Treatment in The Orchard, (Систематизация устройств для обработки почвы в садах), *Bulgarian Journal of Crop Science (Растениевъдни науки), 2016, 53(1-3), 88-97*. https://agriacad.eu/ojs/index.php/bjcs/article/view/3193/2819

[8] Liu, C., Yang, K., Chen, Y., Gong, H., Feng, X., Tang, Z. (2023) Benefits of Mechanical Weeding for Weed Control, Rice Growth Characteristics and Yield in Paddy Fields. *Field Crops Res.*, 293, 108852. https://doi.org/10.1016/j.fcr.2023.108852

[9] Manaenkov K. A., Koldin M. S., Arkova Z. A., (2017) Improvement of tillage in row strips intensive gardens (Совершенствование обработки почвы в приствольных полосах интенсивных садов), *Food and processing industry technologies (Технологии пищевой и перерабатывающей промышленности)*- N3.28-34 pp. https://cyberleninka.ru/article/n/sovershenstvovanie-obrabotki-pochvy-v-pristvolnyh-polosah-intensivnyh-sadov/viewer

[10] Manzone M., Demeneghi M., Marucco P., (2020) Technical solutions for under-row weed control in vineyards: Efficacy, costs and environmental aspects analysis. *Journal of agricultural engineering* 51(1): pp. 36-42. https://doi.org/10.4081/jae.2020.991

[11] Morin, L. (2020) Progress in Biological Control of Weeds with Plant Pathogens. *Annu. Rev. Phytopathol.* 58, 201–213. https://doi.org/10.1146/annurev-phyto-010820-012823

[12] Papyan S., Harutyunyan G., (2024) Research and Development of a Mechanism for Fixing the Hydraulic Cylinder for Controlling the External Working Element of a Garden Milling Machine and Determining its Optimal Parameters, Scientific journal of ANAU *"AgriScience and Technology"* 4(88), 279-283. https://doi.org/10.52276/25792822-2024.4-279

[13] Parasca, S., Spaeth, M., Rusu, T., Bogdan, I., (2024) Mechanical Weed Control: Sensor-based Inter-row Hoeing in Sugar Beet (Beta vulgaris L.) in the Transylvanian Depression. *Agronomy*, 14, 176. https://doi.org/10.3390/agronomy14010176

[14] Pergher, G., Gubiani, R., Mainardis, M., (2019) Mainardis Field Testing of a Biomass-Fueled Flamer for In-Row Weed Control in the Vineyard. *Agriculture*, 9, 210. https://doi.org/10.3390/agriculture9100210

[15] Rzaliev A.S., Serikbayev A.U., Zhunusbaev A.B., (2025) Theoretical study on the substantiation of the parameters of a vertical-axis rotary tiller for cultivation of the near-trunk zone of fruit trees (Теоретические исследования по обоснованию параметров фрезы с вертикально-роторным валом вращения для обработки приствольной зоны плодовых деревьев), *Journal Izdenister natigeler*, №3 (107), 605-616 pp. https://doi.org/10.37884/3-2025/60

[16] Smirnov D. A., (2014) Kinematic analysis of a one-degree-of-freedom slotted-link mechanism with fixed revolute kinematic pairs (Киематический анализ кулисного механизма с одной степенью свободы с неподвижными вращательными кинематическими парами), *Fundamental research* (*Фундаментальные исследования*), № 8(5). Nizhny Novgorod, 1069-1074 pp. https://fundamental-research.ru/ru/article/view?id=34719

[17] Wang, Y., Kang, J., Peng, Q., Chen, Y., Fang, H., Niu, M., Wang, S. (2023) Design and Experiment of Obstacle Avoidance Weeding Machine for Fruit Trees. *J. Jilin Univ. Eng. Technol. Ed*., 53, 2410–2420. https://doi.org/10.13229/j.cnki.jdxbgxb.20211121

[18] Zawada, M., Legutko, S., Goscianska-Lowinska J., Szymczyk, S., Nijak, M., Wojciechowski, J. (2023). Mechanical Weed Control Systems: Methods and Effectiveness. *Sustainability*, 15, 15206. https://doi.org/10.3390/su152115206

OPTIMAL DESIGN AND SIMULATION-BASED VALIDATION OF A TOBACCO PLANTER BASED ON MULTIPLE BIRD-BEAK CHARACTERISTIC CURVES
/
基于多鸟喙特征曲线的烟草栽植器优化设计与仿真验证

Sheng DING[1)], Ao SHAN[2)], Chencan XIAO [3)], Qing JIANG[1,2,*)]

[1)] School of Mechanical and Vehicle Engineering, Anhui Agricultural University, Hefei 230036 / China;
[2)] Anhui Provincial Engineering Research Center of Intelligent Agricultural Machinery, Hefei 230036. / China
Tel: 13349292716; E-mail: jtao@ahau.edu.cn
DOI: https://doi.org/10.35633/inmateh-79-101

Keywords: *biomimetic tobacco planter; penetration resistance; soil adhesion; discrete element method; Box–Behnken design*

ABSTRACT
To address the high penetration resistance and severe soil adhesion of tobacco planting devices operating in wet, clayey soil, a biomimetic planting device was designed using a Gaussian multi-peak function and characteristic curves derived from multiple bird beaks. The peak parameters, including height, position, and width, were optimized using discrete element method (DEM) simulations and response surface methodology. The resulting biomimetic profile reduced penetration resistance and soil adhesion, thereby improving tobacco transplanting performance. The optimized prototype exhibited a penetration resistance of 18.7 N and an adhered soil mass of 14.98 g, representing reductions of 60.47% and 40.56%, respectively, compared with the conventional prototype.

摘要
为解决烟草栽植器在湿黏土壤中阻力大、粘附严重的问题，本文基于高斯多峰函数融合多种鸟喙特征曲线，研制了一款仿生栽植器。结合离散元 (DEM) 仿真，利用响应面法优化了波峰参数（高度、位置和宽度）。该仿生曲线可以有效降低了渗透阻力、改善了土壤附着力，并提升了烟草移栽性能。优化后样机穿透阻力为 18.7 N，黏附质量为 14.98 g，相比于传统样机，分别减少了 60.47% 和 40.56%。

INTRODUCTION
Mechanized tobacco transplanting is strongly influenced by the interaction between the planter and the soil environment. As the primary soil-engaging component, the planter repeatedly penetrates the soil and plastic mulch during transplanting operations. Under wet and cohesive clay conditions, this repeated penetration may generate considerable penetration resistance and severe soil adhesion on the planter surface (*Obour et al., 2019; Xu et al., 2024*). These problems not only increase operational resistance and accelerate the wear of soil-engaging components, but may also adversely affect transplanting quality by causing excessive mulch damage, irregular planting holes, and seedling displacement. Therefore, reducing penetration resistance and soil adhesion is essential for improving the operational performance and reliability of tobacco planting equipment.

Biomimetic design has been increasingly applied to agricultural soil-engaging components by transferring the functional geometric or surface characteristics of biological organisms to engineering structures. Existing biomimetic approaches can generally be divided into two categories: surface microstructure modification and macroscopic contour optimization. Surface-based biomimetic designs typically reproduce the non-smooth or low-adhesion characteristics of biological surfaces. *Tong et al.* investigated the geometric features and wettability of dung beetle cuticles and demonstrated their potential for reducing soil adhesion on tillage implements (*Tong et al., 2005*). *Chen et al.* developed a pangolin-inspired concave microstructure that disrupted the interfacial water film and reduced the jacking force by 18.7% (*Chen et al., 2020*). *El Salem et al* verified that convex bionic surface configurations can break the continuity of soil-tool interfacial water films, decrease the actual contact area between soil and metal matrix, and achieve favorable anti-adhesion performance within viscous wet clay environments (*El Salem et al., 2023*).

Sheng Ding, M.S. Stud. Eng; Ao Shan, M.S. Stud.Eng; Chencan Xiao, M.S. Stud. Eng; Qing Jiang, Prof. Ph.D. Eng.

Similar discontinuous surface structures have also shown potential for reducing tillage resistance and soil adhesion under wet and cohesive soil conditions (*Niu et al., 2022; Zhang et al., 2025*).

In contrast, macroscopic contour optimization focuses on extracting and reproducing characteristic geometries from biological digging, burrowing, or penetrating organs. *Liu et al.* combined the morphological characteristics of the oriental mole cricket foreleg with soil mechanics to improve the digging performance of a cassava harvester (*Liu et al., 2014*). *Li et al. (2026)* investigated the soil burrowing mechanism of earthworms and *Liu et al. (2023)* developed a biomimetic furrow opener based on the head contour of an earthworm, whereas *Wu et al. (2021)* established a biomimetic mathematical model for subsoiling components based on biological geometric characteristics. These studies demonstrated that biomimetic contour optimization can effectively modify soil–tool interaction and reduce soil-engaging resistance. More recently, composite biomimetic strategies have been explored by combining different biological characteristics. *Guan et al. (2022*) integrated biological morphology with hydrophobic surface modification, while *Liu et al. (2024)* combined earthworm- and pangolin-inspired characteristics to reduce soil contact and adhesion.

Despite these advances, most existing biomimetic soil-engaging components are still based on simplified representations of a single biological feature (*Lei et al., 2024; Li et al., 2016; Lin et al., 2025; Sun et al., 2020; Wang et al., 2025*). Such single-feature designs may not fully satisfy the simultaneous requirements of low penetration resistance and reduced soil adhesion under the repeated dynamic penetration conditions encountered during tobacco transplanting. In addition, a unified mathematical framework capable of integrating complementary geometric characteristics from multiple biological prototypes into a continuously adjustable and optimizable contour remains insufficiently developed. Therefore, a multi-source biomimetic design method is needed to systematically combine different morphological characteristics and quantitatively optimize the resulting planter geometry.

To address this limitation, this study proposes a Gaussian multi-peak biomimetic design method for tobacco planters by integrating the characteristic beak contours of four bird species: the Common Kingfisher, Common Quail, Water Rail, and Common Ostrich. These biological prototypes were selected because they exhibit distinctly different beak geometries, including slender, short and robust, decurved, and broad profiles. The extracted contours were represented using a unified Gaussian multi-peak function, which enabled continuous and quantitative adjustment of peak height, peak position, and peak width. A Plackett–Burman screening design and a Box–Behnken response surface methodology were combined with discrete element method (DEM) simulations to identify the key geometric parameters and optimize the planter with respect to penetration resistance and soil adhesion. Furthermore, soil-particle velocity fields and disturbance characteristics were analyzed to investigate the mechanisms by which the optimized multi-peak contour promotes lateral soil diversion, tangential particle motion, and reduction of the frontal compression zone. The results provide a theoretical and methodological basis for designing tobacco planting components with reduced penetration resistance and improved anti-adhesion performance.

MATERIALS AND METHODS

Bionic Design

To address the high penetration resistance and severe soil adhesion encountered by tobacco planters during high-speed and repeated penetration into wet and cohesive soil, four bird species with distinctly different beak morphologies were selected as biological prototypes: the Common Kingfisher (S1), Common Quail (S2), Water Rail (S3), and Common Ostrich (S4), as shown in Fig. 1. The Common Kingfisher has a slender and approximately conical beak with a relatively small tip angle and a smooth longitudinal profile *(Crandell et al., 2019*). The Common Quail has a shorter and more robust beak with concentrated curvature variation near the anterior region (*Zhang X.Y. et al., 2021*). The Water Rail has a slender and moderately decurved beak *(Bouzid et al., 2023*), whereas the Common Ostrich has a broader profile with a comparatively large obtuse tip angle (*Zhang R. et al., 2021*). These four beak geometries represent different morphological characteristics and provide a diverse geometric basis for multi-source biomimetic contour integration and subsequent parametric optimization.

The bird images used for contour extraction were obtained from publicly available online sources, with an approximate original resolution of 1200 × 800 pixels. Original camera and lens metadata were not available because the images were obtained from public online sources. Therefore, image selection was controlled by lateral-view orientation, clear beak boundaries, and the absence of obvious perspective distortion. To ensure reliable contour extraction, only images showing the beak approximately in lateral view, with clear and unobstructed boundaries and no obvious perspective distortion, were selected.

Because this study focused on normalized geometric profiles rather than absolute biological dimensions, all extracted coordinates were normalized to a dimensionless scale before curve fitting to minimize the effects of differences in image scale.

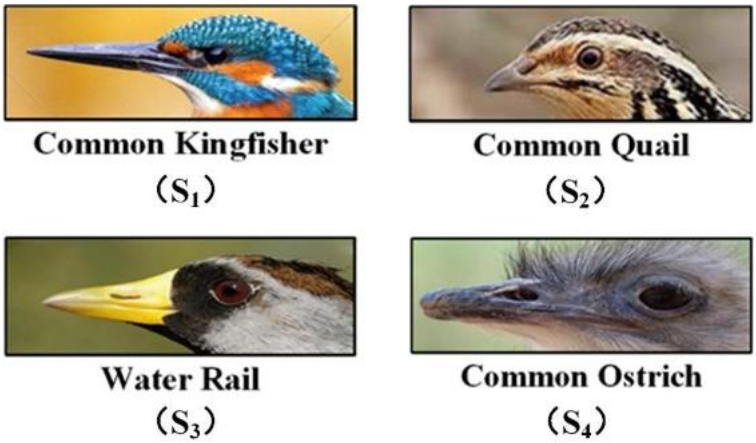


Fig. 1 - Images of the bionic prototypes for the selected bird beaks

The beak-contour extraction procedure is illustrated in Fig. 2. Image processing was performed using MATLAB R2023b (MathWorks, Natick, MA, USA). Grayscale conversion, Otsu thresholding, Canny edge detection, and contour-coordinate extraction were successively conducted. The extracted upper-beak contour was then resampled into 100 equally spaced points along the arc length for subsequent dimensionless normalization and Gaussian multi-peak fitting. The extracted contours were then corrected by affine transformation so that the beak tip coincided with the coordinate origin and the principal longitudinal axis was aligned with the horizontal axis. The normalization equations were:

$$x^* = \frac{x - x_{min}}{x_{max} - x_{\min}}, y^* = \frac{y - y_{\min}}{y_{max} - y_{\min}} \quad (1)$$

x and y are the original contour coordinates; x_{min} and x_{max} are the minimum and maximum values of the x-coordinates, respectively; y_{min} and y_{max} are the minimum and maximum values of the y-coordinates, respectively; and x^* and y^* are the normalized dimensionless coordinates.

To achieve a unified parametric representation of the different bird-beak contours, a Gaussian multi-peak function was used to fit the normalized contour data:

$$f(x) = \sum_{i=1}^{n} a_i e^{-\left(\frac{x-b_i}{c_i}\right)^2} \quad (2)$$

where: $f(x)$ is the fitted value at position x; n is the total number of Gaussian terms; i denotes the current Gaussian component; and a_i, b_i, and c_i represent the peak height, peak position, and peak width of the i -th Gaussian component, respectively.

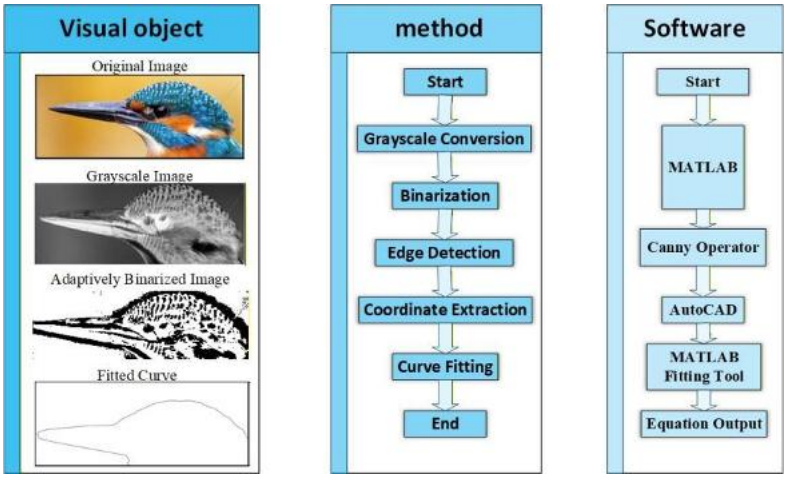


Fig. 2 - Flowchart of image processing and contour extraction

The Gaussian multi-peak function was selected because it can flexibly describe complex biological contours using a limited number of independent parameters, while each parameter has an explicit geometric meaning that allows complex beak morphologies to be converted into continuous, adjustable, and quantifiable engineering design variables. In addition, this parametric representation facilitates subsequent Plackett–Burman screening and Box–Behnken response-surface optimization, thereby reducing the dimensionality of the optimization problem and improving computational efficiency.

The goodness of fit was evaluated using both the coefficient of determination (R^2) and the root mean square error ($RMSE$), calculated as:

$$RMSE = \sqrt{\frac{1}{N}\sum_{j=1}^{N}\left(y_j - \hat{y}_j\right)^2} \quad (3)$$

where:

N is the number of sampled contour points; y_j is the actual normalized contour coordinate of the j-th sampling point; and $\hat{y}_j$ is the corresponding fitted value. The Gaussian multi-peak parameters and fitting evaluation indices of the four bird-beak contours are summarized in Table 1. The R^2 values ranged from 0.9506 to 0.9908, while the $RMSE$ values ranged from 0.0192 to 0.0445, indicating that the Gaussian multi-peak function adequately represented the principal geometric characteristics of the four bird-beak contours.

Table 1

Bionic planter curve parameters

Coefficient	Beak ID			
	S_1	**S_2**	**S_3**	**S_4**
a_1	0.9851	0.9894	0.9722	0.9486
b_1	0.9078	0.9900	0.9272	0.8856
c_1	0.4116	0.3577	0.3673	0.4189
a_2	0.30348	0.3574	0.4918	0.3559
b_2	0.2880	0.3532	0.3462	0.2378
c_2	0.1851	0.1847	0.1861	0.1322
R^2	0.9854	0.9908	0.9727	0.9506
RMSE	0.0241	0.0192	0.0336	0.0445

Structural Design

The planter is the main soil-engaging component in tobacco transplanting and adopts a symmetrical double-valve structure to perform hole formation and seedling release simultaneously. The overall structure is shown in Fig. 3. Its motion is controlled by a linkage mechanism consisting of a pull rod, a rotating shaft, and two movable plates. During the downward stroke, the external driving mechanism actuates the pull rod, causing the two movable plates to rotate outward around the shaft and open the duckbill at the predetermined depth. During the return stroke, the assembly returns to its initial position under the combined effects of the return spring and gravity, preparing for the next working cycle.

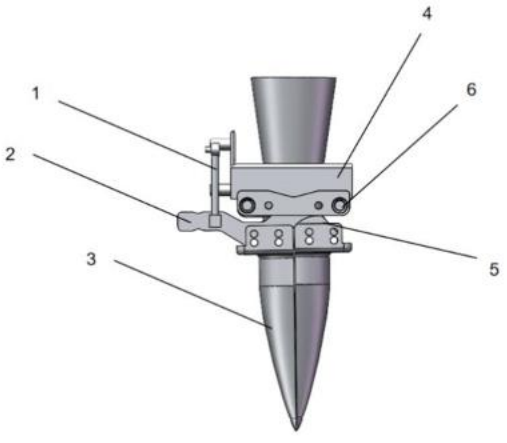


Fig. 3 - Overall structure diagram of the bionic planter

(1) Pull rod (2) Movable plate I (3) Planter (4) Planter bracket (5) Movable plate II; (6) Rotating shaft

The three-dimensional model of the planter was developed using SolidWorks 2024. The main body was designed using 304 stainless steel and was intended for fabrication by metal additive manufacturing. The planter geometry was exported from SolidWorks 2024 as a binary STL surface model and imported into EDEM. A custom STL export resolution was used, with the unit set to millimeters, a surface deviation tolerance of 0.154 mm, and an angular tolerance of 10°. The overall dimensions of the planter were 110 mm × 250 mm × 100 mm, with a wall thickness of 2 mm. The calculated mass based on the CAD model was 0.676 kg, and a nominal dimensional tolerance of ±0.5 mm was specified in the design.

The internal cavity of the planter was dimensioned to ensure compatibility with seedlings cultivated in standard 128-cell plug trays. The seedling plug had an upper diameter of 30 mm, a lower diameter of 10 mm, and a height of 40 mm, as shown in Fig. 4(a). For the subsequent discrete element simulation, the complex morphology of the actual tobacco seedling was simplified and represented by a regular geometric model to establish the internal geometric boundary of the planter, as shown in Fig. 4(b). This simplification reduced the computational complexity associated with complex leaves, stems, and irregular plug geometry. Since the present study mainly focused on the interaction between the external planter surface and wet cohesive soil, particularly the maximum penetration resistance and soil adhesion mass, the detailed morphology of the actual seedling was not explicitly modeled. However, this simplification may neglect local contact and posture variations between the actual seedling and the inner wall of the planter. No separate sensitivity analysis was conducted for the simplified seedling geometry; therefore, its influence on simulation accuracy was not quantitatively assessed. The proposed design was intended to address two major constraints associated with the regional soil conditions: the strong interfacial adhesion of high-moisture clay, which causes severe soil adhesion and accumulation on the planter surface, and the high penetration resistance generated by compacted soil. Typical field soil conditions are shown in Fig. 5. Therefore, the integration of multiple bird-beak characteristic curves into the planter design is intended to reduce soil adhesion and penetration resistance.

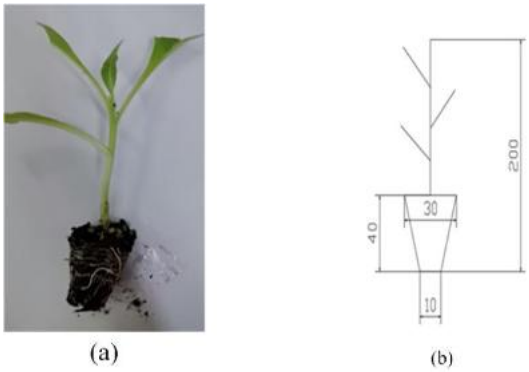


Fig. 4 - Morphological characteristics of the target tobacco seedling

(a) actual biological specimen; (b) simplified geometric model.



Fig. 5 - Field soil exhibiting high penetration resistance and strong adhesion

Experimental Design

To identify the main factors controlling the soil-engaging performance of the planter, the experimental design was conducted in two stages.

First, a Plackett–Burman (PB) screening design was used to evaluate the six morphological parameters (a_1, b_1, c_1, a_2, b_2, and c_2) and identify the factors influencing the maximum penetration resistance (Y_1) and soil adhesion mass (Y_2). These six parameters were derived from the two-term Gaussian multi-peak function, in which each Gaussian term was defined by three independent parameters corresponding to peak height, peak position, and peak width. Therefore, the six parameters jointly characterized the complete geometry of the biomimetic contour.

The maximum penetration resistance (Y_1) was selected to characterize the mechanical resistance encountered by the planter during soil penetration and was closely related to operational energy consumption. The soil adhesion mass (Y_2) was used to quantify the amount of wet cohesive soil retained on the planter surface, which may affect the continuous operating performance of the planter.

The factor levels, configured as high (+1) and low (-1) levels, were determined according to the geometric parameter ranges extracted from the four bird-beak prototypes, thereby ensuring that the investigated design space had a clear biological basis. The factor levels are given in Table 2.

Second, based on the PB screening results, the three factors exerting the greatest influence on soil-engaging performance were selected for further analysis of interaction effects and parameter optimization using a three-factor, three-level Box–Behnken design (BBD), with coded levels of -1, 0, and +1. For three factors, the standard BBD consisted of 12 factorial combination points and five center-point runs, resulting in a total of 17 experimental runs. All design points were simulated under identical numerical settings. The five center-point runs were used to estimate the pure error and evaluate the numerical repeatability of the response surface model.

Table 2

Factors and levels of the Plackett-Burman experimental design

Factor	Low level (-1)	High level (+1)
a_1	0.9486	0.9894
b_1	0.8856	0.9900
c_1	0.3577	0.4189
a_2	0.3034	0.4918
b_2	0.2378	0.3532
c_2	0.1322	0.1861

The interaction dynamics of these experimental runs were simulated using EDEM 2024 software. The Hertz-Mindlin with JKR cohesion contact model was used to represent the cohesive behavior and interfacial adhesion characteristics of wet cohesive clay.

The soil particles were represented by three types of particle aggregates, namely single-sphere, double-sphere, and triple-sphere particles, with particle sizes ranging from 1.5 to 3.0 mm. The proportions of single-sphere, double-sphere, and triple-sphere particles were 60%, 25%, and 15%, respectively, and a total of 100,000 particles were generated in the soil bin.

The particles were generated, allowed to settle under gravity, and then statically compacted using a flat compaction plate to reproduce natural field soil conditions. The penetration simulation was started after the compacted soil bed became stable, as indicated by a low and nearly constant total kinetic energy and no obvious change in bed height. The planter material was modeled as 304 stainless steel.

The setup of the simulation model is shown in Fig. 6, and the complete list of the intrinsic and contact mechanics parameters is given in Table 3.

The Euler integration scheme was adopted, with a fixed time step of 6.47855×10^{-5} s, corresponding to 20% of the Rayleigh time step. The total simulation time was 2.5 s, and simulation data were saved at intervals of 0.001 s. The simulations were performed using the CPU solver with 12 CPU cores. All simulations were conducted on a workstation equipped with a 12th Gen Intel Core i5-12400F processor and 32 GB of RAM.

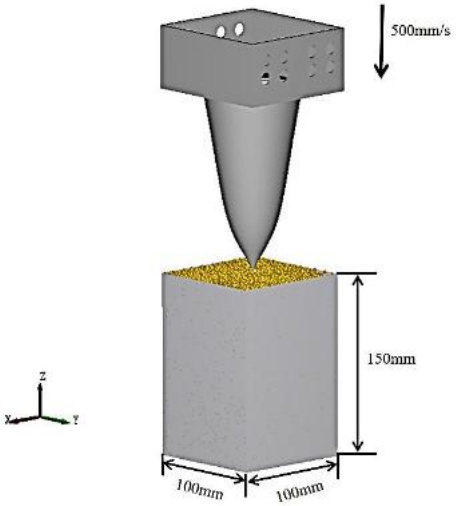


Fig. 6 - Discrete Element Method (DEM) simulation model

Table 3

Intrinsic and contact parameters of the discrete element simulation model

Item	Parameter	Value
Soil properties	Soil density / kg·m⁻³	2760
	Soil Poisson's ratio	0.35
	Soil shear modulus / MPa	1.5
Stainless-steel properties	Stainless steel density / kg·m⁻³	7850
	Stainless steel Poisson's ratio	0.3
	Stainless steel shear modulus / MPa	7x10^4
Soil-soil contact parameters	Soil-soil JKR surface energy / J·m⁻²	4.982
	Coefficient of restitution	0.411
	Coefficient of static friction	0.78
	Coefficient of rolling friction	0.148
Soil–stainless-steel contact parameters	Soil-stainless steel JKR surface energy / J·m⁻²	2.027
	Coefficient of restitution	0.599
	Coefficient of static friction	0.711
	Coefficient of rolling friction	0.015

Statistical analysis and response surface modeling were performed using Design-Expert 13.0.5.0 software (Stat-Ease Inc., Minneapolis, MN, USA), with the significance level set at α = 0.05. The adequacy of the regression models was evaluated using ANOVA, R^2, adjusted R^2, predicted R^2, lack-of-fit test, and adequate precision. Residual diagnostics were conducted using normal probability plots of residuals, residuals versus predicted values, and Cook's distance. The predictive performance of the models was further evaluated by comparing the predicted responses with the corresponding results from independent DEM numerical verification.

RESULTS

Analysis of Key Parameter Screening Tests

The Plackett–Burman screening results are shown in Table 4. The maximum penetration resistance (Y_1) ranged from 25.21 N to 34.12 N, and the soil adhesion mass (Y_2) ranged from 12.40 g to 21.80 g, indicating that the Gaussian contour parameters had an obvious influence on the soil-engaging performance of the planter.

To quantify the relative influence of each parameter, the main effects and percentage contributions were calculated from the screening results. For penetration resistance, a_2 showed the largest positive effect, with a contribution of 54.83%, followed by c_2 and b_2, with contributions of 27.38% and 13.50%, respectively. This indicates that the front-end peak height was the dominant factor increasing penetration resistance, while a larger peak width helped reduce resistance by producing a smoother surface transition.

For soil adhesion mass, c_2 was the dominant factor, with a contribution of 72.00%, followed by a_2, with a contribution of 12.79%. This result indicates that the peak width mainly controlled soil adhesion by affecting the smoothness of the planter surface and the sliding behavior of wet cohesive soil. The effects of the back-end parameters a_1, b_1, and c_1 were relatively small for both response variables.

As shown in the standardized Pareto charts in Fig. 7, the front-end Gaussian parameters a_2, b_2, and c_2 had greater effects on the two response variables than the back-end parameters. Therefore, a_2, b_2, and c_2 were selected as the key design variables for the subsequent Box–Behnken response surface optimization, while a_1, b_1, and c_1 were fixed in the following optimization process.

Table 4

Plackett-Burman experimental design scheme and response results

Test No.	Factor						Penetration Resistance [N]	Soil adhesion mass [g]
	a_1	b_1	c_1	a_2	b_2	c_2		
1	+1	+1	-1	+1	+1	+1	29.86	15.6
2	-1	+1	+1	-1	+1	+1	25.21	12.4
3	+1	-1	+1	+1	-1	+1	28.14	13.8
4	-1	+1	-1	+1	+1	-1	33.85	21.5
5	-1	-1	+1	-1	+1	+1	25.68	12.9
6	-1	-1	-1	+1	-1	+1	27.92	13.5
7	+1	-1	-1	-1	+1	-1	29.15	18.1
8	+1	+1	-1	-1	-1	+1	26.54	16.4
9	+1	+1	+1	-1	-1	-1	26.88	16.8
10	-1	+1	+1	+1	-1	-1	30.06	18.3
11	+1	-1	+1	+1	+1	-1	34.12	21.8
12	-1	-1	-1	-1	-1	-1	26.35	16.1

Table 5

Main effects and percentage contributions of the Plackett–Burman screening results

Factor	Effect on Y_1 [N]	Contribution to Y_1 [%]	Effect on Y_2 [g]	Contribution to Y_2 [%]
a_1	0.94	2.97	1.30	5.59
b_1	0.17	0.10	0.80	2.12
c_1	-0.60	1.21	-0.87	2.48
a_2	4.02	54.83	1.97	12.79
b_2	2.00	13.50	1.23	5.03
c_2	-2.84	27.38	-4.67	72.00

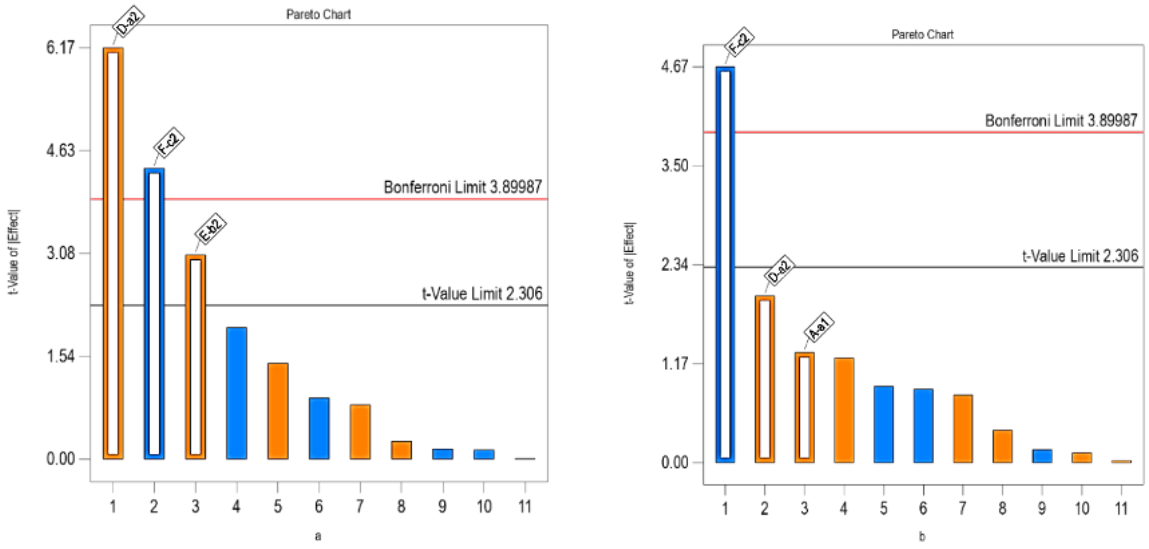


Fig. 7 - Standardized Pareto charts of main effects

(a) penetration resistance; (b) soil adhesion mass.

Box–Behnken Design and Response Surface Model Fitting

According to the Plackett–Burman screening results, the peak height (a_2), peak position (b_2), and peak width (c_2) were selected as the main biomimetic parameters affecting the soil-engaging performance of the planter. A three-factor, three-level Box–Behnken design was used to analyze the effects of these parameters and their interactions on the maximum penetration resistance (Y_1) and soil adhesion mass (Y_2). The coded levels of the three factors are listed in Table 6, and the design matrix and corresponding EDEM simulation results are shown in Table 7.

Table 6

Factors and coded levels of Box-Behnken design

Coded level	Factor		
	a_2	b_2	c_2
1	0.4918	0.3532	0.1861
0	0.3983	0.2955	0.1592
-1	0.3048	0.2378	0.1322

Table 7

Response surface experimental design and EDEM simulation results

Standard Order	Factor			Penetration Resistance [N]	soil adhesion mass [g]
	a_2	b_2	c_2		
1	-1	-1	0	21.9	14.21
2	1	-1	0	35.11	21.24
3	-1	1	0	18.8	12.56
4	1	1	0	32.46	20.54
5	-1	0	-1	20.54	15.56
6	1	0	-1	33.85	20.35
7	-1	0	1	18.6	12.48
8	1	0	1	28.34	18.43
9	0	-1	-1	22.59	17.36
10	0	1	-1	19.46	18.96
11	0	-1	1	20.85	15.12
12	0	1	1	17.65	15.86
13	0	0	0	24.15	16.52
14	0	0	0	23.98	16.41
15	0	0	0	24.32	16.65
16	0	0	0	24.05	16.38
17	0	0	0	24.21	16.55

As shown in Table 7, the maximum penetration resistance ranged from 17.65 N to 35.11 N, and the soil adhesion mass ranged from 12.48 g to 21.24 g. The five center-point runs showed small variations. The penetration resistance values of the center points were 24.15, 23.98, 24.32, 24.05, and 24.21 N, with a mean value of 24.14 N and a standard deviation of 0.13 N. The corresponding soil adhesion mass were 16.52, 16.41, 16.65, 16.38, and 16.55 g, with a mean value of 16.50 g and a standard deviation of 0.11 g. These results indicate that the DEM simulation had good numerical repeatability under the same simulation conditions.

The ANOVA results of the fitted models are shown in Table 8. The quadratic model for penetration resistance was extremely significant (p < 0.0001), with R^2, adjusted R^2, and predicted R^2 values of 0.9916, 0.9808, and 0.8676, respectively. The adequate precision was 30.7602, which was much higher than the recommended threshold of 4. For penetration resistance, the linear terms a_2, b_2 and c_2 were all extremely significant (p < 0.01). The interaction term a_2c_2 was significant (p = 0.0467), while a_2b_2 and b_2c_2 were not significant. The quadratic terms a_2^2, b_2^2, and c_2^2 were also significant, indicating a nonlinear relationship between the front-end contour parameters and penetration resistance.

The linear model for soil adhesion mass was also extremely significant (p < 0.0001), with R^2, adjusted R^2, and predicted R^2 values of 0.9343, 0.9192, and 0.8665, respectively. The adequate precision was 25.7831, indicating that the model had sufficient signal for response prediction within the selected design space.

For soil adhesion mass, a_2 and c_2 were extremely significant (p < 0.01), whereas b_2 was not significant (p = 0.9962). This result indicates that soil adhesion was mainly affected by peak height and peak width rather than peak position.

Although the lack-of-fit terms of both models were significant (p < 0.05), this may be attributed to the nonlinear friction, collision, cohesion, and adhesion behavior between wet clay particles and the biomimetic planter surface in the DEM simulation. Considering the high model significance, high R^2 values, and adequate precision values, the fitted models were considered acceptable for empirical optimization within the selected design space. However, they should not be interpreted as universal prediction models outside the investigated factor ranges.

The PRESS values of the penetration resistance model and soil adhesion mass model were 60.39 and 13.76, respectively. These values, together with the predicted R^2 values, were used to evaluate the predictive performance of the fitted regression models within the selected design space.

Table 8

Analysis of variance (ANOVA) for the regression models of penetration resistance and soil adhesion

Source	Penetration resistance (Y_1)			Soil adhesion (Y_2)		
	df	F-value	p-value	df	F-value	p-value
Model	9	91.62	<0.0001**	3	61.64	<0.0001**
A-a_2	1	568.07	<0.0001**	1	159.25	<0.0001**
B-b_2	1	33.27	0.0007**	1	0	0.9962ns
C-c_2	1	27.58	0.0012**	1	25.68	0.0002**
AB	1	0.0923	0.7701ns	-	-	-
AC	1	5.81	0.0467*	-	-	-
BC	1	0.0022	0.9636ns	-	-	-
A^2	1	126.59	<0.0001**	-	-	-
B^2	1	9.89	0.0163*	-	-	-
C^2	1	63.24	<0.0001**	-	-	-
Lack of Fit	3	70.67	0.0006*	9	62.36	0.0006*
R^2	0.9916			0.9343		
Adjusted R^2	0.9808			0.9192		
Predicted R^2	0.8676			0.8665		
Adeq Precision	30.7602			25.7831		
PRESS	60.39			13.76		

*Note: ** indicates extremely significant (p < 0.01); * indicates significant (p < 0.05); ns indicates not significant (p > 0.05); "-" indicates that the model does not include this term.*

Model Diagnostic Analysis

The diagnostic plots of the fitted response surface models are shown in Fig.8. For both response models, most residual points were approximately distributed along the reference line in the normal probability plots, indicating that no serious deviation from normality was observed. In the residuals versus predicted values plots, the residuals were generally distributed around zero, suggesting that the fitted models could describe the response trends within the selected design space.

The Cook's distance plots showed that several design points had relatively high influence on the fitted models. This may be related to the nonlinear friction, collision, cohesion, and adhesion behavior of wet cohesive soil particles during DEM simulation. These points were not removed because they corresponded to valid parameter combinations in the Box–Behnken design. Therefore, the regression models were used as empirical optimization models within the investigated factor ranges, and the optimized results were further evaluated by independent DEM numerical verification.

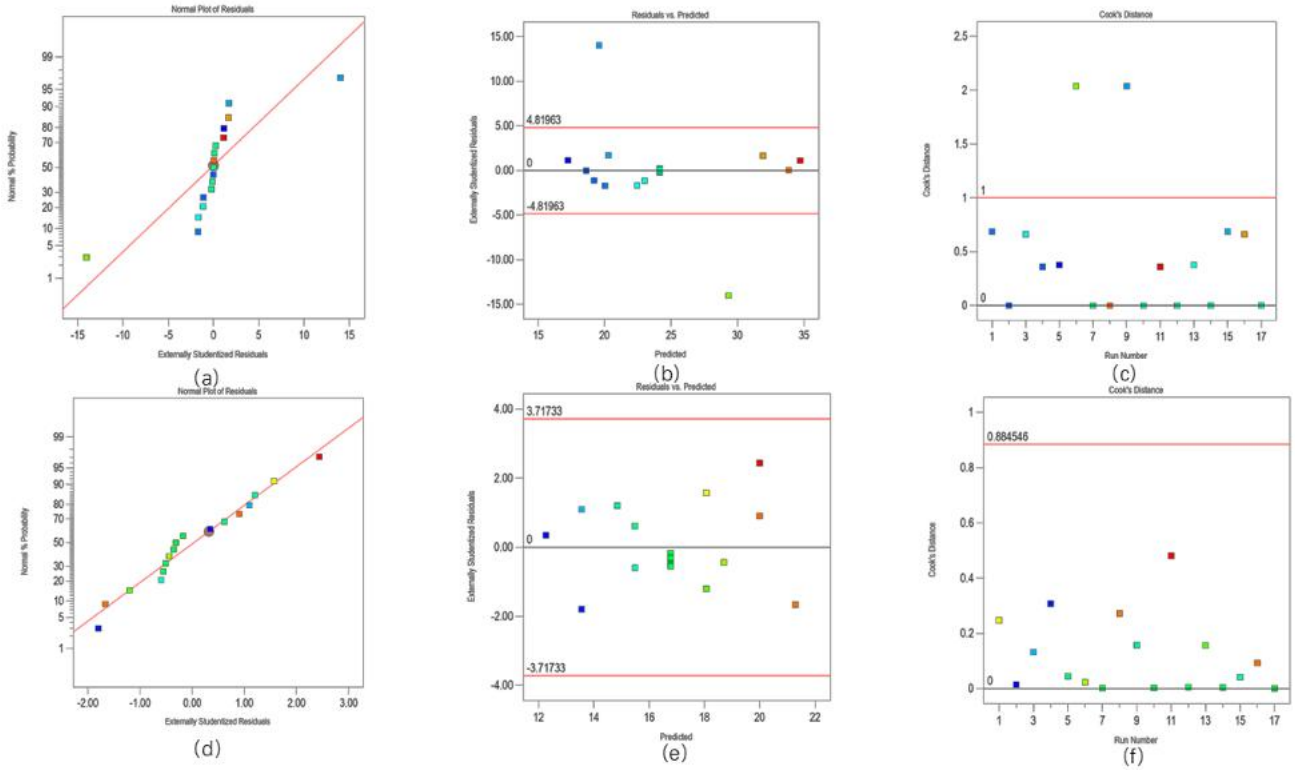


Fig. 8 - Diagnostic plots of the fitted response surface models

(a) normal probability plot of residuals for Y_1; (b) residuals versus predicted values for Y_1; (c) Cook's distance for Y_1; (d) normal probability plot of residuals for Y_2; (e) residuals versus predicted values for Y_2; (f) Cook's distance for Y_2.

According to the BBD analysis, the real factor regression equations of maximum penetration resistance (Y_1) and the soil adhesion mass (Y_2) for the peak height (a_2), peak position (b_2) and peak width (c_2) are as follows:

$$Y_1 = -63.274 - 253.027a_2 + 168.751b_2 + 1351.039c_2 + 20.853a_2b_2 - 354.191a_2c_2 - 11.254b_2c_2 + 464.440{a_2}^2 - 340.838{b_2}^2 - 3951.177{c_2}^2 \quad (4)$$

$$Y_2 = 10.703 + 34.425a_2 - 0.022b_2 - 47.959c_2 \quad (5)$$

Response Surface Analysis

The response surface plots are shown in Fig. 9. For penetration resistance, the response surfaces of the a_2 b_2 and b_2 c_2 interactions were relatively smooth, which is consistent with the ANOVA results showing that these two interaction terms were not significant (p > 0.05). This indicates that changing the peak position (b_2) did not strongly alter the effect of peak height or peak width on penetration resistance.

In contrast, the interaction between a_2 and c_2 had a significant effect on penetration resistance (p < 0.05). When a_2 was high, the penetration resistance remained relatively high, because a larger front-end peak increased the frontal soil-breaking area and enhanced soil compression. When a_2 was low and c_2 was high, the penetration resistance decreased. This indicates that a lower peak height helped reduce frontal compression, while a larger peak width produced a smoother surface transition and promoted soil sliding along the planter surface.

For soil adhesion mass, the response surface showed an approximately linear trend. Soil adhesion increased with increasing a_2 and decreased with increasing c_2. This result indicates that the peak height and peak width mainly controlled soil adhesion by changing the local contact and sliding behavior between wet clay and the planter surface. Therefore, the protrusion height and surface smoothness should be jointly optimized to achieve both resistance reduction and adhesion reduction.

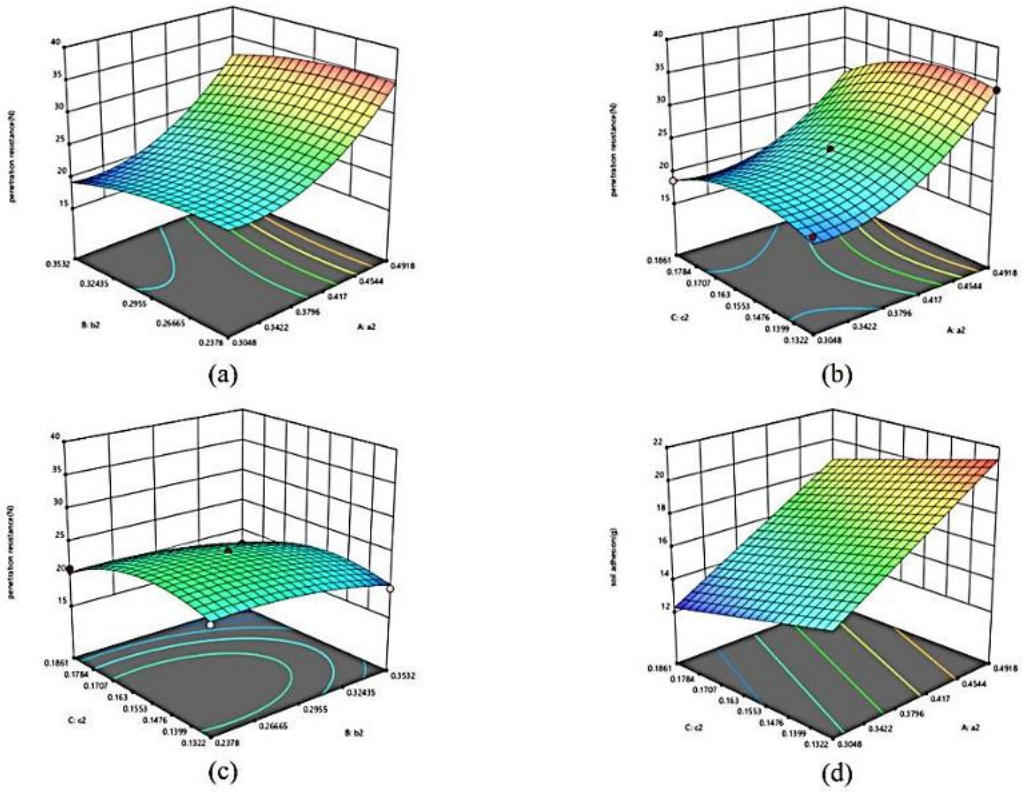


Fig. 9 - Response surface plots illustrating the interactive effects of biomimetic parameters

(a) a_2 and b_2 on penetration resistance (Y_1); (b) b_2 and c_2 on Y_1; (c) a_2 and c_2 on Y_1; (d) a_2 and c_2 on soil adhesion (Y_2)

Objective Function Establishment and Parameter Optimization

The objective is to minimize both the maximum penetration resistance (Y_1) and soil adhesion (Y_2) with the physical constraints of the planter's structure.

The optimization model is as follows:

$$\begin{cases} min\, Y_1 = f_1(a_2, b_2, c_2) \\ min\, Y_2 = f_2(a_2, b_2, c_2) \\ s.t. \\ 0.3048 \le a_2 \le 0.4918 \\ 0.2378 \le b_2 \le 0.3532 \\ 0.1322 \le c_2 \le 0.1861 \end{cases} \quad (6)$$

The desirability function method was used to integrate the two response variables into an overall desirability index (D) calculated as follows:

$$D = (d_1(Y_1) \times d_2(Y_2))^{\frac{1}{2}} \quad (7)$$

where: d_1 and d_2 are the individual desirability values for penetration resistance and soil adhesion.

The optimization objective was to minimize both the maximum penetration resistance (Y_1) and soil adhesion mass (Y_2) within the selected design space. The desirability function method in Design-Expert was used to integrate the two response variables into a comprehensive desirability index. The optimized parameter combination was a_2 = 0.30, b_2 = 0.35, and c_2 = 0.19, with an overall desirability value of 0.893. Under this condition, the predicted penetration resistance and soil adhesion mass were 16.14 N and 12.40 g, respectively.

Other optimization algorithms, such as genetic algorithms and particle swarm optimization, were also considered. However, the present optimization problem involved only three continuous design variables and two response objectives, and the fitted response surface models provided explicit regression equations within the selected design space. Therefore, the desirability function method was adopted because it could directly integrate penetration resistance and soil adhesion mass into a single interpretable optimization index. Population-based optimization algorithms may be considered in future work when more design variables, structural constraints, or experimental validation data are included.

Parameter Optimization and Numerical Verification

To evaluate the optimized parameter combination, the optimized planter model was reconstructed and an independent DEM simulation was conducted under the same numerical conditions. Since this study focused on numerical optimization, the verification was based on DEM simulation rather than laboratory or field experiments. Therefore, the verification results should be interpreted as numerical verification within the DEM framework. The soil particle velocity fields of the conventional prototype, the four single bird-beak biomimetic profiles (S_1–S_4), and the optimized multi-peak profile are shown in Fig. 10.

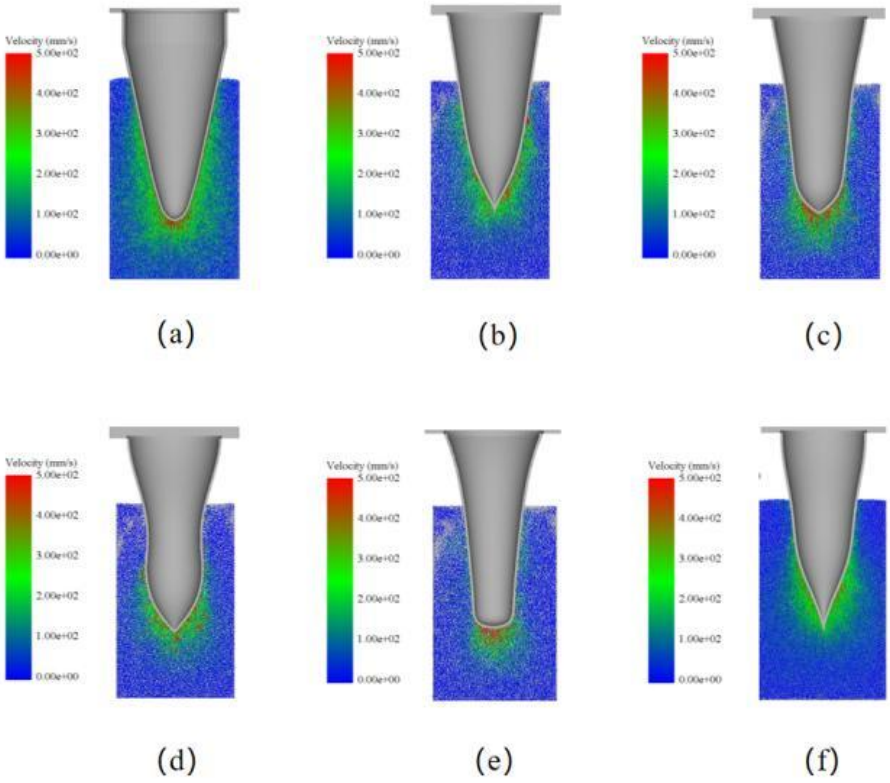


Fig. 10 - Comparison of soil particle velocity fields for different planter profiles

(a) Conventional (b-e) Bionic prototypes S_1-S_4 (f) Optimized multi-peak bionic profile

As shown in Fig. 10(a), the conventional planter produced a wide V-shaped high-velocity disturbance zone during soil penetration, indicating strong frontal compression and large-scale soil disturbance. In contrast, the optimized multi-peak biomimetic planter generated a narrower and more streamlined disturbance zone, and the soil particles tended to move along the planter surface, as shown in Fig. 10(f). This indicates that the dominant soil motion changed from frontal compression to tangential sliding, thereby reducing local soil compaction and weakening soil accumulation on the planter surface.

To quantitatively evaluate the resistance-reduction and anti-adhesion effects, the penetration resistance and soil adhesion mass were extracted for all planter profiles, as shown in Fig. 11. The maximum penetration resistance of the conventional prototype was 47.30 N, whereas that of the optimized biomimetic planter was 18.70 N, corresponding to a reduction of 60.47%. The soil adhesion mass decreased from 25.20 g for the conventional prototype to 14.98 g for the optimized planter, corresponding to a reduction of 40.56%.

As shown in Table 9, the predicted penetration resistance and soil adhesion mass were 16.14 N and 12.40 g, respectively, while the corresponding DEM verification values were 18.70 N and 14.98 g. The relative errors were 15.86% and 20.81%, respectively. Although the DEM verification values were higher than the predicted values, the optimized model showed a consistent reduction trend and was therefore acceptable for evaluating the optimization direction. Mechanistically, the optimized peak height and peak width produced a smoother transition of the planter surface, which reduced frontal soil compression and promoted tangential soil sliding. This change in soil motion reduced penetration resistance and weakened the retention of wet cohesive soil on the planter surface. Overall, the optimized multi-peak configuration achieved coupled reductions in penetration resistance and soil adhesion mass.

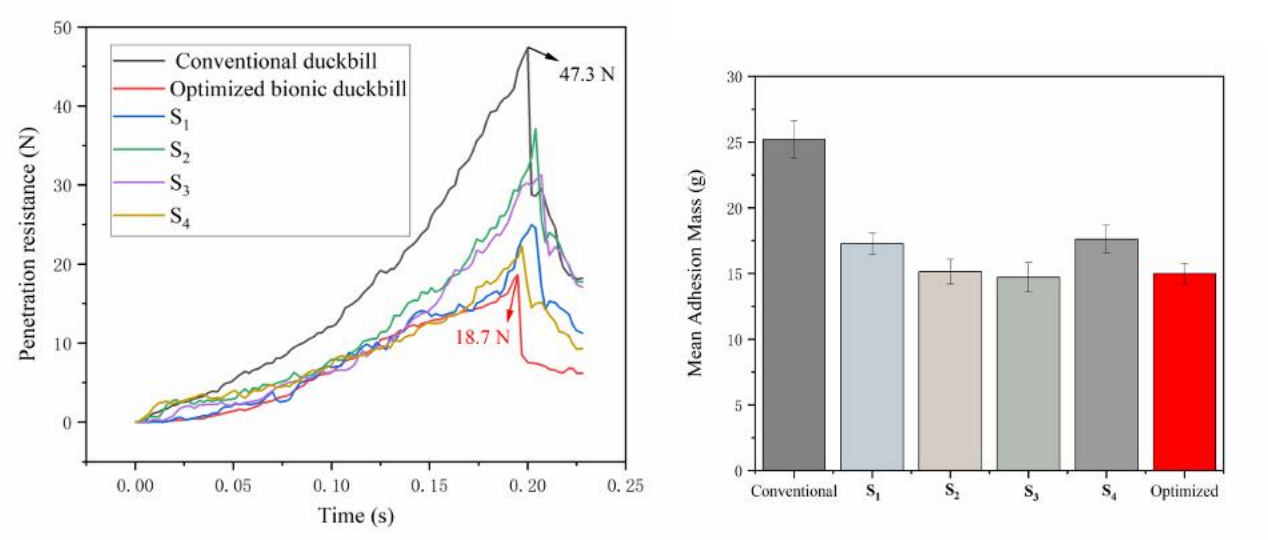


Fig. 11 - Soil-engaging performance of different planter profiles

(a) Penetration resistance curves (b) Mean adhesion mass

Table 9

Numerical verification results of the optimized parameter combination

Response	Predicted value	DEM verification value	Relative error [%]
Y_1 / [N]	16.14	18.70	15.86
Y_2 / [g]	12.40	14.98	20.81

CONCLUSIONS

In this study, a Gaussian multi-peak biomimetic tobacco planter was designed by integrating the characteristic beak contours of multiple bird species. DEM simulation, Plackett–Burman screening, Box–Behnken response surface optimization, and independent DEM numerical verification were used to evaluate the effects of the biomimetic contour parameters on penetration resistance and soil adhesion mass.

The Plackett–Burman screening results showed that the front-end Gaussian parameters a_2, b_2, and c_2 had greater effects on penetration resistance and soil adhesion mass than the back-end parameters. Therefore, a_2, b_2, and c_2 were selected as the key variables for response surface optimization. Based on the Box–Behnken design and desirability function method, the optimized parameter combination was obtained as a_2 = 0.30, b_2 = 0.35, and c_2 = 0.19. Under this condition, the predicted penetration resistance and soil adhesion mass were 16.14 N and 12.40 g, respectively. The independent DEM verification values were 18.70 N and 14.98 g, with relative errors of 15.86% and 20.81%, respectively.

Compared with the conventional planter, the optimized multi-peak biomimetic planter reduced the maximum penetration resistance from 47.30 N to 18.70 N and reduced the soil adhesion mass from 25.20 g to 14.98 g, corresponding to reductions of 60.47% and 40.56%, respectively. The optimized profile also showed better combined resistance-reduction and anti-adhesion performance than the single bird-beak biomimetic profiles.

The soil particle velocity field showed that the optimized multi-peak profile reduced the wide V-shaped frontal disturbance zone and promoted soil motion along the planter surface. This indicates that the dominant soil motion changed from frontal compression to tangential sliding, thereby reducing local soil compaction and weakening the retention of wet cohesive soil on the planter surface.

It should be noted that the verification in this study was based on independent DEM simulation rather than laboratory or field experiments. Therefore, the results should be interpreted as numerical verification within the selected design space. Future work will focus on prototype fabrication and experimental validation under actual tobacco transplanting conditions.

REFERENCES

[1] Bouzid A., Samraoui F., & Samraoui B. (2023). A survey of the distribution of the water rail Rallus aquaticus in Algeria and its first recorded breeding in the Algerian Sahara. *African journal of ecology*. https://doi.org/10.1111/aje.13119

[2] Chen D.H., Yang X., Dai T.D., Sun Y.H., & Chang Z.Y. (2020). Bionic Design to Reduce Jacking Force for Trenchless Installations in Clay Soil. *Journal of bionic engineering*, 17(4), 686–694. https://doi.org/10.1007/s42235-020-0066-8

[3] Crandell K.E., Howe R.O., & Falkingham P.L. (2019). Repeated evolution of drag reduction at the air-water interface in diving kingfishers. *Journal of the royal society interface*, 16(154), Article 20190125. https://doi.org/10.1098/rsif.2019.0125

[4] El Salem A., Zhang G., Wang H., Salem H., Abdalla M., & Ghazy A. (2023). The effect of integrating a bio-inspired convex structure with a low-surface energy polymer on soil adhesion and friction. *Journal of Terramechanics*, 109, 93–100. https://doi.org/10.1016/j.jterra.2023.06.003

[5] Guan C.S., Fu J.J., Xu L., Jiang X.Z., Wang S.L., & Cui Z.C. (2022). Study on the reduction of soil adhesion and tillage force of bionic cutter teeth in secondary soil crushing. *Biosystems engineering*, 213, 133–147. https://doi.org/10.1016/j.biosystemseng.2021.11.018

[6] Lei C., Xie F., Wu F.C., & Yan Q. (2024). Research on bionic design of cylindrical milling cutter based on the curvilinear configuration of the rake face of beaver teeth. *International journal of advanced manufacturing technology*, 130(9-10), 4905–4917. https://doi.org/10.1007/s00170-024-12951-y

[7] Li B., Chen Y., & Chen J. (2016). Modeling of soil-claw interaction using the discrete element method (DEM). *Soil & Tillage research*, 158, 177–185. https://doi.org/10.1016/j.still.2015.12.010

[8] Li K., Nagy D., Keller T., & Tamás K. (2026). Evaluating the effects of earthworm tip geometry on burrowing forces using cone penetration analogues and GPU-based discrete element method (DEM) simulations. Soil & Tillage research, 259, 16, Article 107069. https://doi.org/10.1016/j.still.2026.107069

[9] Lin S.B., Sun H.Y., Yan G.E., Que K.X., Xu S.J., Tang Z., Wang G.Q., & Li J.L. (2025). Structural Design and Analysis of Bionic Shovel Based on the Geometry of Mole Cricket Forefoot. *Agriculture*-Basel, 15(8), Article 854. https://doi.org/10.3390/agriculture15080854

[10] Liu G., Yao J., Chen Z., Han X., & Zou M. (2023). Mesoscopic analysis of drag reduction performance of bionic furrow opener based on the discrete element method. *Plos One*, 18(11), e0293750. https://doi.org/10.1371/journal.pone.0293750

[11] Liu G.M., Han X.K., Wang Z.Y., Wang K., Zhang Z.S., & Duan Z.A. (2024). Viscosity Reduction and Drag Reduction Performance Analysis of Bionic Excavator Buckets Based on Discrete Element Method. *Biomimetics*, 9(11), Article 686. https://doi.org/10.3390/biomimetics9110686

[12] Liu S.H., Weng S.J., Liao Y.L., & Zhu D.Y. (2014). Structural bionic design for digging shovel of cassava harvester considering soil mechanics. *Applied bionics and biomechanics*, 11(1-2), 1–11. https://doi.org/10.3233/ABB-140089

[13] Niu J.P., Luo T.Y., Xie J.Q., Cai H.X., Zhou Z.K., Chen J., & Zhang S. (2022). Simulation and experimental study on drag reduction and anti-adhesion of subsoiler with bionic surface. *International journal of agricultural and biological engineering*, 15(4), 57–64. https://doi.org/10.25165/j.ijabe.20221504.6531

[14] Obour P.B., Keller T., Jensen J.L., Edwards G., Lamande M., Watts C.W., Sorensen C.G., & Munkholm L.J. (2019). Soil water contents for tillage: A comparison of approaches and consequences for the number of workable days. *Soil and Tillage Research*, 195. https://doi.org/10.1016/j.still.2019.104384

[15] Sun J.F., Chen H.M., Wang Z.M., Ou Z.W., Yang Z., Liu Z., & Duan J.L. (2020). Study on plowing performance of EDEM low-resistance animal bionic device based on red soil. *Soil and Tillage Research*, 196, Article 104336. https://doi.org/10.1016/j.still.2019.104336

[16] Tong J., Sun J.Y., Chen D.H., & Zhang S.J. (2005). Geometrical features and wettability of dung beetles and potential biomimetic engineering applications in tillage implements. *Soil and Tillage Research*, 80(1-2), 1–12. https://doi.org/10.1016/j.still.2003.12.012

[17] Wang H.H., Li Y.M., Wu Y., Ji K.Z., & Liu Y.B. (2025). Design and experimental study of bionic digging shovel based on vole's front middle toe. *Journal of agricultural engineering*, 56(4), Article 1831. https://doi.org/10.4081/jae.2025.1831

[18] Wu B.G., Zhang R.Z., Hou P.F., Tong J., Zhou D.Y., Yu H.Y., Zhang Q., Zhang J.S., & Xin Y.L. (2021). Bionic Nonsmooth Drag Reduction Mathematical Model Construction and Subsoiling Verification. *Applied bionics and biomechanics*, 2021, Article 5113453. https://doi.org/10.1155/2021/5113453

[19] Xu Z.H., Qi H.Y., Gao P., Wang S., Liu X.T., & Ma Y.H. (2024). Biomimetic Design of Soil-Engaging Components: A Review. *Biomimetics*, 9(6), Article 358. https://doi.org/10.3390/biomimetics9060358

[20] Zhang F.B., Luo Z.T., Zheng E.L., Han L., Qian J., Yao H.P., Shi Y.Y., & Wang X.C. (2025). Imitating pangolin scale structure for reducing adhesion and resistance of rotary tillage in wet-adhesive soil. *Soil and Tillage Research*, 245, Article 106306. https://doi.org/10.1016/j.still.2024.106306

[21] Zhang R., Li G.Y., Ma S.S., Pang H., Ren L., Zhang H., & Su B. (2021). Frictional performance of ostrich (Struthio camelus) foot sole on sand in all directions. *Biomechanics and modeling in mechanobiology*, 20(2), 671–681. https://doi.org/10.1007/s10237-020-01409-1

[22] Zhang X.Y., Wang X., Wang W., Xu R.X., Li C.L., & Zhang F. (2021). Effects of Personality Traits on the Food-Scratching Behaviour and Food Intake of Japanese Quail (Coturnix japonica). *Animals*, 11(12), Article 3423. https://doi.org/10.3390/ani11123423

DUST GENERATION MECHANISMS AND EFFECTS OF OPERATING PARAMETERS IN A FLAIL-TYPE STRAW PICKUP HEADER USING DEM AND CFD

/

基于 DEM 与 CFD 的锤爪式秸秆捡拾割台扬尘机理与作业参数影响

Jinghao FAN[1,2], Haiqing TIAN*[1,2], Chunxiang ZHUO[1,2], Kai ZHAO[1,2], Qiang YUE[1,2], Ruiyi XU[1,2]

[1)] College of Mechanical and Electrical Engineering, Inner Mongolia Agricultural University, Hohhot 010018, China.

[2)] Inner Mongolia Engineering Research Centre of Intelligent Equipment for the Entire Process of Forage and Feed Production, Hohhot 010018, China.

Tel: 15947019846; E-mail: hqtian@126.com

DOI: https://doi.org/10.35633/inmateh-79-102

Keywords: *flail-type pickup header; dust generation; discrete element method; computational fluid dynamics; particulate matter*

ABSTRACT

Airborne dust generated during straw pickup can impair operating visibility and local air quality; however, the respective contributions of mechanical particle detachment and aerodynamic entrainment in flail-type pickup headers remain insufficiently quantified. This study combined discrete element method (DEM) and computational fluid dynamics (CFD) analyses with field measurements to investigate these two processes. A bonded corn root stubble–soil DEM model was established in EDEM, and the bond fracture rate was used to characterize the relative degree of particle detachment. The effects of ground clearance (30–90 mm), rotor speed (4100–5300 rpm), forward speed (0.5–1.5 m/s), plant spacing (200–300 mm), and row spacing (300–500 mm) were evaluated. CFD simulations were then used to characterize the time-averaged airflow field within the pickup-header housing. Increasing the ground clearance from 30 to 90 mm reduced the bond fracture rate by 44.5%, whereas increasing the rotor speed from 4100 to 5300 rpm increased it by 52.3%. By relating the DEM particle-detachment states to the CFD flow-field characteristics, three dust-generation pathways were identified: stubble fragmentation, root extraction, and direct entrainment of loose surface particles. Rotor speed affected both mechanical detachment and airflow entrainment at the header inlet. Field measurements showed that the selected low-dust operating condition, with a ground clearance of 75 mm, rotor speed of 4400 rpm, and forward speed of 0.75 m/s, reduced total suspended particulate (TSP), PM_{10}, and $PM_{2.5}$ concentrations by 62.2%, 58.4%, and 53.8%, respectively, compared with the dust-intensive condition. By linking particle detachment, airflow entrainment, and field measurements within a mechanism-based framework, this study clarifies the effects of operating parameters on dust generation and provides a basis for selecting low-dust operating parameters and improving pickup-header inlet design.

摘要

秸秆捡拾过程中产生的扬尘会降低作业视野并恶化局部空气质量，但锤爪式捡拾割台中机械颗粒脱离与气流卷吸各自对扬尘形成的作用仍缺乏充分的定量认识。本研究将相互独立的离散元法(DEM)分析、计算流体动力学(CFD)分析与田间测试相结合，对上述两类过程进行了研究。利用 EDEM 建立玉米根茬—土壤粘结颗粒模型，并采用粘结键断裂率表征颗粒相对脱离程度，考察离地高度(30-90 mm)、锤爪转速(4100-5300 r m)、前进速度(0.5-1.5 m/s)、株距(200-300 mm)和行距(300-500 mm)的影响。随后利用 CFD 模拟分析捡拾割台壳体内部的时均气流特征。离地高度由 30 mm 增加至 90 mm 时，粘结键断裂率降低 44.5%；锤爪转速由 4100 r m 增加至 5300 r m 时，粘结键断裂率提高 52.3%。通过将 DEM 获得的颗粒脱离状态与 CFD 流场特征对应分析，推断出三条扬尘产生途径：根茬破碎、根茬拔除以及土壤表面松散颗粒的直接气流卷吸。锤爪转速同时影响机械颗粒脱离和入口气流卷吸。田间试验表明，相较于高扬尘工况，离地高度 5 mm、锤爪转速 4400 r m、前进速度 0.5 m/s 的低尘工况使 TSP、PM_{10}和 $PM_{2.5}$浓度分别降低 62.2%、58.4%和 53.8%。本研究通过在统一的机理框架下关联颗粒脱离、气流卷吸和田间实测结果，阐明了作业参数影响扬尘形成的作用途径，可为低尘作业参数选择及捡拾割台入口结构改进提供依据。

INTRODUCTION

Agricultural field operations can generate substantial airborne particulate matter through the disturbance of soil and crop residues. Total suspended particulate (TSP), particulate matter with an aerodynamic diameter below 10 μm (PM_{10}), and particulate matter below 2.5 μm ($PM_{2.5}$) can deteriorate local air quality and operating conditions, and their emission levels vary with machinery type, soil condition, and operating intensity (*Çarman*

et al., 2023; Chen et al., 2017; Zhang et al., 2023; Chen et al., 2024). Mechanized straw recovery reduces open-field residue burning, but straw pickup itself can generate considerable dust (*Yang et al., 2022*). In a flail-type pickup header, high-speed flails fragment root stubble and detach adhered soil, while rotor-induced negative pressure at the housing inlet entrains detached and loose surface particles. Reported TSP concentrations during harvesting can reach 1500-3000 μg/m^3, and $PM_{2.5}$ may account for 30%-45% of airborne dust (*Zhang et al., 2021; Xu et al., 2022a*). Therefore, source-oriented dust control should address both mechanical detachment and aerodynamic entrainment.

The discrete element method (DEM) has been extensively applied to agricultural machinery–soil interactions. Bonded-particle approaches provide a means of representing cohesive failure and particle separation in granular materials (*Cundall and Strack, 1980; Potyondy and Cundall, 2004*). Agricultural DEM studies have investigated soil–tool interaction, tillage and furrow opening, soil-aggregate fracture, rotary-tillage burial and mixing, and straw–soil–cutting processes (*Zhao et al., 2021; Aikins et al., 2021; Aikins et al., 2023; Du et al., 2022; Foldager et al., 2022; Li et al., 2025*). However, the use of bond failure to characterize particle detachment specifically during high-speed flail interaction with a root stubble–soil composite remains limited.

Computational fluid dynamics (CFD) is well suited to resolving airflow organization and particle-transport conditions within agricultural machinery. Previous studies have applied CFD to optimize airflow distribution in combine-harvester cleaning systems, analyze dust diffusion during harvesting, and evaluate dust-suppression structures (*Liang et al., 2020; Xu et al., 2022b; Xu et al., 2023*). These studies demonstrate that internal airflow plays an important role in dust transport and dispersion. However, existing CFD research has mainly focused on cleaning devices, overall dust diffusion, or suppression structures, while the relationship between the near-ground inlet flow of a flail-type pickup header and the formation of different dust-generation pathways remains insufficiently quantified.

Accordingly, two limitations remain relevant to flail-type straw pickup. First, the mechanical detachment of particles from the root stubble-soil system and their subsequent aerodynamic entrainment have generally been examined as separate processes. Second, the extent to which controllable operating parameters simultaneously affect these two processes has not been clarified through field validation. Therefore, the present study used independent DEM and CFD analyses, rather than a fully coupled DEM-CFD model, and integrated their results with field measurements. The objectives were to: (1) quantify the effects of ground clearance, rotor speed, forward speed, plant spacing, and row spacing on particle detachment; (2) characterize the time-averaged internal flow field and relate its principal regions to potential dust-generation pathways; and (3) evaluate a selected low-dust operating condition using field measurements of TSP, PM_{10}, and $PM_{2.5}$. The main contribution is a mechanism-based framework linking operating parameters to both mechanical detachment and aerodynamic entrainment.

MATERIALS AND METHODS

Structure and Working Principle of the Flail-Type Pickup Header

The flail-type pickup header consists mainly of a flail rotor, housing, mounting frame, transmission system, deflector, and conveying auger (Fig. 1). The main structural parameters are listed in Table 1.

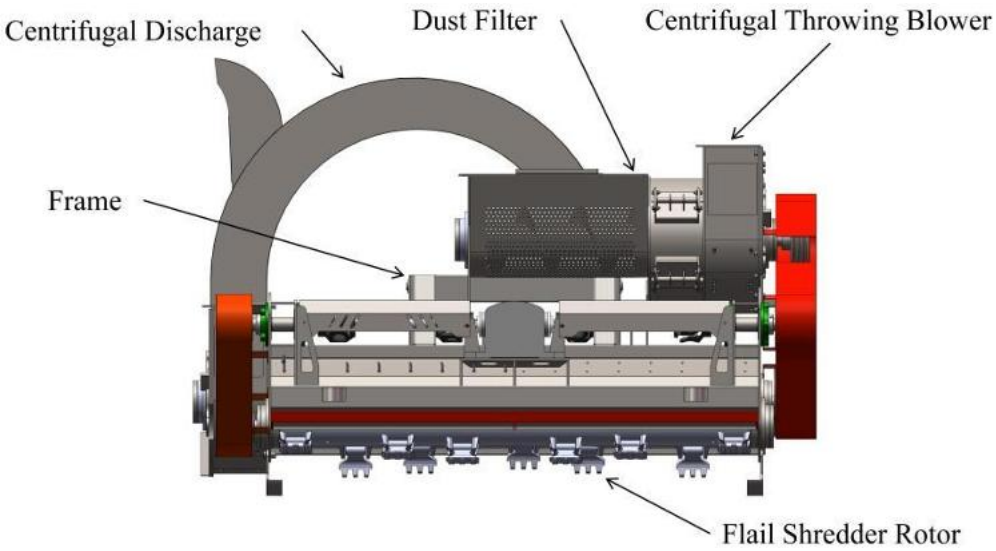


Fig. 1 - Overall Structure

Table 1

Main structural parameters of flail-type pickup header

Parameter	Value
Diameter of flail roller (mm)	180
Length of flail roller (mm)	2200
Number of flails	22
Length of flail (mm)	160

During operation, the rotor turns at 4100-5300 rpm while the machine advances. The flails strike the exposed root stubble without directly contacting the soil surface. Detached material is thrown upward and transported along the housing by the flails and the rotor-induced airflow before entering the conveying auger.

Discrete Element Model of the Root Stubble-Soil Composite

A DEM model of the corn root stubble-soil composite was established in EDEM. Root stubble and 0-100 mm surface-soil samples were obtained from the test field. Material, bonding, and contact parameters were adopted from previously calibrated and validated models for the same material system and operating region (*Zhuo et al., 2025; Xu et al., 2024*).

Table 2

Intrinsic material parameters

Material	Density (kg/m³)	Poisson's Ratio	Shear Modulus (MPa)
Corn Root Stubble	107.5	0.3	6.5
Soil Particles	1646	0.42	4.6
Flail	7850	0.3	79000

The Hertz-Mindlin with Bonding V2 contact model was applied to soil particles and root stubble, as this model can effectively simulate the cohesive forces between moist soil particles (*Potyondy and Cundall, 2004; Aikins et al., 2021*). The bonding parameters are listed in Table 3.

Table 3

Bonding parameters

Contact Pair	Stiffness per Unit Area (N/m³)	Critical Stress (MPa)	Bonding Radius (mm)
Root-Root	2.2×10^6	2.45	1.38
Soil-Soil	5×10^5	0.31	1.65
Root-Soil	6.5×10^5	0.31	1.38

The contact parameters are listed in Table 4.

Table 4

Contact parameters

Contact Type	Coefficient of Static Friction	Coefficient of Rolling Friction	Coefficient of Restitution
Soil-Soil	0.62	0.1	0.55
Soil-Root Stubble	0.42	0.21	0.6
Soil-Flail	0.60	0.10	0.3
Root Stubble-Flail	0.60	0.10	0.5

The soil bin was generated by natural packing. Root stubble was represented by 2-4 mm bonded spheres, with an approximate diameter of 25 mm and burial depth of 200 mm. Stubble units were arranged according to the prescribed plant and row spacings. The pickup geometry was imported from SolidWorks, and the rotor was assigned simultaneous rotation and forward translation. The time step was 3.6% of the Rayleigh time step.

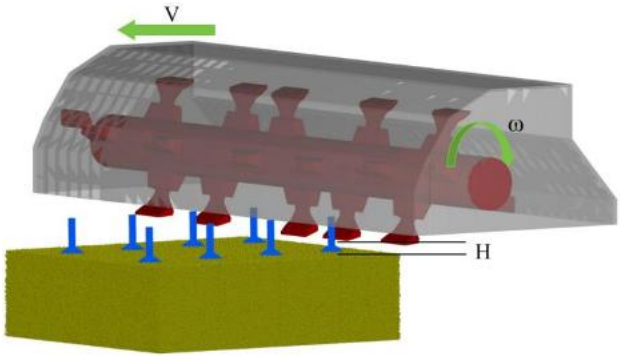


Fig. 2 - Schematic diagram of flail–root stubble interaction

Key Indicators

Because the flails did not directly contact the soil surface, bond failure was used to characterize particle detachment from the stubble-soil matrix. A bond was considered broken when the local stress exceeded its strength limit; the released particles could then be ejected by mechanical impact and subsequently entrained by airflow.

The bond fracture rate η was calculated as the ratio of the number of broken bonds, N_b, to the initial number of bonds, N_0:

$$\eta = \frac{N_b}{N_0} \times 100\% \quad (1)$$

The index was extracted from EDEM post-processing and used to compare the relative degree of particle detachment among operating conditions.

Single-Factor Experiment Design

Five factors were evaluated by single-factor simulations: ground clearance (H), rotor speed (ω), forward speed (v), plant spacing (Δx), and row spacing (Δy). When one factor was varied, the remaining factors were fixed at their intermediate levels (Table 5).

Table 5

Single-factor simulation scheme

Test Number	Operational parameters				
	Ground Clearance	Rotor Speed	Forward Speed	Plant Spacing	Row Spacing
	H (mm)	*ω* (rpm)	*v* (m/s)	Δ*x* (mm)	Δ*y* (mm)
1	30	4700	1	250	400
2	45	4700	1	250	400
3	60	4700	1	250	400
4	75	4700	1	250	400
5	90	4700	1	250	400
6	60	4100	1	250	400
7	60	4400	1	250	400
8	60	4700	1	250	400
9	60	5000	1	250	400
10	60	5300	1	250	400

Test Number	Operational parameters				
	Ground Clearance	Rotor Speed	Forward Speed	Plant Spacing	Row Spacing
	H (mm)	*ω* (rpm)	*v* (m/s)	Δ*x* (mm)	Δ*y* (mm)
11	60	4700	0.5	250	400
12	60	4700	0.75	250	400
13	60	4700	1	250	400
14	60	4700	1.25	250	400
15	60	4700	1.5	250	400
16	60	4700	1	200	400
17	60	4700	1	225	400
18	60	4700	1	250	400
19	60	4700	1	275	400
20	60	4700	1	300	400
21	60	4700	1	250	300
22	60	4700	1	250	350
23	60	4700	1	250	400
24	60	4700	1	250	450
25	60	4700	1	250	500

In addition to the single-factor simulations, two combined operating conditions were simulated for comparison with the subsequent field measurements. The selected low-dust condition was set at a ground clearance of 75 mm, a rotor speed of 4400 rpm, and a forward speed of 0.75 m/s, whereas the dust-intensive condition was set at 30 mm, 5300 rpm, and 1.0 m/s, respectively. Plant spacing and row spacing were maintained at 250 and 400 mm for both conditions. The DEM model parameters and bond-fracture-rate calculation method were kept consistent with those used in the single-factor simulations.

CFD Model of the Internal Flow Field of the Pickup Header

The internal flow field was modeled in ANSYS Fluent 2020R2. The housing, rotor region, inlet, outlet, and a closed ground boundary were retained, while small features with negligible aerodynamic influence were omitted (Fig. 3).

The computational domain was divided into a rotating rotor region and a stationary housing region connected by an interface. A steady multiple-reference-frame (MRF) model was used to obtain the time-averaged flow field. The MRF approach had previously been validated for the same pickup system by comparing simulated and measured inlet pressure distributions at 35 bench-test points *(Wang et al., 2024b)*.

The mesh contained 14.8 million cells. A pressure-based steady solver, the realizable k-ε turbulence model *(Shih et al., 1995)*, and air as the continuous phase were used. The inlet was specified as a pressure inlet, the conveying channel as the outlet, and the rotor walls moved with the rotating reference frame.

The DEM and CFD simulations were conducted independently and did not constitute a fully coupled DEM-CFD simulation. The DEM analysis was used to characterize the relative degree and spatial features of particle detachment from the root stubble-soil system, whereas the CFD analysis was used to characterize the time-averaged airflow within the pickup-header housing. To relate the two analyses, the locations and modes of particle detachment obtained from DEM were compared with the characteristic airflow regions predicted by CFD. Detachment caused by direct flail impact was examined in relation to the high-speed rotation zone, while disturbance at the root-soil interface was evaluated together with the near-ground inlet flow. In addition, the near-ground inlet velocity was compared with the estimated entrainment thresholds to assess the potential for direct lifting of loose surface particles. Accordingly, the proposed dust-generation pathways were interpreted from complementary mechanical and aerodynamic evidence rather than derived from particle trajectories in a coupled DEM-CFD simulation.

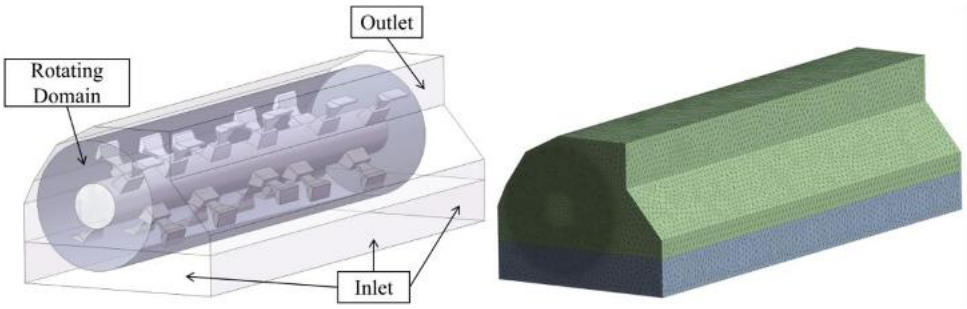


Fig. 3 - Computational Domain and Grid for the Flow Field

Field Experiment

Field tests were conducted in a corn field in Togtoh County, Inner Mongolia, China (40°20′N, 111°30′E; Fig. 4). Measured plant spacing (240-260 mm), row spacing (390-410 mm), and stubble diameter (23-28 mm) were consistent with the DEM settings.

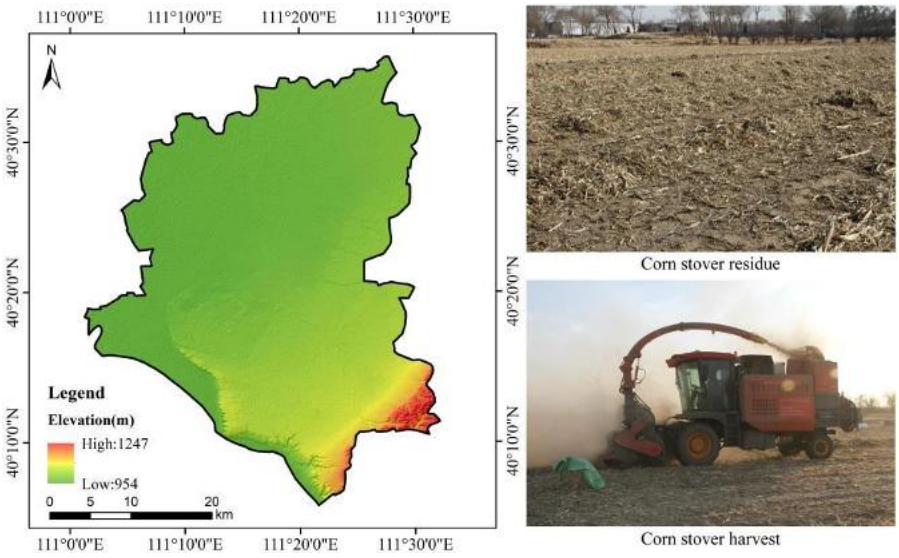


Fig. 4 - Overview of the study area

Two operating conditions were compared using a 4JKZ-240 straw feed baler harvester: a selected low-dust condition (75 mm ground clearance, 4400 rpm rotor speed, and 0.75 m/s forward speed) and a dust-intensive condition (30 mm, 5300 rpm, and 1.0 m/s). The sampling point was located directly above the pickup header (Fig. 5).



Fig. 5 - Installation Location of the Particulate Sampler

Each operating condition was evaluated in three independent field runs (n = 3). Each replicate consisted of a separate 10-min harvesting pass conducted under the same operating-parameter setting, with particulate sampling performed independently for each run.

The measured concentrations are reported as mean ± standard deviation. TSP was collected on glass-fiber filters with a KB-6120 atmospheric sampler at 100 L/min and determined gravimetrically; size-fractionated samples were collected simultaneously. Filters were conditioned for 24 h at 25 ± 1°C and 50 ± 5% relative humidity before weighing.

$$C = \frac{(m_2 - m_1)}{(Q \times t)} \times 10^6 \quad (2)$$

In Eq. (2), C is the TSP mass concentration (μg/m^3), m_1 and m_2 are the filter masses before and after sampling (g), Q is the sampling flow rate (m^3/min; 0.100 m^3/min in the present experiments), and t is the sampling duration (min). Each replicate was sampled for 10 min.

Statistical comparisons between the two operating conditions were performed using a two-sided Welch's t-test because the measured variability differed between conditions. Statistical significance was evaluated at $p < 0.05$. Given the limited number of field replicates (n = 3 per condition), the statistical results were interpreted together with the observed effect magnitude and descriptive variability.

Aerodynamic Entrainment Threshold Calculation

To evaluate the aerodynamic entrainment potential of soil particles near the pickup-header inlet, the threshold friction velocity was estimated using the simplified relationship proposed by *Shao and Lu (2000)*. The reported wind-speed dependence of agricultural-soil dust flux (*Wang et al., 2021; Wang et al., 2024a*) was further used to estimate the relative change in entrainment intensity among different rotor speeds.

$$u_{*t} = \sqrt{A_N \left[\frac{(\rho_p - \rho_a)}{\rho_a} gd \right]} \quad (3)$$

where u_{*t} is the threshold friction velocity (m/s), A_N is the dimensionless coefficient in the Shao-Lu model, ρ_p and ρ_a are the particle and air densities, respectively, g is gravitational acceleration, and d is the particle diameter. In this study, A_N was set to 0.0123 according to *Shao and Lu (2000)*.

The original Shao-Lu relationship is expressed in terms of friction velocity, whereas the CFD results provide the characteristic mean velocity in the inlet entrainment region. Therefore, the threshold friction velocity was converted into an equivalent mean-flow threshold velocity as follows:

$$U_t = \frac{U}{u_*} u_{*t} = A \sqrt{\left[\frac{(\rho_p - \rho_a)}{\rho_a} gd \right]} \quad (4)$$

where U_t is the equivalent mean-flow threshold velocity, U is the characteristic mean inlet velocity, u_* is the corresponding friction velocity, and A is the effective velocity-conversion coefficient:

$$A = \sqrt{A_N} \frac{U}{u_*} \quad (5)$$

For a first-order engineering estimate, the relationship between the mean velocity and friction velocity was obtained from the Darcy-Weisbach formulation:

$$\frac{U}{u_*} = \sqrt{\frac{8}{f}} \quad (6)$$

where f is the Darcy friction factor. The Blasius correlation for smooth turbulent flow, $f = 0.3164\ \mathrm{Re}^{-0.25}$, was adopted. Based on a characteristic inlet velocity of 5-18 m/s, a hydraulic diameter of approximately 0.2 m, and an air kinematic viscosity of 1.5×10^{-5} m^2/s, the Reynolds number was estimated to be 6.7×10^4-2.4×10^5. The corresponding Darcy friction factor was 0.0143-0.0197, giving $U/u_* \approx 20.2 - 23.7$. Substitution into Eq. (5) yielded an effective coefficient range of 2.24-2.62. A representative intermediate value of $A = 2.43$ was therefore adopted to calculate the equivalent mean-flow threshold velocities of particles with different diameters.

The threshold-exceedance ratio was calculated as the ratio of the upper inlet velocity obtained from CFD to the equivalent mean-flow threshold velocity of each representative particle diameter. The relative entrainment flux among rotor speeds was estimated using the cubic relationship between dust flux and airflow velocity reported in previous studies.

The conversion was introduced to enable a consistent comparison between the threshold friction velocity derived from the Shao-Lu relationship and the characteristic inlet velocity obtained from CFD.

The resulting equivalent mean-flow threshold velocity therefore serves as a comparative criterion for evaluating the aerodynamic entrainment potential of particles under different rotor-speed conditions. The Darcy-Weisbach and Blasius relationships provide the velocity-conversion framework under turbulent-flow conditions, while the actual pickup-header inlet flow remains spatially non-uniform because of rotor-induced rotation and local acceleration. Accordingly, the calculated threshold-exceedance ratio is used to compare relative entrainment intensity among operating conditions rather than to represent an exact local entrainment threshold at every point in the inlet region. Similarly, the cubic relationship between dust flux and airflow velocity is used to estimate the relative change in entrainment intensity rather than the absolute dust mass flux.

RESULTS

Effects of Operating Parameters on Particle Detachment

Under the reference condition of a rotor speed of 4700 rpm, a ground clearance of 60 mm, and a forward speed of 1.0 m/s, the dynamic flail-root stubble interaction was divided into four stages according to the flail position, stubble deformation, and particle detachment state: approach, impact, cutting and fragmentation, and separation and ejection (Fig. 6). Substantial bond breakage occurred during the impact and cutting stages. The detached particles acquired initial velocity from the flail impact and could subsequently be entrained and transported by the airflow inside the housing. The effects of the five operating parameters on bond fracture rate are presented in Figs. 7 and 8.

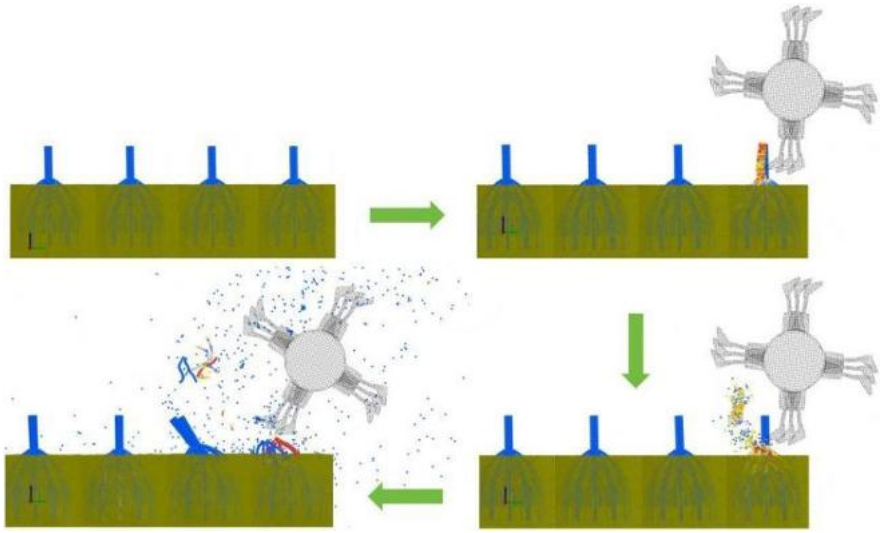


Fig. 6 - Dynamic interaction process between the flail and root stubble

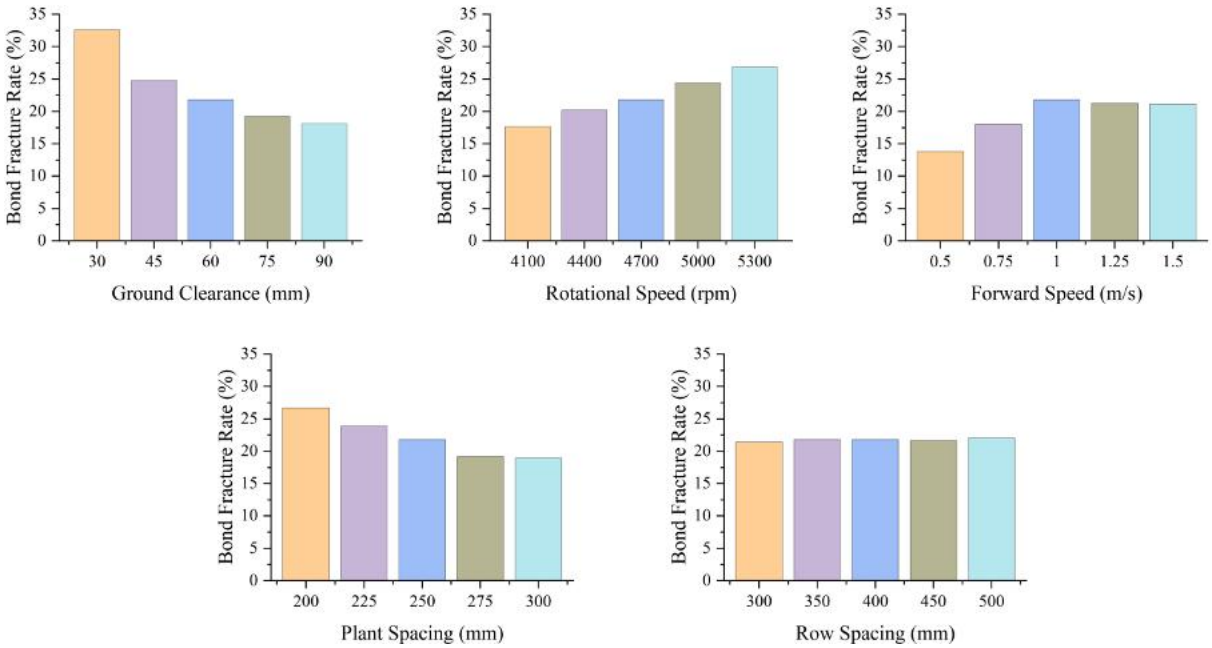


Fig. 7 - Effects of Operating Parameters on the Bond Fracture Rate

Increasing ground clearance from 30 to 90 mm reduced the bond fracture rate from 32.6% to 18.1% (44.5%), because higher clearance shifted flail action upward and reduced disturbance of the strongly bonded root-soil region.

Increasing rotor speed from 4100 to 5300 rpm raised the bond fracture rate from 17.6% to 26.8% (52.3%), as higher speed increased both impact energy and the number of impacts per unit travel distance.

Increasing forward speed from 0.5 to 1.5 m/s raised the bond fracture rate from 13.8% to 21.1%, although the change was only 0.7 percentage points between 1.0 and 1.5 m/s. Forward speed mainly affected the number of stubble contacts per unit time rather than the energy of individual impacts.

Increasing plant spacing from 200 to 300 mm reduced the bond fracture rate from 26.7% to 18.9% because fewer stubble units were encountered per unit area. Plant spacing is an inherent field condition rather than an adjustable machine parameter; therefore, it was evaluated only to characterize its influence on bond fracture rate and was not included in the selection of operating parameters.

Row spacing had the weakest effect: the bond fracture rate varied only from 21.4% to 22.0% over 300-500 mm, with no consistent monotonic trend.

The absolute variation associated with each factor is compared in Fig. 8.

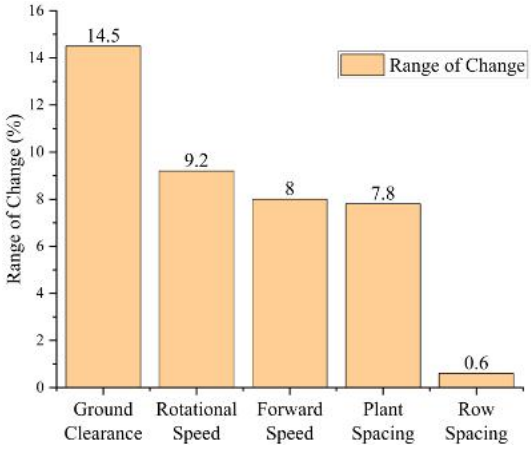


Fig. 8 - Comparison of Factors' Influence on Bond Fracture Rate

The influence order was ground clearance (14.5 percentage points) > rotor speed (9.2) > forward speed (8.0) > plant spacing (7.8) > row spacing (0.6). Thus, ground clearance and rotor speed were the principal controllable factors.

Based on the bond fracture trends within the tested parameter ranges, the candidate low-dust ranges were 60-75 mm for ground clearance, 4400-4700 rpm for rotor speed, and 0.75-1.0 m/s for forward speed. A condition of 75 mm ground clearance, 4400 rpm rotor speed, and 0.75 m/s forward speed was selected for subsequent combined DEM simulation and field comparison.

The observed effects of ground clearance and rotor speed are consistent with the general trend reported in previous agricultural-dust studies that stronger mechanical disturbance tends to increase particulate emissions. Significant differences in dust emissions have been reported among different tillage implements, with more intensive soil disturbance generally associated with higher particulate concentrations (*Çarman et al., 2023*). Agricultural tillage, planting, and harvesting operations have also been shown to generate measurable PM10 and PM2.5 emissions under field conditions (*Chen et al., 2017*). The present results extend these observations to a flail-type straw pickup header and further indicate that ground clearance and rotor speed are the principal controllable parameters governing mechanical particle detachment. The aerodynamic role of rotor speed is further examined through the CFD analysis in the following section.

Internal Flow Field of the Pickup Header and Analysis of Dust Sources

Steady MRF calculations were performed at 4100, 4700, and 5300 rpm to characterize the time-averaged internal flow field and its role in dust entrainment.

Velocity Field Distribution Characteristics

At 4700 rpm, the flow field was divided into four regions according to velocity magnitude and direction:

(1) High-speed rotation zone: airflow adjacent to the rotor formed a strong tangential shear layer, with typical velocities of 80-137 m/s and localized peaks of 153.3 m/s.

(2) Wall-guidance zone: airflow followed the curved inner housing wall at 30-60 m/s, supporting upward material transport.

(3) Inlet entrainment zone: negative pressure drew external air inward and upward through the lower opening at 5-18 m/s, providing the principal pathway for near-ground particle entrainment.

(4) Conveying-channel zone: downstream airflow was comparatively stable at 15-30 m/s and aligned with the channel axis.

The velocity distributions at the three rotor speeds are shown in Fig. 9.

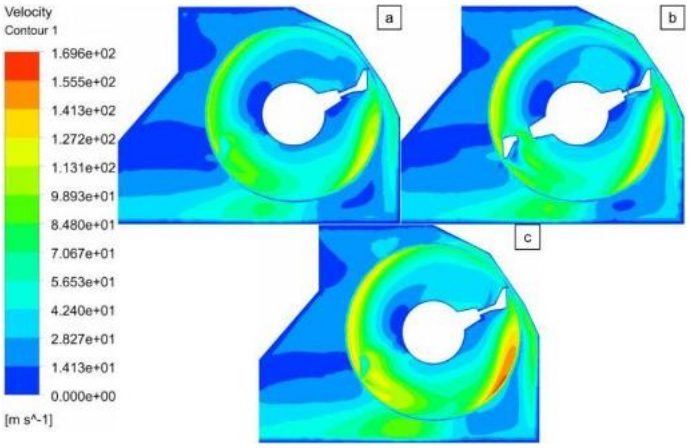


Fig. 9 - Velocity Contour Plot. (a) 4100 rpm; (b) 4700 rpm; (c) 5300 rpm

Increasing rotor speed raised velocities throughout the housing. For each 600 rpm increase, the upper velocity range in the high-speed zone increased by approximately 15-20 m/s, while the upper velocity in the inlet entrainment zone increased by about 4 m/s. The latter trend directly strengthened aerodynamic dust entrainment.

Mechanistic Interpretation of Dust Sources

Three dust-generation pathways were interpreted by relating the DEM detachment states to the corresponding CFD flow regions. Stubble-fragmentation dust originated from direct flail impact and was subsequently transported by the rotating airflow; root-extraction dust resulted from low-clearance disturbance of the root-soil interface followed by near-ground airflow entrainment; and airflow-entrainment dust consisted of loose surface particles lifted directly by the inlet flow. The first pathway increased with rotor speed, whereas the second was mainly associated with ground clearance.

Threshold-Based Comparison of Airflow Entrainment

The measured soil particle-size distribution and the calculated threshold velocities are shown in Fig. 10 and Table 6, respectively.

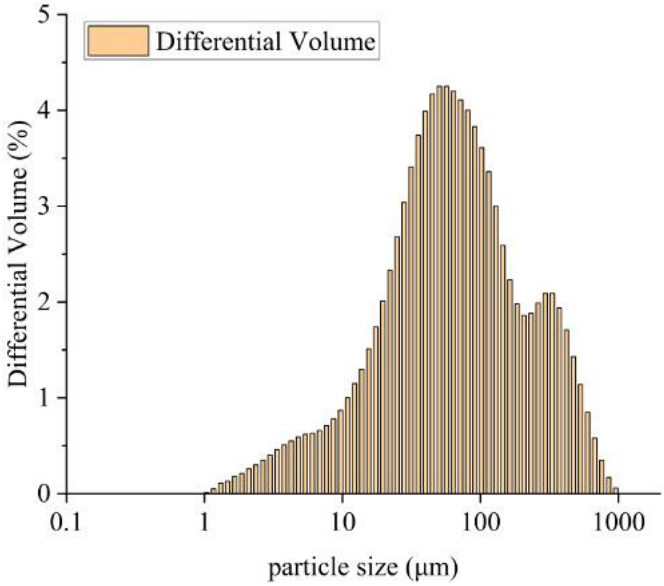


Fig. 10 - Particle Size Distribution

Table 6

Estimated threshold velocities for different particle size fractions

Particle Size (μm)	Equivalent Threshold Velocity (m/s)	Cumulative Volume Percentage (%)
10	0.89	9.38
50	1.99	48.95
100	2.81	68.70
200	3.97	83.72
300	4.87	89.68
500	6.29	96.85

Five monitoring points were placed on a horizontal plane 5 mm above the ground (Fig. 11). The upper inlet velocities of 12.7-16.1 m/s exceeded the recalculated equivalent mean-flow threshold velocities for all representative particle diameters up to 500 μm. Differences among rotor speeds therefore reflected the degree of threshold exceedance rather than whether entrainment occurred.

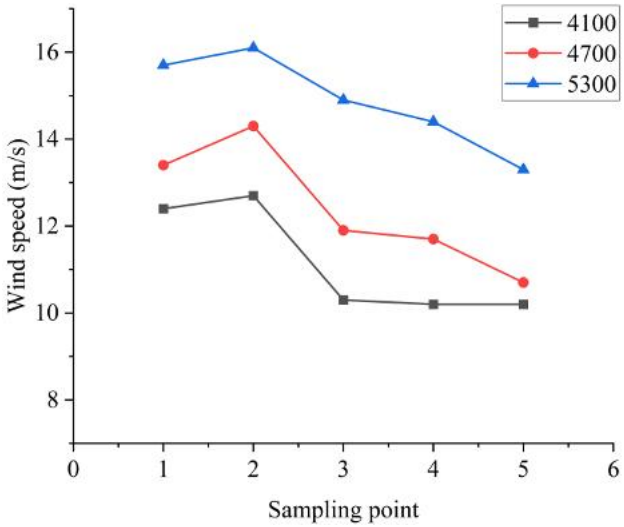


Fig. 11 - Wind Speed Comparison at Measuring Points

The threshold-exceedance ratios and bond fracture rates are compared in Table 7.

Table 7

Comprehensive comparison of airflow entrainment intensity and bond fracture rate at different rotor speeds

Rotor Speed (rpm)	Inlet Velocity Upper Limit (m/s)	Threshold-Exceedance Ratio U/U_t			Bond Fracture Rate (%)
		10-μm particle	50-μm particle	300-μm particle	
4100	12.7	14.3×	6.4×	2.6×	17.6
4700	14.3	16.1×	7.2×	2.9×	21.8
5300	16.1	18.1×	8.1×	3.3×	26.8

From 4100 to 5300 rpm, the velocity-to-threshold ratio increased by 26.8% for representative 10, 50, and 300 μm particles. Based on the calculation method described above, the estimated relative entrainment flux at 5300 rpm was approximately 2.04 times that at 4100 rpm.

Over the same speed range, the bond fracture rate increased by 52.3%. Rotor speed therefore produced a combined mechanical-aerodynamic effect: it increased the quantity of detached particles and simultaneously strengthened their entrainment. This mechanism predicts a larger change in measured dust concentration than in bond fracture rate alone and supports limiting rotor speed to 4400-4700 rpm.

Field Validation and Size-Resolved Particulate Concentrations

The background TSP concentration measured at the sampling point before operation was 56 μg/m³.

The combined DEM simulations yielded bond fracture rates of 34.6% for the dust-intensive condition and 19.1% for the selected low-dust condition, corresponding to a reduction of 44.8%. Field measurements showed the same trend: mean TSP concentration decreased from 3696.0 ± 515.6 to 1397.1 ± 229.2 μg/m3 (62.2%). The difference in TSP concentration between the two operating conditions was statistically significant according to a two-sided Welch's t-test (t = 7.057, p = 0.0076). The larger measured reduction relative to the bond fracture rate is consistent with simultaneous suppression of mechanical detachment and airflow entrainment.

The bond fracture rate should be interpreted as an indicator of the relative degree of particle detachment rather than as a direct predictor of airborne dust concentration. This index quantifies bond failure within the DEM model but does not account for particle size, the fraction of detached particles that actually becomes airborne, subsequent transport and deposition, re-entrainment of loose surface material, or ambient background particles. Therefore, the 44.8% reduction in bond fracture rate and the 62.2% reduction in measured TSP should not be expected to exhibit a one-to-one quantitative relationship. Their consistent trend supports the proposed mechanical-detachment mechanism, while the larger reduction in measured TSP is compatible with the simultaneous weakening of aerodynamic entrainment.

Size-fractionated measurements were used to determine whether the selected low-dust condition also reduced respirable and fine particulate concentrations.

Under the selected low-dust condition, PM_{10} and $PM_{2.5}$ accounted for 68.4% and 22.3% of TSP, respectively; under the dust-intensive condition, the corresponding proportions were 62.2% and 18.3% (Fig. 12).

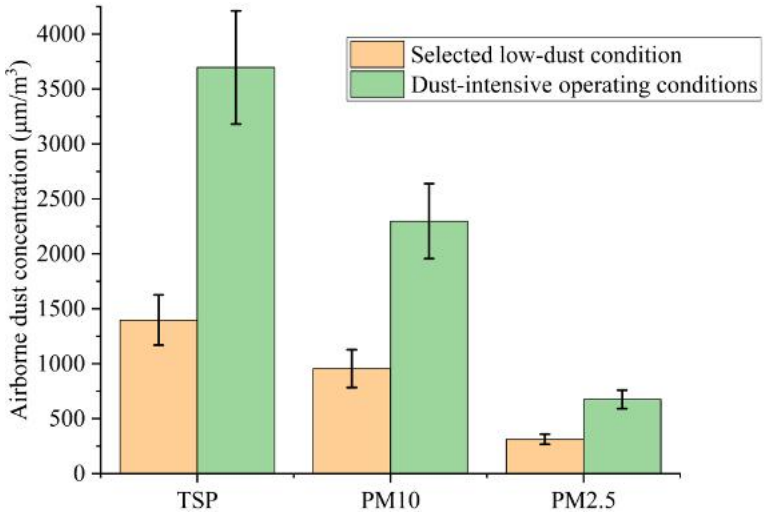


Fig. 12 - Particulate matter concentrations under different operating conditions.

Although the fine-particle proportions were slightly lower under the dust-intensive condition because coarse fragmentation debris increased, the absolute PM_{10} and $PM_{2.5}$ concentrations rose from 955.4 and 312.2 μg/m³ to 2297.4 and 675.2 μg/m³. The selected low-dust condition therefore reduced PM_{10} and $PM_{2.5}$ concentrations by 58.4% and 53.8%, respectively.

The measured TSP concentrations also provide useful context relative to previous harvesting studies. The TSP concentration of 1397.1 μg/m³ under the selected low-dust condition was slightly below the previously reported range of approximately 1500-3000 μg/m³ for harvesting operations, whereas the dust-intensive condition reached 3696.0 μg/m³ and exceeded this range (*Zhang et al., 2021; Xu et al., 2022a*). $PM_{2.5}$ accounted for 18.3%-22.3% of TSP in the present tests, which was lower than the 30%-45% proportion reported in previous harvesting studies (*Zhang et al., 2021; Xu et al., 2022a*). This difference may reflect variations in crop type, soil condition, machine structure, sampling position, and the relatively large contribution of coarse fragments generated by high-speed flail impact. Therefore, direct comparison of absolute concentrations among studies should be made cautiously.

These results demonstrate that parameter adjustment reduced both total and fine particulate emissions; however, the short sampling duration and fixed sampling location do not constitute a full occupational exposure assessment.

CONCLUSIONS

Ground clearance and rotor speed governed dust generation through different but interacting mechanisms. Ground clearance primarily affected mechanical particle detachment by changing the position of flail interaction relative to the strongly bonded root-soil region, whereas rotor speed influenced both impact-induced detachment and the strength of the inlet airflow. Relating the DEM particle-detachment characteristics to the CFD flow-field regions supported three mechanism-based dust-generation pathways: stubble fragmentation, root extraction, and direct airflow entrainment of loose surface particles.

Field measurements further showed that the selected combination of increased ground clearance and moderate rotor speed substantially reduced TSP, PM_{10}, and $PM_{2.5}$ concentrations relative to the dust-intensive condition, demonstrating the practical potential of operating-parameter adjustment for dust mitigation. The results also indicate that reducing excessive inlet negative pressure while maintaining pickup performance represents a promising direction for structural improvement.

Several limitations should be acknowledged. The DEM and CFD analyses were conducted independently rather than through fully coupled particle-flow simulation, and the bond fracture rate represents particle detachment rather than airborne dust concentration itself. Field validation was also limited to two operating conditions, a single field environment, three short-duration replicates per condition, and a fixed sampling position. Future studies should therefore examine a wider range of crops, soil conditions, and operating parameters; employ longer-duration and multi-point field measurements; investigate transient or coupled particle-airflow interactions; and evaluate pickup-header inlet modifications that reduce direct particle entrainment without compromising pickup efficiency.

ACKNOWLEDGEMENTS

This work was supported financially by the National Natural Science Foundation of China [52365035], the First-class Discipline Research Special Projects of the Inner Mongolia Autonomous Region [YLXKZX-NND-046], and the Natural Science Foundation of Inner Mongolia Autonomous Region [2025MS03015].

REFERENCES

[1] Aikins K. A., Ucgul M., Barr J. B., Jensen T. A., Antille D. L., Desbiolles J. M. A. (2021). Determination of discrete element model parameters for a cohesive soil and validation through narrow point opener performance analysis. *Soil and Tillage Research*, 213, 105123. https://doi.org/10.1016/J.STILL.2021.105123.

[2] Aikins K. A., Ucgul M., Barr J. B., Awuah E., Antille D. L., Jensen T. A., Desbiolles J. M. A. (2023). Review of discrete element method simulations of soil tillage and furrow opening. *Agriculture*, 13(3), 541. https://doi.org/10.3390/AGRICULTURE13030541.

[3] Chen G., Wang Q., Li H., He J., Lu C., Qin W., Mao L. (2024). Monitoring of farmland dust during tillage and sowing operations and comparative analysis of cultivation modes in the suburban areas of Beijing. *Soil & Tillage Research*, 237, 105991. https://doi.org/10.1016/J.STILL.2023.105991.

[4] Çarman K., Taner A., Mikailsoy F., Selvi K. Ç., Ungureanu N., Vlăduț N. V. (2023). Application of Computational Intelligence in Describing Dust Emissions in Different Soil Tillage Applications in Middle Anatolia. *Agriculture*, 13(5), 1011. https://doi.org/10.3390/agriculture13051011.

[5] Chen W., Tong D. Q., Zhang S., Zhang X., Zhao H. (2017). Local PM10 and PM2.5 emission inventories from agricultural tillage and harvest in northeastern China. Journal of Environmental Sciences, 57, 15–23. https://doi.org/10.1016/j.jes.2016.02.024.

[6] Cundall P. A., Strack O. D. L. (1980). A discrete numerical model for granular assemblies. *Géotechnique*, 30(3), 331–336. https://doi.org/10.1680/geot.1980.30.3.331.

[7] Du J., Heng Y., Zheng K., Luo C., Zhu Y., Zhang J., Xia J. (2022). Investigation of the burial and mixing performance of a rotary tiller using discrete element method. *Soil and Tillage Research*, 215, 105349. https://doi.org/10.1016/J.STILL.2022.105349.

[8] Foldager F. F., Munkholm L. J., Balling O., Serban R., Negrut D., Heck R., Green O. (2022). Modeling soil aggregate fracture using the discrete element method. *Soil and Tillage Research*, 218, 105295. https://doi.org/10.1016/J.STILL.2021.105295.

[9] Li R., Li H., Yang S., Lu C., Wu Z., Wang Z. (2025). DEM simulation of straw-soil-cutting system interactions for performance assessment of a spin-descent straw cutter. *Computers and Electronics in Agriculture*. https://doi.org/10.1016/J.COMPAG.2025.111022.

[10] Liang Z., Xu L., De Baerdemaeker J., Li Y., Saeys W. (2020). Optimisation of a multi-duct cleaning device for rice combine harvesters utilising CFD and experiments. *Biosystems Engineering*, 190, 25–40. https://doi.org/10.1016/j.biosystemseng.2019.11.016.

[11] Potyondy D. O., Cundall P. A. (2004). A bonded-particle model for rock. *International Journal of Rock Mechanics and Mining Sciences*, 41(8), 1329–1364. https://doi.org/10.1016/j.ijrmms.2004.09.011.

[12] Shao Y., Lu H. (2000). A simple expression for wind erosion threshold friction velocity. *Journal of Geophysical Research: Atmospheres*, 105(D17), 22437–22443. https://doi.org/10.1029/2000JD900304.

[13] Shih T. H., Liou W. W., Shabbir A., Yang Z., Zhu J. (1995). A new k-ε eddy viscosity model for high Reynolds number turbulent flows. *Computers and Fluids*, 24(3), 227–238. https://doi.org/10.1016/0045-7930(94)00032-T.

[14] Wang R., Li Q., Wang R., Chang C., Guo Z., Li J., Zhou N. (2021). Influence of wind velocity and soil size distribution on emitted dust size distribution: A wind tunnel study. *Journal of Geophysical Research: Atmospheres*, 126(7). https://doi.org/10.1029/2020JD033768.

[15] Wang R., Zhang Y., Zhang S., Li Q., Wang R., Li Z., Chang C., Guo Z., Zhou N. (2024). Comprehensive effect of soil particle size composition and wind speed on dust emission efficiency. *Journal of Geophysical Research: Atmospheres*, 129(3), e2023JD039618. https://doi.org/10.1029/2023JD039618.

[16] Wang X., Tian H., Xiao Z., Zhao K., Li D., Wang D. (2024). Numerical simulation and experimental study of corn straw grinding process based on computational fluid dynamics–discrete element method. *Agriculture*, 14(2), 325. https://doi.org/10.3390/agriculture14020325.

[17] Xu H., Zhang P., Hu Z., Mao E., You Z., Du Y. (2022). Analysis of dust emission characteristics of peanut whole-feed harvesting based on total amount collection method. *International Journal of Environmental Research and Public Health*, 19(23), 15937. https://doi.org/10.3390/IJERPH192315937.

[18] Xu H., Zhang P., Hu Z., Mao E., Yan J., Yang H. (2022). Analysis of dust diffusion from a self-propelled peanut combine using computational fluid dynamics. *Biosystems Engineering*, 215, 104–114. https://doi.org/10.1016/J.BIOSYSTEMSENG.2022.01.004.

[19] Xu H., Zhang P., Gu F., Hu Z., Yang H., Mao E., Du Y. (2023). Numerical simulation and experiment of dust suppression device of peanut whole-feed combine using computational fluid dynamics. *Agriculture*, 13(2), 329. https://doi.org/10.3390/AGRICULTURE13020329.

[20] Xu T., Gou Y., Huang D., Yu J., Li C., Wang J. (2024). Modeling and parameter selection of the corn straw-soil composite model based on the DEM. *Agriculture*, 14(11), 2075. https://doi.org/10.3390/AGRICULTURE14112075.

[21] Yang W., Li X., Zhang Y. (2022). Research progress and the development trend of the utilization of crop straw biomass resources in China. *Frontiers in Chemistry*, 10, 904660. https://doi.org/10.3389/FCHEM.2022.904660.

[22] Zhang P., Xu H., Hu Z., Chen Y., Cao M., Yu Z., Mao E. (2021). Characteristics of agricultural dust emissions from harvesting operations: Case study of a whole-feed peanut combine. *Agriculture*, 11(11), 1068. https://doi.org/10.3390/agriculture11111068.

[23] Zhang P., Xu H., Hu Z., Wang Q. (2023). Effects of agricultural machinery operations on PM2.5, PM10 and TSP in farmland under different tillage patterns. *Agriculture*, 13(5), 930. https://doi.org/10.3390/agriculture13050930.

[24] Zhao H., Huang Y., Liu Z., Liu W., Zheng Z. (2021). Applications of Discrete Element Method in the Research of Agricultural Machinery: A Review. *Agriculture*, 11(5), 425. https://doi.org/10.3390/AGRICULTURE11050425.

[25] Zhuo C., Tian H., Xiao Z., Mu Q., Tang L., Zhao K. (2025). Simulation analysis of mechanical response and failure mechanisms of maize stubble-soil composite based on discrete element method and fiber bundle model. *Computers and Electronics in Agriculture*, 236, 110452. https://doi.org/10.1016/J.COMPAG.2025.110452.

DESIGN AND TESTING OF A COMPOSITE POTATO PICKUP DEVICE BASED ON EDEM
/
基于 EDEM 的复合式马铃薯捡拾装置设计与试验

Zheng MA[1,2)], Jianjiao HUANG[1,2)], Shuai WANG[1,2,*)], Yaoming LI[1,2)], Zhiqiang SONG[1,2)] [1]
[1)] School of Agricultural Engineering, Jiangsu University, Zhenjiang 212013, Jiangsu, China
[2)] Key Laboratory for Theory and Technology of Intelligent Agricultural Machinery and Equipment, Jiangsu University, Zhenjiang 212013, Jiangsu, China
Corresponding author's Tel: 18261977691; E-mail: swang@ujs.edu.cn
DOI: https://doi.org/10.35633/inmateh-79-103

Keywords: *potato; pickup device; discrete element; structural optimization; low damage*

ABSTRACT
To address the problems of low manual pickup efficiency and severe soil accumulation in existing shovel-type pickup devices used for segmented potato harvesting, a composite pickup device consisting of a grid-type segmented pickup shovel and a flexible lifting wheel was designed. A potato-soil-machine discrete element simulation model was established using EDEM to optimize structural parameters, including grid spacing, and to investigate the effects of operating parameters, including forward speed, digging depth, and lifting-wheel speed, on pickup performance. The simulation results showed that grid spacing was negatively correlated with the loss rate and positively correlated with the damage rate. An optimized grid spacing of 25 mm reduced the damage rate to 2.21% and the loss rate to 3.70%, while effectively reducing potato jamming. As the forward speed and lifting-wheel speed increased, the loss rate decreased, whereas the damage rate increased. Digging depth had a nonlinear effect on the loss rate, which initially decreased and then increased, reaching its minimum at a digging depth of 100 mm, whereas the damage rate continuously decreased with increasing digging depth. Field tests yielded an average loss rate of 3.88% and an average damage rate of 2.24%, meeting the operational requirements for potato harvesting.

摘要
针对马铃薯分段收获中人工捡拾效率低和现有铲式捡拾装置易壅土的问题，设计了一种由栅栏分段式捡拾铲与柔性拨薯轮组成的复合式捡拾装置。基于 EDEM 软件建立了薯-土-机离散元仿真模型，优化栅栏间距等结构参数并探究了前进速度、入土深度和拨薯轮转速等作业参数对捡拾性能的影响。仿真结果表明：栅栏间距与损失率负相关，与伤薯率正相关；优化后的 25 mm 栅栏间距使伤薯率降至 2.21%，损失率为 3.70%，显著减少了薯块卡滞现象；前进速度和拨薯轮转速增加时，损失率下降而伤薯率上升，入土深度对损失率呈先降后升的非线性影响，100 mm 时最优，对伤薯率则持续降低。田间试验平均损失率为 3.88%，伤薯率为 2.24%，满足马铃薯收获作业要求。

INTRODUCTION
Potato mechanized harvesting can be divided into combine harvesting and segmented harvesting. At present, segmented harvesting is still the predominant method in hilly areas with many small fields *(Wang et al., 2023)*. In segmented harvesting, the preliminary operations such as vine killing, digging, separation, and windrowing have achieved a relatively high level of mechanization. However, the pickup operation still relies heavily on manual labor, resulting in high labor intensity and low efficiency (*Dorokhov et al., 2022*). Therefore, developing a low-damage, high-efficiency potato pickup device is of great significance for improving the mechanization level of segmented potato harvesting and reducing labor costs.

Existing pickup devices can be mainly divided into two categories. The first category is shovel-type pickup devices represented by flat shovels, triangular shovels, and bionic shovels, which are currently widely used and usually adopt a single-stage flat structure. These devices have high forward resistance and severe soil accumulation, which easily cause potatoes to roll back into the furrow and increase the loss rate. However, they can achieve continuous feeding and high operational efficiency *(Beznosyuk et al., 2022; Yang et al., 2025; Mamatov and Karimov, 2023)*.

[1] *Zheng Ma (Professor), Jianjiao Huang (Master's degree student), Shuai Wang (Assistant Researcher), Yaoming Li (Professor), Zhiqiang Song (Assistant Researcher)*

The second category is rotary pickup devices represented by spring-tooth and disc types. They achieve intermittent grasping through rotating components, which avoids large amounts of soil being drawn in, enables targeted picking of potatoes, reduces operational resistance, and alleviates the burden of subsequent potato-soil separation. Nevertheless, these devices are prone to causing damage due to collisions with potatoes, and the forward speed and rotational speed cannot be too high; otherwise, missing picking may occur, limiting the overall operational efficiency *(Lu et al., 2023; Yang et al., 2024; Toure and Wei, 2023)*. Addressing the shortcomings of existing pickup devices, this study designed a composite pickup device consisting of a grid-segmented pickup shovel and a flexible lifting wheel. The device uses the grid structure of the pickup shovel to perform preliminary screening of the potato-soil mixture to alleviate soil accumulation, improves the pickup rate through the horizontal section of the segmented shovel surface, and reduces collision damage by means of the flexible lifting wheel's active rotary conveying action.

The discrete element method has been widely applied in research on potato-soil separation, digging resistance analysis, and structural optimization of equipment, as it can effectively simulate the complex interactions among potatoes, soil, and machinery. Based on this method, this study established a potato-soil-machine discrete element simulation model using EDEM software. The grid spacing of the pickup shovel was taken as a key parameter for optimization, and single-factor simulation experiments were conducted to systematically analyze the effects of forward speed, digging depth, and lifting wheel speed on picking performance. Finally, the operational performance of the device was verified through field experiments, confirming that the composite pickup device under optimized parameters meets the requirements for low-damage and low-loss potato pickup harvesting. This study provides a theoretical basis and technical reference for the optimal design of potato pickup equipment.

MATERIALS AND METHODS

Design of the composite pickup device

The specific structure of the composite pickup device is shown in Fig. 1. It mainly consists of a depth-limiting wheel, a height adjustment plate, a pickup shovel, a lifting wheel, a frame, etc. Its core is a composite structure in which the pickup shovel and the lifting wheel work synergistically: combining the advantages of continuous feeding and high efficiency of the traditional flat pickup shovel, while drawing on the targeted picking concept of the spring-tooth pickup device. By using the active conveying of the lifting wheel to replace the passive pushing of the shovel surface, effective pickup of potatoes is achieved.

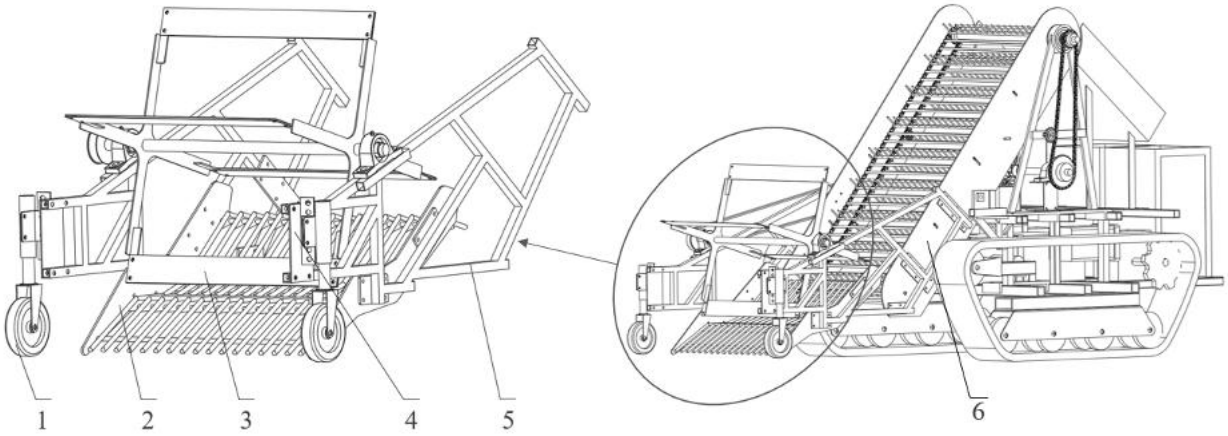


Fig. 1 - Structural schematic of the combined pickup device

1. Depth-limiting wheel 2. Pickup shovel 3. Lifting wheel 4.Height adjustment plate 5. Frame 6. Conveying and lifting device

Before operation, the depth-limiting wheel is adjusted to fit the side of the ridge. During operation, the potato-soil mixture is initially screened by the grid structure of the pickup shovel, and the potatoes remain on the shovel surface. The lifting wheel rotates to generate an active conveying force, smoothly pushing the potatoes off the shovel surface and onto the subsequent conveying and lifting device, finally completing the collection and bagging of potatoes. To adapt to terrain fluctuations, a compression spring is built into the depth-limiting wheel: when compressed, the spring drives the wheel to lift adaptively, buffering impacts and maintaining the working depth, thereby ensuring pickup quality. The main parameters of the composite pickup device are shown in Table 1.

Table 1

Main parameters of the composite pickup device

Item	Value
Overall dimensions (L×W×H) / (mm×mm×mm)	1039 × 818 × 906
Working width / mm	600
Applicable ridge width / mm	≤800
Applicable ridge height / mm	100–200
Number of ridges worked	1

Grid-segmented pickup shovel

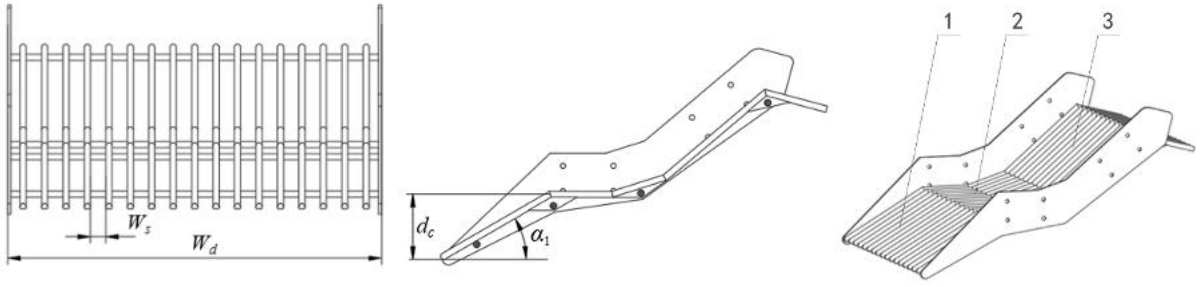
The pickup shovel is the core component of the pickup device. Structural innovations were made based on the traditional flat pickup shovel:

(1) The traditional shovel surface was optimized into a grid structure to preliminarily screen the potato-soil mixture and reduce traveling resistance.

(2) The single-stage shovel surface was reconstructed into a three-stage "inclined–horizontal–inclined" structure: the digging stage screens the soil and picks up underground potatoes (those buried beneath the soil surface); the horizontal stage forms a zero-inclination pickup platform to improve the pickup rate; a smooth transition section is added at the junction between the horizontal stage and the lifting stage to eliminate geometric discontinuities and enhance the low-damage performance of the device; the lifting stage works together with the lifting wheel to raise the potatoes to a certain height for subsequent conveying; and a guide section is provided at the end of the lifting stage to achieve impact-free connection with the conveying and lifting device.

According to the agrotechnical requirements for potato planting in hilly areas, the ridge width ranges from 600 to 800 mm. After digging, potatoes are scattered on the ridge surface with a distribution width of approximately 450 mm and a surface distribution depth of less than 40 mm *(Ahmad and Sharma, 2023)*. To ensure that the pickup shovel completely covers the potato distribution area, the shovel width W_d was designed as 600 mm. The resistance on the shovel surface increases with the entry angle, considering energy saving and soil penetration performance, the entry angle α_1 is generally taken as 20°- 30° *(Wei et al., 2023)*. To shorten the horizontal projection length of the pickup shovel, the upper limit of the entry angle, 30°, was chosen. The digging depth d_c of the pickup shovel should be controlled between 80 -120 mm. Based on this, the length of the first segment of the pickup shovel was set to 200 mm.

The three-axis size distribution of potatoes ranges from 30 to 160 mm *(Wang et al., 2023)*. To prevent small-sized potatoes from becoming embedded or stuck in the grid gaps, the grid spacing of the pickup shovel should be smaller than the minor axis of potatoes. In existing potato harvesting equipment, the grid spacing is mostly designed with reference to the bar spacing of the conveying and lifting chain or the separation conveyor chain, with typical values of 30 - 40 mm *(Bulgakov et al., 2021)*. During such conveying processes, potatoes mainly move with the conveyor chain under their own weight, without significant active pressing action between the potatoes and the grid; therefore, the grid spacing is mainly determined based on passing ability and soil sieving performance. Unlike conventional conveying structures, the pickup device designed in this study uses a lifting wheel to actively convey the potato tubers. When passing through the grid area, potatoes are subjected not only to gravity but also to the contact thrust applied by the lifting wheel, which may press them into the grid gaps. Consequently, the traditional grid spacing parameters are not directly applicable to the design of the present device. Considering the potato size distribution and existing equipment design experience *(Wei et al., 2023)*, the grid spacing W_s was preliminarily set to 30 mm, which will be further optimized through discrete element simulations. The specific structure and parameters of the grid-segmented pickup shovel are shown in Fig. 2.



(a) Front view of pickup shovel (b) Left view of pickup shovel (c) Axonometric view of pickup shovel

Fig. 2 - Structural diagram of the pickup shovel

1.Digging stage; 2.Horizontal stage; 3.Lifting stage

Flexible lifting wheel

Although the grid structure of the pickup shovel enables preliminary screening of the potato-soil mixture, thereby alleviating soil accumulation and reducing loss due to accumulation as well as forward resistance, it also brings a new problem: after soil and potatoes are separated, the potatoes lose the pushing effect of the soil, becoming stranded on the pickup stage of the shovel and difficult to effectively pushed forward and lifted. To address this issue, a lifting wheel is added above the pickup shovel. The lifting wheel is covered with a flexible material (canvas) and generates an active conveying force when rotating. When potatoes remain on the shovel surface, the paddles of the lifting wheel, with a relatively large contact area, smoothly push the potatoes off the shovel surface, avoiding the surface bruising and impact damage caused by the direct rigid collision of spring teeth or fingers in existing studies.

Although the lifting wheel draws on the active conveying concept of the spring-tooth pickup device, its mode of action is different: the spring-tooth pickup device relies on the spring teeth to directly grasp potatoes on the soil surface, and if the grasping fails, it results in missed pickups. In contrast, in the present design, potatoes continuously enter the shovel surface through the forward motion of the pickup shovel, and the lifting wheel only plays an auxiliary pushing role without undertaking the "grasping" function, thus not causing missed pickups. Therefore, the pickup efficiency is mainly inherited from the high-efficiency continuous feeding characteristic of the traditional flat shovel, achieving a balance between targeted potato picking and a high pickup rate.

To facilitate the smooth entry of potatoes into the subsequent elevator conveyor, the lifting wheel needs to push the potatoes up along the lifting section of the pickup shovel to a certain height. As shown in Fig. 3, from point A to point B for the potato, the relationship between the lifting wheel radius and the potato lifting height is given by the following formula:

$$H = \sqrt{2Rd - d^2}sin\beta + dcos\beta + R - Rcos\beta \quad (1)$$

where: H is the potato lifting height, mm;

β is the inclination angle of the third segment of the pickup shovel, (°);

d is the short-axis dimension of the potato, mm;

R is the minimum radius of the lifting wheel, mm.

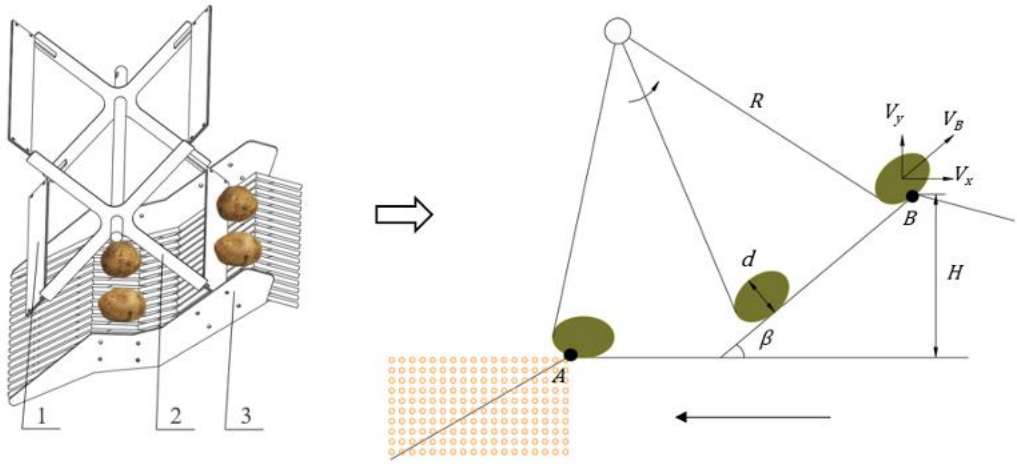


Fig. 3 - Schematic diagram of potato processing

1.Paddle; 2. Lifting wheel; 3. Pickup shovel

At the detachment position (point B), when the potato reaches the highest point with the lifting wheel, it is thrown out along the lifting stage of the pickup shovel and enters the subsequent conveying and lifting device. To facilitate the detachment of the potato from the lifting wheel paddle, the horizontal component of velocity V_X should be greater than the vertical component V_Y, i.e., $V_B cos\beta > V_B sin\beta$. From this, β should be less than 45°. To shorten the horizontal dimension of the pickup shovel and achieve better lifting effect, the inclination angle β of the lifting stage of the pickup shovel was preset to 40°.

Based on the measured distribution range of potato three-axis dimensions, the minimum short-axis dimension d of the potato was taken as 30 mm. To ensure the potato smoothly enters the subsequent conveying and lifting device, the minimum lifting height was set to 150 mm. From equation (1), the lifting wheel radius $R \geq 231$ mm, so R = 300 mm was adopted.

Establishment of the discrete element model

Soil and potato particle models

Soil particles were modeled using spherical particles with a radius of 5 mm. To characterize the actual soil particle size distribution, based on the investigation results of soil particle size in hilly areas (<1 mm: 8.44%, 1- 2 mm: 23.12%, 2 - 5 mm: 37.68%, >5 mm: 30.76%) *(Issa et al., 2025; Chen et al., 2024)*, scaling factors of 0.1, 0.3, 0.5, and 2.0 times were set in the EDEM particle factory, corresponding to generated spherical particles with diameters of 0.5, 1.5, 2.5, and 10.0 mm, and the number generated was allocated according to the mass proportions.

Based on the measured average three-axis dimensions of potatoes, two types of simulation particle models were established: spherical-like and ellipsoidal. The spherical-like potato model had a short axis of 60 mm and a long axis of 66 mm; the ellipsoidal potato model had a short axis of 50 mm and a long axis of 85 mm. These were formed as discrete element models using multi-sphere aggregates. The two types of potato particle models are shown in Fig. 4. To reflect the size variation of tubers in the field, a random scaling factor of 0.6 -1.5 times was applied to the base models in the EDEM particle factory to generate particles covering the range of small, medium, and large tubers.



(a) Spherical-like potato (b) Ellipsoidal potato

Fig. 4 - Simulation model of potato particles

Referring to field conditions, a soil bin and potato ridge model were established: the soil bin length was 7000 mm, the ridge bottom width was 800 mm, the ridge surface width was 600 mm, and the ridge height was 150 mm. The particle factory for potatoes was placed at a height of 400 mm above the soil surface, allowing the potato tubers to fall freely and form a distribution close to the field scattering state. Based on the estimated actual potato yield, a total of 21 kg of potatoes was generated.

Simulation parameter settings

The basic characteristic parameters of the materials are shown in Table 2 *(Li et al., 2023; Wang et al., 2023; Pan et al., 2025)*. The Hertz–Mindlin (no slip) model was used for contacts between particles and the machine components, whereas the Hertz–Mindlin with JKR model was used for particle–particle contacts. The rolling friction model was the standard rolling friction model. The interaction parameters for contact are shown in Table 3 *(Yan et al., 2023; Pan et al., 2026; Foldager et al., 2022)*. The simulation time step was set to 20% of the Rayleigh time step, calculated to be approximately 1.2×10^{-5} s. The data save interval was set to 0.01 s *(Maraveas et al., 2025).*

Table 2

Basic simulation parameters

Parameter	Poisson's ratio	Density / (kg/m³)	Shear modulus / Pa
Potato	0.47	1047	1.99×10^6
Soil	0.25	1240	1.00×10^6
Steel	0.30	7800	7.00×10^{10}
Rubber plate	0.30	1800	3.85×10^7

Table 3

Interaction simulation parameters

Interaction pair	Coefficient of restitution	Coefficient of static friction	Coefficient of rolling friction
Potato-Potato	0.60	0.48	0.03
Soil-Soil	0.13	0.56	0.27
Potato-Soil	0.53	0.50	0.01
Potato-Steel	0.65	0.28	0.16
Soil-Steel	0.28	0.49	0.57
Soil-**Canvas**	0.12	0.66	0.54
Potato-**Canvas**	0.71	0.51	0.20

Evaluation indicators

Referring to the quality evaluation indicators for self-propelled potato combine harvesters in JB/T 14285-2022 "Potato Harvesting Machinery" *(JB/T 14285-2022, 2022)*, and considering the actual working conditions of pickup operations, the performance evaluation indicators for the device were determined as follows: loss rate ≤ 4%, damage rate ≤ 2.5%.

Previous studies typically take the potato extrusion force damage threshold as 100 N *(Yang et al., 2024)*. However, multiple low-stress collisions may also cause cumulative tissue damage. To establish a more practical warning value, a preloading test was conducted on the potato variety used in this study (Qingshu No.9). The results showed that when the extrusion force reached approximately 60 N, slight surface indentations and softening began to appear on the tubers. Therefore, referring to existing damage thresholds and combining with the observations from the pre-test, a more conservative value of 60 N was adopted as the damage risk warning value, which is used to characterize potentially high-risk force events rather than the critical value for actual visible damage.

RESULTS AND ANALYSIS

Initial simulation and problem diagnosis under baseline operating parameters

In the initial design, the grid spacing of the pickup shovel was set to 30 mm. To diagnose whether there were any jamming or damage issues under this structural parameter, referring to typical potato harvesting operating conditions and the design experience of similar pickup devices *(Lu et al., 2023)*, a set of conventional operating parameters was selected as the baseline: forward speed of 0.40 m/s, digging depth of 100 mm, and lifting wheel speed of 20 r/min. A simulation of the pickup process was carried out under these operating conditions, as shown in Fig. 5.

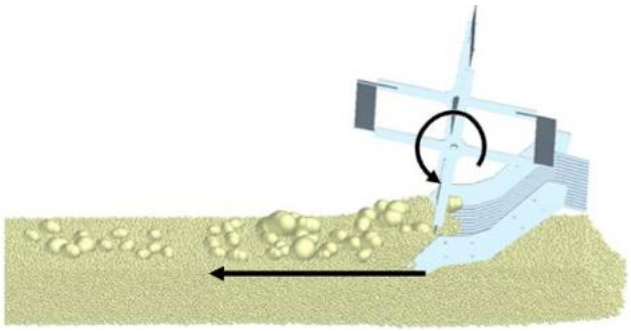


Fig. 5 - Simulation experiment of the pickup process

The time-history curve of the maximum extrusion force during the pickup process was extracted, as shown in Fig. 6. The maximum extrusion force on potatoes during pickup was recorded at intervals of 0.1 s. The red horizontal line in the figure indicates the damage risk warning value of 60 N.

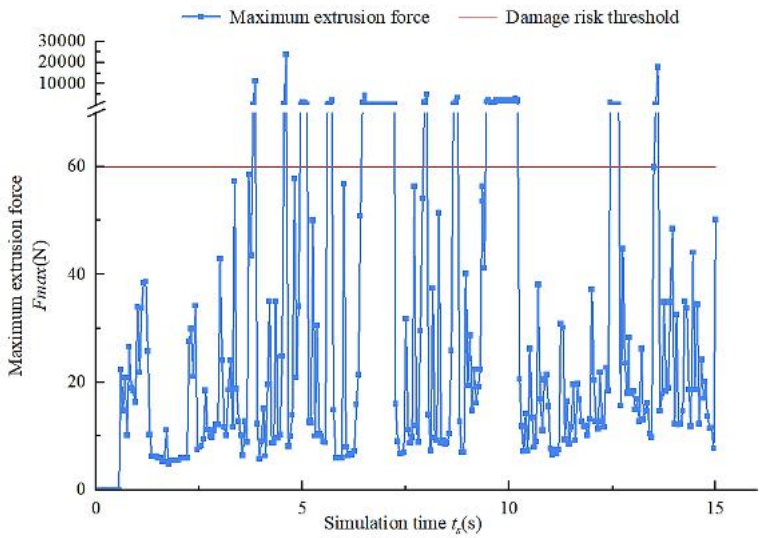
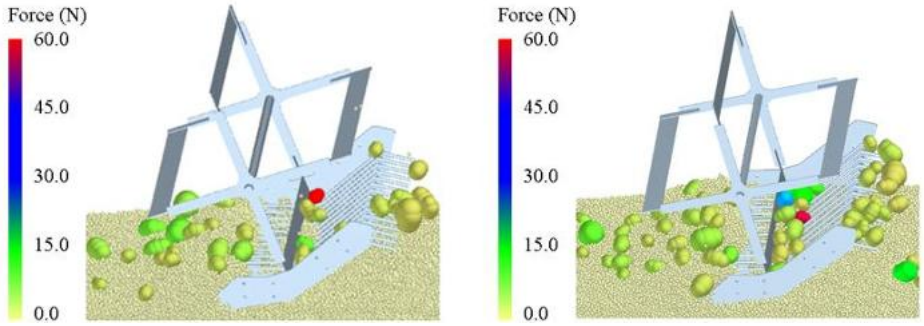


Fig. 6 - Time-history curve of extrusion force during potato pickup process (grid spacing 30 mm)

As shown in Fig. 6, during the 15 s pickup process, a total of 10 damage risk events with extrusion force exceeding 60 N occurred, with an average frequency of approximately once every 1.5 s. Among them, during the intervals of 6.4 - 7.2 s and 9.5 - 10.2 s, the high extrusion force states lasted for about 0.9 s and 0.8 s, respectively, and the risk events were mainly concentrated in the period of 3.8 - 13.6 s, indicating that under the initial grid spacing of 30 mm, the potatoes experienced a significant sustained compression phenomenon during the pickup process. To further analyze the causes of high extrusion forces, typical risk periods were selected for observation, and the results are shown in Fig. 7. It can be seen that during the periods of 6.4 -7.2 s and 9.5 - 10.2 s, potato jamming in the grid gaps occurred. After small-sized potatoes or the tips of potatoes became embedded in the grid gaps, they were constrained by the grid structure under the continuous conveying action of the lifting wheel, making it difficult to detach in time, thus forming a sustained compression state.



(a) Potato jam at simulation time 6.4-7.2 s (b) Potato jam at simulation time 9.5-10.2 s

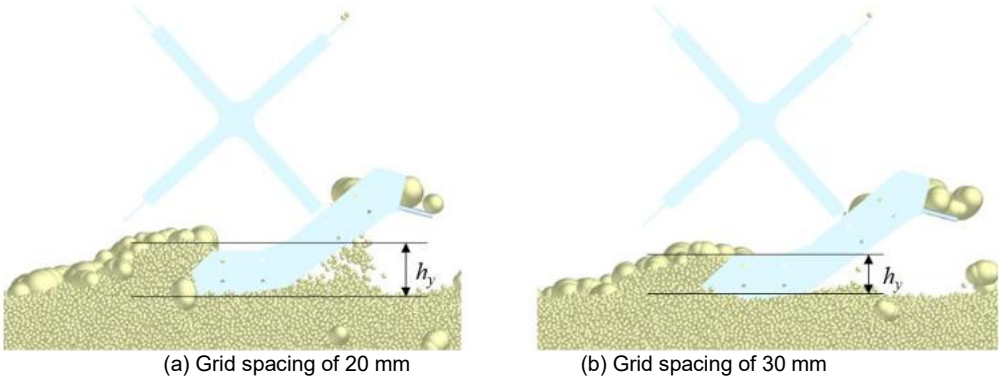
Fig. 7 - Abnormal conditions of potato during pickup process (grid spacing 30 mm)

The analysis suggests that although the 30 mm grid spacing can theoretically effectively prevent small-sized potatoes from falling through the gaps, due to the irregular shapes and random postures of the potatoes, their tips or local protruding parts are still prone to becoming embedded in the grid gaps. Once a potato tuber is embedded, under the continuous conveying action of the lifting wheel, it is easy to form a local "embedding–sustained compression" state, causing the extrusion force to remain at a high level for a certain period, with consecutive sampling points exceeding the 60 N risk warning value.

Combining the analysis of the extrusion force time-history curve and the particle motion state, it can be seen that the high extrusion force events did not occur randomly but showed a clear correspondence with potato jamming, exhibiting a certain regularity. This indicates that the initial 30 mm grid spacing is close to the minor axis size of some small-sized potato tubers, which easily induces tuber embedding and sustained compression. Therefore, it is necessary to further optimize the grid spacing parameter to reduce the risks of potato jamming and mechanical damage.

Single-factor optimization of grid spacing

Based on the clogging and potato damage risks observed in the initial simulation, a single-factor sensitivity analysis was conducted using grid spacing as the test factor. Five levels were selected: 20, 22.5, 25, 27.5, and 30 mm, among which 30 mm was the initial design value. The operating parameters were kept constant for all treatments: forward speed of 0.40 m/s, digging depth of 100 mm, and lifting wheel rotational speed of 20 r/min. Each treatment was simulated three times.



(a) Grid spacing of 20 mm (b) Grid spacing of 30 mm

Fig. 8 - Soil accumulation under different grid spacings of the pickup device

The simulation results showed that grid spacing had a significant influence on soil screening performance and potato conveying behavior. As shown in Fig. 8, when the grid spacing was small (e.g. 20 mm), the soil passed slowly through the grid gaps, resulting in obvious soil accumulation at the front of the pickup shovel. Potatoes tended to accumulate on the shovel surface. As the device moved forward, the accumulated soil caused potatoes in front of the shovel to roll backward or fall back into the ridge bottom, preventing them from entering the pickup shovel smoothly and thereby increasing the loss rate. With increasing grid spacing (e.g. 30 mm), the soil screening capacity improved, the soil accumulation height h_y at the front of the pickup shovel decreased significantly, and the potato passing performance improved, resulting in a lower loss rate.

However, when the grid spacing became excessively large, although soil separation was improved, potatoes were more likely to become embedded in the grid gaps and jam between adjacent rods. Under the continuous conveying action of the lifting wheel, this led to sustained compression and an increase in potato damage rate. The variation trends of simulated damage rate and simulated loss rate under different grid spacings are shown in Fig. 9.

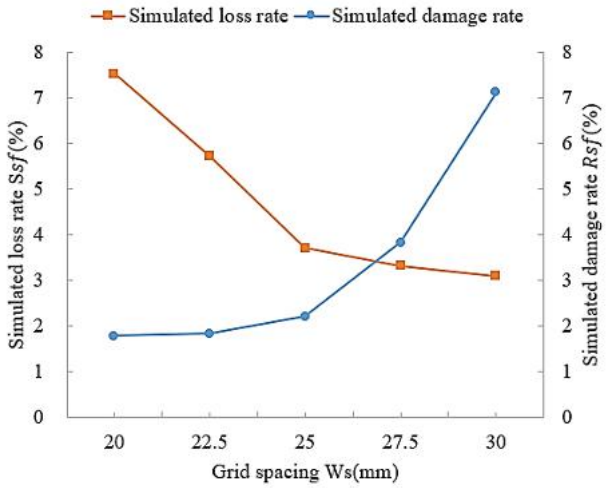


Fig. 9 - Simulated damage rate and simulated loss rate under different grid spacings

As shown in Fig. 9, with the increase of grid spacing, the simulated loss rate showed an overall downward trend, indicating that a larger spacing is beneficial for soil sieving and potato passage. When the grid spacing increased from 20 mm to 30 mm, the simulated loss rate decreased from 7.52% to 3.10%. At the same time, the simulated damage rate increased from 1.79% to 7.11%, indicating that excessive grid spacing significantly increases the risk of potatoes becoming embedded in the gaps and experiencing jamming and compression. Among the tested spacings, the damage rates at 20 mm and 22.5 mm were relatively low, but the loss rates reached 7.52% and 5.71%, respectively, indicating poor pickup performance. At 27.5 mm and 30 mm, the loss rates were low, but the damage rates increased significantly. A comprehensive comparison of the results shows that, under the premise that the damage rate does not exceed the design requirement of 2.5%, the grid spacing of 25 mm corresponds to the lowest loss rate of 3.70%, with a damage rate of 2.21%, demonstrating the best overall performance. Therefore, 25 mm was determined as the optimal grid spacing.

Force validation after optimization

Simulation was conducted again using the optimized grid spacing of 25 mm, and the time-history curve of potato extrusion force during the pickup process was extracted, as shown in Fig. 10. A total of 150 valid sampling points were obtained. Among them, only four isolated sampling points exceeded the 60 N damage warning threshold, occurring at 2.7 s (89.2 N), 5.6 s (90.0 N), 10.0 s (63.5 N), and 11.1 s (97.3 N), accounting for approximately 2.6% of the total sampling points. For the remaining 97.4% of the sampling points, the maximum extrusion force remained within the safe range.

Compared with the initial 30 mm grid spacing, the optimized 25 mm grid structure no longer showed continuous jamming events involving multiple consecutive sampling points exceeding the threshold. The peak extrusion force was controlled below 100 N, and the overall loading level was significantly reduced. This indicates that the optimized grid spacing effectively alleviated sustained compression of potatoes during the pickup process.

The analysis suggests that after reducing the grid spacing, potatoes were less likely to become embedded in the grid gaps. The contact mode gradually changed from “embedded compression” to “surface sliding contact”, thereby reducing the probability of continuous high-load events. In addition, the average extrusion force remained at a relatively low level after optimization, indicating that the interaction between the lifting wheel and potatoes was mainly characterized by transient contact and flexible conveying, without obvious accumulation or sustained compression.

These results demonstrate that the 25 mm grid spacing not only ensures effective soil screening and smooth potato passage, but also effectively suppresses tuber embedding and jamming, significantly reducing the risk of mechanical damage. Therefore, it can be considered an optimal structural parameter that achieves a good balance between low loss rate and low damage rate.

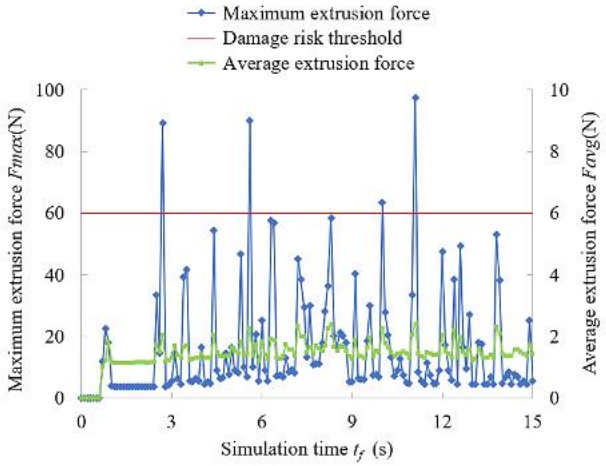
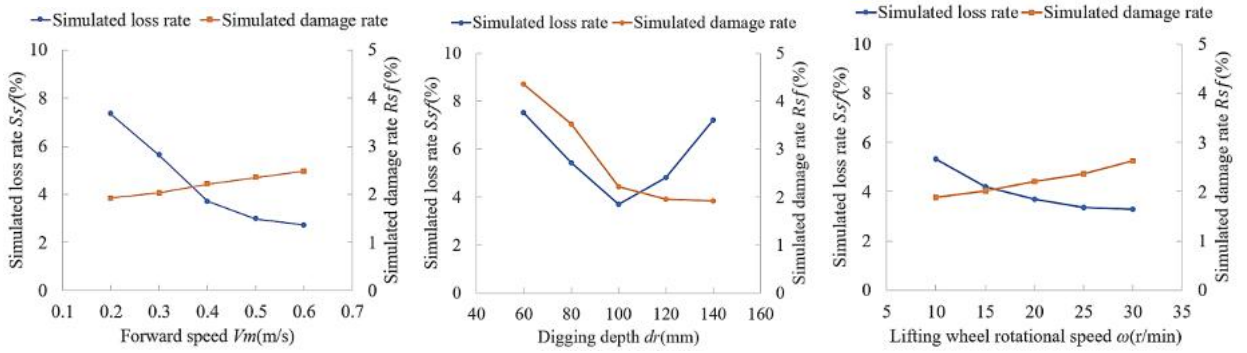


Fig. 10 - Time-history curve of extrusion force during the potato pickup process (optimized grid spacing 25 mm)

Single-factor analysis of the influence of operating parameters on pickup performance

On the basis of determining the optimal grid spacing (25 mm), single-factor simulation tests were carried out to further investigate the influence trends of the overall forward speed, digging depth of the pickup shovel, and lifting wheel speed on the pickup performance. The value ranges of forward speed and digging depth were set with reference to relevant studies on shovel-type pickup devices *(Yang et al., 2024)*, while the value range of lifting wheel speed was determined based on the operating parameters of a spring-tooth pick up device with a similar radius *(Lu et al., 2023*). Accordingly, the forward speed was preliminarily set at 0.2 - 0.6 m/s, the digging depth at 60 - 140 mm, and the lifting wheel speed at 10 - 30 r/min. When testing one factor, the other two factors were kept at their intermediate levels (forward speed 0.40 m/s, digging depth 100 mm, lifting wheel speed 20 r/min). Each parameter combination was simulated three times, and the average values were taken. The influence trends of forward speed, digging depth, and lifting wheel speed on the simulated loss rate and simulated damage rate are shown in Fig. 11(a), (b), and (c), respectively.



(a) Effect of forward speed on pickup performance

(b) Effect of digging depth on pickup performance

(c) Effect of lifting wheel speed on pickup performance

Fig. 11- Effect of operating parameters on picking performance

Analysis of the experimental results yields:

(1) Effect of forward speed: As the forward speed increased from 0.20 m/s to 0.60 m/s, the simulated loss rate decreased significantly (from 7.35% to 2.72%), while the simulated damage rate increased slowly (from 1.92% to 2.48%). A higher forward speed gives the potato-soil mixture sufficient inertia to be transported backward quickly, reducing soil accumulation and buildup, thereby lowering the loss rate.

However, a higher speed also increases the relative collision speed between potatoes and the pickup shovel, leading to a slight increase in the damage rate. When the forward speed exceeded 0.50 m/s, the damage rate approached the design upper limit of 2.5%, and the decrease in loss rate leveled off, indicating that further increasing the forward speed has limited marginal effect on improving pickup performance.

(2) Effect of digging depth: The simulated loss rate exhibited a U-shaped curve with increasing digging depth, first decreasing and then increasing. It was highest at 60 mm (7.52%), lowest at 100 mm (3.70%), and then rose to 7.20% at 140 mm. The simulated damage rate, in contrast, continuously decreased (from 4.36% at 60 mm to 1.92% at 140 mm). When the digging depth was too shallow (60 mm), the end of the digging stage of the pickup shovel was prone to emerge from the soil surface, causing potatoes to stagnate and roll off, resulting in a high loss rate. Moreover, the shallow depth meant less soil and more direct collisions, leading to a higher damage rate. As the digging depth increased, the buffering effect of the soil was enhanced, and the damage rate continued to decrease. However, when the depth exceeded 100 mm, soil accumulation worsened, causing the loss rate to rise again.

(3) Effect of lifting wheel speed: As the lifting wheel speed increased from 10 r/min to 30 r/min, the simulated loss rate continuously decreased from 5.34% to 3.28%, while the simulated damage rate continuously increased from 1.89% to 2.63%. Increasing the speed effectively alleviated soil accumulation and enhanced the active conveying capacity, thereby reducing missed pickup losses. However, excessively high speeds increased the frequency and velocity of collisions between the paddles and the potatoes, leading to a higher damage rate.

Field experiment and simulation comparison

Experimental conditions

The field experiment was conducted in November 2025 at the potato experimental field of the College of Agricultural Engineering, Jiangsu University (Fig. 12). Measurements showed that the ridge bottom width was 800 mm, the ridge surface width was 600 mm, the ridge height was 150–200 mm, and the soil was loam. Before the experiment, the soil moisture content and bulk density were measured: moisture content was determined by the oven-drying method, and bulk density by the cutting ring method, with five sampling points and three repetitions for each. The results showed an average soil moisture content of 14.2% and an average bulk density of 1.28 g/cm³. The test variety was "Qingshu No. 9". Potatoes were manually and randomly placed on the ridge surface according to their field distribution state, with some buried 5–6 cm into the soil to simulate exposed and buried potatoes. The test area length was 10 m, and the total mass of potatoes placed was approximately 30–35 kg. After the test, the picked and missed potatoes were separately collected and weighed, and the damaged potatoes were also picked out and weighed.



Fig. 12 - Field test of potato pickup harvesting

Experimental results and comparison with simulation

Field tests were conducted using the optimized parameter combination (grid spacing of 25 mm, forward speed of 0.40 m/s, digging depth of 100 mm, lifting wheel speed of 20 r/min), and the results are shown in Table 4.

Table 4

Field experiment results of potato pickup harvesting

Indicator	1	2	3	4	5	Mean ± SD
Loss rate Y_1 (%)	3.45	4.24	3.76	4.15	3.82	3.88 ± 0.32
Damage rate Y_2 (%)	2.18	2.31	2.22	2.34	2.15	2.24 ± 0.08

From Table 4, it can be seen that the average loss rate in the field test was 3.88% and the average damage rate was 2.24%, indicating that the designed composite pickup device can meet the operational requirements for potato pickup and harvesting under the optimized grid spacing. Meanwhile, the test results are in good agreement with the simulated predicted values (loss rate 3.70%, damage rate 2.21%), with relative deviations of 4.97% and 1.4%, respectively, further verifying the reliability of the EDEM simulation model and the damage warning method. The deviations mainly stem from the presence of soil clods, stones, and slightly higher surface unevenness in the field compared to the simulation settings, which caused localized soil accumulation and a very small number of missed potatoes. In summary, the composite pickup device with a grid spacing of 25 mm can achieve both low loss and low damage operational requirements.

CONCLUSIONS

(1) To address the problems of low manual picking efficiency, susceptibility to soil accumulation, and high damage rate of existing pickup devices during segmented potato harvesting, a composite potato pickup device consisting of a grid-segmented pickup shovel and a flexible lifting wheel was designed. This device enables preliminary screening of the potato-soil mixture and active conveying, effectively reducing soil accumulation and mechanical damage to potatoes.

(2) A potato–soil–machine discrete element simulation model was established using EDEM to optimize the grid spacing and conduct single-factor simulation analyses. The results showed that increasing the grid spacing was beneficial for reducing the loss rate but increased the risk of potato embedding and jamming, leading to a higher damage rate. After comprehensive comparison, a grid spacing of 25 mm was determined as the optimal value, corresponding to a simulated loss rate of 3.70% and a simulated damage rate of 2.21%. The single-factor simulation analyses also indicated that as the forward speed and lifting wheel speed increased, the simulated loss rate showed an overall decreasing trend while the simulated damage rate gradually increased. Digging depth exhibited a non-linear effect on pickup performance: the simulated loss rate first decreased and then increased with increasing digging depth, whereas the simulated damage rate decreased overall.

(3) Field tests were conducted using the optimized grid spacing (25 mm) and operating parameters. The results showed an average loss rate of 3.88% and an average damage rate of 2.24%, both better than the industry standard requirements (loss rate $\leq$ 4%, damage rate $\leq$ 2.5%), verifying that the designed composite pickup device under the optimized parameters can meet the operational requirements of low loss and low damage.

ACKNOWLEDGEMENT

This research was financially supported by the National Natural Science Foundation of China (32401691) and the Ministry of Agriculture and Rural Affairs Key Project (NK202216050102).

REFERENCES

1. Ahmad, U., & Sharma, L. (2023). A review of Best Management Practices for potato crop using Precision Agricultural Technologies. *Smart Agricultural Technology*, 4, 100220. https://doi.org/10.1016/j.atech.2023.100220
2. Beznosyuk, R.V., Evtekhov, D.V., Borychev, S.N., Kostenko, M.Y., & Rembalovich, G.K. (2022). Justification of parameters of a finger hump of potato harvesters when vibrating canvas. *IOP Conference Series: Earth and Environmental Science*, 981, 042051. https://doi.org/10.1088/1755-1315/981/4/042051
3. Bulgakov, V., Bonchik, V., Holovach, I., Fedosiy, I., Volskiy, V., Melnik, V., Ihnatiev, Y., & Olt, J. (2021). Justification of parameters for novel rotary potato harvesting machine. *Agronomy Research,* 19(S2), 994-1007. https://doi.org/10.15159/AR.21.079
4. Chen, Y., Wang, Z., Zhang, H., Liu, X., Li, H., Sun, W., & Li, H. (2024). Investigation of the Traveling Performance of the Tracked Chassis of a Potato Combine Harvester in Hilly and Mountainous Areas. *Agriculture,* 14(9), 1625. https://doi.org/10.3390/agriculture14091625
5. Dorokhov, A., Didmanidze, O., Aksenov, A., Sibirev, A., Sazonov, N., Mosyakov, M., Godyaeva, M. (2022). The Results of Studies on the Assessment of the Destruction of Soil Clods during Combine Harvesting of Potatoes. *Agriculture*, 12(12), 2024. https://doi.org/10.3390/agriculture12122024
6. Foldager, F.F., Munkholm, L.J., Balling, O., Serban, R., Negrut, D., Heck, R.J., Green, O. (2022). Modeling soil aggregate fracture using the discrete element method. *Soil and Tillage Research*, 218, 105295. https://doi.org/10.1016/j.still.2021.105295

7. Issa, I.I.M., Zhang, Z.G., ElKolaly, W., Wang, F.A., & Wang, Y. (2025). Innovated design, simulation and evaluation of potato harvester excavation and separation conveyors. *International Journal of Agricultural and Biological Engineering,* 18(2), 132–145. https://doi.org/10.25165/j.ijabe.20251802.9164
8. JB/T 14285-2022. (2022). Potato harvesting machinery. Chinese Machinery Industry Standard.
9. Li, J., Li, X., Hu, B., Gu, T., Wang, Z., Wang, H. (2023) Analysis of the resistance reduction mechanism of potato bionic digging shovels in clay and heavy soil conditions. *Computers and Electronics in Agriculture* 214: 108315. https://doi.org/10.1016/j.compag.2023.108315
10. Lu, K., Xie, S., Gai, X., Ji, X. (2024). Design and Experiment of Toggle Lever-Type Potato Picker. *Agriculture,* 14, 826. https://doi.org/10.3390/agriculture14060826
11. Mamatov, F., & Karimov, A. (2023). Potato digger with latticed plowshares and oscillating rods. *E3S Web of Conferences*, 401, 04029. https://doi.org/10.1051/e3sconf/202340104029
12. Maraveas, C., Tsigkas, N., & Bartzanas, T. (2025). Agricultural processes simulation using discrete element method: a review. Computers and Electronics in Agriculture, 237(C), 110733. https://doi.org/10.1016/j.compag.2025.110733
13. Pan, Y., Zhang, J., Zhao, A., Lv, S., Liu, W., Yang, R. (2026). Dynamic Response Analysis and Multi-Objective Optimization of a Potato–Soil Separation Conveyor Based on DEM–MBD Coupling and Field Validation. *Agriculture*, 16, 473. https://doi.org/10.3390/agriculture16040473
14. Pan, Y.F., Yang, R.B., Zhang, H., Zhang, J., Zha, X.T., Qiu, Z.C. (2025). Experiment and optimization of the potato-soil separation and conveying device for a harvester using RecurDyn-EDEM coupling simulation. *International Journal of Agricultural and Biological Engineering*, 18(4), 149-156. https://doi.org/10.25165/j.ijabe.20251804.9219
15. Toure, P. A. J., Wei, S. (2023) Design and characteristic parameters of vibrating potato digger for small farms. *International Journal of Student Project Reporting*, 1(3): 203-231. https://doi.org/10.1504/IJSPR.2023.132509
16. Wang, F., Cao, Q., Li, Y., Pang, Y., Xie, K., & Zhang, Z. (2023). Design and trafficability experiment of self-propelled potato harvester in hilly and mountainous areas（丘陵山区自走式马铃薯联合收获机设计与通过性试验）. *Transactions of the Chinese Society for Agricultural Machinery*, 54(s2), 10-19. https://doi.org/10.6041/j.issn.1000-1298.2023.S2.002
17. Wang, H., Zhao, W., Sun, W., Zhang, H., Liu, X., & Li, H. (2023). Research progress on the technology and equipment for potato mechanized harvesting (马铃薯机械化收获技术与装备研究进展). *Transactions of the Chinese Society of Agricultural Engineering*, 39(14), 1-22. https://dx.doi.org/10.11975/j.issn.1002-6819.202303056
18. Wang, W., Yang, R., Pan, Z., Qing, Y., Zhang, J., Chen, D., Guo, X., & Lyu, S. (2024). Design and Experimental Study of Single Plant Harvester for Potato Breeding Experiments. *Agriculture,* 14(1), 71. https://doi.org/10.3390/agriculture14010071
19. Wang, X., Yang, D., Liu, M., Li, Y., Chen, X., & Cheng, Z. (2023). Parameter optimization and experiment of picking device of self-propelled potato picker（自走式马铃薯捡拾机捡拾装置参数优化与试验）. *Transactions of the Chinese Society for Agricultural Machinery*, 54(s2), 20-29. https://doi.org/10.6041/j.issn.1000-1298.2023.S2.003
20. Wei, Z., Wang, X., Li, X., Wang, F., Li, Z., & Jin, C. (2023). Design and Experiment of Crawler Self-propelled Sorting Type Potato Harvester（履带自走式分拣型马铃薯收获机设计与试验）. *Transactions of the Chinese Society for Agricultural Machinery*, 54(2), 95-106. http://dx.doi.org/10.6041/j.issn.1000-1298.2023.02.009
21. Yan, D., Deng, W., Xie, S., Liu, C., Ren, Z., Zhao, H., Cai, Y., & Zhao, Z. (2023). Discrete Element-Based Simulation Analysis and Research of Potato Soil Agglomerate Fragmentation and Separation. *Applied Sciences*, 13(14), 8416. https://doi.org/10.3390/app13148416
22. Yang, D., Wang, X., Liu, M., Li, Y., Chen, X., & Cheng, Z. (2024). Design and experiment of self-propelled potato collecting and bagging machine（自走式马铃薯捡拾装袋机设计与试验）. *Transactions of the Chinese Society for Agricultural Machinery*, 2024, 55(1): 85-95. http://dx.doi.org/10.6041/j.issn.1000-1298.2024.01.008
23. Yang, R., Xu, W., Pan, Z., Zhang, H., Deng, Z. (2025). Design and experiment of a bionic drag-reducing digger for tuberous crops under heavy soil conditions. *PLOS ONE*, 20(2), e0318526. https://doi.org/10.1371/journal.pone.0318526

BASELINE CHARACTERISATION AND MULTI-YEAR ELEMENTAL MONITORING OF BIOMASS CROPS ON POST-MINING LAND IN PETRILA, ROMANIA
/
CARACTERIZAREA INIȚIALĂ ȘI MONITORIZAREA MULTIANUALĂ A COMPOZIȚIEI ELEMENTARE A CULTURILOR DE BIOMASĂ PE TEREN POST-MINIER DIN PETRILA, ROMÂNIA

Emilia-Cornelia DUNCA[1)], Sorin Mihai RADU[1)], Mădălina-Flavia IONIȚĂ[1)], Sabin Ioan IRIMIE[1)], Daniela-Ionela CIOLEA[1)], Cristian Marian SORICĂ[2*)]

[1)] Universitatea din Petroșani, 20 Universității Street, Petroșani, Romania
[2)] INMA Bucharest, 6 Ion Ionescu de la Brad Blvd., Bucharest, Romania
**E-mail: cri_sor2002@yahoo.com*
DOI: https://doi.org/10.35633/inmateh-79-104

Keywords: *post-mining land, biomass crops, soil penetration resistance, potentially toxic elements, ICP-MS, crop rotation, multi-year monitoring*

ABSTRACT
Post-mining substrates are spatially heterogeneous and require site-specific diagnosis before biomass cultivation. This study documents the establishment and three-year monitoring of a 4,500 m² field platform on a coal-mining waste dump in Petrila, Romania. Nine 500 m² plots were used: three fixed-crop reference plots (designated as controls in the original project records) and six plots under a balanced cyclic rotation of maize (Zea mays), soybean (Glycine max) and sweet sorghum (Sorghum bicolor). Amendment treatments formed part of the wider experimental layout but are not evaluated in the present manuscript. Baseline measurements at eight points in June 2023 included instrument-reported volumetric water content (VWC), temperature, penetration resistance, field pH and semi-quantitative N-P-K screening, complemented by preliminary potentially toxic element screening. Mean VWC was 26.6 ± 4.2% at 5 cm and 20.0 ± 4.3% at 15 cm; mean temperatures were 18.2 ± 1.3 and 16.7 ± 1.1°C. Mean penetration resistance across seven complete profiles was 1.05 ± 0.28 MPa and increased with depth. Field pH averaged 7.1 ± 0.1, and the available laboratory summary prioritised Cu and Ni for follow-up. All crops reached reproductive development. Preliminary operational harvest totals were 85, 263 and 487 kg in 2023, 2024 and 2025, respectively; these values are reported descriptively only and are not interpreted as crop yield because harvested area, crop-specific contributions and moisture basis were not documented consistently. The nine crop-year elemental records are likewise treated as single descriptive observations displaying apparent crop-year differences in the reported Cu, Ni, Zn and Pb values; no inferential comparison among crops or years and no conclusion on soil-to-plant transfer or bioaccumulation is made.

REZUMAT
Substraturile post-miniere sunt eterogene spațial și necesită diagnoză specifică înaintea cultivării biomasei. Studiul documentează înființarea și monitorizarea pe trei ani a unei platforme de 4.500 m² pe halda Petrila. Au fost utilizate nouă parcele de 500 m²: trei parcele de referință cu cultură fixă (desemnate drept martor în documentația inițială a proiectului) și șase cu rotație echilibrată de porumb (Zea mays), soia (Glycine max) și sorg zaharat (Sorghum bicolor). Tratamentele cu amendamente au făcut parte din configurația experimentală extinsă, dar nu sunt evaluate în prezentul manuscris. Caracterizarea inițială din iunie 2023, în opt puncte, a inclus umiditatea volumetrică raportată de instrument, temperatura, rezistența la penetrare, pH-ul de teren și screeningul N-P-K, completate de screeningul preliminar al elementelor potențial toxice. Umiditatea medie a fost 26,6 ± 4,2% la 5 cm și 20,0 ± 4,3% la 15 cm, iar temperaturile 18,2 ± 1,3 și 16,7 ± 1,1°C. Rezistența medie la penetrare pentru șapte profile complete a fost 1,05 ± 0,28 MPa și a crescut cu adâncimea. pH-ul mediu a fost 7,1 ± 0,1, iar sinteza de laborator a prioritizat Cu și Ni pentru monitorizare. Toate culturile au ajuns la dezvoltare reproductivă. Totalurile operaționale preliminare ale biomasei recoltate au fost de 85, 263 și 487 kg în 2023, 2024 și, respectiv, 2025; aceste valori sunt raportate exclusiv descriptiv și nu sunt interpretate ca producții agricole, deoarece suprafața recoltată, contribuțiile specifice fiecărei culturi și baza de umiditate nu au fost documentate consecvent. Cele nouă înregistrări cultură-an privind compoziția elementală sunt, de asemenea, tratate ca observații descriptive individuale, evidențiind diferențe aparente între combinațiile cultură-an în valorile raportate pentru Cu, Ni, Zn și Pb; nu se realizează comparații inferențiale între culturi sau ani și nu se formulează concluzii privind transferul sol-plantă ori bioacumularea.

INTRODUCTION

Post-mining substrates are radically different from agricultural soils in that the excavation, transportation and deposition of the substrate disturb natural horizons and produce combinations of coarse fragments, poorly aggregated fine material and low organic matter matrices. These conditions can limit water retention, nutritional availability and root penetration, and metal(loid)s may add further limitations (*Agbeshie et al., 2024; Castellanos-Barliza and León-Peláez, 2023; Ghosh et al., 2020; Ruiz et al., 2023; Uzarowicz et al., 2025*). Thus, revegetation at field scale should be based on site-specific baseline data to distinguish between initial physical and chemical constraints and later changes during vegetation development (*Miguel et al., 2023; Yuan et al., 2023*).

However, total concentrations of potentially toxic elements (PTEs) alone do not allow proving mobility, bioavailability or ecological risk. Phytomanagement, which integrates monitoring of contaminants and the establishment of vegetation and functional indicators of soil, is increasingly proposed for the production of non-food biomass on degraded land (*Borbón-Palomares et al., 2024; Ceacero-Moreno et al., 2026; Conesa et al., 2026; Paniagua-López et al., 2024*). Maize, soybean and sweet sorghum differ in architecture, nutritional demand and environmental tolerance; sorghum is particularly relevant as a high-biomass crop under marginal conditions (*Kharytonov et al., 2019; Osman et al., 2023*). Mining-derived substrates can also be explored for non-food conversion routes, however feedstock origin can influence product composition and consequently needs elemental supervision before valorisation (*Roman et al., 2025*). Results from conventional maize-soybean systems cannot be easily extrapolated to post-mining substrates without field validation (*Hou et al., 2025*).

Recent geochemical investigations from the broader Petrila mining-waste setting provide important context for the present study. *Dunca et al. (2025)* documented pronounced spatial heterogeneity in heavy-metal burdens and used the geoaccumulation index (Igeo) and contamination factor (Cf) to identify Ni as a main contaminant requiring priority monitoring. *Ioniță (2026)* reported, based on a 2022-2024 dataset covering Ramura 1-4, a gradual decrease in mean pH (from 6.72 to 6.31), an increase in Eh (from 312 to 342 mV), and an annual increases of approximately 3-7% in total Cr, Cu and Ni. A separate redox-focused investigation *(Ioniță et al., 2026)* demonstrated marked intra-dump heterogeneity, including oxidising alkaline upper sectors, wetter near-neutral to slightly acidic/reducing lower sectors, and local extractable Cr(VI) hotspots. Together, these studies show that geochemical conditions across the broader Petrila mining-waste setting are spatially and temporally heterogeneous and strengthen the need for temporally resolved, paired substrate-plant monitoring; they are used here as contextual evidence and are not merged with the present biomass-monitoring dataset.

From an agricultural-engineering perspective, crop establishment on reconstructed or post-mining land is controlled by coupled soil-machine-crop interactions. Heavy machinery traffic can increase soil strength and penetration resistance and can reduce hydraulic functioning, while restored mine soils are particularly vulnerable to recompaction *(Schäffer et al., 2007; Obour and Ugarte, 2021)*. Mechanical reconstruction and surface/subsurface tillage can improve mine-soil physical conditions and vegetation establishment *(Fulton and Wells, 2005; Angel et al., 2018)*. In soils with a high coarse skeletal fraction, stone content directly affects planter workability, admissible forward speed and sowing quality *(Toscano et al., 2022)*. For perennial and other energy crops, georeferenced UAV and multispectral monitoring can complement ground observations with spatially explicit information on canopy development and biomass *(Impollonia et al., 2022)*.

A practical knowledge gap exists between laboratory-scale remediation studies and the engineering steps to convert an untreated heterogeneous mining surface into a repeatable field platform. The site-specific baseline method is in agreement with European and FAO soil-management frameworks (*European Commission, 2021; FAO, 2017*). This study fills that gap using the Petrila platform, and views the 2023-2025 record as a descriptive baseline, not as a demonstration of remediation efficacy. The originality of this work is documentation of field-scale platform establishment, balanced crop rotation and multi-year elemental surveillance under clearly controlled inferential settings. We asked four questions: (Q1) what was the spatial and depth-related variability of VWC, temperature, penetration resistance, and pH characteristic of the baseline campaign; (Q2) which PTEs were prioritised for follow-up by preliminary laboratory screening; (Q3) could maize, soybean and sweet sorghum be repeatedly established under the operational constraints of a coarse post-mining substrate; and (Q4) what interannual patterns were observed in harvested biomass and elemental composition during 2023-2025 in the absence of plot-level analytical replication?

Previous studies have generally addressed individual components of this chain - mine-soil reconstruction/tillage, traffic-induced compaction, planter performance on stony soils, or remote crop monitoring - rather than documenting the end-to-end conversion of an untreated coarse post-mining surface into a repeatable field platform. The specific contribution of the Petrila study is therefore the integrated engineering workflow linking baseline diagnosis, adaptation of mechanical preparation to site constraints, operational crop establishment and multi-year surveillance on the same 4,500 m² field platform. The novelty lies in this field-scale integration and traceable workflow, not in demonstrating amendment efficacy or statistically confirmed yield improvement.

MATERIALS AND METHODS

Study site and environmental context

The field study was conducted on Branch IV of the Petrila coal-mining waste-dump complex, Valea Jiului, Hunedoara County, Romania (locality-level reference ≈45.450° N, 23.419° E; central elevation ≈708 m a.s.l.). Waste deposition in the wider sector ceased in 2015. The mining-derived substrate contains weathered marl and sandstone fragments, a clay-rich matrix, coal fragments and abundant coarse material; before preparation, vegetation consisted of discontinuous herbs, shrubs and birch regrowth. No previous agricultural use or systematic soil-amendment programme was documented (*Sorică et al., 2024*).

Baseline measurements and soil sampling were performed in June 2023 and sowing was completed in late June. Petroșani station data for May-June 2023 (13.3°C/77 mm and 19.8°C/113 mm, respectively) are reported only as campaign context. Comparable seasonal meteorological series for 2024-2025 were not retained in the manuscript dataset; therefore, climate-year effects were not modelled and cannot be separated from interannual crop responses.

Official annual and seasonal climatological characterisations published by the Romanian National Meteorological Administration for 2023-2025 were consulted *(ANM, 2023-2025)*. They confirm substantial interannual thermal and pluviometric differences, but a complete Petroșani station-level growing-season series directly comparable with the archived May-June 2023 station values could not be reconstructed for all three years. To avoid mixing local station observations with non-equivalent national or seasonal summaries, meteorology is retained as contextual information only and is not used as an explanatory covariate for year-to-year biomass differences.

Experimental design and inferential scope

A 5,000 m^2 perimeter was delimited, with approximately 4,500 m^2 used as nine 500 m^2 main plots. Three plots were designated as fixed-crop controls in the original project records and are treated here as fixed-crop reference plots (L1-1 maize, L2-1 soybean and L3-1 sweet sorghum). Six plots followed a balanced three-year cyclic rotation: L1-2/L1-3 maize→sorghum→soybean; L2-2/L2-3 soybean→maize→sorghum; and L3-2/L3-3 sorghum→soybean→maize. The wider project layout also contained amendment subplots. However, treatment identity, application rate, composition and application metadata are not available in the archived dataset used for this manuscript. Accordingly, amendment treatments are excluded from analysis and interpretation; no comparison of biochar versus digestate and no causal amendment effect is estimated.



Fig. 1 - Field establishment workflow for the Petrila biomass-crop platform

Baseline in situ measurements and traceability

Eight operationally selected points (P11-P14 and P21-P24) provided spatial coverage while avoiding plot margins, traffic tracks and conspicuous stone accumulations, consistent with the sampling-strategy principles of ISO 18400-104:2018 but not with a probability-based survey. Instrument-reported VWC and soil temperature were measured at 5 and 15 cm. The equipment inventory lists a FieldScout TDR 300 and an ML2x probe, but the archived field table does not identify which probe generated the reported VWC values; the readings are therefore not interpreted as substrate-calibrated absolute water contents. Penetration resistance was measured with a FieldScout SC 900 at 2.5 cm increments from 2.5 to 15 cm, with one profile per point; P11 showed refusal below 5 cm. Cone geometry, insertion speed and repeated insertions were not retained. Field pH and N-P-K were screened once per point with an electronic tester; N-P-K outputs are used only as semi-quantitative screening.

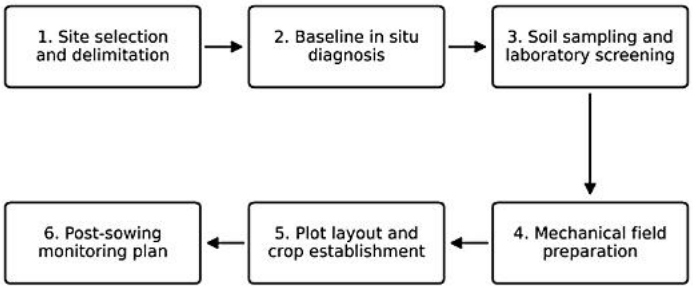


Fig. 2 - Baseline measurement, sampling and crop-establishment workflow

Soil sampling and laboratory screening

Soil samples associated with the in situ network were dried, homogenised and prepared according to the project laboratory workflow and the pretreatment principles of ISO 11464:2006. The available project summary was compared with Romanian reference values from Order no. 756/1997 and identified Cu and Ni as elements requiring follow-up. Sample-level concentrations, digestion details, calibration records, blanks, duplicates, certified reference materials, recoveries and LOD/LOQ were not available in the manuscript dataset. Accordingly, the soil laboratory evidence is used only for qualitative prioritisation, not for contamination classification, bioavailability assessment or risk calculation.

Mechanical preparation and crop establishment

Coarse stones and spontaneous vegetation were removed, the perimeter was staked, and shallow surface mobilisation was performed with a tracked hydraulic excavator because coarse fragments and irregular microrelief obstructed small conventional equipment. Maize hybrid Oituz, soybean variety Eugen and sweet sorghum variety SAȘM 2 were established at crop-appropriate depths using a common 50 × 20 cm geometry (100,000 planting positions ha^{-1}) to standardise field operations (Jităreanu et al., 2020). A one-row manual seeder was abandoned after repeated clogging, and planting positions were opened and covered manually. The common geometry is an operational standardisation, not an agronomic optimum for all three species. Detailed annual records of re-sowing, irrigation, supplementary fertilisation, soybean inoculation, plant-protection interventions and harvest stage were not retained in the manuscript dataset.

The maize, soybean and sweet sorghum crops were used here as experimental biomass crops on degraded post-mining land. Harvested material from the trial was not intended for human food or animal feed, and the present dataset is not used to support any food-chain safety claim.

Biomass elemental-composition monitoring

Above-ground biomass (stems and leaves) of maize, soybean and sorghum was monitored annually from 2023 to 2025. The archived analytical workflow records grinding, homogenisation, acid digestion with HNO_3/H_2O_2 and measurement by ICP-MS (PerkinElmer NexION 1000) for Cu, Pb, Co, Ni, Cr, Zn, Ba, Cd, B, Mo, As and Hg, reported in mg/kg. The supplied dataset contains one reported value for each crop-year combination and does not retain biological replication, plot/subplot identity, detailed sample-drying and aliquot procedures, instrument-calibration parameters, internal standards, blanks, certified reference materials, recoveries or element-specific LOD/LOQ. Therefore, values are reproduced as reported and interpreted descriptively. A dash in the 2023 file for Ba, As or Hg denotes absence of a reported value, not non-detection.

The original laboratory certificates/reports and the missing calibration/QA-QC records were not available in the archived dataset. Consequently, the elemental entries in Tables 2a-2b are retained as archived project-reported values for transparency only. Repeated exact entries such as 1.00 and 0.25 mg/kg are not treated as confirmed quantified concentrations, reporting limits or non-detects, and no regulatory, threshold-based or accumulation interpretation is assigned to them.

Statistical analysis

Analyses were descriptive because point selection was operational, the baseline comprised one campaign and the biomass file lacked plot-linked replication. VWC, temperature and pH were summarised by mean, SD, coefficient of variation and range across eight points; 5- versus 15-cm differences were summarised descriptively. For penetration resistance, site summaries used seven complete profiles, while the valid P11 readings were retained graphically. Biomass elemental values were tabulated by crop-year only. Reported annual harvested-biomass totals (85, 263 and 487 kg) were retained as operational totals only because harvested area, crop-specific mass and moisture basis were not documented consistently. No hypothesis tests, treatment-effect estimates, bioaccumulation factors or soil-to-plant transfer factors were calculated.

Table 1 and Figures 3-4 therefore present descriptive summary statistics only (mean, SD, CV, range and depth-wise summaries), not inferential hypothesis tests. For biomass elemental composition, each crop-year entry is a single reported analytical record; crop species or years cannot be treated as statistical replicates without pseudoreplication. Consequently, additional inferential tests on the archived biomass values would not be statistically valid.

RESULTS AND DISCUSSION

Operational establishment

The 4,500 m² platform was established despite stoniness, irregular microrelief and local slope. Tracked-excavator surface mobilisation followed by manual seed placement provided a workable field solution after the one-row seeder repeatedly clogged. This demonstrates operational feasibility, not superiority of the preparation method or agronomic optimality. Similar constraints from coarse fragments and reconstructed structure are widely reported for post-mining substrates (*Agbeshie et al., 2024; Ruiz et al., 2023; Uzarowicz et al., 2025*).

The field sequence also illustrates the engineering constraint imposed by the coarse skeletal fraction: equipment capable of shallow surface mobilisation remained workable, whereas the one-row seeder repeatedly clogged and could not maintain reliable seed placement. This is consistent with planter-workability studies showing that stoniness reduces admissible operating speed and increases dynamic loads at the soil-planter interface *(Toscano et al., 2022)*.

Crop rotation, reproductive development and harvested biomass

Maize, soybean and sweet sorghum reached reproductive development in all three years. The field notes describe ears in maize, panicles in sorghum and pods in soybean; because these observations were not quantified at plot level, they are treated only as evidence of reproductive establishment. The reported annual harvested-biomass totals were 85 kg in 2023, 263 kg in 2024 and 487 kg in 2025. These values are not interpreted as yield improvement because harvested area, crop-specific contributions and fresh-/dry-mass basis were not retained consistently. The balanced rotation reduced persistent association of a crop with a single field position, but the non-randomised layout and missing plot-level harvest data prevent causal partitioning of crop, rotation, amendment and year effects.

Accordingly, the manuscript uses these masses only as operational harvest totals and not as statistically validated crop-yield estimates.

Baseline water, temperature, pH and N-P-K response

During the June 2023 campaign, instrument-reported VWC ranged from 19.0-30.9% at 5 cm (26.6 ± 4.2%; CV 16.0%) and 12.2-25.3% at 15 cm (20.0 ± 4.3%; CV 21.5%). All eight points were wetter at 5 cm, with a paired depth difference of 6.6 ± 1.9 percentage points. Mean temperature was 18.2 ± 1.3°C at 5 cm and 16.7 ± 1.1°C at 15 cm. Field pH ranged from 7.0 to 7.3 (7.1 ± 0.1), whereas the semi-quantitative N-P-K response was 'very low' at all points. These observations describe one campaign only; near-neutral pH does not imply adequate fertility or low PTE pressure (*Haghighizadeh et al., 2024; Ceacero-Moreno et al., 2026*). Standardised laboratory pH and nutrient analyses are required for agronomic interpretation.

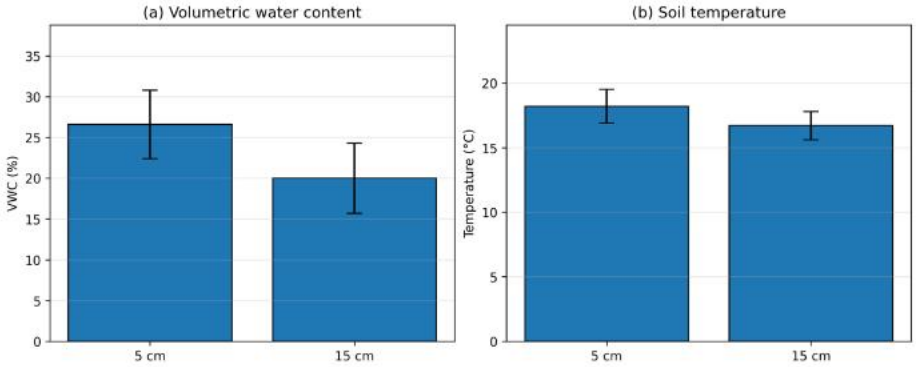


Fig. 3 - Mean VWC and soil temperature at 5 and 15 cm in June 2023 (mean ± SD; n = 8)

Table 1

Baseline observations from the June 2023 campaign

Point	VWC 5 cm (%)	VWC 15 cm (%)	T 5 cm (°C)	T 15 cm (°C)	Field pH	Mean PR 2.5-15 cm (MPa)
P11	19.0	12.2	18.2	17.5	7.0	NA*
P12	27.3	18.0	18.0	16.7	7.3	1.13
P13	21.6	16.3	20.5	17.0	7.3	0.79
P14	29.9	22.0	17.7	15.9	7.0	0.87
P21	29.4	20.7	18.4	18.7	7.2	0.76
P22	25.7	21.6	17.5	16.1	7.0	1.51
P23	30.9	25.3	16.0	15.2	7.2	0.98
P24	28.8	23.9	19.5	16.7	7.1	1.29
Mean ± SD	26.6 ± 4.2	20.0 ± 4.3	18.2 ± 1.3	16.7 ± 1.1	7.1 ± 0.1	1.05 ± 0.28†

** P11 had valid penetration readings only at 2.5 and 5.0 cm and was excluded from the complete-profile mean. † n = 7 complete profiles. N-P-K response was „very low" at all eight points.*

Penetration resistance

Across the seven complete profiles, mean penetration resistance was 1.05 ± 0.28 MPa (CV 26.5%), with point means from 0.76 to 1.51 MPa. The depth-specific mean increased from 0.49 MPa at 2.5 cm to 1.52 MPa at 15 cm; P11 was incomplete because of local refusal below 5 cm. The profile demonstrates small-scale mechanical heterogeneity and greater resistance to root penetration in the deeper measured layer under the moisture conditions of the baseline campaign. It does not justify a universal compacted/not-compacted classification because penetration resistance also depends on water content, particle-size distribution, bulk density, coarse fragments and measurement protocol (*Miguel et al., 2023; Ruiz et al., 2023*).

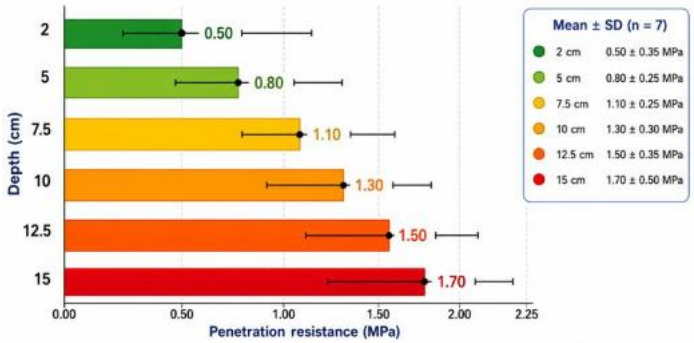


Fig. 4 - Mean penetration-resistance profile for seven complete baseline profiles.

Penetration resistance increased with depth, indicating greater mechanical resistance to root penetration in the deeper measured layer under the moisture conditions of the baseline campaign.

In agricultural-engineering terms, the observed profile links substrate mechanics with crop establishment. Increasing penetration resistance implies a progressively less favourable mechanical environment for root elongation, while machinery traffic can further increase soil strength; therefore, preparation should create a workable rooting layer while limiting unnecessary traffic and recompaction

(Schäffer et al., 2007; Obour and Ugarte, 2021). On reclaimed mine soils, ripping and combined surface/subsurface tillage have been shown to reduce soil strength and improve vegetation establishment *(Angel et al., 2018)*. At Petrila, increasing penetration resistance indicated a root-zone mechanical constraint that motivated site-adapted surface preparation and low-traffic operations; the coarse skeletal fraction subsequently limited seeder operation, necessitating manual seed placement, after which all three crops reached reproductive development. Root growth itself was not measured, so this sequence is interpreted mechanistically rather than as a measured root-response pathway.

Preliminary Potentially Toxic Elements screening

The available laboratory summary prioritised Cu and Ni for follow-up: Cu was described as above the Romanian normal value but below the sensitive-use alert threshold, while some Ni results were described as near or locally above that alert threshold. Pb and Cd were not identified as relevant exceedances in the summary. Because sample-level concentrations and analytical QA/QC were unavailable, Order no. 756/1997 (*Ministry of Waters, Forests and Environmental Protection, 1997*) is used only as a historical screening reference, and no site-wide contamination, mobility or ecological-risk class is assigned. This distinction is important because total concentration does not directly represent bioavailability or plant exposure (*Borbón-Palomares et al., 2024; Ceacero-Moreno et al., 2026; Paniagua-López et al., 2024*).

This qualitative prioritisation is consistent with recent dump-scale studies, which identified Ni as a major contamination priority and showed that pH/Eh conditions and metal concentrations vary in both space and time across the Petrila complex *(Dunca et al., 2025; Ioniță, 2026; Ioniță et al., 2026)*. These external geochemical results support the need for continued monitoring but do not substitute for paired, plot-linked substrate and plant measurements in the present experiment.

Archived biomass elemental records, 2023-2025

The archived biomass file comprised nine crop-year elemental records, reproduced in Tables 2a-2b for transparency. Because the corresponding analytical certificates, full calibration/QA-QC documentation, LOD/LOQ information and plot-linked replication were unavailable, these entries are treated as nominal project-reported values rather than analytically validated concentrations for quantitative comparison. The manuscript therefore does not rank crops or years by elemental concentration, calculate annual concentration means for inference, compare the values with regulatory thresholds, or infer species-specific accumulation capacity.

Because these are single crop-year records rather than replicated plot-level observations, no statistical test of differences among crops or years is performed, and the apparent differences are treated as preliminary, hypothesis-generating patterns only.

The apparent differences among the archived crop-year records may plausibly reflect crop identity, seasonal conditions, growth dilution, substrate mineralogy, pH/redox status and changes in element availability, but these mechanisms were not tested here. Without verified analytical reporting metadata and paired plot-level substrate-plant data, the elemental records cannot be interpreted quantitatively as temporal trends, bioaccumulation or soil-to-plant transfer. Cu and Ni remain priorities for future replicated monitoring because they were also identified as relevant in the separate soil-screening and site-geochemistry datasets. Exact repeated values (1.00 and 0.25 mg/kg) and missing Ba/As/Hg entries must be resolved from laboratory certificates before any quantitative use.

Table 2a

Archived reported biomass elemental values, 2023-2025 (units as supplied: mg/kg): Cu, Pb, Co, Ni, Cr and Zn

Sample	Crop	Year	Cu	Pb	Co	Ni	Cr	Zn
L1_porumb2023	Maize	2023	20.57	1.60	0.97	10.18	6.11	36.18
L2_soia2023	Soybean	2023	41.37	3.67	3.09	26.50	17.27	87.01
L3_sorg2023	Sorghum	2023	23.80	0.95	1.15	12.11	5.75	30.17
L1_porumb2024	Maize	2024	4.51	1.00	1.00	2.54	7.63	35.28
L2_soia2024	Soybean	2024	3.31	1.08	1.00	2.78	6.37	35.25
L3_sorg2024	Sorghum	2024	8.52	2.15	1.89	12.85	6.39	27.21
L1_porumb2025	Maize	2025	8.77	4.75	1.00	10.96	6.21	38.01
L2_soia2025	Soybean	2025	10.64	6.46	1.00	12.92	7.75	47.11
L3_sorg2025	Sorghum	2025	9.14	4.32	1.00	7.48	8.06	42.36

Table 2b

Archived reported biomass elemental values, 2023-2025 (units as supplied: mg/kg): Ba, Cd, B, Mo, As and Hg

Sample	Ba	Cd	B	Mo	As	Hg
L1_porumb2023	-	0.04	12.93	0.99	-	-
L2_soia2023	-	0.02	83.33	1.35	-	-
L3_sorg2023	-	0.19	7.87	0.67	-	-
L1_porumb2024	3.17	1.00	8.12	1.00	1.03	0.25
L2_soia2024	3.28	1.00	8.05	1.00	1.10	0.25
L3_sorg2024	36.85	1.00	28.25	1.00	1.27	0.25
L1_porumb2025	5.85	1.00	16.81	1.00	1.00	1.00
L2_soia2025	6.00	1.00	22.80	1.00	1.00	1.00
L3_sorg2025	9.30	1.00	19.93	1.00	1.00	1.00

Note:„-" *indicates that no value was present in the supplied dataset and does not mean zero or <LOD. Exact values of 1.00 and 0.25 mg/kg are reproduced as reported and require confirmation against laboratory certificates before interpretation as quantified values or reporting limits.*

Implications for subsequent biomass monitoring

The current record establishes an initial elemental-surveillance baseline but does not demonstrate biomass safety. If non-food thermochemical conversion is pursued, PTEs should be quantified in replicated harvested tissues and conversion products because feedstock origin and process conditions can influence product composition (*Roman et al., 2025*). Future work should preserve plot/subplot identity, use replicated paired substrate-plant sampling, document full QA/QC and LOD/LOQ, and report crop-specific dry-matter yield per unit area.

Future monitoring can also be strengthened by georeferenced UAV/multispectral surveys synchronized with field observations. Vegetation indices, canopy height and repeated spatial imagery can provide non-destructive information on crop development and biomass heterogeneity and can guide plot-level sampling; such approaches have been demonstrated for high-throughput phenotyping and biomass/yield prediction in Miscanthus *(Impollonia et al., 2022)*.

In addition, perennial non-food energy crops such as Miscanthus should be evaluated in future field trials as complementary candidates under the evolving pH and redox conditions documented at the Petrila dump.

Study limitations

Two limitation groups constrain inference. Design limitations include one operationally selected baseline network, one baseline campaign and systematic rather than randomised crop/treatment allocation. Data-retention limitations include missing amendment dose/composition metadata, incomplete annual crop-management and meteorological records, non-normalised harvest totals, crop-year aggregation of elemental data, absence of plot-linked biological/analytical replication, and incomplete laboratory QA/QC and LOD/LOQ documentation. The absence of plot-linked analytical replication is a design/data-retention limitation, not evidence of treatment equivalence. Consequently, treatment effects, statistically confirmed temporal trends, bioaccumulation factors, soil-plant transfer factors and safe-valorisation thresholds cannot be inferred from the present dataset.

The present results should therefore be considered preliminary and hypothesis-generating; confirmatory conclusions require additional seasons with replicated, plot-linked measurements and complete analytical QA/QC.

CONCLUSIONS

- A 4,500 m² field platform with nine 500 m² plots was operationally established on a heterogeneous mining-derived substrate in Petrila; maize, soybean and sweet sorghum reached reproductive development under the adopted field preparation and crop-rotation scheme.

- The reported 2023-2025 harvested masses are operational totals only; because harvested area, crop-specific contributions and fresh-/dry-mass basis were not documented consistently, they are not comparable agricultural yields and no year-to-year yield increase is inferred.

- The June 2023 baseline showed clear spatial and depth-related heterogeneity: the 5-cm layer was wetter and warmer than the 15-cm layer, field pH was near neutral, N-P-K screening was very low, and penetration resistance increased with depth under the measured moisture conditions.

- Preliminary laboratory screening prioritised Cu and Ni for follow-up, while the archived 2023-2025 biomass records displayed apparent crop-year differences in the reported Cu, Ni, Zn and Pb values. No conclusion is drawn regarding either the presence or the absence of soil-to-plant transfer or bioaccumulation, because paired substrate-plant data and plot-level replication were unavailable; treatment effects likewise cannot be inferred.

- Subsequent monitoring should retain plot/subplot identity, quantify crop-specific dry-matter yield, pair substrate and plant samples, document amendment properties and seasonal conditions, and apply full analytical QA/QC with explicit LOD/LOQ before evaluating remediation performance or biomass valorisation safety.

- The findings are preliminary and should be used to design confirmatory monitoring rather than to support causal, food-chain-safety or remediation-efficacy claims.

ACKNOWLEDGEMENT

This work was developed within the project „Establishment and Operationalization of a Competence Centre for Soil Health and Food Safety", Specific Project 2: „Restoring Soil Health on Non-Productive Land through Biomass Crops for Sustainable Energy - Soil-Biomass-Sustainability (SoBioSus)", Contract no. 760005/30.12.2022, code 2. The authors acknowledge the project partners' contributions to field mapping, measurements, laboratory screening and crop establishment.

REFERENCES

[1] Agbeshie A.A., Awuah R., Ofori-Adjei N.B., Ennison M., Atta-Darkwa T., (2024), Assessment of soil quality degradation impacted by topsoil stockpiling of a surface mining operation in a tropical climate, *Scientific African*, Vol. 26, e02481, https://doi.org/10.1016/j.sciaf.2024.e02481.

[2] Administrația Națională de Meteorologie - ANM, (2023-2025), Annual and seasonal climatological characterisations for Romania, MeteoRomania, Bucharest/Romania, https://www.meteoromania.ro/clim/.

[3] Angel H.Z., Stovall J.P., Williams H.M., Farrish K.W., Oswald B.P., Young J.L., (2018), Surface and subsurface tillage effects on mine soil properties and vegetative response, Soil Science Society of America Journal, Vol. 82(2), pp. 475-482, https://doi.org/10.2136/sssaj2017.09.0329.

[4] Borbón-Palomares D.B., González-Méndez B., Loredo-Portales R. et al., (2024), Phytostabilization alternatives for an abandoned mine tailing deposit in northwestern Mexico, *Plant and Soil*, Vol. 497, pp. 199-218, https://doi.org/10.1007/s11104-023-06095-3.

[5] Castellanos-Barliza J., León-Peláez J.D., (2023), Soil recovery in a chronosequence of revegetated coal mine spoils in Colombian drylands: a view from the assessment of physical-chemical and biological properties, *Geoderma Regional*, Vol. 33, e00652, https://doi.org/10.1016/j.geodrs.2023.e00652.

[6] Ceacero-Moreno M., Álvarez-Rogel J., González-Alcaraz M.N., (2026), Soil chemical and functional indicators reveal limitations of restoration measures in abandoned metal mine soils of SE Spain: implications for ongoing and future management, *Environmental Geochemistry and Health*, Vol. 48, 477, https://doi.org/10.1007/s10653-026-03378-3.

[7] Conesa H.M., Franco J.A., Ceacero-Moreno M., Martínez-Sánchez J.-J., González-Alcaraz M.N., Álvarez-Rogel J., (2026), Response of field-grown native plant species to a combined amendment for phytomanaging metal(loid)-mine tailings, *Plant and Soil*, Vol. 518, pp. 1431-1447, https://doi.org/10.1007/s11104-025-08084-0.

[8] Dunca E.-C., Ioniță M.-F., Radu S.M., (2025), Soil Contamination and Related Ecological Risks: Complex Analysis of the Defor Petrila Tailings Dump, Romania, *Land*, Vol. 14(7), 1492, https://doi.org/10.3390/land14071492.

[9] Fulton J.P., Wells L.G., (2005), Evaluation of a mechanical system for reconstructing soil on surface mined land, *Applied Engineering in Agriculture*, Vol. 21(1), pp. 43-51, https://doi.org/10.13031/2013.17905.

[10] Ghosh D., Masto R.E., Maiti S.K., (2020), Ameliorative effect of Lantana camara biochar on coal mine spoil and growth of maize (Zea mays),*Soil Use and Management*, 36, 726–739. DOI: 10.1111/sum.12626.

[11] Haghighizadeh A., Rajabi O., Nezarat A., Hajyani Z., Haghmohammadi M., Hedayatikhah S., Delnabi Asl S., Aghababai Beni A., (2024), Comprehensive analysis of heavy metal soil contamination in mining

environments: Impacts, monitoring techniques, and remediation strategies, *Arabian Journal of Chemistry*, Vol. 17(6), 105777, https://doi.org/10.1016/j.arabjc.2024.105777.

[12] Hou L., Wang Y., Wang Z., Gao R., Zhou X., Yang S., Luo X., Jiang Z., Liu Z., (2025), Effects of biochar on soil quality in a maize soybean rotation on Mollisols, *Agronomy*, Vol. 15(5), 1226, https://doi.org/10.3390/agronomy15051226.

[13] Ioniță M.-F., (2026), Temporal Trends of Heavy Metals and Geochemical Parameters in Ramura 1, 2, 3 and 4 Petrila Tailings Dump, *Revista Minelor - Mining Revue*, Vol. 32(1), pp. 77-84, https://doi.org/10.2478/minrv-2026-0007.

[14] Ioniță M.-F., Dunca E.-C., Radu S.M., Irimie S.I., (2026), Extractable Cr(VI) Hotspots in the Defor Petrila Tailings Dump, Romania: A Redox-Based Hazard Screening Approach, *Toxics*, Vol. 14(6), 479, https://doi.org/10.3390/toxics14060479.

[15] Impollonia G., Croci M., Ferrarini A., Brook J., Martani E., Blandinières H., Marcone A., Awty-Carroll D., Ashman C., Kam J., Kiesel A., Trindade L.M., Boschetti M., Clifton-Brown J., Amaducci S., (2022), UAV Remote Sensing for High-Throughput Phenotyping and for Yield Prediction of Miscanthus by Machine Learning Techniques, Remote Sensing, Vol. 14(12), 2927, https://doi.org/10.3390/rs14122927.

[16] Jităreanu G., Ciontu C., Penescu A., Rusu T., Bogdan I., Pop A., Moraru P., Rurac M., Dobre M., Ailincăi C., Țopa D., Calistru A.E., Manea D., Alda S., (2020), *Treatise of agrotechnics (Tratat de agrotehnică - in Romanian)*, "Ion Ionescu de la Brad" Publishing House, Iași/Romania.

[17] Kharytonov M.M., Martynova N.V., Tokar A.V., Rula I.V., Babenko M.G., Bagorka M.O., (2019), Sweet sorghum biomass quantitative and qualitative characteristic depending on hybrid and type of soil, *INMATEH Agricultural Engineering*, vol. 59, no. 3/2019, pp. 189-196, https://doi.org/10.35633/INMATEH-59-21.

[18] Miguel P., Stumpf L., Pinto L.F.S., Pauletto E.A., Rodrigues M.F., Barboza L.S., Rocha J.V.P., (2023), Physical restoration of a minesoil after 10.6 years of revegetation, *Soil and Tillage Research*, Vol. 227, 105599, https://doi.org/10.1016/j.still.2022.105599.

[19] Obour P.B., Ugarte C.M., (2021), A meta-analysis of the impact of traffic-induced compaction on soil physical properties and grain yield, Soil and Tillage Research, Vol. 211, 105019, https://doi.org/10.1016/j.still.2021.105019.

[20] Osman H.E., Fadhlallah R.S., Alamoudi W.M., Eid E.M., Abdelhafez A.A., (2023), Phytoremediation potential of sorghum as a bioenergy crop in Pb-amendment soil, *Sustainability*, Vol. 15(3), 2178, https://doi.org/10.3390/su15032178.

[21] Paniagua-López M., García-Robles H., Aguilar-Garrido A., Romero-Freire A., Lorite J., Sierra-Aragón M., (2024), Vegetation establishment in soils polluted by heavy metal(loid)s after assisted natural remediation, *Plant and Soil*, Vol. 497, pp. 257-275, https://doi.org/10.1007/s11104-024-06521-0.

[22] Roman A., Bucura F., Botoran O.R., Radu G.L., Niculescu V.C., Soare A., Ion-Ebrasu D., Vagner I., Dunca E.C., Șandru C., Constantinescu M., (2025), Thermochemical processing of agricultural waste into biochar with potential application for coal mining degraded soils, *Results in Engineering*, Vol. 26, 105497, https://doi.org/10.1016/j.rineng.2025.105497.

[23] Ruiz F., Safanelli J.L., Perlatti F., Cherubin M.R., Demattê J.A.M., Cerri C.E.P., Otero X.L., Rumpel C., Ferreira T.O., (2023), Constructing soils for climate-smart mining, *Communications Earth & Environment*, Vol. 4, 219, https://doi.org/10.1038/s43247-023-00862-x.

[24] Schäffer B., Attinger W., Schulin R., (2007), Compaction of restored soil by heavy agricultural machinery - Soil physical and mechanical aspects, *Soil and Tillage Research*, Vol. 93(1), pp. 28-43, https://doi.org/10.1016/j.still.2006.03.007.

[25] Sorică C.M., Vlăduț N.V., Sorică E., Vlăduțoiu L., Oprescu R.M., Gavrilă V., Dunca E., Rusănescu C.O., Chiriță A.P., (2024), Research on the in-situ evaluation of certain physico-chemical properties of the soil, in order to establish biomass crops on tailings dumps, Proceedings of ISB-INMA'TEH 2024 International Symposium, pp. 610-619, http://isbinmateh.inma.ro/index.html;

[26] Toscano P., Cutini M., Filisetti A., Premoli E., Porcu M., Catalano N., Bisaglia C., Brambilla M., (2022), Workability Assessment of Different Stony Soils by Soil-Planter Interface Noise and Acceleration Measurement, AgriEngineering, Vol. 4(4), pp. 1139-1152, https://doi.org/10.3390/agriengineering4040070.

[27] Uzarowicz Ł., Kwasowski W., Lasota J., Błońska E., Górka-Kostrubiec B., Tarnawczyk M., Murach D., Gilewska M., Gryczan W., Pawłowicz E., Jankowski P., (2025), Vegetation cover as an important factor affecting the properties and evolution of Spolic Technosols: A case study from a dump of the abandoned

iron ore mine in central Poland, *Catena*, Vol. 254, 108906, https://doi.org/10.1016/j.catena.2025.108906.

[28] Yuan C., Wu F., Wu Q., Fornara D.A., Heděnec P., Peng Y., Zhu G., Zhao Z., Yue K., (2023), Vegetation restoration effects on soil carbon and nutrient concentrations and enzymatic activities in post-mining lands are mediated by mine type, climate, and former soil properties, *Science of the Total Environment*, Vol. 879, 163059, https://doi.org/10.1016/j.scitotenv.2023.163059.

[29] ***European Commission, (2021), *EU Soil Strategy for 2030*: Reaping the benefits of healthy soils for people, food, nature and climate, Brussels/Belgium.

[30] ***Food and Agriculture Organization of the United Nations - FAO, (2017), *Voluntary Guidelines for Sustainable Soil Management*, Rome/Italy.

[31] *** ISO 11464:2006, Soil quality - Pretreatment of samples for physico-chemical analysis, *International Organization for Standardization*, Geneva/Switzerland.

[32] *** ISO 18400-104:2018, Soil quality - Sampling - Part 104: Strategies, *International Organization for Standardization*, Geneva/Switzerland.

[33] *** ISO 11464:2006, Soil quality - Pretreatment of samples for physico-chemical analysis, *International Organization for Standardization*, Geneva/Switzerland.

[34] *** ISO 18400-104:2018, Soil quality - Sampling - Part 104: Strategies, *International Organization for Standardization*, Geneva/Switzerland.

[35] *** Ministry of Waters, *Forests and Environmental Protection*, (1997), Order no. 756/1997 approving the regulation on environmental pollution assessment, as amended (original title in Romanian), Bucharest/Romania.

INTEGRATION OF SMART TRAPS AND WEATHER SENSORS INTO A DIGITAL PRECISION AGRICULTURE SYSTEM
/
INTEGRAREA CAPCANELOR INTELIGENTE ŞI A SENZORILOR METEO ÎNTR-UN SISTEM DIGITAL PENTRU AGRICULTURA DE PRECIZIE

Cătălin PERSU[1)], Dan CUJBESCU [*1)], Florin-Cristian MARIN[2)], Alin ONCESCU[1)], Iuliana GĂGEANU[1)], Robert CRISTEA[1)], Alexandru IONESCU[1)], Carmen BĂLȚATU[1)], Ana-Maria TĂBĂRAȘU[1)]

[1)] National Institute of Research – Development for Machines and Installations Designed to Agriculture and Food Industry, Romania

[2)] Research Institute for Fruit Growing Pitesti-Maracineni, 117450 Maracineni, Arges, Romania

E-mail: persucatalin@yahoo.com

Correspondence: E-mail: dcujbescu@yahoo.com; Tel: +40740272076

DOI: https://doi.org/10.35633/inmateh-79-105

Keywords: *precision agriculture; digital monitoring; orchard crops; smart trap; weather sensors; pest monitoring; autonomous system; data transmission; agricultural IoT; microclimate*

ABSTRACT

Precision agriculture requires advanced digital solutions capable of continuously monitoring environmental conditions and pest dynamics in orchard ecosystems. This paper presents the development, integration, and experimental validation of a digital system dedicated to orchard crop monitoring. The proposed system integrates a smart pheromone trap equipped with an HD camera, a meteorological monitoring station, an autonomous photovoltaic power supply system, and a wireless communication module for real-time data transmission. The experimental model was designed to support automatic pest detection and continuous acquisition of climatic parameters associated with pest and pathogen development. The monitoring architecture combines environmental sensing, image acquisition, local data processing, and cloud-based communication. Functional testing was conducted under controlled orchard conditions over a 30-day monitoring period. The obtained results demonstrated stable autonomous operation, reliable wireless communication, and accurate environmental monitoring. The average deviations compared with a reference meteorological station were within ±0.4 °C for air temperature, ±2.5% for relative humidity, and ±0.3 m/s for wind speed. The smart trap achieved pest identification accuracy higher than 90% for target species. The photovoltaic system ensured autonomous operation for more than 72 h without direct solar radiation. The developed digital platform represents a scalable solution for integrated pest management and precision orchard monitoring applications.

REZUMAT

Agricultura de precizie necesită soluții digitale avansate, capabile să monitorizeze continuu condițiile de mediu și dinamica dăunătorilor din ecosistemele pomicole. Lucrarea prezintă dezvoltarea, integrarea și validarea experimentală a unui sistem digital destinat monitorizării culturilor pomicole. Sistemul propus integrează o capcană inteligentă cu feromoni, echipată cu cameră HD, o stație meteorologică, un sistem autonom de alimentare fotovoltaică și un modul de comunicație wireless pentru transmiterea datelor în timp real. Modelul experimental a fost proiectat pentru detectarea automată a dăunătorilor și achiziția continuă a parametrilor climatici asociați dezvoltării dăunătorilor și patogenilor. Arhitectura sistemului combină senzori de mediu, achiziție de imagini, procesare locală a datelor și comunicație prin platformă cloud. Testarea funcțională a fost realizată în condiții controlate de livadă, pe o perioadă de monitorizare de 30 zile. Rezultatele obținute au demonstrat funcționare autonomă stabilă, comunicație wireless fiabilă și monitorizare meteorologică precisă. Abaterile medii față de o stație meteorologică de referință au fost de ±0,4 °C pentru temperatura aerului, ±2,5% pentru umiditatea relativă și ±0,3 m/s pentru viteza vântului. Capcana inteligentă a obținut o precizie de identificare a dăunătorilor mai mare de 90% pentru speciile țintă. Sistemul fotovoltaic a asigurat funcționarea autonomă timp de peste 72 h fără radiație solară directă. Platforma digitală dezvoltată reprezintă o soluție scalabilă pentru managementul integrat al dăunătorilor și monitorizarea de precizie a culturilor pomicole.

INTRODUCTION

The transition toward precision agriculture has accelerated the development of intelligent monitoring systems capable of continuously evaluating environmental conditions and phytosanitary risks in orchard ecosystems. Modern orchard management requires rapid access to accurate information regarding climatic variability, pest dynamics, and pathogen development in order to optimize crop protection strategies and reduce production losses (*Nicolì et al., 2024; Yakovenko et al., 2023*).

Conventional monitoring methods are generally based on manual field inspections and periodic observations performed by specialists. These approaches require significant labor resources, generate delayed responses, and are strongly influenced by operator experience. In addition, traditional monitoring does not provide continuous data acquisition, which limits the possibility of identifying early infestation stages and accurately predicting pest evolution (*Karar et al., 2021; Rustia et al., 2023*).

Recent advances in digital agriculture enabled the integration of environmental sensors, wireless communication technologies, artificial intelligence, and image processing systems into autonomous monitoring platforms. These technologies support real-time acquisition and analysis of environmental and biological data, allowing rapid identification of critical conditions associated with pest outbreaks and disease development (*Fuentes-Peñailillo et al., 2024; Karunathilake et al., 2023; Masi et al., 2023; Zude-Sasse et al., 2021*).

Smart pheromone traps represent one of the most important technological solutions currently used for integrated pest management in orchard crops. By combining pheromone attraction systems with digital imaging and automated analysis algorithms, these devices can continuously monitor insect populations and reduce the dependence on manual observations. Studies demonstrated that machine vision and neural network approaches can significantly improve pest identification accuracy and increase monitoring efficiency in orchard ecosystems (*Čirjak et al., 2022; İtmeç and Zorlu, 2025; Kumar et al., 2025; Suto, 2022*).

Meteorological parameters also have a major influence on pest and pathogen activity. Air temperature, relative humidity, precipitation, solar radiation, and wind conditions directly affect insect development cycles, infection risks, and migration intensity. Consequently, integrating weather monitoring with automatic pest detection provides a more accurate basis for predictive phytosanitary management (*Rajput et al., 2024*; *Tudi et al., 2021; Yeshiwas et al., 2026*).

Experimental studies conducted in precision horticulture demonstrated that intelligent monitoring systems based on environmental sensors, wireless communication modules, and automated image acquisition can provide accurate and continuous information regarding pest activity and orchard microclimate conditions. Field experiments performed in orchard ecosystems confirmed that integrating meteorological monitoring with digital pest detection improves the efficiency of phytosanitary management and supports early identification of infestation risks (*Łągiewska and Panek-Chwastyk, 2025; Pascoal et al., 2024; Wang et al., 2025*).

Developments in Internet of Things technologies and cloud-based agricultural platforms also demonstrated the applicability of autonomous monitoring infrastructures in orchard crops. The integration of wireless sensor networks, automated image acquisition systems, and real-time communication platforms enables continuous monitoring over extended agricultural areas while reducing labor requirements and operational costs. Several studies reported that intelligent monitoring architectures contribute to improved pest surveillance efficiency, optimized pesticide application, and increased sustainability of horticultural production systems (*Liakos et al., 2018; Pivoto et al., 2021; Talaviya et al., 2020; Verdouw et al., 2021*).

The main objective of the research was the realization of a functional experimental model capable of continuously monitoring environmental parameters and pest activity under orchard conditions. The study also aimed to evaluate the operational stability, energy autonomy, communication reliability, and monitoring accuracy of the developed system. The proposed monitoring platform contributes to the implementation of precision horticulture technologies by supporting real-time decision-making, reducing manual intervention, and improving the efficiency of integrated pest management strategies in orchard ecosystems.

MATERIALS AND METHODS

1. General architecture of the experimental monitoring system

The experimental model was developed as an integrated digital system dedicated to continuous monitoring of orchard crops. The monitoring platform combined environmental sensing modules, smart pest detection equipment, autonomous energy supply, and wireless communication infrastructure within a unified operational architecture.

The developed system included the following main components:

- intelligent meteorological station;
- smart pheromone trap equipped with HD camera;
- electronic acquisition and control module;
- autonomous photovoltaic power supply system;
- wireless communication infrastructure;
- cloud-based monitoring platform.

The experimental model was developed as an integrated digital system dedicated to continuous monitoring of orchard crops. The monitoring platform combined environmental sensing modules, smart pest detection equipment, autonomous energy supply, and wireless communication infrastructure within a unified operational architecture.

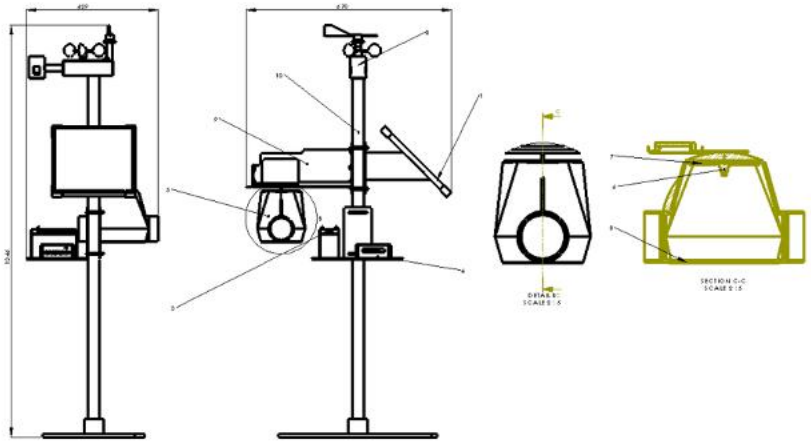


Fig. 1 – General architecture of the experimental orchard monitoring system

1 – solar panel with support arm; 2 – smart meteorological station; 3 – 12 V battery; 4 – support plate for the control unit; 5 – pheromone insect trap; 6 – pest monitoring camera; 7 – LED strip; 8 – adhesive pheromone plate; 9 – pheromone trap mounting arm; 10 – support pipe structure

2. Smart meteorological station

The meteorological station was designed for continuous monitoring of climatic parameters associated with pest activity and pathogen development in orchard ecosystems.

The monitoring station integrated: air temperature sensor; relative humidity sensor; anemometer; wind direction sensor; rainfall sensor; solar radiation sensor.

The sensors were mounted on an anodized aluminum support structure resistant to corrosion and outdoor environmental exposure.

The monitored parameters included: air temperature, °C; relative humidity, %; wind speed, m/s; precipitation intensity, mm/h; solar radiation, W/m².



Fig. 2 – Experimental meteorological station used for continuous orchard environmental monitoring

The experimental meteorological station was installed under orchard field conditions and connected to the acquisition and communication module for real-time environmental monitoring. Table 1 presents the main climatic parameters monitored by the experimental meteorological station together with the corresponding measurement units and sensing components used within the developed monitoring platform.

Table 1

Climatic parameters monitored by the experimental station

Parameter	MU	Sensor type
Air temperature	°C	Digital thermal sensor
Relative humidity	%	Capacitive sensor
Wind speed	m/s	Anemometer
Wind direction	°	Wind vane
Precipitation	mm	Rain gauge
Solar radiation	W/m²	Pyranometer
Parameter	Unit	Sensor

3. Smart pheromone trap

The smart pheromone trap represented the central monitoring component of the experimental system. The trap was designed for automatic detection and monitoring of orchard pests, especially Lepidoptera and Diptera species. The trap structure included: UV-resistant polymer housing; pheromone compartment; HD digital camera; LED illumination system; support and suspension elements.

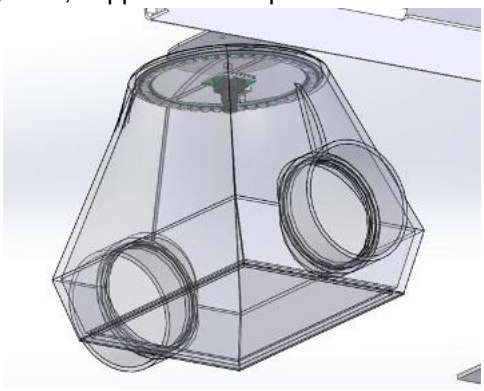


Fig. 3 – Smart pheromone trap integrated into the monitoring system

The HD camera periodically captured images of the adhesive monitoring surface. The integrated LED system ensured uniform illumination during low-light acquisition conditions.

4. Electronic acquisition and control module

The electronic acquisition module coordinated all sensing, communication, and energy management operations within the experimental monitoring system.

The module performed: environmental data acquisition; image acquisition control; LED activation management; local data storage; wireless communication control; energy monitoring.

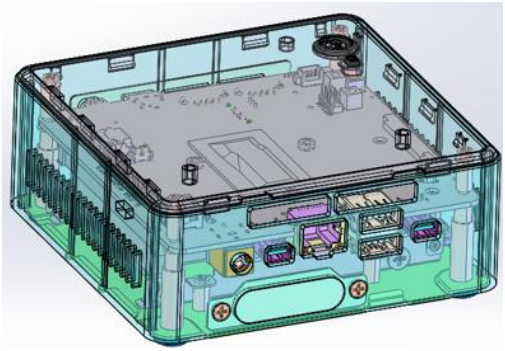


Fig. 4 – Electronic acquisition and control module integrating communication, sensing, and energy management subsystems

The electronic components were integrated into an IP65 protective enclosure to ensure operational stability under field conditions.

5. Autonomous photovoltaic power supply system

The developed monitoring platform used an autonomous photovoltaic energy system for continuous operation under orchard conditions.

The energy subsystem included: monocrystalline photovoltaic panel, 50 W; accumulator, 12 Ah; solar charge controller.

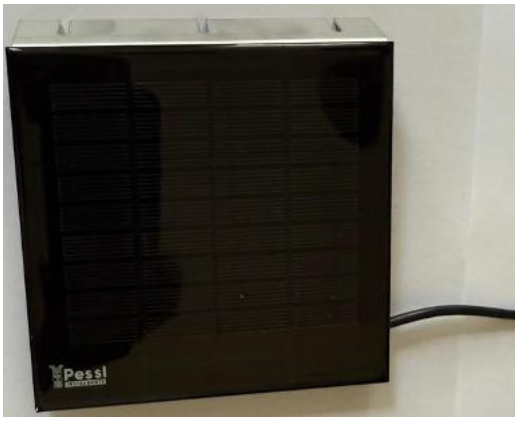


Fig. 5 – Monocrystalline photovoltaic panel integrated into the autonomous orchard monitoring system

The photovoltaic panel was mounted on an adjustable metallic structure oriented southward to maximize solar energy conversion efficiency.

6. Wireless communication and data transmission

The developed monitoring system used wireless communication technologies for remote data transmission and cloud synchronization.

The communication subsystem supported: Wi-Fi communication; 4G transmission; local data storage during signal interruption; automatic synchronization after communication recovery.

Table 2

Data acquisition and transmission configuration

Monitoring operation	Acquisition interval
Meteorological measurements	30 min
Automatic image acquisition	6 h
Data synchronization	12 h

The acquired environmental data and captured images were periodically transmitted to a cloud-based monitoring platform.

7. Experimental setup and monitoring procedure

The experimental monitoring system was installed in an apple orchard located in a lowland horticultural area. The monitoring campaign was conducted during the vegetation season over a period of 30 consecutive days.



Fig. 6 – Integrated experimental monitoring platform installed under orchard field conditions

The experimental monitoring campaign was conducted in an apple orchard at the Research Institute for Fruit Growing Pitești-Mărăcineni, Mărăcineni, Argeș County, Romania, over 30 consecutive days during the vegetation season. The meteorological monitoring unit incorporated Pessl Instruments sensors for air temperature, relative humidity, wind speed and direction, precipitation, and global solar radiation. Air temperature and relative humidity were measured using a HYT221-based sensor, with an operating temperature range of −40 to +125 °C and a relative humidity range of 0–100% RH; the nominal accuracies were ±0.2 °C within the 0–60 °C range and ±2% RH at 23 °C within the 0–90% RH range. Wind speed was measured using a three-cup anemometer with a measurement range of 0–30 m/s and a nominal tolerance of ±0.5 m/s for wind speeds up to 5 m/s and ±10% above 5 m/s. Wind direction was measured over a range of 0–359°, with a nominal tolerance of ±5°. Precipitation was recorded using a double tipping-bucket rain gauge with a resolution of 0.2 mm and a nominal accuracy of ±5%. Global solar radiation was measured using a Pessl Instruments IM506D pyranometer, based on a photodiode sensing element, with a measurement range of 0–2000 W/m², a spectral response of 300–1100 nm, and a maximum absolute error of ±5% (typically approximately ±3%).

The smart pheromone trap was equipped with a Raspberry Pi High Quality Camera based on a Sony IMX477R stacked, back-illuminated CMOS sensor, with a resolution of 12.3 megapixels (4056 × 3040 pixels), a sensor diagonal of 7.9 mm, and a pixel size of 1.55 × 1.55 µm. The camera was fitted with an 8 mm C/CS-mount lens, providing a fixed optical configuration for imaging the adhesive monitoring surface. Images of the adhesive plate were automatically acquired at 6 h intervals. An integrated LED illumination system provided uniform illumination of the monitoring area under low-light conditions, thereby reducing variations in image quality caused by ambient lighting conditions.

The smart-trap evaluation targeted the codling moth (Cydia pomonella) using a conventional pheromone trap with an adhesive plate and a species-specific pheromone lure. A total of 120 images acquired during the 30-day monitoring campaign were evaluated by comparing automatic detections with manual visual counts. Identification accuracy was calculated as the percentage of correctly identified target insects relative to the total number manually confirmed. Energy autonomy was evaluated with the 12 Ah battery fully charged and without direct solar radiation, while maintaining normal acquisition and communication intervals. The system remained fully operational for more than 72 h without external charging.

8. Functional performance evaluation

The environmental measurements obtained from the developed meteorological station were compared with the values recorded by a reference weather station installed in the same orchard area.

The transmission efficiency was evaluated using the relation:

$$\eta = \frac{N_r}{N_t} \cdot 100 \ [\%] \tag{1}$$

where:

η – transmission success rate, [%];
N_r – received data packets, [-];
N_t – transmitted data packets, [-].

The mean deviation of environmental measurements was calculated using:

$$MAD = \frac{1}{n} \cdot \sum_{i=1}^{n} |x_i - x_{ref}| \tag{2}$$

where:

MAD – mean absolute deviation, [°C, m/s, mm, W/m²];
x_i – measured value, [°C, m/s, mm, W/m²];
x_{ref} – measured value, [°C, m/s, mm, W/m²].
n – number of measurements, [-].

The pest detection accuracy of the smart trap was evaluated by comparing automatically detected insect counts with manual observations performed during the experimental monitoring campaign.

RESULTS

1. *Functional validation of the experimental monitoring system*

The developed experimental system operated continuously during the monitoring campaign under orchard environmental conditions. The integrated platform successfully performed simultaneous acquisition of meteorological parameters and automatic pest monitoring using the smart pheromone trap equipped with HD image acquisition capabilities.

The experimental model demonstrated stable operation during continuous field deployment, while the wireless communication subsystem ensured periodic transmission of environmental and biological data to the cloud-based monitoring platform. No significant interruptions of operation were observed during the experimental period.

The modular architecture of the developed monitoring system also facilitated rapid installation, maintenance operations, and reconfiguration according to orchard monitoring requirements.

2. *Environmental monitoring results*

The environmental monitoring subsystem continuously recorded climatic parameters associated with pest activity and pathogen development during the experimental orchard monitoring campaign.

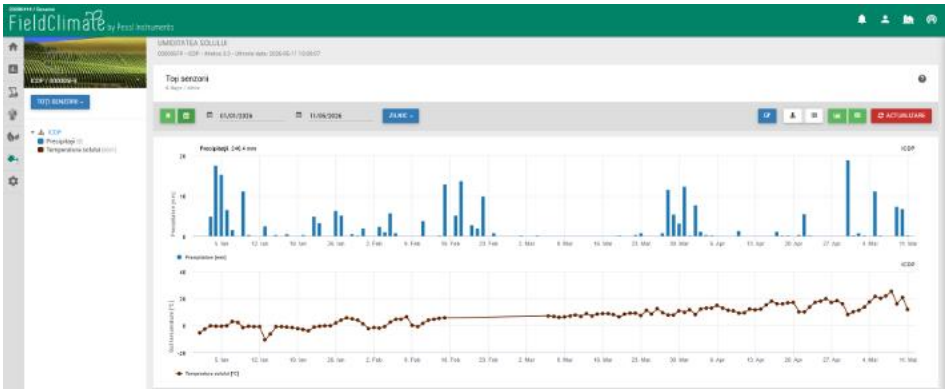


Fig. 7 – Cumulative precipitation recorded during the experimental orchard monitoring campaign

The cumulative precipitation values progressively increased throughout the monitoring campaign, exceeding 120 mm during the analyzed period. Several rainfall accumulation intervals above 15-20 mm were recorded during short time periods, generating elevated humidity conditions within the orchard ecosystem. These environmental conditions favored fungal pathogen development and increased the phytopathological vulnerability of monitored crops.

The environmental monitoring results demonstrated significant climatic variability during the experimental campaign. The cumulative precipitation exceeded 120 mm, while accumulated chilling units surpassed 800 units and accumulated degree-days exceeded 250 °C above the 10 °C thermal threshold. The recorded temperature values varied between approximately -4 °C and 28 °C, with several daily thermal amplitudes above 12 °C. These environmental conditions generated favorable intervals for pest biological activity and phytopathological development. The continuous monitoring platform successfully identified critical climatic periods associated with increased infestation and infection risks, confirming the applicability of the developed system for predictive orchard management and precision phytosanitary monitoring.

3. *Monitoring pest activity in pome fruit crops*

The developed monitoring platform successfully identified the correlation between environmental conditions and phytopathological risks in orchard crops during the experimental campaign. The recorded climatic data indicated cumulative precipitation exceeding 120 mm, accumulated degree-days above 250 °C, and temperatures ranging from approximately -4 °C to 28 °C. Under these conditions, the estimated aphid attack risk exceeded 60% during intervals characterized by temperatures above 18 °C and relative humidity values higher than 70%, while codling moth activity intensified at temperatures between 20 °C and 24 °C. The monitoring system also detected increased fire blight and apple scab infection risks following precipitation accumulation periods above 5-10 mm and relative humidity levels exceeding 80%, confirming the applicability of the developed platform for predictive phytopathological monitoring and precision orchard management.



Fig. 8 – Peach leaf curl infection risk estimated during the experimental monitoring campaign

The obtained results demonstrated that continuous acquisition and integration of climatic and biological data enabled rapid identification of critical environmental intervals associated with increased pest activity and pathogen infection probability in orchard ecosystems.

4. Monitoring phytopathological risks in stone fruit crops

The developed monitoring platform successfully identified the correlation between environmental conditions and phytopathological risks in orchard crops during the experimental campaign. The recorded climatic data indicated cumulative precipitation values exceeding 120 mm, accumulated degree-days above 250 °C, and temperatures ranging from approximately -4 °C to 28 °C. Under these environmental conditions, elevated pest activity and increased pathogen infection probability were observed, especially during intervals characterized by relative humidity values higher than 70-80% and moderate temperatures favorable for biological development.

Table 3 presents the main environmental conditions recorded during the experimental campaign together with the estimated phytopathological and pest infestation risks identified using the developed digital monitoring platform.

Table 3

Estimated phytopathological risks identified during the experimental monitoring campaign

Monitored parameter	Observed condition	Estimated risk level
Aphid infestation risk	RH > 70%; T > 18 °C	Moderate to high
Codling moth activity	T = 20-24 °C	High
Fire blight infection risk	Precipitation > 10 mm	Moderate to high
Apple scab infection risk	RH > 80%	High
Shot-hole disease risk	Prolonged humidity	Moderate
Moniliosis infection risk	T = 17-23 °C; RH > 75%	High
Peach leaf curl infection risk	T = 10-18 °C	Moderate to high

The obtained results demonstrated that increased humidity conditions, precipitation accumulation above 5-10 mm, and temperatures between 18 °C and 24 °C generated favorable environments for pest biological activity and pathogen development. The developed monitoring platform successfully identified critical phytopathological risk intervals and enabled continuous evaluation of orchard environmental conditions during the experimental campaign.

5. Communication performance and operational stability

The wireless communication subsystem ensured stable transmission of environmental and biological data throughout the experimental campaign. The transmission success rate exceeded 99% under stable communication conditions and remained above 90% in areas characterized by reduced signal intensity.

The implemented retransmission mechanism prevented significant data losses during temporary communication interruptions. The photovoltaic energy subsystem also ensured continuous autonomous operation for more than 72 h without direct solar radiation exposure.

The obtained results confirmed the operational stability, autonomous capability, and applicability of the developed digital monitoring platform for long-term precision orchard management applications.

CONCLUSIONS

The developed platform combined environmental sensing technologies, smart pheromone traps, autonomous photovoltaic energy supply, wireless communication infrastructure, and cloud-based data visualization within a unified precision agriculture architecture.

The experimental results confirmed stable and reliable operation of the monitoring system under orchard field conditions during the 30-day monitoring campaign. The environmental monitoring subsystem successfully recorded climatic parameters associated with pest activity and pathogen development, while the smart pheromone trap enabled automatic monitoring of insect population dynamics.

The obtained results demonstrated that cumulative precipitation values exceeding 120 mm, accumulated degree-days above 250 °C, and relative humidity values higher than 70-80% generated favorable environmental conditions for increased pest activity and phytopathological risk development. Elevated codling moth activity was observed at temperatures between 20 °C and 24 °C, while fungal infection risks intensified following precipitation accumulation periods above 5-10 mm.

The wireless communication subsystem ensured reliable real-time data transmission, with transmission success rates exceeding 99% under stable signal conditions. The photovoltaic power supply system also demonstrated high operational autonomy, maintaining continuous system functionality for more than 72 h without direct solar radiation exposure.

The developed digital monitoring platform proved suitable for predictive phytopathological management and precision orchard monitoring applications. The integration of climatic monitoring, automated pest detection, and real-time communication technologies enabled rapid identification of critical environmental intervals associated with increased infestation and infection probability.

The obtained results confirmed the applicability of the proposed monitoring architecture for modern precision horticulture systems, contributing to improved crop protection efficiency, reduced manual intervention, and enhanced sustainability of orchard management practices.

ACKNOWLEDGEMENT

This work was supported by the Romanian Research and Innovation Ministry, through the Project entitled “ADER 25.2.1 Digital system for monitoring orchard crops” – Ctr. 25.2.1./20.09.2023

REFERENCES

[1] Čirjak, D., Miklečić, I., Lemić, D., Kos, T., & Pajač Živković, I. 2022. Automatic Pest Monitoring Systems in Apple Production under Changing Climatic Conditions. *Horticulturae*, *8*(6), 520.
[2] https://doi.org/10.3390/horticulturae8060520
[3] Fuentes-Peñailillo, F., Gutter, K., Vega, R., & Silva, G. C. 2024. Transformative Technologies in Digital Agriculture: Leveraging Internet of Things, Remote Sensing, and Artificial Intelligence for Smart Crop Management. *Journal of Sensor and Actuator Networks*, *13*(4), 39.
[4] https://doi.org/10.3390/jsan13040039
[5] İtmeç, M., & Zorlu, B. 2025. Pest Monitoring with AI-Enabled Camera-Based Pheromone Traps in Orchards with Different Climatic and Topographic Characteristics. *International Journal of Agriculture Environment and Food Sciences*, *9*(Special), 162-171. DOI:10.31015/2025.si.24
[6] Karar, M. E., Alsunaydi, F., Albusaymi, S., & Alotaibi, S. 2021. A new mobile application of agricultural pests recognition using deep learning in cloud computing system. *Alexandria Engineering Journal*, *60*(5), 4423-4432. https://doi.org/10.1016/j.aej.2021.03.009
[7] Karunathilake, E. M. B. M., Le, A. T., Heo, S., Chung, Y. S., & Mansoor, S. 2023. The Path to Smart Farming: Innovations and Opportunities in Precision Agriculture. *Agriculture*, *13*(8), 1593.
[8] https://doi.org/10.3390/agriculture13081593
[9] Kumar, N., Naveen, G., Padhan, S., Hembram, S., Rathore, T., Mohanta, S., & Mani, A. 2025. PHEROMONE TRAPS IN INSECT PEST MANAGEMENT: A COMPREHENSIVE REVIEW OF THEIR APPLICATIONS, EFFICACY AND FUTURE DIRECTIONS IN INTEGRATED PEST MANAGEMENT. *Plant Archives (09725210)*, *25*(1).
[10] Łągiewska, M., & Panek-Chwastyk, E. 2025. Integrating Remote Sensing and Autonomous Robotics in Precision Agriculture: Current Applications and Workflow Challenges. *Agronomy*, *15*(10), 2314.
[11] https://doi.org/10.3390/agronomy15102314
[12] Liakos, K. G., Busato, P., Moshou, D., Pearson, S., & Bochtis, D. 2018. Machine Learning in Agriculture: A Review. *Sensors*, *18*(8), 2674. https://doi.org/10.3390/s18082674

[13] Masi, M., Di Pasquale, J., Vecchio, Y., & Capitanio, F. 2023. Precision Farming: Barriers of Variable Rate Technology Adoption in Italy. *Land*, *12*(5), 1084. https://doi.org/10.3390/land12051084

[14] Nicolì, F., Anaclerio, M., Maldera, F., Nigro, F., & Camposeo, S. 2024. Deficit Irrigation Regime Improves Phytosanitary Status of Cultivar Arbosana Grown in a Super High-Density Olive Orchard. *Agronomy*, *14*(10), 2380. https://doi.org/10.3390/agronomy14102380

[15] Pascoal, D., Silva, N., Adão, T., Lopes, R. D., Peres, E., & Morais, R. 2024. A technical survey on practical applications and guidelines for IoT sensors in precision agriculture and viticulture. *Scientific Reports*, *14*(1), 29793. https://doi.org/10.1038/s41598-024-80924-y

[16] Pivoto, D., Talamini, E., Finocchio, C.P.S., Dalla Corte, V.F., de Vargas Mores, G., da Silva, A.L., 2021. Smart farming: Towards a sustainable agri-food system. *British Food Journal, 123*(9), pp. 3085-3108. https://doi.org/10.1108/BFJ-12-2020-1125

[17] Rajput, N. A., Atiq, M., Baig, M., Jamal, N., Wahab, M., & Ali, F. (2024). Analyzing pest risk in the context of climate change. In *Plant Quarantine Challenges under Climate Change Anxiety* (pp. 359-405). Cham: Springer Nature Switzerland. DOI:10.1007/978-3-031-56011-8_12

[18] Rustia, D. J. A., Lee, W. C., Lu, C. Y., Wu, Y. F., Shih, P. Y., Chen, S. K., Chung J. Y. & Lin, T. T. 2023. Edge-based wireless imaging system for continuous monitoring of insect pests in a remote outdoor mango orchard. *Computers and Electronics in Agriculture*, *211*, 108019. 10.1016/j.compag.2023.108019

[19] Sharma, K., & Shivandu, S. K. 2024. Integrating artificial intelligence and Internet of Things (IoT) for enhanced crop monitoring and management in precision agriculture. *Sensors International*, *5*, 100292.

[20] Suto, J. 2022. Codling Moth Monitoring with Camera-Equipped Automated Traps: A Review. *Agriculture*, *12*(10), 1721. https://doi.org/10.3390/agriculture12101721

[21] Talaviya, T., Shah, D., Patel, N., Yagnik, H., Shah, M., 2020. Implementation of artificial intelligence in agriculture for optimisation of irrigation and application of pesticides and herbicides. *Artificial Intelligence in Agriculture, 4*, pp. 58-73. https://doi.org/10.1016/j.aiia.2020.04.002

[22] Tudi, M., Daniel Ruan, H., Wang, L., Lyu, J., Sadler, R., Connell, D., Chu, C., & Phung, D. T. 2021. Agriculture Development, Pesticide Application and Its Impact on the Environment. *International Journal of Environmental Research and Public Health*, *18*(3), 1112. https://doi.org/10.3390/ijerph18031112

[23] Verdouw, C., Tekinerdogan, B., Beulens, A., Wolfert, S., 2021. Digital twins in smart farming. *Agricultural Systems, 189*, 103046. https://doi.org/10.1016/j.agsy.2020.103046

[24] Wang, Y., Zhang, Z., Jia, W., Ou, M., Dong, X., & Dai, S. 2025. A Review of Environmental Sensing Technologies for Targeted Spraying in Orchards. *Horticulturae*, *11*(5), 551. https://doi.org/10.3390/horticulturae11050551

[25] Yakovenko, R. V., Kopytko, P. G., Yakovenko, O. O., Sirius-Agro, L. L. C., & CHEPURNYI, V. 2023. Productivity of the orchard agroecosystem. *Collection of Scientific Papers of Uman National University of Horticulture*, *102*(1), 17-25. DOI: 10.32782/2415-8240-2023-102-1-17-25

[26] Yeshiwas, Y., Tadele, E., Mohammed, A., & Hu, X. 2026. Impacts of climate change on horticultural systems with focus on socio-economic implications, production and postharvest challenges, and adaptive pathways. *Discover Environment*, *4*(1), 55. DOI:10.1007/s44274-026-00539-0

[27] Zude-Sasse, M., Akbari, E., Tsoulias, N., Psiroukis, V., Fountas, S., & Ehsani, R. 2021. Sensing in precision horticulture. *Sensing approaches for precision agriculture*, 221-251. DOI:10.1007/978-3-030-78431-7_8

RESEARCH ON THE INFLUENCE OF TEMPORARY GRASSLAND ROTATION ON ARABLE CROPS SUITABLE FOR THE FAGARAS COUNTRY
/
CERCETĂRI PRIVIND INFLUENȚA ROTAȚIEI PAJIȘTILOR TEMPORARE ASUPRA CULTURILOR ARABILE PRETABILE PENTRU ȚARA FĂGĂRAȘULUI

Tudor Adrian ENE *[1)], Vasile MOCANU [1)]
[1)] Research-Development Institute for Grassland Brașov / Romania;
Tel: +40735713143; E-mail: tudor.ene@pajisti-grassland.ro
DOI: https://doi.org/10.35633/inmateh-79-106

Keywords: *crop rotation, grasslands influence, yields, temporary grassland*

ABSTRACT
Temporary grasslands are recognized both for their ecological functions, such as nutrient cycling, soil quality, and also for their potential role within crop rotation frameworks. While many studies have shown the agronomic and environmental benefits of permanent grasslands, fewer have analysed the impact of temporary grassland phases as precursors, influencing coming crops in terms of system stability or yield. Results are often mixed or contradictory in the academic literature, due to methodological limitations or insufficient statistical power. The current long-term study (2008-2014) investigates the role of grassland as a precursor to suitable arable crops (potatoes, spring wheat, silage maize and forage turnips), on a rotation-based empiric design, focusing on temporal variability, yield fluctuations and the broader agronomical context in which these changes occur. Using multi-year data, we look at crop yield performance, and discuss results offering suggestions for future research. To account for structural yield differences among crops, yields were standardized within crop categories, allowing for a unified analytical framework. Results from factorial ANOVA models indicate that grassland phases contribute to yield stabilization rather than a uniform increase in production of other crops, with outcomes influenced by crop type and stationary area conditions. Our results suggest that grasslands have the potential to enhance system resilience and are valuable for sustainable crop production under increased environmental uncertainty.

REZUMAT
Pajiștile temporare sunt recunoscute atât pentru funcțiile lor ecologice, cum ar fi ciclul nutrienților, calitatea solului, cât și pentru rolul lor potențial în cadrul rotației culturilor. Deși multe studii au arătat beneficiile agronomice și de mediu ale pajiștilor permanente, mai puține au analizat impactul pajiștilor temporare ca precursori, influențând culturile viitoare în ceea ce privește stabilitatea sistemului sau producţiei. Rezultatele sunt adesea mixte sau contradictorii în literatura academică, din cauza limitărilor metodologice sau a statisticii insuficiente. Studiul actual, pe termen lung (2008-2014), investighează rolul pajiștilor ca precursor al culturilor pretabile în arabil (cartof, grâu de primăvară, porumb siloz și sfeclă furajeră), pe baza unui design empiric bazat pe rotație, concentrându-se pe variabilitatea temporală, fluctuațiile producţiei și contextul agronomic mai larg în care au loc aceste schimbări. Folosind date multianuale, analizăm performanța producţiei culturilor și discutăm rezultatele oferind sugestii pentru cercetări viitoare. Pentru a ține cont de diferențele structurale de randament între culturi, randamentele au fost standardizate în cadrul categoriilor de culturi, permițând un cadru analitic unificat. Rezultatele modelelor factoriale ANOVA indică faptul că pajiștile contribuie la stabilizarea producţiei, mai degrabă decât la o creștere uniformă a producției altor culturi, rezultatele fiind influențate de tipul de cultură și de condițiile staționare zonale. Rezultatele noastre sugerează că pajiștile au potențialul de a spori rezistența sistemului și sunt valoroase pentru producția agricolă durabilă în condiții de incertitudine crescută a mediului.

INTRODUCTION
Sustainable agricultural systems emphasize the use of crop rotation systems and the inclusion of temporary grasslands as strategies to enhance soil fertility, increase nutrient retention and boost system resilience. Temporary grasslands are commonly linked to improved soil structure, favourable biological activity and enhanced organic matter contents, factors that can increase yield in the right climatic conditions (*Bender et al., 2018, Dragomir et al., 2023*).

Despite the aforementioned theoretical advantages, empirical results in field data remain inconsistent, often exhibiting mixed results. Some studies report yield increases in arable crops after a grassland precursor, while others observe neutral or crop-specific effects. A key limitation of the academic literature lies in the heterogeneity of crop types, different soil types found in a wide variety of climatic conditions, and data collected from vastly different experimental designs, which often limit the statistical power of statistical analyses.

This study tries to address some limitations by adopting an integrated analytical model which evaluates yield responses across crops. As reflected by the domain-specific literature, the main advantages that crop rotation provides are: improving soil fertility (*Al-Musawi et al., 2025, Yang et al., 2024*), reducing soil erosion *(Moldavan et al., 2024*), weeds control (*Bender et al., 2018, Weisberger et al., 2019*), increasing soil water uptake and storage (*Shah et al., 2021, Xiao et al., 2025*) reducing greenhouse gas emission from agricultural fields (*Murakami and Iizumi 2025, Saghai et al., 2025, Yang et al. 2024*), reducing mineral fertilizer requirements (*Gokhale and Sharma, 2023, Tzemi et al., 2024*) and improving yields (*Murakami and Iizumi, 2025, Syromiatnykov et al., 2026*).

The inclusion of grasslands in crop rotation presents advantages in terms of productivity (*Wozniak, 2021, Szkutnik-Sroka et al., 2024, Xiao et al., 2025*) and economical returns (*Hassaan et al., 2024, Otto et al., 2023, Smith et al., 2017*), as well as taking into account other functions, such as the protection of water quality (*Mancinelli et al., 2025*), soils (*Francis et al., 2024, Struijk et al., 2026, Ungureanu et al., 2015*), biodiversity (*Li et al., 2019, Chopin et al., 2026, Choudhary et al., 2026*), landscape conservation and its regulatory role of biogeochemical cycles (*Dragomir et al., 2023, Mocanu, 2018, Page et al., 2025*).

Grasslands leave an appreciable amount of biomass in the soil that improves soil fertility (*Li et al., 2019, Frelih-Larsen et al., 2022, Szkutnik-Sroka et al., 2024*). Organic fertilization of land is an operation that has a positive influence on the humus content and physical properties of the soil (*Ball et al., 2005, Zhong et al., 2021, Zheng et al., 2023*). Since the usage of organic fertilizers can be difficult and expensive, the recommended procedure is to perform a rotation between grasslands and crops that are suitable for a specific area (*Fang et al., 2025, Socolar et al., 2021*).

This paper presents the results obtained by the Research-Development Institute for Grassland Brașov from Romania, in the experimental field from Făgăraș Country, during the period 2008-2014. The objective of long-term study was to investigate the role of grassland as a precursor to suitable arable crops, on a rotation-based empiric design, focusing on temporal variability, yield fluctuations and the broader agronomical context in which these changes occur. Although data collection ended in 2014, our multi-year design remains directly relevant to current climate-adaptation and sustainability frameworks, which continue to rely on crop diversification practices, including temporary grasslands as a low-input strategy for stabilizing yields under increased climate variability.

MATERIALS AND METHODS

The experimental field was located in the Făgăraş Country (a central zone of Romania), on the land of a mixed farm in Drăguș, Brașov County, at an altitude of 520 m. The soil type of the experimental field was Podzolic, with the soil acidity ranging from weak to moderate acid, with value of pH between 4.8 to 4.9 and moderate excess humidity *(Mocanu et al., 2018*). The block method was used, with the experimental field being composed of 3 blocks, each block having 5 variations alternated in 4 repetitions. The experimental field scheme is shown in Fig. 1.

The crop rotation took into account suitable crops for this area and the farm requirements, and consisted of: temporary grassland (grasses + perennial legumes), potato, forage turnips, spring wheat, and silage maize (*Mocanu et al., 2018*).

A complex mineral fertilizer, for the temporary grassland variants, was applied as follows (Mocanu et al., 2018): in 2008 – $N_{100}P_{100}K_{100}$, in 2009 – $N_{50}P_{50}K_{50}$, in 2010 – $N_{50}P_{50}K_{50}$, in 2012 – $N_{50}P_{50}K_{50}$, in 2013 – $N_{100}P_{100}K_{100}$ and in 2014 – $N_{50}P_{50}K_{50}$.

For the temporary grassland, a mixture was used in the following percentage: Grasses 70% and Legumes 30% (*Dragomir et al., 2023, Mocanu et al., 2018*), consisting of species and varieties such as: perennial grasses (*Dactylis glomerata* MAGDA, *Festuca pratensis* TRANSILVAN, *Festuca arundinacea* ADELA, *Phleum pratense* TIROM and *Lolium perenne* MATHILDE) and perennial legumes (*Trifolium pratense* ALTASWEDE, *Trifolium repens* RIVENDEL and *Lotus corniculatus* – LOTANOVA).



Fig. 1 - Scheme of the experimental field in Făgăraș Country
(Mocanu et al., 2018)

Climatic conditions varied among years (Table 1): 2012, 2013, 2014 were dry, 2010 was rainy, and 2008, 2009 and 2011 had normal values, with precipitation amounts close to the multiannual average (*Mocanu et al., 2018*).

[Table 1]

Climatic conditions in Făgăraș Country (*Mocanu et al., 2018*)

		2008	2009	2010	2011	2012	2013	2014
Average air temperatures, [°C]	Annual average	8.5	8.9	9.3	10.6	8.8	9.1	9.5
	MAA	7.9	7.9	7.9	8.0	8.0	8.0	8.0
	Deviation	0.6	+1.0	+1.4	+2.6	+0.8	+1.1	+1.5
Atmospheric precipitation [l·m^{-2}]	Annual amount	633.6	674.6	841.3	573.5	493.0	491.7	491.3
	MAA	651.5	647	647	600.0	600.0	600.0	600.0
	Deviation	-17.9	+27.6	+194.3	-26.5	-107.0	-108.3	-108.7

MAA-Multi Annual Average

From the data presented in Table 2, it results that the soil on which the experimental field was located, in the 0...10 cm profile, is strongly acidic, poorly supplied in P and moderately supplied in K, and in the 10...20 cm area, the soil is strongly acidic, very poorly supplied in P and poorly supplied in K.

[Table 2]

The main agrochemical properties of the soil (*Mocanu et al., 2018*)

No.	**Sampling depth** (cm)	**pH**	**Hydrolytic Acidity**	**Sum of Bases**	**V** (%)	**Humus** (%)	**Nitrogen Index**	**P-AL**	**K-AL**
			me at 100 g soil					(ppm)	(ppm)
1	0...10	4.8	10.5	4.8	31.3	1.84	3.70	10.8	90.0
2	10...20	4.9	10.0	4.0	28.5	7.87	2.24	7.4	36.0

Next, the yields of potato, spring wheat, silage maize, and forage turnip grown in rotation after at least one year of temporary grassland are analysed.

Potato yields

In 2009 (normal values in terms of precipitation), potato production was 25.60 t/ha for the A1 alternative (preceding crop: temporary grassland 1st Year) and 35.10 t/ha for the B2 option (preceding crop: temporary grassland 1st Year).

In 2010 (rainy), potato production was 29.50 t/ha for the A5 option (preceding crop: 2009-temporary grassland 1st Year; 2008-silage maize), 27.20 t/ha for B1 (preceding crop: 2009-temporary grassland 2nd Year; 2008-temporary grassland 1st Year), 26.30 t/ha for C2 (preceding crop: 2009-temporary grassland 2nd Year; 2008-temporary grassland 1st Year).

In 2012 (dry), potato production was 11.47 t/ha for the B4 option (preceding crop: 2011- temporary grassland 1st Year; 2010-silage maize; 2009-forage turnip; 2008-temporary grassland 1st Year), compared to 13.97 t/ha for C1 (preceding crop: temporary grassland, 4th Year).

In 2013 (dry), potato production was 22.16 t/ha for the A3 group (preceding crop: 2012-temporary grassland 2nd Year; 2011-temporary grassland 1st Year; 2010-silage maize; 2009-forage turnip; 2008-spring wheat), compared to 31.27 t/ha for the B2 option (preceding crop: 2012-forage turnip; 2011-temporary grassland 1st Year; 2010-spring wheat; 2009-potato; 2008-temporary grassland 1st Year) and respectively 29.14 t/ha for C2 (preceding crop: 2012-silage maize; 2011-temporary grassland 1st Year; 2010-potato; 2009-temporary grassland 2nd Year; 2008-temporary grassland 1st Year).

In 2014 (dry) potato production was 29.90 t/ha for the A2 option (preceding crop: 2013-forage turnip; 2012-temporary grassland 2nd Year; 2011-temporary grassland 1st Year; 2010-forage turnip; 2009-spring wheat; 2008-potato), compared to 41.70 t/ha for B3 (preceding crop: 2013-spring wheat; 2012-silage maize; 2011-temporary grassland 1st Year; 2010-forage turnip; 2009-spring wheat; 2008-temporary grassland 1st Year) and respectively 37.70 t/ha for the C4 alternative (preceding crop: 2013-forage turnip; 2012-spring wheat; 2011-temporary grassland 1st Year; 2010-forage turnip; 2009-temporary grassland 2nd Year; 2008-temporary grassland 1st Year).

Spring wheat yields

In 2009 (standard in terms of precipitation), the spring wheat production was 3.580 t/ha for option A2 (preceding crop: 2008-potato) and 4.370 t/ha for B3 (preceding crop: temporary grassland 1st Year). In the case of option B3, a positive influence of temporary grassland on spring wheat yield is observed, materializing as a 22 % production increase.

In 2010 (a rainy year) the spring wheat production was 2.075 t/ha in the case of option A1 (preceding crop: 2009-potato; 2008-temporary grassland 1st Year), 1.990 t/ha for option B2 (preceding crop: 2009-potato; 2008-temporary grassland 1st Year), 2.112 t/ha in the case of C3 (preceding crop: 2009-temporary grassland 2nd Year; 2008-temporary grassland 1st Year).

In 2012 (a dry year), the spring wheat production was 4.253 t/ha for the B1 option (preceding crop: 2011-temporary grassland 1st Year; 2010-potato; 2009-temporary grassland 2nd Year; 2008-temporary grassland 1st Year), compared to 3.858 t/ha in the case of C4 (preceding crop: 2011-temporary grassland 1st Year; 2010-forage turnip; 2009-temporary grassland 2nd Year; 2008-temporary grassland 1st Year). It can observe that a good production was obtained in both variants, after temporary grassland 2nd Year followed by a potato and forage turnip crop, respectively.

In 2013 (a dry year), the spring wheat production was 2.553 t/ha in the case of option A4 (preceding crop: 2012-temporary grassland 3rd Year; 2011-temporary grassland 2nd Year; 2010-temporary grassland 1st Year; 2009-silage maize; 2008-forage turnip), compared to 3.267 t/ha for B3 (preceding crop: 2012-silage maize; 2011-temporary grassland 1st Year; 2010-forage turnip; 2009-spring wheat; 2008-temporary grassland 1st Year) and respectively 3.508 t/ha for option C5 (preceding crop: 2012-temporary grassland 1st Year; 2011-temporary grassland 1st Year; 2010-silage maize; 2009-temporary grassland 2nd Year; 2008-temporary grassland 1st Year).

In 2014 (a dry year), the spring wheat production was 4.312 t/ha for option A3 (preceding crop: 2013-potato; 2012-temporary grassland 2nd Year; 2011-temporary grassland 1st Year; 2010-silage maize; 2009-forage turnip; 2008-spring wheat), compared to 3.190 t/ha in the case of B2 (preceding crop: 2013-potato; 2012-forage turnip; 2011-temporary grassland 1st Year; 2010-spring wheat; 2009-potato; 2008-temporary grassland 1st Year) and respectively 3.550 t/ha for the C3 option (preceding crop: 2013-silage maize; 2012-forage turnip; 2011-temporary grassland 1st Year; 2010-spring wheat; 2009-temporary grassland 2nd Year; 2008-temporary grassland 1st Year).

Silage maize yields

In 2009 (standard levels of precipitation) the silage maize yield was 47.81 t/ha GM-Green Mass (19.64 t/ha DM-Dry Matter) in case of option A4 (preceding crop: 2008-forage turnip) and 48.48 t/ha GM (21.31 t/ha DM) in case of B5 (preceding crop: temporary grassland 1st Year). In B5, a positive effect of meadow on silage maize yield was observed, resulting in a 1.4% increase.

In 2010 (a rainy year), the silage maize production was 41.63 t/ha GM (14.89 t/ha DM) in the case of A3 (after: 2009-forage turnip; 2008-spring wheat), 37.60 t/ha GM (12.60 t/ha DM) for B4 (preceding crop: 2009-forage turnip; 2008-temporary grassland 1st Year), 53.10 t/ha GM (16.45 t/ha DM) in the case of C5 (preceding crop: 2009-temporary grassland 2nd Year; 2008-temporary grassland 1st Year).

In 2012 (a dry year), the silage maize production was 8.95 t/ha GM (5.09 t/ha DM) in B3 (preceding crop: 2011-temporary grassland 1st Year; 2010-forage turnip; 2009-spring wheat; 2008-temporary grassland 1st Year), compared to 10.10 t/ha GM (6.17 t/ha DM) in the case of C2 (preceding crop: 2011- temporary grassland 1st Year; 2010-potato; 2009-temporary grassland 2nd Year; 2008-temporary grassland 1st Year). In option C2, a positive influence of the temporary grassland on the silage maize production is observed, with a production increase of 12.85 %.

In 2013 (a dry year), silage maize production was 64.51 t/ha GM (25.28 t/ha DM) in the case of A5 (preceding crop: 2012-temporary grassland 2nd Year; 2011-temporary grassland 1st Year; 2010-potato; 2009-temporary grassland 1st Year; 2008- silage maize), compared to 50.81 t/ha GM (19.95 t/ha DM) in the B1 option (preceding crop: 2012-spring wheat; 2011-temporary grassland 1st Year; 2010-potato; 2009- temporary grassland 2nd Year; 2008-temporary grassland 1st Year) and respectively 52.73 t/ha GM (22.28 t/ha DM) for C3 (preceding crop: 2012-forage turnip; 2011-temporary grassland 1st Year; 2010-spring wheat; 2009-temporary grassland 2nd Year; 2008-temporary grassland 1st Year). For option A5, a positive influence of meadow (preceding crop: meadow 2 years) on silage maize production is observed, with a production increase of 26.96 % compared to B1 and 22.34 % compared to option C3.

In 2014 (a dry year), silage maize production was 45.12 t/ha GM (17.53 t/ha DM) in the case of the A4 design (preceding crop: 2013-spring wheat; 2012-temporary grassland 3rd Year; 2011-temporary grassland 2nd Year; 2010-temporary grassland 1st Year; 2009-silage maize; 2008- forage turnip), compared to 32.00 t/ha GM (12.84 t/ha DM) for B5 (preceding crop: 2013-temporary grassland 4th Year; 2012-temporary grassland 3rd Year; 2011-temporary grassland 2nd Year; 2010-temporary grassland 1st Year; 2009-silage maize; 2008-temporary grassland 1st Year) and respectively 45.00 t/ha GM (16.96 t/ha DM) on option C1 (preceding crop: 2013-temporary grassland 1st Year; 2012- potato; 2011-temporary grassland 4th Year; 2010-temporary grassland 3rd Year; 2009-temporary grassland 2nd Year; 2008-temporary grassland 1st Year).

Forage turnip yields

In 2009 (standard year in terms of precipitation), the production of forage turnip was 56.30 t/ha in A3 (preceding crop: 2008-spring wheat) and 51.80 t/ha in B4 (preceding crop: temporary grassland 1st Year). For option B4, a negative influence of meadow on forage turnip production is observed, with a production decrease of 7.99 %.

In 2010 (a rainy year), the production of forage turnip was 68.10 t/ha in the A2 design (after: 2009-spring wheat; 2008-potato), 51.85 t/ha for B3 (preceding crop: 2009-spring wheat; 2008-temporary grassland 1st Year), 72.55 t/ha for option C4 (preceding crop: 2009-temporary grassland 2nd Year; 2008-temporary grassland 1st Year). In the case of C4, a positive influence of the meadow on the production of forage turnip is observed, with a production increase of 39.92 % compared to option B3 and a production increase of 6.53 % compared to A2.

In 2012 (a dry year), the production of forage turnip was 28.50 t/ha in B2 (preceding crop: 2011-temporary grassland 1st Year; 2010-spring wheat; 2009-potato; 2008-temporary grassland 1st Year), compared to 30.50 t/ha in C3 (preceding crop: 2011-temporary grassland 1st Year; 2010-spring wheat; 2009-temporary grassland 2nd Year; 2008-temporary grassland 1st Year). In the case of option C3, a positive influence of the grassland on the production of forage turnip is observed, with an increase in production of 7.02 %.

In 2013 (a dry year), the production of forage turnip was 40.82 t/ha for A2 (preceding crop: 2012-temporary grassland 2nd Year; 2011-temporary grassland 1st Year; 2010-forage turnip; 2009-spring wheat; 2008-potato), compared to 40.07 t/ha MV in the B4 alternative (preceding crop: 2012-potato; 2011-temporary grassland 1st Year; 2010-silage maize; 2009-forage turnip; 2008-temporary grassland 1st Year) and respectively 35.85 t/ha for C4 (preceding crop: 2012-spring wheat; 2011-temporary grassland 1st Year; 2010-forage turnip; 2009-temporary grassland 2nd Year; 2008-temporary grassland 1st Year). In A2, a positive

influence of the grassland (preceding crop: temporary grassland 2nd Year) on the production of forage turnip is observed, with a production increase of 2.00 % compared to B4 and respectively 13.86 % compared to C4.

In 2014 (a dry year), the production of forage turnip was 58.45 t/ha for A5 (preceding crop: 2013-silage maize; 2012-temporary grassland 2nd Year; 2011-temporary grassland 1st Year; 2010-potato; 2009-temporary grassland 1st Year; 2008-silage maize), compared to 43.50 t/ha in B1 (preceding crop: 2013-silage maize; 2012-spring wheat; 2011-temporary grassland 1st Year; 2010-potato; 2009-temporary grassland 2nd Year; 2008-temporary grassland 1st Year) and respectively 50.08 t/ha for C5 (preceding crop: 2013-spring wheat; 2012-temporary grassland 2nd Year; 2011-temporary grassland 1st Year; 2010-silage maize; 2009-temporary grassland 2nd Year; 2008-temporary grassland 1st Year).

Hypotheses

This study aims to investigate the role of temporary grassland as a precursor in arable crop rotation using a multi-year plot-based experimental design. The overall main objective is to assess whether the duration of grassland preceding an arable crop can influence yield, and whether this effect varies across crops and annual climatic conditions.

H1: Grassland duration produces a general effect on crop yields across a multi-crop design.

H2: The effect of grassland duration differs among crop types.

H3: Inter-annual variability and climatic conditions have an effect on the relation between the variables in H1 and H2.

Data structure and empirical analyses

This study exhibits a plot-based crop rotation dataset (as previously referenced in Figure 1), followed across several consecutive years. The structure of the data collected over the years follows a longitudinal structure, with each row corresponding to a unique year and plot variant combination, including current crop, previous crop, and yield (t/ha). Statistical analyses were conducted using SPSS Version 26.

As exhibited in Figure 1, 2011 is a rest year, in which grassland was used to preserve crop rotation continuity and to compute grassland duration as a precursor for the next crops. This does not bias the statistical analyses, because the yield was a dependent variable measured only for the arable crops, therefore grassland yield is not an outcome in the present study.

Our variables of interest are:

-The independent variable (IV): grassland duration as a precursor, which was coded for statistical analyses into two categories, namely a) grass_consec_years, which represents the number of consecutive grassland years immediately preceding the current year, and b) grass_duration_cat, the categorical version for analysis (0- no grassland, 1- temporary grassland 1st Year, 2- temporary grassland 2nd Year, 3 and 3+ years- 3 or more years of consecutive grassland);

-The dependent variable (DV): yield, measured in tonnes per hectare (t/ha), analysed separately for each arable crop (potatoes, spring wheat, silage maize and forage turnips);

-Context variable: year, representing the inter-annual variability and the climatic context and year-specific management. 'NPK' (the complex mineral fertilizer applied on the plots of land) is collinear with 'year' because the annual dose is constant across crops within the same year.

Climatic conditions were classified into three categories, namely dry, normal or rainy, based on the aggregated annual rainfall patterns.

RESULTS

Given the small sample size per crop, factorial models with interactions (duration x year) could lead to unstable estimates, therefore, these analyses have been avoided. Also, due to the large inherent differences in absolute yield levels, direct comparison of raw yield figures would have been misleading. To address this and ensure accuracy, yields were standardized within each crop category using Z-scores. This statistical procedure preserves within-crop variability, while enabling a unified analysis across crops. This way, we were able to focus on relative yield performance rather than absolute magnitudes.

Factorial analysis of variance (ANOVA) models was applied using Type III sums of squares to account for unbalanced designs. The primary model included crop type, year, and grassland duration as fixed factors, along with the interaction between grassland and crop.

A secondary model examined the influence of climatic category in place of year, in order to avoid degrees-of-freedom limitations. Statistical significance was evaluated at $\alpha = 0.05$. Effect sizes were quantified using partial eta squared (ηp^2).

It appears that the overall model explained a substantial proportion of yield variability (R^2=0.587, adjusted R^2=0.443).

A significant main effect of year was observed (F=6.63, p<0.001, ηp^2=0.334), indicating a strong interannual variability in yield across the study period.

It has been noted that the main effect of grassland duration did not appear to reach conventional significance level (p=0.098) suggesting that grassland duration alone does not impose a uniform influence on yield across all crops.

In contrast the interaction between crop type and grassland duration was highly significant (F=4.90, p<0.001, ηp^2=0.450). This interaction accounted for a significant size of explained variance and demonstrating that the yield response to grassland duration differs significantly amongst crops.

As shown in Figure 2 and Table 3, mean standardized yields vary little across grassland duration categories, while variability increases noticeably for longer grassland phases.

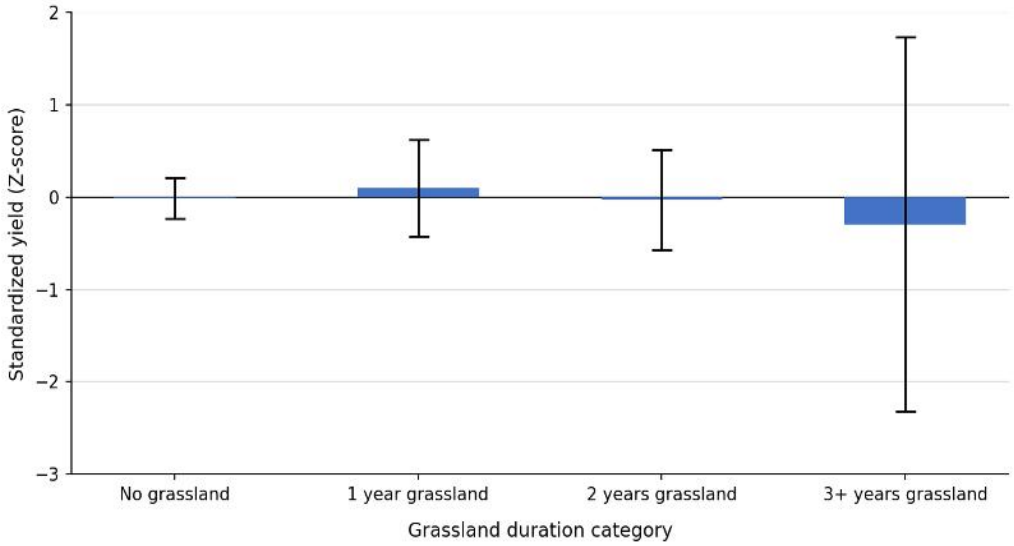


Fig. 2 - Mean standardized crop yield (Z-score) across grassland duration categories

Error bars represent 95 % confidence intervals. Yield values were standardized within crop types to account for inherent yield differences among crops. Short-term grassland phases (1–2 years) are associated with stable or slightly positive standardized yields, while the 3+ years category exhibits high variability due to limited sample size and should be interpreted with caution.

In addition, the main effect of the crop type itself was not significant once yields were standardized thus confirming that the study focus on interaction dynamics rather than crop level differences.

In the climate-based model, the climatic category showed a significant main effect on standardized yields (F=4.70, p=0.012, ηp^2=0.125) highlighting the importance of environmental conditions.

At the same time, the crop x grassland duration interaction remained highly significant (p<0.001) indicating that the crop specific nature of grassland effects carry-on across climatic context. The interaction between climate and grassland duration was not significant suggesting that the climate variates overall yield levels rather than fundamentally altering grassland response patterns.

Table 3

Mean standardized crop yield (Z-score) by grassland duration category

Z-score (yield)			
Grass_duration_cat	**N**	**Mean**	**Std. Deviation**
No grassland	47	-.0133900	.73873321
1 year grassland	25	.1001461	1.27145984
2 years grassland	13	-.0306740	.90286311
3+ years grassland	5	-.2951118	1.62858376
Total	90	.0000000	.97726976

CONCLUSIONS

The results provide insight on effects of temporary grassland on crop yields are not uniform across cropping system. Instead of depicting a universal yield enhancing factor, the grassland duration interacts strongly with specific crops by producing divergent responses depending on crop specific physiological and agronomic characteristics.

Yield values were standardized within crop types. The 3+ years category shows increased dispersion due to limited sample size and should be interpreted with caution.

The absence of a significant main effect of grassland duration should not be interpreted as proof of ineffectiveness. Instead, it reflects the ecological reality that the soil-mediated benefits of grasslands are context-dependent. Crops with higher nutrient demands or greater sensitivity to soil structure appear to benefit differently from grassland phases than crops with lower input requirements.

The strong year effect highlights the role of interannual variability, reinforcing the importance of a long-term observation for further evaluating rotational effects. Climatic conditions further influenced yields but did not negate the crop dependent nature of grassland impacts.

Overall, these findings support the interpretation of temporary grasslands as a stabilizing component within crop rotations. Their primary contribution appears to consolidate yield variability and enhancing system resilience rather than maximizing mean yields across all crops.

In terms of limitations, we noted the use of the aforementioned complex mineral fertilizer NPK whose effect cannot be separated from year effects as they are constant within year across all crops. Another limitation reflects the small sample size per crop and sparse duration categories, which limits inference strength. To address any analysis-related constraints, yields were standardized within crops and analysed collectively. This approach prioritizes the detection of interaction patterns and of system-level responses when it comes to mean differences for a crop. Results must be interpreted with caution, as this exploratory study should be replicated on more crops and repetitions, in order to gather a wider variety of data for ease of comparison. Future research should combine more numerous datasets with mixed-effects statistical modeling, to further identify crop variations in different environmental conditions.

Our study is explorative research which has opened up valuable avenues for future research, while also consolidating existing academic knowledge on crop variation. It investigated the role of temporary grassland as a precursor for arable crop rotation, with the main result indicating that grassland influence crop yields primarily through crop-specific interactions, rather than a uniform main effect on crops. Grassland duration strongly interacts with the crop type, generating yield stability across variable climatic conditions. These findings challenge simplistic assumptions of universal yield enhancement, following grassland phases and instead emphasize the role of grasslands in promoting resilience and functional diversity within agricultural systems. From both an agronomic and methodological perspective, evaluating interaction structures across crops provides a more realistic understanding of rotational benefits in sustainable agriculture.

ACKNOWLEDGEMENT

The authors have recognitions for researchers from National Research-Development Institute for Pedology, Agrochemistry and Environment Protection Bucharest, Romania for support during the research.

REFERENCES

[1] Al-Musawi, Z. K., Vona, V. and Kulmány, I. M. (2025). Utilizing Different Crop Rotation Systems for Agricultural and Environmental Sustainability: A Review. *Agronomy*, 15(8), 1966. https://doi.org/10.3390/agronomy15081966

[2] Ball, B. C., Bingham, I., Rees, B., Litterick, C. W. A. (2005). The role of crop rotations in determining soil structure and crop growth conditions. *Canadian Journal of Soil Science*, 85(5), 557-577. doi: 10.4141/S04-078;

[3] Bender A., Tamm S., Aavola R. (2018). Herbage legume enhance soil fertility in crop rotation, *Grassland Science in Europe*, 23, 583-585

[4] Chopin, P., Hermouet, S., Watson, C., Öborn, I., Bergkvist, G. (2026). A novel framework to study the evolution of crop rotation diversity reveals changes towards regional crop type specialisation in Sweden. *European Journal of Agronomy*, 172, 127848. https://doi.org/10.1016/j.eja.2025.127848

[5] Choudhary, S., Rajpoot, S. K., Tripathi, A., Choudhary, M., Radha, L., Sen, M. (2026). Diversified Cropping Systems for Improving the Crop Productivity and Soil Health of Dryland Ecosystem. *Land Degradation & Development*, 37, 419–437. http://doi.org/10.1002/ldr.70140

[6] Dragomir N., Mocanu V., Dragomir N. (2023). Multifunctional of Grasslands – Permanent Way of Sustainable Utilization of Regional Resources in Romania. *Journal of Energy and Natural Resources*, 12(4), 38-46. https://doi.org/10.11648/j.jenr.20231204.11

[7] Fang Y., Li Q., He C., Wang K., Wang F. (2025). Effect of crop rotation and straw return on soil microbiome in a southern paddy field, *Chilean Journal of Agriculture Research*, 85(1), 57-76. http://dx.doi.org/10.4067/S0718-58392025000100057

[8] Francis, C.A., Blanco-Conqui, H., Creech, C.F. (2024). Adaptive rotations for improving soil productivity and profits. *CABI Reviews*, 19:1. https://doi.org/10.1079/cabireviews.2024.0045

[9] Frelih-Larsen A., Riedel A., Oluwatoyin R., Gattinger A., Niether W. (2022). Improved crop rotation. *Umweltbundesamt*, German Environment Agency;

[10] Gokhale S.C. and Sharma N. (2023). Optimizing crop rotations via Parrondo's paradox for sustainable agriculture. *Royal Society Open Science*, 10:221401. https://doi.org/10.1098/rsos.221401

[11] Hassaan, M. A., Alishba, H., Aslam, S., Danyal, M., Abbas, Z., Ullah, A., Muhammad Babar, M., Haider, Z., Iqbal, A. (2024). Crop rotation as an economic strategy for small-scale farmers: evidence from Punjab, Pakistan. *Journal of Oasis Agriculture and Sustainable Development*, 6(02), 31–39. https://doi.org/10.56027/JOASD.192024

[12] Li, J., Huang, L., Zhang, J., Coulter, J.A., Li, L., Gan, Y. (2019). Diversifying crop rotation improves system robustness. *Agronomy for Sustainable Development*, 39, 38. https://doi.org/10.1007/s13593-019-0584-0

[13] Otto, S., Masin, R., Nikolić, N., Berti, A., Zanin, G. (2023). Effect of 20-years crop rotation and different strategies of fertilization on weed seedbank. *Agriculture, Ecosystems and Environment*, 354, 108580. https://doi.org/10.1016/j.agee.2023.108580

[14] Mancinelli, R., Atait, M., Allam, M., Radicetti, E. (2025). Soil Tillage and Crop Rotation: Pivotal Practices of the Organic Cropping System Management. *Advances in Organic Farming*, 225-234. https://doi.org/10.1079/9781800626850.0024

[15] Mocanu V., Ene T.A., Marusca T., Blaj A.V., Andreoiu A., Mocanu V. (2018). Temporary grassland – an optimal alternative in crop rotation systems. *Grassland Science in Europe*, 28, 996-998;

[16] Moldavan, L., Pimenowa, O., Wasilewski M., Wasilewska, N. (2024). Crop Rotation Management in the Context of Sustainable Development of Agriculture in Ukraine. *Agriculture* 14, 934. http://doi.org/10.3390/agriculture14060934

[17] Murakami, K., Iizumi, T. (2025). Optimization of crop rotation calendar to maximize system-level productivity under climate change. *Environmental Research Communications*, 7, 101010. https://doi.org/10.1088/2515-7620/ae15de

[18] Page, L. D., Strauss, J., Jacobs, K. (2025). The effect of crop-rotation systems in regenerative agricultural environments on the rhizosphere microbiome of dry-land winter wheat. *Sustainable Microbiology*, 2, 4, qvaf020. https://doi.org/10.1093/sumbio/qvaf020

[19] Reddy, P.P. (2017). Crop Rotation. In: Agro-ecological Approaches to Pest Management for Sustainable Agriculture. *Springer*, Singapore. https://doi.org/10.1007/978-981-10-4325-3_15

[20] Saghai, A., Smith M. E., Vico, G., Banerjee, S., Edlinger A., Garcia-Palacios, P., Garland, G., van der Heijden, M.G.A., Herzog, C., Maestre, F. T., Pescador, D. S., Philippot, L., Rillig, M. C., Romdhane, S., Bommarco, R., Hallin, S. (2025). Diverse crop rotations off-set yield-scaled nitrogen losses via denitrification. *bioRxiv*. https://doi.org/10.1101/2025.03.15.643431

[21] Shah, K. K., Modi, B., Pandey, H. P., Subedi, A., Aryal, G., Pandey, M., Shrestha, J. (2021). Diversified Crop Rotation: An Approach for Sustainable Agriculture Production. *Advances in Agriculture*, 8924087. https://doi.org/10.1155/2021/8924087

[22] Shivashankar, M. S., Emmiganur, K., Pandey, S. K. (2024). Crop rotation and intercropping techniques. In book: *Modern Concept in Agronomy* (Edition I), ISBN: 978-81-972002-0-5. http://doi.org/10.5281/zenodo.11051201

[23] Smith, E.G., Zentner, R.P., Campbell, C.A., Lemke, R., Brandt, K. (2017). Long-Term Crop Rotation Effects on Production, Grain Quality, Profitability, and Risk in the Northern Great Plains. *Agronomy Journal*, 109(3), 957-967. https://doi.org/10.2134/agronj2016.07.0420

[24] Socolar, Y., Goldstein, B. R., de Valpine, P., Bowles, T. M. (2021). Biophysical and policy factors predict simplified crop rotations in the US Midwest. *Environmental Research Letters*, 16(5), 054045. https://doi.org/10.1088/1748-9326/abf9ca

[25] Struijk, M., Degani, E., Leigh, S., Bowen, E., Thomas, S., Mortimer, S., Whitmore, A. P., Ashwood, F., Clark, S. J., Sizmur, T., (2026). Crop rotation phase has a greater impact on soil biology than crop rotation diversity. *Agriculture, Ecosystems & Environment*, 396, 110023. https://doi:10.1016/j.agee.2025.110023

[26] Syromiatnykov, Y., Ishniyazova, S., Troyanovskaya, I., Voinash, S., Garkin, I., Malikov, V., Orekhovskaya, A. (2026). Optimizing Crop Rotation and Cereal Saturation for Sustainable Winter Wheat Production Under Semiarid Conditions of Uzbekistan. *Advances in Agriculture*, 5863850. https://doi.org/10.1155/aia/5863850

[27] Szkutnik-Sroka J., Kacorzyk P., Szewczyk W. (2024). The influence of grasses and legumes as a forecrop on the biological activity of the soil. *Grassland Science in Europe*, 29, 226-228, eISBN: 978-90-903-8494-8

[28] Tzemi, D., Ramo, J., Palosuo, T., Peltonen-Sainio, P., Wejberg, H., Lehtonen, H. (2024). The introduction of legume-based crop rotations: an impact assessment on cereal cropping farms in Finland. *International Journal of Agricultural Sustainability*, 22(1), 2335085. https://doi.org/10.1080/14735903.2024.2335085

[29] Ungureanu, N., Croitoru, S., Biris, S., Voicu, G., Vladut, V., Selvi, K.Ç., Boruz, S., Marin, E., Matache, M., Manea, D., Constantin, G., Ionescu, M., (2015) Agricultural Soil Compaction Under the Action of Agricultural Machinery. *Aktualni Zadaci Mehanizacije Poljoprivrede* 43, 31-42;

[30] Weisberger, D., Nichols, V. and Liebman, M. (2019). Does diversifying crop rotations suppress weeds? A meta-analysis. *PLoS ONE*, 14(7), e0219847. https://doi.org/10.1371/journal.pone.0219847

[31] Wozniak, A. (2021). Production efficiency of different crop rotations and tillage systems. *Spanish Journal of Agricultural Research*, 19(4), e0907. https://doi.org/10.5424/sjar/2021194-17023

[32] Xiao, L., Wang, Y., Zhang, C., Zhao, K., Zhao, R., Xie Z. (2025). Crop rotation enhances yield and water productivity: Uncovering potential drivers through global field experiment synthesis. *Agricultural Water Management*, 317, 109644. https://doi.org/10.1016/j.agwat.2025.109644

[33] Yang, X., Xiong, J., Du, T., Ju, X., Gan Y., Li, S., Xia, L., Shen, Y., Pacenka, S., Steenhuis, T. S., Siddique, K. H. M., Kang, S., Butterbach-Bahl, K. (2024). Diversifying crop rotation increases food production, reduces net greenhouse gas emissions and improves soil health. *Nature Communications*, 15:198. https://doi.org/10.1038/s41467-023-44464-9

[34] Zheng, F., Liu, X., Ding, W., Song, X., Li, S., Wu, X. (2023). Positive effects of crop rotation on soil aggregation and associated organic carbon are mainly controlled by climate and initial soil carbon content: A meta-analysis. *Agriculture, Ecosystems & Environment*, 355, 1, 108600. https://doi.org/10.1016/j.agee.2023.108600

[35] Zhong S., Sheng Z., Zheng L., Zheng X., Yang Y., Xiao D., Ai B., Zeng H. (2021), Impacts of 25-year rotation and tillage management on soil quality in a semi-arid tropical climate. *Chilean Journal of Agricultural Research*, 81(1), 3-13. http://dx.doi.org/10.4067/S0718-58392021000100003

ENERGY AND EXERGY ANALYSES OF TWO-TEMPERATURE-LEVEL VAPOR COMPRESSION REFRIGERATION SYSTEMS FOR APPLICATIONS IN THE FOOD INDUSTRY
/
ANALIZA ENERGETICĂ ȘI EXERGETICĂ A SISTEMELOR FRIGORIFICE CU COMPRIMARE MECANICĂ DE VAPORI CU DOUĂ NIVELURI DE TEMPERATURĂ DESTINATE APLICAȚIILOR DIN INDUSTRIA ALIMENTARĂ

Daniel DIMA [1)], George Daniel GHIȚĂ [*1)], Mihai Florin BIZDADEA [*1)], Horațiu POP [1)], Valentin APOSTOL [1)], Valentin CIOBANU [1)], Cristian Marian SORICĂ [2*)]
[1)] National University of Science and Technology POLITEHNICA Bucharest / Romania;
[2)] National Institute of Research – Development for Machines and Installations Designed to Agriculture and Food Industry - INMA Bucharest, Romania
Ghiță George Daniel; E-mail: george_daniel.ghita@upb.ro
Bizdadea Mihai Florin; E-mail: mihai.bizdadea@upb.ro
DOI: https://doi.org/10.35633/inmateh-79-107

Keywords: *exergy analysis, two-temperature-level, refrigeration and freezing system, throttling process, exergy destruction, coefficient of performance, low-GWP refrigerants.*

ABSTRACT
This study compares energy and exergy performance of two vapour-compression refrigeration systems designed to provide simultaneous refrigeration and freezing at two distinct temperature levels for food-industry applications. The simulation results indicated that R1234yf provided the best overall performance for both configurations. The exergy analysis showed that the throttling processes in the first configuration had the fastest increase in exergy destruction with the variation of ambient temperature. The structural improvement of the second configuration led to an increase in overall system performance, confirming the importance of refrigerant selection and structural optimisation of the refrigeration system. For R1234yf, the energy coefficient of performance increased from 2.69 to 2.97 at an ambient temperature of 35 °C and from 1.98 to 2.24 at 45 °C when configuration (b) was used instead of configuration (a).

REZUMAT
Acest studiu compară performanța energetică și exergetică a două sisteme frigorifice cu comprimare mecanică de vapori, proiectate pentru a asigura simultan refrigerarea și congelarea la două niveluri distincte de temperatura, pentru aplicații din industria alimentara. Rezultatele simulărilor au indicat faptul ca R1234yf a oferit cea mai bună performanță globală pentru ambele configurații. Analiza exergetică a arătat ca procesele de laminare din prima configurație au prezentat cea mai rapida creștere a distrugerii de exergie odată cu variația temperaturii ambiante. Îmbunătățirea structurala a celei de-a doua configurații a condus la creșterea performantei globale a sistemului, confirmând importanta selecției agentului frigorific si a optimizării structurale a sistemului frigorific.

INTRODUCTION

In agri-food applications, temperature requirements vary according to the specific characteristics of each product and its intended technological use. Some products must be stored under refrigeration conditions, whereas others require freezing conditions. Two-temperature-level refrigeration systems are used in food storage facilities, commercial units and cold-chain applications where different thermal conditions must be provided simultaneously. These systems can provide one temperature level for refrigeration and another for freezing, either within the same installation or through interconnected refrigeration configurations, such as cascade systems or other forms of thermal coupling.

Refrigeration and freezing are essential technologies for the preservation of agri-food products, as low temperatures reduce microbial activity, slow down enzymatic reactions and limit quality losses. Horticultural and food products have a high water content and deteriorate rapidly during storage, transport and distribution. For this reason, the use of artificial cold through refrigeration or freezing represents one of the most effective methods for preserving perishable products (*Sorică et al., 2023*).

For fresh fruit, storage in climate-controlled rooms contributes to maintaining appearance, firmness and nutritional characteristics during storage (*Hou et al., 2023*). Low-temperature storage is also important for grain preservation, where accurate temperature control can limit biological deterioration and maintain storage conditions. *Han and Leng (2026)* investigated an intelligent control strategy for low-temperature grain storage, demonstrating the potential of precise thermal regulation for agricultural product preservation. For food products of animal origin, refrigeration, partial freezing, and controlled-atmosphere packaging have been investigated as solutions for maintaining quality and extending storage life (*Hou et al., 2024*). For fish and other frozen products, freezing time is a key parameter because it influences product structure, water loss and final quality. *Ren et al. (2026)* experimentally investigated an industrial horizontal plate freezer integrated into a CO_2 refrigeration system. Decreasing the mean evaporating temperature from (-36.1°C) to (-48.6°C) reduced the average freezing time by 35.3%. However, the authors showed that lowering the evaporating temperature reduced the coefficient of performance (COP), while the specific energy consumption remained nearly unchanged because the shorter freezing time partly compensated for the lower performance of the refrigeration cycle.

Another major issue in the agri-food industry is the energy consumption of refrigeration systems. The food chain has a high energy demand, and the choice of refrigeration technology can significantly influence operating costs and environmental impact. *Ferretto et al. (2025)* analysed refrigeration systems for commercial food refrigeration and showed that the refrigerant and system configuration should be selected according to the application and climatic conditions. At the same time, the performance of refrigeration systems is sensitive to ambient temperature, particularly in commercial applications where operation is continuous and the refrigeration load varies over time (*Ferretto et al., 2025; Tsimpoukis et al., 2024*).

The selection of the refrigerant is influenced by regulations aimed at reducing fluorinated greenhouse gas emissions. Refrigerants with a high global warming potential are being progressively restricted, while low-GWP working fluids are increasingly used in commercial and industrial refrigeration systems. *Regulation (EU) 2024/573* establishes the current framework for fluorinated greenhouse gases and replaces *Regulations (EU) No 517/2014*. In this context, R448A, R449A, R454C and R1234yf were considered as working fluids in relation to the requirements established by the aforementioned EU Regulation. R449A and R454C have been investigated in commercial refrigeration systems and food applications, whereas R448A is used in supermarket refrigeration installations (*Ferretto et al., 2025; Giménez-Prades et al., 2024; Tsimpoukis et al., 2024*). R1234yf has also been analysed as a low-GWP refrigerant in studies concerning the energy and exergy performance of vapour-compression refrigeration systems (*Aized et al., 2022*).

Energy analysis is used to assess the overall performance of refrigeration systems through the coefficient of performance. However, exergy analysis is used to evaluate individual processes, as it identifies exergy destruction in each component and highlights the main sources of irreversibility. *Altinkaynak (2021)* analysed R448A and R449A as alternatives to R404A and compared their coefficient of performance, exergy efficiency, and distribution of exergy destruction. *Aized et al. (2022)* applied energy and exergy analyses to several low-GWP refrigerants, including R1234yf. In industrial cold-storage applications, exergy analysis is used to identify components with high exergy destruction and to establish directions for the optimisation of refrigeration systems (*Aksoy and « erçi, 2026)*. In the same context, the development of IoT systems for refrigeration installations has shown that real-time data acquisition, thermodynamic calculations and control functions can support the transition from passive monitoring to the intelligent operation of refrigeration systems (*Bizdadea et al., 2025*).

Recent studies have applied exergy analysis to evaluate and optimise refrigeration systems and other thermal systems at both component and overall system levels (*Aized et al., 2022; Mamut and Sciubba, 2025; Roy and Mandal, 2023*). In the present study, exergy analysis was used to investigate the individual thermodynamic processes occurring within each refrigeration system. The distribution of exergy destruction was analysed to identify the components and processes that limit the performance of the two configurations and account for the differences in their overall performance. Building on the previous study by Ciobanu et al. [6], which compared several two-temperature-level refrigeration configurations mainly from an energy-performance perspective, the present work focuses on two selected configurations and extends the analysis by including a detailed exergy assessment, the distribution of exergy destruction among the main processes, and the influence of ambient temperature. The aim of this paper is therefore to compare the energy and exergy performance of these two vapour-compression refrigeration systems for simultaneous refrigeration and freezing applications in the food industry, using R448A, R449A, R454C and R1234yf as working fluids.

MATERIALS AND METHODS

Selection of Working Fluids

The refrigerants were preliminarily selected based on the literature review, current European Union requirements, environmental characteristics, safety classification and thermodynamic properties. Particular attention was given to the saturation pressure at the freezing-chamber evaporation temperature. Table 1 summarises the relevant characteristics of the candidate fluids at (-29°C) (*ASHRAE-UNEP, 2024; Danfoss Group, 2024*).

R448A, R449A, R454C and R1234yf were retained for the comparative analysis. By contrast, R1233zd(E) and R1234ze(E) were excluded because their saturation pressures at (−29°C) were below atmospheric pressure, which would require sub-atmospheric operation on the low-pressure side under the considered operating conditions. Unlike the previous study by *Ciobanu et al. (2025)*, where compression was assumed to be adiabatic and reversible, both compressors in the present study were modelled as adiabatic devices with a constant isentropic efficiency of 0.80, thereby accounting for compressor irreversibility. This value was selected based on the 0.80-0.90 range reported by *« engel et al. (2019)* for well-designed compressors and on the recent study by *Liu et al. (2026)*, in which compressor isentropic efficiencies between 0.65 and 0.85, including 0.80, were investigated for an R1234yf refrigeration system. Pressure losses in the refrigerant lines and heat exchangers were neglected. The intermediate pressure was defined as the saturation pressure corresponding to the evaporation temperature of the refrigeration chamber.

Table 1

Characteristics of the refrigerants considered in the study and saturation pressure at the freezing-chamber evaporation temperature

No.	Refrigerant	ODP	GWP	Safety class	Refrigerant type	Saturation pressure at −29 °C [bar]
1.	R448A	0	1387	A1	Zeotropic blend	1.68
2.	R449A	0	1397	A1	Zeotropic blend	1.68
3.	R454C	0	148	A2L	Zeotropic blend	1.50
4.	R1234yf	0	4	A2L	Pure fluid	1.03
5.	R1233zd(E)	0	4.5	A1	Pure fluid	0.11
6.	R1234ze(E)	0	7	A2L	Pure fluid	0.64

Description of the Refrigeration Systems

Two configurations of two-temperature-level vapour-compression refrigeration systems were analysed. Both configurations were designed to provide refrigeration and freezing simultaneously, under the same operating conditions. The main parameters used in the comparative energy and exergy analyses are presented in Table 2.

Table 2

Main operating parameters used in the analysis

No.	Parameter	Symbol	Value	UM
1.	Freezing-chamber temperature	t_f	-25	°C
2.	Refrigeration-chamber temperature	t_r	0	°C
3.	Ambient temperature, decision variable	t_0	35˜45	°C
4.	Minimum temperature difference in the heat exchangers	ΔT_{HE}	5	K
5.	Cooling capacity corresponding to the refrigeration load	$\dot{Q}_{\mathrm{ev},r}$	1	kW
6.	Cooling capacity corresponding to the freezing load	$\dot{Q}_{\mathrm{ev},f}$	0.421	kW

The schematic diagram of refrigeration system (a) and the corresponding thermodynamic cycle are shown in Fig. 1. Refrigeration system (a) comprises a refrigeration evaporator (Ev_r), a freezing evaporator (Ev_f), three throttling valves (Tv_1, Tv_2 *and* Tv_3), a high-stage compressor (C_{p1}), a low-stage compressor (C_{p2}), a condenser (Cd), and a liquid separator (*Sl*).

The refrigeration evaporator (Ev_r) provides the refrigeration load, whereas the freezing evaporator (Ev_f) provides the freezing load. The refrigerant from vapour leaving the freezing evaporator (Evf) is compressed by the low-stage compressor (C_{p2}), while the high-stage compressor (C_{p1}) raises the pressure of the combined refrigerant flow to the condensing pressure. Expansion valve (Tv_3) is installed upstream of the liquid separator (*Sl*) and reduces the pressure of part of the liquid refrigerant leaving the condenser to the intermediate-pressure level. The liquid separator connects the refrigerant branches operating at the two pressure levels.

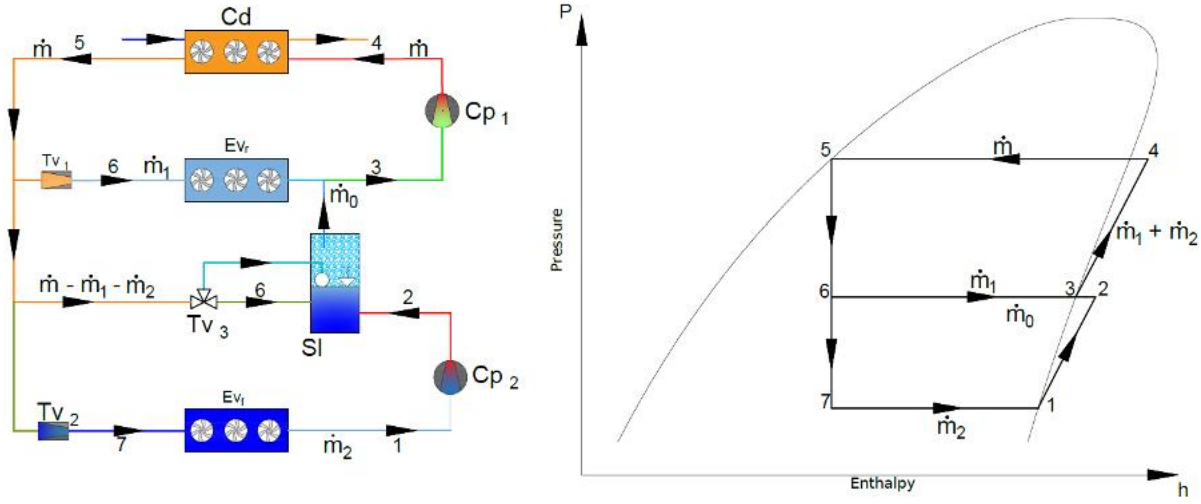


Fig. 1 – Two-temperature-level refrigeration and freezing system (a): schematic diagram (left) and corresponding thermodynamic cycle in the p-h diagram (right)

C_{p1} – high-stage compressor; C_{p2} – low-stage compressor; Cd – condenser; Ev_r – refrigeration evaporator; Ev_f – freezing evaporator; Tv_1,Tv_2 and Tv_3 – throttling valves; Sl –liquid separator; $\dot{m}$,$\dot{m}_0$,$\dot{m}_1$ and $\dot{m}_2$– refrigerant mass flow rates; 1–7 – thermodynamic state points.; p – pressure; h – specific enthalpy. Source: adapted from Ciobanu et al. (2025).

Refrigeration system (b) includes the same main components as refrigeration system (a). However, the connection of the liquid separator (*Sl*) and the arrangement of the freezing branch differ from those of system (a). In system (b), the refrigerant discharged by the low-stage compressor (C_{p2}) enters the liquid separator, together with the two-phase refrigerant stream produced by throttling through expansion valve (Tv_3). Intercooling and phase separation occur in (*Sl*) at the intermediate-pressure level. The vapour leaving the liquid separator mixes with the refrigerant flow from the refrigeration evaporator (Ev_r) before entering the high-stage compressor (C_{p1}). The liquid phase leaving the separator is expanded through (Tv_2) and subsequently supplied to the freezing evaporator (Ev_f). The schematic diagram of refrigeration system (b) and the corresponding thermodynamic cycle are presented in Fig. 2.

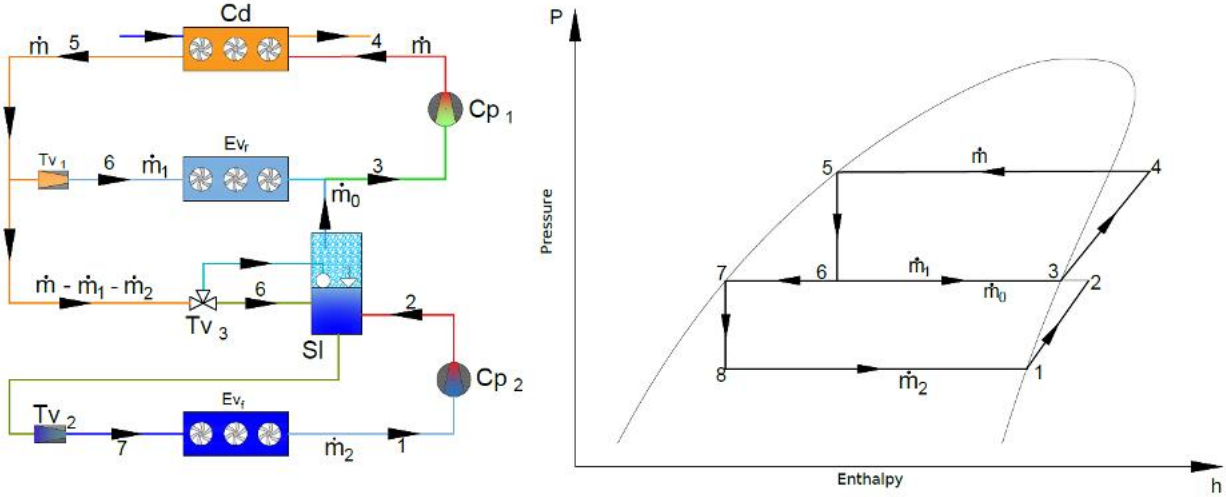


Fig. 2 – Two-temperature-level refrigeration and freezing system (b): schematic diagram (left) and corresponding thermodynamic cycle in the p-h diagram (right)

Cd – condenser; C_{p1} – high-stage compressor; C_{p2} – low-stage compressor; Ev_r – refrigeration evaporator; Ev_f – freezing evaporator; Tv_1,Tv_2 and Tv_3 – throttling valves; Sl –liquid separator; $\dot{m}$,$\dot{m}_0$,$\dot{m}_1$ and $\dot{m}_2$– refrigerant mass flow rates; 1–8 – thermodynamic state points.; p – pressure; h – specific enthalpy.
Source: adapted from Ciobanu et al. (2025).

Mathematical Model of Refrigeration System (a)

After establishing the refrigeration loads and the main operating parameters of the two systems according to the data presented in Table 2, the mathematical models were developed. Energy balances were used to evaluate the overall performance of the systems, whereas exergy analysis was applied to identify the processes associated with the highest exergy destruction. The mathematical models were implemented using Engineering Equation Solver (EES) software (F-Chart Software, n.d.).

Refrigeration system (a), presented in Fig. 1, provides the required cooling loads at two temperature levels, corresponding to refrigeration and freezing applications. Based on the overall energy balance derived from the first law of thermodynamics, the following relationship can be written *(Russell and Adebiyi, 1993)*:

$$\dot{Q}^a_{ev_f} + \dot{Q}^a_{ev_r} + \dot{W}^a_{cp_1} + \dot{W}^a_{cp_2} = \dot{Q}^a_{cd} \quad (1)$$

where: $\dot{Q}^a_{ev_f} and \dot{Q}^a_{ev_r}$ are the cooling capacities corresponding to the freezing and refrigeration loads, respectively, [kW]; $\dot{W}^a_{cp_1} and\ \dot{W}^a_{cp_2}$ are the power inputs of the high-stage and low-stage compressors, respectively, [kW]; $\dot{Q}^a_{cd}$ is the heat transfer rate from the refrigerant to the surroundings in the condenser, [kW]; and superscript a denotes refrigeration system (a).

The cooling capacity corresponding to the freezing load is calculated as:

$$\dot{Q}^a_{ev_f} = \dot{m}_2(h_1 - h_7) \quad (2)$$

The cooling capacity corresponding to the refrigeration load is calculated as:

$$\dot{Q}^a_{ev_r} = \dot{m}_1(h_3 - h_6) \quad (3)$$

where: $\dot{m}_1 and\ \dot{m}_2$ are the refrigerant mass flow rates through the refrigeration and freezing evaporators, respectively, [kg/s], while $h_1, h_3, h_6\ and\ h_7$ are the specific enthalpies at the corresponding thermodynamic state points, [kJ/kg].

The power input of the high-stage compressor is:

$$\dot{W}^a_{cp_1} = \dot{m}(h_4 - h_3) \quad (4)$$

The power input of the low-stage compressor is:

$$\dot{W}^a_{cp_2} = \dot{m}_2(h_2 - h_1) \quad (5)$$

where: $\dot{m}$ is the total refrigerant mass flow rate through the high-stage compressor, [kg/s], and $h_1, h_2, h_3\ and\ h_4$ are the specific enthalpies at the corresponding compressor inlet and outlet state points, [kJ/kg].

The heat transfer rate rejected by the condenser is:

$$\dot{Q}^a_{cd} = \dot{m}(h_5 - h_4) \quad (6)$$

where: h_5 is the specific enthalpy at the condenser outlet, [kJ/kg].

The overall energy coefficient of performance of refrigeration system (a) is defined as:

$$COP^a_{en} = \frac{\dot{Q}^a_{ev_f} + \dot{Q}^a_{ev_r}}{\dot{W}^a_{cp_1} + \dot{W}^a_{cp_2}} \quad (7)$$

Exergy analysis was applied to evaluate the thermodynamic performance of the individual processes. For the complete refrigeration system operating under steady-state conditions, the general exergy balance is written as follows (*Radcenco, 1977*).

$$\sum \dot{E}x^{T_i}_{Q_i} + \sum \dot{I}_i = \sum \dot{W}_i \quad (8)$$

where: $\dot{E}x^{T_i}_{Q_i}$ is the exergy transfer rate associated with heat transfer at temperature T_i, [kW]; $\dot{W}_i$ is the power transfer rate, [kW]; $\dot{I}_i$ is the exergy destruction rate of component or process i, [kW]; and T_i is the absolute temperature at which heat transfer occurs, [K].

Applying Equation (8) to refrigeration system (a) gives:

$$\dot{E}x^{T_{7-1}}_{Q^a_{ev_f}} + \dot{E}x^{T_{6-3}}_{Q^a_{ev_r}} + \dot{I}^a_{cp_1} + \dot{I}^a_{cp_2} + \dot{I}^a_{tv_1} + \dot{I}^a_{tv_2} + \dot{I}^a_{tv_3} + \dot{I}^a_{ls} + \dot{I}^a_{cd} = \dot{W}^a_{cp_1} + \dot{W}^a_{cp_2} \quad (9)$$

where: $\dot{E}x^{T_{7-1}}_{Q^a_{ev_f}}$ and $\dot{E}x^{T_{6-3}}_{Q^a_{ev_r}}$ are the exergy transfer rates associated with the heat absorbed in the freezing and refrigeration evaporators, respectively, [kW]; $\dot{I}^a_{cp_1}$ and $\dot{I}^a_{cp_2}$ are the exergy destruction rates in the high-stage and low-stage compressors, respectively, [kW]; $\dot{I}^a_{tv_1}, \dot{I}^a_{tv_2}$ and $\dot{I}^a_{tv_3}$ are the exergy destruction rates associated with the throttling processes, [kW]; $\dot{I}^a_{ls}$ is the exergy destruction rate in the liquid separator, [kW]; and $\dot{I}^a_{cd}$ is the exergy destruction rate in the condenser, [kW].

After identifying the exergy fuel and exergy product of the system, *Equation (9)* can be expressed in fuel-product form as follows:

$$\dot{W}^a_{cp_1} + \dot{W}^a_{cp_2} = \dot{E}x^{T_f}_{Q^a_{ev_f}} + \dot{E}x^{T_r}_{Q^a_{ev_r}} + \dot{I}^a_{cp_1} + \dot{I}^a_{cp_2} + \dot{I}^a_{ev_f} + \dot{I}^a_{ev_r} + \dot{I}^a_{tv_1} + \dot{I}^a_{tv_2} + \dot{I}^a_{tv_3} + \dot{I}^a_{ls} + \dot{I}^a_{cd} \quad (10)$$

The exergy coefficient of performance of refrigeration system (a) is calculated as:

$$\eta^a_{ex} = \frac{\dot{E}x^{T_f}_{Q^a_{ev_f}} + \dot{E}x^{T_r}_{Q^a_{ev_r}}}{\dot{W}^a_{cp_1} + \dot{W}^a_{cp_2}} \cdot 100 \quad (11)$$

where: η^a_{ex} is the exergy coefficient of performance of refrigeration system (a), [%].

Mathematical Model of Refrigeration System (b)

The configuration shown in Fig. 2 represents refrigeration system (b), which is also designed to meet refrigeration and freezing loads at two distinct temperature levels. The corresponding energy and exergy relations are developed below for this system arrangement.

The energy balance derived from the first law of thermodynamics and applied to refrigeration system (b) is written as follows:

$$\dot{Q}^b_{ev_f} + \dot{Q}^b_{ev_r} + \dot{W}^b_{cp_1} + \dot{W}^b_{cp_2} = \dot{Q}^b_{cd} \quad (12)$$

where: superscript b denotes refrigeration system (b), while the remaining terms have the same meanings and units as those defined for *Equation (1)*.

The overall energy coefficient of performance of refrigeration system (b) is calculated:

$$\mathrm{COP}^b_{en} = \frac{\dot{Q}^b_{ev_f} + \dot{Q}^b_{ev_r}}{\dot{W}^b_{cp_1} + \dot{W}^b_{cp_2}} \quad (13)$$

where: COP^b_{en} is the overall energy coefficient of performance of refrigeration system (b), [–].

The exergy balance of refrigeration system (b), expressed in terms of exergy fuel, exergy product and exergy destruction, is written as:

$$\dot{W}^b_{cp_1} + \dot{W}^b_{cp_2} = \dot{E}x^{T_f}_{Q^b_{ev_f}} + \dot{E}x^{T_r}_{Q^b_{ev_r}} + \dot{I}^b_{cp_1} + \dot{I}^b_{cp_2} + \dot{I}^b_{ev_f} + \dot{I}^b_{ev_r} + \dot{I}^b_{tv_1} + \dot{I}^b_{tv_2} + \dot{I}^b_{tv_3} + \dot{I}^b_{ls} + \dot{I}^b_{cd} \quad (14)$$

where: the exergy-transfer and exergy-destruction terms have the same meanings and units as those defined for refrigeration system (a), while superscript b indicates that the terms refer to refrigeration system (b).

The exergy efficiency of refrigeration system (b) is calculated as:

$$\eta^b_{ex} = \frac{\dot{E}x^{T_f}_{Q^b_{ev_f}} + \dot{E}x^{T_r}_{Q^b_{ev_r}}}{\dot{W}^b_{cp_1} + \dot{W}^b_{cp_2}} \cdot 100 \quad (15)$$

where: η^b_{ex} is the exergy efficiency of refrigeration system (b), [%].

The exergy transfer rate associated with heat transfer is calculated as:

$$\dot{E}x^{T_i}_{Q_i} = \dot{Q}_i \left(\frac{T_0}{T_i} - 1\right) \quad (16)$$

where: $\dot{E}x^{T_i}_{Q_i}$ is the exergy transfer rate associated with heat transfer in process i, [kW]; $\dot{Q}_i$ is the corresponding heat transfer rate, [kW]; T_0 is the ambient reference temperature, [K]; and T_i is the absolute temperature at which heat transfer occurs, [K].

The exergy destruction rate of each process is calculated as:

$$\dot{I}_i = T_0 \dot{S}_{gen_i} \quad (17)$$

where: $\dot{I}_i$ is the exergy destruction rate of process i, [kW], and $\dot{S}_{gen_i}$ is the entropy generation rate associated with the process, [kW/K].

The relative exergy destruction associated with each process, expressed with respect to the total compressor power input, is calculated as:

$$\psi_i = \frac{\dot{I}_i}{\sum_i \dot{W}_i} \cdot 100 \quad (18)$$

where: ψ_i is the relative exergy associated with each process i, [%], and $\sum_i \dot{W}_i$ is the total compressor power input, [kW].

RESULTS

To identify the working fluid providing the highest overall performance for the two investigated refrigeration systems, the overall energy and exergy coefficients of performance were evaluated for R448A, R449A, R454C and R1234yf. The ambient temperature, t_0, was varied from 35 °C to 45 °C and was used as the independent variable in the sensitivity analysis.

For refrigeration system (a), the overall energy coefficient of performance decreased with increasing ambient temperature for all the investigated refrigerants, as shown in Fig.3. R1234yf provided the highest values over the entire temperature range, followed by R448A, R449A and R454C. The energy coefficient of performance obtained with R1234yf decreased from approximately 2.69 at 35°C to approximately 1.98 at 45°C.

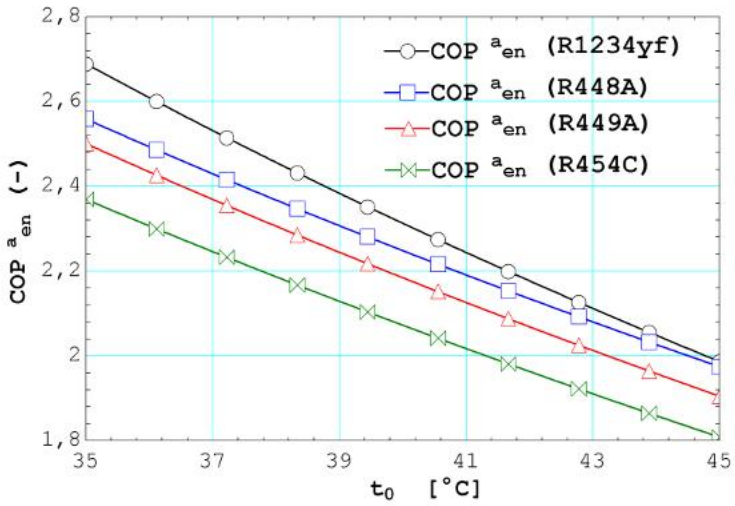


Fig. 3 - Variation of the overall energy coefficient of performance of refrigeration system (a) with ambient temperature for the investigated refrigerants

A similar tendency was obtained for the exergy coefficient of performance of refrigeration system (a), as presented in Fig. 4. The values decreased as the ambient temperature increased, while the ranking of the refrigerants remained unchanged. R1234yf provided the highest exergy coefficient of performance, which decreased from approximately 43.6% to 39.7% over the investigated temperature range. R454C showed the lowest values.

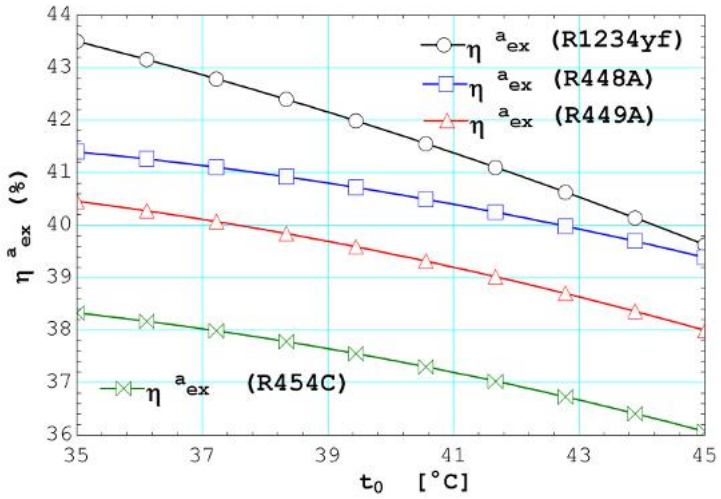


Fig. 4 - Variation of the exergy coefficient of performance of refrigeration system (a) with ambient temperature for the investigated refrigerants

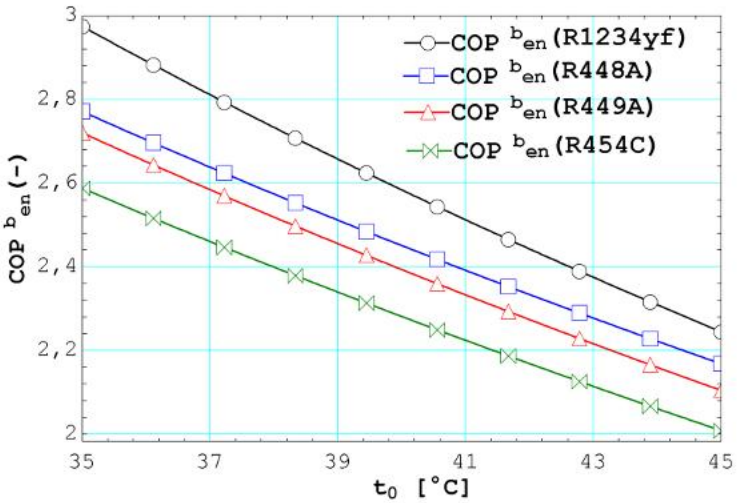


Fig. 5 - Variation of the overall energy coefficient of performance of refrigeration system (b) with ambient temperature for the investigated refrigerants

The results obtained for refrigeration system (b) are presented in Figs. 5 and 6. The overall energy coefficient of performance decreased with increasing ambient temperature for all four refrigerants. R1234yf again provided the highest values, followed by R448A, R449A and R454C. For R1234yf, the energy coefficient of performance decreased from approximately 2.97 at 35 °*C* to approximately 2.24 at 45 °*C*.

The exergy coefficient of performance of refrigeration system (b) followed the same decreasing tendency, as shown in Fig. 6. R1234yf provided the highest values, ranging from approximately 48.0% at 35 °*C* to approximately 44.7% at 45 °*C*. R454C presented the lowest exergy performance throughout the investigated range.

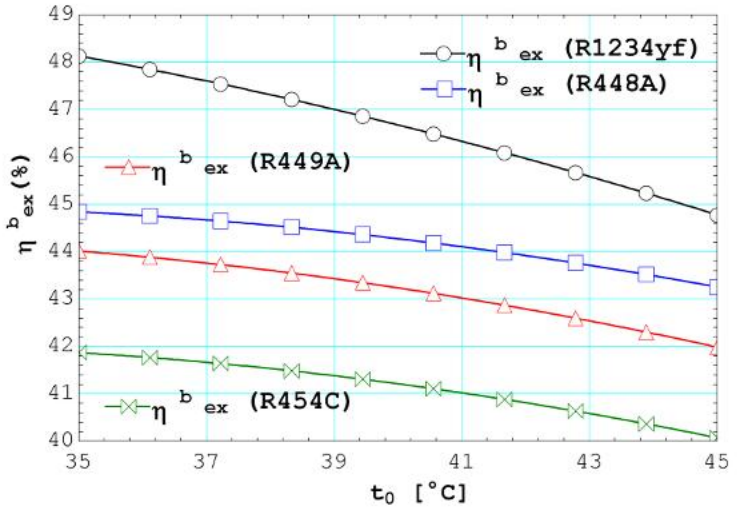


Fig. 6 - Variation of the exergy coefficient of performance of refrigeration system (b) with ambient temperature for the investigated refrigerants

The comparison of the results presented in Figs. 3–6 showed that refrigeration system (b) achieved higher energy and exergy performance than refrigeration system (a) under the same operating conditions. The influence of the system configuration was observed for all the investigated refrigerants. Based on the overall results, R1234yf was selected for the component-level exergy analysis of the two refrigeration systems.

The relative exergy destruction associated with the individual processes of refrigeration system (a) is presented in Fig. 7. The relative exergy destruction associated with the first and second throttling processes increased considerably with ambient temperature. The contribution of the high-stage compressor remained almost constant, whereas the relative contributions of the condenser, low-stage compressor and evaporators generally decreased over the investigated temperature range.

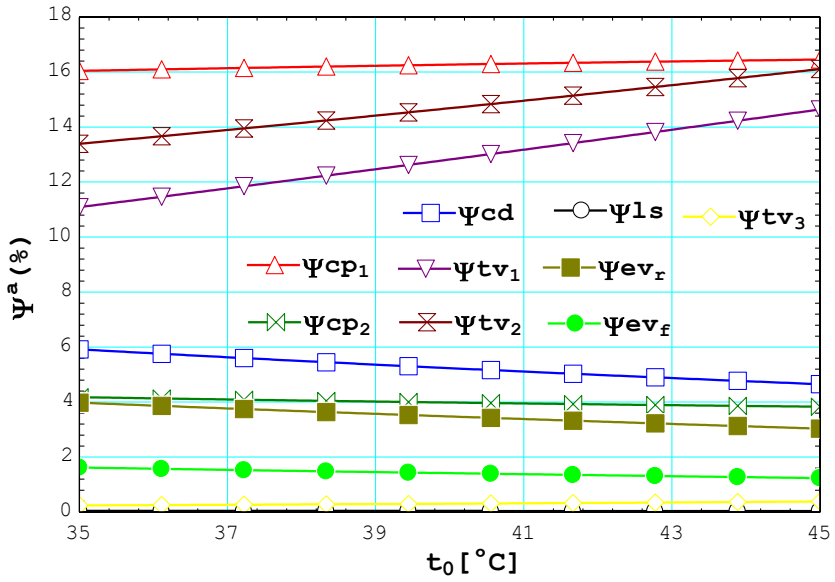


Fig. 7 - Relative exergy destruction associated with the individual processes of refrigeration system (a) using R1234yf

ψ^a– relative exergy destruction associated with system a

For refrigeration system (b), the distribution of relative exergy destruction is shown in Fig. 8. The contribution of the first throttling process increased with ambient temperature, while the third throttling process also showed an increasing tendency. The relative exergy destruction of the second throttling process remained comparatively low. The high-stage compressor represented one of the largest individual contributions, but its variation with ambient temperature is limited.

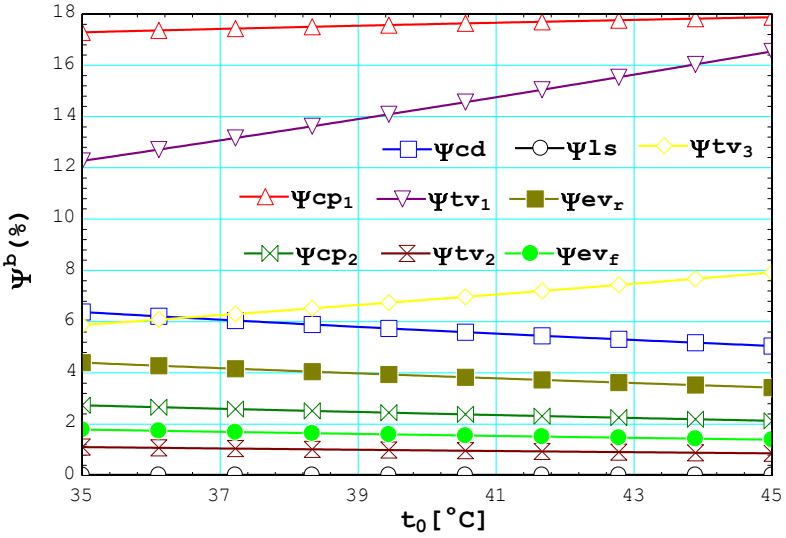


Fig. 8 - Relative exergy destruction associated with the individual processes of refrigeration system (b) using R1234yf

ψ^b– relative exergy destruction associated with system b

The total relative exergy destruction associated with the throttling processes of the two refrigeration systems is compared in Fig. 9. In both configurations, the total value increased with ambient temperature and followed a similar tendency. However, refrigeration system (b) maintained lower values throughout the investigated temperature range. For refrigeration system (a), the total relative exergy destruction of the throttling processes increased from approximately 24.6 % at 35 °C to approximately 31.1 % at 45°C. For refrigeration system (b), the corresponding values increased from approximately 19.1 % to approximately 25.2%.

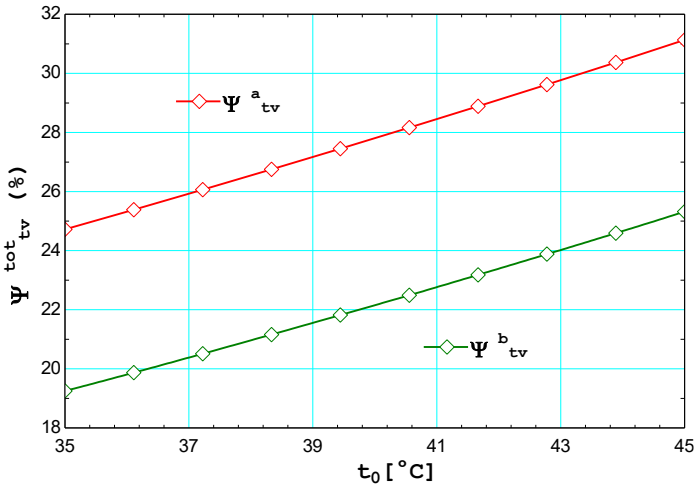


Fig. 9 - Total relative exergy destruction associated with the throttling processes of refrigeration systems (a) and (b) using R1234yf

ψ_{tv}^{tot} – total relative exergy destruction associated with the throttling processes; superscripts a and b denote refrigeration systems (a) and (b), respectively.

The comparison of Figs. 3–6 confirms the superior performance of refrigeration system (b) under the same operating conditions. For R1234yf, the COP of system (b) was approximately 10.4% higher than that of system (a) at 35 °C and 13.1% higher at 45 °C, while the corresponding improvements in exergy efficiency were approximately 10.1% and 12.6%, respectively. This performance advantage is consistent with the lower irreversibilities associated with the throttling processes in configuration (b), for which the total relative exergy destruction remained below that of configuration (a) over the entire investigated temperature range. These results indicate that the modified flow arrangement and intermediate-pressure separation in system (b) provide a thermodynamically more favourable distribution of irreversibilities.

CONCLUSIONS

An energy and exergy analysis was carried out for two refrigeration system configurations capable of simultaneously providing the temperature levels required for refrigeration and freezing. Their performances were evaluated using R448A, R449A, R454C and R1234yf under different ambient-temperature conditions.

The comparative analysis showed that the working fluid had a significant influence on the overall energy and exergy performance of both systems. Among the investigated refrigerants, R1234yf provided the highest energy and exergy coefficients of performance over the entire ambient-temperature range, while both indicators decreased as ambient temperature increased.

Although refrigeration systems (a) and (b) contained the same main components, their different structural arrangements led to different overall performances. Under the same operating conditions, system (b) provided higher energy and exergy coefficients of performance than system (a).

The process-level exergy analysis showed that the relative exergy destruction associated with the throttling processes presented the greatest sensitivity to ambient temperature. The staged throttling arrangement adopted in refrigeration system (b) reduced the total relative exergy destruction associated with these processes throughout the investigated temperature range. This reduction explained the improved overall performance of system (b).

Therefore, refrigerant selection and system configuration should be considered jointly when designing and optimising two-temperature-level refrigeration systems. Exergy analysis proved useful for identifying the main sources of irreversibility and supporting the development of more efficient systems for simultaneous refrigeration and freezing.

As a final conclusion, out of the two configurations investigated in the present paper, configuration (b) is the one recommended to be used in the food industry where both freezing and refrigeration are needed. Among the two configurations investigated, configuration (b) is recommended for food-industry applications requiring simultaneous refrigeration and freezing under the operating conditions and cooling capacities considered in this study. Further analysis is required before extending this conclusion to significantly larger-capacity refrigeration systems.

REFERENCES

[1] Aized T., Rashid M., Riaz F., Hamza A., Nabi H.Z., Sultan M., Ashraf W.M., Krzywanski J., (2022), Energy and exergy analysis of vapor compression refrigeration system with low-GWP refrigerants, *Energies*, vol. 15, no. 19, article 7246. DOI: https://doi.org/10.3390/en15197246

[2] Aksoy A.B., Çerçi Y., (2026), Energy–exergy–exergoeconomic evaluation of a two-stage ammonia refrigeration cycle under industrial operating conditions, *Applied Sciences*, vol. 16, no. 3, article 1163. DOI: https://doi.org/10.3390/app16031163

[3] Altinkaynak M., (2021), Exergetic performance analysis of low GWP alternative refrigerants for R404A in a refrigeration system, *International Journal of Low-Carbon Technologies*, vol. 16, no. 3, pp. 842–850. DOI: https://doi.org/10.1093/ijlct/ctaa104

[4] Bizdadea M.F., Ghiță G.D., Apostol V.G., Pop H.L., Grămescu B., (2025), Modular Internet of Things system for monitoring, control and alerting in refrigeration systems using ESP32 and Raspberry Pi 4, *EAI Endorsed Transactions on Digital Transformation of Industrial Processes*, vol. 1, no. 3. DOI: https://doi.org/10.4108/dtip.9792

[5] Çengel Y.A., Boles M.A., Kanoğlu M., (2019), *Thermodynamics: An Engineering Approach, 9th edition*, McGraw-Hill Education, New York, NY/USA. ISBN 978-1-259-82267-4.

[6] Ciobanu V., Apostol V., Pop H., Ioniță C., Dima D., (2025), Comparative performance analysis of commercial refrigeration systems with two temperature levels considering different refrigerants, *International Conference on Thermal Engineering – ICTEA*, vol. 1, no. 1.

[7] F-Chart Software, (n.d.), Engineering Equation Solver (EES). Available at: *https://fchartsoftware.com/ees/* (accessed on 20 July 2026)

[8] Ferretto W., Molinaroli L., Codella F., (2025), Performance assessment of R-454C, R-449A, and R-744 in food retail refrigeration systems, *Energies*, vol. 18, no. 3, article 667. DOI: https://doi.org/10.3390/en18030667

[9] Giménez-Prades P., Navarro-Esbrí J., Udroiu C.-M., Mota-Babiloni A., (2024), Influence of subcooling in R-449A supermarket refrigeration system and screening of refrigerant mixtures for its energetic and environmental improvement, *Applied Thermal Engineering*, vol. 236, article 121787. DOI: https://doi.org/10.1016/j.applthermaleng.2023.121787

[10] Han F., Leng Z., (2026), Multimodal scenario control method for low-temperature grain storage based on the AdaBelief algorithm (基于 AdaBelief 算法的低温粮食储存多模态场景控制方法), *INMATEH – Agricultural Engineering*, vol. 78, no. 1, pp. 192–202, Bucharest/Romania. DOI: https://doi.org/10.35633/inmateh-78-15

[11] Hou H., Cui S., Li D., Li Z., Chen Y., (2023), Effect of low-voltage electrostatic-field (LVEF) assisting refrigeration on preservation quality of strawberry (低压静电场辅助冷藏对草莓贮藏品质的影响), *INMATEH – Agricultural Engineering*, vol. 71, no. 3, pp. 657–666, Bucharest/Romania. DOI: https://doi.org/10.35633/inmateh-71-57

[12] Hou H., Li D., Zhang S., Niu W., Cui Q., Chen Y., (2024), Impact of partial freezing with modified atmosphere packaging on pork's quality (气调微冻对猪肉品质的影响), *INMATEH – Agricultural Engineering*, vol. 74, no. 3, pp. 127–136, Bucharest/Romania. DOI: https://doi.org/10.35633/inmateh-74-11

[13] Liu Y., Xie Y., Wang Z., Yang Z., Yang L., Dou B., (2026), Experimental research and simulation optimization of compression-type R1234yf hydrate cool storage system, *International Journal of Refrigeration*, vol. 185, pp. 336–348. DOI: https://doi.org/10.1016/j.ijrefrig.2026.02.028

[14] Mamut E., Sciubba E., (2025), Multi-scale extended exergy analysis of the "system Romania": A tool for monitoring the UN-2030 SDGs, *Energy*, vol. 314, article 134055. DOI: https://doi.org/10.1016/j.energy.2024.134055

[15] Pon Pavithiran C.K., Sakthivadivel D., Agarwal A., Agarwal A., (2025), Experimental investigation and thermo-enviro-economic analysis of a novel biomass driven dual-bed vapor adsorption refrigeration system for a cold storage room and bulk milk chiller for rural applications, *Thermal Science and Engineering Progress*, vol. 59, article 103327. DOI: https://doi.org/10.1016/j.tsep.2025.103327

[16] Radcenco V., (1977), *Optimization Criteria for Irreversible Thermal Processes (Criterii de optimizare a proceselor termice (ireversibile))*, Technical Publishing House (Editura Tehnică), Bucharest/Romania. (in Romanian)

[17] Ren S., Hadamitzky P., Hafner A., Widell K.N., (2026), Experimental analysis of freezing times for fish and dummy loads in a horizontal CO_2 plate freezer at −50 °C evaporation temperature, *International Journal of Refrigeration*, vol. 184, pp. 14–29. DOI: https://doi.org/10.1016/j.ijrefrig.2026.01.017

[18] Roy R., Mandal B.K., (2023), Energy, exergy and economic optimization of a two-stage refrigeration system using low-GWP alternative refrigerants for high-temperature lift applications, *Journal of the Brazilian Society of Mechanical Sciences and Engineering*, vol. 45, article 403. DOI: https://doi.org/10.1007/s40430-023-04320-9

[19] Russell L.D., Adebiyi G.A., (1993), *Classical Thermodynamics*, Oxford University Press, New York, NY/USA.

[20] Sorică C.M., Vlăduț N.-V., Grigore A.I., Cristea M., Sorică E., Oprescu R.M., Ionescu A., Vlăduțoiu L.C., Dumitrescu L., (2023), Cryogenic freezing of some berry species using an experimental model of multi-functional quick-freezing equipment (Congelarea criogenică a unor specii de fructe de pădure utilizând un model experimental de echipament multifuncțional de congelare rapidă), *INMATEH – Agricultural Engineering*, vol. 71, no. 3, pp. 451–458, Bucharest/Romania. DOI: https://doi.org/10.35633/inmateh-71-39

[21] Tsimpoukis D., Syngounas E., Bellos E., Koukou M., Tzivanidis C., Anagnostatos S., Vrachopoulos M.G., (2024), Data-driven energy efficiency comparison between operating R744 and R448A supermarket refrigeration systems based on hybrid experimental-simulation analysis, *Thermal Science and Engineering Progress*, vol. 53, article 102776. DOI: https://doi.org/10.1016/j.tsep.2024.102776

[22] *** ASHRAE–UNEP, (2026), Update on New Refrigerants Designations and Safety Classifications, Factsheet 1, *American Society of Heating, Refrigerating and Air-Conditioning Engineers and United Nations Environment Programme*. Available at: https://www.ashrae.org/file%20library/professional%20development/ashrae-unep/unep---ashrae-factsheet--english.pdf (accessed on 20 July 2026)

[23] *** Danfoss Group, (n.d.), *Refrigerants with low GWP*. Available at: https://www.danfoss.com/en/about-danfoss/our-businesses/cooling/refrigerants-and-energy-efficiency/refrigerants-for-lowering-the-gwp/ (accessed on 20 July 2026)

[24] *** European Union, (2024), Regulation (EU) 2024/573 of the European Parliament and of the Council of 7 February 2024 on fluorinated greenhouse gases, amending Directive (EU) 2019/1937 and repealing Regulation (EU) No 517/2014, *Official Journal of the European Union*, L 2024/573, 20 February 2024. Available at: https://eur-lex.europa.eu/eli/reg/2024/573/oj/eng

SORGHUM GRAIN CLASSIFICATION AND DETECTION USING YOLOV8 WITH DECOUPLED FULLY CONNECTED ATTENTION MECHANISM AND MULTI-SCALE FEATURE FUSION

/

融合解耦全连接注意力机制与多尺度特征融合的 YOLOv8 高粱籽粒分类检测方法

Yinzeng LIU[1)], Chengpeng CUI[1,2)], Kaixing ZHANG[3)], Lu LIU [4)], Fandi ZENG[1)], Mingming LIU[1)], Hongwei DIAO[1)], Tiexin WANG[2)], Zhihuan ZHAO[*1)]

[1)] Mechanical and Electronic Engineering College, Shandong Agriculture and Engineering University, Jinan / China;

[2)] Shandong Unia Agricultural Machinery Co., Ltd, Dezhou / China;

[3)] College of Mechanical and Electrical Engineering, Shandong Agricultural University, Tai'an / China;

[4)] Production Unit Directly-Affiliated to Xinjiang Production and Construction Corps / China

Corresponding authors: Zhihuan Zhao; Tel: +86-134-0696-7329.; E-mail: zhaozhihuan@sdaeu.edu.cn

DOI: https://doi.org/10.35633/inmateh-79-108

Keywords: *YOLOv8, Sorghum grain classification, BiFPN, Dynamic Head*

ABSTRACT

The quality inspection of sorghum grains after drying is critical for ensuring storage stability and processing quality. However, traditional manual inspection methods are inefficient, time-consuming, and prone to subjective biases. To address these challenges, this study proposes an improved YOLOv8s model, named YOLOv8s-GBD, for accurate sorghum grain classification and detection. The proposed model integrates three key enhancements. First, the DFC Attention-based bottleneck structure from GhostNetV2 is incorporated into the C2f module to enhance global context awareness and improve detection accuracy. Second, a bi-directional feature pyramid network (BiFPN) is introduced to optimize multi-scale feature fusion. Third, a dynamic head framework based on attention mechanisms is adopted to strengthen feature representation, further boosting the model's accuracy and robustness. Experimental results demonstrate that the YOLOv8-GBD model achieves 95.2% precision, 98.0% recall, 98.7% mAP1, 97.5% mAP2, and 96.6% F1-score. Compared to the original YOLOv8s model, these metrics show improvements of 3.1%, 1.7%, 1.2%, 1.0%, and 2.4%, respectively. Furthermore, the YOLOv8-GBD model outperforms other YOLO series models in sorghum grain classification and detection tasks. In conclusion, the YOLOv8s-GBD model meets the requirements for high accuracy in sorghum grain quality inspection, offering a robust solution for practical applications.

摘要

干燥后高粱籽粒的品质检测对保障仓储稳定性与加工品质至关重要。然而传统人工检测方式效率低下、耗时长，且容易存在主观偏差。针对上述问题，本文提出一种改进 YOLOv8s 模型 YOLOv8s-GBD，实现高粱籽粒精准分类与检测。该模型包含三项核心改进：第一，在 C2f 模块中嵌入 GhostNetV2 的 DFC 注意力瓶颈结构，增强模型全局上下文感知能力，提升检测精度；第二，引入双向特征金字塔网络（BiFPN）优化多尺度特征融合；第三，采用基于注意力机制的动态检测头框架强化特征表征能力，进一步提升模型精度与鲁棒性。实验结果表明：YOLOv8s-GBD 模型精确率 95.2%、召回率 98.0%、mAP1 为 98.7%、mAP2 为 97.5%、F1 分数 96.6%。相较于原始 YOLOv8s 模型，各项指标分别提升 3.1%、1.7%、1.2%、1.0%、2.4%。同时，在高粱籽粒分类检测任务中，YOLOv8s-GBD 模型性能优于其他 YOLO 系列模型。综上，YOLOv8s-GBD 模型能够满足高粱籽粒品质检测的高精度需求，可为实际工程应用提供可靠方案。

INTRODUCTION

Sorghum is one of the important food crops in China. In the processing, transportation, storage, acquisition, sales and other links, the quality of sorghum grains needs to be tested. Its quality directly affects food security and economic benefits. However, during the acquisition and drying process, the grain will inevitably be affected by environmental factors such as temperature, which will lead to a series of quality changes, such as mildew, lesions and mechanical damage (*Olgun M et al., 2016; Tsuzuki W et al., 2014*). Sorghum grains with defects or damage but still have use value are called imperfect grains. The national standard GB/T8231-2024 defines imperfect grains as: diseased, moth-eaten, damaged, sprouted, mouldy and heat-damaged.

During the harvesting process of sorghum, some sorghum seeds are wrapped with glume-protected and useful grains called shelled grains. Sorghum grading indicators such as moisture, capacity, and thousand grain weight need to be completed on-site before sorghum enters storage after the drying session. Some indicators such as imperfect grains and shelled grains cannot be completely eliminated. Small samples need to be tested to ensure grain quality, guide grain storage management and prevent economic losses. Therefore, research on sorghum quality evaluation methods and techniques is of great practical significance to meet the market demand and ensure sorghum storage safety.

The traditional classification of imperfect grains and shelled grains is mainly detected by manual visual inspection. This method is not only inefficient, but also easily affected by subjective factors, resulting in poor accuracy and reliability of the detection results (*Zhang W. et al., 2021; Wang L. et al., 2022; Ni C et al., 2019*). At present, many scholars use physical and chemical detection methods to study the imperfect particles (*Guo M. et al., 2019; Liu J. et al., 2024; Pearson et al., 2007; Yang et al., 2021*), such as analysing the time-domain characteristics of the acoustic wave, or studying the interaction between the acoustic wave and the medium to achieve the detection of imperfect particles (*Sun et al., 2021*). This method is fast, but highly dependent on the acoustic propagation medium, and is highly susceptible to the influence of noise. Chemical detection methods can achieve rapid screening of fungal contamination and mycotoxins in grain, but the repetition rate is very poor and prone to environmental pollution (*Gab-Allah et al., 2021*).

With the rapid development of modern information technology, such as machine vision technology, near-infrared spectroscopic detection technology, hyperspectral detection technology are more and more widely used in the field of agricultural products (*Na et al., 2019; Qi et al., 2024; Qin et al., 2017*). Meanwhile, target detection technology based on deep learning shows great potential in the field of agricultural product quality inspection.

The use of hyperspectral imaging and near-infrared spectroscopy can be used to directly measure the mould condition and disease spots of grain kernels (*Delwiche et al., 2019; He et al., 2021; Sendin et al., 2017*). *Liu Zhang et al., (2021),* proposed a data calibration model based on multi-angle near-infrared hyperspectral, using four sides of wheat grain images combined with machine learning models to detect wheat damaged by rice weevil, and the accuracy rate reached 97%. *Li et al., (2022),* proposed a method for identifying unsound wheat kernels based on a deep convolutional Generative Adversarial Network (DCGAN) and near-infrared hyper-spectral imaging to identify unsound wheat seeds. Experiments show that the recognition accuracy based on the joint model of DCGAN and CNN reaches up to 96.67%. *Fengshuang Liu et al. (2023)* proposed a new spectral-spatial feature extraction-enhanced fully-connected neural network (SSFE-FCNN) to achieve the detection of pixel-level mechanical dam-ages in glutinous maize, and the experiments show that the accuracy of this method reaches up to 98.09%. It can be achieved for the grading operation of maize. Although the use of hyperspectral imaging technology, near infrared spectroscopy technology can achieve the detection of grain defects, germination, etc., but its cost is high and the effect is limited for the detection of grain shape, disease spots and other appearance characteristics.

In recent years, many researchers have used machine vision methods to detect defective grains. The commonly used methods are traditional image processing methods and artificial neural network methods (*Chen Z. et al., 2022; Shen R. et al., 2023*). The traditional image pro-cessing method detects by extracting features such as colour and shape. This method has low accuracy and poor robustness. Therefore, there are more related researches on target detection using deep learning techniques. *Zhang et al., (2025),* proposed a method for identifying unsound wheat seeds based on multi-scale parallel convolutional neural networks. Experiments showed that the accuracy of this method reached 98.798 %. *Lin W. et al.,* (*2023*), proposed an online classification method for soybean seeds based on deep learning. This method can accurately classify normal, damaged, abnormal and unclassifiable soybeans. The accuracy rate reaches 95.63% on NVIDIA Jetson TX2, which lays the foundation for online soybean quality evaluation. *Gao et al., (2022),* studied the identification of wheat unsound kernels based on machine vision and deep learning network models. By comparing the advantages and disadvantages of GoogleNet, DenseNet, IX-Resnet, Res2Net and other networks, a Res24_D_CBAM_Atrous wheat imperfect kernel detection method was proposed, with an accuracy rate of 94 %.

In summary, the combination of machine vision and deep learning enables the detection of imperfect grains at a low cost. Currently, it is widely used in crops such as wheat, corn and soybean, but there are few literatures on the detection of imperfect grains and husked grains of sorghum. Therefore, identifying imperfect, perfect, and shelled grains in sorghum is of great practical importance, but the wide variety places higher demands on the generalisation ability of the model.

To address the aforementioned challenges, an improved model YOLOv8s-GBD (YOLOv8s-C2f_Ghostblockv2-BiFPN-DymiHead) based on YOLOv8s is proposed to achieve accurate recognition of sorghum seed categories. In this study, the C2f module in the YOLOv8s backbone feature extraction network is improved by incorporating the DFC Attention-based Bottleneck structure from GhostNetV2 into the C2f module. This modification strengthens the global context-awareness of feature representation and enhances the detection accuracy of the model. Additionally, a bidirectional feature pyramid network (BiFPN) is incorporated to enhance multi-scale feature fusion performance and thereby improve the accuracy of small-target detection. Finally, to further boost the model's feature expression capability, a target detection head framework based on the attention mechanism (Dynamic Head) is introduced. This not only improves the model's accuracy and robustness but also ensures accurate classification of sorghum seed categories.

MATERIALS AND METHODS

Sorghum grain dataset

The training of the YOLOv8s-GBD algorithm proposed in this study requires labelled sorghum grain datasets. However, existing open-source datasets lack a specific dataset for sorghum grain classification. Consequently, this study constructed a dedicated sorghum grain dataset by collecting images of sorghum grains. The dataset was systematically classified and labelled, with each grain individually enclosed in an independent bounding box.

Materials

Sorghum samples were provided by Bengbu Chuqian Trading Co., Ltd. Three different types of sorghum grains—perfect grains, imperfect grains, and shelled grains-from the Hongyingzi variety were used as research objects. Due to sample limitations, this study focused solely on three types of imperfect grains: lesion grains, damaged grains, and insect-damaged grains. Prior to the experiment, the seeds were dried to ensure that the moisture content of the sorghum grain samples was (13.5 ± 0.5)%. Subsequently, perfect grains, imperfect grains, and shelled grains were carefully selected from the samples.

Sorghum grain image acquisition

In this study, high-resolution industrial cameras were used to collect images of sorghum grains. The industrial camera is a colour camera with a resolution of 25 MP and a 25 mm focal length lens. The industrial camera is connected to the host computer through GigE to ensure the high speed and stability of data transmission.

In the process of image acquisition, the industrial camera is fixed on the array platform, which is 25 cm away from the sorghum grain. The image acquisition device is shown in Fig. 1. In order to reduce environmental interference, the collection site is in the laboratory, and the collection time is selected during the period of stable light (10 a.m. to 2 p.m.). The selected three different types of sorghum grains were randomly spread on a black worktable. Through the SDK software of the industrial camera, the parameters are reasonably set to obtain a colour image with a resolution of 5120 × 5120, which is stored in the jpg format, and a total of 167 colour images are collected.

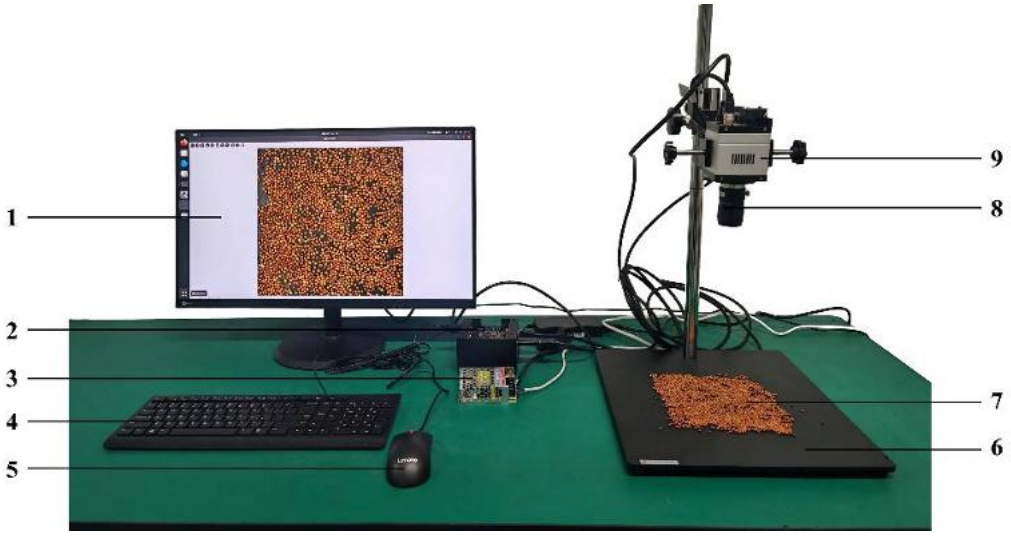


Fig. 1 - Image acquisition platform

1 - Monitor; 2 - Host computer; 3 - Switch power supply; 4 - Keyboard; 5 - Mouse; 6 - Worktable; 7 - Sorghum seed; 8 - Lens; 9 - Industrial camera

Dataset construction

The images collected by industrial cameras contain multiple sorghum grains, making them difficult to label. Therefore, this study employs threshold segmentation, morphological processing and contour search algorithms to divide the images into several sub-images, as shown in Fig. 2. The image dataset consists of sub-images containing only one complete grain. Sorghum grains are classified based on their appearance, epidermal characteristics, and integrity, as illustrated in Fig. 3. The open-source LabelImg image annotation tool (https://github.com/tzutalin/labelImg) is utilized to annotate perfect grains, imperfect grains, and shelled grains within the images. The three types of sorghum grain images are described as follows:

(1) Perfect grain: complete and shiny sorghum grain.

(2) Imperfect grain: lesion grains, damaged grains and insect-damaged grains.

(3) Shelled grain: Sorghum grain with guard glumes (shells).

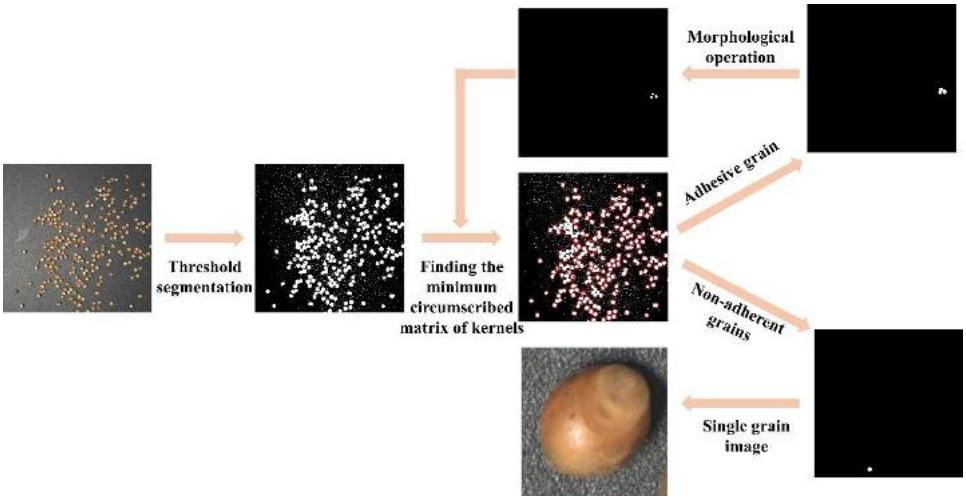


Fig. 2 - Image pre-processing

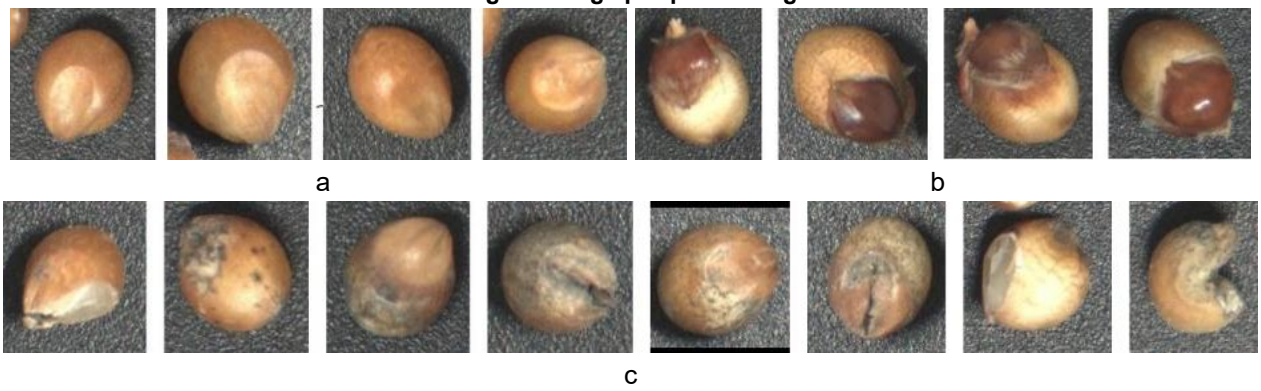


Fig. 3 - Sample of sorghum grain

a - Perfect grain; b - Shelled grain; c - Imperfect grains.

To improve the model's generalization ability and enhance detection performance. The dataset was augmented using preprocessing techniques such as random image rotation and brightness-contrast. The final dataset contained 6330 perfect grains, 7590 imperfect grains, and 5980 shelled grains. To train and validate the model, the three types of sorghum grain images were divided into training, validation and test sets in the ratio of 7:2:1, respectively.

Deep Learning Network Construction

YOLOv8

YOLOv8 is a state-of-the-art single-stage object detection model developed by Ultralytics. The model consists of four parts: Input, Backbone, Neck and Output (*Chitraningrum et al., 2024; Jiang, P et al., 2022*). In the backbone network and Neck section, the design concept of YOLOv7 is referenced. The backbone network employs the C2f module to extract multi-scale features. In the Head section, a decoupled head structure is adopted to separate the classification and detection tasks. Meanwhile, YOLOv8 adopts Task-Aligned Assigner positive-negative sample matching and introduces Distribution Focal Loss (DFL) to improve the training stability and generalisation performance. In addition, the operation of disabling Mosaic augmentation during

the last 10 epochs of YOLOX training is introduced in the data augmentation phase, which effectively enhances the model's accuracy. These changes make YOLOv8 perform well in the classification recognition task. By comparing the model training results of different scales of YOLOv8, as shown in Table 1. Although YOLOv8n has the fewest model parameters, its small number of residual structures results in relatively low detection accuracy. However, YOLOv8m, YOLOv8l, and YOLOv8x have a larger number of parameters, making it difficult to meet the requirements for lightweight and real-time performance. Therefore, this study selected YOLOv8s as the basis for designing a new sorghum grain classification and detection model algorithm, as shown in Fig. 4.

Table 1

Comparison of the performance of different versions of YOLOv8

Model	Size	mAP50	mAP 50-95	Parameters/×106 M	Weight size/MB
Yolov8n	640	0.694	0.653	3.2	5.9
Yolov8s	640	0.707	0.759	11.7	21.4
Yolov8m	640	0.712	0.734	26.0	49.5
Yolov8l	640	0.708	0.721	43.7	83.5
Yolov8x	640	0.703	0.719	68.2	130

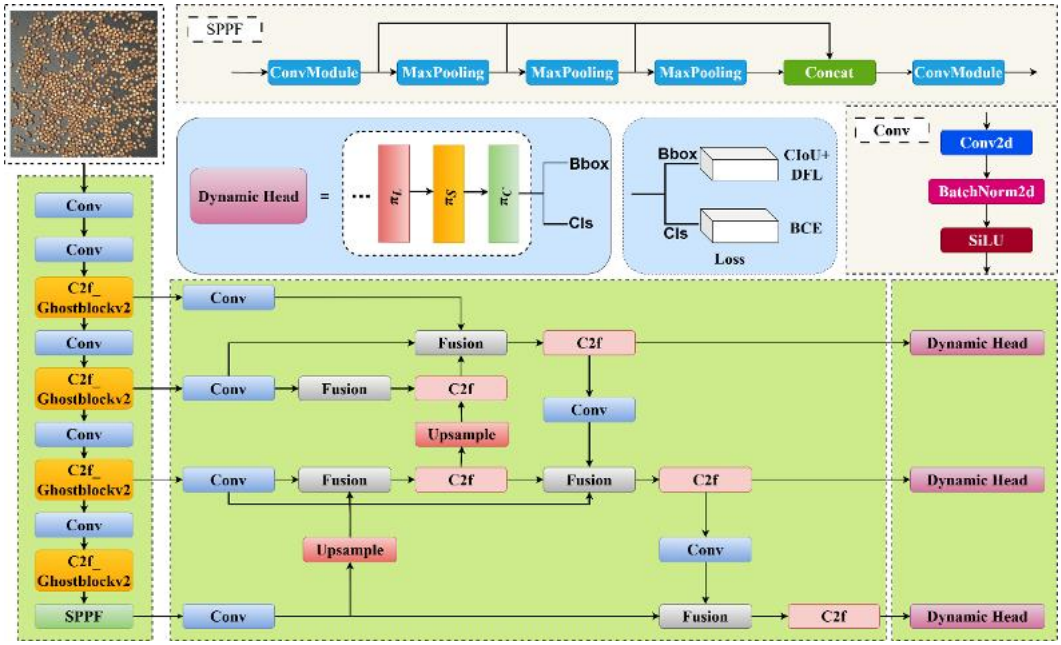


Fig. 4 - Improved YOLOv8 model

C2f_Ghostblockv2

The backbone feature extraction network of the model has the greatest impact on the model accuracy. GhostNetV2 proposed by *Tang et al., (2022),* is a lightweight model, which reduces the number of parameters while ensuring a certain accuracy. In this study, the Bottleneck structure of GhostNetV2 is introduced into the C2f network structure to replace the original convolution layer to form a new network structure C2f_Ghostblockv2, as shown in Fig. 5. This structure solves the problem of recognition accuracy of the model.

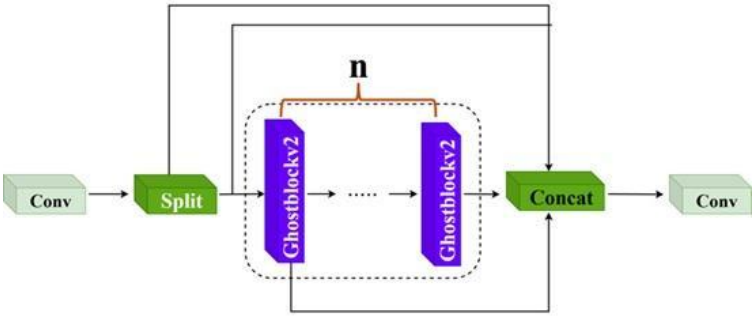


Fig. 5 - Structure of C2f _ Ghostblockv2

The Bottleneck structure of GhostNetV2 consists of two Inverted Residual Bottle-neck structures based on the Ghost Module, as shown in Fig. 6. Specifically, the first Ghost module expands the number of output channels via an extension layer to generate extended features, while the second Ghost module reduces the number of channels to align with the shortcut path's output. To enhance the model's representational capacity, GhostNetV2 integrates the DFC (Decoupled Fully Connected) attention mechanism within the first Ghost module. The DFC attention operates in parallel with the first Ghost module to produce an attention map, which is element-wise multiplied with the extended features to strengthen their representational power. These enhanced features are then passed through the second Ghost module to generate the final output features. The DFC attention captures long-range spatial dependencies by decomposing a fully connected layer into two separate fully connected layers along the horizontal and vertical directions, aggregating pixel information in both dimensions independently. When identifying different types of sorghum grains, this mechanism allows the model to maximize its performance, thereby improving the recognition accuracy of the improved model.

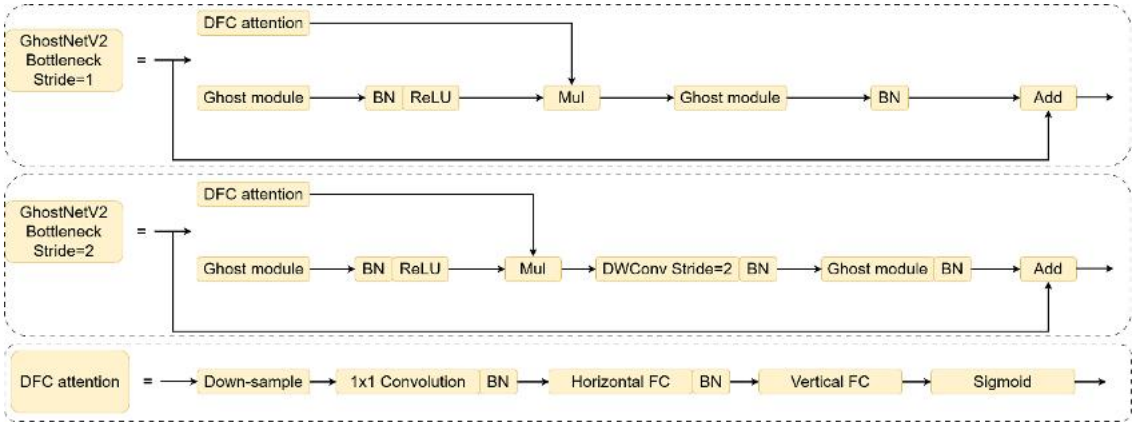


Fig. 6 - Bottleneck structure of GhostNetV2

Feature Fusion Network (BiFPN)

In the original YOLOv8s network, the multi-scale feature maps extracted by the backbone network are input into the PANet structure for feature fusion, the structure of which is shown in Fig. 7(a). The PANet structure uses the summation of different features to achieve the fusion of different feature layers. However, there are many types of sorghum grains, and the sizes of damaged grains and shelled grains in perfect grains and imperfect grains are different. If only simple feature-layer summation is performed, it will result in uneven contributions of different input features to the fused output features. To avoid this problem and make the network better capture multi-scale feature information, this study introduces BiFPN (*Li N. et al., 2024*) to improve the YOLOv8s network, as illustrated in Fig. 7(b).

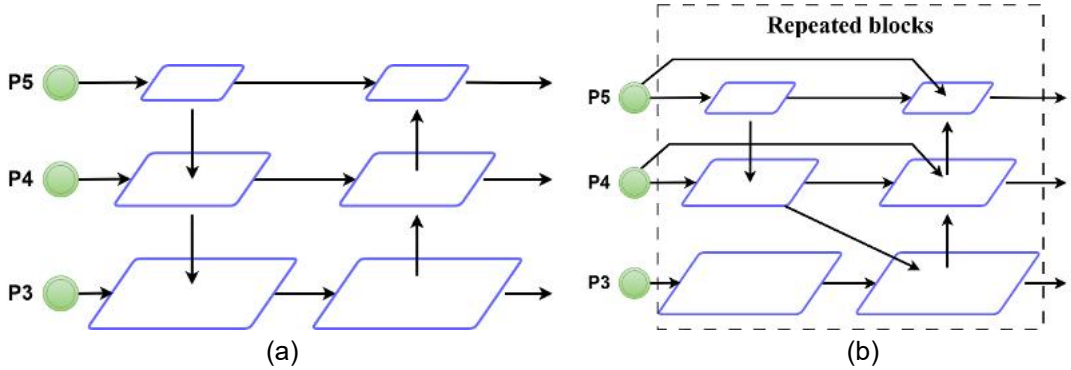


Fig. 7 - Structure of PANet, BiFPN

BiFPN introduces a bi-directional fusion mechanism, where features are fused through bi-directional paths (top-down and bottom-up). In the top-down path, high-level features are fused with low-level features by upsampling. In the bottom-up path, low-level features are fused with high-level features through downsampling. This bi-directional flow enhances the expressive power of the features and allows the different scale features to complement each other. The structure automatically adjusts the importance of different scale features through a weighted fusion mechanism to achieve more accurate feature fusion and improve target detection performance. Meanwhile, the BiFPN module can be repeatedly stacked to enhance information fusion.

By replacing the Neck structure in the YOLOv8s network with the BiFPN network, the model integrates the local and global features of different types of sorghum grains. This approach retains shallower semantic information while preserving deeper location information. Consequently, accurate detection of different types of sorghum seeds at different scales is achieved.

DymiHead

The Head part of the YOLOv8 network architecture receives multi-scale feature maps from the Backbone and Neck networks. These feature maps have different resolutions and are used to detect targets of different sizes. However, the difference of grain size in sorghum grain images is small, only some damaged grains are significantly different from other grain sizes, and other types of grain sizes are relatively close. Therefore, this study introduces a dynamic head framework based on attention mechanism to enhance the feature expression ability of the model.

Dynamic Head consists of Scale-aware Attention, Spatial-aware Attention and Task-aware Attention, and its structure is shown in Fig. 8. The Scale-aware Attention module (π_L) consists of Mean Pooling, 1×1 Convolution, ReLU Activation function and Hard Sigmoid function. This module adaptively enhances important features and suppresses redundant information by computing the spatial and channel attention of the feature map, enabling the model to better capture multi-scale targets. The spatial-aware attention module (π_S) consists of offset learning and 3× 3 convolution. This module focuses on the spatial location information of the feature map and uses the global context information to enhance the response of the target region. The task-aware attention module (π_C) is implemented by global average pooling, two fully connected layers, a normalisation layer, and a shifted sigmoid function. This module exploits task-specific attention mechanisms to enhance the performance of the model in multi-task learning.

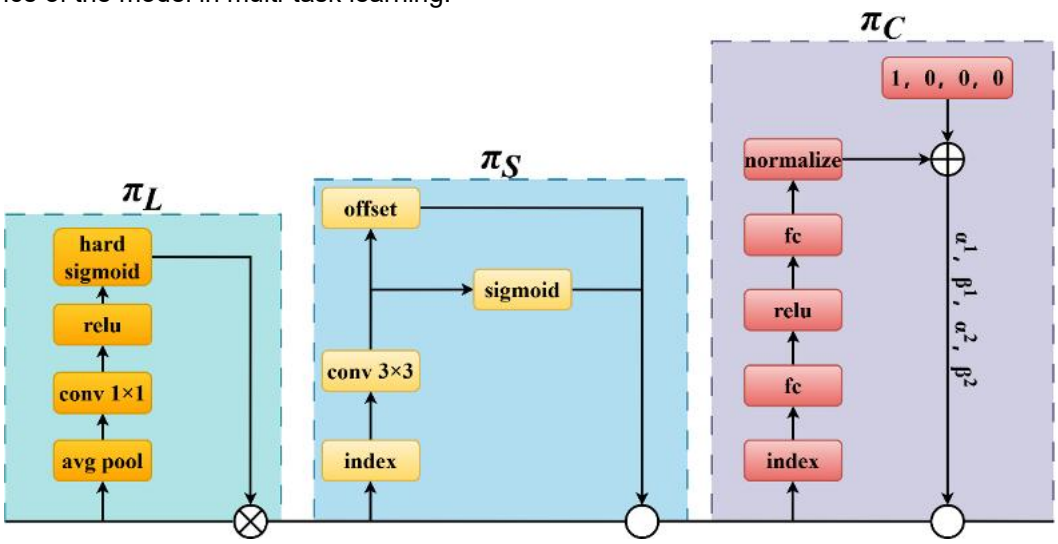


Fig. 8 - Dynamic Head structure

The multi-scale feature maps of sorghum grains extracted by the backbone net-work and Neck network were input into Dynamic Head. Different attention mechanisms operate in different dimensions, complement each other, and collectively enhance the representation ability of the target detection head. By dynamically adjusting the feature weights, the accuracy and robustness of sorghum seed target detection are significantly improved.

Loss calculation

In sorghum kernel classification and detection, the trained model predicts the class of each detected kernel. The prediction results can include both correct and incorrect classifications; therefore, it is essential to evaluate whether the predicted kernel class matches the ground-truth label. The final classification result is determined based on this comparison, enabling the identification of different sorghum kernel types.

This study uses the loss function in the original YOLOv8s network structure, which consists of two parts: category classification loss and border regression loss. Classification Loss uses cross entropy loss. This method measures the performance of the model by calculating the cross entropy of the probability distribution predicted by the model and the probability distribution of the real label. The YOLOv8s target detection model uses CIOU as the regression loss function, which is defined as:

$$CIoU = IoU - \left(\frac{\rho^2(b,b^{gt})}{d^2} + \alpha v\right) \quad (1)$$

$$v = \frac{4}{\pi^2}(arctan\frac{w^{gt}}{h^{gt}} - arctan\frac{w}{h})^2 \quad (2)$$

$$\alpha = \frac{v}{(1-IoU)+v} \quad (3)$$

where ρ is the Euclidean distance, d is the diagonal of the minimum bounding box, v is the trade-off parameter, and α is the corresponding trade-off parameter.

The boundary loss is then in the form of CIoU (Complete Iou) Loss+DFL. Both the distance and overlap rate between the detection frame and the target frame are considered, as well as the influence of the length ratio of the detection frame on regression.

RESULTS

Experimental environment and parameters

The experiments were conducted on a Windows 10 system equipped with an Intel Core i5-12600KF CPU operating at 3.70 GHz, an NVIDIA GeForce RTX 4060 Ti GPU with 16 GB of video memory, and 32 GB of system RAM. The PyTorch deep learning framework (version 1.12.1) was used, with PyCharm 2020.2.1 as the development environment. GPU acceleration was configured using CUDA 11.6 and cuDNN 8.9.7. Python 3.8.5 was used together with torchvision 0.13.1 and torchaudio 0.12.1.

Table 2

Hyperparameters used for deep learning training

Parameter	Parameter Value
Initial learning rate	0.01
Final learning rate	0.01
Weight decay factor	0.0005
IoU threshold	0.7
Momentum	0.9
Learning Rate Adjustment Strategy	steps
Image size	160pixel × 160pixel
Batch-size	32
Number of epochs	200

Before training, the hyperparameters were optimized, with particular attention to key settings such as the input image size and batch size. Examination of the loss curve showed that, when the number of training epochs was set to 200, the model loss gradually stabilized, indicating that the model had reached convergence. Therefore, the number of training epochs was set to 200 in this study. The detailed experimental hyperparameters are presented in Table 2.

Evaluation indicators

In machine learning and deep learning, the prediction results of classification tasks are classified into the following four categories:

(1) *True Positive (TP)*: the prediction is positive, the label value is also positive, and the prediction is correct.

(2) *False Negative (FN)*: Predicted as a negative case, labelled as a positive case, wrong prediction

(3) *False Positive (FP):* the prediction is positive, the label value is negative, the prediction is wrong

(4) *True Negative (TN):* predicted as a negative case, the label value is negative, the prediction is correct

In this study, *P (Precision, %), R (Recall, %), mAP1 (mAP50), mAP2 (mAP50-95)* and *F1* were used to evaluate the performance of the network model. The corresponding equations for these five metrics are as follows:

$$P = \frac{TP}{TP+FP} \times 100\% \quad (4)$$

$$R = \frac{TP}{TP+FN} \times 100\% \quad (5)$$

$$F1 = \frac{P*R*2}{P+R} \quad (6)$$

$$AP = \int_0^1 P(R)dR \quad (7)$$

$$mAP = \frac{1}{M}\sum_{k=1}^{M} AP(k) \times 100\% \quad (8)$$

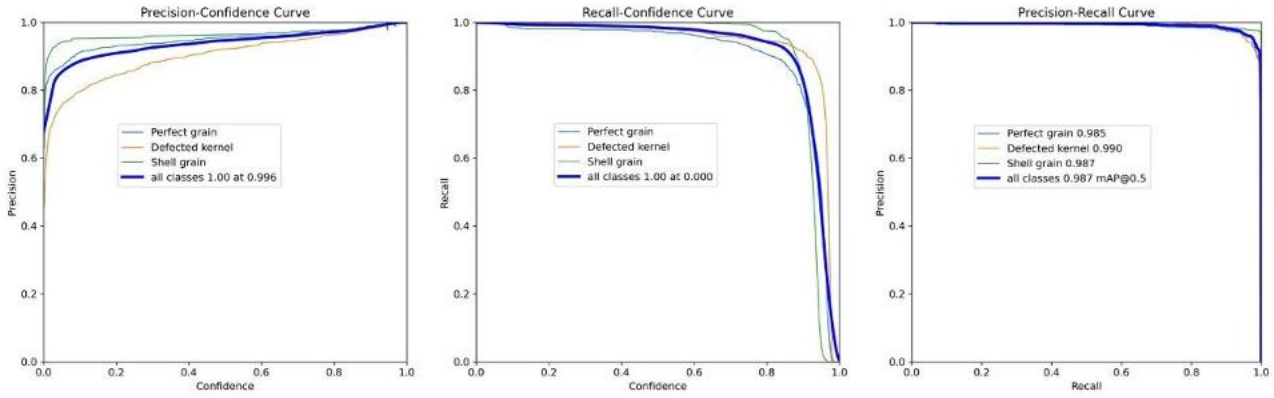
As indicated by the above equations, a higher P corresponds to fewer false positives (FP), meaning that fewer samples from other classes are incorrectly predicted as the target class. A higher $Recall$ corresponds to fewer false negatives (FN), indicating fewer missed detections of positive samples. Because a model may

achieve high P but relatively low $Recall$, or vice versa, the $F1$-score was used to provide a balanced evaluation of P and $Recall$. As the harmonic mean of P and $Recall$, the $F1$-score is strongly influenced by the lower of the two values and therefore helps prevent model selection based on only one favourable metric. The mean average precision (mAP) provides an overall measure of object detection performance across classes and IoU thresholds, depending on the specific mAP definition used.

Improved detection performance of the YOLOv8 algorithm

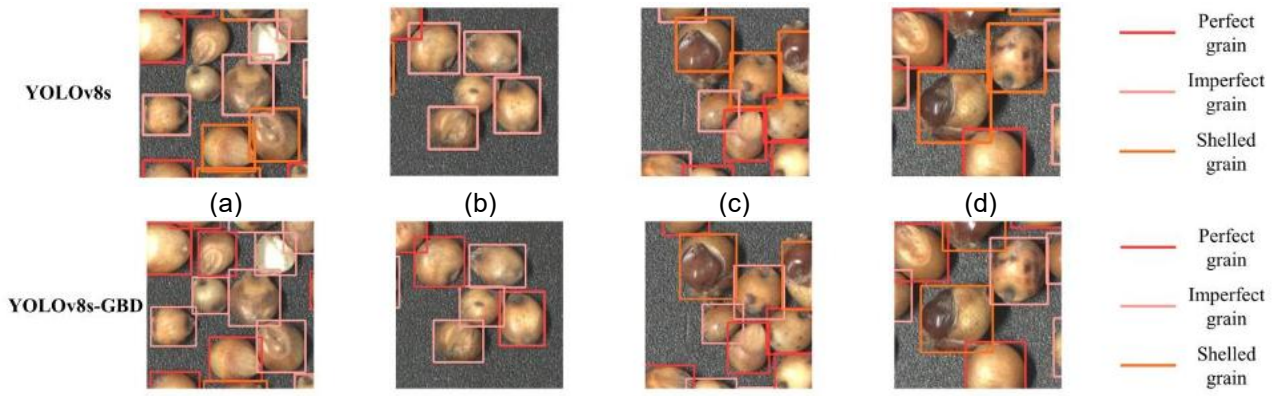
The YOLOv8s-GBD sorghum kernel classification and detection model proposed in this study was trained using transfer learning. The precision P, R, and PR curves obtained during training are shown in Fig.9.

As shown in Fig. 9, the precision values for the Perfect grain, Defected kernel, and Shell grain categories were 0.985, 0.990, and 0.987, respectively. Furthermore, the mean $Average\ Precision\ (mAP1)$ achieves a value of 0.987. These results indicate that the proposed model achieved high classification and detection performance for different sorghum kernel categories.



(a) (b) (c)

Fig. 9 - P, R, PR curves



(a) (b) (c) (d)

(e) (f) (g) (h)

Fig. 10 - Image details of different models

a - Leak detection 2, False detection; b - Leak detection, False detection 1; c - False detection 1, Inaccurate bounding box; d - False detection 1, Inaccurate bounding box 1; e - No leak detection, No false detection; f - No leak detection, No false detection; g - No false detection, Bounding box accuracy; h - No false detection, Bounding box accuracy

The model outputs in this study identify different types of sorghum kernels using rectangular bounding boxes overlaid on the images. For clearer visualization, representative regions of the sorghum kernel detection images were cropped and enlarged. YOLOv8s was used as the baseline model for comparison, as shown in Fig. 10. The comparison results show that dense kernel distributions can lead to severe overlap and adhesion between adjacent kernels. Under these conditions, although YOLOv8s can detect some targets, it is more prone to false detections, missed detections, and inaccurate bounding-box localization. In contrast, the YOLOv8-GBD model detects densely distributed kernels more reliably and provides more accurate classification of kernel types.

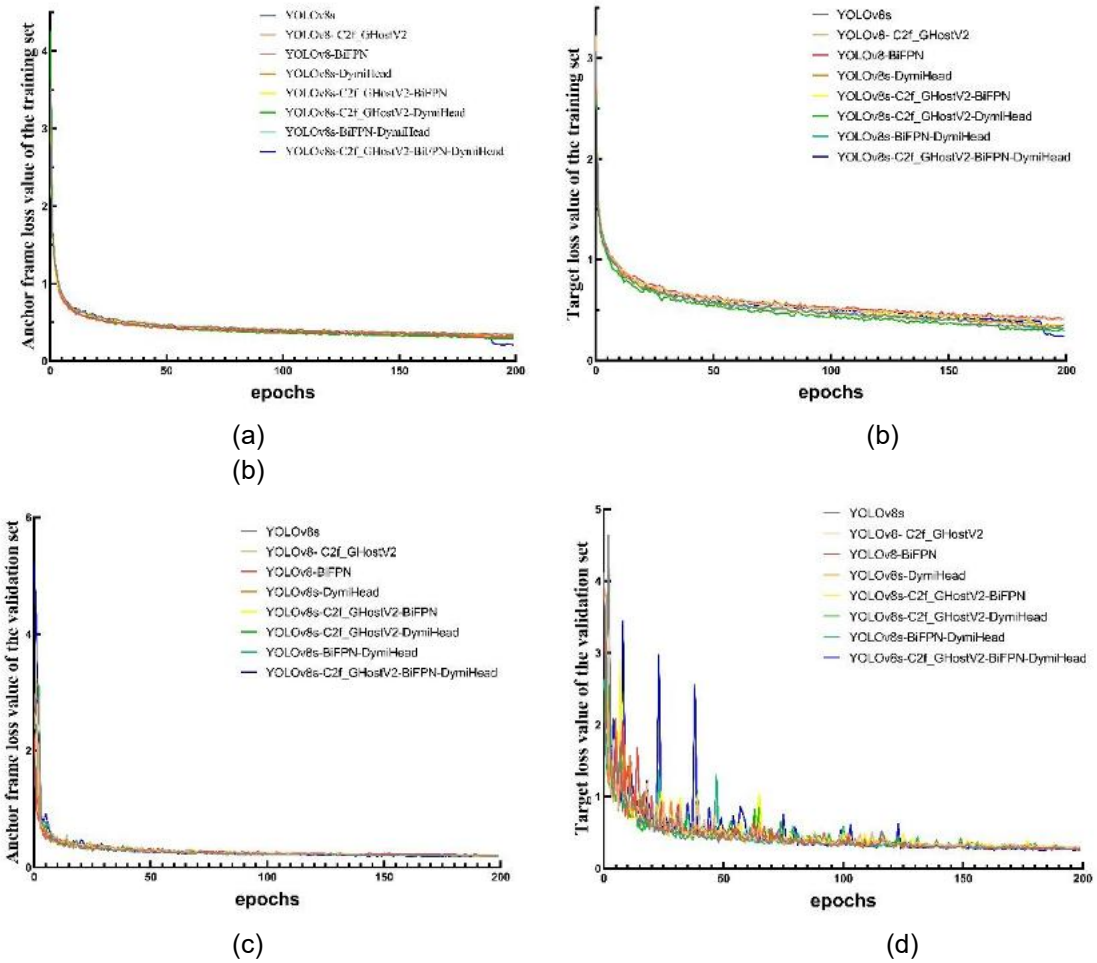
Ablation study

Using the same training, validation, and test sets, ablation experiments were conducted to evaluate the contribution and effectiveness of the different optimization strategies. Based on the YOLOv8s architecture, the Backbone, Neck, and Head components were modified separately. In the Backbone, the GhostNetV2 bottleneck was introduced into the C2f structure to incorporate a long-range attention mechanism and improve feature extraction accuracy. In the Neck, a BiFPN structure was employed for multi-scale feature fusion. In the Head, the original detection head was replaced with a Dynamic Head to enhance feature representation capability. Each modified model was trained for 200 epochs, and the best-performing model was selected for evaluation. The performance metrics of the different models are presented in Table 3.

Table 3

Performance metrics of different models

Model	P/%	R/%	mAP1/ %	mAP2/ %	F1/%
YOLOv8s	92.1	96.3	97.5	96.5	94.2
YOLOv8- C2f_Ghostblockv2	94.4	95.7	98.1	96.6	95.0
YOLOv8-BiFPN	93.3	96.9	98.2	96.7	95.4
YOLOv8-DymiHead	93.7	95.9	98.5	97.2	94.8
YOLOv8- C2f_Ghostblockv2-BiFPN	93.9	96.9	98.1	96.8	95.4
YOLOv8-C2f_Ghostblockv2-DymiHead	94.3	96.3	98.4	97.4	94.8
YOLOv8-BiFPN-DymiHead	93.9	96.5	98.4	97.4	95.2
YOLOv8s-C2f_Ghostblockv2-BiFPN-DymiHead	95.2	98.0	98.7	97.5	96.6



(a) (b)

(c) (d)

Fig. 11 - Training and validation loss curves of different models

As shown in Table 3, introducing C2f_GhostBlockV2, BiFPN, and DymiHead individually resulted in varying improvements in model precision, recall, and mean average precision. The baseline YOLOv8s model achieved a precision of 92.1% for sorghum kernel classification and detection. After introducing C2f_GhostBlockV2, BiFPN, and DynamicHead separately, the precision increased to 94.4%, 93.3%, and 93.7%, respectively, corresponding to improvements of 2.3, 1.2, and 1.6 percentage points relative to the baseline model. Among the individual modifications, C2f_GhostBlockV2 produced the largest improvement in precision. However, only BiFPN improved recall compared with the baseline model. These results indicate that optimizing a single network component provides only limited overall performance gains.

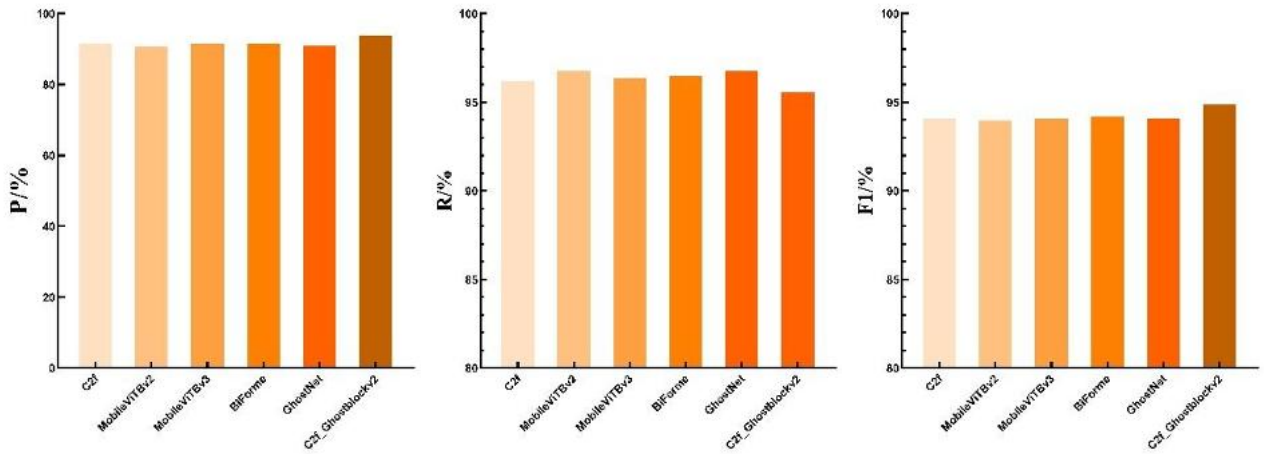
When two optimization strategies were combined, the detection model generally achieved further improvements in precision, recall, and mean average precision, with no obvious deterioration in overall performance. Among the tested combinations, BiFPN combined with DymiHead provided the best overall performance. Compared with the baseline YOLOv8s model, this combination improved precision, recall, mAP1, and mAP2 by 1.8, 0.2, 0.9, and 0.9 percentage points, respectively.

The above experiments show that optimizing the Backbone, Neck, and Head components of YOLOv8s can improve model performance for sorghum kernel classification and detection. Accordingly, the three optimization strategies described above were integrated to develop the proposed YOLOv8s-GBD sorghum kernel classification and detection model. Compared with the baseline YOLOv8s model, YOLOv8s-GBD improved P, R, mAP1, mAP2 and F1 by 3.1, 1.7, 1.2, 1.0, and 2.4 percentage points, respectively. Fig. 11 shows the loss curves for the different model configurations. As shown in the figure, the YOLOv8s-GBD model exhibited relatively high initial training and validation loss values. The losses decreased rapidly during the first 50 epochs and gradually stabilized after approximately 100 epochs, indicating that the model approached convergence.

Comparison experiment of different feature extraction networks

To evaluate the performance of the improved feature extraction network, this study replaces the original C2f module of yolov8s with mainstream network structures such as MobileViTBv2, MobileViTBv3, BiFormer, and GhostNet. The training set, validation set and test set used in this study are used for training, and the training effect is compared with that of C2f_Ghostblockv2 as shown in Fig. 12.

In this study, there are many categories of sorghum grains, especially imperfect grains, with large differences in appearance size, and high requirements for the accuracy and F1 value of the model. From Fig. 12, it can be seen that the C2f _ Ghost-blockv2 structure has the largest gain in the accuracy and F1 value of sorghum grain classification and recognition. Compared with other structures, C2f _ Ghostblockv2 has a small difference in accuracy and recall rate, which can effectively avoid the short board effect and is more suitable for the needs of this study.



(a) (b) (c)

Fig. 12 - Accuracy, recall and F1 value for different feature extraction networks

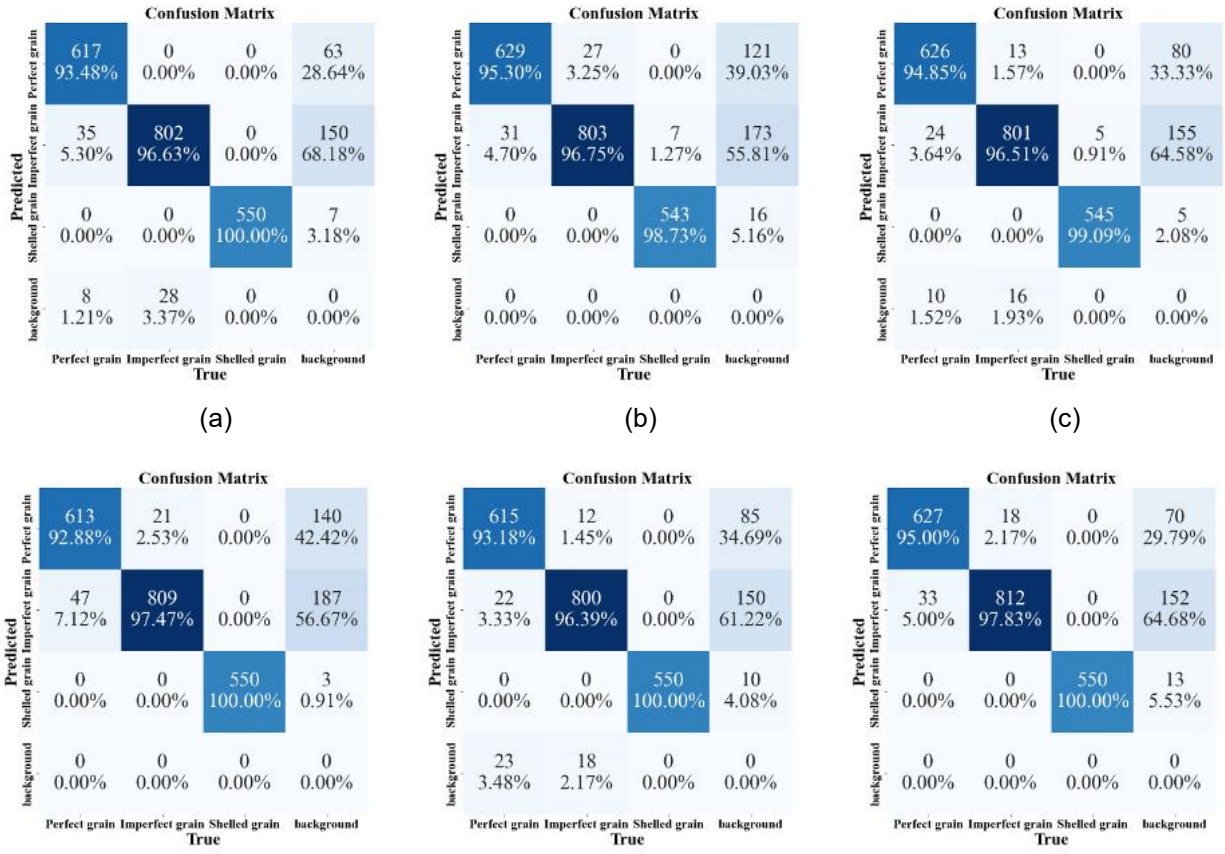


Fig. 13 - Confusion matrix of test effects of different feature extraction networks

As illustrated in Fig. 13, C2f_Ghostblockv2 has the highest classification accuracy for imperfect grains among the six models. Although the classification accuracy of C2f_Ghostblockv2 perfect grains is slightly lower than that of MobileViTBv2, it is still higher than the other network structures. Among the six models, the classification accuracy of C2f_Ghostblockv2 perfect grains is not the best, but its overall classification accuracy is the highest among all models. It shows that C2f_Ghostblockv2 has superior performance in sorghum grain classification.

Comparison of different models

To further evaluate the effectiveness of the YOLOv8s-GBD algorithm for sorghum grain classification and recognition, model training was performed on different versions of the YOLO target detection algorithm using the same training, validation and test sets. The participating comparison detection networks are YOLOv5, YOLOv7-tiny, YOLOv9, YOLOv10, and YOLOv11, and the test results are shown in Table 4.

As shown in Table 4, the YOLOv8s-GBD algorithm achieves 95.2%, 98.0%, 98.7% and 97.5% in P, R, mAP1 and mAP2 values, respectively. It is superior to other YOLO models in terms of P and mAP1, and only the R value and mAP2 value are slightly lower than YOLOv11, and much higher than other YOLO models. Therefore, the com-prehensive recognition performance of YOLOv8s-GBD algorithm is better than other YOLO models. The algorithm proposed in this study can realize the recognition of sorghum grain classification.

Table 4

Parameters of performance indicators for different models

Model	P/%	R/%	mAP1/ %	mAP2/ %	F1/%
YOLOv5	90.1	97.9	96.4	93.7	93.8
YOLOv7-tiny	87.2	92.9	92.7	90.4	90.0
YOLOv9	91.2	96.0	98.6	96.1	93.5
YOLOv10	92.7	96.1	97.7	95.1	94.4
YOLOv11	93.1	98.7	98.5	97.9	95.8
YOLOv8s-C2f_Ghostblockv2-BiFPN-DymiHead	95.2	98.0	98.7	97.5	96.6

Generalization experiment

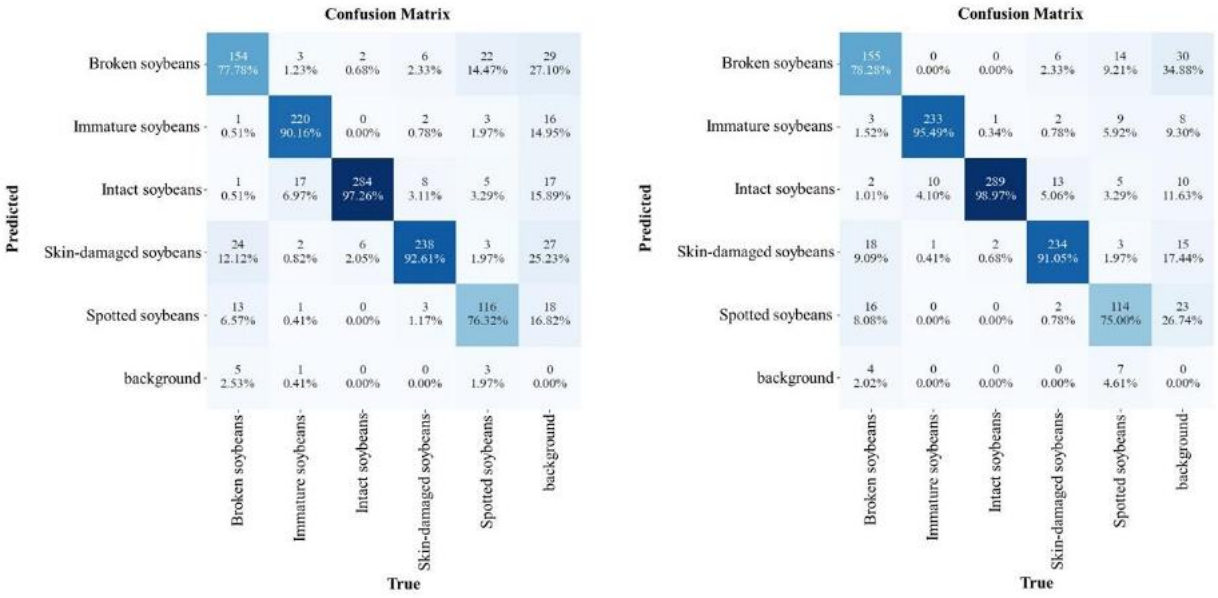
In order to verify the generalization of the algorithm proposed in this study, YOLOv8s-GBD and YOLOv8s were compared on other data sets. The soybean seed dataset purchased from CSDN platform was used in this experiment. The dataset contains five categories of soybean seed images such as intact, speckled, immature, broken and lost, which are very similar to the sorghum seed classification in this study. In this study, 5513 soybean seed images were screened and divided into training, validation, and test sets according to the ratio of 7:2:1.

Table 5

Soybean data set comparison test

Model	P/%	R/%	mAP1/%	mAP2/%	F1/%
YOLOv8s	84.2	86.0	92.3	79.8	93.8
YOLOv8s-GBD	87.2	92.9	92.7	90.4	90.0

The test environment and parameter configurations were kept consistent with the sorghum seed classification test, and the test results are shown in Table 5. Compared with YOLOv8s, YOLOv8s-GBD improves the accuracy and recall by 3 and 6.9 per-centage points, which effectively reduces the problem of misdetection and omission of soybean seeds; and improves the mAP1 and mA2 by 0.4 and 10.6 percentage points, which indicates that YOLOv8s-GBD has a higher detection precision. The detection effect of the two models on the soybean seed data set is shown in Fig. 14. It can be seen from Fig. 14 that the comprehensive detection accuracy of YOLOv8s-GBD on soybean seed test set is high, which proves the generalization of this research method.



(a) (b)

Fig. 14 - Confusion matrix of YOLOv8s and YOLOv8s-GBD test results

CONCLUSIONS

(1) To address the low efficiency and time-consuming nature of conventional quality inspection methods for dried sorghum kernels, an improved YOLOv8s-GBD model was developed based on YOLOv8s. In the Backbone, the C2f module was enhanced by incorporating a GhostNetV2 bottleneck with DFC attention to strengthen feature extraction. BiFPN was introduced in the Neck to improve multi-scale feature fusion, while a Dynamic Head attention mechanism was adopted to enhance feature representation and improve model accuracy and robustness.

(2) The different optimization strategies were trained using the same training and validation sets and evaluated on a common test set. The proposed YOLOv8s-GBD model achieved P, R, mAP1, mAP2 and F1-score values of 95.2%, 98.0%, 98.7%, 97.5%, and 96.6%, respectively. Compared with the baseline YOLOv8s model, these metrics increased by 3.1, 1.7, 1.2, 1.0, and 2.4 percentage points, respectively. The results indicate that YOLOv8s-GBD provides improved performance for sorghum kernel classification and detection and satisfies the accuracy requirements of dried sorghum quality inspection.

(3) Future research should expand both the number of samples and the range of defective-kernel categories. The present study considered only lesion-damaged, mechanically damaged, and insect-damaged kernels among the defective classes. Future work should include additional types of defective kernels to improve the comprehensiveness and accuracy of sorghum kernel classification and detection.

ACKNOWLEDGEMENT

This work was funded by the Key R&D Program of Shandong Province, China (2024CXGC010901) and the integrated pilot project of agricultural machinery Research and Development, Manufacturing and Application in Shandong Province (NJYTHSD−202311). We also sincerely appreciate the editors and anonymous reviewers for their valuable comments and constructive suggestions to improve the quality of this paper.

REFERENCES

[1] Chitraningrum, N., Banowati, L., Herdiana, D., Mulyati, B., Sakti, I., Fudholi, A., ... & Andria, A. (2024). Comparison study of corn leaf disease detection based on deep learning YOLO-v5 and YOLO-v8. *Journal of Engineering and Technological Sciences*, 56(1), 61-70. https://doi.org/10.5614/j.eng.technol.sci.2024.56.1.5

[2] Chen, Z., Fan, W., Luo, Z., & Guo, B. (2022). Soybean seed counting and broken seed recognition based on image sequence of falling seeds. *Computers and Electronics in Agriculture*, 196, 106870. https://doi.org/10.1016/j.compag.2022.106870

[3] Delwiche, S. R., Rodriguez, I. T., Rausch, S. R., & Graybosch, R. A. (2019). Estimating percentages of fusarium-damaged kernels in hard wheat by near-infrared hyperspectral imaging. *Journal of Cereal Science*, 87, 18-24. https://doi.org/10.1016/j.jcs.2019.02.008

[4] Gao, H., Zhen, T., & Li, Z. (2022). Detection of wheat unsound kernels based on improved ResNet. *IEEE access*, 10, 20092-20101. https://ieeexplore.ieee.org/stamp/stamp.jsp?arnumber=9698037

[5] Guo, M., Ma, Y., Yang, X., & Mankin, R. W. (2019). Detection of damaged wheat kernels using an impact acoustic signal processing technique based on gaussian modelling and an improved extreme learning machine algorithm. *Biosystems Engineering*, 184, 37-44. https://doi.org/10.1016/j.biosystemseng.2019.04.022

[6] Gab-Allah, M.A., Choi, K., & Kim, B. (2021). Accurate determination of type b trichothecenes and conjugated deoxynivalenol in grains by isotope dilution–liquid chromatography tandem mass spectrometry. Food Control, 121, 107557-. https://doi.org/10.1016/j.foodcont.2020.107557

[7] He, X., Yan, C., Jiang, X., Shen, F., & Fang, Y. (2021). Classification of aflatoxin B_1 naturally contaminated peanut using visible and near-infrared hyperspectral imaging by integrating spectral and texture features. *Infrared Physics & Technology*, 103652. https://doi.org/10.1016/j.infrared.2021.103652

[8] Jiang, P., Ergu, D., Liu, F., Cai, Y., & Ma, B. (2022). A Review of Yolo algorithm developments. *Procedia computer science*, 199, 1066-1073. https://doi.org/10.1016/j.procs.2022.01.135

[9] Li, H., Zhang, L., Sun, H., Rao, Z., & Ji, H. (2022). Discrimination of unsound wheat kernels based on deep convolutional generative adversarial network and near-infrared hyperspectral imaging technology. *Spectrochimica Acta Part A: Molecular and Biomolecular Spectroscopy*, 268, 120722-. https://doi.org/10.1016/j.saa.2021.120722

[10] Liu, J., Yang, M., He, M., Xu, M., Chen, Y., & Zhang, F. (2024). Rapid and selective detection of AFB1 by direct mass spectrometry using immunoaffinity paper substrate. *Microchemical Journal*, 196, 109439. https://doi.org/10.1016/j.microc.2023.109439

[11] Liu, F., Fu, J., & Zhao, R. (2023). Pixel-wise mechanical damage detection of waxy maize using spectral-spatial feature extraction and hyperspectral image. *Computers and Electronics in Agriculture*, 209. https://doi.org/10.1016/j.compag.2023.107853.

[12] Liu, Z., Sun, H., Zhu, Z., Yan, L., & Luo, T. (2021). Identification of rice-weevil (Sitophilus oryzae L.) damaged wheat kernels using multi-angle NIR hyperspectral data. *Journal of Cereal Science*, 101. https://doi.org/10.1016/j.jcs.2021.103313

[13] Lin, W., Shu, L., Zhong, W., Lu, W., Ma, D., & Meng, Y. (2023). Online classification of soybean seeds based on deep learning. *Engineering Applications of Artificial Intelligence*, 123, 106434. https://doi.org/10.1016/j.engappai.2023.106434

[14] Li, N., Ye, T., Zhou, Z., Gao, C., & Zhang, P. (2024). Enhanced YOLOv8 with BiFPN-SimAM for precise defect detection in miniature capacitors. *Applied Sciences*, 14(1), 429. https://doi.org/10.3390/app14010429

[15] Ni, C., Wang, D., Vinson, R., Holmes, M., & Tao, Y. (2019). Automatic inspection machine for maize kernels based on deep convolutional neural networks. *Biosystems Engineering*, 178, 131–144. https://doi.org/10.1016/j.biosystemseng.2018.11.010

[16] Na, L., Dong, W., Shi-fang, W., & Ping, H. (2019). Progress in terahertz technique for quality inspection of agro-food products. *Spectroscopy and Spectral Analysis*, 39(2), 349-356.

[17] Olgun, M., Onarcan, A. O., Özkan, K., Işik, Ş., Sezer, O., Özgişi, K., Ayter, N. G., Başçiftçi, Z. B., Ardiç, M., & Koyuncu, O. (2016). Wheat grain classification by using dense SIFT features with SVM classifier. *Computers and Electronics in Agriculture*, 122, 185–190. https://doi.org/10.1016/j.compag.2016.01.033

[18] Pearson, T. C., Cetin, A. E., Tewfik, A. H., & Haff, R. P. (2007). Feasibility of impact-acoustic emissions for detection of damaged wheat kernels. *Digital Signal Processing*, 17(3), 617-633. https://doi.org/10.1016/j.dsp.2005.08.002

[19] Qi, H., Luo, J., Wu, X., & Zhang, C. (2024). Application of nondestructive techniques for peach (Prunus persica) quality inspection: *A review. Journal of Food Science*, 89(11), 6863–6887. https://doi.org/10.1111/1750-3841.17388

[20] Qin, J., Kim, M. S., Chao, K., Chan, D. E., Delwiche, S. R., & Cho, B. K. (2017). Line-scan hyperspectral imaging techniques for food safety and quality applications. *Applied Sciences*, 7(2), 125. https://doi.org/10.3390/app7020125

[21] Shen, R., Zhen, T., & Li, Z. (2023). Segmentation of unsound wheat kernels based on improved Mask RCNN. *Sensors*, 23(7), 3379. https://doi.org/10.3390/s23073379

[22] Sun, X., Guo, M., Ma, M., & Mankin, R. W. (2018). Identification and classification of damaged corn kernels with impact acoustics multi-domain patterns. *Computers and Electronics in Agriculture*, 150, 152–161. https://doi.org/10.1016/j.compag.2018.04.008

[23] Sendin, K., Manley, M., & Williams, P. J. (2017). Classification of white maize defects with multispectral imaging. *Food Chemistry*, 243, 311-318. http://dx.doi.org/10.1016/j.foodchem.2017.09.133

[24] Tang, Y., Han, K., Guo, J., Xu, C., Xu, C., & Wang, Y. (2022). GhostNetv2: Enhance cheap operation with long-range attention. *Advances in Neural Information Processing Systems*, 35, 9969–9982. https://doi.org/10.48550/arXiv.2211.12905

[25] Tsuzuki, W., Suzuki, Y., Araki, T., Ohta, S., & Horigane, A. (2014). Effect of oxygen absorber on accumulation of free fatty acids in brown rice and whole grain wheat during storage. *LWT – Food Science and Technology*, 58(1), 222–229. https://doi.org/10.1016/j.lwt.2014.02.015

[26] Wang, L., Liu, J., Zhang, J., Wang, J., & Fan, X. (2022). Corn seed defect detection based on watershed algorithm and two-pathway convolutional neural networks. *Frontiers in Plant Science*, 13, 730190. https://doi.org/10.3389/fpls.2022.730190

[27] Yang, X., Guo, M., Lyu, Q., & Ma, M. (2021). Detection and classification of damaged wheat kernels based on progressive neural architecture search. *Biosystems engineering*, 208, 176-185. https://doi.org/10.1016/j.biosystemseng.2021.05.016

[28] Zhang, Q., Zhen, T., Li, Z., & Gao, H. (2025). MSPCNeXt: Multi-scale parallel convolution for identifying unsound kernels in stored wheat. *Journal of Stored Products Research*, 111, 102559. https://doi.org/10.1016/j.jspr.2025.102559

[29] Zhang, W., Ma, H., Li, X., Liu, X., Jiao, J., Zhang, P., ... & Cao, S. (2021). Imperfect wheat grain recognition combined with an attention mechanism and residual network. *Applied sciences*, 11(11), 5139. https://doi.org/10.3390/app11115139

SA-YOLO FOR MAIZE SEEDLING ROW SEGMENTATION: TOWARD RELIABLE NAVIGATION LINE EXTRACTION IN AGRICULTURAL FIELDS
/
基于改进 YOLOv12n-seg 网络的苗期玉米作物行识别方法

Delin SHANG[1,2], Yu YANG[3], Xingchen QIAO[3], Zhiwei HU[3], Changchun FAN[3], Yuanwei JIANG[3], Ziyang QIN[3], Kuanyan ZHANG[3], Xiaole WANG[3], Tie ZHANG*[1,2], Zhenchao WU*[3], Gang ZHANG*[4]

[1] State Key Laboratory of Agricultural Equipment Technology, Beijing 100083, China;
[2] Chinese Academy of Agricultural Mechanization Sciences Group Co., Ltd., Beijing 100083, China;
[3] School of Engineering, Anhui Agricultural University, Anhui 230036, Hefei, China;
[4] School of Intelligent Manufacturing, Anhui Science and Technology University, Chuzhou 239000, China
Corresponding author: Tie Zhang; Zhenchao Wu; Gang Zhang
Tel: +8613691110166; +8613204655989; +8618756564355; E-mail: zhangtie1979@126.com; wuzhenchao@ahau.edu.cn; zhangg@ahstu.edu.cn
DOI: https://doi.org/10.35633/inmateh-79-109

Keywords: *Crop row recognition; Maize seedlings; Deep learning model; Centreline extraction*

ABSTRACT
The seedling stage is a relatively short but critical period in the maize growth cycle, during which rapid weeding, pesticide application, and fertilization are required. Crop row centreline extraction technology based on computer vision can assist agricultural machinery in performing automated field operations, thereby improving work efficiency. Therefore, improving the accuracy of crop row centreline extraction imposes higher requirements on existing models and algorithms. In this study, a model named Synergistic Attention YOLO (SA-YOLO) was proposed. The feature extraction capability for crop rows was enhanced by introducing the spatial and channel synergistic attention module and designing the A2C2f module integrated with switchable atrous convolution. In addition, a crop topological skeleton feature point extraction strategy and a collaborative fitting method combining principal component analysis and least squares was integrated to accurately extract crop row centrelines from the skeleton feature points of crop pixels within the segmented region of interest. Comparative experiments showed that the SA-YOLO model achieved competitive performance, with an average precision at IoU threshold 0.5 (AP_{50}) of 99.1%, and a mask Intersection over Union (IoU_{mask}) of 83.8%, while maintaining a lightweight architecture with only 3.72 M parameters. The mean angle error (A_{mean}) of crop row centerline extraction was 0.590°, and the mean normalized lateral error (L_{mean}^{norm}) was 0.357%. This study provides a new approach for exploring crop row centerline extraction in agriculture and can further enrich the theoretical and technical foundation for visual navigation of agricultural robots.

摘要
苗期是玉米生长周期中相对较短但关键的时期，需要快速完成除草、施药、施肥等工作。基于计算机视觉的作物行中心线提取技术可以辅助农业机械进行自动化田间作业提高工作效率。因此，作物行中心线提取精度的提升对现有模型与算法提出了更高的要求。本研究提出了一种名为 SA-YOLO 的模型，通过引入 SCSA 注意力模块和设计的 A2C2f_SAConv 模块增强了对作物行特征的提取能力。此外，还集成了作物拓扑骨架特征点提取策略与 PCA-LSM 协同拟合方法，通过分割输出的 ROI 区域内作物像素的骨架特征点来精确提取作物行中心线。对比实验表明，SA-YOLO 模型实现了具有竞争力的性能，其 AP_{50} 为 99.1％，IoU_{mask} 为 83.8％，同时保持轻量级架构，参数仅为 3.72M。作物行中心线提取产生的平均角度误差为 0.590°，归一化横向误差为 0.357%。该研究为探索农业作物行中心线提取提供了新的思路，可以进一步丰富农业机器人视觉导航的理论和技术基础。

1. INTRODUCTION
As one of the most important food crops worldwide, maize plays a key role in global food security. Achieving efficient and intelligent maize production is an important pathway to ensure food supply capacity. In field management during the maize seedling stage *(Shahid et al., 2024)*, rapid and accurate recognition of maize row centrelines is an important foundation for autonomous navigation of agricultural machinery *(Liu et al., 2023; Liu et al., 2024b)*, precision agricultural operations *(Chamara et al., 2023; Huang et al., 2020)*, and crop phenotyping analysis.

Therefore, constructing an accurate and efficient maize row centreline recognition method through intelligent means is of great significance for improving maize production efficiency and sustainable development capability.

With the gradual introduction of sensor technology and agricultural Internet of Things technology into modern agriculture, the methods for crop row centreline extraction have become increasingly diversified. Current research mainly focuses on extracting centrelines from two types of data: crop images *(Song et al., 2023)* and point clouds *(Jiang et al., 2025)*. Among these, crop point cloud data are often acquired using sensors such as light detection and ranging (LiDAR) *(Liu et al., 2024a)* and ultrasonic sensors *(Bronson et al., 2021)*. Point clouds can directly reflect the row structure of crops in three-dimensional space, but the high complexity of acquisition and processing limits their widespread application in field operations requiring high real-time performance *(Luo et al., 2021; Fan et al., 2023)*. In contrast, RGB image-based methods have become the most commonly used data source for field row extraction due to their low acquisition cost and fast processing speed. However, relying solely on colour information makes it difficult to stably distinguish crops from soil under complex conditions such as illumination changes and weed interference, necessitating enhanced crop feature representation. Traditional methods enhance crop row features through operations such as excess green segmentation *(Ban et al., 2024)* and morphological operations *(Cai et al., 2026)* on RGB images. However, these methods are susceptible to field illumination, weeds, and other factors. In complex field environments, maize seedlings are short and sparse, occupy few pixels in the image, and lack sufficient morphological and textural information, making it difficult to effectively distinguish them from soil, residual film, and early-stage weeds *(Kim et al., 2023)*.

Recently, with the continuous development of deep learning technologies, many studies have improved the accuracy of crop row centrelines by continuously refining deep learning networks and post-processing fitting methods. In terms of deep learning networks, multi-scale feature extraction modules, attention mechanisms, or lightweight convolutions have been designed to improve segmentation accuracy while maintaining real-time performance *(Wang et al., 2023)*.

Lv et al. (2026) proposed a DAC feature fusion architecture based on YOLOv11s and adopted LAMP pruning optimization. The resulting YOLO-DP network achieved 93.8% mAP_{50} in complex orchard environments. In the post-processing fitting stage, depending on different annotation strategies, feature point extraction methods also vary. Existing annotation strategies are mainly divided into two categories: annotating specific parts of each crop plant and annotating each entire crop row as a whole. Current research on annotating specific parts of each crop plant has gradually refined from the whole plant to more morphologically stable parts such as plant cores or stems *(Diao et al., 2023; Li et al., 2023)*. This method, however, incurs high annotation cost and may lead to large errors in crop row centrelines due to missed or false detections. In contrast, the method of annotating an entire crop row as a connected region can directly guide the network to learn the row structure features of crops and significantly reduce annotation cost.

Some researchers have extracted feature points by methods such as vertical cutting of pixel strips to obtain centroids or centre points *(Han et al., 2026)*. Yet, this feature point extraction method requires high segmentation accuracy. Because the row spacing of maize seedlings is narrow, adjacent rows are prone to visual adhesion, and uneven emergence or high planting density may cause local staggered interruptions *(Gao et al., 2023)*, all of which can lead to deviation of the fitted centreline. Other researchers have combined deep learning algorithms with traditional feature enhancement methods to extract feature points.

For example, the Excess Green operator and Otsu method are used to segment crops and soil background in the region of interest (ROI), and then Features from Accelerated Segment Test (FAST) corner detection is used to extract crop feature points *(Yang et al., 2023)*. Nevertheless, the FAST corner detection method *(Chen et al., 2021)* mainly targets edges and texture-rich areas and does not act on the crop main stem, which may eventually cause deviation and instability in feature point extraction. In the stage of centreline fitting based on extracted feature points, studies have used fitting algorithms such as the Least Squares Method (LSM) *(Luo et al., 2025)*, Hough Transform (HT) *(Chen et al., 2020)*, and Random Sample Consensus (RANSAC) *(Jin et al., 2025)* to extract crop centrelines. However, the LSM algorithm is sensitive to outliers; the HT algorithm has high computational complexity and introduces errors due to discretization of the parameter space; and the RANSAC algorithm suffers from fluctuating fitting results due to the instability of iterative random sampling and high computational overhead, with centreline errors mostly exceeding 3°, making it difficult to meet the high accuracy requirements of agricultural machinery navigation.

Therefore, the specific contributions of this study to address the above main problems are summarized as follows:

(a) This study provides an open-source Corn Seedling Row (CSR) dataset, which offers a data foundation for related agricultural navigation research. The dataset can be publicly accessed at https://github.com/Possibility007/Corn-Seedling-Row.

(b) This study develops an open-source deep learning model, Synergistic Attention YOLO (SA-YOLO), which can accurately and efficiently segment crop rows, providing a lightweight perception solution for autonomous visual navigation of agricultural robots.

(c) This study proposes a principal component analysis and least squares method (PCA-LSM) collaborative optimization method based on crop topological skeleton feature points for crop row centreline extraction.

(d) The code is publicly available at https://github.com/yyyyyyu-git/SA-YOLO.

2. MATERIALS AND METHODS

The proposed method consists of five main processes. First, an RGB camera was used to collect maize seedling images. The rows were annotated to establish a maize seedling row dataset. Maize seedling rows were segmented based on the SA-YOLO model. ROI extraction and Jet mapping were used to enhance maize seedling features. Finally, based on the extracted skeleton feature points, principal component analysis (PCA) was used to determine the main direction, and then LSM was used to recognize the row centrelines. A schematic overview of the method is shown in Fig. 1.

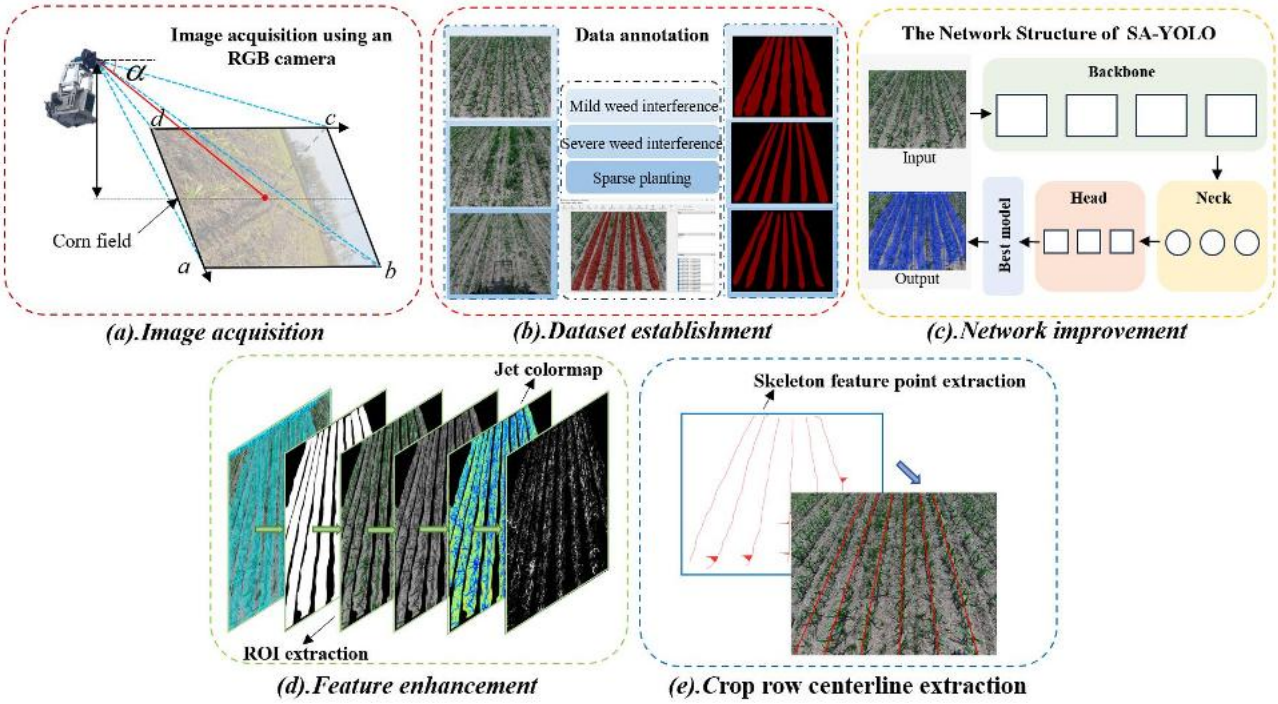


Fig. 1 - Schematic diagram of the overall workflow

2.1 Field image acquisition of maize seedlings

The maize seedling images used in this study were captured at the WanDong Comprehensive Experimental Station of Anhui Agricultural University in Mingguang County, Chuzhou City, Anhui Province (latitude 32°45′20.6″ N, longitude 118°6′55.9″ E, altitude 46 m), from July 5 to July 10, 2025. The image acquisition device was an Ailiguang ALI2312-SCH-SABA-IP67 monocular RGB camera, capturing images at 1920×1536 pixels. The camera was installed at a vertical height of 2.5 m above the ground, with a tilt angle of 50°. A total of 941 original images were collected, all saved in JPG format. The image acquisition scene and method are shown in Fig. 2.

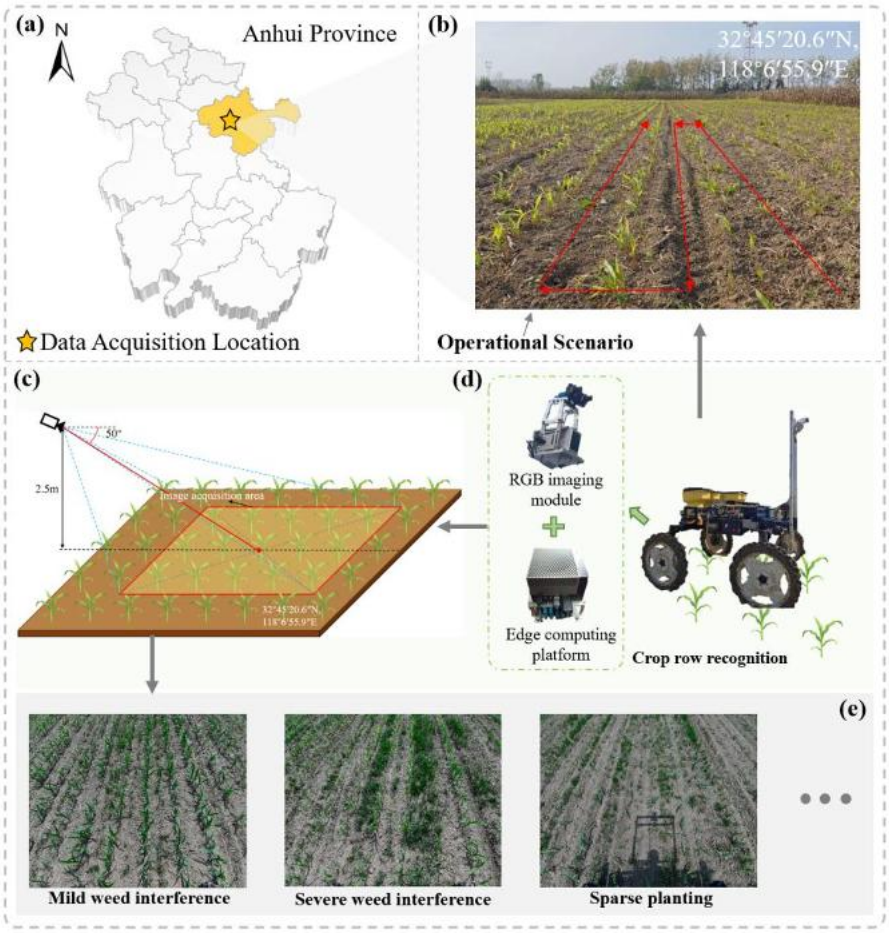


Fig. 2 - Schematic diagram of image acquisition location and method

(a) Data acquisition location; (b) Data acquisition scene; (c) Data acquisition method; (d) Data acquisition device; (b) (e) Example of acquired image.

2.2 Image Annotation and Data Preprocessing

The model in this study is an instance segmentation model for maize seedling rows. Labelme was used for image annotation, and each maize row was annotated separately. Each maize row was annotated as an independent instance, with its mask covering an entire row of maize seedlings, forming a continuous management unit. The generated .json files were converted into .txt files required for model training. After annotation, the image dataset was split for better model training. The image dataset contained a total of 941 images, which were divided into training, validation, and test sets at a ratio of 7:1:2. An annotation example for the seedling maize dataset is shown in Fig. 3, including multiple scenes such as mild weed interference, severe weed interference, and sparse planting.

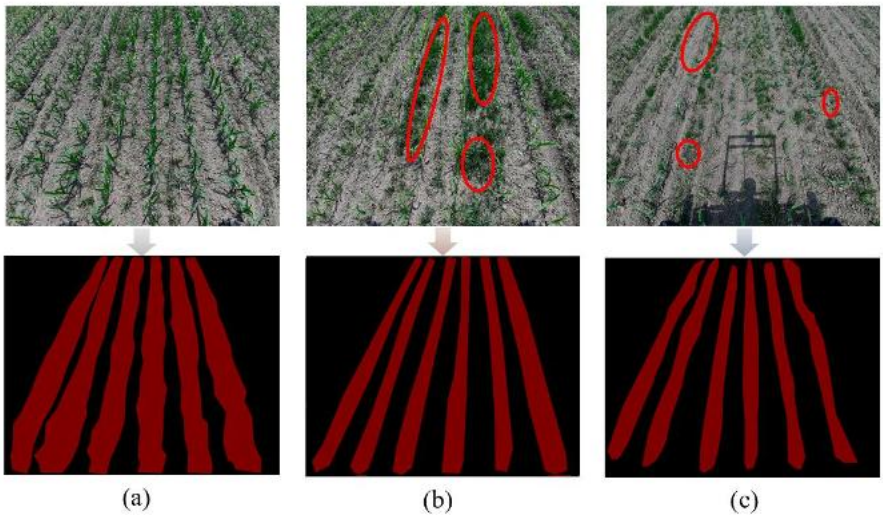


Fig. 3 - Example of dataset annotation

(a) Mild weed interference scene; (b) Severe weed interference scene; (c) Sparse planting scene.

2.3 SA-YOLO model

To address the problems of small plants, inter-row adhesion, and complex background in maize seedling row segmentation, an improved model named SA-YOLO was proposed based on YOLOv12n-seg. The SCSA attention module was introduced into the fast pooling layer of the backbone network to enhance the perception of row structure, and the designed A2C2f_SAConv module was introduced into the neck network to improve feature extraction capability, thereby improving segmentation accuracy while maintaining lightweight characteristics. The structure of the improved SA-YOLO is shown in Fig. 4.

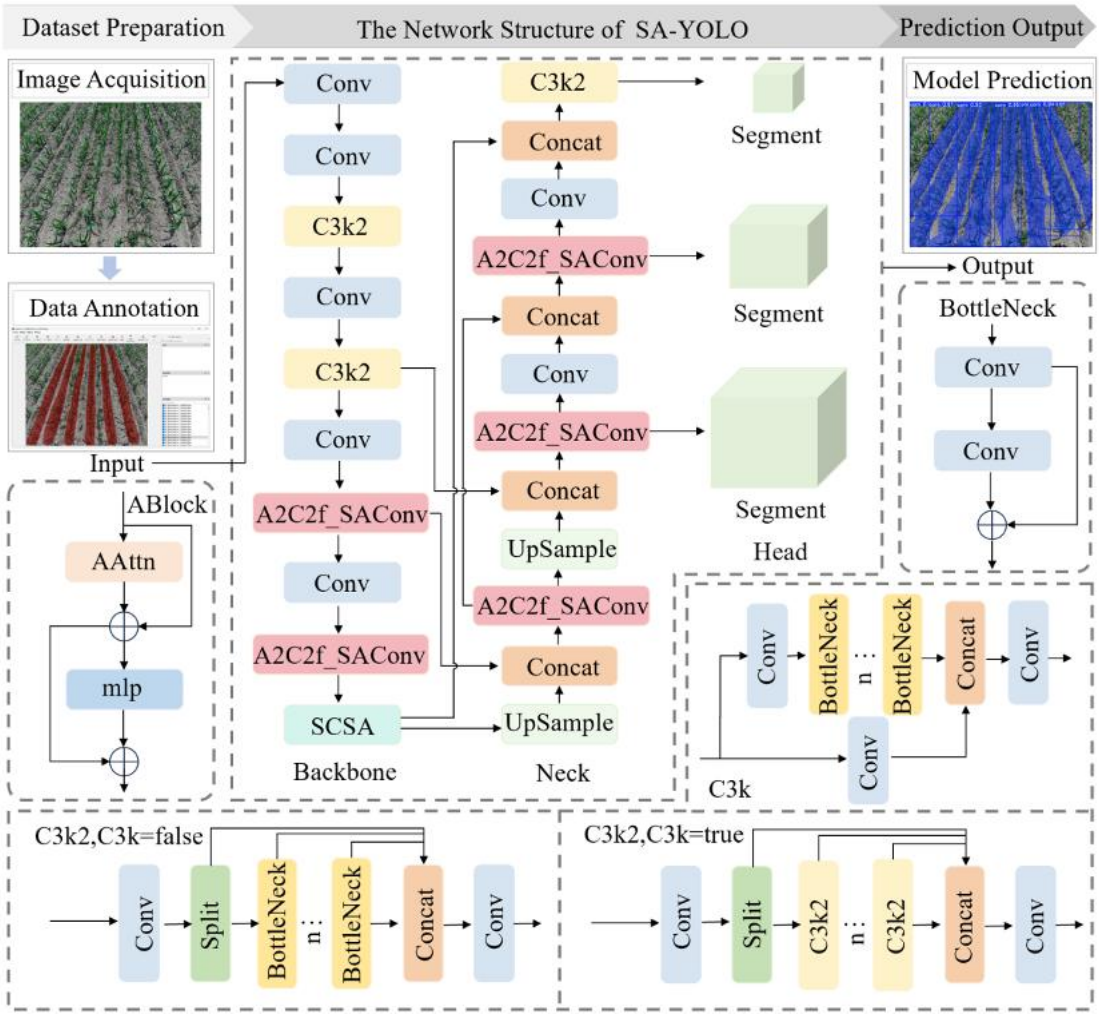


Fig. 4 - Structure of the SA-YOLO model

2.3.1 YOLOv12n-seg model

YOLOv12n-seg is a lightweight instance segmentation version of the YOLOv12 series. Its structure mainly consists of four parts: the input layer, attention-enhanced backbone, multi-scale fusion neck, and segmentation detection head. The input layer preprocesses the image to improve model robustness to different sizes and lighting conditions. The backbone network adopts the region attention module (A^2) and the residual efficient layer aggregation network (R-ELAN), reducing computational complexity while enhancing feature extraction capability. The neck network fuses multi-scale semantic and detail information through a bidirectional feature pyramid structure, improving model convergence and feature representation. The segmentation detection head integrates object localization, classification, and pixel-level segmentation to output instance bounding boxes and precise masks. Although this baseline model performs well in general scenes, in complex field environments, maize seedling row segmentation still faces challenges such as detail loss and mis-segmentation in adhesive regions, necessitating targeted improvements.

2.3.2 SCSA attention module

To enhance the model's perception of the spatial layout and key features of seedling rows, the Spatial and Channel Synergistic Attention (SCSA) module *(Si et al.,2025)* was introduced after the fast pooling layer of the YOLOv12n-seg backbone network. SCSA consists of a Shared Multi-Semantic Spatial Attention (SMSA) module and a Progressive Channel-wise Self-Attention (PCSA) module connected in series. Its structure is shown in Fig. 5.

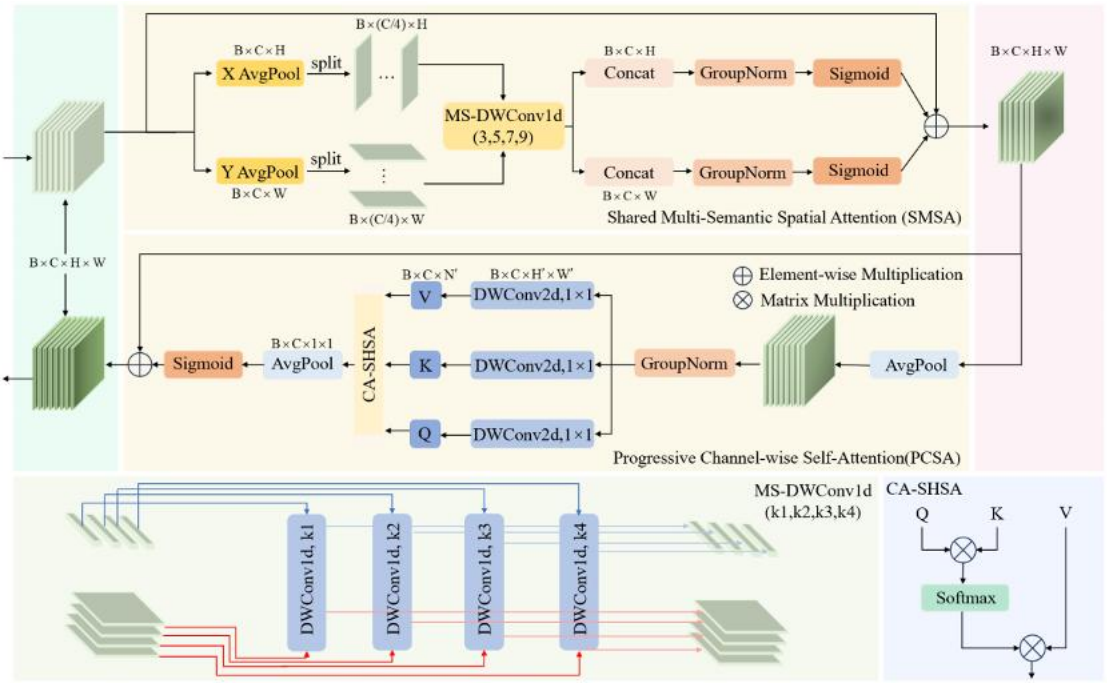


Fig. 5 - Structure of the SCSA attention mechanism module

The SMSA module first performs global average pooling on the input feature map along the height and width dimensions, obtaining two one-dimensional feature sequences. Each sequence is then evenly divided into K sub-features to extract spatial information at different semantic levels in parallel. For each sub-feature, one-dimensional depthwise separable convolutions with kernel sizes of 3, 5, 7, and 9 are used to capture multi-scale spatial context. The height and width dimension features are then aligned through shared convolution, and after concatenating the sub-features, group normalization and Sigmoid activation are applied to generate spatial attention weights. The calculation formulas are shown in (1)~(3).

$$\mathrm{Attn_H}=\sigma\left(\mathrm{GH_K^N}\left(\mathrm{Concat}\left(\mathrm{H_1^{\tilde{X}}},\mathrm{H_2^{\tilde{X}}},\cdots,\mathrm{H_K^{\tilde{X}}}\right)\right)\right) \tag{1}$$

$$\mathrm{Attn_W}=\sigma\left(\mathrm{GW_K^N}\left(\mathrm{Concat}\left(\mathrm{W_1^{\tilde{X}}},\mathrm{W_2^{\tilde{X}}},\cdots,\mathrm{W_K^{\tilde{X}}}\right)\right)\right) \tag{2}$$

$$\mathrm{SWSA(X)=X_s=Attn_H\times Attn_W\times X} \tag{3}$$

where:

$\sigma(\cdot)$ denotes Sigmoid normalization, and $GH_K^N(\cdot)$ and $GW_K^N(\cdot)$ denote group normalization along the H and W dimensions with K groups, respectively.

The PCSA module further performs channel-wise self-attention enhancement on the spatial features output by SMSA. First, progressive average pooling is applied to X_S to reduce resolution while preserving key spatial structure. Then, three independent two-dimensional depthwise convolutions are used to generate Query (Q), Key (K), and Value (V). Single-head self-attention is performed in the channel domain to model inter-channel dependencies. Finally, global pooling and Sigmoid activation are applied to generate channel attention weights, which are multiplied by X_S to obtain the final output. The calculation formulas are shown in (4)~(7).

$$\mathrm{X_p=Pool_{(7,7)}^{(H,W)\to(H',W')}(X_s)} \tag{4}$$

$$\mathrm{Q=F_{proj}^{Q}(X_p),K=F_{proj}^{K}(X_p),V=F_{proj}^{V}(X_p)} \tag{5}$$

$$\mathrm{X_{attn}=Attn(Q,K,V)=Softmax}\left(\frac{\mathrm{QK^T}}{\sqrt{C}}\right)\mathrm{V} \tag{6}$$

$$\mathrm{PCSA(X_s)=X_c=X_s\times\sigma}\left(\mathrm{Pool_{(H',W')}^{(H',W')\to(1,1)}(X_{attn})}\right) \tag{7}$$

where: $Pool_{(k,k)}^{(H,W)\to(H',W')}(\cdot)$ denotes a pooling operation with kernel size $k\times k$ that resizes the resolution from (H,W) to (H',W'). $Fproj(\cdot)$ denotes the linear projections for generating query, key, and value.

SMSA effectively captures multi-semantic spatial information of seedlings in complex field environments through multi-scale convolution, while PCSA enhances feature consistency and suppresses redundancy through progressive channel interaction. The SCSA module significantly improves the model's representation ability of fine seedling features and their spatial row distribution while maintaining low computational overhead, providing more robust feature input for subsequent segmentation tasks.

2.3.3 A2C2f_SAConv module

To address the limitation of standard convolution with a fixed receptive field that cannot adaptively match features at different scales, the A2C2f module in the network was replaced with an improved module incorporating Switchable Atrous Convolution (SAConv) *(Qiao et al.,2021)*, named A2C2f with Switchable Atrous Convolution (A2C2f_SAConv). Its structure is shown in Fig. 6b. SAConv dynamically adjusts the dilation rate and incorporates a context-aware mechanism, enabling the network to optimize multi-scale feature fusion.

The core idea of SAConv is to extend the traditional static atrous convolution into a dynamic, spatially adaptive feature extraction mechanism. Its structure is shown in Fig. 6a. It employs multiple convolution branches with different dilation rates in parallel and dynamically fuses the outputs of each branch through a lightweight, pixel-wise learned switch function, allowing each spatial position to autonomously select the most suitable receptive field based on local context. In addition, SAConv integrates global context preprocessing and postprocessing modules, which perform global average pooling and convolution to calibrate features globally, further improving feature consistency and discriminability. The calculation formulas are shown in (8) and (9).

$$S(x)=\sigma\left(Conv_{1\times1}\left(AvgPool_{5\times5}(x)\right)\right) \tag{8}$$

$$y=S(x)\cdot Conv(x,w,1)+\left(1-S(x)\right)\cdot Conv(x,w+\Delta w,r) \tag{9}$$

where:

The switch function *S(x)* is generated by a 5×5 average pooling layer followed by a 1×1 convolutional layer and normalized by the activation function σ. Conv(x,w,r) denotes the convolution operation with weight *w*, hyperparameter *r*, and trainable weight Δw.

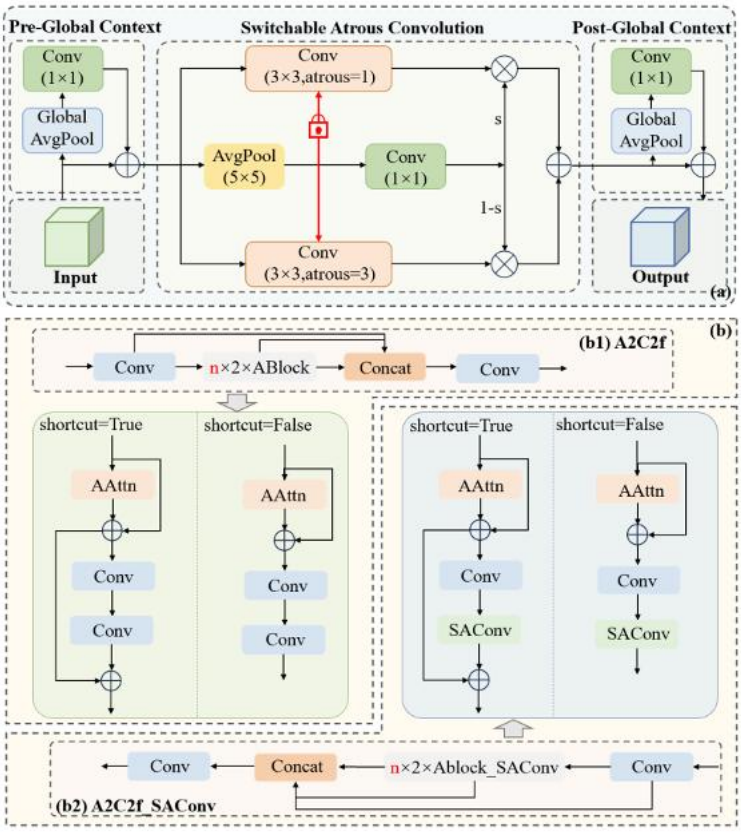


Fig. 6 - Structure of the SAConv module

(a) SAConv structure; (b) Difference between the A2C2f module and the A2C2f_SAConv module.

2.4 Crop row centreline fitting

In the crop row centreline fitting process, contour detection is a key factor affecting the accuracy of the fitted centreline. In this study, the segmentation results were used to extract the ROI region, and the skeleton feature points were extracted from the binary image of crops within the ROI region. Finally, PCA was used to determine the main direction, and LSM was used to fit these skeleton feature points to obtain the centrelines of maize seedling rows.

2.4.1 Crop row skeleton feature point extraction

The improved SA-YOLO model was used to infer the positions of maize seedling rows through instance segmentation. Masks were generated from the inferred segmentation regions, and bitwise operations were performed with the original image to extract the ROI region *(Luz et al.,2024)*, which eliminated a large amount of interference information and saved computational cost. The extraction process is shown in Fig. 7. After the ROI region was extracted, grayscale processing was applied to the image *(Rodríguez et al., 2021)*. However, because the colour features of maize seedlings and ground soil are similar in grayscale images, direct binarization made it difficult to effectively segment maize. Pseudo-colour processing technology *(Bayareh et al.,2021)* significantly enhances image distinguishability by assigning different colour maps to different gray values; this method has been widely used in fields such as medical imaging and meteorological analysis. Among them, the Jet mapping, as a typical pseudo-colour algorithm, is often used to highlight detailed features in images due to its high colour contrast. After Jet mapping, the visual features of the maize seedling regions were significantly enhanced, creating favourable conditions for subsequent processing. After maize seedling feature enhancement, binarization was applied to the image *(Surulivelu et al.,2026)*. Skeleton feature points were extracted from the binarized image. A morphological skeletonization method was used to iteratively delete edge pixels while preserving region connectivity, gradually thinning the crop rows into a single-pixel-wide topological skeleton. This process not only extracted the central feature points of the crop rows but also fully preserved their overall directional trend. The resulting skeleton feature point set was continuous, dense, and geometrically meaningful, faithfully reflecting the morphological characteristics of the crop rows.

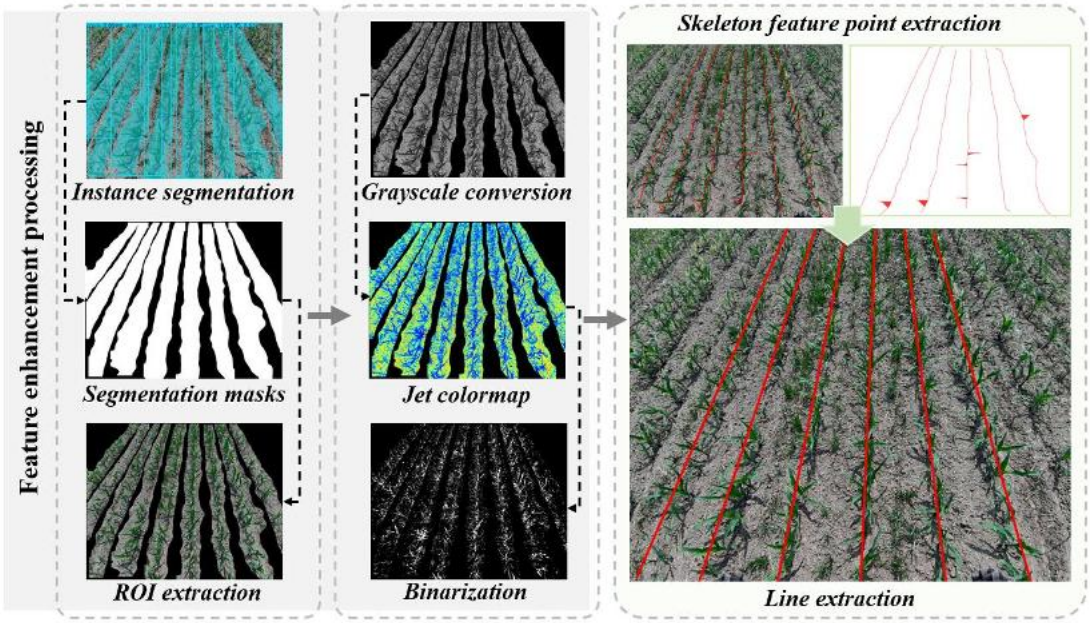


Fig. 7 - Flowchart of crop row centreline fitting

2.4.2 Crop row centreline fitting

PCA robustly estimates the dominant direction of a point set, which corresponds to the eigenvector associated with the largest eigenvalue. However, because the fitted straight line is determined only by the direction of the first principal component without optimizing errors in specific directions, it remains sensitive to outliers. Using LSM alone, although it minimizes the error along a preset independent variable direction, if that direction does not match the actual deviation direction of interest, the resulting line fails to accurately reflect the geometric characteristics of the data. Moreover, its robustness to outliers is poor, and a few outliers can cause the fitting result to deviate significantly from the true trend.

Therefore, this study proposed a collaborative PCA-LSM method. The skeleton feature points were used to fit a straight line that best represents the crop rows. First, PCA was used to determine the main direction of the point set. Then, based on the relative inclination angle between this main direction and the coordinate axes, an appropriate LSM form was selected. This method combines the directional robustness of PCA with the precise fitting capability of LSM, providing better tolerance to outliers and enabling extraction of crop row centrelines that conform to the overall distribution of the data. A schematic comparison of the three methods is shown in Fig. 8.

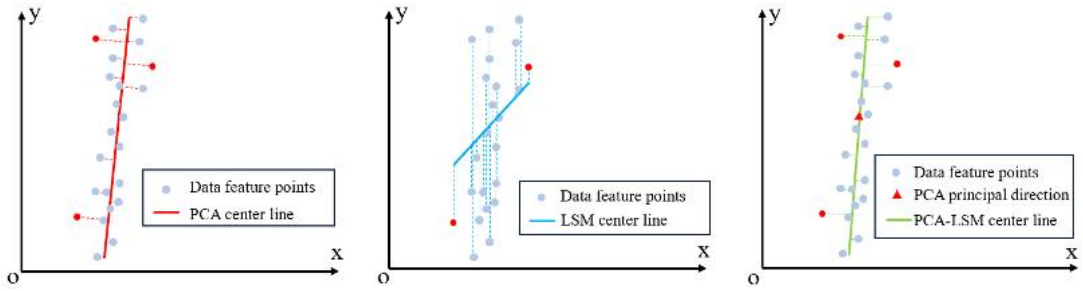
The calculation formula for the PCA principal direction is shown in Equation (10):

$$C=\frac{1}{N-1}\sum_{i=1}^{N}(p_i-\bar{p})(p_i-\bar{p})^T \tag{10}$$

where: $\bar{P}$ is the centroid of the point set, $P_i=(x_i,y_i)$, and the principal direction vector is denoted as $v=(v_x,v_y)$.

The method for selecting the appropriate least squares form is shown in Equation (11):

$$S_{\epsilon}^2=\begin{cases}\min\limits_{k,b}\sum_{i=1}^{N}\left(x_i-(ky_i+b)\right)^2, & \text{if } |v_y|>|v_x|\\ \min\limits_{m,b}\sum_{i=1}^{N}\left(y_i-(mx_i+b)\right)^2, & \text{if } |v_y|<|v_x|\end{cases} \tag{11}$$



(a) (b) (c)

Fig. 8 - Schematic diagrams of three methods

(a) Schematic diagram of the PCA method; (b) Schematic diagram of the LSM method; (c) Schematic diagram of the PCA-LSM method.

3. RESULTS AND DISCUSSION

3.1 Training environment and evaluation metrics

3.1.1 Parameter settings and model training

The model training platform in this experiment used an NVIDIA GeForce RTX 4050 GPU, a 13th Gen Intel(R) Core(TM) i7-13620H processor, 6 GB of video memory, and the Windows 11 operating system. The programming language was Python 3.12, the software platform was PyCharm 2023.2.4, the PyTorch framework version was 2.0.0, and the CUDA version was 11.8. Stochastic gradient descent was used for training. The image resolution was set to 640×640 pixels, the momentum was 0.937, and the weight decay coefficient was 0.0005. The initial learning rate was set to 0.01, and the number of training epochs was 100.

3.1.2 Segmentation evaluation

To evaluate the performance of the improved network for maize seedling row segmentation in field scenes, metrics at the mask level, including Precision (*P*), Recall (*R*), Average Precision (AP_{50}), and mask Intersection over Union (IoU_{mask}), were adopted to assess model performance. Among them, AP_{50} is the area under the precision-recall curve, which comprehensively measures the model's detection capability for a single class and serves as the core metric for evaluating overall network performance. The calculation formulas for the specific parameters are shown in Equations (12)~(15).

$$P=\frac{TP}{TP+FP} \tag{12}$$

$$R=\frac{TP}{TP+FN} \tag{13}$$

$$AP_i=\int_0^1 P_i(R_i)dR_i \tag{14}$$

$$IoU_{mask}=\frac{Area(Mask_{predicted}\cap Mask_{ground\_truth})}{Area(Mask_{predicted}\cup Mask_{ground\_truth})} \tag{15}$$

where:

TP (True Positive), FP (False Positive), and FN (False Negative) in Equations (12)~(14) are defined at the instance level: TP is the number of correctly segmented maize seedling row instances, FP is the number of incorrectly segmented instances, and FN is the number of missed instances. Equation (15) computes the pixel-level mask IoU for a single matched instance using mask areas.

3.1.3 Centreline extraction evaluation

To quantify the accuracy of the extracted crop row centrelines, evaluation metrics based on the lateral error and angle error between the predicted centreline and the ground truth centreline were constructed. The test image set was defined as S_{images}, the total number of images was $k = |S_{images}|$, i=1, 2, …, k. The mean normalized lateral error (L_{mean}^{norm}), the standard deviation of lateral error (L_{std}^{norm}), the mean angle error (A_{mean}), and the standard deviation of angle error (A_{std}) were used to reflect the average deviation level of the predicted navigation line relative to the ground truth centerline across all images. Smaller values indicate higher overall fitting accuracy. The calculation principle of this method is shown in Fig. 9. The formulas for comprehensive evaluation of navigation line accuracy and stability are shown in Equations (16)~(19).

$$L_{mean}^{norm} = \frac{1}{k} \sum_{s \in S_{images}} L_s^{norm} \tag{16}$$

$$L_{std}^{norm} = \sqrt{\frac{1}{k} \sum_{s \in S_{images}} (L_S^{norm} - L_{mean}^{norm})^2} \tag{17}$$

$$A_{mean} = \frac{1}{k} \sum_{i=1}^{k} \theta_i \tag{18}$$

$$A_{std} = \sqrt{\frac{1}{k-1} \sum_{i=1}^{k} (\theta_i - A_{mean})^2} \tag{19}$$

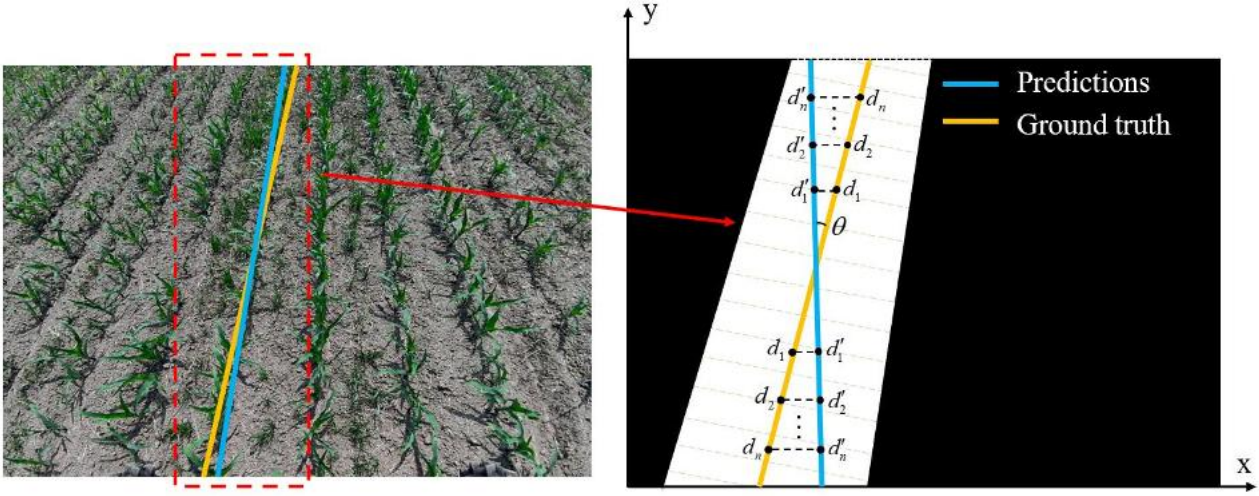


Fig. 9 - Schematic diagram of centreline extraction accuracy evaluation

3.2 Comparison of different segmentation models

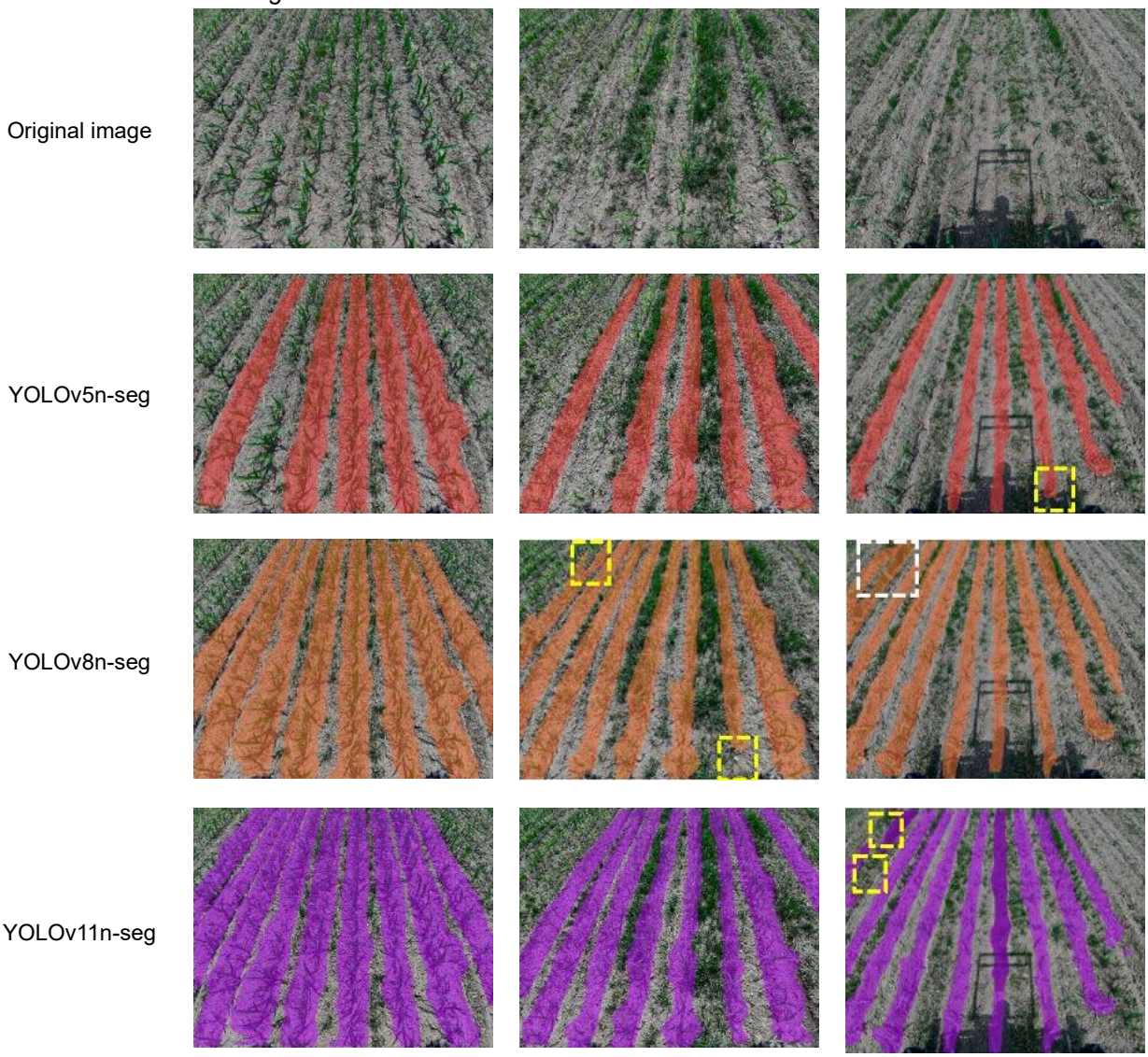
To validate the performance of the SA-YOLO model, comparative experiments were conducted against YOLOv5n-seg, YOLOv8n-seg, YOLOv11n-seg, and the baseline YOLOv12n-seg in a complex maize field environment at the seedling stage. The results are shown in Table 1. The SA-YOLO model achieved the best segmentation accuracy, with an AP_{50} of 99.1% and an IoU_{mask} of 83.8%, which was 1.5% higher than the suboptimal YOLOv8n-seg model. It also maintained leading performance in both precision and recall, indicating that the model can more completely and accurately identify maize row regions. From a lightweight perspective, although YOLOv5n-seg had the smallest number of parameters, its AP_{50} was relatively low. The YOLOv11n-seg model achieves the same P and AP_{50} as the SA-YOLO model, but its IoU_{mask} is 2.0 percentage points lower. Under a lightweight configuration with only 3.72 M parameters and 8.9 Giga Floating Point Operations (GFLOPs) of computation, SA-YOLO achieved an inference speed of 161.29 Frames Per Second (FPS), which was an improvement over the baseline YOLOv12n-seg's 153.85 FPS. Compared with the baseline YOLOv12n-seg, SA-YOLO increased AP_{50} by 0.3 percentage points and IoU_{mask} by 5.0 percentage points, validating the effectiveness of the proposed improved modules in enhancing feature extraction capability and segmentation accuracy.

Table 1

Comparison of detection performance of different network models

Model	P (%)	R (%)	AP_{50} (%)	AP_{50-95} (%)	IoU_{mask} (%)	FPS	Inference Times (ms)	Parameters (M)	GFLOPs	Model size (MB)
YOLOv5n-seg	96.5	94.7	98.5	65.2	82.2	117.65	8.5	**1.88**	**6.7**	**4.1**
YOLOv8n-seg	**96.6**	98.0	98.9	**66.8**	82.3	**232.56**	**4.3**	3.26	12.0	6.8
YOLOv11n-seg	96.5	**98.4**	**99.1**	65.2	81.8	185.19	5.4	2.83	10.2	6.0
YOLOv12n-seg	95.6	97.4	98.8	64.2	78.8	153.85	6.5	2.81	10.2	6.1
SA-YOLO	96.5	98.0	**99.1**	64.0	**83.8**	161.29	6.2	3.72	8.9	7.8

Maize seedling row images from different scenes, including mild weed interference, severe weed interference, and sparse planting, were randomly selected from the dataset for recognition experiments. As shown in Fig. 10, under the mild weed interference scene, the SA-YOLO model successfully segments 9 rows of maize seedlings, while other models all suffered from missed segmentation. Under the severe weed interference scene, YOLOv8n-seg had incomplete segmentation boundaries within the yellow box, affecting row continuity, and YOLOv12n-seg had false detection of weeds as maize rows within the red box. Under the sparse planting scene, the models exhibited blurred boundaries. YOLOv8n-seg and SA-YOLO showed some adhesion between rows within the white box. Across the three scenes, SA-YOLO successfully segmented the most rows of maize seedlings.



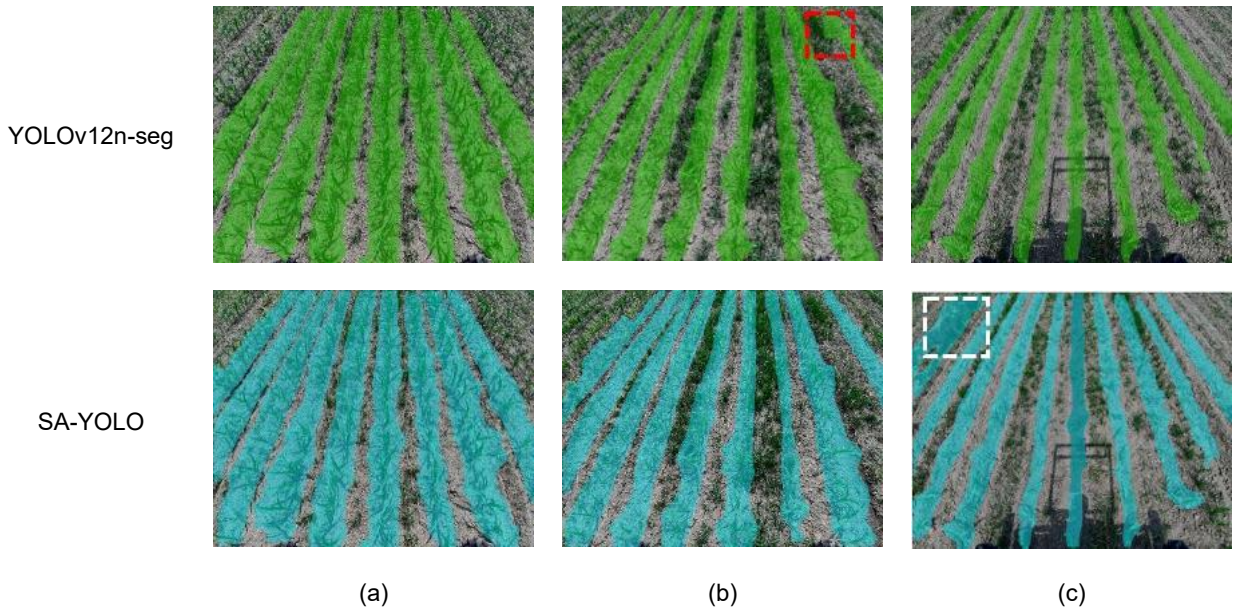


Fig. 10 - Segmentation results of five models under different scenes

(a) Segmentation results in mild weed interference scene; (b) Segmentation results in severe weed interference scene; (c) Segmentation results in sparse planting scene. The yellow boxes indicate incomplete segmentation regions, the white boxes indicate inter-row adhesion regions, and the red boxes indicate false segmentation of weeds.

Based on the above data, the improved SA-YOLO model in this study can accurately segment maize seedling rows in the above scenes, demonstrating that the introduction of the SCSA attention mechanism and the designed A2C2f_SAConv module can achieve better maize row segmentation accuracy in complex field environments, providing theoretical and technical support for the application of agricultural navigation systems *(Lopes et al., 2025)*.

3.3 Ablation experiments

To validate the effectiveness of each improved module, ablation experiments were conducted by sequentially introducing A2C2f_SAConv, SCSA and CBAM modules into the YOLOv12n-seg baseline model. The results are shown in Table 2. The baseline model achieved AP_{50}, AP_{50-95}, and IoU_{mask} of 98.8%, 64.2%, and 78.8%, respectively, on the test set. After introducing only the A2C2f_SAConv module, AP_{50} increased to 99.1%, IoU_{mask} increased by 5.0 percentage points to 83.8%, and the parameter count increased by only 0.91 M, indicating that this module effectively enhances multi-scale feature extraction capability through switchable atrous convolution while maintaining lightweight advantages *(Hu et al., 2025)*. Adding only the SCSA attention module achieved an AP_{50} of 98.9% and an IoU_{mask} of 81.6% with no increase in parameter count, validating the effectiveness of the SCSA spatial and channel synergistic attention mechanism. In contrast, introducing only the Convolutional Block Attention Module (CBAM) module gave an AP_{50} of 98.9% and an IoU_{mask} of 82.5%, with a slight increase in parameters *(Arthur et al., 2025; Guo et al., 2023)*.

Table 2

Ablation experiment results of YOLOv12n-seg

A2C2f_SA Conv	SCSA	CBAM	P (%)	R (%)	AP_{50} (%)	AP_{50-95} (%)	IoU_{mask} (%)	FPS	Inference Times (ms)	Parameters (M)	GFLOPs	Model size (MB)
×	×	×	95.6	97.4	98.8	64.2	78.8	153.85	6.5	**2.81**	10.2	**6.1**
√	×	×	96.3	**98.3**	**99.1**	64.6	**83.8**	178.57	5.6	3.72	8.9	7.7
×	√	×	95.9	98.1	98.9	64.6	81.6	163.93	6.1	**2.81**	10.2	**6.1**
×	×	√	95.6	98.0	98.9	**65.4**	82.5	**196.08**	**5.1**	2.83	9.6	**6.1**
√	√	×	96.5	98.0	**99.1**	64.0	**83.8**	161.29	6.2	3.72	8.9	7.8
√	×	√	**97.2**	96.8	99.0	64.9	83.5	181.82	5.5	3.73	**8.3**	7.8

Although optimization with a single module can improve model performance, more significant breakthroughs rely on synergy and combination among modules *(Liu et al.,2022; Shao et al., 2026; Gao et al., 2024; Meng et al., 2024)*. When both A2C2f_SAConv and SCSA were introduced, the model achieved the best performance, with AP_{50} of 99.1%, IoU_{mask} of 83.8%, *P* and *R* of 96.5% and 98.0%, respectively, and an inference speed of 161.29 FPS. However, introducing both A2C2f_SAConv and CBAM did not bring gains and reduced recall by 1.2 percentage points. Fig. 11 shows the performance curves of the ablation experiments, intuitively demonstrating the improvement in segmentation performance before and after the improvements.

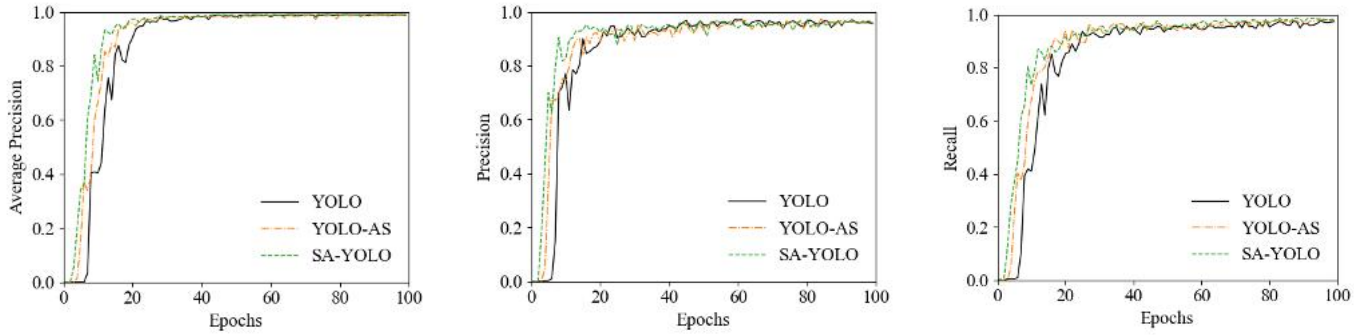


Fig. 11 - Performance curve comparison of improved algorithms

(a) Comparison of average precision curves of YOLOv12; (b) Comparison of precision curves of YOLOv12; (c) Comparison of recall curves of YOLOv12. YOLO refers to the YOLOv12n-seg model, and YOLO-AS refers to YOLOv12n-seg with the A2C2f_SAConv module.

To further visually compare and evaluate segmentation accuracy and understand the model's decision basis, heatmaps of maize seedling row image detection were used, as shown in Fig. 12. It can be seen that the heatmap of the SA-YOLO model is closer to the actual maize seedling row regions. In Fig. 12a, the boundaries indicated by the two straight lines are the boundaries that the model should accurately segment. Fig. 12b shows the heatmap of the YOLOv12n-seg baseline model, where the soil regions between adjacent crop rows exhibited weak boundary discrimination ability, leading to blurred boundaries between rows and incomplete segmentation at farther distances. Fig. 12c and Fig. 12d are heatmaps of the models with the A2C2f_SAConv convolution module and the SCSA attention mechanism module, respectively. The introduction of the A2C2f_SAConv module provided more complete activation of long maize seedling rows by expanding the receptive field, and the heatmap values at the far right were higher than those of the baseline model. The introduction of the SCSA attention mechanism module helped the model better distinguish the difference between maize seedling rows and the background, resulting in higher heatmap values at the maize seedling rows and clearer differentiation at the boundaries. Fig.12e shows the heatmap of the SA-YOLO model. Compared with the YOLOv12n-seg baseline model, the boundaries are clearer and the activation of maize seedling rows is more complete.

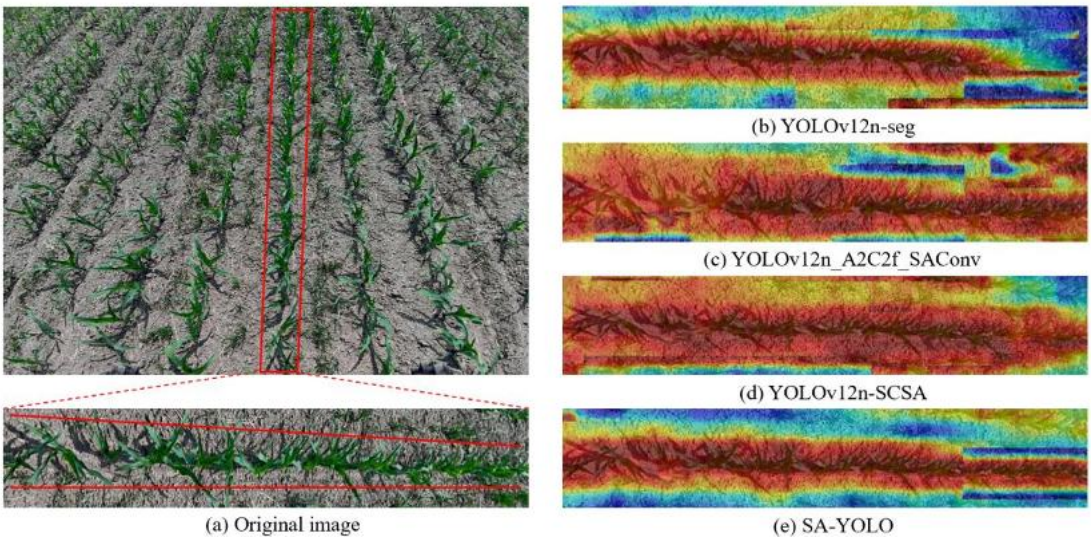


Fig. 12 - Heatmaps of maize seedling row image detection

The red regions represent the areas of greatest focus for the model, the yellow regions represent areas of secondary importance, and the blue regions represent areas with the least influence, typically representing redundant information.

3.4 Crop row centreline detection experiments

3.4.1 Crop row centreline detection using different methods

From a test dataset of 189 maize seedling row images, crop row centrelines were extracted using PCA *(Zhang et al.,2024a)*, LSM *(Ju et al.,2024)*, and the proposed PCA-LSM method, and were also compared with the traditional HT method *(Chen et al.,2025)* and the RANSAC method *(Zhang et al.,2024b)*. The quantitative results are shown in Table 3. As shown in the table, the PCA method achieved a A_{mean} of 0.613°, a L_{mean}^{norm} of 0.359%, and a mean pixel lateral error of 6.90 pixels. The LSM method achieved a A_{mean} of 0.590°, a L_{mean}^{norm} of 0.357%, and a mean pixel lateral error of 6.85 pixels. The results of the PCA-LSM method were exactly the same as those of the LSM method, with all metrics identical. The reason for this is that the maize rows in the test images were approximately vertical, causing PCA-LSM to always select the vertical fitting form, which is mathematically equivalent to LSM. Although PCA was slightly better in stability, LSM had a slight advantage in mean values. Overall, all three methods could effectively extract crop row centrelines, with angle errors all below 0.7° and pixel errors below 7 pixels, meeting the basic accuracy requirements for visual navigation of agricultural robots. The PCA-LSM method automatically degenerated to LSM on the vertical row dataset, verifying the correctness of its adaptive selection.

Table 3 Comparison of crop row centreline detection results using different methods

Fitting method	Scene	Mean angle error (°)	Mean normalized lateral error (%)	Mean pixel lateral error (px)
HT *(Chen et al.,2025)*	Maize seedling	2.600	-	10.78
RANSAC *(Zhang et al.,2024b)*	Rice transplanting	0.776	0.730	4.69
PCA	Maize seedling	0.613	0.359	6.90
LSM	Maize seedling	0.590	0.357	6.85
This study	Maize seedling	0.590	0.357	6.85

Compared with the RANSAC method, its A_{mean} of 0.776° and L_{mean}^{norm} of 0.730% were both higher than those of the proposed algorithm, while its mean pixel lateral error of 4.69 pixels was better than that of our method because of the different image resolutions. The image size in this study was 1920×1536 pixels, while the image size in that study was 1280×1024 pixels. Under the same maize seedling scene, the HT method achieved a A_{mean} of 2.600°, far higher than that of the PCA-LSM method used in this study. The reason for this is discussed as follows. Most fitting algorithms are based on object detection methods, using the center point or bottom midpoint of the detection box as feature points, which may introduce fitting errors due to discrete or missing plants. Alternatively, instance segmentation or semantic segmentation methods obtain feature points by calculating the centroids of connected regions or directly extract the skeleton of inter-row regions, both of which can cause overall deviation of the navigation line due to segmentation breaks or mis-segmentation. Centreline extraction methods that directly act on the crop itself usually use corner detection algorithms such as FAST to extract feature points. The feature points extracted by such methods are mainly from the leaf regions of the crop rather than the main stem regions of the crop rows, ultimately resulting in fitted centrelines that deviate from the crop main stem and are unstable. Compared with existing mainstream methods, the row-unit instance segmentation annotation adopted in this study provides a more structurally consistent learning target for the model. Meanwhile, the skeleton feature point extraction method proposed in this study directly acts on the crop itself, using an image thinning algorithm to extract the topological midline of the crop. This method not only preserves the complete geometric orientation information of the crop rows but also has a natural ability to suppress noise at segmentation edges. Traditional methods require high segmentation accuracy, whereas this study only uses segmentation to extract the ROI region to reduce noise interference, avoiding overall deviation of the navigation line due to segmentation breaks or mis-segmentation, and providing a feature point set with more uniform spatial distribution and higher geometric fidelity for subsequent navigation line fitting.

3.4.2 Crop row centreline detection of different models in complex scenes

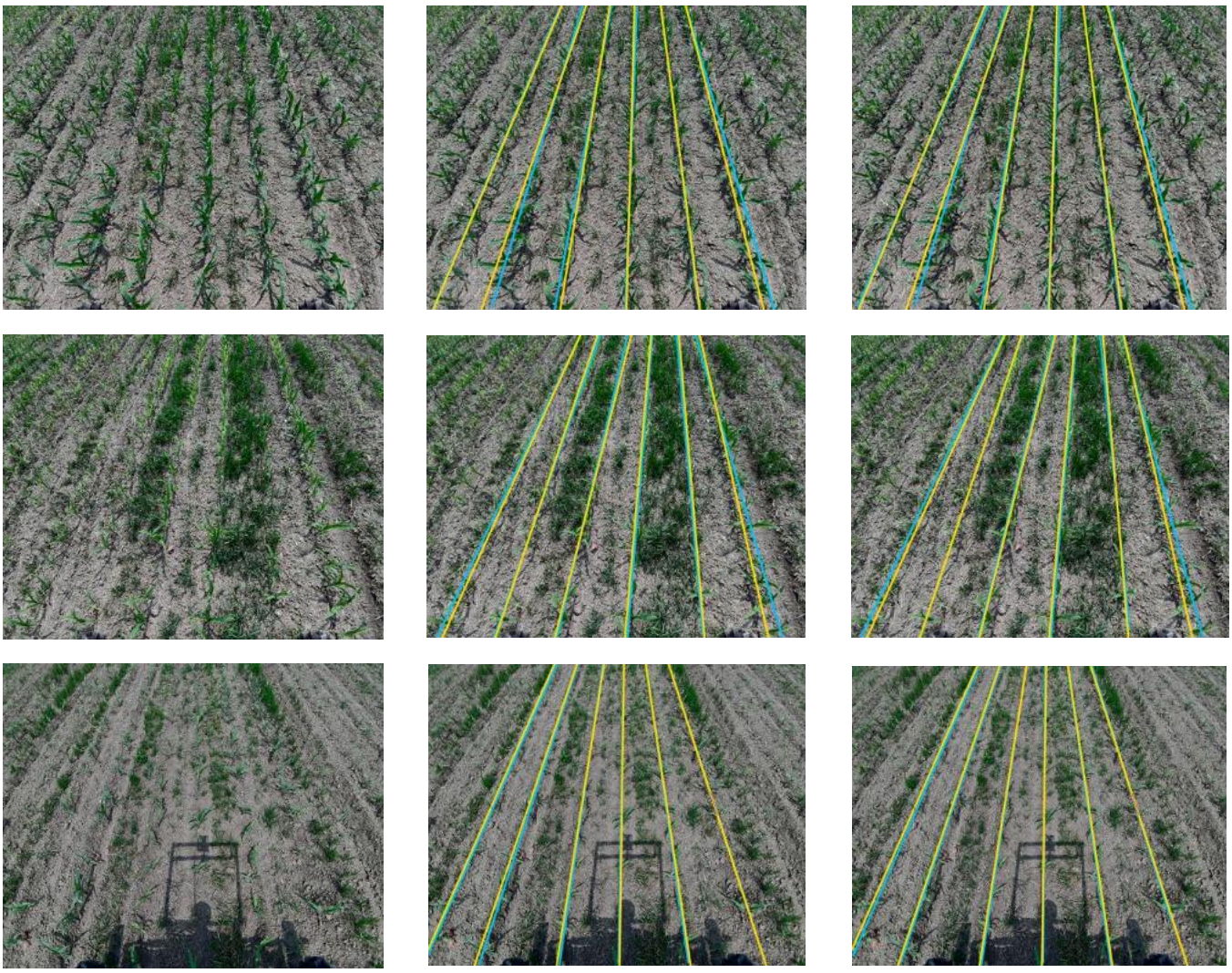
To validate the effectiveness of the proposed SA-YOLO model in crop row centreline extraction, comparative experiments were conducted against the baseline YOLOv12n-seg model. The error statistics of the two models are shown in Table 4.

Table 4

Comparison of crop row centreline detection results of different models

Model	Angle error (°)		Normalized lateral error (%)	
	Mean	Std	Mean	Std
YOLOv12n-seg	0.622	0.530	0.379	0.433
SA-YOLO	0.590	0.498	0.357	0.428

The proposed SA-YOLO model outperformed the baseline YOLOv12n-seg model in all metrics. In terms of angle error, the mean of SA-YOLO decreased from 0.622° to 0.590°, a relative reduction of 5.1%; the standard deviation decreased from 0.530° to 0.498°, a relative reduction of 6.0%. This indicates that the row lines extracted by SA-YOLO are closer to the ground truth rows, with better stability across different scenes. In terms of normalized lateral error, the mean of SA-YOLO decreased from 0.379% to 0.357%, a relative reduction of 5.8%. The standard deviation remained essentially unchanged, indicating that SA-YOLO improved accuracy while maintaining stability. The introduction and design of the SCSA attention module and the A2C2f_SAConv module enriched contextual information and preserved shallow details, enabling the model to more accurately locate crop row centres. Fig. 13 shows the crop row centreline detection performance of YOLOv12n-seg and SA-YOLO in mild weed interference, severe weed interference, and sparse planting scenes, respectively.



(a) (b) (c)

Fig. 13 - Crop row centreline detection results under different scenes

(a) Detection scenes; (b) Detection results of YOLOv12n-seg model; (c) Detection results of SA-YOLO model.

3.4.3 Comparison with related studies

To further evaluate the superiority of the proposed navigation method, our method was compared with other related studies. As shown in Table 5, under field crop environments, our method achieved lower mean angle error and mean normalized lateral error than other state-of-the-art deep learning methods. In addition, it is worth noting that the mean pixel errors of the navigation line generation methods using YOLOX-Nano and Faster R-CNN architectures in jujube orchard and kiwifruit orchard environments, respectively *(Zheng et al., 2023; Ma et al., 2021)*, were slightly lower than our mean lateral pixel error in the maize seedling field. This phenomenon can be explained by the fact that the field scene is more complex than orchards, with weaker illumination, more occlusion, and unstructured environments. The main reason is also the larger image width in this study compared with those studies. Compared with other advanced methods *(Lai et al., 2026)*, the proposed method has stronger robustness and generalization ability and can meet the navigation requirements of maize seedling fields.

Table 5

Performance comparison of different crop row line extraction methods

Reference	Scene	Network	Mean angle error (°)	Mean normalized lateral error (%)	Mean pixel lateral error (px)
(Kong et al., 2025)	Heading rice	SEU-Enet	1.910	-	-
(Lai et al., 2026)	Multiple seedling crops	YOLO-SSR	-	0.720	-
(Zheng et al., 2023)	Jujube orchard	YOLOX-Nano	2.550	0.700	4.49
(Ma et al., 2021)	Kiwifruit orchard	Faster R-CNN	3.200	0.340	5.10
This study	Maize seedling	SA-YOLO	0.590	0.357	6.85

Although the proposed method has clear advantages in accuracy, there are still some limitations. The parameter count of the model is 3.72 M, which is higher than that of the SEU-Enet model of *Kong et al. (2025)* (approximately 0.094 M), leaving room for optimization in extreme lightweight scenarios. This study mainly focused on the accuracy analysis of navigation line extraction and has not yet performed end-to-end real-time testing on actual agricultural machinery platforms.

4. CONCLUSIONS

In this study, to address the problem of crop row centreline extraction for visual navigation of agricultural robots, the SA-YOLO model was constructed, and a crop-based skeleton feature point extraction method and a corresponding crop row centreline extraction method were designed. The model enhanced feature extraction capability by introducing the SCSA attention module and replacing the original A2C2f module with the designed A2C2f_SAConv module, achieving accurate segmentation of crop row regions. In the crop row centreline extraction stage, the constructed skeleton feature point extraction and PCA-LSM joint optimization method effectively improved the accuracy of crop row centrelines. The experimental results showed that the IoU_{mask}, AP_{50}, P, and R scores of the SA-YOLO model were 83.8%, 99.1%, 96.5%, and 98.0%, respectively. Compared with the other four models, it exhibited higher recognition accuracy while maintaining faster segmentation speed. Second, regarding the proposed algorithm, the A_{mean} is reduced to 0.590° and its A_{std} to 0.498°, while the L_{mean}^{norm} is reduced to 0.357% and its L_{std}^{norm} to 0.428%. All the above metrics satisfy the precision requirements of autonomous agricultural machinery. However, several aspects of the proposed model require further improvement. The validation of the model was mainly focused on the crop seedling stage, and its applicability in other growth stage scenes needs further verification. Therefore, future work will include more crop species, more growth stages, and more samples from complex environments to promote the practical application of the algorithm.

5. ACKNOWLEDGEMENT

This work was supported by Opening Fund of National Key Laboratory of Agricultural Equipment Technology (SKL-2025-005), Scientific Research Start-up Foundation of Anhui Agricultural University (rc412405).

6. REFERENCES

[1] Arthur L., Mahnan S., He L., Hussain M., Heinemann P., Brunharo C., (2025). YOLOv7-CBAM and DeepSORT with pixel grid analysis for real-time weed localization and intra-row density estimation in apple orchards, *Computers and Electronics in Agriculture*, vol.239, article no.111071, Amsterdam/Netherlands. DOI: https://doi.org/10.1016/j.compag.2025.111071

[2] Ban C., Wang L., Chi R., Su T., Ma Y., (2024). A camera-LiDAR-IMU fusion method for real-time extraction of navigation line between maize field rows, *Computers and Electronics in Agriculture*, vol.223, article no.109114, Amsterdam/Netherlands. DOI: https://doi.org/10.1016/j.compag.2024.109114

[3] Bayareh Mancilla R., Tấn B., Daul C., Gutiérrez Martínez J., Leija Salas L., Wolf D., Vera Hernández A., (2021). Anatomical 3D modeling using IR sensors and radiometric processing based on structure from motion: Towards a tool for the diabetic foot diagnosis, *Sensors*, vol.21, no.11, article no.3918, Basel/Switzerland. DOI: https://doi.org/10.3390/s21113918

[4] Bronson K.F., French A.N., Conley M.M., Barnes E.M., (2021). Use of an ultrasonic sensor for plant height estimation in irrigated cotton, *Agronomy Journal*, vol.113, no.2, pp.2175-2183, Madison/USA. DOI: https://doi.org/10.1002/agj2.20552

[5] Cai C., Deng Y., Zhou Z., Zhang Y., Yu J., (2026). An end-to-end automated framework for pavement crack detection and dimensional quantification using foundation models and learned skeletonization, *Engineering Applications of Artificial Intelligence*, vol.171, article no.114239, Amsterdam/Netherlands. DOI: https://doi.org/10.1016/j.engappai.2026.114239

[6] Chamara N., Bai G., Ge Y., (2023). AICropCAM: Deploying classification, segmentation, detection, and counting deep-learning models for crop monitoring on the edge, *Computers and Electronics in Agriculture*, vol.215, article no.108420, Amsterdam/Netherlands. DOI: https://doi.org/10.1016/j.compag.2023.108420

[7] Chen J., Qiang H., Wu J., Xu G., Wang Z., Liu X., (2020). Extracting the navigation path of a tomato-cucumber greenhouse robot based on a median point Hough transform, *Computers and Electronics in Agriculture*, vol.174, article no.105472, Amsterdam/Netherlands. DOI: https://doi.org/10.1016/j.compag.2020.105472

[8] Chen Q., Chen J., Jiang Z., Huang L., Gai J., Li P., Zhang M., (2025). Research on efficient and fast extraction of vineyard navigation path based on key point detection, *Engineering Applications of Artificial Intelligence*, vol.159, part A, article no.111549, Amsterdam/Netherlands. DOI: https://doi.org/10.1016/j.engappai.2025.111549

[9] Chen Y., Geng C., Wang Y., Zhu G., Shen R., (2021). Extraction method for centerlines of rice seedings based on Fast-SCNN semantic segmentation (基于 Fast-SCNN 语义分割的秧苗列中心线提取方法), *INMATEH Agricultural Engineering*, vol.64, no.2, pp.335-344, Bucharest/Romania. DOI: https://doi.org/10.35633/inmateh-64-33

[10] Diao Z., Guo P., Zhang B., Zhang D., Yan J., He Z., Zhao S., Zhao C., Zhang J., (2023). Navigation line extraction algorithm for corn spraying robot based on improved YOLOv8s network, *Computers and Electronics in Agriculture*, vol.212, article no.108049, Amsterdam/Netherlands. DOI: https://doi.org/10.1016/j.compag.2023.108049

[11] Fan J., Li Y., Yu S., Gou W., Guo X., Zhao C., (2023). Application of Internet of Things to agriculture—The LQ-FieldPheno platform: A high-throughput platform for obtaining crop phenotypes in field, *Research*, vol.6, article no.0059, Washington/USA. DOI: https://doi.org/10.34133/research.0059

[12] Gao X., Zan X., Yang S., Zhang R., Chen S., Zhang X., Liu Z., Ma Y., Zhao Y., Li S., (2023). Maize seedling information extraction from UAV images based on semi-automatic sample generation and Mask R-CNN model, *European Journal of Agronomy*, vol.147, article no.126845, Amsterdam/Netherlands. DOI: https://doi.org/10.1016/j.eja.2023.126845

[13] Gao X., Wang G., Qi J., Wang Q., Xiang M., Song K., Zhou Z., (2024). Improved YOLOv7 for sustainable agriculture significantly improves precision rate for Chinese cabbage (Brassica pekinensis Rupr.) seedling belt detection, *Sustainability*, vol.16, no.11, article no.4759, Basel/Switzerland. DOI: https://doi.org/10.3390/su16114759

[14] Guo Y., Aggrey S.E., Yang X., Oladeinde A., Qiao Y., Chai L., (2023). Detecting broiler chickens on litter floor with the YOLOv5-CBAM deep learning model, *Artificial Intelligence in Agriculture*, vol.9, pp.36-45, Beijing/China. DOI: https://doi.org/10.1016/j.aiia.2023.08.002

[15] Han W., Xiang Y., Wu M., Zeng Y., Zou R., Jiang X., Quan W., (2026). Ridge navigation line extraction for rapeseed transplanters based on R-YOLOv11-Prune, *Smart Agricultural Technology*, vol.13, article no.101797, Amsterdam/Netherlands. DOI: https://doi.org/10.1016/j.atech.2026.101797

[16] Hu B., Qin Y., Chen R., Ren T., Zhang Z., Wu R., Yuan X., Chen Z., Wang Q., (2025). YOLOv8n-COSD: A lightweight multi-mechanism network for straw plastic impurity detection, *Smart Agricultural Technology*, vol.12, article no.101204, Amsterdam/Netherlands. DOI: https://doi.org/10.1016/j.atech.2025.101204

[17] Huang S., Wu S., Sun C., Ma X., Jiang Y., Qi L., (2020). Deep localization model for intra-row crop detection in paddy field, *Computers and Electronics in Agriculture*, vol.169, article no.105203, Amsterdam/Netherlands. DOI: https://doi.org/10.1016/j.compag.2019.105203

[18] Jiang Y., Li W., Liu J., ur Rehman M.M., Xie B., Wang J., (2025). Generalized perception of tree-row with distribution-peak feature in 3D point cloud for various orchards navigation, *Smart Agricultural Technology*, vol.12, article no.101137, Amsterdam/Netherlands. DOI: https://doi.org/10.1016/j.atech.2025.101137

[19] Jin L., Duan A., Shi Y., Fang H., (2025). EFNetPX: An improved panoptic perception network for inter-row navigation in orchard, *Computers and Electronics in Agriculture*, vol.239, part C, article no.111133, Amsterdam/Netherlands. DOI: https://doi.org/10.1016/j.compag.2025.111133

[20] Ju J., Chen G., Lv Z., Zhao M., Sun L., Wang Z., Wang J., (2024). Design and experiment of an adaptive cruise weeding robot for paddy fields based on improved YOLOv5, *Computers and Electronics in Agriculture*, vol.219, article no.108824, Amsterdam/Netherlands. DOI: https://doi.org/10.1016/j.compag.2024.108824

[21] Kim Y.H., Lee S.J., Yun C., Im S.J., Park K.R., (2023). LCW-Net: Low-light-image-based crop and weed segmentation network using attention module in two decoders, *Engineering Applications of Artificial Intelligence*, vol.126, article no.106890, Amsterdam/Netherlands. DOI: https://doi.org/10.1016/j.engappai.2023.106890

[22] Kong X., Guo Y., Liang Z., Zhang R., Hong Z., Xue W., (2025). A method for recognizing inter-row navigation lines of rice heading stage based on improved ENet network, *Measurement*, vol.241, article no.115677, Amsterdam/Netherlands. DOI: https://doi.org/10.1016/j.measurement.2024.115677

[23] Lai X., Huang J., Mo Y., Li H., Dong T., Wu T., He D., (2026). A lightweight deep learning model for synchronized crop stem detection and row segmentation at the seedling stage: Exploring their contribution to agricultural navigation line extraction, *Computers and Electronics in Agriculture*, vol.243, article no.111385, Amsterdam/Netherlands. DOI: https://doi.org/10.1016/j.compag.2025.111385

[24] Li D., Li B., Long S., Feng H., Xi T., Kang S., Wang J., (2023). Rice seedling row detection based on morphological anchor points of rice stems, *Biosystems Engineering*, vol.226, pp.71-85, Amsterdam/Netherlands. DOI: https://doi.org/10.1016/j.biosystemseng.2022.12.012

[25] Liu S., Jin Y., Ruan Z., Ma Z., Gao R., Su Z., (2022). Real-time detection of seedling maize weeds in sustainable agriculture, *Sustainability*, vol.14, no.22, article no.15088, Basel/Switzerland. DOI: https://doi.org/10.3390/su142215088

[26] Liu T., Zhu S., Yang T., Zhang W., Xu Y., Zhou K., Wu W., Zhao Y., Yao Z., Yang G., Wang Y., Sun C., Sun J., (2024a). Maize height estimation using combined unmanned aerial vehicle oblique photography and LiDAR canopy dynamic characteristics, *Computers and Electronics in Agriculture*, vol.218, article no.108685, Amsterdam/Netherlands. DOI: https://doi.org/10.1016/j.compag.2024.108685

[27] Liu W., Zhou Z., Xu X., Gu Q., Zou S., He W., Luo X., Huang J., Lin J., Jiang R., (2023). Evaluation method of rowing performance and its optimization for UAV-based shot seeding device on rice sowing, *Computers and Electronics in Agriculture*, vol.207, article no.107718, Amsterdam/Netherlands. DOI: https://doi.org/10.1016/j.compag.2023.107718

[28] Liu Y., Guo Y., Wang X., Yang Y., Zhang J., An D., Han H., Zhang S., Bai T., (2024b). Crop root rows detection based on crop canopy image, *Agriculture*, vol.14, no.7, article no.969, Basel/Switzerland. DOI: https://doi.org/10.3390/agriculture14070969

[29] Lopes R.A., Carvalho M.V.L., Kitani E., Zampirolli F.A., Yoshioka L., Celiberto Junior L.A., Ibusuki U., (2025). Deep learning-based instance segmentation for enhanced navigation of agricultural vehicles, *Revista de Informática Teórica e Aplicada*, vol.32, no.1, pp.136-142, Porto Alegre/Brazil. DOI: https://doi.org/10.22456/2175-2745.143329

[30] Luo S., Liu W., Zhang Y., Wang C., Xi X., Nie S., Ma D., Lin Y., Zhou G., (2021). Maize and soybean heights estimation from unmanned aerial vehicle (UAV) LiDAR data, Computers and Electronics in Agriculture, vol.182, article no.106005, *Amsterdam/Netherlands*. DOI: https://doi.org/10.1016/j.compag.2021.106005

[31] Luo Y., Gao G., Jiang P., Sun C., Xu M., Zhou Z., Hu W., Tan Y., (2025). A navigation line extraction method based on semantic segmentation and centerline fitting, *Smart Agricultural Technology*, vol.12, article no.101492, Amsterdam/Netherlands. DOI: https://doi.org/10.1016/j.atech.2025.101492

[32] Luz G.P.C.P. da, Sato G.M., Gomez Gonzalez L.F., Borin J.F., (2024). Smart parking with pixel-wise ROI selection for vehicle detection using YOLOv8, YOLOv9, YOLOv10, and YOLOv11, *arXiv preprint*, article no.2412.01983, Ithaca/USA. DOI: https://doi.org/10.48550/arXiv.2412.01983

[33] Lv P., Xue J., Wei W., Liu S., Gao W., Sun H., Miao H., Wang W., (2026). An advanced detector and dual-shortest distance intersection algorithm for navigation path extraction in complex orchards, *Engineering Applications of Artificial Intelligence*, vol.165, part A, article no.113246, Amsterdam/Netherlands. DOI: https://doi.org/10.1016/j.engappai.2025.113246

[34] Ma C., Dong Z., Chen Z., Zhu Y., Shi F., (2021). Research on navigation line generation of kiwi orchard between rows based on root point substitution (基于根点替代的猕猴桃果园行间导航线生成方法研究), *Agricultural Research in the Arid Areas*, vol.39, no.5, pp.222-230, Yangling/China. DOI: https://doi.org/10.7606/j.issn.1000-7601.2021.05.29

[35] Meng F., Yan C., Yang Y., Xing R., Zhu D., Zhang A., Tang Q., Liao J., (2024). A lightweight improved YOLOv5s model-based rice blast detection method and mobile deployment (基于轻量化改进 YOLOv5s 模型的稻瘟病检测方法及移动部署), *INMATEH Agricultural Engineering*, vol.74, no.3, pp.771-786, Bucharest/Romania. DOI: https://doi.org/10.35633/inmateh-74-68

[36] Qiao S., Chen L.-C., Yuille A., (2021). DetectoRS: Detecting objects with recursive feature pyramid and switchable atrous convolution, *Proceedings of the 2021 IEEE/CVF Conference on Computer Vision and Pattern Recognition (CVPR)*, pp.10208-10219, Nashville/USA. DOI: https://doi.org/10.1109/CVPR46437.2021.01008

[37] Rodríguez Rodríguez L.A., Castañeda-Miranda C.L., Moreno Lució M., Solís-Sánchez L.O., Castañeda-Miranda R., (2021). Quarternion color image processing as an alternative to classical grayscale conversion approaches for pest detection using yellow sticky traps, *Mathematics and Computers in Simulation*, vol.182, pp.646-660, Amsterdam/Netherlands. DOI: https://doi.org/10.1016/j.matcom.2020.11.022

[38] Shahid R., Qureshi W.S., Khan U.S., Munir A., Zeb A., Moazzam S.I., (2024). Aerial imagery-based tobacco plant counting framework for efficient crop emergence estimation, *Computers and Electronics in Agriculture*, vol.217, article no.108557, Amsterdam/Netherlands. DOI: https://doi.org/10.1016/j.compag.2023.108557

[39] Shao J., Zhao Q., Gong Z., Guo X., Geng S., Li Z., Li D., (2026). ENT-YOLO: An improved lightweight YOLO for cotton organ detection in mulched drip irrigation systems in southern Xinjiang, *Agricultural Water Management*, vol.323, article no.110054, Amsterdam/Netherlands. DOI: https://doi.org/10.1016/j.agwat.2025.110054

[40] Si Y., Xu H., Zhu X., Zhang W., Dong Y., Chen Y., Li H., (2025). SCSA: Exploring the synergistic effects between spatial and channel attention, *Neurocomputing*, vol.634, article no.129866, Amsterdam/Netherlands. DOI: https://doi.org/10.1016/j.neucom.2025.129866

[41] Song Y., Xu F., Yao Q., Liu J., Yang S., (2023). Navigation algorithm based on semantic segmentation in wheat fields using an RGB-D camera, *Information Processing in Agriculture*, vol.10, no.4, pp.475-490, Beijing/China. DOI: https://doi.org/10.1016/j.inpa.2022.05.002

[42] Surulivelu M., Hemanand D., Babu R.G., Subash T.D., (2026). AI-based tuberculosis detection and localization in chest X-rays using a binarized simplicial convolutional neural network for efficient and

accurate diagnosis, *Biomedical Signal Processing and Control*, vol.113, article no.108928, Amsterdam/Netherlands. DOI: https://doi.org/10.1016/j.bspc.2025.108928

[43] Wang S., Yu S., Zhang W., Wang X., Li J., (2023). The seedling line extraction of automatic weeding machinery in paddy field, *Computers and Electronics in Agriculture*, vol.205, article no.107648, Amsterdam/Netherlands. DOI: https://doi.org/10.1016/j.compag.2023.107648

[44] Yang Y., Zhou Y., Yue X., Zhang G., Wen X., Ma B., Xu L., Chen L., (2023). Real-time detection of crop rows in maize fields based on autonomous extraction of ROI, *Expert Systems with Applications*, vol.213, part A, article no.118826, Amsterdam/Netherlands. DOI: https://doi.org/10.1016/j.eswa.2022.118826

[45] Zhang H., Ge Y., Xia H., Sun C., (2024a). Safflower picking points localization method during the full harvest period based on SBP-YOLOv8s-seg network, *Computers and Electronics in Agriculture*, vol.227, part 2, article no.109646, Amsterdam/Netherlands. DOI: https://doi.org/10.1016/j.compag.2024.109646

[46] Zhang X., Lu X., Zhang Z., Yang G., He Y., Fang H., (2024b). Simultaneous detection of reference lines in paddy fields using a machine vision-based framework, *Computers and Electronics in Agriculture*, vol.221, article no.108923, Amsterdam/Netherlands. DOI: https://doi.org/10.1016/j.compag.2024.108923

[47] Zheng Z., Hu Y., Li X., Huang Y., (2023). Autonomous navigation method of jujube catch-and-shake harvesting robot based on convolutional neural networks, *Computers and Electronics in Agriculture*, vol.215, article no.108469, Amsterdam/Netherlands. DOI: https://doi.org/10.1016/j.compag.2023.108469

PERFORMANCE EVALUATION OF A SURFACE-MOUNTED THERMOELECTRIC GENERATOR, DESIGNED FOR RECOVERING RESIDUAL HEAT
/
EVALUAREA PERFORMANȚEI UNUI GENERATOR TERMOELECTRIC MONTAT PE SUPRAFAȚĂ, PROIECTAT PENTRU RECUPERAREA CĂLDURII REZIDUALE

Alexandru IONESCU[1)], Florin NENCIU[1)], Mihai MATACHE[1)], Costin MIRCEA[1)], Nicolae-Valentin VLĂDUȚ[1)], Cătălin PERSU[1)], Laurențiu VLĂDUȚOIU[1)], Nicoleta VANGHELE[1)*], Robert BLEJAN[2)]

[1)] National Institute of Research – Development for Machines and Installations Designed to Agriculture and Food Industry - INMA Bucharest / Romania;

[2)] National Institute of Research & Development for Optoelectronics / INOE 2000, Subsidiary Hydraulics and Pneumatics Research Institute / IHP / Romania

Tel: +40726496637; E-mail: vanghelelrc@gmail.com

DOI: https://doi.org/10.35633/inmateh-79-110

Keywords: *energy harvesting, thermoelectric generator, waste heat recovery, carbon-neutral energy, biochar pyrolysis, Seebeck effect*

ABSTRACT

This study explores the potential of harvesting and utilizing thermoelectric energy generated during biochar production. Biochar, a carbon-rich material produced from biomass pyrolysis, offers a sustainable pathway for waste management and soil improvement. However, the biochar production process also generates significant heat, much of which remains underutilized. This research investigates the integration of thermoelectric generators (TEGs) into biochar production equipment to convert waste heat into electricity. The system's design and optimization aim to enhance energy efficiency while supporting renewable energy goals, by using the harvested energy to power up small devices, such as sensors. Experimental results demonstrate the feasibility of capturing thermal energy and converting it into usable electrical power, contributing to the overall sustainability of the process. The experimental results revealed a maximum output voltage of 1.226 V, recorded at a temperature gradient of approximately 42.0 °C, a peak power output of approximately 37.6 mW, an overall maximum temperature gradient of approximately 42.8 °C reached slightly before the voltage peak, and a cumulative harvested energy of 288.92 J. The findings also highlight key factors influencing thermoelectric conversion efficiency, including temperature gradients, TEG material properties, and system integration challenges. This approach not only mitigates energy losses but also aligns with global efforts toward carbon neutrality and resource optimization. The study underscores the dual benefit of biochar production: providing agricultural benefits while supporting energy sustainability.

REZUMAT

Acest studiu explorează potențialul de captare și utilizare a energiei termoelectrice generate în timpul producției de biochar. Biocharul, un material bogat în carbon obținut prin piroliza biomasei, oferă o cale sustenabilă pentru gestionarea deșeurilor și îmbunătățirea solului. Totuși, procesul de producere a biocharului generează, de asemenea, cantități semnificative de căldură, mare parte din aceasta rămânând nevalorificată. Această cercetare investighează integrarea generatoarelor termoelectrice (TEG) în echipamentele de producere a biocharului, pentru a transforma căldura reziduală în energie electrică. Proiectarea și optimizarea sistemului urmăresc creșterea eficienței energetice și susținerea obiectivelor de energie regenerabilă, prin utilizarea energiei recuperate pentru alimentarea unor dispozitive de mici dimensiuni, cum ar fi senzorii. Rezultatele experimentale demonstrează fezabilitatea captării energiei termice și conversiei acesteia în energie electrică utilizabilă, contribuind la sustenabilitatea generală a procesului. Rezultatele experimentale au evidențiat o tensiune maximă de ieșire de 1,226 V, înregistrată la un gradient de temperatură de aproximativ 42,0 °C, o putere maximă de aproximativ 37,6 mW, un gradient maxim general de temperatură de aproximativ 42,8 °C, atins cu puțin timp înaintea vârfului de tensiune, și o energie totală recoltată de 288,92 J. Constatările evidențiază, de asemenea, factorii cheie care influențează eficiența conversiei termoelectrice, inclusiv gradientele de temperatură, proprietățile materialelor TEG și provocările legate de integrarea sistemului. Această abordare nu doar reduce pierderile de energie, ci se aliniază și eforturilor globale pentru neutralitate carbonică și optimizarea resurselor. Studiul subliniază beneficiul dublu al producției de biochar: oferirea de avantaje agricole și susținerea sustenabilității energetice.

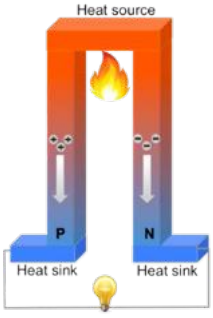
INTRODUCTION

In the context of increasing global energy demand and the need to reduce greenhouse gas emissions, the efficient use of available energy resources has become a critical research priority (*Cui X. et al., 2024; Moriarty P. & Honnery, D., 2016*). A significant share of the energy generated in industrial, agricultural, and biomass-processing systems is dissipated as residual heat, often without being valorized (*Jiang, Y. et al., 2024*), a situation particularly evident in processes such as biomass pyrolysis and biochar production, where high operating temperatures coexist with relatively low overall energy efficiency (*Champier D., 2017*); Seebeck-based recovery from biomass carbonization heat has recently been explored in simulation (*Badaka H. K. & Morega A. M., 2024*). In power stations, for example, approximately two-thirds of the energy produced is lost as waste heat, mainly discharged through cooling towers, since most electricity generation relies on gas- or steam-powered turbine systems in which fuel combustion is first converted into mechanical energy and only subsequently into electricity (*Sanin-Villa D., 2022*). As a result, only about one-third of the energy released from the fuel reaches the power lines leaving the plant.

Several technologies exist for recovering this thermal energy, including Organic Rankine Cycles (ORC), turbo-compounding, and thermoelectric generators (TEGs). Among these, TEGs are a promising solution for the direct conversion of waste heat into electricity. Based on the Seebeck effect, they enable solid-state energy conversion without moving parts, offering high reliability, low maintenance requirements, and scalability (*Ridwan M., 2025*), and have been increasingly investigated for waste-heat recovery from internal combustion engines, industrial processes, and biomass-based systems (*Williams, N. P. et al., 2022*), including automotive exhaust-heat recovery, where structural design and optimization remain active research topics (*Wang Y. et al., 2025*). Thermoelectric recovery from such systems typically relies on arrays of thermoelectric modules (TEMs) applied to surfaces with non-uniform temperature distributions, reducing fuel consumption and pollutant emissions in the process (*Săvescu C. et al., 2025*).

The Seebeck effect arises from the diffusion of charge carriers along a temperature gradient in a conductor or semiconductor, generating a potential difference between the hot and cold sides; the sign of this potential- and of the corresponding Seebeck coefficient identifies the material as p-type (positive) or n-type (negative) (*Quan R. et al., 2020*). The Seebeck coefficient quantifies the ratio between the induced voltage and the applied temperature gradient, and is obtained using a thermoelectric circuit formed of two dissimilar materials, typically two semiconductors with opposite-sign coefficients, joined at junctions held at different temperatures (*Deng Y. et al., 2022*). Materials with a high Seebeck coefficient are the most efficient at converting thermal energy into electricity; the effect underlies applications ranging from thermoelectric generators and thermocouple temperature sensors to wearable devices that harvest body heat.

Despite these advantages, wider adoption of thermoelectric systems remains limited by relatively low conversion efficiencies and by challenges related to thermal integration (*Liu Z. et al., 2023*). TEG performance depends not only on the intrinsic properties of the thermoelectric materials but also on external factors such as the temperature gradient, heat-transfer conditions, and the quality of thermal contact between the heat source and the modules (*Ciupercă R. et al., 2022*). Surface-mounted configurations are particularly sensitive to heat-transfer effectiveness across multiple interfaces, where thermal resistances and contact imperfections can substantially reduce the achievable temperature difference (ΔT) and, consequently, the electrical output (*Mastrullo R. et al., 2019*). The complementary Peltier effect, in which an electric current passed through the junction of two dissimilar materials causes heat to be absorbed at one junction and released at the other, governs the reverse operating mode of the same devices, used for active cooling, and reflects the same carrier-transport mechanism that underlies Seebeck-based power generation (*Chelladorai P. et al., 2024; Maican E., 2015*).



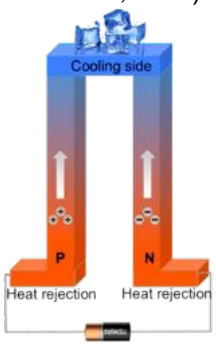


Fig. 1 - Seebeck effect *(Kim M., et al., 2025)*

Fig. 2 - Peltier effect *(Kim M., et al., 2025)*

MATERIALS AND METHODS

Thermoelectric generators (TEG)

A thermoelectric generator (TEG) directly converts heat into electrical energy through the Seebeck effect: when a temperature difference is applied across a conductive or semiconductive material, charge carriers diffuse from the hot end to the cold end, producing an electric current. A practical TEG is built from multiple thermocouples, each an n-type and a p-type semiconductor pair, connected electrically in series and thermally in parallel; the conversion efficiency depends on the thermoelectric material used and is quantified by the dimensionless figure of merit (ZT), which combines electrical conductivity, the Seebeck coefficient, absolute temperature and thermal conductivity (*Ridwan M., 2025*).

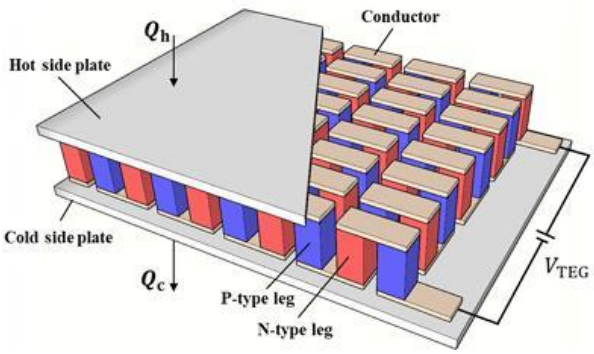


Fig. 3 - Graphic representation of a thermoelectric generator *(Yaman K., et al., 2025)*

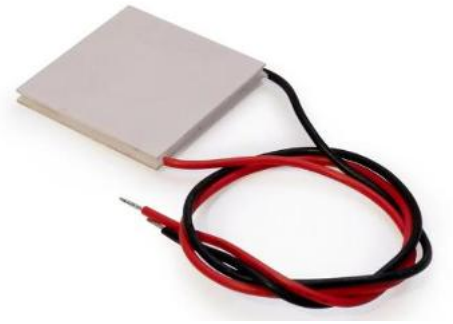


Fig. 4 - Thermoelectric generator module *(Iavnic T., et al., 2024)*

Bismuth telluride (Bi_2Te_3), the active material in the TEC1-12706 Peltier modules used in this study, is among the most widely used thermoelectric materials for near-room-temperature applications (typically 200-300 °C), owing to its favorable electrical conductivity and Seebeck coefficient and its correspondingly high figure of merit (ZT) at low-to-medium temperatures; it is likewise the basis for the reverse (cooling) operating mode of the same devices in thermoelectric refrigeration.

- **Heat source**

The biochar production equipment (Fig. 7) generates high temperatures during the pyrolysis process. The external surfaces of the equipment have been identified as a consistent source of residual heat, making them ideal for mounting Peltier modules.

Although thermally insulated, the heat generated by the six 2000 W heating elements is sufficient for four series-connected Peltier modules to generate a significant electric potential.



Fig. 5 - Bismuth telluride in natural form *(Hqgraphene.com)*

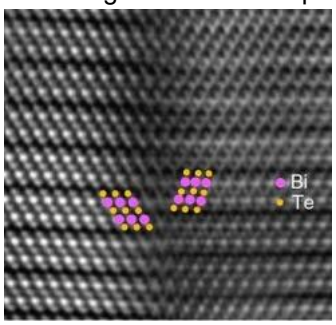


Fig. 6 - Bismuth telluride under microscope *(Hqgraphene.com)*



Fig. 7 - Biochar production equipment

- **TEG modules**

The core of the system comprises four TEC1-12706 modules. While these are primarily designed as Peltier modules for thermoelectric cooling and heating, they can be repurposed as thermoelectric generators (TEGs) when subjected to a temperature gradient. In this configuration, they convert heat into electrical energy through the Seebeck effect. To maximize the voltage output from the TEGs, the four modules are connected in series. This configuration ensures that the voltage generated by each module adds up, resulting in a combined output equal to the sum of individual module voltages. This is particularly advantageous when the application requires higher voltages to power downstream electronics or charge batteries.

For a better cooling distribution on the cold side of the generator, a heat sink was mounted on each of the four modules with thermal paste. (Fig. 8)

Being a low-powered application, it is important to minimize the voltage drop as much as possible. The voltage drop across conductive materials is governed by Ohm's law:

$$U = I \cdot R \quad (1)$$

where U is the voltage drop, I is the current, and R is the resistance of the wire. The resistance (R) of a wire is proportional to its length (L) and resistivity (ρ) and inversely proportional to its cross-sectional area (S):

$$R = \rho \cdot \frac{L}{S} \quad (2)$$

To minimize the resistance of the wiring used with thermoelectric generator (TEG) modules and consequently reduce the voltage drop, the wire length (L) was minimized in this design. This approach ensures that the electrical energy generated by the TEG modules is efficiently transferred to the load or storage system. Shortening the wire length not only reduces resistive losses but also minimizes the thermal resistance introduced by longer wires, which can interfere with the thermal gradient for TEG operation. This optimization step is particularly critical in low-voltage systems, where even minor losses can significantly impact overall performance.

Before conducting the actual experiments, preliminary tests were performed to determine the correct polarity of the thermoelectric generator (TEG) modules and to confirm their functionality based on the Seebeck effect. These tests involved applying a temperature gradient across the module surfaces.

To simulate a temperature differential, heat was applied to the hot side of the TEG module using a handheld lighter, while ice was placed on the cold side. This setup ensured a significant thermal gradient necessary to generate an electromotive force. Using a multimeter, the output voltage and polarity were measured to verify the module's orientation and ensure proper connectivity for subsequent testing. The results confirmed the expected behavior, with the TEG generating a voltage consistent with the Seebeck effect and the designated polarity. This step was a qualitative orientation check preceding the formal experimental campaign described in the following sections, and is reported here only as such, not as part of the formal measurement procedure.

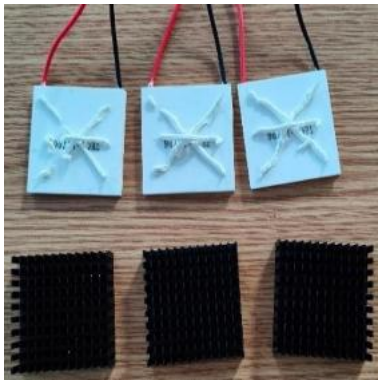


Fig. 8 - Heat-sink mounting using thermal paste



Fig. 9 - Applying ice on the cold side

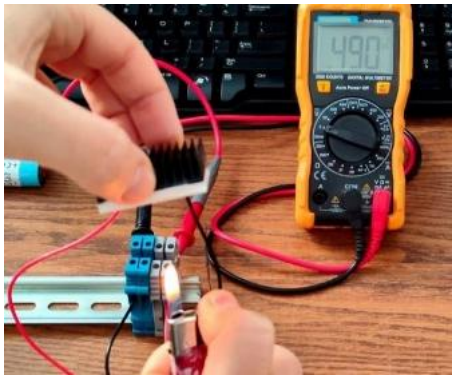
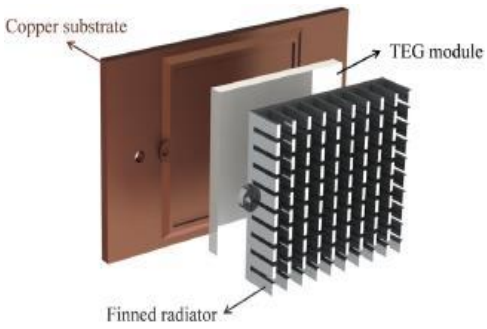


Fig. 10 - Applying high temperature on hot side

For ensuring an efficient and uniform heat distribution across the hot-side surfaces of the Peltier modules, they were mounted on a copper plate, due to its superior thermal conductivity properties. Subsequently, the assembled structure was attached to the equipment using a thermally conductive double-sided adhesive tape, providing both mechanical stability and adequate thermal contact. In order to enhance thermal dissipation and reduce the temperature at the cold junction, the setup utilized four heat sinks, each with dimensions of 40x40 mm.



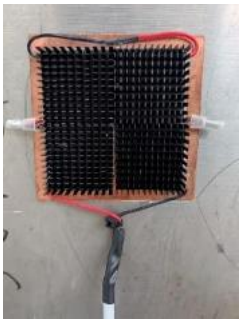


Figure 11. Geometric model of a TEG module with a finned heat sink and copper plate
(Jiang, Y. et. al., 2024)

Figure 12. TEG modules setup

Other instrumentation used

The output voltage and current supplied to the resistive load (Fig. 16) were measured with a PANCONTROL PAN Profimeter digital multimeter (CAT III 600 V), with a DC voltage range of 0.1 mV–600 V and a manufacturer- specified accuracy of 0.7%–4.0% depending on range and function.

Thermal measurements were performed using a UNI-T UTi32 thermal imaging camera. The device operates over a temperature measurement range of −20 °C to 1000 °C and features an infrared (IR) resolution of 32 × 32 pixels. The thermal images were displayed on a 2.4-inch IPS screen with a resolution of 480 × 320 pixels. In addition, the integrated digital camera provides visible-light images at a resolution of 640 × 480 pixels. The camera supports three visualization modes: thermal, visible, and fusion, allowing thermal data to be analyzed alongside conventional imagery. According to the manufacturer's specifications, the instrument has a stated temperature-measurement accuracy of ±2 °C or ±2%, whichever is greater, and a thermal sensitivity (NETD) of 0.15 °C.

Temperature regulation was performed using a Gefran 650 PID temperature controller, a compact 1/16 DIN process controller designed for accurate and stable thermal regulation in industrial applications. The controller has a 48 × 48 mm front-panel format and an approximate depth of 80 mm. Its universal main input can be configured for different temperature sensors, including J, K, R, S, T, C and D thermocouples, as well as PT100 and JPT100 resistance temperature detectors (RTDs). Linear input signals of 0–60 mV, 0–1 V, 0–5 V, 0–10 V and 0/4–20 mA are also supported.

Temperature at the module hot side was sensed with a Gefran TC8-D-1-K thermocouple (Type K), connected to the Gefran 650 controller, with a manufacturer-stated tolerance of IEC 60584-2 Class 2: ±2.5 °C for −40...+333 °C, or ±0.0075×|t| for t > 333 °C (i.e., approximately ±3 °C at the ~400 °C internal operating temperature reached in this study).

The 10 Ω load resistor was a general-purpose commercial resistor with a typical tolerance of ±5%, as manufacturer-specific tolerance data were not available for this component.

Methodology

The measurements were conducted in Bucharest on December 11, 2025. Ambient temperature data were obtained from the website weatherspark.com. The measurements were carried out over a period of 335 minutes, from 9:00 a.m. to approximately 3:30 p.m., with ambient temperatures ranging between 3°C and 12°C. In addition, temperature and output voltage measurements were recorded at 5-minute intervals throughout the duration of the experiment.

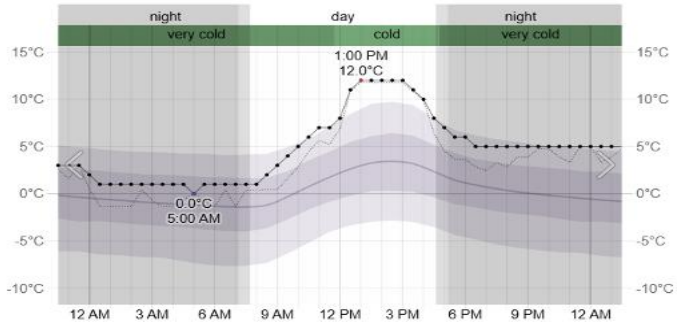


Fig. 13 - Ambient temperatures in Bucharest, 11 Dec 2025 *(Weatherspark.com)*

For the experimental determination of the electrical parameters (current, and output power), a resistive load of 10 Ω was connected across the terminals of the thermoelectric modules. The selection of this load value was based on the maximum power transfer principle, which states that the power delivered to the load is maximized when the load resistance is approximately equal to the internal resistance of the source.

Each thermoelectric module exhibits an internal electrical resistance of approximately 2.5 Ω. With the four modules connected in series, as described above, the equivalent internal resistance of the source is 4 × 2.5 Ω = 10 Ω, which matches the selected load resistance exactly. Therefore, the use of a 10 Ω load closely satisfies the impedance matching condition, enabling an accurate experimental assessment of the maximum extractable power from the system; this equivalence between the source and load resistance is also what justifies halving the total output voltage in Eq. (3) below.

$$V_{load} = \frac{V_{out}}{2} \quad (3)$$

$$I = \frac{V_{load}}{R_L} \quad (4)$$

$$P = V_{load} \cdot I = \frac{V_{load}^2}{R_L} \quad (5)$$

$$\eta = \frac{P}{Q} \quad (6)$$

where:

V_{load} – voltage measured across the load resistor [V]

I – electrical current flowing through the circuit [A]

P – electrical power delivered to the load [W]

P_{avg} – average electrical power delivered to the load [W]

η – yield, expressed here as a conversion ratio relative to the fixed reference power Q_{ref} = 180 W (see Results), rather than a directly measured thermoelectric conversion efficiency [%]

The average electrical power obtained during the experimental campaign was 14.37432 mW. The total duration of the experiment was 335 minutes, corresponding to 20,100 seconds. Based on these values, the total electrical energy generated by the system was calculated as the product of average power and time.

$$E \approx P_{avg} \cdot t \approx 0.01437432 \cdot 20100 \approx 288.92 \text{ [J]} \quad (7)$$

where:

E – electrical energy produced by the system [J]

Theoretical model

The electrical voltage generated by the thermoelectric modules is governed by the Seebeck effect, which establishes a direct proportionality between the generated voltage and the temperature difference across the module.

$$V = \alpha \cdot \Delta T + b \quad (8)$$

where:

V - output voltage [V];

α - Seebeck coefficient [V/K];

ΔT - temperature difference across the module [K].

The thermoelectric modules were mounted on the external surface of the biochar production equipment. Therefore, the temperature difference was defined as:

$$\Delta T = T_{hot} - T_{cold} \quad (9)$$

To determine the temperatures at the ceramic surfaces of the TEGs (Thot and Tcold), it had to be accounted the fact that heat doesn't transfer perfectly from the heat source to the modules as there is thermal friction (thermal resistance) in the copper plate and especially in the thermally conductive tape used.

When heat flows through any material, it loses "pressure" (temperature). The temperature at the actual Peltier junction is always lower than the source and higher than the ambient air.

$$T_{hot} = T_{ext} - (Q \cdot R_{hot}) \quad (10)$$

$$T_{cold} = T_{amb} + (Q \cdot R_{cold}) \quad (11)$$

$$Q = \frac{T_{top} - T_{bottom}}{R_{th}} \quad (12)$$

where:

Q - heat flow [W]

R - thermal resistance [K/W]

T_{top} – temperature on the top of a material [°C]

T_{bottom} – temperature on the bottom of a material [°C]

- **Hot side thermal resistance model**

To determine the temperature drop between the measured external temperature, *T*ext, and the actual hot-side surface temperature of the TEG, *T*hot, Fourier's law of heat conduction and a thermal-resistance model were applied.

$$R_{th} = \frac{L}{k \cdot A} \quad (13)$$

where:

L – thickness of the material (m)

k – thermal conductivity (W/mK)

A – surface area (m²)

$$T_{drop} = Q \cdot R_{th} \quad (14)$$

where:

T_{drop} – Temperature drop across a layer [°C]

The thickness of the copper plate is 1mm, while the other dimensions are 40x40 mm, it results:

$$R_{copper} = \frac{L_{copper}}{k_{copper} \cdot A_{copper}} = \frac{0.001}{401 \cdot 0.0064} \approx 0.00039 \text{ [K/W]} \quad (15)$$

It means that the thermal resistance of the copper plate is negligible, the copper plate itself barely causing any temperature drop (less than 0.1°C).

As for the thermally conductive tape, its thickness was measured as 0.2 mm, while the dimensions are 40x40 mm. Therefore:

$$R_{band} = \frac{L_{band}}{k_{band} \cdot A_{band}} = \frac{0.0002}{1.5 \cdot 0.0064} \approx 0.02083 \text{ [K/W]} \quad (16)$$

- **Cold side thermal resistance model**

Although copper has high thermal conductivity, air has much lower thermal conductivity. As a result, heat dissipation from the heat sinks to the surrounding air is limited, causing the cold side of the TEG module to remain warmer than the ambient temperature.

The effective cold side temperature T_{cold} is calculated by adding the temperature loss factors to the ambient air temperature:

$$T_{cold} = T_{amb} + T_{convective} + T_{conduction} \quad (17)$$

The total cold side resistance (R_{cold}), consists of three components:

- Interface Resistance (R_{int}) - thermal resistance at the contact interface between the TEG module and the heat sink.
- Conduction Resistance ($R_{conduction}$) - thermal resistance associated with heat conduction through the aluminum base of the heat sink.
- Convective Resistance ($R_{convective}$) - thermal resistance associated with heat transfer from the heat-sink fins to the surrounding air; this component typically accounts for the largest temperature drop.

$$R_{convective} = \frac{1}{h \cdot A} = \frac{1}{50 \cdot 0.0064} \approx 3.125 \text{ [K/W]} \quad (18)$$

The convective heat-transfer coefficient adopted in Eq.(18) (h = 50 W/(m²K)) reflects a natural-convection regime for the finned heat sinks used, since no forced-air cooling (fan or blower) was applied during testing.

The other two terms in Eq. (19) — the interface resistance between the TEG module and the heat sink, associated with the thin layer of thermal paste, and the conduction resistance through the thin aluminum base of the heat sink — are, by the same reasoning applied to the copper plate on the hot side in Eq. (15), several orders of magnitude smaller than the convective resistance calculated in Eq. (18). They were therefore neglected. Consequently, the cold-side temperature rise is dominated by the convective resistance, with $R_{convective} \approx 3.125$ K/W.

The heat flow, Q, rejected at the cold side consists of the heat transferred from the hot side together with the internally generated Joule heat:

$$T_{rise} = Q_{total} \cdot (R_{int} + R_{conduction} + R_{convection}) \quad (19)$$

Because the convective thermal resistance of the heat sink $R_{convection}$ is determined primarily by the heat-sink geometry and airflow conditions, a higher heat flow results in a larger temperature difference across the cold-side thermal resistance.

The Seebeck coefficient was determined using linear regression applied to the experimental dataset, according to the relation:

$$\alpha = \frac{V_{out}}{\Delta T} \quad (20)$$

Since the experiment was conducted using 4 modules mounted in series:

$$V_{out} = 4 \cdot \alpha \cdot \Delta T \quad (21)$$

The linear regression fitted to the full V_{out} versus ΔT dataset (Figure 21) gives a slope of 0.0293 V/°C for the four-module series, corresponding to a per-module Seebeck coefficient of:

$$\alpha_{module} = \frac{0.0293}{4} = 0.00733 \text{ [V/K]} \quad (22)$$

As a consistency check, the Seebeck coefficient was also estimated from a single stable data point near the plateau, where the open-circuit output voltage was V_{out} = 1.226 V and ΔT ≈ 42.0 °C.

$$\alpha_{module} = \frac{V_{out}}{4 \cdot \Delta T} = \frac{1.226}{4 \cdot 42.0} = 0.00729 \text{ [V/K]} \quad (23)$$

where: α - the effective Seebeck coefficient of the thermoelectric module under real operating conditions [V/K]

ΔT - temperature difference between the hot and cold side of the module [°C]

V_{out} - voltage measured at the corresponding temperature difference ΔT [V]

The close agreement between the regression-based estimate (0.00733 V/K) and the single-point value (0.00729 V/K) confirms the consistency of the Seebeck coefficient obtained under real operating conditions, and both are in line with the expected performance of commercial thermoelectric modules operating under non-ideal thermal conditions. As shown in Figures 21 and 23, the heating and cooling phases form two visibly distinct branches around this regression line, a hysteresis attributable to the thermal inertia of the system discussed above; the reported slope represents an average across both branches rather than a single-valued instantaneous relationship.

RESULTS

The biochar production unit, acting as the thermal source, reached the target internal temperature of 400 °C in approximately one hour. This temperature was maintained for a duration of about two hours, after which a gradual decrease was observed.

A pronounced thermal inertia of the system was identified. While the internal temperature attained its maximum value within the first hour, the external surface temperature exhibited a delayed response, reaching a peak of 71 °C after approximately three hours from the start of the process. This behavior highlights the transient heat transfer dynamics and the thermal buffering capacity of the system.



Fig. 14 - Measurement of the equipment surface temperature

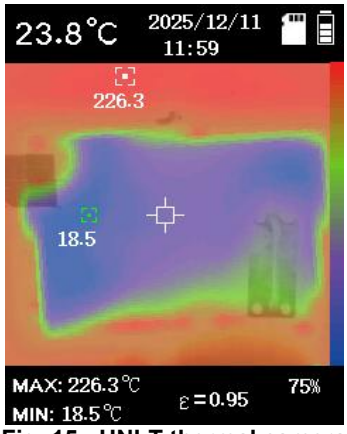


Fig. 15 - UNI-T thermal camera screenshot



Fig. 16 - Measuring the output voltage

Although the theoretical model predicts a linear relationship between output voltage and temperature difference, the experimental results show deviations from ideal linearity. These deviations may be attributed to several factors, including thermal contact resistance between the module and the equipment surface, insufficient heat dissipation from the cold side, transient thermal conditions during measurement, and nonuniform temperature distribution within the module. These values indicate that the system is suitable for low-power applications such as environmental monitoring or autonomous sensing systems.

The experimental measurements performed over a total duration of 335 minutes highlight the temporal evolution of the thermal regime of the biochar reactor and its direct influence on thermoelectric energy generation.

- **Thermal evolution of the system**

The internal temperature of the heat source exhibited a rapid increase during the initial phase, rising from near-ambient values to approximately 400 °C within the first 60–65 minutes. After reaching this peak, the system maintained a quasi-steady thermal plateau at ~400 °C for a significant duration (approximately 65 to 190 minutes), followed by a gradual cooling phase.

In contrast, the external temperature of the heat source and the temperatures measured at the thermoelectric module interfaces (hot and cold sides) showed a delayed and attenuated response. The hot-side temperature increased progressively from ~5.8 °C to a maximum of approximately 62.4 °C, while the cold-

side temperature rose from ~3.5 °C to about 20.6 °C. This resulted in a maximum recorded temperature difference (ΔT) of approximately 42.8 °C.

The data clearly indicate the presence of thermal gradients and heat transfer limitations between the reactor core and the thermoelectric modules, as the external and interface temperatures remained significantly lower than the internal reactor temperature throughout the experiment.

- **Voltage generation and correlation with temperature gradient**

The electrical output of the thermoelectric modules followed the evolution of the temperature gradient across their surfaces. At low ΔT values (approximately 2–3 °C), the generated voltage was minimal (~0.02 V). As ΔT increased, the output voltage rose steadily, reaching a maximum value of 1.226 V at ΔT ≈ 42 °C.

During the steady-state thermal regime (approximately 160–190 minutes), both ΔT and voltage output stabilized, with voltage values consistently around 1.20–1.22 V. This indicates a strong correlation between thermal stability and consistent electrical generation.

Following the decline in reactor temperature, both ΔT and output voltage decreased proportionally, confirming the direct dependence of thermoelectric performance on the available temperature gradient.

- **Electrical performance under load**

The electrical characterization of the system using a 10 Ω resistive load provided insight into the practical energy harvesting capability. The measured current increased with ΔT, ranging from approximately 1 mA at low temperature differences to 61.3 mA at peak conditions.

The corresponding electrical power output reached a maximum value of approximately 37.6 mW at ΔT ≈ 42 °C. At intermediate conditions (ΔT ≈ 26.3 °C), the system produced around 10.8 mW, while at low ΔT values (~2–3 °C), the power output was negligible (~0.01 mW).

These results confirm that the usable electrical power is highly sensitive to the temperature gradient and increases nonlinearly with ΔT.

- **Energy conversion efficiency**

The calculated P/Q_{ref} conversion ratio (yield) remained low throughout the experiment, with values ranging from 0.0001% at minimal ΔT to a maximum of approximately 0.021% at peak operating conditions. Even under stable high-temperature conditions, this ratio did not exceed that value; as explained above, it is referred to the fixed reference power Q_{ref} = 180 W rather than to a per-point modelled heat flow, so it should not be interpreted as a directly measured thermoelectric conversion efficiency.

This limited efficiency reflects both the inherent constraints of thermoelectric conversion at relatively low temperature gradients and the thermal losses occurring within the system.

- **Observed thermal effects influencing performance**

The experimental data reveal several important physical phenomena affecting system performance:

- ✓ A temperature lag between the internal reactor temperature and the thermoelectric module temperatures, indicating significant thermal inertia.
- ✓ A reduced effective ΔT across the modules compared to the available thermal potential, suggesting heat transfer limitations.
- ✓ A gradual rather than instantaneous response of voltage output to temperature changes, further supporting the presence of thermal inertia in the system.

Additionally, the relatively low hot-side temperatures compared to the reactor interior suggest the presence of thermal resistance along the heat transfer path, which limits the effective utilization of the available heat.

Table 1

Summary of key operating points across the thermal cycle

Time point	T_ext (°C)	T_int (°C)	T_hot (°C)	T_cold (°C)	ΔT (°C)	V_out (V)	I (mA)	P (mW)	η (%)	Qref (W)
Start (t = 5 min)	6.3	8.3	5.8	3.5	2.3	0.020	1.0	0.010	0.0000056	180
Plateau onset (t = 65 min)	27.5	401.0	24.1	8.4	15.8	0.359	17.95	3.222	0.00179	180
Mid-plateau (t = 125 min)	55.1	400.0	47.9	14.2	33.7	0.864	43.2	18.662	0.01037	180
Plateau end / peak (t = 185 min)	71.4	400.0	62.4	20.4	42.0	1.226	61.3	37.577	0.02088	180

Late cooling (t = 335 min)	14.6	15.0	13.8	10.3	3.6	0.084	4.2	0.176	0.0000098	180

Table 1 consolidates the recorded and derived quantities at five representative points of the thermal cycle, read directly from the logged dataset underlying Figures 17–24.

The heat flow used as the denominator in Eq. (6), Q_{ref} = 180 W, is a fixed reference power adopted for all five operating points, not a per-point value measured or derived from the thermal-resistance model developed in Materials and Methods; as discussed below, the hot-side and cold-side branches of that model imply markedly different per-point heat flows that cannot yet be reconciled into a single value, so a fixed reference was preferred for this comparison. Accordingly, the derived quantity reported in the η (%) column throughout this study is a conversion ratio referred to this fixed reference power, and should not be read as a directly measured thermoelectric conversion efficiency.

- **Uncertainty analysis**

A brief propagation-of-uncertainty estimate was performed for the peak operating point (Plateau end, t = 185 min). The temperature-gradient uncertainty is dominated by the thermal camera's manufacturer-stated accuracy (±2 °C or ±2%, whichever is greater). Since $\Delta T = T_{hot} - T_{cold}$ is derived from two such independent readings, the combined uncertainty is $\Delta(\Delta T) = \sqrt{(\Delta T_{hot}^2 + \Delta T_{cold}^2)} \approx \pm 2.8$ °C, i.e., approximately ±7% of the peak $\Delta T \approx 42.0$ °C. The output voltage and current were measured with a manufacturer-stated accuracy of 0.7-4.0%, taking a representative mid-range value of ≈2%, the corresponding uncertainty at the peak point is $\Delta V_{out} \approx \pm 0.02$ V and $\Delta I \approx \pm 1.2$ mA. Propagating these through $P = V \cdot I$ gives $\Delta P/P = \sqrt{((\Delta V/V)^2 + (\Delta I/I)^2)} \approx \pm 2.8\%$, i.e., $\Delta P \approx \pm 1.1$ mW on the peak power of 37.6 mW. These figures should be read as indicative rather than a full metrological budget, since the campaign consisted of a single run and repeatability could not be independently assessed; a repeated campaign under similar conditions would be needed to establish the run-to-run (Type A) component of the uncertainty.

- **Extrapolating the results**

Based on the experimental results obtained using a limited number of thermoelectric modules, a theoretical scaling of the system was performed to estimate the potential electrical output when utilizing the entire available heated surface of the reactor door. The total surface area of the door is approximately 2178.75 cm², and excluding the handle area, it remains with a usable area of 2128.75 cm². Assuming the use of standard thermoelectric modules with approximate dimensions of 4 × 4 cm (16 cm² per module), the maximum number of modules that can be mounted is 133 modules. By extrapolation, the total theoretical electrical power becomes approximately 1.25 W. Such power levels are sufficient for several agricultural and autonomous applications, including powering wireless sensor nodes (soil moisture, temperature, humidity), supplying microcontrollers and data logging systems, charging small batteries or supercapacitors for intermittent operation and supporting low-power IoT communication modules, such as LoRa-based systems.

This extrapolated value of 1.25 W should be read as an upper-bound estimate rather than an expected operating point. It assumes a uniform temperature gradient across the entire 2128.75 cm² usable door surface, equal to the $\Delta T \approx 42$ °C measured at the single, most favorably located four-module array in the present setup, and a linear scaling of the cooling capacity of the cold-side heat sinks with the number of modules. In a real 133-module array, both assumptions would degrade: the temperature gradient is expected to be non-uniform across such a large surface, and the shared ambient air volume would reduce the effective convective heat-transfer coefficient per module as module density increases, so the true achievable output at that scale is expected to fall below this estimate.

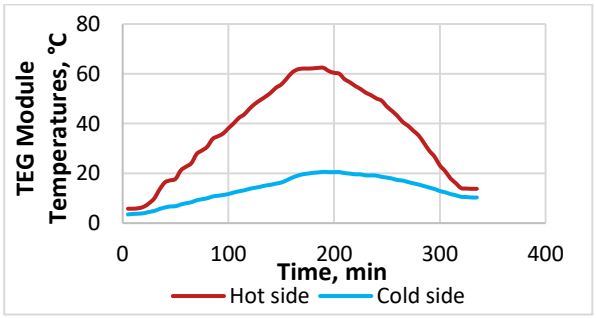


Fig. 17 - Temperatures of Peltier modules over time

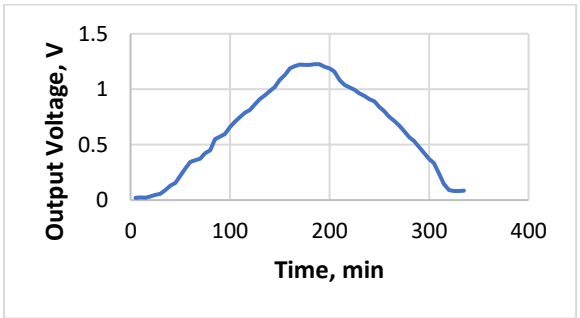


Fig. 18 - Output voltage over time

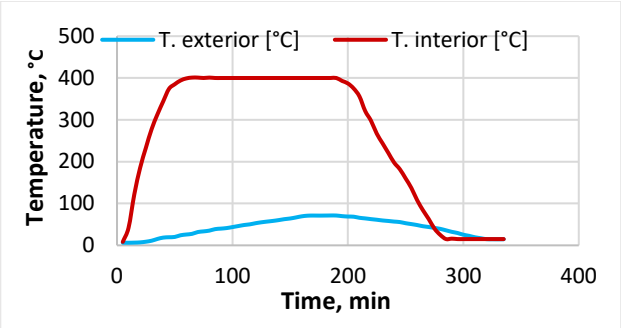


Fig. 19 - Heat source temperature over time

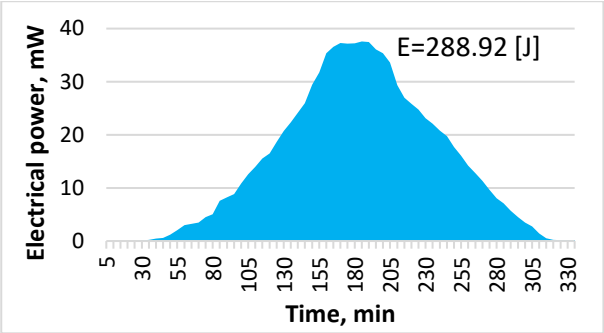


Fig. 20 - Electrical power over time

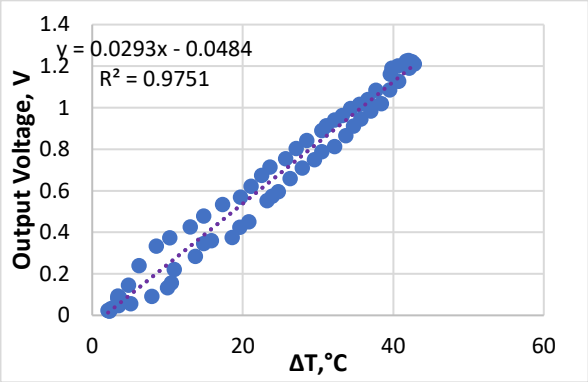


Fig. 21 - Dependence of Output Voltage on Temperature Gradient (ΔT)

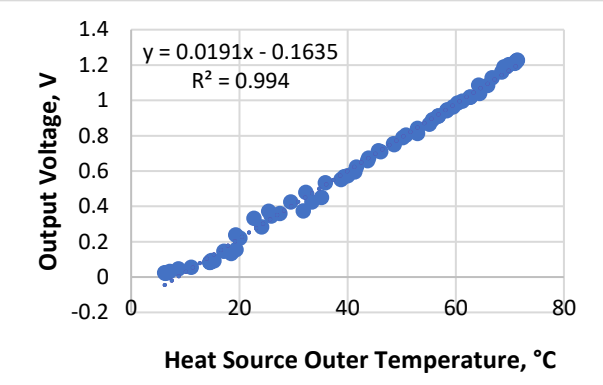


Fig. 22 - Dependence of Output Voltage on heat source outer temperature

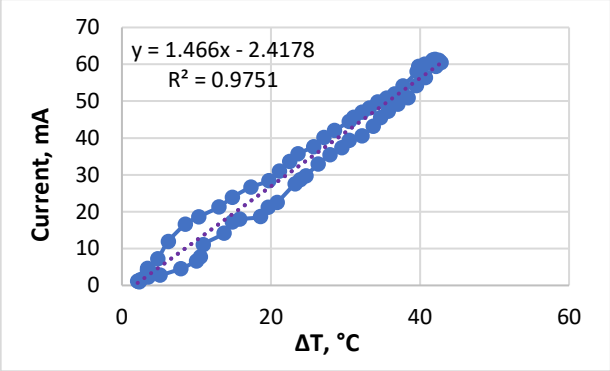


Fig. 23 - Dependence of Current on Temperature Gradient (ΔT)

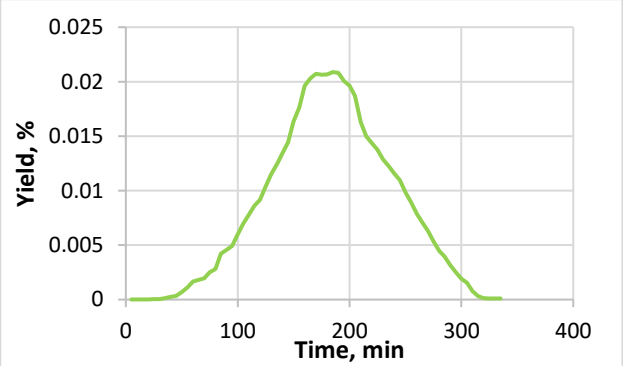


Fig. 24 - Dependence of Yield over time

DISCUSSION AND PERSPECTIVES

Despite the successful generation of electrical power, the overall P/Qref conversion ratio (yield) remained low, with a maximum value of approximately 0.021%. This limited value can be attributed to several factors, including:

- the relatively small temperature gradient across the modules compared to the high source temperature;
- thermal losses due to insufficient heat exchanger optimization;
- the intrinsic limitations of commercially available Peltier modules when used as thermoelectric generators.

Another significant limiting factor identified is the imperfect thermal contact between the heat source and the thermoelectric modules. This interface-related issue represents one of the primary causes of temperature loss in the system. Due to surface irregularities, non-uniform pressure distribution, and microscopic air gaps, a portion of the available thermal energy is not effectively transferred to the hot side of the Peltier modules. This phenomenon is inherently difficult to quantify experimentally, as it depends on contact quality at a micro-scale level, which cannot be directly measured with conventional instrumentation. As a result, it introduces uncertainty in the effective temperature gradient and reduces the overall system performance.

Furthermore, the data suggest that the external temperature of the heat source increased significantly more slowly than the internal temperature, indicating thermal resistance between the reactor core and the module interface. This highlights a critical design limitation and suggests that improved thermal coupling mechanisms, for example enhanced heat sinks, conductive interfaces, or forced cooling on the cold side could substantially increase ΔT and, consequently, electrical output.

One of the primary perspectives for improving system performance lies in the optimization of thermal coupling between the heat source and the thermoelectric modules. As identified in the present study, imperfect contact surfaces and intermediate layers introduce significant thermal resistance.

Future work should focus on:

- the use of advanced thermal interface materials with higher conductivity,
- improved mechanical fixation methods to ensure uniform pressure distribution,
- surface treatment techniques for example polishing or machining to reduce micro-scale air gaps; and the integration of phase-change materials to buffer transient thermal loads and stabilize the temperature gradient across the modules, as recently demonstrated for other TEG configurations (*Karadirek G. et al., 2025*).

The experimental results demonstrate that thermoelectric energy recovery from a biochar production system is feasible, albeit currently limited by low conversion efficiency and thermal losses. However, the obtained data also provide a solid basis for extrapolating the system performance under improved design and scaling conditions.

A key perspective for enhancing the overall electrical output lies in the geometric scalability of the thermoelectric system. In the present configuration, only a limited number of Peltier modules were installed. Considering the available surface of the reactor door, approximately 52.5 × 41.5 cm, excluding a 5 × 10 cm area occupied by the handle, a significantly larger number of modules could be mounted in a dense arrangement.

From a theoretical standpoint, increasing the number of modules proportionally increases the total electrical output, provided that similar thermal conditions (ΔT) are maintained. Under such conditions, the system could transition from milliwatt-level generation, tens of mW measured experimentally with four modules, toward the sub-2 W range estimated in this study for a full-door array of 133 modules (see the extrapolation above); reaching higher power levels would require a larger heated surface, a higher module density, or thermal management improvements beyond the present door-mounted geometry.

This scaling potential enables the consideration of practical applications within the agricultural sector, particularly for low-power and distributed systems. The generated energy could be used for:

- powering wireless environmental sensors, such as soil moisture, temperature, humidity;
- supplying data acquisition and transmission modules in precision agriculture systems;
- charging low-power batteries or supercapacitors for autonomous field devices;
- supporting IoT-based monitoring platforms integrated into biochar or biomass processing units.

Such applications are especially relevant in remote or off-grid agricultural environments, where energy autonomy and sustainability are critical.

An additional promising aspect identified in this study is the presence of secondary heated surfaces within the biochar equipment, reaching temperatures of up to approximately 250 °C. These areas represent an untapped thermal resource that could be exploited using specialized high-temperature thermoelectric modules (e.g., modules based on materials optimized for medium-to-high temperature gradients).

The integration of such modules could significantly increase the overall energy recovery potential of the system by:

- expanding the effective heat exchange surface,
- utilizing multiple thermal zones with different temperature levels,
- enabling a more efficient distribution of thermoelectric conversion across the equipment.

In a combined configuration—where both the reactor door and secondary heated surfaces are utilized—the system could evolve into a multi-source thermoelectric harvesting platform, substantially improving total electrical output and system viability.

Nevertheless, achieving these improvements requires addressing the limitations identified in the current study, particularly:

- reducing thermal contact resistance;
- optimizing heat transfer pathways;
- improving cold-side cooling efficiency.

Overall, while the present experimental setup yields relatively low electrical efficiency, the results clearly indicate that through scaling, improved thermal integration, and the use of advanced thermoelectric materials, biochar production systems have the potential to power low-consumption auxiliary electronics — such as wireless sensor nodes, data loggers, and IoT communication modules — rather than to serve as a primary energy source, given the very low P/Qref conversion ratio (~0.021%) obtained in this study. In this targeted, auxiliary-power role, the approach can still contribute to energy self-sufficiency and sustainability in agricultural applications.

CONCLUSIONS

This research demonstrates that thermoelectric energy recovery from a biochar production system is technically feasible: the surface-mounted TEG array reached a maximum output voltage of 1.226 V, a peak power of 37.6 mW, and a maximum temperature gradient of 42.8 °C over a 335-minute heating cycle, consistent with the expected Seebeck-effect behavior.

The overall P/Q_{ref} conversion ratio, referred to the fixed reference power $Q_{ref} = 180$ W rather than to a per-point modelled heat flow (see Results), nonetheless remained very low (maximum ≈ 0.021%), driven primarily by imperfect thermal contact between the heat source and the module hot side and by the intrinsic limitations of Peltier modules repurposed as generators, as discussed above.

Scaling to the full reactor-door surface indicates that a multi-module array could reach power levels sufficient for low-consumption auxiliary electronics — wireless sensor nodes, data loggers, and IoT communication modules — though not for primary power generation.

Taken together, these results position TEG-based waste heat recovery from biochar production as a viable auxiliary-power source for agricultural monitoring applications, contributing to energy self-sufficiency in a targeted, realistic role rather than as a primary generation method.

ACKNOWLEDGEMENT

This paper was supported by the NUCLEU Program, through Project 9N/ 01.01.2023, "Technology for the valuation of vegetable residues in the form of biochar for the improvement of soil quality," carried out with the support of ANCSI.

REFERENCES

[1] Badaka, H. K., & Morega, A. M. (2024). Simulation of biomass carbonization and heat recovery for electricity production using Seebeck modules. *Revue Roumaine des Sciences Techniques – Série Électrotechnique et Énergétique*. https://doi.org/10.59277/RRST-EE.2024.69.3.17

[2] Champier, D. (2017). Thermoelectric generators: A review of applications. *Energy Conversion and Management, 140, 167–181*. https://doi.org/10.1016/j.enconman.2017.02.070

[3] Chelladorai, P., Atekov, P., Balakrishnan, N., Kashyap, A., Chakravarty, P., & Naresh, G. (2024). Computational and Experimental Evaluation of Thermoelectric Generator for Waste Heat Recovery in Internal Combustion Engine Applications. *SAE Technical Paper 2024-01-5076*.

[4] Ciupercă, R., Constantin, A.-M., Zaica, A., & Ștefan, V. (2022). Recovery of solar thermal energy and energy from the composting process. *INMATEH – Agricultural Engineering, 68*(3), 896–905. https://doi.org/10.35633/inmateh-68-89

[5] Cui, X., Chen, X., & Gao, Z. (2024). Research on the power generation performance and optimization of thermoelectric generators for recycling remaining cold energy. *Energy, 299, 131422*. https://doi.org/10.1016/j.energy.2024.131422

[6] Deng, Y., Liu, X., & Su, C. (2022). Experimental investigation of thermoelectric generator for waste heat recovery from biomass combustion systems. *Renewable Energy, 189*, 1234–1243. https://doi.org/10.1016/j.renene.2022.03.045

[7] Hqgraphene, available online: https://www.hqgraphene.com/Bi2Te3.php Bi2Te3 – Bismuth Telluride (product page). Accessed August 2026.

[8] Iavnic, T., Puiu, D., & Popescu, A. (2024). Energy recovery from waste heat using thermoelectric generators. *Buletinul Institutului Politehnic din Iași, 69*(4), 21–35. https://doi.org/10.2478/bipcm-2023-0032

[9] Jiang, Y., Wang, Y., Yan, J., Shen, L., & Qin, J. (2024). Research on the performance of thermoelectric self-powered systems for wireless sensors based on industrial waste heat. *Sensors, 24(18), 5983*, MDPI. https://doi.org/10.3390/s24185983

[10] Karadirek, G., Taylan, G., Baykara, T., & Helvacı, H. U. (2025). Experimental performance evaluation of phase change material integrated thermoelectric generator. *International Journal of Energy Studies, 10(3), 963–981*. https://doi.org/10.58559/ijes.1686912

[11] Liu, Z., Zhang, H., & Wang, X. (2023). Performance analysis of thermoelectric generators for low-grade waste heat recovery: A review. *Energy Conversion and Management, 278, 116657*. https://doi.org/10.1016/j.enconman.2023.116657

[12] Maican, E. (2015). Renewable energy systems / Sisteme de energii regenerabile, *Printech Publishing House*, Bucharest/Romania

[13] Mastrullo, R., Mauro, A. W., & Vanoli, G. P. (2019). Thermoelectric generators for energy recovery from industrial processes: A review. *Energy Procedia, 158*, 120–125. https://doi.org/10.1016/j.egypro.2019.01.062

[14] Kim, M., Park, D., & Kim, J. (2025). A review on recent selenium- and tellurium-based thermoelectric materials and chalcogenide/organic flexible thermoelectric applications. *Materials Chemistry and Physics, Volume 337*, 1 June 2025, 130571. https://doi.org/10.1016/j.matchemphys.2025.130571

[15] Moriarty, P., & Honnery, D. (2016). Can renewable energy power the future? *Energy Policy, Vol. 93*, pp. 3-7, ISSN 0301-4215

[16] Ridwan, M. (2025). Principle and applications of thermoelectric generators: A review. *Sensors, 25(8), 2484*. https://doi.org/10.3390/s25082484

[17] Quan, R., Li, T., Yue, Y., Chang, Y., & Tan, B. (2020). Experimental study on a thermoelectric generator for industrial waste heat recovery based on a hexagonal heat exchanger. *Energies, 13(12), 3137*, MDPI. https://doi.org/10.3390/en13123137

[18] Sanin-Villa, D. (2022). Recent developments in thermoelectric generation: A review. *Sustainability, 14(24), 16821*, MDPI. https://doi.org/10.3390/su142416821

[19] Săvescu, C., Morega, A. M., Roman, M., & Nechifor, C. (2025). Experimentally validated studies of thermoelectric generators installed on a compressor test bench. *Revue Roumaine des Sciences Techniques – Série Électrotechnique et Énergétique*. https://doi.org/10.59277/RRST-EE.2025.2.7

[20] Wang, Y., Wang, R., Chai, R., Ding, R., Ye, Q., Sun, Z., Meng, X., & Sun, D. (2025). Review of automotive thermoelectric generator structure design and optimization for performance enhancement. *Processes, 13(6), 1931*. https://doi.org/10.3390/pr13061931

[21] Weatherspark. Historical Weather on December 11, 2025 in Bucharest, Romania. Accessed August 2026. Available online: https://weatherspark.com/h/d/93241/2025/12/11/Historical-Weather-on-Thursday-December-11-2025-in-Bucharest-Romania#Figures-Temperature

[22] Williams, N. P., Power, J., Trimble, D., & O'Shaughnessy, S. M. (2022). An experimental evaluation of thermoelectric generator performance under cyclic heating regimes. *Heat and Mass Transfer, 60*, 1991–2003. https://doi.org/10.1007/s00231-022-03280-5

[23] Yaman, K., Dölek, S., & Arslan, G. (2025). Performance analysis of a thermoelectric generator (TEG) for waste heat recovery. *WAPRIME, 2(1), 13–20*. https://doi.org/10.5281/zenodo.16980562

DESIGN AND TESTING OF AN AIR SUCTION ORCHARD FRUIT-BAG COLLECTION MACHINE
/
气吸式果园套袋纸回收机设计与试验

Caiqi HU[1,2], Junbo WANG[1,2], Fengjie TENG[1,2], Rendong SUI*[1,2]
[1)] College of Mechanical and Electrical Engineering, Qingdao Agricultural University, Shandong / China;
[2)] Shandong Provincial Key Laboratory of Smart Agricultural Equipment for Protected Horticulture / China
Tel: 8613475835919; E-mail: 827435160@qq.com
Corresponding author: Rendong SUI
DOI: https://doi.org/10.35633/inmateh-79-111

Keywords: *orchard fruit-bag collection; air suction; airflow field analysis; orchard field test*

ABSTRACT
To address the environmental pollution caused by discarded non-biodegradable fruit bags in orchards, an air-suction orchard fruit-bag collection machine was developed. First, theoretical calculations and analyses were conducted on the key machine components to determine the main operating parameters. Kinematic analysis was then performed using ADAMS, and the airflow field was simulated using Fluent. Next, a prototype was manufactured. Based on multivariable response surface analysis conducted in Design-Expert, the optimal parameter combination was identified as a travel speed of 2 km/h, a suction-inlet air velocity of 15.5 m/s, and a helical-conveyor rotational speed of 66 r/min. Orchard field tests showed that, under the optimal operating conditions, the actual collection rate reached 82.5%, confirming that the machine met the intended design requirements.

摘要
针对果园废弃套袋纸不易降解、污染环境等问题，提出了气吸式果园套袋纸回收机的设计。首先对关键装置进行理论计算与分析，确定影响作业效果的关键因素，以此为基础进行ADAMS运动学分析和Fluent气流场仿真分析。然后进行样机研制，通过 Design-Expert 进行多因素响应面分析，确定整机的工作参数最佳组合为：行进速度为2 km/h、吸入口风速为15.5 m/s、螺旋输送装置转速为66 r/min。果园试验表明，在最佳工作参数下，样机试验回收率为82.5%, 验证本设计能够实现预期的工作效果。

INTRODUCTION
The bagging of young fruit on trees has been widely adopted in orchards for crops such as apples, pears, and peaches. Taking apple orchards as an example, fruit bags not only help reduce pest and disease incidence and limit pesticide exposure but also significantly improve fruit appearance and quality *(Liu et al., 2024; Yu et al., 2022)*. To promote uniform coloration, the bags are generally removed approximately two weeks before harvest, after which they are often discarded in the orchard *(Hong et al., 2020; Kim et al., 2013)*. Because these fruit bags are primarily made from wood pulp with a high fiber content and also contain wet-strength agents and other additives, their natural degradation is limited *(Chen et al., 2024)*. Therefore, collecting the discarded fruit bags can reduce resource waste and help protect the orchard production environment *(Luo et al., 2011; Zhang et al., 2014)*.

Currently, waste fruit bags are collected primarily by hand, a process characterized by high labor requirements, high costs, and low efficiency. These limitations reduce orchard growers' willingness to participate in collection activities *(He et al., 2022; Cao et al., 2019)*. The lack of efficient mechanical collection equipment has therefore become a major constraint on the sustainable development of the fruit industry *(Cai et al., 2024; Bishnoi et al., 2023)*. Research on machinery specifically designed to collect discarded fruit bags in orchards remains limited both in China and internationally; however, relevant studies have been conducted on related collection equipment.

For example, Guo Wensong of China Agricultural University developed a brush-tooth mechanically driven film-separation device for collecting residual plastic film *(Guo et al., 2020; Wang et al., 2019)*. The brush teeth dislodged the residual film, after which negative-pressure airflow at the suction inlet lifted the film.

The collected material was then discharged by a centrifugal fan and separated using a mesh screen. In addition, Liu Enshui and colleagues at Tarim University used Fluent to simulate a gravity settling chamber and determine the optimal operating parameters of the collection device *(Liu et al., 2021; Wang et al., 2012)*.

Existing studies have focused mainly on residual-film collection machinery *(Peng et al., 2020; Hou et al., 2023; Wang et al., 2024)*, whereas research specifically addressing air-suction machines for collecting discarded fruit bags remains limited *(Ken et al., 2024; Ma et al., 2024)*. Although several machines based on relatively simple operating principles have been investigated, innovation in their collection mechanisms has been insufficient, limiting their ability to meet the practical requirements of large-scale discarded fruit-bag collection.

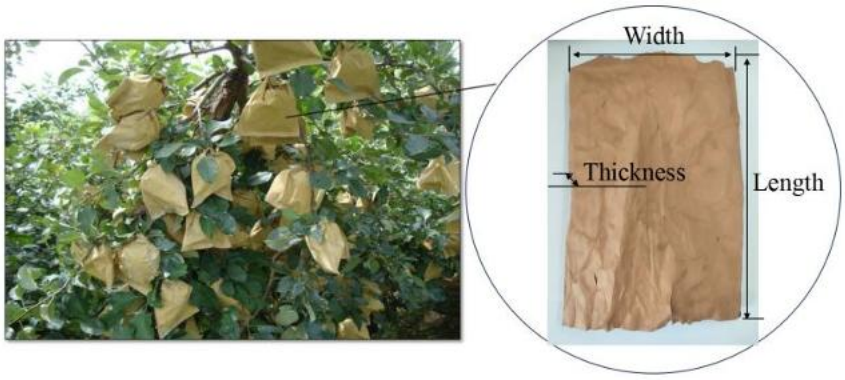
To address these challenges, an air-suction orchard fruit-bag collection machine was developed. The key components were analyzed theoretically to determine the main operating parameters. Kinematic simulations were then conducted in ADAMS, and computational fluid dynamics simulations were performed in Fluent to evaluate the mechanical and aerodynamic performance of the machine. A prototype was subsequently manufactured based on the theoretical analysis and simulation results. Response surface methodology was used to determine the optimal combination of operating parameters, with the collection rate selected as the response variable. Experimental results confirmed that the machine met the intended design requirements.

MATERIALS AND METHODS

Physical Characteristics of Discarded Fruit Bags

The physical characteristics of discarded fruit bags from apple orchards were determined through systematic sampling. A total of 100 discarded fruit bags were randomly collected and divided equally into 10 groups for statistical analysis. Their main physical properties were as follows: the mean length was 180 mm, the mean width was 147 mm, and the mean thickness was 2.2 mm. The coefficient of friction and the mean mass of a single bag were 0.52 and 5.6 × 10^{-3} kg, respectively. Representative fruit bags are shown in Fig. 1.

The terminal velocities of the fruit bags ranged from 2.9 to 5.6 m/s, whereas those of soil-clod impurities ranged from 11.5 to 15.0 m/s.



(a) Fruit bags on an apple tree (b) Enlarged view of a fruit bag

Fig. 1- Fruit bags and their dimensional characteristics

Overall Structure and Operating Principle

The air-suction fruit-bag collection machine mainly consists of a centrifugal fan, an air duct, a settling chamber, a helical conveyor, a direction-changing mechanism, a vertical scraper, a filter screen, a compression device, an engine, and a transmission system. The overall structure of the machine is shown in Fig. 2.

Power is transmitted from the power take-off shaft to the centrifugal fan through a belt-and-pulley drive, while the helical conveyor and vertical scraper are driven by chain-and-sprocket mechanisms. The rotating blades on both sides of the vertical scraper move the fruit bags toward the center, after which the helical conveyor further conveys them to the central collection area. A filter screen mounted at the bottom provides preliminary removal of impurities. The negative-pressure airflow generated by the centrifugal fan then draws the concentrated fruit bags into the settling chamber, where larger impurities are separated.

The cleaned fruit bags are subsequently conveyed through the air duct to the collection bin. Finally, the compression device compacts the bags, thereby completing the collection process.

The vertical scraper, helical conveyor, and settling chamber are the key components of the air-suction fruit-bag collection machine. Accordingly, the design and analysis of these components constitute the main focus of this study.

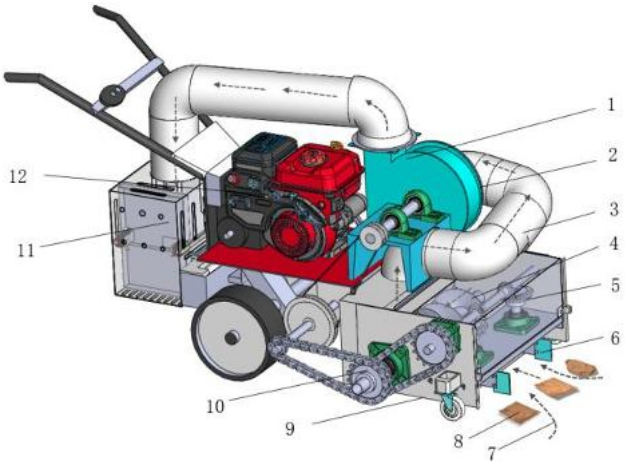


Fig. 2 - Structure of the air-suction fruit-bag collection machine

1. Centrifugal fan; 2. Air duct; 3. Settling chamber; 4. Helical conveyor; 5. Direction-changing mechanism; 6. Vertical scraper; 7. Fruit-bag trajectory; 8. Fruit bag; 9. Filter screen; 10. Transmission system; 11. Compression device; 12. Engine.

Design of the Vertical Scraper Collection Mechanism

The vertical scraper collection mechanism mainly consists of a horizontal drive shaft, two vertical rotating shafts, an adjustment plate, bearing housings, and two symmetrically arranged vertical scraper blades connected through a reversing mechanism. Power is supplied by the engine, and the rotational speed is reduced through belt, chain, and bevel-gear transmissions. The two meshing bevel-gear pairs rotate in opposite directions, ensuring that the left and right scraper blades move the fruit bags toward the center.

The operating principle of the vertical scraper collection mechanism is shown in Fig. 3. Power is transmitted to the horizontal drive shaft through a chain drive, causing the shaft to rotate clockwise. A small bevel gear mounted on the drive shaft engages with a large bevel gear, thereby driving the scraper blades on both sides to rotate inward and move the fruit bags toward the center. To ensure stable fruit-bag collection, an appropriate rotational speed of the scraper blades must be determined.

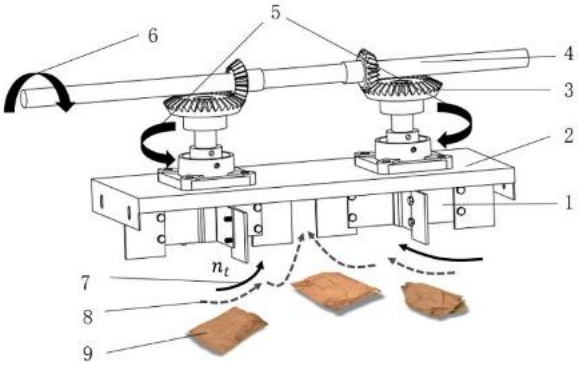


Fig. 3 - Operating principle of the vertical scraper collection mechanism

1. Scraper blades; 2. Adjustment plate; 3. Direction-changing mechanism; 4. Horizontal drive shaft; 5. Rotation direction of the vertical shafts; 6. Rotation direction of the drive shaft; 7. Rotation direction of the scraper blades; 8. Fruit-bag trajectory; 9. Fruit bag.

During operation, the vertical scraper collection mechanism relies primarily on the centrifugal force generated by the rotating scraper blades to move the fruit bags toward the center. A force analysis was conducted for the scraper blade, fruit bag, and bottom plate, and a rectangular coordinate system was established, as shown in Fig. 4. At the position illustrated, the fruit bag is subjected to the centrifugal force exerted by the scraper blade, the friction force acting along the bottom plate, the normal support force from the bottom plate, and its own weight.

Force equilibrium along the bottom plate indicates that the fruit bag can be conveyed into the collection mechanism only when the component of centrifugal force in the conveying direction exceeds the sum of the friction force and the component of gravity acting along the bottom plate.

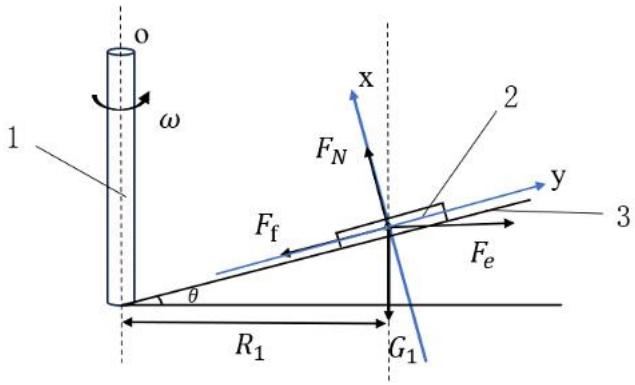


Fig. 4 - Force analysis of a fruit bag on the bottom plate

1. Vertical rotating shaft; 2. Fruit bag; 3. Bottom plate.

Force analysis:

$$\begin{cases} F_f + G_1 \sin\theta \le F_e \cos\theta \\ F_N = G_1 \cos\theta + F_e \sin\theta \end{cases} \quad (1)$$

where:

$$G_1 = m_l g \quad (2)$$

$$F_f = \mu F_N = \mu(m_l g \cos\theta + F_e \sin\theta) \quad (3)$$

where, F_e is the centrifugal force acting on the fruit bag, N; F_f is the friction force acting on the fruit bag, N; G_1 is the weight of the fruit bag, N; F_N is the normal support force exerted by the bottom plate, N; m_l is the mass of a single fruit bag, kg ; θ is the inclination angle of the bottom plate, set to 7°; μ is the coefficient of friction between the fruit bag and the bottom plate, set to 0.52.

Based on the measured physical characteristics, the mass of a single fruit bag was 5.6×10^{-3} kg. Substitution of the relevant parameters into Eqs. (1)–(3) showed that the centrifugal force acting on the fruit bag must exceed 3.77×10^{-2} N for the bag to be conveyed smoothly along the bottom plate and into the collection mechanism.

The centrifugal force generated during blade rotation is related to the blade rotational speed as follows:

$$F_e = m_l \omega_t^2 R_1 \quad (4)$$

$$\omega_t = \frac{\pi n_t}{30} \quad (5)$$

where, ω_t is the angular velocity of the scraper blades, rad·s^{-1}; R_l is the radial distance from the axis of rotation to the fruit bag, m; n_t is the rotational speed of the scraper blades, r·min^{-1}.

The minimum centrifugal force required for successful collection by the vertical scraper mechanism was calculated to be 3.77×10^{-2} N. According to Eqs. (4) and (5), when the blade radius was 0.18 m, the corresponding rotational speed of the scraper blades was 58.39 r·min^{-1}. Therefore, the vertical scraper mechanism can collect the fruit bags smoothly when the blade rotational speed exceeds 58.39 r·min^{-1}.

Design of the Helical Conveyor

To convey the fruit bags toward the center of the machine, a helical conveyor was designed. Helical blades were welded symmetrically to both sides of a hollow shaft, with equal numbers of blades arranged in opposite helical directions. Arc-shaped baffles closely followed the curvature of the rotating blades, thereby helping to prevent fruit-bag accumulation. A filter screen mounted at the bottom removed impurities such as weeds and soil clods. As shown in Fig. 5, the helical conveyor mainly consists of a hollow shaft, helical blades, arc-shaped baffles, a filter screen, and shock-absorbing wheels.

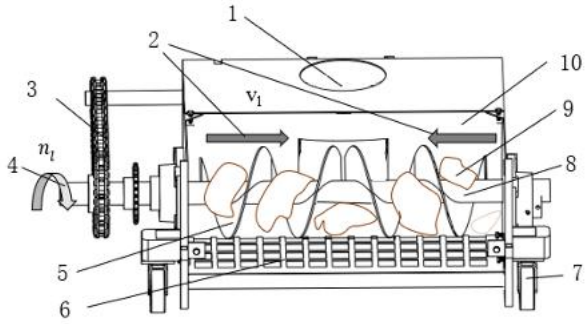


Fig. 5 - Structure and operating principle of the helical conveyor

1. Fruit-bag inlet; 2. Direction of fruit-bag movement; 3. Chain. 4. Rotation direction of the hollow shaft; 5. Helical blades; 6. Filter screen. 7. Shock-absorbing wheel. 8. Hollow shaft. 9. Fruit bag. 10. Arc-shaped baffle.

Based on the operating requirements of the collection machine, the principal geometric parameters of the helical blades were designed, including the outer diameter D_l, shaft diameter d_l, and pitch S_l.

To ensure that the fruit bags entered the helical conveyor smoothly and were conveyed from both sides toward the center, the helical-blade dimensions were selected according to the measured dimensions of the fruit bags. The structural parameters of the conveyor were determined with reference to the fruit-bag characteristics and the *Agricultural Machinery Design Manual*. Considering the physical properties of the fruit bags and the orchard operating environment, the blade outer diameter D_l, pitch S_l, and shaft diameter d_l were set to 160, 160, and 40 mm, respectively, to improve conveying efficiency.

During operation, an excessively low rotational speed of the helical blades may prevent the fruit bags from being conveyed promptly toward the center, resulting in accumulation on both sides. Conversely, an excessively high rotational speed may cause the blades to strike the bags, making them bounce and disrupting their movement toward the center. This may cause the bags to fall out of the conveying area. Therefore, the critical rotational speed of the helical conveyor must be determined.

To prevent accumulation and bouncing, the rotational speed of the helical conveyor should be maintained between the minimum speed required for effective conveying and the critical speed at which the fruit bags begin to lose stable contact with the conveyor. The critical condition was determined by comparing the centrifugal force acting on a fruit bag with its weight:

$$\frac{m_l \omega_l^2 D_l}{2} \leq m_l g \tag{6}$$

where:

$$\omega_l = \frac{\pi n_l}{30} \tag{7}$$

where, m_l is the mass of a single fruit bag, kg; ω_l is the angular velocity of the helical conveyor, rad·s^{-1}; g is the gravitational acceleration, m·s^{-2}; n_l is the rotational speed of the helical blades, r·min^{-1}.

Substituting Eq. (6) into Eq. (7) gives:

$$n_l \leq \frac{30}{\pi}\sqrt{\frac{2g}{D_l}} \tag{8}$$

The calculated critical rotational speed of the helical blades was 106.76 r·min^{-1}. Therefore, considering the previously determined minimum operating speed, the helical conveyor should operate within the range of 58.39–106.76 r·min^{-1}. Within this range, the conveyor can meet the requirements for stable fruit-bag conveying and collection while reducing the risks of blockage and bag bouncing.

Kinematic Simulation of the Helical Conveyor

To evaluate the conveying performance of fruit bags in the helical conveyor, a kinematic simulation was conducted using ADAMS. Before analyzing the motion of the conveyor, kinematic constraints between the components and contact constraints between the fruit bags and the relevant machine parts were defined in the model. The simulation duration was set to 8 s, with 500 calculation steps. The constraint relationships are

listed in Table 1. Because the shape of the fruit bags varied, three representative bag shapes were included in the simulation, as shown in Fig. 6.

Table 1

Constraint relationships in the helical conveyor model

No.	Constraint type	Constrained components
1	Fixed joint	Frame–ground
2	Fixed joint	Helical blades–auger shaft
3	Revolute joint	Auger shaft–frame
4	contact	Fruit bag–frame
5	contact	Fruit bag–helical blades
6	contact	Fruit bag–auger shaft

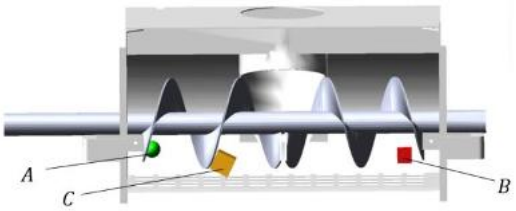
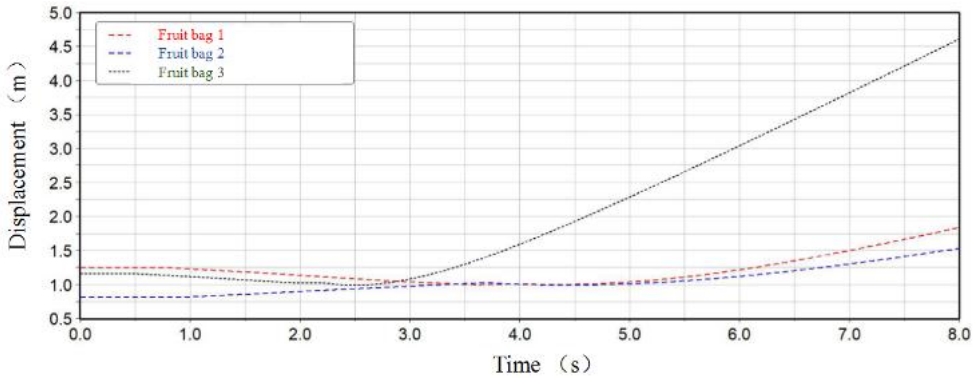


Fig. 6 - ADAMS model of the helical conveyor and representative fruit-bag shapes

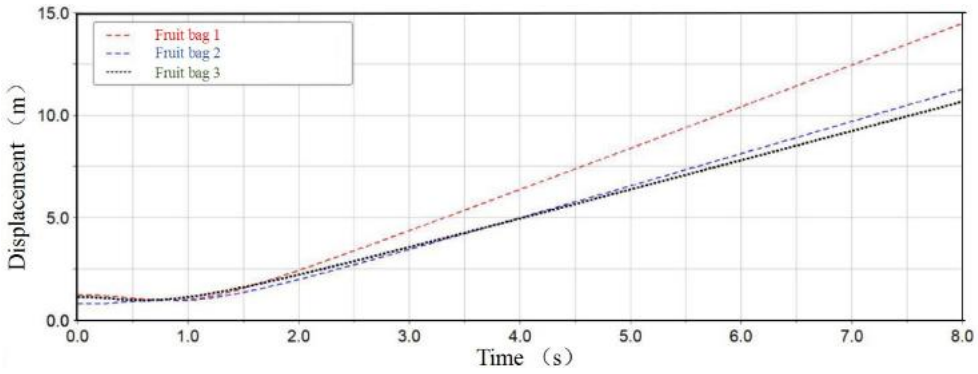
A, fruit bag 1, B, fruit bag 2, C, fruit bag 3.

Based on the simulation results, the displacement curves of the fruit bags at different helical-blade rotational speeds are shown in Fig. 7.



(a) Helical-blade rotational speed of 58.39 r·min⁻¹

(b)



(b) Helical-blade rotational speed of 106.76 r·min⁻¹

Fig. 7 - Displacement curves of the fruit bags at different helical-blade rotational speeds

As shown in Fig. 7, comparison of the displacement curves at helical-blade rotational speeds of 58.39 and 106.76 r·min⁻¹ indicates that a higher rotational speed produced greater fruit-bag displacement over the same period. All three representative fruit bags exhibited stable and smooth motion. These results demonstrate that the helical conveyor can reliably convey the fruit bags toward the center of the machine.

Design of the Settling Chamber

The settling chamber uses gravity-induced settling to separate fruit bags from impurities. It plays an important role in both fruit-bag recovery and impurity removal. The chamber mainly consists of a settling section, an inlet, and an outlet. Its structure and operating principle are shown in Fig. 8.

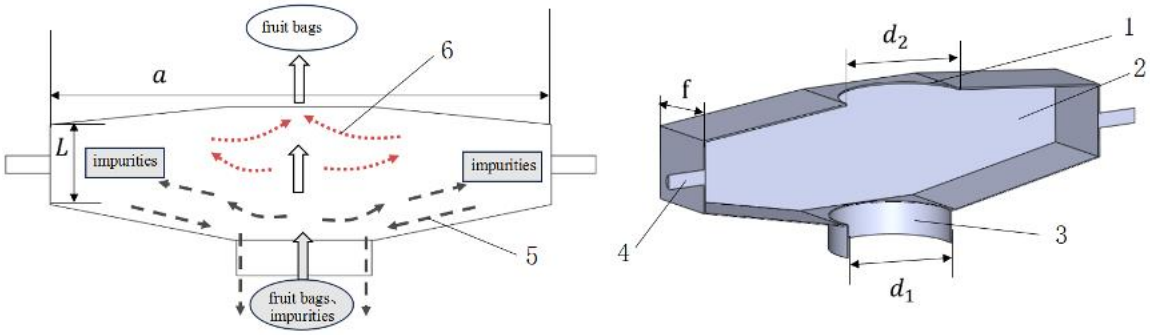


Fig. 8 - Structure and operating principle of the settling chamber

1. Air outlet; 2. Settling section; 3. Inlet; 4. Fixed shaft; 5. Impurity trajectory; 6. Fruit-bag trajectory. a, length of the settling chamber; f, half-width of the settling chamber; L, height of the settling chamber; d_1 is the inlet diameter; d_2, air-duct diameter.

Field investigations showed that, during fruit-bag collection, brittle weed residues were broken into smaller fragments by the vertical scraper and helical conveyor and were subsequently removed through the bottom filter screen. Only a small amount of large weed material entered the settling chamber. Therefore, the impurities reaching the settling chamber consisted mainly of small soil clods. To achieve effective separation of the fruit bags from the soil clods, the airflow velocity in the settling chamber had to be higher than the terminal velocity of the fruit bags but lower than that of the soil clods.

Assuming a constant volumetric airflow rate through the system, different airflow velocities can be obtained by designing the inlet and settling section with different cross-sectional areas. The corresponding airflow velocities were calculated using Eq. (9):

$$Q = v_1 A_1 = v_2 ab \tag{9}$$

where, Q is the volumetric airflow rate supplied by the centrifugal fan, m³·s⁻¹; v_1 is the airflow velocity at the inlet, m·s⁻¹; A_1 is the cross-sectional area of the inlet, m²; is the airflow velocity in the settling section, m·s⁻¹; *a* and *b* are the length and width of the settling section, respectively, m.

Considering that the mean fruit-bag length was 180 mm and that sufficient clearance was required for pneumatic conveying, both the air-duct diameter and the inlet diameter were set to 200 mm. Based on the measured terminal velocities of the fruit bags and soil clods, the airflow velocity in the settling chamber was set to 5.6 m·s⁻¹ to facilitate impurity separation. The settling-chamber length was set to 500 mm so that it was compatible with the overall dimensions of the collection mechanism. According to Eq. (9), the required settling-chamber width was calculated to be 224 mm.

Because the cross-sectional area gradually increased from the suction inlet to the settling chamber, the airflow velocity decreased through this transition region, thereby reducing the aerodynamic force acting on both the fruit bags and the soil clods. Effective separation occurred when the aerodynamic lifting force was sufficient to entrain the fruit bags but insufficient to carry the soil clods. Under these conditions, the fruit bags were conveyed upward by the airflow, whereas the soil clods settled under gravity and were discharged through the bottom screen rather than entering the collection bin. The resultant force acting on a soil clod is expressed by Eq. (10):

$$F = Kmv_2^{\,2} - mg = Kmv_2^{\,2} - Kmv_t^{\,2} = ma_1 \tag{10}$$

where, F is the resultant force acting on the soil clod, N; m is the mass of the soil clod, in kilograms，kg; g is the gravitational acceleration, taken as 9.8 m·s⁻²; K is the aerodynamic or buoyancy coefficient of the soil clod; v_t is the terminal velocity of the soil clod, m·s⁻¹; a_1 is the acceleration of the soil clod, m·s⁻².

As the aerodynamic lifting force gradually decreased, the soil clods moved upward under deceleration until their velocity decreased to zero, with the resultant acceleration being non-positive.

The upward travel distance of the soil clods was used to determine the required height of the settling chamber. This distance is expressed by Eq. (11):

$$-v_3^2 = 2a_1 h \tag{11}$$

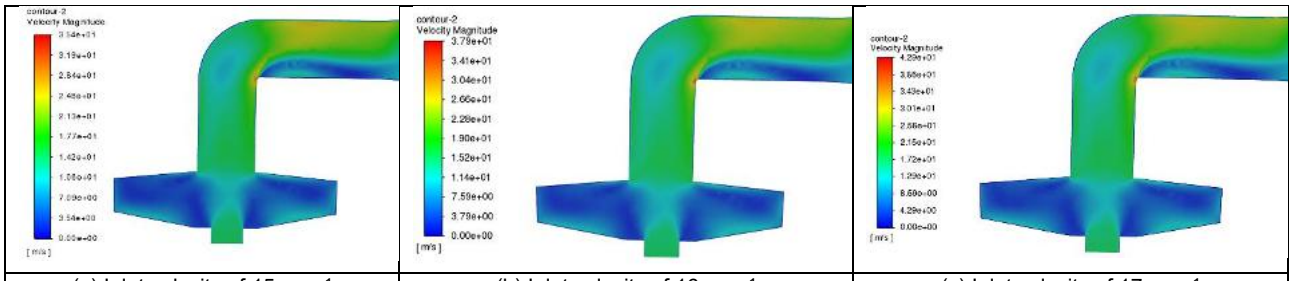
where, h is the upward travel distance of the soil clod, m; v_3 is the initial upward velocity of the soil clod at the bottom of the settling chamber, m·s⁻¹.

Based on the structural requirements of the machine, the initial velocity of the soil clod at the bottom of the settling chamber was set to 5.6 m·s⁻¹. Substitution of the relevant parameters into Eq. (11) yielded a required settling-chamber height of 123 mm.

Airflow-Field Simulation Analysis of the Settling Chamber

The airflow field in the fruit-bag conveying system is highly complex. To characterize the airflow behavior, simulation analysis was conducted using Fluent. Velocity distributions were analyzed on cross-sections of both the settling chamber and the conveying duct, allowing the transport behavior of the fruit bags to be observed visually.

The measured terminal velocity of the fruit bags ranged from 2.9 to 5.6 m·s⁻¹. According to the empirical coefficient, the conveying airflow velocity should be 2.6-5.0 times the terminal velocity of the fruit bags. Considering the practical operating conditions and the need for impurity removal, the inlet airflow velocity should not be set excessively high. Based on a comprehensive assessment, inlet velocities of 15, 16, and 17 m·s⁻¹ were selected. The simulated airflow-velocity contours under these three inlet conditions are shown in Fig. 9.



(a) Inlet velocity of 15 m·s⁻¹ (b) Inlet velocity of 16 m·s⁻¹ (c) Inlet velocity of 17 m·s⁻¹

Fig. 9 - Airflow-velocity contours at different inlet velocities

As shown in Fig. 9(a), at an inlet velocity of 15 m·s⁻¹, the airflow velocity near the lower section of the settling chamber reached approximately 17 m·s⁻¹, allowing the fruit bags and impurities to be rapidly drawn into the chamber. As the cross-sectional area of the settling chamber increased, the airflow velocity gradually decreased from the central region toward both ends. The velocity at both ends was approximately 5.6 m·s⁻¹, which facilitated separation of the fruit bags from the impurities. In the upper section of the settling chamber, the cross-sectional area decreased abruptly, causing the airflow velocity to increase to approximately 18 m·s⁻¹ and enabling the fruit bags to be conveyed smoothly through the outlet.

As shown in Fig. 9(b), the conveying performance at an inlet velocity of 16 m·s⁻¹ was similar to that observed at 15 m·s⁻¹. Under this condition, the fruit bags were effectively separated from the impurities and conveyed smoothly through the outlet.

As shown in Fig. 9(c), when the inlet velocity was set to 17 m·s⁻¹, the airflow velocity near the lower section of the settling chamber reached approximately 21 m·s⁻¹, allowing both the fruit bags and impurities to enter the chamber. However, the airflow velocity in the middle section ranged from 8.59 to 12.9 m·s⁻¹. This range exceeded the terminal velocity of the soil-clod impurities, resulting in incomplete separation of the impurities from the fruit bags.

Based on these results, the inlet airflow velocity should be maintained between 15 and 16 m·s⁻¹ to ensure effective separation of the fruit bags from impurities and stable conveying through the system.

RESULTS

Orchard Field Test

Based on the preceding design and simulation analyses, a prototype was manufactured and tested in an apple orchard. The tree-row spacing ranged from 1,400 to 2,000 mm, while the within-row tree spacing ranged from 1,100 to 1,400 mm. The machine travel speed was varied from 1 to 3 km·h⁻¹. The orchard field test is shown in Fig. 10.



Fig. 10 - Orchard field test of the prototype

Experimental Design and Parameter Optimization

To determine the optimal combination of operating parameters, a three-factor, three-level response surface experiment was designed using Design-Expert. The selected test factors were machine travel speed (1~3 km·h⁻¹), inlet airflow velocity (15~16 m·s⁻¹), and *helical-conveyor* rotational speed (62~68 r·min⁻¹). The coded levels of these factors are presented in Table 2. The fruit-bag collection rate was selected as the response variable and was calculated as follows:

$$Y_1 = (1 - \frac{M_2}{M_1}) \times 100\% \quad (12)$$

where, Y_1 is the fruit-bag collection rate, %; M_2 is the mass of fruit bags remaining in the field after operation, kg; M_1 is the initial mass of fruit bags in the field before operation, kg.

Table 2

Coded levels of the experimental factors

Coded level	Factors		
	Travel speed (km·h⁻¹)	Inlet airflow velocity (m·s⁻¹)	Helical-conveyor rotational speed (r·min⁻¹)
-1	1	15	62
0	2	15.5	65
1	3	16	68

According to the experimental design, 17 experimental runs were conducted. The experimental design matrix and corresponding results are presented in Table 3. In the table, X_1, X_2, and X_3 represent the coded values of the three factors, while Y_1 denotes the fruit-bag collection rate.

Table 3

Experimental design matrix and collection-rate results

Run	Factors			Fruit-bag collection rate Y_1/%
	Travel speed X_1	Inlet airflow velocity X_2	Helical-conveyor rotational speed X_3	
1	1	1	0	74.8
2	0	0	0	83.5

Run	Factors			Fruit-bag collection rate Y_1/%
	Travel speed X_1	Inlet airflow velocity X_2	Helical-conveyor rotational speed X_3	
3	0	0	0	82
4	0	1	-1	78.1
5	1	-1	0	72.7
6	-1	-1	0	74.5
7	-1	0	1	80
8	0	-1	1	82.1
9	0	-1	-1	78.9
10	0	0	0	83.1
11	-1	1	0	71
12	1	0	1	78.5
13	0	0	0	82.7
14	0	0	0	83
15	1	0	-1	75.2
16	0	1	1	80.7
17	-1	0	-1	78.4

Multiple regression analysis was performed on the experimental data, and the analysis of variance (ANOVA) results are presented in Table 4. The overall regression model was highly significant ($P < 0.05$), whereas the lack of fit was not significant ($P > 0.05$), indicating that the model adequately described the experimental data. The terms X_3, X_1^2, and X_2^2 had highly significant effects on the fruit-bag collection rate. According to the reported *P*-values, X_1, X_2, and the interaction term X_1X_2 also had significant effects, whereas the remaining terms were not significant. Based on the reported main-effect results, the factors were ranked in descending order of their influence on the collection rate, Y_1, as follows: helical-conveyor rotational speed (X_3), inlet airflow velocity (X_2), and machine travel speed (X_1).

Table 4

Analysis of variance for the regression model of fruit-bag collection rate

Source	Collection rate				
	Sum of squares	df	Mean Square	*F*-value	*P*-value
model	238.81	9	26.53	26.37	< 0.0001**
X_1	0.9112	1	0.9112	0.9055	0.037*
X_2	1.62	1	1.62	1.61	0.024*
X_3	14.31	1	14.31	14.22	0.007**
X_1X_2	7.84	1	7.84	7.79	0.0269*
X_1X_3	0.7225	1	0.7225	0.7179	0.4248
X_2X_3	0.09	1	0.09	0.894	0.7736
X_1^2	140.06	1	140.06	139.17	< 0.0001**
X_2^2	62.17	1	62.17	61.77	< 0.0001**
X_3^2	3.66	1	3.66	3.64	0.0981
Residual	7.04	7	1.01		
Lack of fit	5.79	3	1.93	6.17	0.0556
Pure error	1.25	4	0.313		
Total	245.85	16			

Note: * Significant at ($0.01 \leq P \leq 0.05$); ** highly significant at ($P<0.01$).

To provide a more intuitive representation of the interaction effects of the factors on the fruit-bag collection rate, the response surface was generated from the experimental results and the regression model, as shown in Fig. 11. When the machine travel speed was held constant, the collection rate first increased and then decreased as the inlet airflow velocity increased, reaching a maximum when the inlet airflow velocity

ranged from 15.2 to 15.8 m·s⁻¹. In addition, the collection rate reached its highest value when the machine travel speed ranged from 1.5 to 2.5 km·h⁻¹.

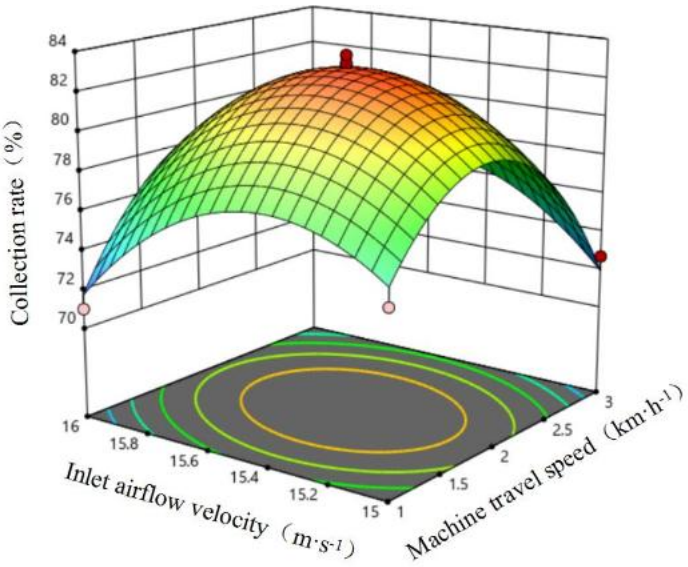


Fig. 11 - Effects of travel speed and inlet airflow velocity on the fruit-bag collection rate

Based on the ANOVA and response surface analyses, the regression equation for the fruit-bag collection rate, Y_1, was obtained as follows:

$$Y_1 = 82.86 - 0.3375X_1 - 0.45X_2 + 1.34X_3 + 1.4X_1X_2 - 5.77X_1^2 - 3.84X_2^2 \quad (13)$$

Considering the operating requirements of the air-suction fruit-bag collection machine, Design-Expert was used to optimize Eq. (13). The optimal parameter combination was a machine travel speed of 1.895 km·h⁻¹, an inlet airflow velocity of 15.509 m·s⁻¹, and a helical-conveyor rotational speed of 66.22 r·min⁻¹. Under these conditions, the model predicted a collection rate of 83.5%.

Experimental Results

The optimized parameters were rounded to practical operating values of 2 km·h⁻¹ for machine travel speed, 15.5 m·s⁻¹ for inlet airflow velocity, and 66 r·min⁻¹ for helical-conveyor rotational speed. Ten orchard field-test runs were conducted under these conditions. The mean collection rate was 82.5%, and the relative error between the predicted and measured values was 1.21%. The close agreement between the two values confirmed the reliability of the optimization model.

CONCLUSIONS

This study systematically investigated the environmental pollution caused by discarded fruit bags in orchards and their potential for recovery. An air-suction fruit-bag collection machine was designed, simulated, manufactured, and experimentally validated. The main conclusions are as follows:

(1) Based on the structural design and theoretical calculations, kinematic simulations of the helical conveyor were conducted using ADAMS, and airflow-field simulations of the settling chamber were performed using Fluent. The results showed that when the inlet airflow velocity ranged from 15 to 16 m·s⁻¹, the fruit bags could be effectively separated from the impurities and conveyed smoothly through the collection system.

(2) A prototype was manufactured based on the theoretical calculations and simulation results, and orchard field tests were conducted. Design-Expert was used to determine the optimal operating parameters. Under the optimized conditions, the measured collection rate was 82.5%. The field-test results confirmed that the machine met the intended design requirements.

ACKNOWLEDGEMENT

This research was funded by the National Natural Science Foundation of China (No: 31971801), the Natural Science Foundation of Shandong Province of China (No: ZR2020ME252, ZR2020ME250), Qingdao Science and Technology Benefit-the-People Demonstration Project (No: 25-1-5-xdny-33-nsh), and the University-enterprise Cooperation Project (No: H20250184).

REFERENCES

[1] Bishnoi, M., Goyal, K, R., Vats, C., Singla, A., (2023). Effect of Pre-Harvest Fruit Bagging on Fruit Quality Characteristics of Different Guava Cultivars during Rainy Season. *International Journal of Plant Soil Science*, 35 (21): 63-71.

[2] Cai, J., Zhang, J., Gao, Z., Wang, X., Guo, G., Baikeli, Y., Tang, X., Wang, Y., (2024). Design and test of a wheel-belt type cotton stalk puller(轮带式棉秆拔取装置的设计与试验). *Int J Agric & Biol Eng*, 17 (2): 102–108.

[3] Cao, C., Luo, K., Peng, M., Wu, Z., Liu, G., Li, Z., (2019). Experimental on winnowing mechanism and winnowing performance of hickory material (山核桃物料风选机理与风选性能试验研究).*Transactions of the Chinese Society for Agricultural Machinery*, 50 (09): 105-112.

[4] Chen,Y; Xing, R.; Liu, X.; Zhang, H.; Li, H. (2024). Design and Test of Potato Seedling Killing and Residual Film Recycling Integrated Machine(马铃薯杀秧与残膜回收联合作业机的设计与试验). *Agronomy*, 14, 2269.

[5] Guo, W., He, X., Wang, L., Zhao, P., Hu, C., Hou, S., Wang X., (2020). Development of a comb tooth loosening and pneumatic stripping plough layer residual film recovery machine (梳齿起膜气力脱膜式耕层残膜回收机研制). *Transactions of the Chinese Society of Agricultural Engineering (Transactions of the CSAE)*, 36 (18): 1-10.

[6] He, J., Cheng, X, T., Gao, Y., Zhang, X., Jia, X., (2022). Comparison of quality and storability among bagged and non-bagged fruits of three apple varieties (3 个苹果品种套袋果与不套袋果品质及耐贮性的比较). *China Fruits*, (06): 6-9.

[7] Hong K L, Sang H Y. (2020). Machine Learning Feature Extraction Based on Binary Pixel Quantification Using Low-Resolution Images for Application of Unmanned Ground Vehicles in Apple Orchards (基于低分辨率图像二值像素量化的机器学习特征提取方法及其在苹果园无人地面车辆中的应用). *Agronomy*, 10 (12): 1926-1926.

[8] Hou, G., Chen, H., Jiang, M., Niu, R., (2023). An Overview of the Application of Machine Vision in Recognition and Localization of Fruit and Vegetable Harvesting Robots. *Agriculture*, 13, 1814.

[9] Ken, T., Daisuke, S., Sadayuki, K., (2024). Comparison of performance between tapered and cylindrical roller bearings for pinion of gear unit subjected to rotation test. *Proceedings of the Institution of Mechanical Engineers*, 238 (3): 332-344.

[10] Kim, K., Lee, M., Eom, T., (2013). Preparation of Emulsion from Biodegradable Polymer (II) - Characteristics of paper treated as PLA and PBS emulsion. *Journal of Korea Technical Association of the Pulp and Paper Industry*, 45 (2): 13-20.

[11] Liu, E., (2021). Optimal design of residual film recovery machine with comb-tooth film lifting and pneumatic film stripping(梳齿式起膜与气力脱膜残膜回收机的优化设计).*Tarim University*.

[12] Liu, X., Ma, T., Zhang, H., Yan, K., Zhou, S., (2024). The accumulation of fungal not bacterial residue carbon is management-dependent under conventional and organic practices in apple-orchard soil. *Geoderma*, 448: 116968-116968.

[13] Luo, Y., Zhang, M, Y., Wang, J., (2011). Comparison experiment of three sizing agents of fruit-bagged paper(三种果袋纸施胶剂的对比实验研究). *Paper and Paper Making*, 30 (06): 6.

[14] Ma, Z., Zhu, Y., Li, J., Song, Z., Yu, J., Li, Y., Xu, L., (2024). Study on the performance of detection air duct and evaluation index of agricultural cleaning centrifugal fans(农用清洁离心风机检测风道性能及评价指标研究). *Biosystems Engineering*, 23981-97.

[15] Peng, Q., Li, C., Kang, J., Shi, G., Zhang, H., (2020). Improved design and test on Pneumatic cylinder sieve Film Hybrid Separator(气力式圆筒筛膜杂分离机改进设计与试验). *Transactions of the Chinese Society for Agricultural Machinery*, 51 (08): 126-135.

[16] Wang, H., Sun, W., Wang, H., Simionescu, P.A. (2024). Automated Mulched Transplanting of Angelica Seedlings Using a Pneumatic Sowing Device. *Agronomy*, 14, 3076.

[17] Wang, J., Xie, H., Li, G., Yan, J., Wei, H., Wu, H. (2019). Design and Simulation of Airflow Uniformity Mechanism for Fixed-Bed Peanut Pod Drying Equipment （固定床式花生荚果烘干设备匀风机构设计与仿真）. *Chinese Journal of Agricultural Machinery and Chemistry*, 40 (04): 84-92.

[18] Wang, W., Wang, C., (2012). Parameter Analysis and Simulation of Toothed Roller Pickup Device(弹齿滚筒式捡拾装置参数分析与仿真). *Transactions of the Chinese Society for Agricultural Machinery*, 43 (10): 82-89.

[19] Yu, M., Wen, Y., Mao, M., (2022). The pattern and development trend of China's apple foreign trade（我国苹果对外贸易格局及发展趋势）. *China Fruits*, (07): 100-104.

[20] Zhang, M., Liu, Y., Wang, X., (2014). Fruit nursery paper production process transformation and cost analysis（果树苗圃纸生产流程改造与成本分析）. *Journal of Shaanxi University of Science & Technology*, 32 (04): 1-4.

DESIGN AND TESTING OF A PRESS-GROOVE UNIFORM SEEDING MACHINE FOR WHEAT IN HIGH-MOISTURE RICE-STUBBLE FIELDS
/
高湿地稻茬麦压沟定深匀播机设计与试验

Zhang XIAO[1)], Tong JIAN[2)], Chen WEI*[1)], Zhaxi LUOBU*[2)], Wu JINJI[1)], Zhu JIPING[1)], Ding YAN[1)], Ma LINGJUAN[3)]
[1)] Nanjing Institute of Agricultural Mechanization, Ministry of Agriculture and Rural Affairs, Nanjing / China;
[2)] Tibet Academy of Agricultural and Animal Husbandry Sciences, Lhasa / China;
[3)] Agricultural Mechanization General Station of the Ministry of Agriculture and Rural Affairs
Tel: +86 025-84346278-68; E-mail: chenwei03@caas.cn
Corresponding author: Chen Wei, Zhaxi Luobu
DOI: https://doi.org/10.35633/inmateh-79-112

Keywords: *high-moisture fields; rice-stubble wheat; seeding machinery; field tests*

ABSTRACT
To address the low quality of mechanized wheat seeding in rice-stubble fields in the middle and lower reaches of the Yangtze River, caused by high soil moisture content and heavy straw coverage, a press-groove uniform seeding machine was designed. Key mechanisms for rotary tillage, precision seedbed preparation, depth-controlled furrow formation, and banded soil covering were developed, and the overall transmission system and blade-roller arrangement were designed to create a wheat seeder suitable for high-moisture rice-stubble fields. Field tests showed that the vegetation coverage rate after operation was 94.2%, the qualified rate of seeding depth was 98.0%, and the coefficient of variation of seeding uniformity was 18.1%. The machine effectively reduced seed skips and exposed seeds during mechanized seeding in high-moisture fields.

摘要
针对长江中下游水旱轮作区稻茬农田土壤含水率高，秸秆覆盖量大等导致小麦机械化播种质量低的问题，本文设计一种压沟匀播机，研发了旋耕、种床精整、定深种沟成型、带状覆土等关键机构，完成了整机传动、刀辊排列等设计，创制一种适用于高湿稻茬农田的小麦播种机，田间试验表明，机具作业植被覆盖率为 94.2%，播深合格率达 98%，播种均匀性变异系数为 18.1%，有效解决了湿烂田机械化播种的“漏播”“露籽”等问题。

INTRODUCTION
The rice-wheat cropping system is the predominant agricultural production system in the paddy-upland rotation regions of the middle and lower reaches of the Yangtze River in China and represents the principal cropping pattern for these two staple grain crops in Jiangsu Province. With an annual planting area of approximately 2.7 million ha, Jiangsu accounts for about 35% of the national rice–wheat rotation area, making it the largest rice-wheat double-cropping region in China (*Gao, 2023; Zhang et al., 2021*). As of 2024, Jiangsu Province had more than 90,000 family farms engaged in grain production, with an average operating area exceeding 170 ha per farm. The continuing expansion of production scale has increased the demand for mechanized field operations, creating a need for further improvements in both the quality and technological level of agricultural mechanization (*Guan et al., 2022; Zhang et al., 2023*).

Because of the abundant seasonal rainfall during the wheat planting period, the soil is often heavy and cloddy, with large amounts of crop residue remaining on the field surface. Existing methods, such as shallow rotary tillage seeding and no-till strip seeding in residue-free fields, are poorly suited to these high-moisture operating conditions. Consequently, the uniformity of seeding depth and seed distribution during mechanized wheat seeding in rice-stubble fields often fails to meet agronomic requirements. Problems such as exposed seeds, seed clustering, seedling gaps, and broken ridges are particularly severe (*Chen et al., 2022*). To ensure an adequate field seed population, the seeding rate must be increased by two- to threefold, substantially increasing production costs (*Sun et al., 2024*). In addition, tractor traffic leaves deep wheel ruts, causing considerable disturbance to the field surface. The resulting seedbed is markedly uneven, which adversely affects subsequent rotary tillage and seeding operations.

Because of differences in cropping systems among countries, research on wheat seeding machinery for rice-stubble fields has been more extensive in China, whereas relatively few similar studies have been reported elsewhere. The main research objectives have been to reduce operating power consumption and improve seeding quality (*Aladdin et al., 2021*).

To address poor operating quality and low efficiency caused by soil adhesion and blockage of the rotary tiller during tillage in rice-stubble fields, *Liu Guoyang et al.* established constitutive and contact models for rice-stubble soil, investigated the soil detachment behavior from rotary tiller components, designed an anti-adhesion rotary tiller, and developed an intelligent vibration-assisted anti-adhesion rotary tiller (*Liu, 2024*).

Li Hongwen et al. designed a wide-width precision reduced-rate seeder for rice-stubble fields based on drainage and seeding requirements. The qualified rate of seeding depth was 86.7%, and that of fertilizer placement depth was 93.3% (*Hong Hu, et al., 2016*). To reduce power consumption during tillage, *Hao Jianjun et al.* designed a wedge-shaped drag-reducing rotary tiller. The results showed that, compared with a rotary tiller conforming to the national standard, the new machine was 8.3% lighter and reduced operating power consumption by 9.29% (*Hao Jianjun, et al., 2019*).

Matin et al. addressed the problem of poor seeding quality in paddy-upland rotation areas of Southeast Asia by designing a blade-roller structure equipped with a single row of six rotary tillage blades. Field tests showed that the new blade roller significantly improved seeding quality (*Matin M.A. et al., 2021*). Behera et al. compared the field performance of a rotary tiller and a combined tillage machine. The results showed that the torque requirement of the rotary tiller was 28% higher than that of the combined tillage machine, whereas its draft resistance and total power consumption were lower (*Behera et al., 2021*).

To address problems such as inconsistent seeding depth and poor seeding uniformity in wheat seeding in rice-stubble fields, the present study investigated a press-groove, depth-controlled uniform seeding technology for wheat in high-moisture rice-stubble fields. The proposed technology integrates rotary tillage and seeding, seedbed preparation under high-moisture conditions, and seeding-depth control. It is intended to improve seeding quality, reduce production costs, enhance operating efficiency and crop yield, and support high-quality, efficient, environmentally sustainable wheat production.

MATERIALS AND METHODS

Overall Design of the Seeding Machine

To meet the requirements for wheat seeding in high-moisture rice-stubble fields, the machine developed in this study integrates seedbed preparation and seeding-depth control functions. The corresponding mechanisms are arranged sequentially according to the operating process of fertilization, seedbed preparation (primary and secondary tillage), seed-furrow formation, in-furrow seeding, and banded soil covering. The machine consists of front and rear sections (Fig.1). The primary tillage unit, seedbed preparation unit, rear depth-control press wheel, and banded soil-covering shaft all use side-drive transmission. The two sections are connected by a three-point hitch, and power is introduced through the intermediate gearbox of the front section. The fertilizer-metering shaft and seed-metering shaft are both motor-driven and controlled by a synchronous control system to improve the field uniformity of seeding and fertilization.

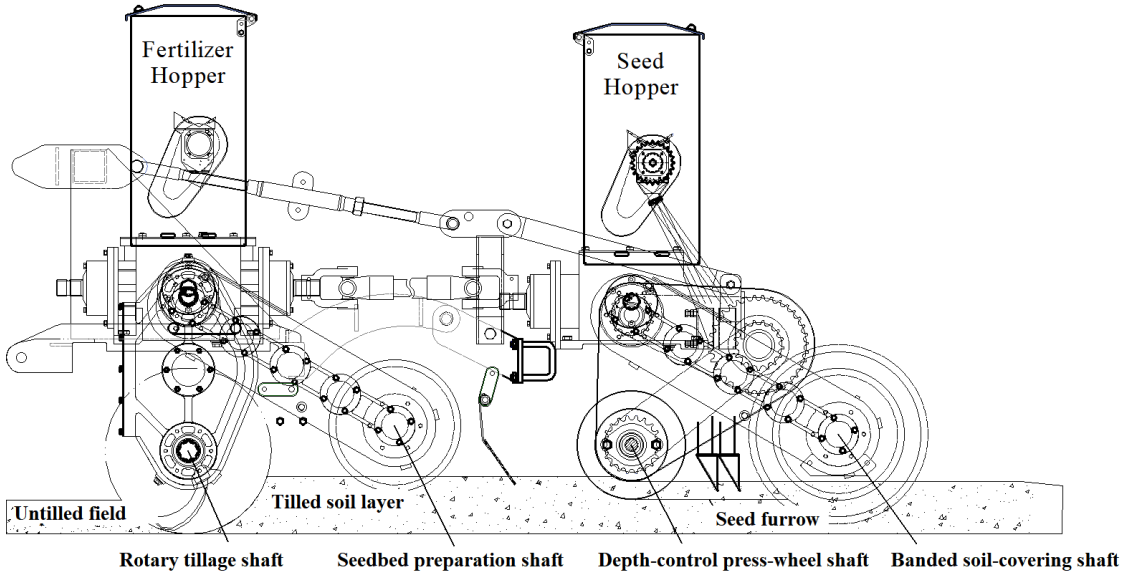
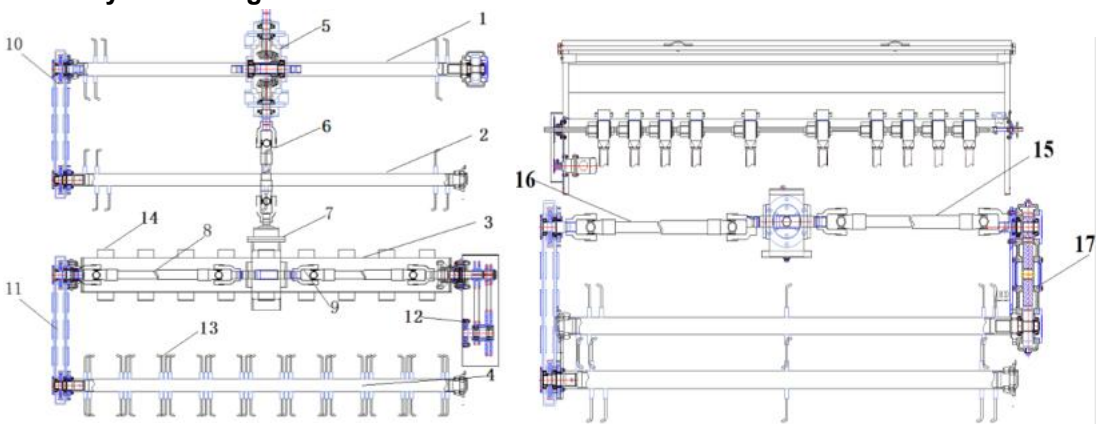


Fig. 1 - Overall schematic design of the seeding machine

The seeder is equipped with four working shafts and therefore has a relatively complex transmission system. Figures 2(a) and 2(b) show the top and front views, respectively, of the overall transmission layout. The transmission process is as follows. The tractor PTO is connected to intermediate gearbox *5*. Power is transmitted through universal-joint drive shaft *15* to side gearbox *17* and then to rotary tillage shaft *1*. Power is also transmitted through universal-joint drive shaft *16* to side gearbox *10* and then to seedbed-finishing shaft *2*. Meanwhile, intermediate gearbox *5* transmits power through universal drive shaft *6* to gearbox *7*, which distributes power to the seed-furrow-forming shaft and gearbox *11*. Gearbox *11* then drives soil-covering shaft *4* to complete the soil-covering operation. The transmission schematic is shown in Fig. 4.

Transmission System Design



(a) top view **(b) front view**

Fig. 2 - Transmission system of the seeding machine

1 - Rotary tillage shaft; 2 - Seedbed preparation shaft; 3 - Depth-control press-wheel shaft; 4 - Banded soil-covering shaft; 5 - Intermediate gearbox; 6 - Universal-joint drive shaft; 7 - Intermediate gearbox; 8 - Universal-joint drive shaft; 9 - Universal-joint drive shaft; 10 - Side gearbox; 11 - Side gearbox; 12 - Side gearbox; 13 - Soil-covering rotary tillage blades; 14 - Depth-control press-wheel; 15 - Right universal joint transmission shaft; 16 - Left universal joint transmission shaft; 17 - Side gearbox

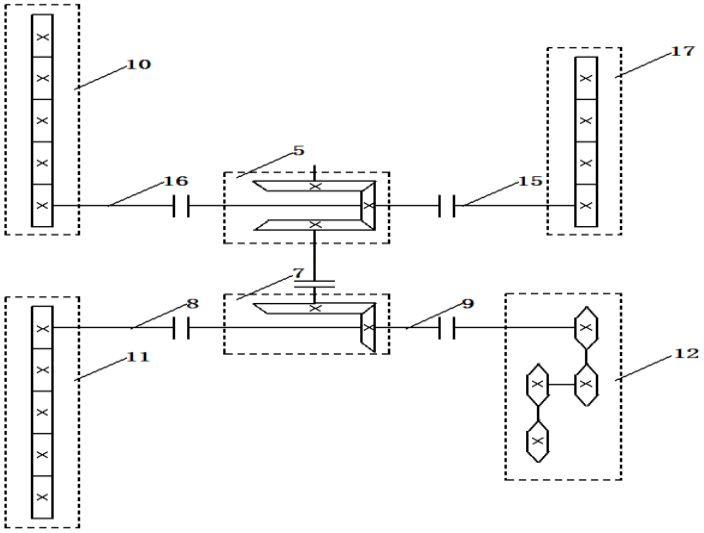


Fig. 3 - Schematic diagram of the transmission mechanism

The rotational speed of the blade shaft was determined using Eq. (1), which accounts for the machine forward speed, blade-shaft rotational speed, and soil-cutting pitch. Because rotary tillage requires a relatively high degree of soil fragmentation, the soil-cutting pitch should not be excessively large; a range of 60–90 mm was considered appropriate.

$$\frac{60V_m}{ZS_{max}} \leq n \leq \frac{60V_m}{ZS_{min}} \quad (1)$$

where: n is the blade-shaft rotational speed, rpm; V_m is the forward speed, m/s; Z is the number of cutting edges. The cutting pitch S was set to 80mm, the forward speed V_m to 1.3m/s, and Z to 2. Based on these values, the rotational speed of the rotary tillage shaft was determined to be 295 rpm, while that of the seedbed preparation shaft was 350 rpm.

Design of key working components

Rotary tiller shaft

The rotary tillage shaft is the main soil-engaging component during tillage and is also a major source of power consumption for the entire machine. Its design should account for force balance, reduced soil blockage, and minimized repeated cutting. In this study, the blades on the rotary tillage shaft were arranged primarily in a helical pattern to ensure balanced loading on both sides. The shaft had a total length of 2304 mm and was equipped with 72 blades, comprising left- and right-curved blades. Two blades were mounted on each cutting plane. The specific arrangement is shown in Fig. 5.

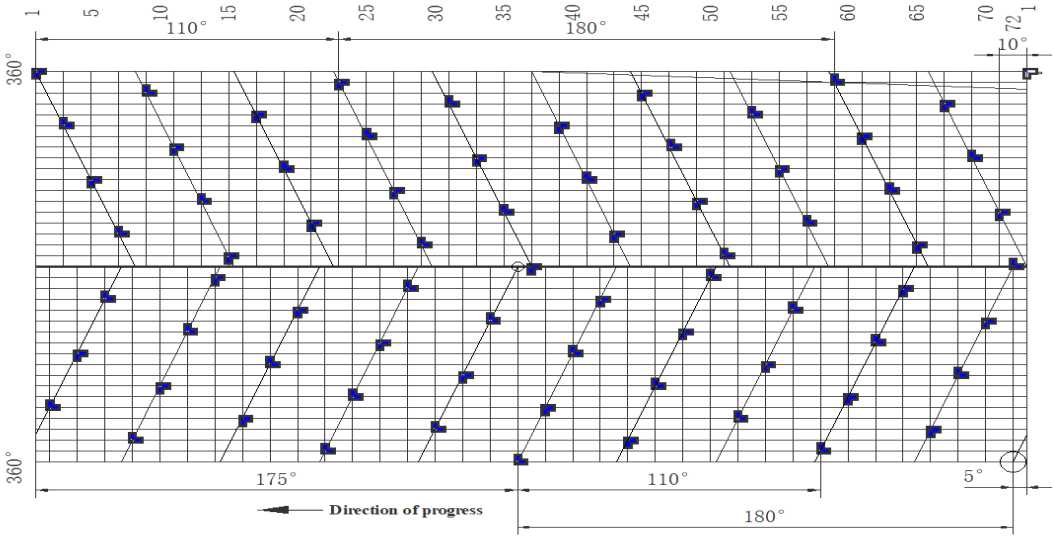


Fig. 4 - Blade arrangement on the rotary tillage shaft

Seedbed preparation shaft

The seedbed soil should be finely tilled and leveled before seeding to facilitate the seeding operation and improve seeding quality. The seedbed preparation shaft is a key component for seedbed preparation. In this study, a high rotational speed and a small rotation radius were adopted based on commonly used blade configurations. The blade rotation radius was set to 175 mm, and the blades were arranged primarily in a helical pattern. The shaft had a total length of 2310 mm and was equipped with 60 blades, comprising left- and right-curved blades. Two blades were mounted on each cutting plane. The specific blade arrangement is shown in Fig. 5.

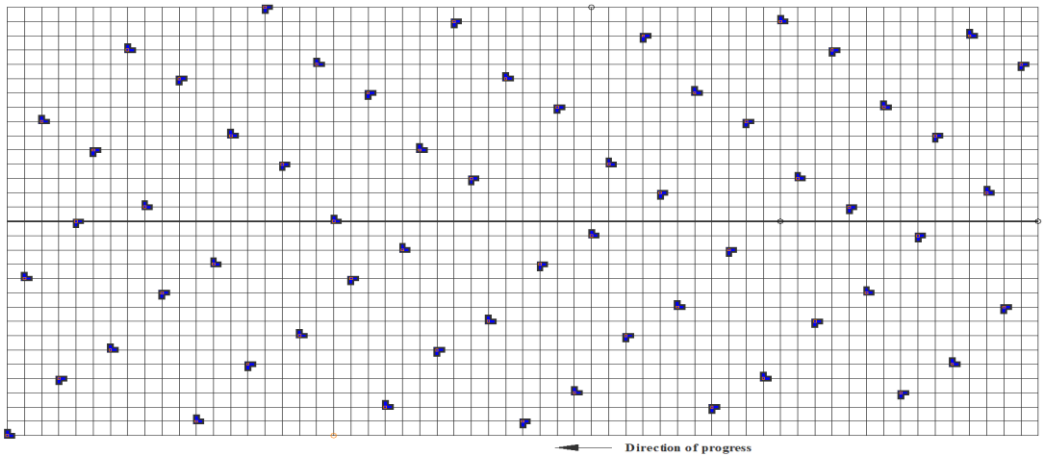


Fig. 5 - Blade arrangement on the seedbed preparation shaft

Depth-limiting press wheel shaft

Seed depth control was one of the technical difficulties in the sowing operation of high-land paddy fields with stubble. This paper aimed to improve the consistency of seed depth and reduce the "exposed seeds" phenomenon. A seed depth forming roller for sowing furrows had been designed. The width of the forming device could be determined according to the width of the seed band, as shown in Figure 6.

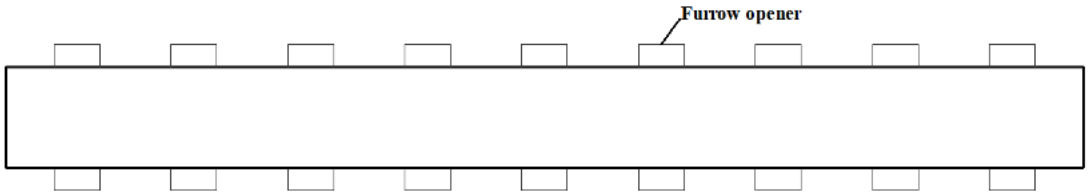


Fig. 6 - Schematic design of the depth-control press-wheel shaft

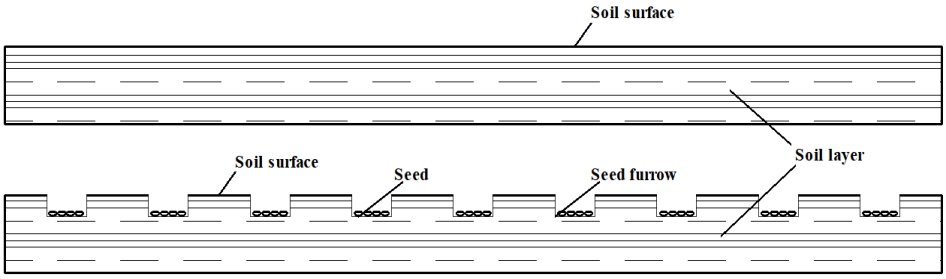


Fig. 7 - Schematic of the seeding operation

Banded soil-covering shaft

Determining the seeding depth is the first step in controlling seed placement depth, while the second step is to achieve a controlled amount of soil covering. Based on the principle of rotary soil covering, a banded soil-covering mechanism was designed, as shown in Fig. 8. The banded soil-covering shaft had a total length of 2304 mm. Nine soil-covering units were arranged in a helical pattern, with six rotary tillage blades in each unit, including four blades at each end, as shown in Fig. 9.

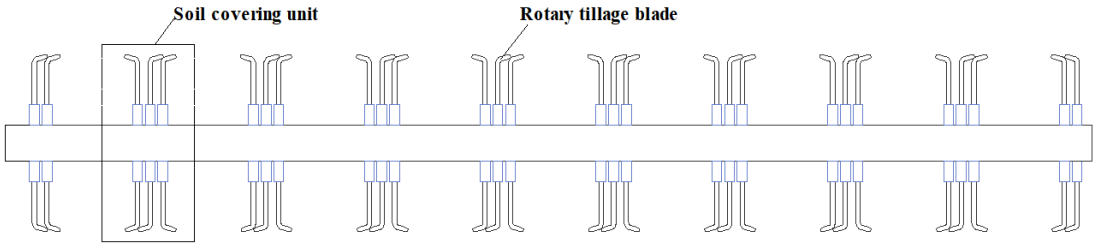


Fig. 8 - Soil-covering unit and rotary tillage blade

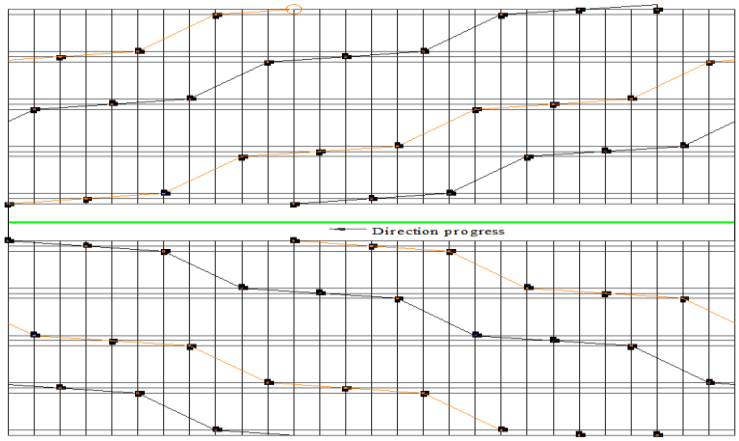


Fig. 9 - Blade arrangement on the banded soil-covering shaft

Experiment and results analysis

Experimental conditions

In October 2024, field tests of the rotary tillage, fertilization, furrow-pressing, and wide-row seeding machine for high-moisture rice-stubble fields were conducted at the Sihong Modern Agricultural Park in Shiji Town, Sihong County, Jiangsu Province. The wheat cultivar used in the tests was ‘Xumai 45’, with a thousand-grain weight of 46.1 g and a bulk density of 803 g/L.

The experimental field was 100 m long and 50 m wide. The rice row spacing was 14 cm, and the stubble height was 22.1 cm. The operating speed was set to 1.3 m/s, and a CFJ2004 tractor was used. The measured soil properties are presented in Table 1, and the field seeding test is shown in Fig. 10. The main instruments used in the tests included a soil moisture meter, soil firmness meter, stopwatch, and measuring tape.

Table 1

Soil properties

Soil depth [cm]	Moisture content	Bulk density [g/cm³]	Soil firmness [MPa]
0 ~ 10	31.2%	1.08	0.59
10 ~ 20	25.3%	1.32	1.68
20 ~ 30	20.5%	1.57	2.48



Fig. 10 - Field seeding operation

Evaluation indicators and methods

To evaluate the operating quality of the machine under high-moisture field conditions, the qualified rate of seeding depth, seeding uniformity, and vegetation coverage rate were selected as the main performance indicators. The specific evaluation methods were as follows.

Vegetation coverage rate

A large amount of straw residue remained on the field surface, which can adversely affect seeding quality and subsequent seedling emergence. Therefore, the vegetation coverage rate was evaluated. The test method followed the national standard GB/T 5668-2017, *Rotary Tiller*. Before and after operation, five sampling points were selected along the diagonal of the test area. At each sampling point, all stubble and straw lying on the soil surface within a 1 m² area were collected and weighed. The mean values before and after operation were then calculated (*Aqsiq et al., 2018*). The vegetation coverage rate was calculated using Eq. (2):

$$F_b = \frac{W_q - W_h}{W_q} \times 100 \quad (2)$$

where: F_b is the vegetation coverage rate, [%]; W_q is the mean mass of vegetation before operation, [g]; W_h is the mean mass of vegetation after operation, [g].

Qualified rate of seeding depth

According to the agricultural machinery evaluation guideline DG/T 027-2024, *Rotary Tiller and Seeder*, five test plots were selected in advance within three operating cycles. Thirty measurement points were established in each plot. After seeding and soil covering, the covering soil was carefully removed, and the thickness of the soil layer above the seeds was measured.

The proportion of measurement points with a seeding depth within (h ± 0.5) cm, where *h* is the locally specified agronomic seeding depth, was calculated as the qualified rate of seeding depth (*Agricultural Mechanization Station, 2024*).

Seeding uniformity

According to the agricultural machinery evaluation guideline DG/T 027-2024, the seeding operation was simulated in an open field at the specified operating speed. Seeds were deposited on a horizontal, straw-free surface. Three test plots were selected in advance. In each plot, six rows were measured, and 10 consecutive measurement sections were selected from each row. The coefficient of variation of seeding uniformity was calculated using Eqs. (3)–(6) (*Agricultural Mechanization Station, 2024*).

$$D = \sum_{i=1}^{3} D_i \quad (3)$$

$$X = \frac{1}{3}\sum_{i=1}^{3} X_i \quad (4)$$

$$G = \sqrt{\frac{1}{D}\sum(x - X)^2} \quad (5)$$

$$V = \frac{G}{X} \times 100\% \quad (6)$$

where:

D is the total number of measurement sections; D_i is the number of measurement sections in each test plot; X is the overall mean number of seeds per section; X_i is the mean number of seeds per section in each test plot; x is the number of seeds in an individual measurement section; G is the overall standard deviation; n is the number of measured rows; V is the coefficient of variation of seeding uniformity.

RESULTS AND ANALYSIS

Straw residue removal rate

Table 2

Straw residue mass before and after seeding

Pre-seeding residue mass		Post-seeding residue mass	
Measurement point	**Residue mass [g/m²]**	**Measurement point**	**Residue mass [g/m²]**
1	330.3	1	28.3
2	413.2	2	18.5
3	351.5	3	17.6
4	345.6	4	20.3
5	326.3	5	18.6
Mean	353.4	**Mean**	20.7
Residue removal rate [%]	94.2		

As shown in Table 2, the mean surface residue mass decreased from 353.4 g/m² before seeding to 20.7 g/m² after seeding, corresponding to a residue removal rate of 94.2%. This substantial reduction in surface residue provided favorable conditions for subsequent seed placement and seedling emergence.

Seeding depth

Table 3

Qualified rate of seeding depth

Indicator	Value
Total number of measurement points	150
Number of qualified points	147
Qualified rate of seeding depth [%]	98

As shown in Table 3, a total of 150 measurement points were evaluated, of which 147 met the specified seeding-depth requirement, resulting in a qualified rate of 98.0%. These results indicate that the machine achieved a high degree of seeding-depth consistency in high-moisture rice-stubble fields.

Seeding uniformity

Table 4

Seeding uniformity indicators

Indicator	Value
D	900
D_0	0
A	0
X	10.6
S	1.91
V [%]	18.1

As shown in Table 4, no empty measurement sections occurred during the seeding operation. The mean number of seeds per section was 10.6, with a standard deviation of 1.91. The coefficient of variation of seeding uniformity was 18.1%, indicating that the seeding performance remained within the acceptable range. The relatively high coefficient of variation may be attributed to the soft and slippery field surface, which could have affected machine travel stability and, consequently, seed distribution.

CONCLUSIONS

Based on the characteristics of the rice-wheat rotation system in the middle and lower reaches of the Yangtze River and the difficulty of controlling seeding depth in high-moisture fields, the following conclusions were drawn:

(1) A press-groove uniform seeding machine was designed, incorporating key mechanisms for seedbed preparation and precise seeding-depth control. The machine was developed to reduce seed skips and exposed seeds during mechanized wheat seeding in high-moisture rice-stubble fields.

(2) The machine incorporated a rotary tillage shaft with a helical blade arrangement, a seedbed preparation shaft, and a banded soil-covering shaft. The overall transmission system was designed and integrated into a complete seeding machine suitable for high-moisture rice-stubble fields. Field tests showed a straw residue removal rate of 94.2%.

(3) Compared with similar machines, it significantly improved the sowing quality. A depth-controlled furrow-pressing seeding method was developed. Field tests showed that the qualified rate of seeding depth reached 98.0%, while the coefficient of variation of seeding uniformity was 18.1%, indicating good seeding-depth consistency and acceptable seeding uniformity under the tested field conditions.

ACKNOWLEDGEMENT

The authors were funded for this project by the Science and Technology Program of Xizang Autonomous Region (XZ202601ZY0114-5), Jiangsu Agricultural Science and Technology Independent Innovation Fund Project (CX(22)1002), Xizang Linzhi City Science and Technology Program Project: Research and Promotion of Key Technologies and Multi-functional Equipment for Mechanized Management in Highland Tea Gardens.

REFERENCES

[1] Aladdin M., Jalil N., Guan N., Rezali K., (2021). Perturbation effect of noise on 7overall fee77ling of discomfort from vertical whole-body vibration in vibro-acoustic environment. *International Journal of Industrial Ergonomics*, 2021, 83: 103136, Netherlands.

[2] AQSIQ, SAC, (2017). Rotary tiller(旋耕机), *National Standards of the People's Republic of China,* Ding Y., Zhu J., et al., Bei Jing/China.

[3] Behera A., Raheman H., Thomas E., (2021). A comparative study on tillage performance of rota-cultivator (a passive-active combination tillage implements) with rotavator (an active tillage implement). *Soil and Tillage Research*, 207: 104861, Netherlands.

[4] Chen W., Ding Y., Tashi N., et al., (2022). Design and experiment of a vertical rotary tillage machine with fixed-layer fertilization function. *INMATEH-Agricultural Engineering*, 67(2):33-40, Romania.

[5] Gao J., (2023). Effects of different compaction treatments on low-temperature resistance of wheat following rice and its physiological mechanism under the return of straw (秸秆还田后不同镇压处理对稻茬小麦低温抗性的影响及其生理机制). *Jiangsu University*, Zhenjiang/China.

[6] Guan C., Fu J., Xu L., Jiang X., Wang S., Cui Z., (2022). Study on the reduction of soil adhesion and tillage force of bionic cutter teeth in secondary soil crushing. *Biosystems Engineering*, 213: 133-147, England.

[7] Hao J., Yu H., Zhao J., Li J., Ma Z., Cai J., (2019). Design and test of wedge drag reduction rotary blade (楔形减阻旋耕刀设计与试验). *Transactions of the Chinese Society of Agricultural Engineering*, 35(8): 55－64, Beijing/China.

[8] Hu H., Li H., Li C., Wang Q., He J, Li W., Zhang X., (2016). Design and experiment of broad width and precision minimal tillage wheat planter in rice stubble field (稻茬田小麦宽幅精量少耕播种机的设计与试验). *Transactions of the Chinese Society of Agricultural Engineering*, 32(4): 24－32, Beijing/China.

[9] Liu G., (2024). Research on Mechanism and device for rotary tillage to reduce adhesion and increase detachment under the sticky soil condition of rice stubble fields in the paddy-upland rotation area (水旱轮作稻茬田粘重土壤旋耕减粘脱附机理及装置研究). *Huazhong agricultural university*, Hubei/China.

[10] MARA, (2024), Rotary-tillage Seeder (旋耕播种机), *Outline for Appraisal for Agricultural Machinery Popularization,* Wang C., Xu F., et al., Bei Jing/China.

[11] Matin M., Hossain M., Gathala M., Timsina J, Krupnik T., (2021). Optimal design and setting of rotary strip-tiller blades to intensify dry season cropping in Asian wet clay soil conditions. Soil and Tillage Research, 207: 104854, Netherlands.

[12] Sun Y., Yang H., Wang Q., Li T., (2024). Development of PLC-based wheat planting and control system for rice stubble wetland. *Journal of Anhui Science and Technology University*, 38(4):102-109, Anhui/China.

[13] Zhang H., Gu F., Wu F., Xu H., Gao X., Hu Z., (2021). General situation and development on mechanized sowing of wheat after rice in Jiangsu Province (江苏省稻茬麦机械化播种概况与发展). *Journal of Chinese Agricultural Mechanization*, 42(11):186-192, Nanjing/China.

[14] Zhang J., Xia M., Chen W., Yuan D., Wu C., Zhu J., (2023). Simulation Analysis and Experiments for Blade-Soil-Straw Interaction under Deep Ploughing Based on the Discrete Element Method. *Agriculture*, 13 136, Switzerland.

WRITING INSTRUCTIONS

Article Types

Three types of manuscripts may be submitted:

1. **Regular articles:** should describe new and carefully confirmed findings, and experimental procedures should be given in sufficient detail for others to verify the work. The length of a full paper should be the minimum required to describe and interpret the work clearly (recommended max.10 pages);
2. **Reviews:** must contain at least three basic elements: an introduction or background information section; the body of the review containing the discussion of sources; and, finally, a conclusion and/or recommendations section to end the paper. The length of a full paper should be the max. 20 pages (if the number of references is 80-100) and max. 45 pages (if the number of references is over 300).

Manuscripts should be written in English (American or British usage is accepted, but not a mixture of these) and submitted directly on the journal website. The 2nd, 3rd and the next versions can be sent by e-mail, ***inmatehjournal@gmail.com*** mentioning the registration number (N…).
Please be sure to include your full affiliation and e-mail address (see Sample manuscript)
The authors are responsible for the accuracy of the whole paper and references.
There are allowed 2 papers by each first author.
The text layout should be in single-column format. To avoid unnecessary errors it is strongly advised to use the "spell-check" and "grammar check" functions of your word processor.

Review Process

All manuscripts are reviewed by 2 members of the Scientifically Review Office. Decisions will be made as rapidly as possible and the journal strives to return reviewers' comments to authors in approx.3 weeks.
The editorial board will re-review manuscripts that are accepted pending revision.

NOTE:

Submission of a manuscript implies: that the work described has not been published before (excepting as an abstract or as part of a published lecture or thesis) that it is not under consideration for publication elsewhere.

1. REGULAR ARTICLES

- Manuscripts should be concise, in ***1.15 line spacing***, and should have 2 cm all over margins. The font should be ***Arial 10 pt.*** Ensure that each new paragraph is clearly indicated, using **TAB at 1 cm**.
- Title will be ***Arial 12 pt***. and explicit figures will be ***Arial 9 pt***.
- Text will be written in English.
- Chapters' titles are written by ***Arial 10 pt, Bold, Uppercase*** (e.g. **INTRODUCTION, MATERIALS AND METHODS**), between chapters is left a space for 10 pt. At the beginning of each paragraph, TAB of 1 cm.
- The paper body will be written in ***Arial 10 pt., Justify alignment***.

TITLE ***Arial 12 pt., Uppercase, Bold, Center*** *(in English language)* and ***Bold Italic*** *(in native language)*.
Should be a brief phrase describing the contents of the paper. Avoid long titles; a running title of no more than 100 characters is encouraged (without spaces).

AUTHORS ***ARIAL 9, Bold, Centre alignment***
Under the paper's title, after a space (enter) 9 pt., write ***authors' names*** and ***affiliations (Arial 8 pt.-Regular)***
When the paper has more than one author, their name will be followed by a mark (Arabic numeral) as superscript if their affiliation is different. Less than 6 authors.
Corresponding author's name (next row), ***(Arial 8 pt.)***. Should be added also: phone, fax and e-mail information, for the paper corresponding author (***font: 8 pt., Italic***).

KEYWORDS ***(In English)*** about 4 to 7 words that will provide indexing references should be listed (title: ***Arial 10pt, bold italic,*** text ***Arial 10 pt., italic***).
A list of non-standard *Abbreviations* should be added. In general, non-standard abbreviations should be used only when the full term is very long and used often. Each abbreviation should be spelled out and introduced in parentheses the first time it is used in the text. Standard abbreviations (such as ATP and DNA) need not to be defined.

ABSTRACT ***(in English and Native language, Arial 10 pt.)***, the title *bold*; the text of abstract: *italic*) should be informative and completely self-explanatory, briefly present the topic, state the scope of the experiments, indicate significant data, and point out major findings and conclusions. The Abstract should be max.250 words. Complete sentences, active verbs, and the third person should be used, and the abstract should be written in the past tense. Standard nomenclature should be used and abbreviations should be avoided. No literature should be cited.

INTRODUCTION (*Arial 10 pt.*) should provide a clear statement of the problem, the relevant literature on the subject, and the proposed approach or solution. It should be understandable to colleagues from a broad range of scientific subjects. We should refer to the current stage of researches performed in the field of the paper to be published, by quoting up-to-date specialty studies, preferably published after 2006, excepting certain referential specialty books/studies, especially papers issued in magazines/journals/conferences/ISI quoted symposia or in other international data bases, which are well known and available.

MATERIALS AND METHODS (*Arial 10 pt.*) should be complete enough to allow experiments to be reproduced. However, only truly new procedures should be described in detail; previously published procedures should be cited, and important modifications of published procedures should be mentioned briefly. Methods in general use need not be described in detail.

RESULTS (*Arial 10 pt.*) should be clarity presented. The results should be written in the past tense when describing findings in the authors' experiments. Results should be explained, but largely, without referring to the literature. Discussion, speculation and detailed interpretation of data should not be included in the Results, but should be put into the Conclusions section.

CONCLUSIONS (*Arial 10 pt.*) The main conclusions drawn from results should be presented in a short Conclusions section. Do not include citations in this section.

Formulae, symbols and abbreviations: Formulae will be typeset in Italics (preferable with the Equation Editor of Microsoft Office 2003) and should be written or marked as such in the manuscript, unless they require a different styling. They should be referred to in the text as Equation (4) or e.g. (4). The formulae should be numbered on the right side, between brackets *(Arial 10 pt.)*:

$$P = F \cdot v \tag{1}$$

Terms of the equation and the unit measure should be explained, e.g.

P is the power, [W];
F – force, [N];
v – speed, [m/s]

SI units must be used throughout.

Tables should be self-explanatory without reference to the text. The details of the methods used in the experiments should preferably be described in the legend instead of in the text. The same data should not be presented both in table and graph form or repeated in the text.
Table's title will be typed ***Arial 9 pt, Bold, Centered***
In the table, each row will be written Arial 9 pt, single-spaced throughout, including headings and footnotes.
The table should be numbered on the right side, ***Arial 10 pt.***

Figures ***(Arial 9 pt., Bold, Center)*** should be typed in numerical order (Arabic numerals). Graphics should be high resolution (e.g.JPEG). Figure number is followed by what represent the figure or graph e.g.:

Fig. 1 – Test stand

Legend: ***Arial 8 pt, Italic, Center,*** e.g.:
1 - plansifter compartments; 2- break rolls; 3 – semolina machines; 4 – reduction rolls; 5 – flour

ACKNOWLEDGMENTS (*Arial 10 pt.*) of people, grants, funds etc should be brief (*if necessarily*).

REFERENCES (*Arial 10 pt.*)
(In alphabetical order, in English and in the original publication language).
Minimum 10 references, last 10 years, minimum 3 references from the last 2 years

It can be used "*References*" tool from the *Word Editor*. **APA Style (American Psychological Association)**
https://apastyle.apa.org/style-grammar-guidelines/references/examples

All references must be provided in English

Authors are fully responsible for the accuracy of the references.

References should be **alphabetically**, with complete details, as follows:

Examples:

Books: https://apastyle.apa.org/style-grammar-guidelines/references/examples/book-references

Jackson, L. M. (2019). *The psychology of prejudice: From attitudes to social action* (2nd ed.). American Psychological Association. https://doi.org/10.1037/0000168-000

Kesharwani, P. (2020). *Nanotechnology based approaches for tuberculosis treatment*. Academic Press.

Sapolsky, R. M. (2017). *Behave: The biology of humans at our best and worst*. Penguin Books.

Torino, G. C., Rivera, D. P., Capodilupo, C. M., Nadal, K. L., & Sue, D. W. (2019). *Microaggression theory: Influence and implications*. John Wiley & Sons. https://doi.org/10.1002/9781119466642

In text:

- ***Parenthetical citations***: (*Jackson, 2019; Sapolsky, 2017*)
- ***Narrative citations***: *Jackson (2019) and Sapolsky (2017)*

Journal Article:
https://apastyle.apa.org/style-grammar-guidelines/references/examples/journal-article-references

Grady, J. S., Her, M., Moreno, G., Perez, C., & Yelinek, J. (2019). Emotions in storybooks: A comparison of storybooks that represent ethnic and racial groups in the United States. *Psychology of Popular Media Culture*, *8*(3), 207–217. https://doi.org/10.1037/ppm0000185

In text:

- ***Parenthetical citation***: (*Grady et al., 2019*)
- ***Narrative citation***: *Grady et al. (2019)*

Conference or Symposium:
https://apastyle.apa.org/style-grammar-guidelines/references/examples/conference-proceeding-references

Duckworth, A. L., Quirk, A., Gallop, R., Hoyle, R. H., Kelly, D. R., & Matthews, M. D. (2019). Cognitive and noncognitive predictors of success. *Proceedings of the National Academy of Sciences*, *USA*, *116*(47), 23499–23504. https://doi.org/10.1073/pnas.1910510116

In text:

- ***Parenthetical citation***: (*Duckworth et al., 2019*)
- ***Narrative citation***: *Duckworth et al. (2019)*

Dissertation / Thesis:
https://apastyle.apa.org/style-grammar-guidelines/references/examples/published-dissertation-references

Zambrano-Vazquez, L. (2016). *The interaction of state and trait worry on response monitoring in those with worry and obsessive-compulsive symptoms* [Doctoral dissertation, University of Arizona]. UA Campus Repository. https://repository.arizona.edu/handle/10150/620615

In text:

- ***Parenthetical citations***: (*Kabir, 2016; Miranda, 2019; Zambrano-Vazquez, 2016*)
- ***Narrative citations***: *Kabir (2016), Miranda (2019), and Zambrano-Vazquez (2016)*

https://apastyle.apa.org/style-grammar-guidelines/references/examples/unpublished-dissertation-references

Harris, L. (2014). *Instructional leadership perceptions and practices of elementary school leaders* [Unpublished doctoral dissertation]. University of Virginia.

In text:

- ***Parenthetical citation***: *(Harris, 2014*)
- ***Narrative citation***: *Harris (2014)*

Patents: Names and initials of authors, year (between brackets), patent title (Italic), patent number, country:
Grant, P. (1989). *Device for Elementary Analyses*. Patent. No.123456. USA.

Legal regulations and laws, organizations:
https://apastyle.apa.org/style-grammar-guidelines/references/examples/iso-standard-references

International Organization for Standardization. (2018). *Occupational health and safety management systems—Requirements with guidance for use* (ISO Standard No. 45001:2018). https://www.iso.org/standard/63787.html

Occupational Safety and Health Administration. (1970). *Occupational safety and health standards: Occupational health and environmental control: Occupational noise exposure* (OSHA Standard No. 1910.95). United States Department of Labor. https://www.osha.gov/laws-regs/regulations/standardnumber/1910/1910.95

In text:

- ***Parenthetical citations***: (International Organization for Standardization, 2018; Occupational Safety and Health Administration, 1970)
- ***Narrative citations***: International Organization for Standardization (2018) and Occupational Safety and Health Administration (1970)

Web references: The full URL should be given in text as a citation, if no other data are known. If the authors, year, and title of the documents are known and the reference is taken from a website, the URL address has to be mentioned after these data.

Citation in text

Please ensure that every reference cited in the text is also present in the reference list (and vice versa).

Do not cite references in the Abstract and Conclusions !.

Unpublished results, personal communications as well as URL addresses are not recommended in the references list.

Making personal quotations (one, at most) should not be allowed, unless the paper proposed to be published is a sequel of the cited paper. Articles in preparation or articles submitted for publication, unpublished, personal communications etc. should not be included in the references list.

Citations style

Text: All citations in the text may be made directly (or parenthetically) as bellow.

- ***single author:*** the author's name (without initials, unless there is ambiguity) and the year of publication:

"as previously demonstrated *(Brown, 2010)*".

- ***two authors:*** both authors' names and the year of publication: *(Adam and Brown, 2008; Smith and Hansel, 2006; Stern and Lars, 2009)*
- ***three or more authors:*** first author's name followed by "et al." and the year of publication: "As has recently been shown *(Werner et al., 2005; Kramer et al., 2000)* have recently shown ...."

Citations of groups of references should be listed first alphabetically, then chronologically.

Units, Abbreviations, Acronyms

- Units should be metric, generally SI, and expressed in standard abbreviated form.
- Acronyms may be acceptable, but must be defined at first usage.

2. REVIEWS

Reviews and perspectives covering topics of current interest in the field, are encouraged and accepted for publication. A review must have at least 80 references. It might give a new interpretation of old material or combine new with old interpretations. Or it might trace the intellectual progression of the field, including major debates. And depending on the situation, the literature review may evaluate the sources and advise the reader on the most pertinent or relevant.

Literature reviews must contain at least three basic elements: an introduction or background information section; the body of the review containing the discussion of sources; and, finally, a conclusion and/or recommendations section to end the paper.

The following provides a brief description of the content of each: Introduction: Gives a quick idea of the topic of the literature review, such as the central theme or organizational pattern. Body: Contains your discussion of sources and is organized either chronologically, thematically, or methodologically. Conclusions / Recommendations: Discuss what you have drawn from reviewing literature so far.

Edited by: INMA Bucharest
6, Ion Ionescu de la Brad Blvd., sect. 1, Bucharest, ROMANIA
Tel: +4021.269.32.60; Fax: +4021.269.32.73
https:// inmateh.eu
e-mail: ***inmatehjournal@gmail.com***